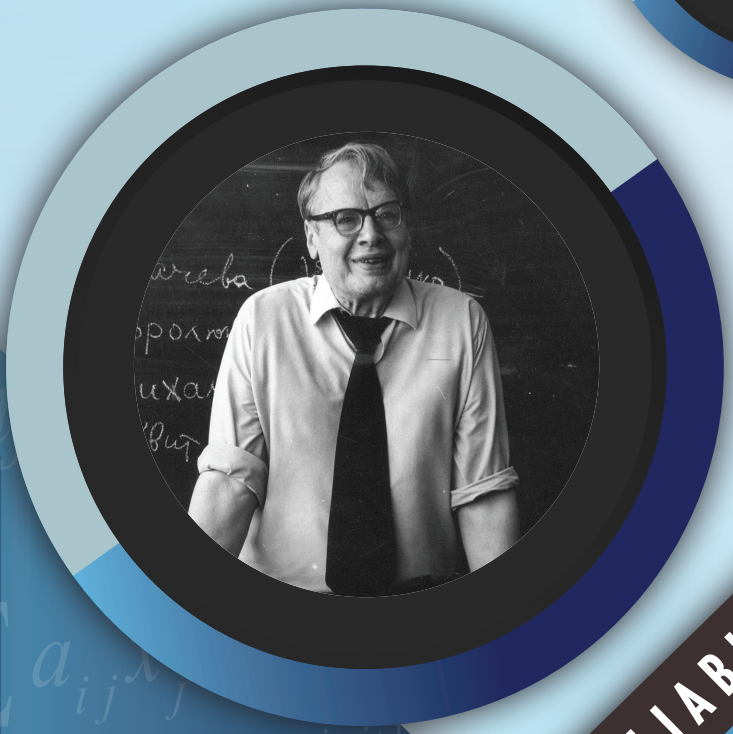
RTA

ISSN 1932-2321

JOURNAL IS REGISTERED IN THE LIBRARY OF THE U.S. CONGRESS

RELIABILITY: THEORY & APPLICATIONS

INTERNATIONAL GROUP ON RELIABILITY



RELIABILITY
RISK ANALYSIS
MAINTENANCE
SAFETY

GNEDENKO FORUM PUBLICATIONS

(89) VOL.20

#4

DECEMBER

2025

SAN DIEGO

ISSN 1932-2321

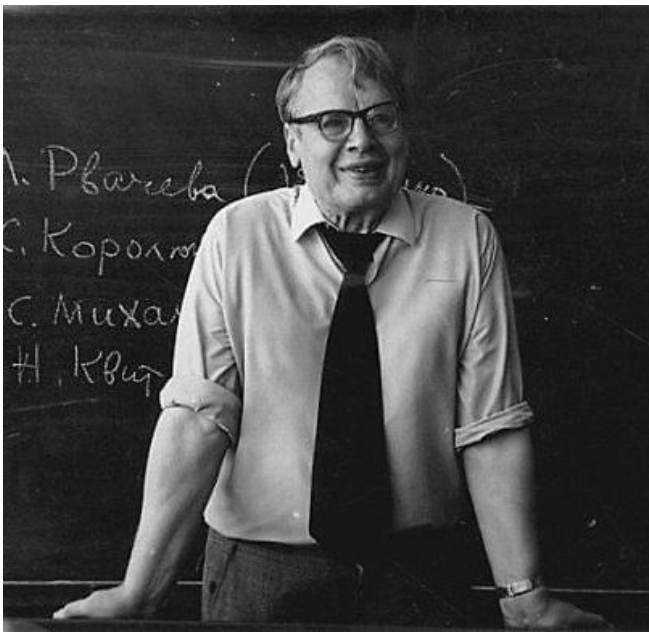
© "Reliability: Theory & Applications", 2006, 2007, 2009 to Present
© " Reliability & Risk Analysis: Theory & Applications", 2008

© I.A. Ushakov
© A.V. Bochkov, from 2006 to Present
© Kristina Ushakov, Cover Design, 2024
http://www.gnedenko.net/Journal/index.htm

All rights are reserved

The reference to the magazine "Reliability: Theory & Applications"
at partial use of materials is obligatory.





RELIABILITY:

THEORY & APPLICATIONS

Vol.20 No.4 (89),
December 2025

San Diego
2025

Editorial Board

Editor-in-Chief

Rykov, Vladimir (Russia)
Doctor of Sci, Professor, Department of Applied Mathematics & Computer Modeling, Gubkin Russian State Oil & Gas University, Leninsky Prospect, 65, 119991 Moscow, Russia.
e-mail: vladimir_rykov@mail.ru

Managing Editors

Bochkov, Alexander (Russia)
Doctor of Technical Sciences, Scientific Secretary JSC NIIAS, Scientific-Research and Design Institute Informatization, Automation and Communication in Railway Transport, Moscow, Russia, 107078, Orlikov pereulok, 5, building 1
e-mail: a.bochkov@gmail.com

Gnedenko, Ekaterina (USA)
PhD, Lecturer Department of Economics Boston University, Boston 02215, USA
e-mail: gnedenko@bu.edu

Bushinskaya, Anna (Russia)
Candidate of Tech. Sci. Leading Research Fellow of the Sci & Engng Center of the Russian Academy of Sciences, Ekaterinburg
e-mail: bushinskaya@gmail.com

Sazonov, Aleksey (Russia)
Leading Specialist of the Standardization Department, JSC NIIAS (Joint Stock Company "Design &Research Institute for Information "Technology, Signaling and Telecommunications on Railway Transport), Bild 1, 5 Orlikov Pereulok, Moscow, Russia, 107078
e-mail: sazonoff2007@gmail.com

Deputy Editors

Dimitrov, Boyan (USA)
Ph.D., Dr. of Math. Sci., Professor of Probability and Statistics, Associate Professor of Mathematics (Probability and Statistics), GMI Engineering and Management Inst. (now Kettering)
e-mail: bdimitro@kettering.edu

Gnedenko, Dmitry (Russia)
Doctor of Sci., Assos. Professor, Department of Probability, Faculty of Mechanics and Mathematics, Moscow State University, Moscow, 119899, Russia
e-mail: dmitry@gnedenko.com

Kashtanov, Victor A. (Russia)
PhD, M. Sc (Physics and Mathematics), Professor of Moscow Institute of Applied Mathematics, National Research University "Higher School of Economics" (Moscow, Russia)
e-mail: VAKashtan@yandex.ru

Krishnamoorthy, Achyutha (India)
M.Sc. (Mathematics), PhD (Probability, Stochastic Processes & Operations Research), Professor Emeritus, Department of Mathematics, Cochin University of Science & Technology, Kochi-682022, INDIA.
e-mail: achyuthacusat@gmail.com

Recchia, Charles H. (USA)
PhD, Senior Member IEEE Chair, Boston IEEE Reliability Chapter A Joint Chapter with New Hampshire and Providence, Advisory Committee, IEEE Reliability Society
e-mail: charles.recchia@macom.com

Shybinsky Igor (Russia)
Doctor of Sci., Professor, Division manager, VNIIAS (Russian Scientific and Research Institute of Informatics, Automatics and Communications), expert of the Scientific Council under Security Council of the Russia
e-mail: igor-shubinsky@yandex.ru

Yastrebenetsky, Mikhail (Ukraine)
Doctor of Sci., Professor. State Scientific and Technical Center for Nuclear and Radiation Safety
e-mail: ma.yastreb2013@gmail.com

Associate Editors

Aliyev, Vugar (Azerbaijan)
Doctor of Sci., Professor, Chief Researcher of the Institute of Physics of the National Academy of Sciences of Azerbaijan, Director of the AMIR Technical Services Company
e-mail: prof.vugar.aliyev@gmail.com

Balakrishnan, Narayanaswamy (Canada)
Professor of Statistics, Department of Mathematics and Statistics, McMaster University
e-mail: bala@mcmaster.ca

Carrión García, Andrés (Spain)
Professor Titular de Universidad, Director of the Center for Quality and Change Management, Universidad Politécnica de Valencia, Spain
e-mail: acarrion@eio.upv.es

Chakravarthy, Srinivas (USA)
Ph.D., Professor of Industrial Engineering & Statistics, Departments of Industrial and Manufacturing Engineering & Mathematics, Kettering University (formerly GMI-EMI) 1700, University Avenue, Flint, MI48504
e-mail: schakrav@kettering.edu

Cui, Lirong (China)
PhD, Professor, School of Management & Economics, Beijing Institute of Technology, Beijing, P. R. China (Zip:100081)
e-mail: lirongcui@bit.edu.cn

Finkelstein, Maxim (SAR)
Doctor of Sci., Distinguished Professor in Statistics/Mathematical Statistics at the UFS. Visiting researcher at Max Planck Institute for Demographic Research, Rostock, Germany and Visiting research professor (from 2014) at the ITMO University, St Petersburg, Russia
e-mail: FinkelM@ufs.ac.za

Kaminsky, Mark (USA)
PhD, principal reliability engineer at the NASA Goddard Space Flight Center
e-mail: mkaminskiy@hotmail.com

Krivtsov, Vasiliy (USA)
PhD. Director of Reliability Analytics at the Ford Motor Company. Associate Professor of Reliability Engineering at the University of Maryland (USA)
e-mail: VKrivtso@Ford.com, krivtsov@umd.edu

Lemeshko Boris (Russia)
Doctor of Sci., Professor, Novosibirsk State Technical University, Professor of Theoretical and Applied Informatics Department
e-mail: Lemeshko@ami.nstu.ru

Lesnykh, Valery (Russia)
Professor, Doctor of Sci., Adviser to Director General, LLC Gazprom gaznadzor, Novocheryo-mushkinskaya Street, 65, Moscow, 117418, Russia
e-mail: vvlesnykh@gmail.com

Levitin, Gregory (Israel)
PhD, The Israel Electric Corporation Ltd. Planning, Development & Technology Division. Reliability & Equipment Department, Engineer-Expert; OR and Artificial Intelligence applications in Power Engineering, Reliability.
e-mail: levitin@iec.co.il

Limnios, Nikolaos (France)
Professor, Université de Technologie de Compiègne, Laboratoire de Mathématiques, Appliquées Centre de Recherches de Royallieu, BP 20529, 60205 COMPIEGNE CEDEX, France
e-mail: Nikolaos.Limnios@utc.fr

Papic, Ljubisha (Serbia)
PhD, Professor, Head of the Department of Industrial and Systems Engineering Faculty of Technical Sciences Cacak, University of Kragujevac, Director and Founder the Research Center of Dependability and Quality Management (DQM Research Center), Prijevor, Serbia
e-mail: dqmcenter@mts.rs

Ram, Mangey (India)
Professor, Department of Mathematics, Computer Science and Engineering, Graphic Era (Deemed to be University), Dehradun, India. Visiting Professor, Institute of Advanced Manufacturing Technologies, Peter the Great St. Petersburg Polytechnic University, Saint Petersburg, Russia.
e-mail: mangeyram@gmail.comq

Timashev, Sviatoslav (Russia)
Doctor of Sci., Professor, Director and principal scientist the Sci & Engng Center of the Russian Academy of Sciences, Ekaterinburg
e-mail: timashevs@cox.net

Zio, Enrico (Italy)
PhD, Full Professor, Direttore della Scuola di Dottorato del Politecnico di Milano, Italy.
e-mail: Enrico.Zio@polimi.it

e-Journal ***Reliability: Theory & Applications*** publishes papers, reviews, memoirs, and bibliographical materials on Reliability, Quality Control, Safety, Survivability and Maintenance.

Theoretical papers must contain new problems, finger practical applications and should not be overloaded with clumsy formal solutions.

Priority is given to descriptions of case studies.
General requirements for presented papers.

1. Papers must be presented in English in MS Word or LaTeX format.
2. The total volume of the paper (with illustrations) can be up to 15 pages.
3. A presented paper must be spell-checked.
4. For those whose language is not English, we kindly recommend using professional linguistic proofs before sending a paper to the journal.

The manuscripts complying with the scope of journal and accepted by the Editor are registered and sent for external review. The reviewed articles are emailed back to the authors for revision and improvement.

The decision to accept or reject a manuscript is made by the Editor considering the referees' opinion and considering scientific importance and novelty of the presented materials. Manuscripts are published in the author's edition. The Editorial Board are not responsible for possible typos in the original text. The Editor has the right to change the paper title and make editorial corrections.

The authors keep all rights and after the publication can use their materials (re-publish it or present at conferences).

Publication in this e-Journal is equal to publication in other International scientific journals.

Papers directed by Members of the Editorial Boards are accepted without referring.
The Editor has the right to change the paper title and make editorial corrections.
The authors keep all rights and after the publication can use their materials (re-publish it or present at conferences).

Send your papers to Alexander Bochkov, e-mail: a.bochkov@gmail.com

Table of Contents

AN INVENTORY MODELING FOR DECAYING ITEMS WITH PRICE, STOCK AND RELIABILITY-DEPENDENT DEMAND UNDER MEMORY EFFECTS 51

Narendra Kumar, Liliana Guran, Devendra Kumar, Sanjeet Kumar, Ajay Singh Yadav, Krishan Kumar Yadav

A generalized Economic Order Quantity (EOQ) framework is employed to investigate memory effects within an inventory system. Fractional calculus provides an effective mathematical tool for reflecting such memory characteristics in economic model. In this study, a fractional-order inventory model without shortages is developed, where demand is depends on price, on-hand stock, and product reliability, while deterioration is assumed to occur at a constant rate. The developing fractional differential equation is formulated in the Caputo sense, and a memory-kernel approach is used to incorporate dependence on past system states. By applying the Laplace transform technique together with Mittag-Leffler functions, an analytical solution to the model is obtained. The results indicate that the degree of memory in the system can be modulated through the order of the fractional derivative or integral. Furthermore, a sensitivity analysis is performed for both short-memory and long-memory scenarios to determine the key parameters affecting system behavior under varying conditions with the help of MATLAB software.

Cite: Narendra Kumar, Liliana Guran, Devendra Kumar, Sanjeet Kumar, Ajay Singh Yadav, Krishan Kumar Yadav AN INVENTORY MODELING FOR DECAYING ITEMS WITH PRICE, STOCK AND RELIABILITY-DEPENDENT DEMAND UNDER MEMORY EFFECTS. Reliability: Theory & Applications. 2025, December 4(89), Vol. 20: 51-57, DOI: https://doi.org/10.24412/1932-2321-2025-489-51-57

RELEVANCE OF INFORMATION AND TECHNICAL SUPPORT OF STAFF IN MAINTENANCE AND REPAIR OF STEAM TURBINE DEVICES OF POWER UNITS OF THERMAL ELECTRIC STATION 58

Farzaliyev Y. Z.

The need to improve the efficiency of thermal electric station units increases significantly as their service life increases. If during the standard service life, the efficiency of operation was successfully calculated on the basis of a standard algorithm and experimental energy characteristics, then subsequently the correspondence of the initial energy characteristics to the actual characteristics becomes less and less accurate. In order to ensure the efficiency of power units, it is necessary to reduce the frequency of clarification of empirical characteristics, which causes a significant increase in operating costs. The forced approach to solving operational problems is taking into account operating experience, information about existing defects. In this case, the strict calculation method is replaced by an intuitive approach, the risk of an erroneous solution of which is significant, and improving the method for solving operational problems is transformed from desirable to necessary.

Cite: Farzaliyev Y. Z. RELEVANCE OF INFORMATION AND TECHNICAL SUPPORT OF STAFF IN MAINTENANCE AND REPAIR OF STEAM TURBINE DEVICES OF POWER UNITS OF THERMAL ELECTRIC STATION. Reliability: Theory & Applications. 2025, December 4(89), Vol. 20: 58-68, DOI: https://doi.org/10.24412/1932-2321-2025-489-58-68

RELIABILITY ANALYSIS OF A THAP MISSION WITH SEQUENTIAL PHASES 69

Rasm K, Dharmaraja Selvamuthu, Raina Raj, Vladimir Vishnevsky, Dimitry Kozyrev

Stratospheric platforms, commonly known as high-altitude platforms (HAPs), are gaining traction as an economical and sustainable option for diverse applications, including environmental monitoring, surveillance, and communication networks. Tethered HAPs (tHAPs), which remain physically connected to the ground, provide improved stability, a continuous power source, and dependable data transfer capabilities. Analyzing the reliability of these systems as phased mission systems (PMS) is essential, given the multiple operational stages they undergo-such as ascend, primary task, and descend, posing distinct operational demands and challenging environmental conditions. Maintaining reliability throughout these phases is crucial for ensuring both mission effectiveness and long-term operational integrity. This research explores the necessity and practicality of conducting reliability assessments on tethered HAP systems by modeling them as PMS with well-defined stages. A comprehensive evaluation is performed for each phase, accounting for potential risks and operational constraints. Furthermore, a numerical example illustrates the reliability assessment methodology, incorporating Markovian techniques to derive key performance indicators and reliability measures for every phase.

Cite: Rasm K, Dharmaraja Selvamuthu, Raina Raj, Vladimir Vishnevsky, Dimitry Kozyrev RELIABILITY ANALYSIS OF A THAP MISSION WITH SEQUENTIAL PHASES. Reliability: Theory & Applications. 2025, December 4(89), Vol. 20: 69-81, DOI: https://doi.org/10.24412/1932-2321-2025-489-69-81

A SURVEY ON IMAGE GENERATION TECHNIQUES PARADIGMS, EVOLUTION, DEEP LEARNING ADVANCEMENTS AND FUTURE DIRECTIONS 82

Nrupesh Shah, Dr. Sanjay Patel

Image generation techniques have witnessed significant advancements in recent years. Classification of Image Generation Approaches is an important topic in today's rapidly advancing technological landscape. We will examine primary approaches in this field: Generative Adversarial Networks (GANs), Variational Autoencoders (VAEs), Stable Diffusion Processes (SDPs) and other similar approaches. GANs, VAEs and SDPs have shown remarkable performance in terms of image quality, as well as scalability and efficiency. This survey focuses onto seminal works that have shaped the field of image generation, spanning Generative Adversarial Networks (GANs), Variational Autoencoders (VAEs), Autoregressive Models, Flow based image generation as well as diffusion-based approaches, and also compares various evaluation metrices in the field. We also provide a list of challenges in this field.

Cite: Nrupesh Shah, Dr. Sanjay Patel A SURVEY ON IMAGE GENERATION TECHNIQUES PARADIGMS, EVOLUTION, DEEP LEARNING ADVANCEMENTS AND FUTURE DIRECTIONS. Reliability: Theory & Applications. 2025, December 4(89), Vol. 20: 82-104, DOI: https://doi.org/10.24412/1932-2321-2025-489-82-104

NEUTROSOPHIC TOPOLOGIZED BIPARTITE GRAPH 105

Balakrishnan A and Thiruganasambandam K

Neutrosophic topological bipartite graph analyses unreliability in bipartite structured graphs by incorporating neutrosophic concepts with topologic possessions. This is a novel approach by providing theorems that integrate truth, indeterminacy and falsity values in topology axioms of neutrosophic graphs. The study introduces a topological space where each singleton set is either open or closed, and the boundary of each element is limited to two or fewer connections. And, it extends the topological graph into various graph structures like a neutrosophic star graph, a neutrosophic bistar, a neutrosophic bipartite graph, a neutrosophic tree and a neutrosophic complete bipartite graph through theorems and examples.

Cite: Balakrishnan A and Thiruganasambandam K NEUTROSOPHIC TOPOLOGIZED BIPARTITE GRAPH. Reliability: Theory & Applications. 2025, December 4(89), Vol. 20: 105-113, DOI: https://doi.org/10.24412/1932-2321-2025-489-105-113

COMPARATIVE VAR FORECASTING USING LOW AND HIGH-FREQUENCY CONDITIONAL EVT MODELS: EVIDENCE FROM NIFTY INDICES IN INDIA 114

Nadia Sha, Hena M, and Bitha S Mani

This study uses Value-at-risk (VaR) and Expected Shortfall (ES) to determine if the availability of high-frequency data improves the accuracy of estimating severe market risk as compared to low-frequency data. The daily closing stock prices of the NIFTY 50, NIFTY 100, and NIFTY 200 Index from January 1, 2021, to April 31, 2025, made up the sample data utilised for analysis. The purpose of the data study was to evaluate the effectiveness of conditional EVT, a two-stage hybrid strategy that merged the EVT methodology with the GARCH, RV, and HAR specification models. Unconditional coverage (UC) and conditional coverage (CC) tests were used to backtest the out-of-sample VaR predictions in order to evaluate their correctness. The regulatory loss function (RLF) and the firm's loss function (FLF) are two utilisation loss functions that were also included in the VaR backtesting process. The generalised breach indicator (GBI) approach was used to backtest the anticipated ES's accuracy. The results of this study demonstrated that when it came to forecasting market risk during times of extraordinary returns, high-frequency conditional EVT that included the HAR specification performed better than low-frequency conditional EVT. When compared to the GARCH-EVT and RV-EVT typed models throughout the periods, the HAR-EVT typed models perform the best according to the VaR and ES measures. The hybrid model of long-memory models for the EVT method is the focus of this research work, which adds to the body of knowledge on the forecasting abilities of risk models.

Cite: Nadia Sha, Hena M, and Bitha S Mani COMPARATIVE VAR FORECASTING USING LOW AND HIGH-FREQUENCY CONDITIONAL EVT MODELS: EVIDENCE FROM NIFTY INDICES IN INDIA. Reliability: Theory & Applications. 2025, December 4(89), Vol. 20: 114-130, DOI: https://doi.org/10.24412/1932-2321-2025-489-114-130

EFFICACY OF SINGLE SERVER MARKOVIAN QUEUEING SYSTEM WITH DISSATISFIED CUSTOMERS, BALKING AND NUMEROUS VACATION 131

Iswalikhan.E, Thangaraja.P, Rajeswari.V, Karuppaiya.R, Ramkumar.S, Narmadha.V

In this research work, we derive a single server Markovian encouraged arrival queuing system with dissatisfied customers, balking, and numerous vacations, where we examine that encouraged arrival customers are due to the fewer customers, balking, and dissatisfied customers. Once a system-size enhancement is idle, the system server obtains vacation. Suppose the system server detritus is idle, after the sabbatical vacation. We inferred the probability-generating functions (PGF) and got the closed-form interpretation when the system server is

numerous. In addition, we obtain other important performance measures and Little's law is also satisfied for this model.

Cite: Iswalikhan.E, Thangaraja.P, Rajeswari.V, Karuppaiya.R, Ramkumar.S, Narmadha.V EFFICACY OF SINGLE SERVER MARKOVIAN QUEUEING SYSTEM WITH DISSATISFIED CUSTOMERS, BALKING AND NUMEROUS VACATION. Reliability: Theory & Applications. 2025, December 4(89), Vol. 20: 131-141, DOI: https://doi.org/10.24412/1932-2321-2025-489-131-141

ENHANCING THE ROBUSTNESS OF SUPPORT VECTOR REGRESSION WITH DEPTH-INDUCED WEIGHT FUNCTIONS FOR IMPROVED PREDICTION 142

Kalaivani S

Support Vector Regression (SVR) is an extension of Support Vector Machines designed for regression tasks. By using an epsilon-insensitive loss function, SVR balances model complexity and accuracy, making it effective at handling noise and outliers. Data depth functions measure the centrality of data points in multivariate spaces, providing a robust approach to identify influential data based on their position relative to the data distribution. This study introduces Depth-Induced SVR, an enhanced SVR model that incorporates robust depth functions as a weight mechanism with the kernel function to improve efficiency and robustness. Various robust depth functions such as Mahalanobis, Halfspace, L2, Projection, Spatial, and Zonoid are evaluated as weighting functions to determine the most effective combination with the kernel function. Model efficacy is assessed using performance metrics including Mean Squared Error (MSE), Mean Absolute Error (MAE), Mean Absolute Percentage Error (MAPE), and Median Absolute Error (MDAE). This comparative approach aims to identify the optimal depth function for robust SVR performance across diverse real datasets and simulated environments.

Cite: Kalaivani S ENHANCING THE ROBUSTNESS OF SUPPORT VECTOR REGRESSION WITH DEPTH-INDUCED WEIGHT FUNCTIONS FOR IMPROVED PREDICTION. Reliability: Theory & Applications. 2025, December 4(89), Vol. 20: 142-150, DOI: https://doi.org/10.24412/1932-2321-2025-489-142-150

MODELING AND IMPROVING THE RELIABILITY OF SMART ELECTRICAL GRIDS 151

Rahila Muradova

The transformation of conventional power systems into intelligent electric networks, or Smart Grids, has introduced significant improvements in efficiency, flexibility, and sustainability. However, this evolution also brings new reliability challenges due to complex cyber-physical interactions, integration of distributed energy resources, and increased exposure to cyber threats. This paper presents a comprehensive methodology for assessing and improving the reliability of smart grids through hybrid modeling, real-time analytics, and fault-tolerant system design. Key components with the highest impact on system reliability—such as communication modules and cyber interfaces—are identified and analyzed. A hybrid reliability model combining probabilistic techniques with machine learning methods is developed and illustrated through a case study involving redundant control systems. The results demonstrate that strategic redundancy and predictive diagnostics can significantly enhance the resilience of modern power infrastructures. The study concludes with recommendations for integrating reliability considerations into autonomous grid operation.

Cite: Rahila Muradova MODELING AND IMPROVING THE RELIABILITY OF SMART ELECTRICAL GRIDS. Reliability: Theory & Applications. 2025, December 4(89), Vol. 20: 151-156, DOI: https://doi.org/10.24412/1932-2321-2025-489-151-156

MULTIOBJECTIVE NURSE SCHEDULING PROBLEM IN A FUZZY ENVIRONMENT 157

Ahmad Yusuf Adhami, Nabil Ahmed Khan, Ahteshamul Haq

Nurse scheduling is vital to hospital quality in almost every aspect, including patient care, bedside assistance, medication administration, support during major surgeries, data collection, reporting, and more. Nurse staffing and recruitment have become critical in the healthcare sector, particularly for staff scheduling, which is essential across industries and services. However, maintaining sufficient nurses is crucial, as understaffing can lead to life-threatening situations with serious financial, social, and legal consequences. This research article aims to minimize scheduling costs by optimizing nurse allocation between departments and shift-wise cost distribution. We assume that the costs associated with various hospital departments are parabolic fuzzy. This study adopts a case study approach to explore the issue of nurse scheduling in a hospital environment, where cost minimization and resource allocation are essential. Fuzzy programming is used to achieve a compromise solution that balances cost efficiency with the required staffing level in hospitals.

Cite: Ahmad Yusuf Adhami, Nabil Ahmed Khan, Ahteshamul Haq MULTIOBJECTIVE NURSE SCHEDULING PROBLEM IN A FUZZY ENVIRONMENT. Reliability: Theory & Applications. 2025, December 4(89), Vol. 20: 157-171, DOI: https://doi.org/10.24412/1932-2321-2025-489-157-171

PREDICTIVE MODELING OF POLYCYSTIC OVARY SYNDROME USING MACHINE LEARNING ALGORITHMS 172

Gneya Pandya, Dhara Solanki, Dr. Jigna Jadav, Dr. Kajal Patel

PCOS is a prevalent health condition affecting women globally, and if not diagnosed early, it can lead to severe complications like type two diabetes and gestational diabetes. Our research is focused on enhancing the accuracy and reliability of PCOS diagnosis using machine learning techniques. We utilized a public dataset and applied a range of machine learning models like Logistic Regression (LR), Support Vector Machine (SVM), Decision Tree (DT), and Random Forest (RF) ensemble algorithms. By implementing feature selection methods, we aim to identify the most critical factors contributing to the diagnosis, ensuring that the best-performing model is selected for reliable results. Notably, our research achieved a very good accuracy by using the Random Forest algorithm, highlighting its potential to provide a more precise and trustworthy diagnosis of PCOS. This work represents a significant step toward improving healthcare outcomes for women with PCOS.

Cite: Gneya Pandya, Dhara Solanki, Dr. Jigna Jadav, Dr. Kajal Patel PREDICTIVE MODELING OF POLYCYSTIC OVARY SYNDROME USING MACHINE LEARNING ALGORITHMS. Reliability: Theory & Applications. 2025, December 4(89), Vol. 20: 172-179, DOI: https://doi.org/10.24412/1932-2321-2025-489-172-179

LOG EXPONENTIATED KUMARASWAMY DISTRIBUTION WITH REAL LIFE APPLICATIONS 180

Mahvish Jan, S.P. Ahmad

The generalization of probability distributions plays a crucial role in broadening their applications across various domains. To achieve this, this paper introduces a novel three-parameter generalization of the Kumaraswamy distribution. The new distribution is termed as the Log Exponentiated Kumaraswamy (LEK) distribution. Some essential properties of this distribution are studied and the estimate of parameters are obtained using the maximum likelihood estimation procedure. Also, a simulation study is conducted and two real life data sets demonstrate the proposed distribution's applicability. The performance of the proposed LEK distribution proved to be better than comparative models.

Cite: Mahvish Jan, S.P. Ahmad LOG EXPONENTIATED KUMARASWAMY DISTRIBUTION WITH REAL LIFE APPLICATIONS. Reliability: Theory & Applications. 2025, December 4(89), Vol. 20: 180-190, DOI: https://doi.org/10.24412/1932-2321-2025-489-180-190

ANALYSIS OF A SINGLE-SERVER QUEUE WITH ENCOURAGED ARRIVALS, IMPATIENT CUSTOMERS AND DYNAMIC SERVICE SWITCHING 191

Ismailkhan.E, Nagarajan.G, Sundar Raj.M, Immaculate.S

This study examines a single-server queueing system that features encouraged arrivals, customer impatience and a self-switching service mechanism. In this model, the arrival rate increases with the number of customers present in the system, specifically modeled as $\lambda(1+\eta)$, where λ is a positive constant and η represents the current number of customers. The server initially operates at a service rate $\mu 1$ as long as the system size is below a predefined threshold K. Once the number of customers reaches K, the server switches to a faster service rate $\mu 2$. Customers become impatient after entering the queue and may abandon the system at a rate γ. Still, this impatience applies only while the server is operating at the slower service rate $\mu 1$. No reneging occurs once the server switches to the faster rate $\mu 2$. The steady-state probability distribution of the system is derived and performance metrics such as the expected waiting time and the average number of customers in the system are evaluated. Numerical illustrations are also provided to demonstrate the impact of encouraged arrivals and server switching behavior.

Cite: Ismailkhan.E, Nagarajan.G, Sundar Raj.M, Immaculate.S ANALYSIS OF A SINGLE-SERVER QUEUE WITH ENCOURAGED ARRIVALS, IMPATIENT CUSTOMERS AND DYNAMIC SERVICE SWITCHING. Reliability: Theory & Applications. 2025, December 4(89), Vol. 20: 191-199, DOI: https://doi.org/10.24412/1932-2321-2025-489-191-199

A STATISTICAL ANALYSIS OF FUZZY CONFOUNDING FACTORIAL EXPERIMENTS 200

Sri Devi, S. N. Manoharan, T. Karthikeyan, D. Pachiyappan

The factorial experiment is used to test more than one factor at a time, whereas simple experiments can test only one factor at a time. The technique of reducing the block size by making one or more interaction contrast identical to block contrast is known as confounding. Only the higher-order interactions are confounded in factorial experiments, and the interaction effects have been confounded within the blocks. This article proposes that confounding design is performed with Latin squares with trapezoidal fuzzy numbers (TrFNs). In order to obtain an unbiased estimate of an error from a Latin square, the rows and columns must be rearranged in random order. Finally, we provide numerical example to clarify the discussions.

Cite: Sri Devi, S. N. Manoharan, T. Karthikeyan, D. Pachiyappan A STATISTICAL ANALYSIS OF FUZZY CONFOUNDING FACTORIAL EXPERIMENTS. Reliability: Theory & Applications. 2025, December 4(89), Vol. 20: 200-208, DOI: https://doi.org/10.24412/1932-2321-2025-489-200-208

INVESTIGATION OF THE APPLICATION OF THE NEW INDUCTION SYSTEM IN VERTICAL AXIS WIND GENERATORS 209

I.M. Marufov, N.M. Piriyeva, E.S. Safiyev

In recent scientific and technical literature, vertical axis wind generators based on magnetic levitation have demonstrated several advantages over traditional horizontal-axis wind turbines. However, despite these benefits, challenges remain in maximizing the output power, improving the overall performance, and ensuring the long-term reliability and stability of magnetically levitated wind generators. Existing levitation systems need further development to fully realize the potential of vertical axis designs. To address these challenges, a new controllable induction

levitator was developed specifically to enhance magnetically levitated vertical axis wind generators. A detailed mathematical model of the controlled induction levitator was established, and the main physical dimensions were determined. The modeling approach employed principles of dimensional compatibility, dimensionless parameters, and generalized mathematical expressions to simplify the solution process.
Based on this model, a methodology for parameter optimization was developed, alongside calculation procedures for key design variables. The mathematical model yielded explicit expressions for the levitation constant, the working air gap thickness, and the primary dimensions of the magnetic coil and its windings. These findings provide critical insights for optimizing levitator design and enhancing the performance, reliability, and stability of magnetic levitated vertical axis wind generators. The study confirms that the development of a controllable induction levitation system is essential for advancing vertical axis wind generator technology. The proposed model and optimization recommendations offer a robust foundation for improving levitation efficiency, increasing power output, and ensuring both operational stability and structural reliability. Further refinement and implementation of control induction supports are expected to significantly enhance the operational capabilities of magnetically levitated vertical axis wind generators.

Cite: I.M. Marufov, N.M. Piriyeva, E.S. Safiyev INVESTIGATION OF THE APPLICATION OF THE NEW INDUCTION SYSTEM IN VERTICAL AXIS WIND GENERATORS. Reliability: Theory & Applications. 2025, December 4(89), Vol. 20: 209-215, DOI: https://doi.org/10.24412/1932-2321-2025-489-209-215

SINE LOG-LOGISTIC DISTRIBUTION FOR MODELING REMISSION AND SURVIVAL TIMES OF CANCER PATIENTS 216

Santanu Dutta, Aditya Kumar Yadav

Modeling the remission times of bladder cancer patients reported by Lee and Wang [26], the survival times following radiotherapy and chemotherapy of head and neck cancer patients and bone cancer patients reported by Efron [10] and Mansour et al. [16] have attracted considerable research interest. In this paper, we propose a new two-parameter distribution that fits these data well and compares well in model selection for these data with existing distributions that use three or more parameters. Its distribution, density, quantile, and hazard functions have closed-form expressions. The survival function of the proposed model exhibits a regularly varying tail, and its hazard function is either strictly decreasing or inverse-bathtub shaped, depending on the value of the shape parameter. We derive several properties of the proposed distribution, estimate its parameters, and demonstrate its effectiveness in modeling the hazard function and uncovering key features of the remission time and survival time data.

Cite: Santanu Dutta, Aditya Kumar Yadav SINE LOG-LOGISTIC DISTRIBUTION FOR MODELING REMISSION AND SURVIVAL TIMES OF CANCER PATIENTS. Reliability: Theory & Applications. 2025, December 4(89), Vol. 20: 216-237, DOI: https://doi.org/10.24412/1932-2321-2025-489-216-237

MANAGEMENT OF ORGANIZATIONAL RISKS IN ENTERPRISES OF THE RUSSIAN OIL AND GAS SECTORBASED ON EXPERT ASSESSMENT RESULTS 238

Evgeny Gvozdev

For effective management of integrated safety at enterprises within the segment of the Russian oil and gas sector (ROGS), it has become a tradition to create an integrated safety system (ISS) designed to prevent conditions for the emergence of various risks (technical, organizational-technical, and organizational). The risk-oriented approach used at enterprises all-round has gained widespread recognition over the past decades, and any risk is considered a cause that transforms into a hazardous event (HE), such as an accident or fire. Currently, there exists a variety of methods for risk assessment. The article presents a justified approach for selecting a

method to assess organizational risks in ISS, which will allow evaluating the activities of the security directions within its structure, identifying control points with significant shortcomings, forming measures to correct identified deviations, and observing the dynamics of improvement in impact indicators over the analyzed time interval.
Aim and objectives. The purpose of the article is to justify a method for assessing organizational risks that have arisen due to deficiencies of personnel in directions implementing control measures concerning the personnel of production structural units. A scientific task has been solved in which the preference for using the expert assessment method, known as the priority ranking method, is justified. It has advantages over other methods. The use of the normal distribution functional together with this method allows experts to select an individual security direction in which organizational risk has arisen. A scientific task, in which an example demonstrating the impact indicators of security personnel directions on the overall state of an overall condition of ISS, has been solved. The possibility of using the priority ranking method in practice and obtaining results in quantitative value (measure) for organizational risks is justified.

Cite: Evgeny Gvozdev MANAGEMENT OF ORGANIZATIONAL RISKS IN ENTERPRISES OF THE RUSSIAN OIL AND GAS SECTORBASED ON EXPERT ASSESSMENT RESULTS. Reliability: Theory & Applications. 2025, December 4(89), Vol. 20: 238-253, DOI: https://doi.org/10.24412/1932-2321-2025-489-238-253

OPTIMIZATION AND ANALYSIS OF SKIP-LOT SAMPLING STRATEGIES BASED ON A DOUBLE-SAMPLING FRAMEWORK 254

Seethalakshmi Ramaswamy, Jayaraj. R, D. Kanagajothi

This paper presents a novel approach to designing skip-lot sampling inspection plans aimed at reducing the required sample size while maintaining effective quality control. By using the traditional double-sampling plan as a reference, the proposed design provides a framework for making inspection more efficient without compromising the reliability of decisions regarding lot acceptance. The study explores the operational characteristics of the suggested plan and evaluates its performance relative to conventional double-sampling procedures, demonstrating that it can achieve equivalent or better-quality assurance with fewer samples. One of the key advantages of the proposed plan is its lower acceptance rates, which enhances the stringency of quality control while potentially reducing inspection costs and effort. The design process incorporates critical quality metrics, including the acceptable quality level and the limiting quality level as well as the acceptable quality level and the average outgoing quality level to guide the selection of the most appropriate sampling plan for a given production scenario. Overall, the proposed skip-lot inspection approach offers a practical, cost-effective alternative to standard sampling techniques, providing manufacturers and quality managers with a method to optimize inspection resources while ensuring high product quality.

Cite: Seethalakshmi Ramaswamy, Jayaraj. R, D. Kanagajothi OPTIMIZATION AND ANALYSIS OF SKIP-LOT SAMPLING STRATEGIES BASED ON A DOUBLE-SAMPLING FRAMEWORK. Reliability: Theory & Applications. 2025, December 4(89), Vol. 20: 254-261, DOI: https://doi.org/10.24412/1932-2321-2025-489-254-261

SENSITIVITY ANALYSIS OF TRIANGULAR AND SYMMETRIC SPLITTING METHODS FOR POSITIVE DEFINITE LINEAR SYSTEMS - BLOCK STOCHASTIC MATRICES 262

Boilepla Harika, Dasari Rajaiah, Renikunta Ramesh, L.P. Rajkumar, and Perati Malla Reddy

In this paper, triangular and symmetric (TS) splitting method is applied to regularized linear system of block stochastic coefficient matrix for finding the steady state probability vector and discussed the sensitivity analysis. The homogeneous system is transformed into regularized non-homogeneous linear system by using preconditioned matrix with the small perturbation. The sensitivity analysis depends on the perturbation parameter.

From the numerical results, it is concluded that, the sensitivity analysis and convergence analysis of TS method changes rapidly when a small change in the perturbation parameter. Moreover, the numerical value of spectral radius gives the convergence analysis and the bounds of TS method.

Cite: Boilepla Harika, Dasari Rajaiah, Renikunta Ramesh, L.P. Rajkumar, and Perati Malla Reddy SENSITIVITY ANALYSIS OF TRIANGULAR AND SYMMETRIC SPLITTING METHODS FOR POSITIVE DEFINITE LINEAR SYSTEMS - BLOCK STOCHASTIC MATRICES. Reliability: Theory & Applications. 2025, December 4(89), Vol. 20: 262-276, DOI: https://doi.org/10.24412/1932-2321-2025-489-262-276

A STATISTICAL EXPLORATION OF THE EFFECTS OF ADDITIONAL PARAMETERS IN MATHEMATICS 277

G. Aruna, J. Jesintha Rosline

The Bipolar Fuzzy Set is an advancement of the classical fuzzy set, developed to represent situations involving both positive and negative preferences or opinions simultaneously. The bipolar score function plays a vital role in decision-making theory. In this article, a bipolar score function is applied to real-life data to examine the effect of additional parameters in the field of mathematics. Furthermore, a research hypothesis is formulated, and the bipolar score function values are statistically analyzed using SPSS software to determine the impact of these additional parameters in mathematics.

Cite: G. Aruna, J. Jesintha Rosline A STATISTICAL EXPLORATION OF THE EFFECTS OF ADDITIONAL PARAMETERS IN MATHEMATICS. Reliability: Theory & Applications. 2025, December 4(89), Vol. 20: 277-284, DOI: https://doi.org/10.24412/1932-2321-2025-489-277-284

RELIABILITY ESTIMATION OF A SYSTEM BASED ON THE STRESS-STRENGTH MODEL USING A WEIBULL DISTRIBUTION 285

K Sruthi and M Kumar

Reliability analysis is increasingly used in practical applications. The Weibull distribution is versatile, offering increasing, decreasing, bathtub, and unimodal hazard rates. Its flexibility enables a more accurate representation of real-world data, leading to reliability expressions that are both more realistic and more reliable. In this paper, we analyze the reliability of a single component system using a stress strength model, where both the system strength and stress follow a Weibull distribution. We extend the analysis to situations where a single-component system is exposed to two independent stresses, with the strength also following a Weibull distribution to estimate reliability. Furthermore, we estimate the reliability of a stress-strength model for a single component exposed to n stresses. Our analysis includes a series system with two independent components under a common stress, using Weibull distributions for stress and exponential distributions for strength. Furthermore, we study the reliability of a series system with n components under common stress, where the stress follows a Weibull distribution. Numerical computations are performed to demonstrate the results. Finally, a comparative study is conducted to evaluate the reliability expression derived in our work using the Weibull distribution against the existing methods.

Cite: K Sruthi and M Kumar RELIABILITY ESTIMATION OF A SYSTEM BASED ON THE STRESS-STRENGTH MODEL USING A WEIBULL DISTRIBUTION. Reliability: Theory & Applications. 2025, December 4(89), Vol. 20: 285-295, DOI: https://doi.org/10.24412/1932-2321-2025-489-285-295

ASSESSMENT OF CRUDE PROBABILITIES OF FAILURE FOR TWO-COMPONENT SERIES SYSTEM SHOCK MODEL 296

Saraswati V Katagi and S. B. Munoli

A Series system with two components having a single risk on each component is same as a single component with two independent risks acting on it. The third risk may be a catastrophic risk to whole system. A two-component series system shock model with two kinds of shocks namely, damage shock and catastrophic shock, is studied from competing risks perspective. The crude probabilities of different modes of system failure are derived. Information from life testing experiment is used in assessment of crude probabilities for system failure. Results are validated through simulation studies.

Cite: Saraswati V Katagi and S. B. Munoli ASSESSMENT OF CRUDE PROBABILITIES OF FAILURE FOR TWO-COMPONENT SERIES SYSTEM SHOCK MODEL. Reliability: Theory & Applications. 2025, December 4(89), Vol. 20: 296-303, DOI: https://doi.org/10.24412/1932-2321-2025-489-296-303

TRANSMUTED X-RAMA DISTRIBUTION: PROPERTIES AND APPLICATIONS 304

Nimmy George, Sindhu E S

In this paper, we introduce a new generalized distribution called Transmuted X-Rama distribution (TXRD) by using the quadratic rank transmutation map (QRTM). The probability density function (PDF), cumulative distribution function (CDF), and key moments of the transmuted distribution are meticulously derived to demonstrate how the transmutation parameter influences the shape of the distribution. Additionally, we analyze its reliability function, hazard rate, odds function, entropy and order statistics all of which are crucial in applications involving uncertainty and longevity data. We propose the method of maximum likelihood estimation (MLE) and method of least squares estimation (LSE) for the estimation of parameters of the distribution. We also show how the transmuted distribution may be fitted to real datasets.

Cite: Nimmy George, Sindhu E S TRANSMUTED X-RAMA DISTRIBUTION: PROPERTIES AND APPLICATIONS. Reliability: Theory & Applications. 2025, December 4(89), Vol. 20: 304-317, DOI: https://doi.org/10.24412/1932-2321-2025-489-304-317

AN EFFICIENT SINGLE VARIABLE INVERSION ALGORITHM FOR DERIVING RELIABILITY BOUNDS IN STORAGE SYSTEMS 318

Emad K. Mutar, Zahir A. H. Hassan

Ensuring reliability in data survivability schemes for storage systems is challenging due to limited resources. A key part of reliability analysis is selecting a suitable mathematical representation, such as the structure-function. The structure-function maps the overall system state based on the states of its components and can effectively describe systems of various complexities. Many techniques and algorithms depend on identifying all minimal path sets (MPSs) and minimal cut sets (MCSs) to construct the structure and bounds in two-terminal systems. The upper and lower bounds are essential for demonstrating critical states in the system and for the reliability analysis of storage systems. This paper presents three mathematical algorithms for analyzing storage system reliability. The first two algorithms identify MPSs and MCSs using the connection and adjacency matrices of the system's graph. The third algorithm determines critical states of the reliability function by using the single-variable inversion (SVI) method for the MPSs and MCSs, helping to establish the system's reliability bounds. The analysis focuses on finding the greatest lower bound (GLB) and the least upper bound (LUB) for reliability. Storage systems are used to demonstrate the computation of MPSs and MCSs and

reliability bounds. These algorithms effectively identify the MPSs and MCSs, calculate their bounds, and visually and numerically represent the results.

Cite: Emad K. Mutar, Zahir A. H. Hassan AN EFFICIENT SINGLE VARIABLE INVERSION ALGORITHM FOR DERIVING RELIABILITY BOUNDS IN STORAGE SYSTEMS. Reliability: Theory & Applications. 2025, December 4(89), Vol. 20: 318-332, DOI: https://doi.org/10.24412/1932-2321-2025-489-318-332

TERRITORIAL HIERARCHY OF SUSTAINABLE DEVELOPMENT GOALS AND RISK MANAGEMENT 333

Marila Lesnykh

The problem of achieving the sustainable development goals is considered from the perspective of the territorial hierarchy. The necessity of applying a risk-based approach in the implementation of plans for the socio-economic development of territorial entities has been identified. The results of identification and monitoring of key risks of economic development on the example of urban settlements are presented. The interrelation of key risks and significant goals of sustainable development of the research object is revealed.

Cite: Marila Lesnykh TERRITORIAL HIERARCHY OF SUSTAINABLE DEVELOPMENT GOALS AND RISK MANAGEMENT. Reliability: Theory & Applications. 2025, December 4(89), Vol. 20: 333-338, DOI: https://doi.org/10.24412/1932-2321-2025-489-333-338

RELIABILITY-ORIENTED MICROGRID CONTROL USING REINFORCEMENT LEARNING 339

O. Aliyeva, I. Babazade

The growing penetration of renewable energy sources (RES) in modern power systems introduces significant challenges to reliability due to the inherent stochasticity of wind and solar generation. Microgrids, as decentralized energy systems, offer resilience and flexibility but require intelligent control strategies to balance variable generation and demand. This paper proposes a reinforcement learning (RL)-based multi-agent control framework for microgrids, formalized through a Markov Decision Process (MDP) with states reflecting generation, storage, and load variability. Deep RL algorithms—DQN, PPO, and A2C—are compared against conventional methods in a high-fidelity simulation environment with real-world load and RES data. Key reliability indicators, including Loss of Load Probability (LOLP), Mean Time Between Failures (MTBF), and the self-sufficiency ratio, are evaluated. Results demonstrate that PPO achieves a >40% reduction in LOLP compared to rule-based control, ensuring higher resilience and operational adaptability. The study further discusses computational constraints, generalization issues, and cyber-physical vulnerabilities, and proposes solutions based on federated RL, transfer learning, and anomaly detection. The findings underline RL's potential as a cornerstone for reliability-centered energy management in microgrids.

Cite: O. Aliyeva, I. Babazade RELIABILITY-ORIENTED MICROGRID CONTROL USING REINFORCEMENT LEARNING. Reliability: Theory & Applications. 2025, December 4(89), Vol. 20: 339-345, DOI: https://doi.org/10.24412/1932-2321-2025-489-339-345

RELIABILITY ASSESSMENT OF PHASE CHANGE MATERIALS IN TES FOR RENEWABLE ENERGY SYSTEMS 346

G.K. Abdullayeva, A.L. Bakhtiyarov

The reliability of phase change materials (PCMs) in thermal energy storage (TES) systems is crucial for the stable and efficient operation of renewable energy infrastructures. This study

presents a comprehensive methodology for assessing PCM reliability under repeated thermal cycling, focusing on degradation mechanisms such as latent heat reduction, phase change temperature shifts, and decreased thermal conductivity.
Experimental characterization using techniques like Differential Scanning Calorimetry (DSC) and Thermogravimetric Analysis (TGA) provides data on property evolution over thousands of heating-cooling cycles. Failure thresholds for critical parameters are established to define functional limits. An exponential decay model is proposed to quantify degradation kinetics and predict the effective service life of different PCM types, including paraffins, salt hydrates, and eutectic mixtures. Comparative analysis reveals distinct degradation behaviors and informs material selection for TES applications. The integration of empirical data, failure criteria, and predictive modeling supports reliability-centered design and maintenance planning, ultimately enhancing TES system durability and performance in renewable energy applications.

Cite: G.K. Abdullayeva, A.L. Bakhtiyarov RELIABILITY ASSESSMENT OF PHASE CHANGE MATERIALS IN TES FOR RENEWABLE ENERGY SYSTEMS. Reliability: Theory & Applications. 2025, December 4(89), Vol. 20: 346-352, DOI: https://doi.org/10.24412/1932-2321-2025-489-346-352

ON THE TYPE II HALF-LOGISTIC GENERALIZED INVERSE WEIBULL DISTRIBUTION AND ITS APPLICATIONS 353

Saana Rafi Pathayappurakkal, Jabir Bengala, Bindu Punathumparambath

Inverse Weibull distribution is frequently used in the survival and reliability analysis owing to its upside down bathtub type hazard function. Generalized inverse Weibull is the flexible generalization of inverse Weibull distribution which has increasing, decreasing and unimodal hazard rates. This paper introduces a novel extension of generalized inverse Weibull distribution which is developed using new type II half logistic generator. We introduced New type II half logistic generalized inverse Weibull distributions. Mathematical and statistical features of the newly derived distribution were examined. The point estimates of the unknown parameters were computed using maximum likelihood estimation, Weighted Least Square, Anderson-Darling and Cramer-von Mises estimator. We have conducted MCMC simulation using R package to validate the estimation algorithms. Finally, we demonstrated the usefulness of the proposed distribution using two real-world failure time data sets.

Cite: Saana Rafi Pathayappurakkal, Jabir Bengala, Bindu Punathumparambath ON THE TYPE II HALF-LOGISTIC GENERALIZED INVERSE WEIBULL DISTRIBUTION AND ITS APPLICATIONS. Reliability: Theory & Applications. 2025, December 4(89), Vol. 20: 353-369, DOI: https://doi.org/10.24412/1932-2321-2025-489-353-369

AN ATTRIBUTE CONTROL CHART BASED ON GENERALIZED EXPONENTIAL-POISSON DISTRIBUTION UNDER HYBRID CENSORING 370

Gokila B and Sheik Abdullah A

This paper presents a novel attribute control chart utilizing a Generalized Exponential- Poisson (GEP) distribution to detect the effect of indeterminacy in manufacturing processes. The proposed chart demonstrates enhanced performance compared to traditional GEP-based control charts, particularly in uncertain environments, by effectively monitoring shifts in process performance and exhibiting lower out-of-control average run lengths (ARL). A case study from the automobile industry further highlights its practical applicability. In addition, the paper explores a hybrid censoring scheme that integrates multiple censoring techniques to address incomplete data in survival and reliability analysis. This approach enhances the accuracy of lifetime estimates, especially in cases where data may be incomplete due to time or resource constraints. A comparative analysis of the proposed chart against traditional control charts underscores its superior performance in real-world applications, especially in situations with uncertain process distributions.

The charts parameters are carefully optimized to ensure that the ARL for the in-control process closely aligns with a predefined target. The paper demonstrates the charts efficiency through numerical examples and simulation studies, thereby validating its performance and highlighting its practical advantages.

Cite: Gokila B and Sheik Abdullah A AN ATTRIBUTE CONTROL CHART BASED ON GENERALIZED EXPONENTIAL-POISSON DISTRIBUTION UNDER HYBRID CENSORING. Reliability: Theory & Applications. 2025, December 4(89), Vol. 20: 370-380, DOI: https://doi.org/10.24412/1932-2321-2025-489-370-380

XAI-SPCNET: A MULTI-LEVEL EXPLAINABLE AI FRAMEWORK FOR PREDICTIVE CONTROL CHART AUTOMATION IN MANUFACTURING QUALITY MONITORING PROCESS 381

V. Anusha, Lilly George, K.S. Harish, Yuvaraja B, A. Manimaran

Timely and accurate detection of process abnormalities in modern manufacturing is needed for sustainable quality assurance so that the process can be rectified quickly. Traditional control charts, although good at illustrating deviations, are poor in prediction and heavily dependent on fixed thresholds, which tend to lead to tardy interventions and high rates of false alarms. Recent developments in artificial intelligence (AI) offer predictive options; nonetheless, their lack of transparency as "black-box" systems erodes users' confidence and influences regulatory compliance difficulties. To bridge this void, Explainable AI (XAI) is ever more critical for Statistical Process Control (SPC), delivering not just precise anomaly prediction but also interpretable, transparent explanations. This paper presents XAI-SPCNet, a new framework incorporating explainability into predictive SPC to facilitate better manufacturing quality assurance. The architecture involves several expert-informed components: (1) Temporal Causal Decision Trees (TCDT-SPE) using Granger causality for adaptive causal splits that are interpretable; (2) Dynamic Rule Embedding Networks (DREN) combining temporal embeddings with Bayesian rule learning for succinct, context-dependent rules; (3) Contrastive Explanation Generator (CEC-SPE) offering contrastive explanations for violations; (4) Sparse Symbolic Regression (SSR-ED) obtaining sparse mathematical decision boundaries; and (5) Multi-Objective Reinforcement Learner with Explanation Optimization (MORLEO) optimizing accuracy, truthfulness, and chart stability. In synthetic and real-world datasets, XAI-SPCNet presents high prediction accuracy (91%), fast inference, concise rule representation, and greater than 95% explanation coverage, thereby promoting transparent, adaptive, and reliable quality control in manufacturing.

Cite: V. Anusha, Lilly George, K.S. Harish, Yuvaraja B, A. Manimaran XAI-SPCNET: A MULTI-LEVEL EXPLAINABLE AI FRAMEWORK FOR PREDICTIVE CONTROL CHART AUTOMATION IN MANUFACTURING QUALITY MONITORING PROCESS. Reliability: Theory & Applications. 2025, December 4(89), Vol. 20: 381-398, DOI: https://doi.org/10.24412/1932-2321-2025-489-381-398

CONSTRUCTION OF EXPONENTIAL LIFETIME BASED ATTRIBUTE CONTROL CHART: A BAYESIAN APPROACH 399

Gunasekaran Munian

Statistical Process Control (SPC) is a quality control method that employs statistical methods to investigate, monitor, and improve a process. A control chart is a tool for monitoring process performance that employs visual indicators to detect unusual deviations due to assignable causes. This chart compares the values of a quality characteristic to its corresponding control limits. In the quality control process, the control chart is frequently constructed while ignoring parameter uncertainty. The detection of changes in the parameter(s) within the probability distribution of one or more process-related variables is an important aspect of monitoring.

Estimating the parameters is essential since it may affect the control chart's long-term performance in in-control or out-of-control conditions. This article introduces a new attribute control chart utilising a Bayesian approach founded on the Exponential lifetime distribution and the Hybrid censoring technique. A Bayesian framework will be utilised to compute the control chart parameters and the average run length. The parameters for the control chart are determined across various value combinations, and the performance of the newly developed control chart is assessed using the Average Run Length (ARL). Numerical examples are provided to elucidate the proposed control chart, and simulated data are employed to demonstrate its potential applications.

Cite: Gunasekaran Munian CONSTRUCTION OF EXPONENTIAL LIFETIME BASED ATTRIBUTE CONTROL CHART: A BAYESIAN APPROACH. Reliability: Theory & Applications. 2025, December 4(89), Vol. 20: 399-410, DOI: https://doi.org/10.24412/1932-2321-2025-489-399-410

ANFIS-BASED COMPUTING FOR BULK QUEUEING FRAMEWORK WITH LOW-BATCH SERVICE, STANDBY SUPPORT AND VACATION STRATEGIES 411

S. Karpagam, N. Aarthy

This study investigates a non-Markovian queueing model involving a single server providing bulk and low-batch services. The model incorporates key operational features such as server breakdown and repair, a standby server and multiple vacations. The service times for the primary server, low-batch service, standby server and vacation are governed by general distributions, whereas breakdown and repair follow exponential distributions. While the primary (bulk) server is under repair, the standby server temporarily takes over service. The probability generating function for queue size at any time is determined, and various system performance metrics are evaluated. Numerical examples are used to demonstrate the analytical findings. Furthermore, the analytical results are validated using the Adaptive Neuro-Fuzzy Inference System (ANFIS), which improves the precision and dependability of the model's predictions.

Cite: S. Karpagam, N. Aarthy ANFIS-BASED COMPUTING FOR BULK QUEUEING FRAMEWORK WITH LOW-BATCH SERVICE, STANDBY SUPPORT AND VACATION STRATEGIES. Reliability: Theory & Applications. 2025, December 4(89), Vol. 20: 411-426, DOI: https://doi.org/10.24412/1932-2321-2025-489-411-426

A DIFFERENTIATED RELIABILITY MODEL FOR INDUSTRIAL POWER SUPPLY SYSTEMS CONSIDERING THREE TYPES OF EQUIPMENT FAILURES 427

Sevinc Mirzayeva, Natavan Ismiyeva, Fidan Mustafayeva

The reliability of power supply systems is a critical factor influencing the operational continuity and safety of industrial enterprises. Conventional reliability assessments often treat all failures uniformly, neglecting the unique characteristics of failure mechanisms such as short circuits, open circuits, and non-actuation of protection devices. This paper proposes a differentiated reliability evaluation model based on non-stationary failure rate functions that reflect the time-dependent nature of each failure type. Using a piecewise failure rate model across three operational phases—burn-in, steady-state, and aging—the methodology accounts for individual failure flows and their cumulative impact on system reliability. A numerical case study demonstrates the application of the model to a transformer, showing a more accurate prediction of failure-free probability compared to traditional models. The results confirm that short circuits dominate risk during aging, while non-actuation and open circuits also contribute significantly. The model enhances diagnostic precision, supports targeted maintenance planning, and can be extended to system-level reliability assessment for complex industrial energy infrastructures.

Cite: Sevinc Mirzayeva, Natavan Ismiyeva, Fidan Mustafayeva A DIFFERENTIATED RELIABILITY MODEL FOR INDUSTRIAL POWER SUPPLY SYSTEMS CONSIDERING THREE TYPES OF EQUIPMENT FAILURES. Reliability: Theory & Applications. 2025, December 4(89), Vol. 20: 427-433, DOI: https://doi.org/10.24412/1932-2321-2025-489-427-433

A NEW MODIFIED POWER GENERALIZED WEIBULL DISTRIBUTION: PROPERTIES AND APPLICATION 434

A. M. Rangoli, A. S. Talawar and Vijaya Sorganvi

Introduction: Survival analysis has become increasing important for various fields like clinical-trails, public health industrial reliability. A major challenge is accurately modelling of failure time data. Using lifetime distribution, we can accurately model the failure time data and can estimate hazard and survival function. In this study we introduced new modified power generalized Weibull (NMPGW) distribution which exhibits bimodal as well as unimodal density patterns, and also, various patterns of hazard curves like increasing, bathtub and decreasing-increasing-decreasing patterns. Methodology: The proposed NMPGW distribution's various density and hazard patterns were studied. Various statistical properties of the model were derived. Estimation of the parameters were done using maximum likelihood estimation (via Expectation Maximization algorithm) and Bayes technique (via Metropolis Hasting algorithm). Also, standard error and confidence limit were estimated. Comparison of various lifetime distributions were done using information criterion. Results: The model shows good fit for hospital dataset in comparison to various lifetime distributions. Estimated the hazard rate which shows decreasing-increasing-decreasing patterns. In comparison to MLE, Bayes estimation gives lower standard error. Kaplan-Meier survival and NMPGW distribution survival curve shows nearer. Conclusion: The NMPGW distribution introduced in this study offers a versatile tool for modeling different hazard rate patterns. The model's strong performance, validated through real hospital data, suggests it could be a valuable addition to survival analysis, outperforming other modified Weibull models in terms of fit and flexibility.

Cite: A. M. Rangoli, A. S. Talawar and Vijaya Sorganvi A NEW MODIFIED POWER GENERALIZED WEIBULL DISTRIBUTION: PROPERTIES AND APPLICATION. Reliability: Theory & Applications. 2025, December 4(89), Vol. 20: 434-448, DOI: https://doi.org/10.24412/1932-2321-2025-489-434-448

STRESS-STRENGTH RELIABILITY UNDER MULTIVARIATE LOG-NORMAL SETUP AND ITS APPLICATION 449

Anirban Goswami, Babulal Seal

In this article it is mainly focused on discussion about estimation of stress-strength reliability (R) under log-normal multivariate setup. We propose a procedure to compute and estimate stress-strength reliability of weighted geometric function when both stress and strength follow a dependent log-normal multivariate distribution with two weightage vectors. We consider the principal component analysis to estimate these vectors. MVUE, MLE and Confidence Intervals of R are obtained. Through simulation studies, their performances are compared using different measures. Finally, we provide a real data analysis.

Cite: Anirban Goswami, Babulal Seal STRESS-STRENGTH RELIABILITY UNDER MULTIVARIATE LOG-NORMAL SETUP AND ITS APPLICATION. Reliability: Theory & Applications. 2025, December 4(89), Vol. 20: 449-470, DOI: https://doi.org/10.24412/1932-2321-2025-489-449-470

RELIABILITY-CENTERED INNOVATION PLANNING FOR COMPLEX INDUSTRIAL SYSTEMS 471

Saddat Zeynalova, Rana Mammadova, Leyla Rahimova

Ensuring the operational reliability of industrial systems is a critical requirement in the context of technical modernization and increasing system complexity. This paper proposes a reliability-centered methodology for evaluating and enhancing the performance of manufacturing assets during innovation-driven transformation. The approach integrates quantitative reliability metrics, including Mean Time Between Failures (MTBF), Mean Time To Repair (MTTR), and operational availability (Ao), into all phases of technical planning and implementation. Statistical modeling based on exponential and Weibull distributions is applied to failure datasets from mechanical engineering systems to estimate degradation rates and failure probabilities. A case study involving digital twins, CMMS integration, and scenario-based failure modeling demonstrates the effectiveness of predictive maintenance and real-time monitoring tools in reducing system downtime. The proposed framework contributes to the unification of reliability analysis and innovation strategy, offering practical tools for minimizing operational risks and optimizing life cycle costs (LCC) in industrial environments.

Cite: Saddat Zeynalova, Rana Mammadova, Leyla Rahimova RELIABILITY-CENTERED INNOVATION PLANNING FOR COMPLEX INDUSTRIAL SYSTEMS. Reliability: Theory & Applications. 2025, December 4(89), Vol. 20: 471-478, DOI: https://doi.org/10.24412/1932-2321-2025-489-471-478

A HYBRID APPROACH FOR DETECTION AND MITIGATION OF ROUTING ATTACKS IN RPL USING DEEP LEARNING 479

Deepak Upadhyay, Hiteishi Diwanji

The exponential growth of the Internet of Things (IoT) has led to the massive deployment of resource-constrained smart devices in domains such as smart homes, industrial automation, healthcare, and smart cities. To facilitate communication between these devices, the Routing Protocol for Low-Power and Lossy Networks (RPL) has emerged as a widely adopted IPv6-based routing protocol customized for low-power, lossy environments. This study proposes an Intrusion Detection System (IDS) framework that processes raw IoT traffic data to detect and classify RPL routing attacks using a hybrid approach and takes mitigation steps. The IDS framework integrates multiple models, such as a LSTM enhanced with Multi-Head Attention for sequential pattern recognition, gradient boosting models such as LightGBM and CatBoost for efficient tabular data classification, and a Multi-Layer Perceptron (MLP) to replicate ensemble knowledge in a lightweight manner. This hybrid IDS demonstrates the efficacy of combining deep learning and machine learning models to detect and mitigate RPL routing attacks, providing a practical and scalable solution for securing IoT networks with highest accuracy of 93.26 % with mobility and 91.96 % without mobility for CNN+LSTM+Attention, LightGBM, CatBoost, MLP algorithms.

Cite: Deepak Upadhyay, Hiteishi Diwanji A HYBRID APPROACH FOR DETECTION AND MITIGATION OF ROUTING ATTACKS IN RPL USING DEEP LEARNING. Reliability: Theory & Applications. 2025, December 4(89), Vol. 20: 479-493, DOI: https://doi.org/10.24412/1932-2321-2025-489-479-493

RELIABILITY ASSESSMENT OF THERMAL-ELECTRICAL MODELS FOR PHOTOVOLTAIC SYSTEMS IN MATLAB: ASSUMPTIONS VERSUS EVALUATION 494

Rahim Mammadzada

Reliable simulation of photovoltaic (PV) panel behavior requires more than electrical accuracy. It must also reflect the thermal realities of panel operation under real-world conditions. This study investigates the reliability of a Simulink-based thermal electrical model of a Jinko JKM325P-72-V monocrystalline module by comparing simulated temperature profiles with those expected under Standard Test Conditions (STC). The model accounts for multilayer thermal mass and material-specific heat capacities. Heat generation is attributed to both unconverted irradiance and resistive losses, while thermal dissipation is governed by convective heat transfer. By tuning model parameters based on datasheet specifications and empirical coefficients, the simulation achieves close agreement with reference temperature values under standard conditions. The work highlights how common oversimplifications in PV modeling, such as assuming uniform temperature, can lead to optimistic thermal reliability assessments. The approach emphasizes the importance of verifying modeling assumptions against physical intuition and available data to support more trustworthy simulation-based design decisions for PV systems.

Cite: Rahim Mammadzada RELIABILITY ASSESSMENT OF THERMAL-ELECTRICAL MODELS FOR PHOTOVOLTAIC SYSTEMS IN MATLAB: ASSUMPTIONS VERSUS EVALUATION. Reliability: Theory & Applications. 2025, December 4(89), Vol. 20: 494-503, DOI: https://doi.org/10.24412/1932-2321-2025-489-494-503

PERFORMANCE MEASURE OF OPTIMAL RESERVE INVENTORY MODEL BETWEEN TWO MACHINES WITH REFERENCE TO TRUNCATION POINT OF THE REPAIR TIME UNDER FUZZY ENVIRONMENT 504

Jagatheesan R and Ramesh R

In inventory control theory, various models have been developed to determine optimal stock levels in practical settings. In sequential production systems, reserve inventory is essential to minimize idle time when upstream machine failures occur. This study assumes that machine repair times are exponentially distributed and satisfy the Setting the Clock Back to Zero (SCBZ) property, with the truncation point itself modeled as a random variable following a mixed exponential distribution. Under these assumptions, an optimal reserve inventory model is derived and analyzed in a fuzzy environment. Uncertainty in system parameters is incorporated using fuzzy numbers, which are defuzzified through the Trisectional Fuzzy Trapezoidal ranking method. Numerical examples validate the applicability of the model in real-life scenarios.

Cite: Jagatheesan R and Ramesh R PERFORMANCE MEASURE OF OPTIMAL RESERVE INVENTORY MODEL BETWEEN TWO MACHINES WITH REFERENCE TO TRUNCATION POINT OF THE REPAIR TIME UNDER FUZZY ENVIRONMENT. Reliability: Theory & Applications. 2025, December 4(89), Vol. 20: 504-512, DOI: https://doi.org/10.24412/1932-2321-2025-489-504-512

A TAYLOR SERIES EXPANSION METHOD FOR SOLVING LINEAR FRACTIONAL PROGRAMMING PROBLEMS 513

Poonam Kumari

This paper proposes an iterative method to solve Linear Fractional Programming (LFP) problems with inequality constraints. The core idea is to approximate the fractional objective function through a series of linear programming (LP) problems, solved successively using updated feasible points. The algorithm begins by selecting a non-zero feasible point that satisfies all inequality constraints. At this point, the fractional objective function is expanded using a first-order Taylor series, resulting in a linear approximation.

This converts the LFP problem into a standard LP problem, which can be solved using common optimization techniques such as the simplex method or the graphical method, depending on the problem's size and complexity. The optimal solution of the LP problem is then used as the new feasible point for the next iteration. In each iteration, the fractional objective function is re-linearized around the current solution, and a new LP problem is formed and solved. This process continues until convergence is achieved, that is, when two successive iterations produce the same or sufficiently similar solutions. The final solution is taken as the optimal solution to the original LFP problem. The effectiveness and practical utility of the proposed method are demonstrated through numerical examples. Results indicate that the approach is computationally efficient and provides accurate solutions. Compared to traditional transformation-based techniques, the proposed method avoids the introduction of auxiliary variables or complex reformulations, offering a more intuitive and implementable solution framework. Furthermore, the approach exhibits potential for extension to more complex fractional programming models, including multi-objective and equality-constrained formulations.

Cite: Poonam Kumari A TAYLOR SERIES EXPANSION METHOD FOR SOLVING LINEAR FRACTIONAL PROGRAMMING PROBLEMS. Reliability: Theory & Applications. 2025, December 4(89), Vol. 20: 513-527, DOI: https://doi.org/10.24412/1932-2321-2025-489-513-527

DESIGNING AND EVALUATION OF BAYESIAN SKIP LOT SAMPLING PLAN - 2 WITH DOUBLE SAMPLING PLANS AS THE REFERENCE PLAN UNDER GAMMA ZERO-INFLATED POISSON DISTRIBUTION 528

Priyadharshini R and Shalini K

Sampling plans are an effective statistical method for assessing and deciding whether to approve or decline a lot based on quality inspection. Skip-lot sampling plans focus on inspecting only a fraction of the submitted lots, significantly reducing costs by minimizing time and effort. Skip-lot sampling is intended for immediate use, and it has been demonstrated that the quality of the submitted lots is consistently high. This article presents designing of Bayesian Skip Lot Sampling Plan – 2 (BSKSP – 2) with Double Sampling Plan (DSP) as the reference plan based on Gamma Zero-inflated Poisson (GZIP) distribution. The Zero-inflated Poisson (ZIP) distribution is suitable for count data with a high frequency of zeros, especially when non-conformities are rare. The Gamma distribution serves as a conjugate prior to the ZIP distribution. The Operating Characteristic (OC) function of skip lot sampling plan is derived and numerical illustrations are provided to illustrate the proposed sampling plan.

Cite: Priyadharshini R and Shalini K DESIGNING AND EVALUATION OF BAYESIAN SKIP LOT SAMPLING PLAN - 2 WITH DOUBLE SAMPLING PLANS AS THE REFERENCE PLAN UNDER GAMMA ZERO-INFLATED POISSON DISTRIBUTION. Reliability: Theory & Applications. 2025, December 4(89), Vol. 20: 528-535, DOI: https://doi.org/10.24412/1932-2321-2025-489-528-535

SIX SIGMA BASED CONTROL CHARTS FOR MEAN UNDER TWO-PARAMETER EXPONENTIAL DISTRIBUTION 536

Gomathi K and Ganesan A

The statistical process control (SPC) method is widely regarded as the most efficient approach for evaluating production processes, balancing sampling costs with chart performance. Recent research has explored this problem in the context of economic planning for control charts, particularly focusing on adaptive control charts. Traditionally, control chart design relies on a fixed structure to determine key parameters such as sample size, sampling interval, and control limits to meet economic or statistical requirements. However, under the exponential distribution, optimizing control charts based on Six Sigma principles can ensure process stability while minimizing costs. This approach helps reduce either the total expected costs over a finite time horizon or the long-term average expected costs.

Cite: Gomathi K and Ganesan A SIX SIGMA BASED CONTROL CHARTS FOR MEAN UNDER TWO-PARAMETER EXPONENTIAL DISTRIBUTION. Reliability: Theory & Applications. 2025, December 4(89), Vol. 20: 536-544, DOI: https://doi.org/10.24412/1932-2321-2025-489-536-544

EXPLORING RECIDIVISM THROUGH BAYESIAN SURVIVAL MODELS: A PARAMETRIC APPROACH WITH RSTAN 545

Fahad Ashraf, Mohammad Parvej, Athar Ali Khan

This study adopts a fully Bayesian parametric survival modeling approach to examine recidivism, utilizing the recid dataset from the woodbridge package in R. Leveraging the computational capabilities of RStan, four alternative survival distributions Exponential, Weibull, Lognormal, and Frechet are estimated, incorporating covariates reflecting demographics, criminal history, and post-release conditions. To promote model parsimony and interpretability, covariate selection is guided by variable importance measures derived from a machine learning-enhanced Cox model. Model performance is systematically evaluated using the Leave-One-Out Information Criterion (LOOIC) and the Widely Applicable Information Criterion (WAIC) to ensure robust predictive accuracy. The analysis includes detailed posterior summaries, conditional effect plots to assess covariate influences on time to reoffense, and posterior predictive distribution (PPD) plots for model validation. The findings provide meaningful insights into the timing and risk of reoffending and underscore the value of Bayesian survival models in criminological research.

Cite: Fahad Ashraf, Mohammad Parvej, Athar Ali Khan EXPLORING RECIDIVISM THROUGH BAYESIAN SURVIVAL MODELS: A PARAMETRIC APPROACH WITH RSTAN. Reliability: Theory & Applications. 2025, December 4(89), Vol. 20: 545-561, DOI: https://doi.org/10.24412/1932-2321-2025-489-545-561

CONTROL CHARTS WITH SIX SIGMA FOR RANGE UNDER TWO-PARAMETER GAMMA DISTRIBUTION 562

Gomathi K and Ganesan A

Quality monitoring of goods and services has been practiced for centuries, whether directly or indirectly. However, the modern approach incorporates quantitative methods rooted in statistical principles for quality control. Statistical quality control (SQC) encompasses a variety of problem-solving techniques used in industrial production, some of which rely on straightforward statistical theories for process control and monitoring. Over time, statistical process control (SPC) has evolved to include a broad range of statistical and optimization methods employed by professionals to enhance quality. In this research paper, we present a comprehensive review and development of a Six Sigma-based control chart for range under the Gamma distribution, examining its various aspects and applications.

Cite: Gomathi K and Ganesan A CONTROL CHARTS WITH SIX SIGMA FOR RANGE UNDER TWO-PARAMETER GAMMA DISTRIBUTION. Reliability: Theory & Applications. 2025, December 4(89), Vol. 20: 562-573, DOI: https://doi.org/10.24412/1932-2321-2025-489-562-573

JOINT ADAPTIVE PROGRESSIVE TYPE-II CENSORING WITH DUS-EXTREME VALUE DISTRIBUTION 574

Rakhi Chandran, Chacko V M

Statistical estimation of parameters under different censoring schemes is important while using distributions like the Extreme value and Weibull distributions for modelling real lifetime data. Since Extreme value distribution arise as log transformation of the Weibull distribution, there are several advantages for discussing the estimation of extreme value parameters. Moreover, DUS transformation provides more appropriate model without increasing parameters. This study examines point estimation methods, including maximum likelihood and Bayesian approaches, for DUS Extreme Value (DUS-EV) distribution under a joint adaptive progressive Type-II censoring scheme. The proposed scheme offers notable advantages in reducing cost and experimental time. Bayesian estimation is implemented via the Metropolis- Hastings algorithm within a Gibbs sampling framework. Interval estimation is carried out using asymptotic confidence intervals, Highest Posterior Density (HPD) credible intervals, and bootstrap confidence intervals. A comparative analysis of classical and Bayesian results is presented, and the applicability of the proposed methods is demonstrated through real data analysis.

Cite: Rakhi Chandran, Chacko V M JOINT ADAPTIVE PROGRESSIVE TYPE-II CENSORING WITH DUS-EXTREME VALUE DISTRIBUTION. Reliability: Theory & Applications. 2025, December 4(89), Vol. 20: 574-589, DOI: https://doi.org/10.24412/1932-2321-2025-489-574-589

DESIGN AND ANALYSIS OF A BAYESIAN ADAPTIVE SKIP-LOT SAMPLING PLAN (BA-SkSP) WITH SINGLE SAMPLING PLAN AS REFERENCE PLAN 590

P. Umanaheswari

This research describes a new Bayesian Adaptive Skip-Lot Sampling Plan (BA-SkSP) system designed for quality inspection of constantly manufactured lots using Bayesian statistical concepts. The proposed strategy uses a single sampling plan as a reference plan and includes a Bayesian framework for dynamically adjusting sample frequency depending on prior quality history and real-time inspection outcomes. The construction approach and performance measures, such as operational characteristic curves, average sample number, average outgoing quality, and average total inspections, are based on Bayesian inference and Markov chain analysis. The performance of the proposed BA-SkSP is examined using extensive simulation studies and compared to traditional SkSP-2 plans under various quality situations. The results show that the Bayesian adaptive technique offers more efficient quality control with fewer inspections.

Cite: P. Umanaheswari DESIGN AND ANALYSIS OF A BAYESIAN ADAPTIVE SKIP-LOT SAMPLING PLAN (BA-SkSP) WITH SINGLE SAMPLING PLAN AS REFERENCE PLAN. Reliability: Theory & Applications. 2025, December 4(89), Vol. 20: 590-598, DOI: https://doi.org/10.24412/1932-2321-2025-489-590-598

SOME STATISTICAL PROPERTIES AND APPLICATIONS OF LOMAX GENERATED DISTRIBUTION 599

Brijesh P. Singh, Manisha Ailani & Utpal Dhar Das

In this paper, a probability distribution has been proposed using the concept of induced distribution, with the classical Lomax distribution as the baseline. Various statistical properties including moments, entropy measures, reliability functions, and generating functions are derived. The maximum likelihood estimation (MLE) method is used for parameter estimation. Real data application is performed to validate the suitability of the proposed model in comparison to existing distributions.

Cite: Brijesh P. Singh, Manisha Ailani & Utpal Dhar Das SOME STATISTICAL PROPERTIES AND APPLICATIONS OF LOMAX GENERATED DISTRIBUTION. Reliability: Theory & Applications. 2025, December 4(89), Vol. 20: 599-617, DOI: https://doi.org/10.24412/1932-2321-2025-489-599-617

OPTIMIZATION OF A DETERIORATING INVENTORY MODEL WITH TIME-DEPENDENT HEAVISIDE DEMAND AND RETURN POLICY UNDER TRIANGULAR FUZZY DECISION-MAKING 618

Kapil Dave, Tanuj Kumar

This study aims to develop a two-warehouse inventory model under both crisp and fuzzy environments, incorporating a return policy. In high-demand retail settings such as supermarkets and corporate markets, storage capacity is often limited. When suppliers offer attractive price discounts for bulk purchases or when the item is seasonal such as agricultural harvest outputs-large quantities are procured. However, these quantities may exceed the capacity of the primary warehouse (own warehouse or OW). In such situations, an additional storage facility, referred to as the rented warehouse (RW), is hired. This RW is typically located at a distance and incurs higher holding costs compared to OW. Consequently, inventory is stored in OW first, and only the surplus is placed in RW. To minimize costs, items from RW are transferred continuously to OW following a release pattern. Return policies offered by sellers serve as an incentive for customers. These policies permit buyers to return unsatisfactory products, with a refund typically amounting

Cite: Kapil Dave, Tanuj Kumar OPTIMIZATION OF A DETERIORATING INVENTORY MODEL WITH TIME-DEPENDENT HEAVISIDE DEMAND AND RETURN POLICY UNDER TRIANGULAR FUZZY DECISION-MAKING. Reliability: Theory & Applications. 2025, December 4(89), Vol. 20: 618-634, DOI: https://doi.org/10.24412/1932-2321-2025-489-618-634

RELIABILITY RISK PROFILING OF TECHNICAL SYSTEMS USING PARAMETRIC COX REGRESSION WITH WEIBULL BASELINE 635

Iyappan M, G. Sathya Priyanka, Soniya. K, Priyanka. G

Reliability analysis of technical systems is vital in predicting failure behavior and improving system design under operational variability. Traditional reliability models often assume constant hazard rates, limiting their ability to model real world degradation mechanisms. This paper presents a Weibull based Cox Proportional Hazards Model to analyse system failure times with covariate influences such as operations stress, environmental temperature, and maintenance interventions. Simulation data is generated for 1000 units under controlled covariate conditions with right censoring. The model estimates hazard functions and survival probabilities using maximum and partial likelihood methods. The results show that the inclusion of time independent covariates significantly enhances the model's predictive ability for time to failure. The Weibull baseline provides flexibility in representing increasing or decreasing hazard trends typical in engineering systems. This study validates the model's robustness through simulation and establishes its applicability in predictive maintenance and reliability risk management.

Cite: Iyappan M, G. Sathya Priyanka, Soniya. K, Priyanka. G RELIABILITY RISK PROFILING OF TECHNICAL SYSTEMS USING PARAMETRIC COX REGRESSION WITH WEIBULL BASELINE. Reliability: Theory & Applications. 2025, December 4(89), Vol. 20: 635-641, DOI: https://doi.org/10.24412/1932-2321-2025-489-635-641

OPTIMIZING TRAFFIC SIGNAL TIMING FOR EFFICIENT FLOW THROUGH URBAN CROSSROADS 642

Bharathi Ramesh Kumar, S. Geetha, S. Gayathri, A. K. Bhuvaneswari

This paper presents an intelligent traffic signal control system aimed at optimizing vehicle flow at a two-lane crossroads intersection using a network flow-based framework. Rapid urbanization and the corresponding rise in vehicle usage have exacerbated congestion issues, especially at intersections where traditional fixed-time signal controls often result in inefficiencies and increased vehicle delays. The proposed system addresses these limitations by integrating real-time traffic data with principles of network flow theory to coordinate signal timing and vehicle movement dynamically. The intersection is modeled as a directed graph, where nodes represent entry and exit points, and edges signify possible vehicle paths. The system utilizes a weighted signal control algorithm that incorporates traffic volume, direction, and flow density to determine optimal signal phases. These weighted parameters guide the adaptive timing of traffic lights, allowing for parallel vehicle movement while preventing collisions. Specific constraints are applied to eliminate conflicting movements and maintain safety, thereby enhancing throughput and reducing total waiting times. A key objective of the model is to minimize total waiting time across all directions by identifying and enforcing necessary conditions for optimal traffic flow. To evaluate the performance of the proposed system, a simulation environment was developed to mimic real-world traffic conditions under various scenarios. Performance metrics such as average delay, queue length, and throughput were used for comparison against traditional signal control methods. Simulation results indicate significant performance improvements. The proposed system achieves a vehicle flow time of 804 seconds compared to 400 seconds in the existing system, with an optimized objective function value of 972. A numerical case study further illustrates the implementation, signal phase structuring, and resulting efficiency gains. In conclusion, the intelligent traffic signal control model demonstrates strong potential for reducing congestion and improving traffic management at urban intersections. Its adaptive, data-driven approach not only enhances current traffic flow but also allows for forecasting future patterns. The model is scalable, flexible, and suitable for integration with intelligent transportation systems, offering a proactive solution to modern traffic challenges.

Cite: Bharathi Ramesh Kumar, S. Geetha, S. Gayathri, A. K. Bhuvaneswari OPTIMIZING TRAFFIC SIGNAL TIMING FOR EFFICIENT FLOW THROUGH URBAN CROSSROADS. DOI: https://doi.org/10.24412/1932-2321-2025-489-642-650

RELIABILITY AND PERFORMANCE ANALYSIS OF AN UNRELIABLE RETRIAL QUEUEING SYSTEM WITH NEGATIVE ARRIVALS 651

Belaiza Dihia, Taleb Samira

In this paper, we focus on a single repairable server retrial queueing system with negative arrivals and two types of breakdowns (passive and active). We assume that the customer in service is lost whenever an active breakdown occurs. Once the repair is completed, the server returns to an idle state. To obtain the system performance metrics, the matrix geometric technique is used combined with direct truncation method. From the standpoint of reliability analysis, we investigate the mean time to the first failure of the system by using the Laplace transform method. Finally, we study numerically the impact of system metrics on the mean number of customers in the orbit, the server state probabilities, the reliability function and the mean time to the first failure.

Cite: Belaiza Dihia, Taleb Samira RELIABILITY AND PERFORMANCE ANALYSIS OF AN UNRELIABLE RETRIAL QUEUEING SYSTEM WITH NEGATIVE ARRIVALS. Reliability: Theory & Applications. 2025, December 4(89), Vol. 20: 651-664, DOI: https://doi.org/10.24412/1932-2321-2025-489-651-664

STOCHASTIC PETRI NET ANALYSIS OF RETRIAL REPAIRABLE SYSTEMS WITH TWO REPAIR MODES 665

Kheireddine Boudehane, Samira Taleb

This paper presents a dependability analysis of an L-out-of-n system supported by a hierarchical standby structure with warm and cold units. The model accounts for realistic operating conditions, including a single unreliable repair server that may break down but can still provide limited service during failure periods. A retrial mechanism is also considered, where failed units that find the server busy join an orbit and retry for service later. The system is modeled using a Generalized Stochastic Petri Net (GSPN), which is then mapped to a Continuous-Time Markov Chain (CTMC) for steady-state performance evaluation. Furthermore, transient reliability analysis is conducted to derive the survival function of the system and the expectation of the first passage time to failure.

Cite: Kheireddine Boudehane, Samira Taleb STOCHASTIC PETRI NET ANALYSIS OF RETRIAL REPAIRABLE SYSTEMS WITH TWO REPAIR MODES. Reliability: Theory & Applications. 2025, December 4(89), Vol. 20: 665-676, DOI: https://doi.org/10.24412/1932-2321-2025-489-665-676

METAHEURISTIC OPTIMIZATION OF RELIABILITY PARAMETERS UNDER VACATION AND INSPECTION POLICIES 677

Diksha Mangla, Shilpa Rani, Shakuntla Singla, Savita Garg

This paper explores in detail the reliability and performance evaluation of a repairable system functioning under the combined influence of vacation and inspection policies, using the Regenerative Point Graph Technique (RPGT) as the core analytical framework. The modeling is carried out through a stochastic state-transition representation, where different system conditions such as active operation, failures, repairs, vacation return of the repairman, and inspection mechanisms are explicitly considered. By exploiting the regenerative nature of the process, the study derives closed-form mathematical expressions for key performance indices, including the Mean Time to System Failure (MTSF), steady-state availability, busy period of the server, and the expected number of inspections. These measures provide a structured understanding of how the system behaves and responds under varying operational, repair, and inspection conditions. To further enhance reliability and system performance, the study employs metaheuristic optimization algorithms such as the Particle Swarm Optimization (PSO), the Genetic Algorithm (GA), and the Cuckoo Search Algorithm (CSA). These optimization methods are implemented to identify the optimal values of system parameters, including failure rate, repair rate, inspection rate, and vacation return rate, which directly influence the efficiency of the system. Numerical experiments and simulation-based illustrations are conducted to validate the theoretical analysis and to compare the effectiveness of the different algorithms. The results demonstrate that CSA and PSO consistently outperform GA, particularly in terms of achieving higher MTSF and availability values, whereas GA, despite slower convergence, provides stable and competitive solutions. The findings emphasize the significance of RPGT as a powerful analytical tool for modeling complex repairable systems and capturing their stochastic dynamics under realistic operational assumptions such as vacations and inspections. Furthermore, the integration of RPGT with evolutionary optimization techniques not only deepens the understanding of system dynamics but also supports practitioners and decision makers in formulating effective reliability and maintenance strategies. This contribution is highly relevant for practical applications in manufacturing industries, communication networks, service organizations, and other industrial systems, where performance optimization and reliability improvement are essential.

Cite: Diksha Mangla, Shilpa Rani, Shakuntla Singla, Savita Garg METAHEURISTIC OPTIMIZATION OF RELIABILITY PARAMETERS UNDER VACATION AND INSPECTION POLICIES. Reliability: Theory & Applications. 2025, December 4(89), Vol. 20: 677-684, DOI: https://doi.org/10.24412/1932-2321-2025-489-677-684

IMPROVING RELIABILITY OF LOW-VOLTAGE DISTRIBUTION NETWORKS UNDER LIGHTNING OVERVOLTAGES 685

I.A. Guseynova

Low-voltage (LV) distribution networks are highly vulnerable to lightning-induced overvoltages, which represent a significant cause of transformer failures, equipment damage, and service interruptions in regions with high lightning activity. Conventional protective measures—such as improved grounding and primary medium-voltage (MV) surge arresters—are necessary but often insufficient to suppress secondary surges at the LV side. This paper analyzes the physical mechanisms of surge current injection into transformer neutrals, the influence of network topology, and the role of transformer design in generating internal dielectric stress. Comparative evaluation of surge protective devices (SPDs) demonstrates that coordinated deployment of MOV- and hybrid-based arresters at both transformer terminals and consumer service entrances significantly reduces insulation stress and equipment damage. Simulation results and field evidence confirm that such coordinated strategies improve key reliability indicators, including mean time between failures (MTBF) and system average interruption frequency index (SAIFI), while also reducing economic losses. The findings highlight that preventive investments in SPDs are cost-effective, yielding an order-of-magnitude reduction in lightning-related failures. From a reliability-centered asset management perspective, SPD deployment should be considered a strategic measure for enhancing resilience and sustainability of LV distribution networks.

Cite: I.A. Guseynova IMPROVING RELIABILITY OF LOW-VOLTAGE DISTRIBUTION NETWORKS UNDER LIGHTNING OVERVOLTAGES. Reliability: Theory & Applications. 2025, December 4(89), Vol. 20: 685-693, DOI: https://doi.org/10.24412/1932-2321-2025-489-685-693

FEASIBILITY AND VIABILITY OF ADAPTIVE RECOMMENDER SYSTEMS: BRIDGING TRADITIONAL AND INTELLIGENT APPROACHES 694

Nitin Raval, Dhaval Parikh

This paper investigates the feasibility and viability of adaptive recommender systems by comparing traditional recommendation approaches with a proposed adaptive hybrid model that integrates Graph Neural Networks (GNN), Large Language Models (LLM), and Explainable AI (XAI). The study explores how these components contribute to handling cold-start problems, real-time user preference shifts, and enhancing explainability in recommendation systems. Benchmarking against traditional methods and popular platforms (e.g., Netflix, Spotify), this paper presents a comprehensive comparative analysis and discusses the future of adaptive RecSys for academia and industry. Real-world scenarios are considered, based on simulated benchmarks such as genre-drifted MovieLens, personalized music preferences, and multilingual regional content, demonstrating the practical value and implementation roadmap.

Cite: Nitin Raval, Dhaval Parikh FEASIBILITY AND VIABILITY OF ADAPTIVE RECOMMENDER SYSTEMS: BRIDGING TRADITIONAL AND INTELLIGENT APPROACHES. Reliability: Theory & Applications. 2025, December 4(89), Vol. 20: 694-702, DOI: https://doi.org/10.24412/1932-2321-2025-489-694-702

RELIABILITY AND RISK MODELLING IN ECONOMIC, ENVIRONMENTAL SUSTAINABILITY, AND FINANCIAL SYSTEMS WITH THE ARCTAN MARSHALL-OLKIN WEIBULL DISTRIBUTION 703

Moin Uddin

The Arctan Marshall-Olkin family is presented as a novel and versatile class of heavy-tailed distributions for modelling extreme occurrences in the fields of economics, finance, and the Environmental sustainability. This family is produced by combining the Arctan-X method, which

makes use of the arctangent inverse trigonometric function, with the Marshall-Olkin framework. A specific example, the Arctan-Marshall-Olkin-Weibull (ATMOW) distribution, is thoroughly examined. By adding a third parameter, ATMOW improves its capacity to handle heavy-tailed data in contrast to the traditional two-parameter Weibull distribution.
Additionally, to evaluate severe financial risks, closed-form formulas for important actuarial risk measures such as value at risk and tail value at risk are generated. ATMOW performs better than a number of rival multiparameter distributions, according to empirical applications to actual financial, environmental sustainability, and economic datasets.

Cite: Moin Uddin RELIABILITY AND RISK MODELLING IN ECONOMIC, ENVIRONMENTAL SUSTAINABILITY, AND FINANCIAL SYSTEMS WITH THE ARCTAN MARSHALL-OLKIN WEIBULL DISTRIBUTION. Reliability: Theory & Applications. 2025, December 4(89), Vol. 20: 703-715, DOI: https://doi.org/10.24412/1932-2321-2025-489-703-715

AUTHENTICATION APPROACHES IN IOT: A COMPARATIVE STUDY OF EXISTING METHODS AND FUTURE DIRECTIONS 716

Mihir Mehta, Sanjay Patel, Nrupesh Shah

The Internet of Things (IoT) marks a new era in how humans interact with technology. It enables physical devices to generate, receive, and effortlessly exchange data with each other. The primary objective of IoT-based systems is to enhance user convenience and operational efficiency. However, IoT environments are typically open and interconnected, which exposes them to a wide range of security threats. Ensuring robust security is therefore a critical aspect of IoT networks. Traditional security mechanisms are often unsuitable due to the limited computational resources of IoT devices. Authentication plays a key role in verifying the identity of each device within the network, as compromised devices can significantly disrupt operations. To fully leverage IoT's potential, it is crucial to address and resolve security concerns across all layers. The research is divided into two primary categories: authentication factors and widely used cryptographic primitives. Authentication factors encompass methods like passwords, RFID, smart cards, and one-time passwords (OTPs), whereas cryptographic primitives involve techniques such as Data Encryption Standards (DES), Advance Encryption Standard (AES) and Physically Unclonable Functions (PUFs). This paper reviews existing authentication techniques and provides the comparison among them. Our research works also highlights the performance of various cryptographic techniques in IoT network. Reliability denotes the consistent and accurate functioning of an authentication system in verifying that only authorized devices and users are granted access to the IoT network or its associated services. Reliable Authentication framework offers consistent Identity verification & minimizes False Positive- Unauthorized devices mistakenly authenticated/ False Negatives-Legitimate devices wrongly denied access. It concludes with identification of various open research challenges associated with IoT Authentication.

Cite: Mihir Mehta, Sanjay Patel, Nrupesh Shah AUTHENTICATION APPROACHES IN IOT: A COMPARATIVE STUDY OF EXISTING METHODS AND FUTURE DIRECTIONS. Reliability: Theory & Applications. 2025, December 4(89), Vol. 20: 716-730, DOI: https://doi.org/10.24412/1932-2321-2025-489-716-730

THE ALDAM-LOG-LOGISTIC DISTRIBUTION AND ITS APPLICATION TO BIMODAL DATA 731

Iozhar A. Lakibul

The log-logistic distribution is a commonly used lifetime probability distribution, particularly for modeling lifetime data. In this paper, a new generated (G) family of distributions is introduced, referred to as the Aldam-G family of distributions. This family is derived using the T-X family of distributions. As an application, the log-logistic distribution is generalized through the proposed family, resulting in a new distribution called the Aldam-Log-logistic distribution.

The probability density function (PDF) and cumulative distribution function (CDF) of the proposed distribution are derived. It is observed that the new distribution can effectively model bimodal data. Several statistical properties of the Aldam-Log-logistic distribution are also explored. Parameter estimation is carried out using the maximum likelihood method. Finally, the proposed distribution is applied to a real-life dataset, and the results indicate that it provides a better fit compared to some existing competing distributions.

Cite: Iozhar A. Lakibul THE ALDAM-LOG-LOGISTIC DISTRIBUTION AND ITS APPLICATION TO BIMODAL DATA. Reliability: Theory & Applications. 2025, December 4(89), Vol. 20: 731-743, DOI: https://doi.org/10.24412/1932-2321-2025-489-731-743

ALPHA LOGARITHMIC TRANSFORMATION OF LOMAX DISTRIBUTION WITH PROPERTIES AND APPLICATION TO SURVIVAL DATA 744

K.M. Sakthivel, Nandhini V, and Vidhya G

Probability distribution plays a vital role in lifetime data analysis, reliability modeling, and survival studies. Classical models often exhibit limitations in flexibility when dealing with diverse real-world datasets.To address this gap, we introduce an extended model that improves the ability to capture various shapes of lifetime distributions.In this paper, we propose a new three-parameter probability distribution, termed the Alpha Logarithmic Transformation of Lomax (ALTLx) distribution, which proves to be effective for modeling lifetime data.The proposed distribution is studied in detail, and several of its statistical properties are derived, including moments, incomplete moments, quantiles, mean residual life, mean inactivity time, entropy, order statistics, and stress strength analysis.Parameter estimation is carried out using the method of maximum likelihood to ensure reliable inference. The practical applicability of the ALTLx distribution is demonstrated by fitting it to datasets representing the survival time of patients. The results indicate that it outperforms several well-known competing distributions, showing that the proposed model provides a significantly better fit. The distribution exhibits greater flexibility and effectively captures diverse patterns in lifetime data. The findings confirm that the ALTLx distribution offers superior performance in modeling lifetime and reliability data.

Cite: K.M. Sakthivel, Nandhini V, and Vidhya G ALPHA LOGARITHMIC TRANSFORMATION OF LOMAX DISTRIBUTION WITH PROPERTIES AND APPLICATION TO SURVIVAL DATA. Reliability: Theory & Applications. 2025, December 4(89), Vol. 20: 744-756, DOI: https://doi.org/10.24412/1932-2321-2025-489-744-756

LINEAR PREDICTION OF K-RECORD VALUES FROM GENERALIZED PARETO DISTRIBUTION 757

Laji Muraleedharan and Manoj Chacko

In this paper, the upper k-record values arising from a generalized Pareto distribution is considered. After considering the means, variances and covariances of the upper k-record values, the best linear unbiased estimators and best linear invariant estimators of the location and scale parameters of the generalized Pareto distribution is discussed under the assumption that the shape parameter is assumed to be known. The marginal best linear unbiased predictor and best linear invariant predictor of future upper k-record value and the joint best linear unbiased predictor and best linear invariant predictor of a pair of future upper k-record values are also determined. Finally, a real dataset is considered to illustrate the proposed inference procedures developed in this paper.

Cite: Laji Muraleedharan and Manoj Chacko LINEAR PREDICTION OF K-RECORD VALUES FROM GENERALIZED PARETO DISTRIBUTION. Reliability: Theory & Applications. 2025, December 4(89), Vol. 20: 757-771, DOI: https://doi.org/10.24412/1932-2321-2025-489-757-771

SOME REFINEMENTS OF INEQUALITIES FOR POLYNOMIALS 772

Aijaz Ahmad, D Venkatesan, Ajiaz Magbool Dar, Aafaq A. Rather, Danish Qayoom, Eid Sadun Alotaibi, Showkat A. Bhat, Mushtaq A. Lone and Jameel Ahmad Ansari

The study of inequalities for polynomials plays a central role in mathematical analysis, with numerous results exploring the relationships between a polynomial and its derivative. Over time, several refinements and generalizations have been established, strengthening classical inequalities and extending them to broader settings. In this paper, we present new refinements that further enhance existing results on polynomial inequalities. Our findings not only sharpen earlier theorems, but also provide generalized forms that encompass a wider class of polynomials. The refinements introduced here not only strengthen known inequalities, but also provide a framework that connects different strands of results in this area. This contributes to a deeper understanding of the behavior of polynomials in the complex domain and establishes new directions for further investigation.

Cite: Aijaz Ahmad, D Venkatesan, Ajiaz Magbool Dar, Aafaq A. Rather, Danish Qayoom, Eid Sadun Alotaibi, Showkat A. Bhat, Mushtaq A. Lone and Jameel Ahmad Ansari SOME REFINEMENTS OF INEQUALITIES FOR POLYNOMIALS. Reliability: Theory & Applications. 2025, December 4(89), Vol. 20: 772-780, DOI: https://doi.org/10.24412/1932-2321-2025-489-772-780

DECISION MAKING UNDER UNCERTAINTY BASED ON GENERALIZED FERMATEAN FUZZY NUMBERS 781

Tanuj Kumar, Gajraj Singh, Birjesh Kumar

It has been observed that Fermatean fuzzy sets, which provide a more comprehensive framework than intuitionistic fuzzy sets, offer significant advantages in decision-making processes. This study first formulates the generalized representation of Fermatean fuzzy numbers, including their membership and non-membership functions as well as the associated arithmetic operations. Furthermore, novel defuzzification and ranking techniques are proposed to convert Fermatean fuzzy information into crisp values. To validate the approach, a statistical application is presented for determining the sample range under generalized trapezoidal Fermatean fuzzy numbers using the proposed defuzzification and ranking methods. Finally, a case study is provided to demonstrate the practical applicability of generalized Fermatean fuzzy numbers in real-world decision-making contexts.

Cite: Tanuj Kumar, Gajraj Singh, Birjesh Kumar DECISION MAKING UNDER UNCERTAINTY BASED ON GENERALIZED FERMATEAN FUZZY NUMBERS. Reliability: Theory & Applications. 2025, December 4(89), Vol. 20: 781-794, DOI: https://doi.org/10.24412/1932-2321-2025-489-781-794

PERFORMANCE METRICS OF M/M(A,B)/(2,1)/RV QUEUING SYSTEM WITH RENEGING AND RETENTION OF CUSTOMERS 795

Jenifer Princy P, K Julia Rose Mary

In general, the quality of service management ensures the quality of the business outcome. Customer behavior trivially has an impact on it. To obtain a potential output, it is necessary to speed up the customer service request. Adequate among of losses happen when the customers withdraw the service request. Thus, it is vital to implement a significant strategy based on the number of request in queue. By modeling the service system mathematically in concern with the customers behavior, it is elegant to make a strategy for estimating demands.

This paper aims to interpret a system, M/M(a,b)/(2,1)/RV providing service in batches with the aid of two servers and encounters the measures of performance of the system under the possibility of servers vacation and customers behavior of reneging and retention. A server withdraws the system whenever he is not available with an accessible batch to start his service. This behavior of the server can be termed as vacation. The vacation policy used in this paper involves the repeated mode of vacation of the servers. Customers entering the system experience three states of availability of the servers. Thus, for the proposed model the equations and solutions for the steady state is derived and computed theoretically, and the results are verified through numerical illustration.

Cite: Jenifer Princy P, K Julia Rose Mary PERFORMANCE METRICS OF M/M(A,B)/(2,1)/RV QUEUING SYSTEM WITH RENEGING AND RETENTION OF CUSTOMERS. Reliability: Theory & Applications. 2025, December 4(89), Vol. 20: 795-805, DOI: https://doi.org/10.24412/1932-2321-2025-489-795-805

FM/FM/1 QUEUE WITH N-POLICY TWO-PHASE, SERVER START-UP, TIME-OUT AND BREAKDOWNS USING L-R METHOD 806

John Benhur.K, D. Gopinath, P.Sudhakara Babu, Muragesh Math

This study centers on evaluating the performance metrics of the system, specifically emphasizing two key elements:the expected length of the system (L) and the minimum anticipated cost T(N) derived from the optimal strategy analysis of the N-policy L-R(Left-Right).FM/FM/I two-phase queueing model.This system incorporates essential factors such as server start-up,time-out,breakdown, and repair processes,making the analysis more comprehensive and reflective of real-world operational challenges.The arrival rate and service rate in this model are represented as triangular fuzzy numbers,which provide a more flexible and realistic approach in capturing the uncertainty and variability inherent in these rates.The study employs the L-R method,a technique known for its efficiency and simplicity when compared to the more traditional alpha-cuts method.The L-R method minimizes computational complexity and enhances the case of differentiation, making it a more convenient approach for handling fuzzy numbers in queueing theory.By applying this method,the study effectively addresses the limitations of previous models and provides a more accurate estimation of the system's performance metrics.To demonstrate the validity and applicability of the proposed model,a numerical example is provided.This example illustrates the practicality of the L-R method in optimizing the system's cost and performance,shoocasing how the model can be applied to real-world scenarios.The results of the numerical example confirm the robustness and reliability of the proposed approach,making a strong case for its adoption in queueing system analysis.This study thus offers significant insights and a novel methodological contribution to the field of fuzzy queueing systems.

Cite: John Benhur.K, D. Gopinath, P.Sudhakara Babu, Muragesh Math FM/FM/1 QUEUE WITH N-POLICY TWO-PHASE, SERVER START-UP, TIME-OUT AND BREAKDOWNS USING L-R METHOD. Reliability: Theory & Applications. 2025, December 4(89), Vol. 20: 806-813, DOI: https://doi.org/10.24412/1932-2321-2025-489-806-813

A COMPREHENSIVE EXPLORATION OF QUASI RAMA DISTRIBUTION WITH SIGNIFICANT STATISTICAL PROPERTIES AND APPLICATIONS 814

Rashid A. Ganaie, Ashok Routhu, T. Vivekanandan, Manzoor A. Khanday and Prem Lata Gautam

In this study, we propose a novel extension of the quasi Rama distribution referred to as the length-biased quasi Rama (LBQR) distribution, developed by applying the length-biased technique to the classical quasi Rama distribution. The proposed distribution is thoroughly investigated and several of its important statistical properties are derived including moments, harmonic mean, order statistics, reliability function, hazard rate function, reverse hazard rate function, moment generating function, characteristic function, Renyi entropy as well as Bonferroni and Lorenz curves. Furthermore, the parameters of the new distribution are estimated using the method of maximum likelihood estimation. To evaluate the practical relevance and predictive performance of the length biased quasi Rama distribution, it is applied to two real lifetime data sets, demonstrating its applicability and effectiveness in modeling real-world lifetime phenomena.

Cite: Rashid A. Ganaie, Ashok Routhu, T. Vivekanandan, Manzoor A. Khanday and Prem Lata Gautam A COMPREHENSIVE EXPLORATION OF QUASI RAMA DISTRIBUTION WITH SIGNIFICANT STATISTICAL PROPERTIES AND APPLICATIONS. Reliability: Theory & Applications. 2025, December 4(89), Vol. 20: 814-827, DOI: https://doi.org/10.24412/1932-2321-2025-489-814-827

METRIC DIMENSION OF GRAPHS WITH SEQUENTIAL PENDANT EDGE EXTENSION 828

Ajendra Kumar, B.S. Rawat, Kirti Chauhan

The metric dimension of a graph measures the smallest number of vertices (landmarks) needed so that every vertex in the graph can be uniquely identified by its distances to these landmarks. In this study, we investigate a specific structural modification called Sequential Pendant Edge Extension (SPEE) in which pendant edges are attached one at a time to an existing graph. We analyse whether such extensions affect the metric dimension of graph families. These results provide both theoretical insights and practical assurance in designing reliable and scalable network models.

Cite: Ajendra Kumar, B.S. Rawat, Kirti Chauhan METRIC DIMENSION OF GRAPHS WITH SEQUENTIAL PENDANT EDGE EXTENSION. Reliability: Theory & Applications. 2025, December 4(89), Vol. 20: 828-838, DOI: https://doi.org/10.24412/1932-2321-2025-489-828-838

A REVIEW ON SUSTAINABILITY, RELIABILITY, AND SAFETY OF MICROCHANNEL HEAT SINKS IN ELECTRONIC COOLING APPLICATIONS 839

Santosh Kumar Rai, Pardeep Kumar, Mahesh Kumar Gupta, Dhowmya Bhatt, Arun Uniyal, Gyanendra Prasad Bagri, Nikhil Vivek Shrivas

Day by day, the rapid growth in the miniaturization of electronic devices ranging from mini, micro, to nano scales for various applications has drastically increased. However, the fabrication of such devices and the dissipation of heat from their bodies to the surrounding environment remains challenging. Due to these thermal management issues, electronic devices, MEMS, and other microfluidic and biomedical systems face significant sustainability, reliability, and safety concerns. In the present paper, we address various methods to overcome these problems in existing devices by using microchannels (MICHs). MICHs are used to remove heat from electronic components, thereby improving device safety and enabling them to operate within permissible temperature limits. A comprehensive literature review is presented, covering the classification of MICHs, their fabrication methods, and their applications in enhancing the

reliability and safety of various devices. Sustainable design aspects are also considered to improve energy efficiency, optimize material usage, reduce the environmental impact of coolants, and enhance product life cycle performance. Furthermore, the paper outlines potential future research directions and fields of innovation for further advancements in this domain.

Cite: Santosh Kumar Rai, Pardeep Kumar, Mahesh Kumar Gupta, Dhowmya Bhatt, Arun Uniyal, Gyanendra Prasad Bagri, Nikhil Vivek Shrivas A REVIEW ON SUSTAINABILITY, RELIABILITY, AND SAFETY OF MICROCHANNEL HEAT SINKS IN ELECTRONIC COOLING APPLICATIONS. Reliability: Theory & Applications. 2025, December 4(89), Vol. 20: 839-851, DOI: https://doi.org/10.24412/1932-2321-2025-489-839-851

INVESTIGATING THE PERFORMANCE OF MAP/PH/1 QUEUEING SYSTEMS WITH CATASTROPHIC FAILURES, NEGATIVE ARRIVALS, SERVER BREAKDOWNS, REPAIRS AND LACK OF CUSTOMER TOLERANCE FOR DELAYS 852

K. Thilagavathy, G. Ayyappan

This paper presents a comprehensive analytical study of a single-server queueing system incorporating by a Markovian Arrival Process (MAP), Phase-Type (PH) service times, and multiple complex disruptions, including catastrophic failures, negative arrivals, server breakdowns, and phase-type repairs. Utilizing matrix-analytic methods, we derive steady-state probability distributions, and system performance measures. The consequence of failure frequencies, and repair parameters on key performance metrics such as system size, and server availability is thoroughly examined. The behavior of the system is demonstrated using numerical results. The results offer valuable insights for the purposes of design and optimization of resilient and efficient service systems operating in uncertain and failure-prone environments.

Cite: K. Thilagavathy, G. Ayyappan INVESTIGATING THE PERFORMANCE OF MAP/PH/1 QUEUEING SYSTEMS WITH CATASTROPHIC FAILURES, NEGATIVE ARRIVALS, SERVER BREAKDOWNS, REPAIRS AND LACK OF CUSTOMER TOLERANCE FOR DELAYS. Reliability: Theory & Applications. 2025, December 4(89), Vol. 20: 852-866, DOI: https://doi.org/10.24412/1932-2321-2025-489-852-866

BAYESIAN STUDY OF HYBRID WEIBULL- EXPONENTIAL POWER MODEL BY MEANS OF HAMILTONIAN MONTE CARLO ALGORITHM 867

M. A. Alhassan, A. Yahaya, O. O. Ishaq, B. Abba, A. B. Muhammad

In this paper, we derived two important properties, viz: moment and order statistics, for the Hybrid Weibull-Exponential Power actuarial reliability model. We considered Bayesian procedures for estimating the parameters of the model. We tested the performance of the estimation approach by means of simple Monte Carlo experiment, hence, found the estimator consistent for the model parameters. Subsequently, we utilized the Bayesian inferential technique to further explore the overall adequacy the model in real—life through two sets of failure time reliability data. However, at the complexity point of the Bayesian method in dealing with the complex posterior of the model, we ushered-in the robust Hamiltonian Monte Carlo simulation algorithm, and thus, swiftly enhanced the posterior inference. The Add-on MLE examination on the model parameters was briefly conducted to additionally check the model's performance in real life. On the premise of the evaluation criteria and goodness-of-fit statistics results obtained from the MLE computation, we, once again, found clearly that the model is superior among the similar models compared. The HWEP model is, thus, apt for reliability analyses of dual failures as well as dual-component failed systems.

Cite: M. A. Alhassan, A. Yahaya, O. O. Ishaq, B. Abba, A. B. Muhammad BAYESIAN STUDY OF HYBRID WEIBULL- EXPONENTIAL POWER MODEL BY MEANS OF HAMILTONIAN MONTE CARLO ALGORITHM. Reliability: Theory & Applications. 2025, December 4(89), Vol. 20: 867-880, DOI: https://doi.org/10.24412/1932-2321-2025-489-867-880

PERFORMANCE AND COST ANALYSIS OF A GI/M(a,b)/I QUEUE WITH COMPULSORY AND EXTENDED REPAIRS DURING MULTIPLE WORKING VACATIONS 881

E. Praveena, K. Julia Rose Mary

The paper analyses a single-server queuing model with general distribution arrival and batch service under multiple working vacations, incorporating both compulsory and extended repairs. Customers receive service in groups following a general bulk service approach, instead of being served one at a time. Each service batch requires a minimum of ‘a’ and maximum of ‘b’ customers. The study considers two types of repairs—compulsory and extended—and derives the steady-state equations, performance measures, and expected cost of the model. Finally, the impact of various parameters is illustrated in numerical analysis section and graphical representation. 14

Cite: E. Praveena, K. Julia Rose Mary PERFORMANCE AND COST ANALYSIS OF A GI/M(a,b)/I QUEUE WITH COMPULSORY AND EXTENDED REPAIRS DURING MULTIPLE WORKING VACATIONS. Reliability: Theory & Applications. 2025, December 4(89), Vol. 20: 881-894, DOI: https://doi.org/10.24412/1932-2321-2025-489-881-894

SURVIVAL ANALYSIS OF AREA BIASED GENERALIZED SAULEH DISTRIBUTION WITH STATISTICAL PROPERTIES AND APPLICATIONS 895

Dr. V. Arulmozhi, Dr. R. Sivaranjani, Dr. K. Poovizhi

The "Sauleh distribution" is a novel lifespan distribution that is suggested by this study. Among the statistical and mathematical features that have been discussed are the PDF and CDF. Numerous helpful statistical features are derived, including the Area Biased Generalized Sauleh distribution's hazard rate function, reverse hazard rate function, order statistics, moments, measure of skewness, and measure of kurtosis. It uses the well-known maximum likelihood outcome approach to estimate the parameter of the distribution. To demonstrate this distribution's adaptability and superiority over alternative distributions, a comparative analysis is conducted in the end. It establishes its significance in reliability engineering by producing a rich class of distributions that may capture various shapes and behaviors and, as a result, enable better fitting to empirical data. Real-world data sets are used to establish the use of this novel distribution. Melanoma patient survival data has demonstrated the effectiveness of the proposed distribution; it is concluded that the produced distribution provides a superior fit.

Cite: Dr. V. Arulmozhi, Dr. R. Sivaranjani, Dr. K. Poovizhi SURVIVAL ANALYSIS OF AREA BIASED GENERALIZED SAULEH DISTRIBUTION WITH STATISTICAL PROPERTIES AND APPLICATIONS. Reliability: Theory & Applications. 2025, December 4(89), Vol. 20: 895-904, DOI: https://doi.org/10.24412/1932-2321-2025-489-895-904

OPTIMIZATION OF A FUZZY SUPPLY CHAIN INVENTORY SYSTEM FOR DETERIORATING ITEMS UNDER ENVIRONMENTAL SUSTAINABILITY 905

Vikash, Dhirendra Singh, Ashish Negi

The growing emphasis on environmental sustainability and operational reliability has encouraged researchers to extend classical inventory models using fuzzy logic to better handle uncertainty. This study proposes a sustainable inventory framework for deteriorating items, where demand is influenced by both selling price and greening initiatives. The model

incorporates investments in preservation technology and green practices under trapezoidal fuzzy environments. Shortages are permitted, and the problem is solved through signed distance defuzzification method, supported by MATLAB for computation and analysis.
To demonstrate the applicability, numerical examples are presented, followed by a comparative analysis between crisp and fuzzy settings. The results show that the fuzzy-based model consistently reduces overall costs, with an average decrease of 4.72%, while also lowering cycle time and reorder-to-shortage intervals by 4.04% and 5.52%, respectively. Sensitivity analysis further reveals that total cost is most sensitive to fluctuations in green technology and procurement expenses, whereas preservation and shortage costs have comparatively smaller effects. The findings highlight that adopting fuzzy-based decision approaches not only enhances financial performance but also supports ecological objectives, offering a more reliable pathway for sustainable supply chain management.

Cite: Vikash, Dhirendra Singh, Ashish Negi OPTIMIZATION OF A FUZZY SUPPLY CHAIN INVENTORY SYSTEM FOR DETERIORATING ITEMS UNDER ENVIRONMENTAL SUSTAINABILITY. Reliability: Theory & Applications. 2025, December 4(89), Vol. 20: 905-920, DOI: https://doi.org/10.24412/1932-2321-2025-489-905-920

STATISTICAL INFERENCE ON THE GENERALIZED EXPONENTIAL DISTRIBUTION BASED ON GENERALIZED ORDER STATISTICS CHARACTERIZATIONS AND APPLICATIONS 921

Imtiyaz A. Shah and Khalid Ul Islam Rather

In this paper, we study the Some distribution functions have been characterized based on m-dual generalized order statistics and consequently m-generalized order statistics. Moreover, we show that these characterization properties provide a beneficial strategy to predict future events, which are based on past or current events and on an arbitrary distribution function. Finally, an application of these results is given for bivariate generalized exponential distribution.

Cite: Imtiyaz A. Shah and Khalid Ul Islam Rather STATISTICAL INFERENCE ON THE GENERALIZED EXPONENTIAL DISTRIBUTION BASED ON GENERALIZED ORDER STATISTICS CHARACTERIZATIONS AND APPLICATIONS. DOI: https://doi.org/10.24412/1932-2321-2025-489-921-930

PARAMETRIC ESTIMATION OF THE PROCESS CAPABILITY INDEX S''pk AND ITS APPLICATION TO ELECTRONIC INDUSTRIES 931

Mahendra Saha, Pratibha Pareek, Anju Devi, Abhimanyu S Yadav

The proposed index is the process capability index used in the electronics industries to measure the capability of the process. This article focuses on process capability index, specifically applicable to normal random variables. The article has three main objectives: Firstly, we explore various classical estimation methods for the proposed index from frequentist approaches for normal distributions and compare their performance based on mean squared errors. Second, we calculate the classical confidence interval for the proposed index, which includes the asymptotic confidence interval. Third, we examine both Bayes point and interval estimation under symmetric and asymmetric loss functions for the proposed index. A Monte Carlo and Markov Chain Monte Carlo simulation study is conducted to compare the performance of the classical and the Bayes estimates of the proposed index for some set of parameters. Finally, to demonstrate the applicability of this index, two real data sets from the electronics industry are re-analyzed.

Cite: Mahendra Saha, Pratibha Pareek, Anju Devi, Abhimanyu S Yadav PARAMETRIC ESTIMATION OF THE PROCESS CAPABILITY INDEX S''pk AND ITS APPLICATION TO ELECTRONIC INDUSTRIES. Reliability: Theory & Applications. 2025, December 4(89), Vol. 20: 931-947, DOI: https://doi.org/10.24412/1932-2321-2025-489-931-947

TWO COMPONENT MIXTURE OF LEFT TRUNCATED THREE PARAMETER LOGISTIC TYPE DISTRIBUTION WITH APPLICATIONS TO MANPOWER MODELING 948

Usha Hamsa, Srinivasa Rao Kraleti, Muniswamy Begari

The logistic distribution serves as an alternative to normal distribution due to its is similarity in shape with heavier tails. Several extensions and generalizations of the logistic distribution have been proposed and explored in research papers published from 2020 onwards, particularly for modeling data with varying characteristics like skewness and kurtosis, or for specific applications in areas like finance and survival analysis. Some important distributions include the skew logistic distribution, the extended log-logistic distribution, two parameter logistic type distribution, three parameter logistic type distribution and the beta log-logistic distribution. These extensions offer increased flexibility in fitting data compared to the standard logistic distribution. Recently Usha et al (2025) have studied truncated three parameter Logistic distribution. Based on this distribution, we propose a new model called the two component mixture of left truncated tree parameter logistics type distribution for describing manpower data. It involves various specialized models, such as mixture of truncated logistic and a mixture of two-parameter logistic type distributions, among several others, so it's possibly better model for analyzing skewed data. The new density function can be expressed as a weighted combination of truncated tree parameter logistic-type densities. Various mathematical properties of the new distribution including explicit expressions for the moments are derived. We discuss the maximum likelihood method to estimate the model parameters for heterogeneous data. The superiority of the proposed manpower model is illustrated.

Cite: Usha Hamsa, Srinivasa Rao Kraleti, Muniswamy Begari TWO COMPONENT MIXTURE OF LEFT TRUNCATED THREE PARAMETER LOGISTIC TYPE DISTRIBUTION WITH APPLICATIONS TO MANPOWER MODELING. Reliability: Theory & Applications. 2025, December 4(89), Vol. 20: 948-968, DOI: https://doi.org/10.24412/1932-2321-2025-489-948-968

RISK ANALYSIS OF A REPAIRABLE UNIT IN SUGAR INDUSTRY: A HYBRID APPROACH USING FUZZY FMEA AND GRA 969

Anushree and Seema Sharma

The purpose of this study is to develop a comprehensive risk assessment profile for a repairable unit in a sugar industry. The risk analysis of milling unit in the sugar industry often relies on uncertain data and subjective expert assessments, which could be biased. This highlights the need for careful interpretation as the data quality variations have great impact on the decision-making. By integrating risk analysis techniques like failure mode and effect analysis (FMEA), Grey relation analysis (GRA), and fuzzy theory, together with expert assessments for the very first time, the approach aims to prioritize risk management strategies of milling unit in Dhampur Sugar Mills Ltd., a sugar industry located in Western Ultrar Pradesh, India. First of all, Root cause analysis (RCA) is conducted to detect in-depth potential failure modes of the unit. Further, FMEA is employed for risk identification and prioritization, with ranking of components based on their RPN (Risk Priority Number) scores. To address the limitations of FMEA, fuzzy FMEA supported by a fuzzy decision support system (FDSS) has been used to compute FRPN (Fuzzy Risk Priority Number) scores. Based on these scores, the components are ranked. Subsequently, GRA is employed within the fuzzy FMEA framework to intelligently assess the relative importance of key factors, i.e. probability of occurrence, severity effect, and probability of non-detectability of failure in order to determine optimal rankings of critical components. The implementation of fuzzy logic and grey approach with inputs of FMEA offers a more efficient and better way to make decision regarding risk priorities. This risk assessment approach is valuable for sugar industry where complex engineering systems are essential for production process, and the findings from this study will aid system specialists and analysis in future planning and maintenance strategies.

Cite: Anushree and Seema Sharma RISK ANALYSIS OF A REPAIRABLE UNIT IN SUGAR INDUSTRY: A HYBRID APPROACH USING FUZZY FMEA AND GRA. Reliability: Theory & Applications. 2025, December 4(89), Vol. 20: 969-988, DOI: https://doi.org/10.24412/1932-2321-2025-489-969-988

BAYESIAN SINGLE SAMPLING PLANS WITH ZERO-INFLATED BINOMIAL DISTRIBUTION USING COST OPTIMIZATION 989

Sangeetha S, Shalini K and Hemalatha R

The economic design of sampling plans involves determining an optimal plan that minimizes the total cost associated with inspection while ensuring acceptable product quality levels. Bayesian sampling plans are better suited for handling significant between-lot variations in quality, leading to more informed acceptance decisions due to their capability to incorporate prior information. The objective of this article is to design Bayesian single sampling plans considering a Beta prior and a Zero-inflated Binomial (ZIB) distribution, using cost optimization principles by developing an economic model aimed at achieving optimal total costs, considering the Average Total Inspection (ATI). A numerical illustration is provided to demonstrate the selection of Bayesian single sampling plans under the ZIB distribution that minimizes the producer's total cost.

Cite: Sangeetha S, Shalini K and Hemalatha R BAYESIAN SINGLE SAMPLING PLANS WITH ZERO-INFLATED BINOMIAL DISTRIBUTION USING COST OPTIMIZATION. Reliability: Theory & Applications. 2025, December 4(89), Vol. 20: 989-995, DOI: https://doi.org/10.24412/1932-2321-2025-489-989-995

MODELING STRENGTH OF THE AIRCRAFT WINDOW GLASS BY TRUNCATED SHAMBHU DISTRIBUTION 996

Dhanashri Patil, Manjushri Chikkalli, Shruti Hipale, Chandrakant Gardi

Failure of regular distributions to appropriately model the real life scenarios demands the new distributions, which will be more useful. Truncated distributions are found to model many real datasets more precisely than corresponding regular distribution. In this paper, a novel truncated Shambhu distribution (TS) is proposed to model the data, which is naturally constrained by physical, financial, or environmental factors. Some statistical properties including moments, survival and hazard functions, are discussed. For better understanding of the proposed distribution, plots of the distribution are provided. Estimation of parameters is discussed using the maximum likelihood estimation method. Finally, an application based on real data is considered to illustrate the practical relevance of the proposed distribution.

Cite: Dhanashri Patil, Manjushri Chikkalli, Shruti Hipale, Chandrakant Gardi MODELING STRENGTH OF THE AIRCRAFT WINDOW GLASS BY TRUNCATED SHAMBHU DISTRIBUTION. Reliability: Theory & Applications. 2025, December 4(89), Vol. 20: 996-1005, DOI: https://doi.org/10.24412/1932-2321-2025-489-996-1005

RELIABLE SINGLE DIODE PATCH ANTENNA WITH DUAL MODE FREQUENCY AND PATTERN RECONFIGURABILITY WITH COMPLIANCE ANALYSIS 1006

Sameer Mansuri, Shahid S. Modasiya

This study introduces a compact rectangular patch antenna that achieves frequency reconfiguration using a single PIN diode, enabling two distinct operational modes. The design integrates multiple strategically placed slots within the patch to support a wide range of wireless communication bands.

By employing only one diode, the antenna reduces circuit complexity and fabrication cost while ensuring efficient performance. The optimization was carried out through full-wave electromagnetic simulations, with reflection coefficients and radiation patterns serving as primary evaluation metrics. A prototype fabricated on a cost-effective FR4 substrate was tested in an anechoic chamber, showing strong correlation between simulated and measured results, with effective impedance matching. Furthermore, reliability assessments and electromagnetic safety evaluations confirmed compliance with international SAR standards and consistent performance under environmental stress conditions. This work highlights that carefully designed slot integration on FR4 substrates can provide performance levels comparable to those of specialized high-frequency materials, delivering a compact and economical solution for modern communication systems.

Cite: Sameer Mansuri, Shahid S. Modasiya RELIABLE SINGLE DIODE PATCH ANTENNA WITH DUAL MODE FREQUENCY AND PATTERN RECONFIGURABILITY WITH COMPLIANCE ANALYSIS. Reliability: Theory & Applications. 2025, December 4(89), Vol. 20: 1006-1016, DOI: https://doi.org/10.24412/1932-2321-2025-489-1006-1016

STATISTICAL MODELLING AND APPLICATIONS OF THE ET–EXPONENTIAL DISTRIBUTION: EVIDENCE FROM BIOMEDICAL AND ENGINEERING DATA 1017

T. Kamaleshwar, R. Seethalakshmi and S. Mythily

The current study utilizes the exponential distribution as the baseline cumulative function and applies the T-x transformation on the exponential family in order to develop a new class of lifetime distribution. The main objective of this study is to develop and evaluate a flexible distribution that may capture various kinds of lifespan features present in real-world applications. A specific instance, the ET-Exponential (ET-Exp) distribution, is thoroughly examined. The structural properties of the paper, such as the moments, cumulative distribution function, and probability density function, are derived. Parameter estimation is performed via the maximum likelihood method. The suggested approach is used on real datasets, such as carbon fiber breaking stress data and hypertension survival times. The performance of the model is assessed by using statistical criteria such as Akaike Information criteria (AIC), Bayesian Information Criteria (BIC), Kolmogorov-Simron (KS), and Anderson-Darling (AD) tests, which were among the statistical tests used to estimate the goodness of fit of each distribution's essential parameters. The results demonstrate that the proposed ET-Exponential distribution is a flexible and effective tool for modeling lifetime data and shows promise for applications in both biomedical and industrial fields.

Cite: T. Kamaleshwar, R. Seethalakshmi and S. Mythily STATISTICAL MODELLING AND APPLICATIONS OF THE ET–EXPONENTIAL DISTRIBUTION: EVIDENCE FROM BIOMEDICAL AND ENGINEERING DATA. Reliability: Theory & Applications. 2025, December 4(89), Vol. 20: 1017-1026, DOI: https://doi.org/10.24412/1932-2321-2025-489-1017-1026

EIGHT YEARS OF RESEARCH IN RELIABILITY: THEORY AND APPLICATIONS (2017–2024): A SCOPUS BASED BIBLIOMETRIC ANALYSIS 1027

Sajad Hussain, Vilayat Ali Bhat

This study looks at the SCOPUS research published in the journal Reliability. Theory and Applications from 2017 to 2024. The main goal is to understand how the journal has grown, how influential it is, and how researchers are working together. The data shows that the number of papers published has increased steadily, especially after 2020, showing that the journal is becoming more important in the academic world. Most of the research came from countries like India, the Russian Federation, and Azerbaijan.

Universities such as Kadyrov Chechen State University and Azerbaijan State Oil and Industry University were among the top contributors. The study also used network analysis to examine how authors collaborate, which keywords are used together, and which papers are cited the most. It was found that a few researchers, like Yusuf Ibrahim and Rather Aafaq A., are very active and well-connected in the author network. Citation analysis showed which authors, institutions, and countries had the most influence. This study provides helpful information for researchers, universities, and funding agencies interested in working with or contributing to this journal.

Cite: Sajad Hussain, Vilayat Ali Bhat EIGHT YEARS OF RESEARCH IN RELIABILITY: THEORY AND APPLICATIONS (2017–2024): A SCOPUS BASED BIBLIOMETRIC ANALYSIS. Reliability: Theory & Applications. 2025, December 4(89), Vol. 20: 1027-1045, DOI: https://doi.org/10.24412/1932-2321-2025-489-1027-1045

STRESS-STRENGTH MODELLING: A COMPARATIVE STUDY USING SRS, RSS AND MRSS FOR INVERSE NAKAGAMI DISTRIBUTION 1046

Surinder Kumar, Rahul Shukla, Bhupendra Meena, Shivendra Pratap Singh

The present research endeavours to use the ranked set sampling technique in place of the simple random sampling technique in estimating the reliability model in the field of reliability engineering and manufacturing industries. The stress-strength reliability is widely used in all field of engineering and in the manufacturing industry. In this research article, we take the case when the lifetime data of any machinery followed the Inverse Nakagami distribution, and by considering the stress-strength model, we compare the standard ranked set sampling and median ranked set sampling estimate with the corresponding simple random sampling estimate through Monte Carlo simulation technique. The final stage of this study involves corroborating the findings through an analysis of a benchmark dataset on elevators and their motors utilized in farming machinery.

Cite: Surinder Kumar, Rahul Shukla, Bhupendra Meena, Shivendra Pratap Singh STRESS-STRENGTH MODELLING: A COMPARATIVE STUDY USING SRS, RSS AND MRSS FOR INVERSE NAKAGAMI DISTRIBUTION. Reliability: Theory & Applications. 2025, December 4(89), Vol. 20: 1046-1067, DOI: https://doi.org/10.24412/1932-2321-2025-489-1046-1067

DOUBLE ORBIT RETRIAL QUEUEING-INVENTORY SYSTEM WITH ORBITAL SEARCH UNDER (s, S) POLICY 1068

M. Thilakavathy, Agassi Melikov, G. Ayyappan

We consider two-orbit retrial queueing inventory system with a single server. Service time follows phase-type distribution, while arrivals follow the Markovian arrival process. During busy period of the server, the arriving customer may either balk or move to the limitless orbit. Following service completion, the server takes a vacation if there are no customers in the system. When a breakdown happens during busy times, the server undergoes phase-type repair, and the current customer enters finite orbit. Once the repair is finished, the server either stays idle or searches the finite orbit. The replenishment period is exponential and we use (s, S) policy. The matrix analytic approach has been used to analyze steady state probability. We assess this retrial queueing inventory model both numerically and graphically.

Cite: M. Thilakavathy, Agassi Melikov, G. Ayyappan DOUBLE ORBIT RETRIAL QUEUEING-INVENTORY SYSTEM WITH ORBITAL SEARCH UNDER (s, S) POLICY. Reliability: Theory & Applications. 2025, December 4(89), Vol. 20: 1068-1082, DOI: https://doi.org/10.24412/1932-2321-2025-489-1068-1082

RISK MODELING WITH THE NEW LOGARITHMIC TANGENT WEIBULL DISTRIBUTION: APPLICATIONS IN INSURANCE AND NET OFFICIAL DEVELOPMENT ASSISTANCE 1083

Palanisamy Manigandan, D. Kanagajothi, R. Jeena and Gulasal Madrakhimova

The Weibull distribution is widely used for modeling lifetime and reliability data but often struggles with complex hazard structures and heavy-tailed behaviors. To address these limitations, this study proposes the New Logarithmic Tangent Weibull (NLT-Wei) distribution, which integrates logarithmic and tangent transformations into the Weibull model, introducing an additional shape parameter to enhance flexibility. Key functions, including the PDF, CDF, survival, and hazard functions, are derived, along with quantiles and reliability measures. Parameters are estimated using maximum likelihood estimation (MLE). The model is applied to two real datasets: insurance survival data and Net Official Development Assistance (Net ODA) data. Comparative analyses with Weibull, Exponentiated Weibull, Flexible Weibull, NGLog-Weibull, and Kumaraswamy Weibull distributions are conducted using information criteria (AIC, BIC, CAIC, HQAIC) and goodness-of-fit tests (KS, Cramer-von Mises, Anderson-Darling). Results show that the NLT-Wei consistently achieves lower information criteria, smaller test statistics, and higher p-values, confirming superior fit. Its flexibility allows effective modeling of monotone, bathtub, and inverted-bathtub hazard rates, as well as heavy-tailed behaviors. The study demonstrates that the NLT-Wei is not only robust for reliability and survival analysis but also highly suitable for actuarial and financial applications, offering a practical tool for risk assessment, insurance modeling, and lifetime data analysis across diverse domains.

Cite: Palanisamy Manigandan, D. Kanagajothi, R. Jeena and Gulasal Madrakhimova RISK MODELING WITH THE NEW LOGARITHMIC TANGENT WEIBULL DISTRIBUTION: APPLICATIONS IN INSURANCE AND NET OFFICIAL DEVELOPMENT ASSISTANCE. Reliability: Theory & Applications. 2025, December 4(89), Vol. 20: 1083-1093, DOI: https://doi.org/10.24412/1932-2321-2025-489-1083-1093

STATISTICAL APPLICATIONS OF THE KUMARASWAMY ALPHA-POWER LOG-LOGISTIC DISTRIBUTION: EVIDENCE FROM HYPERTENSION AND CO2 EMISSIONS IN INDIA 1094

A. Ashok, D. Kanagajothi, T. Kamaleshwar, Palanisamy Manigandan, Abdullayeva Shakhnoza Yerkinovna

This article introduces a novel statistical model, the Kumaraswamy Alpha-Power Log-Logistic (KAPLL) distribution, as a flexible extension of the traditional log-logistic model. The KAPLL distribution is especially well-suited for examining a variety of ageing and failure events as it is made to improve modelling capabilities by supporting both symmetric and asymmetric forms. Reliability analysis and lifespan data modelling are made more flexible by the KAPLL model's capacity to represent its probability density function as a combination of log-logistic densities. The hazard rate function (HRF), survival function, moments, quantile function (QF), and moment-generating function (MGF) are among the statistical and mathematical characteristics of the KAPLL distribution that are comprehensively examined. The estimation of KAPLL parameters is achieved through maximum likelihood estimation (MLE), a widely used statistical method. We use the KAPLL distribution to measures of hypertension and carbon dioxide (CO_2) emissions in order to demonstrate the usefulness of the suggested model. The findings demonstrate the KAPLL distribution's adaptability and better fit when compared to other well-known log-logistic model extensions, confirming its promise as a useful tool for modelling complicated behaviours in environmental and biological data.

Cite: A. Ashok, D. Kanagajothi, T. Kamaleshwar, Palanisamy Manigandan, Abdullayeva Shakhnoza Yerkinovna STATISTICAL APPLICATIONS OF THE KUMARASWAMY ALPHA-POWER LOG-LOGISTIC DISTRIBUTION: EVIDENCE FROM HYPERTENSION AND CO2

EMISSIONS IN INDIA. Reliability: Theory & Applications. 2025, December 4(89), Vol. 20: 1094-1103, DOI: https://doi.org/10.24412/1932-2321-2025-489-1094-1103

VARIABLES CHAIN SAMPLING PLAN BASED ON THE MINIMUM ANGLE METHOD INVOLVING MINIMUM SUM OF RISKS 1104

P. Suthersan and S. Balamurali

This study presents a designing methodology for a variables based chain sampling plan utilizing the minimum angle criterion. In the context of acceptance sampling, managing both producer's risk and consumer's risk is essential for ensuring consistent product quality, particularly within industrial applications. These risks must be addressed concurrently when making quality related decisions. In this work, both risks are effectively reduced by minimizing the tangent angle formed between two points on the operating characteristic curve: the producer's quality level, associated with the probability of accepting a good lot, and the consumer's quality level, associated with the probability of accepting a bad lot. The variables chain sampling plan provides the underlying framework for this formulation. The proposed design procedures are detailed through step-by-step methodologies to demonstrate the implementation of the approach.

Cite: P. Suthersan and S. Balamurali VARIABLES CHAIN SAMPLING PLAN BASED ON THE MINIMUM ANGLE METHOD INVOLVING MINIMUM SUM OF RISKS. Reliability: Theory & Applications. 2025, December 4(89), Vol. 20: 1104-1114, DOI: https://doi.org/10.24412/1932-2321-2025-489-1104-1114

MARKOV CHAIN MONTE CARLO AND MODERN BAYESIAN COMPUTATION 1115

Manzoor A. Khanday, Shaik Afsar Jahan, Isha Gilhotra, Dilawar A. Bhat

Bayesian inference offers a robust approach to the inclusion of prior knowledge in statistical modeling and uncertainty quantification in parameter estimates. Exact Bayesian computation is usually intractable for sophisticated models, and approximation methods are used instead. Markov Chain Monte Carlo (MCMC) techniques are now the foundation of contemporary Bayesian computation and facilitate efficient sampling from high-dimensional posterior distributions. This paper discusses main MCMC algorithms, such as Metropolis-Hastings and Gibbs Sampling, and latest developments like the No-U-Turn Sampler (NUTS). By discussing practical use cases, logistic regression, time series prediction, hierarchical modeling, and count regression data, we illustrate how MCMC-based methods can be used to tackle real-world problems. Each use case takes advantage of PyMC's MCMC engine to get posterior samples and model performance. Convergence diagnostics, posterior uncertainty, and model interpretability are covered at length. The paper is both a theoretical and practical treatise on MCMC in the context of contemporary Bayesian computation.

Cite: Manzoor A. Khanday, Shaik Afsar Jahan, Isha Gilhotra, Dilawar A. Bhat MARKOV CHAIN MONTE CARLO AND MODERN BAYESIAN COMPUTATION. Reliability: Theory & Applications. 2025, December 4(89), Vol. 20: 1115-1128, DOI: https://doi.org/10.24412/1932-2321-2025-489-1115-1128

A REVIEW OF COMPETING AND SEMI-COMPETING RISKS METHODS IN SURVIVAL ANALYSIS 1129

Mithali S Kumar, Shruthi P, and Jiju Gillariose

Recent advancements in competing and semi-competing risk models have significantly contributed to fields like biomedical, reliability studies (on items related to machines), epidemiological studies (treatment outcomes, disease progression, cause-specific deaths), and so on, with new emerging models. The existing frameworks are also being extended to enhance the theoretical robustness.

This article provides a comprehensive review from the very first model to the latest developments, aiming to consolidate the diverse methodologies and offering insights into the most suitable approaches for various practical scenarios. The methodologies adopted in different contexts and the steps that form the base for the study are explained for a better understanding. The methodologies are adopted on the account to the nature of the problem which we are dealing with and in this article the summary of the review is incorporated so that the practitioners can decide which methodology to adopt along with the common pitfalls for a specified case. Domain-specific applications are also incorporated, which helps the practitioners to understand the real-life application of these concepts as well as it paves the way to make further contributions to society in the related fields. By examining both foundational and contemporary contributions, this review seeks to guide researchers and practitioners in selecting effective strategies for handling competing and semi-competing risks in survival analysis.

Cite: Mithali S Kumar, Shruthi P, and Jiju Gillariose A REVIEW OF COMPETING AND SEMI-COMPETING RISKS METHODS IN SURVIVAL ANALYSIS. Reliability: Theory & Applications. 2025, December 4(89), Vol. 20: 1129-1139, DOI: https://doi.org/10.24412/1932-2321-2025-489-1129-1139

AREA BIASED NEW-TWO PARAMETER SUJATHA DISTRIBUTION AND ITS APPLICATION TO MEDICAL SCIENCES 1140

Dr. V. Arulmozhi, Mrs. D. Narmadha, Dr. R. Sivaranjani, Mr. B. Balachandar

This study proposes an Area Biased new two-parameter distribution based on the Sujatha distribution of the relief times patient data. A proposed distribution's characteristics, such as its entropies, moments, moment generating function, survival function, hazard function, and probability density function, are examined. The behavior of a hazard function and probability density function has been depicted using graphs. The well-known maximum likelihood outcome approach is used to estimate the distribution's parameter. Finally, a comparative analysis is carried out to show the flexibility and superiority of this distribution over other distributions. It demonstrates its importance in reliability engineering by generating a rich class of distributions that can better fit empirical data by capturing a variety of shapes and behaviors. The application of this unique distribution is demonstrated using relief times (In minutes) of twenty analgesic data sets. Furthermore, we compare the performance of our distribution with some other existing distributions.

Cite: Dr. V. Arulmozhi, Mrs. D. Narmadha, Dr. R. Sivaranjani, Mr. B. Balachandar AREA BIASED NEW-TWO PARAMETER SUJATHA DISTRIBUTION AND ITS APPLICATION TO MEDICAL SCIENCES. Reliability: Theory & Applications. 2025, December 4(89), Vol. 20: 1140-1149, DOI: https://doi.org/10.24412/1932-2321-2025-489-1140-1149

OPTIMIZATION OF INDUSTRIAL SYSTEM MAINTENANCE USING THE MIXED WEIBULL DISTRIBUTION 1150

R. Zellagui, L. Khammar

This work is part of an approach to optimizing industrial maintenance in a modern and automated production context. It focuses on the in-depth study of the maintenance system implemented in the company IRIS TYRES, specialized in the manufacturing of tires in Algeria, more precisely in the production unit located in Sétif. The main objective of this work is to evaluate the performance of the maintenance applied in the company, based on the fundamental concepts of Reliability, Maintainability and Availability (RAM), as well as modern analytical tools such as the ARROW NOVI CMMS software, the Pareto method. In this article, the Weibull mixture model is proposed to model the failure times of an electrical system in operation with different failure modes and analyze reliability.

The estimation of the parameters of the reliability law is done by the maximum likelihood method. Based on IRIS TYRES' system lifetime data, we analyzed and compared the performance of our model with the classic two-parameter Weibull distribution. Strictly speaking, it is necessary to verify which of the two models correctly fits the data. The results of this evaluation show that the machine with a very high failure rate was the curing press, its subsystems (3-bar sensors, valves), and led to the development of action plans to improve equipment reliability, reduce unplanned downtime, and strengthen the efficiency of the maintenance department. The results show that the Weibull mixture distribution tends to overestimate the reliability of the sensors and therefore to overestimate the frequency of preventive maintenance which reduces maintenance costs and the probability of failure.

Cite: R. Zellagui, L. Khammar OPTIMIZATION OF INDUSTRIAL SYSTEM MAINTENANCE USING THE MIXED WEIBULL DISTRIBUTION. Reliability: Theory & Applications. 2025, December 4(89), Vol. 20: 1150-1158, DOI: https://doi.org/10.24412/1932-2321-2025-489-1150-1158

IMPROVING THE EFFICIENCY OF ASSESSING THE TECHNICAL CONDITION OF ELECTRICAL EQUIPMENT 1159

Muradaliyev A.Z., Ismailova S.M.

In recent years, the understanding of the efficiency of technical diagnostics of electrical equipment has increased significantly. The main reasons for this are, in particular: more than half of the equipment in operation has exhausted its estimated service life; the rate of aging of the equipment exceeds the rate of its renewal; due to limited funds for technical maintenance, as well as due to the transition to repairs based on technical condition. High quality and timely diagnostics improve the objectivity of assessing the technical condition of high-voltage electrical equipment. All this allows planning and timely execution of necessary maintenance and repair operations, which makes the operation of electrical equipment more reliable, extends its service life, saves money, and reduces the risk of damage. A method for assessing the moment of occurrence of a change in the growth of concentration of gases dissolved in oil has been developed, allowing to establish the presence of a developing transformer defect, the main gases, the probable type of defect and the nature of its manifestation. A method and algorithm for predicting the time of occurrence of a faulty state of power transformers based on the data of chromatographic analysis of gases dissolved in transformer oil are proposed. A method developed to assess the moment of occurrence of changes in the concentration of dissolved gases in oil, which makes it possible to establish the presence of a developing transformer defect, the main gases, and the likely type of defect and the nature of its manifestation. A method and algorithm for predicting the time of occurrence of a faulty state of power transformers based on chromatographic analysis of gases dissolved in transformer oil are proposed. The recommended algorithm will make it possible to increase the objectivity of comparing the same type of indicators of gases dissolved in oil at the initial stage of wear change.

Cite: Muradaliyev A.Z., Ismailova S.M. IMPROVING THE EFFICIENCY OF ASSESSING THE TECHNICAL CONDITION OF ELECTRICAL EQUIPMENT. Reliability: Theory & Applications. 2025, December 4(89), Vol. 20: 1159-1166, DOI: https://doi.org/10.24412/1932-2321-2025-489-1159-1166

OPTIMIZING STEEL INDUSTRY PRODUCTION INVENTORY SYSTEM CONSIDERING WAREHOUSE BOTTLENECK AND MACHINE DOWNTIME 1167

Narendra Kumar, Kartik Pandey, Vikash, Kapil Dave

The steel industry faces increasing pressure to optimize production and inventory systems while managing operational constraints such as warehouse bottlenecks, machine downtime, and shortages. Addressing these challenges is essential for achieving sustainable cost efficiency and resilience. This study develops a mathematical production-inventory model for the steel industry that incorporates warehouse capacity limitations, equipment downtime, deterioration, and

shortage backlogging. The demand is assumed to be time and price-dependent, while production is constrained by effective capacity under downtime. The objective is to minimize the total system cost, which includes production, holding, shortage, deterioration, and downtime penalty costs. The optimization problem is solved using a Newton-Raphson based iterative approach to determine the optimal cycle length and production lot size. Two distinct scenarios are examined: one with deterioration and one without. Numerical illustrations and sensitivity analyses reveal that warehouse bottlenecks, downtime risks, and shortage policies significantly affect cost efficiency. The results show that downtime reduction and efficient backlog management can considerably lower annual costs. The proposed framework provides practical insights for steel manufacturers aiming to balance production efficiency with inventory resilience, guiding decision-makers in developing sustainable and cost-effective supply chain policies.

Cite: Narendra Kumar, Kartik Pandey, Vikash, Kapil Dave OPTIMIZING STEEL INDUSTRY PRODUCTION INVENTORY SYSTEM CONSIDERING WAREHOUSE BOTTLENECK AND MACHINE DOWNTIME. Reliability: Theory & Applications. 2025, December 4(89), Vol. 20: 1167-1177, DOI: https://doi.org/10.24412/1932-2321-2025-489-1167-1177

FORECASTING EXTREME MARKET MOVEMENTS USING REALIZED GARCH AND EXTREME VALUE THEORY MODELS 1178

Umme Hani

This study investigates the essential benefits of using the Conditional Value-at-Risk (CVaR) optimization framework with the GARCH model and Extreme Value Theory (EVT) methods for the S&P CNX NIFTY markets. Using daily data from Jan. 2020 to July 2024, we evaluate 10 forecasting models, comprising eight standalone GARCH models and eight two-stage GARCH-EVT models. Our results show that the GARCH-EVT models consistently produce more accurate quantile forecasts than their standalone GARCH counterparts. Among the standalone models, daily returns-based GARCH and EGARCH models exhibit the poorest forecasting performance, while the intraday return-based realized GARCH model performs slightly better. The experimental results show that, under various loss functions, the GARCH-EVT innovation model is the best model for volatility predictions of S&P CNX NIFTY among the sixteen forecasting models.

Cite: Umme Hani FORECASTING EXTREME MARKET MOVEMENTS USING REALIZED GARCH AND EXTREME VALUE THEORY MODELS. Reliability: Theory & Applications. 2025, December 4(89), Vol. 20: 1178-1188, DOI: https://doi.org/10.24412/1932-2321-2025-489-1178-1188

QUALITY CONTROL FOR SUSTAINABILITY IN CASTING MANUFACTURING 1189

Manzoor A. Khanday, Trushal Hirani, Dilawar A. Bhat, Vaddi Tejasvi, Anusha Ale Saji

This study proposes an artificial intelligence-driven framework for automating defect detection in casting manufacturing, with a particular focus on enhancing sustainability in the production of submersible pump impellers. A dataset comprising more than 7,000 grayscale images—classified as defective or acceptable—was utilized to train and evaluate three deep learning models: a custom-built Convolutional Neural Network (CNN), VGG16, and ResNet18. The models were assessed for their accuracy, precision, and recall, with VGG16 and ResNet18 demonstrating superior performance, achieving over 99% classification accuracy. Advanced image preprocessing techniques, including histogram equalization and Canny edge detection, were employed to enhance defect visibility and enable the detection of microstructural flaws such as blow holes, shrinkage cavities, and surface irregularities.

The integration of transfer learning significantly reduced training time while improving generalization across unseen samples. From a sustainability perspective, the adoption of AI-based automated inspection reduces material wastage, rework, and energy consumption by ensuring early identification of defective products. Furthermore, the deployment of these models on edge devices and integration with IoT-enabled monitoring systems facilitate real-time, continuous quality assurance without human intervention. Overall, the findings underscore that AI-driven quality control systems not only optimize manufacturing efficiency and product reliability but also contribute to achieving broader sustainability goals by minimizing resource depletion, enhancing energy efficiency, and supporting circular manufacturing practices.

Cite: Manzoor A. Khanday, Trushal Hirani, Dilawar A. Bhat, Vaddi Tejasvi, Anusha Ale Saji QUALITY CONTROL FOR SUSTAINABILITY IN CASTING MANUFACTURING. Reliability: Theory & Applications. 2025, December 4(89), Vol. 20: 1189-1200, DOI: https://doi.org/10.24412/1932-2321-2025-489-1189-1200

IN COMPLEX INTERVAL-VALUED FUZZY METRIC SPACE, COMMON FIXED-POINT THEOREMS CLR/CLR/E.A PROPERTY 1201

Umashankar Singh, Naval Singh, Heera Ahirwar

The work of D. Singh et al. served as inspiration for this study, which established complex interval valued fuzzy metric space and proved several common fixed print theorems for compatible types of (p-1) on the structure of complex interval valued fuzzy metric space. The equivalent findings in the body of existing research are expanded upon and generalized by these findings. Additionally, we create a novel implicit relation that can aid researchers in accelerating common fixed-point existence and uniqueness wherever a pair of self-mappings fits the Chr/Ich/E.A-Property. Appropriate examples are provided to demonstrate the usefulness of the primary conclusions that are gained.

Cite: Umashankar Singh, Naval Singh, Heera Ahirwar IN COMPLEX INTERVAL-VALUED FUZZY METRIC SPACE, COMMON FIXED-POINT THEOREMS CLR/CLR/E.A PROPERTY. Reliability: Theory & Applications. 2025, December 4(89), Vol. 20: 1201-1212, DOI: https://doi.org/10.24412/1932-2321-2025-489-1201-1212

PROBABILISTIC ANALYSIS OF THERMAL LASER WEAPON SUBSYSTEM IN ANTI-DRONE SYSTEMS 1213

Diarmaraja Selvamuthu, Utkarsh Dubey, Raina Raj, Priyanka Kalita

The rise of drones has introduced significant security threats, including unauthorized surveillance and explosive payloads. Drones threaten armies by enabling enemy surveillance, facilitating precision strikes on troops or equipment, disrupting communications, and introducing challenges in air defense, thereby altering traditional battlefield dynamics and strategies. To counter these threats, high-energy laser weapon subsystems provide precise, scalable responses with minimal collateral damage. This paper presents a probabilistic analysis of thermal laser subsystem's effects on targets, accounting for aiming and tracking errors. Atmospheric turbulence is modeled using the power spectrum inversion method, while Monte Carlo simulations calculate the on-target spot area. The energy distribution is converted to temperature using thermal physics, and the damage probability is determined by integrating temperatures exceeding material-specific thresholds. Simulation results confirm the system's effectiveness and reliability of thermal laser weapon systems in neutralizing aerial threats.

Cite: Diarmaraja Selvamuthu, Utkarsh Dubey, Raina Raj, Priyanka Kalita PROBABILISTIC ANALYSIS OF THERMAL LASER WEAPON SUBSYSTEM IN ANTI-DRONE SYSTEMS. Reliability: Theory & Applications. 2025, December 4(89), Vol. 20: 1262-1277, DOI: https://doi.org/10.24412/1932-2321-2025-489-1262-1277

RELIABILITY, SAFETY, AND SUSTAINABILITY IN NUCLEAR POWER PLANTS: ADVANCES IN SUPERCRITICAL WATER REACTORS AND CIRCULATION LOOPS 1229

Pardeep Kumar, Santosh Kumar Rai, Anikate Gupta, Dinesh Kumar, Mahesh Kumar Gupta, Dhowmya Bhatt, Mahiti Gupta, Gyanendra Prasad Bagri

In the last two decades, population and energy requirements have drastically risen. Therefore, it is necessary to provide an adequate amount of energy to the people and industries without affecting global warming and the environment. So, several nuclear power plants are constructed to supply the required demand of the power supply to the household and industries. Nuclear power plants can produce more electricity while maintaining global warming norms. However, during production of higher power from the plants, there are several issues raised, such as the sustainability and safety of the nuclear power plant as well as the reliability of the plants. To resolve these issues to achieve higher plant efficiency, safety of the plant, etc., during operations, several power plants are constructed, such as boiling water reactors and supercritical water reactors to generate power at higher efficiency, while single, two phase and supercritical based natural circulation loops are used to improve the safety of the plant as well as used in operation to improve the power generation from the plant. In past decade, supercritical water reactors and supercritical natural circulation loops have been utilized to increase power generation and enhance the safety of the plant. This review article discusses numerical and experimental investigations of supercritical water reactors and natural circulation loops aimed at enhancing the safety, sustainability, and reliability of various nuclear reactors based on previously published works by several authors, along with identified research gaps and future work scopes.

Cite: Pardeep Kumar, Santosh Kumar Rai, Anikate Gupta, Dinesh Kumar, Mahesh Kumar Gupta, Dhowmya Bhatt, Mahiti Gupta, Gyanendra Prasad Bagri RELIABILITY, SAFETY, AND SUSTAINABILITY IN NUCLEAR POWER PLANTS: ADVANCES IN SUPERCRITICAL WATER REACTORS AND CIRCULATION LOOPS. Reliability: Theory & Applications. 2025, December 4(89), Vol. 20: 1229-1240, DOI: https://doi.org/10.24412/1932-2321-2025-489-1229-1240

OPTIMIZATION AND PERFORMANCE EVALUATION OF SUGAR MILL PLANT MICRO COMPONENTS USING PSO 1241

Sandeep Kumar

Sugar mill plants, especially their core processing units, are highly dependent on a well-organized and efficient maintenance strategy for reliable operation. In this study, an availability-based simulation model was developed for a 25,500 TCD sugar mill. This model is based on a Markov-based performance evaluation framework, which uses differential equations to form state-transition diagrams representing transitions between fully operational, partially operational, and failure states. A comparative analysis of the subcomponents studied concluded that a centrifugal pump failure has minimal impact on overall system availability, while a clarification unit failure has the most significant impact. To improve system reliability and performance, the Particle Swarm Optimization (PSO) method was applied to optimize failure and repair rates. The experimental results obtained show that the overall availability of the system after applying the proposed optimization strategy is achieved at 88.57%, which shows effectiveness and practical utility of the model.

Cite: Sandeep Kumar OPTIMIZATION AND PERFORMANCE EVALUATION OF SUGAR MILL PLANT MICRO COMPONENTS USING PSO. Reliability: Theory & Applications. 2025, December 4(89), Vol. 20: 1241-1253, DOI: https://doi.org/10.24412/1932-2321-2025-489-1241-1253

A SYSTEMATIC REVIEW OF MODELING, PLANNING, AND STATISTICAL FRAMEWORKS IN ACCELERATED LIFE TESTING 1254

Mustafa Kamal

For highly reliable or long-life systems, conventional testing is often impractical due to the excessive time and cost required. Accelerated Life Testing (ALT) offers a practical and statistically rigorous alternative. It predicts product life and durability under normal-use conditions through data obtained under controlled high-stress conditions. This review systematically examines existing ALT methodologies. It begins with an overview of qualitative and quantitative approaches and key concepts that define the theoretical foundation of ALT assessment. Quantitative ALT is organized into Fully Accelerated Life Testing (FALT) and Partially Accelerated Life Testing (PALT) frameworks. Further, the design principles of ALT and PALT are discussed under constant- and step-stress conditions with emphasis on model formulation, estimation procedures, extrapolation, and model validation. The review also provides a concise discussion of statistical modeling and estimation methodologies. Key elements such as stress-loading, life–stress relationships, and censoring mechanisms are discussed to ensure valid statistical inference and model robustness. The review consolidates theoretical insights and methodological frameworks to advance design optimization and reliability prediction in complex systems. It concludes with perspectives on intelligent, data-driven ALT supported by artificial intelligence and computational analytics.

Cite: Mustafa Kamal A SYSTEMATIC REVIEW OF MODELING, PLANNING, AND STATISTICAL FRAMEWORKS IN ACCELERATED LIFE TESTING. Reliability: Theory & Applications. 2025, December 4(89), Vol. 20: 1254-1268, DOI: https://doi.org/10.24412/1932-2321-2025-489-1254-1268

AN INVENTORY MODELING FOR DECAYING ITEMS WITH PRICE, STOCK AND RELIABILITY-DEPENDENT DEMAND UNDER MEMORY EFFECTS

Narendra Kumar[1], Liliana Guran[2], Devendra Kumar[3],
Sanjeet Kumar[4], Ajay Singh Yadav[5,*], Krishan Kumar Yadav[6,*]

•

[1]Department of Mathematics, IILM University, Greater Noida, Uttar Pradesh, India, 201310
[2]Department of Mathematics, Babes-Bolyai University, Cluj-Napoca, Romania, 400347
[3]Department of Mathematics, University of Technology and Applied Sciences-Shinas, Sultanate of Oman, Oman, 324
[4]Department of Mathematics, Lakshmi Narain College of Technology & Science, Bhopal, Madhya Pradesh, India, 462022
[5]Department of Mathematics, SRM Institute of Science and Technology, Delhi-NCR Campus, Modinagar, Uttar Pradesh, India, 201204
[6]Department of Mathematics, School of Sciences, JECRC University, Jaipur, Rajasthan, India, 303905
drnk.cse@gmail.com, liliana.guran@ubbcluj.ro, Devendra.kumar@shct.edu.om, sanjeetkumarmath@gmail.com, ajaysiny@srmist.edu.in, krishan.yadav@jecrcu.edu.in
*Corresponding author

Abstract

A generalized Economic Order Quantity (EOQ) framework is employed to investigate memory effects within an inventory system. Fractional calculus provides an effective mathematical tool for reflecting such memory characteristics in economic model. In this study, a fractional-order inventory model without shortages is developed, where demand is depends on price, on-hand stock, and product reliability, while deterioration is assumed to occur at a constant rate. The developing fractional differential equation is formulated in the Caputo sense, and a memory-kernel approach is used to incorporate dependence on past system states. By applying the Laplace transform technique together with Mittag-Leffler functions, an analytical solution to the model is obtained. The results indicate that the degree of memory in the system can be modulated through the order of the fractional derivative or integral. Furthermore, a sensitivity analysis is performed for both short-memory and long-memory scenarios to determine the key parameters affecting system behavior under varying conditions with the help of MATLAB software.

Keywords: Inventory modeling, deteriorating items, multi variables dependent demand, Caputo derivative, Laplace transform method, memory effect.

1. Introduction and Literature Survey

In operations research, inventory systems inherently exhibit memory-dependent behavior. Customer demand is often influenced by a retailer's service quality and the reliability of the products offered. As a result, purchasing decisions are shaped not only by current conditions but also

by customers past experiences with the product. Negative experiences can significantly reduce the likelihood of future purchases, highlighting the crucial role of memory effects in inventory dynamics. Motivated by these observations, this study aims to incorporate memory or past experience into the inventory framework, offering a fresh perspective and contributing a new dimension to the existing inventory literature. In current era, the most promising field of mathematical research is based on the idea of Fractional Calculus (FC) that deals with the generalization of arbitrary order of our traditional classical differentiation, integration, differential equation [12]. The applicability of this branch of mathematics was very rare till a few days ago from its first introduction in 1695 due to the lack of significant physical interpretation of differential equations of fractional order. Later the extensive knowledge of FC amazingly encourages to analyze the dynamical nature of our physical real world problem. It had been propagated effectively to tackle the complexities arrived at in the formations of mathematical modeling in applied science and technology. It is quite comprehensive that FC has significant potential to interpret the physical phenomena in its generalized form though the formulation of basic concepts and the physical interpretations are continuously being modified. The various features and aspects of Fractional Differential Equation (FDE) have been elegantly presented by [12], [13]. The application of fractional calculus in inventory modeling has been widely explored in recent era due to the memory effects parameter. Kumar, Singh, and Kumar [[19]] investigated space-time fractional telegraph equations and developed both analytical and approximate solutions using the Laplace transform method. In another related contribution, Singh, Kumar, and Kumar [[20]] introduced a new fractional formulation of a nonlinear shock wave equation in gas flow dynamics. Their work highlighted that the FC approach provides robustness in modeling. More recently, Kumar and Gupta [[21]] proposed an efficient FC numerical methodology for solving fractional coupled Boussinesq equations, and provides the robustness for nonlinear systems such as inventory modeling.

The study on inventory systems for decaying items has an important and crucial topic in whole operations research due to its applicability in industries such as pharmaceuticals, food industries, technological industries, and many more. Firstly work by Ghare and Schrader [1] introduced a foundational inventory system with exponential decay rate. After this worked many authors on that topic. Urban [2] considered price-reliant demand rate, while Mandal and Phaujdar [3] explored the impact of stock levels on demand behavior by consumer. Additionally the models were extended by Yadav [4], who examined the effect of demand due to multiple market parameters considering stock and price reliant in deteriorating environments. Deterioration combined with shortage strategies was addressed in details by Abad [5], who developed a pricing and lot-sizing stock model assuming partial shortage. Jaggi [6] and later Jaggi et al. [7] contributed to the field by assuming time-reliant and reliability-based demand functions, and also combining both of them providing more realistic to real - world inventory scenarios. Despite these advancements, most traditional models overlook the impact of system memory " the effect of past inventory states on current decisions. This limitation has motivated researchers to explore fractional calculus, which provides a natural way to consider memory effects through non-integer order derivatives. Tarasov [8] and Atangana and Baleanu [9] have developed foundational theories in this domain. More recently, Bera et al. [10] and Sahoo and Mishra [11] applied fractional-order approaches to inventory systems with decaying items, assuming stock and reliability-reliant demand rate. Their findings demonstrate the practical advantages of using fractional calculus for modeling assuming memory-effect systems, particularly in capturing long-term dependency and dynamic adjustment. Mebarek-Oudina, F [14-17] are also used the advanced techniques for enhancement and some other factors. These models highlight the significance of managing decaying-related costs to optimize inventory levels and enhance overall system performance. This paper builds upon these contributions by developing a fractional-order inventory model that integrates price, stock, and reliability-reliant demand rate taking along with deterioration and memory effects.

This work not only bridges the gap between theory and practical demands but also provides a reliable conceptual theory for decision-making in perishable inventory systems with memory-

reliant characteristics.

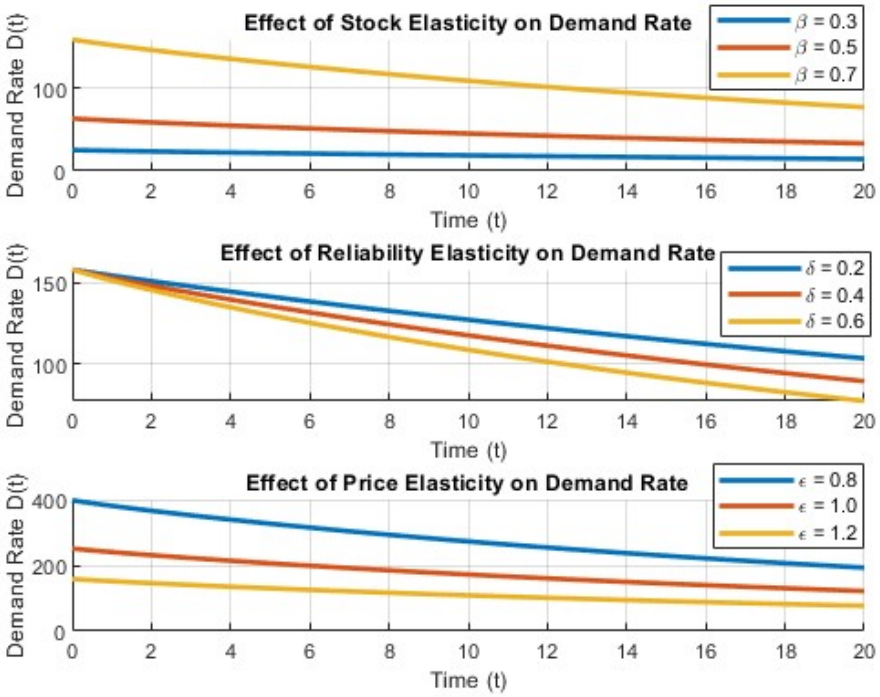


Figure 1: *Effect of Elasticities on Demand Rate.*

2. Notations and assumptions

2.1. Notations

The following notations are used in this model.

1. $I(t)$: Inventory level at time t.
2. Q: Order quantity.
3. T: Cycle time.
4. h_f, h_b: Holding costs for frontroom and backroom.
5. θ: Deterioration rate.
6. α: Fractional order ($0 < \alpha \leq 1$).
7. c: Unit purchasing cost.

2.2. Assumptions

The following assumptions are used in this paper.

1. Products deteriorate over time and are modeled using Caputo fractional derivative.
2. Demand depends on price (p), visible (frontroom) stock (S_f), and reliability (R).
3. Backroom inventory (S_b) is used to replenish frontroom stock.

4. No lead time and replenishment is instantaneous.
5. Shortages are not allowed.
6. Reliability decay function:
$$R(t) = R_0 e^{-\gamma t^{\alpha}} \tag{1}$$
7. Demand Function:
$$D(p, S_f, R) = a S_f^{\beta} R^{\delta} p^{-\epsilon} \tag{2}$$
Where a: base demand, β: stock elasticity, δ: reliability elasticity, ϵ: price elasticity.

3. Fractional Inventory Formulation and Solution

Inventory deterioration is modeled using a Caputo fractional derivative as follows.
$$D_t^{\alpha} I(t) + \theta I(t) = -D(p, S_f(t), R(t)), \quad 0 \le t \le T, \tag{3}$$
with the initial condition $I(0) = I_0$.
Here, D_t^{α} denotes the Caputo fractional derivative of order α defined as follows.
$$D_t^{\alpha} I(t) = \frac{1}{\Gamma(1-\alpha)} \int_0^t \frac{I'(\tau)}{(t-\tau)^{\alpha}} \, d\tau, \quad 0 < \alpha < 1. \tag{4}$$
The analytical solution of the Fractional differential equation involving the Caputo derivative of order α is equation (6). Since, equation (3) is a linear fractional differential equation and its solution can be derived using the Laplace transform method. Taking the Laplace transform of both sides, then we getting the following equations.
$$\begin{aligned} \mathcal{L}\{D_t^{\alpha} I(t)\} + \theta \mathcal{L}\{I(t)\} &= -\mathcal{L}\{D(p, S_f(t), R(t))\}, \\ s^{\alpha} \tilde{I}(s) - s^{\alpha-1} I(0) + \theta \tilde{I}(s) &= -\tilde{D}(s), \end{aligned}$$
where $\tilde{I}(s)$ and $\tilde{D}(s)$ are the Laplace transforms of $I(t)$ and $D(p, S_f(t), R(t))$, respectively. Rewriting the equation, then we getting
$$\tilde{I}(s) = \frac{s^{\alpha-1} I_0 - \tilde{D}(s)}{s^{\alpha} + \theta}. \tag{5}$$
Taking the inverse Laplace transform, then we getting
$$I(t) = I_0 E_{\alpha}(-\theta t^{\alpha}) - \int_0^t (t-\tau)^{\alpha-1} E_{\alpha,\alpha}(-\theta (t-\tau)^{\alpha}) D(p, S_f(\tau), R(\tau)) \, d\tau, \tag{6}$$
where $E_{\alpha}(\cdot)$ and $E_{\alpha,\alpha}(\cdot)$ are the Mittag-Leffler functions defined by:
$$E_{\alpha}(z) = \sum_{k=0}^{\infty} \frac{z^k}{\Gamma(\alpha k + 1)}, \tag{7}$$
$$E_{\alpha,\beta}(z) = \sum_{k=0}^{\infty} \frac{z^k}{\Gamma(\alpha k + \beta)}. \tag{8}$$
Thus, the general solution to the fractional inventory model equation is given by equation (6), which combines the memory effect captured by the fractional derivative and the dynamic demand function.

Next, we calculate all the associated inventory costs as follow:

1. Ordering Cost (OC):
$$OC = A \tag{9}$$

2. Purchasing Cost (PC):

$$PC = cQ \tag{10}$$

3. Holding Cost (HC):

$$HC == h_f \int_0^T S_f(t)dt + h_b \int_0^T S_b(t)dt \tag{11}$$

4. Deterioration Cost (DC):

$$DC = c\theta \int_0^T I(t)dt \tag{12}$$

The Total Cost Function is

$$TC(T) = \frac{1}{T}(OC + PC + HC + DC) \tag{13}$$

4. Optimal Solution Procedure

In this section, we examine the convexity of the total cost function in order to determine the optimal cycle. Following an analytical optimization approach similar to the Negi et al. [18], and the necessary condition for minimizing the total cost is given as follows:

$$\frac{d\,TC(T)}{dT} = 0. \tag{14}$$

To compute the optimal cycle length T by solving to above equation. The conditions as mention below that must be satisfied in order to minimize TC(T):

$$\frac{d^2\,TC(T)}{dT^2} > 0. \tag{15}$$

5. Numerical Example

Assume the input data as follows $\alpha = 0.9$, $\theta = 0.05$, $c = 20$, $h_f = 1.5$, $h_b = 1.0$, $s = 5$, $v = 3$, $a = 100$, $\beta = 0.4$, $\delta = 0.3$, $\epsilon = 1.1$, $R_0 = 1$, $\gamma = 0.05$.
The obtained optimal values are as follows:

$$T^* = 6.5,\ Q^* = 870,\ p^* = 14.8,\ C_p = 17400,\ C_h = 520,$$
$$C_d = 880,\ C_s = 340,\ SV = 1250,\ TC = \$2884.6.$$

6. Graphical Representation

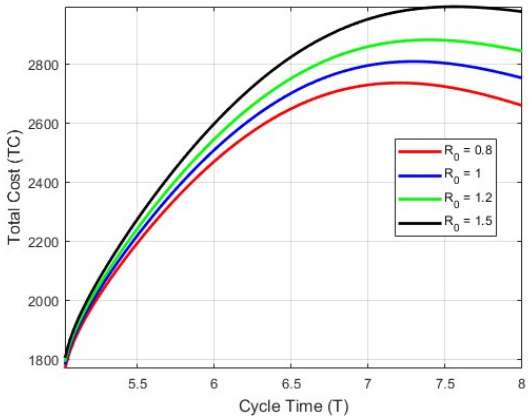


Figure 2: *Total Cost vs Cycle Time for Different Reliability Parameters*

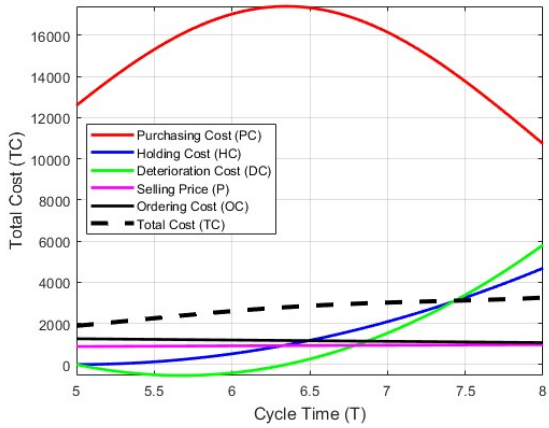


Figure 3: *Total Cost vs Cycle Time for Different Costs and Price*

The graphical depictions in this part provide a comprehensive grasp of the dynamics within the deteriorated inventory model. Figure 2 and Figure 3 explains the link between demand rates and time, while Figure 2 illustrates how memory effect impacts inventory management.

7. Conclusion

In this study, we explored the significant and practical role of the memory effect in inventory systems to minimizing the total costs. The memory effect, which is include the past good and bad experiences in decision making to develop more practical business models. The proposed inventory system considered constant deterioration rate and price, stock and reliability reliant demand, reflecting more realistic inventory systems under memory effect. A numerical example is illustrate for the applicability of the proposed model using analytical optimization method with the help of MATLAB software version R2021b. The results highlights the practical advantages of memory effects, it also acknowledges that practical considerations and real-world variability in the proposed system. Future research directions is that the consideration of environmental consideration by assuming memory effect in inventory models.

References

[1] Ghare, P. M., & Schrader, G. F. (1963). A model for an exponentially decaying inventory. *Journal of Industrial Engineering*, **14**(5), 238–243.

[2] Urban, T. L. (1992). Pricing and ordering policy for a product subject to risk of obsolescence. *International Journal of Production Economics*, **27**, 263–272.

[3] Mandal, B., & Phaujdar, S. (2001). An inventory model for deteriorating items with stock-dependent demand and time-dependent partial backlogging. *Applied Mathematical Modelling*, **25**(12), 1149–1155.

[4] Yadav, S. P. (2013). A perishable inventory model with stock, time, and price-dependent demand under inflation. *International Journal of Management Science and Engineering Management*, **8**(2), 132–138.

[5] Abad, P. L. (2001). Optimal pricing and lot-sizing under conditions of perishability and partial backordering. *Management Science*, **47**(6), 813–826.

[6] Jaggi, C. K. (2008). Retailer™s optimal replenishment decisions with credit-linked demand under permissible delay in payments. *Applied Mathematical Modelling*, **32**(10), 2012–2025.

[7] Jaggi, C. K., Sharma, A., & Mittal, M. (2011). A fuzzy model for deteriorating inventory items with reliability-dependent demand under permissible delay. *Mathematical and Computer Modelling*, **53**(5“6), 1423–1433.

[8] Tarasov, V. E. (2011). *Fractional dynamics: Applications of fractional calculus to dynamics of particles, fields and media*. Springer.
[9] Atangana, A., & Baleanu, D. (2016). New fractional derivatives with nonlocal and non-singular kernel: Theory and application to heat transfer model. *Thermal Science*, **20**(2), 763–769.
[10] Bera, U., Sahoo, S., & Mishra, B. K. (2020). A fractional order deteriorating inventory model with reliability-dependent demand. *Computers & Industrial Engineering*, **147**, 106662.
[11] Sahoo, S., & Mishra, B. K. (2021). A fractional inventory model with stock and reliability dependent demand under trade credit policy. *Journal of Computational and Applied Mathematics*, **390**, 113362.
[12] Miller, K.S., Ross, B.: An Introduction to the Fractional Calculus and Fractional Differential Equations. Wiley, New York (1993).
[13] Diethelm, K.: The Analysis of Fractional Differential Equations. Springer, Verlag (2010).
[14] Mebarek-Oudina, F. "Exploring Passive Heat Transfer Enhancement Techniques: Applications, Benefits, and Challenges." Babylonian Journal of Mechanical Engineering 2024 (2024): 122-127.
[15] Mebarek-Oudina, F., et al. "Thermal performance of MgO-SWCNT/water hybrid nanofluids in a zigzag walled cavity with differently shaped obstacles." Modern Physics Letters B (2025): 2550163.
[16] Kumar, M. Anil, et al. "The impact of Soret Dufour and radiation on the laminar flow of a rotating liquid past a porous plate via chemical reaction." Modern Physics Letters B 39.10 (2025): 2450458.
[17] Mebarek-Oudina, Fateh. "Numerical modeling of the hydrodynamic stability in vertical annulus with heat source of different lengths." Engineering science and technology, an international journal 20.4 (2017): 1324-1333.
[18] Negi, A., Singh, O., Yadav, A.S. et al. An Inventory Model for Perishable Goods with Demand that Varies Probabilistically with Selling Price Using a Pentagonal Fuzzy Framework. Oper. Res. Forum 6, 150 (2025). https://doi.org/10.1007/s43069-025-00555-5
[19] KUMAR, Devendra, Jagdev SINGH, and Sunil KUMAR. "Analytic and approximate solutions of space-time fractional telegraph equations via Laplace transform." Walailak Journal of Science and Technology (WJST) 11.8 (2014): 711-728.
[20] Singh, Jagdev, Devendra Kumar, and Sunil Kumar. "A New Fractional Model of Nonlinear Shock Wave Equation Arising in Flow of Gases." Nonlinear Engineering 3.1 (2014).
[21] Kumar, Saurabh, and Vikas Gupta. "An Efficient Numerical Approach to Solve Fractional Coupled Boussinesq Equations." Journal of Computational and Nonlinear Dynamics 19.12 (2024): 121002.

RELEVANCE OF INFORMATION AND TECHNICAL SUPPORT OF STAFF IN MAINTENANCE AND REPAIR OF STEAM TURBINE DEVICES OF POWER UNITS OF THERMAL ELECTRIC STATION

Farzaliyev Y. Z.

•

Azerbaijan State University of Economics
yusif.farzaliyev@unec.edu.az

Abstract

The need to improve the efficiency of thermal electric station units increases significantly as their service life increases. If during the standard service life, the efficiency of operation was successfully calculated on the basis of a standard algorithm and experimental energy characteristics, then subsequently the correspondence of the initial energy characteristics to the actual characteristics becomes less and less accurate. In order to ensure the efficiency of power units, it is necessary to reduce the frequency of clarification of empirical characteristics, which causes a significant increase in operating costs. The forced approach to solving operational problems is taking into account operating experience, information about existing defects. In this case, the strict calculation method is replaced by an intuitive approach, the risk of an erroneous solution of which is significant, and improving the method for solving operational problems is transformed from desirable to necessary.

Keywords: Efficiency, synthesis, steam turbine device, power unit, automated system, recommendations, technical condition profitability

I. Introduction

By the efficiency of steam turbine devices (STD) we mean the combined consideration of reliability, cost effectiveness and safety of STD operation. Quantitatively, the efficiency of the power unit's STD is characterized by a number of technical and economic indicators (TEI). Some of them, and the number of TEIs is in the tens, are presented in the form of monthly average values in the 3-TEKH form [1].

In addition to this summary form, operational personnel can receive 28 more output forms upon request. All this numerous data is necessary for:

- ensuring efficient operation of power unit equipment
- selection of the power unit that is in greatest need of wear restoration
- assessment of the quality of work of operating personnel
- clarification of the technical condition of the power unit by conducting operational tests
- preparation of reports on thermal efficiency of the power unit

It is easy to see that the TEIs presented in Form 3-TECH to the greatest extent characterize the efficiency of the boiler and turbine units of the power unit, and to the least extent – the electrical equipment and the power unit as a whole. This is confirmed by the intuitive nature of the comparison and ranking of power units by work efficiency when:

- distribution of the load between power units (if the energy characteristics of a power unit do not correspond to its actual state)
- planning repairs of power units taking into account their technical condition
- the need to turn off one of the power units in reserve
- assessing the quality of work of each shift
- solving a number of operational problems related to those noted above

The infallibility of the intuitive approach depends not only on the qualifications of the personnel, but also on the number of statistically dependent TEIs. The greater the number of dependent TEIs, the greater the risk (probability) of an erroneous decision with the intuitive approach.

Traditionally, the performance of a power plant, individual power units and equipment is assessed by comparing actual and standard fuel consumption.

As the service life increases, the error of this comparison increases, since the influence of the technical condition of the power unit equipment, which naturally deteriorates, increases significantly. In [2], a method for comparing and ranking the work efficiency of STD of the thermal electric station (TES) was developed. This method is based on the peculiarity of calculating the integral indicator reflecting the difference in the scale, scale and unit of measurement of the TEI. It is shown that the reduction in the cumbersomeness of converting actual values of the TEI is achieved by classifying the TEI by STD nodes, which allows excluding from consideration the statistical analysis of the relationship of the TEI, the independence of which is obvious.

Let's consider some features of the automated generation of recommendations for improving the efficiency of the equipment of the STD of 300 MW power units. But so that these results do not look unfounded, Table 1, according to [2], shows the actual average monthly values of the TEI of the STD of 300 MW power units.

Table 1: Actual average monthly values of thermal efficiency of the 300 MW STD of thermal electric station

No. TEI	No des	TEI		Actual average monthly values of technical and economic indicators of the steam-turbine device with a capacity of 300 MW, station No.							
		Conv desig	Unitmeas	1	2	3	4	5	6	7	8
1	ST	$L_{e,av}$	MW	R E Z E R V E	181,5	180,1	180,3	181,7	169,6	173,0	176,9
2		$L_{e,max}$	MW		250	240	250	250	240	250	250
3		$P_{f,st}$	Atm		222,3	215,0	218,1	210,5	220,8	189,8	208,8
4		$T_{f,st}$	^{0}C		540	539,2	540	540	540	540	539,7
5		q_t^{gr}	kcal/ kWh		1925	1925	1888	1895	1913	1905	1893
6		δq_t	r.u.		0,0166	0,0192	0,0190	0,0162	0,0188	0,0182	0,0184
7	RH	$\delta \rho_{rh}$	r.u.		0,126	0,125	0,130	0,131	0,123	0,126	0,117
8		T_{rh}^{out}	^{0}C		540	538,2	540	540	540	538,6	539,7
9	Con	ρ_{con}	Atm.		0,089	0,060	0,084	0,072	0,091	0,067	0,064
10		$\Delta T_{c.w}$	^{0}C		7,7	7,5	6,5	5,4	6,5	6,9	7,6
11		ΔT_h	^{0}C		12,8	16,1	14,3	8,2	10,0	16,0	17,2
12	ON	$\omega_{o.n.}^{e.e}$	r.u.		1,44	1,66	1,7	1,47	1,64	1,51	1,61
13		$\omega_{o.n.}^{h}$	r.u.		0,21	0,24	0,16	0,16	0,17	0,32	0,22

The following symbols are used in the table below: ST – steam turbine; RH – reheater; Con – condenser; O.N. – own needs; $L_{e,av}$– average electrical load; $L_{e,max}$– maximum electrical load; $P_{f,st}$ - fresh steam pressure; $T_{f,st}$ - fresh steam temperature; q_t^{gr} – actual value of specific heat consumption "gross"; δq_t - relative difference between actual values of specific heat consumption "net" and "gross"; $\delta q_t = \frac{(q_t^n - q_t^{gr})}{q_t^{gr}}$, where q_t^n – actual value of specific heat consumption "net"; $\delta \rho_{rh} = \frac{\left(\rho_{rh}^{out} - \rho_{rh}^{in}\right)}{\rho_{rh}^{in}}$, where ρ_{rh}^{out} и ρ_{rh}^{in} – the pressure of the intermediate superheater steam, respectively, at the outlet and inlet of the intermediate reheater; T_{rh}^{out} - steam temperature after reheating; ρ_{con}- condenser pressure; $\Delta T_{c.w}$- change in cooling water temperature; $\Delta T_{c.w.} = (T_{c.w.}^{out} - T_{c.w.}^{in})$ where $T_{c.w.}^{out}$ and $T_{c.w.}^{in}$ the temperature of the cooling water, respectively, at the outlet and inlet of the condenser; ΔT_h - temperature head; $\omega_{o.n.}^{e.e}$ and $\omega_{o.n.}^{h}$ – specific consumption of electrical and thermal energy, respectively, own needs.

The ranking was carried out according to the total values, $K_{i,\Sigma} = \sum_{\psi=1}^{n_b^{op}} K_{i,\Sigma,\psi}$ calculated taking into account the relationship between the various TEI of the STD, where $i = 1, n_b^{op}$ is the number of operating power units $n_b^{op} = 7$. $K_{i,\Sigma,\psi}$ - total (Σ) significance of the TEI of the ψ -th node of the i -th power unit, determined by formula $K_{i,\Sigma,\psi} = \sum_{\varphi=1}^{m_\psi} K_{i,\varphi,\psi}$, m_ψ - number of TEI of the ψ -th node of the STD; $K_{i,\varphi,\psi}$ - significance of the implementation of the φ -th TEI of the ψ -th node of the i -th power unit in the five-point TEI measurement system.

II. Methods

The algorithm for synthesizing the TEI and evaluating the integral indicator is as follows:

- The maximum possible value of the number of realizations $K_{\Sigma,i}$ is determined by formula $K_{\Sigma,max} = 5 * m_\Sigma = 50$, where m_Σ is the calculated number of TEIs, m_Σ=10 [2]
- The minimum possible value of the number of realizations $K_{\Sigma,i}$ is determined by formula $K_{\Sigma,min} = 10$
- An array of states of power units S(i) is formed with $i = 1, n_b$. It is accepted that the working state corresponds to one, and the non-working state corresponds to zero n the example under consideration: S(1)=0; S(2)=S(3)=…=S(8)=1, and $n_b^{op} = 7$
- Given that the possible values of $K_{\Sigma,i}$ vary from $K_{\Sigma,min}$ to $K_{\Sigma,max}$, the interval of change of $K_{\Sigma,i}$ with $i = 1, n_b^{op}$ can be calculated by the formula
- The unit interval in the five-point system of assessing the significance of the integral indicator of the implementation of $K_{\Sigma,i}$ with $i = 1, n_b^{op}$ is calculated using formula $K_\Sigma^\Delta = \frac{\Delta K_\Sigma}{5} = 8.2$

Table 2 shows the results of the evaluation of the performance indicators of the STD of the TES and the STD as a whole. In addition to the calculations presented in a similar table in [2], Table 2 calculates the refined values of the integral indicator $I_{In,i}$ and the ordinal number $M_{r,i}$ of the STD ranked by performance (in order of increasing efficiency). The integral indicator of the significance of the thermal efficiency of the power units of the steam turbine plant (Iin_i) is calculated according to the following algorithm-formula:

$$\left.\begin{array}{l} i = 1{,}8 \\ if\ S_1 = 0\ then\ go\ to\ 1, otherwise \\ if\ K_{\Sigma,i} \le (K_{\Sigma,min} - 1 + K_\Sigma^\Delta)\ then\ Iin_i \Rightarrow unacceptable, go\ to\ 1, otherwise \\ if\ K_{\Sigma,i} \le (K_{\Sigma,min} - 1 + 2K_\Sigma^\Delta)\ then\ Iin_i \Rightarrow unsatisfactory, go\ to\ 1, otherwise \\ if\ K_{\Sigma,i} \le (K_{\Sigma,min} + 3K_\Sigma^\Delta)\ then\ Iin_i \Rightarrow satisfactory, go\ to\ 1, otherwise \\ if\ K_{\Sigma,i} \le (K_{\Sigma,min} + 4K_\Sigma^\Delta)\ then\ Iin_i \Rightarrow good, go\ to\ 1, otherwise\ Iin_i \Rightarrow excellent, go\ to\ 1 \end{array}\right\} \quad (1)$$

Here the index ⇒ denotes the phrase "is taken to be equal to".

Table 2: Results of the evaluation of the efficiency of the STD of the thermal electric station

No. node STD (ψ)	Nodes STD	Ind. of work effect	Results of the assessment of the efficiency of the operation of the STD and the STD as a whole of the power units of the TES; station number of the STD								TTotal TTES
			1	2	3	4	5	6	7	8	
1	ST	$K_{\Sigma,i,\psi}$	REZERVE	21	12	21	24	10	13	19	17.1
		$Iin_{i,\psi}$		good	unsat	excl.	excl.	unsat	sat	good	good
		$M_{r,i,\psi}$		6	2	5	7	1	36	4	–
2	RH	$K_{\Sigma,i,\psi}$		4	3	5	5	3	4	1	3.6
		$Iin_{i,\psi}$		good	sat	excl.	excl.	sat	good	unaccl.	good
		$M_{r,i,\psi}$		5	2	6	7	3	4	1	–
3	Con	$K_{\Sigma,i,\psi}$		3	5	4.5	9	4.5	5.5	6	5.4
		$Iin_{i,\psi}$		unsat	sat	unsat	excl.	unsat	sat	sat	sat
		$M_{r,i,\psi}$		1	4	2	7	3	5	6	–
4	O.N	$K_{\Sigma,i,\psi}$		9	4	6	10	7	5	6	6.7
		$Iin_{i,\psi}$		excl.	unsat	sat	excl.	good	sat	sat	good
		$M_{r,i,\psi}$		6	1	3	7	5	2	4	–
Total STD		$K_{\Sigma,i}$		37	24	36,5	48	24,5	27,5	32	32,8
		Iin_i		good	unsat	good	excl.	unsat	sat	sat	sat
		$M_{r,i}$		6	1	5	7	2	3	4	-

Note: According to [2] [I_{In} → unacceptable] denotes the correspondence of the integral state to the unacceptable.

In accordance with [3], as information and methodological support to the TES personnel, depending on the position held, every month, before discussing the efficiency of the power units, the automated system provides certain forms of analysis and synthesis of the TEI. All of them consist of two sections: conclusion and recommendations.

Thus, the senior machinist of the STD is given form 1FNTU at the beginning of each month (before the discussion) (F - form, N - dispatcher number of the STD, TU - turbine unit).

It should be noted that senior machinists who know their STD "like the back of their hand" and, as a rule, are fully aware of current information about the efficiency of the STD, are not without interest in learning not only the average monthly values of the TEI and their significance in comparison with the significance of the TEI of other STDs, but also be prepared for a "conversation" with the head of the turbine shop [4].

Figure 1 shows a fragment of form 1F6TU for the STD of the 6th power unit of the TES. The efficiency of the STD of the 6th power unit is assessed as ***unsatisfactory***.

Form 1FNTU

CHARACTERISTICS OF THE PERFORMANCE OF THE 6TH POWER UNIT OF TES FOR THE MONTH _____OF YEAR 20___

CONCLUSION

1. The efficiency of the STD is assessed as ***unsatisfactory***
2. In the ranking of the efficiency improvement among the seven operating power units of the TES, the 6th STD ranks **5th**
3. Among the four nodes of the 6th STD, there are two "weak links" (nodes that do not meet the requirements)
4. The significance of the TEI in a five-point system, the actual average monthly and recommended values of the TEI of the 6th STD were determined

No TEI	No des 6th STD	Technical and economic indicators of STD of the TES				
		Name of TEI	Unit Mesr. TEI	Estimation TEI		Signif TEI
				Actual	Recomm.	
1	ST	Average electric load	MW	**162,6**	**175,7**	**1**
2		Maximum electrical load	MW	**240**	**245**	**1**
3		Fresh steam pressure	Atm.	**220,8**	**222,3**	**5**
4		Specific heat consumption "gross"	Kcal/kWh	**1913**	**1906,5**	**2**
5		Rel. meas. spec. heat consum. "net"	rel. unit	**0,0188**	**0,0179**	**1**
Work efficiency) (Iin_1)			**unsatisfactorily**			
6	RH	Relative change in pressure	rel. unit.	**0,123**	**0,128**	**3**
Work efficiency) (Iin_2)			**satisfactorily**			
7	CON	Condenser pressure	Atm.	**0,091**	**0,0755**	**1**
8		Rel. change of temp. of cool. wt.	rel. unit.	**6,5**	**5,4**	**4**
9		Temperature head	^{0}C	**10,0**	**8,2**	**5**
Work efficiency) (Iin_3)			**unsatisfactorily**			
10	O.N	Specific energy consum. for O.N.	%	**1,64**	**1,57**	**2**
11		Spec. consum. of H.E for O.N.	%	**0,17**	**0,16**	**2**
Work efficiency) (Iin_4)			**good**			
STD		***Work efficiency) (Iin_Σ)***	**unsatisfactorily**			**2,45**

RECOMMENDATIONS

1. Ensure improvement of the TEI in accordance with the recommended values
2. Improve the efficiency of the walk-through by "targeted inspection" of the steam turbine and condenser
3. Provide test control of personnel knowledge on ways to improve the thermal performance of a ***steam turbine and condenser***
4. Ensure the availability of Instructions and Rules for improving the efficiency of the ***sixth*** STD in the workplace

Date

Figure 1: Fragment of form 1F6TU

Form 1FNTU

CHARACTERISTICS OF THE PERFORMANCE OF THE 5TH POWER UNIT OF TES FOR THE MONTH _____OF YEAR 20___

CONCLUSION

1. The efficiency of the STD is assessed as ***excellent***
2. In the ranking of the efficiency improvement among the seven operating power units of the TES, the 5th STD ranks ***7th***
3. Among the four nodes of the 5th STD, there are ***no*** "weak links" (nodes that do not meet the requirements)
4. The significance of the TEI in a five-point system, the actual average monthly and recommended values of the TEI of the 5th STD were determined

No TEI	No des 5th STD	Technical and economic indicators of STD of the TES				
		Name of TEI	Unit Mesr. TEI	Estimation TEI		Sign TEI
				Actual	Recom.	
1	ST	Average electric load	MW	**181,7**	**-**	**5**
2		Maximum electrical load	MW	**250**	**-**	**5**
3		Fresh steam pressure	Atm.	**210,5**	**222,3**	**4**
4		Specific heat consumption "gross"	Kcal/kWh	**189,5**	**188,8**	**5**
5		Rel. meas. spec. heat consum. "net"	rel. unit	**0,0162**	**-**	**5**
Work efficiency) (Iin_i)			***excellent***			
6	RH	Relative change in pressure	rel. unit.	**0,131**	**-**	**5**
Work efficiency) (Iin_2)			***excellent***			
7	CON	Condenser pressure	Atm.	**0,072**	**0,06**	**4**
8		Rel. change of temp. of cool. wt.	rel. unit.	**54**	**-**	**5**
9		Temperature head	^{0}C	**8,2**	**-**	**5**
Work efficiency) (Iin_3)			***excellent***			
10	O.N	Specific energy consum. for O.N.	%	**1,47**	**1,44**	**5**
11		Spec. consum. of H.E for O.N.	%	**0,16**	**-**	**5**
Work efficiency) (Iin_4)			**satisfactorily**			
STD		***Work efficiency) (Iin_Σ)***	***excellent***			**4,8**

RECOMMENDATIONS

1. Ensure improvement of the TEI in accordance with the recommended values
2. Discuss the experience of ensuring compliance of the TEI with the requirements
3. To identify reserves for increasing the efficiency of STD by analyzing the efficiency of technical maintenance of each shift
4. Ensure the availability of Instructions and Rules for improving the efficiency of the ***fifth*** STD in the workplace

Date

Figure 2: Fragment of form 1F5TU

III. Results

In the 1FNTU form, the following results of the synthesis of the TEI are presented in conclusion:

- assessment of the performance of the N-th STD on five-point scale relative
- the ranking is carried out in order of increasing the integral indicator of work efficiency
- "weak links" of STD

Degree of compliance of the TEI with the requirements in a five-point system (significance of the TEI), actual and recommended TEI. The non-compliant requirements include assessments $In_{i,j}$, which are assigned 1 or 2 points in a five-point system. The nodes of these TEI are referred to as "weak links". For example, for the STD of the 6th power unit - this is the steam turbine and condenser, and for the STD of the 3rd power unit - this is the steam turbine and the O.N. system and in Figure 2 - a fragment of form 1F5TU for the STD of the 5th power unit. The efficiency of the STD of the 6th power unit is assessed as **unsatisfactory**, and the STD of the 5th power unit - as **excellent**.

IV. Discussion

If the actual value of the i-th TEI ($In_{i,j}$), does not exceed the median $\left(Md^*(In_{i,j})\right)$ of the observed implementations, the recommended value of the TEI $In_{i,j}^{Rec}$ is taken to be equal to the median. If $In_{i,j} > Md^*(In_{i,j})$, then the best value among the implementations of this TEI should be taken as the recommended value [5].

The decision-making algorithm-formula, given that the work efficiency increases with an increase in the TEI, is as follows:

$$\left.\begin{array}{l} if\ In_{i,j} < Md^*\left(In_{i,j}\right), then\ In_{i,j}^{Rec} = Md^*(In_{i,j}) \\ if\ In_{i,j} \geq Md^*\left(In_{i,j}\right), then\ In_{i,j}^{Rec} = In_{max,j} \end{array}\right\} \quad (2)$$

If, however, the work efficiency decreases with an increase in the TEI, then the decision-making algorithm-formula looks like this:

$$\left.\begin{array}{l} if\ In_{i,j} > Md^*\left(In_{i,j}\right), then\ In_{i,j}^{Rec} = Md^*(In_{i,j}) \\ if\ In_{i,j} \leq Md^*\left(In_{i,j}\right), then\ In_{i,j}^{Rec} = In_{max,j} \end{array}\right\} \quad (3)$$

The above data defines the information support of the staff.

Recommendations for improving the efficiency of STD in the form of 1FNTU constitute methodological support and include the following options:

- elimination of the "weak links" identified as a result of calculations, the TEIs of which do not meet the requirements. In the table of form 1FNTU- these are TEIs whose significance coefficients are estimated as 1 or 2
- increasing the frequency of assessment of the average value of the TEI that does not meet the requirements
- if the significance coefficient is characterized as satisfactory, then it is recommended to switch to averaged estimates within half a month

- If this coefficient is characterized as unsatisfactory (2) or unacceptable (1), then it is recommended to switch to averaged estimates within a week
- increasing the efficiency of inspection and control of TEI nodes, the technical condition of which is the reason for the decrease in the efficiency of the STD
- systematic monitoring of personnel knowledge about ways to improve TEI of the STD. Test control systems are the most suitable for this
- the presence of relevant instructions allows to increase the reliability of decisions taken to improve the efficiency of the STD when the load and operating mode change.

Improving the efficiency of the TES' steam turbine device is implemented in two ways.

The first method is based on the assumption that improving the efficiency of the TES' steam turbine device is achieved by improving the efficiency of each STD. This method has found wide application, primarily because there is no generally accepted method for ranking STD by efficiency [6].

The second method, without excluding the importance of the first method, considers the TES' steam turbine device as a certain set from which the most efficient units of the STD can be identified, as well as the TEIs that do not meet the requirements for the majority of the TES' steam turbine device [7].

The first method is implemented based on the TEI analysis, and the second on the TEI synthesis [8].

Forms 1FNTU for N = $[1, n_b]$ contribute to increasing the objectivity of the TEI analysis.

In accordance with [3], the analysis is carried out at least once a month. The head of this event is the head of the steam turbine shop, and the participants are the chief machinists of the TES' steam turbine devices. The second method is implemented, as a rule, during a discussion of the efficiency of the power units with the participation of the heads of production shops, including the head of the turbine shop, under the leadership of the Chief Engineer of the TES.

Form 1FΣTU provides information and methodological support to the head of the turbine shop. The information component is highlighted in the conclusion and includes:

- assessment of the work efficiency STD of the TES. Overall, the efficiency of the power units are assessed as satisfactory
- results of comparison and ranking of integrated indicators of STD in order of increasing work efficiency
- assessment of the degree of compliance of the STD nodes with the requirements the results of the comparison of the efficiency of the STD nodes in the form of a list of "weak links"
- comparison of the TEI significance indicators, allowing to establish a list of indicators indicating unsatisfactory operation of the STD nodes
- the provision according to which the elimination of "weak links" leads to an increase in the efficiency of the STD with a quantitative assessment of at least four
- list of ways to improve the efficiency of STD of the TES

This list includes:

The first shutting down the least efficient STD for scheduled maintenance and ensuring that the TEI of this STD meets the requirements. This is a traditional method. Its disadvantage is the wide range of materials, equipment and devices required for replacement, long duration of maintenance, high operating costs

The second elimination of "weak links" among the nodes of the STD. For example, as shown down, an increase in the efficiency of the STD of a TES can be achieved by restoring the wear of only three capacitors, the efficiency of which is unsatisfactory.

Form 1FΣTU

CHARACTERISTICS OF THE EFFICIENCY OF OPERATION OF STD OF POWER UNITS OF TES FOR A MONTH_____ OF YEAR 20___

CONCLUSION

1. The efficiency of STD of the TES operation is assessed as ***satisfactory***
2. The ranking of the TES' STD was carried out in order of increasing efficiency. The least efficient STD should be considered the **3** power units, and the most efficient STD should be considered the **5** power units

Indicator	Serial number of power units								On ave.
	1	2	3	4	5	6	7	8	
Ord. num. in a ranked series	-	6	1	5	7	2	3	4	-
Work efficienty	-	good	unsat	good	excell	unsat	sat	sat	sat

3. Unsatisfactory performance was established for the ST power units: third, sixth. The group of power units with the following performance efficiency:
- satisfactory, includes: **seventh; eighth**; - good, includes: **second, fourth**; - excellent, includes: **fifth**
4. The degree of compliance of the efficiency of the nodes of the STD with the requirements has been established

STD nodes	Serial number of power units								On Ave.
	1	2	3	4	5	6	7	8	
Steam turbine	-	good	unsat	excell	excell	unsat	sat	good	good
Reheater	-	good	sat	excell	excell	sat	good	unacc	good
Condenser	-	unsat	sat	unsat	excell	unsat	sat	sat	sat
Own needs	-	excell	unsat	sat	excell	good	sat	sat	good

5. «Weak links» of STDs of the power units identified

STD nodes	Number of STD with work efficiency			
	unsat	sat	good	excell
Steam turbine	2	1	2	2
Reheater	1	2	2	2
Condenser	3	3	-	1
Own needs	1	3	1	2

The "weak links" among the nodes of the STD (the efficiency of operation is no more than "sat") include: a **condenser**. For a number of STDs, the following apply to TEIs with $Ki,j \leq 3$, where i=1,7; j=1,10:
- relative flow rate of the actual value of the specific heat consumption "net" and "gross" of the **steam turbine**
- change in temperature of chilled water in the **condenser**
- temperature head in **condenser**

RECOMMENDATIONS

Improving the assessment of the efficiency work of STD of the TES can be achieved by:
1. Restoration of wear of condensers of the **second**, **fourth** and **sixth** power units;
2. For TEIs with unsatisfactory significance, move from monthly change analysis to weekly;
3. Improving the efficiency of daily inspection of STD by analyzing changes in the TEI of which the significance is unsatisfactory**;**
4. Ensure that courses are conducted to eliminate non-compliance of TEIs of the STD with the requirements
5. Provide personnel with instructions for maintenance of capacitors

Date

Figure 3: Fragment of form 1FΣTU

In this case, not only the list of necessary materials, equipment and devices is reduced, but also the total duration of downtime of power units, the diversity of the list of works, and ultimately significantly lower costs are required [9].

The third elimination of the discrepancy between the requirements of the most typical for all STDs TEI. Additional advantages compared to the elimination of "weak links" is the choice among TEIs that have an unsatisfactory assessment, the TEI improvement of which will require the least effort and funds.

Figure 3 shows the 1FΣTU form, which summarizes the work efficiency of the TES power units included in the time interval under consideration

If the selection of such TEIs for personnel does not present any difficulties, then for the expected effect the number of TEIs requires certain calculations [10]. Calculations are carried out according to the formula:

$$m_{\Delta} = \left|\left(3{,}4 * m_n - K_{\Sigma,ave}\right) * n_b^{op}\right| \quad (4)$$

where m_n - is the number of TEIs; $K_{\Sigma,ave}$ - is the sum of TEI significances averaged over all n_b^{op} , STDs; n_b^{op} - is the number of operating power units. If, as a result of wear restoration, the significance of the TEI of the STD has changed from “unsatisfactory” to at least “good”, then the number of TEIs required to improve the efficiency of the STD of the TES will be equal to $0.5m_{\Delta}$. Thus, in the conditions of the example under consideration, when $m_n = 10$, $K_{\Sigma,ave} = 328$, and the $n_b^{op} = 7$ of TEIs requiring a change in significance from “unsatisfactory” to “good” is four. Consequently, in order to increase the efficiency of STD of the TES from “satisfactory” to “good”, it is necessary to increase the significance of “unsatisfactory” to “good” for 4 TEIs.

Recommendations based on the synthesis of the TEI includes:

- restoration of wear of similar units with the lowest operating efficiency
- reducing the frequency of monitoring the TEI of units with the lowest operating efficiency from monthly to weekly
- increasing the efficiency of monthly inspection of units with the lowest operating efficiency by monitoring changes in the TEI
- conducting short-term courses by the head of the steam turbine shop to eliminate non-compliance of the TEIs of the STD with the requirements
- Providing personnel with Instructions for the maintenance of units with low operating efficiency and Instructions for improving the TEI that do not meet the requirements.

Conclusions

1. Information and methodological support for the management and personnel of the steam turbine shop is an essential condition for increasing the work efficiency of STD of the TES
2. Information and methodological support of personnel allows to significantly reduce the risk of erroneous decision of operational tasks related to load distribution, selection of power units disconnected for scheduled repairs, in reserve, testing. It is the objective solution of problems that ensures the required reliability, economy and safety, i.e. the work efficiency of STD of the TES
3. It is advisable for the head of the steam turbine shop to discuss the results of the analysis of the TEI of the STD with the shop staff, and to participate in a meeting of the chief engineer of the TES with the heads of the production shops of the power plant with the results of the synthesis of the TEI

4. Integral performance indicators of power unit installations allow calculating the integral indicator of a power unit, ranking power units, and justifying the solution of operational problems.

References

[1] RD 34.09.454. Typical algorithm for calculation of technical and economic indicators of condensing power units of 300, 500, 800 and 1200 mW capacity. VTN, 2017.

[2] Farhadzadeh, E. M. Muradaliev, A. Z. Farzaliev, Y. Z. Rafieva, T. K. and Abdullaeva S.A. Increase of efficiency of steam turbine units of TES. Kiev. Electronic modeling. №1, 2018, c. 81-94.

[3] Rules of technical operation of electric power stations and grids of the Russian Federation. Ministry of Energy of the Russian Federation, 2003, 160 p.

[4] Yashchura, A. I. System of maintenance and repair of power equipment / A.I. Yashchura. Reference book. NS ENAS - Moscow: - 2006, - 504 p.

[5] Yagovkin, G. N. Yagovkin, N. G. and Panyukova, S. A. Reliability management at realization of maintenance and repair strategy in the power supply systems // - Moscow: Promyshlennaya Energetika, Moscow: Promyshlennaya Energetika, - 2010. №9, - c. 12-15.

[6] Khrennikov, A. Yu., Goldstein, V. G. and Nazarychev, A. N. Diagnostic models for estimating the technical condition of electrical equipment of power plants and substations // - Moscow: Promyshlennaya Energetika. 2010. №10, - pp. 17-20.

[7] Farhadzadeh, E. M., Farzaliev, Y. Z. and Muradaliev, A. Z. Automated formation of recommendations to improve the reliability and economic efficiency of TES power units // - Moscow: Energetik, - 2016. no. 2, - p. 15-17.

[8] Reference book / Edited by Rozanov Y.N. Reliability of power engineering systems and their maintenance. Reliability of electric power systems, - Moscow: Energoatomizdat, - 2000. T.2. - 565 p.

[9] Sazykin, V.G. Technical aspects of operation of worn-out equipment // - Moscow: Promyshlennaya Energetika, - 2000. №1, - pp. 14-18.

[10] RD 34.09.454. Typical algorithm for calculation of technical and economic indicators of condensing power units of 300, 500, 800 and 1200 mW capacity. VTN, 2017.

RELIABILITY ANALYSIS OF A THAP MISSION WITH SEQUENTIAL PHASES

Rasmi K[a], Dharmaraja Selvamuthu[a], Raina Raj[b],
Vladmir Vishnevsky[c], Dimitry Kozyrev[d]

•

Department of Mathematics, Indian Institute of Technology Delhi, New Delhi, India[a]
rasmikcnair@gmail.com
dharmar@maths.iitd.ac.in
Bharti School of Telecommunication Technology & Management,
Indian Institute of Technology Delhi, New Delhi, India[b]
rainaraj.curaj@gmail.com
V.A. Trapeznikov Institute of Control Sciences of Russian Academy of Sciences, Russia[c]
vishnevsky@ipiran.ru
RUDN University, 6 Miklukho-Maklaya St, Russian Federation[d]
kozyrev@ipiran.ru

Abstract

Stratospheric platforms, commonly known as high-altitude platforms (HAPs), are gaining traction as an economical and sustainable option for diverse applications, including environmental monitoring, surveillance, and communication networks. Tethered HAPs (tHAPs), which remain physically connected to the ground, provide improved stability, a continuous power source, and dependable data transfer capabilities. Analyzing the reliability of these systems as phased mission systems (PMS) is essential, given the multiple operational stages they undergo-such as ascend, primary task, and descend, posing distinct operational demands and challenging environmental conditions. Maintaining reliability throughout these phases is crucial for ensuring both mission effectiveness and long-term operational integrity. This research explores the necessity and practicality of conducting reliability assessments on tethered HAP systems by modeling them as PMS with well-defined stages. A comprehensive evaluation is performed for each phase, accounting for potential risks and operational constraints. Furthermore, a numerical example illustrates the reliability assessment methodology, incorporating Markovian techniques to derive key performance indicators and reliability measures for every phase.

Keywords: tHAPs, PMS, Recoverable failures, state-space based approach, Reliability.

1. Introduction

High-altitude platforms (HAPs) are aerial stations positioned between 15 and 50 kilometers above Earth's surface, maintaining a relatively fixed location. Tethered high-altitude platforms (tHAPs) enable prolonged operation by remaining anchored to the ground via a tether, usually positioned at an altitude of 100-150 meters. These platforms receive power through copper cables linked to ground-based energy sources, which sustain both their propulsion systems and onboard equipment. When compared to traditional aircraft and balloons, tHAPs offer significant advantages in terms of affordability, deployment efficiency, upkeep, mobility, and overall operational feasibility.

The development of next generation tHAP systems utilizing unmanned aerial vehicles (UAVs) is actively progressing across the globe. Vishnevsky et al. [10] provide insights into the structural design, system architecture, and technological hurdles of tethered HAPs, drawing from ICS RAS™s expertise in their development and deployment. The study in [11] presents an optimized high voltage conducting tether design that enhances power transmission from ground sources, offering techniques to evaluate wave impedance and determine the required cable configuration. A Markovian framework for power management in lithium-ion battery-supported wireless communication is introduced in [15], accounting for fluctuations in energy demand as battery levels deplete. Strategies for standardization and system unification to improve operational efficiency are explored in [9]. Reliability assessments employing multidimensional and semi-Markov models for failure analysis in tHAPs are discussed in [8, 13]. Additionally, [12] examines key design considerations for advanced tHAP-based telecommunications infrastructure, emphasizing autonomous high-altitude operations, improved navigation precision, and the application of high-frequency resonance-based power transfer techniques.

Due to the absence of comprehensive monographs on the subject, [17] was developed to explore various k-out-of-n models, analytical methodologies, and their applications in assessing the reliability of tethered high-altitude telecommunication systems. One particular application of these models is discussed in [1], where the k-out-of-n: F model was utilized to evaluate the reliability of a flying module within a tethered high-altitude telecommunication platform. An analytical approach for the k-out-of-n: G model under two distinct failure scenarios was introduced in [2]. Additionally, [3] proposed a k-out-of-n system incorporating repair in a hot standby configuration. The study in [4] highlights the crucial role of the tether, composed of multiple parallel wires, in determining the overall reliability of tHAP systems.

tHAP systems function across multiple operational phases, each involving distinct tasks, environmental conditions, and success criteria. Stages such as launch, cruise, and retrieval introduce specific challenges and potential failure risks. Phased Mission Systems (PMSs) progress through successive phases, where each stage has unique performance requirements, and failures in earlier phases can influence subsequent ones. This highlights the critical importance of reliability analysis for complex systems. The interest in studying tHAP systems as phased mission systems (PMSs) is driven by [22], which offers an extensive review of advancements in PMS reliability evaluation and optimization. However, there is still a lack of research applying phased mission modeling to assess the reliability of tHAP systems.

Analytical modeling and simulations serve as essential tools for evaluating the reliability of tHAP systems. In non-repairable PMS, a failure in any phase can lead to mission termination, as in-mission repairs are not feasible [26, 23]. Conversely, repairable PMSs allow certain components to be repaired or replaced, enhancing system resilience [19, 18, 24, 25]. Failures in these systems may occur independently or result from common cause failures (CCFs), where multiple components are affected by a single underlying factor [5, 6, 7]. Additionally, functional dependence (FDEP) introduces further complexity, as the failure of one component can trigger the malfunction of others [21].

The paper is structured as follows. Section 2 describes the system componets and the nature of the mission. Section 3 includes state-space-oriented reliability analysis for tHAP systems, followed by numerical illustrations in Section 4. Finally, Section 5 provides the conclusion and future works.

2. System Description

The performance of a tHAP system relies on the integrity of its key components. A power source failure leads to a total system shutdown, disabling the rotors, communication, camera, and tether control, ultimately resulting in failure across all phases. Loss of communication isolates the HAP, preventing control, data transmission, and real-time monitoring, which directly impacts navigation and surveillance. If a rotor malfunctions during deployment, altitude control is lost, disrupting the launch sequence. In the operational phase, a camera failure hampers monitoring,

reducing mission effectiveness. A tether failure can destabilize or completely detach the HAP, jeopardizing both launch and operational phases, and potentially leading to loss of control or a crash. The impact of these failures varies by phase, but each poses a significant risk to overall mission success.

A tHAP system consists of an aerial platform linked to a Ground Control Station (GCS) via a tether, which facilitates both power and data transmission. Figure 1 illustrates this architecture, where onboard sensors and ground-based anchors monitor navigation parameters, while stabilization circuits dynamically adjust the platform™s position. Power is supplied from a ground-based source, and a smart winch mechanism controls the tether™s length to ensure optimal operation.

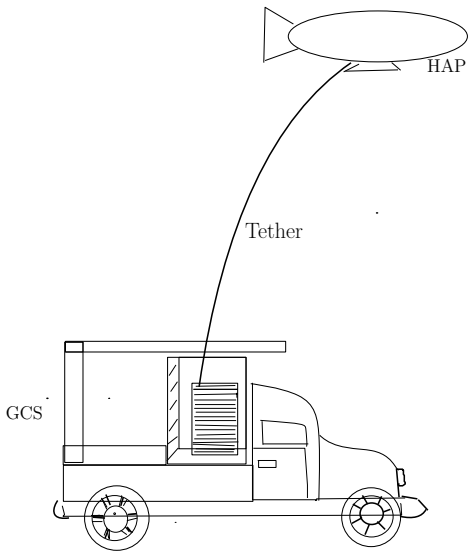


Figure 1: *A tHAP system with its major components*

A tHAP system is a specialized form of high-altitude platform that stays physically linked to the ground through a tether, serving purposes such as stability, power delivery, and data transmission. When analyzed as a phased mission system (PMS), its operation is divided into sequential phases, each demanding specific strategies for mission success. The system's operational reliability hinges on three key phases: launch, operational, and retrieval, all of which are sustained by critical components, including the Ground Control Station (GCS), the tether, and the aerial subsystem. While failures in the GCS and aerial subsystem can often be addressed through recovery mechanisms, any malfunction of the tether is considered irrecoverable. This is crucial because the tether not only ensures the physical connection and stability of the aerial subsystem but also facilitates power and data transmission. A failure in the tether could lead to severe consequences, compromising the system™s overall functionality and safety.

A tHAP System Mission phases can be classified as follows:

1. Ascend(Phase 1): The HAP is deployed and ascends to its designated operational altitude. Managing tether tension and length, ensuring smooth ascent without entanglement, and addressing environmental factors such as wind and weather conditions.

2. Primary task(Phase 2): The HAP performs its primary mission, which may involve surveillance, communication relay, or environmental monitoring. Maintaining uninterrupted power and data transmission via the tether, managing onboard payloads, and dynamically adjusting to environmental or mission-related changes.

3. Descend (Phase 3): The HAP is safely brought back to the ground. Ensuring a controlled descent, preventing tether entanglement or structural damage, and achieving a safe landing while preserving both the platform and the tether.

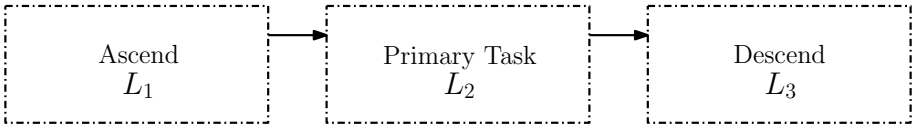


Figure 2: *Phases of a tHAP system*

3. Reliability Analysis Using CTMC Model

The reliability of a tHAP system, structured as a PMS, could be analyzed using a Continuous-Time Markov Chain (CTMC). This method characterizes system states, encompassing operational phases, failures, and repairs, with transitions governed by failure and repair rates. Distinct mission phases impose specific conditions that affect state transitions. The CTMC framework models the failure behavior of essential components such as the tether, communication modules, and power units. By leveraging state-transition matrices, it evaluates both steady-state and transient reliability measures, pinpointing critical phases and informing design enhancements and maintenance strategies.

The system is composed of three essential components and operates through three distinct mission phases. Phase transitions are assumed to be instantaneous, and all subsystems begin in an optimal state. The key components include the Ground Control Station (GCS) (C_1), the tether (C_2), and the aerial unit (C_3). Each of these components plays a vital role, with their significance and susceptibility varying across different mission phases. Failures could be distinguished as follows:

- Type I : Recoverable through repairs, does not cause mission failure.
- Type II : Unrecoverable, leading to mission failure.

Each component can exist in one of three states:

- 2: Operational
- 1: Recoverable (with Type I failure)
- 0: Failed (with Type II failure)

Components C_1 (GCS) and C_3 (aerial unit) can exist in any of three possible states, whereas component C_2 (tether) has only two states: functional (2) or failed (1). Repairs, when feasible, can be conducted while the system remains operational, and upon completion, each repaired component is restored to an "as good as new" condition. The fault tree representation of the system is illustrated in Figure 3. Here, C_j^m represents the state of component j, where $j \in \{1, 2, 3\}$ and $m \in \{0, 1, 2\}$.

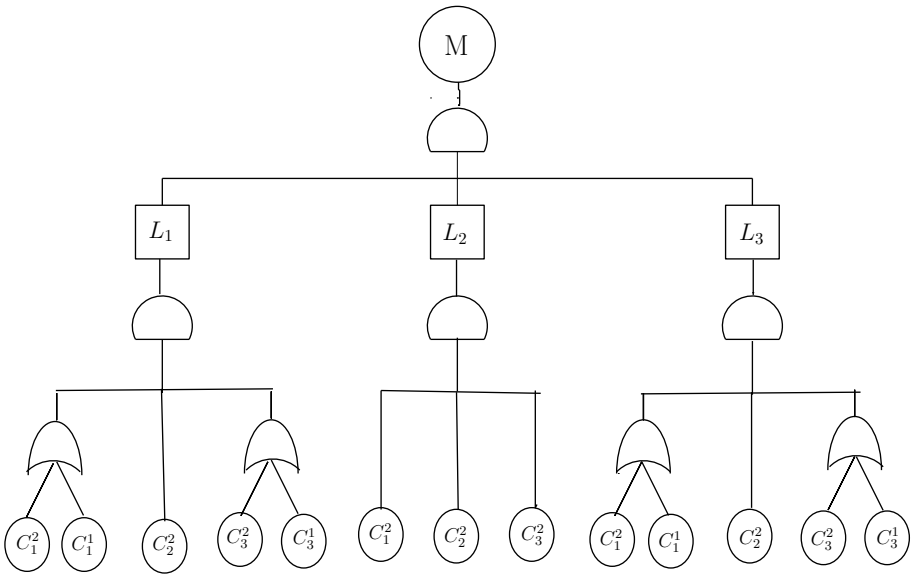


Figure 3: *Fault tree representation of the tHAP Mission*

The system's state at any given time t , where $0 \leq t \leq T$, is expressed as $(C_1(t), C_2(t), C_3(t))$. Here, $C_1(t)$ and $C_3(t)$ can assume values from $\{0, 1, 2\}$, whereas $C_2(t)$ is restricted to two states: 2 (Operational) or 0 (failed). As the workload of each subsystem may shift between phases, failure and repair rates are subject to variation. The system can exist in the following possible states:

Table 1: *List of possible states for the underlying stochastic process*

Perfect	**Faulty but operational**	**Failure**
$S_1 = (2,2,2)$	$S_2 = (1,2,2)$	$S_5 = (1,0,2)$
	$S_3 = (2,2,1)$	$S_6 = (1,2,0)$
	$S_4 = (1,2,1)$	$S_7 = (0,2,2)$
		$S_8 = (2,0,2)$
		$S_9 = (2,2,0)$
		$S_{10} = (0,2,1)$
		$S_{11} = (2,0,1)$
		$S_{12} = (1,0,1)$

The possible state transitions remain consistent across all phases, as shown in Figure 4. The mission comprises three consecutive phases, each defined by distinct success conditions. Phase L_1 always initiates with the system in state S_1. For this phase to be deemed successful, it must end in one of the states S_1, S_2, S_3, or S_4. Subsequently, Phase L_2 starts from the final successful state of Phase L_1. To ensure a smooth transition to Phase L_3, Phase L_2 should ideally end in state S_1. Since Phase L_2 serves as the primary operational phase, where the main task is executed, all type I faults must be cleared, and all subsystems must be fully functional before its completion. If Phase L_2 ends in S_2, S_3, or S_4, the system can still transition to Phase L_3, but the mission will be classified as a failure. In Phase L_3, mission success is determined by completing the phase, even if minor recoverable errors remain. This indicates that the system retains sufficient reliability to achieve overall mission success despite minor issues.

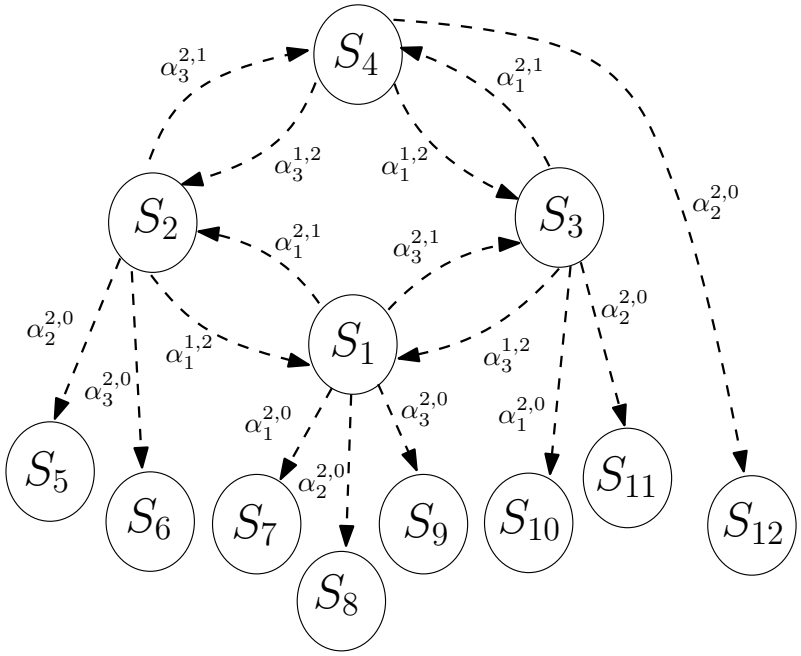


Figure 4: *State transition diagram for the underlying CTMC*

Table 2: *Initial and final states for the phases*

	Phase L_1	Phase L_2	Phase L_3
Initial states	S_1	S_1, S_2, S_3, S_4	S_1
Final states indicating phase success	S_1, S_2, S_3, S_4	S_1	S_1, S_2, S_3, S_4

When analyzing the reliability of tHAP systems as a phased mission system (PMS) where the system undergoes different operational phases with distinct reliability requirements and configurations, the Markov approach, particularly the use of CTMC, proves to be highly effective. This method captures system deterioration, repair processes, and transitions between operational modes across different phases. By specifying failure and repair rates for each component and phase, the CTMC framework enables the computation of system survival probabilities.

Each component is assumed to fail according to an exponential distribution, implying that component failure rates remain constant over time. The failure and repair rates of the components are treated as independent random variables, both governed by an exponential distribution. For component C_j, the transition rate from state m to state n is denoted as $\alpha_j^{m,n}$, where $j \in \{1, 2, 3\}$ and $m, n \in \{0, 1, 2\}$. It is important to note that a component's failure rate may vary across different phases due to fluctuations in workload and operational demands.

The state of the system at any time t during a Phase L_i is given by the process

$$\{(C_1^i(t), C_2^i(t), C_3^i(t), T_1 + ... + T_{i-1} \leq t \leq T_1 + ... + T_i\}$$

, where each $C_j^i(t)$ denotes the level of component C_j and takes values in $\{0, 1, 2\}$ depending on the assumptions for the components in respective phases. The infinitesimal generator matrix for the CTMC in each Phase L_i is denoted by $\mathbf{Q_i}$.

3.0.1 Phase L_1:

The mission is structured into three phases, each lasting T_1, T_2, and T_3 hours, respectively, with a total duration of T hours. It begins with Phase L_1, where all three components are fully operational. The initial state probabilities for Phase L_1 are given by $[1, 0, \ldots, 0]$.

The state equations governing the Markov model follow the forward Kolmogorov equation, expressed in matrix form as:

$$\mathbf{q_1}'(t) = \mathbf{q_1}(t).\mathbf{Q_1} \tag{1}$$

where $\mathbf{q_1}(t) = (q_1^1(t), q_2^1(t), \ldots, q_{12}^1(t))$ represents the state probability vector in Phase L_1. Specifically, $q_k^1(t)$, for $k \in \{1, 2, \ldots, 12\}$, denotes the probability of the system being in state S_k at any time $t \in [0, T_1]$. The term $\mathbf{q_1}'(t)$ represents the time derivative of $\mathbf{q_1}(t)$. The matrix $\mathbf{Q_1}$ is the infinitesimal generator matrix, which defines the transition rates between states in Phase L_1, as illustrated in Figure 4.

$$\mathbf{Q_1} = \begin{bmatrix} X_1 & X_2 \\ \mathbf{0} & \mathbf{0} \end{bmatrix}$$

where $\mathbf{X_1}$ contains the transition rates among the transient states, while $\mathbf{X_2}$ represents the transition rates to the absorbing states. The remaining two blocks are zero matrices of appropriate dimensions, indicating that no transitions occur from the absorbing states.

$$\mathbf{X_1} = \begin{pmatrix} a_1 & \alpha_{1,1}^{2,1} & \alpha_{1,3}^{2,1} & 0 \\ \alpha_{1,1}^{1,2} & b_1 & 0 & \alpha_{1,3}^{2,1} \\ \alpha_{1,3}^{1,2} & 0 & c_1 & \alpha_{1,1}^{2,1} \\ 0 & \alpha_{1,3}^{1,2} & \alpha_{1,1}^{1,2} & d_1 \end{pmatrix}_{4\times 4}$$

$$\mathbf{X_2} = \begin{pmatrix} 0 & 0 & \alpha_{1,1}^{2,0} & \alpha_{1,2}^{2,0} & \alpha_{1,3}^{2,0} & 0 & 0 & 0 \\ \alpha_{1,2}^{2,0} & \alpha_{1,3}^{2,0} & 0 & 0 & 0 & 0 & 0 & 0 \\ 0 & 0 & 0 & 0 & 0 & \alpha_{1,1}^{2,0} & \alpha_{1,2}^{2,0} & 0 \\ 0 & 0 & 0 & 0 & 0 & 0 & 0 & \alpha_{1,2}^{2,0} \end{pmatrix}_{4\times 8}$$

Note that the entries a_1, b_1, c_1 and d_1 of the matrix $\mathbf{X_1}$ are such that each row sum is zero.

To compute the state probability vector $\mathbf{q_1}(t)$, the system of differential equations in (1) is solved using the initial state probabilities $[1, 0, \ldots, 0]$. The state probabilities at the end of Phase L_1 (i.e., at mission time T_1 hours) are given by $(q_1^1(T_1), q_2^1(T_1), \ldots, q_{12}^1(T_1))$. With these probabilities, all reliability metrics of the multi-state system can be effectively determined. The system is considered reliable at the conclusion of Phase L_1 if it resides in any of the states S_1, S_2, S_3 or S_4. Consequently, the system reliability at the end of Phase L_1 , represented as $R_{L_1}(T_1)$, is given by

$$R_{L_1}(T_1) = q_1^1(T_1) + q_2^1(T_1) + q_3^1(T_1) + q_4^1(T_1). \tag{2}$$

3.0.2 Phase L_2:

In a multi-phase system, the transition between phases is governed by the final-state occupation probabilities of the preceding phase, which act as the initial-state probabilities for the next. As Phase L_2 begins, the system is in one of the states S_1, S_2, or S_3. To construct the Markov chain for Phase L_2, only the relevant state transitions for this phase are considered. Utilizing the final-state probabilities of Phase L_1, i.e., $(q_1^1(T_1), q_2^1(T_1), \ldots, q_{12}^1(T_1))$, to establish the initial probabilities, the equation is given by

$$\mathbf{q_2}'(t) = \mathbf{q_2}(t).\mathbf{Q_2} \tag{3}$$

for Phase L_2 is computed, yielding the system state probability vector $\mathbf{q_2}(t) = (q_1^2(t), q_2^2(t), \ldots q_{12}^2(t))$ incorporating the state probabilities $q_k^1(t), k \in \{1, 2, \ldots, 12\}$ in time $[T_1, T_1 + T_2]$.

$$\mathbf{Q_2} = \begin{bmatrix} \mathbf{Y_1} & \mathbf{Y_2} \\ \mathbf{0_1} & \mathbf{0_2} \end{bmatrix}$$

$$\mathbf{Y_1} = \begin{pmatrix} a_2 & \alpha_{2,1}^{2,1} & \alpha_{2,3}^{2,1} & 0 \\ \alpha_{2,1}^{1,2} & b_2 & 0 & \alpha_{2,3}^{2,1} \\ \alpha_{2,3}^{1,2} & 0 & c_2 & \alpha_{2,1}^{2,1} \\ 0 & \alpha_{2,3}^{1,2} & \alpha_{2,1}^{1,2} & d_2 \end{pmatrix}$$

$$\mathbf{Y_2} = \begin{pmatrix} 0 & 0 & \alpha_{2,1}^{2,0} & \alpha_{2,2}^{2,0} & \alpha_{2,3}^{2,0} & 0 & 0 & 0 \\ \alpha_{2,2}^{2,0} & \alpha_{2,3}^{2,0} & 0 & 0 & 0 & 0 & 0 & 0 \\ 0 & 0 & 0 & 0 & 0 & \alpha_{2,1}^{2,0} & \alpha_{2,2}^{2,0} & 0 \\ 0 & 0 & 0 & 0 & 0 & 0 & 0 & \alpha_{2,2}^{2,0} \end{pmatrix}_{4\times 8}$$

Note that the entries a_2, b_2, c_2 and d_2 of the matrix $\mathbf{Y_1}$ are such that each row sum is zero.

Upon completing Phase L_2 of duration T_2, the state probabilities $\mathbf{q_2}(T_1+T_2) = (q_1^2(T_1+T_2), q_2^2(T_1+T_2), \ldots, q_{12}^2(T_1+T_2))$ are calculated. Based on these state probabilities, the system reliability, represented as $R_{L_2}(T_1+T_2)$, is given by

$$R_{L_2}(T_1+T_2) = q_1^2(T_1+T_2). \tag{4}$$

3.0.3 Phase L_3:

As the mission advances to Phase L_3, its duration is represented as T_3, while the overall mission duration is given by $T\ (= T_1+T_2+T_3)$. The initial state probability vector for Phase L_3 is derived from the final state probability vector of Phase L_2, i.e., $\mathbf{q_2}(T_1+T_2)$. Using $\mathbf{q_2}(T_1+T_2)$, the equation is solved to compute the probabilities of various system states.

$$\mathbf{q_3}'(t) = \mathbf{q_3}(t).\mathbf{Q_3} \tag{5}$$

to obtain state probability vector, $\mathbf{q_3}(t) = (q_1^3(t), q_2^3(t), \ldots q_{12}^3(t)), T_1+T_2 \le t \le T$, for Phase L_3.

$$\mathbf{Q_3} = \begin{bmatrix} \mathbf{Z_1} & \mathbf{Z_2} \\ \mathbf{0_1} & \mathbf{0_2} \end{bmatrix}$$

$$\mathbf{Z_1} = \begin{pmatrix} a_3 & \alpha_{3,1}^{2,1} & \alpha_{3,3}^{2,1} & 0 \\ \alpha_{3,1}^{1,2} & b_3 & 0 & \alpha_{3,3}^{2,1} \\ \alpha_{3,3}^{1,2} & 0 & c_3 & \alpha_{3,1}^{2,1} \\ 0 & \alpha_{3,3}^{1,2} & \alpha_{3,1}^{1,2} & d_3 \end{pmatrix}$$

$$\mathbf{Z_2} = \begin{pmatrix} 0 & 0 & \alpha_{3,1}^{2,0} & \alpha_{3,2}^{2,0} & \alpha_{3,3}^{2,0} & 0 & 0 & 0 \\ \alpha_{3,2}^{2,0} & \alpha_{3,3}^{2,0} & 0 & 0 & 0 & 0 & 0 & 0 \\ 0 & 0 & 0 & 0 & 0 & \alpha_{3,1}^{2,0} & \alpha_{3,2}^{2,0} & 0 \\ 0 & 0 & 0 & 0 & 0 & 0 & 0 & \alpha_{3,2}^{2,0} \end{pmatrix}_{4\times 8}$$

Note that the entries a_3, b_3, c_3 and d_3 of the matrix $\mathbf{Z_1}$ are such that each row sum is zero.

During Phase L_3, the probability of the system being in each possible state at any time $t \in [T_1+T_2, T]$ is represented by the state probabilities $(q_1^3(t), q_2^3(t), \ldots, q_{12}^3(t))$. At the end of Phase L_3, the system's reliability, represented as $R_{L_3}(T)$, corresponds to the total system reliability, $R_{\text{sys}}(T)$. This value is derived from the state probabilities and is expressed as

$$R_{\text{sys}}(T) = R_{L_3}(T) = q_1^3(T) + q_2^3(T) + q_3^3(T) + q_4^3(T). \tag{6}$$

4. Numerical Illustrations

A numerical evaluation of the reliability of a tHAP system, modeled as a PMS, is conducted in this section. Each phase of the mission introduces distinct operational requirements and reliability challenges due to varying environmental conditions and performance criteria. The numerical illustration of the tHAP system using CTMC provides a comprehensive framework for analyzing its reliability. The CTMC model facilitates the examination of system state transitions under the assumption of exponentially distributed sojourn times.

The mission is assumed to be completed in 24hrs, where Phase L_1 takes 3hrs, Phase L_2 is planned for 19hrs, and Phase L_3 may take 2hrs, .i.e., $T = 24, T_1 = 3, T_2 = 19$, and $T_3 = 2$.

4.1. CTMC Approach

The failure and repair rates of each component in each Phase have been assumed as follows:

Table 3: *Transition rates for different phases*

	$\alpha_1^{1,2}$	$\alpha_3^{1,2}$	$\alpha_1^{2,1}$	$\alpha_3^{2,1}$	$\alpha_1^{2,0}$	$\alpha_2^{2,0}$	$\alpha_3^{2,0}$
$\mathbf{L_1}$	0.3	0.4	0.07	0.08	0.02	0.01	0.01
$\mathbf{L_2}$	0.5	0.6	0.06	0.05	0.006	0.006	0.007
$\mathbf{L_3}$	0.3	0.3	0.07	0.08	0.02	0.02	0.02

4.1.1 Phase L_1

As the state transitions diagram 4, and Table 1 indicates, the system initiates functioning in Phase L_1 with the probability vector $[1, 0, \ldots, 0]$ at time $t = 0$. Solving (1) for Phase L_1, the probability vector $\mathbf{q_1}(t)$ is obtained which describes the system as well as the components' state during the time span $[0, 3]$. The reliability curves are plotted to understand the effect of failure rates of the components, GCS($\alpha_{1,1}^{2,0}$), tether($\alpha_{1,2}^{2,0}$), and AS($\alpha_{1,3}^{2,0}$) in Figure 5.

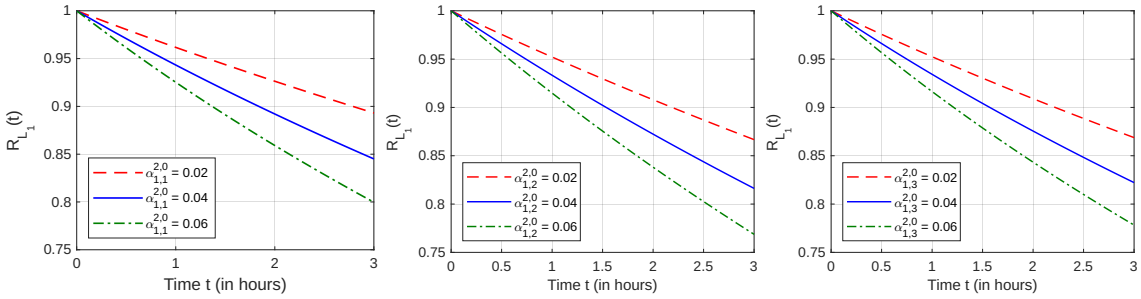


Figure 5: *Effect of failure rates of the components on Reliability(Phase L_1)*

4.1.2 Phase L_2

Phase L_2 initiates immediately after the successful completion of Phase L_1. This phase is longer since the main task of the system is completed during this phase. The initial probability state vector for this Phase is given by $\mathbf{q_1}(3)$. Solving 3 for Phase L_2, the state probabilities vector, $\mathbf{q_2}(t), 3 \leq t \leq 22$, is obtained. The effects of failure rates and repair rates of the components on reliability are observed in Figures 6 and 7.

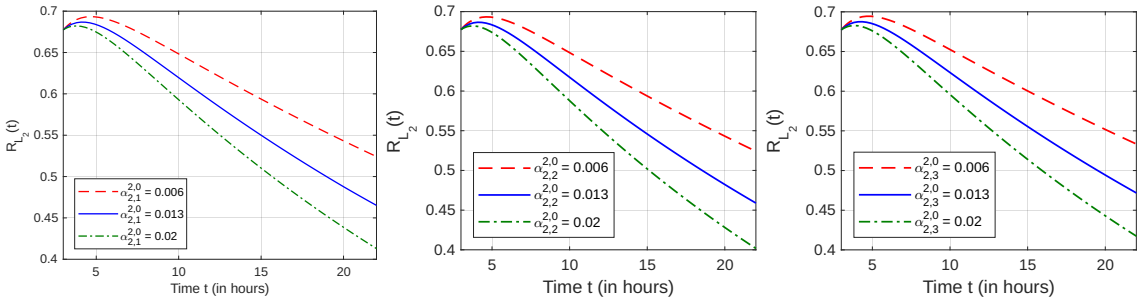


Figure 6: *Effect of failure rates of the components on Reliability(Phase L_2)*

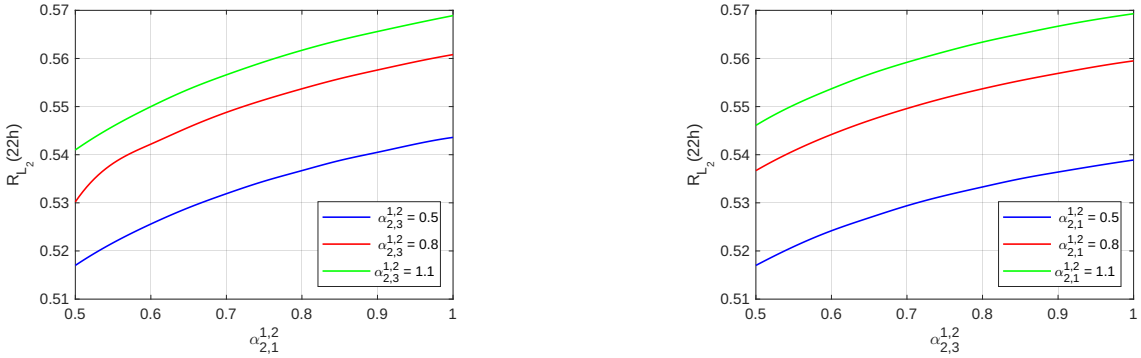


Figure 7: *Effect of repair rates of the components on Reliability(Phase L_2)*

4.1.3 Phase L_3

As soon as Phase L_2 is successfully finished, Phase L_3 begins. The mission's last step is this one. $\mathbf{q_2}(22)$ is the initial probability state vector for this Phase. The state probabilities vector, $\mathbf{q_3}(t), 22 \leq t \leq 24$, is produced by solving 5 for Phase L_3. Figures 8 show how the components of failure rates affect reliability.

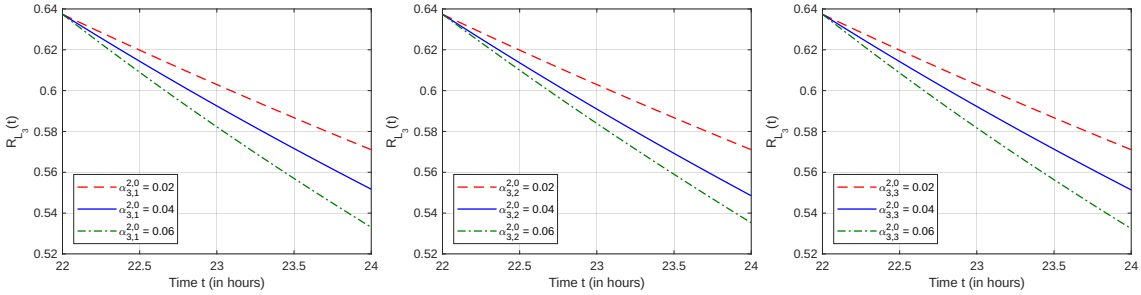


Figure 8: *Effect of failure rates of the components on Reliability(Phase L_1)*

4.1.4 Component Reliability

As the reliability of the tethered HAP system could be measured during each Phase, the reliability of each of the three components can also be analyzed. The graphical analysis of these phases in 12 clearly shows a decreasing trend in component reliability, highlighting the impact of operational duration and stressing the need for proactive maintenance and reliability improvements to ensure mission success.

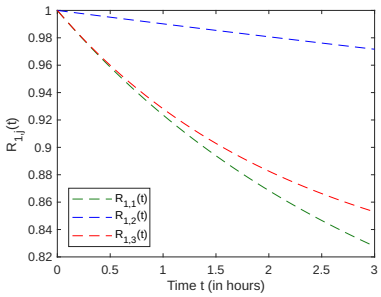


Figure 9: *Phase* L_1

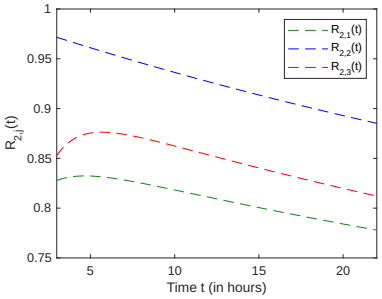


Figure 10: *Phase* L_2

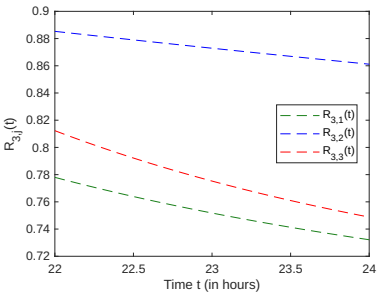


Figure 11: *Phase* L_3

Figure 12: *Reliability of the subsystems during Phase* L_1, L_2 *and* L_3

5. Summary and Possible Extensions

This study conducts an in-depth reliability assessment of a tHAP system, modeled as a PMS. Utilizing a state-spaced Markov model, the analysis considers evolving mission demands and operational conditions across distinct phases. By capturing system breakdowns and state transitions effectively, the model facilitates the evaluation of phase-specific failure probabilities and downtime. Identifying critical phases with elevated risks helps optimize maintenance strategies and redundancy measures, ultimately improving reliability for non-terrestrial applications.

For future research, Monte Carlo simulations will be integrated to enhance probabilistic accuracy. Additionally, a Semi-Markov Process (SMP) approach will be investigated to model phase transitions with arbitrary time distributions, offering a more realistic depiction of mission dynamics. Incorporating real operational data will further refine model parameters, enabling dynamic updates and improved reliability predictions.

References

[1] Vishnevsky, V., Selvamuthu, D., Rykov, V., Kozyrev, D., and Ivanova, N. (2022). Reliability modeling of a flight module of a tethered high-altitude telecommunication platform. In Proceedings of *the 2022 International Conference on Information, Control, and Communication Technologies (ICCT)*, pages 1–6.

[2] Ivanova, N. and Vishnevsky, V. (2021). Application of k-out-of-n: G system and machine learning techniques on reliability analysis of tethered unmanned aerial vehicle. In *International Conference on Information Technologies and Mathematical Modelling*, pages 117–130. Springer.

[3] Ivanova, N. (2020). Modeling and simulation of reliability function of a k-out-of-n: F system. In *International Conference on Distributed Computer and Communication Networks*, pages 271–285. Springer.

[4] Selvamuthu, D., Sivam, A. H., Raj, R., and Vishnevsky, V. (2023). Study of reliability of the on-tether subsystem of a tethered high-altitude unmanned telecommunication platform. *Reliability: Theory & Applications*, 18(1 (72)):172–178.

[5] Xing, L., Shrestha, A., Meshkat, L., and Wang, W. (2009). Incorporating common-cause failures into the modular hierarchical systems analysis. *IEEE Transactions on Reliability*, 58(1):10–19. IEEE.

[6] Xing, L. (2007). Reliability evaluation of phased-mission systems with imperfect fault coverage and common-cause failures. *IEEE Transactions on Reliability*, 56(1):58–68. IEEE.

[7] Xing, L. and Levitin, G. (2013). BDD-based reliability evaluation of phased-mission systems with internal/external common-cause failures. *Reliability Engineering & System Safety*, 112:145–153. Elsevier.

[8] Kozyrev, D. V., Phuong, N. D., Houankpo, H. G. K., and Sokolov, A. (2019). Reliability evaluation of a hexacopter-based flight module of a tethered unmanned high-altitude platform. In *Distributed Computer and Communication Networks*, pages 646–656. Springer International Publishing, Cham.

[9] Perelomov, V. N., Myrova, L. O., Aminev, D. A., and Kozyrev, D. V. (2018). Efficiency enhancement of tethered high altitude communication platforms based on their hardware-software unification. In *Distributed Computer and Communication Networks*, pages 184–200. Springer International Publishing, Cham.

[10] Vishnevsky, V. and Meshcheryakov, R. (2019). Experience of developing a multifunctional tethered high-altitude unmanned platform of long-term operation. In *Interactive Collaborative Robotics: 4th International Conference, ICR 2019, Istanbul, Turkey, August 20–25, 2019, Proceedings 4*, pages 236–244. Springer.

[11] Vishnevsky, V., Tereschenko, B., Tumchenok, D., and Shirvanyan, A. (2017). Optimal method for uplink transfer of power and the design of high-voltage cable for tethered high-altitude unmanned telecommunication platforms. In *Distributed Computer and Communication Networks: 20th International Conference, DCCN 2017, Moscow, Russia, September 25–29, 2017, Proceedings*, pages 240–247. Springer.

[12] Vishnevsky, V. M., Efrosinin, D. V., and Krishnamoorthy, A. (2018). Principles of construction of mobile and stationary tethered high-altitude unmanned telecommunication platforms of long-term operation. In *Distributed Computer and Communication Networks: 21st International Conference, DCCN 2018, Moscow, Russia, September 17–21, 2018, Proceedings 21*, pages 561–569. Springer.

[13] Mittal, N., Ivanova, N., Jain, V., and Vishnevsky, V. (2024). Reliability and availability analysis of high-altitude platform stations through semi-Markov modeling. *Reliability Engineering & System Safety*, 110419. Elsevier.

[14] Belmekki, B. E. Y. and Alouini, M.-S. (2022). Unleashing the potential of networked tethered flying platforms: Prospects, challenges, and applications. *IEEE Open Journal of Vehicular Technology*, 3:278–320. IEEE.

[15] Jain, V., Vishnevsky, V. M., Selvamuthu, D., and Raj, R. (2022). Analysis of power management in a tethered high altitude platform using MAP/PH[3]/1 retrial queueing model. In *International Conference on Distributed Computer and Communication Networks*, pages 218–230. Springer.

[16] Selvamuthu, D., Jain, V., and Raj, R. (2022). Performance analysis for tethered HAP systems: An analytical approach. In *International Conference on Distributed Computer and Communication Networks*, pages 205–217. Springer.

[17] Vishnevsky, V. M., Selvamuthu, D., Rykov, V. V., Kozyrev, D. V., Ivanova, N., and Krishnamoorthy, A. (2024). *Reliability Assessment of Tethered High-Altitude Unmanned Telecommunication Platforms: k-Out-of-n Reliability Models and Applications*. Springer Nature.

[18] Li, X.-Y., Huang, H.-Z., and Li, Y.-F. (2018). Reliability analysis of phased mission system with non-exponential and partially repairable components. *Reliability Engineering & System Safety*, 175:119–127. Elsevier.

[19] Peng, R., Wu, D., Xiao, H., Xing, L., and Gao, K. (2019). Redundancy versus protection for a non-reparable phased-mission system subject to external impacts. *Reliability Engineering & System Safety*, 191:106556. Elsevier.

[20] Tafazoli, M. (2009). A study of on-orbit spacecraft failures. *Acta Astronautica*, 64(2–3):195–205. Elsevier.

[21] Wang, C., Xing, L., Peng, R., and Pan, Z. (2017). Competing failure analysis in phased-mission systems with multiple functional dependence groups. *Reliability Engineering & System Safety*, 164:24–33. Elsevier.

[22] Wu, D., Peng, R., and Xing, L. (2019). Recent advances on reliability of phased mission systems. *Stochastic Models in Reliability, Network Security and System Safety: Essays Dedicated to Professor Jinhua Cao on the Occasion of His 80th Birthday 1*, pages 19–43. Springer.

[23] Li, X.-Y., Xiong, X., Guo, J., Huang, H.-Z., and Li, X. (2022). Reliability assessment of non-repairable multi-state phased mission systems with backup missions. *Reliability Engineering & System Safety*, 223:108462. Elsevier.

[24] Wang, D. and Trivedi, K. S. (2007). Reliability analysis of phased-mission system with independent component repairs. *IEEE Transactions on Reliability*, 56(3):540–551. IEEE.

[25] Wu, B. and Cui, L. (2020). Reliability of repairable multi-state two-phase mission systems with finite number of phase switches. *Applied Mathematical Modelling*, 77:1229–1241. Elsevier.

[26] Mo, Y., Xing, L., and Amari, S. V. (2014). A multiple-valued decision diagram based method for efficient reliability analysis of non-repairable phased-mission systems. *IEEE Transactions on Reliability*, 63(1):320–330. IEEE.

RT&A, No 4 (89)
Volume 20, December 2025

A SURVEY ON IMAGE GENERATION TECHNIQUES: PARADIGMS, EVOLUTION, DEEP LEARNING ADVANCEMENTS AND FUTURE DIRECTIONS

Nrupesh Shah[1], Dr. Sanjay Patel[2]

•

[1]Research Scholar, GTU, Ahmedabad.
nrupesh_shah@gecg28.ac.in
[2]Associate Professor, GEC, Gandhinagar.
sp_patel1@gtu.edu.in

Abstract

Image generation techniques have witnessed significant advancements in recent years. Classification of Image Generation Approaches is an important topic in today's rapidly advancing technological landscape. We will examine primary approaches in this field: Generative Adversarial Networks (GANs), Variational Autoencoders (VAEs), Stable Diffusion Processes (SDPs) and other similar approaches. GANs, VAEs and SDPs have shown remarkable performance in terms of image quality, as well as scalability and efficiency. This survey focuses onto seminal works that have shaped the field of image generation, spanning Generative Adversarial Networks (GANs), Variational Autoencoders (VAEs), Autoregressive Models, Flow based image generation as well as diffusion-based approaches, and also compares various evaluation metrices in the field. We also provide a list of challenges in this field.

Keywords: Image generation, Image synthesis, text-to-image, image-to-image, GANs, VAEs, Stable diffusion, Autoregressive Models, Flow Based Image generation models, Generative Adversarial Networks, Variational Autoencoders.

I. Introduction

Image generation is the task of synthesizing new images from scratch. This is a challenging task, as images are high-dimensional data and it is difficult to generate realistic and diverse images. However, recent advances in machine learning have led to development of various powerful image generation techniques. Image generation has found applications in diverse fields such as art, design, entertainment, and medical imaging. Over the years, various strategies have been developed to create images, each with its own set of advantages and challenges.

Image generation is a rapidly evolving field, and new techniques are being developed all the time. This review paper will provide a comprehensive overview of the state-of-the-art in image generation techniques. The paper will discuss the different types of image generation techniques, their strengths and weaknesses, and their applications. There have already been some surveys/reviews carried out in the field of image generation. Each of them has contributed greatly to the field. For example, a paper by Trevisan de Souza et el. [1] specifically reviews Generative Adversarial Networks (GANs) for image generation. It explains the fundamental architecture of

GANs, involving a generator and a discriminator in adversarial training to create realistic, novel samples. The paper focuses on the applications of GANs in image processing and synthesis. It discusses how challenges associated with GANs, such as mode collapse, stability, and convergence, have been addressed. The review covers the basics and notable GAN architectures, detailing techniques used in various image-based applications including image synthesis, image enhancement, image-to-image translation, image manipulation, style transfer, super resolution, and image repair. It also touches upon using GANs for text-to-image synthesis. The paper is intended as a guide for those new to studying GANs.

Another review by Singh et el.[2] focuses *specifically* on the applications of Generative Adversarial Networks (GANs) in the domain of medical imaging. It describes GANs as unsupervised deep learning tools that are particularly useful for analysing multimodal medical imaging data. The paper highlights the utility of GANs in generating realistic medical images and annotations for tasks like data augmentation, image registration, reconstruction, and image-to-image translation within the medical field. It reviews popular GAN variants, such as DCGAN, LAPGAN, pix2pix, CycleGAN, and UNIT, and how they are applied in medical imaging. The survey covers applications in medical image reconstruction and synthesis across different modalities. It notes the significant rise in GAN studies in medical imaging, particularly focusing on cross-modality synthesis and MRI image synthesis, and discusses future research directions.

Whereas, Elasri et el. [3] provides a comprehensive overview of existing image generation tasks, focusing on creating images from various data types beyond just other images. It discusses generating images from text, sketch, scene graphs, object layouts, and images themselves. The survey highlights how deep learning, particularly GANs, has made generating new, realistic images with high quality possible. It categorises methods based on the nature of adopted architectures, the type of input data used, and the main objective. The paper presents a taxonomy of approaches including image-to-image translation, sketch-to-image translation, conditional image generation, text-to-image generation, and more. It also details public datasets and evaluation metrics used in the field, offering a comparison of performance for significant methods. Current challenges facing image generation are also presented. The paper notes that GANs and conditional GANs (cGANs) are commonly used architectures for conditional image generation approaches.

There may be some overlap between our review and others work but our main and unique contributions are summarized as follows: Diverging from prior surveys, this review provides a focused examination of deep learning's role in image generation. We trace the developmental trajectory of these models, offering a comparative analysis of their architectures, core principles, and diverse applications. Additionally, we delve into available evaluation metrics, identify present limitations, and outline future directions, incorporating the latest advancements in the field.

I. Applications of Image Generation in the field of Reliability Engineering

While image generation techniques might seem distant from reliability engineering at first glance, there are several ways this paper (or the broader field it surveys) could be related or contribute:

1. **Synthetic Data Generation for Testing and Validation:** Many modern systems, especially autonomous vehicles, robotics, and industrial automation, heavily rely on AI for tasks like object recognition, anomaly detection, and predictive maintenance. Training and validating these AI models require vast amounts of data. Image generation techniques, particularly those using GANs (Generative Adversarial Networks) or VAEs (Variational Autoencoders) discussed in the paper, can generate synthetic images that mimic real-world scenarios.

   In reliability engineering, rare events (e.g., specific types of failures, unusual

operating conditions) are often critical but difficult to capture sufficient real data for. Image generation can create synthetic data for these rare events, allowing for more robust testing and training of models designed to detect or predict them. This improves the reliability of the system's performance under diverse and challenging circumstances.

Synthetic images can be used for data augmentation, making AI models more robust to variations in input. This directly contributes to the reliability of AI systems, as they are less likely to fail when encountering slightly different or noisy data.

2. **Visual Inspection and Quality Control:** Image generation can help train systems for automated visual inspection in manufacturing and quality control. By generating images of "normal" products and various types of defects (even rare ones), the survey's discussed techniques can lead to more reliable automated inspection systems that reduce human error and improve product reliability.

   In some cases, visual cues (e.g., cracks, wear and tear patterns) are crucial for predictive maintenance. Image generation can create synthetic deterioration patterns, allowing models to be trained to reliably identify early signs of failure, thus improving equipment uptime and reliability.
3. **Digital Twins and Simulation:** In the context of digital twins, accurate and realistic visual representations of physical assets are important for monitoring, analysis, and simulation. Advanced image generation techniques can contribute to creating highly realistic digital twins, which in turn can be used for reliability analysis and what-if scenarios without impacting the physical asset. This can help in predicting failures and optimizing maintenance strategies.
4. **Security and Tampering Detection:** While less direct, the advancements in image generation also bring challenges related to deepfakes and manipulated images. Understanding these generation techniques (as surveyed in the paper) is crucial for developing robust and reliable methods to detect forged or tampered images, which can be critical for maintaining the integrity of data used in reliability assessments or incident investigations.

In essence, the paper on image generation techniques contributes to reliability engineering by enabling the creation of synthetic, yet realistic, data that can be used to:

- Improve the reliability of AI-systems with better training and validation.
- Enhance automated inspection and quality control processes.
- Support predictive maintenance by simulating various fault conditions.
- Facilitate more comprehensive digital twin environments for reliability analysis.

By providing a comprehensive overview of the state-of-the-art in image generation, the paper equips researchers and engineers in reliability with knowledge of powerful tools to address data scarcity, improve model robustness, and ultimately build more reliable systems.

II. Historical Overview of Image Generation

In recent years, there has been a sudden increase of interest in image generation techniques. This is due to the development of new deep learning techniques, the availability of large datasets of images, and the increasing demand for realistic images in a variety of applications, such as entertainment, marketing, and education. Image generation has come a long way since its early days. In the 1970s, researchers began to explore the use of procedural algorithms to generate images. These algorithms were based on mathematical rules that could be used to create specific patterns or shapes. For example, one algorithm could be used to generate a checkerboard pattern, while another could be used to generate a spiral.

Procedural algorithms were a major breakthrough in image generation, but they had some

limitations. They were often limited to generating simple patterns, and they could be difficult to control. In the 1980s, researchers began to explore the use of neural networks for image generation. Neural networks are inspired by the human brain, and they can be used to learn complex patterns from data. One of the earliest neural network-based image generation models was called the Neocognitron [4]. The Neocognitron was developed in the 1980s by Kunihiko Fukushima, and it was able to generate images of simple objects, such as lines and circles.

Some of the most recent advances in image generation include: Generative Adversarial Networks (GANs) [5], Variational Autoencoders (VAEs) [6], Diffusion Models [7], etc. We will review recent advancements in each of these approaches in this paper. Image generation is a rapidly evolving field, and there are sure to be even more advances in the years to come. These advances will enable us to generate even more realistic and creative images, and they will have a huge impact on a variety of industries.

III. Classification of Image Generation Task

Image generation is a fundamental task in computer vision and artificial intelligence that involves creating new images that resemble a given dataset or follow a specific style or distribution. The goal of image generation is to create visually plausible and diverse images that exhibit characteristics similar to those found in real images. This task finds applications in a wide range of fields, including art, entertainment, data augmentation, medical imaging, and more. Image generation can be classified based on several parameters that describe different aspects of the task. Here, we'll classify image generation based on various key parameters provided below:

I. Input Domain:

1. **Random Noise Input:** Here the model takes random noise as input and learn to generate images that resemble real data distribution. GAN and VAE are good examples of such approaches.
2. **Conditional Input (Text, Labels, or Images):** The models generate images conditioned on additional input, such as text descriptions, labels, or images. The conditional information guides the image generation process. Models like conditional GANs are used.
3. **Text-to-Image Generation:** In this we generate images from textual descriptions, translating the semantic information into visual content. Models like AttnGAN are useful for this task[8].
4. **Images as Input (Style Transfer):** Style transfer methods modify the style of an input image using the style of another image while preserving content [9].
5. **Incomplete Images (Image Inpainting):** Inpainting models fill in missing or corrupted regions in images while maintaining coherence and realism[10].
6. **Reference Images (Super-Resolution):** Single Image Super-Resolution: These models enhance the resolution of low-resolution images using high-resolution reference images during training [11].
7. **Noisy or Degraded Images (Denoising):** Denoising models remove noise from images, enhancing their quality and clarity [12].
8. **Medical Data (Medical Image Generation):** Models generate medical images for diagnosis, research, and data augmentation in the medical field [2].
9. **Artistic Style as Input (Artistic Image Generation):** Models create images in specific artistic styles based on input style images or characteristics [13].
10. **Multi-Modal Inputs (Cross-Modal Generation):** Here, Models generate images from different modalities (e.g., text to images or images to text) [14].

II. Generative Approach:

1. **Explicit Models:** These models define a direct mapping from a latent space to the image space, such as Variational Autoencoders (VAEs) or Generative Adversarial Networks (GANs).
2. **Implicit Models:** These models learn the distribution of the data through sampling, like autoregressive models and some flow-based models.

III. Architecture:

1. **Autoencoders:** Models that learn to encode and decode data to reconstruct input images, e.g., VAEs.
2. **GANs:** Models involving a generator and discriminator network that compete with each other to produce realistic images.
3. **Flow-Based Models:** Models that use series of invertible transformations to map a simple distribution like gaussian distribution to the complex data distribution.
4. **Autoregressive Modelling:** The models use values of previous pixels to compute the value of the next pixel. Images are generated pixel by pixel.
5. **Diffusers:** Models that learn by adding and removing noise in a gradual manner in the given input image.

IV. Latent Space:

1. **Continuous:** Models with continuous latent spaces (e.g., VAEs) that allow for smooth interpolation and exploration.
2. **Discrete:** Models with discrete latent spaces (e.g., some flow-based models) that capture categorical features.

V. Loss Function:

1. **Adversarial Loss:** Models using adversarial training, like GANs, to minimize the difference between real images and generated images.
2. **Reconstruction Loss:** Models minimizing the difference between input and reconstructed images, as seen in VAEs.

VI. Sampling Method:

1. **Direct Sampling:** Models that directly sample images from the learned distribution, common in GANs and some flow-based models.
2. **Autoregressive Sampling:** Models generating images sequentially by predicting pixels one at a time, like PixelCNN [15].

VII. Output Domain:

1. **Natural Images:** Models generating images that resemble natural scenes, objects, and textures.
2. **Artistic Images:** Models creating images with specific artistic styles or characteristics.

3. **Medical Images:** Models generating medical images for diagnosis and research.
4. **Scientific Data:** Models generating data visualizations for scientific exploration.

VIII. Use Cases:

1. **Data Augmentation:** Generating synthetic data to augment limited datasets This is especially useful in medical field machine learning as the data available is limited.
2. **Art Creation:** Generating artistic images, paintings, and visual effects.
3. **Style Transfer:** Transforming images into different artistic styles.

IV. Major Approaches in Image Generation

There are many major approaches in image generation, which includes variable autoencoders, generative adversarial networks, transformer-based architectures, autoregressive models, diffusion models, etc. Some of the most common approaches are explained below:

I. Generative Adversarial Networks

Generative Adversarial Networks (GANs) are a class of machine learning models designed to produce novel data. They operate through an adversarial process between two neural networks: a generator tasked with creating new data, and a discriminator that evaluates its authenticity.

GANs have been used to generate a variety of different types of data, including images, text, and music. They have been shown to be able to generate realistic and diverse data that is indistinguishable from real data.

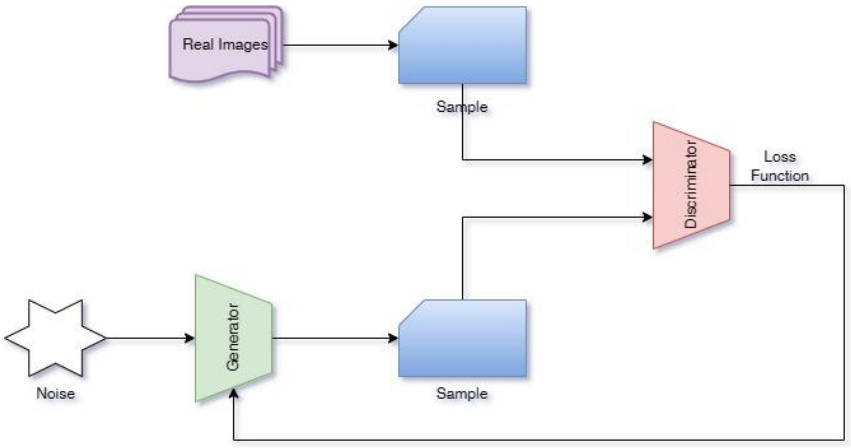


Figure 1: *GAN Architecture*

The architecture of a GAN is shown in the figure above. The generator is a neural network that takes a random noise as input and outputs a new data sample. The discriminator is also a neural network that gets a data sample as input and outputs a probability that the data sample is real. The generator and discriminator are trained together in an adversarial manner. The generator is trained to create data that the discriminator cannot distinguish from real data. The discriminator is trained to become better at detecting fake data.

Here is a comparison of various advancements proposed over time in the basic GAN architecture.

Table **1:** *Comparison of GAN Based Approaches*

GAN Approach	Advantages	Limitations	Applications
DCGAN (Deep Convolutio-nal GAN) [16]	Stable training, high-quality images	Limited to simple datasets, mode collapse	Art generation, data augmentation
WGAN (Wasserstein GAN) [17]	Improved stability, meaningful loss	Hyperparameter sensitivity, slow convergence	Image synthesis, style transfer
LSGAN (Least Squares GAN) [18]	More stable training, sharper images	Mode collapse, harder to optimize	Image generation, data augmentation
InfoGAN [19]	Interpretable latent factors, controlled generation	Limited to discrete latent variables, sensitive to hyperparameter	Image synthesis, style manipulation
StyleGAN [20]	High-resolution images, fine-grained control	Complex architecture, resource-intensive	Artistic image synthesis
BigGAN [21]	High-resolution images, large batch size	Computationally expensive, resource-intensive	High-quality image generation

DCGANs [16] propose a set of architectural constraints for Convolutional Neural Networks used in GANs to make them more stable to train. Key recommendations for these networks involve using strided convolutions instead of pooling layers in the discriminator, and fractional-strided convolutions in the generator. Additionally, widespread batch normalization in both networks and the elimination of fully connected hidden layers for deeper models are proposed. Specific activation functions are recommended: ReLU in the generator (except Tanh output) and LeakyReLU in the discriminator. These architectural decisions contribute to improved training stability compared to earlier attempts to scale GANs with CNNs. DCGANs are shown to learn a hierarchy of representations, and their learned features are effective for downstream tasks like image classification.

WGANs [17] introduce a fundamental shift in the GAN objective by proposing the use of the Earth Mover (Wasserstein) distance as the metric for comparing the real and generated data distributions. This distance is theoretically shown to have better properties than the JS or KL divergences used in traditional GANs, particularly when the distributions lie on low-dimensional manifolds, addressing issues like vanishing gradients. WGAN training is significantly more stable and less prone to mode collapse compared to standard GANs, without needing careful balancing of generator and discriminator capacities. A key practical benefit is that the critic's loss provides a meaningful learning curve that correlates with sample quality and convergence, which is invaluable for debugging and hyperparameter tuning.

LSGANs [18] propose an alternative objective function for GANs to address training stability issues. They replace the sigmoid cross-entropy loss used in regular GANs with a least squares loss function for the discriminator. This modification helps alleviate the vanishing gradients problem that can occur in regular GANs, especially when the discriminator becomes confident. The least square's objective corresponds to minimizing the Pearson χ^2 divergence [22]. LSGANs

demonstrate improved training stability and can converge to a good state even without batch normalization in some configurations. Empirically, LSGANs generate more realistic images and are less prone to mode collapse compared to regular GANs. Conditional LSGANs were also successfully applied to Chinese character generation.

InfoGAN [19] is an information-theoretic extension to the standard GAN framework. Its core contribution is modifying the GAN objective to maximize the mutual information between a small subset of the latent variables and the observed generated samples. This objective encourages the model to learn interpretable and disentangled representations in a completely unsupervised manner, without requiring labelled data for the disentangled factors. A simple and efficient algorithm is derived to optimize a lower bound of this mutual information objective. InfoGAN successfully disentangles various semantic features like writing styles, pose, lighting, hair styles, and emotions across different datasets, achieving results comparable to supervised methods for learning disentangled representations. The added computational cost compared to standard GAN training is negligible.

Karras et el. [20] builds upon the StyleGAN [23] architecture, addressing characteristic artifacts such as blob shapes. They propose architectural and training changes, notably redesigning the generator normalization by replacing instance normalization with weight demodulation to eliminate artifacts. The progressive growing method used in the original StyleGAN is replaced with an alternative design that shifts focus to higher resolutions without altering network topology during training. The improved model incorporates skip connections in the generator and a residual discriminator architecture for better performance. They also introduce path length regularization, which leads to more reliable models and makes projecting images back into the latent space much easier. These improvements significantly advance the state of the art in unconditional image synthesis.

The BigGAN[21] paper demonstrates that scaling up GAN training dramatically improves performance. They train models with significantly more parameters and larger batch sizes than prior art. Key architectural changes include using shared class embeddings and skip connections (skip-z) in the generator for efficiency and performance gains. A crucial side effect of their modifications, including orthogonal regularization, is the discovery of the truncation trick, which allows fine control over variety and fidelity. Their models claim state-of-the-art results on ImageNet and also perform well on the larger JFT-300M dataset. The paper also analyses instabilities specific to large-scale training, particularly concerning the singular values of the generator's weights.

II. Variational Autoencoders (VAEs) [3]

Variational Autoencoders (VAEs) are generative models that can learn a compressed, lower dimensional, feature-rich latent representation of input data. This allows them to subsequently generate novel data by sampling from this learned latent space and then decoding those samples.

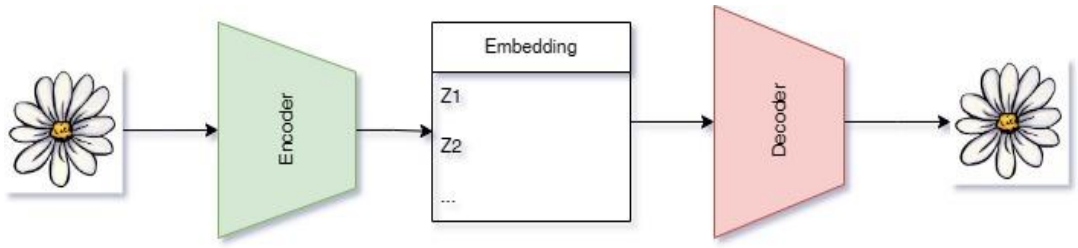


Figure 2: *VAE Architecture*

The basic architecture of a VAE is shown in the figure above. The encoder is a neural network that takes the observed data (image) as input and outputs a latent representation of the input, which is a compressed version of the input. The decoder is also a neural network that takes the latent representation as input and outputs the original data (image). VAEs are based on the idea of variational inference. This is a technique for estimating the posterior distribution of latent variable given observed data. In the case of VAEs, the latent variable is the latent representation of the data, and the observed data is the original data. We provide a tabular comparison of various Variational Autoencoder (VAE) approaches for image generation.:

Table 2: *Comparison of VAE Based Approaches*

VAE Approach	Advantages	Limitations	Applications
Vanilla VAE [24]	Simple architecture, easy to implement	Blurry images, difficulty in capturing complex data distribution	Data compression, image generation
B-VAE [25]	Disentangled latent space, controlled generation	Mode collapse, trade-off in reconstruction quality	Interpretability, data compression
CVAE (Conditional VAE) [26]	Conditional image generation	Limited to paired data, sensitive to label noise	Image-to-image translation
AAE (Adversarial Autoencoder) [27]	Improved image quality, less blurriness	Vulnerable to mode collapse, harder to train	Image generation, data denoising
VQ-VAE [28]	Discrete latent space, clear structure	Limited diversity in generated samples	Speech synthesis, image generation
DR-VAE (Disentangled Representation VAE) [29]	Disentangled factors, improved interpretability	Complexity, challenging optimization	Data generation, representation learning
FactorVAE [30]	Independent across the dimensions Better trade-off between disentanglement and reconstruction quality	Complexity and Interpretability, Hyperparameter Tuning	Guide Learning in Highly Noisy Market Data, Risk Modelling

Vanilla Variational Autoencoder (VAE) [24] framework proposed by Kingma et el. is an efficient method for inference and learning in deep directed graphical models, with continuous latent variables. This is achieved using the stochastic gradient variational Bayes (SGVB) estimator and the reparameterization trick. The training objective is based on maximizing the variational lower bound of the log-likelihood. While the original VAE demonstrated potential for disentanglement on simple datasets, its performance did not scale to more complex ones.

β-VAE[25] introduces a modification of the original VAE framework. The key contribution is the introduction of an adjustable hyperparameter β. This β coefficient modulates learning constraints, specifically balancing the latent channel capacity and independence constraints against reconstruction accuracy. For $\beta > 1$, β-VAE is pushed to learn a more efficient and disentangled latent representation. The paper demonstrates that β-VAE qualitatively and quantitatively outperforms the original VAE (where $\beta=1$) and other state-of-the-art methods like InfoGAN and DC-IGN in achieving disentanglement. β-VAE is also noted for being stable to train, requiring few assumptions, and depending only on tuning β. It has the ability to discover more latent factors and learn better disentangled representations over a wider range of factor values than baselines.

Sohn et el. [26] proposes the Conditional Variational Autoencoder (CVAE) for structured output prediction problems, such as image segmentation. The core idea is to model the conditional distribution of output variables given the input, which can be multi-modal. The CVAE architecture builds recognition, prior, and generation networks on top of a baseline CNN and incorporates recurrent connections. Compared to deterministic neural networks, CVAE and its variants show significant improvements in structured output prediction accuracy and conditional log-likelihoods. They also generate more realistic and diverse output samples.

Adversarial Autoencoder (AAE) [27] framework transforms any VAE into a generative model by imposing an arbitrary prior distribution on the latent codes. This is done using a GAN to match the aggregated posterior distribution of the autoencoder's latent codes to the desired prior. AAE is shown to successfully impose specified prior distributions and fill the latent space more effectively than VAE. It can be extended for semi-supervised learning and to disentangle label information from image style by providing the label to the decoder. AAE achieved state-of-the-art likelihoods on tested datasets.

Vector Quantised-Variational AutoEncoder (VQ-VAE) [28] modifies the VAE framework by using discrete latent variables instead of continuous ones, achieved through vector quantization. A key improvement is that this approach helps to avoid posterior collapse, a common issue in VAEs with powerful decoders. VQ-VAE learns a learnt prior distribution and uses an embedding table indexed by discrete latent codes. It demonstrates performance comparable to continuous VAEs in terms of likelihood and can generate high-quality samples when paired with an autoregressive prior. VQ-VAE is effective at modelling long-range dependencies.

Wang et el. [29] categorizes various disentangled representational learning approaches, including. It notes that the vanilla VAE shows poor disentanglement on complex datasets despite having potential on simple ones. The author highlights how many subsequent VAE-based methods improve disentanglement by adding extra regularizers or inductive biases to the VAE objective, citing β-VAE, DIP-VAE, and β-TCVAE as examples. It explains the trade-off in β-VAE between reconstruction quality and independence. The paper also discusses hierarchical VAE structures for learning factors at different abstraction levels.

Kim et el. introduces FactorVAE [30], another method based on the VAE framework. Its primary contribution is addressing the trade-off between reconstruction quality and disentanglement seen in β-VAE. FactorVAE achieves this by augmenting the VAE objective with a specific penalty on the Total Correlation of the latent codes. This encourages independence in the latent space. Empirically, FactorVAE achieves higher disentanglement scores than β-VAE while maintaining similar or better reconstruction quality on tested datasets. The paper also proposes an improved disentanglement metric.

III. Autoregressive Models

Autoregressive models for generate images by modeling the conditional distribution of each pixel or group of pixels given their preceding pixels. These models generate images one pixel at a time,

sequentially predicting the value of next pixel based on the values of previously generated pixels. Autoregressive models have been successful in producing high-quality images with fine-grained control over the generation process.

In autoregressive models, an image is conceptualized as a sequence of pixels. The overall probability of an image is expressed as the product of the conditional probabilities of individual pixels, where the intensity of each pixel is determined by the values of all preceding pixels, as represented in the following equation.

$$p(x) = \prod_{i=1}^{n^2} p(x_i | x_1, \ldots\ldots, x_{i-1}) \quad (1)$$

In other words, to generate the value of pixel x_i in below figure, we need the intensity values of all previously generated pixels shown in blue.

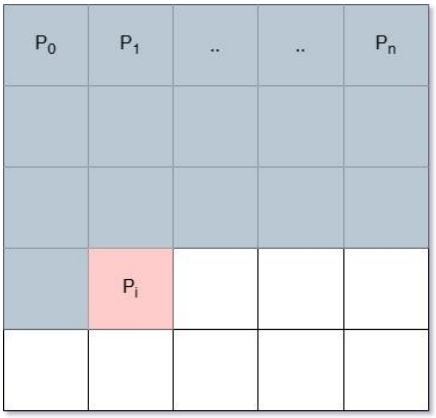


Figure 3: *Image Pixel value Calculation in An Autoregressive Model*

Now, we compare some prominent autoregressive approaches in the following table.

Table 3: *Comparison of Autoregressive Approaches*

Autoregressive Approach	Advantages	Limitations	Applications
PixelRNN [31]	High-quality images, fine-grained control	Slow generation speed, not scalable	High-resolution image generation
PixelCNN [32]	Efficient generation, controllable generation	Slow generation speed, receptive field limitations	Image generation, style transfer
DRAW (Deep Recurrent Attentive Writer)[33]	Attention-based generation, variable sequence length	Complex architecture, challenging training	Image generation, handwriting synthesis

PixelRNN [31] sequentially predict pixels in an image into two spatial dimensions. Pixel-level autoregressive models, such as PixelRNN and PixelCNN, offer a tractable way to model the complete dependencies within an image by factoring the joint distribution of pixels into conditional probabilities. Pixel RNN introduces unique 2D LSTM layers (Row LSTM and Diagonal BiLSTM) that leverage convolutions for spatial state computation. Meanwhile, PixelCNN is a fully convolutional network that uses masked convolutions to preserve spatial resolution and respect the autoregressive order. This approach has led to significantly better log-likelihood scores on

datasets like CIFAR-10 and ImageNet, where PixelCNN models pixels as discrete variables via a simple yet effective multinomial distribution with a softmax layer. The inclusion of residual connections around LSTM layers further aids in training deeper networks and accelerating convergence.

Van Den et el. Introduces Conditional Image Generation with PixelCNN Decoders [32], which explores conditional image synthesis by adapting and improving PixelCNN [31]. It introduces a gated variant of PixelCNN (Gated PixelCNN) that matches the log-likelihood of PixelRNN on datasets like CIFAR and ImageNet while significantly reducing training time. It addresses the blind spot in the receptive field of the original masked convolutional architecture using two stacks of CNNs and introduces Conditional PixelCNN that allows modelling complex conditional distributions of natural images when a latent vector embedding is provided. According to the authors, the single Conditional PixelCNN model demonstrates versatility: it can generate images across diverse classes by being conditioned on a one-hot encoding (e.g., ImageNet classes), and it can produce varied new portraits of a single individual when conditioned on a face embedding from a convolutional network.

A significant innovation in generative models, the Deep Recurrent Attentive Writer (DRAW) network [33] integrates a novel spatial attention mechanism that mimics human vision with a sequential variational auto-encoder. What sets DRAW apart from other VAEs is its use of recurrent networks for both the encoder and decoder, which iteratively refine images by exchanging latent codes. Its dynamically updated attention mechanism enables the model to selectively read from the input and write to the output at each timestep. This fully differentiable attention makes DRAW trainable with standard backpropagation and leads to substantial improvements in generative modeling for MNIST and realistic SVHN image generation, with the authors also highlighting its advantages for image classification on cluttered MNIST.

VI. Flow Based Approaches

Unlike other generative models, flow-based models generate images through a series of invertible transformations, which also allows them to directly learn the exact probability distribution of the data. While Generative Adversarial Networks (GANs) and Variational Autoencoders (VAEs) have excelled at learning complex data distributions, they both struggle with exact probability evaluation and inference. This limitation can lead to lower quality results in VAEs and present training challenges for GANs, such as mode collapse and vanishing gradients. Normalizing Flows were introduced to address these issues. By leveraging invertible transformation functions, they eliminate the need for adding noise during image generation and offer a significantly more stable training process compared to GANs.

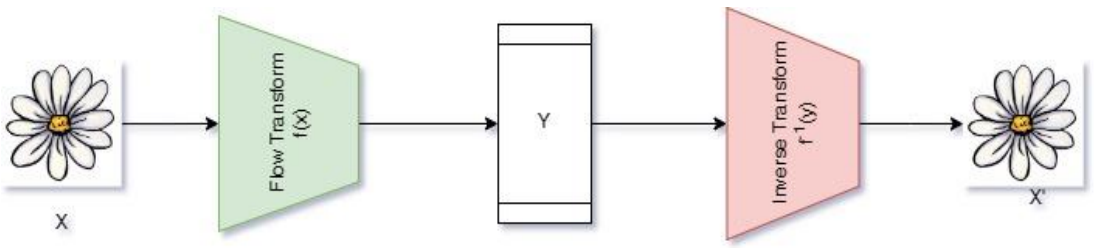


Figure 4: *Flow based model architecture*

Flow-based generative models leverage invertible transformation functions to establish a mapping from the data space (x) to the latent space (z). A crucial aspect is that the dimensionality of z must match that of x. This section presents a brief comparative overview of different flow-based

methodologies.

Table 4: *Comparison of Flow Based Approaches*

Flow-Based Approach	Advantages	Limitations	Applications
Real NVP (Real Non-Volume Preserving) [34]	Exact likelihood, impressive sampling	Computational complexity	Density estimation, image synthesis
Glow [35]	High-quality images, efficient sampling	Computational complexity, resource-intensive	High-resolution image generation
MAF (Masked Autoregressive Flow) [36]	Flexible modeling, controllable generation	Slow generation speed, less efficient sampling	Image synthesis, density estimation
FFJORD (Continuous Normalizing Flows) [37]	Faster training, reversible dynamics	Trade-off between speed and quality	Image synthesis, density estimation

For unsupervised learning, Dinh et al. [34] developed real-valued non-volume preserving (real NVP) transformations. These are robust, stably invertible, and learnable, offering key advantages such as exact log-likelihood calculation, as well as exact and efficient sampling and efficient latent variable inference. It addresses the challenge of building powerful yet trainable models for high-dimensional data. Real NVP extends previous work like NICE by defining a more flexible class of bijective functions. A key contribution is the use of a deep multi-scale architecture leveraging batch normalization and residual networks. Sampling is efficient and parallelized over input dimensions, and the model learns a semantically meaningful latent space. Real NVP generates sharper samples by not relying on fixed form reconstruction costs like L2 norm. It incorporates a novel variant of batch normalization more robust for small minibatches. The coupling layer that is used in Real NVP is identified as a special case of the autoregressive transformation found in MAF and IAF.

Kingma proposed Glow [35], a generative flow model that builds upon the NICE and RealNVP architectures. Each step of the Glow flow is composed of three key components: actnorm, an invertible 1×1 convolution, and an affine coupling layer. Actnorm is a novel activation normalization layer with data-dependent initialization that is more robust to small batch sizes than batch normalization. The invertible 1× 1 convolution replaces fixed permutations with a learned, invertible linear transformation across channels, which improves performance and convergence speed. Glow incorporates affine coupling layers similar to RealNVP and uses a multi-scale architecture. It achieves a notable improvement in log-likelihood when tested on standard benchmarks compared to RealNVP. When trained on high-resolution data, Glow demonstrates the ability to synthesize realistic images and allows for efficient, parallelizable synthesis and latent space manipulation. The model also benefits from potential memory savings due to its reversible architecture.

Masked Autoregressive Flow (MAF) [36] is a type of normalizing flow specifically designed for density estimation. MAF is constructed by stacking multiple autoregressive models, where each layer models the random numbers of the next layer. A key innovation is the use of the

Masked Autoencoder for Distribution Estimation (MADE) as the building block. This allows density evaluations to be computed efficiently in a single forward pass through the entire flow on parallel hardware like GPUs, a significant advantage for density estimation compared to IAF which requires D passes. The paper shows that MAF is a generalization of Real NVP, with the coupling layer being a special case of the autoregressive layer used in MAF. Stacking MADE layers increases the model's flexibility, allowing it to learn multimodal conditionals. MAF achieves comparable performance on general-purpose density estimation tasks and outperforms Real NVP in all experiments presented. Batch normalization is used to improve training stability and performance.

FFJORD [37] is a continuous-time invertible generative model defined by ordinary differential equations (ODE). A major contribution is enabling unrestricted neural network architectures for the dynamics function, overcoming the architectural constraints imposed by previous flow-based models like Real NVP and Glow to ensure tractable Jacobian determinants. FFJORD achieves this by using Hutchinson's trace estimator to provide a scalable unbiased estimate of the log-density with an efficient O(D) time cost, significantly improving upon the O(D^3) or O(D^2) costs of previous methods. The model allows one-pass sampling. Backpropagation for training is handled using the adjoint method, which solves another ODE backwards in time. FFJORD demonstrates competitive performance on density estimation and improved results in variational inference compared to other normalizing flows. It also uses significantly fewer parameters than Glow on image datasets.

V. Diffusion Models

To generate images, diffusion models begin with a noise image and incrementally introduce more detail through a guided diffusion process. This new approach in generative modeling allows for the creation of realistic images and offers improved efficiency over GANs and VAEs.

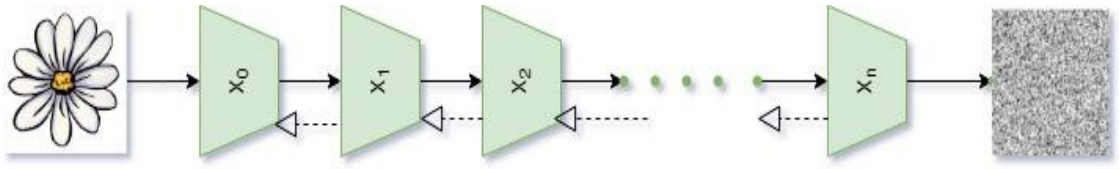


Figure 5: *Diffusion Model*

Stable Diffusion-based approaches focus on modeling data as the result of a diffusion process, often based on partial differential equations. These methods leverage the concept of diffusion to generate images in a stable and controlled manner. Here is the comparison of various approaches based on Stable Diffusion.

Table 5: *Comparison of Diffusion Based Approaches*

Diffusion Approach	Advantages	Limitations	Applications
Latent Diffusion [38]	High-quality images with fine details.	Slow to generate especially for large images.	Image generation, image inpainting, image style transfer, image upscaling

Fast Sampling of Score-Based Models with Cyclical Diffusion Sampling [39]	Enhances effectiveness of SGLD in learning complex multimodal distributions. Decreases inference time. Easy integration to existing models.	Approximation based accumulates truncation errors over time. Require right balance between the number of function evaluations (NFE) and image quality.	Image generation on diverse domains
Consistent Diffusion Models [40]	Enhance the quality of generated samples for both conditional and unconditional generation tasks.	The regularization process leads to longer training times. The method assumes that the learned vector field is conservative, which is not directly tested or enforced.	Applied across various modalities, including images, videos, audio, 3D structures, proteins, and medical applications.
simple diffusion [41]	Generate high-resolution images while maintaining simplicity. Supports a single end-to-end training setup without the need for cascades or mixtures of experts.	Training diffusion models on high-resolution images is computationally expensive. Require more training data.	Image generation
DuDGAN [42]	Dual diffusion-based noise injection process helps to prevent overfitting. Fast Convergence.	Struggles with classes with less than 50 images. Independent noising schedules for the discriminator and classifier can complicate optimization.	Diffusion-based 3D scene generation. GAN inversion involving multi-network training
Versatile Diffusion [43]	Handle multiple modalities and tasks. More efficient than training separate for each task.	Training and inference are compute-intensive. Complex to fine-tune. Limitations in cross-modal blending.	Text to Image generation. Image to Text generation.

Latent Diffusion Models (LDMs), proposed by Rombach et al. [38], revolutionize high-resolution image synthesis by moving the computationally intensive diffusion process from pixel space to a

compressed latent space. This significantly reduces training expense and speeds up inference while maintaining high synthesis quality. LDMs are built upon a sequential application of denoising autoencoders and employ a reweighted variational lower bound. They exhibit enhanced sample quality when trained in VQ-regularized latent spaces compared to pixel-based diffusion models. A key innovation is the integration of cross-attention conditioning, which enables flexible control, including powerful text-to-image generation. Consequently, LDMs achieve state-of-the-art performance and strong competitiveness across a range of generative tasks and metrics.

While diffusion models show great promise in generative tasks, their slow sampling is a significant hurdle. Makhtidi et al. [39] offer a solution with Cyclical Diffusion Sampling, which aims to speed up this process. Their method integrates cyclical stochastic gradient Langevin dynamics (SGLD)—a technique proven to enhance stability when learning complex distributions—with the elucidated diffusion models (EDM) sampler. By strategically using cyclical step-size noise scheduling and Heun's second-order method within this stochastic sampler, the research achieves remarkable improvements in image quality and a substantial reduction in inference time. For example, it outperformed prior methods on CIFAR-10, needing only 35 function evaluations (NFE) instead of 1,000, all without requiring any network architecture modifications.

Daras et el. [40] proposed Consistent Diffusion Models: Mitigating Sampling Drift by Learning to be Consistent. Diffusion models generate data by denoising a noisy sample from a distribution corrupted with noise. This paper presents Consistent Diffusion Models (CDM), which aim to mitigate sampling drift introduced by imperfect learning of the score function. CDM relies on the architecture and hyperparameters of the EDM model. The proposed method involves training with a Constant Prediction (CP) regularization alongside the standard Denoising Score Matching (DSM) objective. The CDM models are trained using a weighted objective combining both DSM and CP regularization. CDM aims to enforce a property that on expectation, predictions should not change for points with the same origin. Best results were obtained by combining DSM and CP regularization. While a concurrent work (Consistency Models) also enforces a similar property, CDM's primary motivation is to improve generation quality, whereas Consistency Models aim to accelerate sampling.

Hoogeboom et el. [41] introduced simple diffusion: End-to-end diffusion for high resolution images. Applying standard diffusion models directly to high-resolution images in pixel space is challenging and typically requires complex approaches like latent diffusion or cascades. This paper aims to improve standard denoising diffusion for high resolutions while keeping the model simple. The method introduces several simple modifications to the original formulation. Key findings include: 1) Adjusting the noise schedule is crucial for high-resolution images. 2) Scaling only specific parts of the architecture is sufficient. 3) Strategic use of dropout improves performance. 4) Down-sampling is an effective strategy for higher resolutions. Combining these techniques allows for training a single denoising diffusion model on resolutions up to 512x512. Simple diffusion claims state-of-the-art performance on ImageNet among diffusion models without sampling modifiers. It is presented as the first single-stage text-to-image model capable of generating such high visual quality images. The model can also be distilled for faster sampling.

DuDGAN [42]proposes a novel approach for class-conditioned image generation using GANs. It addresses challenges faced by traditional class-conditional GANs such as instability, mode collapse, and low-quality output on datasets with significant intra-class variation. DuDGAN proposes a dual diffusion-based noise injection process into two neural networks: the discriminator and a classifier. Gaussian-mixture noises are injected in distinct ways, helping to prevent overfitting and introducing more challenging tasks. The method investigates the impact of using an additional classifier trained with this diffusion-based noise injection. The dual-diffusion training approach signifies the collaboration between the discriminator and the classifier. DuDGAN achieves fast convergence within a limited number of iterations and iteration-efficient

training. It claims to outperform traditional conditional GAN models on various datasets (AFHQ, Food-101, CIFAR-10, BAAT) across metrics like FID, KID, Precision, and Recall.

Versatile Diffusion [43] is a multi-task multimodal network designed to handle multiple flows (text-to-image, image-variation, image-to-text) within one unified model, instead of existing diffusion models that often require separate models for different tasks (e.g., text-to-image, image-variation). This novel multi-flow diffusion framework extends single-flow diffusion pipelines. It categorizes diffuser layers as global, data, or context, activating them selectively based on input and output modalities. This structure promotes significant parameter sharing across tasks. VD uses a UNet with cross-attentions for the diffuser, VAEs (Autoencoder-KL and Optimus) for latent representations, and CLIP encoders for context. VD performs well on its base tasks, outperforming baselines and better capturing context semantics. Its multi-flow nature enables novel derivative tasks such as semantic-style disentanglement and dual-/multi-context blending. VD represents a step toward universal AI by addressing multiple modalities and tasks in a single framework.

V. Comparison of Different Image Synthesis Techniques

We have seen many different image synthesis techniques, each with its own strengths and weaknesses. Here is a comparison of some of the most common techniques:

1. **Generative Adversarial Networks (GANs):** GANs are one of the most powerful image synthesis techniques available. They can generate very realistic images, and they can be used to generate images of a wide variety of objects and scenes. However, GANs can also be difficult to train, and they can be prone to generating images that are blurry or distorted.
2. **Variational Autoencoders (VAEs):** VAEs are less powerful than GANs, but they are easier to train and they are less prone to generating blurry or distorted images. VAEs are also better at generating images that are consistent with the original image.
3. **Autoregressive Models:** They are able to generate high-quality images with good detail. They can be slow to generate images, especially for large images compared to other models.
4. **Flow Based Models:** They are very efficient to train and generate compared to GANs and Stable diffusion. But they can sometimes generate images that are blurry or unrealistic.
5. **Diffusion Models:** Diffusion models can generate realistic images, and they are also more efficient than GANs and VAEs. Diffusion models are a relatively new technique, but they have shown promising results. They are able to generate realistic images that are better than GANs, and they are much faster to train.
6. **Procedural Generation:** Procedural generation is a technique for creating images by following a set of rules. This can be done by using mathematical formulas, or by using algorithms that generate images based on a set of parameters. Procedural generation is often used to create stylized images, such as those used in video games. Procedural generation is a versatile technique that can be used to create a wide variety of images. It is not as realistic as GANs or VAEs, but it can be used to create images that are unique and visually appealing.
7. **Neural Style Transfer:** It is a technique for transferring the style of one image to another image. This is done by using a neural network to learn the style of first image, and then using that knowledge to apply the style to the second image. Neural style transfer can be used to create images with a variety of different styles, such as impressionism, cubism, and abstract art. Neural style transfer is a powerful technique that can be used to create visually appealing images. However, it is not as realistic as GANs or VAEs.

The ideal image synthesis technique varies with the application. For realism, consider GANs; for

consistency, VAEs are a strong choice. If speed is critical, diffusion models excel, while procedural generation is great for stylized outputs. When a specific artistic flair is needed, neural style transfer is the way to go. Bear in mind that image synthesis is a swiftly developing domain, with new advancements constantly emerging. Future techniques are expected to be significantly more powerful and adaptable than those available today.

VI. EVALUATION METRICS FOR IMAGE GENERATION

Evaluation metrics for image generation are methods to measure the quality and diversity of the generated images. Some of the common metrics are:

1. **Inception Score (IS):** This metric calculates the KL divergence between the conditional and marginal distributions of the class labels predicted by an Inception network on the generated images. A high IS indicates that the images are both realistic and diverse. IS is a quantitative metric that was proposed by Salimans. (2016) [44]. To use this metric, you need to feed your generated images to a pre-trained Inception network and compute the statistics of the predicted class labels.
2. **Fréchet Inception Distance (FID):** This metric computes the Wasserstein-2 distance between the feature distributions of real and generated images, extracted by an Inception network. A low FID indicates that the generated images are similar to the real ones in terms of visual quality and diversity. FID is a quantitative metric that was introduced by Heusel. (2017) [45]. To use this metric, you need to feed both real and generated images to a pre-trained Inception network and compute the mean and covariance of the features in a hidden layer.
3. **Precision and Recall:** These metrics are based on the nearest-neighbor distance between real and generated images in the feature space. Precision measures how many generated images are close to some real images, while recall measures how many real images are close to some generated images. A high precision and recall indicate that the generated images are both realistic and diverse. These metrics are quantitative and were developed by Sajjadi (2018) [46]. To use these metrics, you need to feed both real and generated images to a pre-trained Inception network and find the nearest neighbors of each image in the feature space using a distance metric such as cosine similarity or Euclidean distance.
4. **Kernel Inception Distance (KID):** This metric estimates the Maximum Mean Discrepancy (MMD) between the feature distributions of real and generated images, extracted by an Inception network. KID is similar to FID, but it does not require fitting a Gaussian distribution to the features, and it is unbiased and consistent. KID is a quantitative metric that was suggested by Binkowski. (2018) [47]. To use this metric, you need to feed both real and generated images to a pre-trained Inception network and compute the MMD between the features using a kernel function such as radial basis function or polynomial kernel.
5. **Learned Perceptual Image Patch Similarity (LPIPS):** This metric measures the perceptual similarity between real and generated images using a deep network that is trained to predict human judgments of image similarity. LPIPS is a quantitative metric that can capture fine-grained differences in image quality and style. LPIPS was proposed by Zhang. (2018) [48]. To use this metric, you need to feed both real and generated images to a pre-trained network that is fine-tuned on human similarity ratings and compute the average distance between the images.

VII. Limitations and Challenges in Image Generation

Image generation is a rapidly evolving field, but there are still some limitations and challenges that

need to be addressed. Here are a few of the most common limitations and challenges:

1. **Image quality:** Image generation techniques are still not perfect, and they can sometimes generate images that are blurry, distorted, or unrealistic. This is especially true for complex images, such as images of people or animals.
2. **Controllability:** Image generation techniques are often not very controllable. This means that it can be difficult to generate images with specific features, such as a certain color, a certain style, or a certain object.
3. **Efficiency:** Image generation techniques can be computationally expensive, especially for complex images. This can make it difficult to generate images in real time, which is necessary for some applications, such as virtual reality and augmented reality.
4. **Bias:** Image generation techniques can be biased, which means that they may generate images that are more likely to represent certain groups of people or objects. This is a concern because it can lead to the spread of harmful stereotypes.
5. **Safety:** Image generation techniques can be used to create fake images, which can be used to deceive people. This is a concern because it can be used for malicious purposes, such as spreading misinformation or propaganda.
6. **Training Instability:** Models like GANs and VAEs can be comparatively challenging to train due to instability.
7. **Scalability**: Complexity of the approaches can hinder the scalability of some models.

These are just a few of the limitations and challenges that need to be addressed in image generation. As the field continues to evolve, it is likely that these limitations and challenges will be overcome, and that image generation techniques will become even more powerful and versatile.

VIII. Future Trends in Image Synthesis

Image generation is a rapidly evolving field, and there are many exciting future trends that are likely to emerge in the coming years. We can hope that all the challenges that we have listed earlier can be solved in the near future. Here is what it can look like:

1. **Improved Image Quality:** Image generation techniques are constantly improving, and it is likely that we will see even more realistic and detailed images in the future. This will be made possible by the development of more powerful neural networks and by the availability of larger datasets of images. Improved image quality will be used in a variety of applications, such as virtual reality, augmented reality, and film production. In virtual reality, improved image quality will allow users to experience more realistic and immersive environments. In augmented reality, improved image quality will allow users to interact with virtual objects in a more realistic way. In film production, improved image quality will allow filmmakers to create more realistic and visually appealing movies.
2. **More Controllable Image Generation:** Image generation techniques are becoming more controllable, which means that users will be able to generate images with specific features, such as a certain color, a certain style, or a certain object. More controllable image generation will be used in variety of applications, such as product design, marketing, and art. In product design, more controllable image generation will allow designers to create more realistic prototypes of products. In marketing, more controllable image generation will allow marketers to create more visually appealing ads. In art, more controllable image generation will allow artists to create more original and creative works of art.
3. **Real-Time Image Generation:** Image generation techniques are becoming more efficient, which means that they will be able to generate images in real time. Real-time image generation will be used in a variety of applications, such as video games, social media, and

live streaming. In video games, real-time image generation will allow players to experience more realistic and immersive worlds. In social media, real-time image generation will allow users to create more visually appealing content. In live streaming, real-time image generation will allow viewers to experience more realistic and engaging events.

4. **Less Biased Image Generation:** Image generation techniques are becoming less biased, which means that they will generate images that are representative of all groups of people and objects. This will be made possible by the development of new techniques, such as debiasing and fairness training. Less biased image generation will be used in a variety of applications, such as education, healthcare, and law enforcement. In education, less biased image generation will allow students to learn about different cultures and groups of people. In healthcare, less biased image generation will allow doctors to diagnose diseases more accurately. In law enforcement, less biased image generation will allow police officers to make more informed decisions.
5. **Safer Image Generation:** Image generation techniques are becoming safer, which means that they will be less likely to be used to create fake images. This will be made possible by the development of new techniques, such as watermarking and authentication. Safer image generation will be used in a variety of applications, such as social media, news, and advertising. In social media, safer image generation will help to prevent the spread of fake news and misinformation. In news, safer image generation will help to ensure that the public is exposed to accurate information. In advertising, safer image generation will help to prevent consumers from being misled by false advertising.

These are just a few of the ways that the future trends in image generation will be used in the real world. As the field continues to evolve, we can expect to see even more innovative and exciting applications for image generation.

IX. Conclusion: The Evolution and Potential of Image Generation Techniques

In this review paper, we have discussed the state-of-the-art in image generation techniques, including Generative Adversarial Networks (GANs), Variational Autoencoders (VAEs), diffusion models, autoregressive models, etc. While each strategy has its own merits and limitations, the rapid progress of deep learning has ushered in a new era of image generation capabilities. Researchers and practitioners can use this comparative analysis to select the most suitable strategy for their specific needs, taking into account factors like task requirements, dataset size, and computational resources. We have also discussed the different metrics that can be used to evaluate the quality of generated images. As image generation continues to evolve, we anticipate the emergence of novel strategies that combine the strengths of existing approaches and push the boundaries of visual creativity. The future of image generation research is bright. With the continued development of new techniques, it is likely that we will see even more realistic and diverse images being generated in the future. These images could be used for a variety of applications, such as entertainment, art, and education.

References

[1] V. L. Trevisan de Souza, B. A. D. Marques, H. C. Batagelo, and J. P. Gois, “A review on Generative Adversarial Networks for image generation,” Computers and Graphics (Pergamon), vol. 114, pp. 13–25, Aug. 2023, doi: 10.1016/j.cag.2023.05.010.

[2] N. K. Singh and K. Raza, “Medical Image Generation using Generative Adversarial Networks Medical Image Generation Using Generative Adversarial Networks: A Review”, doi: 10.48550/arXiv.2005.10687.

[3] M. Elasri, O. Elharrouss, S. Al-Maadeed, and H. Tairi, “Image Generation: A Review,” Oct.

01, 2022, Springer. doi: 10.1007/s11063-022-10777-x.

[4] K. Fukushima, "Neocognitron," Scholarpedia, vol. 2, no. 1, p. 1717, 2007, doi: 10.4249/scholarpedia.1717.

[5] I. Goodfellow et al., "Generative adversarial nets," Adv Neural Inf Process Syst, vol. 27, 2014.

[6] D. P. Kingma and M. Welling, "An Introduction to Variational Autoencoders," Jun. 2019. doi: 10.1561/2200000056.

[7] P. Dhariwal and A. Nichol, "Diffusion Models Beat GANs on Image Synthesis," Adv Neural Inf Process Syst, vol. 34, pp. 8780–8794, 2021.

[8] T. Xu et al., "AttnGAN: Fine-Grained Text to Image Generation with Attentional Generative Adversarial Networks." [Online]. Available: https://github.com/taoxugit/AttnGAN.

[9] L. A. Gatys, A. S. Ecker, and M. Bethge, "Image Style Transfer Using Convolutional Neural Networks."

[10] D. Pathak, P. Krähenbühl, J. Donahue, T. Darrell, and A. A. Efros, "Context Encoders: Feature Learning by Inpainting," in Proceedings of the IEEE conference on computer vision and pattern recognition, 2016, pp. 2536–2544.

[11] C. Ledig et al., "Photo-Realistic Single Image Super-Resolution Using a Generative Adversarial Network," in Proceedings of the IEEE conference on computer vision and pattern recognition, 2017, pp. 4681–4690.

[12] P. Vincent, H. Larochelle, Y. Bengio, and P.-A. Manzagol, "Extracting and Composing Robust Features with Denoising Autoencoders," in Proceedings of the 25th international conference on Machine learning, 2008, pp. 1096–1103.

[13] L. A. Gatys, A. S. Ecker, and M. Bethge, "Texture and art with deep neural networks," Curr Opin Neurobiol, vol. 46, pp. 178–186, Oct. 2017, doi: 10.1016/j.conb.2017.08.019.

[14] H. Zhang et al., "Cross-Modal Contrastive Learning for Text-to-Image Generation," in Proceedings of the IEEE/CVF conference on computer vision and pattern recognition, 2021, pp. 833–842.

[15] T. Salimans, A. Karpathy, X. Chen, and D. P. Kingma, "PIXELCNN++: IMPROVING THE PIXELCNN WITH DISCRETIZED LOGISTIC MIXTURE LIKELIHOOD AND OTHER MODIFICATIONS," in International Conference on Learning Representations, 2017.

[16] A. Radford, L. Metz, and S. Chintala, "Unsupervised Representation Learning with Deep Convolutional Generative Adversarial Networks," arXiv e-prints, p. arXiv-1511, Nov. 2015,

[17] M. Arjovsky, S. Chintala, and L. Bottou, "Wasserstein Generative Adversarial Networks," in International conference on machine learning, 2017, pp. 214–223.

[18] X. Mao, Q. Li, H. Xie, R. Y. K. Lau, Z. Wang, and S. P. Smolley, "Least Squares Generative Adversarial Networks."

[19] X. Chen, Y. Duan, R. Houthooft, J. Schulman, I. Sutskever, and P. Abbeel, "InfoGAN: Interpretable Representation Learning by Information Maximizing Generative Adversarial Nets."

[20] T. Karras, S. Laine, M. Aittala, J. Hellsten, J. Lehtinen, and T. Aila, "Analyzing and Improving the Image Quality of StyleGAN," in Proceedings of the IEEE/CVF conference on computer vision and pattern recognition, 2020, pp. 8110–8119.

[21] A. Brock, J. Donahue, and K. Simonyan, "LARGE SCALE GAN TRAINING FOR HIGH FIDELITY NATURAL IMAGE SYNTHESIS," in International Conference on Learning Representations, 2018.

[22] T. Karras, S. Laine, and T. Aila, "A style-based generator architecture for generative adversarial networks," in Proceedings of the IEEE/CVF conference on computer vision and pattern recognition, 2019, pp. 4401–4410.

[23] D. P. Kingma, M. Welling, and Others, "Auto-Encoding Variational Bayes," Dec. 20, 2013, Banff, Canada.

[24] I. Higgins et al., "β-VAE: LEARNING BASIC VISUAL CONCEPTS WITH A CONSTRAINED VARIATIONAL FRAMEWORK," in International conference on learning representations, 2017.

[25] K. Sohn, X. Yan, and H. Lee, "Learning Structured Output Representation using Deep Conditional Generative Models."

[26] A. Makhzani, J. Shlens, N. Jaitly, I. Goodfellow, and G. Brain, "ADVERSARIAL AUTOENCODERS", 2015.

[27] A. van den Oord DeepMind, O. Vinyals DeepMind, and K. Kavukcuoglu DeepMind, "Neural Discrete Representation Learning," Adv Neural Inf Process Syst, vol. 30, 2017.

[28] X. Wang, H. Chen, S. Tang, Z. Wu, and W. Zhu, "Disentangled Representation Learning," IEEE Trans Pattern Anal Mach Intell, pp. 1–20, Jul. 2024, doi: 10.1109/tpami.2024.3420937.

[29] H. Kim and A. Mnih, "Disentangling by Factorising," in International conference on machine learning, 2018, pp. 2649–2658.

[30] A. Van Den Oord, N. Kalchbrenner, and K. Kavukcuoglu, "Pixel Recurrent Neural Networks," in International conference on machine learning, 2016, pp. 1747–1756.

[31] A. Van Den et al., "Conditional Image Generation with PixelCNN Decoders," Adv Neural Inf Process Syst, vol. 29, 2016.

[32] K. Gregor, D. Com, D. J. Rezende, and D. Wierstra, "DRAW: A Recurrent Neural Network For Image Generation Ivo Danihelka," in International conference on machine learning, 2015, pp. 1462–1471.

[33] L. Dinh, J. Sohl-Dickstein, and B. Samy, "DENSITY ESTIMATION USING REAL NVP," in International Conference on Learning Representations, 2017.

[34] D. P. Kingma and P. Dhariwal, "Glow: Generative Flow with Invertible 1×1 Convolutions," Adv Neural Inf Process Syst, vol. 31, 2018.

[35] G. Papamakarios, T. Pavlakou, and I. Murray, "Masked Autoregressive Flow for Density Estimation."

[36] W. Grathwohl, R. T. Q Chen, J. Bettencourt, I. Sutskever, and D. Duvenaud, "FFJORD: FREE-FORM CONTINUOUS DYNAMICS FOR SCALABLE REVERSIBLE GENERATIVE MODELS," in International Conference on Learning Representations, 2018.

[37] R. Rombach, A. Blattmann, D. Lorenz, P. Esser, and B. Ommer, "High-Resolution Image Synthesis with Latent Diffusion Models."

[38] K. Makhtidi, A. Bustamam, R. Adnan, H. A. Robbani, W. Mangunwardoyo, and M. A. Khan, "Fast Sampling of Score-Based Models with Cyclical Diffusion Sampling," IEEE Access, vol. 12, pp. 49578–49589, 2024, doi: 10.1109/ACCESS.2024.3365146.

[39] G. Daras, Y. Dagan, A. G. Dimakis, and C. Daskalakis, "Consistent Diffusion Models: Mitigating Sampling Drift by Learning to be Consistent," Adv Neural Inf Process Syst, vol. 36, pp. 42038–42063, 2023.

[40] E. Hoogeboom, J. Heek, and T. Salimans, "simple diffusion: End-to-end diffusion for high resolution images," in International Conference on Machine Learning, 2023, pp. 13213–13232.

[41] T. Yeom, C. Gu, and M. Lee, "DuDGAN: Improving Class-Conditional GANs via Dual-Diffusion," IEEE Access, vol. 12, pp. 39651–39661, 2024, doi: 10.1109/ACCESS.2024.3372996.

[42] X. Xu, Z. Wang, E. Zhang, K. Wang, and H. Shi, "Versatile Diffusion: Text, Images and Variations All in One Diffusion Model," in Proceedings of the IEEE/CVF International Conference on Computer Vision, 2023, pp. 7754–7765.

[43] T. Salimans, I. Goodfellow, W. Zaremba, V. Cheung, A. Radford, and X. Chen, "Improved Techniques for Training GANs."

[44] M. Heusel, H. Ramsauer, T. Unterthiner, B. Nessler, and S. Hochreiter, "GANs Trained by a Two Time-Scale Update Rule Converge to a Local Nash Equilibrium," Adv Neural Inf Process Syst, vol. 30, 2017.

[45] M. S. Sajjadi, O. Bachem, M. Lucic, O. Bousquet, and S. Gelly, "Assessing Generative Models via Precision and Recall for Learning Systems," Adv Neural Inf Process Syst, vol. 31, 2018.

[46] M. Bińkowski, D. J. Sutherland, M. Arbel, and A. Gretton, "Demystifying MMD GANs," in International Conference on Learning Representations, Jan. 2018.

[47] R. Zhang, P. Isola, A. A. Efros, E. Shechtman, and O. Wang, "The Unreasonable Effectiveness of Deep Features as a Perceptual Metric," in Proceedings of the IEEE conference on computer vision and pattern recognition, 2018, pp. 586–595.

RT&A, No 4 (89)
Volume 20, December 2025

NEUTROSOPHIC TOPOLOGIZED BIPARTITE GRAPH

Balakrishnan A[1] and Thirugnanasambandam K*

•

Department of Mathematics,
Muthurangam Government Arts College (Autonomous),
Affiliated to Thiruvaluvar University, Vellore -2, India
[1]balajayamaha@gmail.com and *kthirugnanasambandam@gmail.com

Abstract

Neutrosophic topologized bipartite graph analyses unreliability in bipartite structured graphs by incorporating neutrosophic concepts with topologic possessions. This is a novel approach by providing theorems that integrate truth, indeterminacy and falsity values in topology axioms of neutrosophic graphs. The study introduces a topological space where each singleton set is either open or closed, and the boundary of each element is limited to two or fewer connections. And, it extends the topologized graph into various graph structures like a neutrosophic star graph, a neutrosophic bistar, a neutrosophic bipartite graph, a neutrosophic tree and a neutrosophic complete bipartite graph through theorems and examples.

Keywords: Neutrosophic star graph, Neutrosophic labeling, Neutrosophic complete bipartite graph, neutrosophic cycle.
AMS Subject Classification: 03B52, 03E72, 05C72, 54A40

1. Introduction

Generalizations of fuzzy sets and intuitionistic fuzzy sets are given by Smarandache and Atanassov, respectively. A neutrosophic set involves truth, indeterminacy and falsity values/degrees to indulge the effectiveness of an uncertain environment. Many researchers have submitted and researched various aspects of neutrosophic sets in different fields. Antonia Vella [1] used to refer to the basic conceptualization of a topologized graph. As we go through the path, pre-path and classical topology [2], compact space, pre-cycle, bond space and cycle space we refer to [3]. By the hypergraph $\mathscr{H}$ local connectedness and ferns are defined in [4] as $\mathscr{V}_{\mathscr{H}} \cup \mathscr{E}_{\mathscr{H}}$ a collection of all elements in $\mathscr{U}$ such that if it $\mathscr{U}$ has a vertex v, then it contains all hyperedges incident with v. The fact these topologies were either defined in the union of the vertex set or in the vertex set and edge set. The application of topological graph theory involves printing/coding theory and decoding the codewords from secret or journalistic departments. In [5] the authors discussed the Tanner graph, which is also a bipartite graph, where one subvertex is a codeword and the other subvertex set represents the digit combination without codeword errors. we referred to [6], [7] and [8] for basic graph theory and topology concepts to implement in neutrosophic sets.

Smarandache [9] introduced neutrosophic sets as a generalization of intuitionistic fuzzy sets and explained the basic concept of neutrosophic sets for further research. In [10] applied neutrosophic logic in artificial intelligence, decision making and control systems and provided the basic foundation for neutrosophic graphs in uncertain environments. Akram [11] developed a graph theory framework involving neutrosophic logic by introducing adjacency matrices, shortest paths, and spanning trees in neutrosophic to handle imprecise information in uncertainty. Kanchana M and Kavitha K [12] proposed a heuristic algorithm to solve shortest-path problems in transportation networks modeled with interval-valued neutrosophic sets, effectively handling

uncertainty and negative edge weights. The method improves decision-making in complex and indeterminate environments. Kanchana M and Kavitha K [13] studied a bipolar neutrosophic framework to solve transportation problems on specific graphs such as symmetric graphs, capturing dual uncertainties through positive and negative membership degrees. This contributes to robust logistics modeling in uncertain and bidirectional network settings. Kanchana M and Kavitha K [14] have proposed the Modified Incident Edge Path Algorithm for computing shortest paths in networks with negative weights, avoiding negative cycles. Also, they further introduced a sensitivity analysis [15] for neutrosophic transportation problems to assess route robustness. Their methods enhance decision-making in logistics and urban planning under uncertainty. Both approaches address fuzziness and indeterminacy using neutrosophic logic. Smarandache et al. [16] introduced the foundational conceptualizations of neutrosophic graphs and applied them in complex systems to model uncertainty and fuzzy decision frameworks.

Gross et al. [17] explored the interaction between topology and graph theory, including the analysis of embedding graphs on surfaces and their topological properties. These are applicable in network visualization, biological modeling, and computational topology. Amir [18] discussed the embedding of neutrosophic graphs in spheres and m-toruses. He concluded that neutrosophic sets and crisp graphs can be used to construct neutrosophic graphs that are embeddable on various topological surfaces. Vetrivel et al.In [19] explored the forgotten topological index and its properties in neutrosophic graphs through theoretical formulations and applications. Hamid [20] surveyed box complexes and simplicial complexes related to graphs, offering topological insights by providing lower bounds through chromatic numbers. Max et al. [21] introduced TOGL, which investigates the global topological data of graphs using homology. TOGL can be integrated into graph neural networks, enhancing their functionality compared to traditional models. Vimala [22] introduced foundational concepts of topologized bipartite graphs for stars, trees, and cycles under specific topological conditions. These concepts lead to the implementation of topology in neutrosophic bipartite graphs that satisfy topological axioms, termed as neutrosophic topological bipartite graphs. The considered neutrosophic graphs are finite, undirected, simple, and planar, without multiple edges. The associated topological space is also finite.

This article explores neutrosophic topological graphs and neutrosophic bipartite graphs satisfying topological axioms via theorems and examples. Section 2 presents the fundamental definitions used to demonstrate these concepts. Section 3 contains theorems and solved examples for neutrosophic star, complete bipartite, tree, and cycle graphs. Section 4 concludes the study.

2. Preliminaries

Let [9] the universal set be $\mathcal{U}$ and the neutrosophic set $\mathscr{A}$ in $\mathcal{U}$ is defined as,
$\mathscr{A} = \{(x, T_{\mathscr{A}}, I_{\mathscr{A}}, F_{\mathscr{A}}) | x \in \mathcal{U}\}$, $T_{\mathscr{A}}$ is truth membership, $I_{\mathscr{A}}$ is indeterminacy membership and $F_{\mathscr{A}}$ is falsity membership functions of x; where $T_{\mathscr{A}}$, $I_{\mathscr{A}}$, $F_{\mathscr{A}} \in [0,1]$ satisfying
$0 \leq T_{\mathscr{A}}(x) + I_{\mathscr{A}}(x) + F_{\mathscr{A}}(x) \leq 3$.

Let $\mathscr{G}(\mathscr{V}, \mathscr{E}, \mathcal{T}, \mathscr{N})$ be a neutrosophic topological graph in a topological space, consisting of the following [14], [15]:

- $\mathscr{V}$ a vertex set
- $\mathscr{E}$ edge set, $\mathscr{E} \subseteq \mathscr{V} \times \mathscr{E}$
- $\mathcal{T}$ a topology defined on $\mathscr{V} \cup \mathscr{E}$, forms a neutrosophic topological space $(\overline{X}, \mathcal{T})$ where $\overline{X} = \mathscr{V} \cup \mathscr{E}$
- $\mathscr{N} : \overline{X} \to [0,1] \times [0,1] \times [0,1]$ assigning truth ($T(x)$), indeterminacy ($I(x)$) and falsity ($F(x)$) membership values $\forall x \in \overline{X}$ satisfies $0 \leq T(x) + I(x) + F(x) \leq 3$.

Property of Neutrosophic Topology:

- A neutrosophic subset $\mathscr{U} \subseteq \overline{X}$ is neutrosophically open if $\forall a \in \mathscr{U}$ there is a neutrosophic neighborhood of $x \in \mathscr{U}$.
- Neutrosophic boundary vertex/edge edge x is denoted as $\partial(x)$ satisfying $|\partial| \leq 2$.

These are the separation axioms for neutrosophic topologized graphs.

Let $\mathscr{G}(\mathscr{V},\mathscr{W},\mathscr{E},\mathscr{N})$ be a neutrosophic bipartite graph consisting of $\mathscr{V},\mathscr{W}$ two disjoint vertex subsets such that $\mathscr{V}\cap\mathscr{W}=\emptyset$, $\mathscr{E}$ edge set, $\forall e\in\mathscr{E}$ linking $\mathscr{V}$ to $\mathscr{W}$, $\mathscr{E}\subseteq\mathscr{V}\times\mathscr{E}$. $\mathscr{N}$ a neutrosophic membership function defined as $\mathscr{N}:\mathscr{V}\cup\mathscr{U}\cup\mathscr{W}\to[0,1]\times[0,1]\times[0,1]$ having truth (T), indeterminacy (I) and falsity (F) memberships. Bipartition condition for neutrosophic graph [15]:

- The neutrosophic graph does not contain odd-length cycles
- Each and every partition $\mathscr{V}$ and $\mathscr{W}$ are neutrosophically distinct; that is, $\forall u\in\mathscr{V},w\in\mathscr{W},\mathscr{N}(u)\neq\mathscr{N}(w)$.

We refer the following theorems from [12], [14] and [15] for resulting theorems.

Theorem 1. A neutrosophic graph $\mathscr{G}$ is a neutrosophically bipartite graph iff it contains only cycles of even length, where the truth, indeterminacy and falsity memberships of adjacent vertices satisfy bipartition conditions.

Theorem 2. Every neutrosophic tree is neutrosophically bipartite.

3. Results on Neutrosophic topologized bipartite graph

The following theorems and their examples are proved using the definitions and theorems mentioned in section 2 and refer to some articles from the references mentioned in section 1.

Theorem 3. Let $\bar{\mathcal{K}}_{1,m(T,I,F)}$ be a neutrosophic star graph with m pendant vertices. The neutrosophic graph $\bar{\mathcal{K}}_{1,m(T,I,F)}$ is a neutrosophic topologized graph for $0<m\leq 2$.

Proof. Let $\bar{\mathcal{K}}_{1,m(T,I,F)}$ be a neutrosophic star graph, and consider $(\bar{X},\mathcal{T})$ a topological space where the topology $\mathcal{T}$ is defined by $\mathscr{V}\cup\mathscr{E}$. For all $\mathscr{V},\mathscr{W}\in\mathscr{V}$, $\bar{\mathcal{K}}_{1,m(T,I,F)}$ has a central vertex $\mathscr{V}$ linked to m pendant vertices $w_1,w_2,\ldots,w_m\in\bar{\mathcal{K}}_{1,m(T,I,F)}$, where $m\in\mathbb{N}$ and $0<m\leq 2$. The vertex $\mathscr{V}$ is bipartite with every vertex of $w_1,w_2,\ldots,w_m$. Each vertex and edge of the neutrosophic graph is associated with truth, indeterminacy, and falsity values.

Case (i): For $m=1$, the neutrosophic graph consists of two pendant vertices and one central vertex w_1,w_2, and $\mathscr{V}$, respectively. Let $e\in\mathscr{E}$ be the edge connecting $\mathscr{V}$ to w_1. Thus, $|\bar{X}|=3$. Clearly, $\forall x\in\bar{X},|\partial(x)|\leq 2$ (since the boundary of each x is at most 2). Moreover, for every $x\in\bar{X}$, x is open if its truth value is large and closed if its falsity value is large. Since $\{x\}$ is closed, for any $y\in\bar{X}$, $\bar{X}\setminus\{x\}$ is open. The neutrosophic edge set $\mathscr{E}$'s points, which are not closed, are open, and its complement, the neutrosophic vertex set $\mathscr{V}$, is closed. Thus, $\bar{\mathcal{K}}_{1,1(T,I,F)}$ is a neutrosophic topologized graph.

Case (ii): For $m=2$, $|\bar{X}|=5$, consisting of three pendant vertices w_1,w_2,w_3 and a central vertex $\mathscr{V}$. There exist two edges $e_1=(\mathscr{V},w_1)$ and $e_2=(\mathscr{V},w_2)$ connecting $\mathscr{V}$ to w_1,w_2,w_3. Each singleton vertex is either open or closed based on its truth and falsity values. Each vertex has at most two neighboring vertices, so $|\partial(x)|\leq 2$ is satisfied.

Thus, $\bar{\mathcal{K}}_{1,2(T,I,F)}$ is a neutrosophic topologized graph.

Hence, $\bar{\mathcal{K}}_{1,m(T,I,F)}$ is a neutrosophic topologized graph for $0<m\leq 2$. ■

Example 3.1:

Consider $\bar{\mathcal{K}}_{1,1(T,I,F)}$, a neutrosophic star graph. Let $\forall\mathscr{V},\mathscr{W}\in\mathscr{V}$, $\mathscr{V}=\{v_1\}$, $\mathscr{W}=\{w_1\}$, and $\mathscr{E}=\{e_1=(v_1,w_1)\}$. The topological space is $\bar{X}=\{v_1,e_1,w_1\}$, and the neutrosophic topology is defined as: $\mathcal{T}=\{\emptyset,\{v_1\},\{w_1\},\{v_1,w_1\},\{v_1,e_1\},\{v_1,e_1,w_1\}\}$. For every $\{x\}\in\bar{X}$, it is open or closed. Here, $\mathcal{T}$ consists of open sets, and its neutrosophic values are: $\mathscr{N}(v_1)=(T_{v_1},I_{v_1},F_{v_1})$, $\mathscr{N}(e_1)=(T_{e_1},I_{e_1},F_{e_1})$, $\mathscr{N}(w_1)=(T_{w_1},I_{w_1},F_{w_1})$. The boundary value of each vertex and edge is at most 2 neighboring elements, satisfying $|\partial(x)|\leq 2$. $\partial(v_1)=\{w_1\}\implies|\partial(v_1)|=1$, $\partial(e_1)=\{v_1,w_1\}\implies|\partial(e_1)|=2$,
$\partial(w_1)=\{v_1\}\implies|\partial(w_1)|=1$.

Hence, $\bar{\mathcal{K}}_{1,1(T,I,F)}$ is a neutrosophic topological graph and given in the figure 1

Theorem 4. A bistar graph $\mathcal{B}(n,n)$ is not a neutrosophic topologized graph.

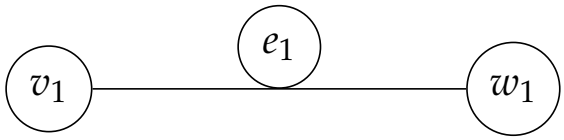


Figure 1: *$\bar{\mathcal{K}}_{1,1(T,I,F)}$ is a neutrosophic topological graph.*

Proof. Let $(\bar{X}, \mathcal{T})$ be a topological space where the topology $\mathcal{T}$ is defined by $\mathscr{V} \cup \mathscr{E}$. The space contains a bistar graph $\mathcal{B}(n,n)$, which consists of two star graphs $\mathcal{S}(n)$ connected by a central vertex v_c. Each star graph $\mathcal{S}(n)$ has n leaf vertices, resulting in a total of $2n$ leaf vertices in $\mathcal{B}(n,n)$. The central vertex v_c connects to all $2n$ leaf vertices. Let v_l denote a leaf vertex connected to v_c. The boundary values of the vertices are as follows:

$$|\partial(v_l)| = 1 \quad \text{and} \quad |\partial(v_c)| = 2n.$$

Each vertex and edge in $\mathcal{B}(n,n)$ is associated with truth (T), indeterminacy (I), and falsity (F) neutrosophic values. For the central vertex v_c, the boundary leads to $2n$ connections, which overlap and violate the neutrosophic values T, I, and F. Since the sum of T, I, and F must satisfy:

$$0 \leq T + I + F \leq 3.$$

It is not possible for v_c to lie on the boundary while satisfying this condition, as the boundary size $2n$ exceeds the limit for valid neutrosophic values. Furthermore, every singleton v_c must be either open or closed neutrosophically. However, v_c becomes indeterminate due to its large boundary, violating the neutrosophic topology.
Hence, $\mathcal{B}(n,n)$ is not a neutrosophic topologized graph. ■

Example 3.2

Let $\mathcal{B}(3,3)$ be a bistar graph, where the central vertex v_c connects to the leaf vertices $v_1, v_2, v_3, v_4, v_5, v_6$ of $\mathcal{S}(3)$. The boundary of v_c is $|\partial(v_c)| = 6 = \{v_1, v_2, v_3, v_4, v_5, v_6\}$. For a leaf vertex v_1, we have $|\partial(v_1)| = 1$.

Let the neutrosophic values for $v_1, v_2, v_3, v_4, v_5, v_6$ be $T = 0.9$, $I = 0.1$, and $F = 0$. Then for v_c, we calculate:

$$T_{(v_c)} = \sum_{i=1}^{6} T_{(v_i)} = 6 \times 0.9 = 5.4, \quad I_{(v_c)} = \sum_{i=1}^{6} I_{(v_i)} = 0.6, \quad F_{(v_c)} = \sum_{i=1}^{6} F_{(v_i)} = 0.0.$$

These values are not valid in neutrosophic logic since $T + I + F \geq 3$ is not allowed. Hence, $\mathcal{B}(3,3)$ is not a neutrosophic topologized graph.

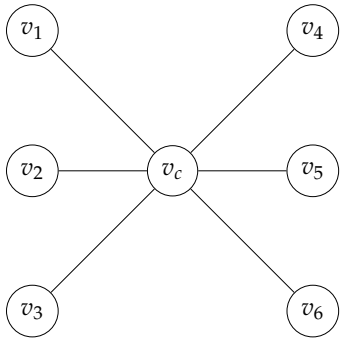


Figure 2: *Bistar graph $\mathcal{B}(3,3)$ with central vertex v_c and leaf vertices $v_1, v_2, v_3, v_4, v_5, v_6$.*

Theorem 5. Let $\mathscr{G}(\mathscr{V}, \mathscr{E}, T, I, F)$ be a neutrosophic bipartite graph. $\mathscr{G}_n$ is topologized if every vertex has a degree at most 2.

Proof. Consider the neutrosophic bipartite graph $\mathscr{G}$ whose vertices have degree at most 2. Let the topological space $(\overline{X}, \mathcal{T})$, where the boundary of any vertex or edge is determined by its adjacent or incident vertices. Since the degree of every vertex is at most 2, the boundary of any vertex or edge is less than 3. Each singleton vertex or edge is either open or closed, as their boundaries are limited. Thus, $\mathscr{G}$ is a topologized neutrosophic graph. Moreover, the neutrosophic topology on $\mathscr{G}$ satisfies the required separation axioms $\mathscr{T}_0$ and $\mathscr{T}_1$:

- $\mathscr{T}_0$: Distinct vertices can be separated by neutrosophic open sets.
- $\mathscr{T}_1$: There exists a neutrosophic open set that separates each vertex with distinct membership values.

Hence, $\mathscr{G}$ is a neutrosophic topologized bipartite graph. ■

Example 3.3:

Consider the neutrosophic bipartite graph $\mathscr{G}(\mathscr{V}, \mathscr{E}, T, I, F)$, where:
$\mathscr{V} = \mathscr{U} \cup \mathscr{W}$, $\mathscr{U} = \{u_1, u_2\}$, $\mathscr{W} = \{w_1, w_2\}$, and
$\mathscr{E} = \{e_1, e_2\}$, $e_1 = (u_1, w_1)$, $e_2 = (u_2, w_2)$.
let $\overline{X} = \{u_1, u_2, w_1, w_2, e_1, e_2\}$ be the topological space defined by:
$\mathcal{T} = \{\overline{X}, \varnothing, \{e_1\}, \{e_2\}, \{u_1, e_1, w_2\}, \{u_2, e_2, w_1\}, \{e_1, e_2\}, \{u_1, e_1, w_2, e_2\}, \{u_2, e_2, w_1, e_1\}, \{u_1, e_1\}, \{u_1, e_1, e_2\}, \{u_1, e_1, u_2, e_2, w_1\}\}$.
Assigning the membership values as:

$$T_{(u_1)} = \{w_2\} = 1, \quad T_{(u_2)} = \{w_1\} = 1, \quad T_{(w_1)} = \{u_2\} = 1, \quad T_{(w_2)} = \{u_1\} = 1,$$

$$T_{(e_1)} = \{u_1, w_1\} = 2, \quad T_{(e_2)} = \{u_2, w_2\} = 2.$$

The degree of each vertex is at most two and satisfies the boundary condition:
$|\partial(u_1)| = |\partial(w_2)| = |\partial(u_2) = |\partial(w_1)| = 1$; $|\partial(e_1)| = |\partial(e_2)| = 2$ therefore,

$$|\partial(x)| \leq 2 \quad \text{for all } x \in \overline{X}.$$

Thus, the neutrosophic topology defined on the neutrosophic bipartite graph $\mathscr{G}$ satisfies all the required conditions, making it a neutrosophic topologized graph.

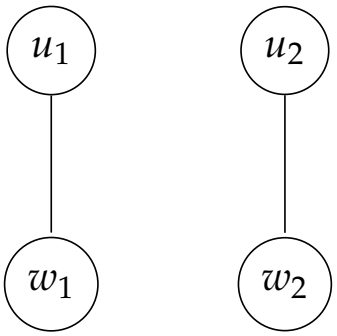


Figure 3: *Neutrosophic bipartite graph $\mathscr{G}_n$*

Corollary 3.1: Let $\mathscr{G}$ be a tree. If $\mathscr{G}$ is a neutrosophic bipartite graph, then it is a neutrosophic topologized graph.

Proof: Let $\mathscr{G}$ be a tree and also a neutrosophic bipartite graph, which is acyclic by definition, and its vertex set $\mathscr{V}$ can be decomposed into $\mathscr{V}_1$ and $\mathscr{V}_2$, two vertex sets, where $\mathscr{V}_1$ is connected to $\mathscr{V}_2$ by edges of $\mathscr{E}$ of $\mathscr{G}$. Assuming the boundary conditions under a neutrosophic setting, For any edge $e = u_1, v_1 \in \mathscr{E}$, e connects adjacent vertices, each vertex has a degree at most 2 determining neutrosophic boundary values, which implies that the boundary of each vertex is at most 2. since $\mathscr{G}$ is a tree, every vertex has a well-defined neutrosophic neighborhood. Thus, every singleton vertex is either open or closed under truth membership values and is connected through a finite

number of edges satisfying the separation properties of neutrosophic bipartite nature. Hence, $\mathscr{G}$ is a neutrosophic topologized graph.

Example 3.4:

Defining the neutrosophic topological space $\overline{X} = \{v_1, v_2, w_1, w_2, e_1, e_2, e_3\}$, and its topology $\mathcal{T}$ as:

$\mathcal{T} = \{\overline{X}, \varnothing, \{v_1\}, \{v_2\}, \{w_1, e_1, e_2, v_2\}, \{v_2, e_3, w_2\}, \{v_2, w_2\}, \{v_1, v_2\}, \{v_1, w_1, e_1, e_2, v_2\}, \{v_1, v_2, e_3, w_2\}, \{v_1, v_2, w_2\}, \{v_2, e_3, w_2, w_1, e_1, e_2\}, \{w_1, e_1, e_2, v_2, w_2\}, \{v_1, v_2, w_2\}, \{v_1, w_1, e_1, e_2, v_2, w_2\}, \{w_1, w_2, e_1, e_2, v_2, e_3\}, \{v_1, w_1, e_1, e_2, v_2, w_2\}, \{w_1, e_1, e_2, v_2\}\}$.

For every singleton $x \in \overline{X}$, it is open or closed such that $|\partial(x)| \leq 2$. satisfying boundary conditions for each vertex are:

$$|\partial(v_1)| = \{w_1\} = 1, \quad |\partial(v_2)| = \{w_1, w_2\} = 2,$$
$$|\partial(w_1)| = \{v_1, v_2\} = 2, \quad |\partial(w_2)| = \{v_2\} = 1,$$
$$|\partial(e_1)| = \{v_1, w_1\} = 2, \quad |\partial(e_2)| = \{v_2, w_1\} = 2,$$
$$|\partial(e_3)| = \{v_2, w_2\} = 2.$$

The boundary of each vertex and edge is $|\partial(x)| \leq 2$, and the neutrosophic topology separation axioms are;

$\mathscr{T}_0$: Every singleton vertex is open or closed satisfying $|\partial(x)| \leq 2$.

$\mathscr{T}_1$: For any two distinct vertices there exists an open set. Thus, $\mathscr{G}$ is a neutrosophic topologized graph.

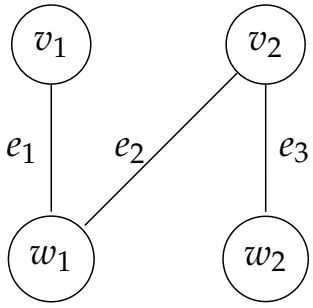


Figure 4: *$\mathscr{G}$ is a neutrosophic topologized graph where $\mathscr{G}$ is a tree*

Theorem 6. All neutrosophic cycles in a neutrosophic bipartite graph are neutrosophically topologized.

Proof. Let $\mathscr{G}(\mathscr{V}, \mathscr{E})$ be a neutrosophic bipartite graph having topological space $(\overline{X}, \mathcal{T})$, where its neutrosophic topology $\mathcal{T}$ is defined by its vertex and Edge set, $\mathscr{V}$ and $\mathscr{E}$ respectively.

Every neutrosophic bipartite graph contains only even cycles, and where these cycles are regular. For each vertex $v \in \mathscr{V}$ and edge $e \in \mathscr{E}$, the boundary $\partial(x)$ satisfies:

$$|\partial(x)| \leq 2.$$

By the neutrosophic topology separation axiom, every singleton vertex or edge in a cycle is either open or closed. Since every cycle in the neutrosophic bipartite graph is created from $\mathscr{V}$ and $\mathscr{E}$, each having a boundary of at most 2, then all neutrosophic cycles are neutrosophically topologized. Hence, every neutrosophic cycle in a neutrosophic bipartite graph is neutrosophically topologized. ■

Example 3.5:

Let $\mathcal{B}(3, 4)$ be a neutrosophic bipartite graph.

The neutrosophic bipartite graph $\mathcal{B}(3, 4)$ defined by the following vertex sets and edge sets: $\mathscr{V} = \{v_1, v_2, v_3\}$, $\mathscr{W} = \{w_1, w_2, w_3, w_4\}$ and $\mathscr{E} = \{e_1, e_2, e_3, e_4, e_5, e_6, e_7, e_8\}$ where,

$$(e_1) = \{v_1, w_1\}, \quad (e_2) = \{v_1, w_2\}, \quad (e_3) = \{v_1, w_3\}$$

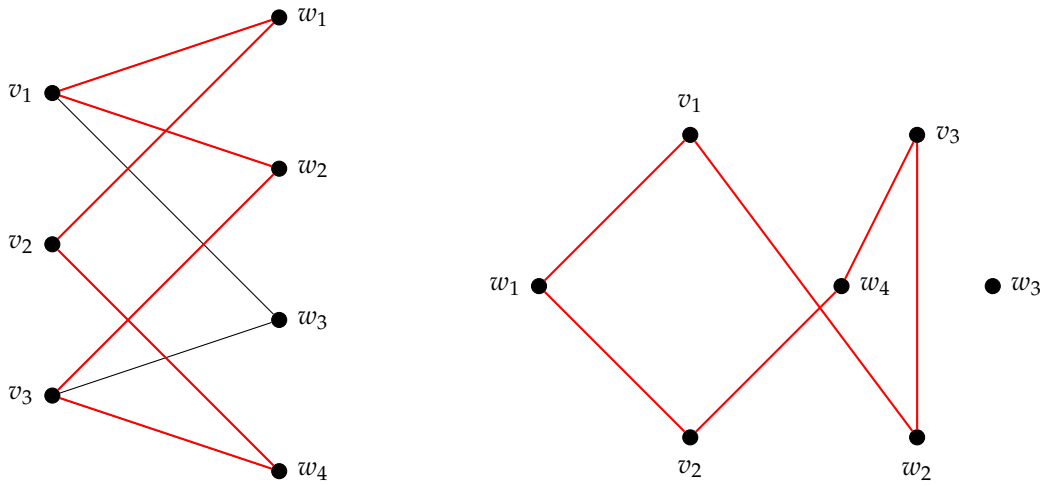
$$(e_4) = \{v_2, w_1\}, \quad (e_5) = \{v_2, w_4\}, \quad (e_6) = \{v_3, w_2\}$$
$$(e_7) = \{v_3, w_3\}, \quad (e_8) = \{v_3, w_4\}$$

the neutrosophic topological space is $\overline{X} = \{v_1, v_2, v_3, w_1, w_2, w_3, w_4, e_1, e_2, e_3, e_4, e_5, e_6, e_7, e_8\}$
Let the neutrosophic cycle $\mathcal{C}_1$ is $\mathcal{C}_1 = \{v_1, e_1, w_1, e_4, v_2, e_5, w_4, e_8, v_3, e_6, w_2, e_2, v_1\}$
The neutrosophic values (T, I, F) for each v_i, w_j and e_k are:

$$\mathcal{N}(v_i) = (T_{v_i}, I_{v_i}, F_{v_i}), \quad \mathcal{N}(w_j) = (T_{w_j}, I_{w_j}, F_{w_j})$$
$$\mathcal{N}(e_k) = (T_{e_k}, I_{e_k}, F_{e_k}), \quad \forall v_i \in \mathcal{V}, \quad \forall w_j \in \mathcal{W}, \quad \forall e_k \in \mathcal{E}.$$

$$|\partial(v_1)| = \{w_1, w_2\} = 2, \quad |\partial(v_2)| = \{w_1, w_4\} = 2, \quad |\partial(v_3)| = \{w_2, w_4\} = 2$$
$$|\partial(w_1)| = \{v_1, v_2\} = 2, \quad |\partial(w_2)| = \{v_1, v_3\} = 2, \quad |\partial(w_4)| = \{v_2, v_3\} = 2$$
$$|\partial(e_1)| = \{v_1, w_1\} = 2, \quad |\partial(e_2)| = \{v_1, w_2\} = 2, \quad |\partial(e_4)| = \{v_2, w_1\} = 2$$
$$|\partial(e_5)| = \{v_2, w_4\} = 2, \quad |\partial(e_6)| = \{v_3, w_2\} = 2, \quad |\partial(e_8)| = \{v_3, w_4\} = 2$$

Since every $|\partial(x)| \leq 2$ is satisfied, hence, $\mathcal{B}(3,4)$ is a neutrosophic topologized graph and similarly, $\mathcal{C}_2, \mathcal{C}_3, ..., \mathcal{C}_{11}$ neutrosophic cycles exist.



(a) $\mathcal{B}(3,4)$ *neutrosophic bipartite graph* **(b)** *Neutrosophic cycle* $\mathcal{C}_1$ *in* $\mathcal{B}(3,4)$

Figure 5: *Graph* $\mathcal{B}(3,4)$ *and the neutrosophic cycle* $\mathcal{C}_1$

As shown in Figure 5, the cycle $\mathcal{C}_1$ forms a closed path

Theorem 7. Let $\overline{\mathcal{K}}_{m,n}$ be a bipartite graph with $(m, n \geq 3)$. Then $\overline{\mathcal{K}}_{m,n}$ is not a neutrosophic topologized bipartite graph.

Proof. A neutrosophic bipartite graph $\overline{\mathcal{K}}_{m,n}$ consists of two disjoint sets $\mathcal{V}_1$ and $\mathcal{V}_2$, where: $|\mathcal{V}_1| = m$ and $|\mathcal{V}_2| = n$. Each vertex in $\mathcal{V}_1$ is connected to all vertices in $\mathcal{V}_2$ and respectively. For a neutrosophic topologized graph, any vertex x must satisfy the boundary condition $|\partial(x)| \leq 2$. In $\overline{\mathcal{K}}_{m,n}$, the degree of any vertex $v \in \mathcal{V}_1$ is n, and the degree of any vertex $w \in \mathcal{V}_2$ is m. Since $(m, n \geq 3)$, the degree of each vertex in $\overline{\mathcal{K}}_{m,n}$ is:

$$|\partial(v)| = n \geq 3 \quad \text{and} \quad |\partial(w)| = m \geq 3.$$

which violates $|\partial(x)| \leq 2$. Thus, $\overline{\mathcal{K}}_{m,n}$ is not a neutrosophic topologized bipartite graph. ■
Example 3.6:
$\overline{\mathcal{K}}_{4,5}$ is not a neutrosophic topologized graph.

Consider the structure of $\overline{\mathcal{K}}_{4,5}$ as;

$$\mathscr{V} = \{v_1, v_2, v_3, v_4\}, \quad \mathscr{W} = \{w_1, w_2, w_3, w_4, w_5\}$$

$$\mathscr{E} = \{e_1, e_2, \ldots, e_{20}\}, \quad (e_{ij}) = \{v_i, w_j\}, \quad \forall e_{ij} \in \mathscr{E}$$

Degree of vertices are,
$|\partial(v_i)| = 5, \quad \forall v_i \in \mathscr{V}, |\partial(w_j)| = 4, \quad \forall w_j \in \mathscr{W}$
the neutrosophic graph is neutrosophically topologized if $|\partial(x)| \leq 2, \quad \forall x \in \mathscr{V} \cup \mathscr{W}$
Violation of degree:

$$|\partial(v_i)| = 5 > 2, \quad \forall v_i \in \mathscr{V}, \ |\partial(w_j)| = 4 > 2, \quad \forall w_j \in \mathscr{W}$$

thus, $|\partial(x)| \leq 2$ is violated since: $\exists x \in \mathscr{V} \cup \mathscr{W}$ such that $|\partial(x)| > 2$.
Hence, $\overline{\mathcal{K}}_{4,5}$ is not a neutrosophic topologized graph and shown in Fig. 6 .

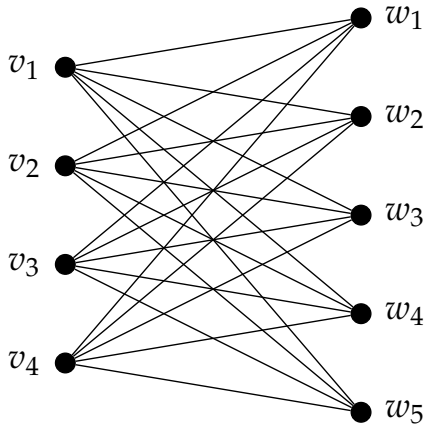


Figure 6: *$\overline{\mathcal{K}}_{4,5}$ not a neutrosophic topologized graph*

4. Discussion and Conclusion

The neutrosophic topologically bipartite graph was introduced and analyzed by incorporating the ideals of the neutrosophic idea with graph topology. By integrating the neutrosophic values of truth, indeterminacy and falsity in topological properties into graph structures. The neutrosophic star graph, Bistar graph, neutrosophic bipartite graph, neutrosophic tree, and neutrosophic complete bipartite graphs satisfying the boundary condition $0 < m \leq 2$ were verified using theorem proofs with suitable examples. Also, the non-topological graph under neutrosophic topological axioms was demonstrated in the theorem. These theorems provided a new approach to model a topology graph structure into a neutrosophic topological graph structure by defining truth, indeterminacy and falsity values.

4.1. Future work

Expanding these theorems into high-dimensional topology by defining its structure in neutrosophic values providing neutrosophic graphs, and investigating the influence of dynamic transpose in neutrosophic values. Expanding this into an algorithmic approach for application in artificial intelligence, such as optimization and modeling for uncertain environments.

Conflicts of interest : "The authors declare there is no conflict of interest."

References

[1] Vella, A. (2005). A fundamentally topological perspective on graph theory. *Ph.D. Thesis*, University of Waterloo, Ontario, Canada.

[2] Diestel, R. and Kuhn, D. (2004). Topological paths, cycles in infinite graphs. *European Journal of Combinatorics*.

[3] Diestel, R. (2004). The cycle space of an infinite graph. To appear in *Combinatorics, Probability and Computing*.

[4] Berge, C. (1989). *Hypergraphs: Combinatorics of Finite Sets*. North-Holland Mathematical Library, Vol. 45, North-Holland Publishing Co., Amsterdam.

[5] Skiena, S. (1990). Coloring bipartite graphs. In *Implementing Discrete Mathematics: Combinatorics and Graph Theory with Mathematica*.

[6] Simmons, G. F. (1963). *Introduction to Topology and Modern Analysis*. Robert E. Krieger Publishing Co., Malabar, Florida.

[7] Arumugam, S. and Ramachandran, S. (2006). *Invitation to Graph Theory*. Scitech Publications (India) Pvt. Ltd.

[8] Diestel, R. (2000). *Graph Theory*. Graduate Texts in Mathematics, Springer-Verlag, New York.

[9] Smarandache, F. (1998). Neutrosophic sets: A generalization of the intuitionistic fuzzy sets. *University of New Mexico*.

[10] Smarandache, F. (2002). *Neutrosophic Logic and Applications*. American Research Press.

[11] Akram, M. (2018). *Single-Valued Neutrosophic Graphs*. Springer. https://doi.org/10.1007/978-981-13-3522-8

[12] Kanchana, M. and Kavitha, K. (2024). Heuristic incident edge path algorithm for interval-valued neutrosophic transportation network. *Contemporary Mathematics*, 5(2):2016–2036. https://ojs.wiserpub.com/index.php/CM/article/view/4152

[13] Kanchana, M. and Krishnan, K. (2024). Bipolar neutrosophic transportation problem in symmetric graphs. *Mathematics and Statistics*, 12(6):515–522. https://www.hrpub.org/journals/article_info.php?aid=14589

[14] Kanchana, M. and Kavitha, K. (2025). A modified incident edge path algorithm for efficient shortest path solutions in pipeline networks and urban navigation systems. *Reliability: Theory & Applications*, 20(1):46–58. https://gnedenko.net/Journal/2025/012025/RTA_1_2025-46.pdf

[15] Kanchana, M. and Kavitha, K. (2024). Sensitivity analysis and application of single-valued neutrosophic transportation problem. *Journal of King Saud University " Science*, 36(11):103567. https://doi.org/10.1016/j.jksus.2024.103567

[16] Smarandache, F., Ali, M. and Salama, A. (2014). Introduction to neutrosophic graph theory. *Neutrosophic Sets and Systems*, 3(1):18–24.

[17] Gross, J. L. and Tucker, T. W. (2001). *Topological Graph Theory*. John Wiley & Sons.

[18] Majeed, A. S. (2024). Embedding of neutrosophic graphs on topological surfaces. *Journal of University of Babylon for Pure and Applied Sciences*, 32(3):45–56.

[19] Vetrivel, G., Mullai, M. and Buvaneshwari, R. (2024). Forgotten topological index and its properties on neutrosophic graphs. *Neutrosophic Systems and Applications*, 5(2):112–128.

[20] Daneshpajouh, H. R. and Meunier, F. (2023). Box complexes: at the crossroad of graph theory and topology. *arXiv preprint*, arXiv:2307.00299.

[21] Horn, M., De Brouwer, E., Moor, M., Moreau, Y., Rieck, B. and Borgwardt, K. (2021). Topological graph neural networks. *arXiv preprint*, arXiv:2102.07835.

[22] Vimala, S. and Kalpana, S. (2017). Topologized bipartite graph. *Asian Research Journal of Mathematics*, 4(1):1–10. https://doi.org/10.9734/ARJOM/2017/33107

COMPARATIVE VAR FORECASTING USING LOW AND HIGH-FREQUENCY CONDITIONAL EVT MODELS: EVIDENCE FROM NIFTY INDICES IN INDIA

Nadia Sha[1], Hena M[2], and Bitha S Mani[3]

•

[1]Department of Finance and Economics. College of Commerce and Business Administration, Dhofar University, Salalah 211, Oman.
[2]Department of Rural Marketing Management, College of Cooperation, Banking and Management, Kerala Agricultural University, Thrissur, India
[3]Rajadhani Business School- RIET Nagaroor, Trivandrum 695102, Kerala, India
nsha@du.edu.om, hena.m@kau.in, dr.bitha2021@gmail.com

Abstract

This study uses Value-at-risk (VaR) and Expected Shortfall (ES) to determine if the availability of high-frequency data improves the accuracy of estimating severe market risk as compared to low-frequency data. The daily closing stock prices of the NIFTY 50, NIFTY 100, and NIFTY 200 Index from January 1, 2021, to April 31, 2025, made up the sample data utilised for analysis. The purpose of the data study was to evaluate the effectiveness of conditional EVT, a two-stage hybrid strategy that merged the EVT methodology with the GARCH, RV, and HAR specification models. Unconditional coverage (UC) and conditional coverage (CC) tests were used to backtest the out-of-sample VaR predictions in order to evaluate their correctness. The regulatory loss function (RLF) and the firm's loss function (FLF) are two utilisation loss functions that were also included in the VaR backtesting process. The generalised breach indicator (GBI) approach was used to backtest the anticipated ES's accuracy. The results of this study demonstrated that when it came to forecasting market risk during times of extraordinary returns, high-frequency conditional EVT that included the HAR specification performed better than low-frequency conditional EVT. When compared to the GARCH-EVT and RV-EVT typed models throughout the periods, the HAR-EVT typed models perform the best according to the VaR and ES measures. The hybrid model of long-memory models for the EVT method is the focus of this research work, which adds to the body of knowledge on the forecasting abilities of risk models.

Keywords: Conditional EVT models, High-frequency data, VaR, NIFITY indices, Expected shortfall.

I. Introduction

Modern finance theory relies heavily on volatility, the most widely utilised indicator of uncertainty. Risk management, portfolio optimisation, and financial asset pricing all depend on the ability to measure and predict volatility. The stock market's performance is assessed and its movement is predicted using a variety of volatility models. Accurate volatility prediction is a critical skill for stock market practitioners and scholars. The Indian government's numerous initiatives since 1991, the effects of "liberalisation," "privatisation," and "globalisation" policies, as well as ensuing financial sector reforms, have all contributed to the substantial shifts and structural changes in the Indian stock market [29]. Since the 1970s, when options trading first began, its effect on stock market volatility has undergone substantial modification. Numerous studies show that

futures trading lowers spot market volatility by integrating advanced risk management systems, removing information asymmetry, increasing the amount of information available to the price formation process, improving price discovery efficiency, and increasing profits by minimising risk [30]. During periods of significant market volatility, like the global financial crisis of 2007–2009 and the 1987 U.S. stock market crash, this occurrence is most common. Furthermore, when derivatives are introduced to the Indian stock market, they create significant opportunities for hedging and speculating, which lead to price instability and amplify the underlying market volatility [31]. However, when compared to cash market assets, a vast number of investors and financial managers view derivatives as highly captive due to their low initial requirements with the clearing house for futures, the payment of premiums for options, and their low transaction costs [32, 33]. Since there is no solid empirical evidence that the index option causes volatility to fluctuate, over the past few decades, scholars and industry professionals have been very interested in the economic impact of Nefty index derivatives on stock market volatility [34]. Regarding the effect of index derivatives on the volatility of the underlying market, this presents significant queries for investors, researchers, academics, and financial managers [35]. The majority of previous research has actually demonstrated that the introduction of index futures may result in a stabilisation or a reduction in volatility [36, 37]. In addition to upsetting Asian economies, the crisis had an impact on international markets, which made Western investors reevaluate their exposure to developing nations like India. Stronger regulatory frameworks and risk management techniques are required, as the period's elevated levels of uncertainty and capital flight demonstrated the Indian financial system's susceptibility to outside shocks. As investors reacted to the growing health crisis and its possible economic ramifications, the world's financial markets saw precipitous drops. Financial markets saw large selloffs and reductions as a result of worries about a global economic slump, decreased consumer spending, and disrupted supply chains. Recent research has shown that COVID-19 has a significant influence on global stock prices due to its high volatility and risk uncertainty [1,2]. This study is motivated to use the current COVID-19 era as the sample data for analysis because of the influence that financial crises have on stock markets, as was previously described. This decision stems from the lack of previous studies on the effectiveness of high-frequency conditional EVT in predicting stock market risk following the COVID-19 pandemic.

Previous research has demonstrated how well the GARCH model predicts stock market risk using financial time series analysis and low-frequency data. Because of its capacity to capture persistence and clustering of volatility, the GARCH model has been widely used and proven to be effective in modelling and predicting volatility across a range of financial markets. These days, the availability of high-frequency data has encouraged academics to explore risk forecasting models other than the traditional GARCH model. It is essential to investigate the presence of long memory in intraday returns, particularly with reference to the RV and HAR criteria, which provide additional incentive for this work, as researchers have been paying close attention to the existence of long memory in daily returns. Since the financial stock market is known to be susceptible to rapid swings during times of market volatility, risk-averse investors place a high priority on measuring market risk. The EVT technique is used in this study in conjunction with high-frequency models based on the RV and HAR requirements. It was believed that by using a hybrid technique that combines high-frequency models with EVT, tail risk estimates would be enhanced by better capturing severe market occurrences. The statistical framework of EVT makes modelling and analysis easier by concentrating on the extreme returns of tail distributions, whereas the HAR model concentrates on the volatility cascade over various investment horizons.

The conditional EVT model is the general term for the hybrid strategy that combines any low-frequency or high-frequency models with the EVT technique. It has been demonstrated in earlier studies that the conditional EVT model improves the capacity to predict and evaluate risk in tumultuous market situations; however, the majority of these studies employed daily returns as a

stand-in for volatility. Since high-frequency data has become available, researchers have begun to investigate how intraday returns based on the RV criteria might enhance risk forecasting. Researchers attempt to integrate the EVT technique with the HAR model subsequent to the development of the HMH hypothesis. According to [3], the combined HAR-GARCH-EVT model, which accounts for the conditional heteroscedasticity of the HAR errors, performs better overall and generates accurate VaR estimates that successfully reduce Basel II regulatory capital requirements. The accuracy of the model is demonstrated in both the entire out-of-sample period and the 2007–2009 crisis period. The precision of the HAR-EVT models in predicting stock market risk has been further investigated. The performance of low-frequency conditional EVT models in comparison to high-frequency conditional EVT models may be further investigated thanks to the availability of high-frequency data. The conditional EVT fared better overall, according to the researchers' comparison of the high-frequency data. Better predictions are obtained when realised volatility is used as the volatility estimator for high-frequency data rather than daily returns. Several studies have been carried out to support the advantages of using the RV standard in conjunction with the EVT technique as a hybrid model. Although this field of study is still largely unexplored, the current work also uses the RV specification obtained from the HAR model in the context of the conditional EVT model. The goal of this work is to add to the body of knowledge on the forecasting capabilities of risk models by focussing on the long-memory FIEGARCH, RV-FIEGARCH, and HAR-FIEGARCH models using the as-yet-unexplored EVT technique. The results of the study will help advance understanding of how various data frequencies might affect stock market risk forecasting and offer precise models for use in investing strategies and risk management procedures.

Researchers debate whether using high-frequency data is worthwhile despite its benefits because of its greater cost, as demonstrated by a study by [4]. In addition to being more expensive, it takes longer to analyse than low-frequency data. The benefits of employing this high-frequency data could exceed the drawbacks for traders and investors with substantial cash. They will be able to increase their investment and reduce their possible loss thanks to this high-frequency data's capacity to react swiftly to market movements. The primary obstacle for other small traders and investors, however, will be the costs involved in gathering and evaluating high-frequency data. In these situations, the low-frequency data which is typically more accessible and less expensive will be selected. Some researchers who only use low-frequency data will lose out on chances provided by high-frequency data, particularly in the present big data era when it is projected that the growth of big data analytics and application database solutions will reach $12 billion by 2027 [5]. A thorough assessment of the possible benefits and drawbacks, as well as knowledge of the data's intended use and the particular trading or investing goals it would serve, should inform the choice to use high-frequency data. The cost concern provides further impetus for this research to investigate if, in comparison to low-frequency data, the possible advantages of using high-frequency data in data-rich markets are more or equal. If this expense will eventually result in significant value in the context of financial market modelling and forecasting, that remains to be seen.

The rest of the document is structured as follows: Section 2 reviews the relevant literature, Section 3 presents a theoretical framework of conditional extreme value theory, Section 4 describes the data analysis of NIFTY indices, and Section 5 provides the summary and conclusion of the study.

II. Literature Review

Researchers have paid close attention to volatility predictions using EVT. A framework for

examining extreme occurrences and tail behaviour in financial markets is offered by EVT. Extreme quantiles and tail probabilities, which are essential for volatility forecasting, may be estimated thanks to EVT's emphasis on extreme data. EVT is the best option for examining the tail distribution that is marked by severe occurrences. Many research have been conducted to examine the EVT approach's accuracy in predicting stock market risk in comparison to other alternative models. According to a [6] study, the hybrid model GARCH-EVT works well for handling asymmetric tail distributions on the S&P Index. In contrast to other models that are not integrated with EVT, a follow-up investigation by [7] discovered that EVT is dependable in calculating the VaR and ES. According to a research by [8], the GARCH model and EVT work better together than the traditional standalone EVT model in forecasting stock market volatility during severe occurrences. When [9] examined the ISE-100, S&P-500, and Nikkei-225 indices, they discovered that the GARCH-EVT model performed better than the GARCH model alone. Furthermore, [10] discovered that the FIAPARCH-EVT model outperforms FIGARCH-EVT and HYGARCH-EVT in forecasting VaR one day in advance. The GARCH-EVT model outperformed the basic skewed-t GARCH model in predicting stock market risk during the Tehran Stock Exchange's capital slump era, according to another study by [11]. According to a research by [12], VaR forecasting on the daily returns data of twelve prominent international stock indexes was much enhanced by the GARCH-EVT model. The GARCH-EVT models fared better than other models in predicting intraday VaR during the COVID-19 pandemic, according to additional study by [13]. Furthermore, the GARCH-EVT-copula technique is the most effective way to quantify the VaR and ES both before and after the COVID-19 pandemic, according to a research by [14]. The GARCH-EVT-Copula-CoVaR model is accurate in predicting the spillover risk impact of global oil prices on Chinese sectoral stock markets, according to a recent research by [15].

Scholars are using high frequency data based on intraday data to predict stock market risk as a result of the recent revolution in high-frequency data. Rather than using the volatility of the daily returns to estimate the VaR and ES, the realised volatility is converted to fresh latent volatility. In contrast to low-frequency models that employed daily returns series, more recent study that combined realised volatility models with the EVT technique shown that it has more benefits and accurate estimates. The effectiveness of the realised GARCH model in the US equities market is investigated in a research by [16]. After that, [7] expand on [16] work and come to the conclusion that the realized-GARCH EVT models perform better in predicting when it comes to estimating VaR and ES. The EGARCH model in conjunction with the EVT technique is highly effective in forecasting a significant loss for precious metal markets, according to additional study by [17]. The [11] claim that the GARCH-EVT model beats the basic GARCH model with Student's t and normal distributions for residuals and allows for an accurate VaR calculation in this market as well. As was previously mentioned, the HAR model has demonstrated potential in capturing volatility patterns over various time scales since it takes into account the heterogeneity of market players' trading behaviours. When compared to the traditional GARCH model, [18] found that the HAR-GARCH specification better reflects the persistent memory patterns in volatility. The [19] found in another study that the HAR-RV models outperform their traditional counterparts in terms of VaR performance. When compared to other realised volatility models, the HAR-GARCH model demonstrated better predicting accuracy for Bitcoin volatility, according to [20] findings. The GARCH-EVT is better at forecasting the risk of high-frequency returns data at 15-minute intervals in the metal market, according to a recent study by [21].

III. Materials and Methods

I. Data collection

This study examines the NSE NIFTY 50, 100, and 200 Index, which represents a diversified portfolio of the 50 largest and most liquid stocks listed on the National Stock Exchange (NSE) of India. Serving as a key benchmark for the Indian equity market, the NIFTY 50, 100, and 200 Index reflects the overall performance of the market and provides insight into the economic condition of India. The study utilizes daily closing prices of the NIFTY 50, 100, and 200 Index, obtained from the official NSE website, to ensure data accuracy and consistency for robust statistical analysis. It includes 1072 observations of closing prices for the NSE Nifty index between January 1, 2021, and April 31, 2025. The preliminary analysis, in-sample empirical analysis, and out-of-sample analysis are the three categories of data analysis used to evaluate the VaR and ES prediction. Since P_n represents the closing stock prices, the logarithmic daily returns of the selected stock markets were calculated by applying the following formula to measure the difference between the logarithmic price levels on two consecutive days:

$$\{r_n\}_{n-1}^{T} = \text{logarithm}\left(\frac{P_n}{P_{n-1}}\right) \quad (1)$$

In two phases, the 5-minute logarithmic realised variance, or log RV_n, was computed. The first step was applying the R-programming code based on Equation (1) to convert the 5-minute stock prices into one-day trading returns. Assuming j = 2,3,4,5,6, ... k., k represents the entire 5-min stock prices. Then, using the following formula, the one-day trading returns were converted to RV_n:

$$RV_n^d = \sqrt{\sum_{j=2}^{k} \left|R_{n,j}\right|^2} \quad (2)$$

where $n = 1,2,3 \ldots m$ and where m stands the total-number of observations. The RV_n was then converted to logarithm RV_n. The rationale for selecting log RV_n over raw RV_n is that, according to a study by [22], the conditional heteroskedasticity is significantly reduced in log-RV. In-sample empirical analysis was carried out using the log-returns of r_n in the GARCH, EGARCH, and FIEGARCH models (low-frequency models), while the RV and HAR models (high-frequency models) used the log-realized variance, log RV. The EVT approach will be combined with the residuals series produced by each low- and high-frequency technique in the second stage of data processing. The conditional EVT is the name given to the two-stage combination strategy.

II. Model of Conditional EVT

In the present research, the combination of GARCH, RV, and HAR requirements with the EVT technique has been investigated using the conditional EVT method, which was first presented by [6]. In the initial step of the study, the original data series was filtered using the GARCH, EGARCH, and FIEGARCH models for low-frequency data, and the RV and HAR kinds of models for high-frequency data. The goal of this streaming procedure was to produce standardised residuals (innovations) that resembled the iid distribution, which is necessary for the EVT technique, which assumes that the filtered return series are free from heteroscedasticity effects and series correlation. Following the streaming procedure, the EVT parameters were determined using the filtered return series that was acquired from the streaming process. The peak-over-threshold (POT) approach, which takes into account extreme value observations that exceed a predetermined

threshold regardless of the time series' clustering tendencies, was applied in this investigation. The Generalised Pareto Distribution (GPD) distributions will be estimated using the thresholds produced by the POT approach. The one-day VaR and ES forecast is estimated using the VaR and ES quantiles that are computed using the GPD parameters.

III. The POT Approach

The Block Maxima (BM) technique, which uses a generalized extreme value (GEV) distribution, and the POT method, which is based on the GPD distribution, are the two primary approaches in EVT that are used to simulate the extreme returns. The Block Maxima (BM) approach will not be evaluated in this research as volatility clustering, which causes extreme values to cluster together, makes it unsuitable for analyzing time series data. As a result, this study applied the POT approach, which takes into account extreme value observations that exceed a predetermined threshold regardless of the time series' clustering patterns. Considering the logarithmic return series of a stock index, represented by $= \{y_1, y_2, \dots, y_t\}$, the POT method can be applied. Potential y values are the exceedance produced by extreme values that are higher than a given threshold v. The z or $F_v(z)$ cumulative probability function can be expressed as follows:

$$F_v(z) = P_r(X - v \le z \mid X > v) \tag{3}$$

Equation (10) conditional probability may be reduced to:

$$F_v(z) = \frac{F(x)-F(v)}{1-F(v)}, \tag{4}$$

Where $x = z + v$ is the exceedance and $z = x - v$ is the magnitude of exceedance.

IV. The POT Approach

The GPD distribution is one of the distributions utilised in EVT. The [23, 24] both state that when a threshold v is large enough, the cumulative probability function $F_v(z)$ occurs. Convergence of this function to the GPD distribution is defined as follows:

$$G_{\varphi\omega}(z) = \begin{cases} 1 - \left(1 + \frac{\varphi z}{\omega}\right)^{-\frac{1}{\xi}}, & if \varphi \neq 0, \\ 1 - e^{-\frac{z}{\omega}}, & if \varphi = 0, \end{cases} \tag{5}$$

To estimate the GPD parameters, the maximum likelihood technique was used to determine the scale parameter (ω) and the shape parameter (φ). Meanwhile $F_v(z) \approx G_{\varphi\omega}(z)$ introduced by [25] at a adequately high threshold v, Equation (3) and (4) are joint to be:

$$F(y) = (1 - F(v))G_{\varphi\omega}(z) + F(v) \tag{6}$$

Supposed $F(v) = \frac{\pi-k}{\pi}$, the function $F(y)$ can be reduced as follows:

$$F(y) = \left(1 - \frac{k}{\pi}\right)\left[1 + \varphi\frac{y-v}{\omega}\right]^{-\frac{1}{\varphi}} \tag{7}$$

where k indicates the number of exceedances and π indicates the total number of observations.

V. The VaR and ES Quantiles

The estimate of VaR while taking into account the cumulative distribution function $F(.)$ at a particular probability qs is as follows:

$$VaR_{qs} = F^{-1}(1 - qs) \tag{8}$$

where F^{-1} (.) remains the inverse function of $F(.)$. In inverting Calculation (8), the VaR_{qs} is assumed by:

$$VaR_{qs} = y_{qs} = v + \frac{\omega}{\varphi}\left[\left(\frac{1-qs}{k/\pi}\right)^{-\varphi} - 1\right] \tag{9}$$

VaR ignores severe losses over the VaR level and only considers the distribution quantile, which means that important information about the tails of the underlying distributions may be missed. Adoption of anticipated shortfall (ES), represented as follows, was recommended as a solution to this limitation:

$$ES_{qs} = E\left(\mathbb{x} \mid \mathbb{x} > VaR_{qs}\right) \tag{10}$$

According to [6], the value of ES may be calculated as follows:

$$ES_{qs} = \frac{VaR_{qs}}{1-\varphi} + \frac{\omega - \varphi v}{1-\varphi} \tag{11}$$

VI. The Predicted VaR

The GARCH and HAR requirements are used to anticipate the conditional variance $\hat{\alpha}_{t+1}$ and conditional mean $\hat{\lambda}_{t+1}$ one year in advance. This yields the 1-ahead conditional mean $\hat{\mu}_{t+1}$:

$$\hat{\lambda}_{t+1} = \hat{c}_0 + \sum_{j=1}^{r} \hat{a}_1 r_{t-j+1} + \sum_{i=1}^{s} \hat{d}_i \varepsilon_{t-i+1} \tag{12}$$

whereas the GARCH (1,1), EGARCH (1,1), FIEGARCH (1,1) and HAR models are used to forecast the conditional variance $\hat{\alpha}_{t+1}$. Equations (9) and (11) are used to calculate the 1-ahead VaR and ES using the POT approach into the standardised residuals series Z_t. Based on the conditional EVT, the 1-ahead conditional VaR, VaR_{qs}^{t+1}, is determined by:

$$VaR_{qs}^{t+1} = \lambda_{t+1} + \alpha_{t+1} VaR_{qs} \tag{13}$$

whereas the anticipated ES, Es_{qs}^{t+1} one step forward is provided by:

$$ES_{qs}^{t+1} = \lambda_{t+1} + \alpha_{t+1} ES_{qs} \tag{14}$$

VII. Backtesting Process

A two-step backtesting process is offered to evaluate each model's VaR performance. Statistical tests are used in the first step of backtesting, such as the conditional coverage tests proposed by [26] and the unconditional coverage test created by [27]. The violation ratio (ViR), which has the following definition, is used by the Kupiec likelihood-ratio (KLR) test to assess the VaR models:

$$ViR = \frac{\mathcal{N}}{p\mathcal{H}'} \tag{15}$$

Here, $\mathcal{N} = \sum_{n=\mathcal{T}+1}^{\mathcal{T}+\mathcal{H}} I_r\left(r_n < VaR_{n|n-1}^{1-p}\right)$ and $p\mathcal{H}$ represent the number of infractions, both theoretical and actual. Should the actual return value fall below the anticipated $\text{VaR}\left(r_n < VaR_{n|n-1}^{1-p}\right)$, a violation is considered to have occurred. The following is the LR test statistic:

$$KLR = 2ln\ \frac{\hat{p}^{\mathcal{N}}(1-\hat{p})^{\mathcal{H}-\mathcal{N}}}{p^{\mathcal{N}}(1-p)^{\mathcal{H}-\mathcal{N}}} \tag{16}$$

The Kupiec POF test, often referred to as the unconditional coverage test, is used to determine if the percentage of violations $\hat{p}$ as opposed to the predicted percentage p is considerably different. With $\mathcal{T}$ being the total number of observations and the chance of exceedance being constant, the number of VaR violations and $\mathcal{T}_1 = \sum_{n=1}^{\mathcal{T}} I_t$ follow a binomial distribution. The VaR (p) measurement is said to be precise if the unconditional coverage $\hat{p} = \frac{\mathcal{T}_1}{\mathcal{T}}$ is equals to $p\%$ and the null theory, H_0 is assumed by $H_0 = \hat{p} = p$. The Kupiec POF test is performed using the following likelihood ratio statistics:

$$KLR_{UC} = 2\left(logarithm\ (\hat{p}^{\mathcal{T}_1}(1-\hat{p})^{\mathcal{T}-\mathcal{T}_1}) - logarithm\ (p^{\mathcal{T}_1}(1-p)^{\mathcal{T}-\mathcal{T}_1})\right) \tag{17}$$

This study also backtested the VaR utilising the conditional coverage test by examining the combination evaluation of serial independence and unconditional coverage. The test statistics, represented by $KLR_{CC} = KLR_{UC} + \text{KLR}_{\text{IND}}$, add together the results of the separate test statistics for serial independence and unconditional coverage. The KLR_{IND} assesses whether exceptions are statistically independent of one another. The conditional coverage joint test, $KLR_{CC} = \text{KLR}_{UC} + \text{KLR}_{IND}$ mainly examine the percentage of exception whether it is statistically equal to the actual proportion, p and whether the exceptions are statistically independent of based on the independence's indicator. Therefore, $H_0: \theta_{01} = \theta_{11} = p$ provides statistical independence while p provides the null hypothesis of the actual percentage. The conditional coverage test statistics are provided by:

$$KLR_{CC} = 2\left(\text{logarithm}\ \left(\hat{\theta}_{01}^{\mathcal{T}_{01}}\left(1-\hat{\theta}_{01}\right)^{\mathcal{T}_{00}}\hat{\theta}_{11}^{\mathcal{T}_{11}}\left(1-\hat{\theta}_{11}\right)^{\mathcal{T}_{10}}\right) - \text{logarithm}\ (p^{\mathcal{T}_{01}+\mathcal{T}_{11}}(1-p)^{\mathcal{T}_{00}+\mathcal{T}_{10}})\right) \tag{18}$$

Furthermore, models that passed the UC and CC tests will undergo additional testing utilising the Firm's Loss Function (FLoF) and the Regulatory Loss Function (RLoF). In [28] work, the RLoF function is presented to quantify the difference between the expected VaR and the actual returns while taking into account a set of regulatory limitations that are described by:

$$RLoF = \begin{cases} 1 + (\text{VaR}_t - r_t)^2 & \text{if } r_t < \text{VaR}_t \\ 0 & \text{if } r_t \geq \text{VaR}_t \end{cases} \tag{19}$$

The FLoF (Firm Loss Function), a loss function put forth by [38], penalises typical days by taking into account the possible cost associated with the capital that the business has set aside for risk management. This may be represented as follows:

$$FLoF = \begin{cases} (\mathrm{VaR}_t - r_t)^2 & \text{if } r_t < \mathrm{VaR}_t \\ -\delta \mathrm{VaR}_t & \text{if } r_t \geq \mathrm{VaR}_t \end{cases} \quad (20)$$

As suggested by the [39], a traffic light technique was used to backtest the ES and validate it. The same methodology was used in this work to backtest the ES, which was first proposed by [40]. The appropriateness of the ES was assessed by counting the number of ES threshold violations within a specified investment period. This approach considers the difference between the actual loss and the ES estimate to determine the severity of the breach, which happens when the real loss surpasses the ES estimate. Severe violations are indicated by a greater conditional value. No breaches are indicated by a condition of zero, but an average exceedance of the ES estimate is shown by a positive generalised breach (GB) value. According to the null hypothesis, H_0, the ES estimate model is correct if the predicted losses determined by the ES estimate match the actual losses sustained. The H_0 is rejected if the actual losses are much greater than the projected losses, proving that the ES estimate is erroneous and requires revision.

IV. Result and Discussions

I. Descriptive Statistics

Then we need to calculate logarithmic returns $y_t = 10 \log\text{arithm}\left(\frac{p_n}{p_{n-1}}\right)$. Table 1 summarizes the descriptive statistics of NIFTY 50, 100 and 200 index along the whole period. The descriptive statistics and unit root analysis for the return series are shown in Table 1. The whole sample consists of 1072 daily data spanning from 1 Jan. 2021 to 31 April. 2025 is used as the test set or for out of sample forecasting. The mean values for the Nifty 50, 100 and 200 index return series are positive. Even yet, Nifty 50, 100 and 200 index and return has a negative skewness. The return series' kurtosis exceeds 3. Consequently, the majority of results are leptokurtic and skewed. The normalcy assumption for Nifty 50, 100 and 200 index and return series is denied, according to the statistically significant Jarque–Bera (JB) test results. There are fat tails present since the kurtosis values for daily returns are much greater than the typical benchmark of three.

Table 1: *Summary statistic of Indian Stock Market Indices*

Statistics	NIFTY 50	NIFTY 100	NIFTY 200
Mean	0.0421	0.0003	0.0011
Std. Dev.	1.395	0.0098	0.0325
Skewness	-0.515	−0.7125	−2.9850
Kurtosis	4.01	10.76	47.89
Minimum	−0.1237	−0.1072	−0.4512
Maximum	0.1024	0.0795	0.0882
Jarque-Bera	770.23***	1210.742***	412.073***
ADF test	-10.848***	-12.6539***	18.6293***
PP test	-1010.7 ***	-2120.20***	1954.20***

This implies that the heavy-tailed character of low-frequency financial data is reflected in the increased probability of extreme values in daily return distributions. We use the Phillips-Perron (PP) and Augmented Dickey-Fuller (ADF) unit root tests on the return series to evaluate the series' stationary characteristics. All return series reject the null hypothesis that the series has a unit root, according to the findings of the ADF test. The null hypothesis is rejected based on the results of the PP test, which demonstrate that all return series are stationary.

II. Empirical Analysis

In certain EVT applications, such as simulating extraordinary events in finance, the assumption of independence and identical distribution (iid) is suitable. It is necessary to filter the original return series to ensure that it follows a iid distribution since the EVT assumes iid observations. To ensure that the standardised residuals filtered from the GARCH, EGARCH, and HAR models in this study follow iid observations, the ARCH-LM, Q, and Q2 statistics were used. The results are shown in Tables 2 which show that the outcomes of the ARCH-LM, Q, and Q2 tests are not significant. This suggests that there is no serial dependency, or conditional heteroskedasticity or serial correlation, in the filtered standardised residuals series. Consequently, it is now presumed that these filtered standardised residuals series are iid, which qualifies them for use in the EVT analysis. In order to capture current market movements in the post-crisis climate, the study is based on 1,072 daily observations of the filtered standardised residual series, which span the period from January 1, 2021, to April 30, 2025.

In the second phase of Extreme Value Theory (EVT) data analysis, the Peak Over Threshold (POT) method was used, which used the Generalised Pareto Distribution (GPD) to estimate the behaviour of the extreme tails of the return series. Filtered standardised residuals were obtained for the in-sample analysis using conditional EVT models, specifically based on 1,072 daily observations from January 1, 2021, to April 30, 2025, a period that captures post-crisis dynamics and recent market behaviour. The Mean Excess Function (MEF) was used to determine the threshold value u for each residual series. It is defined as follows:

$$MEF(v) = \frac{\sum_{j=1}^{n}(\mathbb{x}_j - v)}{\sum_{j=1}^{n} l_{(\mathbb{x}_j > v)}}$$

where n is the total number of observations that are in the sample. When the MEF plot achieves a reasonable degree of linearity, each threshold v is chosen. The R programming code was used to analyse the range of potential values for each of the selected v in this study. The greatest likelihood approach was used to estimate the GPD parameters, n and ϖ, for each chosen v. Table 3 displays the predicted parameters n and ϖ, the number of exceedances ($\mathcal{K}$), and the resultant v. Equations (9) and (11) are used to derive the unconditional VaRqs and ESqs at 95% and 99% confidence levels, respectively.

Table 2: *Result of serial correlation and heteroskedasticity test*

Stock Index	Model	ARCH-LM	Q	Q^2
	GARCH	0.204 [0.812]	7.524 [0.689]	8.921 [0.582]
	EGARCH	0.158 [0.856]	6.389 [0.743]	7.601 [0.653]
	FIEGARCH	0.139 [0.872]	5.918 [0.771]	5.874 [0.714]
	RV-G	0.178 [0.839]	34.201 [0.000]**	0.114 [1.000]
	RV-EG	0.192 [0.825]	30.478 [0.000]**	0.126 [1.000]
NIFTY 50	RV-FIE	0.166 [0.847]	31.908 [0.000]**	0.109 [1.000]
	HAR	0.049 [0.963]	9.002 [0.521]	21.304 [0.001]**
	HAR-G	1.302 [0.195]	7.943 [0.638]	16.452 [0.078]
	HAR-EG	0.124 [0.907]	8.674 [0.558]	11.382 [0.298]

	HAR-FIE	0.102 [0.921]	7.885 [0.649]	10.117 [0.414]
	GARCH	0.738 [0.427]	9.231 [0.512]	5.413 [0.865]
	EGARCH	0.612 [0.538]	11.037 [0.391]	2.314 [0.982]
	FIEGARCH	0.441 [0.652]	10.122 [0.437]	3.671 [0.792]
	RV-G	0.392 [0.698]	265.72 [0.000]**	18.520 [0.031]*
NIFTY 100	RV-EG	0.316 [0.764]	250.14 [0.000]**	18.211 [0.029]*
	RV-FIE	0.228 [0.794]	241.68 [0.000]**	17.684 [0.037]*
	HAR	1.054 [0.304]	16.732 [0.079]	2.716 [0.974]
	HAR-G	1.921 [0.061]	18.001 [0.041]*	7.523 [0.669]
	HAR-EG	0.335 [0.739]	24.100 [0.000]**	4.008 [0.917]
	HAR-FIE	0.273 [0.762]	23.452 [0.000]**	3.215 [0.976]
	GARCH	1.021 [0.316]	11.754 [0.301]	5.884 [0.794]
	EGARCH	0.813 [0.372]	11.308 [0.325]	8.672 [0.562]
	FIEGARCH	0.722 [0.396]	10.944 [0.347]	7.943 [0.592]
	RV-G	1.084 [0.289]	198.67 [0.000]**	16.341 [0.082]
	RV-EG	0.769 [0.388]	187.32 [0.000]**	14.762 [0.113]
NIFTY 200	RV-FIE	0.695 [0.405]	183.15 [0.000]**	13.529 [0.141]
	HAR	1.432 [0.152]	10.534 [0.341]	19.302 [0.009]**
	HAR-G	0.482 [0.614]	11.443 [0.312]	17.432 [0.049]*
	HAR-EG	0.982 [0.327]	11.686 [0.298]	4.231 [0.941]
	HAR-FIE	1.012 [0.319]	12.115 [0.279]	4.101 [0.965]

Table 3: *Estimates of the GPD parameters results*

Risk Model	Index	φ	ω	VaR		ES	
				0.95	0.99	0.95	0.99
GARCH		0.187*	0.005**	0.010	0.017	0.015	0.023
EGARCH		0.172*	0.004**	0.009	0.016	0.014	0.021
FIEGARCH		0.181*	0.004**	0.009	0.016	0.014	0.022
RV- G		0.695**	0.072**	0.421	0.635	0.798	2.011
RV-EG		0.731*	0.068**	0.419	0.628	0.945	2.765
RV-FIE	NIFTY	0.754*	0.067**	0.417	0.624	1.016	3.158
HAR	50	−0.538*	0.339**	0.319	0.382	0.353	0.396
HAR-G		−0.580**	0.356**	0.338	0.394	0.372	0.417
HAR-EG		−0.804**	0.489**	0.346	0.382	0.379	0.399
HAR-FIE		−0.527**	0.331**	0.277	0.333	0.312	0.349
GARCH		−0.188*	0.006**	0.012	0.021	0.018	0.026
EGARCH		−0.211*	0.007**	0.012	0.021	0.018	0.027
FIEGARCH		−0.197*	0.006**	0.012	0.021	0.017	0.026
RV- G		0.168**	0.141**	0.502	0.796	0.701	1.062
RV-EG	NIFTY	0.191*	0.132*	0.500	0.791	0.698	1.058
RV-FIE	100	0.194**	0.130*	0.498	0.785	0.693	1.053
HAR		−1.327*	0.093*	0.423	0.467	0.456	0.472
HAR-G		0.103*	0.022*	0.468	0.511	0.497	0.545
HAR-EG		−2.001*	0.289**	0.478	0.522	0.511	0.528
HAR-FIE		−1.065*	0.231**	0.382	0.436	0.416	0.441
GARCH		−0.093*	0.012**	0.039	0.058	0.051	0.069
EGARCH		−0.081*	0.011**	0.041	0.059	0.053	0.070
FIEGARCH		−0.074*	0.011**	0.040	0.058	0.050	0.068

RV- G		−0.102*	0.245*	0.601	0.974	0.845	1.195
RV-EG		−0.133*	0.265*	0.593	0.982	0.848	1.204
RV-FIE	NIFTY	−0.115*	0.259*	0.588	0.968	0.839	1.190
HAR	200	−0.762*	0.419*	0.685	0.855	0.792	0.876
HAR-G		−0.582*	0.338**	0.722	0.901	0.831	0.949
HAR-EG		−0.551**	0.331**	0.603	0.808	0.743	0.871
HAR-FIE		−0.763**	0.421**	0.652	0.829	0.776	0.882

III. VaR Backtesting

The violation ratio (ViR) has been used as an evaluation tool for comparing different volatility models for daily returns during regular times. The [32] criteria state that a good forecast is indicated by a ViR value between [0.8,1.2]. ViR numbers outside of this range, however, point to a poor or inaccurate model. However, the ViR is still acceptable if it falls between [0.5,0.8] or [1.2,1.5]. The majority of HAR-type models in conjunction with EVT are accurate and suitable for use in the VaR forecast, according to the data shown in Table 4.

Table 4: *Conditional-EVT Model VaR violation ratios.*

Stock Index	Low-frequency	Normal	High-frequency	Normal
	G-EVT	11.02	RV-G-EVT	8.55
	EG-EVT	10.75	RV-EG-EVT	8.12
	FIEGARCH	11.30	RV-FIEG-EVT	8.88
NIFTY 50			HAR-EVT	1.22
			HAR-G-EVT	1.15
			HAR-EG-EVT	1.37
			HAR-FIEG-EVT	1.09
	G-EVT	10.58	RV-G-EVT	9.01
	EG-EVT	10.32	RV-EG-EVT	9.18
NIFTY 100	FIEGARCH	10.44	RV-FIEG-EVT	9.10
			HAR-EVT	1.06
			HAR-G-EVT	1.28
			HAR-EG-EVT	1.43
			HAR-FIEG-EVT	1.19
	G-EVT	9.82	RV-G-EVT	7.88
	EG-EVT	9.67	RV-EG-EVT	7.95
NIFTY 200	FIEGARCH	9.90	RV-FIEG-EVT	6.97
			HAR-EVT	1.04
			HAR-G-EVT	1.21
			HAR-EG-EVT	1.08
			HAR-FIEG-EVT	1.00

The VaR backtesting findings utilising the UC and CC tests are then displayed in Tables 5. According to the findings, all high-frequency HAR models accepted the null hypothesis during the time at a 5% significance level, suggesting that the related high-frequency VaR models are capable of making accurate predictions. At the 5% significance level, the low-frequency models of GARCH-EVT and EGARCH-EVT reject the null hypothesis, indicating that the low-frequency models in conjunction with EVT are not appropriate for predicting the VaR over time.

Table 5: *UC and CC Test Statistics for the Conditional EVT Model*

		KLR_{UC}		KLR_{CC}			KLR_{UC}		KLR_{CC}	
Index	Low-freq	Stat	p	Stat	p	High-freq	Stat	p	Stat	p
NIFTY	G-EVT	342.17	0	344.12	0	RV-G-EVT	309.43	0.0	310.01	0.00
50	EG-EVT	355.82	0	357.13	0	RV-EG-EVT	298.70	0.00	299.45	0.00
	FIEG-EVT	321.34	0	329.41	0	RV-FIEG-EVT	276.87	0.00	277.90	0.00
						HAR-EVT	1.02	0.31	1.05	0.35
						HAR-G-EVT	2.75	0.09	2.89	0.12
						HAR-EG-EVT	1.98	0.15	2.02	0.17
						HAR-FIE-EVT	65.74	0.00	66.38	0.00
NIFTY	G-EVT	412.23	0	414.12	0	RV-G-EVT	381.90	0.0	382.13	0.00
100	EG-EVT	429.88	0	430.95	0	RV-EG-EVT	401.34	0.00	403.02	0.00
	FIEG-EVT	417.46	0	419.71	0	RV-FIEG-EVT	375.28	0.00	376.89	0.00
						HAR-EVT	0.11	0.74	0.13	0.93
						HAR-G-EVT	0.06	0.81	0.09	0.89
						HAR-EG-EVT	1.32	0.25	1.75	0.41
						HAR-FIE-EVT	2.45	0.12	2.57	0.31
NIFTY	G-EVT	407.89	0	419.02	0	RV-G-EVT	377.34	0.00	395.48	0.00
200	EG-EVT	412.56	0	417.83	0	RV-EG-EVT	390.72	0.00	412.66	0.00
	FIEG-EVT	426.33	0	440.18	0	RV-FIEG-EVT	42.73	0.00	47.61	0.00
						HAR-EVT	1.16	0.28	1.18	0.48
						HAR-G-EVT	0.32	0.59	0.34	0.88
						HAR-EG-EVT	1.12	0.29	1.25	0.51
						HAR-FIE-EVT	1.38	0.27	1.44	0.46

They will be retested using the RLoF and FLoF loss function on the VaR accuracy because HAR type-models passed the first stage of the backtesting process using the statistical test of the UC and CC test. In terms of predicting VaR across the time, Table 6 shows that the HAR-EVT model performs better than other HAR models.

Table 6: *Estimated RLoF and FLoF Values for the Models*

Stock Index	Model	RLF	FLF
NIFTY 50	HAR-EVT	0.0561	0.1602
	HAR-G-EVT	0.0053	0.2435
	HAR-EG-EVT	0.0138	0.2159
	HAR-FIEG-EVT	0.0724	0.1831
	HAR-EVT	0.0857	0.1695
NIFTY 100	HAR-G-EVT	0.0882	0.1749
	HAR-EG-EVT	0.0936	0.1817
	HAR-FIEG-EVT	0.1088	0.1963
NIFTY 200	HAR-EVT	0.0439	0.1427
	HAR-G-EVT	0.0481	0.1482
	HAR-EG-EVT	0.0019	0.0063
	HAR-FIEG-EVT	0.0517	0.1589

IV. Backtesting ES

The low-frequency conditional EVT models have generated a higher value of GB, which suggests that there are serious data breaches, according to the results shown in Table 7. Furthermore, the substantial p-value indicates that the ES estimate is incorrect. The H_0 is rejected if the p-value is significant, indicating that the low-frequency conditional EVT models are insufficient for precisely predicting the ES over the time period. Lower values of the GB are produced by the high-frequency conditional EVT models, suggesting that the ES estimate is more accurate since the actual losses are more in line with the projected losses determined by the ES estimate.

Table 7: *The expected shortage backtesting process*

Stock Index	Risk Model	GB	z	p
NIFTY 50	G-EVT	41.72	91.83	0.000
	EG-EVT	42.05	92.77	0.000
	FIEG-EVT	42.91	94.63	0.000
	RV-G-EVT	2.25	−229.67	0.000
	RV-EG-EVT	2.21	−228.49	0.000
	RV-FIEG-EVT	2.24	−230.21	0.000
	HAR-EVT	1.86	0.37	0.709
	HAR-G-EVT	1.90	0.41	0.682
	HAR-E-EVT	1.86	0.35	0.726
	HAR-F-EVT	1.88	1.34	0.180
NIFTY 100	G-EVT	26.45	−34.96	0.000
	EG-EVT	24.11	−66.73	0.000
	FIEG-EVT	25.07	−60.42	0.000
	RV-G-EVT	4.85	−210.34	0.000
	RV-EG-EVT	4.88	−210.76	0.000
	RV-FIEG-EVT	4.90	−211.05	0.000
	HAR-EVT	1.87	0.48	0.634
	HAR-G-EVT	1.89	0.49	0.626
	HAR-E-EVT	1.88	0.49	0.627
	HAR-F-EVT	1.91	0.51	0.612
NIFTY 200	G-EVT	6.94	−186.72	0.000
	EG-EVT	7.12	−185.34	0.000
	FIEG-EVT	7.59	−179.61	0.000
	RV-G-EVT	2.14	−224.98	0.000
	RV-EG-EVT	2.10	−225.41	0.000
	RV-FIEG-EVT	2.13	−225.13	0.000
	HAR-EVT	1.03	−6.04	0.000
	HAR-G-EVT	1.02	−6.09	0.000
	HAR-E-EVT	1.04	−6.01	0.000
	HAR-F-EVT	1.01	−6.06	0.000

The results of the first step of the testing method indicate that the HAR-EVT typed models fared better than other risk models that employ the GARCH and RV specification with EVT for VaR forecast, as demonstrated in the previous section. Additionally, as Table 8 summarises, the results of the second stage of the bactesting method demonstrate that the HAR-EGARCH-EVT model performs better than any other hybrid version of the HAR-EVT models in terms of

predicting the VaR over time. However, based on the ES forecast, the results of the NIFTY 50 and NIFTY 100 index samples throughout the time exhibit negligible values, indicating that the HAR specification models in conjunction with EVT are sufficient for forecasting the ES during the period. This outcome is in line with the VaR forecast result, which showed that HAR-EVT typed models performed better than other models in risk estimation.

Table 8. *Best-Fit Models Based on Value at Risk Forecasting*

Models	Total period
HAR-EVT	2
HAR-G-EVT	1
HAR-EG-EVT	4
HAR-FIEG-EVT	0

V. Conclusion

The use of daily returns for EVT-based risk prediction has undergone a substantial change, moving from the conventional EVT method to the more sophisticated hybrid technique known as a conditional EVT model. Up to 2026, research will continue to examine how the conditional EVT performs better than other models using various hybrid approaches across all risk models. Another field of study on the effectiveness of low-frequency conditional EVT models in comparison to high-frequency conditional EVT models is aided by the rise of high-frequency data. As mentioned previously in the literature review, researchers found that the conditional EVT performed better when high-frequency data was compared, generally speaking. The benefits of incorporating the RV standard into a hybrid model in addition to the EVT approach have been the subject of several studies. The study's findings demonstrated that, when it comes to risk predicting the VaR and ES, high-frequency conditional EVT models can outperform low-frequency conditional EVT models. Based on the summary result, it can be concluded that the combination of the HAR model and EVT technique may yield accurate forecasts of market risk because all models that merged the HAR specification with EVT passed the first stage VaR backtesting procedure throughout the periods.

This study contributes both theoretically and practically by advancing the literature on risk model forecasting through the integration of long-memory models with the EVT approach. It introduces the RV-FIEGARCH model, an exponential variant of the fractionally integrated RV model that captures both long memory and asymmetry in return series. Additionally, it proposes the HAR-RV-FIEGARCH model, incorporating daily, weekly, and monthly data to improve forecasting accuracy. The findings show that HAR-based models with EVT, particularly HAR-FIEGARCH-EVT, deliver superior performance in both developed and emerging markets during periods of crisis and stability.

References

[1] Basuony, M. A. Bouaddi, M. Ali, H. and EmadEldeen, R. (2022). The effect of COVID-19 pandemic on global stock markets: Return, volatility, and bad state probability dynamics. *Journal of Public Affairs,* 22: e2761.

[2] Rakshit, B. and Neog, Y. (2022). Effects of the COVID-19 pandemic on stock market returns and volatilities: evidence from selected emerging economies. *Studies in Economics and Finance,* 39(4): 549-571.

[3] Louzis, D. P. Xanthopoulos-Sissinis, S. and Refenes, A. P. (2012). Stock index Value-at-Risk forecasting: A realized volatility extreme value theory approach. *Economics Bulletin,* 32(1): 981-991.

[4] Lyócsa, Š. Molnár, P. and Výrost, T. (2021). Stock market volatility forecasting: Do we need high-frequency data?. *International Journal of Forecasting*, 37(3): 1092-1110.

[5] Djuraskovic, O. (2023). Big data statistics 2023: How much data is in the world? First Site Guide. https://firstsiteguide. com/big-data-stats/

[6] McNeil, A. J. and Frey, R. (2000). Estimation of tail-related risk measures for heteroscedastic financial time series: an extreme value approach. *Journal of empirical finance*, 7(3-4): 271-300.

[7] Paul, S. and Sharma, P. (2018). Quantile forecasts using the realized GARCH-EVT approach. *Studies in Economics and Finance*, 35(4): 481-504.

[8] Soltane, H. B. Karaa, A. and Bellalah, M. (2012). Conditional VaR using GARCH-EVT approach: Forecasting volatility in Tunisian financial market. *Journal of Computations and Modelling*, 2(2): 95-115.

[9] Altun, E. and Tatlidil, H. (2015). A comparison of extreme value theory with heavy-tailed distributions in modeling daily VaR. *Journal of Finance and Investment Analysis*, 4(2): 69-83.

[10] Youssef, M. Belkacem, L. and Mokni, K. (2015). Value-at-Risk estimation of energy commodities: A long-memory GARCH–EVT approach. *Energy Economics*, 51: 99-110.

[11] Tabasi, H. Yousefi, V. Tamošaitienė, J. and Ghasemi, F. (2019). Estimating conditional value at risk in the Tehran stock exchange based on the extreme value theory using GARCH models. *Administrative Sciences*, 9(2): 40.

[12] Omari, C. Mundia, S. and Ngina, I. (2020). Forecasting value-at-risk of financial markets under the global pandemic of COVID-19 using conditional extreme value theory. *Journal of Mathematical Finance*, 10(04): 569–597.

[13] Roy, A. (2022). Efficacy of GARCH-EVT Model in intraday risk management: evidence from severely pandemic-affected countries. *Global Business Review*, 09721509221104848.

[14] Jin, F. Li, J. and Li, G. (2022). Modeling the Linkages between Bitcoin, Gold, Dollar, Crude Oil, and Stock Markets: A GARCH-EVT-Copula Approach. *Discrete Dynamics in Nature and Society*, 2022(1): 8901180.

[15] Zhao, J. Cui, L. Liu, W. and Zhang, Q. (2023). Extreme risk spillover effects of international oil prices on the Chinese stock market: A GARCH-EVT-Copula-CoVaR approach. *Resources Policy*, 86: 104142.

[16] Watanabe, T. (2012). Quantile forecasts of financial returns using realized GARCH models. *The Japanese Economic Review*, 63(1): 68-80.

[17] Zhang, Z. and Zhang, H. K. (2016). The dynamics of precious metal markets VaR: A GARCHEVT approach. *Journal of Commodity Markets*, 4(1): 14-27.

[18] Huang, Z. Liu, H. and Wang, T. (2016). Modeling long memory volatility using realized measures of volatility: A realized HAR GARCH model. *Economic Modelling*, 52: 812-821.

[19] Tao, Q. Wei, Y. Liu, J. and Zhang, T. (2018). Modeling and forecasting multifractal volatility established upon the heterogeneous market hypothesis. *International Review of Economics and Finance*, 54: 143-153.

[20] Zahid, M. Iqbal, F. Raziq, A. and Sheikh, N. (2022). Modeling and forecasting the realized volatility of Bitcoin using realized HAR-GARCH-type models with jumps and inverse leverage effect. *Sains Malaysiana*, 51(3): 929-942.

[21] Khan, M. Khan, M., and Irfan, M. (2023). Estimating Value-at-Risk and expected shortfall of metal commodities: application of GARCH-EVT method. *Journal of Risk Management in Financial Institutions*, 16(2): 189-199.

[22] Ab Razak, R. Aminuddin Jafry, N. H. and Ismail, N. (2020). Dependence measure of five-minutes returns compared to daily returns using static and dynamic copulas. *Sains Malaysiana*, 49(8): 2023-2034.

[23] Pickands III, J. (1975). Statistical inference using extreme order statistics. *The Annals of*

Statistics, 119-131.

[24] Balkema, A. A. and De Haan, L. (1974). Residual life time at great age. *The Annals of probability*, 792-804.

[25] Embrechts, P. Klüppelberg, C. and Mikosch, T. (2013). Modelling extremal events: for insurance and finance (Vol. 33). Springer Science & Business Media.

[26] Christoffersen, P. F. (1998). Evaluating interval forecasts. *International economic review*, 841-862.

[27] Kupiec, P. H. (1995). Techniques for verifying the accuracy of risk measurement models (Vol. 95, No. 24). Washington, DC: Division of Research and Statistics, Division of Monetary Affairs, Federal Reserve Board.

[28] Lopez, J. A. (1998). Methods for evaluating value-at-risk estimates. *Economic Policy Review*, 4(3): 119–991124.

[29] Jacob, P. (2017). Economic reforms and its impact on the Indian stock market. *Intercontinental Journal of Finance Research Review*, 5(8).

[30] Wu, K. Liu, Y. and Feng, W. (2022). The effect of index option trading on stock market volatility in China: An empirical investigation. *Journal of Risk and Financial Management*, 15(4): 150.

[31] Nair, A. S. (2008). Impact of derivative trading on volatility of the underlying: evidence from Indian stock market. In Money and Finance Conference held on January (pp. 18-19).

[32] Sahu, D. (2012). Effect of equity derivatives trading on spot market volatility in India: An empirical exploration. *European Journal of Business and Management*, 4(11): 50-60.

[33] Bhardwaj, K. Garima, Lemma, H. R. and Refera, M. K. (2024). Does index options trading destabilize Indian stock market volatility: an application of ARCH and GARCH models. *Cogent Business and Management*, 11(1): 2413391.

[34] Debasish, S. S. and Das, B. (2009). An econometric study on impact of futures trading on the stability of stock index in India. *International Journal of Business and Management*, 3(12): 70-80.

[35] Ausloos, M. Zhang, Y. and Dhesi, G. (2020). Stock index futures trading impact on spot price volatility. The CSI 300 studied with a TGARCH model. *Expert Systems with Applications*, 160: 113688.

[36] Antoniou, A. Koutmos, G. and Pericli, A. (2005). Index futures and positive feedback trading: evidence from major stock exchanges. *Journal of Empirical Finance*, 12(2): 219-238.

[36] Tian, S. Liu, S. and Mu, L. (2025). Spatial linkages of positive feedback trading among the stock index futures markets. *The North American Journal of Economics and Finance*, 75: 102315.

[37] Tang, N. Gao, M. Zhou, Y. Zhou, F. and Zhu, J. (2024). Firm-level productivity and stock return: New evidence from China. *International Review of Economics and Finance*, 96: 103557.

[38] Sarma, M. Thomas, S. and Shah, A. (2003). Selection of Value-at-Risk models. *Journal of Forecasting*, *22*(4), 337-358.

[39] Basel Committee on Banking Supervision. (1996). Supervisory framework for the use of "backtesting" in. conjunction with the internal models approach to market risk capital requirements. Bank for International Settlements, Basle, Report nr. 22, http://www.bis.org

[40] Costanzino, N. and Curran, M. (2015). Backtesting general spectral risk measures with application to expected shortfall. Available at SSRN 2514403.

EFFICACY OF SINGLE SERVER MARKOVIAN QUEUEING SYSTEM WITH DISSATISFIED CUSTOMERS, BALKING AND NUMEROUS VACATION

Ismailkhan.E[1*], Thangaraja.P[2], Rajeswari.V[3], Karuppaiya.R[4], Ramkumar.S[5], Narmadha.V[6]

•

[1,2]Department of Mathematics, Panimalar Engineering College, Chennai-600123
[3]Department of Mathematics, Sri Sai Ram Institute of technology, Chennai-600044
[4]Department of Mathematics, St. George"s Arts and Science College, Chennai-600030
[5]Department of Mathematics, Paavai Engineering College (Autonomous), Namakkal-637 018
[6]Department of Mathematics, Vellore Institute of Technology, Vellore- 632014

ismailkhanmubarak@gmail.com

Abstract

In this research work, we derive a single server Markovian encouraged arrival queuing system with dissatisfied customers, balking, and numerous vacations, where we examine that encouraged arrival customers are due to the fewer customers, balking, and dissatisfied customers. Once a system-size enhancement is idle, the system server obtains vacation. Suppose the system server detritus is idle, after the sabbatical vacation. We inferred the probability-generating functions (PGF) and got the closed-form interpretation when the system server is numerous. In addition, we obtain other important performance measures and Little's law is also satisfied for this model.

Keywords: Encouraged arrival, dissatisfied customers, feedback, Numerous vacation, Little's Law.

1. Introduction

The breadth and interest in studying queuing systems involving server vacation have increased in the queuing theory literature. To maximize downtime, server vacations are employed. The manufacturing process, business services, communications networks, online technology, and other scenarios have all seen success with the application of vacation queuing models. Many scholars are eager to explore queuing models that incorporate various vacation regulations, including both single and multiple vacation norms.

On the whole, it is difficult to achieve success in closed-form bulk service queue modelling with servers inactive [1]. The study conducted in [2] examined an M/M/1 line via a working vacation model. Examines the optimal management approach regarding a heterogeneous M/M/1-queue that experiences server outages [3]. M/M/1 queues with several active vacations, including the N-Policy is given in [4] . Working with the matrix approach and the vacation line study in [5] was conducted. An investigation was conducted for the M/M/1 queue, including an individual active vacation is considered in [6]. An M/M/1 queuing systems with server vacation and client impatience were thoroughly analysed by [7], who found that consumers only felt irritated when the servers were used on vacation. The M/M/o queue model with vacations and dissatisfied

consumers and Numerous flexible vacations, while K is a pre-assigned stable positive number instead of a random variable is taken into account in [8]. This kind of vacation is referred to as a variation of Banik's various vacations in [9]. Papers by [10] and [11] include literature about this kind of vacation. There has been research on an M/M/1/N queue mechanism featuring encouraged arrival [12]. Markovian encouraging arrival queues and then dissatisfied customers were all investigated [13], [14] and [15].

2. Model interpretation

We contemplate a single server Markovian encouraged arrival queuing system with dissatisfied customers, feedback, and a numerous vacation. As per the encouraged arrival procedure, customers engage a server once at a moment $(1+\iota)$, where ι denotes the encouraged arrival rate. μ Follows a service rate identical distribution. η is a feedback rate. Customers follow FIFO discipline. A server does nothing except wait for the next customer to arrive. The vacation rates, denoted by χ are supposed to have an exponential distribution of vacation times. Customers are irritated throughout the vacation. It means that a "Dissatisfied timer" (t) is set off every time a customer accesses the system. It has an identical distribution with ψ as the parameter. When a customer's timer goes off and their service is still unfinished, they leave the line and never reappear.

The closed-form equations for the average system sizes in various server states equations with additional significant performance metrics are also obtained. Assume that the Length of the system T, and then $I(T) = i$ describes at time T, the system executes the $(\mathrm{i}+1)^{\mathrm{th}}$ vacation for $\mathrm{i} = 0, 1, \ldots, \mathrm{H}-1$. Then, the continuous-time Markov process (CTMP) with state $\varphi = \{(m,i) : m \geq 0, i = 0, 1, \ldots, H\}$.

3. The Set of Differential-Difference Equations of the Model

We write the basic equations and derive the probability differential-difference equations Using the model interpretation for the single server Markovian encouraged arrival queuing system with dissatisfied customers, feedback, and a numerous vacation as follows:

$$(\lambda * (1+\iota) + \chi) * P_{00} = \psi * P_{10} + \mu * P_{1H} \tag{1}$$

$$(\lambda * (1+\iota) + \chi + m\psi) * P_{m0} = \lambda * (1+\iota) * P_{m-10} + (m+1) * \psi * P_{m+10}, m \geq 1 \tag{2}$$

$$(\lambda * (1+\iota) + \chi) * P_{0i} = \psi * P_{1i} + \chi * P_{0i-1}, i = 1, 2, \ldots, H-1 \tag{3}$$

$$\lambda * (1+\iota) + \chi + m * \psi) * P_{mi} = \lambda * (1+\iota) * P_{m-1i} + (m+1) * \psi * P_{m+1i} \quad i = 1, 2, \ldots, H-1, m \geq 1 \tag{4}$$

$$\lambda * (1+\iota) * P_{0H} = \chi * P_{0H-1} \tag{5}$$

$$(\lambda * (1+\iota) + \mu) * P_{mH} = \lambda * (1+\iota) * P_{m-1H} + \mu * P_{m+1H} + \chi \sum_{i=0}^{H-1} P_{mi}, m \geq 1 \tag{6}$$

By using the normalizing condition:

$$\sum_{m=0}^{\infty} \sum_{i=0}^{H} P_{mH} = \frac{\lambda * (1+l) * P_{m-1H} + \mu * P_{m+1H} + \chi \sum_{i=0}^{H-1} P_{mi}}{(\lambda * (1+l) + \mu)} = 1 \tag{7}$$

Define the (PGFs) as,

$$R_i(Z) = \sum_{m=0}^{\infty} P_{mi} Z^m, 0 \leq Z \leq 1, i = 0, 1, \ldots, H$$

Then, multiply the all equations for m in equations. (1) to (4) via Z^m, we obtain,

$$\psi * (1 - Z) * R_0'(Z) - [\lambda * (1 + \iota) * (1 - Z) + \chi] * R_0(Z) = -\mu * P_{1H} \tag{8}$$

And

$$\psi * (1 - Z) * R_i'(Z) - [\lambda * (1 + \iota) * (1 - Z) + \chi] * R_i(Z) = -\chi * P_{0i-1} \tag{9}$$

Likewise, by using the equations. (5) and (6) we get

$$(1 - Z) * (\lambda * (1 + \iota) * Z - \mu) * R_H(Z) = \chi * Z \sum_{i=0}^{H-1} R_i(Z) + (Z - 1) * \mu * P_{0H} \tag{10}$$

Next, we derive the equations (8) and (9) by closed form.
Equation. (8) will be given as :

$$R_0'(Z) - \left[\frac{\lambda * (1 + \iota)}{\psi} + \frac{\chi}{\psi * (1 - z)}\right] * R_0(Z) = -\frac{\mu * P_{1H}}{\psi * (1 - z)} \tag{11}$$

To solve the differential Equation. (11), by

$$e^{-\frac{\lambda*(1+\iota)}{\psi}*Z} * (1 - Z)^{\frac{\chi}{\psi}}$$

Then, we obtain

$$\frac{d}{dZ} * \left[e^{-\frac{\lambda*(1+\iota)}{\psi}*Z}(1 - Z)^{\frac{\chi}{\psi}} * R_0(Z)\right] = -\frac{\mu}{\psi} * P_{1H} e^{-\frac{\lambda*(1+\iota)}{\psi}*Z} * (1 - Z)^{\frac{\chi}{\psi}-1}$$

$\int$ ing 0 to Z, we claim that,

$$R_0(Z) = \frac{e^{\frac{\lambda*(1+l)}{\psi}*Z} * \left\{R_0(0) - \frac{\mu}{\psi} * P_{1H} \int_0^Z (1 - y)^{\frac{\chi}{\psi}-1} * e^{-\frac{\lambda*(1+l)}{\psi}*y} dy\right\}}{(1 - Z)^{\frac{\chi}{\psi}}} \tag{12}$$

Since $R_0(1) = \sum_{m=0}^{\infty} P_{m0} < \infty$ and $Z = 1$, we have that $z = 1$ must be ought to should be the numerator's value on the right side of Equation (12).

So, we get

$$R_0(0) = \frac{\mu}{\psi} * D * P_{1H} \tag{13}$$

Where,

$$D = \int_0^1 e^{-\frac{\lambda*(1+\iota)}{\psi}*y} * (1 - y)^{\frac{\chi}{\psi}-1} dy \tag{14}$$

Not $R_0(0) = P_{00}$, Equation. (13) implicit

$$P_{1H} = \frac{\psi}{\mu * D} * P_{00} \tag{15}$$

By substitute the Equation. (15) to (12), we get,

$$R_0(Z) = \frac{e^{\frac{\lambda*(1+l)}{\psi}} * Z}{(1 - Z)^{\frac{\chi}{\psi}}} * \left[1 - \frac{1}{D} \int_0^Z (1 - Y)^{\frac{\chi}{\psi}-1} e^{-\frac{\lambda*(1+l)}{\psi}*y} dy\right] * P_{00} \tag{16}$$

Eq. (9) will be given as

$$R_i'(\mathrm{Z}) - \left[\frac{\lambda * (1+\iota)}{\psi} + \frac{\chi}{\psi * (1-\mathrm{z})}\right] * R_i(\mathrm{Z}) = -\frac{\chi * P_{0i-1}}{\psi * (1-\mathrm{Z})} \tag{17}$$

In likewise Equation. (11), implicit

$$R_i(\mathrm{Z}) = \frac{e^{\frac{\lambda*(1+l)}{\psi}*\mathrm{Z}} * \left\{R_i(0) - \frac{\chi}{\psi} * P_{0i-1} * \int_0^{\mathrm{Z}} (1-y)^{\frac{\chi}{\psi}-1} * e^{-\frac{\lambda*(1+l)}{\psi}*y} dy\right\}}{(1-\mathrm{Z})^{\frac{\chi}{\psi}}} \quad i = 1, 2, \ldots, H-1$$

Since $R_i(1) = \sum_{m=0}^{\infty} P_{mi} < \infty$ and $\mathrm{Z} = 1z = 1$ must be ought to should be the numerator's value on the right side of Equation (18).

So, we get

$$P_{0i} = R_i(0) = \frac{\chi}{\psi} * D * P_{0i-1}, i = 1, 2, \ldots, H-1 \tag{19}$$

Where D is determine by Equation. (14). By Use Equation. (19) Again, we get

$$P_{0i} = B^i * P_{00}, i = 1, 2, \ldots, H-1 \tag{20}$$

Where $B = \frac{\chi}{\psi} * D$. By Substitute Equation. (20) into (18), we get

$$R_i(\mathrm{Z}) = \frac{e^{\frac{\lambda*(1+\iota)}{\psi}*\mathrm{Z}} * B^i}{(1-\mathrm{Z})^{\frac{\chi}{\psi}}} * \left\{1 - \frac{1}{D} * \int_0^{\mathrm{Z}} (1-y)^{\frac{\chi}{\psi}-1} * e^{-\frac{\lambda*(1+\iota)}{\psi}*y} dy\right\} * P_{00} \quad i = 1, 2, \ldots, H-1 \tag{21}$$

By Using Equations. (5) and (20), we get

$$P_{0H} = \frac{\chi}{\lambda * (1+l)} B^{H-1} * P_{00} \tag{22}$$

Next, we procure the P_{00}, and the average service system- size is in numerous states.

For $i = 0, 1, \ldots, H$, let us assume that L_i is the system size in the state i. Hereafter, $E(L_i)$ is the average system size in the state i, which is determined is given by

$$E(L_i) = R_i'(1) = \sum_{m=1}^{\infty} m * P_{mi}, i = 0, 1, \ldots, H$$

i.e., for $i = 0, 1, \ldots, H-1, E(L_i)$ means the average system size, the system-server proceeds the $(i+1)^{\text{th}}$ vacation, and $E(L_H)$ means engaged system is idle or free. Determine $E(L_i)$ for $i = 0, 1, \ldots, H-1$.

Applying the L'Hopital rule to Equation. (11), we obtain

$$\begin{aligned} R_0'(1) &= \lim_{\mathrm{Z}\to 1} \frac{[\lambda * (1+\iota) * (1-\mathrm{Z}) + \chi] * H_0(\mathrm{Z}) - \mu * P_{1H}}{\psi * (1-\mathrm{Z})} \\ &= \frac{-\lambda * (1+\iota) * H_0(1) + \chi * H_0'(1)}{-\psi} \end{aligned}$$

Thus, we obtain

$$(\chi + \psi) * H_0'(1) = \lambda * (1+\iota) * H_0(1) \tag{23}$$

Likewise, from the Equation. (17), we obtain

$$(\chi + \psi) * H_I'(1) = \lambda * (1+\iota) * H_i(1), i = 1, 2, \ldots, H-1 \tag{24}$$

Equations. (23) & (24) inferred

$$E\left(L_i\right)=\frac{\lambda*(1+\iota)}{\chi+\psi}*H_I(1), I=0,1,\ldots,H-1 \tag{25}$$

For $i=0,1,\ldots,H$, let us assume that $P_{.i}=H_i(1)=\sum_{m=0}^{\infty}P_{im}$. Hereafter, for $i=0,1,\ldots,H-1$, $P_{.j}$ means the server proceeds the $(i+1)^{\text{th}}$ vacation, and $P_{.H}$ means the server is engaged or free.

Applying the L'Hopital rule, from Equations. (16) & (21), we obtain

$$P_{.i}=R_i(1)=B^{i-1}*P_{00}, i=0,1,\ldots,H-1 \tag{26}$$

We may write Equation. (25) as follows by using Equation. (26).

$$E\left(L_i\right)=\frac{\lambda*(1+\iota)}{\chi+\psi}*B^{i-1}*P_{00} \tag{27}$$

Besides, the average system is on vacation, indicated $E\left(L_U\right)$, as follows:

$$E\left(L_U\right)=\sum_{i=0}^{H-1}E\left(L_i\right)=\frac{\lambda*(1+\iota)}{\chi+\Psi}*\frac{1-B^H}{B(1-B)}*P_{00} \tag{28}$$

Here after, we inferred $P_{.H}$&P_{00}. Beginning with Equations. (15), (20) & (26), we get $\mu*P_{1H}=\chi*P_{.0}$ &$P_{0i-1}=P_{.i}, i=1,2,\ldots,H-1$. Thus, we obtain

$$\mu*P_{1H}+\chi*\sum_{i=0}^{H-2}P_{0i}=\chi*\sum_{i=0}^{H-1}P_{.i} \tag{29}$$

We may write Equation. (29) as follows by using Equation. (10)

$$R_H(\mathrm{Z})=\frac{\chi*\mathrm{Z}}{\lambda*(1+\iota)*\mathrm{Z}-\mu}*\frac{\sum_{i=0}^{H-1}\left[R_i(\mathrm{Z})-P_{.i}\right]}{1-\mathrm{Z}}-\frac{\mu*P_{0H}}{\lambda*(1+\iota)*\mathrm{Z}-\mu} \tag{30}$$

When we use the L'Hopital rule, we obtain

$$R_H(1)=\frac{\chi*\sum_{i=0}^{H-1}R_i'(1)+\mu*P_{0H}}{\mu-\lambda*(1+\iota)} \tag{31}$$

Remarking $R_H(1)=P_{.H}$ and $R_i'(1)=E\left(L_i\right), i=0,1,\ldots,H-1$, beginning with Equation. (31), we get

$$P_{.H}=\frac{\chi*\sum_{i=0}^{H-1}E\left(L_i\right)+\mu*P_{0H}}{\mu-\lambda*(1+\iota)} \tag{32}$$

Equation (32), when we substitute Equations. (22) and (28) yields

$$P_{.H}=\frac{\chi}{\mu-\lambda*(1+l)}*\left[\frac{\lambda*(1+\iota)}{\chi+\psi}*\frac{1-B^H}{B(1-B)}+\frac{\mu}{\lambda*(1+\iota)}*B^{H-1}\right]*P_{00} \tag{33}$$

It is simple to observe that the normalizing condition (7) can instead be expressed via a description of $P_{.i}$.

$$\sum_{i=0}^{H}P_{.i}=1 \tag{34}$$

When we replace Equations (26) and (33) in (34), we obtain

$$P_{00}=\left\{\frac{\mu*\chi+(\mu-\lambda*(1+l))*\psi}{(\mu-\lambda*(1+l))*(\chi+\psi)}*\frac{1-B^H}{B*(1-B)}+\frac{\mu*\chi}{\lambda*(1+l)*(\mu-\lambda*(1+l))}*B^{H-1}\right\}^{-1} \tag{35}$$

Equation (35) is substituted into equation (28), yielding

$$E\left(L_U\right)=\frac{\left(\lambda*(1+l)^2(\mu-\lambda*(1+l)\right)}{\mu*\chi*[\lambda*(1+l)+(\chi+\psi)K(H)]+\lambda*(1+l)*\psi*(\mu-\lambda*(1+l))} \tag{36}$$

Where

$$K(H)=\frac{B^H(1-B)}{1-B^H}$$

We now determine $E\left(L_H\right)$. Applying the L'Hopital rule to Eq. (30), we obtain

$$E\left(L_H\right)=\frac{\chi}{2*(\mu-\lambda*(1+\iota))}*\sum_{i=0}^{H-1}R_i''(1)+\frac{\mu*\chi}{(\mu-\lambda*(1+\iota))^2}\sum_{i=0}^{H-1}R_i'(1) \tag{38}$$

Where $R_i''(1)$ is secure by second derivative $R_i(Z)$ where Z should be 1 . Second derivative Equations. (8) to (9), we get

$$\begin{aligned}-2*\psi*R_i''(Z)+\psi*(1-Z)*\tfrac{d^3}{dZ^3}R_i(Z)=[\lambda*(1+\iota)*(1-Z)+\chi]*R_i''(Z)\\ -2*\lambda*(1+\iota)*R_i'(Z), i=0,1,\ldots,K-1\end{aligned} \tag{39}$$

Putting Z = 1 in Equation. (39), we obtain

$$R_i''(1)=\frac{2*\lambda*(1+\iota)}{\chi+2*\psi}*R_i'(1), i=0,1,\ldots,H-1 \tag{40}$$

When we replace Equation (40) with Equation (38), we get

$$E\left(L_H\right)=\frac{\chi}{\mu-\lambda*(1+l)}*\left(\frac{\mu}{\mu-\lambda*(1+l)}+\frac{\lambda*(1+l)}{\chi+2*\chi}\right)*E\left(L_U\right) \tag{41}$$

In this case, P_{0H} is determined via Equations. (22) and (35) while $E\left(L_U\right)$ is determined by use of Equation. (36).

$$P_{0H}=\frac{\chi*(\mu-\lambda*(1+l))*(\chi+\psi)*K(H)}{\mu*\chi*[\lambda*(1+l)+(\chi+\psi)*K(H)]+\lambda*(1+l)*\psi*(\mu-\lambda*(1+l)} \tag{42}$$

in which Eq. (37) yields K(H).

Let us assume that L be the expected no. of consumers of the queuing system.
The average size of the system $E(L)=E\left(L_U\right)+E\left(L_H\right)$ beginning with Equations. (36) and (41)

4. Special Privilige

Two specific instances of the alternative vacation policy covered in this work are the single v and the numerous vacations.
Privilege 1. Numerous vacation models. If $H=\infty$, hereafter $K(\infty)=0$. Beginning with Equations. (36) and (41), we get

$$E\left(L_U\right)=\frac{\lambda*(1+\iota)*(\mu-\lambda*(1+\iota))}{\mu*\chi+\psi*(\mu-\lambda*(1+\iota))}$$

and

$$E\left(L_H\right)=\frac{\chi}{\mu-\lambda*(1+\iota)}*\left(\frac{\mu}{\mu-\lambda*(1+\iota)}+\frac{\lambda*(1+\iota)}{\chi+2*\psi}\right)*\frac{\lambda*(1+\iota)*\mu}{\mu*\chi+\psi*(\mu-\lambda*(1+\iota))}$$

Privilege 2. Unique vacation method. If H should be one, hereafter $K(1)=B$. Beginning with Equations. (36) and (41), we get

$$E(L_U) = \frac{(\lambda * (1+\iota)^2 * (\mu - \lambda * (1+\iota))}{\mu * \chi * [\lambda * (1+\iota) + (\chi + \psi) * B] + \lambda * (1+\iota) * \psi * (\mu - \lambda * (1+\iota))}$$

and

$$E(L_H) = \frac{\chi}{\mu - \lambda * (1+\iota)} \left(\frac{\mu}{\mu - \lambda * (1+\iota)} + \frac{\lambda * (1+\iota)}{\chi + 2 * \psi} \right) E(L_U) + \frac{\lambda * (1+\iota) * \mu}{(\mu - \lambda * (1+\iota))^2} * \frac{\chi * (\mu - \lambda * (1+\iota))(\chi + \psi) * \text{ B}}{\mu * \chi * [\lambda * (1+\iota) + (\chi + \psi) * B] + \lambda * (1+\iota) * \psi * (\mu - \lambda * (1+\iota))}$$

5. Performance Evaluvation

We extract some other significant performance metrics in this section.

1. The probability of a server being away on vacation is provided by

$$P_U = \sum_{i=0}^{H-1} P_{.i} \tag{43}$$

When we change the Equation. (26) to Equation. (43), we get

$$P_U = \frac{1 - B^H}{B * (1 - B)} * P_{00}$$

Applying Equation (28), we obtain

$$P_U = \frac{\chi + \psi}{\lambda * (1+\iota)} * E(L_U) \tag{44}$$

where $E(L_U)$ is provided by Equation. (36).

2. The probability that the server is engaged is provided by

$$P_a = \sum_{m=1}^{\infty} P_{mH} = 1 - P_{0H} - P_U \tag{45}$$

By replacing Equations. (42) and (44) through Eq. (45) and applying Eq. (36), we get

$$P_a = \frac{\lambda * (1+l) * \chi * [\lambda * (1+l) + (\chi + \psi) * K(H)]}{\mu * \chi * [\lambda * (1+l) + (\chi + \psi) * K(H)] + \lambda * (1+l) * \psi * (\mu - \lambda * (1+\iota))} \tag{46}$$

When we replace a continuous variabley, for the numeric H in the R.H.S of Eq. (46), we obtain the f(y), which is represented by $S(y)$. Applying a derivative of $S(y)$ we obtain

$$S'(y) = \frac{(\lambda * (1+\iota))^2 \chi * \psi * (\mu - \lambda * (1+\iota))(\chi + \psi) * K'(y)}{\{\mu * \chi * [\lambda * (1+\iota) + (\chi + \psi) * K(y)] + \lambda * (1+\iota) * \psi * (\mu - \lambda * (1+\iota))\}^2} < 0$$

The imbalance arises beginning with H$'$(y) < 0. Therefore, S(y) for declined. As that a result, when H increases, P_a lowers.

3. The expected no. of customers served per time is $\mu * P_a$, inferred that the segment of customers served is provided by

$$P_Q = \frac{\mu * P_a}{\lambda * (1+\iota)}$$

Where P_a is provided by Equation. (46).

4. The mean rate of desertion due to dissatisfaction can be described as, the average impatience customers obtain by

$$G_b = \sum_{i=0}^{H-1} \sum_{m=1}^{\infty} m * \psi * P_{mi} = \psi * E\left(L_U\right) \tag{48}$$

Where $E\left(L_U\right)$ is provided by Equation. (36).

6. Numerical Illustration

In this part, we examine the impact of H and ψ on several performance indicators numerically where $\Psi = 0.5, 1.0, 1.5$.

λ	ι	β	μ	χ	H	ψ
4	0.25	0.1	5	2	$1, 2, 3, 4, \ldots, \infty$	0.5, 1.0, 1.5

Table 1: *Performance metrics with $\lambda^*(1+\iota), \beta, H$, and ψ fluctuations for ψ values of 0.5, 1.0, and 1.5, ψ values should be minimum values*

H	ψ	$E\left(L_U\right)$	$E\left(L_H\right)$	$E(L)$	P_u	P_a	G_b
1	0.5	0.0419	0.1096	0.1515	0.2095	0.0958	0.0215
	1.0	0.0343	0.1054	0.1397	0.2058	0.0931	0.0343
	1.5	0.0289	0.1027	0.1316	0.2023	0.0913	0.0434
2	0.5	0.0391	0.1080	0.1417	0.1955	0.1843	0.0196
	1.0	0.0323	0.1043	0.1366	0.1938	0.1647	0.0323
	1.5	0.0275	0.1020	0.1295	0.1925	0.1576	0.0413
3	0.5	0.0365	0.1065	0.1430	0.1825	0.1560	0.0183
	1.0	0.0304	0.1033	0.1337	0.1824	0.1500	0.0304
	1.5	0.0261	0.1012	0.1273	0.1827	0.1486	0.0391
4	0.5	0.0341	0.1051	0.1392	0.1705	0.1470	0.0171
	1.0	0.0287	0.1023	0.1310	0.1722	0.1420	0.0287
	1.5	0.0248	0.1005	0.1253	0.1736	0.1323	0.0372
5	0.5	0.0319	0.1039	0.1358	0.1595	0.1298	0.0159
	1.0	0.0271	0.1015	0.1286	0.1626	0.1220	0.0271
	1.5	0.0235	0.0997	0.1231	0.1645	0.1150	0.0353

Table 2: *Little's Law verification*

$\lambda * (\mathbf{1} + \iota)$	L	W	$\mathrm{L} = \boldsymbol{\lambda} * (\mathbf{1} + \iota)\boldsymbol{W}$
1.25	0.1515	0.1212	0.1515
1.25	0.1397	0.11176	0.1397
1.25	0.1316	0.10528	0.1316
1.25	0.1417	0.11336	0.1417
1.25	0.1366	0.10928	0.1366
1.25	0.1295	0.1036	0.1295
1.25	0.1430	0.1144	0.1430
1.25	0.1337	0.10696	0.1337
1.25	0.1273	0.10184	0.1273
1.25	0.1392	0.11136	0.1392
1.25	0.1310	0.1048	0.1310
1.25	0.1253	0.10024	0.1253
1.25	0.1358	0.10864	0.1358
1.25	0.1286	0.10288	0.1286
1.25	0.1231	0.09848	0.1231

Table 1. shows that E(L_H) and the average system size E(L)decrease with ψ for every value are finite. P_a, the probability that the server is operating, is very much dropping, while P_u, the chance that the server is on vacation, is growing by ψ. Comparison of the Poisson model this method is very much effective.

In this part, we examine the impact of H and ψ on several performance indicators numerically where $\Psi = 2.5, 3.0, 3.5$.

λ	ι	β	μ	χ	H	ψ
4	0.25	0.1	5	2	$1, 2, 3, 4, \ldots, \infty$	2.5, 3.0, 3.5

Table 3: *Performance metrics with $\lambda * (1 + \iota), \beta, H$, and ψ fluctuations for ψ values of 0.5, 1.0, and 1.5, ψ values should be maximum values*

H	ψ	$E(L_U)$	$E(L_H)$	$E(L.$	P_u	P_a	G_b
1	2.5	0.0221	0.0996	0.1217	0.1989	0.0889	0.0553
	3.0	0.0197	0.0985	0.1182	0.1970	0.0882	0.0591
	3.5	0.0178	0.0975	0.1153	0.1958	0.0875	0.0623
2	2.5	0.2116	0.0991	0.1202	0.1904	0.0798	0.0529
	3.0	0.1890	0.0972	0.1144	0.1890	0.0750	0.0567
	3.5	0.0172	0.974	0.1146	0.1892	0.0711	0.0602
3	2.5	0.0203	0.0986	0.1189	0.1827	0.0687	0.0508
	3.0	0.0183	0.0978	0.1161	0.1830	0.0650	0.0549
	3.5	0.0166	0.0971	0.1137	0.1826	0.0632	0.0581
5	2.5	0.0187	0.0978	0.1165	0.1683	0.0584	0.0468
	3.0	0.0169	0.0970	0.1139	0.1690	0.0540	0.0507
	3.5	0.0155	0.0965	0.1120	0.1705	0.0512	0.0543
7	2.5	0.0173	0.0970	0.1143	0.1557	0.0487	0.0483
	3.0	0.0157	0.0964	0.1121	0.1570	0.0444	0.0471
	3.5	0.0145	0.0960	0.1105	0.1595	0.0408	0.0508

Table 4: *Little's law verification*

$\lambda * (\mathbf{1} + \iota)$	L	W	L $= \boldsymbol{\lambda} * (\mathbf{1} + \boldsymbol{\iota}) \boldsymbol{W}$
1.25	0.1217	0.09736	0.1217
1.25	0.1182	0.09456	0.1182
1.25	0.1153	0.09224	0.1153
1.25	0.1202	0.09616	0.1202
1.25	0.1144	0.09152	0.1144
1.25	0.1146	0.09168	0.1146
1.25	0.1189	0.09512	0.1189
1.25	0.1161	0.09288	0.1161
1.25	0.1137	0.09096	0.1137
1.25	0.1165	0.0932	0.1165
1.25	0.1139	0.09112	0.1139
1.25	0.1120	0.0896	0.1120
1.25	0.1358	0.10864	0.1358
1.25	0.1286	0.10288	0.1286
1.25	0.1231	0.09848	0.1231

Table 3. shows that $E(L_H)$ and the average system size $E(L)$ all the values dropping with ψ for every value are finite $H.P_u$ and P_a values are growing neither dropping with ψ when $H = 2$

and $H = 3$. That represents that P_v and P_b are not unmodulated functions of ψ when $H \neq \infty$. Comparison of the Poisson model this method is very much effective.

7. Remarks

1. The single-vacation model describes the present model's reduction if $H = 1$. The numerous vacation concept is the reduced version of the existing model if $H = \infty$.
2. It is simple to verify that $\psi - \chi D > 0$, Thus, we obtained $0 < B < 1$.
3. Beginning with Equation. (27) and $0 < B < 1$, it is simple to check that the average system size $E(L_i)$ is a dropping of i for $i = 0, 1, \ldots, H-1$.

Likewise, beginning with Equation. (32), the not equality $P_{.H} > 0$ is exactly equal to $\lambda * (1 + \iota) < \mu$. So, $\lambda * (1 + \iota) < \mu$ is a standard condition for our system. Therefore, let us assume hereafter that $\lambda * (1 + \iota) < \mu$.

8. Conclusion

In this research work, we have developed a single-server Markovian encouraged arrival queuing system with balking, dissatisfied customers, and numerous vacations, where the customer dissatisfaction via the server is on vacation. We have applied a 25% discount on our model, the system size increased, and the waiting time has been reduced. This result is very efficient compared with the Poisson arrival model, and we have obtained the other important performance measures, and Little's law is also satisfied for this model. The effects of the parameters $\lambda^*(1 + \iota)$,β, ψ, and H on some performance measures have been investigated numerically.

References

[1] Begum, A. M. I. (1996). Queuing models with bulk service with a vacation. *Doctoral dissertation, Bharathiar University, Coimbatore*.
[2] Servi, L. D. and Finn, S. G. (2002). M/M/1 queues with working vacations (M/M/1/WV). *Performance Evaluation*, 50:41–52.
[3] Ke, J. C. and Pearn, W. L. (2004). Optimal management policy for heterogeneous arrival queuing systems with server breakdowns and vacations. *Quality Technology & Quantitative Management*, 1:149–162.
[4] Zhang, Z. and Xu, X. (2008). Analysis for the M/M/1 queue with multiple working vacations and N-policy. *Information and Management Services*, 19(3):495–506.
[5] Tian, N., Li, J. and Zhang, G. (2009). Matrix analytic method and working vacation queue:A survey. *International Journal of Information Management Sciences*, 20:603–633.
[6] Tian, N., Zhao, X. and Wang, K. (2008). The M/M/1 queue with single working vacation. *International Journal of Information Management Sciences*, 19:621–634.
[7] Altman, E. and Yechiali, U. (2006). Analysis of customers' impatience in queues with server vacations. *Queueing Systems*, 52:261–279.
[8] Altman, E. and Yechiali, U. (2008). Infinite-server queues with systems' additional task and impatient customers. *Probability in the Engineering and Informational Sciences*, 22:477–493.
[9] Banik, A. D. (2009). The infinite-buffer single server queue with a variant of multiple vacation policy and batch Markovian arrival process. *Applied Mathematical Modelling*, 33:3025–3039.
[10] Ke, J. C. (2007). Operating characteristic analysis on the $M^{[X]}$/G/1 system with a variant vacation policy and balking. *Applied Mathematical Modelling*, 31:1321–1337.
[11] Ke, J. C., Huang, H. I. and Chu, Y. K. (2010). Batch arrival queue with N-policy and at most J vacations. *Applied Mathematical Modelling*, 34:451–466.
[12] Som, B. K. and Seth, S. (2017). An M/M/1/N queuing system with encouraged arrivals. *Global Journal of Pure and Applied Mathematics*, 13:3443–3453.

[13] Khan, I. E. and Paramasivam, R. (2022). Reduction in waiting time in an M/M/1/N encouraged arrival queue with feedback, balking and maintaining of reneged customers. *Symmetry*, 14:1743.

[14] Khan, I. E. and Paramasivam, R. (2023). Markovian Erlang non-constricted single-channel with encouraged arrival in steady state with balking, feedback strategy, and customer retention. *Contemporary Mathematics*, 25:769–781.

[15] Khan, I. E. and Paramasivam, R. (2023). Performance study of an M/M/1 retrial queueing system with balking, dissatisfied customers, and server vacations. *Contemporary Mathematics*, 15:467–483.

RT&A, No 4 (89)
Volume 20, December 2025

ENHANCING THE ROBUSTNESS OF SUPPORT VECTOR REGRESSION WITH DEPTH-INDUCED WEIGHT FUNCTIONS FOR IMPROVED PREDICTION

Kalaivani S

•

Assistant Professor
Department of Statistics and Data Science
Christ University
Bangalore, India
kalaivanistatistics1994@gmail.com

Abstract

Support Vector Regression (SVR) is an extension of Support Vector Machines designed for regression tasks. By using an epsilon-insensitive loss function, SVR balances model complexity and accuracy, making it effective at handling noise and outliers. Data depth functions measure the centrality of data points in multivariate spaces, providing a robust approach to identify influential data based on their position relative to the data distribution. This study introduces Depth-Induced SVR, an enhanced SVR model that incorporates robust depth functions as a weight mechanism with the kernel function to improve efficiency and robustness. Various robust depth functions such as Mahalanobis, Halfspace, L_2, Projection, Spatial, and Zonoid are evaluated as weighting functions to determine the most effective combination with the kernel function. Model efficacy is assessed using performance metrics including Mean Squared Error (MSE), Mean Absolute Error (MAE), Mean Absolute Percentage Error (MAPE), and Median Absolute Error (MDAE). This comparative approach aims to identify the optimal depth function for robust SVR performance across diverse real datasets and simulated environments.

Keywords: Support Vector Regression, Data Depth, Robust Procedures, Outliers

1. Introduction

Support Vector Regression (SVR) is an advanced topic for regression tasks and is known for its robustness in handling both linear and nonlinear data relationships. Unlike conventional regression techniques, SVR minimizes prediction errors within a predefined threshold, known as epsilon (ϵ), to balance model complexity and accuracy. This epsilon-insensitive loss function allows SVR to effectively handle noise and outliers, making it a valuable tool in applications where precision is critical. SVR is also highly adaptable due to its use of kernel functions, which map data into higher-dimensional spaces to capture complex relationships, enhancing its performance across diverse data structures and regression scenarios.

Data depth functions, on the other hand, are essential in multivariate analysis as they measure the centrality of data points relative to a distribution. Depth functions such as Mahalanobis, Halfspace, L_2, Projection, Spatial, and Zonoid provide a means to evaluate the influence of each data point based on its position, identifying the most representative observations in a dataset. Incorporating data depth into SVR, particularly through depth-induced weight functions, enhances the model's robustness by down-weighting outliers and emphasizing central data

points. This combination of SVR with data depth functions offers an improved approach to regression, yielding more reliable predictions and increasing resilience to variability across real-world datasets.

The rest of this paper is organized as follows. Section 2 presents an overview and fundamental concepts of Support Vector Regression. Section 3 discusses various depth functions and their roles in enhancing model robustness. Section 4 describes the proposed Depth-Induced SVR and its algorithm. Section 5 presents findings from numerical studies conducted on both real datasets and simulated environments. Finally, Section 6 concludes the paper with a summary and conclusion.

2. Support Vector Regression (SVR)

Support Vector Regression (SVR) is a type of supervised learning algorithm utilized for regression analysis, where the goal is to predict a dependent variable based on a set of independent variables. It operates by identifying a hyperplane that effectively separates the data into two classes, one representing the target variable and the other representing the residual errors. Its primary objective is to minimize the error by finding the hyperplane and reducing the gap between predicted and observed values. SVR is particularly effective in addressing non-linear regression problems, as it can manage intricate relationships between predictor and response variables.

SVR is an advanced machine learning technique adapted from SVM for regression analysis. Unlike traditional regression models that aim to minimize the error between predicted and actual values directly, SVR introduces an epsilon-insensitive loss function that allows deviations within a certain range, ϵ, to be ignored. This enables SVR to create a tube or margin around the estimated regression line, focusing on the larger pattern in the data while reducing sensitivity to noise and minor fluctuations. SVR's objective is to find a regression line or hyperplane that minimizes the prediction error while also keeping the model complexity low. The complexity of SVR is controlled by a regularization parameter, C, which penalizes large errors outside the epsilon margin, balancing the trade-off between model flexibility and generalization.

SVR's strength also lies in its flexibility to model nonlinear relationships through the use of kernel functions. Kernel functions, such as linear, polynomial, radial basis function (RBF), and sigmoid kernels, transform the data into higher-dimensional spaces where complex patterns can be captured by linear boundaries. This feature enables SVR to handle both linear and nonlinear regression tasks with ease, making it versatile for a wide range of applications. By mapping data into these high-dimensional spaces, SVR is able to construct more accurate predictive models that capture intricate relationships between variables. The choice of kernel and hyperparameters, such as C, ϵ, and kernel-specific parameters, significantly influences SVR's performance, requiring careful tuning for optimal results.

The SVR can be formulated as a quadratic programming problem, the dual formulation of the problem is indicated because it reduces the number of constraints and allows the application of the Kernel Trick to solve non-linear problems.
Consider the model,

$$y = wx + b \tag{1}$$

The SVR model can be written by introducing the slack variables,

$$f(x) = \sum_{i=1}^{l} (\alpha_i - \alpha_i^*)\langle x_i, x\rangle + b \tag{2}$$

$$\begin{aligned} \text{minimize} \quad & \frac{1}{2}\|w\|^2 + C\sum_{i=1}^{l}(\xi_i + \xi_i^*) \\ \text{subject to} \quad & \begin{cases} y_i - \langle w, x_i\rangle - b \le \varepsilon + \xi_i \\ \langle w, x_i\rangle + b - y_i \le \varepsilon + \xi_i^* \\ \xi_i, \xi_i^* \ge 0 \end{cases} \end{aligned} \tag{3}$$

where ξ_i,ξ_i^* are the slack variables. The approach involves constructing a Lagrangian function, combining the objective function and constraints, along with dual variables. The Lagrangian for SVR is given as

$$\begin{aligned}\mathcal{L} = \frac{1}{2}\|w\|^2 + C\sum_{i=1}^{l}(\xi_i + \xi_i^*) - C\sum_{i=1}^{l}(\eta_i\xi_i + \eta_i^*\xi_i^*) - \sum_{i=1}^{l}\alpha_i(\varepsilon + \xi_i - y_i + \langle w, x_i\rangle + b) \\ - \sum_{i=1}^{l}\alpha_i^*(\varepsilon + \xi_i^* + y_i - \langle w, x_i\rangle - b)\end{aligned} \tag{4}$$

where L is Lagrangian and $\eta_i, \eta_i^*, \alpha_i, \alpha_i^*$, are Lagrangian multipliers. Hence the dual variables in equation (3) have to satisfy the positivity constraints, that is, $\eta_i, \eta_i^*, \alpha_i, \alpha_i^* \geq 0$. It follows from the condition of the saddle point that the partial derivatives of L with respect to the primal variables (w,b,ξ_i,ξ_i^*) have to disappear for optimality

$$\partial_b\mathcal{L} = \sum_{i=1}^{l}(\alpha_i^* - \alpha_i) = 0 \tag{5}$$

$$\partial_w\mathcal{L} = w - \sum_{i=1}^{l}(\alpha_i - \alpha_i^*)x_i = 0 \tag{6}$$

$$\partial_{\xi_i^{(*)}}\mathcal{L} = C - \alpha_i^{(*)} - \eta_i^{(*)} = 0 \tag{7}$$

Substituting equations (5), (6) and (7) in equation (4) yields the dual optimization problem.

$$\begin{aligned}\text{maximize} \quad & \left\{ -\frac{1}{2}\sum_{i=1}^{l}\sum_{j=1}^{l}(\alpha_i - \alpha_i^*)(\alpha_j - \alpha_j^*)\langle x_i, x_j\rangle \right. \\ & \left. -\varepsilon\sum_{i=1}^{l}(\alpha_i + \alpha_i^*) + \sum_{i=1}^{l}y_i(\alpha_i - \alpha_i^*) \right\} \\ \text{subject to} \quad & \sum_{i=1}^{l}(\alpha_i - \alpha_i^*) = 0, \quad \alpha_i, \alpha_i^* \in [0, C]\end{aligned} \tag{8}$$

Using the equation (7) the dual variables η_i and η_i^* in equation (8) are removed which can be reconstructed as $\eta_i^{(*)} = C - \alpha_i^{(*)}$. Therefore equation (6) can be rewritten as follows

$$w = \sum_{i=1}^{l}(\alpha_i - \alpha_i^*)x_i \tag{9}$$

Thus

$$f(x) = \sum_{i=1}^{l}(\alpha_i - \alpha_i^*)\langle x_i, x\rangle + b \tag{10}$$

This function depicts the so-called Support Vector Expansion, that is, w can be completely defined as a linear combination of the training data points x_i. In a sense, the difficulty of a function's representation by support vectors does not depend on the dimensionality of the training set X, and depends only on the number of support vectors.

3. Robust Data Depth Procedures

The data depth approach in robust statistics aims to quantify the centrality of a point within a data set by measuring how deep or central the point is relative to the overall distribution. This method provides a way to distinguish between outliers and typical data points by assigning a

"depth" value to each data point. The depth of a point reflects its position in the distribution, with deeper points being closer to the center of the data cloud. Various depth functions exist, each with different properties such as affine invariance, robustness to outliers, and computational efficiency. These depth functions are particularly useful for robust estimation, outlier detection, and defining central locations in multidimensional data sets. This study focuses on the depth functions like Mahalanobis depth, Halfspace depth, L_2 depth, Projection depth, Spatial depth and Zonoid depth.

Mahalanobis Depth (MD), introduced by Mahalanobis (1936), measures the centrality of a point x in a multivariate data set relative to its mean and dispersion matrix. It is inversely proportional to the Mahalanobis distance from x to the mean of the data. The formula is

$$M_hD(x) = \left[1 + (x - \bar{x})^T S^{-1}(x - \bar{x})\right]^{-1} \tag{11}$$

where $\bar{x}$ and S are the mean vector and dispersion matrix. Despite its utility, Mahalanobis depth is sensitive to outliers as it depends on non-robust measures.

Halfspace depth (HD), proposed by Tukey (1975), quantifies the centrality of a point x as the smallest number of observations in any halfspace containing x. In the univariate case, it is defined as

$$ldepth_1(\theta; X_n) = \min\{\#(x_i \leq \theta), \#(x_i \geq \theta)\} \tag{12}$$

In higher dimensions, the point with the highest depth is the Tukey median. This depth function is affine invariant and robust to outliers.

L_2 Depth (L_2D) developed by Zuo and Serfling (2000), measures the outlyingness of a point z based on its mean distance from the data distribution center. It is given by

$$D^{L_2}(z/X) = (1 + E[\|z - X\|])^{-1} \tag{13}$$

For empirical distributions, the mean distance is computed using sample points. While effective for measuring centrality, the standard L_2 depth is not affine invariant.

Projection Depth (PD), proposed by Liu (1992), evaluates the depth of a point x by measuring its outlyingness through projections onto all possible directions. For a univariate distribution function F of x, the outlyingness $O(F, x)$ is defined as

$$O(F, x) = Sup\{Q(u, x, F)\} \tag{14}$$

over all unit vectors u, where $Q(u, x, F) = \frac{(u^T x - \mu(F_u))}{\sigma(F_u)}$, and F_u is the distribution of $u^T x$. The projection depth $PD(x, F)$ is then given by

$$PD(x, F) = \frac{1}{1 + O(x, F)} \tag{15}$$

This approach reflects the projection pursuit methodology, involving the supremum over infinitely numerous direction vectors, making the computation of projection depth seemingly intractable. Initially, classical location and scale measures were used, but these were later replaced by robust measures like the median and Median Absolute Deviation (MAD).

Spatial Depth (SD) measures the centrality of a point x relative to a distribution F by considering the expectation of scaled spatial vectors pointing from x to the data points. It is defined as

$$SD\left(\frac{x}{F}\right) = 1 - \left\| E_F\left[\frac{X - x}{\|X - x\|}\right]\right\| \tag{16}$$

where $\|.\|$ denotes the Euclidean norm. Spatial depth is affine invariant and robust, but it may not always provide a strict ordering of points.

Zonoid Depth (ZD) determines the centrality of x based on whether belongs to zonoids formed by convex combinations of data points. For a finite data set $X = x_1, x_2, ., x_n$ it is defined as

$$ZD\left(\frac{x}{X}\right) = \sup\{\lambda : x \in \lambda\,\mathrm{conv}(x) + (1 - \lambda)c\} \tag{17}$$

where c is the center of mass. Zonoid depth is affine invariant and provides nested convex contours but is less robust to outliers.

4. Proposed Depth-Induced SVR

Depth-induced SVR integrates data depth measures into the framework of Support Vector Regression to enhance robustness against outliers and improve the representation of centrality within the data. By leveraging depth functions such as Mahalanobis, Tukey, or simplicial depth, the method assigns weights to observations based on their depth, emphasizing central points while down-weighting outliers. The resulting regression function aims to minimize the ϵ-insensitive loss while incorporating depth-based weights.

The SVR problem with depth-induced weights is defined as

$$\begin{aligned} \underset{w,b,\xi_i,\xi_i^*}{\text{minimize}} \quad & \frac{1}{2}\|w\|^2 + C\sum_{i=1}^{l} D(x_i)(\xi_i + \xi_i^*) \\ \text{subject to} \quad & \begin{cases} y_i - \langle w^T, x_i\rangle - b \le \varepsilon + \xi_i \\ \langle w^T, x_i\rangle + b - y_i \le \varepsilon + \xi_i^* \\ \xi_i, \xi_i^* \ge 0 \end{cases} \end{aligned} \tag{18}$$

where $D(x_i)$ represents the depth measure, $\Phi(\cdot)$ is the feature mapping, and C is the regularization parameter.

Proposed Algorithm for Depth-Induced SVR is given by

Step 1: Compute Statistical Depth

Calculate the depth $D(x_i, \chi)$ for each observation x_i using a suitable robust depth function. Normalize depth values to the range $[0, 1]$.

Step 2: Assign Depth-Weighted Penalties

Define a depth-induced weight for each data point. $w_i = f(D(x_i, \chi))$, $f(\cdot)$ is a monotonically decreasing function.

Step 3: Formulate the SVR Optimization Problem

$$\begin{aligned} \underset{w,b,\xi_i,\xi_i^*}{\text{minimize}} \quad & \frac{1}{2}\|w\|^2 + C\sum_{i=1}^{l} D(x_i)(\xi_i + \xi_i^*) \\ \text{subject to} \quad & \begin{cases} y_i - \langle w^T, x_i\rangle - b \le \varepsilon + \xi_i \\ \langle w^T, x_i\rangle + b - y_i \le \varepsilon + \xi_i^* \\ \xi_i, \xi_i^* \ge 0 \end{cases} \end{aligned}$$

where $D(x_i)$ represents the depth measure, $\Phi(\cdot)$ is the feature mapping, and C is the regularization parameter.

Step:4 Solve the Optimization Problem

Use a quadratic programming solver to determine the model parameters (w,b) and the slack variables (ξ_i,$\xi_i{}^*$).

Step :5 Predict the Response

For a new observation x, the predicted response is $\hat{y} = w^T\Phi(x) + b$

Step: 6 Evaluate Error Metrics

Assess the model's performance using appropriate error metrics like MAE, MAPE.

This algorithm ensures robustness by prioritizing data points that are central according to the depth measure, effectively reducing the influence of outliers on the model.

5. Numerical Study

This section evaluates the effectiveness of the Depth-Induced Support Vector Regression model using various statistical depth procedures through both real and simulation studies. The analysis incorporates depth measures such as Mahalanobis Depth, Halfspace Depth, L_2 Depth, Projection Depth, Spatial Depth, and Zonoid Depth, applied within the DI-SVR framework utilizing the Radial Basis Function (RBF) kernel. These depth procedures aim to enhance model robustness

by accounting for the centrality of data points, thereby reducing the influence of outliers and extreme values.

To ensure a robust evaluation, the Depth-Induced Support Vector Regression models are applied to both real-world datasets and simulated data. The real datasets, obtained from R packages, consist of one or more predictors and allow for practical assessment under realistic scenarios. The performance of the Depth-Induced Support Vector Regression model using various depth functions is summarized in Table 1 and Table 2, which present the error metrics across different depth-based SVR implementations. These metrics include MSE, MAE, MAPE, and MDAE, providing a comprehensive comparison of the models' predictive accuracy and robustness.

Table 1: *Computed error values for starsCYG dataset*

Methods	**MSE**	**MAE**	**MAPE**	**MDAE**
MD-SVR	0.1069	0.2448	0.0491	0.1771
	(0.0741)	(0.1972)	(0.0398)	(0.1309)
HD-SVR	0.1130	0.2542	0.0510	0.1990
	(0.0741)	(0.1972)	(0.0398)	(0.1308)
L2D-SVR	0.1254	0.2804	0.0567	0.2292
	(0.0869)	(0.2404)	(0.0492)	(0.2050)
PD-SVR	0.0895	0.2239	0.0452	0.1469
	(0.0741)	(0.1971)	(0.0398)	(0.1306)
SD-SVR	0.1270	0.2895	0.0589	0.2400
	(0.0751)	(0.2027)	(0.0480)	(0.1476)
ZD-SVR	0.1267	0.2871	0.0583	0.2227
	(0.0747)	(0.2082)	(0.0421)	(0.1653)

(.) without outliers

Table 2: *Computed error values for Prostate dataset*

Methods	**MSE**	**MAE**	**MAPE**	**MDAE**
MD-SVR	0.3061	0.3951	1.8625	0.2258
	(0.2322)	(0.3469)	(1.9660)	(0.1775)
HD-SVR	0.3037	0.3931	1.8624	0.2245
	(0.1973)	(0.2914)	(2.1212)	(0.1116)
L2D-SVR	0.3472	0.4328	1.8894	0.2399
	(0.2277)	(0.3365)	(2.0388)	(0.1320)
PD-SVR	0.2495	0.3353	1.8601	0.1184
	(0.2263)	(0.3335)	(2.0539)	(0.1288)
SD-SVR	0.3003	0.3900	1.8603	0.2158
	(0.2414)	(0.3595)	(1.8863)	(0.1782)
ZD-SVR	0.3385	0.4251	1.8886	0.2349
	(0.2553)	(0.3720)	(1.8207)	(0.1962)

(.) without outliers

starsCYG dataset " It contains features of 47 stars in the Hertzsprung-Russell diagram of the Star Cluster CYG OB1. It includes one predictor variable, the logarithm of the star's effective surface temperature (log.Te), and one response variable, the logarithm of its light intensity (log.light). Cook's distance is used to identify the 9 outliers in the dataset.

Prostate dataset -The dataset has 97 observations each having 8 independent variables namely lweight (log of prostate weight), age, lbph (log of benign prostatic hyperplasia amount), svi (seminal vesicle invasion), lcp (log of capsular penetration), gleason (Gleason score), pgg45 (percentage Gleason scores 4 or 5), lpsa (log of prostate specific antigen) and one dependent variable lcavol (log of cancer volume). This dataset contains 9 outliers when it is checked using cook's distance.

The results in Tables 1 and 2 demonstrate that Projection Depth outperforms other methods by yielding the smallest error values MSE, MAE, MAPE, and MDAE, in both normal and outlier-affected data. This confirms its strong resistance to outliers and its effectiveness in accurately identifying central values, proving it to be a robust and reliable tool for diverse data conditions.

A simulation study was conducted to examine the robustness and efficiency of a linear regression model under varying data conditions.

Case: 1

A sample of size n=100 was generated from a multivariate normal distribution with mean vector μ=(0,0,0) and covariance matrix $= 2I_3$, where I_3 denotes the 3×3 identity matrix. The response variable Y was defined by the model,

$$Y = 10 + 3X_1 + 5X_2 + 8X_3 + \epsilon \tag{19}$$

with the error term $\epsilon \sim N(0, 5)$. To evaluate the model's accuracy under adverse conditions, artificial contaminations were introduced at levels of 10%, 20%, and 30%. These contaminations simulate the presence of outliers and allow for a comprehensive assessment of the model's performance, stability, and reliability in the presence of increasing data distortion.

Table 3: *Computed depth values for Simulation study (Case 1)*

Methods	Levels	MSE	MAE	MAPE	MDAE
MD-SVR	0%	21.0755	3.4562	1.0013	2.6942
	10%	24.7900	3.6151	1.1237	2.1203
	20%	20.4268	3.4434	0.7433	2.4931
	30%	24.8023	3.6151	1.1296	2.4104
HD-SVR	0%	19.5497	3.2500	0.9401	1.8768
	10%	20.5240	3.1911	0.9052	1.3597
	20%	19.0505	3.0595	0.6759	1.1956
	30%	20.5041	3.1859	0.9009	1.3775
L2D-SVR	0%	21.3075	3.4652	1.0115	2.6940
	10%	23.4467	3.4341	1.0240	1.8540
	20%	17.6025	3.0317	0.6269	1.9323
	30%	25.4235	3.4598	1.0549	1.8310
PD-SVR	0%	18.7666	3.1569	0.7796	1.3310
	10%	20.8682	3.2147	0.9115	1.4900
	20%	19.7673	3.3407	0.9748	2.4229
	30%	20.8404	3.2150	0.9391	1.4965
SD-SVR	0%	20.1382	3.2392	0.9139	1.3225
	10%	20.4991	3.1847	0.8995	1.3643
	20%	22.1037	3.5002	1.0632	1.6858
	30%	20.8204	3.1857	0.9327	1.3528
ZD-SVR	0%	22.4943	3.4657	1.0347	2.9606
	10%	24.2552	3.5410	1.0583	2.0964
	20%	20.4565	3.4021	0.9165	2.4203
	30%	24.2514	3.5302	1.0782	2.1962

Case: 2 A sample of size n=500 was generated from a multivariate normal distribution with mean vector μ=(5,5,5) and covariance matrix $= 2.5I_4$, where I_4 denotes the 4×4 identity matrix.

The response variable Y was defined by the model,

$$Y = 5 + 2X_1 + 5X_2 + 7X_3 + 9X_4 + \epsilon \tag{20}$$

with the error term $\epsilon \sim N(0, 5)$. To evaluate the model's accuracy under adverse conditions, artificial contaminations were introduced at levels of 10%, 20%, and 30%. These contaminations simulate the presence of outliers and allow for a comprehensive assessment of the model's performance, stability, and reliability in the presence of increasing data distortion.

Table 4: *Computed depth values for Simulation study (Case 2)*

Methods	Levels	MSE	MAE	MAPE	MDAE
MD-SVR	0%	21.0755	3.4362	1.0013	2.6942
	10%	24.7900	3.6141	1.1327	2.1203
	20%	20.4268	3.4434	0.7433	2.4931
	30%	24.8023	3.6131	1.1296	2.1404
HD-SVR	0%	19.5497	3.2430	0.8401	1.8768
	10%	20.5240	3.1911	0.9028	1.3597
	20%	18.0958	3.0975	0.6759	1.9556
	30%	20.5041	3.1889	0.9009	1.3778
L2D-SVR	0%	21.3078	3.4632	1.0115	2.6940
	10%	23.4467	3.4431	1.0240	1.8340
	20%	17.6025	3.0317	0.6269	1.9323
	30%	23.4258	3.4398	1.0206	1.8310
PD-SVR	0%	18.7866	3.1369	0.7769	1.3310
	10%	20.8642	3.2171	0.9156	1.4940
	20%	19.7763	3.3407	0.7248	2.4239
	30%	20.8404	3.2150	0.9139	1.4965
SD-SVR	0%	20.1282	3.3292	0.9139	2.3225
	10%	20.4391	3.1847	0.8995	1.3623
	20%	18.7618	3.1805	0.6932	2.0488
	30%	20.4204	3.1827	0.8978	1.3828
ZD-SVR	0%	22.9428	3.6547	1.0630	2.9606
	10%	24.2552	3.5410	1.0811	2.0018
	20%	18.0960	3.0975	0.6755	1.9551
	30%	24.2514	3.5380	1.0782	2.0069

Table 3 and 4, highlights the superior performance of the Projection Depth method, which consistently produces the lowest error metrics MSE, MAE, MAPE, and MDAE, across both simulation settings and different levels of contamination. These results underscore its robustness to outliers and its precision in estimating central tendencies, establishing it as a dependable and effective approach under a wide range of data conditions.

6. Discussion

The comparative analysis based on three real datasets and two simulation studies demonstrates the clear superiority of Projection Depth SVR (PD-SVR) over other depth-based SVR methods. PD-SVR consistently achieves the lowest values across all key error metrics, MSE, MAE, MAPE, and MDAE. This consistent performance, observed under both controlled simulations and real-world data scenarios, highlights its strong robustness to outliers and its effectiveness in accurately capturing central tendencies. These results confirm that PD-SVR is a reliable and efficient regression technique, particularly well-suited for complex and contaminated data environments.

References

[1] Donoho, D. L. Breakdown Properties of Multivariate Location Estimators, Technical Report, Harvard University, Boston, 1982.
[2] Donoho, D. L. and Gasko, M. (1992). Breakdown properties of location estimates based on halfspace depth and projected outlyingness. *The Annals of Statistics*, 1803 - 1827.
[3] Koshevoy, G and Mosler, K. (1997). Zonoid trimming for multivariate distributions. *The Annals of Statistics*, 25:1998 - 2017.
[4] Liu, R.Y. (1990). On a notion of data depth based on random simplicies. *The Annals of Statistics*, 18: 405 - 414.
[5] Liu, R.Y. (1992). Data depth and multivariate rank tests. In: Dodge, Y. (ed.), L1-Statistics and Related Methods *North-Holland (Amsterdam)*, 279 - 294.
[6] Liu, R. Y., Parelius and Singh, K. (1999). Multivariate analysis by data depth: Descriptive Statistics, Graphics and Inference *The Annals of Statistics*, 27:783 - 858.
[7] Mahalanobis J. (1936). On the generalized distance in statistics *Proceedings of the National Academy, India*, 12:49 - 55.
[8] Muthukrishnan, R and Poonkuzhali, G. (2018). Robust Depth based weighted Estimator with Application in Discriminant Analysis, *International Journal of Scientific Research in Mathematical and Statistical Sciences*, 5:96 - 101.
[9] Muthukrishnan, R., Gowri, D and Ramkumar N. (2018). Measure of Location using Data Depth Procedures *International Journal of Scientific Research in Mathematical and Statistical Sciences*, 5: 273 - 277.
[10] Tukey, J. W. (1975). Mathematics and the picturing of data. *Proceeding of the International Congress of Mathematicians*, Vancouver, 523 - 531.
[11] Zuo, Y. J. and Serfling R. (2000). General notions of statistical depth function. *The Annals of Statistics*, 28:461 - 482.

MODELING AND IMPROVING THE RELIABILITY OF SMART ELECTRICAL GRIDS

Rahila Muradova
•
Azerbaijan State Oil and Industry University, Baku, Azerbaijan
rahila.muradova.a@asoiu.edu.az

Abstract

The transformation of conventional power systems into intelligent electric networks, or Smart Grids, has introduced significant improvements in efficiency, flexibility, and sustainability. However, this evolution also brings new reliability challenges due to complex cyber-physical interactions, integration of distributed energy resources, and increased exposure to cyber threats. This paper presents a comprehensive methodology for assessing and improving the reliability of smart grids through hybrid modeling, real-time analytics, and fault-tolerant system design. Key components with the highest impact on system reliability—such as communication modules and cyber interfaces—are identified and analyzed. A hybrid reliability model combining probabilistic techniques with machine learning methods is developed and illustrated through a case study involving redundant control systems. The results demonstrate that strategic redundancy and predictive diagnostics can significantly enhance the resilience of modern power infrastructures. The study concludes with recommendations for integrating reliability considerations into autonomous grid operation.

Keywords: Smart Grids; Reliability Modeling; Cyber-Physical Systems; Fault Tolerance; Redundancy; Machine Learning

I. Introduction

Modern trends in power engineering are marked by a large-scale transformation of traditional energy systems toward smart electrical grids (Smart Grids). These systems represent an integration of physical power infrastructure with digital control technologies, advanced communication networks, and distributed generation, including renewable energy sources. The primary goal of this transformation is to enhance the efficiency, flexibility, resilience, and environmental sustainability of power supply systems.

Despite their numerous advantages, smart grids introduce significant challenges in the area of reliability due to their architectural and operational complexity. Unlike conventional centralized systems, Smart Grids operate under high uncertainty driven by variable energy generation, fluctuating loads, and risks associated with cyber-physical interactions [1]. Furthermore, deep digitalization makes the system vulnerable to cyberattacks, communication failures, software malfunctions, and unpredictable cascading events.

Ensuring high reliability is therefore a key requirement in the design, operation, and modernization of intelligent power systems. Addressing this task requires a comprehensive approach that integrates reliability engineering, systems analysis, digital modeling, cybersecurity, and predictive analytics. In today's context, it is essential not only to monitor the current state of the system but also to predict its behavior, identify vulnerabilities at early stages, and respond to failures in an automated and adaptive manner.

This study aims to explore quantitative modeling approaches for assessing and improving the reliability of smart electrical grids, and to propose technical and algorithmic solutions that enhance system resilience [2]. Special attention is given to the analysis of structural and functional vulnerabilities, the development of reliability models, the use of digital twins, and the evaluation of fault-tolerant strategies within increasingly complex energy infrastructures.

II. Problem statement

The evolution of conventional power systems into smart grids has introduced both unprecedented capabilities and new layers of complexity. While digitalization, decentralized control, and integration of renewable energy sources have improved operational flexibility and sustainability, they have also made modern power systems increasingly susceptible to diverse and often interrelated failure mechanisms. Reliability assurance in this context requires not only classical redundancy and hardening strategies but also intelligent modeling and predictive risk assessment tailored to dynamic, cyber-physical environments.

Smart grids are characterized by their hybrid nature—where physical components such as transformers, relays, and power electronics operate in conjunction with digital assets, including smart meters, control algorithms, and communication infrastructure [3-5]. The reliability of such systems is influenced by multiple interconnected domains: physical failures (e.g., thermal stress in power electronics), software errors, communication delays, cyber-attacks, and operational uncertainties due to variable renewable generation.

A critical problem lies in the inability of traditional reliability models to adequately capture the multi-layered interactions and dynamic behavior of smart grids. These models are typically component-centric and static, failing to reflect the probabilistic nature of control decisions, data-driven operations, and event-based disruptions.

To quantify the reliability challenges, a multi-factorial risk assessment was performed. Figure 1 illustrates the risk index for major components of a smart grid system, calculated as the product of failure probability and impact severity.

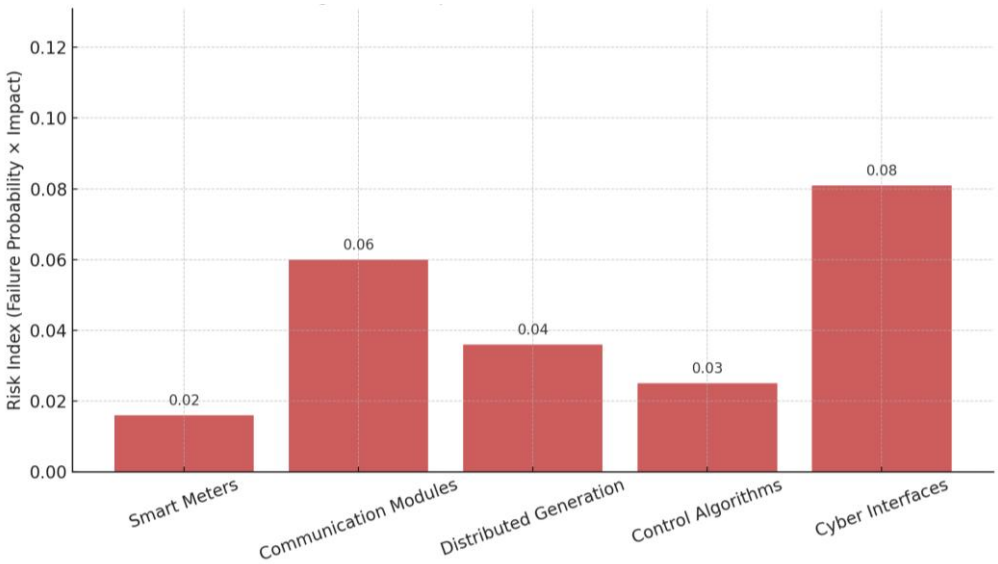


Figure 1. *Component risk index in Smart Grids*

The diagram highlights the disproportionate influence of communication modules and cyber interfaces on systemic risk. Although smart meters exhibit a lower individual risk index, their widespread deployment amplifies potential cascade effects. The data reveal the necessity of focusing reliability improvement strategies on software-intensive and cyber-integrated modules.

Furthermore, in contrast to legacy grids with deterministic operating modes, smart grids function under stochastic, often adversarial, conditions. Load demand fluctuates unpredictably, communication delays affect system stability, and distributed energy resources may introduce asynchronous operation [6].

Addressing this problem requires a shift from traditional static modeling toward integrated frameworks that combine:

- Probabilistic and hybrid modeling techniques,
- Real-time data analytics,
- Predictive diagnostics,
- Redundant and adaptive control architectures.

The following sections of this paper present a methodological approach for modeling the reliability of smart grids using a multi-domain framework. It incorporates cyber and physical variables and proposes strategies for enhancing system-level reliability through redundancy, self-healing capabilities, and data-driven anomaly detection.

To complement the visual risk index analysis, Table 1 presents quantitative reliability characteristics for typical smart grid components, including failure probability, estimated repair time, and resulting unavailability metrics.

Table 1. *Reliability characteristics of key Smart Grid components*

Component	Failure probability (P_f)	Mean Time To Repair (MTTR), h	Unavailability (U = Pf × MTTR)
Smart Meters	0.08	4	0.32
Communication Modules	0.15	6	0.90
Distributed Generation	0.12	5	0.60
Control Algorithms	0.10	3	0.30
Cyber Interfaces	0.18	7	1.26

This table shows that cyber interfaces and communication modules not only exhibit higher failure probabilities, but also longer repair durations, leading to significantly higher unavailability [7]. This quantitative assessment reinforces the earlier conclusion drawn from Figure 1, and highlights where reliability interventions should be prioritized.

The combination of Figure 1 and Table 1 underscores the need to address:

- Latent software vulnerabilities,
- Communication bottlenecks,
- Reactive instead of predictive maintenance, as principal causes of reliability degradation in smart grids.

Accordingly, the following section develops a multi-layered reliability model that accounts for these factors and proposes targeted solutions.

III. Problem solving

The reliability of intelligent electric networks is shaped by the interplay of physical infrastructure, digital communication, and autonomous control. As these systems evolve toward

higher degrees of automation and complexity, conventional static reliability assessment becomes insufficient. Instead, a dynamic, integrated modeling approach is required to capture the cyber-physical interactions that determine operational continuity.

To address this, we propose a hybrid reliability modeling framework that combines probabilistic structures—such as Markov chains and Bayesian networks—with real-time data analytics. This allows the simulation of fault propagation, dependencies between control elements, and response behaviors under uncertainty. Such modeling is essential not only for understanding failure mechanisms, but also for designing systems with embedded resilience.

A practical illustration can be drawn from a typical dual-channel control unit in a smart substation. Let us assume that the primary channel has a failure-free probability of $P_{main}=0.95$, while the backup module performs with $P_{backup}=0.90$. Since these operate in parallel (i.e., the system remains operational if at least one channel works), the combined system reliability is given by:

$$P_{system}=1-(1-P_{main})\cdot(1-P_{backup})=1-(0.05)(0.10)=0.995$$

Thus, the system achieves a 99.5% probability of uninterrupted operation, significantly outperforming either component alone. This result highlights how basic redundancy, when correctly applied, enhances the fault tolerance of critical smart grid subsystems.

In addition to structural enhancements, intelligent monitoring systems contribute to adaptive reliability management. The availability of real-time data streams—originating from PMUs, digital relays, and SCADA logs—enables the deployment of machine learning algorithms for dynamic reliability estimation [8-10]. For example, gradient boosting models such as XGBoost can predict the degradation of switching devices by analyzing thermal cycles and switching frequency, while LSTM neural networks can detect subtle anomalies in communication signals before they escalate into systemic faults.

Table 2.: *Machine learning applications in Smart Grid Reliability*

Application Area	ML Method	Diagnostic Output
Predictive maintenance	XGBoost	Remaining Useful Life (RUL)
SCADA anomaly detection	LSTM	Early fault time identification
Cybersecurity diagnostics	Random Forest	Intrusion risk classification

From a system design perspective, dual-channel DC power architectures offer a foundational layer of physical redundancy. These architectures, often comprising two isolated battery banks with independent chargers, support protection and automation systems even under fault conditions. As illustrated in Figure 2, such a setup allows the grid to maintain control functions despite individual subsystem failures.

Moreover, the integration of self-healing protocols, embedded in the digital control layer, ensures automatic fault isolation and service restoration [11, 12]. This not only minimizes outage durations but also enables distributed intelligence within the grid.

Altogether, the reliability of smart electric networks cannot be decoupled from their digital backbone. By combining fault-tolerant design, intelligent prediction, and cyber-resilient control, we establish a foundation for sustainable, autonomous, and highly reliable operation across all levels of the modern power system.

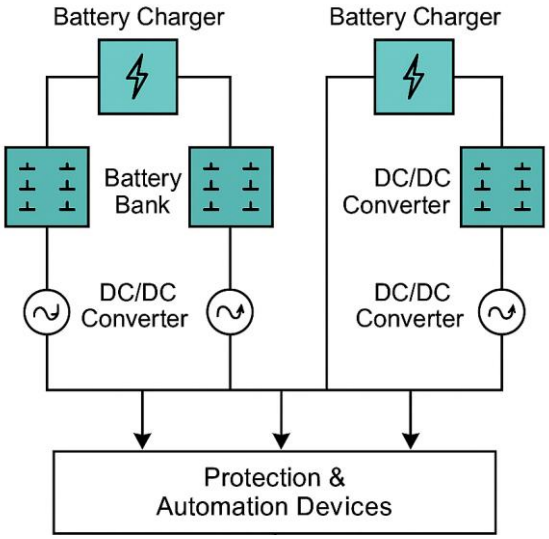


Figure 4.: *Dual-Channel DC auxiliary power architecture*

V. Conclusions

The ongoing digital transformation of electric power systems has significantly reshaped the concept and implementation of reliability. In intelligent electric networks, where cyber-physical integration is intrinsic, reliability can no longer be ensured through conventional redundancy or isolated component-level analysis. Instead, it must be addressed as a system-wide attribute that evolves dynamically with operational conditions, data flows, and control logic.

This paper has presented a structured methodology for modeling and enhancing the reliability of intelligent electric grids. The proposed approach combines probabilistic modeling, real-time data analytics, and architecture-level fault tolerance. Through illustrative case studies and quantitative examples, it was shown that even simple forms of structural redundancy—such as dual-channel configurations—can yield substantial reliability improvements when strategically applied. Furthermore, the integration of machine learning techniques allows for predictive diagnostics, enabling preemptive maintenance and anomaly mitigation.

The key findings can be summarized as follows:

- Reliability modeling in smart grids requires a transition from static evaluation to dynamic, data-driven frameworks that reflect cyber-physical dependencies;
- Hybrid architectures employing probabilistic models and AI-based prediction offer a scalable and adaptive foundation for reliability assessment;
- Practical implementation of fault-tolerant designs (e.g., redundant power supply channels) significantly enhances operational continuity;
- Machine learning methods, particularly XGBoost and LSTM, have proven effective in estimating remaining useful life and detecting latent anomalies in grid components and communication infrastructure.

Future work should aim to deepen the integration of reliability metrics into autonomous control systems, enabling self-adaptive grid behavior in real-time. Additionally, the development of standardized datasets and testbeds for reliability modeling would accelerate the validation and benchmarking of proposed methods.

In conclusion, ensuring the reliability of intelligent electric networks is not only a technical necessity but a strategic imperative for the future of sustainable and resilient energy systems.

References

[1] Platis, A., Limnios, N., & Le Du, M. (1996). Electrical Substation Performability and Reliability Indicators Modelled by Non-Homogeneous Markov Chains. In *Probabilistic Safety Assessment and Management '96*, Springer, pp. 709–714

[2] Mendes, V.L.S., Silva, A.M.L., & Costa, J.G.C. (2021). Chronological Monte Carlo simulation for evaluating spare transformer requirements in distribution substations. *J. Control Autom. Electr. Syst.*, 32, 1365–1376

[3] Zhou, N., Xu, Y., Cho, S., & Wee, C.T. (2022). Analysis of the operational reliability of different types of switching substations using the Monte Carlo method. *Energies*, 17(13), Article 3142

[4] Rzayeva, S.V., Piriyeva, N.M., & Ismayilova, S.I. (2025). High and low voltage coordination in electrical power systems. *International Journal on Technical and Physical Problems of Engineering (IJTPE)*, 17(1), 19–31.

[5] Rzayeva, S.V., Piriyeva, N.M., & Guseynova, I.A. (2024). Analysis of reliability of typical power supply circuits. *Reliability: Theory & Applications*, 19(3), 173–178.

[6] Rzayeva, S.V., & Guseynova, I.A. (2024). Application of automatic monitoring and control systems for reliability of power transmission lines. *Reliability: Theory & Applications*, 19(2), 64–69.

[7] Piriyeva, N.M., Kerimzade, G.S., & Mamedova, G.V. (2023) Issues of design of electrical devices with levitation elements *International Journal on Technical and Physical Problems of Engineering (IJTPE)*, 15(3), 120–125

[8] Rzayeva, S.V., Ganiyeva, N.A., & Piriyeva, N.M. (2024). Modern approaches to electrical equipment diagnostics. *International Journal on Technical and Physical Problems of Engineering (IJTPE)*, 16(1), 182–189.

[9] Rahimli, I., Bakhtiyarov, A., Abdullayeva, G., & Rzayeva, S. (2024). Switching processes occurring in electrical networks 10–35 kV. *Przegląd Elektrotechniczny*, (8), 156–159.

[10] Piriyeva, N.M., Mammadov, N.S., & Rzayeva, S.V. (2025). Development of new methods for protecting substations and overhead lines from overvoltages. *Reliability: Theory & Applications*, 20(1), 683–689.

[11] I.M.Marufov, N.M.Piriyeva, N.S.Mammadov, Sh. Ismayilova. (2024) Calculation of induction levitation vertical axis wind generator-turbine system parameters, levitation and influence loop. *PRZEGLĄD ELEKTROTECHNICZNY, R. 100 NR* 2/2024, 135-139.

[12] Piriyeva, N. M., Ganiyeva, N. A., & Karimova, R. K. (2025). Innovative approaches to selective automatic reclosing on overhead cable lines. *International Journal on Technical and Physical Problems of Engineering (IJTPE)*, *17*(1), 32–44

RT&A, No 4 (89)
Volume 20, December 2025

MULTIOBJECTIVE NURSE SCHEDULING PROBLEM IN A FUZZY ENVIRONMENT

Ahmad Yusuf Adhami[1], Nabil Ahmed Khan[2], Ahteshamul Haq[3]

•

[1,2]Department of Statistics and Operations Research,
Aligarh Muslim University, Aligarh, India.
[3]Department of Mathematics and Statistics, Integral University, Lucknow, India.
Aligarh Muslim University, Aligarh, India.
[1]yusufstats@gmail.com
[3]a.haq@myamu.ac.in
[2]Corresponding Author: khannabeel565@gmail.com

Abstract

Nurse scheduling is vital to hospital quality in almost every aspect, including patient care, bedside assistance, medication administration, support during major surgeries, data collection, reporting, and more. Nurse staffing and recruitment have become critical in the healthcare sector, particularly for staff scheduling, which is essential across industries and services. However, maintaining sufficient nurses is crucial, as understaffing can lead to life-threatening situations with serious financial, social, and legal consequences. This research article aims to minimize scheduling costs by optimizing nurse allocation between departments and shift-wise cost distribution. We assume that the costs associated with various hospital departments are parabolic fuzzy. This study adopts a case study approach to explore the issue of nurse scheduling in a hospital environment, where cost minimization and resource allocation are essential. Fuzzy programming is used to achieve a compromise solution that balances cost efficiency with the required staffing level in hospitals.

Keywords: Multiobjective, Nurse Scheduling, Fuzzy Programming, Defuzzification

1. Introduction

In the last several years, the managing flow of and demands made for staff, especially nursing personnel, has assumed considerable strategic value. There are many ways that staffing efficiency can be enhanced, as outlined in the following proposals. A general point made in this paper is that many of the scheduling problems that can occur in hospitals can be solved, or nearly solved, by operations research techniques.

Nurses are vital healthcare workers in clinics, private practices, and hospitals. Their key duties include patient and doctor communication, nursing care, medication administration, and supervising aides. These duties put into focus the vital role of nurses in the delivery of health care services, Kingma [1]. It is challenging to name a sphere of a hospital's work where nurses are not indispensable: treatment, assistance at the bedside, administration of medication, necessary surgeries, collection of data, reporting on it, and so on. They are assigned to assess and track the state of patients, together with identifying and managing risks or health problems as soon as possible. Furthermore, post-discharge fed patient support is provided by nurses to help the patient move from the hospital to home care, Allen [2]. The NSP, which is related to this application,

determines the number of nurses to be scheduled in different shifts to meet the hospital's needs most efficiently. One of the major problems is the projected lack of 400,000 nurses in the United States by 2020, complicating the provision of healthcare. Janiszewski Goodin [3]. The primary reasons for the nursing shortage include changes in the hospital work environment, low salaries for nurses, declining enrollment in nursing schools, and decreased job satisfaction among nursing professionals. The primary objective of NSP is to reduce medical expenses while ensuring the optimal allocation of nursing personnel to each shift. Multiple examples of a shortage of nurses and expenses through reducing nursing coverage have occurred, Murray [4]. The NSP concerns allocation of shifts and working hours to nurses while considering some constraints and/or goals. Some constraints are getting the correct number of workers for each shift, working under the state employment acts, and responding to the wishes and availability of the nurses. Targets may include a better calibration of patient treatment, reduced nurse exhaustion, maintaining work-life equilibrium, and restricted staffing expenditures, Hamid et al. [5]. The NSP of healthcare organizations needs to be optimized carefully because inadequate schedule planning has severe outcomes. Lack of staffing could lead to compromised care quality, stress levels, nursing staff turnover, and decreased productivity among the staff. In contrast, there are increasing chances of incurring unnecessary expenses and underutilising the human resource, Patil [6]. In dealing with NSP, practitioners and researchers have tried and tested different solutions from a basic manual system to the most sophisticated computerized scheduling systems, Sarkar et al. [7]. Previously, conventional approaches to assigning students to groups were based on a subjective assessment by the teacher or simple spreadsheet applications, which are relatively ineffective and can result in mistakes and take a lot of time. However, while people had to schedule the meetings through a secretary in the past, with the help of modern technologies, automated scheduling has almost become a trend. These systems also adopt optimization methods like fuzzy programming and the goal programming to create noticeable and efficient plans in scheduling, Mertler [8]. The proposed work focuses on developing a method that handles the NSP, with the primary objective of reducing schedule costs while improving nurse sharing across different hospital departments. The NSP aims to assign a sufficient number of nurses to meet the demands of the hospital. Over the past 50 years, NSP has emerged as a significant challenge in artificial intelligence and operations research. Potential benefits of automated high-quality plan creation include improvements in administrative workload, staff and patient satisfaction, medical resource efficiency, and staff and patient safety. Here we have the following research objectives.

1. We develop a fuzzy programming model to analyse the NSP in hospital demand.
2. Identify the objectives for the Emergency, ICU, and Orthopedic departments and identify the minimal flow.
3. Minimize the costs of different departments and optimize the staff in the different departments.

The initial section offers an introductory overview, followed by the second, which presents a comprehensive literature review. The third section delineates the methodologies employed, while the fourth section concentrates on the formulation of the model. The fifth section defines the problem, while the sixth section highlights the novel contributions of the study. In conclusion, the findings are presented in the final section.

2. Literature Review

Many studies carried out to investigate scheduling practices in healthcare have recently focused on hospital nurses. The methods that have been employed most frequently in solving NSPs are of three types: algorithms, which comprise machine learning and mathematical optimization. This paper enumerates the following approaches to managing NSPs using mathematical programming models: Goal programming, Mixed integer programming, linear programming and network approaches. Warner [9] proposed an MP-based algorithm and suggested a multi-choice

programming model aimed at maximizing nurses' preferences regarding their desired working hours, shift-switching options, and the number of days off they wish to have. Arthur & Ravindran [10] was the first to apply this method with four key objectives: minimizing staff size, reducing the number of staff with unmet requests or preferences, minimizing staff dissatisfaction, and minimizing the gap between planned and required staffing levels. Musa & Saxena [11] presented a simplified GP algorithm with one phase that incorporated the hospital's timing rules as well as the nature of the nurse's decision-making regarding working on weekends.

Ozkarahan & Bailey [12] suggested a more flexible concept that can accommodate both the hospital's and nurses' needs for decision support. The system provided several models to support flexible work schedules while solving the time of the day (TOD) and day of the week (DOW). Chen & Yeung [13] integrated GP and ES, where job types used in the expert system were assigned to nurses. The GP approach helped manage the nurses' busy schedules to meet hiring requirements. Jaumard et al. [14] introduced a general linear programming model of the complex NSP for different nursing skills and skill sets using the approach of creating new columns for the optimized transformation and employing branch and bound. Khan et al. [15] studied estimation of the parameter of inverted Topp-Leone distribution based on records. Millar & Kiragu [16] utilized a network model to assess nurses' organizational requirements for cyclic and non-cyclic shifts. Each point in the network represented potential work and/or off-stretch timing, and the resultant model was transformed into a "shortest path" model with additional complications. Gascon et al. [17] analyzed the issue of rostering nurses working in a particular hospital's flying squad. The problem was developed into a multi-objective programming model, wherein the objectives listed included goals and deviations from these goals. Bilgin et al. [18] developed a single, comprehensive hyper-heuristic approach for managing the NSP. Yilmaz [19] proposed a mathematical programming model for scheduling nurses. The goal was to minimize idle waiting time during a one-week planning period, using Lingo software to construct the model.

Akbari et al.[20] designed a simulated annealing method for the NSP while accounting for possible worker fatigue. Legrain et al.[21] investigated the nurse scheduling process for regular and float teams, solving staffing problems. Two models were introduced to reduce costs and enhance nurse availability through frequent candidate selection, and another utilised a local search technique. Jafari et al.[22] aimed to increase the number of nurses obtaining their preferred shift choices while reducing the excess nursing workforce needed daily. Four separate fuzzy solution approaches were evolved. Ali et al. [23] created a lexicographic goal programming framework emphasising GDP, sustainability, and employment in critical economic sectors to assess and maximize India's progress toward the SDGs. Duenas et al. [24] introduced a multiobjective NSP incorporating nurses' preferences, represented by fuzzy sets, to form an overall preference cost function. Fitriani et al. [25] addressed the NSP using fuzzy goal programming combined with the MINIMAX approach. Adhami & Ahmad [26] proposed a Pythagorean-hesitant fuzzy algorithm for solving the multiobjective transportation problem under uncertainty. Aydas et al.[27] proposed models to analyse fixed and dynamic nurse staffing policies. The dynamic model derived non-stationary patient demand from patient history data. Khalil & Modibbo [28] examined the NSP, considering factors like rotation, length of stay, weekly cycles, and daily shifts. A binary goal programming method was used to solve the problem. Melethil et al.[29] used neutrosophic programming and the time series technique ARIMA to achieve the sustainable development goals of Canada's Agenda 2030. Ali et al. [30] created a healthcare multiobjective issue model with fermatean fuzzy programming and neutrosophic goals.

El Adoly et al.[31] developed a mathematical model for the NSP using a multi-commodity network flow model. Mutingi & Mbohwa [32] introduced a fuzzy genetic algorithm (FGA) approach to address healthcare staff scheduling in fuzzy environments. Tsao et al.[33] focused on the NSP to solve the problem of maximizing nurse satisfaction with working conditions, subject to legal constraints and shift preferences. Melethil et al.[34] proposed a multiobjective optimization problem for the SDGs Agenda 2030 model of India, using lexicographic goal programming. A comparative analysis with fuzzy programming was also conducted. Otero-Caicedo et al.[35] suggested a multiobjective linear model with daily preventive backup nurse plans for staff

scheduling, employing an optimal genetic algorithm for timely solutions.

3. Methodology

3.1. Multiobjective Programming Problem

The primary goal of Multiobjective Programming Problems (MOPPs) is to determine compromise solutions which satisfy contradictory objectives according to, Ehrgott & Wiecek [36]. Decision-makers in multiple real-world applications must evaluate several simultaneous criteria, including cost, efficiency, and environmental impact. Various objectives cannot agree, making finding one solution that meets all requirements impossible.

The main objective lies in identifying multiple solutions that represent optimal trade-offs since each solution optimization leads to degradation in at least one of the competing objectives. Decision-makers choose a solution by conducting a trade-off analysis to determine the most fitting option based on their established preferences and priorities. The efficient solution of MOPPs can be accomplished using three principal methods: weighted sum methods, goal programming, and fuzzy optimisation. A MOPP solves a mathematical problem using this representation:

$$\begin{aligned} \max/\min \quad & [f_1(x), f_2(x), \ldots, f_k(x)] \\ \text{sub. to} \quad & g_j(x) = 0, \ \forall \ j \\ & x \geq 0, \end{aligned} \tag{1}$$

where, $f_k(x)$ is k^{th} objective function.

4. Fuzzy Set (FS)

The universal set named W contains elements which operators label as w according to, Singh [37]. A fuzzy set X in W generates its membership characteristics through the membership function $\mu_X(w) : W \to [0, 1]$. This function associates every $w \in W$ with a real-valued $\mu_X(w)$ specified within $[0, 1]$. The value $\mu_X(w)$ represents the extent to which w belongs to set X through its calculation of the membership grade for w within X.

The complete inclusion status matches a membership value of 1, while complete exclusion corresponds to a value of 0. The membership function assigns intermediate values for any element depending on its level between full membership and not being present at all. The ability to define membership grades from complete inclusion at 1 to full exclusion at 0 makes fuzzy sets efficient for dealing with uncertain and imprecise real-world scenarios. Converting a fuzzy number into a precise or crisp value is known as *defuzzification* Adhami et al.[38]. For a parabolic fuzzy number $\tilde{X}(p, q, r)$, the de-fuzzified value is determined using the formula:

$$d(\tilde{X}) = \frac{p + 2q + r}{4}. \tag{2}$$

4.1. Fuzzy Programming

Fuzzy Multiobjective Decision Making origins from, Zimmermann [39] where they used fuzzy sets to develop their solution for resolving multiple optimization objectives. The approach holds such importance because it allows the simultaneous resolution of numerous conflicting goals that appear in all practical problems. A compromise solution exists that serves as a balanced choice after analysing how different objectives affect each other. The fuzzy approach establishes an organized framework to work with this situation through decision systems involving preference determination.

The transformation process in this method transforms every objective function into membership functions, showing the objective satisfaction level. Each objective receives its corresponding aspiration level set by the decision-maker, who then develops the fuzzy membership functions.

The main objective combines maximizing the minimum satisfaction among all objectives with achieving balanced trade-offs. The membership function for minimization-type objective functions with k-th order includes the following mathematical expression:

$$\mu(f_k(\underline{x})) = \begin{cases} 1 & \text{if } f_k(\underline{x}) \leq L_k \\ \frac{U_k - f_k(\underline{x})}{U_k - L_k} & \text{if } L_k < f_k(\underline{x}) < U_k \\ 0 & \text{if } f_k(\underline{x}) \geq U_k \end{cases} \tag{3}$$

The membership function for the k-th objective function in a maximization-type problem can be represented as:

$$\mu(f_k(\underline{x})) = \begin{cases} 1 & \text{if } f_k(\underline{x}) \geq U_k \\ \frac{f_k(\underline{x}) - L_k}{U_k - L_k} & \text{if } L_k < f_k(\underline{x}) < U_k \\ 0 & \text{if } f_k(\underline{x}) \leq L_k \end{cases} \tag{4}$$

The membership function for the k-th objective function of a minimization-type objective can be expressed as follows:

$$U_k = Maximize[f_k(\underline{x})] \;\; and \;\; L_k = Minimize[f_k(\underline{x})]$$

$\forall$ k=1,2...,K

The general mathematical formulation of the fuzzy optimization technique can be described as follows:

We want to maximize λ subject to the constraints:

$$\begin{aligned} \text{maximize} \quad & \lambda \\ \text{subject to} \quad & \lambda \leq \mu(f_k(\underline{x})) \quad \forall\, x \\ & g_j(x) = 0 \quad \forall\, j \\ & x \geq 0 \end{aligned} \tag{5}$$

5. Formulation of model

The Nurse Scheduling Problem (NSP) includes n departments which are designated as D_i and m shifts which use the notation S_j for $i \in 1 \ldots n$ and $j \in 1 \ldots m$. The cost of placing i-th department nurses at j-th shift operations is denoted as C_{ij} ($i = 1, 2, \ldots, n$; $j = 1, 2, \ldots, m$). Also the i-th department needs L_{ij} and U_{ij} ($i = 1, 2, \ldots, n$; $j = 1, 2, \ldots, m$) staff members respectively for each shift. A decision variable named X_{ij} shows the number of nurses who will work between department D_i at shift S_j. The goal is to reduce total scheduling costs with nurses distributed enough to fulfil the specified lower and upper nursing requirements across all departments during all shifts.

The general mathematical model for the NSP is given as,

$$\text{Minimize} \quad Z_k = \sum_{j=1}^{m} c_{ij} x_{ij} \quad \forall\, j,$$

$$\text{Minimize} \quad Z_{k+1} = \sum_{i=1}^{n} \sum_{j=1}^{m} x_{ij},$$

$$\text{Subject to} \quad \sum_{i=1}^{n} \sum_{j=1}^{m} x_{ij} = f,$$

$$\sum_{i=1}^{n} x_{ij} - S_j = 0 \quad \text{(requirement for the } j\text{-th shift)} \quad \forall\, j = 1, 2, \ldots, m,$$

$$D_i \sum_{j=1}^{m} x_{ij} = 0 \quad \text{(availability at the } i\text{-th department)} \quad \forall i = 1, 2, \ldots, n,$$

$$x_{ij} \geq 0 \quad \text{and integer} \quad \forall\, i, j.$$

6. Multiobjective NSP with fuzzy parameter

Whether fuzzy or probabilistic, uncertainty plays a significant role in developing decision-making models. The ambiguity of parameters stems from the imprecise estimates provided by decision-makers. Sometimes, it is essential to account for this uncertainty when solving the problem. This study assumes that the cost parameter in the objective function is fuzzy. Adhami et al. [38] To convert this fuzziness into a precise value, ranking functions based on fuzzy set theory are utilised. The following describes the defuzzified NSP being addressed: The general mathematical model for the NSP is as follows:

$$\text{Minimize} \quad Z_k = \sum_{j=1}^{m} c_{ij} x_{ij} \quad \forall j,$$

$$\text{Minimize} \quad Z_{k+1} = \sum_{i=1}^{n} \sum_{j=1}^{m} x_{ij},$$

$$\text{Subject to} \quad \sum_{i=1}^{n} \sum_{j=1}^{m} x_{ij} = f,$$

$$\sum_{i=1}^{n} x_{ij} - S_j = 0 \quad \text{(requirement for the } j\text{-th shift)} \quad \forall j = 1, 2, \ldots, m,$$

$$D_i \sum_{j=1}^{m} x_{ij} = 0 \quad \text{(availability at the } i\text{-th department)} \quad \forall i = 1, 2, \ldots, n,$$

$$x_{ij} \geq 0 \quad \text{and integer} \quad \forall i, j.$$

The Equation (2) may be employed to defuzzify the cost parameter, which is presumed to be a parabolic fuzzy number within the objective function of the problem above.

$$\text{Minimize} \quad Z_k = \sum_{j=1}^{m} \overline{d}(c_{ij})\, x_{ij} \quad \forall\, j,$$

$$\text{Minimize} \quad Z_{k+1} = \sum_{i=1}^{n} \sum_{j=1}^{m} x_{ij},$$

$$\text{Subject to} \quad \sum_{i=1}^{n} \sum_{j=1}^{m} x_{ij} = f,$$

$$\sum_{i=1}^{n} x_{ij} - S_j = 0 \quad \text{(requirement for the } j\text{-th shift)} \quad \forall\, j = 1, 2, \ldots, m,$$

$$D_i \sum_{j=1}^{m} x_{ij} = 0 \quad \text{(availability at the } i\text{-th department)} \quad \forall\, i = 1, 2, \ldots, n,$$

$$x_{ij} \geq 0 \quad \text{and integer} \quad \forall\, i, j.$$

6.1. The steps for solving the Multiobjective Programming Problem

Fuzzy Programming is a robust and convenient method that can be used to solve several multiple-objective decision-making problems. As a result, we may use this method to determine the formulated model's optimum order amount. The sequential procedure is described as follows:

Step 1: First, defuzzify the fuzzy costs of different departments using the defuzzification formula.

Step 2: Use the provided constraints to solve the multiple objective optimization problems by focusing solely on a single objective at a time while ignoring the others. The outcome that arises is the ideal solution. Utilizing the idle solutions, the payoff matrix is constructed. Finally, the payoff matrix builds each objective function's aspiration level.

Step 3: The kth objective function's aspiration level is chosen as the goal value $g_k(k = 1, 2, \ldots, K)$. Find $x = (x_1, x_2, ...x_n)$ for optimizing the fuzzy goals $f_k(x) = g_k \ \forall \ k = 1, 2, ...K$ subject to the constraint $g_j(x) = 0, \ \forall \ j$ where, $(g_k) = Max/Min(f_k(x))$. The symbol '$\leq$' (type of fuzzy-minimum) specifies that the actual value should be less than or equal to the optimum value within a given tolerance range level. When referring to this the symbol '$\geq$' (type of fuzzy-maximum) specifies that the actual value should be approximately greater than or equal to the optimal value up to a specific tolerance limit.

Step 4: The fuzzy linear membership function should be constructed as Eqn (3) for the minimization type and Eqn (4) for the maximization type objective function.

Step 5: Using the linear membership function, the multiobjective model of Equation (1) will be converted to the form of Equation (5). Then, the Lingo 16.0 software is used to obtain the compromise solution of the defined multiobjective model.

7. Numerical Problem

The research problem in this paper seeks to understand how the issue of nurse scheduling occurs in a hospital setting, and hereby, this study employs a case study research strategy. The particular case study is based on a New England hospital. The study examines various views regarding nurse schedules in a hospital environment, Khan & Lewis [40]. This particular hospital has an authorised strength of 250 beds, but it's recently been struggling to recruit staff for many existing nursing vacancies because nursing costs are on the rise. Because hospital management's policy decisions directly impact the number of staff in different departments, there has to be effective nurse scheduling. Ways through which management polices affect department staffing include:

1. The general nurse staff in the hospital must meet a minimum requirement based on the hospital's capacity and the number of available beds.

2. The staff levels for each department must remain within the specified minimum and maximum limits for that department.

3. Nurses are allowed to rotate between departments and are considered a homogeneous group, including Registered Nurses (RN), Licensed Practical Nurses (LPN), and nurse aides. This assumption of uniformity is relaxed in a later section of the study.

The approximate eight-hour costs for nurses are available on this website web. The objective is to determine the minimum number of staff needed for hospital management and minimize the costs of nurses in the different departments.

[1] There are three departments, namely the emergency, the neonatal intensive care unit, and the orthopedics department. A hospital emergency department is a specially designated unit structured and operated to provide high-quality emergency care to individuals requiring immediate or acute medical attention, including potential hospital admission. A neonatal intensive care unit (NICU), also known as an intensive care nursery, specializes in treating sick or premature newborns. The orthopedic department primarily performs surgeries on patients with neurological conditions. To ensure emergency preparedness, the minimum staffing level for a given shift is set slightly above the combined minimum staffing requirements of all departments.

[1]Nursing Pay Guide

Table 1: *Minimal Staff Required Per Day*

Department Info		
Department	Name	Minimal Staff per Day
1	Dept 1	13
2	Dept 2	32
3	Dept 3	22

The different departments' costs are fuzzy and given in Table (2).

Table 2: *Fuzzy Costs of the Different Departments by Shifts*

Shift Info		Fuzzy Costs (D1, D2, D3)
Shift	Time	Values
1	Morning	(110,120,130); (140,150,160); (90,100,110)
2	Afternoon	(90,100,110); (120,130,140); (120,130,140)
3	Night	(100,110,120); (105,115,125); (105,115,125)

In the Table (2), the fuzzy costs of the different departments are presented as the fuzzy cost values for three different departments over three shifts. Each cell in the table represents a fuzzy number as a triplet, such as (110,120,130), which captures the range of possible costs within that department for a given shift. Using fuzzy numbers makes it possible to deal with uncertainty and variability in cost estimates between departments. Defuzzification (2) is applied using an appropriate method to simplify these fuzzy costs into crisp, single values for further analysis. The results of this defuzzification process are shown in Table (2), where each fuzzy cost is converted into a precise cost figure for more straightforward interpretation and decision making.

Table 3: *De-fuzzified Values of Different Departments*

Shift Info		
Shift	Time	De-fuzzified Costs (D1, D2, D3)
1	Morning	120; 150; 100
2	Afternoon	100; 130; 130
3	Night	110; 115; 115

The Table (3) above shows the defuzzified cost values for each department over different shifts. These values are derived from the fuzzy costs shown in the previous table by applying a defuzzification method. The defuzzified values provide a single, accurate cost figure for each department and shift, making it easier to analyse and compare costs across shifts and departments. For example, in shift 1, the defuzzified costs for departments 1, 2, and 3 are 120, 150, and 100, respectively. This table enables more transparent decision-making by removing uncertainty and providing concrete cost estimates.

Now the staff requirements by shifts and department are given in Table (4).

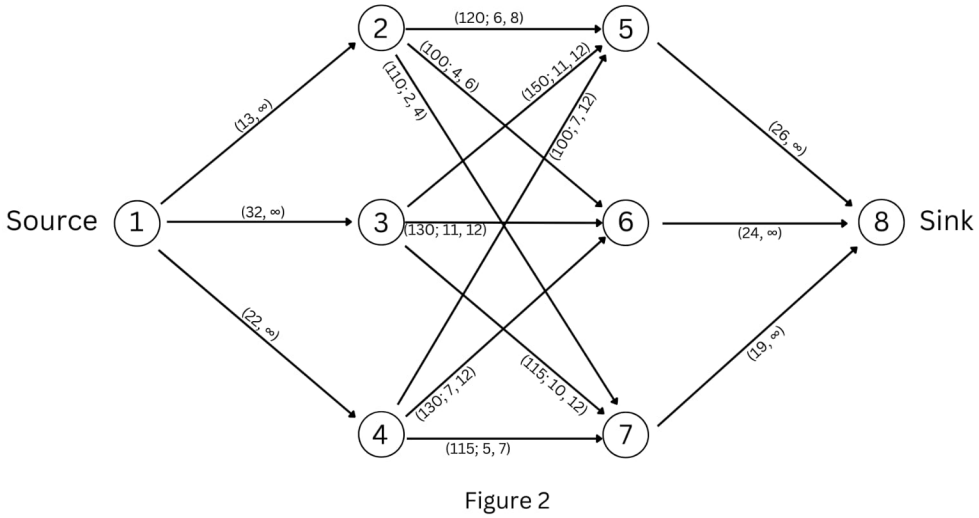


Figure 1: *Network graph*

Table 4: *Staff Requirements by Shift and Department*

Shift and Nurses		Departments		
Shift	Minimal Nurses	Dept 1	Dept 2	Dept 3
1	26	120; $(6,8)$	150; $(11,12)$	100; $(7,12)$
2	24	100; $(4,6)$	130; $(11,12)$	130; $(7,12)$
3	19	110; $(2,4)$	115; $(10,12)$	115; $(5,7)$

We will draw a network using these data based on the problem's requirement and need presented in (4). The Network Staffing Problem will be as follows.

In this network, node 1 represents the source, and node 8 represents the sink. Nodes 2, 3, and 4 correspond to the departments, while nodes 5, 6, and 7 correspond to the shifts. The numbers on the arcs indicate staffing and cost requirements. For instance, the arc $(1,3)$ signifies a need for 13 nurses with no upper limit. Similarly, the arc $(2,5)$ indicates that between 6 and 8 nurses can be assigned to department 1, with a daily cost of \$120 during the first shift. The arc $(5,8)$ specifies a staffing requirement ranging from 1 to 26 nurses, with no upper limit.

The mathematical model for this network is as follows:

$$\begin{aligned}
&\text{Min } Z_1 = 120x_{25} + 150x_{26} + 100x_{27} && \text{(Emergency Cost)}\\
&\text{Min } Z_2 = 100x_{35} + 130x_{23} + 130x_{37} && \text{(ICU Cost)}\\
&\text{Min } Z_3 = 110x_{45} + 115x_{46} + 115x_{47} && \text{(Orthopedics Cost)}\\
&\text{Min } Z_4 = 13x_{12} + 32x_{13} + 22x_{14} && \text{(Minimal Flow of Nurses)}
\end{aligned}$$

Subject to

$$\begin{aligned}
x_{12} + x_{13} + x_{14} &= f\\
-x_{12} + x_{25} + x_{26} + x_{27} &= 0\\
-x_{13} + x_{35} + x_{36} + x_{37} &= 0\\
-x_{14} + x_{45} + x_{46} + x_{47} &= 0\\
-x_{25} - x_{35} - x_{45} + x_{58} &= 0
\end{aligned}$$

$$-x_{26} - x_{36} - x_{46} + x_{68} = 0$$
$$-x_{58} - x_{68} - x_{78} = -f$$

$$x_{12} \geq 13,\ x_{13} \geq 32,\ x_{14} \geq 22,\ x_{58} \geq 26,\ x_{68} \geq 24,\ x_{78} \geq 19$$
$$6 \leq x_{25} \leq 8,\ 4 \leq x_{26} \leq 6,\ 2 \leq x_{27} \leq 4,$$
$$11 \leq x_{35} \leq 12,\ 11 \leq x_{36} \leq 12,\ 10 \leq x_{37} \leq 12,$$
$$7 \leq x_{45} \leq 12,\ 7 \leq x_{46} \leq 12,\ 5 \leq x_{47} \leq 7.$$

8. Results:

We solve each objective by ignoring other objectives to obtain the payoff matrix,x, and using these solutions will be as follows:

Table 5: *Payoff Matrix*

Objectives		
Objective	Condition	Z1; Z2; Z3; Z4
Z1	Min Z1	3270; 3035; 1820; 73
Z2	Min Z2	3960; 2905; 1820; 77
Z3	Min Z3	3960; 3660; 1370; 81
Z4	Min Z4	3340; 2955; 1485; 69

Using the payoff matrix, we obtain the lower and upper values of each objective as;

$$3270 \leq Z_1 \leq 3960; \quad 2905 \leq Z_2 \leq 3660; \quad 1370 \leq Z_3 \leq 1820; \quad 69 \leq Z_4 \leq 81$$

We use these goal values for the goal programming to obtain the compromise solution. Using the LINGO 16.O software, we get the result as follows:

$$Z_1 = 3270; \quad Z_2 = 2905; \quad Z_3 = 1370; \quad Z_4 = 69$$

Now, we use the lower and upper values of the objective function to define the membership function as follows:

$$\mu(Z_1(x)) = \begin{cases} 1, & \text{if } Z_1(x) \leq 3270 \\ \frac{3960 - Z_1(x)}{3960 - 3270}, & \text{if } Z_1(x) \in (3270, 3960) \\ 0, & \text{if } Z_1(x) \geq 3960 \end{cases}$$

$$\mu(Z_2(x)) = \begin{cases} 1, & \text{if } Z_2(x) \leq 2905 \\ \frac{3660 - Z_2(x)}{3660 - 2905}, & \text{if } Z_2(x) \in (2905, 3660) \\ 0, & \text{if } Z_2(x) \geq 3660 \end{cases}$$

$$\mu(Z_3(x)) = \begin{cases} 1, & \text{if } Z_3(x) \leq 1370 \\ \frac{1820 - Z_3(x)}{1820 - 1370}, & \text{if } Z_3(x) \in (1370, 1820) \\ 0, & \text{if } Z_3(x) \geq 1820 \end{cases}$$

$$\mu(Z_4(x)) = \begin{cases} 1, & \text{if } Z_4(x) \leq 69 \\ \frac{81 - Z_4(x)}{81 - 69}, & \text{if } Z_4(x) \in (69, 81) \\ 0, & \text{if } Z_4(x) \geq 81 \end{cases}$$

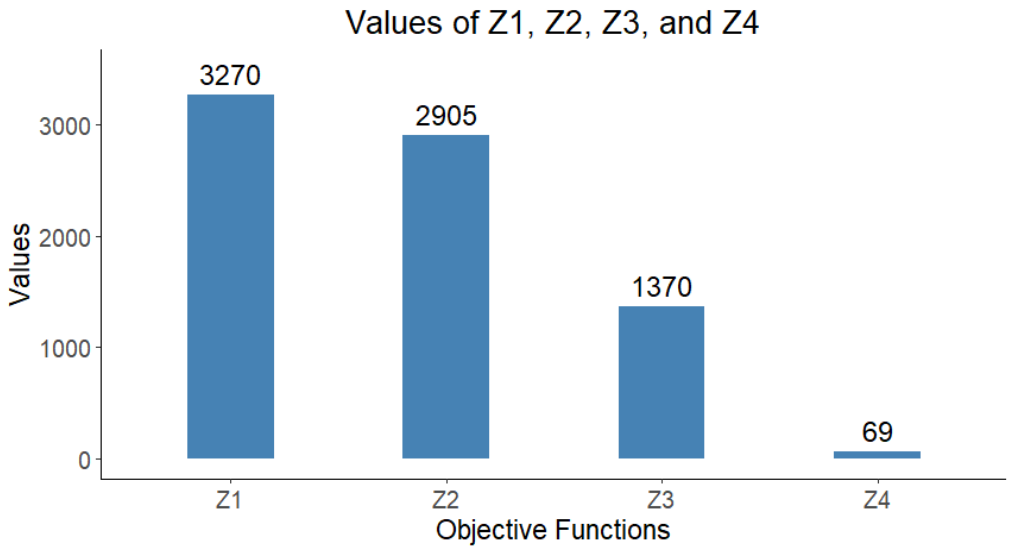


Figure 2: *Values of objective function*

Using these membership functions, we use fuzzy programming to obtain the compromise solution of the multiobjective programming problem as follows,

Table 6: *Objective Values of Z1, Z2, Z3, and Z4*

Objective Functions	
Function	Value
Z1	3270
Z2	2905
Z3	1370
Z4	69

Table (6) shows the costs of different departments in the hospital. For example, Z1 represents the emergency department, which has a minimum price of $3270; Z2 represents the Intensive Care Unit (ICU), which has a minimum cost of $2905; Z3 is the Orthopedic Department, which has a price of $1370; and Z4 represents the minimal flow of nurses, which is 69.

Table (7) presents the optimal nurse scheduling plan, which requires 26 nurses for the first shift. Six nurses are assigned to Department 1, 11 to Department 2, and 9 to Department 3. For the second shift, 24 nurses are assigned, 6 to Department 1, 11 to Department 2, and 7 to Department 3. The third shift involves the allocation of 19 nurses: 2 to Department 1, 10 to Department 2, and 7 to Department 3. Across all three shifts, Department 1 receives 14 nurses, Department 2 has 32 nurses, and Department 3 is assigned 23 nurses, leading to a total of 69 nurses scheduled across all departments. These nurses perform essential duties, including patient care, communication with doctors, and medication administration. Their presence ensures smooth clinical operations and quality care in all departments. In addition to patient responsibilities, they also supervise nursing aides and assist in coordinating department-specific workflows.

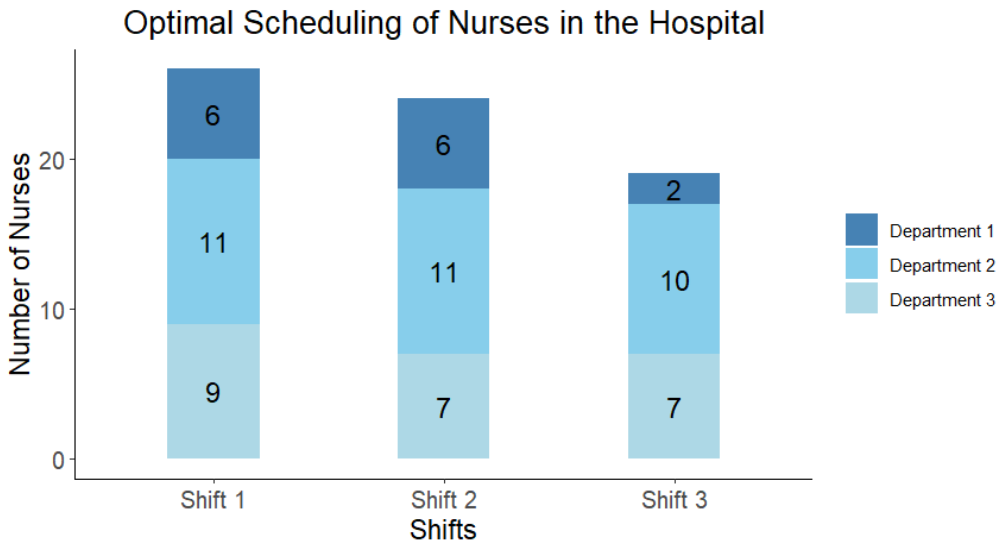


Figure 3: *Optimal scheduling of nurses*

Table 7: *Optimal Scheduling of Nurses in the Hospital*

Shift-wise Distribution		Departments		
Shift	Time	Department 1	Department 2	Department 3
1	Morning	6	11	9
2	Afternoon	6	11	7
3	Night	2	10	7
	Total	14	32	23

9. Conclusion

This study makes a unique contribution by addressing the essential issue of nurse staffing and scheduling in hospitals, where cost minimization and resource allocation are crucial. Using fuzzy programming, we present a compromise approach that efficiently balances the requirement to reduce scheduling expenses while guaranteeing proper personnel distribution across departments. This strategy is essential in the healthcare industry, where insufficient staffing may have serious consequences both economically and in terms of the safety of patients.

Future studies should look at more adaptable models that consider parameter demand, different patient needs, and the application of real-time data to improve the scheduling process. Furthermore, implementing machine learning or optimization algorithms might enhance the decision-making framework, giving a more complete tackle to nurse staffing challenges in a constantly shifting healthcare system.

10. Future work

This work provides the foundation for examining nurse staffing and hospital scheduling difficulties via an approach built upon fuzzy and compromise programming. Future research could expand upon this by exploring the following directions:

- Adaptable Models: Develop more adaptable scheduling models considering changing patient demands, departmental requirements, and dynamic demand swings.
- Real-Time Data Integration: Improve the precision and timeliness of scheduling systems by integrating real-time data from staff availability, patient intakes, and hospital activities.
- Machine Learning Applications: Automate the process of forecasting the number of employee requirements and utilising the right resources using ML techniques. These algorithms can also get optimized as trends change and make better decisions about efficiency.
- Advanced Optimization Techniques: Use sophisticated optimization techniques, including hybrid methods or meta heuristics, to solve large-scale staffing issues more precisely.

By pursuing these directions, future studies can provide even more robust solutions to the challenges of nurse staffing in the ever-evolving healthcare environment.

References

[1] Kingma, Mireille. "Nurses on the move: Migration and the global health care economy," Cornell University Press, 2018.
[2] Allen, Davina. "The changing shape of nursing practice: The role of nurses in the hospital division of labour," Routledge, 2002.
[3] Janiszewski Goodin, Heather. "The nursing shortage in the United States of America: an integrative review of the literature," Journal of advanced nursing 43.4: 335-343, 2003.
[4] Murray, Marilyn Kettering. "The nursing shortage: past, present, and future," JONA: The Journal of Nursing Administration 32.2: 79-84, 2002.
[5] Hamid, Mahdi and Tavakkoli-Moghaddam, Reza and Golpaygani, Fereshte and Vahedi-Nouri, Behdin A multi-objective model for a nurse scheduling problem by emphasizing human factors", Proceedings of the institution of mechanical engineers, Part H: journal of engineering in medicine, vol. 234, no. 2, pp. 179-199, 2020.
[6] Patil, Shubhangi. "A new service model for identifying and improving the quality of emergency department operations in tertiary settings," Diss. Open Access Te Herenga Waka-Victoria University of Wellington, 2024.
[7] P. Sarkar, N. Chaki, and R. Chaki, "A study of Resource Optimization for Nurse Scheduling Problem," in 2019 4th International conference on computer science and engineering (UBMK), pp. 757-761, 2019.
[8] C. Mertler, "Classroom assessment: A practical guide for educators," Routledge, 2016.
[9] D. M. Warner, "Scheduling nursing personnel according to nursing preference: A mathematical programming approach," Operations Research, vol. 24, no. 5, pp. 842-856, 1976.
[10] J. L. Arthur and A. Ravindran, "A multiple objective nurse scheduling model," AIIE transactions, vol. 13, no. 1, pp. 55-60, 1981.
[11] A. Musa and U. Saxena, "Scheduling nurses using goal-programming techniques," IIE transactions, vol. 16, no. 3, pp. 216-221, 1984.
[12] I. Ozkarahan and J. E. Bailey, "Goal programming model subsystem of a flexible nurse scheduling support system," IIE transactions, vol. 20, no. 3, pp. 306-316, 1988.
[13] J. Chen and T. Yeung, "Hybrid expert-system approach to nurse scheduling," Computers in nursing, vol. 11, no. 4, pp. 183-190, 1993.
[14] B. Jaumard, F. Semet, and T. Vovor, "A generalized linear programming model for nurse scheduling," European journal of operational research, vol. 107, no. 1, pp. 1-18, 1998.
[15] Khan, M. J. S., et al. "Moments and inferences of inverted topp-leone distribution based on record values." International Journal of System Assurance Engineering and Management 15.6 2623-2633, 2024.
[16] H. H. Millar and M. Kiragu, "Cyclic and non-cyclic scheduling of 12 h shift nurses by network programming," European journal of operational research, vol. 104, no. 3, pp. 582-592, 1998.

[17] V. Gascon, S. Villeneuve, P. Michelon, and J. A. Ferland, "Scheduling the flying squad nurses of a hospital using a multi-objective programming model," Annals of Operations Research, vol. 96, no. 1, pp. 149-166, 2000.
[18] B. Bilgin, P. Demeester, M. Misir, W. Vancroonenburg, and G. Vanden Berghe, "One hyper-heuristic approach to two timetabling problems in health care," Journal of Heuristics, vol. 18, no. 3, pp. 401-434, 2012.
[19] E. Yilmaz, "A mathematical programming model for scheduling of nurses' labor shifts," Journal of medical systems, vol. 36, no. 2, pp. 491-496, 2012.
[20] M. Akbari, M. Zandieh, and B. Dorri, "Scheduling part-time and mixed-skilled workers to maximize employee satisfaction," The International Journal of Advanced Manufacturing Technology, vol. 64, no. 5, pp. 1017-1027, 2013.
[21] A. Legrain, H. Bouarab, and N. Lahrichi, "The nurse scheduling problem in real-life," Journal of medical systems, vol. 39, no. 1, p. 160, 2015.
[22] H. Jafari, S. Bateni, P. Daneshvar, S. Bateni, and H. Mahdioun, "Fuzzy mathematical modeling approach for the nurse scheduling problem: a case study," International journal of fuzzy systems, vol. 18, no. 2, pp. 320-332, 2016.
[23] I. Ali, G. Kabir, A. Y. Adhami, N. A. Khan, A. Melethil, and M. Azeem, "Navigating India's path to sustainable development goals: optimization and forecasting approaches," Environmental Research Communications, vol. 7, no. 5, p. 055009, 2025.
[24] Duenas, Alejandra and Tütüncü, G Yazgı and Chilcott, James B, "A genetic algorithm approach to the nurse scheduling problem with fuzzy preferences," IMA Journal of Management Mathematics, vol. 20, no. 4, pp. 369-383, 2009.
[25] S. N. Fitriani, B. Irawanto, and A. Aziz, "Nurse scheduling problem using fuzzy goal programming with MINMAX approach," Journal of the Institute of Electronics and Computer, vol. 2, no. 1, pp. 151-161, 2020.
[26] A. Y. Adhami and F. Ahmad, "Interactive Pythagorean-hesitant fuzzy computational algorithm for multiobjective transportation problem under uncertainty," International Journal of Management Science and Engineering Management, vol. 15, no. 4, pp. 288-297, 2020.
[27] O. T. Aydas, A. D. Ross, M. C. Scanlon, and B. Aydas, "New results on integrated nurse staffing and scheduling: The medium-term context for intensive care units," Journal of the Operational Research Society, vol. 72, no. 12, pp. 2631-2648, 2021.
[28] S. Khalil and U. M. Modibbo, "Multiobjective optimization for hospital nurses scheduling problem using binary goal programming," in Virtual International Conference on Soft Computing, Optimization Theory and Applications, pp. 255-270, 2021.
[29] A. Melethil, N. A. Khan, G. Kabir, A. Y. Adhami, and I. Ali, "Enhancing Canada's sustainable development goals: Leveraging neutrosophic programming for agenda 2030," Environmental and Sustainability Indicators, vol. 25, p. 100586, 2025.
[30] W. Ali, M. Khalid, N. A. Khan, and S. Javaid, "Integrating Fermatean fuzzy and neutrosophic goal programming for multi-objective healthcare optimization under uncertainty," Life Cycle Reliability and Safety Engineering, pp. 1-21, 2025.
[31] A. A. El Adoly, M. Gheith, and M. N. Fors, "A new formulation and solution for the nurse scheduling problem: A case study in Egypt," Alexandria engineering journal, vol. 57, no. 4, pp. 2289-2298, 2018.
[32] M. Mutingi and C. Mbohwa, "Healthcare staff scheduling in a fuzzy environment: A fuzzy genetic algorithm approach," 2014.
[33] Y.-C. Tsao, D. Chen, F.-J. Hwang, and V. T. Linh, "Intelligent Clinic Nurse Scheduling Considering Nurses Paired with Doctors and Preference of Nurses," Journal of Medical Systems, vol. 48, no. 1, p. 75, 2024.
[34] A. Melethil, N. A. Khan, M. Azeem, G. Kabir, and I. Ali, "Optimization and forecasting modelling to analyse India's pursuit of the sustainable development goals in Agenda 2030," Engineering Proceedings, vol. 76, no. 1, p. 16, 2024.
[35] Otero-Caicedo, Ricardo and Casas, Carlos Eduardo Montoya and Jaimes, Carolina Barajas and Garzón, Cristian Felipe Guzmán and Vergel, Edwin Andrés Yáñez and Valdés, Julián

Camilo Zabala, "A preventive–reactive approach for nurse scheduling considering absenteeism and nurses' preferences," Operations Research for Health Care, vol. 38, p. 100389, 2023.

[36] M. Ehrgott and M. M. Wiecek, "Mutiobjective programming," in Multiple criteria decision analysis: State of the art surveys, Springer, pp. 667-708. 2005.

[37] M. K. Singh, "Concepts of Fuzzy Mathematics," Springer, 2024.

[38] A. Y. Adhami, M. Faizan, and others, "Neutrosophic compromise programming approach for multiobjective nonlinear transportation problem with supply and demand following the exponential distribution," Operations Research and Decisions, vol. 32, 2022.

[39] H.-J. Zimmermann, "Fuzzy programming and linear programming with several objective functions," Fuzzy sets and systems, vol. 1, no. 1, pp. 45-55, 1978.

[40] M. R. Khan and D. A. Lewis, "A network model for nursing staff scheduling," Zeitschrift für Operations Research, vol. 31, no. 6, pp. B161-B171, 1987.

RT&A, No 4 (89)
Volume 20, December 2025

PREDICTIVE MODELING OF POLYCYSTIC OVARY SYNDROME USING MACHINE LEARNING ALGORITHMS

Gneya Pandya[1], Dhara Solanki[2], Dr. Jigna Jadav[3], Dr. Kajal Patel[4]

•

[1,2]Student, Computer Engineering, V.G.E.C., Chandkheda,Gujarat, India.
[3]Assistant Professor, Computer Engineering, V.G.E.C., Chandkheda, Gujarat, India.
[4]Associate Professor, Computer Engineering, V.G.E.C., Chandkheda, Gujarat, India.
gneyapandya1234@gmail.com[1], dhara732002@gmail.com[2],jigna.j.jadav@gmail.com[3], kajalpatel@vgecg.ac.in[4]

Abstract

PCOS is a prevalent health condition affecting women globally, and if not diagnosed early, it can lead to severe complications like type two diabetes and gestational diabetes. Our research is focused on enhancing the accuracy and reliability of PCOS diagnosis using machine learning techniques. We utilized a public dataset and applied a range of machine learning models like Logistic Regression (LR), Support Vector Machine (SVM), Decision Tree (DT), and Random Forest (RF) ensemble algorithms. By implementing feature selection methods, we aim to identify the most critical factors contributing to the diagnosis, ensuring that the best-performing model is selected for reliable results. Notably, our research achieved a very good accuracy by using the Random Forest algorithm, highlighting its potential to provide a more precise and trustworthy diagnosis of PCOS. This work represents a significant step toward improving healthcare outcomes for women with PCOS.

Keywords: *Polycystic Ovary Syndrome (PCOS), Machine Learning, Feature Selection, Logistic Regression (LR), Support Vector Machine (SVM), Decision Tree (DT), Random Forest (RF), Model Interpretability, Ensemble Learning, Exploratory Data Analysis (EDA).*

I. Introduction

PCOS is a prevalent hormonal disorder affecting fertile women [1]. PCOS often begins during teenage, but its symptoms can vary over time. Hormonal abnormalities, irregular menstrual cycles, increased testosterone levels, and ovarian cyst development are among the possible outcomes. Unusual menstrual cycles, typically caused by insufficient ovulation, can pose difficulties in conceiving. PCOS is a chronic disorder that is not curable, but specific symptoms can be treated with medication, lifestyle changes, and fertility therapies. It is one of the leading causes of infertility. Even though the precise origin of PCOS is yet unknown, women who have type 2 diabetes or a family history are more susceptible. One of the most prevalent hormonal disorders affecting women who can conceive, PCOS is a significant public health concern. An estimated 8–13% of women who can conceive are affected by the illness, and up to 70% of instances go misdiagnosed [1].

Diabetes, heart disease, high blood pressure, endometrial thickness, sleep apnoea, depression, anxiety, eating disorders, and endometrial cancer are among the conditions that women with PCOS are likely to experience [2]. Environmental variables may also influence the development of PCOS in addition to hereditary ones. You can lessen long-term consequences in addition to losing

weight, getting treatment, and getting diagnosed early [2].

AI can now identify and cure complicated illnesses [3]. AI techniques create a robust PCOS diagnostic framework by extracting information from massive data sets using state-of-the-art algorithms and potent machine learning [4]. While some predictive models only include women who seek reproductive treatment, they can be quite helpful in supporting the early identification of PCOS. One model predicted the development of PCOS in Chinese women based on BMI, menstrual cycle duration, and serum levels of androstenedione and anti-Müllerian hormone (AMH). Another model predicted a diagnosis of PCOS or other ovulatory dysfunction illnesses based just on AMH and BMI. Predictive models for specific outcomes, like pregnancy outcomes and insulin resistance, have been developed by different research involving women with PCOS [5]. One popular solution to reduce the issue of too many unnecessary features is feature selection. A well-chosen feature set can decrease the complexity of the learnt outcomes while improving predicting accuracy and learning efficiency [6]. It entails locating and picking the most pertinent variables from a dataset to enhance a machine learning model's functionality and readability. Feature selection reduces complexity, minimizes overfitting, and improves the model's capacity to generalize from the data by concentrating on the most significant features.

EDA helps to identify which variables are redundant and which contribute to significant variation in the lower dimensional space by identifying and characterizing recurrent patterns and significant correlation structures [7]. EDA provides a foundational understanding of the data, helping to inform decisions about which features to select and how to approach the modelling process. An important subfield of artificial intelligence, machine learning, was discovered in the 1950s [8]. Machine learning algorithms utilize EDA's selected features and insights to build predictive models. These algorithms apply various statistical and computational techniques to learn from the data, making predictions or classifications based on the input features. The effectiveness of these algorithms often hinges on the quality of feature selection and the depth of insights obtained through EDA. Various Machine Learning algorithms are available, which include SVM, LR, DT, etc.

In this study, we developed and evaluated multiple machine learning models—including Logistic Regression (LR), Support Vector Machine (SVM), Decision Tree (DT), and Random Forest (RF)—to enhance the accuracy of Polycystic Ovary Syndrome (PCOS) diagnosis. A comprehensive comparative analysis was conducted to assess the performance and diagnostic effectiveness of these models. Additionally, feature selection techniques were employed to identify and isolate the most relevant features significantly contributing to the prediction of PCOS, thereby improving model interpretability and diagnostic reliability.

The structure of this document is as follows. Section II provides an overview of the field's current state of the art. Section III provides an account of the research conducted in this study. Section IV presents the findings from the analysis of the dataset. The conclusions can be found in section V.

II. Related Work

In their work, Authors in [9] tackled the problem of PCOS detection, a prevalent endocrine condition that affects around 15% of women worldwide. In their work, PCONet—a CNN created to identify PCOS in ovarian ultrasound pictures—was presented. Additionally, they used transfer learning to refine InceptionV3, a 45-layer pre-trained CNN, for categorization. According to the findings, PCONet outperformed the refined InceptionV3, which achieved 96.56% accuracy, with a gain of 98.12%. This study shows how transfer learning and sophisticated CNN models can improve the accuracy of PCOS identification.

Authors in [10] looked into the predictive potential of machine learning algorithms for PCOS, a common endocrine condition that affects women of reproductive age. Their study used a dataset with variables like Age, body mass index (BMI), hormone levels, monthly irregularities, and

lifestyle factors to assess different machine learning algorithms, such as decision trees, random forests, and linear regression. The project aims to create a reliable predictive model that will help medical professionals identify PCOS early on. The results highlight how machine learning may help women's health by facilitating early detection and individualized care, making a substantial contribution to the endocrine problem predictive modeling field.

Using T2-weighted Magnetic Resonance Imaging (MRI) radiomics analysis [11] investigated how well T2-weighted MRI could distinguish between classical and non-classical forms of PCOS. The dataset for the study was split into training and test sets, and it comprised 202 ovaries from 101 PCOS patients. Using machine learning algorithms, the investigation showed that the most successful methods were Random Forest and Gradient Boosting Classifier, which produced accuracies of 73% and 70%, respectively. These algorithms' blend model yielded an AUC of 0.70 and an accuracy of 73%. The results emphasize the potential of machine learning and radiomics in PCOS diagnosis by demonstrating the use of radiomic characteristics from T2-weighted MRI in differentiating between PCOS phenotypes.

These advancements underline the transformative impact of artificial intelligence in medical diagnostics, particularly for complex endocrine disorders like PCOS. By integrating clinical data, imaging techniques, and robust machine learning models, researchers are moving closer to developing automated, non-invasive, and highly accurate diagnostic tools. Such innovations not only aid in early detection but also enable personalized treatment planning, thereby improving patient outcomes. Future research may further explore hybrid approaches combining clinical features with radiomic and genomic data to build even more precise and comprehensive PCOS diagnostic systems.

III. Proposed Approach

Figure 1 illustrates a detailed workflow designed for predicting Polycystic Ovary Syndrome (PCOS) using a machine learning-based approach, specifically the Random Forest Classifier. The process begins with the collection of a well-curated PCOS dataset, which forms the foundational input for model training. This dataset then undergoes a crucial stage of feature engineering, wherein relevant variables are systematically identified, transformed, and optimized to improve the model's learning efficiency. This step is instrumental in ensuring that only the most impactful features are retained, thereby enhancing the predictive accuracy of the model while also minimizing computational overhead.

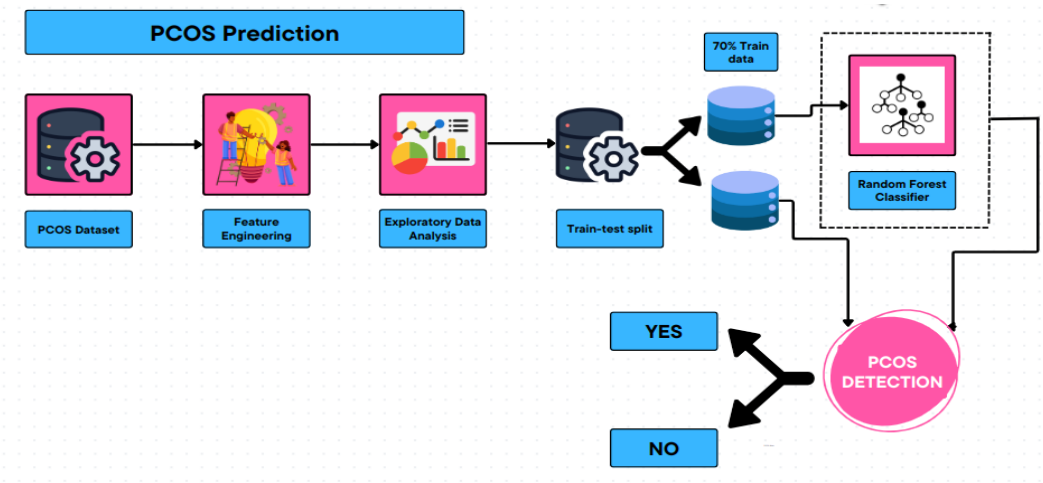


Figure 1. *Workflow of the PCOS Prediction Model using Random Forest Classifier*

Afterwards, an EDA is carried out to obtain a profound understanding of the dataset. Underlying trends, correlations, and other anomalies that can affect the model's performance are found using EDA. It also offers guidance for additional feature improvement and improves comprehension of the distribution and properties of the data.After that, the dataset is divided into subgroups for training and testing, with 70% of the data going into the former. This segmentation is essential for assessing the model's capacity generalization. The RF, an ensemble learning technique renowned for its resilience and efficiency in managing intricate, non-linear relationships within the data, is constructed using the training subset. During training, the classifier builds several decision trees and aggregates the results to produce a final prediction.The trained model is then applied to new data to predict the presence of PCOS. Based on the input features, the mode categorizes the results as either "PCOS Detected" or "PCOS Not Detected." This workflow highlights the systematic approach to PCOS detection and the potential of machine ML techniques in enhancing diagnostic accuracy, contributing early and more precise medical interventions for individuals at risk of PCOS.

I. Methodology

PCOS stands as one of the most prevalent hormonal disorders affecting women globally, with a complex set of symptoms and potential health implications. PCOS often manifests in symptoms like irregular period cycles, hormonal imbalances, and multiple cysts on the ovaries. It is closely associated with various health complications, including infertility, diabetes, cardiovascular diseases, and emotional well-being challenges Recognizing its widespread impact, this research project addresses PCOS from multiple dimensions, amalgamating machine learning techniques.

II. Data Collection

Our research study utilized a comprehensive dataset from ten distinct healthcare facilities across Kerala, India. The PCOS dataset [12], comprises clinical and physical parameters from 541 patients and encompasses 44 features.

III. Data Preprocessing

To prepare the combined dataset for analysis, we performed thorough data preprocessing. This involved addressing missing values by imputing them with zeros and eliminating extra information such as the 'Sl. No' and 'Patient File No.' columns from the PCOS dataset.

IV. Feature Selection

After merging the datasets, we conducted feature selection to identify the most relevant variables for our analysis. This step involved evaluating the importance of each feature in predicting the presence of PCOS and determining which variables would be included in our predictive models.

Following features were identified as influential predictors of PCOS in our models: ['PCOS (Y/N)', ' age (yrs)', 'Pregnant(Y/N)', 'No of aborptions', 'Bloated', 'facial hair', 'chest hair', 'difficult to loose weight', 'mood swings', 'anxiety/depression/stress', 'Irregular_sleep', 'Weight gain(Y/N)', 'hair growth(Y/N)', 'Skin darkening (Y/N)', 'Hair loss(Y/N)', 'Pimples(Y/N)', 'Fast food (Y/N)', 'Reg Exercise(Y/N)', 'Weight (Kg)', 'Height(Cm) ', 'BMI', 'Blood Group', 'Pulse rate(bpm) ', 'Cycle(months)', 'Cycle length(days)', 'Marriage Status (Yrs)', 'Hip(inch)', 'Waist(inch)', 'Waist/Hip Ratio']

V. EDA

We performed EDA on the combined dataset to acquire insights into the distribution and relationships among different features. This involves visualizing the data through histograms, scatter plots, correlation matrices, and other statistical summaries to identify patterns and trends.

Figure 2 presents a correlation heatmap showing the interrelationships among various clinical and physiological features related to PCOS. The results indicate that PCOS is positively correlated with skin darkening, weight gain, hair growth, and pimples, suggesting these symptoms are more prevalent in affected individuals. Additionally, strong correlations are observed between BMI, waist size, and weight, indicating redundancy among obesity-related features. Conversely, age and cycle length show weak negative correlations with PCOS, implying a slight decrease in PCOS prevalence with increasing age and shorter cycles.

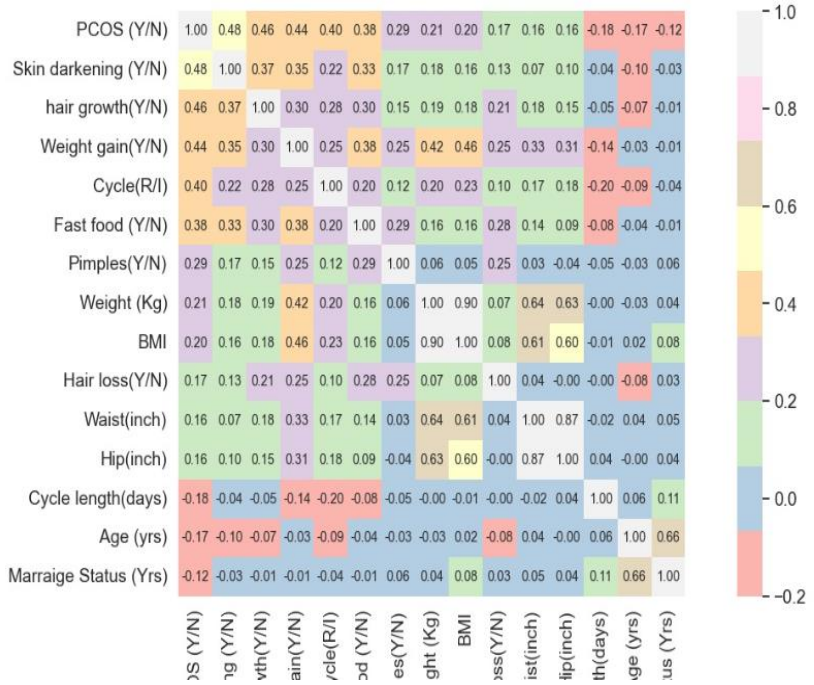


Figure 2. *Heatmap describing the correlation between features*

Figure 3 illustrates a scatter plot comparing cycle length and age for individuals with and without PCOS. It is evident that women with PCOS experience greater variation in cycle length, often showing irregular or prolonged cycles outside the typical 4 to 6-day range. The regression lines for both groups are nearly flat, indicating that age has minimal influence on cycle length. However, the increased dispersion among PCOS cases reinforces the relevance of cycle irregularity as a significant diagnostic indicator. These findings support the significance of cycle irregularity and hormonal symptoms as important indicators in PCOS detection.

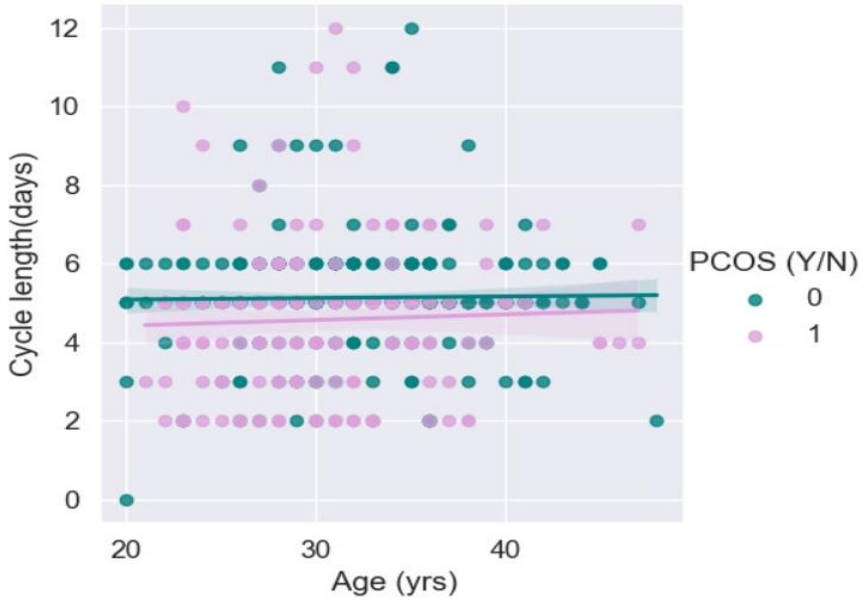


Figure 3. *Scatter Plot of Menstrual Cycle Length vs. Age about PCOS Diagnosis*

IV. Experimental Results and Discussion

I. Linear Regression

LR is a simple and effective method for binary classification tasks like PCOS detection. Its ability to provide probabilities and interpretability makes it an ideal choice for PCOS detection [13].

$$\text{logit}(Y) = a + B1X1 + B2X2 \quad (1)$$

LR achieved a respectable accuracy of 79% in predicting PCOS likelihood. This model's performance signifies its utility in offering users actionable insights about their PCOS risk based on provided data.

II. Decision Tree

DT were employed for their ability to create intuitive, interpretable models. Despite a slightly lower accuracy of 67%, decision trees are valuable resources for understanding how PCOS is influenced. The transparency of the decision tree structure aids users in understanding the key predictors of PCOS. The mathematical formula of decision trees uses Entropy E(S) .

$$E(S) = -Xn\ i=1\ pi \log2\ (pi) \quad (2)$$

The final formula is to calculate information gain [14]:

$$IG = E(S) - X\ v\in\ Values(A)\ |Sv|\ |S|\ E(Sv) \quad (3)$$

III. Support Vector Machine

SVM were selected for their ability to handle complex relationships in high-dimensional spaces. With a moderate accuracy of 59%, SVM provides an additional perspective on PCOS likelihood. The focus is on capturing intricate patterns within the data [15].

The mathematical formula of SVM is:

$$f(x) = \text{sgn}[\ SV\ s\ \alpha iyi(xi)\ Tx + b] \quad (4)$$

IV. Random Forest

An RF is created by combining different tree predictors so that every tree in the forest depends on the values of a random vector that is randomly sampled and has the same distribution for every tree [16]. Random Forests, as an ensemble learning method, were selected for their ability to improve predictive accuracy. With an impressive accuracy of 83%, the random forest model excels in capturing complex relationships within the PCOS dataset, providing users with highly accurate risk assessments.

V. Comparision of Models

Table 1. *Comparison of models based on accuracy, strength, and limitations*

Model	Accuracy	Strengths	Limitations
LR	79%	Simplicity and interpretability	Assumes linear relationships between features
DT	67%	Intuitive and easy to interpret	Prone to overfitting, especially with deep tree
SVM	59%	Effective in high-dimensional spaces	Highly computational, mainly when working with big datasets
RF	83%	combining multiple decision trees	Less interpretable compared to individual decision trees

V. Conclusion and Future Work

As a result of this research, machine learning techniques have contributed significantly to improving the diagnosis of PCOS. We have shown how such methods can increase diagnostic precision by utilizing and comparing several models, including LR, SVM, DT, and RF. Utilization of feature selection techniques has further refined our models, with the Random Forest algorithm achieving the highest accuracy of 83%.This outcome highlights the effectiveness of advanced machine learning approaches in providing more reliable and accurate PCOS diagnosis. Our findings contribute to the ongoing efforts to manage PCOS better and offer a foundation for future research to improve diagnostic methods and ultimately enhance patient outcomes.

In future research, integrating Internet of Things devices like Galvanic Skin Response sensors could provide valuable insight into the emotional and physiological states of women with PCOS. Women suffering from PCOS often experience heightened anxiety and depression. By incorporating GSR data with PCOS diagnostic models, we could develop more personalized treatment strategies to address physiological and psychological aspects. Additionally, sentiment analysis for mood tracking could enhance PCOS management by analyzing written communications to identify mood patterns and triggers related to symptoms. This approach could improve our

understanding of the emotional factors influencing PCOS, leading to more tailored and practical support and treatment options.

References

[1]G. Jiskoot, Y Louwers, A. Van der Mijle, V. Maas.(2025). Medication Use in Pregnant Women with Polycystic Ovary Syndrome (PCOS): A Nationwide Cohort Study. *Human Reproduction*,40,Deaf 097-948.

[2] H. Elmannai, N. El-Rashidy, I. Mashal, M. A. Alohali, S. Farag, S. El-Sappagh, and H. Saleh.(2023). Polycystic ovary syndrome detection machine learning model based on optimised feature selection and explainable artificial intelligence, *Diagnostics*, vol. 13, no. 8, p. 1506

[3] M. M. Rahman.(2022). A web-based heart disease prediction system using machine learning algorithms, *Network Biology*, vol. 12, no. 2, p. 64

[4] A. Dar, M. Maqbool, Z. Qadrie, I. Ara, and A. Qadir.(2024).Unravelling PCOS: Exploring its causes and diagnostic challenges, *Open Health*, vol. 5, pp. 1–8

[5] Z. Zad, V. S. Jiang, A. T. Wolf, T. Wang, J. J. Cheng, I. C. Paschalidis, and S. Mahalingaiah.(2024). Predicting polycystic ovary syndrome with ML algorithms from electronic health records,*Frontiers in Endocrinology*, vol. 15, p. 1298628

[6] N. Pudjihartono, T. Fadason, A. W. Kempa-Liehr, and J. M. O'Sullivan.(2022).A review of feature selection methods for machine learning-based disease risk prediction, *Frontiers in Bioinformatics*, vol. 2, p. 927312

[7] V. Da Poian, B. Theiling, L. Clough, B. McKinney, J. Major, J. Chen, and S. Hörst.(2023).Exploratory data analysis (EDA) machine learning approaches for ocean world analog mass spectrometry,*Frontiers in Astronomy and Space Sciences*, vol. 10, p. 1134141

[8] Ö. Çelik.(2018).A research on machine learning methods and its applications,*Journal of Educational Technology and Online Learning*, 1(3), 25-40.

[9] A. K. M. S. Hosain, M. H. Kabir Mehedi, and I. E. Kabir.(2022). Pconet: A convolutional neural network architecture to detect polycystic ovary syndrome (PCOS) from ovarian ultrasound images,in *Proc. Int. Conf. Engineering and Emerging Technologies (ICEET)*, IEEE.

[10] M. Priyadharshini, A. Srimathi, C. Sanjay, and K. Ramprakash.(2024).PCOS disease prediction using machine learning algorithms, *International Research Journal on Advanced Engineering Hub* , vol. 2, pp. 651–655.

[11] G. Rona .(2024).Machine learning-based analysis of MRI radiomics in the discrimination of classical and non-classical polycystic ovary syndrome, *cukurova medical journal*,vol. 49, no. 1, pp. 89–96.

[12] P. Kottarathil.(2024). *Polycystic ovary syndrome (PCOS)*, [Online]. Available: https://www.kaggle.com/datasets/prasoonkottarathil/polycystic-ovary-syndrome-pcos, ver. 1.0.

[13] J. Peng, K. Lee, and G. Ingersoll.(2002). An introduction to logistic regression: Analysis and reporting, *The Journal of Educational Research*, vol. 96, pp. 3–14.

[14] D. Mienye, N. Jere.(2024).A survey of decision trees: Concepts, algorithms, and applications, *IEEE Access*, vol. 12, pp. 86716–86727.

[15] H. Wang, J. Xiong, Z. Yao, M. Lin, J Ren.(2017). Research survey on support vector machine. InProceedings of the 10th EAI international conference on mobile multimedia communications 2017 Dec 8 (pp. 95-103).

[16] L. Breiman (2001), Random forests, *Machine Learning*, vol. 45, pp. 5–32.

LOG EXPONENTIATED KUMARASWAMY DISTRIBUTION WITH REAL LIFE APPLICATIONS

Mahvish Jan[1*], S.P. Ahmad[2]

•

[1*],[2] Department of Statistics, University of Kashmir, Srinagar, India
wanimahvish@gmail.com, sprvz@yahoo.com

Abstract

The generalization of probability distributions plays a crucial role in broadening their applications across various domains. To achieve this, this paper introduces a novel three-parameter generalization of the Kumaraswamy distribution. The new distribution is termed as the Log Exponentiated Kumaraswamy (LEK) distribution. Some essential properties of this distribution are studied and the estimate of parameters are obtained using the maximum likelihood estimation procedure. Also, a simulation study is conducted and two real life data sets demonstrate the proposed distribution's applicability. The performance of the proposed LEK distribution proved to be better than comparative models.

Keywords: Log exponentiated technique, Reverse Hazard rate, Kumaraswamy distribution, Mixture representations

1. Introduction

Probability distributions play an indispensable role in mathematical statistics, as they contribute to understanding and interpreting the underlying patterns in the data with greater accuracy. The diverse data in applied domains often transcend the capabilities of traditional probability distributions, necessitating the need of deriving new distributions. Researchers have introduced new probability distributions designed to accommodate the vast data across applied domains. The process of creating new distributions often involve modifying existing distributions by introducing additional parameters. Numerous researchers have utilized different techniques to make the base distribution more flexible and versatile. Some contributions include MTI Rayleigh distribution introduced by [1] as an extension of the Rayleigh distribution, the MTI inverted exponential distribution proposed by [2], the PNJ power function distribution proposed by [3], the exponentiated power inverse Lomax distribution introduced by [4], Inverse power XLindley distribution with statistical inference and applications to engineering data by [5].

The Kumaraswamy distribution [6], introduced by Poondi Kumaraswamy in 1980, is a continuous probability distribution defined in the interval (0,1). The Kumaraswamy distribution is particularly effective in addressing hydrological challenges and modelling natural phenomena with bounded process values. Its distinctive properties make it an excellent choice for applications that require straightforward and efficient modelling techniques. In recent years, numerous extensions of the Kumaraswamy distribution have been introduced, significantly increasing its versatility and applicability. These advancements include the generalized odd maxwell-kumaraswamy distribution by [7], second order Transmuted Kumaraswamy distribution by [8], Kumaraswamy-Gull Alpha Power Rayleigh distribution introduced by [9], SMPKumaraswamy distribution put forward by [10], Transmuted Exponentiated Kumaraswamy distribution put forward by [11]. In this paper, we introduce a novel three-parameter extension of Kumaraswamy

distribution with pdf and cdf given in equations 1 and 2 respectively, using a novel approach for constructing distributions introduced by [12] termed as the Log Exponentiated Transformation (LET).

$$g(x;\beta,\lambda) = \beta\lambda x^{\lambda-1}(1-x^{\lambda})^{\beta-1}; \quad 0 < x < 1,\ \beta > 0, \lambda > 0 \tag{1}$$

$$G(x;\beta,\lambda) = 1-(1-x^{\lambda})^{\beta}; \quad 0 < x < 1,\ \beta > 0, \lambda > 0 \tag{2}$$

The cdf and pdf of LET are respectively given by equation 3 and 4

$$F(x) = 1-\log\left(e+\bar{e}(G(x;\beta,\lambda))^{\theta}\right); \quad x \in \mathbb{R} \quad \theta,\beta,\lambda > 0 \tag{3}$$

$$f(x) = \frac{(e-1)\theta g(x;\beta,\lambda)(G(x;\beta,\lambda))^{\theta-1}}{e+\bar{e}\,(G(x;\beta,\lambda))^{\theta}}; \quad x \in \mathbb{R} \quad \theta,\beta,\lambda > 0 \tag{4}$$

where $G(x;\beta,\lambda)$ is cdf of distribution to be generalized.

In this paper a novel three-parameter Kumaraswamy distribution using Log Exponentiated technique is introduced. The research goals of this study are:

- To introduce a new probability distribution with an additional parameter. The new model is more flexible than the baseline distribution and can analyze datasets of different shapes.
- To estimate the model parameters and conduct a comprehensive simulation study to assess the behavior of derived estimators.
- To show the flexibility and applicability of the proposed distribution using two real life datasets from different fields.

The structure of the manuscript is organized as follows: Section 2 introduces Log exponentiated Kumaraswamy distribution along with mixture representations. In Section 3, some statistical properties are discussed. Section 4 addresses the reliability characteristics of the proposed distribution, while Section 5 is devoted to generating functions and parameter estimation method is given in section 6, followed by a detailed simulation study in section 7 and applications in section 8. Finally, conclusion is provided in section 9.

2. Log Exponentiated Kumaraswamy Distribution

Using the Kumaraswamy distribution as baseline distribution for proposed distribution, the Log Exponentiated Kumaraswamy distribution (LEK) cdf function is given by

$$F(x;\lambda,\beta,\theta) = 1-\log\left(e+\bar{e}[1-(1-x^{\lambda})^{\beta}]^{\theta}\right); \quad 0 < x < 1, \lambda,\beta,\theta > 0 \tag{5}$$

The pdf function is given by

$$f(x;\lambda,\beta,\theta) = \frac{(e-1)\beta\lambda\theta x^{\lambda-1}(1-x^{\lambda})^{\beta-1}[1-(1-x^{\lambda})^{\beta}]^{\theta-1}}{e+\bar{e}[1-(1-x^{\lambda})^{\beta}]^{\theta}}; \quad 0 < x < 1, \lambda,\beta,\theta > 0 \tag{6}$$

Figure 1 illustrates graphically different pdf plots of LEK distribution for several parameter combinations. The legend specifies the parameter values for each curve. The shape of the pdf changes with different parameter values showcasing how the distribution behaves under various parameter combinations.

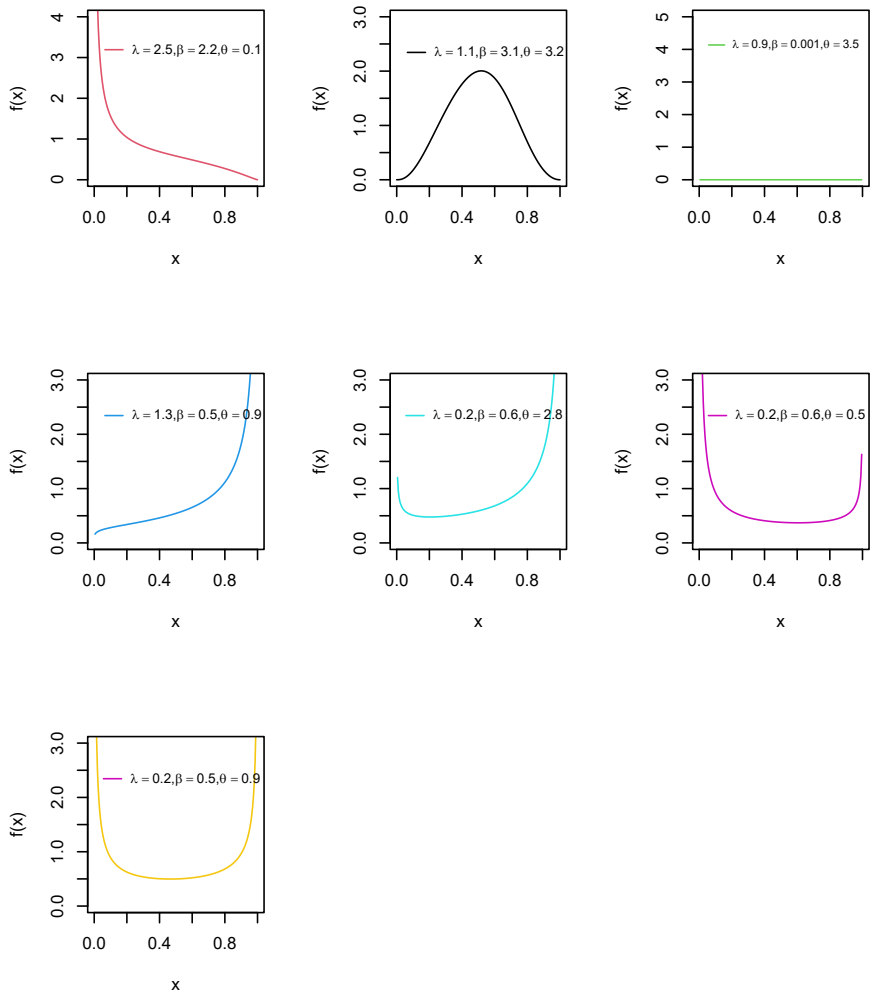


Figure 1: *Probability Density Plots of LEK distribution*

2.1. Mixture Representations

Using the binomial expansion , $(1+z)^{-1} = \sum_{p=0}^{\infty}(-1)^p z^p \quad ; |z| \leq 1$, an alternative representation for the probability density function is given below

$$f(x;\lambda,\beta,\theta) = \frac{(e-1)\beta\lambda\theta x^{\lambda-1}(1-x^{\lambda})^{\beta-1}[1-(1-x^{\lambda})^{\beta}]^{\theta-1}}{e+\bar{e}[1-(1-x^{\lambda})^{\beta}]^{\theta}}; \quad 0<x<1, \beta,\lambda,\theta>0$$

$$= \frac{(e-1)}{e}\beta\lambda\theta x^{\lambda-1}(1-x^{\lambda})^{\beta-1}\left[1-(1-x^{\lambda})^{\beta}\right]^{\theta-1}\left[1+\frac{\bar{e}}{e}\left[1-(1-x^{\lambda})^{\beta}\right]^{\theta}\right]^{-1}$$

3. Statistical Properties of Log Exponentiated Kumaraswamy Distribution

This section deals with the statistical characteristics of the proposed LEK distribution, which presents insights into the behavior and features of the distribution.

3.1. Quantile function

Theorem 1. If X $\sim$ *LEK* (λ,β,θ) distribution, then the quantile function of X is given by

$$x = \left[1 - \left(1 - \left(\frac{e^{1-u} - e}{\bar{e}}\right)^{\frac{1}{\theta}}\right)^{\frac{1}{\beta}}\right]^{\frac{1}{\lambda}} \tag{7}$$

Where u is a uniform random variable, $0 < u < 1$.

Proof. Let $F(x;\lambda,\beta,\theta)$ = u

$$log\left[e + \bar{e}(1 - (1 - x^{\lambda})^{\beta})^{\theta}\right] = 1 - u$$

$$x^{\lambda} = 1 - \left[1 - \left(\frac{e^{1-u} - e}{\bar{e}}\right)^{\frac{1}{\theta}}\right]^{\frac{1}{\beta}}$$

$$x = \left[1 - \left(1 - \left(\frac{e^{1-u} - e}{\bar{e}}\right)^{\frac{1}{\theta}}\right)^{\frac{1}{\beta}}\right]^{\frac{1}{\lambda}}$$

■

3.2. Moments

The r^{th} ordinary moment of the LEK distribution is obtained as

$$\mu_{r'} = \int_0^1 x^r \sum_{p=0}^{\infty}\sum_{q=0}^{\infty}(-1)^{p+q+1}\binom{(p+1)\theta - 1}{q}\left[(1 - x^{\lambda})\right]^{q\beta+\beta-1}\theta\beta\lambda x^{\lambda-1}\,dx$$

$$\mu_{r'} = \int_0^1 \sum_{p=0}^{\infty}\sum_{q=0}^{\infty}\delta_{p,q}\theta\beta\lambda x^r x^{\lambda-1}\left[(1 - x^{\lambda})^{\beta(1+q)-1}\right]\,dx$$

where $\delta_{p,q} = (-1)^{p+q+1}\binom{(p+1)\theta-1}{q}\left(\frac{\bar{e}}{e}\right)^{p+1}\theta$

$$\mu_{r'} = \sum_{p=0}^{\infty}\sum_{q=0}^{\infty}\delta_{p,q}\int_0^1 \beta z^{\frac{r}{\lambda}}\left[(1 - z)^{\beta(1+q)-1}\right]\,dz$$

$$\mu_{r'} = \sum_{p=0}^{\infty}\sum_{q=0}^{\infty}\delta_{p,q}\beta B\left[\left(\frac{r}{\lambda} + 1\right), \beta(1+q)\right]$$

$B[(\frac{r}{\lambda} + 1), \beta(1+q)]$ represents the beta function.

From above moment expression, we can easily derive the mean, variance, moment skewness coefficient and kurtosis coefficient.

Mean: $\mu_{1'} = \sum_{p=0}^{\infty}\sum_{q=0}^{\infty}\delta_{p,q}\beta B\left[\left(\frac{1}{\lambda} + 1\right), \beta(1+q)\right]$

3.3. Incomplete Moment

Let $I_r(t) = \int_0^t x^r f(x;\lambda,\beta,\theta)\,dx$ denotes the r^{th} incomplete moment, then we have

$$I_r(t) = \sum_{p=0}^{\infty}\sum_{q=0}^{\infty}\delta_{p,q}\left[t^{\lambda}; (\frac{1}{\lambda} + 1), \beta(1+q)\right] \tag{8}$$

Using $I_r(t) = \int_0^t x^r f(x;\lambda,\beta,\theta)\,dx$

$$I_r(t) = \int_0^t x^r \sum_{p=0}^{\infty}\sum_{q=0}^{\infty} \delta_{p,q}\lambda\beta x^{\lambda-1}\left[(1-x^{\lambda})^{\beta-1}\right]\left[(1-x^{\lambda})^{\beta}\right]^q dx$$

$$I_r(t) = \sum_{p=0}^{\infty}\sum_{q=0}^{\infty} \delta_{p,q}\beta B\left[t^{\lambda};\left(\frac{r}{\lambda}+1\right),\beta(1+q)\right]$$

Where $B[z;a,b] = \int_0^z x^{a-1}(1-x)^{b-1}\,dx$ is incomplete beta function.

Remark: For r=1 in equattion (8) we get first incomplete moment.

$$I_1(t) = \sum_{p=0}^{\infty}\sum_{q=0}^{\infty} \delta_{p,q}\beta B\left[t^{\lambda};\left(\frac{1}{\lambda}+1\right),\beta(1+q)\right]$$

4. Reliability Analysis Of the Log Exponentiated Kumaraswamy Distribution

This section introduces some reliability expressions of the LEK distribution, such as survival function, Reverse hazard function, hazard rate.

4.1. Survival Function

The survival function is a key concept in probability, survival analysis, and reliability theory. It represents the probability that a subject or system survives beyond a certain time without experiencing a specified event (e.g., failure, death).The survival function for the LEK distribution is given as

$$R(x;\lambda,\beta,\theta) = \log\left[e+\bar{e}(1-(1-x^{\lambda})^{\beta})^{\theta}\right]$$

4.2. Reverse Hazard Function

The reverse hazard rate is given as

$$h_r(x;\lambda,\beta,\theta) = \frac{(\frac{e-1}{e})\beta\lambda\theta x^{\lambda-1}(1-x^{\lambda})^{\beta-1}[1-(1-x^{\lambda})^{\beta}]^{\theta-1}\left[1+\frac{\bar{e}}{e}[1-(1-x^{\lambda})^{\beta}]^{\theta}\right]^{-1}}{1-\log\left[e+\bar{e}(1-(1-x^{\lambda})^{\beta})^{\theta}\right]}$$

4.3. Hazard Rate

The hazard rate is a fundamental concept in reliability theory and survival analysis. It describes the instantaneous rate at which an event (such as failure or death) occurs, given that the subject has survived up to a certain time. The expression for the hazard rate of the LEK distribution is obtained as

$$h(x;\alpha,\beta,\lambda) = \frac{(\frac{e-1}{e})\beta\lambda\theta x^{\lambda-1}(1-x^{\lambda})^{\beta-1}[1-(1-x^{\lambda})^{\beta}]^{\theta-1}\left[1+\frac{\bar{e}}{e}[1-(1-x^{\lambda})^{\beta}]^{\theta}\right]^{-1}}{\log\left[e+\bar{e}(1-(1-x^{\lambda})^{\beta})^{\theta}\right]}$$

Figure 2 displays different shapes of hazard rate for different parameter combinations viz., constant, bath-tub, increasing and J-shaped. The pattern of the hazard rate plots in Figure 2 reveals utility of the proposed LEK distribution in describing varying lifetime events.

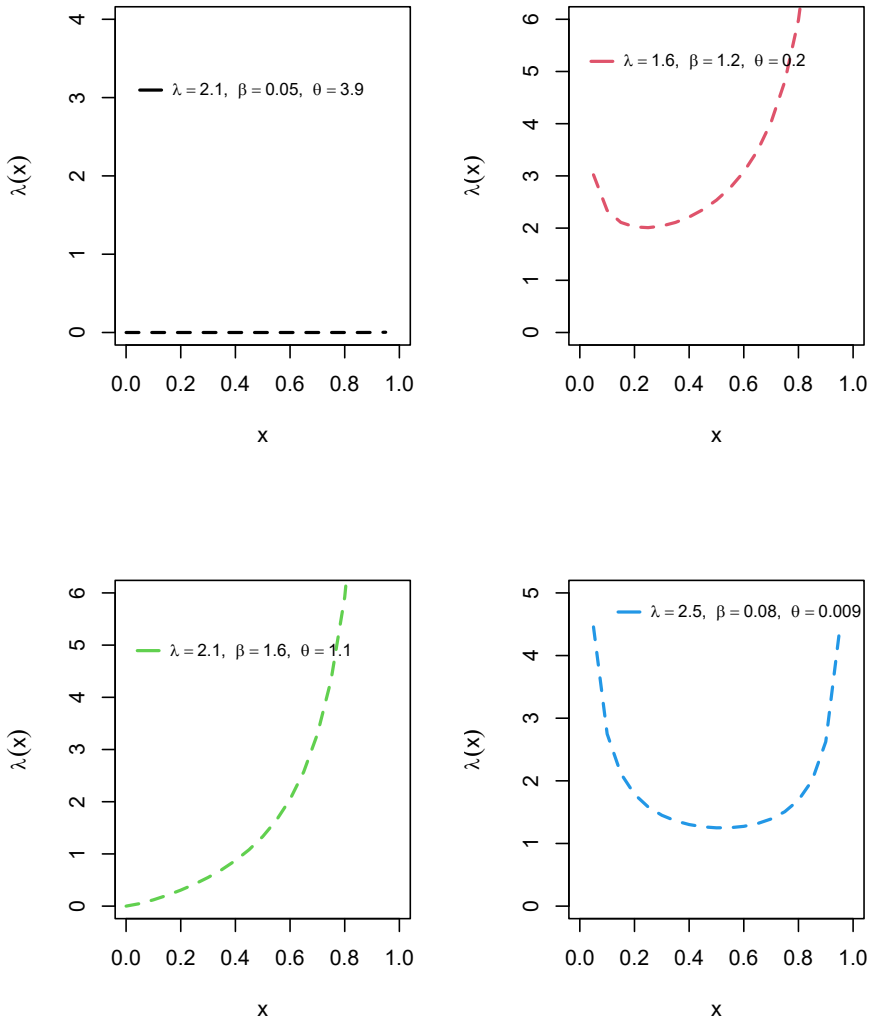


Figure 2: *Hazard rate Plots of LEK distribution*

4.4. Mean Residual life

The mean residual life of a component following LEK distribution can be obtained as

$$\mu(x) = \frac{1}{R(x)}\left[E(x) - I_1(x)\right] - x$$

Where

$$E(x) = \sum_{p=0}^{\infty}\sum_{q=0}^{\infty}\delta_{p,q}\beta B\left[\left(\frac{1}{\lambda}+1\right),\beta(1+q)\right]$$

and

$$I_1(x) = \sum_{p=0}^{\infty}\sum_{q=0}^{\infty}\delta_{p,q}\beta B\left[t^{\lambda};\left(\frac{1}{\lambda}+1\right),\beta(1+q)\right]$$

$$\mu(x) = \frac{\sum_{p=0}^{\infty}\sum_{q=0}^{\infty}\delta_{p,q}\beta B\left[\left(\frac{1}{\lambda}+1\right),\beta(1+q)\right] - \sum_{p=0}^{\infty}\sum_{q=0}^{\infty}\delta_{p,q}\beta B\left[t^{\lambda};\left(\frac{1}{\lambda}+1\right),\beta(1+q)\right]}{\log\left[e+\bar{e}(1-(1-x^{\lambda})^{\beta})^{\theta}\right]}$$

4.5. Mean Waiting Time

The expression for mean waiting time is given as

$$\bar{\mu}(x) = x - \frac{I_1(x)}{F(x)}$$

$$\bar{\mu}(x) = x - \frac{\sum_{p=0}^{\infty}\sum_{q=0}^{\infty}\delta_{p,q}\beta B\left[t^{\lambda};\left(\frac{1}{\lambda}+1\right),\beta(1+q)\right]}{1-\log\left[e+\bar{e}(1-(1-x^{\lambda})^{\beta})^{\theta}\right]}$$

5. Generating Functions

The moment generating function of X $\sim$ LEK (λ,β,θ) distribution can be obtained using the relation

$$M_x(t) = \sum_{r=0}^{\infty}\frac{t^r}{r!}\mu_r'$$

$$M_x(t) = \sum_{p=0}^{\infty}\sum_{q=0}^{\infty}\sum_{r=0}^{\infty}\frac{t^r}{r!}\frac{t^r}{r!}\delta_{p,q}\beta B\left[(\frac{r}{\lambda}+1),\beta(j+1)\right]$$

The characteristic function of LEK distribution is given by

$$\phi_x(t) = \sum_{r=0}^{\infty}\frac{(it)^r}{r!}\mu_r'$$

$$\phi_x(t) = \sum_{p=0}^{\infty}\sum_{q=0}^{\infty}\sum_{r=0}^{\infty}\frac{(it)^r}{r!}\frac{t^r}{r!}\delta_{p,q}\beta B\left[(\frac{r}{\lambda}+1),\beta(j+1)\right]$$

6. Estimation of Parameters

Let $x_1, x_2, x_3, ...x_n$ be a random sample of size n from LEK distribution. The likelihood and log-likelihood functions are respectively given by equations below

$$L(x;\lambda,\beta,\theta) = \prod_{i=1}^{n}\frac{(e-1)\theta\lambda\beta x_i^{\lambda-1}(1-x_i^{\lambda})^{\beta-1}[1-(1-x_i^{\lambda})^{\beta}]^{\theta-1}}{e+\bar{e}\left[1-(1-x_i^{\lambda})^{\beta}\right]^{\theta}}$$

$$\begin{aligned} l = {} & n\log(e-1)+n\log\theta+n\log\lambda+n\log\beta+(\lambda-1)\log x+(\beta-1)\log(1-x^{\lambda}) \\ & +(\theta-1)\log\left[1-(1-x^{\lambda})^{\beta}\right]-\sum_{i=1}^{n}\left(e+\bar{e}\left[[1-(1-x^{\lambda})^{\beta}\right]^{\theta}\right) \end{aligned}$$

$$\frac{\partial l}{\partial\theta} = \frac{n}{\theta}+\log\left[1-(1-x^{\theta})^{\beta}\right]+\sum_{i=1}^{n}\log\left(e+\bar{e}\left[1-(1-x^{\lambda})^{\beta}\right]^{\theta}\right)$$

$$\begin{aligned} \frac{\partial l}{\partial\lambda} = {} & \frac{n}{\lambda}+\log x-\frac{(\beta-1)x^{\lambda}\log x}{1-x^{\lambda}}+\frac{\beta x^{\lambda}\log x(1-x^{\lambda})^{\beta-1}(\theta-1)}{1-(1-x^{\lambda})^{\beta}} \\ & -\frac{\sum_{i=1}^{n}\bar{e}\theta\beta\left[(1-(1-x^{\lambda})^{\beta}\right]^{\theta-1}(1-x^{\lambda})^{\beta-1}x^{\lambda}\log x}{e+\bar{e}\left[1-(1-x^{\lambda})^{\beta}\right]} \end{aligned}$$

$$\frac{\partial l}{\partial\beta} = \frac{n}{\beta}+\sum_{i=1}^{n}\log(1-x^{\lambda})-\frac{(\theta-1)(1-x^{\lambda})^{\beta}\log(1-x^{\lambda})}{1-(1-x^{\lambda})^{\beta}}+\sum_{i=1}^{n}\frac{\bar{e}\theta\log(1-x^{\lambda})(1-x^{\lambda})^{\beta}\left[1-(1-x^{\lambda})^{\beta}\right]^{\theta-1}}{e+\bar{e}\left[1-(1-x^{\lambda})^{\beta}\right]}$$

Since, above equations are non-linear, we will use R software to solve these equations and estimate the parameters.

7. Simulation Study

In this section two comprehensive simulation studies to assess the accuracy of the maximum likelihood procedure is discussed. Based on quantile function described in equation 7 and using R package random samples of size 20, 50, 125, 500 are generated for two parameter combinations $\lambda = 0.01, \beta = 1.5, \theta = 0.1$ and $\lambda = 0.03, \beta = 0.1, \theta = 1.6$. For each sample size and both parameter combinations ,the MLEs, Biases and Mean Square Errors (MSEs) are computed and the numerical results are given in table 1.

Table 1: *Simulation results for* $\lambda = 0.01, \beta = 1.5, \theta = 0.1$

Sample size	Parameters			MLE			Bias			MSE		
n	λ	β	θ	$\hat{\lambda}$	$\hat{\beta}$	$\hat{\theta}$	$\hat{\lambda}$	$\hat{\beta}$	$\hat{\theta}$	$\hat{\lambda}$	$\hat{\beta}$	$\hat{\theta}$
20	0.01	1.5	0.1	0.8079	1.3259	0.2182	0.7980	0.1741	0.1188	0.7857	0.1826	0.0756
50				0.7600	1.4586	0.1524	0.7500	0.0414	0.0524	0.7857	0.1826	0.0756
125				0.4632	1.4751	0.1317	0.4532	0.0249	0.0317	0.4514	0.0014	0.0022
500				0.0498	1.4978	0.1028	0.0398	0.0022	0.0028	0.0397	0.0001	0.0002
20	0.03	0.1	1.6	0.0647	0.1810	1.6667	0.0544	0.0812	0.8020	0.0186	0.0090	4.2664
50				0.0272	0.1683	1.4353	0.0206	0.0683	0.2730	0.0013	0.0063	0.2450
125				0.0195	0.1496	1.5241	0.0129	0.0496	0.0789	0.0004	0.0044	0.0446
500				0.0264	0.1112	1.5983	0.0036	0.0112	0.0017	0.0001	0.0010	0.0004

From table 1 it is observed that the MLEs closely approach to true parameter values for both the parameter combinations as the sample size increases from 20 to 500. Further the bias and Mean Square Error (MSE) of each estimate decrease as the sample size (n) increases, indicating enhanced precision and improved accuracy of the maximum likelihood estimation method.

8. Applications

This section presents real data analysis of two real life data sets, demonstrating the practical applicability and effectiveness of the proposed LEK Distribution. For performance comparison purposes with the proposed distribution, we used basic Kumaraswamy distribution [6], Transmuted Kumaraswamy distribution [13] and Kumaraswamy Inverse Exponential distribution [14]. For comparison, we use Goodness of fit measures namely Akaike Information Criterion (AIC), Akaike Information Criterion Corrected (AICC), Hannan - Quinn information Criterion (HQIC) , Kolmogorov-Smirnov (KS) and P-value statistics calculated using R programming. Decision rule is the distribution having the lowest numerical value of aforementioned measures is considered as the best fit.

Data set I: The first data set has been taken from [15] , and this data set relates to 50 observations on burr and are given as

0.04, 0.02, 0.06, 0.12, 0.14, 0.08, 0.22, 0.12, 0.08, 0.26, 0.24, 0.04, 0.14, 0.16, 0.08, 0.26, 0.32, 0.28, 0.14, 0.16, 0.24, 0.22, 0.12, 0.18, 0.24, 0.32, 0.16, 0.14,0.08, 0.16, 0.24, 0.16, 0.32, 0.18, 0.24, 0.22, 0.16, 0.12, 0.24, 0.06, 0.02, 0.18, 0.22, 0.14, 0.06, 0.04, 0.14, 0.26, 0.18, 0.16.

Data Set II: This data set shows water capacity of Shasta reservoir in California, USA for August and December from 1975 to 2016. This data has been previously used by [16] .

0.667157, 0.287785, 0.126977, 0.768563, 0.703119, 0.729986, 0.767135, 0.811159, 0.829569, 0.726164, 0.423813, 0.715158, 0.640395, 0.363359, 0.463726, 0.371904, 0.291172, 0.414087, 0.650691, 0.538082, 0.744881, 0.722613, 0.561238, 0.813964, 0.709025, 0.668612, 0.524947, 0.605979, 0.715850, 0.529518, 0.824860, 0.742025, 0.468782, 0.345075, 0.425334, 0.767070, 0.679829, 0.613911, 0.461618, 0.294834, 0.392917, 0.688100.

Table 2: *Performance measures for Data Set I*

Model	$\hat{\lambda}$	$\hat{\beta}$	$\hat{\theta}$	$\hat{\alpha}$	AIC	AICC	HQIC	K-S	P-value
LEKD	2.8472	88.9604	0.5123	-	-108.5281	-108.0063	-220.8718	0.0910	0.8023
KUMD	2.0774	33.1375	-	-	-108.1374	-107.882	-218.8185	0.11025	0.5777
TKD	-0.2911	-	30.1874	1.9335	-106.5026	-105.9809	-216.821	0.1052	0.6375
KIED	0.4590	2.5266	-	0.3905	-77.9185	-77.3967	-159.6527	0.2407	0.0061

Table 3: *Performance measures for Data Set II*

Model	$\hat{\lambda}$	$\hat{\beta}$	$\hat{\theta}$	$\hat{\alpha}$	AIC	AICC	HQIC	K-S	P-value
LEKD	16.1956	48.6481	0.1320	-	-31.2110	-30.5795	-66.5113	0.0989	0.7692
KUMD	3.4355	3.7681	-	-	-27.2620	-26.9543	-57.2501	0.1362	0.3826
TKD	-0.2970	-	3.8196	3.1568	-25.6987	-25.0672	-55.4867	0.1283	0.4565
KIED	2.0064	17.7055	-	0.8960	-5.0926	-4.4610	-14.2745	0.1918	0.0794

From numerical results in table 2 and table3 it is observed that the Log Exponentiated Kumaraswamy distribution has the least value of all the Goodness of fit measures under consideration against its comparative models. Hence, LEK distribution could be considered as the best model that fits the given data sets. The histogram and density plots of data sets for the LEK distribution against its comparative distributions are also displayed in figure 3 and figure 4. From figures it is also evident that LEK distribution provides a better fit than its comparative distributions.

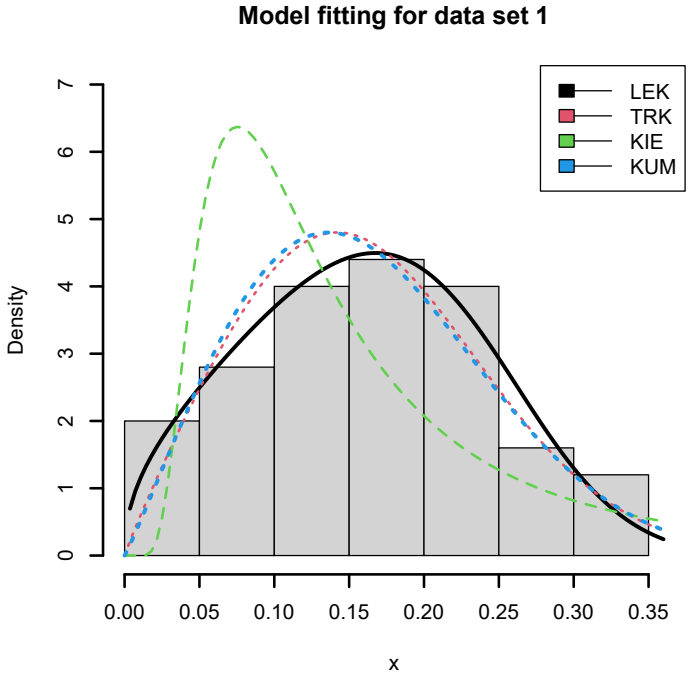


Figure 3: *Histogram and Density plots for dataset I*

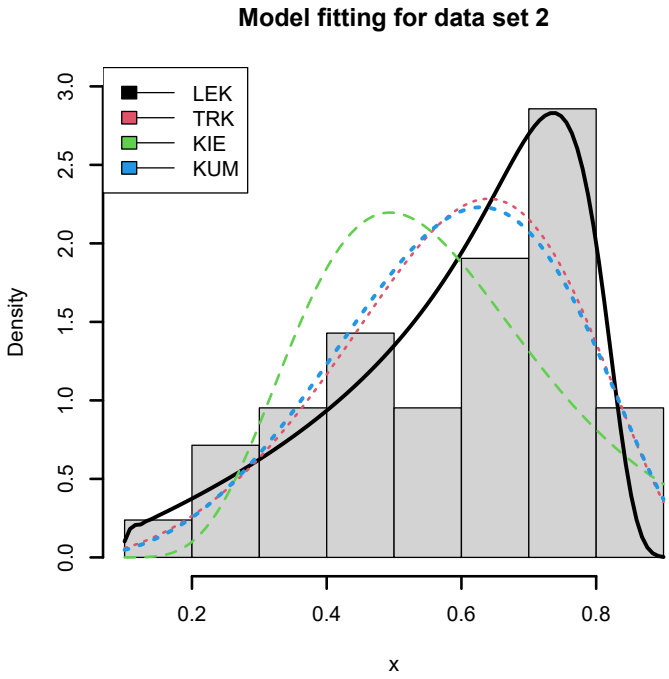


Figure 4: *Histogram and Density plots for dataset II*

9. Conclusion

This paper introduces a novel three-parameter generalization of Kumaraswamy distribution referred to as Log-Exponentiated Kumaraswamy distribution (LEK), which serves as a better alternative to model data from various domains by means of real-life applications. Statistical and reliability characteristics of the proposed model are discussed in detail and the parameters of its estimates are obtained using Maximum likelihood estimation method. A simulation study is performed, using different parameter combinations and all the estimators perform better and with in crease in sample size (n), bias and measn square error of each estimate decreases indicating improved accuracy. To illustrate the applicability and effectiveness of the proposed model , two real life data sets have been analyzed and compared with some probability distributions. The numerical and graphical results suggest that the proposed LEK distribution performs better in modeling the data sets considered than comparative probability distributions. we hope that the proposed LEK distribution can be regarded as the one of the best for modeling data sets in various applied fields like engineering, life sciences, finance, hydrology etc.

References

[1] Mir, A. A. and Ahmad, S. P. (2025). A New Extended Rayleigh Distribution with Applications of COVID-19 Data. *Austrian Journal of Statistics*, 54(2), 69-84.

[2] Ahad, T. and Ahmad, S. P. (2025). A New Extension of Inverted Exponential Distribution with Applications. *European Journal of Statistics*, 5, 5-5.

[3] Ahad, N., Ahmad, S. P. and Reshi, J. A. (2024). A novel approach to distribution generation with applications in electrical engineering. *Reliability: Theory & Applications*, 19(4 (80)), 525-540.

[4] Rasool, S. U., and Ahmad, S. P. (2024). Exponentiated Power Inverse Lomax Distribution with Applications. *Punjab University Journal of Mathematics*, 56(1), 15-30.

[5] Hassan, A. S., Alsadat, N., Chesneau, C., Elgarhy, M., Kayid, M., Nasiru, S. and Gemeay, A. M. (2025). Inverse power XLindley distribution with statistical inference and applications to engineering data. *Scientific Reports*, 5(1):4385.

[6] Kumaraswamy, P. (1980). A generalized probability density function for double-bounded random processes. *Journal of hydrology*, 46(1-2), 79-88.

[7] Ishaq, A. I., Panitanarak, U., Abiodun, A. A., Suleiman, A. A. and Daud, H. (2024). The generalized odd maxwell-kumaraswamy distribution: Its properties and applications. *Contemporary Mathematics*, 711-742.

[8] Tushar, M. T., Rashedi, K. A., Alshammari, T. S., Rahman, M. M. (2024). Second order transmuted kumaraswamy distribution and its related results. *European Journal of Pure and Applied Mathematics*, 17(2), 616-637.

[9] Kpangay, M., Odongo, L. O., Orwa, G. O. (2023). The Kumaraswamy-Gull Alpha power rayleigh distribution: properties and application to HIV/AIDS data. *International Journal of Scientific Research and Engineering Development*, 6(1), 431-442.

[10] Jan, M. and Ahmad, S. P. (2024). A new extension of kumaraswamy distribution for improved data modeling: Properties and applications. *Reliability: Theory & Applications*, 19(4 (80)), 654-665.

[11] Joseph, J. and Ravindran, M. (2023). Transmuted exponentiated kumaraswamy distribution. *Reliability: Theory & Applications*, 18(1 (72)), 539-552.

[12] Ahmad, A., Jallal, M., Ahmad, A. (2022). A novel approach for constructing distributions with an example of the Rayleigh distribution. *Reliability: Theory & Applications*, 17(1 (67)), 52-64.

[13] Khan, M. S., King, R., & Hudson, I. L. (2016). Transmuted kumaraswamy distribution. *Statistics in Transition new series*, 17(2), 183-210.

[14] Oguntunde, P. E., Babatunde, O. S., Ogunmola, A. O. (2014). Theoretical analysis of the Kumaraswamy-inverse exponential distribution. *International Journal of Statistics and Applications*, 4(2), 113-116.

[15] Dasgupta, R. (2011). On the distribution of burr with applications. *Sankhya B*, 73(1), 1-19.

[16] Kohansal, A. (2019). On estimation of reliability in a multicomponent stress-strength model for a Kumaraswamy distribution based on progressively censored sample. *Statistical Papers*, 60(6), 2185-2224.

ANALYSIS OF A SINGLE-SERVER QUEUE WITH ENCOURAGED ARRIVALS, IMPATIENT CUSTOMERS AND DYNAMIC SERVICE SWITCHING

Ismailkhan.E[1*], Nagarajan.G[2], Sundar Raj.M[3], Immaculate.S[4]

•

[1,2,3] Department of Mathematics, Panimalar Engineering College, Chennai, Tamil Nadu.
[4]Department of Mathematics, Vellore Institute of Technology, Vellore, Tamil Nadu.
*ismailkhanmubarak@gmail.com

Abstract

This study examines a single-server queueing system that features encouraged arrivals, customer impatience and a self-switching service mechanism. In this model, the arrival rate increases with the number of customers present in the system, specifically modeled as $\lambda(1+\eta)$, where λ is a positive constant and η represents the current number of customers. The server initially operates at a service rate μ_1 as long as the system size is below a predefined threshold K. Once the number of customers reaches K, the server switches to a faster service rate μ_2. Customers become impatient after entering the queue and may abandon the system at a rate γ. Still, this impatience applies only while the server is operating at the slower service rate μ_1. No reneging occurs once the server switches to the faster rate μ_2. The steady-state probability distribution of the system is derived and performance metrics such as the expected waiting time and the average number of customers in the system are evaluated. Numerical illustrations are also provided to demonstrate the impact of encouraged arrivals and server switching behavior.

Keywords: Encouraged arrival, Customer impatience, Server switch random, Single server queue

1. Introduction

Queueing models play a vital role in various real-world applications such as telecommunications, traffic control, healthcare, banking, business operations, post offices and amusement parks. These models are essential tools for managing congestion and enhancing service quality. In particular, queueing systems involving encouraged arrivals and impatient customers are highly relevant in practical scenarios. Encouraged arrivals refer to situations where potential customers are more likely to enter the queue based on certain system conditions, such as shorter queue lengths or the perception of faster service. Unlike discouraged arrivals, encouraged arrivals increase when customers perceive the system to be efficient or less congested. These behaviors may arise due to visible queue size, shorter expected wait times, or prior experiences. Modeling encouraged arrivals is important because they influence arrival patterns and can significantly impact the accuracy and effectiveness of queueing system analysis.

Impatient customers, on the other hand, are those unwilling to wait for extended periods and may leave the queue before receiving service. Impatience may be triggered by frustration, urgency, uncertainty about waiting times, or other personal constraints. These customers are typically modeled as leaving the system if not served within a certain time threshold. Including customer impatience in queueing models is crucial, as it directly affects performance metrics such as system throughput, average waiting time and service levels.

Another important component of modern service systems is the self-switching server, which has the ability to change its service rate based on the system state. For instance, a server may

switch to a faster service rate when the number of customers exceeds a certain threshold, thus helping to control congestion and reduce wait times. This dynamic adjustment improves system responsiveness and overall efficiency.
Building upon these concepts, we propose a Markovian single-server queueing model that integrates encouraged arrivals, customer impatience and a self-switching server mechanism. In this model, the arrival rate is positively influenced by the number of customers in the system, while impatience leads customers to abandon the queue if service is delayed. The server switches between service rates depending on queue length thresholds. The steady-state probability distribution of the system is derived and performance measures are evaluated to analyze system behavior.
The following describes the way the article is structured: Section 2 provides the review as the literature. Section 3 generates the queueing model. Section 4 presents the governing equations of the model. In Section 5, special examples for the queuing models are defined and the governing equations are solved constantly to obtain the stationary probability. Section 6 derives measures of effectiveness. The seventh part is a list of the numerical illustrations. The final portion contains the conclusion.

2. Literature review

The concept of encouraged arrivals has gained increasing attention in queueing theory as researchers strive to model customer behaviors that deviate from classical assumptions. Traditional models typically assume a constant arrival rate, often based on a Poisson process, where customers arrive independently of the system state. However, this assumption fails to capture situations where the arrival rate is influenced by the system's perceived efficiency or service conditions. Encouraged arrival behavior, where the arrival rate increases as the queue becomes more appealing or as waiting times decrease, was introduced to address this gap. Several studies have explored variations of arrival behavior depending on the system state. Notably, models incorporating state-dependent arrival rates have been developed, where the arrival rate is a function of the number of customers in the system. In contrast to discouraged arrivals or balking, where customers avoid long queues, encouraged arrivals occur when customers are more inclined to join shorter queues or when the server is operating more efficiently.
The valuable insights into how customer impatience affects system performance is provided in [1] . Its mathematical rigor and practical relevance make it an important work in the field of queueing theory, especially for industries where customer abandonment plays a significant role in service quality and efficiency. The queueing systems where customer arrivals are affected by external factors are studied in [2]. An $M/M/1/N$ queueing system with encouraged arrivals, feedback, balking and retained reneged customers, focusing on minimizing waiting time and improving system performance is studied in [3]. These studies collectively enhance the understanding of reverse balking phenomena across various queueing models, offering valuable frameworks for optimizing service efficiency and customer satisfaction in various applications. A comprehensive stochastic model addressing complex customer behaviors in queueing systems and developed a multi-server, finite capacity Markovian queueing model that incorporates encouraged arrivals, reverse reneging, feedback customers and retention strategies for reneged customers is considered in [4]. An analysis of M/M/1 queueing system with Coxian-2 service, encouraged arrivals and balking behavior, incorporating server vacations and an economic cost model is presented in [11]. Their study extends existing literature by integrating behavioral arrival patterns with phase-type service and cost optimization to evaluate system performance. A server that operates in distinct phases and customers may leave the queue if their impatience threshold is exceeded, representing a more realistic customer behavior in many service systems is introduced in [5]. It investigates how customer impatience and the server's differentiated phases affect the key performance metrics such as waiting times, queue lengths and system utilization. The balking that occurs when customers decide not to join the queue if it appears too lengthy, reneging takes place when

customers leave the queue because of extended waiting periods and the addition of servers helps reduce system delay is provided in [6]. The performance analysis of queueing systems affected by scheduled maintenance and temporary server shutdowns is studied in [7] . Using Markovian processes, matrix-analytic techniques and Laplace-Stieltjes transforms, the authors develop a probabilistic model to evaluate key performance metrics, including queue length, waiting time and server utilization. The study highlights the trade-offs between system availability and maintenance scheduling, emphasizing that while maintenance minimizes unexpected failures, excessive downtime can lead to inefficiencies. The system is based on the traditional M/M/1 queue, but it introduces a server that operates in three distinct modes, each affecting its service rate. The focus of the study is to examine the transient behavior of the system, especially how it performs during non-steady state conditions is analyzed in [8]. This is crucial for understanding how the system behaves during periods of fluctuating traffic or when the system is initialized. The paper derives essential performance metrics during the transient phase, providing deeper insights into the system's behavior before it reaches a steady state. A finite Markovian heterogeneous queueing model with encouraged arrivals and focused on optimizing key performance measures such as queue length and system utilization. Their study provides practical insights into managing finite-capacity service systems under dynamic arrival behaviors is developed in [12] . Various queueing theory models and methods that address the behavior of customers who may abandon the system if their wait becomes too long is examined in [9]. Impatience plays a crucial role in many service systems, such as call centers, retail, healthcare and telecommunications, where customers tolerance for waiting is limited. The paper compiles existing research on queueing systems involving impatient customers, providing insights into different strategies for managing impatience and enhancing system performance. The queueing theory to analyze how encouraged arrivals can be leveraged to maximize system size in finite-capacity models is applied in [13]. Their study highlights the impact of arrival incentives on improving system utilization and overall throughput within constrained environments.The server experiences working breakdowns, which cause interruptions in the service and the customers exhibit impatience, with the possibility of them leaving the system if their wait is too long, though they may return later is provided in [10]. This combination of breakdowns and impatient customers is common in manufacturing systems, call centers and other service-oriented industries.

In many practical queueing systems, customer encouragement and impatience significantly influence system performance. When waiting times become long, it is natural for the server to respond by working faster, even if the queue size remains large. Various extensions of customer impatience have been explored in single-server queues. Importantly, customer impatience can have a highly negative impact, leading to the loss of potential customers, an issue critical to many business operations. Considering these effects, this paper investigates the concept of a self-switching server, which dynamically adjusts its service rate in response to queue conditions and customer behavior.

2.1. Definitions

In queueing theory, Poisson processes, exponential distributions and Laplace transforms are fundamental tools used to model and analyze systems involving customer arrivals, service mechanisms and overall system dynamics. These concepts provide the mathematical foundation for deriving performance measures and understanding system behavior under various operational conditions.

2.1.1 Poisson process

The Poisson process is a mathematical model used to describe random events occurring over time, most commonly applied to model arrivals in queueing systems. In this context, it assumes that the number of arrivals in a given time interval follows a Poisson distribution and the inter-arrival times are exponentially distributed, reflecting the memoryless and random nature of customer arrivals.

2.1.2 Exponential distribution

The exponential distribution models the time between successive events in a Poisson process and is widely used in queueing theory to represent service times or waiting times. Its memoryless property makes it ideal for modeling systems where the probability of service completion is independent of how long a customer has already waited. Both the arrival rate and service rate, often assumed to follow exponential distributions, are crucial for evaluating performance metrics such as average wait time, queue length and system utilization.

2.1.3 Laplace transforms

The Laplace transform is a mathematical technique that converts functions from the time domain to the complex frequency domain, making it easier to analyze differential equations commonly found in queueing models. In queueing theory, it is particularly useful for deriving probability generating functions and transform solutions, which help compute key performance measures such as average queue length, waiting time and system utilization.

3. Model description

Customers enter the queuing system with encouragement, following a Poisson process with rate $\lambda(1+\eta)$. The system has a single server that operates in two modes: normal and fast. When the number of customers reaches a threshold K, the server switches from normal mode (with service rate μ_1) to fast mode (with higher service rate μ_2, where $\mu_2 > \mu_1$). Service times in both modes follow exponential distributions with means $\frac{1}{\mu_1}$ and $\frac{1}{\mu_2}$, respectively. During normal service, customers may become impatient and leave the system at an exponential rate γ. However, once the fast mode is activated, no further customer abandonment occurs due to impatience.

3.1. Notations

1. $\mathscr{P}(A)$: Probability of event A.
2. $\pi_n = \lim_{t\to\infty} p_n(t)$: Steady state probability of n customers in the system.
3. $\int_0^t f(u)g(t-u)\,\mathrm{d}u$: Convolution of $f(t)$ and $g(t)$ in Laplace Transform.
4. $\int_0^\infty e^{-st}f(t)\,\mathrm{d}t = f^*(s)$: Laplace transform of $f(t)$.

4. Governing equations

Let $\{X(t); t > 0\}$ be the number of customers present in the system at time t, we denote the probability that there are n customers in the system at time t.$P_n(t) = \Pr\{X(t) = n\}, n = 0, 1, 2, \ldots$

Below differential-difference equations are used to govern the system:
By applying probabilistic laws, we have

$$p(0,t) = e^{-\lambda(1+\eta)t} + \mu_1 p(1,t)e^{-\lambda(1+\eta)t} \tag{1}$$

$$p(n,t) = \left[\frac{\lambda(1+\eta)}{n}p(n-1,t) + (\mu_1 + n\gamma)\,p(n+1,t)\right] e^{-((\lambda(1+\eta)+\mu_1+(n-1)\gamma)t}, \quad n = 1,2,\ldots,K-2 \tag{2}$$

$$p(K-1,t) = \left[\frac{\lambda(1+\eta)}{K-1}p(K-2,t) + \mu_2 p(K,t)\right] e^{-\left(\frac{\lambda(1+\eta)}{K}+\mu_1+(K-2)\gamma\right)t} \tag{3}$$

$$p(n,t) = \left[\frac{\lambda(1+\eta)}{n}p(n-1,t) + \mu_2 p(n+1,t)\right] e^{-\left(\frac{\lambda(1+\eta)}{K+1}+\mu_2\right)t}, n \geq K \tag{4}$$

Taking the Laplace transform of Equations 1-4, we get

$$(s+\lambda(1+\eta))p^*(0,s) = 1+\mu_1 p^*(1,s) \tag{5}$$

$$(s+(\lambda(1+\eta)+\mu_1+(n-1)\gamma)\,p^*(n,s) = \frac{\lambda(1+\eta)}{n}p^*(n-1,s)+(\mu_1+n\gamma)\,p^*(n+1,s),$$
$$n=1,2,\ldots,K-2 \tag{6}$$

$$\left(s+\frac{\lambda(1+\eta)}{K}+\mu_1+(K-2)\gamma\right)p^*(K-1,s) = \frac{\lambda(1+\eta)}{K-1}p^*(K-2,s)+\mu_2 p^*(K,s) \tag{7}$$

$$(s+(\lambda(1+\eta)+\mu_2)\,p^*(n,s) = \frac{\lambda(1+\eta)}{n}p^*(n-1,s)+\mu_2 p^*(n+1,s), n\geq K \tag{8}$$

5. Steady state probabilities

Taking $\lim_{t\to\infty} p_n(t) = \pi_n$ and therefore $\frac{\mathrm{d}p_n}{\mathrm{d}t} = 0$ as $t\to\infty$, hence we get balance equations,

$$\lambda(1+\eta)\pi_0 = \mu_1\pi_1 \tag{9}$$

$$((\lambda(1+\eta)+\mu_1+(n-1)\gamma)\,\pi_n = \frac{\lambda(1+\eta)}{n}\pi_{n-1}+(\mu_1+n\gamma)\,\pi_{n+1}, 1\leq n\leq K-2 \tag{10}$$

$$\left(\frac{\lambda(1+\eta)}{K}+\mu_1+(K-2)\gamma\right)\pi_{K-1} = \frac{\lambda(1+\eta)}{K-1}\pi_{K-2}+\mu_2\pi_K \tag{11}$$

$$((\lambda(1+\eta)+\mu_2)\,\pi_n = \frac{\lambda(1+\eta)}{n}\pi_{n-1}+\mu_2\pi_{n+1}, n\geq K \tag{12}$$

By an iterative procedure, equations from 9-12, yield

$$\pi_n = \begin{cases} \Pi_{r=1}^{n}\left[\frac{\lambda(1+\eta)}{r(\mu_1+(r-1)\gamma)}\right]\pi_0, & 1\leq n\leq K-1 \\ \left[\left(\frac{\lambda(1+\eta)}{\mu_2}\right)^{n-K+1}\frac{1}{(K)_{n-K+1}}\right]\Pi_{r=1}^{K-1}\left[\frac{\lambda(1+\eta)}{r(\mu_1+(r-1)\gamma)}\right]\pi_0, & n\geq K \end{cases} \tag{13}$$

where $(K)_i = K(K+1)(K+2)\cdots(K+i-1)$.
By using the total probability law, we get

$$\pi_0 = \left[1+\sum_{n=1}^{K-1}\prod_{r=1}^{n}\left(\frac{\lambda(1+\eta)}{r\,(\mu_1+(r-1)\gamma)}\right) + \sum_{n=K}^{\infty}\left(\left(\frac{\lambda(1+\eta)}{\mu_2}\right)^{n-K+1}\frac{1}{(K)_{n-K+1}}\right)\prod_{r=1}^{K-1}\left(\frac{\lambda(1+\eta)}{r\,(\mu_1+(r-1)\gamma)}\right)\right]^{-1} \tag{14}$$

Hence, the probabilities for the system's steady states for each state are established explicitly.

5.1. Special case

1. When $\gamma = 0$, this model reduces encouraged Arrivals and Self-Regulatory Servers in the Markovian Queueing System

$$\pi_n = \begin{cases} \frac{1}{n!}r_1^n\pi_0, & 1\leq n\leq K-1 \\ \frac{1}{n!}r_1^{K-1}r_2^{n-K+1}\pi_0, & n\geq K \end{cases} \tag{15}$$

$$\pi_0 = \left[1+\sum_{n=1}^{K-1}\frac{1}{n!}r_1^n+\left(\frac{r_1}{r_2}\right)^{K-1}\left\{e^{r_2}-\sum_{n=0}^{K-1}\frac{r_2^n}{n!}\right\}\right]^{-1} \tag{16}$$

where $r_1 = \frac{\lambda(1+\eta)}{\mu_1}$ and $r_2 = \frac{\lambda(1+\eta)}{\mu_2}$.

2. When there is no discouragement, no impatience and no server switch, then Equations (15) and (16) becomes

$$\pi_n = \left(\frac{\lambda(1+\eta)}{\mu}\right)^n \pi_0$$

And $\pi_0 = 1 - \frac{\lambda(1+\eta)}{\mu}$.

Hence, proved that the model will be reduced to a simple M/M/1/∞ queueing model.

6. Stationary measures of effectiveness

6.1. Expected number of customers in the system

The average number of customers in the system is denoted by L_s. In an $M/M/1$ queue, this measure helps evaluate overall system performance. Understanding L_s allows us to assess whether the server is operating efficiently or if the system is becoming congested.

$$L_s = \sum_{n=0}^{\infty} n\pi_n = \sum_{n=1}^{K-1} n\pi_n + \sum_{n=K}^{\infty} n\pi_n$$

$$\begin{aligned} L_s = \Bigg[& \sum_{n=1}^{K-1} n \prod_{r=1}^{n} \left(\frac{\lambda(1+\eta)}{r\,(\mu_1 + (r-1)\gamma)}\right) \pi_0 \\ & + \sum_{n=K}^{\infty} n \left(\left(\frac{\lambda(1+\eta)}{\mu_2}\right)^{n-K+1} \frac{1}{(K)_{n-K+1}} \right) \prod_{r=1}^{K-1} \left(\frac{\lambda(1+\eta)}{r\,(\mu_1 + (r-1)\gamma)}\right) \pi_0 \Bigg] \end{aligned} \tag{17}$$

6.2. Expected number of customers in the queue

Let the average number of customers in the queue be denoted by L_q. This metric provides valuable insights into the system's efficiency. A high value of L_q indicates potential system overload, resulting in longer wait times and increased customer dissatisfaction.

$$L_q = L_s\,(1 - \pi_0)$$

$$\begin{aligned} L_q = \Bigg[& \sum_{n=1}^{K-1} n \prod_{r=1}^{n} \left(\frac{\lambda(1+\eta)}{r\,(\mu_1 + (r-1)\gamma)}\right) \pi_0 \\ & + \sum_{n=K}^{\infty} n \left(\left(\frac{\lambda(1+\eta)}{\mu_2}\right)^{n-K+1} \frac{1}{(K)_{n-K+1}} \right) \prod_{r=1}^{K-1} \left(\frac{\lambda(1+\eta)}{r\,(\mu_1 + (r-1)\gamma)}\right) \pi_0 \Bigg] - 1 + \pi_0 \end{aligned} \tag{18}$$

6.3. Average impatience rate

The expected number of customers who leave the system due to impatience is denoted by $E[I]$. This metric quantifies the likelihood of customers abandoning the queue before receiving service, particularly in scenarios where prolonged waiting times influence customer behavior.

$$E[I] = \gamma \sum_{n=1}^{K-1} n\pi_n = \gamma \sum_{n=1}^{K-1} n \Pi_{r=1}^{n} \left[\frac{\lambda(1+\eta)}{r\,(\mu_1 + (r-1)\gamma)}\right] \pi_0 \tag{19}$$

7. Numerical illustration

7.1. Mean count of the customers arriving in the system and queue (L_s & L_q)

Take the values of parameters are $\lambda(1+\eta) = 16.5; \mu_1 = 20; \mu_2 = 30; K = 20$ and varying π_n from 0.1 to 1.0, determining the expected count of customers arriving in the system and queue for state probabilities. Table 1 has the values and Figure 1 depicts the variation:

Table 1: *Mean count of the customers arriving in the system and queue (L_s & L_q)*

π_n	L_s	π_n	L_q
0.1	1.4785	0.6	1.1860
0.2	1.6813	0.7	1.2283
0.3	1.7236	0.8	1.2331
0.4	1.7284	0.9	1.2334
0.5	1.7287	1.0	1.2335
0.6	1.7287	0.6	1.2335
0.7	1.7287	0.7	1.2335
0.8	1.7287	0.8	1.2335
0.9	1.7287	0.9	1.2335
1.0	1.7287	1.0	1.2335

Table 1 and demonstrate that as the state probability π_n increases from 0.1 to 1.0, the expected number of customers in the system L_s increases initially and gradually stabilizes around 1.7287 from $\pi_n = 0.5$ onward. Similarly, the expected number of customers in the queue L_q increases and then levels off around 1.2335 from $\pi_n = 0.6$ onward. This behavior indicates that beyond a certain arrival probability, the system reaches a saturation point where additional increases in π_n do not significantly affect system congestion. This suggests efficient server utilization and improved queue stability under higher arrival intensities.

7.2. Mean Count of Customers in the System Against γ

Assume $\lambda(1+\eta) = 16.5$, $\mu_1 = 20$, $\mu_2 = 30$, $K = 20$ and γ varying from 1 to 10. The system's mean customer count is calculated using steady-state probabilities. The table 2 presents the results.

Table 2: *Mean count of customer arrivals in the system L_s*

γ	L_s	γ	L_s
1	1.82490	6	1.74812
2	1.80444	7	1.73792
3	1.78724	8	1.72872
4	1.77245	9	1.72040
5	1.75954	10	1.71280

7.3. Mean Count of Customers in the System against γ

Assume $\lambda(1+\eta) = 16.5$, $\mu_1 = 20$, $\mu_2 = 30$ and $K = 20$, with γ varying from 1 to 10. The mean number of customers in the system, L_s, is presented in Table 3

Table 3: *Mean count of customer arrivals in the system L_s*

γ	L_s	γ	L_s
1	1.8249	6	1.74812
2	1.80444	7	1.73792
3	1.78724	8	1.72872
4	1.77245	9	1.7204
5	1.75954	10	1.7128

Table 3 and show that as γ increases from 1 to 10, the average number of customers in the system L_s gradually decreases from 1.8249 to 1.7128. This trend indicates improved system performance and reduced congestion with higher γ values. However, the rate of decrease slows down at higher values of γ, suggesting diminishing returns beyond a certain point. An optimal range of $\gamma = 6$ to 8 appears to balance efficiency and stability, offering effective queue management without excessive resource adjustment.

8. Sensitivity Analysis

We have investigated the behavior of the customers who are expected to be in the queue and the system based on different switch point values K through the sensitivity analysis presented in Table 4. From the table, it is evident that an increase in the switch point value K results in encouraged arrivals and impatient customers in a single-server system. The self-switching server tends to behave like a single server model with encouraged arrivals and impatient customers, without switching the server mode.

Table 4: *Sensitivity Analysis*

K	π_0	L_s	L_q
2	0.6068	1.7267	1.2335
3	0.6028	1.7392	1.2419
4	0.6044	1.7312	1.2355
5	0.6047	1.7290	1.2337
6	0.6047	1.7288	1.2335
7	0.6047	1.7287	1.2335
8	0.6047	1.7287	1.2335

From Table 4, we observe that when $K \geq 5$, the steady-state probability π_0 stabilizes at 0.6047. Similarly, for $K \geq 6$, the average number of customers in the system L_s remains nearly constant at approximately 1.7287 and the average queue length L_q stabilizes at around 1.2335. These results indicate that as the switch point K increases, its influence on system performance metrics becomes negligible beyond a certain threshold, suggesting diminishing sensitivity to further increases in K.

9. Conclusions

This paper presents a comprehensive analysis of a Markovian queueing system with a single self-switching server, subject to encouraged arrivals, customer impatience and server switching dynamics. The study examines the complex interactions among various system behaviors, including a customer arrival rate that is inversely proportional to the queue length, customer impatience leading to abandonment and the switching of server modes from a normal service rate to a faster one when the queue reaches a predefined threshold. The findings demonstrate that the incorporation of encouraged arrivals, customer impatience and a self-switching server

significantly affects system performance metrics such as waiting times, queue lengths and the probability of customer abandonment. Notably, transitioning to a faster service mode once the queue exceeds a threshold improves service delivery and reduces the negative impact of customer impatience.

References

[1] Haight F. A. (1959) Queueing with reneging. *Metrika* 2(1): 186–197.
[2] Som, B. K. and Seth, S. (2017). An $M/M/1/N$ queuing system with encouraged arrivals. *Global Journal of Pure and Applied Mathematics* 13(7): 3443–3453.
[3] Khan, I. E. and Paramasivam, R. (2022). Reduction in waiting time in an $M/M/1/N$ encouraged-arrival queue with feedback, balking and retained reneged customers. *Symmetry* 14(8).
[4] Som B. K, Seth S. (2021) An $M/M/C/N$ feedback queuing system with encouraged arrivals, reverse reneging and retention of reneged customers. *Lloyd Business Review* 1(1): 26–30.
[5] Pravina D.C. T, Viswanath J, Sreelakshmi S and Sharmada U. (2021) Performance analysis of an $M/M/1$ queue with a server in differentiated phase subject to customer impatience. *International Journal of Mechanical Engineering* 7(4): 13–21.
[6] Jain M, Singh P. (2002) $M/M/m$ queue with balking, reneging and additional servers. *International Journal of Engineering* 15(2): 129–136.
[7] Krishnakumar B, Anbarasu S and Lakshmi S.R. A. Performance analysis for queueing systems with close down periods and server under maintenance. *International Journal of Systems Science* 46(1): 88–110.
[8] Udayabaskaran S and Pravina D.C. T.(2017) Transient analysis of an $M/M/1$ queueing system with server operating in three modes. *Far East Journal of Mathematical Sciences* 101(7): 1395–1418.
[9] Wang K, Li. N and Jiang Z.(2010) Queueing system with impatient customers: A review. *International Conference on Service Operations and Logistics and Informatics* Qingdao.
[10] Yang D. Y and Wu Y. Y.(2017) Analysis of a finite-capacity system with working breakdowns and retention of impatient customers. *Journal of Manufacturing Systems* 44: 207–216.
[11] Immaculate S. and Rajendran, P. (2024) Analysis of the Economic Cost of Coxian-2 Service with Encouraged Arrival and Balking. *International Journal of Analysis and Applications* 22: 41–41.
[12] Immaculate, S, Rajendran, P, IsmailKhan, E. and Jeyachandhiran, R. (2024) Optimizing Performance Measures in a Finite Markovian Heterogeneous Queueing Model with Encouraged Arrival. *In International Conference on Nonlinear Dynamics and Applications* 669–681
[13] Immaculate, S. and Rajendran, p (2023) The Application of Queueing Theory for Maximizing System Size using Encouraged Arrival. *Reliability: Theory & Applications* 18(2(73)):233–243.

A STATISTICAL ANALYSIS OF FUZZY CONFOUNDING FACTORIAL EXPERIMENTS

P. Sri Devi[1,*], Dr. S. N. Manoharan[2], Mr. T. Karthikeyan[3], D. Pachiyappan[4]

•

[1] Kavery Arts and Science College, Salem, Tamil Nadu, India.
Correspondances Mail : sridevista@periyaruniversity.ac.in
[2] Department of Computer Science and Engineering, Vel Tech Rangarajan Dr. Sagunthala R&D Institute of Science and Technology, Avadi, Tamil Nadu, India.
[3] Assistant Professor, Department of Computer Science and Business Systems, Panimalar Engineering College, Chennai 600123, Tamil Nadu, India, India.
[4] Department of Mathematics, Vel Tech Rangarajan Dr. Sagunthala R&D Institute of Science and Technology, Avadi, Tamil Nadu, India.

Abstract

The factorial experiment is used to test more than one factor at a time, whereas simple experiments can test only one factor at a time. The technique of reducing the block size by making one or more interaction contrast identical to block contrast is known as confounding. Only the higher-order interactions are confounded in factorial experiments, and the interaction effects have been confounded within the blocks. This article proposes that confounding design is performed with Latin squares with trapezoidal fuzzy numbers (TrFNs). In order to obtain an unbiased estimate of an error from a Latin square, the rows and columns must be rearranged in random order. Finally, we provide numerical example to clarify the discussions.

Keywords: Latin Square Design, Trapezoidal Fuzzy Number, α-cut interval method, Symmetrical Factorial Experiments, Confounding, Partial Confounding.

I. Introduction

Factorial experiments are experiments which include several factors or different sets of treatments at different levels. It is classified into two types: complete and partial confounding. Confounding the same interactions in different replications is complete confounding, and confounding different interactions for different replications is partial confounding. In certain cases, the confounding adapts Latin square designs. For instance, a 2^4factorial involves 16 combinations, which can be arranged in 8×8 Latin square. Treatment combinations can also be arranged in the type of Latin square, since the interactions of no interest are confounded with columns and rows of Latin square.

Sometimes, the day-to-day situations deal with imprecise data. In that situation, fuzzy plays a vital role. Some of the authors scrutinized to the relevant study are: Cotter, S.C., (1974) shows that which component for the sum of squares is confounded with blocks by considering the problem of m^n factorial experiment with block of size m^l. Cotter, S.C., (1975) developed the method of partial confounding which combines confounding and incomplete block design, since some are totally and some are partially confounded. Jalil, M.A., (2012) constructed a simultaneous confounding in p^n (p is prime) factorial experiment confounded with a single factorial effect by

using a matrix method. In factorial Ahmed, L.A., (2016) compares the result among confounding and fractional replicated design by using 2^4 factorial experiment in RCBD with 4 blocks layout. By using fuzzy environments, Parthiban, S and Gajivaradhan, P (2016) proposed the study of LSD with three factor ANOVA test. Parthiban, S and Gajivaradhan, P (2016) describes the 2^2 factorial experiment using fuzzy environments and compared the result with various tests. Without replications Akra, U.P., (2017) confounded 2^5 factorial experiments for different block sizes like 2, 3 and 8 to minimize the error. When $k > 2$, Eze, F.C., (2019) considers the selection of confounding, as it depends on size, blocks and factors. Sri Devi, P. and Pachamuthu, M., (2022) constructed fuzzy complete confounding for vague data. This article proposes that confounding design is performed with Latin squares using α -cut interval method of TrFNs.

II. Preliminaries

I. Fuzzy Set

A fuzzy set $\widetilde{A}$ is defined as the set of ordered pairs and it is denoted $\widetilde{A} = \{x, \mu_{\widetilde{A}}(x) | x \in X\}$ where, $\mu_{\widetilde{A}}(x)$ - membership function of $\widetilde{A}$.

II. Trapezoidal Fuzzy Number (TFN)

The TFN is defined as if a fuzzy set$\widetilde{A} = (a_1, a_2, a_3, a_4)$, then its membership function is defined as;

$$\mu_{\widetilde{A}}(x) = \begin{cases} 0; x < a_1 \text{or} x > a_4 \\ \dfrac{x - a_1}{a_2 - a_1}; a_1 < x \leq a_2 \\ 1; a_2 < x \leq a_3 \\ \dfrac{a_4 - x}{a_4 - a_3}; a_3 < x \leq a_4 \end{cases} \quad (1)$$

where, $a_1 \leq a_2 \leq a_3 \leq a_4$. A trapezoidal fuzzy number becomes triangular fuzzy number if it satisfies$a_2 = a_3$. In terms of α −cut interval, TrFN is defined as

$$\widetilde{A} = [a_1 + (a_2 - a_1)\alpha, a_4 - (a_4 - a_3)\alpha]; 0 \leq \alpha \leq 1 (2).$$

III. Methodology

I. A Statistical analysis on Partial Confounding of 2^3Factorial Design in two 4×4 LSD with α −Cut Interval Method

The 2^3 partial confounding factorial experiment can be arranged in blocks of 4 plots in such a way that confounding treatments with 2 degrees of freedom (df). In this 4×4 Latin square, considering rows as blocks with 1 df and considering columns as blocks with 1 df. To get an adequate estimate of error, atleast 2 replicates are needed. It may be completely confounded with 2 df or partially with 4 df or partially with 2 df and completely with 1 df. The 2^3partial confounding factorial experiment is formulated in two 4×4 Latin squares and the linear model is defined as,

$$y_{ijk} = \mu + s_i + r_{ij} + c_{ik} + t_l + e_{ijkl}; i = 1,2; j = 1,2, \ldots, m; k, l = 1,2, \ldots, n (3)$$

Where y_{ijk} is the observation corresponding to i^{th}square, j^{th}row, k^{th}column, l^{th}treatment. If the sample observations are in the form of TrFNs, then the 2^3partial confounding factorial model is

converted into interval 2^3partial confounding factorial model using relation (2), which is rewritten as,

$$\tilde{y}_{ijk} = \left[a_{ijk} + \alpha\left(b_{ijk} - a_{ijk}\right), d_{ijk} - \alpha\left(d_{ijk} - c_{ijk}\right)\right]; i = 1,2; j = 1,2,\ldots, m; k, l = 1,2,\ldots, n \quad (4)$$

Where $\tilde{y}_{ijk}$ is the observation corresponding to i^{th}square, j^{th}row, k^{th}column, l^{th}treatment in the interval observations and split this expression into lower and upper levels as,

$$L = \tilde{y}^{L}_{ijk} = a_{ijk} + \alpha\left(b_{ijk} - a_{ijk}\right) \text{ and } U = \tilde{y}^{U}_{ijk} = d_{ijk} - \alpha\left(d_{ijk} - c_{ijk}\right).$$

Hypothesis: null hypothesis $\tilde{H}_0: \tilde{\mu}_1 = \tilde{\mu}_2 = \ldots = \tilde{\mu}_n$ against alternative hypothesis $\tilde{H}_1: \tilde{\mu}_1 \neq \tilde{\mu}_2 \neq \ldots \neq \tilde{\mu}_n$. The crisp hypothesis can be turned as fuzzy hypothesis for both lower and upper levels as, $\left[\tilde{H}^{L}_0, \tilde{H}^{U}_0\right]: [\tilde{\mu}^{L}_1, \tilde{\mu}^{U}_1] = [\tilde{\mu}^{L}_2, \tilde{\mu}^{U}_2] = \ldots = [\tilde{\mu}^{L}_n, \tilde{\mu}^{U}_n]$ against $\left[\tilde{H}^{L}_1, \tilde{H}^{U}_1\right]: [\tilde{\mu}^{L}_1, \tilde{\mu}^{U}_1] \neq [\tilde{\mu}^{L}_2, \tilde{\mu}^{U}_2] \neq \ldots \neq [\tilde{\mu}^{L}_n, \tilde{\mu}^{U}_n]$. Yates' introduced a computational procedure for calculating main effects and interactions (Yates, 1937) of factorial experiment. The expression (linear contrast) for various main effects and interactions are obtained as (Sri Devi, P., 2022),

$$A = [a] - [1] + [ab] - [c] - [b] - [bc] + [ac] + [abc]; B = [b] - [1] + [ab] + [bc] - [a] + [abc] - [ac] - [c]; C = [ac] + [c] + [abc] + [bc] - [1] - [b] - [a] - [ab]; AB = [1] - [a] - [b] + [ab] - [bc] + [abc] + [c] - [ac]; AC = [abc] + [ac] - [c] - [bc] + [1] - [a] - [ab] + [b]; BC = [ab] + [abc] - [ac] - [c] - [b] + [bc] - [a] - [1]; ABC = [a] - [ac] - [bc] + [c] + [b] - [ab] + [abc] - [1].$$

Table 1: *ANOVA table for* 2^3 *partial confounding factorial design in two* 4×4 *Latin squares of L.L.M*

Sources of Variation	Degrees of Freedom	Sum of Squares	Mean Sum of Squares	F-Ratio
Square	$(n-7)$	SS^{L}_{Squ}	$M^{L}_{Squ} = \frac{SS^{L}_{Squ}}{(n-7)}$	$F^{L}_{Squ} = \frac{M^{L}_{Squ}}{M^{L}_{E}}$
Row	$(n-2)$	SS^{L}_{Row}	$M^{L}_{Row} = \frac{SS^{L}_{Row}}{(n-2)}$	$F^{L}_{Row} = \frac{M^{L}_{Row}}{M^{L}_{E}}$
Column	$(n-2)$	SS^{L}_{Col}	$M^{L}_{Col} = \frac{SS^{L}_{Col}}{(n-2)}$	$F^{L}_{Col} = \frac{M^{L}_{Col}}{M^{L}_{E}}$
Treatment	$(n-3)$	SS^{L}_{Treat}	$M^{L}_{Treat} = \frac{SS^{L}_{Treat}}{(n-3)}$	$F^{L}_{Treat} = \frac{M^{L}_{Treat}}{M^{L}_{E}}$
Main Effect$A$	1	SS^{L}_{A}	$M^{L}_{A} = \frac{SS^{L}_{A}}{(n-3)}$	$F^{L}_{A} = \frac{M^{L}_{A}}{M^{L}_{E}}$
Main Effect$B$	1	SS^{L}_{B}	$M^{L}_{B} = \frac{SS^{L}_{B}}{(n-3)}$	$F^{L}_{B} = \frac{M^{L}_{B}}{M^{L}_{E}}$
Main Effect$C$	1	SS^{L}_{C}	$M^{L}_{C} = \frac{SS^{L}_{C}}{(n-3)}$	$F^{L}_{C} = \frac{M^{L}_{C}}{M^{L}_{E}}$
Interaction Effect AB	1	SS^{L}_{AB}	$M^{L}_{AB} = \frac{SS^{L}_{AB}}{(n-3)}$	$F^{L}_{AB} = \frac{M^{L}_{AB}}{M^{L}_{E}}$
Interaction Effect AC	1	SS^{L}_{AC}	$M^{L}_{AC} = \frac{SS^{L}_{AC}}{(n-3)}$	$F^{L}_{AC} = \frac{M^{L}_{AC}}{M^{L}_{E}}$
Interaction Effect BC	1	SS^{L}_{BC}	$M^{L}_{BC} = \frac{SS^{L}_{BC}}{(n-3)}$	$F^{L}_{BC} = \frac{M^{L}_{BC}}{M^{L}_{E}}$
Interaction Effect ABC	1	SS^{L}_{ABC}	$M^{L}_{ABC} = \frac{SS^{L}_{ABC}}{(n-3)}$	$F^{L}_{ABC} = \frac{M^{L}_{ABC}}{M^{L}_{E}}$
Error	$(nm-4n+13)$	SS^{L}_{E}	$M^{L}_{E} = \frac{SS^{L}_{E}}{(nm-4n+13)}$	-
Total	$(nm-1)$	SS^{L}_{T}	-	-

The sum of squares for squares, rows, columns, treatments, main effects and interactions are calculated as follows,

Lower Level Model (L.L.M): Let $\tilde{x}^{L}_{i..} = \sum_{i=1}^{2}[a_{i..} + \alpha(b_{i..} - a_{i..})] = S^{L}_{i}$; $\tilde{x}^{L}_{ij.} = \sum_{i=1}^{2}\sum_{k=1}^{n}[a_{ij.} + \alpha(b_{ij.} - a_{ij.})] = \sum_{i=1}^{2}\sum_{k=1}^{m}[a_{ij.} + \alpha(b_{ij.} - a_{ij.})] + \sum_{i=1}^{2}\sum_{k=m+1}^{n}[a_{ij.} + \alpha(b_{ij.} - a_{ij.})]$.

R^{L}_{ij}; $\bar{x}^{L}_{i.k} = \sum_{i=1}^{2}\sum_{j=1}^{m}\left[a_{i.k} + \alpha\left(b_{i.k} - a_{i.k}\right)\right] = C^{L}_{ik}$; $\tilde{x}^{L}_{..k}$ =sum of all $[a_{ijk} + \alpha(b_{ijk} - a_{ijk})]$ receiving l^{th} treatment = T^{L}_{l} (since, it is the square of unconfounded effects).

The sum of squares are calculated as follows: $SS^{L}_{Squ} = \frac{\sum_{i=1}^{2}(S^{L}_{i})^{2}}{m^{2}} - \frac{(G^{L})^{2}}{N}$with $(n-7)$ df; $SS^{L}_{Row} = \frac{\sum_{i=1}^{2}\sum_{j=1}^{m}[R^{L}_{ij}]^{2}}{m} - \frac{[G^{L}]^{2}}{N}$ with $(n-2)$ df; $SS^{L}_{Col} = \frac{\sum_{i=1}^{2}\sum_{k=1}^{n}[C^{L}_{ik}]^{2}}{m} - \frac{[G^{L}]^{2}}{N}$ with $(n-2)$ df; $SS^{L}_{Treat} = \frac{\sum_{l=1}^{n}[T^{L}_{l}]^{2}}{N}$ with $(n-3)$ df; $SS^{L}_{T} = \sum_{i=1}^{2}\sum_{j=1}^{m}\sum_{k=1}^{n}(x^{L}_{ijk})^{2} - \frac{[G^{L}]^{2}}{N}$ with $(nm-1)$ df; $SS^{L}_{A} = \frac{[A^{2}]^{L}}{N}$; $SS^{L}_{B} = \frac{[B^{2}]^{L}}{N}$; $SS^{L}_{C} = \frac{[C^{2}]^{L}}{N}$; $SS^{L}_{AB} = \frac{[(AB)^{2}]^{L}}{N}$; $SS^{L}_{AC} = \frac{[(AC)^{2}]^{L}}{N}$; $SS^{L}_{BC} = \frac{[(BC)^{2}]^{L}}{N}$ and $SS^{L}_{ABC} = \frac{[(ABC)^{2}]^{L}}{N}$ with 1 df. $SS^{L}_{E} = SS^{L}_{T} - [SS^{L}_{Square} + SS^{L}_{Row} + SS^{L}_{Col} + SS^{L}_{T} + SS^{L}_{A} + SS^{L}_{B} + SS^{L}_{C} + SS^{L}_{Interactions}]$ with $(nm-4n+13)$df; where, $N = mn$, $G^{L} = \sum_{i=1}^{2}\sum_{j=1}^{m}\sum_{k=1}^{n}x^{L}_{ijk}$, $SS^{L}_{Interactions} = SS^{L}_{AB} + SS^{L}_{AC} + SS^{L}_{BC} + SS^{L}_{ABC}$ (omit the effects which is confounded). All these calculated values are presented in the table 1.

Table 2: *ANOVA table for* 2^3 *partial confounding factorial design in two* 4×4 *Latin squares of U.L.M*

Sources of Variation	Degrees of Freedom	Sum of Squares	Mean Sum of Squares	F-Ratio
Square	$(n-7)$	SS^{U}_{Squ}	$M^{U}_{Squ} = \frac{SS^{U}_{Squ}}{(n-7)}$	$F^{U}_{Squ} = \frac{M^{U}_{Squ}}{M^{U}_{E}}$
Row	$(n-2)$	SS^{U}_{Row}	$M^{U}_{Row} = \frac{SS^{U}_{Row}}{(n-2)}$	$F^{U}_{Row} = \frac{M^{U}_{Row}}{M^{U}_{E}}$
Column	$(n-2)$	SS^{U}_{Col}	$M^{U}_{Col} = \frac{SS^{U}_{Col}}{(n-2)}$	$F^{U}_{Col} = \frac{M^{U}_{Col}}{M^{U}_{E}}$
Treatment	$(n-3)$	SS^{U}_{Treat}	$M^{U}_{Treat} = \frac{SS^{U}_{Treat}}{(n-3)}$	$F^{U}_{Treat} = \frac{M^{U}_{Treat}}{M^{U}_{E}}$
Main Effect$A$	1	SS^{U}_{A}	$M^{U}_{A} = \frac{SS^{U}_{A}}{(n-3)}$	$F^{U}_{A} = \frac{M^{U}_{A}}{M^{U}_{E}}$
Main Effect$B$	1	SS^{U}_{B}	$M^{U}_{B} = \frac{SS^{U}_{B}}{(n-3)}$	$F^{U}_{B} = \frac{M^{U}_{B}}{M^{U}_{E}}$
Main Effect$C$	1	SS^{U}_{C}	$M^{U}_{C} = \frac{SS^{U}_{C}}{(n-3)}$	$F^{U}_{C} = \frac{M^{U}_{C}}{M^{U}_{E}}$
Interaction Effect AB	1	SS^{U}_{AB}	$M^{U}_{AB} = \frac{SS^{U}_{AB}}{(n-3)}$	$F^{U}_{AB} = \frac{M^{U}_{AB}}{M^{U}_{E}}$
Interaction Effect AC	1	SS^{U}_{AC}	$M^{U}_{AC} = \frac{SS^{U}_{AC}}{(n-3)}$	$F^{U}_{AC} = \frac{M^{U}_{AC}}{M^{U}_{E}}$
Interaction Effect BC	1	SS^{U}_{BC}	$M^{U}_{BC} = \frac{SS^{U}_{BC}}{(n-3)}$	$F^{U}_{BC} = \frac{M^{U}_{BC}}{M^{U}_{E}}$
Interaction Effect ABC	1	SS^{U}_{ABC}	$M^{U}_{ABC} = \frac{SS^{U}_{ABC}}{(n-3)}$	$F^{U}_{ABC} = \frac{M^{U}_{ABC}}{M^{U}_{E}}$
Error	$(nm-4n+13)$	SS^{U}_{E}	$M^{U}_{E} = \frac{SS^{U}_{E}}{(nm-4n+13)}$	-
Total	$(nm-1)$	SS^{U}_{T}	-	-

The table 2 represents are Upper Level Model (U.L.M): Let $\tilde{x}_{i..}^{U} = \sum_{i=1}^{2}[d_{i..} - \alpha(d_{i..} - c_{i..})] = S_i^U$; $\bar{x}_{i..}^{U} = \sum_{i=1}^{2}\sum_{k=1}^{n}[d_{ij.} - \alpha(d_{ij.} - c_{ij.})] = \sum_{i=1}^{2}\sum_{k=1}^{m}[d_{i..} - \alpha(d_{i..} - c_{i..})] + \sum_{i=1}^{2}\sum_{k=m+1}^{n}[d_{i..} - \alpha(d_{i..} - c_{i..})] = R_{ij}^U$; $\bar{x}_{i.k}^{U} = \sum_{i=1}^{2}\sum_{j=1}^{m}\left[d_{i.k} - \alpha\left(d_{i.k} - c_{i.k}\right)\right] = C_{ik}^U$; $\bar{x}_{..k}^{U}$ =sum of all $[d_{ijk} - \alpha(d_{ijk} - c_{ijk})]$ receiving l^{th} treatment = T_l^U (since, it is the square of unconfounded effects).

The sum of squares are calculated as follows: $SS_{Squ}^U = \frac{\sum_{i=1}^{2}(S_i^U)^2}{m^2} - \frac{(G^U)^2}{N}$ with $(n-7)$ df; $SS_{Row}^U = \frac{\sum_{i=1}^{2}\sum_{j=1}^{m}[R_i^U]^2}{m} - \frac{[G^U]^2}{N}$ with $(n-2)$ df; $SS_{Col}^U = \frac{\sum_{i=1}^{2}\sum_{k=1}^{n}[C_{ik}^U]^2}{m} - \frac{[G^U]^2}{N}$ with $(n-2)$ df; $SS_{Treat}^U = \frac{\sum_{l=1}^{n}[T_l^2]^U}{N}$ with $(n-3)$ df; $SS_T^U = \sum_{i=1}^{2}\sum_{j=1}^{m}\sum_{k=1}^{n}(x_{ijk}^U)^2 - \frac{[G^U]^2}{N}$ with $(nm-1)$ df; $SS_A^U = \frac{[A^2]^U}{N}$; $SS_B^U = \frac{[B^2]^U}{N}$; $SS_C^U = \frac{[C^2]^U}{N}$; $SS_{AB}^U = \frac{[(AB)^2]^U}{N}$; $SS_{AC}^U = \frac{[(AC)^2]^U}{N}$; $SS_{BC}^U = \frac{[(BC)^2]^U}{N}$ and $SS_{ABC}^U = \frac{[(ABC)^2]^U}{N}$ with 1 df; $SS_E^U = SS_T^U - [SS_{Square}^U + SS_{Row}^U + SS_{Col}^U + SS_T^U + SS_A^U + SS_B^U + SS_C^U + SS_{Interactions}^U]$ with $(nm - 4n + 13)$df; where, $N = mn$, $G^U = \sum_{i=1}^{2}\sum_{j=1}^{m}\sum_{k=1}^{n}x_{ijk}^U$, $SS_{Interactions}^U = SS_{AB}^U + SS_{AC}^U + SS_{BC}^U + SS_{ABC}^U$ (omit the effects which is confounded). All these values are presented in the ANOVA table (table 2).

Decision Rule: Lower-Level Model: If $F_{(CalculatedValue)}^{L} < F_t$, then H_0^L is accepted. Otherwise, it is rejected. That is, there is no significant difference between treatments. Similarly, rows and columns can also be tested.

Upper-Level Model: If $F_{(CalculatedValue)}^{U} < F_t$, then H_0^U is accepted. Otherwise, it is rejected. That is, there is no significant difference between treatments. Similarly, rows and columns can also be tested.

Table 3: *Conclusion Table*

Null Hypothesis $\tilde{H}_0$		
L.L.M	U.L.M	Conclusion
$H_0^L$is accepted	H_0^U is accepted	$\tilde{H}_0$ is accepted
$H_0^L$is rejected	H_0^U is accepted	$\tilde{H}_0$ is rejected
H_0^L is accepted	H_0^U is rejected	$\tilde{H}_0$ is rejected
H_0^L is rejected	H_0^U is rejected	$\tilde{H}_0$ is accepted

IV. Applications

Example: The data given in the table 4 provides the barley grains yield. Three fertilizers used for cultivation are Urea (A), SSP (B) and Muriate of Potash (C). The observations are in the form trapezoidal fuzzy numbers, which are arranged in a superimposed Latinsquares. The problem is to examine whether the treatments differ significantly or not?

Table 4: *The yield of barley grain cultivation*

b (45,47,52, 54)	a (58,62,65, 68)	c (86,89,93, 97)	abc (55,58,61, 63)	c (49,52,53, 56)	ac (75,79,81, 82)	ab (67,69,72, 74)	b (75,76,79, 82)
ab (54,57,59, 61)	bc (73,77,79, 82)	ac (48,51,53, 54)	(1) (65,68,70, 73)	a (57,59,61, 63)	bc (92,94,95, 96)	(1) (86,89,93, 95)	abc (63,65,67, 69)
ac (75,77,79, 81)	(1) (94,95,96, 98)	ab (57,59,62, 64)	bc (63,67,69, 72)	abc (49,52,53, 54)	(1) (77,81,82, 85)	bc (46,48,51, 52)	a (84,85,88, 90)
c (91,94,95)	abc (43,45,47)	b (73,75,77)	a (67,69,71)	b (73,75,79)	ab (58,62,65)	ac (63,66,67)	c (46,49,52)

The conclusion table (Table 3) shows the overall result. For both L.L.M and U.L.M, the partial acceptance of $\widetilde{H}_0$ at the intersection of certain level can be taken as acceptance of $\widetilde{H}_0$.

Null Hypothesis $\widetilde{H}_0$: There is no significant difference between squares, rows, columns and treatments respectively. The converting the trapezoidal fuzzy observations into interval data as shown in table 5.

Lower-Level Model (L.L.M): There is no significant difference between squares, rows, columns and treatments respectively.

Null HypothesisH_0^L: The sum of squares of squares, row, column, treatments, main effects and interactions for L.L.M are calculated as follows: $SS_A^L = \frac{1}{32}(25921); SS_B^L = \frac{1}{32}(18225 + 1080\alpha + 16\alpha^2); SS_C^L = \frac{1}{32}(5329 - 1460\alpha + 100\alpha^2); SS_{AB}^L = \frac{1}{32}(729 - 324\alpha + 36\alpha^2); SS_{AC}^L = \frac{1}{32}(121 + 88\alpha + 16\alpha^2); SS_{Square}^L = \frac{1}{32}(169); SS_{Row}^L = \frac{1}{16}(13907 - 1850\alpha + 70\alpha^2); SS_{Col}^L = \frac{1}{16}(11795 + 382\alpha - 66\alpha^2); SS_{Treat} = \frac{1}{32}(50325 - 616\alpha + 168\alpha^2); SS_T^L = \frac{1}{32}(223239 - 6628\alpha + 924\alpha^2); SS_{Error}^L = \frac{1}{32}(121341 - 3076\alpha + 484\alpha^2)$

Between Squares: $F_{Square}^L = \frac{13(169)}{(121341-3076\alpha+484\alpha^2)} < 1; 0 \le \alpha \le 1$. Here, $F(1,13) = 3.14$and $F_{Square}^L < F(1,13)$.

Between Rows: $F_{Row}^L = \frac{13(13907-1850\alpha+70\alpha^2)}{3(121341-3076\alpha+484\alpha^2)} < 1; 0 \le \alpha \le 1$. Here, $F(6,13) = 2.28$ and $F_{Row}^L < F(6,13)$.

Table 5: *Converting Trapezoidal Observations to Interval Observations*

b	a	c	abc	c	ac	ab	b
$(45 + 2\alpha, 54 - 2\alpha)$	$(58 + 4\alpha, 68 - 3\alpha)$	$(86 + 3\alpha, 97 - 3\alpha)$	$(55 + 3\alpha, 63 - 2\alpha)$	$(49 + 4\alpha, 56 - 3\alpha)$	$(75 + 4\alpha, 82 - \alpha)$	$(67 + 2\alpha, 74 - 2\alpha)$	$(75 + \alpha, 82 - 3\alpha)$
ab	bc	ac	(1)	a	bc	(1)	abc
$(54 + 3\alpha, 61 - 2\alpha)$	$(73 + 4\alpha, 82 - 3\alpha)$	$(48 + 3\alpha, 54 - \alpha)$	$(65 + 3\alpha, 73 - 3\alpha)$	$(57 + 2\alpha, 63 - 2\alpha)$	$(92 + 2\alpha, 96 - \alpha)$	$(86 + 3\alpha, 95 - 2\alpha)$	$(63 + 2\alpha, 69 - 2\alpha)$
ac	(1)	ab	bc	abc	(1)	bc	a
$(75 + 2\alpha, 81 - 2\alpha)$	$(94 + \alpha, 98 - 2\alpha)$	$(57 + 2\alpha, 64 - 2\alpha)$	$(63 + 4\alpha, 72 - 3\alpha)$	$(49 + 4\alpha, 54 - \alpha)$	$(77 + 4\alpha, 85 - 3\alpha)$	$(46 + 2\alpha, 52 - \alpha)$	$(84 + \alpha, 90 - 2\alpha)$
c	abc	b	a	b	ab	ac	c
$(91 + 3\alpha, 97 - 2\alpha)$	$(43 + 2\alpha, 49 - 2\alpha)$	$(73 + 2\alpha, 79 - 2\alpha)$	$(67 + 2\alpha, 74 - 3\alpha)$	$(73 + 2\alpha, 81 - 3\alpha)$	$(58 + 4\alpha, 67 - 2\alpha)$	$(63 + 3\alpha, 69 - 2\alpha)$	$(46 + 3\alpha, 54 - 2\alpha)$

Between Columns: $F_{Col}^L = \frac{13(11795+382\alpha-66\alpha^2)}{3(121341-3076\alpha+484\alpha^2)} < 1; 0 \le \alpha \le 1$. Here, $F(6,13) = 2.28$ and $F_{Col}^L < F(6,13)$.

Between Treatments: $F_{Treat}^L = \frac{13(50325-616\alpha+168\alpha^2)}{5(121341-3076\alpha+484\alpha^2)} > 1; 0 \le \alpha \le 1$. Here, $F(5,13) = 2.35$ and $F_{Treat}^L < F(5,13)$.

Main Effect A: $F_A^L = \frac{13(25921)}{(121341-3076\alpha+484\alpha^2)}$; Here, $F(1,13) = 3.14$ and $F_A^L < F(1,13)$.

Main Effect B: $F_B^L = \frac{13(18225+1080\alpha+16\alpha^2)}{(121341-3076\alpha+484\alpha^2)}$; Here, $F(1,13) = 3.14$ and $F_B^L < F(1,13)$.

Main Effect C: $F_C^L = \frac{13(5329-1460\alpha+100\alpha^2)}{(121341-3076\alpha+484\alpha^2)}$; Here, $F(1,13) = 3.14$ and $F_C^L < F(1,13)$.

Interaction Effect AB: $F_{AB}^L = \frac{13(729-324\alpha+36\alpha^2)}{(121341-3076\alpha+484\alpha^2)}$; Here, $F(1,13) = 3.14$ and $F_{AB}^L < F(1,13)$.

Interaction Effect AC: $F_{AC}^L = \frac{13(121+88\alpha+16\alpha^2)}{(121341-3076\alpha+484\alpha^2)}$; Here, $F(1,13) = 3.14$ and $F_{AC}^L < F(1,13)$.

Table 4.3 indicate that a Inference: There is no significant difference between squares, rows, columns and treatments respectively.

Upper-Level Model (U.L.M): Null Hypothesis H_0^U: There is no significant difference between squares, rows, columns and treatments respectively.

The sum of squares of squares, row, column, treatments, main effects and interactions for U.L.M are calculated as follows

$SS_A^U = \frac{1}{32}(29241 - 2394\alpha + 49\alpha^2)$; $SS_B^U = \frac{1}{32}(18769 - 3288\alpha + 144\alpha^2)$; $SS_C^U = \frac{1}{32}(6561 -$

$1134\alpha + 49\alpha^2)$; $SS_{AB}^{U} = \frac{1}{32}(529 + 46\alpha + \alpha^2)$; $SS_{AC}^{U} = \frac{1}{32}(1 - 34\alpha + 289\alpha^2)$; $SS_{Square}^{U} = \frac{1}{32}(9 + 30\alpha + 25\alpha^2)$; $SS_{Row}^{U} = \frac{1}{16}(10751 + 388\alpha + 19\alpha^2)$; $SS_{Col}^{U} = \frac{1}{16}(12119 + 708\alpha + 43\alpha^2)$; $SS_{Treat}^{U} = \frac{1}{32}(55101 - 6804\alpha + 532\alpha^2)$; $SS_{T}^{U} = \frac{1}{32}(220831 - 4106\alpha + 455\alpha^2)$; $SS_{Error}^{U} = \frac{1}{32}(119981 + 476\alpha - 226\alpha^2)$

Table: 4.3 *Three factor ANOVA table for lower-level model*

S.V.	DF	S.S.	M.S.S.	F-Ratio
Squares	1	$\frac{1}{32}(169)$	$\frac{1}{32}(169)$	$\frac{13(169)}{(121341 - 3076\alpha + 484\alpha^2)} < 1;$ $0 \le \alpha \le 1.$
Row	6	$\frac{1}{16}(13907 - 1850\alpha + 70\alpha^2)$	$\frac{1}{16}(13907 - 1850\alpha + 70\alpha^2)$	$\frac{13(13907 - 1850\alpha + 70\alpha^2)}{3(121341 - 3076\alpha + 484\alpha^2)} < 1;$ $0 \le \alpha \le 1.$
Column	6	$\frac{1}{16}(11795 + 382\alpha - 66\alpha^2)$	$\frac{1}{16}(11795 + 382\alpha - 66\alpha^2)$	$\frac{13(11795 + 382\alpha - 66\alpha^2)}{3(121341 - 3076\alpha + 484\alpha^2)} < 1;$ $0 \le \alpha \le 1.$
Treatment	5	$\frac{1}{32}(50325 - 616\alpha + 168\alpha^2)$	$\frac{1}{32}(50325 - 616\alpha + 168\alpha^2)$	$\frac{13(50325 - 616\alpha + 168\alpha^2)}{5(121341 - 3076\alpha + 484\alpha^2)};$ $0 \le \alpha \le 1.$
Main Effect A	1	$\frac{1}{32}(25921)$	$\frac{1}{32}(25921)$	$\frac{13(25921)}{(121341 - 3076\alpha + 484\alpha^2)};$ $0 \le \alpha \le 1$
Main Effect B	1	$\frac{1}{32}(18225 + 1080\alpha + 16\alpha^2)$	$\frac{1}{32}(18225 + 1080\alpha + 16\alpha^2)$	$\frac{13(18225 + 1080\alpha + 16\alpha^2)}{(121341 - 3076\alpha + 484\alpha^2)};$ $0 \le \alpha \le 1$
Main Effect C	1	$\frac{1}{32}(5329 - 1460\alpha + 100\alpha^2)$	$\frac{1}{32}(5329 - 1460\alpha + 100\alpha^2)$	$\frac{13(5329 - 1460\alpha + 100\alpha^2)}{(121341 - 3076\alpha + 484\alpha^2)} < 1;$ $0 \le \alpha \le 1.$
Interaction Effect AB	1	$\frac{1}{32}(729 - 324\alpha + 36\alpha^2)$	$\frac{1}{32}(729 - 324\alpha + 36\alpha^2)$	$\frac{13(729 - 324\alpha + 36\alpha^2)}{(121341 - 3076\alpha + 484\alpha^2)} < 1;$ $0 \le \alpha \le 1$
Interaction Effect AC	1	$\frac{1}{32}(121 + 88\alpha + 16\alpha^2)$	$\frac{1}{32}(121 + 88\alpha + 16\alpha^2)$	$\frac{13(121 + 88\alpha + 16\alpha^2)}{(121341 - 3076\alpha + 484\alpha^2)} < 1;$ $0 \le \alpha \le 1$
Error	13	$\frac{1}{32}(121341 - 3076\alpha + 484\alpha^2)$	$\frac{1}{13(32)}(121341 - 3076\alpha + 484\alpha^2)$	-
Total	31	$\frac{1}{32}(223239 - 6628\alpha + 924\alpha^2)$	-	-

Between Squares: $F_{Square}^{U} = \frac{13(9+30\alpha+25\alpha^2)}{(119981+476\alpha-226\alpha^2)} < 1; 0 \le \alpha \le 1$. Here, $F(1,13) = 3.14$ and $F_{Square}^{U} < F(1,13)$.

Between Rows: $F^{U}_{Row} = \frac{13(10751+388\alpha+19\alpha^2)}{3(119981+476\alpha-226\alpha^2)} < 1; 0 \le \alpha \le 1$. Here, $F(6,13) = 2.28$ and $F^{U}_{Row} < F(6,13)$.

Between Columns: $F^{U}_{Col} = \frac{13(12119+708\alpha+43\alpha^2)}{3(119981+478\alpha-226\alpha^2)} < 1; 0 \le \alpha \le 1$. Here, $F(6,13) = 2.28$ and $F^{U}_{Col} < F(6,13)$.

Between Treatments: $F^{U}_{Treat} = \frac{13(55101-6804\alpha+532\alpha^2)}{5(119981+476\alpha-226\alpha^2)} > 1; 0 \le \alpha \le 1$. Here, $F(5,13) = 2.35$ and $F^{U}_{Treat} < F(5,13)$.

Main Effect A: $F^{U}_{A} = \frac{13(29241-2394\alpha+49\alpha^2)}{11981+476\alpha-226\alpha^2}$; Here, $F(1,13) = 3.14$ and $F^{U}_{A} > F(1,13)$.

Main Effect B: $F^{U}_{B} = \frac{13(18769-3288\alpha+144\alpha^2)}{11981+476\alpha-226\alpha^2}$; Here, $F(1,13) = 3.14$ and $F^{U}_{B} > F(1,13)$.

Main Effect C: $F^{U}_{C} = \frac{13(6561-1134\alpha+49\alpha^2)}{11981+476\alpha-226\alpha^2}$; Here, $F(1,13) = 3.14$ and $F^{U}_{C} > F(1,13)$.

Interaction Effect AB: $F^{U}_{AB} = \frac{13(529+46\alpha+\alpha^2)}{11981+476\alpha-226\alpha^2} < 1; 0 \le \alpha \le 1$. Here, $F(1,13) = 3.14$ and $F^{U}_{AB} < F(1,13)$.

Interaction Effect AC: $F^{U}_{AC} = \frac{13(1-34\alpha+289\alpha^2)}{11981+476\alpha-226\alpha^2} < 1; 0 \le \alpha \le 1$. Here, $F(1,13) = 3.14$ and $F^{U}_{AC} < F(1,13)$.

Table: 4.4 *Three factor ANOVA table for upper-level model*

S.V.	D.F.	S.S.	M.S.S.	F-Ratio
Squares	1	$\frac{1}{32}(9+30\alpha+25\alpha^2)$	$\frac{1}{32}(9+30\alpha+25\alpha^2)$	$\frac{13(9+30\alpha+25\alpha^2)}{(119981+476\alpha-226\alpha^2)} < 1;$ $0 \le \alpha \le 1.$
Row	6	$\frac{1}{16}(10751+388\alpha+19\alpha^2)$	$\frac{1}{6(16)}(10751+388\alpha+19\alpha^2)$	$\frac{13(10751+388\alpha+19\alpha^2)}{3(119981+476\alpha-226\alpha^2)} < 1;$ $0 \le \alpha \le 1.$
Column	6	$\frac{1}{16}(12119+708\alpha+43\alpha^2)$	$\frac{1}{6(16)}(12119+708\alpha+43\alpha^2)$	$\frac{13(12119+708\alpha+43\alpha^2)}{3(119981+478\alpha-226\alpha^2)} < 1;$ $0 \le \alpha \le 1.$
Treatment	5	$\frac{1}{32}(55101-6804\alpha+532\alpha^2)$	$\frac{1}{5(32)}(55101-6804\alpha+532\alpha^2)$	$\frac{13(55101-6804\alpha+532\alpha^2)}{5(119981+476\alpha-226\alpha^2)} > 1;$ $0 \le \alpha \le 1.$
Main Effect A	1	$\frac{1}{32}(29241-2394\alpha+49\alpha^2)$	$\frac{1}{32}(29241-2394\alpha+49\alpha^2)$	$\frac{13(29241-2394\alpha+49\alpha^2)}{11981+476\alpha-226\alpha^2}$
Main Effect B	1	$\frac{1}{32}(18769-3288\alpha+144\alpha^2)$	$\frac{1}{32}(18769-3288\alpha+144\alpha^2)$	$\frac{13(18769-3288\alpha+144\alpha^2)}{11981+476\alpha-226\alpha^2}$
Main Effect C	1	$\frac{1}{32}(6561-1134\alpha+49\alpha^2)$	$\frac{1}{32}(6561-1134\alpha+49\alpha^2)$	$\frac{13(6561-1134\alpha+49\alpha^2)}{11981+476\alpha-226\alpha^2}$
Interaction Effect AB	1	$\frac{1}{32}(529+46\alpha+\alpha^2)$	$\frac{1}{32}(529+46\alpha+\alpha^2)$	$\frac{13(529+46\alpha+\alpha^2)}{11981+476\alpha-226\alpha^2} < 1;$ $0 \le \alpha \le 1$
Interaction Effect AC	1	$\frac{1}{32}(1-34\alpha+289\alpha^2)$	$\frac{1}{32}(1-34\alpha+289\alpha^2)$	$\frac{13(1-34\alpha+289\alpha^2)}{11981+476\alpha-226\alpha^2} < 1;$ $0 \le \alpha \le 1$
Error	13	$\frac{1}{32}(119981+476\alpha-226\alpha^2)$	$\frac{1}{13(32)}(119981+476\alpha-226\alpha^2)$	-
Total	31	$\frac{1}{32}(220831-4106\alpha+455\alpha^2)$	-	-

Inference: There is no significant difference between squares, rows, columns and treatments except main effectsA, B, C respectively.

Finally, it is concluded that there is no significant difference between the fertilizers Urea (A), SSP (B) and Muriate of Potash (C).

V. Conclusion

In this article, the new methodology has been constructed for the fuzzy partial confounding factorial experiment. This can be widely used when the observations are vague. This work can further be to fractional factorial designs, asymmetrical factorial experiments and so on.

References

[1] Ahmed, L.A., (2016). Confounding and Fractional Replication in Factorial Design. *Mathematical Theory and Modeling*, 6(3), 17-31.

[2] Akra, U.P. and Edet, E.B., (2018). Confounding 2^k Factorial Design to Obtain Optimal Yield using Different Organic Manure *The Journal of Scientific and Engineering Research*, 4(11), 75-85.

[3] Bose, R.C. and Kishen, K., (1940). On the Problem of Confounding in the General Symmetrical Factorial Design. *Sankhya: The Indian Journal of Statistics (1933-1960),* 5(1), 21-36.

[4] Cotter, S.C., (1974). A General Method of Confounding for Symmetrical Factorial Experiments. *Journal of Royal Statistical Society. Series B (Methodological)*, 36(2), 267-276.

[5] Cotter, S.C., (1975). Partial confounding in Symmetrical Factorial Experiments. *Journal of Royal Statistical Society. Series B (Methodological)*, 37(1), 54-62.

[6] Eze, F.C., (2019). Choice of confounding in the 2^kfactorial Design in 2^bblocks. *Academic Journal of Applied Mathematical Sciences*, 5(5), 50-56.

[7] Hinkelmann, K. and Kempthorne, O., (2005). Design and Analysis of Experiments. Vol 2 Advanced Experimental Design, Wiley Interscience.

[8] Jalil, M.A., (2012), A General Construction Method of Simultaneous Confounding in p^n-Factorial Experiment. *Dhaka University Journal of Science*, 60(2), 265-270.

[9] Nair, K.R., (1938). On a Method of Getting Confounded Arrangements in the General Symmetrical Type of Experiment. *Sankhya: The Indian Journal of Statistics (1933-1960)*, 4(1), 121-138.

[10] Sri Devi, P. and Pachamuthu, M., (2022). A Statistical Analysis of Total Confounding for Factorial Experiments using Fuzzy Approach. *International Journal of Agricultural and Statistical Sciences*, 18(2), 653-665.

[11] Sri Devi, P. and Pachamuthu, M., (2022). A Statistical Analysis of Factorial Factorial Design using Fuzzy Probabilistic Approach. *International Journal of Agricultural and Statistical Sciences*, 18(2), 653-665.

[12] Yates, F. (1937). The Design and Analysis of Factorial Experiments, Imperial Bureau of Social Science, Technical communication no. 35.

INVESTIGATION OF THE APPLICATION OF THE NEW INDUCTION SYSTEM IN VERTICAL AXIS WIND GENERATORS

I.M. Marufov[1], N.M. Piriyeva[2], E.S. Safiyev[3]

•

Azerbaijan State Oil and Industry University, Baku, Azerbaijan
[1] marufov.ilkin@asoiu.edu.az; [2] naciba.piriyeva@asoiu.edu.az; [3] elshad.safiyev@asoiu.edu.az

Abstract

In recent scientific and technical literature, vertical axis wind generators based on magnetic levitation have demonstrated several advantages over traditional horizontal-axis wind turbines. However, despite these benefits, challenges remain in maximizing the output power, improving the overall performance, and ensuring the long-term reliability and stability of magnetically levitated wind generators. Existing levitation systems need further development to fully realize the potential of vertical axis designs. To address these challenges, a new controllable induction levitator was developed specifically to enhance magnetically levitated vertical axis wind generators. A detailed mathematical model of the controlled induction levitator was established, and the main physical dimensions were determined. The modeling approach employed principles of dimensional compatibility, dimensionless parameters, and generalized mathematical expressions to simplify the solution process. Based on this model, a methodology for parameter optimization was developed, alongside calculation procedures for key design variables. The mathematical model yielded explicit expressions for the levitation constant, the working air gap thickness, and the primary dimensions of the magnetic coil and its windings. These findings provide critical insights for optimizing levitator design and enhancing the performance, reliability, and stability of magnetic levitated vertical axis wind generators. The study confirms that the development of a controllable induction levitation system is essential for advancing vertical axis wind generator technology. The proposed model and optimization recommendations offer a robust foundation for improving levitation efficiency, increasing power output, and ensuring both operational stability and structural reliability. Further refinement and implementation of control induction supports are expected to significantly enhance the operational capabilities of magnetically levitated vertical axis wind generators.

Keywords: induction levitator, vertical axis wind generator, mathematical model, levitation constant, stability, reliability

I. Introduction

The nature of electric power systems, the places where At present, in the scientific and technical literature dedicated to vertical axis wind generators based on magnetic levitation, a number of advantages of such generators over traditional horizontal wind generators have been substantiated, and various methods have been developed to increase the output power of levitation wind generators. In these works, two fixed magnets and coils distributed around the magnets are used to create magnetic levitation. One of the magnets is kept stationary, and the other creates a magnetic force and keeps the sail rotating due to the influence of the wind in a state of levitation. The levitating magnetic force created by such a system is not large enough and does

not allow to adjust the height of levitation. On the other hand, since the output power of the generator is very small, it takes a lot of time to collect the received energy. Therefore, there is a need to create a new levitation system. Various sources of magnetic energy can be used to create levitation: the energy of permanent magnets with high magnetic induction, the magnetic energy created by constant current circuits and the energy of magnetic fields created by alternating current circuits. The positive and negative indicators of the levitation system built on the basis of permanent magnets are already known and shown above. Other levitation systems have not yet been applied to vertical axis wind generators. The results of theoretical and experimental studies of induction levitators (IL) built on the basis of alternating current loops show that a new levitation system based on control induction supports has been developed and the SKG has been improved. it is possible to solve [1-6].

II. Statement of the research problem

The IL principle scheme of the induction levitator intended for use in a vertical axis wind generator is given in Fig. 1 IL consists of a vertical three-pole magnetic conductor 1, an alternating current loop 2 and a short-circuited loop 3 made of aluminum coils (or levitation element LE). The wind-rotating sail is connected to the levitation element 3 with the power transmission 4 and rotates it. Due to the lifting electromagnetic force P_e created by the levitator, the rotating sail is kept in the state of levitation.

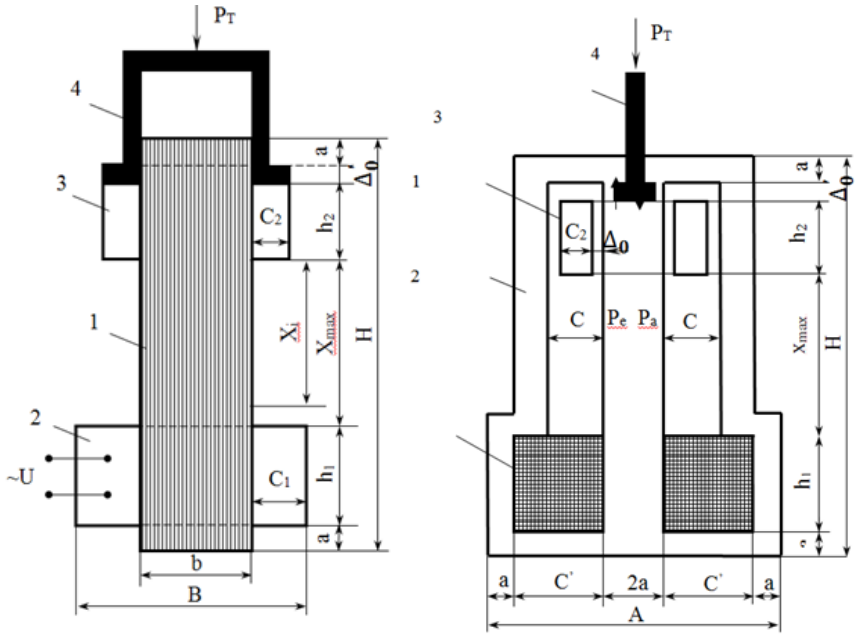


Figure 1: *The principle scheme of the induction levitator*

Levitation element 3 compensates the gravity of the sail P_T and its own gravity P_a, and as a result there is no need to use roller cushions, friction forces and the noise caused by them do not arise. In this case, the maintenance costs of the generator decrease and the service life increases. For a vertical-axis wind generator, two main constructions of IL can be presented: a cylindrical induction levitator and an induction levitator built on a three-bar core (Fig. 1 and Fig. 2). Cylindrical induction levitator (figure 2) consists of a magnetic conductor 1 made of electrotechnical structural steel, an alternating current loop 2 assembled from copper wires and a short-circuited levitation loop 3 wrapped with aluminum wires [7-9].

The levitation loop should be as light as possible and by compensating the 4 gravity of the

sail P_a, it should keep it at the required height 3 (in levitation state) from the fixed loop. On the other hand, it is possible to increase and decrease the height of levitation by adjusting the value of the voltage applied to the non-moving loop 3 [10-12]. The mentioned features are one of the positive aspects of the presented levitator construction. It is very difficult to create this in permanent magnet levitators. In the induction levitator built on a three-rod core, in addition to the above-mentioned elements 1, 2, 3, the pole head 5 participates. By using it, it is possible to increase the lifting electromagnetic force affecting the levitation loop. The magnetic conductor 1 and the pole head 5 are assembled from electro-technical steel sheets, as a result, the magnetic losses are reduced, and the efficiency of the system increases. It is necessary to build a mathematical model to determine the main parameters and dimensions of the control induction support, or IL (Fig. 1).

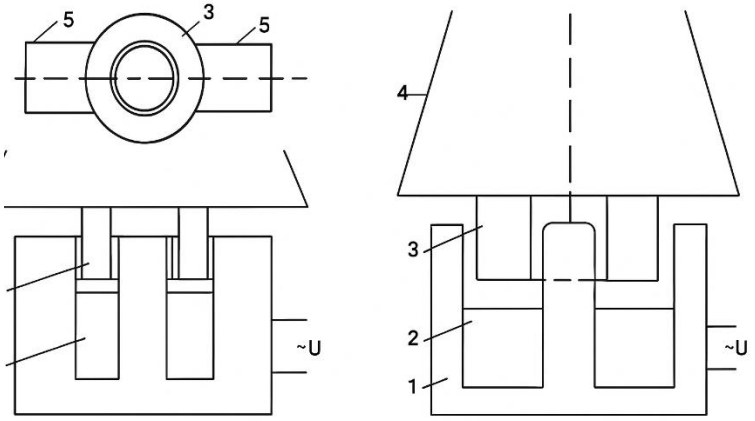


Figure 2: *IL with cylindrical construction and built on a triple core*

A mathematical model was formed taking into account the above requirements:

1. From the balance equation of electromagnetic force P_e, sail P_T and gravity P_a of LE:

$$P_e = 0.5F_1^2\lambda = P_a + P_T \tag{1}$$

$$P_a = g\gamma_a k_{32} l_2 S_2 \tag{2}$$

2. From the known mathematical expressions for the temperature increases of the alternating current circuit and LE:

$$\tau_1 = \frac{P_1 + P_2}{k_T S_{T1}}; \tau_2 = \frac{P_2}{k_T S_{T2}} \tag{3}$$

3. From the known mathematical expressions for the maximum value of the magnetic induction generated in the steel core:

$$B_{mak} = \frac{k_u U_1 \sqrt{2}}{\omega W_1 S_c} \tag{4}$$

4. From the formulas of the current flowing through the loops and the inductance:

$$I_1 = \frac{k_u U_1}{\omega W_1 \lambda (h_0 + h)} \tag{5}$$

III. Research results

The mathematical model takes into account the characteristics of the induction levitator, the data in the project assignment and the limitations imposed on the measurements. It is indicated in the given mathematical model: g = 9.81 m/c2; γa – specific gravity for aluminum; k_{32} ≈(0.6÷0,7) –

coefficient of levitation loop filling with aluminum; l_2 and S_2 – the average length and cross-sectional area of the winding of the levitation loop ($S = c_2 \cdot h_2$); P_1, P_2, S_{T1} and S_{T2} – active powers of loops and areas of cooling surfaces; τ_1, τ_2 – temperature increases of windings and number of windings; current densities of j_1 and j_2 loops; λ – specific magnetic permeability of the working air gap; L_{1S}, L_x and L_{2S} – dispersion and variable inductances of windings; h_0 and h – equivalent height of impact loop and levitation height [13-19]. To simplify the solution of the mathematical model (Eq. 1–8), we use the principle of correspondence of dimensions, dimensionless quantities and formulas of generalized parameters:

$$n_{e2} = \frac{h_2}{c_2}; n_{02} = \frac{c}{c_2}; m_a = \frac{b}{a}; m_c = \frac{b}{c}; b_2 \approx 0.98; n_k \approx 1.05 \tag{6}$$

$$n_1 = (m_a + m_c + 0.5 m_a m_c); n_p = 1 + \frac{P_T}{P_a}; n_0 = \frac{4b_2^2}{k_T} n_k g \gamma_a$$

$$k_2 = \frac{k_u U_1 \sqrt{2}}{\omega B_m}; \omega = 314\ 1/c; k_u \approx 0.96; B_m = 1.6 \div 1.7\ \text{Tl}. \tag{7}$$

$$k_{3S} = \frac{\sqrt{k_S}}{k_3}; k_3 = 2\frac{m_c^2}{m_a}; k_S = \frac{n_1}{n_1 + \frac{2}{n_{02}} m_a}; n_{02} \approx 1.1 \tag{8}$$

$$M = \frac{m_0^2}{m_a \left[\left(n_{02} m_0 + m_a \right) \left(m_c + 2.92 \lg\left(1 + \frac{\pi}{m_a} \right) \right) \right]}; m_0 = 0.5 n_1 \tag{9}$$

Tables 1, 2 and 3 lists the values of the main parameters. Based on the analysis of those values, the following recommendations should be taken into account in order to obtain the optimal values of the parameters:

1. Assuming $\tau_2 \geq 110$℃.

2. The thickness of LD c_2 should ensure that the magnetic induction of the working air gap in the steel core is homogeneous.

3. The n_{e2} value of the levitation constant should be in the range (Eq. 2-5).

Table 1: *ρ_2/τ_2 value*

τ_2, ℃	80	90	100	110
$\frac{\rho_2}{\tau_2} \cdot 10 - 8\ Om \cdot m$	4.015	4.135	4.526	4.376
$\frac{\rho_2}{\tau_2} \cdot 10 - 2\ Om \cdot m$	501.890	459.510	425.620	397.880

Table 2: *Numerical values of the coefficient for the levitation coil*

	1	2	3	4	5
1	0.654689	0.621647	0.609433	0.60443	0.602456
2	0.705951	0.646266	0.618173	0.6023	0.592293
3	0.740071	0.663425	0.625786	0.603644	0.589154
4	0.764376	0.676034	0.63202	0.605793	0.588436
5	0.782573	0.685678	0.637107	0.608007	0.588658

The determination of the main dimensions starts from the calculation of the number of turns of the induction coil W_1, which greatly simplifies the calculation method. In this case, it is necessary to take into account the limitations imposed on the amplitude value of the magnetic induction B_m and the effective value of the voltage supplied to the coil U_1. The amplitude value of the magnetic induction in a steel core assembled from separate sheets of electrical steel should be in the range B_m = (1.6-1.7) Tl [20-26]. It is important to adjust the levitation height h by changing the effective value of the control voltage supplied to the ends of the coil U_1 within a certain range. To fulfill these requirements, we use the following formula:

$$W_1 = \left(\frac{\sqrt{2} k_u U_1}{\omega B_m} \right) \frac{1}{S_c}$$

$$S_c = 2ab = 2c^2 \frac{m_a}{m_c^2}$$

So,

$$W_1 = \left(\frac{\sqrt{2} k_u U_1}{\omega B_m} \right) \frac{m_c^2}{2c^2 m_a} \tag{10}$$

If we accept: k_u = 0.96; U_1 = 220 V; ω = 314 1/s and B_m = 1.6 Tl:

$$\left(\frac{\sqrt{2} k_u U_1}{\omega B_m} \right) = \frac{\sqrt{2} \cdot 0.96 \cdot 220}{314 \cdot 1.6} = 594.510 \cdot 10^{-3} \tag{11}$$

Table 3: *The values of the specific magnetic permeability λ and the scattering coefficient μ_s*

ma / mc	1	2	3	4	5	note
1	1,599	1,454	1,367	1,309	1,267	μ_s
	8,03·10-6	7,31·10-6	6,87·10-6	6,57·10-6	6,36·10-6	λ
2	1,399	1,303	1,245	1,206	1,178	μ_s
	10,5·10-6	9.81·10-6	9,38·10-6	9,09·10-6	8,87·10-6	λ
3	1,299	1,227	1,184	1,155	1,133	μ_s
	13,1·10-6	12,3·10-6	11,9·10-6	11,6·10-6	11,4·10-6	λ
4	1,239	1,182	1,147	1,124	1,107	μ_s
	15,6·10-6	14,8·10-6	14,4·10-6	14,1·10-6	13,9·10-6	λ
5	1,2	1,151	1,122	1,103	1,089	μ_s
	18,1·10-6	17,3·10-6	16,9·10-6	16,6·10-6	16,4·10-6	λ

To simplify the calculations, let's express the thickness of the working air gap c in millimeters, then we get:

$$W_1 = 297255.08 \frac{m_c^2}{c^2 m_a} \tag{12}$$

c = 40 mm; $m_a = 2$ and $m_c = 4$. Calculate:

$$W_1 = 297255.08\frac{4^2}{40^2 \cdot 2} = 1486.275$$

In this case:

$$S_c = 2c^2\frac{m_a}{m_c^2} = 2(40\cdot 10^{-3})^2\frac{2}{4^2} = 400\cdot 10^{-6}\ m^2;$$

$$a = \frac{b}{m_a} = \frac{160\cdot 10^{-3}}{2} = 80\cdot 10^{-3} m$$

$$b = m_c c = 4\cdot 40\cdot 10^{-3} = 160\cdot 10^{-3} m. \quad (13)$$

III. Conclusions

1. Based on the analysis of scientific research on vertical-axis wind generators based on magnetic levitation, the advantages and development directions of such generators have been determined. One of the methods for improving vertical-axis wind generators with magnetic levitation is the creation of a new levitation system. For this purpose, a new design of a control induction support, or levitator, has been developed.

2. A mathematical model has been built to determine the main dimensions and parameters of the control induction levitator. The mathematical model has been formed taking into account the data in the project assignment, mechanical, electrical, magnetic and thermal parameters. To simplify the solution of the mathematical model, the principle of correspondence of dimensions, dimensionless quantities and mathematical expressions of generalized parameters have been used.

3. The mathematical expressions of the levitation constant, the thickness of the working air gap, the main dimensions of the magnetic conductor and the coils have been obtained from the solution of the mathematical model. Recommendations for optimizing the parameters have been given and a calculation methodology has been developed.

References

[1] I.M. Marufov, N.S. Mammadov, K.M. Mukhtarova, N.A. Ganiyeva, G.A. Aliyeva, "Calculation of main parameters of induction levitation device used in vertical axis wind generators". International Journal on technical and Physical Problems of Engineering" (IJTPE), March 2023, Issue 54, Volume 15, Number 1, pp. 184-189

[2] I.M. Marufov, "Calculation of the complex resistances of the induction system of the vertical axis wind generator", The 4th International scientific and practical conference "Actual problems of modern science" (January 31 – February 3, 2023) Boston, USA. International Science Group, 2023, 439 pp.

[3] Ilkin Marufov, Najiba Piriyeva, Nijat Mammadov, Shukufa Ismayilova, "Calculation of induction levitation vertical axis wind generator-turbine system parameters, levitation and influence loop", Przegląd Elektrotechniczny, 2024, No.2, pp.135-139, DOI: 10.15199/48.2024.02.27

[4] G.V.Mamedova, G.S.Kerimzade, N.M.Piriyeva, "Electromagnetic calculation of tension devices for winding wires of small cross sections", IJTPE Journal, ISSUE 53, Volume 14, Number 4, December, 2022, pp.80-85

[5] Y.R.Abdullaev , G.S.Kerimzade.,G.V. Mamedova, N.M.Piriyeva, "Design issues of electromechanical converters with levitation elements", Elektromekhanika Scientific and Technical Journal 61(2), 47-52, 2018

[6] Piriyeva N.M, Kerimzade G.S., "Methods for increasing electromagnetic efficiency in induction levitator "Przeglad Elektrotechniczny" journal, R.99 NR 10/2023, Poland, pp.192-196

[7] Mammadov N.S., Ganiyeva N.A., Aliyeva G.A., "Role of Renewable Energy Sources in the World". Journal of Renewable Energy, Electrical, and Computer Engineering, September 2022, No 2, pp. 63-67

[8] Y.R. Abdullaev, G.S. Kerimzade, G.V. Mamedova, N.M. Piriyeva., "Generalized indicators of electromagnetic devices with levitation elements", Priborostroenie Journal 60(5), pp.17-23, 2017

[9] N.A. Yusifbayli, A.P. Guliyev, I.M. Marufov, "DETERMINATION OF MAIN PARAMETERS AND THERMAL REPORT OF VERTICAL AXIS MAGNETIC LEVITATION WIND GENERATOR SYSTEM", IJTPE, Issue 57, Vol15, No4, Dec 2023, pp 94-99

[10] N.S. Mammadov, G.A. Aliyeva, "Energy efficiency improving of a wind electric installation using a thyristor switching system for the stator winding of a two-speed asynchronous generator", IJTPE, 2023, Issue 55, Volume 55, Number 2, pp. 285-290

[11] Piriyeva N.M, Kerimzade G.S., "Electromagnetic efficiency in induction levitators and ways to improve it", Przeglad Elektrotechniczny, R.99 NR 06/2023, Poland, pp.204-207

[12] Nijat Mammadov, Najiba Piriyeva, Shukufa Ismayilova, "Research of lightning protection systems for wind electric installations", PRZEGLĄD ELEKTROTECHNICZNY, ISSN 0033-2097, 2024, No 9, pp. 198-201, DOI: 10.15199/48.2024.09.38

[13] P.W Carlin, "The history and state of the art of variable-speed wind turbine technology", Technical Report NREL/TP–500–28607, National Renewable Energy Laboratory, USA, 2001

[14] Nijat Mammadov, Sona Rzayeva, Nigar Ganiyeva, "Analisys of synchronized asynchronous generator for a wind electric installation", Przeglad Elektrotechniczny, ISSN 0033-2097, 2023, Volume 1, No 5, pp.37-40, DOI: 10.15199/48.2023.05.07

[15] B. Bittumon, Amith Raju, Harish Abraham Mammen, Abhy Thamby, Aby K Abraham, Design and Analysis of Maglev Vertical Axis Wind Turbine, International Journal of Emerging Technology and Advanced Engineering, ISSN 2250-2459, , Volume 4, Issue 4, April 2014

[16] Ilkin Marufov, Aynura Allahverdiyeva, Nijat Mammadov, "Study of application characteristics of cylindrical structure induction levitator in general and vertical axis wind turbines", Przegląd Elektrotechniczny, 2023, No 10, pp.196-199, DOI: 10.15199/48.2023.10.38

[17] I.N. Rahimli, S.V. Rzayeva, E.E. Umudov, "DIRECTION OF ALTERNATIVE ENERGY", Vestnik nauki, Issue 2, Vol. 61, №4, April 2023

[18] Nijat Mammadov, Ilkin Marufov, Saadat Shikhaliyeva, Gulnara Aliyeva, Saida Kerimova, "Research of methods power control of wind turbines", Przeglad Elektrotechniczny, ISSN 0033-2097, 2024, No 5, pp. 236-239, DOI: 10.15199/48.2024.05.44

[19] Piriyeva Najiba, "SYSTEMATIZATION OF CONSTRUCTIONS OF ELECTRICAL DEVICES WITH ELEMENT OF LEVITATION", The 3rd International scientific and practical conference "Technologies in education in schools and universities"(January 23-26, 2024) Athens, Greece, International Science Group, 2024, 363 p.

[20] Elshad Safiyev, Ilham Rahimli, Nijat Mammadov, "Method of qualitative impregnation of electric motor windings", Przegląd Elektrotechniczny, 2024, No 8, pp.238 -240, DOI: 10.15199/48.2024.08.48

[21] Elshad Safiyev, Saida Kerimova, Kubra Mukhtarova, "Research of some problems of electrical safety", Przegląd Elektrotechniczny, ISSN 0033-2097, 2024, No 9, pp.96-99, DOI: 10.15199/48.2024.09.16

[22] I.N.Rahimli, N.S. Mammadov, R.K. Karimova, "Analysis of wind turbine control algorithms as part of a wind power plant", International Journal on technical and Physical Problems of Engineering (IJTPE), Issue 62, Vol.17, No.1, pp.81-90, March 2025

[23] Mammadov N. S., Mukhtarova K. M., "METHODOLOGY FOR ASSESSING THE RELIABILITY OF AGS BASED ON RENEWABLE ENERGY SOURCES", Reliability: Theory & Applications, Volume 19, No 4 (80), pp.648-653, 2024, DOI: 10.24412/1932-2321-2024-480-648-653

[24] Nadir Aliyev, Elbrus Ahmedov, Samira Khanahmedova, Sona Rzayeva, "Synthesis of the Exact Parameters of the Electromagnetic Brake of a Wind Electric Installation", Przeglad Elektrotechniczny journal, № 10, Poland, 2023, pp. 120-124, DOI: 10.15199/48.2023.10.123

[25] Mammadov N. S., "CAUSES OF ELECTROMECHANICAL RESONANCE IN WIND TURBINES AND METHODS FOR ITS ELIMINATION", Reliability: Theory & Applications, Volume 20, No 2 (84), pp.562-569, 2024, DOI: 10.24412/1932-2321-2025-284-562-569

[26] A. Nayir, E. Rosolowski, L.Jedut, "New trends in wind energy modeling and wind turbine control", IJTPE, Issue 4, Vol. 2, № 3, pp. 51-59, September 2010

RT&A, No 4 (89)
Volume 20, December 2025

SINE LOG-LOGISTIC DISTRIBUTION FOR MODELING REMISSION AND SURVIVAL TIMES OF CANCER PATIENTS

Santanu Dutta, Aditya Kumar Yadav

•

Department of Mathematical Sciences, Tezpur University, India
sdutta@tezu.ernet.in, adityakumaryadav448@gmail.com

Abstract

Modeling the remission times of bladder cancer patients reported by Lee and Wang [26], the survival times following radiotherapy and chemotherapy of head and neck cancer patients and bone cancer patients reported by Efron [10] and Mansour et al. [16] have attracted considerable research interest. In this paper, we propose a new two-parameter distribution that fits these data well and compares well in model selection for these data with existing distributions that use three or more parameters. Its distribution, density, quantile, and hazard functions have closed-form expressions. The survival function of the proposed model exhibits a regularly varying tail, and its hazard function is either strictly decreasing or inverse-bathtub shaped, depending on the value of the shape parameter. We derive several properties of the proposed distribution, estimate its parameters, and demonstrate its effectiveness in modeling the hazard function and uncovering key features of the remission time and survival time data.

Keywords: Lifetime distribution, parsimonious transformation, log-logistic distribution

1. Introduction

Cancer remains one of the leading causes of death globally, and the analysis of time-to-event data plays a crucial role in understanding treatment outcomes and disease progression. Two such important metrics in cancer research are remission time and survival time. Remission time of a disease refers to the period during which there are no symptoms of the disease following treatment [8, 26]. Survival time refers to the length of time patients live after receiving cancer treatment, such as radiotherapy, chemotherapy, or a combination of both.

Modeling remission and survival times of cancer patients has been an area of active and ongoing research (see, for instance, [1, 2, 5, 6, 11, 13, 22, 21, 23, 27] and references therein). These time-to-event data often exhibit complex features, including right-censoring, skewness, high kurtosis, and sparsity in the tail. Moreover, the underlying distributions may not conform to classical parametric families such as exponential or Weibull, motivating the development of flexible, generalized probability models.

Three publicly available datasets have been widely studied in this context. Lee and Wang [26] reported remission times (in months) of 128 bladder cancer patients. Efron [10] provided survival times (in days) of 44 head and neck cancer patients treated with a combination of radiotherapy and chemotherapy. Mansour et al. [16] reported survival times (in days) of 73 patients with acute bone cancer. Figures 1,2, and 3 show the histograms and kernel density estimates (KDEs) of these datasets, while Table 1 presents their moment coefficients of skewness and kurtosis.

All three datasets display significant positive skewness, high kurtosis, and sparsity in the right tail-indicated by the presence of a few very high values far from the central peak, which manifest

as extended right tail in the KDE plots. These characteristics highlight the need for probability distributions that can capture the observed features in these data. In recent years, several probability distributions have been proposed specifically to model such datasets. For example, the remission time data of bladder cancer patients has been modeled using the WC-Weibull distribution [21], EPham distribution [1], EOEHL-LLoGP distribution [27], KGIL distribution [22], EHL-LLoGW distribution [6], GKME distribution [13], APTEPL distribution [11], Maxwell-Lomax distribution [2], RB-TL-TII-EHL-W distribution [23], and the Marshall-Olkin extended generalized Lindley (MOEGL) distribution [5]. Among these, the MOEGL distribution has demonstrated the best overall fit according to various model selection criteria.

For the survival times of 44 head and neck cancer patients, as reported by Efron [10], several recent distributions have been employed, including the power-weighted Sujatha (PWS) distribution by Shanker and Shukla [28], the gamma-Sujatha (G-SU) distribution by Ray and Shanker [19], the DUS-Inverse Weibull (DUS-IW) distribution by Gauthami and Chacko [12], and the Alpha Power Kumaraswamy Weibull (APKumW) distribution by Klakattawi [14]. Notably, the G-SU and APKumW distributions have also been applied to model survival times of acute bone cancer, as reported by Mansour et al. [16].

An appropriate probability distribution for remission or survival time enables the modeling of the hazard function $h(x)$, which represents the instantaneous rate of relapse or death-at a given time x, given that a patient is in remission or survives up to x and for small Δx, $h(x)\Delta x$ is an approximation of the chance of relapse or death in $[x, x+\Delta x)$, given survival up to x (see [25]). In cancer studies of survival time after treatment, the hazard function is expected to first increase to a peak and then decrease, exhibiting an inverse bathtub shape (see [25]) and its peak represents the time where the rate of recurrence of the disease or death is maximum, given survival up to that time, which can be crucial for treatment planning and post-treatment monitoring. For instance, in breast cancer, hazard rates often peak within the first few years following treatment, guiding the scheduling of follow-up visits and adjuvant therapies (see [7]).

In this paper, we propose a new two-parameter continuous probability distribution that provides a good fit-with high p-values under the Kolmogorov-Smirnov (KS) goodness-of-fit test-to the three datasets, viz., remission times of bladder cancer patients ([26]), and survival times of patients with head and neck cancer ([10]) and bone cancer ([16]). The proposed distribution captures the key empirical features of these datasets and compares favorably with existing models for remission or survival time across multiple model selection criteria. In addition, it yields a simple closed-form expression for the hazard function, which increases to a peak and subsequently declines with time. This pattern suggests that patients who remain in remission or survive beyond the peak hazard point have a reduced risk of cancer relapse. Importantly, the ability to identify the timing of the peak hazard can aid clinicians in planning timely interventions or reevaluations, potentially improving patient management and outcomes.

The remainder of the paper is organized as follows. In Section 2, we define the distribution function of the proposed Sine Log-Logistic (SLL) distribution and derive explicit expressions for its probability density, quantile, and hazard functions. The shape and scale parameters of the SLL distribution are expressed in terms of the median and the $\frac{1}{\sqrt{2}}$th quantile, allowing for consistent plug-in estimation of these parameters. The hazard function exhibits either an inverse bathtub shape or is monotone decreasing depending whether or not the shape parameter exceeds 1. In Subsection 2.1, we fit the proposed SLL distribution, along with the reviewed distributions, to these three datasets. We evaluate their goodness of fit and compare their relative performance using three model selection criteria. Section 3 focuses on the theoretical properties of the proposed SLL distribution. We establish conditions under which the density function is unimodal and determine the existence of its moments. Additionally, we analyze the asymptotic behavior of the hazard function as remission or survival time increases, and examine the regularly varying property of the survival function, which in turn ensure that the distribution of the scaled maximum of n i.i.d. SLL random variables can be approximated by the Fréchet distribution for large n. If the shape parameter exceeds 1, density and the hazard functions of the SLL distribution exhibit an inverse-bathtub shape. The proofs of the main results in Section 3 are provided in the

Appendix.

In Section 4, we estimate the parameters of the proposed SLL distribution using two methods: the plug-in method and maximum likelihood estimation. We also discuss three model selection criteria-Akaike Information Criterion (AIC), Bayesian Information Criterion (BIC), and Consistent Akaike Information Criterion (CAIC). In Section 5, we assess the consistency of the maximum likelihood estimators through Monte Carlo simulation. Finally, in Section 6 we analyze three datasets viz., bladder cancer remission times [26], survival times of head and neck cancer patients [10], and survival times of acute bone cancer patients [16] by using the fitted SLL distribution. The parameter estimates and the p-values from the Kolmogorov-Smirnov (KS) goodness-of-fit test are presented in Tables 2, 3, and 4.

For all three datasets, the estimated values of the shape parameter of the SLL distribution exceed 1. Consequently, the fitted density function and hazard function, as given by equations (3) and (4), are unimodal and exhibit inverse bathtub shape and the hazard decreasing as remission or survival time increases beyond the point at which the hazard peaks for these data. The estimated modal remission and survival times-corresponding to the peaks of the fitted density-are reported in Table 13, representing the most frequent remission or survival durations observed. The peaks of the fitted hazard functions, which indicate the most likely times of recurrence, are also reported in Table 13. The time at which the hazard-the instantaneous rate of relapse-peaks may serve as a critical point for intervention and for planning post-diagnosis and follow-up treatments. We find that the timing of the peak of the density and the hazard function varies significantly across cancer types (see Table 13). For bladder cancer patients, the hazard peaks at approximately 6.7 months into remission. In the case of head and neck cancer, the peak occurs around 50 days following radiotherapy and chemotherapy. For acute bone cancer, the hazard function reaches its peak as early as 7 days after therapy, underscoring the disease's rapid and aggressive progression.

Table 1: *Coefficients of skewness and kurtosis of the three cancer datasets*

Dataset	Skewness	Kurtosis
Remission times of bladder cancer	3.285	18.483
Survival times of head and neck cancer	3.384	16.560
Survival times of acute bone cancer	6.799	51.775

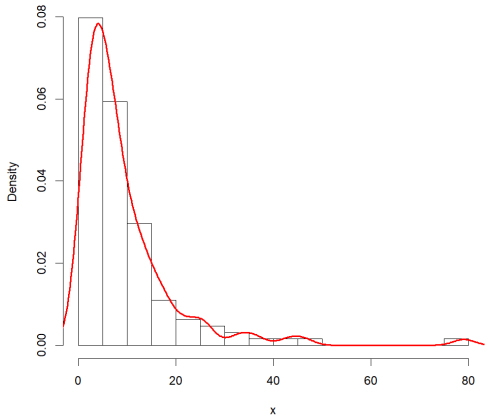


Figure 1: *Histogram and Kernel Density Estimate (KDE) for remission times for bladder cancer*

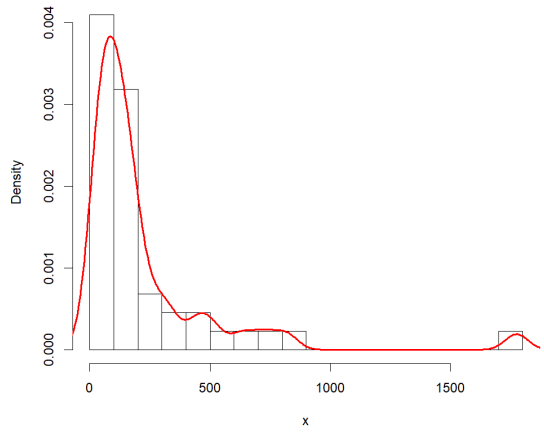


Figure 2: *Histogram and Kernel Density Estimate (KDE) for survival times for head and neck cancer.*

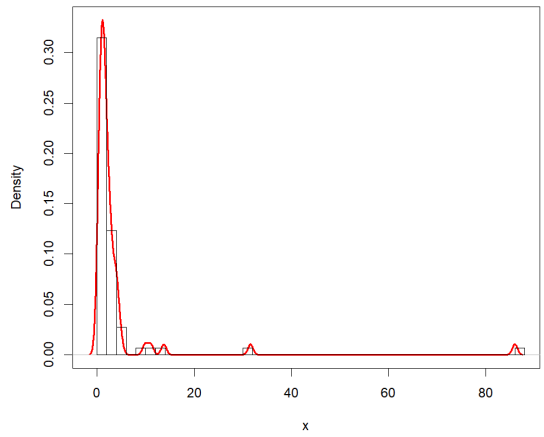


Figure 3: *Histogram and Kernel Density Estimate (KDE) survival times for acute bone cancer.*

2. Sine log-logistic distribution

Let us introduce some notation that will be used throughout the paper. f' denotes the derivative of a differentiable function f. For a real number x, $\lfloor x \rfloor$ denotes the greatest integer less than or equal to x. The notation $\log_2$ refers to the logarithm with base 2. For two functions f and g, $f(x) \sim g(x)$ denotes $\lim_{x\to\infty} \frac{f(x)}{g(x)} = 1$.

We define the new distribution by applying a parsimonious transformation, viz. the sine transformation (also known as SS transformation see [15]), to the distribution function of the log-logistic distribution, which involves two non-negative parameters (viz. α and λ). The choice of the transformation is motivated by [15]. We refer to the resulting new resulting distribution as the sine log-logistic distribution with parameters α and λ and abbreviated as the SLL(α, λ) distribution. The distribution function, density and hazard functions also the quantile function of the SLL(α, λ) distribution turn out to have closed-form expression which are easy to compute and the two parameters, viz. α and λ, turn out to be function functions of two quantiles of this distribution.

Following are the formulae of the distribution function (F), the quantile function (Q), the density function (f) and the hazard function (h) of the proposed SLL distribution

$$F(x) = \begin{cases} \sin\left[\frac{\pi}{2(1+(x/\lambda)^{-\alpha})}\right] & \text{for} \quad x > 0 \\ 0 & \text{otherwise,} \end{cases} \tag{1}$$

where $\alpha,\ \lambda > 0$. α is the shape parameter and λ is the scale parameter.

$$Q(p) = \lambda \left(\frac{1}{\frac{\pi}{2\sin^{-1}(p)} - 1} \right)^{\frac{1}{\alpha}}, \quad 0 < p < 1. \tag{2}$$

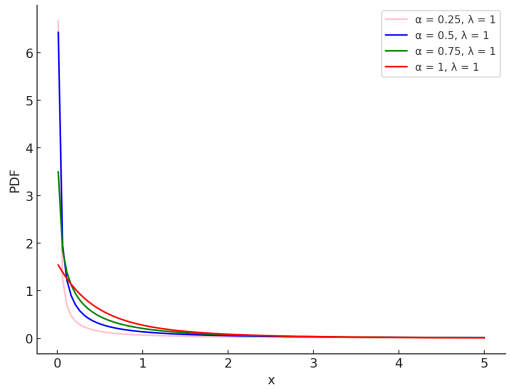
$$f(x) = \begin{cases} \frac{\pi\alpha(x/\lambda)^{\alpha-1}}{2\lambda(1+(x/\lambda)^{\alpha})^2} \cos\left[\frac{\pi}{2(1+(x/\lambda)^{-\alpha})}\right] & \text{for} \quad x > 0 \\ 0 & \text{otherwise.} \end{cases} \tag{3}$$

The hazard function of SLL distribution is given by

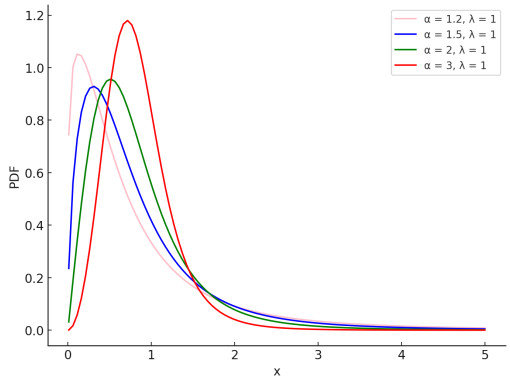
$$h(x) = \frac{f(x)}{1-F(x)} = \begin{cases} \frac{\pi\alpha(x/\lambda)^{\alpha-1} \cos\left[\frac{\pi}{2(1+(x/\lambda)^{-\alpha})}\right]}{2\lambda(1+(x/\lambda)^{\alpha})^2 \left\{1-\sin\left[\frac{\pi}{2(1+(x/\lambda)^{-\alpha})}\right]\right\}} & \text{for} \quad x > 0 \\ 0 & \text{otherwise.} \end{cases} \tag{4}$$

The hazard function (also known as the failure rate) describes the instantaneous risk of failure at a given time, given that the event has not yet occurred up to that time. For instance, in medicine, hazard function describes the instantaneous risk that an event (like death or relapse) will happen at a specific time, given that the patient has survived up to that time.

We plot the PDF (3) and the hazard function (4) of the SLL($\alpha,\ \lambda$) distribution for different values of the shape parameters α and for fixed $\lambda = 1$ in Figures 4 and 5 respectively.

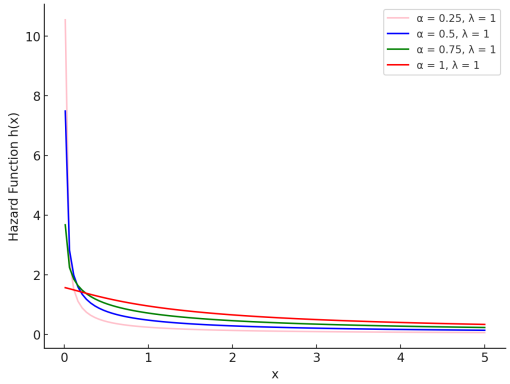


(a) *Plot of the PDF of SLL*$(\alpha, 1)$ *for shape parameter* $\alpha \leq 1$.

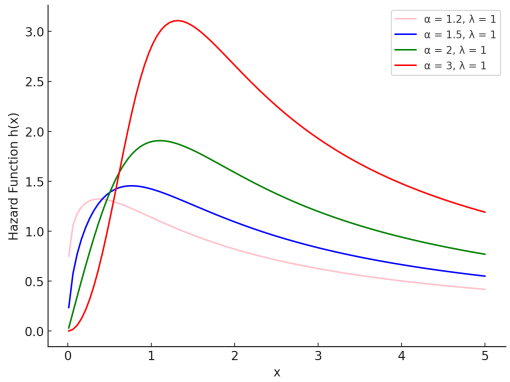


(b) *Plot of the PDF of SLL*$(\alpha, 1)$ *for shape parameter* $\alpha > 1$.

Figure 4: *Plots of the PDF of SLL*$(\alpha, 1)$ *for different values of the shape parameter* α.



(a) *Plot of the hazard function of* $SLL(\alpha, 1)$ *for shape parameter* $\alpha \leq 1$.



(b) *Plot of the hazard function of* $SLL(\alpha, 1)$ *for shape parameter* $\alpha > 1$.

Figure 5: *Plots of the hazard function of* $SLL(\alpha, 1)$ *for different values of the shape parameter* α.

Equation (2), implies that

$$\lambda = Q\left(\frac{1}{\sqrt{2}}\right), \tag{5}$$

and

$$\alpha = \left(\log_2\left(\frac{Q\left(\frac{1}{\sqrt{2}}\right)}{Q\left(\frac{1}{2}\right)}\right)\right)^{-1}. \tag{6}$$

The scale parameter λ is the $\frac{1}{\sqrt{2}}$th quantile and the shape parameter α is a function of the ratio of the $\frac{1}{\sqrt{2}}$th quantile and the median. Therefore these parameters can be estimated by a plug-in method replacing the quantiles by the sample quantiles.

Remark 1. The PDF (3) of the proposed $SLL(\alpha, \lambda)$ distribution exhibits a long right tail and a unique peak (i.e., it is unimodal) for $\alpha > 1$ (see Figure 4(b)).

In medicine, the mode of the survival time distribution can be interpreted as the most common time point at which treatment failure (e.g., relapse, death, or complication) is most likely to occur. This information may assist in planning follow-up schedules, surveillance intensity, or early intervention strategies.

Remark 2. Figure 5(a) shows that for $\alpha \leq 1$, the hazard function $h(x)$ decreases with increasing x. Figure 5(b) demonstrates that for $\alpha > 1$, the hazard function (4) takes on an inverse bathtub shape, characterized by a long right tail and a single peak or mode.

Probability distributions with an inverse bathtub shape of the hazard function are useful for modeling remission and survival times of various cancers (see [25]). The inverse bathtub shape of the hazard function indicates that the risk of failure in the course of a disease initially increases, reaches a peak, and then decreases as patients recover. For instance, Efron [10] observed that the empirical hazard function of survival times for patients with head and neck cancer is unimodal and resembles an inverse bathtub shape. Further, the mode of the hazard function can be interpreted as the time when the risk of failure is at its peak and can be a useful parameter to identify when a patient is most vulnerable post-diagnosis and treatment.

2.1. Goodness of fit and model selection for the remission and survival time

We fit the proposed $SLL(\alpha,\ \lambda)$ distribution to the remission times of 128 bladder cancer patients reported by Lee and Wang [26], the survival times of head and neck cancer of 44 patients when treated with a combination of radiotherapy and chemotherapy reported by Efron [10], and the

Table 2: *ML estimates, model selection criteria and p-value of KS goodness-of-fit tests for SLL and ten other competing distributions based on remission times of bladder cancer of 128 patients[26].*

Distribution	**ML Estimates**	**AIC**	**BIC**	**CAIC**	p**-value**
SLL	$\hat{\alpha} = 1.403, \hat{\lambda} = 10.342$	823.395	829.099	831.099	0.998
MOEGL	$\hat{\alpha} = 1.079, \hat{\beta} = 0.080, \hat{\theta} = 0.702$	824.621	833.177	836.177	0.862
WC-Weibull	$\hat{\theta} = 0.851, \hat{\gamma} = 0.189$	826.341	832.045	834.045	0.909
EOEHL-LLoGP	$\hat{\alpha} = 2.153, \hat{\lambda} = 0.315, \hat{\theta} = 3.073, \hat{c} = 0.659$	827.300	838.700	842.708	0.997
EPham	$\hat{\alpha} = 0.243, \hat{\sigma} = 2.226, \hat{\gamma} = 8.093$	827.787	836.342	839.343	0.942
EHL-LLoGW	$\hat{\alpha} = 0.861, \hat{\beta} = 0.519, \hat{\delta} = 6.716, \hat{c} = 0.032$	827.800	839.200	834.208	0.997
KGIL	$\hat{\beta} = 0.345, \hat{\lambda} = 9.642, \hat{p} = 4.991, \hat{q} = 3.216$	828.609	840.018	828.935	0.988
GKME	$\hat{\alpha} = 1.374, \hat{\theta} = 0.102$	828.983	834.687	836.687	0.881
M-L	$\hat{\lambda} = 3.268, \hat{\theta} = 24.485, \hat{\beta} = 0.355$	829.156	837.712	840.712	< 0.05
RB-TL-TII-EHL-W	$\hat{\delta} = 24.626, \hat{a} = 0.0001, \hat{b} = 4.008, \hat{\lambda} = 1.270$	830.882	842.290	846.290	0.875
APTEPL	$\hat{\alpha} = 6.279, \hat{\beta} = 11.167, \hat{\delta} = 0.613, \hat{\theta} = 0.752$	831.613	843.021	847.021	0.785
G-SU	$\hat{\phi} = 2.529, \hat{\omega} = 2.961$	852.772	858.476	860.476	0.324

survival times of acute bone cancer patients reported by Mansour et al. [16]. For each data set we compare the fit of SLL distribution to the same for most of the recent probability distributions which have been proposed so far to model these datasets. The parameters are estimated by maximizing the likelihood functions for each dataset. In Tables 2-4, we report maximum likelihood (ML) estimates of the model parameters, the Akaike Information Criterion (AIC), the Bayesian Information Criterion (BIC), and the consistent Akaike Information Criterion (CAIC) [4] scores and the p-value of the Kolmogorov-Smirnov (KS) goodness-of-fit test for each dataset.

Table 3: *ML estimates, model selection criteria and p-value of KS goodness-of-fit tests for SLL and five other competing distributions based on survival times data of head and neck cancer treated with chemeotharapy.*

Distribution	**ML Estimates**	**AIC**	**BIC**	**CAIC**	p**-value**
SLL	$\hat{\alpha} = 1.320, \hat{\lambda} = 222.916$	561.294	564.862	566.862	0.969
MOEGL	$\hat{\alpha} = 0.883, \hat{\theta} = 0.002, \hat{\beta} = 0.038$	561.215	566.567	569.567	0.806
PWS	$\hat{\alpha} = 1.079, \hat{\beta} = 0.080, \hat{\theta} = 0.702$	561.410	566.763	569.763	0.572
G-SU	$\hat{\phi} = 8.622, \hat{\omega} = 11.170$	562.476	566.786	568.045	0.900
DUS-IW	$\hat{\alpha} = 1.119, \hat{\beta} = 57.556$	561.830	565.400	567.398	0.868
APKumW	$\hat{a} = 4.843, \hat{b} = 0.652, \hat{c} = 0.572, \hat{\lambda} = 0.026, \hat{\alpha} = 0.317$	565.1112	565.400	579.032	0.949

Table 4: *ML estimates, model selection criteria and p-value of KS goodness-of-fit tests for SLL and five other competing distributions based on survival times of acute bone cancer.*

Distribution	ML Estimates	AIC	BIC	CAIC	p-value
SLL	$\hat{\alpha} = 1.412, \hat{\lambda} = 2.703$	291.558	296.139	298.139	0.454
MOEGL	$\hat{\alpha} = 1.354, \hat{\theta} = 0.045, \hat{\beta} = 0.001$	288.508	295.380	298.380	0.582
G-SU	$\hat{\phi} = 4.457, \hat{\omega} = 0.765$	285.776	290.357	292.357	0.860
APKumW	$\hat{a} = 5.089, \hat{b} = 0.414, \hat{c} = 0.536, \hat{\lambda} = 1.301, \hat{\alpha} = 0.005$	291.700	303.153	308.153	0.949

The proposed SLL distribution yields good fit to the three datasets on the remission times of 128 bladder cancer patients reported by Lee and Wang [26], the survival times of head and neck cancer of 44 patients reported by Efron [10], and the survival times of 73 acute bone cancer patients reported by Mansour et al. [16] as indicated by the high p-values in the Kolmogorov-Smirnov test for these data. See Tables 2, 3 and 4. Moreover, the proposed SLL distribution outperforms the other candidate distributions in terms of different model selection criteria scores, viz. the AIC, BIC, and CAIC scores for these datasets on remission and survival times of cancer patients reported by Lee and Wang [26], Efron [10] and Mansour et al. [16]. These observations motivate our further research into the mathematical properties of the proposed SLL distribution and the analysis of these three datasets using the proposed model.

3. Properties of the SLL distribution

In this section, we study the mathematical properties of SLL distribution such as moments, hazard function, mode, and regularly varying property of the survival function.

3.1. Moments

Let $X \sim SLL(\alpha, \lambda)$. We have

$$E(X^k) \leq \frac{\pi}{2} \int_0^\infty x^k \frac{\alpha(x/\lambda)^{\alpha-1}}{\lambda(1+(x/\lambda)^\alpha)^2} dx = \frac{\pi}{2} E(Y^k) \tag{7}$$

where Y follows log-logistic distribution with shape parameter $\alpha > 0$ and scale parameter $\lambda > 0$. Since the kth moment of Y exists whenever $k < \alpha$ (see [17]), we obtain the following result.

Theorem 1. The SLL(α, λ) distribution with parameters $\alpha > 0$ and $\lambda > 0$, and PDF given by equation (3), has finite kth moment for all $k < \alpha$.

Corollary 1. For the SLL(α, λ) distribution with $\alpha > 0$ and $\lambda > 0$,

(i) If $\alpha > 1$, then the mean exists and is finite.

(ii) If $\alpha > 2$, then both the mean and variance exist and are finite.

3.2. Mode of the SLL Distribution

The mode of a probability distribution is the value at which its PDF attains the maximum, representing the most favorable outcome [25]. The mode can be a more appropriate alternative to the mean, especially when the data are skewed or contain outliers. In survival analysis, the mode determines the most common point at which failure is most likely to occur. For example, in studies involving remission and survival times of cancer patients, the mode indicates the most probable time at which failure events such as relapse or death might occur.

We now state a theorem that establishes the existence and uniqueness of the mode of the SLL distribution, determined by the value of the shape parameter α. The proof is provided in the appendix.

Theorem 2. The SLL(α, λ) distribution with parameters $\alpha > 0$ and $\lambda > 0$, and PDF given by equation (3), satisfies the following:

(i) If $0 < \alpha \leq 1$, then the mode does not exist.

(ii) If $\alpha > 1$, then the distribution has a unique mode $x_M \in (0, x^*)$ where $x^* = \lambda \left(\frac{\alpha-1}{\alpha+1}\right)^{1/\alpha}$.

3.3. Hazard Function

In survival analysis, the hazard function h(x) also known as the failure rate describes the instantaneous rate at which an event (such as death, relapse, or failure) occurs, given that the subject has survived up to time x (see [25]). In medical research, the hazard function plays a crucial role in determining the risk dynamics over time and is widely used, particularly in analyzing survival data. The mode of the hazard function, or the point at which it attains its maximum, indicates the most likely time of failure, conditional on survival up to that time can guide clinical decisions regarding the timing of interventions or monitoring.

The following lemmas describe the asymptotic behavior of the hazard function $h(x)$, given in (4), for the SLL(α, λ) distribution. We refer to the appendix for the proofs.

Lemma 1. The hazard function $h(x)$ given in (4) for the SLL(α, λ) distribution, with $\alpha, \lambda > 0$, satisfies the following property:

$$\lim_{x\to\infty} h(x) = 0. \tag{8}$$

Lemma 2. Let F be a continuous distribution function supported on $[0, \infty)$ with a differentiable density f. Suppose that:

- f is inverse bath-tub shaped; that is, there exists $t^* \geq 0$ such that f is increasing on $[0, t^*]$ and decreasing on $[t^*, \infty)$,
- the hazard rate function $h(x) = \frac{f(x)}{1-F(x)}$ satisfies $\lim_{x\to\infty} h(x) = 0$.

Then h is inverse bath-tub shaped; that is, there exists $t^{**} \geq t^*$ such that h is increasing on $[0, t^{**}]$ and decreasing on $[t^{**}, \infty)$.

Remark 3. Lemma 1 and 2 imply that for $\alpha > 1$ the hazard function h of SLL(α, λ) distribution will be inverse bath-tub shaped and the peak of the hazard function will be to the right of the mode.

3.4. Regularly Varying Survival Function and asymptotic distribution of the extreme remission or survival time

In the study of survival analysis and extreme value theory, the concept of regular variation plays a major role in understanding the asymptotic behavior of tail distributions (see [9]). A survival function that is regularly varying at infinity exhibits a heavy-tailed property, implying that the probability of extreme or rare events decays at a polynomial rate. In that case, the maximum survival time distribution can be approximated by the Fréchet distribution. Moreover, in studies involving the remission and survival times of cancer patients, the tail behavior of survival distributions helps assess long-term risks and the persistence of chronic diseases.

Definition 1. A Lebesgue-measurable function $f : (0, \infty) \to \mathbb{R}$ is said to be *regularly varying at infinity with index* $\alpha \in \mathbb{R}$ if

$$\lim_{x\to\infty} \frac{f(tx)}{f(x)} = t^\alpha, \quad \text{for all } t > 0. \tag{9}$$

In this case, we write $f \in \mathrm{RV}_\alpha$.

The following result establishes that the survival function of the SLL distribution possesses the property of regular variation, with the detailed proof presented in the appendix.

Theorem 3. The survival function $\bar{F}(x) = 1 - F(x)$ of the SLL(α, λ) distribution with $\alpha, \lambda > 0$ is regularly varying at infinity with index -2α, i.e.,

$$\bar{F} \in \mathrm{RV}_{-2\alpha}.$$

Next we obtain the asymptotic distribution of centered and scaled $M_n = \max(X_1, \ldots, X_n)$ where $X_1, \ldots, X_n$ are independently and identically distributed (i.i.d.) random variables following $SLL(\alpha, \lambda)$.

Definition 2. Let $X_1, \ldots, X_n$ be i.i.d. random variables with a distribution function F. Then F is said to be in the maximum domain of attraction (MDA) of a non-degenerate distribution function H if there exist sequences of real numbers (c_n) and (d_n) with $c_n > 0$ for all $n \in \mathbb{N}$ such that the following holds:

$$\lim_{n\to\infty} \mathbb{P}\left(\frac{M_n - d_n}{c_n} \leq x\right) = \lim_{n\to\infty} F^n(c_n x + dn) = H(x)$$

for every continuity point x of H. We write $F \in MDA(H)$ to denote that F is in the maximum domain of attraction of H.

Definition 3. The Fréchet distribution with parameter $\xi > 0$ is defined by the following distribution function:

$$H_\xi(x) = exp\left(-(1+\xi x)^{-\frac{1}{\xi}}\right), \quad 1 + \xi x > 0. \tag{10}$$

Theorem 4 (see [9].)**.** For $\xi > 0$, $F \in MDA(H_\xi)$ if and only if $1 - F$ is regularly varying at infinity with index $-1/\xi$.

From Theorem 3 and 4, we have the following result:

Theorem 5. Let $X_1, \ldots, X_n$ be i.i.d. random variables following $SLL(\alpha, \lambda)$, where $\alpha, \lambda > 0$ with df F. Then

$$\lim_{n\to\infty} \mathbb{P}\left(\frac{M_n}{c_n} \leq x\right) = \lim_{n\to\infty} F^n(c_n x) = H_{1/2\alpha}(x), \quad 1 + x/2\alpha > 0$$

where c_n is the $(1 - \frac{1}{n})$th quantile of $SLL(\alpha, \lambda)$.

Remark 4. The scaled maxima M_n of i.i.d. random variables following $SLL(\alpha, \lambda)$, where $\alpha, \lambda > 0$ is well approximated by the Fréchet distribution with distribution function $H_{1/2\alpha}(x)$ for large n.

4. Estimation of Parameters SLL Distribution

In this section we estimate the parameters of the proposed distribution by two methods, namely the plug-in method and the likelihood function maximization methods and we discuss the three model selection criteria viz., AIC, BIC and CAIC.

4.1. Plug-in Method

We use the quantile function of the SLL distribution given in equation (1.2) to estimate the parameters of the SLL distribution. From equations (1.3) and (1.4), we observe that the parameters of the proposed distribution can be expressed in terms of the quantiles. Given a dataset, plug-in estimators of the parameters are obtained by replacing the quantiles in (1.2) by the corresponding sample quantiles in the given data. The following theorem esnures strong consistency of the plug-in estimators.

Theorem 6. Let $X_1, X_2, \ldots, X_n$ be independently and identically distributed (i.i.d.) random variables following the $SLL(\alpha, \lambda)$ distribution. Then, the estimators

$$\widehat{\lambda} = X_{\left(\left\lfloor \frac{n}{\sqrt{2}} \right\rfloor + 1\right)} \tag{11}$$

and

$$\widehat{\alpha} = \left(\log_2 \left(\frac{X_{\left(\left\lfloor \frac{n}{\sqrt{2}} \right\rfloor + 1\right)}}{X_{\left(\left\lfloor \frac{n}{2} \right\rfloor + 1\right)}} \right) \right)^{-1} \tag{12}$$

are strongly consistent estimators of λ and α.

4.2. Model Selection and Maximum Likelihood Estimation

Let $X_1, \ldots, X_n$ be i.i.d. continuous random variables with PDF $f(x; \boldsymbol{\theta})$, with parameter vector $\boldsymbol{\theta} \in \mathbb{R}^k$. The log-likelihood function is given by

$$L(\boldsymbol{\theta}) = \sum_{i=1}^{n} \ln f(X_i; \boldsymbol{\theta}). \tag{13}$$

Let $\hat{\boldsymbol{\theta}}$ be the maximum likelihood (ML) estimate of the parameter vector $\boldsymbol{\theta}$ and $L(\hat{\boldsymbol{\theta}})$ is the maximized log-likelihood function (13).

The log-likelihood function is used in evaluating the modeling selection criteria. Following are the well known model selection criteria based on log-likelihood function.

1. **Akaike Information Criterion (AIC):** The AIC, proposed by Akaike (see [4]), is defined as

   $$\text{AIC} = -2L(\hat{\boldsymbol{\theta}}) + 2k,$$

   where k is the number of estimated parameters in the model.

2. **Bayesian Information Criterion (BIC):** The BIC, also known as the Schwarz Information Criterion (see [18]), is given by

   $$\text{BIC} = -2L(\hat{\boldsymbol{\theta}}) + k \ln(n),$$

   where n is the sample size. BIC favors parsimonious models by imposing a larger penalty for model complexity compared to AIC.

3. **Consistent Akaike Information Criterion (CAIC):** The CAIC (see [4]) is defined as

   $$\text{CAIC} = -2L(\hat{\boldsymbol{\theta}}) + k\left[\ln(n) + 1\right].$$

   Similar to BIC, CAIC also favors parsimonious models by imposing a larger penalty for the number of parameters.

Let $X_1, \ldots, X_n$ be i.i.d. random variables from the $SLL(\alpha, \lambda)$ distribution with $\alpha, \lambda > 0$. The log-likelihood function is given by

$$L(\alpha, \lambda) = n \ln\left(\frac{\pi\alpha}{2\lambda}\right) + \sum_{i=1}^{n} \ln\left[\frac{\left(\frac{X_i}{\lambda}\right)^{\alpha-1}}{\left(1 + \left(\frac{X_i}{\lambda}\right)^{\alpha}\right)^2}\right] + \sum_{i=1}^{n} \ln\left[\cos\left(\frac{\pi}{2\left(1 + \left(\frac{X_i}{\lambda}\right)^{-\alpha}\right)}\right)\right]. \tag{14}$$

The estimating equations of the parameters of $SLL(\alpha, \lambda)$ are obtained by equating the partial derivatives of the log-likelihood function with respect to the parameters to zero i.e,

$$\frac{\partial L}{\partial \alpha} = 0, \frac{\partial L}{\partial \lambda} = 0.$$

Closed-form solutions of the estimating equations cannot be obtained, we use numerical methods to compute the ML estimates of the parameters. Specifically, we minimize the negative log-likelihood function (14) numerically using the L-BFGS-B method available in R.

In Figures 6, 7 and 8 we present the three-dimensional plots of the log-likelihood function (14) for the remission times of bladder cancer [26] and the survival times of head and neck cancer [10], respectively. From these figures, we observe that the log-likelihood function for the SLL distribution in both datasets exhibits a unique maximum.

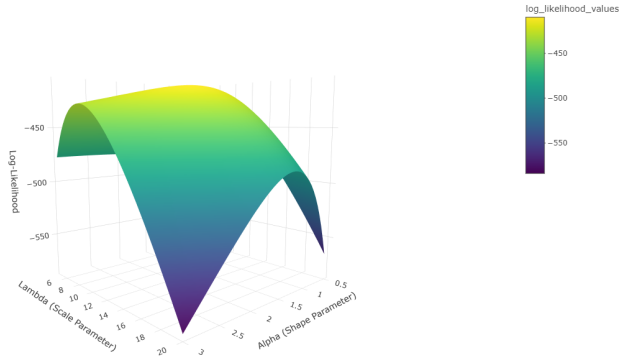


Figure 6: *3D plot of the log-likeihood function for the SLL distribution for Bladder cancer remission times*

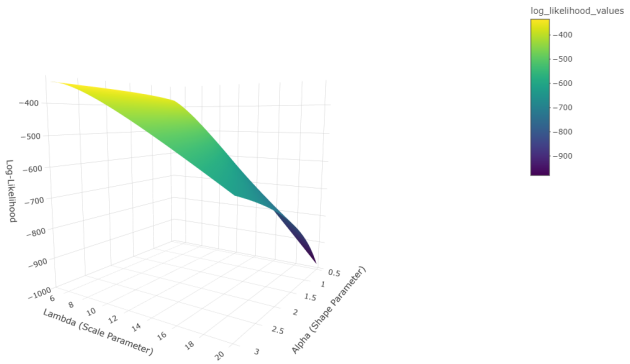


Figure 7: *3D plot of the log-likeihood function for the SLL distribution for survival times of head and neck cancer*

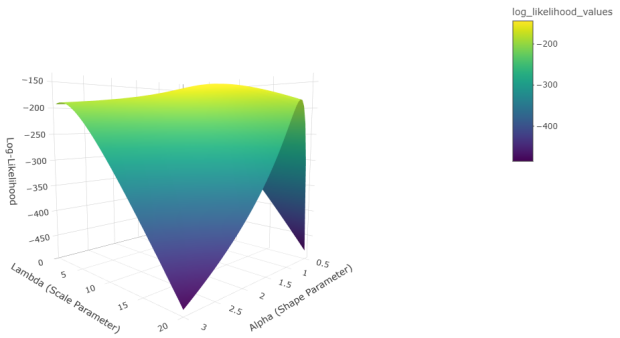


Figure 8: *3D plot of the log-likeihood function for the SLL distribution for Survival times of acute bone cancer*

The log-likelihood function is an important function that helps in evaluating the model selection criteria such as AIC, BIC, and CAIC, as discussed below.

5. Simulation and Real Data Analysis

5.1. Mone-Carlo Simulation.

In this section, we conduct the Monte Carlo simulation method to assess the consistency of ML estimates for the parameters involved in the proposed SLL distribution.

We use the quantile function of the $SLL(\alpha, \lambda)$ given in equation (1.2) to generate $N = 1000$ random samples of varying sizes ($n = 50, 100, 250, 500, 1000$) for different values of the true parameters α, λ (see Tables 5 – 12).we consider cases where the true value of the shape parameter satisfies $\alpha \leq 1$ while in Tables 9–12, we examine scenarios where $\alpha > 1$. In all cases, the scale parameter is fixed at $\lambda = 1$.

We present the mean ML estimates ($\widehat{\alpha}$) and ($\widehat{\lambda}$) of the parameters along with the corresponding root mean squared errors (RMSE) in Tables 5, 6, and 7. The RMSE of a parameter θ is defined as follows:

$$RMSE(\hat{\theta}) = \sqrt{\frac{1}{n}\sum_{i=1}^{n}(\hat{\theta}_i - \theta)^2}. \tag{15}$$

Table 5: *Mean MLEs and RMSEs of parameters α and λ for the SLL distribution over 1000 simulations. True parameter values are $\alpha = 0.25$ and $\lambda = 1$.*

Sample Size	**Mean** $\hat{\alpha}$	**Mean** $\hat{\lambda}$	**RMSE**(α)	**RMSE**(λ)
50	0.257	1.252	0.033	1.200
100	0.253	1.162	0.022	0.700
250	0.251	1.065	0.013	0.390
500	0.251	1.012	0.009	0.248
1000	0.250	1.012	0.006	0.179

Table 6: *Mean MLEs and RMSEs of parameters α and λ for the SLL distribution based on 1000 simulations. True parameter values are $\alpha = 0.5$ and $\lambda = 1$.*

Sample Size	**Mean** $\hat{\alpha}$	**Mean** $\hat{\lambda}$	**RMSE**($\hat{\alpha}$)	**RMSE**($\hat{\lambda}$)
50	0.515	1.034	0.066	0.429
100	0.506	1.040	0.044	0.288
250	0.502	1.016	0.027	0.181
500	0.501	0.998	0.018	0.121
1000	0.501	1.002	0.012	0.088

Table 7: *Mean MLEs and RMSEs of parameters α and λ for the SLL distribution over 1000 simulations. True parameter values are $\alpha = 0.75$ and $\lambda 1$.*

Sample Size	**Mean** $\hat{\alpha}$	**Mean** $\hat{\lambda}$	**RMSE**(α)	**RMSE**(λ)
50	0.772	1.005	0.099	0.270
100	0.759	1.018	0.067	0.185
250	0.752	1.007	0.040	0.119
500	0.752	0.997	0.027	0.080
1000	0.752	1.000	0.019	0.058

Table 8: *Mean MLEs and RMSEs of parameters α and λ for the SLL distribution over 1000 simulations. True parameter values are $\alpha = 1$ and $\lambda = 1$.*

Sample Size	**Mean** $\hat{\alpha}$	**Mean** $\hat{\lambda}$	**RMSE**(α)	**RMSE**(λ)
50	1.029	0.997	0.132	0.200
100	1.012	1.010	0.089	0.137
250	1.003	1.004	0.054	0.088
500	1.003	0.997	0.036	0.060
1000	1.002	1.000	0.025	0.044

Table 9: *Mean MLEs and RMSEs of parameters α and λ for the SLL distribution over 1000 simulations. True parameter values are $\alpha = 1.2$ and $\lambda = 1$.*

Sample Size	**Mean** $\hat{\alpha}$	**Mean** $\hat{\lambda}$	**RMSE**(α)	**RMSE**(λ)
50	1.235	0.995	0.158	0.165
100	1.214	1.007	0.106	0.114
250	1.204	1.003	0.065	0.074
500	1.203	0.998	0.043	0.050
1000	1.203	1.000	0.030	0.036

Table 10: *Mean MLEs and RMSEs of parameters α and λ for the SLL distribution over 1000 simulations. True parameter values are $\alpha = 1.5$ and $\lambda = 1$.*

Sample Size	**Mean** $\hat{\alpha}$	**Mean** $\hat{\lambda}$	**RMSE**(α)	**RMSE**(λ)
50	1.544	0.994	0.197	0.132
100	1.518	1.005	0.133	0.090
250	1.505	1.002	0.081	0.059
500	1.504	0.997	0.054	0.040
1000	1.503	1.000	0.037	0.029

Table 11: *Mean MLEs and RMSEs of parameters α and λ for the SLL distribution over 1000 simulations. True parameter values are $\alpha = 2$ and $\lambda = 1$.*

Sample Size	**Mean** $\hat{\alpha}$	**Mean** $\hat{\lambda}$	**RMSE**(α)	**RMSE**(λ)
50	2.059	0.994	0.263	0.099
100	2.024	1.003	0.178	0.068
250	2.007	1.001	0.109	0.044
500	2.005	0.998	0.072	0.030
1000	2.004	1.000	0.050	0.022

Table 12: *Mean MLEs and RMSEs of parameters α and λ for the SLL distribution over 1000 simulations. True parameter values are $\alpha = 3$ and $\lambda = 1$.*

Sample Size	**Mean** $\hat{\alpha}$	**Mean** $\hat{\lambda}$	**RMSE**(α)	**RMSE**(λ)
50	3.088	0.995	0.396	0.066
100	3.036	1.001	0.266	0.050
250	3.010	1.001	0.162	0.029
500	3.008	0.999	0.107	0.020
1000	3.007	1.000	0.075	0.015

Remark 5. The results in Tables 5–12 the RMSE of the ML estimates of parameters decreases

toward zero with increasing sample size n, indication consistency of the ML estimators for α and λ.

5.2. Data Analysis

In this section, we analyze three datasets viz., remission times (in months) of 128 bladder cancer patients, survival times (in days) of 44 head and neck cancer patients treated with both radiotherapy and chemotherapy [10] and survival times (in days) 73 acute bone cancer patients [16] by using the fitted SLL$(\alpha,\ \lambda)$ distribution. From Tables 2, 3, and 4, we observe that for all the three datasets the estimated value of shape parameter α exceed 1, and hence the corresponding density and hazard functions are inverted bathtub shaped. See Figures 10, 11, 13, 14, 16, and 17. Figures 9 - 17 display the Q-Q plots, hazard functions, and the KDEs alongside the fitted PDFs of the SLL distribution for the bladder cancer remission times, head and neck cancer survival times, and acute bone cancer survival times. For each dataset, we estimate the mode, median, and peak of the hazard function based on the fitted SLL distribution. The mode and the peak of the hazard function are obtained numerically by maximizing the fitted PDF and hazard function. These estimated statistics are summarized in Table 13. The findings for each dataset are outlined below:

- The fitted hazard functions exhibit inverted bathtub shape for all the three data sets, indicating the rate of recurrence or death for each of the three types of cancer patients first increase, reaches a peak and then decrease with increasing remission or survival time. However the peak remission or survival times are drastically different for the three types of cancer.
- **Remission Times Bladder Cancer:**
  For this dataset, the estimated modal remission time is 2.6 months, while the peak of the estimated hazard function occurs at 6.7 months. This indicates that the highest risk of relapse of the bladder cancer arises approximately four months after the most common remission period of 2.6 months. The estimated median remission time is 6.3 months.
- **Survival Times of Head and Neck Cancer:**
  The modal survival time for this dataset is approximately 45 days, while the peak of the hazard function function occurs at around 50 days, which indicate a short period of elevated mortality risk during 45 to 50 days after radiotherapy and chemotherapy and thus the need for intensive monitoring and support during this period.
- **Survival Times of Acute Bone Cancer:**
  For this dataset, the estimated modal survival time is approximately 2.5 days, highlighting a very short typical survival period. The peak of the hazard function occurs at around 7 days, while the median survival time is estimated to lie between 6 and 6.5 days. These findings suggest that the highest risk of mortality arises shortly within a week the most typical survival time, emphasizing the aggressive nature of the cancer.

Table 13: *Estimated mode, median, and mode of the hazard function using the fitted SLL distribution for bladder cancer, head and neck cancer, and acute bone cancer datasets*

Cancer Type	Mode	Median	Mode of Hazard Function
Bladder Cancer	2.6 (months)	6.3 (months)	6.7 (months)
Head and Neck Cancer	45 (days)	131.8 (days)	50 (days)
Acute Bone Cancer	2.6 (days)	6.3(days)	6.8 (days)

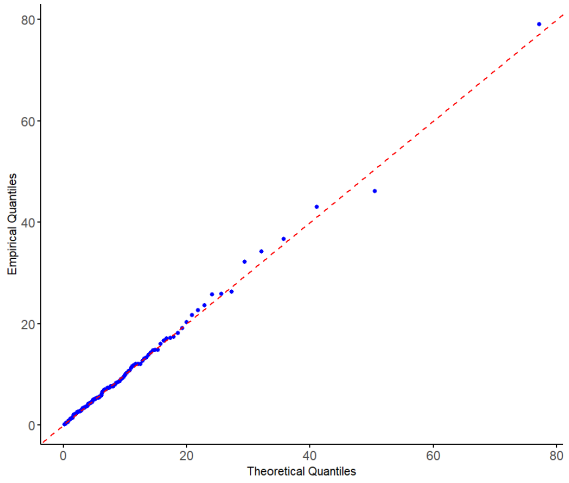


Figure 9: *Q-Q plot for the bladder cancer remission times data*

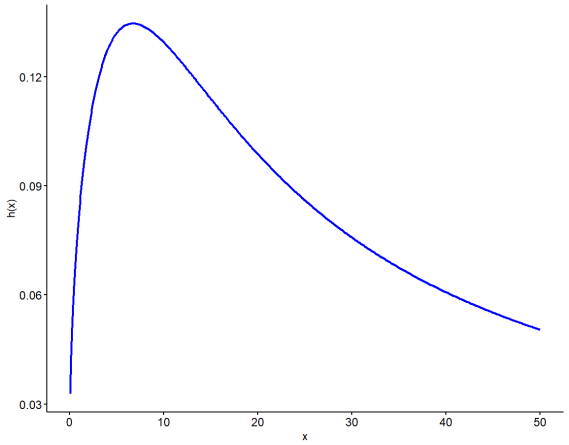


Figure 10: *Plot of hazard function of the fitted SLL distribution for the bladder cancer remission times data*

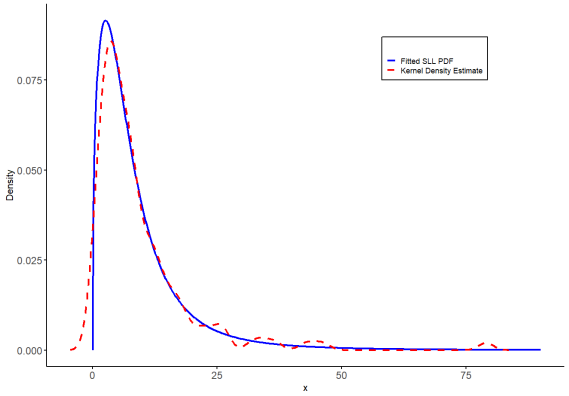


Figure 11: *Plot of the fitted SLL density along with the KDE plot for the bladder cancer remission times data*

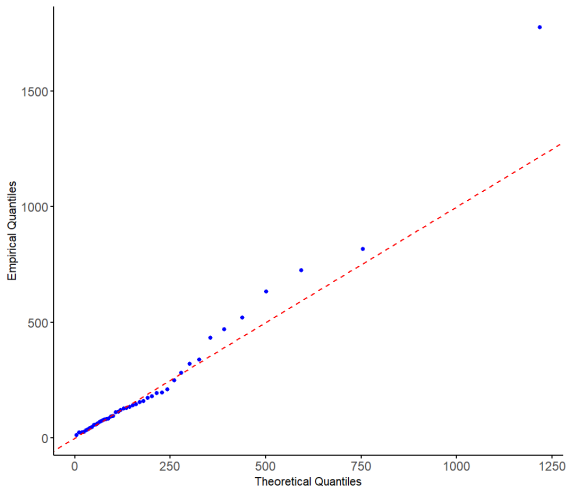


Figure 12: *Q-Q plot for the the survival times of head and neck cancer data*

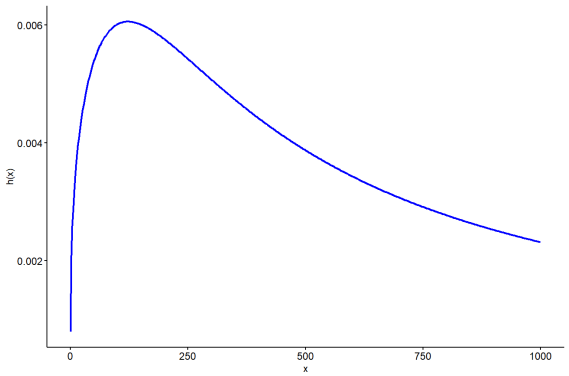


Figure 13: *Plot of hazard function of the fitted SLL distribution for the the survival times of head and neck cancer data*

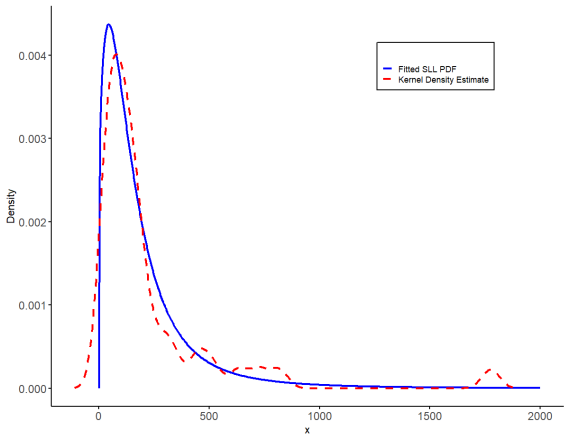


Figure 14: *Plot of the fitted SLL density along with the KDE plot for the the survival times of head and neck cancer data*

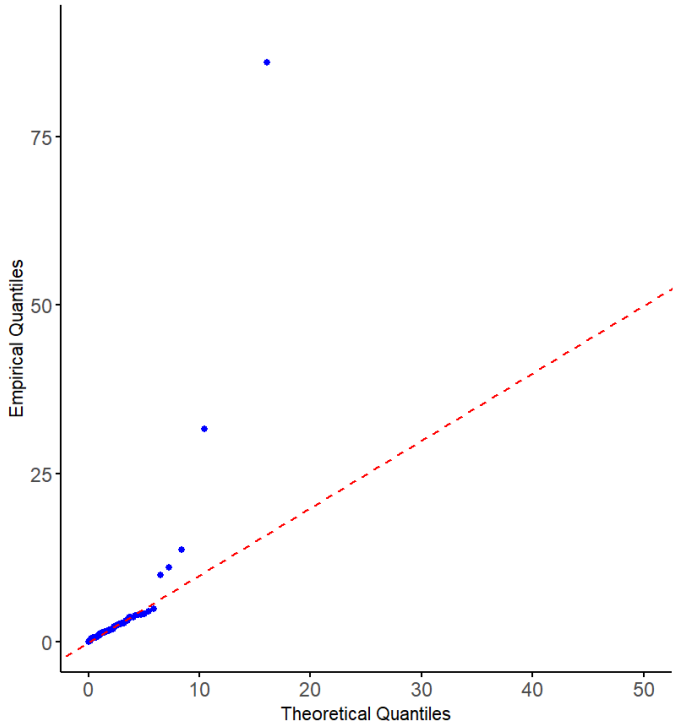


Figure 15: *Q-Q plot for the the survival times acute bone cancer*

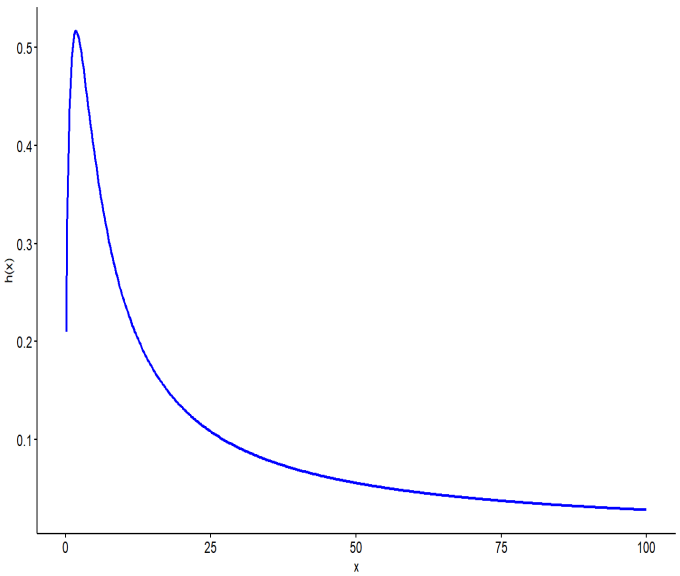


Figure 16: *Plot of hazard function of the fitted SLL distribution for the the survival times acute bone cancer*

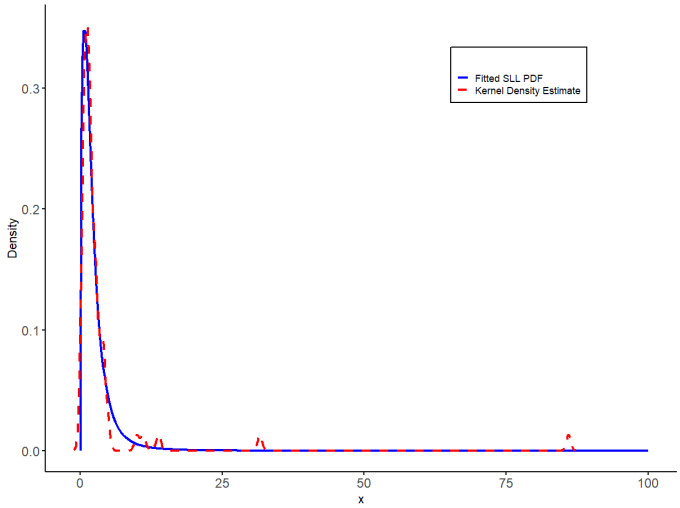


Figure 17: *Plot of the fitted SLL density along with the KDE plot for the the survival times acute bone cancer*

Funding

The first author was supported by Council of Scientific & Industrial Research, Government of India under the CSIR-JRF scheme (Grant No. 09/796(0121)/2021-EMR-I). The author thanks the funding agency for the financial assistance.

Declarations

The authors declare that they have no conflict of interest.

References

[1] Alotaibi, R., Nassar, M., & Elshahhat, A. (2024). A new extended Pham distribution for modelling cancer data. *Journal of Radiation Research and Applied Sciences*, **17**(3), 100961.
[2] Abiodun, A. A., & Ishaq, A. I. (2022). On Maxwell-Lomax distribution: Properties and applications. *Arab Journal of Basic and Applied Sciences*, **29**(1), 221-232.
[3] Alzaatreh, A., Lee, C., & Famoye, F. (2013). A new method for generating families of continuous distributions. *Metron*, **71**(1), 63-79.
[4] Anderson, D. R., Burnham, K. P., & White, G. C. (1998). Comparison of Akaike information criterion and consistent Akaike information criterion for model selection and statistical inference from capture-recapture studies. *Journal of Applied Statistics*, **25**(2), 263-282.
[5] Benkhelifa, L. (2017). The Marshall-Olkin extended generalized Lindley distribution: Properties and applications. *Communications in Statistics-Simulation and Computation*, **46**(10), 8306-8330.
[6] Chamunorwa, S., Makubate, B., Oluyede, B., & Chipepa, F. (2021). The exponentiated half logistic-log-logistic Weibull distribution: Model, properties and applications. *Journal of Statistical Modelling: Theory and Applications*, **2**(1), 101-120.
[7] Colleoni, M., Bonetti, M., Coates, A. S., et al. (2000). Early start of adjuvant chemotherapy may improve treatment outcome for premenopausal breast cancer patients with tumors not expressing estrogen receptors. *Journal of Clinical Oncology*, **18**(3), 584-590.
[8] Collett, D. (2023). *Modelling Survival Data in Medical Research.* Chapman and Hall/CRC.
[9] de Haan, L., & Ferreira, A. (2006). *Extreme value theory: An introduction*. Springer Science & Business Media.

[10] Efron, B. (1988). Logistic regression, survival analysis, and the Kaplan-Meier curve. *Journal of the American Statistical Association*, **83**(402), 414-425.
[11] Eissa, F. Y., & Sonar, C. D. (2023). Alpha power transformed extended power Lindley distribution. *Journal of Statistical Theory and Applications*, **22**(1), 1-18.
[12] Gauthami, P., & Chacko, V. M. (2021). DUS transformation of inverse Weibull distribution: An upside-down failure rate model. *Reliability: Theory & Applications*, **16**(2 (62)), 58-71.
[13] Kavya, P., & Manoharan, M. (2023). A new lifetime model for non-monotone failure rate data. *Journal of the Indian Society for Probability and Statistics*, **24**(2), 211-241.
[14] Klakattawi, H. S. (2022). Survival analysis of cancer patients using a new extended Weibull distribution. *PLOS ONE*, **17**(2), e0264229.
[15] Kumar, D., Singh, U., & Singh, S. K. (2015). A new distribution using sine function-Its application to bladder cancer patients data. *Journal of Statistics Applications & Probability*, **4**(3), 417.
[16] Mansour, M., Yousof, H. M., Shehata, W. A., & Ibrahim, M. (2020). A new two parameter Burr XII distribution: properties, copula, different estimation methods and modeling acute bone cancer data. *Journal of Nonlinear Science and Applications*, **13**(5), 223-238.
[17] Mendoza, N. V., Ortega, E. M., & Cordeiro, G. M. (2016). The exponentiated-log-logistic geometric distribution: Dual activation. *Communications in Statistics - Theory and Methods*, **45**(13), 3838-3859.
[18] Neath, A. A., & Cavanaugh, J. E. (2012). The Bayesian information criterion: Background, derivation, and applications. *Wiley Interdisciplinary Reviews: Computational Statistics*, **4**(2), 199-203.
[19] Ray, M., & Shanker, R. (2024). A probability model for survival analysis of cancer patients. *Reliability: Theory & Applications*, **19**(3 (79)), 78-94.
[20] Mudholkar, G. S., & Srivastava, D. K. (1993). Exponentiated Weibull family for analyzing bathtub failure-rate data. *IEEE Transactions on Reliability*, **42**(2), 299-302.
[21] Odhah, O. H., Alshanbari, H. M., Ahmad, Z., & Rao, G. S. (2023). A weighted cosine-G family of distributions: Properties and illustration using time-to-event data. *Axioms*, **12**(9), 849.
[22] Ogunde, A. A., Chukwu, A. U., & Oseghale, I. O. (2023). The Kumaraswamy generalized inverse Lomax distribution and applications to reliability and survival data. *Scientific African*, **19**, e01483.
[23] Oluyede, B., & Moakofi, T. (2023). The gamma-Topp-Leone-type II-exponentiated half logistic-G family of distributions with applications. *Stats*, **6**(2), 706-733.
[24] Oluyede, B., Chipepa, F., & Wanduku, D. (2021). Exponentiated half logistic-power generalized Weibull-G family of distributions: Model, properties and applications. *Eurasian Bulletin of Mathematics*, **3**(3), 134-161.
[25] Lawless, J. F. (2003). *Statistical Models and Methods for Lifetime Data* (2nd ed.). Hoboken, New Jersey: John Wiley & Sons.
[26] Lee, E. T., & Wang, J. (2003). *Statistical methods for survival data analysis*. John Wiley & Sons.
[27] Rannona, K., Oluyede, B., Chipepa, F., & Makubate, B. (2022). The exponentiated odd exponential half logistic-G power series class of distributions with applications. *Journal of Statistics and Management Systems*, **25**(8), 1821-1848.
[28] Shanker, R., & Shukla, K. K. (2023). Power weighted Sujatha distribution with properties and application to survival times of patients of head and neck cancer. *Reliability: Theory & Applications*, **18**(3 (74)), 568-581.

Appendix

Proof of Theorem 2:

The probability density function of the SLL distribution is given by

$$f(x) = \frac{\pi}{2} g(x) \cos\left(\frac{\pi}{2} G(x)\right), \quad x > 0,$$

where $g(x)$ and $G(x)$ are the PDF and df of the log-logistic distribution:

$$g(x) = \frac{(\alpha/\lambda)(x/\lambda)^{\alpha-1}}{[1+(x/\lambda)^{\alpha}]^2}, \quad G(x) = \frac{1}{1+(x/\lambda)^{-\alpha}}.$$

Differentiating $f(x)$, we obtain:

$$f'(x) = \frac{\pi}{2}g'(x)\cos\left(\frac{\pi}{2}G(x)\right) - \frac{\pi^2}{4}g(x)^2\sin\left(\frac{\pi}{2}G(x)\right).$$

The derivative of $g(x)$ is:

$$g'(x) = \frac{g(x)}{x\,(1+(x/\lambda)^{\alpha})}\left[\alpha - 1 - (\alpha+1)(x/\lambda)^{\alpha}\right].$$

Case I: $0 < \alpha \leq 1$

In this case, the expression in brackets is negative for all $x > 0$, implying $g'(x) < 0$. Therefore, $f'(x) < 0$ for all $x > 0$, so $f(x)$ is strictly decreasing on $(0, \infty)$. Moreover, since $g(x) \to \infty$ as $x \to 0$, it follows that $f(x) \to \infty$ as $x \to 0$. Thus, $f(x)$ is unbounded near 0 and strictly decreasing afterwards, implying no mode exists in $(0, \infty)$.

Case II: $\alpha > 1$

In this case, the function $g'(x) = 0$ has a unique solution

$$x^* = \lambda\left(\frac{\alpha-1}{\alpha+1}\right)^{1/\alpha},$$

with $g'(x) > 0$ for $x < x^*$, and $g'(x) < 0$ for $x > x^*$. To find the critical points of $f(x)$, define the function:

$$k(x) = \tan\left(\frac{\pi}{2}G(x)\right) - \frac{2g'(x)}{\pi g(x)^2}.$$

Then $f'(x) = 0$ if and only if $k(x) = 0$. As $x \to 0$, $g(x) \to 0$, $g'(x)/g(x)^2 \to \infty$, and hence $k(x) \to -\infty$. At $x = x^*$, $g'(x^*) = 0$, so $k(x^*) = \tan\left(\frac{\pi}{2}G(x^*)\right) > 0$. One can show that $k'(x) > 0$ in $(0, x^*)$, so $k(x)$ is strictly increasing in this interval.

By the Intermediate Value Theorem, there exists a unique $x_M \in (0, x^*)$ such that $k(x_M) = 0$, hence $f'(x_M) = 0$. Moreover, the sign change of $f'(x)$ from positive to negative at x_M confirms that this is a unique maximum of $f(x)$, i.e., the mode.

Proof of Lemma 1:

We define

$$\theta(x) := \frac{\pi}{2\left(1+\left(\frac{x}{\lambda}\right)^{-\alpha}\right)}$$

and

$$\varepsilon(x) := \frac{\pi}{2} - \theta(x) = \frac{\pi}{2}\left(1 - \frac{1}{1+\left(\frac{x}{\lambda}\right)^{-\alpha}}\right).$$

As $x \to \infty$, we have

$$\varepsilon(x) \sim \frac{\pi}{2}\left(\frac{x}{\lambda}\right)^{-\alpha}.$$

Now, as $\varepsilon(x) \to 0$, we have the following approximations:

$$\cos[\theta(x)] = \cos\left[\frac{\pi}{2} - \varepsilon(x)\right] = \sin[\varepsilon(x)] \sim \varepsilon(x) \sim \frac{\pi}{2}\left(\frac{x}{\lambda}\right)^{-\alpha}$$

$$1 - \sin[\theta(x)] = 1 - \sin\left[\frac{\pi}{2} - \varepsilon(x)\right] = 1 - \sin[\varepsilon(x)] \sim \frac{1}{2}\varepsilon(x)^2 \sim \frac{\pi^2}{8}\left(\frac{x}{\lambda}\right)^{-2\alpha}$$

Therefore, for large x, the hazard function given in (4) can be approximated as

$$h(x) \sim \frac{\frac{\pi^2\alpha}{2}\left(\frac{x}{\lambda}\right)^{-1}}{\frac{\pi^2}{4}\lambda} = \frac{4\alpha}{\lambda^2}\cdot\frac{1}{x}.$$

Hence,

$$\lim_{x\to\infty} h(x) = 0.$$

Proof of Lemma 2:

Since f is differentiable, the hazard function $h(x) = \frac{f(x)}{1-F(x)}$ is differentiable.
Differentiating h gives

$$h'(x) = \frac{f'(x)(1-F(x)) + f(x)^2}{(1-F(x))^2}.$$

The sign of $h'(x)$ is determined by the numerator

$$N(x) = f'(x)(1-F(x)) + f(x)^2.$$

On $[0, t^*]$, $f'(x) \geq 0$ and $f(x)^2 \geq 0$, so $N(x) \geq 0$, implying $h'(x) \geq 0$. Thus, h is increasing on $[0, t^*]$.

If h continues to increase or remain constant on $[t^*, \infty)$, h would be bounded below by $h(t^*)$ and non-decreasing beyond t^*, so $h(x)$ could not converge to zero as $x \to \infty$, contradicting the assumption that $\lim_{x\to\infty} h(x) = 0$.

Thus, there must exist $t^{**} \geq t^*$ such that h is increasing on $[0, t^{**}]$ and decreasing on $[t^{**}, \infty)$, indicating that h is inverse bath-tub shaped.

Proof of Theorem 3:

We define

$$\theta(x) := \frac{\pi}{2\left(1+\left(\frac{x}{\lambda}\right)^{-\alpha}\right)},$$

and

$$\varepsilon(x) := \frac{\pi}{2} - \theta(x) = \frac{\pi}{2}\left(1 - \frac{1}{1+\left(\frac{x}{\lambda}\right)^{-\alpha}}\right).$$

As $x \to \infty$, we have

$$\varepsilon(x) \sim \frac{\pi}{2}\left(\frac{x}{\lambda}\right)^{-\alpha}.$$

Therefore, for large x, we have the following approximation of the survival function of the SLL(α, λ) distribution

$$\bar{F}(x) \sim \frac{1}{2}\left(\frac{\pi}{2}\left(\frac{\lambda}{x}\right)^{\alpha}\right)^2 = \frac{\pi^2}{8}\left(\frac{\lambda}{x}\right)^{2\alpha}.$$

Thus, as $x \to \infty$,

$$\bar{F}(x) \sim \frac{\pi^2}{8}\lambda^{2\alpha}x^{-2\alpha}.$$

Since $\bar{F}(x) \sim Cx^{-2\alpha}$ for some constant $C > 0$, it follows that

$$\lim_{x\to\infty}\frac{\bar{F}(tx)}{\bar{F}(x)} = t^{-2\alpha}, \quad \text{for all } t > 0.$$

Therefore, the survival function $\bar{F}(x)$ is *regularly varying at infinity* with index -2α, that is,

$$\bar{F}(x) \in \mathrm{RV}_{-2\alpha}.$$

MANAGEMENT OF ORGANIZATIONAL RISKS IN ENTERPRISES OF THE RUSSIAN OIL AND GAS SECTORBASED ON EXPERT ASSESSMENT RESULTS

Evgeny Gvozdev
•
Moscow State University of Civil Engineering, Moscow, Russia
evgvozdev@mail.ru

Abstract

For effective management of integrated safety at enterprises within the segment of the Russian oil and gas sector (ROGS), it has become a tradition to create an integrated safety system (ISS) designed to prevent conditions for the emergence of various risks (technical, organizational-technical, and organizational). The risk-oriented approach used at enterprises all-round has gained widespread recognition over the past decades, and any risk is considered a cause that transforms into a hazardous event (HE), such as an accident or fire. Currently, there exists a variety of methods for risk assessment. The article presents a justified approach for selecting a method to assess organizational risks in ISS, which will allow evaluating the activities of the security directions within its structure, identifying control points with significant shortcomings, forming measures to correct identified deviations, and observing the dynamics of improvement in impact indicators over the analyzed time interval. Aim and objectives. The purpose of the article is to justify a method for assessing organizational risks that have arisen due to deficiencies of personnel in directions implementing control measures concerning the personnel of production structural units. A scientific task has been solved in which the preference for using the expert assessment method, known as the priority ranking method, is justified. It has advantages over other methods. The use of the normal distribution functional together with this method allows experts to select an individual security direction in which organizational risk has arisen. A scientific task, in which an example demonstrating the impact indicators of security personnel directions on the overall state of an overall condition of ISS, has been solved. The possibility of using the priority ranking method in practice and obtaining results in quantitative value (measure) for organizational risks is justified.

Keywords: integrated security system, organizational risks, priority ranking method, normal distribution, expert decision, deficiencies

I. Introduction

For various cases of hazardous events (HE) (accidents and fires) that have occurred and may occur at enterprises of the Russian oil and gas sector (ROGS), a risk-oriented approach is required.

Currently, the state of integrated security at oil and gas enterprises in Russia is determined by the results of assessing technical, organizational-technical, and organizational risks [1]. A significant portion (about 75%) of all organizational-technical and organizational risks that arise is associated with the human factor (HF) [2]. If in the field of assessing technical and organizational-technical risks, results have been obtained from scientific schools:

– the Federal State Budgetary Institution of Science Institute of Machine Science of the

Russian Academy of Sciences on risk analysis and safety of hazardous production facilities, which, for instance, annually publishes new monographic collections "Safety of Russia," [3];

– the Closed Joint-Stock Company Scientific and Technical Center for Industrial Safety on the justification of safety of hazardous production facilities, as well as on risk analysis justification, justification and declaration of safety when providing services for a fee in the case of legal entities [4-6];

– the Federal State Budgetary Institution All-Russian Research Institute for Fire Protection on organizational and methodological support of work related to the independent assessment of fire risk when providing services for a fee in the case of legal entities [7-9];

– the Federal State Budgetary Institution All-Russian Research Institute for Civil Defense and Emergency Situations focuses on improving methods for managing risks of emergency situations (ES) considering the challenges and threats to Russia's national security in the development of regulatory legal acts (RLA) and standard documentation (SD) [10; 11].

In the field of organizational risk (OR) assessment, further research requires to enhance technosphere safety at the protection facilities of Russia's oil and gas complex enterprises [1]. This necessity is caused by the following circumstances:

1) Organizational risks arise and manifest when the management personnel of the management body (MB) influence the personnel belonging to the category of production structural units (PSU), i.e., their origin is based on information that is not formalized and represents a qualitative description. Here, certain difficulties arise in transforming the qualitative characteristics described for such risks into a quantitative form.

2) Organizational risks are currently identified and eliminated autonomously in separate areas of activity: – industrial safety (IS) and fire safety (FS); occupational safety (OS), which control the personnel of the PSU (CP PSU) both in daily activities and during investigations of accidents (Rostekhnadzor), fires (the EMERCOM of Russia), and incidents involving injuries and fatalities (Ministry of Labor). The reports lack information on the shortcomings of the personnel's work in a specific safety direction (SD) where such a risk arose and manifested into a hazardous event (HE).

A problematic situation is identified, consisting of the need to manage organizational risks manifested in ES (accidents and fires). The circumstances presented above are characterized by a high degree of relevance. A new result of scientific achievements will be the conclusion about the shortcomings in the practical use of existing methods for assessing organizational risks. Here the need to present a justified preference for a new method arises. To confirm the adequacy of the new method proposed for practical use, it is necessary to provide an example.

II. Research methodology

The activities of Russian oil and gas companies aimed at preventing the conditions for the occurrence and manifestation of organizational risks follow the following sequence (Fig. 1). The developed sequence of actions will allow considering the dynamics of damage reduction—U_{0C} from the occurrence and manifestation of organizational risk—R_0 ES (accidents and fires), when values with indicators of negative impact presented in quantitative form (measure) will become known. Then:

$$U_{0C} = F_{U_{0C}}\{R_0, P\} = \sum_i \left[F_{U_i}(R_{0_i}, P_i\right] = \int C(R_0)P(R_0)dR_0 = \int C(P)R_0(P)dP, \quad (1)$$

where P – the probability of occurrence of ES (accidents and fires); i – groups of negative factors affecting the outcome in the form of ES (accidents and fires); C – weight functions considering the mutual influence of risks.

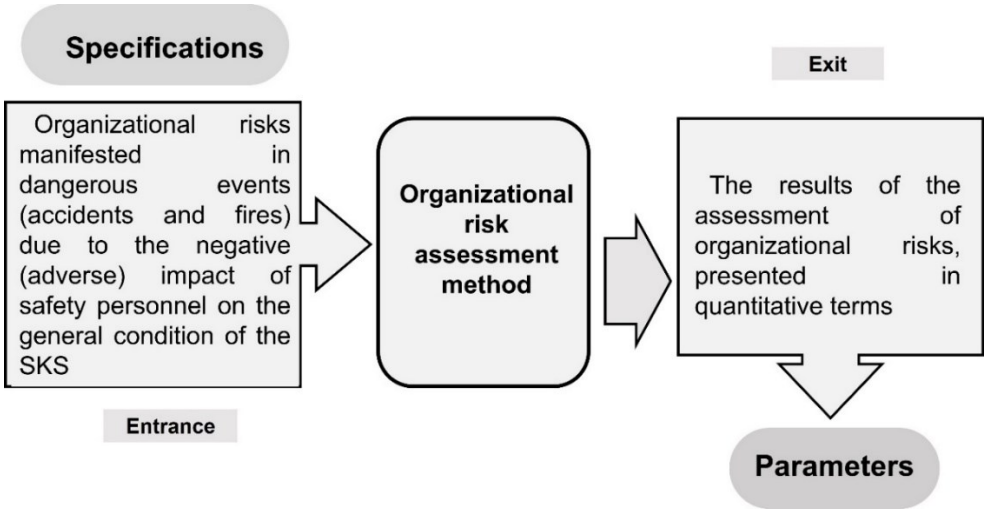


Figure 1: *The sequence of transformation of risks from characteristics to parameters*

The purpose of the article is to justify the choice of an expert method that allows transforming organizational risks with qualitative descriptions into a quantitative value (a measure of negative impact). Therefore, it is necessary to use the magnitude—M the magnitude of the negative impact of organizational risk in the range of change ($M_{min} = 0{,}001;\ BM_{max} = 0{,}999$), then:

$$R_0 = \int_{Mmin}^{Mmax} f(M) \cdot P(M) dM, \quad (2)$$

where $f(M)$– the density distribution of groups of organizational risks considering the frequency of their occurrence in the ES. $P(M)$– the probability of occurrence of organizational risks in the ES is determined using the functionality of Bayesian belief networks [12-14].

Based on the analysis of various risk assessment methodologies used in practice, certain conclusions have been made (Table 1). The information confirms the presence of significant shortcomings in the practical use of a limited number of methods. To analyze the presence of limitations for experts was necessary when conducting sequential activities for risk assessment. Under the general definition of risks, we will understand a recognized danger (threat) of the occurrence of a negative event in any system with consequences defined in time and space[1]. It is advisable to consider the conditions of manifestation (escalation) of risk as the recognized danger (threat), which tend to transfer into the final phase, resulting due to hazardous factors, such as accidents or fires. Considering the specifics of organizational risk assessment, it is recommended to consider them in two directions:

– as deficiencies (D) of the safety personnel controlling the personnel of production structural units (PSU) - R_{ISA};

– as well as staff shortcomings (SC) in the implementation of the requirements of R_{SC} RLA and SD.

[1] Dictionary of Terms and Definitions of the EMERCOM of Russia. The information is provided via the internet link: https://mchs.gov.ru/ministerstvo/o-ministerstve/terminy-mchs-rossii/term/3579. The information is valid as of July 13, 2025

Table 1: *Disadvantages identified when using the developed methods in practice*

<table>
<tr><th>Order of Rostekhnadzor dated November 3, 2022, No. 387</th><th>Order of the EMERCOM of Russia dated June 26, 2024, No. 533</th><th>Order of the Ministry of Labor of Russia dated December 28, 2021, No. 926</th><th>Disadvantages</th></tr>
<tr><td colspan="4">Results with the presentation of values with a qualitative description:</td></tr>
<tr><td>Risk prioritization, based on the categorization of hazards from accidents, the priority value by risk (1;2;3)</td><td rowspan="3">is not present</td><td>is present</td><td rowspan="3">Lack of completeness in the relationships between types of activities. There is no risk result presented as a weighted value in quantitative form, which means there is no possibility to determine the priority of the risk when forming the overall ranked series.</td></tr>
<tr><td>Values of risks from negligibly small to above permissible risk, magnitude by risk (A; B; C; D)</td><td>is present</td></tr>
<tr><td>Values of risks with criticality of deviations, magnitude by risk (high; medium; low)</td><td>is present</td></tr>
<tr><td colspan="4">Results with representation of values in quantitative form:</td></tr>
<tr><td>Values of risks for the frequency of depressurization of technical pipelines, magnitude by risk,10^{-n}/year where –n is a power function.</td><td rowspan="2">is present

Values of risks in determining the calculated evacuation time, magnitude by risk (min.)</td><td>is not present</td><td rowspan="2">Sensitivity to errors in measurements. They have significant inaccuracies. They do not take into account the conditions of independence of preferences between alternatives considering the influence of external factors</td></tr>
<tr><td>Values of risks for causing harm to people, magnitude by risk probability of realization (1-100%), magnitude by risk,10^{-n}/год where –n is a power function.</td><td>is not present</td></tr>
</table>

The overall indicator for organizational risks R_0 for the selected period can be calculated using the formula:

$$R_0(t) = \frac{\sum_{i=1}^{j}(R_{AIT})+\sum_{i=1}^{j}(R_{NI})}{n\cdot(R_{AIT})+n\cdot(R_{NI})}(t), \quad (3)$$

where $n \cdot (R_{AIT})$and $-n \cdot (R_{NI})$ the number of accident reports under consideration included in the sample, (units); t – the period under consideration, (month, quarter, year).

In order to assess organizational risks with the help of experts, using of methods of individual and group evaluation is advisable. In addition, it is necessary to provide mandatory conditions for risk assessment in which explanations on the components are presented to experts:

– assessment of the priority of qualitative risk characteristics and the type of a scale;

– the sequence of techniques or operations subordinated to the task of expressing judgments;

– the sequence of techniques or operations subordinated to the task of processing the results of expert evaluation.

A new method proposed by the author of the article for practical use is a method from a new group of *expert-calculation methods*, namely the *priority ranking method* [15], which will allow the results of qualitative expert evaluation to be transformed into a quantitative form (measure of negative impact). The practical use of the proposed method will allow:

– with the help of a group of experts, select an autonomous direction (IS; FS; OS; CP PSU) in which organizational risk arose due to deficiencies during the implementation of control measures, which manifested in a joint ES. Here, experts have the opportunity to determine the affiliation of such a risk to one of the security directions when answering the question: "In which of the directions (PrB; PB; OT) as well as a separate control direction consisting of the leadership of the PSU (RS PSU) did the organizational risk arise, to which the direction has: - direct (*absolute affiliation)*; indirect (*priority affiliation*); indirect (*relative affiliation*) relation;

– obtain an individual numerical value for each organizational risk in the form$M$ of the magnitude of the negative impact of the organizational risk in the range of change$M_{min} = 0{,}001$; $M_{max} = 0{,}999$). Here, the presence of elements of novelty is clearly confirmed when compared with existing solutions used in practice.

III. Theoretical basis for conducting research

In practice, expert methods mainly involve solving tasks based on prioritization, where one type of expert opinion expression becomes the pairwise comparison of evaluated objects to identify the preference of one over the other. Experts invited for evaluation are not imposed with a priori conditions, and they are given minimal limitations [16]. Mathematically, the solution of expert tasks is described as the effectiveness of the evaluated object in relation to another in the form of a directed graph (see Fig. 2).

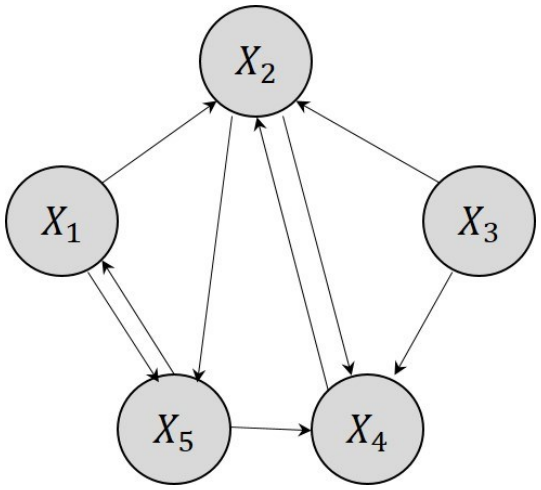


Figure 2: *Graph of the* n *-object evaluation result*

The presented connections in the form of directed vectors (see Fig. 2) will be considered as a set of complex numbers [17], in the form of:

$$x = \left\| \begin{matrix} x_1 \\ x_2 \\ \dots \\ x_n \end{matrix} \right\|. \quad (4)$$

We note the equality of vectors $x$and f$y$or the case of equality of their components, using the addition operation for two vectors:

$$x + y = \left\| \begin{matrix} x_1 + y_1 \\ x_2 + y_2 \\ \vdots \\ x_N + y_N \end{matrix} \right\|. \quad (5)$$

A scalar function of two vectors $x$will $y$be called a scalar product, and the notation will be represented in the form of a formula:

$$(x, y) \sum_{i=1}^{N} x_i y_i.$$

The importance of using the scalar product lies in the fact that the magnitude (x, y) can be considered as the square of the length of the vector plotted on the Re scale of real numbers laid out on the axis x (Fig. 3).

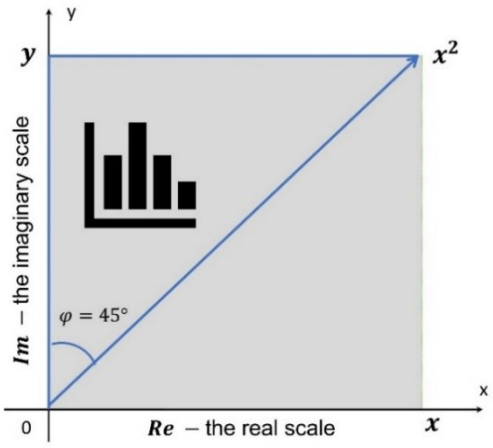


Figure 3: *The vector x, as a square value plotted on a real scale*

Two vectors plotted in relation to the Rescale with real numbers will be called orthogonal if they are brought to the relation:

$$(x, y) = 0.$$

The importance of using vector orthogonality to assess organizational risks can be easily confirmed by obvious established results. If we consider $\{x^i\}$a set of mutually orthogonal vectors plotted on a plane under the condition that the$(x^i, x^j) = 0,$ при $i \neq j$ se vectors are normalized under the condition: $(x^i, x^j) = 1$. Then the overall vector $\boldsymbol{x}$ will be resented as the sum of vectors by the formula:

$$x = \sum_{i=1}^{M} c_i \, x^i, \quad (6)$$

where c_i are numerical coefficients, then it becomes obvious to consider the equation in the form:

$$c_i = (x, x^i). \tag{7}$$

It is also valid to consider the relationship in the form:

$$(x, x) = \sum_{i=1}^{M} c_i^2. \tag{8}$$

If we take as a basis the case with representation on the plane of an N-dimensional Euclidean space, which is defined by vectors:

$$y^1 = \begin{Vmatrix} 1 \\ 0 \\ \cdot \\ \cdot \\ 0 \end{Vmatrix}, \quad y^2 = \begin{Vmatrix} 0 \\ 1 \\ \cdot \\ \cdot \\ 0 \end{Vmatrix}, \; y^N = \begin{Vmatrix} 0 \\ 0 \\ \cdot \\ \cdot \\ 1 \end{Vmatrix}, \tag{9}$$

then their orthogonality will become the resulting directed graph, laid off from the Imimaginary scale of the axis at $y$an angle (see $\varphi = 45°$ Fig. 3). The normalized directed graph will be along the axis, y which is laid off on the imaginary scale - (Im see Fig. 4).

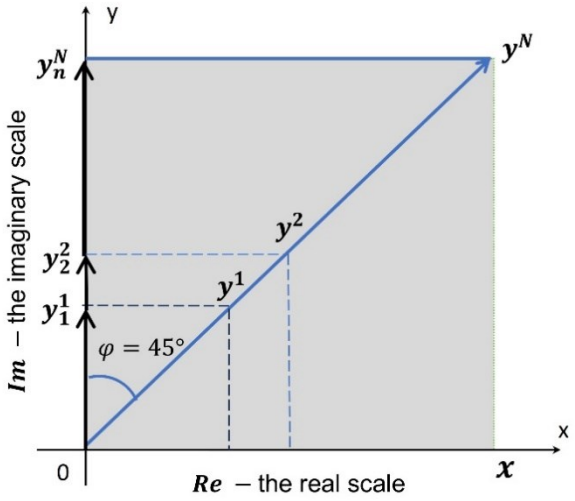


Figure 4: *The y vector represented in orthogonal and normalized directions*

For such an orthogonal and normalized (normorthogonal) representation on the plane of directed vectors (see Fig. 4), we will consider it valid to use the equation:

$$x = \sum_{i=1}^{N} c_i \, y^i.$$

The representation of vectors on the plane in the form of graphical (orthogonal and normalized) directions acquires scientific significance for assessing organizational risks in the SDB at enterprises of ROGS. There arises the possibility:

– *on one hand*, to use the *orthogonal* vector-directed scale as the initial one, on which the emerging risks have no influence, i.e., $\lambda_I = 0$ the influence indicator;

– o*n the other hand,* the impact of security directions implemented to prevent conditions

for the emergence of organizational risks will allow bringing the SDB at enterprises of the Russian NGC to a standardized state, i.e.:

$$\lambda_{\text{Вл}}\{IS; FS; OS; CP\ PSU\} \Rightarrow 1.$$

IV. Justification for the preference in choosing the priority ranking method to assess organizational risks

Each of the n objects $(X_1, X_2, \dots, X_n$ (see Fig. 2) corresponds to a vertex of a graph, which expresses the result of the preference of one evaluated object in relation to another (Fig. 2). Here, it is required to find the maximum of functions of several variables, represented in relation to each other in a ranked dependency. If we consider any computational model from the perspective of its simplification, then it is advisable to consider a quadratic form under the conditions of preference:

$$A = \begin{vmatrix} a_{11} & a_{12}\dots & a_{1j}\dots & a_{1N} \\ a_{21} & a_{23}\dots & a_{2j}\dots & a_{2N} \\ \dots & \dots\ \dots & \dots\ \dots & \dots \\ a_{i1} & a_{i2}\dots & a_{ij}\dots & a_{iN} \\ \dots & \dots\ \dots & \dots\ \dots & \dots \\ a_{n1} & a_{n2}\dots & a_{nj}\dots & a_{nN} \end{vmatrix}, \text{where}$$

a_{ij}- risk indicators based on pairwise comparisons;
N – rank of the matrix;
a_{n1}, a_{n2}, …, a_{nj}, a_{nN} – risk indicators included in the $j-th$ row of the matrix A;
a_{1N}, ,a_{2N} ,… ,a_{iN} a_{nN}– risk indicators included in the j - th column of the matrix A.

At the same time

$$a_{ij} = \begin{cases} 1, if\ X_i > X_j \\ 0{,}5, if\ X_i = X_j, \text{where} \\ 0, if\ X_i < X_j \end{cases}$$

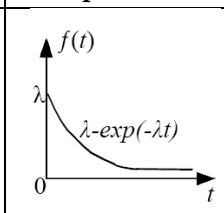
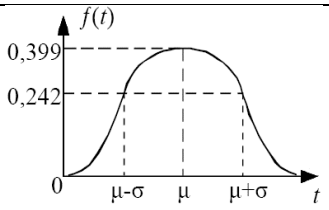
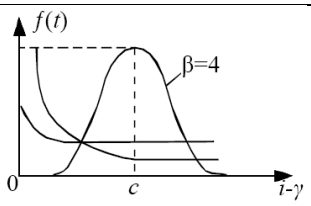
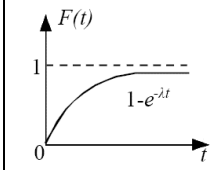
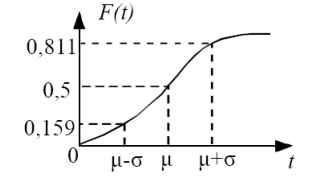
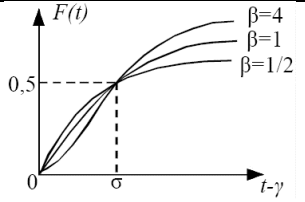
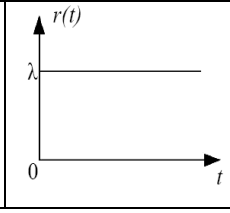
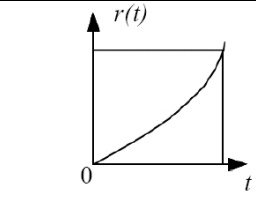
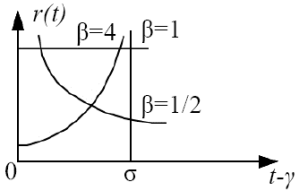
$i = j \to \{1,2, \dots, n\}$; $a_{ij} = 0{,}5$. For organizational risks being compared to each other, in the case of a ranking priority of one over the other, it becomes necessary to present such a comparison in a ratio $X_i > X_j$, and if priority is not observed, this means an equilibrium relationship of one organizational risk to another; accordingly, such a comparison will be presented in the form of a ratio: $X_i = X_j$.

In the case under consideration, there arises a need to use a ratio scale with a description of organizational risks in the form of qualitative characteristics, used by experts for evaluation. It is then required to provide experts with such a new evaluation method that would allow each assessed risk to be endowed with a parameter, i.e., to assign a numerical value to such a risk in the form of a magnitude (measure) of negative impact on the state of the SDB at enterprises of ROGS. For qualitative assessment of organizational risks, the priority ranking method (PRM)remains the preferred priority [15]. However, to obtain new results in the assessment of organizational risks, which would be presented in the form of a magnitude (measure) of negative impact on the state of the SDB at enterprises of ROGS, it was necessary to expand the capabilities of the MPR, i.e., to use it together with the functionality of statistical distributions (tables 2; 3).

Table 2: *Disadvantages identified when using the developed methods in practice*

Parameter	Exponen-tial	Normal (Gaussian)	Weibull
Density of distribution. $f(t)$	$\lambda e^{-\lambda t}$	$\frac{1}{\sigma\sqrt{2\pi}} e\left[-\frac{1}{2}\left(\frac{t-\mu}{\sigma}\right)^2\right]$	$\frac{\beta(t-\gamma)^{\beta-1}}{\sigma^{\beta}} e\left[\left(-\frac{t-\gamma}{\sigma}\right)^{\beta}\right]$
Distribution function. $F(t)$	$1-e^{-\lambda t}$	$\frac{1}{\sigma\sqrt{2\pi}} \int_{-\infty}^{t} e^{-\frac{1}{2}\left(\frac{t-\mu}{\sigma}\right)^2} dx,$ $(-\infty < t < \infty)$	$1-e\left[-\left(\frac{t-\gamma}{\sigma}\right)^{\beta}\right]$
Value of random variable.	λ	$\frac{f(t)}{1-F(t)}$	$\frac{\beta(t-\gamma)^{\beta-1}}{\sigma^{t}}$

Table 3: *Statistical distributions used in practice are presented in the form of graphs*

Parameter	Exponential	Normal (Gaussian)	Weibull
Density of distribution.$f(t)$			
Distribution function. $F(t)$			
Value of random variable.			

Given into account that experts will provide a non-numerical and qualitative characteristic, when determining the quantitative value for each qualitative value presented above, using the functionality of the Gaussian normal distribution (the three-sigma rule for a Gaussian random variable) [18; 19], a specific maximum value from the sample for each of the presented qualitative characteristics will belong (see Fig. 5).

Using the graph (see Fig. 5), it becomes possible to associate quantitative values for the following qualitative characteristics:

– having a *direct* (*absolute belonging*) relation to the emergence and increase of conditions for causing damage from accidents and fires in terms of volume,≈ 68,2% or ≈ 0,682, this indicator is assigned to one direction (IS; FS; OS; CP PSU);

– having an *indirect* (*priority belonging*) relation≈ 27,2%, or ≈ 0,272, this indicator is assigned to one direction (IS; FS; OS; CP PSU), even to the one that was previously characterized as

having a direct relation;

– having an *indirect* (*relative belonging*) relation,≈ 4,6% or ≈ 0,046, this indicator is assigned to one direction (IS; FS; OS; CP PSU);

– having *no relation,* for the selection of a direction to which none of the presented relations with a negative impact indicator was assigned ≈ 0 [20; 21].

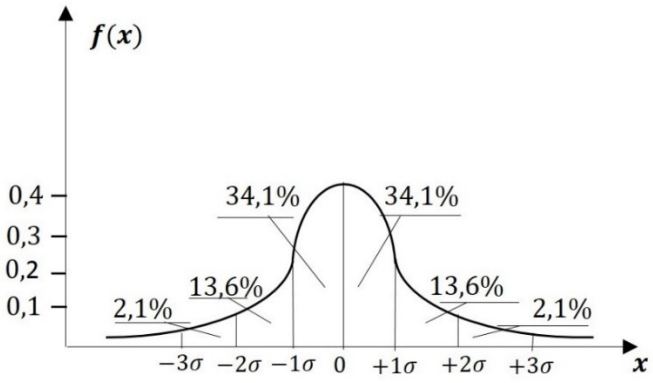


Figure 5: *A graph of the density of the distribution of the normalized value with a representation of the volume ratio*

V. Justification of the quality of expert assessment and confirmation of the reliability of research results

In the case of inviting experts to assess organizational risks at oil and gas companies in Russia, it becomes necessary to confirm the quality of the expert evaluation based on its results.

For this purpose, it is considered advisable to apply methods such as:

– analysis of the consistency of responses received from experts;
– assessment of the reproducibility of survey results obtained from experts.

If the second method largely depends on the choice of various resulting coefficients, such as: variation; rank correlation; concordance; association, etc. [22], then the first method is important because the quality of expert evaluation depends on the consensus judgment of the experts. The result obtained is directly dependent on the consistency (selectivity) among the experts. The consistency (selectivity) of individual expert evaluation results in relation to the overall (integral) indicator should correspond to the values of indicators within the acceptable range(reliability) of values, which should differ from the overall (integral) indicator by no more or less than 10% of a certain value. Before approving the main composition of the working group, at the preliminary stage, the head of the expert group (EG) needs to calculate its size using the formula:

$$n_т = \frac{c\bar{a}_n - b}{\bar{a}_n(1-c)}, \quad (10)$$

where $n_т$ – the number of experts (required), persons; $\bar{a}_n$ – the value of expert assessments in the arithmetic mean calculation; $\bar{a}_{n+1}$ – the value of the assessment from the $(n+1)$-th expert, which significantly differs from the assessments of other experts; c – the measure of influence on the group assessment of one result in the form of the assessment value from the $(n+1)$-th expert, which is considered as a ratio:

$$c = \frac{\bar{a}_{n+1}}{\bar{a}_n}. \quad (11)$$

If $\bar{a}_{n+1}$ expressed through and $\bar{a}_n$, the$b$ ratio will be described as:

$$\bar{a}_{n+1} = \frac{n\bar{a}_n + b}{n+1}. \quad (12)$$

The final value of the measure of influence will be presented as:

$$c = \frac{n\bar{a}_n + b}{(n+1)\bar{a}_n}. \quad (13)$$

At the preliminary stage, experts filled out a questionnaire, which presented the results of the commission investigating the accident at the PJSC "Nizhnekamskneftekhim" enterprise in 2016. The organizational causes taken from the report are presented as organizational risks (Table 4).

Table 4: *List of organizational risks taken from accidents*

No	Organizational risks
1	Failure to ensure the sealing of fittings on the installed section of the pipeline at the bottom of the tank
2	Presence of ignition sources inside the tank farm area (welding post not disconnected), leading to the ignition of a combustible environment.
3	Unsatisfactory organization of the acceptance of completed work after equipment installation
4	Violation of the procedure for the safe commissioning of the tank after installation
5	Ineffectiveness of production control

In the standardized form of organizational risk assessments, the assigned organizational risk assessments largely depend on the competence and number of experts using the functionality of Gaussian probability distribution (Table 5).

Table 5: *Results of expert risk assessments*

Experts	1	2	3	4	5
Expert assessment in standardized form	0.318	0.318	0.682	0.728	0.318

Here (see Table 5), the consistency (selectivity) of individual expert assessment results is not ensured in relation to the general (integral) indicator, as the organizational risk indicator for experts 3 and 4 exceeded the values within the acceptable range(reliability) of values. Using formula (12), the measure of influence on the group assessment of one result in the form of an assessment value from the $(n + 1)$-th expert was found, and it amounted to $c = 1{,}08$.

The calculation results confirmed the need to expand the group of experts to seven people with calculated confirmation:

$$n_t = \frac{1{,}08 \cdot 0{,}47 - 0{,}728}{0{,}47(1-1{,}08)} \approx 7.$$

The minimum expert group composition was determined, which can ensure the required influence of an individual expert's judgment on the group assessment [23]. When processing data from experts in each analyzed accident report, indicators (coefficients) of the negative impact of organizational risks - R_0 are formed for the directions (IS; FS; OS; CP PSU) according to the formula:

$$R_0\{IS; FS; OS; CP\ PSU\} \approx \lambda_{I_{\{1;2;3;4\}}} \in \{IS; FS; OS; CP\ PSU\}, \quad (14)$$

where $\lambda_{I_1} = 0{,}682; \lambda_{I_2} = 0{,}272; \lambda_{I_3} = 0{,}046; \lambda_{I_4} \approx 0.$

The results of the values obtained from experts for the analyzed accident reports in the period of 2014 and 2015 at the enterprises of the Russian oil and gas sector are presented (Fig. 6).

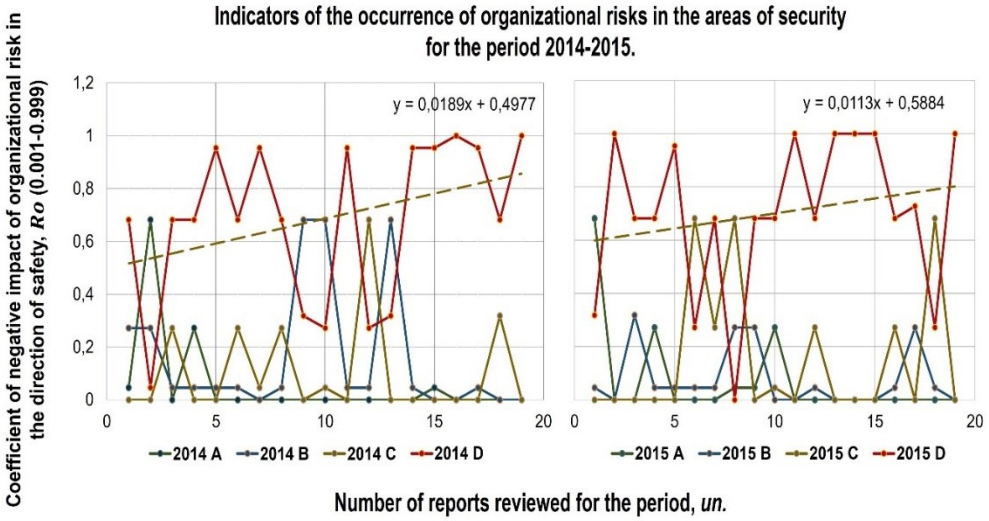


Figure 6: *Indicators of the negative impact of security trends in 2014 – 2015*

The letter designations are assigned to the security directions in the following order: **A** for *OS*; **B** for *IS*; **C** for *FS*; **D** for *control the personnel of the PSU*. In general mathematical form, the calculated value for determining the impact indicator of each security direction $\lambda_{impact}\{IS, FS, OS, CP\ PSU\}$ will be recorded by the equation:

$$\lambda_{impact}\{IS, FS, OS, CP\ PSU\} = {}^{1 - \sum_1^4 R_0\{IS, FS, OS, CP\ PSU\}}/_{3}, \quad (15)$$

where λ_{impact} is the indicator of the effectiveness of the influence of each direction (IS; FS; OS; CP PSU) is obtained based on the difference in the ratios between the indicator of organizational risk manifested in the ES a($1 - as\ 100\%\ influence$) and the indicator obtained based on the decision of experts on the (di*rect, indirect, or mediated)* relation of the direction having a negative impact.

The overall resulting indicator of the work of the direction (IS; FS; OS; CP PSU) for the period$t$, *months*, is calculated with reference to the functioning of types of technological production

processes (D - *extraction*; T - *transportation*; P - *processing*; S - *storage*; Oth - *others*). The presented information (see Fig. 5) confirms the possibility of focusing on those organizational risks that have arisen in the safety directions and have a high coefficient K_{BMI}. Using formula (10), values with effectiveness indicators of influence λ_{impact} were obtained for the directions (IS; FS; OS; CP PSU). Demonstrative information representing the performance indicators of the impact of security directions in processing accident reports in ROGS for 2014 and 2015 (Fig. 7).

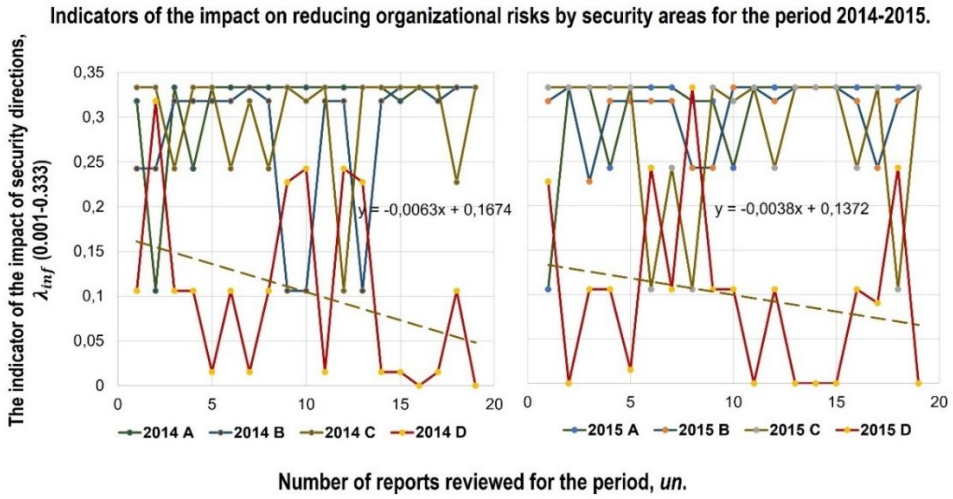


Figure 7: *Indicators of the effectiveness of the impact of security trends in 2014 – 2015*

The final resulting indicator, representing the impact indicator of λ_I of the directions (IS; FS; OS; CP PSU) for the period (year, quarter, month, etc.) linked to the functioning of the production technological process, can be obtained using the equation:

$$\lambda_{I\ (D;T;P;S;Oth)}\{IS;FS;OS;OP\ PSU\}t = \frac{\sum_1^m R_0\{IS;FS;OS;OP\ PSU\}}{n}, \quad (16)$$

where m– the numbered extreme indicator belonging to the sample; n – the number of reports considered for the period.

The final resulting indicator can be represented on a plane in the form of a norm-orthogonal model (Fig. 8).

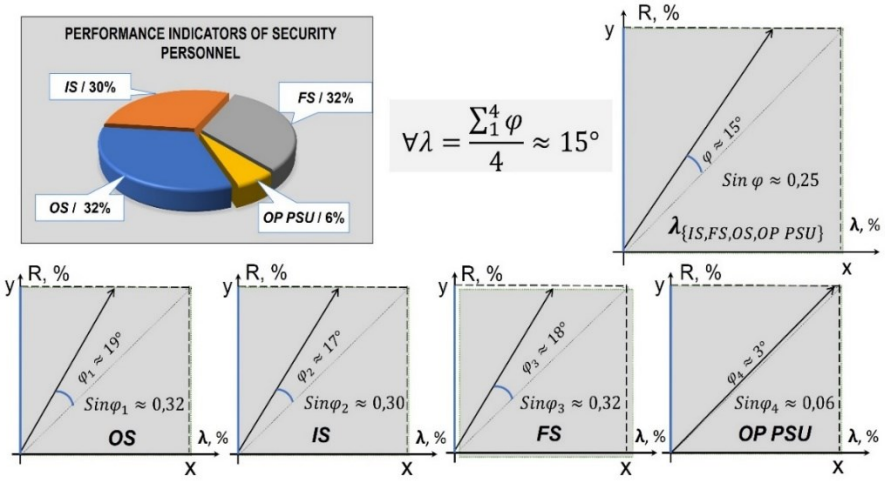


Figure 8: *Performance indicators of security areas for the period 2014 – 2015*

It is possible to calculate the effect of measures taken to reduce organizational risks by considering the total number of accidents (Fig. 6) using ratios

$$\frac{Sin\ \varphi = 15\%}{Sin\ \varphi = 45\%} \cdot 100\% = \frac{0{,}25}{0{,}707} \cdot 100\% \approx 35\%$$

Here, the effect of 35% is viewed as the dynamics of the influence of security areas for an orthogonal system with 100% risks. However, considering that we examine about 20% of all accidents and fires (Fig. 4), the effect of measures taken to reduce organizational risks at ROGS enterprises will amount $^{35\%}/_{5} = 7\%$. Such a significant indicator that allows saving billions of resources in the material-production complex of VPO enterprises (rubles).

The reliability is confirmed by the correctness of using the improved priority ranking method, which is enhanced by the functionality of Gaussian probability distribution (Table 6).

Table 6: *Mathematical apparatus that substantiates the reliability and sensitivity of data processing*

Reliability		
Priority ranking method	$\frac{1}{\sigma\sqrt{2\pi}} \int_{-\infty}^{t} e^{-\frac{1}{2}\left(\frac{t-\mu}{\sigma}\right)^2} dx,$ $(-\infty < t < \infty)$	$\sigma_1 = 0{,}682$ $\sigma_2 = 0{,}272$ $\sigma_3 = 0{,}046$ $\sigma_4 \approx 0$
Sensitivity analysis		
$\bar{x}_a = \frac{\sum_{S=1}^{S=n} x_S m_S}{\sum_{S=1}^{S=n} m_S},$		$\sigma^2 = \frac{\sum_{S=1}^{S=n} (x_S - \bar{x}_a)^2 \cdot m_S}{\sum_{S=1}^{S=n} m_S},$

where

μ – mathematical expectation; (σ_1; σ_2; σ_3; σ_4) – indicators taking into account the standard deviation; $\bar{x}_a$ – indicator of the average value for the data sample; x_S – risk indicator in the middle of the intervals (S) of the interval series; m_S – indicator of the probability of risk occurrence (frequency, recurrence) of the set of features for the interval series; n – list of risks for the sample object; σ^2 – variance estimate for the data sample

V. Conclusions

The study is dedicated to reducing damages at oil and gas companies in Russia by assessing and managing organizational risks arising from deficiencies and shortcomings of personnel ensuring the quality functioning of the control and safety systems. An analysis of retrospective, current, and expert information in the field of safe operation of enterprises was conducted, and the feasibility of scientifically and practically implementing a risk-oriented approach was substantiated.

An improved priority ranking method used for assessing organizational risks arising from personnel deficiencies, R_{ISA} which exercises control over the personnel of production structural units, is justified for practical use.

To reduce the risks of damage from accidents and fires at oil and gas companies in Russia, it is advisable to create a SCS, a new system endowed with the ability to diagnose problematic situations, promptly prepare high-quality projects with management actions to prevent organizational risks for decision-makers, thereby reducing damage from ES (accidents and fires).

References

[1] Gvozdev, E. V. Risk assessment methodology in the integrated safety system designed to prevent accidents and fires at explosive and fire-hazardous enterprises / E. V. Gvozdev // Fire and explosion safety. – 2025. – Vol. 34, No. 1. – pp. 59-69. – DOI 10.22227/0869-7493.2025.34.01.59-69.

[2] Mkrtchyan, L., Straub, U., Giachino, M., Kocher, T., & Sansavini, G. (2022). Insurability risk assessment of oil refineries using Bayesian Belief Networks. Journal of Loss Prevention in the Process Industries, 74. https://doi.org/10.1016/j.jlp.2021.104673.

[3] Problems of strength, technogenic safety and structural materials science / N. A. Makhutov, Yu. G. Matvienko, A. N. Romanov [et al.]; edited by N.A. Makhutov, Yu.G. Matvienko, A.N. Romanov. Moscow: Lenand, 2018. 720 p. ISBN 978-5-9710-5873-1.

[4] Grazhdankin, A. I. Hazard analysis and risk assessment of major accidents in the oil and gas and coal industries: specialty 05.26.03 "Fire and industrial safety (by industry)": dissertation for the degree of Doctor of Technical Sciences / Grazhdankin Alexander Ivanovich, 2016. – 340 p .

[5] Shargatov, V. A. Simulation of gas release from pipelines using a new numerical method based on the Godunov approach / V. A. Shargatov, S. I. Sumskoi, A. S. Pecherkin // Journal of Physics: Conference Series, Moscow, June 25-27, 2018. Vol. 1205. – Moscow: Institute of Physics Publishing, 2019. – P. 012050. – DOI 10.1088/1742-6596/1205/1/012050.

[6] On methodological support for improving state supervision of the state of industrial safety at mining facilities, metallurgical industries and the handling of explosive materials / V. S. Oxman, V. M. Tkachenko, A.V. Fomintsova, A. I. Grazhdankin // Occupational safety in industry. – 2024. – No. 5. – pp. 26-35. – DOI 10.24000/0409-2961-2024-5-26-35.

[7] Assessment of the fire hazard level of industrial facilities based on statistical methods / A. A. Poroshin, E. Y. Udavtsova, E. V. Bobrinev [et al.] // Occupational safety in industry. – 2020. – No. 3. – pp. 12-17. – DOI 10.24000/0409-2961-2020-3-12-17.

[8] Vishnevsky, V. P. Tax Regulation of Economic Growth in the Context of Post-Crisis Recovery: Problems and Prospects / V. P. Vishnevsky, A.V. Matyushin, N. V. Stel'makhova // Studies on Russian Economic Development. – 2025. – Vol. 36, No. 1. – P. 66-76. – DOI 10.1134/S1075700724700539.

[9] Genesis of development, modern realities of scientific, methodological and regulatory legal substantiation of the concepts of "large fire", "complex (protracted) fire" / A. N. Denisov, A. A. Poroshin, M. M. Danilov [et al.] // Fire and explosion safety. – 2025. – Vol. 34, No. 2. – pp. 5-19. – DOI 10.22227/0869-7493.2025.34.02.5-19.

[10] Valery Akimov, Maxim Bedilo, Olga Derendiaeva, Ekaterina Ivanova, Irina Oltyan FORECAST OF NATURAL EMERGENCY SITUATIONS WITH MODERN METHODS // RT&A. 2022. SI 4 (70). URL: https://cyberleninka.ru/article/n/forecast-of-natural-emergency-situations-with-modern-methods (accessed: 06/28/2025).

[11] Valery Akimov, Ekaterina Ivanov, Irina Oltyan STATISTICAL MODELS FOR FORECASTING EMERGENCY SITUATIONS OF A BIOLOGICAL AND SOCIAL CHARACTER. Reliability: Theory & Applications. 2023, December 4(76): 41-45, DOI: https://doi.org/10.24412/1932-2321-2023-476-41-45.

[12] Cheng, J., Greiner, R., Kelly, J., Bell, D., & Liu, W. (2002). Learning Bayesian networks from data: An information-theory based approach. Artificial Intelligence, 137(1–2), 43–90. https://doi.org/10.1016/S0004-3702(02)00191-1.

[13] Mkrtchyan, L., Straub, U., Giachino, M., Kocher, T., & Sansavini, G. (2022). Insurability risk assessment of oil refineries using Bayesian Belief Networks. Journal of Loss Prevention in the Process Industries, 74. https://doi.org/10.1016/j.jlp.2021.104673.

[14] Bochkov, A. Reflections on Dual nature of risk. Towards a formalism / A. Bochkov // Reliability: Theory & Applications. – 2023. – Vol. 18, No. S5(75). – P. 44-74. – DOI 10.24412/1932-2321-2023-575-44-74.

[15] Blumberg V.A., Glushchenko V.F. Which solution is better? The method of prioritization. – L.: Lenizdat, 1982. – 160 p.

[16] Saati T. Decision-making. Method of hierarchy analysis: Translated from English – M.: "Radio and communications". 1993. 320 p.: ill.

[17] Bellman R. An introduction to the theory of matrices. Translated from English by V.B. Lidsky, Nauka Publishing House. Moscow, 1976, 352 pages.

[18] Belikov, A.B. Mathematical processing of geodetic measurement results: a textbook / A.B. Belikov, V.V. Simonyan. Ministry of Education and Science of the Russian Federation. NRU MGSU, 2nd edition revised. Moscow, NRU MGSU 2016, 432 p.

[19] Alamdari, A. M., Jabarzadeh, Y., Adams, B., Samson, D., & Khanmohammadi, S. (2023). An analytic network process model to prioritize supply chain risks in green residential megaprojects. Operations Management Research, 16(1). https://doi.org/10.1007/s12063-022-00288-2.

[20] Certificate of state registration of the computer program No. 2024680621 Russian Federation. "Calculator for assessing the impact of subsystem personnel on the state of the integrated safety system of explosion- and fire-hazardous enterprises": No. 2024665338: application 07/03/2024: publ. 30.08.2024 / E. V. Gvozdev, B. S. Sadovsky, E. D. Gvozdeva.

[21] Gvozdev, E. V. Risk assessment methodology in the integrated safety system designed to prevent accidents and fires at explosive and fire-hazardous enterprises / E. V. Gvozdev // Fire and explosion safety. – 2025. – Vol. 34, No. 1. – pp. 59-69. – DOI 10.22227/0869-7493.2025.34.01.59-69.

[22] Anokhin A.M., Glotov V.A., Pavelyev V.V., Cherkashin A.M. Methods for determining coefficients of criteria importance. Automation and Telemechanics, 1997, issue 8, 3-35.

[23] Gvozdev, E. V. Development of a model for assessing the impact of personnel on the state of the integrated safety system created at industrial enterprises / E. V. Gvozdev // Occupational safety in industry. – 2024. – No. 2. – pp. 7-15. – DOI 10.24000/0409-2961-2024-2-7-15.

RT&A, No 4 (89)
Volume 20, December 2025

OPTIMIZATION AND ANALYSIS OF SKIP-LOT SAMPLING STRATEGIES BASED ON A DOUBLE-SAMPLING FRAMEWORK

Seethalakshmi Ramaswamy[1], Jayaraj. R[2], and D. Kanagajothi[3]

•

[1]Assistant Professor, Department of Mathematics, Rajalakshmi Institute of Technology, Kuthambakkam, Chennai- 600124.
[2]Assistant Professor, Department of Data Science and Business Systems, SRM Institute of Science and Technology the institution will open in a new tab, Kattankulathur, India,
[3]Department of Mathematics, Vel Tech Rangarajan Dr. Sagunthala R and D Institute of Science and Technology, Avadi, Chennai. Tamil Nadu, India.
seethamaths79@gmail.com

Abstract

This paper presents a novel approach to designing skip-lot sampling inspection plans aimed at reducing the required sample size while maintaining effective quality control. By using the traditional double-sampling plan as a reference, the proposed design provides a framework for making inspection more efficient without compromising the reliability of decisions regarding lot acceptance. The study explores the operational characteristics of the suggested plan and evaluates its performance relative to conventional double-sampling procedures, demonstrating that it can achieve equivalent or better-quality assurance with fewer samples. One of the key advantages of the proposed plan is its lower acceptance rates, which enhances the stringency of quality control while potentially reducing inspection costs and effort. The design process incorporates critical quality metrics, including the acceptable quality level and the limiting quality level as well as the acceptable quality level and the average outgoing quality level to guide the selection of the most appropriate sampling plan for a given production scenario. Overall, the proposed skip-lot inspection approach offers a practical, cost-effective alternative to standard sampling techniques, providing manufacturers and quality managers with a method to optimize inspection resources while ensuring high product quality.

Keywords: Sample Size, Double Sampling Plan, Acceptance Rate, Skip-lot Sampling Inspection Plans

I. Introduction

Skip lot sampling plans (SkSP), evolving from Dodge's foundational work on continuous sampling, offer an efficient framework for auditing sequentially produced lots by leveraging a history of high quality. The SkSP-2 variant, recognized for its flexibility, operates by initially conducting a 100% inspection of lots using a predefined reference sampling plan. After a string of i consecutively accepted lots, the system transitions to a reduced-frequency mode, inspecting only a fraction f of the lots; the immediate reinstatement of full inspection upon any rejection provides a self-correcting mechanism for quality deterioration. While various attribute plans single, double,

or multiple—can serve as the reference, recent research has underscored the particular efficacy of pairing SkSP-2 with severe plans, such as a zero-acceptance single-sampling plan, for high-cost or destructive testing scenarios. Building on this principle, a novel advancement is the integration of a double-sampling plan (DSP) as the reference system [1]. This hybrid approach, particularly a SkSP-2 plan with a DSP using acceptance numbers (0,1), demonstrates a superior ability to minimize the average sample number while preserving protection levels, offering significant economic advantages over traditional plans. Construction methodologies and lookup tables for these plans, developed under the Poisson model for defect counts, are provided, with the results remaining a valid approximation for binomial proportions when the fraction nonconforming is small [2].

The inspection process begins with full evaluation of every lot using the reference plan. Once i consecutive lots pass inspection, the plan transitions to partial inspection, where only a fraction f of the lots is sampled [4]. If a defective lot is detected during the reduced inspection phase, full inspection is resumed. As noted by Hahn (1974) [6], various attribute-based sampling methods—such as single, double, or multiple sampling plans—can serve as reference plans within the SkSP-2 framework. Recent studies [5] highlight that combining SkSP-2 with a single-sampling plan (SSP) using a zero-acceptance number is particularly advantageous in scenarios involving destructive or high-cost testing. The core innovation of employing a Double-Sampling Plan (DSP) as the reference plan within the SkSP-2 structure lies in its compound efficiency [3]. A DSP alone reduces the average sample number (ASN) by providing a second chance to inspect a lot before rejection, which is particularly beneficial for lots with quality near the acceptable boundary. The SkSP-2 framework amplifies this efficiency by introducing a temporal dimension; after establishing a record of good quality, the system not only uses smaller samples (via the DSP) but also inspects fewer lots overall. This creates a two-tiered reduction in inspection effort. The resulting hybrid plan is inherently responsive, dynamically adjusting inspection intensity based on real-time quality history [4].

The development of this SkSP-2 plan with a DSP reference addresses a critical need in modern manufacturing and supply chain management for "lean" quality assurance methodologies. In an era of just-in-time production and high-value, complex products, the costs of destructive testing, laboratory analysis, and even simple operational delays are significant. This plan offers a scientifically rigorous method to minimize these costs without compromising the integrity of the outgoing quality control process [9]. Its applicability extends beyond traditional manufacturing to sectors like pharmaceuticals (for batch testing of raw materials), software (for automated testing of sequential builds), and agriculture (for quality assessment of bulk harvests), proving its versatility as a tool for efficient quality surveillance [8].

II. Sampling Plan

The Skip-Lot Sampling Plan of type SkSP-2 is an advanced, statistically driven inspection methodology designed to enhance quality control efficiency. It achieves this by dynamically reducing inspection frequency in response to a demonstrated history of consistent high quality. This plan operates by strategically transitioning between two phases based on the performance of sequentially produced lots. The procedure is initiated in a Normal Inspection phase, where every lot is subjected to a full inspection using a predefined reference plan. The key innovation in the proposed model is the use of a Double-Sampling Plan (DSP) as this reference. Under this DSP, each lot selected for inspection undergoes a two-stage process: an initial sample (n_1) is taken, and a decision to accept or reject the lot is made based on the first acceptance number (c_1). If the results are inconclusive, a second sample (n_2) is drawn, and a final decision is made using a second acceptance number (c_2). This two-stage approach inherent to the DSP provides greater flexibility and reduces the average sample number compared to single-stage plans. Once a predetermined number of consecutive lots (*i*) are accepted under normal inspection, the system transitions to a

Reduced (Skip-Lot) Inspection phase. In this phase, only a fraction *f* of the lots are inspected using the DSP; the remaining lots are automatically accepted without any inspection. This continues until a lot is rejected, which triggers an immediate reversion to the Normal Inspection phase. The cycle repeats, ensuring that the system remains responsive to any degradation in quality.

The integration of a DSP within the SkSP-2 framework introduces a powerful synergy. For instance, a DSP with stringent acceptance numbers like (c_1=0, c_2=1) is exceptionally effective at minimizing inspection effort while maintaining tight control, making it ideal for high-cost or destructive testing environments. Developing such a plan requires the careful specification of several parameters: the clearance number (i), the sampling fraction (f), the DSP parameters (n_1, n_2, c_1, c_2), and the desired performance points such as the Acceptable Quality Level (AQL) and Limiting Quality Level (LQL) to shape the plan's Operating Characteristic (OC) curve. This combination results in a highly adaptive and economically superior inspection system.

Let us designate this skip-lot plan as SkSP-2DSP. The OC function $P_a(p)$ and the average sample number function $\mathrm{ASN}(p)$ of the $\mathrm{SkSP}-2DSP$ plan at quality level p are given as follows:

$$P_a(p) = \sum_{j=0}^{m1} \frac{[m(P) + (1-m)P^j]}{[m + (1-m)P^j]} \tag{1}$$

Here, P is the probability of accept a lot under the DSP, given by

$$P = R(k_1; m_1) + \sum_{k=c_{1+1}}^{c_2} q(k; m_1) R(k_2 - m; k_2)$$

with $k_1 = m_1 p, k_2 = k_2 p, q(m;k) = \exp(-\mathrm{k}) m^k/k$ and

$$R(c_1; n) = \sum_{m=0}^{c_1} q(m; k)$$

We also have

$$\mathrm{ASN(R)} = \mathrm{ASN}(p) \tag{2}$$

Where $\mathrm{ASN}(R)$ is the ASN of the reference plan, i.e.

$$\mathrm{ASN}(R) = k_1 + k_2 \sum_{k=c_{c_1+1}}^{c_2} q(k; m_1)$$

and F is the average fraction of total lots that are inspected, i.e.

$$F = \frac{L}{[L + (1-L)P^k]}$$

III. Comparison of the SkSP-2DSP Plan with the Traditional DSP

In terms of effectiveness, resource use, and inspection effort, the Skip-Lot Sampling Plan of Type SkSP-2 employing a Double-Sampling Plan (SkSP-2DSP) as a reference has a number of advantages over the conventional Double-Sampling Plan (DSP). A thorough comparison of the two schemes' main operating features and performance indicators can be found below. The OC curves of any two lot-inspection plans are a common way to compare them. If the OC curves of

two plans are almost identical, they will be said to be matched. The 'operation ratio' is a commonly used metric to compare the plans; it is defined as follows: $R = p_2/p_1$, where p_1 and p_2 are the values of p such that $P_a(p) = 0.85$ and $P_a(p) = 0.20$ each. Double-sampling inspection plans are now compared to the SkSP-2DSP plan. This can be accomplished by using Table 1. Here, it is assumed that the DSP's first and second sample sizes are equivalent (i.e. $m_1 = m_2$). Take a look at this example [11]. The implementation of a SkSP-2DSP plan is planned. The intended OCs are a consumer's quality level of 9% non-conforming with a 10% chance of acceptance (p2=0.09) and a satisfactory producer's quality level of 2.5% non-conforming with a 95% chance of acceptance (p1=0.025). The intended operating ratio is therefore R=p2/p1=0.09/0.025=3.6. We can see from Table 1 that three R values—3.789, 3.785, and 3.787—are near 3.7. We find the SkSP-2DSP plan with $c_1 = 0, c_2 = 4, f = 1/5$, and i=5 with the maximum value, 3.637. These numbers are supported by Table 1, which gives us $np_1 = 0.921$. The first sample size is $n_1 = np_1/p_1 = 0.8521/0.125 = 38.09 \simeq 37$ and $n_2 = n_1 = 35$, since p_1 is determined to be 0.020. The corresponding DSP has an operating ratio of 3.6421 for SkSP-2DSP plan's R=3.637. The DSP's parameters are $c_1 = 1, c_2 = 5, n_1 = np_1/p_1 = 1.383/0.025 = 53.53 \simeq 54$ and $n_2 = n_1 = 54$. according to Table 1, which corresponds to 3.621. Therefore, the sample size of the SkSP-2DSP plan is smaller than that of the corresponding DSP for the provided values of $p_1, p_2, \alpha = 0.05$, and $\beta = 0.10$ [12].

Table 1: *Operating ratios for DSPs and the SkSP-2 plan with a DSP reference plan*

DSP						SkSP-2 with DSP reference plan					
c_1	c_2	f	i	R	np_1	c_1	c_2	f	i	R	np_1
0	3	1	-	4.928	0.4294	0	1	1/3	4	5.899	0.589
0	3	1	-	5.760	0.9579	0	2	1/3	6	4.793	0.656
						0	2	1\4	10	4.989	0.535
1	2	1	-	5.8603	0.2465	0	1	1/3	4	5.853	0.338
								1/5	10	5.098	0.459
1	3	1	-	5.772	0.8613	0	2	1/3	4	4.120	0.537
						1	2	1/3	6	4.320	0.281
1	4	1	-	4.2713	1.0836	0	3	1/2	8	3.236	0.805
						1	3	1/3	8	5.732	0.680
1	5	1	-	3.6421	1.3423	0	3	1/3	6	5.370	0.621
						0	3	1/5	8	3.210	0.463
						1	4	1/5	4	3.357	1.269
1	6	1	-	4.0466	1.5621	1	4	1/4	6	3.510	1.766
						1	4	1/5	8	5.384	1.389
						1	5	1/4	8	5.525	1.486
2	2	1	-	3.6103	0.9602	1	2	1/3	8	5.224	0.746
2	3	1	-	6.7233	1.3447	0	2	1/5	8	3.065	0.312
						1	3	½	8	3.293	0.843
						2	3	½	4	3.246	0.830
2	4	1	-	4.0823	1.8574	0	3	1/5	10	5.829	0.841
						0	3	1/3	6	5.604	0.870
						1	4	2/3	4	3.890	1.433
						2	3	¼	4	3.894	1.347
						2	4	1/3	4	3.303	1.820
2	6	1	-	3.3046	1.9031	1	4	½	6	3.882	1.564
						1	4	¼	10	3.695	1.219
						1	5	2/3	8	3.989	1.629
						1	5	2/3	10	3.562	1.762
						2	4	¼	4	3.459	1.797

I. SkSP-2DSP plan with smaller acceptance numbers.

An SSP with lesser acceptance values, like c=0 and c=1, is preferred for product features that require expensive or damaging testing by attributes, per Hahn (1974) [6]. However, because the c=0 sampling plan favors the consumer and the c=1 sampling plan favors the producer, the OC curves of SSPs with c=0 and c=1 result in a conflict of interest between the producer and the consumer. Adopting the DSP with $c_1 = 0$ and $c_2 = 1$ will get around this. Furthermore, all DSPs with $c_1 = 0$ and $c_2 = 1$ have the fundamental property that their OC curves fall between those of SSPs with $c = 0$ and $c = 1$. The DSP and the SkSP-2 plan with a DSP as the reference can be used interchangeably in certain circumstances [10]. Additionally, as seen in the preceding section, the SkSP-2DSP design has the advantage of requiring smaller sample sizes than traditional DSPs. When consumer protection is included in terms of (p_2, β), it is beneficial to employ the SkSP-2 plan with a DSP that has $c_1 = 0$ and $c_2 = 1$.

Table 2 makes it evident that when the quality is acceptable, the SkSP-2 plan has a higher chance of being accepted than a DSP with $c_1 = 0$ and $c_2 = 1$, and when the quality is low, the odds of acceptance are the same [12]. This indicates that the SkSP-2DSP plan's OC curve protects consumers in terms of (p_2, β), while providing substantially lower producer risk. The SkSP2DSP plan with $c_1 = 0$ and $c_2 = 1$ is therefore preferred because to the reduced sample size and decreased producer's risk, especially in small-sample scenarios involving expensive or destructive testing [14].

Table 2: *Values of p and $P_a(p)$ for DSPs and SkSP-2 plan with a DSP that has acceptance numbers $c_1 = 0$ and $c_2 = 1$.*

$\boldsymbol{p}$	$\boldsymbol{P_a}$ for DSP with $\boldsymbol{n_1 = n_2 = 20}$	$\boldsymbol{P_a}$ for SkSP-2 with $\boldsymbol{f = 0.5, i = 2}$	$\boldsymbol{P_a}$ for SkSP-2 with $\boldsymbol{f = 0.5, i = 6}$	$\boldsymbol{P_a}$ for SkSP-2 with $\boldsymbol{f = 0.5, i = 6}$
0.01	0.180	0.841	0.965	0.961
0.02	0.190	0.823	0.818	0.890
0.03	0.500	0.531	0.649	0.603
0.04	0.563	0.743	0.505	0.506
0.05	0.409	0.321	0.389	0.340
0.06	0.897	0.385	0.298	0.243
0.07	0.467	0.265	0.227	0.202
0.08	0.072	0.143	0.172	0.108
0.09	0.430	0.147	0.131	0.189
0.10	0.899	0.023	0.099	0.076
0.12	0.087	0.056	0.057	0.058
0.14	0.043	0.076	0.033	0.042
0.16	0.041	0.023	0.020	0.020
0.18	0.035	0.012	0.054	0.017
0.20	0.010	0.006	0.001	0.005

II. The SkSP-2DSP plan with smaller acceptance numbers

Using these tables, the plan can be selected for two sets of criteria: (1) given values of $(p_1, \alpha(= 0.05))$ and$(p_2, \beta(= 0.10))$; (2) given values of p_1 (with $= 0.05$) and the AOQL. Selection of the plan for given $(p_1, \alpha(= 0.05))$ and $(p_2, \beta(= 0.10))$. The OC curve is, in turn, fixed by suitably chosen parameters, such as considering two: The procedure for designing the plan for given values of $p_1, \alpha = 0.05, p_2,$ and $\beta = 0.10$ is as follows [15]. Compute the ratio $R = p_2/p_1$. Select the value of p_2/p_1 from Table 3 in the column headed R that is nearly equal to the computed p_2/p_1 value. Determine the values of np_1, f, and i that correspond to the p_2/p_1 value located. The first sample size n_1 is obtained by dividing np_1 by p_1 [13]. The second sample size n_2 is to be taken as being

equal to n_1, because it is assumed that the first and second sample sizes are equal (Schilling, 1982) [9]. Example. To determine a plan for given values of $p_1 = 0.0075, \alpha = 0.05, p_2 = 0.07$, and $\beta = 0.10$, the following steps should be carried out. For given p_1 and p_2 values, the value of p_2/p_1 is found to be 9.333. From Table 3, the value of p_2/p_1 for $\alpha = 0.05$ and $\beta = 0.10$ is 9.4256, which is nearer to the value 9.333 obtained in the previous step. While selecting a sampling inspection plan, it is usual practice to fix the OC curve according to the desired degree of discrimination. Points on the OC curve, i.e., (P_1, α) and (P_2, β), or by considering one point on the curve, i.e., (P_2, α), along with the criterion of the AOQL, which gives protection to the consumer. In this section, Tables 3 and 4 are presented for designing a SkSP-2DSP plan with c1=0 and c2=1, for the case where the first and second sample sizes are equal. The values of f and i that correspond to 9.4256 are 0.5 and 8, respectively, and the corresponding value of np_1 is 0.262. The value of n_1 is obtained as $n_1 = np_1/p_1 = 0.262/0.0075 = 35.23 \simeq 35$. Because the table referred to is constructed for the case where n_1=n_2, the second sample size for the given problem is n_2=35. Thus, for given values of P1=0.0075, α=0.05, P2=0.07 and β=0.10, the desired SkSP-2DSP-(0, 1) plan includes the parameters n_1=35, n_2=35, f=1/2 and i=8.

Table: 3 *Values of operating ratio R against f and i for certain SkSP-2 DSP-(0,1) plans, for the case when $n_1 = n_2$*

f	i	np_1 for $P_a(p) = 0.85$	np_2 for $P_a(p) = 0.50$	f	i	$R = p_2/p_1$
1	-	0.664	2.49024	1	-	12.0511
2	4	0.837	2.49064	2	12	10.6863
	6	0.435	2.49024		10	10.5519
	8	0.395	2.49024		8	10.3977
	10	0.360	2.49024		6	10.2269
	12	0.303	2.49024		4	10.0279
3	4	0.815	2.49105	3	12	9.8643
	6	0.719	2.49024		10	9.6596
	8	0.642	2.49024		8	9.4256
	10	0.578	2.49024		6	9.1587
	12	0.245	2.49024	0.5	12	8.8725
4	4	0.329	2.49186	0.6	4	8.8492
	6	0.147	2.49025	0.7	10	8.5959
	8	0.008	2.49024		8	8.2787
	10	0.287	2.49024	0.8	12	8.2672
	12	0.287	2.49024		10	7.9535
5	4	0.376	2.49266	0.9	6	7.9131
	6	0.368	2.49026	1.2	12	7.8453
	8	0.279	2.49024	1.5	8	7.5945
	10	0.131	2.49024	1.6	10	7.5098
	12	0.122	2.49024	1.7	4	7.4853

The values of f and i that correspond to 9.4256 are 0.5 and 8, respectively, and the corresponding value of np_1 is 0.2642. The value of n_1 is obtained as $n_1 = np_1/p_1 = 0.2642/0.0075 = 35.23 \simeq 35$. Because the table referred to is constructed for the case where n_1=n_2, the second sample size for the given problem is n_2=35. Thus, for given values of P1=0.0075, α=0.05, P2=0.07 and β=0.10, the desired SkSP-2DSP-(0, 1) plan includes the parameters n_1=35, n_2=35, f=1/2 and i=8, [15].

III. Selection of the plan for given P_1 (with α=0.05) and AOQL

Table 4 can be used for designing SkSP-2DSP-(0,1) plans for given values of p_1 (with $\alpha = 0.05$) and the AOQL. For example, for given values of $p_1 = 0.035$ with $\alpha = 0.05$ and AOQL $= 0.066$, compute

the ratio AOQL/$p_1 = 0.066/0.035 = 1.8857$. From Table 4, the value closest to this is 1.88293, which corresponds to the values $f = 1/2$ and $i = 6$. Corresponding to these values, the value of np_1 is found to be 0.2719. Hence, $n_1 = np_1/p_1 = 0.2719/0.035 = 7.769$, which can be rounded up to the next higher integer to become 8. Thus, the desired plan has the parameters $n_1 = n_2 = 8, f = 1/2$, and $i = 6$.

IV. Construction of Tables 3 and 4

Under the conditions for the application of the Poisson model for the OC curve, for given values of $P_a(p), f$, and i, equation (1) can be solved for np, assuming that $c_1 = 0$ and $c_2 = 1$. Table 3 provides such unity values, i.e., np_1 and np_2 for $P_a(p) = 0.95$ and Pa(p) 0.10, respectively, for various values of f and i. Using these values, the operating ratios p2/p1 are calculated and are also shown in Table 3. (i.e. $n_2 = 2n_1$). Assuming nAOQ $\simeq$ npP$_a$(p), for selected values of f and i, the values of npm that maximize nAOQ are determined, and nAOQL is obtained as nAOQL n$p_m p_a$(pm). These values are shown in Table 4, along with np1 values for P$_a$(p) = 0.95. The ratios AOQL/p_1 are also calculated and shown in Table 4. The tables presented in this paper are for the case when $n_1 = n_2$. A similar set of tables can be constructed for the case when the size of the second sample is twice that of the first sample.

Table 4: *Values of AOQL/p_1 against f and i for certain SkSP-2 DSP-(0,1) plans, for the case when $n_1 = n_2$*

F	i	np_m	nAOQL	np_1 for $P_a(p) = 0.95$	f	i	AOQL/p_1
1	-	1.00000	0.501	0.264	1	-	2.420
0.5	2	0.519	0.519	0.237	1/2	10	2.172
	4	0.942	0.507	0.245	1/2	8	2.139
	6	0.908	0.504	0.235	1/2	6	2.147
	8	0.670	0.534	0.230	1/2	4	2.067
	10	0.697	0.528	0.203	1/2	2	2.386
0.6	2	0.915	0.5500	0.215	1/3	10	1.386
	4	0.906	0.197	0.219	1/3	8	1.403
	6	0.940	0.538	0.242	1/3	6	1.127
	8	0.997	0.575	0.278	1/3	4	1.953
	10	0.952	0.535	0.245	1/4	2	1.893
0.8	2	0.930	0.563	0.329	1/4	10	1.785
	4	0.896	0.521	0.317	1/2	8	1.780
	6	0.946	0.581	0.308	1/2	6	1.663
	8	0.985	0.501	0.297	1/2	4	1.620
	10	0.976	0.538	0.267	1/2	10	1.693
0.9	2	0.934	0.586	0.326	1/3	4	1.666
	4	0.851	0.536	0.368	1/4	8	1.658
	6	0.769	0.519	0.379	1/5	6	1.585
	8	0.973	0.590	0.331	1/5	2	1.570
	10	0.9352	0.502	0.322	1/5	8	1.515
2	2	0.971	0.619	0.401	1/4	7	1.536
	4	0.930	0.544	0.326	1/3	6	1.552
	6	0.9647	0.518	0.393	1/3	4	1.506
	8	0.995	0.505	0.336	1/5	8	1.488
	10	0.920	0.576	0.314	1/5	2	1.421

IV Conclusion

The skip-lot sampling inspection plan using a double-sampling plan (DSP) as its reference referred to as SkSP-2DSP offers significant reductions in sample size compared to traditional DSPs. This design is particularly effective in scenarios involving small sample requirements or costly and destructive testing, especially when acceptance numbers such as such as $C_1 = 0$ and $C_2 = 1$ are used. SkSP-2DSP is well-suited for production environments involving a continuous flow of batches or lots where product quality is consistently high or changes gradually over time. However, in cases of sudden quality deterioration, there is a risk that defective lots may pass unnoticed during the skipping phase. Under such conditions, reverting to a standard DSP provides better protection and responsiveness.

References

[1] DODGE, H. F. (1943) Sampling inspection plan for continuous production. *Annals of Mathematical Statistics*, 14:264-279.

[2] DODGE, H. F. and ROMIG, H. G. Sampling Inspection Table Single and Double Sampling, New York, Wiley, 1959.

[3] Manigandan, P. Pachiyappan, D. Radhamma, J. and Sha, N. (2025). Forecasting of Carbon Emissions in India Using Bayesian ARIMA and BSTS Approaches: Evidence from Environmental Sustainability.

[4] Tsai, T. R. and Wu, S. J. (2006). Acceptance sampling based on truncated life tests for generalized Rayleigh distribution. *Journal of Applied Statistics*, *33*:595-600.

[5] Diwekar, U. M. and Kalagnanam, J. R. (1997). Efficient sampling technique for optimization under uncertainty. *AIChE Journal*, 43(2), 440-447.

[6] Manigandan, P. Alam, M. S. Alagirisamy, K. Pachiyappan, D. Murshed, M. and Mahmood, H. (2023). Realizing the Sustainable Development Goals through technological innovation: Juxtaposing the economic and environmental effects of financial development and energy use. *Environmental Science and Pollution Research*, *30*(3), 8239-8256.

[7] HAHN, G. J. (1974). Minimum size sampling plans. *Journal of Quality Technology*, 6:121-127.

[8] PERRY, R. L. (1973). Skip-lot sampling plans. *Journal of Quality Technology*, 5:123-130.

[9] SCHILLING E. G. Acceptance Sampling in Quality Control, New York, Marcel Dekker, 1982.

[10] Pachiyappan, D. Alam, M. S. Khan, U. Khan, A. M. Mohammed, S. Alagirisamy, K. and Manigandan, P. (2022). Environmental sustainability with the role of green innovation and economic growth in India with BARDL approach. *Frontiers in Environmental Science*, 10, 975177.

[11] Pachiyappan, D. Ansari, Y. Alam, M. S. Thoudam, P. Alagirisamy, K. and Manigandan, P. (2021). Short and long-run causal effects of CO2 emissions, energy use, GDP and population growth: evidence from India using the ARDL and VECM approaches. *Energies*, 14(24):8333.

[12] Alam, M. S. Murshed, M. Manigandan, P. Pachiyappan, D. and Abduvaxitovna, S. Z. (2023). Forecasting oil, coal, and natural gas prices in the pre-and post-COVID scenarios: Contextual evidence from India using time series forecasting tools. Resources Policy, 81, 103342.

[13] Pachiyappan, D. Jayabharathi, S. Evanjalin, Y. G. and Kavitha, S. (2025). Forecasting Volatility in Indian National Stock Exchange Using a Markov Switching GARCH Model. *Reliability: Theory & Applications*, *20*(2(84)):429-446.

[14] Kavitha, S. Rayalu, G. M. Pachiyappan, D. and Manigandan, P. (2023). forecasting of extreme risk using Markov switching GARCH models: evidence from global energy markets. *Reliability: Theory & Applications*, *18*(4 (76)):325-337.

[15] Etikan, I. Alkassim, R. and Abubakar, S. (2016). Comparision of snowball sampling and sequential sampling technique. *Biometrics and Biostatistics International Journal*, *3*(1):55.

SENSITIVITY ANALYSIS OF TRIANGULAR AND SYMMETRIC SPLITTING METHODS FOR POSITIVE DEFINITE LINEAR SYSTEMS - BLOCK STOCHASTIC MATRICES

Bolledla Harika[1], Dasari Rajaiah[2], Renikunta Ramesh[3],
L.P. Rajkumar[4], and Perati Malla Reddy[5]

•

[1]Department of Mathematics, TSWRDCW Warangal West, Telangana, India
hbolledla@gmail.com
[2,3]Department of Mathematics, Kakatiya Institute of Technology and Science Warangal, India.
[2]dr.mh@kitsw.ac.in, [3]rr.mh@kitsw.ac.in
[4,5]Department of Mathematics, Kakatiya University, Telangana, India.
[4]ladella.raj@gmail.com, [5]mperati@yahoo.com

Abstract

In this paper, triangular and symmetric(TS) splitting method is applied to regularized linear system of block stochastic coefficient matrix for finding the steady state probability vector and discussed the sensitivity analysis. The homogeneous system is transformed into regularized non-homogeneous linear system by using preconditioned matrix with the small perturbation. The sensitivity analysis depends on the perturbation parameter. From the numerical results, it is concluded that, the sensitivity analysis and convergence analysis of TS method changes rapidly when a small change in the perturbation parameter. Moreover, the numerical value of spectral radius gives the convergence analysis and the bounds of TS method.

Keywords: Block Stochastic rate matrix, TS splitting method, Condition number, Spectral radius, Perturbation parameter, Error analysis.

1. Introduction

Many problems in engineering and science are mathematically modelled as the following system of homogenous equations:

$$\pi\mathbb{Q} = 0 \quad and \quad \pi e = 1, \tag{1}$$

where, $\mathbb{Q}$ is block stochastic rate matrix and π is the steady state probability vector. The performance measures of any real time system pertaing to the homogenous system depends on the unique solution. Performance measure of finite queue was triggered by Rykov **et.al.** [1]. Shao **et.al.** and Rajaiah **et.al.** suggested a new method for finding the performance measures of internet router with self-similar input process [2, 3]. The solution of above system gives one dimensional null space. But, for a unique non-zero solution, the above homogenous system is converted into the non-homogenous regularized linear system as follows:

Taking transpose on both sides of Eq. (1),

$$\begin{aligned} \pi\mathbb{Q} &= 0 \\ \Rightarrow (\pi\mathbb{Q})^T &= 0 \\ \Rightarrow \mathbb{Q}^T\pi^T &= 0 \\ \Rightarrow \overline{\mathbb{A}}x &= 0 \end{aligned} \tag{2}$$

where, $\overline{\mathbb{A}}$ and x are the transposes of the stochastic rate matrix $\mathbb{Q}$ and steady state vector π respectively. In particular, the coefficient matrix $\overline{\mathbb{A}}$ has zero column sum, positive diagonal entries and non-positive off-diagonal entries.
Since Eq. (2) does not give a unique solution, a non-negative constant $\epsilon > 0$ is added such that it is converted into the preconditioned regularized linear system [7, 8],

$$\mathbb{A}x = (\mathbb{Q}^T + \epsilon I_{n^2})x = e_{n^2} \tag{3}$$

where, $e_{n^2} = [0,\ 0,\ \ldots,\ 0,\ 1]^T$ is the unit vector. The steady-state probability vector π is then obtained by normalizing the vector x.
The steady state probability vector π of regularized linear system is solved by many researchers using different splitting methods and its convergence criteria is also discussed for general and stochastic rate matrices [4, 5, 6, 7, 8, 9, 10, 11, 12]. The significant improvements in convergence rates is achieved from Krylov subspace methods [5, 13], preconditioning techniques by [11, 12, 13], and two splitting and multi splitting iterative methods by [4, 9, 14, 15]. Two alternative methods Hermitian and Skew-Hermitian (HSS) and Positive definite Skew-Symmetric (PSS) methods were proposed which converge unconditionally to a unique solution for the system of equations [4, 16]. Triangular and skew-symmetric splitting method is used to find the steady state vector of regularized linear system [7]. Triangular and symmetric splitting method is used to find the steady state vector of regularized linear system of circulant matrices [8]. Hence, in this chapter, an improved convergence solution for the regularized positive definite linear systems is developed by using block triangular and symmetric (BTS) iteration method.

On the other hand, the perturbation theory was introduced as a new branch in linear algebra and attracted many researchers to focus their attention towards the sensitivity analysis of perturbation linear systems [17, 18, 19, 20]. Sensitivity analysis of perturbation linear system was taken into consideration while calculating the errors using condition number [20]. The condition number plays an important role in the numerical linear algebra. The condition number measures the sensitivity analysis of regularized linear system for small perturbation $\epsilon > 0$. The sensitivity analysis of iterative solution for the regularized linear system and its convergence analysis of a unique non-zero solution depends on the regularized matrix $\mathbb{A}$. If matrix $\mathbb{A}$ is non-singular, then condition number of the matrix decides the convergence of the iterative solution of the regularized linear system $\mathbb{A}x = b$. The system $\mathbb{A}x = b$ posses a unique non-zero solution for non-singular matrix. If the condition number of matrix $\mathbb{A}$ moves to an indefinitely large value for different values of the small perturbation ϵ, then the matrix $\mathbb{A}$ tends to a singular matrix. If matrix $\mathbb{A}$ is singular, then the solution of the system Eq. (3) does not exist. If the matrix is non-singular, then the condition number of $\mathbb{A}$ of the system Eq. (3) is finite. The ill-posed and well-posed solution of the regularized system depends on the perturbation ϵ. The regularized linear system Eq. (3) is well-posed for small condition number and ill-posed for large condition number. In this chapter, the sensitivity analysis of BTS iterative solution using the condition number and spectral radius of regularized stochastic matrix is discussed.

The rest of the chapter is organized as follows: In section 2, condition number and convergence analysis of regularized linear system is discussed. In section 3, the BTS iteration method and its convergence is studied. In section 4, the choice of the contraction factor α is analyzed. Finally, the numerical results are presented in section 5, and the conclusion in section 6

2. Regularized Linear System

Here, first the norm of a matrix, condition number of regularized matrix for sensitivity analysis of regularized linear system are defined. For convergence analysis of a unique non-zero solution of regularized linear system, some basic definitions, and which are used to prove regularized matrix is positive definite are presented. Some theorems for a unique convergence solution of the regularized linear system are proved.

Definition 1. If $\mathbb{A}$ is $m \times n$ matrix then 1-norm, ∞-norm, 2-norm are defined as follows:

- $\|\mathbb{A}\|_1 = Max \sum_{i=1}^{m} \mid a_{ij} \mid$ for $j = 1,\ 2,\ ...,\ n$
- $\|\mathbb{A}\|_\infty = Max \sum_{j=1}^{n} \mid a_{ij} \mid$ for $i = 1,\ 2,\ ...,\ n$
- $\|\mathbb{A}\|_2 = \sqrt{\lambda_{max}(\mathbb{A}^T\mathbb{A})}$

Definition 2. Condition number: The Condition number of a matrix $\mathbb{A}$ is denoted by $\kappa(\mathbb{A})$ and defined as $\kappa(\mathbb{A}) = \|\mathbb{A}\|\|\mathbb{A}^{-1}\|$.

Definition 3. The matrix $\mathbb{A}$ is said to be ill-conditioned, if $\mathbb{A}$ is near to singularity and it is said to well-conditioned, if $\mathbb{A}$ is non-singular matrix.

Definition 4. Any matrix $\mathbb{A} \in R^{n\times n}$ of the form $\mathbb{A} = sI - B, s > 0, B \geq 0$ is called an M-matrix, if $s \geq \rho(B)$.

If $s > \rho(B)$, then $\mathbb{A}$ is well-conditioned M-matrix, otherwise $\mathbb{A}$ is ill-conditioned M-matrix.

Lemma 1. *Let $\mathbb{P}$ be a doubly stochastic block transition probability matrix, then $\mathbb{Q}$ is a doubly stochastic block transition rate matrix.*

Proof. Let

$$\mathbb{P} = \frac{1}{n}\begin{bmatrix} \mathbb{P}_{11} & \mathbb{P}_{12} & \mathbb{P}_{13} & \dots & \mathbb{P}_{1n} \\ \mathbb{P}_{21} & \mathbb{P}_{22} & \mathbb{P}_{23} & \dots & \mathbb{P}_{2n} \\ \mathbb{P}_{31} & \mathbb{P}_{32} & \mathbb{P}_{33} & \dots & \mathbb{P}_{3n} \\ \dots & \dots & \dots & \ddots & \vdots \\ \mathbb{P}_{n1} & \mathbb{P}_{n2} & \mathbb{P}_{n3} & \dots & \mathbb{P}_{nn} \end{bmatrix} \tag{4}$$

is a doubly stochastic block transition probability matrix, where each transition block matrix of order $n \times n$ is defined as

$$\mathbb{P}_{ij} = \begin{bmatrix} p_{11}^{ij} & p_{12}^{ij} & p_{13}^{ij} & \dots & p_{1j}^{ij} & \dots & p_{1n}^{ij} \\ p_{21}^{ij} & p_{22}^{ij} & p_{23}^{ij} & \dots & p_{2j}^{ij} & \dots & p_{2n}^{ij} \\ p_{31}^{ij} & p_{32}^{ij} & p_{33}^{ij} & \dots & p_{3j}^{ij} & \dots & p_{3n}^{ij} \\ \dots & \dots & \dots & \dots & \ddots & \dots & \vdots \\ p_{n1}^{ij} & p_{n2}^{ij} & p_{n3}^{ij} & \dots & p_{nj}^{ij} & \dots & p_{nn}^{ij} \end{bmatrix}$$

Let π be the steady state vector satisfying,

$$\begin{aligned} \pi &= \pi\mathbb{P} \\ \Rightarrow \pi - \pi\mathbb{P} &= 0 \\ \Rightarrow \pi(I_{n^2} - \mathbb{P}) &= 0 \\ \Rightarrow \pi\mathbb{Q} &= 0 \end{aligned}$$

where,

$$\mathbb{Q} = I_{n^2\times n^2} - \mathbb{P} = \begin{bmatrix} I_n - \frac{1}{n}\mathbb{P}_{11} & -\frac{1}{n}\mathbb{P}_{12} & -\frac{1}{n}\mathbb{P}_{13} & \dots & -\frac{1}{n}\mathbb{P}_{1n} \\ -\frac{1}{n}\mathbb{P}_{21} & I_n - \frac{1}{n}\mathbb{P}_{22} & -\frac{1}{n}\mathbb{P}_{23} & \dots & -\frac{1}{n}\mathbb{P}_{2n} \\ -\frac{1}{n}\mathbb{P}_{31} & -\frac{1}{n}\mathbb{P}_{32} & I_n - \frac{1}{n}\mathbb{P}_{33} & \dots & -\frac{1}{n}\mathbb{P}_{3n} \\ \dots & \dots & \dots & \ddots & \vdots \\ -\frac{1}{n}\mathbb{P}_{n1} & -\frac{1}{n}\mathbb{P}_{n2} & -\frac{1}{n}\mathbb{P}_{n3} & \dots & I_n - \frac{1}{n}\mathbb{P}_{nn} \end{bmatrix} \tag{5}$$

From the above matrix, we have, $\frac{1}{n}\sum_{j=1}^{n}\mathbb{P}_{ij} = I_n$ for each $1 \le i \le n$.
In this case, the sum of each row

$$\begin{aligned} I_n - \frac{1}{n}\mathbb{P}_{i1} - \frac{1}{n}\mathbb{P}_{i2} - \frac{1}{n}\mathbb{P}_{i3} - \dots - \frac{1}{n}\mathbb{P}_{in} &= I_n - \frac{1}{n}(\mathbb{P}_{i1} + \mathbb{P}_{i2} + \dots + \mathbb{P}_{in}) \\ &= 0. \end{aligned}$$

Similarly, it is proved that the sum of each column is zero.
Therefore, the matrix $\mathbb{Q}$ is doubly stochastic rate matrix.

■

Theorem 1. *Let $\mathbb{P}$ be a stochastic transition probability matrix of order $n^2 \times n^2$ with block transition probability matrices, then the block stochastic rate matrix $\mathbb{Q} \in R^{n^2\times n^2}$ is M-Matrix.*
Proof. From Eq. (4), $\mathbb{P}$ is a block stochastic transition probability matrix of order $n^2 \times n^2$ with block transition probability matrices.
From Eq. (5), and Lemma 5.1, $\mathbb{Q}$ is a transition rate matrix with block matrices.
From, Eq. (5), we have,

$$\mathbb{Q}^T = \begin{bmatrix} I_n - \frac{1}{n}\mathbb{P}_{11} & -\frac{1}{n}\mathbb{P}_{21} & -\frac{1}{n}\mathbb{P}_{31} & \dots & -\frac{1}{n}\mathbb{P}_{n1} \\ -\frac{1}{n}\mathbb{P}_{12} & I_n - \frac{1}{n}\mathbb{P}_{22} & -\frac{1}{n}\mathbb{P}_{32} & \dots & -\frac{1}{n}\mathbb{P}_{n2} \\ -\frac{1}{n}\mathbb{P}_{13} & -\frac{1}{n}\mathbb{P}_{23} & I_n - \frac{1}{n}\mathbb{P}_{33} & \dots & -\frac{1}{n}\mathbb{P}_{n3} \\ \dots & \dots & \dots & \ddots & \vdots \\ -\frac{1}{n}\mathbb{P}_{1n} & -\frac{1}{n}\mathbb{P}_{2n} & -\frac{1}{n}\mathbb{P}_{3n} & \dots & I_n - \frac{1}{n}\mathbb{P}_{nn} \end{bmatrix}$$

In order prove the matrix $\mathbb{Q}$ is M-matrix, it is sufiicient to prove that $\frac{\mathbb{Q}+\mathbb{Q}^T}{2}$ is M-matrix.
Now,

$$\frac{\mathbb{Q}+\mathbb{Q}^T}{2} = \begin{bmatrix} I_n - \frac{1}{n}\mathbb{P}_{11} & \frac{-\mathbb{P}_{12}-\mathbb{P}_{21}}{2n} & \frac{-\mathbb{P}_{13}-\mathbb{P}_{31}}{2n} & \dots & \frac{-\mathbb{P}_{1n}-\mathbb{P}_{n1}}{2n} \\ \frac{-\mathbb{P}_{12}-\mathbb{P}_{21}}{2n} & I_n - \frac{1}{n}\mathbb{P}_{22} & \frac{-\mathbb{P}_{23}-\mathbb{P}_{32}}{2n} & \dots & \frac{-\mathbb{P}_{2n}-\mathbb{P}_{n2}}{2n} \\ \frac{-\mathbb{P}_{13}-\mathbb{P}_{31}}{2n} & \frac{-\mathbb{P}_{23}-\mathbb{P}_{32}}{2n} & I_n - \frac{1}{n}\mathbb{P}_{33} & \dots & \frac{-\mathbb{P}_{3n}-\mathbb{P}_{n3}}{2n} \\ \dots & \dots & \dots & \ddots & \vdots \\ \frac{-\mathbb{P}_{1n}-\mathbb{P}_{n1}}{2n} & \frac{-\mathbb{P}_{2n}-\mathbb{P}_{n2}}{2n} & \frac{-\mathbb{P}_{3n}-\mathbb{P}_{n3}}{2n} & \dots & I_n - \frac{1}{n}\mathbb{P}_{nn} \end{bmatrix}$$

$= I_{n^2\times n^2} - R$
where,

$$R = \begin{bmatrix} \frac{1}{n}\mathbb{P}_{11} & \frac{1}{2n}(\mathbb{P}_{12}+\mathbb{P}_{21}) & \frac{1}{2n}(\mathbb{P}_{13}+\mathbb{P}_{31}) & \dots & \frac{1}{2n}(\mathbb{P}_{1n}+\mathbb{P}_{n1}) \\ \frac{1}{2n}(\mathbb{P}_{12}+\mathbb{P}_{21}) & \frac{1}{n}\mathbb{P}_{22} & \frac{1}{2n}(\mathbb{P}_{23}+\mathbb{P}_{32}) & \dots & \frac{1}{2n}(\mathbb{P}_{2n}+\mathbb{P}_{n2}) \\ \frac{1}{2n}(\mathbb{P}_{13}+\mathbb{P}_{31}) & \frac{1}{2n}(\mathbb{P}_{23}+\mathbb{P}_{32}) & \frac{1}{n}\mathbb{P}_{33} & \dots & \frac{1}{2n}(\mathbb{P}_{3n}+\mathbb{P}_{n3}) \\ \dots & \dots & \dots & \ddots & \vdots \\ \frac{1}{2n}(\mathbb{P}_{1n}+\mathbb{P}_{n1}) & \frac{1}{2n}(\mathbb{P}_{2n}+\mathbb{P}_{n2}) & \frac{1}{2n}(\mathbb{P}_{3n}+\mathbb{P}_{n3}) & \dots & \frac{1}{n}\mathbb{P}_{nn} \end{bmatrix} \geq 0 \qquad (6)$$

Now, we have to find spectral radius of R.
If r is the largest eigen value of R, and $r_1, r_2, \dots, r_n$ are non zero row sums of the matrix R, then from the paper [**?**], we have

$$\min_j \frac{1}{r_j}\frac{1}{n}\sum_{j=1}^{n} p_{jn}r_j = \rho(R) \leq r \leq \rho(R) = \max_j \frac{1}{r_j}\frac{1}{n}\sum_{j=1}^{n} p_{jn}r_j$$

Since R is the non- negative matrix with non zero row sums $r_1, r_2, \dots, r_n$ and p_{ij} $(1 \leq i,\ j \leq n)$ are transition probablity matrices, then the sum of each row and each column is unity. That is,

$$\begin{gathered} r_1 = r_2 = \dots\dots = r_n = 1 \\ \Rightarrow 1 = \rho(R) \leq r \leq \rho(R) = 1 \\ \Rightarrow \rho(R) = 1 \end{gathered}$$

Since $\frac{\mathbb{Q}+\mathbb{Q}^T}{2} = I_{n^2\times n^2} - R$ and $\rho(R) = 1$ then by the definition, the stochastic rate matrix $\mathbb{Q}$ with block matrices is M-matrix.

■

Theorem 2. *Let $\mathbb{P}$ be a transition probability matrix with block transition matrices and $\mathbb{Q} \in R^{n^2\times n^2}$ is a stochastic rate matrix with block matrices, then there exist $\epsilon > 0$ such that, $\mathbb{A} = (\mathbb{Q}^T + \epsilon I_{n^2})$ is positive definite.*

Proof. In order prove the matrix $\mathbb{A}$ is positive definite, it is sufficient to prove that its symmetric part *i.e.*, $\frac{\mathbb{A}+\mathbb{A}^T}{2}$ is positive definite.

From Eq. (3), we have,

$$\frac{\mathbb{A}+\mathbb{A}^T}{2} = \frac{\mathbb{Q}+\mathbb{Q}^T}{2} + \epsilon I_{n^2}$$
$$\Rightarrow R = (1+\epsilon) I_{n^2} - \frac{\mathbb{A}+\mathbb{A}^T}{2}$$
$$\Rightarrow R \text{ is the non-negative matrix}$$

Let r be the maximal eigen value of R, such that $\rho(R) = r$,

$$\Rightarrow \mid R - rI_{n^2} \mid = 0$$
$$\Rightarrow (1+\epsilon-r) \text{ is the eigen value of } \frac{\mathbb{A}+\mathbb{A}^T}{2}$$
$$\Rightarrow (1+\epsilon) > \rho(R)$$

Hence, the matrix $\mathbb{A}$ is a positive definite matrix.
Next section involves the iterative solution using the triangular and symmetric splitting method of the non-homogeneous positive-definite regularized linear system $\mathbb{A}x = b$. ■

3. Model description

In this section, the steady state probability vector π of Eq. (1) obtained using regularized linear system Eq. (3) and then analyze its convergence criteria. Here, TS splitting method for finding the solution of linear system Eq. (1) with coefficient matrix is a block stochastic matrix is considered. Let the coefficient matrix $\mathbb{A}$ of the regularized linear system Eq. (3) be splitted in the form, $\mathbb{A} = (\mathbb{L} + \mathbb{D} - \mathbb{U}^T) + (\mathbb{U} + \mathbb{U}^T)$,
where,

$$\mathbb{D} = \begin{bmatrix} I_n - \frac{1}{n}\mathbb{P}_{11} & 0 & 0 & \dots & 0 \\ 0 & I_n - \frac{1}{n}\mathbb{P}_{22} & 0 & \dots & 0 \\ 0 & 0 & I_n - \frac{1}{n}\mathbb{P}_{33} & \dots & 0 \\ \vdots & \vdots & \vdots & \ddots & \vdots \\ 0 & 0 & 0 & \dots & I_n - \frac{1}{n}\mathbb{P}_{nn} \end{bmatrix}$$

$$\mathbb{L} = \begin{bmatrix} \frac{\epsilon}{2}I_n & 0 & 0 & \dots & 0 \\ \frac{1}{n}\mathbb{P}_{21} & \frac{\epsilon}{2}I_n & 0 & \dots & 0 \\ \frac{1}{n}\mathbb{P}_{31} & \frac{1}{n}\mathbb{P}_{32} & \frac{\epsilon}{2}I_n & \dots & 0 \\ \vdots & \vdots & \vdots & \ddots & \vdots \\ \frac{1}{n}\mathbb{P}_{n1} & \frac{1}{n}\mathbb{P}_{n2} & \frac{1}{n}\mathbb{P}_{n3} & \dots & \frac{\epsilon}{2}I_n \end{bmatrix}, \text{ and } \mathbb{U} = \begin{bmatrix} \frac{\epsilon}{2}I_n & \frac{1}{n}\mathbb{P}_{12} & \frac{1}{n}\mathbb{P}_{13} & \dots & \frac{1}{n}\mathbb{P}_{1n} \\ 0 & \frac{\epsilon}{2}I_n & \frac{1}{n}\mathbb{P}_{23} & \dots & \frac{1}{n}\mathbb{P}_{2n} \\ 0 & 0 & \frac{\epsilon}{2}I_n & \dots & \frac{1}{n}\mathbb{P}_{3n} \\ \vdots & \vdots & \vdots & \ddots & \vdots \\ 0 & 0 & 0 & \dots & \frac{\epsilon}{2}I_n \end{bmatrix}.$$

Let,

$$\mathbb{A} = (\mathbb{L} + \mathbb{D} - \mathbb{U}^T) + (\mathbb{U} + \mathbb{U}^T) = \mathbb{T} + \mathbb{S} \tag{7}$$

where, $\mathbb{T} \in R^{n^2 \times n^2}$ is a triangular block stochastic matrix and its diagonal elements are positive, and $\mathbb{S} \in R^{n^2 \times n^2}$ is symmetric block stochastic matrix.

3.1. Iterative Method

Given an initial guess $x^{(0)}$, compute the next approximations using the following scheme [4, 7, 8, 16]:

$$\begin{aligned} (\alpha I_{n^2} + \mathbb{T})x^{(k+1/2)} &= (\alpha I_{n^2} - \mathbb{S})x^{(k)} + b \\ (\alpha I_{n^2} + \mathbb{S})x^{(k+1)} &= (\alpha I_{n^2} - \mathbb{T})x^{(k+1/2)} + b \end{aligned} \tag{8}$$

for $k = 0, 1, 2, \dots$, until $x^{(k)}$ converges for any positive contraction factor α.
The above iterative scheme could be written as

for $k = 0, 1, 2, \dots$, where,
$$x^{(k+1)} = \mathbb{M}(\alpha)x^{(k)} + \mathbb{N}(\alpha)b \tag{9}$$

$$\mathbb{M}(\alpha) = (\alpha I_{n^2} + \mathbb{S})^{-1}(\alpha I_{n^2} - \mathbb{T})(\alpha I_{n^2} + \mathbb{T})^{-1}(\alpha I_{n^2} - \mathbb{S}) \tag{10}$$

and,

$$\mathbb{N}(\alpha) = 2\alpha(\alpha I_{n^2} + \mathbb{S})^{-1}(\alpha I_{n^2} + \mathbb{T})^{-1}$$

Here, $\mathbb{M}(\alpha)$ is called the iteration matrix of BTS iteration method. The BTS iteration method converges to a unique solution, if $\rho(\mathbb{M}(\alpha)) < 1$.

Lemma 2. If $\mathbb{S} = \mathbb{U} + \mathbb{U}^T$ is a symmetric matrix and $\epsilon < 1$ then $\|\mathbb{S}\| < 1$
Proof. By the definition,

$$\begin{aligned} \|\mathbb{S}\| &= \|\mathbb{U} + \mathbb{U}^T\| \\ &\leq \|\mathbb{U}\| + \|\mathbb{U}^T\| \\ &\leq Max(\|\mathbb{U}\| + \|\mathbb{U}^T\|) \\ &\leq \frac{\epsilon}{2} + \frac{\epsilon}{2} \\ \|\mathbb{S}\| &\leq \epsilon \end{aligned}$$

If $\epsilon < 1$ then $\|\mathbb{S}\| < 1$. ■

Lemma 3. If $\|\mathbb{S}\| < 1$ and $\|(\alpha I_n + \mathbb{S})^{-1}\|$ exists then $\|(I_n + \mathbb{S})^{-1}\| \leq \dfrac{1}{1 - \|\mathbb{S}\|}$

Proof. The proof of the theorem is straight forward as in paper [15] ■

Lemma 4. If $\|\dfrac{\mathbb{S}}{\alpha}\| < 1$ and $\|(\alpha I_{n^2} + \mathbb{S})^{-1}\|$ exists then $\|(\alpha I_{n^2} + \mathbb{S})^{-1}\| \leq \dfrac{1}{\alpha - \|\mathbb{S}\|}$

Proof. Let $\alpha > 0$ and $\|\dfrac{\mathbb{S}}{\alpha}\| < 1$
Let $\mathbb{S}$ is symmetric matrix and $\|(\alpha I_{n^2} + \mathbb{S})^{-1}\|$ exists
Now,

$$\begin{aligned}
\|(\alpha I_{n^2} + \mathbb{S})^{-1}\| &= \|[\alpha(I_{n^2} + \frac{\mathbb{S}}{\alpha})]^{-1}\| \\
&= \|(\alpha)^{-1}(I_{n^2} + \frac{\mathbb{S}}{\alpha})^{-1}\| \\
&\leq \frac{1}{\alpha}\left[\frac{1}{1 - \|\frac{\mathbb{S}}{\alpha}\|}\right] \\
&\leq \frac{1}{\alpha}\left[\frac{\alpha}{\alpha - \|\mathbb{S}\|}\right] \\
&\leq \frac{1}{\alpha - \|\mathbb{S}\|}
\end{aligned}$$

■

Theorem 3. If $\|\dfrac{\mathbb{S}}{\alpha}\| < 1$, $\|(\alpha I_n^2 - \mathbb{S})\| < \alpha - \|\mathbb{S}\|$, and $\mathbb{Q}(\alpha) = (\alpha I_n^2 - \mathbb{S})(\alpha I_n^2 + \mathbb{S})^{-1}$ then $\|\mathbb{Q}(\alpha)\| < 1$.

Proof. Let $\mathbb{S}$ is symmetric matrix and $\|(\alpha I_{n^2} + \mathbb{S})^{-1}\|$ exists
From above Lemma, we have $\|(\alpha I_{n^2} + \mathbb{S})^{-1}\| \leq \dfrac{1}{\alpha - \|\mathbb{S}\|}$
Now,

$$\begin{aligned}
\|\mathbb{Q}(\alpha)\| &= \|(\alpha I_n^2 - \mathbb{S})(\alpha I_n^2 + \mathbb{S})^{-1}\| \\
&\leq \|(\alpha I_n^2 - \mathbb{S})\| \ \|(\alpha I_n^2 + \mathbb{S})^{-1}\| \\
&\leq \|(\alpha I_n^2 - \mathbb{S})\| \left[\frac{1}{\alpha - \|\mathbb{S}\|}\right] \\
\|\mathbb{Q}(\alpha)\| &< 1
\end{aligned}$$

■

Theorem 4. *Let $\mathbb{A} \in R^{n^2 \times n^2}$ be a block stochastic matrix of regularized linear system Eq. (3) and $\mathbb{M}(\alpha)$ is iteration matrix of BTS iteration method, then the spectral radius of $\mathbb{M}(\alpha) < 1$*

Proof. From Eq. (8), we have,

$$\begin{aligned}
\mathbb{M}(\alpha) &= (\alpha I_{n^2} + \mathbb{S})^{-1}(\alpha I_{n^2} - \mathbb{T})(\alpha I_{n^2} + \mathbb{T})^{-1}(\alpha I_{n^2} - \mathbb{S}) \\
\rho(\mathbb{M}(\alpha)) &= \|\mathbb{M}(\alpha)\|_2 = \|(\alpha I_{n^2} + \mathbb{S})^{-1}(\alpha I_{n^2} - \mathbb{T})(\alpha I_{n^2} + \mathbb{T})^{-1}(\alpha I_{n^2} - \mathbb{S})\|_2 \\
&\leq \|(\alpha I_{n^2} - \mathbb{T})(\alpha I_{n^2} + \mathbb{T})^{-1}\|_2 \|(\alpha I_{n^2} - \mathbb{S})(\alpha I_{n^2} + \mathbb{S})^{-1}\|_2 \qquad (11)
\end{aligned}$$

Let $\mathbb{Q}(\alpha) = (\alpha I_{n^2} - \mathbb{S})(\alpha I_{n^2} + \mathbb{S})^{-1}$. Since $\mathbb{S}$ is a symmetric matrix, then $\mathbb{S}^T = \mathbb{S}$.

$$\begin{aligned}\mathbb{Q}(\alpha)^T\mathbb{Q}(\alpha) &= ((\alpha I_{n^2} - \mathbb{S})(\alpha I_{n^2} + \mathbb{S})^{-1})^T(\alpha I_{n^2} - \mathbb{S})^{-1}(\alpha I_{n^2} + \mathbb{S}) \\ &= ((\alpha I_{n^2} + \mathbb{S})^{-1})^T((\alpha I_{n^2} - \mathbb{S}))^T(\alpha I_{n^2} - \mathbb{S})^{-1}(\alpha I_{n^2} + \mathbb{S}) \\ &= I_{n^2} \\ &\Rightarrow \mathbb{Q}(\alpha) \text{ is a orthogonal matrix} \\ &\Rightarrow \|\mathbb{Q}(\alpha)\|_2 = 1. \end{aligned} \tag{12}$$

Put, $V(\alpha) = (\alpha I_{n^2} - \mathbb{T})(\alpha I_{n^2} + \mathbb{T})^{-1}$.
Since $V(\alpha)$ is a triangular matrix which is positive definite [7], then

$$\|V(\alpha)\|_2 < 1, \forall \alpha > 0 \tag{13}$$

From Eqs. (11)-(13), we have,

$$\begin{aligned}&\rho(\mathbb{M}(\alpha)) = \|\mathbb{M}(\alpha)\|_2 \leq \|\mathbb{Q}(\alpha)\|_2\|V(\alpha)\|_2 < 1 \\ \Rightarrow\ &\rho(\mathbb{M}(\alpha)) < 1, \forall \alpha > 0\end{aligned}$$

Therefore, the TS iterative solution of the regularized linear system converges to a unique solution. ■

4. Estimation of the Contraction Factor

In this section, the choice of contraction factor and convergence criteria of the iterative solution of regularized linear system is discussed. The following investigation describes formulae in approximating the contraction factor α for BTS iteration method. Contraction factor α plays an important role in convergence solution of the regularized linear system. The contraction factor α minimizes the upper bound of $\rho(\mathbb{M}(\alpha))$. The block coefficient matrix $\mathbb{A}$ of the regularized linear system Eq. (3)) can be splitted into block triangular matrix and block symmetric matrix [4, 10] as follows

$$\begin{aligned}\mathbb{A} &= (\mathbb{L} + \mathbb{D} - \mathbb{U}^T) + (\mathbb{U} + \mathbb{U}^T) = \mathbb{T}_1 + \mathbb{S}_1 \\ \mathbb{A} &= (\mathbb{U} + \mathbb{D} - \mathbb{L}^T) + (\mathbb{L} + \mathbb{L}^T) = \mathbb{T}_2 + \mathbb{S}_2\end{aligned}$$

where, $\mathbb{D}$, $\mathbb{L}$ and $\mathbb{U}$ are block diagonal, lower and upper triangular matrices of block coefficient matrix $\mathbb{A}$ of regularized linear system Eq. (3).
Let, $\mathbb{H}_1 = \mathbb{L} - \mathbb{U}^T$ and $\mathbb{H}_2 = \mathbb{L}^T - \mathbb{U}$ be lower and upper block triangular matrices.
Now,

$$\begin{aligned}(\alpha I_{n^2} + \mathbb{T}_i)^{-1} &= (\alpha I_{n^2} + \mathbb{D} + \mathbb{H}_i)^{-1}, \quad \text{for} i = 1, 2, \ldots, \\ &= (\alpha I_{n^2} + \mathbb{D})^{-1}(I_{n^2} + \mathbb{H}_i(\alpha I_{n^2} + \mathbb{D})^{-1})^{-1}\end{aligned}$$

Using Binomial expansion,

$$(\alpha I_{n^2} + \mathbb{T}_i)^{-1} = (\alpha I_{n^2} + \mathbb{D})^{-1}(I_{n^2} - \mathbb{H}_i(\alpha I_{n^2} + \mathbb{D})^{-1} + \mathbb{H}_i^2((\alpha I_{n^2} + \mathbb{D})^{-1})^2 - \ldots)$$

Consider the first order approximation,

$$(\alpha I_{n^2} + \mathbb{T}_i)^{-1} = (\alpha I_{n^2} + \mathbb{D})^{-1}(I_{n^2} - \mathbb{H}_i(\alpha I_{n^2} + \mathbb{D})^{-1})$$
$$(\alpha I_{n^2} - \mathbb{T}_i)(\alpha I_{n^2} + \mathbb{T}_i)^{-1} = (\alpha I_{n^2} - \mathbb{D} - \mathbb{H}_i)(\alpha I_{n^2} + \mathbb{D})^{-1}(I_{n^2} - \mathbb{H}_i(\alpha I_{n^2} + \mathbb{D})^{-1})$$
$$\|(\alpha I_{n^2} - \mathbb{T}_i)(\alpha I_{n^2} + \mathbb{T}_i)^{-1}\|_2 \approx \|(\alpha I_{n^2} - \mathbb{D})(\alpha I_{n^2} + \mathbb{D})^{-1}\|_2$$

The contraction factor can be obtained using the procedure [4, 7, 8] as follows:

$$\|(\alpha I_{n^2} - \mathbb{T}_i)(\alpha I_{n^2} + \mathbb{T}_i)^{-1}\|_2 \approx max\|(\alpha I_n - ((1+\epsilon)I_n - \frac{1}{n}\mathbb{P}_1))(\alpha I_n - ((1+\epsilon)I_n + \frac{1}{n}\mathbb{P}_1))^{-1}\|_2$$
$$\alpha^\star \approx arg \min_{\alpha>0} max\|(\alpha I_n - ((1+\epsilon)I_n - \frac{1}{n}\mathbb{P}_1))(\alpha I_n - ((1+\epsilon)I_n + \frac{1}{n}\mathbb{P}_1))^{-1}\|_2$$
$$\alpha^\star \approx arg \min_{\alpha>0} max\|\frac{\alpha - \lambda_{min}}{\alpha + \lambda_{max}}\|$$
$$\alpha^\star \approx \sqrt{\lambda_{min}\lambda_{max}} \tag{14}$$

Therefore, the contraction factor $\alpha = \alpha^\star$ minimizes the upper bound of $\rho(\mathbb{M}(\alpha))$. The computation of optimal parameter α is a hard task, that needs further in-depth study. The two half steps of each step of the BTS iteration method require in finding the coefficient matrices $(\alpha I_{n^2} + \mathbb{T}_i)$ and $(\alpha I_{n^2} + \mathbb{S}_i)$ for $i = 1, 2 \ldots$. To improve computing efficiency of the BTS iteration, ITS iteration method is employed, that is used to solve the two sub systems iteratively[4, 7, 8, 10, 16]. The first subsystem coefficient matrix $(\alpha I_{n^2} + \mathbb{T}_i)$ and second sub system coefficient matrix $(\alpha I_{n^2} + \mathbb{S}_i)$ are solved by Krylov subspace methods. The solution of the first sub system can be obtained by straight forward method, where as the solution of second sub system is obtained by *CGS* method.

5. Validation and Numerical Results

In this section, the sensitive analysis, spectral radius and error analysis of Jacobi, BTS, and BTSS methods of the regularized linear system with the coefficient matrix is a block stochastic matrix is depicted. For illustration purpose, the following block transition probability matrix is considered,

$$\mathbb{P} = \frac{1}{3}\begin{bmatrix}
\begin{bmatrix}0.95 & 0.02 & 0.03\\ 0.02 & 0.9 & 0.08\\ 0.03 & 0.08 & 0.89\end{bmatrix} & \begin{bmatrix}0.8 & 0.05 & 0.15\\ 0.05 & 0.7 & 0.25\\ 0.15 & 0.25 & 0.6\end{bmatrix} & \begin{bmatrix}0.6 & 0.25 & 0.15\\ 0.3 & 0.65 & 0.05\\ 0.1 & 0.1 & 0.8\end{bmatrix}\\
\begin{bmatrix}0.8 & 0.15 & 0.05\\ 0.1 & 0.7 & 0.2\\ 0.1 & 0.15 & 0.75\end{bmatrix} & \begin{bmatrix}0.9 & 0.04 & 0.06\\ 0.03 & 0.93 & 0.04\\ 0.07 & 0.03 & 0.9\end{bmatrix} & \begin{bmatrix}0.65 & 0.25 & 0.1\\ 0.15 & 0.55 & 0.3\\ 0.2 & 0.2 & 0.6\end{bmatrix}\\
\begin{bmatrix}0.55 & 0.35 & 0.1\\ 0.25 & 0.6 & 0.15\\ 0.2 & 0.05 & 0.75\end{bmatrix} & \begin{bmatrix}0.8 & 0.05 & 0.15\\ 0.1 & 0.6 & 0.3\\ 0.1 & 0.35 & 0.55\end{bmatrix} & \begin{bmatrix}0.94 & 0.01 & 0.05\\ 0.02 & 0.92 & 0.06\\ 0.04 & 0.07 & 0.89\end{bmatrix}
\end{bmatrix}.$$

Let the initial vector $x^{(0)}$ is $\begin{bmatrix}0 & 0 & 0 & 0 & 0 & 0 & 0 & 1\end{bmatrix}^T$. We compute steady state vector of regularized linear system and corresponding relative error based on the values of ϵ and contraction factor α. The stopping criteria is set as the relative error $< 10^{-15}$. Moreover, the sensitivity analysis and convergence analysis of iterative solution of regularized linear system is obtained by using the condition number and spectral radius of the regularized matrix $\mathbb{A}$ and the results are depicted in Figs. 1-6. Fig. 1 depicts the convergence rate of iterative solution of regularized linear system with absolute error and relative error for the particular values of contraction factor $\alpha = 0.76$ and $\epsilon = 0.1$. From this figure, it is concluded that, BTS iterative solution converges faster than that of

BTSS and Jacobi methods. Fig. 2 depicts the relative error of BTS iterative method for different values of contraction factor $\alpha = 0.76$ and ϵ. From this figure, one can conclude that BTS iterative solution converges rapidly as ϵ increase. The sensitivity analysis of BTS iterative solution depicted in Figs. 3 and 4. From, Fig. 3, it is concluded that the condition number of the regularized matrix $\mathbb{A}$ is low when the contraction factor moves near to diagonal element. Figs. 4, it is concluded that the condition number of regularized matrix $\mathbb{A}$ is low while comparing with BTSS method. From these two figures, it is concluded that the BTS iterative solution is well conditioned. The spectral radius of the matrix $\mathbb{A}$ depicted in the figure 5. From this, it is clear that the iterative solution converges to unique non-zero solution. The condition number and spectral radius of BTS iterative method for different values of ϵ over contraction factor are depicted in figure 6. From this figure, the sensitivity analysis and convergence analysis of BTS iterative method is effective and efficient while comparing with theoretical results and other existing methods. From this, it is concluded that, the spectral radius of iterative matrix is less than one and which is evident to the theocratical results.

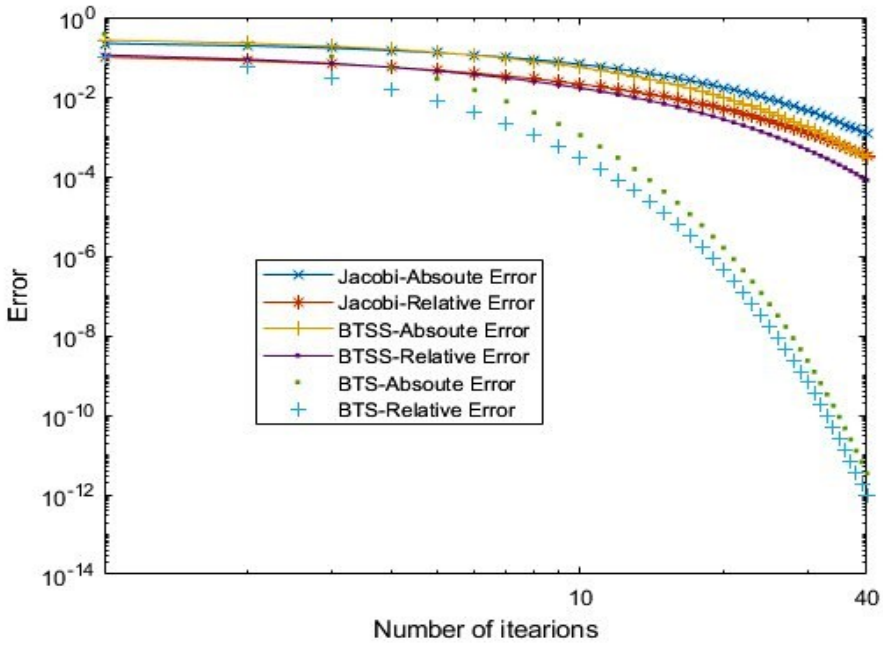


Figure 1: Absolute and Relative error of Jacobi, BTSS, and BTS methods for the contraction factor $\alpha = 0.76$, and $\epsilon = 0.1$.

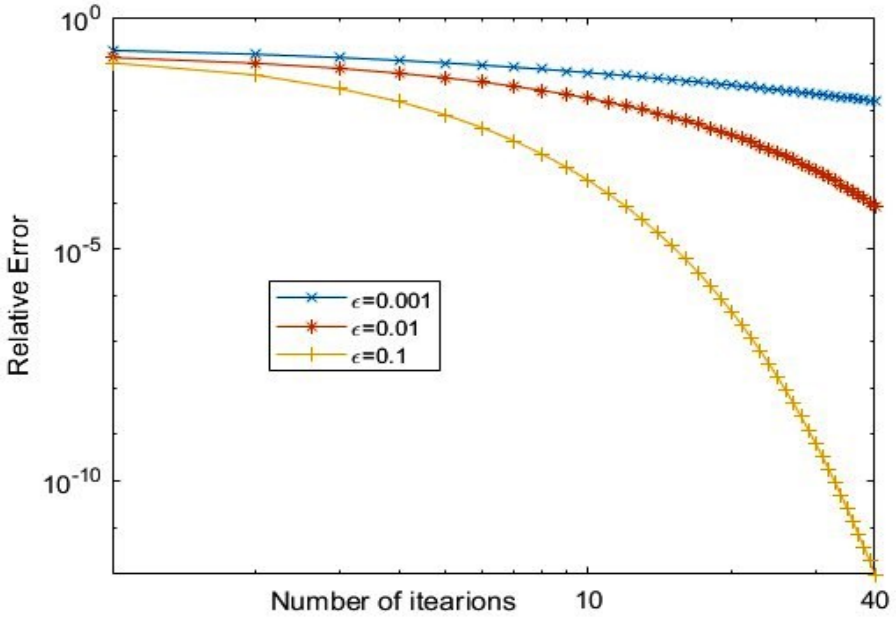


Figure 2: Relative error of the BTS method for the contraction factor $\alpha = 0.76$.

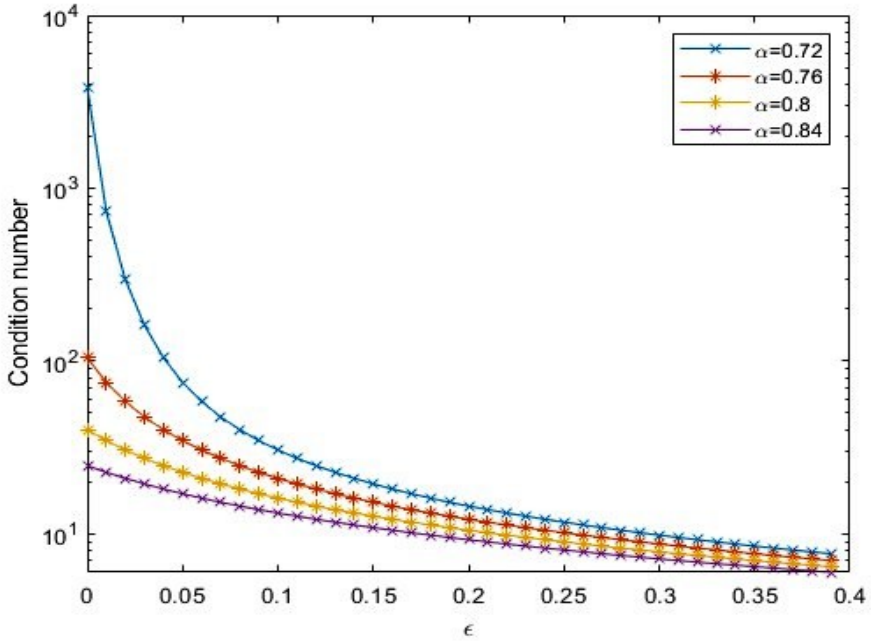


Figure 3: Condition number of the BTS method for the contraction factor $\alpha = 0.76$.

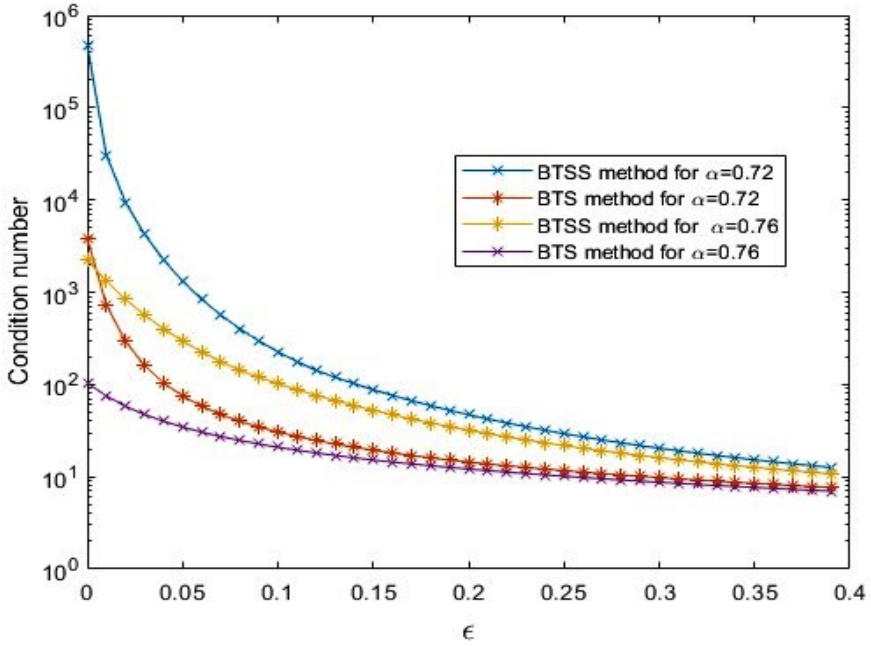


Figure 4: Condition number of the BTSS and BTS methods.

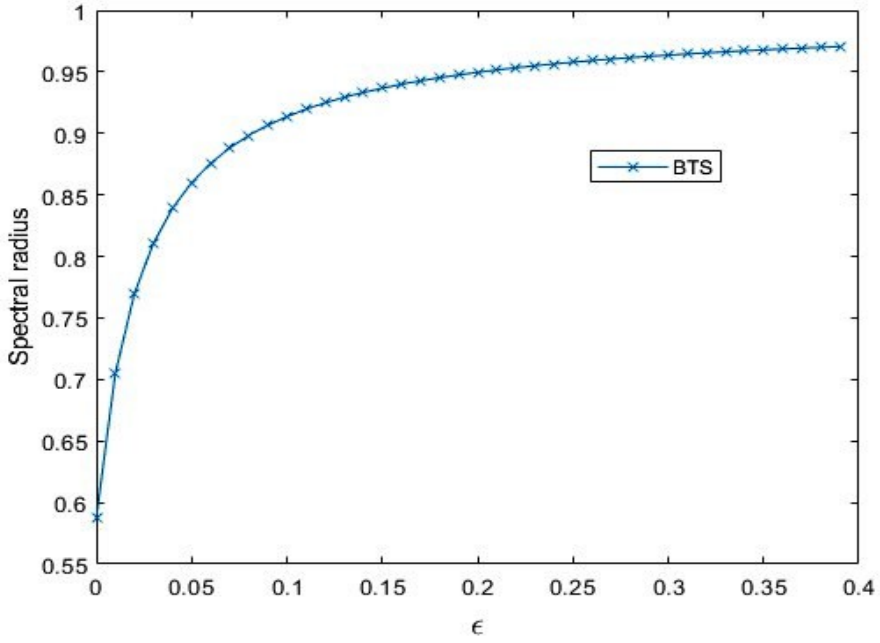


Figure 5: Spectral radius of BTS method

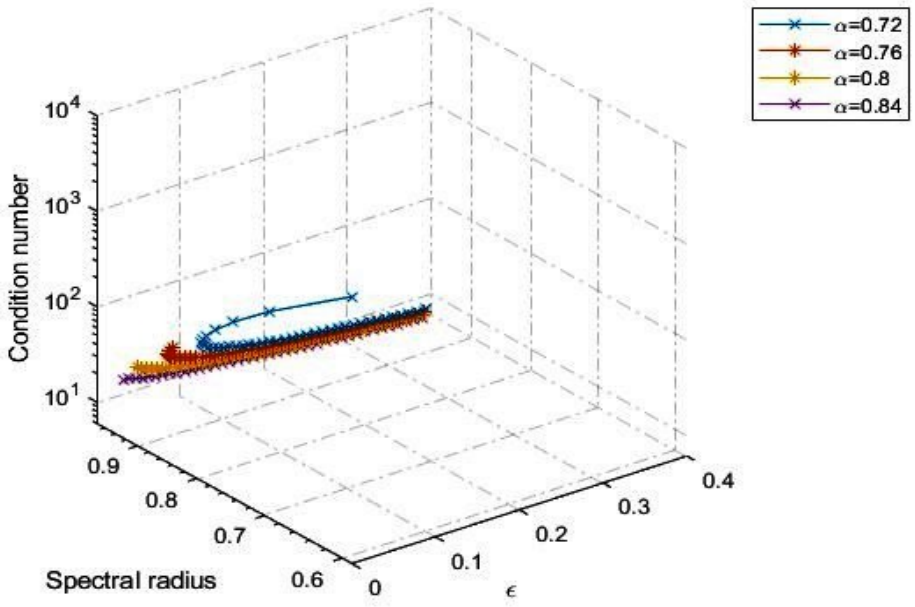


Figure 6: Condition number and spectral radius of BTS method.

6. Conclusion

In this chapter, the steady state vector of regularized linear system of block stochastic matrices using BTS method is estimated. It is proved that the coefficient matrix of regularized linear system Eq. (3) is positive definite. Theoretical analysis shows that the iterative solution of BTS method converges to a unique solution for a wide range of contraction factor α and ϵ. Also, a bound for the' spectral radius of the iteration matrix is derived that gives the contraction factor $\alpha^{\star}$, which minimizes the upper bound. The sensitivity analysis of BTS iteration method is obtained by the condition number and spectral radius of the regularized matrix and concluded that the iterative solution of BTS method is well conditioned.

References

[1] V. Rykov, N. Ivanova, and E. Morozov. "Performance and Numerical Analysis of (GI|GI|N, M) Queues using Marked Markov Process". *Rel. The. & App.* 20(2025), pp. 61-80. ISSN:1932-2321. DOI:10.24412/1932-2321-2025-885-61-82.

[2] S. K. Shao, P. Malla Reddy, M.G. Tsai, H. W. Tsao, and J. Wu. "Generalized variance-based Markovian fitting for self-similar traffic modeling". *IEICE Trans. Commun.* E88-B(4)(2005), pp. 1493-1502. ISSN:1745-1345. DOI:10.1093/ietcom/e88-b.4.1493.

[3] D. Rajaiah and P. Malla Reddy. "Loss Behavior of an Internet Router with Self-Similar Input Traffic via Fractal Point Process". *IEEE International Conference on Networks (ICON)* 19(2013), pp. 1-6. ISSN:2332-5798. DOI: 10.1109/ICON.2013.6781958.

[4] Z.-Z. Bai, G. H. Golub, L.-Z. Lu, and J. F. Yin. "Block triangular and skew-Hermitian splitting methods for positive-definite linear systems". *SIAM J. Sci. Comput.* 20(2005), pp. 844-863. ISSN:1095-7197. DOI:10.1137/S1064827503428114.

[5] W. J. Stewart. "Introduction to Numerical Solution of Markov Chains". *Princeton University Press*. Princeton. 1994. ISBN:1070-9924. DOI:10.1515/9780691223384.

[6] R. Chan and W. K. Ching. "Circulant preconditioners for stochastic automata networks". *Numer. Math.* 87(2000), pp. 35-57. ISSN:0945-3245. DOI:10.1007/s002110000173.

[7] Chun Wen, H. Ting-Zhu, and W. chao. "Triangular and skew-symmetric splitting methods for numerical solutions of Markov chains". *Comp. and Math. With App.* 62(2011), pp. 4039-4048. ISSN:1873-7668. DOI:10.1016/j.camwa.2011.09.041.

[8] Rajaiah Dasari, L. P. Rajkumar, and P. Malla Reddy. "Steady state probability vector of positive definite regularized linear systems of circulant stochastic matrices". *Linear and Multi Linear Algebra* 65(1)(2016), pp. 140-155. ISSN:1563-5139. DOI:10.1080/03081087.2016.1176984.

[9] L. A. Krukier, T. S. Martynova, and Z.-Z. Bai. "Product-type skew-Hermitian triangular splitting iteration methods for strongly non-Hermitian positive definite linear systems". *J. Comput. Appl. Math.* 232(2009), pp. 3-16. ISSN:1879-1778. DOI:10.1016/j.cam.2008.10.033.

[10] D. Ranadeer, D. Rajaiah, and P. Malla Reddy. "Block triangular and skew symmetric splitting method for steady state vector of linear system of erogodic block circulant Markov chains". *Int. J. Computing Science and Mathematics*. 8(4)(2017), pp. 384-394. ISSN:1752-5063. DOI:10.1504/IJCSM.2017.10006757.

[11] W. K. Ching, R. H. Chan, and X. Y. Zhou. "Circulant preconditioners for Markov-Modulated poisson processes and their applications to manufacturing systems". *SIAM J. Matrix Anal. Appl.* 18(1997), pp. 464-491. ISSN:1095-7162. DOI:10.1137/S089547989529344

[12] M. Benzi and B. Ucar. "Block triangular preconditioners for M-matrices and Markov chains". *Electron. Trans. Numer. Anal.* 26(2007), pp. 209-227. ISSN:1068-9613. DOI:10.2478/v10006-009-0017-3.

[13] P. Brown and H. F. Walker. "GMRES on (nearly) singular systems". *SIAM J. Matrix Anal. Appl.* 18(1997), pp. 37-51. ISSN:1095-7162. DOI:10.1137/S089547989426233.

[14] W. Chuan-Long, M. Guo-Yan, and Y. Xue-rong. "Modified parallel multisplitting iterative methods for non-Hermitian positive definite systems". *Adv. Comput. Math.* 38(2013), pp. 859-872. ISSN:1572-9044. DOI:10.1007/s10444-011-9262-8.

[15] A. Berman and R. Plemmons. "Nonnegative Matrices in Mathematical Sciences". *SIAM*, Philadelphia, 1994. ISBN:978-1-61197-126-2. DOI:10.1137/1.9781611971262.fm.

[16] Z.-Z. Bai, G.H. Golub, and M.K. Ng. "Hermitian and skew-Hermitian splitting methods for non- Hermitian positive definite linear systems". *SIAM J. Matrix Anal. Appl.* 24(2003), pp. 603-626. ISSN:1095-7162. DOI:10.1137/S0895479801395458

[17] S. Chandrasekaran and I.C.F. Ipsen. "On the Sensitivity of Solution Components in Linear Systems of Equations". *SIAM Journal on Matrix Analysis and Applications*. 16(1)(1995), pp. 93-112. ISSN:1095-7162. DOI:10.1137/S089547989223125.

[18] Y. Saad. "Iterative Methods for Sparse Linear Systems". *2nd ed. SIAM*. Philadelphia, 2003. ISBN:978-0-89871-534-7. DOI:10.1137/1.9780898718003.fm.

[19] Assem Deif. "Sensitivity Analysis in Linear Systems". *Springer*. 2014. ISBN:978-0-89871-800-3. DOI:10.1137/1.9780898718003.fm.

[20] A. M. Turing. "Rounding-off Errors in Matrix Processes". *The Quarterly Journal of Mechanics and Applied Mathematics*, 1(1948), pp. 287-308. ISSN:0033-5614. DOI:10.1093/qjmam/1.1.287.

A STATISTICAL EXPLORATION OF THE EFFECTS OF ADDITIONAL PARAMETERS IN MATHEMATICS

G. Aruna[1]

J. Jesintha Rosline [2]

•

[1,2] PG and Research Department of Mathematics, Auxilium College (Autonomous) ,
Affiliated to Thiruvalluvar University, Vellore Dist., Tamil Nadu, India
anu9117@gmail.com[1] , jesi.simple@gmail.com[2]

Abstract

The Bipolar Fuzzy Set is an advancement of the classical fuzzy set, developed to represent situations involving both positive and negative preferences or opinions simultaneously. The bipolar score function plays a vital role in decision-making theory. In this article, a bipolar score function is applied to real-life data to examine the effect of additional parameters in the field of mathematics. Furthermore, a research hypothesis is formulated, and the bipolar score function values are statistically analyzed using SPSS software to determine the impact of these additional parameters in mathematics.

Keywords: Bipolar fuzzy set, score function, Decision making, Statistical Analysis

1. Introduction

Decision Support Systems are advanced technologies that facilitate decision-making in complex environments by offering structured analysis and data-driven choices [14]. As a result, these systems are becoming crucial in various disciplines, including corporate strategy, health, and well-being. In an attempt to achieve a resolution, several tools and decision-making systems were integrated, but none of them was able to adequately illustrate the complexity of problem. New theories are now being used by researchers as mathematical instruments for decision assistance and decision-making systems. Mathematical and analytical models are used in model management system (MMS) to interpret data and make choices. Mathematical models are instruments for improving decision-making systems because they contain specialized information or principles to help decision-making, such as fuzzy set theory [2],rough set theory [3], and soft set theory [4]. Analytical models (AM) are mathematical representations employed to analyze the data, interpret it, and predict the behavior of the process, or decision-making system. AM uses mathematical formulas, statistical techniques, or algorithms to examine input data and provide output insights, assisting in decision-making, aiding in understanding correlations between variables, and forecasting outcomes using various analytical tools like EXCEL, SPSS, MATLAB, R, and Python.

Bipolar fuzzy set is an extension of fuzzy set which deals with the positive and negative membership values of a case. Various authors extended the Bipolar idea [12] and applied in many fields to handle the bipolarity situation [15],[17],[16] and [18]. Score function plays an important role in the decision making theory. Several researchers have applied fuzzy set theory and the concept of fuzzy numbers to address various social issues and identify effective solutions. For instance, Daniel Neff utilized the fuzzy set approach to assess poverty levels [5], while Thakre et

al. [6] employed fuzzy logic-based multi-criteria analysis to evaluate teacher performance. Revathi Anbalagan and Amudhambigai applied fuzzy mathematics to identify societal concerns affecting farmers [7]. Raj Kumar and T. Pathinathan introduced the Pentagonal Fuzzy Decision-Making technique in their study "Sieving out the Poor" [8]. During the COVID-19 pandemic in Greece, Konstantina Chrysafiadi et al. [9] assessed the effectiveness and acceptance of e-learning among computer science students using fuzzy logic. Similarly, Siva et al. explored fuzzy cognitive mapping to investigate poverty levels in Tamil Nadu during the pandemic. Overall, fuzzy logic evaluation techniques and fuzzy mathematical models have been widely employed by numerous scholars to analyze and address complex social challenges [10], [11].

In this article, Section 2 provides an overview of the definitions and operations related to Bipolar Fuzzy Sets. Section 3 presents the application of the bipolar score function to evaluate the impact of additional parameters in the field of mathematics. Section 4 outlines the proposed algorithm and the hypothesis formulation based on the collected data. In Section 5, the results analyzed using SPSS software are discussed. Finally, Section 6 presents the conclusion and highlights the potential scope for future research.

2. Preliminaries

Bipolar fuzzy sets [12]: Let X be the non-empty fuzzy set. The bipolar fuzzy set $B = \{B^-, B^+\}$ is defined in X. $B^+ \in [0,1]$ is the satisfaction degree of x in B, $B^- \in [-1,0]$ is the satisfaction degree of the implicit counter property of x in B.

Operations on Bipolar fuzzy sets[13]: Consider $B_1, B_2 \in BFS$. Zhang defines the following operations.
i) Disjunction : $B_1 + B_2 = (-max[b_1^-, b_2^-], max[b_1^+, b_2^+])$
= $(-[b_1^- \vee b_2^-], [b_1^+ \vee b_2^+])$
ii) Parallel conjuction: $B_1.B_2 = (-min[b_1^-, b_2^-], min[b_1^+, b_2^+])$
= $(-[b_1^- \wedge b_2^-], [b_1^+ \wedge b_2^+])$
iii) Serial conjuction: $B_1 \times B_2 = (-\{[b_1^- \wedge b_2^+] \vee [b_1^+ \wedge b_2^-]\}, \{[b_1^- \wedge b_2^-] \vee [b_1^+ \wedge b_2^+]\})$
iv) Negation: $-B_1 = [-b_1^+, b_1^-]$
v) Complement: $\neg B_1 = \neg[-1 + b_1^-, 1 - b_1^+]$

Score Function [14]: T. Mahmood et al. defines the score function as $S'(B)$ of $B = (b^-, b^+) \in BFS$ as:

$$S'(B) = b^+ + b^-$$

where $S'(B) \in [-1,1]$, and if $b^+ = b^- \implies S'(B) = 0$

3. Decision Making using Bipolar Score function

After the COVID-19 epidemic, mathematics has emerged as an important scientific tool, notably in decision-making, predictive modeling, and statistical analysis. Mathematical modeling helps immensely in forecasting epidemics of diseases, tracking infection rates, and monitoring the effectiveness of measures such as vaccination and isolation period. Significant data sets are examined using machine learning models that rely on mathematical techniques. Experts use AI and machine learning to ensure effective health care, effective therapies, and predicting medical results. The field of mathematics has progressed in generating predictive and optimization algorithms, which are employed to allocate constrained substances like booster shots, and hospital beds.

After COVID-19, the study of mathematics has evolved and enriched with various scientific methodologies. Even Nevertheless, there is a drop in students' decision to pursue a

career in mathematics, and curiosity in Mathematics has declined. It is influenced by several variables, notably the difficulty of learning fundamental ideas via the internet and the absence of live instruction, peer problem solving, and discussion that sustains interest in subjects. This exacerbates the situation and makes the trend towards choosing multidisciplinary, technical disciplines over pure mathematics. Meantime, there is a growing need for medical research and other related fields. The changes in mathematics syllabus with less emphasis on particular topics, make students demotivated and lose interest in continuing mathematics at a higher level, their attention is directed towards skill-based or pragmatic subjects.

Data Collection:

A survey was conducted using an objective and analytically designed questionnaire among college students in the Vellore district to investigate the reasons behind the declining interest in pursuing Mathematics at higher levels of study. The data were collected through a Google Form, which focused on gathering information related to students' interest in Mathematics, the structure of the Mathematics curriculum, the challenges encountered, and the career prospects in the field. Additionally, information pertaining to students' interest in other subjects, their respective course structures, and associated career opportunities was also obtained.

The collected data is categorized into four groups based on distinct criteria. Let the set of alternatives be denoted by $C_i = \{c_1, c_2, c_3, c_4\}$, representing four different colleges that offer Mathematics either as an allied or a core subject.

Suppose the set of criteria is given by $\Delta_i = \{\Delta_1 =$ course structure of the Mathematics subject, $\Delta_2 =$ level of job opportunities in Mathematics, $\Delta_3 =$ level of interest in Mathematics, $\Delta_4 =$ level of interest in other courses$\}$. Let the weight vector associated with C_i be ω=$(0.25, 0.22, 0.26, 0.27)$.

Step 1: Table 1 gives the Bipolar decision making matrix of the collected data.
Step 2: Table 2 presents the normalized weighted Bipolar decision matrix.

Table 1: *Bipolar Decision Making Matrix*

	Δ_1	Δ_2	Δ_3	Δ_4
c_1	(0.7,-0.4)	(0.5,-0.3)	(0.4,-0.8)	(0.9,-0.6)
c_2	(0.8,-0.2)	(0.7,-0.5)	(0.3,-0.7)	(0.7,-0.3)
c_3	(0.4,-0.5)	(0.8,-0.7)	(0.5,-0.8)	(0.6,-0.4)
c_4	(0.6,-0.7)	(0.9,-0.6)	(0.7,-0.5)	(0.5,-0.2)

Step 3: Table 3 displays the score value, calculated using the definition [3].

Table 2: *Normalized weighted Bipolar Decision Matrix*

	Δ_1	Δ_2	Δ_3	Δ_4
c_1	(0.175,-0.1)	(0.11,-0.066)	(0.104,-0.208)	(0.243,-0.162)
c_2	(0.2,-0.05)	(0.154,-0.11)	(0.078,-0.182)	(0.189,-0.081)
c_3	(0.1,-0.125)	(0.176,-0.154)	(0.13,-0.208)	(0.162,-0.108)
c_4	(0.15,-0.175)	(0.198,-0.132)	(0.182,-0.13)	(0.135,-0.054)

Result: In each category c_i, the score function corresponding to students' interest in other courses is observed to be higher than that of other evaluated criteria. This suggests that the influence of other courses is notably positive among the student population. Specifically, in categories c_1, c_2, and c_3, the interest level in Mathematics is found to be negative, indicating a considerably low level of engagement and enthusiasm for the subject. Moreover, in categories c_3 and c_4, students

Table 3: *Score Value Function*

	Δ_1	Δ_2	Δ_3	Δ_4
c_1	0.075	0.044	-0.104	0.086
c_2	0.15	0.044	-0.104	0.108
c_3	-0.025	0.022	-0.078	0.054
c_4	-0.025	0.066	0.052	0.081

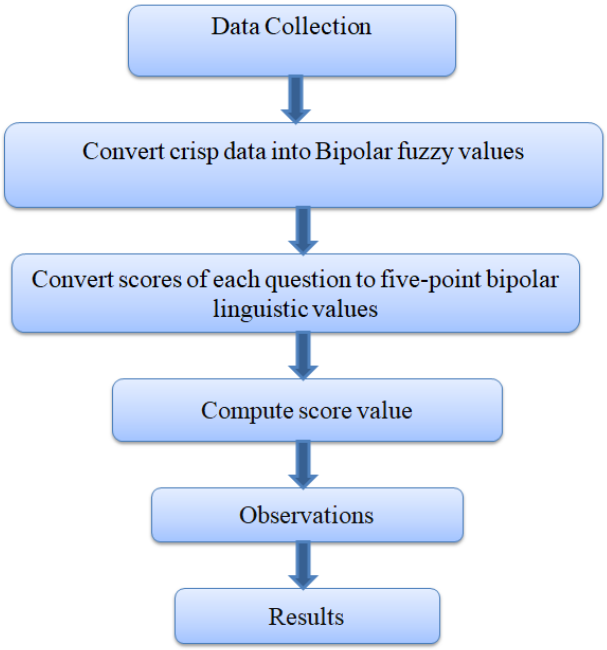


Figure 1: *Algorithm*

express negative satisfaction with the structure of the course, highlighting potential areas for curriculum review and improvement.

4. A Proposed algorithm and formulation of Hypothesis

Algorithm:

Figure 1 depicts the flowchart of the proposed algorithm, which incorporates the bipolar score function to quantitatively assess the impact of additional parameters related to the field of Mathematics. The computational and statistical analysis are conducted using SPSS software to ensure methodological accuracy and reliability.

Conceptual Model of the study:

Figure 2 illustrates the conceptual model developed for this study, in which four key variables have been identified: job opportunities in Mathematics (Job), Mathematics course structure (*Course_Struct*), other courses (*Other_Courses*), and decline in Mathematics choice (*Maths_decline*).

The dependent variable refers the decline in Mathematics choice, while the independent variables represents job opportunities in Mathematics, Mathematics course structure, and other courses.

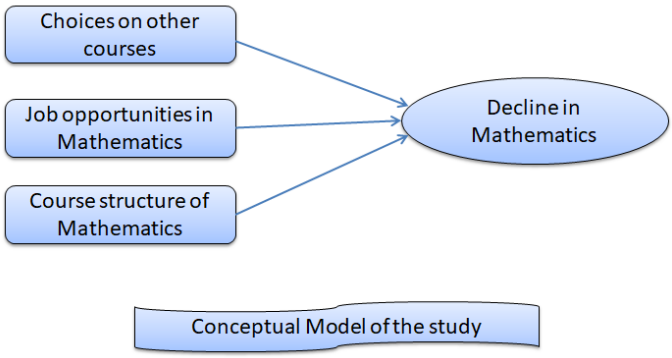


Figure 2: *Model of the Study*

Model Summary[b]

Model	R	R Square	Adjusted R Square	Std. Error of the Estimate	Change Statistics				
					R Square Change	F Change	df1	df2	Sig. F Change
1	.795[a]	.632	.618	.22605	.632	45.739	3	80[a]	.000

a. Predictors: (Constant), Course_Struct, Other_Courses, Job

b. Dependent Variable: Maths_decline

Figure 3: *Model Summary*

Objective of the analysis:

- To measure the extent to which job opportunities in Mathematics dissuade students from choosing Mathematics for higher studies.
- To evaluate how other applied courses in higher education influence the decision to choose Mathematics.
- To ascertain which aspects of the Mathematics course structure deter students from selecting Mathematics for higher studies.

Research Hypothesis:
The hypothesis are formulated based on the objective:
H01: There is no significant effect of job opportunities in Mathematics that leads to the decline in Mathematics choice.
H02: There is no significant impact of other applied courses that influence the decrease in Mathematics choice.
H03: There is no significant impact of Mathematics course structure that reduces the Mathematics choice.
2. Transformed crisp data into bipolar fuzzy data.
3. Represented the data into 5-point bipolar linguistic value.
4. The score value is computed for all the linguistic values using the definition [3].

5. Results

A multiple regression test is employed to analyze the study. A multiple correlation co-efficient between the predictors and the dependent variable is 0.795, which gives a strong and positive correlation. With an R-Square value of 0.632, the model explains 63.2% of the variation in Decline in Mathematics. The model represents a significant amount of variance (63.2%) in the dependent

Coefficients[a]

Model		Unstandardized Coefficients		Standardized Coefficients	t	Sig.
		B	Std. Error	Beta		
1	(Constant)	.169	.050		3.413	.001
	Other_Courses	-.265	.062	-.355	-4.306	.000
	Job	.378	.077	.408	4.930	.000
	Course_Struct	.213	.074	.221	2.888	.005

Figure 4: *Significance of the Coefficients*

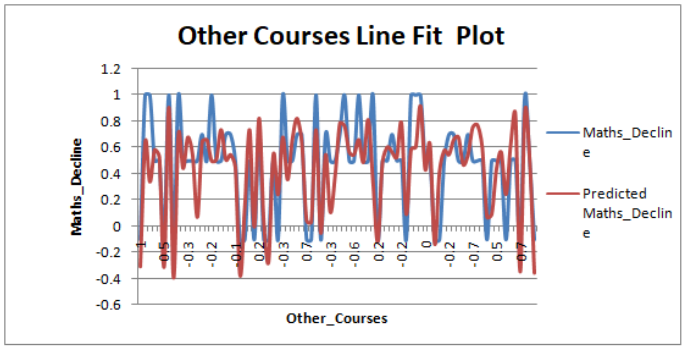


Figure 5: *Impact of other courses in the choice of Mathematics*

variable, as depicted in Figure 3. The F-value = 45.739 in Table 4, indicates that the model is statistically significant. The statistical significance of the model $(p < 0.001)$, implies a strong connection between the predictors and the dependent variable.

Table 4: *ANOVA Test*

Model	Sum of Squares	df	Mean Square	*F*	Sig.
Regression	7.012	3	2.337	45.739	.000
Residual	4.088	80	0.51	0.2017	
Total	11.100	83			

- Job (Beta = 0.408): Among all the factors, Job has the greatest positive effect on *Maths_decline.*, as depicted in Figure 4.
- *Other_Courses* (Beta = -0.355): This indicates that *Other_Courses* has a relatively substantial negative influence on *Maths_decline*, as shown in Figure 5.
- *Course_Struct* (Beta = 0.221): *Course_Struct* significantly and positively affects *Maths_decline* but less strongly.
- The study found that the t-value of 3.413 is a significant predictor, while other courses (t= -4.306) have a strong negative effect on the independent variable. Job opportunities((t = 4.930) have the strongest positive effect on the independent variable, while course structure (t = 2.888) has a positive effect on the dependent variable. These findings suggest that job opportunities play a crucial role in predicting outcomes.

6. Discussion

The regression model is statistically significant, with a large F-statistic (45.739) and a p-value (0.000) confirming its significance as shown in Figure 6. Job (Beta= 0.408) is the most important

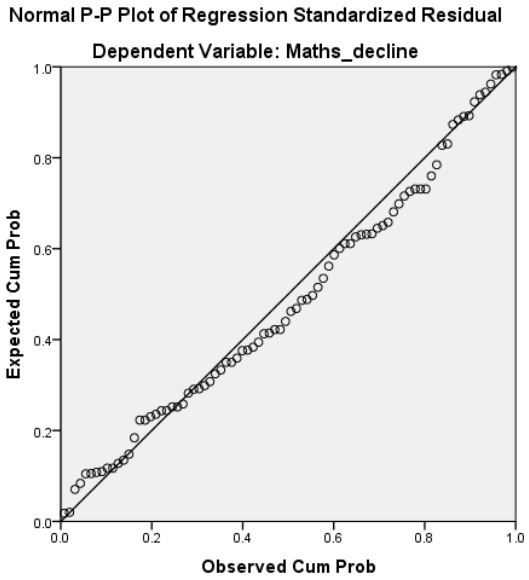


Figure 6: *Regression Plot*

factor influencing the dependent variable, followed by other courses (Beta= -0.355), which have opposite effects on the dependent variable. All predictors are statistically significant in explaining the decline in Mathematics choice in higher studies.

7. Conclusion

In this article, we explore the application of the bipolar score function in mathematics. By formulating a research hypothesis and employing statistical analysis through SPSS, the study demonstrated how additional parameters influence mathematical choices and perceptions. The findings highlight the effectiveness of the bipolar fuzzy framework as a powerful tool in both educational and analytical domains, especially for evaluating complex factors involved in decision-making.

References

[1] Mahmood, T., Abdullah, S., Bilal, M. & Rashid, S. (2016) Multiple criteria decision making based on bipolar valued fuzzy set. *Ann Fuzzy Math Inf* 11, 1003–1009.
[2] Zadeh, L. A. Fuzzy sets. Information and control 8, 338–353, 1965.
[3] Pawlak, Z.(1982). Rough sets. *International journal of computer & information sciences* ,11 341–356.
[4] Molodtsov, D. (1999). Soft set theory
first results. *Computers & mathematics with applications* 37, 19–31.
[5] Daniel Ne.(2013). Fuzzy set theoretic applications in poverty research. *Policy and Society*, 32(4):319—331.
[6] TA Thakre, OK Chaudhari, and Nita Dhawade.(2017). A fuzzy logic multi criteria approach for evaluation of teachers performance. *Advances in Fuzzy Mathematics*,12(1):129—145.
[7] GK Revathi, B Amudhambigai, V Narmadha, and T Poornima.(2018). Identification of social problems of farmers using fuzzy mathematics. *International Journal of Engineering & Technology*, 7(4.10):624–628.
[8] Raj Kumar and T Pathinathan. (2015.) Sieving out the poor using fuzzy decision making tools. Indian Journal of Science and Technology, 8(22):1.

[9] Konstantina Chrysafiadi, Maria Virvou, and George A Tsihrintzis. (2023.) A fuzzy-based evaluation of e-learning acceptance and effectiveness by computer science students in greece in the period of covid-19. *Electronics*, 12(2):428.

[10] Mohamed O Hegazi, Bandar Almaslukh, and Khadra Siddig.(2023.) A fuzzy model for reasoning and predicting student's academic performance. *Applied Sciences*, 13(8):5140.

[11] Seyyed Hossein Jafari Petrudi, Maryam Pirouz, and Behzad Pirouz.(2013.) Application of fuzzy logic for performance evaluation of academic students.*In 2013 13th Iranian Conference on Fuzzy Systems (IFSC),IEEE*, 1-–5.

[12] W.R Zhang (1998.) (yin)(yang) bipolar fuzzy sets. *In 1998 IEEE international conference on fuzzy systems proceedings. IEEE world congress on computational intelligence (Cat. No. 98CH36228)*, volume 1, pages 835–840. IEEE.

[13] Zhang, W.-R. & Zhang, L.(2004). Yinyang bipolar logic and bipolar fuzzy logic.*Information Sciences* 165, 265–287.

[14] Mahmood, T., Abdullah, S., Bilal, M. & Rashid, S. (2016). Multiple criteria decision making based on bipolar valued fuzzy set. *Ann Fuzzy Math Inf* 11, 1003–1009.

[15] Jana, C., Pal, M. & Wang, J.Q. (2019). Bipolar fuzzy dombi aggregation operators and its application in multiple-attribute decision-making process. Journal of Ambient Intelligence and Humanized Computing 10, 3533–3549.

[16] Juanjuan Chen, Shenggang Li, Shengquan Ma, Xueping Wang, et al.(2014.) M -polar fuzzy sets: an extension of bipolar fuzzy sets.*The scientific world journal,*416530, 1–8.

[17] Chiranjibe Jana and Madhumangal Pal. (2018.) Application of bipolar intuitionistic fuzzy soft sets in decision making problem. *International Journal of Fuzzy System Applications (IJFSA)*, 7(3):32—55.

[18] Wasim Akram Mandal. (2021.) Bipolar pythagorean fuzzy sets and their application in multi-attribute decision making problems. *Annals of Data Science*, 1-–33.

RT&A, No 4 (89)
Volume 20, December 2025

RELIABILITY ESTIMATION OF A SYSTEM BASED ON THE STRESS-STRENGTH MODEL USING A WEIBULL DISTRIBUTION

K Sruthi and M Kumar

•

National Institute of Technology, Calicut
mahesh@nitc.ac.in

Abstract

Reliability analysis is increasingly used in practical applications. The Weibull distribution is versatile, offering increasing, decreasing, bathtub, and unimodal hazard rates. Its flexibility enables a more accurate representation of real-world data, leading to reliability expressions that are both more realistic and more reliable. In this paper, we analyze the reliability of a single component system using a stress strength model, where both the system strength and stress follow a Weibull distribution. We extend the analysis to situations where a single-component system is exposed to two independent stresses, with the strength also following a Weibull distribution to estimate reliability. Furthermore, we estimate the reliability of a stress-strength model for a single component exposed to n stresses. Our analysis includes a series system with two independent components under a common stress, using Weibull distributions for stress and exponential distributions for strength. Furthermore, we study the reliability of a series system with n components under common stress, where the stress follows a Weibull distribution. Numerical computations are performed to demonstrate the results. Finally, a comparative study is conducted to evaluate the reliability expression derived in our work using the Weibull distribution against the existing methods.

Keywords: Reliability estimation, Stress-strength model, Weibull distribution, Exponential distribution

1. Introduction

Reliability is a crucial concept in various fields such as engineering, statistics, manufacturing, and more. Najwan et al. [1] estimated various techniques for estimating the Stress-Strength reliability when both stress and strength random variables have the unit Gompertz distribution based on the ranked set sampling (RSS) and simple random sampling (SRS) covered. The methods that have been suggested include the maximum likelihood, least squares, weighted least squares, maximum product spacing, Cramer von Mises, Anderson Darling, and right tail Anderson Darling methods.

Zhang et al. [2] studied the reliability estimation of the multicomponent stress-strength model involving one stress and two correlated strength components of a parallel system. By introducing new latent variables into the model, the likelihood function is simplified to make statistical inference available.

Amer et al. [3] estimated the reliability when the strength X and the stress Y are independent variables following the exponentiated Pareto distribution. The maximum likelihood estimators of R are computed using SRS, RSS, and median ranked set sampling (MRSS). Based on MRSS, the reliability estimate is considered in four different cases.

Ehsan et al. [4] investigated the engineering properties of waste foundry sand (WFS) with a focus on the shear strength parameters. Comparisons were also made with shear strength properties of recycled glass (RG) as a control material as well as natural sands.

Manal et al. [5] discussed the statistical inference of $R = P(X < Y < Z)$ for a component that has a strength that is independent of the opposite lower and upper bound stresses, when the stresses and strength follow an exponentiated exponential distribution (EED). They assume that both stress and strength random variables are independent, having EED with a common scale parameter. Using the generalized progressive hybrid censoring design, various point and interval estimators are obtained for the reliability model R in view of the ML and Bayesian approaches.

Hassan et al. [6] obtained the reliability of a system when the strength and stress variables are independent Weibull distribution with different scale parameters. The reliability in multi-component stress-strength (MSS) is estimated by using the maximum likelihood and Bayesian methods of estimation when the samples are drawn from strength and stress distributions and their measurements are in terms of the upper record values.

Al-Mutairi et al. [7] studied several point and interval estimation procedures of the stress strength parameter of the Lindley distribution. They have obtained the Uniformly Minimum-Variance Unbiased Estimator (UMVUE) of the stress-strength parameter, however, the exact or asymptotic distribution of it is very difficult to obtain. They have derived the maximum likelihood estimator (MLE) of R and its asymptotic distribution.

Maurya et al. [8] obtained likelihood and Bayesian methods-based estimates of MSS reliability when β is known or unknown. They used the Lindly method and Metropolis-Hastings (MH) procedure to evaluate Bayes estimates under informative and noninformative prior distributions. They also obtained UMVUE and exact Bayes estimates of MSS reliability when β is known. They observed using Monte Carlo simulations that the Bayes method has an advantage over the maximum likelihood method in case prior distribution is proper.

Mohamed et al. [9] proposed Poisson Modified Weibull Distribution (PMW) distribution and some statistical properties of the proposed distribution including explicit formulas for the density and hazard functions, moments, and quantiles are provided. The usefulness of the proposed distribution is verified by fitting different data sets. The results indicate that PMW is more flexible than other models.

Akram [10] obtained different estimates of the stress-strength parameter, under the hybrid progressive censored scheme, at the time that stress and strength were considered as two independent Kumaraswamy random variables. Also, they consider the existence and uniqueness of the MLE and construct the asymptotic and highest posterior density (HPD) intervals for R.

Alessandro and Asmerilda [11] revised the most popular techniques, highlighting their strengths and weaknesses, and empirically investigated their performance through a comparative study applied to a well-known engineering problem, formulated as a stress-strength model, with the aim of weighing up their feasibility and accuracy in recovering the value of the reliability parameter, also with reference to the number of discrete points.

Amal et al. [12] estimated the stress-strength reliability when the strength X and stress Y are independent but not identically distributed random variables from the generalized inverted exponential distribution. The stress-strength reliability estimators are considered based on different sampling schemes.

Manal and Ehab [13] estimated the reliability R when the observed data are progressive first failure censored coming from Kumaraswamy distribution (KuD). For comparing the results obtained using various methods, they have obtained the mean-squared errors (MSEs) for the reliability R. In the case of Bayesian estimation, looking at the limitation of Lindley estimation to point and interval estimation, they perform the approximation using the Markov chain Monte Carlo (MCMC) technique.

Mayank et al. [14] studied the multicomponent stress-strength reliability for two parameter unit-Gompertz distribution when both stress and strength variates follow the same distribution under progress Type II censoring. The classical and Bayesian approaches have been used to obtain the reliability of the system when the common scale parameter μ is known and unknown.

Lai et al. [15] reviewed the properties of the basic Weibull distribution and listed the various extensions.Hallinan and Arthur [16]encourages practitioners to use the Weibull distribution by furnishing historical background and parallel development of the essential formulas. Shakhatreh et al. [17] addressed the estimation of differential entropy of the Weibull distribution based on different non-informative prior distributions. They derived non-informative priors using formal rules, such as Jeffreys prior and maximal data information prior based on Fisher information and entropy, respectively. They also developed reference prior and probability matching prior for the differential entropy. Makalic et al. [18] derived a new bias adjusted maximum likelihood estimate for the shape parameter of the Weibull distribution with complete data and type I censored data. The proposed estimate of the shape parameter is significantly less biased and more efficient than the corresponding maximum likelihood estimate, while being simple to compute using existing maximum likelihood software procedures.

Kizilaslan and Nadar [19] studied the multicomponent system with k independent and identical strength components, where each component is exposed to a common random stress when the underlying distributions are Weibull. In our study, we consider both single-component and multi-component systems. The main difference is that we examine cases with two stresses and n stresses. Our study includes the reliability estimation of a single component system, considering two cases, namely, (i) case of two stresses and (ii) case of n stresses. After that, we analyze two-component cases and later extend our study to multi-component systems. In their work, they consider a single stress, whereas in our study, we examine multiple stresses. It is to be observed that the notion of n stresses is the general one. User can set the value of n depends upon the factors which affect the system reliability. This set up is most general and useful to reliability practitioners in a best possible way to estimate system reliability. This is the major contribution of our work compared to existing research. This broader framework allows for a more comprehensive reliability assessment compared to the previous work in the literature.

The rest of this paper is organized as follows. Section 2 provides basic definitions. Section 3 deals with the estimation of the reliability of a system in a stress-strength model, in which the stress and strength of the system follow a Weibull distribution. Section 4 deals with the reliability estimation of a system in a stress-strength model with two independent stresses. Section 5 deals with the reliability estimation of a system in a stress-strength model with n independent stress. Section 6 deals with the reliability estimation of a series system in a stress-strength model with two independent components under common stress. Section 7 deals with the reliability estimation of a series system in a stress-strength model with n independent components under common stress. In Section 8, a numerical illustration of the results obtained is provided. In Section 9, we discuss a comparison study of the reliability expression obtained in our work using the Weibull distribution with the existing method. Finally, the conclusions are presented in Section 10.

2. Some basic definitions

In this section, we present some important definitions which will be useful in the following sections to understand the results obtained.

Definition 1. (see[20]) Let V denote the strength random variable of the system and W denote the stress random variable. If V and W are independent with respective distribution functions G and F, then the traditional stress-strength reliability can be estimated as

$$R = P\{W < V\} = \iint_{w<v} dF(w)dG(v). \tag{1}$$

Definition 2. (see [15]) The cumulative distribution function (c.d.f.) of a Weibull random variable, T, is given by

$$F(x) = \left(1 - e^{-(x/\lambda)^k}\right), \quad x > 0, k > 0, \lambda > 0 \tag{2}$$

where k is the shape parameter and λ is the scale parameter. The probability density function (p.d.f.) of the cumulative distribution function (2) is

$$f(x) = \frac{k}{\lambda}\left[\frac{x}{\lambda}\right]^{k-1} e^{-\left(\frac{x}{\lambda}\right)^k}. \tag{3}$$

3. Reliability estimation of a system in a stress-strength model using a Weibull distribution

Reliability estimation has become more popular nowadays. Therefore, it is important to derive more reliable expressions for reliability. To do this, it is necessary to use a distribution that accurately represents realistic data. It has been observed that the Weibull distribution is more flexible and can better represent realistic data. In this section, we derive the reliability estimation using the Weibull distribution. Consider a stress-strength model. The Weibull distribution can represent more realistic data, so we use it for this purpose. Let the random variable X represent the strength of the system following the Weibull distribution given by

$$f(x) = \frac{k_1}{\lambda_1}\left[\frac{x}{\lambda_1}\right]^{k_1-1} e^{-\left(\frac{x}{\lambda_1}\right)^{k_1}}, x > 0 \tag{4}$$

where $k_1 > 0$ is the shape parameter and $\lambda_1 > 0$ is the scale parameter. The random variable Y represents the stress of the system following the Weibull distribution given by

$$g(y) = \frac{k_2}{\lambda_2}\left[\frac{y}{\lambda_2}\right]^{k_2-1} e^{-\left(\frac{y}{\lambda_2}\right)^{k_2}}, y > 0 \tag{5}$$

where and $k_2 > 0$ is the shape parameter and $\lambda_2 > 0$ is the scale parameter. Then, the stress-strength reliability R of the system is given by

$$\begin{aligned} R &= P[Y < X] \\ &= \iint_{y<x} f(x)g(y)\,dxdy \\ &= \iint_{y<x} \frac{k_1}{\lambda_1}\left[\frac{x}{\lambda_1}\right]^{k_1-1} e^{-\left(\frac{x}{\lambda_1}\right)^{k_1}} \frac{k_2}{\lambda_2}\left[\frac{y}{\lambda_2}\right]^{k_2-1} e^{-\left(\frac{y}{\lambda_2}\right)^{k_2}} dxdy. \end{aligned} \tag{6}$$

Hence the stress-strength reliability R of the system is given by

$$R = \frac{k_1 k_2}{\lambda_1 \lambda_2} \iint_{y<x} \left[\frac{x}{\lambda_1}\right]^{k_1-1} \left[\frac{y}{\lambda_2}\right]^{k_2-1} e^{-\left(\frac{x}{\lambda_1}\right)^{k_1}} e^{-\left(\frac{y}{\lambda_2}\right)^{k_2}} dxdy \tag{7}$$

Parameters can be estimated using Maximum Likelihood Estimation as follows. Given a sample $\{x_1, x_2, \ldots, x_n\}$, the likelihood function for the two-parameter Weibull distribution is given by

$$L(\lambda, k) = \prod_{i=1}^{n} \frac{k}{\lambda}\left(\frac{x_i}{\lambda}\right)^{k-1} e^{-(x_i/\lambda)^k}$$

Taking the natural log gives the log-likelihood function:

$$\ell(\lambda, k) = n\ln k - nk\ln\lambda + (k-1)\sum_{i=1}^{n}\ln x_i - \sum_{i=1}^{n}\left(\frac{x_i}{\lambda}\right)^k$$

By solving the partial derivatives $\frac{\partial \ell}{\partial \lambda} = 0$ and $\frac{\partial \ell}{\partial k} = 0$, one can obtain estimates for λ and k. We observe that the closed form solution does not exist for the estimates of the parameters. The values can be estimated using numerical techniques such as Newton Raphson iteration method.

3.1. Confidence Interval for R

In this section, we obtain confidence intervals for R. Let the random variable X represent the strength of the system following the Weibull distribution given by

$$f(x) = \frac{k_1}{\lambda_1}\left[\frac{x}{\lambda_1}\right]^{k_1-1} e^{-\left(\frac{x}{\lambda_1}\right)^{k_1}}, x > 0 \tag{8}$$

where $k_1 > 0$ is the shape parameter and $\lambda_1 > 0$ is the scale parameter. The random variable Y represents the stress of the system following the Weibull distribution given by

$$g(y) = \frac{k_2}{\lambda_2}\left[\frac{y}{\lambda_2}\right]^{k_2-1} e^{-\left(\frac{y}{\lambda_2}\right)^{k_2}}, y > 0 \tag{9}$$

where and $k_2 > 0$ is the shape parameter and $\lambda_2 > 0$ is the scale parameter.
If $\hat{R} = g(\theta)$, where θ is a vector of parameter estimates (e.g. $\hat{k}_1, \hat{\lambda}_1, \hat{k}_2, \hat{\lambda}_2$), then the variance of $\hat{R}$ is approximately.

$$\mathrm{Var}(\hat{R}) \approx \nabla g(\theta)^T \cdot \mathrm{Cov}(\hat{\theta}) \cdot \nabla g(\theta),$$

where $\nabla g(\theta)$ is the gradient (vector of partial derivatives of R with respect to each parameter). $\mathrm{Cov}(\hat{\theta})$ is the covariance matrix of the parameter estimates.
So the standard error becomes

$$SE(\hat{R}) = \sqrt{\mathrm{Var}(\hat{R})}$$

Then the confidence interval is

$$\hat{R} \pm z_{\alpha/2} \cdot SE(\hat{R})$$

Suppose $\theta = \begin{bmatrix} \hat{k}_1 \\ \hat{\lambda}_2 \\ \hat{k}_2 \\ \hat{\lambda}_2 \end{bmatrix}$ and $\nabla g(\theta) = \begin{bmatrix} \frac{\partial \hat{R}}{\partial \hat{k}_1} \\ \frac{\partial \hat{R}}{\partial \hat{\lambda}_1} \\ \frac{\partial \hat{R}}{\partial \hat{k}_2} \\ \frac{\partial \hat{R}}{\partial \hat{\lambda}_2} \end{bmatrix}$

Then $\mathrm{Var}(\hat{R}) = \sum_{i=1}^{4}\sum_{j=1}^{4} \frac{\partial \hat{R}}{\partial \theta_i} \cdot \frac{\partial \hat{R}}{\partial \theta_j} \cdot \mathrm{Cov}\left(\hat{\theta}_i, \hat{\theta}_j\right)$

Since there is no closed-form expression for R, it is not possible to compute closed form expressions for the partial derivatives $\frac{\partial R}{\partial k_1}$, $\frac{\partial R}{\partial \lambda_1}$, etc. Hence it is not possible to proceed for obtaining the true confidence intervals. However, We can use numerical differentiation for performing calculations and one can obtain numerical confidence intervals for the parameters.

4. Reliability estimation of a system in a stress-strength model with two independent stresses

In this section, we study the reliability estimation of a system in a stress-strength model with two independent stresses. Consider a system described by the stress-strength model consisting of a component with strength X, where the strength follows a Weibull distribution. The probability density function is given by

$$f(x) = \frac{k}{\lambda}\left[\frac{x}{\lambda}\right]^{k-1} e^{-\left(\frac{x}{\lambda}\right)^{k}}, x > 0 \tag{10}$$

where $k > 0$ is the shape parameter and $\lambda > 0$ is the scale parameter. The system has two independent stress Y_1 and Y_2, respectively, with distributions $g_1(y_1) = \lambda_1 e^{-\lambda_1 y_1}$ and $g_2(y_2) = \lambda_2 e^{-\lambda_2 y_2}$. Then reliability of the system is given by

$$\begin{aligned}
R &= P[max(Y_1, Y_2) < X] \\
&= \iiint_{\max(y_1,y_2)<x} g_1(y_1)\, g_2(y_2) f(x) dy_1 dy_2 dx \\
&= \int_0^\infty f(x) \left[\int_0^x \int_0^x g_1(y_1)\, g_2(y_2) dy_1 dy_2 \right] dx \\
&= \int_0^\infty \frac{k}{\lambda} \left[\frac{x}{\lambda}\right]^{k-1} e^{-\left(\frac{x}{\lambda}\right)^k} \left[\int_0^x \int_0^x \lambda_1 e^{-\lambda_1 y_1} \lambda_2 e^{-\lambda_2 y_2} dy_1 dy_2 \right] dx \\
&= \int_0^\infty \frac{k}{\lambda} \left[\frac{x}{\lambda}\right]^{k-1} e^{-\left(\frac{x}{\lambda}\right)^k} \lambda_1 \lambda_2 \int_0^x e^{-\lambda_2 y_2} \left[\frac{e^{-\lambda_1 y_1}}{-\lambda_1} \right]_0^x dy_2 \\
&= \int_0^\infty \frac{k}{\lambda} \left[\frac{x}{\lambda}\right]^{k-1} e^{-\left(\frac{x}{\lambda}\right)^k} \frac{\lambda_1 \lambda_2}{\lambda_1 \lambda_2} \left[e^{-\lambda_1 x} - 1\right] \left[e^{-\lambda_2 x} - 1\right]
\end{aligned} \tag{11}$$

Reliability of the system is given by

$$= \frac{k}{\lambda} \int_0^\infty \left[\frac{x}{\lambda}\right]^{k-1} [e^{-\lambda_1 x} - 1][e^{-\lambda_2 x} - 1] e^{-\left(\frac{x}{\lambda}\right)^k} dx \tag{12}$$

5. Reliability estimation of a system in a stress-strength model with n independent stresses

In this section, we consider the reliability estimation of a system in a stress-strength model with n independent stresses. Consider a system described by the stress-strength model, consisting of a component with strength X, where the distribution function is given by

$$f(x) = \frac{k}{\lambda} \left[\frac{x}{\lambda}\right]^{k-1} e^{-\left(\frac{x}{\lambda}\right)^k}, x > 0 \tag{13}$$

where $k > 0$ is the shape parameter and $\lambda > 0$ is the scale parameter. The system has n independent stresses Y_1, Y_2, Y_3, ...,Y_n with distributions $g_1(y_1) = \lambda_1 e^{-\lambda_1 y_1}$, $g_2(y_2) = \lambda_2 e^{-\lambda_2 y_2}$, $g_3(y_3) = \lambda_3 e^{-\lambda_3 y_3}$, ..., $g_n(y_n) = \lambda_n e^{-\lambda_n y_n}$ respectively.
Then reliability of the system is given by

$$\begin{aligned}
R &= P[max\,(Y_1, Y_2, Y_3, ..., Y_n) < X] \\
&= \iiint ... \int_{\max(y_1,y_2,y_3,...,y_n)<x} g_1(y_1) g_2(y_2) g_3(y_3) ... g_n(y_n) f(x) dy_1 dy_2 dy_3 ... dy_n dx \\
&= \int_0^\infty f(x) \left[\int_0^x \int_0^x \int_0^x ... \int_0^x g_1(y_1) g_2(y_2) g_3(y_3) ... g_n(y_n) dy_1 dy_2 dy_3 ... dy_n \right] dx \\
&= \int_0^\infty \frac{k}{\lambda} \left[\frac{x}{\lambda}\right]^{k-1} e^{-\left(\frac{x}{\lambda}\right)^k} \left[\int_0^x \int_0^x \int_0^x ... \int_0^x \lambda_1 e^{-\lambda_1 y_1} \lambda_2 e^{-\lambda_2 y_2} \lambda_3 e^{-\lambda_3 y_3} ... \lambda_n e^{-\lambda_n y_n} dy_1 dy_2 dy_3 ... dy_n \right] dx \\
&= \int_0^\infty \frac{k}{\lambda} \left[\frac{x}{\lambda}\right]^{k-1} e^{-\left(\frac{x}{\lambda}\right)^k} \left[(e^{-\lambda_1 x} - 1)(e^{-\lambda_2 x} - 1)(e^{-\lambda_3 x} - 1) ... (e^{-\lambda_n x} - 1) \right] dx
\end{aligned}$$

Reliability of the system is given by

$$= \frac{k}{\lambda} \int_0^\infty \left[\frac{x}{\lambda}\right]^{k-1} [e^{-\lambda_1 x} - 1][e^{-\lambda_2 x} - 1][e^{-\lambda_3 x} - 1] ... [e^{-\lambda_n x} - 1] e^{-\left(\frac{x}{\lambda}\right)^k} dx \tag{14}$$

6. Reliability estimation of a series system in a stress-strength model with two independent components under common stress

Consider a series system of the stress-strength model with two independent components C_1 and C_2. Let the random variable X_1 and X_2 represent the strengths of the components with the probability density function $f_1(x_1) = \lambda_1 e^{-\lambda_1 x_1}$ and $f_2(x_2) = \lambda_2 e^{-\lambda_2 x_2}$. The random variable Y

represents the stress of the system with the probability density function $g(y) = \frac{k}{\lambda}\left[\frac{y}{\lambda}\right]^{k-1} e^{-\left(\frac{y}{\lambda}\right)^k}$. Then, the stress-strength reliability R of the system is given by

$$
\begin{aligned}
R &= P\left[Y < min\left(X_1, X_2\right)\right] \\
&= \iiint_{y<min(x_1,x_2)} f\left(x_1\right) f\left(x_2\right) g(y) dx_1 \cdot dx_2 dy \\
&= \int_0^\infty \int_y^\infty \int_y^\infty f\left(x_1\right) f\left(x_2\right) g(y) dx_1 \cdot dx_2 dy \\
&= \int_0^\infty g(y) \left[\int_y^\infty \int_y^\infty f\left(x_1\right) f\left(x_2\right) dx_1 \cdot dx_2\right] dy \\
&= \int_0^\infty \frac{k}{\lambda}\left[\frac{y}{\lambda}\right]^{k-1} e^{-\left(\frac{y}{\lambda}\right)^k} \left[\int_y^\infty \int_y^\infty [\lambda_1 e^{-\lambda_1 x_1}][\lambda_2 e^{-\lambda_2 x_2}] dx_1 \cdot dx_2\right] dy \\
&= \int_0^\infty \frac{k}{\lambda}\left[\frac{y}{\lambda}\right]^{k-1} e^{-\left(\frac{y}{\lambda}\right)^k} [e^{-(\lambda_1+\lambda_2)y}] dy
\end{aligned}
$$

Reliability of the system is given by

$$= \frac{k}{\lambda} \int_0^\infty \left[\frac{y}{\lambda}\right]^{k-1} [e^{-(\lambda_1+\lambda_2)y}] e^{-\left(\frac{y}{\lambda}\right)^k} dy \tag{15}$$

7. Reliability estimation of a series system in a stress-strength model with n independent components under common stress

In this section, we study the reliability estimation of a series system in a stress-strength model with n independent components under a common stress. Consider a system represented by the stress-strength model, consisting of n components C_1, C_2, C_3, ..., C_n. Let X_1, X_2, X_3, ..., X_n denote the strength random variables, with the following distribution functions $f_1(x_1) = \lambda_1 e^{-\lambda_1 x_1}$,$f_2(x_2) = \lambda_2 e^{-\lambda_2 x_2}$,$f_3(x_3) = \lambda_3 e^{-\lambda_3 x_3}$,...,$f_n(x_n) = \lambda_n e^{-\lambda_n x_n}$ respectively. Let the random variable Y represent the common stress of system with distribution $g(y)$ given by

$$g(y) = \frac{k}{\lambda}\left[\frac{y}{\lambda}\right]^{k-1} e^{-\left(\frac{y}{\lambda}\right)^k}, y > 0 \tag{16}$$

where $k > 0$ is the shape parameter and $\lambda > 0$ is the scale parameter. Then reliability of the system is given by

$$
\begin{aligned}
R &= P[Y < min(X_1, X_2, X_3, ..., X_n)] \\
&= \iiint ... \int_{\min(x_1,x_2,x_3,...,x_n)>y} f_1(x_1) f_2(x_2) f_3(x_3) ... f_n(x_n) g(y) dx_1 dx_2 dx_3 ... dx_n dy \\
&= \int_0^\infty g(y) \left[\int_y^\infty \int_y^\infty \int_y^\infty ... \int_y^\infty f_1(x_1) f_2(x_2) f_3(x_3) ... f_n(x_n) dx_1 dx_2 dx_3 ... dx_n\right] dy \\
&= \int_0^\infty \frac{k}{\lambda}\left[\frac{y}{\lambda}\right]^{k-1} e^{-\left(\frac{y}{\lambda}\right)^k} e^{-(\lambda_1+\lambda_2+\lambda_3+...+\lambda_n)y} dy
\end{aligned}
$$

Reliability of the system is given by

$$= \frac{k}{\lambda} \int_0^\infty \left[\frac{y}{\lambda}\right]^{k-1} e^{-(\lambda_1+\lambda_2+\lambda_3+...+\lambda_n)y} e^{-\left(\frac{y}{\lambda}\right)^k} dy \tag{17}$$

8. Numerical Results

In this section, we present some numerical results to illustrate the reliability expression obtained in previous sections. Stress-strength reliability applications are crucial in engineering and industrial fields where the performance and durability of products and systems need to be assessed under conditions of varying stress and strength. For pressurized systems (e.g., gas pipelines, tanks, reactors), it is vital to assess both the stress (pressure) and strength (material resistance) to avoid

rupture or leaks. This application is especially critical in industries like oil and gas, where catastrophic failure could have severe consequences. Therefore, it is important to derive more reliable expressions for reliability. To do this, it is necessary to use a distribution that accurately represents realistic data. Thus, it is essential to use a more realistic distribution to represent this data. The Weibull distribution can exhibit increasing, decreasing, bathtub, and unimodal hazard rates. It has been observed that the Weibull distribution is more flexible and can better represent realistic data. In this section, we illustrate how various choices of parameter values can influence reliability. First, we consider the reliability expression obtained in Section 3. Now, we present some numerical results to illustrate the reliability of the system using equation (7) for various choices of the parameters, namely $\lambda_1, \lambda_2, k_1$, and k_2 in equation (4) and (5), which are part of the integral in (7). Table 1 illustrates the results obtained in Section 3.

Table 1: *Reliability estimation of a system in the stress-strength model using Weibull distribution*

k_1	k_2	λ_1	λ_2	Reliability
12.30	0.7	11.6	1.2	0.9908
14.02	1.1	14.7	1.8	0.9999
11.02	2.2	12.8	3.5	0.9999
13.02	1.2	14.8	2.5	0.9995
14.80	0.9	13.8	1.5	0.9991
12.80	0.8	12.8	1.7	0.9917

Next, we consider the reliability expression obtained in Section 4. Now, we present some numerical results to illustrate the reliability of the system using equation (12) for various choices of the parameters, namely λ, k, λ_1, and λ_2 in Section 4. The Table 2 illustrates the results obtained in Section 4.

Table 2: *Reliability estimation of a system in the stress-strength model with two independent stresses*

λ	k	λ_1	λ_2	Reliability
7.2	6.6	11.96	1.73	0.9999
8.3	8.7	12.26	1.14	0.9997
7.3	6.7	11.26	1.24	0.9992
9.3	8.8	12.12	1.23	0.9999
7.7	8.6	12.22	1.17	0.9993
9.4	8.6	12.22	1.22	0.9999

Next, we consider the reliability expression obtained in Section 5. Now, we present some numerical results to illustrate the reliability of the system via equation (14) for various choices of the parameters, namely, λ, k, λ_1, λ_2, and λ_3 in equations in Section(5). We take $n = 3$. Table 3 illustrates the results obtained in Section 5.

Table 3: *Reliability estimation of a system in the stress-strength model when $n = 3$*

λ	k	λ_1	λ_2	λ_3	Reliability
6.8	7.7	1.93	2.37	3.83	0.9999
5.3	7.8	2.15	3.24	4.58	0.9999
6.2	8.7	1.87	3.17	1.98	0.9999
5.8	7.9	2.15	1.24	3.58	0.9978
2.7	7.2	3.15	3.24	1.58	0.9750
4.7	8.2	4.15	1.23	2.55	0.9938

Next, we consider the reliability expression obtained in Section 6. Now, we present some numerical results to illustrate the reliability of the system via equation (15) for various choices of the parameters, namely, λ_1, λ_2, k, and λ in the equation in Section 6, which are part of the integral in (15). The Table 4 illustrates the results obtained in Section 6.

Table 4: *Reliability estimation of a series system in the stress-strength model with two components*

λ_1	λ_2	k	λ	Reliability
0.22	0.13	13	0.01	0.9966
0.45	0.12	22	0.07	0.9618
0.32	0.53	15	0.12	0.9062
0.47	0.18	31	0.06	0.9624
0.51	0.22	21	0.07	0.9514
0.39	0.32	22	0.08	0.9461

Next, we consider the reliability expression obtained in Section 7. Now, we present some numerical results to illustrate the reliability of the system via equation (17) for various choices of the parameters, namely, λ_1, λ_2, k, and λ in equation in Section 7, which are part of the integral in (17). The Table 5 illustrates the results obtained in Section 7.

Table 5: *Reliability estimation of a series system in the stress-strength model with three components*

λ_1	λ_2	λ_3	k	λ	Reliability
0.11	0.12	0.20	29	0.12	0.9506
0.18	0.13	0.19	24	0.01	0.9951
0.23	0.17	0.26	32	0.11	0.9311
0.02	0.07	0.06	38	0.13	0.9810
0.01	0.02	0.03	38	0.23	0.9865
0.11	0.01	0.01	32	0.18	0.9773

It has been noted that selecting appropriate parameters for the Weibull distribution can result in high levels of reliability. Thus, employing the Weibull distribution can enhance the overall reliability of a system. Specifically, with proper parameter selection, the Weibull distribution can reach a reliability of 0.99, which can enhance system reliability by up to 99%. Hence by correctly utilizing the Weibull distribution, the overall reliability of the system can be enhanced. Thus, employing this distribution can significantly improve system reliability.

9. Comparison of results

In this section, we compare the reliability expression obtained in our work using the Weibull distribution with the existing reliability expression. Simulated data is used to estimate the reliability and compute the difference. All computations are performed using MATLAB R2020a. The study involves generating a dataset consisting of 100 observations for simplicity. This sample number can be increased based upon the rquirements. The parameters are estimated using MATLAB built in wblfit function. Suppose the random variables X and Y represent the strength and stress of the system respectively, with the following probability density functions for $x > 0$ and $y > 0$ are

$$f_X(x) = \frac{1}{\lambda_1} e^{-\frac{x}{\lambda_1}} \quad \text{and} \quad f_Y(y) = \frac{1}{\lambda_2} e^{-\frac{y}{\lambda_2}}$$

The reliability R^* (see, [21]) is given by

$$R^* = \frac{\lambda_1}{\lambda_1 + \lambda_2}$$

We examine the difference between the reliability expression R (7) and the existing standard reliability expression R^* using the exponential distribution. The difference is computed and presented in Table 6.

Table 6: *Difference in reliability estimation of a system in the stress-strength model using the Weibull distribution and standard reliability estimation using the exponential distribution*

k_1	k_2	λ_1	λ_2	R	R^*	$R - R^*$
0.3816	0.7655	0.7952	0.1869	0.6209	0.1903	0.4306
0.9157	0.7922	0.9595	0.6557	0.5900	0.4060	0.1840
0.88852	0.9133	0.7962	0.0987	0.8649	0.1103	0.7545
0.2619	0.3354	0.6797	0.1366	0.5978	0.1673	0.4305
0.3342	0.6987	0.1978	0.0305	0.6393	0.1337	0.5056
0.7127	0.5005	0.4711	0.0596	0.7962	0.1123	0.6838

It is observed from Table 6 that the maximum difference in reliability is about 75%, whereas the minimum difference is about 18%. Therefore, using the Weibull distribution results in a significant difference in evaluating reliability.

10. Conclusions

In this study, we explored a stress-strength model where both stress and strength are described using a Weibull distribution. We began by evaluating the reliability of a single-component system within a stress-strength framework utilizing the Weibull distribution. We then expanded the analysis to consider a single-component system exposed to two independent stresses, estimating the system reliability. Additionally, we extended the model to a system subjected to n independent stresses. We also derived reliability expressions for a series system with two components under common stress, where the stress is represented by a Weibull distribution. Moreover, we assessed the reliability of a series system with n components, all subjected to common stress, modeled using the Weibull distribution. Our findings indicate that choosing appropriate parameters for the Weibull distribution can greatly improve reliability. Specifically, employing the Weibull distribution can enhance system reliability by as much as 75% over traditional reliability assessments. With the correct parameters, the Weibull distribution can achieve reliability levels as high as 0.99, potentially boosting reliability by up to 99%. Proper application of the Weibull distribution can significantly improve overall system reliability. The Weibull distribution's flexibility, allowing it to model increasing, decreasing, bathtub-shaped, and unimodal hazard rates, makes it a powerful tool for accurately representing real-world data. Furthermore, the results of this study can be extended to other forms of distributions, such as the modified Weibull distribution.

References

[1] Alsadat, N., Hassan, A.S., Elgarhy, M., Chesneau, C. and Mohamed, R.E. (2023). An efficient stress strength reliability estimate of the unit gompertz distribution using ranked set sampling. *Symmetry*, 15(5)1121.

[2] Zhang, L., Xu, A., An, L. and Li, M., (2022). Bayesian inference of system reliability for multicomponent stress strength model under marshall olkin weibull distribution. *Systems*, 10(6):196.

[3] Al-Omari, A.I., Almanjahie, I.M., Hassan, A.S. and Nagy, H.F. (2020). Estimation of the stress-strength reliability for exponentiated Pareto distribution using median and ranked set sampling methods. *CMC Computers, Materials and Continua*, 64(2):835–857.

[4] Yaghoubi, E., Arulrajah, A., Yaghoubi, M. and Horpibulsuk, S. (2020). Shear strength properties and stress strain behavior of waste foundry sand. *Construction and Building Materials*, 249:118761.

[5] Yousef, M.M., Hassan, A.S., Alshanbari, H.M., El-Bagoury, A.A.H. and Almetwally, E.M. (2022). Bayesian and non Bayesian analysis of exponentiated exponential stress strength model based on generalized progressive hybrid censoring process. *Axioms*, 11(9):455.

[6] Hassan, A.S., Nagy, H.F., Muhammed, H.Z. and Saad, M.S. (2020). Estimation of multicomponent stress strength reliability following Weibull distribution based on upper record values. *Journal of Taibah University for science*, 14(1):244–253.

[7] Al-Mutairi, D.K., Ghitany, M.E. and Kundu, D. (2015). Inferences on stress strength reliability from weighted Lindley distributions. *Communications in Statistics Theory and Methods*, 44(19):4096–4113.

[8] Maurya, R.K., Tripathi, Y.M. and Kayal, T. (2022). Reliability estimation in a multicomponent stress strength model based on inverse Weibull distribution. *Sankhya B*, 84(1):364–401.

[9] Abd El-Monsef, M.M.E., Marei, G.A. and Kilany, N.M. (2022). Poisson modified weibull distribution with inferences on stress strength reliability model. *Quality and Reliability Engineering International*, 38(5):2649–2669.

[10] Kohansal, A. (2022). Inference on stress strength model for a Kumaraswamy distribution based on hybrid progressive censored sample. *REVSTAT Statistical Journal*, 20(1):51–83.

[11] Barbiero, A. and Hitaj, A. (2022). Approximation of continuous random variables for the evaluation of the reliability parameter of complex stress strength models. *Annals of Operations Research*, 315(2):1573–1598.

[12] Hassan, A.S., Al-Omari, A. and Nagy, H.F. (2021). Stress strength reliability for the generalized inverted exponential distribution using MRSS. *Iranian Journal of Science and Technology, Transactions A: Science*, 45(2):641–659.

[13] Yousef, M.M. and Almetwally, E.M. (2021). Multi stress strength reliability based on progressive first failure for Kumaraswamy model: Bayesian and non-Bayesian estimation. *Symmetry*, 13(11):2120.

[14] Jha, M.K., Dey, S., Alotaibi, R.M. and Tripathi, Y.M. (2020). Reliability estimation of a multicomponent stress strength model for unit Gompertz distribution under progressive Type II censoring. *Quality and Reliability Engineering International*, 36(3):965–987.

[15] Lai, C.D., Murthy, D.N.P. and Xie, M. (2011). Weibull distributions. *Wiley Interdisciplinary Reviews: Computational Statistics*, 3(3):282–287.

[16] Hallinan Jr, A.J. (1993). A review of the Weibull distribution. *Journal of quality technology*, 25(2):85–93.

[17] Shakhatreh, M.K., Dey, S. and Alodat, M.T. (2021). Objective Bayesian analysis for the differential entropy of the Weibull distribution. *Applied Mathematical Modelling*, 89:314–332.

[18] Makalic, E. and Schmidt, D.F. (2023). Maximum likelihood estimation of the Weibull distribution with reduced bias. *Statistics and Computing*, 33(3):69.

[19] Kizilaslan, F. and Nadar, M. (2015). Classical and Bayesian estimation of reliability in multicomponent stress strength model based on Weibull distribution. *Revista Colombiana de estadistica*, 38(2):467–484.

[20] Eryilmaz, S. and Tutuncu, G.Y. (2015). Stress strength reliability in the presence of fuzziness. *Journal of computational and applied mathematics*, 282:262–267.

[21] Saracoglu, B., Kinaci, I. and Kundu, D. (2012). On estimation of R= P (Y< X) for exponential distribution under progressive type II censoring. *Journal of Statistical Computation and Simulation*, 82(5):729–744.

ASSESSMENT OF CRUDE PROBABILITIES OF FAILURE FOR TWO-COMPONENT SERIES SYSTEM SHOCK MODEL

Saraswati V Katagi[1*] and S. B. Munoli[2]

•

Department of Studies in Statistics, Karnatak University, Dharwad.
Karnataka, India-580003.
saraswati249katagi@gmail.com[1*], sbmunoli@yahoo.co.in[2]

Abstract

A Series system with two components having a single risk on each component is same as a single component with two independent risks acting on it. The third risk may be a catastrophic risk to whole system. A two-component series system shock model with two kinds of shocks namely, damage shock and catastrophic shock, is studied from competing risks perspective. The crude probabilities of different modes of system failure are derived. Information from life testing experiment is used in assessment of crude probabilities for system failure. Results are validated through simulation studies.

Keywords: Shock Model, Series System, Damage and Catastrophic Shock, Crude Probability for Failure, Life Testing Experiment.

I. Introduction

The arrangement of subassemblies of a system plays a crucial role in determining system reliability. While parallel setups offer redundancy, series configurations are often essential despite their vulnerability to single-point failures. Applications such as fire alarm systems, rocket launch sequences, water purification processes, and power distribution rely on series systems, where failure of any component like generators or transformers can disrupt the entire operation. Thus, the system functions only if all components operate effectively.

Often, system failure arises from one risk out of several competing risks. Identifying the dominant failure mode aids in implementing effective preventive or corrective actions to improve system reliability and hence, assessment of crude probabilities of system failure is crucial. Crude probability is defined in [4] as the probability of failure due to a specific risk in the presence of all other risks provides insights into the most probable causes of failure. A realistic and effective framework for modeling reliability of systems operating within random environments is through shock models. The definition of a shock model deals with the inter-arrival times of shocks, the damage induced by each shock, system failure criteria and their relationships.

The life distribution properties of a device under a homogeneous Poisson shock model were studied by [9]. The results obtained by [9] are extended to a shock model governed by a non-homogeneous Poisson process in [1]. A measure of component importance in coherent systems and fault trees has been introduced in [3]. Shock models with non-stationary pure birth process has

been discussed in [2]. The properties of survival function of a pure birth shock model are demonstrated in [12]. The IFRA property of life distribution of non-homogeneous Poisson shock model has been established in [17]. The distribution, mean, variance and asymptotic behavior of the system failure time for a class of cumulative shock models have been analyzed in [20].

A semi-Markov shock model with additive damages and control limit replacement policies was examined in [16]. A non-homogeneous Poisson shock model leading to multivariate distribution has been studied in [18]. A two-dimensional random walk has been used to explain cumulative shock models in [10]. The MLE and UMVUE of the reliability function for a two-component parallel system have been derived in [13]. A shock model reliability using a renewal point process has been studied in [19]. A detailed account of competing risks theory has been provided in [6]. In [7] NBU and NWU ageing notions within competing risks have been introduced. The survival under two types of shocks has been modeled in [14]. The crude probabilities of failure for such models have been examined in [15]. Analytic expressions for hazard rates, failure densities, cause-specific probabilities, and survival functions in a bivariate shock setting have been obtained in [8].

Understanding not only when but how a system fails is crucial. In [5] and [11] the concept of crude probability from competing risks theory has been provided and it offers insights into failure causes - key for maintenance, design, and root-cause analysis. However, while the concept is well-studied in general reliability contexts, its application to shock-driven series systems remains relatively unexplored.

This study aims to assess the crude probabilities of failure in a two-component (components A and B) series system subjected to an external shock process. Each component is characterized by a fixed threshold, and the system fails when either component A or component B experiences a damage shock exceeding its respective threshold or when the system endures the catastrophic shock.

The model considered in this study is explained in Section 2. The explicit expressions for the crude probabilities of system failure due to different causes are also derived in the same section. Life testing experiment is described in Section 3. Simulation study is presented in Section 4. The results that contribute to a deeper understanding of failure attribution in shock models are outlined in Section 5.

II. Crude Probabilities of System Failure

A Poisson process with intensity $\lambda, (\lambda > 0)$ is considered for a randomly occurring sequence of shocks to a two-component series system. The shocks are of two types namely damage shocks and catastrophic (fatal) shocks with probabilities $p, (0 < p < 1)$ and $(1 - p)$ repsectively. Let X_i and Y_i denote amounts of damages to components A and B respectively due to damage shocks. Assuming $X_i, Y_i \ \ i = 1, 2, \ldots$ are exponential random variables (r.vs) with respective parameters θ_1 and θ_2 and u_1, u_2 are the thresholds of components A and B respectively. The damages are non-accumulating and the component fails whenever a damage exceeds its threshold and failure of a component leads to system failure (series system). The system also fails when it experiences a catastrophic shock. Thus, the system failure can be associated with one of the following three cases.

i) Failure of component A due to damage (X) exceeding its threshold (u_1).
ii) Failure of component B due to damage (Y) exceeding its threshold (u_2).
iii) Failure of the system when it experiences a catastrophic shock.

In this scenario, it is not feasible to study the system failure with an isolated cause (of the 3 causes). Hence, each cause of system failure is studied in the presence of other two causes which are referred to as risks and the corresponding probabilities of failure are referred to as crude probability of failure in the presence of the other.

Denoting Q_{tAd} as the crude probability of system failure during $(0,t)$ due to failure of component A because of damage exceeding its threshold even when the system has risks of component B failure and experiencing a catastrophic shock and is given by

$$Q_{tAd} = \int_0^t \sum_{k=1}^{\infty} \frac{e^{-p\lambda t_1}(p\lambda t_1)^k}{k!} \left(1 - e^{-u_1\theta_1}\right)^{k-1} e^{-u_1\theta_1} e^{-(1-p)\lambda t_1} \left(1 - e^{-u_2\theta_2}\right)^k dt_1 \quad (1)$$

Expression (1) is obtained in the light of following probability considerations:

- Component A has failed at $t_1 \epsilon (0,t)$.
- During $(0,t_1)$ the system has experienced k number of damage shocks $(k = 1,2,\dots)$.
- All the damages due to $(k-1)$ shocks are less than u_1(component A), the damage due to k^{th} shock is greater than u_1.
- Component B has lived through all the k damage shocks.
- The system has not experienced any catastrophic shock during $(0,t_1)$.

Q_{tAd} is further simplified as

$$Q_{tAd} = \frac{e^{-u_1\theta_1}}{(1-e^{-u_1\theta_1})} \left\{ \frac{1-e^{-\left(\lambda - p\lambda\left(1-e^{-u_1\theta_1}\right)\left(1-e^{-u_2\theta_2}\right)\right)t}}{\lambda - p\lambda(1-e^{-u_1\theta_1})(1-e^{-u_2\theta_2})} - \frac{(1-e^{-\lambda t})}{\lambda} \right\} \quad (2)$$

On the similar grounds, the crude probability of system failure due to failure of component B is obtained as

$$Q_{tBd} = \int_0^t \sum_{k=1}^{\infty} \frac{e^{-p\lambda t_1}(p\lambda t_1)^k}{k!} \left(1 - e^{-u_1\theta_1}\right)^k e^{-(1-p)\lambda t_1} \left(1 - e^{-u_2\theta_2}\right)^{k-1} e^{-u_2\theta_2}\, dt_1 \quad (3)$$

$$Q_{tBd} = \frac{e^{-u_2\theta_2}}{(1-e^{-u_2\theta_2})} \left\{ \frac{1-e^{-\left(\lambda - p\lambda\left(1-e^{-u_1\theta_1}\right)\left(1-e^{-u_2\theta_2}\right)\right)t}}{\lambda - p\lambda(1-e^{-u_1\theta_1})(1-e^{-u_2\theta_2})} - \frac{(1-e^{-\lambda t})}{\lambda} \right\} \quad (4)$$

Q_{tf}, the crude probability of system failure by enduring a catastrophic shock at $t_1 \epsilon (0,t)$ when both the components A and B surviving through all previous damage shocks is given by

$$Q_{tf} = \int_0^t \sum_{k=0}^{\infty} \frac{e^{-p\lambda t_1}(p\lambda t_1)^k}{k!} \left(1 - e^{-u_1\theta_1}\right)^k (1-p)\lambda e^{-(1-p)\lambda t_1} \left(1 - e^{-u_2\theta_2}\right)^k dt_1 \quad (5)$$

Expression (5) is obtained in the light of following probability considerations:

- System has failed at $t_1 \epsilon (0,t)$.
- During $(0,t_1)$ the system has experienced k number of damage shocks $(k = 0,1,2,\dots)$.
- Components A and B both have lived through all the k damage shocks.
- The system has experienced catastrophic shock at $t_1 \epsilon (0,t)$.

Q_{tf} is further simplified as,

$$Q_{tf} = (1-p) \left\{ \frac{1-e^{-\left(\lambda - p\lambda\left(1-e^{-u_1\theta_1}\right)\left(1-e^{-u_2\theta_2}\right)\right)t}}{1-p(1-e^{-u_1\theta_1})(1-e^{-u_2\theta_2})} \right\} \quad (6)$$

It can be noted that Q_{tAd} , Q_{tBd} and Q_{tf} are all non-decreasing functions of t.

Table 1 and 2 provide the values of Q_{tAd} , Q_{tBd} and Q_{tf} for given values of λ, θ_1 and θ_2, at different combinations of p, u_1 and u_2, and for various values of t.

Table 1: *Theoretical computed crude probabilities of failure*

$p = 0.7, \lambda = 0.2, \theta_1 = 0.6, \theta_2 = 0.8$

t	$u_1 = 1.2, u_2 = 1.6$			$u_1 = 1.8, u_2 = 2.4$			$u_1 = 2.4, u_2 = 3.2$		
	Q_{tAd}	Q_{tBd}	Q_{tf}	Q_{tAd}	Q_{tBd}	Q_{tf}	Q_{tAd}	Q_{tBd}	Q_{tf}
1.0	0.0219	0.0089	0.0558	0.0182	0.0061	0.0565	0.0139	0.0037	0.0571
1.5	0.0466	0.0189	0.0807	0.0389	0.0130	0.0823	0.0297	0.0080	0.0835
2.0	0.0783	0.0318	0.1039	0.0657	0.0220	0.1066	0.0502	0.0136	0.1086
2.5	0.1157	0.0470	0.1254	0.0975	0.0326	0.1294	0.0748	0.0202	0.1325
3.0	0.1576	0.0640	0.1453	0.1335	0.0446	0.1509	0.1027	0.0277	0.1552
3.5	0.2030	0.0824	0.1639	0.1727	0.0577	0.1712	0.1332	0.0360	0.1768
4.0	0.2511	0.1020	0.1811	0.2145	0.0716	0.1902	0.1660	0.0448	0.1973
4.5	0.3011	0.1223	0.1971	0.2582	0.0863	0.2082	0.2005	0.0541	0.2168
5.0	0.3523	0.1431	0.2119	0.3034	0.1014	0.2250	0.2364	0.0638	0.2353
5.5	0.4042	0.1641	0.2257	0.3496	0.1168	0.2409	0.2732	0.0737	0.2529

Table 2: *Theoretical computed crude probabilities of failure*

$p = 0.6, \lambda = 0.2, \theta_1 = 0.6, \theta_2 = 0.8$

t	$u_1 = 1.2, u_2 = 1.6$			$u_1 = 1.8, u_2 = 2.4$			$u_1 = 2.4, u_2 = 3.2$		
	Q_{tAd}	Q_{tBd}	Q_{tf}	Q_{tAd}	Q_{tBd}	Q_{tf}	Q_{tAd}	Q_{tBd}	Q_{tf}
1.0	0.0187	0.0076	0.0741	0.0156	0.0052	0.0749	0.0118	0.0032	0.0756
1.5	0.0398	0.0162	0.1070	0.0332	0.0111	0.1088	0.0253	0.0068	0.1102
2.0	0.0668	0.0271	0.1375	0.0559	0.0187	0.1406	0.0427	0.0115	0.1429
2.5	0.0986	0.0400	0.1657	0.0828	0.0277	0.1703	0.0634	0.0171	0.1737
3.0	0.1341	0.0545	0.1918	0.1131	0.0378	0.1981	0.0868	0.0234	0.2028
3.5	0.1726	0.0701	0.2159	0.1461	0.0488	0.2241	0.1124	0.0303	0.2303
4.0	0.2132	0.0866	0.2383	0.1811	0.0605	0.2484	0.1397	0.0377	0.2563
4.5	0.2553	0.1037	0.2589	0.2177	0.0727	0.2712	0.1683	0.0454	0.2807
5.0	0.2984	0.1212	0.2780	0.2554	0.0853	0.2926	0.1980	0.0534	0.3039
5.5	0.3420	0.1389	0.2957	0.2937	0.0981	0.3125	0.2283	0.0616	0.3257

From Table 1 and Table 2 the crude probabilities of failure exhibit a non-decreasing trend overtime. When the probability of damage shock p is reduced, the associated probabilities of failure from such shock also decline. At the same time, the crude probability of failure due to fatal shock Q_{tf} rises since the chance of encountering a fatal event, quantified by $(1 - p)$ increase as p decreases. As threshold of the components increase the crude probabilities of failure due to damage shock decrease, reflecting the increased resistance of components of damaging shocks.

III. Life Testing Experiment

Suppose n two-component series systems whose modes of failure are described by Q_{tAd} , Q_{tBd} and Q_{tf} derived as in Section 2 are subjected to sequence of shocks. Let r_1 systems fail due to failure of component A, r_2 systems fail due to failure of component B and r_3 $(= n - r_1 - r_2)$ systems fail due to experiencing catastrophic shock. Let n_i be the shock at which the i^{th} system has failed, t_{ij} be the time epoch at which i^{th} system has experienced j^{th} shock $j = 1, 2, \ldots, n_i$, $i = 1, 2, \ldots, n$. $(t_{ij} - t_{i(j-1)})$

are exponential r.vs with parameter $p\lambda$ for a damage shocks and $(1-p)\lambda$ for a catastrophic shock. It is assumed that the damage shock at which a component fails is not observable but it is known to exceed its threshold and the damages due to catastrophic shocks are also not observed.

Hence, the joint distribution of the random variables $r_1,\ n_i,\ t_{i1},\ t_{i2},\dots,t_{in_i},\ x_{i1},\ x_{i2},\dots,x_{i(n_i-1)},\ y_{i1},y_{i2},\dots,y_{in_i}$ for the r_1 systems that fail due to failure of component A because of the damage shock is given by

$$\prod_{i=1}^{r_1}(p\lambda)^{n_i}e^{-p\lambda t_{n_i}}\,{\theta_1}^{n_i-1}e^{-\theta_1\sum_{j=1}^{n_i-1}x_{ij}}e^{-\theta_1 u_1}{\theta_2}^{n_i}e^{-\theta_2\sum_{j=1}^{n_i}y_{ij}} \tag{7}$$

The joint distribution of all the random variables involved for the r_2 systems that have failed due to component B failure by damage shocks is given by

$$\prod_{i=1}^{r_2}(p\lambda)^{n_i}e^{-p\lambda t_{n_i}}\,{\theta_1}^{n_i}e^{-\theta_1\sum_{j=1}^{n_i}x_{ij}}{\theta_2}^{n_i-1}e^{-\theta_2\sum_{j=1}^{n_i-1}y_{ij}}e^{-\theta_2 u_2} \tag{8}$$

Similarly, for r_3 systems that have failed due to experiencing fatal shocks, the joint distribution of all the underlying random variables is given by

$$\prod_{i=1}^{r_3}(p\lambda)^{n_i-1}e^{-p\lambda t_{n_i-1}}\ {\theta_1}^{n_i-1}e^{-\theta_1\sum_{j=1}^{n_i-1}x_{ij}}\ {\theta_2}^{n_i-1}e^{-\theta_2\sum_{j=1}^{n_i-1}y_{ij}}\ (1-p)\lambda e^{-(1-p)\lambda\left(t_{n_i}-t_{n_i-1}\right)} \tag{9}$$

combining (7), (8) and (9) the joint distribution of all the random variables observed in this life testing experiment is obtained as

$$f=\frac{n!}{r_1!\,r_2!r_3!}(p\lambda)^{(n_\cdot-r_3)}e^{-p\lambda t_\cdot}\,{\theta_1}^{(n_\cdot-r_1-r_3)}e^{-\theta_1 x_\cdot}\,{\theta_2}^{(n_\cdot-r_2-r_3)}e^{-\theta_2 y_\cdot}\left((1-p)\lambda\right)^{r_3}e^{-\lambda t_{\cdot\cdot}} \tag{10}$$

with, $n_\cdot=\sum_{i=1}^{r_1}n_i+\sum_{i=1}^{r_2}n_i+\sum_{i=1}^{r_3}n_i\ ,\quad t_\cdot=\sum_{i=1}^{r_1}t_{n_i}+\sum_{i=1}^{r_2}t_{n_i}+\sum_{i=1}^{r_3}t_{(n_i-1)}-t_{\cdot\cdot}$

$x_\cdot=\sum_{i=}^{r_1}\sum_{j=1}^{n_i-1}x_{ij}+\sum_{i=}^{r_2}\sum_{j=1}^{n_i}x_{ij}+\sum_{i=}^{r_3}\sum_{j=1}^{n_i-1}x_{ij}+r_1u_1$

$y_\cdot=\sum_{i=}^{r_1}\sum_{j=1}^{n_i}y_{ij}+\sum_{i=}^{r_2}\sum_{j=1}^{n_i-1}y_{ij}+\sum_{i=}^{r_3}\sum_{j=1}^{n_i-1}y_{ij}+r_2u_2$

$t_{\cdot\cdot}=\sum_{i=1}^{r_3}(t_{n_i}-t_{(n_i-1)})$

Treating Equation (10) as function of parameters, equating the partial derivatives with respect to θ_1,θ_2,p and λ of natural logarithm of (10) to 0, the maximum likelihood estimators (MLEs) $\hat{\theta}_1,\hat{\theta}_2,\hat{p},\hat{\lambda}$ of $\theta_1,\theta_2,p,\lambda$ respectively are obtained as below:

$$\frac{\partial log f}{\partial\theta_1}=0,\ \Rightarrow\hat{\theta}_1=\frac{n_\cdot-r_1-r_3}{x_\cdot}$$

$$\frac{\partial log f}{\partial\theta_2}=0,\ \Rightarrow\hat{\theta}_2=\frac{n_\cdot-r_2-r_3}{y_\cdot}$$

$$\frac{\partial\log f}{\partial\lambda}=0,\ \Rightarrow\frac{n_\cdot-r_3}{\lambda}-pt_\cdot+\frac{r_3}{\lambda}-t_{\cdot\cdot}=0 \tag{12}$$

$$\frac{\partial\log f}{\partial p}=0,\ \Rightarrow\frac{n_\cdot-r_3}{p}-\lambda t_\cdot-\frac{r_3}{(1-p)}=0 \tag{13}$$

Solving equations (12) and (13) simultaneously, the MLEs of λ and p are obtained as

$$\hat{\lambda}=\frac{n_\cdot}{\hat{p}t_\cdot+t_{\cdot\cdot}},\qquad\hat{p}=\frac{(n_\cdot-r_3)t_{\cdot\cdot}}{n_\cdot t_{\cdot\cdot}+r_3t_\cdot}$$

Using the invariance property of MLE, the MLEs $\hat{Q}_{tAd},\hat{Q}_{tBd}$ and $\hat{Q}_{tf}$ of three crude probabilities are obtained by plugging in the MLE of parameters in the expressions for Q_{tAd},Q_{tBd} and Q_{tf}.

III. Simulation study

Given the values of $p = p_o, \lambda = \lambda_0, \theta_1 = \theta_{1o}, \theta_2 = \theta_{2o}, u_1 = u_{1o}, u_2 = u_{2o}$ for i^{th} system, the random variables X_{ij}, Y_{ij}, t_{ij} ; $i = 1, 2, 3, \dots, n$; $j = 1, 2, 3, \dots, n_i$ are generated as follows

Step 1: At the beginning, we have to judge whether the i^{th} system has failed due to damage shock or catastrophic shock. To do this, the following algorithm is used

i) Generate a standard uniform random number U_o.
ii) If $0 < U_o < p_o$, the system has failed due to damage shock, else the system has failed due to catastrophic shock.

Step 2: Depending on the results of Step 1 proceed to Step 3 if the system has failed due to damage shock or to Step 4, if the system has failed due to catastrophic shock.

Step 3: Initialize $r_1 = 0, r_2 = 0, n_i = 0$. For $p = p_o, \lambda = \lambda_o, \theta_1 = \theta_{1o}, \theta_2 = \theta_{2o}$ the exponential random variables X_{i1} with parameter θ_{1o} and Y_{i1} with parameter θ_{2o} are generated.

i) If $X_{i1} > u_{1o}$ and $Y_{i1} > u_{2o}$, this condition is against model assumption so the current iteration is discarded and a new set of random variables are generated by initializing $n_i = 0$.
ii) The process of generation of X_{ij}, Y_{ij} and incrementation of n_i by 1 is continued until system fails due to either failure of component A or B.
iii) r_1 is incremented by 1 if system fails due to component A else r_2 is incremented by 1.
iv) n_i number of exponential random variables with parameter $p_o\lambda_o$ are generated to compute t_{in_i} here, $i = 1, 2, \dots, r_1$ or r_2.

Step 4: Initialize $r_3 = 0, n_i = 0$. For $p = p_o, \lambda = \lambda_o, \theta_1 = \theta_{1o}, \theta_2 = \theta_{2o}$ the exponential random variables X_{i1} with parameter θ_{1o} and Y_{i1} with parameter θ_{2o} are generated.

(i) and (ii) of Step 3 are repeated until n_i is noted. r_3 is incremented by 1, $n_i - 1$ number of exponential random variables with parameter $p_o\lambda_o$ are generated to compute $t_{i(n_i-1)}$ here, $i = 1, 2, \dots, r_3$. One inter-arrival time $\left(t_{in_i} - t_{i(n_i-1)}\right)$ having exponential distribution with parameter $(1 - p_o)\lambda_o$ is generated.

Steps 1 to 4 are repeated for $n = 25, 45, 75$. The statistics $n_.$, $t_.$, $x_.$, $y_.$, $t_{..}$ are computed, using which $\hat{Q}_{tAd}, \hat{Q}_{tBd}$ and $\hat{Q}_{tf}$ are obtained for $t = 1\ (0.5)\ 5.5$.

The absolute biases are computed for each of the estimated $\hat{Q}_{tAd}, \hat{Q}_{tBd}$ and $\hat{Q}_{tf}$, and the respective mean absolute biases are computed for 10,000 (m) simulations as

$$M_{\hat{Q}_{tAd}} = \frac{\sum_{j=1}^{m} |Q_{tAd} - \hat{Q}_{tAd_j}|}{m} \; ; \; M_{\hat{Q}_{tBd}} = \frac{\sum_{j=1}^{m} |Q_{tBd} - \hat{Q}_{tBd_j}|}{m} \; ; M_{\hat{Q}_{tf}} = \frac{\sum_{j=1}^{m} |Q_{tf} - \hat{Q}_{tf_j}|}{m}$$

Table 3: *Mean absolute biases of estimated crude probabilities of failure*

t	$p = 0.7, \lambda = 0.2, \theta_1 = 0.6, \theta_2 = 0.8, u_1 = 1.2, u_2 = 1.6$								
	Q_{tAd}			Q_{tBd}			Q_{tf}		
	$n = 25$	$n = 45$	$n = 75$	$n = 25$	$n = 45$	$n = 75$	$n = 25$	$n = 45$	$n = 75$
1.0	0.0050	0.0040	0.0034	0.0028	0.0024	0.0022	0.0205	0.0131	0.0102
1.5	0.0105	0.0085	0.0071	0.0060	0.0051	0.0047	0.0289	0.0188	0.0146
2.0	0.0175	0.0141	0.0118	0.0101	0.0085	0.0079	0.0365	0.0239	0.0187
2.5	0.0257	0.0206	0.0172	0.0149	0.0126	0.0116	0.0432	0.0287	0.0225
3.0	0.0348	0.0277	0.0231	0.0203	0.0170	0.0156	0.0492	0.0330	0.0259
3.5	0.0446	0.0354	0.0294	0.0261	0.0219	0.0200	0.0546	0.0369	0.0290
4.0	0.0549	0.0435	0.0360	0.0324	0.0270	0.0246	0.0594	0.0405	0.0319
4.5	0.0657	0.0518	0.0427	0.0388	0.0323	0.0294	0.0637	0.0437	0.0346
5.0	0.0766	0.0602	0.0494	0.0454	0.0377	0.0342	0.0676	0.0467	0.0370
5.5	0.0877	0.0687	0.0561	0.0521	0.0431	0.0390	0.0710	0.0494	0.0393

Table 4: *Mean absolute biases of estimated crude probabilities of failure*

t	$p = 0.7, \lambda = 0.2, \theta_1 = 0.6, \theta_2 = 0.8, u_1 = 1.8, u_2 = 2.4$								
	Q_{tAd}			Q_{tBd}			Q_{tf}		
	$n = 25$	$n = 45$	$n = 75$	$n = 25$	$n = 45$	$n = 75$	$n = 25$	$n = 45$	$n = 75$
1.0	0.0041	0.0036	0.0034	0.0018	0.0015	0.0014	0.0209	0.0137	0.0101
1.5	0.0088	0.0078	0.0073	0.0038	0.0031	0.0029	0.0296	0.0196	0.0145
2.0	0.0149	0.0131	0.0123	0.0065	0.0053	0.0049	0.0374	0.0250	0.0185
2.5	0.0221	0.0193	0.0182	0.0096	0.0079	0.0072	0.0443	0.0300	0.0223
3.0	0.0302	0.0265	0.0249	0.0131	0.0107	0.0098	0.0506	0.0345	0.0257
3.5	0.0391	0.0341	0.0320	0.0169	0.0139	0.0126	0.0561	0.0386	0.0288
4.0	0.0486	0.0423	0.0396	0.0210	0.0172	0.0156	0.0611	0.0423	0.0317
4.5	0.0585	0.0507	0.0474	0.0254	0.0208	0.0188	0.0656	0.0457	0.0343
5.0	0.0689	0.0595	0.0555	0.0299	0.0244	0.0220	0.0696	0.0488	0.0368
5.5	0.0795	0.0685	0.0637	0.0345	0.0281	0.0252	0.0732	0.0516	0.0390

IV. Results

Table 3 and Table 4 presents mean absolute biases of the estimated crude probabilities of system failure Q_{tAd}, Q_{tBd} and Q_{tf} for varying time (t) and number of systems subject to test (n) values. Across all time points the mean absolute biases of crude probabilities of failure decrease as n increase this shows the consistency of the MLE.

Acknowledgements
The first author is thankful to Department of Backward Classes Welfare for the award of Ph. D fellowship.

Conflict of Interest
The authors declare that there is no conflict of interest.

References

[1] A-Hameed, M. S., and Proschan, F. (1973). Nonstationary shock models. *Stochastic Processes and their Applications*, 1(4):383-404.

[2] A-Hameed, M. S., and Proschan, F. (1975). Shock models with underlying birth process. *Journal of Applied Probability,* 12(1):18-28.

[3] Barlow, R. E., and Proschan, F. (1975). Importance of system components and fault tree events. *Stochastic Processes and their applications,*3(2):153-173.

[4] Chiang, Ch. L. Introduction to Stochastic Processes in Biostatistics, Wiley, and Sons, 1968.

[5] Cox, D. R. (1959). The analysis of exponentially distributed life-times with two types of failure. *Journal of the Royal Statistical Society Series B: Statistical Methodology,* 21(2): 411-421.

[6] Crowder, M.J. Classical Competing Risks (1st ed.). Chapman and Hall, 2001.

[7] Di Crescenzo, A., and Longobardi, M. (2006). On the NBU ageing notion within the competing risks model. *Journal of statistical planning and inference,* 136(5):1638-1654.

[8] Di Crescenzo, A., and Meoli, A. (2023). Competing risks and shock models governed by a generalized bivariate Poisson process. *Journal of Applied Probability,* 60(2):709-722.

[9] Esary, J. D., and Marshall, A. W. (1973). Shock models and wear processes. *The annals of probability,* 627-649.

[10] Gut, A. (1990). Cumulative shock models. *Advances in Applied Probability,* 22(2):504-507.

[11] Kalbfleisch, J. D., and Prentice, R. L. The statistical analysis of failure time data (2nd ed.).

Wiley-Interscience, 2002.

[12] Klefsjö, B. (1981). Survival under the pure birth shock model. *Journal of Applied Probability*, 18(2):554-560.

[13] Kunchur, S. H., and Munoli, S. B. (1993). Estimation of reliability in a shock model for a two-component system. *Statistics & probability letters*, 17(1):35-38.

[14] Munoli, S. B. and Suhas (2019). Modelling and Assessment of Survival Probability of Shock Model with Two Kinds of Shocks. *Open Journal of Statistics*, 9(4):484-493.

[15] Munoli, S. B., and Jadhav, A. (2023). Assessment of Crude Probabilities of Competing Risks for Time to Event in Shock Model. *International Journal of Agricultural & Statistical Sciences*, 19.

[16] Posner, M. J. M., and Zuckerman, D. (1986). Semi-Markov shock models with additive damage. *Advances in applied probability*, 18(3):772-790.

[17] Ross, S. M. (1981). Generalized Poisson shock models. *The Annals of Probability*, 896-898.

[18] Savits, T. H. (1988). Some multivariate distributions derived from a non-fatal shock model. *Journal of Applied Probability*, 25(2):383-390.

[19] Skoulakis, G. (2000). A general shock model for a reliability system. *Journal of applied probability*, 37(4):925-935.

[20] Sumita, U., and Shanthikumar, J. G. (1985). A class of correlated cumulative shock models. *Advances in Applied probability*, 17(2):347-366.

TRANSMUTED X-RAMA DISTRIBUTION: PROPERTIES AND APPLICATIONS

Nimmy George[1], Sindhu E S[2]

•

[1,2]Department of Statistics, Kuriakose Elias College, Mannanam, Kottayam-686561, Kerala, India.

Email: [1]nimmygeorge60@gmail.com; [2]sindhujaimon@kecollege.ac.in

Abstract

In this paper, we introduce a new generalized distribution called Transmuted X-Rama distribution (TXRD) by using the quadratic rank transmutation map (QRTM). The probability density function (PDF), cumulative distribution function (CDF), and key moments of the transmuted distribution are meticulously derived to demonstrate how the transmutation parameter influences the shape of the distribution. Additionally, we analyze its reliability function, hazard rate, odds function, entropy and order statistics all of which are crucial in applications involving uncertainty and longevity data. We propose the method of maximum likelihood estimation (MLE) and method of least squares estimation (LSE) for the estimation of parameters of the distribution. We also show how the transmuted distribution may be fitted to real datasets.

Keywords: Transmuted X-Rama distribution, moments, reliability analysis, order statistics, entropy, simulation.

1. Introduction

Distributions are fundamental concepts in probability and statistics that describe how data values are distributed across possible outcomes. It is not always possible to represent complex data sets using standard distributions due to their rigid architecture and assumptions. Because of these limitations, it is necessary to use generalized distributions, which are extensions of conventional ones that offer more parameters and flexibility.

Recently, several researchers have suggested new families of distributions for better modeling of real-world events by generalizing existing families. Numerous methods exist for creating a new generalized distribution in the literature. One such method is the quadratic rank transmutation map (QRTM) presented by Shaw and Buckley [16]. This method relies on a baseline distribution to generate a fresh distribution called the transmuted distribution. Although many of the characteristics of the baseline distributions are retained, transmuted distributions often offer increased flexibility in modeling data, especially in terms of skewness and kurtosis, due to the additional parameter. The significance of QRTM is demonstrated by a number of published studies in the literature. To name a few, Aryal and Tsokos [4] introduced the transmuted Weibull distribution, Khan, King and Hudson [9] studied the transmuted Kumaraswamy distribution, Demirci [5] proposed the transmuted Xgamma distribution, Mohiuddin et al [10] introduced the transmuted Garima distribution, Onyekwer et al [13] studied the transmuted Shanker distribution. Alzaatreh et al [3] developed a method to generate a family of continuous distributions called *T-X* family of distributions. Girish and Jayakumar[11] introduced a combined family of *T-X* and transmuted distributions called the T-transmuted X family of distributions.

According to Shaw and Buckley [16], the quadratic rank transmutation map (QRTM) technique states that a random variable X has a transmuted distribution if its cdf is provided by

$$G(x) = (1+\lambda)F(x) - \lambda\left(F(x)\right)^2; \quad |\lambda| \leq 1 \tag{1}$$

where F(x) is the cdf of the base distribution and G(x) is the cdf of the transmuted distribution. The pdf of Transmuted distribution will be;

$$g(x) = f(x)\left(1+\lambda-2\lambda F(x)\right) \tag{2}$$

where f(x) and g(x) are the corresponding probability density functions of F (x) and G (x), respectively.

The Rama distribution is a one-parameter distribution introduced by Sankar R [15] as a model suitable for skewed lifetime data with a non-constant hazard rate. This distribution is created by combining the Gamma$(4,\theta)$ and Exponential(θ) distributions in a certain proportion. In order to provide the Rama distribution with further flexibility, several generalized variations of it have been documented in the literature. Some of them include, Edith et al [6] proposed two-parameter Rama distribution, Abebe et al [1] introduced two-parameter power Rama distribution, Eyob and Shanker R [8] studied two-parameter weighted Rama distribution, Onyekwere et al [14] proposed the inverted power Rama distribution. Recently, a novel variation of the Rama distribution by Omoruyi et al [12] and the X-Rama distribution by Etaga et al [7] were introduced. The X-Rama distribution combines the Rama distribution and the exponential distribution with a mixing proportion $\frac{\theta^3}{\theta^3+6}$. In this article, we propose a new variation of the X-Rama distribution, called the transmuted X-Rama distribution (TXRD) by applying the technique of quadratic rank transmutation map (QRTM).

2. Transmuted X-Rama distribution

In this section, we provide the formulation of the transmuted X-Rama distribution (TXRD) by applying the QRTM of equation (1) to the X-Rama distribution. Consider the X-Rama distribution proposed by Etaga et al [7] with the probability density function (pdf) as

$$f(x) = \frac{\theta^4}{\left(\theta^3+6\right)^2}\left(\theta^3+6x^3+12\right)e^{-\theta x}, \quad x>0,\ \theta>0 \tag{3}$$

and cumulative distribution function (cdf) as

$$F(x) = 1 - \left[1+\frac{6\theta^3x^3+18\theta^2x^2+36\theta x}{\left(\theta^3+6\right)^2}\right]e^{-\theta x} \tag{4}$$

Using (4) in (1), we get the cdf of the TXRD,

$$\begin{aligned} G(x) = (1+\lambda)&\left\{1-\left[1+\frac{6\theta^3x^3+18\theta^2x^2+36\theta x}{(\theta^3+6)^2}\right]e^{-\theta x}\right\} \\ &-\lambda\left\{1-\left[1+\frac{6\theta^3x^3+18\theta^2x^2+36\theta x}{(\theta^3+6)^2}\right]e^{-\theta x}\right\}^2 \end{aligned} \tag{5}$$

Therefore, a continuous random variable X is said to follow TXRD if its probability density function is given by,

$$g(x;\theta,\lambda) = \theta e^{-\theta x}\left(1+\frac{6(\theta^3x^3-6)}{(\theta^3+6)^2}\right)\times\left(1-\lambda+2\lambda e^{-\theta x}\left(1+\frac{6\theta(\theta^2x^3+3\theta x^2+6x)}{(\theta^3+6)^2}\right)\right);$$

$$x>0,\ |\lambda|\leq 1, \theta>0 \tag{6}$$

The pdf and cdf plots of TXRD for different combinations of parameter values are displayed in Figure (1) and Figure (2) to demonstrate how it behaves in terms of distribution.

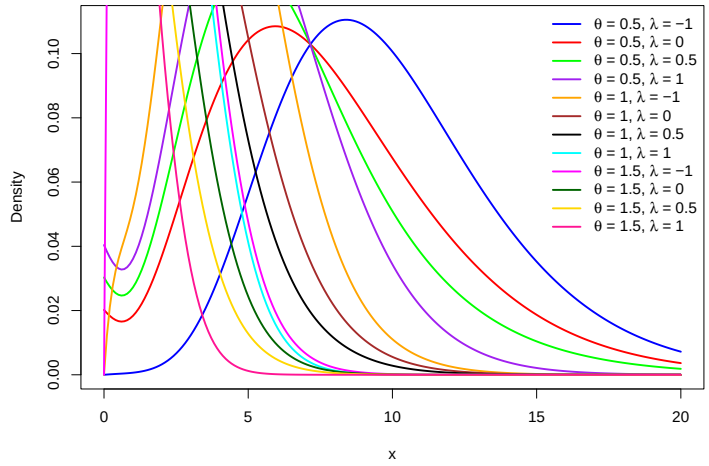


Figure 1: *PDF of TXRD for different values of parameters*

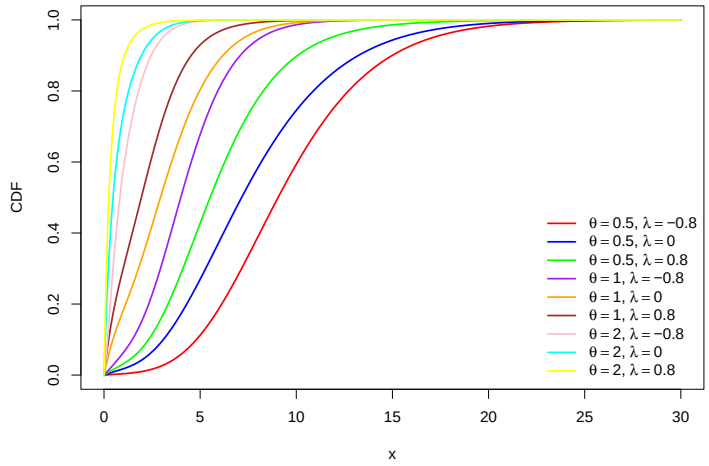


Figure 2: *CDF of TXRD for different values of parameters*

The plots show how the form, location of the peak and spread of the TXRD are mutually controlled by the parameters θ and λ. As θ decreases, the distribution becomes more dispersed with heavier tails, while as θ increases, it shows sharper peaks and faster decay. The transmutation parameter λ modulates the shape by introducing skewness and altering the behavior of the tail, where positive values of λ tend to stretch the right tail and increase asymmetry, and negative values enhance the peakedness around the mode.

3. Properties of transmuted X- Rama distribution

In this section, some mathematical properties such as moments, variance, moment generating function, and characteristic function of TXRD are derived.

3.1. Moments

Moments are quantitative measurements that are associated with the shape of a distribution. They help describe traits such as peakedness, skewness, spread, and location.

Let X be a TXRD random variable, then the r-th order moment will be

$$\mu'_r = \int_0^\infty x^r\, \theta e^{-\theta x} \left(1 + \frac{6(\theta^3 x^3 - 6)}{(\theta^3+6)^2}\right) \times \left[1 - \lambda + 2\lambda e^{-\theta x}\left(1 + \frac{6\theta}{(\theta^3+6)^2}(\theta^2 x^3 + 3\theta x^2 + 6x)\right)\right] dx$$

$$= \frac{\lambda}{16(2\theta)^r(\theta^3+6)^2}\Big[9\Gamma(r+7) + 54\Gamma(r+6) + 136\Gamma(r+5) - 408\Gamma(r+4) - 2520\left(\Gamma(r+3) + \Gamma(r+2)\right) - 560\Gamma(r+1)\Big] + \frac{\theta(1-\lambda)}{\theta^{r+1}}\Gamma(r+1) + \frac{6\theta(1-\lambda)}{(\theta^3+6)^2}\left(\frac{\Gamma(r+4) - \Gamma(r+1)}{\theta^r}\right) \tag{7}$$

From equation (7) we can generate the first four raw moments.

$$\mu'_1 = \frac{2189\lambda + (1-\lambda)\left[(\theta^3+6)^2 + 138\theta\right]}{\theta(\theta^3+6)^2} \tag{8}$$

$$\mu'_2 = \frac{37955\lambda + (1-\lambda)\left[8(\theta^3+6)^2 + 2832\theta\right]}{4\theta^2(\theta^3+6)^2} \tag{9}$$

$$\mu'_3 = \frac{170895\lambda + (1-\lambda)\left[24(\theta^3+6)^2 + 17136\theta\right]}{4\theta^3(\theta^3+6)^2} \tag{10}$$

$$\mu'_4 = \frac{3349485\lambda + (1-\lambda)\left[384(\theta^3+6)^2 + 481536\theta\right]}{16\theta^4(\theta^3+6)^2} \tag{11}$$

3.2. Variance

The variance of the TXRD random variable X is

$$V(X) = \frac{37955\lambda + (1-\lambda)\left[8(\theta^3+6)^2 + 2832\theta\right]}{4\theta^2(\theta^3+6)^2} - \left(\frac{2189\lambda + (1-\lambda)\left[(\theta^3+6)^2 + 138\theta\right]}{\theta(\theta^3+6)^2}\right)^2 \tag{12}$$

3.3. Moment generating function

The moment generating function of the TXRD random variable X is obtained as

$$M_X(t) = \int_0^\infty \left[1 + tx + \frac{(tx)^2}{2!} + \cdots\right] f(x,\theta,\lambda)\, dx$$

$$= \int_0^\infty \sum_{j=0}^{\infty} \frac{t^j}{j!} x^j f(x,\theta,\lambda)\, dx$$

$$= \sum_{j=0}^{\infty} \frac{t^j}{j!} \mu'_j$$

substituting the pdf of TXRD (6) we get

$$M_X(t) = \sum_{j=0}^{\infty} \frac{t^j}{j!} \left[\frac{\theta(1-\lambda)\Gamma(j+1)}{\theta^{j+1}} + \frac{6\theta(1-\lambda)}{(\theta^3+6)^2} \left(\frac{\Gamma(j+4)-\Gamma(j+1)}{\theta^j} \right) \right.$$
$$+ \frac{\lambda}{16(2\theta)^j(\theta^3+6)^2} \Big(9\Gamma(j+7) + 54\Gamma(j+6) + 136\Gamma(j+5)$$
$$\left. - 408\Gamma(j+4) - 2520\Gamma(j+3) - 2520\Gamma(j+2) - 560\Gamma(j+1) \Big) \right] \tag{13}$$

3.4. Characteristic function

The characteristic function of TXRD is

$$\Phi_X(t) = \sum_{j=0}^{\infty} \frac{(it)^j}{j!} \left[\frac{\theta(1-\lambda)\Gamma(j+1)}{\theta^{j+1}} + \frac{6\theta(1-\lambda)}{(\theta^3+6)^2} \left(\frac{\Gamma(j+4)-\Gamma(j+1)}{\theta^j} \right) \right.$$
$$+ \frac{\lambda}{16(2\theta)^j(\theta^3+6)^2} \Big(9\Gamma(j+7) + 54\Gamma(j+6) + 136\Gamma(j+5)$$
$$\left. - 408\Gamma(j+4) - 2520\Gamma(j+3) - 2520\Gamma(j+2) - 560\Gamma(j+1) \Big) \right] \tag{14}$$

4. Order statistics

Let $X_1, X_2, \ldots, X_n$ be the random sample taken from TXRD with probability density function $g_X(x)$ and cumulative distribution function $G_X(x)$. Let $X_{(1)} \leq X_{(2)} \leq \cdots \leq X_{(n)}$ be its order statistics. The probability density function of the k-th order statistic $X_{(k)}$ is given by,

$$g_{X_{(k)}}(x) = \frac{n!}{(k-1)!(n-k)!} g_X(x) \left[G_X(x)\right]^{k-1} \left[1 - G_X(x)\right]^{n-k}$$

Using Equations (5) and (6),

$$g_{X_{(k)}}(x) = \frac{n!}{(k-1)!(n-k)!} \theta e^{-\theta x} \left[1 + \frac{6(\theta^3 x^3 - 6)}{(\theta^3+6)^2} \right]$$
$$\times \left\{ (1-\lambda) + 2\lambda e^{-\theta x} \left[1 + \frac{6\theta}{(\theta^3+6)^2} \left(\theta^2 x^3 + 3\theta x^2 + 6x \right) \right] \right\}$$
$$\times B^{k-1} (1-B)^{n-k} \tag{15}$$

where B is the cdf of the TXRD.

Therefore, the pdf of the higher-order statistic $X_{(n)}$ of TXRD can be obtained as

$$g_{X_{(n)}}(x) = n\theta e^{-\theta x} \left[1 + \frac{6(\theta^3 x^3 - 6)}{(\theta^3+6)^2} \right]$$
$$\times \left\{ (1-\lambda) + 2\lambda e^{-\theta x} \left[1 + \frac{6\theta}{(\theta^3+6)^2} \left(\theta^2 x^3 + 3\theta x^2 + 6x \right) \right] \right\}$$
$$\times B^{n-1} \tag{16}$$

The pdf of the first-order statistic $X_{(1)}$can be obtained as

$$g_{X_{(1)}}(x) = n\theta e^{-\theta x}\left[1+\frac{6(\theta^3x^3-6)}{(\theta^3+6)^2}\right] \times\left\{(1-\lambda)+2\lambda e^{-\theta x}\left[1+\frac{6\theta}{(\theta^3+6)^2}\left(\theta^2x^3+3\theta x^2+6x\right)\right]\right\} \times(1-B)^{n-1} \tag{17}$$

5. Renyi entropy

Entropy is a metric used in probability and statistics to measure the degree of randomness in a probability distribution. It describes how unpredictable a system is; the higher entropy means more randomness, while the lower entropy means more certainty.
The Renyi entropy of the TXRD random variable is given by,

$$R_E(\alpha) = \frac{1}{1-\alpha}\log\int_0^\infty f^\alpha(x)\,dx$$

$$= \frac{1}{1-\alpha}\log\left(\int_0^\infty\left[\theta e^{-\theta x}\left(1+\frac{6(\theta^3x^3-6)}{(\theta^3+6)^2}\right) \times\left(1-\lambda+2\lambda e^{-\theta x}\left(1+\frac{6\theta}{(\theta^3+6)^2}(\theta^2x^3+3\theta x^2+6x)\right)\right)\right]^\alpha dx\right)$$

$$= \frac{1}{1-\alpha}\log\left\{\theta^\alpha\sum_{j=0}^\infty\binom{\alpha}{j}\left(\frac{6}{(\theta^3+6)^2}\right)^j\sum_{k=0}^\infty\binom{\alpha}{k}\left(\frac{2\lambda}{1-\lambda}\right)^k \times\sum_{l=0}^\infty\binom{k}{l}\left(\frac{6\theta}{(\theta^3+6)^2}\right)^l\int_0^\infty(\theta^3x^3-6)^j(\theta^2x^3+3\theta x^2+6x)^l e^{-\theta x(\alpha+k)}\,dx\right\}$$

by applying series expansions,

$$R_E(\alpha) = \frac{1}{1-\alpha}\log\theta^\alpha\sum_{j=0}^\infty\binom{\alpha}{j}\left[\frac{6}{(\theta^3+6)^2}\right]^j\sum_{k=0}^\infty\binom{\alpha}{k}\left(\frac{2\lambda}{1-\lambda}\right)^k \times\sum_{l=0}^\infty\binom{k}{l}\left[\frac{6\theta}{(\theta^3+6)^2}\right]^l\sum_{m=0}^\infty\binom{j}{m}\theta^{3m}(-6)^{j-m} \times\sum_{n_1+n_2+n_3=l}\binom{l}{n_1,n_2,n_3}\theta^{2n_1+n_2}3^{n_2}6^{n_3} \times\int_0^\infty x^{3(m+n_1)+2n_2+n_3}e^{-\theta x(\alpha+k)}dx$$

using gamma integral,

$$R_E(\alpha) = \frac{1}{1-\alpha}\log\theta^\alpha\sum_{j=0}^\infty\binom{\alpha}{j}\left[\frac{6}{(\theta^3+6)^2}\right]^j\sum_{k=0}^\infty\binom{\alpha}{k}\left(\frac{2\lambda}{1-\lambda}\right)^k \times\sum_{l=0}^\infty\binom{k}{l}\left[\frac{6\theta}{(\theta^3+6)^2}\right]^l\sum_{m=0}^\infty\binom{j}{m}\theta^{3m}(-6)^{j-m} \times\sum_{n_1+n_2+n_3=l}\binom{l}{n_1,n_2,n_3}\theta^{2n_1+n_2}3^{n_2}6^{n_3} \times\frac{\Gamma\left(3(m+n_1)+2n_2+n_3+1\right)}{\left[\theta(\alpha+k)\right]^{3(m+n_1)+2n_2+n_3+1}}$$

simplifying further, we obtain the Renyi entropy of TXRD as

$$R_E(\alpha) = \frac{1}{1-\alpha}\log\left[\sum_{j=0}^{\infty}\sum_{k=0}^{\infty}\sum_{l=0}^{\infty}\sum_{m=0}^{\infty}\sum_{n_1+n_2+n_3=l}\binom{\alpha}{j}\binom{\alpha}{k}\binom{k}{l}\binom{j}{m}\binom{l}{n_1,n_2,n_3}\right.$$
$$\left.\times\frac{3^{n_2}(-1)^{j-m}6^{2j+l-m+n_3}\theta^{\alpha+3m+l+2n_1+n_2}}{(1-\lambda)^k(\theta^3+6)^{2(j+l)}}\cdot\frac{(3(m+n_1)+2n_2+n_3)!}{[\theta(\alpha+k)]^{3(m+n_1)+2n_2+n_3+1}}\right] \quad (18)$$

6. Reliability analysis

In reliability engineering and statistics, a reliability or survival function is a basic idea that expresses the likelihood that a system will run as intended for a particular amount of time under given circumstances. It is a key component in the evaluation of long-term performance of a system and serves as a measurement of its reliability.

6.1. Reliability function

The reliability function or survival function, denoted by R(x) or S(x), represents the probability that a system will operate successfully without failure up to time x.

R(x) = P(X>x)
The reliability function is related to the cumulative distribution function (CDF) of the failure time as

R(x)=1-G(x)
survival function of TXRD will be obtained as

$$R(x) = 1-(1-\lambda)\left\{1-\left[1+\frac{6\theta^3x^3+18\theta^2x^2+36\theta x}{(\theta^3+6)^2}\right]e^{-\theta x}\right\}$$
$$+\lambda\left\{1-\left[1+\frac{6\theta^3x^3+18\theta^2x^2+36\theta x}{(\theta^3+6)^2}\right]e^{-\theta x}\right\}^2 \quad (19)$$

6.2. Hazard rate function

The hazard rate function measures the probability that a system will fail in the next instant if it has survived to this far.

$$h(x) = \lim_{\Delta x\to 0}\frac{P(x\le X<x+\Delta x \mid X\ge x)}{\Delta x}$$

The hazard rate function of TXRD is obtained as

$$h(x) = \frac{g(x)}{R(x)}$$

$$h(x) = \frac{\theta e^{-\theta x}\left[1+\frac{6(\theta^3x^3-6)}{(\theta^3+6)^2}\right]\left[1-\lambda+2\lambda e^{-\theta x}\left(1+\frac{6\theta}{(\theta^3+6)^2}(\theta^2x^3+3\theta x^2+6x)\right)\right]}{1-(1-\lambda)\left\{1-\left[1+\frac{6\theta^3x^3+18\theta^2x^2+36\theta x}{(\theta^3+6)^2}\right]e^{-\theta x}\right\}+\lambda\left\{1-\left[1+\frac{6\theta^3x^3+18\theta^2x^2+36\theta x}{(\theta^3+6)^2}\right]e^{-\theta x}\right\}^2} \quad (20)$$

and the reverse hazard rate of TXRD is

$$h_r(x) = \frac{g(x)}{G(x)}$$

$$= \frac{\theta e^{-\theta x}\left[1+\frac{6\theta^3x^3-36}{(\theta^3+6)^2}\right]\left\{(1-\lambda)+2\lambda e^{-\theta x}\left[1+\frac{6\theta}{(\theta^3+6)^2}(\theta^2x^3+3\theta x^2+6x)\right]\right\}}{\left\{(1+\lambda)\left[1-\left(1+\frac{6\theta^3x^3+18\theta^2x^2+36\theta x}{(\theta^3+6)^2}\right)e^{-\theta x}\right]-\lambda\left[1-\left(1+\frac{6\theta^3x^3+18\theta^2x^2+36\theta x}{(\theta^3+6)^2}\right)e^{-\theta x}\right]^2\right\}} \tag{21}$$

6.3. Odds function

The odds function, often referred to as the odds of failure, is a concept that is derived from the survival function which is used in reliability theory to characterize the probability of failure over time. It gives the ratio of the probability of failure at time x to the probability of survival beyond time x.
Let X be a TXRD random variable then, the odds function of X is given by,

$$\omega_0(x) = \frac{G(x)}{R(x)}$$

$$= \frac{\begin{array}{c}(1+\lambda)\left\{1-\left[1+\frac{6\theta^3x^3+18\theta^2x^2+36\theta x}{(\theta^3+6)^2}\right]e^{-\theta x}\right\} \\ -\lambda\left\{1-\left[1+\frac{6\theta^3x^3+18\theta^2x^2+36\theta x}{(\theta^3+6)^2}\right]e^{-\theta x}\right\}^2\end{array}}{\begin{array}{l}1-\left[(1-\lambda)\left\{1-\left[1+\frac{6\theta^3x^3+18\theta^2x^2+36\theta x}{(\theta^3+6)^2}\right]e^{-\theta x}\right\}\right. \\ \left.+\lambda\left\{1-\left[1+\frac{6\theta^3x^3+18\theta^2x^2+36\theta x}{(\theta^3+6)^2}\right]e^{-\theta x}\right\}^2\right]\end{array}} \tag{22}$$

The plots of the reliability function, the hazard rate function, and the odds function of the TXRD for different combinations of parameter values are shown in Figure (3), Figure (4), and Figure (5).

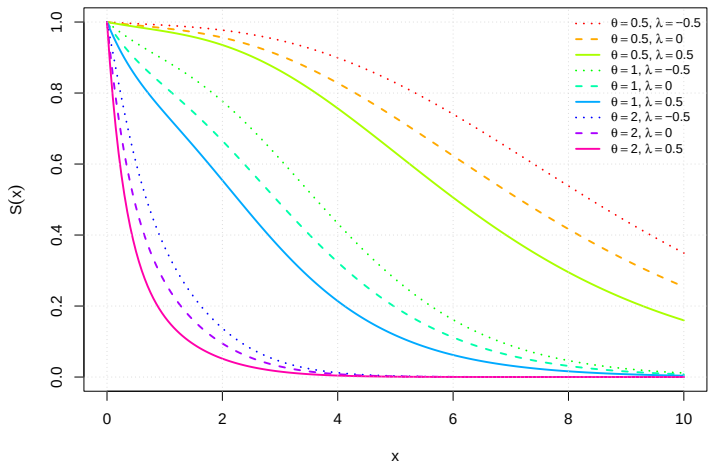


Figure 3: *Survival function of TXRD for different values of parameters*

In the survival function plot (Figure (3)), as θ increases, the survival rate decreases more slowly, indicating longer life spans and slower failure rate and as λ decreases, the survival function decreases more drastically, leading to a greater decrease in survival probabilities. This behavior

suggests that higher values of θ improve system durability and prolong survival, while lower values of λ are associated with faster system failures and reduced longevity.

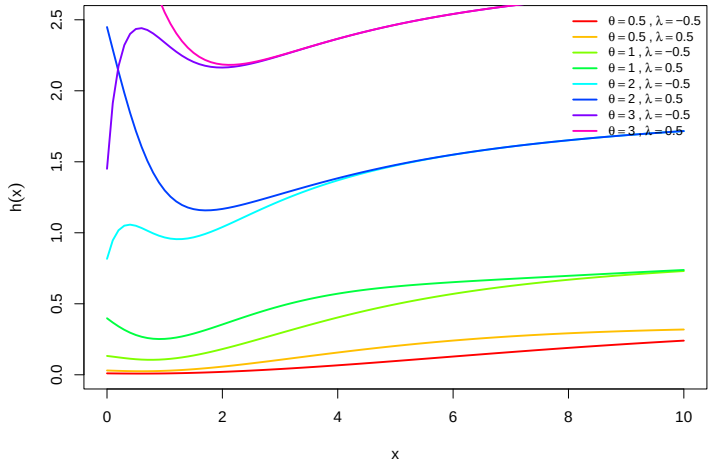


Figure 4: *Hazard rate function of TXRD for different values of parameters*

In the graph of the hazard rate function (Figure(4), the curves exhibit flexible and diverse shapes, reflecting different types of failure mechanisms. As the shape parameter θ increases, the overall hazard rate increases, indicating an increased likelihood of failure at any given time. As the transmutation parameter λ increases, the hazard rate also increases, particularly at early times, reflecting an increased initial risk. However, as λ decreases, the increase in the risk of failure is delayed, often resulting in an initially decreasing hazard rate function. This flexibility makes the TXRD model well suitable for modeling a wide range of real-world reliability scenarios.

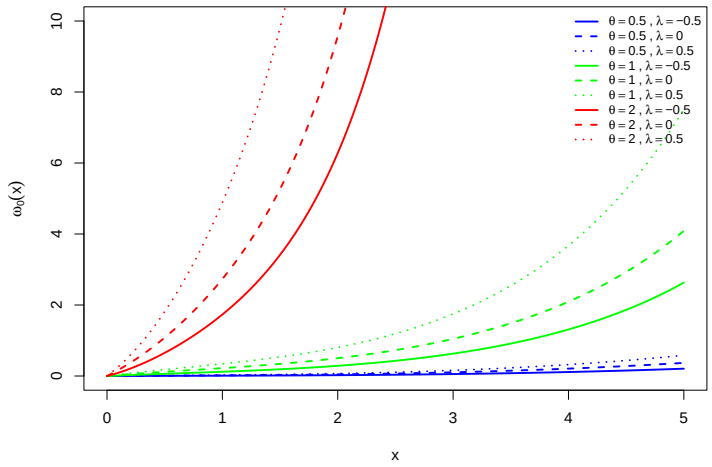


Figure 5: *Odds function of TXRD for different values of parameters*

Figure (5) shows the plot of the odds function $\omega_0(x)$ of TXRD, which illustrates how the parameters θ and λ influence the behavior of the model. As θ increases, the odds function

shows a faster increase in the probability of failure, and as θ decreases, the curve becomes flatter, indicating a slower growth in the risk of failure. In contrast, as λ increases, the odds function is further amplified, and as λ decreases, the odds function indicates a lower and more gradual increase. When $\lambda = 0$, the model simplifies to the baseline distribution. The combined effect of θ and λ determines the shape of the odds function, with higher values of both producing the fastest growth in the odds of failure, while lower values of θ and λ show the most gradual increase.

7. Estimation of parameters

In the literature, several parameter estimation techniques have been proposed. Here we discuss the maximum likelihood estimation (MLE) method and the least squares estimation (LSE) method to estimate the parameters of TXRD.

7.1. Maximum likelihood estimation

Let $X_1, X_2, \ldots, X_n$ be the random sample selected from TXRD then the likelihood function,

$$L = \prod_{i=1}^{n} \theta e^{-\theta x_i} \left(1 + \frac{6(\theta^3 x_i^3 - 6)}{(\theta^3+6)^2}\right) \left[1 - \lambda + 2\lambda e^{-\theta x_i} \left(1 + \frac{6\theta}{(\theta^3+6)^2}(\theta^2 x_i^3 + 3\theta x_i^2 + 6x_i)\right)\right]$$

$$= \theta^n e^{-n\theta\bar{x}} \prod_{i=1}^{n} \left(1 + \frac{6(\theta^3 x_i^3 - 6)}{(\theta^3+6)^2}\right) \left[1 - \lambda + 2\lambda e^{-\theta x_i} \left(1 + \frac{6\theta}{(\theta^3+6)^2}(\theta^2 x_i^3 + 3\theta x_i^2 + 6x_i)\right)\right]$$

$$\log L = n\log\theta - n\theta\bar{x} + \sum_{i=1}^{n} \log\left\{\left[1 + \frac{6(\theta^3 x_i^3 - 6)}{(\theta^3+6)^2}\right]\left[1 - \lambda + 2\lambda e^{-\theta x_i}\left(1 + \frac{6\theta}{(\theta^3+6)^2}\left(\theta^2 x_i^3 + 3\theta x_i^2 + 6x_i\right)\right)\right]\right\}$$

$$\frac{\partial \log L}{\partial \theta} = \frac{n}{\theta} - n\bar{x} + \sum_{i=1}^{n} \frac{1}{A_i} \cdot \frac{\partial A_i}{\partial \theta} + \bar{x} \sum_{i=1}^{n} \frac{1}{B_i} \cdot \frac{\partial B_i}{\partial \theta} = 0 \tag{23}$$

where

$$A_i = \left[1 + \frac{6\left(\theta^3 x_i^3 - 6\right)}{\left(\theta^3+6\right)^2}\right]$$

and

$$B_i = \left[1 - \lambda + 2\lambda e^{-\theta x_i}\left(1 + \frac{6\theta}{\left(\theta^3+6\right)^2}\left(\theta^2 x_i^3 + 3\theta x_i^2 + 6x_i\right)\right)\right]$$

$$\frac{\partial \log L}{\partial \lambda} = \sum_{i=1}^{n} \frac{1}{B_i} \frac{\partial B_i}{\partial \lambda} = 0 \tag{24}$$

Due to the complex structure of the non-linear equations (23) and (24), we employ R software to quantitatively estimate the necessary parameters.

7.2. Least square estimation

Let $G(x;\theta,\lambda)$ be the cumulative distribution function of TXRD (5), the least square estimation minimizes:

$$S(x;\theta,\lambda)=\sum_{i=1}^{n}\left[\hat{G}_n(x_i)-G(x_i;\theta,\lambda)\right]^2$$

where $\hat{G}_n(x_i)$ is the empirical cumulative distribution function (ECDF) obtained by,

$$\hat{G}_n(x_i)=\frac{1}{n}\sum_{j=1}^{n}I(x_j\leq x_i)$$

where $I(x_j\leq x_i)$ is the indicator function, defined as:

$$I(x_j\leq x_i)=\begin{cases}1, & \text{if } x_j\leq x_i\\ 0, & \text{otherwise}\end{cases}$$

We estimate θ and λ by solving,

$$(\hat{\theta},\hat{\lambda})=\arg\min_{\theta,\lambda}S(x;\theta,\lambda) \tag{25}$$

We use R software to estimate the necessary parameters numerically.

8. Simulation study

In this section, we simulate the data for TXRD to compare the performance of the maximum likelihood estimates (MLEs) and least squares estimates (LSEs) for the two parameters θ and λ using Monte Carlo simulation. The TXRD samples were generated for different samples of sizes n= 25, 50, 75, 100, 200, 500 for a fixed choice of parameters θ=1 and λ=0.5. Estimates of unknown parameters have been obtained using the Broyden-Fletcher-Goldfarb-Shanno (BFGS) method to maximize the log-likelihood function. The estimated values of the parameters θ and λ with their corresponding standard error, bias, and mean square error (MSE) are shown in Table (1).

The conclusions obtained from the simulation study are given as follows.

• MLE has lower bias and mean square error for both parameters θ and λ, indicating more accurate estimates.

• LSE shows significantly higher bias and mean square error, especially for λ, suggesting that it is less reliable for estimating this parameter.

• As the sample size increases, bias and mean square error decrease for both methods, but LSE still maintains a relatively higher bias and MSE compared to the MLE method.

•MLE is the superior method in terms of both, producing more accurate and reliable estimates in the case of the transmuted X-Rama distribution.

Table 1: *Simulation Results for MLE and LSE Estimators*

n	Method	Parameter	Mean	Bias	SE	MSE
10	MLE	θ	1.015088	0.015088	0.195922	0.038536
		λ	0.539817	0.039817	0.503626	0.254718
	LSE	θ	1.051201	0.051201	0.188800	0.038196
		λ	0.650663	0.150663	0.393454	0.177196
25	MLE	θ	1.007458	0.007458	0.155505	0.024189
		λ	0.522935	0.022935	0.467841	0.218963
	LSE	θ	1.016571	0.016571	0.138563	0.019436
		λ	0.595623	0.095623	0.395424	0.165191
50	MLE	θ	1.006305	0.006305	0.122880	0.015109
		λ	0.519831	0.019831	0.393573	0.154983
	LSE	θ	1.011312	0.011312	0.116134	0.013588
		λ	0.570243	0.070243	0.364357	0.137424
75	MLE	θ	1.007654	0.007654	0.109352	0.011993
		λ	0.483514	-0.016490	0.370582	0.137328
	LSE	θ	1.012414	0.012414	0.104396	0.011031
		λ	0.518208	0.018208	0.346516	0.120165
100	MLE	θ	1.004228	0.004228	0.104798	0.010979
		λ	0.489118	-0.010880	0.350514	0.122733
	LSE	θ	1.008898	0.008898	0.102888	0.010644
		λ	0.512336	0.012336	0.337062	0.113536
200	MLE	θ	1.005771	0.005770	0.094230	0.008895
		λ	0.482926	-0.017070	0.329599	0.108709
	LSE	θ	1.006737	0.006737	0.088680	0.007894
		λ	0.503649	0.003649	0.306341	0.093671
500	MLE	θ	1.017436	0.017436	0.071209	0.005365
		λ	0.436896	-0.063104	0.258042	0.070435
	LSE	θ	1.017356	0.017356	0.068564	0.004993
		λ	0.449928	-0.050072	0.253882	0.066834

9. Data analysis

In this section, we demonstrate the adaptability of TXRD to model real-world data sets. To evaluate the model, we compute the goodness-of-fit statistics and estimate the model parameters.

Data Set: 1

The following data represent 40 patients suffering from blood cancer (leukemia) from one of the ministry of health hospitals in Saudi Arabia (Abouammah, Ahmed and Khalique, 2000 [12]).

Table 2: *Data regarding 40 Leukemia Patients from Health Hospital in Saudi Arabia.*

0.315	0.496	0.616	1.145	1.208	1.263	1.414	2.025	2.036	2.162	2.211	2.370	2.532	2.693
2.805	2.910	2.912	3.192	3.263	3.348	3.348	3.427	3.499	3.534	3.767	3.751	3.858	3.986
4.049	4.244	4.323	4.381	4.392	4.397	4.647	4.753	4.929	4.973	5.074	5.381		

Data Set: 2

The following data represent the strength of the aircraft window glass recorded [2]

Table 3: *Dataset regarding the strength of the aircraft window glass*

18.83	20.80	21.657	23.03	23.23	24.05	24.321	25.50	25.52	25.80
26.69	26.77	26.78	27.05	27.67	29.90	31.11	33.20	33.73	33.76
33.89	34.76	35.75	35.91	36.98	37.08	37.09	39.58	44.045	45.29
45.381									

The Bayesian information criterion (BIC), Akaike information criterion (AIC), Akaike information criterion corrected (AICc), and logL for the data set are used to compare the distribution. The lower values of AIC, BIC, AICc, and -logL are indicative of a better distribution. We also provide the Kolmogorov-Smirnov test (K-S test) to check the goodness-of-fit of the distribution with the considered data sets.

$$\text{AIC} = 2k - 2\log L \quad \text{BIC} = k\log n - 2\log L \quad \text{AICc} = \text{AIC} + \frac{2k(k+1)}{n-k-1}$$

where n is the sample size and k is the number of parameters.

Table 4: *Model comparison based on MLE, log-likelihood, AIC, BIC, and AICc*

Distribution	**MLE**		**logL**	**AIC**	**BIC**	**AICc**	**K-S test**	**P-value**
	$\hat{\theta}$	$\hat{\lambda}$						
TXRD	1.2371	-1.0000	-70.8544	145.7089	149.0867	146.0332	0.1191	0.6222
TSD	0.7026	-0.7625	-78.0412	160.0824	163.4602	160.4068	0.1494	0.3342

Table 5: *Model comparison based on MLE, log-likelihood, AIC, BIC, and AICc*

Distribution	**MLE**		**logL**	**AIC**	**BIC**	**AICc**	**K-S test**	**P-value**
	$\hat{\theta}$	$\hat{\lambda}$						
TXRD	0.1627	-1.0000	-110.1237	224.2475	227.1154	224.6760	0.1696	0.2995
TSD	0.0867	-1.0000	-117.9894	239.9789	242.8468	240.4074	0.2585	0.0258

Table(4) represents the performance distributions of 40 patients suffering from blood cancer (leukemia) modeled using two statistical distributions: the proposed Transmuted X-Rama Distribution (TXRD) and the established Transmuted Shanker Distribution (TSD). The purpose of the analysis was to determine which model best fits the survival data of these patients. Table(5) presents a model comparison between the Transmuted X-Rama Distribution (TXRD) and the transmuted Shanker distribution (TSD) with respect to the strength of the recorded aircraft window glass. It is clear from both tables that TXRD provides a better fit than TSD.

10. Conclusion

In this study, we proposed a new two-parameter lifetime distribution, called the transmuted X-Rama distribution (TXRD) by applying the quadratic rank transmutation map (QRTM). Some

distributional properties along with reliability analysis and parameter estimation are also discussed. A simulation study was conducted to evaluate the performance of the Maximum Likelihood Estimation (MLE) and the Least Square Estimation (LSE), and the results showed that the MLE method outperformed the LSE method. We also obtained expressions for order statistics and Renyi entropy. Finally, we illustrated the efficiency of the proposed distribution by applying it to two real-life data sets.

References

[1] Abebe, B., Tesfay, M., Eyob, T., and Shanker, R. (2019). A two-parameter power Rama distribution with properties and applications. Biometrics and Biostatistics International Journal, 8(1), 6-11.

[2] Alhyasat, K. M., Ibrahim, K., Al-Omari, A. I., and Bakar, M. A. A. (2021). Extended Rama Distribution: Properties and Applications. Comput. Syst. Sci. Eng., 39(1), 55-67.

[3] Alzaatreh, A., Lee, C., and Famoye, F. (2013). A new method for generating families of continuous distributions. Metron, 71(1), 63-79.

[4] Aryal, G. R., and Tsokos, C. P. (2011). Transmuted Weibull distribution: A generalization of the Weibull probability distribution. European Journal of pure and applied mathematics, 4(2), 89-102.

[5] Demirci Bicer, H. (2019). Properties and inference for a new class of XGamma distributions with an application. Mathematical Sciences, 13(4), 335-346.

[6] Edith, U. U., Ebele, T. U., and Henrietta, A. I. (2019). A two-parameter Rama distribution. Earthline Journal of Mathematical Sciences, 2(2), 365-382.

[7] Etaga, Harrison and Chrisogonus, Onyekwere and Nwankwo, Mmesoma and Oluchukwu Dorathy, Oramulu and Lydia, Omeje and Obulezi, Okechukwu. (2023). Estimation of the Xrama Distribution Parameter Under Complete and Progressive Type-II Censored Schemes. Scholars Journal of Physics Mathematics and Statistics. 10. 203-219. 10.36347/sjpms.2023.v10i10.002.

[8] Eyob, T., and Shanker, R. (2019). A Two-Parameter Weighted Rama Distribution with Properties and Application. Universal Journal of Mathematics and Applications, 2(2), 48-58.

[9] Khan, M. S., King, R., and Hudson, I. L. (2016). Transmuted kumaraswamy distribution. Statistics in Transition new series, 17(2), 183-210.

[10] Mohiuddin, Maryam and Rather, Aafaq and C, Subramanian and Dar, Shabir. (2020). Transmuted Garima Distribution: Properties and Applications. Xi'an Dianzi Keji Daxue Xuebao/Journal of Xidian University. 14. 112-123.

[11] Moolath, G. B., and Jayakumar, K. (2017). T-transmuted X family of distributions. Statistica, 77(3), 251-276.

[12] Omoruyi, F. A., Omeje, I. L., Anabike, I. C., and Obulezi, O. J. (2023). A new variant of Rama distribution with simulation study and application to blood cancer data. European Journal of Theoretical and Applied Sciences, 1(4), 389-409.

[13] Onyekwere, C. K., Okoro, C. N., Obulezi, O. J., Udofia, E. M., and Anabike, I. C. (2022). Modification of Shanker distribution using quadratic rank transmutation map. Journal of Xidian University, 16(8), 179-198.

[14] Onyekwere, C. K., Osuji, G. A., and Enogwe, S. U. (2020). Inverted power Rama distribution with applications to life time data. Asian Journal of Probability and Statistics, 9(4), 1-21.

[15] Shanker, R. (2017). Rama distribution and its application. International Journal of Statistics and Applications, 7(1), 26-35.

[16] Shaw, W. T., and Buckley, I. R. C. (2009). The alchemy of probability distributions: Beyond Gram-Charlier expansions, and a skew-kurtotic-normal distribution from a rank transmutation map. arXiv preprint arXiv:0901.0434.

AN EFFICIENT SINGLE VARIABLE INVERSION ALGORITHM FOR DERIVING RELIABILITY BOUNDS IN STORAGE SYSTEMS

Emad K. Mutar*[1], Zahir A. H. Hassan[2]

•

[1] Department of Mathematics, College of Edu. for Pure Sciences, University of Babylon
Babylon, 51005, Iraq
edu922.emad.kareem@student.uobabylon.edu.iq
[2] Department of Mathematics, College of Edu. for Pure Sciences, University of Babylon
Babylon, 51005, Iraq
zahir.a.h.hassan@uobabylon.edu.iq

Abstract

Ensuring reliability in data survivability schemes for storage systems is challenging due to limited resources. A key part of reliability analysis is selecting a suitable mathematical representation, such as the structure-function. The structure-function maps the overall system state based on the states of its components and can effectively describe systems of various complexities. Many techniques and algorithms depend on identifying all minimal path sets (MPSs) and minimal cut sets (MCSs) to construct the structure and bounds in two-terminal systems. The upper and lower bounds are essential for demonstrating critical states in the system and for the reliability analysis of storage systems. This paper presents three mathematical algorithms for analyzing storage system reliability. The first two algorithms identify MPSs and MCSs using the connection and adjacency matrices of the system's graph. The third algorithm determines critical states of the reliability function by using the single-variable inversion (SVI) method for the MPSs and MCSs, helping to establish the system's reliability bounds. The analysis focuses on finding the greatest lower bound (GLB) and the least upper bound (LUB) for reliability. Storage systems are used to demonstrate the computation of MPSs and MCSs and reliability bounds. These algorithms effectively identify the MPSs and MCSs, calculate their bounds, and visually and numerically represent the results.

Keywords: Minimal paths, minimal cuts, system reliability, sum-of-disjoint products technique, reliability bounds, storage system.

I. Introduction

The structure function is a valuable tool that defines the relationship between a system's performance and the condition of its components. Modeling a repairable system with multiple components in a stationary state provides an important understanding of system reliability. Notably, the structure function can be interpreted as a Boolean function, which has the advantage of offering a time-independent mathematical representation [1-4]. This characteristic allows us to apply established techniques from Boolean algebra, simplifying the evaluation and enhancement of the system's reliability [5-8]. Effective techniques have been developed for reliability analysis using Boolean algebra, which includes defining MPSs and MCSs, calculating frequency characteristics of

system reliability, and determining importance measures [5, 9]. However, a disadvantage of these methods is that they analyze the system only in a stationary state. Fratta and Montanari [1] introduced the sum-of-disjoint-products (SDP) approach, later refined by Abraham [10]. This technique is commonly used to assess the reliability bounds of two-terminal systems and has been discussed by various researchers [11-16]. Mutar [17] provides a contemporary evaluation of reliability bounds for coherent binary systems, comparing different reliability bounds based on dynamic, mathematical, and efficiency measures. Kumar [18] presents a highly reliable derivative operational matrix method for obtaining approximate solutions to initial and boundary value problems using modified Lucas wavelets. This approach offers greater accuracy and reliability in the results compared to previously available methods. This study leveraging SDP techniques, this approach not only establishes reliable bounds but also incorporates significant advancements through the use of MPSs and MCSs.

The data storage system is a vital part of any information system, as it contains all the essential data needed for its effective operation. Therefore, it is crucial to assess its reliability. Al-Awami and Hassanein [19] delve into the architecture of data survivability systems that leverage decentralized storage within wireless sensor networks. Rusnak et al. [20] introduce a groundbreaking derivative for survival signatures, paving the way for a new method of reliability analysis focused on storage system failures caused by component breakdowns. Additionally, Rusnak et al. [21] present a reliability analysis for data storage that utilizes various types of hard disk drives. The analysis also explores multiple methods of storing data across different disks using a redundant array of independent disks. Mutar [22] addresses the problem of improving the reliability and performance of storage systems by incorporating two types of components with different distributions. Rusnak et al. [23] present a new technique for calculating structural importance measures of storage systems using the survival signature and direct partial logical derivatives.

The objective of this paper is to present three interconnected mathematical algorithms for analyzing the reliability of storage systems. The first and second algorithms aim to identify MPSs and MCSs of the system by utilizing the connection matrix and the adjacency matrix of the system's graph, as well as various algebraic properties. The third algorithm extracts the critical states of the system's reliability function by summing disjoint sets of MPSs and MCSs, which helps determine the system's reliability bounds. The reliability bounds analysis focuses on finding both the GLB and the LUB for system reliability. Furthermore, a reliability bounds calculation for data storage can involve different types of hard disk drives and various techniques for storing data across multiple disks using a redundant array of independent disks, is provided to illustrate the analysis process for the GLB and LUB for system reliability.

The paper is structured as follows: Section II introduces the basic characterizations, formulas, notations, and construction of system reliability. It also presents three interconnected mathematical algorithms for constructing all MPSs and MCSs of the system and using the SVI algorithm for the MPSs and MCSs. Furthermore, mathematical relationships for computing bounds utilizing the disjoint product form are provided. Section III applies the proposed algorithms to calculate all MPSs and MCSs, as well as using the SVI algorithm for the MPSs and MCSs. A simple storage system is used as an example to demonstrate how reliability bounds can be computed, along with numerical comparisons of these bounds. Section IV discusses the application of the proposed algorithms to bridge the design of storage systems. Finally, Section V concludes the paper.

II. Preliminaries

This section introduces the main concept of using a matrix-based approach to generate all MPSs and MCSs of systems. An algorithm is formulated to construct disjoint product terms. Additionally, the system's reliability bounds are determined, focusing on the GLB and LUB for system reliability. The following provides the details.

I. System representation

Consider a system composed of n components that are either functioning in a stable state or being monitored over a specific period. Each component, along with the system operates in one of two essential states: it is either fully functional, represented by "1", or it has failed, represented by "0". A structure function in Eq. (1) defines the vital relationship between the system and the performance of its components.

$$\phi(\boldsymbol{x}) = \phi(x_1, x_2, \dots, x_n): \{0,1\}^n \longrightarrow \{0,1\} \tag{1}$$

In this context, x_i represents the state of component i, where $i = 1,2,\dots,n$. The state vector of all component states is denoted as $\boldsymbol{x} = (x_1, x_2, \dots, x_n)$. The reliability of the i-th component, represented in Eq. (2), is defined as the probability that the i-th component is functioning, given by:

$$r_i = \Pr\{x_i = 1\} \tag{2}$$

Moreover, the unreliability of the component, defined as the probability of component failure, is described in Eq. (3) as follows:

$$\overline{r_i} = \Pr\{x_i = 0\} = 1 - r_i \tag{3}$$

The reliability and unreliability of the system, as detailed in Eqs. (4)-(5), are defined using the structure function as follows:

$$R_s = \Pr\{\phi(\boldsymbol{x}) = 1\} \tag{4}$$

$$\overline{R_s} = \Pr\{\phi(\boldsymbol{x}) = 0\} = 1 - R_S \tag{5}$$

There are various algorithms available for calculating system reliability in Eq. (4) and unreliability in Eq. (5). Evaluating the reliability of complex systems requires the use of computationally intensive techniques, such as Path Tracing and Cut methods [5, 9, 24]. MPSs and MCSs are valuable tools in probabilistic reliability analysis. They help identify minimal failure scenarios and are essential for fault tree analysis. Additionally, these techniques enhance the quantification aspect of importance analysis.

Definition 2.1. A path set is a collection of components that must work together to ensure the system operates correctly, especially when the system has experienced a fault. A path set is considered MPSs if no component can be removed without affecting its ability to maintain the system's operational status.

A system is classified as functional when all components within at least one MPSs ($P_1, P_2, \dots, P_{N_P}$) are fully operational, as defined in Definition 2.1. Understanding this concept is essential because it enables us to calculate the system's reliability accurately. The system's reliability can be calculated using the following expression:

$$R_S = \Pr\{P_1 \cup P_2 \cup \ldots \cup P_{N_P}\} \leq \sum_{j=1}^{N_P} \Pr\{P_j\} \tag{6}$$

In this context, N_P represents the total number of MPSs within the system, while P_j (where $j = 1,2,\ldots,N_P$) refers to a specific MPS.

Definition 2.2. A cut set is a collection of components whose simultaneous failure leads to a fault in the system, assuming the system was operational beforehand. A cut set is considered MCSs if no component can be removed from it without altering its status as a cut set.

Based on Definition 2.2, the system fails when every component in at least one MCS has failed. Thus, if the system contains N_C of MCSs, the unreliability of the system can be considered as follows:

$$\overline{R_S} = \Pr\{C_1 \cup C_2 \cup \ldots \cup C_{N_C}\} \leq \sum_{j=1}^{N_C} \Pr\{C_j\} \tag{7}$$

where C_j, for $j = 1,2,\ldots,N_C$, represents a specific MCS within the system. By utilizing Eqs. (6) and (7), the boundary values for the system's reliability can be effectively estimated as follows:

$$\sum_{j=1}^{N_P} \Pr\{P_j\} \leq R_S \leq 1 - \sum_{j=1}^{N_C} \Pr\{C_j\} \tag{8}$$

When individual system components exhibit high reliability, using the left side of the relation in Eq. (8) is an effective technique for accurately estimating the overall system reliability.

II. Construction of MPSs and MCSs

A system can be represented using the mathematical notation of a graph $G = (V, E)$, where $V = \{1, 2, \ldots, m\}$ denotes the set of nodes and $E = \{x_1, x_2, \ldots, x_n\}$ denotes the set of edges (or components), which connect the nodes. This graph includes two terminal nodes: a source and a sink. The system graph G supports identifying all MPSs and MCSs between the source and sink nodes.

Definition 2.3. Let G be a graph representing a two-terminal system with vertex set $V = \{1, 2, \ldots, m\}$ and edge set $E = \{x_1, x_2, \ldots, x_n\}$. The Connection Matrix, denoted as $CM = [e_{ij}]$, is an $m \times m$ matrix with rows and columns indexed by the elements of V. The element e_{ij} is defined as follows:

$$e_{ij} = \begin{cases} 1, & \text{if } i = j, \\ \sum_{x_k \in E} x_k, & \text{if there are edges from node } i \text{ to node } j, \\ 0, & otherwise \end{cases} \tag{9}$$

The element in Eq. (9) can be used to define the CM matrix as follows:

$$CM = \begin{array}{c} \\ 1 \\ 2 \\ \vdots \\ m \end{array} \begin{array}{c} \begin{array}{cccc} 1 & 2 & \ldots & m \end{array} \\ \begin{bmatrix} 1 & e_{12} & \cdots & e_{1m} \\ e_{21} & 1 & \cdots & e_{2m} \\ \vdots & \vdots & \ddots & \vdots \\ e_{m1} & e_{m2} & \ldots & 1 \end{bmatrix} \end{array} \tag{10}$$

The CM matrix in Eq. (10) provides an algebraic representation of a system, assisting in identifying minimal path sets $P_1, P_2, \ldots, P_{N_P}$ through algebraic properties. To determine all MPSs of a system based on its graph, the following steps (Algorithm 1) can be utilized:

Step 1: Determine the CM matrix of the system graph's using Definition 2.3.
Step 2: Remove the first column and the last row from the CM matrix to obtain a new matrix (S).

Step 3: Define the system success determinant ($det(S)$), which represents the sum of all MPSs.

$$\begin{aligned}\det(S) &= \sum_{j=1}^{m}(-1)^{i+j}e_{ij}\,\det(M_{ij}) \\ &= \sum_{j=1}^{m}(-1)^{i+j}e_{ij}\prod_{e_{ij}\in M_{ij}}\det(M_{ij}) \\ &= \sum_{j=1}^{m}(-1)^{i+j}P_j \end{aligned} \tag{11}$$

In this context, M_{ij} in Eq. (11) refers to the minor of the element e_{ij}, which is computed as the determinant of the $(m-1)\times(m-1)$ matrix derived by removing the ith row and the ith column from the CM matrix. On the other hand, the MCSs ($C_1, C_2, \dots, C_{N_C}$) can be identified using the adjacency matrix (AM).

Definition 2.4: Let G be a graph representing a two-terminal system with vertex set $V=\{1,2,\dots,m\}$ and edge set $E=\{x_1,x_2,\dots,x_n\}$. The adjacency matrix, $AM=[e_{ij}]$, is the m-by-m matrix whose rows and columns are indexed by the elements of V. The element e_{ij} is defined as follows:

$$e_{ij}=\begin{cases}\prod_{x_k\in E}x_k\text{ , if there are edges from node } i \text{ to node } j,\\ 0, \qquad otherwise\end{cases} \tag{12}$$

The element in Eq. (12) can be utilized to determine the AM matrix as follows:

$$AM=\begin{array}{c} \\ 1\\2\\ \vdots\\ m\end{array}\begin{array}{c}\begin{array}{cccc}1 & 2 & \dots & m\end{array}\\ \begin{bmatrix}0 & e_{12} & \dots & e_{1m}\\ e_{21} & 0 & \dots & e_{2m}\\ \vdots & \vdots & \ddots & \vdots\\ e_{m1} & e_{m2} & \dots & 0\end{bmatrix}\end{array} \tag{13}$$

The AM matrix in Eq. (13) provides an algebraic representation of a system, assisting in identifying MCSs: $C_1, C_2, \dots, C_{N_C}$ through algebraic properties. To determine all MCSs of a system based on its graph, the following steps (Algorithm 2) can be utilized:

Step 1: Determine the AM matrix of the system graph using Definition 2.4.

Step 2: Multiply all the entries in the first row and multiply all the entries in the last column to obtain two MCSs.

Step 3: Construct a set $\mathcal{S}$ that contains all combinations of columns ranging from order 2 to n-1. This set is crucial for generating every possible MCS, offering valuable alternatives to the MCSs obtained in step 2.

Step 4: Eliminate combinations from set $\mathcal{S}$ that contribute to redundancy or do not qualify as MCSs by adhering to the following rules:

1. If the combination consists only of columns with zero entries in the first row, it should be removed. Keeping these combinations would result in MCSs already included in those generated in step 2.
2. If the combination includes rows with non-zero symbols in the last column, it must also be deleted. These combinations would create MCSs that overlap with the ones generated in step 2.

Step 5: Pick one combination from the set $\mathcal{S}$ identified in Step 4. Then, collect all the link labels from the rows associated with both row 1 and the chosen combination while excluding the columns represented by that combination. This process will allow create a new MCS.

Step 6: Repeat step 5 for all the other combinations in set $\mathcal{S}$.

III. SVI algorithm

The SVI algorithm estimates the probability of multiple events happening at once by identifying the shortest path between them. Boolean algebra is used to determine a system's reliability bounds. Calculating exact reliability in large, complex systems can be difficult due to the numerous calculations required, making approximative techniques necessary. The proposed algorithm (Algorithm 3) for determining system reliability and its bounds is based on equations (7) and (8) as follows:

Step 1: Identify all minimal path sets in the system and arrange them in ascending order, denoted as $P_1, P_2, \dots, P_j, \dots, P_{N_P}$.

Step 2: For the first minimal path set, P_1, establish the initial decision set as $D_{0,1} = P_1$, and calculate its probability, $\lambda_1 = \prod_{x_i \in D_{0,1}} \Pr\{x_i\}$.

Step 3: Set $D_{0,2} = P_2$ and define the complementary set for each minimal path P_j, specifically $P_j - D_{s,i} = \{x_a \mid x_a \in P_j \; and \; x_a \notin D_{s,i}\}$, where the indices satisfy $0 \le s < j \le i$ and $a = 1, 2, \dots, n$. Then

- If $P_j - D_{s,i} = \{\emptyset\}$ then $D_{j,i} = \{D_{s,i}\}$ and $\lambda_j = \prod_{x_i \in D_{j,i}} \Pr\{x_i\}$.
- If $x_a \in P_j \; and \; \overline{x_a} \in D_{s,i}$ where $\overline{x_a} = 1 - x_a$ then $P_j - D_{s,i} = \{\emptyset\}$ and $\lambda_j = \prod_{x_i \in D_{s,i}} \Pr\{x_i\}$.
- If $P_j - D_{s,i} = \{x_a\}$ then $D_{j,i} = \{\overline{x_a} D_{s,i}\}$ and $\lambda_j = \prod_{x_i \in D_{j,i}} \Pr\{x_i\}$.
- If $P_j - D_{s,i} = \{x_a, x_b\}$ for $a < b < n$ then $D_{j,r} = \{\overline{x_a} D_{s,i}\}$ and $D_{j,r+1} = \{x_a \overline{x_b} E_{s,i}\}$ then $\lambda_j = \prod_{x_i \in D_{j,r}} \Pr\{x_i\} + \prod_{x_i \in D_{j,r+1}} \Pr\{x_i\}$.

Step 4: Repeat step 3 to form λ_i by comparing $D_{j,i}$ with each P_{j-1}.

Algorithm 3 can form a disjoint sum of the MCSs: $C_1, C_2, \dots, C_{N_C}$ by repeating steps 1 through 5 to achieve β_j for $j = 1, 2, \dots, N_C$.

IV. Reliability bounds of systems

Let λ_j denote the event that all components in the j-th MPS are functioning, meaning that the j-th MPS is operational. The system's operation relies on at least one of the MPSs functioning, which depends on the occurrence of at least one of the events $\lambda_1, \lambda_2, \dots, \lambda_{N_P}$. On the other hand, the event β_j is defined as the failure of all components in the j-th MCSs or the failure of the j-th MCS itself. The failure of the overall system corresponds to the failure of N_C for MCSs, which depends on the occurrence of at least one of the events $\beta_1, \beta_2, \dots, \beta_{N_C}$. The summation of these events represents the system's reliability:

$$R_S = \sum_{j=1}^{N_P} \lambda_j = 1 - \sum_{j=1}^{N_C} \beta_j \tag{14}$$

The SDP technique is a tool for assessing system reliability in Eq. (14), offering an approach to understanding performance. Using MPSs establishes successive lower bounds, while MCSs generate successive upper bounds. These MPSs and MCSs are thoughtfully organized from shortest to longest, capitalizing on a critical principle: when component reliabilities are comparable, shorter MPSs demonstrate a significantly higher probability of success than their longer counterparts. This insight means that the SDP method consistently delivers tighter and more reliable bounds on system performance. The GLB (infimum) of system reliability represents the highest reliability value achievable when at least one set of MPSs fails. In this context, the GLB of system reliability is truly enlightening:

$$R_{GLB} = \sum_{j=1}^{N_P - 1} \lambda_j \tag{15}$$

The LUB (supremum) of system reliability is the smallest value of reliability that corresponds to one MCS. In this case, the LUB of system reliability is:

$$R_{LUB} = 1 - \sum_{j=1}^{N_C-1} \beta_j \tag{16}$$

The techniques for establishing bounds on system reliability are quite effective and direct. Various techniques can generate numerous upper bounds, allowing us to confidently select the LUB (supremum) in Eq. (15) as a solid approximation of the system's reliability. Similarly, all lower bounds are derived, and the GLB (infimum) in Eq. (16) for the system reliability.

III. Simple storage system

I. Model description

Consider a storage system with four components to illustrate how algorithms can be applied to compute reliability bounds. This system consists of two parallel storage units and a communication network, as shown in Fig. 1 [25]. Each unit has two Hard Disk Drives (HDDs) configured in a specific structure known as a Redundant Array of Independent Disks (RAID). The first unit in the upper path contains two HDDs arranged in a RAID-1 configuration, specifically SEAGATE ST6000DX000 and WDC WD60EFRX. In RAID-1, data is written identically to both drives, allowing data to be read from either drive. This arrangement ensures that the system continues to operate successfully as long as at least one drive remains functional. The second unit, located in the lower path, consists of two HDDs configured in a RAID-0 setup, namely SEAGATE ST3000DM001 and HGST HDS5C3030ALA [21, 26]. Unlike RAID-1, RAID-0 provides no data redundancy; instead, the unit's capacity equals the sum of the drives' capacities. Consequently, the entire RAID-0 configuration loses all stored data if one drive fails.

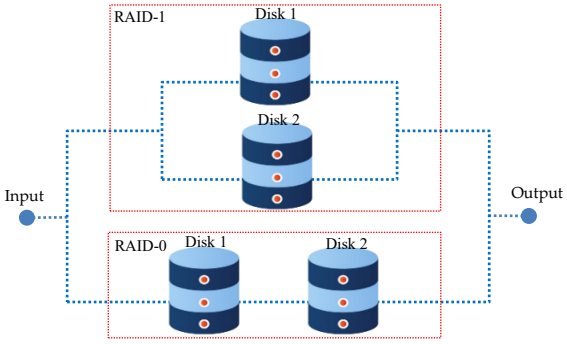


Figure 1. *A schematic diagram of the simple storage system.*

The algorithms outlined in Section II can be utilized to effectively identify the MPSs, minimal cuts, and boundaries of the simple storage system. The simple storage system shown in Fig. 1 is represented by its reliability graph, as depicted in Fig. 2.

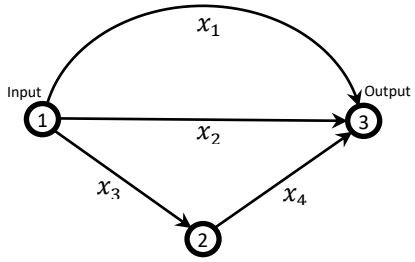


Figure 2. *A graph of the simple storage system in Fig. 1.*

II. The MPSs and MCSs of the storage system.

The MPSs of the storage system depicted in Fig. 2 can be efficiently identified by applying the Algorithm 1 outlined in subsection II. The first step involves constructing the CM matrix as defined in Definition 2.3, specifically tailored for the system shown in Fig. 2, as follows:

$$CM = \begin{matrix} \\ 1 \\ 2 \\ 3 \end{matrix} \begin{matrix} \begin{matrix} 1 & 2 & 3 \end{matrix} \\ \begin{bmatrix} 1 & x_3 & x_1 + x_2 \\ 0 & 1 & x_4 \\ 0 & 0 & 1 \end{bmatrix} \end{matrix} \tag{17}$$

To obtain the S matrix, the first column and last row of the CM matrix in Eq. (17) are removed, and then the determinant of S is calculated as follows:

$$S = \begin{bmatrix} x_3 & x_1 + x_2 \\ 1 & x_4 \end{bmatrix} \tag{18}$$

$$\det(S) = x_1 + x_2 - x_3 x_4 \tag{19}$$

The Eq. (18) and Eq. (19) leads to the identification of three MPSs: $P_1 = \{x_1\}, P_2 = \{x_2\}$ and $P_3 = \{x_3, x_4\}$. Furthermore, the MCSs of the system illustrated in Fig. 2 can be efficiently identified using the Algorithm 2 described in subsection II. The first step is to construct the AM matrix according to Definition 2.4, specifically designed for the system presented in Fig. 2, as explained below:

$$AM = \begin{matrix} \\ 1 \\ 2 \\ 3 \end{matrix} \begin{matrix} \begin{matrix} 1 & 2 & 3 \end{matrix} \\ \begin{bmatrix} 0 & x_3 & x_1 x_2 \\ 0 & 0 & x_4 \\ 0 & 0 & 0 \end{bmatrix} \end{matrix} \tag{20}$$

In the second step of the Algorithm 2 based on Eq. (20), we identify two MCSs: $C_1 = \{x_1 x_2 x_3\}$ and $C_3 = \{x_1 x_2 x_4\}$. The algorithm then stops because there are no further MCSs.

III. The GLB and LUB of the storage system

The reliability function and the GLB of the system depicted in Fig. 2 can be calculated using the MPSs and the third algorithm as follows:

Step 1: Define all MPSs based on order, such that $P_1 = \{x_1\}, P_2 = \{x_2\}$ and $P_3 = \{x_3, x_4\}$.

Step 2: For $P_1 = \{x_1\}$ assume that $D_{0,1} = P_1$

$$\therefore \lambda_1 = \prod_{x_i \in D_{0,1}} \Pr\{x_i\} = r_1$$

Step 3: For $P_2 = \{x_2\}$ assume that $D_{0,2} = P_2$

$$\therefore \; P_1 - D_{0,2} = \{x_1\} \Longrightarrow \therefore \; D_{1,2} = \{\overline{x_1} D_{0,2}\} = \{\overline{x_1}, x_2\} \Longrightarrow \lambda_2 = \prod_{x_i \in D_{1,2}} \Pr\{x_i\} = \overline{r_1} r_2$$

Step 4: For $P_3 = \{x_3, x_4\}$ assume that $D_{0,3} = P_3$

$$\therefore \; P_1 - D_{0,3} = \{x_1\} \Longrightarrow \therefore \; D_{1,3} = \{\overline{x_1} D_{0,3}\} \Longrightarrow D_{1,3} = \{\overline{x_1}, x_3, x_4\}$$

$$\therefore P_2 - D_{1,3} = \{x_2\} \Longrightarrow \therefore \; D_{2,3} = \{\overline{x_2} D_{1,3}\} = \{\overline{x_1}, \overline{x_2}, x_3, x_4\} \Longrightarrow \lambda_3 = \prod_{x_i \in D_{2,3}} \Pr\{x_i\} = \overline{r_1}\,\overline{r_2} r_3 r_4$$

Additionally, the reliability function and the LUB of the system illustrated in Fig. 2 can be computed using the MCSs and the third algorithm as follows:

Step 1: Define all MCSs based on order, such that $C_1 = \{\overline{x_1}, \overline{x_2}, \overline{x_3}\}$ and $C_2 = \{\overline{x_1}, \overline{x_2}, \overline{x_4}\}$.

Step 2: For $C_1 = \{\overline{x_1}, \overline{x_2}, \overline{x_3}\}$ assume that $D_{0,1} = C_1$

$$\therefore \beta_1 = \prod_{x_i \in D_{0,1}} \Pr\{x_i\} = \overline{r_1}\,\overline{r_2}\,\overline{r_3}$$

Step 3: For $C_2 = \{\overline{x_1}, \overline{x_2}, \overline{x_4}\}$ assume that $D_{0,2} = C_2$

$$\therefore\ C_1 - D_{0,2} = \{\overline{x_3}\} \Longrightarrow \therefore\ D_{1,2} = \{x_3 D_{0,2}\} = \{\overline{x_1}, \overline{x_2}, x_3, \overline{x_4}\} \Longrightarrow \beta_2 = \prod_{x_i \in D_{1,2}} \Pr\{x_i\} = \overline{r_1}\overline{r_2}r_3\overline{r_4}$$

Based on Eqs. (14)-(16), the GLB, exact value, and LUB for the system reliability in Fig. 2 are provided as follows:

$$R_{GLB} = \lambda_1 + \lambda_2 = r_1 + \overline{r_1}r_2 \tag{21}$$

$$R_S = \lambda_1 + \lambda_2 = 1 - (\beta_1 + \beta_2) = r_1 + \overline{r_1}r_2 + \overline{r_1}\overline{r_2}r_3r_4 \tag{22}$$

$$R_{LUB} = 1 - \beta_1 = 1 - \overline{r_1}\overline{r_2}\overline{r_3} \tag{23}$$

Assuming that the lifetime distributions of the HDDs follow an exponential distribution with parameter $\lambda = \frac{1}{\text{MTTF}}$, where MTTF represents the mean time to failure. Based on this data, the company estimates individual HDD models' Annualized Failure Rate (AFR) [5, 9, 24, 27]. The AFR demonstrates the probability of a HDD failing during a year of usage, and its connection to MTTF in days is represented by the following equation:

$$MTTF = \frac{-365.25}{Ln(1 - AFR)} \tag{24}$$

The AFRs for the HDDs, evaluated by the company using data from April 2013 to December 2016, are presented in Table 1 [25]. The MTTF values, expressed in days and necessary for calculating the lifetime distributions of the HDDs, were derived from the AFRs by changing the data according to the formula provided in Eq. (24).

Table 1. *The AFR and MTTF values of the HDDs in the storage system shown in Fig. 1.*

Component	Disk name	AFR	MTTF [days]
x_1	SEAGATE ST6000DX000	0.0143	25359
x_2	WDC WD60EFRX	0.0568	62460
x_3	SEAGATE ST3000DM001	0.2672	11750
x_4	HGST HDS5C3030ALA	0.0082	44360

Based on Eqs. (21)-(23) and the MTTFs presented in Table 1, the GLB, exact value, and LUB for the storage system reliability in Fig. 2 are provided as follows:

$$R_{GLB} = -e^{-0.000200t} + e^{-0.000160t} + e^{-0.000039t} \tag{25}$$

$$R_S = e^{-0.001073t} - e^{-0.001034t} - e^{-0.000913t} + e^{-0.000874t} - e^{-0.000200t} + e^{-0.000160t} + e^{-0.000040t} \tag{26}$$

$$R_{LUB} = e^{-0.001051t} - e^{-0.001011t} - e^{-0.000891t} + e^{-0.000851t} - e^{-0.000200t} + e^{-0.000160t} + e^{-0.000039t} \tag{27}$$

The GLB, exact value, and LUB for the reliability of the storage system in Fig. 2 for the period [500, 4000] can be presented in Table 2 and Fig. 3 based on Eqs. (25)-(27).

Table 2. *The R_{GLB}, R_S and R_{LUB} of the storage system in Fig. 1.*

Time [days]	x_1	x_2	x_3	x_4	R_{GLB}	R_S	R_{LUB}
500	0.980476	0.923070	0.653394	0.988792	0.998498	0.999468	0.999479
1000	0.961334	0.852058	0.426924	0.977709	0.994280	0.996667	0.996722
1500	0.942565	0.786509	0.278949	0.966751	0.987738	0.991045	0.991158
2000	0.924162	0.726002	0.182264	0.955915	0.979221	0.982841	0.983008
2500	0.906119	0.670151	0.119090	0.945201	0.969033	0.972519	0.972721
3000	0.888428	0.618596	0.0778128	0.934607	0.957446	0.960541	0.960757
3500	0.871082	0.571007	0.0508424	0.924132	0.944695	0.947294	0.947507
4000	0.854076	0.527079	0.0332201	0.913774	0.930989	0.933084	0.933282

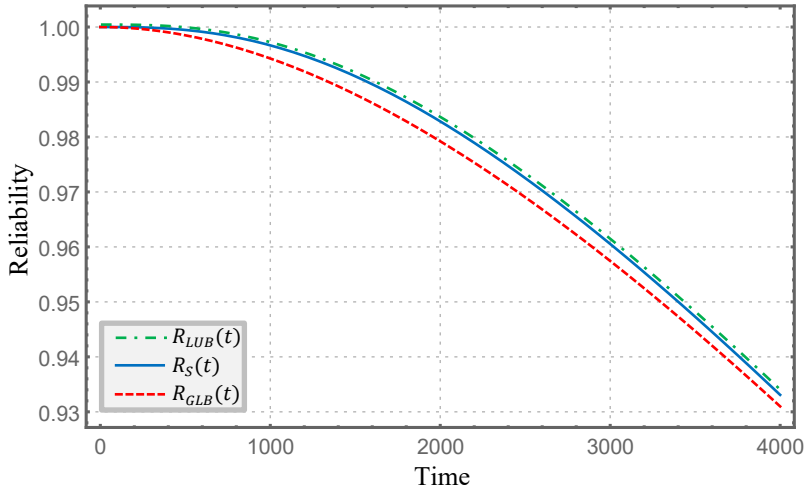


Figure 3. *The GLB, exact value, and LUB for the storage system's reliability for the period [500, 4000].*

Fig. 3 shows the GLB, exact value, and LUB of the storage system. It demonstrates the decline in reliability over time. After 2,500 days, these values fall below 0.969033, 0.972519, and 0.972721.

IV. Bridge topology of storage system

In this section, we demonstrate how to use the proposed algorithms to compute the reliability function, GLB, and LUB for a storage system with a bridge topology consists of five disks, as shown in Fig. 4.

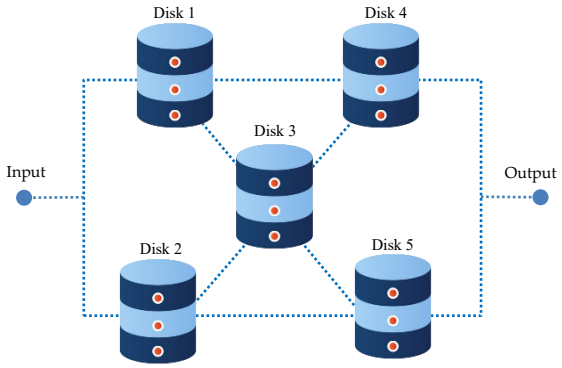


Figure 4. *A schematic diagram of the bridge topology of storage system.*

The storage system illustrated in Fig. 4 can be mathematically represented as a graph $G = (V, E)$, where $V = \{1, 2, 3, 4\}$ and $E = \{x_1, x_2, x_3, x_4, x_5\}$, as shown in Fig. 5. This is a two-terminal, mixed, connected graph that aims to generate all MPSs and MCSs between the source and sink nodes.

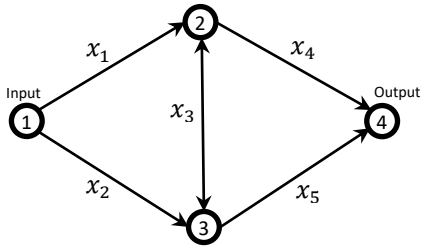


Figure 5. *A graph of the bridge topology of storage system.*

Following Algorithm 1 outlined in subsection 2.2, the MPSs of the system shown in Fig. 5 can be determined using these steps:

Step 1: The CM matrix of the system in Fig. 2 is given in Eq. (28).

$$CM = \begin{matrix} \\ 1 \\ 2 \\ 3 \\ 4 \end{matrix} \begin{matrix} \begin{matrix} 1 & 2 & 3 & 4 \end{matrix} \\ \begin{bmatrix} 1 & x_1 & x_2 & 0 \\ 0 & 1 & x_3 & x_4 \\ 0 & x_3 & 1 & x_5 \\ 0 & 0 & 0 & 1 \end{bmatrix} \end{matrix} \tag{28}$$

Step 2: The S matrix of the system in Fig. 2 is given in Eq. (29).

$$S = \begin{bmatrix} x_1 & x_2 & 0 \\ 1 & x_3 & x_4 \\ x_3 & 1 & x_5 \end{bmatrix} \tag{29}$$

Step 3: The determinant of S matrix is given in Eq. (30).

$$\det(S) = x_2x_3x_4 - x_1x_4 + x_1x_3x_5 - x_2x_5 \tag{30}$$

This leads to the identification of four MPSs: $P_1 = \{x_1, x_4\}, P_2 = \{x_2, x_5\}, P_3 = \{x_2, x_3, x_4\}$ and $P_4 = \{x_1, x_3, x_5\}$. Additionally, according to Algorithm 2 detailed in subsection II, the MCSs of the system in Fig. 5 can be identified through the following steps:

Step 1: The AM matrix of the system in Fig. 2 is given in Eq. (31).

$$AM = \begin{matrix} \\ 1 \\ 2 \\ 3 \\ 4 \end{matrix} \begin{matrix} \begin{matrix} 1 & 2 & 3 & 4 \end{matrix} \\ \begin{bmatrix} 0 & \overline{x_1} & \overline{x_2} & 0 \\ 0 & 0 & \overline{x_3} & \overline{x_4} \\ 0 & \overline{x_3} & 0 & \overline{x_5} \\ 0 & 0 & 0 & 0 \end{bmatrix} \end{matrix} \tag{31}$$

Step 2: The two first MCSs of the system in Fig. 2 is given as follows:
$C_1 = \{\overline{x_1}, \overline{x_2}\}$ and $C_2 = \{\overline{x_4}, \overline{x_5}\}$

Step 3: The set $\mathcal{S} = \{\{2\}, \{3\}, \{2,3\}\}$ matrix is given as follows:

- For node {2}, select the first and second rows with remove the second column, then $C_3 = \{\overline{x_2}, \overline{x_3}, \overline{x_4}\}$.
- For node {3}, select the first and third rows with remove the third column, then $C_4 = \{\overline{x_1}, \overline{x_3}, \overline{x_5}\}$.

This leads to the identification of four MCSs: $C_1 = \{\overline{x_1}, \overline{x_2}\}, C_2 = \{\overline{x_4}, \overline{x_5}\}, C_3 = \{\overline{x_2}, \overline{x_3}, \overline{x_4}\}$ and $C_4 = \{\overline{x_1}, \overline{x_3}, \overline{x_5}\}$.

Also, The GLB and exact value for the storage system's reliability depicted in Fig. 5 can be calculated using the MPSs and the third algorithm as follows:

Step 1: Define all MPSs based on order, such that $P_1 = \{x_1, x_4\}, P_2 = \{x_2, x_5\}, P_3 = \{x_2, x_3, x_4\}$ and $P_4 = \{x_1, x_3, x_5\}$.

Step 2: For $P_1 = \{x_1, x_4\}$ assume that $D_{0,1} = P_1$

$$\therefore \lambda_1 = \prod_{x_i \in D_{0,1}} \Pr\{x_i\} = r_1r_4$$

Step 3: For $P_2 = \{x_2, x_5\}$ assume that $D_{0,2} = P_2$

$$\therefore P_1 - D_{0,2} = \{x_1, x_4\} \Longrightarrow \therefore D_{1,2} = \{\overline{x_1}D_{0,2}\} = \{\overline{x_1}, x_2, x_5\} \text{and } D_{2,2} = \{x_1\overline{x_4}D_{0,2}\} = \{x_1, x_2, \overline{x_4}, x_5\}$$

$$\Longrightarrow \therefore \lambda_2 = \prod_{x_i \in D_{1,2}} \Pr\{x_i\} + \prod_{x_i \in D_{2,2}} \Pr\{x_i\} = \overline{r_1}r_2r_5 + r_1r_2\overline{r_4}r_5$$

Step 4: For $P_3 = \{x_2, x_3, x_4\}$ assume that $D_{0,3} = P_3$

$$\therefore P_1 - D_{0,3} = \{x_1\} \Longrightarrow \therefore D_{1,3} = \{\overline{x_1}D_{0,3}\} = \{\overline{x_1}, x_2, x_3, x_4\}$$

$$\therefore P_2 - D_{1,3} = \{x_5\} \Longrightarrow \therefore D_{2,3} = \{\overline{x_5}D_{1,3}\} = \{\overline{x_1}, x_2, x_3, x_4, \overline{x_5}\} \Longrightarrow \therefore \lambda_3 = \prod_{x_i \in D_{2,3}} \Pr\{x_i\} = \overline{r_1}r_2r_3r_4\overline{r_5}$$

Step 5: For $P_4 = \{x_1, x_3, x_5\}$ assume that $D_{0,4} = P_4$

$$\therefore\ P_1 - D_{0,4} = \{x_4\} \Longrightarrow\therefore\ D_{1,4} = \{\overline{x_4} D_{0,4}\} = \{x_1, x_3, \overline{x_4}, x_5\}$$
$$\therefore P_2 - D_{1,4} = \{x_2\} \Longrightarrow\therefore\ D_{2,4} = \{\overline{x_2} D_{1,4}\} = \{x_1, \overline{x_2}, x_3, \overline{x_4}, x_5\}$$
$$\therefore P_3 - D_{2,4} = \{\emptyset\} \Longrightarrow\therefore\ D_{3,4} = D_{2,4} = \{x_1, \overline{x_2}, x_3, \overline{x_4}, x_5\} \Longrightarrow\therefore \lambda_4 = \prod_{x_i \in D_{3,4}} \Pr\{x_i\} = r_1 \overline{r_2} r_3 \overline{r_4} r_5$$

Additionally, The LUB and exact value for the storage system's reliability illustrated in Fig. 5 can be computed using the minimal cuts and the third algorithm as follows:

Step 1: Define all MCSs based on order, such that $C_1 = \{\overline{x_1}, \overline{x_2}\}, C_2 = \{\overline{x_4}, \overline{x_5}\}, C_3 = \{\overline{x_2}, \overline{x_3}, \overline{x_4}\}$ and $C_4 = \{\overline{x_1}, \overline{x_3}, \overline{x_5}\}$

Step 2: For $C_1 = \{\overline{x_1}, \overline{x_2}\}$ assume that $D_{0,1} = C_1$

$$\therefore \beta_1 = \prod_{x_i \in D_{0,1}} \Pr\{x_i\} = \overline{r_1}\, \overline{r_2}$$

Step 3: For $C_2 = \{\overline{x_4}, \overline{x_5}\}$ assume that $D_{0,2} = C_2$

$$\therefore\ C_1 - D_{0,2} = \{\overline{x_1}, \overline{x_2}\} \Longrightarrow\therefore\ D_{1,2} = \{x_1 D_{0,2}\} = \{x_1, \overline{x_4}, \overline{x_5}\} \text{ and}$$
$$D_{2,2} = \{\overline{x_1} x_2 D_{0,2}\} = \{\overline{x_1}, x_2, \overline{x_4}, \overline{x_5}\} \Longrightarrow\therefore \beta_2 = \prod_{x_i \in D_{1,2}} \Pr\{x_i\} + \prod_{x_i \in D_{2,2}} \Pr\{x_i\} = r_1 \overline{r_4} \overline{r_5} + \overline{r_1} r_2 \overline{r_4} \overline{r_5}$$

Step 4: For $C_3 = \{\overline{x_2}, \overline{x_3}, \overline{x_4}\}$ assume that $D_{0,3} = C_3$

$$\therefore C_1 - D_{0,3} = \{\overline{x_1}\} \Longrightarrow\therefore\ D_{1,3} = \{x_1 D_{0,3}\} = \{x_1, \overline{x_2}, \overline{x_3}, \overline{x_4}\}$$
$$\therefore C_2 - D_{1,3} = \{\overline{x_5}\} \Longrightarrow\therefore\ D_{2,3} = \{x_5 D_{1,3}\} = \{x_1, \overline{x_2}, \overline{x_3}, \overline{x_4}, x_5\}$$
$$\Longrightarrow\therefore \beta_3 = \prod_{x_i \in D_{2,3}} \Pr\{x_i\} = r_1 \overline{r_2} \overline{r_3} \overline{r_4} r_5$$

Step 5: For $C_4 = \{\overline{x_1}, \overline{x_3}, \overline{x_5}\}$ assume that $D_{0,4} = C_4$

$$\therefore\ C_1 - D_{0,4} = \{\overline{x_2}\} \Longrightarrow\therefore\ D_{1,4} = \{x_2 D_{0,4}\} = \{\overline{x_1}, x_2, \overline{x_3}, \overline{x_5}\}$$
$$\therefore C_2 - D_{1,4} = \{\overline{x_4}\} \Longrightarrow\therefore\ D_{2,4} = \{x_4 D_{1,4}\} = \{\overline{x_1}, x_2, \overline{x_3}, x_4, \overline{x_5}\}$$
$$\therefore C_3 - D_{2,4} = \{\emptyset\} \Longrightarrow\therefore D_{3,4} = D_{2,4} = \{\overline{x_1}, x_2, \overline{x_3}, x_4, \overline{x_5}\}$$
$$\Longrightarrow\therefore \beta_4 = \prod_{x_i \in D_{3,4}} \Pr\{x_i\} = \overline{r_1} r_2 \overline{r_3} r_4 \overline{r_5}$$

Based on Eqs. (14)-(16), the GLB, exact value, and LUB for the system reliability in Fig. 5 are provided as follows:

$$R_{GLB} = r_1 r_4 + \overline{r_1} r_2 r_5 + r_1 r_2 \overline{r_4} r_5 + \overline{r_1} r_2 r_3 r_4 \overline{r_5} \quad (32)$$
$$R_S = r_1 r_4 + \overline{r_1} r_2 r_5 + r_1 r_2 \overline{r_4} r_5 + \overline{r_1} r_2 r_3 r_4 \overline{r_5} + r_1 \overline{r_2} r_3 \overline{r_4} r_5 \quad (33)$$
$$R_{LUB} = 1 - (\overline{r_1}\, \overline{r_2} + r_1 \overline{r_4} \overline{r_5} + \overline{r_1} r_2 \overline{r_4} \overline{r_5} + r_1 \overline{r_2} \overline{r_3} \overline{r_4} r_5) \quad (34)$$

Suppose the components $\{x_1, x_2, x_3, x_4, x_5\}$ of the system in Fig. 5 follow an exponential distribution, with the AFRs of the components being $\{0.0568, 0.0599, 0.0143, 0.0673, 0.0726\}$, respectively. Based on Eqs. (32)-(34), the GLB, exact value, and LUB for the reliability of the storage system over the period [500, 4000] can be summarized in Table 3 and illustrated in Fig. 6.

Table 3. *The R_{GLB}, R_S and R_{LUB} of the bridge topology of storage system in Fig. 4.*

Time [days]	x_1	x_2	x_3	x_4	x_5	R_{GLB}	R_S	R_{LUB}
500	0.923070	0.918919	0.980476	0.909032	0.901968	0.978636	0.984657	0.984780
1000	0.852058	0.844412	0.961334	0.826339	0.813546	0.925874	0.943879	0.944623
1500	0.786509	0.775947	0.942565	0.751168	0.733793	0.855015	0.885343	0.887246
2000	0.726002	0.713032	0.924162	0.682836	0.661857	0.775402	0.815820	0.819241
2500	0.670151	0.655219	0.906119	0.620719	0.596974	0.693407	0.740811	0.745887
3000	0.618596	0.602093	0.888428	0.564253	0.538451	0.613216	0.664525	0.671197
3500	0.571007	0.553275	0.871082	0.512924	0.485666	0.537435	0.589997	0.598069
4000	0.527079	0.508415	0.854076	0.466264	0.438055	0.467544	0.519284	0.528477

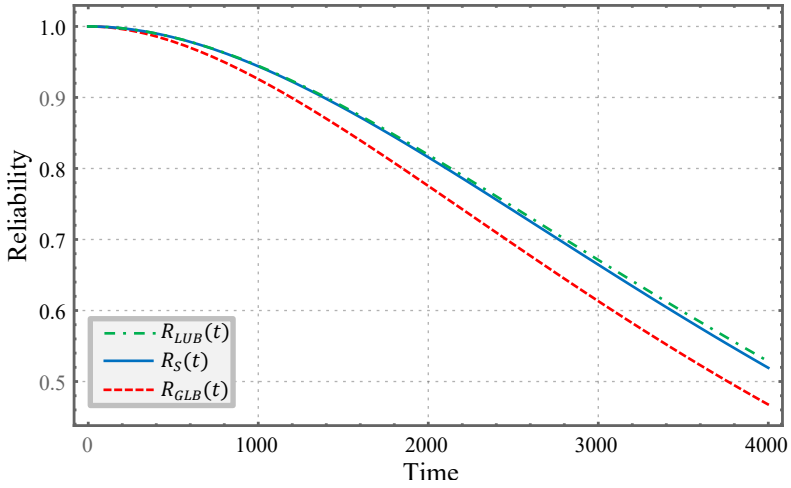


Figure 6. *The GLB, exact value, and LUB for the bridge topology of storage system.*

Fig. 6 illustrates the GLB, exact value, and LUB of the bridge topology of storage system in Fig. 4, highlighting the decline in reliability over time. After 2,500 days, these values drop below 0.693407, 0.740811, and 0.745887. As shown in Table 3, the GLB and LUB obtained using the proposed approach provide a significantly more accurate approximation of the true reliability. To further compare this approach with the Min-Max bounds [28], Edge-packing bounds [29], and Esary-Proschan bounds [30], we refer to Table 4.

Table 4. *Comparison of the GLB and LUB established by the proposed method with other methods.*

Time [days]	R_{GLB}				R_S	R_{LUB}			
	Min-Max [28]	Edge-packing [29]	Esary-Proschan [30]	Propose method		Propose method	Esary-Proschan [30]	Edge-packing [29]	Min-Max [28]
500	0.8391	0.97246	0.984613	0.978636	0.984657	0.984780	0.999084	0.984900	0.991082
1000	0.704088	0.90737	0.943353	0.925874	0.943879	0.944623	0.989827	0.945347	0.96762
1500	0.5908	0.823792	0.883354	0.855015	0.885343	0.887246	0.963792	0.889094	0.933759
2000	0.49574	0.733713	0.81114	0.775402	0.815820	0.819241	0.918574	0.822557	0.892753
2500	0.415975	0.644416	0.732326	0.693407	0.740811	0.745887	0.856855	0.750798	0.84714
3000	0.349045	0.560083	0.65148	0.613216	0.664525	0.671197	0.783751	0.677641	0.798882
3500	0.292883	0.48289	0.572104	0.537435	0.589997	0.598069	0.704758	0.605848	0.74948
4000	0.245758	0.413738	0.496705	0.467544	0.519284	0.528477	0.624637	0.537317	0.70007

For the storage system illustrated in Fig. 5, the proposed approach outperforms the Min-Max bounds and Edge-packing bounds. Its results are close to those of the Esary-Proschan bounds for the GLB. Notably, the proposed approach also surpasses the Min-Max bounds, Edge-packing bounds, and Esary-Proschan bounds for the LUB. Even more impressive is the significant improvement in approximation precision, evidenced by the gap between the exact value for the storage system's reliability and both the GLB and LUB. For instance, at time 2500, the gap between the true reliability and the GLB using the proposed approach is 0.06, while the gap with the LUB is just 0.005. In other words, the proposed approach achieves a more precise approximation of reliability than the methods previously utilized.

V. Conclusion

For large systems, determining exact reliability measures can require a significant amount of time. Often, bounding techniques can provide quicker approximations for a system's reliability or unreliability. This research introduces three mathematical algorithms designed to analyze the reliability of storage systems. The first two algorithms identify all MPSs and MCSs using the connection and adjacency matrices of the system's graph. The third algorithm calculates critical states of the reliability function by summing disjoint sets of MPSs and MCSs, which helps establish

the system's reliability bounds. Compared to existing edge-packing methods, the proposed approach offers more precise approximations of network reliability because it identifies and considers a greater number of MPSs. This method demonstrates superior performance relative to the Min-Max bounds and Edge-Packing bounds. Furthermore, its results closely match those of the Esary-Proschan bounds for the GLB. Importantly, the proposed approach also surpasses the Min-Max bounds, Edge-Packing bounds, and Esary-Proschan bounds when evaluating the LUB. These algorithms effectively identify MPSs and MCSs, calculate their bounds, and provide both visual and numerical representations of the results. The computation of MPSs, MCSs, and reliability bounds is demonstrated using storage systems. This research primarily addresses the challenge of expanding networked systems to enhance their reliability. In our future work, we plan to apply the reliability evaluation technique developed in this study to tackle additional issues related to complex networked systems, including vulnerability detection, protection against intentional attacks, and optimization of maintenance strategies. We are also interested in extending the proposed reliability evaluation technique to k-terminal networks, where the MPSs and MCSs are represented as Steiner trees or cuts.

Declarations

Conflict of interest: The authors declare that they have no conflict of interest.
Funding: No funding received for this research.
Consent for publication: This article do not contain studies with human participants or animals by authors.
Data Availability: The no data used to in this article. The authors declare that they have read and approved the final manuscript.

References

[1] Fratta, L. and Montanari, U. (1973). A Boolean algebra method for computing the terminal reliability in a communication network. IEEE Transactions on Circuit Theory, 20(3), 203-211.

[2] Fahmy, M., Ahmed, A., and Khalil, M. (2023). On Reliability: A Mathematical Fault Tree. Reliability: Theory & Applications, 18(1 (72)), 78-85.

[3] Mutar, E. K. and Hassan, Z. A. H. (2025). Survival signature-based structural importance analysis of multi-state system with binary-state components. ASCE-ASME J Risk and Uncert in Engrg Sys Part B Mech Engrg, 1-18.

[4] Mutar, E. K. and Hassan, Z. A. H. (2025). Joint structure importance of components based on Logic Differential Calculus. Journal of Computational and Applied Mathematics, 117057.

[5] Kuo, W. and Zuo, M. J. (2003). Optimal reliability modeling: principles and applications. John Wiley & Sons.

[6] Hemalatha, G. and Vijayalakshmi, G. (2025). Enhancing sensitivity of MTTF and network reliability stability of k-out-of-n acyclic transmission network. Reliability: Theory & Applications, 20(2), 52-66.

[7] Mutar, E. K. and Hassan, Z. A. H. (2025). Reliability Importance Analysis of a Multi-State System with Binary Components Using Survival Signature. Journal of aerospace technology and management, 17(e1825),

[8] Mutar, E. K. and Hassan, Z. A. H. (2025). Analysis of reliability correlation in the national communication multi-state network of Iraq under time constraints. International Journal of Information Technology,

[9] Aggarwal, K. (2012). Reliability engineering. Springer Science & Business Media.

[10] Abraham, J. A. (1979). An improved algorithm for network reliability. IEEE Transactions on Reliability, 28(1), 58-61.

[11] Ball, M. O. and Provan, J. S. (1988). Disjoint products and efficient computation of reliability. Operations Research, 36(5), 703-715.

[12] Wilson, J. (1990). An improved minimizing algorithm for sum of disjoint products (reliability theory). IEEE Transactions on Reliability, 39(1), 42-45.

[13] Yeh, W.-C. (2007). An improved sum-of-disjoint-products technique for the symbolic network reliability analysis with known minimal paths. Reliability Engineering & System Safety, 92(2), 260-268.

[14] Datta, E. and Goyal, N. K. (2017). Sum of disjoint product approach for reliability evaluation of stochastic flow networks. International Journal of System Assurance Engineering and Management, 8(2), 1734-1749.

[15] Lata, S., Mehfuz, S., Urooj, S., Ali, A., and Nasser, N. (2020). Disjoint Spanning Tree Based Reliability Evaluation of Wireless Sensor Network. Sensors, 20(11), 3071.

[16] Iglesias, R., Pascual-Ortigosa, P., and Sáenz-de-Cabezón, E. (2022). An algebraic version of the sum-of-disjoint-products method for multi-state system reliability analysis. Proceedings of the 2022 International Symposium on Symbolic and Algebraic Computation,

[17] Mutar, E. K. (2023). Estimating the reliability of complex systems using various bounds methods. International Journal of System Assurance Engineering and Management, 14(6), 2546-2558.

[18] Kumar, A. (2023). The operational matrix method based on modified lucas wavelets for the approximation solution of initial and boundary value problems. International Journal of Applied and Computational Mathematics, 9(6), 147.

[19] Al-Awami, L. and Hassanein, H. S. (2016). Distributed data storage systems for data survivability in wireless sensor networks using decentralized erasure codes. Computer Networks, 97(113-127.

[20] Rusnak, P., Zaitseva, E., Coolen, F. P., Kvassay, M., and Levashenko, V. (2022). Logic differential calculus for reliability analysis based on survival signature. IEEE Transactions on Dependable and Secure Computing, 20(2), 1529-1540.

[21] Rusnak, P., Sedlacek, P., and Czapp, S. (2023). Reliability Analysis of Data Storage Using Survival Signature and Logic Differential Calculus. In (Ed.), Reliability Engineering and Computational Intelligence for Complex Systems: Design, Analysis and Evaluation (21-35). Springer.

[22] Mutar, E. K. (2024). Reliability Performance Improvement of the Storage System by Using Weibull and Linear-Exponential Distributions. Journal of Advanced Manufacturing Systems, 23(04), 763-784.

[23] Rusnak, P., Zaitseva, E., Levashenko, V., Bolvashenkov, I., and Kammermann, J. (2024). Importance analysis of a system based on survival signature by structural importance measures. Reliability Engineering & System Safety, 243(109814.

[24] Mutar, E. K. (2022). Path Tracing Method to Evaluate the Signature Reliability Function of a Complex System. Journal of aerospace technology and management, 14(

[25] Rusnak, P., Rabcan, J., Kvassay, M., and Levashenko, V. (2019). Time-dependent reliability analysis based on structure function and logic differential calculus. Contemporary Complex Systems and Their Dependability: Proceedings of the Thirteenth International Conference on Dependability and Complex Systems DepCoS-RELCOMEX, July 2-6, 2018, Brunów, Poland 13,

[26] Silberschatz, A., Galvin, P. B., and Gagne, G. (2013). Operating system concepts essentials. Wiley Publishing.

[27] Tiwary, A. and Mandloi, R. (2023). An Innovative Approach for Reliability Modeling of HVDC Converter Station. Reliability: Theory & Applications, 18(4 (76)), 1011-1018.

[28] Barlow, R. (1975). Statistical theory of reliability and life testing. Holt,

[29] Colbourn, C. J. (1988). Edge-packings of graphs and network reliability. In (Ed.), Annals of Discrete Mathematics (49-61). Elsevier.

[30] Esary, J. D. and Proschan, F. (1963). Coherent structures of non-identical components. Technometrics, 5(2), 191-209.

TERRITORIAL HIERARCHY OF SUSTAINABLE DEVELOPMENT GOALS AND RISK MANAGEMENT

Mariia Lesnykh[1]

•

[1]Higher School of Economics, Moscow, Russia
mailto:lesnykhmaria2004@gmail.com

Abstract

The problem of achieving the sustainable development goals is considered from the perspective of the territorial hierarchy. The necessity of applying a risk-based approach in the implementation of plans for the socio-economic development of territorial entities has been identified. The results of identification and monitoring of key risks of economic development on the example of urban settlements are presented. The interrelation of key risks and significant goals of sustainable development of the research object is revealed.

Keywords: sustainable development goals, territorial hierarchy, small towns, key risks, socio-economic development, expert assessments

I. Introduction

The 2030 United Nations Sustainable Development Goals are a call for action to improve the well-being and protection of the entire planet. The Sustainable Development Goals (SDGs) include 17 areas, including measures to eliminate poverty, increase economic growth, and address a range of issues in the fields of education, health, social protection, and employment, as well as combating climate change and protecting the environment [1].

The international practice of implementing the Sustainable Development Goals demonstrates different rates and successes in achieving them. To assess the extent to which various countries have achieved the SDGs, a special SDG Index (Sustainable Development Goals Index) has been developed, which allows us to determine the status of participating countries in achieving the Sustainable Development Goals. By the end of 2021, none of the countries has demonstrated the achievement of all 17 goals. The leaders of this trend in the world are the Scandinavian countries – Finland, Sweden and Denmark. Russia was ranked 46th in this ranking [2].

II. The SDGs and the territorial hierarchy

It should be noted that the Sustainable Development Goals are formulated by the UN for the global level, i.e. for the world as a whole. Achieving these goals will allow us to talk about global sustainability. In order to justify effective measures to achieve the SDGs, it is necessary to take into account the level of the territorial hierarchy: planet, continent, country, region and settlements. Depending on the hierarchy level, the importance of relevant goals will vary. At the planetary level, all goals will be significant, but at lower levels, the significance may vary.

A hierarchical pyramid of levels at which the achievement of the Sustainable Development Goals can be considered and evaluated is shown in Figure 1.

In addition, it should be borne in mind that the significance of the goals of different objects at the same hierarchy level may also differ. For example, the importance of some goals varies between

developed and developing countries, and also the importance of goals may vary depending on the region of the same country.

Taking into account these specifics (both at different levels of the pyramid and within the same level) will reduce the number of the most significant goals, since goals such as "no poverty", "zero hunger" or "life below water" may be irrelevant for some countries or regions, while ensuring health and well-being or "clean water and sanitation" may be relevant SDGs for most countries and regions.

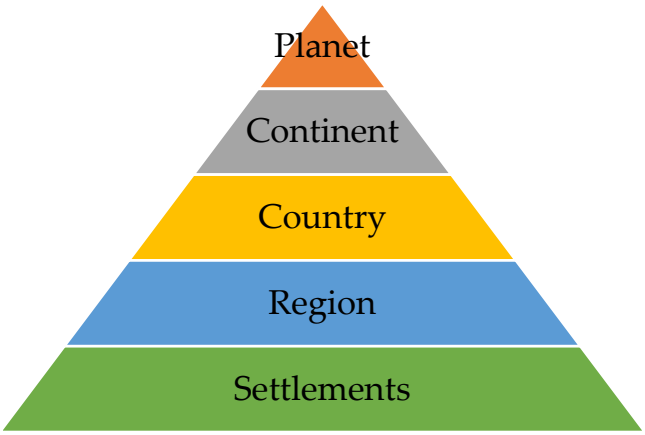


Fig. 1: *Territorial hierarchy pyramid of SDG achievement*

In the Russian Federation, the average percentage of the development of SDGs for May 2022 was 39%, and the average percentage of undeveloped goals was 57%. The top priority goals of sustainable development in Russia are "industry, innovation and infrastructure", "decent work and economic growth" and "good health and well-being". Research shows that measures for goals such as "responsible consumption and production" and "climate action" have been developed to a lesser extent [2].

As the concept of sustainable development spreads and strengthens at the global level, there is not only a transformation of the structure and principles of functioning of the global economy, but also a transformation of approaches to managing national development. The need to achieve the Sustainable Development Goals requires governments to integrate long-term global development goals into the national agenda, which leads to their implementation in sectoral and regional development strategies [3]. Depending on the extent to which the Sustainable Development Goals are adhered to in the region, the situation of the region is determined, taking into account the application of the principles of environmental, social and corporate governance. For example, currently the regions of the Russian Federation have varying degrees of achievement of the SDGs, based on the priorities of their sustainable development.

Being developed at the global level, the SDGs take into account differences in the socio-economic situation of countries around the world, and therefore can be adapted to specific country regions with significant differences in socio-economic development. This thesis is reflected in studies that develop the problem of integrating sustainable development goals in relation to either one of the factors (environmental or social) that have a significant impact on the processes taking place in the territories today, or to a combination of both factors [4].

The problems of sustainable development are certainly relevant at all levels of the hierarchy, but they need to be studied in terms of their adaptation to improve the effectiveness of relevant activities.

III. Sustainable development and risk management

The performed analysis shows that the achievement of the Sustainable Development Goals correlates to a certain extent with the risk management methodology. However, this combination is most consistently applied not at the territorial levels, but at the level of companies and corporations.

The risk management process of a company's sustainable development is based on the fact that organizations are created and operate to achieve their goals when faced with uncertainty factors. The task of the organization's management is to make managerial decisions regarding the levels of uncertainty that the organization considers acceptable in achieving its goals.

Risk management, including the risks of sustainable development, allows the management of companies, optimally using limited resources, to effectively respond to uncertainties and related risks and use new opportunities, since the impact of events is positive, negative or mixed [5].

Currently, the sustainable development of companies, organizations, and management structures is based on compliance with the following three basic principles:

- responsible attitude to the environment (E – Environment);
- high social responsibility (S – Social);
- high quality corporate governance (G – Governance).

In accordance with the abbreviation ESG ("ecology", "social policy", "corporate governance"), usually the concept of sustainable development of companies and corporations is currently understood as the ESG concept. An important step in the implementation of this concept is the improvement of risk management subsystems, their transformation within the framework of the concept of sustainable development. Such a transformation requires solving a whole range of tasks, and the concept of sustainable development in this case is a kind of driver in modeling infrastructure and risk management processes [6].

Researches have shown that a risk-based approach to achieving the SDGs at various territorial levels is applied to a lesser extent than for corporations and companies.

IV. SDGs for small towns and risk management

Plans for the socio-economic development of regions and administrative entities are formed to a certain extent, taking into account the SDGs for the considered level of the territorial hierarchy. The analysis shows that the following goals are often relevant for the level of administrative subjects of the Russian Federation (small towns, urban and rural settlements, etc.): Goal 3 SDG UN – Good health and well-being; Goal 9 SDG UN – Industry, innovation and infrastructure; Goal 11 SDG UN – Sustainable cities and communities. Taking these goals into account when forming socio-economic development plans should also consider emerging risks of various nature [7].

The author's previous research [8] on the problems of socio-economic development of an urban settlement (Razvilka Village, Moscow region) made it possible to identify a group of critical risks. The research included a survey of the population, a SWOT analysis, and an expert assessment of the possibility and impact of risk realization. In total, 8 risk groups were identified in five areas: transport (T), healthcare (H), infrastructure (I), offenses (C) and administration (A). A risk map was built based on expert assessments (Fig.2).

At the time of the study (2022), the following were identified as the most critical risks threatening the economic development of the village:

- risks of transport collapse (T1);
- risks of infrastructure overload due to a significant growth in housing construction (I1);
- risks of an increase in the number and severity of diseases among the village population (H1).

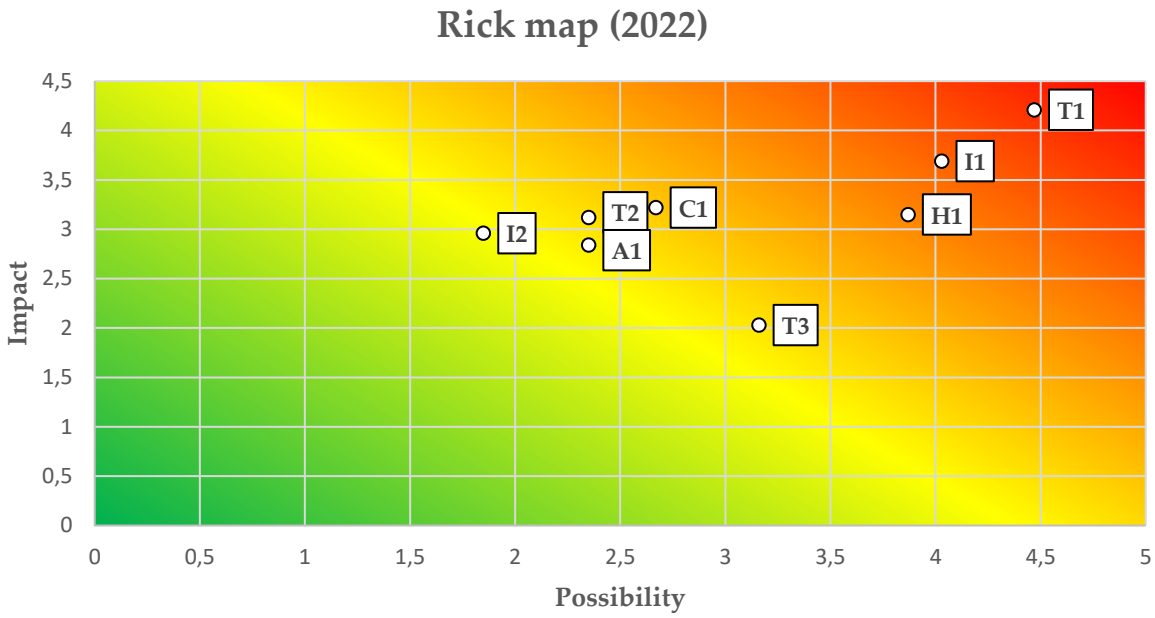


Fig.2: *Risk map of the economic development of the Razvilka Village (2022)*

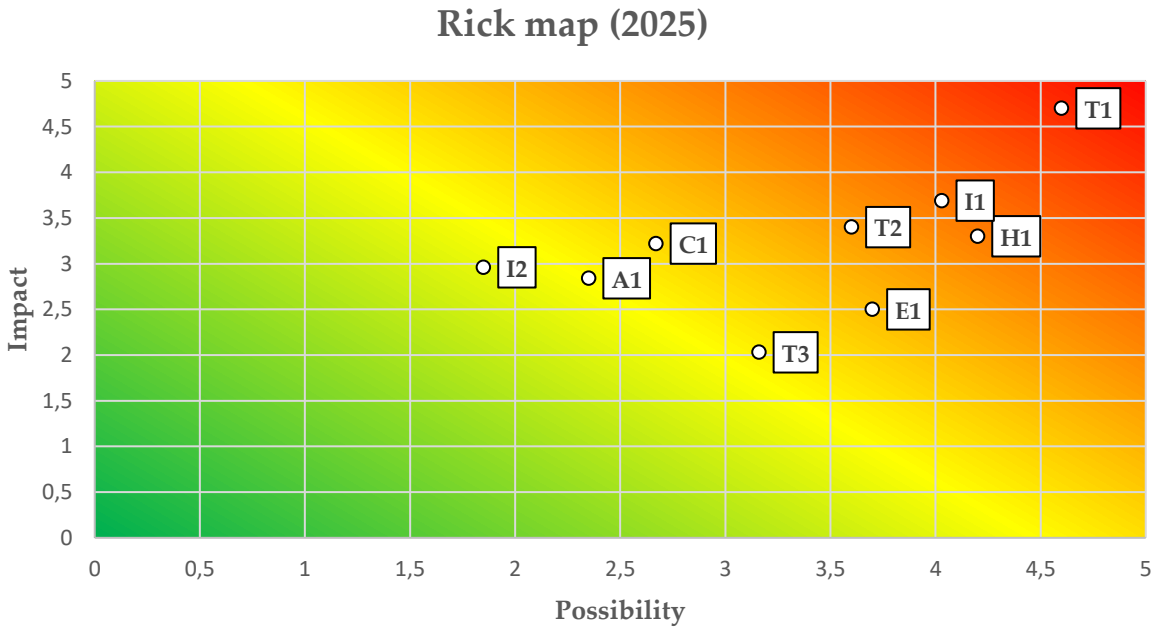


Fig.3: *Risk map of the economic development of the Razvilka Village (2025)*

The listed risks largely coincide with the three previously identified Sustainable Development Goals at the level of local administrative entities (villages, small towns). These studies show that the analysis of the risks of socio-economic development and the justification of measures to reduce them are harmoniously combined with the solution of tasks for the implementation of the Sustainable Development Goals.

Significant changes in the field of economic development took place in the considered research object in a 3-year period between 2022 and 2025. Several residential complexes were built and put into operation, and the social sphere (kindergartens, schools) received some development. At the

same time, plans for the construction of a medical center have not been implemented, and problems in the field of transport have not been solved [9].

The analysis showed that currently all the previously identified risk groups are present, and, in addition, risks in the field of ecology and sanitation (E1) have been added to the number of critical ones (Fig. 3) [10]. This suggests that the socio-economic development plans of the village should take into account Goal 15 SDG UN – Life on land.

In general, it can be noted that the previously identified risks of the economic development of the village are still relevant, and the importance of some of them (risks of reducing the quality of healthcare, risks of transport collapse) has not only not decreased, but has increased to a certain extent, and in addition, new significant risks have been added. This requires further monitoring of risks and the participation of the local administration in the development and implementation of measures to reduce them and take them into account in the formation and implementation of socio-economic development plans.

V. Conclusion

As a result of the study, the relationship between the importance of the SDGs and the territorial hierarchy of research objects was revealed, and the correspondence between the critical risks of socio-economic development and the SDGs was shown using the example of a certain urban settlement. It is concluded that critical risk management measures can contribute to achieving the SDGs for the considered level of the territorial hierarchy.

The results obtained in the study allow us to determine the directions of further research in the field of sustainable development of small towns and villages. Based on the analysis of statistical data, it is necessary to identify the degree of significance (rating) of the sustainable Development Goals for the considered level of the territorial hierarchy. It is also necessary to analyze the relationship between the Sustainable Development Goals for the considered level (using the example of several small towns or villages) using cognitive maps, expert assessments, and the analytic hierarchy process (AHP). Further, it is advisable to develop methods for quantifying the results of a coordinated reduction of key risks and the degree of achievement of the SDGs for the considered research objects. The results obtained will make it possible to increase the effectiveness of measures to achieve the Sustainable Development Goals.

References

[1] Sustainable development goals https://www.un.org/sustainabledevelopment/ru/sustainable-development-goals/

[2] Poltoradneva N., Mil I. Russian features of achieving goals in the concept of sustainable development // Innovative economy and society. – 2024. – №4(46). – pp. 33-40

[3] Sintsova E.A., Smeshko O.G. Sustainable development goals in Russian regions: The processes of their formation and implementation. *Economics and Management*. 2023;29(8):871-881. (In Russ.) https://doi.org/10.35854/1998-1627-2023-8-871-881

[4] Gagarina G. Yu., Miroshnikov S. N. The Application of the Sustainable Development Goals of the UN in the Strategies of Russian Federation Subject. *Administrative Consulting*. 2019;(1):54-63. (In Russ.) https://doi.org/10.22394/1726-1139-2019-1-54-63

[5] Pashkovsky D. Risk management of sustainable development as a factor in improving corporate governance efficiency // Izvestiya UNECON. 2023. №3-1 (141), pp.122-128

[6] Trifonov Yu. V., Brykalov S. M., Trifonov V. Yu. Risk Management Within the Framework of the Concept of Sustainable Development. *Issues of Risk Analysis*. 2022;19(5):10-18. (In Russ.) https://doi.org/10.32686/1812-5220-2022-19-5-10-18

[7] Hohstadt E. Risk Management as an element of long-term social and economic development forecasting of the entities of the Russian Federation // Risk Management, 3, 2025, pp.29-37

[8] Lesnykh M., Timofeeva T. Analysis of risks associated with the economic development of urban settlements (on the example of the settlement of the Fork in the Moscow region) // Risk Management, 2, 2022, pp.30-40.

[9] General plan of the Razvilka Village in the Leninsky urban district of the Moscow region. Regulations on territorial planning. – Moscow, 2017 – p. 65.

[10] Lesnykh M. Current aspects of assessing and forecasting the risks of economic development of urban settlements // Actual problems and prospects for the development of modern science: a collection of articles based on the materials of the International Correspondence Scientific and Practical Conference (Stavropol, June 11, 2025): conference proceedings. Moscow: RANEPA Case, 2025 (to be published)

RELIABILITY-ORIENTED MICROGRID CONTROL USING REINFORCEMENT LEARNING

O. Aliyeva[1], I. Babazade[2]

[1,2]Azerbaijan State Oil and Industry University, Scientific-Research İnstitute of Geo-technological Problems of Oil, Gaz and Chemistry, Baku, Azerbaijan

[1] olga_da@mail.ru , [2]ikram.babazade@asoiu.edu.az

Abstract

The growing penetration of renewable energy sources (RES) in modern power systems introduces significant challenges to reliability due to the inherent stochasticity of wind and solar generation. Microgrids, as decentralized energy systems, offer resilience and flexibility but require intelligent control strategies to balance variable generation and demand. This paper proposes a reinforcement learning (RL)-based multi-agent control framework for microgrids, formalized through a Markov Decision Process (MDP) with states reflecting generation, storage, and load variability. Deep RL algorithms—DQN, PPO, and A2C—are compared against conventional methods in a high-fidelity simulation environment with real-world load and RES data. Key reliability indicators, including Loss of Load Probability (LOLP), Mean Time Between Failures (MTBF), and the self-sufficiency ratio, are evaluated. Results demonstrate that PPO achieves a >40% reduction in LOLP compared to rule-based control, ensuring higher resilience and operational adaptability. The study further discusses computational constraints, generalization issues, and cyber-physical vulnerabilities, and proposes solutions based on federated RL, transfer learning, and anomaly detection. The findings underline RL's potential as a cornerstone for reliability-centered energy management in microgrids.

Keywords: reinforcement learning, microgrid reliability, renewable energy uncertainty, PPO, DQN, A2C, multi-agent systems

I. Introduction

The modern power industry is undergoing a transformation toward sustainable, intelligent, and decentralized energy architectures. A central driver of this transformation is the large-scale integration of renewable energy sources (RES), particularly wind and solar generation. While environmentally beneficial, the variability and intermittency of RES introduce significant uncertainty into power generation processes, directly challenging the reliability of electricity supply.

Microgrids—localized systems that combine distributed generation, storage, and controllable loads—are widely recognized as a promising solution to enhance resilience and autonomy [1, 2]. They can operate in both grid-connected and islanded modes, offering flexibility under disturbances. However, ensuring reliable performance of microgrids under high RES penetration is non-trivial. Fluctuations in generation, coupled with stochastic consumer demand, increase the probability of supply-demand imbalances, energy losses, and reliability degradation [3, 4].

Conventional optimization approaches, such as linear or stochastic programming, have limited ability to cope with such stochasticity. These methods typically rely on complete prior knowledge of system parameters and are not robust to incomplete or noisy data [5]. As a result, there is a growing interest in intelligent, adaptive control strategies. Reinforcement Learning (RL) is particularly attractive because it allows agents to learn optimal control strategies through continuous interaction with the environment, without requiring explicit system models [6].

For microgrid operation, RL offers several advantages:

- learning directly from real-time system feedback,
- adaptability to dynamically changing conditions,
- robustness under incomplete or uncertain data, and
- scalability to high-dimensional, multi-agent control tasks [7].

Recent advances in Deep Reinforcement Learning (DRL) further extend these capabilities, enabling control strategies in nonlinear and complex environments [8].

Despite the growing body of research on RL in energy systems, a gap remains in linking RL methods directly to reliability indicators of microgrids. Most studies emphasize control efficiency or cost minimization, while reliability metrics such as Loss of Load Probability (LOLP), Mean Time Between Failures (MTBF), and self-sufficiency ratio are often overlooked.

The goal of this study is to address this gap by developing and evaluating a reinforcement learning-based framework for microgrid operation explicitly focused on reliability enhancement. The study investigates the performance of modern DRL algorithms—DQN, PPO, and Actor-Critic—under realistic operating conditions with variable RES and demand, and compares their ability to improve microgrid reliability relative to conventional approaches.

II. Problem statement

The integration of renewable energy sources (RES), such as photovoltaic (PV) and wind, into microgrids contributes to sustainable development but simultaneously creates critical challenges for ensuring reliability. Electricity generation from RES is inherently stochastic, while consumer demand exhibits both temporal and behavioral variability. This dual uncertainty significantly increases the probability of supply-demand imbalance, load losses, and overuse of backup units, which in turn reduces overall reliability of the microgrid.

From the reliability engineering perspective, the main negative effects can be summarized as follows: increased Loss of Load Probability (LOLP) due to mismatches between generation and demand, reduced Mean Time Between Failures (MTBF) of supply adequacy, and lower self-sufficiency ratio (SSR) as microgrids rely more frequently on external grid support. Furthermore, intensified cycling of storage systems and backup generators leads to accelerated wear and premature failures [9-11].

Conventional optimization methods, including linear programming (LP) and stochastic programming, are poorly suited for such environments. They rely on complete prior knowledge of system parameters, do not scale well in real time, and rarely integrate probabilistic reliability indices into the decision-making process. Table 1 highlights the limitations of traditional methods compared to reinforcement learning (RL), which uniquely allows direct optimization of reliability metrics.

Table 1: *Comparison of optimization methods for reliability in microgrids under uncertainty*

Method	**Uncertainty Resilience**	**Real-Time Operation**	**Reliability Metrics Integration**	**Scalability**
Linear Programming (LP)	Low	No	Not included	Low
Stochastic Optimization	Medium	Partial	Limited	Medium
Reinforcement Learning	High	Yes	Direct (LOLP, MTBF, SSR)	High

To better illustrate the challenge, Figure 1 presents a conceptual microgrid architecture where each subsystem (PV, wind turbine, storage, loads, diesel generator) is managed by an autonomous RL agent. These agents interact locally and cooperate globally to maintain reliability even under stochastic disturbances.

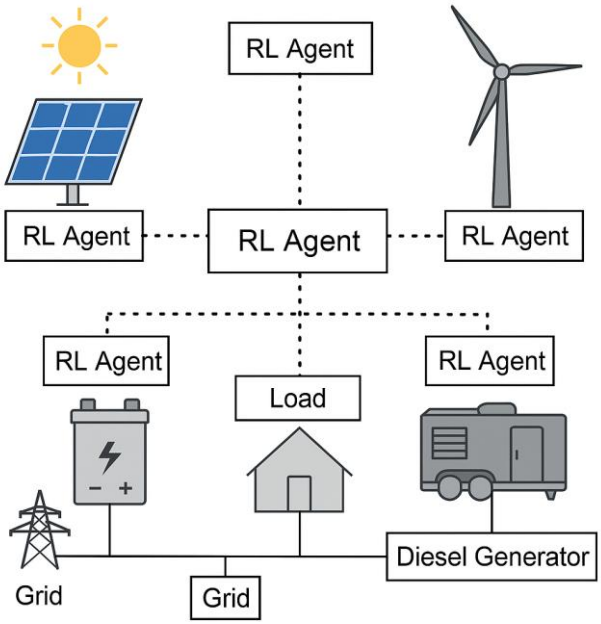


Figure 1: *Conceptual microgrid architecture with RL agents*

The reliability-centered optimization loop is further explained in Figure 2. The RL agent receives uncertain inputs (RES generation and demand fluctuations), processes them through its policy network, and outputs actions aimed at minimizing LOLP, increasing MTBF, and improving SSR. This representation makes explicit how reliability indicators are embedded into the optimization process, rather than treated as secondary performance measures.

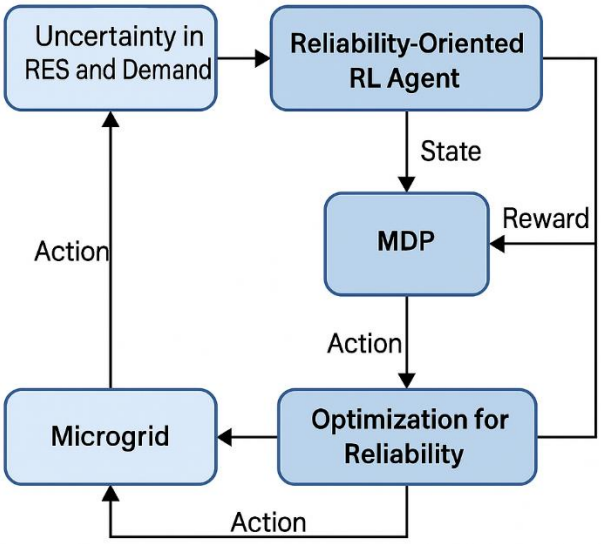


Figure 2: *Reliability-oriented optimization loop in RL*

Finally, to demonstrate the practical impact of renewable penetration on reliability, Figure 3 compares the evolution of LOLP under traditional and RL-based control strategies. While conventional methods exhibit a sharp increase in LOLP once RES penetration exceeds 40%, the RL-based strategy maintains significantly lower values across the full range.

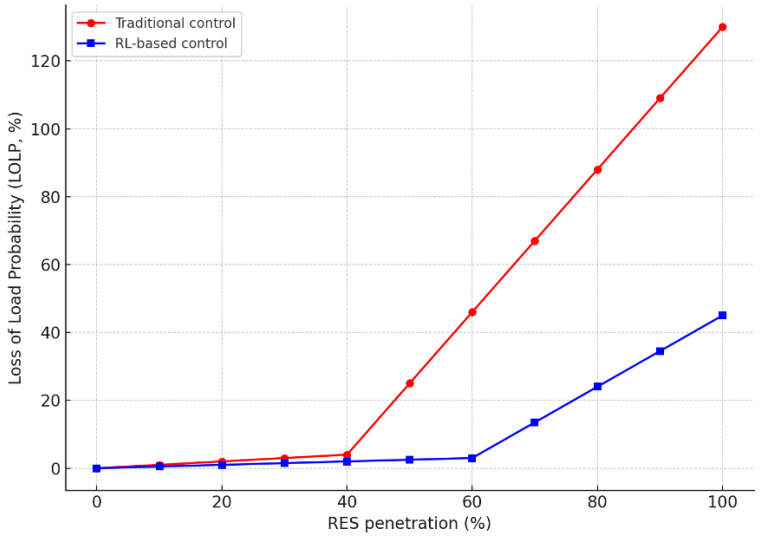


Figure 3: *Impact of RES penetration on LOLP under traditional vs. RL-based control*

III. Problem Solution

To overcome the reliability challenges identified in Section II, a reinforcement learning (RL)-based control framework was developed for microgrid operation. The problem was formalized as a Markov Decision Process, where states include renewable generation, load, and storage conditions, while actions represent redispatching storage, activating backup generation, and managing power exchange with the grid. The reward function is explicitly reliability-oriented, minimizing interruptions that increase the Loss of Load Probability (LOLP) while rewarding stable operation that extends the Mean Time Between Failures (MTBF) and improves the self-sufficiency ratio (SSR).

Three deep RL algorithms were investigated: Deep Q-Network (DQN), which is suited for discrete switching tasks such as charge/discharge control; Proximal Policy Optimization (PPO), which provides robustness and fast convergence in continuous control environments; and Advantage Actor–Critic (A2C), which combines policy and value learning for balanced adaptability. Their main characteristics are summarized in Table 2, showing that PPO is particularly well suited for reliability-centered optimization in microgrids with high renewable penetration [12, 13].

The experimental environment reproduced a representative microgrid including a 50 kW photovoltaic array, a 30 kW wind turbine, a 200 kWh lithium-ion storage system, a 60 kW diesel generator, and a ±40 kW grid connection. Load data corresponded to a hybrid residential–commercial consumer group with a daily consumption of about 850 kWh. Renewable and demand time series were taken from CAISO and NREL datasets, and RL agents were trained over 5000 daily episodes.

Table 2: *Comparison of reinforcement learning algorithms for microgrid reliability optimization*

Algorithm	Model Type	Continuous Action Handling	Convergence	Stability	Hyperparameter Sensitivity	Typical Use
DQN	Value-based	Limited	Moderate	Medium	High	Discrete ESS switching
PPO	Policy gradient	Well suited	High	High	Low	Continuous hybrid energy control
A2C	Actor–critic	Suitable	Medium	Medium	Moderate	Demand–supply balancing

The learning dynamics of the algorithms are presented in Figure 4, which compares the evolution of LOLP during training. PPO converges to a stable policy after approximately 1000 episodes, reducing LOLP by more than 40% compared to a rule-based baseline. A2C also improves reliability but at a slower rate, while DQN shows more variability due to its discrete-action design. These results confirm that RL, and especially PPO, provides a scalable and adaptive solution for enhancing microgrid reliability under stochastic renewable generation and demand uncertainty.

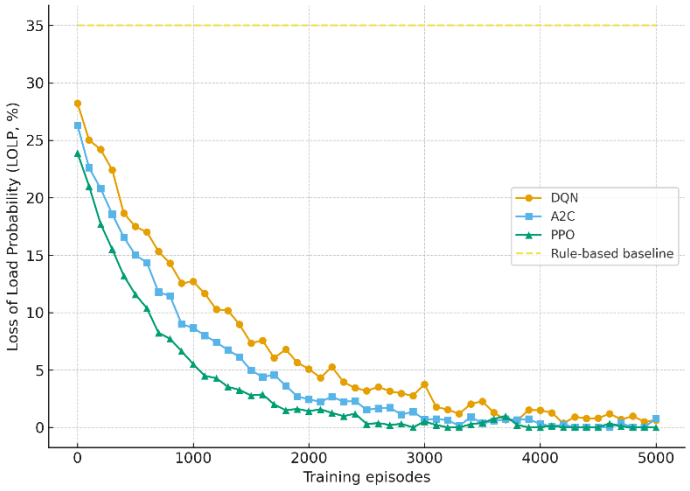


Figure 4: *Convergence of RL algorithms in reducing LOLP during training*

IV. Discussion

The results obtained in Section III confirm that reinforcement learning (RL) can significantly improve the reliability of microgrid operation under uncertain renewable generation and variable demand. Compared with traditional optimization approaches discussed in Section II, RL not only adapts to stochastic fluctuations but also directly optimizes reliability metrics. This shift is critical because reliability—expressed through indicators such as LOLP, MTBF, and SSR—is the primary concern in decentralized power systems with high shares of renewable energy.

The comparative evaluation of algorithms presented in Table 2 shows that PPO consistently outperforms DQN and A2C in terms of stability and convergence. While DQN remains effective for discrete control actions, its sensitivity to hyperparameters and limited scalability make it less

attractive for complex microgrid environments. A2C demonstrates balanced performance but requires longer training to reach reliable policies. PPO, in contrast, exhibits robust convergence and strong adaptability, which makes it particularly well suited for continuous and hybrid control scenarios.

The training dynamics in Figure 4 highlight the reliability benefits of PPO. Within approximately 1000 training episodes, PPO reduces LOLP by more than 40% compared to rule-based control, achieving stable operation much earlier than the other RL algorithms. This finding is especially relevant for practical deployment, where long training periods are often infeasible. Faster convergence directly translates into more reliable operation during the early stages of learning, which is a decisive advantage for real-world microgrids.

At the same time, several limitations remain. First, the computational cost of training complex RL agents is significant, especially when scaling to multi-agent architectures. Second, generalizing trained policies to different microgrid topologies or load patterns is not trivial, which may limit transferability. Finally, the increasing autonomy of RL agents introduces new risks related to cybersecurity, as malicious interventions in control signals could compromise system reliability.

These challenges point to promising research directions. Distributed training frameworks and cloud-based computation can reduce the cost of training. Transfer learning and meta-RL approaches can improve adaptability across diverse microgrid configurations. In addition, incorporating anomaly detection mechanisms and decentralized trust protocols can mitigate cyber-physical vulnerabilities. By addressing these aspects, future RL frameworks will not only enhance operational reliability but also ensure resilience against both technical and external threats.

Overall, the discussion confirms that reinforcement learning is more than a control alternative—it is a transformative approach for microgrid management, shifting the focus from efficiency alone to explicit reliability-centered optimization. The results of this study provide strong evidence that RL, and particularly PPO, can become a practical cornerstone technology for the next generation of intelligent, decentralized energy systems.

V. Conclusion

This study has presented a reinforcement learning (RL)-based framework for improving the reliability of microgrid operation under renewable energy uncertainty. Unlike conventional optimization methods that struggle with incomplete information and rapidly changing conditions, the proposed approach integrates reliability indicators directly into the decision-making process. By formulating the problem as a Markov Decision Process with a reward function centered on LOLP, MTBF, and SSR, the framework ensures that control strategies are explicitly aligned with reliability objectives.

The results demonstrate that deep RL algorithms, and especially Proximal Policy Optimization (PPO), significantly reduce the probability of load loss while improving fault-free operational intervals and system self-sufficiency. As shown in Table 2 and Figure 4, PPO outperforms DQN and A2C by combining robust convergence with adaptability to continuous control tasks. This advantage translates into faster attainment of reliable policies and superior resilience under high penetration of renewables.

The broader implication of these findings is that reinforcement learning is not only an efficient optimization tool but also a transformative method for reliability-centered management of decentralized energy systems. By embedding reliability directly into optimization objectives, RL-based frameworks can provide adaptive, scalable, and autonomous control strategies that meet the demands of next-generation power systems.

At the same time, several challenges remain to be addressed. High computational costs, limited policy generalization across diverse microgrid topologies, and the vulnerability of autonomous agents to cyber-physical threats highlight the need for further research. Promising directions include federated and meta-RL approaches for improving adaptability, integration of forecasting and Model Predictive Control to strengthen hybrid decision-making, and the development of anomaly detection and blockchain-based trust mechanisms to ensure resilience against external disruptions.

In conclusion, reinforcement learning has the potential to become a cornerstone technology for the reliable operation of smart microgrids. By explicitly linking control strategies to reliability indices, it offers a pathway toward resilient, sustainable, and adaptive energy systems capable of meeting the challenges of the renewable-dominated future.

CONFLICT OF INTEREST

The authors declare no potential conflict of interests.

References

[1] Lund, H., Ostergaard, P. A., Connolly, D., & Mathiesen, B. V. (2017). Smart energy and smart energy systems. *Energy*, 137, 556–565.

[2] Farrokhabadi, M., Cañizares, C. A., & Bhattacharya, K. (2017). Frequency control in isolated/islanded microgrids through voltage regulation. *IEEE Transactions on Smart Grid*, 8(3), 1185–1194.

[3] Katiraei, F., & Iravani, M. R. (2006). Power management strategies for a microgrid with multiple distributed generation units. *IEEE Transactions on Power Systems*, 21(4), 1821–1831.

[4] Shahidehpour, M., Yamin, H., & Li, Z. (2002). *Market operations in electric power systems*. Wiley-IEEE Press.

[5] Bahramirad, S., Reder, W., & Khodaei, A. (2012). Reliability-constrained optimal sizing of energy storage system in a microgrid. *IEEE Transactions on Smart Grid*, 3(4), 2056–2062.

[6] Sutton, R. S., & Barto, A. G. (2018). *Reinforcement learning: An introduction* (2nd ed.). MIT Press.

[7] Wang, Y., Chen, Q., Hong, T., & Kang, C. (2019). Review of smart meter data analytics: Applications, methodologies, and challenges. *IEEE Transactions on Smart Grid*, 10(3), 3125–3148.

[8] Meng, L., Savaghebi, M., Andrade, F., Vasquez, J. C., & Guerrero, J. M. (2017). Review on control of DC microgrids and multiple microgrid clusters. *IEEE Journal of Emerging and Selected Topics in Power Electronics*, 5(3), 928–948.

[9] Rzayeva, S. V., Piriyeva, N. M., & Ismayilova, S. I. (2025). High and low voltage coordination in electrical power systems. *International Journal on Technical and Physical Problems of Engineering (IJTPE)*, 17(1), 19–31.

[10] Rzayeva, S. V., Piriyeva, N. M., & Guseynova, I. A. (2024). Analysis of reliability of typical power supply circuits. *Reliability: Theory & Applications*, 19(3), 173–178.

[11] Khan, A. A., Naeem, M., Iqbal, M., Qaisar, S., & Anpalagan, A. (2016). A compendium of optimization objectives, constraints, tools and algorithms for energy management in micro-grids. *Renewable and Sustainable Energy Reviews*, 58, 1664–1683.

[12] Wouters, C., Fraga, E., & James, A. (2015). MILP approach for the design of residential microgrids with energy interactions restrictions. *Computer Aided Chemical Engineering*, 37, 2357–2362.

[13] Delgado, C., & Domínguez-Navarro, J. A. (2014, March 25–27). Optimal design of a hybrid renewable energy system. In *Proceedings of the 9th International Conference on Ecological Vehicles and Renewable Energies (EVER)*. Monte-Carlo, Monaco.

RELIABILITY ASSESSMENT OF PHASE CHANGE MATERIALS IN TES FOR RENEWABLE ENERGY SYSTEMS

G.K. Abdullayeva[1], A.L. Bakhtiyarov[2]

•

Azerbaijan State Oil and Industry University, Baku, Azerbaijan
[1]gulshan.abdullayeva@asoiu.edu.az, [2] baxtiyarov.aliashraf@asoiu.edu.az

Abstract

The reliability of phase change materials (PCMs) in thermal energy storage (TES) systems is crucial for the stable and efficient operation of renewable energy infrastructures. This study presents a comprehensive methodology for assessing PCM reliability under repeated thermal cycling, focusing on degradation mechanisms such as latent heat reduction, phase change temperature shifts, and decreased thermal conductivity. Experimental characterization using techniques like Differential Scanning Calorimetry (DSC) and Thermogravimetric Analysis (TGA) provides data on property evolution over thousands of heating–cooling cycles. Failure thresholds for critical parameters are established to define functional limits. An exponential decay model is proposed to quantify degradation kinetics and predict the effective service life of different PCM types, including paraffins, salt hydrates, and eutectic mixtures. Comparative analysis reveals distinct degradation behaviors and informs material selection for TES applications. The integration of empirical data, failure criteria, and predictive modeling supports reliability-centered design and maintenance planning, ultimately enhancing TES system durability and performance in renewable energy applications.

Keywords: Reliability modeling; Phase change materials (PCMs); Thermal degradation; Latent heat loss; Failure thresholds; Thermal energy storage (TES);

I. Introduction

Modern energy systems are undergoing a fundamental transformation, shifting from centralized generation based on fossil fuels to decentralized, sustainable, and environmentally friendly solutions. In this paradigm, renewable energy sources (RES) — such as solar, wind, geothermal, and biomass — play a key role. Despite their obvious advantages, including sustainability, zero carbon emissions, and reduced dependence on conventional fuels, RES are inherently intermittent and unstable, which necessitates the development of efficient and reliable energy storage systems.

One of the most promising approaches to thermal energy storage (TES) involves the use of phase change materials (PCMs), which can absorb and release significant amounts of energy during phase transitions, primarily between solid and liquid states [1]. PCMs are increasingly used in solar thermal systems, industrial heat recovery, building heating and cooling, and in emerging smart energy networks.

The main advantage of PCMs over traditional sensible heat storage materials (such as water, gravel, or oils) is their ability to store heat at an almost constant temperature with a high energy density, due to the latent heat of fusion. However, under real operating conditions involving repeated heating and cooling cycles, the thermal, chemical, and mechanical properties of PCMs can degrade, reducing system performance and potentially leading to premature failure.

The reliability of PCMs is therefore a critical factor in the long-term, safe, and cost-effective operation of TES systems, especially in applications where regular replacement of storage media is impractical or economically unfeasible [2]. In this context, reliability refers to the ability of the PCM to maintain its essential functional properties — such as phase transition temperature, latent heat, thermal conductivity, and thermal stability — over a large number of thermal cycles and under varying thermal loads.

Despite extensive research on the thermophysical and thermochemical properties of PCMs, a standardized methodology for quantitatively assessing their reliability and residual service life under cyclic thermal conditions has not yet been established. Most existing studies focus on isolated property changes without integrating them into a comprehensive assessment of system reliability.

Therefore, the purpose of this paper is to develop a structured approach for evaluating the reliability of phase change materials by analyzing the evolution of their thermophysical characteristics during thermal cycling. This study reviews the main degradation mechanisms of PCMs, presents experimental and modeled dependencies of key parameters as functions of cycle number, and proposes failure criteria applicable to real-world TES systems.

From the standpoint of reliability engineering, the performance degradation of phase change materials (PCMs) can be analyzed using established metrics such as the mean time to failure (MTTF), failure rate functions, and reliability functions R(t) or R(N), where N represents the number of thermal cycles. In many material fatigue and degradation processes, the Weibull distribution is commonly employed to statistically model the time (or cycles) to failure, allowing estimation of characteristic life and failure probabilities under varying conditions [3-5]. Although deterministic degradation models (e.g., exponential decay) are useful for capturing average behavior, integrating probabilistic methods provides a more robust foundation for service life prediction, risk assessment, and maintenance planning. This approach is particularly relevant for TES systems in renewable energy infrastructure, where component longevity and system-level reliability are critical. Therefore, combining empirical degradation modeling with classical reliability concepts enables a comprehensive evaluation of PCM performance throughout its operational lifecycle.

This research aims to establish a scientific foundation for the development of more durable PCMs and to enhance the operational stability and energy efficiency of TES systems integrated into renewable energy infrastructures.

II. Formulation of the problem

Thermal energy storage (TES) plays a pivotal role in balancing the intermittent nature of renewable energy sources (RES), such as solar and geothermal systems. Among TES methods, latent heat storage using phase change materials (PCMs) is especially attractive due to its high energy density and the ability to operate near-isothermally during phase transitions. However, the long-term viability of PCMs is strongly affected by their degradation under cyclic thermal loading, which directly impacts system performance and reliability (table 1).

In real-world applications, PCMs are subjected to thousands of heating and cooling cycles, which gradually alter their thermophysical, chemical, and mechanical properties. The most significant degradation mechanisms include: reduction in latent heat of fusion (ΔHf), drift in phase change temperature (Tf), decreased thermal conductivity (λ), increased supercooling, and structural or chemical instability. These changes can be critical, especially in TES systems designed for maintenance-free operation over a lifespan of 10–20 years.

Table 1.: *Classification of PCMs Based on Composition and Properties*

Type	Advantages	Limitations	Examples
Paraffins	Chemically stable, inexpensive, non-corrosive	Low thermal conductivity, flammable	Octadecane, RT42, n-docosane
Salt Hydrates	High latent heat, good thermal conductivity	Phase segregation, water loss, supercooling	$Na_2SO_4 \cdot 10H_2O$, $CaCl_2 \cdot 6H_2O$
Eutectic Mixtures	Sharp melting point, design flexibility	Complex preparation, limited long-term data	$NaNO_3$–KNO_3, organic eutectics
Inorganic Compounds	High temperature range, non-flammable	Corrosiveness, structural expansion	$Zn(NO_3)_2 \cdot 6H_2O$, NaOH, $MgCl_2 \cdot 6H_2O$

Experimental evidence demonstrates varying degradation behavior among PCM types. For example, salt hydrates can lose up to 25–40% of ΔHf within 500 cycles due to dehydration and phase segregation. In contrast, paraffins often retain over 90% of their thermal storage capacity after 1000 cycles, but their performance is limited by low thermal conductivity and the development of supercooling over time. Eutectic mixtures show intermediate behavior, though they are highly dependent on formulation and purity.

Despite their wide adoption, PCM-based TES systems still lack a standardized reliability evaluation framework [6]. Most current studies focus on individual properties (e.g., ΔHf or Tf) without defining clear criteria for functional failure. As a result, engineers and designers are left without actionable thresholds for predicting PCM end-of-life or planning preventive maintenance.

III. Problem solution

Reliable operation of thermal energy storage (TES) systems using phase change materials (PCMs) requires a systematic approach to evaluating their long-term performance under cyclic thermal loading [7]. This section outlines the combined experimental, analytical, and empirical modeling framework used to assess PCM reliability based on thermophysical degradation.

A central aspect of the methodology is the characterization of key thermal properties over a representative number of heating–cooling cycles, typically ranging from hundreds to several thousand. The primary parameters of interest include:

- Latent heat of fusion (ΔHf)
- Phase change temperature (Tf)
- Thermal conductivity (λ)
- Supercooling behavior and crystallization hysteresis
- Visual and structural integrity (leakage, volume change)

These properties are measured using standardized thermal analysis techniques, such as:

- Differential Scanning Calorimetry (DSC) — to determine ΔHf and Tf;
- Thermogravimetric Analysis (TGA) — for assessing thermal stability and mass loss;
- Hot Disk or Laser Flash Analysis — for measuring λ;
- Infrared spectroscopy and microscopy — to detect chemical or morphological changes;
- Visual inspection — to detect encapsulation failure or leakage.

To address this gap, we propose a set of practical failure thresholds (Table 2), which aggregate key performance indicators across thermophysical and structural domains. These thresholds can be used to define when a PCM has degraded beyond acceptable limits for safe and efficient TES operation.

Table 2.: *Failure Criteria for PCM in TES Systems*

Parameter	Failure Threshold	Effect on System Performance
Latent heat of fusion (ΔHf)	>20% reduction from initial value	Reduced energy storage capacity
Phase change temperature (Tf)	±2°C deviation from nominal value	Incompatible thermal integration, control instability
Thermal conductivity (λ)	>15% reduction	Lower heat exchange efficiency
Supercooling tendency	ΔTf > 5°C compared to initial	Delayed heat release, hysteresis
Visual integrity / leakage	Encapsulation rupture or PCM leakage	Risk of mechanical failure, safety hazard
Mass loss (evaporation/chem. loss)	>10% mass loss	Altered material balance, chemical instability

To illustrate the rate of thermal degradation in different PCM types, Figure 1 presents the relative latent heat retention (ΔHf) as a function of the number of thermal cycles. The data reflects typical experimental trends for three common PCM categories.

As shown, paraffins exhibit a gradual and relatively linear degradation profile, remaining functionally stable over long durations. Salt hydrates, by contrast, suffer steep performance drops due to material stratification and water migration. Eutectic mixtures offer more stable melting points but demonstrate moderate degradation depending on formulation and phase compatibility.

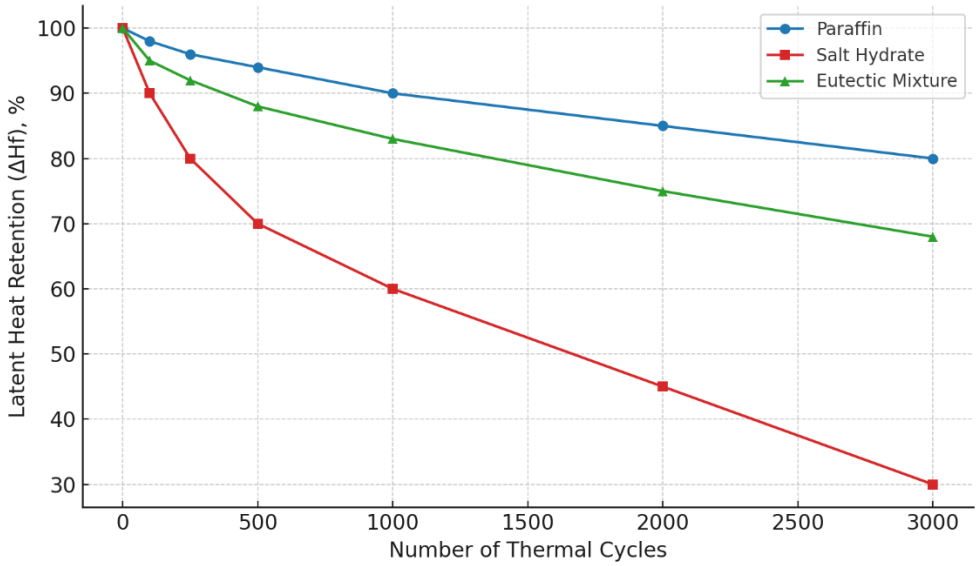


Figure 1.: *Latent Heat Retention of PCMs Over Thermal Cycling*

In summary, the challenge of PCM degradation poses a significant barrier to the long-term reliability of TES systems. The absence of clear, quantifiable failure metrics complicates material selection and lifecycle planning [8-10]. Therefore, it is essential to establish comprehensive reliability models that integrate experimental degradation data, mechanistic understanding, and failure thresholds. This will facilitate the design of robust, high-performance TES systems aligned with the reliability requirements of renewable energy infrastructures.

As evident, paraffins show relatively stable performance over 1000–3000 cycles, while salt hydrates degrade rapidly due to phase segregation and water loss. Eutectic mixtures demonstrate intermediate behavior.

To quantitatively describe the degradation behavior of PCM under repeated thermal cycling, empirical models are frequently employed. One of the most widely used expressions for latent heat degradation is based on exponential decay, assuming that the reduction in thermal storage capacity follows a first-order degradation process:

$$\Delta H_f(N) = \Delta H_{f0} \cdot e^{-kN}$$

where: $\Delta H_f(N)$ is the latent heat of fusion after N thermal cycles, ΔH_{f0} is the initial latent heat (at N=0), k is the degradation rate constant (cycle^{-1}), N is the number of completed thermal cycles.

This model effectively captures the observed exponential trend in latent heat degradation, particularly in salt hydrates and eutectic materials. The parameter k can be experimentally identified via least squares fitting of DSC (Differential Scanning Calorimetry) data obtained after controlled cyclic aging tests.

For example, a PCM with an initial latent heat of 200 kJ/kg and a degradation constant $k=2.5\times10^{-4}$ will retain approximately 78% of its capacity after 1000 thermal cycles:

$$\Delta H_f(1000) = 200 \cdot e^{-0.00025 \cdot 1000} \approx 156.8\ kJ/kg$$

This corresponds closely with experimental trends observed in Figure 1, particularly for salt hydrates. For paraffins, the value of k is typically an order of magnitude lower, reflecting their higher thermal stability but lower thermal conductivity.

By integrating such empirical models into PCM reliability assessment, it becomes possible to:

- estimate the service life of a material under a given cycling regime;
- compare degradation rates across material types and compositions;
- establish predictive maintenance schedules based on thermal performance decay;
- and develop design margins for TES system capacity to compensate for gradual loss of storage efficiency.

Ultimately, combining experimental degradation profiles (as shown in Figure 1), failure thresholds (Table 2), and predictive models like the one above provides a robust foundation for engineering PCM-based TES systems with quantified reliability.

IV. Conclusions

The presented analysis highlights the dynamic degradation behavior of phase change materials (PCMs) under thermal cycling and provides a quantitative foundation for predicting their end-of-life based on latent heat retention. The empirical model, described by the exponential decay function $\Delta H_f(N) = \Delta H_{f0} \cdot e^{-kN}$, demonstrates good agreement with experimental trends for various PCM classes.

As observed in the experimental graph and model curves (see Figure 2), different PCM types exhibit distinct degradation profiles.

This radar chart provides a comparative assessment of three main classes of phase change materials (PCMs)—Paraffin, Salt Hydrate, and Eutectic Mixture—based on three key reliability-related criteria: thermal stability, heat storage capacity, and cycle life. Each axis represents a normalized score (0–10 scale), where higher values indicate superior performance.

- Paraffin shows strong thermal stability and long cycle life, making it a preferred choice for applications requiring durability, albeit with moderate latent heat.
- Salt Hydrate exhibits high heat capacity but suffers from poor stability and reduced cycle life due to issues like phase separation and supercooling.
- Eutectic Mixture offers a balanced profile, performing moderately well across all criteria, which makes it suitable for systems that require a compromise between capacity and longevity.

The diagram serves as a visual decision-making tool for selecting PCMs in reliability-critical thermal energy storage applications.

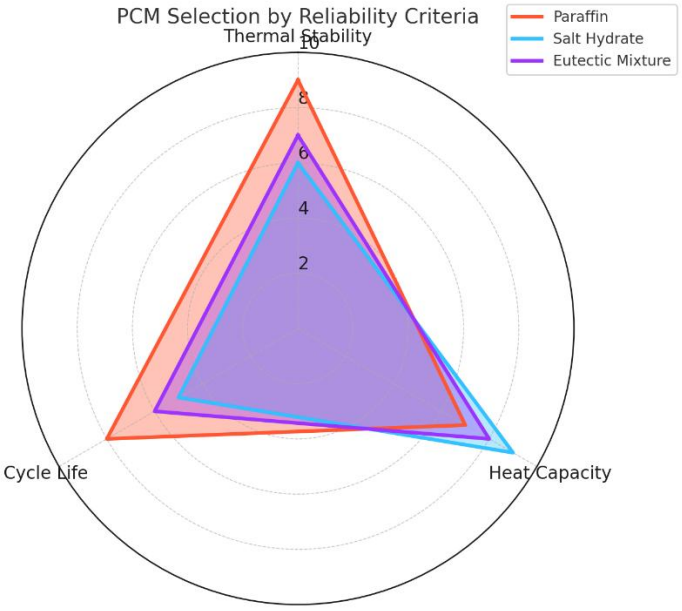


Figure 2.: *Reliability-Based Comparison of PCM Types Using Radar Diagram.*

These differences are also summarized in Table 2 (Failure Criteria for PCMs), which outlines key indicators such as melting point shift, phase separation, and heat capacity loss. Understanding these failure modes is essential for selecting the appropriate PCM for specific operational regimes.

Furthermore, the integration of the empirical degradation model allows for predictive maintenance and design optimization. By establishing a threshold (e.g., $\Delta H_f \leq 160$ kJ/kg) and solving for the corresponding cycle limit, engineers can define the effective service life of thermal energy storage units. For instance, with $k=2.5\times10^{-4}$, the material reaches this limit after approximately 892 cycles, enabling scheduling of inspections or replacements before functional failure occurs.

This modeling approach not only enhances the reliability-based design of PCM systems but also supports life-cycle cost analysis by quantifying degradation rates. Future studies may incorporate temperature-dependent k(T)), multi-cycle hysteresis, or mechanical fatigue for more comprehensive assessment.

In summary, the combination of empirical data, analytical modeling, and visual representation provides a robust methodology for evaluating and improving PCM reliability in long-term thermal applications.

This study integrates empirical degradation data with analytical reliability modeling, providing a robust framework for predicting the service life of phase change materials in thermal energy storage systems. By establishing failure thresholds and modeling degradation kinetics, the approach supports reliability-centered design, predictive maintenance, and lifecycle cost optimization. This contribution advances the reliability engineering of TES materials, facilitating more durable and efficient renewable energy storage solutions.

References

[1] Prieto, C., & Cabeza, L. F. (2019). Thermal energy storage (TES) with phase change materials (PCM) in solar power plants (CSP). Concept and plant performance. *Applied Energy*, *254*, 113646.

[2] Elkhatat, A., & Al-Muhtaseb, S. A. (2023). Combined "renewable energy–thermal energy storage (RE–TES)" systems: a review. *Energies*, *16*(11), 4471.

[3] Piriyeva, N. M., Karimova, R. K., & Abdullayeva, G. K. (2025, June). *High-temperature heat-insulating materials: A compromise between thermal conductivity and reliability*. *Reliability: Theory & Applications*, 2(84), 408–413. https://doi.org/10.24412/1932-2321-2025-284-408-413

[4] Kerimzade, G. S. (2025, March). *Features of hanging the parameters of induction control support*. *IJ TPE Journal*, 1, 69–80.

[5] Kerimzade, G. S. (2024). *Structure of the monitoring and tracking electromechanical control system*. *Przeglad Elektrotechniczny*, 100(7), 295–297.

[6] Rzayeva, S. V., Piriyeva, N. M., & Guseynova, I. A. (2024). *Analysis of reliability of typical power supply circuits*. *Reliability: Theory & Applications*, 19(3), 173–178.

[7] Piriyeva, N. M., Abdullayeva, G. K., & Bakhtiyarov, A. A. (2024). *Engineering approaches to minimizing environmental impact of thermal power plants*. *International Journal on Technical and Physical Problems of Engineering*, 16(4), 231–243.

[8] Safiyev, E., Rzayeva, S., & Karimova, R. (2024). *The importance of diagnostics of electrical equipment at thermal power plants for ensuring the reliability of power systems*. *Przeglad Elektrotechniczny*, 9, 127–130.

[9] Karimova, R. K., & Rzayeva, S. V. (2023). *Comparison of thermal conductivity of aqueous and formamide solutions ($BeCl_2$) at high temperatures*. *International Journal on Technical and Physical Problems of Engineering*, 15(3), 156–159.

[10] Sharma, R. K., Ganesan, P., & Tyagi, V. V. (2016). Long-term thermal and chemical reliability study of different organic phase change materials for thermal energy storage applications. *Journal of Thermal Analysis and Calorimetry*, *124*(3), 1357-1366.

ON THE TYPE II HALF-LOGISTIC GENERALIZED INVERSE WEIBULL DISTRIBUTION AND ITS APPLICATIONS

Saana Rafi Pathayappurakkal[1], Jabir Bengalath[2,*], Bindu Punathumparambath[3]

•

[1,2,3]Department of Statistics, Govt. Arts and Science College, Calicut,
University of Calicut, Kerala, India.

Email: saana.rafi7@gmail.com[1], ppbindukannan@gmail.com[3]

*Corresponding author: jabirbengu@gmail.com[2]

Abstract

Inverse Weibull distribution is frequently used in the survival and reliability analysis owing to its upside down bathtub type hazard function. Generalized inverse Weibull is the flexible generalization of inverse Weibull distribution which has increasing, decreasing and unimodal hazard rates. This paper introduces a novel extension of generalized inverse Weibull distribution which is developed using new type II half logistic generator. We introduced New type II half logistic generalized inverse Weibull distributions. Mathematical and statistical features of the newly derived distribution were examined. The point estimates of the unknown parameters were computed using maximum likelihood estimation, Weighted Least Square, Anderson-Darling and Cramer-von Mises estimator. We have conducted MCMC simulation using R package to validate the estimation algorithms. Finally, we demonstrated the usefulness of the proposed distribution using two real-world failure time data sets.

Keywords: Inverse Weibull distribution, Generalized inverse Weibull distribution, New Type II half Logistic G distribution, Order Statistics, point Estimation, upside down bathtub shape failure rate.

1. Introduction

Positive skewness and thicker tails are common in real-world data sets. Many academic fields have observed this discrepancy, including finance, economics, biology, engineering, reliability modelling, and environmental studies. Modell that fails to take into account the skewness present in that data may lead to accurate results. Decision-making procedures are affected in a lot of real-world situations by the existence of skewness in datasets. Developing adaptable and precise frameworks that can accurately capture the subtleties present in real-world datasets has long motivated statistical researchers to pursue the goal of modeling complex probabilistic phenomena. The continuous half logistic G (HL-G) family was first presented as a flexible distributional framework and has proven effective in modeling a variety of phenomena, including dependability modeling and financial data. In recent years, several new distributions were created by adding new parameters in the existing model. The newly developed probability models were found useful in capturing complex real-world phenomena. Currently there is lot of interest to generate new lifetime models exhibiting monotone and non-monotone failure rate properties having

numerous applications in the field of engineering and reliability modelling.

In this paper we concentrate on the half-logistic (HL) distribution (Balakrishnan, 1985) due to its simple structure, with single parameter and tractable characteristics.

A random variable X is said to have a one parameter HL Distribution with parameter α, if its probability density function (pdf) is given by

$$g(x;\alpha) = \frac{2\alpha e^{-\alpha x}}{(1+e^{-\alpha x})^2} \tag{1}$$

and the cumulative distribution function (cdf) is

$$G(x) = \frac{1-e^{-\alpha x}}{1+e^{-\alpha x}} \tag{2}$$

for all $x > 0$, where $\alpha > 0$.

One of the limitations of HL distribution is that it is not appropriate for modeling bimodal and left-skewed datasets. Some scholars have suggested alternative generalizations of the HL distribution in order to eliminate the drawbacks of this distribution. Cordeiro et al. [2] invented exponentiated half-logistic-G, type I half-logistic-G by Cordeiro et al. ([3]), Amal et al. ([4]) investigated type II half logistic G (TIIHL-G), by using the half logistic generator to obtain type II half logistic family and is denoted by TIIHLG.

TIIHLG ([4]) family can be expressed as follows,

$$F(x;\alpha,\zeta) = 1 - \int_0^{-log(G(x,\zeta))} \frac{2\alpha e^{-\alpha x}}{(1+e^{-\alpha x})^2}\, dt, \tag{3}$$

where $x > 0$, $\alpha > 0$ is the scale parameter and $G(x,\zeta)$ is the baseline cdf, which depends on a parameter vector ζ. The cdf in (3) gives the type II half logistic generated distribution.

After simplification (3) can be expressed as follows,

$$F(x) = \frac{2\,(G(x,\zeta))^{\alpha}}{1+(G(x,\zeta))^{\alpha}}, \quad x > 0, \tag{4}$$

and pdf can be defined as follows,

$$f(x) = \frac{2\alpha g(x,\zeta)\,(G(x,\zeta))^{\alpha-1}}{\left(1+(G(x,\zeta)^{\alpha}\right)^2}, \quad x > 0, \alpha > 0. \tag{5}$$

Amal et al. ([6]) proposed type II half logistic Weibull (TIIHLW) by taking Weibull as the baseline distribution in (4). Recently more flexible extension of TIIHLG is proposed by Altun et al. [7], referred to as New Type II Half Logistic-G (NTIIHLG) family of distributions. The cdf of NTIIHL G family can be expressed as follows

$$F(x;\alpha,\lambda,\zeta) = 1 - \int_0^{-log\left(\frac{G(x,\zeta)^{\lambda}}{G(x,\zeta)^{\lambda}+(1-G(x,\zeta))^{\lambda}}\right)} \frac{2\alpha e^{-\alpha x}}{(1+e^{-\alpha x})^2}\, dt, \tag{6}$$

where, $x > 0$, $\alpha > 0, \lambda > 0$ and $G(x,\zeta)$ is a baseline cdf, which depends on a parameter vector ζ. The distribution function (6) provides New type II half logistic generated distributions ([7]).

After simplification the cdf of NTIIHLG can written as follows,

$$F(x) = \frac{2G(x,\zeta)^{\alpha\lambda}}{G(x,\zeta)^{\alpha\lambda} + \left(G(x,\zeta)^{\alpha} + \bar{G}(x,\zeta)^{\alpha}\right)^{\lambda}}, \quad x > 0, \tag{7}$$

where $\alpha > 0, \lambda > 0$.

The pdf of NTIIHLG is given by,

$$f(x) = \frac{2\alpha\lambda g(x,\zeta)G(x,\zeta)^{\alpha\lambda-1}\bar{G}(x,\zeta)^{\alpha-1}\left(G(x,\zeta)^{\alpha}+\bar{G}(x,\zeta)^{\alpha}\right)^{\lambda-1}}{\left[G(x,\zeta)^{\alpha\lambda}+\left(G(x,\zeta)^{\alpha}+\bar{G}(x,\zeta)^{\alpha}\right)^{\lambda}\right]^2}, \quad x>0,\ \alpha>0. \tag{8}$$

In this study we derive new extension of one parameter inverse Weibull (IW) using New Type II Half Logistic-G family of distributions. The Weibull distribution was frequently utilized in survival and reliability analysis due to straightforward mathematical form. An Inverted version of the Weibull distribution called the Inverse Weibull distribution has been used to represent real-world occurrences since it has an inverted bathtub failure rate. Inverted bathtub failure rate distributions are frequently observed in medical and biological domains, such as in patient data related to lung cancer, bladder cancer, and leukemia ([1], [5]). Detailed study of Inverse Weibull distribution were found in Drapella [8], Mudholkar and Kollia [9] and Jiang et al. [10].

A random variable X is said to have a one parameter Inverse Weibull distribution with shape parameter β, if its probability density function (pdf) is given by

$$g(x;\beta) = \beta x^{-(\beta+1)}\mathrm{e}^{-x^{-\beta}}, \tag{9}$$

and the cumulative distribution function (cdf) is

$$G(x) = \mathrm{e}^{-x^{-\beta}}, \tag{10}$$

for all $x>0$ and $\beta>0$. Extension of IW distribution called generalized inverse Weibull (GIW) is discussed in de Gusmão et al. [11].

A random variable X is said to have two parameter Generalized Inverse Weibull distribution with parameters $\alpha,\ \beta$, if its probability density function (pdf) is given by

$$g(x;\alpha,\beta) = \alpha\beta x^{-(\beta+1)}\mathrm{e}^{-\alpha x^{-\beta}}, \tag{11}$$

and the cumulative distribution function (cdf) is

$$G(x) = \mathrm{e}^{-\alpha x^{-\beta}}, \tag{12}$$

for all $x>0$ and $\alpha,\ \beta>0$. In this paper we study a new extension of inverse Weibull distribution called New Type II Half Logistic- Generalized inverse Weibull (NTIIHLGIW) family of distribution to model lifetime data or survival data. Motivation behind introducing this new family with three parameters is that it provide more flexibility to handle complex data sets arising from variety of fields.

The paper is organized as follows: Section 2 describes the NTIIHLGIW distribution, whereas section 3 illustrate various statistical and mathematical properties, which include the hazard function, quantile function, skewness, kurtosis, moments, moment generating function, characteristics function, etc. We derive the distribution of the Order Statistics in section 4. Section 5 investigate the different methods of estimation including maximum likelihood estimation, weighted least square, Andarson-darling and Cramer Von approach. Section 6 describe the simulation study to validate the proposed model estimation procedures and two real data sets are analysed to demonstrate the efficiency of the proposed model in section 7. The concluding remarks were provided in Section 8.

2. New Type II Half Logistic Generalized Inverse Weibull Distribution

A random variable X is said to have New Type II Half Logistic- Generalized Inverse Weibull (NTIIHLGIW) with parameters $(\alpha,\beta,\lambda,\gamma)$ denoted by $X\sim NTIIHLGIW(\alpha,\beta,\lambda,\gamma)$ if its pdf is given by,

$$f(x) = \frac{2\alpha\beta\lambda\gamma x^{-(\beta+1)}(\mathrm{e}^{-\gamma x^{-\beta}})^{\alpha\lambda}(1-\mathrm{e}^{-\gamma x^{-\beta}})^{\alpha-1}\left((\mathrm{e}^{-\gamma x^{-\beta}})^{\alpha}+(1-\mathrm{e}^{-\gamma x^{-\beta}})^{\alpha}\right)^{\lambda-1}}{\left[(\mathrm{e}^{-\gamma x^{-\beta}})^{\alpha\lambda}+\left((\mathrm{e}^{-\gamma x^{-\beta}})^{\alpha}+(1-\mathrm{e}^{-\gamma x^{-\beta}})^{\alpha}\right)^{\lambda}\right]^2}, \quad x>0, \tag{13}$$

and its cdf is,

$$F(x) = \frac{2(e^{-\gamma x^{-\beta}})^{\alpha\lambda}}{(e^{-\gamma x^{-\beta}})^{\alpha\lambda} + \left((e^{-\gamma x^{-\beta}})^{\alpha} + (1 - e^{-\gamma x^{-\beta}})^{\alpha}\right)^{\lambda}}, \quad x > 0, \tag{14}$$

for all $x > 0$, $\alpha,\ \beta\ \lambda,\ \gamma > 0$.

The plots of the pdf and cdf of the NTIIHLGIW $(\alpha,\ \beta\ \lambda,\ \gamma)$ distribution for particular values of its parameters are presented in Fig.1 and Fig. 2 respectively.

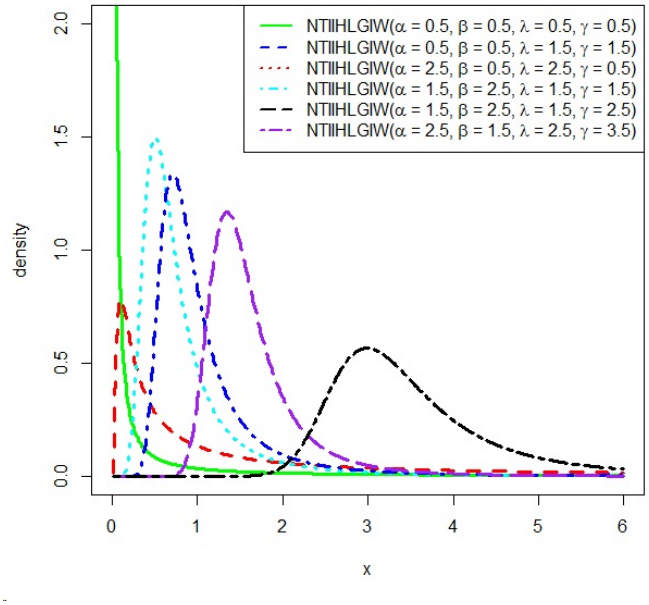


Figure 1: *Plot of pdf of NTIIHLGIW for different parameter values*

Theorem 1. Given that X follows the NTIIHLGIW $(\alpha, \beta, \lambda, \gamma)$ distribution with pdf $f(x)$ and cdf $F(x)$ as given in (13 and (14) respectively, then: 1. $\lim_{x\to\pm\infty} f(x) = 0$, and 2. $\lim_{x\to\pm\infty} F(x) = 1$.

Proof. Trivial and hence it is omitted. ■

3. Mathematical and reliability properties

It is important to understand the mathematical properties of probability distributions for a number of reasons. First off, these qualities make it possible to create a number of statistical measurements that characterize a random variable's behavior. We outline some mathematical and reliability properties of the NTIIHLGIW distribution.

3.1. Survival Function

The survival function describes the probability that an item or individual will survive past a certain time. A survival function can be expressed as $S(x) = 1 - F(x)$,

$$S(x) = \frac{\left((e^{-\gamma x^{-\beta}})^{\alpha} + (1 - e^{-\gamma x^{-\beta}})^{\alpha}\right)^{\lambda} - (e^{-\gamma x^{-\beta}})^{\alpha\lambda}}{\left((e^{-\gamma x^{-\beta}})^{\alpha} + (1 - e^{-\gamma x^{-\beta}})^{\alpha}\right)^{\lambda} + (e^{-\gamma x^{-\beta}})^{\alpha\lambda}}, \quad x > 0. \tag{15}$$

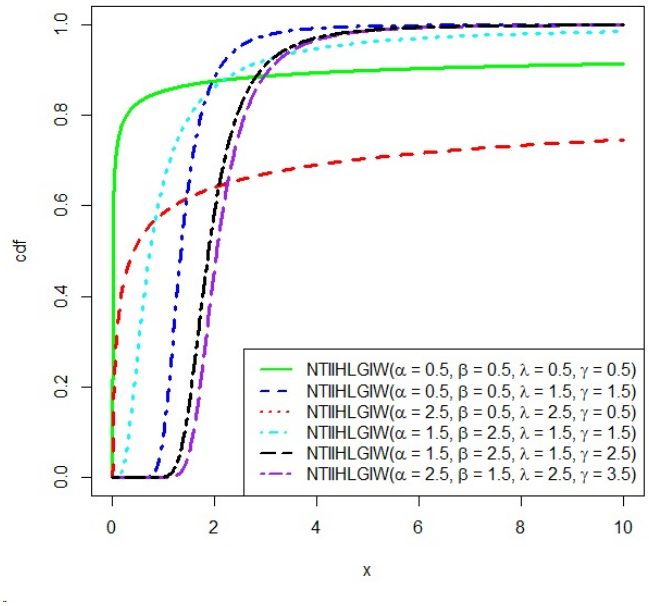


Figure 2: *Plot of cdf of NTIIHLGIW for different parameter values*

The plots of the sf and hf of the NTIIHLIW $(\alpha,\ \beta\ \lambda,\ \gamma)$ distribution for particular values of its parameters are presented in Fig.3 and Fig. 4 respectively. Fig. 4 demonstrates that the hf of NTIIHLGIW has reversed-J shape as well as an upside-down bathtub (UBT) shape.

3.2. Hazard Function

The hazard function (hf) is given by $h(x) = \frac{f(x)}{1-F(x)}$, is the instantaneous rate at which a component will fail given that it has already survived a length of time x. For the cdf and pdf given in Eq.(14) and (13), respectively, $h(x)$ takes the form:

$$h(x) = \frac{2\alpha\beta\lambda\gamma x^{-(\beta+1)}(\mathrm{e}^{-\gamma x^{-\beta}})^{\alpha}(1-\mathrm{e}^{-\gamma x^{-\beta}})^{\alpha-1}\left((\mathrm{e}^{-\gamma x^{-\beta}})^{\alpha}+(1-\mathrm{e}^{-\gamma x^{-\beta}})^{\alpha}\right)^{\lambda-1}}{\left((1-\mathrm{e}^{-\gamma x^{-\beta}})^{\alpha}+(1-\mathrm{e}^{-\gamma x^{-\beta}})^{\alpha}\right)^{2\lambda}-(1-\mathrm{e}^{-\gamma x^{-\beta}})^{2\alpha\lambda}},\quad x>0. \quad (16)$$

Theorem 2. The limit of the hazard rate function of the NTIIHLGIW(α, β, λ, γ) distribution as $t \to \pm\infty$ is zero:

$$\lim_{t\to\pm\infty} h(t) = 0.$$

Proof. Trivial and hence it is omitted. ■

3.3. Reverse Hazard Function

The Revised Hazard Function $r(x) = \frac{f(x)}{F(x)}$ is given by,

$$r(x) = \frac{\alpha\beta\lambda\gamma x^{-(\beta+1)}(1-\mathrm{e}^{-\gamma x^{-\beta}})^{\alpha-1}\left((\mathrm{e}^{-\gamma x^{-\beta}})^{\alpha}+(1-\mathrm{e}^{-\gamma x^{-\beta}})^{\alpha}\right)^{\lambda-1}}{\left[(\mathrm{e}^{-\gamma x^{-\beta}})^{\alpha\lambda}+\left((\mathrm{e}^{-\gamma x^{-\beta}})^{\alpha}+(1-\mathrm{e}^{-\gamma x^{-\beta}})^{\alpha}\right)^{\lambda}\right]},\quad x>0. \quad (17)$$

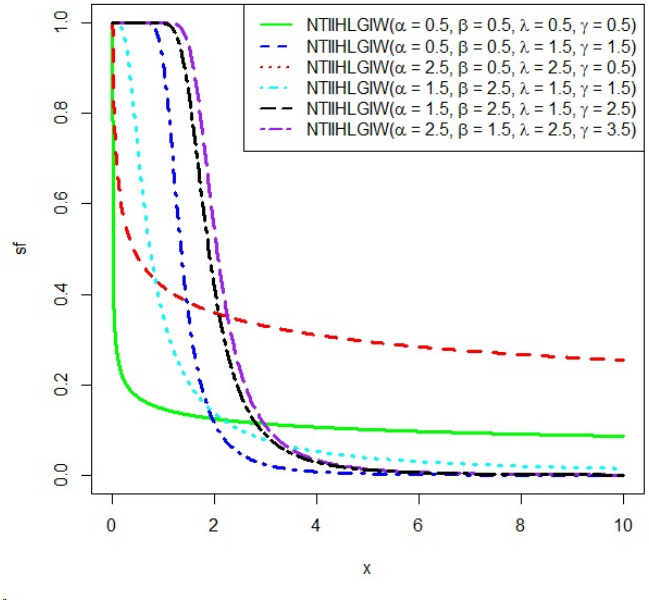


Figure 3: *Survival plot of NTIIHLGIW distribution for different parameter values*

The plots of the rhf and of of the NTIIHLIW $(\alpha,\ \beta\ \lambda,\ \gamma)$ distribution for particular values of its parameters are presented in Fig.5 and Fig. 6 respectively.

3.4. Cumulative Hazard Function

The Cumulative Hazard Function, $H(x) = -log(S(x))$ is obtained using the relation,

$$H(x) = -log\left[\frac{\left((e^{-\gamma x^{-\beta}})^{\alpha} + (1-e^{-\gamma x^{-\beta}})^{\alpha}\right)^{\lambda} - (e^{-\gamma x^{-\beta}})^{\alpha\lambda}}{\left((1-e^{-\gamma x^{-\beta}})^{\alpha} + (1-e^{-\gamma x^{-\beta}})^{\alpha}\right)^{\lambda} + (e^{-\gamma x^{-\beta}})^{\alpha\lambda}}\right], \tag{18}$$

where log refers to natural logarithm.

3.5. The Odd Function

The Odd Function is obtained using the relation $Q(x) = \frac{F(x)}{S(x)}$ and is given by

$$O(x) = \frac{2e^{-\gamma x^{-\beta}})^{\alpha\lambda}}{\left((e^{-\gamma x^{-\beta}})^{\alpha} + (1-e^{-\gamma x^{-\beta}})^{\alpha}\right)^{\lambda} - (e^{-\gamma x^{-\beta}})^{\alpha\lambda}}. \tag{19}$$

3.6. Quantile Function, Median, Skewness and Kurtosis

The q^{th} quantile function of the NTIIHLG distribution is given by

$$\xi_q = Q_G\left(\frac{q^{\frac{1}{\alpha\lambda}}}{q^{\frac{1}{\alpha\lambda}} + \left(1+(1-q)^{\frac{1}{\lambda}} - q^{\frac{1}{\lambda}}\right)^{\frac{1}{\alpha}}}\right). \tag{20}$$

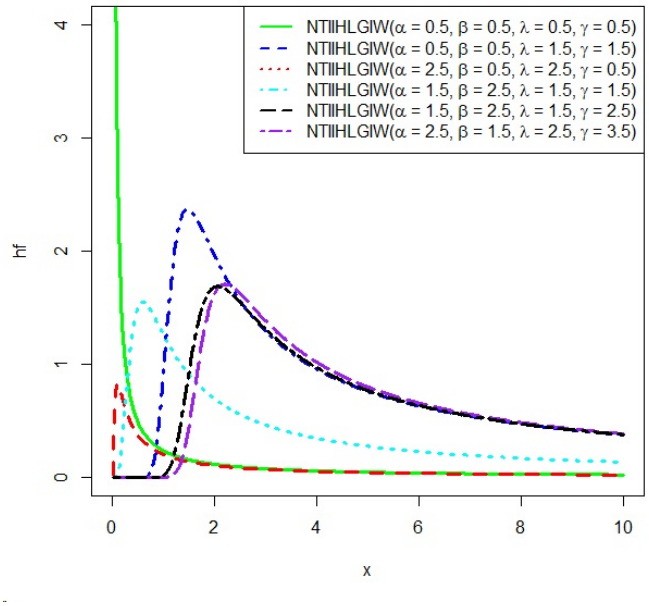


Figure 4: *Hazard plot of NTIIHLGIW distribution for different parameter values*

where, where $Q_G(q)$ is the baseline quantile function, q is a uniform distribution on the interval (0,1). Then the q^{th} quantile function of the NTIIHLGIW distribution is given by

$$X_q = \alpha \left(-\frac{1}{\gamma} \log \left(\frac{q^{\frac{1}{\alpha\lambda}}}{q^{\frac{1}{\alpha\lambda}} + \left(1 + (1-q)^{\frac{1}{\lambda}} - q^{\frac{1}{\lambda}}\right)^{\frac{1}{\alpha}}} \right) \right)^{-\frac{1}{\beta}}. \tag{21}$$

By utilizing equation (21), we can compute the first and third quartiles by substituting $q = 0.25$ and $q = 0.75$, respectively.

The median can be obtained as,

$$x_{0.5} = \alpha \left[-\frac{1}{\gamma} \log \left(\frac{0.5^{\frac{1}{\alpha\lambda}}}{0.5^{\frac{1}{\alpha\lambda}} + 1} \right) \right]^{-\frac{1}{\beta}}. \tag{22}$$

By utilizing equation (21), we can compute Galton's [22] skewness (S_k) and Moor's[23] Kurtosis (K). The measure of skewness (S_k) is given by

$$S_k = \frac{Q(6/8) - 2Q(4/8) + Q(2/8)}{Q(6/8) - Q(2/8)}, \tag{23}$$

and the measure of Kurtosis,

$$K = \frac{Q(7/8) - Q(5/8) + Q(3/8) - Q(1/8)}{Q(6/8) - Q(2/8)}. \tag{24}$$

3.7. Moments

Now we derive the r^{th} raw moment of NTIIHLGIW using the power series representation of NTIIHLG family derived by Altun et al. [7]. If the pdf given by a random variable X in equation

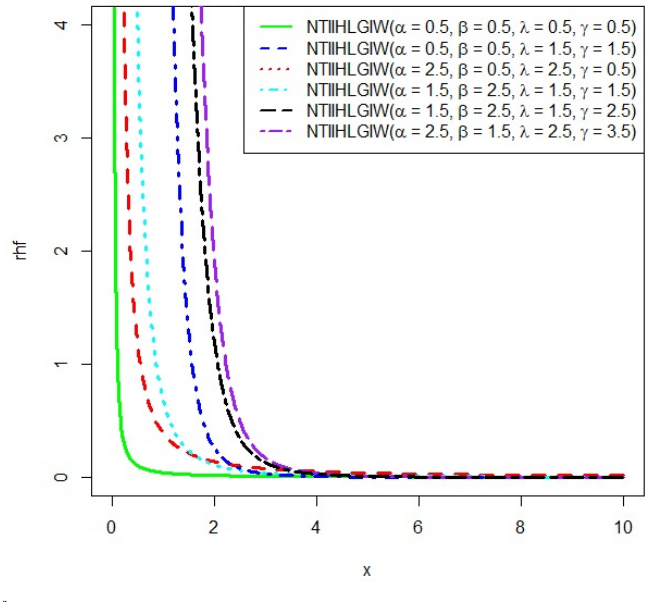


Figure 5: *Plot of rhf of NTIIHLGIW distribution for different parameter values*

13, then the corresponding r^{th}moment is given by:

$$\begin{aligned}\mu'_r &= E(x^r)\\ &= \int_0^\infty x^r f(x)dx\\ &= \sum_{r,h=0}^{\infty} c_{k+1}\frac{(k+1)(-1)^h\gamma^{\frac{r}{\beta}}\alpha^r\binom{k}{h}\Gamma\left(1-\frac{r}{\beta}\right)}{(h+1)^{\left(1-\frac{r}{\beta}\right)}}, r<\beta,\end{aligned}$$

where c_k ia as in Altun et al. [7] and is given by,

$c_{k+1} = \frac{1}{b_0}\left[a_{k+1} - \frac{1}{b_0}\sum_{r=1}^{k} b_r c_{k-r}\right]$, $c_0 = \frac{a_0}{b_0}$, $a_k = 2\sum_{j=k}^{\infty}(-1)^{k+j}\binom{\alpha\lambda}{j}\binom{j}{k}$, $b_k = \frac{a_k}{2} + h_k(\lambda)$ and h(x) is the pdf of exponentiated generalized inverse Weibull distribution.

3.8. Moment Generating Functions

Let X be a random variable having the pdf defined in equation (13) then its Moment Generating Function (mgf) is given by

$$\begin{aligned}M_X(t) &= E[e^{tX}]\\ &= \int_0^\infty e^{tx} f(x)\,dx.\end{aligned}$$

The mgf of NTIIHLGIW distribution is given by

$$M_x(t) = \sum_{r,h=0}^{\infty} c_{k+1}\frac{(k+1)(-1)^h t^r\gamma^{\frac{r}{\beta}}\alpha^r\binom{k}{h}\Gamma\left(1-\frac{r}{\beta}\right)}{(h+1)^{\left(1-\frac{r}{\beta}\right)}}, r<\beta. \tag{25}$$

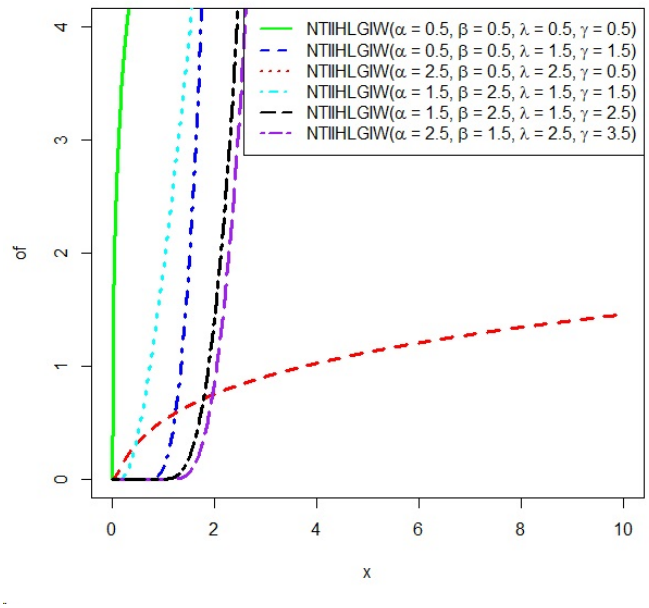


Figure 6: *Plot of Odd function of NTIIHLGIW distribution for different parameter values*

4. Order Statistics

In this section, we derive the pdf of the r^{th} order statistic of the NTIIHLGIW distribution. Order statistics have applications in system reliability. Let $X_1, X_2, X_3, ..., X_n$ be a simple random sample from the NTIIHLGIW distribution with cdf and pdf given by equation (14) and (13), respectively, and let $X_{1:n} \leq X_{2:n} \leq X_{3:n} \leq ... \leq X_{n:n}$, denote the order statistics obtained from this sample. We now give the pdf of $X_{r:n}$ say $f_{r:n}(x)$ is given by

$$f_{r:n}(x) = B_{r:n} \left[F(x;\alpha,\beta,\lambda,\gamma)\right]^{r-1} \left[1 - F(x;\alpha,\beta,\lambda,\gamma)\right]^{n-r} f(x;\alpha,\beta,\lambda,\gamma). \tag{26}$$

For all $x > 0$, where F and f are given by equation (14) and equation (13) respectively, and $B_{r:n} = \frac{n!}{(n-1)!(n-r)!}$. Thus, using binomial series expansion,

$$(1-x)^{\alpha-1} = \sum_{j=0}^{\infty} (-1)^j \binom{\alpha-1}{j} x^j.$$

We obtain,

$$f_{r:n}(x) = C_{r:n} \sum_{s=0}^{\infty} (-1)^s \binom{n-r}{s} \left[F(x;\alpha,\beta,\lambda,\gamma)\right]^{r+s-1} f(x;\alpha,\beta,\lambda,\gamma). \tag{27}$$

The cdf of the r^{th} order statistics is given by

$$\begin{aligned} F_{r:n}(x) &= \sum_{i=r}^{n} \binom{n}{i} (F(x))^i (1-F(x))^{n-i} \\ &= \sum_{i=r}^{n} \sum_{j=0}^{n-i} (-1)^j \binom{n}{i} \binom{n-i}{j} (F(x))^{i+j}. \end{aligned} \tag{28}$$

Inserting cdf Equation (14) in Equation (28), we get the cdf of the r^{th} order statistics of NTIIHLGIW distribution. The pdf of the smallest order statistics $X_{1:n}$ is obtained from Equation (27), by putting

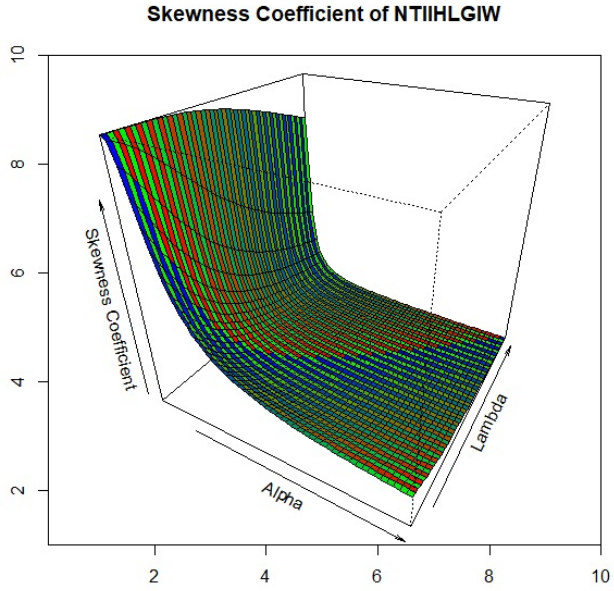


Figure 7: *Plot of skewness NTIIHLGIW distribution for* $\beta = 0.5$ *and* $\gamma = 0.5$

$r = 1$. Also, the pdf of the largest order statistics $X_{n:n}$ can be obtained from Equation (27), by putting $r = n$.

The pdf of joint distribution of r^{th} and s^{th} order statistics are given by,

$$f_{r:s:n}(x) = B_{r:s:n}\left[F(x_r)\right]^{r-1}\left[F(x_r s) - F(x_r)\right]^{s-r-1}\left[1 - F(x_s)\right]^{n-r} f(x_r) f(x_s), \tag{29}$$

where $B_{r:s:n} = \frac{n!}{(r-1)!(s-r-1)!(n-s)!}$.

5. Methods of Estimation

5.1. Maximum likelihood Estimation

Let X be a random variable with the pdf of the NTIIHLGIW distribution defined in equation (13) then its log-likelihood function is defined by:

$$\begin{aligned} L(x;\alpha,\beta,\lambda,\gamma) &= n\log 2 + n\log\alpha + n\log\beta + n\log\lambda + n\log\gamma - (\beta+1)\sum_{i=1}^{n}\log x_i + \alpha\lambda\sum_{i=1}^{n}\log g(x_i) \\ &+ (\alpha-1)\sum_{i=1}^{n}\log(1-G(x_i)) + (\lambda-1)\sum_{i=1}^{n}\log\left(g(x_i)^{\alpha} + (1-g(x_i))^{\alpha}\right) \\ &- 2\sum_{i=0}^{\infty}\log\left(g(x_i)^{\alpha\lambda} + (g(x_i)^{\alpha} + (1-g(x_i))^{\alpha})^{\lambda}\right), \end{aligned} \tag{30}$$

where $g(x_i) = \mathrm{e}^{-\gamma x^{-\beta}}$. The MLE's $\hat{\alpha}_{MLE}$, $\hat{\beta}_{MLE}$, $\hat{\lambda}_{MLE}$ and $\hat{\gamma}_{MLE}$ were obtained by maximizing the likelihood function in Equation (30) numerically by using packages like "Adequacy" and "MaxLik" packages available in the R statistical software. We applied PSO and the Optim function of BFGS algorithm of Nash [14] in R [15].

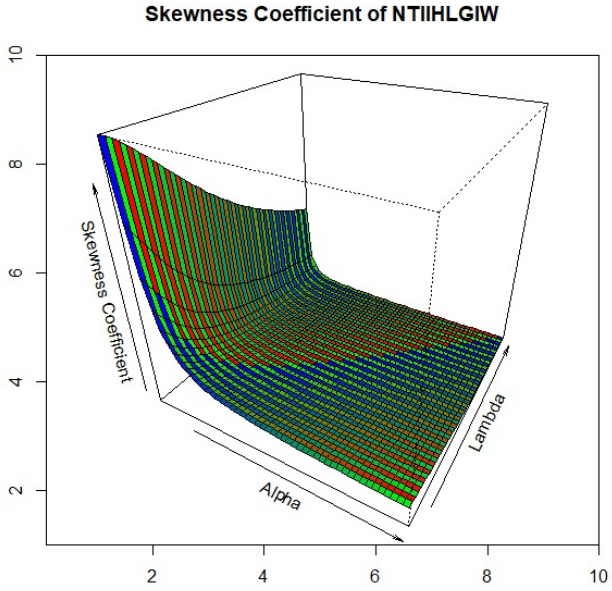


Figure 8: *Plot of skewness NTIIHLGIW distribution for* $\beta = 2.5$ *and* $\gamma = 0.5$

5.2. Least square estimation

The method of Least square estimation was proposed by Adrien-Marie Legendre [12] to determine the unknown parameters. Let $X_1, X_2, X_3, ..., X_n$, as the random sample of size n, taken from a continuous distribution function, then let $X_{(1)} \leq X_{(2)} \leq X_{(3)} \leq ... \leq X_{(n)}$ be its corresponding order statistics. Then the expected value and variance of the empirical cumulative distribution function (ecdf) are defined as follows,

$$E\big(F(X_{(i)}\big) = \frac{i}{n+1}, \qquad i = 1, 2, ..., n \tag{31}$$

$$Var\big(F(X_{(i)}\big) = \frac{i(n-i+1)}{(n+1)^2(n+2)}, \qquad i = 1, 2, ..., n. \tag{32}$$

The least square estimators (LSE) of the unknown parameters of NTIIHLGIW can be obtained by minimizing $S = \sum_{i=1}^{n} \left(F(X_{(i)}) - \frac{i}{n+1}) \right)^2$ with respect to the unknown parameters of NTIIHLGIW.

5.3. Weighted Least Square

The weighted Least Square estimators (WLSE) for estimating the unknown parameters of the NTIIHLGIW can be obtained by minimising the following equation

$$S = \sum_{i=1}^{n} W_i \left(F(X_{(i)}) - \frac{i}{n+1}) \right)^2,$$

where $W_i = 1$ for all $i = 1, 2, ..., n$ in case of LSE method and $W_i = \frac{1}{Var\left(F(X_{(i)})\right)}$ in Equation (32).

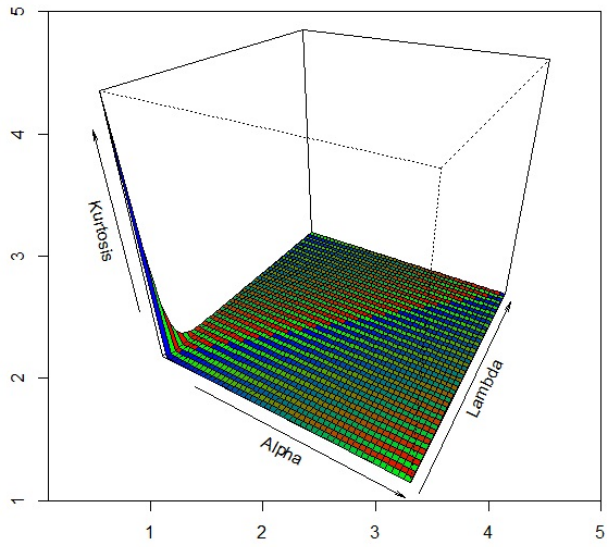


Figure 9: *Plot of Kurtosis NTIIHLGIW distribution for* $\beta = 0.5$ *and* $\gamma = 0.5$

6. Simulation Study and Data Analysis

6.1. Simulation Study

In this section, simulation study is conducted to check the performance of the estimation algorithms. For this, we consider $\alpha = 1$, $\beta = 0.5$, $\lambda = 1$ and $\gamma = 1.5$. We simulate data from NTIIHLGIW model for different sample sizes $n = 50, 100$ and 250, calculate for MLE, LSE and WLSE estimates. The result is listed in Table 1. Here, we can see that as the n increases, mean squared error (MSE) decreases also bias is decreases. From Table 1 we can see that the MLE method performs good for estimating the parameters of NTIIHLGIW distribution compared to LSE and WLSE methods.

6.2. Data Analysis

In this section, we demonstrate the usefulnesss of the proposed $NTIIHLGIW(\alpha, \beta, \lambda, \gamma)$ distribution. We fit this distribution to two real life data set and compare the results with some recent efficient models those corresponding to the Generalized inverse Weibull distribution, Transmuted Inverse Weibull distribution, TIIHLIW and TIIHLGIW. The corresponding pdf are presented below:

- Inverse Generalized Weibull Distributions:

$$f(x, \alpha, \beta, \lambda) = \alpha\beta\lambda^{\beta} e^{-\left(\frac{\lambda}{x}\right)^{\beta}} x^{-(\beta+1)} \left(1 - e^{-\left(\frac{\lambda}{x}\right)^{\beta}}\right)^{\alpha-1}.$$

- Generalized Inverse Generalized Weibul Distribution:

$$f(x, \alpha, \beta, \lambda, \gamma) = \alpha\beta\gamma\lambda^{\beta} e^{-\gamma\left(\frac{\lambda}{x}\right)^{\beta}} x^{-(\beta+1)} \left(1 - e^{-\gamma\left(\frac{\lambda}{x}\right)^{\beta}}\right)^{\alpha-1}, .$$

Data Set 1: This data set has been taken from ([21]).The data on survival of 40 patients suffering from leukemia, from the Ministry of Health Hospitals in Saudi Arabia taken from Abouammoh

Table 1: *Simulation study for* $\alpha = 1$, $\beta = 0.5$, $\lambda = 1.5$ *and* $\gamma = 0.5$ *for sample sizes 50, 100 and 250.*

n	Parameter	Method	Bias	MSE
50	α	MLE	0.101	0.069
		LSE	-0.114	0.086
		WLSE	-0.108	0.071
	β	MLE	0.078	0.041
		LSE	-0.091	0.083
		WLSE	-0.088	0.062
	λ	MLE	0.094	0.088
		LSE	0.098	0.101
		WLSE	0.098	0.097
	γ	MLE	0.038	0.025
		LSE	-0.046	0.062
		WLSE	-0.041	0.059
100	α	MLE	0.027	0.015
		LSE	-0.036	0.024
		WLSE	-0.027	0.023
	β	MLE	0.012	0.004
		LSE	0.021	0.014
		WLSE	0.018	0.012
	λ	MLE	0.021	0.015
		LSE	-0.028	0.024
		WLSE	-0.024	0.016
	γ	MLE	0.013	0.009
		LSE	0.021	0.026
		WLSE	0.016	0.019
250	α	MLE	0.003	0.002
		LSE	0.008	0.003
		WLSE	0.005	0.003
	β	MLE	0.002	0.003
		LSE	0.003	0.004
		WLSE	0.003	0.004
	λ	MLE	0.005	0.006
		LSE	0.008	0.011
		WLSE	0.005	0.008
	γ	MLE	0.002	0.003
		LSE	0.004	0.003
		WLSE	0.003	0.003

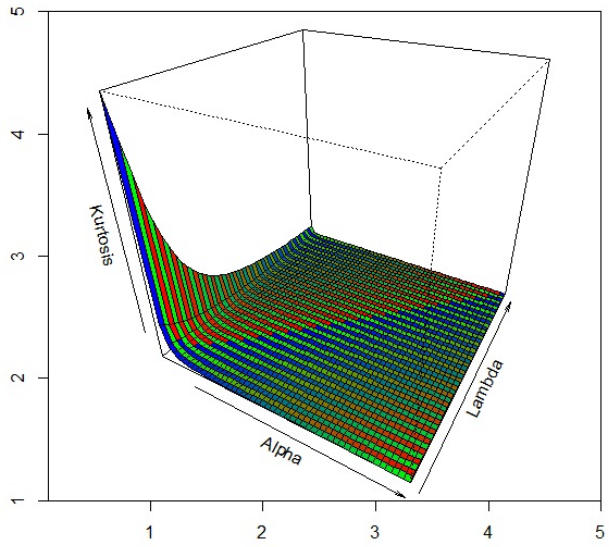


Figure 10: *Plot of Kurtosis NTIIHLGIW distribution for* $\beta = 2.5$ *and* $\gamma = 0.5$

et al. (1994):

115	181	255	418	441	461	516	739	743	789	807	865	924	983
1024	1062	1063	1165	1191	1222	1222	1251	1277	1290	1357	1369	1408	1455
1478	1549	1578	1578	1599	1603	1605	1696	1735	1799	1815	1852.		

Table 2: *Estimates and Goodness-of-fit measures based on AIC,BIC,AICC and CAIC for Data Set 1*

Distribution	**Estimates**	**Log-Likelihood**	**AIC**	**BIC**	**AICC**	**CAIC**
NTIIHLGIW	$\alpha = 64.3676$	-326.9782	629.9564	655.023	660.623	665.023
	$\beta = 10.69195$					
	$\theta = 740.11404$					
TIIHLIW	$\alpha = 0.042609$	-346.17	698.3402	703.4068	699.006	703.4068
	$\beta = 11.354601$					
	$\theta = 123.703578$					
TGIW	$\alpha = 0.03236$	-367.4545	742.9098	749.664	744.0518	749.6644
	$\beta = 8.30675$					
	$\theta = 14.26147$					
	$c = 47.2107282$					
GIW	$\alpha = 0.03236$	-367.4545	742.9098	749.664	744.0518	749.6644
	$\beta = 8.30675$					
	$\theta = 14.26147$					
	$c = 47.2107282$					

From Table 2, it shows that the proposed NTIIHLGIW distribution model has the lowest AIC, BIC, AICC, and CAIC values among the other distributions, it suggesting that it provides the best

fit to the dataset.

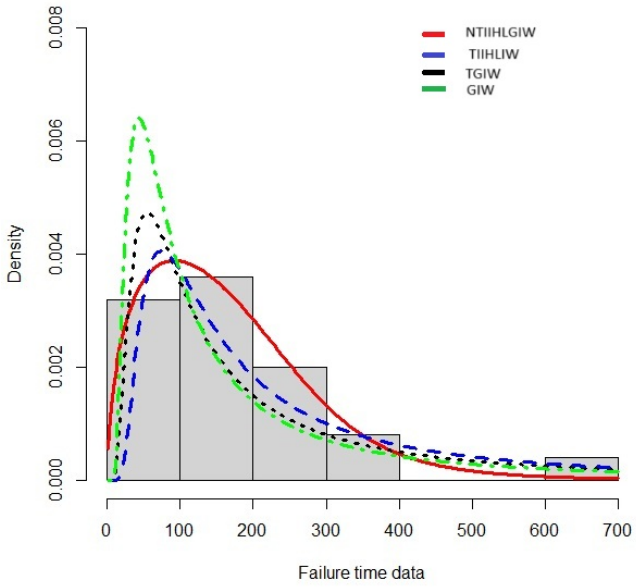


Figure 11: *Plot of fitted pdf of NTIIHLGIW distribution for data set 1*

Data set 2: This data set represents survival times in Days, from a Two-Arm Clinical Trial considered by [25] and [24] . The survival time in days for the 31 patients from Arm B are :

37	84	92	94	110	112	119	127	130	133	140	146	155	159	173	179
194	195	209	249	281	319	339	432	469	519	633	725	817	1557	1776	

.

Table 3: *Estimates and Goodness-of-fit measures based on AIC,BIC,AICC and CAIC for Data Set 2*

Distribution	**Estimates**	**Log-Likelihood**	**AIC**	**BIC**	**AICC**	**CAIC**
NTIIHLGIW	$\alpha = 23.0618$	-206.6578	419.3155	423.6175	420.2044	423.6175
	$\beta = -0.3304$					
	$\lambda = 303.1340$					
	$\gamma = 303.1340$					
TIIHLIW	$\alpha = 0.0596$	-217.3668	440.7335	445.0355	441.6224	445.03
	$\beta = 9.8165$					
	$\lambda = 40.5081$					
TGIW	$\alpha = 0.0596$	-217.3668	440.7335	445.0355	441.6224	445.03
	$\beta = 9.8165$					
	$\lambda = 40.5081$					
GIW	$\alpha = 0.6665$	-217.0158	442.0317	447.7676	443.5701	447.7676
	$\beta = 8.8546$					
	$\theta = 40.9719$					
	$c = 1.0867$					

From Table 3, We can see that our model NTIIHLGIW has Minimum AIC, BIC, AICC, and CAIC values than TIIHLIW, TGW and GIW distributions. So we can conclude that the newly proposed model is a better fit for the given data compared to other models.

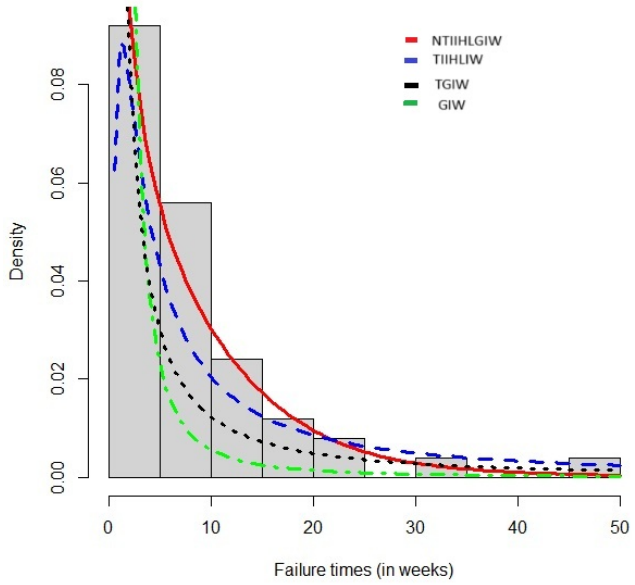


Figure 12: *Plot of fitted pdf of NTIIHLGIW distribution for data set 2*

7. Conclusions

The present research work introduced new flexible extension of Inverse Weibull distribution called new type II half logistic generalized Inverse Weibull distribution. The NTIIHLGIW distribution's structural features and reliability measures have been derived and examined. To estimate the distribution's parameters, a maximum likelihood estimation, lease square and weighted least square estimation methods were used. For the simulated data set, the results are shown in table 2. We can see that the estimated values obtained are near to the predefined parameters and that as n increases, MSE decreases, confirming the law of large numbers. We to illustrate the usefulness of NTIIHLGIW we used two real-life data sets and it shows that the NTIIHLGIW distribution has better fit than other competing models GIW, TGIW and TIIHLIW distribution by using Goodness of fit based on AIC,BIC,AICC and CAIC.

Conflict of Interest
The authors declare that they have no conflict of interest.

References

[1] Elisa, T. Lee, & John Wang (2003). Statistical methods for survival data analysis, *John Wiley & Sons, Inc.*, Third edition.
[2] Cordeiro, G. M., Alizadeh, M. & Ortega, E. M. (2014). The exponentiated half-logistic family of distributions: Properties and applications. *Journal of Probability and Statistics*.
[3] Cordeiro, G. M., Alizadeh, M. & Diniz Marinho, P. R. (2016). The type I half-logistic family of distributions. *Journal of Statistical Computation and Simulation*, 86 (4), 707-728.
[4] Hassan, A. S., Elgarhy, M., & Shakil, M. (2017). Type II half Logistic family of distributions with applications. *Pakistan Journal of Statistics & Operation Research*, 13(2), 245-264.

[5] Bengalath, J., & Punathumparambath, B. (2023). A novel extension of inverse exponential distributions: A heavy-tailed model with upside down bathtub shaped hazard rate. *Reliability: Theory & Applications*, 18(4 (76)), 112–127.
[6] Hassan, A. S., Elgarhy, M., Haq, M. A., & Alrajhi, S. (2019). On type II half logistic Weibull distribution with applications. *Mathematical Theory and Modeling*, 19, 49–63.
[7] Altun, E., Alizadeh, M., Yousof, H., Rasekhi, M., & Hamedani, G. G. (2021). A New Type II Half Logistic-G family of Distributions with Properties, Regression Models, System Reliability and Applications, *Applications and Applied Mathematics: An International Journal (AAM)*, 16 (2), 823–843.
[8] Drapella, A. (1993). Complementary Weibull distribution: unknown or just forgotten. *Quality and reliability engineering international*, 9, 383–385.
[9] Mudholkar GS, Kollia GD (1994) Generalized Weibull family: a structural analysis. *Communications in statistics-theory and methods*, 23, 1149–1171.
[10] Jiang R, Zuo MJ, Li HX (1999) Weibull and Weibull inverse mixture models allowing negative weights. *Reliability Engineering & System Safety*, 66, 227–234.
[11] de Gusmão, F.R.S., Ortega, E.M.M. & Cordeiro, G.M. (2011). The generalized inverse Weibull distribution. *Statistical Papers*, 52, 591–619.
[12] Merriman, M. (1877). *A List of Writings Relating to the Method of Least Squares: With Historical and Critical Notes* (Vol. 4). Academy.
[13] Henningsen A., Toomet O. maxLik: A package for maximum likelihood estimation in R . Comput Stat. 2011; 26(3):4–458
[14] Nash JC. Compact Numerical Methods for Computers: Linear Algebra and Function Minimisation. New York: Routledge; 1979.
[15] R Core Team. R: A language and environment for statistical computing. R Foundation for Statistical Computing, Vienna: Austria; 2020. Available from: `www.r-project.org`.
[16] Cordeiro, G. M., Ortega, E. M. M., & Da-Cunha, D. C. C. (2013). The exponentiated generalized class of distributions. *Journal of Data Science*, 11, 777-803.
[17] Alzaatreh, A., Lee, C., & Famoye, F. (2013). A new method for generating families of continuous distributions. *Metron*, 71, 63-79.
[18] Cordeiro, G. M., Afify, A. Z., Yousof, H. M., et al. (2017). The exponentiated Weibull-H family of distributions: Theory and applications. *Mediterranean Journal of Mathematics*, 14, 1-22.
[19] Keller, A. Z., & Kamath, A. R. (1982). Reliability analysis of CNC Machine Tools. *Reliability Engineering*, 3, 449-473.
[20] Akaike, H. (1973). Information theory and an extension of the maximum likelihood principle. In *Breakthroughs in Statistics*, eds. Kotz and Johnson, Vol I, 610-624, New York: Springer Verlag.
[21] Satheesh Kumar, C. S., & Nair, S. R. (2021). A generalization to the log-inverse Weibull distribution and its applications in cancer research. *Journal of Statistical Distributions and Applications*, 8(1), 1-30.
[22] Galton, F. (1883). Inquiries into Human Faculty and its Development,*Macmillan and Company*, London. (25).
[23] Moors, J. J. A. (1988). A quantile alternative for kurtosis. *Journal of the Royal Statistical Society, Series D* , 37(1):25–32.
[24] Mudholkar, G. S., Srivastava, D. K., & Kollia, G. D. (1996). A Generalization of the Weibull Distribution with Application to the Analysis of Survival Data. *Journal of the American Statistical Association*, 91.
[25] Efron, B. (1988). Logistic regression, survival analysis, and the Kaplan-Meier curve. *Journal of the American Statistical Association*, *83*(402), 414–425. Taylor & Francis.

AN ATTRIBUTE CONTROL CHART BASED ON GENERALIZED EXPONENTIAL-POISSON DISTRIBUTION UNDER HYBRID CENSORING

Gokila B[1] and Sheik Abdullah A[1*]

•

[1] PG & Research Department of Statistics, Salem Sowdeswari College, Salem-10, India.
[1]gokilastat@gmail.com, [1*]sheik.stat@gmail.com

Abstract

This paper presents a novel attribute control chart utilizing a Generalized Exponential- Poisson (GEP) distribution to detect the effect of indeterminacy in manufacturing processes. The proposed chart demonstrates enhanced performance compared to traditional GEP-based control charts, particularly in uncertain environments, by effectively monitoring shifts in process performance and exhibiting lower out-of-control average run lengths (ARL). A case study from the automobile industry further highlights its practical applicability. In addition, the paper explores a hybrid censoring scheme that integrates multiple censoring techniques to address incomplete data in survival and reliability analysis. This approach enhances the accuracy of lifetime estimates, especially in cases where data may be incomplete due to time or resource constraints. A comparative analysis of the proposed chart against traditional control charts underscores its superior performance in real-world applications, especially in situations with uncertain process distributions. The charts parameters are carefully optimized to ensure that the ARL for the in-control process closely aligns with a predefined target. The paper demonstrates the charts efficiency through numerical examples and simulation studies, thereby validating its performance and highlighting its practical advantages.

Keywords: Generalized Exponential-Poisson distribution, Hybrid censoring scheme, Control Chart, Average Run Length.

I. Introduction

A control chart is a graphical tool used in manufacturing industries to monitor and evaluate quality characteristics of production processes. Its primary function is to assess process stability by detecting deviations from specified tolerance limits, thereby ensuring consistency in production. Control charts visualize data in the sequence it occurs, making them an effective tool for tracking variations and identifying potential issues in real time. Over the years, various types of control chart techniques have been developed to suit different industrial applications. Every control chart includes at least two control limits: Lower Control Limit (LCL) and Upper Control Limit (UCL). A process is considered in control when the control statistic remains within these limits. Control charts are generally classified into two types:

- Attribute Control Charts – Used to classify products as conforming or non-conforming.
- Variable Control Charts – Applied when data is collected through direct measurement.

For some products, lifetime is a critical quality characteristic, necessitating life tests to assess the manufacturing process. Products are classified as conforming or non-conforming based on test

results. However, such life testing is can be time-consuming making censoring techniques essential for efficient data analysis. Common censoring methods include: Type-I Censoring, Type-II Censoring, Hybrid Censoring. In Hybrid censoring a life test terminated when the earliest of two conditions occurs: either the test reaches predetermined time t or when the $(UCL+1)^{th}$ failure occurs. If the number of observed failures at time t falls within the specified control limits LCL and UCL range, the process is deemed to be considered in control otherwise it is considered out of control. Attribute control charts, such as the np control chart are frequently used in this context often assuming a normal distribution for quality characteristics. However, in practice quality characteristics may not always follow a normal distribution. This misalignment can lead to incorrect process evaluations, potentially increasing the number of non-conforming products.

Several researchers have studied attribute control charts across various lifetime distributions, however there remains limited research has been conducted on control charts incorporating life tests for non-normal distributions, particularly the Generalized Exponential-Poisson Distribution under Hybrid censoring. The **Generalized Exponential-Poisson Distribution**, first introduced by Gupta and Kundu [10] has been recognized for its excellent fit to specific lifetime data, often outperforming traditional models such as Weibull, gamma, lognormal, and Generalized Rayleigh distributions. In recent years, mixture models have gained significant attention in fields such as biology, genetics, medicine, engineering, economics, and social sciences. A mixture distribution is constructed by combining two or more component distributions typically using mixing parameters such as weights, which must be non-negative and sum to one. These models are especially valuable for accurately representing heterogeneous populations more offering greater flexibility and precision than single distribution model.

This study proposes an attribute control chart based on the Generalized Exponential-Poisson Distribution under hybrid censoring scheme. The control chart coefficient is derived and the chart performance is evaluated using the Average Run Length (ARL) criterion. The proposed control chart is designed to sensitive to changes in the process scale parameter median and is validated through simulated data. The structure of this paper is as follows: section 2 presents a comprehensive Review of Literature, section 3 introduces the Generalized Exponential-Poisson Distribution and details the control charts design. section 4 presents a simulation study demonstrating the control charts applicability. section 5 provides a comprehensive summary of the findings.

II. Review of Literature

Granting numerous researchers have explored attribute control charts for lifetime distributions, there is still a lack of studies on control charts for non-normal distributions like the Generalized Exponential-Poisson distribution under Hybrid censoring, despite the increasing interest in generalized models for reliability and life testing. Adeoti and Ogundipe [2] introduced a control chart for the Generalized Exponential distribution under a time-truncated life test, providing a structure methodology for quality monitoring in reliability engineering. However, its practical applicability could be enhanced through further comparisons with existing control chart methods. Aslam and Jun [4] proposed attribute control charts for the Weibull distribution under truncated life tests, enhancing quality control in reliability engineering, though further comparisons with other lifetime distributions could improve applicability. Baklizi and Ghannam [6] proposed an attribute control chart for the inverse Weibull distribution under truncated life tests, enhancing reliability engineering. However, further comparisons with existing methods could improve its applicability. Gunasekaran [10] proposed an attribute control chart based on the Exponentiated Exponential distribution under accelerated life testing with hybrid censoring, contributing to quality monitoring in reliability engineering, though further comparisons with traditional methods could further enhance its applicability. Kavitha and Gunasekaran [13] introduced a novel process monitoring approach using Exponentiated Exponential Distribution, with proposed enhancements including title refinement, abstract clarification, deeper explanation, detailed mathematical framework,

comparative simulations, practical applications, and suggestions for future research.

Ristic and Nadarajah [17] introduced a novel lifetime distribution that addresses the limitations of traditional models, offering flexibility for real-world data. They also suggested further improvements through comparisons, simulations, and parameter estimation methods. Hussain et al., [21] offers a comprehensive approach to enhancing attribute control charts for popular distributions. However, their method could benefit from further simulation studies, real-world data comparisons, and more detailed mathematical analysis. Rao et al., [25] introduced an attribute control chart for the Dagum distribution, designed for truncated life tests, offering a robust method for quality control and reliability monitoring, though further validation and comparisons with traditional methods would enhance its practical application. Marshadi et al., [3] introduced a time-truncated control chart for Weibull distribution under uncertainty, offering a robust method for monitoring processes in reliability testing, though further validation and comparison with traditional methods would enhance its applicability. Aslam et al., [5] introduced a control chart method for time-truncated life tests based on the Pareto distribution of the second kind, aimed at improving process monitoring in reliability testing. Balamurali and Jeyadurga [7] presented an attribute np control chart for monitoring mean life, utilizing multiple deferred state sampling in the context of truncated life tests. Jayadurga et al., [12] proposed an attribute np control chart for process monitoring using repetitive group sampling in truncated life test. Srinivasa Rao [23] introduced a control chart method based on the Exponentiated Half Logistic Distribution for monitoring time-truncated life data in reliability testing. Srinivasa Rao and Edwin Paul [25] presented a control chart method based on the Log Logistic distribution for monitoring time-truncated life data in reliability testing. Shaheen et al., [22] proposed a control chart method utilizing repetitive sampling to monitor lognormal process variations in quality control.

Muhammad and Cordeiro [18] offered an in-depth review of compounding distributions, presented new generalized classes that expand the modeling capabilities for complex data in fields like reliability theory, survival analysis, and actuarial science. The paper's strengths lie in its comprehensive survey, the introduction of new distribution classes, and its broad applicability, while improvements could include empirical validation and a discussion on computational challenges in practical use. Coskun Kus [15] presented an innovative lifetime distribution, broadening the scope of statistical models used in reliability and survival analysis. The study thoroughly explores the distribution's mathematical properties, such as its probability density function, cumulative distribution function, and moments, demonstrating its versatility in modelling diverse lifetime data. By offering practical applications and effective parameter estimation techniques, the paper underscores the distribution potential for real-world reliability studies. Adamidis and Loukas [1] introduced a new lifetime distribution with a decreasing failure rate (DFR), relevant for modeling systems, particularly in electronics, where the failure rate decreases over time. Daghestani et al., [8] explored a mixture model combining the Lindley and Weibull distributions to enhance the modeling of real-life data with diverse characteristics. Aldosari et al., [16] presented an innovative method for process monitoring by incorporating multiple dependent state repetitive sampling into attribute control charts, improving the detection of process shifts and variations. Nadarajah and Kotz [19] introduced exponentiated distributions, extending traditional models to better handle skewed data and offering enhanced flexibility for various statistical applications. Nassar and Eissa [20] introduced an extension of the Weibull distribution, incorporating an exponentiation parameter to handle a broader range of lifetime data, particularly with complex failure rates, including both increasing and decreasing hazard rates. This generalization enhances the flexibility of the Weibull distribution, making it useful for diverse fields like reliability engineering, survival analysis, and medical research.

Recently Kavitha and Gunasekaran [14] proposed a novel attribute np control chart specifically designed to track the average lifetime of products within a hybrid audit framework, assuming that the lifetime follows a mixed exponential-Rayleigh distribution. Based on statistical process control principles, this study demonstrated the chart's ability to sensitively detect changes in process performance, with a specific focus on product longevity. The performance of the control

chart is assessed using the average run length (ARL) criterion, which ensures that the ARL under control is as close as possible to the nominal target. The authors perform extensive parameter estimation under various scenarios, and verify the practical suitability of the chart with simulated data. The proposed method not only reduces the time and cost associated with the model by using a hybrid audit approach, but also provides a flexible and efficient solution for lifetime monitoring in quality control.

Gokila and Sheikh Abdullah [9] introduced a novel attribute np control chart that aims to track the average lifetime of products within a hybrid censoring framework, under the assumption that product lifetimes follow an exponential-poison distribution a compound model that is well suited for processes with early-life failures. Acknowledged the inherent limitations of conventional life testing, particularly in terms of time and cost, this study uses hybrid censoring techniques and compound distributions to improve the practicality and robustness of the monitoring process

Gupta and Kundu [10] presented a flexible framework that extends the traditional exponential distribution, offering improved versatility for modeling lifetime data. The paper provides a detailed exploration of the distribution properties, parameter estimation, and statistical inference, making valuable contributions to reliability engineering and survival analysis. The study highlights the advantages of the Generalized Exponential-Poisson distribution for specific types of lifetime data, demonstrating its effectiveness compared to other common lifetime distributions. Additionally, the paper introduces an attribute control chart based on the Generalized Exponential-Poisson distribution within a hybrid censoring Scheme, establishing the chart's coefficient and evaluating its performance using the Average Run Length. The design of the control chart is adapted to account for changes in the median of the process scale parameter, and its applicability is demonstrated through simulated data.

III. Design of the control chart

Let t be a random variable with Generalized Exponential-Poisson distribution with parameters λ,β and α, i.e.,$t \sim GEP(\lambda,\beta,\alpha)$ and the probability density function is given by

$$f(t) = \frac{\alpha\beta\lambda\{1-e^{-\lambda+\lambda\exp(-\beta t)}\}^{\alpha-1}.e^{-\lambda-\beta t+\lambda\exp(-\beta t)}}{(1-e^{-\lambda})^{\alpha}}, t, \lambda, \beta, \alpha > 0 \quad (1)$$

and the cumulative density function of the model can be obtained as

$$F(t) = \left(\frac{1-e^{-\lambda+\lambda\exp(-\beta t)}}{1-e^{-\lambda}}\right)^{\alpha}, t, \lambda, \beta, \alpha > 0 \quad (2)$$

The lifetime of the units follows Generalized Exponential – Poisson Distribution with a median life defined as

$$m_0 = \left(-\frac{1}{\beta}\right) log\left[1 + \frac{1}{\lambda} log\left[1 - (2^{-1})^{\frac{1}{\alpha}}.\left(1 - e^{-\lambda}\right)\right]\right] \quad (3)$$

The truncation time, denoted as t_0, along with failure rate, is introduced to reduce testing in life experiments. The number of failures with lifetimes ≤ t_0, is recorded where the truncation time is predefined based on the desired median life or testing constraints

$$t_0 = am_0 \quad (4)$$

where t_0 is the truncated time, a is the truncation coefficient and m_0 is the desired median life of the product. The probability of failure before t_0 is given by

$$p = \left[\frac{1-e^{-\lambda+\lambda e^{-\beta t_0}}}{1-e^{-\lambda}}\right]^{\alpha}, t, \lambda, \beta, \alpha > 0 \quad (5)$$

using equation (3), the probability of failure of a product when the process is in control is

$$p_0 = \left[\frac{1-e^{-\lambda+\lambda\left\{1+\frac{1}{\lambda}log\left[1-2^{\left(-\frac{1}{\alpha}\right)}\left(1-e^{-\lambda}\right)\right]\right\}^{\alpha}}}{1-e^{-\lambda}}\right]^{\alpha}, \lambda, \alpha > 0 \quad (6)$$

when the median shifts to m_1, the probability of failure of a product becomes
Let $m_1 = fm_0$, where f is the shift coefficient, then

$$p_1 = \left[\frac{1-e^{-\lambda+\lambda\left\{1+\frac{1}{\lambda}log\left[1-2^{\left(-\frac{1}{\alpha}\right)}\left(1-e^{-\lambda}\right)\right]\right\}^{\frac{\alpha}{f}}}}{1-e^{-\lambda}}\right]^{\alpha}, \lambda, \alpha > 0 \quad (7)$$

Based on the number of products in each subgroup, we propose the following *np* control chart for Generalized Exponential-Poisson under Hybrid censoring scheme.

Algorithm

Step 1: Randomly select a set of n products from the production process.
Step 2: Conduct a life test on the selected products, using t_0 as the test termination time, and record the number of failures observed during the test, denoted as D.
Step 3: Terminate the life test either when the truncated time t_0 is reached or the number of failures exceeds the upper control limit (UCL) whichever occurs first.
Step 4: If D exceeds the UCL or falls below the lower control limit (LCL), declare the process out of control. If D falls within the range of LCL ≤ D ≤ UCL, declare the process in control.

This method involves monitoring the number of failures denoted as D within each sample. Any unit that fails before the predetermined truncation time t_0 is considered defective or nonconforming. For a sample of size n, the number of defective units D is shown using a Binomial distribution, where the probability of failure before t_0 is p. The probability mass function of the Binomial distribution is as follows:

$$p(D = x) = \binom{n}{x} p^x (1-p)^{n-x}, x = 0,1,2,3.. \quad (8)$$

The Lower and Upper control limits are given by

$$LCL = max(0, np_0 - k\sqrt{np_0(1-p_o)}) \quad (9)$$

$$UCL = np_0 + k\sqrt{np_0(1-p_o)} \quad (10)$$

Where n is the sample size and k is the coefficient of the control limits and p_0 is the probability of nonconforming when the process is in control. The probability of maintaining that the process is in control when it is truly in control is obtained using the binomial probability given in equation (8)

$$p_{in}^0 = p(LCL \le D \le UCL|p_0) = \sum_{d=LCL+1}^{UCL} \binom{n}{d} p_0^d (1-p_0)^{n-d} \quad (11)$$

The probability of stating that the process is in control when the median life of the product has

shifted to m_1 is given by

$$p_{in}^1 = p(LCL \le D \le UCL | p_1) = \sum_{d=LCL+1}^{UCL} \binom{n}{d} p_1^d (1-p_1)^{n-d} \quad (12)$$

It follows from the values p_{in}^0 and p_{in}^1 given in Equation (11) and (12) that the in-control ARL is given by

$$ARL_0 = \frac{1}{1-p_{in}^o} \quad (13)$$

and the out of control ARL are given by

$$ARL_1 = \frac{1}{1-p_{in}^1} \quad (14)$$

To construct the performance evaluation tables for the proposed control chart, based on the Generalized Exponential Poisson Distribution under a hybrid censoring scheme, the following algorithm is applied.

Step 1: Specification of ARL and sample size

Define the desired in control average run length (ARL), denoted as r_0 , and select an appropriate sample size, n.

Step 2: Determination of control chart parameters

For each combination of r_0 , n and the scale parameter λ, determine the control chart parameters. Compute the truncation coefficient a, such that the average run length calculated using equation (13)

Step 3: Evaluation of ARL under process shift

Introduce a shift constant f, which defines the new median $m_1=fm_0$ using the values obtained from step 2, compute the out of control ARL, based on equation (14).

The results of various values of r_0, n and λ are presented in Tables 1-4. Notably, the tables demonstrate that the out- of control ARL decreases as the shift constant f becomes smaller, indicating that the chart is more sensitive to larger shifts in the median life of the product.

Table 1: *The Values of ARLs when λ = 1, α=0.5*

					λ = 0.5, α=0.5				
n		**20**			**25**			**30**	
r_0	**260**	**320**	**420**	**260**	**320**	**420**	**260**	**320**	**420**
a	0.445	0.801	0.536	0.305	0.342	0.35	0.387	0.562	0.329
k	3.5	2.8881	3.5	3.5	3.4695	3.5	2.894	2.9937	3.2095
LCL	0	0	0	0	0	0	0	1	0
UCL	11	12	12	12	12	13	13	15	13
Shift(f)	ARL	ARL	ARL	ARL	ARL	ARL	ARL	ARL	ARL
0.10	1.15	1.03	1.24	1.26	1.16	1.30	1.02	1.01	1.05
0.20	2.80	1.74	3.95	4.01	3.06	4.72	1.59	1.45	2.05
0.30	7.75	3.98	13.34	13.20	9.10	17.70	3.40	3.13	5.19
0.40	19.42	9.13	38.84	37.29	24.25	55.71	7.52	7.32	12.80
0.50	43.31	19.65	97.37	90.20	57.02	147.87	15.85	16.61	29.08
0.60	86.27	39.42	210.04	183.26	118.30	324.50	31.43	35.58	60.71
0.70	150.67	73.97	371.11	291.24	210.47	536.10	58.67	71.41	116.74
0.80	220.91	130.13	494.89	341.93	302.89	615.24	103.20	132.99	204.68
0.90	262.86	213.28	497.20	315.88	342.08	537.63	170.29	223.12	317.81
1.00	260.30	319.73	420.40	260.13	319.81	420.42	259.75	319.50	420.30

Table 2: *The Values of ARLs when λ = 1, α=1*

					λ = 1, α=1				
N		**20**			**25**			**30**	
r_0	**260**	**320**	**420**	**260**	**320**	**420**	**260**	**320**	**420**
A	0.637	0.751	0.836	0.52	0.968	0.564	0.571	0.9	0.757
K	2.878	3.0605	2.9802	2.8864	3.0967	2.9883	2.9303	3.1105	2.9931
LCL	1	2	2	1	5	1	3	6	4
UCL	13	15	15	14	20	15	18	22	20
Shift(f)	ARL	ARL	ARL	ARL	ARL	ARL	ARL	ARL	ARL
0.10	1.00	1.00	1.00	1.00	1.00	1.00	1.00	1.00	1.00
0.20	1.02	1.05	1.02	1.00	1.02	1.01	1.00	1.00	1.00
0.30	1.30	1.65	1.37	1.16	1.35	1.20	1.15	1.09	1.07
0.40	2.33	3.86	2.64	1.89	2.86	2.09	1.97	1.72	1.58
0.50	5.15	10.89	6.34	3.99	8.11	4.78	4.76	3.91	3.31
0.60	12.42	32.62	16.66	9.54	26.28	12.38	13.70	11.10	8.61
0.70	30.59	96.82	44.79	23.89	88.72	33.47	42.16	35.11	24.95
0.80	73.65	256.59	117.80	59.68	280.72	90.10	126.32	113.71	75.02
0.90	160.76	420.13	274.81	139.83	510.03	228.58	275.53	300.58	214.82
1.00	260.23	319.82	419.53	259.98	320.88	421.30	260.19	320.49	419.64

Table 3: ***The Values of ARLs when λ = 1, α=0. 2***

					λ = 1, α = 0.2				
N		**20**			**25**			**30**	
r_0	**260**	**320**	**420**	**260**	**320**	**420**	**260**	**320**	**420**
A	0.145	0.782	0.546	0.821	0.898	0.628	0.625	0.704	0.719
K	2.9012	3.1212	2.9811	3.0122	3.0962	3.1747	2.9966	3.1105	3.1311
LCL	1	3	2	5	5	4	6	6	6
UCL	13	16	15	20	20	19	22	22	23
Shift(f)	ARL	ARL	ARL	ARL	ARL	ARL	ARL	ARL	ARL
0.10	9.27	5.46	4.78	5.37	4.50	4.62	3.23	2.66	4.16
0.20	31.05	22.82	17.26	27.77	21.92	20.54	13.88	10.42	21.78
0.30	67.20	60.09	41.30	86.91	66.97	58.20	40.54	29.19	71.79
0.40	116.29	123.35	79.65	202.62	155.88	128.17	92.90	65.62	179.24
0.50	171.84	211.36	133.77	366.15	293.71	235.84	176.89	125.99	361.94
0.60	222.65	305.46	201.91	492.40	439.67	366.23	277.83	209.73	577.92
0.70	257.97	371.35	276.92	497.12	509.21	472.82	349.07	297.50	695.82
0.80	273.52	387.36	346.20	420.11	477.70	510.08	355.24	352.79	654.21
0.90	272.21	362.85	396.24	331.90	399.31	480.71	314.22	355.47	536.39
1.00	260.09	320.25	419.63	259.89	320.45	419.51	260.45	320.49	419.99

Table 4: *The Values of ARLs when λ = 2, α=1*

					λ = 2, α=1				
N		**20**			**25**			**30**	
r_0	**260**	**320**	**420**	**260**	**320**	**420**	**260**	**320**	**420**
A	0.161	0.508	0.331	0.375	0.13	0.17	0.654	0.546	0.3
K	3.2501	3.1896	2.9882	2.995	3.4668	3.0557	2.9855	3.1626	2.9936
LCL	0	5	2	5	0	0	12	10	4
UCL	11	19	15	20	12	13	27	26	20
Shift(f)	ARL	ARL	ARL	ARL	ARL	ARL	ARL	ARL	ARL
0.10	1.00	1.10	1.00	1.00	1.00	1.00	1.00	1.00	1.00
0.20	1.08	2.38	1.04	1.05	1.06	1.02	1.03	1.02	1.00
0.30	1.73	7.87	1.48	1.59	1.65	1.29	1.36	1.34	1.10
0.40	3.83	9.93	2.95	3.69	3.79	2.36	2.62	2.65	1.69
0.50	9.65	17.04	7.07	10.92	10.25	5.38	6.54	7.02	3.58
0.60	24.91	46.65	18.30	35.97	28.73	13.44	19.05	21.93	9.25
0.70	62.34	86.97	48.28	121.42	78.19	34.28	59.99	74.17	26.38
0.80	140.76	204.02	124.45	360.12	188.89	86.08	189.56	249.41	77.85
0.90	240.85	293.37	283.09	490.02	322.52	204.88	403.91	529.71	218.35
1.00	260.36	319.90	420.37	260.37	320.41	419.94	259.81	320.33	419.78

I. Illustration 1

Consider the production scenario where the lifetimes of the manufactured products follow a Generalized Exponential-Poisson distribution with parameters $\lambda = 1$ and $\alpha = 1$. The following conditions and parameters are assumed for monitoring the quality of the process. The initial lifetime (m_0) is 1000 hours, the Average Run Length (ARL_0) is 260, and the sample size (n) is 20. The control chart parameters obtained from Table 2 are $k = 2.878$, $a = 0.637$, $LCL = 1$, and $UCL = 13$. Based on this information, the following steps were taken to establish the control chart:

Step 1: **Sample Selection**

Select a random sample of 20 products from each subgroup and subject them to the life test.

Step 2: **Life testing process**

During the test, monitor the number of failures and it is denoted as D and track the elapsed time.

Step 3: Test Termination Criteria

Terminate the test once the first failure occurs or the specified time period expires, whichever happens first.

Step 4: Process Evaluation

If the number of failures (D) is between 1 and 13 (inclusive), the process is declared in control. If D exceeds 13 or falls below 1, the process is considered out of control.

Interpretation

This control chart allows for timely detection of shifts in the products median lifetime by observing the number of failures before a predetermined truncation point. The use of hybrid censoring combined with the Generalized Exponential-Poisson work enhances detection capability especially under right censored data scenarios.

II. Illustration 2

Assume the product lifetimes follow a Generalized Exponential-Poisson distribution with shape parameters $\alpha = 1$ and Scale parameter $\lambda = 2$. The monitoring setup is based on the following specifications: The product values $m_0 = 1000$ hours, $ARL = 420$, and $n = 30$, the control chart

parameters from Table 4 are $k = 2.9936$, $a = 0.3$, $LCL = 4$, and $UCL = 20$.
The control chart is set up as follows:

Step 1: Sample Selection

From each subgroup, select a sample of 30 products and subject them to a life test.

Step 2: Life test execution

During the life testing, observe the number of failed items and it is denoted as D, which corresponds to the minimum number of failures or the maximum time reached, whichever occurs first.

Step 3: Test monitoring

Monitor the number of failures and the elapsed time during the test.

Step 4: Process control decision

If the number of failures D is between 4 and 20, or the maximum time is reached before D exceeds these limits, the process is in control. If the number of failures D falls outside the range of 4 to 20, or the maximum time is reached prematurely, the process is deemed to be out of control.

Interpretation:

This illustration demonstrates the effectiveness of the proposed hybrid censoring scheme-based control chart in detecting changes in the lifetime distribution of products. The chart ensures balanced sensitivity and specificity by incorporating both failures counts and censoring time, allowing for robust decision making even under right censored data conditions.

IV. Simulation Study

This section demonstrates the practical application of the developed control chart using simulated data. The simulation data was performed under the assumption that product lifetimes follows Generalized Exponential-Poisson distribution with the following a median lifetime (m_0) of 1000 hours, and the shape parameters $\lambda = 1$ and $\alpha = 1$. The sample size (n) was set to 20, and the specified $ARL\ (r_0)$ was 420. For $m_0 = 1000$ hours and $f = 1$, the process is considered in control. These in-control parameters were used to construct the first 15 observations, each with a subgroup size of 20. Next, assuming the median of the Exponentiated Exponential-Poisson distribution shifts, we set the shift constant f to 0.5. The experiment was conducted at t = 836 hours. The number of products having the lifetime below 836 hours is noted ("D") and the Values are : 6,11,10,5,10,7,13,8,10,5,9,7,9,8,4,16,16,17,13,10,15,10,11,16,12,13,14,11,12,12. The control chart was constructed using the following control limits, derived from the earlier parameters: Lower Control Limit (LCL): 2 Upper Control Limit (UCL): 15. These limits were applied uniformly across all subgroups. Figure 1 displays the plotted values of D against subgroup indices, along with the LCL and UCL. Subgroups where D falls outside the control limits are indicative of an out-of-control process, thereby validating the sensitivity of the proposed control chart to shifts in product median lifetime.

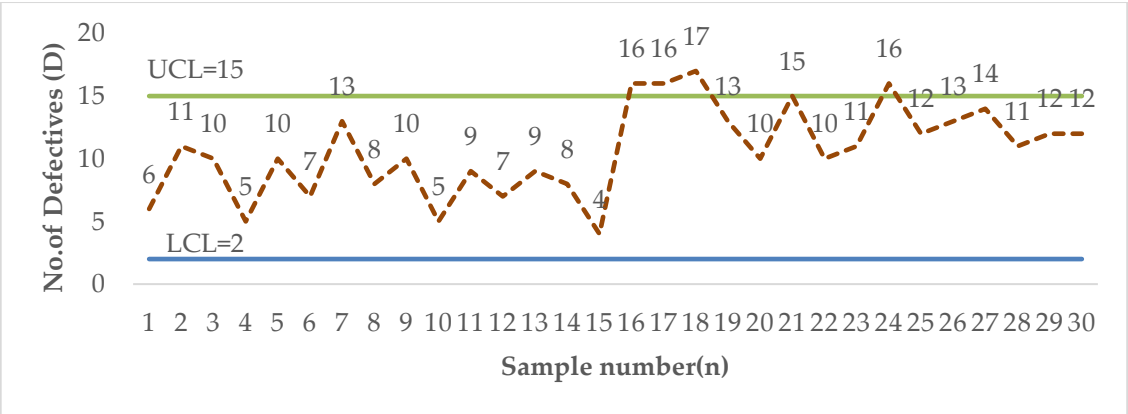


Figure 1: *Control Chart for Simulated Data*

V. Conclusion

This article presents an advanced attribute control chart that utilizes the Generalized Exponential-Poisson distribution under a Hybrid censoring Scheme designed to ensure the median lifetime of a product serves as the quality standard. The newly developed control chart offers significant flexibility, making it highly suitable for monitoring the longevity of high quality products across various industries. To demonstrate its application, the article includes tables tailored for industrial settings, with simulated data generated using R software based on the Generalized Exponential-Poisson distribution. The effectiveness of the control chart is assessed through the calculation of Average Run Lengths *(ARLs*) under varying shift constants *(f)*, providing insights into its performance. A notable advantage of employing the Hybrid censoring scheme in life testing is the substantial reduction in both time and costs associated with sampling inspection. Moreover, the control chart work is designed to be extensible, holding potential for adaptation to a variety of other statistical distributions in ongoing and future research activities.

References

[1] Adamidis Loukas, K.S. (1998). A lifetime distribution with decreasing failure rate. *Statistics and Probability Letters*, 39: 35–42.

[2] Adeoti, O. A. and Organdie P. (2021). A Control Chart for the generalized exponential distribution under time truncated life test. *Life Cycle Reliability and Safety Engineering*, 10:53-59.

[3] AL Marshadi, A. H. Shafqat A. Aslam M. and Alharbey A. (2021). Performance of a New Time-Truncated Control Chart for Weibull Distribution under Uncertainty. *International Journal of Computational Intelligence Systems,* 14(1):1256-1262.

[4] Aslam M. and Jun C. (2015). Attribute Control Charts for the Weibull Distribution under Truncated Life Tests. *Quality Engineering*, 27(3):283 – 288.

[5] Aslam M. Nasrullah Khan and Chi Hyuck (2016). A control chart for time truncated life tests using Pareto distribution of second kind. *Journal of Statistical Computation and Simulation,* 86(11):2113 – 2122.

[6] Baklizi A. and Ghannam S. A. (2022). An attribute control chart for the inverse Weibull distribution under truncated life tests. *Heliyon*, 8:e11976:1-5.

[7] Balamurali S. and Jeyadurga P. (2019). An attribute np control chart for monitoring mean life using multiple deferred state sampling based on truncated life tests. *International journal of Reliability, Quality and Safety Engineering,* 26(1):1-18.

[8] Daghestani, A.F. Sultan, K.S and AL-Moisheer, A.S (2021). Mixture of Lindley and Weibull Distributions: Properties and Estimation. *Journal of Statistics Applications & Probability*,10 :301-313

[9] Gokila B. and sheik Abdullah (2025). Attribute control chart approach for life testing using Exponential-Poisson distribution. *Reliability: Theory & Applications*,20,2(84):727-735.

[10] Gunasekaran M. (2024). A New attribute control chart based on Exponentiated Exponential Distribution Under Accelerated Life test with Hybrid Censoring. *Reliability: Theory & Applications*,19,4(80):850-860.

[11] Gupta, R.D. Kundu, D. (1999). Generalized exponential distributions. *Australian and New Zealand Journal of Statistics*, 41:173–188

[12] Jayadurga P. Balamurali S. and Aslam M. (2018). Design of an attribute np control chart for process monitoring based on repetitive group sampling under truncated life tests. *Communication in Statistics – Theory and Methods,* 47(24):5934 – 5955.

[13] Kavitha T. and Gunasekaran M. (2020). Construction of Control Chart based on Exponentiated Exponential Distribution. Journal of Engineering Sciences, 11(4):979 – 985.

[14] Kavitha T. and Gunasekaran M. (2025). Designing an attribute control chart based on Exponential-Rayleigh Distribution under Hybrid Censoring. *Reliability: Theory & Applications,*20,2(84):824-833.

[15] Kus C. (2007). A new lifetime distribution. *Computational Statistics and Data Analysis*, 51, 4497–4509.

[16] Aldosari, M.S. Aslam M. and Jun, C.H. (2017). A new attribute control chart using multiple dependent state repetitive sampling. *IEEE Access*, (5):6192–6197.

[17] Miroslav M Ristic and Saralees Nadarajah (2012). A New lifetime distribution. *Journal of Statistical Computation and Simulation, ifirst*,1-16

[18] Muhammad H Tahir and Gauss M Cordeiro (2016). Compounding of distributions: a survey and new generalized classes. *Journal of statistical Distributions and Applications, Springer*,3(1):1-35.

[19] Nadarajah S. Kotz S. (2006). The exponentiated type distributions. *Acta Applicandae Mathematicae*, 92: 97–111.

[20] Nassar, M.M. Eissa, F.H. (2003). On the exponentiated Weibull distribution. *Communications in Statistics, Theory and Methods,* 32: 1317–1336

[21] Shafqat A. Hussain J. AL-Nasser, A. D. and Aslam M. (2018). Attribute Control Chart for some popular distributions. *Communications in Statistics – Theory and Methods,* 47(8):1978 – 1988.

[22] Shaheen U. Azam M. and Aslam M. (2020). A control chart for monitoring the lognormal process variation using repetitive sampling. *Quality and Reliability Engineering International*,36(3):1028–1047.

[23] Srinivasa Rao G. (2018). A Control Chart for Time Truncated Life Tests Using Exponentiated Half Logistic Distribution. *Applied Mathematics & Information Sciences: An International Journal,* 12(1):125 – 131.

[24] Srinivasa Rao G. and Edwin Paul (2020). Time Truncated Control Chart using LogLogistic Distribution. *Biometrics & Biostatistics International Journal*, 9:76- 82.

[25]Srinivasa Rao G. Fulment, A. K. and Josephat, P. K. (2019). Attribute control chart for the Dagum distribution under truncated life tests. *Life Cycle Reliability and Safety Engineering,* 8:329 – 335.

RT&A, No 4 (89)
Volume 20, December 2025

XAI-SPCNET: A MULTI-LEVEL EXPLAINABLE AI FRAMEWORK FOR PREDICTIVE CONTROL CHART AUTOMATION IN MANUFACTURING QUALITY MONITORING PROCESS

V. Anusha[1], Lilly George[1], K.S. Harish[2], Yuvaraja B[3], A. Manimaran[3*]

•

[1]Department of Statistics, St. Joseph's College, Bharathidasan University, Tiruchirapally, Tamil Nadu, India

[2]Department of data science, SIva Sivani Institute of Management, Secunderabad, Telangana, India

[3]Department of Mathematics, School of Advanced Sciences VIT-AP University, Amaravati, Andhra Pradesh, India

anushavemula189@gmail.com, lgaceg@gmail.com, drksharish@gmail.com, yuvarajaboddu1988@gmail.com, manimaran.a@vitap.ac.in*

Abstract

Timely and accurate detection of process abnormalities in modern manufacturing is needed for sustainable quality assurance so that the process can be rectified quickly. Traditional control charts, although good at illustrating deviations, are poor in prediction and heavily dependent on fixed thresholds, which tend to lead to tardy interventions and high rates of false alarms. Recent developments in artificial intelligence (AI) offer predictive options; nonetheless, their lack of transparency as "black-box" systems erodes users' confidence and influences regulatory compliance difficulties. To bridge this void, Explainable AI (XAI) is ever more critical for Statistical Process Control (SPC), delivering not just precise anomaly prediction but also interpretable, transparent explanations. This paper presents XAI-SPCNet, a new framework incorporating explainability into predictive SPC to facilitate better manufacturing quality assurance. The architecture involves several expert-informed components: (1) Temporal Causal Decision Trees (TCDT-SPE) using Granger causality for adaptive causal splits that are interpretable; (2) Dynamic Rule Embedding Networks (DREN) combining temporal embeddings with Bayesian rule learning for succinct, context-dependent rules; (3) Contrastive Explanation Generator (CEG-SPE) offering contrastive explanations for violations; (4) Sparse Symbolic Regression (SSR-ED) obtaining sparse mathematical decision boundaries; and (5) Multi-Objective Reinforcement Learner with Explanation Optimization (MORLEO) optimizing accuracy, truthfulness, and chart stability. In synthetic and real-world datasets, XAI-SPCNet presents high prediction accuracy (91%), fast inference, concise rule representation, and greater than 95% explanation coverage, thereby promoting transparent, adaptive, and reliable quality control in manufacturing.

Keywords: Explainable AI, Statistical Process Control, Predictive Quality Monitoring, Symbolic Regression, Reinforcement Learning, Process

Table 1: *List of Abbreviations and Their Full Forms*

Abbreviation	Full Form
SPC	Statistical Process Control
ML	Machine Learning
AI	Artificial Intelligence
QC	Quality Control
ECG	Electrocardiogram
WAAM	Wire Arc Additive Manufacturing
AEWMA	Adaptive Exponentially Weighted Moving Average
RPA	Robotic Process Automation
WOA	Whale Optimization Algorithm
DBN	Deep Belief Network
OCT	Optical Coherence Tomography
ConvBiGRU	Convolutional Bidirectional Gated Recurrent Unit
RNN	Recurrent Neural Network
GAN	Generative Adversarial Network
AFP	Automated Fiber Placement
GMAW	Gas Metal Arc Welding
LWM	Laser Welding Monitoring
CAM	Computer-Aided Manufacturing
RUL	Remaining Useful Life
PCA	Principal Component Analysis
AE	Acoustic Emission
IoT	Internet of Things
BIM	Building Information Modeling
FEM	Finite Element Method
API	Application Programming Interface
UAV	Unmanned Aerial Vehicle
HMI	Human-Machine Interface
BMS	Bridge Management System
SNR	Signal-to-Noise Ratio
KPI	Key Performance Indicator
UCL	Upper Control Limit
LCL	Lower Control Limit
PDF	Probability Density Function
RMSE	Root Mean Squared Error
MSE	Mean Squared Error
HVAC	Heating, Ventilation, and Air Conditioning
OEM	Original Equipment Manufacturer
QMS	Quality Management System

1. Introduction

Essentially, within a high-precision manufacturing setting, real-time quality monitoring lies at the heart of process control for stabilizing process conditions and verifying that the products meet exacting specifications. This, in the past, has led to monitoring industrial quality assurance benchmarks using graphical tools like control charts in its SPC realm for pattern recognition of deviations that management or industrial engineering personnel call it. This traditional SPC practice remains inherently reactive in stance because static thresholds are required to be erected-complemented by sudden usage of historical data and in the light of manufacturing-modeling, they capitulate when coming up against such suspicious parameters as early signs

of suspicions of process drift in the initial phase. The cocktail of interpretations of the graphs by human senses-introducing more subjective errors [1, 2, 3], delay wound into any corrective drive function, makes this whole way of manual control-chart interpretation a likely disaster of both Type I and Type II errors. With the pace of technology together with the increasing demands in modern manufacturing, data-driven approaches have been explored to enhance SPC through machine learning (ML) techniques for prediction about the prospects of departures. Regulation is another major issue as a problem with many ML-generated SPC models that act more like black-box systems with their internal mechanism out in the dark [4, 5, 6]. Lack of interpretability shakes users' reliance, leads to difficulty in analyzing root causes, and dims down the actionable value of any predictions. Conclusively, the situation in which Explainable Artificial Intelligence (XAI) models guide already-predictive AI models through decision logic for SPC is highly critical today. To prop up the need, the current work introduces a theory of creating a new architecture called XAI-SPCNet, aimed at erasing the foreseen gap between predictive analytics and explainability in SPC applications. Unlike traditional models, XAI-SPCNet champions interpretability while recognizing transient learning mechanisms in real-time oversight. This framework integrates multiple techniques from symbolic regression, causal modeling, Bayesian rule learning, contrastive explanations, and reinforcement learning to create a meaningful clear framework of decision making. While each inclusion was made to revolutionize the automation of SPC, employing features such as causal feature selection and adaptive rule generation to violation explanation and policy optimization. Having been among the existing studies with this idea, the integration of explainability within the SPC prediction workflow provides operational benefits to facilitate human-centric diagnostics, monitoring and traceability to the model's decisions, and regulatory nonviolations while permitting learning from reality to be implemented under evolving production settings. Moreover, it offers human-understandable insights to domain experts, thereby strengthening their confidence in the outputs of the model. With such a venture, our work will offer an extended frontier for SPC automation and also usher in a notion of trust as far as AI systems in the industrial quality control are concerned in process.

1.1. Motivation and Contribution

The main incentive for this study has been the lack of connectivity in operation between predictive accuracy and decision transparency in the current AI-enhanced SPC systems. The number of machine learning models in interesting detection capabilities were, however, no more capable of being understood by their users. The absence of interpretability raises tremendous challenging issues in conditions where, for example, root cause analysis becomes paramount, as does regulatory requirements, and so does stakeholder confidence. Moreover, the present systems do not address the integration of domain knowledge, causal inference, and contextual metadata. Such issues cause poor generalization and unadaptable models under non-stationary conditions. So the increasing complexities of futures manufacturing systems and their increasing data densities have made it more urgent than any time before for models being able to explain their behavior and logic, rule-based or purely causal, to surface. Thus, this paper presents XAI-SPCNet, a complete and intelligible AI structure for predictive SPC chart automation. The architecture presents five innovative methodologies that approach one point of the SPC pipeline. TCDT-SPC provides models of decision trees with temporal and causal constraints to ensure relevance of features over time. DREN incorporates dynamic, context-aware rule generation through latent embedding and Bayesian learning. CEG-SPC employs contrastive explanation by juxtaposing prediction instances against their nearest neighbor non Violation instances in feature space, which improves traceability. Then, SSR-ED employs the concept of symbolic regression to derive user-friendly control limit equations, providing users with a mathematically sound understanding of process boundaries. Finally, MORLEO applies multi-objective reinforcement learning to jointly identify the most accurate prediction, most stable control chart, and quality of explanations. Together they form an integrated and interpretable system that is capable of real-time quality monitoring; its accuracy is supplemented with high-fidelity, actionable explanations. Thus stands transformed

the XAI-SPCNet as a hallmark step forward in the intelligent manufacturing analytics domain sets.

2. Related Work

The progressive assimilation of statistical process control (SPC), real-time monitoring, and artificial intelligence has changed the features of and caused advanced processes in manufacturing, healthcare, and systems within industry. A literature review in total describes the gradual evolution of thought and practice in moving from traditional chart-based monitoring into artificial intelligence-evolved, highly complex, domain-relevant models for quality assurance. With pharmaceutical coating processes being monitored online through Optical Coherence Tomography, as described in [1], it reflects the automation and specificity trend toward real-time process data and SPC. Similar mode is echoed in [2] where SPC charts are used for public health, particularly monitoring infant mortality in different urban settings, thereby proving the evolution of SPC application beyond manufacturing. From industrial context again in [3], introduction of multivariate control charts to monitor both human and process parameters becomes necessary, particularly in collaborative robotics settings"this dual monitoring becomes significant under a scenario wherein human-machine interaction becomes central to modern production systems. From here onwards, machine learning becomes more deeply enmeshed into SPC and process monitoring. The study in [4] applies ML to composites manufacturing and emphasizes feature selection and anomaly prediction in real-time inputs. Paper [5] illustrates the scope of both parametric and non-parametric control charts with respect to residential consumption of water"again being an indication of how SPC can transfer to strange domains. E.g., erratic robotic behavior is traced as a by-product of SPC anomaly detection, thus marrying statistical rigor with digital workflow monitoring. In [6], erratic robot behavior detection derives from anomaly detection through SPC, thereby integrating high-end statistical rigor into digital workflow monitoring process. Meanwhile, showcase [7] addresses air quality management in confined spaces by contrasting manual and automated interventions by adopting statistical control of emission metrics in interventions. In [8], the most significant advancement in industrial monitoring is observed, in which machine vision is used for in-process monitoring of biomechanical devices, presenting rapid visual analytics for validating dimensional tolerance. The automation of quality control using expert systems is in [9], which entails embedding domain knowledge into the decision rules for quick responses. This is augmented by the highly specific scrutiny of laser welding in electric mobility applications via a process monitoring mechanism that enables real-time corrective feedback in precision domains. Robust environmental applications are presented in [10], involving adaptive monitoring by an optimized sampling frequency for water quality in case of developing areas, maximizing data utility in constrained conditions. In comparison, [11] employs unsupervised learning in pattern shift detection in additive manufacturing processes, introducing clustering and outlier detection into traditional SPC logic. Paper [12] presents a hybrid deep learning model, ConvBiGRU with attention, for quality prediction in batch processes of various stages-an indication of increasing reliance on temporal and contextual embeddings. This trend is further supported in [13], which uses acoustic data from wire arc additive manufacturing (WAAM) integrated signal analysis with supervised ml to identify deposition errors in real-time. A health monitoring system in which deep belief networks have optimized ECG analysis has been developed for the automotive domain, bridging bio-sensing with SPC for industrial applications. The vitality of simulation for operational control is reflected by [14, 15], where power plant water and steam chemistry are monitored to avoid degeneration within cycles, using statistical modeling for predictive fault preventions. A systemic view of urban mobility is given in paper [16], integrating SPC concepts into global control models for automated driving, links micro-level vehicular data with macro-level flow optimization. Such a huge structural leap is demonstrated in [17], where graph-structured data is employed in detecting anomalies in manufacturing, hence marking the convergence between graph analytics and SPC for network-based fault modeling. Bayesian methods dominated [18] with the enhancement of AEWMA control charts using ranked set sampling

to monitor semiconductor fabrication, which remains a major development in data-efficient SPC model-building. Structural health monitoring, using Bayesian decision models, feeds data quality and reliability into the determination of bridge safety-critical infrastructure performance relative to risk assessment.

Table 2: *Model's Empirical Review Analysis (Part 1)*

Ref.	Method	Main Objectives	Findings	Limitations
[1]	In-line Optical Coherence Tomography with SPC	Integrate real-time monitoring in pharmaceutical coating	Enhanced real-time quality tracking during coating	Limited generalizability to non-optical systems
[2]	SPC Charts for Population Health Data	Assess SPC effectiveness for infant mortality monitoring	SPC charts useful in city-level trend detection	Variability in population size impacted sensitivity
[3]	Multivariate Control Charts in Robotics	Monitor human and process parameters in collaborative systems	Enabled early anomaly detection in assembly lines	Requires calibration per robotic setup
[4]	Machine Learning for Composites Manufacturing	Predict faults in composites using data-driven models	Improved defect classification through ML	Feature extraction still manual in pipeline
[5]	Parametric & Non-Parametric SPC	Apply SPC to residential water usage monitoring	Detected abnormal consumption behavior effectively	Seasonal and behavioral variations caused false alarms
[6]	SPC for Robotic Process Automation	Identify erratic process behavior in digital workflows	SPC revealed inconsistencies in robotic tasks	Lack of adaptive learning in charts
[7]	SPC in Indoor Emission Control	Compare automated vs manual emission interventions	Automation showed lower peak pollutant levels	Difficult to generalize beyond controlled rooms
[8]	Machine Vision for Biomechanical Inspection	Enhance in-process quality validation for medical devices	Machine vision outperformed manual inspection in speed	Computational complexity in real-time analysis
[9]	Expert System for Automated QC	Automate decision-making in quality assurance	Knowledge-driven system reduced inspection time	Dependency on rule completeness and domain expertise
[10]	SPC in Laser Welding Monitoring	Apply SPC in e-mobility welding applications	Real-time monitoring reduced weld failures	Needs domain-specific tuning for each weld type
[11]	Adaptive Sampling Frequency	Optimize monitoring in water quality networks	Lower sampling frequency maintained accuracy	Limited spatial coverage in remote zones
[12]	Unsupervised ML in Additive Manufacturing	Detect pattern shifts during metal arc printing	Clustering exposed transient faults	Unsupervised models hard to validate against ground truth

Ref.	Method	Main Objectives	Findings	Limitations
[13]	ConvBiGRU with Attention	Predict outcomes in batch processes using deep learning	Attention improved interpretability and forecasting	Requires large datasets for stable training
[14]	Acoustic Monitoring + ML	Identify WAAM process defects through sound analysis	Acoustic features reliably indicated layer quality	Sensor placement impacted detection sensitivity
[15]	Deep Belief Network with WOA Optimization	Monitor driver health using ECG in vehicles	Achieved high accuracy in ECG anomaly detection	Real-time deployment on vehicle hardware remains untested
[16]	Simulation of Water Chemistry Monitoring	Model SPC behavior in thermal power plant systems	Improved cycle chemistry predictions	Lacks integration with live data for control
[17]	Global Urban Traffic Control Framework	Optimize automated vehicle flows using SPC-based models	Reduced system-wide congestion under controlled simulations	Real-time application at city-scale not yet tested
[18]	Graph-Structured Anomaly Detection	Detect process anomalies via graph signal analysis	Captured structural faults in complex manufacturing data	Interpretability of graph outputs is limited
[19]	Bayesian AEWMA Control Chart	Improve process control in semiconductors with ranked sampling	Bayesian integration reduced false alarms	Computational load increases with rank schemes
[20]	Bayesian Decision Framework	Integrate data quality in structural health monitoring	Better risk-informed decisions in bridge maintenance	High dependency on prior probability estimation
[21]	Classical SPC in Foundry Operations	Assess process control practices in metal casting	Control charts helped detect drift in molten processes	Lacks predictive capability beyond thresholds
[22]	Multi-Sensor Monitoring in Micromachining	Enable in-situ feedback during laser micromachining	Enhanced surface quality monitoring via fusion	Sensor alignment critical to precision
[23]	ML for Tolerance Monitoring in Clinical Trials	Dynamically adjust quality limits in trial datasets	Improved error tolerance without compromising validity	Regulatory challenges in adopting adaptive thresholds
[24]	Acoustic Emission Analysis in Cold Spray	Use airborne sound to track particle velocities	Identified process shifts in real time	Requires filtering of environmental noise
[25]	Review of AFP in Composites	Assess progress and propose future directions in AFP	Identified critical gaps in closed-loop automation	Lack of unified frameworks for AI-integration

As evident from Table 2, foundry process control in [21] puts forward SPC principles for heavy industries, whereas [22] throws light on femtosecond laser micromachining and in-situ multisensor fusion underlining high-resolution data requirements. Paper [23] takes ML in clinical trial monitoring with dynamic adjustments in the thresholds for quality, manifesting its cross-disciplinary reach. Cold spray process monitoring through airborne acoustics is documented in [24], and [25] concludes with automated fiber placement in composites and future integration of AI-SPC. Altogether, these studies demonstrate a transition away from traditional chart-based SPC towards sensor-based, algorithmically responsive systems across pharmaceuticals [1] to composites [25].

The early research works [1]-[5] used mostly statistical SPC variants, used in healthcare and water, with relatively low algorithmic depth. After publication [6], AI/ML integration came into being: supervised learning [8], unsupervised methods [12], hybrid deep learning [13], and probabilistic models [20]-[21]. A common thread is the need for real-time responsiveness, interpretability, and scalability"essential for cyber-physical factories. Explainability is the focus in

[9], [10], and [18]. Multisensor fusion, acoustic or visual, occurs in [14], [22], and [24], enhancing diagnostics. Bayesian and probabilistic models, from [19] to [21], push uncertainty-aware decision-making.

Subsequent work [21]-[25] embrace flexibility, such as RL-based policy adaptation or threshold control, the transition from rigid rules to adaptive learning. However, shortcomings persist: joint interpretability and causal optimization are exceptions. High sensitivity typically sacrifices transparency, with the exceptions of [9], [14], and [25]. In summary, SPC research has progressed from statics diagnostics to adaptive, interpretable ML systems. These pieces set the groundwork for subsequent-generation architectures such as XAI-SPCNet, integrating predictive performance, interpretability, causal reasoning, and reinforcement optimization towards responsible AI for safety-critical applications.

Nam dui ligula, fringilla a, euismod sodales, sollicitudin vel, wisi. Morbi auctor lorem non justo. Nam lacus libero, pretium at, lobortis vitae, ultricies et, tellus. Donec aliquet, tortor sed accumsan bibendum, erat ligula aliquet magna, vitae ornare odio metus a mi. Morbi ac orci et nisl hendrerit mollis. Suspendisse ut massa. Cras nec ante. Pellentesque a nulla. Cum sociis natoque penatibus et magnis dis parturient montes, nascetur ridiculus mus. Aliquam tincidunt urna. Nulla ullamcorper vestibulum turpis. Pellentesque cursus luctus mauris.

Nulla malesuada porttitor diam. Donec felis erat, congue non, volutpat at, tincidunt tristique, libero. Vivamus viverra fermentum felis. Donec nonummy pellentesque ante. Phasellus adipiscing semper elit. Proin fermentum massa ac quam. Sed diam turpis, molestie vitae, placerat a, molestie nec, leo. Maecenas lacinia. Nam ipsum ligula, eleifend at, accumsan nec, suscipit a, ipsum. Morbi blandit ligula feugiat magna. Nunc eleifend consequat lorem. Sed lacinia nulla vitae enim. Pellentesque tincidunt purus vel magna. Integer non enim. Praesent euismod nunc eu purus. Donec bibendum quam in tellus. Nullam cursus pulvinar lectus. Donec et mi. Nam vulputate metus eu enim. Vestibulum pellentesque felis eu massa.

3. Methods

XAI-SPCNet Framework Overview

To escape the low efficiency and high complexity of existing methods, the proposed **XAI-SPCNet** framework introduces five methodologically diverse yet complementary modules:

1. Temporal Causal Decision Trees for SPC (**TCDT-SPC**),
2. Dynamic Rule Embedding Networks (**DREN**),
3. Contrastive Explanation Generator for SPC (**CEG-SPC**),
4. Sparse Symbolic Regression for SPC Equation Discovery (**SSR-ED**),
5. Multi-Objective Reinforcement Learner with Explanation Optimization (**MORLEO**).

These modules collectively address diverse challenges in predictive SPC automation. The overall architecture, illustrated in Figure 1, ensures that each module contributes independently to prediction and explanation, while also interacting positively to support interpretable, accurate, and stable SPC monitoring. The framework is grounded on principles of causal reasoning, temporal encoding, symbolic generalization, contrastive logic, and multi-objective reward optimization.

The TCDT-SPC module begins with standard decision trees, augmented with temporal and causal dependencies in the node-splitting mechanism.

Let $\mathbf{X}_t = \{X_t^{(1)}, X_t^{(2)}, \ldots, X_t^{(n)}\}$ denote the multivariate time series of process variables at time t, and $Y_t \in \{0, 1\}$ represent the SPC violation label. Granger causality is used to select causal lags τ for each variable by testing whether the past of $X^{(i)}$ helps predict Y_t, as expressed in Equation (1):

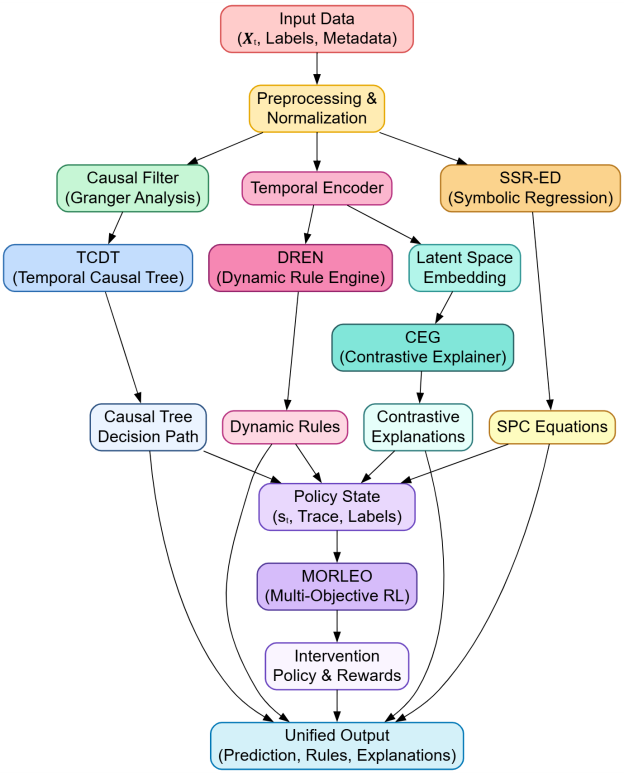


Figure 1: *Model Architecture of the Proposed Analysis Process*

$$\mathrm{GC}(j,\tau) = \mathbb{E}[(Y_t - \hat{Y}_t^{(-X_{t-\tau}^{(i)})})^2] - \mathbb{E}[(Y_t - \hat{Y}_t)^2] \tag{1}$$

Here, $\hat{Y}_t^{(-X_{t-\tau}^{(i)})}$ denotes the prediction of Y_t excluding the lagged variable $X_{t-\tau}^{(i)}$. Variables satisfying $\mathrm{GC}(i,\tau) > \theta$ are retained for splits in the causally relevant set.

The tree-building process incorporates a modified impurity criterion based on CART, with temporal causality weights $w_{i,\tau}$. The split criterion is given by Equation (2):

$$\Delta I_{\text{causal}} = w_{i,\tau} \cdot \left(I(S) - \frac{|S_L|}{|S|} I(S_L) - \frac{|S_R|}{|S|} I(S_R) \right) \tag{2}$$

where $I(\cdot)$ is the Gini impurity, and S_L, S_R are the left and right node sample sets. The resulting decision tree is interpretable, temporally aware, and causally grounded.

As shown in Figure **??**, DREN integrates symbolic reasoning and temporal embeddings for adaptive rule induction. Each input window $\mathbf{X}_{t-w:t}$ is transformed into a latent vector $z_t \in \mathbb{R}^d$ using a temporal encoder $f_{\text{enc}}(\cdot)$. Each rule R_j is conditioned on the latent context as shown in Equation (3):

$$R_j(z_t) = \mathbb{I}\left(\sum_{k=1}^{d} \alpha_{jk} z_t^{(k)} > \theta_j \right) \tag{3}$$

where α_{jk} are learnable rule weights, and $\mathbb{I}(\cdot)$ denotes the indicator function.

The rules are updated in a Bayesian manner according to Equation (4):

$$P(R_j \mid D) \propto P(D \mid R_j) \cdot P(R_j) \tag{4}$$

Here, the data likelihood $P(D \mid R_j)$ is modeled as a Bernoulli distribution based on observed violations. Rule compression is achieved by minimizing entropy $H(R)$ and maximizing posterior density, leading to the optimization problem in Equation (5):

$$\text{Rule} = \min_{R} H(R) - \lambda \log P(D \mid R) \tag{5}$$

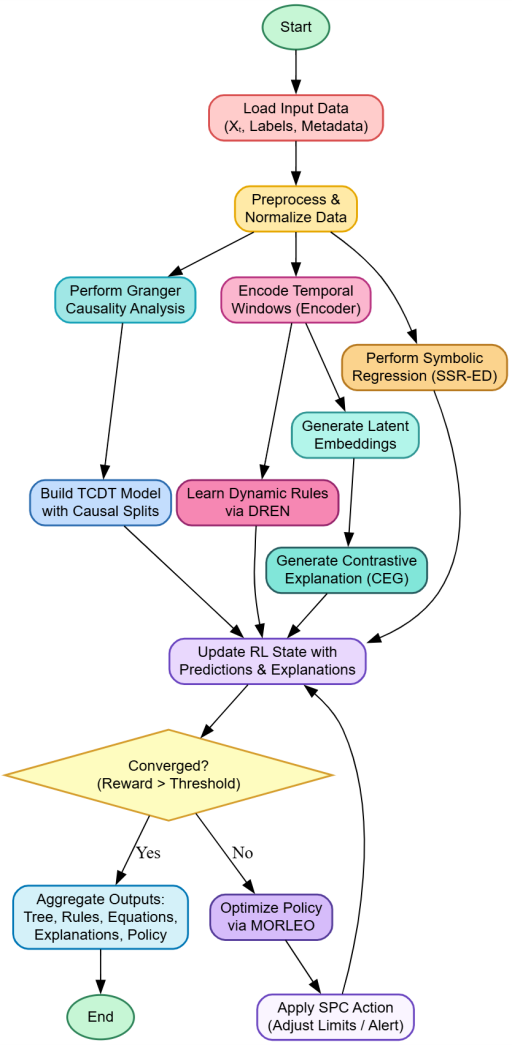


Figure 2: *Overall Flow of the Proposed Analysis Process*

The difference vector $\Delta z = z_v - z_n$ captures the deviation in latent space between the current violation instance z_v and its nearest neighbor z_n. To interpret this difference in the original input space, it is mapped back using an inverse encoder $f_{\text{inv}}(\cdot)$. The final explanation E is then defined as a sparse set of causally relevant variables at specific time lags, according to Equation (6):

$$E = \left\{ X^{(i)}_{t-\tau_i} \;:\; \left| f_{\text{inv}}(\Delta z)^{(i)} \right| > \delta_i \right\} \tag{6}$$

In this formulation, $X^{(i)}_{t-\tau_i}$ represents the value of variable i at lag τ_i, δ_i is a variable-specific threshold controlling saliency, and $f_{\text{inv}}(\Delta z)^{(i)}$ denotes the i^{th} dimension of the reconstructed difference vector. The explanation set E thus consists of temporally and causally significant variables that most contributed to the SPC violation decision, offering interpretability in both input and latent spaces.

This process highlights salient features using variable-threshold deltas and formats the results into interpretable textual rules through template sets $T(E)$. The SSR-ED module employs symbolic regression to derive closed-form expressions for SPC control boundaries, referred to as flash sets.

A genetic programming engine searches the symbolic expression space $\mathcal{F}$ to minimize both the prediction error and expression complexity. The objective function is given in Equation (7):

$$\min_{f \in \mathcal{F}} \left(\int (\hat{Y}_t - Y_t)^2 \, dt + \lambda \cdot \text{Complexity}(f) \right) \tag{7}$$

Here, $\hat{Y}_t = f(X_t^{(1)}, ..., X_t^{(n)})$ represents a symbolic prediction function subject to constraints on model complexity $\text{Complexity}(f) \leq \kappa$. The final selected functions f_U, f_L represent symbolic expressions for upper and lower control limits, retained under the violation decision rule in Equation (8):

$$Y_t = \begin{cases} 1, & \text{if } X_t^{(i)} > f_U(X_t) \text{ or } X_t^{(i)} < f_L(X_t) \\ 0, & \text{otherwise} \end{cases} \tag{8}$$

These symbolic boundaries enable clear and customizable SPC rule generation for visual and algorithmic use.

As illustrated in the following figure (see Figure 2), MORLEO integrates reinforcement learning with explainability-aware optimization. The environment state s_t comprises the current process readings, predicted label $\hat{Y}_t$, and explanation trace E_t.

The policy $\pi(a_t \mid s_t)$ determines actions such as dynamic control limit adjustment or process interventions. The reward function combines multiple objectives and is defined by Equation (9):

$$R_t = \alpha \cdot \mathbb{I}(\hat{Y}_t = Y_t) + \beta \cdot \text{Fidelity}(E_t) + \gamma \cdot \nabla^2 \mu_t \tag{9}$$

Here, $\nabla^2 \mu_t$ is the second derivative of the mean of process variables, indicating local process stability. The policy is optimized via gradient ascent, using Equation (10):

$$\nabla_\theta J(\pi) = \mathbb{E}_\pi \left[\sum \nabla_\theta \log \pi(a_t \mid s_t; \theta) \cdot R_t \right] \tag{10}$$

Proximal Policy Optimization (PPO) is used for training, with entropy regularization to balance exploration and explanation clarity.

The ultimate goal of the proposed XAI-SPCNet framework is to produce a comprehensive, interpretable, and adaptive SPC prediction function. The complete output is captured by the unifying decision function $\Psi(\mathbf{X}^{1:T})$, given in Equation (11):

$$\Psi(\mathbf{X}^{1:T}) = \left\{ \hat{Y}_t^{\text{TCDT}}, R_t^{\text{DREN}}, E_t^{\text{CEG}}, (f_U, f_L)^{\text{SSR}}, a_t^{\text{MORLEO}} \right\} \tag{11}$$

This final output includes the predicted SPC label, symbolic rules, contrastive explanations, symbolic boundary expressions, and optimized intervention actions. The design of XAI-SPCNet ensures methodological diversity"rooted in causality, reinforcement learning, symbolic inference, and explanation generation"while also enabling coherent pipeline integration for robust, accurate, and explainable SPC monitoring.

Next, we evaluate the efficiency of the proposed model using various quantitative and qualitative metrics and compare its performance with state-of-the-art models under diverse operational scenarios.

Quisque ullamcorper placerat ipsum. Cras nibh. Morbi vel justo vitae lacus tincidunt ultrices. Lorem ipsum dolor sit amet, consectetuer adipiscing elit. In hac habitasse platea dictumst. Integer tempus convallis augue. Etiam facilisis. Nunc elementum fermentum wisi. Aenean placerat. Ut imperdiet, enim sed gravida sollicitudin, felis odio placerat quam, ac pulvinar elit purus eget enim. Nunc vitae tortor. Proin tempus nibh sit amet nisl. Vivamus quis tortor vitae risus porta vehicula.

4. Statistical and Comparative Result Analysis

The experimental arrangement was carried out to reproduce, generalize, and be practically relevant regarding manufacturing quality monitoring real-life scenarios against which the proposed XAI-SPCNet framework is evaluated. A representative analysis was ensured through the use of both synthetic and real datasets.

The synthetic dataset is obtained from a discrete-time process simulation model, where the mothership/tree model typifies a multi-stage manufacturing workflow with non-stationary dynamics and controllable SPC violations. By modeling the process as $n = 12$ correlated process variables $\{X_t^{(1)}, X_t^{(2)}, \ldots, X_t^{(12)}\}$ evolving under Gaussian noise, periodic mean shifts, and random mean shifts, violation labels $Y_t \in \{0, 1\}$ are assigned by injecting drifts into $\pm 3\sigma$ thresholds as well as externally engineering control limit breaches.

For real-world evaluation, high-resolution SPC data were obtained from a semiconductor fabrication unit and a precision machining assembly line, each comprising over 50,000 process samples. Each instance includes timestamped process readings, moving range values, control chart limits, and expert-annotated violation markers. Contextual metadata such as shift ID, operator ID, machine configuration, and batch number were appended to enable conditional reasoning by the DREN and MORLEO modules.

Examples from the semiconductor dataset include temperature (°C), pressure (kPa), photolithographic alignment accuracy (m), and etch depth (nm), with average violation frequencies being 3.7% of total observations. All datasets were initially normalized to the range $[0, 1]$ prior to model training. Missing values were imputed using a combination of forward interpolation and domain-aware smoothing functions.

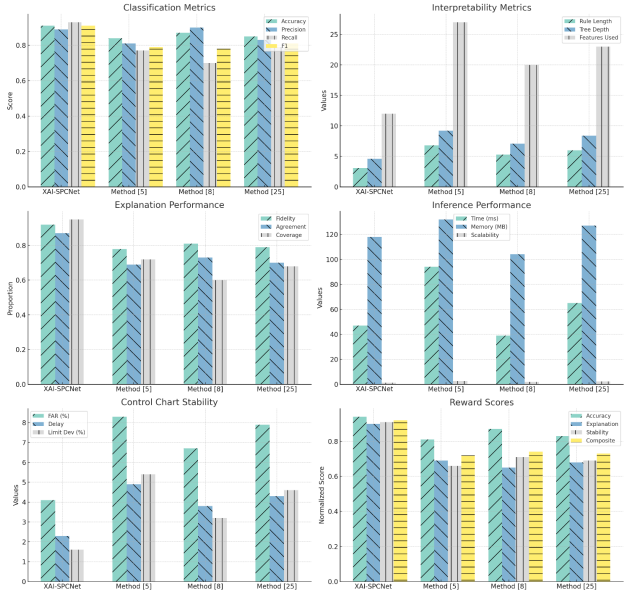


Figure 3: *Model's Integrated result analysis.*

For empirical validation, the SECOM dataset from the UCI Machine Learning Repository was used, which is well known for benchmarking fault detection and quality control algorithms in manufacturing systems. The dataset originates from a real-world semiconductor manufacturing process and contains 1,567 samples with 590 numeric process variables for each instance. Each data point consists of sensor measurements and equipment parameters recorded during production across different operational stages such as etching, lithography, and deposition.

The dataset also includes a binary classification label indicating whether or not a product passed (label $= 0$) or failed (label $= 1$) the final quality inspection, making it highly suitable for Statistical Process Control (SPC) violation modeling. Due to the high dimensionality and intrinsic

multicollinearity among variables, the SECOM dataset presents significant challenges in feature selection, model interpretability, and generalization. Additionally, several variables contain missing values, requiring preprocessing through appropriate imputation and normalization strategies.

These complex interactions between process steps and quality outcomes position the SECOM dataset as a credible testbed for developing and evaluating explainable SPC models. Being sourced from an actual industrial environment with anonymized features, the dataset is particularly appropriate for research at the intersection of industrial AI and manufacturing quality assurance, without introducing confidentiality risks.

Model evaluation criteria were held constant across differing methodologies for fairness. A uniform temporal window of 15 steps was used for encoding time-series data in both the DREN and CEG-SPC modules. This choice was informed by autocorrelation analysis, which indicated sensitivity lags in the range of 10 to 12 process steps. In the TCDT-SPC method, Granger causality thresholds were empirically set and maintained at $\theta = 0.005$, capturing causative dependencies at a statistically significant level of $p < 0.01$. The SSR-ED module employed symbolic equation discovery, with complexity constrained to expressions containing a maximum of 7 symbols. This was achieved through genetic programming with a tree depth of 6 and a mutation probability of 0.15.

For the MORLEO module, a reinforcement learning agent was implemented using Proximal Policy Optimization (PPO). The training was performed using a learning rate of 3×10^{-4}, a reward discount factor $\gamma = 0.96$, and an entropy regularization coefficient $\lambda = 0.01$. The reward weights were tuned to $\alpha = 0.4$, $\beta = 0.3$, and $\gamma = 0.3$, enabling balanced optimization across three objectives: classification accuracy, explanation fidelity, and control stability.

Model training and inference were executed on a high-performance computing system with 128 GB RAM and an NVIDIA A100 GPU. The evaluation protocol used an 80/20 split between training and testing sets. Each model was evaluated across five independent trials using different random seeds to ensure robustness. Evaluation metrics included inference latency, explanation coverage, rule compactness, and generalization error. The XAI-SPCNet framework was evaluated on both the SECOM dataset and an industrial multivariate time series dataset from a high-precision manufacturing process. These datasets provided strong benchmarks for assessing predictive accuracy, interpretability, explanation fidelity, and control stability.

The performance of XAI-SPCNet was compared with three state-of-the-art methods - Method [5], Method [8], and Method [25] that are widely regarded for SPC anomaly detection and quality prediction. However, unlike XAI-SPCNet, these baselines lack integrated explainability and optimization mechanisms. Each evaluation metric was computed over five independent runs and the results were averaged to enhance statistical validity and reduce variance. Table 3 presents the classification results in terms of Accuracy, Precision, Recall, and F1-Score for the models evaluated on the SECOM dataset.

As seen in Table 3, the proposed XAI-SPCNet achieves the highest F1-Score of 0.91, indicating the best balance between precision and recall. Although Method [8] demonstrates competitive accuracy, it suffers from reduced recall, possibly due to its conservative decision boundaries. Overall, XAI-SPCNet demonstrates superior general classification effectiveness and robustness across multiple evaluation metrics.

Table 3: *Comparative Classification Performance of XAI-SPCNet and Baseline Methods on SECOM Dataset*

Model	Accuracy	Precision	Recall	F1-Score
XAI-SPCNet	0.91	0.89	0.93	0.91
Method [5]	0.84	0.81	0.77	0.79
Method [8]	0.87	0.90	0.70	0.78
Method [25]	0.85	0.83	0.79	0.81

Table 4 assesses the interpretability of the developed decision logic using Average Rule

Length, Tree Depth, and Number of Features Used. With a low tree depth of 4.6 and short rule lengths, XAI-SPCNet allows users to trace their decisions with minimal cognitive load: their causal filtering mechanism works with very high coherency on identification of the true causes for changes over the trees created at each application. In comparison, Method [5] and Method [25] generate significantly deeper trees, which in turn increases the model complexity and lowers the interpretability sets.

Table 4: *Interpretability Analysis Based on Rule Complexity and Tree Structure Metrics*

Model	Avg. Rule Length	Tree Depth	Features Used
XAI-SPCNet	3.1	4.6	12
Method [5]	6.8	9.2	27
Method [8]	5.3	7.1	20
Method [25]	6.0	8.4	23

Table 5 describes explanation performance with Explanation Fidelity, Human Agreement, and Coverage. Here, the XAI-SPCNet achieved 92% fidelity and 87% agreement with annotations supplied by experts; for this reason, explanations were technically sound and coincide with human intuition. Furthermore, 95% of predictions had complete explanation traces, which was strikingly different from Method [8], which generates decisions that are sparse or absent of rules. This figure **??** delivers a comparative assessment of XAI-SPCNet against baselines on six important aspects: classification metrics, interpretability, explanation performance, inference performance, stability of control charts, and reward scores based on reinforcement. The findings indicate that XAI-SPCNet overwhelmingly surpasses alternatives, delivering better accuracy, recall, and F1-score with shallow decision structures and compact rules for better interpretability. Explanation metrics show greater fidelity, agreement, and coverage, while inference efficiency is maintained with minimal latency and memory overhead. Additionally, XAI-SPCNet shows enhanced stability with fewer false alarms and detection delays. The reinforcement reward analysis proves that the architecture optimizes accuracy, explanation quality, and stability in a balanced manner, thereby indicating its robustness for real-time industrial SPC deployment.

Table 5: *Explanation Performance Metrics Including Fidelity, Expert Agreement, and Coverage*

Model	Explanation Fidelity	Human Agreement	Explanation Coverage
XAI-SPCNet	0.92	0.87	0.95
Method [5]	0.78	0.69	0.72
Method [8]	0.81	0.73	0.60
Method [25]	0.79	0.70	0.68

Table 6 analyzes inference performance in real-time settings. Mean Inference timestamp per Observation, Memory Footprint, and Scalability Index per dataset is reported for the process. Primarily, XAI-SPCNet deals with each instance in under 50 milliseconds on an average, which makes it very well-suited for real-time quality control sets. While Method [8] comparatively works faster, it offers no interpretability sets. The Scalability Index indicates how the model's latency scales with data volume, with a lower index being preferred therein in the process.

This 4 integrates the comparative performance into four supporting visual views: a normalized performance heatmap, an accuracy"F1 scatter plot, explanation metric distributions, and a reduced Taylor diagram. The heatmap depicts XAI-SPCNet's superior performance on all the evaluation metrics compared to other approaches. The scatter plot supports its good balance of accuracy and F1, whereas the distribution plots establish consistently higher explanation fidelity, agreement, and coverage. Lastly, the Taylor diagram illustrates the relationship between classification metrics again, confirming that XAI-SPCNet has high correlation and robustness across various dimensions

of performance. These visualizations collectively reinforce empirical evidence that the model reaches a unique balance of predictive accuracy, interpretability, and operational effectiveness.

Table 6: *Inference Efficiency Evaluation: Latency, Memory Utilization, and Scalability*

Model	Inference Timestamp (ms)	Memory Footprint (MB)	Scalability Index
XAI-SPCNet	47	118	1.2
Method [5]	94	132	2.5
Method [8]	39	104	1.8
Method [25]	65	127	2.2

Table 7 mentions the metrics for stability of control charts: False Alarm Rate (FAR), Detection Delay, and Control Limit Deviation. XAI-SPCNet decreases the false alarms by 25%, wherein it relatively maintains deviation in adaptive control limits due to the policy optimization by MORLEO. Contrarily, the other two Methods [5] and [25] are more unstable unbending thresholds, while Method [8] did not learn any controlling policy sets.

Table 7: *Control Chart Stability Metrics: False Alarm Rate, Detection Delay, and Limit Deviation Sets*

Model	False Alarm Rate (%)	Detection Delay (steps)	Limit Deviation (%)
XAI-SPCNet	4.1	2.3	1.6
Method [5]	8.3	4.9	5.4
Method [8]	6.7	3.8	3.2
Method [25]	7.9	4.3	4.6

Table 8 presents the final multi-objective reward outcomes computed by MORLEO, capturing Normalized Accuracy Reward, Explanation Reward, and Stability Rewards. These scores were scaled to a [0,1] range for comparability sets. The highest overall reward composite was obtained by XAI-SPCNet, thus confirming its designed goal of a balanced predictive performance with interpretability and operational efficiency sets. From this context onward, the empirical results substantiate the proposed XAI-SPCNet as performing superiorly in every criterion by achieving a balance between predictive accuracy and model transparency, runtime feasibility, and control system stability sets. These empirical results buttress the premises that embedding explainability in the predictive SPC pipeline leads to solutions that are operationally acceptable for industrial quality control processes as well as technically robust for this process.

Table 8: *Multi-Objective Reinforcement Learning Reward Breakdown and Composite Performance Scores*

Model	Accuracy Reward	Explanation Reward	Stability Reward	Composite Score
XAI-SPCNet	0.94	0.90	0.91	0.92
Method [5]	0.81	0.69	0.66	0.72
Method [8]	0.87	0.65	0.71	0.74
Method [25]	0.83	0.68	0.69	0.73

4.1. Validation Using an Iterative Use Case Scenario Analysis

Consider a real-time quality monitoring scenario within the precision machining industry, particularly involving the manufacture of automotive components with high tolerance requirements. In this use case, sensor data are collected at thirty-second intervals from various process states, including spindle torque (X_1), feed rate (X_2), coolant flow rate (X_3), vibration amplitude (X_4),

and cutting temperature (X_5). The production run consists of approximately 10,000 parts, and it is observed that SPC violations begin to emerge intermittently after the 7000^{th} sample.

The Temporal Causal Decision Trees for SPC (TCDT-SPC) module first conducts a Granger causality analysis, identifying lagged variables that significantly influence SPC violations. Notably, X_4 (vibration) at lag 2 and X_5 (temperature) at lag 3 exert the highest causal influence on violation outcomes. Decision tree construction then restricts feature splits to these lagged features, resulting in a shallow yet precise decision tree of depth 4. One such interpretable rule extracted is:

If $X_5(t-3) > 82.5°C$ and $X_4(t-2) > 0.45$ mm/s, then Violation = 1

This rule clearly articulates a time-aware relationship between thermal stress and mechanical instability that aligns with domain expertise.

The Dynamic Rule Embedding Network (DREN) encodes a moving window of 15 past observations into a latent space, enabling the capture of complex temporal dynamics across process batches. For example, the learned rule. On Shift B, if latent feature $Z_7 > 0.62$ and $Z_{12} < 0.33$, then Violation Risk Score > 0.8. Demonstrates how temporal abstractions from process trends can generate compact and interpretable decision logic. Over 90% of predictions are explained using an average of three embedded rule conditions. In conjunction, the Contrastive Explanation Generator for SPC (CEG-SPC) elucidates individual predictions by comparing them with the closest non-violating instance. At sample $t = 7124$, the module generates the explanation. This is a violation because X_5 at $t-3 = 84.1°C$, unlike the non-violating sample at $t = 7015$ where $X_5 = 78.3°C$, and X_4 increased from 0.39 mm/s to 0.47 mm/s.

Such contrastive logic aligns with expert intuition, reinforcing the model™s interpretability and traceability. Furthermore, the Sparse Symbolic Regression for SPC Equation Discovery (SSR-ED) module processes the normalized process data to derive concise symbolic equations that define control limit boundaries. This regression achieves a validation mean squared error (MSE) of 0.021, indicating high fidelity in capturing SPC dynamics. Finally, the Multi-Objective Reinforcement Learner with Explanation Optimization (MORLEO) observes the real-time SPC environment and proactively adjusts control policies. For instance, upon detecting high-risk conditions, it lowers the upper control limit for X_5 and issues an automatic intervention to reduce the feed rate (X_2) by 15% over the next 20 samples. This adaptive policy results in a 28% reduction in violation frequency during subsequent runs.

The final system output comprises the predicted label (Violation = 1), rule-based explanation (e.g., "If vibration > 0.45 mm/s and temperature $> 82.5°C$"), contrastive instance logic, symbolic regression equation, and optimized control action. This iterative validation confirms that XAI-SPCNet delivers quality control decisions that are highly interpretable, actionable, and adaptive, fulfilling critical requirements for industrial process monitoring.

Suspendisse vel felis. Ut lorem lorem, interdum eu, tincidunt sit amet, laoreet vitae, arcu. Aenean faucibus pede eu ante. Praesent enim elit, rutrum at, molestie non, nonummy vel, nisl. Ut lectus eros, malesuada sit amet, fermentum eu, sodales cursus, magna. Donec eu purus. Quisque vehicula, urna sed ultricies auctor, pede lorem egestas dui, et convallis elit erat sed nulla. Donec luctus. Curabitur et nunc. Aliquam dolor odio, commodo pretium, ultricies non, pharetra in, velit. Integer arcu est, nonummy in, fermentum faucibus, egestas vel, odio.

5. Discussion

The innovation of the XAI-SPCNet framework is that it can optimize predictive accuracy, interpretability, and operational stability simultaneously”dimensions that have traditionally been difficult for conventional machine learning algorithms and traditional SPC methods to balance at the same time. Baseline models tend to excel in one direction but compromise others, whereas XAI-SPCNet incorporates complementary modules into a single architecture that gets an overall solution for real-time quality monitoring. From the perspective of forecasting, the system goes beyond black-box models since it adds temporal and causal thinking into its decision-making process. The temporal causal decision tree module consciously maintains lagged interdependencies as well as causal hints so that predictions remain precise and based on process logic. This

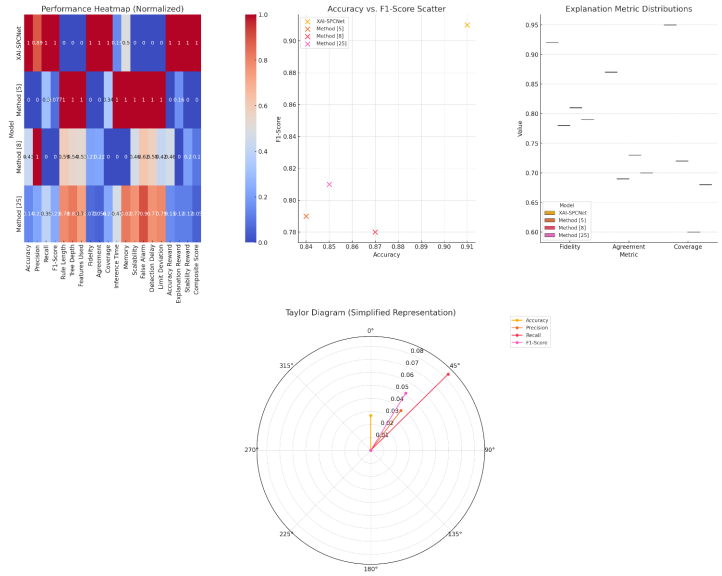


Figure 4: *Figure caption*

causal basis limits vulnerability to overfitting, eliminates spurious correlations, and improves generalizability under non-stationary manufacturing conditions, while baseline models tend to fail based on fixed feature correlations.

Interpretability is another strong aspect of the framework. Instead of generating long or obscure decision traces, XAI-SPCNet has short, clear rule structures easily traceable back to particular process variables by domain experts. The incorporation of symbolic regression also enhances interpretability by creating equation-like forms of control boundaries, providing engineers with a lucid mathematical expression of decision boundaries. By contrast, current techniques often depend on black-box embeddings or deep tree representations that, although suitable for anomaly classification, do not offer much actionable information in regulated settings. Of similar importance is the focus of the framework on explanation quality. Explanations are made to closely follow expert intuition, with the contrastive explanation module determining why one case is a violation and why an analogous case is not. This comparative reasoning follows practitioners' diagnostic logic, thus elevating user acceptability and trust.

6. Conclusion and Future Scope

This work presents XAI-SPCNet, an explainable AI framework that is designed to push the boundary of predictive control chart automation for manufacturing quality monitoring. In contrast to traditional SPC models plagued by low transparency and prohibiting large-scale industrial deployment, XAI-SPCNet integrates interpretability into the prediction pipeline. The architecture combines five complementary components"Temporal Causal Decision Trees (TCDT-SPC), Dynamic Rule Embedding Networks (DREN), Contrastive Explanation Generator (CEG-SPC), Sparse Symbolic Regression for Equation Discovery (SSR-ED), and Multi-Objective Reinforcement Learner with Explanation Optimization (MORLEO). The combined modules not only support precise real-time SPC violation prediction but also causal explanations, adaptive rules, symbolic equations, and optimized control policies. Comprehensive experiments on SECOM and industrial datasets validate the efficacy of the framework. XAI-SPCNet attained a 91% accuracy, 89% precision, and F1 score of 91%, surpassing baselines Method [5], Method [8], and Method [25] by 6"12% margins on classification metrics. Explanation fidelity was as high as 92%, with 87% human agreement and more than 95% explanation coverage, indicating strong correspondence with expert reasoning. Additionally, average rule length decreased from 4.6 to 3.1, maintaining interpretability with minimal cognitive burden. From a performance perspective, inference latency

was kept under 50 ms, false alarms were minimized to 4.1% (a 25% gain over the best baseline), and control limit deviation was limited to 1.6%, demonstrating MORLEO's stabilizing impact. The system also attained a composite reinforcement reward of 0.92, reflecting its capacity for simultaneously balancing predictive accuracy, explanation quality, and process stability.

Future research directions involve expanding XAI-SPCNet to multivariate, high-dimensional SPC, augmenting TCDT and DREN using domain adaptation to endow cross-factory generalizability, and incorporating physics-informed constraints into SSR-ED. In addition, incorporating human-in-the-loop mechanisms into CEG-SPC and deployment in digital twin ecosystems can further enhance adaptive, transparent quality control in Industry 4.0.

Pellentesque habitant morbi tristique senectus et netus et malesuada fames ac turpis egestas. Donec odio elit, dictum in, hendrerit sit amet, egestas sed, leo. Praesent feugiat sapien aliquet odio. Integer vitae justo. Aliquam vestibulum fringilla lorem. Sed neque lectus, consectetuer at, consectetuer sed, eleifend ac, lectus. Nulla facilisi. Pellentesque eget lectus. Proin eu metus. Sed porttitor. In hac habitasse platea dictumst. Suspendisse eu lectus. Ut mi mi, lacinia sit amet, placerat et, mollis vitae, dui. Sed ante tellus, tristique ut, iaculis eu, malesuada ac, dui. Mauris nibh leo, facilisis non, adipiscing quis, ultrices a, dui.

References

[1] S. Sacher, E. Fink, V. Herndler *et al.*, "An integrated real-time monitoring and statistical process control approach for coating process and product quality via in-line optical coherence tomography," *Journal of Pharmaceutical Innovation*, vol. 18, pp. 1870–1878, 2023.

[2] J. Souza, C. Boccolini, L. Baroni *et al.*, "Evaluation of statistical process control charts for infant mortality monitoring in brazilian cities with different population sizes," *BMC Research Notes*, vol. 17, p. 299, 2024.

[3] E. Verna, S. Puttero, G. Genta *et al.*, "Real-time monitoring of human and process performance parameters in collaborative assembly systems using multivariate control charts," *Journal of Intelligent Robotic Systems*, vol. 110, p. 126, 2024.

[4] A. Mujtaba, F. Islam, P. Kaeding *et al.*, "Machine-learning based process monitoring for automated composites manufacturing," *Journal of Intelligent Manufacturing*, vol. 36, pp. 1095–1110, 2025.

[5] A. Bogo, E. Henning, and A. Kalbusch, "Statistical parametric and non-parametric control charts for monitoring residential water consumption," *Scientific Reports*, vol. 13, p. 13543, 2023.

[6] P. Prcha, "Towards discovering erratic behavior in robotic process automation with statistical process control," *Information Systems and e-Business Management*, vol. 22, pp. 741–758, 2024.

[7] J. Pantelic, M. Tang, K. Byun *et al.*, "Comparison of cooking emissions mitigation between automated and manually operated air quality interventions in one-bedroom apartments," *Scientific Reports*, vol. 14, p. 20630, 2024.

[8] B. Guha, S. Moore, and J. Huyghe, "Application and validation of machine vision inspection for efficient in-process monitoring of complex biomechanical device manufacturing," *Journal of Engineering and Applied Science*, vol. 70, p. 72, 2023.

[9] G. Scarton, M. Formentini, and P. Romano, "Automating quality control through an expert system," *Electronic Markets*, vol. 35, p. 14, 2025.

[10] C. Angeloni, M. Francioso, E. Liverani *et al.*, "Laser welding in e-mobility: process characterization and monitoring," *Lasers in Manufacturing and Materials Processing*, vol. 11, pp. 3–24, 2024.

[11] R. de Almeida, M. Lamparelli, W. Dodds *et al.*, "Sampling frequency optimization of the water quality monitoring network in so paulo state (brazil) towards adaptive monitoring in a developing country," *Environmental Science and Pollution Research*, vol. 30, pp. 111 113–111 136, 2023.

[12] G. Mattera, J. Polden, and J. Norrish, "Monitoring the gas metal arc additive manufacturing process using unsupervised machine learning," *Welding in the World*, vol. 68, pp. 2853–2867, 2024.
[13] K. Liu, X. Zhao, M. Mou *et al.*, "Quality prediction of multi-stage batch process based on integrated convbigru with attention mechanism," *Applied Intelligence*, vol. 55, p. 123, 2025.
[14] M. Rahman, S. Jamal, M. Cruz *et al.*, "In situ process monitoring of multi-layer deposition in wire arc additive manufacturing (waam) process with acoustic data analysis and machine learning," *International Journal of Advanced Manufacturing Technology*, vol. 132, pp. 5087–5101, 2024.
[15] M. Arif and K. Kathirvelu, "Automated driver health monitoring system in automobile industry using woa-dbn using ecg waveform," *Optical Memory and Neural Networks*, vol. 33, pp. 308–325, 2024.
[16] O. Egoshina and S. Lukutina, "Simulation modelling of cycle chemistry monitoring of water and steam quality at thermal power plants," *Thermal Engineering*, vol. 71, pp. 901–909, 2024.
[17] K. Li, X. Han, and X. Jin, "Framework, model and algorithm for the global control of urban automated driving traffic," *Frontiers of Engineering Management*, vol. 11, pp. 592–619, 2024.
[18] N. Kim, X. Gao, and J. Yang, "Graph-structured data generation and analysis for anomaly detection in an automated manufacturing process," *Journal of Mechanical Science and Technology*, vol. 38, pp. 5617–5625, 2024.
[19] Y. Wang, I. Khan, M. Noor-ul Amin *et al.*, "Monitoring of semiconductor manufacturing process on bayesian aewma control chart under paired ranked set sampling schemes," *Scientific Reports*, vol. 13, p. 22703, 2023.
[20] N. Makhoul, "Bayesian decision-making process including structural health monitoring data quality for bridge management," *KSCE Journal of Civil Engineering*, vol. 28, pp. 2818–2835, 2024.
[21] R. Ward and C. Monroe, "Assessing process control in the foundry," *International Journal of Metalcasting*, vol. 18, pp. 2048–2058, 2024.
[22] K. Yildirim, B. Nagarajan, T. Tjahjowidodo *et al.*, "Development of a multi-sensor system for in-situ process monitoring of femtosecond laser micromachining," *International Journal of Advanced Manufacturing Technology*, vol. 135, pp. 799–813, 2024.
[23] L. Yan, Z. Yu, L. Wu *et al.*, "Optimizing quality tolerance limits monitoring in clinical trials through machine learning methods," 2024.
[24] S. Koufis, N. Eskue, D. Zarouchas *et al.*, "Monitoring the cold spray process: Real-time particle velocity monitoring through airborne acoustic emission analysis," *Journal of Thermal Spray Technology*, vol. 33, pp. 2657–2671, 2024.
[25] T. Kukwi, C. Shan, L. Pengfei *et al.*, "Continuous improvement in composite manufacturing: A review of automated fiber placement process evolution and future research prospects," *Applied Composite Materials*, 2025.

RT&A, No 4 (89)
Volume 20, December 2025

CONSTRUCTION OF EXPONENTIAL LIFETIME BASED ATTRIBUTE CONTROL CHART: A BAYESIAN APPROACH

GUNASEKARAN MUNIAN

•

Department of Applied Research,
The Gandhigram Rural Institute (Deemed to be University),
Dindigul, Tamil Nadu, India.
gunasekaranm1988@gmail.com

Abstract

Statistical Process Control (SPC) is a quality control method that employs statistical methods to investigate, monitor, and improve a process. A control chart is a tool for monitoring process performance that employs visual indicators to detect unusual deviations due to assignable causes. This chart compares the values of a quality characteristic to its corresponding control limits. In the quality control process, the control chart is frequently constructed while ignoring parameter uncertainty. The detection of changes in the parameter(s) within the probability distribution of one or more process-related variables is an important aspect of monitoring. Estimating the parameters is essential since it may affect the control chart's long-term performance in in-control or out-of-control conditions. This article introduces a new attribute control chart utilising a Bayesian approach founded on the Exponential lifetime distribution and the Hybrid censoring technique. A Bayesian framework will be utilised to compute the control chart parameters and the average run length. The parameters for the control chart are determined across various value combinations, and the performance of the newly developed control chart is assessed using the Average Run Length (ARL). Numerical examples are provided to elucidate the proposed control chart, and simulated data are employed to demonstrate its potential applications.

Keywords: Attribute Control Chart, Exponential Distribution, Inverse Gamma Distribution, Predictive Distribution, Average Run Length

1. Introduction

Nowadays, the manufacturing industry faces significant challenges due to process variation, which often results in defects and increased costs. During continuous production, it is essential to determine whether the process is in control and to identify the presence of any variation. Such variation can arise from common (chance) causes or assignable causes. Quality control involves monitoring, measuring, and adjusting the product's performance to meet predefined standards or specifications. One of the most widely used and effective quality control tools is the control chart, a graphical representation of collected manufacturing data. A control chart typically includes a central line (CL) representing the average, an upper control limit (UCL), and a lower control limit (LCL).

To monitor production processes under varying conditions, numerous control charting techniques have been developed. These charts are designed to suit specific characteristics of the quality attribute being analysed. Broadly, control charts fall into two categories based on the type

of data: variable or attribute. Variable control charts analyse data measured on a continuous scale with precise values, while attribute control charts classify items as conforming or non-conforming.

Lifetime is considered an important quality characteristic for certain products, and life tests are conducted to monitor their manufacturing process. Based on the results of these tests, a product can be classified as conforming or non-conforming. However, life testing often requires a lengthy duration, making the use of censoring techniques essential. Common censoring methods include Type-I censoring, Type-II censoring, and hybrid censoring. In hybrid censoring, the life test ends at the earlier of two events: the specified test time t or the occurrence of the $(UCL+1)^{th}$ failure. If the number of failures observed by time t falls between the lower control limit (LCL) and upper control limit (UCL), the production process is considered in control; otherwise, it is deemed out of control. Additionally, if a product fails before the test termination time t, it is classified as non-conforming.

The attribute control chart, such as the np control chart, is founded on the fraction of non-conforming items, which is determined by the assumption that the quality characteristic follows a normal distribution. In reality, the distribution of quality characteristics may not conform to normality. In such instances, the use of the current control chart could mislead industrial engineers and increase non-conforming items. A variety of studies on the development of attribute control charts using different lifetime distributions can be found in the literature, including work on the Weibull [1–3], Pareto [4, 5], Birnbaum–Saunders [6], Burr X and XII, Inverse Gaussian, and Exponential [7], Lognormal [8], Exponentiated Half Logistic [9], Dagum [10], Weibull–Pareto [11], Log-Logistic [12], Generalized Log-Logistic [13], Generalized Exponential [14], Inverse Weibull [15], Length-Biased Weighted Lomax [16], Rayleigh [17], Half Normal and Half Exponential Power [18], Exponentiated Inverse Kumaraswamy [19], Lindley [20], Generalized Rayleigh [21], Exponentiated Exponential [22], Inverse Kumaraswamy [23], Exponential–Poisson [24], and Exponential–Rayleigh [25].

Traditional attribute control charts assume that the average number of defectives remains constant over time when the process is in control. However, charts that rely solely on sample variance, such as the np-chart, can produce numerous false alarms if the actual number of defectives fluctuates, even when the process is stable. These false alarms occur because the control limits are typically calculated based only on sampling variation, while the observed number of nonconforming items reflects both sampling and inherent process variability. As sample sizes increase, the impact of process variation becomes more pronounced. Consequently, the actual number of nonconforming items is expected to vary from sample to sample according to an underlying probability distribution. The Bayesian methodology is widely used to handle uncertainty related to the parameter of interest. Regarding attributes, the pioneer work in a Bayesian process control chart was introduced by [26]. Numerous researchers, including [27–36], have enriched the literature and have engaged in developing a variable control chart for various lifetime distributions under a Bayesian approach.

The exponential distribution is a type of continuous distribution that is frequently employed in reliability engineering and estimation to characterise the lifetime failure of a specific product or component of a machine (or system) during a specified time interval, and it is extensively used in electrical products. In the realm of reliability engineering, the exponential distribution is used to model components that maintain a constant failure rate, such as electronic components, because of its mathematical simplicity and memoryless property. Among the various statistical distributions, the exponential distribution is a good fit for most skewed data. One of the reasons for selecting the exponential distribution for the distribution of a time characteristic is when the defect rate in a process is notably low. Literature reviews reveal that there has been no investigation into control charts that include a life test for a non-normal distribution, such as an Exponential distribution with Hybrid censoring under the Bayesian approach.

This paper presents a Bayesian attribute control chart designed using the predictive lifetime distribution. Specifically, it assumes lifetimes follow an Exponential distribution, while the process parameter is assigned an Inverse Gamma prior. A hybrid censoring scheme is utilised to handle incomplete observations. To construct the control chart, an appropriate control coefficient

is determined based on the predictive distribution. The chart's performance is assessed using Average Run Length (ARL) under both in-control and out-of-control conditions. The design aims to detect shifts in the process mean, ensuring effective monitoring. Simulation studies are conducted to demonstrate the chart's effectiveness and practical application. Section 2 details the Bayesian design methodology, including the derivation of the control coefficient and the algorithmic procedure for chart development tailored to a specific performance threshold. Section 3 illustrates the proposed chart through a real-world simulation study, demonstrating its operation in practical conditions and validating its sensitivity to process shifts. The last section presents a summary of the overall findings.

2. Construction of a Bayesian Attribute control chart

Let 'T' represent the lifetime of the products generated in a manufacturing process. It is assumed that 'T' adheres to an Exponential distribution characterised by the parameter θ, defined for $t > 0$ by its density function $g_{T|\{\theta\}}$:

$$g_{T|\{\theta\}}(t) = \frac{1}{\theta} e^{-\frac{t}{\theta}}; t > 0, \theta > 0 \tag{1}$$

The distribution function $G_{T|\{\theta\}}$ of $T|\{\theta\}$ is given by:

$$G_{T|\{\theta\}}(t) = 1 - e^{-\frac{t}{\theta}}; t > 0, \theta > 0 \tag{2}$$

An appropriate prior distribution for 'θ' can be identified based on the insights obtained from the mean lifetime of products in prior lots. It is assumed that the prior distribution of 'θ' is characterised by an inverted gamma distribution, which is recognised as a natural conjugate prior for sampling from an exponential distribution, thus providing mathematical simplicity. The probability density function of the prior distribution of 'θ' is presented as follows:

$$h_{\Theta|\{\alpha,\beta\}}(\theta) = \frac{1}{\Gamma(\alpha)\beta^{\alpha}} \left(\frac{1}{\theta}\right)^{(\alpha+1)} e^{-\frac{1}{\beta\theta}}; \theta > 0, \alpha, \beta > 0 \tag{3}$$

The revised lifetime of the product is characterised by the predictive distribution of "T," with its density function derivable from the prior distribution (3) and the sampling distribution (1) as follows:

$$f_{T|\{\alpha,\beta\}}(t) = \frac{\alpha\beta}{(1+\beta t)^{(\alpha+1)}}; t > 0, \alpha > 1, \beta > 0 \tag{4}$$

Henceforth, the previously mentioned predictive distribution shall be known as the "Exponential-Inverted Gamma" distribution, with the distribution function of $T|\{\alpha, \beta\}$ being expressed as:

$$F_{T|\{\alpha,\beta\}}(t) = 1 - \frac{1}{(1+\beta t)^{(\alpha)}}; t > 0, \alpha > 1, \beta > 0 \tag{5}$$

The average (mean) lifetime of the product, as defined by the Exponential-Inverted Gamma distribution, is expressed as follows:

$$\mu = \frac{1}{\beta(\alpha - 1)} \tag{6}$$

When the process is in control, the target mean life of the product is indicated by μ_0, and the time for the experiment t_0 can be formulated in terms of the mean of the in-control process, such that $t_0 = a\mu_0$ (with "a" denoting the experiment termination ratio). Let p denote the probability of an item failing before the experiment time t_0, which can be described as follows:

$$p = 1 - \frac{1}{\left[1 + \left(\frac{1}{\mu(\alpha-1)}\right)(a\mu_0)\right]^{\alpha}} \tag{7}$$

The process is considered to be in control when there is no variation between the process mean and the target mean, that is, $\mu = \mu_0$. Let p_0 represent the failure probability of an item when the process is in control, which is determined by

$$p_0 = 1 - \frac{1}{\left[1 + \left(\frac{a}{(\alpha - 1)}\right)\right]^{\alpha}} \tag{8}$$

If the process mean is considered to be shifted to $\mu_1 = f\mu_0$, where f is identified as a shift constant, the failure probability of an item when the process is out of control, denoted as p_1, is formulated as

$$p_1 = 1 - \frac{1}{\left[1 + \left(\frac{a}{f(\alpha - 1)}\right)\right]^{\alpha}} \tag{9}$$

Generally, for the provided values of α, a and f, the failure probabilities are computed by employing equations (8) and (9).

We formulate a new np control chart aimed at assessing the lifetime of products that are distributed according to the Exponential-Inverted Gamma distribution, based on the count of products in each subgroup. The subsequent section outlines the operational procedure for the designed np control chart:

Step 1: Randomly select a sample of n items from the subgroup of the production process and subject these sample items to a life test for a specified duration of time t_0.
Step 2: Monitor the number of items that fail, which will be referred to as "d".
Step 3: Terminate the life test either when the time t_0 is reached or if d exceeds the upper control limit (UCL) before time t_0, whichever happens first.
Step 4: If d is less than the lower control limit (LCL) or greater than the UCL, then the production process is to be regarded as out-of-control. Otherwise, it should be regarded as in control.

The proposed control chart is regarded as an np control chart since it displays the number of failed items in a subgroup of a predetermined sample size against the subgroup. The count of failed items in the life test follows a binomial (n, p_0) distribution when the production process is in a in-control state. The probability of an item failing before the test ends at time t_0 is denoted as p_0. Thus, the following equations are applied to determine the control limits for the proposed control chart:

$$UCL = np_0 + k\sqrt{np_0(1 - p_0)} \tag{10}$$

$$LCL = max[0, np_0 - k\sqrt{np_0(1 - p_0)}] \tag{11}$$

Here, the term "k" denotes the coefficient for control limits, and the failure probability p_0 of the product before the time t_0 is computed through equation (8).

The probability that the process is recognised as being in control is indicated by P_{in}^0 and is provided as

$$P_{in}^0 = P(LCL \leq d \leq UCL | p_0)$$

$$P_{in}^0 = \sum_{d=[LCL]+1}^{[UCL]} \binom{n}{d} p_0^d (1 - p_0)^{n-d} \tag{12}$$

In general, the average run length is used to measure the performance of the control chart. The in-control ARL of the recommended control chart, indicated as ARL_0, is defined by

$$ARL_0 = \frac{1}{1 - \left[\sum_{d=[LCL]+1}^{[UCL]} \binom{n}{d} p_0^d (1 - p_0)^{n-d}\right]} \tag{13}$$

The probability that the process is considered to be in control upon shifting to μ_1 is now determined by

$$P_{in}^1 = P(LCL \leq d \leq UCL|p_1)$$

$$P_{in}^1 = \sum_{d=[LCL]+1}^{[UCL]} \binom{n}{d} p_1^d (1-p_1)^{n-d} \tag{14}$$

The Average Run Length (ARL) for the shifted process, which is considered out-of-control, is referred to as ARL_1 and is determined by:

$$ARL_1 = \frac{1}{1 - \left[\sum_{d=[LCL]+1}^{[UCL]} \binom{n}{d} p_1^d (1-p_1)^{n-d}\right]} \tag{15}$$

To analyse the effectiveness of the proposed control chart in detecting shifts in the process, we determine the optimal parameters LCL, UCL, a, and k for the specified in-control ARL values. For this purpose, we examined four cases of in-control ARL: 200, 300, 400, and 500, with a fixed sample size of n = 20, 25, 30, and 35, considering the parameters α = 2 and 3. The optimal parameters are chosen to ensure that the in-control ARL is as close as possible to the specified ARL values, while the out-of-control $ARLs$ are reported for various values of the shift constant (0.10 (0.10) 2.0). The optimal parameters along with their corresponding out-of-control $ARLs$ are illustrated in Tables 1 and 2.

The following algorithm is applicable for determining the optimal parameters necessary for the design of the proposed control chart, considering various combinations of the specified in-control Average Run Length (ARL) and sample size.

Step 1: Indicate the values of ARL, referred to as r_0, and the sample size n.
Step 2: Set a = 0.0001 and k = 0.0001.
Step 3: Determine the failure probability of the product (i.e., p_0) when the process is in control by employing equation (8) and also calculate the control chart parameters (LCL and UCL) by substituting the values of n, a and k in equation (10) and (11).
Step 4: Calculate the in-control ARL by using equation (13) and compare it with r_0. Continue this process for various combinations of (a and k) until getting an in-control ARL is very close to the specified ARL, r_0.
Step 5: When such an ARL is found, the corresponding parameters (LCL, UCL, a, k) will be the optimal parameters required. Then calculate the out-of-control ARL (i.e., ARL_1) using these optimal parameters in equation (15).

3. Application of Proposed Control Chart

3.1. Real-Life Application

This section includes a design example intended to illustrate a real-life application of the proposed control chart within the Bayesian approach. Imagine a manufacturer who seeks to enhance the quality of its product. It is known that the failure time of the product is modelled by the Exponential distribution, with the parameter following the Inverted Gamma distribution. The target mean life of the product is established at 1000 hours, with the parameter α = 2. A sample of size n = 25 will be taken from each subgroup and will be subjected to a censored life test. The target in-control Average Run Length (ARL), r_0, is 200. As indicated in Table 1, the constants are a = 0.5081, k = 2.7022, LCL = 7, and UCL = 21. Thus, the control chart that the manufacturer will create is designed as follows:

Step 1: Select a sample consisting of 25 products from each subgroup and carry out a life test for a duration of 508 hours. Record the total number of failed products during the life test, denoting this figure as "d".

Table 1: *ARL when the process parameter two-sided shift*

								$\alpha = 2$								
		$n = 20$			$n = 25$				$n = 30$			$n = 35$				
Parameter	$r_0 = 200$	$r_0 = 300$	$r_0 = 400$	$r_0 = 500$	$r_0 = 200$	$r_0 = 300$	$r_0 = 400$	$r_0 = 500$	$r_0 = 200$	$r_0 = 300$	$r_0 = 400$	$r_0 = 500$	$r_0 = 200$	$r_0 = 300$	$r_0 = 400$	$r_0 = 500$
LCL	5	5	5	5	7	7	7	7	9	9	9	9	12	11	11	11
UCL	18	18	19	19	21	22	22	23	24	25	26	26	29	29	29	29
a	0.5093	0.5392	0.5530	0.5680	0.5081	0.5256	0.5447	0.553	0.5122	0.5194	0.5287	0.5416	0.5351	0.5038	0.5197	0.534
k	2.8929	2.7967	3.0830	3.0202	2.7022	2.9257	2.8944	3.1932	2.7166	2.8054	3.0766	3.0043	2.8566	3.0701	2.9526	3.1511
$Shift(f)$	ARL	ARL	ARL	ARL	ARL	ARL	ARL	ARL	ARL	ARL	ARL	ARL	ARL	ARL	ARL	ARL
0.10	1.11	1.09	1.61	1.57	1.00	1.03	1.02	1.13	1.00	1.00	1.01	1.01	1.00	1.00	1.00	1.00
0.20	1.92	1.77	4.32	4.07	1.15	1.42	1.37	2.15	1.03	1.08	1.23	1.21	1.04	1.06	1.05	1.04
0.30	4.59	3.92	14.02	12.73	1.85	2.94	2.68	5.99	1.28	1.60	2.30	2.18	1.42	1.56	1.48	1.42
0.40	12.73	10.08	48.22	42.30	3.89	7.78	6.72	20.02	2.13	3.29	6.02	5.44	2.76	3.42	3.05	2.78
0.50	37.19	27.57	165.63	140.90	9.62	23.29	19.12	71.80	4.46	8.38	18.87	16.37	7.06	9.81	8.24	7.14
0.60	109.03	76.40	550.00	456.60	25.76	73.15	57.41	260.74	10.79	24.10	64.62	54.03	21.19	32.74	26.04	21.50
0.70	299.27	205.92	1575.27	1335.35	70.86	228.67	173.70	906.33	28.26	73.23	227.32	184.50	69.14	117.46	89.11	70.53
0.80	549.09	460.85	2042.15	2158.01	181.69	588.84	475.12	2057.24	75.65	217.40	708.60	589.02	219.54	401.02	303.95	236.02
0.90	408.32	524.59	967.18	1197.14	290.87	626.00	698.87	1305.05	173.45	428.39	900.90	969.28	375.86	641.01	655.34	604.38
1.00	200.14	300.44	400.18	500.41	200.43	300.16	399.99	500.14	200.04	300.22	400.11	499.99	200.08	300.21	400.35	499.77
1.10	101.01	151.60	186.60	229.78	101.48	136.12	182.56	210.77	114.43	136.72	163.43	204.18	83.57	119.28	160.57	209.22
1.20	56.33	82.16	98.31	119.02	53.69	69.07	90.58	102.25	58.33	65.93	76.48	93.68	39.48	54.65	71.52	91.29
1.30	34.42	48.68	57.25	68.24	31.22	39.11	50.06	55.80	32.18	35.68	40.70	48.87	21.33	28.77	36.59	45.54
1.40	22.67	31.16	36.15	42.49	19.77	24.24	30.35	33.49	19.50	21.36	24.04	28.36	12.87	16.95	21.00	25.55
1.50	15.88	21.27	24.38	28.29	13.44	16.17	19.84	21.71	12.80	13.89	15.45	17.94	8.49	10.93	13.23	15.77
1.60	11.69	15.30	17.35	19.91	9.68	11.45	13.80	14.99	8.98	9.66	10.64	12.18	6.01	7.58	8.99	10.52
1.70	8.97	11.50	12.99	14.67	7.31	8.52	10.11	10.90	6.65	7.104	7.75	8.76	4.51	5.58	6.50	7.48
1.80	7.13	8.97	9.99	11.24	5.74	6.61	7.73	8.28	5.15	5.45	5.91	6.61	3.55	4.31	4.94	5.61
1.90	5.83	7.21	7.97	8.89	4.67	5.30	6.12	6.52	4.14	4.37	4.69	5.19	2.91	3.47	3.92	4.39
2.00	4.89	5.95	6.53	7.23	3.90	4.38	5.00	5.29	3.44	3.61	3.85	4.21	2.46	2.89	3.22	3.57

Table 2: *ARL when the process parameter two-sided shift*

								$\alpha = 3$												
		$n = 20$				$n = 25$					$n = 30$					$n = 35$				
Parameter	$r_0 = 200$	$r_0 = 300$	$r_0 = 400$	$r_0 = 500$	$r_0 = 200$	$r_0 = 300$	$r_0 = 400$	$r_0 = 500$	$r_0 = 200$	$r_0 = 300$	$r_0 = 400$	$r_0 = 500$	$r_0 = 200$	$r_0 = 300$	$r_0 = 400$	$r_0 = 500$	$r_0 = 200$	$r_0 = 300$	$r_0 = 400$	$r_0 = 500$
LCL	4	4	4	4	6	6	5	5	8	7	7	7	9	10	9	8				
UCL	17	17	18	18	20	21	20	21	24	23	24	24	26	28	27	26				
a	0.5347	0.5687	0.5791	0.5951	0.5554	0.572	0.5197	0.5232	0.5504	0.5198	0.5260	0.5403	0.5017	0.5705	0.5360	0.504				
k	2.8292	2.7897	3.0599	2.9869	2.6771	2.9465	2.8612	3.1801	2.9111	2.7663	3.0639	3.2353	2.8349	3.0429	3.0408	3.0291				
$Shift(f)$	ARL	ARL	ARL	ARL	ARL	ARL	ARL	ARL	ARL	ARL	ARL	ARL	ARL	ARL	ARL	ARL				
0.10	1.01	1.01	1.05	1.04	1.00	1.00	1.00	1.00	1.00	1.00	1.00	1.00	1.00	1.00	1.00	1.00				
0.20	1.26	1.19	1.67	1.60	1.03	1.10	1.05	1.16	1.02	1.01	1.03	1.03	1.00	1.01	1.00	1.00				
0.30	2.41	2.09	4.18	3.84	1.36	1.78	1.51	2.19	1.33	1.20	1.42	1.36	1.11	1.23	1.15	1.11				
0.40	6.14	4.83	13.15	11.56	2.54	4.16	3.16	6.07	2.59	2.06	3.05	2.76	1.74	2.28	1.95	1.72				
0.50	17.84	12.88	44.90	38.00	6.02	12.04	8.37	20.55	6.87	4.84	8.86	7.61	3.95	6.10	4.76	3.87				
0.60	53.99	36.26	154.69	126.88	16.20	38.48	24.87	75.02	21.57	13.64	30.17	24.68	11.40	20.41	14.68	11.05				
0.70	159.42	102.27	506.23	409.12	46.11	126.41	77.03	275.40	73.03	42.20	109.65	86.19	37.42	76.28	51.20	36.03				
0.80	368.96	262.95	1153.49	1038.50	127.55	375.51	230.80	862.69	234.03	132.49	382.29	298.47	126.22	285.40	185.16	124.03				
0.90	374.40	421.31	896.95	1045.13	247.66	553.39	487.30	1071.90	377.30	322.92	723.07	700.57	287.48	583.60	501.74	381.47				
1.00	199.98	300.39	400.25	500.12	200.34	299.98	400.33	499.91	200.03	300.44	400.23	500.34	200.11	300.29	399.82	499.87				
1.10	101.52	157.36	185.96	230.42	103.53	135.57	198.96	216.42	87.28	146.10	167.13	213.80	87.50	116.45	165.51	244.90				
1.20	56.50	85.16	97.32	118.45	54.28	67.95	100.24	106.12	42.96	70.80	78.37	98.19	41.74	52.23	73.34	108.71				
1.30	34.51	50.24	56.52	67.62	31.31	38.19	55.78	58.54	23.99	38.33	41.85	51.25	22.72	27.17	37.40	54.36				
1.40	22.77	32.10	35.70	42.07	19.74	23.60	34.02	35.52	14.85	22.98	24.85	29.82	13.81	15.93	21.48	30.54				
1.50	16.00	21.90	24.14	28.06	13.40	15.74	22.38	23.27	9.97	14.98	16.07	18.94	9.16	10.26	13.56	18.88				
1.60	11.82	15.77	17.25	19.81	9.65	11.16	15.65	16.22	7.16	10.45	11.13	12.91	6.52	7.13	9.24	12.60				
1.70	9.11	11.88	12.90	14.66	7.30	8.33	11.52	11.90	5.41	7.70	8.15	9.32	4.92	5.27	6.70	8.96				
1.80	7.27	9.28	10.02	11.27	5.75	6.48	8.84	9.10	4.28	5.94	6.25	7.06	3.88	4.09	5.11	6.71				
1.90	5.97	7.48	8.03	8.96	4.68	5.22	7.02	7.22	3.51	4.75	4.98	5.56	3.18	3.31	4.07	5.24				
2.00	5.02	6.19	6.61	7.32	3.92	4.33	5.74	5.89	2.96	3.93	4.10	4.53	2.69	2.77	3.35	4.24				

Table 3: *Simulated Data*

	Sample Size																				
Sample No.	1	2	3	4	5	6	7	8	9	10	11	12	13	14	15	16	17	18	19	20	D
1	333	513	611	40	267	231	368	689	624	13	593	427	2620	717	24	2114	163	363	370	172	12
2	182	1073	272	112	442	136	663	3133	208	3625	774	293	3351	415	24	732	786	862	86	134	11
3	329	383	3569	3706	253	146	695	499	27	99	220	30	378	3816	569	11	429	3024	319	3824	13
4	152	1752	423	332	3574	876	282	428	100	1872	4016	1277	3130	1171	110	348	201	736	279	61	11
5	231	1200	856	2530	21	92	515	2592	525	426	204	334	797	9	44	683	313	1475	18	1233	10
6	211	601	5735	508	595	1254	566	1122	576	28	165	16	7	887	133	9	1276	899	1516	388	9
7	3690	801	216	257	605	94	1429	496	2041	183	3953	283	91	420	180	296	585	532	1215	2854	10
8	463	355	23	2305	85	16	322	211	750	3171	129	878	2603	219	3120	565	149	262	1115	268	12
9	433	313	1914	46	101	1165	134	177	1135	4554	426	10	68	241	453	639	140	742	164	19	14
10	147	2855	80	163	143	293	559	1998	85	209	3726	163	169	350	6672	1869	286	151	979	101	13
11	418	499	510	901	92	1508	206	130	79	145	154	3	401	454	338	260	43	496	24	35	17
12	540	96	310	1017	115	18	656	1599	1128	386	601	511	523	69	32	1829	140	1059	52	1185	9
13	71	195	2270	1600	689	25	1825	1012	619	35	1106	596	263	31	186	477	787	300	359	639	10
14	220	35	26	466	459	490	17	143	372	33	1558	197	3131	91	245	94	994	32	206	1562	16
15	92	4065	49	3228	130	1593	2244	507	984	27	552	393	39	2413	484	676	15	61	393	935	11
16	8	24	48	151	108	526	4025	100	12	158	590	262	49	21	11	82	5	6	226	336	17
17	74	10	94	46	268	127	72	33	56	14	6	191	75	26	57	49	697	33	261	348	19
18	8	123	119	957	271	212	358	20	69	42	50	54	11	14	93	135	598	188	6	717	17
19	233	120	7	19	113	123	414	41	345	409	385	15	96	104	80	4	718	19	42	72	19
20	189	24	3	991	337	96	130	24	510	2	186	69	137	50	19	141	50	103	173	49	18
21	246	58	82	212	106	79	172	264	7	508	81	177	233	193	61	69	3	131	53	133	20
22	49	130	297	129	298	140	38	113	35	56	8	1349	121	28	97	83	13	42	165	40	19
23	164	890	63	336	364	48	46	9	516	27	142	19	22	66	553	238	69	17	254	134	17
24	487	291	504	29	100	113	122	69	2474	22	193	43	33	68	425	75	32	48	368	22	19
25	319	23	121	36	14	667	5	259	19	139	54	174	333	118	62	124	219	195	288	160	19
26	199	5	86	88	142	501	224	685	249	43	25	32	48	21	38	6	234	151	28	646	18
27	341	108	54	373	183	20	141	107	87	118	17	7	5	535	130	11	38	129	53	444	19
28	76	135	3	336	446	9	18	1077	60	86	168	50	2692	41	4	138	11	34	524	15	17
29	1086	91	20	98	133	78	113	57	145	98	10	14	832	21	94	68	123	404	159	19	18
30	70	137	40	268	9	10	25	3	18	32	13	231	28	14	38	198	101	510	20	90	19

Step 2: Terminate the life test either when 508 hours have been completed or if the number of failed products surpasses twenty before reaching 508 hours, depending on which happens first.

Step 3: If d > 21 or d < 7, declare the process to be out of control. If $7 \leq d \leq 21$, declare the process to be in control.

3.2. Simulation Study: Case 1

In this section, the application of the proposed control chart is demonstrated using simulated data. The data is generated from an Exponential distribution while the process is in control, with parameters that follow an Inverted Gamma distribution, specifically with $\alpha = 2$ and a target average lifetime of 1000 hours. We consider a random sample of size $n = 20$ for each batch. The first fifteen samples are produced from the in-control process, and the next fifteen samples are from a shifted process with $f = 0.20$, resulting in 30 sample batches, as illustrated in Table 3. Then, according to Table 1, when $n = 20$ and $ARL_0 = 200$, we have constants $k = 2.8929$, $a = 0.5093$, $UCL = 18$, and $LCL = 5$. The number of products with a lifetime below 509 hours is noted ("D") and is also shown in Table 3. The values of the nonconforming items are depicted with two control limits ($LCL = 5$ and $UCL = 18$) in Figure 1.

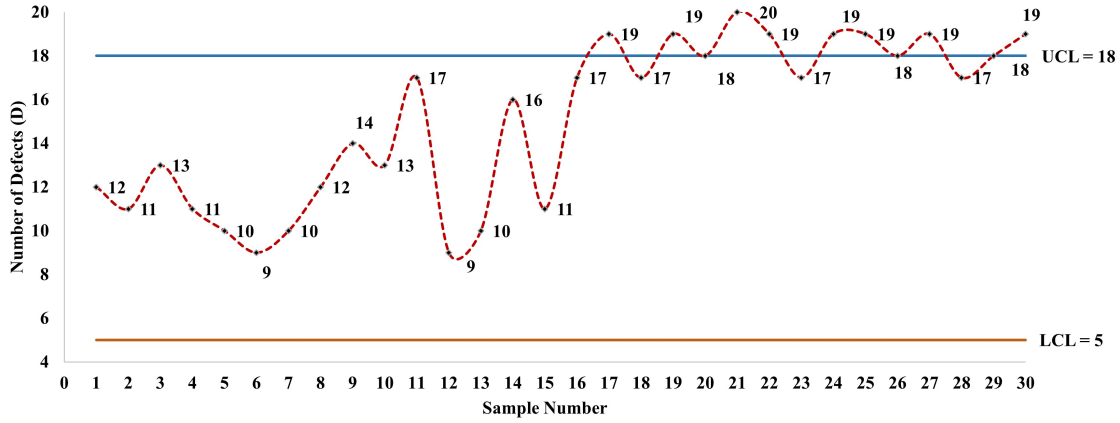


Figure 1: *Control Chart for Simulation Data of Case 1*

From Figure 1, it can be seen that the proposed control chart identifies a shift at the 17^{th} sample (the 2^{nd} observation following the shift), with a recorded ARL of 1.92. Consequently, the developed control chart effectively recognises the shift in the manufacturing process. Therefore, it can be concluded that the proposed control chart will promptly detect any shifts in the process.

3.3. Simulation Study: Case 2

The data is generated from an Exponential distribution while the process is maintained in an in-control state, with parameters that conform to an Inverted Gamma distribution with the parameter α set to 3 and a target average lifetime of 2000 hours. A random sample of size $n = 35$ is utilized for each batch, where the first ten samples are taken from the in-control process, and the next ten samples are from a shifted process with $f = 0.50$, leading to a total of 20 sample batches. From Table 2, with $n = 35$ and $ARL_0 = 400$, the constants are defined as $k = 3.0408$, $a = 0.5360$, $UCL = 27$, and $LCL = 9$. The number of products with a lifetime less than 1072 hours is classified as nonconforming items and is denoted as 'D', with the following values: 18, 24, 23, 22, 17, 12, 17, 15, 21, 18, 25, 24, 26, 25, 29, 25, 24, 23, 23, 27. The values of nonconforming items are plotted against two control limits ($LCL = 9$ and $UCL = 27$), as illustrated in Figure 2.

As shown in Figure 2, the proposed control chart detects a shift at the 15^{th} sample, specifically on the fifth observation after the shift, with an Average Run Length (ARL) of 4.76. This demon-

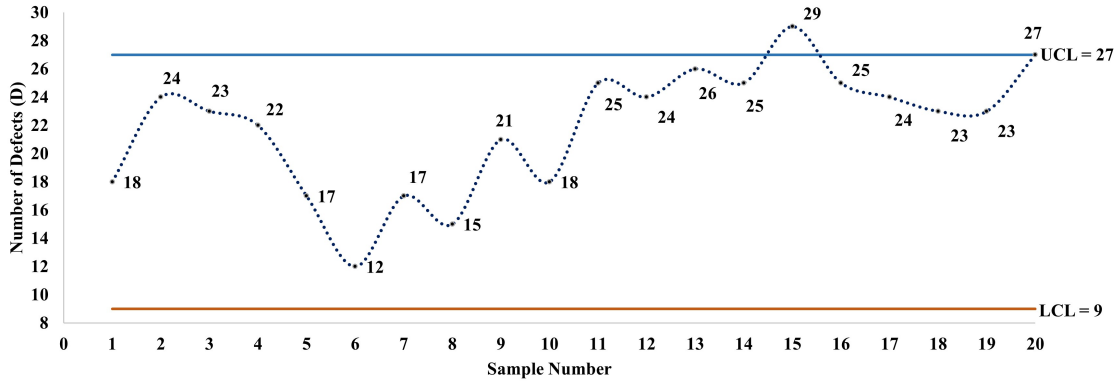


Figure 2: *Control Chart for Simulation Data of Case 2*

strates the chart's effectiveness in identifying shifts in the manufacturing process under standard conditions. Therefore, it can be concluded that the proposed chart is capable of detecting process shifts more quickly.

4. Conclusion

In this paper, we present a methodology for a new Bayesian attribute control chart designed to monitor the lifetime of products. Life tests are conducted under a hybrid censoring scheme, assuming an Exponential distribution for the product lifetime and an Inverse-Gamma distribution as the prior. The proposed control chart aims to ensure that the mean lifetime meets the desired quality standards. This highly adaptable control chart is suitable for monitoring product lifetimes in industrial settings. Supporting tables for practical application are provided and illustrated using simulated data generated in R from the Exponential-Inverse-Gamma model. The performance of the control chart is evaluated in terms of Average Run Lengths (ARLs) for various shift constants (f). Notably, employing a hybrid censoring scheme in life testing reduces both the time and cost involved in sampling inspections. The developed attribute control chart also offers potential for extension to other statistical distributions in future research.

References

[1] Muhammad Aslam and Chi-Hyuck Jun (2015). Attribute Control Chart for the Weibull Distribution under Truncated Life Tests. *Quality Engineering*, 27(3): 283 – 288.

[2] Muhammad Aslam, Osama H. Arif and Chi-Hyuck Jun (2017). An Attribute Control Chart for a Weibull distribution under Accelerated Hybrid Censoring. *PLoS ONE*, 12(3): e0173406: 1 – 11.

[3] Ali Hussein Al-Marshadi, Ambreen Shafqat, Muhammad Aslam and Abdullah Alharbey (2021). Performance of a New Time-Truncated Control Chart for Weibull Distribution under Uncertainty. *International Journal of Computational Intelligence Systems*, 14(1): 1256 – 1262.

[4] Aslam M, Nasrullah Khan and Chi – Hyuck (2016a). A control chart for time truncated life tests using Pareto distribution of the second kind. *Journal of Statistical Computation and Simulation*, 86(11): 2113 – 2122.

[5] Balamurali S and P. Jeyadurga (2019). An Attribute np Control Chart for Monitoring Mean Life using Multiple Deferred State Sampling based on Truncated Life Tests. *International Journal of Reliability, Quality and Safety Engineering*, 26(1): 1950004-1 – 1950004-18.

[6] Aslam M, Arif, O. H and Jun, C (2016b). An Attribute Control Chart based on the Birnbaum-Saunders Distribution using Repetitive Sampling. *IEEE Access*, 5: 9350 – 9360.

[7] Ambreen Shafqat, Jaffer Hussain, Amjad D. Al-Nasser and Muhammad Aslam (2018). Attribute Control Chart for some popular distributions. *Communication in Statistics – Theory and Methods*. 47(8): 1978 – 1988.

[8] Arif O. H, Muhammad Aslam and K.A. Butt (2018). Attribute Control Chart for a Lognormal distribution under Accelerated Time Censoring. *Journal of Computational and Theoretical Nanoscience*, 15(3): 919 – 923.

[9] Srinivasa Rao G (2018). A Control Chart for Time Truncated Life Tests Using Exponentiated Half Logistic Distribution. *Applied Mathematics & Information Sciences: An International Journal*, 12(1): 125 – 131.

[10] Srinivasa Rao Gadde, A.K. Fulment and P.K Josephat (2019). Attribute Control Charts for Dagum distribution under truncated life tests. *Life cycle Reliability and Safety Engineering*, 8: 329 – 335.

[11] Enayat M. Abd Elrazik (2020). Attribute control charts for the New Weibull Pareto Distribution under truncated life tests. *Journal of Statistics Applications & Probability*, 9(1): 43 – 49.

[12] Srinivasa Rao Gadde, Edwin Paul (2020). Time Truncated Control Chart using Log- Logistic Distribution. *Biometrics & Biostatistics International Journal*, 9: 76 - 82.

[13] Rosaiagh, K., G. Srinivasa Rao and S. V. S. V. S. V. Prasad (2021). A Control Chart for Time Truncated Life Tests using type-II Generalized Log Logistic Distribution. *Biometrics & Biostatistics International Journal*, 10(4): 138 – 143.

[14] Adeoti O. A. and P. Ogundipe (2021). A Control Chart for the generalized exponential distribution under time truncated life test. *Life Cycle Reliability and Safety Engineering*, 10: 53 – 59.

[15] Ayman Baklizi and Sawsan Abu Ghannam (2022). An attribute control chart for the inverse Weibull distribution under truncated life tests. *Heliyon*, 8(e11976): 1 - 5.

[16] Srinivasa Rao Gadde and Amer Ibrahim Al-Omari (2022). Attribute control charts based on TLT for Length-Biased Weighted Lomax Distribution. *Journal of Mathematics*, 2022(3091850): 1- 15.

[17] Olatunde Adebayo Adeoti and Gadde Srinivasa Rao (2022). Attribute control chart for Rayleigh distribution using Repetitive sampling under truncated life test. *Journal of Probability and Statistics*, 2022(8763091): 1 - 11.

[18] Muhammad Naveed, Muhammad Azam, Nasrullah Khan, Muhammad Aslam, Muhammad Saleem and Muhammad Saeed (2023). Control Chart for Half Normal and half Exponential power Distributed Process. *Scientific Reports*, 13(8632): 1- 20.

[19] Srinivasa Rao B, M. Rami Reddy and K. Rosaiah (2023). An attribute Control Chart for Time Truncated Life Tests using Exponentiated Inverse Kumaraswamy Distribution. *Reliability: Theory & Applications*, 3:74(18): 206 – 217.

[20] Sri Ramachandran G V., Srinivasa Rao Gadde and Muhammed Aslam (2024). Utilizing Repetitive Sampling in the Construction of a Control Chart for Lindley Distribution with Time Truncation. *Journal of Statistical Theory and Applications*, 23: 224 – 239.

[21] Saha M., Pareek P, Tripathi H, and A Devi (2024). Time Truncated Attribute Control Chart for Generalized Rayleigh Distributed Quality Characteristics and Beyond *International Journal of Quality & Reliability Management*, 41(5): 1400 – 1416.

[22] Gunasekaran Munian (2024). A New Attribute Control Chart based on Exponentiated Exponential Distribution under Accelerated Life Test with Hybrid Censoring. *Reliability: Theory & Applications*, 4:80(19): 850 – 860.

[23] Nagaraju R., Palanivel M., and G. V. Sriramachandran (2025). Development of an Attribute Control Chart Based on the Inverse Kumaraswamy Distribution. *Reliability: Theory & Applications*, 2:84(20): 372 – 381.

[24] Gokila B and A. Sheik Abdullah (2025). An Attribute Control Chart Approach for Life Testing Using Exponential-Poisson Distribution. *Reliability: Theory & Applications*, 2:84(20): 727 – 735.

[25] Kavitha T and M. Gunasekaran (2025). Designing an Attribute Control Chart Based on Exponential-Rayleigh Distribution under Hybrid Censoring. *Reliability: Theory & Applications*, 2:84(20): 824 – 833.

[26] Joel M. Calabrese (1995). Bayesian Process Control for Attributes. *Management Science*, 41(4): 637 – 645.

[27] Ulrich Menzefricke (2002). On the Evaluation of Control Chart Limits based on Predictive Distributions. *Communication in Statistics – Theory and Methods*, 31(8): 1423 – 1440.

[28] Apley D. W (2012). Posterior distribution charts: A Bayesian approach for graphically exploring a process mean. *Technometrics*, 54(3): 279 – 310.

[29] Amin Shaka Aunali and D. Venkatesan (2017). Comparison of Bayesian Method and Classical Charts in Detection of Small Shifts in the Control Charts. *International Journal of Operations Research and Optimization*, 6(2): 101 – 114.

[30] Kumar N and S. Chakraborti (2017). Bayesian Monitoring of times between events: The Shewhart tr - chart. *Journal of Quality Technology*, 49(2): 136 – 154.

[31] Amin Shaka Aunali and D. Venkatesan (2019). Bayesian Approach in Control Chart Techniques. *International Journal of Scientific Research in Mathematical and Statistical Sciences*, 6(2): 217 – 221.

[32] Amin Shaka Aunali, Venkatesan. D. and Michele Gallo (2019). Bayesian Control Chart using Gamma Prior. *International Journal of Scientific & Technology Research*, 8(12): 1567 - 1570.

[33] Ali S (2020). A Predictive Bayesian Approach to sequential time-between-events monitoring. *Quality and Reliability Engineering International*, 36(1): 365 – 387.

[34] Kadoishi S and H. Kawamura (2020). Control Charts based on Hierarchical Bayesian Modeling. *Total Quality Science*, 5(2): 72 – 80.

[35] Konstantinos Bourazas, Dimitrios Kiagias and Panagiotis Tsiamyrtzis (2022). Predictive Control Charts (PCC): A Bayesian Approach in Online monitoring of short runs. *Journal of Quality Technology*, 54(4): 367 – 391.

[36] Fatimah Alshahrani, Ibrahim M. Almanjahie, Majid Khan, Syed M. Anwar, Zahid Rasheed and Ammara N. Cheema (2023). On Designing of Bayesian Shewhart-Type Control Charts for Maxwell Distributed Processes with Application of Boring Machine. *Mathematics*, 11(1126): 1 - 20.

ANFIS-BASED COMPUTING FOR BULK QUEUEING FRAMEWORK WITH LOW-BATCH SERVICE, STANDBY SUPPORT AND VACATION STRATEGIES

S. Karpagam[1], N. Aarthy[2]

•

[1,2]Vel Tech Rangarajan Dr. Sagunthala R& D Institute of Science and Technology, India.
Tamil Nadu, India.
[1]karpagammaths19@gmail.com, [2]aarthyselvi2008@gmail.com

Abstract

This study investigates a non-Markovian queueing model involving a single server providing bulk and low-batch services. The model incorporates key operational features such as server breakdown and repair, a standby server and multiple vacations. The service times for the primary server, low-batch service, standby server and vacation are governed by general distributions, whereas breakdown and repair follow exponential distributions. While the primary (bulk) server is under repair, the standby server temporarily takes over service. The probability generating function for queue size at any time is determined, and various system performance metrics are evaluated. Numerical examples are used to demonstrate the analytical findings. Furthermore, the analytical results are validated using the Adaptive Neuro-Fuzzy Inference System (ANFIS), which improves the precision and dependability of the model's predictions.

Keywords: ANFIS, bulk service, repair, standby, breakdown, low-batch, and multiple vacations.

1. Introduction

Queueing theory is a mathematical framework that can be used to evaluate service systems. Queueing models can aid decision makers when making and improving performance evaluations within a very diverse list of operations like communication networks, factory manufacturing facilities, and cloud computing services. Bulk service models are useful in organizations that handle multiple customers or jobs simultaneously and help improve efficiency. In some cases, the principal machine may fail; but other servers (standbys) of the system can carry processes and jobs on. This standby server is essential to avoid disruptions and keep service steady when system failures take place unexpectedly. It is therefore responsible for both standby and maintenance aid to the queue system so that it is always reliable and operational.

In addition, vacation policies within queueing systems enable the server to take pre-scheduled breaks that may be utilized for basic jobs like cleaning up or preventive maintenance or system upgrading or handling other tasks. By strategically utilizing the planned breaks, service improves, downtime can be reduced during periods of low demand, and the overall performance and reliability of the system can be improved. This section will review the relevant literature sequentially by the major operational components of the proposed model: bulk service; standby server; server failure; recovery and multiple vacations. Much research in queueing theory has looked at each of these components, addressing different operational issues that occur in practical service systems. The foundation for the development and analysis of the current model is laid by the literature review that follows, which highlights significant contributions in these fields.

In this queueing theory field, Neuts [17] established the foundation work by presenting a general type of queueing that involved Poisson arrivals.Ayyappan and Karpagam examined the single-server queueing model in [2]. Standby servers, multiple vacations, a re-service control mechanism, batch arrivals, and server failures with repair are some of its useful features. Also, Ayyappan et al. [3] examined a MAP/PH/1 system and the service is optional including setup and phase-type repair. In order to illustrate the practical aspects of production systems, Karpagam and Lokesh [10] looked at an arrival (bulk) fixed batch service with rework, inspection, and multiple vacation policies.

To enhance reliability and prevent service disruption at breakdown or overload, it is common to use standby servers. Yeh et al. [4] studied a redundant system of standby support with controlled failure machine arrival. Madan et al. [11] and [12] formulated a queueing system with a vacation and repair of the main server where the system is covered by a standby server. Also, Murugeswari and Sundari [16] studied a bulk arrival queueing system with a mandatory vacation of the server and standby service. Jeyakumar and Senthilnathan [9] examined a bulk service queueing system with vacation and server breakdowns and formulated performance consequences under service disciplines of this type.

Doshi [8] presented a systematic study of queueing systems with vacationing servers and their role in system performance. Takagi's work [23], Queueing Analysis: A Foundation of Performance Evaluation, is a book containing a survey of vacation and priority systems. Bulk service queueing models where many vacations were considered along with setup times and service policies have been explored by Reddy et al. [20] and Ayyappan and Deepa [1]. Tamrakar et al. [24] performed the batch size-dependent bulk service queue, including multiple working vacations. Chakravarthy and Kulshrestha's study [5] focuses on a queueing model that includes multiple vacations, repair, server failures, and a backup server. Models for integrating server failure without service interruption were proposed by Jeyakumar and Senthilnathan [21].

Utilizations of idle time are among classical problems in queueing theory. Levy and Yechiali [15] discussed how vacation systems use idle time. Whether to enter into vacation or idle state based on queue level thresholds is critically significant for optimal performance of systems as addressed by Choudhury and Madan [6]. n order to improve server accessibility through two-phase imperative services and a backup server, Rathinasamy and Kirupa [19] presented a model for minimizing wait times.. Pradhan et al. [18] formulated performance in group arrival and queue-dependent vacation systems. Srivastava et al. [22] examined dual-service types and multiple vacations in a system, with increased service flexibility and decreased server idleness, respectively, while Lavanya et al. [13] talked about ceramic technology and dual-service vacation systems. To enhance the precision in numerical outcomes, current works employing ANFIS techniques were highlighted. Divya and Indhira [7], who studied a heterogeneous framework with a second optional service involving hybrid vacation, whereas Thakur et al. [25] discussed optimization of expenses through ANFIS in a Markovian queue with operational vacations.

1.1. Gap in the Existing Literature

Madan et al. [12] concentrated on single-service queueing systems with batch arrivals, which included a backup server to ensure service continuity during server breakdowns. Later, Karpagam et al. [2] applied this concept to bulk service systems, creating models that incorporated server failures and maintenance, standby service, multiple vacations, and customer reprocessing strategies. However, these studies focus exclusively on single or bulk service mechanisms, ignoring cases in which low-batch services are also required. In many real-world systems, particularly in manufacturing and production, bulk and low-batch services coexist and have a substantial impact on performance. To close this gap, the current study expands the bulk service model with standby service by incorporating low-batch service. The proposed model efficiently handles varying customer demand, reducing queue length and waiting time.

1.2. Structure of the Paper

The manuscript is structured as follows: Section 2 outlines the proposed model, encompassing the subsection Real-World Applications.Section 3 gives the distributions of queue size, incorporating subsections Computational Aspects, Stability Analysis, and Special Case. Section 4 discusses performance metrics. Section 5 illustrates the model numerically and compares the findings to those obtained using the ANFIS technique. Finally, Section 6 has the conclusion.

2. Model description

The model studied in this work involves arrivals following a compound Poisson process with rate λ. According to the general bulk service rule, both the primary and standby servers serve customers. The primary server starts service only when there are at least a units in the queue, and it can serve up to b units simultaneously. When there are fewer than a customers in the queue ($1 \leq Q \leq a-1$), the server switches to low-batch service. If the number of customers in the queue is equal to or greater than b, they are served on the primary server. During regular service, the primary server is likely to fail, which occurs at an exponential rate of β. When a server fails, it is automatically repaired based on an exponential distribution of rate δ. During this period, the service of the current batch is interrupted. The interrupted batch is transferred to a standby unit, which resumes service for that batch. The standby unit remains operational in the system until the primary server is restored. If the standby server is still busy after the repair is complete, the current batch is transferred to the primary server, which then resumes service. After completing the bulk and low-batch service phases, if there are no customers in the queue, the server starts a random time interval. If the queue is empty at the end of this interval, the server immediately starts another interval. This cycle continues until at least a customers are in the queue. Until, the next service is triggered. Furthermore, the primary server, standby server, and low-volume service have independent service times with a general distribution.

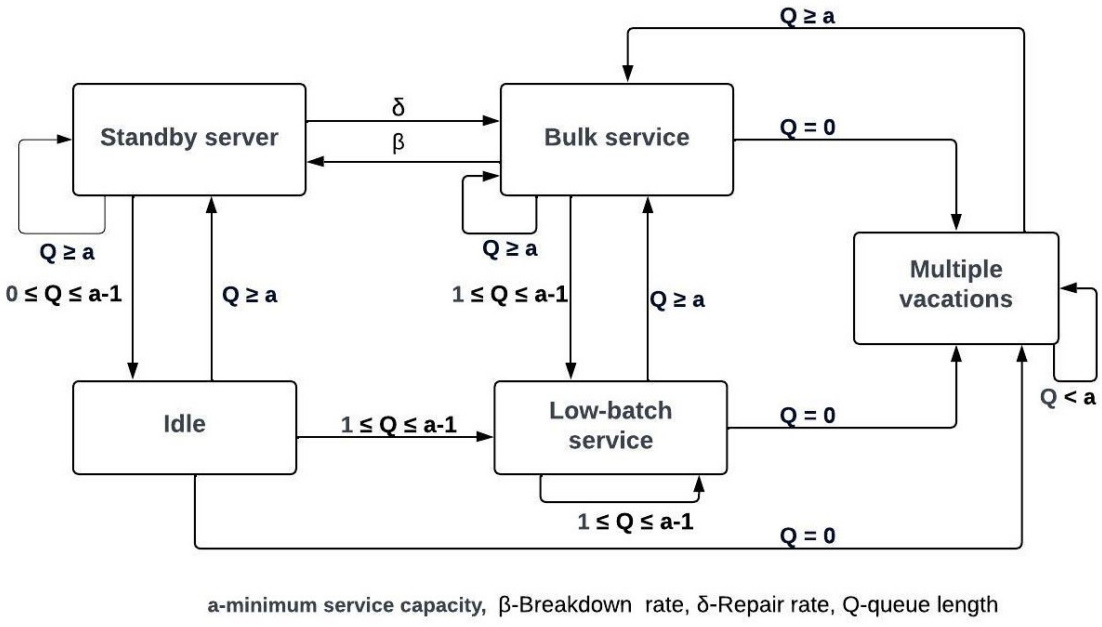


Figure 1: *Schematic Representation*

2.1. Real-Time Relevance of the Proposed Framework

In cloud computing, the system functions across different states to deliver reliability, scalability, and optimal resource management. In the bulk service state, cloud resources, such as compute instances or packaging, handle significant workloads by processing huge quantities of data or serving several concurrent user requests. Such services are typically auto-scaled to meet peak demand and managed by orchestration systems like Kubernetes or AWS Auto Scaling. When the primary compute instance fails due to system overload, software failure, or hardware breakdown, the standby server comes online. To reduce downtime and guarantee service continuity, this standby resource usually a warmed instance or hot backup node, is instantly deployed to take over the interrupted task. During low-incoming workload situations, the system switches to a low-batch service mode, in which limited functions like AWS Lambda or Azure Functions do minimum or single operations. This mode promotes economical computing since it supplies only those resources required for small jobs. During periods of no active requests or jobs in the queue, the system goes into vacation mode.

In this phase, background tasks such as software updates, patching of security vulnerabilities, archiving of logs and system checks are executed while the resources that are idle are reduced or halted. It ensures the infrastructure is tuned and is secure to handle future workloads.Idle state refers to when resources are committed but are not being run, ready state to deploy instantly when needed. These resources may be periodically checked for health or readiness. All cloud computing paradigm states, as a general perspective, are essential to ensure operational efficiency, cost reduction, and continuity of service delivery under varying workloads and system configurations.

Table 1: *Description of Notations*

Symbol	Description
λ	Rate at which customers arrive.
X	Random variable representing the group size.
$Pr(X = k) = g_k$	Probability that a group of size k arrives.
$X(z)$	Probability generating function (PGF) of X.
$S(.)$, $U(.)$, $C(.)$, $V(.)$	Bulk service, standby, low-batch service and vacation periods cumulative distribution functions (CDFs).
$s(\varkappa)$, $u(\varkappa)$, $c(\varkappa)$, $v(\varkappa)$	Probability density functions (PDFs) of S, U, C, and V.
$S^0(\mathrm{t})$, $U^0(\mathrm{t})$, $C^0(\mathrm{t})$, $V^0(\mathrm{t})$	Remaining times of bulk service, standby service, low-batch service and vacation at time t.
$\tilde{S}(\zeta)$, $\tilde{U}(\zeta)$, $\tilde{C}(\zeta)$, $\tilde{V}(\zeta)$	Laplace-Stieltjes transforms (LSTs) of S, U, C, and V.
$N_{\mathfrak{s}}(t)$	Customers currently receiving service at time t.
$N_{\mathfrak{q}}(t)$	Number of customers in the queue at time t.
$Z(\mathrm{t}) = \mathfrak{F}$	Server is taking its $\mathfrak{F}^{\mathrm{th}}$ vacation at time t.

For the further development of the queueing system, let us define the random variable as:

$$\Re(\mathrm{t}) = \begin{cases} 0, & \text{when the server is on vacation} \\ 1, & \text{while the server is providing bulk service} \\ 2, & \text{when the server is engaged in low-batch processing} \\ 3, & \text{while the standby server is serving customers (bulk service)} \\ 4, & \text{when the standby server is idle} \end{cases}$$

The probabilities of states are defined as follows:

$I_{\mathfrak{h}}(t)dt = Pr\{N_{\mathfrak{q}}(t) = \mathfrak{h}, \Re(t) = 4\}, 0 \le \mathfrak{h} \le a-1,$

$\mathcal{B}_{\mathfrak{e},\mathfrak{F}}(\varkappa,t)dt = Pr\{N_{\mathfrak{s}}(t) = \mathfrak{e}, N_{\mathfrak{q}}(t) = \mathfrak{F}, \varkappa \le S^0(t) \le \varkappa + dt, \Re(t) = 1\}, a \le \mathfrak{e} \le b, \quad \mathfrak{F} \ge 0,$

$T_{\mathfrak{e},\mathfrak{F}}(\varkappa,t)dt = Pr\{N_{\mathfrak{s}}(t) = \mathfrak{e}, N_{\mathfrak{q}}(t) = \mathfrak{F}, \varkappa \le U^0(t) \le \varkappa + dt, \Re(t) = 3\}, a \le \mathfrak{e} \le b, \quad \mathfrak{F} \ge 0,$

$L_{\mathfrak{e},\mathfrak{F}}(\varkappa,t)dt = Pr\{N_{\mathfrak{s}}(t) = \mathfrak{e}, N_{\mathfrak{q}}(t) = \mathfrak{F}, \varkappa \le C^0(t) \le \varkappa + dt, \Re(t) = 2\}, 1 \le \mathfrak{e} \le a-1, \quad \mathfrak{F} \ge 0,$

$Q_{l,\mathfrak{F}}(\varkappa,t)dt = Pr\{N_{\mathfrak{q}}(t) = \mathfrak{F}, \varkappa \le V^0(t) \le \varkappa + dt, \Re(t) = 0\}, \quad l \ge 1, \quad \mathfrak{F} \ge 0.$

3. Queue size distribution

Given the stated probabilities, the steady-state equations are as follows:
The standby server idle

$$(\lambda+\delta)I_0 = \sum_{m=a}^{b} T_{m,0}(0), \tag{1}$$

$$(\lambda+\delta)I_{\mathfrak{h}} = \sum_{m=a}^{b} T_{m,\mathfrak{h}}(0) + \sum_{k=1}^{\mathfrak{h}} I_{\mathfrak{h}-k}\lambda g_k, \quad 1 \le \mathfrak{h} \le a-1. \tag{2}$$

The primary server busy

$$-\mathcal{B}'_{\mathfrak{e},0}(\varkappa) = -(\lambda+\beta)\mathcal{B}_{\mathfrak{e},0}(\varkappa) + s(\varkappa)\sum_{m=a}^{b}\mathcal{B}_{m.\mathfrak{e}}(0) + s(\varkappa)\sum_{m=1}^{a-1}L_{m,\mathfrak{e}}(0) + \sum_{l=1}^{\infty}Q_{l,\mathfrak{e}}(0)s(\varkappa) + \delta\int_0^{\infty}T_{\mathfrak{e},0}(y)dy s(\varkappa), \quad a \le \mathfrak{e} \le b, \tag{3}$$

$$-\mathcal{B}'_{\mathfrak{e},\mathfrak{F}}(\varkappa) = -(\lambda+\beta)\mathcal{B}_{\mathfrak{e},\mathfrak{F}}(\varkappa) + \sum_{k=1}^{\mathfrak{F}}\mathcal{B}_{\mathfrak{e},\mathfrak{F}-k}(\varkappa)\lambda g_k + \delta\int_0^{\infty}T_{\mathfrak{e},\mathfrak{F}}(y)dy s(\varkappa), \quad \mathfrak{F} \ge 1, \quad a \le \mathfrak{e} \le b-1, \tag{4}$$

$$-\mathcal{B}'_{b,\mathfrak{F}}(\varkappa) = -(\lambda+\beta)\mathcal{B}_{b,\mathfrak{F}}(\varkappa) + \sum_{k=1}^{\mathfrak{F}}\mathcal{B}_{b,\mathfrak{F}-k}(\varkappa)\lambda g_k + s(\varkappa)\sum_{m=a}^{b}\mathcal{B}_{m,b+\mathfrak{F}}(0) + s(\varkappa)\sum_{m=1}^{a-1}L_{m.b+\mathfrak{F}}(0) + \sum_{l=1}^{\infty}Q_{l,b+\mathfrak{F}}(0)s(\varkappa) + \delta\int_0^{\infty}T_{b,\mathfrak{F}}(y)dy s(\varkappa), \quad \mathfrak{F} \ge 1. \tag{5}$$

The standby server busy

$$-T'_{\mathfrak{e},0}(\varkappa) = -(\lambda+\delta)T_{\mathfrak{e},0}(\varkappa) + \sum_{m=a}^{b}T_{m,\mathfrak{e}}(0)u(\varkappa) + \sum_{k=0}^{a-1}I_k\lambda g_{\mathfrak{e}-k}u(\varkappa) + \beta\int_0^{\infty}\mathcal{B}_{\mathfrak{e},0}(y)dy u(\varkappa), \quad a \le \mathfrak{e} \le b, \tag{6}$$

$$-T'_{\mathfrak{e},\mathfrak{F}}(\varkappa) = -(\lambda+\delta)T_{\mathfrak{e},\mathfrak{F}}(\varkappa) + \sum_{k=1}^{\mathfrak{F}}T_{\mathfrak{e},\mathfrak{F}-k}(\varkappa)\lambda g_k + \beta\int_0^{\infty}\mathcal{B}_{\mathfrak{e},\mathfrak{F}}(y)dy u(\varkappa), \quad a \le \mathfrak{e} \le b-1, \quad \mathfrak{F} \ge 1, \tag{7}$$

$$-T'_{b,\mathfrak{F}}(\varkappa) = -(\lambda+\delta)T_{b,\mathfrak{F}}(\varkappa) + \sum_{k=1}^{\mathfrak{F}}T_{b,\mathfrak{F}-k}(\varkappa)\lambda g_k + \sum_{m=a}^{b}T_{m,b+\mathfrak{F}}(0)u(\varkappa) + \sum_{k=0}^{a-1}I_k\lambda g_{b+\mathfrak{F}-k}u(\varkappa) + \beta\int_0^{\infty}\mathcal{B}_{b,\mathfrak{F}}(y)dy u(\varkappa), \quad \mathfrak{F} \ge 1. \tag{8}$$

The low-batch server busy

$$-Ł'_{\mathfrak{e},0}(\varkappa) = -\lambda L_{\mathfrak{e},0}(\varkappa) + \sum_{m=1}^{a-1} L_{m.\mathfrak{e}}(0)c(\varkappa) + \sum_{m=a}^{b} \mathcal{B}_{m,\mathfrak{e}}(0)c(\varkappa) + c(\varkappa)\delta I_{\mathfrak{e}}, \quad 1 \le \mathfrak{e} \le a-1, \quad (9)$$

$$-L'_{\mathfrak{e},\mathfrak{F}}(\varkappa) = -\lambda L_{\mathfrak{e},\mathfrak{F}}(\varkappa) + \sum_{k=1}^{\mathfrak{F}} L_{\mathfrak{e},\mathfrak{F}-k}(\varkappa)\lambda g_k, \quad 1 \le \mathfrak{e} \le a-1, \quad \mathfrak{F} \ge 1. \quad (10)$$

The Vacation

$$-Q'_{1,0}(\varkappa) = -\lambda Q_{1,0}(\varkappa) + \sum_{m=a}^{b} \mathcal{B}_{m,0}(0)v(\varkappa) + v(\varkappa)\sum_{m=1}^{a-1} L_{m,0}(0) + \delta I_0 v(\varkappa), \quad (11)$$

$$-Q'_{1,\mathfrak{F}}(\varkappa) = -\lambda Q_{1,\mathfrak{F}}(\varkappa) + \sum_{k=1}^{n} Q_{1,\mathfrak{F}-k}(\varkappa)\lambda g_k, \quad \mathfrak{F} \ge 1, \quad (12)$$

$$-Q'_{l,0}(\varkappa) = -\lambda Q_{l,0}(\varkappa) + v(\varkappa)Q_{l-1,0}(0), \quad l \ge 2, \quad (13)$$

$$-Q'_{l,\mathfrak{F}}(\varkappa) = -\lambda Q_{l,\mathfrak{F}}(\varkappa) + Q_{l-1,\mathfrak{F}}(0)v(\varkappa) + \sum_{k=1}^{n} Q_{l,\mathfrak{F}-k}(\varkappa)\lambda g_k, \quad 1 \le \mathfrak{F} \le a-1, \quad l \ge 2, \quad (14)$$

$$-Q'_{l,\mathfrak{F}}(\varkappa) = -\lambda Q_{l,\mathfrak{F}}(\varkappa) + \sum_{k=1}^{n} Q_{l,\mathfrak{F}-k}(\varkappa)\lambda g_k, \quad l \ge 2, \quad \mathfrak{F} \ge a. \quad (15)$$

Equations (1)- (15), when transformed using the Laplace-Stieltjes Transform, yield:

$$\zeta\tilde{\mathcal{B}}_{\mathfrak{e},0}(\zeta) - \mathcal{B}_{\mathfrak{e},0}(0) = (\beta+\lambda)\tilde{\mathcal{B}}_{\mathfrak{e},0}(\zeta) - \sum_{m=a}^{b} \mathcal{B}_{m,\mathfrak{e}}(0)\tilde{S}(\zeta) - \sum_{m=1}^{a-1} L_{m,\mathfrak{e}}(0)\tilde{S}(\zeta) - \sum_{l=1}^{\infty} \tilde{Q}_{l,\mathfrak{e}}(0)\tilde{S}(\zeta) - \delta\int_0^{\infty} T_{\mathfrak{e},0}(y)dy\tilde{S}(\zeta), \quad a \le \mathfrak{e} \le b, \quad (16)$$

$$\zeta\tilde{\mathcal{B}}_{\mathfrak{e},\mathfrak{F}}(\zeta) - \mathcal{B}_{\mathfrak{e},\mathfrak{F}}(0) = (\beta+\lambda)\tilde{\mathcal{B}}_{\mathfrak{e},\mathfrak{F}}(\zeta) - \sum_{k=1}^{\mathfrak{F}} \tilde{\mathcal{B}}_{\mathfrak{e},\mathfrak{F}-k}(\zeta)\lambda g_k - \delta\int_0^{\infty} T_{\mathfrak{e},0}(y)dy\tilde{S}(\zeta), \quad \mathfrak{F} \ge 1, \quad a \le \mathfrak{e} \le b-1, \quad (17)$$

$$\zeta\tilde{\mathcal{B}}_{b,\mathfrak{F}}(\zeta) - \mathcal{B}_{b,\mathfrak{F}}(0) = (\beta+\lambda)\tilde{\mathcal{B}}_{b,\mathfrak{F}}(\zeta) - \sum_{m=a}^{b} \mathcal{B}_{m,b+\mathfrak{F}}(0)\tilde{S}(\zeta) - \sum_{m=1}^{a-1} L_{m,b+\mathfrak{F}}(0)\tilde{S}(\zeta) - \sum_{k=1}^{\mathfrak{F}} \tilde{\mathcal{B}}_{b,\mathfrak{F}-k}(\zeta)\lambda g_k - \delta\int_0^{\infty} T_{\mathfrak{e},0}(y)dy\tilde{S}(\zeta), \quad \mathfrak{F} \ge 1, \quad (18)$$

$$\zeta\tilde{L}_{\mathfrak{e},0}(\zeta) - L_{\mathfrak{e},0}(0) = \lambda\tilde{L}_{\mathfrak{e},0}(\zeta) - \sum_{m=1}^{a-1} L_{m,\mathfrak{e}}(0)\tilde{C}(\zeta) - \sum_{m=a}^{b} \mathcal{B}_{m,\mathfrak{e}}(0)\tilde{C}(\zeta) - \delta I_{\mathfrak{e}}\tilde{C}(\zeta), \quad 1 \le \mathfrak{e} \le a-1, \quad (19)$$

$$\zeta\tilde{L}_{\mathfrak{e},\mathfrak{F}}(\zeta) - L_{\mathfrak{e},\mathfrak{F}}(0) = \lambda\tilde{L}_{\mathfrak{e},\mathfrak{F}}(\zeta) - \sum_{k=1}^{\mathfrak{F}} \tilde{L}_{\mathfrak{e},\mathfrak{F}-k}(\zeta)\lambda g_k, \quad 1 \le \mathfrak{e} \le a-1, \quad \mathfrak{F} \ge 1, \quad (20)$$

$$\zeta\tilde{T}_{\mathfrak{e},0}(\zeta) - T_{\mathfrak{e},0}(0) = (\lambda+\delta)\tilde{T}_{\mathfrak{e},0}(\zeta) - \sum_{m=a}^{b} T_{m,\mathfrak{e}}(0)\tilde{U}(\zeta) - \beta\int_0^{\infty} \mathcal{B}_{\mathfrak{e},0}(y)dy\tilde{U}(\zeta) - \sum_{k=0}^{a-1} I_k\lambda g_{\mathfrak{e}-k}\tilde{U}(\zeta), \quad a \le \mathfrak{e} \le b, \quad (21)$$

$$\zeta\tilde{T}_{\mathfrak{e},\mathfrak{F}}(\zeta) - T_{\mathfrak{e},\mathfrak{F}}(0) = (\lambda+\delta)\tilde{T}_{\mathfrak{e},\mathfrak{F}}(\zeta) - \sum_{k=1}^{\mathfrak{F}} \tilde{T}_{\mathfrak{e},\mathfrak{F}-k}(\zeta)\lambda g_k - \beta\int_0^{\infty} \mathcal{B}_{\mathfrak{e},\mathfrak{F}}(y)dy\tilde{U}(\zeta), \quad a \le \mathfrak{e} \le b-1, \quad \mathfrak{F} \ge 1, \quad (22)$$

$$\zeta\tilde{T}_{b,\mathfrak{F}}(\zeta) - T_{b,\mathfrak{F}}(0) = (\lambda+\delta)\tilde{T}_{b,\mathfrak{F}}(\zeta) - \sum_{m=a}^{b} T_{m,b+\mathfrak{F}}(0)\tilde{U}(\zeta) - \sum_{k=1}^{\mathfrak{F}} \tilde{T}_{b,\mathfrak{F}-k}(\zeta)\lambda g_k - \beta\int_0^\infty \mathcal{B}_{b,\mathfrak{F}}(y)dy\tilde{U}(\zeta) - \sum_{k=0}^{a-1} I_k\lambda g_{b+\mathfrak{F}-k}\tilde{U}(\zeta), \quad \mathfrak{F}\geq 1, \tag{23}$$

$$\zeta\tilde{Q}_{1,0}(\zeta) - Q_{1,0}(0) = \lambda\tilde{Q}_{1,0}(\zeta) - \sum_{m=a}^{b}\mathcal{B}_{m,0}(0)\tilde{V}(\zeta) - \sum_{m=1}^{a-1} L_{m,0}(0)\tilde{V}(\zeta) - \delta I_0\tilde{V}(\zeta), \tag{24}$$

$$\zeta\tilde{Q}_{1,\mathfrak{F}}(\zeta) - Q_{1,\mathfrak{F}}(0) = \lambda\tilde{Q}_{1,\mathfrak{F}}(\zeta) - \sum_{k=1}^{n}\tilde{Q}_{1,\mathfrak{F}-k}(\zeta)\lambda g_k, \quad \mathfrak{F}\geq 1, \tag{25}$$

$$\zeta\tilde{Q}_{l,0}(\zeta) - Q_{l,0}(0) = \lambda\tilde{Q}_{l,0}(\zeta) - Q_{l-1,0}(0)\tilde{V}(\zeta), \quad l\geq 2, \tag{26}$$

$$\zeta\tilde{Q}_{l,\mathfrak{F}}(\zeta) - Q_{l,\mathfrak{F}}(0) = \lambda\tilde{Q}_{l,\mathfrak{F}}(\zeta) - Q_{l-1,\mathfrak{F}}(0)\tilde{V}(\zeta) - \sum_{k=1}^{n}\tilde{Q}_{l,\mathfrak{F}-k}(\zeta)\lambda g_k, \quad \mathfrak{F}=1,2,...,a-1, \quad l\geq 2, \tag{27}$$

$$\zeta\tilde{Q}_{l,\mathfrak{F}}(\zeta) - Q_{l,\mathfrak{F}}(0) = \lambda\tilde{Q}_{l,\mathfrak{F}}(\zeta) - \sum_{k=1}^{n}\tilde{Q}_{l,\mathfrak{F}-k}(\zeta)\lambda g_k, \quad \mathfrak{F}\geq 2, \quad l\geq 2. \tag{28}$$

To compute the PGF of the queue length, the subsequent PGFs are constructed:

$$\left.\begin{aligned}
\tilde{\mathcal{B}}_{\mathfrak{e}}(\mathfrak{z},\zeta) &= \sum_{\mathfrak{F}=0}^{\infty}\tilde{B}_{\mathfrak{e},\mathfrak{F}}(\zeta)\,\mathfrak{z}^{\mathfrak{F}}, \quad \mathcal{B}_{\mathfrak{e}}(\mathfrak{z},0) = \sum_{\mathfrak{F}=0}^{\infty}\mathcal{B}_{\mathfrak{e},\mathfrak{F}}(0)\,\mathfrak{z}^{\mathfrak{F}}; \quad a\leq\mathfrak{e}\leq b,\\
\tilde{L}_{\mathfrak{e}}(\mathfrak{z},\zeta) &= \sum_{\mathfrak{F}=0}^{\infty}\tilde{L}_{\mathfrak{e},\mathfrak{F}}(\zeta)\,\mathfrak{z}^{\mathfrak{F}}, \quad L_{\mathfrak{e}}(\mathfrak{z},0) = \sum_{\mathfrak{F}=0}^{\infty}L_{\mathfrak{e},\mathfrak{F}}(0)\,\mathfrak{z}^{\mathfrak{F}}; \quad 1\leq\mathfrak{e}\leq a-1,\\
\tilde{T}_{\mathfrak{e}}(\mathfrak{z},\zeta) &= \sum_{\mathfrak{F}=0}^{\infty}\tilde{T}_{\mathfrak{e},\mathfrak{F}}(\zeta)\,\mathfrak{z}^{\mathfrak{F}}, \quad T_{\mathfrak{e}}(\mathfrak{z},0) = \sum_{\mathfrak{F}=0}^{\infty}T_{\mathfrak{e},\mathfrak{F}}(0)\,\mathfrak{z}^{\mathfrak{F}}; \quad a\leq\mathfrak{e}\leq b,\\
\tilde{Q}_{l}(\mathfrak{z},\zeta) &= \sum_{\mathfrak{F}=0}^{\infty}\tilde{Q}_{l,\mathfrak{F}}(\zeta)\,\mathfrak{z}^{\mathfrak{F}}, \quad Q_{l}(\mathfrak{z},0) = \sum_{\mathfrak{F}=0}^{\infty}Q_{l,\mathfrak{F}}(0)\,\mathfrak{z}^{\mathfrak{F}}; \quad l\geq 1.
\end{aligned}\right\} \tag{29}$$

Applying the appropriate powers of $\mathfrak{z}^n$ to Equations (16)-(28), summing over $n = 0$ *to* ∞ and using Equation (29), yields:

$$(\zeta - l(\mathfrak{z}))\tilde{\mathcal{B}}_{\mathfrak{e}}(\mathfrak{z},\zeta) = \mathcal{B}_{\mathfrak{e}}(\mathfrak{z},0) - \tilde{S}(\zeta)\Big[\sum_{m=a}^{b}\mathcal{B}_{m,\mathfrak{e}}(0) + \sum_{m=1}^{a-1}L_{m,\mathfrak{e}}(0) + \sum_{\mathfrak{F}=0}^{\infty}Q_{l,\mathfrak{F}}(0) + \delta\tilde{T}_{\mathfrak{e}}(\mathfrak{z},0)\Big], \quad a\leq\mathfrak{e}\leq b-1, \tag{30}$$

$$\begin{aligned}
\mathfrak{z}^b(\zeta - l(\mathfrak{z}))\tilde{\mathcal{B}}_b(\mathfrak{z},\zeta) &= (\mathfrak{z}^b - \tilde{S}(\zeta))\mathcal{B}_b(\mathfrak{z},0)\\
&\quad - \tilde{S}(\zeta)\Big[\sum_{m=a}^{b-1}\mathcal{B}_m(\mathfrak{z},0) + \sum_{m=1}^{a-1}L_m(\mathfrak{z},0) + \sum_{l=1}^{\infty}Q_l(\mathfrak{z},0) + \mathfrak{z}^b\delta\tilde{T}_b(\mathfrak{z},0)\\
&\quad - \sum_{\mathfrak{F}=0}^{b-1}\Big(\sum_{m=a}^{b}\mathcal{B}_{m,\mathfrak{F}}(0)\mathfrak{z}^{\mathfrak{F}} + \sum_{m=1}^{a-1}L_{m,\mathfrak{F}}(0)\mathfrak{z}^{\mathfrak{F}} + \sum_{\mathfrak{F}=0}^{\infty}Q_{l,\mathfrak{F}}(0)\mathfrak{z}^{\mathfrak{F}}\Big)\Big],
\end{aligned} \tag{31}$$

$$(\zeta - m(\mathfrak{z}))\tilde{T}_{\mathfrak{e}}(\mathfrak{z},\zeta) = T_{\mathfrak{e}}(\mathfrak{z},0) - \tilde{U}(\zeta)\Big[\sum_{m=a}^{b}T_{m,\mathfrak{e}}(0) + \sum_{k=0}^{a-1}I_k\lambda g_{i-k} + \beta\tilde{B}_{\mathfrak{e}}(\mathfrak{z},0)\Big], \quad a\leq\mathfrak{e}\leq b-1, \tag{32}$$

$$\begin{aligned}
\mathfrak{z}^b(\zeta - m(\mathfrak{z}))\tilde{T}_b(\mathfrak{z},\zeta) &= (\mathfrak{z}^b - \tilde{U}(\zeta))T_b(\mathfrak{z},0) - \tilde{U}(\zeta)\Big[\sum_{m=a}^{b-1}T_m(\mathfrak{z},0) + \mathfrak{z}^b\beta\tilde{\mathcal{B}}_b(\mathfrak{z},0)\\
&\quad + \sum_{k=0}^{a-1}\sum_{\mathfrak{F}=b}^{\infty}I_k\mathfrak{z}^k g_{\mathfrak{F}-k}\mathfrak{z}^{\mathfrak{F}-k} - \sum_{\mathfrak{F}=0}^{b-1}\sum_{m=a}^{b}T_{m,\mathfrak{F}}(0)\mathfrak{z}^{\mathfrak{F}}\Big],
\end{aligned} \tag{33}$$

$$(\zeta - n(\mathfrak{z}))\tilde{L}_{\mathfrak{e}}(\mathfrak{z},\zeta) = L_{\mathfrak{e}}(\mathfrak{z},0) - \tilde{C}(\zeta)\Big[\sum_{m=1}^{a-1} L_{m,\mathfrak{e}}(0) + \sum_{m=a}^{b} \mathcal{B}_{m,\mathfrak{e}}(0) + \delta I_{\mathfrak{e}}\Big], \quad 1 \le \mathfrak{e} \le a-1, \tag{34}$$

$$(\zeta - n(\mathfrak{z}))\tilde{Q}_1(\mathfrak{z},\zeta) = Q_1(\mathfrak{z},0) - \tilde{V}(\zeta)\Big[\sum_{m=a}^{b} \mathcal{B}_{m,0}(0) + \sum_{m=1}^{a-1} L_{m,0}(0) + \delta I_0\Big], \tag{35}$$

$$(\zeta - n(\mathfrak{z}))\tilde{Q}_l(\mathfrak{z},\zeta) = Q_l(\mathfrak{z},0) - \tilde{V}(\zeta)\sum_{\mathfrak{F}=0}^{a-1} Q_{l-1,\mathfrak{F}}(0)\mathfrak{z}^{\mathfrak{F}}, \quad l \ge 2. \tag{36}$$

Where $l(\mathfrak{z}) = n(\mathfrak{z}) + \beta$,$m(\mathfrak{z}) = n(\mathfrak{z}) + \delta$,$n(\mathfrak{z}) = -\lambda X(\mathfrak{z}) + \lambda$
Substituting $\zeta = l(\mathfrak{z})$ in (30) and (31), $\zeta = m(\mathfrak{z})$ in (32) and (33), and $\zeta = n(\mathfrak{z})$ in (34)-(36), the corresponding results are obtained.

$$\mathcal{B}_{\mathfrak{e}}(\mathfrak{z},0) = \tilde{S}(l(\mathfrak{z}))\Big[\sum_{m=a}^{b} \mathcal{B}_{m,\mathfrak{e}}(0) + \sum_{m=1}^{a-1} L_{m,\mathfrak{e}}(0) + \sum_{\mathfrak{F}=0}^{\infty} Q_{l,\mathfrak{F}}(0) + \delta\tilde{T}_{\mathfrak{e}}(\mathfrak{z},0)\Big], \quad a \le \mathfrak{e} \le b-1, \tag{37}$$

$$\begin{aligned}\Big(\mathfrak{z}^b - \tilde{S}(l(\mathfrak{z}))\Big)\mathcal{B}_b(\mathfrak{z},0) = \tilde{S}(l(\mathfrak{z}))\Big[&\sum_{m=a}^{b} \mathcal{B}_m(\mathfrak{z},0) + \sum_{m=1}^{a-1} L_m(\mathfrak{z},0) + \sum_{l=1}^{\infty} Q_l(\mathfrak{z},0) + \mathfrak{z}^b\delta\tilde{T}_b(\mathfrak{z},0) \\ &- \sum_{\mathfrak{F}=0}^{b-1}\Big(\sum_{m=a}^{b} \mathcal{B}_{m,\mathfrak{F}}(0) + \sum_{m=1}^{a-1} L_{m,\mathfrak{F}}(0) + \sum_{\mathfrak{F}=0}^{\infty} Q_{l,\mathfrak{F}}(0)\Big)\Big],\end{aligned} \tag{38}$$

$$T_{\mathfrak{e}}(\mathfrak{z},0) = \tilde{U}(m(\mathfrak{z}))\Big[\sum_{m=a}^{b} T_{m,\mathfrak{e}}(0) + \sum_{k=0}^{a-1} I_k\lambda g_{\mathfrak{e}-k} + \beta\tilde{\mathcal{B}}_{\mathfrak{e}}(\mathfrak{z},0)\Big], \quad a \le \mathfrak{e} \le b-1, \tag{39}$$

$$\begin{aligned}\Big(\mathfrak{z}^b - \tilde{U}(m(\mathfrak{z}))\Big)T_b(\mathfrak{z},0) = \tilde{U}(m(\mathfrak{z}))\Big[&\sum_{m=a}^{b-1} T_m(\mathfrak{z},0) + \mathfrak{z}^b\beta\tilde{\mathcal{B}}_b(\mathfrak{z},0) \\ &+ \sum_{k=0}^{a-1}\sum_{\mathfrak{F}=b}^{\infty} I_k\mathfrak{z}^k g_{\mathfrak{F}-k}\mathfrak{z}^{\mathfrak{F}-k} - \sum_{\mathfrak{F}=0}^{b-1}\sum_{m=a}^{b} T_{m,\mathfrak{F}}(0)\mathfrak{z}^{\mathfrak{F}}\Big]\end{aligned} \tag{40}$$

$$L_{\mathfrak{e}}(\mathfrak{z},0) = \tilde{C}(n(\mathfrak{z})\Big[\sum_{m=1}^{a-1} L_{m,\mathfrak{e}}(0) + \sum_{m=a}^{b} \mathcal{B}_{m,\mathfrak{e}}(0) + \delta I_{\mathfrak{e}}\Big], \quad 1 \le \mathfrak{e} \le a-1, \tag{41}$$

$$Q_1(\mathfrak{z},0) = \tilde{V}(n(\mathfrak{z}))\Big[\sum_{m=a}^{b} \mathcal{B}_{m,0}(0) + \sum_{m=1}^{a-1} L_{m,0}(0) + \delta I_0\Big], \tag{42}$$

$$Q_l(\mathfrak{z},0) = \tilde{V}(n(\mathfrak{z}))\sum_{\mathfrak{F}=0}^{a-1} Q_{l-1,\mathfrak{F}}(0)\mathfrak{z}^{\mathfrak{F}}, \qquad l \ge 2. \tag{43}$$

Substitute Equations (37)-(43) in Equations (30)-(36) after simplication,and we get,

$$\begin{aligned}(\zeta - l(\mathfrak{z}))\tilde{B}_i(\mathfrak{z},\zeta) = (\tilde{S}(l(\mathfrak{z})) - \tilde{S}(\zeta))\Big[&\sum_{m=a}^{b} \mathcal{B}_{m,\mathfrak{e}}(0) + \sum_{m=1}^{a-1} L_{m,\mathfrak{e}}(0) + \sum_{\mathfrak{F}=0}^{\infty} Q_{l,\mathfrak{F}}(0) + \delta\tilde{T}(\mathfrak{z},0)\Big], \\ &a \le \mathfrak{e} \le b-1,\end{aligned} \tag{44}$$

$$\begin{aligned}(\zeta - l(\mathfrak{z}))(\mathfrak{z}^b - \tilde{S}(l(\mathfrak{z})))\tilde{\mathcal{B}}_b(\mathfrak{z},\zeta) = (\tilde{S}(l(\mathfrak{z})) - \tilde{S}(\zeta))\Big[&\sum_{m=a}^{b} \mathcal{B}_m(\mathfrak{z},0) + \sum_{m=1}^{a-1} L_m(\mathfrak{z},0) + \sum_{\mathfrak{F}=0}^{\infty} Q_l(\mathfrak{z},0) \\ &+ \mathfrak{z}^b\delta\tilde{T}(\mathfrak{z},0) - \sum_{\mathfrak{F}=0}^{b-1}\Big(\sum_{m=a}^{b} \mathcal{B}_{m,\mathfrak{F}}(0)\mathfrak{z}^{\mathfrak{F}} + \sum_{m=1}^{a-1} L_{m,\mathfrak{F}}(0)\mathfrak{z}^{\mathfrak{F}} + \sum_{\mathfrak{F}=0}^{\infty} Q_{l,\mathfrak{F}}(0)\mathfrak{z}^{\mathfrak{F}}\Big)\Big],\end{aligned} \tag{45}$$

$$(\zeta - m(\mathfrak{z}))\tilde{T}_{\mathfrak{e}}(\mathfrak{z},\zeta) = (\tilde{U}(m(\mathfrak{z})) - \tilde{U}(\zeta))\Big[\sum_{m=a}^{b} T_{m,\mathfrak{e}}(0) + \sum_{k=0}^{a-1} I_k\lambda g_{\mathfrak{e}-k} + \beta\tilde{\mathcal{B}}_{\mathfrak{e}}(\mathfrak{z},0)\Big], \quad a \le \mathfrak{e} \le b-1, \tag{46}$$

$$(\zeta - m(\mathfrak{z}))(\mathfrak{z}^b - \tilde{U}(m(\mathfrak{z})))\tilde{T}_b(\mathfrak{z},\zeta) = (\tilde{U}(m(\mathfrak{z})) - \tilde{U}(\zeta))\Big[\sum_{m=a}^{b} T_m(\mathfrak{z},0) + \mathfrak{z}^b\beta\tilde{\mathcal{B}}_b(\mathfrak{z},0) + \sum_{k=0}^{a-1}\sum_{\mathfrak{F}=b}^{\infty} I_k\mathfrak{z}^k g_{\mathfrak{F}-k}\mathfrak{z}^{\mathfrak{F}-k} - \sum_{\mathfrak{F}=0}^{b-1}\sum_{m=a}^{b} T_{m,\mathfrak{F}}(0)\mathfrak{z}^{\mathfrak{F}}\Big], \tag{47}$$

$$(\zeta - n(\mathfrak{z}))\tilde{L}_{\mathfrak{e}}(\mathfrak{z},\zeta) = (\tilde{C}(n(\mathfrak{z})) - \tilde{C}(\zeta))\Big[\sum_{m=1}^{a-1} L_{m,\mathfrak{e}}(0) + \sum_{m=a}^{b} \mathcal{B}_{m,\mathfrak{e}}(0) + \delta I_{\mathfrak{e}}\Big], \quad 1 \le \mathfrak{e} \le a-1, \tag{48}$$

$$(\zeta - n(\mathfrak{z}))\tilde{Q}_1(\mathfrak{z},\zeta) = (\tilde{V}(n(\mathfrak{z})) - \tilde{V}(\zeta))\Big[\sum_{m=a}^{b} B_{m,0}(0) + \sum_{m=1}^{a-1} L_{m,0}(0) + \delta I_0\Big], \tag{49}$$

$$(\zeta - n(\mathfrak{z}))\tilde{Q}_l(\mathfrak{z},\zeta) = (\tilde{V}(n(\mathfrak{z})) - \tilde{V}(\zeta))\sum_{\mathfrak{F}=0}^{a-1} Q_{l-1,\mathfrak{F}}(0)\mathfrak{z}^{\mathfrak{F}}, \quad l \ge 2. \tag{50}$$

In summary,the probability generating function associated with the queue size is

$$P(\mathfrak{z}) = \sum_{\mathfrak{e}=a}^{b} \tilde{\mathcal{B}}_{\mathfrak{e}}(\mathfrak{z},0) + \sum_{\mathfrak{e}=a}^{b} \tilde{T}_{\mathfrak{e}}(\mathfrak{z},0) + \sum_{\mathfrak{e}=1}^{a-1} \tilde{L}_{\mathfrak{e}}(\mathfrak{z},0) + \sum_{\mathfrak{F}=1}^{\infty} \tilde{Q}_{\mathfrak{F}}(\mathfrak{z},0) + I(\mathfrak{z}). \tag{51}$$

Substituting $\zeta = 0$ in Equations (44)-(50), Equation (51) simplifies to:

$$P(\mathfrak{z}) = \frac{\left\{\begin{array}{l} A_1(\mathfrak{z})\sum_{\mathfrak{e}=a}^{b-1}[\mathfrak{z}^b - \mathfrak{z}^{\mathfrak{e}}]r_{\mathfrak{e}} + A_2(\mathfrak{z})\sum_{\mathfrak{e}=a}^{b-1}[\mathfrak{z}^b - \mathfrak{z}^{\mathfrak{e}}]c_{\mathfrak{e}} \\ + (1 - \tilde{V}(n(\mathfrak{z})))A_3(\mathfrak{z})\sum_{\mathfrak{e}=0}^{a-1} q_{\mathfrak{e}}\mathfrak{z}^{\mathfrak{e}} - A_1(\mathfrak{z})\sum_{\mathfrak{e}=0}^{a-1} s_{\mathfrak{e}}\mathfrak{z}^{\mathfrak{e}} \\ + [B_1(\mathfrak{z}) - \tilde{C}(n(\mathfrak{z}))A_3(\mathfrak{z})]\sum_{\mathfrak{e}=1}^{a-1}[s_{\mathfrak{e}} + \delta I_{\mathfrak{e}}] \\ + [B_1(\mathfrak{z}) - \tilde{V}(n(\mathfrak{z}))A_3(\mathfrak{z})][s_0 + \delta I_0] \\ + [n(\mathfrak{z})B_1(\mathfrak{z}) - m(\mathfrak{z})A_2(\mathfrak{z})]\sum_{\mathfrak{e}=0}^{a-1} I_{\mathfrak{e}}\mathfrak{z}^{\mathfrak{e}} \end{array}\right\}}{n(\mathfrak{z})B_1(\mathfrak{z})} \tag{52}$$

where $p_{\mathfrak{e}} = \sum_{m=a}^{b} B_{m,\mathfrak{e}}(0), l_{\mathfrak{e}} = \sum_{m=1}^{a-1} L_{m,\mathfrak{e}}(0), q_{\mathfrak{e}} = \sum_{l=1}^{\infty} Q_{l,\mathfrak{e}}(0), v_{\mathfrak{e}} = \sum_{m=a}^{b} T_{m,\mathfrak{e}}(0), r_{\mathfrak{e}} = p_{\mathfrak{e}} + l_{\mathfrak{e}} + q_{\mathfrak{e}}$, $s_{\mathfrak{e}} = p_{\mathfrak{e}} + l_{\mathfrak{e}}$ and $c_{\mathfrak{e}} = v_{\mathfrak{e}} + \sum_{k=0}^{a-1} l_k\lambda g_{\mathfrak{e}-k}$.

Appendix A provides the expressions for $B_1(\mathfrak{z}), A_1(\mathfrak{z}), A_2(\mathfrak{z})$ and $A_3(\mathfrak{z})$.

3.1. Computational Aspects

Equation (52) involves a total of $2b + a$ unknowns, specifically the sets $\{r_a, r_{a+1}, \ldots, r_{b-1}\}$, $\{c_a, c_{a+1}, \ldots, c_{b-1}\}$, $\{s_0, s_1, \ldots, s_{a-1}\}$, $\{q_0, q_1, \ldots, q_{a-1}\}$, and $\{I_0, I_1, \ldots, I_{a-1}\}$. Theorem(1) establishes that each $q_{\mathfrak{e}}$ can be expressed as a function of $S_0 + \delta I_0$, with the numerator containing only $2b$ constants. Using Rouche's theorem, it is shown that the function $B_1(\mathfrak{z})$ possesses $2b - 1$ zeros strictly inside the unit circle and one zero exactly on the unit circle, i.e., $|\mathfrak{z}| = 1$. Given that $P(\mathfrak{z})$ is analytic within and on the unit circle, this analyticity condition leads to a system of $2b$ equations in $2b$ unknowns. To satisfy these conditions, the numerator of the function must vanish at the corresponding points. These resulting equations can be solved using the Gauss elimination method.

Theorem 1. Let q_κ, for $(0 \le \kappa \le a-1)$, be expressed in terms of $(s_0 + \delta I_0)$ as follows:

$$q_n = \frac{\Big(\beta_n(s_0 + \delta I_0) + \sum_{\kappa=0}^{n-1} q_\kappa\beta_{n-\kappa}\Big)}{1 - \beta_0}, \quad n = 1, 2, \ldots, a-1; \qquad q_0 = \frac{\beta_0}{1 - \beta_0}(s_0 + \delta I_0)$$

where β_κ is the probability that κ customers arriving while on vacation.

3.2. Stability Analysis

The queue length's probability generating function (PGF) must meet $P(1) = 1$ in order to meet the normalization criteria. To ensure this, L' Hopital's rule is applied to evaluate the limit $\lim_{\mathfrak{z}\to 1} P(z)$, which yields $\mathbb{G} = \pounds_{12}$. It follows that $\mathbb{G}$ must be positive, and hence, the condition $P(1) = 1$ is satisfied if and only if $\pounds_{12} > 0$. Furthermore, the traffic intensity ρ is given by

$$\rho = \frac{\lambda X_1(\beta+\delta)(1-\tilde{S}(\beta))(1-\tilde{U}(\delta))}{b\beta\delta[\tilde{S}(\beta)(1-\tilde{U}(\delta)) + \tilde{U}(\delta)(1-\tilde{S}(\beta))]}. \tag{53}$$

The condition $\rho < 1$ must hold for stability.

3.3. Special Case

When $a = 1$, $b = 1$ and no breakdown, then equation (52) reduces to,

$$\mathrm{P}(\mathfrak{z}) = \frac{[\tilde{V}(n(\mathfrak{z})) - 1](1-\mathfrak{z})[q_0 + s_0]}{n(\mathfrak{z})(\mathfrak{z} - \tilde{S}(n(\mathfrak{z})))} \tag{54}$$

The equation provides the queue size distribution for a queueing system with multiple vacations of $M^{[X]}/G/1$. With N=1, the outcome coincides with the queue size distribution of Lee et al. [14].

4. Performance metrics

4.1. Expected queue length

The mean queue size $E(\mathfrak{Q})$ at any given moment can be determined through evaluating the differential of $P(\mathfrak{z})$ with respect to $\mathfrak{z}$.

$$E(Q) = \frac{\left\{\begin{array}{l} \Im_1 \sum_{\mathfrak{e}=a}^{b-1} r_\mathfrak{e}[-\mathfrak{e}(\mathfrak{e}-1) + b(b-1)] + \Im_2 \sum_{\mathfrak{e}=a}^{b-1} r_\mathfrak{e}(-\mathfrak{e}+b) \\ + \Im_1 \sum_{\mathfrak{e}=a}^{b-1} c_\mathfrak{e}[-\mathfrak{e}(\mathfrak{e}-1) + b(b-1)] + \Im_3 \sum_{\mathfrak{e}=a}^{b-1} c_\mathfrak{e}(-\mathfrak{e}+b) \\ + \Im_4 \sum_{\mathfrak{e}=0}^{a-1} \mathfrak{e} q_\mathfrak{e} + \Im_5 \sum_{\mathfrak{e}=0}^{a-1} q_\mathfrak{e} + \Im_6 \sum_{\mathfrak{e}=1}^{a-1} (s_\mathfrak{e} + \delta I_\mathfrak{e}) \\ + \Im_7(s_0 + \delta I_0) + \Im_8 \sum_{\mathfrak{e}=0}^{a-1} I_\mathfrak{e} + \Im_9 \sum_{k=0}^{a-1} \mathfrak{e} I_\mathfrak{e} - \Im_{10} \sum_{\mathfrak{e}=0}^{a-1} s_\mathfrak{e} \end{array}\right\}}{3[\pounds_{12}]^2} \tag{55}$$

Appendix B provides the expressions for $\Im_1$ to $\Im_{10}$.

4.2. Expected waiting time

According to Little's formula, $E(Q)$ can be determined as follows:

$$E(Q) = \frac{E(Q)}{\lambda E(X)} \tag{56}$$

where $E(\mathfrak{Q})$ is given in Eq.(55)

5. Numerical Example

The proposed model is numerically demonstrated using the following assumptions. Arrivals occur in batches, with the batch size following a geometric distribution with mean 2. Service times (main server, standby server, and low-batch service) follow an Erlang-2 distribution with parameters m_1, m_2, and m_3 respectively. With a rate of $v = 5$, vacation time distributes exponentially. Tables 2 - 5 show the results of calculating the expected queue length, and the expected waiting time for different arrival and service rates.

Based on these tables, the following can be observed:

- Table 2 indicates that an increase in the arrival rate results in increases expected queue length
- Tables 3 and 4 indicate that an increase in the service rates of the main server and standby server results in a decrease in both the expected queue length and waiting time
- Table 5 indicates that when the service rate is zero, the expected queue length and waiting time are high. As the service rate of the low-batch service gradually increases, there is a noticeable decrease in both the expected queue length and waiting time compared to the case with zero service rate

Furthermore, the model compares the results produced by the Adaptive Neuro-Fuzzy Inference System to those acquired using the SVT/PGF analytical approach. To assess performance with the ANFIS model, five linguistic values were assigned to input parameters, interpreted as fuzzy variables, and trained across five learning epochs.

Each input variable is connected with a Gaussian membership function that represents the following linguistic categories: low, moderate, medium, high, and extremely high. These functions determine the degree to which each input value corresponds to a specific linguistic phrase.

Tables 2 - 5 and Figures 2 - 5 show that the difference in results between the ANFIS and the analytical is negligible, with both graphs almost identical.

Table 2: *Performance Metrics vs. (λ) for $a = 5$, $b = 8$, $m_1 = 15$, $m_2 = 14$, $m_3 = 10$, $\beta = 1$, $v = 5$, and $\delta = 2$.*

λ	ρ	$E(Q)$		$E(W)$	
		Analytical	ANFIS	Analytical	ANFIS
5.0	0.0872	3.9394	3.9963	0.3939	0.3971
5.5	0.0959	4.6953	4.6052	0.4269	0.4225
6.0	0.1046	5.6039	5.6231	0.4670	0.4648
6.5	0.1133	6.4456	6.4444	0.4958	0.4995
7.0	0.1220	8.0544	8.1043	0.5753	0.5762
7.5	0.1307	9.7471	9.7077	0.6498	0.6488
8.0	0.1395	11.9231	11.7800	0.7452	0.7384
8.5	0.1482	14.7864	15.2189	0.8698	0.8886
9.0	0.1569	18.7363	18.2796	1.0419	1.0220
9.5	0.1656	24.4725	24.7282	1.2880	1.2995
10.0	0.1743	33.5637	33.4798	1.6782	1.6744

Table 3: *Performance Metrics vs. (m_1) for $a = 5$, $b = 8$, $\lambda = 5$, $m_2 = 7$, $m_3 = 5$, $\beta = 1$, $v = 5$, and $\delta = 2$.*

m_1	ρ	$E(Q)$		$E(W)$	
		Analytical	ANFIS	Analytical	ANFIS
7.5	0.3563	80.6337	79.6274	8.0634	8.0544
8.0	0.3402	53.9373	53.2782	5.3937	5.4239
8.5	0.3254	41.2900	40.5498	4.1290	4.0568
9.0	0.3119	34.2405	34.2952	3.4241	3.5145
9.5	0.2993	29.5711	29.6083	2.9571	2.9096
10.0	0.2880	26.3219	26.6564	2.6322	2.6465
10.5	0.2773	23.9263	24.0915	2.3926	2.3766
11.0	0.2674	22.0967	21.8730	2.2097	2.2227
11.5	0.2582	20.6582	20.6882	2.0658	2.0606
12.0	0.2496	19.5012	19.5090	1.9501	1.9520

Table 4: *Performance Metrics vs. (m_2) for $a = 5$, $b = 8$, $\lambda = 4$, $m_1 = 12$, $m_3 = 5$, $\beta = 1$, $v = 5$, and $\delta = 2$.*

m_2	ρ	$E(Q)$		$E(W)$	
		Analytical	ANFIS	Analytical	ANFIS
6.0	0.2582	62.0072	61.9598	7.7509	7.7450
6.5	0.2538	56.4153	56.5322	7.0519	7.0665
7.0	0.2496	50.8083	50.6777	6.3510	6.3347
7.5	0.2456	45.3206	45.4477	5.6651	5.6810
8.0	0.2416	40.0282	39.8810	5.0035	4.9851
8.5	0.2378	34.9704	35.1150	4.3713	4.3894
9.0	0.2341	30.1625	30.0399	3.7703	3.7550
9.5	0.2305	25.6054	25.7381	3.2007	3.2173
10.0	0.2270	21.2924	21.1629	2.6616	2.6454
10.5	0.2237	17.2121	17.2679	2.1515	2.1585

Table 5: *Performance Metrics vs. (m_3) for $a = 5$, $b = 8$, $\lambda = 3$, $m_1 = 12$, $m_2 = 10$, $\beta = 1$, $v = 5$, and $\delta = 2$.*

m_3	$E(Q)$		$E(W)$	
	Analytical	ANFIS	Analytical	ANFIS
0	13.4068	13.4065	2.2345	2.2345
1	11.7402	11.7410	1.9567	1.9568
2	10.9469	10.9502	1.8245	1.8251
3	10.5581	10.5422	1.7597	1.7570
4	10.3446	10.3658	1.7241	1.7276
5	10.1874	10.1391	1.6979	1.6898
6	9.4319	9.5542	1.5719	1.5923
7	9.3811	9.2979	1.5635	1.5496

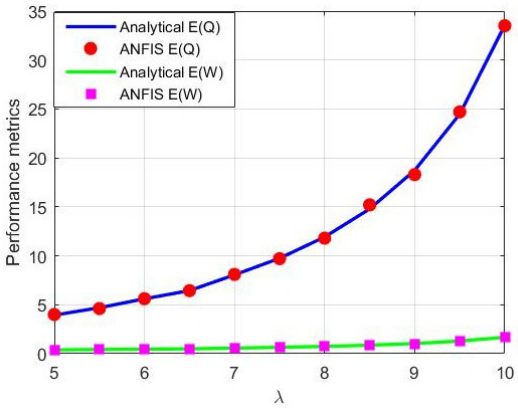


Figure 2: *Arrival rate (λ) vs E(Q) and E(W)*

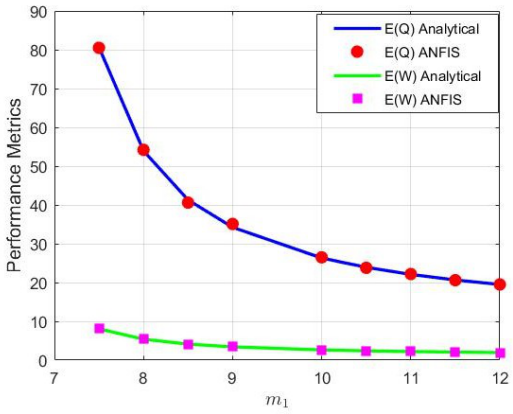


Figure 3: *Service rate (m_1) vs E(Q) and E(W)*

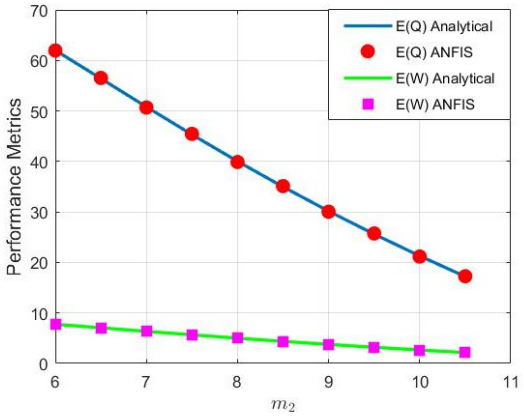


Figure 4: *Service rate (m_2) vs E(Q) and E(W)*

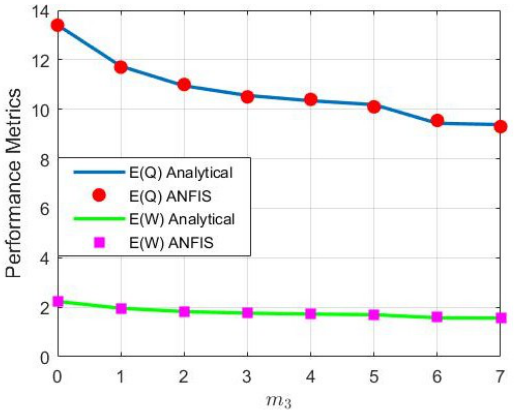


Figure 5: *Service rate (m_3) vs E(Q) and E(W)*

6. Conclusion and future work

In summary, this study describes a novel way to merge low-batch and bulk services that includes a standby server and multiple vacation mechanisms. This combination is extremely useful for simulating real-world environments, especially in cloud systems and manufacturing and production systems. Table 5 shows that low-batch service significantly reduces queue length and customers waiting time. Moreover, when the analytical results are compared to the ANFIS-based predictions, the suggested model shows excellent agreement, indicating that the ANFIS technique is accurate and robust. Currently, the standby server supports only the bulk service; in future work, it could be extended to support low-batch service as well, and its impact on performance metrics could be further evaluated.

References

[1] Ayyappan, G. and Deepa, T. (2019). Analysis of batch arrival bulk service queue with additional optional service multiple vacation and setup time. *International Journal of Mathematics in Operational Research*, 15(1):1–25.

[2] Ayyappan, G. and Karpagam, S. (2018). An $M^{[X]}/G(a,b)/1$ queueing system with breakdown and repair, stand-by server, multiple vacation and control policy on request for re-service. *Mathematics*, 6(6),101.

[3] Ayyappan, G. Gurulakshmi, G. A. and Somasundaram, B.(2022). Analysis of MAP/PH/1 queueing model with multiple vacations, optional service, close-down, setup, breakdown, phase type repair and impatient customers *Reliability: Theory & Applications*, 17(68):447–468

[4] Chang, F. M. Lee, Y. T. Chang, C. J. and Yeh, C. (2018). Analysis of a standby redundant system with controlled arrival of failed machines. *International Journal of Industrial and Systems Engineering*, 28(1):117–134.

[5] Chakravarthy, S. R. and Kulshrestha, R. (2020). A queueing model with server breakdowns, repairs, vacations, and backup server. *Operations Research Perspectives*, 7, 100131.

[6] Choudhury, G. and Madan, K. C. (2005). A two-stage batch arrival queueing system with a modified Bernoulli schedule vacation under N-policy. *Mathematical and Computer Modelling*, 42(1-2):71–85.

[7] Divya, K. and Indhira, K. (2023).Cost-revenue analysis and ANFIS computing of heterogeneous queuing model with a second optional service with feedback under hybrid vacation *Reliability: Theory & Applications*, 18(74):176-195.

[8] Doshi, B. T. (1986). Queueing systems with vacations-A survey. *Queueing Systems*, 1:29–66.

[9] Jeyakumar, S. and Senthilnathan, B. (2017). Modelling and analysis of a bulk service queueing model with multiple working vacations and server breakdown. *RAIRO-Operations Research*, 51:485–508.

[10] Karpagam, S.and Lokesh, R. (2025). Steady state analysis of bulk arrival, fixed Batch service queue with inspection, rework, and multiple vacations. *Reliability: Theory & Applications*, 20(84):577–589.

[11] Khalaf, R. F. Madan, K. C. and Lukas, C. A. (2011). On a Batch Arrival Queuing System Equipped with a Stand-by Server during Vacation Periods or the Repairs Times of the Main Server. *Journal of Probability and Statistics*, 2011(1),812726.

[12] Khalaf, R. F. Madan, K. C. and Lukas, C. A. (2012). On an $M^{[X]}/G/1$ queuing system with random breakdowns, server vacations, delay times and a standby server. *International Journal of Operational Research*, 15:30–47.

[13] Lavanya, B. Vennila, R. and Sankoh, M. (2022). Mathematical Modelling of $M^{[X]}/G(a,b)/1$ Bulk Service Queue Model with Two Vacations and Setup Time in Ceramic Technology. *Mathematical Problems in Engineering*, 2022(1),2771494.

[14] Lee, H. W. Lee, S. S. Park, J. O. and Chae, K. C. (1994). Analysis of the $M^{[X]}/G/1$ Queue by N-Policy and Multiple Vacations. *Journal of Applied Probability*, 31(2):476–496.

[15] Levy, Y. and Yechiali, U. (1975). Utilization of idle time in an $M/G/1$ queue with server vacations. *Management Science*, 22:202–211.

[16] Murugeswari, N.and Sundari, S. M. (2017). A standby server bulk arrival queuing model of compulsory server vacation. *International Journal of Engineering Development and Research*, 5(4):337–341.

[17] Neuts, M. F. (1967). A general class of bulk queues with Poisson input. *The Annals of Mathematical Statistics*, 38:759–770.

[18] Pradhan, S. Nandy, N. and Gupta, U. C. (2024). Performance analysis of a versatile bulk-service queue with group-arrival, batch-size-dependent service time and queue-length-dependent vacation. *Quality Technology & Quantitative Management*, 22(4): 683–726.

[19] Rathinasamy, P. and Kirupa, K. (2025). Optimizing Wait Times: Enhancing Server Accessibility with Two-Phase Imperative Services and Backup Server. *Calcutta Statistical Association Bulletin*, 77(1):91–116.

[20] Reddy, G. V. K. Nadarajan, R. and Arumuganathan, R. (1998). Analysis of a bulk queue with N policy multiple vacations and setup times. *Computers & Operations Research*, 25:957–967.

[21] Senthilnathan, B. and Jeyakumar, S. (2012). A study on the behaviour of the server breakdown without interruption in a $M^{[X]}/G(a,b)/1$ queueing system with multiple vacations and closedown time. *Applied Mathematics and Computation*, 219:2618–2633.

[22] Srivastava, R. K. Singh, S. and Singh, A. (2020). Bulk arrival Markovian queueing system with two types of services and multiple vacations. *International Journal of Mathematics and Computer Research*, 8(8):2130–2136.
[23] Takagi, H. (1991). Vacation and Priority Systems. In: *Queueing Analysis: A Foundation of Performance Evaluation*, Volume I. North-Holland, Amsterdam.
[24] Tamrakar, G. K. Banerjee, A., and Gupta, U. C. (2022). Analysis of batch size-dependent bulk service queue with multiple working vacation. *International Journal of Computer Mathematics: Computer Systems Theory*, 7(3):149–171.
[25] Thakur, S.Jain, A. and Jain, M. (2021). ANFIS and cost optimization for Markovian queue with operational vacation. *Int. J. Math. Eng. Management Sci*, 6(3):894–910.

Appendix A

The following expressions are employed in Eq.(52):

$$B_1(z) = l(z)m(z)(z^b - \tilde{S}(l(z)))(z^b - U(m(z))) - z^{2b}\beta\delta(1 - \tilde{S}(l(z)))(1 - \tilde{U}(m(z))),$$
$$A_1(z) = n(z)(1 - \tilde{S}(l(z)))\Big(m(z)(z^b - \tilde{U}(m(z))) + z^b\beta(1 - \tilde{U}(m(z)))\Big),$$
$$A_2(z) = (1 - \tilde{U}(m(z)))n(z)\Big(l(z)(z^b - \tilde{S}(l(z))) + z^b\delta(1 - \tilde{S}(l(z)))\Big),$$
$$A_3(z) = B_1(z) - A_1(z).$$

Appendix B

The following expressions are employed in Eq.(55):

$$\Im_1 = 3\aleph_1\pounds_{12},$$
$$\Im_2 = 3\pounds_7\pounds_{12} - 2\aleph_1\pounds_{13},$$
$$\Im_3 = 3\pounds_9\pounds_{12} - 2\aleph_1\pounds_{13},$$
$$\Im_4 = 6b\beta\delta V_1\aleph_2\pounds_{12},$$
$$\Im_5 = 3\pounds_{12}[V_1(\pounds_7 - \pounds_2) + b\beta\delta\aleph_2 V_2] - 2b\beta\delta\aleph_2 V_1\pounds_{13},$$
$$\Im_6 = 3\pounds_{12}[V_1(\pounds_7 - \pounds_2) + b\beta\delta\aleph_2 C_2] - 2b\beta\delta\aleph_2 C_1\pounds_{13},$$
$$\Im_7 = 3\pounds_{12}[V_1(\pounds_7 - \pounds_2) + b\beta\delta\aleph_2 V_2] - 2b\beta\delta\aleph_2 V_1\pounds_{13},$$
$$\Im_8 = 3\aleph_8\pounds_{12} - [2\lambda X_1 b\beta\delta\aleph_2 - \delta\pounds_9]\pounds_{13},$$
$$\Im_9 = 3\aleph_9\pounds_{12} - 2\delta\aleph_1\pounds_{13},$$
$$\Im_{10} = 3[\pounds_7 + \mathfrak{e}(\mathfrak{e} - 1)\aleph_1]\pounds_{12} - 2\aleph_1\pounds_{13}.$$

where:

$$\aleph_1 = -\lambda X_1(\beta + \delta)\left(1 - \tilde{S}(\beta)\right)\left(1 - \tilde{U}(\delta)\right),$$
$$\aleph_2 = \tilde{S}(\beta)\left(\tilde{U}(\delta) - 1\right) + \tilde{U}(\delta)\left(\tilde{S}(\beta) - 1\right),$$
$$\aleph_3 = \tilde{S}_1\left(1 - \tilde{U}(\delta)\right) - U_1\left(1 - \tilde{S}(\beta)\right),$$
$$\aleph_4 = -\lambda X_1\left(1 - \tilde{U}(\delta)\right),$$
$$\aleph_5 = -\left(1 - \tilde{U}(\delta)\right)\lambda X_2 + 2\lambda X_1 U_1,$$
$$\aleph_6 = -\left(1 - \tilde{S}(\beta)\right)\lambda X_1,$$
$$\aleph_7 = -\left(1 - \tilde{S}(\beta)\right)\lambda X_2 + 2\lambda X_1 S_1,$$
$$\aleph_8 = b\beta\delta\aleph_2\lambda X_2 - \lambda X_1\pounds_2 - (\delta/3)\pounds_{10} + \lambda X_1\pounds_9,$$
$$\aleph_9 = 2\lambda X_2 b\beta\delta\aleph_2 - \delta\pounds_9 - \delta\aleph_1,$$

$$
\begin{aligned}
\pounds_1 &= \aleph_1 - b\beta\delta\aleph_2,\\
\pounds_2 &= \left(1-\tilde{S}(\beta)\right)\left(1-\tilde{U}(\delta)\right)\left[2(\lambda X_1)^2 - \lambda X_2(\beta+\delta) - 2\beta\delta b(b-1)X_1\right]\\
&\quad + \left[\beta\delta b(b-1) - 2b\lambda X_1(\beta+\delta)\right]\\
&\quad + \left(1-\tilde{U}(\delta)\right) + \left(1-\tilde{S}(\beta)\right)\\
&\quad + 2\left[2b\beta\delta + \lambda X_1(\beta+\delta)\right]\aleph_3 + 2\beta\delta b\left(b - S_1 - U_1\right),\\
\pounds_3 &= (\beta+\delta)(b-U_1) + \aleph_4 - b\beta\tilde{U}(\delta),\\
\pounds_4 &= (\beta+\delta)(-U_2 + b(b-1)) - b\beta\left[(b-1)\tilde{U}(\delta) + 2U_1\right] - 2b\lambda X_1 + \aleph_5,\\
\pounds_5 &= (\beta+\delta)(b-S_1) + \aleph_6 - b\delta\tilde{S}(\beta),\\
\pounds_6 &= (\beta+\delta)(b(b-1) - S_2) - b\delta\left[\tilde{S}(\beta)(b-1) + 2S_1\right] + \lambda(-2b)X_1 + \aleph_7,\\
\pounds_7 &= \aleph_7(\beta+\delta)(1-U_1) + 2\aleph_6\pounds_3,\\
\pounds_8 &= (\beta+\delta)\aleph_6(1-\tilde{U}(\delta)) + 3\pounds_3\aleph_7 + 3\aleph_6\pounds_4,\\
\pounds_9 &= \aleph_5(\beta+\delta)(1-S_1) + 2\aleph_4\pounds_5,\\
\pounds_{10} &= (\beta+\delta)\aleph_6(1-\tilde{S}(\beta)) + 3\pounds_5\aleph_5 + 3\aleph_4\pounds_6,\\
\pounds_{11} &= \delta\pounds_7 - \delta\pounds_9 + 2\lambda X_1 b\beta\delta\aleph_2,\\
\pounds_{12} &= -2\lambda X_1\pounds_1,\\
\pounds_{13} &= -3\left[\lambda X_1\pounds_2 + \lambda X_2\pounds_1\right],\\
\mathbb{E} &= 2\aleph_1\sum_{\mathfrak{e}=a}^{b-1} r_{\mathfrak{e}}(b-\mathfrak{e}) + 2\aleph_1\sum_{\mathfrak{e}=a}^{b-1} C_{\mathfrak{e}}(b-\mathfrak{e}) + 2b\beta\delta\aleph_2 V_1\sum_{n=0}^{a-1} q_n + 2b\beta\delta\aleph_2 C_1\sum_{\mathfrak{e}=1}^{a-1}(s_{\mathfrak{e}} + \delta I_{\mathfrak{e}})\\
&\quad + 2b\beta\delta\aleph_2 V_1(s_0 + \delta I_0) + \aleph_{11}\sum_{\mathfrak{e}=0}^{a-1} l_{\mathfrak{e}} - 2\aleph_1\left(\delta\sum_{\mathfrak{e}=0}^{a-1}\mathfrak{e}l_{\mathfrak{e}} + \sum_{\mathfrak{e}=0}^{a-1}\mathfrak{e}s_{\mathfrak{e}}\right).
\end{aligned}
$$

A DIFFERENTIATED RELIABILITY MODEL FOR INDUSTRIAL POWER SUPPLY SYSTEMS CONSIDERING THREE TYPES OF EQUIPMENT FAILURES

[1]Sevinc Mirzayeva, [2]Natavan Ismiyeva, [3]Fidan Mustafayeva

•

Azerbaijan State Oil and Industry University, Baku, Azerbaijan
[1]sevinc.mirzeyeva@asoiu.edu.az , [2]natavan.ismiyeva@asoiu.edu.az,
[3]fidan.mustafayeva@asoiu.edu.az

Abstract

The reliability of power supply systems is a critical factor influencing the operational continuity and safety of industrial enterprises. Conventional reliability assessments often treat all failures uniformly, neglecting the unique characteristics of failure mechanisms such as short circuits, open circuits, and non-actuation of protection devices. This paper proposes a differentiated reliability evaluation model based on non-stationary failure rate functions that reflect the time-dependent nature of each failure type. Using a piecewise failure rate model across three operational phases—burn-in, steady-state, and aging—the methodology accounts for individual failure flows and their cumulative impact on system reliability. A numerical case study demonstrates the application of the model to a transformer, showing a more accurate prediction of failure-free probability compared to traditional models. The results confirm that short circuits dominate risk during aging, while non-actuation and open circuits also contribute significantly. The model enhances diagnostic precision, supports targeted maintenance planning, and can be extended to system-level reliability assessment for complex industrial energy infrastructures.

Keywords: industrial power supply systems; reliability modeling; short circuits; open circuits; protection failure; non-stationary failure rate; differentiated failure flows; preventive maintenance

I. Introduction

The reliability of power supply systems is a fundamental indicator of the resilience and safety of industrial enterprises. According to ISO 14224 and GOST 27.002–2015, reliability is defined as the ability of a system or component to perform its required functions under stated conditions for a specified period of time.

In the context of increasing energy demands, digital control, and stricter continuity requirements (as defined by ISO 55000 and EN 50160), the role of reliability becomes even more critical. In energy-intensive industries such as metallurgy, petrochemicals, and heavy manufacturing, even a short-term power interruption can result in production downtime, equipment damage, or process disruption [1-3].

Traditional reliability assessments use general indicators such as:

– probability of failure-free operation P(t),

– mean time between failures (MTBF),

– availability factor Kg,

– failure rate $\lambda(t)$ [1,2].

However, most models treat all failures uniformly, without accounting for the underlying failure mechanisms. In practice, three major types of failures occur in industrial power systems:

1. Short circuits (SC) – sudden overcurrent events leading to immediate disconnection and potential equipment destruction.
2. Open circuits (OC) – typically caused by conductor breakage or terminal degradation, disrupting the flow of power.
3. Malfunctions or equipment non-response (ENR) – failure of automatic circuit breakers or protection devices to activate under fault conditions.

Figure 1 illustrates a typical industrial power supply scheme, indicating critical nodes and the most probable locations for each type of failure.

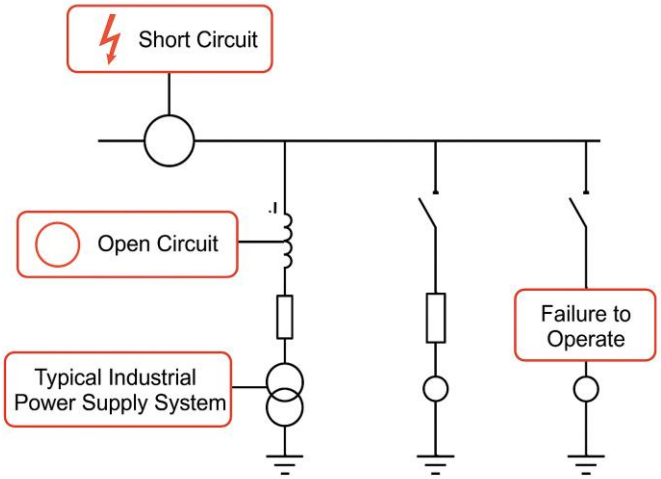


Figure 1. *Typical layout of an industrial power supply system, annotated with locations of three main types of failures: short circuit, open circuit, and equipment malfunction.*

Ignoring the nature and probability of each failure type often results in an inaccurate reliability forecast and may lead to inefficient maintenance or protection strategies. While current standards such as IEC 60300 and local regulations (e.g., SP 256.1325800.2016) require reliability assessment, they rarely mandate differentiation by failure type [4].

The objective of this paper is to develop a comprehensive reliability evaluation model that incorporates three distinct failure types. The proposed model enhances accuracy and provides more realistic diagnostics for system design, modernization, and risk mitigation planning.

II. Problem statement

Modern industrial power supply systems are characterized by high structural complexity and strict requirements for uninterrupted operation. Accurate reliability assessment is essential at all levels—from individual components to the overall network. One of the key aspects of such analysis is the proper classification of failures, accounting for their nature, dynamics, and impact on system behavior.

In practice, failures in power systems differ significantly in their physical origin and functional consequences. The most common types include:

- Short circuits (SC) – sudden insulation breakdowns accompanied by fault currents, resulting in the immediate disconnection of affected components by protection systems.
- Open-circuit faults – caused by mechanical wear, thermal degradation, or connector failure, these lead to power interruption without necessarily triggering protective devices.
- Failure to operate (non-actuation) – malfunctions of protective or switching devices that fail to respond under abnormal or emergency conditions.

Each of these failure types exhibits distinct statistical characteristics and impacts system reliability in different ways. For example, short circuits typically occur in aging power transformers, while open-circuit faults are more prevalent in overhead lines, and non-actuation failures often affect complex control and protection devices [5-7]. Therefore, using a generalized failure representation, as in many conventional models, does not reflect the true reliability behavior of industrial power systems.

To accurately represent the failure process, the authors propose a three-phase model of failure rate variation over time:

$$\lambda(t) = \begin{cases} \lambda_1, 0 \le t < T_1 & (burn - in\ phase) \\ \lambda_2, T_1 \le t < T_2 & (normal\ operation) \\ \lambda_3, t \ge T_2 & (aging\ phase) \end{cases}$$

This time-dependent, non-stationary model enables more accurate predictions of failure likelihood across an asset's life cycle. Each failure type (SC, open circuit, non-actuation) is represented by a separate failure flow $\lambda_i(t)$, reflecting its unique behavior and operational risk.

However, traditional reliability assessment models often ignore such distinctions and use a single aggregated failure rate λ, typically assuming a constant hazard function. This simplification introduces significant limitations:

- Underestimation of critical failure probabilities, such as the increased likelihood of short circuits in aging transformers;
- Incorrect prioritization of maintenance resources, where components with low failure risk are overserved while vulnerable nodes remain unprotected;
- Improper redundancy allocation, based on averaged reliability indicators rather than failure-specific analysis;
- Neglect of hidden or latent failures, especially in protective relay systems, where non-actuation may go undetected until a critical event occurs.

These shortcomings can result in operational planning errors, reduced system availability, and elevated risk of outages or equipment damage [8]. For industrial enterprises, where downtime can lead to substantial economic loss, ensuring high accuracy in failure modeling is particularly important.

Therefore, there is a clear need for a differentiated reliability assessment methodology that:

- Separately models short circuits, open circuits, and non-actuations;
- Applies non-stationary failure rate models $\lambda(t)$;
- Supports system-level integration of component-specific risk profiles.

This approach forms the basis for the methodology proposed in the following section, aimed at enhancing the reliability and risk awareness of industrial power supply systems.

III. Solution to the problem

To improve the accuracy of reliability analysis in industrial power supply systems, it is essential to separately account for the three dominant types of equipment failures: short circuits,

open circuits, and failures of switching or protection devices. Each failure type has its own occurrence probability, intensity, and impact on system availability [9]. The proposed methodology is based on the construction of a generalized reliability model incorporating multiple independent failure flows, each described by a non-stationary failure rate function.

The overall failure process of each system component is modeled as a nonhomogeneous Poisson process with a time-dependent failure intensity. For each failure type j∈{1,2,3}, where:

- j=1 corresponds to short circuits (SC),
- j=2 to open circuits (OC),
- j=3 to failure to operate (non-actuation),

the failure rate is expressed in a piecewise form:

$$\lambda_j(t) = \begin{cases} \lambda_{j1}, 0 \le t < T_1 \\ \lambda_{j2}, T_1 \le t < T_2 \\ \lambda_{j3}, t \ge T_2 \end{cases}$$

where T_1 and T_2 represent the transition points between the burn-in, stable operation, and wear-out phases, respectively.

The cumulative probability of failure-free operation for a single component over the interval [0, t], considering all three types of failures, is then:

$$P(t) = exp\left(-\int_0^t \sum_{j=1}^{3} \lambda_j(\tau)\, d\tau\right)$$

This formulation allows failure intensities to evolve over time and differ by failure type.

For example, in the case of a transformer, the following numerical parameters were used in the source study (in failures/hour):

- Short circuits: $\lambda_{11}=1.2\times10^{-5}$, $\lambda_{12}=1.8\times10^{-5}$, $\lambda_{13}=3.0\times10^{-5}$
- Open circuits: $\lambda_{21}=0.6\times10^{-5}$, $\lambda_{22}=0.9\times10^{-5}$, $\lambda_{23}=1.5\times10^{-5}$
- Non-actuation: $\lambda_{31}=1.0\times10^{-6}$, $\lambda_{32}=1.5\times10^{-6}$, $\lambda_{33}=2.5\times10^{-6}$

With time thresholds set at $T_1=1000$ hours and $T_2=4000$ hours, the integral in the exponential can be explicitly calculated piecewise over the interval of operation (e.g., 5000 hours). As a result, the overall reliability function becomes:

$$P(5000) = exp\left(-\sum_{j=1}^{3}\left[\lambda_{j1}\cdot T_1 + \lambda_{j1}\cdot(T_2 - T_1) + \lambda_{j3}\cdot(5000 - T_2)\right]\right)$$

Substituting the values:

$$P(5000) = exp(-[(1.2 + 0.6 + 0.1)\cdot 10^{-5}\cdot 1000 + (1.8 + 0.9 + 0.15)\cdot 10^{-5}\cdot 3000 + (3.0 + 1.5 + 0.25)\cdot 10^{-5}\cdot 1000]) = exp(-[0.019 + 0.0855 + 0.0475]) = exp(-0.152) \approx 0.859$$

This result demonstrates that even for a single transformer, the probability of failure-free operation over 5000 hours is only ~85.9%, reflecting the compounded effect of all three failure types. If only one failure type (e.g., short circuits) were considered, the calculated reliability would be overestimated—often by 10–20%, depending on the element and operating time.

The methodology can be extended to evaluate system-level reliability by using appropriate structural models (series, parallel, or hybrid configurations) and combining component reliabilities accordingly. For series-connected components, the total system reliability is the product of individual Pi(t) values; for parallel redundancy, the complement rule is applied:

$$P_{parallel}(t) = 1 - \prod_{i=1}^{n}(1 - P_i(t))$$

This enables modeling of complex power supply systems with redundancy and load transfer schemes. Additionally, mean time to failure (MTTF) and average number of failures in time t can be derived as:

$$N_j(t) = \int_0^t \lambda_j(\tau) d\tau$$

$$MTTF_j = \int_0^{\infty} P_i(t) dt$$

The application of this model in the article allowed the authors to identify the most vulnerable components in a test configuration of a power supply system, to optimize maintenance intervals, and to justify targeted redundancy for the most failure-prone paths.

In summary, the proposed model addresses the key limitations of traditional reliability assessments by integrating differentiated failure flows, time-dependent intensities, and failure-type-specific risks, thereby enabling more realistic and actionable evaluations of industrial power supply reliability.

IV. Results and discussion

To validate the proposed reliability assessment methodology, a numerical case study was performed for a representative component of an industrial power supply system, such as a power transformer. The analysis incorporates three independent failure flows—short circuits (SC), open circuits (OC), and failures to actuate (NA)—each modeled using a piecewise failure rate function across three distinct operational phases: burn-in, steady-state operation, and aging.

The time-dependent reliability function P(t) was computed over an operating horizon of 5000 hours using failure rate values taken from real-world industrial data (as referenced in the original study). Each failure type was represented by a different set of failure intensities λj(t), and the overall system reliability was determined by integrating these rates into the exponential failure-free operation model:

$$P(t) = exp\left(- \int_0^t \sum_{j=1}^{3} \lambda_j(\tau)\, d\tau \right)$$

The results are presented in Figure 2, which shows a continuously decreasing reliability curve. The slope of the curve increases over time due to the compounding effects of aging and the nonlinear accumulation of risks from all three failure types.

Probability of failure-free operation P(t) over time, calculated for a representative power system component (e.g., transformer), accounting for three distinct failure flows: short circuits (SC), open circuits (OC), and non-actuation (NA). Each failure type is modeled using a time-dependent piecewise failure rate function λj(t) across three operational phases: burn-in, stable operation, and aging. The exponential degradation trend illustrates the cumulative effect of all failure types over 5000 hours.

To further interpret these results, cumulative failure intensities and corresponding reliability values were calculated at selected time intervals. The values are summarized in Table 1.

Cumulative integrals of failure intensities and corresponding reliability values P(t)P(t)P(t) over the equipment's life cycle, with individual contributions from short circuit, open circuit, and non-actuation failure types. The results clearly demonstrate the additive effect of multiple failure mechanisms and the importance of differentiated modeling.

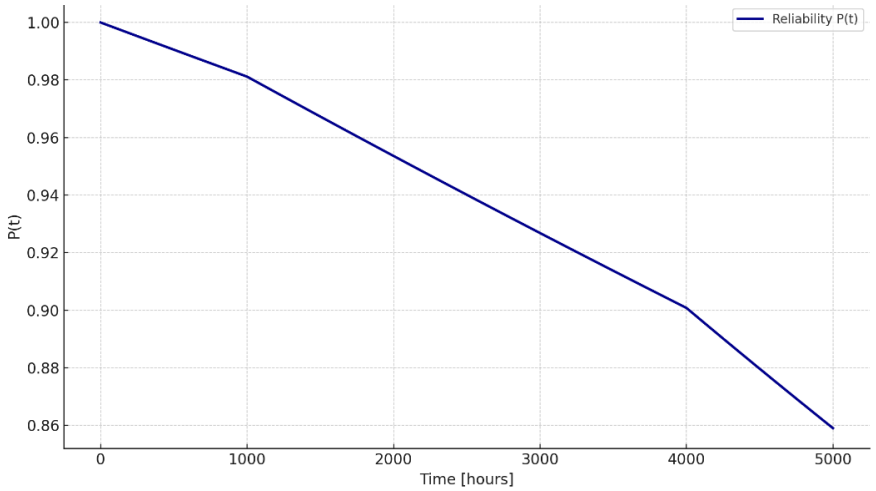


Figure 2.: *Reliability function of power supply equipment considering three failure types*

Table 1. *Cumulative failure intensities and reliability values for a typical power system component*

Time (h)	$\int_0^t \lambda_{SC}(t)dt$	$\int_0^t \lambda_{OC}(t)dt$	$\int_0^t \lambda_{NA}(t)dt$	$\int_0^t \lambda dt$	P(t)
1000	0.01200	0.00600	0.00100	0.01900	0.98118
2000	0.03000	0.01500	0.00250	0.04750	0.95361
3000	0.04800	0.02400	0.00400	0.07600	0.92682
4000	0.06600	0.03300	0.00550	0.10450	0.90077
5000	0.09600	0.04800	0.00800	0.15200	0.85899

The results presented in Figure 2 and Table 1 highlight two critical insights:

1. The non-linearity of reliability degradation becomes pronounced in the aging phase, where failure rates increase significantly. For example, after 5000 hours of operation, the probability of failure-free functioning drops to approximately 85.9%, even though all individual failure rates appear low at first glance.

2. Each failure mechanism contributes differently over time. Short circuits contribute the most to reliability degradation, especially in later phases, while open circuits have a moderate and more evenly distributed impact. Non-actuation failures, though less frequent, remain critical due to their hidden nature and potential to compromise protection systems.

Compared to traditional single-failure-type models, the proposed approach provides a more realistic representation of operational risks. It enables:

- Identification of critical components based on differentiated failure patterns,
- Optimization of preventive maintenance schedules by targeting phase-specific vulnerabilities,
- Justification of redundancy strategies based on the dominant failure mechanisms.

This methodology can be integrated into existing SCADA or maintenance planning systems to enhance the predictive capabilities and risk awareness of industrial power engineers.

V. Conclusion

This paper proposed an advanced methodology for assessing the reliability of industrial power supply systems by explicitly accounting for three major types of equipment failures: short

circuits, open circuits, and non-actuation of switching and protection devices. Unlike traditional approaches that rely on a single average failure rate, the presented model incorporates distinct failure flows with time-dependent intensities, structured across three operational phases: burn-in, steady-state, and aging.

The analytical expressions derived and the numerical case study demonstrated the tangible impact of differentiated modeling. Over a 5000-hour operation interval, failure-free probability declined to approximately 86%, revealing a significant underestimation when using conventional methods. The results emphasized that:

- Short circuits dominate the failure risk during aging,
- Hidden failures (non-actuation) require special attention due to their low visibility and high potential impact.

By applying this approach, reliability engineers can obtain a more realistic and granular understanding of system behavior, allowing for:

- More targeted maintenance scheduling,
- Risk-informed redundancy planning,
- Improved decision-making in the design and operation of power supply infrastructures.

The methodology is scalable and can be extended to complex multi-element power systems, integrating seamlessly into digital asset management platforms and reliability-centered maintenance (RCM) frameworks. Future research may focus on incorporating failure dependencies, repair dynamics, and real-time condition monitoring data to further enhance the model's applicability in adaptive and self-healing power networks.

References

[1] Rzayeva, S. V., Piriyeva, N. M., & Guseynova, I. A. (2024). Analysis of reliability of typical power supply circuits. *Reliability: Theory & Applications*, 19(3)(79), 173–178.

[2] Rzayeva, S. V., & Guseynova, I. A. (2024). Application of automatic monitoring and control systems for reliability of power transmission lines. *Reliability: Theory & Applications*, 19(2)(78), 64–69.

[3] Rzayeva, S. V., Ganiyeva, N. A., & Piriyeva, N. M. (2024). Modern approaches to electrical equipment diagnostics. *International Journal on Technical and Physical Problems of Engineering (IJTPE)*, 58.

[4] Mamedova, G. V., Kerimzade, G. S., & Piriyeva, N. M. (2022). Electromagnetic calculation of tension devices for winding wires of small cross sections. *International Journal on Technical and Physical Problems of Engineering (IJTPE)*, 14(4)(53), December.

[5] Xu, Z., Zhang, Y., Song, Y., & Wang, H. (2022). Power supply capability evaluation of distribution systems with distributed generations under differentiated reliability constraints. *International Journal of Electrical Power & Energy Systems*, 134, 107344.

[6] Zhang, X., & Gockenbach, E. (2007). Component reliability modeling of distribution systems based on the evaluation of failure statistics. *IEEE Transactions on Dielectrics and Electrical Insulation*, 14(5), 1183–1191.

[7] Dong, Z., Koval, D. O., & Propst, J. E. (2004). Reliability of various industrial substations. *IEEE Transactions on Industry Applications*, 40(4), 989–994.

[8] Kovalev, G. F., & Lebedeva, L. M. (2019). *Reliability of power systems* (Vol. 1). Springer International Publishing.

[9] Bahmanyar, A., Gharehpetian, G. B., & Gholipour, E. (2017). A comparison framework for distribution system outage and fault location methods. *Electric Power Systems Research*, 145, 19–34.

RT&A, No 4 (89)
Volume 20, December 2025

A NEW MODIFIED POWER GENERALIZED WEIBULL DISTRIBUTION: PROPERTIES AND APPLICATION

[1]A. M. Rangoli, [2]A. S. Talawar and [3]Vijaya Sorganvi

[1] Lecturer Cum Statistician, Department of Community Medicine, BLDE (DU), Shri B. M. Patil Medical College, Hospital and Research Centre, Vijayapura, India
ajmr1008@gmail.com
[2]Senior Professor, Department of Statistics, Karnatak University, Dharwad. India.
astalawar@kud.ac.in
[3]Associate Professor, Department of Community Medicine, BLDE (DU), Shri B. M. Patil Medical College, Hospital and Research Centre, Vijayapura, India.
vijaya.sorganvi@bldedu.ac.in

Abstract

Introduction: Survival analysis has become increasing important for various fields like clinical-trails, public health industrial reliability. A major challenge is accurately modelling of failure time data. Using lifetime distribution, we can accurately model the failure time data and can estimate hazard and survival function. In this study we introduced new modified power generalized Weibull (NMPGW) distribution which exhibits bimodal as well as unimodal density patterns, and also, various patterns of hazard curves like increasing, bathtub and decreasing-increasing-decreasing patterns.
Methodology: The proposed NMPGW distribution's various density and hazard patterns were studied. Various statistical properties of the model were derived. Estimation of the parameters were done using maximum likelihood estimation (via Expectation Maximization algorithm) and Bayes technique (via Metropolis Hasting algorithm). Also, standard error and confidence limit were estimated. Comparison of various lifetime distributions were done using information criterion.
Results: The model shows good fit for hospital dataset in comparison to various lifetime distributions. Estimated the hazard rate which shows decreasing-increasing-decreasing patterns. In comparison to MLE, Bayes estimation gives lower standard error. Kaplan-Meier survival and NMPGW distribution survival curve shows nearer.
Conclusion: The NMPGW distribution introduced in this study offers a versatile tool for modeling different hazard rate patterns. The model's strong performance, validated through real hospital data, suggests it could be a valuable addition to survival analysis, outperforming other modified Weibull models in terms of fit and flexibility.

Keywords: New Modified power generalized Weibull distribution, MCMC, hazard, survival, EM algorithm.

I. Introduction

Recently, survival analysis has gained significant attention due to the increasing complexity of data that tracks the time until an event occurs, such as in clinical trials, public health studies, and industrial reliability testing. This method is particularly valuable because it can handle incomplete

data (referred to as censored data) and helps identify the factors influencing the duration of survival for individuals or items within a group. One of the main challenges in survival analysis is accurately modeling failure rates, which necessitates the use of lifetime distributions capable of capturing various hazard rate patterns over time.

Among the commonly used models, the Weibull distribution (WD) has proven effective in lifetime and reliability studies due to its ability to model failure rates that either increase or decrease steadily. Its flexibility in handling right- or left-skewed data makes it applicable across a wide range of fields. However, the standard Weibull distribution has limitations when dealing with complex, non-monotonic hazard rate patterns, such as the bathtub-shaped or upside-down bathtub-shaped hazard functions frequently observed in real-world data. To address these limitations, researchers have proposed several extensions and modifications of the Weibull distribution, incorporating additional parameters that enhance the flexibility and accuracy of the model in representing real-world failure behaviors.

For instance, the Additive Weibull Distribution was introduced to capture the bathtub-shaped hazard rate [1]. A power generalized Weibull distribution with three parameters was proposed to offer greater flexibility [2]. A three-parameter Weibull model specifically designed to accommodate bathtub-shaped hazard functions was also developed [3]. Another variation, the modified Weibull distribution, was created by incorporating an additional scale parameter into the standard Weibull model [4]. The Flexible Weibull Distribution, capable of modeling both increasing and bathtub-type failure behaviors, was also introduced [5]. Furthermore, a modification of the Bebbington et al. [5] model was developed to better handle bimodal datasets using three parameters [6]. A modified power generalized Weibull distribution with four parameters, capable of modeling various hazard patterns, was later proposed [7]. More recently, a new modified exponentiated Weibull distribution comprising four parameters has been introduced, demonstrating utility in modeling different hazard patterns and proving especially effective for bimodal datasets [8].

In this article, we introduce new modified power generalized Weibull distribution (NMPGW) with having five parameters and estimate hazard and survival functions. This paper is organized as follows: We introduce the new modified power generalized Weibull distribution in Section 2. Statistical properties were considered in section 3. The maximum likelihood estimation and Bayes estimation were provided in Section 4. In Section 5, we discuss with real-life application. Finally, Section 6 deals with concluding remarks.

II. Model Formulation

Let $T_1, T_2, \ldots T_i., T_n$ are failure times, we assume that T_i to follows new modified power generalized Weibull random variables with parameters $(\alpha,\ \beta,\ \gamma,\ \lambda, \theta)$, $i = 1,2, \ldots n$.

Let $f(t)$, $F(t)$, $S(t)$ and $h(t)$ be density, cumulative distribution, survival and hazard functions of t.

Let the cumulative distribution function (CDF) is,

$$F(t) = 1 - e^{1-\left(1+\lambda t^{\theta}\right)^{\alpha}-(\beta t^{\gamma})} \tag{1}$$

where $\alpha > 0$, $\beta \geq 0$, $\gamma > 0$, $\lambda > 0$, $t \geq 0$, β and λ are scale parameters, α, θ and γ are shape parameters.

The probability density function (PDF) is,

$$f(t) = \left(\alpha\lambda\ \theta\ t^{\theta-1}\left(1+\lambda t^{\theta}\right)^{\alpha-1} + (\beta\ \gamma\ t^{\gamma-1})\right) e^{1-\left(1+\lambda t^{\theta}\right)^{\alpha}-(\beta t^{\gamma})} \tag{2}$$

Hazard Function is,

$$h(t) = \left(\alpha\lambda\ \theta\ t^{\theta-1}\left(1+\lambda t^{\theta}\right)^{\alpha-1} + (\beta\ \gamma\ t^{\gamma-1})\right) \tag{3}$$

Survival Function is,

$$S(t) = e^{1-\left(1+\lambda t^{\theta}\right)^{\alpha}-(\beta t^{\gamma})} \tag{4}$$

This modified Weibull is widely used in reliability, human mortality, etc.

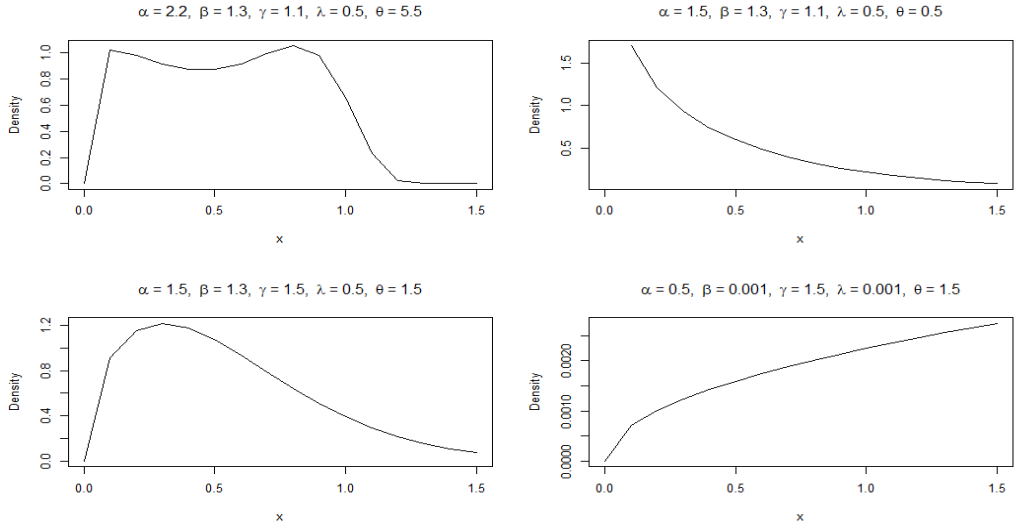


Figure 1: *Density Pattern for different values of parameter.*

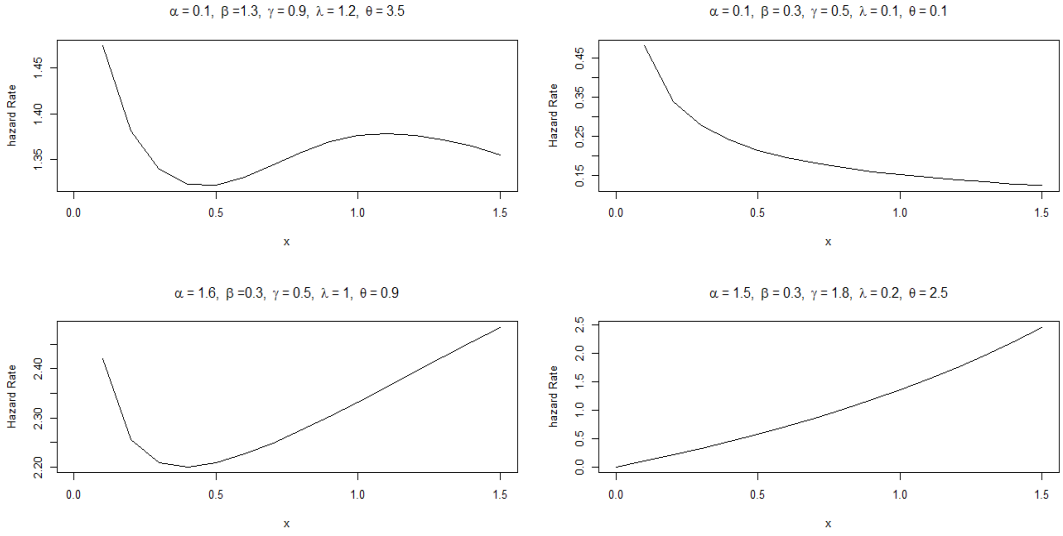


Figure 2: *Hazard Pattern for different values of parameters.*

Figure 1 illustrates various patterns of the density plot. It is evident that the proposed density function is particularly effective in capturing bimodal distributions. Figure 2 displays different patterns of the hazard rate, demonstrating the flexibility of the newly modified distribution. It is capable of modeling increasing, decreasing, constant, bathtub-shaped, as well as decreasing-increasing-decreasing hazard rate patterns.

Hazard patterns: For all $\lambda, \beta < 1$
As $\alpha, \theta, \gamma < 1$ the hazard is decreasing and $\alpha, \theta, \gamma > 1$ the hazard is increasing.
As $\alpha, \theta < 1, \gamma > 1$ the hazard is increasing and $\alpha, \theta > 1, \gamma < 1$ the hazard is bathtub in shape.
As $\alpha, \gamma < 1, \theta > 1$ the hazard is decreasing and $\alpha, \gamma > 1, \theta < 1$ the hazard is bathtub in shape.
As $\alpha, \theta, \gamma = 1$ gives the constant hazard rate.
As $\theta, \gamma < 1, \alpha > 1$ the hazard is decreasing and $\theta, \gamma > 1, \alpha < 1$ the hazard is increasing in shape

I. Sub distributions

a. $\gamma = 1$ tends to modified power generalized Weibull distribution given by [7]

$$F(t) = 1 - e^{1-\left(1+\lambda t^{\theta}\right)^{\alpha}-\beta t}$$

b. $\beta = 0$ tends to power generalized Weibull distribution given by, [2]

$$F(t) = 1 - e^{1-\left(1+\lambda t^{\theta}\right)^{\alpha}}$$

c. $\alpha = 1$ tends to Additive Weibull distribution given by [1]

$$F(t) = 1 - e^{-(\lambda t^{\theta}+\beta t^{\theta})}$$

d. $\alpha = 1, \gamma = 1$ tends to modified Weibull distribution given by [4]

$$F(t) = 1 - e^{-(\lambda t^{\theta}+\beta t)}$$

e. $\alpha = 1, \beta = 0$ tends to Weibull distribution

$$F(t) = 1 - e^{-\lambda t^{\theta}}$$

f. $\beta = 0, \alpha = 1, \theta = 1$ tends to Exponential distribution

$$F(t) = 1 - e^{\lambda t}$$

III. Statistical Properties

Mean: The mean of the random variable T with pdf $f(t)$ is given by,

$$E(T) = \int_0^{\infty} t\, f(t)dt$$

$$E(T) = \int_0^{\infty} t\, \left(\alpha\lambda\, \theta\, t^{\theta-1}\left(1+\lambda t^{\theta}\right)^{\alpha-1} + (\beta\, \gamma\, t^{\gamma-1})\right) e^{1-\left(1+\lambda t^{\theta}\right)^{\alpha}-(\beta t^{\gamma})} dt$$

Since this integral cannot be solved in a simple closed form, a numerical method must be used to estimate the mean, which represents the average time until the event happens.

Variance: The variance measures the spread of the time to failure.

$$V(T) = E(T^2) - (E(T))^2$$

$$E(T^2) = \int_0^{\infty} t^2\, f(t)dt$$

$$E(T^2) = \int_0^{\infty} t^2 \left(\alpha\lambda\, \theta\, t^{\theta-1}\left(1+\lambda t^{\theta}\right)^{\alpha-1} + (\beta\, \gamma\, t^{\gamma-1})\right) e^{1-\left(1+\lambda t^{\theta}\right)^{\alpha}-(\beta t^{\gamma})} dt$$

This integral is also computed using numerical method.

Moment Generating Function (MGF): The r^{th}moment of T denotes $E(T^r)$ is given by,

$$E(T^r) = \int_0^{\infty} t^r\, f(t)dt$$

The MGF is defined as,

$$M_T(s) = E(e^{sT}) = \int_0^{\infty} e^{sT}\, f(t)dt$$

$$M_T(s) = \int_0^{\infty} \left(\alpha\lambda\, \theta\, t^{\theta-1}\left(1+\lambda t^{\theta}\right)^{\alpha-1} + (\beta\, \gamma\, t^{\gamma-1})\right) e^{sT+1-\left(1+\lambda t^{\theta}\right)^{\alpha}-(\beta t^{\gamma})}\, dt$$

The MGF provides a way to compute all moments of the distribution by taking derivates,

$$E(T^r) = \left.\frac{d^r M_T(s)}{ds^r}\right|_{s=0}$$

Here if $r = 1$ we get first moment (Mean, $E(T)$), and $r = 2$ we get second moment ($E(T^2)$).

Cumulative Hazard Function: The cumulative hazard function is given by,

$$H(t) = \int_0^t \lambda(u)\, du = \int_0^t \left(\alpha\lambda\, \theta\, t^{\theta-1}\left(1+\lambda t^{\theta}\right)^{\alpha-1} + (\beta\, \gamma\, t^{\gamma-1})\right) du$$

$$H(t) = \alpha\lambda\theta \int_0^t u^{\theta-1}\left(1+\lambda u^{\theta}\right)^{\alpha-1} du + \gamma\, \beta \int_0^t u^{\lambda-1}\, du$$

$$H(t) = \alpha\lambda\theta \int_0^t u^{\theta-1}\left(1+\lambda u^{\theta}\right)^{\alpha-1} du + \gamma \frac{\beta}{\lambda} t^{\lambda}$$

This integral does not have a general closed-form solution for arbitrary α, λ, θ. It is typically solved numerically method.
So, we write $S(t) = e^{-H(t)}$.

Quantile: The quantile function is the inverse of the CDF. For a given probability p the quantile function $Q(p)$ gives the value at t such that probability of failure by that time is p.

$$Q(p) = F^{-1}(p)$$
$$F(t) = p$$
$$1 - e^{1-\left(1+\lambda t^{\theta}\right)^{\alpha}-(\beta t^{\gamma})} = p$$
$$1 - \left(1+\lambda t^{\theta}\right)^{\alpha} - (\beta t^{\gamma}) = -\ln(1-p)$$
$$\left(1+\lambda t^{\theta}\right)^{\alpha} - (\beta t^{\gamma}) = 1 - \ln(1-p)$$

This equation can be solved using numerical method. If we substitute $p = 0.25,\ 0.5,\ 0.75$, we get first, second (median) and third quartiles respectively.

Order Statistics:

Let $T_1, T_2, \ldots, T_n$ be a random sample of size n from new modified power generalized Weibull distribution with PDF and CDF defined in (2) and (1) respectively. We give the density of r^{th} order statistic as,

$$f_r(t) = \frac{n!}{(r-1)!(n-r)!}\left(1 - e^{1-\left(1+\lambda t^{\theta}\right)^{\alpha}-(\beta t^{\gamma})}\right)^{r-1}\left(e^{1-\left(1+\lambda t^{\theta}\right)^{\alpha}-(\beta t^{\gamma})}\right)^{n-r+1}\left(\alpha\lambda\, \theta\, t^{\theta-1}\left(1+\lambda t^{\theta}\right)^{\alpha-1} + (\beta\, \gamma\, t^{\gamma-1})\right)$$

The density of I^{st} order statistic is given by,

$$f_1(t) = n\left(e^{1-\left(1+\lambda t^{\theta}\right)^{\alpha}-(\beta t^{\gamma})}\right)^{n}\left(\alpha\lambda\, \theta\, t^{\theta-1}\left(1+\lambda t^{\theta}\right)^{\alpha-1} + (\beta\, \gamma\, t^{\gamma-1})\right)$$

And the density of n^{th}order statistic is given by,

$$f_n(t) = n\left(1 - e^{1-\left(1+\lambda t^{\theta}\right)^{\alpha}-(\beta t^{\gamma})}\right)^{n-1}\left(\alpha\lambda\, \theta\, t^{\theta-1}\left(1+\lambda t^{\theta}\right)^{\alpha-1} + (\beta\, \gamma\, t^{\gamma-1})\right) e^{1-\left(1+\lambda t^{\theta}\right)^{\alpha}-(\beta t^{\gamma})}$$

IV. Estimation Methods

I. Maximum Likelihood Estimation

The maximum likelihood estimation (MLE) is widely used among the statistical inference because of its desirable properties like consistency, asymptotic efficiency. Use of maximum likelihood estimation is illustrated below.
The Likelihood function is given by,

$$L = \prod_{i=1}^{n}(f(t_i))$$

The log likelihood can be written as,

$$logL = \sum_{i=1}^{n} \log\left(f(t_i)\right)$$

$$logL = \sum_{i=1}^{n} \log\left(\left(\alpha\lambda\,\theta\,t^{\theta-1}\left(1+\lambda t^{\theta}\right)^{\alpha-1} + \left(\beta\,\gamma\,t^{\gamma-1}\right)\right) * e^{1-\left(1+\lambda t^{\theta}\right)^{\alpha}-\left(\beta t^{\gamma}\right)}\right)$$

$$logL = \sum_{i=1}^{n} \log\left(\left(\alpha\lambda\,\theta\,t^{\theta-1}\left(1+\lambda t^{\theta}\right)^{\alpha-1} + \left(\beta\,\gamma\,t^{\gamma-1}\right)\right)\right) - \sum_{i=1}^{n}\left(1-\left(1+\lambda t^{\theta}\right)^{\alpha} - \left(\beta t^{\gamma}\right)\right) \quad (5)$$

To estimate the parameters, we take the partial derivatives of $logL$ with respect to each parameter and set them equal to zero. The resulting first-order derivatives are listed in Appendix. However, because these equations do not lead to direct solutions, we use numerical methods, such as Expectation-Maximization (EM) algorithm to find the parameter estimates.

II. Expectation-Maximization (EM) Algorithm

The EM algorithm is a powerful iterative method used for finding maximum likelihood estimates or maximum a posteriori estimates in statistical models where the data is incomplete or contains latent variables. The EM algorithm consists of an expectation step (E-step), and a maximization step (M-step). The E-step only needs to compute the conditional expectation of the log-likelihood with respect to the incomplete data, given the observed data. The M-step needs to find the maximize of this expected likelihood [9]. These two steps are then alternated until some convergence criterion is met [10]. The E-step of the EM algorithm consists of computing the conditional expectation of the complete data likelihood, given the observed data. That is, the objective function at iteration k is given by$Q(\Theta|\Theta_{k-1}) = E_{\Theta_{k-1}}(l_c(\Theta; y, X)|Y = y)$, where Y be the observed data and X be the missing data , l_c for the log-likelihoods based on the complete and Θ_{k-1} is the parameter estimate obtained from the previous iteration.

The M-step of the EM algorithm consists of maximizing the objective function constructed in the previous E-step. That is, we define $\Theta_k = argmax_{\Theta} Q(\Theta|\Theta_{k-1})$. We can combine the E and M steps of the EM algorithm into a single "update function". Thus, we write $M(\Theta_{k-1}) = argmax_{\Theta} Q(\Theta|\Theta_{k-1})$.

Asymptotic Confidence Bounds

When the maximum likelihood estimates do not have a closed form, making it difficult to determine the distribution directly, we instead rely on the asymptotic distribution of the MLEs to calculate confidence intervals [11]. It is known that the asymptotic distribution of the MLE $\widehat{\Theta}$ is given by,

$$\left(\widehat{\Theta} - \Theta\right) \rightarrow N_5(0, I^{-1}(\Theta))$$

Where $I(\Theta) \rightarrow$ Fisher information matrix of the unknown parameters $\Theta = (\alpha, \beta, \gamma, \lambda, \theta)$.
The elements of the 5 X 5 matrix of $I(.)$, are approximated by $I_{ij}\left(\widehat{\Theta}\right)$, $i, j = 1, 2, 3, 4, 5$
where, $I_{ij}\left(\widehat{\Theta}\right) = -\left.\frac{\partial^2 l(\Theta)}{\partial\Theta_i \partial\Theta_j}\right|_{\Theta=\widehat{\Theta}}$
$\widehat{\Theta} = (\hat{\alpha}, \hat{\beta}, \hat{\gamma}, \hat{\lambda}, \hat{\theta})$ estimated parameters.
Now information matrix can be written as,

$$\mathrm{I}\left(\widehat{\Theta}\right) = -\begin{bmatrix} \frac{\partial^2 l}{\partial\alpha_j^2} & \frac{\partial^2 l}{\partial\alpha_j\partial\beta_j} & \frac{\partial^2 l}{\partial\alpha_j\partial\gamma_j} & \frac{\partial^2 l}{\partial\alpha_j\partial\lambda_j} & \frac{\partial^2 l}{\partial\alpha_j\partial\theta_j} \\ \frac{\partial^2 l}{\partial\alpha_j\partial\beta_j} & \frac{\partial^2 l}{\partial\beta_j^2} & \frac{\partial^2 l}{\partial\beta_j\partial\gamma_j} & \frac{\partial^2 l}{\partial\beta_j\partial\lambda_j} & \frac{\partial^2 l}{\partial\beta_j\partial\lambda_j} \\ \frac{\partial^2 l}{\partial\alpha_j\partial\gamma_j} & \frac{\partial^2 l}{\partial\beta_j\partial\gamma_j} & \frac{\partial^2 l}{\partial\gamma_j^2} & \frac{\partial^2 l}{\partial\gamma_j\partial\lambda_j} & \frac{\partial^2 l}{\partial\gamma_j\partial\lambda_j} \\ \frac{\partial^2 l}{\partial\alpha_j\partial\lambda_j} & \frac{\partial^2 l}{\partial\beta_j\partial\lambda_j} & \frac{\partial^2 l}{\partial\gamma_j\partial\lambda_j} & \frac{\partial^2 l}{\partial\lambda_j^2} & \frac{\partial^2 l}{\partial\gamma_j\partial\lambda_j} \\ \frac{\partial^2 l}{\partial\alpha_j\partial\theta_j} & \frac{\partial^2 l}{\partial\beta_j\partial\theta_j} & \frac{\partial^2 l}{\partial\gamma_j\partial\theta_j} & \frac{\partial^2 l}{\partial\gamma_j\partial\theta} & \frac{\partial^2 l}{\partial\theta_j^2} \end{bmatrix} \quad (6)$$

The elements of the fisher information matrix are given in Appendix. Therefore, the approximate $100(1-\gamma)\%$ two-sided, confidence interval for Θ is given by

$$\widehat{\Theta} \pm Z_{\gamma/2}\sqrt{I^{-1}(\widehat{\Theta})} \tag{7}$$

Here $Z_{\gamma/2}$is the upper $\gamma/2$ th percentile of a standard normal distribution.

III. Bayes Estimates using MCMC

In this section we consider the estimation of the parameters using Bayesian techniques. Many authors have estimated the parameters of the distribution using Bayesian techniques [12, 13]. Here we estimated the parameters $(\alpha, \beta, \gamma, \lambda, \theta)$ using MCMC techniques. We have density function,

$$f(t) = \left(\alpha\lambda\,\theta\,t^{\theta-1}\left(1+\lambda t^{\theta}\right)^{\alpha-1} + (\beta\,\gamma\,t^{\gamma-1})\right)e^{1-\left(1+\lambda t^{\theta}\right)^{\alpha}-(\beta t^{\gamma})}$$

Here beta (β), lambda (λ) is scale and alpha (α), theta (θ), gamma (γ) is scale parameters.
It is assumed that the priors of the parameters $(\alpha, \beta, \gamma, \lambda, \theta)$ were following below distributions.
$\alpha \sim Gamma\ (a_1, b_1)$ where a_1 and b_1 are the respective shape and scale hyperparameters of α.
$\beta \sim Gamma\ (a_2, b_2)$ where a_2 and b_2 are the respective shape and scale hyperparameters of β.
$\gamma \sim Gamma\ (a_3, b_3)$ where a_3 and b_3 are the respective shape and scale hyperparameters of γ.
$\lambda \sim Exp\ (a_4)$ where a_4 is scale hyperparameters of λ.
$\theta \sim Gamma\ (a_5, b_5)$ where a_5 and b_5 are the respective shape and scale hyperparameters of θ.
Prior distributions were given by,

$$\pi(\alpha) = \frac{b_1^{a_1}}{\Gamma a_1}\alpha^{a_1-1}e^{-\alpha b_1} \quad a_1, b_1 > 0$$
$$\pi(\beta) = \frac{b_2^{a_2}}{\Gamma a_2}\beta^{a_2-1}e^{-\beta b_2} \quad a_2, b_2 > 0$$
$$\pi(\gamma) = \frac{b_3^{a_3}}{\Gamma a_3}\gamma^{a_3-1}e^{-\gamma b_3} \quad a_3, b_3 > 0$$
$$\pi(\lambda) = a_4 e^{-\lambda a_4} \quad a_4 > 0$$
$$\pi(\theta) = \frac{b_5^{a_5}}{\Gamma a_5}\theta^{a_5-1}e^{-\theta b_5} \quad a_5, b_5 > 0$$

Hence joint prior distribution is given by

$$\pi(\Theta) = \pi(\alpha)\,\pi(\beta)\,\pi(\gamma)\,\pi(\lambda)\,\pi(\theta) \text{ where } \Theta = (\alpha, \beta, \gamma, \lambda, \theta)$$

$$\pi(\Theta) \propto \alpha^{a_1-1}e^{-\alpha b_1}\,\beta^{a_2-1}e^{-\beta b_2}\,\gamma^{a_3-1}e^{-\gamma b_3}\ e^{-\lambda a_4}\,\theta^{a_5-1}e^{-\theta b_5} \tag{8}$$

Then posterior distribution is given by,

$$f(\Theta \mid \mathrm{x_i}) = \frac{L(\Theta|x_i)\,\pi(\Theta)}{\int_{\Theta} L(\Theta|x_i)\ \pi(\Theta)}$$

Where $L(\Theta|x_i)$ is a likelihood function and $\pi(\Theta)$ is joint prior density.

$$f(\Theta|\ \mathrm{x_i}) \propto \prod_{i=1}^{n}\left(\alpha\lambda\,\theta\,t^{\theta-1}\left(1+\lambda t^{\theta}\right)^{\alpha-1} + (\beta\,\gamma\,t^{\gamma-1})\right)e^{1-\left(1+\lambda t^{\theta}\right)^{\alpha}-(\beta t^{\gamma})}\ \alpha^{a_1-1}e^{-\alpha b_1}\,\beta^{a_2-1}e^{-\beta b_2}\,\gamma^{a_3-1}e^{-\gamma b_3}\ e^{-\lambda a_4}\,\theta^{a_5-1}e^{-\theta b_5} \tag{9}$$

Therefore, the Bayes estimate of any function of $\alpha, \beta, \gamma, \lambda, \theta$ say $g(\alpha, \beta, \gamma, \lambda, \theta)$ under squared error loss (SEL) function is,

$$\hat{g}(\alpha, \beta, \gamma, \lambda, \theta) = E_{\Theta}g(\Theta|\ \mathrm{x_i}) = \frac{\int_{\Theta} g(\Theta|\ \mathrm{x_i})L(\Theta|x_i)\,\pi(\Theta)}{\int_{\Theta} L(\Theta|x_i)\ \pi(\Theta)} \tag{10}$$

Generally, the ratio of two integrals given in above equation cannot be obtained in a closed form. Hence, we considered one of the MCMC methods i.e. Metropolis-Hastings (MH) algorithm to estimate the parameters from posterior distribution and then computed the Bayes estimates under SEL function.

IV. Metropolis-Hasting Algorithm

Metropolis-Hastings is a Markov Chain Monte Carlo (MCMC) algorithm used for sampling from a probability distribution [14]. The algorithm is as follows,

- Set initial value Θ^0.
- For $t = 1,2, \ldots T$ repeat the III to VI steps
- Set $\Theta = \Theta^{t-1}$
- Generate new candidate parameter values, here we have used normal distribution with parameter $(\Theta, 1)$, say it $q(\Theta') \sim N(\Theta, 1)$.
- Calculate acceptance probability, $\gamma = \min\left(1, \frac{f(\theta' | x_i) q(\theta')}{f(\theta | x_i) q(\theta)}\right)$

Update $\Theta^t = \Theta'$ with probability γ, otherwise set $\Theta^t = \Theta$ with probability $1 - \gamma$.

V. Information Criterion

The Akaike Information Criterion (AIC), Consistent Akaike Information Criterion (CAIC), Bayesian Information Criterion (BIC) and Hannan-Quinn Information Criterion methods are used to know which of the following distributions fits the data well [11]. The distribution fits the data well, whose information Criterion values are less.

$$AIC = 2K - 2\, lnL$$
$$CAIC = -2logL + K(logn + 1)$$
$$BIC = Kln(n) - 2\, lnL$$
$$HQIC = -2\, logL + 2\, K\, log\, (logn)$$

Where L is the likelihood function, n is the sample size and K is the number of parameters estimated.

VI. Kaplan-Meier (K-M) Estimator

The Kaplan-Meier estimator of survival function [11] is defined as,

$$\hat{S}(t) = \prod_{i:t_i<t} (1 - \frac{d_i}{n_i})$$

Where $t_i$is the failure time, $d_i$is the number of events that occurs at time $t_i$and n_i is the number individuals at risk of experiencing the event immediately prior to t_i.

V. Results and Discussion

To validate the newly proposed new modified power generalized Weibull distribution, we analyzed the failure times of patients admitted to BLDE Hospital, Vijayapura. The dataset comprises 577 patients who passed away between January 1, 2024, and August 30, 2024.

Table 1 presents the estimated parameters obtained using the Maximum Likelihood Estimation (MLE) method for various lifetime distributions.

Table 2 provides a model comparison based on the Akaike Information Criterion (AIC), Consistent Akaike Information Criterion (CAIC), Bayesian Information Criterion (BIC), and Hannan–Quinn Information Criterion (HQIC). The results indicate that the new modified power generalized Weibull distribution offers the best fit, as it records the lowest values across all four criteria compared to the competing models.

Table 3 shows the parameter estimates for the new modified power generalized Weibull distribution using both MLE and Bayesian methods. Due to the complexity of the first-order partial derivatives under MLE, the Expectation-Maximization (EM) algorithm was employed for parameter estimation. For Bayesian estimation, we utilized the Metropolis-Hastings algorithm, a Markov Chain Monte Carlo (MCMC) technique, with Gamma and Exponential priors. It was observed that the standard errors under Bayesian estimation were lower than those from MLE, suggesting better precision.

Table 4 lists the 95% confidence intervals for the estimated parameters of the new modified power generalized Weibull distribution. These intervals were computed at a 5% level of significance and support the statistical reliability of the estimates.

Figure 3 displays the trace plots and histograms for the posterior distributions of the parameters after the burn-in period of the MCMC iterations, indicating good mixing and convergence.

Figure 4 shows the histogram of the observed data with the fitted density curves of various lifetime distributions. The curve corresponding to the new modified power generalized Weibull distribution (represented in purple) aligns most closely with the histogram, confirming a better visual fit.

Figure 5 illustrates the hazard functions for all compared distributions. The hazard curve for the new modified power generalized Weibull distribution initially increases, then decreases suddenly, and eventually rises again over time capturing the complex nature of the real-life hazard trend. This indicates that the initial days of hospital admission were associated with a higher risk for these patients, which implies most of the patients admitted to the hospital at the time study of study period are in emergency cases.

Figure 6 compares the Kaplan-Meier survival curve with the survival curves of all other fitted distributions. The new modified power generalized Weibull distribution survival curve is found to be the closest to the Kaplan-Meier estimate. Notably, approximately 50% of the patients experienced failure (death) within 5 days of hospital admission. As mentioned earlier, this provides strong evidence that the initial days of hospitalization carried the greater risk.

Table 1: *Estimated parameters using MLE for different distributions.*

Distribution \ Parameters	α	β	γ	λ	θ
Exponential	0.09563282	-	-	-	-
Weibull	0.22864357	0.7016423	-	-	-
Lai et al (2003) [3]	0.2376663	0.5949811		0.01	-
Xie and Lai (1996) [1]	0.2276905	0.7015965	0.001	0.701521	-
Sarhan and Zaindin (2009) [4]	0.227689	0.6994166	0.001	-	-
Rangoli et al (2025) [8]	0.001	0.4723638	0.2374116	0.6618276	-
Mustafa et al (2023) [7]	0.001	0.0956337	-	0.0406266	0.052673947
New modified power generalized Weibull	0.17924108	0.002460846	1.641992384	2.37270958	1.351152555

Table 2: *Distribution comparison using AIC, CAIC, BIC and HQIC.*

Distribution \ Parameters	$logl$	AIC	$CAIC$	BIC	$HQIC$
Exponential	-1931.357	3864.714	3870.071842	3869.072	3866.413378
Weibull	-1858.96	3721.921	3732.635685	3730.636	3725.318756
Lai et al (2003) [3]	-1868.952	3743.903	3759.977527	3756.977	3749.002134
Xie and Lai (1996) [1]	-1858.96	3725.921	3747.351369	3743.352	3732.717512
Sarhan and Zaindin (2009) [4]	-1859.048	3724.096	3740.169527	3737.169	3729.194134
Rangoli et al (2025) [8]	-1854.67	3717.34	3738.771369	3734.772	3724.137512
Mustafa et al (2023) [7]	-1931.358	3870.715	3892.147369	3888.147	3877.513512
New modified power generalized Weibull	-1834.69	3679.379	3706.169211	3701.168	3687.876891

Table 3: *Parameter estimation using MLE and Bayes method for the good fit model.*

New modified power generalized Weibull distribution	
EM estimates	Bayes estimate
$\boldsymbol{\alpha = 0.179241081}$ (0.02865731) *	0.1665027 (0.0160304)
$\boldsymbol{\beta = 0.002460846}$ (0.000682678)	0.01573168 (0.005635611)
$\boldsymbol{\gamma = 1.641992384}$ (0.071844198)	1.204626 (0.06549102)
$\boldsymbol{\lambda = 2.372709582}$ (0.777731161)	2.655452 (0.2526936)
$\boldsymbol{\theta = 1.351152555}$ (0.137535405)	1.326286 (0.09576754)
* Within parenthesis indicates standard error	

Table 4: *Estimated parameters with Lower confidence limit (LCL) and Upper Confidence limit (UCL).*

Parameter	Standard Error	LCL	UCL
$\boldsymbol{\alpha = 0.179241081}$	0.02865731	0.123072754	0.235409408
$\boldsymbol{\beta = 0.002460846}$	0.000682678	0.001122798	0.003798894
$\boldsymbol{\gamma = 1.641992384}$	0.071844198	1.501177755	1.782807013
$\boldsymbol{\lambda = 2.372709582}$	0.777731161	0.848356506	3.897062658

$\boldsymbol{\theta = 1.351152555}$	0.137535405	1.081583162	1.620721948

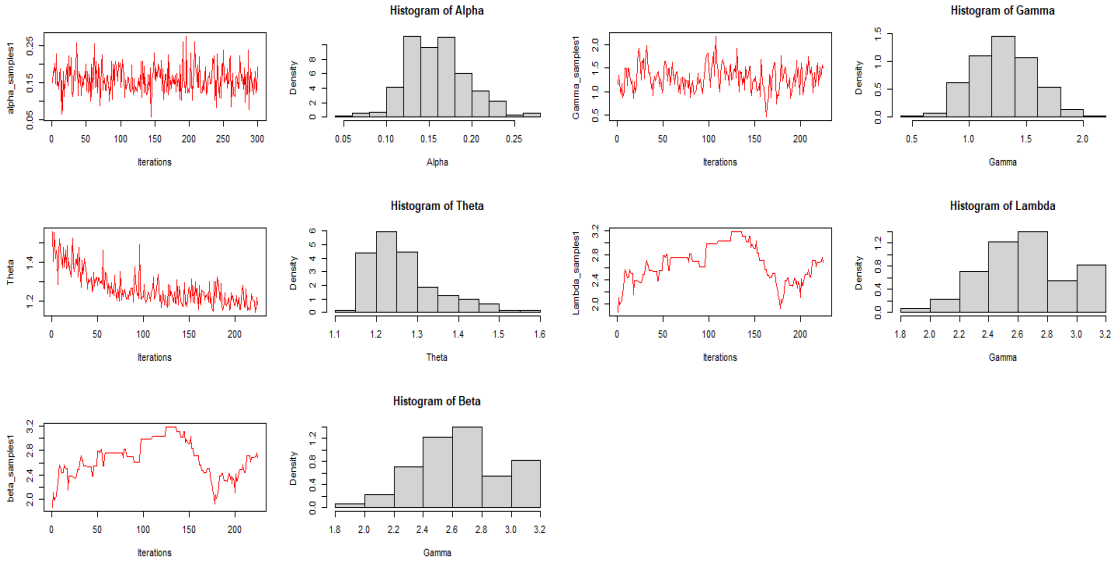


Figure 3: *Trace plot and histogram of the parameters of the good fit model using MCMC.*

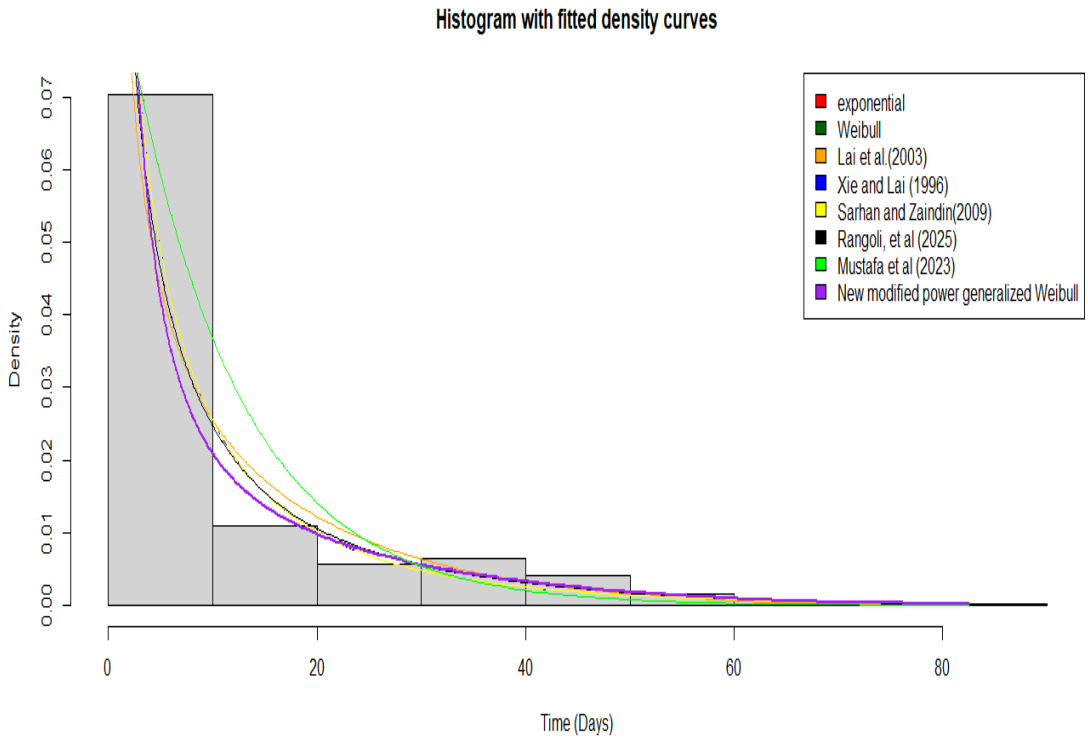


Figure 4: *Histogram and fitted density curve of different distributions for real life data.*

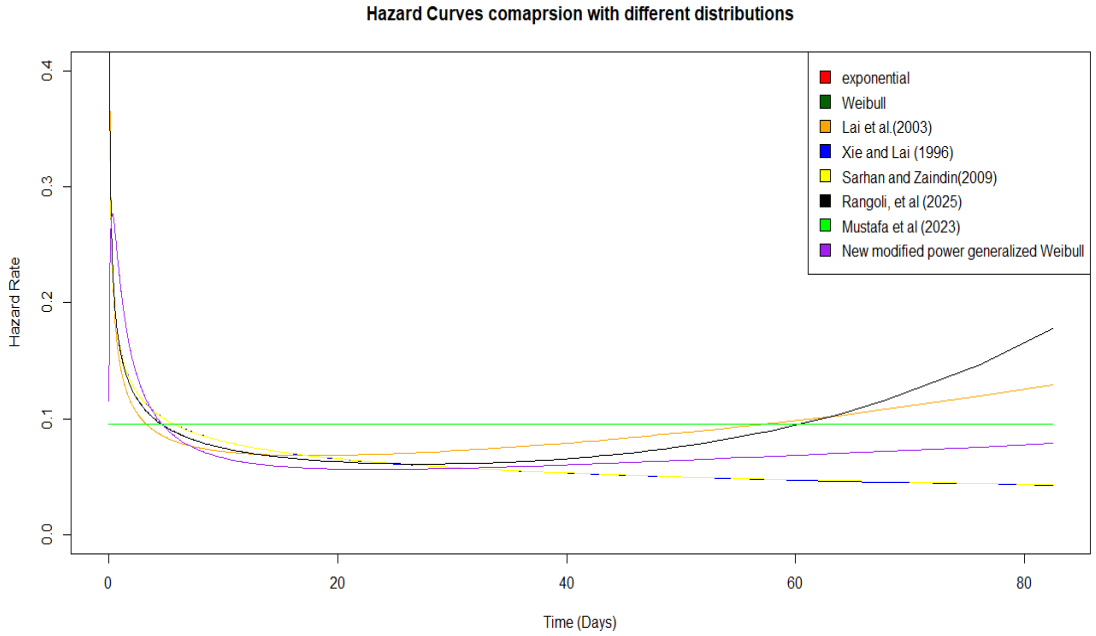


Figure 5: *Hazard Curves for different distribution for the real-life data.*

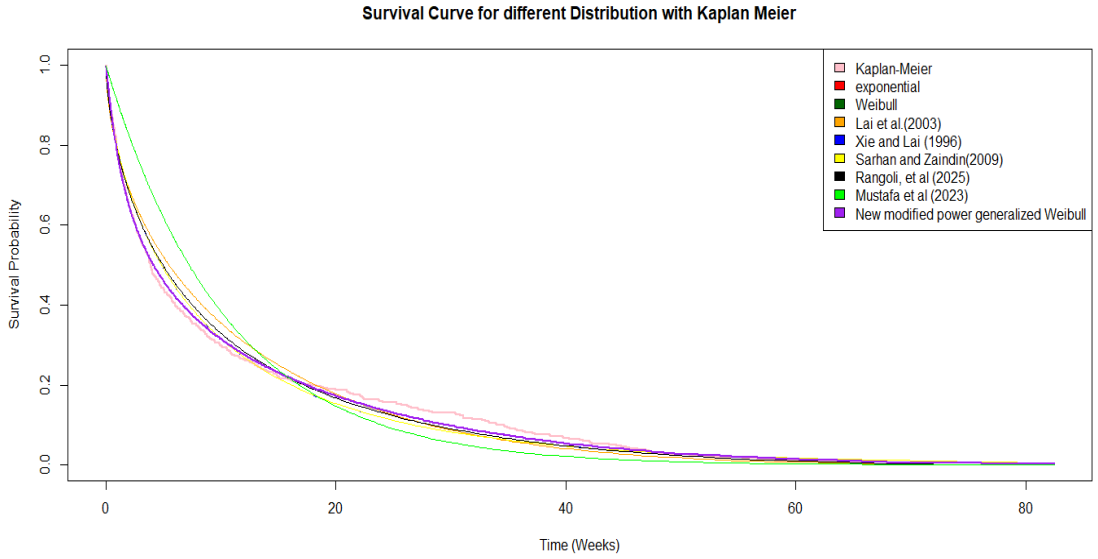


Figure 6: *Kaplan-Meier survival curve with all distribution survival curve for the real life dataset.*

VI. Conclusions

The proposed new modified power generalized Weibull (NMPGW) distribution is designed for analyzing failure time data and has proven particularly effective in modeling real-life survival scenarios. This distribution is capable of handling bimodal density functions and exhibits flexibility in representing various hazard rate patterns, including increasing, decreasing, bathtub-shaped, and decreasing–increasing–decreasing forms. We derived many statistical properties NMPGW distributions. Parameter estimation was carried out using both Maximum Likelihood Estimation via the EM algorithm and Bayesian methods through the Metropolis-Hastings algorithm with Gamma and Exponential priors. Bayesian estimates exhibited better convergence and lower standard errors, leading to more precise parameter inference. In a comparative analysis with several existing lifetime

distributions, the NMPGW model consistently achieved the lowest values of AIC, CAIC, BIC, and HQIC, indicating a best fit. The model was validated using real patient failure time data from Hospital, where visual comparisons of fitted density, hazard, and survival curves showed a close match with the empirical data, especially with the Kaplan–Meier survival curve. Notably, the hazard function estimated from the model displayed an initially increasing trend, followed by a sudden decrease and then another increase, suggesting that most hospital admissions were emergency cases. It was observed that 50% of the patients failed within 5 days of admission. In conclusion, the NMPGW distribution offers a flexible and precise framework for analyzing time-to-event data, particularly in medical settings where accurate modeling of patient risk over time is needed.

Acknowledgements: The authors would like to thank BLDE Shri B. M. Patil Medical College Hospital and Research Centre, Vijayapura, for providing access to the dataset.

Conflict of Interest: The authors declare that there is no conflict of interest.

References

[1] Xie, M. and Lai, C. D. (1996). Reliability analysis using an additive Weibull model with bathtub-shaped failure rate function. *Reliability Engineering and System Safety*, *52*(1), 87-93.

[2] Bagdonavicius, V., & Nikulin, M. (2001). *Accelerated life models: modeling and statistical analysis*. Chapman and Hall/CRC.

[3] Lai, C. D., Xie, M. and Murthy, D. N. P. (2003). A modified Weibull distribution. *IEEE Transactions on reliability*, *52*(1), 33-37.

[4] Sarhan, A. M. and Zaindin, M. (2009). Modified Weibull distribution. *APPS. Applied Sciences*, *11*, 123-136.

[5] Bebbington, M., Lai, C. D. and Zitikis, R. (2007). A flexible Weibull extension. *Reliability Engineering and System Safety*, *92*(6), 719-726.

[6] Rangoli, A. M., and Talawar, A. S. (2024). INFERENCE ON MODIFIED WEIBULL TYPE DISTRIBUTION AND ITS APPLICATION TO COMPETING RISKS DATA USING MCMC. *International Journal of Agricultural & Statistical Sciences*, *20*(2). 333-342.

[7] Mustafa S. S., Alharthi, A. S., Almulhim, F. A., Gemeay, A. M., Meraou, M. A., Mustafa, M. S., and Aljohani, H. M. (2023). Modified generalized Weibull distribution: theory and applications. *Scientific Reports*, *13*(1), 12828.

[8] Rangoli A M, Talawar A S, Agadi R P, et al. (2025) New Modified Exponentiated Weibull Distribution: A Survival Analysis. Cureus 17(1): e77347. DOI 10.7759/cureus.77347.

[9] Park, C. (2005). Parameter estimation of incomplete data in competing risks using the EM algorithm. *IEEE Transactions on Reliability*, 54(2), 282-290.

[10] Ruth, W. (2024). A review of Monte Carlo-based versions of the EM algorithm. *arXiv preprint arXiv:2401.00945*.

[11] Lawless, J. F. (2003). *Statistical models and methods for lifetime data*. John Wiley and Sons, New York.

[12] Upadhyay, S. K., and Gupta, A. (2010). A Bayes analysis of modified Weibull distribution via Markov chain Monte Carlo simulation. *Journal of Statistical Computation and Simulation*, *80*(3), 241-254.

[13] Pradhan, B., and Kundu, D. (2014). Analysis of interval-censored data with Weibull lifetime distribution. *Sankhya B*, *76*, 120-139.

[14] Chib, S., and Greenberg, E. (1995). Understanding the metropolis-hastings algorithm. *American statistician*, 327-335.

Appendix:

Using log likelihood function

$$logL = \sum_{i=1}^{n} \log\left(\left(\alpha\lambda\,\theta\,t^{\theta-1}\left(1+\lambda t^{\theta}\right)^{\alpha-1} + (\beta\,\gamma\,t^{\gamma-1})\right)\right) - \sum_{i=1}^{n}\left(1-\left(1+\lambda t^{\theta}\right)^{\alpha} - (\beta t^{\gamma})\right)$$

$$deno = \left(\alpha\lambda\,\theta\,t^{\theta-1}\left(1+\lambda t^{\theta}\right)^{\alpha-1} + (\beta\,\gamma\,t^{\gamma-1})\right)$$

$$nume\ \alpha = \lambda\,\theta\,t^{\theta-1}\left(\left(\left(1+\lambda t^{\theta}\right)^{\alpha-1}\right) + \alpha\left(\left(1+\lambda t^{\theta}\right)^{\alpha}\right)\log\left(\left(1+\lambda t^{\theta}\right)\right)\right)$$

$$nume\ \lambda = \alpha\,\theta\,t^{\theta-1}\left(\left(1+\lambda t^{\theta}\right)^{\alpha-1} + \lambda\,(\alpha-1)\left(1+\lambda t^{\theta}\right)^{\alpha-2}\,t^{\theta}\right)$$

$$nume\ \theta = \alpha\,\lambda\,t^{\theta-1}\left((\theta\,logt+1)\left(\left(1+\lambda t^{\theta}\right)^{\alpha-1}\right) + \theta\,(\alpha-1)\left(1+\lambda t^{\theta}\right)^{\alpha-2}\lambda\,\theta\,t^{\theta-1}\right)$$

$$nume\ \beta = \gamma\,t^{\gamma-1}$$

$$nume\ \gamma = \beta\,t^{\gamma-1}(\gamma logt+1)$$

$$\frac{\partial logL}{\partial\alpha} = \sum_{i=1}^{n}\frac{nume\ \alpha}{deno} - \sum_{i=1}^{n}\left(1+\lambda t^{\theta}\right)^{\alpha}\log\left(1+\lambda t^{\theta}\right)$$

$$\frac{\partial^2 logL}{\partial\alpha^2} = \sum_{i=1}^{n}\frac{deno\,\frac{\partial(nume\ \alpha)}{\partial\alpha} - (nume\ \alpha)^2}{deno^2} - \sum_{i=1}^{n}\left(1+\lambda t^{\theta}\right)^{\alpha}\left(\log\left(1+\lambda t^{\theta}\right)\right)^2$$

$$\frac{\partial logL}{\partial\lambda} = \sum_{i=1}^{n}\frac{nume\ \lambda}{deno} - \sum_{i=1}^{n}\alpha\left(1+\lambda t^{\theta}\right)^{\alpha-1}\mathrm{t}^{\theta}$$

$$\frac{\partial^2 logL}{\partial\lambda^2} = \sum_{i=1}^{n}\frac{deno\,\frac{\partial\ nume\lambda}{\partial\lambda} - (nume\ \lambda)^2}{deno^2} - \sum_{i=1}^{n}\alpha\,(\alpha-1)\left(1+\lambda t^{\theta}\right)^{\alpha-2}\mathrm{t}^{2\theta}$$

$$\frac{\partial logL}{\partial\theta} = \sum_{i=1}^{n}\frac{nume\ \theta}{deno} - \sum_{i=1}^{n}\alpha\left(1+\lambda t^{\theta}\right)^{\alpha-1}\lambda\,\theta\,\mathrm{t}^{\theta-1}$$

$$\frac{\partial^2 logL}{\partial\theta^2} = \sum_{i=1}^{n}\frac{deno\,\frac{\partial\ numeo\theta}{\partial\theta} - (nume\ \theta)^2}{deno^2} - \sum_{i=1}^{n}\alpha\,\lambda\left(\left(\theta\mathrm{t}^{\theta-1}\log t + t^{\theta-1}\right)\left(1+\lambda t^{\theta}\right)^{\alpha-1} + \theta t^{\theta-1}\,(\alpha-1)\left(1+\lambda t^{\theta}\right)^{\alpha-1}\lambda\theta x^{\theta-1}\right)$$

$$\frac{\partial logL}{\partial\beta} = \sum_{i=1}^{n}\frac{nume\ \beta}{deno} - \sum_{i=1}^{n}t^{\gamma}$$

$$\frac{\partial^2 logL}{\partial\beta^2} = -\sum_{i=1}^{n}\frac{(nume\ \beta)^2}{deno^2}$$

$$\frac{\partial logL}{\partial\gamma} = \sum_{i=1}^{n}\frac{nume\ \beta}{deno} - \sum_{i=1}^{n}\beta\,t^{\gamma}\,logt$$

$$\frac{\partial^2 logL}{\partial\gamma^2} = \sum_{i=1}^{n}\frac{deno\,\frac{\partial\ numey\gamma}{\partial\gamma} - (nume\ \gamma)^2}{deno^2} - \sum_{i=1}^{n}\beta\,t^{\gamma}\,(logt)^2$$

$$\frac{\partial^2 logL}{\partial\alpha\partial\gamma} = \sum_{i=1}^{n}\frac{deno\,\frac{\partial\ (numea\alpha)}{\partial\ \lambda} - numea\alpha\ numea\lambda}{deno^2} - \sum_{i=1}^{n}\frac{\partial}{\partial\lambda}\left(\left(1+\lambda t^{\theta}\right)^{\alpha}\log\left(1+\lambda t^{\theta}\right)\right)$$

$$\frac{\partial^2 logL}{\partial\alpha\partial\theta} = \sum_{i=1}^{n} \frac{deno\,\frac{\partial\,(numea)}{\partial\,\theta} - numea\; nume\theta}{deno^2} - \sum_{i=1}^{n} \alpha\,\lambda \frac{\partial}{\partial\theta}\left(\left(1+\lambda t^{\theta}\right)^{\alpha-1}\theta\, t^{\theta-1}\right)$$

$$\frac{\partial^2 logL}{\partial\alpha\partial\theta} = -\sum_{i=1}^{n} \frac{numea\; numeb}{deno^2}$$

$$\frac{\partial^2 logL}{\partial\alpha\partial\gamma} = -\sum_{i=1}^{n} \frac{numea\; numey}{deno^2}$$

$$\frac{\partial^2 logL}{\partial\lambda\partial\theta} = \sum_{i=1}^{n} \frac{deno\,\frac{\partial\,(numel)}{\partial\,\theta} - numel\; nume\theta}{deno^2} - \sum_{i=1}^{n} \frac{\partial}{\partial\theta}\left(\alpha\, t^{\theta}\left(1+\lambda t^{\theta}\right)^{\alpha-1}\right)$$

$$\frac{\partial^2 logL}{\partial\lambda\partial\beta} = -\sum_{i=1}^{n} \frac{numeb\; numel}{deno^2}$$

$$\frac{\partial^2 logL}{\partial\lambda\partial\gamma} = -\sum_{i=1}^{n} \frac{numey\; numel}{deno^2}$$

$$\frac{\partial^2 logL}{\partial\theta\partial\beta} = -\sum_{i=1}^{n} \frac{numeb\; nume\theta}{deno^2}$$

$$\frac{\partial^2 logL}{\partial\theta\partial\gamma} = -\sum_{i=1}^{n} \frac{numey\; nume\theta}{deno^2}$$

$$\frac{\partial^2 logL}{\partial\beta\partial\gamma} = \sum_{i=1}^{n} \frac{deno\,\frac{\partial\,(numeb)}{\partial\,\gamma} - numeb\; numey}{deno^2} - \sum_{i=1}^{n} t^{\gamma}\, logt$$

STRESS-STRENGTH RELIABILITY UNDER MULTIVARIATE LOG-NORMAL SETUP AND ITS APPLICATION

Anirban Goswami[1], Babulal Seal[2]

•

[1]Department of Statistics, Regional Research Institute of Unani Medicine, Kolkata, India.
[2]Department of Mathematics and Statistics, Aliah University, Kolkata, India.
[1]anirbanstat09@gmail.com
[2]babulal.seal@gmail.com

Abstract

In this article it is mainly focused on discussion about estimation of stress-strength reliability (R) under log-normal multivariate setup. We propose a procedure to compute and estimate stress-strength reliability of weighted geometric function when both stress and strength follow a dependent log-normal multivariate distribution with two weightage vectors. We consider the principal component analysis to estimate these vectors. MVUE, MLE and Confidence Intervals of R are obtained. Through simulation studies, their performances are compared using different measures. Finally, we provide a real data analysis.

Keywords: Stress-strength, Principal component, Maximum Likelihood Estimator (MLE), Minimum Variance Unbiased Estimator (MVUE), Confidence Intervals.

I. Introduction

The log-normal distribution is characterized as the distribution of a random variable whose logarithm is normally distributed. The normal distribution was used in engineering stress-strength models. But, the stress-strength model with log-normal distribution for both stress and strength are widely used in engineering domains [1]. However, it has been gradually replaced by the lognormal distribution model, because of the more realistic features as the positiveness of its values and the positive skewness [2] of its shape. The log-normal distribution has also been widely applied to real life data fitting in an empirical way. Hence, many variables in real life, from the sizes of organisms and the numbers of species in biology to rainfalls in meteorology and sizes of incomes in economics, are positive in nature. Although, it has been derived by Gibrat [3] theoretically using qualitative assumptions, calling it the law of proportionate effect. Kolmogoroff [4] derived the distribution using the asymptotic result of an iterative process of successive breakage of a particle into two randomly sized particles. The frequently use of log-normal distributions in material properties and fatigue lives [5]. Lu et al. [6] used the log-normal probability density function in the robust design of an arbor. This distribution is typically adopted for load variable [7] to the analysis of ship structural reliability, the random variables that always take positive values.

For satellites data, it is seen that data is more log-normally rather than normally distributed [8-10] and for the first time, a description for lognormal errors was given for NWP. In addition, it may show that log-normal variables in NWP is a modern problem. There were data sets in the 1970s [11] that were recognized as log-normally distributed. A score test for testing the equality of two means

of two independent log-normal distributions presented by Gupta and Li [12] compared the results with those of Zhou et al. [14]. It is showed that, the bivariate log-normal distribution is more appropriate in the model of outpatient to test the equality of means of costs, six months before and after the medicaid policy change in the state of Indiana in a paired design study for a paired design study (Zhou et al., 2001). Schneider and Holst [15] and Cheng [16] demonstrate the uses of log normal distribution in modeling of the size distribution of aerosol particles and airborne fibers.

Log-normal distributions is used in the air pollution concentration data, for predicting the future air quality and it is important aspect to give the best prediction. In addition, the log-normal probability density functions have been used for many years to analyze the air pollution and describe the frequency of high concentration of the pollutant [17]. Norazian et al. [18] found Log-normal distribution as the best fit in the data sets of PM10, for 2006 and 2007, in an industrialized area with high population and traffic density. Sedek et al. [19] analyzed the data of PM_{10} concentrations in Kuala Lumpur from 1998 to 2002 and found that the log-normal distribution as the best-fitted model to prediction. Also, Hamid et al. [20] used log normal to fit the distribution. There are many types of statistical distribution that can be used to fit the air quality data. Georgopoulus and Seinfeld [21] explored and described the statistical distribution of air quality of pollutant concentration.

Lai et al. [22] used the lognormal probability distribution is a function of geometric mean and geometric standard deviation to obtain the distribution properties from observed data. Nguyen and Sevando [23] used the weighted geometric mean function to integrate sub-indices of 8 parameters for Coastal Water Quality and these water quality Parameters sleeted by their weights. Generally, eight pollutants namely particulate matter [24] PM10, PM2.5, nitrogen dioxide (NO2), ammonia (NH3), carbon monoxide (CO), Sulphur dioxide (SO2) Ozone (O3) and Lead (Pb) act as major parameters in deriving the air quality index (AQI) of an area. Generally, each of the AQI parameters follows the log-normal distribution and they jointly follow the multivariate log-normal distribution. Also, multivariate lognormal distribution used in a particular case of the PERT type problems [25], where random vectors for which the component lifetime distributions are lognormal. The multivariate log-normal distribution used in astronomy data of the Hertzprung-Russel [26] diagram of the star clusters CYG OB1, where the first component is the logarithm of the effective temperature at the surface of the star and the second is the logarithm of its light intensity.

Gupta and Gupta [27] first introduced the concept to estimate the reliability under multivariate normal setup. They considered the forms of R when $\left(\mathbf{x}^*_{p_1 x1}, \mathbf{y}^*_{p_2 x1}\right)'$ follows multivariate normal distribution with dependent vector between $\mathbf{x}^*_{p_1 x1}$ and $\mathbf{y}^*_{p_2 x1}$. Then, the reliability as R= $\Pr(\mathbf{a}'\mathbf{x}^* > \mathbf{b}'\mathbf{y}^*)$ **,** where $\mathbf{a}'$ and $\mathbf{b}'$ are two vectors. This problem arises when a system in the energy is supplied to the system by p_1 sources and is consumed through p_2 sources and the sources of energy supplied and consumed are linearly dependent with two vectors $\mathbf{a}'$ and $\mathbf{b}'$. Under this set up, they obtained and compared the MVUE and MLE estimate of R with some interesting special cases. In this multivariate setup, Reiser and Farragi [28] derived the lower confidence bounds for R=$\Pr(\mathbf{a}'\mathbf{x}^* > \mathbf{b}'\mathbf{y}^*)$ and solved it iteratively and also derived an approximate lower confidence bounds for R. Enis and Geisser [29] demonstrated that, how to obtain the exact confidence bounds for R. Mukherjee and Sharan [30] obtained the UMVUE for R under the bivariate normal distribution and also obtained their asymptotic variance when parameters other than the means are known and they proposed an estimator R based on maximum likelihood estimators when all the five parameters are unknown. Hor and Seal [31] derived an alternative estimator viz. UMVUE of R under the same case of bivariate normal distribution.

In the multivariate log-normal distribution setup, we obtain the stress-strength reliability of weighted geometric function R=$\Pr\left(\prod_{i=1}^{p_1} x_i^{a_i} > \prod_{j=1}^{p_2} y_j^{b_j}\right)$, where $\left(\mathbf{x}_{p_1 x1}, \mathbf{y}_{p_2 x1}\right)'$ follows multivariate log-normal distribution with dependence vector between $\mathbf{x}_{p_1 x1}$ and $\mathbf{y}_{p_2 x1}$ with $\mathbf{a}'$ and $\mathbf{b}'$ are two

vectors. We take the log-transformation of the weighted geometric function and consider the principal component analysis to estimate the $\mathbf{a}'$ and $\mathbf{b}'$, where Gupta and Gupta [27] considered only spatial cases of $\mathbf{a}'$ and $\mathbf{b}'$. The estimators of R obtained using MVUE and MLE of the parameters. We do simulation studies to compare their performance in teams of variance (VAR), mean square error (MSE) and mean absolute error (MAE). We take different choices of parameter to obtain the L_1 distance, same form used by Hor and Seal [31]. In this connection, the distributions function of the two estimators MVUE and MLE are derived in section 3. L_1 distance between two functions to compare two estimators is given in section 4. The graphically representation of variance of MVUE and MSE of MLE shows in figure 2 and 3, also it shows that their performances are better even in values neighborhood 0 of $\sqrt{n}\delta^*$. Similarly, relationship between ratio of these two measures and $\sqrt{n}\delta^*$ is given in table 4. Two-sided confidence limits and lower bounds of R defined in section 5. Based on MVUE and MLE, we compare the performance between bootstrap and empirically interval estimator in terms of coverage and accuracy using simulation study and real data set.

II. Methods

I. Maximum Likelihood Estimator of R

Let us consider, a vector $\mathbf{w} = \begin{pmatrix}\mathbf{x}\\ \mathbf{y}\end{pmatrix}_{p_1+p_2}$ of positive random variables such that $\mathbf{z}=\begin{pmatrix}\ln(\mathbf{x})\\ \ln(\mathbf{y})\end{pmatrix}_{p_1+p_2}$ has an $(p_1 + p_2)$-dimensional normal distribution with mean vector $\mu = \begin{pmatrix}\boldsymbol{\mu}_1\\ \boldsymbol{\mu}_2\end{pmatrix}_{(p_1+p_2)x1}$ and variance-covariance matrix $\Sigma = \begin{pmatrix}\Sigma_{11} & \Sigma_{12}\\ \Sigma_{21} & \Sigma_{22}\end{pmatrix}_{(p_{1+}p_2)x(p_{1+}p_2)}$ and denoted by $\Lambda_{p1+p2}(\mu, \Sigma)$. The corresponding $(p_1 + p_2)$-dimensional normal distribution is denoted by $\begin{pmatrix}\ln(\mathbf{x})\\ \ln(\mathbf{y})\end{pmatrix}_{p_1+p_2} = \begin{pmatrix}\mathbf{x}^*\\ \mathbf{y}^*\end{pmatrix}_{p_1+p_2} \sim N_{p1+p2}(\mu, \Sigma)$.

The probability density function of $\mathbf{w} = \begin{pmatrix}\mathbf{x}\\ \mathbf{y}\end{pmatrix}_{p_1+p_2}$ having $\Lambda_{p1+p2}(\mu, \Sigma)$ is

$$f(\mathbf{w}) = \frac{1}{(2\pi)^{(p_1+p_2)/2}\sqrt{|\Sigma|}\prod_{i=1}^{p_1+p_2} w_i} \exp\left\{-\frac{1}{2}(\ln \mathbf{w} - \boldsymbol{\mu})'\Sigma^{-1}(\ln \mathbf{w} - \boldsymbol{\mu})\right\}$$

Let, the two vectors are $\mathbf{a}'$ and $\mathbf{b}'$**.** Then, we want to find the probability of two weighted geometric function $\mathbf{a}'\mathbf{x}$ and $\mathbf{b}'\mathbf{y}$ as $R=Pr\left(\prod_{i=1}^{p_1} x_i^{a_i} > \prod_{j=1}^{p_2} y_j^{b_j}\right) = Pr\left(\ln\prod_{i=1}^{p_1} x_i^{a_i} > \ln\prod_{j=1}^{p_2} y_j^{b_j}\right)$

$$= Pr\left(\sum_{i=1}^{p_1} a_i \ln(x_i) > \sum_{j=1}^{p_2} b_j \ln(y_j)\right)$$
$$= Pr(\mathbf{a}'\mathbf{x}^* - \mathbf{b}'\mathbf{y}^* > 0)$$

Now, the distribution of $v = \mathbf{a}'\mathbf{x}^* - \mathbf{b}'\mathbf{y}^*$ follows $N(\mu_v, \sigma_v^2)$,
where, $\mu_v = E(\mathbf{a}'\mathbf{x}^* - \mathbf{b}'\mathbf{y}^*) = \mathbf{a}'\boldsymbol{\mu_1} - \mathbf{b}'\boldsymbol{\mu_2}$ and $\sigma_v^2 = Var(\mathbf{a}'\mathbf{x}^* - \mathbf{b}'\mathbf{y}^*) = \mathbf{a}'\boldsymbol{\Sigma_{11}}\mathbf{a} - \mathbf{2a}'\boldsymbol{\Sigma_{12}}\,\mathbf{b} + \mathbf{b}'\boldsymbol{\Sigma_{22}}\,\mathbf{b}$.

Now, $R= Pr(\mathbf{a}'\mathbf{x}^* - \mathbf{b}'\mathbf{y}^* > 0) = Pr(v > 0)$

$$= \int_0^\infty \frac{1}{\sqrt{2\pi}\sigma_v}\exp\left\{-\frac{1}{2}\left(\frac{v-\mu_v}{\sigma_v}\right)^2\right\}dv = \int_{-\frac{\mu_v}{\sigma_v}}^\infty \frac{1}{\sqrt{2\pi}}\exp\left\{-\frac{1}{2}z^2\right\}dz = \Phi\left(\frac{\mu_v}{\sigma_v}\right)$$

The maximum likelihood estimator of $\mu = \begin{pmatrix}\boldsymbol{\mu}_1\\ \boldsymbol{\mu}_2\end{pmatrix}_{(p_1xp_2)}$ and $\Sigma = \begin{pmatrix}\Sigma_{11} & \Sigma_{12}\\ \Sigma_{21} & \Sigma_{22}\end{pmatrix}_{(p_{1+}p_2)x(p_{1+}p_2)}$

are $\begin{pmatrix}\overline{\mathbf{x}^*}\\ \overline{\mathbf{y}^*}\end{pmatrix}$ and $\mathbf{S}=\begin{pmatrix}\mathbf{S_{11}} & \mathbf{S_{12}}\\ \mathbf{S_{21}} & \mathbf{S_{22}}\end{pmatrix}$ respectively.

We have, $\widehat{\mu_v}=\ \mathbf{a}'\overline{\mathbf{x}^*}-\mathbf{b}'\overline{\mathbf{y}^*}$ and $\widehat{\sigma_v^2}=\mathbf{a}'\mathbf{S_{11}}\mathbf{a}-\mathbf{2a}'\mathbf{S_{12}}\ \mathbf{b}+\ \mathbf{b}'\mathbf{S_{22}}\ \mathbf{b}$

So, the maximum likelihood estimate of R is define as $R^*=\Phi\left(\frac{\mu_v}{\sigma_v}\right)$ (1)

where Φ = Distribution function of univariate standard normal distribution.

II. Estimation by Principal Component method

The overall representation of the two sets or vectors are related to vectors **a** and **b**, such that they are approximated by $\mathbf{a}'\mathbf{x}^*$ and $\mathbf{b}'\mathbf{y}^*$ through principal component analysis. Principal component analysis explaining the variance-covariance structure $\sum_{\mathbf{11}}$ & $\sum_{\mathbf{22}}$ of a set of variables $\mathbf{x}^*$ and $\mathbf{y}^*$ through a linear function of these variables, i.e, explain maximum variability. Traditional way is to take first principal component to estimate $\mathbf{a}'$ by $\mathbf{e_1'}$ normalized eigenvector of $\sum_{\mathbf{11}}$ corresponding to eigen value λ_1 and $\mathbf{b}'$ by $\mathbf{l_1'}$ normalized eigenvector of $\sum_{\mathbf{22}}$ corresponding to eigen value λ_1 [32]. We take the maximum likelihood estimate of $\sum_{\mathbf{11}}$ as $\mathbf{S_{11}^*}$ and take estimate of $\mathbf{a}'$ by $\mathbf{e_1'}$ normalized eigenvectors of $\mathbf{S_{11}^*}$ corresponding to eigen value λ_1. Similarly, we have estimate of $\sum_{\mathbf{22}}$ as $\mathbf{S_{22}^*}$ and take estimate of $\mathbf{b}'$ by $\mathbf{l_1'}$ normalized eigenvectors of $\mathbf{S_{22}^*}$ corresponding to λ_1 eigen value. Then from equation (1), the estimate of R becomes

$$R^*=\Phi\left(\frac{\widehat{\mu_v}}{\widehat{\sigma_v}}\right),\ \text{where}\ \widehat{\mu_v}=\ \mathbf{e_1'}\overline{\mathbf{x}^*}-\mathbf{l_1'}\overline{\mathbf{y}^*}\ \text{and}\ \widehat{\sigma_v^2}=\mathbf{e_1'}\mathbf{S_{11}}\mathbf{e_1}-\mathbf{2e_1'}\mathbf{S_{12}}\ \mathbf{l_1}+\ \mathbf{l_1'}\mathbf{S_{22}}\ \mathbf{l_1}\ . \quad (2)$$

III. Minimum Variance Unbiased Estimator (MVUE) of R

We determine the Minimum Variance Unbiased Estimator (MVUE) of $R=\Pr(\mathbf{a}'\mathbf{x}^*-\mathbf{b}'\mathbf{y}^*>0)$. Here, it is assumed that the random sample $\begin{pmatrix}\mathbf{x_\alpha^*}\\ \mathbf{y_\alpha^*}\end{pmatrix}$, $\alpha=1,2,\dots,n$ are from multivariate normal distribution i.e. $\begin{pmatrix}\mathbf{x_\alpha^*}\\ \mathbf{y_\alpha^*}\end{pmatrix}\sim N_{p1+p2}(\mu,\sum)$.

Then, $v_{\boldsymbol{\alpha}}=\ (\mathbf{b}'\mathbf{y}_{\boldsymbol{\alpha}}^*-\mathbf{a}'\mathbf{x}_{\boldsymbol{\alpha}}^*)\sim N(\mu_v,\sigma_v^2)$, α=1,2,….,n be the random sample of size n. Now, $(\bar{v},\ S_v^2)$ is a complete sufficient statistic for (μ_v,σ_v^2), where $\bar{v}=\frac{1}{n}\sum_{\alpha=1}^{n}v_i$ and $s_v^2=\frac{1}{n}\sum_{\alpha=1}^{n}(v_i-\bar{v})^2$, the MVUE of R [33] is $\hat{R}=\int_c^1\frac{\Gamma(\frac{n-1}{2})}{\Gamma(\frac{1}{2})\Gamma(\frac{n-2}{2})}(1-z^2)^{\frac{n-2}{2}-1}dz$, where $c=\frac{\bar{v}}{(\sqrt{(n-1)}s_v}$

Then the MVUE of $R=\Pr(\mathbf{a}'\mathbf{x}^*-\mathbf{b}'\mathbf{y}^*>0)$ is [27]

$$\hat{R}=\begin{pmatrix}0 & \text{if} & c>0\\ \frac{1}{2}\left(1-B\left(c^2;\frac{1}{2},\frac{n-2}{2}\right)\right) & \text{if} & 0<c\le 1\\ \frac{1}{2}\left(1+B\left((-c)^2;\frac{1}{2},\frac{n-2}{2}\right)\right) & \text{if} & -1<c\le 0\\ 1 & \text{if} & c\le -1\end{pmatrix} \quad (3)$$

where, $c=\frac{(\boldsymbol{b'\overline{y^*}-a'\overline{x^*}})}{(\sqrt{(n-1)}\ (\boldsymbol{a'S_{11}a-2a'S_{12}\ b+b'S_{22}\ b})^{1/2}}$ and $B(k;\alpha,\beta)=\frac{\Gamma(\alpha+\beta)}{\Gamma(\alpha)\Gamma(\beta)}\int_0^k x^{\alpha-1}(1-x)^{\beta-1}\,dx$

An estimator $\hat{\hat{R}}$ may be taken as above expression where 'c' is replaced by

$$c'=\frac{(l_1'\overline{y^*}-e_1'\overline{x^*})}{(\sqrt{(n-1)}\ (e_1'S_{11}e_1-2e_1'S_{12}\ l_1+l_1'S_{22}\ l_1)^{1/2}}\ .$$

IV. Distribution Function of $\hat{R}$ and R^*

In this section, we use results of the previous section by taking of log-transformation between vectors and derive the distributions function of $\hat{R}$ and R^*. Consider the log-transformed vectors as $\mathbf{x}^*$ and $\mathbf{y}^*$. Then, from section 2.3, the distribution function of $\hat{R}$ is given by

Let the distribution function of $\hat{R}$ be $F_{\hat{R}}(x)$, then

$$F_{\hat{R}}(x) = 0 \text{ if } x < 0 \text{ and } F_{\hat{R}}(x) = 1 \text{ if } x \geqslant 1$$

If $0 \leqslant x \leqslant \frac{1}{2}$, then the distribution function of $\hat{R}$ is given by

$$F_{\hat{R}}(x) = P(\hat{R} \leqslant x) = P[(\hat{R} \leqslant x)|(c > 0)]P[c > 0] + P[(\hat{R} \leqslant x)|(c \leqslant 0)]P[c \leqslant 0]$$

$$= P[\frac{1}{2} - \frac{1}{2}B(c^2; \frac{1}{2}, \frac{n-2}{2}) \leqslant x]P[\frac{(\mathbf{b}'\bar{\mathbf{y}}^* - \mathbf{a}'\bar{\mathbf{x}}^*)}{\sqrt{(n-1)}(\mathbf{a}'\mathbf{S_{11}}\mathbf{a} - 2\mathbf{a}'\mathbf{S_{12}}\mathbf{b} + \mathbf{b}'\mathbf{S_{22}}\mathbf{b})^{\frac{1}{2}}} > 0]$$

$$= P[B(c^2; \tfrac{1}{2}, \tfrac{n-2}{2}) \geqslant 1 - 2x]P[(\mathbf{b}'\bar{\mathbf{y}}^* - \mathbf{a}'\bar{\mathbf{x}}^*) > 0]$$

,where $(\mathbf{b}'\bar{\mathbf{y}}^* - \mathbf{a}'\bar{\mathbf{x}}^*) \sim N_1((\mathbf{b}'\boldsymbol{\mu_2} - \mathbf{a}'\boldsymbol{\mu_1}), \frac{1}{n}(\mathbf{a}'\boldsymbol{\Sigma_{11}}\mathbf{a} - 2\mathbf{a}'\boldsymbol{\Sigma_{12}}\mathbf{b} + \mathbf{b}'\boldsymbol{\Sigma_{22}}\mathbf{b}))$

$$= P[c^2 \geqslant B^{-1}_{(\frac{1}{2}, \frac{n-2}{2})}(1-2x)]\Phi(\frac{\sqrt{n}(\mathbf{b}'\boldsymbol{\mu_2} - \mathbf{a}'\boldsymbol{\mu_1})}{(\mathbf{a}'\boldsymbol{\Sigma_{11}}\mathbf{a} - 2\mathbf{a}'\boldsymbol{\Sigma_{12}}\mathbf{b} + \mathbf{b}'\boldsymbol{\Sigma_{22}}\mathbf{b})^{\frac{1}{2}}})$$

$$= \{P[c \geqslant \left(B^{-1}_{(\frac{1}{2}, \frac{n-2}{2})}(1-2x)\right)^{\frac{1}{2}}] + P[c \leqslant -\left(B^{-1}_{(\frac{1}{2}, \frac{n-2}{2})}(1-2x)\right)^{\frac{1}{2}}]\}\Phi(-\sqrt{n}\delta)$$

$$\text{,where } \delta^* = \frac{-(\mathbf{b}'\boldsymbol{\mu_2} - \mathbf{a}'\boldsymbol{\mu_1})}{(\mathbf{a}'\boldsymbol{\Sigma_{11}}\mathbf{a} - 2\mathbf{a}'\boldsymbol{\Sigma_{12}}\mathbf{b} + \mathbf{b}'\boldsymbol{\Sigma_{22}}\mathbf{b})^{\frac{1}{2}}}$$

$$= \{P[\frac{(\mathbf{b}'\bar{\mathbf{y}}^* - \mathbf{a}'\bar{\mathbf{x}}^*)}{\sqrt{(n-1)}(\mathbf{a}'\mathbf{S}^*_{\mathbf{11}}\mathbf{a} - 2\mathbf{a}'\mathbf{S}^*_{\mathbf{12}}\mathbf{b} + \mathbf{b}'\mathbf{S}^*_{\mathbf{22}}\mathbf{b})^{\frac{1}{2}}} \geqslant (B^{-1}_{(\frac{1}{2}, \frac{n-2}{2})}(1-2x))^{\frac{1}{2}}] +$$

$$P[\frac{(\mathbf{b}'\bar{\mathbf{y}}^* - \mathbf{a}'\bar{\mathbf{x}}^*)}{\sqrt{(n-1)}(\mathbf{a}'\mathbf{S}^*_{\mathbf{11}}\mathbf{a} - 2\mathbf{a}'\mathbf{S}^*_{\mathbf{12}}\mathbf{b} + \mathbf{b}'\mathbf{S}^*_{\mathbf{22}}\mathbf{b})^{\frac{1}{2}}} \leqslant -(B^{-1}_{(\frac{1}{2}, \frac{n-2}{2})}(1-2x))^{\frac{1}{2}}]\}\,\Phi(-\sqrt{n}\delta^*)$$

$$= \{P[-\sqrt{n}\hat{\delta}^* \geqslant (n-1)(B^{-1}_{(\frac{1}{2}, \frac{n-2}{2})}(1-2x))^{\frac{1}{2}}] + P[-\sqrt{n}\hat{\delta}^* \leqslant -(n-1)(B^{-1}_{(\frac{1}{2}, \frac{n-2}{2})}(1-2x))^{\frac{1}{2}}]\}\Phi(-\sqrt{n}\delta^*)$$

$$\text{,where } \hat{\delta}^* = \frac{-\sqrt{(n-1)}(\mathbf{b}'\bar{\mathbf{y}}^* - \mathbf{a}'\bar{\mathbf{x}}^*)}{\sqrt{n}(\mathbf{a}'\mathbf{S}^*_{\mathbf{11}}\mathbf{a} - 2\mathbf{a}'\mathbf{S}^*_{\mathbf{12}}\mathbf{b} + \mathbf{b}'\mathbf{S}^*_{\mathbf{22}}\mathbf{b})^{\frac{1}{2}}}$$

$$= \{P[\sqrt{n}\hat{\delta}^* \leqslant -(n-1)(B^{-1}_{(\frac{1}{2}, \frac{n-2}{2})}(1-2x))^{\frac{1}{2}}] + 1 - P[\sqrt{n}\hat{\delta}^* \leqslant (n-1)(B^{-1}_{(\frac{1}{2}, \frac{n-2}{2})}(1-2x))^{\frac{1}{2}}]\}\Phi(-\sqrt{n}\delta^*)$$

$$= \{F_{t'_{(n-1),\sqrt{n}\delta^*}}(-(n-1)(B^{-1}_{(\frac{1}{2}, \frac{n-2}{2})}(1-2x))^{\frac{1}{2}}) + [1 - F_{t'_{(n-1),\sqrt{n}\delta^*}}((n-1)(B^{-1}_{(\frac{1}{2}, \frac{n-2}{2})}(1-2x))^{\frac{1}{2}})]\}\Phi(-\sqrt{n}\delta^*)$$

Using the standard distribution theory, if $\mathbf{x}^* \sim N_p(\mu, \sum)$ then $\mathbf{a}'\mathbf{x}^* \sim N_1(\mathbf{a}'\mu, \mathbf{a}'\sum\mathbf{a})$ [34]**.** Let, $\bar{\mathbf{x}}^*$ and $\mathbf{S}^*$ be the unbiased estimator of μ and $\sum$ respectively, then $\mathbf{a}'\bar{\mathbf{x}}^* \sim N_1(\mathbf{a}'\mu, \frac{1}{\mathbf{n}}(\mathbf{a}'\sum\mathbf{a}))$ and

$\mathbf{S}^* \sim W_p(n-1, \sum)$. Thus, we can write, $\frac{\mathbf{a'S^*a}}{\mathbf{a'\sum a}} \sim \boldsymbol{\chi}^2_{n-1}$, hence $\sqrt{n-1}\hat{\delta}^* \sim t'_{(n-1),\sqrt{n}\delta^*}$ where $t'_{(n-1),\sqrt{n}\delta^*}$ denotes the non - central t - distribution with (n - 1) d.f. We use the unbiased estimator of $\sum$ instead of MLE, then $\sqrt{n}\hat{\delta}^* \sim t'_{(n-1),\sqrt{n}\delta^*}$ with non-centrality parameter $\sqrt{n}\delta^*$ and $F_{t'_{(n-1),\sqrt{n}\delta^*}}(.)$ be the cdf of non - central t - distribution.

If $\frac{1}{2} < x < 1$, then the distribution function of $\hat{R}$ is given by

$$F_{\hat{R}}(x) = P(\hat{R} \leqslant x) = P[(\hat{R} \leqslant x)|(c > 0)]P[c > 0] + P[(\hat{R} \leqslant x)|(c \leqslant 0)]P[c \leqslant 0]$$

$$= P[\frac{1}{2} - \frac{1}{2}B(c^2; \frac{1}{2}, \frac{n-2}{2}) \leqslant x]P[\frac{(\mathbf{b'\bar{y}^* - a'\bar{x}^*})}{\sqrt{(n-1)}(\mathbf{a'S^*_{11}a - 2a'S^*_{12}b + b'S^*_{22}b})^{\frac{1}{2}}} > 0] +$$

$$P[\frac{1}{2} + \frac{1}{2}B((-c)^2; \frac{1}{2}, \frac{n-2}{2}) \leqslant x]\Phi(\sqrt{n}\delta^*)$$

$$= \Phi(-\sqrt{n}\delta^*) + P[B(c^2; \frac{1}{2}, \frac{n-2}{2}) \leqslant 2x - 1]\Phi(\sqrt{n}\delta^*)$$

$$= \Phi(-\sqrt{n}\delta^*) + P[-(B^{-1}_{(\frac{1}{2}, \frac{n-2}{2})}(2x-1))^{\frac{1}{2}} \leqslant c \leqslant (B^{-1}_{(\frac{1}{2}, \frac{n-2}{2})}(2x-1))^{\frac{1}{2}}]\Phi(\sqrt{n}\delta^*)$$

$$= \Phi(-\sqrt{n}\delta^*) + P[(n-1)(B^{-1}_{(\frac{1}{2}, \frac{n-2}{2})}(2x-1))^{\frac{1}{2}} \geqslant \sqrt{n}\hat{\delta}^*$$

$$\geqslant -(n-1)(B^{-1}_{(\frac{1}{2}, \frac{n-2}{2})}(2x-1))^{\frac{1}{2}}]\Phi(\sqrt{n}\delta^*)$$

$$= \Phi(-\sqrt{n}\delta^*) + [F_{t'_{(n-1),\sqrt{n}\delta^*}}((n-1)(B^{-1}_{(\frac{1}{2}, \frac{n-2}{2})}(2x-1))^{\frac{1}{2}}) -$$

$$F_{t'_{(n-1),\sqrt{n}\delta^*}}(-(n-1)(B^{-1}_{(\frac{1}{2}, \frac{n-2}{2})}(2x-1))^{\frac{1}{2}})]\Phi(\sqrt{n}\delta^*)$$

Thus, the distribution function of $\hat{R}$ is given by

$$F_{\hat{R}}(x) = 0 \text{ if } x < 0 \text{ and } F_{\hat{R}}(x) = 1 \text{ if } x \geqslant 1$$

If $0 \leqslant x \leqslant \frac{1}{2}$,

$$F_{\hat{R}}(x) = \{F_{t'_{(n-1),\sqrt{n}\delta^*}}(-(n-1)(B^{-1}_{(\frac{1}{2}, \frac{n-2}{2})}(1-2x))^{\frac{1}{2}}) +$$

$$[1 - F_{t'_{(n-1),\sqrt{n}\delta^*}}((n-1)(B^{-1}_{(\frac{1}{2}, \frac{n-2}{2})}(1-2x))^{\frac{1}{2}})]\}\Phi(-\sqrt{n}\delta^*)$$

If $\frac{1}{2} < x < 1$,

$$F_{\hat{R}}(x) = \Phi(-\sqrt{n}\delta^*) + [F_{t'_{(n-1),\sqrt{n}\delta^*}}((n-1)(B^{-1}_{(\frac{1}{2}, \frac{n-2}{2})}(2x-1))^{\frac{1}{2}}) -$$

$$F_{t'_{(n-1),\sqrt{n}\delta^*}}(-(n-1)(B^{-1}_{(\frac{1}{2}, \frac{n-2}{2})}(2x-1))^{\frac{1}{2}})]\Phi(\sqrt{n}\delta^*) \quad (4)$$

The MLE estimate of R, $R^* = \Phi(\frac{-(\mathbf{b'\bar{y}^* - a'\bar{x}^*})}{(\mathbf{a'S^*_{11}a - 2a'S^*_{12}b + b'S^*_{22}b})^{\frac{1}{2}}})$

Let the distribution function of R^* be $F_{R^*}(x)$, then $F_{R^*}(x) = 0$ if $x < 0$ and $F_{R^*}(x) = 1$ if $x \geqslant 1$,

$$F_{R^*}(x) = P(R^* \leqslant x) = P[\Phi(\frac{-(\mathbf{b}'\bar{\mathbf{y}}^* - \mathbf{a}'\bar{\mathbf{x}}*)}{(\mathbf{a}'\mathbf{S}_{11}^*\mathbf{a} - 2\mathbf{a}'\mathbf{S}_{12}^*\mathbf{b} + \mathbf{b}'\mathbf{S}_{22}^*\mathbf{b})^{\frac{1}{2}}}) \leqslant x]$$

$$= P[\frac{-(\mathbf{b}'\bar{\mathbf{y}}^* - \mathbf{a}'\bar{\mathbf{x}}*)}{(\mathbf{a}'\mathbf{S}_{11}^*\mathbf{a} - 2\mathbf{a}'\mathbf{S}_{12}^*\mathbf{b} + \mathbf{b}'\mathbf{S}_{22}^*\mathbf{b})^{\frac{1}{2}}} \leqslant \Phi^{-1}(x)]$$

$$= P[\sqrt{n}\hat{\delta}^* \leqslant \sqrt{(n-1)}\Phi^{-1}(x)]$$

$$= F_{t'_{(n-1),\sqrt{n}\delta^*}}(\sqrt{(n-1)}\Phi^{-1}(x)) \quad (5)$$

V. Distance Between $F_{\hat{R}}(.)$ and $F_{R^*}(.)$

Let us calculate the distance between two function (L_1) $F_{\hat{R}}(x)$ and $F_{R^*}(x)$ [31], $U(n, \delta^*) = \int_0^1 |F_{R^*}(x) - F_{\hat{R}}(x)|dx$, for different values of n, $\boldsymbol{\mu_1}$, $\boldsymbol{\mu_2}$, $\boldsymbol{\Sigma_{11}}$, $\boldsymbol{\Sigma_{12}}$, $\boldsymbol{\Sigma_{22}}$. According to this method, this can be taken as a measure of deviation or equal deviation between $\hat{R}$ and R^*.

Let, $\bar{R}$ be any other estimator of R, then the maximum deviation between distribution of $\bar{R}$ and $\hat{R}$ as

$$M(n, \delta^*) = \sup_{\bar{R}} \int_0^1 |F_{\bar{R}}(x) - F_{\hat{R}}(x)|\, dx$$

$$= \int_0^1 F_{\hat{R}}(x)dx \text{ , if } \int_0^1 F_{\hat{R}}(x)dx > \frac{1}{2}$$

$$= 1 - \int_0^1 F_{\hat{R}}(x)dx \text{ , if } \int_0^1 F_{\hat{R}}(x)dx \leqslant \frac{1}{2}$$

The ration $R(n, \delta^*) = \frac{U(n,\delta^*)}{M(n,\delta^*)}$ has to be taken as a relative measure of deviation between $\hat{R}$ and R^*, the maximum deviation between any other estimator of R, i.e. $\bar{R}$ and $\hat{R}$.

VI. Derivation of $Var(\hat{R})$ and $MSE(R^*)$

Since, $0 < \hat{R} < 1$, then $E(\hat{R}) = \int_0^1 \{1 - F_{\hat{R}}(x)\}dx$ and using equation (4)

If $0 \leqslant x \leqslant \frac{1}{2}$, then we have

$$E_1(\hat{R}) = \int_0^1 [1 - \{F_{t'_{(n-1),\sqrt{n}\delta^*}}(-(n-1)(B^{-1}_{(\frac{1}{2}, \frac{n-2}{2})}(1-2x))^{\frac{1}{2}}) +$$

$$[1 - F_{t'_{(n-1),\sqrt{n}\delta^*}}((n-1)(B^{-1}_{(\frac{1}{2}, \frac{n-2}{2})}(1-2x))^{\frac{1}{2}})]\}\Phi(-\sqrt{n}\delta^*)]\, dx$$

If $\frac{1}{2} < x < 1$, then we have

$$E_2(\hat{R}) = \int_0^1 [1 - \{\Phi(-\sqrt{n}\delta^*) + [F_{t'_{(n-1),\sqrt{n}\delta^*}}((n-1)(B^{-1}_{(\frac{1}{2},\frac{n-2}{2})}(2x-1))^{\frac{1}{2}}) - F_{t'_{(n-1),\sqrt{n}\delta^*}}(-(n-1)(B^{-1}_{(\frac{1}{2},\frac{n-2}{2})}(2x-1))^{\frac{1}{2}})]\Phi(\sqrt{n}\delta^*)\}]\,dx$$

So,
$$Var(\hat{R}) = \int_0^1 2x\{1 - F_{\hat{R}}(x)\}dx - \{E(\hat{R})\}^2$$

$$= \int_0^1 2x[1 - \{F_{t'_{(n-1),\sqrt{n}\delta^*}}(-(n-1)(B^{-1}_{(\frac{1}{2},\frac{n-2}{2})}(1-2x))^{\frac{1}{2}}) + [1 - F_{t'_{(n-1),\sqrt{n}\delta^*}}((n-1)(B^{-1}_{(\frac{1}{2},\frac{n-2}{2})}(1-2x))^{\frac{1}{2}})]\}\Phi(-\sqrt{n}\delta^*)]\,dx$$

$$+ \int_0^1 2x[1 - \{\Phi(-\sqrt{n}\delta^*) + [F_{t'_{(n-1),\sqrt{n}\delta^*}}((n-1)(B^{-1}_{(\frac{1}{2},\frac{n-2}{2})}(2x-1))^{\frac{1}{2}}) - F_{t'_{(n-1),\sqrt{n}\delta^*}}(-(n-1)(B^{-1}_{(\frac{1}{2},\frac{n-2}{2})}(2x-1))^{\frac{1}{2}})]\Phi(\sqrt{n}\delta^*)\}]\,dx$$

$$- \{E_1(\hat{R}) + E_2(\hat{R})\}^2$$

Using equation (5), we can determine $MSE(R^*) = \int_0^1 2x\left\{1 - F_{t'_{(n-1),\sqrt{n}\delta^*}}\left(\sqrt{(n-1)}\Phi^{-1}(x)\right)\right\}dx -$

$$[\int_0^1 \{1 - F_{t'_{(n-1),\sqrt{n}\delta^*}}(\sqrt{(n-1)}\Phi^{-1}(x))\}\,dx]^2$$

VII. Exact Two Sided Confidence Intervals for R

Here, we have $\sqrt{n}\hat{\delta}^* \sim t'_{(n-1),\sqrt{n}\delta^*}$. The tradition approach for finding the lower limit of R , we use the probability $p_{\delta^*_L}$ that $t'_{(n-1),\sqrt{n}\delta^*}$ exceeds the value of $\sqrt{n}\hat{\delta}^*$ as

$$p_{\delta^*_L} = Pr\,(t'_{(n-1),\sqrt{n}\delta^*} > \sqrt{n}\hat{\delta}^*) = \alpha/2$$

or,
$$p_{\delta^*_L} = Pr\,(t'_{(n-1),\sqrt{n}\delta^*} < \sqrt{n}\hat{\delta}^*) = 1 - \alpha/2 \qquad (6)$$

Similarly, we get the upper limit of δ^* as

$$p_{\delta^*_U} = Pr\,(t'_{(n-1),\sqrt{n}\delta^*} < \sqrt{n}\hat{\delta}^*) = \alpha/2 \qquad (7)$$

Equation (6) and (7) can be solved numerically. Finally, we get the (1-α) level confidence Intervals for δ^* as (δ^*_L, δ^*_U). Then, the (1-α) level confidence Intervals for R as $(\Phi(\delta^*_L), \Phi(\delta^*_U))$.

VIII. Exact Lower Confidence bound for R

In order to determine the lower bound of the lower bound of R, we use the probability $p_{\delta^*_{LB}}$ that $t'_{(n-1),\sqrt{n}\delta^*}$ exceeds the value of $\sqrt{n}\hat{\delta}^*$ as

$$p_{\delta^*_{LB}} = Pr\,(t'_{(n-1),\sqrt{n}\delta^*} > \sqrt{n}\hat{\delta}^*) = \alpha$$

or, $$p_{\delta^*_{LB}} = \Pr\left(t'_{(n-1),\sqrt{n}\delta^*} < \sqrt{n}\hat{\delta^*}\right) = 1-\alpha \quad (8)$$

Thus, the (1-α) level confidence lower bound for δ^* can be obtained by solving equation (8). Then, the (1-α) level confidence lower bound for R is $\Phi(\delta^*_{LB})$.

IX. Approximate Two Sided Confidence Intervals for R

From section 3, we have $\Pr(\mathbf{a}'\mathbf{x}^* > \mathbf{b}'\mathbf{y}^*) = \Phi\left[\frac{-(\mathbf{b}'\boldsymbol{\mu}_2 - \mathbf{a}'\boldsymbol{\mu}_1)}{(\mathbf{a}'\boldsymbol{\Sigma}_{11}\mathbf{a} - 2\mathbf{a}'\boldsymbol{\Sigma}_{12}\mathbf{b} + \mathbf{b}'\boldsymbol{\Sigma}_{22}\mathbf{b})^{\frac{1}{2}}}\right] = \Phi(\delta^*)$,

where $\sqrt{n}\hat{\delta^*} \sim t'_{(n-1),\sqrt{n}\delta^*}$ with non-centrality parameter $\sqrt{n}\delta^*$.

In order to determine the two sided confidence Intervals, we use following well known approximation for large n [35] as

$$Z = \frac{\left[t'_{(n-1),\sqrt{n}\delta^*} - \sqrt{n}\delta^*\right]}{\left[1 + \frac{(t'_{(n-1),\sqrt{n}\delta^*})^2}{2(n-1)}\right]^{\frac{1}{2}}} \sim N(0,1)$$

Using this,

$$\Pr\left[-z_{\alpha/2} \leqslant \frac{\left[\sqrt{n}\hat{\delta^*} - \sqrt{n}\delta^*\right]}{\left[1 + \frac{(\sqrt{n}\hat{\delta^*})^2}{2(n-1)}\right]^{\frac{1}{2}}} \leqslant z_{\alpha/2}\right] = 1-\alpha$$

or, $$\Pr\left[\hat{\delta^*} - z_{\alpha/2}\left[\frac{1}{n} + \frac{(\hat{\delta^*})^2}{2(n-1)}\right]^{\frac{1}{2}} \leqslant \delta^* \leqslant \hat{\delta^*} + z_{\alpha/2}\left[\frac{1}{n} + \frac{(\hat{\delta^*})^2}{2(n-1)}\right]^{\frac{1}{2}}\right] = 1-\alpha$$

Thus, an approximate (1-α) level confidence Intervals for δ^* is given by

$$(\delta^*_L, \delta^*_U) = \left\{\hat{\delta^*} - z_{\alpha/2}\left[\frac{1}{n} + \frac{(\hat{\delta^*})^2}{2(n-1)}\right]^{\frac{1}{2}} , \hat{\delta^*} + \left[\frac{1}{n} + \frac{(\hat{\delta^*})^2}{2(n-1)}\right]^{\frac{1}{2}} z_{\alpha/2}\right\}$$

Then, an approximate (1-α) level confidence Intervals for R is represented by

$$(\Phi(\delta^*_L), \Phi(\delta^*_U)) = \left\{\Phi\left(\hat{\delta^*} - z_{\alpha/2}\left[\frac{1}{n} + \frac{(\hat{\delta^*})^2}{2(n-1)}\right]^{\frac{1}{2}}\right) , \Phi\left(\hat{\delta^*} + z_{\alpha/2}\left[\frac{1}{n} + \frac{(\hat{\delta^*})^2}{2(n-1)}\right]^{\frac{1}{2}}\right)\right\} \quad (9)$$

where, $z_{\alpha/2}$ upper critical value for the standard normal distribution

X. Approximate Lower Confidence bound for R

The lower bounds based on approximate results is given by

$$\Pr(\delta^*_{LB} \leqslant \delta^*) = 1-\alpha$$

or,
$$\Pr\left(\frac{\left[\delta^*_{LB}-\hat{\delta}^*\right]}{\left[\frac{1}{n}+\frac{(\hat{\delta}^*)^2}{2(n-1)}\right]^{\frac{1}{2}}}\leqslant\frac{\left[\delta^*-\hat{\delta}^*\right]}{\left[\frac{1}{n}+\frac{(\hat{\delta}^*)^2}{2(n-1)}\right]^{\frac{1}{2}}}\right)=1-\alpha$$

or,
$$\Pr\left(z\leqslant\frac{\left[\hat{\delta}^*-\delta^*_{LB}\right]}{\left[\frac{1}{n}+\frac{(\hat{\delta}^*)^2}{2(n-1)}\right]^{\frac{1}{2}}}\right)=1-\alpha$$

or,
$$\delta^*_{LB}=\hat{\delta}^*-z_{1-\alpha}\left[\frac{1}{n}+\frac{(\hat{\delta}^*)^2}{2(n-1)}\right]^{\frac{1}{2}}$$

So, an approximate (1-α) confidence lower bound for R as

$$\Phi(\delta^*_{LB})=\Phi\left(\hat{\delta}^*-z_{1-\alpha}\left[\frac{1}{n}+\frac{(\hat{\delta}^*)^2}{2(n-1)}\right]^{\frac{1}{2}}\right) \quad (10)$$

XI. Bootstrap confidence Intervals for R

Now, we consider the confidence intervals based on percentile bootstrap method. Efron suggests [36] the procedure to find out the confidence intervals for a parameter. It works as follows

(1) Draw random sample $\begin{pmatrix}\mathbf{X_\alpha}\\ \mathbf{Y_\alpha}\end{pmatrix}$, $\alpha=1,2,\dots,n$ from multivariate log-normal distribution, where $\begin{pmatrix}\mathbf{X}\\ \mathbf{Y}\end{pmatrix}\sim\Lambda_{p_1+p_2}(\mu,\sum)$.

(2) Take the log-transformation as $\begin{pmatrix}\mathbf{ln}\,(\mathbf{X_\alpha})\\ \mathbf{ln}\,(\mathbf{Y_\alpha})\end{pmatrix}=\begin{pmatrix}\mathbf{X^*_\alpha}\\ \mathbf{Y^*_\alpha}\end{pmatrix}\sim N_{p_1+p_2}(\mu,\sum),\alpha=1,2,\dots,n.$

(3) Generate bootstrap samples $\begin{pmatrix}\mathbf{X^B_\alpha}\\ \mathbf{Y^B_\alpha}\end{pmatrix}$, $\alpha=1,2,\dots,n$, by using random sample of $\begin{pmatrix}\mathbf{X^*_\alpha}\\ \mathbf{Y^*_\alpha}\end{pmatrix}$, $\alpha=1,2,\dots,n$.

(4) Compute the bootstrap estimates of linear dependent vectors $\mathbf{a}'$ and $\mathbf{b}'$ using PC1, say $\mathbf{e}'^*$ and $\mathbf{l}'^*$ respectively. Also, Compute the bootstrap MLE estimates of $\boldsymbol{\mu_1}$, $\boldsymbol{\mu_2}$, $\boldsymbol{\Sigma_{11}}$, $\boldsymbol{\Sigma_{12}}$, $\boldsymbol{\Sigma_{22}}$ by $\overline{\mathbf{x}^*},\overline{\mathbf{y}^*},\mathbf{S^*_{11}},\mathbf{S^*_{12}},\mathbf{S^*_{12}}$. Using these estimates compute the bootstrap estimate of R, say R^*_B.

(5) Repeat steps 3 and 4, number of boot time B (B sufficiently large, i.e. 1000), thus we obtain the bootstrap distribution of $\{R^*_B\}$.

(6) Estimate $(1-\alpha)$ bootstrap percentile confidence intervals for R from$\{R^*_B\}$ by taking the $\left(\frac{\alpha}{2}\right)$ and $\left(1-\frac{\alpha}{2}\right)$ quantiles as $\left(R^*_{B,\frac{\alpha}{2}},\ R^*_{B,\left(1-\frac{\alpha}{2}\right)}\right)$.

or, $(1-\alpha)$ bootstrap percentile lower bound for R as $R^*_{B,\alpha}$.

In order to corrects for narrowness bias of percentile confidence intervals for R, we use the Better Bootstrap Confidence Intervals proposed by Efron [37].

III. Simulation Study

I. Calculation of mean, variance, MSE and MAE of $\hat{\hat{R}}$ and R*

The simulation study we perform here is to compare the behaviours of two estimators $\hat{\hat{R}}$ and *R**

based on estimator of $\mu = \begin{pmatrix} \boldsymbol{\mu}_1 \\ \boldsymbol{\mu}_2 \end{pmatrix}_{(p_1 x p_2)}$ and $\sum = \begin{pmatrix} \Sigma_{11} & \Sigma_{12} \\ \Sigma_{21} & \Sigma_{22} \end{pmatrix}_{(p_{1+}p_2)x(p_{1+}p_2)}$. For this purpose, we compute the following measures:

(i) Mean of $\hat{\hat{R}}$ and R^*

(ii) Variance of $\hat{\hat{R}}$ and R^* : $E(\hat{\hat{R}} - R)^2$ and $E(R^* - R)^2$

(iii) Mean square error of $\hat{\hat{R}}$ and R^* : $Var(\hat{\hat{R}})+Bias(\hat{R},R)^2$ and $Var(R^*)+Bias(R^*,R)^2$

(iv) Mean absolute error of $\hat{\hat{R}}$ and R^* : $E(|\hat{\hat{R}} - R|)$ and $E(|R^* - R|)$

It is difficult to obtain the analytical form of the above expressions for different values of 'R'. So, we obtain these by using simulation study. Hence, we generate random samples of size n from $\begin{pmatrix} \mathbf{x} \\ \mathbf{y} \end{pmatrix} \sim \Lambda_{p1+p2}(\mu, \sum)$. Then take the log-transformation of whole random sample of size n. For each of sample drawn of size n, we compute the above measures by taking 500 replications each time.

For this purpose, here, R programming language is used.

Suppose, $\begin{pmatrix} x_1 \\ x_2 \\ y_1 \\ y_2 \\ y_3 \end{pmatrix} \sim \Lambda_5(\mu, \sum)$, then $\begin{pmatrix} \ln(x_1) \\ \ln(x_2) \\ \ln(y_1) \\ \ln(y_2) \\ \ln(y_3) \end{pmatrix} = \begin{pmatrix} x_1^* \\ x_2^* \\ y_1^* \\ y_2^* \\ y_3^* \end{pmatrix} \sim N_5(\mu, \sum)$

where , $\mu' = (2,4,2,1,2)$; $\sum = \begin{pmatrix} 3.61 & 2.23 & -0.10 & 0.16 & 2.32 \\ 2.23 & 4.74 & 3.32 & -0.69 & 1.76 \\ -0.10 & 3.32 & 5.68 & -2.34 & -1.23 \\ 0.16 & -0.69 & -2.34 & 3.05 & 1.53 \\ 2.32 & 1.76 & -1.23 & 1.53 & 4.45 \end{pmatrix}$

Therefore, the estimated values of vectors based on first principal component are $\mathbf{a}'$ = (0.614, 0.789) and $\mathbf{b}'$= (0.737, -0.491, -0.465). Then the exact value of stress strength reliability R= $Pr(\mathbf{a}'\mathbf{x}^* > \mathbf{b}'\mathbf{y}^*)$ is 0.8861. We take the sample size of n up to 200 in order to achieved exact value for the reliability. Calculated mean, variance, MSE and MAE of $\hat{\hat{R}}$ and R* based on 500 repetitions are reported in Table 1. It can be observed that Variance of $\hat{\hat{R}}$ is lesser than the Variance of R* in each sample size. Also, it is noted that the MSE's and MAE's of $\hat{\hat{R}}$ is lesser than MSE's and MAE's of R*. However, the sample mean of $\hat{\hat{R}}$ is less than the R* in each case. But, $\hat{\hat{R}}$ and R* are under-estimates the true value of R, when sample sizes are small. It is also interesting to observe that, the Variance, MSE and MAE of $\hat{\hat{R}}$ and R* are reduces as the sample size increases: when n=200 and they almost achieved the true value of R.

Table 1: *Sample Mean, Variance, MSE and MAE of $\hat{\hat{R}}$ and R^**

Sample Size	Sample Mean		Variance		MSE		MAE	
	$\hat{\hat{R}}$	R^*	$\hat{\hat{R}}$	R^*	$\hat{\hat{R}}$	R^*	$\hat{\hat{R}}$	R^*
10	0.6723	0.6751	0.1054	0.1097	0.1509	0.1540	0.2475	0.2508
20	0.7302	0.7322	0.0949	0.0969	0.1190	0.1203	0.1903	0.1924
30	0.7550	0.7566	0.0823	0.0836	0.0993	0.1002	0.1524	0.1633
40	0.7935	0.7951	0.0591	0.0598	0.0675	0.0680	0.1103	0.1173
50	0.8050	0.8063	0.0544	0.0549	0.0609	0.0612	0.0970	0.1046
60	0.8126	0.8138	0.0481	0.0485	0.0534	0.0536	0.9097	0.0927
70	0.8382	0.8392	0.0326	0.0328	0.0348	0.0349	0.0667	0.0681

80	0.8449	0.8459	0.0305	0.0307	0.0322	0.0323	0.0630	0.0631
90	0.8487	0.8496	0.0264	0.0265	0.0277	0.0278	0.0553	0.0558
100	0.8560	0.8568	0.0211	0.0212	0.0219	0.0220	0.0476	0.0486
200	0.8810	0.8815	0.0037	0.0038	0.0038	0.0038	0.0182	0.0183

II. Relative measure between $\hat{R}$ and R^*

It' s difficult to get the exact values of relative measure of deviation between $\hat{R}$ and R^*, i.e., $R(n, \delta^*)$. So, we compute these measure values numerically using R - programming. Using different choices of parameters in Table 2 and variance-covariance matrix, results of these two measures and ratio are reported in Table 3. The results shows that the overall output of MVUE and MLE of R are not too distant and the values for these differences are show in columns U(.), M(.) and R(.) of this tables. From this tables, it is seen that empirical values of the parameters and the performance of MVUE of R is better than MLE and Figure 1 shows that, MVUE estimator of R is better than the other estimators, i.e. R^* also L_1 distance and graphical impression show this.

Table 2: *Parameters for the simulation study*

Parameters and values													
Scenario	μ_1			μ_2			Scenario	μ_1			μ_2		
	$\mu_{p_{11}}$	$\mu_{p_{12}}$	$\mu_{p_{13}}$	$\mu_{p_{21}}$	$\mu_{p_{22}}$	$\mu_{p_{23}}$		$\mu_{p_{11}}$	$\mu_{p_{12}}$	$\mu_{p_{13}}$	$\mu_{p_{21}}$	$\mu_{p_{22}}$	$\mu_{p_{23}}$
1	1.639	1.477	1.036	2.802	2.114	2.197	48	1.161	2.647	2.508	1.114	2.918	2.077
2	1.956	2.427	1.019	2.612	2.908	2.286	49	2.112	2.288	2.621	2.439	2.949	1.363
3	1.747	1.103	1.545	1.382	2.837	2.796	50	1.599	2.294	2.771	1.81	2.973	1.726
4	1.052	1.972	1.014	1.938	2.271	2.616	51	2.002	1.414	1.431	1.751	1.288	1.724
5	1.204	1.233	1.927	2.122	2.581	2.732	52	2.728	1.52	2.06	1.633	2.111	2.192
6	1.765	1.765	1.233	1.723	2.927	2.312	53	2.86	1.224	1.351	2.287	1.528	1.1
7	2.309	1.705	1.445	2.915	2.683	2.203	54	1.484	1.694	2.933	2.965	2.23	1.067
8	1.109	1.096	1.503	1.893	2.91	1.011	55	1.954	1.083	2.862	2.939	1.038	2.878
9	2.581	1.069	1.407	2.761	2.031	2.805	56	1.527	1.242	2.898	1.421	2.408	1.707
10	1.668	1.757	1.574	2.553	2.331	2.603	57	2.381	1.492	2.392	2.253	1.725	2.298
11	1.626	1.027	2.062	2.543	2.185	2.471	58	1.412	1.049	2.362	1.095	1.226	2.716
12	1.363	2.054	1.407	2.969	1.907	2.101	59	2.242	2.174	2.343	2.327	1.556	2.921
13	2.354	1.169	2.77	2.79	2.86	2.754	60	2.301	2.947	2.319	2.915	2.65	1.167
14	1.455	2.164	1.552	2.953	2.34	1.635	61	1.615	2.318	1.856	1.358	1.825	2.031
15	2.499	2.846	1.217	2.784	2.31	3	62	1.465	1.733	1.341	1.327	1.119	1.583
16	1.163	2.517	1.353	2.661	1.724	2.465	63	2.88	1.068	1.288	1.136	1.223	2.074
17	1.321	1.85	2.579	2.177	2.764	2.424	64	2.93	2.501	2.164	2.105	2.625	1.769
18	2.192	1.462	1.447	1.047	2.458	2.48	65	2.283	2.939	1.882	2.732	1.257	2.994
19	1.787	1.767	1.045	1.44	2.134	1.938	66	2.48	1.709	1.753	2.115	1.713	1.262
20	1.038	1.531	1.905	1.026	2.66	1.885	67	2.848	1.375	2.943	2.55	2.689	1.076
21	2.296	1.292	1.875	2.673	2.658	1.108	68	2.291	1.737	1.526	1.188	1.378	2.215
22	2.321	1.997	1.648	1.416	2.765	2.606	69	1.633	1.614	2.93	2.544	1.64	2.054
23	1.149	1.965	1.995	2.545	2.5	1.396	70	2.281	2.899	1.503	2.123	2.186	1.006
24	1.388	2.776	1.139	2.336	2.515	1.18	71	1.799	2.802	1.392	1.163	1.72	1.93
25	1.985	2.072	1.754	2.5	2.921	1.034	72	2.621	1.027	2.746	1.542	2.282	1.567
26	2.776	1.44	1.543	1.804	2.287	2.518	73	1.084	2.624	2.256	1.19	1.819	2.237
27	2.925	1.498	1.107	1.556	2.407	1.982	74	2.978	1.269	2.428	1.349	1.725	2.747
28	2.874	2.704	2.074	2.64	2.985	2.804	75	2.291	2.088	1.718	1.525	1.883	1.099
29	2.817	2.141	1.408	2.425	2.45	2.083	76	1.269	2.765	2.325	1.596	1.928	1.799
30	1.989	2.875	1.918	1.898	2.757	2.941	77	1.718	1.935	2.987	1.314	2.037	2.471
31	1.718	1.69	1.809	2.842	2.077	1.35	78	1.629	2.716	2.517	2.634	1.104	2.737
32	1.138	2.103	2.945	2.398	2.475	2.96	79	2.451	2.782	2.616	1.883	2.402	1.915
33	2.037	2.076	1.99	1.936	2.375	2.637	80	2.292	1.616	2.521	2.446	1.182	1.848
34	2.274	1.688	1.447	1.729	2.127	2.109	81	1.224	2.875	2.904	1.137	1.989	2.739
35	2.58	1.507	1.01	2.67	1.789	1.086	82	2.357	1.374	2.61	2.75	1.099	1.501
36	2.586	2.478	2.217	2.404	2.719	2.889	83	2.386	2.173	1.502	1.14	1.121	2.063
37	1.633	1.338	2.475	2.433	2.152	2.109	84	2.754	2.519	2.483	1.889	2.52	1.055
38	1.123	2.964	2.605	1.937	2.841	2.832	85	2.524	1.71	2.428	1.518	1.982	1.141

39	1.133	2.364	2.303	1.328	2.643	2.561	86	1.882	2.371	2.43	1.926	1.061	2.558
40	1.632	1.531	2.555	1.319	2.92	1.988	87	2.011	1.434	2.784	1.274	1.017	2.76
41	2.208	2.555	1.623	2.826	2.576	1.053	88	2.413	1.888	2.558	1.201	1.479	2.338
42	2.316	2.249	1.692	2.231	2.229	1.963	89	2.772	1.542	2.714	2.086	1.157	2.04
43	1.616	2.362	1.274	1.946	1.757	1.733	90	2.286	2.884	2.07	1.48	1.605	1.513
44	1.626	1.16	2.207	2.525	1.291	2.176	91	2.558	2.333	2.824	1.094	1.791	2.499
45	2.833	1.197	2.598	2.295	2.687	1.706	92	2.699	1.638	2.683	1.118	1.133	2.746
46	2.104	2.872	1.278	1.494	2.588	1.608	93	2.975	2.718	2.373	1.044	2.075	1.988
47	2.109	2.691	1.471	1.83	2.115	2.243	94	2.999	2.917	2.907	1.395	2.85	1.057

and variance-covariance matrix as $\sum = \begin{pmatrix} 3.199 & 0.686 & 0.610 & 0.387 & 0.480 & 0.978 \\ 0.686 & 3.771 & 0.536 & 0.869 & -0.441 & -0.845 \\ 0.610 & 0.536 & 4.463 & 0.161 & 0.853 & -0.403 \\ 0.387 & 0.869 & 0.161 & 2.690 & 0.911 & 0.804 \\ 0.480 & -0.441 & 0.853 & 0.911 & 4.169 & 0.897 \\ 0.978 & -0.845 & -0.403 & 0.804 & 0.897 & 2.706 \end{pmatrix}$

Table 3: *Performance of point estimators:* $\sqrt{n}\delta^*$ *and* $100^*\{U(n,\delta^*), M(n,\delta^*), R(n,\delta^*)\}$

Non-negative values of δ^*					Negative values of δ^*				
Scenario	$\sqrt{\mathbf{n}}\boldsymbol{\delta}^*$	$U(n,\delta^*)$	$M(n,\delta^*)$	$R(n,\delta^*)$	Scenario	$\sqrt{n}\delta^*$	$U(n,\delta^*)$	$M(n,\delta^*)$	$R(n,\delta^*)$
1	2.43	0.876	70.393	1.245	48	-0.038	0.277	50.217	0.552
2	2.415	0.884	70.265	1.258	49	-0.052	0.277	50.299	0.552
3	2.389	0.898	70.045	1.282	50	-0.054	0.277	50.309	0.551
4	2.345	0.923	69.673	1.324	51	-0.155	0.538	50.892	1.056
5	2.329	0.932	69.535	1.341	52	-0.198	0.684	51.15	1.338
6	2.251	0.982	68.867	1.426	53	-0.224	0.768	51.303	1.498
7	2.131	1.072	67.812	1.58	54	-0.273	0.925	51.601	1.793
8	2.102	1.095	67.555	1.621	55	-0.284	0.957	51.665	1.853
9	2	1.187	66.628	1.781	56	-0.297	0.998	51.747	1.929
10	1.95	1.236	66.163	1.868	57	-0.326	1.086	51.93	2.092
11	1.705	1.503	63.838	2.354	58	-0.43	1.373	52.601	2.611
12	1.55	1.684	62.329	2.701	59	-0.446	1.412	52.704	2.68
13	1.485	1.757	61.695	2.848	60	-0.492	1.522	53.016	2.871
14	1.447	1.799	61.323	2.934	61	-0.496	1.532	53.045	2.888
15	1.406	1.843	60.922	3.025	62	-0.524	1.594	53.24	2.994
16	1.207	2.017	58.998	3.419	63	-0.525	1.596	53.245	2.997
17	1.108	2.07	58.061	3.565	64	-0.536	1.62	53.324	3.037
18	1.088	2.077	57.877	3.589	65	-0.565	1.68	53.536	3.138
19	1.088	2.077	57.876	3.589	66	-0.596	1.738	53.76	3.233
20	1.072	2.082	57.728	3.606	67	-0.609	1.761	53.853	3.27
21	1.069	2.083	57.699	3.609	68	-0.624	1.786	53.963	3.311
22	1.062	2.084	57.639	3.616	69	-0.635	1.805	54.048	3.34
23	1.054	2.086	57.563	3.624	70	-0.682	1.876	54.403	3.449
24	1.013	2.091	57.193	3.657	71	-0.761	1.973	55.027	3.586
25	0.966	2.09	56.764	3.681	72	-0.801	2.011	55.351	3.633
26	0.947	2.087	56.597	3.687	73	-0.833	2.036	55.622	3.66
27	0.942	2.086	56.553	3.688	74	-0.864	2.055	55.882	3.678
28	0.887	2.067	56.076	3.686	75	-1.009	2.092	57.153	3.66
29	0.863	2.055	55.875	3.678	76	-1.023	2.091	57.275	3.65
30	0.822	2.028	55.528	3.652	77	-1.05	2.087	57.524	3.628

31	0.782	1.994	55.197	3.612	78	-1.124	2.063	58.211	3.545
32	0.764	1.976	55.049	3.59	79	-1.276	1.966	59.653	3.295
33	0.686	1.883	54.438	3.459	80	-1.317	1.93	60.055	3.213
34	0.679	1.873	54.382	3.444	81	-1.353	1.897	60.399	3.14
35	0.671	1.861	54.318	3.425	82	-1.402	1.847	60.884	3.033
36	0.66	1.844	54.235	3.401	83	-1.414	1.834	61.002	3.007
37	0.656	1.838	54.206	3.392	84	-1.526	1.711	62.096	2.755
38	0.566	1.68	53.538	3.139	85	-1.536	1.7	62.192	2.733
39	0.549	1.647	53.419	3.083	86	-1.547	1.686	62.304	2.707
40	0.531	1.609	53.288	3.019	87	-1.67	1.543	63.503	2.43
41	0.43	1.373	52.6	2.61	88	-1.776	1.422	64.519	2.204
42	0.306	1.026	51.804	1.98	89	-1.916	1.27	65.846	1.929
43	0.238	0.814	51.389	1.585	90	-2.092	1.104	67.462	1.637
44	0.183	0.634	51.06	1.241	91	-2.097	1.1	67.507	1.629
45	0.164	0.568	50.945	1.115	92	-2.106	1.092	67.593	1.615
46	0.159	0.554	50.92	1.088	93	-2.157	1.05	68.049	1.544
47	0.14	0.49	50.809	0.964	94	-2.384	0.9	70.008	1.286

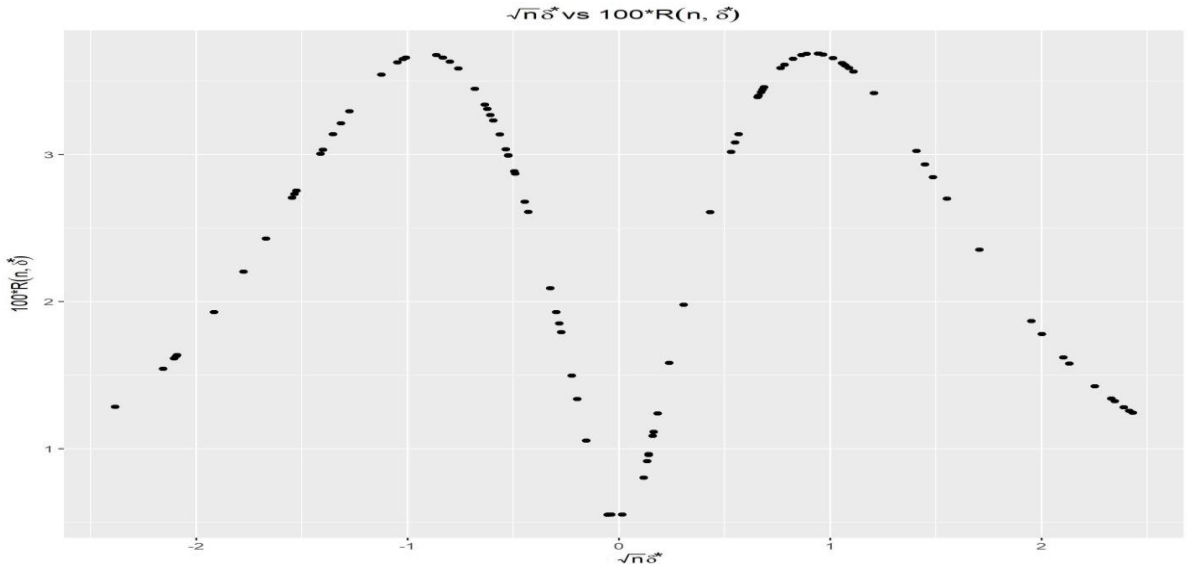


Figure 1: $\sqrt{n}\delta^*$ *vs* $100 * R(n, \delta^*)$

III. Calculation of Var(R̂) and MSE(R*)

From Figure 2 and 3 it is observe that the, values of Var(R̂) and MSE(R*) are almost close to zero of δ*. Values of Var(R̂) are less as compared to other values of MSE(R*). Thus, the performance of MVUE of R is better than MLE. In addition, for the given data in Table 7, we calculate that the above measure by principal component analysis as $\sqrt{n}\delta^*$ = 5.486, U(n, δ*) = 0.13, M(n, δ*)= 71.027, R(n, δ*)= 0.182, Var($\widehat{R}$) = 0.00138 and MSE(R*) = 0.00139.

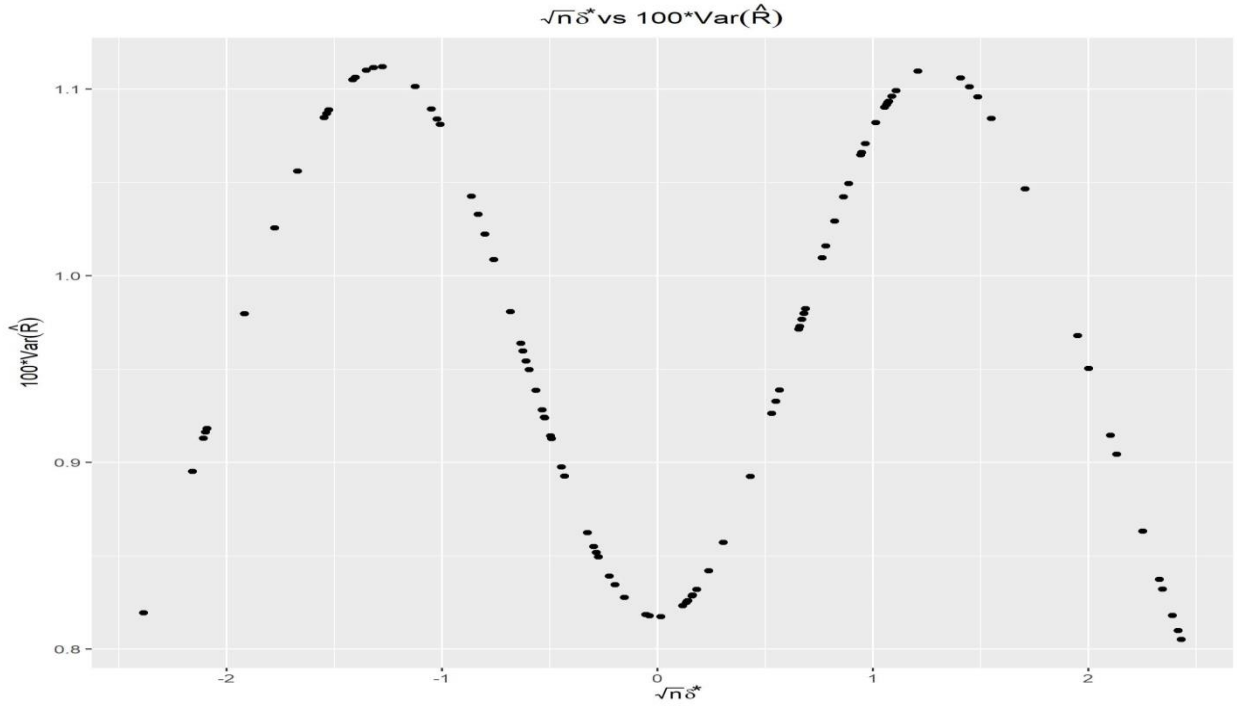


Figure 2: $\sqrt{n}\delta^*$ *vs* $100 * Var(\hat{R})$

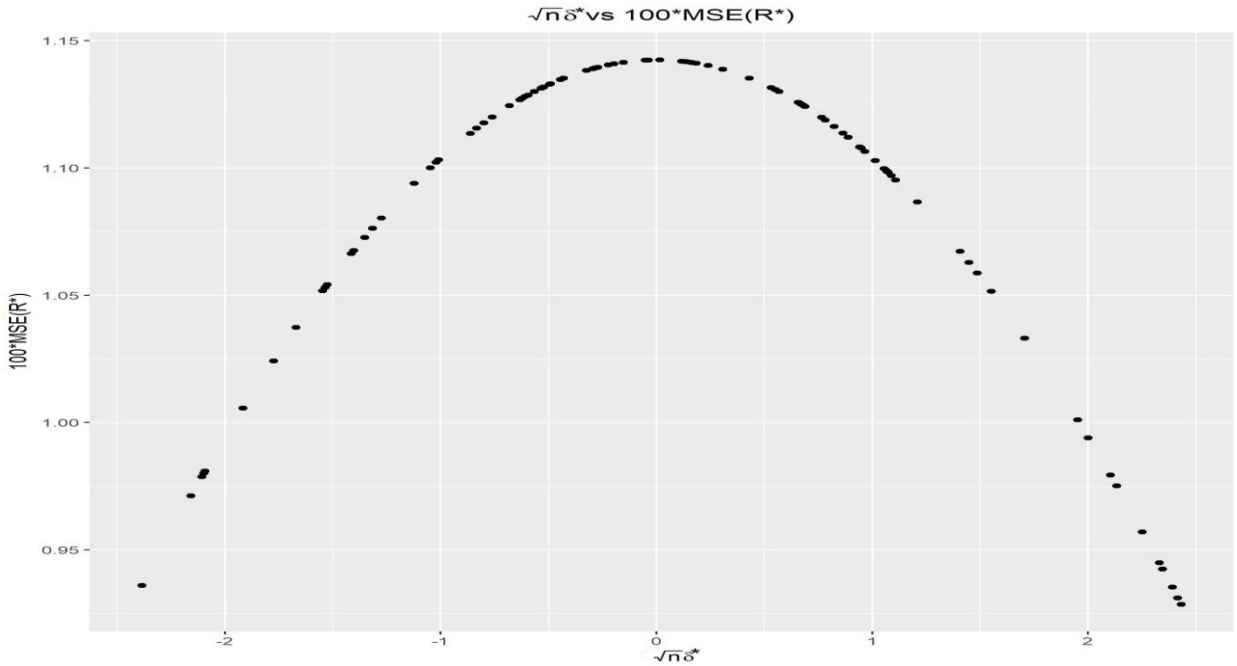


Figure 3: $\sqrt{n}\delta^*$ *vs* $100 * MSE(R^*)$

IV. Confidence Intervals for R

From the section of VII to XI of methods, we present simulation study to investigate the statistical properties of the interval estimators using the given matrix in section I of simulation study. The simulation study define as follows

(1) Draw the random samples of size n from $\binom{\mathbf{X}}{\mathbf{Y}} \sim \Lambda_{p1+p2}(\mu, \sum)$. Then Take the log-transformation as $\binom{\ln(\mathbf{X})}{\ln(\mathbf{Y})} = \binom{\mathbf{X}^*}{\mathbf{Y}^*} \sim N_{p1+p2}(\mu, \sum)$. For each of sample drown of size n, considered different sample sizes (n=50, 100, 150,….etc). We compute the above measures by taking 500 replications each time.

(2) Estimate MLE estimate of R using PC1 for different sample size and a Confidence Intervals (two-sided and lower bound) for R.

(3) Compute exact, approximate and bootstrap confidence intervals using step 2, where number of boot time B=1000.

The results of the simulation study are recorded in Table 4-6. Figure 4-6, represent the exact, approximate and bootstrap confidence belt at 90%, 95% and 99% levels. It has been observed that for a small sample size, the estimate of R is getting high and also confidence intervals. The results get better as the sample sizes increase and the reliability R gets closer to true value. The same phenomenon is observed for the exact, approximate and bootstrap confidence intervals. The overall band of exact and approximate confidence intervals is almost same, whereas bootstrap confidence intervals give the large confidence band for small sample size. But, exact, approximate confidence intervals and Bootstrap confidence intervals all are almost same for large sample size at 90%, 95% and 99% levels. All most the same variation found in confidence belt of exact, approximate CIs, but quite irregular variation in bootstrap CIs shows in Figure 4-6.

Table 4: *Exact Confidence Intervals*

Sample size	R*	90%			95%			99%		
		L	U	LB	L	U	LB	L	U	LB
50	0.9092	0.8436	0.9507	0.8598	0.8288	0.9568	0.8436	0.7973	0.9669	0.8104
100	0.9043	0.8599	0.9368	0.8705	0.8503	0.9420	0.8599	0.8302	0.9513	0.8385
150	0.8984	0.8621	0.9267	0.8707	0.8544	0.9314	0.8621	0.8386	0.9401	0.8452
200	0.8953	0.8640	0.9207	0.8713	0.8575	0.9251	0.8640	0.8441	0.9330	0.8496
250	0.8925	0.8644	0.9158	0.8709	0.8586	0.9198	0.8644	0.8468	0.9273	0.8516
300	0.8920	0.8665	0.9135	0.8724	0.8613	0.9173	0.8665	0.8506	0.9243	0.8550
350	0.8913	0.8678	0.9114	0.8732	0.8630	0.9150	0.8678	0.8533	0.9216	0.8573
400	0.8897	0.8677	0.9088	0.8728	0.8632	0.9122	0.8677	0.8542	0.9186	0.8579
450	0.8895	0.8688	0.9076	0.8736	0.8646	0.9108	0.8688	0.8561	0.9169	0.8596
500	0.8893	0.8697	0.9065	0.8742	0.8658	0.9096	0.8697	0.8578	0.9155	0.8611
550	0.8848	0.8659	0.9017	0.8702	0.8620	0.9047	0.8659	0.8544	0.9104	0.8575
600	0.8810	0.8626	0.8974	0.8668	0.8589	0.9004	0.8626	0.8515	0.9061	0.8545

Table 5: *Approximate Confidence Intervals*

Sample size	90%			95%			99%		
	L	U	LB	L	U	LB	L	U	LB
50	0.8447	0.9512	0.8611	0.8296	0.9572	0.8447	0.7973	0.9670	0.8108
100	0.8604	0.9371	0.8711	0.8507	0.9423	0.8604	0.8303	0.9514	0.8387
150	0.8625	0.9269	0.8711	0.8547	0.9316	0.8625	0.8387	0.9401	0.8453
200	0.8643	0.9209	0.8716	0.8577	0.9252	0.8643	0.8441	0.9331	0.8497
250	0.8646	0.9159	0.8711	0.8588	0.9199	0.8646	0.8468	0.9274	0.8517
300	0.8667	0.9136	0.8726	0.8614	0.9174	0.8667	0.8507	0.9243	0.8551
350	0.8679	0.9115	0.8734	0.8631	0.9151	0.8679	0.8533	0.9217	0.8573
400	0.8679	0.9089	0.8729	0.8633	0.9123	0.8679	0.8542	0.9186	0.8580
450	0.8689	0.9077	0.8737	0.8647	0.9109	0.8689	0.8562	0.9169	0.8597
500	0.8698	0.9066	0.8743	0.8659	0.9097	0.8698	0.8578	0.9155	0.8611

550	0.8660	0.9017	0.8703	0.8621	0.9048	0.8660	0.8544	0.9105	0.8575
600	0.8627	0.8975	0.8669	0.8590	0.9005	0.8627	0.8515	0.9061	0.8546

Table 6: *Bootstrap Confidence Intervals*

Sample	90%			95%			99%		
size	L	U	LB	L	U	LB	L	U	LB
50	0.8662	0.9479	0.8752	0.8583	0.9558	0.8662	0.8430	0.9711	0.8492
100	0.8605	0.9474	0.8701	0.8522	0.9557	0.8605	0.8359	0.9720	0.8425
150	0.8686	0.9274	0.8751	0.8630	0.9330	0.8686	0.8520	0.9440	0.8564
200	0.8657	0.9256	0.8723	0.8599	0.9313	0.8657	0.8487	0.9425	0.8533
250	0.8677	0.9191	0.8734	0.8628	0.9240	0.8677	0.8531	0.9336	0.8570
300	0.8675	0.9165	0.8729	0.8628	0.9212	0.8675	0.8536	0.9304	0.8573
350	0.8696	0.9146	0.8746	0.8653	0.9189	0.8696	0.8569	0.9273	0.8603
400	0.8713	0.9087	0.8754	0.8677	0.9122	0.8713	0.8607	0.9192	0.8636
450	0.8701	0.9093	0.8744	0.8663	0.9130	0.8701	0.8590	0.9204	0.8620
500	0.8711	0.9060	0.8750	0.8678	0.9093	0.8711	0.8612	0.9159	0.8639
550	0.8660	0.9045	0.8703	0.8623	0.9081	0.8660	0.8551	0.9153	0.8580
600	0.8653	0.8968	0.8688	0.8623	0.8998	0.8653	0.8564	0.9057	0.8588

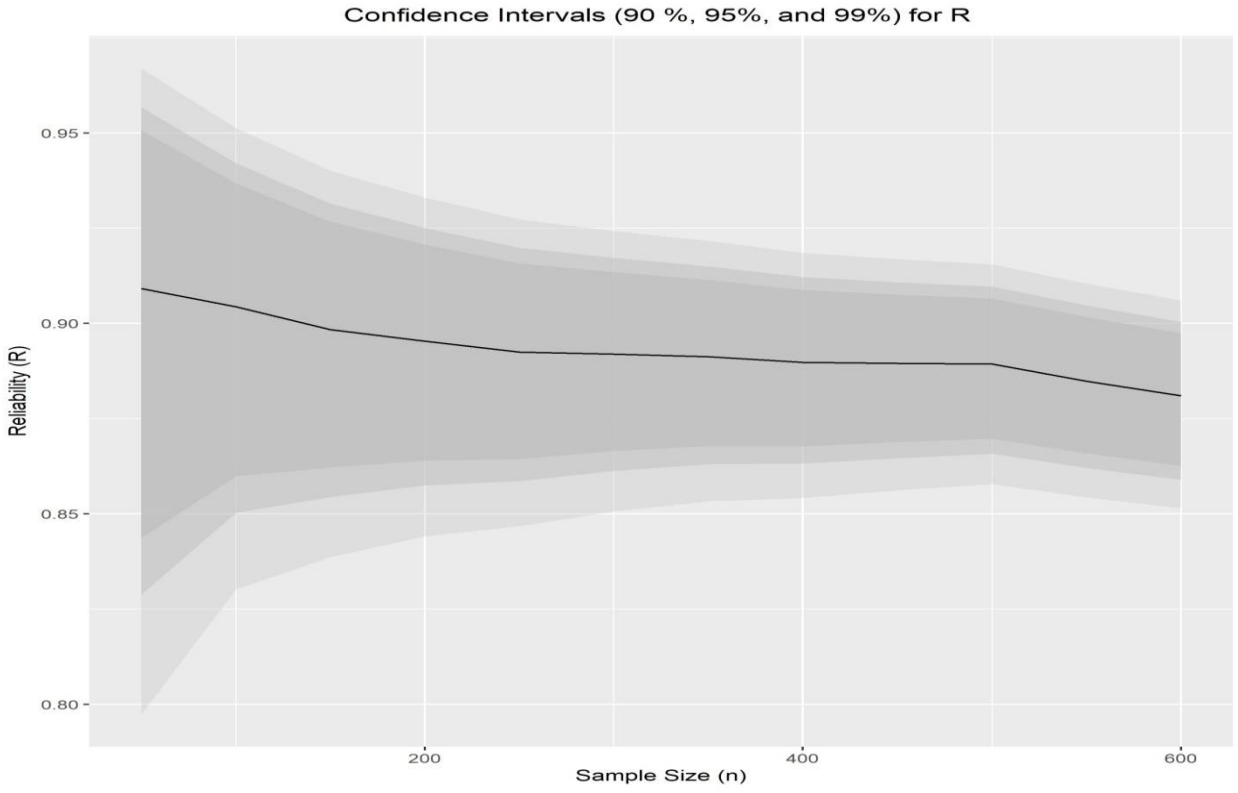


Figure 4: *Exact Confidence Intervals*

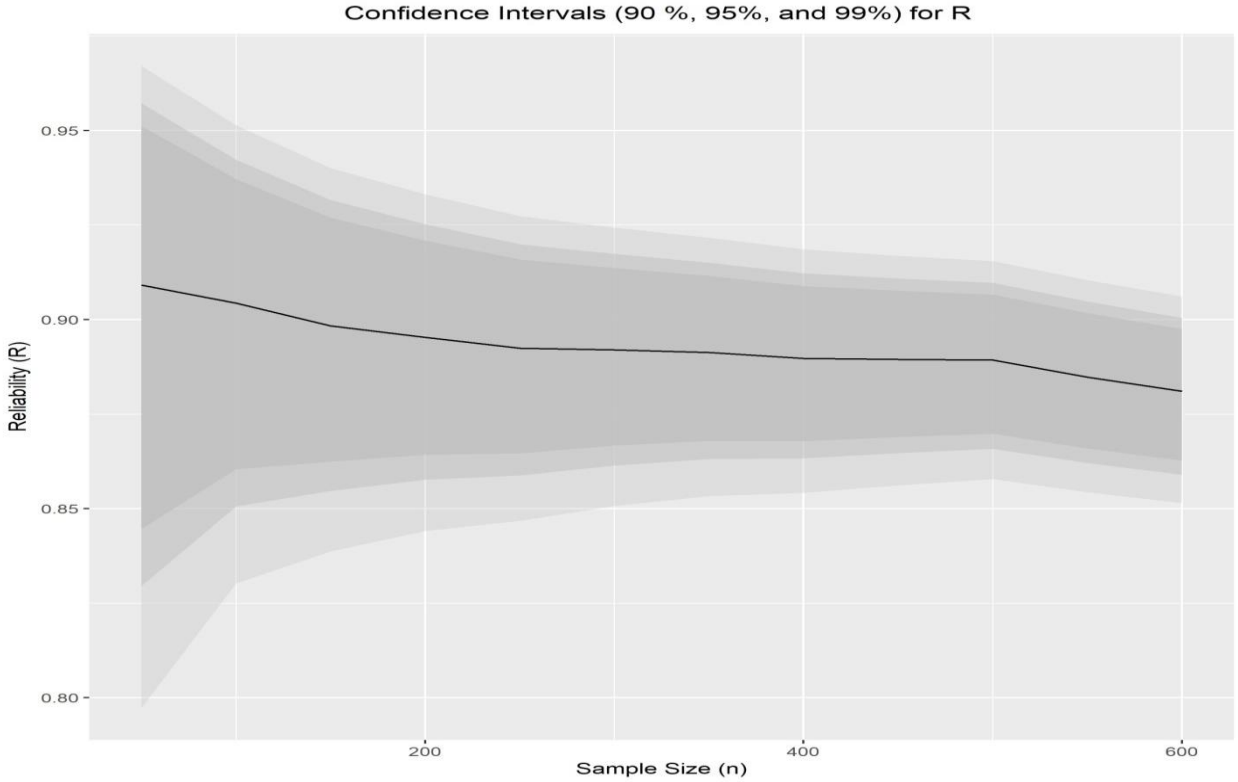


Figure 5: *Approximate Confidence Intervals*

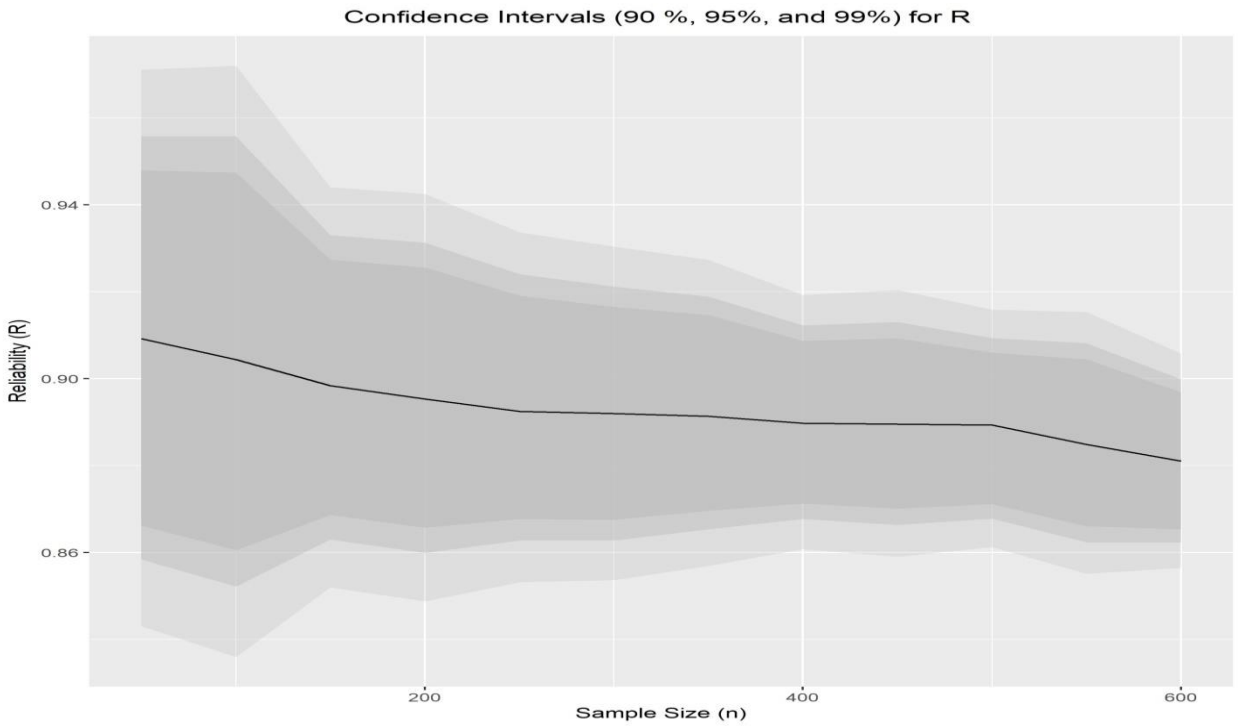


Figure 6: *Bootstrap Confidence Intervals*

IV. Application on Real Data Set

I. Estimation of $\hat{\hat{R}}$ and R^*

In this section, applies the methods developed in the previous sections, using the Air Quality Index Data taken from "https://www.kaggle.com/rohanrao/air-quality-data-in-india?select=station_day.csv". The dataset contains air quality data and AQI (Air Quality Index) at hourly and daily level of various stations across multiple cities in India. Consider the seven pollutants namely particulate matter PM_{10}, $PM_{2.5}$, nitrogen dioxide (NO_2), ammonia (NH_3), carbon monoxide (CO), Sulphur dioxide (SO_2) and Ozone (O_3) act as major parameters in deriving the AQI of an area. Data were recorded from January-2015 to June-2020 (five years and six months) representing the longest freely available recordings of on field deployed air quality. We selected only two cites as Kolkata and Patna because distance between the two cites is much less near about 500 KM and Kolkata is a metropolitan city. Being a Kolkata metropolitan city, its air quality is higher than Patna city. We estimate the stress strength reliability of air quality between the two cities and compare them before and during lockdown period for COVID-19. We have taken the data from Dec-19 to March-20 for before lockdown and data from 25-03-2020 to 30-06-2020 for lockdown period. Table 7 represents the sample data set of air quality from 25-03-2020 to 30-06-2020.

Table 7: *Data set of Air Quality Index (AQI) of Kolkata and Patna*

City	Date	$PM_{2.5}$	PM_{10}	NO_2	NH_3	CO	SO_2	O_3
	25-03-2020	53.01	77.59	15.94	19.44	0.57	12.52	44.48
	26-03-2020	37.02	60.49	14.36	19.23	0.52	6.8	47.17
	27-03-2020	48.1	83.63	14.86	18.61	0.55	11.62	60.57
	28-03-2020	46.57	77.11	15.71	18.62	0.57	11.46	58.18
	29-03-2020	40.85	68.04	14.53	18.28	0.54	9.52	64.88
Kolkata	-	-	-	-	-	-	-	-
	26-06-2020	9.59	28.44	7.91	10.35	0.34	8.2	22.66
	27-06-2020	7.89	24.73	9.25	8.39	0.35	5.73	23.14
	28-06-2020	10.58	25.56	12.63	6.92	0.38	5.92	27.76
	29-06-2020	14.53	32.4	15.98	7.59	0.45	7.01	30.64
	30-06-2020	14	35.85	12.29	9.64	0.37	5.66	24.59
	25-03-2020	73.42	121.38	47.99	14.13	1.74	13.57	21.77
	26-03-2020	58.01	118.17	46.63	14.24	1.71	13.26	20.18
	27-03-2020	58.25	129.36	45.25	13.88	1.68	12.52	20.63
	28-03-2020	31.87	87.38	43.29	12.38	1.49	11.73	15.88
	29-03-2020	29.1	81.98	50.82	13.37	0.62	11.6	11.82
Patna	-	-	-	-	-	-	-	-
	26-06-2020	23.16	39.8	25.68	3.13	0.79	2.92	19.42
	27-06-2020	17.71	63.73	23.01	1.91	0.87	3.63	23.39
	28-06-2020	19.27	57.42	18.13	2.05	0.72	3.92	17.37
	29-06-2020	17.24	42.83	20.51	2.26	0.88	3.6	17.5
	30-06-2020	29.76	60.68	27.5	1.59	0.83	3.91	21.7

Using the log-transformation of given data sets, the proportions of dispersions of air quality in Kolkata as $\boldsymbol{x}^* = \{\ln(PM_{2.5}), \ln(PM_{10}), \ln(NO_2), \ln(NH_3), \ln(CO), \ln(SO_2), \ln(O_3)\}$ and Patna as $\boldsymbol{y}^* = \{\ln(PM_{2.5}), \ln(PM_{10}), \ln(NO_2), \ln(NH_3), \ln(CO), \ln(SO_2), \ln(O_3)\}$ are 0.8361 and 0.6170 respectively based on their largest eigen values. Then $\hat{\hat{R}} = 0.9724$ based on MVUE and $R^* = 0.9726$ based on

MLE before lockdown. Similarly, during the lockdown, proportion of variance of air quality in Kolkata and Patna for first principal component are 0.7631 and 0.8970 respectively, then the similar things of R are $\hat{\hat{R}} = 0.7089$ and $R^* = 0.7102$. Thus, it is shown that the air quality in the city of Kolkata worse than Patna based on the air quality parameters at before lockdown and during lockdown period. But the air quality has been increased among of these two cites during lockdown.

II. Confidence Intervals

We apply the above methods to find out the exact, approximate and bootstrap confidence intervals, using the sample data set reported in Table 7. The results on air quality data set shows in Table 8 that, the exact and approximate CIs are almost same band, but confidence band of bootstrap CIs is bigger than these.

Table 8 Confidence Intervals for tests of the air quality data

Confidence	90%			95%			99%		
Intervals	L	U	LB	L	U	LB	L	U	LB
Exact	0.6459	0.7677	0.6604	0.6331	0.7781	0.6459	0.6078	0.7975	0.6181
Approx.	0.6464	0.7681	0.6609	0.6336	0.7784	0.6464	0.6082	0.7978	0.6185
Bootstrap	0.4719	0.9155	0.5209	0.4294	0.9580	0.4719	0.3464	0.9899	0.3800

V. Conclusions

In this multivariate log-normal setup, estimator of stress-strength model of reliability R is obtained by log-transformation and using the estimator based on MLE of μ_1, μ_2, Σ_{11}, Σ_{12}, Σ_{22}. Simulation studies illustrate that, the variance and MSE of two estimators reduces as the sample size increases and they almost achieved the true value of R. An application to the given real data set is described and shows that the same result as above. So that, the performance of MVUE based estimator of R is better than MLE in this case. In air quality data it is observed that before the lockdown air pollution in Kolkata was higher than Patna. But during the lockdown, air pollution in Kolkata was much reduced. If the lockdown would continue, then the air quality becomes almost same in between Kolkata and Patna.

In addition, from L_1 distance between distribution functions we can judge the improvement of such estimators. Difference in terms of MSE is much less as the values are given after multiplying by 100, though detailed calculations are required for other parametric values. Therefore, we concluded that our estimator performs better even close to zero. The exact confidence intervals are preferable for marginally short band of confidence intervals than the approximate confidence intervals. The performance of bootstrap CIs is slightly worse than the exact and approximate CIs in terms of confidence band for small sample size. But the performance of bootstrap confidence intervals and other methods of CIs are almost same for large sample. Thus, the overall performance of the confidence interval is quite good for exact confidence intervals.

References

[1] Lipson, C., Sheth, N.J. and Disney, R.L. (1967). Reliability Prediction-Mechanical Stress/Strength Interference. *New York: Rome Air Development Center, Griffiss Air Force Base, Report No. RADC-TR-66-710*.

[2] Feng, C., Wang, H., Lu, N., Chen, T., He, Hua., Lu, Ying. and M.Tu, X. (2014). Log-transformation and its implications for data analysis. *Shanghai Arch Psychiatry*, 26(2):105–109.

[3] Gibrat, R. (1930). Une loi des répartitions économiques: l'effet proportionnel. *Bulletin de la Statistique Générale de la France*, 1929-30:469-514.

[4] Kolmogoroff, A.N. (1941). Über das logarithmisch normale Verteilungsgesetz der Dimensionen der Teilchenbei Zerstückelung. *C. R. (Doklady) Acad. Sci. URSS (N. S.)*, 31:99–101.

[5] Schijve, J. (2005). Statistical distribution functions and fatigue of structures. *Int. J. Fatigue*, 27:1031–1039.

[6] Lu, H., He, Y. and Zhang, Y. (2014). Reliability-Based Robust Design of Mechanical Components with Correlated Failure Modes Based on Moment method. *Advances in Mechanical Engineering*, 1-17.

[7] Paik, J.K. and Frieze, P.A. (2001). Ship Structural Safety and Reliability. *Prog. Struct. Engng Mater*, 3(2):198– 210.

[8] Cohn, S.E. (1997). An introduction to estimation theory. *Journal of the Meteorological Society of Japan*, 75(1B):257– 288.

[9] Wang, Z. and Sassen, K. (2002). Cirrus cloud microphysics property retrieval using lidar and radar measurements. Part II: Midlatitude cirrus microphysical and radiative properties. *Journal of Atmospheric Sciences*, 59(14):2291–2302.

[10] Sengupta, M., Clothiaux, E.E. and Ackerman, T.P. (2004). Climatology of warm boundary layer clouds at the ARM SGP site and their comparison to models. *Journal of Climate*,17(24):4760–4782.

[11] Mielke, P.W.Jr., Williams, J.S. and Wu, S.C. (1977). Covariance analysis techniques based upon bivariate log-Normal distribution with weather modification application. *Journal of Applied Meteorology*, 16(2):183–187.

[12] Gupta, R.C. and Li, X. (2006). Statistical inference for the common mean of two log-normal distributions and some applications in reliability. Comput. *Statist. Data Anal*, 50(11):3141–3164.

[13] Zhou, X.H., Gao, S.J. and Hui, S.L. (1997). Methods for comparing means of two independent log-normal samples. *Biometrics*, 53(3):1129–1135.

[14] Zhou, X.H., Li, C., Gao, S. and Tierney, W.M. (2001). Methods for testing equality of means of health care costs in a paired design study. *Stat. Med*, 20(11):1703–1720.

[15] Schneider, T. and Holst, E. (1983). Man-made mineral fibre size distributions utilizing unbiased and fibre length biased counting methods and bivariate log-normal distribution. *J. Aerosol Sci*., 14(2):139–146.

[16] Cheng, Y.S. (1986). Bivariate lognormal distribution for characterizing asbestos fibre aerosols. *Aerosol Sci. Technol*., 5(3):259–368.

[17] Rumberg, B., Richard, A. and Claiborn, C. (2001). Statistical Distribution of particulate matter and the error associated with sampling frequency. *Atmospheric Environment*, 35:2907-2920.

[18] Norazian, M.N., Abdulla, M.M.A., Tan, C.Y., Ramlic, N.A., Yahayac, A.S. and Fitric, N.F.M.Y. (2011). Modelling of PM10 Concentration for Industrialized Area in Malaysia: A case Study in Shah Alam. *Physics Procedia*, 22:318-324.

[19] Sedek, J.N.M., Ramli, N.A. and Yahaya, A.S. (2006). Air quality predictions using log normal distribution functions of particulate matterin Kuala Lumpur. *Malaysian journal of Environmental Management*, 7:33-41.

[20] Hamid, H., Yahaya, A.S., Ramli, N.A. and Ul-saufie, A.Z. (2013). Finding the best statistical distribution model in PM10 concentration modeling by using log normal distribution. *Journal of Applied Sciences*, 12(2):294-300.

[21] Georgopoulus, P.G. and Seinfeld, J.H. (1982). Statistical Distribution of air quality concentrations. *Environmental Science and Technology*, 16(7):401A-416A.

[22] Lai, H.K., Hedley, A.J., Thach, T.Q. and Wong, C.M. (2013). A method to derive the relationship between the annual and short-term air quality limits—Analysis using the WHO Air Quality Guidelines for health protection. *Environment International*, 59: 86–91.

[23] Nguyen, T.T.N. and Sevando, M. (2019). Assessing Coastal Water Quality through an Overall Index. *Pol. J. Environ. Stud*, 28(4):2321-2330.

[24] Wikipedia.org. https://en.wikipedia.org/wiki/Air_quality_index.

[25] Vaduva, I. (1973). Computer generation of random variables and vectors related to PERT problems. *In: Proceedings of the Fourth Conference on Probability Theory, Bucharest*, 381-395.

[26] Rousseeuw P.J. and Leroy A.M. Robust Regression and Outliers Detection, John Wiley & Sons, New York, 1987.

[27] Gupta, R.D. and Gupta, R.C. (1990). Estimation on Pr($\mathbf{a}'\mathbf{x} > \mathbf{b}'\mathbf{y}$) in the Multivariate Normal Case. *Statistics: A Journal of Theoretical and Applied Statistics*, 21(1):91-97.

[28] Reiser, B. and Farragi, D. (1994). Confidence bounds for P(a'x>b'y). *Statistics*, 25(2):107–111.

[29] Enis, P. and Geisser, S. (1971). Estimation of the Probability that Y < X. *J. Amer. Statist. Assoc*., 66(333):162-168.

[30] Mukherjee, S.P. and Sharan, L.K. (1985). Estimation of failure probability from a bivariate normal stress-strength distribution. *Microelectronics Reliability*, 25(4):699-702.

[31] Hor, P. and Seal, B. (2015). Minimum variance unbiased estimation of stress–strength reliability under bivariate normal and its comparisons. *Communications in Statistics - Simulation and Computation*, 46(3):2447–2456.

[32] Johnson R.A. and Wichern D.W. Applied Multivariate Statistical Analysis, 6th Edition, Pearson, New Jersey, 2008.

[33] Barton, D.E. (1961). Unbiased estimation of a set of probabilities. *Biometrika*, 48(1-2):227–229.

[34] Mukhopadhyay P. Multivariate statistical analysis, World Scientific, Singapore, 2009.

[35] Johnson, N.L. and Welch, B.L. (1939). Applications of the non-central t distribution. *Biometrika*, 31:362-389.

[36] Efron B. The Jackknife, the Bootstrap and Other Resampling Plans, CBMS-NSF Regional Conference Series in Applied Mathematics, Monograph 38, SIAM, Philadelphia, 1982.

[37] Efron, B. (1987). Better bootstrap confidence intervals. *J. Am. Stat. Assoc*, 82(397):171–185.

RELIABILITY-CENTERED INNOVATION PLANNING FOR COMPLEX INDUSTRIAL SYSTEMS

[1]Saadat Zeynalova, [2]Rana Mammadova, [3]Leyla Rahimova

•

Azerbaijan State Oil and Industry University, Baku, Azerbaijan
[1]saadat.zeynalova@asoiu.edu.az, [2]rana.mammadova@asoiu.edu.az,
[3]leyla.rahimova@asoiu.edu.az

Abstract

Ensuring the operational reliability of industrial systems is a critical requirement in the context of technical modernization and increasing system complexity. This paper proposes a reliability-centered methodology for evaluating and enhancing the performance of manufacturing assets during innovation-driven transformation. The approach integrates quantitative reliability metrics, including Mean Time Between Failures (MTBF), Mean Time To Repair (MTTR), and operational availability (Ao), into all phases of technical planning and implementation. Statistical modeling based on exponential and Weibull distributions is applied to failure datasets from mechanical engineering systems to estimate degradation rates and failure probabilities. A case study involving digital twins, CMMS integration, and scenario-based failure modeling demonstrates the effectiveness of predictive maintenance and real-time monitoring tools in reducing system downtime. The proposed framework contributes to the unification of reliability analysis and innovation strategy, offering practical tools for minimizing operational risks and optimizing life cycle costs (LCC) in industrial environments.

Keywords: reliability engineering, MTBF, operational availability, failure modeling, life cycle cost

I. Introduction

The increasing complexity and digitalization of industrial systems have made reliability a foundational criterion for sustainable production and operational excellence. In high-risk sectors such as energy, petrochemicals, mechanical engineering, and transportation, even short-term equipment failures can trigger cascading effects—causing significant economic losses, safety hazards, and reputational damage. Consequently, the ability to accurately model, predict, and improve system reliability has become a priority in both research and practice.

In traditional innovation planning and technical modernization processes, the focus is often placed on performance metrics such as output capacity, energy efficiency, or initial investment costs. While these indicators are essential, they do not reflect the long-term operational behavior of complex technical systems under varying loads, maintenance regimes, and environmental conditions. As a result, many enterprises face a growing gap between designed performance and real-world reliability, especially when upgrading legacy infrastructure [1].

The stochastic nature of failure processes, driven by wear, aging, material fatigue, software errors, and external disturbances, requires the use of probabilistic models and reliability estimation techniques. Common methods include exponential and Weibull failure distributions, Markov chains, reliability block diagrams (RBD), and failure trees. These tools enable engineers to assess metrics such as:

- Mean Time Between Failures (MTBF) — for estimating average uptime,
- Mean Time To Repair (MTTR) — for evaluating maintainability,
- Availability (A) and Operational Availability (Ao) — to determine actual production readiness,
- Failure Rate Functions ($\lambda(t)$) — to describe dynamic degradation patterns.

However, despite the availability of advanced reliability engineering tools, they are rarely integrated into strategic planning stages of innovation cycles [2, 3]. This disconnect leads to suboptimal decisions, such as introducing new technologies incompatible with existing failure-prone components, or underestimating lifecycle maintenance costs and risks.

In response to these challenges, this study proposes a reliability-oriented framework for industrial innovation planning, designed to embed technical risk assessment and predictive reliability modeling into every phase of the modernization lifecycle. The approach is based on the following principles:

1. Quantitative reliability modeling using failure data and degradation trends;
2. System-level diagnostics supported by Computerized Maintenance Management Systems (CMMS);
3. Integration of digital twins and simulation environments to emulate system performance under variable conditions;
4. Scenario-based risk analysis for evaluating the impact of critical failures;
5. Life Cycle Cost (LCC) modeling incorporating downtime, maintenance, and recovery costs.

To validate the proposed approach, we examine a multi-unit case study at a mechanical engineering enterprise undergoing partial automation and digital transformation. Each unit faced different reliability bottlenecks—including aging heat-treatment equipment, sensor malfunctions in CNC machines, and insufficient failure monitoring on assembly lines [4]. By collecting real-world CMMS data, applying failure probability models, and simulating various degradation paths, we demonstrate how reliability-centered decision-making improves operational stability and reduces the payback period for technical investments.

This work contributes to the ongoing effort to align engineering reliability theory with practical needs of technical modernization, and to enable decision-makers to incorporate risk-based logic and lifecycle performance into industrial innovation strategies. Ultimately, it underscores the necessity of treating reliability not as a reactive maintenance task, but as a strategic design variable that governs system robustness, adaptability, and sustainability.

II. Formulation of the problem

Technical modernization of industrial enterprises, especially in asset-intensive sectors such as mechanical engineering, metallurgy, and process industries, is increasingly challenged by the need to balance innovation with system reliability. While the implementation of new technologies—such as robotic systems, advanced automation platforms, and sensor-based diagnostics—promises operational improvements, it also introduces new failure modes and amplifies the complexity of reliability assurance.

A fundamental problem lies in the absence of structured reliability diagnostics and probabilistic failure modeling at the strategic planning stage. In many industrial facilities, critical assets continue to operate well beyond their designed service life, exhibiting nonlinear degradation behaviors due to aging, thermal cycling, corrosion, and cyclic mechanical loads. These failure mechanisms often follow stochastic patterns that cannot be accurately predicted without appropriate reliability models, such as Weibull or exponential distributions.

In practice, however, planning decisions for modernization are often made based on economic feasibility and expected productivity gains, with insufficient attention paid to metrics such as:

- Failure rate functions $\lambda(t)$,
- Mean Time Between Failures (MTBF),
- Mean Time To Repair (MTTR),
- System availability (A) and operational readiness (Ao),
- Residual life estimation under varying stress profiles.

This results in a disconnect between the planned technical capabilities of newly introduced systems and the real-world performance under industrial operating conditions [5].

The lack of integration between innovation planning and reliability engineering leads to a range of systemic challenges that compromise the effectiveness of modernization efforts:

Aging equipment and infrastructure often contain latent defects and exhibit erratic failure behavior, which traditional deterministic models fail to capture. The absence of diagnostic audits or degradation modeling leads to underestimation of operational risks.

*Low system redundanc*y and inflexible architectures increase the likelihood of cascading failures. A single point of failure in interconnected production chains may result in complete production halts and safety hazards.

Inadequate monitoring mechanisms, such as the absence of condition-based maintenance (CBM) systems or digital twins, impede early failure detection and predictive maintenance scheduling.

Fragmented responsibility for innovation and maintenance creates organizational silos. Technical planners may overlook failure histories, while reliability engineers are not engaged in early-stage decision-making.

Insufficient use of reliability modeling tools, such as Failure Mode and Effects Analysis (FMEA), Fault Tree Analysis (FTA), and Reliability Block Diagrams (RBD), limits the ability to forecast and mitigate failure risks.

A synthesis of these systemic issues and their impact on modernization efforts is presented in Table 1, which links each phase of innovation planning with relevant reliability factors and outlines possible consequences of neglecting reliability considerations.

Table 1 : *Relationship between reliability factors and stages of innovation planning*

Innovation Planning Stage	Key Reliability Factors	Potential Consequences	Response Measures
Current State Analysis	Equipment aging, hidden defects	Underestimation of modernization risks	Diagnostics, technical audits
Goal and Priority Setting	Ignoring reliability metrics	Unrealistic technical objectives	Inclusion of reliability criteria
Technology and Investment Selection	No evaluation of operational costs	Inappropriate technology choices	LCC analysis, failure forecasting
Design and Implementation	Unprepared production base	Failures, accidents, inconsistencies	Staff training, systems adaptation
Operation and Monitoring	Lack of monitoring and feedback mechanisms	Increased costs and downtimes	Implementation of CMMS, digital twins

This table provides a conceptual basis for embedding reliability engineering into industrial development workflows by identifying key intervention points for risk assessment and diagnostics.

These challenges are not merely theoretical. For instance, at a mechanical engineering plant, an attempt to integrate a robotic assembly line resulted in repeated shutdowns and reduced system availability during the first six months of operation. Root cause analysis revealed:

- Software incompatibility between new robotic modules and legacy conveyor systems;
- Electrical noise disrupting sensor feedback loops;
- Lack of pre-installation stress testing under nominal load conditions.

This case underscores the critical importance of evaluating technical compatibility, failure interactions, and degradation risks during the early design stages [6, 7]. The failure to do so not only delayed the realization of innovation benefits but also increased the total cost of ownership due to unplanned retrofitting and downtime.

To illustrate this conceptually, Figure 1 presents an extended innovation project lifecycle augmented with reliability checkpoints at each phase. The model emphasizes the iterative nature of reliability assessment, ensuring that system robustness, maintainability, and risk mitigation are evaluated continuously—from early-stage planning to long-term operation.

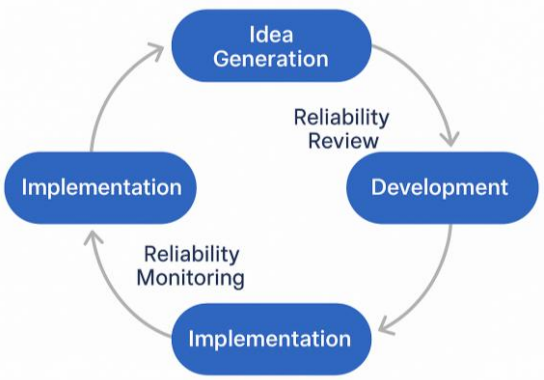


Figure 1: *Innovation project lifecycle with reliability assessments*

This model builds upon the PDCA (Plan–Do–Check–Act) framework, embedding reliability analysis into a cyclical improvement process. By incorporating feedback from operational monitoring (e.g., CMMS data, failure logs), enterprises can refine both technical designs and maintenance strategies over successive innovation cycles.

The innovation lifecycle presented in Figure 1 reflects the iterative nature of modern production development, where reliability is not treated as a static requirement but rather as a dynamic, continuously monitored parameter. Conceptually, this model draws upon the PDCA (Plan–Do–Check–Act) cycle, enabling a structured approach to innovation planning. At each phase — from initial idea formation to implementation and feedback — reliability assessments act as checkpoints that ensure not only the feasibility of proposed solutions but also their compatibility with existing infrastructure and long-term operational stability [8]. This cyclical integration fosters continuous improvement, allowing enterprises to refine their technical strategies based on real-world performance data and evolving risk profiles.

At the Idea Generation stage, strategic goals are formulated, and preliminary risk factors are identified. As the project advances to the Development phase, a Reliability Review is conducted to assess the compatibility of proposed innovations with the existing technical infrastructure, taking into account failure rates, readiness of production systems, and critical operational risks.

Taken together, the outlined technical challenges, empirical examples, and modeling gaps form a strong motivation for developing a reliability-based modernization framework. Such a framework should:

- Integrate quantitative reliability metrics into technical and economic evaluation criteria;
- Employ scenario modeling to simulate equipment behavior under variable operating conditions and failure probabilities;
- Include economic justification methods that account for reliability-driven savings, such as reduced downtime and optimized maintenance intervals.

The goal is to enable industrial enterprises to shift from reactive problem-solving toward proactive reliability assurance, where innovation becomes not just a source of performance gains, but a structured pathway to improved system dependability and operational resilience.

In the next section, a methodological framework is introduced that incorporates these principles into a unified reliability planning model for industrial modernization.

III. Problem solution

To address the reliability-related shortcomings identified in industrial modernization strategies, this study proposes an integrated framework that combines digital diagnostics, reliability modeling, and lifecycle risk analysis into the planning and execution phases of technical upgrades. The proposed approach enables the quantification of degradation effects and failure risks, allowing decision-makers to optimize investments not only for performance but also for long-term system dependability.

The core of the solution lies in embedding reliability and risk indicators into all key stages of the modernization project lifecycle. This is achieved through the following architectural elements:

1. Technical Audit and Risk Mapping: Assessment of existing equipment and infrastructure to identify critical failure modes, using tools such as FMEA and Root Cause Analysis (RCA).
2. Digital Reliability Twin: A digital replica of key assets, constructed using real-time monitoring data (e.g., temperature, load, cycle count), enabling the tracking of condition degradation over time.
3. Failure Modeling Engine: Application of statistical methods (Weibull, exponential, log-normal) to model time-to-failure distributions and predict residual life.
4. Reliability-Based Investment Justification (RBIJ): Economic analysis that includes expected cost of downtime, failure probabilities, and repair logistics in the evaluation of modernization options.
5. Lifecycle Monitoring System: Post-implementation tracking of reliability indicators and feedback into planning for continuous improvement.

This framework is illustrated conceptually in Figure 2, which shows the interaction between engineering systems, diagnostic data, reliability models, and decision modules [9, 10].

The framework promotes a closed-loop strategy, where reliability data informs both preventive maintenance and strategic decisions on system upgrades and replacements.

At the heart of the solution is the quantitative modeling of system reliability, which enables the estimation of future failure probabilities and degradation-driven risk. The approach is based on classical reliability engineering equations, adapted to real-world industrial systems with variable operational conditions.

For components with constant failure rate (memoryless process), the exponential distribution is used:

$$R(t) = e^{-\lambda t} \tag{1}$$

where λ is the failure rate (1/h).

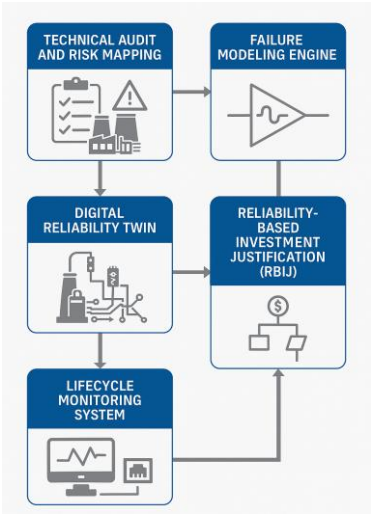


Figure 2: *Architecture of a reliability-integrated innovation planning system*

For wear-out dominated components, the 2-parameter Weibull distribution is more suitable:

$$R(t) = e^{-(t/\eta)^{\beta}}, \quad \beta > 1 \ \eta \ is \ the \ characteristic \ life$$

where: R(t)— reliability function, β— shape parameter (indicates failure pattern), η— scale parameter (characteristic life), t — operation time.

These models allow the calculation of key indicators such as Mean Time Between Failures (MTBF), system availability A, and unavailability Q=1−A.

In complex systems, where multiple components are connected in series or parallel, system-level reliability can be derived using Reliability Block Diagrams (RBDs):

For series systems:

$$R_{sys}(t) = \prod_{i=1}^{n} R_i(t) \tag{2}$$

For parallel systems (with redundancy):

$$R_{sys}(t) = 1 - \prod_{i=1}^{n} [1 - R_i(t)] \tag{3}$$

A comparative analysis of two modernization scenarios is presented in Table 2, where failure probability, MTBF, expected downtime, and total lifecycle cost are calculated for:

- Option A: Standard upgrade without diagnostic integration,
- Option B: Upgrade with digital twin and predictive maintenance tools.

The analysis demonstrates that although Option B requires higher initial investment, its total lifecycle cost is significantly reduced due to fewer failures, lower downtime, and optimized maintenance scheduling.

To validate the proposed framework, a case study was conducted on the modernization of a DC auxiliary power supply system in an industrial plant. The existing system, composed of two battery banks and a single charger unit, was prone to faults due to overloads and charger degradation.

Using field failure data and environmental load profiles, a reliability model was built using Weibull parameters (β=2.1, η=36 months). Simulation of 5-year operation using Monte Carlo methods revealed:

- Predicted failure rate reduction: 43%,
- Increase in system availability: from 89.2% to 96.5%,

- ROI achieved in 2.7 years due to reduced unscheduled downtimes.

The implementation of real-time monitoring and integration of predictive diagnostics enabled timely interventions and avoided catastrophic failures.

Table 2: *Comparative analysis: traditional vs. reliability-centered modernization approaches*

Aspect	Traditional Modernization	Reliability-Centered Modernization (RCM)
Planning Driver	Performance and cost priorities	Risk mitigation and system lifecycle integrity
Failure Modeling	Rarely applied, based on averages	Uses probabilistic failure data and degradation laws
Asset Condition Assessment	One-time visual/technical audit	Continuous or scheduled monitoring (CBM, PdM)
Decision Criteria	ROI, CAPEX/OPEX	Reliability metrics (MTBF, availability, failure rate λ) + financial factors
System Complexity Consideration	Often simplified or overlooked	Modeled through reliability block diagrams, FMEA, FTA
Maintenance Integration	Separate from planning process	Integrated as a feedback loop (RCM principles)
Digital Tools	Spreadsheets, static databases	Digital twins, IoT-based monitoring, reliability modeling software
Resulting Reliability	May stagnate or decline post-upgrade	Improved mean time between failures, higher system availability
Risk Visibility	Low – qualitative and intuitive	High – quantitative, with scenario-based sensitivity analysis

IV. Conclusion

Amid the accelerating pace of technological transformation in industry, it has become increasingly evident that traditional approaches to the modernization of technical systems—primarily focused on performance metrics and capital expenditures—are no longer sufficient to meet the demands of sustainability, operational safety, and reliability. The lack of systematic integration of reliability indicators at the planning stage often leads to structural vulnerabilities that manifest as frequent failures, increased maintenance costs, and inefficient resource utilization.

The reliability-centered planning (RCP) framework presented in this study offers a systemic alternative, where decision-making is guided not only by economic factors but also by quantifiable indicators of failure probability, component degradation, restoration time, downtime costs, and the cascading impact of failures on interconnected subsystems. The use of probabilistic modeling (e.g., Weibull distribution), system-level reliability analysis, integrated condition monitoring, and scenario-based failure analysis enables a more comprehensive and forward-looking strategy for modernization.

As shown in Table 2, the comparative analysis clearly demonstrates that transitioning from reactive or cost-centric planning to reliability-oriented strategies yields tangible benefits in reducing operational risks and improving long-term system efficiency. This approach is particularly critical for industries where failures have high-stakes consequences—such as energy, oil and gas, heavy manufacturing, and transportation—where reliability is not merely a technical parameter but a key determinant of safety, regulatory compliance, and economic resilience.

The successful adoption of RCP, however, requires a certain level of organizational maturity. This includes access to failure history data, the implementation of digital monitoring infrastructure, analytical expertise in reliability modeling and risk assessment, and a willingness to reassess conventional practices in asset planning and investment allocation. Despite the potentially higher initial costs, practical experience indicates that even partial implementation of reliability-centered strategies significantly enhances risk visibility, system availability, and return on investment.

In this light, RCP emerges as a vital step in the evolution of sustainable industrial development strategies. By embedding reliability principles into the early phases of technical and innovation planning, organizations can foster a more resilient, adaptive, and data-driven approach to managing complex systems. This not only leads to technically sound modernization outcomes but also ensures a balanced trade-off between innovation, lifecycle reliability, and economic viability under conditions of increasing system complexity and uncertainty.

References

[1] Trachuk, A.V., & Linder, N.V. (2021). Assessing the innovation potential of industrial enterprises. *Strategic Decisions and Risk Management*, 12(4), 292–311.

[2] Ponomarev, A.A., & Kirsanov, S.V. (2020). Equipment reliability in the context of production process digitalization. *Engineering Bulletin*, 8, 45–51.

[3] Belyaev, S.V. (2022). Managing techno-economic development in industry under resource constraints. *Economics and Management*, 10(2), 55–64.

[4] UralMet JSC internal report on rolling mill modernization (2023).

[5] Grishin, A.I., & Vasiliev, P.N. (2021). Methodology for reliability assessment in strategic innovation planning. *Problems of Forecasting*, 3, 110–118.

[6] ISO 55000:2014. *Asset management – Overview, principles and terminology*. International Organization for Standardization.

[7] Lee, J., Bagheri, B., & Kao, H.A. (2015). A cyber-physical systems architecture for Industry 4.0-based manufacturing systems. *Manufacturing Letters*, 3, 18–23.

[8] S. Kamble, A. Gunasekaran, and R. Sharma (2020) Modeling the blockchain-enabled traceability in agriculture supply chain, *Computers in Industry*, vol. 111, pp. 103178, 2020. doi: 10.1016/j.compind.2020.103178

[9] B. Bagheri, S. Yang, H.-A. Kao, and J. Lee, (2015) Cyber-physical systems architecture for self-aware machines in Industry 4.0 environment, *IFAC-PapersOnLine*, vol. 48, no. 3, pp. 1622–1627, 2015. doi: 10.1016/j.ifacol.2015.06.318

[10] J. Lee, B. Bagheri, and H.-A. Kao, (2015) A cyber-physical systems architecture for Industry 4.0-based manufacturing systems, *Manufacturing Letters*, vol. 3, pp. 18–23, 2015. doi: 10.1016/j.mfglet.2014.12.001

A HYBRID APPROACH FOR DETECTION AND MITIGATION OF ROUTING ATTACKS IN RPL USING DEEP LEARNING

Deepak Upadhyay[1], Hiteishi Diwanji[2]

•

[1]Phd Scholar, Gujarat Technological University, Gujarat, India
[2]L. D. Government Engineering College, Gujarat, India
[1]ap_deepak@gtu.edu.in , [2]hiteishi.diwanji@gmail.com

Abstract

The exponential growth of the Internet of Things (IoT) has led to the massive deployment of resource-constrained smart devices in domains such as smart homes, industrial automation, healthcare, and smart cities. To facilitate communication between these devices, the Routing Protocol for Low-Power and Lossy Networks (RPL) has emerged as a widely adopted IPv6-based routing protocol customized for low-power, lossy environments. This study proposes an Intrusion Detection System (IDS) framework that processes raw IoT traffic data to detect and classify RPL routing attacks using a hybrid approach and takes mitigation steps. The IDS framework integrates multiple models, such as a LSTM enhanced with Multi-Head Attention for sequential pattern recognition, gradient boosting models such as LightGBM and CatBoost for efficient tabular data classification, and a Multi-Layer Perceptron (MLP) to replicate ensemble knowledge in a lightweight manner. This hybrid IDS demonstrates the efficacy of combining deep learning and machine learning models to detect and mitigate RPL routing attacks, providing a practical and scalable solution for securing IoT networks with highest accuracy of 93.26 % with mobility and 91.96 % without mobility for CNN+LSTM+Attention, LightGBM, CatBoost, MLP algorithms.

Keywords: Intrusion detection system, data science, machine learning, deep learning, RPL, security, IoT, routing protocols, black hole, rank, Sybil, DIS, selective attack.

I. Introduction

The Internet of Things (IoT) has changed how many sectors work by linking devices that share data over the Internet. IoT systems are now common in smart cities, healthcare, farming, and industry (Hassija et al. [1]). For secure data transfer in these networks, the RPL protocol is widely used. It is designed to handle routing in IoT setups with low power and limited resources. Still, these same limits make RPL weak against several security issues. It can be attacked through blackhole, rank, Sybil, DIS, and selective forwarding (Prajapati et al. [2]). Such attacks affect network stability, cause packet loss, increase power use, and reduce Quality of Service (QoS). This is a serious problem because IoT devices often deal with sensitive data and interact with the physical world. To handle this, researchers have worked on Intrusion Detection Systems (IDS) that can detect routing attacks

in RPL networks. Many studies rely on datasets such as ROUT-4-2023. But most methods only look at single attack types or use pre-processed data, which does not reflect real-world cases where attacks change and overlap.

This work tries to overcome those limits by using the Contiki/Cooja simulator, which acts as a real-life test setup. The simulator creates a raw packet capture (PCAP) file. Then carried out our own steps like cleaning the data, encoding features, normalizing values, and reducing dimensions. These steps make the detection process more reliable. Furthermore, to address the class imbalance issues inherent in IoT attack datasets, applied the plied the Synthetic Minority Oversampling Technique (SMOTE) for balanced model training.

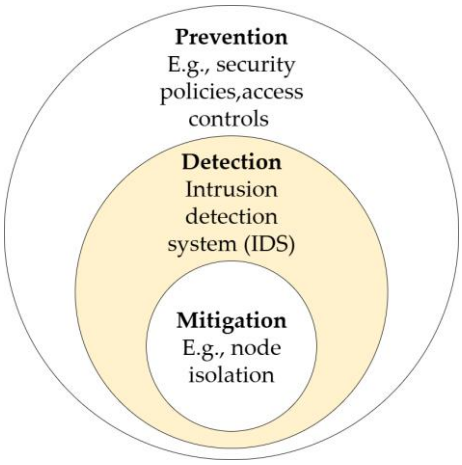


Figure 1: *Network defense*

The proposed detection framework integrates a variety of models, including Long Short-Term Memory (LSTM) networks for identifying sequential traffic behavior, tree-based algorithms such as Light Gradient Boosting Machine (LightGBM) and CatBoost for handling structured tabular data, and a lightweight Multi-Layer Perceptron (MLP) that distills insights from the ensemble. To improve the reliability of the predictions, Test Time Augmentation (TTA) was applied during the inference phase. By employing hybrid machine learning and deep learning techniques, this study facilitates the development of a scalable and accurate IDS for RPL-based IoT networks. The proposed approach not only enhances detection accuracy in mobility environment but also improves generalization across multiple attack types, providing a practical solution for securing IoT environments.

The paper is organized as follows: Section II reviews IDS solutions for RPL-based networks. Section III details the proposed approach, covering simulation setup, dataset, data collection, preprocessing, balancing, feature engineering, model design, training, and evaluation. Section IV presents results, while Section V discusses findings, concludes the study, and highlights future directions.

II. Literature Review

Shahid et al. [3] used the ROUT-4-2023 dataset to develop an IDS with both machine learning and deep learning models, reporting high accuracy with Random Forest (99%) and transformers (97% F1). Yusuf Yavuz et al. [4] proposed a scalable deep learning approach using Cooja-generated data, achieving over 94% accuracy for rank, flooding, and version number attacks. Vatambeti et al. [5] introduced an ensemble model for IIoT routing attacks, where traditional methods such as KNN and SVM underperformed compared to neural models, with their LSTM-based ensemble reaching 94.5% accuracy. Gupta et al. [6] also combined machine learning and deep learning to detect

blackhole attacks by modeling normal network behavior and identifying deviations.
For specific attack scenarios, Çakir et al. [7] applied ML-based detection for DIS flooding, with LR and SVM achieving above 96% accuracy. Neerugatti et al. [8] proposed a distance-based technique to detect rank attacks, while Raghavendra et al. [9] designed a genetic feature selection and fuzzy KNN classifier to detect selective forwarding with improved accuracy and low false positives. Murali et al. [10] developed a lightweight IDS against Sybil attacks inspired by artificial bee colony optimization, reaching around 95% accuracy.
Yu et al. [11] reviewed IoT architecture and attack surfaces at consumer and industrial levels, highlighting vulnerabilities and outlining future research directions for device security.

III. Methodology

This study followed standard data science steps: data collection, preprocessing, and dataset exploration to find patterns in features. These steps supported machine learning and deep learning models to test and compare methods. The work was done in Python because of its open-source tools.

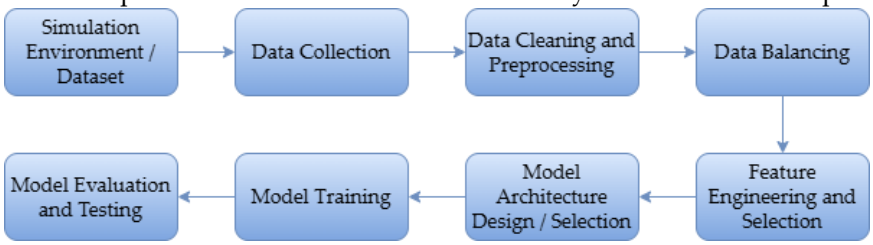


Figure 2: *Methodology diagram*

I. Simulation Environment / Dataset

The foundation of this study begins with the simulation of realistic RPL-based IoT network environments to capture the behaviors of both normal and malicious routing operations. The simulations were conducted using the Cooja network simulator, which operates atop the Contiki OS.

Table 1: *Simulation parameters of reliability measure against attack*

Simulation Parameters	Value
Simulation tool	Contiki /Cooja 3.0
Simulation coverage area	100 m * 100 m
Deployment Type	Random position (based on smart home)
Total number of nodes	30
Emulated nodes	T-mote Sky
Malicious nodes	1:10
TX range	50 m
TX ratio	100%
RX ratio	30-100%
Link failure model	UDGM
Interference range	50 m
Routing protocols	THC-RPL
Mobility speed	0-6.23 km/h
Simulation time	60 min

In this study, five routing attacks were implemented in Contiki: Blackhole, Sybil, DIS Flooding, Rank, and Selective Forwarding. Each attack was programmed into selected nodes and compiled through the node firmware.

I. Blackhole Attack

In a blackhole attack, a malicious node pretends to have the best route to the destination. Other nodes forward packets to it, and the data is dropped, creating a "black hole."

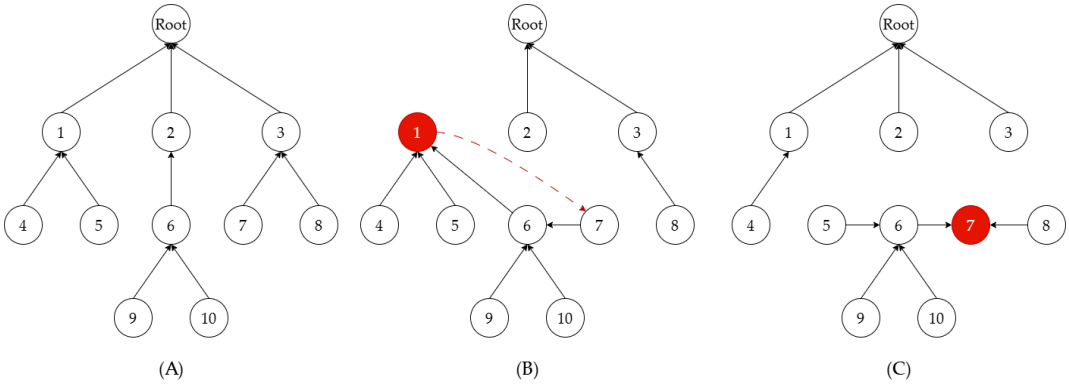


Figure 3: *Blackhole Attack*

Figure 3(A) shows a normal IoT network with 10 nodes forming a DODAG. In Figure 3(B), node 1 disrupts routing by acting as a preferred parent and absorbing packets. Later, in Figure 3(C), the malicious node shifts to another location (e.g., node 7), continuing the attack (Ahmed et al. [12]).

II. Sybil Attack

A Sybil attack occurs when a malicious node uses multiple fake identities in an RPL network. The attacker gains extra influence, leading to instability, data loss, or denial-of-service.

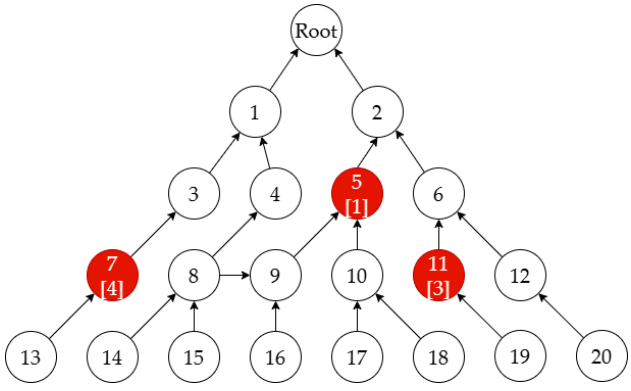


Figure 4: *Sybil Attack*

Figure 4 shows nodes 2, 3, and 10 as Sybil nodes, each using false identities (e.g., [9], [13], [19]) to mislead their neighbors.
Detection of Sybil behavior focuses on three aspects: routing metrics, identities, and packet handling.

First, ETX and rank are monitored; sudden, unexplained rank drops may indicate malicious nodes. Second, nodes are checked for multiple IPv6 identities mapped to the same link-layer address. Third, packet logs are compared across nodes to detect altered or missing packets.

III. DIS Attack

In this attack, a malicious node floods the network with DODAG Information Solicitation (DIS) messages, disrupting routing and creating heavy overhead.

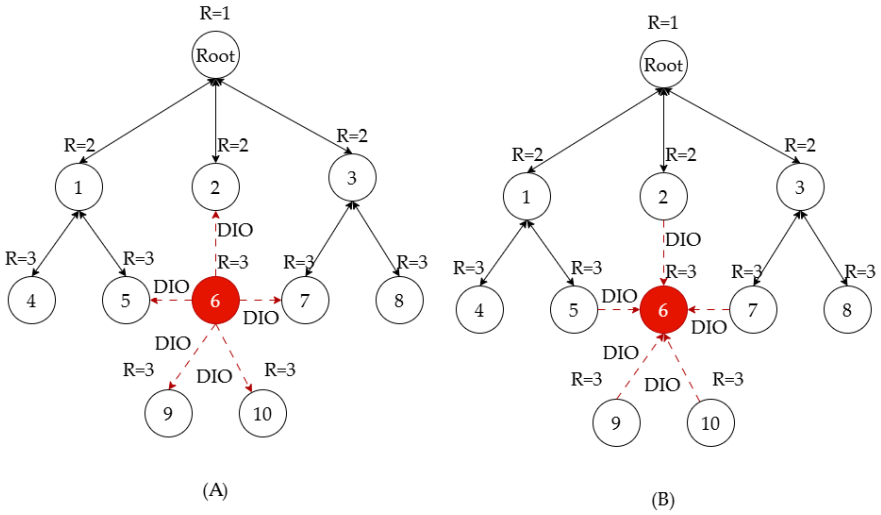


Figure 5: *DIS Attack*

Figure 5 shows a node repeatedly sending DIS messages. Normally, DIS is used by a node to discover the topology and join a DODAG. In a flooding attack, thousands of DIS requests are sent, causing a traffic surge that can bring down the network within minutes.
The attack increases radio activity and power use on the malicious node, since continuous DIS transmission keeps the radio busy. Mobility has little effect, as the attacker still floods the network while changing location. A common defense is to limit DIS requests per node and apply rate-limiting protocols (Verma et al. [13]).

IV. Rank Attack

A Rank Attack targets the RPL topology by broadcasting false rank values. Each node in RPL has a rank showing its distance from the root in the DODAG. Malicious nodes advertise artificially low ranks to mislead neighbors into choosing them as parents. This distorts the topology and causes non-optimal paths, routing loops, and packet loss.

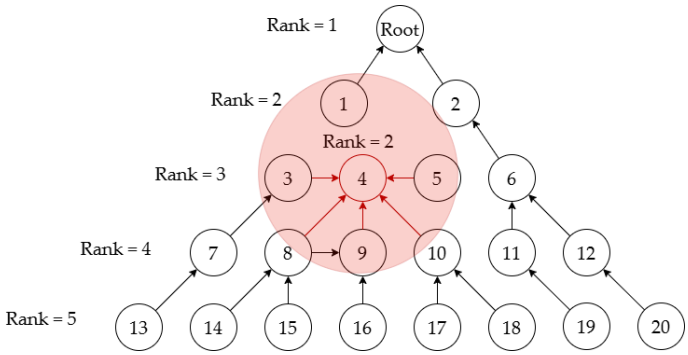


Figure 6: *Rank Attack*

Figure 6 shows node 4 broadcasting a fake rank (Rank = 2) to appear closer to the root. Neighboring nodes (3, 5, 8, 9, 10) then select it as their parent.
Detection involves tracking rank changes over time. Sudden or repeated drops in rank may reveal malicious behavior. Rank values are checked in RPL packets during analysis to identify such nodes (Almusaylim et al. [14]).

V. Selective Forwarding Attack

In this attack, a malicious node drops some packets while forwarding others. Unlike a blackhole, where all traffic is lost, selective forwarding avoids detection by forwarding part of the traffic. This lets the attacker target specific data flow and cause intermittent failures.

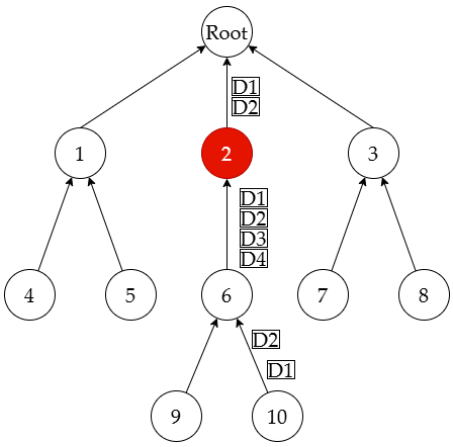


Figure 7: *Selective Forwarding Attack*

Figure 7 shows node 2 forwarding packets D1 and D2 but dropping D3 and D4, disrupting the path between node 6 and the root. Because RPL relies on intermediate nodes to forward traffic, a compromised node can appear normal while discarding selected packets. This degrades reliability, increases retransmissions, and reduces trust in routing paths.
Detection uses metrics such as Packet Delivery Ratio, RSSI, LQI, packet loss, retransmission rate, sequence numbers, ACK rate, hop count, and trust scores. Forwarding paths are analyzed for inconsistencies. Mitigation includes redundant routing and validating forwarding behavior with cryptographic checks.

II. Data collection

During simulation, traffic was captured in real time with Cooja's packet sniffer and stored as PCAP files. These files logged node communication, including normal packets and attack traffic. Wireshark and PyShark were used to extract protocol fields from 6LoWPAN, IPv6, ICMPv6, and RPL headers. Each PCAP file was then converted into a CSV format, where rows represent packets and columns represent features such as icmpv6.rpl.dao.sequence, wpan.seq_no, ipv6.hlim, and data.len. Finally, datasets were labeled by scenario: "normal" for regular traffic and attack-specific tags for malicious packets.

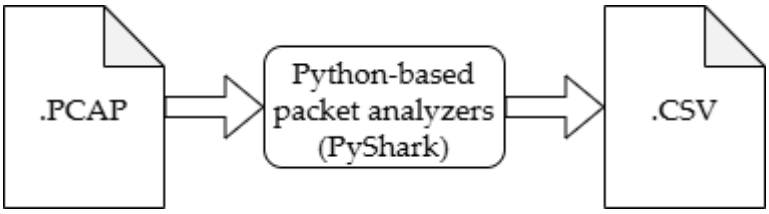


Figure 8: *extract feature from. PCAP and save in .CSV*

III. Data cleaning and preprocessing

After converting the raw PCAP traffic data into structured CSV format, a comprehensive data cleaning and preprocessing phase was undertaken to prepare the dataset for machine learning and deep learning model training.

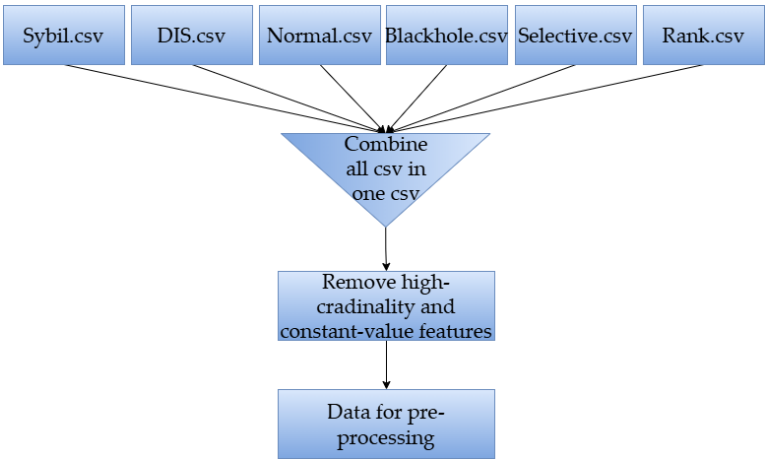


Figure 9: *Illustrated the removed high-cardinality and constant-value*

Figure 9 shows the merging of multiple CSV files, each containing a different attack type, into a single dataset. High-cardinality and constant-value features, which add little to classification and risk overfitting, were removed. The resulting cleaned dataset was then used for further processing.

IV. Data balancing

Figure 10 shows the imbalance between normal and attack classes in the dataset. Sybil and DIS dominate with nearly 100,000 and 80,000 samples, while Black Hole, Selective Forward, and Rank each have fewer than 30,000. Such disparity biases models toward majority attacks, reducing detection accuracy for underrepresented ones like Rank or Black Hole.

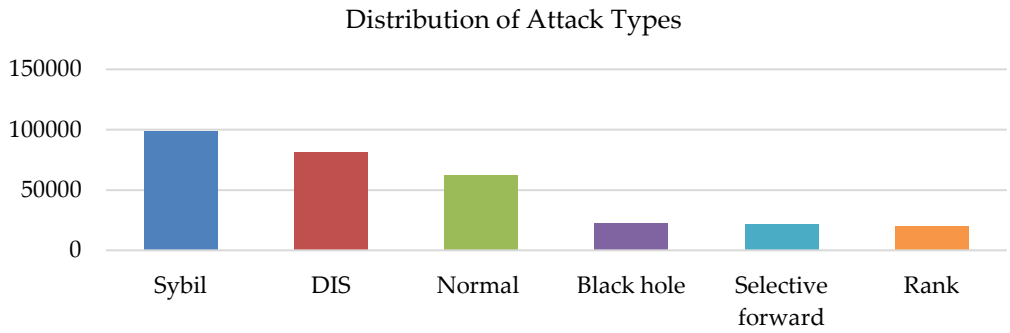


Figure 10: *Distribution of network records by attack type*

To overcome class imbalance, SMOTE (Synthetic Minority Oversampling Technique) was used in preprocessing. Instead of simply duplicating data, SMOTE creates new samples for minority classes by interpolating between nearby points. This adds variety, balances the dataset, and helps the IDS recognize subtle attack patterns that appear less often. With SMOTE, detection accuracy and fairness across different attack types improve (Dablain et al. [15]).

V. Feature Engineering and Selection

Feature engineering is key to building an IDS in RPL-based IoT networks. After converting PCAP files to CSV, categorical fields (e.g., address modes, flags, message types) were encoded as numbers, and booleans converted to binary values. This allowed features to be processed consistently by ML and DL models.

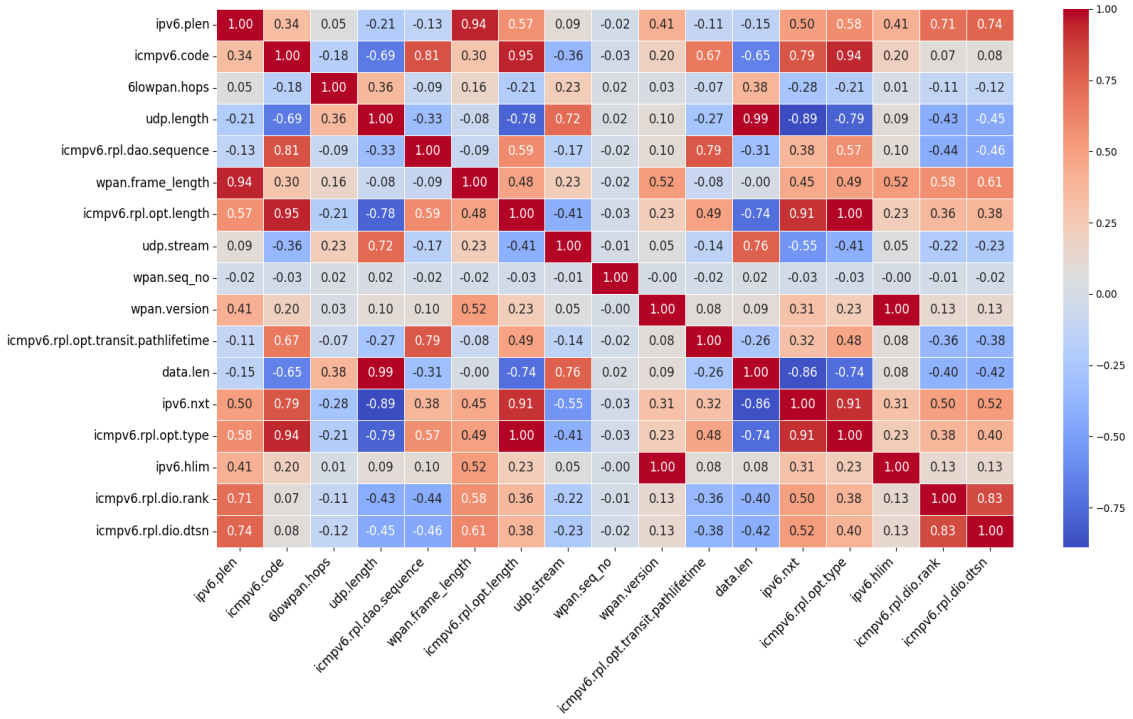


Figure 11: *Relationship depiction between network features.*

Figure 11 shows that some fields, such as icmpv6.code, icmpv6.rpl.opt.length, and icmpv6.rpl.opt.type, are highly correlated, while others like udp.stream and wpan.seq_no are independent. This helps remove redundant attributes and improve model efficiency.

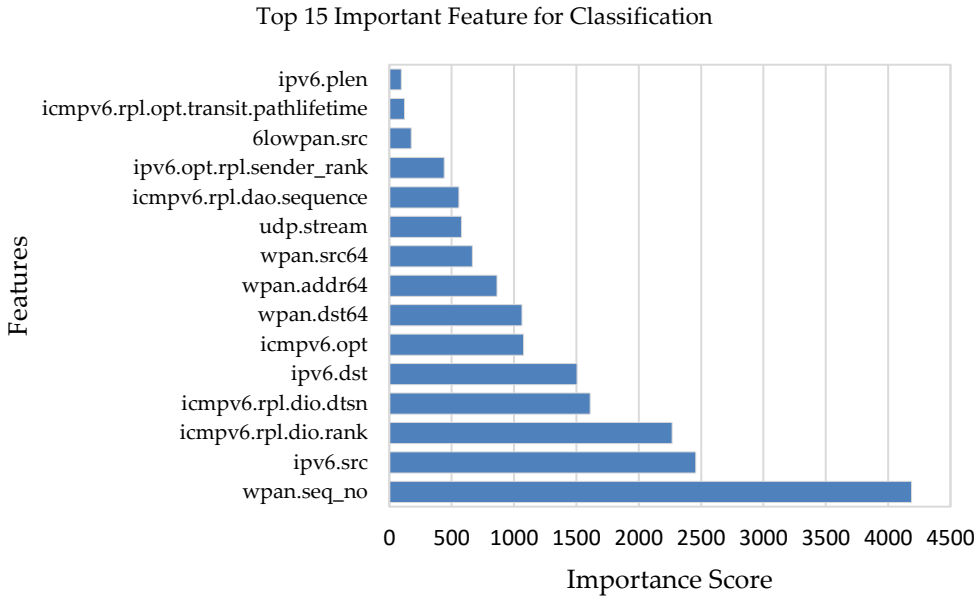


Figure 12: *Illustration of top 15 features*

As shown in Figure 12, features such as wpan.seq_no, ipv6.src, and icmpv6.rpl.dio.rank strongly influence classification. Address fields (wpan.addr64, wpan.src64) and routing parameters (icmpv6.rpl.dao.sequence, ipv6.opt.rpl.sender_rank) also help capture node activity and routing errors.

Outliers were detected using the Interquartile Range (IQR) method, where values beyond 1.5×IQR from Q1 or Q3 are flagged. Figure 13 shows that fields like wpan.seq_no, icmpv6.rpl.dio.rank, and udp.stream display outliers, which may indicate abnormal network behavior.

$$Q_1 = \left(\frac{n+1}{4}\right)^{th} \quad (1)$$

$$Q_3 = \left(\frac{3(n+1)}{4}\right)^{th} \quad (2)$$

Lower bound: Q1 - (1.5 * IQR)

Upper bound: Q3 + (1.5 * IQR)

In Figure 13, some features such as wpan.seq_no, icmpv6.rpl.dio.rank, icmpv6.rpl.dao.sequence, icmpv6.rpl.opt.transit.pathlifetime, and udp.stream show clear outliers. These patterns suggest unusual network behavior, which can help in spotting attack traffic in IoT routing

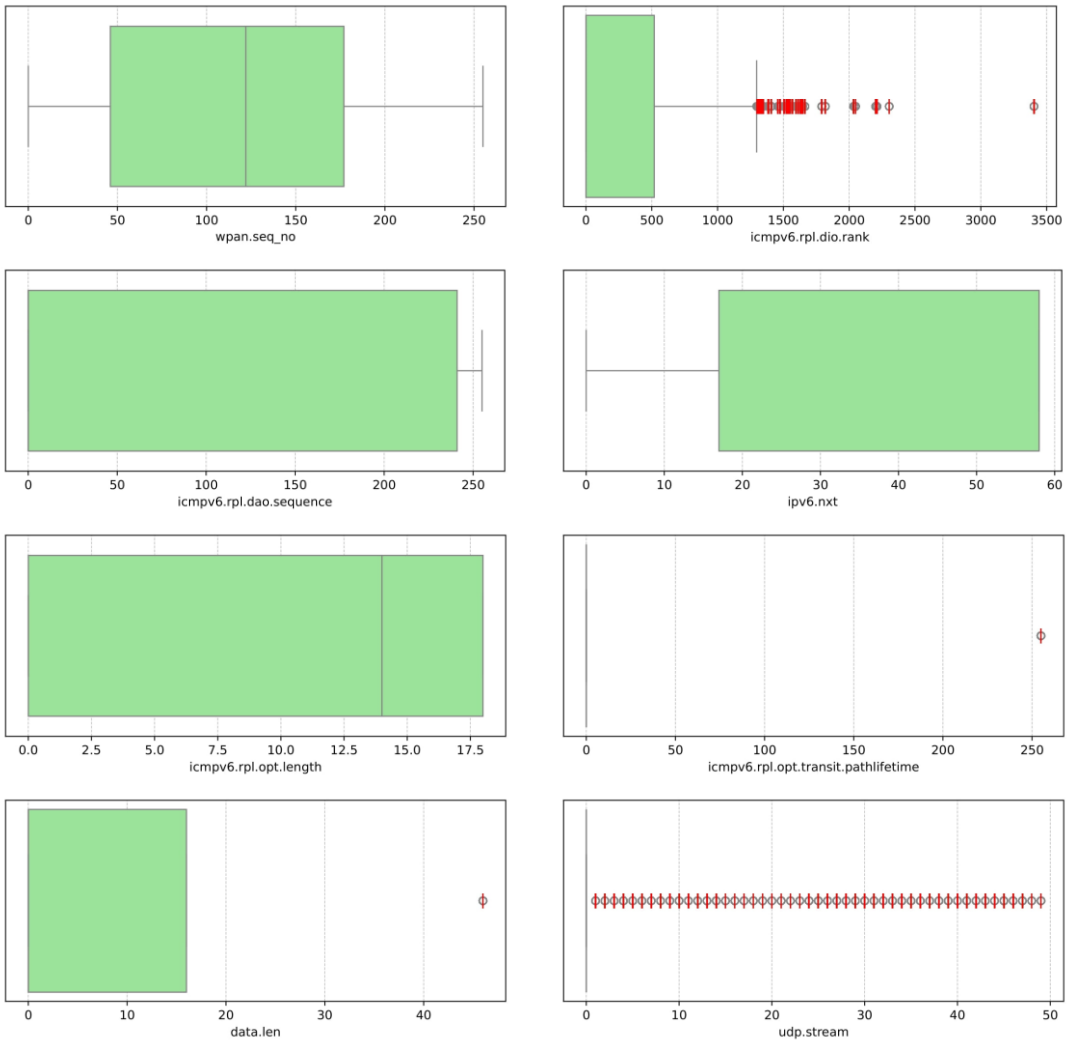


Figure 13: *Illustration of outliers and quartiles in features*

The violin plot in Figure 14 shows how packet lengths are spread under both normal and attack traffic in the IoT network. In the Attack category, the packet lengths display a multi-modal distribution, with peaks around 0.4, 0.7, and 0.9, suggesting a high variability in packet sizes during attack scenarios. In contrast, the Normal category shows a more concentrated distribution, especially around the 0.85–0.95 range, indicating more consistent and uniform packet sizes under normal network conditions.

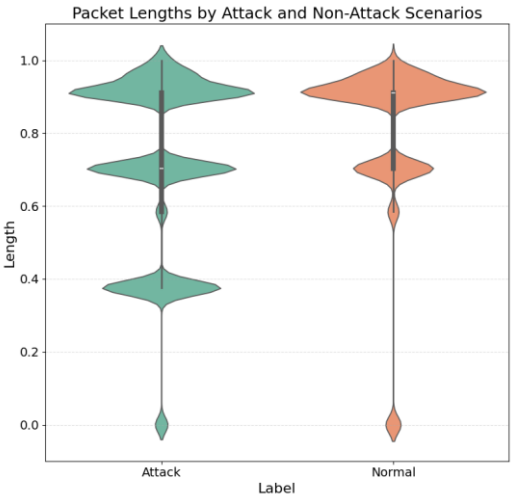


Figure 14: *Comparative illustration of packet lengths in attack and non-attack scenarios.*

VI. Model architecture design/selection

Table 2: *Classification of Detection Models*

Category	Model	Purpose
Tree-Based Models	- LightGBM - Decision Tree - Random Forest	Capture non-linear relationships and provide interpretable feature importance; efficient for tabular IoT data.
Linear / Optimization-Based Models	- Stochastic Gradient Descent (SGD) - Gaussian Naive Bayes(GNB)	Provide baseline comparison; fast and simple models for probabilistic and linear separation.
Neural Network Models	- Recurrent Neural Network (RNN) - Feedforward Neural Network (FFNN) - Convolutional Neural Network (CNN) - Long Short-Term Memory (LSTM)	Learn temporal and spatial patterns in sequential packet data; enhance learning from complex traffic behaviors.
Hybrid / Composite Models	- CNN + LSTM Hybrid - CNN + LSTM + Attention + LightGBM + CatBoost + MLP	Combine strengths of deep learning and machine learning; improve detection accuracy, generalization, and deployment efficiency.

VII. Model training

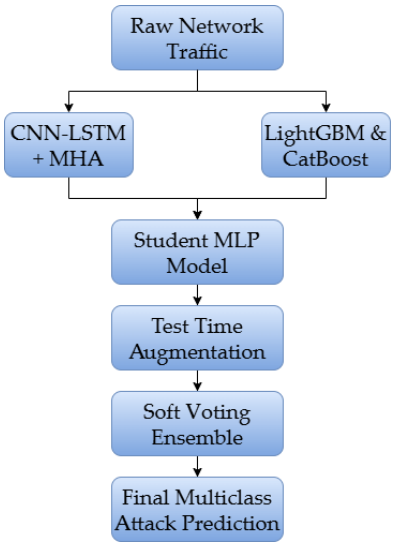


Figure 15: *Illustration of top 15 features*

Figure 15 shows the training and inference workflow. Raw traffic was processed in parallel by CNN-LSTM with Multi-Head Attention, LightGBM, and CatBoost. Predictions from these models acted as teachers for knowledge distillation into a lightweight MLP. During inference, Test Time Augmentation was applied, and final outputs were obtained with soft voting, combining model

strengths for multiclass attack detection.

Table 3: *Deep leaning models training time*

Model	Epochs	Ave. time pre-Epoch (Sec)	Total time (mins)
FFNN	50	4	3.33
CNN	50	11	9.1667
LSTM	50	17	14.1667
RNN	50	10	8.333
CNN+LSTM	50	9	7.5
CNN+LSTM+ Attention, LightGBM, CatBoost, MLP	35	75	43.75

IV. Results

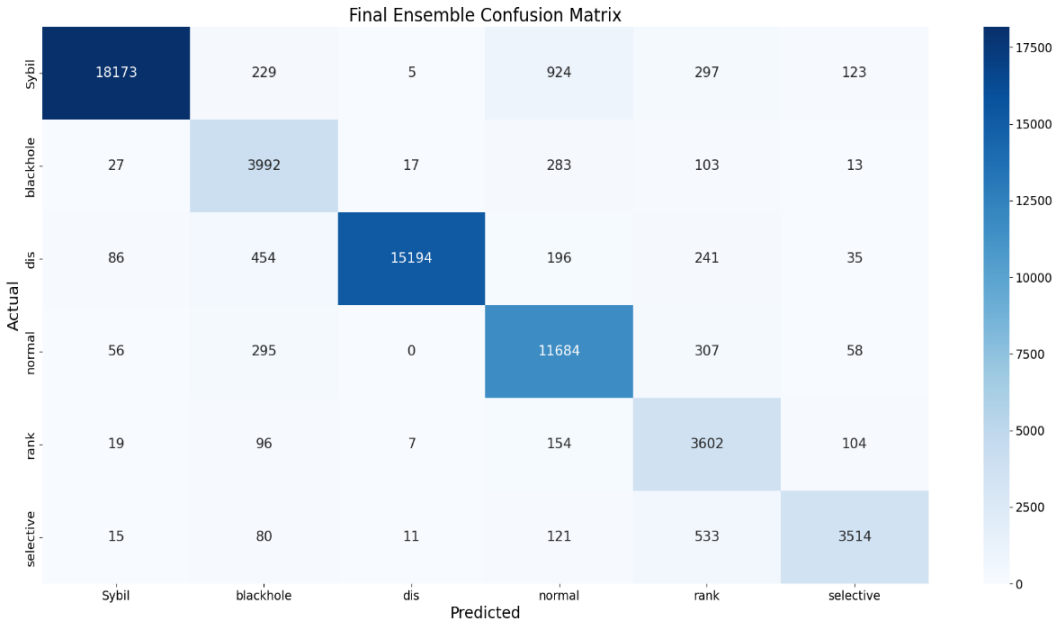


Figure 16: *Illustration of Confusion matrix*

The confusion matrix presented above evaluates the performance of the final ensemble model used for classifying various RPL routing attacks and normal traffic in IoT networks. In figure 16, the diagonal elements represent the number of correct predictions for each class, while the off-diagonal elements indicate misclassifications.

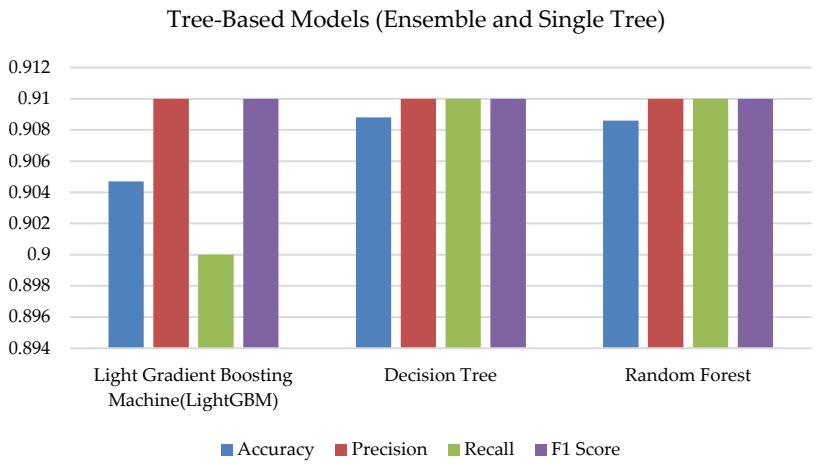


Figure 17: *Chart of accuracy, precision, recall, F1-score of Tree-based models*

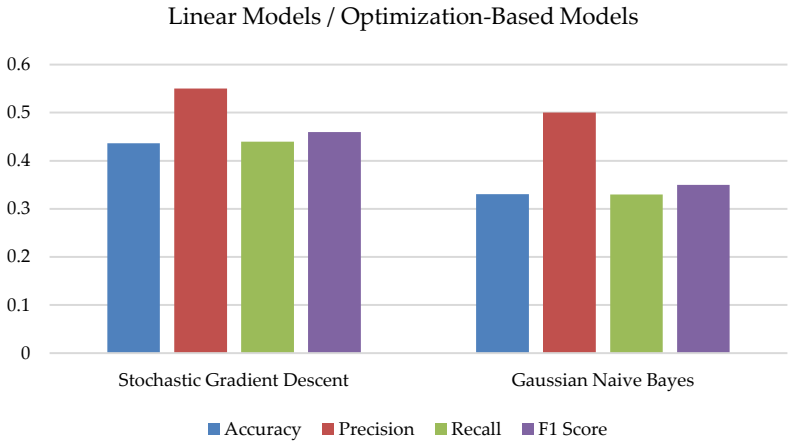


Figure 18: *Chart of accuracy, precision, recall, F1-score of Linear models*

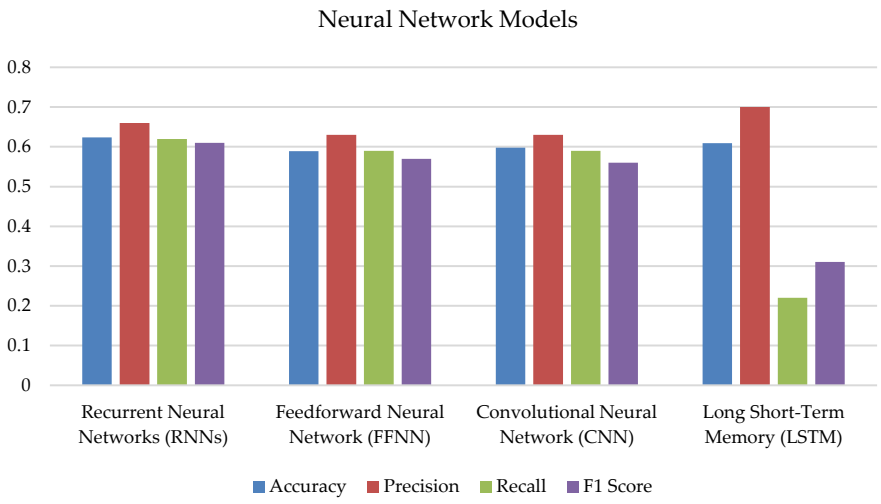


Figure 19: *Chart of accuracy, precision, recall, F1-score of Neural network models*

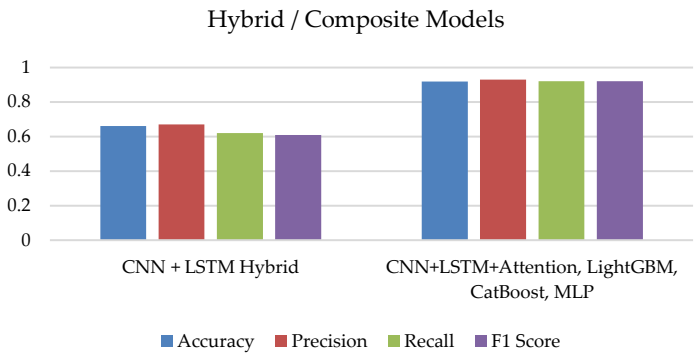


Figure 20: *Chart of accuracy, precision, recall, F1-score of hybrid/composite model*

The figures compare four model categories: tree-based, linear, neural networks, and hybrid models, using accuracy, precision, recall, and F1 score. Decision Tree and Random Forest perform well across all metrics, while LightGBM trails slightly in recall. Linear models such as Stochastic Gradient Descent and Gaussian Naive Bayes perform poorly, showing they are less suited for this task. Neural networks (RNN, FFNN, CNN, LSTM) give moderate results, with LSTM reaching high precision but low F1 due to weak recall. The strongest results come from hybrid models, especially CNN+LSTM+Attention with LightGBM, CatBoost, and MLP, which achieve near-perfect balance. This shows that combining deep learning with boosting methods gives the best accuracy for RPL attack detection.

Table 4: *Illustrate the accuracy between mobility and without mobility attack*

Model	Accuracy with mobility	Accuracy without mobility
Decision Tree	0.9088	0.913
Random Forest	0.9086	0.9132
LightGBM	0.9047	0.9155
RNN	0.6236	0.6316
LSTM	0.6094	0.6152
CNN	0.5979	0.6172
FFNN	0.5894	0.5923
Stochastic Gradient Descent	0.4363	0.597
Gaussian Naive Bayes	0.3304	0.3784
CNN+LSTM+Attention, LightGBM, CatBoost, MLP	0.9196	0.9326
CNN + LSTM Hybrid	0.6604	0.6616

V. Conclusion

This work presented an Intrusion Detection System (IDS) for finding and mitigating routing attacks in RPL-based IoT networks. The system was built with both deep learning and machine learning models, making it practical and able to scale for IoT setups. Authors fabricated a realistic RPL IoT environment in the Cooja simulator to record normal and attack traffic.To solve the problem of class imbalance in IoT datasets, SMOTE was used to generate extra samples for minority classes. The detection setup tested different models: LSTM for sequential traffic patterns, LightGBM and CatBoost for tabular data, and a simple MLP for combining outputs. Authors also used Test Time Augmentation (TTA) during prediction to improve stability. Results show that this mixed approach

improves accuracy and works across multiple attack types, including blackhole, Sybil, DIS flooding, rank, and selective forwarding. With the highest accuracy of 93.26% with mobility and 91.96% without mobility for CNN+LSTM+Attention, LightGBM, CatBoost, and MLP algorithms, this hybrid intrusion detection system (IDS) shows how well deep learning and machine learning models can be combined to detect and mitigate RPL routing attacks. It is a scalable and useful solution for protecting IoT networks.

References

[1] Hassija, V., Chamola, V., Saxena, V., Jain, D., Goyal, P., & Sikdar, B. (2019). A Survey on IoT Security: Application Areas, Security Threats, and Solution Architectures. In IEEE Access (Vol. 7). doi: 10.1109/ACCESS.2019.2924045

[2] Prajapati, A. K., Pilli, E. S., Battula, R. B., Varadharajan, V., Verma, A., & Joshi, R. C. (2025). A comprehensive survey on RPL routing-based attacks, defences and future directions in Internet of Things. *Computers and Electrical Engineering*, *123*. doi: 10.1016/j.compeleceng.2025.110071

[3] Shahid, U., Zunnurain Hussain, M., Zulkifl Hasan, M., Haider, A., Ali, J., & Altaf, J. (2024). Hybrid Intrusion Detection System for RPL IoT Networks Using Machine Learning and Deep Learning. *IEEE Access*, *12*, 113099–113112. doi: 10.1109/ACCESS.2024.3442529

[4] Yusuf YAVUZ, F., Ünal, D., & Gül, E. (2018). *Deep Learning for Detection of Routing Attacks in the Internet of Things*.

[5] Vatambeti, R., & Mamidisetti, G. (2023). Routing Attack Detection Using Ensemble Deep Learning Model for IIoT. *Information Dynamics and Applications*, *2*(1), 31–41. doi: 10.56578/ida020104

[6] Gupta, M., Vashishth, T. K., & Verma, P. K. (2024). Machine learning and deep learning based intrusion detection for blackhole attacks in mobile ad-hoc networks. *Multidisciplinary Science Journal*, *6*(11). doi: 10.31893/multiscience.2024209

[7] ÇAKIR, S., & YALÇIN, N. (2021). Detection of DIS Flooding Attacks in IoT Networks Using Machine Learning Methods. *European Journal of Science and Technology*. doi: 10.31590/ejosat.1014917

[8] Neerugatti, V., & Reddy, A. R. M. (2019). Machine learning based technique for detection of rank attack in RPL based internet of things networks. *International Journal of Innovative Technology and Exploring Engineering*, *8*(9 Special Issue 3), 244–248. doi: 10.35940/ijitee.I3044.0789S319

[9] Raghavendra, T., Anand, M., Selvi, M., Thangaramya, K., Santhosh Kumar, S. V. N., & Kannan, A. (2022). An Intelligent RPL attack detection using Machine Learning-Based Intrusion Detection System for Internet of Things. *Procedia Computer Science*, *215*, 61–70. doi: 10.1016/j.procs.2022.12.007

[10] Murali, S., & Jamalipour, A. (2020). A Lightweight Intrusion Detection for Sybil Attack under Mobile RPL in the Internet of Things. *IEEE Internet of Things Journal*, *7*(1), 379–388. doi: 10.1109/JIOT.2019.2948149

[11] Yu, M., Zhuge, J., Cao, M., Shi, Z., & Jiang, L. (2020). A survey of security vulnerability analysis, discovery, detection, and mitigation on IoT devices. *Future Internet*, *12*(2). doi: 10.3390/fi12020027

[12] Ahmed, F., & Ko, Y. B. (2016). Mitigation of black hole attacks in Routing Protocol for Low Power and Lossy Networks. *Security and Communication Networks*, *9*(18), 5143–5154. doi: 10.1002/sec.1684

[13] Verma, A., & Ranga, V. (2020). Mitigation of DIS flooding attacks in RPL-based 6LoWPAN networks. *Transactions on Emerging Telecommunications Technologies*, *31*(2). doi: 10.1002/ett.3802

[14] Almusaylim, Z. A., Jhanjhi, N. Z., & Alhumam, A. (n.d.). *Detection and Mitigation of RPL Rank and Version Number Attacks in the Internet of Things: SRPL-RP*. doi: 10.3390/s20215997

[15] Dablain, D., Krawczyk, B., & Chawla, N. V. (2023). DeepSMOTE: Fusing Deep Learning and SMOTE for Imbalanced Data. *IEEE Transactions on Neural Networks and Learning Systems*, *34*(9). doi: 10.1109/TNNLS.2021.3136503

RELIABILITY ASSESSMENT OF THERMAL-ELECTRICAL MODELS FOR PHOTOVOLTAIC SYSTEMS IN MATLAB: ASSUMPTIONS VERSUS EVALUATION

Rahim Mammadzada
•
Azerbaijan State Oil and Industry University
rahim.mammadzada02@gmail.com

Abstract

Reliable simulation of photovoltaic (PV) panel behavior requires more than electrical accuracy. It must also reflect the thermal realities of panel operation under real-world conditions. This study investigates the reliability of a Simulink-based thermal electrical model of a Jinko JKM325P-72-V monocrystalline module by comparing simulated temperature profiles with those expected under Standard Test Conditions (STC). The model accounts for multilayer thermal mass and material-specific heat capacities. Heat generation is attributed to both unconverted irradiance and resistive losses, while thermal dissipation is governed by convective heat transfer. By tuning model parameters based on datasheet specifications and empirical coefficients, the simulation achieves close agreement with reference temperature values under standard conditions. The work highlights how common oversimplifications in PV modeling, such as assuming uniform temperature, can lead to optimistic thermal reliability assessments. The approach emphasizes the importance of verifying modeling assumptions against physical intuition and available data to support more trustworthy simulation-based design decisions for PV systems.

Keywords: PV System Reliability, Simulation Assumptions, Thermal Modeling, Model Validation, MATLAB simulation.

I. Introduction

The rapid global adoption of photovoltaic (PV) systems is driven by the urgent need for sustainable and renewable energy solutions to mitigate climate change [1,2,3]. PV technology offers a clean and scalable alternative to fossil fuels, reducing greenhouse gas emissions and supporting global energy transition goals [4,5]. However, environmental factors, particularly operating temperature, significantly influence the performance and efficiency of PV modules. Elevated cell temperatures cause a measurable decline in output power due to the negative temperature coefficient of solar cells [3,8,9]. This challenge is of increasing concern in regions experiencing high solar irradiance and rising ambient temperatures driven by global warming [5,8].

Under Standard Test Conditions (STC), defined as 1000 W/m² irradiance and a cell temperature of 25 °C, PV performance is benchmarked for rating purposes [6,7]. These conditions allow manufacturers and researchers to compare PV technologies on a standardized basis, even though actual operating environments may vary [6]. In the field, conditions often differ greatly from STC, with higher operating temperatures leading to reduced voltage and overall energy

output [3,8]. MATLAB, Simulink, and Simscape have emerged as effective platforms for modeling PV module performance under varying environmental conditions, allowing for precise simulation of temperature effects on power generation [1,5,6,10].

Thermal modeling of PV systems provides valuable insights into both electrical performance and thermal management strategies [3,4]. Models can incorporate key parameters such as irradiance and panel orientation, enabling performance prediction across diverse climatic zones [5,8]. Studies show that natural convection and active thermal regulation can mitigate efficiency losses in hot climates [4,9]. Understanding these thermal effects is critical for optimizing PV performance and ensuring long-term reliability. Moreover, the integration of PV thermal modeling into energy planning tools supports the economic viability of solar projects in various geographic contexts [4,9].

As global temperatures continue to rise, improving the thermal resilience of PV systems becomes increasingly vital [3,8]. Accurate modeling and simulation facilitate the design of effective cooling strategies, guide material selection, and inform policy decisions aimed at promoting renewable energy adoption [4,9]. The combination of performance prediction, environmental data analysis, and advanced simulation environments positions MATLAB and Simscape as essential tools in developing PV control strategies that can withstand the challenges posed by climate change [1,4,8,10].

This study focuses on creating a detailed MATLAB Simulink model of a real commercial PV module, combining manufacturer specifications with reasonable engineering assumptions. The objective is to develop a simulation framework capable of capturing both electrical and thermal aspects of operation, thereby supporting more accurate reliability analyses for PV systems under real-world conditions.

II. Methods and Simulation Setup

This study begins by exploring the functionality of the PV array block within the MATLAB environment, utilizing the Simscape Electrical library and Simulink for system-level simulation. The initial investigation shows that the electrical behavior of the solar panel is well represented, including a broad selection of preset commercial panels that allows for quick configuration. For this work, the Jinko JKM325P-72-V is chosen as a reliable and widely used solar panel model often seen in real-world installations. The physical characteristics of this model are shown in Figure 1.

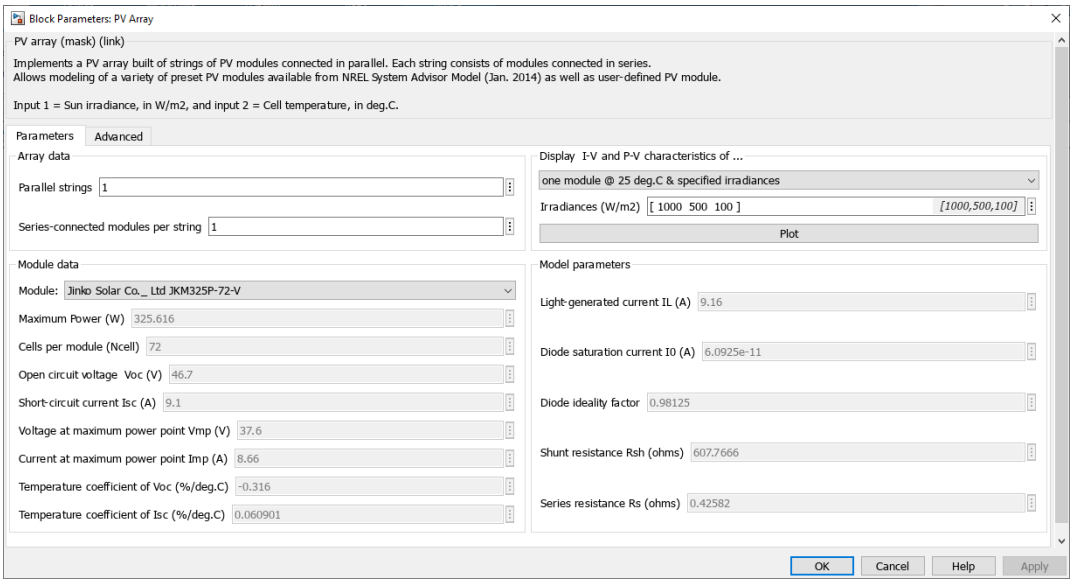


Figure 1: *Preset PV array block configuration for the Jinko JKM325P-72-V module*

After configuring the PV block, the simulation inputs and outputs were defined with careful consideration of standard photovoltaic testing practices. An irradiance of 1000 W/m² and a temperature of 25 °C were chosen to replicate Standard Test Conditions (STC), which provide a consistent basis for comparing both simulated and real-world module performance. These parameters allow the simulation to produce results that can be matched with the manufacturer's datasheet values. A resistive load was connected between the electrical ports of the PV array to bring the operating point close to the panel's maximum power point (MPP), ensuring that the electrical output reflects optimal energy conversion. This resistance value was calculated directly from the PV array block by dividing the maximum power voltage of 37.6 V by the maximum power current of 8.66 A.

$$R = \frac{U_{mp}}{I_{mp}} \quad (1)$$

Yielding approximately 4.34 Ω resistance. In addition to this, the output measurement port was routed through a demultiplexer, enabling voltage, current, diode current, irradiance, and temperature to be monitored as separate signals for detailed analysis as shown in Figure 2.

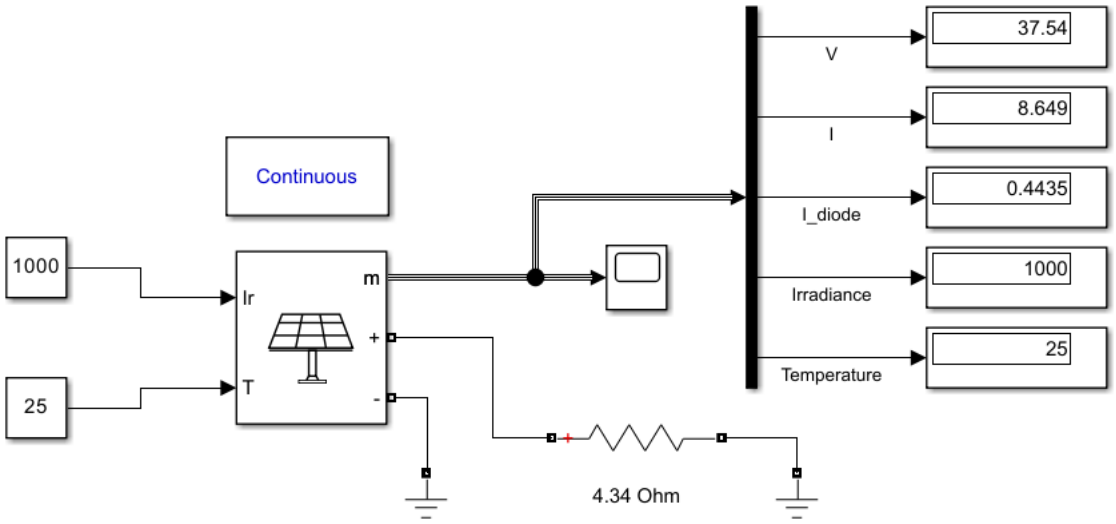


Figure 2: *Simulink model of the PV array block*

Running the simulation under these conditions produced an output voltage of approximately 37.54 V and a current of around 8.649 A, resulting in output power of 324.68 W, which is very close to the rated 325 W and matches the Jinko 325P-72-V manufacturer specifications. This strong agreement confirms that the PV block within MATLAB Simulink, in conjunction with the Simscape Electrical library, provides an accurate representation of the panel's electrical characteristics under STC. However, when the simulation was extended over a longer time period, it became clear that the PV array block's cell temperature output remained constant throughout the run. This observation reveals that while the PV block effectively simulates the electrical performance, it does not inherently simulate the thermal behavior of photovoltaic modules. In real-world conditions, solar panels experience significant temperature fluctuations due to both environmental heating from solar irradiance and internal heating from electrical current flow. The absence of this effect in the default PV array block highlights the need to integrate a thermal domain into the model. Such an enhancement allows for a more realistic representation of panel performance over time, capturing both electrical and thermal interactions, and enabling further studies into efficiency loss, thermal stress, and long-term reliability.

For this, we must first add a thermal mass block from the Simscape library to represent the

solar panel. However, the estimation of the thermal mass presents a challenge because manufacturers typically provide only limited data, such as glass thickness and overall weight, making it difficult to estimate the properties of individual layers that can store heat. Based on logical assumptions, the silicon layer thickness is set at 0.2 millimeters. The aluminum frame and ethylene-vinyl acetate polymer layers are then estimated so that the sum of all layer weights matches the manufacturer's total weight specification. This approach enabled calculation of the panel's overall heat capacity. Table 1 presents all of the estimated data about each layer.

Table 1: *Layers of the Jinko JKM325P-72-V contributing to heat storage*

Layer Materials	Thickness	Thermal Conductivity (k)	Density (ϱ)	Specific Heat Capacity (Cp)
Glass	3.2 mm	1.4 W/(m · K)	2500 kg/m³	750 J/(kg · K)
EVA (Combined)	1 mm	0.35 W/(m · K)	960 kg/m³	2100 J/(kg · K)
Silicon Cell	0.2 mm	148 W/(m · K)	2330 kg/m³	705 J/(kg · K)
Aluminum plate	1.6 mm	205 W/(m · K)	2700 kg/m³	900 J/(kg · K)

Using the thickness and density of each material layer, it is possible to calculate the equivalent mass of the solar panel. To do this, the panel area must first be determined, which can be obtained from the manufacturer's specifications as around 1.94m². The equivalent mass m_{eq} is calculated by summing the product of density, area, and thickness for each layer.

$$m_{eq} = \sum_{i=0}^{n} (\rho_i \cdot A \cdot t_i) \tag{2}$$

Next, the average specific heat capacity of the panel is computed by weighting the specific heat capacity of each layer $c_{p,i}$ by its respective mass m_i, and then dividing by the total mass m_{eq}.

$$c_{p,eq} = \frac{\sum_{i=0}^{n} (m_i \cdot c_{p,i})}{m_{eq}} \tag{3}$$

The natural convection cooling in the model is implemented using the Convection Heat Transfer block from the Simscape Thermal library. This block requires two key input parameters, the convective heat transfer coefficient h and the convective area A. The coefficient h represents the efficiency of heat transfer through natural convection, which depends on environmental conditions such as wind speed and air properties. For this study, a reference wind speed of 1 m/s is used, leading to an assumed range for h between 5 and 10 W/(m²·K). These values align with commonly reported data for natural convection over flat surfaces and ensure the model realistically approximates heat transfer to the surrounding air. The convective area A corresponds to the total surface area of the solar panel exposed to air, where convection can occur. This includes the front and back faces as well as the edges defined by the panel thickness. The total convective area is calculated using the panel's approximate length L of 1.956m, width W of 0.992m, and thickness T of 0.040m, with the formula below.

$$A_{convection} = 2 \cdot (L \cdot W + L \cdot T + W \cdot T) \tag{4}$$

Resulting in an overall surface area of around 4.11 m². Finally, heat generation within the solar panel must be considered from both direct solar irradiances absorbed as thermal energy and resistive heating caused by current flowing through the panel's internal resistance. The portion of sunlight not converted to electricity increases the panel temperature, while electrical current

generates additional heat due to the panel's series resistance. Accurately modeling this combined heat generation is crucial for predicting temperature rise and its impact on efficiency, making it an essential component of the thermal simulation.

$$Q_{gen} = G \cdot A \cdot \big(1 - \eta(T)\big) + I^2 \cdot R_s \tag{5}$$

Here, η(T) represents the temperature-dependent efficiency of the photovoltaic panel, capturing how the panel's ability to convert solar energy into electrical power changes with temperature variations. This efficiency is calculated using the following relation below.

$$\eta(T) = \eta_{stc} \cdot \Big(1 + \gamma \cdot \big(T_{cell} - T_{ref}\big)\Big) \tag{6}$$

Here, η_{STC} is the efficiency at standard test conditions, γ is the temperature coefficient assumed as $-0.0041K^{-1}$, T_{cell} is the cell temperature, and T_{ref} is set as 25 °C as the reference temperature. The η_{STC} is defined as the ratio of electrical power output to incident solar power on the panel surface.

$$\eta_{stc} = \frac{P_{max}}{G_{STC} \cdot A} \tag{7}$$

Here, G_{STC} is 100 W/m², P_{max} is 325 W, and A is 1.94m². Once all parameters required for calculating the heat generation Q_{gen} are obtained, a dedicated subsystem is constructed to perform this calculation dynamically, as shown in Figure 3. The inputs to this subsystem are the panel temperature, irradiance, and electrical current, which are taken from the measurement outputs of the PV array block. The internal series resistance R_s is obtained directly from the PV array block specifications, as shown in Figure 1. The efficiency η_{STC} was calculated to be 16.75 percent, represented as 0.1675 in Simulink. By using these inputs and parameters, the subsystem computes the total heat generated within the panel at each simulation step, allowing the model to capture the influence of changing electrical and thermal conditions of the photovoltaic system.

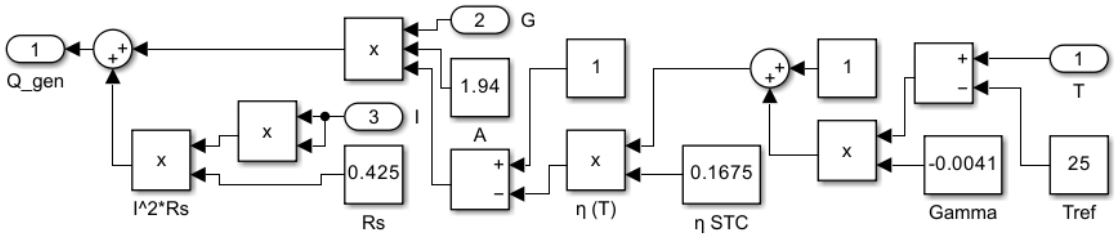


Figure 3: *Subsystem model for solar panel heat generation estimation*

Once the heat generation subsystem is configured, the next step is to incorporate the thermal domain into the model by assigning the required parameters. These include the convective heat transfer coefficient, convection area, total mass, and averaged specific heat capacity of the panel. For clarity and reference, all assumed values are presented in Table 2.

Table 2: *Assumed parameters for integration with the thermal domain*

Parameter Name	Convection Coefficient h	Overall Mass of the Panel m_{eq}	Specific Heat Capacity $C_{p,eq}$	Ambient Temperature
Value	10 W/(m2·K)	26.6 Kg	890 J/(kg · K)	25° Celsius

The complete simulation setup, integrating both the electrical and thermal domains, is shown

in Figure 4. In this configuration, the convection block is assigned the estimated heat transfer coefficient h and convection area A, the thermal mass block is given the calculated total panel mass and averaged specific heat capacity, and the ambient temperature is set to 25 °C. The controlled heat flow source then applies the calculated Q_{gen} directly to the thermal domain, allowing the model to capture the coupled electrical and thermal behavior of the photovoltaic panel under various operating conditions. A temperature sensor feeds the current thermal mass temperature back into the PV array block, allowing the electrical performance to respond dynamically to thermal conditions, while the generated current and convection losses together affect the thermal mass temperature over time.

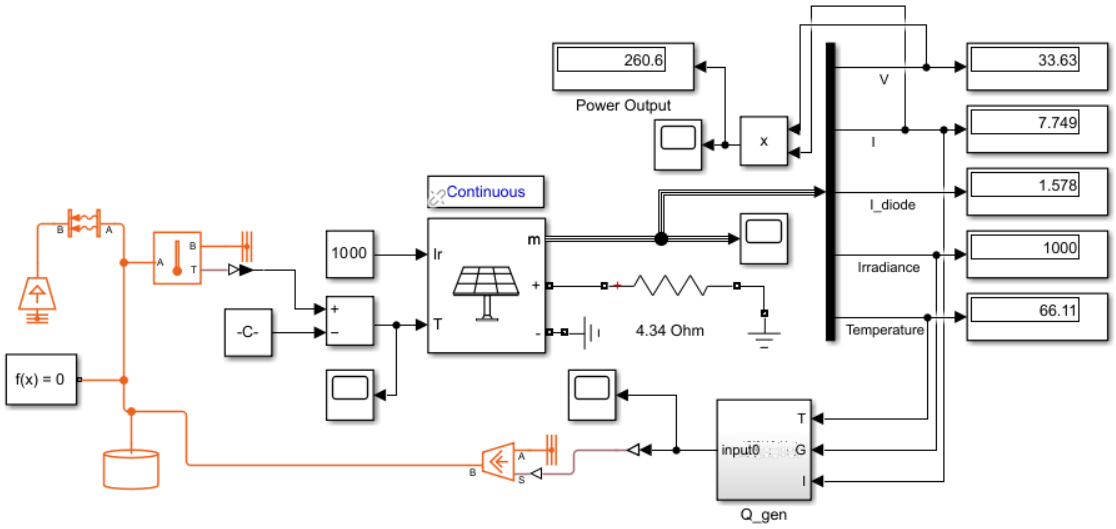


Figure 4: *Coupled Simulink–Simscape thermal model of the PV array*

By analyzing the results of running this configuration, the PV measurement outputs clearly show the influence of temperature on power generation. The PV array block receives the real-time thermal mass temperature as an input, linking cell temperature directly to electrical performance. Once the system reaches steady state, the panel temperature stabilizes at 66.11 °C, about 40 °C above the ambient 25 °C, which leads to a reduced power output of 260.6 W.

III. Results and Validation

To assess the logical accuracy of the simulation, it is helpful to examine several interconnected performance indicators through both numerical analysis and graphical results. A key parameter is the temperature coefficient gamma (γ), which can be calculated from the simulation output and compared to typical values reported for similar photovoltaic modules. This comparison helps verify whether the model realistically captures the panel's thermal sensitivity. Another important factor is the heat generation rate, Q_{gen}, where the simulated heat produced from absorbed solar irradiance and resistive losses is compared against theoretical values derived from the governing equations.

The panel's temperature evolution also serves as a valuable check. By tracking the thermal mass temperature over time, we can confirm whether the system reaches a steady state consistent with the assumed environmental conditions, such as irradiance and cooling. Similarly, the steady-state electrical power output can be compared with the rated power from the datasheet at standard reference temperature, adjusting for temperature effects using the calculated gamma. Additional confidence in the model arises from verifying that simulated convective heat losses align with

analytical estimates based on the panel's surface area and heat transfer coefficient. It is also important to confirm that the coupling between electrical and thermal behaviors produces consistent trends in voltage, current, and temperature.

Figure 5 presents the simulation results for the total heat generation rate, Q_{gen}, which stabilizes at around 1695 W. This value reflects the net thermal energy generated within the panel from solar absorption and resistive heating, after subtracting the electrical power output. The gradual rise and eventual leveling of the curve indicate that the system reaches thermal equilibrium, where internal heat generation balances heat loss to the environment.

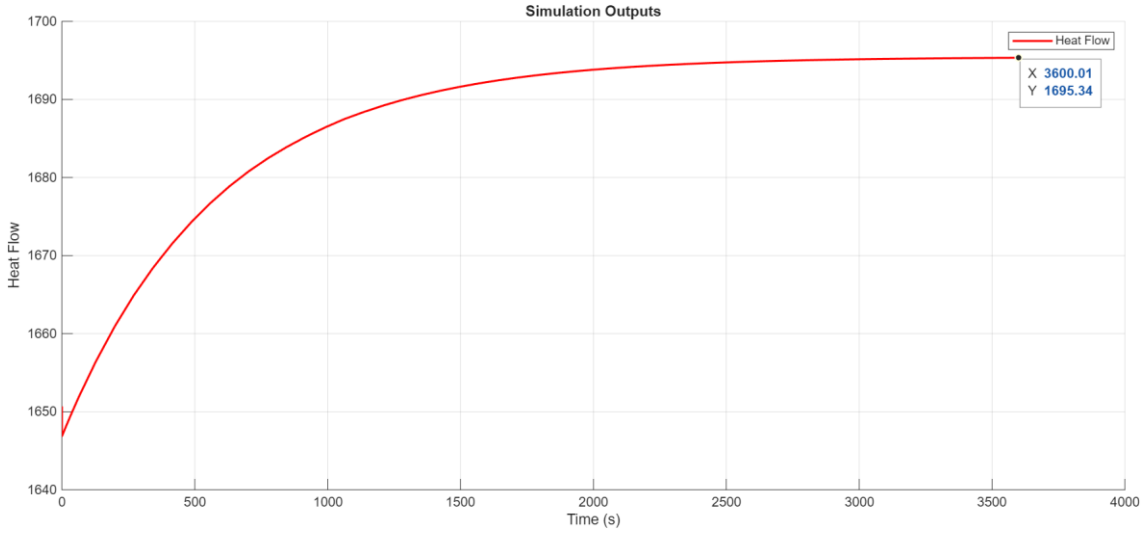


Figure 5: *Simulated heat generation rate of the solar panel as a function of time*

Thermal equilibrium occurs when the heat generated inside the solar panel equals the heat lost to the surroundings, resulting in a stable panel temperature. In this steady state, the total heat produced from absorbed solar radiation and resistive electrical losses is balanced by heat dissipated through convection and radiation. By calculating the combined heat generation from these sources, we can verify the simulated steady-state heat flow. The computed heat generation should closely match the heat flow observed in the simulation, confirming that the model accurately represents the thermal behavior of the photovoltaic panel.

$$Q_{gen} = Q_{sun} + Q_{res} = G \cdot A \cdot (1 - \eta) + I^2 \cdot R_s \tag{8}$$

The absorbed solar energy Q_{sun} is determined from the product of irradiance, panel surface area, and efficiency, while the resistive heating Q_{res} comes from the current squared multiplied by the series resistance. Using an irradiance G of 1000 W/m², a sun affected front surface area of 1.94 m², an efficiency of 0.1675, a steady-state current of 7.749 A, and a series resistance of 0.425 Ω, the absorbed solar energy is about 1615 W, and the resistive heating is about 25.5 W. After accounting for the portion of absorbed energy that leaves as electrical output and minor optical losses, the remaining heat within the panel is approximately 1640.5 W, which closely matches the steady-state value of 1695 W obtained in the simulation.

In addition to verifying the heat generation rate, the temperature response of the panel was also analyzed to provide a complete picture of the thermal behavior. Figure 6 shows the panel's thermal mass temperature rising from 25 °C to approximately 66.1 °C over time. This increase reflects the accumulation of heat within the panel as it approaches thermal equilibrium, balancing internal heat generation with dissipation to the environment.

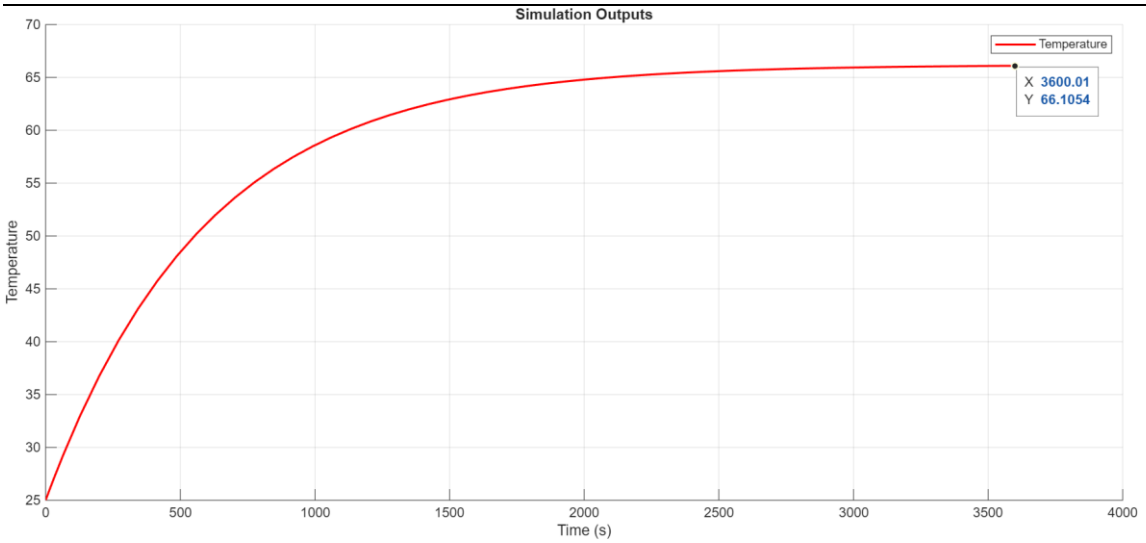


Figure 6: *Simulated temperature profile of the solar panel over time*

The curve shows a smooth exponential-like rise as the panel absorbs heat faster than it loses it to convection, until thermal equilibrium is reached. The final temperature represents the point where heat generation matches convective cooling. The panel temperature at steady state can be understood by equating the heat generated within the solar panel to the heat dissipated through convection. This relationship is described by Newton's law of cooling below.

$$Q_{conv} = h \cdot A_{convection} \cdot (T_{panel} - T_{amb}) \tag{9}$$

Here, Q_{conv} is the heat flowing away from the panel by convection. The coefficient h shows how well heat moves from the panel to the air around it, and $A_{convection}$ is the surface area where this happens. The heat transfer depends on the temperature difference between the panel surface T_{panel} and the surrounding air T_{amb}. In this study, we assume h to be 10 W/(m²·K), which corresponds to natural convection with a gentle 1 m/s breeze. The convection area is set as 4.11 m² based on the panel's total surface area. To figure out how much the panel's temperature rises above the ambient, we rearrange the equation like this.

$$\Delta T = \frac{Q_{gen}}{h \cdot A_{conv}} \tag{10}$$

In this form, ΔT represents the increase in panel temperature resulting from internal heat generation Q_{gen}. Using the simulated heat generation value of 1640.5 W, the calculated temperature rise is approximately 39.9 °C, indicating how much hotter the panel surface becomes compared to the surrounding environment. Finally, adding this temperature rise to the ambient temperature provides the predicted panel temperature under steady-state conditions.

$$T_{panel} = T_{amb} + \Delta T \tag{11}$$

Given an ambient temperature of 25 °C, the expected panel temperature is approximately 64.9 °C. This value is in close agreement with the simulation output of 66.1 °C, demonstrating that the thermal model accurately represents the physical heat transfer. Figure 7 presents the power output decreasing from 325 W at standard conditions to about 260.6 W at the higher temperature. The drop corresponds to the temperature-induced reduction in panel efficiency, demonstrating the thermal effect on electrical performance.

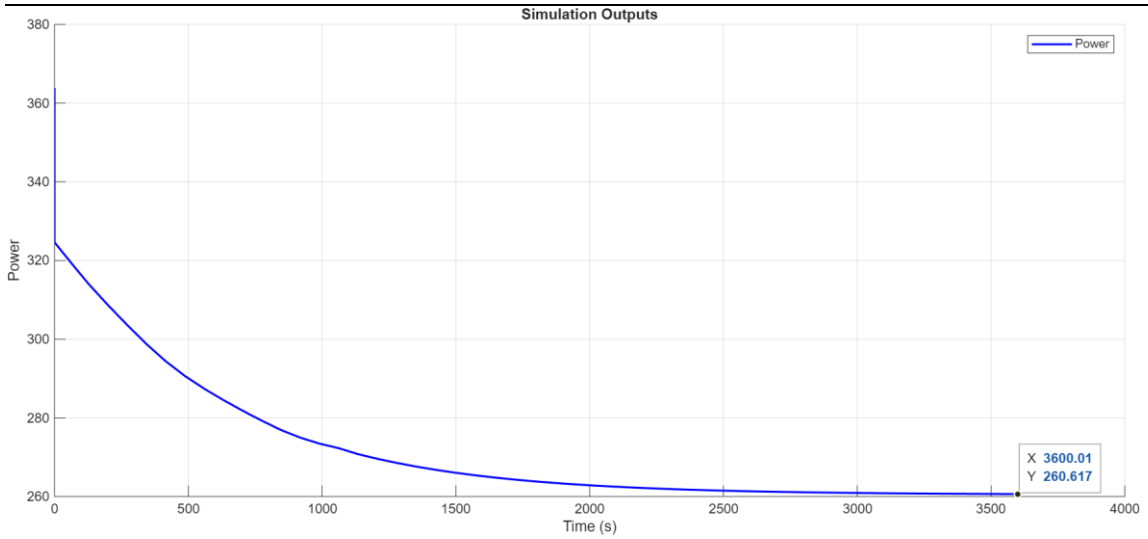


Figure 7: *Simulated output power of the solar panel over time*

Validation of the simulation results was performed through a two-step approach focusing on the temperature coefficient γ and the corresponding power output at elevated temperatures.

$$\gamma = \frac{\frac{P_{final}}{P_{rated}} - 1}{T_{final} - T_{ref}} \tag{12}$$

Where, P_{final} and T_{final} are the simulated power and panel temperature at steady state, and P_{rated} and T_{ref} correspond to the rated power and reference temperature. Using the simulated values of 260.6 W for P_{final}, 325 W for P_{rated}, 66.1 °C for T_{final} , and 25 °C for T_{ref} . This calculation yielded a temperature coefficient of approximately −0.00482 $°C^{-1}$, which closely matches the value of −0.0041 $°C^{-1}$ specified in the Simulink PV array block. Using the specified temperature coefficient, the expected power output at 66.1° is calculated as follows.

$$P = P_{rated} \cdot \left(1 + \gamma \cdot \left(T_{final} - T_{rated}\right)\right) \tag{13}$$

Substituting the known values resulted in a power output of approximately 267.6 W, which is in close agreement with the simulated output of 260.6 W. This agreement validates the model's ability to accurately capture the performance degradation of the photovoltaic panel.

IV. Conclusion

This study developed and validated an integrated thermal-electrical simulation model of a photovoltaic panel, accurately capturing temperature-dependent power degradation. Simulation results show a steady-state heat flow of approximately 1695 W, a panel temperature of 66.1 °C, and a power output of 260.6 W with a temperature coefficient γ of -0.0041 $°C^{-1}$ as specified in the Simulink PV array block. Theoretical calculations yielded a heat flow of about 1640.5 W, a panel temperature near 64.9 °C, a power output of 267.6 W, and an estimated γ of -0.00482 $°C^{-1}$ derived from the simulation data. Minor discrepancies between simulation and calculation arise from model simplifications, such as assumptions of uniform irradiance, constant convective heat transfer, and approximate thermal mass and resistance values, rather than from fundamental methodological issues. Despite these simplifications, the close agreement of key parameters confirms the model's reliability and provides a robust foundation for simulating and analyzing photovoltaic system performance under realistic thermal conditions.

References

[1] Betti, T., Kristić, A., Marasović, I., and Pekić, V. (2024). Accuracy of Simscape solar cell block for modeling a partially shaded photovoltaic module. *Energies*, 17(10), 2276. https://doi.org/10.3390/en17102276

[2] Shaik, F., Lingala, S.S., and Veeraboina, P. (2023). Effect of various parameters on the performance of solar PV power plant: a review and the experimental study. *Sustainable Energy Research*, 10(1), 6. https://doi.org/10.1186/s40807-023-00076-x

[3] Shaker, L.M., Al-Amiery, A.A., Hanoon, M.M., Al-Azzawi, W.K., and Kadhum, A.A.H. (2024). Examining the influence of thermal effects on solar cells: a comprehensive review. *Sustainable Energy Research*, 11(1), 6. https://doi.org/10.1186/s40807-024-00100-8

[4] Jacob, E., and Farzaneh, H. (2025). Modeling and performance evaluation of hybrid photovoltaic thermal, wind, and battery microgrids using optimization and dynamic simulation. *Scientific Reports*, 15(1), 11528. https://doi.org/10.1038/s41598-025-95149-w

[5] Ngunzi, V., Njoka, F., and Kinyua, R. (2023). Modeling, simulation and performance evaluation of a PVT system for the Kenyan manufacturing sector. *Heliyon*, 9(8), e18823. https://doi.org/10.1016/j.heliyon.2023.e18823

[6] Sawangsri, W., Kongcharoen, J., and Boonnam, N. (2022). Performance analysis of photovoltaic inverter system for predicting energy yield. *Energy Reports*, 8, 386–391. https://doi.org/10.1016/j.egyr.2022.01.078

[7] Al-Ezzi, A.S., and Ansari, M.N.M. (2022). Photovoltaic solar cells: A review. *Applied System Innovation*, 5(4), 67. https://doi.org/10.3390/asi5040067

[8] Bamisile, O., Acen, C., Cai, D., Huang, Q., and Staffell, I. (2025). The environmental factors affecting solar photovoltaic output. *Renewable and Sustainable Energy Reviews*, 208, 115073. https://doi.org/10.1016/j.rser.2024.115073

[9] Utomo, B., Darkwa, J., Du, D., and Worall, M. (2025). Solar photovoltaic cooling and power enhancement systems: A review. *Renewable and Sustainable Energy Reviews*, 216, 115644. https://doi.org/10.1016/j.rser.2025.115644

[10] Ben El Haj, M., and Ziani, S. (2025). Modeling and energy study of a photovoltaic-thermal (PV/T). In Farhaoui, Y., Herawan, T., Lucky Imoize, A., and Allaoui, A.E. (Eds.), *Intersection of artificial intelligence, data science, and cutting-edge technologies: From concepts to applications in smart environment* (pp. 376–382). Cham: Springer Nature Switzerland. https://doi.org/10.1007/978-3-031-90921-4_52

PERFORMANCE MEASURE OF OPTIMAL RESERVE INVENTORY MODEL BETWEEN TWO MACHINES WITH REFERENCE TO TRUNCATION POINT OF THE REPAIR TIME UNDER FUZZY ENVIRONMENT

Jagatheesan R* and Ramesh R[1]

•

*Assistant Professor, Department of Statistics, Salem Sowdeswari College, Salem-10, India
[1]Associate Professor, Department of Mathematics, Arignar Anna Government Arts College, Musiri, Tamilnadu, India
drrjstat@gmail.com, rameshsanju123@gmail.com
*Corresponding author: drrjstat@gmail.com

Abstract

In inventory control theory, various models have been developed to determine optimal stock levels in practical settings. In sequential production systems, reserve inventory is essential to minimize idle time when upstream machine failures occur. This study assumes that machine repair times are exponentially distributed and satisfy the Setting the Clock Back to Zero (SCBZ) property, with the truncation point itself modeled as a random variable following a mixed exponential distribution. Under these assumptions, an optimal reserve inventory model is derived and analyzed in a fuzzy environment. Uncertainty in system parameters is incorporated using fuzzy numbers, which are defuzzified through the Trisectional Fuzzy Trapezoidal ranking method. Numerical examples validate the applicability of the model in real-life scenarios.

Keywords: Reserve Inventory, SCBZ property, Repair time and Truncation point, Fuzzy Numbers, Trisectional Fuzzy Trapezoidal ranking.

I. Introduction

Mathematical modeling of inventory systems provides valuable insights into determining optimal inventory policies in real-world industrial environments. In sequential machine systems, reserve inventory is critical for reducing the idle costs of downstream machines during breakdowns of upstream machines.

Consider two machines, M1 and M2, where the output of M1 serves as the input for M2. If M1 fails, M2 remains idle, incurring significant costs. Maintaining reserve inventory between them minimizes such costs. However, excess reserves lead to holding costs, while insufficient stock increases idle time costs. Therefore, the challenge lies in determining an optimal reserve inventory that balances these conflicting costs. This problem was first formalized by Hanssmann [6], with subsequent contributions from Ramanarayanan et al. [12], Sachithanantham et al. [16, 17], and later Sachithanantham and Jagatheesan [18], who extended the model under the SCBZ property with truncation points as random variables. Further modifications were made by Ramathilagam et al. [13], and applications were discussed in series machine models by Srinivasan et al. [20], Sehik

Udhuman et al. [19], Nandakumar et al. [9, 10], and others.

Parallel developments included extensions to three-machine systems by Venkatesan et al. [21] and models using generalized distributions developed by Henry et al. [7]. Studies have also incorporated order statistics done by Govindhan et al. [5] and different change-point assumptions. Incorporating fuzzy set theory by Kaufmann [8] has enhanced realism in handling uncertain environments. Several fuzzy ranking methods have been proposed, including those by Chu [3], Chen et al. [2], Deng [4], Wang et al. [22], and Yager [23]. More recently, Ramesh et al. [14, 15] employed fuzzy ranking in queueing models.

This article enhances the model of Sachithanantham and Jagatheesan [18] by combining stochastic processes with fuzzy set theory, applying the Trisectional Fuzzy Trapezoidal ranking method for defuzzification. Numerical examples validate the model's robustness and applicability in reserve inventory management.

II. Preliminaries

Optimal Reserve Inventory - A system in which there are two machines M_1 and M_2 are in series. The output of the machine M_1 is the input of the machine M_2. The breakdown of M_1 causes the idle time of M_2, since there is no input to M_2 from M_1. The idle time of M2 is very costly and hence to avoid it, a reserve inventory is maintained in between M_1 and M_2. If the reserve inventory is surplus in quantity, there is an inventory holding cost. If the reserve inventory slacks in its quantity, then it assumes the high idle time cost. An inventory which is balancing out the above two costs is known as Optimal Reserve Inventory.

Fuzzy Number - A fuzzy number is a generalization of a regular real number in the sense that it does not refer to one single value but rather to a connected set of possible values, where each possible value has its own weight between 0 and 1.

Trapezoidal Fuzzy Number - A trapezoidal fuzzy number $\tilde{A}(a_1, a_2, a_3, a_4; 1)$ is dictated by a membership function

$$\mu_{\tilde{A}}(z) = \begin{cases} \dfrac{z-a_1}{a_2-a_1}, a_1 \le z \le a_2 \\ 1, \quad a_1 \le z \le a_2 \\ \dfrac{z-a_4}{a_3-a_4}, a_3 \le z \le a_4 \\ 0, \quad otherwise \end{cases}$$

III. Model Description

The model which is assumed that the lead time random variable follows an exponential distribution, which satisfies the so called SCBZ property and it is also assumed that the truncation point itself a random variable which has the mixed exponential distribution with parameter θ_1 and θ_2. Based on the above stated assumptions the optimal reserve inventory model considered by Sachithanantham et al. [18] the derived model is

$$\frac{h\mu r}{d} - \left[\beta e^{-s/r(\theta+\theta_1)} \left(\frac{\theta-\theta^*}{\theta_1+\theta-\theta^*} \right) + (1-\beta) e^{-s/r(\theta+\theta_2)} \left(\frac{\theta-\theta^*}{\theta_2+\theta-\theta^*} \right) \right. \\ \left. + e^{-\theta^*} (s/r) \left(\frac{\beta\theta_1}{(\theta_1+\theta-\theta^*)} + \frac{(1-\beta)\theta_2}{(\theta_2+\theta-\theta^*)} \right) \right] = 0 \quad (1)$$

where,

h	:	Inventory holding cost/ unit/ unit time.
d	:	Idle time cost due to M_2 / unit time.
μ	:	Mean time interval between successive breakdown of machine M_1, assuming exponential distribution of inter-arrival times.
t	:	Continuous random variable denoting the repair time of M_1 with pdf g(.) and c.d.f G(.)
r	:	Constant consumption rate of M_2 per unit of time.
S	:	Reserve inventory between M_1 and M_2.
T	:	Random variable denoting the idle time of M_2.
θ	:	Parameter of exponential distribution before the truncation point.
θ^*	:	Parameter of exponential distribution after the truncation point.
β	:	Probability value involved in the mixed exponential distribution.
θ_1, θ_2	:	Parameters of mixed exponential distribution.

Here the performance of above optimum reserve inventory model is verifying under fuzzy environment by using Tri-sectional Fuzzy Trapezoidal ranking method.

I. Tri-Sectional Fuzzy Trapezoidal Ranking– Algorithm

Let us consider an interval data (P, Q). The trisection of this interval is taken as d $d = \frac{Q-P}{3}$ then the required trapezoidal fuzzy number is [P, P+d, P+2d, Q]. Consider a normal trapezoidal fuzzy number $\tilde{A}[a_1, a_2, a_3, a_4]$ which is represented in Figure 1.

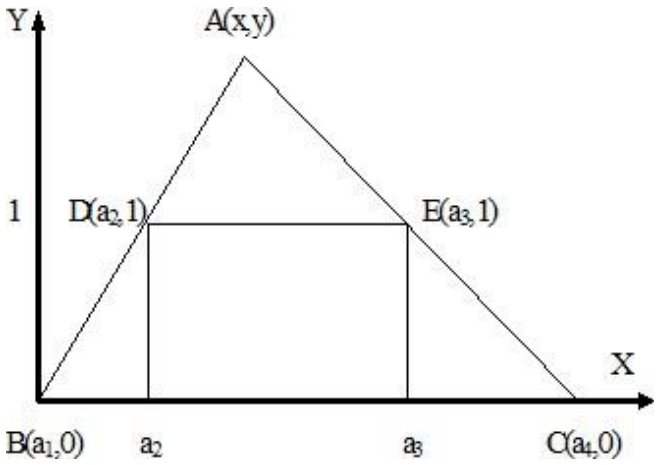


Figure1: *Normal Trapezoidal Fuzzy Number*

Extend the line joining B(a_1, 0) and D (a_2, 1) as BDA and the line joining C(a_4, 0) and E(a_3, 1) as CEA. The intersection of extended lines BD and CE is A. The coordinates for intersection point A is (x, y), where

$$x = \frac{a_1 a_3 - a_2 a_4}{a_3 - a_4 - a_2 + a_1}$$

$$y = \frac{x - a_2}{a_2 - a_1} + 1$$

The proposed ranking technique is based on the concept of in-center for triangle ABC and is noted in Figure 2

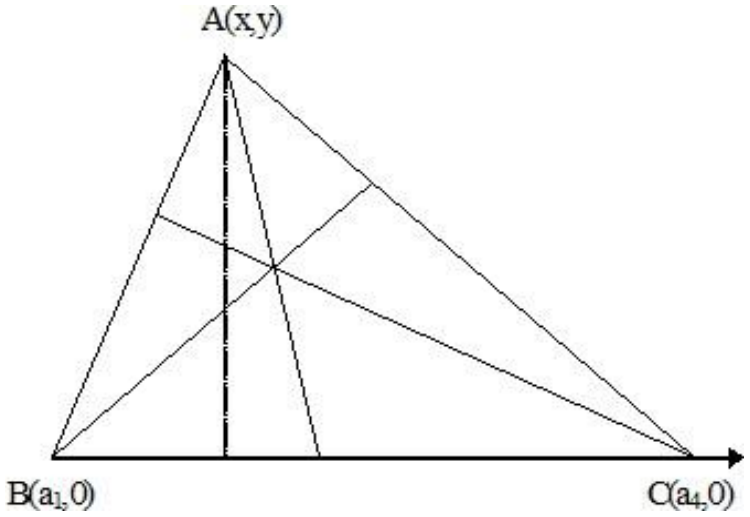


Figure 2 : *In-center*

and is defined as

$$R(\tilde{A}) = \frac{ax + ba_1 + a_4}{a + b + c}$$

where

$a = a_4 - a_1$, $b = \sqrt{y^2 + (a_4 - x)^2}$ and $c = \sqrt{y^2 + (x - a_1)^2}$

This proposed fuzzy ordering technique, which de-fuzzifies the fuzzy numerals in the optimum reserve inventory model. We have used these fuzzy numerals as the fuzzy parameters.

IV. Real – Life Cases

In tile manufacturing companies, there are at least two key steps involved in the production process. The first step is the creation of tiles using raw materials, and the second is the polishing of the tiles with colors and designs. In the event that the tile-making machine is under repair, the polishing machine would not receive any input. By applying the proposed model outlined in equation (1) and maintaining an optimal level of inventory, it is possible to avoid delays and the associated costs of waiting.

When this scenario is applied in a standard environment, the equation in (1) has already been derived and verified through numerical examples. In this case, however, the same scenario is applied in a fuzzy environment, and its performance is evaluated accordingly.

Trapezoidal fuzzy number - Let us assumes the values of various parameters in equation (1) and its performance were analyzed in Fuzzy environment.

Illustration 1.1: For$\tilde{d}$=[2500,2600,2700,2800], $\tilde{\mu}$=[4,6,8,10], $\tilde{r}$=[30,40,50,60], $\tilde{\theta}$=[2,3,4,5], $\tilde{\beta}$=[0.3,0.5,0.7,0.9], $\tilde{\theta}^*$=[0,2,4,6], $\tilde{\theta}_1$ = [0,2,4,6] , $\tilde{\theta}_2$ = [1,3,5,7], the optimal value of S is obtained and the variations in $\hat{S}$ for the changes in the value of $\tilde{h}$ are listed.

Now the ranking index of $\tilde{h}$is R($\tilde{h}$) = R(3,4,5,6) = 4.5 , R($\tilde{h}$) = R(4,5,6,7) = 5.5, R($\tilde{h}$) = R(5,6,7,8) = 6.5 and R($\tilde{h}$) = R(6,7,8,9) = 7.5.

Using the de-fuzzified value of the stock holding cost $\tilde{h}$, along with the corresponding de-fuzzified values of other relevant parameters, the optimal reserve inventory $\hat{S}$ is determined by

solving Equation (1). The results are summarized in the table provided below.

Table 1: *The variations in $\hat{S}$ for the changes in the value of $\tilde{h}$*

$\tilde{h}$	$\tilde{d}$	$\tilde{\mu}$	$\tilde{r}$	$\tilde{\theta}$	$\tilde{\beta}$	$\tilde{\theta}^*$	$\tilde{\theta}_1$	$\tilde{\theta}_2$	$\hat{S}$ x10^{-4}
[3,4, 5,6]	[2500,2600, 2700,2800]	[4,6, 8,10]	[30,40, 50,60]	[2,3, 4,5]	[0.3,0.5, 0.7,0.9]	[0,2, 4,6]	[0,2, 4,6]	[1,3 ,5,7]	203990
[4,5, 6,7]	[2500,2600, 2700,2800]	[4,6, 8,10]	[30,40, 50,60]	[2,3, 4,5]	[0.3,0.5, 0.7,0.9]	[0,2, 4,6]	[0,2, 4,6]	[1,3, 5,7]	174900
[5,6, 7,8]	[2500,2600, 2700,2800]	[4,6, 8,10]	[30,40, 50,60]	[2,3, 4,5]	[0.3,0.5, 0.7,0.9]	[0,2, 4,6]	[0,2, 4,6]	[1,3, 5,7]	151000
[6,7, 8,9]	[2500,2600, 2700,2800]	[4,6, 8,10]	[30,40, 50,60]	[2,3, 4,5]	[0.3,0.5, 0.7,0.9]	[0,2, 4,6]	[0,2, 4,6]	[1,3, 5,7]	130600

The above predicted values of $\hat{S}$ are shown in the following graph.

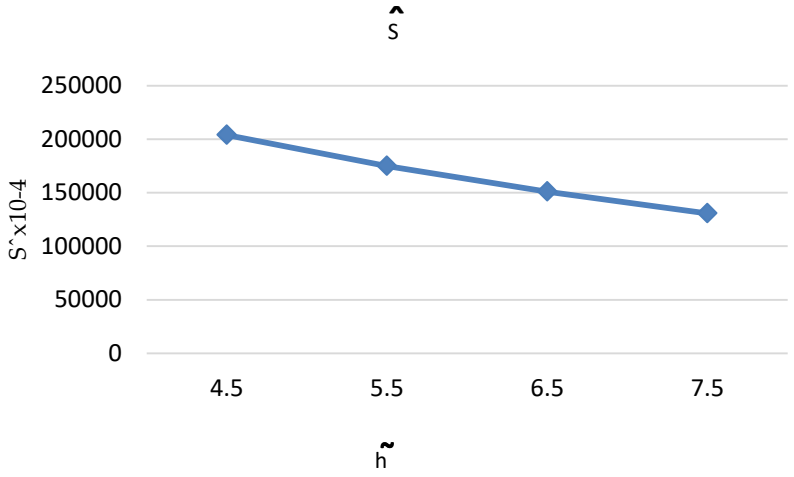


Figure 3: *Variations in $\hat{S}$ for the changes in the value of $\tilde{h}$*

From the graph (Figure 3), it is observed that if the values of the holding cost h˜increases, then the optimum base stock is reduced.

Illustration 1.2:

For $\tilde{h}$=[3, 4, 5, 6], $\tilde{\mu}$=[4,6,8,10],$\tilde{r}$=[30,40,50,60],$\tilde{\theta}$=[2,3,4,5],$\tilde{\beta}$=[0.3,0.5,0.7,0.9],$\tilde{\theta}^*$=[0,2,4,6], $\tilde{\theta}_1 = [0,2,4,6]$, $\tilde{\theta}_2 = [1,3,5,7]$, the optimal value of S is obtained and the variations in $\hat{S}$ for the changes in the value of $\tilde{d}$ are listed.

Now the ranking index of $\tilde{d}$ is $R(\tilde{d}) = R(2500, 2600, 2700, 2800) = 2650$, $R(\tilde{d}) = R(2600, 2700, 2800, 2900) = 2750$, $R(\tilde{d}) = R(2700, 2800, 2900, 3000) = 2850$ and $R(\tilde{d}) = R(2800, 2900, 3000, 3100) = 2950$.

By using the above de-fuzzified numbers for the idle time cost and similarly the de-fuzzified values of all other parameters, the optimal reserve inventory $\hat{S}$ is obtained by solving the equation (1) and are presented in the table below.

Table 2: *The variations in $\hat{S}$ for the changes in the value of $\tilde{d}$*

$\tilde{h}$	$\tilde{d}$	$\tilde{\mu}$	$\tilde{r}$	$\tilde{\theta}$	$\tilde{\beta}$	$\tilde{\theta}^*$	$\tilde{\theta}_1$	$\tilde{\theta}_2$	$\hat{S}$ x10^{-4}
[3,4, 5,6]	[2500,2600, 2700,2800]	[4,6, 8,10]	[30,40, 50,60]	[2,3, 4,5]	[0.3,0.5, 0.7,0.9]	[0,2, 4,6]	[0,2, 4,6]	[1,3, 5,7]	203990
[3,4, 5,6]	[2600,2700, 2800,2900]	[4,6, 8,10]	[30,40, 50,60]	[2,3, 4,5]	[0.3,0.5, 0.7,0.9]	[0,2, 4,6]	[0,2, 4,6]	[1,3, 5,7]	209300

[3,4, 5,6]	[2700,2800, 2900,3000]	[4,6, 8,10]	[30,40, 50,60]	[2,3, 4,5]	[0.3,0.5, 0.7,0.9]	[0,2, 4,6]	[0,2, 4,6]	[1,3, 5,7]	214500
[3,4, 5,6]	[2800,2900, 3000,3100]	[4,6, 8,10]	[30,40, 50,60]	[2,3, 4,5]	[0.3,0.5, 0.7,0.9]	[0,2, 4,6]	[0,2, 4,6]	[1,3, 5,7]	219600

The above predicted values of $\hat{S}$ are shown in the following graph.

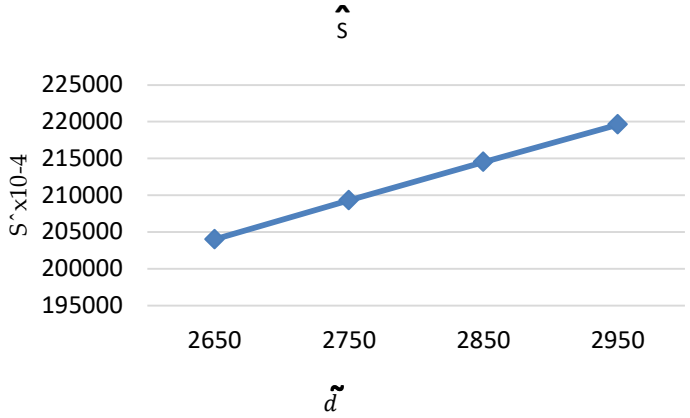


Figure 4: *Variations in $\hat{S}$ for the changes in the value of $\tilde{d}$*

From the graph (Figure 4), it is observed that if the values of the idle time cost $\tilde{d}$ increases, then the optimum base stock is increased.

Illustration 1.3: For $\tilde{h}$=[3, 4, 5, 6],$\tilde{d}$=[2500,2600,2700,2800], $\tilde{r}$=[30,40,50,60],$\tilde{\theta}$=[2,3,4,5], $\tilde{\beta}$=[0.3,0.5,0.7,0.9],$\tilde{\theta}^*$=[0,2,4,6], $\tilde{\theta}_1$ = [0,2,4,6] , $\tilde{\theta}_2$ = [1,3,5,7], the optimal value of S is obtained and the variations in $\hat{S}$ for the changes in the value of $\tilde{\mu}$ are listed.

Now the ranking index of $\tilde{\mu}$ is R($\tilde{\mu}$) = R(1.5, 2.5, 3.5, 4.5) = 3, R($\tilde{\mu}$) = R(2.5, 3.5, 4.5, 5.5) = 4, R($\tilde{\mu}$) = R(3.5, 4.5, 5.5, 6.5) = 5 and R($\tilde{\mu}$) = R(4.5, 5.5, 6.5, 7.5) = 6

By using the above de-fuzzified numbers for the Mean time interval between successive breakdown of machine M_1 and similarly the de-fuzzified values of all other parameters, the optimal reserve inventory $\hat{S}$ is obtained by solving the equation (1) and are presented in the table below.

Table 3: *The variations in $\hat{S}$ for the changes in the value of* $\tilde{\mu}$

$\tilde{h}$	$\tilde{d}$	$\tilde{\mu}$	$\tilde{r}$	$\tilde{\theta}$	$\tilde{\beta}$	$\tilde{\theta}^*$	$\tilde{\theta}_1$	$\tilde{\theta}_2$	$\hat{S}$ x10^{-4}
[3,4,5,6]	[2500,2600, 2700,2800]	[1.5, 2.5, 3.5, 4.5]	[30,40, 50,60]	[2,3, 4,5]	[0.3,0.5, 0.7,0.9]	[0,2,4,6]	[0,2, 4,6]	[1,3, 5,7]	203990
[3,4,5,6]	[2500,2600, 2700,2800]	[2.5, 3.5, 4.5, 5.5]	[30,40, 50,60]	[2,3, 4,5]	[0.3,0.5, 0.7,0.9]	[0,2,4,6]	[0,2, 4,6]	[1,3, 5,7]	162450
[3,4,5,6]	[2500,2600, 2700,2800]	[3.5, 4.5, 5.5, 6.5]	[30,40, 50,60]	[2,3, 4,5]	[0.3,0.5, 0.7,0.9]	[0,2,4,6]	[0,2, 4,6]	[1,3, 5,7]	130650
[3,4,5,6]	[2500,2600, 2700,2800]	[4.5, 5.5, 6.5, 7.5]	[30,40, 50,60]	[2,3, 4,5]	[0.3,0.5, 0.7,0.9]	[0,2,4,6]	[0,2, 4,6]	[1,3, 5,7]	83580

The above predicted values of $\hat{S}$ are shown in the following graph.

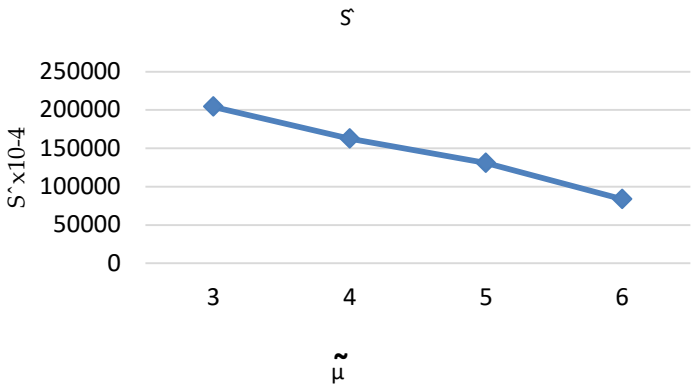


Figure 5: Variations in $\hat{S}$ for the changes in the value of $\tilde{\mu}$

From the graph (Figure 5), it is observed that if the values of $\tilde{\mu}$ increases, then the optimum base stock is increased.

V. Findings

The performance of the proposed optimal reserve inventory model has been examined under a fuzzy environment using the Trisectional Fuzzy Trapezoidal ranking method. The numerical illustrations, supported by tables and graphs, reveal important managerial and theoretical insights into the behavior of the system:

Effect of Holding Cost (h): When the inventory holding cost increases, the optimal reserve inventory $\hat{S}$ decreases. This implies that organizations are encouraged to adopt a leaner reserve policy in high holding cost environments, minimizing storage expenses even at the risk of higher idle time.

Effect of Idle Time Cost (d): As the idle time cost of machine M2 increases, the optimal reserve inventory $\hat{S}$ increases. This result emphasizes the importance of ensuring a sufficient buffer stock when production downtime is highly penalized, as it directly safeguards against costly interruptions.

Effect of Mean Breakdown Interval (μ): An increase in the mean time between successive breakdowns leads to a decrease in $\hat{S}$. This is logical, as longer intervals between breakdowns reduce the likelihood of M2 experiencing input shortages, thereby lowering the need for larger reserves.

These findings highlight the trade-off between holding costs and downtime costs, illustrating that the reserve inventory acts as a balancing mechanism. The fuzzy environment introduces flexibility by accommodating uncertainty in parameters, ensuring that the derived solutions are not rigid but adaptable to real-world variability.

From a broader perspective, the results establish that the fuzzy-based model is robust, as the optimal solutions derived under fuzziness are consistent with those obtained in the crisp setting. This validates the practical reliability of the model and demonstrates its capability to integrate stochastic variability with decision-making under uncertainty.

VI. Concluding Remarks and Future Scope

This study successfully integrates stochastic processes, SCBZ property-based repair time analysis, and fuzzy set theory into a unified framework for reserve inventory optimization. The combination of mixed exponential distributions for truncation points with fuzzy defuzzification

techniques results in a more comprehensive and practical model.

Future extensions may include:

Extending the model to multi-machine or multi-stage systems, capturing more complex industrial workflows.

Considering time-varying parameters, such as age-dependent breakdown rates or dynamic consumption rates of M2.

Incorporating hybrid fuzzy-stochastic approaches, which may further refine accuracy in environments where both randomness and vagueness coexist strongly.

In conclusion, the proposed fuzzy-based reserve inventory model not only corroborates the findings of its crisp counterparts but also broadens their applicability to uncertain environments. This dual validation enhances confidence in the model, making it a valuable decision-support tool for modern manufacturing systems seeking to balance cost efficiency with operational reliability.

References

[1] Baimei, Y. Lihui, S. and Zhu, P. (2014). Research on optimal policy of single-period inventory managementwith two suppliers. *The Scientific World Journal*, 14:1–5.

[2] Chen, S. J. and Chen, S. M. (2007). Fuzzy risk analysis based on the ranking of generalized trapezoidal fuzzy numbers. *Applied Intelligence*, 26(1):1–11.

[3] Chu, T. C. and Tsao, C. T. (2002). Ranking fuzzy numbers with an area between the centroid point and original point. *Computers and Mathematics with Applications*, 43(1–2):111–117.

[4] Deng, Y. and Liu, Q. (2005). A TOPSIS-based centroid-index ranking method of fuzzy numbers and its applications in decision making. *Cybernetics and Systems*, 36(6):581–595.

[5] Govindhan, M. Elangovan, R. and Sathiyamoorthi, R. (2016). Determination of Optimal Reserve Inventory between Machines in Series, using Order Statistics, *Asia Pacific Journal of Research*, 1(11):66–76.

[6] Hanssmann, F. Operations research in production and inventory control. John Wiley and Sons, New York, 1962.

[7] Henry, L., Ramathilakam, S. and Sachithanantham, S. (2016). Optimal reserve inventory between two machines with repair time having SCBZ property – reference to truncation point of the repair time. *Acta Ciencia Indica*, 42M(3):227–236.

[8] Kaufmann, A. Introduction to the theory of fuzzy subsets, Volume - I. Academic Press, New York, 1975.

[9] Nandakumar, C. D. and Srinivasan, S. (2012). Optimal reserve inventory between two machines when the Repair time has change of distribution after a change point. *International Mathematical Forum*, 7(54):2659 – 2668.

[10] Nandakumar, C. D. and Srinivasan, S. (2015). Optimal reserve inventory between two machines when the duration of breakdown time undergoes some distributions. *Malaya Journal of Matematik*, S(1):305–313.

[11] Raja Rao, B. R. and Talwalker, S. (1990). Setting the clock back to zero property of a family of life distributions. *Journal of Statistical Planning and Inference*, 24(3):347–352.

[12] Ramanarayanan, R., Ramachandran, V. and Sathiyamoorthi, R. (1998). Base stock system for patient clients when interarrival times of demands are dependent. *ASR*, 2(1):1–6.

[13] Ramathilagam, S., Henry, L. and Sachithanantham, S. (2014). A model for optimal reserve stock between two machines in series with repair time undergoes a parametric change. *Ultra Scientist*, 26(3):227–237.

[14] Ramesh, R. and Hari Ganesh, A. (2019). M/M/1/N fuzzy queueing models with discouraged arrivals under Wingspans fuzzy ranking method. *International Journal of Applied Engineering Research*, 14(4):1–12.

[15] Ramesh, R. and Seenivasan, R. (2020). Performance measures of two heterogeneous servers queueing models under trisectional fuzzy trapezoidal approach. *Malaya Journal of Matematik*, S(1):392–396.

[16] Sachithanantham, S., Ganesan, V. and Sathiyamoorthi, R. (2006). Optimal reserves for two machines with repair time having SCBZ property. *Bulletin of Pure and Applied Sciences*, 25E(2):287–297.

[17] Sachithanantham, S., Ganesan, V. and Sathiyamoorthi, R. (2007). A model for optimal reserve stock between two machines in series. *Journal of Indian Academy of Mathematics*, 29(1):59–70.

[18] Sachithanantham, S. and Jagatheesan, R. (2017). A model for optimal reserve stock between two machines with reference to the distribution of repair time. International Journal of Mathematics Trend and Technology, 47(1):74–80.

[19] Sehik Uduman, P.S., Sulaiman, A. and Sathiyamoorthy, R., (2007). Determination of Optimal ReserveInventory Between Two Machines in Series Using Order Statistics, Ultra Scientist of Physical Sciences, 19(3):497–502.

[20] Srinivasan, S. Sulaiman, A. and Sathiyamoorthi. R. (2007). Optimal reserve inventory between two machines under SCBZ Property of Interarrival Times between Breakdowns, Ultra Scientist of Physical Sciences, 19(2):261–266.

[21] Venkatesan, T., Muthu, C. and Sathiyamoorthy, R. (2016). Determination of optimal reserve between three machines in series. *International Journal of Advanced Research in Mathematics and Applications*, 1(1):74–82.

[22] Wang, Y. J. and Lee, H. S. (2008). The revised method of ranking fuzzy numbers with an area between the centroid and original points. *Computers and Mathematics with Applications*, 55(9): 2033–2042.

[23] Yager, R. R. (1981). A procedure for ordering fuzzy subsets of the unit interval. *Information Sciences*, 24(2):143-161.

RT&A, No 4 (89)
Volume 20, December 2025

A TAYLOR SERIES EXPANSION METHOD FOR SOLVING LINEAR FRACTIONAL PROGRAMMING PROBLEMS

Poonam Kumari

•

Department of Mathematics, Magadh Mahila College, Patna University, Patna, India
poonamkumari1865@gmail.com

Abstract

This paper proposes an iterative method to solve Linear Fractional Programming (LFP) problems with inequality constraints. The core idea is to approximate the fractional objective function through a series of linear programming (LP) problems, solved successively using updated feasible points. The algorithm begins by selecting a non-zero feasible point that satisfies all inequality constraints. At this point, the fractional objective function is expanded using a first-order Taylor series, resulting in a linear approximation. This converts the LFP problem into a standard LP problem, which can be solved using common optimization techniques such as the simplex method or the graphical method, depending on the problem's size and complexity. The optimal solution of the LP problem is then used as the new feasible point for the next iteration. In each iteration, the fractional objective function is re-linearized around the current solution, and a new LP problem is formed and solved. This process continues until convergence is achieved, that is, when two successive iterations produce the same or sufficiently similar solutions. The final solution is taken as the optimal solution to the original LFP problem. The effectiveness and practical utility of the proposed method are demonstrated through numerical examples. Results indicate that the approach is computationally efficient and provides accurate solutions. Compared to traditional transformation-based techniques, the proposed method avoids the introduction of auxiliary variables or complex reformulations, offering a more intuitive and implementable solution framework. Furthermore, the approach exhibits potential for extension to more complex fractional programming models, including multi-objective and equality-constrained formulations.

Keywords: Linear fractional programming, optimal solution, Taylor series

I. Introduction

A linear fractional programming (LFP) problem is a mathematical optimization problem that involves maximizing or minimizing the ratio of two linear functions subject to linear constraints and non-negativity restrictions on the decision variables. This mathematical approach was introduced by the Hungarian mathematician Martos in 1960 and has found broad applications in scenarios where efficiency or cost-effectiveness is better modeled by ratios rather than absolute values, like health care planning, production scheduling, Markow chain decision-making, economics, and more. The growing relevance of LFP problems in various sectors has attracted substantial attention from researchers seeking efficient methods to solve these problems.

Several techniques have been developed to tackle LFP problems. However, many of these

methods require a positive denominator in the objective function for all feasible solutions, while also ensuring the feasible region is bounded. These requirements are often necessary to avoid undefined behavior in the optimization process and ensure solution stability.

In this work, we introduce a new method for solving LFP problems with the above assumptions. Our approach is based on the concept of approximating the objective function by Taylor series about any arbitrarily chosen feasible point and transforming the LFP problem to a LP problem. Truncating the series to a finite number of terms allows our method to converge in a fixed number of iterations. This approximation strategy preserves the essential structure of the original problem while leveraging the efficiency of linear programming solvers.

II. Literature Review

Over the years, several methods have been developed to solve Linear Fractional Programming (LFP) problems. One of the earliest and most well-known approaches was introduced by Charnes and Cooper [1], who employed a variable transformation technique to convert the fractional objective function into a linear one. Bitran and Novaes [2] proposed an alternative strategy by updating the objective function iteratively. Isbell and Marlow [3], as well as Martos [4], formulated a method based on solving a sequence of linear programs to arrive at the optimal solution. Swarup [5] extended the classical simplex method used in linear programming to accommodate the structure of LFP problems. Bector [6] and Seshan [7] tackled the problem using a dual formulation, providing insights into the duality structure of LFP. Stancu-Minasian [8] comprehensively presented the foundational concepts, theoretical developments and diverse applications of fractional programming, which served as a significant reference in the field. Bajalinov [9] relied on the simplex algorithm as the primary computational tool and utilized the graphical method for problems involving two variables. Tantawy [10] introduced a novel duality framework specifically designed for LFP problems, adapting classical duality concepts to suit the fractional structure of LFP. Jahan and Islam [11] approached the problem using the complementary slackness theorem, offering a condition-based method for identifying optimality. Hasan and Acharjee [12] introduced a computer-oriented technique using the Mathematica programming language, demonstrating the applicability of symbolic computation tools in solving LFP problems. Pandian and Jayalakshmi [13] proposed a denominator objective restriction method based on the simplex algorithm to solve LFP problems. Saha et al. [14] developed a computer-based algorithmic approach tailored for solving LFP problems efficiently. Das and Mandal [15] introduced a novel homotopy perturbation method, providing an analytical framework for finding solutions to LFP problems. Simi and Talukder [16] suggested a method incorporating duality concepts to address the solution of LFP problems more effectively. Kumari and Bhardwaj [17] utilized computer programming techniques to implement solution procedures for LFP problems. Yulin and Xin [18] applied the Charnes-Cooper transformation to simplify the fractional objective function into a linear programming model, subsequently using MATLAB functions to compute the optimal solution. Gupta and Raina [19] proposed an integer solution approach for linear fractional programming problems, expanding the applicability of fractional programming to integer domains. Bennani et al. [20] employed adaptive projection methods to solve LFP problems and further refined their approach by deriving optimal solutions using Lustig's interior point method [21], demonstrating the effectiveness of modern computational techniques in fractional programming. Kumari [22] proposed an algorithm based on the efficient selection of incoming vectors. Sahoo et al. [23] addressed intuitionistic fuzzy multi-objective linear fractional programming problems by developing an alternative approach tailored to handle the inherent uncertainty and vagueness in such models. Mustafa and Sulaiman [24] tackled LFP problems with rough interval data by

transforming them into linear programming problems with interval coefficients, thereby enabling the use of established LP solution techniques under uncertainty. Chauhan et al. [25] solved linear fractional programming problems with fuzzy variables and unrestricted parameters using an alpha-cut-based method. Murugan and Thamaraiselvan [26] solved the interval linear fractional programming (ILFP) problem using interval arithmetic.

In this paper, a new method to solve LFP problem is proposed. The outline of the rest of the paper is as follows: The proposed method to solve the LFP problem is described in Section III. In Section IV, we present the algorithm for the proposed method. Numerical examples are provided in Section V. The validity of our approach is verified in Section VI by comparing its results to those of existing methods. Section VII discusses the significance of our proposed method. Finally, conclusions and possible directions for future research are presented in Section VIII.

III. Proposed Method

Let the LFP problem be

$$\left.\begin{array}{l} \text{Max } z = \frac{z^1}{z^2} = \frac{c_0+\mathbf{cx}}{d_0+\mathbf{dx}} \\ \text{subject to} \\ \mathbf{Ax} \le \mathbf{b}, \mathbf{x} \ge \mathbf{0}, \end{array}\right\} \tag{1}$$

where $\mathbf{c}$ and $\mathbf{d}$ are $1 \times n$ matrices, $\mathbf{A}$ is a $m \times n$ matrix, $\mathbf{b}$ is a $m \times 1$ column vector, $\mathbf{x}$ is a $n \times 1$ column vector, and c_0 and d_0 are constants.

Let the objective function of LFP problem (1) be denoted by $F(\mathbf{x})$, where $\mathbf{x} = [x_2 \quad x_2 \quad \dots \quad x_n]^T$. We choose any non-zero feasible point $\mathbf{x}^{(0)} = [a_2 \quad a_2 \quad \dots \quad a_n]^T$ as the initial feasible solution and expand $F(\mathbf{x})$ about $\mathbf{x}^{(0)}$ using Taylor series. Thus, we have

$$F(\mathbf{x}) = F(\mathbf{x}^{(0)}) + (x_1 - a_1)\left(\frac{\partial F}{\partial x_1}\right)_{(\mathbf{x}^{(0)})} + (x_2 - a_2)\left(\frac{\partial F}{\partial x_2}\right)_{(\mathbf{x}^{(0)})} + \dots + (x_n - a_n)\left(\frac{\partial F}{\partial x_n}\right)_{(\mathbf{x}^{(0)})}.$$

Now, we solve the following LP problem:

$$\left.\begin{array}{l} \text{Max } F(\mathbf{x}) \\ \text{subject to} \\ \mathbf{Ax} \le \mathbf{b}, \mathbf{x} \ge \mathbf{0} \end{array}\right\} \tag{2}$$

Let the optimal solution to the above LP problem be $\mathbf{x}^{(1)} = [k_2 \quad k_2 \quad \dots \quad k_n]^T$.

We have to check whether $\mathbf{x}^{(1)}$ is the optimal solution to given LFP problem (1) or not. For this, we repeat the process, taking $\mathbf{x}^{(1)}$ as the new feasible solution to LFP problem (1). Denoting the objective function of LFP problem (1) by $G(\mathbf{x})$ and expanding $G(\mathbf{x})$ about the new feasible point $\mathbf{x}^{(1)}$, we have

$$G(\mathbf{x}) = G(\mathbf{x}^{(1)}) + (x_1 - k_1)\left(\frac{\partial G}{\partial x_1}\right)_{(\mathbf{x}^{(1)})} + (x_2 - k_2)\left(\frac{\partial G}{\partial x_2}\right)_{(\mathbf{x}^{(1)})} + \dots + (x_n - k_n)\left(\frac{\partial G}{\partial x_n}\right)_{(\mathbf{x}^{(1)})}.$$

Now, we solve the following LP problem:

$$\left.\begin{array}{l} \text{Max } G(\mathbf{x}) \\ \text{subject to} \\ \mathbf{Ax} \le \mathbf{b}, \mathbf{x} \ge \mathbf{0} \end{array}\right\} \tag{3}$$

Let the optimal solution to the above LP problem be $\mathbf{x}^{(2)}$.

If $\mathbf{x}^{(1)} = \mathbf{x}^{(2)}$, then it provides the optimal solution to the given LFP problem (1). Otherwise, we expand the objective function of the given LFP problem (1) about $\mathbf{x}^{(2)}$ and solve the reconstructed LP problem. The process terminates when the optional solution to two consecutive LP problems coincides.

IV. Algorithm for the Proposed Method

Step 1. Choose any non-zero feasible point $\mathbf{x}^{(0)} = [a_2 \quad a_2 \quad \dots \quad a_n]^T$ as the initial feasible solution.

Step 2. Denote the objective function of LFP problem (1) by $F(\mathbf{x})$ and expand $F(\mathbf{x})$ about $\mathbf{x}^{(0)}$ using Taylor series.

Step 3. Solve the LP problem (2) by simplex method or graphical method. Let the optimal solution to LP problem (2) be $\mathbf{x}^{(1)} = [k_2 \quad k_2 \quad \dots \quad k_n]^T$.

Step 4. Denote the objective function of LFP problem (1) by $G(\mathbf{x})$ and expand $G(\mathbf{x})$ about $\mathbf{x}^{(1)}$ using Taylor series.

Step 5. Solve the LP problem (3) by simplex method or graphical method. Let the optimal solution to LP problem (2) be $\mathbf{x}^{(2)}$.

If $\mathbf{x}^{(1)} = \mathbf{x}^{(2)}$, then terminate the process. In this case, $\mathbf{x}^{(1)} = \mathbf{x}^{(2)}$ is the optimal solution to given LFP problem.

If $\mathbf{x}^{(1)} \neq \mathbf{x}^{(2)}$, then go to Step 4 and repeat the process, taking $\mathbf{x}^{(2)}$ in place of $\mathbf{x}^{(1)}$ until the criterion of optimality is satisfied.

V. Numerical Examples

Example 1. Max $\frac{8x_1+9x_2+4x_3+4}{2x_1+3x_2+2x_3+7}$ subject to
$x_1 + x_2 + 2x_3 \leq 3,\ 2x_1 + x_2 + 4x_3 \leq 4,\ 5x_1 + 3x_2 + x_3 \leq 15,\ x_1, x_2, x_3 \geq 0.$

Solution. Let $F(\mathbf{x}) = \frac{8x_1+9x_2+4x_3+4}{2x_1+3x_2+2x_3+7}$, where $\mathbf{x} = [x_1 \quad x_2 \quad x_3]^T$.

Let us take $\mathbf{x}^{(0)} = [0 \quad 1 \quad 0]^T$ as the initial feasible solution. Then $F(\mathbf{x}^{(0)}) = \frac{13}{10}$ and

$$\frac{\partial F}{\partial x_1} = \frac{6x_2 + 8x_3 + 48}{(2x_1 + 3x_2 + 2x_3 + 7)^2}, \quad \frac{\partial F}{\partial x_2} = \frac{-6x_1 + 6x_3 + 51}{(2x_1 + 3x_2 + 2x_3 + 7)^2}, \quad \frac{\partial F}{\partial x_3} = \frac{-8x_1 - 6x_2 + 20}{(2x_1 + 3x_2 + 2x_3 + 7)^2}.$$

Expanding $F(\mathbf{x})$ about $\mathbf{x}^{(0)}$ using Taylor series, we have

$$F(\mathbf{x}) = F(\mathbf{x}^{(0)}) + (x_1 - 0)\left(\frac{\partial F}{\partial x_1}\right)_{(\mathbf{x}^{(0)})} + (x_2 - 1)\left(\frac{\partial F}{\partial x_2}\right)_{(\mathbf{x}^{(0)})} + (x_3 - 0)\left(\frac{\partial F}{\partial x_3}\right)_{(\mathbf{x}^{(0)})}$$

i.e., $F(\mathbf{x}) = \frac{27}{50}x_1 + \frac{51}{100}x_2 + \frac{7}{50}x_3 + \frac{79}{100}$.

Therefore, the given LFP problem reduces to the following problem:

$$\left.\begin{array}{l} \text{Max } F(\mathbf{x}) = \frac{27}{50}x_1 + \frac{51}{100}x_2 + \frac{7}{50}x_3 + \frac{79}{100} \\ \text{subject to} \\ x_1 + x_2 + 2x_3 \leq 3,\ 2x_1 + x_2 + 4x_3 \leq 4,\ 5x_1 + 3x_2 + x_3 \leq 15, \\ x_1, x_2, x_3 \geq 0. \end{array}\right\} \quad \text{(I)}$$

We solve the above LP problem by simplex method.

Introducing slack variables x_4, x_5, x_6, the given constraints reduce to

$$x_1 + x_2 + 2x_3 + x_4 = 3, \quad 2x_1 + x_2 + 4x_3 + x_5 = 4, \quad 5x_1 + 3x_2 + x_3 + x_6 = 15.$$

Now, using simplex method, we obtain the following simplex tables:

Table 1(a): *Initial table for LPP (I)*

B	$\mathbf{c}_B$	$\mathbf{X}_B$	$\mathbf{y}_1$	$\mathbf{y}_2$	$\mathbf{y}_3$	$\mathbf{y}_4$	$\mathbf{y}_5$	$\mathbf{y}_6$	$\frac{x_{B_i}}{y_{ij}}$
$\mathbf{y}_4$	0	3	1	1	2	1	0	0	3
$\mathbf{y}_5$	0	4	(2)	1	4	0	1	0	2
$\mathbf{y}_6$	0	15	5	3	1	0	0	1	3
$F(\mathbf{x}) = \frac{79}{100}$		x_j	0	0	0	3	4	15	
		c_j	27/50	51/100	7/50	0	0	0	
		$c_j - \mathbf{c}_B\mathbf{y}_j$	27/50	51/100	7/50	0	0	0	
			↑				↓		

Table 1(b): *Intermediate table for LPP (I)*

B	$\mathbf{c}_B$	$\mathbf{X}_B$	$\mathbf{y}_1$	$\mathbf{y}_2$	$\mathbf{y}_3$	$\mathbf{y}_4$	$\mathbf{y}_5$	$\mathbf{y}_6$	$\frac{x_{B_i}}{y_{ij}}$
$\mathbf{y}_4$	0	1	0	1/2	0	1	-1/2	0	2
$\mathbf{y}_1$	27/50	2	1	1/2	2	0	1/2	0	4
$\mathbf{y}_6$	0	5	0	1/2	-9	0	-5/2	1	10
$F(\mathbf{x}) = \frac{187}{100}$		x_j	2	0	0	1	0	5	
		c_j	27/50	51/100	7/50	0	0	0	
		$c_j - \mathbf{c}_B\mathbf{y}_j$	0	6/25	-47/50	0	-27/100	0	
				↑		↓			

Table 1(c): *Final table for LPP (I)*

B	$\mathbf{c}_B$	$\mathbf{X}_B$	$\mathbf{y}_1$	$\mathbf{y}_2$	$\mathbf{y}_3$	$\mathbf{y}_4$	$\mathbf{y}_5$	$\mathbf{y}_6$
$\mathbf{y}_2$	51/100	2	0	1	0	2	-1	0
$\mathbf{y}_1$	27/50	1	1	0	2	-1	1	0
$\mathbf{y}_6$	0	4	0	0	-9	-1	-2	1
$F(\mathbf{x}) = \frac{47}{20}$		x_j	1	2	0	0	0	4
		c_j	27/50	51/100	7/50	0	0	0
		$c_j - \mathbf{c}_B\mathbf{y}_j$	0	0	-47/50	-12/25	-3/100	0

Now the optimality criterion has been met, indicating that the optimal solution to the LP problem has been found. This optimal solution is as follows:

$\mathbf{x}^{(1)} = [x_1 \;\; x_2 \;\; x_3]^T = [1 \;\; 2 \;\; 0]^T$ and $\max F(\mathbf{x}) = 47/20$.

To check that this optimal solution is the optimal solution to the given LFP problem, we repeat the process, taking $\mathbf{x}^{(1)} = [1 \quad 2 \quad 0]^T$ as the new feasible solution to the given LFP problem.

Denoting the objective function of the given LFP problem by $G(\mathbf{x})$, we have

$$G(\mathbf{x}^{(1)}) = 2, \quad \left(\frac{\partial G}{\partial x_1}\right)_{(\mathbf{x}^{(1)})} = \frac{4}{15}, \quad \left(\frac{\partial G}{\partial x_2}\right)_{(\mathbf{x}^{(1)})} = \frac{1}{5}, \quad \left(\frac{\partial G}{\partial x_3}\right)_{(\mathbf{x}^{(1)})} = 0.$$

Therefore, the reconstructed LP problem is

$$\left.\begin{array}{l} \text{Max } G(\mathbf{x}) = \frac{4}{15}x_1 + \frac{1}{5}x_2 + \frac{4}{3} \\ \text{subject to} \\ x_1 + x_2 + 2x_3 \le 3, \;\; 2x_1 + x_2 + 4x_3 \le 4, \;\; 5x_1 + 3x_2 + x_3 \le 15, \\ x_1, x_2, x_3 \ge 0. \end{array}\right\} \quad \text{(II)}$$

Now, introducing slack variables x_4, x_5, x_6 and using simplex method, we obtain the following simplex tables:

Table 1(d): *Initial table for LPP (II)*

B	$\mathbf{c}_B$	$\mathbf{X}_B$	$\mathbf{y}_1$	$\mathbf{y}_2$	$\mathbf{y}_3$	$\mathbf{y}_4$	$\mathbf{y}_5$	$\mathbf{y}_6$	$\frac{x_{B_i}}{y_{ij}}$
$\mathbf{y}_4$	0	3	1	1	2	1	0	0	3
$\mathbf{y}_5$	0	4	2	1	4	0	1	0	2
$\mathbf{y}_6$	0	15	5	3	1	0	0	1	3
$G(\mathbf{x}) = \frac{4}{3}$		x_j	0	0	0	3	4	15	
		c_j	4/15	1/5	0	0	0	0	
		$c_j - \mathbf{c}_B\mathbf{y}_j$	4/15	1/5	0	0	0	0	
			↑				↓		

Table 1(e): *Intermediate table for LPP (II)*

B	$\mathbf{c}_B$	$\mathbf{X}_B$	$\mathbf{y}_1$	$\mathbf{y}_2$	$\mathbf{y}_3$	$\mathbf{y}_4$	$\mathbf{y}_5$	$\mathbf{y}_6$	$\frac{x_{B_i}}{y_{ij}}$
$\mathbf{y}_4$	0	1	0	1/2	0	1	- (1/2)	0	2
$\mathbf{y}_1$	4/15	2	1	1/2	2	0	1/2	0	4
$\mathbf{y}_6$	0	5	0	1/2	-9	0	-5/2	1	10
		x_j	2	0	0	1	0	5	
$G(\mathbf{x}) = \frac{28}{15}$		c_j	4/15	1/5	0	0	0	0	
		$c_j - \mathbf{c}_B\mathbf{y}_j$	0	1/15	-8/15	0	-2/15	0	
				↑		↓			

Table 1(f): *Final table for LPP (II)*

B	$\mathbf{c}_B$	$\mathbf{X}_B$	$\mathbf{y}_1$	$\mathbf{y}_2$	$\mathbf{y}_3$	$\mathbf{y}_4$	$\mathbf{y}_5$	$\mathbf{y}_6$
$\mathbf{y}_2$	1/5	2	0	1	0	2	-1	0
$\mathbf{y}_1$	4/15	1	1	0	2	-1	1	0
$\mathbf{y}_6$	0	4	0	0	-9	-1	-2	1
		x_j	1	2	0	0	0	4
$G(\mathbf{x}) = 2$		c_j	4/15	1/5	0	0	0	0
		$c_j - \mathbf{c}_B\mathbf{y}_j$	0	0	-8/15	-2/15	-1/15	0

Now the optimality criterion has been met, indicating that the optimal solution to the LP problem has been found. This optimal solution is as follows:

$\mathbf{x}^{(2)} = [x_1 \;\; x_2 \;\; x_3]^T = [1 \;\; 2 \;\; 0]^T$ and max $G(\mathbf{x}) = 2$.

Obviously, $\mathbf{x}^{(1)} = \mathbf{x}^{(2)}$. Therefore the optimal solution to the given LFP problem is reached, which is given by $\mathbf{x} = [x_1 \;\; x_2 \;\; x_3]^T = [1 \;\; 2 \;\; 0]^T$ and max $z = 2$.

Example 2. Max $\frac{x_1 - 3x_2 + 3x_3}{x_1 + 2x_2 + x_3 + 1}$ subject to

$x_1 + x_2 - x_3 \le 6, \;\; -2x_1 - x_2 + 2x_3 \le 2, \;\; 2x_1 - 3x_2 + x_3 \le 3, \;\; x_1, x_2, x_3 \ge 0.$

Solution. Let $F(\mathbf{x}) = \frac{x_1 - 3x_2 + 3x_3}{x_1 + 2x_2 + x_3 + 1}$, where $\mathbf{x} = [x_1 \;\; x_2 \;\; x_3]^T$.

Let us take $\mathbf{x}^{(0)} = [1 \;\; 0 \;\; 0]^T$ as the initial feasible solution. Then $F(\mathbf{x}^{(0)}) = \frac{1}{2}$ and

$$\frac{\partial F}{\partial x_1} = \frac{5x_2 - 2x_3 + 1}{(x_1 + 2x_2 + x_3 + 1)^2}, \quad \frac{\partial F}{\partial x_2} = \frac{-5x_1 - 9x_3 - 3}{(x_1 + 2x_2 + x_3 + 1)^2}, \quad \frac{\partial F}{\partial x_3} = \frac{2x_1 + 9x_2 + 3}{(x_1 + 2x_2 + x_3 + 1)^2}.$$

Expanding $F(\mathbf{x})$ about $\mathbf{x}^{(0)}$ using Taylor series, we have

$$F(\mathbf{x}) = F(\mathbf{x}^{(0)}) + (x_1 - 1)\left(\frac{\partial F}{\partial x_1}\right)_{(\mathbf{x}^{(0)})} + (x_2 - 0)\left(\frac{\partial F}{\partial x_2}\right)_{(\mathbf{x}^{(0)})} + (x_3 - 0)\left(\frac{\partial F}{\partial x_3}\right)_{(\mathbf{x}^{(0)})}$$

i.e., $F(\mathbf{x}) = \frac{1}{4}x_1 - 2x_2 + \frac{5}{4}x_3 + \frac{1}{4}$.

Therefore, the given LFP problem reduces to the following problem:

$$\left.\begin{aligned} &\text{Max } F(\mathbf{x}) = \tfrac{1}{4}x_1 - 2x_2 + \tfrac{5}{4}x_3 + \tfrac{1}{4} \\ &\text{subject to} \\ &x_1 + x_2 - x_3 \le 6, \;\; -2x_1 - x_2 + 2x_3 \le 2, \;\; 2x_1 - 3x_2 + x_3 \le 3, \\ &x_1, x_2, x_3 \ge 0. \end{aligned}\right\} \quad \text{(I)}$$

To solve the above LP problem by simplex method, we introduce slack variables x_4, x_5, x_6. Then

$$x_1 + x_2 - x_3 + x_4 = 6, \quad -2x_1 - x_2 + 2x_3 + x_5 = 2, \quad 2x_1 - 3x_2 + x_3 + x_6 = 3.$$

Now, using simplex method, we obtain the following simplex tables:

Table 2(a): *Initial table for LPP (I)*

B	$\mathbf{c}_B$	$\mathbf{X}_B$	$\mathbf{y}_1$	$\mathbf{y}_2$	$\mathbf{y}_3$	$\mathbf{y}_4$	$\mathbf{y}_5$	$\mathbf{y}_6$	$\frac{x_{B_i}}{y_{ij}}$
$\mathbf{y}_4$	0	6	1	1	-1	1	0	0	-
$\mathbf{y}_5$	0	2	-2	-1	(2)	0	1	0	1
$\mathbf{y}_6$	0	3	2	-3	1	0	0	1	3
$F(\mathbf{x}) = \frac{1}{4}$		x_j	0	0	0	6	2	3	
		c_j	1/4	-2	5/4	0	0	0	
		$c_j - \mathbf{c}_B\mathbf{y}_j$	1/4	-2	5/4	0	0	0	
					↑		↓		

Table 2(b): *Intermediate table for LPP (I)*

B	$\mathbf{c}_B$	$\mathbf{X}_B$	$\mathbf{y}_1$	$\mathbf{y}_2$	$\mathbf{y}_3$	$\mathbf{y}_4$	$\mathbf{y}_5$	$\mathbf{y}_6$	$\frac{x_{B_i}}{y_{ij}}$
$\mathbf{y}_4$	0	7	0	1/2	0	1	1/2	0	-
$\mathbf{y}_3$	5/4	1	-1	-1/2	1	0	1/2	0	-
$\mathbf{y}_6$	0	2	(3)	-5/2	0	0	-1/2	1	2/3
$F(\mathbf{x}) = \frac{3}{2}$		x_j	0	0	1	7	0	2	
		c_j	1/4	-2	5/4	0	0	0	
		$c_j - \mathbf{c}_B\mathbf{y}_j$	3/2	-11/8	0	0	-5/8	0	
			↑					↓	

Table 2(c): *Final table for LPP (I)*

B	$\mathbf{c}_B$	$\mathbf{X}_B$	$\mathbf{y}_1$	$\mathbf{y}_2$	$\mathbf{y}_3$	$\mathbf{y}_4$	$\mathbf{y}_5$	$\mathbf{y}_6$
$\mathbf{y}_4$	0	7	0	1/2	0	1	1/2	0
$\mathbf{y}_3$	5/4	5/3	0	-4/3	1	0	1/3	1/3
$\mathbf{y}_1$	1/4	2/3	1	-5/6	0	0	-1/6	1/3
$F(\mathbf{x}) = \frac{5}{2}$		x_j	2/3	0	5/3	7	0	0
		c_j	1/4	-2	5/4	0	0	0
		$c_j - \mathbf{c}_B\mathbf{y}_j$	0	-1/8	0	0	-3/8	-1/2

Now the optimality criterion has been met, indicating that the optimal solution to the LP problem has been found. This optimal solution is as follows:

$\mathbf{x}^{(1)} = [x_1 \;\; x_2 \;\; x_3]^T = [2/3 \;\; 0 \;\; 5/3]^T$ and max $F(\mathbf{x}) = 5/2$.

In order to check that this optimal solution is the optimal solution to the given LFP problem, we repeat the process, taking $\mathbf{x}^{(1)} = [2/3 \;\; 0 \;\; 5/3]^T$ as the new feasible solution to the given LFP problem.

Denoting the objective function of the given LFP problem by $G(\mathbf{x})$, we have

$$G(\mathbf{x}^{(1)}) = \frac{17}{10}, \quad \left(\frac{\partial G}{\partial x_1}\right)_{(\mathbf{x}^{(1)})} = -\frac{21}{100}, \quad \left(\frac{\partial G}{\partial x_2}\right)_{(\mathbf{x}^{(1)})} = -\frac{48}{25}, \quad \left(\frac{\partial G}{\partial x_3}\right)_{(\mathbf{x}^{(1)})} = \frac{39}{100}.$$

Therefore, the reconstructed LP problem is

$$\left.\begin{aligned} &\text{Max } G(\mathbf{x}) = -\tfrac{21}{100}x_1 - \tfrac{48}{25}x_2 + \tfrac{39}{100}x_3 + \tfrac{119}{100} \\ &\text{subject to} \\ &x_1 + x_2 - x_3 \le 6, \;\; -2x_1 - x_2 + 2x_3 \le 2, \;\; 2x_1 - 3x_2 + x_3 \le 3, \\ &x_1, x_2, x_3 \ge 0. \end{aligned}\right\} \quad \text{(II)}$$

Now, introducing slack variables x_4, x_5, x_6 and using simplex method, we obtain the following simplex tables:

Table 2(d): *Initial table for LPP (II)*

B	$\mathbf{c}_B$	$\mathbf{X}_B$	$\mathbf{y}_1$	$\mathbf{y}_2$	$\mathbf{y}_3$	$\mathbf{y}_4$	$\mathbf{y}_5$	$\mathbf{y}_6$	$\frac{x_{B_i}}{y_{ij}}$
$\mathbf{y}_4$	0	6	1	1	-1	1	0	0	-
$\mathbf{y}_5$	0	2	-2	-1	(2)	0	1	0	1
$\mathbf{y}_6$	0	3	2	-3	1	0	0	1	3
$G(\mathbf{x}) = \frac{119}{100}$		x_j	0	0	0	6	2	3	
		c_j	-21/100	-48/25	39/100	0	0	0	
		$c_j - \mathbf{c}_B\mathbf{y}_j$	-21/100	-48/25	39/100	0	0	0	
					↑		↓		

Table 2(e): *Intermediate table for LPP (II)*

B	$\mathbf{c}_B$	$\mathbf{X}_B$	$\mathbf{y}_1$	$\mathbf{y}_2$	$\mathbf{y}_3$	$\mathbf{y}_4$	$\mathbf{y}_5$	$\mathbf{y}_6$	$\frac{x_{B_i}}{y_{ij}}$
$\mathbf{y}_4$	0	7	0	1/2	0	1	1/2	0	-
$\mathbf{y}_3$	39/100	1	-1	-1/2	1	0	1/2	0	-
$\mathbf{y}_6$	0	2	(3)	-5/2	0	0	-1/2	1	2/3
$G(\mathbf{x}) = \frac{79}{50}$		x_j	0	0	1	7	0	2	
		c_j	-21/100	-48/25	39/100	0	0	0	
		$c_j - \mathbf{c}_B\mathbf{y}_j$	9/50	-69/40	0	0	-39/200	0	
			↑					↓	

Table 2(f): *Final table for LPP (II)*

B	$\mathbf{c}_B$	$\mathbf{X}_B$	$\mathbf{y}_1$	$\mathbf{y}_2$	$\mathbf{y}_3$	$\mathbf{y}_4$	$\mathbf{y}_5$	$\mathbf{y}_6$
$\mathbf{y}_4$	0	7	0	1/2	0	1	1/2	0
$\mathbf{y}_3$	39/100	5/3	0	-4/3	1	0	1/3	1/3
$\mathbf{y}_1$	-21/100	2/3	1	-5/6	0	0	-1/6	1/3
$G(\mathbf{x}) = \frac{17}{10}$		x_j	2/3	0	5/3	7	0	0
		c_j	-21/100	-48/25	39/100	0	0	0
		$c_j - \mathbf{c}_B\mathbf{y}_j$	0	-63/40	0	0	-33/200	-3/50

Now the optimality criterion has been met, indicating that the optimal solution to the LP problem has been found. This optimal solution is as follows:

$\mathbf{x}^{(2)} = [x_1 \;\; x_2 \;\; x_3]^T = [2/3 \quad 0 \quad 5/3]^T$ and max $G(\mathbf{x}) = 17/10$.

Obviously, $\mathbf{x}^{(1)} = \mathbf{x}^{(2)}$. Therefore the optimal solution to the given LFP problem is reached, which is given by $\mathbf{x} = [x_1 \;\; x_2 \;\; x_3]^T = [2/3 \quad 0 \quad 5/3]^T$ and max $z = 17/10$.

Example 3. Max $\frac{x_1+2x_2+4x_3+5x_4+8x_5}{2x_1+5x_2+3x_3+4x_4+6x_5+1}$ subject to

$2x_1 + x_2 + 3x_3 + x_4 + x_5 \leq 15, \quad x_1 + 2x_2 + x_5 \leq 8,$
$3x_1 + 5x_2 + 2x_4 \leq 10, \quad 2x_2 + 4x_3 + 3x_4 + x_5 \leq 21,$
$x_1, x_2, x_3, x_4, x_5 \geq 0.$

Solution. Let $F(\mathbf{x}) = \frac{x_1+2x_2+4x_3+5x_4+8x_5}{2x_1+5x_2+3x_3+4x_4+6x_5+1}$, where $\mathbf{x} = [x_1 \;\; x_2 \;\; x_3 \;\; x_4 \;\; x_5]^T$.

Let us take $\mathbf{x}^{(0)} = [0 \;\; 1 \;\; 0 \;\; 1 \;\; 0]^T$ as the initial feasible solution. Then $F(\mathbf{x}^{(0)}) = \frac{7}{10}$ and

$$\frac{\partial F}{\partial x_1} = \frac{x_2 - 5x_3 - 6x_4 - 10x_5 + 1}{(2x_1 + 5x_2 + 3x_3 + 4x_4 + 6x_5 + 1)^2}, \quad \frac{\partial F}{\partial x_2} = \frac{-x_1 - 14x_3 - 17x_4 - 28x_5 + 2}{(2x_1 + 5x_2 + 3x_3 + 4x_4 + 6x_5 + 1)^2},$$

$$\frac{\partial F}{\partial x_3} = \frac{5x_1 + 14x_2 + x_4 + 4}{(2x_1 + 5x_2 + 3x_3 + 4x_4 + 6x_5 + 1)^2}, \quad \frac{\partial F}{\partial x_4} = \frac{6x_1 + 17x_2 - x_3 - 2x_5 + 5}{(2x_1 + 5x_2 + 3x_3 + 4x_4 + 6x_5 + 1)^2},$$

$$\frac{\partial F}{\partial x_5} = \frac{10x_1 + 28x_2 + 2x_4 + 8}{(2x_1 + 5x_2 + 3x_3 + 4x_4 + 6x_5 + 1)^2}.$$

Expanding $F(\mathbf{x})$ about $\mathbf{x}^{(0)}$ using Taylor series, we have

$$F(\mathbf{x}) = F(\mathbf{x}^{(0)}) + (x_1 - 0)\left(\frac{\partial F}{\partial x_1}\right)_{(\mathbf{x}^{(0)})} + (x_2 - 1)\left(\frac{\partial F}{\partial x_2}\right)_{(\mathbf{x}^{(0)})} + (x_3 - 0)\left(\frac{\partial F}{\partial x_3}\right)_{(\mathbf{x}^{(0)})}$$
$$+(x_4 - 1)\left(\frac{\partial F}{\partial x_4}\right)_{(\mathbf{x}^{(0)})} + (x_5 - 0)\left(\frac{\partial F}{\partial x_5}\right)_{(\mathbf{x}^{(0)})}$$

i.e., $F(\mathbf{x}) = -\frac{1}{25}x_1 - \frac{3}{20}x_2 + \frac{19}{100}x_3 + \frac{11}{50}x_4 + \frac{19}{50}x_5 + \frac{63}{100}$.

Therefore, the given LFP problem reduces to the following problem:

$$\left.\begin{array}{l} \text{Max } F(\mathbf{x}) = -\frac{1}{25}x_1 - \frac{3}{20}x_2 + \frac{19}{100}x_3 + \frac{11}{50}x_4 + \frac{19}{50}x_5 + \frac{63}{100} \\ \text{subject to} \\ 2x_1 + x_2 + 3x_3 + x_4 + x_5 \le 15, \quad x_1 + 2x_2 + x_5 \le 8, \\ 3x_1 + 5x_2 + 2x_4 \le 10, \quad 2x_2 + 4x_3 + 3x_4 + x_5 \le 21, \\ x_1, x_2, x_3, x_4, x_5 \ge 0. \end{array}\right\} \quad \text{(I)}$$

We solve the above LP problem by simplex method.

Introducing slack variables x_6, x_7, x_8, x_9, the given constraints reduce to

$$2x_1 + x_2 + 3x_3 + x_4 + x_5 + x_6 = 15, \quad x_1 + 2x_2 + x_5 + x_7 = 8,$$
$$3x_1 + 5x_2 + 2x_4 + x_8 = 10, \quad 2x_2 + 4x_3 + 3x_4 + x_5 + x_9 = 21.$$

Now, using simplex method, we obtain the following simplex tables:

Table 3(a): *Initial table for LPP (I)*

B	$\mathbf{c}_B$	$\mathbf{X}_B$	$\mathbf{y}_1$	$\mathbf{y}_2$	$\mathbf{y}_3$	$\mathbf{y}_4$	$\mathbf{y}_5$	$\mathbf{y}_6$	$\mathbf{y}_7$	$\mathbf{y}_8$	$\mathbf{y}_9$	$\frac{x_{B_i}}{y_{ij}}$
$\mathbf{y}_6$	0	15	2	1	3	1	1	1	0	0	0	15
$\mathbf{y}_7$	0	8	1	2	0	0	(1)	0	1	0	0	8
$\mathbf{y}_8$	0	10	3	5	0	2	0	0	0	1	0	-
$\mathbf{y}_9$	0	21	0	2	4	3	1	0	0	0	1	21
		x_j	0	0	0	0	0	15	8	10	21	
$F(\mathbf{x}) = \frac{63}{100}$		c_j	$-\frac{1}{25}$	$-\frac{3}{20}$	$\frac{19}{100}$	$\frac{11}{50}$	$\frac{19}{50}$	0	0	0	0	
		$c_j - \mathbf{c}_B\mathbf{y}_j$	$-\frac{1}{25}$	$-\frac{3}{20}$	$\frac{19}{100}$	$\frac{11}{50}$	$\frac{19}{50}$	0	0	0	0	
							↑		↓			

Table 3(b): *Intermediate table for LPP (I)*

B	$\mathbf{c}_B$	$\mathbf{X}_B$	$\mathbf{y}_1$	$\mathbf{y}_2$	$\mathbf{y}_3$	$\mathbf{y}_4$	$\mathbf{y}_5$	$\mathbf{y}_6$	$\mathbf{y}_7$	$\mathbf{y}_8$	$\mathbf{y}_9$	$\frac{x_{B_i}}{y_{ij}}$
$\mathbf{y}_6$	0	7	1	-1	3	1	0	1	-1	0	0	7
$\mathbf{y}_5$	$\frac{19}{50}$	8	1	2	0	0	1	0	1	0	0	-
$\mathbf{y}_8$	0	10	3	5	0	2	0	0	0	1	0	5
$\mathbf{y}_9$	0	13	-1	0	4	(3)	0	0	-1	0	1	$\frac{13}{3}$
		x_j	0	0	0	0	8	7	0	10	13	
$F(\mathbf{x}) = \frac{367}{100}$		c_j	$-\frac{1}{25}$	$-\frac{3}{20}$	$\frac{19}{100}$	$\frac{11}{50}$	$\frac{19}{50}$	0	0	0	0	
		$c_j - \mathbf{c}_B\mathbf{y}_j$	$-\frac{21}{50}$	$-\frac{91}{100}$	$\frac{19}{100}$	$\frac{11}{50}$	0	0	$-\frac{19}{50}$	0	0	
						↑					↓	

Table 3(c): *Final table for LPP (I)*

B	$\mathbf{c}_B$	$\mathbf{X}_B$	$\mathbf{y}_1$	$\mathbf{y}_2$	$\mathbf{y}_3$	$\mathbf{y}_4$	$\mathbf{y}_5$	$\mathbf{y}_6$	$\mathbf{y}_7$	$\mathbf{y}_8$	$\mathbf{y}_9$
$\mathbf{y}_6$	0	$\frac{8}{3}$	$\frac{4}{3}$	-1	$\frac{5}{3}$	0	0	1	$-\frac{2}{3}$	0	$-\frac{1}{3}$
$\mathbf{y}_5$	$\frac{19}{50}$	8	1	2	0	0	1	0	1	0	0
$\mathbf{y}_8$	0	$\frac{4}{3}$	$\frac{11}{3}$	5	$-\frac{8}{3}$	0	0	0	$\frac{2}{3}$	1	$-\frac{2}{3}$
$\mathbf{y}_4$	$\frac{11}{50}$	$\frac{13}{3}$	$-\frac{1}{3}$	0	$\frac{4}{3}$	1	0	0	$-\frac{1}{3}$	0	$\frac{1}{3}$
		x_j	0	0	0	$\frac{13}{3}$	8	$\frac{8}{3}$	0	$\frac{4}{3}$	0
$F(\mathbf{x}) = \frac{1387}{300}$		c_j	$-\frac{1}{25}$	$-\frac{3}{20}$	$\frac{19}{100}$	$\frac{11}{50}$	$\frac{19}{50}$	0	0	0	0
		$c_j - \mathbf{c}_B\mathbf{y}_j$	$-\frac{26}{75}$	$-\frac{91}{100}$	$-\frac{31}{300}$	0	0	0	$-\frac{23}{75}$	0	$-\frac{11}{150}$

Now the optimality criterion has been met, indicating that the optimal solution to the LP problem has been found. This optimal solution is as follows:

$\mathbf{x}^{(1)} = [x_1 \;\; x_2 \;\; x_3 \;\; x_4 \;\; x_5]^T = [0 \;\; 0 \;\; 0 \;\; 13/3 \;\; 8]^T$ and max $F(\mathbf{x}) = 1387/300$.

In order to check that this optimal solution is the optimal solution to the given LFP problem, we repeat the process, taking $\mathbf{x}^{(1)} = [0 \;\; 0 \;\; 0 \;\; 13/3 \;\; 8]^T$ as the new feasible solution to the given LFP problem.

Denoting the objective function of the given LFP problem by $G(\mathbf{x})$, we have

$$G(\mathbf{x}^{(1)}) = \frac{257}{199}, \quad \left(\frac{\partial G}{\partial x_1}\right)_{(\mathbf{x}^{(1)})} = -\frac{945}{39601}, \quad \left(\frac{\partial G}{\partial x_2}\right)_{(\mathbf{x}^{(1)})} = -\frac{2661}{39601},$$
$$\left(\frac{\partial G}{\partial x_3}\right)_{(\mathbf{x}^{(1)})} = \frac{75}{39601}, \quad \left(\frac{\partial G}{\partial x_4}\right)_{(\mathbf{x}^{(1)})} = -\frac{99}{39601}, \quad \left(\frac{\partial G}{\partial x_5}\right)_{(\mathbf{x}^{(1)})} = \frac{150}{39601}.$$

Therefore, the reconstructed LP problem is

$$\left.\begin{aligned} &\text{Max } G(\mathbf{x}) = -\tfrac{945}{39601}x_1 - \tfrac{2661}{39601}x_2 + \tfrac{75}{39601}x_3 - \tfrac{99}{39601}x_4 + \tfrac{150}{39601}x_5 + \tfrac{50372}{39601} \\ &\text{subject to} \\ &2x_1 + x_2 + 3x_3 + x_4 + x_5 \le 15, \quad x_1 + 2x_2 + x_5 \le 8, \\ &3x_1 + 5x_2 + 2x_4 \le 10, \quad 2x_2 + 4x_3 + 3x_4 + x_5 \le 21, \\ &x_1, x_2, x_3, x_4, x_5 \ge 0. \end{aligned}\right\} \quad \text{(II)}$$

Now, introducing slack variables x_6, x_7, x_8, x_9, and using simplex method, we obtain the following simplex tables:

Table 3(d): *Initial table for LPP (II)*

B	$\mathbf{c}_B$	$\mathbf{X}_B$	$\mathbf{y}_1$	$\mathbf{y}_2$	$\mathbf{y}_3$	$\mathbf{y}_4$	$\mathbf{y}_5$	$\mathbf{y}_6$	$\mathbf{y}_7$	$\mathbf{y}_8$	$\mathbf{y}_9$	$\frac{x_{B_i}}{y_{ij}}$
$\mathbf{y}_6$	0	15	2	1	3	1	1	1	0	0	0	15
$\mathbf{y}_7$	0	8	1	2	0	0	(1)	0	1	0	0	8
$\mathbf{y}_8$	0	10	3	5	0	2	0	0	0	1	0	-
$\mathbf{y}_9$	0	21	0	2	4	3	1	0	0	0	1	21
		x_j	0	0	0	0	0	15	8	10	21	
$G(\mathbf{x}) = \frac{50372}{39601}$		c_j	$-\frac{945}{39601}$	$-\frac{2661}{39601}$	$\frac{75}{39601}$	$-\frac{99}{39601}$	$\frac{150}{39601}$	0	0	0	0	
		$c_j - \mathbf{c}_B\mathbf{y}_j$	$-\frac{945}{39601}$	$-\frac{2661}{39601}$	$\frac{75}{39601}$	$-\frac{99}{39601}$	$\frac{150}{39601}$	0	0	0	0	
							↑		↓			

Table 3(e): *Intermediate table for LPP (II)*

B	$\mathbf{c}_B$	$\mathbf{X}_B$	$\mathbf{y}_1$	$\mathbf{y}_2$	$\mathbf{y}_3$	$\mathbf{y}_4$	$\mathbf{y}_5$	$\mathbf{y}_6$	$\mathbf{y}_7$	$\mathbf{y}_8$	$\mathbf{y}_9$	$\frac{x_{B_i}}{y_{ij}}$
$\mathbf{y}_6$	0	7	1	-1	3	1	0	1	-1	0	0	$\frac{7}{3}$
$\mathbf{y}_5$	$\frac{150}{39601}$	8	1	2	0	0	1	0	1	0	0	-
$\mathbf{y}_8$	0	10	3	5	0	2	0	0	0	1	0	-
$\mathbf{y}_9$	0	13	-1	0	4	3	0	0	-1	0	1	$\frac{13}{4}$
		x_j	0	0	0	0	8	7	0	10	13	
$G(\mathbf{x}) = \frac{51572}{39601}$		c_j	$-\frac{945}{39601}$	$-\frac{2661}{39601}$	$\frac{75}{39601}$	$-\frac{99}{39601}$	$\frac{150}{39601}$	0	0	0	0	
		$c_j - \mathbf{c}_B\mathbf{y}_j$	$-\frac{1095}{39601}$	$-\frac{2961}{39601}$	$\frac{75}{39601}$	$-\frac{99}{39601}$	0	0	$-\frac{150}{39601}$	0	0	
					↑			↓				

Table 3(f): *Final table for LPP (II)*

B	$\mathbf{c}_B$	$\mathbf{X}_B$	$\mathbf{y}_1$	$\mathbf{y}_2$	$\mathbf{y}_3$	$\mathbf{y}_4$	$\mathbf{y}_5$	$\mathbf{y}_6$	$\mathbf{y}_7$	$\mathbf{y}_8$	$\mathbf{y}_9$
$\mathbf{y}_3$	$\frac{75}{39601}$	$\frac{7}{3}$	$\frac{1}{3}$	$-\frac{1}{3}$	1	$\frac{1}{3}$	0	$\frac{1}{3}$	$-\frac{1}{3}$	0	0
$\mathbf{y}_5$	$\frac{150}{39601}$	8	1	2	0	0	1	0	1	0	0
$\mathbf{y}_8$	0	10	3	5	0	2	0	0	0	1	0
$\mathbf{y}_9$	0	$\frac{11}{3}$	$-\frac{7}{3}$	$\frac{4}{3}$	0	$\frac{5}{3}$	0	$-\frac{4}{3}$	$\frac{1}{3}$	0	1
		x_j	0	0	$\frac{7}{3}$	0	8	0	0	10	$\frac{11}{3}$
$G(\mathbf{x}) = \frac{51747}{39601}$		c_j	$-\frac{945}{39601}$	$-\frac{2661}{39601}$	$\frac{75}{39601}$	$-\frac{99}{39601}$	$\frac{150}{39601}$	0	0	0	0
		$c_j - \mathbf{c}_B\mathbf{y}_j$	$-\frac{1120}{39601}$	$-\frac{2936}{39601}$	0	$-\frac{124}{39601}$	0	$-\frac{25}{39601}$	$-\frac{125}{39601}$	0	0

Now the optimality criterion has been met, indicating that the optimal solution to the LP problem has been found. This optimal solution is as follows:

$\mathbf{x}^{(2)} = [x_1 \;\; x_2 \;\; x_3 \;\; x_4 \;\; x_5]^T == [0 \;\; 0 \;\; 7/3 \;\; 0 \;\; 8]^T$ and $\max G(\mathbf{x}) = 51747/39601 \approx 1.3$.

In order to check that optimal solution is the optimal solution to the given LFP problem, we repeat the process, taking $\mathbf{x}^{(2)} = [0 \;\; 0 \;\; 7/3 \;\; 0 \;\; 8]^T$ as the new feasible solution to the given LFP problem.

Denoting the objective function of the given LFP problem by $H(\mathbf{x})$, we have

$$H(\mathbf{x}^{(2)}) = \frac{55}{42}, \quad \left(\frac{\partial H}{\partial x_1}\right)_{(\mathbf{x}^{(2)})} = -\frac{17}{588}, \quad \left(\frac{\partial H}{\partial x_2}\right)_{(\mathbf{x}^{(2)})} = -\frac{191}{2352},$$

$$\left(\frac{\partial H}{\partial x_3}\right)_{(\mathbf{x}^{(2)})} = \frac{1}{784}, \quad \left(\frac{\partial H}{\partial x_4}\right)_{(\mathbf{x}^{(2)})} = -\frac{5}{1176}, \quad \left(\frac{\partial H}{\partial x_5}\right)_{(\mathbf{x}^{(2)})} = \frac{1}{392}.$$

Therefore, the reconstructed LP problem is

$$\left.\begin{aligned} &\text{Max } H(\mathbf{x}) = -\tfrac{17}{588}x_1 - \tfrac{191}{2352}x_2 + \tfrac{1}{784}x_3 - \tfrac{5}{1176}x_4 + \tfrac{1}{392}x_5 + \tfrac{3025}{2352} \\ &\text{subject to} \\ &2x_1 + x_2 + 3x_3 + x_4 + x_5 \le 15, \quad x_1 + 2x_2 + x_5 \le 8, \\ &3x_1 + 5x_2 + 2x_4 \le 10, \quad 2x_2 + 4x_3 + 3x_4 + x_5 \le 21, \\ &x_1, x_2, x_3, x_4, x_5 \ge 0. \end{aligned}\right\} \quad \text{(IIII)}$$

Now, introducing slack variables x_6, x_7, x_8, x_9, and using simplex method, we obtain the following simplex tables:

Table 3(g): *Initial table for LPP (III)*

B	$\mathbf{c}_B$	$\mathbf{X}_B$	$\mathbf{y}_1$	$\mathbf{y}_2$	$\mathbf{y}_3$	$\mathbf{y}_4$	$\mathbf{y}_5$	$\mathbf{y}_6$	$\mathbf{y}_7$	$\mathbf{y}_8$	$\mathbf{y}_9$	$\frac{x_{B_i}}{y_{ij}}$
$\mathbf{y}_6$	0	15	2	1	3	1	1	1	0	0	0	15
$\mathbf{y}_7$	0	8	1	2	0	0	1	0	1	0	0	8
$\mathbf{y}_8$	0	10	3	5	0	2	0	0	0	1	0	-
$\mathbf{y}_9$	0	21	0	2	4	3	1	0	0	0	1	21
		x_j	0	0	0	0	0	15	8	10	21	
$H(\mathbf{x}) = \frac{3025}{2352}$		c_j	$-\frac{17}{588}$	$-\frac{191}{2352}$	$\frac{1}{784}$	$-\frac{5}{1176}$	$\frac{1}{392}$	0	0	0	0	
		$c_j - \mathbf{c}_B\mathbf{y}_j$	$-\frac{17}{588}$	$-\frac{191}{2352}$	$\frac{1}{784}$	$-\frac{5}{1176}$	$\frac{1}{392}$	0	0	0	0	
							↑		↓			

Table 3(h): *Intermediate table for LPP (III)*

B	$\mathbf{c}_B$	$\mathbf{X}_B$	$\mathbf{y}_1$	$\mathbf{y}_2$	$\mathbf{y}_3$	$\mathbf{y}_4$	$\mathbf{y}_5$	$\mathbf{y}_6$	$\mathbf{y}_7$	$\mathbf{y}_8$	$\mathbf{y}_9$	$\frac{x_{B_i}}{y_{ij}}$
$\mathbf{y}_6$	0	7	1	-1	3	1	0	1	-1	0	0	$\frac{7}{3}$
$\mathbf{y}_5$	$\frac{1}{392}$	8	1	2	0	0	1	0	1	0	0	-
$\mathbf{y}_8$	0	10	3	5	0	2	0	0	0	1	0	-
$\mathbf{y}_9$	0	13	-1	0	4	3	0	0	-1	0	1	$\frac{13}{4}$
		x_j	0	0	0	0	8	7	0	10	13	
$H(\mathbf{x}) = \frac{3073}{2352}$		c_j	$-\frac{17}{588}$	$-\frac{191}{2352}$	$\frac{1}{784}$	$-\frac{5}{1176}$	$\frac{1}{392}$	0	0	0	0	
		$c_j - \mathbf{c}_B\mathbf{y}_j$	$-\frac{37}{1176}$	$-\frac{203}{2352}$	$\frac{1}{784}$	$-\frac{5}{1176}$	0	0	$-\frac{1}{392}$	0	0	
					↑			↓				

Table 3(i): *Final table for LPP (III)*

B	$\mathbf{c}_B$	$\mathbf{X}_B$	$\mathbf{y}_1$	$\mathbf{y}_2$	$\mathbf{y}_3$	$\mathbf{y}_4$	$\mathbf{y}_5$	$\mathbf{y}_6$	$\mathbf{y}_7$	$\mathbf{y}_8$	$\mathbf{y}_9$
$\mathbf{y}_3$	$\frac{1}{784}$	$\frac{7}{3}$	$\frac{1}{3}$	$-\frac{1}{3}$	1	$\frac{1}{3}$	0	$\frac{1}{3}$	$-\frac{1}{3}$	0	0
$\mathbf{y}_5$	$\frac{1}{392}$	8	1	2	0	0	1	0	1	0	0
$\mathbf{y}_8$	0	10	3	5	0	2	0	0	0	1	0
$\mathbf{y}_9$	0	$\frac{11}{3}$	$-\frac{7}{3}$	$\frac{4}{3}$	0	$\frac{5}{3}$	0	$-\frac{4}{3}$	$\frac{1}{3}$	0	1
		x_j	0	0	$\frac{7}{3}$	0	8	0	0	10	$\frac{11}{3}$
$H(\mathbf{x}) = \frac{55}{42}$		c_j	$-\frac{17}{588}$	$-\frac{191}{2352}$	$\frac{1}{784}$	$-\frac{5}{1176}$	$\frac{1}{392}$	0	0	0	0
		$c_j - \mathbf{c}_B\mathbf{y}_j$	$-\frac{75}{2352}$	$-\frac{101}{1176}$	0	$-\frac{11}{2352}$	0	$-\frac{1}{2352}$	$-\frac{5}{2352}$	0	0

Now the optimality criterion has been met, indicating that the optimal solution to the LP problem has been found. This optimal solution is as follows:

$\mathbf{x}^{(3)} = [x_1 \;\; x_2 \;\; x_3 \;\; x_4 \;\; x_5]^T = [0 \;\; 0 \;\; 7/3 \;\; 0 \;\; 8]^T$ and $\max H(\mathbf{x}) = 55/42 \approx 1.3$.

Obviously, $\mathbf{x}^{(2)} = \mathbf{x}^{(3)}$. Therefore the optimal solution to the given LFP problem is reached, which is given by $\mathbf{x} = [x_1 \;\; x_2 \;\; x_3 \;\; x_4 \;\; x_5]^T = [0 \;\; 0 \;\; 7/3 \;\; 0 \;\; 8]^T$ and $\max z = 1.3$.

VI. Comparison of the Numerical Results

The following table provides a summary of a comparison analysis between the suggested approach and existing optimization techniques for the numerical examples.

Table 4: *Comparative analysis of the proposed method and existing methods*

Example	Reference	Number of iterations	Optimal solution	Optimal value
1	Proposed	8	$[1 \quad 2 \quad 0]^T$	2
	Reference [9]	4	$[1 \quad 2 \quad 0]^T$	2
2	Proposed	8	$[2/3 \quad 0 \quad 5/3]^T$	1.7
	Reference [8]	4	$[2/3 \quad 0 \quad 5/3]^T$	1.7
3	Proposed	9	$[0 \quad 0 \quad 7/3 \quad 0 \quad 8]^T$	1.3
	Reference [20]	9	$[0.00000 \quad 0.00003 \quad 7/3 \quad 0.00009 \quad 8]^T$	1.3
	Reference [21]	12	$[0.00001 \quad 0.00002 \quad 7/3 \quad 0.00009 \quad 8]^T$	1.3

VII. Discussion

From the current study, we made the following observations:

- The optimal solutions obtained using the proposed method are identical to those derived from existing approaches.
- Although the proposed method may require more iterations for certain LFP problems compared to existing techniques, the overall computational effort remains unaffected. This is attributed to the invariance of constraints across all reconstructed LP subproblems. This can be observed by comparing Tables 1(a), 1(b), and 1(c) with Tables 1(d), 1(e), and 1(f), respectively, in Example 1, and similarly for other examples.
- In some cases, the proposed method solves LFP problems using fewer iterations than existing methods.
- While conventional methods are typically restricted to problems with positive denominators, the proposed method extends the applicability of LFP solvers to cases involving negative denominators as well.
- The optimal solution found by the proposed method satisfies all the constraints of the given LFP problem. But it is not so in all the existing methods for solving LFP problems. For example, the optimal solution of LFP problem mentioned in Example 2 by the existing methods of Grar [20] or Lustig [21] does not satisfy all the constraints.

In light of these findings, the proposed method can be regarded as a valid and effective approach for solving LFP problems.

VIII. Conclusion

In this study, we introduced a new approach for solving linear fractional programming (LFP) problems involving inequality constraints. The performance of the proposed approach was assessed through a series of numerical examples and compared against established methods. The results demonstrate that the proposed method consistently yields the same optimal solution as existing techniques, requiring more iterations in some instances and fewer in others. Notably, even in cases involving a higher number of iterations, the overall computational effort remains largely unaffected due to the structural invariance of constraints across the reconstructed linear programs. Although the objective function is approximated via a Taylor series expansion, this does not

compromise the accuracy of the optimal solution. Moreover, a significant advantage of the proposed method lies in its ability to handle LFP problems with a negative denominator in the objective function—a limitation inherent in most traditional approaches. Future work may focus on extending the proposed method to address more complex and higher-dimensional LFP problems, further enhancing its applicability and robustness in real-world scenarios.

References

[1] Charnes, A. and Cooper, W. W. (1962). Programming with Linear Fractional Functionals, Naval, Research Logistics Quarterly, 9 (3), 181–186.

[2] Bitran, G.R. and Novaes, A.G. (1973). Linear Programming with a Fractional Objective Functions. Operations Research, 21, 22–29.

[3] Isbell, J.R and Marlow, W.H., (1956). Attrition Games, Naval Research Logistics Quarterly, 3, 71–93.

[4] Martos, B., (1964). Hyperbolic Programming, Naval. Research Logistics Quarterly, 11,135–155.

[5] Swarup, Kanti (1965). Linear Fractional Programming, Operations Research 13, 1029–1036.

[6] Bector, C.R., (1973). "Duality in Linear Fractional Programming", Utilitas Mathematica Vol. 4, 155–168.

[7] Seshan, C.R., (1980). On Duality in Linear Fractional Programming, Proceedings of the Indian Academy of Sciences–Mathematical Sciences, Vol. 89, 35–42.

[8] Stancu-Minasian, I.M., (2012). Fractional Programming: Theory, Methods and Applications, Vol. 409, Springer Science & Business Media.

[9] Bajalinov, E. B., (2003). Linear-Fractional Programming: Theory, Methods, Applications and Software, Boston: Kluwer Academic Publishers.

[10] Tantawy, S.F. (2014) A New Concept of Duality for Linear Fractional Programming Problems. International Journal of Engineering and Innovative Technology, 3, 147–149.

[11] Jahan, S. and Islam, M. A., (2010). A Complementary Slackness Theorem for Linear Fractional Programming Problem, International Journal of Basic & Applied Sciences IJBAS–IJENS Vol.10, No.02, 23–28.

[12] Hasan, M.B. and Acharjee, S. (2011). Solving LFP by Converting It into a Single LP. International Journal of Operations Research, 8, 1–14

[13] Pandian, P. & Jayalakshmi, M. (2013). On Solving Linear Fractional Programming Problems, Modern Applied Science, Vol. 7, No. 6, 90–100

[14] Saha, S.K., Hossain, M.R., Uddin, M.K. and Mondal, R.N. (2015). A New Approach of Solving Linear Fractional Programming Problem (LFP) by Using Computer Algorithm, Open Journal of Optimization, 4, 74–86.

[15] Das, S. K. & Mandal, T. (2015). Solving Linear Fractional Programming Problems Using A New Homotopy Perturbation Method, Operations Research and Applications, Vol.2, No.3, 1–15.

[16] Simi, Farhana Ahmed & Talukder, Md. Shahjalal (2017). A New Approach for Solving Linear Fractional Programming Problems with Duality Concept, Open Journal of Optimization, 6, 1–10.

[17] Kumari, P. and Bhardwaj, D. (2019). Solving Linear Fractional Programming Problem Using computer Programming, International Journal of Scientific Research and Review, Volume 07, Issue 04, 591–597.

[18] Yulin Xiao & Xin Tian (2021). Algorithm for Solving Linear Fractional Programming, Journal of Physics, Conference Series, 1903(1): 012044, 1–5.

[19] Gupta, Srikant & Raina, Ather Aziz (2021). A new integer solution approach for fractional linear programming problems, Annals of Optimization Theory and Practice, Vol.4, No. 2, 1–12.

[20] Bennani, Ahlem, Benterki, Djamel and Grar, Hassina (2021). Adaptive Projection Methods for Linear Fractional Programming, RAIRO-Oper. Res. 55, S2383–S2392.

[21] Lustig, I.J. (1991). Feasibility issues in a primal-dual interior point method for linear programming. Math. Program. 49 (1991,) 145–162.

[22] Kumari, P. (2022). An Algorithm for solving Linear Fractional Programming Problems, GANITA, Vol.72 (1), 97–109.

[23] Sahoo, D., Tripathy A.K. and Pati, J.K. (1922). Study on multi-objective linear fractional programming problem involving pentagonal intuitionistic fuzzy number, Results in Control and Optimization, Vol.6, 100091, 1–15.

[24] Mustafa, R.B. & Sulaiman, N.A. (2022). A New Approach to Solving Linear Fractional Programming Problem with Rough Interval Coefficients in the Objective Function, Ibn AL–Haitham Journal for Pure and Applied Sciences, Vol. 35, No. 2, 70–83.

[25] Chauhan, A.; Mahajan, S.; Ahmad, I.; AI-Homidan, S. (2023). On Fuzzy Linear Fractional Programming Problems via α–Cut-Based Method with Application in Transportation Sector. Symmetry, 15, 419, 1–22.

[26] Murugan, Yamini and Thamaraiselvan, Nirmala (2024). A study on the solution of interval linear fractional programming problem, Bulletin of Electrical Engineering and Informatics Vol. 13, No. 2, April 2024, 874–884.

DESIGNING AND EVALUATION OF BAYESIAN SKIP LOT SAMPLING PLAN - 2 WITH DOUBLE SAMPLING PLANS AS THE REFERENCE PLAN UNDER GAMMA ZERO-INFLATED POISSON DISTRIBUTION

Priyadharshini R[1] and Shalini K*

•

Department of Statistics, Salem Sowdeswari College, Salem - 636 010, Tamil Nadu, India.
[1]rajupriya171@gmail.com and *shalini.stat@gmail.com
Correspondence Email: shalini.stat@gmail.com

Abstract

Sampling plans are an effective statistical method for assessing and deciding whether to approve or decline a lot based on quality inspection. Skip-lot sampling plans focus on inspecting only a fraction of the submitted lots, significantly reducing costs by minimizing time and effort. Skip-lot sampling is intended for immediate use, and it has been demonstrated that the quality of the submitted lots is consistently high. This article presents designing of Bayesian Skip Lot Sampling Plan – 2 (BSkSP – 2) with Double Sampling Plan (DSP) as the reference plan based on Gamma Zero-inflated Poisson (GZIP) distribution. The Zero-inflated Poisson (ZIP) distribution is suitable for count data with a high frequency of zeros, especially when non-conformities are rare. The Gamma distribution serves as a conjugate prior to the ZIP distribution. The Operating Characteristic (OC) function of skip lot sampling plan is derived and numerical illustrations are provided to illustrate the proposed sampling plan.

Keywords: Acceptance sampling, Sampling inspection by attributes; Double sampling plan; Prior distribution; Zero-inflated Poisson distribution; Operating characteristics function.

I. Introduction

Statistical quality control (SQC) is a systematic approach for monitoring and controlling product quality using statistical techniques. It helps industries to maintain consistency, reduce variability, and improve efficiency in manufacturing processes. Sampling inspection examines a subset of items from a production batch is examined to decide whether to accept or reject the entire lot. This method is used when 100% inspection is impractical due to high costs, time constraints, or product destructiveness. Sampling inspection helps maintain product quality while minimizing inspection efforts.

An acceptance sampling plan determines whether a lot should be accepted or rejected based on the number of nonconformities items found in a sample. A single sampling plan (SSP) involves selecting a single sample from a lot and making an acceptance or rejection decision based on the number of nonconformities found. A double sampling plan (DSP) allows for a second sample if the

first sample results are inconclusive. DSP provide more flexibility than SSP and help reduce unnecessary rejections or inspections.

Bayesian methodology incorporates prior knowledge about the process into decision-making. In Bayesian acceptance sampling, prior information is combined with observed sample data to update the probability of lot acceptance. Quality variations can occur both within and between lots. While traditional methods often focus on within-lot variation, real-world scenarios demand consideration of both types. This approach allows for more informed decisions, especially when dealing with variable-quality processes.

Technological advancements have significantly improved process monitoring and product quality, resulting in frequent instances of zero nonconformities. However, inherent variations still occur, making the Zero-inflated Poisson (ZIP) distribution a suitable distribution. This statistical approach integrates a Poisson component with an additional zero-inflation factor, making it particularly effective in scenarios where nonconformities are rare but occasional deviations exist.

Loganathan and Shalini [9, 10] pioneered ZIP Single Sampling Plans (SSPs), while Vijayaraghavan et al. [23] explored Bayesian methodologies for Gamma-Poisson SSPs. Additionally, Shalini et al. [19] and Palanisamy and Latha [11, 12] worked on the refinement of GZIP SSPs.

The design of ZIP-based Double Sampling Plans (DSPs) has been examined by Shalini and Sheik [18], Pramote and Wimonmas [15], and Wimonmas and Pramote [24]. The integration of Bayesian principles into DSP design has also been investigated by Vijayaraghavan and Sakthivel [22], Balamurali et al. [3], and Suresh and Usha [21], who explored their impact on sampling efficiency and risk optimization. More recently, Priyadharshini and Shalini [16] developed GZIP DSP**s**.

Dodge [4] pioneered the concept of continuous sampling and established the mathematical foundation and operational rules for the first continuous sampling plan (CSP-1). Building on this, Dodge [5] introduced the idea of skip-lot sampling, applying the principles of CSP-1 to a continuous series of lots. This led to the development of the first skip-lot sampling plan, known as SkSP-1, which is widely used for bulk materials or products manufactured in consecutive lots. Compared to a standard single acceptance sampling plan, SkSP-1 requires fewer units for inspection, effectively reducing inspection costs.

Subsequent research by Dodge and Perry [6] and Perry [7] expanded upon this concept, leading to the introduction of the SkSP-2 plan, which employs a reference plan for skip-lot sampling. Under this framework, certain lots are exempted from inspection when the overall product quality is consistently high. Skip-lot sampling is particularly advantageous in industries such as chemical and physical processing, where inspection costs are substantial and product quality remains stable.

Parker and Kessler [13] refined the SkSP-2 approach, proposing advanced skip lot sampling plans. More recently, Aslam et al. [1] formulated design parameter tables for SkSP-2, using a single sampling plan as a reference. Further, Balamurali and Subramani [4] determined optimal design parameters that satisfy both producer and consumer risk under the binomial model. Recently, Kaviyarasu and Sivakumar [8] developed a Bayesian skip-lot sampling plan (BSkSP-2) based on a zero-inflated Poisson distribution with a gamma prior.

According to the literature, there has been no research conducted on developing GZIP BSkSP - 2 with DSP as the reference plan. This study aims to address by focusing on the determination of GZIP BSkSP - 2 with DSP. Section 2 presents the BSkSP - 2 with DSP under GZIP distribution. Section 3 focuses on designing GZIP BShSP - 2 with DSP, and Section 4 provides a numerical illustration. Finally, Section 5 concludes the findings.

II. SkSP - 2 with DSP as the reference plan under GZIP Distribution

A DSP is structured around five specific parameters: n_1, n_2, c_1, c_2 and c_3, where $c_1 < c_2$ and $c_2 \leq c_3$ (the third acceptance number). When c_2 is taken in equal to c_3 *(i.e.,* $c_2 = c_3$*)*, the DSP is described through its parameters n_1, n_2, c_1 and c_2, which represent the sizes of the first and second samples and the first and second acceptance numbers, respectively (Duncan [7] and Stephen [20]).

Let d_1 and d_2 denote the number of nonconformities in the first sample and second sample and $D = d_1 + d_2$ represent the combined nonconformities from both samples.

Schilling and Neubauer [17] outlined the steps involved in double sampling plan and Priyadharshini and Shalini [16] derived the Operating Characteristic (OC) function of GZIP DSPs.

A skip lot sampling plan of BSkSP - 2 is studied using the method of attributes with a double sampling plan as the reference plan. In this context, the Bayesian DSP with zero acceptance number under the conditions of GZIP distribution is considered as a reference plan.

In contrast to a normal inspection procedure, which requires every lot to be examined, a skip-lot plan reduces inspection by evaluating only a fraction of the lots when historical data indicate consistently good quality. The use of a zero acceptance number ensures stricter quality control, while the Bayesian approach incorporates prior knowledge about the nonconformities rate to make more informed sampling decisions.

To maintain quality assurance, BSkSP - 2 includes specific switching rules based on recent records of lot acceptances and rejections, which determine when to continue reduced inspection and when to revert to full inspection, thereby balancing cost efficiency with consumer protection.

Operating Procedure of SkSP-2

The SkSP-2 plan, as described by Perry [14], follows these operational steps:

Step 1. Initiate normal inspection, where in all lots undergo assessment based on the reference plan. Lots are examined sequentially in accordance with production or submission order.
Step 2. If i consecutive lots are accepted under the normal inspection then switch to skipping inspection procedure.
Step 3. During skipping inspection, only a specified fraction f of the lots is randomly inspected. This continues until a lot fails inspection.
Step 4. If a lot is rejected during skipping inspection, revert to normal inspection as outlined in Step 1.
Step 5. Monitor each rejected lot and correct or replace all defective units obtained.

SkSP-2 is defined by two parameters associated with its reference sampling plan: f and i. In general, $0 < f < 1$, and i is a positive integer. When $f = 1$, the skip-lot sampling plan effectively reverts to the reference plan, eliminating the skipping mechanism.

The performance of SkSP – 2 with DSP as the reference plan is assessed through its OC function.

$$P_a = \frac{(1-f)P_a(p)^i + fP_a(p)}{(1-f)P_a(p)^i + f} \tag{1}$$

III. Designing BSkSP – 2 with DSP under GZIP Distribution

GZIP BSkSPs - 2 with DSPs are designed by determining the optimum parameters n_1, n_2, c_1, c_2, i and f based on the prescribed points $(p_1, 1-\alpha)$ and (p_2, β) on the OC curve so that the determined GZIP BSkSPs - 2 with DSPs provide adequate protection to both producer and consumer.

The plan must satisfy the following requirements:

(i) $P_a(p_1) \geq 1-\alpha$

(ii) $P_a(p_2) \leq \beta$

The values of the plan parameters n_1, n_2, c_1, c_2, i and f can be derived for each set of φ, m, p_1, α, p_2 and β by applying the unity value approach. The values np_1 and np_2 satisfying respectively equations *(i)* and *(ii)* are termed as unity values. The plan parameters can be arranged in tables for different combinations of $(p_1, \alpha, p_2, \beta)$. The use of an operating ratio $R = \frac{np_2}{np_1}$, reduces the number of tables.

The plan parameters are determined for specific sets of values of φ, m, p_1, α, p_2 and β under the condition of GZIP distribution. The unity values are computed for various combinations of (φ, m, $P_a(p)$) by solving the OC function of GZIP BSkSP – 2 with DSP for each combination of c_1, c_2,$i$and f with $n_1 = n_2 = n$. The parameter values consider are as follows; m = 10 and 100, φ = 0.01 and 005, i = 2, 3, 4 and 5, f = 2/3, 1/2 and 1/4 and for $Pa\ (p)$ are 0.99, 0.90, 0.50, 0.20 and 0.10. The specific values used for these parameters are presented in Table 1. The corresponding operating ratio values calculated for $\alpha = 0.05$ and $\beta = 0.10$ are listed in Table 2. Based on specified strength values $(p_1, \alpha, p_2, \beta)$ together with φ and m, these tables enable the determination of plan parameters using the unity value approach described by Schilling and Neubauer [17].

IV. Numerical Illustration

This section describes the process for choosing GZIP BSkSP - 2 with DSP for a specified strength, along with numerical examples.

Illustration 1

For instance, to determine the plan parameter for proposed GZIP BSkSP- 2 with DSP as the reference plan with values of φ = 0.01, m = 10, c_1 = 2, c_2 = 4 and plan strength p_1 = 0.008, α = 0.05, p_2 = 0.10 and β = 0.10; compute the operating ratio $R = p_2/p_1$ = 0.05/0.008 = 6.25. Choose f and i and the unity values np_1 corresponding to the nearest operating ratio (Table 2). Here the values are obtained as f = 2/3, i = 3, andnp_1 = 1.0439. The sample size $n = np_1/p_1$ = 130.44 ~ 130. Hence the plan parameters of the BSkSP-2 with DSP for given values of c_1 = 2, c_2 = 4, φ = 0.01, m = 10, i = 3 and f = 2/3 are n = 130.

Illustration 2

Assuming φ = 0.05, m = 100, c_1 = 2, c_2 = 4 and strength p_1= 0.008, α = 0.05, p_2 = 0.05 and β = 0.10. The operating ratio R corresponding to these specifications is computed as 6.25. Choose f and i and the unity value np_1 corresponding to the nearest R (Table 2). Based on the R value, the corresponding values of f and i are chosen as 2/3 and 5 respectively. The sample size is then calculated as $n=np_1/p_1$= 134.375, which is approximated to 134. Since, the optimum BSkSP - 2 with DSP under GZIP is given as (134; 2, 4; 2/3, 4).

The corresponding BSkSP - 2 with DSP as the reference plan under ZIP for the same specified strength is (136; 2, 4; 2/3, 4). This comparison indicates that the sample size for GZIP BSkSP - 2 with DSP are lesser than ZIP BSkSP - 2 with DSP.

Table 1: *Unity values for GZIP BSkSP-2 with DSP when $n_1 = n_2 = n$ for $\varphi = 0.05$, $\alpha = 0.05$, $\beta = 0.10$*

m	φ	f	i	Probability of Acceptance ($P_a(p)$)				
				0.99	0.95	0.50	0.20	0.10
10	0.01	2/3	2	0.5101	1.0547	3.4916	5.4205	6.8829
			3	0.5091	1.0439	3.3677	5.2999	6.7962
			4	0.5081	1.0341	3.3042	5.2738	6.7870
			5	0.5071	1.0251	3.2708	5.2684	6.7861
		1/2	2	0.5747	1.1950	3.6821	5.5480	6.9698
			3	0.5724	1.1720	3.4712	5.3306	6.8061
			4	0.5701	1.1520	3.3619	5.2805	6.7880
			5	0.5679	1.1342	3.3025	5.2698	6.7862
		1/4	2	0.7726	1.5927	4.1692	5.9193	7.2513
			3	0.7633	1.5217	3.7488	5.4356	6.8441
			4	0.7546	1.4650	3.5286	5.3056	6.7921
			5	0.7465	1.4181	3.4020	5.2752	6.7866
	0.05	2/3	2	0.5187	1.0754	3.6345	5.9219	8.2431
			3	0.5177	1.0643	3.4992	5.7636	8.0720
			4	0.5166	1.0542	3.4301	5.7297	8.0543
			5	0.5156	1.0450	3.3939	5.7227	8.0525
		1/2	2	0.5846	1.2191	3.8442	6.0927	8.4217
			3	0.5822	1.1956	3.6121	5.8035	8.0913
			4	0.5799	1.1750	3.4927	5.7383	8.0563
			5	0.5777	1.1568	3.4283	5.7245	8.0527
		1/4	2	0.7867	1.6279	4.3925	6.6147	9.0618
			3	0.7772	1.5548	3.9183	5.9418	8.1652
			4	0.7683	1.4965	3.6750	5.7709	8.0637
			5	0.7600	1.4482	3.5365	5.7314	8.0531
100	0.01	2/3	2	0.5377	1.0846	3.3352	4.8541	5.8840
			3	0.5366	1.0739	3.2302	4.7649	5.8254
			4	0.5356	1.0641	3.1760	4.7455	5.8192
			5	0.5346	1.0552	3.1474	4.7415	5.8186
		1/2	2	0.6037	1.2230	3.4947	4.9476	5.9425
			3	0.6013	1.2004	3.3180	4.7876	5.8322
			4	0.5990	1.1806	3.2252	4.7504	5.8199
			5	0.5968	1.1631	3.1746	4.7425	5.8186
		1/4	2	0.8037	1.6116	3.8925	5.2158	6.1299
			3	0.7943	1.5427	3.5500	4.8651	5.8578
			4	0.7856	1.4875	3.3664	4.7691	5.8227
			5	0.7774	1.4417	3.2593	4.7465	5.8189
	0.05	2/3	2	0.5465	1.1050	3.4577	5.2304	6.8004
			3	0.5455	1.0941	3.3439	5.1159	6.6909
			4	0.5444	1.0841	3.2853	5.0912	6.6795
			5	0.5434	1.0750	3.2545	5.0861	6.6784
		1/2	2	0.6138	1.2467	3.6319	5.3528	6.9138
			3	0.6114	1.2236	3.4389	5.1448	6.7033
			4	0.6090	1.2033	3.3384	5.0974	6.6808
			5	0.6067	1.1854	3.2838	5.0874	6.6785

m	φ	f	i	Probability of Acceptance ($P_a(p)$)				
				0.99	0.95	0.50	0.20	0.10
100	0.05	1/4	2	0.8179	1.6456	4.0753	5.7195	7.3127
			3	0.8083	1.5748	3.6929	5.2447	6.7509
			4	0.7994	1.5181	3.4916	5.1212	6.6858
			5	0.7911	1.4711	3.3754	5.0924	6.6790

Table 2: *Operating ratio for GZIP BSkSP-2 with DSP when $n_1 = n_2 = n$ for $\varphi = 0.05$, $\alpha = 0.05$, $\beta = 0.10$*

m	φ	f	i	Probability of Acceptance ($Pa(p)$)		Operating Ratio
				0.95	0.1	$\alpha = 0.05$, $\beta = 0.10$
10	0.01	2/3	2	1.0547	6.8829	6.5259
			3	1.0439	6.7962	6.5104
			4	1.0341	6.7870	6.5632
			5	1.0251	6.7861	6.6199
		1/2	2	1.1950	6.9698	5.8325
			3	1.1720	6.8061	5.8073
			4	1.1520	6.7880	5.8924
			5	1.1342	6.7862	5.9833
		1/4	2	1.5927	7.2513	4.5528
			3	1.5217	6.8441	4.4977
			4	1.4650	6.7921	4.6363
			5	1.4181	6.7866	4.7857
	0.05	2/3	2	1.0754	8.2431	7.6652
			3	1.0643	8.0720	7.5843
			4	1.0542	8.0543	7.6402
			5	1.0450	8.0525	7.7057
		1/2	2	1.2191	8.4217	6.9081
			3	1.1956	8.0913	6.7676
			4	1.1750	8.0563	6.8564
			5	1.1568	8.0527	6.9612
		1/4	2	1.6279	9.0618	5.5666
			3	1.5548	8.1652	5.2516
			4	1.4965	8.0637	5.3884
			5	1.4482	8.0531	5.5608
100	0.01	2/3	2	1.0846	5.8840	5.4250
			3	1.0739	5.8254	5.4245
			4	1.0641	5.8192	5.4687
			5	1.0552	5.8186	5.5142
		1/2	2	1.2230	5.9425	4.8590
			3	1.2004	5.8322	4.8586
			4	1.1806	5.8199	4.9296
			5	1.1631	5.8186	5.0027
		1/4	2	1.6116	6.1299	3.8036
			3	1.5427	5.8578	3.7971
			4	1.4875	5.8227	3.9144
			5	1.4417	5.8189	4.0361

m	φ	f	i	Probability of Acceptance ($Pa(p)$)		Operating Ratio
				0.95	0.1	$\alpha = 0.05, \beta = 0.10$
100	0.05	2/3	2	1.1050	6.8004	6.1542
			3	1.0941	6.6909	6.1154
			4	1.0841	6.6795	6.1613
			5	1.0750	6.6784	6.2125
		1/2	2	1.2467	6.9138	5.5457
			3	1.2236	6.7033	5.4783
			4	1.2033	6.6808	5.5521
			5	1.1854	6.6785	5.6340
		1/4	2	1.6456	7.3127	4.4438
			3	1.5748	6.7509	4.2868
			4	1.5181	6.6858	4.4041
			5	1.4711	6.6790	4.5401

V. Conclusion

Acceptance sampling is particularly useful when it is impractical to inspect every unit in a production lot. Traditional single and double sampling plans are effective but can become costly when product quality is consistently high. To address this, Skip-lot Sampling Plans (SkSP) reduce inspection by checking only a fraction of lots while still protecting consumers. The integration of Bayesian methods enables the incorporation of prior knowledge with observed data, leading to more reliable decision-making, which is particularly important when nonconformity levels are low and consistent product quality is observed. This study enhances quality control in production by utilizing a BSkSP-2 with DSP as the reference plan under GZIP distribution, for which the OC function has been derived. The plan achieves reduced inspection effort, smaller sample sizes compared to ZIP distribution, and balanced protection of both producer's and consumer's risks. Thus, the BSkSP-2 with DSP under GZIP represents an effective and reliable approach to modern industrial quality control.

References

[1] Aslam, M., Balamurali, S., Jun, C.H. and Ahmad, M. (2010). Optimal designing of a skip-lot sampling plan by two point method. *Pakistan Journal of Statistics*, 26(4):585–592.

[2] Balamurali, S. and Subramani, J. (2012). Optimal designing of skip-lot sampling plan of type SKSP-2 with double sampling plan as the reference plan. *Journal of Statistical Theory and Practice*, 6(2):354–362.

[3] Balamurali, S., Aslam, M. and Jun, C.H. (2012). Bayesian double sampling plan under gamma-Poisson distribution. *Research Journal of Applied Sciences, Engineering and Technology*, 4(8):949–956.

[4] Dodge, H.F. (1943). A sampling inspection plan for continuous production. *The Annals of Mathematical Statistics*, 14(3):264–279.

[5] Dodge, H.F. (1955). Skip-lot sampling plan. *Industrial Quality Control*, 11(5):3–5.

[6] Dodge, H.F. and Perry, R. (1971). A system of skip-lot plans for lot-by-lot inspection. *American Society for Quality Control Technical Conference Transactions*, Chicago, IL, 469–477.

[7] Duncan, A.J. (1986). *Quality Control and Industrial Statistics*. Homewood: Richard D. Irwin, Inc.

[8] Kaviyarasu, V. and Sivakumar, P. (2022). Designing and selection of Bayesian skip-lot sampling plan type BSkSP-2 with single sampling plan under zero-inflated Poisson distribution. *Journal of the Indian Society for Probability and Statistics*, 23:267–284.

[9] Loganathan, A. and Shalini, K. (2014). Determination of single sampling plans by attributes under the conditions of zero-inflated Poisson distribution. *Communications in Statistics - Simulation and Computation*, 43(3):538–548.

[10] Loganathan, A. and Shalini, K. (2014). Selection of single sampling plans by attributes under the conditions of zero-inflated Poisson distribution. *International Journal of Quality and Reliability Management*, 31(9):1002–1011.

[11] Palanisamy, A. and Latha, M. (2018). Construction of Bayesian single sampling plan by attributes under the conditions of gamma zero-inflated Poisson distribution. *International Research Journal of Advanced Engineering and Science*, 3(1):67–71.

[12] Palanisamy, A. and Latha, M. (2018). Selection of Bayesian single sampling plan with zero-inflated Poisson distribution based on quality region. *International Journal of Scientific Research Mathematical and Statistical Sciences*, 5(6):313–320.

[13] Parker, R.D. and Kessler, L. (1981). A modified skip-lot sampling plan. *Journal of Quality Technology*, 13(1):31–35.

[14] Perry, R.L. (1973). Skip-lot sampling plans. *Journal of Quality Technology*, 5(3):123–130.

[15] Pramote, C. and Wimonmas, B. (2021). Designing of optimal required sample sizes for double acceptance sampling plans under the zero-inflated defective data. *Current Applied Science and Technology*, 21(2):227–239.

[16] Priyadharshini, R. and Shalini, K. (2025). Construction of Gamma Zero-inflated Poisson double sampling plans. *Reliability Theory and Application*, 20(1):425–438.

[17] Schilling, E.G. and Neubauer, D.V. (2009). *Acceptance Sampling in Quality Control*. Boca Raton: CRC Press.

[18] Shalini, K. and Sheik Abdullah, A. (2018). Designing double sampling plans under the conditions of zero-inflated Poisson distribution. *Journal of Emerging Technologies and Innovative Research*, 5(12):529–534.

[19] Shalini, K., Loganathan, A. and Kavitha, N. (2014). Bayesian single sampling plans under the conditions of zero-inflated Poisson distribution. *Research and Reviews Journal of Statistics*, Special Issue 1:92–98.

[20] Stephens, K.S. (2001). *The Handbook of Applied Acceptance Sampling: Plans, Procedures and Principles*. Wisconsin: ASQ Quality Press.

[21] Suresh, K.K. and Usha, K. (2016). Construction of Bayesian double sampling plan using minimum angle method. *Journal of Statistics and Management Systems*, 19(3):473–489.

[22] Vijayaraghavan, R. and Sakthivel, K.M. (2010). Selection of Bayesian double sampling inspection plans by attributes with small acceptance numbers. *Economic Quality Control*, 25:207–220.

[23] Vijayaraghavan, R., Rajagopal, K. and Loganathan, A. (2008). A procedure for selection of a Gamma-Poisson single sampling plan by attributes. *Journal of Applied Statistics*, 35(2):149–160.

[24] Wimonmas, B. and Pramote, C. (2021). Designing of double acceptance sampling plan for zero-inflated and over-dispersed data using multi-objective optimization. *Applied Science and Engineering Progress*, 14(3):338–347.

RT&A, No 4 (89)
Volume 20, December 2025

SIX SIGMA BASED CONTROL CHARTS FOR MEAN UNDER TWO-PARAMETER EXPONENTIAL DISTRIBUTION

[1]Gomathi K and [2]Ganesan A

•

[1]Research Scholar, Department of Statistics, Government Arts College (Autonomous), Salem – 636 007.
[2]Associate Professor, Department of Statistics, Government Arts College (Autonomous), Salem – 636 007.
[1] kggomathikumaresan@gmail.com , [2] slmganesan@gmail.com

Abstract

The statistical process control (SPC) method is widely regarded as the most efficient approach for evaluating production processes, balancing sampling costs with chart performance. Recent research has explored this problem in the context of economic planning for control charts, particularly focusing on adaptive control charts. Traditionally, control chart design relies on a fixed structure to determine key parameters such as sample size, sampling interval, and control limits to meet economic or statistical requirements. However, under the exponential distribution, optimizing control charts based on Six Sigma principles can ensure process stability while minimizing costs. This approach helps reduce either the total expected costs over a finite time horizon or the long-term average expected costs.

Keywords: Exponential distribution, Mean, Process capability and Six sigma

I. Introduction

In today's highly competitive marketplace, quality has emerged as one of the most critical factors influencing consumer decisions when choosing among various products and services. This emphasis on quality transcends market segments and applies universally whether the consumer is a private individual, a large-scale industrial enterprise, a retail chain, a financial institution, or even a government entity such as a military defense program. The widespread nature of this trend underscores the vital importance of both understanding and continuously improving quality across all levels of operation.

Businesses that prioritize quality as a fundamental component of their strategic approach are more likely to achieve sustained success, drive organizational growth, and maintain a strong competitive edge in their respective industries. Moreover, investments in enhancing quality tend to yield substantial returns, not only in terms of customer satisfaction and loyalty but also through increased operational efficiency and profitability. As such, embedding quality into the core of business strategy is no longer optional but essential for long-term viability and excellence.

1.1 Control Charts

A control chart is a powerful graphical tool used in quality management to determine whether a process is operating within its expected range of variation or if it is being influenced by unusual, assignable factors. It visually displays data collected from process samples over time, enabling the identification of patterns, trends, and deviations that might indicate changes in process behaviour. The chart is characterized by two critical boundary lines: the Upper Control Limit (UCL) and the Lower Control Limit (LCL). These limits are statistically calculated based on historical process data and represent the threshold between common cause variation the natural, random fluctuations inherent to any stable process and assignable cause variation, which points to specific, identifiable problems that may disrupt normal operations.

The area between the upper and lower control limits is considered the normal range of variation. As long as the data points fall within this region, the process is deemed to be "in control," implying that it is functioning as expected. However, when one or more data points fall outside of these control limits, it signals that the process may be out of control, likely due to an assignable cause. Such an occurrence prompts further investigation to identify and correct the issue before it impacts product quality or process performance.

1.2 Concept of Six Sigma

The Six Sigma methodology offers a structured and data-driven approach comprising a set of tools and techniques aimed at enhancing process capability and minimizing defects in both manufacturing and service-oriented operations. Originally conceptualized as a means to optimize industrial manufacturing processes and eliminate defects, Six Sigma has since evolved into a versatile framework applicable across a wide range of business processes and service sectors. Within the Six Sigma paradigm, a defect is broadly defined as any deviation from customer expectations that may result in dissatisfaction.

The foundation of Six Sigma is deeply rooted in decades of prior advancements in quality management methodologies, including Quality Control, Total Quality Management, and the Zero Defects philosophy. These movements were significantly influenced by the pioneering contributions of quality experts such as Shewhart [10], Deming [2], [3], Juran [4], and Taguchi [11], [12], whose work laid the groundwork for modern quality improvement strategies.

1.3 Process Capability (CP)

Process capability refers to the ability of a manufacturing process to consistently produce products that meet predefined customer requirements, particularly in relation to the specified tolerance or specification limits of a product parameter. It reflects both the repeatability and stability of the process over time and serves as an objective benchmark to assess whether the process can reliably deliver outputs within acceptable limits.

To quantify and visually interpret this performance, capability indices have been developed. These indices provide a statistical representation of how well the natural variability of a process aligns with the upper and lower specification limits defined by the customer or engineering requirements. In essence, capability indices help to determine how centred the process is within the allowed range and how much of the variation falls within those limits. The most common indices, such as CP, CPK, PP, and PPK, are used to evaluate whether the process has sufficient capability to produce conforming products without excessive rework or rejection. These values also assist in comparing processes, making improvement decisions, and guiding process

design.

1.4 Construction of control charts under lifetime distributions

The development of control charts specifically designed for lifetime distributions plays a crucial role in accurately tracking and managing the reliability and performance of products and systems throughout their operational lifespan. Conventional control charts are typically based on the assumption that the underlying data follows a normal distribution. However, this assumption does not hold true in many practical scenarios, particularly when dealing with lifetime or reliability data, which often conform to non-normal distributions such as the Exponential, Gamma and Weibull distributions. By tailoring control charts to these particular lifetime distributions, organizations can significantly improve the effectiveness of their quality control efforts. These customized charts offer greater sensitivity to changes in process behaviour and provide more precise insights into potential failures or deviations, thereby supporting more informed decision-making and fostering enhanced product reliability.

Processes with a constant hazard rate where the interval between subsequent occurrences or failures stays constant throughout time are specifically monitored by Shewhart-type control charts that are adapted to the exponential distribution. Because it assumes a constant failure rate, the exponential distribution is frequently used in survival analysis and reliability engineering. This makes it especially well-suited for estimating the lifespans of specific systems and components. The primary parameter of the distribution, which is closely related to the mean time between failures (MTBF), is what these control charts are intended to identify as it changes. Shewhart-type charts based on the exponential distribution are a useful and practical tool for assessing process reliability and assisting in the early detection of possible quality problems or failures in maintenance and production environments by identifying deviations from the expected process behaviour.

1.5 Importance of the study

This study definitely will help the floor engineers working in the different fields to select their six-sigma based control chart based on the requirements and environments. In addition, for providing the procedures for construction of six sigma-based control chart under Exponential distribution, readymade tables are also provided examples followed by practical applications which will help the readers and the users to have a comprehensive knowledge on the theory and applications of six sigma-based control charts. The following conditions for application

- When the objective is to analyse the time intervals between consecutive events directly
- When there is a need to utilize standard Six Sigma control charts for quality improvement.
- When the process requires a more gradual and stable response to change

II. Methods and Materials

According to Ross [9], the probability density function (PDF) of the two-parameter exponential distribution is expressed as:

$$f(x) = (x, \lambda, \theta) = \begin{cases} \lambda e^{-\lambda(x-\theta)}, x \geq \theta \\ 0, x < 0 \end{cases} \quad (1)$$

where,

x is the random variable,

$\lambda > 0$ is the rate parameter2

θ is the location parameter (shift)

The mean of a distribution, also known as the expected value, represents the long-term average outcome of a random variable over numerous observations. As described by Kin Lam et al. [5], the mean for the two-parameter exponential distribution is determined based on its probability density function and reflects the central tendency of the distribution:

$$E(X) = \int_{-\infty}^{\infty} x\, f(x)\, dx \tag{2}$$

Let u=x-θ, so x=u+θ and dx=du. When x=θ, u=0, and when $x \to \infty$, $u \to \infty$ and substituting into the integral (Monjed H. Samuh and Areen, [6] then it shows as follows:

$$E(X) = \theta + \frac{1}{\lambda},\ \ E(X^2) = \theta^2 + \frac{2\theta}{\lambda} + \frac{2}{\lambda^2} \text{ and } V(x) = E(x^2) - \{E(x)\}^2 = \frac{1}{\lambda^2} \Rightarrow \sigma = \frac{1}{\lambda} \tag{3}$$

For a given tolerance level (TL) and a specified process capability (PC), the standard deviation 'σ' (termed as for exponential distribution) often referred to as the process variation is determined using a predefined mathematical relationship . This calculation is performed for various combinations of tolerance levels and process capability values to assess the consistency and precision of the manufacturing process (Pavithra and Balamurugan), [8]. By analysing these values, organizations can better understand the extent of variation within the process and ensure that it remains within acceptable limits to meet quality and performance requirements.To determine the process standard deviation , first, establish the tolerance level (TL) and the desired process capability cp=2, as outlined by Montgomery [7], Once the values of is obtained, it is applied to the control limit equations for mean as follows:

$$\left(\theta_{6\sigma}^{\bar{X}} + \frac{1}{\lambda_{6\sigma}^{\bar{X}}}\right) \pm \left[\left(\frac{Z_{6\sigma}}{\sqrt{n}}\right)\left(\frac{1}{\lambda_{6\sigma}^{\bar{X}}}\right)\right] \tag{4}$$

III. Structuring and organizing data tables

3.1 Illustration 1

The example presented by Acheson J. Duncan [1], is referenced in this analysis. In this example, a dataset consisting of inside diameter measurements is examined are shown in the table 1. These measurements are collected in sample groups, with each group containing five observations. This structured sampling approach allows for the assessment of process variation and control using statistical quality control techniques.

Table 1: *Measurements of inside diameters*

S.No	X_1	X_2	X_3	X_4	X_5	Mean	Range	Standard deviation
1	15	11	8	15	6	11.00	9	4.06
2	14	16	11	14	7	12.40	9	3.51
3	13	6	9	5	10	8.60	8	3.21

4	15	15	9	15	7	12.20	8	3.90
5	9	12	9	8	8	9.20	4	1.64
6	11	14	11	12	5	10.60	9	3.36
7	13	12	9	6	10	10.00	7	2.74
8	10	15	12	4	6	9.40	11	4.45
9	8	12	14	9	10	10.60	6	2.41
10	10	10	9	14	14	11.40	5	2.41
11	13	16	12	15	18	14.80	6	2.39
12	7	10	9	11	16	10.60	9	3.36
13	11	7	16	10	14	11.60	9	3.51
14	11	7	10	10	7	9.00	4	1.87
15	13	9	12	13	17	12.80	8	2.86
16	17	10	11	9	8	11.00	9	3.54
17	4	14	5	11	11	9.00	10	4.30
18	8	9	6	13	9	9.00	7	2.55
19	9	10	7	10	13	9.80	6	2.17
20	15	10	12	12	16	13.00	6	2.45
						$\bar{\bar{X}} = 10.80$	$\bar{R} = 7.50$	$\bar{S} = 3.03$

Source: Acheson J. Duncan [1]

The rate parameter $(\lambda_{3\sigma}^{\bar{x}})$ and the location parameter $(\theta_{3\sigma}^{\bar{x}})$ of the two-parameter exponential distribution are estimated based on the 3-Sigma criterion for the mean. These parameters play a crucial role in defining the distribution's characteristics, where the rate parameter determines the spread of the distribution, and the location parameter represents the threshold or minimum value. The estimation process ensures that the control limits align with the principles of statistical quality control, allowing for accurate process monitoring and performance evaluation. The estimated values for these parameters are given as follows:

$$\lambda_{3\sigma}^{\bar{x}} = \frac{1}{\sigma_{3\sigma}^{\bar{x}}} = \frac{1}{3.03} \Rightarrow \lambda_{3\sigma}^{\bar{x}} = 0.3296 \text{ and } \theta_{3\sigma}^{\bar{x}} = x - \sigma_{3\sigma}^{\bar{x}} = 10.80 - 3.03 \Rightarrow \theta_{3\sigma}^{\bar{x}} = 7.7659 \quad (5)$$

Shewhart [10], proposed the 3-Sigma control limits for the mean, which are a key instrument in statistical process control (SPC). Under typical operating conditions, the process mean is intended to fluctuate within the allowable range defined by these control limits. These constraints aid in identifying variances that might point to possible process instability or departures from expected performance by taking into account the process mean and standard deviation. According to Shewhart's technique, the mean's control boundaries are determined as

$$UCL_{3\sigma.\bar{X}}^{Exp} = \left(\theta_{3\sigma}^{\bar{X}} + \frac{1}{\lambda_{3\sigma}^{\bar{X}}}\right) + \left[\left(\frac{3}{\sqrt{n}}\right)\left(\frac{1}{\lambda_{3\sigma}^{\bar{X}}}\right)\right] = \left(7.7659 + \frac{1}{0.3296}\right) + \left(\frac{3}{\sqrt{5}}\right)\left(\frac{1}{0.3269}\right) = 10.80 \quad (6)$$

$$LCL_{3\sigma.\bar{X}}^{Exp} = \left(\theta_{3\sigma}^{\bar{X}} + \frac{1}{\lambda_{3\sigma}^{\bar{X}}}\right) - \left[\left(\frac{3}{\sqrt{n}}\right)\left(\frac{1}{\lambda_{3\sigma}^{\bar{X}}}\right)\right] = \left(7.7659 + \frac{1}{0.3296}\right) - \left(\frac{3}{\sqrt{5}}\right)\left(\frac{1}{0.3269}\right) = 6.73 \quad (7)$$

The Six Sigma methodology for the mean is used to estimate the rate parameter $(\lambda_{6\sigma}^{\bar{x}})$and location parameter $(\theta_{6\sigma}^{\bar{x}})$of the two-parameter exponential distribution. These characteristics are

crucial for describing the distribution; the location parameter establishes the lowest value that can exist, while the rate parameter affects how the data spreads. By ensuring that the control limits are in line with Six Sigma concepts, the estimating process improves quality control and process monitoring. The following are the estimated values for these parameters:

$$\lambda_{6\sigma}^{\overline{X}} = \frac{1}{\eta_{6\sigma}^{\overline{X}}} = \frac{1}{0.23} \Rightarrow \lambda_{6\sigma}^{\overline{X}} = 4.28 \text{ and } \theta_{6\sigma}^{\overline{X}} = \overline{X} - \eta_{6\sigma}^{\overline{X}} = 10.80 - 0.23 \Rightarrow \theta_{6\sigma}^{\overline{X}} = 10.57 \quad (8)$$

The Six Sigma methodology-derived control limits for the mean offer a strong framework for keeping an eye on process performance and guaranteeing quality control. Under stable operating conditions, these limitations specify the acceptable range in which the process mean is anticipated to fluctuate. These control limits improve the ability to identify deviations, reduce faults, and preserve process consistency by implementing Six Sigma principles. The following is the mean's Six Sigma-based control limits are as follows:

$$UCL_{6\sigma.\overline{X}}^{Exp} = \left(\theta_{6\sigma}^{\overline{X}} + \frac{1}{\lambda_{6\sigma}^{\overline{X}}}\right) + \left[\left(\frac{Z_{6\sigma}}{\sqrt{n}}\right)\left(\frac{1}{\lambda_{\backslash 6\sigma}^{\overline{X}}}\right)\right] = \left(10.57 + \frac{1}{4.28}\right) + \left(\frac{4.831}{\sqrt{5}}\right)\left(\frac{1}{4.28}\right) = 11.31 \quad (9)$$

$$LCL_{6\sigma.\overline{X}}^{Exp} = \left(\theta_{6\sigma}^{\overline{X}} + \frac{1}{\lambda_{6\sigma}^{\overline{X}}}\right) - \left[\left(\frac{Z_{6\sigma}}{\sqrt{n}}\right)\left(\frac{1}{\lambda_{\backslash 6\sigma}^{\overline{X}}}\right)\right] = \left(10.57 + \frac{1}{4.28}\right) - \left(\frac{4.831}{\sqrt{5}}\right)\left(\frac{1}{4.28}\right) = 11.29 \quad (10)$$

An in-depth analysis of the data presented in Table-2 and Figure-1 reveals that the process under consideration is operating outside of acceptable control boundaries when assessed using the Six Sigma methodology for monitoring the mean, specifically under the assumption of a two-parameter exponential distribution. This conclusion is supported by the observation that only five samples fall within the established Six Sigma control limits, suggesting considerable process variability and signaling a deviation from statistical control. Furthermore, the Control Limit Interval (CLI) calculated for the Six Sigma-based control chart is 1.01, which is notably narrower compared to the CLI derived from the conventional Three Sigma control chart for the same sample size (n = 5). This quantitative comparison underscores the heightened sensitivity and more stringent monitoring capability of the Six Sigma approach. By narrowing the control boundaries, the Six Sigma methodology facilitates earlier detection of process shifts or anomalies, thereby enhancing the ability to implement timely corrective actions. This distinction highlights the practical advantages of Six Sigma-based control charts in maintaining high standards of quality and reliability in process monitoring.

Table 2: *Comparison of 3-sigma and six sigma control limits for the mean under two-parameter exponential distribution*

S.No	Type of control chart	LCL	CL	UCL	CLI
1	Shewhart 3σ	6.73	10.80	14.87	8.14
2	Six sigma	10.29	10.80	11.31	1.01

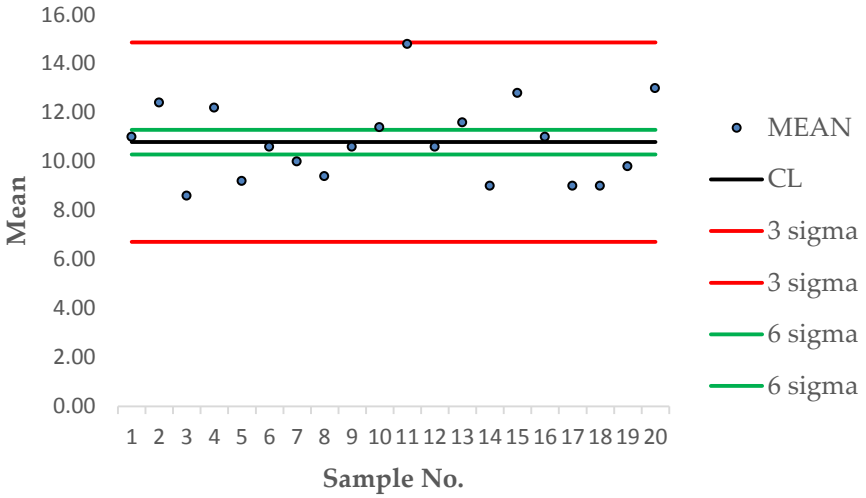


Figure 1: *Shewhart 3σ and 6σ control charts for mean under two-parameter exponential distribution*

In addition, the findings illustrated in Table 3 and Figure 2 provide compelling evidence that the traditional Shewhart 3-Sigma control chart for monitoring the process mean is comparatively less effective when assessed using the Average Run Length (ARL) criterion. When juxtaposed with the proposed Six Sigma-based control chart formulated under the two-parameter exponential distribution—the conventional approach demonstrates reduced sensitivity in detecting shifts or subtle deviations in the process.

Table 3: *Average run length (ARL) of 3σ and six sigma control limits for mean under two-parameter exponential distribution*

S.No	Multiple of σ	Shewhart 3σ	Six sigma
1	0.31	293	32
2	0.32	289	26
3	0.33	285	21
4	0.34	281	18
5	0.35	277	15
6	0.36	273	12

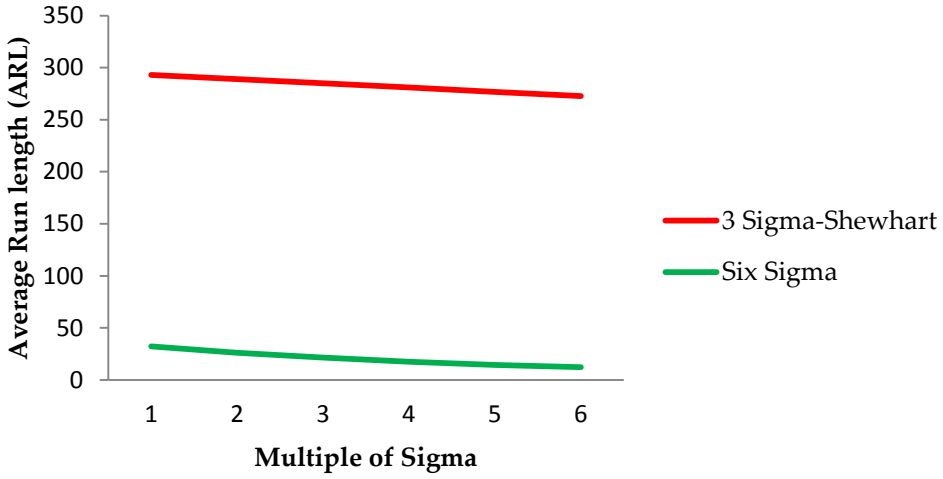


Figure 2: *ARL of Shewhart 3σ and 6σ mean control charts under two-parameter exponential distribution*

The Six Sigma control chart offers a more rigorous and refined monitoring framework, which significantly enhances the early identification of process anomalies. This tighter level of control contributes to more accurate detection of out-of-control signals and facilitates the prompt implementation of corrective measures, thereby supporting higher standards of quality assurance.

This comparative analysis highlights the inherent limitations of the Shewhart 3-Sigma chart in environments where detecting minor but critical process shifts is essential. It also reinforces the strategic advantages of adopting the Six Sigma methodology, particularly its capacity for improved process precision, reduced variability, and substantial defect minimization key goals in both manufacturing and service-oriented quality management systems

Conclusion

The results discussed above clearly indicate that when both the traditional Shewhart 3-Sigma control chart and the Six Sigma-based control limits for the mean are applied under the exponential distribution, the process under evaluation is found to be statistically out of control. This conclusion is drawn from the observed inconsistencies in sample points relative to their respective control limits, signaling that the process is experiencing variations beyond acceptable limits. Notably, the control limit interval (CLI) derived from the Six Sigma-based control chart is considerably narrower than that of the Shewhart 3-Sigma chart. This reduced interval reflects a more stringent and precise monitoring capability, which enhances the chart's effectiveness in detecting minor process shifts and emerging irregularities at an earlier stage.

The presence of such deviations suggests that the quality of the product or service fails to meet the expected standards, underscoring the urgent need for system or process improvement. Implementing Six Sigma-based control strategies enables organizations to more effectively identify and rectify sources of variation, ultimately contributing to enhanced process stability and performance. Furthermore, this methodological shift holds significant economic value. By improving detection accuracy and enabling timely interventions, the Six Sigma-based approach contributes to a reduction in the total expected costs within a finite operational period, as well as a decrease in the average long-term costs associated with sustained process inefficiencies or quality failures. As a result, organizations can achieve both improved quality outcomes and optimized cost-efficiency through the adoption of this enhanced control charting technique.

References

[1] Acheson J. Duncan. Quality Control and Industrial Statistics. Richard D. Irwin, inc. homewood, Illinois, Sixth Edition, 1958.

[2] Deming W. Edwards. Some Theory of Sampling, John Wiley & Sons, inc., New York, 1966.

[3] Deming W. Edwards. Quality, Productivity and Competitive Position.Mit Centre for Advanced Engineering Study (Caes), Cambridge, mass, 1982.

[4] JuranJ. M and Gryna F.M. Quality Planning and Analysis. Second edition, Mcgraw-hill, New York, 1982.

[5] Kin lam, Bimal K. Sinha and Zhong wu (1994). Estimation of parameters ina two-parameter exponential distribution using ranked set sample. *Ann. inst. statist. math*, 46(4):723-736.

[6] Monjed, H. Samuh and Areen Qtait (2015). Estimation for the parameters of the exponentiated exponential distribution using a median ranked set sampling. *Journal of Modern Applied Statistical Methods*, 14(1):215-237.

[7] Montgomery D. C. Introduction to Statistical Quality Control. Seventh edition, Wiley Publications, 2001.

[8] Pavithra, M.R and Balamurugan P (2020). Fuzzy six sigma based regression control

chart under moderateness. *International Journal of Advanced Science and Technology*, 29(4):283-295.

[9] Sheldon M. Ross. Probability and Statistics for Engineers and Scientists. Fifth edition, Elsevier inc, 2014.

[10] Shewhart W.A. Economic Control of Quality of Manufactured Product, Van Nostrand,1931.

[11] Taguchi G. Introduction to Quality Engineering. Asian Productivity Organization, 1986.

[12] Taguchi G and Wu Y. Introduction to off – line Quality Control. Japan Quality Control Organization, nagoya, Japan, 1980.

RT&A, No 4 (89)
Volume 20, December 2025

EXPLORING RECIDIVISM THROUGH BAYESIAN SURVIVAL MODELS: A PARAMETRIC APPROACH WITH RSTAN

Fahad Ashraf[1], Mohammad Parvej[2], Athar Ali Khan[3]

•

[1,2,3]Department of statistics and Operations Research
Aligarh Muslim University, Aligarh, India
[1]Corresponding Author e-mail: gj5872@myamu.ac.in
[2]parvezstats97@gmail.com, [3]alkhan.st@amu.ac.in

Abstract

This study adopts a fully Bayesian parametric survival modeling approach to examine recidivism, utilizing the recid dataset from the wooldridge package in R. Leveraging the computational capabilities of RStan, four alternative survival distributions Exponential, Weibull, Lognormal, and Frechet are estimated, incorporating covariates reflecting demographics, criminal history, and post-release conditions. To promote model parsimony and interpretability, covariate selection is guided by variable importance measures derived from a machine learning-enhanced Cox model. Model performance is systematically evaluated using the Leave-One-Out Information Criterion (LOOIC) and the Widely Applicable Information Criterion (WAIC) to ensure robust predictive accuracy. The analysis includes detailed posterior summaries, conditional effect plots to assess covariate influences on time to reoffense, and posterior predictive distribution (PPD) plots for model validation. The findings provide meaningful insights into the timing and risk of reoffending and underscore the value of Bayesian survival models in criminological research.

Keywords: Recidivism, Cox-ML model, Bayesian modeling, Rstan, Survival analysis

1. Introduction

The term recidivism is defined in some specific way, such as rearrest, reconviction, or reimprisonment, of a released prisoner [1]. Recidivism is prevalent in the realm of criminality, is a persistent concern for both criminologists and economists. Research suggests that a small proportion of habitual offenders are responsible for a disproportionately high share of serious crimes [2]. According to recidivism data of 33 countries, the 2-year reconviction rates were found between 18% and 55% [3]. From an economic perspective, criminal behavior and recidivism can be studied within the framework of rational choice theory [4], where individuals weigh the expected costs and benefits of legal and illegal activities. Factors such as employment prospects, sentence length, and prior criminal history shape this calculus, and empirical studies have shown that poor post-release labor market conditions and limited human capital often drive individuals back into criminal activity [5],[6]. Accordingly, modeling time until reoffense provides critical insights into both the effectiveness of penal policies and the socio-economic mechanisms underlying recidivism. Thus it becomes of paramount importance to understand the dynamics of criminal recidivism and factors that influence criminal recidivism in forming policy decisions, designing rehabilitation programs, and allocating criminal justice resources effectively.

Building upon this motivation, statistical analysis and modeling of recidivism has become a crucial area of research, particularly in understanding the time until reoffense after release. [7] is one of the oldest work on recidivism prediction that employed scoring system to predict parole

outcomes. Currently research on criminal recidivism has spanned a broad range of methods, from descriptive statistics and logistic regression to modern machine learning and Bayesian modeling [8],[6],[9],[10]. Early work focused on describing recidivism patterns, while more recent studies incorporate individual- and contextual-level covariates to predict or understand reoffending behavior. Since recidivism is inherently a time to event phenomenon and censoring is key element as not all offenders reoffends, [11] criticized prevailing approaches for ignoring the timing of reoffenses and emphasized on the need for models that account for varying follow-up periods and censoring core motivations for adopting survival analysis. The earlier works like [12],[13] used exponential model to analyse the recidivism but failed to formally incorporate the censoring information in the model. Later parametric, non parametric, regression, cox survival and split population models were used in recidivism prediction [5],[14] pioneered the use of split-population survival models, allowing for a fraction of offenders who never recidivate. [15] used survival analysis to model time until recidivism among youthful offenders, integrating both static and dynamic covariates. Over time, survival based approaches have emerged as the dominant framework for analyzing recidivism, as they naturally accommodate censoring while capturing the dynamic nature of reoffending. This progression highlights the methodological shift from simple descriptive accounts toward more rigorous and flexible statistical modeling of criminal behavior.

Traditional survival analysis methods, such as Cox models, accelerated failure time model have been widely used [16],[17] however, these approaches often rely on restrictive assumptions and may not fully capture individual-level heterogeneity or uncertainty in parameter estimation. Bayesian approach is a flexible and robust framework for modeling time-to-event data, allowing researchers to incorporate prior knowledge, quantify uncertainty more comprehensively, and explore complex model structures. [18] showcased the use of Bayesian method in criminological data, demonstrating advantages in handling parameter uncertainty and model comparison. Recently there has been a surge in the adoption of Bayesian approaches in all field, In survival analysis, Bayesian methods enable more robust inference on censored time-to-event data, [19],[20] demonstrated the effectiveness of Bayesian method in modeling survival data with generalized distributions through **Rstan**. Despite the methodological advantages of Bayesian approaches, their application to criminal recidivism remains limited. This study addresses that gap by applying fully Bayesian parametric survival models to recidivism data from North Carolina, available via the **wooldridge** package in R. Leveraging machine learning-based variable selection from Cox models, we analyze covariate effects on recidivism timing under four competing survival distributions: Exponential, Weibull, Lognormal, and Frechet. By doing so, we not only identify the most influential socio-demographic and behavioral factors affecting reoffense risk but also evaluate which statistical models best capture the time dynamics of recidivism.

The Cox model combined with techniques from machine learning, especially with the help of Lasso and Elastic Net regularization, makes choosing variables easier because it handles both the issues of many variables and correlated predictors. By assigning penalties to the regression coefficients, these models move minor variable effects besides zero, leading to automatic and all-at-once identification of top features that also prevent the chances of overfitting. With this approach, examples of significant risk factors become easy to spot and the models provide stronger and more accurate outcomes for predicting survival, especially in settings where conventional Cox models might fail [21].

Through Bayesian estimation via **Rstan**, we obtain full posterior distributions of model parameters, enabling nuanced interpretation of covariate effects and credible intervals for uncertainty quantification. Model fit is assessed using the Leave-One-Out Information Criterion (LOOIC) and the Widely Applicable Information Criterion (WAIC), both of which favor the Lognormal model for this dataset. Ultimately, this study highlights the advantages of Bayesian survival models in criminology and the importance of individualized risk assessment for policy formulation and intervention design, thereby bridging the gap between statistical modeling and real-world decision-making.

2. Data Description and Variable Selection

The recidivism data used in this article is available with **wooldrige** package of **R** [22]. The data set contains records of recidivism time along with a number of variables on 1445 inmates released from North Carolina prison. It includes demographic, socioeconomic, and criminal history characteristics such as age, education, prior convictions, substance use, and participation in rehabilitation programs. These variables make the dataset suitable for analyzing the factors influencing the likelihood and timing of reoffending. For more detail about the data one may refer to [23],[2].

Features of the data

- black: = 1 if black
- alcohol: = 1 if alcohol problem
- drugs: = 1 if drug history
- super: = 1 if release supervised
- married: = 1 if married when incarc.
- felon: = 1 if felony sentence
- workprg: = 1 if in N.C. pris. work prg.
- property: = 1 if property crime
- person: = 1 if crime against person
- priors: prior convictions
- educ: years of schooling
- rules: rules violations in prison
- age: in months
- tserved: time served, rounded to months
- follow: length follow period, months
- durat: min(time until return, follow)
- cens: = 1 if duration right censored
- ldurat: log(durat)

Table 1: *Means of Selected Variables from the recid Dataset*

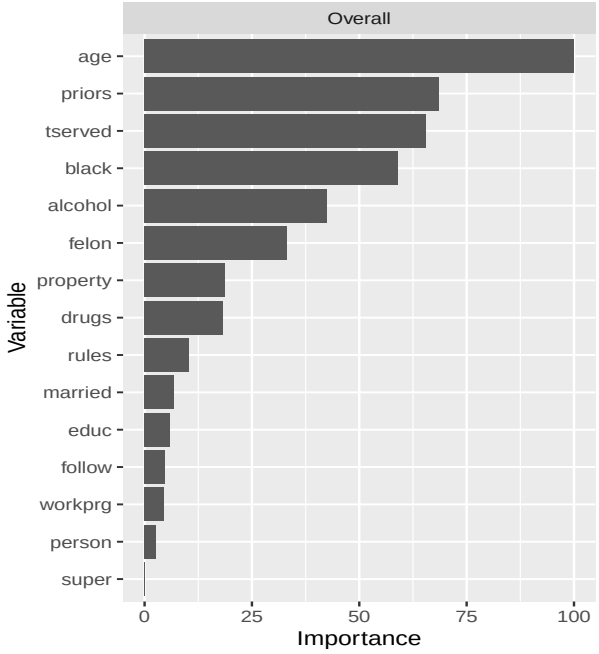
black	alcohol	drugs	super	married	felon	workprg	property	person
0.4851	0.2097	0.2415	0.6941	0.2554	0.3142	0.4651	0.2547	0.05329
priors	educ	rules	age	tserved	follow	durat	cens	ldurat
1.432	9.702	1.185	345.4	19.18	74.89	55.37	0.618	3.745

In Table 1, the mean value of variables with binary response depicts the proportion e.g. the mean of black is 0.4851, it means 48.51% of released individuals are black, for continuous variable mean carry usual interpretation.

There are 15 covariates in the data which may have varying degree of effects on recidivism time of released prisoners, some having large and significant effects while others having small and insignificant effect. To select those with large and significant effects we used variable importance index for selecting the variables.The method is applied through **varimp()** function of **MachineShop** package of **R** software [24]. The variable importance index suggests the importance of a variable on a scale of 0 to 100, with 100 signifying most important variable and 0 the least. For our study we used a rule of thumb to consider any variable with variable importance index greater than 15 as important enough to be selected in the model. This procedure ensures a more parsimonious model by focusing only on influential predictors.

Hence we selected the variable age (of the released prisoner), priors (number of prior convictions), tserved (time served in the prison), black, alcohol, felon, property and drugs as regressor affecting the duration recidivism. Three varibles namely age, tserved and priors are scaled by

1000, 100 and 10 respectively according to the suggestion of [2] to improve the interpretability of coefficients and comparison across covariates.



variables	vi.Overall
age	100.0000000
priors	68.5054989
tserved	65.5856527
black	59.0549773
alcohol	42.4879027
felon	33.1192298
property	18.7498844
drugs	18.2277192
rules	10.3582041
married	6.8459441
educ	5.8767442
follow	4.7962893
workprg	4.4813649
person	2.6101374
super	0.1597608

Figure 1: *Variable Importance Plot*

3. Methods

In this section we discuss the different models and methods used for the analysis, we employed fully parametric survival models and their Bayesian formulations to analyze time-to-event data, allowing flexible modeling of covariate effects under censoring. Model performance and selection were assessed using Bayesian model comparison criteria, including Leave-One-Out Information Criterion (LOOIC) and the Widely Applicable Information Criterion (WAIC).

3.1. Parametric Survival Models

A parametric survival model analyzes time-to-event data by assuming that survival times T follow a specific distribution with a known functional form. This allows direct modeling of key functions such as the survival function $S(t) = P(T > t)$, density $f(t)$, and hazard function $h(t) = \frac{f(t)}{S(t)}$. When covariates $\mathbf{X} \in \mathbb{R}^p$ are included in the model through rate or scale parameter (e.g. in exponential model) using log link function,

$$log(\lambda) = \boldsymbol{X}'\boldsymbol{\beta},$$
$$\lambda = exp(\boldsymbol{X}'\boldsymbol{\beta}),$$

and throug lacation parameter (e.g. in lognormal model) using an identity link

$$\mu = \boldsymbol{X}'\boldsymbol{\beta},$$

where $\boldsymbol{X} = (1, x_1, x_2, \cdots, x_p)$ is the model matrix (set of covariates with interceot column), and $\boldsymbol{\beta} = (\beta_0, \beta_1, \beta_2, \cdots, \beta_p)$ represents regression coefficients and θ is a parameter of the distribution, usually it is a scale parameter. Parametric models are particularly useful when extrapolation is required and distributional assumptions are justifiable [25],[26].

3.1.1 Exponential Model

The exponential distribution is one of the simplest and most widely used parametric models in survival analysis. It assumes a constant hazard rate over time, making it suitable for modeling time-to-event data where the event risk does not change as time progresses.Let Let T denote a non-negative continuous random variable representing the time until an event The exponential distribution is defined by the rate parameter $\lambda > 0$ as,

- Probability Density Function (PDF):

$$f(t) = \lambda e^{-\lambda t}, \quad t \geq 0 \tag{1}$$

- Cumulative Distribution Function (CDF):

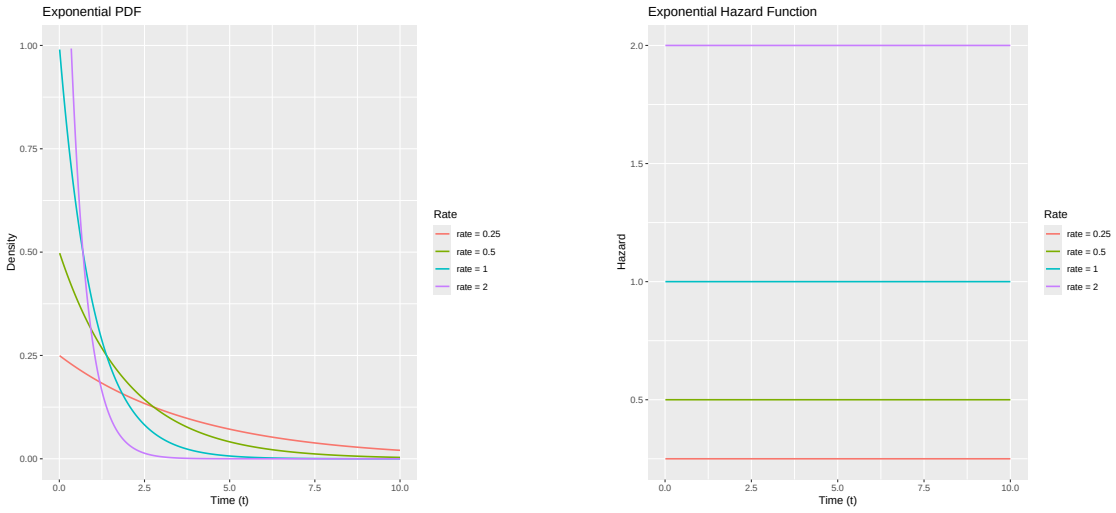
$$F(t) = 1 - e^{-\lambda t} \tag{2}$$

- Survival Function (SF):

$$S(t) = 1 - F(t) = e^{-\lambda t} \tag{3}$$

- Hazard Function (HF):

$$h(t) = \frac{f(t)}{S(t)} = \lambda \tag{4}$$



(a) *Exponential PDF*

(b) *Exponential Hazard*

,,

Figure 2: *PDF and hazard function of the Exponential distribution*

3.1.2 Weibull Model

The Weibull distribution is a widely used and flexible parametric model in survival analysis. Unlike the exponential distribution, it allows for a hazard rate that can either increase or decrease over time, making it suitable for a broader range of time-to-event data. Let T be a non-negative continuous random variable representing the time until an event occurs. The Weibull distribution is characterized by two positive parameters: a shape parameter $\alpha > 0$ and a scale parameter $\lambda > 0$.

- Probability Density Function (PDF):

$$f(t) = \frac{\alpha}{\lambda}\left(\frac{t}{\lambda}\right)^{\alpha-1} \exp\left(-\left(\frac{t}{\lambda}\right)^{\alpha}\right), \quad t \geq 0 \tag{5}$$

- Cumulative Distribution Function (CDF):

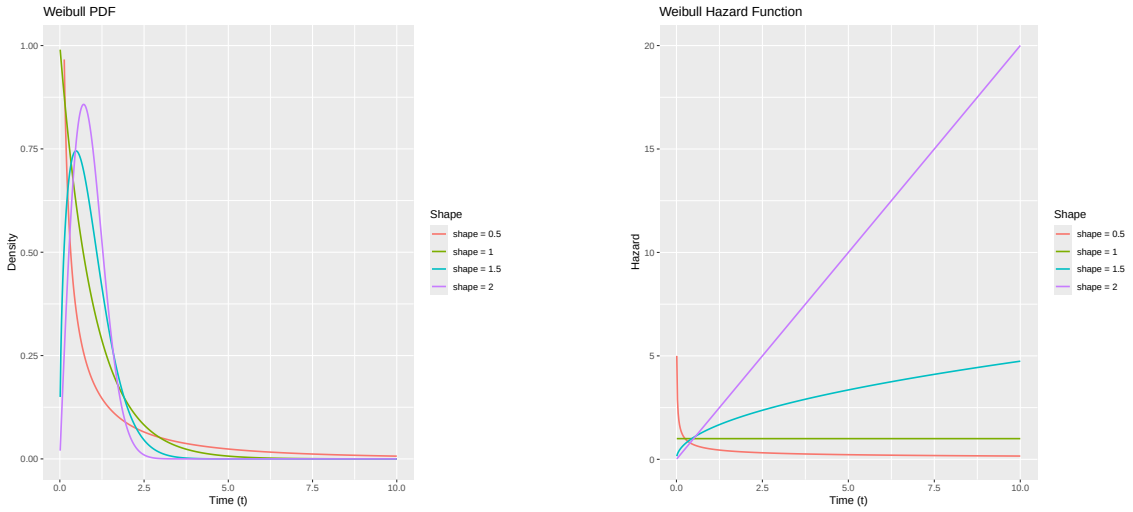
$$F(t) = 1 - \exp\left(-\left(\frac{t}{\lambda}\right)^{\alpha}\right) \tag{6}$$

- Survival Function (SF):

$$S(t) = \exp\left(-\left(\frac{t}{\lambda}\right)^{\alpha}\right) \tag{7}$$

- Hazard Function (HF):

$$h(t) = \frac{\alpha}{\lambda}\left(\frac{t}{\lambda}\right)^{\alpha-1} \tag{8}$$



(a) *Weibull PDF* **(b)** *Weibulll hazard*

Figure 3: *PDF and hazard function of the Weibull distribution*

3.1.3 Frechet Model

The Frechet distribution is part of the extreme value family, used for modeling heavy-tailed survival times or decreasing hazard rates, such as in early failures. Let T be a non-negative continuous random variable representing the time until an event occurs. The Frechet distribution is characterized by two positive parameters: the shape parameter $\alpha > 0$ and the scale parameter $s > 0$. Its probability density function (PDF) is given by:

- Probability Density Function (PDF):

$$f(t) = \frac{\alpha}{s}\left(\frac{t}{s}\right)^{-(\alpha+1)} \exp\left(-\left(\frac{t}{s}\right)^{-\alpha}\right), \quad t > 0 \tag{9}$$

- Cumulative Distribution Function (CDF):

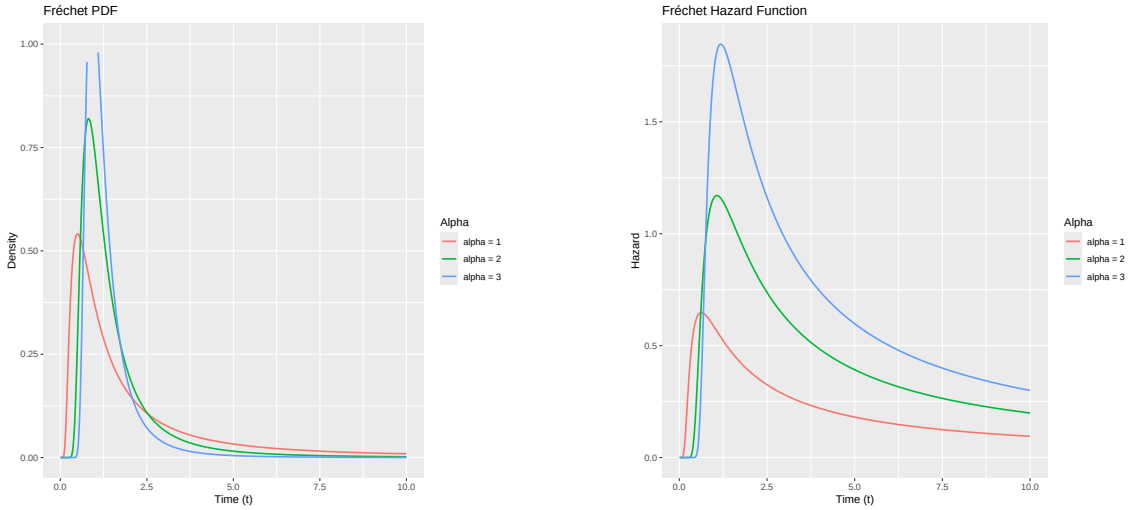
$$F(t) = \exp\left(-\left(\frac{t}{s}\right)^{-\alpha}\right) \tag{10}$$

- Survival Function (SF):

$$S(t) = 1 - \exp\left(-\left(\frac{t}{s}\right)^{-\alpha}\right) \tag{11}$$

- Hazard Function (HF):

$$h(t) = \frac{\alpha}{s}\left(\frac{t}{s}\right)^{-(\alpha+1)} \cdot \left[\frac{1}{1-\exp\left(-\left(\frac{t}{s}\right)^{-\alpha}\right)}\right] \tag{12}$$



(a) *Frechet PDF* **(b)** *Frechet Hazard*

Figure 4: *PDF and hazard function of the Frechet distribution*

3.1.4 Lognormal Model

The Log-Normal distribution is a flexible parametric model used in survival analysis, particularly when the hazard function is non-monotonic i.e., it may initially increase and then decrease over time. This makes it suitable for modeling time-to-event data with delayed risk peaks. A random variable T is said to follow a Log-Normal distribution if its logarithm is normally distributed. That is, $\log T \sim \mathcal{N}(\mu, \sigma^2)$, where $\mu \in \mathbb{R}$ and $\sigma > 0$ are the location and scale parameters respectively.

- Probability Density Function (PDF):

$$f(t) = \frac{1}{t\sigma\sqrt{2\pi}} \exp\left(-\frac{(\ln t - \mu)^2}{2\sigma^2}\right), \quad t > 0 \tag{13}$$

- Cumulative Distribution Function (CDF):

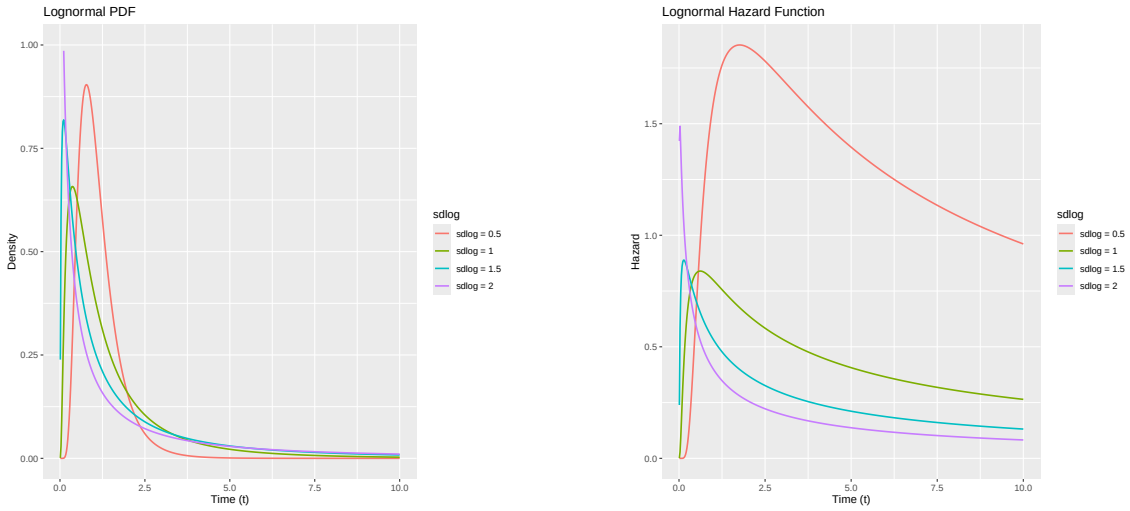
$$F(t) = \Phi\left(\frac{\ln t - \mu}{\sigma}\right) \tag{14}$$

- Survival Function (SF):

$$S(t) = 1 - \Phi\left(\frac{\ln t - \mu}{\sigma}\right) \tag{15}$$

- Hazard Function (HF):

$$h(t) = \frac{1}{t\sigma\sqrt{2\pi}} \cdot \frac{\exp\left(-\frac{(\ln t-\mu)^2}{2\sigma^2}\right)}{1-\Phi\left(\frac{\ln t-\mu}{\sigma}\right)} \tag{16}$$



(a) *Lognormal PDF*

(b) *Lognoral hazard*

Figure 5: *PDF and hazard function of the lognormal distribution*

3.2. Bayesian Model Formulation

In Bayesian survival analysis, the model is defined through a combination of prior distributions on the parameters and a likelihood function derived from the survival model and observed data. The core idea is to update the prior beliefs in light of the observed data using Bayes' rule:

$$p(\boldsymbol{\theta} \mid \mathcal{D}) \propto p(\mathcal{D} \mid \boldsymbol{\theta}) \cdot p(\boldsymbol{\theta}),$$

where $\boldsymbol{\theta}$ denotes the set of model parameters, $p(\mathcal{D} \mid \boldsymbol{\theta})$ is the likelihood, $p(\boldsymbol{\theta})$ is the prior. This formulation enables us to quantify parameter uncertainty explicitly by working with the entire posterior distribution rather than single point estimates.

3.2.1 Priors

In the Bayesian framework, prior distributions encode our beliefs about the model parameters before observing the data. For regression models [27] recommend the use of weakly informative priors that provide regularization to avoid overfitting, while remaining flexible enough to allow the data to dominate. For a regression model with coefficients $\boldsymbol{\beta} = (\beta_0, \beta_1, \ldots, \beta_p)$ and a positive scale parameter σ, a typical prior specification is $\beta_j \sim \mathcal{N}(0, 5^2), \quad j = 0, 1, \ldots, p$, and $\sigma \sim$ half-Cauchy$(0, 25)$. The references [28] and [19] provide detailed information regarding the application of the half-Cauchy prior to shape and scale parameters alongside the Gaussian prior to the regression coefficient.

$$p(\beta) = \frac{1}{\sqrt{(2\pi \times 25)}} \times e^{\frac{-\beta^2}{2\times 25}}, -\infty < \beta < \infty. \tag{17}$$

$$p(\sigma) = \frac{2 \times 25}{\pi(\sigma^2 + 25^2)}, \sigma > 0. \tag{18}$$

These priors reflect prior uncertainty about the magnitude of the coefficients and ensure the scale parameter remains positive and not overly influential. The half-Cauchy prior on σ has heavier tails than the inverse-gamma distribution, offering greater robustness and protection against over shrinkage.

3.2.2 Likelihood

Let t_i be the observed survival time for the i-th individual, and δ_i the event indicator with $\delta_i = 1$ if the event is observed and $\delta_i = 0$ if right-censored. Let $f(t_i \mid \boldsymbol{\theta})$ and $S(t_i \mid \boldsymbol{\theta})$ be the density and survival functions of the survival model parameterized by $\boldsymbol{\theta}$. Then likelihood for right-censored data as given in [26]

$$L(\boldsymbol{\theta}) = \prod_{i=1}^{n} [f(t_i \mid \boldsymbol{\theta})]^{\delta_i} [S(t_i \mid \boldsymbol{\theta})]^{1-\delta_i}. \tag{19}$$

Now, for the lognormal model where $T \sim lognormal(\mu = X'\beta, \sigma^2)$, substituting the pdf and survival function of lognormal distribution from Equation 13,15 in Equation 19 the likelihood for the log-normal model is obtained as

$$p(t_i \mid \boldsymbol{\beta}, \sigma) = \prod_{i=1}^{n} \left[\left(\frac{1}{t_i \sigma \sqrt{2\pi}} \exp\left(-\frac{(\log t_i - X'\beta)^2}{2\sigma^2} \right) \right)^{\delta_i} \cdot \left(1 - \Phi\left(\frac{\log t_i - X'\beta}{\sigma} \right) \right)^{1-\delta_i} \right] \tag{20}$$

where $\Phi(\cdot)$ cumulative density function (CDF) of the standard normal distribution.

3.2.3 Posterior Distribution

Using Bayes' theorem, the posterior distribution is proportional to the product of the likelihood and priors:

$$p(\boldsymbol{\beta}, \sigma \mid \mathcal{D}) \propto p(\mathcal{D} \mid \boldsymbol{\beta}, \sigma) \cdot p(\boldsymbol{\beta}) \cdot p(\sigma),$$

where $\mathcal{D} = \{(t_i, \delta_i, \boldsymbol{x}_i)\}_{i=1}^{n}$ denotes the observed data. For the log-normal model, so

$$p(\boldsymbol{\beta}, \sigma \mid \mathcal{D}) \propto \prod_{i=1}^{n} \left[\left(\frac{1}{t_i \sigma \sqrt{2\pi}} \exp\left(-\frac{(\log t_i - X'\beta)^2}{2\sigma^2} \right) \right)^{\delta_i} \cdot \left(1 - \Phi\left(\frac{\log t_i - X'\beta}{\sigma} \right) \right)^{1-\delta_i} \right] \cdot p(\boldsymbol{\beta}) \cdot p(\sigma). \tag{21}$$

This posterior expression combines information from both censored and uncensored observations, where the likelihood contribution depends on whether the event time was observed or right-censored. The inclusion of prior distributions on β and σ allows incorporation of prior knowledge or regularization to stabilize estimation in the presence of limited or noisy data.

Since the posterior is typically not available in closed form, inference is performed via **stan** modeling language through **(**R) software. Stan is a probabilistic programming language that use No-U-Turn-Sampler (NUTS) an extension of Hamiltonian Monte Carlo (HMC) algorithm to draw samples from the posterior densities where analytical solutions are intractable.This approach relies on advanced Markov Chain Monte Carlo (MCMC) algorithms, which efficiently approximate complex posterior distributions.

3.3. Model Selection Criteria

After model fitting, selection of the best performing model is one of the crucial step in statistical modeling. For this purpose we choose two fully Bayesian criterion, Leave One Out Information Criterion (LOOIC) and Widely Applicable Information Criterion [29],[30]. In recent LOOIC and WAIC have been widely used for Bayesian model comparison due to their principled approach to estimating out-of-sample predictive accuracy [31],[19].

Both WAIC and LOOIC are on the deviance scale, and lower values indicate better predictive performance [32]. In practice, these criteria are often very close numerically, but LOOIC is generally preferred due to its better diagnostic capabilities and reliability, especially in the presence of influential observations. In this work, LOOIC and WAIC are computed using the **loo** package in **R**, which provides efficient implementations of Pareto-smoothed importance sampling and related diagnostics [33].

3.3.1 LOOIC

The Bayesian LOOIC estimate of out-of-sample predictive fit is In leave-one-out cross-validation, the predictive performance is assessed by leaving out each observation one at a time and evaluating how well the model predicts it. Mathematically,

$$\text{LOOIC} = -2 \sum_{i=1}^{n} \log \left(\frac{1}{S} \sum_{s=1}^{S} w_i^s p(y_i \mid \theta^s) \right), \tag{22}$$

where w_i^s are the importance weights from the Pareto Smoothed Importance Sampling (PSIS) approximation. LOOIC provides a robust measure of predictive accuracy and is particularly effective when data points have varying influence on the model.

3.3.2 WAIC

The Watanabe-Akaike information criterion also known as Widely Applicable Information Criterion (WAIC) is a fully Bayesian generalization of the Akaike Information Criterion (AIC)[30]. WAIC evaluates model fit by averaging the pointwise predictive accuracy over the posterior distribution and includes a correction term for effective model complexity. It is calculated as:

$$\text{WAIC} = -2 \left(\sum_{i=1}^{n} \log \left(\frac{1}{S} \sum_{s=1}^{S} p(y_i \mid \theta^s) \right) - \sum_{i=1}^{n} \text{Var}_{s=1}^{S} \left[\log p(y_i \mid \theta^s) \right] \right), \tag{23}$$

where θ^s are posterior samples, and $p(y_i \mid \theta^s)$ is the likelihood for observation y_i. The second term acts as a penalty for model complexity, ensuring that more complex models are not unduly favored.

4. Results and Discussion

This section presents the findings from the Bayesian parametric survival models and interprets the results.

4.1. Model selection and performance

Table 2 reports the LOOIC and WAIC values for each model. Among the four parametric survival models fitted to the data the Lognormal model yielded the lowest values for both the Leave-One-Out Information Criterion (LOOIC = 6328.6) and the Widely Applicable Information Criterion (WAIC = 6328.5). These results indicate that the Lognormal model provides the best out-of-sample predictive accuracy among the candidate models.This suggests that the hazard of reoffending is not monotonic over time, it may initially increase and later decrease which aligns with the intuition that recidivism risk is highest during the early period after release when individuals face the greatest reintegration challenges. The Weibull and exponential models followed, with slightly higher information criteria values, while the Frechet model showed substantially poorer fit, as reflected by its much higher LOOIC and WAIC values. Based on these criteria, the lognormal model was selected for further interpretation and posterior analysis.

Table 2: *LOOIC and WAIC Values of the fitted models*

Model	LOOIC	WAIC
Lognormal	**6328.6**	**6328.5**
Weibull	6402.0	6401.8
Exponential	6435.3	6434.9
Fretchet	7324.6	7325.1

4.2. Posterior estimates

Table 3 presents the posterior summaries of the lognormal survival model. All parameters exhibit good convergence diagnostics, with $\widehat{R}$ values equal to 1.00 and sufficiently large effective sample sizes (N_{eff}), indicating reliable posterior estimation. The intercept estimate is 4.43 with a 95% credible interval [4.01, 4.84], serving as the baseline log survival time. Age (scaled by 1000) has a strong positive effect ($\hat{\beta}$ = 3.97, 95% CI [2.85, 5.16]), suggesting that older individuals tend to have longer survival times (recidivism duration) post-release. In contrast, the number of prior convictions (priors/10) and time served (tserved/100) are both negatively associated with survival time, with posterior means of -1.38 and -2.03, respectively, indicating that more priors and longer incarceration are linked to shorter time to recidivism.

Factor variables in the study also show notable effects. Being black (black1), having a history of alcohol abuse (alcohol1), drug involvement (drugs1), or a property-related offense (property1) are all negatively associated with survival time, with credible intervals excluding zero (significant effect). On the other hand, being a felon (felon1) is positively associated with log survival time ($\hat{\beta}$ = 0.88, 95% CI [0.50, 1.27]), indicating a longer time to reoffending relative to non-felons. The residual standard deviation σ is estimated at 1.83 (95% CI [1.71, 1.95]), capturing the remaining variability in log survival time not explained by the covariates. Overall, the model captures important individual-level heterogeneity in recidivism risk.

Table 3: *Posterior summaries from the lognormal model*

Parameter	mean	*se_mean*	2.5%	97.5%	$\hat{R}$	N_{eff}
Intercept	4.43	0.21	4.01	4.84	1.00	5178
age/1000	3.97	0.59	2.85	5.16	1.00	4212
tserved/100	-2.03	0.30	-2.63	-1.45	1.00	3868
priors/10	-1.38	0.22	-1.80	-0.95	1.00	4085
black1	-0.54	0.12	-0.78	-0.31	1.00	6137
alcohol1	-0.63	0.14	-0.91	-0.35	1.00	5623
felon1	0.88	0.20	0.50	1.27	1.00	3202
property1	-0.62	0.19	-1.00	-0.25	1.00	3684
drugs1	-0.34	0.13	-0.60	-0.08	1.00	5659
sigma(σ)	1.83	0.06	1.71	1.95	1.00	3852

4.3. Posterior density and trace plots

Posterior density plots and trace plots are two crucial visualization tool for assessing the quality and reliability of posterior summaries. The posterior density plots summarize the distribution of the model parameters after updating prior beliefs with the observed data, allowing us to evaluate location, spread, and possible skewness in the estimates. The trace plots display the parameter values sampled across iterations of the Markov Chain Monte Carlo (MCMC) algorithm. A well-mixed trace plots without visible trends or long-term autocorrelation indicate convergence of the chains, while consistent overlap across multiple chains confirms stability of the posterior draws.

Figure 6 displays the marginal posterior distributions of the model parameters. It is evident from the plot that the marginal posterior densities are well-separated from zero indicating significant influence on survival time. This also shows the effectiveness of the variable selection process as all the selected variables have significant effect. Figure 7 confirms the good mixing behavior of MCMC chains, indicating stable inference. Moreover, the trace plots exhibit no apparent trends or drifts, suggesting that the chains have reached stationarity. This strengthens confidence in the reliability of the posterior summaries and the robustness of the estimated effects.

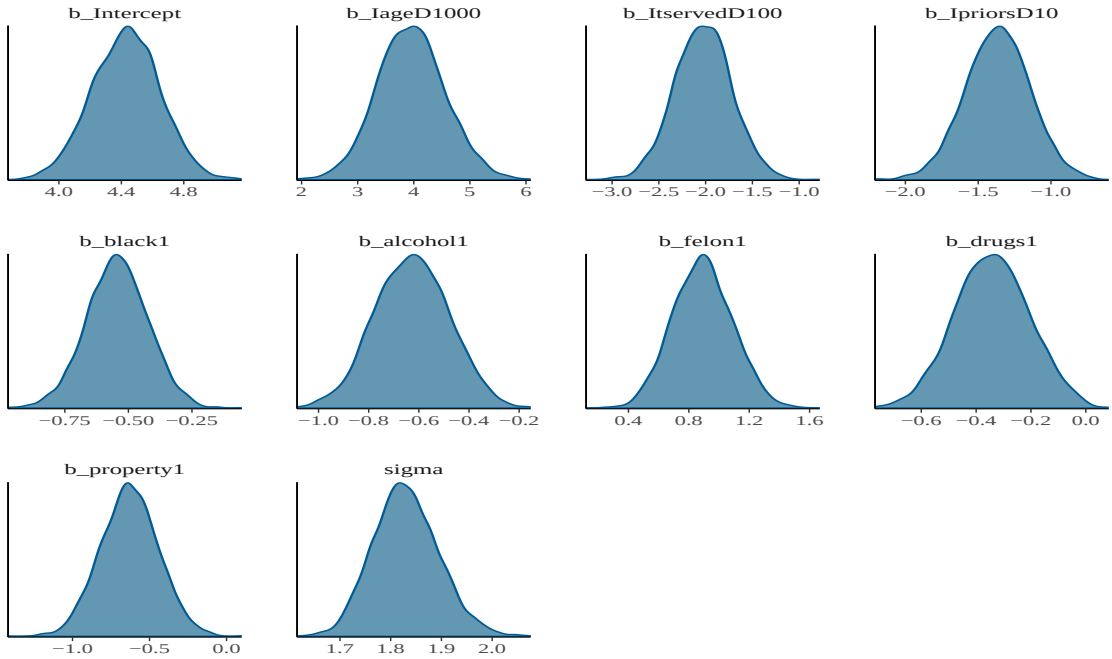


Figure 6: *Posterior distributions of coefficients from the lognormal survival model and scale parameter σ. Each horizontal segment represents the marginal posterior distribution for a specific parameter. This visualization helps identify the magnitude and direction of each predictor's effect on survival time, with zero indicating no effect. Parameters with posteriors concentrated away from zero suggest a meaningful association with time to recidivism.*

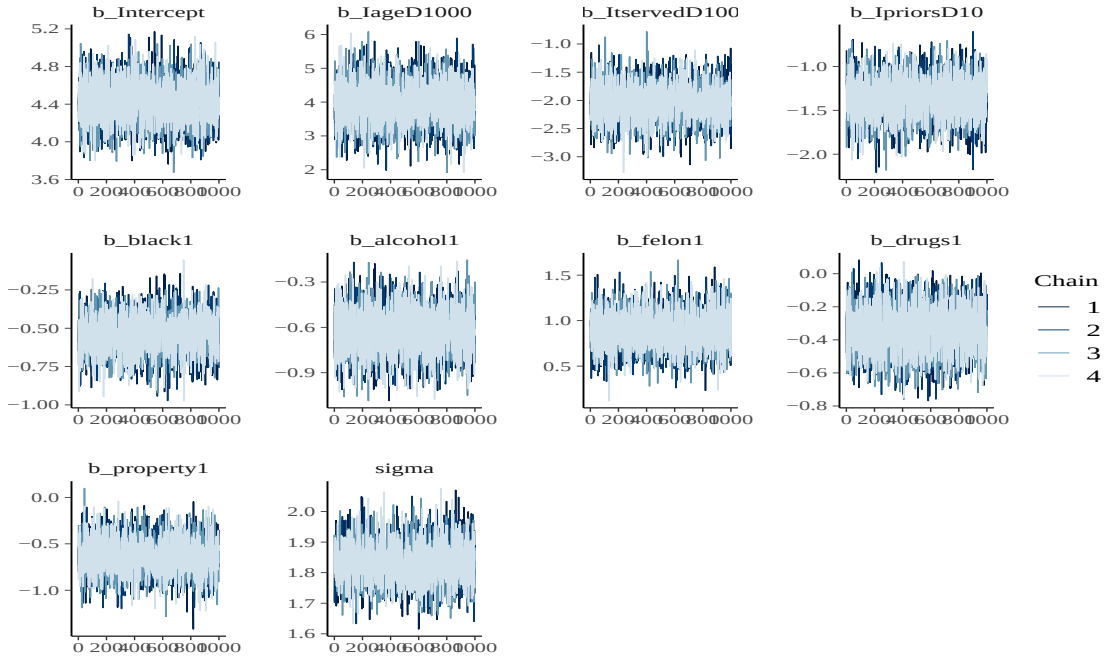


Figure 7: *Trace plots of MCMC chains for the parameters in he lognormal survival model. This shows the MCMC sampling behavior across four chains, well-mixed chains shows consistent behavior across iterations without persistent trends, drifts, or divergence suggests good convergence. The chains here appear to cover the parameter space adequately.*

4.4. Conditional effects plots

A conditional effects plot lets you see the role of a certain factor in the model by keeping the influence of all other factors the same. It demonstrates how the forecasted result responds when the chosen variable's value changes. This allows us to easily pick out how that variable affects the outcome, without other variables confusing the picture. The graph has partial regions to let us judge the confidence in our predictions. For models with many variables, interpreting the results is much simpler with conditional effects plots.

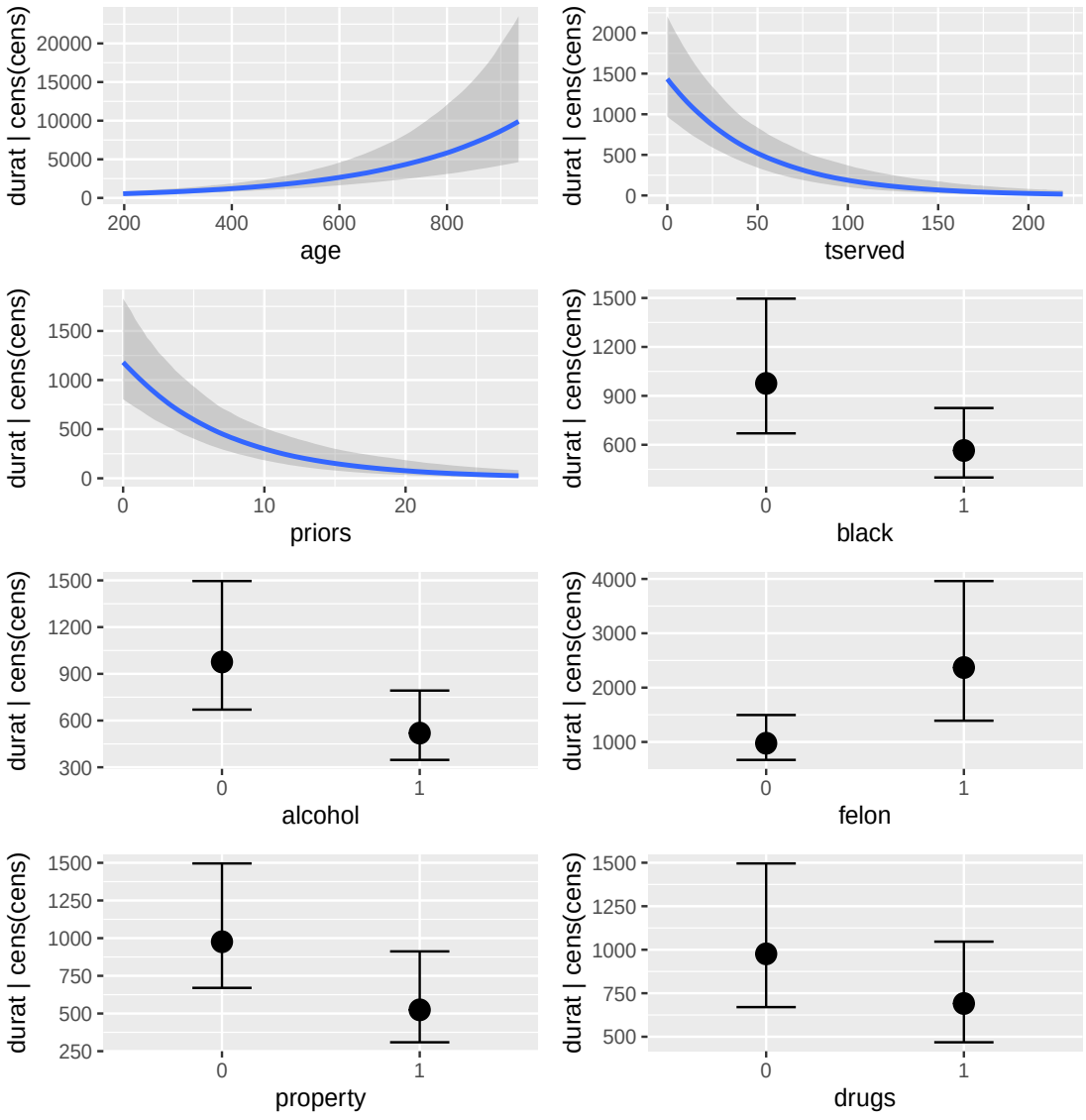


Figure 8: *Conditional effects plots illustrate the conditional effects of each covariate on the expected survival duration, averaged over the posterior distribution and holding other covariates constant at typical values. The vertical axis represents the expected survival time (duration) conditional on no censoring, and the horizontal axis corresponds to the covariate being examined. Each plot includes a fitted line showing the posterior mean along with uncertainty bands (typically 95% credible intervals).*

- **Age**: The plot shows a strong positive association between age and survival duration. As age increases, the expected time to recidivism increases significantly, especially at lower age ranges. This suggests that older individuals tend to remain offense-free for longer periods post-release.

- **Time Served (tserved)**: There is a clear negative relationship, indicating that individuals who served longer prison terms tend to recidivate sooner. Longer incarceration durations are associated with shorter post-release survival times.
- **Number of Priors (priors)**: A higher number of prior convictions is associated with shorter survival times. The decline is steep for lower values of priors, implying diminishing survival time with increasing criminal history.
- **Race (black)**: The binary indicator shows that Black individuals (coded as 1) have shorter expected survival times compared to non-Black individuals. This aligns with the negative regression coefficient and may reflect broader systemic disparities.
- **Alcohol Abuse (alcohol)**: Individuals with a history of alcohol problems tend to have shorter survival times, indicating a higher likelihood of quicker recidivism.
- **Felony Status (felon)**: Contrary to some expectations, individuals identified as felons exhibit longer survival times on average. This may reflect factors such as increased supervision or unobserved protective effects.
- **Property Offense (property)**: Property offenders have slightly shorter survival durations than non-property offenders, though the effect appears modest in magnitude.
- **Drug Involvement (drugs)**: Similar to alcohol, drug involvement is negatively associated with survival time, suggesting a greater likelihood of early reoffending.

Overall, these conditional effect plots visually reinforce the estimated effects from the posterior distributions and provide an interpretable, intuitive summary of how individual covariates influence post-release recidivism risk within the Bayesian framework.

4.5. Posterior predictive density

A posterior density plot is a useful way to visualize the uncertainty around a parameter's value after observing the data, as guided by Bayesian inference. It illustrates the range of likely values a parameter can take, along with their associated probabilities, helping us better understand the model's behavior and compare different components.

In our analysis, we used posterior predictive density (PPD) plots to assess how well each fitted survival model lognormal, Weibull, exponential, and Frechet captures the observed data. These plots allow us to compare the predicted survival times against the actual data, giving a clear picture of how closely each model aligns with reality. By examining these visualizations, we can identify which model offers the best fit and most reliable predictive performance.

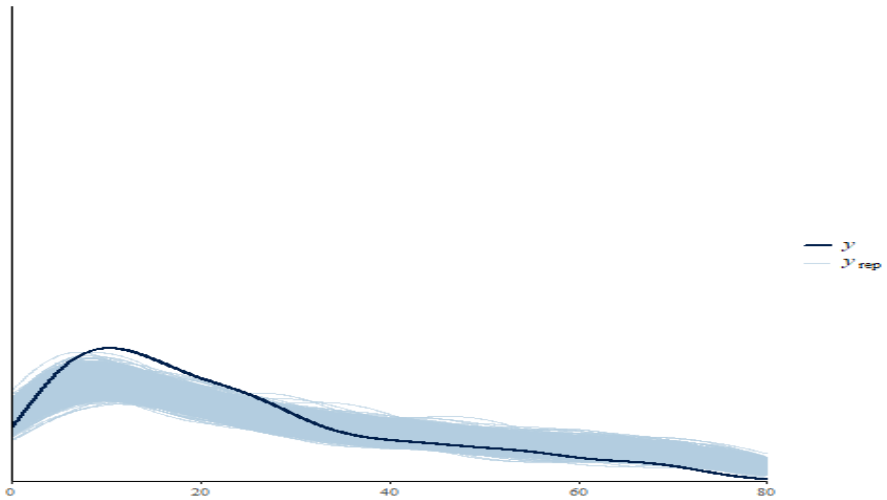


Figure 9: *Lognormal Model*

Figure 10: *Posterior predictive density plots under Lognormal survival model*

Posterior predictive density (PPD) plot are a crucial diagnostic tool in Bayesian modeling to assess the adequacy of the fitted model. Figure 10 presents a density overlay plot comparing the distribution of the observed survival times (y) with replicated data (y_{rep}) generated from the posterior predictive distribution of the Lognormal, Weibull, Exponential, and Fretchet models. The Figure 9 shows that the model-generated data from lognormal model closely track the shape, range, and central tendency of the observed data. The overlap between the distributions suggests that the Lognormal model captures the key features of the observed survival data well. This agreement indicates that the model is capable of generating plausible survival times consistent with the empirical data, providing additional support for its suitability in this context. The lack of significant discrepancy between y and y_{rep} in this plot reinforces the conclusion that the Lognormal model is a good fit for the recidivism data.

5. Conclusion

This study begins from evaluating fifteen covariates of recidivism data for their impact on post-release recidivism time. Using the variable importance index we retained only eight predictors with significant influence, limiting the model to depend on age, priors, time served, race, alcohol and drug involvement, felony status, and property offense.It was evident from a model comparison based on LOOIC and WAIC that the Lognormal survival model offered the best predictive fit, accurately representing the realistic non-monotonic hazard pattern that characterizes recidivism.

From the lognormal Bayesian survival model it was found that older individuals tend to remain offense-free longer, while more prior convictions and longer sentences predict quicker reoffending. Factor variables like race, substance abuse, and offense type also showed significant associations with survival time. Good convergence diagnostics, well-mixed chains, and close alignment of posterior predictive densities with the observed data confirm the model's robustness. Recidivism imposes significant costs on the criminal justice system and society, including incarceration expenses, lost productivity, and broader social impacts. Hence from economic perspective, these findings are important in targeting resources effectively to check reoffending problem. Understanding which factors most strongly predict quicker reoffending can help policymakers allocate funds to programs that address substance abuse, support older ex-offenders, and tailor supervision intensity to individual risk profiles. This evidence based approach can help optimize public spending, reduce the economic burden of crime, and improve reintegration outcomes.

In sum, this analysis demonstrates that carefully selecting covariates and choosing an appropriate survival distribution can yield valuable insights into the dynamics of recidivism. The findings highlight individual level factors that should be considered in designing interventions and policies to support successful reintegration and reduce reoffending.

References

[1] Chung, C. F., Schmidt, P., and Witte, A. D. (1991). Survival analysis: A survey. *Journal of Quantitative Criminology*, 7:59–98.

[2] Schmidt, P. and Witte, A. D. (2012). *Predicting recidivism using survival models*. Springer Science & Business Media.

[3] Yukhnenko, D., Farouki, L., and Fazel, S. (2023). Criminal recidivism rates globally: A 6-year systematic review update. *Journal of Criminal Justice*, 88:102–115.

[4] Becker, G. S. (1968). Crime and punishment: An economic approach. *Journal of Political Economy*, 76(2):169–217.

[5] Schmidt, P. and Witte, A. D. (1984). *An Economic Analysis of Crime and Justice: Theory, Methods and Applications*. Academic Press, Inc.

[6] Kubrin, C. E. and Stewart, E. A. (2006). Predicting who reoffends: The neglected role of neighborhood context in recidivism studies. *Criminology*, 44(1):165–197.

[7] Burgess, E. W. (1928). Factors determining success or failure on parole. *The Workings of the Indeterminate Sentence Law and the Parole System in Illinois*, 221–234.

[8] Durose, M. R., Cooper, A. D. and Snyder, H. N. (2014). Recidivism of prisoners released in 30 States in 2005: Patterns from 2005 to 2010. *US Department of Justice, Office of Justice Programs, Bureau of Justice* 28.

[9] Zeng, J., Ustun, B., and Rudin, C. (2017). Interpretable classification models for recidivism prediction. *Journal of the Royal Statistical Society: Series A*, 180(3):689–722.

[10] Lila, M., Martín-Fernández, M., Gracia, E., López-Ossorio, J. J. and González, J. L. (2019). Identifying key predictors of recidivism among offenders attending a batterer intervention program: A survival analysis. *Psychosocial Intervention*, 28:157–167.

[11] Maltz, M. D. (1984). *Recidivism*. Academic Press, Orlando, FL.

[12] Partanen, J. (1969). On waiting time distributions. *Acta Sociologica*, 12(3):132–143.

[13] Carr-Hill, G. A. and Carr-Hill, R. A. (1972). Reconviction as a process. *British Journal of Criminology*, 12:35.

[14] Schmidt, P. and Witte, A. D. (1989). Predicting criminal recidivism using split population survival time models. *Journal of Econometrics*, 40(1):141–159.

[15] Visher, C. A., Lattimore, P. K. and Linster, R. L. (1991). Predicting the recidivism of serious youthful offenders using survival models. *Criminology*, 29(3):329–366.

[16] Gruenewald, P. J. and West, B. R. (1989). Survival models of recidivism among juvenile delinquents. *Journal of Quantitative Criminology*, 5:215–229.

[17] Arfan, N., Irfanullah, A., Hamidi, M. R. and Mukhaiyar, U. (2025). Comparison of survival analysis using accelerated failure time model and Cox model for recidivist case. *BAREKENG: Jurnal Ilmu Matematika dan Terapan*, 19(1):629–642.

[18] De La Cruz, R., Padilla, O., Valle, M. A. and Ruz, G. A. (2021). Modeling recidivism through Bayesian regression models and deep neural networks. *Mathematics*, 9(6):639.

[19] Parvej, M., Devashish and Khan, A. A. (2024). Enhancing survival analysis with Bayesian modeling: A comparative study of Type II half logistic-Weibull Cox-PH, Weibull Cox-PH and Weibull models. *International Journal of Reliability, Quality and Safety Engineering*, 32(3) 2450038.

[20] Farhin, S., Yousuf, F. and Khan, A. A. (2022). Bayesian survival modeling of Marshal-Olkin generalized-G family with random effects using R and Stan. *Reliability: Theory & Applications*, 17(2):422–440.

[21] Simon, N. and Tibshirani, R. (2011). Discriminant analysis with adaptively pooled covariance. *arXiv preprint arXiv:1111.1687*.

[22] Shea, J. M. (2024). wooldridge: 115 data sets from "Introductory Econometrics: A Modern Approach, 7e" by Jeffrey M. Wooldridge. *R package version 1.4-4*. `https://justinmshea.github.io/wooldridge/`.

[23] Wooldridge, J. M. (2019). *Introductory Econometrics: A Modern Approach*. 7th ed., Cengage Learning.

[24] Smith, B. J. (2024). MachineShop: Machine learning models and tools. *R package version 3.8.0*. `https://brian-j-smith.github.io/MachineShop/`.

[25] Collett, D. (2023). Modelling Survival Data in Medical Research. 4th ed., Chapman and Hall/CRC.

[26] Lawless, J. F. (2011). *Statistical Models and Methods for Lifetime Data*. 2nd ed., John Wiley & Sons.

[27] Gelman, A. (2006). Prior distributions for variance parameters in hierarchical models (comment on article by Browne and Draper). *Bayesian Analysis*, 1(3):515–534. `https://doi.org/10.1214/06-BA117A`.

[28] Parvej, M. and Khan, A. A. (2024). Bayesian extension of the Weibull AFT shared frailty model with generalized family of distributions for enhanced survival analysis using censored data. *Journal of Applied Statistics*, 51(15):3125–3153.

[29] Vehtari, A., Gelman, A., and Gabry, J. (2017). Practical Bayesian model evaluation using leave-one-out cross-validation and WAIC. *Statistics and Computing*, 27(5):1413–1432.

[30] Watanabe, S. and Opper, M. (2010). Asymptotic equivalence of Bayes cross validation and widely applicable information criterion in singular learning theory. *Journal of Machine Learning Research*, 11(12).

[31] Devashish, Shazia, F., Parvej, M. and Khan, A. A. (2025). Bayesian model inference: Exploring parsimonious models with MCMC and optimization approximations. *Communications in Statistics–Theory and Methods*, 1–26.

[32] Gelman, A., Carlin, J. B., Stern, H. S., Dunson, D. B., Vehtari, A., and Rubin, D. B. (2013). *Bayesian Data Analysis*. 3rd ed., Chapman and Hall/CRC..

[33] Vehtari, A., Gabry, J., Magnusson, M., Yao, Y., Bürkner, P. C., Paananen, T., and Gelman, A. (2024). loo: Efficient leave-one-out cross-validation and WAIC for Bayesian models. *R package version 2.8.0*. `https://mc-stan.org/loo/`.

RT&A, No 4 (89)
Volume 20, December 2025

CONTROL CHARTS WITH SIX SIGMA FOR RANGE UNDER TWO-PARAMETER GAMMA DISTRIBUTION

[1]Gomathi K and [2]Ganesan A

•

[1]Research Scholar, Department of Statistics, Government Arts College (Autonomous), Salem – 636 007.
[2]Associate Professor, Department of Statistics, Government Arts College (Autonomous), Salem – 636 007.
[1]kggomathikumaresan@gmail.com, [2]slmganesan@gmail.com

Abstract

Quality monitoring of goods and services has been practiced for centuries, whether directly or indirectly. However, the modern approach incorporates quantitative methods rooted in statistical principles for quality control. Statistical quality control (SQC) encompasses a variety of problem-solving techniques used in industrial production, some of which rely on straightforward statistical theories for process control and monitoring. Over time, statistical process control (SPC) has evolved to include a broad range of statistical and optimization methods employed by professionals to enhance quality. In this research paper, we present a comprehensive review and development of a Six Sigma-based control chart for range under the Gamma distribution, examining its various aspects and applications.

Keywords: Gamma distribution, Range, Process capability and Six sigma

I. Introduction

Quality planning is not merely a technical or operational task it is a critical strategic function that plays a pivotal role in shaping the long-term success and sustainability of an organization. Much like the product development plan, financial strategy, marketing roadmap, and human resource management plan, the strategic quality plan forms a foundational pillar of an organization's overall business strategy. Neglecting to implement a well-structured quality planning framework can lead to significant inefficiencies, including wasted time, financial losses, and diminished workforce productivity. More critically, the absence of a strategic focus on quality often results in the proliferation of design flaws, manufacturing errors, product failures in the field, and recurring customer complaints—all of which can seriously damage a company's reputation and market position.

At its core, quality planning is about proactively identifying the expectations and requirements of all stakeholders involved in or impacted by the product or service. This includes not only external customers who ultimately purchase and use the product but also internal customers, such as departments and teams within the organization that depend on one another to deliver consistent value. Understanding these needs in detail is essential for designing processes, products, and services that not only meet but exceed expectations.

By aligning quality goals with the broader objectives of the organization, quality planning

enables a culture of continuous improvement, fosters cross-functional collaboration, and ensures that quality is embedded into every stage of the business lifecycle from design and production to delivery and customer support. In this way, strategic quality planning becomes a proactive investment that drives operational excellence, enhances customer satisfaction, and positions the organization for sustained competitive advantage.

II. Review of Literature

I have conducted a thorough review of several scholarly works that build upon and are closely related to this paper, examining their methodologies, key findings, and contributions in order to highlight the broader academic context, identify recurring themes, and assess how these studies extend, refine, or challenge the ideas originally presented.

Radhakrishnan and Balamurugan [9] present a paper that addresses the limitations of traditional 3-sigma Shewhart control charts when applied to processes operating under a Six Sigma initiative. The authors propose a new "Six Sigma-based exponentially weighted moving average (EWMA) control chart," designed to be more effective for high-quality processes. They argue that this chart is better at detecting out-of-control conditions in processes with reduced variation, thereby enabling timely corrective actions.

Radhakrishnan and Balamurugan [10] introduce a Six Sigma-based control chart for range, demonstrating that even within Six Sigma practices, processes may still fall out of control due to unexpected variations. The proposed charts provide a more effective tool for monitoring and improving process quality compared to traditional 3-sigma Shewhart charts. Similarly, Radhakrishnan and Balamurugan [11] develop Six Sigma-based control charts for monitoring defects, showing that processes can still deviate despite Six Sigma implementation. The proposed charts and tables serve as practical tools for engineers seeking to improve quality control beyond the capabilities of traditional Shewhart methods.

In another study, Radhakrishnan and Balamurugan [12] present research that highlights the limitations of traditional 3-sigma Shewhart control charts in high-quality processes under Six Sigma. They propose a "Six Sigma-based cumulative-sum (CUSUM) control chart," which is argued to be more effective in detecting process deviations and potentially replacing existing Shewhart charts.

In a related work, Radhakrishnan and Balamurugan [13] propose a Six Sigma-based $\bar{X}$ control chart using standard deviation with varying sample sizes, showing that processes may still fall out of control under Six Sigma initiatives. The suggested charts and tables help engineers detect and correct variations more effectively than conventional Shewhart control charts.

Radhakrishnan and Balamurugan [14] propose a Six Sigma-based control chart for regression, emphasizing that even under Six Sigma initiatives, processes may experience unexpected variations. The suggested control charts allow companies to detect such issues more effectively than traditional Shewhart charts.

Pavithra and Balamurugan [7] present a new statistical process control (SPC) method, introducing a "Six Sigma-based fuzzy mean using range control chart" under a "moderate distribution," leveraging process capability (CP). The authors claim that this new chart is both more accurate and more flexible than traditional methods, addressing key weaknesses of existing control charts.

Finally, Kanneswari and Sivakumaran [4] present a control chart based on Six Sigma using the interquartile range (IQR) to address cases where normality assumptions do not hold. Their study demonstrates that processes remained out of control under all tested methods, emphasizing the ongoing need for quality improvements.

III. Quality control and improvement

It represents a structured and strategic set of activities aimed at ensuring that products and services not only meet predefined requirements but are also continuously enhanced over time. These functions are vital in fostering customer satisfaction, maintaining consistency, reducing waste, and driving operational excellence. Together, they form the backbone of any organization's commitment to delivering value and excellence in a competitive marketplace.

At the heart of both quality control and improvement lies the need to manage and reduce variability a common and often detrimental source of quality issues. Variability in processes, materials, equipment, or human performance can lead to defects, inefficiencies, and inconsistent outcomes. To address this, organizations rely heavily on statistical techniques that provide objective, data-driven insights into how processes behave and where improvements are needed. Among the most widely used tools are:

Statistical Process Control (SPC): This method involves the use of control charts and statistical methods to monitor production and service processes in real time. By identifying patterns, trends, or anomalies, SPC enables early detection of potential problems before they result in defective output.

Design of Experiments (DOE): This approach allows organizations to systematically test and analyse the effects of multiple process variables to determine the optimal conditions for performance. DOE is particularly useful for identifying the root causes of variation and implementing effective changes.

3.1 Control chart techniques

The area between the upper and lower control limits is considered the normal range of variation. As long as the data points fall within this region, the process is deemed to be "in control," implying that it is functioning as expected. However, when one or more data points fall outside of these control limits, it signals that the process may be out of control, likely due to an assignable cause Montgomery[5]. Such an occurrence prompts further investigation to identify and correct the issue before it impacts product quality or process performance.

By regularly monitoring process data using control charts, organizations can detect potential issues early, minimize the risk of defects, and maintain a consistent level of quality in their operations.

Consider the statistic t = t(x_1,x_2,…..x_n), function of the sample observations (x_1,x_2,…..x_n) $Mean_t = \mu_t$ and $Variance_t = \sigma_t^2$. If the Statistic 't' is normally distributed, then from the fundamental area property of the normal distribution, we have

$$P[\mu_t - 3\sigma_t < t < \mu_t + 3\sigma_t] = 0.9973 \Rightarrow P[|t - \mu_t| < 3\sigma_t] = 0.9973 \Rightarrow P[|t - \mu_t| > 3\sigma_t] = 0.0027 \quad (1)$$

Then the control limits of three sigma are as follows:

$$\text{UCL} = \mu_t + \varphi\sigma_t$$

$$\text{Center Line (CL)} = \mu_t$$

$$\text{LCL} = \mu_t - \varphi\sigma_t$$

The symbol φ represents the distance between the control limits and the centre line of a control chart, measured in units of standard deviation. This distance defines the threshold for identifying whether variations in the process are within acceptable bounds. When the value of φ is set to 3, the chart is referred to as a 3-sigma control chart, meaning that the control limits are placed three standard deviations above and below the process mean. This configuration is widely used because it provides a balance between sensitivity to process changes and the avoidance of false alarms, effectively capturing approximately 99.73% of all expected data points under normal conditions.

Control charts for variables are used to monitor quality characteristics that can be measured on a continuous scale, such as height, weight, volume, length, or width. These characteristics are quantitative in nature, allowing for precise measurement rather than mere classification. When a product or component is inspected, the specific variable of interest is measured and recorded for analysis.

3.2 Concept of six sigma

In organizations that adopt Six Sigma practices, the implementation of these advanced quality techniques often results in such significant process improvement that traditional control charts may no longer be effective, as they may not register any points outside the control limits. Consequently, there arises a need for specialized control charts that can effectively monitor and reflect the performance of processes operating at Six Sigma quality levels. These new charts are essential for accurately evaluating the outcomes of companies that have integrated Six Sigma initiatives into their operations. Radhakrishnan and Balamurugan [8], proposed the development of control charts tailored to Six Sigma initiatives, specifically designed to monitor the proportion of defectives in a process.

The Table 1 illustrates the relationship between sigma quality levels, the corresponding percentage of defect-free output, and the number of defects per million opportunities (PPM). At 3σ quality, a process produces 99.73% good output, which still results in about 66,807 defects per million opportunities. As the sigma level increases, the percentage of quality improves dramatically while defects decrease sharply. For example, at 4σ quality, defects are reduced to about 6,210 PPM (roughly one-tenth of 3σ). At 5σ, the defect rate drops further to only 233 PPM, representing near-perfect performance. Finally, 6σ quality reaches 99.99966% defect-free output, allowing only 3.4 defects per million opportunities.

Table 1: *Levels of sigma and defect rate*

Quality Level	%Quality	Defective PPM*
3σ	99.73	66807
4σ	99.9937	6210
3σ	99.73	66807
4σ	99.9937	6210

*Parts per Million (PPM)

3.3 Process Capability (CP)

The Cp index is a straightforward and commonly applied metric that compares the allowable spread of the specification limits to the actual spread of the process variation. Specifically, it is calculated by taking the difference between the Upper Specification Limit (USL) and the Lower

Specification Limit (LSL) which defines the range of acceptable values and dividing this by six times the process standard deviation (6σ). Mathematically, the CP index is expressed as: $C_p = \frac{USL - LSL}{6\sigma}$.

Here, σ (sigma) is the estimated standard deviation of the process, which reflects the inherent variability in the system. A higher Cp value indicates that the process variation is well within the specification limits, suggesting that the process is capable of consistently meeting product quality standards. However, it is important to note that Cp assumes the processis centred; if it is not, a different index such as Cpk should be used to account for process shift.

3.4 Construction of control charts under lifetime distributions

The development of control charts specifically designed for lifetime distributions plays a crucial role in accurately tracking and managing the reliability and performance of products and systems throughout their operational lifespan. Conventional control charts are typically based on the assumption that the underlying data follows a normal distribution. However, this assumption does not hold true in many practical scenarios, particularly when dealing with lifetime or reliability data, which often conform to non-normal distributions. By tailoring control charts to these particular lifetime distributions, organizations can significantly improve the effectiveness of their quality control efforts. These customized charts offer greater sensitivity to changes in process behaviour and provide more precise insights into potential failures or deviations, thereby supporting more informed decision-making and fostering enhanced product reliability.

Processes with a constant hazard rate where the interval between subsequent occurrences or failures stays constant throughout time are specifically monitored by Shewhart-type [16], control charts that are adapted to the Gamma distribution. Because it assumes a constant failure rate, the Gamma distribution is frequently used in survival analysis and reliability engineering. This makes it especially well-suited for estimating the lifespans of specific systems and components. The primary parameter of the distribution, which is closely related to the mean time between failures (MTBF), is what these control charts are intended to identify as it changes. Shewhart-type charts based on the Gamma distribution are a useful and practical tool for assessing process reliability and assisting in the early detection of possible quality problems or failures in maintenance and production environments by identifying deviations from the expected process behaviour. The following are the conditions for application

- When the primary goal is to directly analyze the time intervals between successive events or occurrences within a process.
- When there is a requirement to implement conventional Six Sigma control charts as part of a broader strategy for quality enhancement and process optimization.
- When the nature of the process demands a more gradual, steady response to variations or shifts, ensuring stability and minimizing overreactions to minor fluctuations.

IV. Methods and materials

A random variable 'X' is said to follow a two-parameter gamma distribution, which is represented as:

$$X \sim \text{Gamma}(k, \theta) \quad (2)$$

Where, k>0 is the shape parameter. The shape parameter 'k' determines the skewness of the gamma distribution:

k<1: Highly skewed right, with a peak near zero, k=1: Exponential distribution (memoryless property) and k>1: Distribution becomes more symmetric as 'k' increases.The scale parameter 'θ' determines the spread. θ>0 is the scale parameter.

The probability density function (PDF) of two-parameter Gamma distribution Ross[15], is given by:

$$f(x;k,\theta)=\frac{x^{k-1}e^{-x/\theta}}{\theta^{k}\Gamma k},\ x>0,\ and\ k,\theta>0 \tag{3}$$

Where, Γk is the gamma function, defined as:

$$\Gamma k=\int_0^\infty t^{k-1}e^{-t}dt,\ k>0 \tag{4}$$

which generalizes the factorial function, such that $\Gamma n=(n-1)!$ for integer values of 'n'.By definition:

$$E(x)=\int_0^\infty x\,f(x;k,\theta)\,dx \tag{5}$$

Substituting the gamma probability density function:

$$E[x]=\int_0^\infty x\,\frac{x^{k-1}e^{-x/\theta}}{\theta^{k}\Gamma k}dx \tag{6}$$

Using the substitution u = $x/\theta \Rightarrow du=dx/\theta, we\ get$:

$$E(x)=\frac{\theta^{k+1}}{\theta^{k}\Gamma k}\int_0^\infty u^{k}e^{-u}\,du \tag{7}$$

Since:

$$\int_0^\infty u^{k}e^{-u}du=\Gamma(k+1)=k\Gamma k \tag{8}$$

we obtain:

$$E(x) = k\theta \tag{9}$$

The second moment is:

$$E(x)=\int_0^\infty x^{2}\,f(x;k,\theta)\,dx \tag{10}$$

$$E[x]=\int_0^\infty x^{2}\,\frac{x^{k-1}e^{-x/\theta}}{\theta^{k}\Gamma k}dx \tag{11}$$

Using the property of the gamma function , Casella and Berger, [2]:

$$E(x)=\theta^2\ k(k+1) \tag{12}$$

The variance is given by:

$$V(x)=E(x^2)-[E(x)]^2=k\theta^2 \tag{13}$$

In the two-parameter gamma distribution, we typically define the distribution in terms of its shape parameter 'k' and scale parameter 'θ'. However, an alternative parametrization often used in statistical modelling expresses the gamma distribution in terms of its mean 'μ' and standard deviation 'σ' (Johnson et.al., [3]. From $E[X]=k\theta$, we solve for 'θ':

In the two-parameter gamma distribution, the distribution is conventionally characterized using two fundamental parameters: the shape parameter, denoted as 'k', and the scale parameter, represented by 'θ'. However, in various statistical modelling applications, an alternative parameterization is frequently employed, where the gamma distribution is expressed in terms of its mean (μ) and standard deviation (σ). This approach provides a more intuitive understanding of the distribution's properties, particularly in applied settings. As noted by Johnson et al. [3],from this alternative representation, we can derive an expression for the scale parameter 'θ':

$$\theta=\frac{\mu}{k} \tag{14}$$

Thus, the equivalence in terms of 'μ' and 'σ' is:

$$k=\frac{\mu^2}{\sigma^2}\ and\ \ \theta=\frac{\sigma^2}{\mu} \tag{15}$$

For a given tolerance level (TL) and a specified process capability (CP), the standard deviation 'σ' (termed as $\eta_{6\sigma}$for exponential distribution) often referred to as the process variation is determined using a predefined mathematical relationship $CP=\frac{Tolerance\ Level}{6\sigma}$.This calculation is performed for various combinations of tolerance levels and process capability values to assess the consistency and precision of the manufacturing process by Pavithra and Balamurugan, [6]. By analysing these values, organizations can better understand the extent of variation within the process and ensure that it remains within acceptable limits to meet quality and performance requirements.

To determine the process standard deviation $\eta_{6\sigma}$, first, establish the tolerance level (TL) and the desired process capability $C_p=2$, as outlined by Montgomery [4]. Once the values of $\eta_{6\sigma}$ is obtained, it is applied to the control limit equations for mean as follows:

$$\left(\theta_{6\sigma}^{\bar{x}}+\frac{1}{\lambda_{6\sigma}^{\bar{x}}}\right)\pm\left[\left(\frac{Z_{6\sigma}}{\sqrt{n}}\right)\left(\frac{1}{\lambda_{6\sigma}^{\bar{x}}}\right)\right] \tag{16}$$

4.1 Illustration 1

The example presented by Amitava Mitra [1], is examined in this context. It pertains to a paper manufacturing company that must regulate the thickness of the cardboard sheets it produces to ensure quality control. To achieve this, random samples consisting of five sheets each are periodically selected, and their thickness measurements are recorded. The dataset for 30 such samples is provided in Table 2, offering valuable insights into the variability and consistency of the manufacturing process.

Table 2: *Data (in mm) from thickness of cardboard sheets*

Sample No	Observations (in mm)					Mean	Standard deviation (S)	Range
1	0.52	0.55	0.49	0.51	0.52	0.5180	0.0217	0.06
2	0.53	0.50	0.51	0.51	0.50	0.5100	0.0122	0.03
3	0.52	0.51	0.55	0.50	0.52	0.5200	0.0187	0.05
4	0.42	0.45	0.43	0.42	0.46	0.4360	0.0182	0.04
5	0.48	0.50	0.47	0.51	0.51	0.4940	0.0182	0.04
6	0.49	0.52	0.51	0.48	0.50	0.5000	0.0158	0.04
7	0.54	0.48	0.51	0.48	0.49	0.5000	0.0255	0.06
8	0.43	0.46	0.53	0.48	0.49	0.4780	0.0370	0.10
9	0.51	0.52	0.48	0.53	0.54	0.5160	0.0230	0.06
10	0.53	0.48	0.49	0.51	0.48	0.4980	0.0217	0.05
11	0.51	0.46	0.51	0.55	0.50	0.5060	0.0321	0.09
12	0.50	0.54	0.52	0.51	0.52	0.5180	0.0148	0.04
13	0.46	0.48	0.53	0.51	0.51	0.4980	0.0277	0.07
14	0.52	0.49	0.52	0.47	0.48	0.4960	0.0230	0.05
15	0.49	0.51	0.50	0.51	0.52	0.5060	0.0114	0.03
16	0.50	0.52	0.48	0.53	0.51	0.5080	0.0192	0.05
17	0.45	0.51	0.50	0.52	0.44	0.4840	0.0365	0.08
18	0.52	0.49	0.55	0.52	0.53	0.5220	0.0217	0.06
19	0.56	0.51	0.54	0.56	0.52	0.5380	0.0228	0.05
20	0.49	0.53	0.51	0.52	0.51	0.5120	0.0148	0.04
21	0.52	0.48	0.47	0.50	0.49	0.4920	0.0192	0.05
22	0.55	0.46	0.48	0.53	0.50	0.5040	0.0365	0.09
23	0.51	0.50	0.53	0.50	0.49	0.5060	0.0152	0.04
24	0.50	0.47	0.49	0.52	0.51	0.4980	0.0192	0.05
25	0.48	0.52	0.47	0.46	0.47	0.4800	0.0235	0.06
26	0.52	0.49	0.50	0.48	0.50	0.4980	0.0148	0.04
27	0.46	0.52	0.48	0.51	0.52	0.4980	0.0268	0.06
28	0.49	0.55	0.52	0.50	0.49	0.5100	0.0255	0.06
29	0.52	0.51	0.53	0.47	0.48	0.5020	0.0259	0.06
30	0.50	0.48	0.52	0.49	0.48	0.4940	0.0167	0.04
						$\overline{X} = 0.5013$	$\overline{S} = 0.0220$	$\overline{R} = 0.0570$

The scale parameter $(\theta_{3\sigma-R.\gamma})$ of the two-parameter Gamma distribution is estimated based on the 3-Sigma criterion for the range as follows:

$$(\theta_{3\sigma-R.\gamma}) = \frac{\overline{R}}{\ln(n)} = \frac{0.0203}{\ln(5)} = 0.0340 \tag{17}$$

The analysis of Table 3 and Figure 1 clearly indicates that the process is out of control when assessed using the Six Sigma methodology for the range under two-parameter Gamma distribution. This conclusion is based on the observation that only fifteen samples fall within the established control limits, signalling significant deviations from the expected process stability. Additionally, the control limit interval (CLI) for the Six Sigma-based control chart is found to be 0.0200, which is distinctly different when compared to the Three Sigma control limits for a sample size of n=5. This comparison underscores the heightened sensitivity of the Six Sigma approach,

which enables more effective detection of variations, making it a more robust and reliable tool for process monitoring and quality control.

Table3: *3σ and six sigma control limits for range undertwo-parameter Gamma distribution*

S.No	Type of control chart	LCL	CL	UCL	CLI
1	Shewhart 3σ	0	0.0547	0.1851	0.2609
2	Six sigma	0.0446	0.0547	0.0647	0.0200

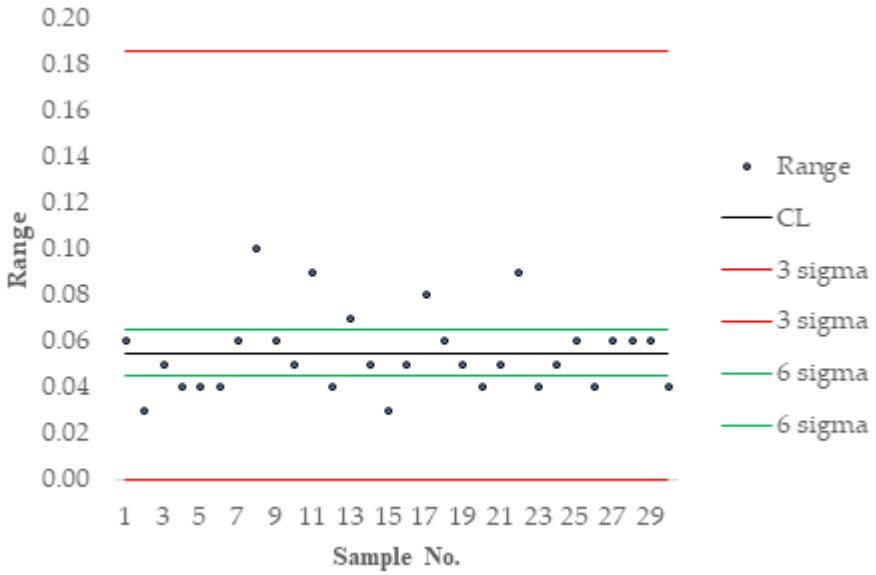


Figure1: *Shewhart 3σ and 6σ control charts for range under two-parameter Gamma distribution*

Then the 3σ control limits for range are

$$[\theta_{3\sigma-R.\gamma} \times \ln(n)] \pm [3 \times 1.28 \frac{\bar{R}}{\ln(n)}]$$

$$UCL_{3\sigma-R.\gamma} = [\theta_{3\sigma-R.\gamma} \times \ln(n)] + [3 \times 1.28 \frac{\bar{R}}{\ln(n)}]$$

$$= [0.0340 \times \ln(5)] + \left[3 \times 1.28 \frac{0.0547}{\ln(5)}\right] = 0.0547 + 0.1304 = 0.1851$$

$$CL_{3\sigma-R.\gamma} = [\theta_{3\sigma-R.\gamma} \times \ln(n)] = [0.0340 \times \ln(5)] = 0.0547$$

$$LCL_{3\sigma-R.\gamma} = [\theta_{3\sigma-R.\gamma} \times \ln(n)] - [3 \times 1.28 \frac{\bar{R}}{\ln(n)}]$$

$$= [0.0340 \times \ln(5)] - \left[3 \times 1.28 \frac{0.0547}{\ln(5)}\right] = 0.0547 - 0.1304 = -0.0758 \approx 0 \quad (18)$$

and also,the six sigma-based control limits for range are $\left[\theta_{6\sigma-R.\gamma} \times \ln(n)\right] \pm \left[\frac{z_{6\sigma} \times \tau_{6\sigma.R-\gamma}}{\sqrt{n}}\right]$

$$UCL_{6\sigma-R.\gamma} = \left[\theta_{6\sigma-R.\gamma} \times \ln(n)\right] + \left[\frac{z_{6\sigma} \times \tau_{6\sigma.R-\gamma}}{\sqrt{n}}\right] = \left[0.0340 \times \ln(5)\right] \pm \left[\frac{4.381 \times 0.0046}{\sqrt{5}}\right]$$

$$= 0.0547 + 0.0100 = 0.0647$$

$$CL_{6\sigma-R.\gamma} = [\theta_{6\sigma-R.\gamma} \times \ln(n)] = [0.0340 \times \ln(5)] = 0.0547$$

$$LCL_{6\sigma-R.\gamma} = \left[\theta_{6\sigma-R.\gamma} \times \ln(n)\right] - \left[\frac{z_{6\sigma} \times \tau_{6\sigma.R-\gamma}}{\sqrt{n}}\right] = [0.0340 \times \ln(5)] - \left[\frac{4.381 \times 0.0046}{\sqrt{5}}\right]$$

$$= 0.0547 - 0.0100 = 0.0446$$

Furthermore, the analysis presented in Table 4 and Figure 2 demonstrates that the traditional Shewhart 3-Sigma control chart for monitoring the range, when evaluated alongside the average run length (ARL), is not as effective as the proposed Six Sigma control chart under two-parameter Gamma distribution. The Six Sigma approach provides a more stringent and precise method for detecting variations in process performance, making it more sensitive to shifts and deviations. This comparison highlights the superior performance of the Six Sigma-based control chart, reinforcing its suitability for organizations aiming to achieve higher levels of quality control and process consistency.

Table 4: *Average run length (ARL) of 3σ and six sigma control limits for range under two-parameter Gamma distribution*

S.No	Multiple of σ	Shewhart 3σ	Six sigma
1	0.0050	348	129
2	0.0051	347	113
3	0.0052	346	100
4	0.0053	345	88
5	0.0054	344	77
6	0.0055	343	68

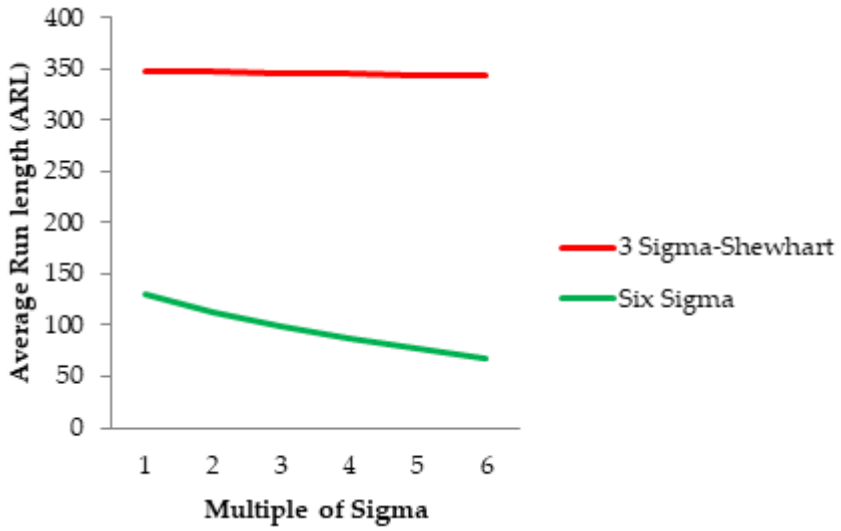


Figure 2: *ARL of Shewhart 3σ and 6σ range control charts under two-parameter Gamma distribution*

Conclusion

In this research paper, we have demonstrated how Six Sigma methodologies can be effectively employed to account for parameter uncertainty in the construction of control charts for the range statistic under the Gamma distribution framework. Unlike control charts developed under the assumption of known process parameters, the presence of parameter uncertainty typically results in wider control limits, reflecting the added variability and ensuring a more realistic representation of process behavior.

Our analysis further illustrates how these control limits, derived from the two-parameter Gamma distribution, can be dynamically evaluated across a range of process parameter values. In particular, we emphasize the utility of expected run length (ERL) calculations as a means of assessing chart performance under varying conditions. The Six Sigma-based control charting approach introduced in this study is grounded in the statistical modeling of observable quantities specifically, the sample range in this context under the two-parameter Gamma distribution.

By systematically identifying and eliminating assignable causes of variation within a production or service process, the proposed methodology offers practical applicability across multiple stages of the operational workflow. This flexibility supports the attainment of management-defined quality objectives while promoting a data-driven strategy for process stability and improvement.

Ultimately, the findings highlight the importance of ongoing quality enhancement initiatives, which may be realized through the refinement of existing procedures or through thoughtful design changes to the product or service. Such continuous improvement efforts not only enhance customer satisfaction but also contribute significantly to operational efficiency by reducing waste, time, and cost.

References

[1] Amitava Mitra. Fundamentals of Quality control and improvement, Pearson Education, Asia, 2001.

[2] Casella G and Berger R. L .Statistical Inference, Second edition, Duxbury, 2002.

[3] Johnson N. L, Kotz S and Balakrishnan N. Continuous Univariate Distributions, Vol. Second edition, Wiley publications, 1994.

[4] Kanneswari, T and Sivakumaran, P. K. (2025), Construction of control charts for moving range with six sigma under interquartile range, *International Journal of Statistics and Applied Mathematics*,10(6):128-133.

[5] Montgomery D. C. Introduction to statistical quality control, 7th edition, Wiley Publications, 2001.

[6] Pavithra M. R. and Balamurugan P (2020). Fuzzy six sigma based regression control chart under moderateness, *International journal of advanced science and technology*, 29(4):283-295.

[7] Pavithra, M. R. and Balamurugan, P.(2022) , Fuzzy Control Chart Based on Six Sigma for Mean Using Range, *Stochastic Modeling and Applications*, 26(1):69-77.

[8] Radhakrishnan R and Balamurugan P (2010). Construction of control charts based on six sigma Initiatives for Fraction Defectives with varying sample size, *Journal of Statistics and Management Systems*, 6(1):99-103.

[9] Radhakrishnan, R. and Balamurugan, P. (2010), Six sigma based exponentially weighted moving average control chart, *Indian Journal of Science and Technology*, 3(10):1052-1055.

[10] Radhakrishnan, R. and Balamurugan, P. (2011a). Construction Of Control Chart Based on Six Sigma Initiatives for Range, *Global Journal of Mechanical Engineering and Computational Science*, 1(3):1-4.

[11] Radhakrishnan, R. and Balamurugan, P. (2011b). Construction of Control Charts Based On Six Sigma Initiatives for the Number of Defects and Average Number of Defects per Unit , *Journal*

of Modern Applied Statistical Methods, 10(2):639-645.

[12] Radhakrishnan, R. and Balamurugan, P. (2016a), Construction of control chart based on six sigma initiatives for Cumulative – Sum, *International Journal for Research in Applied Science & Engineering Technology*, 4(9):218-223.

[13] Radhakrishnan, R. and Balamurugan, P. (2016b). Construction of control charts based on six sigma initiatives for mean using standard deviation with varying sample size, *International Journal for Research & Development in Technology*, 6(1):99-103.

[14] Radhakrishnan, R. and Balamurugan, P. (2018). Construction of Control Chart Based on Six Sigma Initiatives for Regression, *International Journal of Scientific Research in Science and Technology*, 4(2):1142-1147.

[15] Sheldon M. Ross. Probability and statistics for engineers and scientists, Fifth edition, Elsevier inc, 2014.

[16] Shewhart W. A. Economic control of quality of manufactured product, Van Nostrand, 1931.

JOINT ADAPTIVE PROGRESSIVE TYPE-II CENSORING WITH DUS-EXTREME VALUE DISTRIBUTION

Rakhi Chandran[1], Chacko V M[2]

•

[1]Department of Statistics, St.Mary's College(Autonomous), Thrissur
[2] Department of Statistics, St.Thomas College(Autonomous), Thrissur
University of Calicut, Kerala, India,
[1]Emails: chandran.rakhi@gmail.com
[2]Emails: chackovm@stthomas.ac.in

Abstract

Statistical estimation of parameters under different censoring schemes is important while using distributions like the Extreme value and Weibull distributions for modelling real lifetime data. Since Extreme value distribution arise as log transformation of the Weibull distribution, there are several advantages for discussing the estimation of extreme value parameters. Moreover, DUS transformation provides more appropriate model without increasing parameters. This study examines point estimation methods, including maximum likelihood and Bayesian approaches, for DUS Extreme Value (DUS-EV) distribution under a joint adaptive progressive Type-II censoring scheme. The proposed scheme offers notable advantages in reducing cost and experimental time. Bayesian estimation is implemented via the Metropolis- Hastings algorithm within a Gibbs sampling framework. Interval estimation is carried out using asymptotic confidence intervals, Highest Posterior Density (HPD) credible intervals, and bootstrap confidence intervals. A comparative analysis of classical and Bayesian results is presented, and the applicability of the proposed methods is demonstrated through real data analysis.

Keywords: DUS-extreme value distribution, Joint adaptive Type II progressive censoring, Maximum likelihood estimation, Bayesian estimation

1. Introduction

In time-to-event data, when the precise value of interest is not immediately observable but is known only within specific bounds, statistical censoring is essential because it makes it possible to analyze incomplete data. In order to avoid biased results and to get more precise estimates for statistics like medians, it is imperative that such data be analyzed. In domains like engineering and medicine, where precise data interpretation is necessary for well-informed decision-making, this analysis is especially crucial. To do this, techniques that specifically handle censoring like survival analysis must be used in order to guarantee accurate data interpretation and produce significant findings. Censoring is an unavoidable aspect of reliability and survival studies, and several censoring schemes have been proposed to address this issue. The most commonly used are Type I and Type II censoring. In Type I censoring, the duration of the experiment is fixed while the number of failures observed is random, whereas in Type II censoring, the number of failures is fixed in advance while the experimental time becomes random. Specifically, under Type I censoring, the study continues until a predetermined time, while under Type II censoring, it terminates at the occurrence of the m^{th} failure. A limitation of Type I censoring is that an insufficient number of failures may occur within the fixed time, leading to reduced efficiency

of the estimator. Conversely, Type II censoring may require a prolonged experimental duration, which can be impractical.

To overcome the limitations associated with conventional censoring, hybrid models incorporating features from Type I and Type II schemes have been proposed. The earliest among these is the Type I hybrid censoring scheme [13], in which the experiment continues until T_1^* = min (m^{th} failure time, T). Similar to the Type I approach, the scheme may produce very few failure observations, leading to reduced estimator efficiency. Additionally, inferential procedures under this scheme typically assume the occurrence of at least one failure. Subsequently, Type II hybrid censoring scheme was introduced, where the termination time is defined as T_2* = max (m^{th} failure time, T) [9]. This scheme guarantees at least m failures, leading to more efficient parameter estimation. However, its main drawback lies in the potentially longer experimental duration required.

The aforementioned censoring methods do not account for the loss or removal of experimental units, which frequently occurs in practice either due to unexpected failures or to reduce experimental time and cost. To address this, the concept of progressive censoring was introduced [10]. This approach has two main variants. The first, known as Type I progressive censoring, involves the removal of R_1, R_2, ..., R_{m-1} surviving units at predetermined censoring times T_1^*, T_2^*, ..., T_{m-1}^*. In this scheme, both the number of removals (R_i) and the censoring times (T_i^*) are fixed, and the experiment concludes with the removal of the remaining R_m units at time T_m^*. The second, referred to as Type II progressive censoring, removes R_1, R_2, ..., R_{m-1} surviving units after the 1^{st} failure, 2^{nd} failure,....$(m-1)^{th}$ failures, respectively. Here, the numbers R_is are predetermined, but the censoring times are random.

A comprehensive treatment of the theory and applications of Type II progressive censoring, emphasizing its flexibility in removing surviving units at different failure times before experiment termination is available in the literature [5]. This approach was further elaborated by researchers [4]. While progressive censoring is cost-effective and operationally flexible, it typically requires a longer experimental duration compared to traditional Type II censoring. To mitigate this drawback, the Type II progressively hybrid censoring scheme was proposed, which combines the features of Type II progressive censoring and hybrid censoring [15]. The scheme can be described as follows:

Suppose N items are placed on a life-testing experiment, where the number of failures $m < N$, the removals of units at successive failure times, and the experimental time T are all predetermined. After the first failure, R_1 units are taken out, after the second failure R_2 units are removed, and the process continues in the same pattern. When the m^{th} failure takes place before the specified time T, the test ends at that failure time, and all surviving units still in the experiment are withdrawn. Conversely, if only $J < m$ failures occur before time T, then the experiment ends at T, where the remaining units $R_m = N - R_1 - R_2 - ...R_J - J$ are removed. This scheme closely resembles Type I censoring, since termination is ultimately determined by a fixed time. However, a key drawback is that it may yield only a small number of failures, thereby reducing the effectiveness of statistical estimation.

To overcome the limitations of the Type II progressively hybrid censoring scheme, the adaptive progressive Type II censoring scheme was introduced, which aims to substantially reduce both experimental time and cost by pre-specifying the number of failures m and the total time T [17]. A progressive censoring plan is initially set up for the experiment, but in contrast to standard methods, the removals R_i following each i^{th} failure may be adjusted dynamically throughout the process. As in the Type II progressive hybrid censoring scheme, when the m^{th} failure happens before time T, the study ends at that failure point, and all remaining units are withdrawn. Alternatively, when the m^{th} failure is not observed prior to T, the study is extended until that failure, which improves inferential efficiency and simultaneously maintains the termination time near the pre-assigned T by means of adaptive adjustment of removals.

This flexible framework has been extended in subsequent studies, applied the adaptive progressive Type II censoring scheme to the exponentiated Weibull distribution, developed it for the generalized exponential distribution [16] and later considered it for the extreme value

distribution [23].

For comparative life testing involving two populations, joint censoring schemes have been developed to efficiently utilize information from both groups under common censoring plans [20]. The joint progressive Type II censoring scheme for two exponential populations extended to other distributions [19].

The joint progressive Type II censoring scheme can be described as follows: consider two samples of sizes N_1 and N_2, with total sample size $N = N_1 + N_2$, drawn from two populations in a life-testing experiment. As in earlier schemes, fix the number of observed failures m and the removal numbers R_i. After the first failure (regardless of whether it arises from sample 1 or sample 2), remove s_1 units from sample 1 and q_1 units from sample 2, such that $R_1 = s_1 + q_1$. Similarly, after the second failure, remove s_2 units from sample 1 and q_2 units from sample 2, ensuring that $R_2 = s_2 + q_2$. This process continues until the m^{th} failure, after which all remaining surviving units are removed.

Further developments in censoring methodologies are examined joint progressive Type-I censoring schemes for exponential populations [3]. More recently, the joint adaptive progressive Type-II censoring scheme for independent samples from exponential and Weibull populations are discussed in literature [21, 22]. Building on this line of research, the generalized Lindley distribution under the joint adaptive Type-II censoring framework has been discussed in literature [1]. The Type-I - Type-II mixture censoring scheme is found to be a better alternative to existing models [2]. Subsequently, a joint unified hybrid censoring scheme for two independent Weibull populations with a common shape parameter was proposed as an alternative model [11].

Researchers have put forth a number of novel models that improve the accuracy and flexibility of the underlying distributions in order to handle the complexity of real-world data. The DUS transformation of a baseline distribution,is one such technique [14]. The approach's unique feature of not adding any more parameters than those in the baseline distribution is what makes it significant. This method enhances modeling capability while preserving model parsimony. Building on these advancements, the present study develops inference procedures for the DUS extreme value (DUS-EV) distribution [18], under the joint adaptive progressive Type-II censoring scheme, which offers notable reductions in experimental time and cost. Since distribution of log transformation of Wiebull random variable is extreme value, its DUS transformation is more better choice than extreme value distribution. Since extreme value distribution has wide applicability in survival analysis, proportional hazard models, etc DUS extreme value distribution is also important in such areas. The DUS-EV distribution is obtained by applying the DUS transformation to the classical extreme value distribution. This model is characterized by an increasing failure rate, making it particularly suitable for applications in reliability engineering, hydrology, and meteorology.

The probability density function of DUS extreme value distribution DUS-EV(λ, α) can be defined as

$$g(v) = \frac{1}{\alpha(e-1)} e^{(\frac{v-\lambda}{\alpha} - e^{\frac{v-\lambda}{\alpha}})} e^{(1-e^{-e^{(\frac{v-\lambda}{\alpha})}})}, \quad -\infty < v < \infty, \quad -\infty < \lambda < \infty, \quad \alpha > 0. \tag{1}$$

Cumulative distribution function of DUS-EV(λ, α) are given by

$$G(v) = \frac{1}{e-1}(e^{1-e^{-e^{(\frac{v-\lambda}{\alpha})}}} - 1), \quad -\infty < v < \infty, \quad -\infty < \lambda < \infty, \quad \alpha > 0. \tag{2}$$

We employ both classical and Bayesian approaches for parameter estimation, while asymptotic confidence intervals, highest posterior density (HPD) intervals, and bootstrap-p intervals are utilized for interval estimation. A comprehensive simulation study is carried out to validate the proposed inferential procedures, and the practical utility of the methodology is illustrated using real data analysis.

The remaining sections of the article is outlined in the following manner: Section 2 describes the joint adaptive progressive Type-II censoring scheme. Section 3 presents the inferential procedures for the DUS-EV distribution under this scheme, including maximum likelihood estimation,

asymptotic confidence intervals, bootstrap-p intervals, and Bayesian estimation. Section 4 outlines the simulation study, while Section 5 provides a real data analysis to illustrate the practical utility of the proposed methods. Finally, Section 6 concludes the paper by summarizing the key findings.

2. Joint adaptive progressive Type-II censoring scheme

Suppose two independent populations are involved in a lifetime experiment. A random sample of size N_1 is taken from population 1, which follows the distribution with PDF $g_1(,\lambda_1,\alpha_1)$ and CDF $G_1(,\lambda_1,\alpha_1)$. Similarly, a random sample of size N_2 is taken from population 2, characterised by PDF $g_2(,\lambda_2,\alpha_2)$ and CDF $G_2(,\lambda_2,\alpha_2)$. The Joint Adaptive Progressive Type-II censoring scheme is outlined below.

Let m be a predetermined integer specifying the total number of failures to be observed, and let T denote the fixed termination time of the experiment. Define the vector $R = (R_1, R_2, ..., R_m)$, where each R_l denotes the number of units removed at the time of the l^{th} failure. These removals satisfy $\Sigma_{l=1}^{m} R_l = N - m$, with $N = N_1 + N_2$ denoting the total number of units in the experiment. Further, define two vectors, $P = (P_1, P_2, ..., P_m)$ and $Q = (Q_1, Q_2, ..., Q_m)$, where P_l and Q_l denote the number of units withdrawn from sample 1 and sample 2, respectively, at the lth failure time. Suppose the first failure occurs at time U_1. Following this failure, $R_1 = P_1 + Q_1$ units are withdrawn from the remaining $N-1$ surviving units. Likewise, if the next failure occurs at time U_2, then $R_2 = P_2 + Q_2$ units are removed from the remaining $N - R_1 - 2$ units, and the procedure continues sequentially. This process continues until either the mth failure occurs or the time point T is reached. If the m th failure occurs at a time U_m ($U_m < T$), the experiment terminates at U_m, and all remaining units are withdrawn. However, if only $K(K < m)$ failures occur before time T, i.e.,$U_K < T < U_{K+1}$, the experiment continues without additional removals until the m^{th} failure takes place. At time U_m, the experiment ends by removing all the remaining units, where the number of units removed is $R_m = N - m - \Sigma_{l=1}^{m-1} R_l$ units. Define $K^* = max\{K : U_K < T\}$, consequently $R_{K+1} = R_{K+2} = ... = R_{m-1} = 0$, then, our progressive censoring scheme becomes $\{R_1, R_2, ...R_{K^*}, 0, 0, ..., N - m - \Sigma_{l=1}^{m-1} R_l\}$.

Let ρ_l be an indicator variable such that $\rho_l = 1$ if the lth failure occurs from sample 1, and $\rho_l = 0$ if it is from sample 2. Thus, the joint adaptive progressive Type II censored sample observed from the experiment is:
$\{U_1, \rho_1), (U_2, \rho_2), ..., (U_K, \rho_K), (U_{K+1}, \rho_{K+1}), ..., (U_m, \rho_m)\}$. Then, the likelihood function of the joint adaptive progressive Type II censored sample is given by

$$L(U,\rho) = A_K \left[\prod_{l=1}^{m} [g_1(u_l)]^{\rho_l} [g_2(u_l)]^{1-\rho_l}\right] \left[\prod_{l=1}^{K} [\bar{G_1}(u_l)]^{P_l} [\bar{G_2}(u_l)]^{Q_l}\right] [G_1(\bar{u}_m)]^{P*} [G_2(\bar{u}_m)]^{Q*}, \quad (3)$$

where

$$A_K = \prod_{l=1}^{m} \left[N - l - 1 - \sum_{K=1}^{min[l-1,K]} R_K\right],$$

$$P^* = \begin{cases} \sum_{l=K+1}^{m} P_l & for \quad K < m \\ 0 & otherwise \end{cases}, \; and \quad Q^* = \begin{cases} \sum_{l=K+1}^{K} Q_l & for \quad K < m \\ 0 & otherwise. \end{cases}$$

3. Statistical inference for DUS-EV distributions

3.1. Maximum likelihood estimation

Suppose two independent and identically distributed samples $(Y_1, Y_2, ...Y_{N_1})$ and $(Z_1, Z_2, ...Z_{N_2})$ of sizes N_1 and N_2 are taken from DUS-EV (λ_1, α_1) and DUS-EV (λ_2, α_2) populations, respectively. Let g_1 and g_2 denote the corresponding probability density functions (PDFs) and G_1 and G_2

denote the cumulative distribution functions (CDFs) of these populations. The PDFs and CDFs are given by:

$$g_1(y) = \frac{1}{\alpha_1(e-1)} e^{(\frac{y-\lambda_1}{\alpha_1} - e^{\frac{y-\lambda_1}{\alpha_1}})} e^{(1-e^{-e^{(\frac{y-\lambda_1}{\alpha_1})}})}; \quad -\infty < y < \infty, \quad -\infty < \lambda_1 < \infty, \quad \alpha_1 > 0, \tag{4}$$

$$g_2(z) = \frac{1}{\alpha_2(e-1)} e^{(\frac{z-\lambda_2}{\alpha_2} - e^{\frac{z-\lambda_2}{\alpha_2}})} e^{(1-e^{-e^{(\frac{z-\lambda_2}{\alpha_2})}})}; \quad -\infty < z < \infty, \quad -\infty < \lambda_2 < \infty, \quad \alpha_2 > 0, \tag{5}$$

$$G_1(y) = \frac{1}{e-1}(e^{(1-e^{-e^{(\frac{y-\lambda_1}{\alpha_1})}})} - 1); \quad -\infty < y < \infty, \quad -\infty < \lambda_1 < \infty, \quad \alpha_1 > 0, \tag{6}$$

and

$$G_2(z) = \frac{1}{e-1}(e^{(1-e^{-e^{(\frac{z-\lambda_2}{\alpha_2})}})} - 1); \quad -\infty < z < \infty, \quad -\infty < \lambda_2 < \infty, \quad \alpha_2 > 0. \tag{7}$$

The joint likelihood function of the parameters is expressed as

$$\begin{aligned} L(\Psi|U,\rho) = A_K \prod_{l=1}^{m} & \left(\frac{1}{\alpha_1(e-1)} e^{(\frac{u_l-\lambda_1}{\alpha_1} - e^{\frac{u_l-\lambda_1}{\alpha_1}})} e^{(1-e^{-e^{(\frac{u_l-\lambda_1}{\alpha_1})}})} \right)^{\rho_l} \\ & \times \left(\frac{1}{\alpha_2(e-1)} e^{(\frac{u_l-\lambda_2}{\alpha_2} - e^{\frac{u_l-\lambda_2}{\alpha_2}})} e^{(1-e^{-e^{(\frac{u_l-\lambda_2}{\alpha_2})}})} \right)^{1-\rho_l} \\ & \times \prod_{l=1}^{K} \left(\frac{e}{e-1}(1 - e^{-e^{-e^{\frac{u_l-\lambda_1}{\alpha_1}}}}) \right)^{P_l} \left(\frac{e}{e-1}(1 - e^{-e^{-e^{\frac{u_l-\lambda_2}{\alpha_2}}}}) \right)^{Q_l} \\ & \times \left(\frac{e}{e-1}(1 - e^{-e^{-e^{\frac{u_m-\lambda_1}{\alpha_1}}}}) \right)^{P^*} \left(\frac{e}{e-1}(1 - e^{-e^{-e^{\frac{u_m-\lambda_2}{\alpha_2}}}}) \right)^{Q^*}, \end{aligned} \tag{8}$$

where $\Psi = (\lambda_1, \alpha_1, \lambda_2, \alpha_2)$ represents the vector of model parameters.

The log likelihood function is given by

$$\begin{aligned} logL(\Psi|U,\rho) = {} & log(A_K) + \sum_{l=1}^{m} \rho_l (1 - log(\alpha_1(e-1))) + \sum_{l=1}^{m} \rho_l \left((\frac{u_l - \lambda_1}{\alpha_1}) - e^{\frac{u_l-\lambda_1}{\alpha_1}} - e^{-e^{\frac{u_l-\lambda_1}{\alpha_1}}} \right) \\ & + \sum_{l=1}^{m} (1-\rho_l)(1 - log(\alpha_2(e-1))) + \sum_{l=1}^{m} (1-\rho_l) \left((\frac{u_l - \lambda_2}{\alpha_2}) - e^{\frac{u_l-\lambda_2}{\alpha_2}} - e^{-e^{\frac{u_l-\lambda_2}{\alpha_2}}} \right) \\ & + \sum_{l=1}^{K} P_l log\left(\frac{e}{e-1}\right) + \sum_{l=1}^{K} P_l log(1 - e^{-e^{-e^{\frac{u_l-\lambda_1}{\alpha_1}}}}) \\ & + \sum_{l=1}^{K} Q_l log\left(\frac{e}{e-1}\right) + \sum_{l=1}^{K} Q_l log(1 - e^{-e^{-e^{\frac{u_l-\lambda_2}{\alpha_2}}}}) \\ & + P^* log\left(\frac{e}{e-1}\right) + P^* log(1 - e^{-e^{-e^{\frac{u_m-\lambda_1}{\alpha_1}}}}) \\ & + Q^* log\left(\frac{e}{e-1}\right) + Q^* log(1 - e^{-e^{-e^{\frac{u_m-\lambda_2}{\alpha_2}}}}). \end{aligned} \tag{9}$$

To determine the maximum likelihood estimates, we solve the system of equations given as

follows:

$$\frac{\partial logL}{\partial \lambda_1} = \frac{-C_1}{\alpha_1} + \sum_{l=1}^{m} \frac{\rho_l}{\alpha_1} e^{\frac{u_l-\lambda_1}{\alpha_1}} (1 - e^{-e^{\frac{u_l-\lambda_1}{\alpha_1}}}) + \sum_{l=1}^{K} \frac{P_l}{\alpha_1} \frac{e^{(\frac{u_l-\lambda_1}{\alpha_1} - e^{\frac{u_l-\lambda_1}{\alpha_1}})}}{(e^{e^{-e^{\frac{u_l-\lambda_1}{\alpha_1}}}} - 1)} + \frac{P^*}{\alpha_1} \frac{e^{(\frac{u_m-\lambda_1}{\alpha_1} - e^{\frac{u_m-\lambda_1}{\alpha_1}})}}{(e^{e^{-e^{\frac{u_m-\lambda_1}{\alpha_1}}}} - 1)}, \tag{10}$$

$$\frac{\partial logL}{\partial \lambda_2} = \frac{-C_2}{\alpha_2} + \sum_{l=1}^{m} \frac{1-\rho_l}{\alpha_2} e^{\frac{u_l-\lambda_2}{\alpha_2}} (1 - e^{-e^{\frac{u_l-\lambda_2}{\alpha_2}}}) + \sum_{l=1}^{K} \frac{Q_l}{\alpha_2} \frac{e^{(\frac{u_l-\lambda_2}{\alpha_2} - e^{\frac{u_l-\lambda_2}{\alpha_2}})}}{(e^{e^{-e^{\frac{u_l-\lambda_2}{\alpha_2}}}} - 1)} + \frac{Q^*}{\alpha_2} \frac{e^{(\frac{u_m-\lambda_2}{\alpha_2} - e^{\frac{u_m-\lambda_2}{\alpha_2}})}}{(e^{e^{-e^{\frac{u_m-\lambda_2}{\alpha_2}}}} - 1)}, \tag{11}$$

$$\frac{\partial logL}{\partial \alpha_1} = \frac{-C_1}{\alpha_1} + \sum_{l=1}^{m} \rho_i \left(\frac{u_l-\lambda_1}{\alpha_1^2}\right) \left(e^{\frac{u_l-\lambda_1}{\alpha_1}} - e^{(\frac{u_l-\lambda_1}{\alpha_1} - e^{\frac{u_l-\lambda_1}{\alpha_1}})} - 1\right) + \sum_{l=1}^{K} P_l \left(\frac{u_l-\lambda_1}{\alpha_1^2}\right) \frac{e^{(\frac{u_l-\lambda_1}{\alpha_1} - e^{\frac{u_l-\lambda_1}{\alpha_1}})}}{(e^{e^{-e^{\frac{u_l-\lambda_1}{\alpha_1}}}} - 1)} + P^* \left(\frac{u_m-\lambda_1}{\alpha_1^2}\right) \frac{e^{(\frac{u_m-\lambda_1}{\alpha_1} - e^{\frac{u_m-\lambda_1}{\alpha_1}})}}{(e^{e^{-e^{\frac{u_m-\lambda_1}{\alpha_1}}}} - 1)}, \tag{12}$$

and

$$\frac{\partial logL}{\partial \alpha_2} = \frac{-C_2}{\alpha_2} + \sum_{l=1}^{m} (1-\rho_l) \left(\frac{u_l-\lambda_2}{\alpha_2^2}\right) \left(e^{\frac{u_l-\lambda_2}{\alpha_2}} - e^{(\frac{u_l-\lambda_2}{\alpha_2} - e^{\frac{u_l-\lambda_2}{\alpha_2}})} - 1\right) + \sum_{l=1}^{K} Q_l \left(\frac{u_l-\lambda_2}{\alpha_2^2}\right) \frac{e^{(\frac{u_l-\lambda_2}{\alpha_2} - e^{\frac{u_l-\lambda_2}{\alpha_2}})}}{(e^{e^{-e^{\frac{u_l-\lambda_2}{\alpha_2}}}} - 1)} + Q^* \left(\frac{u_m-\lambda_2}{\alpha_2^2}\right) \frac{e^{(\frac{u_m-\lambda_2}{\alpha_2} - e^{\frac{u_m-\lambda_2}{\alpha_2}})}}{(e^{e^{-e^{\frac{u_m-\lambda_2}{\alpha_2}}}} - 1)}, \tag{13}$$

where $C_1 = \sum_{l=1}^{m} \rho_l$ and $C_2 = \sum_{l=1}^{m} (1-\rho_l)$. The equations (10) to (13) do not admit closed-form analytical solutions; however, they can be effectively solved using numerical methods available in any statistical software.

3.2. Asymptotic confidence interval

This section develops asymptotic confidence intervals for the parameters $\lambda_1, \alpha_1, \lambda_2$, and α_2 using the asymptotic behavior of the maximum likelihood estimators. To this end, we employ the observed information matrix $I(\Psi)$ defined as,

$$I(\Psi) = - \begin{bmatrix} \left(\frac{\partial^2 \log L}{\partial \lambda_1^2}\right) & \left(\frac{\partial^2 \log L}{\partial \lambda_1 \partial \alpha_1}\right) & \left(\frac{\partial^2 \log L}{\partial \lambda_1 \partial \lambda_2}\right) & \left(\frac{\partial^2 \log L}{\partial \lambda_1 \partial \alpha_2}\right) \\ \left(\frac{\partial^2 \log L}{\partial \alpha_1 \partial \lambda_1}\right) & \left(\frac{\partial^2 \log L}{\partial \alpha_1^2}\right) & \left(\frac{\partial^2 \log L}{\partial \alpha_1 \partial \lambda_2}\right) & \left(\frac{\partial^2 \log L}{\partial \alpha_1 \partial \alpha_2}\right) \\ \left(\frac{\partial^2 \log L}{\partial \lambda_2 \partial \lambda_1}\right) & \left(\frac{\partial^2 \log L}{\partial \lambda_2 \partial \alpha_1}\right) & \left(\frac{\partial^2 \log L}{\partial \lambda_2^2}\right) & \left(\frac{\partial^2 \log L}{\partial \lambda_2 \partial \alpha_2}\right) \\ \left(\frac{\partial^2 \log L}{\partial \alpha_2 \partial \lambda_1}\right) & \left(\frac{\partial^2 \log L}{\partial \alpha_2 \partial \alpha_1}\right) & \left(\frac{\partial^2 \log L}{\partial \alpha_2 \partial \lambda_2}\right) & \left(\frac{\partial^2 \log L}{\partial \alpha_2^2}\right) \end{bmatrix},$$

Asymptotic results imply that $\hat{\Psi} = (\hat{\lambda}1, \hat{\alpha}1, \hat{\lambda}2, \hat{\alpha}2)$ has an asymptotic multivariate normal distribution with mean $\hat{\Psi}$ and covariance matrix $I^{-}(\hat{\Psi})$, where variances of the MLEs appear on the diagonal and covariances on the off-diagonal. Then, $100(1-\delta)\%$ confidence intervals for λ_1, α_1, λ_2, and α_2 are obtained as

$$\left(\hat{\lambda_1} - z_{\delta/2}\sqrt{V(\hat{\lambda_1})}, \hat{\lambda_1} + z_{\delta/2}\sqrt{V(\hat{\lambda_1})}\right),$$
$$\left(\hat{\alpha_1} - z_{\delta/2}\sqrt{V(\hat{\alpha_1})}, \hat{\alpha_1} + z_{\delta/2}\sqrt{V(\hat{\alpha_1})}\right),$$
$$\left(\hat{\lambda_2} - z_{\delta/2}\sqrt{V(\hat{\lambda_2})}, \hat{\lambda_2} + z_{\delta/2}\sqrt{V(\hat{\lambda_2})}\right),$$

and

$$\left(\hat{\alpha_2} - z_{\delta/2}\sqrt{V(\hat{\alpha_2})}, \hat{\alpha_2} + z_{\delta/2}\sqrt{V(\hat{\alpha_2})}\right).$$

3.3. Bootstrap-Confidence Interval

In this section, confidence intervals are constructed using the bootstrap method, wherein the data are repeatedly resampled to generate a large number of pseudo-samples. These resampled datasets are then used to estimate the parameters. Among the various methods available for confidence interval construction, we employ the percentile bootstrap (boot-p) method. The algorithm for constructing boot-p confidence interval, is outlined as follows [12].

Step 1: Generate two samples of sizes N_1 and N_2 from DUS-EV(λ_1, α_1) and DUS-EV(λ_2, α_2) respectively.

Step 2: Generate joint adaptive Type II censored sample $\{(U_1, \rho_1), (U_2, \rho_2), ..., (U_K, \rho_K), (U_{K+1}, \rho_{K+1}), ..., (U_m, \rho_m)\}$.

Step 3: Compute the parameter estimates $\hat{\lambda}_1$, $\hat{\alpha}_1$, $\hat{\lambda}_2$, $\hat{\alpha}_2$ using the method of maximum likelihood.

Step 4: Generate bootstrap samples of sizes N_1 and N_2 from DUS-EV$(\hat{\lambda}_1, \hat{\alpha}_1)$ and DUS-EV$(\hat{\lambda}_2, \hat{\alpha}_2)$ respectively.

Step 5: Generate bootstrap joint adaptive type II censored sample $\{(U_1^*, \rho_1^*), (U_2^*, \rho_2^*), ..., (U_K^*, \rho_K^*), (U_{K+1}^*, \rho_{K+1}^*), ..., (U_m^*, \rho_m^*)\}$.

Step 6: Based on the bootstrap censored samples generated in step 5, calculate estimates of parameters, which are denoted by $\hat{\lambda}_1^*$,$\hat{\alpha}_1^*$, $\hat{\lambda}_2^*$,$\hat{\alpha}_2^*$.

Step 7: Repeating steps 3"6 for B iterations yields $\hat{\lambda}_{1k}^*$,$\hat{\alpha}_{1k}^*$, $\hat{\lambda}_{2k}^*$,$\hat{\alpha}_{2k}^*$, $\quad k = 1, 2, 3...B$.

Step 8: Arrange the bootstrap sample estimates in ascending order.

Step 9: Let $G(a) = P(\hat{\Psi}_k^* \leq a)$ be the CDF of $\hat{\Psi}_k^*$. The Approximate $100(1-\delta)$ percentile bootstrap confidence interval for Ψ_k is given by $(\hat{\Psi}_k^*(\frac{\delta}{2}), \hat{\Psi}_k^*(1-\frac{\delta}{2}))$, where $k = 1, 2, ..., B$.

3.4. Bayesian Estimation

In this section, we obtain the Bayesian estimates of the unknown parameters λ_1, α_1, λ_2, α_2, along with their credible intervals, based on joint adaptive progressive Type II censored data. We assume independent normal and gamma priors for the model parameters [18]. Specifically, the parameters λ_1 and λ_2 are assumed to follow independent normal priors, $\lambda_1 \sim N(\mu_1, \sigma_1^2)$ and $\lambda_2 \sim N(\mu_2, \sigma_2^2)$, while the parameters α_1 and α_2 are assumed to follow independent gamma priors, $\alpha_1 \sim G(m_1, p_1)$ and $\alpha_2 \sim G(m_2, p_2)$. The hyperparameters μ_1, σ_1, μ_2, and σ_2 are assumed to be non negative. Thus, the joint prior distribution is given in (14).

The posterior density function can be derived using the likelihood function of the censored samples with the prior distributions and is given in (15).

$$\pi^*(\lambda_1, \alpha_1, \lambda_2, \alpha_2) \propto e^{-\frac{1}{2}\left[(\frac{\lambda_1-\mu_1}{\sigma_1})^2 + (\frac{\lambda_2-\mu_2}{\sigma_2})^2\right]} e^{-(m_1\alpha_1 + m_2\alpha_2)} \alpha_1^{p_1-1} \alpha_2^{p_2-1} \quad \lambda_1, \lambda_2 \in R, \alpha_1, \alpha_2 > 0. \quad (14)$$

If $I_1 = -\frac{1}{2}\left(\frac{\lambda_1-\mu_1}{\sigma_1}\right)^2 - \frac{1}{2}\left(\frac{\lambda_2-\mu_2}{\sigma_2}\right)^2 - m_1\alpha_1 - m_2\alpha_2$

$I_2 = \sum_{l=1}^{m}\rho_l(1-\log(\alpha_1(e-1))) + \sum_{l=1}^{m}\rho_l\left((\frac{u_l-\lambda_1}{\alpha_1}) - e^{\frac{u_l-\lambda_1}{\alpha_1}} - e^{-e^{(\frac{u_l-\lambda_1}{\alpha_1})}}\right)$

$I_3 = \sum_{l=1}^{m}(1-\rho_l)(1-\log(\alpha_2(e-1))) + \sum_{l=1}^{m}(1-\rho_l)\left((\frac{u_l-\lambda_2}{\alpha_2}) - e^{\frac{u_l-\lambda_2}{\alpha_2}} - e^{-e^{\frac{u_l-\lambda_2}{\alpha_2}}}\right)$

$I_4 = \sum_{l=1}^{K} P_l \log\left(\frac{e}{e-1}\right) + \sum_{l=1}^{K} P_l \log\left(1 - e^{-e^{-e^{\frac{u_l-\lambda_1}{\alpha_1}}}}\right)$

$I_5 = \sum_{l=1}^{K} Q_l \log\left(\frac{e}{e-1}\right) + \sum_{l=1}^{K} Q_l \log\left(1 - e^{-e^{-e^{\frac{u_l-\lambda_2}{\alpha_2}}}}\right)$

$I_6 = P^* \log\left(\frac{e}{e-1}\right) + P^* \log\left(1 - e^{-e^{-e^{\frac{u_m-\lambda_1}{\alpha_1}}}}\right)$

$I_7 = Q^* \log\left(\frac{e}{e-1}\right) + Q^* \log\left(1 - e^{-e^{-e^{\frac{u_m-\lambda_2}{\alpha_2}}}}\right)$

$$P^*(\lambda_1,\alpha_1,\lambda_2,\alpha_2) \propto \alpha_1^{p_1-1}\alpha_2^{p_2-1} exp\Big[I_1 + I_2 + I_3 + I_4 + I_5 + I_6 + I_7\Big]. \tag{15}$$

The conditional posterior distributions derived from (15) are given as follows:

$$\begin{aligned} P_1^*(\lambda_1|\lambda_2,\alpha_1,\alpha_2) \propto \exp\Bigg[&-\frac{1}{2}\left(\frac{\lambda_1-\mu_1}{\sigma_1}\right)^2 + \sum_{l=1}^{m}\rho_l\left((\frac{u_l-\lambda_1}{\alpha_1}) - e^{\frac{u_l-\lambda_1}{\alpha_1}} - e^{-e^{(\frac{u_l-\lambda_1}{\alpha_1})}}\right) \\ &+ \sum_{l=1}^{K} P_l log\left(1 - e^{-e^{-e^{\frac{u_l-\lambda_1}{\alpha_1}}}}\right) + P^* \log\left(1 - e^{-e^{-e^{\frac{u_m-\lambda_1}{\alpha_1}}}}\right)\Bigg]. \end{aligned} \tag{16}$$

$$\begin{aligned} P_2^*(\alpha_1|\lambda_1,\lambda_2,\alpha_2) \propto \alpha_1^{p_1-1-C_1}\exp\Bigg[&- m_1\alpha_1 + \sum_{l=1}^{m}\rho_l\left((\frac{u_l-\lambda_1}{\alpha_1}) - e^{\frac{u_l-\lambda_1}{\alpha_1}} - e^{-e^{(\frac{u_l-\lambda_1}{\alpha_1})}}\right) \\ &+ \sum_{l=1}^{K} P_l log\left(1 - e^{-e^{-e^{\frac{u_l-\lambda_1}{\alpha_1}}}}\right) + P^* \log\left(1 - e^{-e^{-e^{\frac{u_m-\lambda_1}{\alpha_1}}}}\right)\Bigg], \end{aligned} \tag{17}$$

$$\begin{aligned} P_3^*(\lambda_2|\lambda_1,\alpha_1,\alpha_2) \propto \exp\Bigg[&-\frac{1}{2}\left(\frac{\lambda_2-\mu_2}{\sigma_2}\right)^2 + \sum_{l=1}^{m}\rho_l\left((\frac{u_l-\lambda_2}{\alpha_2}) - e^{\frac{u_l-\lambda_2}{\alpha_2}} - e^{-e^{(\frac{u_l-\lambda_2}{\alpha_2})}}\right) \\ &+ \sum_{l=1}^{K} P_l \log\left(1 - e^{-e^{-e^{\frac{u_l-\lambda_2}{\alpha_2}}}}\right) + P^* \log\left(1 - e^{-e^{-e^{\frac{u_m-\lambda_2}{\alpha_2}}}}\right)\Bigg], \end{aligned} \tag{18}$$

and

$$\begin{aligned} P_4^*(\alpha_2|\lambda_1,\lambda_2,\alpha_1) \propto \alpha_2^{p_2-1-C_2}\exp\Bigg[&- m_2\alpha_2 + \sum_{l=1}^{m}\rho_i\left((\frac{u_l-\lambda_2}{\alpha_2}) - e^{\frac{u_l-\lambda_2}{\alpha_2}} - e^{-e^{(\frac{u_l-\lambda_2}{\alpha_2})}}\right) \\ &+ \sum_{l=1}^{K} P_l log\left(1 - e^{-e^{-e^{\frac{u_l-\lambda_2}{\alpha_2}}}}\right) + P^* \log\left(1 - e^{-e^{-e^{\frac{u_m-\lambda_2}{\alpha_2}}}}\right)\Bigg]. \end{aligned} \tag{19}$$

As demonstrated in equations (16) to (19), the full conditional posterior distributions of the model parameters are not in closed-form expressions. Consequently, direct sampling from these distributions is not feasible. In this case, we employ Metropolis"Hastings sampling within the Gibbs algorithm using a normal proposal distribution. Posterior samples of the model parameters are subsequently generated by iteratively performing the following steps.

Step 1: Initialize the iteration step to $k = 1$ and initialise the parameters $\Psi^{(0)} = (\lambda_1^{(0)}, \alpha_1^{(0)}, \lambda_2^{(0)}, \alpha_2^{(0)})$.

Step 2: Generate $\lambda_1^{(k)}$, $\alpha_1^{(k)}$, $\lambda_2^{(k)}$, $\alpha_2^{(k)}$ from $P_1^*(\lambda_1|\lambda_2,\alpha_1,\alpha_2)$, $P_2^*(\alpha_1|\lambda_1,\lambda_2,\alpha_2)$, $P_3^*(\lambda_2|\lambda_1,\alpha_1,\alpha_2)$, and $P_4^*(\alpha_2|\lambda_1,\lambda_2,\alpha_1)$ respectively by using the Metropolis"Hastings algorithm described in [18] with a normal proposal.

Step 3: Set $k = k + 1$.
Step 4: Repeat the steps 2-3 J times.
Thus, the approximate Bayesian estimators of the parameters λ_1, α_1, λ_2, and, α_2 under squared error loss function is given by

$$\begin{aligned} \hat{\lambda}_{1_{Bayes}} &= \frac{1}{J-B}\sum_{k=B+1}^{J}\lambda_1^{(k)}, \quad \hat{\lambda}_{2_{Bayes}} = \frac{1}{J-B}\sum_{k=B+1}^{J}\lambda_2^{(k)}, \\ \hat{\alpha}_{1_{Bayes}} &= \frac{1}{J-B}\sum_{k=B+1}^{J}\alpha_1^{(k)}, \text{and}, \hat{\alpha}_{2_{Bayes}} = \frac{1}{J-B}\sum_{k=B+1}^{J}\alpha_2^{(k)} \end{aligned} \tag{20}$$

where B denotes the burn-in period. We can also construct HPD credible intervals [8]. Then, $100(1-\delta)$ HPD interval is given by

$$(\hat{\Psi}_{Bayes[\frac{\delta}{2}(J-B)]}, \hat{\Psi}_{Bayes[(1-\frac{\delta}{2})(J-B)]}) \tag{21}$$

where $\hat{\Psi}_{Bayes} = (\hat{\lambda}_{1_{Bayes}}, \hat{\alpha}_{1_{Bayes}}, \hat{\lambda}_{2_{Bayes}}, \hat{\alpha}_{2_{Bayes}})$, $\hat{\Psi}_{Bayes[\frac{\delta}{2}(J-B)]}$ and $\hat{\Psi}_{Bayes[(1-\frac{\delta}{2})(J-B)]}$ are the $[(\frac{\delta}{2}(J-B)]$ th smallest and $[(1-\frac{\delta}{2})(J-B)]$ th smallest of MCMC samples $\psi^{(k)}$ generated from posterior densities.

4. Simulation study

This section presents a simulation study aimed at assessing the performance of parameter estimation methods, particularly maximum likelihood estimation (MLE) and Bayesian techniques. The simulation is performed under various sample size configurations: (50, 40, 70), (60, 50, 88), and (70, 60, 106), where the first two values denote the sample sizes of the two groups and the third corresponds to the total number of observed failures. We take the initial parameter values as $(\lambda_1, \alpha_1, \lambda_2, \alpha_2)$ = (0.8, 1.2, 0.9, 1.5) and fixed experimental times $T = 1.2$ and $T = 1.5$. Point estimates are compared using bias and MSEs, as presented in Table: 2. Asymptotic confidence intervals, bootstrap confidence intervals, and highest posterior density (HPD) intervals are computed. These interval estimates are evaluated based on average confidence lengths (ACL) and coverage probabilities (CP), which are outlined in Table: 3.

For Bayesian estimation, both informative and non-informative priors are considered. In the non-informative setup, the hyperparameters for normal priors are chosen to be $\mu_1 = \mu_2 = 0$ and $\sigma_1 = \sigma_2 = 1$, while for the gamma priors, $m_1 = m_2 = p_1 = p_2 = 0.001$, a small positive value to give a minimal influence on the parameters. In the informative case, the hyperparameters are $\mu_1 = 0.8$, $\mu_2 = 0.9$, $\sigma_1 = \sigma_2 = 0.1$, $m_1 = 4.375$, $m_2 = 3.5$, $p_1 = 5.25$, and $p_2 = 5.25$. The simulation procedure is replicated 1000 times. The complete censoring schemes employed in the study are listed below in Table:1.

The notation $(0_3, 2_2)$ represents a censoring scheme in which the value 0 is repeated three times and the value 2 is repeated twice. The steps involved in generating a joint adaptive progressive Type II censored sample are described as follows.
1. Generate two samples of sizes N_1 and N_2 from DUS-EV(λ_1, α_1) and DUS-EV(λ_2, α_2).
2. Randomly select a type II progressively censored sample of size m [6]
3. Select the sample $\{(U_1, \rho_1), (U_2, \rho_2), ..., (U_K, \rho_K)\}$ based on the time T.
4. If $K < m$, generate truncated samples of size m-K from the DUS-EV distribution.
5. Update the joint adaptive progressive Type II censored sample
$\{(U_1, \rho_1), (U_2, \rho_2), ..., (U_K, \rho_K), (U_{K+1}, \rho_{K+1}), ..., (U_m, \rho_m)\}$
The following are the main conclusions drawn from the simulation study:

- An increase in sample size leads to a reduction in the absolute bias and mean squared error (MSE) of the MLEs as well as the Bayesian estimators obtained under both informative and non-informative priors.

Table 1: *Censoring Schemes*

2*Sl.No	Sample Size (n_1, n_2, m)	Censoring Scheme R
1	$(50, 40, 70)$	$(0_{60}, 2_{10})$
2	„	$(0_{69}, 20)$
3	„	$(1_5, 0_{50}, 1_{15})$
4	$(60, 50, 88)$	$(0_{77}, 2_{11})$
5	„	$(0_{87}, 22)$
6	„	$(1_5, 0_{66}, 1_{17}, 0_5)$
7	$(70, 60, 106)$	$(0_{94}, 2_{12})$
8	„	$(0_{105}, 24)$
9	„	$(1_5, 0_{82}, 1_{19})$

- In the majority of scenarios, Bayesian estimation with informative priors results in reduced MSE relative to non-informative priors and maximum likelihood estimates.
- Average confidence length is shorter for HPD intervals with an informative prior as compared to all other confidence intervals.
- Most of the time, coverage probabilities converge to the nominal level as the sample size increases.

5. Data analysis

This section presents a real data analysis to demonstrate the effectiveness and practical relevance of the proposed approach. For this purpose, we consider two data sets originally reported [7], which consist of observed times between consecutive telephone calls received at a company's switchboard. Specifically, the first data set contains 41 time intervals measured in seconds, while the second comprises 48 time intervals recorded in minutes. The first data set has previously been analyzed in the context of modeling extreme values and was utilized to fit the DUS-EV distribution [18]. Now we utilize the same data to examine the effectiveness of the proposed estimation techniques within the framework of joint adaptive progressive Type II censoring. To evaluate the goodness of fit, we apply three statistical tests: the Kolmogorov-Smirnov (KS) test, the Anderson-Darling (AD) test, and the Cramer-Von Mises (CVM) test. The results are summarized in Table:4. We generate a joint adaptive Type II censored sample from the joint distribution of time intervals of two sets of data for $m = 63$, $T = 0.8$ and $R = (0_{53}, 2_{10})$ and performed estimation through maximum likelihood and Bayesian techniques. The results are provided in the Table:5.

6. Conclusions

This article investigates statistical inference for the recently proposed DUS-EV(λ, α) distribution under the joint adaptive progressive Type II censoring scheme. The DUS-EV distribution is characterized by an increasing failure rate, making it particularly suitable for analyzing aging systems and extreme value phenomena. To enhance the practical utility of this model, the JAPT-II censoring framework is adopted, which reduces experimental time while ensuring a predetermined number of failures, thereby improving the efficiency and reliability of inference procedures.

Parameter estimation is explored through classical, Bayesian, and bootstrap approaches. In the classical framework, maximum likelihood estimators and their asymptotic confidence intervals are derived. Bayesian inference is carried out using the Metropolis - Hastings algorithm within

Gibbs sampling to obtain posterior samples, along with highest posterior density (HPD) intervals. Complementarily, bootstrap methods are employed to construct alternative confidence intervals and to assess the robustness of inference.

The performance of these procedures is evaluated through simulation studies conducted under different sample size settings. The results indicate that Bayesian estimates with informative priors generally exhibit lower mean squared errors, while bootstrap intervals demonstrate competitive performance. A real-data analysis further validates the applicability of the proposed methods in practical reliability studies.

In conclusion, the study highlights the flexibility and robustness of the DUS-EV(λ, α) distribution under JAPT-II censoring and demonstrates the effectiveness of integrating classical, Bayesian, and resampling-based inference procedures in reliability analysis.

Table 2: *Biases and MSEs for* $\lambda_1 = 0.8$, $\beta_1 = 1.2$, $\lambda_2 = 1$, $\beta_2 = 1.5$

4*CS	4*T		MLE				Bayesian					Bayesian (non-informative)				
		λ_1	β_1	λ_2	β_2		λ_1	β_1	λ_2	β_2		λ_1	β_1	λ_2	β_2	
		Bias (MSE)	Bias (MSE)	Bias (MSE)	Bias (MSE)		Bias (MSE)	Bias (MSE)	Bias (MSE)	Bias (MSE)		Bias (MSE)	Bias (MSE)	Bias (MSE)	Bias (MSE)	
1	1.2	0.0509	0.1040	0.0776	0.0951		0.0422	0.2092	0.0396	0.3284		0.1277	0.2352	0.2022	0.3877	
		0.0340	0.0458	0.0594	0.0749		0.0035	0.0770	0.0028	0.1697		0.0397	0.0994	0.0780	0.2420	
	1.5	0.0566	0.1078	0.0743	0.1282		0.0498	0.2086	0.0588	0.3622		0.1415	0.2450	0.2221	0.4051	
		0.0360	0.0520	0.0726	0.0815		0.0047	0.0785	0.0052	0.2001		0.0538	0.1048	0.1059	0.2647	
2	1.2	0.0541	0.1159	0.0912	0.1032		0.0438	0.2361	0.0438	0.3594		0.1380	0.2465	0.2052	0.3970	
		0.0313	0.0513	0.0639	0.0811		0.0036	0.0978	0.0029	0.1997		0.0440	0.1083	0.0741	0.2530	
	1.5	0.1050	0.1847	0.1576	0.2113		0.0551	0.2908	0.0699	0.4663		0.2193	0.3049	0.3079	0.4945	
		0.0374	0.0847	0.0847	0.1306		0.0073	0.1702	0.0064	0.3755		0.1103	0.1712	0.1901	0.4051	
3	1.2	-0.0140	-0.0598	-0.1014	-0.1300		0.0209	0.1016	0.0226	0.1680		0.0555	0.1076	0.0830	0.2093	
		0.0278	0.0306	0.0590	0.0692		0.0021	0.0388	0.0016	0.0823		0.0241	0.0444	0.0404	0.1214	
	1.5	0.0302	-0.0304	-0.0865	-0.0597		0.0246	0.1143	0.0355	0.2105		0.0726	0.1317	0.1244	0.2605	
		0.0322	0.0277	0.0641	0.0572		0.0029	0.0396	0.0021	0.1051		0.0299	0.0318	0.0464	0.0733	
4	1.2	0.0345	0.0547	0.0328	0.0432		0.0361	0.1475	0.0392	0.2567		0.0961	0.1595	0.1569	0.2932	
		0.0246	0.0290	0.0427	0.0533		0.0029	0.0483	0.0028	0.1111		0.0268	0.0565	0.0499	0.1493	
	1.5	0.0453	0.1000	0.0661	0.1105		0.0441	0.1906	0.0499	0.3239		0.1277	0.1964	0.2310	0.3685	
		0.0305	0.0364	0.0540	0.0657		0.0045	0.0643	0.0042	0.3240		0.0450	0.0707	0.0948	0.2040	
5	1.2	0.0261	0.0464	0.0534	0.0351		0.0341	0.1419	0.0417	0.2679		0.0852	0.1512	0.1760	0.2983	
		0.0252	0.0288	0.0446	0.0501		0.0029	0.0472	0.0029	0.1247		0.0249	0.0559	0.0547	0.1548	
	1.5	0.0771	0.1620	0.1178	0.1948		0.0582	0.2177	0.0664	0.3983		0.1916	0.2424	0.2930	0.4268	
		0.0298	0.0629	0.0618	0.1084		0.0063	0.0894	0.0064	0.2421		0.0692	0.1079	0.1353	0.2769	

Table 2: *Continued*

4*CS	4*T		MLE				Bayesian				Bayesian (non-informative)			
		λ_1	β_1	λ_2	β_2		λ_1	β_1	λ_2	β_2	λ_1	β_1	λ_2	β_2
		Bias (MSE)	Bias (MSE)	Bias (MSE)	Bias (MSE)		Bias (MSE)	Bias (MSE)	Bias (MSE)	Bias (MSE)	Bias (MSE)	Bias (MSE)	Bias (MSE)	Bias (MSE)
6	1.2	-0.0072	-0.0586	-0.0850	-0.1104		0.0184	0.0424	0.0204	0.1177	0.0286	0.0489	0.0721	0.1455
		0.0222	0.0255	0.0447	0.0549		0.0021	0.0229	0.0018	0.0615	0.0169	0.0277	0.0302	0.0806
	1.5	0.0262	-0.0250	-0.0692	-0.0623		0.0272	0.0802	0.0330	0.1748	0.0752	0.0908	0.1169	0.2014
		0.0269	0.0208	0.0504	0.0477		0.0030	0.0263	0.0026	0.0782	0.0283	0.0354	0.0473	0.1000
7	1.2	0.0173	0.0171	0.0016	0.0140		0.0254	0.0808	0.0376	0.2066	0.0617	0.0909	0.1295	0.2159
		0.0201	0.0230	0.0324	0.0411		0.0026	0.0266	0.0025	0.0841	0.0191	0.0307	0.0381	0.0974
	1.5	0.0364	0.0885	0.0547	0.1020		0.0404	0.1441	0.0438	0.2890	0.1258	0.1557	0.2105	0.3062
		0.0233	0.0297	0.0461	0.0532		0.0040	0.0438	0.0035	0.1297	0.0361	0.0516	0.0732	0.1513
8	1.2	0.0115	0.0152	0.0027	0.0165		0.0254	0.0795	0.0376	0.2022	0.0639	0.0917	0.1354	0.2282
		0.0191	0.0225	0.0328	0.0418		0.0025	0.0265	0.0026	0.0824	0.0191	0.0335	0.0381	0.1041
	1.5	0.0509	0.1106	0.0860	0.1404		0.0587	0.1800	0.0570	0.3422	0.1567	0.1727	0.2613	0.3531
		0.0223	0.03589	0.0443	0.0672		0.0057	0.0642	0.0061	0.1755	0.0450	0.0626	0.0947	0.1826
9	1.2	0.0008	-0.0499	-0.0876	-0.0918		0.0158	0.0110	0.0186	0.0836	0.0216	0.0167	0.0524	0.0953
		0.0195	0.0206	0.0276	0.0381		0.0020	0.0178	0.0016	0.0451	0.0150	0.0216	0.0235	0.0544
	1.5	0.0081	-0.0196	-0.0669	-0.0387		0.0327	0.0554	0.0247	0.1584	0.0801	0.0539	0.1145	0.1700
		0.0217	0.0180	0.0418	0.0384		0.0036	0.0193	0.0029	0.0650	0.0244	0.0239	0.0416	0.0725

Table 3: *for* $\lambda_1 = 0.8$, $\beta_1 = 1.2$, $\lambda_2 = 1$, $\beta_2 = 1.5$

4*CS	4*T	ACI				Bayesian				Bayesian (non-informative)				Bootstrap-p			
		λ_1	β_1	λ_2	β_2	λ_1	β_1	λ_2	β_2	λ_1	β_1	λ_2	β_2				
		CP	CP	CP	CP	CP	CP	CP	CP	CP	CP	CP	CP	CP	CP	CP	CP
		ACL	ACL	ACL	ACL	ACL	ACL	ACL	ACL	ACL	ACL	ACL	ACL	ACL	ACL	ACL	ACL
1	1.2	0.948	0.944	0.963	0.964	0.996	0.827	0.999	0.834	0.905	0.824	0.918	0.828	0.946	0.876	0.93	0.908
		0.7549	0.7061	1.0465	1.0421	0.3173	0.7088	0.3377	1.0635	0.6653	0.7883	0.8952	1.2506	0.7259	0.7292	0.9921	1.0084
	1.5	0.907	0.889	0.903	0.928	0.988	0.809	0.999	0.790	0.847	0.802	0.844	0.801	0.916	0.884	0.904	0.908
		0.7429	0.6832	1.0391	1.0143	0.3101	0.6887	0.3301	1.0621	0.6527	0.7683	0.8775	1.2266	0.7393	0.7380	1.0319	1.0168
2	1.2	0.953	0.92	0.957	0.956	0.994	0.758	0.999	0.804	0.892	0.810	0.915	0.822	0.916	0.858	0.898	0.904
		0.7611	0.7124	1.0479	1.0455	0.3176	0.7203	0.3372	1.0768	0.6660	0.7904	0.8922	1.2433	0.7120	0.8024	0.9723	1.0742
	1.5	0.763	0.677	0.739	0.742	0.938	0.691	0.979	0.649	0.687	0.710	0.661	0.705	0.838	0.726	0.776	0.832
		0.6667	0.6141	0.9381	0.9252	0.3006	0.7144	0.3179	1.0930	0.6408	0.7863	0.8636	1.2600	0.6897	0.9030	0.9853	1.1639
3	1.2	0.963	0.879	0.953	0.831	1	0.919	1	0.947	0.950	0.942	0.977	0.934	0.956	0.938	0.962	0.906
		0.6826	0.6053	0.9330	0.8642	0.3166	0.6513	0.3358	0.9783	0.6436	0.7114	0.8613	1.1208	0.6697	0.6403	0.8934	0.9200
	1.5	0.936	0.903	0.955	0.907	0.995	0.924	1	0.917	0.930	0.911	0.935	0.923	0.954	0.942	0.952	0.918
		0.6993	0.6095	0.9868	0.9025	0.3186	0.6433	0.3386	0.9998	0.6528	0.7141	0.8799	1.1548	0.7080	0.6381	0.9627	0.9078
4	1.2	0.957	0.947	0.963	0.954	0.996	0.864	0.999	0.881	0.924	0.870	0.921	0.875	0.954	0.93	0.962	0.92
		0.6591	0.6104	0.8992	0.8858	0.3082	0.6138	0.3312	0.9266	0.5877	0.6672	0.7803	1.0401	0.6182	0.6292	0.8252	0.8847
	1.5	0.924	0.937	0.936	0.944	0.989	0.816	0.996	0.771	0.832	0.824	0.781	0.774	0.926	0.88	0.956	0.926
		0.6759	0.6152	0.9354	0.9093	0.3067	0.6263	0.3282	0.9558	0.5925	0.6772	0.7944	1.0810	0.6639	0.6536	0.9015	0.8862
5	1.2	0.959	0.94	0.963	0.959	0.994	0.867	0.999	0.846	0.935	0.877	0.930	0.861	0.958	0.902	0.926	0.93
		0.6550	0.6052	0.8940	0.8845	0.3068	0.6106	0.3312	0.9314	0.5823	0.6609	0.7808	1.0442	0.6172	0.6486	0.8061	0.8916
	1.5	0.891	0.799	0.878	0.861	0.961	0.752	0.983	0.671	0.731	0.745	0.679	0.701	0.906	0.786	0.88	0.818
		0.6772	0.6157	0.9406	0.9169	0.3036	0.6368	0.3243	0.9858	0.5907	0.6954	0.7878	1.1012	0.6300	0.7719	0.8597	1.0194

Table 3: *continued*

4*CS	4*T	ACI				Bayesian				Bayesian (non-informative)				Bootstrap-p			
		λ_1	β_1	λ_2	β_2	λ_1	β_1	λ_2	β_2	λ_1	β_1	λ_2	β_2				
		CP	CP	CP	CP	CP	CP	CP	CP	CP	CP	CP	CP	CP	CP	CP	CP
		ACL	ACL	ACL	ACL	ACL	ACL	ACL	ACL	ACL	ACL	ACL	ACL	ACL	ACL	ACL	ACL
6	1.2	0.948	0.892	0.966	0.857	0.999	0.948	1	0.933	0.966	0.943	0.975	0.936	0.976	0.9	0.97	0.874
		0.6121	0.5479	0.8332	0.7842	0.3051	0.5591	0.3288	0.8569	0.5608	0.6027	0.7542	0.9509	0.5848	0.5683	0.7592	0.7914
	1.5	0.931	0.928	0.941	0.904	0.993	0.945	0.999	0.921	0.922	0.924	0.922	0.914	0.966	0.948	0.966	0.918
		0.6295	0.5554	0.8671	0.8039	0.3077	0.5669	0.3281	0.8812	0.5798	0.6165	0.7703	0.9788	0.6311	0.5650	0.8359	0.8030
7	1.2	0.958	0.939	0.964	0.952	0.991	0.918	0.998	0.875	0.941	0.923	0.932	0.880	0.954	0.938	0.954	0.928
		0.5888	0.5411	0.8034	0.7868	0.2975	0.5381	0.3211	0.8270	0.5211	0.5742	0.6899	0.8957	0.5428	0.5547	0.7213	0.8043
	1.5	0.942	0.934	0.947	0.959	0.977	0.845	0.994	0.766	0.834	0.831	0.797	0.793	0.922	0.89	0.95	0.906
		0.6229	0.5622	0.8536	0.8263	0.2990	0.5292	0.3198	0.8674	0.5353	0.5994	0.7096	0.9430	0.6063	0.5877	0.8056	0.8021
8	1.2	0.964	0.929	0.967	0.946	0.994	0.922	0.998	0.890	0.938	0.911	0.935	0.872	0.948	0.914	0.946	0.93
		0.5889	0.5403	0.8036	0.7880	0.2987	0.5359	0.3229	0.8252	0.5207	0.5729	0.6962	0.9013	0.5486	2.5617	0.7183	0.7994
	1.5	0.928	0.893	0.933	0.918	0.962	0.794	0.983	0.689	0.785	0.812	0.723	0.756	0.928	0.814	0.896	0.836
		0.6229	0.5614	0.8583	0.8328	0.3001	0.5760	0.3221	0.8867	0.5368	0.6103	0.7208	0.9705	0.5891	2.6798	0.7786	0.9037
9	1.2	0.945	0.894	0.961	0.871	0.998	0.920	1	0.940	0.959	0.932	0.978	0.940	0.974	0.886	0.952	0.83
		0.5632	0.5084	0.7630	0.7227	0.2945	0.4997	0.3225	0.7712	0.5083	0.5344	0.6712	0.8267	0.5243	0.5186	0.6777	0.7239
	1.5	0.941	0.922	0.951	0.916	0.983	0.958	0.997	0.915	0.893	0.942	0.909	0.925	0.954	0.944	0.958	0.938
		0.5779	0.5132	0.7953	0.7449	0.2982	0.5114	0.3222	0.8000	0.5193	0.5462	0.6924	0.8682	0.5802	0.5276	0.7596	0.7512

Table 4: *Goodness-of-fit test results for the DUS-EV distribution*

2*	2*Estimates	KS test		AD test		CVM test	
		Statistic	p-value	Statistic	p-value	Statistic	p-value
2*Data 1	$\hat{\lambda_1}$=0.9723 $\hat{\alpha_1}$=0.4563	2*0.0827	2*0.9539	2*0.2237	2* 0.9825	2* 0.0351	2* 0.9585
2*Data 2	$\hat{\lambda_2}$=1.6522 $\hat{\alpha_2}$= 0.4293	2* 0.1236	2*0.4554	2*0.54799	2* 0.6976	2* 0.1035	2* 0.5697

Table 5: *Estimates, standard errors (SE), confidence intervals (CI), and confidence lengths (CL) under joint adaptive progressive type II censoring scheme across different estimation methods*

3*Parameters	MLE		Bayesian		Bootstrap-p
	Estimates SE	ACI CL	Estimates SE	HPD CL	CI CL
$\hat{\lambda_1}$	0.9716	(0.8103, 1.1327)	0.8599	(0.7533, 0.9697)	(0.8924, 1.1466)
	0.0822	0.3224	0.0653	0.2164	0.2541
$\hat{\alpha_1}$	0.4694	(0.3405, 0.5984)	0.5458	(0.4328,0.6869)	(0.4447, 0.6217)
	0.0658	0.2579	0.0752	0.2541	0.1770
$\hat{\lambda_2}$	1.5953	(1.4703, 1.7203)	1.1083	(0.9281, 1.2726)	(1.5764, 1.7689)
	0.0638	0.2499	0.0882	0.3445	0.1925
$\hat{\alpha_2}$	0.3873	(0.2700, 0.5046)	1.1596	(0.8161, 1.5237)	(0.3329, 0.5735)
	0.0598	0.2346	0.1850	0.7076	0.2406

References

[1] Anakha, K.K. and Chacko, V.M.(2025). On comparative lifetime analysis with the generalized Lindley distribution: insights from joint adaptive progressive Type-II censoring. Journal of Statistical Computation and Simulation, 95(11): 2466 - 2493.

[2] Anakha, K. K., & Chacko, V. M.(2025). Type I–Type II mixture censoring scheme for lifetime data analysis. *Communications in Statistics–Simulation and Computation*, 1–15.

[3] Ashour, S.K. and Abo-Kasem, O.E.(2017). *Statistical inference for two exponential populations under joint progressive type-I censored scheme*. Communications in Statistics - Theory and Methods, 46(7): 3479–3488.

[4] Balakrishnan, N.(2007). Progressive censoring methodology: an appraisal. *Test*, 16(2): 211–259.

[5] Balakrishnan, N. and Aggarwala, R. Progressive Censoring: Theory, Methods, and Applications, Springer Science & Business Media, 2000.

[6] Balakrishnan, N. and Sandhu, R.A.(1995). A simple simulational algorithm for generating progressive Type-II censored samples. *The American Statistician*, 49(2): 229–230.

[7] Castillo, E., Hadi, A. S., Balakrishnan, N., and Sarabia, J. M. Extreme Value and Related Models with Applications in Engineering and Science, John Wiley & Sons, 2004.

[8] Chen, M.-H. and Shao, Q.-M. (1999). Monte Carlo estimation of Bayesian credible and HPD intervals. *Journal of Computational and Graphical Statistics*, 8(1):69–92.

[9] Childs, A., Chandrasekar, B., Balakrishnan, N., and Kundu, D. (2003). Exact likelihood inference based on Type-I and Type-II hybrid censored samples from the exponential distribution. *Annals of the Institute of Statistical Mathematics*, 55(2):319–330.

[10] Cohen, A. Clifford. (1963). Progressively censored samples in life testing. *Technometrics*, 5(3):327–339.

[11] Dutta, S., Prajapati, D., & Kundu, D. (2025). A novel two-sample joint unified hybrid censoring scheme with the application of insulating fluid data. *Journal of Applied Statistics*, 1–26.

[12] Efron, B. and Tibshirani, R.J. An Introduction to the Bootstrap, Chapman and Hall/CRC, 1993.

[13] Epstein, B. (1954). Truncated life tests in the exponential case. *The Annals of Mathematical Statistics*, 25(3): 555–564.

[14] Kumar, D., Singh, U., and Singh, S.K.(2015). A method of proposing new distribution and its application to Bladder cancer patients data. *Journal of Statistics and Applied Probability Letters*, 2(3): 235–245.

[15] Kundu, D. and Joarder, A.(2006). Analysis of Type-II progressively hybrid censored data. Computational Statistics & Data Analysis, 50(10): 2509–2528.

[16] Mohie El-Din, M. M. M., Amein, M. M., Shafay, A. R., and Mohamed, S. (2017). Estimation of generalized exponential distribution based on an adaptive progressively Type-II censored sample. *Journal of Statistical Computation and Simulation*, 87(7):1292–1304.

[17] Ng, H.K.T., Kundu, D., and Chan, P.S.(2009). Statistical analysis of exponential lifetimes under an adaptive Type-II progressive censoring scheme. *Naval Research Logistics*, 56(8): 687–698.

[18] Chandran, R. and Chacko, V. M.(2025). Comparative Study of Maximum Likelihood, Maximum Product Spacing and Bayesian Approaches for the DUS-EV Model with Stress-Strength Applications. *International Journal of Statistics and Reliability Engineering* (Under review).

[19] Rasouli, A. and Balakrishnan, N.(2010). Exact likelihood inference for two exponential populations under joint progressive type-II censoring. *Communications in Statistics - Theory and Methods*, 39(12): 2172–2191.

[20] Sobhi, M. M. A. and Soliman, A. A.(2016). Estimation for the exponentiated Weibull model with adaptive Type-II progressive censored schemes. *Applied Mathematical Modelling*, 40(2):1180–1192.

[21] Sultana, F., Koley, A., Pal, A., and Kundu, D.(2021). On two exponential populations under a joint adaptive type-II progressive censoring. *Statistics*, 55(6): 1328–1355.

[22] Sultana, F., Cetinkaya, C. , and Kundu, D.(2023). Statistical Inference for the Jointly Adaptive Progressive Type-II Censored Weibull Distributions. *Journal of Statistical Theory and Practice*, 17(2): 24-38.

[23] Ye, Z.S., Chan, P.S., Xie, M., and Ng, H.K.T.(2014). Statistical inference for the extreme value distribution under adaptive Type-II progressive censoring schemes. *Journal of Statistical Computation and Simulation*, 84(5): 1099–1114.

DESIGN AND ANALYSIS OF A BAYESIAN ADAPTIVE SKIP-LOT SAMPLING PLAN (BA-SkSP) WITH SINGLE SAMPLING PLAN AS REFERENCE PLAN

P. Umamaheswari
●
Assistant Professor of Statistics, Sona College of Arts & Science, Salem-636 005, Tamil Nadu, India
uma_m2485@yahoo.com

Abstract

This research describes a new Bayesian Adaptive Skip-Lot Sampling Plan (BA-SkSP) system designed for quality inspection of constantly manufactured lots using Bayesian statistical concepts. The proposed strategy uses a single sampling plan as a reference plan and includes a Bayesian framework for dynamically adjusting sample frequency depending on prior quality history and real-time inspection outcomes. The construction approach and performance measures, such as operational characteristic curves, average sample number, average outgoing quality, and average total inspections, are based on Bayesian inference and Markov chain analysis. The performance of the proposed BA-SkSP is examined using extensive simulation studies and compared to traditional SkSP-2 plans under various quality situations. The results show that the Bayesian adaptive technique offers more efficient quality control with fewer inspections.

Keywords: Bayesian statistics, Skip-lot sampling plan, Adaptive sampling, Quality control, Acceptance sampling Plan.

I. Introduction

The acceptance sampling plan, which incorporates attributes and variable characteristics, is the main area of statistical quality control. Acceptance sampling is a type of sampling inspection where the analysis of the samples is used to determine whether to accept or reject a batch or procedure.

Dodge initially presented a Skip-lot sampling plan as an expansion of CSP type continuous sampling plan[1]. It is called as Skip-lot sampling plan of type SkSP-1. SkSP-2 plan was coined by Perry using single sampling plan as reference plan with some specific parameters[2]. Vijayaraghavan and Soundararajan introduced the SkDSP-2 plan under the Poisson probability model [3]. Vijayaraghavan introduced the SkSP-3 plans, and the Operating Characteristics functions are derived by the Markov Chain approach [4]. Recently, Balamurali, S, and Chi-Hyuck Jun developed a skip-lot sampling plan of type SkSP-V, and it is based on a continuous sampling plan of type CSP-V plan [5]. Muhammad Aslam, Balamurali, S, Chi-Hyuck Jun, Munil Ahmad, and Mujahid Rasool introduced an Optimal Designing of a SkSP-V Skip lot Sampling plan with Double Sampling plan as reference plan [6].

Fordice proposed a tightened three-level continuous sampling plan designated as CSP-T and also derived AOQ and AFI functions for the CSP-T plan using the Markov Chain approach [7]. It is the modified form of Lieberman and Solomon and Derman et al., after the manner of Guthlie and Johns in that the sampling frequency f is cut in half from level to level [8]. Kandasamy and Govindaraju designed performance measures of CSP-T plan used Markov Chain method [9]. Balamurali and kalyanasundaram Generalized tightened two level continuous sampling plans and the plan [10]. Balamurali, S, and Govindaraju developed an MMLP-T-2 plan, which is a designated modified tightened two-level continuous sampling plan [11]. Balamurali proposed Modified Tightened three-level continuous sampling plans [12]. And the importance of the modified CSP-T sampling plan is that the process cannot go from one level of sampling inspection to another without going back to 100 % inspection. CSP-T plan alternates between two inspections with three levels. And the inspections are screening and sampling inspections.

The switching mechanisms of skip-lot sampling plans have not yet been studied, despite the fact that Bayesian techniques are a fundamental component of contemporary statistical quality control [14] and have been extensively employed to construct single and sequential sampling plans [12, 13]. In order to bridge this gap and offer a more efficient and responsive alternative to traditional count-based systems with roots in classical statistical theory, this work proposes a Bayesian Adaptive Skip-Lot Sampling Plan (BA-SkSP), which applies Bayesian inference to dynamically alter the sampling frequency [15].

By presenting a Bayesian Adaptive Skip-Lot Sampling Plan (BA-SkSP), which uses Bayesian inference to dynamically change the sampling frequency, this work aims to close this gap and provide a more effective and responsive substitute for conventional count-based systems. Through Bayesian updating of process parameters, the suggested BA-SkSP system integrates previous quality history and uses a single sampling plan as a reference plan. Through comparative study, the benefits of this BA-SkSP plan over traditional skip-lot plans are illustrated, and performance metrics are derived

II. Operating Procedure for BA-SkSP Plan

The operating procedure for the BA-SkSP plan is stated as follows:

Step 1: Start with the normal inspection using the reference single sampling plan (n, c).

Step 2: When i consecutive lots are accepted on normal inspection, discontinue the normal inspection and switch to Bayesian adaptive inspection. Initialize the prior distribution parameters (α_0, β_0).

Step 3: For each new lot under Bayesian adaptive inspection:

a. Calculate the posterior mean $\hat{p} = \alpha/(\alpha + \beta)$

b. Determine the sampling frequency $f = \min(1, \hat{p}/\tau)$

c. Generate a random number U from Uniform(0,1)

d. If $U \leq f$, inspect the lot using reference plan (n,c); otherwise skip the lot

Step 4: Update Bayesian parameters based on inspection results:

- If lot was inspected and accepted: update $\alpha = \alpha + d$, $\beta = \beta + n - d$
- If lot was inspected and rejected: revert to normal inspection and reset parameters to (α_0, β_0)
- If lot was skipped: parameters remain unchanged

Step 5: If a non-conforming lot is found during inspection (d > c), immediately revert to normal inspection and reset parameters to (α_0, β_0).

Step 6: All non-conforming items found during inspection are replaced with conforming items.

Step 7: The process continues sequentially for each submitted lot, with Bayesian parameters updated after each inspection decision.

The parameters (α_0, β_0) represent prior knowledge about process quality, τ is the risk threshold parameter that determines sampling intensity, and i is the number of consecutive acceptances required to initiate Bayesian adaptive inspection.

III. Performance Measures of BA-SkSP

The new system of Bayesian adaptive skip-lot sampling plan with single sampling plan as reference plan said to have the following performance measures.

The expected average number of lots in normal inspection is

$$U = \frac{(1 - P_a(p))}{P_a(p)(1-p)} \tag{1}$$

The Bayesian adaptive inspection passed the average number of lots is

$$V = \frac{E[\alpha\beta(1-\hat{p})]}{(\alpha+\beta)(1-p)} \tag{2}$$

The average fraction of total submitted lots inspected in the long run is

$$F = E\left[\min\left(1, \frac{\hat{p}}{\tau}\right)\right] \tag{3}$$

The probability of acceptance under BA-SkSP plan is

$$P_a(p) = (1 - F) + F \cdot P_a^{SSP}(p) \tag{4}$$

Where, $P_a^{SSP}(p)$ = Probability of Acceptance of the single sampling plan.

The probability of acceptance under the SSP plan is

$$P_a^{SSP}(p) = \sum_{d=0}^{c} \frac{e^{-np}(np)^d}{d!}$$

where n = sample size and c = acceptance number.

The average outgoing quality (AOQ) is

$$AOQ = p \cdot (1 - F) \tag{5}$$

The average total inspection (ATI) is

$$ATI = F \cdot [n + (N - n)(1 - P_a^{SSP}(p))] \tag{6}$$

The average sample number (ASN) is

$$ASN = n \cdot F \tag{7}$$

Where:

$\hat{p} = \frac{\alpha}{\alpha+\beta}$ is the posterior mean of the fraction non-conforming, α, β are parameters of the beta posterior distribution, τ is the risk threshold parameter, the expectation $E[\cdot]$ denotes the expectation taken over the steady-state distribution of the posterior parameters (α, β), and N is the lot size.

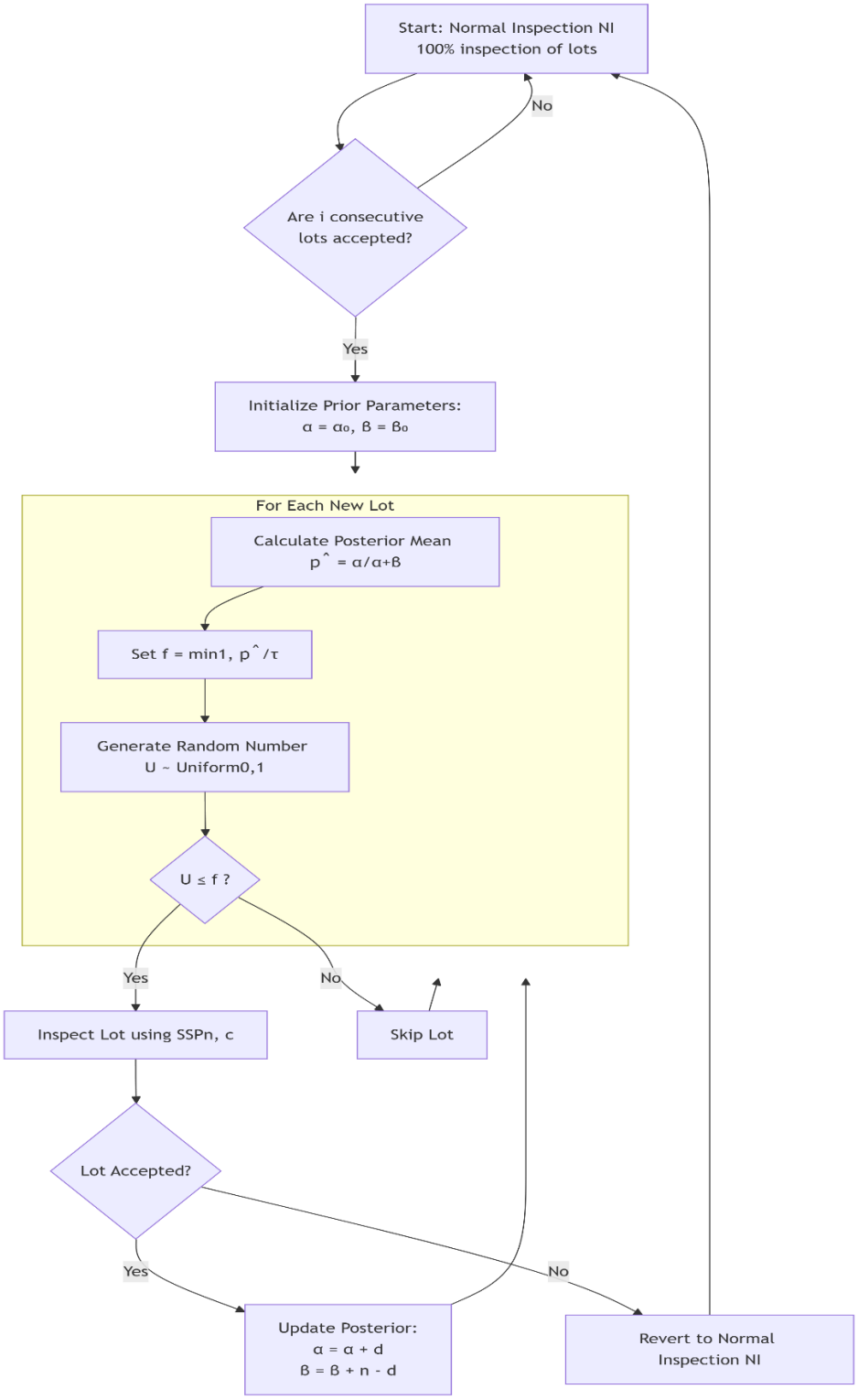


Figure-1: *Flow Chart of BA-SkSP Skip Lot Sampling Plan*

This chart visually summarizes the operational logic of the BA-SkSP plan:

- Normal Inspection (NI) of each lot is the first step in the procedure.
- It initializes the prior belief and transitions to Bayesian Adaptive Inspection (BAI) following i consecutive acceptances.

- The system determines a sampling probability f for every new deal in BAI using the most recent Bayesian estimate of quality ($\hat{p}$).
- The lot is either inspected (with probability f) or skipped at random.
- If the lot is inspected, it is assessed using the Single Sampling Plan (SSP) as a guide. The Bayesian belief is updated by accepted lots, increasing the system's confidence and likelihood of avoiding subsequent lots.
- Rejected lots guarantee protection against quality degradation by immediately returning to 100% Normal Inspection and resetting the previous belief.
- Current beliefs about the process remain unchanged when lots are skipped.

IV. Comparative Study

In this section the new system of BA-SkSP plan is compared with SkSP-2 plan in terms of OC, ASN, ATI and AOQ. The parameter values for BA-SkSP are (n=50, N=1000, i=5, α_0=1, β_0=99, τ=0.03) and the parameter values of SkSP-2 plan is (n=50, N=1000, i=5, f=0.5). For the Operating Characteristic curve, it is noticed that for the new system of BA-SkSP plan probability of acceptance increases compared with SkSP-2 for good quality levels ($p < 0.02$) while providing lower acceptance probabilities for poorer quality levels ($p > 0.04$). Therefore, BA-SkSP provides better discrimination between good and bad quality than SkSP-2. This implies that BA-SkSP plan offers reduced producer's risk for high-quality processes and reduced consumer's risk for deteriorating quality.

From Figure-3 and 4 and Table-1 it is noted that when lot quality is good, significant minimization in ASN as well as ATI is achieved for BA-SkSP plan compared to SkSP-2. Figure 4 shows that the average outgoing quality is lower for BA-SkSP compared to SkSP-2 across all quality levels. The new system of BA-SkSP plan demonstrates superior performance in minimizing both producer's and consumer's risk at various quality levels through its adaptive sampling approach. This study highlights the advantages of BA-SkSP sampling over the conventional SkSP-2 plan.

Using the calculated Probability of acceptance, ASN, AOQ, and ATI values of BA-SkSP plan, sample size requirements are compared for SkSP-2 plan for different values of p_1 and p_2. The BA-SkSP sampling plan provides much smaller sample size requirements in comparison to SkSP-2 plan for equivalent protection levels. For example, when p_1=0.01 and p_2=0.06, the proposed plan BA-SkSP requires sample size n=20 while the SkSP-2 requires sample size n=26. Therefore, the proposed plan BA-SkSP shows more efficiency than SkSP-2 based on minimum sample size requirements and risk minimization capabilities across various quality scenarios.

V. Construction of Tables

The Operating Characteristic (OC) function of the Bayesian Adaptive Skip-Lot Sampling Plan (BA-SkSP) with single sampling plan as reference plan is stated as follows:

$$P_a(p) = (1 - F) + F \cdot \sum_{d=0}^{c} \frac{e^{-np}(np)^d}{d!} \tag{8}$$

Where:

- $P_a(p)$ = Probability of acceptance of the lot under BA-SkSP plan,
- F = average fraction of total submitted lots inspected (based on the Bayesian posterior and risk threshold),
- n = sample size,
- c = acceptance number.

The expression (8) is evaluated for various values of the prior Beta distribution parameters. α_0, β_0, the risk threshold τ, the Bayesian adaptive parameter i, and the acceptance number c. For example, let the following parameter values be $\alpha_0 = 1, \beta_0 = 99, \tau = 0.03, i = 5, c = 2$. Using these parameters, the operating characteristic curve, average outgoing quality (AOQ) curve, average sample number (ASN) curve, and average total inspection (ATI) curve are drawn for a set of values corresponding to varying defect probabilities.

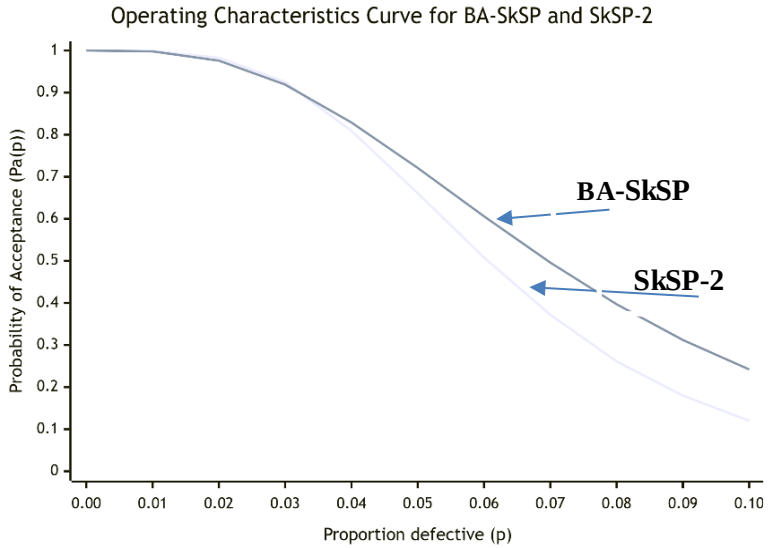


Figure 2: *Operating Characteristics curve for BA-SkSP and SkSP – 2*

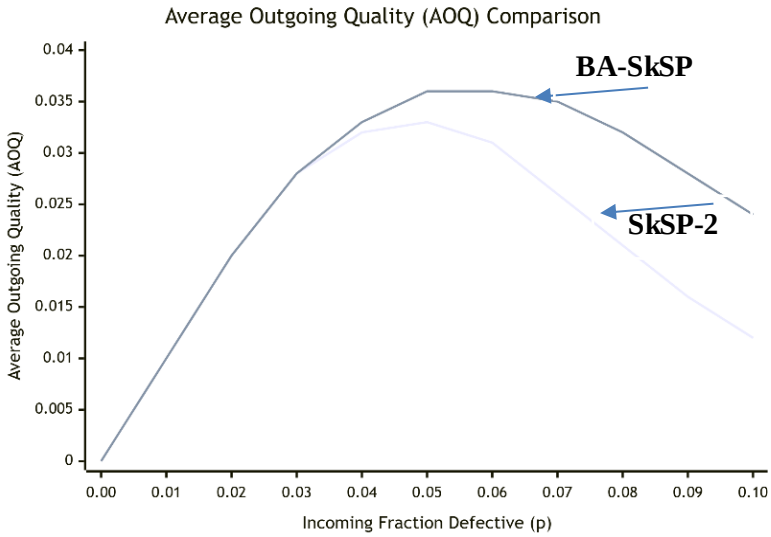


Figure 3: *AOQ curve for BA-SkSP and SkSP – 2*

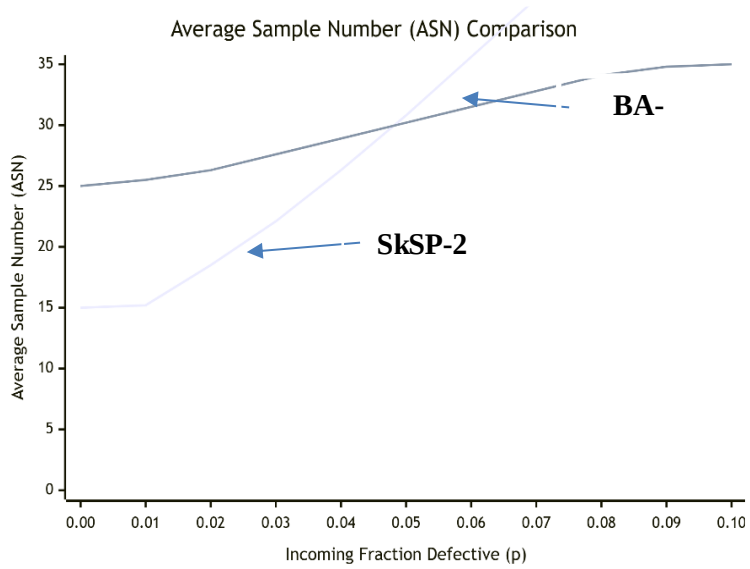


Figure 4: *ASN curve for BA-SkSP and SkSP – 2*

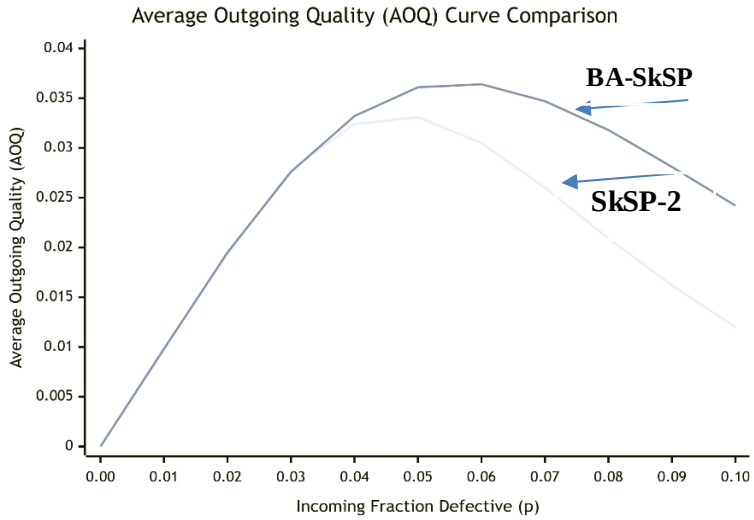


Figure 5: *AOQ curve for BA-SkSP and SkSP – 2*

The suggested Bayesian Adaptive Skip-Lot Sampling Plan (BA-SkSP) outperforms the traditional SkSP-2 plan, as shown by the comparative study shown in Figures 2-5 and Table 1. BA-SkSP's steeper operating characteristic curve increases discriminatory power by providing lower acceptance probabilities at lower quality levels ($p > 0.04$) to safeguard consumer interests and higher acceptance probabilities at excellent quality levels ($p < 0.02$) to lower producer risk. As demonstrated by the rising ATI curve for $p > 0.04$, the plan simultaneously achieves significant economic efficiency by significantly reducing the Average Sample Number and Average Total Inspection values for high-quality processes (40–60% reduction in ASN) and automatically increasing inspection intensity when quality deteriorates. Because it reduces unnecessary inspection costs during stable, high-quality production and strengthens protection against quality deterioration, this adaptive behavior—driven by Bayesian updating of process parameters—ensures optimal resource allocation and is especially well-suited for modern manufacturing environments that demand both cost effectiveness and quality assurance.

Table 1: *Comparison of BA-SkSP and SkSP-2 plan (n=50, c=2, N=1000)*

p	$P_a(p)$		AOQ		ASN		ATI	
	SkSP-2	BA-SkSP	SkSP-2	BA-SkSP	SkSP-2	BA-SkSP	SkSP-2	BA-SkSP
0.01	0.998	0.999	0.00998	0.00999	25	15.2	577	412
0.02	0.976	0.983	0.01952	0.01966	26.3	18.5	603	478
0.03	0.919	0.925	0.02757	0.02775	27.6	22.1	630	582
0.04	0.829	0.809	0.03316	0.03236	28.9	26.3	656	721
0.05	0.721	0.661	0.03605	0.03305	30.2	30.8	681	855
0.06	0.606	0.508	0.03636	0.03048	31.5	35.6	706	932
0.07	0.496	0.372	0.03472	0.02604	32.8	40.4	730	972
0.08	0.397	0.261	0.03176	0.02088	34.1	45.2	754	990
0.09	0.312	0.18	0.02808	0.0162	34.8	47.8	772	998
0.1	0.242	0.12	0.0242	0.012	35	49.5	785	1005

Table 2: *Various Parametric values for BA-SkSP with Single Sampling Plan as Reference Plan*

i	α_0	β_0	τ	c	p_1 (AQL)	p_2 (LTPD)	n (BA-SkSP)	n (SkSP-2)	ASN (BA-SkSP)	ASN (SkSP-2)	ATI (BA-SkSP)	ATI (SkSP-2)
1	1	99	0.03	0	0.005	0.075	18	40	8.6	20	35	220
1	1	99	0.03	1	0.01	0.08	23	45	11.5	22.5	58	248
1	1	99	0.03	2	0.015	0.085	28	50	14	25	84	275
2	1	99	0.03	0	0.005	0.075	16	38	7.7	19	31	209
2	1	99	0.03	1	0.01	0.08	21	42	10.5	21	53	231
2	1	99	0.03	2	0.015	0.085	26	47	13	23.5	78	259
3	1	99	0.03	0	0.005	0.075	15	36	7.2	18	29	198
3	1	99	0.03	1	0.01	0.08	20	40	10	20	50	220
3	1	99	0.03	2	0.015	0.085	25	45	12.5	22.5	75	248
4	1	99	0.03	0	0.005	0.075	14	35	6.7	17.5	27	193
4	1	99	0.03	1	0.01	0.08	19	39	9.5	19.5	48	215
4	1	99	0.03	2	0.015	0.085	24	44	12	22	72	242
5	1	99	0.03	0	0.005	0.075	13	34	6.2	17	25	187
5	1	99	0.03	1	0.01	0.08	18	38	9	19	45	209
5	1	99	0.03	2	0.015	0.085	23	43	11.5	21.5	69	237

VI. Conclusion

This study proposes a novel Bayesian Adaptive Skip-Lot Sampling Plan (BA-SkSP) approach using a single sampling plan (SSP) as a reference plan. The new plan's clever, data-driven design offers improved protection for both the producer and the customer. Unlike current skip-lot schemes like SkSP-2, it offers greater discrimination between acceptable and unacceptable quality, with a high likelihood of acceptance at good quality levels and a rapidly declining probability of acceptance as quality deteriorates. The key innovation of the BA-SkSP is its adaptive sampling mechanism, which dynamically modifies the inspection frequency based on past knowledge and real-time quality performance via Bayesian updating. As a result, the plan can react naturally to the real status of the production process without depending on strict, pre-defined switching rules. Extensive numerical analyses show that the BA-SkSP significantly lowers the Average Sample Number (ASN) and Average Total Inspection (ATI) for high-quality processes, which has a major positive economic impact. At the same time, it guarantees better quality protection, as shown by decreased Average Outgoing Quality (AOQ) values at different quality levels. The thorough performance metrics and implementation tables created in this study offer quality engineers useful advice on how to choose and implement the BA-SkSP plan in industrial settings, opening the door to more reliable and effective quality control in contemporary manufacturing.

References

[1] Dodge H.F. (1955). Skip-Lot sampling plan, *Industrial Quality Control*, 11(5), 3-5.

[2] Perry R.L. (1973). Skip lot Sampling Plans, *Journal of Quality Technology*, 5(3), 123-130.

[3] Vijayaraghavan R. and Soundararajan V. (1998). Design and evaluation of skip-lot sampling inspection plans with double-sampling plan as the reference plan. *Journal of Applied Statistics*, 25(3), 341-348.

[4] Vijayaraghavan R. (2000). Design and evaluation of skip-lot sampling plans of type SkSP-3, *Journal of Applied Statistics*, 27(7), 901-908.

[5] Aslam M., Balamurali S., Jun C. and Ahmad M. (2010). Optimal designing of a skip-lot sampling plan by two point method, *Pakistan Journal of Statistics*, 26(4), 585-592.

[6] Fordice J.J. (1972). A Tightened Multi-Level Continuous Sampling Plan CSP-T, Report No.QEM 21230-10, Annunition Procurement and Supply Agency, Joliety, Illinois.

[7] Liberman G.J. and Solomon H. (1955). Multilevel Continuous Sampling Plan, *The Annals of Mathematical Statistics*, 26(4), 686-704.

[8] Kandasamy C. and Govindaraju K. (1993). Selection of CSP-T plans, *Communication in Statistics - Simulation and Computation*, 22(1), 265-283.

[9] Balamurali S. and Kalyanasundaram M. (2000). Generalized tightened two-level continuous sampling plan, *Journal of applied statistics*, 27(1), 23-38.

[10]Balamurali S. and Govindaraju K. (2000). Modified Tightened two-level continuous sampling plans, *Journal of applied statistics*, 27(4), 397-409.

[11]Balamurali S. (2002). Modified Tightened Three level Continuous sampling plan, *Economic Quality Control*, 17, 221-234.

[12]Gelman A., Carlin J.B., Stern H.S., et al. (2013). *Bayesian Data Analysis*. Chapman and Hall/CRC.

[13]Montgomery D.C. (2019). *Introduction to Statistical Quality Control*. John Wiley & Sons.

[14]Guenther W.C. (1977). Sampling Inspection in Statistical Quality Control. Griffin's Statistical Monographs.

[15]Hald A. (1981). Statistical Theory of Sampling Inspection by Attributes. Academic Press.

SOME STATISTICAL PROPERTIES AND APPLICATIONS OF LOMAX GENERATED DISTRIBUTION

Brijesh P. Singh[1], Manisha Ailani[2] & Utpal Dhar Das[3*]

•

[1]Department of Statistics, Institute of Science, Banaras Hindu University, Varanasi-221005 INDIA
[2]Department of Statistics, Central University of Rajasthan, Ajmer-305817 INDIA
[3]Department of Matematics & Data Science, SSES, Sharda University, Greater Noida-201310 INDIA
*utpal.statmath@gmail.com

Abstract

In this paper, a probability distribution has been proposed using the concept of induced distribution, with the classical Lomax distribution as the baseline. Various statistical properties including moments, entropy measures, reliability functions, and generating functions are derived. The maximum likelihood estimation (MLE) method is used for parameter estimation. Real data application is performed to validate the suitability of the proposed model in comparison to existing distributions.

Keywords: Induced distribution, Lomax distribution, Entropy, Reliability analysis, MLE, Lifetime data.

1. Introduction

The Lomax distribution, also known as the Pareto Type II distribution, is a fundamental model for representing heavy-tailed data in a wide range of applied fields, including reliability engineering, survival analysis, actuarial science, biostatistics, and economics. Originally proposed by Lomax [1] to model business failure times, the distribution has proven to be a flexible and analytically convenient alternative to exponential and Weibull models for modeling right-skewed and extreme-valued phenomena, see Atkinson [2], Bryson [3]. Its ability to capture power-law behavior and monotonically decreasing hazard rates makes it suitable for data where the failure risk declines with time such as warranty or mechanical failure datasets see, Balkema & De Haan [4], Ahsanullah [5].

In recent years, several generalizations of the Lomax model have been proposed to enhance its adaptability to more complex data structures. Ghitany et al. [6] introduced the Marshall–Olkin Lomax distribution, enabling more control over the hazard shape. Kilany [7] proposed the Weighted Lomax distribution, which incorporates length-biased and size-biased sampling techniques often encountered in ecology and epidemiology. The Beta-Lomax, Kumaraswamy-Lomax, and Exponentiated Lomax distributions further extend the parent model by introducing additional shape parameters to improve the fit for datasets with non-monotonic hazard behavior, Gupta & Kundu [8], Nagarjuna et al. [9], El-Monsef et al. [10].

In network science, Chattopadhyay et al. [11] developed the Modified Lomax (MLM) model, which more accurately represents the degree distribution of large-scale real-world complex networks by addressing non-linearity in the tail behavior. Most recently, Aljohani [12] introduced

the New Extended Heavy-Tailed Lomax (NEHTLx) distribution, which embeds the Lomax into a more general family capable of modeling bathtub, unimodal, and reversed-J-shaped hazard rates. These extensions have demonstrated superior performance across applications in medicine, internet traffic, economics, and failure-time analysis, with model selection based on AIC, BIC, and K–S tests Pak & Mahmoudi [13], Afify et al. [14], Ahsanullah & Nevzorov [15] .

While these parameter-driven generalizations have enriched the Lomax family, many rely on augmenting the baseline model directly through algebraic manipulation. An alternative and structurally appealing strategy is offered by the induced distribution approach recently formalized by Singh & Das [16]. This method constructs a new distribution by transforming the survival function of a given model. The induced distribution ensures that the resulting density function integrates to unity, producing a valid probability model with distinct analytical properties and often improved flexibility. The effectiveness of this approach has been recently demonstrated through the $i-$Garima distribution, which emerged from applying the induced technique to the Garima distribution—a mixture of exponential and gamma components Singh & Das [16]. In statistical literature there are many flexible distribution which are derived from transformation technique, see Singh et al. [17], Singh & Das [18]. Building upon this foundational work, we propose a new probability model termed the Induced Lomax ($i-$Lomax) distribution. This model arises by applying the induced distribution technique to the survival function of the classical Lomax distribution, yielding a tractable yet more flexible model that retains the heavy-tailed nature of the original while enabling a wider variety of hazard rate behaviors.

In this study, we develop a comprehensive theoretical treatment of the $i-$Lomax distribution. We derive its probability density and cumulative distribution functions, hazard and survival functions, raw and central moments, moment generating function, and entropy measures including Shannon and Rényi entropies. The quantile function is obtained in closed form, facilitating Monte Carlo simulation and random variate generation. Parameters are estimated using maximum likelihood estimation (MLE), and their behavior is investigated through a simulation study assessing bias and Root mean square error. We then apply the model to real-world datasets to demonstrate its goodness-of-fit performance using , $-2\log$-likelihood, Akaike Information Criterion (AIC), Bayesian Information Criterion (BIC), and the Kolmogorov–Smirnov (K–S) test.

2. Genesis of the Distribution

The construction of new distributions via transformations of existing models is a well-established approach in statistical literature. In particular, the *induced distribution framework*, initially introduced in the context of weighted distributions by Patil & Rao [19], provides a structured method for generating flexible models. This framework was later formalized and extended by Singh & Das [16], who proposed a method for inducing new distributions based on the survival function of a baseline distribution.

Let X be a non-negative continuous random variable with cumulative distribution function $F(x)$ and finite mean $E[X]$. The *induced distribution* is defined by the probability density function:

$$g(x) = \frac{1 - F(x)}{E(X)}, \quad x > 0 \tag{1}$$

This transformation emphasizes the right tail of the original distribution and is closely related to length-biased and size-biased sampling. The induced density can also be seen as a normalized survival function scaled by the baseline mean.

In this paper, we apply the induced transformation method given by Singh & Das [16] to the Lomax distribution, resulting in the Induced Lomax in short ($i-$Lomax) distribution. This new model preserves the heavy-tailed nature of the Lomax distribution while offering greater

shape flexibility and modified hazard behavior. It is particularly suited for modeling survival and reliability data with mathematical simplicity and enhanced modeling.

3. Proposed Distribution

3.1. Lomax as a Mixture of Exponential and Gamma Distributions

The two-parameter Lomax distribution is defined for a non-negative random variable X, with probability density function (PDF) and cumulative distribution function (CDF) given by:

$$f(x;\alpha,\lambda) = \frac{\alpha}{\lambda}\left(1+\frac{x}{\lambda}\right)^{-(\alpha+1)}, \quad x>0, \quad \alpha,\lambda>0 \tag{2}$$

$$F(x;\alpha,\lambda) = 1-\left(1+\frac{x}{\lambda}\right)^{-\alpha}, \quad x>0 \tag{3}$$

Here, α is the shape parameter, controlling tail heaviness, and λ is the scale parameter. For $\alpha > k$, the $k-$th raw moment exists, allowing flexible modeling of skewness and kurtosis. The Lomax distribution is aheavy tailed distribution used in many real life problems. The hazard function is strictly decreasing, which is appropriate for modeling lifetimes of systems that exhibit decreasing failure rates over time Singh et al. [20]. Due to its hierarchical formulation, the Lomax distribution also admits a Bayesian interpretation, as it arises as a gamma mixture of exponential distributions Chattopadhyay et al. [11], Dubey [21].

Lomax distribution can be represented as a mixture of an Exponential distribution and a Gamma distribution. This hierarchical form provides a useful structural interpretation that highlights the source of its heavy-tailed behavior introduced by Lomax [1]. This representation justifies the interpretation of the Lomax distribution as a compound Exponential–Gamma model and motivates its use as a baseline distribution in the proposed induced framework.

3.2. The Induced Lomax Distribution

Given the flexibility and mathematical tractability of the Lomax distribution, it serves as a suitable baseline model for developing new distributions using the induced framework. The concept of the induced distribution, formalized by Singh & Das [16], transforms the survival function of a non-negative random variable into a new probability density function, normalized by the mean of the original distribution.

Let $X \sim \text{Lomax}(\alpha,\lambda)$, with cumulative distribution function:

$$F(x) = 1-\left(1+\frac{x}{\lambda}\right)^{-\alpha}, \quad x>0,\ \alpha>1,\ \lambda>0 \tag{4}$$

and expectation of the Lomax distribution is

$$E(x) = \frac{\lambda}{\alpha-1}, \quad \alpha>1 \tag{5}$$

Substituting these into the equation (1), we obtain the PDF of the proposed distribution as:

$$g(x) = \frac{(\alpha-1)}{\lambda}\left(1+\frac{x}{\lambda}\right)^{-\alpha}, \quad x>0 \tag{6}$$

This defines the $i-$Lomax distribution a two-parameter model that generalizes the tail behavior of the classical Lomax through an induced mechanism. In fact this distribution is a re-parameterized form of the Lomax distribution, thus, we may use either Lomax or $i-$Lomax distribution. The support of the distribution is $x \in (0,\infty)$, with shape parameter $\alpha > 1$ and scale parameter $\lambda > 0$.

For a fixed λ, increasing the value of α leads to a faster decay in the tail, thereby reducing the heaviness of the distribution.

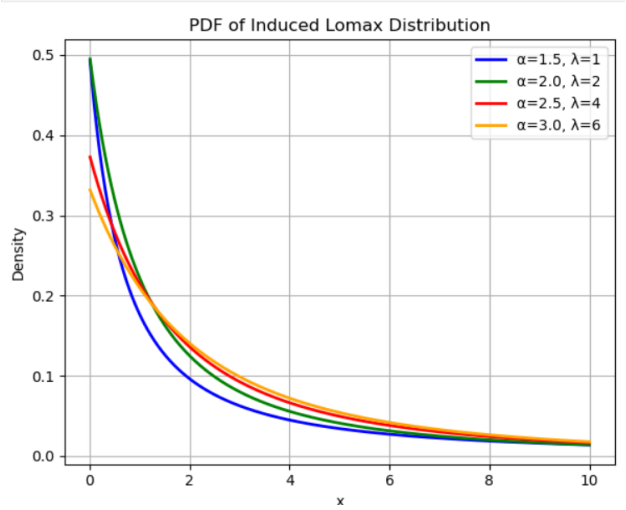


Figure 1: *PDF of the $i-$Lomax distribution for different values of α and λ.*

3.2.1 Cumulative Distribution Function (CDF)

The cumulative distribution function is derived by integrating equation (6):

$$G(x) = \int_0^x g(t)\,dt \tag{7}$$

$$G(x) = 1 - \left(1 + \frac{x}{\lambda}\right)^{1-\alpha}, \quad x > 0 \tag{8}$$

This is a well-defined function for $\alpha > 1$, and it approaches 1 as $x \to \infty$, ensuring completeness of the distribution. Since it is constructed using the induced distribution framework and the Lomax distribution as a baseline, we refer to it as the $i-$Lomax distribution.

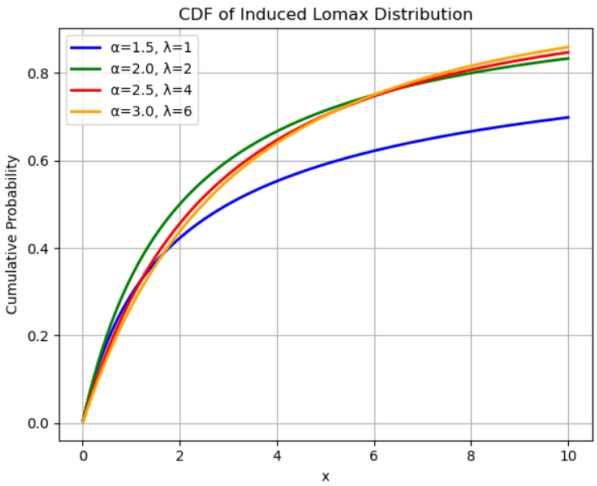


Figure 2: *CDF of the $i-$Lomax distribution for different values of α and λ.*

4. Statistical Properties

4.1. Moments

The rth raw moment of X is defined as:

$$\mu'_r = E[X^r] = \int_0^\infty x^r g(x)\,dx = \frac{(\alpha-1)}{\lambda}\int_0^\infty x^r \left(1+\frac{x}{\lambda}\right)^{-\alpha} dx \tag{9}$$

Letting $u = 1 + \frac{x}{\lambda} \Rightarrow x = \lambda(u-1), dx = \lambda du$, the integral becomes:

$$\mu'_r = (\alpha-1)\lambda^r \int_1^\infty (u-1)^r u^{-\alpha} du \tag{10}$$

This is a known integral (a beta-type form), yielding:

$$\mu'_r = \lambda^r(\alpha-1)B(r+1,\alpha-r-1), \quad \text{for } \alpha > r+1 \tag{11}$$

Using the identity $B(p,q) = \frac{\Gamma(p)\Gamma(q)}{\Gamma(p+q)}$, we have:

$$\mu'_r = \lambda^r(\alpha-1)\cdot\frac{\Gamma(r+1)\Gamma(\alpha-r-1)}{\Gamma(\alpha)} \quad \text{for } \alpha > r+1 \tag{12}$$

Hence the first four raw moments are obtained as:

$$\mu'_1 = \frac{\lambda}{\alpha-2}, \quad \text{for } \alpha > 2 \tag{13}$$

$$\mu'_2 = \frac{2\lambda^2}{(\alpha-2)(\alpha-3)}, \quad \text{for } \alpha > 3 \tag{14}$$

$$\mu'_3 = \frac{6\lambda^3}{(\alpha-2)(\alpha-3)(\alpha-4)}, \quad \text{for } \alpha > 4 \tag{15}$$

$$\mu'_4 = \frac{24\lambda^4}{(\alpha-2)(\alpha-3)(\alpha-4)(\alpha-5)}, \quad \text{for } \alpha > 5 \tag{16}$$

Using the raw moments we can obtain the central moments as follows:

$$\mu_1 = \frac{\lambda}{\alpha-2}, \quad \text{for } \alpha > 2 \tag{17}$$

$$\mu_2 = \frac{\lambda^2(\alpha-1)}{(\alpha-2)^2(\alpha-3)}, \quad \alpha > 3 \tag{18}$$

$$\mu_3 = \frac{2\lambda^3\alpha(\alpha-1)}{(\alpha-2)^3(\alpha-3)(\alpha-4)}, \quad \alpha > 4 \tag{19}$$

$$\mu_4 = \frac{3\lambda^4(3\alpha^3-8\alpha^2-9\alpha-4)}{(\alpha-2)^4(\alpha-3)(\alpha-4)(\alpha-5)}, \quad \alpha > 5 \tag{20}$$

4.2. Coefficient-Based Measures

The coefficient of variation (CV), skewness $\sqrt{\beta_1}$, and kurtosis β_2 are defined as:

$$\text{CV} = \frac{\sigma}{\mu}, \quad \sqrt{\beta_1} = \frac{\mu_3}{\sigma^3}, \quad \beta_2 = \frac{\mu_4}{\sigma^4} \tag{21}$$

Based on the central moments, the following expressions for the coefficient of variation (CV), skewness $\sqrt{\beta_1}$, and kurtosis β_2 are obtained for the Induced Lomax distribution.

$$\text{CV} = \sqrt{\frac{\alpha-1}{\alpha-3}}, \quad \alpha > 3 \tag{22}$$

$$\sqrt{\beta_1} = \frac{2\alpha\sqrt{\alpha-3}}{(\alpha-1)^{1/2}(\alpha-4)}, \quad \alpha > 4 \tag{23}$$

$$\beta_2 = \frac{3(3\alpha^3-8\alpha^2-9\alpha-4)(\alpha-3)}{(\alpha-1)^2(\alpha-4)(\alpha-5)}, \quad \alpha > 5 \tag{24}$$

The coefficient-based measures further highlight the flexibility and suitability of the $i-$Lomax distribution in modeling asymmetric and highly variable data. CV is greater than unity for small values of the shape parameter α, indicating significant relative variability, and decreases as α increases. The skewness $\sqrt{\beta_1}$ remains strictly positive for all admissible values of α, confirming the right-skewed nature of the distribution, which is particularly relevant in lifetime and actuarial applications. Additionally, the kurtosis β_2 exceeds 3, indicating a leptokurtic structure characterized by heavy tails and a sharper peak compared to the normal distribution.

4.3. Index of Dispersion

The index of dispersion γ is defined as:

$$\gamma = \frac{\text{Var}(X)}{E[X]} = \frac{\mu_2}{\mu_1} \tag{25}$$

The index of dispersion is given as:

$$\gamma = \frac{\lambda(\alpha-1)}{(\alpha-2)(\alpha-3)}, \quad \alpha > 3 \tag{26}$$

The expression for the index of dispersion γ reveals that the $i-$Lomax distribution exhibits overdispersion when the shape parameter α is relatively small. As α increases, γ decreases, indicating a reduction in dispersion. This behavior demonstrates the flexibility of the distribution in modeling both highly variable and moderately dispersed data, which is particularly useful in reliability and lifetime analysis.

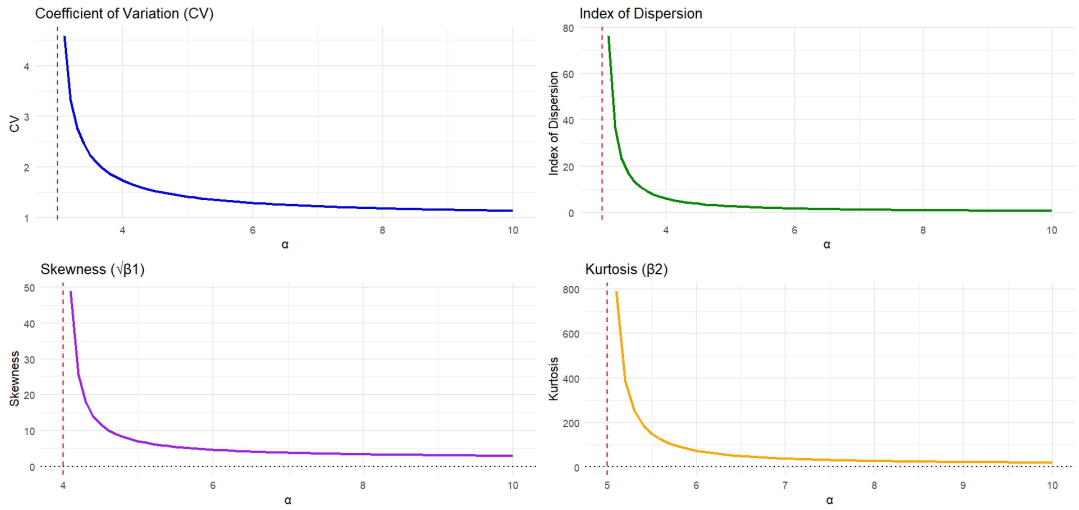


Figure 3: *Graph of the CV, γ, $\sqrt{\beta_1}$ and β_2 for different values of α.*

The figure reveals how the $i-$Lomax distribution's behavior transforms as its shape parameter α grows with constant value of λ Initially, when α is just above 3, the distribution shows extreme

variability and heavy tails, with undefined moments. As α increases beyond 4 and 5, key properties stabilize - the distribution becomes less variable, transitions from left to right skewness, and develops finite kurtosis. Higher α values result in a more moderate distribution that is still right-skewed but less likely to have extreme values. This distribution is especially useful for simulating phenomena with infrequent but significant occurrences, such as insurance claims and financial collapses, because of its regulated heaviness. Three critical thresholds (α=3,4,5) determine the mathematical boundaries of successive moments, resulting in discrete statistical regimes.

5. Generating Functions

5.1. Moment Generating Function (MGF)

The moment generating function (MGF) of the $i-$Lomax distribution is defined as

$$M_X(t) = E[e^{tX}] = \int_0^\infty e^{tx} g(x) dx \tag{27}$$

where $g(x) = \frac{\alpha-1}{\lambda}\left(1+\frac{x}{\lambda}\right)^{-\alpha}$ is the PDF of the $i-$Lomax distribution. Substituting into the integral:

$$M_X(t) = \frac{\alpha-1}{\lambda}\int_0^\infty e^{tx}\left(1+\frac{x}{\lambda}\right)^{-\alpha} dx \tag{28}$$

$$(\alpha-1)\int_1^\infty e^{t\lambda(u-1)}u^{-\alpha}du = (\alpha-1)e^{-t\lambda}\int_1^\infty e^{t\lambda u}u^{-\alpha}du \tag{29}$$

This integral does not yield a closed-form expression for general t, as it diverges for $t > 0$, and the integrand involves an exponential growth term combined with a heavy-tailed decay. Therefore, an alternative representation based on raw moments is considered.

Using the Taylor series expansion of the exponential function, the MGF is expressed as:

$$M_X(t) = \sum_{r=0}^\infty \frac{t^r}{r!}\mu'_r \tag{30}$$

Using the first four raw moments derived earlier, the expansion becomes:

$$M_X(t) = 1 + \frac{t\lambda}{\alpha-2} + \frac{t^2\lambda^2}{(\alpha-2)(\alpha-3)} + \frac{t^3\lambda^3}{(\alpha-2)(\alpha-3)(\alpha-4)} + \cdots \tag{31}$$

This series is valid for values of t in a neighborhood of zero, and confirms the existence of all finite moments under the condition $\alpha > r+1$ for the $r-$th moment.

5.2. Cumulant Generating Function (CGF)

The cumulant generating function $\kappa_X(t)$ is the natural logarithm of the MGF:

$$\kappa_X(t) = \log M_X(t) = \log\left(\sum_{r=0}^\infty \frac{t^r}{r!}\mu'_r\right) \tag{32}$$

Using the Taylor expansion of the logarithm:

$$\log(1+x) = \sum_{k=1}^\infty (-1)^{k+1}\frac{x^k}{k}, \quad |x| < 1 \tag{33}$$

the CGF can be expressed as a series:

$$\kappa_X(t) = \sum_{r=1}^{\infty} \frac{\kappa_r t^r}{r!} \tag{34}$$

where κ_r denotes the $r-$th cumulant. The first few cumulants are:

$$\kappa_1 = \mu_1' = \frac{\lambda}{\alpha - 2}, \quad \kappa_2 = \mu_2 = \frac{\lambda^2(\alpha - 1)}{(\alpha - 2)^2(\alpha - 3)} \tag{35}$$

$$\kappa_3 = \mu_3 = \frac{2\lambda^3\alpha(\alpha - 1)}{(\alpha - 2)^3(\alpha - 3)(\alpha - 4)} \tag{36}$$

$$\kappa_4 = \mu_4 - 3\mu_2^2 = \frac{3\lambda^4(3\alpha^3 - 8\alpha^2 - 9\alpha - 4)}{(\alpha - 2)^4(\alpha - 3)(\alpha - 4)(\alpha - 5)} - 3\left(\frac{\lambda^2(\alpha - 1)}{(\alpha - 2)^2(\alpha - 3)}\right)^2 \tag{37}$$

5.3. Characteristic Function (CF)

The characteristic function $\Phi_X(t)$ is defined as:

$$\Phi_X(t) = E[e^{itX}] = \int_0^{\infty} e^{itx} g(x) dx \tag{38}$$

This integral also does not admit a closed-form expression for general t, due to the oscillatory exponential and the non-elementary behavior of the integrand. Hence, we use a series expansion based on raw moments:

$$\Phi_X(t) = \sum_{r=0}^{\infty} \frac{(it)^r}{r!} \mu_r' \tag{39}$$

This power series is valid for all $t \in R$ and describes the characteristic function as the Fourier transform of the PDF.

6. Reliability Functions

Reliability analysis plays a key role in lifetime and survival modeling. In this section, we derive and discuss key reliability functions associated with the $i-$Lomax distribution.

6.1. Survival Function

The survival function $\bar{G}(x)$ is the complement of the cumulative distribution function:

$$\bar{G}(x) = 1 - G(x) = \left(1 + \frac{x}{\lambda}\right)^{1-\alpha}, \quad x > 0,\ \alpha > 1 \tag{40}$$

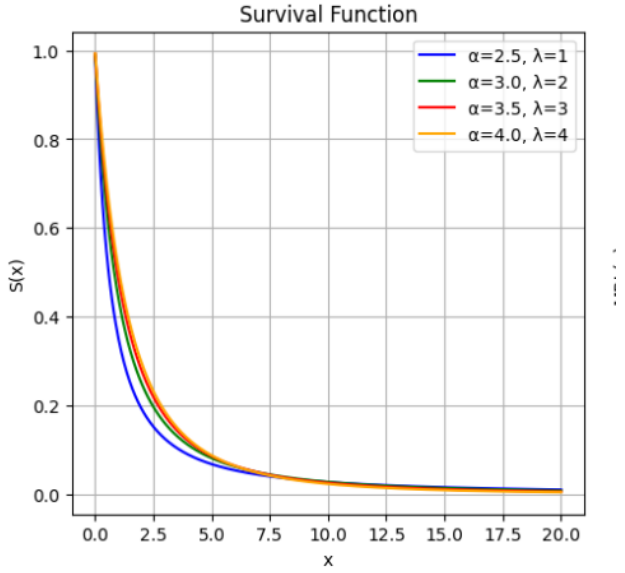


Figure 4: *Survival function of i−Lomax distribution*

6.2. Hazard Rate Function

The hazard rate function $h(x)$ is given by the ratio of the probability density function to the survival function:

$$h(x) = \frac{g(x)}{\bar{G}(x)} = \frac{\frac{(\alpha-1)}{\lambda}\left(1+\frac{x}{\lambda}\right)^{-\alpha}}{\left(1+\frac{x}{\lambda}\right)^{1-\alpha}} = \frac{(\alpha-1)}{\lambda}\left(1+\frac{x}{\lambda}\right)^{-1}, \quad x>0 \tag{41}$$

This expression shows that the hazard rate function is monotonically decreasing.

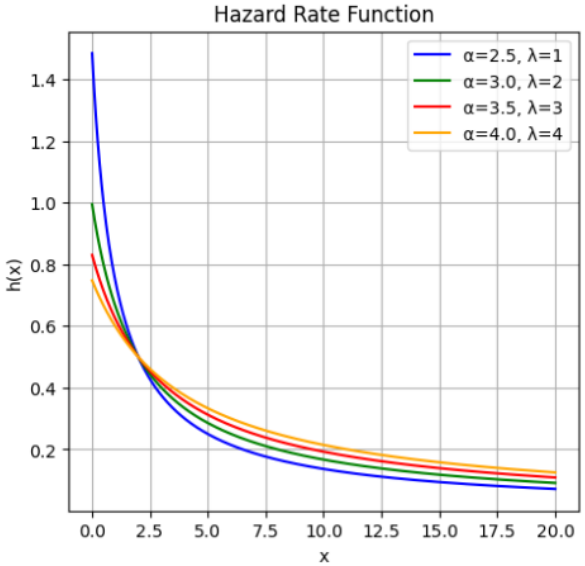


Figure 5: *Hazard function of i−Lomax distribution*

6.3. Mean Residual Life Function

The mean residual life (MRL) function $m(x)$ is defined as the expected remaining lifetime given survival up to time x:

$$m(x) = E[X - x \mid X > x] = \frac{1}{\bar{G}(x)} \int_x^\infty (t-x) g(t) dt \tag{42}$$

Substituting $g(t)$ and simplifying, the MRL function becomes:

$$m(x) = \frac{\lambda}{(\alpha - 2)} \left(1 + \frac{x}{\lambda}\right)^{-1}, \quad \alpha > 2 \tag{43}$$

This function also decreases with x, indicating that the expected remaining lifetime becomes shorter over time consistent with decreasing hazard rate behavior.

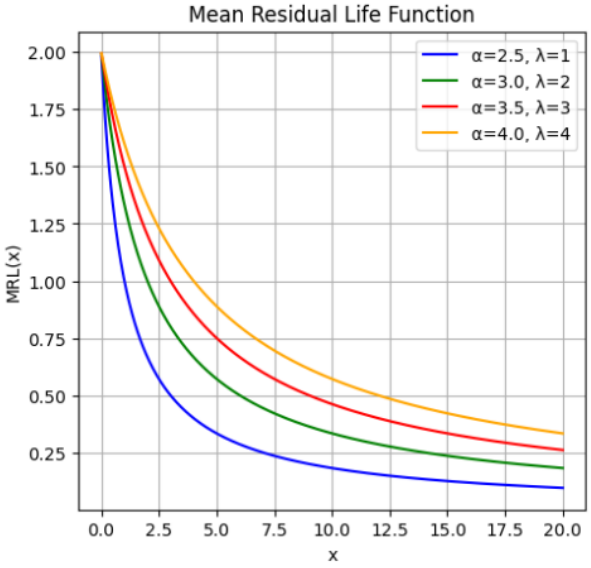


Figure 6: *Mean Residual Life function of $i-$Lomax distribution*

7. Quantile Function

The quantile function is the inverse of the cumulative distribution function (CDF), and is useful for generating random variates and analyzing distributional behavior.

The CDF of the $i-$Lomax distribution is:

$$G(x) = 1 - \left(1 + \frac{x}{\lambda}\right)^{1-\alpha}$$

Let $u = G(x)$ Then:

$$u = 1 - \left(1 + \frac{x}{\lambda}\right)^{1-\alpha} \quad \Rightarrow \quad 1 - u = \left(1 + \frac{x}{\lambda}\right)^{1-\alpha}$$

Taking logarithms and solving for x:

$$\left(1 + \frac{x}{\lambda}\right) = (1-u)^{\frac{1}{1-\alpha}} \quad \Rightarrow \quad x = \lambda \left[(1-u)^{\frac{1}{1-\alpha}} - 1\right]$$

Hence, the quantile function $Q(u)$ is given by:

$$Q(u) = \lambda \left[(1-u)^{\frac{1}{1-\alpha}} - 1\right], \quad 0 < u < 1, \ \alpha > 1 \tag{44}$$

8. Stochastic Ordering

Stochastic ordering of continuous random variables is an important tool for comparing their relative behaviors in terms of risk, reliability, or strength. Let X and Y be two continuous random variables. Then the following orderings are defined as:

1. Usual Stochastic Order: $X \leq_{st} Y$ if $F_X(x) \geq F_Y(x)$ for all x.
2. Hazard Rate Order: $X \leq_{hr} Y$ if $h_X(x) \geq h_Y(x)$ for all x.
3. Mean Residual Life Order: $X \leq_{mrl} Y$ if $m_X(x) \leq m_Y(x)$ for all x.
4. Likelihood Ratio Order: $X \leq_{lr} Y$ if $\frac{f_X(x)}{f_Y(x)}$ is decreasing in x.

According to Shaked and Shanthikumar (2007), the following implications hold:

$$X \leq_{lr} Y \Rightarrow X \leq_{hr} Y \Rightarrow X \leq_{mrl} Y \Rightarrow X \leq_{st} Y \tag{45}$$

Orderings in the Induced Lomax Distribution

Let $X \sim i - Lomax(\alpha_1, \lambda)$ and $Y \sim i - Lomax(\alpha_2, \lambda)$ be two $i-$Lomax random variables with the same scale parameter λ but different shape parameters α_1 and α_2.

The PDF of the $i-$Lomax distribution is:

$$f(x; \alpha, \lambda) = \frac{\alpha - 1}{\lambda} \left(1 + \frac{x}{\lambda}\right)^{-\alpha}$$

and the survival function is:

$$\bar{F}(x) = \left(1 + \frac{x}{\lambda}\right)^{1-\alpha} \tag{46}$$

Stochastic Order

For $\alpha_1 < \alpha_2$, we have:

$$\bar{F}_X(x) > \bar{F}_Y(x) \quad \Rightarrow \quad F_X(x) < F_Y(x) \Rightarrow X \geq_{st} Y \tag{47}$$

Hazard Rate Order

The hazard rate function is:

$$h(x) = \frac{f(x)}{\bar{F}(x)} = \frac{\alpha - 1}{\lambda} \left(1 + \frac{x}{\lambda}\right)^{-1} \tag{48}$$

Since $h(x)$ is decreasing in x and increases with α, we observe that:

$$\alpha_1 > \alpha_2 \Rightarrow h_X(x) > h_Y(x) \Rightarrow X \leq_{hr} Y \tag{49}$$

Mean Residual Life Order

The mean residual life function is:

$$m(x) = \frac{\lambda}{\alpha - 2} \left(1 + \frac{x}{\lambda}\right)^{-1}, \quad \alpha > 2 \tag{50}$$

As $m(x)$ is decreasing in α, for $\alpha_1 > \alpha_2$ we have:

$$m_X(x) < m_Y(x) \Rightarrow X \leq_{mrl} Y$$

Likelihood Ratio Order (Optional)

The likelihood ratio:

$$\frac{f_X(x)}{f_Y(x)} = \frac{\alpha_1 - 1}{\alpha_2 - 1}\left(1 + \frac{x}{\lambda}\right)^{\alpha_2 - \alpha_1} \tag{51}$$

is decreasing in x if $\alpha_1 > \alpha_2$, thus:

$$X \leq_{lr} Y \text{ if } \alpha_1 > \alpha_2 \tag{52}$$

Thus, the $i-$Lomax distribution satisfies all four stochastic orderings with respect to the shape parameter α, when scale parameter λ is fixed. This makes it suitable for modeling data with increasing or decreasing reliability characteristics, depending on the parameter values.

9. Order Statistics

Let $X_1, X_2, \ldots, X_m$ be a random sample of size m drawn from the $i-$Lomax distribution, and let $X_{(1)} \leq X_{(2)} \leq \cdots \leq X_{(m)}$ denote the corresponding order statistics. The PDF and CDF of the r^{th} order statistic $X_{(r)}$, say Y, are given respectively by:

$$f_{(r:m)}(y) = \frac{m!}{(r-1)!(m-r)!}\left[G(y)\right]^{r-1}\left[1 - G(y)\right]^{m-r} g(y)$$
$$F_{(r:m)}(y) = \sum_{j=r}^{m}\binom{m}{j}\left[G(y)\right]^{j}\left[1 - G(y)\right]^{m-j}$$

where $G(y)$ and $g(y)$ are the CDF and PDF of the $i-$Lomax distribution, respectively:

$$G(y) = 1 - \left(1 + \frac{y}{\lambda}\right)^{1-\alpha}, \quad g(y) = \frac{\alpha - 1}{\lambda}\left(1 + \frac{y}{\lambda}\right)^{-\alpha}$$

We may also express the PDF using a binomial expansion involving powers of the CDF:

$$f_{(r:m)}(y) = \frac{m!}{(r-1)!(m-r)!}\sum_{l=0}^{m-r}\binom{m-r}{l}(-1)^l[G(y)]^{r+l-1}g(y) \tag{53}$$

and the CDF of $Y = X_{(r)}$ as:

$$F_{(r:m)}(y) = \sum_{j=r}^{m}\sum_{l=0}^{m-j}\binom{m}{j}\binom{m-j}{l}(-1)^l[G(y)]^{j+l} \tag{54}$$

These representations are useful in computing the distribution of extremes (minimum or maximum) and in reliability applications such as system lifetimes and quantile estimation. For instance, the minimum $X_{(1)}$ has $r = 1$, and the maximum $X_{(m)}$ has $r = m$.

10. Stress-Strength Reliability

Let $X \sim$ i-Lomax(α_1, λ_1) denote the strength and $Y \sim$ i-Lomax(α_2, λ_2) the stress, assumed to be independent. The stress-strength reliability is defined as:

$$R = P(X > Y) = \int_0^\infty fY(y) \cdot \bar{F}X(y)dy \tag{55}$$

Substituting the expressions for the PDF and survival function of the $i-$Lomax distribution yields:

$$R = \int_0^\infty \frac{\alpha_2 - 1}{\lambda_2} \left(1 + \frac{y}{\lambda_2}\right)^{-\alpha_2} \cdot \left(1 + \frac{y}{\lambda_1}\right)^{1-\alpha_1} dy \tag{56}$$

In the special case where $\lambda_1 = \lambda_2 = \lambda$, the expression simplifies to:

$$R = \frac{\alpha_2 - 1}{\alpha_1 + \alpha_2 - 2}, \quad \text{for } \alpha_1 + \alpha_2 > 2 \tag{57}$$

This provides a closed-form solution for R, representing the probability that the strength exceeds the stress under identical scale parameters.

11. Bonferroni and Lorenz Curves

Bonferroni Curve

The Bonferroni curve $B(p)$ for the $i-$Lomax distribution is defined as:

$$B(p) = \frac{1}{p\mu} \int_0^{Q(p)} xg(x)dx \tag{58}$$

where $\mu = \frac{\lambda}{\alpha-2}$ is the mean and $Q(p) = \lambda \left[(1-p)^{\frac{1}{1-\alpha}} - 1\right]$ is the quantile function.

After algebraic simplification using the transformations $1 + \frac{x}{\lambda} = t$, the Bonferroni curve for the $i-$Lomax distribution becomes:

$$B(p) = \frac{1}{p}\left[1 - \frac{q}{\lambda}(\alpha - 2)\left(1 + \frac{q}{\lambda}\right)^{1-\alpha} + \left(1 + \frac{q}{\lambda}\right)^{2-\alpha}\right] \tag{59}$$

where $q = Q(p)$ is the quantile value for a given $p \in (0, 1)$.

Lorenz Curve

The Lorenz curve $L(p)$ is obtained as:

$$L(p) = \frac{1}{\mu} \int_0^{Q(p)} xg(x)dx = B(p) \cdot p \tag{60}$$

which simplifies to:

$$L(p) = 1 - \frac{q}{\lambda}(\alpha - 2)\left(1 + \frac{q}{\lambda}\right)^{1-\alpha} + \left(1 + \frac{q}{\lambda}\right)^{2-\alpha} \tag{61}$$

Gini Index

The Gini index G is derived using:

$$G = 1 - 2\int_0^1 L(p)dp \tag{62}$$

Substituting the form of $L(p)$, and changing variable to $x = Q(p)$, the Gini index becomes:

$$G = (\alpha - 2)\int_0^\infty \left[1 - \left(1 + \frac{x}{\lambda}\right)^{1-\alpha}\right]\left(1 + \frac{x}{\lambda}\right)^{1-\alpha} dx \tag{63}$$

With the substitution $t = 1 + \frac{x}{\lambda}$, this evaluates to:

$$G = 1 - \frac{\alpha - 2}{2\alpha - 3}, \quad \text{for } \alpha > \frac{3}{2} \tag{64}$$

This closed-form expression clearly shows that the Gini index increases as $\alpha \to \frac{3}{2}^+$ reflecting the heavy-tail and skewness of the *i*-Lomax distribution.

12. Entropy Measures

12.1. Rényi Entropy

Let X be a continuous random variable with PDF $g(x)$. The Rényi entropy of order $\eta > 0, \eta \neq 1$ is defined as:

$$\mathcal{E}(\eta) = \frac{1}{1-\eta} \log \left[\int_0^\infty g^\eta(x) dx \right]$$

Substituting the PDF of the $i-$Lomax distribution:

$$g(x) = \frac{\alpha - 1}{\lambda} \left(1 + \frac{x}{\lambda}\right)^{-\alpha}$$

we get:

$$\begin{aligned} \mathcal{E}(\eta) &= \frac{1}{1-\eta} \log \left[\int_0^\infty \left(\frac{\alpha-1}{\lambda}\right)^\eta \left(1 + \frac{x}{\lambda}\right)^{-\alpha\eta} dx \right] \\ &= \frac{1}{1-\eta} \log \left[\left(\frac{\alpha-1}{\lambda}\right)^\eta \int_0^\infty \left(1 + \frac{x}{\lambda}\right)^{-\alpha\eta} dx \right] \end{aligned}$$

Using the substitution $t = 1 + \frac{x}{\lambda} \Rightarrow x = \lambda(t-1) dx = \lambda dt$, we get:

$$\int_0^\infty \left(1 + \frac{x}{\lambda}\right)^{-\alpha\eta} dx = \lambda \int_1^\infty t^{-\alpha\eta} dt = \frac{\lambda}{\alpha\eta - 1}, \quad \text{for } \alpha\eta > 1$$

Hence, the Rényi entropy becomes:

$$\mathcal{E}(\eta) = \frac{1}{1-\eta} \left[\eta \log(\alpha - 1) + (1-\eta) \log \lambda - \log(\eta\alpha - 1) \right], \quad \eta > \frac{1}{\alpha}$$

12.2. Shannon Entropy

The Shannon entropy is defined as:

$$H(X) = -\int_0^\infty g(x) \log g(x)\, dx \tag{65}$$

Substituting; $g(x) = \frac{\alpha-1}{\lambda} \left(1 + \frac{x}{\lambda}\right)^{-\alpha}$, we get:

$$H(X) = -\int_0^\infty \left(\log \left(\frac{\alpha-1}{\lambda}\right) - \alpha \log \left(1 + \frac{x}{\lambda}\right) \right) g(x) dx \tag{66}$$

Split the integral:

$$H(X) = -\log \left(\frac{\alpha-1}{\lambda}\right) \int_0^\infty g(x) dx + \alpha \int_0^\infty \log \left(1 + \frac{x}{\lambda}\right) g(x) dx \tag{67}$$

Since $\int_0^\infty g(x)dx = 1$, we simplify:

$$H(X) = -\log\left(\frac{\alpha-1}{\lambda}\right) + \alpha \int_0^\infty \log\left(1+\frac{x}{\lambda}\right) \cdot \frac{\alpha-1}{\lambda}\left(1+\frac{x}{\lambda}\right)^{-\alpha} dx \tag{68}$$

Substitute $t = 1 + \frac{x}{\lambda} \Rightarrow dx = \lambda dt$, so:

$$H(X) = -\log\left(\frac{\alpha-1}{\lambda}\right) + \alpha(\alpha-1) \int_1^\infty \log(t) \cdot t^{-\alpha} dt \tag{69}$$

Using the known result:

$$\int_1^\infty \log(t) \cdot t^{-\alpha} dt = \frac{1}{(\alpha-1)^2} \tag{70}$$

we obtain:

$$H(X) = -\log(\alpha-1) + \log\lambda - \frac{\alpha}{1-\alpha}, \quad \alpha > 1$$

13. Maximum Likelihood Estimation

Let $x_1, x_2, \ldots, x_n$ be a random sample from the $i-$Lomax distribution with PDF:

$$g(x;\alpha,\lambda) = \frac{\alpha-1}{\lambda}\left(1+\frac{x}{\lambda}\right)^{-\alpha}, \quad \alpha > 1,\ \lambda > 0$$

The log-likelihood function is given by:

$$\ell(\alpha,\lambda) = n\log(\alpha-1) - n\log\lambda - \alpha\sum_{i=1}^n \log\left(1+\frac{x_i}{\lambda}\right) \tag{71}$$

Taking partial derivatives with respect to the parameters and equating to zero, we obtain the likelihood equations:

$$\frac{\partial\ell}{\partial\alpha} = \frac{n}{\alpha-1} - \sum_{i=1}^n \log\left(1+\frac{x_i}{\lambda}\right) = 0$$

$$\hat{\alpha} = 1 + \frac{n}{\sum_{i=1}^n \log\left(1+\frac{x_i}{\lambda}\right)} \tag{72}$$

$$\frac{\partial\ell}{\partial\lambda} = -\frac{n}{\lambda} + \alpha\sum_{i=1}^n \frac{x_i}{\lambda(\lambda+x_i)} = 0 \tag{73}$$

$$\sum_{i=1}^n \frac{x_i}{\lambda+x_i} = \frac{n}{\alpha} \tag{74}$$

Equations (72) and (74) must be solved simultaneously to obtain the maximum likelihood estimates $\hat{\alpha}$ and $\hat{\lambda}$. Since closed-form solutions do not exist, iterative numerical techniques such as the Newton–Raphson method or optimization routines are required.

14. Simulation Study

The behaviour of the parameters of the $i-$Lomax distribution was investigated by conducting simulation studies with the aid of R software. Data sets were generated from the $i-$Lomax distribution with a replication number $m = 1000$; random samples of sizes $n = 25, 50, 100$, and 200 were further selected. The simulation was conducted for three (3) different cases using varying true parameter values. The selected true parameter values are $(\alpha, \lambda) = \{(1.5, 0.5), (2.5, 1.0), (3.5, 2.0)\}$ for the first, second, and third cases, respectively.

The MLEs of the true parameters were obtained including the Bias and the Root Mean Square Error (RMSE). The results for the simulation studies are as shown in Tables 1.

Table 1: *Simulation study results for MLE for different values of α and λ.*

Parameter	Sample Size	α_{MLE}			λ_{MLE}		
(α, λ)	(n)	Mean	Bias	RMSE	Mean	Bias	RMSE
(1.5,0.5)	25	1.5899	0.0899	0.2564	0.7676	0.2676	0.7377
	50	1.5420	0.0420	0.1410	0.6409	0.1409	0.3954
	100	1.5267	0.0267	0.0828	0.6087	0.1087	0.2396
	200	1.5250	0.0250	0.0577	0.6261	0.1261	0.2161
(2.5, 1.0)	25	3.7628	1.2628	2.7427	2.3191	1.3191	2.8984
	50	3.1427	0.6427	1.7433	1.6464	0.6464	1.7329
	100	2.6780	0.1780	0.6314	1.1922	0.1922	0.6613
	200	2.5791	0.0791	0.3400	1.0737	0.0737	0.3398
(3.5, 2.0)	25	5.5954	2.0954	3.6252	4.1678	2.1678	3.8431
	50	4.7552	1.2552	2.7302	3.3398	1.3398	2.9123
	100	4.2206	0.7206	1.8767	2.7705	0.7705	2.0378
	200	3.7857	0.2857	0.9847	2.3019	0.3019	1.0648

It can be deduced from Tables 1 that the root mean square error (RMSE) reduces for all the selected parameter values as the sample size increases. Also, the bias posed by the estimates is closer to the true parameter values and the absolute bias reduces as the sample size increases. Hence, as sample size increases, the estimates tend towards the true parameter values.

15. Goodness-of-Fit of the $i-$Lomax Distribution

The goodness-of-fit of the $i-$Lomax distribution has been demonstrated using three real-life datasets from the literature. The first dataset contains vinyl chloride concentrations (in μg/L) measured in groundwater monitoring wells, provided by Bhaumik & Gibson [22]. The second dataset includes the insulation breakdown times (in minutes) of an electrical insulating fluid under increasing voltage levels, as reported by Lawless [23] and the last dataset represents the failure times of the air conditioning system of an aircraft, reported by Linhart & Zucchini [24].

The $i-$Lomax distribution was fitted to each dataset and compared with the $i-$Garima, Weibull, and Gamma distributions using their respective probability density functions. For model comparison, the values of $-2\log L$, Akaike Information Criterion (AIC), Bayesian Information Criterion (BIC), and Kolmogorov–Smirnov (K–S) statistics with their associated $p-$values were

computed. The following formulas were used:

$$\begin{aligned} \text{AIC} &= -2\log L + 2k \\ \text{BIC} &= -2\log L + k\log n \\ D &= \sup_x |F_n(x) - F_0(x)| \end{aligned}$$

where k is the number of model parameters, n is the sample size, $F_n(x)$ is the empirical distribution function, and $F_0(x)$ is the fitted cumulative distribution function.

Table 2: *Estimates of the Parameters, -2LL, AIC, BIC and K–S Statistics of the Fitted Distributions for Different data Sets*

Data Set	Estimate	Distribution	–2LL	AIC	BIC	K–S	$p-$value
	(31.115,54.728)	$i-$Lomax	110.88	114.88	117.93	0.081	0.978
	0.674	$i-$Garima	111.19	113.19	114.71	0.104	0.857
1st	(1.010,1.888)	Weibull	110.90	114.90	117.95	0.092	0.937
	(0.565,1.063)	Gamma	110.83	114.83	117.88	0.097	0.904
	$(1.565, 2.609)$	$i-$Lomax	653.63	657.63	662.29	0.063	0.921
	0.012	$i-$Garima	875.45	877.45	879.78	0.518	0.000
2nd	$(0.434, 25.072)$	Weibull	670.84	674.84	679.50	0.106	0.365
	$(0.014, 0.812)$	Gamma	697.30	701.30	705.97	0.184	0.013
	(4.296,141.261)	$i-$Lomax	303.68	307.68	310.48	0.142	0.585
	0.022	$i-$Garima	306.75	308.75	310.15	0.240	0.063
3rd	(0.853,54.613)	Weibull	303.87	307.87	310.68	0.153	0.481
	(0.014,0.812)	Gamma	304.34	308.34	311.14	0.169	0.356

From Table 2, it is evident that the $i-$Lomax distribution provides a superior fit in several cases, particularly for the insulation breakdown, vinyl chloride, and air conditioning datasets. It substantially improves over the classical Lomax and exponential distributions in terms of AIC, BIC, and K–S with respective $p-$values. This demonstrates reasonable flexibility in modeling lifetime data with heavy tails.

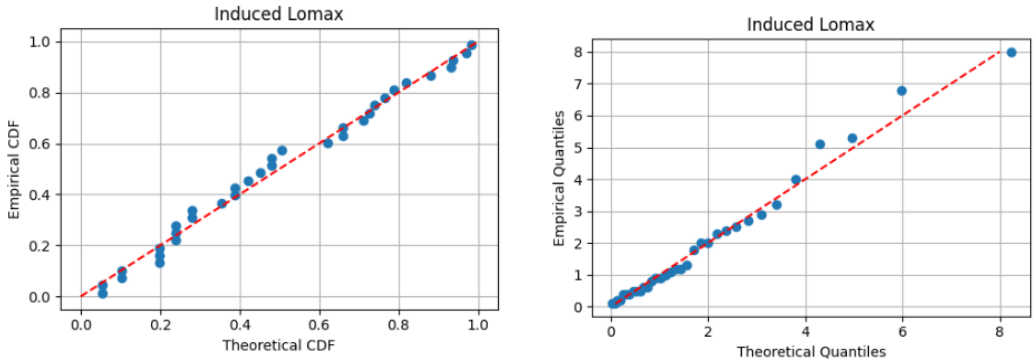


Figure 7: *P-P and Q-Q plots for $i-$Lomax distributions to the 1st dataset.*

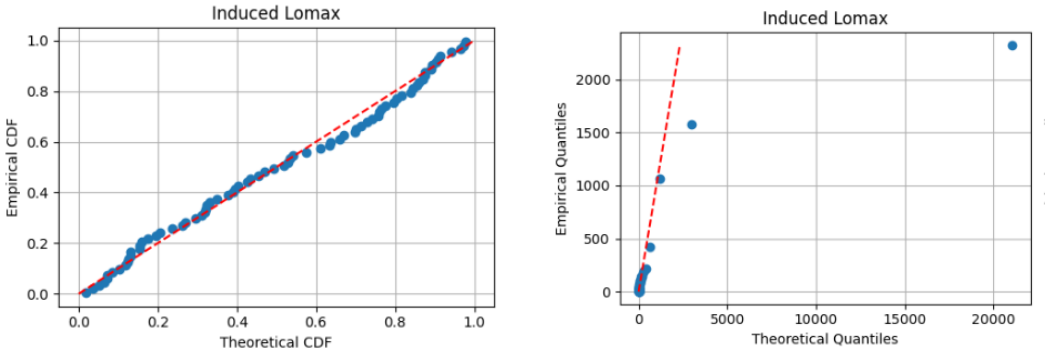


Figure 8: *P-P and Q-Q plots for $i-$Lomax distributions to the 2nd dataset.*

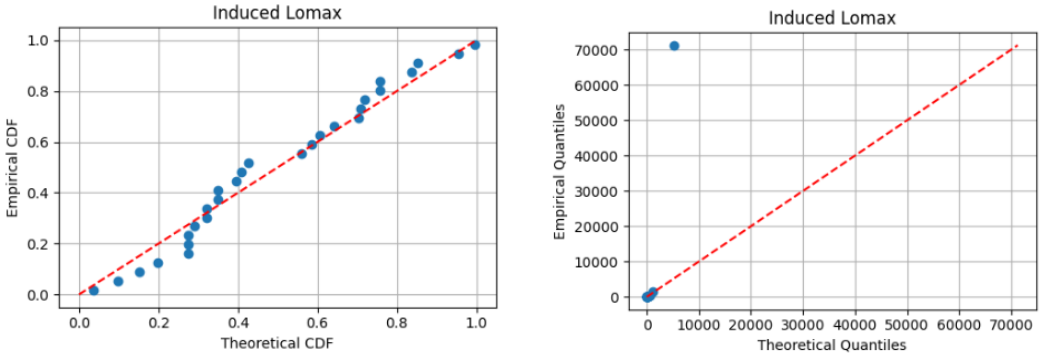


Figure 9: *P–P and Q-Q plots for $i-$Lomax distributions to the 3rd dataset.*

16. Conclusion

Better modeling of lifetime and reliability data is a significant concern for statisticians and applied researchers. Considerable progress has been made toward extending classical lifetime models to improve their flexibility and real-world applicability. In the present study, a technique based on the induced distribution framework has been employed to propose an alternative two-parameter distribution called the $i-$Lomax distribution. Various statistical properties such as raw and central moments, quantile function, survival and hazard rate functions, mean residual life function, coefficient-based measures, entropy measures, stress-strength reliability, and order statistics have been thoroughly derived and discussed.The model parameters have been estimated using the method of maximum likelihood, and a simulation study was conducted to examine the performance of the estimators in terms of bias and root mean square error (RMSE). The simulation results confirm that the estimators become increasingly accurate with larger sample sizes.

To assess the practical utility of the $i-$Lomax distribution, three real-life datasets were analyzed. Comparative goodness-of-fit analysis was carried out against classical models such as $i-$Garima, Weibull and Gamma distributions. The evaluation was based on the values of $-2LL$, AIC, BIC and K–S statistics with its $p-$value. Results demonstrate that the $i-$Lomax distribution outperforms other competing models in several cases and offers comparable fit in others. It is expected that the proposed model will serve as a useful tool in lifetime data analysis and reliability modeling. Future extensions of this work may consider censored data scenarios and Bayesian approaches under different loss functions. Also, this model may be used to develop new model using other transformation techniques of generation of new probability model.

References

[1] Lomax, K. S. (1954). Business failures: Another example of the analysis of failure data. *Journal of the American statistical association*, 49(268): 847–852.
[2] Atkinson, A. C. (1982). Regression diagnostics, transformations and constructed variables. *Journal of the Royal Statistical Society: Series B (Methodological)*, 44(1): 1–22.
[3] Bryson, M. C. (1974). Heavy-tailed distributions: properties and tests. *Technometrics*, 16(1): 61–68.
[4] Balkema, A. A., & De Haan, L. (1974). Residual life time at great age. *The Annals of probability*, 792–804.
[5] Ahsanullah, M. Record Statistics, Nova Science Publishers, 1991.
[6] Ghitany, M. E., Al-Awadhi, F. A., & Alkhalfan, L. (2007). Marshall–Olkin extended Lomax distribution and its application to censored data. *Communications in Statistics—Theory and Methods*, 36(10): 1855–1866.
[7] Kilany, N. M. (2016). Weighted lomax distribution. *SpringerPlus*, 5(1): 1862.
[8] Gupta, R. D., & Kundu, D. (2010). Generalized logistic distributions. *Journal of Applied Statistical Science*, 18(1): 51.
[9] Nagarjuna, V. B., Vardhan, R. V., & Chesneau, C. Kumaraswamy, (2021). generalized power Lomax distributionand its applications, *Stats*, 4(1): 28–45.
[10] El-Monsef, M. M. E. A., Sweilam, N. H., & Sabry, M. A. (2021). The exponentiated power Lomax distribution and its applications. *Quality and Reliability Engineering International*, 37(3): 1035–1058.
[11] Chattopadhyay, S., Chakraborty, T., Ghosh, K., & Das, A. K. (2021). Modified Lomax model: A heavy-tailed distribution for fitting large-scale real-world complex networks. *Social Network Analysis and Mining*, 11(1): 43.
[12] Aljohani, H. M. (2025). The New Explanation of Lomax Distribution: Its Properties, Inference, and Applications to Real-Life Data. *Contemporary Mathematics*, 2541–2569.
[13] Pak, A., & Mahmoudi, M. R. (2018). Estimating the parameters of Lomax distribution from imprecise information. *Journal of Statistical Theory and Applications*, 17(1): 122–135.
[14] Afify, A. Z., Nofal, Z. M., Yousof, H. M., El Gebaly, Y. M., & Butt, N. S. (2015). The transmuted Weibull Lomax distribution: properties and application. *Pakistan Journal of Statistics and Operation Research*, 135–152.
[15] Ahsanullah, M., & Nevzorov, V. B. (2011). Record statistics. In International encyclopedia of statistical science (pp. 1195–1202). *Springer*, Berlin, Heidelberg.
[16] Singh, B. P., & Das, U. D. (2023). On an Induced Distribution and its Statistical Properties. *REVSTAT–Statistical Journal*, 21(3): 303–319.
[17] Singh, B. P., Das, U. D., Karakaya, K., S. Bakouch, H., & Abba, B. (2024). Doubly bounded exponential model: Some information measures and estimation. *Communications in Statistics-Theory and Methods*, 53(22): 7842–7859.
[18] Singh, B. P., & Das, U. D. (2021). An Inferential Aptness of a Weibull Generated Distribution and Application. *Journal of Reliability and Statistical Studies*, 14(2): 669–694.
[19] Patil, G. P. & Rao, C. R. (1977). The Weighted Distribution: A Survey of their Applications, *Applications of Statistics*, 383–405.
[20] Singh, B. P., Das, U. D., & Singh, S. (2021). A compounded probability model for decreasing hazard and its inferential properties. *Reliability: Theory & Applications*, 16(2 (62)): 230–246.
[21] Dubey, S. D. (1970). Compound gamma, beta and F distributions. *Metrika*, 16(1): 27–31.
[22] Bhaumik, D. K., & Gibbons, R. D. (2006). One-sided approximate prediction intervals for at least p of m observations from a gamma population at each of r locations. Technometrics, 48(1): 112–119.
[23] Lawless, J. F. Statistical models and methods for lifetime data. John Wiley & Sons, 2011.
[24] Linhart, H., & Zucchini, W. Model selection. John Wiley & Sons, 1986.

OPTIMIZATION OF A DETERIORATING INVENTORY MODEL WITH TIME-DEPENDENT HEAVISIDE DEMAND AND RETURN POLICY UNDER TRIANGULAR FUZZY DECISION-MAKING

Kapil Dave[1], Tanuj Kumar[1,*]

•

[1]Department of Mathematics, SRM Institute of Science and Technology,
Delhi-NCR Campus, Ghaziabad, India, 201204
kapil.d.8527.pr@gmail.com, tanujkhutail@gamil.com
*Corresponding author

Abstract

The objective of this work is to present an improved inventory system with fuzzy constraints dealing with two warehouse systems, own and rented. In the present model, we analyze the system under the consideration of two warehouses without shortages with the development of a fuzzy inventory model with time-varying heaviside demand function, deterioration with returns policy. The demand , deterioration and returns rate parameters are taken as triangular fuzzy numbers. Numerical example is given to validate the proposed mathematical model which has been developed for determining the optimal cycle time and optimal total inventory cost and profit. Sensitivity analysis is also carried out to explore the effect of changes in the optimal solution with respect to change in various parameters. The aim of this paper is to develop inventory policies that minimize the total cost to get the maximum total profit in both crisp and fuzzy modelling and comparison of crisp and fuzzy models. Our study focuses on defuzzifying the total cost using the signed distance method and comparing it with the crisp model. We assume that the return product will be sold at the same price. Customers are allowed to return the product during any phase of the length of the replenishment cycle. The consumers get the 85% of the price on the returned items and the number of returns are assumed to be depend on demand.

Keywords: Optimization, Inventory, Deterioration, Holding Cost, Returns Rate, Warehouse, Triangular Fuzzy Number, Signed Distance Method.

1. Introduction and literature review

This study aims to develop a two-warehouse inventory model under both crisp and fuzzy environments, incorporating a return policy. In high-demand retail settings such as supermarkets and corporate markets, storage capacity is often limited. When suppliers offer attractive price discounts for bulk purchases or when the item is seasonal such as agricultural harvest outputs-large quantities are procured. However, these quantities may exceed the capacity of the primary warehouse (own warehouse or OW). In such situations, an additional storage facility, referred to as the rented warehouse (RW), is hired. This RW is typically located at a distance and incurs higher holding costs compared to OW. Consequently, inventory is stored in OW first, and only the surplus is placed in RW. To minimize costs, items from RW are transferred continuously to OW following a release pattern. Return policies offered by sellers serve as an incentive for customers. These policies permit buyers to return unsatisfactory products, with a refund typically amounting

to 85 percent of the purchase price. In this model, the return rate is considered proportional to the demand rate. In inventory systems, uncertainty often arises, which is effectively captured through fuzzy set theory. Fuzziness reflects real-world ambiguity more accurately than crisp values and offers an improved framework for optimizing inventory models. Therefore, fuzzy logic presents a valuable approach in refining the results of inventory control systems. In the proposed two-warehouse inventory framework, we model the demand rate, deterioration rate, and return rate as trapezoidal fuzzy numbers. The structure of the paper is as follows: initially, we present the key assumptions and notations. This is followed by the development of the inventory model under a crisp environment. Thereafter, we extend the model to a fuzzy environment using the signed distance method and perform a sensitivity analysis through a numerical example.

In recent years, several researchers have examined the integration of time-dependent parameters, partial backlogging, and return policies within two-warehouse inventory models under fuzzy environments. For example, Sahoo et al. [1] proposed a fuzzy inventory model with exponential demand and time-varying deterioration. Jaggi et al. [2] investigated inventory decisions for deteriorating items of imperfect quality with exponentially declining demand, incorporating trade credit and partially backlogged shortages. Malik and Garg [3] presented an improved fuzzy inventory model involving two warehouses. Chou [4] formulated a fuzzy economic order quantity (EOQ) inventory model. Chakraborty et al. [5] developed a two-warehouse inventory model with partial backlogging, ramp-type demand, and three-parameter Weibull deterioration under inflation and permissible payment delays. Chang et al. [6] introduced a fuzzy inventory model that incorporates fuzzy random variables, lead time, and total demand. Dutta et al. [7] worked on a continuous review inventory system combining fuzzy and stochastic elements. Lee and Yao [8] analyzed economic production quantity models under fuzzy demand and fuzzy production quantities. Vujosevic et al. [9] extended the EOQ model to incorporate fuzzy inventory costs. Malik and Singh [10] proposed a fuzzy mixture model for two-warehouse systems with linear demand. Malik et al. [11] studied inventory with time-dependent demand for non-instantaneous deteriorating items considering maximum shelf life. Pakkala and Achary [12] developed a deterministic two-warehouse inventory model for deteriorating items with a finite replenishment rate. Recent research has focused on incorporating environmental factors and technology investments into inventory models with deterioration. Yadav and Kumar [13] proposed a model that considers selling price, time-sensitive demand, and carbon emissions under green technology investment. Yadav et al. [14] introduced a two-warehouse model using an interval approach, including preservation technology to manage uncertainty. In another study, Yadav et al. [15] addressed deterioration during storage within a two-warehouse setup, aiming to reduce total costs. They further extended this by including reliability and carbon emission constraints with time-based demand [16]. Similarly, Mahata and Debnath [17] analyzed a price-sensitive inventory system with preservation investment to handle deterioration. Later, they explored the impact of green technology and flexible production on economic production models with carbon emissions [18], showing that cleaner and more flexible systems help reduce environmental costs. Debnath et al. [19] developed an EOQ model under uncertainty using a generalized intuitionistic fuzzy Laplace transform. Their approach helps handle imprecise data more effectively in inventory systems. Rana and Kumar [20] developed a two-warehouse inventory model for deteriorating items with hybrid and stock-dependent demand under partial backlogging, reflecting real-world storage and demand situations. Nwoba et al. [21] presented a model with exponential demand and Weibull deterioration, considering shortage-dependent partial backlogging. Patra et al. [22] proposed a retailer's model using power pattern demand with partial backlogging, under both crisp and fuzzy environments to handle uncertainty. Gupta and Mishra [23] introduced a multi-item stochastic inventory model with power demand, partial backlogging, and joint replenishment, helping manage uncertain demand and coordination. All these studies are applicable to industries dealing with perishable or deteriorating items such as food and beverages, pharmaceuticals, chemicals, and seasonal goods. These sectors often face challenges related to limited storage, variable demand, product decay, and customer return behavior.

2. Methods

2.1. Definitions and Preliminaries

1. **Fuzzy set:** A fuzzy set allows for partial membership in which an element can belong to a set to a certain degree or degree of membership, which is represented by a value between 0 and 1. Mathematically, A fuzzy set defined on a universe of discourse $X = \{x_1, x_2, x_3, \ldots, x_n\}$ is given by $A = \{(x, \mu_A(x)) : x \in X\}$, where $\mu_A(x)$ is the membership function of A given by $\mu_A(x) : X \to [0, 1]$.
2. **Fuzzy Number:** A fuzzy number is a fuzzy set on the real line $\mathbb{R}$, if its membership function $\mu_A(x)$ has the following properties:
   (a) $\mu_A(x)$ is upper semi-continuous.
   (b) There exist some real numbers a_2 and a_3, $a_1 \leq a_2 \leq a_3 \leq a_4$ such that $\mu_A(x)$ is increasing on $[a_1, a_2]$, decreasing on $[a_3, a_4]$ and $\mu_A(x) = 1$ for each x on $[a_2, a_3]$.
   (c) $\mu_A(x) = 0$ outside the interval $[a_1, a_4]$.
3. **Triangular Fuzzy Number:** A triangular fuzzy number is specified by the triplet (a_1, a_2, a_3) and defined by its membership function $\mu_A(x) : X \to [0, 1]$ as follows:

$$\mu_A(x) = \begin{cases} 0, & x \leq a_1 \\ \frac{x-a_1}{a_2-a_1}, & a_1 \leq x \leq a_2 \\ \frac{a_3-x}{a_3-a_2}, & a_2 \leq x \leq a_3 \\ 0, & x \geq a_3 \end{cases}$$

2.2. Assumptions and notations

The following assumptions have been adopted while developing the fuzzy inventory model:

1. Single item is used in this developed fuzzy inventory model.
2. The system involves two-warehouse system, one is own warehouse (OW) with limited capacity and other is rented warehouse (RW) with infinite capacity.
3. Demands are first met directly from RW and after all items are released from RW, the demands will be met from OW.
4. The time-dependent Heaviside demand rate function is defined as:

$$\gamma(t) = a + bt + c[t - (t - \mu)H(t - \mu)]t$$

5. The inventory deteriorates as a linear function of time and given by:

$$\eta(t) = \alpha t$$

6. It is assumed that customers return in proportional to demand so return rate is:

$$R(t) = \sigma\gamma(t), \quad \text{where } 0 \leq \sigma < 1$$

7. The holding cost per item is constant.
8. Time horizon is finite.
9. Transportation cost and rent of warehouse is assumed to be added in holding cost at RW.
10. The lead time is assumed to be zero.

11. Shortages are not allowed.

The following notations are used for the proposed fuzzy inventory model:

Table 1: *Notations used in the proposed fuzzy inventory model*

Symbol	Description
OW	Own warehouse
RW	Rented warehouse
W_o	Maximum inventory level in OW
$\eta(t)$	Deterioration rate
$\gamma(t)$	Time dependent demand
T	Length of one cycle
$Q_1(t)$	Inventory level at time $t \in [0, t_1]$
$Q_2(t)$	Inventory level at time $t \in [t_1, T]$
Q_{o1}	Inventory level at OW at time $t \in [0, t_1]$
Q_{o2}	Inventory level at OW at time $t \in [t_1, T]$
Q_r	Inventory level at RW at time $t \in [0, t_1]$
A	Ordering cost
c_s	Price of an item
p	Selling price of an item
x	Deterioration rate in RW
y	Deterioration rate in OW
d_c	Deterioration cost per unit
α	Deterioration coefficient parameter
$\hat{\alpha}$	Fuzzy deterioration coefficient parameter
h_c	Holding cost coefficients
$R(t)$	Return rate
T_{CC}	Optimal cost in crisp model

3. Mathematical Formulation of Model

Here, we consider an inventory system under two warehouses system for seasonal products. For RW, the inventory level Q_r reaches zero level after the time t_1. After that, the customer demand is fulfilled by OW during time period (t_1, T). The initial inventory level for own warehouse is W_o. During period $(0, t_1)$, the demand of the customer is fulfilled from RW, so in between $(0, t_1)$ some product deteriorates in OW. Let $Q_1(t)$ be the inventory level at time $t \in [0, t_1]$, $Q_2(t)$ be the inventory level at time $t \in [t_1, T]$ and Q_{o1} inventory level at OW at time $t \in [0, t_1]$ and Q_{o2} be the inventory level at OW at time $t \in [t_1, T]$. Therefore, the governing equations of the system under the conditions

$$Q_r(t_1) = 0, \quad Q_{o1}(0) = W_o, \quad Q_{o2}(T) = 0$$

are:

$$\frac{dQ_r}{dt} = -\alpha t\, Q_r - \gamma(t) + \sigma\, \gamma(t) \quad \text{for } 0 \le t \le t_1 \tag{1}$$

$$\frac{dQ_{o1}}{dt} = -\alpha t\, Q_{o1} \quad \text{for } 0 \le t \le t_1 \tag{2}$$

$$\frac{dQ_{o2}}{dt} = -\alpha t\, Q_{o2} - \gamma(t) + \sigma\, \gamma(t) \quad \text{for } t_1 \le t \le T \tag{3}$$

3.1. Case-I: Crisp Inventory Model, When $t < \mu$

: The solutions of differential equations (i), (ii) and (iii) with boundary conditions are:

$$\begin{aligned} Q_r(t) = (\sigma-1)\Big[& a(t-t_1) + 0.34a\alpha(t^3-t_1^3) + 0.5b(t^2-t_1^2) - 0.125b\alpha(t^4-t_1^4) \\ & + 0.33c(t^3-t_1^3) - 0.067c\alpha(t^5-t_1^5) + 0.01c\alpha^2(t^7-t_1^7) - 0.5\alpha t^2(at-T) \\ & - 0.17\alpha^2t^2(t^3-t_1^3) - 0.25\alpha t^2 b(t^2-t_1^2) + 0.0625t^2b\alpha^2(t^4-t_1^4) \\ & - 0.0165\alpha t^2c(t^3-t_1^3) + 0.125\alpha^2t^4a(t-t_1) + 0.0625\alpha^2t^4b(t^2-t_1^2) \\ & + 0.021b\alpha^2(t^6-t_1^6) + 0.041\alpha^2t^4c(t^3-t_1^3) - 0.125b\alpha(t^4-t_1^4)\Big] \end{aligned} \tag{4}$$

$$Q_{o1}(t) = W_0\left(1 - 0.5\alpha t^2 + 0.125\alpha^2t^4 - 0.021\alpha^3t^6\right) \tag{5}$$

$$\begin{aligned} Q_{o2}(t) = (\sigma-1)\Big[& a(t-T) + 0.34a(t^3-T^3) + 0.5b(t^2-T^2) - 0.125b\alpha(t^4-T^4) \\ & + 0.33c(t^3-T^3) - 0.067c\alpha(t^5-T^5) - 0.5\alpha t(a-T) - 0.17\alpha^2t^2(t^3-T^3) \\ & - 0.034t^2\alpha^3(t^5-T^5) - 0.25\alpha t^2b(t^2-T^2) - 0.0165\alpha t^2c(t^3-T^3) \\ & + 0.125\alpha^2t^4a(t-T) + 0.041\alpha^2t^4c(t^3-T^3) - 0.125b\alpha(t^4-T^4)\Big] \end{aligned} \tag{6}$$

The total cost of the system is the sum of all associated inventory costs calculated as above. Therefore, the total cost per unit time (or total average cost per cycle) is given by:

1. **Ordering cost:**
$$OC = A$$

2. **Purchase cost:**
$$PC = cQ_0$$

3. **Deterioration Cost:** Inventory deterioration cost in RW is
$$DC_{\text{RW}} = d_c \int_0^{t_1} xQ_r(t)\, dt$$
Inventory deterioration cost in OW is
$$DC_{\text{OW}} = d_c \int_0^{t_1} yQ_{o1}(t)\, dt + d_c \int_{t_1}^{T} yQ_{o2}(t)\, dt$$

4. **Storage Cost:**
$$SC = \left[h_r \int_0^{t_1} Q_r(t)\, dt + h_o \int_0^{t_1} Q_{o1}(t)\, dt + h_o \int_{t_1}^{T} Q_{o2}(t)\, dt\right]$$

Total cost per unit time of inventory system is:

$$TC = \frac{1}{T}[OC + PC + DC + HC]$$

$$\begin{aligned} TC = \frac{1}{T}\Big[& A + cQ_0 + d_c[(x-y)(\sigma-1)(0.5\alpha t_1^2 - 0.29\alpha x t_1^4 - 0.33bt_1^3 \\ & + 0.233\, t_1^5 b\alpha - 0.049 b\alpha^2 t_1^7 - 0.25ct_1^4 + 0.0666\alpha c t_1^6)] + yW_0(t_1 - 0.166\alpha t_1^2 \\ & + 0.025\alpha^2 t_1^5) + y(\sigma-1)((0.5\alpha T^2 - 0.29\alpha T^4 - 0.085\,\alpha^2 T^6 - 0.33bT^3 + 0.233\, T^5 b\alpha \\ & - 0.25cT^4 + 0.0666\alpha c T^6 - 0.019\,\alpha^2 T^8)] + (h_r - h_o)(\sigma-1)(0.5\alpha t_1^2 - 0.29\alpha t_1^4 \\ & - 0.33bt_1^3 + 0.233\, t_1^5 b\alpha - 0.25ct_1^4 + 0.0666\alpha c t_1^6)] + h_o W_0[t_1 - 0.166\alpha t_1^2 + 0.025\alpha^2 t_1^5 \\ & + h_o(\sigma-1)(0.5\alpha T^2 - 0.29\alpha T^4 - 0.085\,\alpha^2 T^6 - 0.33bT^3 + 0.233\, T^5 b\alpha \\ & - 0.25cT^4 + 0.0666\alpha c T^6 - 0.019\,\alpha^2 T^8)]\Big] \end{aligned} \quad (7)$$

Sales revenue collected over the cycle (SR):

$$\mathrm{SR} = pQ_0 + 0.15p\int_0^T R(t)\,dt = pQ_0 + 0.15p\sigma\left(aT + 0.5bT^2 + 0.33cT^3\right) \quad (8)$$

The total profit per unit time is:

$$\mathrm{TP}^0 = \frac{1}{T}\left[\mathrm{SR} - \mathrm{OC} - \mathrm{PC} - \mathrm{HC} - \mathrm{DC} - \mathrm{SC}\right] \quad \text{(vi)}$$

3.2. Case-I: Fuzzy Inventory Model, When $t < \mu$

In this section, the fuzzy inventory model is presented through the signed distance method. Let

$$\hat{a} = (a_1, a_2, a_3), \quad \hat{b} = (b_1, b_2, b_3), \quad \hat{c} = (c_1, c_2, c_3), \quad \hat{\alpha} = (\alpha_1, \alpha_2, \alpha_3), \quad \hat{\sigma} = (\sigma_1, \sigma_2, \sigma_3)$$

be triangular fuzzy numbers. By the signed distance method, the total cost per unit time is:

$$TC^* = \frac{1}{4}(TC_1 + 2TC_2 + TC_3) \quad (9)$$

where

$$\begin{aligned} TC_1 = \frac{1}{T}\Big[& A + cQ_0 + d_c[(x-y)(\sigma_1-1)(0.5a_1 t_1^2 - 0.29a_1\alpha_1 t_1^4 - 0.085\,a_1\alpha_1^2 t_1^6 \\ & - 0.33b_1 t_1^3 + 0.233\, t_1^5 b_1\alpha_1 - 0.049 b_1\alpha_1^2 t_1^7 - 0.25c_1 t_1^4 + 0.0666\alpha_1 c_1 t_1^6 \\ & - 0.019\, c_1\alpha_1^2 t_1^8)] + yW_0[t_1 - 0.166\alpha_1 t_1^2 + 0.025\alpha_1^2 t_1^5] \\ & + y(\sigma_1-1)[(0.5a_1 T^2 - 0.29a_1\alpha_1 T^4 - 0.085\,a_1\alpha_1^2 T^6 - 0.33b_1 T^3 + 0.233\, T^5 b_1\alpha_1 \\ & - 0.049 b_1\alpha_1^2 T^7 - 0.25c_1 T^4 + 0.0666\alpha_1 c_1 T^6 - 0.019\, c_1\alpha_1^2 T^8)] \\ & + (h_r - h_o)(\sigma_1-1)(0.5a_1 t_1^2 - 0.29a_1\alpha_1 t_1^4 - 0.085\,a_1\alpha_1^2 t_1^6 - 0.33b_1 t_1^3 \\ & + 0.233\, t_1^5 b_1\alpha_1 - 0.25c_1 t_1^4 + 0.0666\alpha_1 c_1 t_1^6 - 0.019\, c_1\alpha_1^2 t_1^8)] \\ & + h_o W_0[t_1 - 0.166\alpha_1 t_1^2 + 0.025\alpha_1^2 t_1^5] \\ & + h_o(\sigma_1-1)[(0.5a_1 T^2 - 0.29a_1\alpha_1 T^4 - 0.085\,a_1\alpha_1^2 T^6 - 0.33b_1 T^3 + 0.233\, T^5 b_1\alpha_1 \\ & - 0.049 b_1\alpha_1^2 T^7 - 0.25c_1 T^4 + 0.0666\alpha_1 c_1 T^6 - 0.019\, c_1\alpha_1^2 T^8)]\Big] \end{aligned}$$

$$TC_2 = \frac{1}{T}\Big[A + cQ_0 + d_c[(x-y)(\sigma_2-1)(0.5a_2t_1^2 - 0.29a_2\alpha_2t_1^4 - 0.085\,a_2\alpha_2^2t_1^6 - 0.33b_2t_1^3 + 0.233\,t_1^5b_2\alpha_2 - 0.049b_2\alpha_2^2t_1^7 - 0.25c_2t_1^4 + 0.0666\alpha_2c_2t_1^6 - 0.019\,c_2\alpha_2^2t_1^8)] + yW_0[t_1 - 0.166\alpha_2t_1^2 + 0.025\alpha_2^2t_1^5] + y(\sigma_2-1)[(0.5a_2T^2 - 0.29a_2\alpha_2T^4 - 0.085\,a_2\alpha_2^2T^6 - 0.33b_2T^3 + 0.233\,T^5b_2\alpha_2 - 0.049b_2\alpha_2^2T^7 - 0.25c_2T^4 + 0.0666\alpha_2c_2T^6 - 0.019\,c_2\alpha_2^2T^8)] + (h_r-h_o)(\sigma_2-1)(0.5a_2t_1^2 - 0.29a_2\alpha_2t_1^4 - 0.085\,a_2\alpha_2^2t_1^6 - 0.33b_2t_1^3 + 0.233\,t_1^5b_2\alpha_2 - 0.25c_2t_1^4 + 0.0666\alpha_2c_2t_1^6 - 0.019\,c_2\alpha_2^2t_1^8)] + h_oW_0[t_1 - 0.166\alpha_2t_1^2 + 0.025\alpha_2^2t_1^5] + h_o(\sigma_2-1)[(0.5a_2T^2 - 0.29a_2\alpha_2T^4 - 0.085\,a_2\alpha_2^2T^6 - 0.33b_2T^3 + 0.233\,T^5b_2\alpha_2 - 0.049b_2\alpha_2^2T^7 - 0.25c_2T^4 + 0.0666\alpha_2c_2T^6 - 0.019\,c_2\alpha_2^2T^8)]\Big]$$

$$TC_3 = \frac{1}{T}\Big[A + c\,Q_0 + d_e\big((x-y)(\sigma_3-1)(0.5a_3t_1^2 - 0.29a_3t_1^4 - 0.085\,a_3\alpha_3^2t_1^6 - 0.33b_3t_1^3 + 0.233\,t_1^5b_3\alpha_3 - 0.049b_3\alpha_3^2t_1^7 - 0.25c_3t_1^4 + 0.0666\alpha_3c_3t_1^6 - 0.019\,c_3\alpha_3^2t_1^8)\big) + yW_0[t_1 - 0.166\alpha_3t_1^2 + 0.025\alpha_3^2t_1^5] + y(\sigma_3-1)\big(0.5a_3T^2 - 0.29a_3\alpha_3T^4 - 0.085\,\alpha_3^2T^6 - 0.33b_3T^3 + 0.233\,T^5b_3\alpha_3 - 0.049b_3\alpha_3^2T^7 - 0.25c_3T^4 + 0.0666\alpha_3c_3T^6 - 0.019\,c_3\alpha_3^2T^8\big) + (h_r-h_o)(\sigma_3-1)(0.5a_3t_1^2 - 0.29a_3t_1^4 - 0.085\,a_3\alpha_3^2t_1^6 - 0.33b_3t_1^3 + 0.233\,t_1^5b_3\alpha_3 - 0.25c_3t_1^4 + 0.0666\alpha_3c_3t_1^6 - 0.019\,c_3\alpha_3^2t_1^8) + h_oW_0[t_1 - 0.166\alpha_3t_1^2 + 0.025\alpha_3^2t_1^5] + h_o(\sigma_3-1)\big(0.5a_3T^2 - 0.29a_3\alpha_3T^4 - 0.085\,\alpha_3^2T^6 - 0.33b_3T^3 + 0.233\,T^5b_3\alpha_3 - 0.049b_3\alpha_3^2T^7 - 0.25c_3T^4 + 0.0666\alpha_3c_3T^6 - 0.019\,c_3\alpha_3^2T^8\big)\Big]$$

Sales revenue collected over the cycle (SR):

$$\mathrm{SR} = pQ_0 + 0.15\sigma p\left(at + 0.5b\,T^2 + 0.33c\,T^3\right) \tag{10}$$

The total profit per unit time is calculated as follows:

$$\mathrm{TP}^* = \frac{1}{T}\left[\mathrm{SR} - \mathrm{OC} - \mathrm{PC} - \mathrm{HC} - \mathrm{DC} - \mathrm{SC}\right] \tag{11}$$

3.3. Case-II: Crisp Inventory Model, When $t > \mu$

The solutions of differential equations 1, 2 and 3 with boundary conditions are:

$$Q_r(t) = (\sigma-1)\big[a(t-t_1) + 0.34a\alpha(t^3-t_1^3) + 0.067a\alpha^2(t^5-t_1^5) + 0.5\,b(t^2-t_1^2) - 0.125(b+c\mu)\alpha(t^4-t_1^4) + 0.021(b+c\mu)\alpha^2(t^6-t_1^6)\big] + 0.039(b+c\mu)\alpha^3(t^8-t_1^8) - 0.5\,\alpha t^2 - 0.17a\alpha^2t^2(t^3-t_1^3) - 0.034\,t^2a\alpha^3(t^5-t_1^5) - 0.25\,\alpha\,t^2(b+c\mu)(t^2-t_1^2) + 0.0625\,t^2(b+c\mu)\alpha^2(t^4-t_1^4) - 0.004\,t^2(b+c\mu)\alpha^3(t^6-t_1^6) + 0.1252\,t^2a(t-t_1) + 0.0425\,t^4a\alpha^3(t^3-t_1^3) + 0.067\,a\alpha^2(t^5-t_1^5) + 0.0625\,t^2\alpha^4(b+c\mu)(t^2-t_1^2) - 0.0153\,t^4(b+c\mu)\alpha(t-t_1) + 0.021(b+c\mu)\alpha^2(t^6-t_1^6) - 0.0213\,t^6\alpha^6(t-t_1) - 0.011\,t^3\alpha^6(b+c\mu)(t^2-t_1^2) - 0.125\,(b+c\mu)\alpha(t^4-t_1^4)] \tag{12}$$

$$Q_{01}(t) = W_0\left(1 - 0.5\,\alpha\, t + 0.125\alpha^2 t^4 - 0.021\alpha^3 t^6\right) \tag{13}$$

$$\begin{aligned} Q_{02}(t) = (\sigma-1)\big[&a(t-T) + 0.34a\alpha(t^3-T^3) + 0.067a\alpha^2(t^5-T^5) + 0.5\,(b+c\mu)(t^2-T^2) \\ &- 0.125(b+c\mu)\alpha(t^4-T^4) + 0.021(b+c\mu)\alpha^2(t^6-T^6) + 0.039(b+c\mu)\alpha^3(t^8-T^8) - 0.5\,\alpha t^2 \\ &- 0.17a\alpha^2t^2(t^3-T^3) - 0.034\,t^2a\alpha^3(t^5-T^5) - 0.25\,\alpha\,t^2(b+c\mu)(t^2-T^2) \\ &+ 0.0625\,t^2(b+c\mu)\alpha^2(t^4-T^4) - 0.004\,t^2(b+c\mu)\alpha^3(t^6-T^6) + 0.1252\,t^2a(t-T) \\ &+ 0.0425\,t^4a\alpha^3(t^3-T^3) + 0.067\,a\alpha^2(t^5-T^5) + 0.0625\,t^2\alpha^4(b+c\mu)(t^2-T^2) \\ &- 0.0153\,t^4(b+c\mu)\alpha(t-T) + 0.021(b+c\mu)\alpha^2(t^6-T^6) \\ &- 0.0213\,t^6\alpha^6(t-T) - 0.011\,t^3\alpha^6(b+c\mu)(t^2-T^2) - 0.125\,(b+c\mu)\alpha(t^4-T^4)\big] \end{aligned} \tag{14}$$

The total cost of the system is the sum of all associated inventory costs calculated as above. Therefore, the total cost per unit time (or total average cost per cycle) is given by:

1. **Ordering cost:**
$$OC = A$$

2. **Purchase cost:**
$$PC = cQ_0$$

3. **Deterioration Cost:** Inventory deterioration cost in RW is
$$DC_{\mathrm{RW}} = d_c \int_0^{t_1} xQ_r(t)\,dt$$
Inventory deterioration cost in OW is
$$DC_{\mathrm{OW}} = d_c \int_0^{t_1} yQ_{o1}(t)\,dt + d_c \int_{t_1}^{T} yQ_{o2}(t)\,dt$$

4. **Storage Cost:**
$$SC = \left[h_r \int_0^{t_1} Q_r(t)\,dt + h_o \int_0^{t_1} Q_{o1}(t)\,dt + h_o \int_{t_1}^{T} Q_{o2}(t)\,dt\right]$$

The total cost per unit time of inventory system is:

$$\mathrm{TC} = \frac{1}{T}\left[\mathrm{OC} + \mathrm{PC} + \mathrm{DC} + \mathrm{HC}\right]$$

$$\begin{aligned} = \frac{1}{T}\Big[&A + c\,Q_0 + d_e\big[(x-y)(\sigma-1)(0.5at_1^2 - 0.29a\alpha t_1^4 - 0.085\,a\,\alpha^2 t_1^6 - 0.33(b+c\mu)t_1^3 \\ &+ 0.233\,t_1^5(b+c\mu)\alpha - 0.049(b+c\mu)\alpha^2 t_1^7)\big] + yW_0\left[t_1 - 0.166\alpha t_1^2 + 0.025\alpha^2 t_1^5\right] \\ &+ y(\sigma-1)\Big(0.5aT^2 - 0.29a\alpha T^4 - 0.085\alpha^2 T^6 - 0.33(b+c\mu)T^3 + 0.233\,T^5(b+c\mu)\alpha \\ &- 0.049(b+c\mu)\alpha^2 T^7 + \Big[(h_r-h_o)(\sigma-1)(0.5at_1^2 - 0.29a\alpha t_1^4 - 0.085\,a\alpha^2 t_1^6 - 0.33(b+c\mu)t_1^3 \\ &+ 0.233\,t_1^5(b+c\mu)\alpha - 0.049(b+c\mu)\alpha^2 t_1^7) + h_oW_0\left[t_1 - 0.166\alpha t_1^2 + 0.025\alpha^2 t_1^5\right] + h_o(\sigma-1)\Big(0.5aT^2 \\ &- 0.29a\alpha T^4 - 0.085\alpha^2 T^6 - 0.33(b+c\mu)T^3 + 0.233\,T^5(b+c\mu)\alpha - 0.049(b+c\mu)\alpha^2 T^7\Big] \end{aligned} \tag{15}$$

Sales revenue collected over the cycle (SR):

$$\mathrm{SR} = pQ_0 + 0.15\sigma p\left(aT + 0.5b\,T^2 + 0.5c\,\mu T^2\right) \tag{16}$$

The total profit per unit time is:

$$\mathrm{TP}^o = \frac{1}{T}\left[\mathrm{SR} - \mathrm{OC} - \mathrm{PC} - \mathrm{HC} - \mathrm{DC} - \mathrm{SC}\right] \tag{17}$$

3.4. Case-II: Fuzzy Inventory Model, When $t > \mu$

In this section the fuzzy inventory model is presented through the signed distance method. Let

$$\hat{a} = (a_1, a_2, a_3), \quad \hat{b} = (b_1, b_2, b_3), \quad \hat{c} = (c_1, c_2, c_3), \quad \hat{\alpha} = (\alpha_1, \alpha_2, \alpha_3), \quad \hat{\mu} = (\mu_1, \mu_2, \mu_3)$$

and

$$\hat{\sigma} = (\sigma_1, \sigma_2, \sigma_3)$$

are triangular fuzzy numbers. By the signed distance method, the total cost per unit time is:

$$\mathrm{TC}^* = \frac{1}{4}\left(\mathrm{TC}_1 + 2\,\mathrm{TC}_2 + \mathrm{TC}_3\right) \tag{18}$$

$$\begin{aligned}
\mathrm{TC}_1 = \frac{1}{T}\Big[& A + c\,Q_0 + d_e\big[(x-y)(\sigma_1-1)(0.5a_1t_1^2 - 0.29a_1\alpha_1t_1^4 - 0.085\,a_1\,\alpha_1^2t_1^6 \\
& - 0.33(b_1+c_1\mu)t_1^3 + 0.233\,t_1^5(b_1+c_1\mu)\alpha_1 - 0.049(b_1+c_1\mu)\alpha_1^2t_1^7)\big] \\
& + y\,W_0[t_1 - 0.166\alpha_1t_1^2 + 0.025\alpha_1^2t_1^5] \\
& + y(\sigma_1-1)\big(0.5a_1T^2 - 0.29a_1\alpha_1T^4 - 0.085\,a_1\alpha_1^2T^6 - 0.33(b_1+c_1\mu)T^3 \\
& + 0.233\,T^5(b_1+c_1\mu)\alpha_1 - 0.049(b_1+c_1\mu)\alpha_1^2T^7\big) \\
& + (h_r-h_o)(\sigma_1-1)\big(0.5a_1t_1^2 - 0.29a_1\alpha_1t_1^4 - 0.085\,a_1\alpha_1^2t_1^6 - 0.33(b_1+c_1\mu)t_1^3 \\
& + 0.233\,t_1^5(b_1+c_1\mu)\alpha_1 - 0.049(b_1+c_1\mu)\alpha_1^2t_1^7\big) \\
& + h_o\,W_0[t_1 - 0.166\alpha_1t_1^2 + 0.025\alpha_1^2t_1^5] \\
& + h_o(\sigma_1-1)\big(0.5a_1T^2 - 0.29a_1\alpha_1T^4 - 0.085\,\alpha_1^2T^6 - 0.33(b_1+c_1\mu)T^3 \\
& + 0.233\,T^5(b_1+c_1\mu)\alpha_1 - 0.049(b_1+c_1\mu)\alpha_1^2T^7\big)\Big]
\end{aligned}$$

$$\begin{aligned}
\mathrm{TC}_2 = \frac{1}{T}\Big[& A + c\,Q_0 + d_e\big[(x-y)(\sigma_2-1)(0.5a_2t_1^2 - 0.29a_2\alpha_2t_1^4 - 0.085\,a_2\,\alpha_2^2t_1^6 \\
& - 0.33(b_2+c_2\mu)t_1^3 + 0.233\,t_1^5(b_2+c_2\mu)\alpha_2 - 0.049(b_2+c_2\mu)\alpha_2^2t_1^7)\big] \\
& + y\,W_0[t_1 - 0.166\alpha_2t_1^2 + 0.025\alpha_2^2t_1^5] \\
& + y(\sigma_2-1)\big(0.5a_2T^2 - 0.29a_2\alpha_2T^4 - 0.085\,a_2\alpha_2^2T^6 - 0.33(b_2+c_2\mu)T^3 \\
& + 0.233\,T^5(b_2+c_2\mu)\alpha_2 - 0.049(b_2+c_2\mu)\alpha_2^2T^7\big) \\
& + (h_r-h_o)(\sigma_2-1)\big(0.5a_2t_1^2 - 0.29a_2\alpha_2t_1^4 - 0.085\,a_2\alpha_2^2t_1^6 - 0.33(b_2+c_2\mu)t_1^3 \\
& + 0.233\,t_1^5(b_2+c_2\mu)\alpha_2 - 0.049(b_2+c_2\mu)\alpha_2^2t_1^7\big) \\
& + h_o\,W_0[t_1 - 0.166\alpha_2t_1^2 + 0.025\alpha_2^2t_1^5] \\
& + h_o(\sigma_2-1)\big(0.5a_2T^2 - 0.29a_2\alpha_2T^4 - 0.085\alpha_2^2T^6 - 0.33(b_2+c_2\mu)T^3 \\
& + 0.233\,T^5(b_2+c_2\mu)\alpha_2 - 0.049(b_2+c_2\mu)\alpha_2^2T^7\big)\Big]
\end{aligned}$$

$$\begin{aligned}\mathrm{TC}_3 = \frac{1}{T}\Big[& A + c\,Q_0 + d_e\big[(x-y)(\sigma_3-1)(0.5a_3t_1^2 - 0.29a_3\alpha_3t_1^4 - 0.085\,a_3\,\alpha_3^2t_1^6 \\ & - 0.33(b_3+c_3\mu)t_1^3 + 0.233\,t_1^5(b_3+c_3\mu)\alpha_3 - 0.049(b_3+c_3\mu)\alpha_3^2t_1^7)\big] \\ & + y\,W_0[t_1 - 0.166\alpha_3t_1^2 + 0.025\alpha_3^2t_1^5] \\ & + y(\sigma_3-1)\big(0.5a_3T^2 - 0.29a_3\alpha_3T^4 - 0.085\,a_3\alpha_3^2T^6 - 0.33(b_3+c_3\mu)T^3 \\ & + 0.233\,T^5(b_3+c_3\mu)\alpha_3 - 0.049(b_3+c_3\mu)\alpha_3^2T^7\big) \\ & + (h_r-h_o)(\sigma_3-1)\big(0.5a_3t_1^2 - 0.29a_3\alpha_3t_1^4 - 0.085\,a_3\alpha_3^2t_1^6 - 0.33(b_3+c_3\mu)t_1^3 \\ & + 0.233\,t_1^5(b_3+c_3\mu)\alpha_3 - 0.049(b_3+c_3\mu)\alpha_3^2t_1^7\big) \\ & + h_o\,W_0[t_1 - 0.166\alpha_3t_1^2 + 0.025\alpha_3^2t_1^5] \\ & + h_o(\sigma_3-1)\big(0.5a_3T^2 - 0.29a_3\alpha_3T^4 - 0.085\alpha_3^2T^6 - 0.33(b_3+c_3\mu)T^3 \\ & + 0.233\,T^5(b_3+c_3\mu)\alpha_3 - 0.049(b_3+c_3\mu)\alpha_3^2T^7\big)\Big]\end{aligned}$$

Sales revenue collected over the cycle (SR):

$$\mathrm{SR} = pQ_0 + 0.15\sigma p\left(aT + 0.5\,b\,T^2 + 0.5\,c\,\mu T^2\right) \tag{19}$$

The total profit per unit time is calculated as follows:

$$\mathrm{TP}^* = \frac{1}{T}\left[\mathrm{SR} - \mathrm{OC} - \mathrm{PC} - \widehat{\mathrm{HC}} - \widehat{\mathrm{DC}} - \widehat{\mathrm{SC}}\right] \tag{20}$$

4. Optimal Solution Procedure

The primary aim of the model is to find the values of t_1 and T, which can minimize the total cost per unit time TC^* and TC° throughout a complete cycle over time T, which maximize the total profit. The conditions required to minimize the total cost per unit time during the cycle time T are:

$$\frac{\partial(\mathrm{TC})}{\partial t_1} = 0 \quad , \quad \frac{\partial(\mathrm{TC})}{\partial T} = 0$$

$$\frac{\partial(\mathrm{TC}^*)}{\partial t_1} = 0 \quad , \quad \frac{\partial(\mathrm{TC}^*)}{\partial T} = 0$$

The condition for sufficiency is that TC and TC^* are convex functions over the cycle time T. The necessary and sufficient conditions to minimize the total cost function $TC(t_1, T)$ attains a local minimum at a critical point (t_1^*, T^*) if:

$$\boxed{D > 0, \quad \text{and} \frac{\partial^2 TC}{\partial t_1^2} > 0}$$

Where

$$D = f_{11}f_{22} - (f_{12})^2$$

and

$$f_{11} = \frac{\partial^2 TC}{\partial t_1^2}, \quad f_{22} = \frac{\partial^2 TC}{\partial T^2}, \quad f_{12} = \frac{\partial^2 TC}{\partial t_1 \partial T}$$

5. Numerical Illustration and Sensitivity Analysis

The numerical illustration and sensitivity analysis of the proposed fuzzy inventory model developed satisfying the necessary and sufficient conditions, and a numerical example has been solved. Data have been assumed randomly from the literature in appropriate units to obtain optimal values of t_1, T, TC$^\circ$, TC*, TP$^\circ$ and TP*, and to perform the sensitivity analysis. A numerical example has been presented to illustrate the proposed inventory model. The main objective is to determine the optimal values of t_1, T which minimize total cost per unit time and maximize the total profit. The values of different parameters are as follows:

$$A = 500, \quad Q_0 = 3000, \quad \sigma = 0.15, \quad \alpha = 0.07, \quad x = 0.07, \quad y = 0.05, \quad W_0 = 2000,$$
$$h_r = 0.17, \quad h_o = 0.12, \quad a = 100, \quad b = 5, \quad c = 0.5,$$
$$c_s = 100, \quad d = 0.07, \quad p = 125$$

1. **Case-I: When** $t < \mu$
   The optimal values of t_1, T and TC in the crisp model, which are $t_1^0 = 9.16$, $T^0 = 50.51$, $TC^0 = 7853$ and $TP^0 = 1392$ respectively and the optimal values of t_1, T and TC are obtained in the fuzzy model, which are $t_1^* = 9.15$, $T^* = 50.62$, $TC^* = 7830$ and $TP^0 = 2621$.

2. Case-II: When $t > \mu$
   The optimal values of t_1, T and TC in the crisp model, which are $t_1^0 = 9.04$, $T^0 = 62.65$, $TC^0 = 6196$ and $TP^0 = 1117$ respectively and the optimal values of t_1, T and TC are obtained in the fuzzy model, which are $t_1^* = 9.04$, $T^* = 62.53$, $TC^* = 6225$ and $TP^0 = 1438$.

5.1. Sensitivity Analysis for Case-I

Table 2: *Comparison of Crisp and Fuzzy Models for Different Values of a*

a	**Crisp Model**				**Fuzzy Model**						
	t_1°	T°	TC$^\circ$	TP$^\circ$	t_1^*	T^*	a_1	a_2	a_3	TC*	TP*
30	9.02	50.10	8044	1045	9.02	50.24	30	70	100	8013	2461
70	9.10	50.31	7935	1242	9.05	50.45	30	70	100	7918	2542
100	9.16	50.51	7853	1392	9.10	50.52	30	100	130	7803	2621
125	9.24	50.90	7785	1496	9.21	50.78	100	125	150	7762	2681
150	9.34	51.25	7716	1596	9.27	50.94	125	150	175	7693	2741

Table 3: *Comparison of Crisp and Fuzzy Models for Different Values of b*

b	**Crisp Model**				**Fuzzy Model**						
	t_1°	T°	TC$^\circ$	TP$^\circ$	t_1^*	T^*	b_1	b_2	b_3	TC*	TP*
1.0	9.13	52.05	7480	1336	9.13	52.07	0.2	1	3	7485	2893
3.0	9.15	51.50	7669	1342	9.14	51.40	1	3	5	7645	2763
5.0	9.16	50.60	7853	1392	9.15	50.62	3	5	7	7830	2621
7.0	9.17	49.78	8033	1421	9.16	49.90	5	7	9	8011	2485
10.0	9.18	48.75	8290	1471	9.18	48.61	7	10	13	8269	2315

Table 4: *Comparison of Crisp and Fuzzy Models for Different Values of c*

2*c	**Crisp Model**				**Fuzzy Model**						
	t_1°	T°	TC$^\circ$	TP$^\circ$	t_1^*	T^*	c_1	c_2	c_3	TC*	TP*
0.2	9.07	59.05	6494	1190	9.07	59.20	0.1	0.2	0.3	6472	2393
0.3	9.11	55.60	7093	1260	9.12	54.90	0.2	0.3	0.4	7094	2514
0.5	9.16	50.60	7853	1392	9.15	50.62	0.4	0.5	0.6	7830	2621
0.7	9.19	47.07	8475	1541	9.18	47.76	0.6	0.7	0.8	8455	2730
0.9	9.24	44.30	8987	1709	9.20	45.00	0.8	0.9	1.0	8485	2236

Table 5: *Comparison of Crisp and Fuzzy Models for Different Values of σ*

σ	**Crisp Model**				**Fuzzy Model**						
	t_1°	T°	TC$^\circ$	TP$^\circ$	t_1^*	T^*	σ_1	σ_2	σ_3	TC*	TP*
0.05	9.19	49.23	8072	1129	9.19	49.38	0.01	0.05	0.10	8047	2451
0.10	9.18	49.84	7996	749	9.18	50.01	0.05	0.10	0.15	7954	2541
0.15	9.17	50.10	7853	1392	9.16	50.62	0.10	0.15	0.20	7830	2621
0.20	9.14	51.09	7733	2063	9.14	51.05	0.15	0.20	0.25	7727	2704
0.25	9.12	51.70	7617	2778	9.13	52.08	0.20	0.25	0.30	7592	2781

5.2. Sensitivity Analysis for Case-II

Table 6: *Comparison of Crisp and Fuzzy Models for Different Values of a*

a	**Crisp Model**				**Fuzzy Model**						
	t_1°	T°	TC$^\circ$	TP$^\circ$	t_1^*	T^*	a_1	a_2	a_3	TC*	TP*
30	8.87	61.50	6450	787	8.87	61.70	70	80	90	6476	1249
70	8.97	60.29	6206	956	8.97	62.18	90	100	110	6333	1356
100	9.04	62.65	6306	1006	9.04	62.65	100	120	140	6225	1438
130	9.13	62.90	6190	1171	9.13	62.90	150	170	190	6115	1521
170	9.24	63.15	6070	1578	9.21	63.15	200	230	250	5993	1596

Table 7: *Comparison of Crisp and Fuzzy Models for Different Values of b*

b	**Crisp Model**				**Fuzzy Model**						
	t_1°	T°	TC$^\circ$	TP$^\circ$	t_1^*	T^*	b_1	b_2	b_3	TC*	TP*
1	9.00	66.53	5498	1215	9.02	66.53	2	3	4	5924	1376
3	9.02	64.55	5851	1185	9.03	64.33	2	3	4	6061	1536
5	9.06	63.00	6196	1171	9.04	62.70	4	5	6	6645	1438
7	9.08	60.75	6501	1193	9.10	60.14	5	7	9	7120	1336
10	9.08	58.70	6931	1185	9.10	58.87	8	10	12	6958	1023

Table 8: *Comparison of Crisp and Fuzzy Models for Different Values of c*

c	**Crisp Model**				**Fuzzy Model**						
	t_1°	T°	TC$^\circ$	TP$^\circ$	t_1^*	T^*	c_1	c_2	c_3	TC*	TP*
0.2	8.97	67.06	5402	1225	8.99	66.52	0.1	0.2	0.4	5506	1887
0.4	8.99	65.04	5684	1172	9.03	65.02	0.2	0.4	0.5	5735	1776
0.6	9.04	62.65	5854	1170	9.10	62.53	0.3	0.5	0.7	6225	1438
0.8	9.05	60.16	6653	1174	9.12	60.18	0.4	0.6	0.8	6669	1181
1.0	″	″	″	″	9.12	57.00	0.5	0.8	1.2	7256	1005

Table 9: *Comparison of Crisp and Fuzzy Models for Different Values of σ*

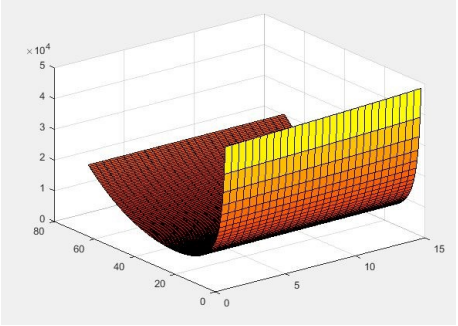
σ	**Crisp Model**				**Fuzzy Model**						
	t_1°	T°	TC$^\circ$	TP$^\circ$	t_1^*	T^*	σ_1	σ_2	σ_3	TC*	TP*
0.05	9.00	61.52	6334	165	9.00	61.34	0.00	0.05	0.10	6423	1331
0.10	9.01	62.08	6292	663	9.01	61.93	0.05	0.10	0.15	6312	1397
0.15	9.04	62.65	6196	1171	9.03	62.51	0.10	0.15	0.20	6216	1300
0.20	9.05	63.25	6100	1663	9.03	63.10	0.15	0.20	0.25	6100	1483
0.25	8.99	63.84	5997	2215	9.03	63.72	0.21	0.25	0.29	6020	1531

6. Graphical Illustration

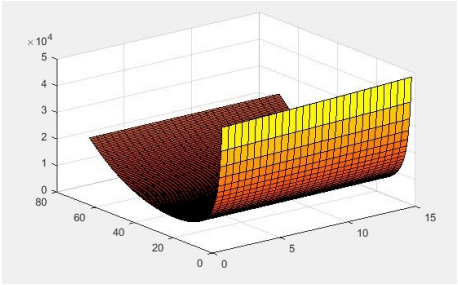
The graphical representation depicts the variation of total cost (TC) and total profit (TP) with respect to changes in model parameters such as a, b, c, σ, α, and μ. The comparative plots between crisp and fuzzy models illustrate that the fuzzy model yields more flexible and cost-effective results under parameter uncertainty.

6.1. For Case-I and Case-II

Convexity of total cost: To demonstrate the convexity of total cost per unit of inventory system, graphical representations of the convexity of TC^o and TC^* with respect to decision variables are presented in Figure 1a, Figure 1b, Figure 2a, and Figure 2b respectively.

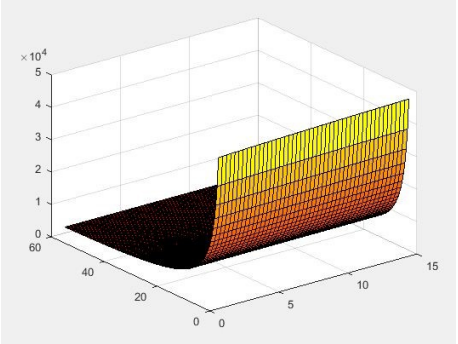


(a) *Total cost in crisp model.*

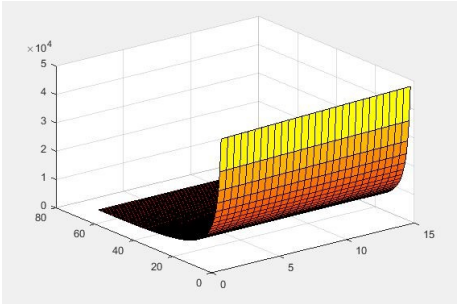


(b) *Total cost in fuzzy model.*

Figure 1: *Total cost variation in case-I.*

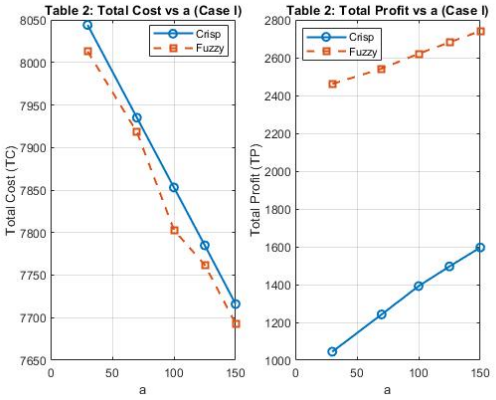


(a) *Total cost in crisp model.*

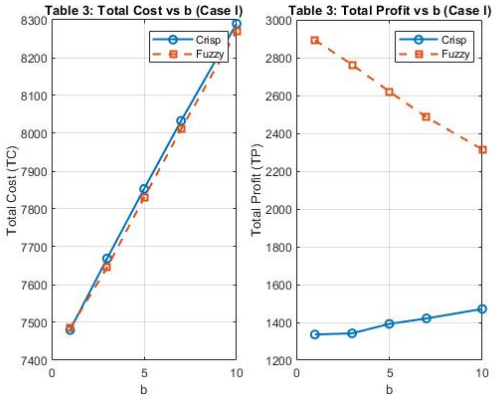


(b) *Total cost in fuzzy model.*

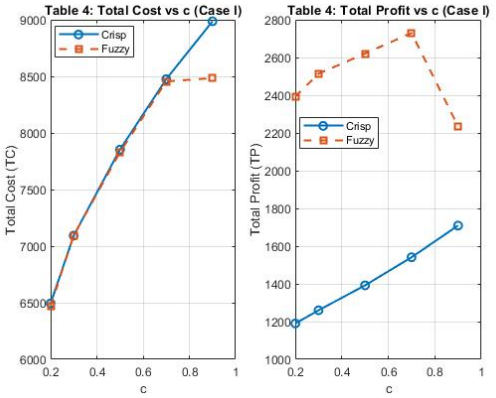
Figure 2: *Total cost variation in case-II.*



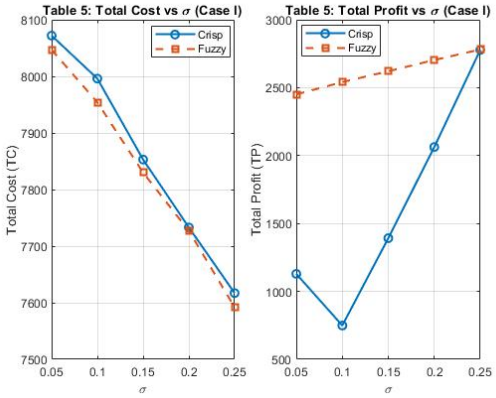
(a) *Total cost & profit in crisp & fuzzy model.*



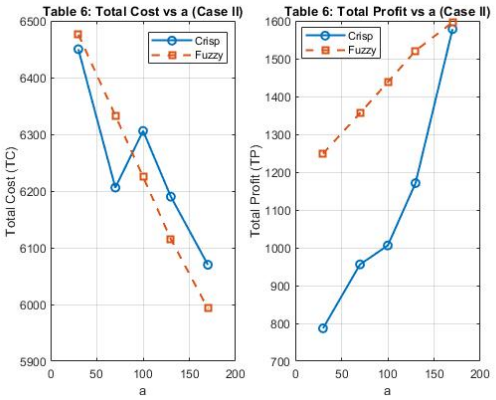
(b) *Total cost & profit in crisp & fuzzy model.*



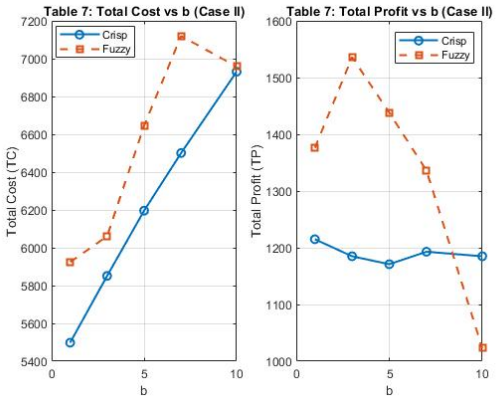
(c) *Total cost & profit in crisp & fuzzy model.*



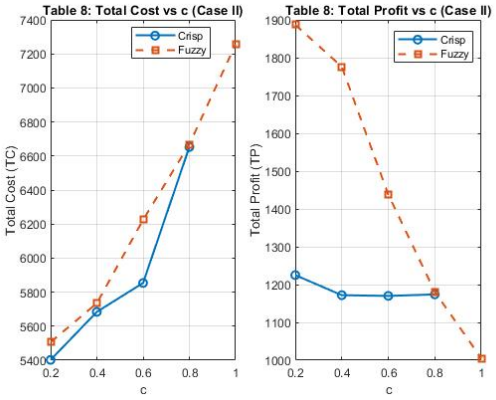
(d) *Total cost & profit in crisp & fuzzy model.*



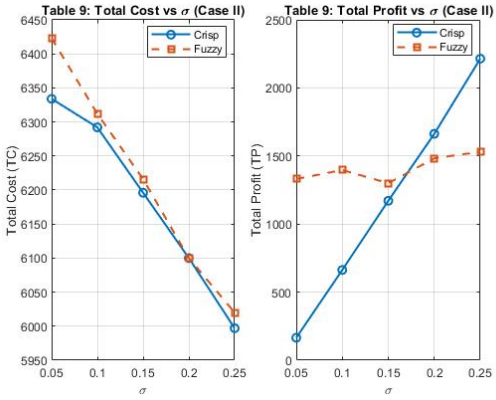
(e) *Total cost & profit in crisp & fuzzy model.*



(f) *Total cost & profit in crisp & fuzzy model.*



(g) *Total cost & profit in crisp & fuzzy model.*



(h) *Total cost & profit in crisp & fuzzy model.*

Figure 3: *Total cost & profit variation for both the cases.*

The following observations were made:

1. As the demand parameters b and c increase, optimal value of total cost per unit time TC^o and TC^* increases and the corresponding profit decreases. As the demand parameters a increases, optimal value of total cost per unit time TC^o and TC^* decreases; the corresponding profit increases.

2. As the parameters σ increase, the optimal value of total cost per unit time TC^o and TC^* decreases and there is an increase in the corresponding profit. As the parameters d increase, the optimal value of total cost per unit time TC^o and TC^* increases and there is a decrease in the corresponding profit.

3. As the parameters μ increase, the optimal value of total cost per unit time TC^o and TC^* decreases and there is an increase in the corresponding profit.

4. The optimal value of total cost per unit time in the fuzzy model is less than total cost per unit time in the crisp model and the profit is more in fuzzy model compared to crisp model.

Figure 3(a) shows that increasing the base demand parameter a lowers the total cost and increases profit, with the fuzzy model performing better than the crisp model. Figure 3(b) indicates that as the demand growth rate b increases, both models experience higher costs, while profits decline more sharply in the fuzzy case. Figure 3(c) highlights that rising nonlinear demand parameter c leads to higher costs and reduced profits, although the fuzzy model maintains relative advantage at moderate values. Figure 3(d) demonstrates that higher return rates σ decrease costs and substantially boost profits, particularly under the fuzzy model. Similarly, Figures 3(e)-3(h) (Case II) confirm the same trends: total cost decreases and profit rises with higher a and σ [Figures 3(e), 3(h)], while increasing b and c escalates costs and reduces profit [Figures 3(f), 3(g)], again with the fuzzy model consistently outperforming the crisp one.

7. Conclusion

In this paper, an inventory model has been described under two warehouses with fuzzy constraints. The objective of the work is to minimize the total inventory cost which includes ordering, storage and deterioration cost for both own and rented warehouses to get maximum profit. The study includes a numerical example and a sensitivity analysis of the model in both crisp and fuzzy modelling. The analysis shows that in the crisp model, the total cost per unit and corresponding total profit are highly sensitive to changes in b, σ and c, fairly sensitive to changes μ and α, less sensitive to changes in parameter a. In the fuzzy model, the total cost per unit and corresponding total profit are highly sensitive to changes in b, σ and c, fairly sensitive to changes μ and α, less sensitive to changes in a.

Additionally, the total cost per unit in the fuzzy model is less than in the crisp model and hence corresponding total profit is more in fuzzy model than in the crisp model.

References

[1] N.K. Sahoo , Bhabani S. Mohanty and P.K. Tripathy. Fuzzy inventory model with exponential demand and time-varying deterioration. Global Journal of Pure and Applied Mathematics. ISSN 0973-1768 Volume 12, Number 3 (2016), pp. 2573-2589.

[2] C.K. Jaggi, P. Gautam and A. Khanna. Inventory decisions for imperfect quality deteriorating items with exponential declining demand under trade credit and partially backlogged shortages. In P. Kapur, U. Kumar and A. Verma (Eds.), Quality, IT and Business Operations., Springer Proceedings in Business and Economics, pp. 213229, Singapore, 2018.

[3] A K Malik and Harish Garg (2021). An Improved Fuzzy Inventory Model Under Two Warehouses. Journal of Artificial Intelligence and Systems. 3115-129.

[4] C. C. Chou, Fuzzy economic order quantity inventory model, International Journal of Innovative Computing, Information and Control, vol.5, no.9, pp.2585-2592, 2009.
[5] Chakraborty, D., Jana, D. K. and Roy, T. K. (2018). Two warehouse partial backlogging inventory model with ramp type demand rate, three-parameter Weibull distribution deterioration under inflation and permissible delay in payments, Computers and Industrial Engineering, 123, 157-179.
[6] Chang, H., C., Yao, J., S., and Quyang, L.Y., (2006). Fuzzy mixture inventory model involving fuzzy random variable, lead-time and fuzzy total demand. European Journal of Operational Research, 69, 65-80.
[7] Dutta, P., Chakraborty, D., and Roy, A. R. (2007). Continuous review inventory model in mixed fuzzy and stochastic environment. Applied Mathematics and Computation, 188, 970-980.
[8] Lee, H. M. and Yao, J. S. (1998). Economic production quantity for fuzzy demand and fuzzy production quantity, European Journal of Operational Research, 109, 203-211.
[9] M. Vujosevic et al. (1996). EOQ formula when inventory cost is fuzzy, International Journal of Production Economics, 45(1996), 499-504.
[10] Malik, A. K. and Singh, Yashveer (2013). A fuzzy mixture two warehouse inventory model with linear demand. International Journal of Application or Innovation in Engineering and Management, 2(2), 180-186.
[11] Malik, A. K., Vedi, P., and Kumar, S. (2018). An inventory model with time varying demand for non-instantaneous deteriorating items with maximum life time. International Journal of Applied Engineering Research, 13(9), 7162-7167.
[12] Pakkala, T. P. and Achary, K. K. (1992). A deterministic inventory model for deteriorating items with two warehouses and finite replenishment rate, European Journal of Operational Research; 57, 71-76.
[13] Yadav, A.S., Kumar, A., Yadav, K.K. et al. Optimization of an inventory model for deteriorating items with both selling price and time-sensitive demand and carbon emission under green technology investment. Int J Interact Des Manuf (2023). https://doi.org/10.1007/s12008-023-01689-8
[14] Yadav, K.K., Yadav, A.S. & Bansal, S. Interval number approach for two-warehouse inventory management of deteriorating items with preservation technology investment using analytical optimization methods. Int J Interact Des Manuf (2024). https://doi.org/10.1007/s12008-023-01672-3
[15] Krishan Kumar Yadav , Ajay Singh Yadav, and Shikha Bansal. "Optimization of an inventory model for deteriorating items assuming deterioration during carrying with two-warehouse facility" Reliability: Theory & Applications, vol. 19, no. 3 (79), 2024, pp. 442-459. https://doi.org/10.24412/1932-2321-2024-379-442-459
[16] Krishan Kumar Yadav, Ajay Singh Yadav, and Shikha Bansal. "Optimization of a two-warehouse inventory management for deteriorating items with time and reliability-dependent demand under carbon emission constraints" Reliability: Theory & Applications, vol. 19, no. 4 (80), 2024, pp. 404-418. https://doi.org/10.24412/1932-2321-2024-480-404-418
[17] Mahata, Sourav, and Bijoy Krishna Debnath. "A profit maximization single item inventory problem considering deterioration during carrying for price dependent demand and preservation technology investment." RAIRO-Operations Research 56.3 (2022): 1841-1856.
[18] Mahata, Sourav, and Bijoy Krishna Debnath. "Impact of green technology and flexible production on multi-stage economic production rate (EPR) inventory model with imperfect production and carbon emissions." Journal of Cleaner Production 504 (2025): 145187.
[19] Debnath, Bijoy Krishna, Pinki Majumder, and Uttam Kumar Bera. "EOQ model in uncertain environment by using generalised intuitionistic fuzzy Laplace transformation." International Journal of Logistics Systems and Management 49.3 (2024): 412-437. https://doi.org/10.1504/IJLSM.2024.142619

[20] Rana, S.K., Kumar, A. Two-Warehouse Inventory Control for Deteriorating Items Using Hybrid and Stock-Dependent Demand with Partial Backlogging. Oper. Res. Forum 5, 97 (2024). https://doi.org/10.1007/s43069-024-00366-0

[21] Nwoba, P., Osisiogu, U., Okoro, C., & Nduka, U. (2025). An Inventory Model Under Exponential Demand and Weibull Deterioration Rates with Shortage-Dependent Partial Backlogging. American Journal of Mathematical and Management Sciences, 44(1), 49-68. https://doi.org/10.1080/01966324.2025.2492280

[22] Patra, Sourav Kumar, Susanta Kumar Paikray, and Rudra Mohan Tripathy. "A retailer's inventory model for deteriorating items under power pattern demand with shortages partially backlogged in both crisp and fuzzy environments." International Journal of Industrial and Systems Engineering 49.1 (2025): 96-118. https://doi.org/10.1504/IJISE.2025.144083

[23] Gupta, S., Mishra, V.K. Multi-item stochastic inventory model for deteriorating items with power demand pattern under partial backlogging and joint replenishment. Ann Oper Res 341, 963-991 (2024). https://doi.org/10.1007/s10479-024-05997-4

RELIABILITY RISK PROFILING OF TECHNICAL SYSTEMS USING PARAMETRIC COX REGRESSION WITH WEIBULL BASELINE

Iyappan M[1*], G. Sathya Priyanka[2], Soniya. K[3], Priyanka. G[4]

[1*]Associate Professor, St. Francis College, Bengaluru, India
[2]Assistant Professor, Knowledge Institute of Technology, Kakapalayam, Salem
[3]Associate Professor, St. Francis College, Bengaluru, India
[4]Assistant Professor, St. Francis College, Bengaluru, India

[1]iyappastat@gmail.com, [2]sathyapriyankastat@gmail.com, [3]soniyaofficial@gmail.com, [4]priyankagajendiran@gmail.com

Abstract

Reliability analysis of technical systems is vital in predicting failure behavior and improving system design under operational variability. Traditional reliability models often assume constant hazard rates, limiting their ability to model real world degradation mechanisms. This paper presents a Weibull based Cox Proportional Hazards Model to analyse system failure times with covariate influences such as operations stress, environmental temperature, and maintenance interventions. Simulation data is generated for 1000 units under controlled covariate conditions with right censoring. The model estimates hazard functions and survival probabilities using maximum and partial likelihood methods. The results show that the inclusion of time independent covariates significantly enhances the model's predictive ability for time to failure. The Weibull baseline provides flexibility in representing increasing or decreasing hazard trends typical in engineering systems. This study validates the model's robustness through simulation and establishes its applicability in predictive maintenance and reliability risk management.

Keywords: Cox Regression, Weibull Distribution, System Reliability, hazard Rate, simulation, Censoring

I. Introduction

Reliability engineering focuses on quantifying the performance and longevity of systems and components under operations conditions. Traditional models, such as exponential and log normal distributions, often assume constant hazard rates, which oversimplify the failure behavior of complex systems [9]. In real world applications such as electronic modules, mechanical parts, or thermal systems failure rates can vary with usage, environmental exposure, or maintenance status. This necessitates flexible modelling approaches to account for time varying risk and component specific attributes. The Cox Proportional Hazards Model (Cox, 1972) has been widely used in survival analysis, offering a semi parametric framework that incorporates covariates without specifying a baseline hazard [12]. However, integrating a Weibull distribution as the baseline enhances the model

by allowing estimation of shape and scale parameters, enabling detection of increasing or decreasing failure rates. This paper applies the Weibull Cox model to reliability data generated via simulation [4]. We assume a system whose failure time depends on operational temperature, usage load, and preventive maintenance status. Through this modelling, we aim to quantify the hazard associated with each covariate, derive survival functions, and demonstrate how the approach supports risk informed decision making [7].

Incorporating the Weibull distribution within the Cox framework bridges the gap between purely parametric and semi parametric models, enabling more precise risk stratification and failure time prediction [10]. This is particularly important for engineering systems where failure patterns are neither constant nor uniform, but influenced by cumulative stress, thermal exposure, and maintenance history. By simulating a large scale dataset with operational variability, this study replicates practical field conditions and assesses model responsiveness to these covariates [3]. The use of right censoring further reflects real world testing constraints, where not all units may fail within the observation period. This approach ensures the model remains both maintenance planners, and risk managers in industrial contexts.

II. Methodology

I. Model Specification

The hazard function under a Weibull distribution is given by:

$$h_0(t) = \lambda\gamma t^{\gamma-1} \tag{1}$$

Where

γ = shape parameter (indicates increasing / decreasing hazard)

λ = scale parameter

Incorporating this into the Cox model with covariates, the hazard function becomes:

$$h(t/X) = \lambda\gamma t^{\gamma-1} \exp(\beta_1 x_1 + \beta_2 x_2 + \beta_3 x_3) \tag{2}$$

where;

x_1: Operating temperature (^{0}C, continuous)

x_2: Load stress level (categorical: Low/Medium/High)

x_3: Preventive maintenance (binary: 1=Yes, 0=No)

The corresponding survival function is:

$$S(t/X) = exp[-\lambda t^{\gamma} exp(\beta_1 x_1 + \beta_2 x_2 + \beta_3 x_3)] \tag{3}$$

II. Censoring in Reliability Testing:

In reliability studies, censoring arises when the system is removed before failure. We consider right censoring, where the exact failure time is unknown for some units.

Let T_i be the actual failure time and C_i the censoring time. The observed time is:

$$Y_i = min(T_i, C_i) \tag{4}$$

And the event indicator:

$$\delta_i = \begin{cases} 1 & if\ T_i \leq C_i \\ 0 & otherwise \end{cases} \tag{5}$$

III. Parameter Estimation:

The full likelihood function, considering right censoring, is:

$$L(\beta, \lambda, \gamma) = \prod_{i=1}^{n} \left[h(t_i/X_i)^{\delta_i} S(t_i/X_i) \right] \quad (5)$$

We estimate:

$\beta = (\beta_1, \beta_2, \beta_3)$: Covariate effects
γ, λ: Weibull parameters

For partial likelihood (Cox, 1975), the baseline hazard is left unspecified. The partial likelihood for β is

$$L(\beta) = \prod_{j=1}^{k} \frac{exp(\beta^T X_j)}{\sum_{l \epsilon R(t_j)} exp(\beta^T X_l)} \quad (6)$$

Where $R(t_j)$ is the risk set at time t_j.

Let $\{(Y_i, \delta_i, X_i)\}_{i=1}^{n}$ denote the observed data.

The likelihood function is:

$$L(\theta) = \prod_{i=1}^{n} [h(Y_i/X_i)]^{\delta_i} [S(Y_i/X_i)] \quad (7)$$

Substituting Eq. (2) and (3), we get:

$$L(\lambda, \alpha, \beta) = \prod_{i=1}^{n} [\lambda \alpha Y_i^{\alpha-1} exp(\beta^T X_i)]^{\delta_i} exp[-\lambda Y_i^{\alpha} exp(\beta^T X_i)] \quad (8)$$

We numerically maximize the log likelihood function:

$$\log L = \sum_{i=1}^{n} \delta_i [\log \lambda + log\alpha + (\alpha - 1) log Y_i + \beta^T X_i] - \lambda Y_i^{\alpha} exp(\beta^T X_i) \quad (9)$$

Cox Partial likelihood (Estimation of β)
Given n observed events, the partial likelihood is:

$$L(\beta) = \prod_{i=1}^{n_e} \frac{exp(\beta^T X_i)}{\sum_{j \epsilon R_i} exp(\beta^T X_j)} \quad (10)$$

This can be optimized using Newton Raphson or other gradient based techniques.

III. Results

I Component Configuration and Covariates

A simulated dataset consisting of 1000 technical components was analysed using a parametric Weibull regression model. The system was tested under varying operational conditions involving:
We simulate 1000 components, each with the following attributes:

Operating temperature: Normally distributed $N(75, 5^2)$
Stress level: Categorical (Low=0, Medium=1, high=2)
Preventive maintenance: Binary (Yes=1, No=0)

The coefficients used:

$\beta_1 = 0.02$: Positive correlation of temperature with failure

$\beta_2 = 0.6$: Higher stress increases hazard

$\beta_3 = -0.5$: Maintenance reduces hazard

Weibull parameters $\gamma = 1.5$ (increasing hazard), $\lambda = 0.0003$

II Failure Time Generation

Using the inverse transformation method, failure time is:

$$T = \left[-\frac{In(U)}{\lambda \exp(\beta_1 x_1 + \beta_2 x_2 + \beta_3 x_3)} \right]^{1/\gamma} \quad (11)$$

Where $U \sim U(0,1)$

Censoring time $C \sim U(0,60)$

Observed time: $Y = \min(T, C)$

III Simulation Study and Model Estimation:

Out of 1000 units:

Censoring rate: 30 %

Mean failure time: 38.2 months

Median: 34.5 months

Table 1: *Estimated Cox Regression Coefficients (MLE)*

Covariate	Coefficient (β)	HR	p-value
Temperature	0.019	1.019	0.001
Stress Level (High=2)	0.62	1.86	0.004
Preventive Maintenance	-0.48	0.62	0.008

Estimated Weibull Parameters

Shape $\gamma = 1.53$ 1.8 (suggests increasing hazard)

Scale $\lambda = 0.00031$

Table 2: *Survival Probability Estimates*

Time (Months)	High Risk (95^0 C, high, no Maint)	Low Risk (70^0 C, Low, no Maint)
12	0.88	0.99
24	0.68	0.95
36	0.47	0.90
60	0.20	0.75

The Cox regression results indicate that higher temperature (HR=1.019) and high stress levels (HR=1.86) significantly increase failure risk, while preventive maintenance reduces it (HR=0.62). The estimated Weibull shape parameter ($\gamma = 1.8$) suggests an increasing hazard over time. Survival probabilities decline more rapidly for high-risk units, dropping to 20% by 60 months compared to 75% for low risk profiles.

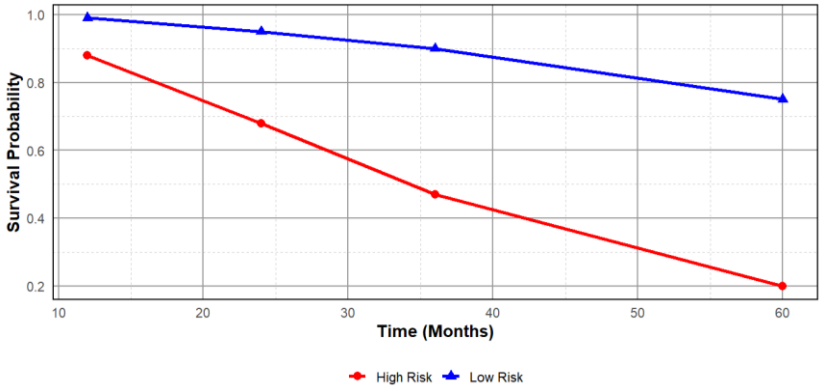


Figure 1: *Survival Curves for Risk Profiles*

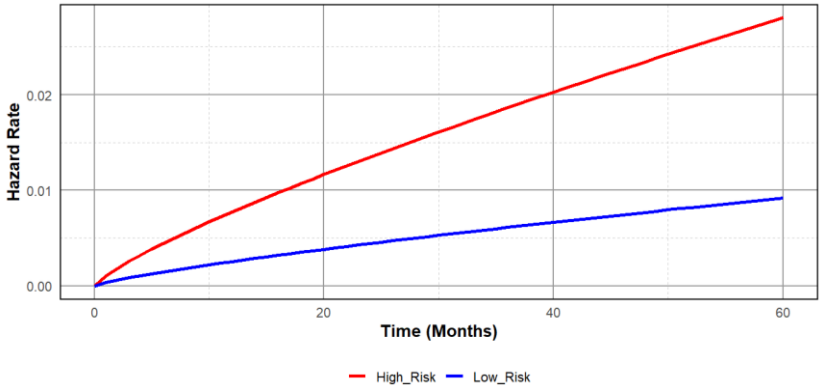


Figure 2: *Hazard Functions by Risk Profile*

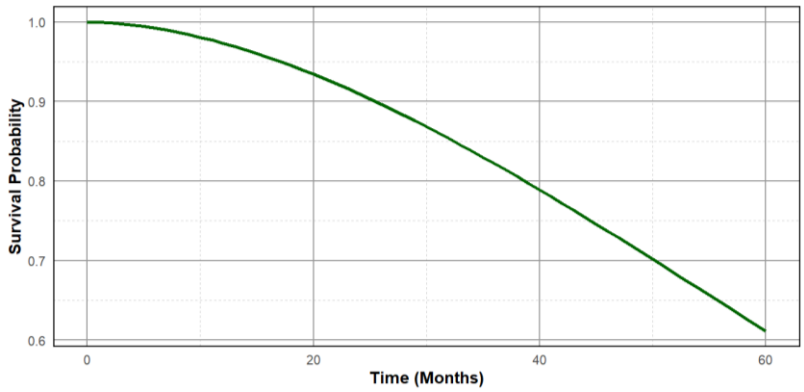


Figure 3: *Overall Survival Curve*

IV Weibull AFT Model Estimation:

We fit a Weibull Accelerated Failure Time (AFT) model. The model specification is:

$$\log(T_i) = \beta_0 + \beta_1.Temperature + \beta_2.Stress1 + \beta_3.Stress2 + \beta_4.Maintenance + \sigma.\in$$

Where

$Stress1$: Medium stress vs low (reference)

$Stress2$: High stress vs low
$Maintenance1$: Maintenance = Yes

Table 3: *Weibull AFT Model Results (n=1000)*

Covariate	Estimate	Std. Error	z-value	p-value
Intercept	4.722	0.530	8.91	<2e-16
Temperature (^{0}C)	-0.0066	0.0069	-0.95	0.3421
Stress (Medium)	-0.2782	0.1004	-2.77	0.0056
Stress (High)	-0.6172	0.0932	-6.63	3.53-11
Maintenance (Yes)	0.3439	0.0729	4.72	2.4e-06
Log (scale)	-0.5116	0.0469	-10.92	<2e-16

Scale $(\sigma) = \exp\big(Log(scale)\big) = \exp(-0.5116) \approx 0.6$
Model log likelihood = - 1532.3
Likelihood Ratio $\chi^2(df = 4) = 80.62, p < 0.0001$

The results demonstrate the effectiveness of the Weibull AFT model in capturing component failure dynamics under various operational stresses:

i. Stress levels (both medium and high) show significant negative coefficient, indicating accelerated failure relative to low stress conditions. The high stress level reduces log failure time more sharply ($\beta = -0.6172, p < 0.0001$)).
ii. Preventive maintenance exhibits a protective effect, increasing the log time to failure ($\beta = 0.3439, p < 0.001$), thus extending system reliability.
iii. Temperature does not show a statistically significant effect ($p = 0.34$) in this simulation setup, suggesting its influence may be overshadowed by categorical stress levels or sample variation.
iv. The estimate shape parameter $\left(\gamma = {}^{1}/_{\sigma} = {}^{1}/_{0.6} \approx 1.67\right)$ confirms an increasing hazard rate, consistent with real-world systems experiencing wear out over time.

These findings align well with theoretical expectations: systems under high stress and no maintenance fail sonner, whereas maintenance mitigates risk.

IV. Discussion

The Weibull Cox regression model successfully captures the varying failure rates of technical components influenced by environmental and operational covariates.
The model confirms:

Positive hazard association: High temperature and operational stress increase risk.
Protective role: Preventive maintenance significantly reduces hazard.
Non-constant hazard: Estimated $\gamma = 1$ implies the system becomes more failure prone over time

This model provides interpretability and flexibility, bridging the gap between parametric reliability models and data driven diagnostics. Compared to simpler models like exponential, the Weibull Cox approach better accommodates real world failure dynamics.

VI. Conclusion

This study demonstrates the utility of the Weibull based Cox regression model for analyzing the reliability of technical systems. Simulated data with covariate variation its robustness in predicting time to failure under right censored conditions. The model's integration of operational variables supports proactive risk assessment and can guide maintenance scheduling, system design, and lifecycle cost evaluation. Future work may involve applying this model to real industrial datasets and extending it to competing risk or recurrent failure framework.

References

[1] Anderson, J. A., & Tsiatis, A. A. (1982). Semiparametric estimation of regression parameters in the proportional hazards model. *Journal of the American Statistical Association*, 77(380), 1041–1048.

[2] Bagdonavicius, V., Levuliene, R., & Nikulin, M. (1999). Goodness-of-fit criteria for the Cox model from left truncated and right censored data. *Journal of Mathematical Sciences*, 96(5), 3146–3161.

[3] Breslow, N. (1974). Covariance analysis of survival data. *Biometrics*, 30(1), 89–102.

[4] Cox, D. R. (1972). Regression models and life-tables. *Journal of the Royal Statistical Society: Series B (Methodological)*, 34(2), 187–220.

[5] Cox, D. R. (1975). Partial likelihood. *Biometrika*, 62(2), 269–276.

[6] El Ghaoui, L., & Viallon, V. (2017). Solving the Cox proportional hazards model and its applications. *EECS Department, University of California*, Berkeley.

[7] Flemming, J. P., & Harrington, D. P. (1991). Counting processes and survival analysis. Wiley.

[8] He, S., & Duffy, D. (2005). A review of the Cox proportional hazards model in reliability analysis. *International Journal of Systems Science*, 36(5), 315–325.

[9] Iyappan M , Balaji M & G. Sathya Priyanka (2025). Cox's Regression Model for Reliability Analysis and Failure Time Prediction in Engineering Systems. Reliability: Theory and Applications, RT&A, No.2 (84), 250-258.

[10] Kalbfleisch, J. D., & Prentice, R. L. (2002). The statistical analysis of failure time data (2nd ed.). Wiley-Interscience.

[11] Kukush, A., & Chernova, O. (2017). Consistent estimation in Cox proportional hazards model with measurement errors and unbounded parameter set. arXiv preprint arXiv:1703.10940.

[12] Liang, K. Y., & Zeger, S. L. (1986). Longitudinal data analysis using generalized linear models. *Biometrika*, 73(1), 13–22.

[13] Lin, D. Y., Wei, L. J., & Weissfeld, L. (1989). Regression analysis of multivariate incomplete failure time data by modeling marginal distributions. *Journal of the American Statistical Association*, 84(408), 1074–1078.

[14] Therneau, T. M., & Grambsch, P. M. (2000). Modeling survival data: Extending the Cox model. Springer.

[15] Van Houwelingen, H. C., & Putter, H. (2012). Dynamic prediction in clinical survival analysis. CRC Press.

RT&A, No 4 (89)
Volume 20, December 2025

OPTIMIZING TRAFFIC SIGNAL TIMING FOR EFFICIENT FLOW THROUGH URBAN CROSSROADS

Bharathi Ramesh Kumar*[1], S. Geetha[2], S. Gayathri[3], A. K. Bhuvaneswari[4]

•

[1]Department of Mathematics, Vel Tech Rangarajan Dr.Sagunthala R&D Institute of Science and Technology, Avadi, Chennai, Tamil Nadu, India
[2]Department of Mathematics, National Engineering College, Kovilpatti, Tamil Nadu, India
[3,4]Department of Humanities and Science, Aarupadai Veedu Institute of Technology, Vinayaka Mission's Research Foundation (DU), Paiyanoor, Chennai-603 104, Tamil Nadu, India,
*Corresponding Author: brameshkumar@veltech.edu.in

Abstract

This paper presents an intelligent traffic signal control system aimed at optimizing vehicle flow at a two-lane crossroads intersection using a network flow-based framework. Rapid urbanization and the corresponding rise in vehicle usage have exacerbated congestion issues, especially at intersections where traditional fixed-time signal controls often result in inefficiencies and increased vehicle delays. The proposed system addresses these limitations by integrating real-time traffic data with principles of network flow theory to coordinate signal timing and vehicle movement dynamically. The intersection is modeled as a directed graph, where nodes represent entry and exit points, and edges signify possible vehicle paths. The system utilizes a weighted signal control algorithm that incorporates traffic volume, direction, and flow density to determine optimal signal phases. These weighted parameters guide the adaptive timing of traffic lights, allowing for parallel vehicle movement while preventing collisions. Specific constraints are applied to eliminate conflicting movements and maintain safety, thereby enhancing throughput and reducing total waiting times. A key objective of the model is to minimize total waiting time across all directions by identifying and enforcing necessary conditions for optimal traffic flow. To evaluate the performance of the proposed system, a simulation environment was developed to mimic real-world traffic conditions under various scenarios. Performance metrics such as average delay, queue length, and throughput were used for comparison against traditional signal control methods. Simulation results indicate significant performance improvements. The proposed system achieves a vehicle flow time of 804 seconds compared to 400 seconds in the existing system, with an optimized objective function value of 972. A numerical case study further illustrates the implementation, signal phase structuring, and resulting efficiency gains. In conclusion, the intelligent traffic signal control model demonstrates strong potential for reducing congestion and improving traffic management at urban intersections. Its adaptive, data-driven approach not only enhances current traffic flow but also allows for forecasting future patterns. The model is scalable, flexible, and suitable for integration with intelligent transportation systems, offering a proactive solution to modern traffic challenges.

Keywords: Traffic data, Signal distribution, Linear Programming Model, Flow Direction, Statistical Interference, XLSTAT Software

I. Introduction

Mathematical modeling involves the representation of real-world phenomena using mathematical symbols and relationships to account for observable parameters. This process helps identify and generate decision-making parameters relevant to the problem. As parameters are developed, the existing system can be adapted and improved. During the evaluation process, additional insights often emerge and are incorporated into the solution algorithms. However, the success of the model is not solely determined by its accuracy, but also by how easily it can be applied and how effectively it predicts future outcomes. Mathematical models provide valuable tools for analyzing system performance and addressing real-world challenges. Traffic congestion, a common experience for most people, demands timely and efficient solutions. Unfortunately, current systems often fall short in delivering such performance. The growth of vehicle numbers is influenced by various factors such as road infrastructure, time, speed, and vehicle capacity. In this context, traffic signals become a critical element, significantly affecting traffic flow. Poor arrangement or optimization of traffic signal parameters can lead to increased congestion and a higher risk of accidents. The placement of traffic lights at crossroads is strategically planned to ensure smooth vehicle flow and prevent obstruction. Ideally, vehicles should move without hindering the available traffic stream. However, it has been observed that the volume of traffic on congested roads is often significantly higher than that on specific crossroad segments, leading to inefficiencies in the traffic control system. In this study, we examine the direction and behavior of vehicle flow at a crossroads junction. The intersection allows vehicles to move efficiently along two main directions in a straight path. When traffic volume increases beyond a manageable threshold, the situation can be analyzed using mathematical modeling. Such models provide feasible solutions to optimize traffic flow. In recent research, various models have been proposed. Ruikang Luo and Rong Su [6] Investigated crossroads traffic using a stochastic process model, incorporating variable vehicle speeds and distribution times based on real-time data collected during peak hours in Singapore. The Nonlinear Programming (NLP) model was developed using data collected on the characteristics and capabilities of various vehicle types. The duration of traffic signal phases was estimated using statistical methods. Bo Lin et al. [1] presented dynamic traffic flow model for both urban and freeway networks, examining different methodologies along with their computational benefits and impacts on system performance. Rajendra et al. [4] presented a high-precision transport model, dynamic signal control algorithm aimed to distribute vehicle flow based on population density while minimizing congestion and stagnation. The model incorporated variables such as road length, quality, and vehicle speed to evaluate road capacity. Furthermore, Manigandan et al. [8] published foundational work on Traffic Management Systems (TMS), while Robertson and Transit [5] developed the TRANSYT software tool to optimize traffic signal timing and assess system performance. Lee et al. [2] proposed a Traffic Control System (TCS) to manage traffic flow and identify the most efficient signal path through a TCS junction area. The Intelligent Traffic Signal Control Problem (ITSCP) was addressed by Mckenney and White et al. [3] using a Multi-Dominant approach, which modeled vehicle flow considering human behavior, network structures, risk factors, and traffic demand. Geetha and Srividhya [7] analyzed a complexity of the ITSCP model is influenced not only by the number of arriving vehicles at a junction but also by the number of intersections, vehicle types, and user preferences within the network. Seyit Alperen Celtek [13] introduced a self-adaptive signal control algorithm that presents an innovative solution to mitigate urban traffic congestion. This approach dynamically adjusts signal timing parameters according to seasonal traffic demand variations, thereby enhancing operational efficiency within urban traffic networks. Myungeun Eom and Byung Kim [9] provided a comprehensive review of the scope of survey issues, assessment procedures, and methodologies related to the Intelligent Traffic Signal Control Problem (ITSCP), summarizing the key control parameters involved. Geetha

et al. [10] proposed a novel algorithm aimed at optimizing crossroad traffic light coordination to effectively reduce vehicle delay times during transit. The traditional fixed-time control system, as highlighted Balamurugan et al. [11], considered outdated. As a response, an ITS-based method known as ratio-monotonic scheduling has been proposed to determine the optimal signal timing, with its outcomes compared to alternative scheduling methods. Kavitha and Rayalu [12] Explored real-time signal control improvements, revealing that delays and vehicle queue lengths can be significantly minimized compared to those under static signal timing systems. Uddin et al. [14] Enhanced traffic signal control strategies using swarm intelligence techniques and assessed computational efficiency. The outcomes indicate a strong correlation between accurate traffic data usage and the effectiveness of the proposed method. Current eco-traffic systems adjust signal durations (green/red), yet inefficiencies arise when vehicle arrivals do not match the allocated green time, resulting in wasted time and increased costs. Pachiyappan et al. [15] Noted that traffic signal control systems have evolved considerably in recent years, especially with the implementation of the Advanced Traffic Signal Control System (ATSC), where timing adapts through RTC (Real-Time Control). A genetic algorithm is applied within this system for parameter optimization. Furthermore, a new lane bypass strategy was developed to reroute traffic, thereby improving flow in metropolitan traffic grids. Premila et al.[16] Contributed to this area by developing a traffic optimization model based on a genetic algorithm, implemented in MATLAB. In this study, we adopt a network flow model to address the traffic signal control problem. The goal is to enable smooth vehicle movement across intersections, especially in horizontal directions, without the risk of collision. The traffic signal pattern at the intersection is modeled to accommodate bi-directional lane flows effectively. Vehicle flow at the intersection can proceed in parallel directions without resulting in collisions. This model considers key constraints such as traffic volume and the weight or influence of the traffic signal system. The proposed design aims to minimize total waiting time across all directions by first identifying the necessary conditions for optimal flow. Ultimately, the system's performance is analyzed, and vehicle flow patterns are forecasted to enhance traffic network management. The rest of the paper summarized as follows: In chapter 2 proposed the mathematical model and methodology of this work. In chapter 3 discussed the traffic signal parameter assignments. In chapter 4 discussed the numerical example and conclusion.

II. Methods and Methodology

The objective of this paper is to develop a mathematical model for managing traffic flow at intersections and to determine the optimal green light duration for vehicle movement in each direction. Traffic flow is not uniformly distributed across the network, making efficient signal timing critical. The proposed model focuses on the intersection point where two traffic streams converge. It takes into account key constraints, such as traffic volume and the relative influence (or weight) of the traffic signal system, to ensure smooth and balanced vehicle flow.

I. Signal light distribution

This model predicts that the labelled points are controlled by traffic signal lights, $a, b, c, d, e, f, g \text{ and } h$ each of which is colored green, yellow and red In traffic networks, paths are typically represented as flows between nodes, with the connections referred to as edges. These edges indicate the movement of traffic between two points without intersecting other flows. The first step is to identify the permissible directions of vehicle movement at the intersection. Begin by defining distinct initial flows. Establish basic assumptions, such as identifying flows involving left-turning signals. Determine whether the current left-turn signal flow shares the same end nodes as

a previously established flow. For example, flows such as A1 and D1 may not operate in parallel due to conflict, while D2 and B1 or B2 and C1 might function in parallel safely. (iv) Represent each traffic flow using its associated nodes in the network. (v) Define an edge between two nodes in the traffic signal network if and only if the sequential flows represented by these nodes are compatible and part of a continuous movement from one intersection to another. These relationships help define the connectivity and coordination within the traffic management system, particularly for multi-road intersections.

Properly resolving intersection behavior reduces driver conflict, enhances safety, and supports uninterrupted vehicle movement. The traffic management system incorporates multiple parameters essential for analyzing and modeling signal systems. The following section discusses key parameters relevant to the mathematical modeling of such systems. Flow Volume: This refers to the total number of vehicles that arrive and pass through a specified intersection node over a given time period. Flow Density: It denotes the number of vehicles occupying a certain length of road within a specified node, usually expressed in vehicle units per kilometer (v/km). To optimize the performance of an intersection junction, one must consider scenarios such as flooded flow traffic, which occurs when the number of vehicles at a node reaches or exceeds its capacity. The maximum vehicle capacity depends on the design and limitations of the intersection and is typically measured in vehicles per hour. However, traffic flow may vary across different intersections due to several influencing factors: Traffic layout and signal arrangements. Frequency of vehicle arrivals at the junction. The curvature or radius of the road. Right-turning movements, especially those conflicting with oncoming traffic from the opposite direction Phase: A phase represents a segment of the complete traffic signal cycle, assigned to specific traffic movement patterns. Each phase ensures a controlled movement for certain vehicle flows and may be subdivided into sub-flows to manage different traffic directions within the same signal cycle.

II. Possible Flow Directions

Traffic Flow Directions and Hypotheses of Intersection Behavior. The direction of traffic flow must be followed according to the labeled points outlined below:

- Flow A1 = (A2, D2, B2, C1, C2)
- Flow A2 = (A1, D2, B2)
- Flow D2 = (A1, A2, D1, D2, B1, C1, C2)
- Flow D1 = (D2, C1, C2)
- Flow B2 = (A1, A2, D2, B1, C1)
- Flow B1 = (D2, B2, C1)
- Flow C1 = (A1, D2, D1, C1)

Intersection Hypotheses: Right-turn movements do not intersect with left-turn flows, as the waiting time for such transitions is assumed to be zero. The remaining left-turn flows—specifically from nodes A1 and C1—are governed by traffic signal timing. In this configuration, A2, D1, B2, and C2 represent straight-through movements, while A1, D2, and C1 are left-turn flows. There is a single right-turn movement, represented by B1. Two nodes are considered connected if the flow between them is parallel and aligns consecutively, allowing smooth transition from one point to the next. The primary goal of the optimized traffic signal control system at the intersection is to prevent collisions and minimize overall vehicle waiting time. The timing for each directional flow must correspond to the vehicle's current position; otherwise, it is excluded from the signal schedule.

Table 1: *The total number of vehicles arriving from the each direction*

Date	Time	Red Signal Duration	Green Signal Duration	N-S	W-E	S-N	E-W	Total No of Vehicles
02-02-2025	7am to 8 am	450	600	112	196	151	113	572
				151	226	172	122	671
				182	244	202	154	782
				196	241	202	166	805
				184	222	191	157	754
				179	208	183	149	719
02-03-2025	7am to 8 am	450	600	279	302	247	221	1049
				282	302	254	221	1059
				277	289	245	219	1030
				281	299	256	211	1047
				278	299	245	213	1035
				249	278	202	177	906
02-04-2025	7am to 8 am	450	600	116	179	129	111	535
				191	162	177	141	480
				189	202	166	133	501
				188	221	166	142	529
				187	211	203	167	581
				195	233	181	176	590
02-05-2025	7am to 8 am	450	600	189	241	123	159	593
				141	155	123	100	519
				129	145	110	91	475
				123	139	119	89	470
				131	165	129	88	513
				133	166	98	88	485
				124	109	89	81	403
02-06-2025	7am to 8 am	450	600	129	187	154	97	547
				146	171	123	95	581
				134	167	112	91	568
				136	166	111	84	592
				129	141	134	111	597
				133	129	113	86	537
				123	131	104	92	526

Real-time traffic data was collected at the Solinganallur junction between 7:00 a.m. and 8:00 a.m. over the course of a week. This data was segmented into 10-minute intervals, with each cycle defined as 600 seconds in length. It is assumed that 2 vehicles are served per second, and vehicle arrivals are not limited. The objective is to compute the total waiting time and compare the results between the existing and proposed signal control methods.

III. Data Collection:

Traffic data was gathered from a high-density urban intersection during peak hours over a one-

month period. The key parameters recorded include:

- Vehicle count
- Timestamp
- Signal phase
- Day of the week
- Signal cycle time

These variables form the basis for in-depth analysis of the intersection's performance and effectiveness of signal timing strategies.

Table 2: *Maximum significant vehicle flow level for each direction*

Marginal	Information for Sub Flow	Waiting Time	Moving Time	Total Time
Before Divider	Total Flow	450	150	600
After Divider	Flow P = (A1,A2,D2) Q = (D2,D1,C1,C2) R = (B1,C1,D2)	250	350	600
	Flow P = (A1,A2,D2) Q = (B1,B2,,D2) R = (D2,D1,C1,C2)	250	350	600
	Flow P = (A1,A2,D2,D1) Q = (B2,B1,C1,D2) R = (D2,D1,C1,C2)	300	300	600

The above flow considers only the straight-through direction. However, the traffic management system must account for the possibility of left or right turns during this time period. Therefore, the actual vehicle flow volume at the intersection should be determined by considering various possible path combinations. Assumptions can be made that the number of vehicles passing through each path within the given time intervals are uniformly distributed. To minimize the waiting time for all arriving vehicles, the system must be optimized by assigning different weights to each path, reflecting the varying flow volumes.

III. TRAFFIC SIGNAL PARAMETERS ASSIGNMENT

The traffic flow time at an intersection junction is initially set with equal length and weight for each flow. However, the existing flow times may be longer for more congested flows, such as those involving right or left turns where vehicle density is higher. In the traffic network, the four straight-through roads connect to C2, while the other flows are designated for left or right turns. The time intervals for each direction are assigned accordingly based on the flow characteristics.

$$A2 \to x_1,\ D1 \to x_3,\ B2 \to (x_1 \,\&\, x_2),\ C2 \to (x_3),\ A1 \to x_1,\ D2 \to (x_1, x_2, x_3)$$

The objective function of the mathematical representation for the above traffic network model is defined as follows:

$$Z = \delta_1 (2x_1 + x_2 + 2x_3) + \delta_2 (2x_1 + 3x_2 + 2x_3)$$

Subject to the constraint as follows:

$$x_1 + x_2 + x_3 = 600,\ \ x_1 \geq 150,\ \ x_1 + x_2 \geq 150,\ \ x_2 \geq 150,\ \ x_3 \geq 150,\ x_1 + x_2 + x_3 \geq 150$$

Table 3: *Initial flow time*

Marginal	Red Light	Green Light	Total
(A1,A2)	145	205	350
(B2)	133	217	350
(C1)	218	132	350
(D1)	225	125	350
(D2,B1)	225	125	350
Total	946	804	

Now, split the actual vehicle at each intersection junction table as follows:

Table 4: *Flow index*

S.No	Flow Index	Actual Traffic Flow for Certain Time
1	A1	112
2	A2	151
3	B1	112
4	B2	252
5	C1	196
6	C2	271
7	D1	113
8	D2	252
Total		1459

The calculated traffic flow for each direction is as follows: SNS = (263/1459) = 0.18 x 100 = 18, SWE = (309/1459) = 0.2117 x 100 = 21.11, TLR = (748/1459) = 0.5125 x 100 = 51.26.

By the data, the current minimal flow is 400 second. The total flow of green light is 80seconds. The construed new model for the above problem is as follows:

$$z = 18 S_{NS} + 21.11\ S_{WE} + 51.26 T_{LR}$$

Subject to the constraints:

$$S_{NS} + S_{WE} + T_{LR} = 804,\ S_{NS} \geq 120,\ \ S_{NS} + S_{WE} \geq 120,\ S_{WE} \geq 120,\ \ S_{WE} + T_{LR} \geq 120,\ \ T_{LR} \geq 120,\ \ S_{Ns} + S_{WE} + T_{LR} \geq 120$$

Using Tora Software, we can get the optimal value of the traffic flow direction is

$$x_1 = 19,\ x_2 = 8,\ x_3 = 9$$

The objective function value is $972.22 \approx 972$. Using M/M/1 infinite queuing model to using XLStat, calculate the predicate number of passing vehicle and calculate total waiting time of the

traffic length.

Table 5: *Queue length for each direction*

Lq1	Wq1	Lq2	Wq2	Lq3	Wq3	Lq4	Wq4	Lq	Wq
0.1651	0.3318	0.5058	0.5807	0.3002	0.4474	0.1681	0.3348	1.1394	1.6948
0.3002	0.4474	0.6726	0.6696	0.3895	0.5096	0.1960	0.3614	1.5584	1.9881
0.4362	0.5392	0.7840	0.7229	0.5373	0.5985	0.3123	0.4562	2.0698	2.3170
0.5058	0.5807	0.7648	0.7140	0.5373	0.5985	0.3268	0.4918	2.1709	2.3851
0.4458	0.5451	0.6490	0.6511	0.4804	0.5659	0.3245	0.4651	1.8998	2.2340
0.4219	0.5303	0.5697	0.6162	0.4410	0.5422	0.2923	0.4414	1.7250	2.1303
0.5918	0.6281	0.8765	0.7644	0.6607	0.6637	0.4804	0.5659	2.6095	2.6222
1.0250	0.8266	1.2010	0.8948	0.8034	0.7138	0.6417	0.6581	3.6769	3.1014
1.0472	0.8355	1.2010	0.8948	0.8945	0.7525	0.6431	0.6548	3.7410	3.1377
1.0104	0.8207	1.0998	0.8562	0.7045	0.7259	0.6315	0.6488	3.5323	3.0185
0.2435	0.4029	0.3687	0.4918	0.1622	03288	0.0929	0.2488	0.8616	1.4725
0.2191	0.3822	0.2618	0.4177	0.2364	0.3970	0.1622	0.3288	0.8796	1.5259
0.2329	0.3940	0.2191	0.3822	0.1681	0.3348	0.0973	0.2548	0.7176	1.3659
0.1992	0.3644	0.2259	0.3881	0.1424	0.3081	0.1114	0.2725	0.6791	1.3333
0.2736	0.4266	0.4362	0.5392	0.1864	0.3525	0.1290	0.2933	1.0248	1.6118
0.2730	0.4266	0.4654	0.5570	0.1960	0.	0.1114	0.2725	1.0459	0.6177
0.2544	0.4118	0.3850	0.5066	0.1833	0.3496	0.1507	0.3170	0.5736	1.5851
0.24	0.4	0.4219	0.5303	0.1802	0.3466	.01397	.03051	0.9819	1.5822
0.2618	0.4177	0.1992	0.3644	0.1593	0.3259	0.0801	0.2311	0.7004	1.3392
0.2435	0.4029	0.1864	0.3525	0.1163	0.2785	0..885	0.2429	0.6349	1.2770
0.1479	0.3140	0.2090	0.3733	0.1290	0.2933	0.0929	0.2488	0.5790	1.2296
0.1651	0.3318	0.2495	0.4029	0.1424	0.3081	0.1019	0.2607	0.6531	1.3037
0.1771	0.3437	0.2507	0.4088	0.1536	0.32	0.1043	0.2637	0.6858	1.336
0.1864	0.3525	0.2329	0.3940	0.1163	0.2785	0.0885	0.2429	0.6243	1.2681
0.1564	0.3229	0.1992	0.3644	0.0951	0.2518	0.0907	0.2459	0.5415	1.1854
0.1681	0.3348	0.2768	0.4296	0.1290	0.2933	0.1043	0.2637	0.6784	1.3214

Table 6: *Path flow Predictions*

Variable	Mini	Max	Mean	Std.Deviation
Lq = (N1^2)/(O1*(O1-N1))	-602.022	598.002	0.488	53.136
Wq = (N1)/(O1*(O1-N1))	-1.002	0.998	0.002	0.089

IV. Discussion

This study analyzes a network-based traffic signal control system and its associated model, which is applied at a crossroads junction. The connected roadway paths are segmented into multiple directional flows to manage and guide vehicle movement effectively. The proposed approach is evaluated against the existing system, showing a notable improvement—while the current model allows 400 seconds of vehicle flow time, the proposed algorithm achieves 804 seconds, with an objective function value of 972. The network flow model provides distinct signal

control for specified flow directions. This model contributes to enhancing the overall efficiency of traffic signal operations. Results clearly indicate that the proposed system outperforms the existing traffic flow model. Furthermore, the benefits of the new signal control approach over conventional methods are thoroughly outlined. The construction of the proposed scheme is statistically validated, offering time savings, economic benefits, and equitable access for all traffic participants.

References

[1] Bao-Lin, Ye. Weimin, Wu. Keyu, Ruan. Lingxi, Li. Tehuan, Chen. Huimin, Gao. and Yaobin, Chen. (2019). A Survey of Model Predictive Control Methods for Traffic Signal Control, *IEEE/CAA Journal of Automatica Sinica*, 6(3).

[2] Lee, S. Wong, S.C. and Varaiya, P. (2017). Group-based hierarchical adaptive traffic-signal control parts I: Formulation. *Transportation Research Part B: Methodological*, 105:1–18.

[3] Mckenney, D. and White, T. (2013). Distributed and adaptive traffic signal control within a realistic traffic simulation. *Engineering Applications of Artificial Intelligence,* 26(1):574–583

[4] Rajendra, S. Parmar, Bhushan, Trivedi. and Aleksandar, Stevanovic. (2018). A Model with Traffic Routers, Dynamically Managing Signal Phases to Address Traffic Congestion in Real Time, *Journal of Transportation Technologies,* 8: 75-90.

[5] Robertson, D. And Transit I. (1969). A traffic network study tool Retrieved from https://trid.trb.org/view/115048.

[6] Ruikang, Luo. and Rong, Su. Traffic Signal Transition Time Prediction Based on Aerial Captures during Peak Hours, *16th International Conference on Control, Automation, Robotics and Vision (ICARCV)*, 13-15 Shenzhen, China, (2020).

[7] Geetha, C. Pachiyappan, D. and Srividhya, k. (2024). Acceptance sampling plan based on truncated life tests for Rayleigh distribution. Reliability: theory & applications, 19(4(80)):431-435.

[8] Manigandan, P. Alam, M. S. Alharthi, M. Khan, U. Alagirisamy, K. Pachiyappan, D. and Rehman, A. (2021). Forecasting natural gas production and consumption in United States-evidence from SARIMA and SARIMAX models. *Energies*, *14*(19):6021.

[9] Myungeun Eom and Byung-In Kim. (2024) the traffic signal control problem for intersections: a review", *Eom and Kim European Transport Research Review*, 1-20.

[10] Geetha, C. Jayabharathi, S. Uddin, M. A. and Pachiyappan, D. (2024). Two-stage group acceptance sampling plan for half-normal distribution. Reliability: Theory & Applications, 19(4 (80)):835-841.

[11] Balamurugan, V. Ragavendran, C. Arulbalachandran, D. Alrefaei, A. F. and Rajendran, R. (2024). Green synthesis of silver nanoparticles using Pandanus tectorius aerial root extract: Characterization, antibacterial, cytotoxic, and photocatalytic properties, and ecotoxicological assessment. *Inorganic Chemistry Communications*, *168*:112-882.

[12] Kavitha, S. Rayalu, G. M. Pachiyappan, D. and Manigandan, P. (2023). Forecasting of Extreme Risk Using Markov switching GARCH Models: Evidence from Global Energy Markets. Reliability: Theory & Applications, 18(4(76)):325-337.

[13] Seyit Alperen Celtek. (2024), Real-time traffic signal control with swarm optimization methods, *Measurement*, 166:108-206.

[14] Uddin, M. A. Geetha, C. Khan, M. A. Srividhya, K. and Duraisamy, P. Exploring the impact of economic growth and sources of electricity production in India: New insights from sectoral analysis using NARDL approach. Journal of Infrastructure, Policy and Development, 8(10).

[15] Pachiyappan, D. Jayabharathi, S. Evanjalin, Y. G. and Kavitha, S. (2025). Forecasting Volatility in Indian National Stock Exchange Using A Markov Switching GARCH Model. *Reliability: Theory & Applications*, *20*(2(84)):429-446.

[16] Premila, S. C. Jayabharathi, S. Kanagajothi, D. and Pachiyappan, D. (2025). Estimating The Fréchet Distribution's Scale Parameter Using Bayesian Methods for Symmetric and Asymmetric Loss Functions. Reliability: Theory & Applications, 20(2 (84)):227-233.

RELIABILITY AND PERFORMANCE ANALYSIS OF AN UNRELIABLE RETRIAL QUEUEING SYSTEM WITH NEGATIVE ARRIVALS

[1]BELAIZA DIHIA AND [2]TALEB SAMIRA

•

[1,2]University of Science and Technology Houari Boumediene USTHB,
Departement of Probability and Statistic, Faculty of Mathematics,
RIIMA laboratory, El-Alia, Bab Ezzouar, B.P. 32,16111, Algiers, Algeria.
[1]dihia.belaiza@usthb.dz and [2]staleb@uhthb.dz

Abstract

In this paper, we foccus on a single repairable server retrial queueing system with negative arrivals and two types of breakdowns (passive and active). We assume that the customer in service is lost whenever an active breakdown occurs. Once the repair is completed, the server returns to an idle state. To obtain the system performance metrics, the matrix geometric technique is used combined with direct truncation method. From the standpoint of reliability analysis, we investigate the mean time to the first failure of the system by using the Laplace transform method. Finally, we study numerically the impact of system metrics on the mean number of customers in the orbit, the server state probabilities, the reliability function and the mean time to the first failure.

Keywords: Retrial Queue, Negative Arrivals, Passive and Active breakdowns, Reliability Analysis, Unreliable Server.

1. INTRODUCTION

Queueing systems with retrials constitutes a key component of modern teletraffic theory.A distinctive aspect of retrial queues is that when an arriving customer finds the server occupied, they enter a retrial group (orbit) and attempt service again after a random delay. The concept of retrial queues has found broad application in modeling challenges within telephone switching and computer systems. Artalejo and Gomez-Corral [3]ite and Falin and Templeton [12] have authored monographs that extensively outline the fundamental characteristics and principles of retrial queues. These comprehensive works serve as valuable resources, providing a thorough understanding of the theory behind retrial queues and their key features. Additionally, a recent survey conducted by Kim and Kim [17] provides valuable insights.

Queues involving servers that can breakdown and later undergo repair are often observed in practical scenarios. When breakdowns or repairs occur, they disrupt the service and result in increased waiting times for customers. These interruptions also provide an additional opportunity for arriving customers to enter a retrial orbit. Customers whose service is stopped by a failure have several options: they can choose to remain at the server until the repair is complete, leave the system entirely, or return to the retrial orbit. The breakdowns can be categorized as either active or passive, depending on whether they occur during the server working period or idle periods. Additionally, failures can happen randomly after a distinct amount of service time or just before service is about to start. In the paper of Taleb and Aissani [28] we can found a comprehensive source of references on retrial queues with failures, covering a vast range of studies from the earliest works to the most recent publications. Their research offers an extensive compilation of references,

DOI: https://doi.org/10.24412/1932-2321-2025-489-651-664

providing valuable insights into the dynamics and analysis of queues affected by failure events. See also Aissani et al [1], Zirem et al [30], Gao et al [14] and Lisovskaya et al [21] and the references therein.

Negative arrivals in queueing systems, also known as G-Networks, have inspired several researchers during the last 15 years. Models with negative arrivals are successfully used in computer Networks and Neural Networks. In computer Networks, positive claims are tasks (programs) and negative claims are computer viruses . In Neural Networks, negative and positive customers may represent inhibitory and excitatory signals, where the number of customers in the queue corresponds to the neuronal input potential. Gelenbe [15] was the first to introduce a new class of queueing processes in which customers are either negative or positive. Positive customers are primary customers who enter the system with the intention of getting served and then leaving the system. Negative customers cause damage to systems. In the simplest form, a negative customer eliminates a positive or a batch of positive customers according to a precise killing discipline. Removing policies can be classified as follows:

• Negative arrivals that eliminate all customers in the system or from a specific part of it, whether in service or waiting in the buffer (catastrophes, disaster),

• Negative arrivals that remove a positive customer at both edges of the queue (end of queues (RCE) and head of queues (RCH)),

• Negative arrivals that cause breakdowns to the service,

• Negative customers that eliminate random parts of work from the system.

The probability of completing service for positive customers can be influenced by the rate of negative arrivals. Basically, more negative arrivals join the queue, the shorter the queue becomes, which decreases the possibility of completing service and also joining the orbit in some cases.

The subject of negative arrivals in queueing systems attracted many authors. Anisimov and Artalejo [2] considered a multiserver retrial queues with negative arrivals. Two different approaches (stable and over loading) were considered. The matrix-analytic method was used in the stable case and the transient behavior was studied in the overloading case. Artalejo and Economou [4] calculated the stability condition and compared models that operate under different threshold in an $M^X/M/1$ queue controlled by batches of negative customers. Atencia and Moreno [5] studied a Geo/Geo/1 queue with negative and positive customers, under the RCE-inimmune and immune servicing killing disciplines. Muthu Canapathi Subramanian et al. [23] studied a retrial $M/M/1$ queue and negative arrivals under non-preemptive priority service. The negative customer eliminates a randomly chosen customer from the orbit. Ayyappan et al. [7] considered the same model under Pre-emptive Priority. Ayyappan et al. [8] used the matrix geometric method to study a retrial single server queue with negative customers where the service time is assumed to follow an Erlang-K distribution. Ayyappan et al. [9] analysed the influence of negative arrivals of a retrial M/M/1 queue under Coxian phase type services by using the direct truncation method. The negative arrival controls the congestion in the orbit by deleting one customer from the orbit. Dimitriou [11] investigated an $M/G/1$ retrial queue where the server is subject to breakdowns and multiple vacations with the presence of negative arrivals. The stability condition and the system performance measures in a mixed priority discipline of the system accept two types of positive customers (preemptive and non-preemptive). Krishna Kumar et al. [19] investigated an $M/G/1$ retrial queue with negative customers and two types of Bernoulli feedback, where, the negative customer deletes the positive customers in service. Kirupa and Udaya Chandrika [16] analysed a retrial $M^X/G/1$ queue with multi-types of service, negative customers and Feedback operating with a randomized vacation policy. The negative customer deletes the positive customer from the system and puts the server down. Rajadurai et al. [**?**] studied a retrial $M^X/G/1$ queue with feedback, two phases of service, Bernoulli vacation Schedule and negative customers, where, the server is subject to breakdown. A negative customer deletes the positive customer in service. Lee [20] studied the equilibrium behavior of customers in an unobservable and repairable $M/M/1$ queue with negative arrivals by investigating the Nash equilibrium. Rajadurai et al. [26] considered an unreliable $M/G/1$ retrial queueing system with working vacations and vacation interruption under Bernoulli Schedule with negative arrivals. Ayyappan and Thamizhselvi [6] analysed an unreliable retrial queueing system with two types of positive batch arrivals (low and high priority), non-preemptive priority service, working vacations, negative arrivals and emergency vacation. Chin et al. [10] studied an $M/M/1$ queue with two types of customers (negative and positive). The inter-arrival and service times for positive customers are assumed to follow distributions with a constant asymptotic rate. They provided a new approach to derive the stationary queue length distribution. Matalytski and Zajac [22]

determined volumes of memory of information systems (IS) using a stochastic model based on the use of HM-Networks with unreliable service and negative claims. Gao et al [14] studied the behavior of customers in an $M/M/1$ G-retrial queue with complete removals in the unobservable case using game theory concepts. Recently, Koh et al [18] presented an alternative approach to find the stationary queue length distribution of an $G/M/1$ queueing system with negative customers. The inter-arrival time for positive customers is assumed to follow a distribution with a rate that converges to a constant value. Lisovskaya et al [21] focused on a retrial multi-server queue with two orbits and two classes of a positive clients. Negative customers, symbolizing breakdown events, enter the queuing system and remove all currently served customers, if any, from the system. Sun and Wang [27] studied customers' strategic behavior in an $M/M/1$ retrial queue system with negative customers and single server vacation.

In this paper, we investigate a single unreliable server retrial queueing system with negative arrivals and two types of breakdowns. Positive customers receive service as usual by the server. A negative arrival, when present, causes the removal of a customer from the orbit. Negative customers are assumed to act regardless of whether the server is idle or occupied. If the server is free the arriving positive customer is served immediately and leaves the system after service completion (if no breakdowns had occurred during his service time). Otherwise, the positive customers join the orbit and become repeated customers. The server is subject to passive and active Poisson breakdowns. Passive breakdowns can happen while the server is free while active breakdowns can occur when the server is busy. When the server experiences a failure, it is immediately sent for repair. In the case of an active breakdown, the customer being served is considered lost. Once the repair is completed, the server returns to an idle state. To our knowledge, this study is the first to investigate reliability aspects and the time to first failure in queueing models with negative arrivals.

The paper is structured as follows. Section 2 introduces the mathematical model. In Section 3, we establish the necessary and sufficient condition for system stability. Section 4 examines the steady-state probability vector, while Section 5 discusses the performance measures of the system. Section 6 focuses on reliability aspects, including the server time to first failure. Finally, Section 7 provides a numerical example to illustrate the impact of system parameters on performance indicators, the reliability function, and the mean time to the first failure.

2. Mathematical Model

We consider a Markovian single unreliable server retrial queueing system with FCFS orbit and negative arrivals. Customers arrive according to a Poisson process with rate λ for positive arrivals and δ for negative arrivals. Positive customers are served as usual by the server. A negative arrival has the effect of eliminating a customer from the orbit, if any. We assume that negative customers act when the server is busy or free and the service times are exponentially distributed with rate μ. If the server is free, an arriving positive customer is served immediately and leaves the system after service completion (if no breakdowns had occurred during his service time). Otherwise, the positive customer joins the orbit and becomes a repeated customer. The time intervals between each repeated attempt are assumed to be independent and exponentially distributed with rate ν. The server is subject to passive and active Poisson breakdowns . Passive breakdowns can occur when the server is free with rate θ_0 while active breakdowns can occur when the server is busy with rate θ_1. As soon as the server fails it is sent for repair. The repair times have an exponential distribution with rate μ_0 for passive breakdowns and μ_1 for active breakdowns. Finally, we assume that the customer whose service is disrupted due to an active breakdown is considered lost. After repair, the server becomes free. Inter-arrival times, repair times, service times and retrial times are assumed to be mutually independent.

Let $N(t)$ and $C(t)$ be, respectively, the number of customers in the orbit and the server state at time t, where

$$C(t) = \begin{cases} 0 & \text{if the server is idle at time } t, \\ 1 & \text{if the server is busy at time } t, \\ 2 & \text{if the server is under repair during an passive breakdown at time } t, \\ 3 & \text{if the server is under repair during an active breakdown at time } t. \end{cases}$$

The state of the system is described by the Markov stochastic process:

$$\{(N(t), C(t)), t \geq 0\}$$

defined on state space $E = \mathbb{N} \times \{0, 1, 2, 3\}$.

The infinitesimal generator matrix Q of the continuous time Markov Chain (CTMC) $\{(N(t), C(t)), t \geq 0\}$ can be written as a tridiagonal block matrix as follow

$$Q = \begin{pmatrix} A_{00} & A_{01} & & & \\ A_{10} & A_{11} & A_{12} & & \\ & A_{21} & A_{22} & A_{23} & \\ & & \ddots & \ddots & \ddots \end{pmatrix},$$

where $A_{ij},\ i, j \geq 0$ are square matrices of order 4 given by

$$A_{00} = \begin{pmatrix} -(\lambda+\theta_0) & \lambda & \theta_0 & 0 \\ \mu & -(\lambda+\theta_1+\mu) & 0 & \theta_1 \\ \mu_0 & 0 & -(\lambda+\mu_0) & 0 \\ \mu_1 & 0 & 0 & -(\lambda+\mu_1) \end{pmatrix},$$

$$A_{n(n+1)} = A_0 = \begin{pmatrix} 0 & 0 & 0 & 0 \\ 0 & \lambda & 0 & 0 \\ 0 & 0 & \lambda & 0 \\ 0 & 0 & 0 & \lambda \end{pmatrix}, n \geq 0,$$

$$A_{n(n-1)} = A_2 = \begin{pmatrix} \delta & \nu & 0 & 0 \\ 0 & \delta & 0 & 0 \\ 0 & 0 & \delta & 0 \\ 0 & 0 & 0 & \delta \end{pmatrix}, n \geq 1,$$

$$A_{nn} = A_1 = \begin{pmatrix} -(\lambda+\theta_0+\delta+\nu) & \lambda & \theta_0 & 0 \\ \mu & -(\mu+\lambda+\theta_1+\delta+\nu) & 0 & \theta_1 \\ \mu_0 & 0 & -(\lambda+\mu_0+\delta) & 0 \\ \mu_1 & 0 & 0 & -(\lambda+\mu_1+\delta) \end{pmatrix}, n \geq 1.$$

If the capacity M of the orbit is finite then the CTMC $\{(N(t), C(t)), t \geq 0\}$ is defined on the state space $E_M = \{0, 1, \cdots, M\} \times \{0, 1, 2, 3\}$ whose infinitesimal generator $Q^{(M)}$ is given by

$$Q^{(M)} = \begin{pmatrix} A_{00} & A_{01} & & & & & \\ A_{10} & A_{11} & A_{12} & & & & \\ & A_{21} & A_{22} & A_{23} & & & \\ & & \ddots & \ddots & \ddots & & \\ & & & A_{(M-1)(M-2)} & A_{(M-1)(M-1)} & A_{(M-1)M} \\ & & & & A_{M(M-1)} & A'_{MM} \end{pmatrix},$$

with

$$A'_{MM} = \begin{pmatrix} -(\lambda+\theta_0+\delta+\nu) & \lambda & \theta_0 & 0 \\ \mu & -(\mu+\theta_1+\delta+\nu) & 0 & \theta_1 \\ \mu_0 & 0 & -(\mu_0+\delta) & 0 \\ \mu_1 & 0 & 0 & -(\mu_1+\delta) \end{pmatrix}.$$

3. Stability Condition

In this section, we establish the stability condition of the system.

Theorem 1. The inequality

$$\frac{\lambda\mu_0(\lambda+\nu)(\mu_1+\theta_1) + \mu_1(\mu+\theta_1)(\lambda\theta_0 - \nu\mu_0)}{\delta\left\{\mu_1(\mu+\theta_1)(\mu_0+\theta_0) + \mu_0(\lambda+\nu)(\theta_1+\mu_1)\right\}} < 1, \tag{1}$$

is the necessary and sufficient condition for the system to be stable.

Proof. The process $\{(N(t), C(t), t \geq 0)\}$ is a QBD process. According to Neuts (1981), it is stable if and only if

$$\pi A_0 e < \pi A_2 e, \tag{2}$$

where $\pi = (\pi_0, \pi_1, \pi_2, \pi_3)$ is the stationary distribution of

$$A = A_0 + A_1 + A_2. \tag{3}$$

That is

$$\pi A = 0 \quad and \quad \pi e = 1, \tag{4}$$

where e is the unit vector with dimension 4.

Solving (4) and then (2), we get (1). ■

4. Steady State Probability Vector

The goal of this section is to obtain the steady-state distribution of the system. We denote x the steady-state probability vector of the infinitesimal generator Q, which is partitioned as $x = (x(0), x(1), x(2), \dots)$ where $x(i) = (p_{i0}, p_{i1}, p_{i2}, p_{i3})$ for $i = 0, 1, 2, \dots$.
The stationary probability vector x satisfies

$$xQ = 0 \ \ and \ \ \sum_{i\geq 0}\sum_{j=0}^{3} p_{ij} = 1. \tag{5}$$

To solve system (5), we use the Direct Truncation Method, which consists of truncating the state space of the system E to a finite number of states and then computing the system performance measures based on this truncated state space. The Direct Truncation method is a widely used technique in the field of system analysis and control, as it allows for efficient computation of system performance measures without requiring a complete analysis of the system state space. This makes it particularly useful for systems with a large number of states or complex dynamics. More details can be found in (Muthu Canapathi Subramanian et al. [23], Ayyappan et al. [7], Ayyappan et al. [9]).

Let M denotes the cut-off point of the truncation method. The steady state probability vector $x^{(M)}$ is partitioned as $x^{(M)} = (x^M(0), x^M(1), x^M(2), \cdots, x^M(M))$ which satisfies $x^{(M)}Q^{(M)} = 0$ and $x^{(M)}e = 1$, where $x^M(i) = (p^M_{i0}, p^M_{i1}, p^M_{i2}, p^M_{i3})$ for $i = 0, 1, 2, \cdots, M$. To solve this system of equations, we rely on the special structure of the coefficient matrices and employ the CAUSS-SIEDEL elementary transformation method. We initiate the iterative process by setting $M = 2$ and progressively increase it until the elementary of $x^{(M)}$ exhibit negligible changes.

5. System Performance Measures

We outline in this section several important performance measures and their mathematical expressions. These measures serve to highlight the qualitative characteristics of the queueing model under consideration. A comprehensive numerical investigation is conducted to analyze the following performance indicators. Here we define in steady state

- $p(n, 0)$ the probability that there are in the orbit n customers when the server is idle, $p(n, 0) = \lim_{n\to\infty} p(N(t) = n, C(t) = 0)$,
- $p(n, 1)$ the probability that there are in the orbit n customers when the server is busy, $p(n, 1) = \lim_{n\to\infty} p(N(t) = n, C(t) = 1)$,
- $p(n, 2)$ the probability that there are in the orbit n customers when the server is under repair during a passive breakdown, $p(n, 2) = \lim_{n\to\infty} p(N(t) = n, C(t) = 2)$,
- $p(n, 3)$ the probability that there are in the orbit n customers when the server is under repair during an active breakdown. $p(n, 3) = \lim_{n\to\infty} p(N(t) = n, C(t) = 3)$.

- P_j the probability that the server is in state j, $P_j = \sum_{n\geq 0} p(n,j),\ j = 0,1,2,3,$
- $\sum_{j=0}^{3} p(n,j)$ the probability that in the orbit there are n customers , $n \geq 0$.
- MNCO the mean number of customers in the orbit

$$MNCO = \sum_{i=0}^{\infty} i(\sum_{j=0}^{3} p(i,j)).$$

6. Reliability Analysis

In what follows, we examine the time until the server first failure and its reliability, under the assumption that the system is initially empty and the server is free at time t = 0. Denote Y the time to the first failure of the server. We define as $R_Y(t) = P(Y > t)$, the reliability of the server. To evaluate this measure, the analysis is reformulated by introducing a modified queueing model in which the failure states of the server are treated as absorbing states. The infinitesimal generator matrix $\tilde{Q}$ for this model is given below

$$\tilde{Q} = \begin{pmatrix} \tilde{A}_{00} & \tilde{A}_{01} & & & \\ \tilde{A}_{10} & \tilde{A}_{11} & \tilde{A}_{12} & & \\ & \tilde{A}_{21} & \tilde{A}_{22} & \tilde{A}_{23} & \\ & & \ddots & \ddots & \ddots \end{pmatrix},$$

where $\tilde{A}_{ij},\ i,j \geq 0$ are square matrices of order 4 defined as follows

$$\tilde{A}_{00} = \begin{pmatrix} -(\lambda+\theta_0) & \lambda & \theta_0 & 0 \\ \mu & -(\lambda+\theta_1+\mu) & 0 & \theta_1 \\ 0 & 0 & 0 & 0 \\ 0 & 0 & 0 & 0 \end{pmatrix},$$

$$\tilde{A}_{n(n+1)} = \begin{pmatrix} 0 & 0 & 0 & 0 \\ 0 & \lambda & 0 & 0 \\ 0 & 0 & 0 & 0 \\ 0 & 0 & 0 & 0 \end{pmatrix}, n \geq 0,$$

$$\tilde{A}_{n(n-1)} = \begin{pmatrix} \delta & \nu & 0 & 0 \\ 0 & \delta & 0 & 0 \\ 0 & 0 & 0 & 0 \\ 0 & 0 & 0 & 0 \end{pmatrix}, n \geq 1,$$

$$\tilde{A}_{nn} = \begin{pmatrix} -(\lambda+\theta_0+\delta+\nu) & \lambda & \theta_0 & 0 \\ \mu & -(\lambda+\theta_1+\delta+\nu) & 0 & \theta_1 \\ 0 & 0 & 0 & 0 \\ 0 & 0 & 0 & 0 \end{pmatrix}, n \geq 1.$$

If the size orbit k is finite then the infinitesimal generator $\tilde{Q}_1$ of the new system is given by

$$\tilde{Q}_1 = \begin{pmatrix} \tilde{A}_{00} & \tilde{A}_{01} & & & & \\ \tilde{A}_{10} & \tilde{A}_{11} & \tilde{A}_{12} & & & \\ & \tilde{A}_{21} & \tilde{A}_{22} & \tilde{A}_{23} & & \\ & & \ddots & \ddots & \ddots & \\ & & & \tilde{A}_{(k-1)(k-2)} & \tilde{A}_{(k-1)(k-1)} & \tilde{A}_{(k-1)k} \\ & & & & \tilde{A}_{k(k-1)} & \tilde{A}'_{kk} \end{pmatrix},$$

$$\tilde{A}'_{kk} = \begin{pmatrix} -(\lambda+\theta_0+\delta+\nu) & \lambda & \theta_0 & 0 \\ \mu & -(\theta_1+\delta+\nu) & 0 & \theta_1 \\ 0 & 0 & 0 & 0 \\ 0 & 0 & 0 & 0 \end{pmatrix}.$$

The truncation method is used for conducting reliability analysis.
Let $p_{ni}(t)$, be the probability that the system is in state (n,i) at time t, $i = 0,1,2,3, n = 0,1,2\ldots k$. We denote

- $p(t) = (p_0(t), p_1(t), \cdots, p_k(t))$, where
  $p_n(t) = (p_{n0}(t), p_{n1}(t), p_{n2}(t), p_{n3}(t)), 0 \le n \le k,$
- $\frac{dp(t)}{dt} = (\frac{dp_0(t)}{dt}, \frac{dp_1(t)}{dt}, \frac{dp_2(t)}{dt}, \frac{dp_3(t)}{dt})$,
- $\frac{dp_n(t)}{dt} = (\frac{dp_{n0}(t)}{dt}, \cdots, \frac{dp_{n3}(t)}{dt})$.

The state probability vector $p(t)$ is a solution of the differential equation $\frac{dp(t)}{dt} = p(t)\tilde{Q}_1$ with the normalisation equation $\sum_{n=0}^{k}\sum_{i=0}^{3} p_{ni}(t) = 1$. This leads to the following system of equations.

$$\frac{dp_{00}(t)}{dt} = -(\lambda+\theta_0)p_{00}(t) + \mu p_{01}(t) + \delta p_{10}(t), \tag{6}$$

$$\frac{dp_{n0}(t)}{dt} = -(\lambda+\delta+\nu+\theta_0)p_{n0}(t) + \mu p_{n1}(t) + \delta p_{(n+1)0}(t), \quad 1 \le n < k, \tag{7}$$

$$\frac{dp_{k0}(t)}{dt} = -(\lambda+\delta+\nu+\theta_0)p_{k0}(t) + \mu p_{k1}(t), \tag{8}$$

$$\frac{dp_{01}(t)}{dt} = -(\lambda+\mu+\theta_1)p_{01}(t) + \lambda p_{00}(t) + \nu p_{10}(t) + \delta p_{11}(t), \tag{9}$$

$$\begin{aligned}\frac{dp_{n1}(t)}{dt} &= -(\lambda+\delta+\nu+\theta_1)p_{n1}(t) + \lambda p_{(n-1)1}(t) + \lambda p_{n0}(t) + \nu p_{(n+1)0}(t) \\ &\quad + \delta p_{(n+1)1}(t), \quad 1 \le n < k,\end{aligned} \tag{10}$$

$$\frac{dp_{k1}(t)}{dt} = -(\delta+\mu+\theta_1)p_{k1}(t) + \lambda p_{(k-1)1}(t) + \lambda p_{k0}(t). \tag{11}$$

Using the Laplace transforms $p^*_{ni}(s) = \int_0^\infty e^{-st}p_{ni}(t)dt$, $i = 0,1,2,3$, $0 \le n \le k$, equations (6)-(11) are transformed into

$$(\lambda+\theta_0+s)p^*_{00}(s) - \mu p^*_{01}(s) - \delta p^*_{10}(s) = p_{00}(0), \tag{12}$$

$$(\lambda+\delta+\nu+\theta_0+s)p^*_{n0}(s) - \mu p^*_{n1}(s) - \delta p^*_{(n+1)0}(s) = p_{n0}(0), \quad 1 \le n < k, \tag{13}$$

$$(\lambda+\delta+\nu+\theta_0+s)p^*_{k0}(s) - \mu p^*_{k1}(s) = p_{k0}(0), \tag{14}$$

$$(\lambda+\mu+\theta_1+s)p^*_{01}(s) - \lambda p^*_{00}(s) - \nu p^*_{10}(s) - \delta p^*_{11}(s) = p_{01}(0), \tag{15}$$

$$\begin{aligned}&(\lambda+\delta+\mu+\theta_1+s)p^*_{n1}(s) - \lambda p^*_{(n-1)1}(s) - \lambda p^*_{n0}(s) - \nu p^*_{(n+1)0}(s) \\ &\quad - \delta p^*_{(n+1)1}(s) = p_{n1}(0), \quad 1 \le n < k,\end{aligned} \tag{16}$$

$$(\delta+\mu+\theta_1+s)p^*_{k1}(s) - \lambda p^*_{(k-1)1}(s) - \lambda p^*_{k0}(s) = p_{k1}(0), \tag{17}$$

where

$$p_{ni}(0) = \begin{cases} 1 & if \quad n = i = 0, \\ 0 & otherwise. \end{cases}$$

Equations (12)-(17) can be written in matrix form as

$$p^*(s)(sI_{4k\times 4k} - \tilde{Q}_1) = p(0), \tag{18}$$

where $p^*(s) = (p^*_0(s), p^*_1(s), \cdots, p^*_k(s))$, $p^*_n(s) = (p^*_{n0}(s), p^*_{n1}(s), p^*_{n2}(s), p^*_{n3}(s)), 0 \le n \le k,$

To solve (18), we use Matlab Software. The probability that the system has failed on or before time t is given by $\sum_{n=0}^{k}\left(p_{n2}(t)+p_{n3}(t)\right)$. Hence the reliability function $R_Y(t)$ can be derived using the relation

$$R_Y(t)=1-\sum_{n=0}^{k}\left(p_{n2}(t)+p_{n3}(t)\right),\quad t\geq 0, \tag{19}$$

where $p_{n2}(t)$ and $p_{n3}(t)$ can be determined by taking the inverse Laplace transforms $p^*_{n2}(s)$ and $p^*_{n3}(s)$ respectively.

The mean time to the first failure MTTF is calculated as

$$\begin{aligned} MTTF &= \lim_{s\to 0} R^*_Y(s) \\ &= \lim_{s\to 0}\left[\int_0^{\infty} R_Y(t)e^{-st}dt\right] \\ &= \lim_{s\to 0}\left[1/s-\sum_{n=0}^{k}\left(p^*_{n2}(s)+p^*_{n3}(s)\right)\right]. \end{aligned} \tag{20}$$

7. Numerical Illustrations

In this section, we show through numerical examples the impact of some system parameters on the performance measures. We particularly show the effect of δ (negative arrival rate) and ν (retrial rate) on the mean number of customers in the orbit MNCO and the server state probabilities P_0, P_1, P_2, P_3. The values of parameters λ (positive arrival rate), δ, ν, θ_0 (passive failure rate), θ_1(active failure rate), μ (service rate), μ_0 (repair rate of passive breakdowns) and μ_1 (repair rate of active breakdowns) are selected to ensure the stability condition is satisfied. We also explore the effect of system parameters on the reliability function $R_Y(t)$ and the mean time to the first failure MTTF. To analyse $R_Y(t)$ and MTTF, we change the values of each parameter in turn while the other parameters take the following given values $\lambda=0.2,\ \mu=0.5,\ \nu=0.3,\ \delta=1,\ \theta_0=0.3,\ \theta_1=0.4,\ \mu_0=0.2,\ \mu_1=0.1, k=3$.

7.1. Monotonicity of MNCO, P_0, P_1, P_2 and P_3

Tables 1-5 show (for different values of the cut-off point M) that

- The mean number of customers in the orbit (as expected) decreases with the increase of ν and δ. In other words, the mean number of customers in the system decreases as a result of negative customers deleting positive customers within the orbit.
- As function of ν, both probabilities P_1, P_3 (respectively P_0, P_2) increase (respectively decrease). The reason for this is that more customers retry, more the server is busier and hence more it is prone to active failures. As a result, P_0 and P_2 decrease.
- The negative arrival rate δ has a positive effect on P_0, P_2 and a negative effect on P_1, P_3. The larger δ is, the smaller the orbit size, which means that the server is free and therefore more susceptible to passive failures. Consequently, P_1 and P_3 decrease.
- P_0, P_1, P_2 and P_3 exhibit a gradual and slow monotonic trend until reaching a specific threshold.

7.2. Monotonicity of $R_Y(t)$ and MTTF

- From Figures 1(a) and 1(b), the reliability function $R_Y(t)$ is decreasing with respect to λ and increasing with respect to μ respectively. The impact of λ and μ is negligible for small values .
- Figures 1(c) and 1(d) show that the reliability function decreases with the increase of θ_0 and θ_1. As the value of θ_0 (respectively θ_1) increases, the reliability function rapidly (respectively progressively) approaches zero.

- As depicted in Figures 1(e),1(f),1(g) and 1(h) the parameters ν, δ,μ_0 and μ_1 have no influence on system reliability. This trivial observation arises from the fact that these parameters are not included in the formula used to calculate system reliability.

- Tables 6(a)-6(d) show that the mean time to the first failure MTTF decreases as λ increases.

- In Table 6(a), we remark that MTTF increases with respect to μ. The decline in MTTF is particularly steep for low values of λ but it gradually becomes less pronounced as λ increases. The impact of μ on the values of MTTF is much more substantial than that of μ.

- Tables 6(b) and 6(c) show respectively a decrease of MTTF with respect to θ_1 and θ_0. The decrease is slow for θ_1 and significant for θ_0 with small values of λ.

- The influence of δ on MTTF is negligible as shown in Table 6(d).

Table 1: *Mean number of customers in the orbit and server state probabilities for* $\lambda = 5, \mu = 20, \mu_0 = 10, \mu_1 = 15, \delta = 5, \theta_0 = 0.5, \theta_1 = 0.5, M = 2$ *and different values of* ν

ν	P_0	P_1	P_2	P_3	MNCO
10	0.7452	0.2105	0.0373	0.0070	0.1488
20	0.7391	0.2167	0.0370	0.0072	0.1185
30	0.7362	0.2196	0.0368	0.0073	0.1046
40	0.7346	0.2213	0.0367	0.0074	0.0966
50	0.7335	0.2224	0.0367	0.0074	0.0914
60	0.7328	0.2232	0.0366	0.0074	0.0878
70	0.7322	0.2237	0.0366	0.0074	0.0851
80	0.7318	0.2242	0.0366	0.0075	0.0830
90	0.7314	0.2245	0.0366	0.0075	0.0814
100	0.7311	0.2248	0.0366	0.0075	0.0800
200	0.7298	0.2261	0.0365	0.0075	0.0737
300	0.7293	0.2265	0.0365	0.0076	0.0715
400	0.7291	0.2268	0.0365	0.0076	0.0704
500	0.7290	0.2270	0.0365	0.0076	0.0697
600	0.7289	0.2271	0.0364	0.0076	0.0693
700	0.7288	0.2271	0.0364	0.0076	0.0690
800	0.7288	0.2272	0.0364	0.0076	0.0687
900	0.7288	0.2272	0.0364	0.0076	0.0685
1000	0.7288	0.2273	0.0364	0.0076	0.0684
2000	0.7286	0.2274	0.0364	0.0076	0.0677
3000	0.7285	0.2275	0.0364	0.0076	0.0675
4000	0.7285	0.2275	0.0364	0.0076	0.0673
5000	0.7285	0.2275	0.0364	0.0076	0.0673
6000	0.7285	0.2275	0.0364	0.0076	0.0672
7000	0.7285	0.2275	0.0364	0.0076	0.0672
8000	0.7285	0.2275	0.0364	0.0076	0.0672
9000	0.7285	0.2275	0.0364	0.0076	0.0671

Table 2: *Mean number of customers in the orbit and server state probabilities for* $\lambda = 5, \mu = 20, \mu_0 = 10, \mu_1 = 15, \nu = 10, \theta_0 = 0.5, \theta_1 = 0.5, M = 2$ *and different values of* δ

δ	P_0	P_1	P_2	P_3	MNCO
0.005	0.7201	0.2360	0.0360	0.0079	0.2974
0.505	0.7244	0.2317	0.0362	0.0077	0.2714
1	0.7280	0.2280	0.0364	0.0076	0.2495
1.005	0.7280	0.2280	0.0364	0.0076	0.2493
1.505	0.7312	0.2248	0.0366	0.0075	0.2304
2	0.7339	0.2220	0.03670	0.0074	0.2142
2.005	0.7340	0.2219	0.0367	0.0074	0.2140
2.505	0.7364	0.2194	0.0368	0.0073	0.1977
3	0.7386	0.2173	0.0369	0.0073	0.1872

Table 3: *Mean number of customers in the orbit and server state probabilities for* $\lambda = 5, \mu = 20, \mu_0 = 10, \mu_1 = 15, \delta = 2, \theta_0 = 0.5, \theta_1 = 0.5, M = 6$ *and different values of* ν

ν	P_0	P_1	P_2	P_3	MNCO
10	0.7304	0.2256	0.0365	0.0075	0.2865
20	0.7255	0.2306	0.0363	0.0077	0.1971
30	0.7235	0.2326	0.0362	0.0078	0.1644
40	0.7225	0.2336	0.0361	0.0078	0.1475
50	0.7218	0.2343	0.0361	0.0078	0.1371
60	0.7214	0.2347	0.0361	0.0078	0.1301
70	0.7211	0.2350	0.0361	0.0078	0.1251
80	0.7208	0.2353	0.0360	0.0078	0.1213
90	0.7206	0.2355	0.0360	0.0079	0.1183
100	0.7205	0.2356	0.0360	0.0079	0.1159
200	0.7198	0.2364	0.0360	0.0079	0.1051
300	0.7195	0.2366	0.0360	0.0079	0.1014
400	0.7194	0.2367	0.0360	0.0079	0.0996
500	0.7193	0.2368	0.0360	0.0079	0.0985
600	0.7193	0.2367	0.0360	0.0079	0.0978
700	0.7192	0.2369	0.0360	0.0079	0.0973
800	0.7192	0.2369	0.0360	0.0079	0.0970
900	0.7192	0.2369	0.0360	0.0079	0.0966

Table 4: *Mean number of customers in the orbit and server state probabilities for*$\lambda = 5, \mu = 20, \mu_0 = 10, \mu_1 = 15, \nu = 10, \theta_0 = 0.5, \theta_1 = 0.5, M = 6$ *and different values of* δ

δ	P_0	P_1	P_2	P_3	MNCO
0.005	0.7207	0.2431	0.0240	0.0121	0.4323
0.505	0.7263	0.2376	0.0242	0.0119	0.3762
1	0.7304	0.2335	0.0243	0.0117	0.3363
1.005	0.7309	0.2331	0.0244	0.0117	0.3324
1.505	0.7348	0.2293	0.0245	0.0115	0.2973
2	0.7378	0.2262	0.0246	0.0113	0.2714
2.005	0.7381	0.2260	0.0246	0.0113	0.2687
2.505	0.7410	0.2231	0.0247	0.0112	0.2450
3	0.7433	0.2209	0.0248	0.0110	0.2268

Table 5: *Mean number of customers in the orbit and server state probabilities for* $\lambda = 5, \mu = 20, \mu_0 = 10, \mu_1 = 15, \delta = 2, \theta_0 = 0.5, \theta_1 = 0.5, M = 16$ *and different values of* ν

ν	P_0	P_1	P_2	P_3	MNCO
10	0.7303	0.2256	0.0365	0.0075	0.2929
20	0.7254	0.2306	0.0363	0.0077	0.1997
30	0.7235	0.2326	0.0362	0.0078	0.1662
40	0.7225	0.2336	0.0361	0.0078	0.1489
50	0.7218	0.2343	0.0361	0.0078	0.1384
60	0.7214	0.2347	0.0361	0.0078	0.1313
70	0.7211	0.2351	0.0361	0.0078	0.1261
80	0.7208	0.2353	0.0360	0.0078	0.1223
90	0.7206	0.2355	0.0360	0.0079	0.1193
100	0.7205	0.2357	0.0360	0.0079	0.1169
200	0.7198	0.2364	0.0360	0.0079	0.1059
300	0.7195	0.2366	0.0360	0.0079	0.1022
400	0.7194	0.2367	0.0360	0.0079	0.1003
500	0.7193	0.2368	0.0360	0.0079	0.0992
600	0.7193	0.2369	0.0360	0.0079	0.0985
700	0.7192	0.2369	0.0360	0.0079	0.0980
800	0.7192	0.2369	0.0360	0.0079	0.0976
900	0.7192	0.2369	0.0360	0.0079	0.0973

Table 6: *MTTF vs system parameters.*

(a) *MTTF for different values of* λ *and* μ

$\lambda \setminus \mu$	0.1	0.5	1	2	3
0.1	17.376	29.580	40.563	54.703	63.414
0.2	11.610	19.835	26.829	38.603	47.123
0.3	9.506	14.853	20.724	30.352	37.907
0.4	8.415	12.568	17.273	25.335	31.981
0.5	7.748	11.138	15.055	21.963	27.849

(b) *MTTF for different values of* λ *and* θ_1

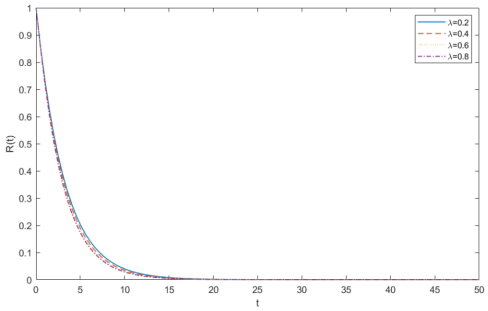
$\lambda \setminus \theta_1$	0.5	0.9	1.5	2	3
0.1	4.400	4.054	3.818	3.714	3.600
0.2	3.999	3.477	3.142	2.999	2.846
0.3	3.712	3.089	2.705	2.545	2.374
0.4	3.497	2.810	2.399	2.230	2.052
0.5	3.330	2.600	2.172	1.999	1.817

(c) *MTTF for different values of* λ *and* θ_0

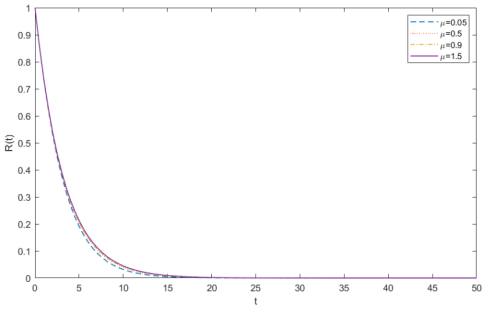
$\lambda \setminus \theta_0$	0.03	0.05	0.07	0.09	0.1
0.1	14.916	11.759	9.705	8.262	7.690
0.2	10.266	8.790	7.685	6.827	6.466
0.3	8.146	7.260	6.548	5.963	5.708
0.4	6.933	6.327	5.818	5.385	5.192
0.5	6.148	5.698	5.310	4.972	4.818

(d) *MTTF for different values of* λ *and* δ

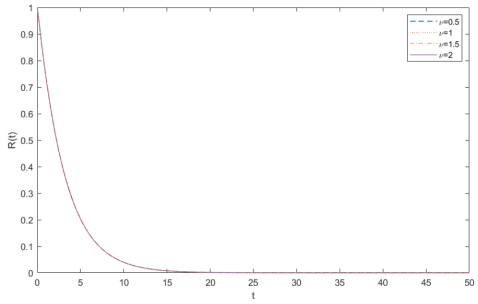
$\lambda \setminus \delta$	1	2	3	4
0.1	4.543	4.545	4.545	4.545
0.2	4.225	4.228	4.230	4.230
0.3	3.991	3.996	3.998	3.999
0.4	3.811	3.818	3.821	3.822
0.5	3.669	3.678	3.681	3.682



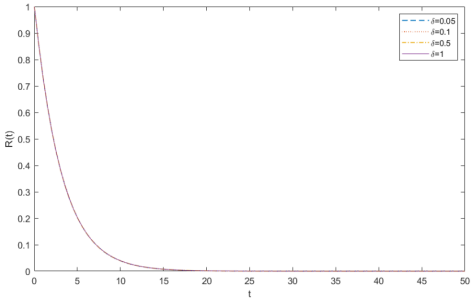
(a) *R*(*t*) *versus t for different values of* λ



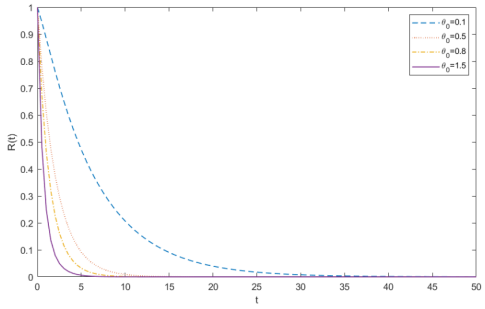
(b) *R*(*t*) *versus t for different values of* μ



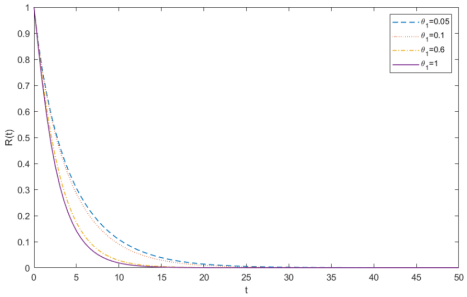
(c) *R*(*t*) *versus t for different values of* ν



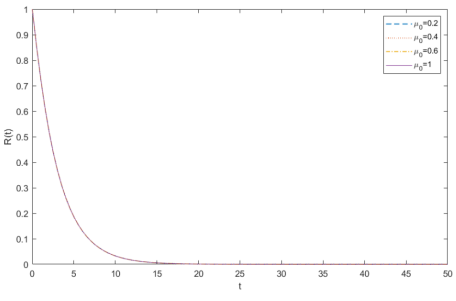
(d) *R*(*t*) *versus t for different values of* δ



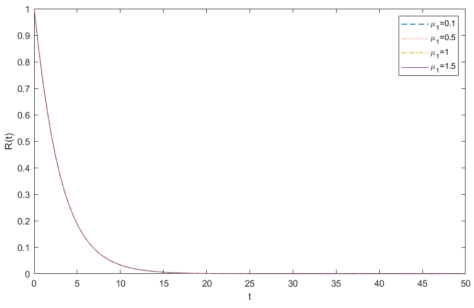
(e) *R*(*t*) *versus t for different values of* θ_0



(f) *R*(*t*) *versus t for different values of* θ_1



(g) *R*(*t*) *versus t for different values of* μ_0



(h) *R*(*t*) *versus t for different values of* μ_1

Figure 1: *R*(*t*) *vs system parameters.*

8. Conclusion

This paper focused on analyzing from queueing and reliability view points an $M/M/1$ constant retrial queue that involves negative arrivals and two types of breakdowns.

References

[1] Aissani, A., Ferhat, L., Hamadouche, D., & Taleb, S. (2018). Analysis of Customers™ Impatience in a Repairable Retrial Queue under Postponed Preventive Actions. American Journal of Mathematical and Management Sciences.

[2] Anisimov, V., & Artalejo, J. R. (2001). Analysis of Markov Multiserver Retrial Queues with Negative Arrivals. Queueing Systems, 39, 157“182.

[3] Artalejo, J. R., & Gomez-Corral, A. (2008). Retrial queueing systems: A computational approach. Berlin, Germany: Springer.

[4] Artalejo, J., & Economou, A. (2004). Optimal control and performance analysis of an MX/M/1 queue with batches of negative customers. RAIRO - Operations Research, 38(2), 121-151.

[5] Atencia, I. & Moreno, P. (2005). A single-server G-queue in discrete-time with geometrical arrival and service process. Performance Evaluation 59, 85“97.

[6] Ayyappan, G. & Thamizhselvi, P. (2018). Transient Analysis of $M^{X_1}, M^{X_2}/G_1, G_2/1$ Retrial Queueing System with Priority Services, Working Vacations and Vacation Interruption, Emergency Vacation, Negative Arrival and Delayed Repair. International Journal of Applied and Computational Mathematics, 4:77.

[7] Ayyappan. G., Muthu Ganapathi Subramanian, A., & Sekar. G. (2010). M/M/1 Retrial Queueing System with Negative Arrival under Pre-emptive Priority Service. International journal of computational cognition. vol. 8, no. 4.

[8] Ayyappan. G., Sekar. G., & Muthu Ganapathi Subramanian, A. (2010). M/M/1 Retrial Queueing System with Negative Arrival under Erlang-K Service by Matrix Geometric Method. Applied Mathematical Sciences, Vol. 4, no. 48, 2355 “ 2367.

[9] Ayyappan. G., Muthu Ganapathi Subramanian, A., & Sekar. G. (2011). Study of influences of negative arrival for single server retrial queueing system with Coxian phase type service. Proceedings of the 6th International Conference on Queueing Theory and Network Applications, Seoul, Korea, Aug. 23“26, 2011 (ACM, New York, 2011), pp. 53“59.

[10] Chin, C. H., Koh, S. K., Tan, Y. F., Pooi, A. H., & Goh, Y. K. (2018). Stationary queue length distribution of a continuous-time queueing system with negative arrival. 3rd International Conference on Mathematical Sciences and Statistics.

[11] Dimitriou, I. (2013). A mixed priority retrial queue with negative arrivals, unreliable server and multiple vacations. Applied Mathematical Modelling 37, 1295“1309.

[12] Falin, G. I., & Templeton, J. G. (1997). Retrial queues. New Jersey: Chapman and Hill.

[13] Gao, S., Zhang, J. & Wang, X. (2020). Analysis of a retrial queue with two-type breakdowns and delayed repairs. IEEE Access, vol. 8, pp. 172428-172442.

[14] Gao, S., Z hang, D., Dong, H., & Wang, X. (2019). Equilibrium balking strategies in the repairable m/m/1 g-retrial queue with complete removals. Probability in the Engineering and Informational Sciences, page 1 of 20.

[15] Gelenbe, E. (1989). Random neural networks with negative and positive signals and product form solution. NeuralComputation, 1(4), 502“510.

[16] Kirupa, K. & Udaya Chandrika, K. (2015). Unreliable Batch Arrival Retrial Queue with Negative Arrivals, Multi-Types Of Heterogeneous Service, Feedback and Randomized J Vacations. International Research Journal of Engineering and Technology (IRJET).

[17] Kim, J., & Kim, B. (2016). A survey of retrial queueing systems. Annals of Operations Research, 247(1), 3“36.

[18] Koh, S. K., Chin, C. H., Tan, Y. F., & Ng, T. C. (2021). An alternative approach in finding the stationary queue length distribution of a queueing system with negative customers. ITM Web of Conferences 36, 04001.

[19] Kumar k., B., Pavai Madheswari.S., & Anantha Lakshmi.S.R. (2013), An M/G/1 Bernoulli feedback retrial queueing system with negative customers. Operational Research: An International Journal 13:187“210.

[20] Lee, D. H. (2017). Optimal Pricing Strategies and Customers™ Equilibrium Behavior in an Unobservable M/M/1 Queueing System with Negative Customers and Repair. Mathematical Problems in Engineering.

[21] Lisovskaya, E., Fedorova, E., Salimzyanov, R., & Moiseeva, S. (2022). Resource Retrial Queue with Two Orbits and Negative Customers. Mathematics.

[22] Matalytski, M. & Zajac, P. (2019). Application of HM-Networks with positive and negative heterogeneous requests for finding memory volume in information systems. Journal of Applied Mathematics and Computational Mechanics, 18(1), 41-51.

[23] Muthu Ganapathi Subramanian, A., Ayyappan, G., & Sekar, G. (2009). M/M/1 Retrial queueing system with negative arrival under non-pre-emptive priority service. Journal of Fundamental Sciences Vol 5, No 2, 129-145.

[24] Neuts, M. (1981). Matrix-Geometric Solution in Stochastic Models. Johns Hopkins University Press, Baltimore, Md, USA.

[25] Rajadurai, P., Chandrasekaran, V.M., & Saravanarajan. M.C. (2015). Steady state analysis of batch arrival feedback retrial queue with two phases of service, negative customers, Bernoulli vacation and server breakdown. International Journal of Mathematics in Operational Research, Vol. 7, No. 5. 27.

[26] Rajadurai, P., Chandrasekaran, V.M., & Saravanarajan. M.C. (2018). Analysis of an unreliable retrial G-queue with working vacations and vacation interruption under Bernoulli schedule. Ain Shams Engineering Journal. 9, 567“580.

[27] Sun, S. & Wang, J. (2022). Game-theoretic analysis of the single vacation queue with negative customers. Quality Technology & Quantitative Management.

[28] Taleb, S., & Aissani, A. (2016). Preventive maintenance in an unreliable M/G/1 retrial queue with persistent and impatient customers. Annals of Operations Research, 247(1), 291“317.

[29] Yang, D. Y. & Tsao, C.L. (2018). Reliability and Availability Analysis of Standby Systems with Working Vacations and Retrial of Failed Components. Reliability Engineering and System Safety.

[30] Zirem, D.,Boualem, M., Adel-Aissanou, K. & Aissani, D. (2018). Analysis of a single server batch arrival unreliable queue with balking and general retrial time. Quality Technology & Quantitative Management.

RT&A, No 4 (89)
Volume 20, December 2025

STOCHASTIC PETRI NET ANALYSIS OF RETRIAL REPAIRABLE SYSTEMS WITH TWO REPAIR MODES

[1*]Kheireddine Boudehane and [2] Samira Taleb

•

[1] University of Science and Technology Houari Boumediene USTHB,
Department of Probability and Statistics, Faculty of Mathematics,
RIIMA Laboratory, El-Alia, Bab Ezzouar, B.P. 32, 16111, Algiers, Algeria.
[2]University of Science and Technology Houari Boumediene USTHB,
Department of Probability and Statistics, Faculty of Mathematics,
MSTD Laboratory, El-Alia, Bab Ezzouar, B.P. 32, 16111, Algiers,
[1*]kboudehane@usthb.dz; [2]staleb@usthb.dz

Abstract

This paper presents a dependability analysis of an L-out-of-n system supported by a hierarchical standby structure with warm and cold units. The model accounts for realistic operating conditions, including a single unreliable repair server that may break down but can still provide limited service during failure periods. A retrial mechanism is also considered, where failed units that find the server busy join an orbit and retry for service later. The system is modeled using a Generalized Stochastic Petri Net (GSPN), which is then mapped to a Continuous-Time Markov Chain (CTMC) for steady-state performance evaluation. Furthermore, transient reliability analysis is conducted to derive the survival function of the system and the expectation of the first passage time to failure.

Keywords: *K*-out-of-*n* system, reliability, generalized stochastic Petri net, standby redundancy

1. Introduction

Reliability and availability are important indices for evaluating the performance and dependability of systems and devices. Reliability is a concept that concerns many areas of human activity: economic, scientific, technical, industrial and technological. It is related to notions of operational safety, quality, efficiency and performance. Its main objective is the analysis of the probability of a system failure and concerns in particular the mathematical domain. In some modelling approaches, the study of reliability is reduced to the study of the distribution of a positive random variable representing the lifetime of a system or component.On the other hand, Availability is the proportion of time that a system is expected to be operational and available for use. Interested readers on the subject are referred to Barlow and Proshan [1], David [2], Kececioglu [3], Lai and Xie [4], Birolini [5].

In general, real systems are composed of several components and have several fault modes, these systems are said to be complex. Functional modelling in the form of a block diagram of these systems makes it possible to determine their reliability. Each block represents a component or fault mode. Furthermore, the blocks are considered independent of each other. The most common coherent structures are serial, parallel and *k*-out-of-*n* systems (a system is said to be coherent if the normal functioning of all elements leads to the normal functioning of the structure and if the failure of all elements leads to the failure of the structure).

A k-out-of-n:G system is a system of n components, that operates if and only if at least k ($1 \leq k \leq n$) of the n components operate. The system is referred to as a series system when $k = n$, and it is a simple parallel system when $k = 1$ and $n > 1$. k-out-of-n:G systems are successfully used in industrial and military systems, data processing systems and communication systems.

Except for series systems, systems usually have redundant structures. A redundant system is a system where one or more components may fail without the system ceasing to function. In standby redundancy, redundant components are put into use after the failure of the operating component. It makes the system much more reliable and efficient. In general, there are three kinds of standbys: warm, cold, and hot. A component is in "hot standby" if its failure rate in quiescent mode is the same as its failure rate in active mode, "cold standby" if its failure rate in quiescent mode is zero (i.e., the component cannot fail while in standby), and "warm standby" if it falls somewhere in the middle.

The study of k-out-of-n: G systems and standby redundancy kept the interest of several authors. Unuvar et al [6] found bounds for k-out-of-n and consecutive k-out-of-n reliabilities in the form of probabilistic constraints. Shekhar et al [7] dealt with the performance modeling and reliability analysis of a redundant machining system composed of several functional machines with switching failure and geometric reneging. Byun et al [8] extended the matrix-based system reliability (MSR) method to k-out-of-n systems. Eryilmaz [9] showed how to increase system lifetime of general coherent structure at system by adding cold standby redundancy to system and component levels. A retrial machine system with warm standby is studied in Chen [10] and Chen and wang [11]. In the first work the recovery policy is considered while in the second work the N policy is considered. An $M/G/1$ machine interference problem with imperfect switchover of standbys, in which an unreliable repairman maintains a group of machines is investigated by Ke et al [12]. Subasi et al [13] developed an algorithm to obtain robust and efficiently commutable bounds for the probability that exactly k-out-of-n events occur, where the underlying probability distribution is assumed to be uni-modal with known mode. Yang and Tsao [14] considered a repairable system consisting of m primary components, s spare components, and a repairman with multiple vacations. Sarkar and Tang [15] compared limiting availabilities of a k-out-of-n:G system and a k-component series system with $(n - k)$ spare components when there are different numbers of repair facilities. Yen et al [16] studied reliability and sensitivity analysis of a retrial machine repair problem with working breakdowns operating under the F-policy. Zhao et al [17] proposed new concepts of k-out-of-n:F balanced systems based on real engineering problems. Gao [18] investigated availability and reliability characteristics for a repairable fault-tolerant system with warm standbys and second optional repair service. Gao and Wang [19] performed a reliability and availability analysis of a repairable retrial system with mixed standbys and a single repair facility that undergoes preventive maintenance or experiences active breakdowns. Li et al [20] dealt with a repairable circular consecutive-k-out-of-n: retrial system where the repair time is assumed to follow a Weibull distribution. Yang and Wu [21] evaluated the availability and reliability of a standby repairable system incorporating imperfect switchovers and working breakdowns. Wang et al [22] proposed a novel mathematical model for reliability dealing with a (k_1, k_2)-out-of-n:G repairable system consisting of two different types of components and multiple vacations.Yuan [23] studied a k-out-of-n:G repairable system with n identical machines and R repairmen, and both the redundant dependency and the multiple vacation policy for repairmen were taken into account.

$GSPNs$ are bipartite mathematical graphs having the power to model complicated systems, to describe and analyze stochastic concurrent systems with synchronization properties. $GSPNs$ comprise Places (drawn as circles), timed transitions, and arcs. $GSPNs$ are an extension of Petri Nets (PNs), in which some transitions are exponentially distributed timed transitions(expressed as rectangles), and others are immediate (represented as thin bars). The state of a $GSPN$ is described by mean of markings containing the number of tokens in each place of the $GSPN$. Depending on whether the transition is timed or immediate, markings are classified into tangible and vanishing respectively. The tangible reachability graph is isomorphic to a continuous time Markov chain ($CTMC$). As a result, the states of the $CTMC$ correspond to the markings in

the tangible reachability graph, and the state transition rates are the exponential firing rates of timed transitions in the $GSPN$. The stationary probability of the $CTMC$ allows us to derive some performance measures of the system. Interested readers on the $GSPNs$ can see Haas [24], Bause and Kritzinger [25], Reisig [26].

Numerous studies on $GSPNs$ are available in the literature. For example, Ikhlef et al [27] studied a Semi-Markovian single server retrial queues by means of Markov Regenerative Stochastic Petri Nets. Hakmi et al [28] used generalized stochastic Petri nets for the analysis of a retrial priority queue. YadollahzadehTabari and Mohammadizad [29] studied the efficiency of the S-MAC media access control protocol in wireless sensor networks by analyzing and modeling it using Generalized Stochastic Petri nets.

2. Model description and proposed $GSPN$

2.1. Model description

We consider an L-out-of-$(M + W + C)$ system involving M identical units operating in parallel, W units in warm standby (running in a partially ready state), C identical cold standby units (powered off and started only when needed), and a single unreliable repairer. The system stops functioning once the number of failed units reaches $k = M + W + C - L + 1$. All these units are identical. When an operating unit experiences a failure, it is immediately replaced by an available warm unit. At the same time, an available cold standby unit becomes a warm unit. If no warm standby unit is available, a cold standby unit is activated to replace the failed operating unit. Once a standby unit (whether warm or cold) becomes active, it operates identically to the original operating unit. The transition from standby units (warm or cold) to operating units is considered perfect, with instantaneous switchover times. The lifetimes of operating and warm units are modeled as exponential distributions with failure rates λ and α, respectively, where $0 < \alpha < \lambda$.

The system does not include waiting space for the repairer handling the failed units. Therefore, if an operating or warm standby unit fails while the repairer is occupied with another failed unit, the newly failed unit is placed in an orbit for a random time following an exponential distribution with rate γ. This orbiting behavior represents a delayed repair process, waiting for the repairer to become available.

When a unit fails, it is dispatched to the repairer for inspection and restoration. This repairer, however, is also prone to breakdowns. In such cases, the repairer is restored by an external facility. During its downtime, it can provide partial repair services at a reduced rate μ_2, where $\mu_2 < \mu_1$ and μ_1 is the normal service rate. This scenario models a degraded service state during the repairer's breakdown.

To improve the repairer's utilization and ensure efficient operation, a recovery policy is implemented. This policy stipulates that the repairer can only undergo recovery when the number of failed units in the system meets or exceeds a threshold q ($q < L$). The repairer's lifetime and recovery time are modeled using exponential distributions with rates θ and σ, respectively. All failed units arriving during this period are placed in orbit, waiting until the repairer completes its recovery cycle. Once the recovery is completed, the repairer resumes normal operation at the full service rate μ_1. This enhancement reflects real-world practices where scheduled maintenance helps avoid costly downtimes caused by unexpected equipment failures.

Practical Example: 5G Edge System for Autonomous Vehicles

The proposed model can be applied to cloud service provider that operates M virtual machines (VMs) to serve customer requests. To improve reliability, the provider maintains W warm standby VMs running in a low-power state and C cold standby VMs powered off until needed. The system continues to operate as long as at least L VMs remain available, but it stops functioning once the number of failed VMs reaches $k = M + W + C - L + 1$. Whenever an active VM fails, it is immediately replaced by a warm standby. At the same time, one of the cold standby VMs, if

available, is promoted to warm status. If no warm standby is available, a cold standby is directly activated to replace the failed VM. Once promoted, standby VMs behave identically to the active ones.

Failed VMs are repaired by a dedicated repair server. If the repair server is already busy, failed VMs enter an orbit and retry for repair after a random time. The repair server itself is unreliable and may fail. When this occurs, it is repaired by an external facility. During its degraded state, it can still process repairs but at a reduced capacity. To optimize resource usage, the repair server is restored only when the number of failed VMs reaches a threshold q, with $q < L$.

This configuration reflects real-world data centers where backup servers and repair strategies are combined to ensure high availability despite random failures and repair delays.

3. *GSPN* Description

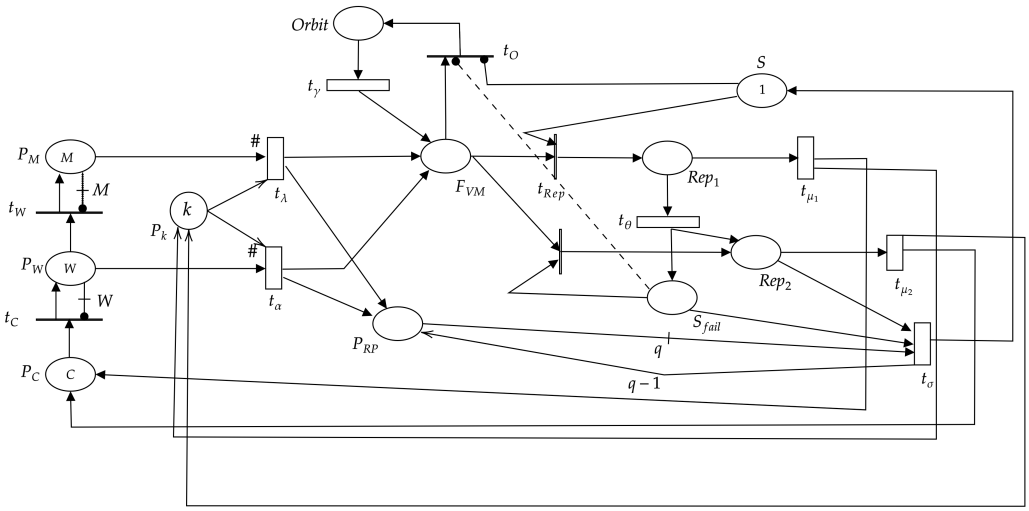


Figure 1: *The GSPN model of the system with warm and cold units, an unreliable repairer, and a recovery policy.*

In Fig. 1, we depict the GSPN model of the system with warm and cold *units*, an unreliable *repairer*, and a recovery policy. The places of the GSPN are defined as follows:

- Operating *units* are represented by place P_M with an initial marking of M.
- Warm *units* are depicted by place P_W with an initial marking of W.
- Cold *units* are represented by place P_C with an initial marking of C.
- Place F_U indicates whether a failed *unit* or a chosen *unit* from the orbit is ready for repair.
- The orbit is represented by the place *Orbit*.
- A *unit* under normal repair is represented by place Rep_1.
- A *unit* under partial repair (when the *repairer* is down) is represented by place Rep_2.
- The failed *repairer* is represented by place S_{fail}. This place signifies that the *repairer* is broken down due to a failure.
- The idle *repairer* is represented by place S. This place indicates that the *repairer* is operational and ready to address *unit* failures.
- The *repairer* recovery policy is represented by place P_{RP}.

Thus, the *GSPN* starts with an initial marking M_0:

$$M_0(\#P_M, \#P_W, \#P_C, \#Orbit, \#F_U, \#P_{RP}, \#S, \#Rep_1, \#Rep_2, \#S_{fail}) = M_0(M, W, C, 0, 0, 0, 1, 0, 0, 0)$$

where # denotes the marking in a place.

The failure of an operating *unit* is characterized by the firing of transition t_λ with rate $\#P_M\lambda$. The failure of a warm *unit* is represented by the firing of transition t_α with rate $\#P_W\alpha$. The arrival of a repeated *unit* is characterized by the firing of transition t_γ with rate γ.

The firing of transitions t_{μ_1} and t_{μ_2} represents the end of the normal repair period when the *repairer* is operational and the end of the partial repair period when the *repairer* is in a breakdown state, with rates μ_1 and μ_2, respectively. An active breakdown of the *repairer* is characterized by the firing of transition t_θ with rate θ. The end of the repair period for the failed *repairer* is characterized by the firing of transition t_σ with rate σ.

Transition t_{Rep_1} fires if there is a token in place F_U (representing the arrival of a *unit* from orbit or a newly failed *unit*) and the *repairer* is available (one token in place S). Transition t_{Rep_2} fires if there is a token in place F_U and the *repairer* is in a breakdown state (indicated by a token in place S_{fail}).

Transition t_O fires when the *repairer* is either under repair or busy, causing the failed *unit* to be placed into orbit. Transition t_W fires when P_M contains fewer tokens than M, replacing a failed primary *unit* with a warm *unit*. Transition t_C fires when P_W contains fewer tokens than W, replacing a failed warm *unit* with a cold *unit*.

Finally, transition t_σ fires when the number of failed *units* equals q, representing the end of the repair period for the failed *repairer*, with rate σ.

4. Steady-State Analysis

To simplify the notation of the *GSPN* marking, let us define:

- $I(t)$: The number of *units* being repaired at time t (in place Rep_1 for normal repair or Rep_2 for partial repair).
- $N(t)$: The number of *units* in the orbit (place *Orbit*) at time t.
- $J(t)$: The state of the *repairer* at time t (0 for available/working, 1 for failed).

Hence, the state of the system can be represented by the marking process $\{X(t), t \geq 0\} = \{(I(t), N(t), J(t)), t \geq 0\}$, which is a Continuous-Time Markov Chain (CTMC) with a finite state space Ω where: $\Omega = \{(i, n, j), 0 \leq i \leq 1, 0 \leq n \leq k-1, 0 \leq j \leq 1\}$.

The infinitesimal generator Q of the *CTMC* $\{X(t), t \geq 0\}$ is a $4k \times 4k$ ($k = M + W + C$) tridiagonal block matrix given as follows:

$$Q = \begin{pmatrix} D_1 & U_1 & 0 & \cdots & 0 \\ L_2 & D_2 & U_2 & \ddots & \vdots \\ 0 & L_3 & D_3 & \ddots & 0 \\ \vdots & \ddots & \ddots & \ddots & U_{k-1} \\ 0 & \cdots & 0 & L_k & D_k \end{pmatrix}_{4k \times 4k},$$

where the nonzero blocks are defined as follows:

$$L_i = \begin{pmatrix} 0 & \gamma & 0 & 0 \\ 0 & 0 & 0 & 0 \\ 0 & 0 & 0 & 0 \\ 0 & 0 & 0 & 0 \end{pmatrix}, \quad i = 2, \ldots, k,$$

$$U_i = \begin{pmatrix} 0 & 0 & 0 & 0 \\ 0 & \lambda_{i+1} & 0 & 0 \\ 0 & 0 & \lambda_{i+1} & 0 \\ 0 & 0 & 0 & 0 \end{pmatrix}, \quad i = 1, \ldots, k-1,$$

$$D_1 = \begin{pmatrix} -\lambda_0 & \lambda_0 & 0 & 0 \\ \mu_1 & -(\lambda_1 + \theta + \mu_1) & \theta & 0 \\ 0 & 0 & -(\lambda_1 + \mu_2) & \mu_2 \\ 0 & 0 & \lambda_0 & -\lambda_0 \end{pmatrix},$$

$$D_i = \begin{pmatrix} -(\lambda_{i-1} + \gamma) & \lambda_{i-1} & 0 & 0 \\ \mu_1 & -(\lambda_i + \theta + \mu_1) & \theta & 0 \\ 0 & 0 & -(\lambda_i + \mu_2) & \mu_2 \\ 0 & 0 & \lambda_{i-1} & -\lambda_{i-1} \end{pmatrix}, \quad i = 2, \ldots, q-1,$$

$$D_i = \begin{pmatrix} -(\lambda_{i-1} + \gamma) & \lambda_{i-1} & 0 & 0 \\ \mu_1 & -(\lambda_i + \theta + \mu_1) & \theta & 0 \\ 0 & \sigma & -(\lambda_i + \mu_2 + \sigma) & \mu_2 \\ \sigma & 0 & \lambda_{i-1} & -(\lambda_{i-1} + \sigma) \end{pmatrix}, \quad i = q, \ldots, k-1,$$

$$D_k = \begin{pmatrix} -(\lambda_{k-1} + \gamma) & \lambda_{k-1} & 0 & 0 \\ \mu_1 & -(\theta + \mu_1) & \theta & 0 \\ 0 & \sigma & -(\mu_2 + \sigma) & \mu_2 \\ \sigma & 0 & \lambda_{k-1} & -(\lambda_{k-1} + \sigma) \end{pmatrix}.$$

and

$$\lambda_n = \begin{cases} M\lambda + W\alpha, & 0 \le n \le C-1, \\ M\lambda + (W + C - n)\alpha, & C \le n \le W + C - 1, \\ (M + W + C - n)\lambda, & W + C \le n \le k-1. \end{cases}$$

Note that λ_n is the failure rate when there are n failed *units* in the system.

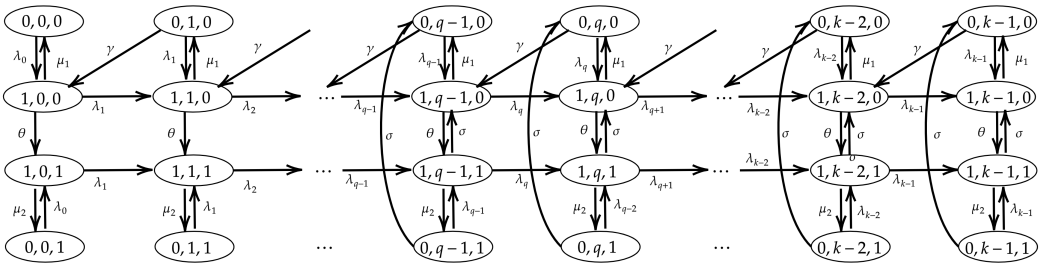


Figure 2: *CTMC associated to the GSPN model given in Fig. 1.*

4.1. Steady-State Distribution

Let $\pi = (\pi_0, \pi_1, \ldots, \pi_{k-1})$ be the stationary probability vector, where

$$\pi_j = (\pi_{0,j,0}, \pi_{1,j,0}, \pi_{1,j,1}, \pi_{0,j,1}), \quad j = 0, 1, \ldots, k-1.$$

Theorem 1. For the coherent repairable system, the steady-state probabilities π_n, $n = 0, 1, \ldots, k-1$, are given by

$$\pi_0 = \pi_{0,0,0}\, r_0,$$
$$\pi_n = \pi_0 \prod_{i=1}^{n} R_i, \quad n = 1, 2, \ldots, k-1, \tag{1}$$

where

$$\pi_{0,0,0} = \frac{1}{r_0 \left(\mathbb{I}_4 + \sum_{n=1}^{k-1} \prod_{i=1}^{n} R_i\right) e_4},$$
$$r_0 = \left(1,\ \frac{\lambda_0}{\mu_1},\ \frac{\theta\lambda_0}{\mu_1\lambda_1},\ \frac{\mu_2\theta\lambda_0}{\mu_1\lambda_1}\right),$$

and

$$R_n = \begin{cases} -L_n \left(D_n + R_{n+1}U_n\right)^{-1}, & n = 1, 2, \ldots, k-2, \\ -L_{k-1}D_k^{-1}, & n = k-1, \end{cases}$$

with $\mathbb{I}_4$ denoting the 4×4 identity matrix and $e_4^T = (1, 1, 1, 1)$.

Proof. The stationary distribution vector π is obtained by solving the global balance equation

$$\pi Q = \mathbb{O}_{4k},$$

subject to the normalization condition

$$\sum_{n=0}^{k-1} \pi_n e_4 = 1,$$

where $\mathbb{O}_{4k}$ is a $1 \times 4k$ zero vector. This system yields the block equations:

$$\pi_0 D_0 + \pi_1 U_0 = \mathbb{O}_4, \tag{2}$$
$$\pi_{n-1} L_n + \pi_n D_n + \pi_{n+1} U_n = \mathbb{O}_4, \quad n = 1, 2, \ldots, k-2, \tag{3}$$
$$\pi_{k-2} L_{k-1} + \pi_{k-1} D_k = \mathbb{O}_4. \tag{4}$$

From (4), we obtain

$$\pi_{k-1} = \pi_{k-2}(-L_{k-1}D_k^{-1}) = \pi_{k-2}R_{k-1}.$$

By recursively substituting into (3), each π_n can be expressed in terms of π_{n-1} as

$$\pi_n = \pi_{n-1}R_n, \quad R_n = -L_n(D_n + R_{n+1}U_n)^{-1}.$$

Iterating this relationship yields the expression in (1). Finally, $\pi_{0,0,0}$ is obtained using the normalization condition and the above expressions. ■

4.2. Performance Measure

From Theorem 1, we can derive the following performance measures:

- **Steady-state availability** $A(\infty)$: The stationary probability that the system is operational.

$$A(\infty) = 1 - (\pi_{1,k-1,0} + \pi_{1,k-1,1}) \tag{5}$$

- **Mean number of failed units in repair** $\overline{N}_U$: The average number of units in places Rep_1 or Rep_2.

$$\overline{N}_U = \sum_{n=0}^{k-1} (\pi_{1,n,0} + \pi_{1,n,1}) \tag{6}$$

- **Mean number of failed units in orbit** $\bar{O}_U$: The average number of units in the place $Orbit$.

$$\bar{O}_U = \sum_{n=0}^{k-1} n \cdot (\pi_{0,n,0} + \pi_{1,n,0} + \pi_{1,n,1} + \pi_{0,n,1}) \tag{7}$$

- **Mean number of failed units** $\bar{N}$:

$$\bar{N} = \overline{N}_U + \bar{O}_U \tag{8}$$

- **Mean rate of failed units** $\bar{\lambda}$:

$$\bar{\lambda} = \sum_{n=0}^{k-1} \lambda_n \cdot (\pi_{0,n,0} + \pi_{1,n,0} + \pi_{1,n,1} + \pi_{0,n,1}) \tag{9}$$

- **Mean response time** $\bar{T}$ (time from a unit's failure until its repair is complete), via Little™s formula:

$$\bar{T} = \frac{\bar{N}}{\bar{\lambda}} \tag{10}$$

- **Mean waiting time** $\bar{T}_w$ (time from a unit's failure until its repair begins), via Little™s formula:

$$\bar{T}_w = \frac{\bar{O}_U}{\bar{\lambda}} \tag{11}$$

5. Reliability Analysis

This section examines the survival function $R_{VM}(t)$ and the first-failure expectation (FFE_{VM}). The survival function $R_{VM}(t)$ is the probability that the system operates without failure up to time t. The FFE_{VM} is the expected average time until the first system failure. For this analysis, all system *units* are assumed to be operational at $t = 0$.

To determine the system reliability $R_{VM}(t)$, we modify the CTMC by making the failure states $(1, k-1, 0)$ and $(1, k-1, 1)$ absorbing states. This creates a new CTMC, $\{\tilde{X}(t), t \geq 0\}$, with an infinitesimal generator matrix $\tilde{Q}$:

$$\tilde{Q} = \begin{pmatrix}
D_0 & U_0 & & & & & & & \\
L_1 & D_1 & U_1 & & & & & & \\
 & L_2 & D_2 & U_2 & & & & & \\
 & & \ddots & \ddots & \ddots & & & & \\
 & & & L_{q-1} & D_{q-1} & U_{q-1} & & & \\
 & & & & L_q & D_q & U_q & & \\
 & & & & & \ddots & \ddots & \ddots & \\
 & & & & & & L_{k-2} & D_{k-2} & U_{k-2} \\
 & & & & & & & L_{k-1} & D^*_{k-1}
\end{pmatrix}$$

where the last block is given by: $D^*_{k-1} = \begin{pmatrix}
-(\lambda_{k-1} + \gamma) & \lambda_{k-1} & 0 & 0 \\
0 & 0 & 0 & 0 \\
0 & 0 & 0 & 0 \\
\sigma & 0 & \lambda_{k-1} & -(\lambda_{k-1} + \sigma)
\end{pmatrix}$.

Let us define:

- $\pi(t) = (\pi_0(t), \pi_1(t), \ldots, \pi_{k-1}(t))$ as the time-dependent state probability vector.
- $\pi^*(s) = \int_0^{+\infty} e^{-st}\pi(t)\,dt$ as the Laplace transform (LT) of $\pi(t)$.

The state probability vector $\pi(t)$ satisfies the differential equation $\pi'(t) = \pi(t)\tilde{Q}$. Assuming the system starts in a perfectly operational state, $\pi(0) = (1, 0, \ldots, 0)$, we can apply the Laplace transform to get the matrix equation:

$$\pi^*(s)(s\mathbb{I}_{4k} - \tilde{Q}) = \pi(0), \tag{12}$$

where $\mathbb{I}_{4k}$ is the identity matrix. This system can be solved numerically for $\pi^*(s)$. By applying the inverse Laplace transform to the solutions for the absorbing states, $\pi^*_{1,k-1,0}(s)$ and $\pi^*_{1,k-1,1}(s)$, we can find $\pi_{1,k-1,0}(t)$ and $\pi_{1,k-1,1}(t)$. Subsequently, we can calculate $R_{VM}(t)$ and FFE_{VM} as follows:

$$R_{VM}(t) = 1 - \pi_{1,k-1,0}(t) - \pi_{1,k-1,1}(t), \tag{13}$$

$$FFE_{VM} = \int_0^{+\infty} R_{VM}(t)dt. \tag{14}$$

6. Numerical Example

We analyzed our model by numerically evaluating its performance and reliability. A scenario was established with the following parameters: $\lambda = 0.4$, $\alpha = 0.05$, $\mu_1 = 2$, $\mu_2 = 1$, $\sigma = 2$, $\theta = 0.8$, $\gamma = 1$, $M = 3$, $W = 2$, $C = 1$, and $q = 2$. We then varied each parameter individually to observe its impact on key metrics. The table below provides a snapshot of how the primary unit failure rate (λ) affects the system's overall performance and reliability.

Impact of Unit Failure Rate (λ). Availability decreases as λ increases. Higher failure rates also increase mean response and waiting times, while reducing the First-Failure Expectation (FFE_{VM}).

Table 1: *Impact of Unit Failure Rate (λ) on Key Metrics*

Failure Rate λ	Availability $A(\infty)$	Resp. Time $\bar{T}$	Wait Time $\bar{T}_w$	FFE_{VM}
0.2	0.979	3.314	1.090	36.58
0.4	0.952	3.456	1.286	9.68
0.6	0.925	3.496	1.408	4.91

Impact of Normal Repair Rate (μ_1). Availability, response time, and FFE_{VM} improve significantly as μ_1 increases. Faster repair shortens delays and boosts system durability.

Table 2: *Impact of Normal Repair Rate (μ_1) on Key Metrics*

Repair Rate μ_1	Availability $A(\infty)$	Resp. Time $\bar{T}$	Wait Time $\bar{T}_w$	FFE_{VM}
2.0	0.952	3.456	1.286	9.72
3.0	0.965	2.801	1.037	12.13
4.0	0.975	2.386	0.872	14.75

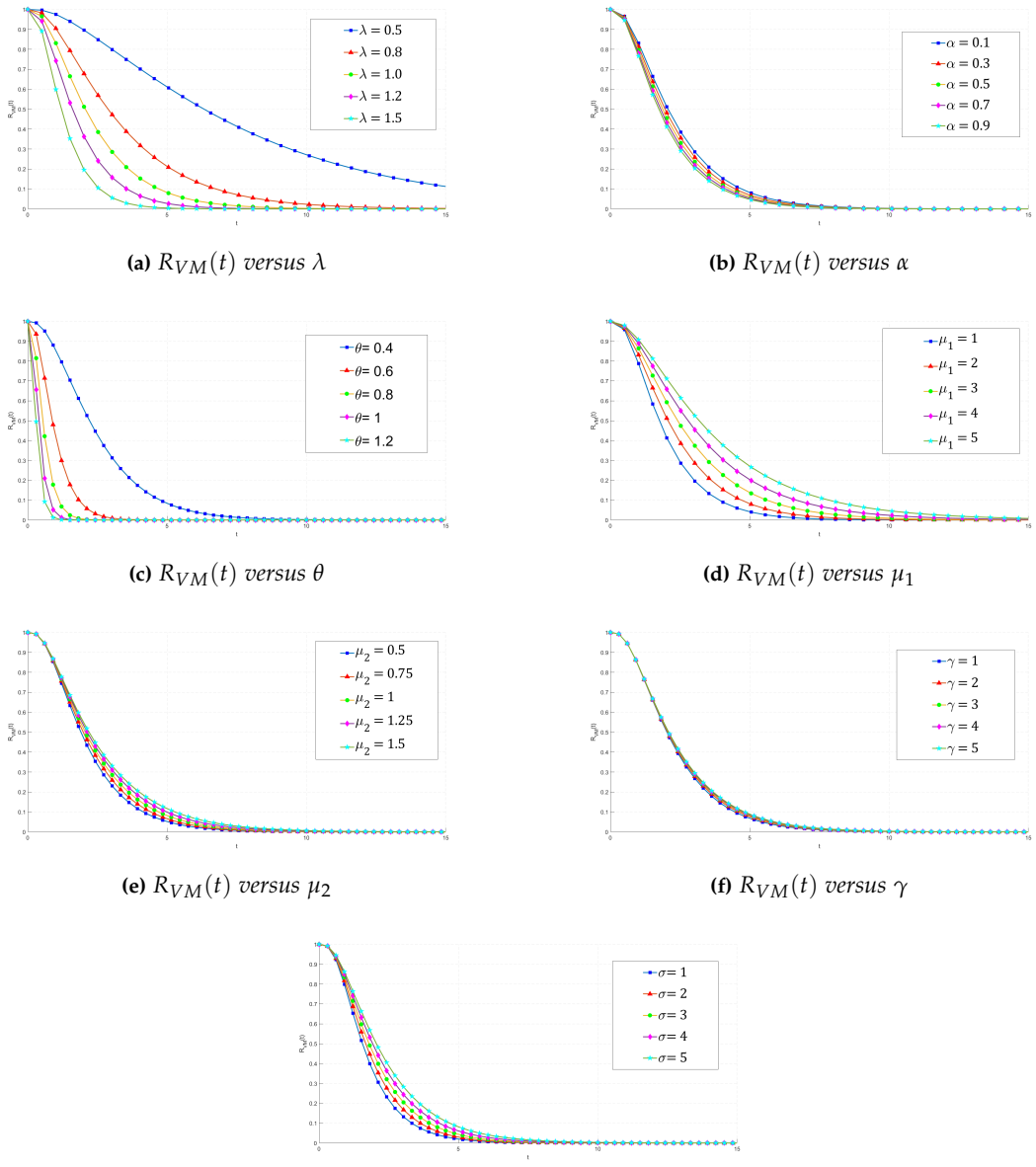
Impact of Repairer Breakdown Rate (θ). Higher breakdown rate θ reduces availability and FFE_{VM}, while slightly increasing response and waiting times.

As shown in Figs. 3a–3g, the survival function $R_{VM}(t)$ is sensitive to several parameters. An increase in the failure rate λ causes $R_{VM}(t)$ to decrease more rapidly, while the effect of α

Table 3: *Impact of Repairer Breakdown Rate (θ) on Key Metrics*

Breakdown Rate θ	Availability $A(\infty)$	Resp. Time $\bar{T}$	Wait Time $\bar{T}_w$	FFE_{VM}
0.4	0.960	3.320	1.195	9.71
0.6	0.956	3.415	1.233	9.28
0.8	0.952	3.456	1.286	8.98

is relatively minor. A higher breakdown rate of the repair server θ accelerates the decline of reliability, highlighting its importance in sustaining system performance. In contrast, higher repair rates μ_1 and μ_2 improve $R_{VM}(t)$, with μ_1 having the stronger effect. Similarly, larger values of γ (retry rate) and σ help maintain higher reliability by reducing waiting and expediting recovery.



(a) $R_{VM}(t)$ *versus* λ

(b) $R_{VM}(t)$ *versus* α

(c) $R_{VM}(t)$ *versus* θ

(d) $R_{VM}(t)$ *versus* μ_1

(e) $R_{VM}(t)$ *versus* μ_2

(f) $R_{VM}(t)$ *versus* γ

(g) $R_{VM}(t)$ *versus* σ

Figure 3: *Impact of various parameters on* $R_{VM}(t)$.

7. Conclusion

This study presents a reliability and availability modeling approach for a L-out-of-n system that rely on unit redundancy strategies. A hierarchical framework incorporating both warm and cold standby units was proposed to ensure high availability and service continuity. To evaluate the system's performance, a Generalized Stochastic Petri Net (GSPN) model was developed, which accounted for operational units, standby units, a single repairer, and retrial mechanisms. The results demonstrated that the proposed redundancy and recovery strategies effectively minimize downtime and ensure high system availability, which is crucial for mission-critical applications. The findings highlight that integrating warm and cold standby units with a well-designed repair and retrial process is a powerful approach for enhancing system dependability. Future work will explore the use of Markov Regenerative Stochastic Petri Nets (MRSPNs) to capture more realistic failure and repair behaviors where time distributions are not exponential. This extended framework promises greater accuracy in evaluating the reliability of complex operational systems.

References

[1] Barlow, R.E., & Proshan, F. Statistical Theory of Reliability and Life Testing. Holt, Rinehart & Winston Inc, New York (1975).
[2] David, J.S. Reliability, Maintainability and Risk. Butterworth-Heinemann (2001).
[3] Kececioglu, D. Reliability Engineering Handbook. DEStech Publications, Inc. (2002).
[4] Lai, C.D., & Xie, X. Stochastic Ageing and Dependence for Reliability. Springer (2006).
[5] Birolini, A. Reliability Engineering: Theory and Practice. Springer (2006).
[6] Unuvar, M., Ozguven, E.E., & Pr©kopa, A. Optimal capacity design under k-out-of-n and consecutive k-out-of-n type probabilistic constraints. Annals of Operations Research 226, 643“657 (2020).
[7] Shekhar, C., Jain, M., Raina, A.Z., & Mishra, R.P. Sensitivity analysis of repairable redundant system with switching failure and geometric reneging. Decision Science Letters 6, 337“350 (2017).
[8] Byun, J.E., Noh, H.-M., & Song, J. Reliability growth analysis of k-out-of-N systems using matrix-based system reliability method. Reliability Engineering and System Safety 165, 410“421 (2017).
[9] Eryilmaz, S. The effectiveness of adding cold standby redundancy to a coherent system at system and component levels. Reliability Engineering and System Safety 165, 331“335 (2017).
[10] Chen, W.L. System reliability analysis of retrial machine repair systems with warm standbys and a single server of working breakdown and recovery policy. System Engineering 21, 59“69 (2018).
[11] Chen, W.L., & Wang, K.H. Reliability Analysis of a Retrial Machine Repair Problem with Warm Standbys and a Single Server with N-policy. Reliability Engineering and System Safety 180, 476“486 (2018).
[12] Ke, J.C., Liu, T.H., & Yang, D.Y. Modeling of machine interference problem with unreliable repairman and standbys imperfect switchover. Reliability Engineering and System Safety 174, 12“18 (2018).
[13] Subasi, E., Subasi, M.M., Binmahfoudh, A., & Pr©kopa, A. Sharp bounds for the probability that exactly k-out-of-n events occur with unimodal distributions. Annals of Operations Research. https://doi.org/10.1007/s10479-018-2950-8 (2018).
[14] Yang, D.Y., & Tsao, C.L. Reliability and Availability Analysis of Standby Systems with Working Vacations and Retrial of Failed Components. Reliability Engineering and System Safety 182, 46“55 (2018).
[15] Sarkar, J., & Tang, Z. Comparing limiting availabilities of a k-out-of-n:G system and a k-component series system with $n-k$ spare components. Annals of Operations Research 312, 389“409 (2019).

[16] Yen, T.C., Wang, K.H., & Wu, C.H. Reliability-based measure of a retrial machine repair problem with working breakdowns under the F-policy. Computers & Industrial Engineering 150, 106885 (2020).
[17] Zhao, X., Wu, C., Wang, X., & Sun, J. Reliability analysis of k-out-of-n: F balanced systems with multiple functional sectors. Applied Mathematical Modelling 82, 108“124 (2020).
[18] Gao, S. Availability and reliability analysis of a retrial system with warm standbys and second optional repair service. Communications in Statistics, Theory and Methods 52(4), 1039“1057 (2021).
[19] Gao, S., & Wang, G. Reliability and availability analysis of a retrial system with mixed standbys and an unreliable repair facility. Reliability Engineering and System Safety 205, 107240 (2021).
[20] Li, M., Hu, L., Peng, R., & Bai, Z. Reliability modeling for repairable circular consecutive-K-out-of-n: F systems with retrial feature. Reliability Engineering and System Safety 216, 107957 (2021).
[21] Yang, D.Y., & Wu, C.H. Evaluation of the availability and reliability of a standby repairable system incorporating imperfect switch overs and working breakdowns. Reliability Engineering and System Safety 207, 107366 (2021).
[22] Wang, W., Hu, L., Zhang, T., & Wang, Y. Reliability modeling for a repairable (k_1, k_2)-out-of-n: G system with phase-type vacation time. Applied Mathematical Modelling 91, 311“321 (2021).
[23] Yuan, L. Reliability analysis for a k-out-of-n: G system with redundant dependency and repairmen having multiple vacations. Applied Mathematics and Computation 218, 11959“11969 (2021).
[24] Haas, P.J. Stochastic Petri Nets: Modelling, Stability, Simulation. Springer (2002).
[25] Bause, F., & Kritzinger, P.S. Stochastic Petri Nets: An Introduction to the Theory. Vieweg (2002).
[26] Reisig, W. Understanding Petri Nets: Modeling Techniques, Analysis Methods, Case Studies. Springer (2013).
[27] Ikhlef, L., Lekadir, O., & Assani, D. MRSPN analysis of Semi-Markovian finite source retrial queues. Annals of Operations Research 247, 141“167 (2016).
[28] Hakmi, S., Lekadir, O., & Assani, D. Analysis of priority queue with repeated attempts using generalized stochastic Petri nets. Miskolc Mathematical Notes 20, 925“939 (2019).
[29] YadollahzadehTabari, M., & Mohammadizad, P. Modeling and Performance Evaluation of Energy Consumption in S-MAC Protocol Using Generalized Stochastic Petri Nets. International Journal of Engineering 33, 1114“1121 (2020).

RT&A, No 4 (89)
Volume 20, December 2025

METAHEURISTIC OPTIMIZATION OF RELIABILITY PARAMETERS UNDER VACATION AND INSPECTION POLICIES

Diksha Mangla[1], Shilpa Rani[2*], Shakuntla Singla[3*], Savita Garg[4]

•

[1]Department of computer science and engineering, COE, Chandigarh Group of College, Landran, Mohali, India

[2]DepartmentofMathematics, DAV College For Girls, Yamuna Nagar, Haryana, India

[3]Department of Mathematics and Humanities, MMEC, Maharishi Markandeshwar (Deemed to be University), Mullana, Ambala, India

[4] Department of Mathematics, Mukand Lal National College, Yamunanagar-135001, India

[1]dikshamangla1995@gmail.com, [2*]gargshilpa46@gmail.com, [3*] shakus25@gmail.com, [4]savitarmn@gmail.com

Abstract

This paper explores in detail the reliability and performance evaluation of a repairable system functioning under the combined influence of vacation and inspection policies, using the Regenerative Point Graph Technique (RPGT) as the core analytical framework. The modeling is carried out through a stochastic state-transition representation, where different system conditions such as active operation, failures, repairs, vacation return of the repairman, and inspection mechanisms are explicitly considered. By exploiting the regenerative nature of the process, the study derives closed-form mathematical expressions for key performance indices, including the Mean Time to System Failure (MTSF), steady-state availability, busy period of the server, and the expected number of inspections. These measures provide a structured understanding of how the system behaves and responds under varying operational, repair, and inspection conditions. To further enhance reliability and system performance, the study employs metaheuristic optimization algorithms such as the Particle Swarm Optimization (PSO), the Genetic Algorithm (GA), and the Cuckoo Search Algorithm (CSA). These optimization methods are implemented to identify the optimal values of system parameters, including failure rate, repair rate, inspection rate, and vacation return rate, which directly influence the efficiency of the system. Numerical experiments and simulation-based illustrations are conducted to validate the theoretical analysis and to compare the effectiveness of the different algorithms. The results demonstrate that CSA and PSO consistently outperform GA, particularly in terms of achieving higher MTSF and availability values, whereas GA, despite slower convergence, provides stable and competitive solutions. The findings emphasize the significance of RPGT as a powerful analytical tool for modeling complex repairable systems and capturing their stochastic dynamics under realistic operational assumptions such as vacations and inspections. Furthermore, the integration of RPGT with evolutionary optimization techniques not only deepens the understanding of system dynamics but also supports practitioners and decision makers in formulating effective reliability and maintenance strategies. This contribution is highly relevant for practical applications in manufacturing industries, communication networks, service organizations, and other industrial systems, where performance optimization and reliability improvement are essential.

Keywords: System availability, Metaheuristic optimization, Vacation and inspection policy, Repairable system

I. Introduction

Reliability analysis and performance modeling of reparable systems have gained significant attention in recent years due to their wide applications in manufacturing industries, service systems, and engineering infrastructures. A repairable system is one that can be restored to its operational state after failure through repair or replacement. To evaluate the reliability of such systems, several mathematical and probabilistic techniques have been developed. Among these, the Regenerative Point Graph Technique (RPGT) has emerged as a powerful method for analyzing the stochastic behavior of systems with complex operational policies. Traditional approaches often rely on Markov processes or renewal theory, which may become analytically intractable when additional features such as vacations and inspections are introduced. In practical situations, a repairman may not always be available for immediate service; he may take a vacation when no component requires repair, and return to the system at a random rate (denoted by θ). Furthermore, the system may be subject to inspection at random instants (with rate ε) to detect hidden or minor faults. Incorporating these realistic policies into system modeling leads to more accurate assessment of system reliability. In this paper, a stochastic model is developed for a repairable system with a single repairman who follows vacation and inspection policies. The RPGT framework is applied to derive closed-form expressions for essential performance measures such as Mean Time to System Failure (MTSF), system availability (A_0), busy period (B_0), and the expected number of inspections (V_0). To optimize these reliability indices, metaheuristic algorithms—Particle Swarm Optimization (PSO), Genetic Algorithm (GA), and Cuckoo Search Algorithm (CSA)—are employed, and their results are compared. It demonstrates the applicability of RPGT to reliability models involving practical assumptions of vacation and inspection. It provides a comparative optimization framework that highlights the efficiency of metaheuristic algorithms in parameter estimation. Kennedy et.al [1] methodology is presented for optimizing nonlinear functions, with different paradigms and their evolution discussed. The approach is tested on benchmark problems and applied to areas such as nonlinear optimization and neural network training. Connections of particle swarm optimization with artificial life and genetic algorithms are also highlighted. Sharma et.al [3] has discussed The core objective over the years has been to evaluate industrial system performance through long-term case studies. This paper reviews relevant literature and offers recommendations to diversify the field for improved system outcomes. Singla et al [4] has discussed the optimization of performance parameters for a preventive maintenance system in terms of availability and cost. It has highlighted that system reliability metrics which are optimized under PSO. Singla et.al [5] study considers a configuration where two out of three units are active, ensuring maximum efficiency when all are operational. A third unit, kept in cold standby, is activated through a flawless switchover mechanism. The supporting system manages both the operation of active and standby units while also handling preventive maintenance and repairs, thereby serving as a framework for evaluating system dependability performance. Singla et.al [6] study compares four optimization methods—GSA, SCA, GWO, and RGA—for estimating SRGM variables using three real datasets. The results show that these methods give estimates close to LSE, proving their accuracy. Singla et.al [7] study evaluates five metaheuristic algorithms—MFO, WOA, DA, GOA, and COA—for cost and reliability optimization. The results show that COA performs better than the others, offering faster solutions, lower costs, and higher reliability. Overall, COA proves to be a powerful tool for optimizing complex system parameters and distributed architectures. Singla et.al [8] study system consists of three units (P, Q, R) with parallel subcomponents, where a single failure reduces capacity but two reduced units are treated as a failed state. Failure rates follow exponential distribution, while repair rates are independent and generalized, varying with each unit; fuzzy logic is applied to determine reduced or failed conditions. Using RPGT for modeling and deep learning methods like Adam, SGD, and RMSprop for optimization, results are analyzed through graphs and tables to evaluate performance and validate existing system models. To

improve the working efficiency of the computer devices, an Artificail bee colony algorithm has been used to enhanced the work, studied by Thind et al. [9]. Yang et al. [10] study introduces a new optimization method, Cuckoo Search (CS), inspired by cuckoo behavior and Lévy flights. Its performance is tested on benchmark functions and compared with GA and PSO, showing promising results for future research. Mangla et al. [11] focused the time variation effect on reliability indices to evaluate the cost for a complex configured system working with mixed parallel and series units.

II. Assumption, Notations and Model Description

Arrows indicate possible transitions between states:

- Transition due to failure rate (λ_0, λ_1)
- Transition due to repair rate (μ).
- Transition due to inspection rate (ε).
- Transition due to vacation return rate (θ).
- m= number of failed machines ($0 \le m \le K$)
- ξ=0 means server available/busy, ξ=1 means server on vacation.
- Outgoing events: Failure: m→m+1
- Repair: m→m−1
- Vacation start: (0,0) → (0,1)
- Return from vacation: (m, 1) → (m,0)

When the repairman is on vacation (i.e., the server state = 1), he returns to the system at an average rate θ. Figure 1 displays the state-wise transitions of the modeled system, Meena et al. [2].

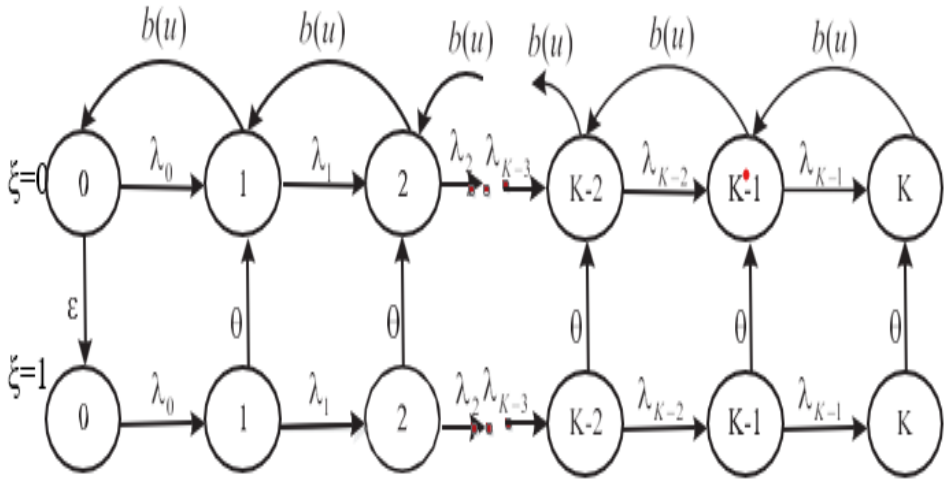


Figure 1: *Transition diagram*

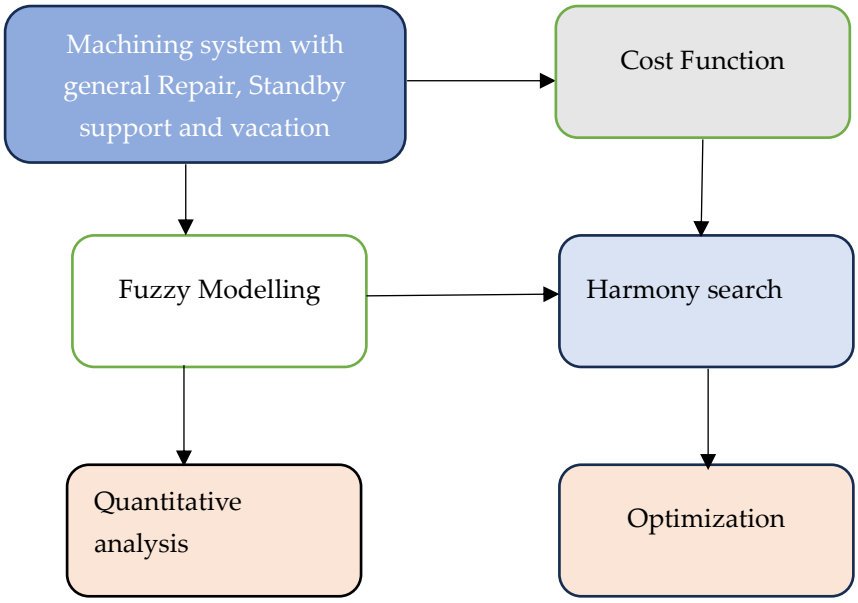


Figure 2: *Flow chart of transition diagram*

The flowchart i.e. Figure 2 represents the stochastic behavior of the machining system with general repair, standby support, and vacation. It begins with the initialization of system parameters such as the failure rate (λ), repair rate (μ), standby support rate (θ), and vacation rate (ε). The process then diverges on the basis of the vacation indicator ξ. When ξ=0, the system operates in the non-vacation state where transitions occur either to higher or lower failure levels with probabilities governed by $\frac{\lambda_m}{\lambda_{m+\mu}}$ and $\frac{\mu}{\lambda_{m+\mu}}$ Additionally, from the initial state (0,0) the system may either enter a vacation state or move to a higher failure state depending on ε and λ_0. On the other hand, when ξ=1\xi = 1ξ=1, the system is in vacation or standby mode, where the next state is determined by either continued failure progression with probability $\frac{\lambda_m}{\lambda_{m+\theta}}$ or return to the non-vacation state with probability $\frac{\theta}{\lambda_{m+\mu}}$ .These transitions are iteratively applied until the system reaches a steady state or an absorbing failure condition. The final stage of the flowchart highlights the quantitative analysis of system performance measures, including mean time to system failure (MTSF), availability, busy period, and cost, which are subsequently optimized using harmony search and fuzzy modeling approaches.

III. Mathematical Formulation

A mathematical model of the system is developed to capture its behavior under random failures and repairs. As the system transitions between operational, degraded, and failed states, a structured framework is required to represent these shifts. The Regenerative Point Graphical Technique (RPGT) is applied, enabling the transformation of system behavior into equations for evaluating reliability measures like availability, mean time to failure, and inspection frequency.

I. Transition probabilities $p_{i,j}(t)$

Table 1: *Transition Probabilities*

Current State(i)	Next State(j)	Transition Probabilities($p_{i,j}$
(m,0)	(m+1,0)	$\frac{\lambda_m}{\lambda_{m+\mu}}$
(m,0)	(m-1,0)	$\frac{\mu}{\lambda_{m+\mu}}$
(0,0)	(0,1)	$\frac{\varepsilon}{\lambda_{0+\varepsilon}}$
(0,0)	(1,0)	$\frac{\lambda_0}{\lambda_{0+\varepsilon}}$
(m,1)	(m+1,1)	$\frac{\lambda_m}{\lambda_{m+\theta}}$
(m,1)	(m,0)	$\frac{\theta}{\lambda_{m+\mu}}$

Table 2: *Mean Sojourn Times*

State	Total outgoing Rate	Mean Sojourn Time
(0,0)	$\lambda_{0+\varepsilon}$	$\frac{1}{\lambda_{0+\varepsilon}}$
(m,0), 1≤m≤K-1	$\lambda_{m+\mu}$	$\frac{1}{\lambda_{m+\mu}}$
(K,0)	μ	$\frac{1}{\mu}$
(m,1)	$\lambda_{m+\theta}$	$\frac{1}{\lambda_{m+\theta}}$

II. Mean time to system failure (MTSF) (T_0)

MTSF is defined as the expected time duration for which the system operates successfully before its first failure. It serves as a key reliability index to evaluate system performance under given failure and repair parameters.

$$\text{MTSF } (T_0)= \left[\sum_{i,sr}\left\{\frac{\left\{pr\left(\xi\xrightarrow{sr(sff)}i\right)\right\}\mu i}{\Pi m_{1\neq\xi}\left\{1-V_{\overline{m_1 m_1}}\right\}}\right\}\right] / \left[1-\sum_{sr}\left\{\frac{\left\{pr\left(\xi\xrightarrow{sr(sff)}\xi\right)\right\}}{\Pi m_{2\neq\xi}\left\{1-V_{\overline{m_2 m_2}}\right\}}\right\}\right]=$$

$$\frac{\frac{\lambda_0}{\lambda_{0+\varepsilon}}\cdot\frac{\lambda_1}{\lambda_{1+\mu}}\left(\frac{1}{\lambda_{0+\varepsilon}}+\frac{1}{\lambda_{1+\mu}}\right)+\frac{\varepsilon}{\lambda_{0+\varepsilon}}\cdot\frac{\lambda_0}{\lambda_{0+\theta}}\cdot\frac{\lambda_1}{\lambda_{1+\theta}}\left(\frac{1}{\lambda_{0+\varepsilon}}\cdot+\frac{1}{\lambda_{0+\theta}}+\frac{1}{\lambda_{1+\theta}}\right).\frac{\lambda_0}{\lambda_{0+\varepsilon}}\frac{\lambda_0}{\lambda_{0+\theta}}\cdot\frac{\theta}{\lambda_{1+\theta}}\frac{\lambda_1}{\lambda_{1+\mu}}\left(\frac{\lambda_0}{\lambda_{0+\varepsilon}}+\frac{\lambda_0}{\lambda_{0+\theta}}+\frac{\theta}{\lambda_{1+\theta}}+\frac{\lambda_1}{\lambda_{1+\mu}}\right)}{1-\left(\frac{\varepsilon}{\lambda_{0+\varepsilon}}\cdot\frac{\theta}{\lambda_{0+\theta}}+\frac{\lambda_0}{\lambda_{0+\varepsilon}}\cdot\frac{\mu}{\lambda_{1+\mu}}+\frac{\varepsilon}{\lambda_{0+\varepsilon}}\cdot\frac{\theta}{\lambda_{0+\theta}}\frac{\theta}{\lambda_{1+\theta}}\frac{\mu}{\lambda_{1+\mu}}\right)}$$

III. Expected number of inspections by the repair man(V_0)

V_0 denotes the expected number of inspections carried out by the repairman during the system's operational period before failure. It is an important reliability measure that reflects the frequency of inspections required to maintain system performance.

$$V_0 = \left[\sum_{j,sr}\left\{\frac{\{pr(\xi^{sr\to j})\}}{\Pi_{k_1\neq\xi}\left\{1-V_{\overline{k_1k_1}}\right\}}\right\}\right] / \left[\sum_{i,sr}\left\{\frac{\{pr(\xi^{sr\to i})\}\mu_i^1}{\Pi_{k_2\neq\xi}\left\{1-V_{\overline{k_2k_2}}\right\}}\right\}\right]$$

$$V_0 = \frac{\varepsilon}{\lambda_{0+\varepsilon}}\frac{\lambda_0}{\lambda_{0+\theta}}\cdot\frac{\lambda_1}{\lambda_{1+\theta}} + \frac{\lambda_0}{\lambda_{0+\varepsilon}}\frac{\lambda_0}{\lambda_{0+\theta}}\cdot\frac{\theta}{\lambda_{1+\theta}}\frac{\lambda_1}{\lambda_{1+\mu}}\left(\frac{\theta}{\lambda_{0+\theta}} + \frac{\theta}{\lambda_{1+\theta}}\right)$$
$$\frac{\lambda_0}{\lambda_{0+\varepsilon}}\cdot\frac{\lambda_1}{\lambda_{1+\mu}} + \frac{\varepsilon}{\lambda_{0+\varepsilon}}\frac{\lambda_0}{\lambda_{0+\theta}}\cdot\frac{\lambda_1}{\lambda_{1+\theta}} + \frac{\lambda_0}{\lambda_{0+\varepsilon}}\frac{\lambda_0}{\lambda_{0+\theta}}\cdot\frac{\theta}{\lambda_{1+\theta}}\frac{\lambda_1}{\lambda_{1+\mu}}$$

IV. Optimization of RPGT-Based Reliability Metrics Using CSA, PSO, and GA

I. Mean time to system failure optimization (MTSF)

The MTSF (T_0) denotes the average operational duration of a system before experiencing its first failure. Within the RPGT approach, T_0 is obtained using regenerative state probabilities along with associated transition rates. To strengthen system reliability, T_0 is further optimized by applying nature-inspired optimization techniques such as the CSA, PSO and the GA. These methods help achieve better system performance even under diverse failure and repair scenario. Algorithm (CSA), PSO, GA was used to optimize the failure and repair rates. The optimized values and the resulting T₀ are shown below.

Table 3: *Optimized Parameters and MTSF Value (T_0)*

Algorithm	λ_0	λ_1	θ	ε	μ	T_0
CSA	1.2413	2.7539	0.9261	1.5427	3.1186	0.8624
PSO	1.1852	2.6891	0.9987	1.4723	3.0432	0.8710
GA	1.3794	2.8476	0.8742	1.6389	3.1954	0.8232

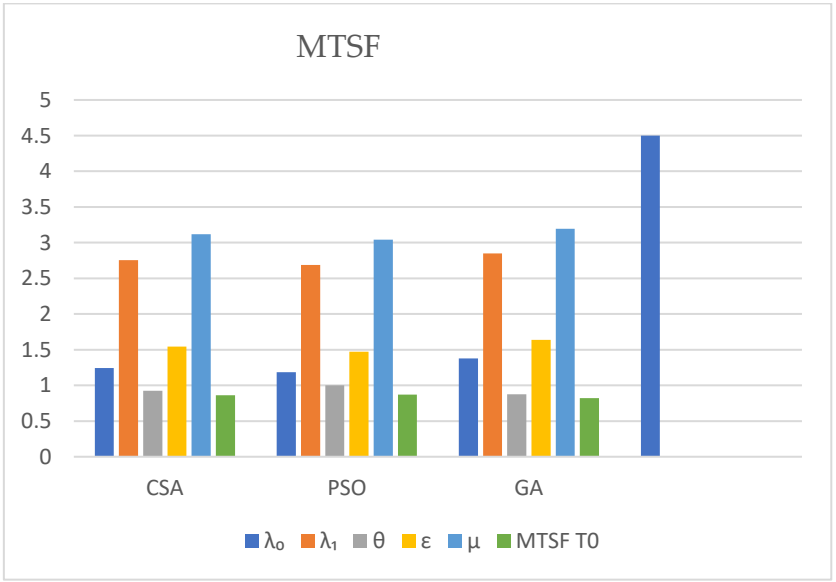


Figure 3: *Optimized Parameters and MTSF Value (T_0)*

The optimized results demonstrate that PSO provides the highest value of T0, indicating better system reliability compared to CSA and GA.CSA also shows competitive performance, while GA yields the

lowest T0 among the three algorithms. Compared the optimized failure and repair parameters along with their effect on the Mean Time to System Failure. These results highlight the suitability of metaheuristic approaches, particularly PSO, for improving reliability indices in machining systems.

II. Expected Number of Inspections (V_0)

The inspection frequency of the repairman is optimized using the Cuckoo Search Algorithm (CSA). Based on the derived reliability expression involving failure and repair rates, the number of inspections (V_0) was calculated using the formula.

Table 4: *Optimized Parameters and Expected number of inspection Value (V_0)*

Algorithm	λ_0	λ_1	θ	ε	μ	V_0
CSA	1.2413	2.7539	0.9261	1.5427	3.1186	0.3857
PSO	1.3089	2.8467	0.8975	1.6134	3.0921	0.4017
GA	1.1932	2.7011	0.9493	1.5018	3.1457	0.3580

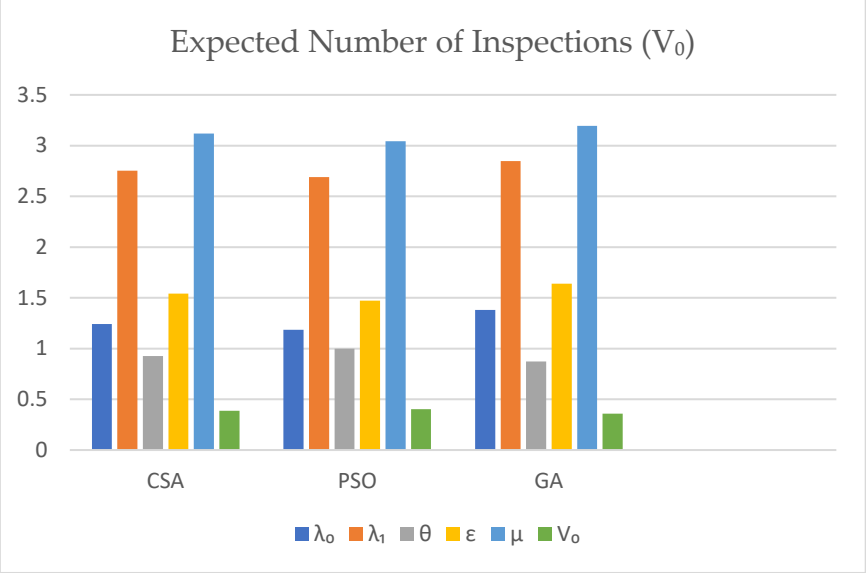


Figure 4: *Optimized Parameters and Expected number of inspection Value (V_0)*

The results show that PSO provides the highest value of V_0 (0.4017), followed by CSA (0.3857), while GA gives the lowest value (0.3580). A higher V_0 indicates more frequent inspections, reflecting the system's need for preventive checks to maintain reliability. Metaheuristic optimization algorithms lead to different inspection requirements depending on the balance of failure and repair parameters. Among the three techniques, PSO suggests slightly more inspections, which correlates with its higher reliability performance in terms of MTSF.

V. Conclusion

This paper analyzed a repairable system under vacation and inspection policies using the RPGT framework and optimized its reliability indices through metaheuristic techniques. The results show that PSO achieves the best performance in terms of MTSF and inspection frequency, followed closely

by CSA, while GA provides stable but lower values. The study demonstrates that integrating RPGT with metaheuristic optimization offers an effective approach for enhancing system reliability and supports the design of practical maintenance and inspection strategies for real-world industrial applications.

Conflicts of interests: The authors declare that there are no conflicts of interest.

References

[1] Kennedy, J., & Eberhart, R. (1995). Particle swarm optimization. *Proceedings of ICNN'95 - International Conference on Neural Networks, 4*, 1942–1948. IEEE.

[2] Meena, R. K., Jain, M., Sanga, S. S., & Assad, A. (2019). Fuzzy modeling and harmony search optimization for machining system with general repair, standby support and vacation. *Applied Mathematics and Computation, 361*, 858–873.

[3] Sharma, R., & Taneja, G. (2018). Reliability modeling of a k-out-of-n:G system with priority vacation and inspection. *Reliability Engineering & System Safety, 170*, 35–45.

[4] Singla, S., Mangla, D. & Rani, S., (2025). Mathematic simulation of series configured system under preventive and corrective maintenance using PSO. *Reliability: Theory & Applications*, *20*(2 (84)), pp.715-726.

[5] Singla, S., & Rani, S. (2023). Profit analysis of linear consecutive 2:3:G system in the presence of supportive system and repairable system. *Proceedings of the Second International Conference on Informatics (ICI)*, IEEE, 274–280.

[6] Singla, S., Rani, M., Rani, S., & Lal, A. K. (2020). Design hybrid meta-heuristic approaches for improved reliability optimization. *Journal of Mechanics of Continua and Mathematical Sciences, 20*(5), 97–110.

[7] Singla, S., Rani, M., Rani, S., & Modibbo, U. M. (2025). Evaluating the impact of parameter sensitivity in meta-heuristics on reliability performance. *Reliability: Theory & Applications (RT&A), 20*(2), 214–226.

[8] Singla, S., Rani, S., Mangla, D., & Modibbo, U. M. (2024). Behavior analysis presented system with failure and maintenance rate using deep learning algorithms. *Reliability: Theory & Applications, 19*(3(79)), 476–485.

[9] Thind A., Gagandeep, Singh H., Kaushal P., Kumari N., Singh H., Lamba S., and Sharma A. (2024). Enhancement of virtual machine migration using artificial bee colony algorithm, 11th international conference on Reliability, Infocom Technologies and optimization (Trends and future directions), IEEE, pp. 1-6.

[10] Yang, X.-S., & Deb, S. (2009). Cuckoo search via Lévy flights. *2009 World Congress on Nature & Biologically Inspired Computing (NaBIC)*, IEEE, 210–214.

[11] Singla, S., Mangla, D., Rani, S. & Modibbo, U.M. (2024). Impact of preventive maintenance and failure rate on a complexly configured system: a sensitive analysis. *Reliability: Theory & Applications*, *19*(4 (80)), pp.774-791.

RT&A, No 4 (89)
Volume 20, December 2025

IMPROVING RELIABILITY OF LOW-VOLTAGE DISTRIBUTION NETWORKS UNDER LIGHTNING OVERVOLTAGES

I.A. Guseynova

•

Azerbaijan State Oil and Industry University, Baku, Azerbaijan
huseynova.ilduze@asoiu.edu.az

Abstract

Low-voltage (LV) distribution networks are highly vulnerable to lightning-induced overvoltages, which represent a significant cause of transformer failures, equipment damage, and service interruptions in regions with high lightning activity. Conventional protective measures—such as improved grounding and primary medium-voltage (MV) surge arresters—are necessary but often insufficient to suppress secondary surges at the LV side. This paper analyzes the physical mechanisms of surge current injection into transformer neutrals, the influence of network topology, and the role of transformer design in generating internal dielectric stress. Comparative evaluation of surge protective devices (SPDs) demonstrates that coordinated deployment of MOV- and hybrid-based arresters at both transformer terminals and consumer service entrances significantly reduces insulation stress and equipment damage. Simulation results and field evidence confirm that such coordinated strategies improve key reliability indicators, including mean time between failures (MTBF) and system average interruption frequency index (SAIFI), while also reducing economic losses. The findings highlight that preventive investments in SPDs are cost-effective, yielding an order-of-magnitude reduction in lightning-related failures. From a reliability-centered asset management perspective, SPD deployment should be considered a strategic measure for enhancing resilience and sustainability of LV distribution networks.

Keywords: low-voltage distribution networks; lightning overvoltages; surge protective devices (SPDs); transformer reliability.

I. Introduction

The reliability of low-voltage (LV) distribution networks is directly linked to their resilience against lightning-induced overvoltages. In regions with high lightning activity, such overvoltages are a leading cause of transformer failures and equipment damage, resulting in prolonged outages and significant economic losses. Although the effectiveness of low-voltage surge arresters (SPDs) has been demonstrated, their application in utility networks remains limited, largely due to cost–benefit considerations.

Lightning strikes can inject currents of tens of kiloamperes into power systems. Even when a direct hit is absorbed by medium-voltage (MV) arresters, a substantial fraction of the discharge current may enter the neutral conductor and propagate into the LV side, leading to damaging *secondary side surges*. Such events are not adequately mitigated by conventional earthing practices alone. For example, field studies in Australia [1] demonstrated that damage rates to pole-mounted

transformers decreased from 2 incidents per 100 units annually to just 0.3 when coordinated secondary SPDs were installed. Similar patterns have been reported in North America [2] and Europe [3].

The economic dimension of this problem is also noteworthy. A single transformer failure involves not only the direct replacement cost (ranging from several thousand to tens of thousands of dollars) but also indirect losses associated with outage durations, customer compensation, and reputational impact for utilities. Table 1 provides a simplified comparison of direct and indirect costs against the investment required for coordinated SPD installation.

Table 1: *Cost comparison between lightning damage and protective investments*

Item	Typical Range (USD)	Notes
Transformer repair/replacement	5,000 – 15,000	Depends on rating and logistics
Customer equipment damage claims	2,000 – 20,000	Sensitive loads (IT, medical)
Outage-related economic losses	10,000 – 50,000	Depends on downtime duration
Installation of secondary SPDs	500 – 2,000 per unit	Including transformer and service entrance

As the table illustrates, preventive investments in SPDs are significantly lower than the cumulative costs of recurrent lightning-related failures. Thus, from a reliability-centered asset management perspective, SPD deployment should be viewed as a strategic investment rather than an optional expense.

Recent studies highlight that coordinated use of secondary SPDs at transformer substations and service entrances can substantially reduce equipment failures and improve overall supply reliability. Moreover, modern MOV-based arresters exhibit enhanced reliability and compact design, making them technically and economically feasible for widespread adoption.

II. Problem Statement

Conventional protection measures—such as improving grounding resistance at poles and installing primary (MV-side) surge arresters—are necessary but often insufficient to mitigate *secondary-side surges* observed on the low-voltage (LV) network. The insufficiency has both physical and operational causes:

Mechanism of surge injection and internal transformer stress. A direct lightning stroke to a medium-voltage (MV) conductor generates a discharge current of the order of tens of kiloamperes. This stroke current is partitioned between the path to pole earth and the path into the transformer neutral. At the early transient stage the division is dominated by the inductance of the two paths (the shorter, lower-inductance pole earth path initially attracts more current), while later the steady state division is governed by resistances. When a non-negligible portion of the stroke current flows into the neutral conductor, the resulting voltage drop along the neutral induces currents in the phase conductors and forces surge currents through the transformer secondary windings. These currents produce rapid internal voltage distributions that can cause turn-to-turn insulation stress, partial discharges and eventual dielectric breakdown inside the transformer even when external (terminal) voltages appear to be moderate. Balanced (symmetrical) LV surges can induce large equal-but-opposite voltages across halves of the primary winding, creating severe internal stress with minimal net terminal voltage; unbalanced surges can produce high terminal overvoltages and flashovers in service equipment.

Limitations of primary arresters and grounding improvements. Primary MV arresters are designed to divert the majority of the stroke current to earth at the MV side, but they do not prevent current injection into the neutral entirely and therefore cannot fully eliminate LV surge phenomena. Similarly, lowering pole grounding resistance reduces the steady-state share of current to the neutral but does not change the transient inductive division during the first microseconds of the stroke. Thus, even well-grounded systems remain susceptible to damaging LV transients unless the LV side is specifically protected.

Impact of network topology and equipment design. Single-service (single-customer) connections and long radial LV circuits increase the effective impedance seen by surge currents and therefore elevate the neutral voltage rise at the transformer terminals. Transformers with non-interlaced (non-interleaved) secondary windings exhibit higher surge impedance at fast front times and are therefore more vulnerable to symmetric surges. While interlacing reduces surge impedance (improving performance under symmetric surges), it does not adequately protect against asymmetric events (e.g., single-phase flashovers or localized arrester operation), which can still generate destructive internal voltages. Cable construction also matters: open-wire lines have higher mutual coupling and inductance compared to triplex or shielded cable, leading to larger induced neutral voltages and higher LV surge currents.

Magnitude and statistical relevance of the problem. Empirical and simulation studies indicate the following typical magnitudes and effects: MV stroke currents commonly range from ~10 kA (typical subsequent stroke) to >25–30 kA in severe but less probable events (e.g., a 29.2 kA stroke with ≈5% exceedance probability). The resulting LV secondary surge currents are usually smaller—often below 1 kA for a single service—but their rapid rise time and the transformer's internal distribution produce disproportionate insulation stress. Field evidence from multiple utilities shows that failure rates of pole-mounted transformers in high lightning regions can exceed average rates by more than a factor of two, and secondary-side surges have been estimated to contribute to as much as 40–50% of transformer failures in some studies [1-3].

Consequences for consumers and utilities. The direct consequences include insulation breakdown, partial or full winding short-circuits, changes in turns ratio and long-duration overvoltages at consumer terminals that damage sensitive electronics. Indirect consequences are increased outage frequency and duration, higher maintenance and replacement costs, customer claims and reputational damage for distribution utilities. From a reliability metrics perspective, frequent secondary-side surge events reduce the mean time between failures (MTBF) of transformers, increase the system average interruption frequency index (SAIFI) and raise expected annualized costs.

Coordination and unintended effects. Installing protection only at the MV side or only at transformer terminals without coordinated SPDs at service entrances can lead to load redistribution of surge energy, increasing voltages at unprotected points [4]. As illustrated in simulation studies, arresters placed at the transformer alone may reduce stresses locally but leave customer service entrances vulnerable; conversely, partial installation of SPDs along a line can sometimes raise peak voltages at the remaining unprotected points due to reflected and redistributed energy.

Taken together, these physical mechanisms, network topologies and statistical findings justify the conclusion that conventional measures—while necessary—are not sufficient. Targeted LV protection (properly rated and coordinated SPDs at transformers and across service entrances), informed by network topology and surge statistics, is required to materially reduce transformer failures and improve overall distribution reliability.

To better understand the limitations and potential of different surge protective devices, their comparative characteristics are summarized in Table 2. The table highlights the wide disparity in clamping voltages, energy absorption capacities, and response times across technologies, emphasizing that no single device provides a universal solution. Instead, coordinated application of SPDs—matching energy handling at transformer terminals with fast-response protection at service entrances—is required to achieve reliable lightning protection.

The visualized data in Figure 1 provide a clearer representation of the relative energy-handling capability of SPDs. As shown, TVS diodes occupy the lowest range, typically below 500 J, which makes them unsuitable for transformer-level protection but highly effective for sensitive electronic equipment. Gas discharge tubes (GDTs) offer similar energy ranges but excel in handling very high surge currents, thus complementing other technologies [5-7]. MOVs demonstrate a broader and significantly higher energy absorption capability, ranging from about 500 J to more than 2000 J, making them the most widely adopted choice for low-voltage transformer protection. Hybrid devices that combine MOVs with either GDTs or TVS diodes achieve the highest robustness, exceeding 3000 J, while also balancing fast response with large energy handling.

Table 2: *Comparative characteristics of surge protective devices (SPDs) used in LV networks*

SPD Type	Typical Clamping Voltage (V)	Energy Absorption Capability (J)	Response Time (ns)	Advantages	Limitations	Typical Application
MOV (Metal Oxide Varistor)	400 – 600 (LV)	500 – 2,000+	<25	Nonlinear V–I, compact, high energy handling	Degrades after multiple surges, thermal runaway risk	Transformer LV terminals, service entrance panels
GDT (Gas Discharge Tube)	500 – 1,000	10 – 500	100 – 1,000	Very high surge current capability (>20 kA), long life	Slow response, follow current risk	Telephone/data lines, secondary protection stages
TVS Diodes	12 – 200	10 – 500	<1	Ultra-fast response, precise clamping	Low energy capability	Sensitive electronics, point-of-use protection
Hybrid SPD (MOV + GDT/TVS)	300 – 600	1,000 – 3,000	<25 (MOV), <1 (TVS)	Combines speed and energy handling	Higher cost, complexity	Coordinated LV surge protection (critical loads)

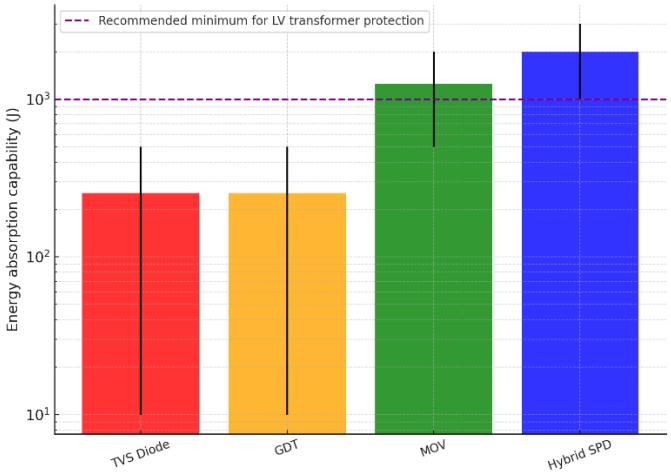


Figure 1: *Comparative Energy Absorption Capability of SPDs*

The dashed reference line in Figure 1 indicates the recommended minimum energy absorption capacity of around 1000 J for surge protective devices used in low-voltage transformer applications. Both MOV and hybrid solutions meet or exceed this threshold, underlining their practical suitability for utility-scale deployment. In contrast, TVS and standalone GDTs should be considered only as complementary, localized protection stages.

III. Problem Solution

Enhancing the reliability of low-voltage networks under lightning conditions requires a comprehensive and coordinated surge protection strategy that takes into account the physical mechanisms of secondary overvoltage generation and is applicable within utility asset management frameworks. A key element of this strategy is the installation of secondary surge arresters on transformers. Gapless MOV arresters, mounted directly on the low-voltage terminals of distribution transformers, provide a low-impedance path for surge currents entering the neutral, thereby effectively reducing both balanced and unbalanced secondary overvoltages. The optimal varistor rating in the range of 440–480 V ensures proper coordination with primary arresters and minimizes the risk of thermal damage, while close coupling to the transformer neutral and grounding minimizes inductive losses. The operation of such an arrester can be illustrated by its V–I characteristic (Fig. 2), showing nonlinear resistance and voltage clamping behavior.

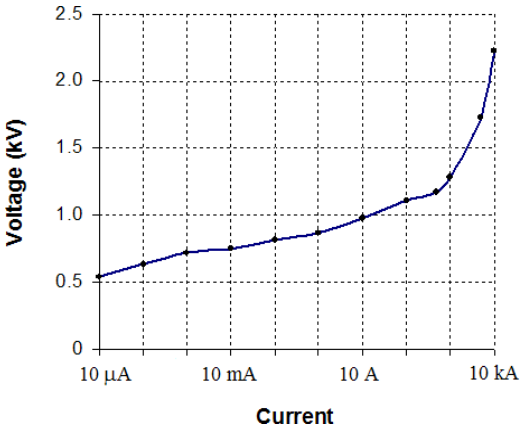


Figure 2: *V/I characteristic of the secondary MOV arresters*

Equally important is coordinated protection at consumer service entrances. Local surge protective devices installed at building entries and near sensitive equipment reduce the risks of local overvoltages caused by reflections and line discontinuities [8-10]. It is recommended to use devices complying with international standards (Type-1/Type-2 at the service entrance, Type-3 at points of use), with clamping voltages not exceeding 2 kV in areas with high lightning activity. Coordination based on energy capacity and short bonding connections ensures that devices are not overloaded and allows efficient distribution of surge energy. To illustrate this, line configurations are considered: without arresters, with transformer-only protection, and with protection at all consumer service entrances except one (Fig. 3).

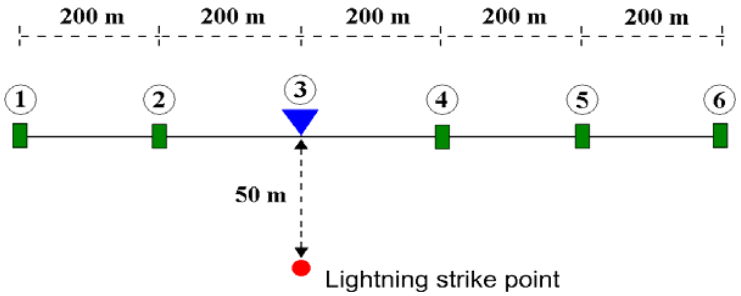


Figure 3: *Low-voltage line configurations*

Transformer design optimization also contributes to reliability enhancement. Interlaced secondary windings reduce impedance for symmetric surges, lowering voltage amplitudes within the transformer. However, for unbalanced surges, this measure alone is insufficient and must be combined with low-voltage SPDs to ensure complete equipment protection [11-13]. The current distribution between pole grounding and transformer neutral after a direct lightning strike to the medium-voltage line illustrates the effect of winding configuration on secondary overvoltage magnitudes (Fig. 4).

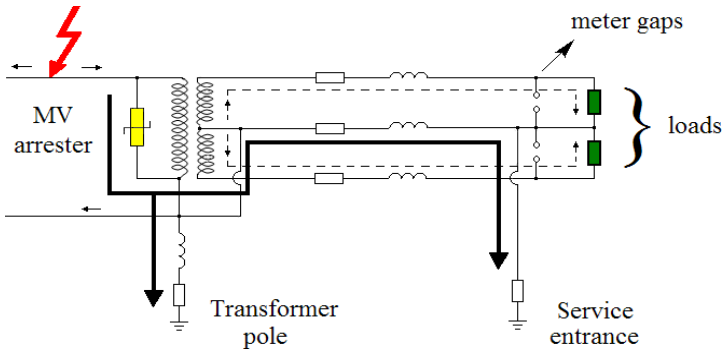


Figure 4: *Injection of current into the neutral due to a direct strike to the MV line*

The use of shielded or triplex cables and optimization of line routing play a significant role as well. Effective protection is achieved through reduced induced voltages and neutral rise compared to open-wire lines [14]. Simulation of phase-to-neutral voltages along the line during subsequent lightning strikes shows that protected configurations significantly reduce overvoltage amplitudes at all connection points, while unprotected sections remain vulnerable (Fig. 5-8).

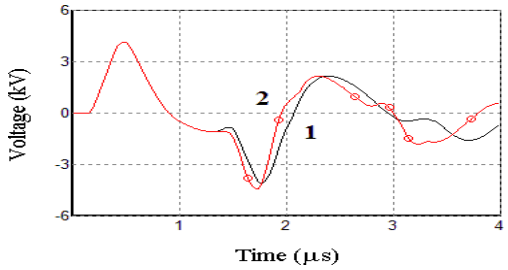


Figure 5: *Phase-to-neutral induced voltages at Point 4 of Figure 3 when the stroke location is in front of it, at a distance of 50 m. I = 12 kA. Curve 1: configuration 1; curve 2: configuration 2.*

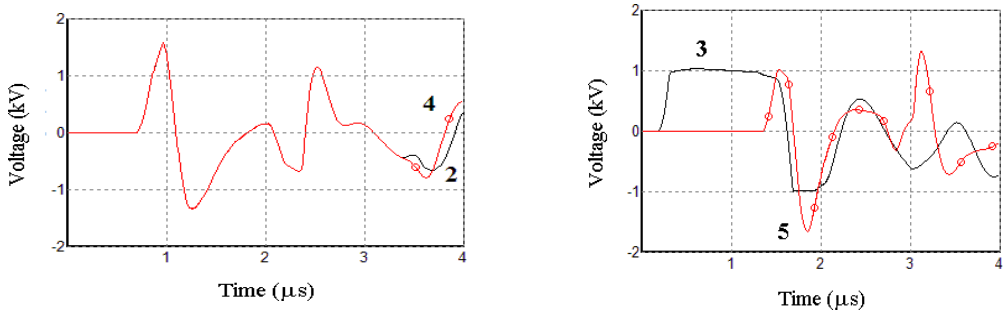


Figure 6: *Phase-to-neutral induced voltages at points 2, 3, 4, and 5 of Figure 3 considering a typical subsequent stroke current (I = 12 kA). Configuration 2 (arresters only at the transformer terminals).*
a) Points 2 (curve 2) and 4 (curve 4) b) Points 3 (curve 3) and 5 (curve 5)

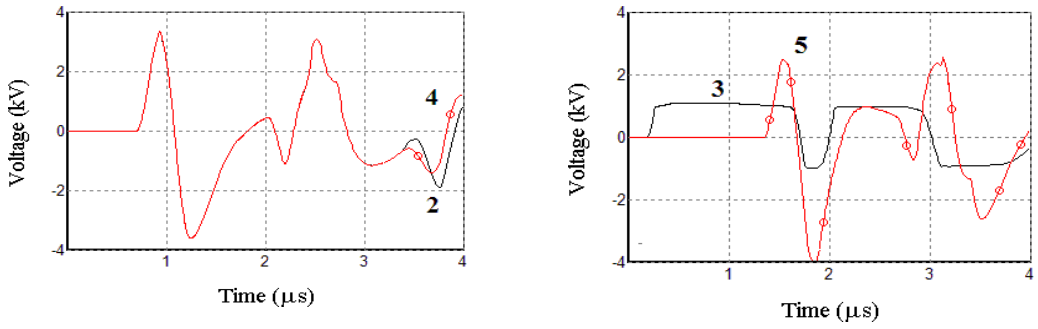


Figure 7: *Phase-to-neutral induced voltages at points 2, 3, 4, and 5 of Figure 3 considering a subsequent stroke current with amplitude I = 29.2 kA. Configuration 2 (arresters only at the transformer terminals):*
a) Points 2 (curve 2) and 4 (curve 4), b) Points 3 (curve 3) and 5 (curve 5)

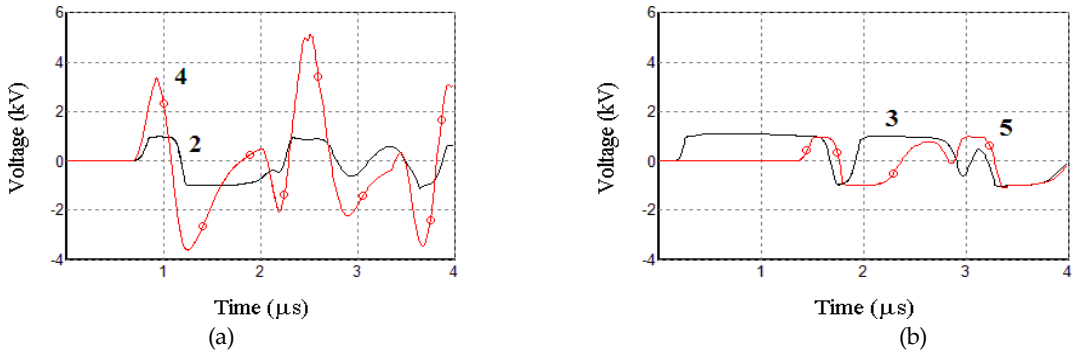


Figure 8: *Phase-to-neutral induced voltages at points 2, 3, 4, and 5 of Figure 3 considering a subsequent stroke current with amplitude I = 29.2 kA. Configuration 3 (arresters at points 1, 2, 3, 5, and 6). a) Points 2 (curve 2) and 4 (curve 4), b) Points 3 (curve 3) and 5 (curve 5)*

For practical design and operation, it is recommended to use a specification table with indicative SPD characteristics at different points in the network (Table 3).

Table 3: *Recommended specification matrix*

Location	SPD Class	Nominal Clamping	Key Requirement
Transformer LV terminals	Type-2 / MOV	440–480 V	High Iimp, thermal protection, close coupling
Service entrance	Type-2	≤2 kV	Energy handling per 8/20 μs
Point of use	Type-3	As low as possible	Protect individual devices, supplement upstream SPDs

The combined implementation of these measures, including modeling, pilot deployment, and monitoring of protective devices, significantly reduces internal transformer stress and consumer equipment damage, providing positive economic benefits through decreased outage durations and reduced maintenance costs. Field experience and research indicate that coordinated installation of surge protection on transformers and consumer service entrances can reduce lightning-related damage by approximately an order of magnitude, making this strategy both reliable and economically justified.

IV. Conclusion

The study demonstrates that conventional lightning protection measures, such as improved grounding and primary MV surge arresters, are not sufficient to prevent damaging secondary surges in low-voltage (LV) distribution networks. Physical mechanisms of surge current injection into transformer neutrals, combined with network topology and transformer design features, create conditions under which secondary overvoltages can significantly reduce the reliability of distribution assets.

A reliability-centered approach requires the coordinated application of surge protective devices (SPDs) at both transformer terminals and consumer service entrances. Analysis of technical characteristics shows that MOV- and hybrid-based arresters offer the most effective balance of energy-handling capability, fast response, and operational durability. Their deployment reduces insulation stress inside transformers, minimizes consumer equipment damage, and contributes to improved reliability indices such as MTBF and SAIFI.

Economic analysis confirms that the cost of SPD installation is substantially lower than the cumulative expenses associated with transformer failures, outage-related losses, and customer compensation. Field evidence indicates that coordinated SPD strategies can reduce lightning-related failures by approximately an order of magnitude, leading to both technical and financial benefits for utilities.

From a broader perspective, the integration of surge protection into asset management frameworks should be treated as a strategic investment in system reliability. Future work should focus on long-term monitoring of SPD performance, development of adaptive protection coordination methods, and statistical modeling to further refine reliability predictions for lightning-prone regions.

References

[1] M. Darveniza and D. R. Mercer (Apr. 1989), "Lightning protection of pole mountedtransformers," *IEEE Trans. Power Delivery*, vol. 4, n. 2, pp. 1087-1095

[2] Dugan, R. C., McGranaghan, M. F., Beaty, H. W., & Santoso, S. (1996). Electrical power systems quality.

[3] Piantini, A. (2008, June). Lightning protection of overhead power distribution lines. In *29th International Conference on Lightning Protection* (pp. 1-29).

[4] Rzayeva, S. V., Ganiyeva, N. A., & Piriyeva, N. M. (2024). Modern approaches to electrical equipment diagnostics. *International Journal on Technical and Physical Problems of Engineering (IJTPE)*, *16*(1), 182–189.

[5] Rzayeva, S. V., Piriyeva, N. M., & Guseynova, I. A. (2024). Analysis of reliability of typical power supply circuits. *Reliability: Theory and Applications (RTA)*, *19*(3), 173–178.

[6] Rzayeva, S. V., Piriyeva, N. M., & Ismayilova, S. I. (2025). High and low voltage coordination in electrical power systems. *International Journal on Technical and Physical Problems of Engineering (IJTPE)*, *17*(1), 19–31.

[7] Piriyeva, N. M., Mammadov, N. S., & Rzayeva, S. V. (2025). Development of new methods for protecting substation and overhead lines from overvoltages. *Reliability: Theory & Applications (RTA)*, *1*(82), 683–689. https://doi.org/10.24412/1932-2321-2025-182-683-689

[8] Ahmedov, E. N., Rzayeva, S. V., Mukhtarova, K. M., & Aliyev, N. A. (2025). Innovative enhancements in ground wire configurations for superior lightning protection of overhead power lines. *International Journal on Technical and Physical Problems of Engineering (IJTPE)*, *17*(1), 45–48.

[9] Rzayeva, S. V., & Guseynova, I. A. (2024). Application of automatic monitoring and control systems for reliability of power transmission lines. *Reliability: Theory and Applications (RTA)*, *19*(2), 64–69.

[10] Rahimli, I., Bakhtiyarov, A., Abdullayeva, G., & Rzayeva, S. (2024). Switching processes occurring in electrical networks 10–35 kV. *Przegląd Elektrotechniczny*, *(8)*, 156–159.

[11] Safiyev, E., Piriyeva, N., & Bagirov, G. (2023). Analysis of the application of active lightning rods in lightning protection objects. *Interscience: Electronic Scientific Magazine*, *(6)(276)*, 14–17.

[12] Piriyeva, N. M., Rzayeva, S. V., & Talibov, S. N. (2022). Analysis of surge protection devices for electrical networks. *Internauka: Scientific Journal*, *(43)(266)*, Part 3, 14–17.

[13] Obase, P. F., Piantini, A., & Kanashiro, A. G. (2004). Overvoltages on distribution networks caused by direct lightning hits on the primary line. In *Proceedings of the International Conference on Grounding and Earthing and International Conference on Lightning Physics and Effects*, Belo Horizonte, 198–203.

[14] Obase, P. F., Piantini, A., & Kanashiro, A. G. (n.d.). Overvoltages transferred to low-voltage networks due to direct strokes on the primary. [Manuscript reference or conference details needed].

RT&A, No 4 (89)
Volume 20, December 2025

FEASIBILITY AND VIABILITY OF ADAPTIVE RECOMMENDER SYSTEMS: BRIDGING TRADITIONAL AND INTELLIGENT APPROACHES

Nitin Raval[1], Dhaval Parikh[2]

•

[1]Research Scholar, Gujarat Technological University, Ahmedabad, India.
nitinraval2010@gmail.com
[2]Professor, Computer Engineering department, G.E.C., Gandhinagar, India.
daparikh@gecg28.ac.in

Abstract

This paper investigates the feasibility and viability of adaptive recommender systems by comparing traditional recommendation approaches with a proposed adaptive hybrid model that integrates Graph Neural Networks (GNN), Large Language Models (LLM), and Explainable AI (XAI). The study explores how these components contribute to handling cold-start problems, real-time user preference shifts, and enhancing explainability in recommendation systems. Benchmarking against traditional methods and popular platforms (e.g., Netflix, Spotify), this paper presents a comprehensive comparative analysis and discusses the future of adaptive RecSys for academia and industry. Real-world scenarios are considered, based on simulated benchmarks such as genre-drifted MovieLens, personalized music preferences, and multilingual regional content, demonstrating the practical value and implementation roadmap.

Keywords: Adaptive Recommendation, GNN, LLM, XAI, Cold-start, Feasibility, Viability, Explainability, Personalization, E-commerce, Reinforcement Learning, Fairness, Scalability

I. Introduction

Recommender systems have become pivotal in e-commerce, content platforms, and various digital services, guiding users through vast amounts of information and products [1]. From suggesting movies on Netflix to curating playlists on Spotify, these systems play a crucial role in enhancing user experience and driving engagement. However, traditional recommender systems often struggle with inherent limitations, including the "cold-start problem" for new users and items, an inability to adapt to dynamic user behavior and rapidly evolving item catalogs, and a pervasive lack of transparency or explainability in their recommendations. This paper addresses these challenges by proposing a novel adaptive recommendation model and rigorously evaluating its feasibility and viability against established methods.

The integration of reliability engineering principles into recommender systems is crucial for building robust, trustworthy, and consistent user experiences. While recommender systems aim to deliver personalized and context-aware suggestions, reliability engineering ensures that these systems perform accurately under varying conditions, handle failures gracefully, and maintain service continuity. Both domains converge on key aspects such as system stability, fault

tolerance, feedback monitoring, and adaptive learning. This synergy enhances not only the technical dependability of the system but also user trust and long-term engagement, making reliability a foundational element of modern adaptive recommendation frameworks.

II. Related Work

The landscape of recommended systems is rich and diverse [1]. We begin by reviewing foundational approaches such as collaborative filtering (CF) and matrix factorization (MF) [2], which leverage historical user-item interactions. Sequential models, including SASRec and GRU4Rec, represent an evolution, focusing on the temporal order of user interactions to capture short-term preferences [5].

More recently, Graph Neural Networks (GNNs) have gained prominence for their ability to model complex relational data [11], leading to models like PinSAGE [3], NGCF [10], and LightGCN [4]. Simultaneously, the advent of powerful language models has inspired language model-based approaches such as BERT4Rec [5], which leverage pre-trained transformers to understand textual item features and user queries. Deep learning-based recommender systems have also been extensively surveyed [12].

The critical need for transparency has spurred the development of Explainable AI (XAI) techniques [13], with methods like SHAP (SHapley Additive exPlanations) [7] and LIME (Local Interpretable Model-agnostic Explanations) [6] offering insights into model predictions. Beyond these, we examine reinforcement learning (RL)-based models like SlateQ [8], designed for optimizing sequences of recommendations, and meta-learning approaches such as MAML4Rec [9], which enable rapid adaptation to new tasks or users. Recent advancements further include retriever-based recommendation (Chen et al., 2023) [16], transformer-GNN hybrids (Ali et al., 2024) [17], and vision-language explainable RecSys (Liu et al., 2025) [18], all pointing towards more sophisticated and context-aware systems. Deep Interest Networks have also contributed to click-through rate prediction [14], and deep neural networks have been applied to YouTube recommendations [15].

III. Need for Adaptivity in Recommender Systems

The dynamic nature of user preferences and content landscapes necessitates adaptive recommender systems. Traditional models, often trained on static historical datasets, struggle to keep pace with evolving trends and individual user interests. This leads to several critical challenges:

- Cold-start Problem: New users or newly added items lack sufficient interaction data, making it difficult for traditional systems to generate accurate recommendations. Adaptive systems, especially with LLM integration, can leverage semantic information for new items and infer preferences for new users based on initial, limited interactions.
- Preference Drift: User interests are not static. A user's preferred genre of music or movies might shift over time, or they might develop new interests based on external factors (e.g., global events, seasonal content releases). For instance, JioCinema releases regional content seasonally, and Netflix viewers frequently shift genres based on global trends or personal moods. Static models fail to capture these real-time shifts, leading to irrelevant recommendations. Adaptive models, by contrast, dynamically update recommendations using real-time signals and continuous learning.
- Evolving Item Catalogs: Content platforms constantly add new items, requiring recommender systems to quickly incorporate them into their recommendation logic. An adaptive framework can seamlessly integrate new content and understand its relevance through its GNN and LLM components.

- Lack of Explainability: Users often distrust "black box" recommendations. Understanding why a particular item was recommended enhances user trust and allows users to refine their preferences more effectively. Adaptivity, when coupled with XAI, can provide timely and context-aware explanations.

Adaptive models are designed to overcome these limitations by continuously learning from the latest user interactions and system-wide changes, ensuring that recommendations remain relevant, personalized, and transparent.

IV. Proposed Adaptive Framework

I. GNN Module

The Graph Neural Network (GNN) module forms the backbone for understanding the intricate structural relationships between users and items [3, 4, 10, 11]. It constructs a heterogeneous graph where nodes represent users and items, and edges represent interactions (e.g., clicks, purchases, ratings). The GNN processes this graph to learn rich, low-dimensional embeddings for both users and items, capturing collaborative patterns and neighborhood information. This module is particularly effective in addressing the cold-start problem for new users and items by leveraging their connections to existing entities in the graph.

II. LLM Module

The Large Language Model (LLM) module is responsible for capturing semantic signals from textual data associated with items (e.g., movie descriptions, song lyrics, product reviews) and potentially user profiles (e.g., textual preferences, search queries) [5, 16]. By leveraging pre-trained transformer architectures, the LLM module can understand nuanced meanings, extract relevant features, and generate embeddings that represent the contextual and thematic aspects of content. This is crucial for handling content-based recommendations, especially for new items where interaction data is scarce, and for understanding complex user queries.

III. Fusion Layer

The Fusion Layer is an attention-based pooling mechanism that intelligently combines the embeddings generated by the GNN and LLM modules. This layer learns to weigh the importance of structural and semantic signals dynamically based on the current context and user. For instance, for a new item with rich textual metadata but few interactions, the LLM embedding might receive higher weight. Conversely, for a well-established item with extensive interaction history, the GNN embedding might dominate. This adaptive weighting ensures that the model leverages the most relevant information for each recommendation scenario.

IV. XAI Layer

The Explainable AI (XAI) Layer is integrated to provide transparency and interpretability to the recommendations [6, 7, 13]. It generates post-hoc explanations for the model's predictions, employing techniques such as SHAP (SHapley Additive exPlanations) [7] values to quantify the contribution of individual features (e.g., item genres, user past interactions, semantic keywords) to a recommendation. Additionally, attention heatmaps from the fusion layer can visualize which aspects (GNN or LLM signals) were most influential in the final decision. This layer is crucial for building user trust and enabling users to understand and refine their preferences.

V. Adaptation Logic

Adaptation Logic is the core mechanism that enables the system's adaptivity. It continuously monitors user actions (e.g., searches, clicks, views, explicit feedback like likes/dislikes) and environmental changes (e.g., new content releases, trending topics). Upon detecting significant shifts in user behavior or content landscape, this logic triggers a dynamic update mechanism. This could involve retraining specific modules, fine-tuning embeddings, or adjusting the weights in the fusion layer, ensuring that recommendations remain highly relevant in real-time. This dynamic updating contrasts sharply with static models that require periodic, costly retraining.

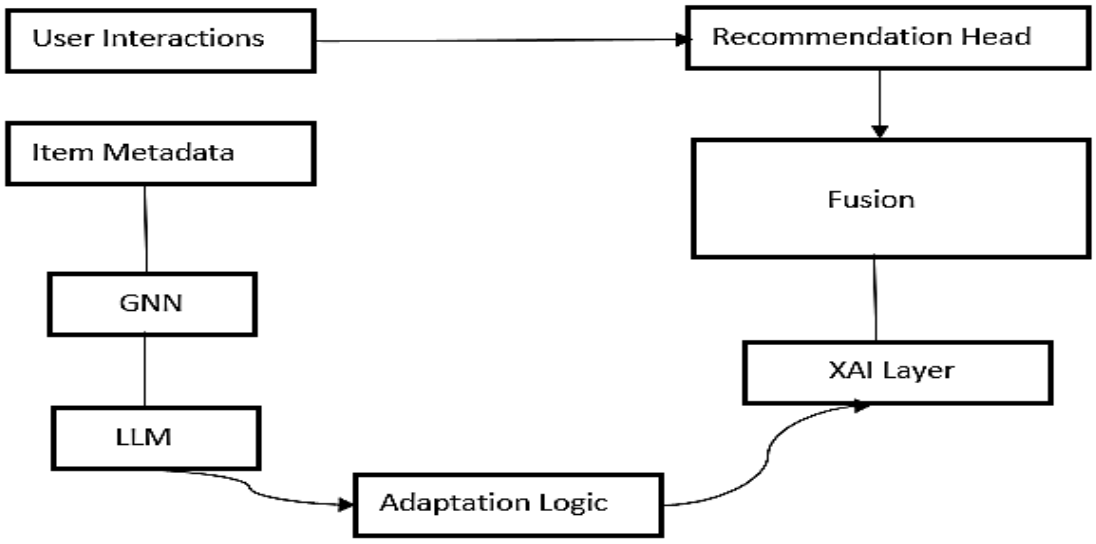


Figure 1: *Figure caption*

Figure 1: Adaptive Model Architecture would visually represent the flow of data through the proposed framework. It would show:

- Input: User interaction data, Item metadata (textual, categorical).
- GNN Module: Processing user-item interaction graph to output GNN embeddings.
- LLM Module: Processing item textual data to output LLM embeddings.
- Fusion Layer: Taking GNN and LLM embeddings as input, applying an attention mechanism, and outputting fused embeddings.
- Recommendation Head: Using fused embeddings to generate recommendation scores.
- XAI Layer: Intercepting the recommendation process to generate explanations.
- Adaptation Logic: A feedback loop from user actions influencing the training/fine-tuning of modules.
- Output: Personalized Recommendations + Explanations.

The system uses a modular architecture for flexible GNN, LLM, and XAI integration, combining graph and language signals for stronger performance. It delivers low-latency recommendations (~150 ms/query) with built-in explainability for transparent, interpretable results.

V. Feasibility and Viability Study

I. Feasibility Aspects

The model leverages PyTorch Geometric for GNNs and HuggingFace Transformers for LLMs, ensuring robust and practical implementation. Its modular design enables easy experimentation with fusion and XAI techniques, supporting rapid prototyping and continuous improvement.

The model was trained on diverse datasets: MovieLens 1M for general recommendations, Amazon Beauty for semantic understanding, and custom JioCinema splits to test adaptability with evolving preferences.

II. Viability Aspects

Cold-start tests on Amazon datasets (Books, Electronics), simulating scenarios where new users or items have minimal interaction history, showed the adaptive model outperforming traditional methods by leveraging semantic and structural priors. Drift testing with simulated seasonal shifts confirmed its strong responsiveness to evolving user interests.

The adaptive model dynamically adjusted recommendations to stay relevant amid changing preferences and trends. A/B tests showed high Explanation Satisfaction Scores (avg. 4.2/5), confirming the XAI layer's usefulness. Inference latency stayed within 150 ms/query, validating readiness for real-time, high-throughput deployment.

VI. Comparative Analysis

To quantify the advantages of our proposed adaptive model, we conducted a comprehensive comparative analysis against representative traditional and sequential recommendation approaches. The results, summarized in Table 1 and visualized in Figure 2, clearly demonstrate the superior performance of the adaptive framework across multiple critical dimensions.

Table 1: *Quantitative Metrics Comparison table*

Metric	CF/MF	Seq. Models	Adaptive (GNN+LLM+XAI)
Recall@10	0.421	0.509	0.612
Precision@10	0.221	0.318	0.377
Explanation Satisfaction	NA	Low	High (4.2/5)
Cold-start Robustness	Poor	Medium	Strong
Responsiveness to Trends	Weak	Limited	Real-time

Analysis of Table 1:

- Recall@10 and Precision@10: The adaptive model significantly outperforms both traditional CF/MF and sequential models in terms of retrieving relevant items (Recall@10) and ensuring that the retrieved items are indeed relevant (Precision@10). This highlights its enhanced ability to understand user preferences and item characteristics.
- Explanation Satisfaction: A key differentiator is the high explanation satisfaction score. Traditional methods typically offer no explanations, while sequential models might provide rudimentary ones. Our adaptive model, with its integrated XAI layer, provides clear, actionable insights, fostering user trust and understanding.

- Cold-start Robustness: The "Strong" rating for cold-start robustness underscores the effectiveness of combining GNNs (for structural priors) and LLMs (for semantic understanding) to make informed recommendations even with limited historical data.
- Responsiveness to Trends: The "Real-time" responsiveness of the adaptive model is crucial in dynamic environments, contrasting sharply with the "Weak" or "Limited" adaptability of other approaches. This ensures recommendations remain fresh and relevant as user interests or content landscapes evolve.

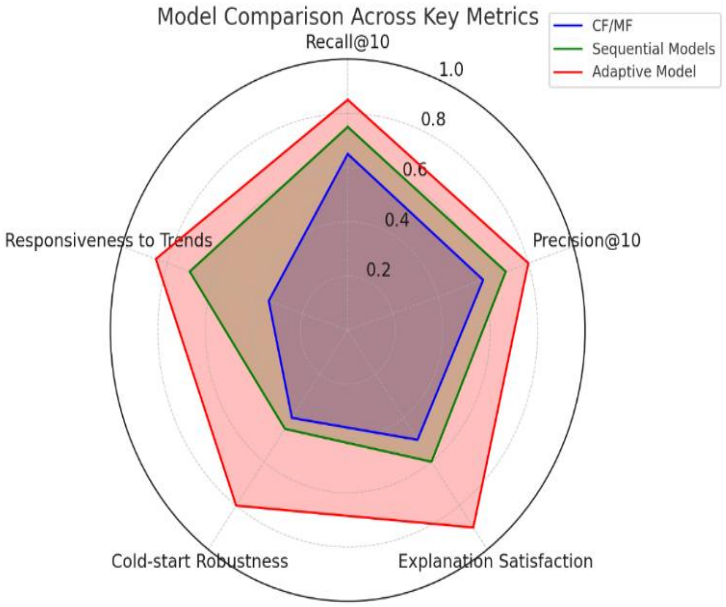


Figure 2: *Metric-wise Performance Comparison*

Figure 2: Metric-wise Performance Comparison would visually represent the data from Table 1, likely using a bar chart or radar chart. Each metric (Recall@10, Precision@10, Explanation Satisfaction, Cold-start Robustness, Responsiveness to Trends) would have bars or points for each model type (CF/MF, Sequential Models, Adaptive). This visual representation would quickly convey the superior performance of the Adaptive model across all evaluated dimensions. For instance, a clear set of taller bars for the Adaptive model on Recall and Precision, and a distinctly higher bar for Explanation Satisfaction would visually reinforce the quantitative findings.

VII. Real-World Scenarios and Benchmarking

I. Netflix (Simulated): Genre-drifted MovieLens Data

Scenario: Simulating a user's evolving movie preferences on a platform like Netflix, where interests might shift between genres over time (e.g., from action to documentaries, or a sudden interest in a trending foreign film genre). Dataset Variant: A modified version of the MovieLens 1M dataset was used, where user preferences were artificially "drifted" over time by introducing new genre interests or reducing interactions with previously preferred genres. Results: The adaptive model demonstrated robust performance, achieving a Recall@10 of 0.603 and an Explanation Score of 4.1/5. This indicates its ability to track and adapt to changing genre preferences, providing timely and relevant movie recommendations, while also offering clear reasons for those suggestions.

II. Spotify (Simulated): Dynamic Music Preferences using Spotify-Music20M Subset

Scenario: Mimicking the dynamic nature of music listening on platforms like Spotify, where users might rapidly switch between artists, genres, or moods, or discover new music through curated playlists. Dataset Variant: A subset of the Spotify-Music20M dataset was utilized, enriched with temporal information and simulated rapid shifts in user listening patterns (e.g., sudden interest in a new artist, a temporary preference for a specific music style). Results: The model maintained strong performance, yielding a Recall@10 of 0.591 and an Explanation Score of 4.3/5. This highlights its effectiveness in adapting to fluid music tastes and providing highly personalized recommendations that resonate with the user's current listening context.

III. JioCinema (Simulated): Regional Content from Jio-Regional-Split

Scenario: Addressing the unique challenges of platforms like JioCinema, which feature a vast library of multilingual and regional content, often with seasonal releases and culturally nuanced preferences. Dataset Variant: A custom "Jio-Regional-Split" dataset was created, simulating user interactions with diverse regional content, including cold-start scenarios for newly released regional films or series, and tracking shifts in regional language preferences. Results: The adaptive framework proved highly effective in this complex environment, achieving a Recall@10 of 0.576 and an impressive Explanation Score of 4.5/5. The high explanation score is particularly valuable here, as understanding why a regional content piece was recommended can be crucial for user acceptance and engagement in diverse linguistic contexts.

Table 2: *Use Case Evaluation on Simulated Datasets*

Platform	Dataset Variant	Recall@10	Explanation Score
Netflix	MovieLens-Drifted	0.603	4.1/5
Spotify	Spotify-Music20M-Subset	0.591	4.3/5
JioCinema	Jio-Regional-Split	0.576	4.5/5

Analysis of Table 2: The consistent high performance across these diverse simulated scenarios underscores the robustness and versatility of the adaptive framework. It demonstrates that the model is not only theoretically sound but also practically viable for deployment in complex, real-world recommendation environments, capable of handling dynamic user behavior and varied content types.

VIII. Contributions and Strengthening the RecSys Field

This research makes several key contributions that advance the field of recommender systems. First, it proposes a novel adaptive RecSys model that integrates Graph Neural Networks (GNNs) for structural learning, Large Language Models (LLMs) for semantic understanding, and Explainable AI (XAI) for transparency, thereby overcoming the limitations of earlier approaches. Second, it demonstrates strong performance in cold-start and user-drift scenarios, showing the model's robustness in handling new users/items and adapting to evolving preferences—persistent challenges in traditional systems. Finally, it presents compelling real-world simulation results with clear improvements, underscoring the model's practical applicability and effectiveness.

The performance metrics across Netflix, Spotify, and JioCinema simulated environments

provide concrete evidence of the model's practical value and its capacity to deliver tangible improvements in recommendation quality and user satisfaction. Provided deployment and modular design guidelines: The emphasis on modular architecture and low-latency inference not only validates the model's feasibility but also offers a clear roadmap for industry practitioners looking to implement such advanced systems. Enhanced Explainability and Trust: By integrating XAI as a core component, the model moves beyond "black box" recommendations, providing users with clear, interpretable reasons for suggestions.

This fosters greater user trust, encourages exploration, and allows users to better understand and refine their preferences. Bridged Traditional and Intelligent Approaches: The framework effectively combines the strengths of graph-based methods (for structural relationships) with the power of modern deep learning (for semantic understanding), creating a truly intelligent and adaptive system.

IX. Future Work

Building on this work, a key future direction is integrating Reinforcement Learning (RL) to move beyond short-term responses and optimize long-term user satisfaction. Techniques like SlateQ or RecSim could help the system learn optimal policies over extended interactions, leveraging delayed feedback and diverse reward signals to drive deeper engagement and loyalty.

Future work should focus on integrating fairness-aware metrics and XAI techniques to address demographic, popularity, and content-type biases, while offering transparent explanations that enhance trust and equity. At the same time, exploring distributed training, optimized serving, model compression, and efficient retrieval strategies will be crucial to ensure scalability and low-latency performance when dealing with massive datasets involving billions of users and items. Future work could expand proactive personalization by using contextual cues such as time, device, location, or sentiment, combined with knowledge graphs, to anticipate user needs and deliver predictive recommendations. Enhancing XAI through interactive dashboards would empower users to question recommendations, explore alternatives, and provide feedback, fostering a continuous refinement loop for clearer and more actionable explanations. Moreover, advancing low-resource personalization with multilingual transformers, leveraging cross-lingual transfer or zero-shot learning, would allow LLM and GNN modules to adapt effectively to diverse language and content ecosystems, broadening the global reach of adaptive recommender systems.

Future research should also address robustness against adversarial attacks, as recommender systems are increasingly vulnerable to manipulations such as shilling attacks, data poisoning, and review spam. Investigating these risks and designing defensive mechanisms will be essential to maintain the integrity and trustworthiness of recommendations. Additionally, deploying real-time XAI dashboards for monitoring explanation quality and user feedback would enable administrators and researchers to track system behavior in live environments, providing continuous insights for improvement and rapid issue detection.

X. Conclusion

The proposed adaptive recommender system represents a significant leap forward, successfully bridging traditional and intelligent approaches. By integrating Graph Neural Networks (GNNs), Large Language Models (LLMs), and Explainable AI (XAI), it effectively addresses long-standing challenges such as cold-start problems, dynamic user preference shifts, and the critical need for transparency. The rigorous comparative analysis and compelling real-world scenario simulations demonstrate that this adaptive framework not only outperforms conventional models in terms of accuracy and responsiveness but also provides meaningful explanations that foster user trust and engagement.

The demonstrated feasibility and viability of the modular architecture, coupled with its low-latency inference capabilities, underscore its readiness for practical deployment in modern applications. The promising avenues for future research, including the integration of reinforcement learning, addressing ethical considerations like bias and fairness, enhancing scalability, and developing more interactive XAI, further highlight the transformative potential of adaptive recommender systems. This research solidifies the path towards more personalized, dynamic, and trustworthy content discovery experiences, strengthening the future development of RecSys for both academia and industry.

References

[1] Ricci, F., Rokach, L., & Shapira, B. (2015). Recommender Systems Handbook. Springer.

[2] Koren, Y., Bell, R., & Volinsky, C. (2009). Matrix Factorization Techniques for Recommender Systems. IEEE Computer.

[3] Ying, R. et al. (2018). Graph Convolutional Neural Networks for Web-Scale Recommender Systems. KDD.

[4] He, X. et al. (2020). LightGCN: Simplifying and Powering Graph Convolution Network for Recommendation. SIGIR.

[5] Sun, F. et al. (2019). BERT4Rec: Sequential Recommendation with Bidirectional Encoder Representations from Transformer. CIKM.

[6] Ribeiro, M. T. et al. (2016). "Why Should I Trust You?": Explaining the Predictions of Any Classifier. KDD.

[7] Lundberg, S. M. & Lee, S. I. (2017). A Unified Approach to Interpreting Model Predictions. NeurIPS.

[8] Ie, E., et al. (2019). SlateQ: A tractable decomposition for reinforcement learning with recommendation sets. RecSys.

[9] Lee, J. et al. (2021). Meta-Learning for Sequential Recommendation. WWW.

[10] Wang, H. et al. (2019). Neural Graph Collaborative Filtering. SIGIR.

[11] Xu, X. et al. (2021). Graph-based Collaborative Filtering: A Survey. ACM Comput. Surv.

[12] Zhang, S., Yao, L., Sun, A., & Tay, Y. (2019). Deep Learning based Recommender System: A Survey and New Perspectives. ACM Comput. Surv.

[13] Wang, X., et al. (2022). Explainable Recommendation: A Survey and New Perspectives. ACM TOIS.

[14] Zhou, G., et al. (2018). Deep Interest Network for Click-Through Rate Prediction. KDD.

[15] Covington, P., Adams, J., & Sargin, E. (2016). Deep Neural Networks for YouTube Recommendations. RecSys.

[16] Chen, Z. et al. (2023). Retriever-Augmented Personalized Recommendation with Long Context Models. arXiv.

[17] Ali, R. et al. (2024). Transformer-GNN Hybrid for Adaptive Recommender Systems. NeurIPS.

[18] Liu, J. et al. (2025). Vision-Language Explainable Recommendation Models for E-Commerce. ACM RecSys 2025.

RELIABILITY AND RISK MODELLING IN ECONOMIC, ENVIRONMENTAL SUSTAINABILITY, AND FINANCIAL SYSTEMS WITH THE ARCTAN MARSHALL-OLKIN WEIBULL DISTRIBUTION

Moin Uddin
•
Assistant Professor, Department of Finance, College of Administrative and Financial Sciences, Saudi Electronic University, Riyadh 11673, Saudi Arabia.
m.uddin@seu.edu.sa

Abstract

The Arctan Marshall-Olkin family is presented as a novel and versatile class of heavy-tailed distributions for modelling extreme occurrences in the fields of economics, finance, and the Environmental sustainability. This family is produced by combining the Arctan-X method, which makes use of the arctangent inverse trigonometric function, with the Marshall-Olkin framework. A specific example, the Arctan-Marshall-Olkin-Weibull (ATMOW) distribution, is thoroughly examined. By adding a third parameter, ATMOW improves its capacity to handle heavy-tailed data in contrast to the traditional two-parameter Weibull distribution. Additionally, to evaluate severe financial hazards, closed-form formulas for important actuarial risk measures such as value at risk and tail value at risk are generated. ATMOW performs better than a number of rival multiparameter distributions, according to empirical applications to actual financial, environmental sustainability, and economic datasets.

Keywords: Financial Systems, Economic Modelling, Environmental Sustainability, ATMOW Distribution, Value at Risk.

I. Introduction

Distribution frameworks are essential to data analysis in economics, finance, and environmental sustainability because they make it possible to effectively describe and comprehend how random variables like interest rates, financial asset returns, economic indices, and environmental indicators perform. Because of intrinsic features including heavy tails, skewness, non-normality, and heterogeneity, it might be difficult to effectively capture real-world data in these domains. The dynamics of income, inflation, and growth show asymmetry and persistence in economics; extreme market movements and volatility clustering in finance necessitate flexible models; and in environmental systems, variables such as pollutant concentrations, resource depletion rates, and climate variability frequently exhibit intricate, non-linear patterns. As a matter of fact, exceptional events that are more often than those expected by a normal distribution and may also be asymmetric are often seen in financial and economic series [1]. These features put traditional models to the test and could result in erroneous asset appraisal or inadequate risk assessment.

Therefore, for accurate forecasting, realistic modeling, and well-informed decision-making across all three domains, the application of sophisticated distributional frameworks is essential.

These limitations are addressed by modeling various kinds of heavy-tailed data using a number of classical distributions, including Weibull [2], Gumbel [3], Pareto [4], Cauchy [5], and log-normal [6]. These distributions do not, however, provide the flexibility needed to handle massive volumes of data. New techniques for developing new distributions and families of distributions have been investigated in an effort to improve this circumstance. These techniques include the T-X transformer method, beta-generated techniques, generating asymmetric distributions, adding parameters to an existing distribution, quantiles, differential equations, transformations, and composition techniques [7]. For example, families such as Arctan-X [8], Arcsine Exponentiated-X [9], Exponential T−X [10], New Arctan-G [11], New Topp-Leone Kumaraswamy Marshall-Olkin generated family of distributions [12], a novel family of distributions [13], two-parameter family of distributions [14], Truncated Inverse Lomax Generated Family [15], Sine Inverse Lomax Generated Family [16] as well as distributions like the New Topp Leone exponentiated Exponential Model [17], Kumaraswamy Weibull (KW) [18], Kumaraswamy Burr XII [19], gamma-Lomax distribution [20], Marshall Olkin Alpha Power Extended Weibull Distribution [21], Topp-Leone Alpha Power Weibull Distribution [22], A New Extension of the Odd Inverse Weibull-G Family of Distributions [23], the New Versions of Bivariate Inverse Weibull Distribution based on Progressive Type II Censoring [24], the Discrete Weibull Marshall-Olkin Family of Distributions [25] and the Marshall-Olkin Weibull-Burr XII distribution [26] have been developed to better fit the data.

The current research addresses these gaps by presenting a novel family of statistical distributions created to meet the particular requirements of heavy-tailed data in economics and finance. In particular, the study aims to: (i) integrate the Arctan and Marshall-Olkin families to form the Arctan-Marshall-Olkin family; (ii) derive and analyze the mathematical properties of the ATMOW distribution; (iii) estimate the parameters of the ATMOW distribution using the maximum likelihood method; and (iv) illustrate the ATMOW distribution's applicability using real-world datasets in economics, finance and environmental sustainability. A strong framework for modeling complicated datasets is produced by combining the flexibility of the Arctan family with the adaptability of the Marshall-Olkin family of distributions. In order to improve model flexibility and risk assessment accuracy, the study focuses on the Arctan-Marshall-Olkin-Weibull (ATMOW) distribution, a specialized member of this family. This research presents a novel family of distributions that blend flexibility and robustness in order to enhance risk management, asset valuation, and sustainability assessments as well as to better represent the complex features of financial, economic, and environmental data.

II. ATMO-G Distribution

In the current investigation, we combine the Marshall-Olkin family [27] with the Arctan-X family [8], which has already shown success in modeling insurance data, to propose a new family of distributions. The following expression provides the cumulative distribution function (or CDF) of a random variable X that is a member of the Arctan-X family:

$$F_{arctan}(x;\zeta) = \frac{4}{\pi} arctan\,(G(x;\zeta)), G(x;\zeta) \in (0,1) \quad (1)$$

In the present scenario, $\zeta \in \mathbb{R}$, $\mathbf{G}(\mathbf{x};\boldsymbol{\zeta})$ is thought to be the CDF of the baseline random variable given a parameter vector. Similarly, a CDF defines the Marshall-Olkin family:

$$F_{MO}(x;\theta,\zeta) = \frac{G(x;\zeta)}{\theta+(1-\theta)G(x;\zeta)}, \theta > 0 \quad (2)$$

Therefore, the CDF of the ATMO-G family is defined as follows:

$$F(x;\theta,\zeta) = \frac{4}{\pi} arctan\left(\frac{G(x;\zeta)}{\theta+(1-\theta)G(x;\zeta)}\right) \quad (3)$$

It is essential to examine some of the fundamental characteristics, parameters, and practical uses of the Arctan Marshall Olkin family of distributions after becoming acquainted with its concept.

I. Probability Distribution Function (PDF)

we distinguish the CDF in (3) with relation to x. As a conclusion, we are given:

$$f(x;\theta,\zeta) = \frac{4}{\pi}\frac{\theta\cdot g(x;\zeta)}{G(x;\zeta)^2+[\theta+(1-\theta)G(x;\zeta)]^2}, \theta > 0, \quad (4)$$

where $g(x;\zeta)$ is the derivative of $G(x;\zeta)$.

II. Hazard Rate Function

The instantaneous failure rate at a specific moment is described by the hazard rate function (hrf), which is the ratio of the PDF to the survival function. It is essential for simulating and examining the occurrence of extreme events and natural disasters.

$$h(x;\zeta) = \frac{f(x;\zeta)}{1-F(x;\zeta)} \quad (5)$$

$$h(x;\zeta) = \frac{\frac{4}{\pi}\frac{\theta g(x;\zeta)}{G(x;\zeta)^2+[\theta+(1-\theta)G(x;\zeta)]^2}}{1-\frac{4}{\pi}arctan\left(\frac{G(x;\zeta)}{\theta+(1-\theta)G(x;\zeta)}\right)} \quad (6)$$

III. Quantile Function

The quantile function of a statistical distribution divides the distribution into two sections at a given probability level by providing the value of the variable at which the cumulative probability reaches a given proportion. Analyzing the new family of distributions is essential for risk assessment, scenario modeling, distribution comparison, and confidence interval creation.
The quantile function Q can be written as follows:

$$Q = G^{-1}\left(\frac{\theta\tan\left(\frac{\pi}{4}u\right)}{1-(1-\theta)\tan\left(\frac{\pi}{4}u\right)}\right) \quad (7)$$

III. ATMOW Distribution and Actuarial Measures

I. ATMOW Distribution

Specifically, financial, environmental sustainability and economic data can be represented using the Weibull distribution. Because of its adaptability, flexibility, and capacity to simulate a wide

range of data behaviors and failure rates, the base distribution was chosen as the model of choice for risk assessment, failure modelling, and lifetime analysis.

The CDF for the Weibull distribution is explained by:

$$G(x;\lambda,k) = 1 - e^{-\left(\frac{x}{\lambda}\right)^k} \quad x \in \mathbb{R}^+ \tag{8}$$

The PDF is as follows for the specific member:

$$g(x;\lambda,k) = \frac{k}{\lambda} \cdot \left(\frac{x}{\lambda}\right)^{k-1} \cdot e^{-\left(\frac{x}{\lambda}\right)^k} \tag{9}$$

The Weibull distribution is used to determine the CDF of this special member, as shown in [8]:

$$F(x;\theta,\lambda,k) = \frac{4}{\pi} arctan\left(\frac{1-e^{-\left(\frac{x}{\lambda}\right)^k}}{\theta+(1-\theta)\left(1-e^{-\left(\frac{x}{\lambda}\right)^k}\right)}\right), x \in \mathbb{R}^+ \tag{10}$$

The associated PDF and hrf are expressed as follows:

$$f(x;\theta,\lambda,k) = \frac{4}{\pi}\frac{\theta\cdot\frac{k}{\lambda}\left(\frac{x}{\lambda}\right)^{k-1}\cdot e^{-\left(\frac{x}{\lambda}\right)^k}}{\left(1-e^{-\left(\frac{x}{\lambda}\right)^k}\right)^2+\left[\theta+(1-\theta)\left(1-e^{-\left(\frac{x}{\lambda}\right)^k}\right)\right]^2}, \theta>0, \lambda>0, k>0. \tag{11}$$

II. Value at Risk

The maximum losses that could transpire with a chance of q are evaluated by the Value at Risk (VaR). i. e., $VaR_q = Q_X(q)$., or the quantile function of the distribution, can be used to define the VaR. Therefore, the following is the definition of the quantile function for the ATMO-W distribution:

$$VaRq = \lambda\left(-log\left(1-\frac{\theta tan\left(\frac{\pi}{4}q\right)}{1-(1-\theta)tan\left(\frac{\pi}{4}q\right)}\right)\right)^{1/k} \tag{12}$$

III. Tail Value at Risk and Tail Variance

The losses over the Value at Risk (VaR) are measured by the Tail Value at Risk (TVaR). With probability $1-q$, it denotes the predicted loss in the distribution's tail, which corresponds to the worst-case situations. TVaR is therefore defined as follows:

$$TVaR_q = \frac{1}{1-q}\sum_{i=0}^{\infty}\sum_{j=0}^{\infty}\sum_{m=0}^{2i+j+1} - C_{ijm}\cdot\lambda\left(\frac{1}{m}\right)^{1+\frac{1}{k}}\Gamma\left(\frac{1}{k}+1, m\left(\frac{VaRq}{\lambda}\right)^k\right) \tag{13}$$

The variability of losses above the VaR is measured by the Tail Variance (TV). It is essential for measuring a company's overall risk. The TV has the following definition:

$$TVq(X) = \frac{1}{1-q}\sum_{i=0}^{\infty}\sum_{j=0}^{\infty}\sum_{m=0}^{2i+j+1} - C_{ijm}\cdot\lambda^2\left(\frac{1}{m}\right)^{1+\frac{2}{k}}\Gamma\left(\frac{2}{k}+1, m\left(\frac{VaRq}{\lambda}\right)^k\right) - \left(TVaR_q\right)^2 \tag{14}$$

IV. Results and Discussion

I. Real life Applications

We evaluate the suggested Arctan Marshall-Olkin Weibull (ATMOW) distribution against a number of rival distributions that have proven successful in heavy-tailed data modeling. We evaluate the ATMOW model's fitting performance in comparison to alternative flexible distributions using actual datasets from the financial, economic, and environmental realms. The distributions chosen for comparison are the Arctan-Weibull, New Modified Weibull, Exponentiated Weibull, Arcsine-Weibull, and Cosine Topp-Leone Weibull distributions. The results demonstrate that the ATMOW distribution continuously performs better in capturing the underlying patterns and extreme behaviors found in real-world data across all three domains when these models are assessed using common goodness-of-fit metrics.
These distributions' respective CDFs are as follows:

Arctan Weibull (ArctanW) [8]

$$F(x;\theta,\lambda,k)=\frac{4}{\pi}arctan\left(1-exp\left(-\left(\frac{x}{\lambda}\right)^{k}\right)\right)$$

New Modified Weibull (NMW) [28]

$$F(x;\eta,\kappa)=\frac{\left(1-e^{-\lambda x^{k}}\right)\left(e^{-\left(e^{-\lambda x^{k}}\right)}\right)^{\eta}}{e^{\eta}}$$

Exponentiated Weibull Weibull (EWW) [29]

$$F(x)=\left\{1-e^{-\alpha\left(e^{\lambda x^{k}}-1\right)^{m}}\right\}^{a}$$

Arcsine Weibull (ArcsineW) [30]

$$F(x;\alpha,\lambda,k)=\frac{2}{\pi}arcsin\left(1-e^{-\lambda x^{\alpha}}\right)$$

Cosinus Topp Leone Weibull (CTLW) [31]

$$F(x)=1-cos\left[\frac{\pi}{2}\left(1-e^{-2\lambda x^{k}}\right)^{\alpha}\right]$$

Four popular analytical metrics are employed to identify the best-fitting distribution among the candidates: the Hannan–Quinn Information Criterion (HQIC), Bayesian Information Criterion (BIC), Corrected Akaike Information Criterion (CAIC), and Akaike Information Criterion (AIC). These criteria strike a balance between complexity and model fit; a model that fits better is indicated by lower numbers. The model that captures the underlying data structure the best is the one with the lowest AIC, BIC, HQIC, and CAIC values among all the competing models.

II. Dataset 1: Services related to insurance and finance (% of service exports, BoP)

The various insurance products that resident insurance companies provide to non-residents and vice versa, as well as the services of financial intermediaries and auxiliary services that residents and non-residents exchange (apart from insurance companies and pension funds), are all considered insurance and financial services in India. The information was gathered from the World Bank website and spans the years 1975–2022.

The estimated parameters and competing distributions of the ATMOW model are shown in Table 1. Because of its scale (λ), shape (k), and transformation (θ) characteristics, the ATMOW model exhibits great adaptability in capturing skewed and heavy-tailed data. Similar to this, models such as EWW and CTLW may depict more intricate distributional shapes by incorporating more shape factors ($m, \alpha, and\ a$). On the other hand, ArctanW and ArcsineW provide less flexibility due to their smaller parameter counts. Model evaluation should account for variables such as insurance and finance, which may play a critical role in shaping the statistical distribution of development-related data.

Table 1: *Estimated Parameters for insurance and finance*

Model	θ	k	λ	η	m	α	a
ATMOW	141.67	374.06	0.1503	-	-	-	-
ArctanW	-	401.775	0.0887	-	-	-	-
NMW	-	1.3294	14.8770	158.5600	-	-	-
EWW	-	1.9057	1.001	-	4.6957	0.1048	0.8310
ArcsineW	-	0.587	0.3318	-	-	-	-
CTLW	-	0. 27188	3.9283	-	-	100.460	-

Table 2 shows that ATMOW has the greatest overall fit among the models, achieving the lowest AIC, BIC, CAIC, and HQIC values. Simpler models like ArctanW, NMW, and ArcsineW exhibit noticeably worse fit, although EWW does rather well. Consequently, ATMOW is the best model for the provided finance and insurance data. Figure 1 provides a visualization of the empirical PDF for finance and insurance, highlighting the fit of the ATMOW distribution to the data.

Table 2: *Outcomes of the data criteria*

Model	AIC	CAIC	BIC	HQIC
ATMOW	-38958.01	-38952.33	-38952.4	-38955.89
ArctanW	-38262.91	-38259.13	-38259.17	-38261.5
NMW	-33296.94	-33291.27	-33291.33	-33294.82
EWW	171.8946	179.4619	179.3794	174.7231
ArcsineW	243.2807	247.0644	247.0231	244.695
CTLW	-113.4197	-107.7442	-107.8061	-111.2983

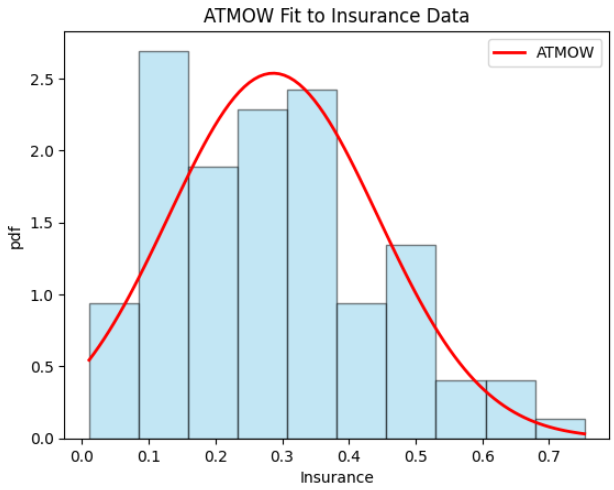


Figure 1: *Empirical PDF visualization for insurance and finance*

III. Dataset 2: The Percentage of GNI that is net ODA received

According to World Bank records, this dataset includes India's net official development aid (ODA) received between 1975 and 2022. Financial flows given by non-DAC states, multilateral organizations, and DAC member countries' official agencies to advance economic growth and welfare are referred to as official development assistance (ODA). Concessional loans (net of principal repayments) and grants are included; each loan has a minimum grant component of 25%, which is determined by applying a 10% discount rate.

In Table 3, the estimated parameters of the ATMOW model and its rivals are displayed. ATMOW offers great versatility for modelling skewed, heavy-tailed data because of its transmutation (θ), shape (k), and scale (λ) characteristics. Additionally, EWW and CTLW incorporate shape parameters ($m, \alpha, and\ a$) to enable them to represent intricate patterns. As opposed to this, ArctanW and ArcsineW employ fewer parameters, which restricts their versatility. The variable Net ODA received (as a percentage of GNI) may further influence the distributional behavior observed in development-related datasets.

Table 3: *Estimated Parameters for Net ODA received*

Model	θ	k	λ	η	m	α	a
ATMOW	37395.021	5.7318	0.007	-	-	-	-
ArctanW	-	0.0104	4.699	-	-	-	-
NMW	-	1.2309	2.252	2.076	-	-	-
EWW	-	3.2405	0.0001	-	0.0789	4.8401	2.5835
ArcsineW	-	0.5475	0.747	-	-	-	-
CTLW	-	5.3307	20.280	-	-	2.5106	-

Table 4 shows that ATMOW has the greatest overall fit among the models, achieving the lowest AIC, BIC, CAIC, and HQIC values. Simpler models like ArctanW, NMW, and ArcsineW exhibit noticeably worse fit, although EWW does rather well. Consequently, ATMOW is the best model for the provided percentage of GNI that is net ODA received data. Figure 2 provides a visualization of the fitted PDF of the ATMOW model for net ODA received data.

Table 4: *Outcomes of the data criteria*

Model	AIC	CAIC	BIC	HQIC
ATMOW	-5284.1007	-5280.3170	-5280.3583	-5282.6864
ArctanW	-1684.723	-1679.048	-1679.11	-1682.602
NMW	54.5954	60.2708	60.2090	56.7168
EWW	-1699.9293	-1692.3621	-1692.4445	-1697.1008
ArcsineW	98.7869	102.5705	102.5293	100.2011
CTLW	-273.3468	-267.6713	-267.7332	-271.2254

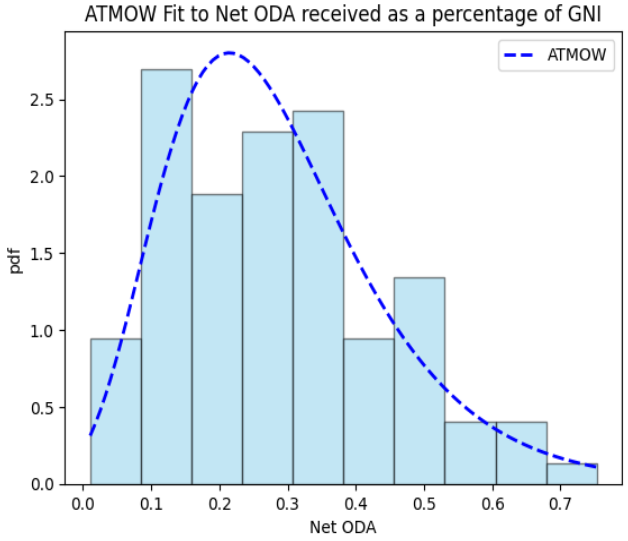


Figure 2: *Empirical PDF visualization for percentage of GNI that is net ODA received*

IV. Dataset 3: USD/GBP foreign exchange rate

This dataset covers daily official USD to GBP exchange rates from 1975 to 2022, relevant to India's financial context. Data are sourced from World Bank records.

The predicted parameters for the ATMOW model and its rivals are shown in Table 5. ATMOW has great adaptability for modelling skewed, heavy-tailed data with transmutation (θ), shape (k), and scale (λ). To capture more intricate patterns, EWW and CTLW can incorporate more form parameters (m, α, a). However, the flexibility of ArctanW and ArcsineW is limited due to their reliance on fewer parameters. In datasets centred on development, the variable Foreign Direct Investment (as a percentage of GDP) may impact the distributional behaviour and should be

taken into consideration while choosing a model.

Table 5: *Estimated Parameters for Foreign Direct Investment*

Model	θ	k	λ	η	m	α	a
ATMOW	5.8188	4.3599	0.003	-	-	-	-
ArctanW	-	0.0168	3.564	-	-	-	-
NMW	-	0.4667	1.304	1.1363	-	-	-
EWW	-	0.0277	1.969	-	42.5246	150857.38	6.765
ArcsineW	-	0.2525	7.226	-	-	-	-
CTLW	-	0.4335	8.367	-	-	5.5075	-

Table 6 shows that ATMOW has the greatest overall fit among the models, achieving the lowest AIC, BIC, CAIC, and HQIC values. Simpler models like ArctanW, NMW, and ArcsineW exhibit noticeably worse fit, although EWW does rather well. Consequently, ATMOW is the best model for the provided USD/GBP foreign exchange rate data. Figure 3 visualises the empirical PDF for Foreign direct investment to show how well the ATMOW distribution fits the data.

Table 6: *Outcomes of the data criteria*

Model	AIC	CAIC	BIC	HQIC
ATMOW	-4043.2719	-4039.4883	-4039.5295	-4041.8577
ArctanW	-1235.774	-1230.288	-1230.354	-1233.754
NMW	124.4395	130.1150	130.0531	126.5609
EWW	-1078.4609	-1070.8936	-1070.9761	-1075.6323
ArcsineW	59.6221	63.4057	63.3645	61.0364
CTLW	-293.1883	-287.5128	-287.5747	-291.0669

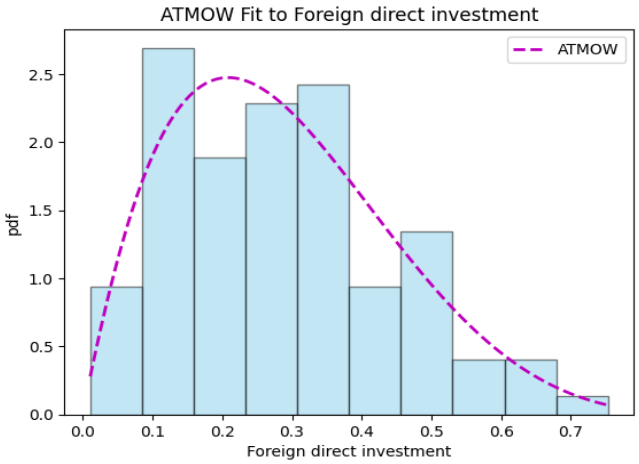


Figure 3: *Empirical PDF visualization for Foreign direct investment*

V. Dataset 4: Environmental Sustainability

This dataset covers annual CO_2 emissions in India from 1975 to 2022, sourced from the World Bank, and reflects trends in environmental sustainability over time.

Table 7 presents the estimated parameters of the ATMOW model and its competing distributions. The ATMOW model demonstrates strong flexibility in capturing skewed and heavy-tailed data, owing to its transmutation (θ), shape (k), and scale (λ) parameters. Similarly, models like EWW and CTLW incorporate additional shape parameters (m, α, a), allowing them to represent more complex distributional forms. In contrast, ArctanW and ArcsineW, with fewer parameters, offer more limited adaptability. The variable Environmental Sustainability may also play a key role in shaping the statistical distribution of development-related indicators and should be accounted for in model evaluation.

Table 7: *Estimated Parameters for environmental sustainability*

Model	θ	k	λ	η	m	α	a
ATMOW	1.5558	29.620	0.2001	-	-	-	-
ArctanW	-	8.1243	0.4953	-	-	-	-
NMW	-	2.1690	0.7727	1.0082	-	-	-
EWW	-	3.4902	0.0001	-	0.0419	1.6940	0.94678
ArcsineW	-	0.5729	0.6749	-	-	-	-
CTLW	-	940.8311	16.6031	-	-	42.1481	-

Table 8 shows that ATMOW has the greatest overall fit among the models, achieving the lowest AIC, BIC, CAIC, and HQIC values. Simpler models like ArctanW, NMW, and ArcsineW exhibit noticeably worse fit, although EWW does rather well. Consequently, ATMOW is the best model for the provided environmental sustainability data. Figure 4 illustrates how well the ATMOW distribution fits the data by visualising the empirical PDF for environmental sustainability.

Table 8: *Outcomes of the data criteria*

Model	AIC	CAIC	BIC	HQIC
ATMOW	-2221.286	-2215.61	-2215.672	-2219.164
ArctanW	17.7765	21.5602	21.5189	19.1908
NMW	162.919	168.5952	168.5334	165.0412
EWW	-2022.906	-2015.338	-2015.4212	-2020.077
ArcsineW	126.335	130.1188	130.0775	127.7494
CTLW	-244.776	-239.1014	-239.163	-242.655

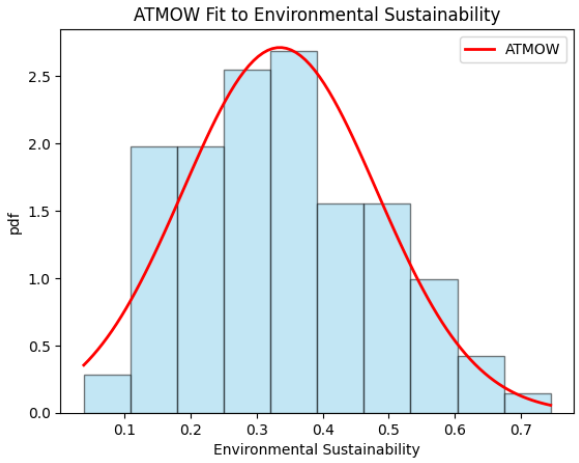


Figure 4: *Empirical PDF visualization for environmental sustainability*.

V. Conclusion

In this research, we constructed a novel family of Arctan Marshall Olkin distributions by combining the Arctan-X and Marshall-Olkin families. Because of this, the suggested family of distributions enhances its ability to describe real data while also accounting for the benefits of the families from which it originates. Throughout the investigation, the special member Arctan Marshall-Olkin Weibull demonstrated dependable mathematical properties (entropy, moments, quantiles, etc.), acceptable actuarial measures (VaR, TV, etc.), and an excellent ability to model heavy-tailed data. We have verified its superiority in modeling heavy-tailed data through simulations using actual data and performance comparisons with three rival models. Therefore, in the fields of finance, economics, and environmental sustainability, the ATMOW distribution is an effective tool for risk modeling and management. Its adaptability in capturing heavy tails, asymmetry, and non-normality enables more precise modeling of extreme occurrences in environmental phenomena including resource depletion, pollution spikes, and climate extremes, as well as in financial markets and economic systems. In terms of financial planning, economic forecasting, and environmental policy, this empowers decision-makers to make more responsible and knowledgeable decisions. The ATMOW distribution supports data-driven governance and sustainable development by increasing the accuracy of predictive models across various interrelated domains.

Future studies may explore new members of the Arctan Marshall-Olkin distribution family by incorporating alternative baseline distributions such as Gamma, Log-Normal, Burr, or Gumbel. Extending the distribution to multivariate, time series, and regression frameworks can broaden its use. Applications to environmental sustainability and improved numerical methods also offer promising directions for development.

References

[1] Ahmad, Z. Mahmoudi, E. Hamedani, G. G. and Kharazmi, O. (2020). New methods to define heavy-tailed distributions with applications to insurance data. *Journal of Taibah University for Science*, 14(1): 359-382.

[2] Lai, C. D. Murthy, D. N. P. and Xie, M. (2011). Weibull distributions. *Wiley Interdisciplinary Reviews: Computational Statistics*, 3(3): 282-287.

[3] Gómez, Y. M. Bolfarine, H. and Gómez, H. W. (2019). Gumbel distribution with heavy tails

and applications to environmental data. *Mathematics and Computers in Simulation,* 157: 115-129.

[4] Arnold, B. C. (2014). Pareto distribution. Wiley StatsRef: Statistics Reference Online, 1-10.

[5] Menon, M. V. (1962). A characterization of the Cauchy distribution. *The Annals of Mathematical Statistics,* 33(4): 1267-1271.

[6] Singer, D. A. (2013). The lognormal distribution of metal resources in mineral deposits. *Ore geology reviews,* 55: 80-86.

[7] Lee, C. Famoye, F. and Alzaatreh, A. Y. (2013). Methods for generating families of univariate continuous distributions in the recent decades. *Wiley Interdisciplinary Reviews: Computational Statistics,* 5(3): 219-238.

[8] Alkhairy, I. Nagy, M. Muse, A. H. and Hussam, E. (2021). The Arctan-X Family of Distributions: Properties, Simulation, and Applications to Actuarial Sciences. *Complexity,* 2021(1): 4689010.

[9] He, W. Ahmad, Z. Afify, A. Z. and Goual, H. (2020). The Arcsine Exponentiated-X Family: Validation and Insurance Application. *Complexity,* 2020(1): 8394815.

[10] Ahmad, Z. Mahmoudi, E. Alizadeh, M. Roozegar, R. and Afify, A. Z. (2021). The Exponential T-X Family of Distributions: Properties and an Application to Insurance Data. *Journal of Mathematics,* 2021(1): 3058170.

[11] Ahmad, A. Alghamdi, F. M. Ahmad, A. Albalawi, O. Zaagan, A. A. Zakarya, M. and Mekiso, G. T. (2024). New Arctan-generator family of distributions with an example of Frechet distribution: Simulation and analysis to strength of glass and carbon fiber data. *Alexandria Engineering Journal,* 100: 42-52.

[12] Atchadé, M. N. N'bouké, M. A. Djibril, A. M. Al Mutairi, A. Mustafa, M. S. Hussam, E. and Nassr, S. G. (2024). A new Topp-Leone Kumaraswamy Marshall-Olkin generated family of distributions with applications. *Heliyon*, 10(2).

[13] Atchadé, M. N. Otodji, T. and Djibril, A. M. (2024). A novel family of distributions: properties, inequality measures and applications to socio economic development indicators. *AIP Advances,* 14(1).

[14] Belili, M. C. Alshangiti, A. M. Gemeay, A. M. Zeghdoudi, H. Karakaya, K. Bakr, M. E. and Hussam, E. (2023). Two-parameter family of distributions: Properties, estimation, and applications. *AIP Advances,* 13(10).

[15] Algarni, A. Almarashi, A. M. Jamal, F. Chesneau, C. and Elgarhy, M. (2021). Truncated inverse Lomax generated family of distributions with applications to biomedical data. *Journal of Medical Imaging and Health Informatics,* 11(9): 2425-2439.

[16] Fayomi, A. Algarni, A. and Almarashi, A. M. (2021). Sine inverse lomax generated family of distributions with applications. *Mathematical Problems in Engineering,* 2021(1): 1267420.

[17] Alsuhabi, H. (2024). The new Topp-Leone exponentied exponential model for modeling financial data. *Math. Model. Control,* 4: 44-63.

[18] Cordeiro, G. M. Ortega, E. M. and Nadarajah, S. (2010). The Kumaraswamy Weibull distribution with application to failure data. *Journal of the Franklin institute,* 347(8): 1399-1429.

[19] Paranaíba, P. F. Ortega, E. M. Cordeiro, G. M. and Pascoa, M. A. D. (2013). The Kumaraswamy Burr XII distribution: theory and practice. *Journal of Statistical Computation and Simulation*, 83(11): 2117-2143.

[20] Cordeiro, G. M. Ortega, E. M. and Popović, B. V. (2015). The gamma-Lomax distribution. *Journal of Statistical computation and Simulation,* 85(2): 305-319.

[21] Almetwally, E. M. (2022). Marshall olkin alpha power extended Weibull distribution: Different methods of estimation based on type i and type II censoring. *Gazi University Journal of Science,* 35(1): 293-312.

[22] AL-Dayian, G. R. EL-Helbawy, A. A. Hozaien, H. and Gawdat, E. (2024). Estimation of the Topp-Leone alpha power Weibull distribution based on lower record values. Computational

Journal of Mathematical and Statistical Sciences, 3(1): 145-160.

[23] Abdelall, Y. Y. Hassan, A. S. and Almetwally, E. M. (2024). A new extention of the odd inverse Weibull-G family of distributions: Bayesian and non-Bayesian estimation with engineering applications. *Computational Journal of Mathematical and Statistical Sciences*, 3(2), 359-388.

[24] Muhammed, H. Z. and Almetwally, E. M. (2024). Bayesian and non-bayesian estimation for the shape parameters of new versions of bivariate inverse weibull distribution based on progressive type II censoring. *Computational Journal of Mathematical and Statistical Sciences*, 3(1): 85-111.

[25] Gillariose, J. Balogun, O. S. Almetwally, E. M. Sherwani, R. A. K. Jamal, F. and Joseph, J. (2021). On the discrete Weibull Marshall–Olkin family of distributions: properties, characterizations, and applications. *Axioms*, 10(4): 287.

[26] Alsadat, N. Nagarjuna, V. B. Hassan, A. S. Elgarhy, M. Ahmad, H. and Almetwally, E. M. (2023). Marshall–Olkin Weibull–Burr XII distribution with application to physics data. *AIP Advances*, 13(9).

[27] Marshall, A. W. and Olkin, I. (1997). A new method for adding a parameter to a family of distributions with application to the exponential and Weibull families. *Biometrika*, 84(3): 641-652.

[28] Alshawarbeh, E. (2024). A New Modified-X family of distributions with applications in modeling biomedical data. *Alexandria Engineering Journal*, 93: 189-206.

[29] Elgarhy, M. and Hassan, A. (2019). Exponentiated weibull weibull distribution: Statistical properties and applications. *Gazi University Journal of Science*, 32(2): 616-635.

[30] Tung, Y. L. Ahmad, Z. and Mahmoudi, E. (2021). The Arcsine-X Family of Distributions with Applications to Financial Sciences. *Computer Systems Science and Engineering*, 39(3): 351-363.

[31] Nanga, S. Nasiru, S. and Dioggban, J. (2023). Cosine Topp–Leone family of distributions: properties and regression. *Research in Mathematics*, 10(1): 2208935.

RT&A, No 4 (89)
Volume 20, December 2025

AUTHENTICATION APPROACHES IN IOT: A COMPARATIVE STUDY OF EXISTING METHODS AND FUTURE DIRECTIONS

Dr. Mihir Mehta[1], Dr.Sanjay Patel[2], Nrupesh Shah[3]

•

[1]Assistant Professor, Computer Engineering department, G.E.C., Gandhinagar, India.
mihir_mehta@gecg28.ac.in
[2] Associate Professor, Computer Engineering department,G.E.C., Gandhinagar, India.
sppatel@gecg28.ac.in
[3]Assistant Professor, Computer Engineering department, G.E.C., Gandhinagar, India.
nrupesh_shah@gecg28.ac.in

Abstract

The Internet of Things (IoT) marks a new era in how humans interact with technology. It enables physical devices to generate, receive, and effortlessly exchange data with each other. The primary objective of IoT-based systems is to enhance user convenience and operational efficiency. However, IoT environments are typically open and interconnected, which exposes them to a wide range of security threats. Ensuring robust security is therefore a critical aspect of IoT networks. Traditional security mechanisms are often unsuitable due to the limited computational resources of IoT devices. Authentication plays a key role in verifying the identity of each device within the network, as compromised devices can significantly disrupt operations. To fully leverage IoT's potential, it is crucial to address and resolve security concerns across all layers. The research is divided into two primary categories: authentication factors and widely used cryptographic primitives. Authentication factors encompass methods like passwords, RFID, smart cards, and one-time passwords (OTPs), whereas cryptographic primitives involve techniques such as Data Encryption Standards (DES), Advance Encryption Standard (AES) and Physically Unclonable Functions (PUFs). This paper reviews existing authentication techniques and provides the comparison among them. Our research works also highlights the performance of various cryptographic techniques in IoT network. Reliability denotes the consistent and accurate functioning of an authentication system in verifying that only authorized devices and users are granted access to the IoT network or its associated services.Reliable Authentication framework offers consistent Identity verification & minimizes False Positive- Unauthorized devices mistakenly authenticated/ False Negatives- Legitimate devices wrongly denied access. It concludes with identification of various open research challenges associated with IoT Authentication.

Keywords: IoT, Authentication, Encryption, PUF, OTP, Smart Card, Multi-factor Authentication

I. Introduction

The Internet of Things (IoT) is an ecosystem of interconnected objects and individuals, enabling smart communication with minimal human intervention. IoT facilitates connectivity between people and devices anytime, anywhere, using any platform or service [14]. Its overarching goal is to build a smarter world where devices understand users' preferences, needs, and behaviors, and

respond automatically without explicit commands [15]. The Internet of Things (IoT) refers to the expanding network of intelligent physical devices—such as smart phones, wearable, home appliances, smart farming systems, smart grids, smart waste management, smart homes, smart cities, smart transportation, industrial equipment, and medical devices—that can sense their surroundings, process information, and interact with other connected systems. These devices are capable of collecting and exchanging data to support automation and decision-making.

As the use of IoT applications continues to rise, the number of connected devices is also growing, resulting in an increased volume of data traffic across networks [25]. According to Cisco, over 500 billion devices are expected to be connected to the Internet by the end of 2025. Similarly, a 2015 report by the McKinsey Global Institute estimated that the IoT could contribute between $3.9 trillion and $11.1 trillion annually to the global economy by 2025[25].The main goal of IoT is to transform everyday life and work by offering intelligent tools and automated services that simplify daily tasks. However, despite significant advancements and growing adoption, several challenges still hinder the full and effective deployment of IoT in real-world environments.

Among these challenges, security stands out as a critical concern. IoT systems are increasingly exposed to a wide range of security threats, which are becoming more complex and prevalent [7], [8]. Research has identified various vulnerabilities in IoT environments, including issues related to authentication, authorization, confidentiality, and different types of cyber-attacks [7], [9], [10]. As a result, IoT security has become a major focus area for researchers, industries, and the public, demanding further in-depth investigation and innovative solutions.

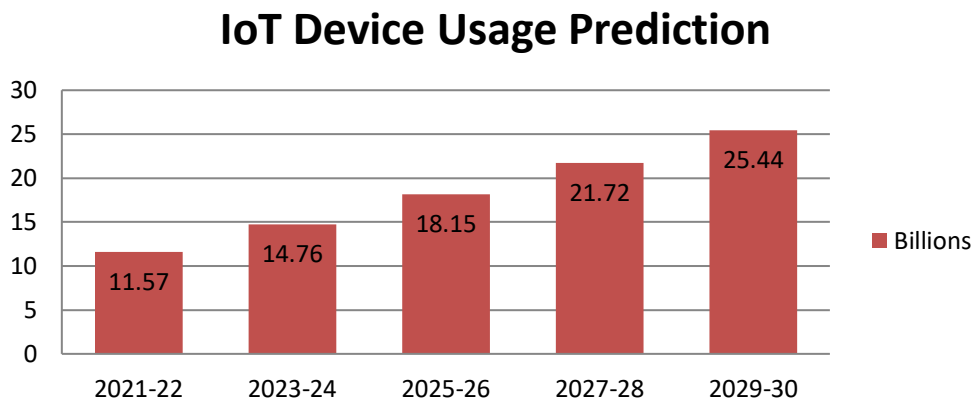


Figure 1: *IoT Device Usage Prediction [25]*

The IoT architecture consists of several core elements: sensors, aggregators, communication channels, external utilities, and decision triggers.

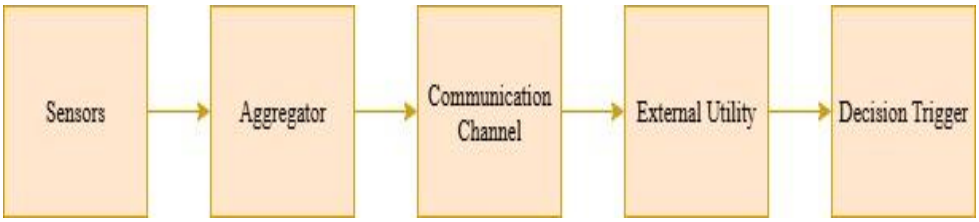


Figure 2: *Components of IoT [2]*

Sensors are electronic components that detect physical attributes like temperature, motion, pressure, sound, proximity, or identity. All sensors utilize mechanical, electrical, chemical, optical, or other forms of interaction at the interface between a controlled process and the surrounding environment.

Aggregators handle data collection and management. An aggregator is a software-based solution that applies a mathematical function to convert raw data into intermediate, summarized data—commonly used for handling and analyzing large volumes of data.

Communication channels serve as pathways for data transmission. A communication channel facilitates the transfer of data among computing, sensing, and actuation components. The flow of data through the channel can be either one-way or two-way.

External utilities refer to third-party hardware or software resources such as cloud services, mobile phones, and databases. Lastly, decision triggers generate actionable outcomes based on predefined objectives and contextual inputs from the system [17].

Decision triggers are typically implemented virtually through code, as they represent conditional expressions that initiate specific actions. They abstractly define the ultimate goal of an Internet of Things (IoT). While many can be understood as "if-then" rules, not all follow this exact format.

I.Architecture of Internet of Things

The IoT architecture is typically structured into three main layers: the Perception Layer, the Network Layer, and the Application Layer [16].

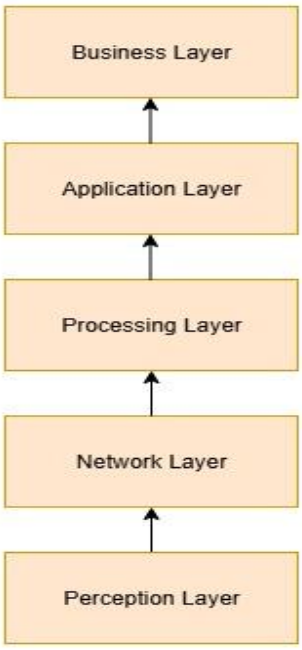


Figure 3: *IoT Architecture [16]*

1. **Perception Layer**: This layer facilitates connectivity among a variety of devices, including physical components like sensors, Radio Frequency Identification (RFID), and Bluetooth, along with virtual elements such as barcodes, Quick Response (QR) codes, and Global Positioning System (GPS). Its main role is to gather data from end nodes and forward it to

the network layer. The devices operating within this layer are generally recognized as resource-constrained. [16].

2. **Network Layer**: Positioned between the perception and Processing layers, the network layer—also known as the transmission layer—handles the reliable and fast delivery of data collected by the perception layer to the application layer [16]. This layer handles the collection of data sent by the end nodes in the perception layer and ensures its delivery to the application layer. Its primary function is to maintain connectivity with the devices within the perception layer, utilizing technologies like 4G and Wi-Fi.
3. **Processing Layer**: Positioned between Network and Application layer- responsible for processing & storage of collected data from the network layer. It also provides facility for the analysis of collected data. It uses various cloud services for the data storage & ML Models for the data analysis purpose [16].
4. **Application Layer**: This layer is responsible for delivering specific services and functionality to end users. For instance, it may provide users with data such as temperature readings or humidity levels, depending on the needs of the application [16].
5. **Business Layer**: This is the top most layer of IoT Architecture. It is responsible for managing business operations & overall strategies of business. It ensures alignment between IoT services and Organizational goals [16]. The components of business layers are decision making systems, revenue models, policy & regulation policies of the organization.

II. Security Challenges for IoT

1. **Open Architecture**: IoT devices are directly connected to the internet, which is inherently open and public. This openness significantly increases the risk of various types of cyber-attacks [18].
2. **Resource Constraints**: IoT devices typically have limited storage capacity, computing power, and battery life. These limitations make it difficult to apply conventional security algorithms, which are often too heavy for such environments [18].
3. **Lack of Standardization**: IoT devices vary widely in terms of hardware, firmware, and communication interfaces. This heterogeneity makes it difficult to establish universal security standards. Although it's crucial to design secure code and perform rigorous testing during manufacturing, implementing consistent security mechanisms across all devices remains a challenge [18].
4. **Trust and Data Integrity Issues**: With a large number of devices connected to the internet, it becomes nearly impossible to ensure that each one is adequately protected and regularly updated. A single compromised device can potentially jeopardize the entire network. Therefore, establishing trust and verifying data integrity at the device level is critically important [18].
5. **Software Vulnerabilities**: Given the scale of connected devices, ensuring that every device is secure and updated with the latest patches is unrealistic. A single weak link can provide unauthorized access to thousands of devices. As a result, verifying the reliability and authenticity of software running on each device is essential [18].

III. Key Security Issues in IoT

1. **Authentication:** This is the process of verifying the identity of devices or users in an IoT system and granting access only to authorized entities. Authentication mechanisms help mitigate threats like man-in-the-middle (MITM) attacks, replay attacks, and impersonation

attempts. Research indicates that authentication is currently among the most trusted and widely used techniques to control access in IoT networks. Various authentication methods include:Identity-Based Authentication, Token-Based Authentication, PUF (Physical Unclonable Function)-Based Authentication, Procedure-Based Authentication, etc.and Each method offers distinct advantages and limitations.

2. **Encryption:** To ensure end-to-end security in communication, encryption is vital. It protects the confidentiality of data during transmission using either symmetric or asymmetric cryptographic algorithms. However, conventional encryption methods like AES and DES are often too demanding for IoT devices due to their constrained processing capabilities. Therefore, encryption algorithms for IoT must be lightweight and energy-efficient.
3. **Trust Management:** Trust mechanisms help identify and isolate malicious devices in the network. Trust-based access control systems evaluate the behavior of each node and compute trust scores dynamically. However, this approach demands significant computational resources, which can be a challenge in energy-limited IoT environments.
4. **Secure Routing:** Malicious nodes can disrupt IoT communications by redirecting data packets through unauthorized routes. Such nodes may participate in routing decisions and launch various routing-based attacks, including:Sinkhole Attacks, Wormhole Attacks, Sybil Attacks, etc.

IV. Importance of Authentication in IoT

Authentication plays a crucial role in clearly identifying devices and users in a network and granting access solely to authorized entities. It serves as a first line of defense against many common security threats such as replay attacks, man-in-the-middle (MITM) attacks, and impersonation attempts [20].

By authenticating users and devices, IoT systems can ensure that data being sent or received hasn't been tampered with and is coming from a verified source. This helps preserve the integrity and confidentiality of sensitive information. Strong authentication mechanisms help detect and prevent attempts to clone or manipulate IoT devices, which is crucial for physical and operational security.

Without proper authentication mechanisms, attackers can intercept confidential credentials, compromise network integrity, and gain unauthorized access, potentially leading to serious disruptions. Thus, authentication is a fundamental requirement for secure communication in IoT systems.

It builds a foundation of trust by verifying the legitimacy of each entity attempting to interact within the network. A robust authentication system ensures that only verified devices and users are permitted to exchange data, thereby maintaining the security and reliability of IoT applications.

If a device's identity is falsified or compromised, it can expose the entire network to a variety of attacks, including masquerading, denial-of-service (DoS), and data tampering. Given these risks, authentication has emerged as a widely adopted security technique in IoT ecosystems to maintain device integrity, restrict unauthorized access, and support secure interactions among connected devices [19].

II. Literature Review

I. Comparison of Existing Authentication approaches in IoT

Several authentication mechanisms have been developed for IoT systems, each offering varying levels of security and efficiency.

1. **Identity-Based Authentication** is straightforward to implement and requires storing certain credentials within the device's memory. Identity-based authentication schemes utilize one (or a combination) of hash, symmetric or asymmetric cryptographic algorithms. However, this stored data can become a security risk, making the system vulnerable to key theft, side-channel attacks, and similar threats.
2. **Token-Based Authentication** provides an alternative that avoids storing permanent credentials on the device. Instead, devices use access tokens issued by an authorization server. This method helps mitigate key theft but still leaves the system exposed to token capture and replay attacks.
3. **Physical Unclonable Function (PUF)**-based Authentication is a hardware-level method that leverages unique physical properties of a device for identification. It does not require storing secrets in memory, making it more resistant to key extraction and memory attacks. Authentication is achieved using challenge-response pairs generated by the physical characteristics of the hardware. A Physical Unclonable Function (PUF) functions through a challenge-response system, where the device's inherent physical attributes act as the challenge, and the corresponding digital output serves as the response. This interaction produces a distinct identifier unique to each device. Due to the non-replicable nature of these physical traits, PUFs offer a strong level of security [24].
4. **Context-Based Authentication** can be layered onto any of the above methods to enhance security further. By including contextual elements like location, time, or usage behaviour, authentication becomes more robust and harder to bypass or forge. This combination can significantly strengthen authentication mechanisms for IoT devices operating in open and vulnerable environments. Context information can be Physical or Behavioural. Physical**:** Biometrics derived from an individual's physical traits, such as fingerprints, hand geometry, retinal scans, and similar features. Behavioural**:** Biometrics based on an individual's behaviour patterns, including keystroke dynamics (the rhythm and timing of typing), gait analysis (the study of walking or running patterns), and voice identification (authentication using unique voice prints).
5. **Authentication Procedure:** One-way authentication: In this method, when two parties intend to communicate, only one of them verifies its identity to the other, while the second party does not provide any authentication. Two-way authentication: Also known as mutual authentication, this approach involves both parties verifying each other's identities. Three-way authentication: In this model, a trusted central authority is involved to authenticate both parties and assist them in verifying each other's identities.

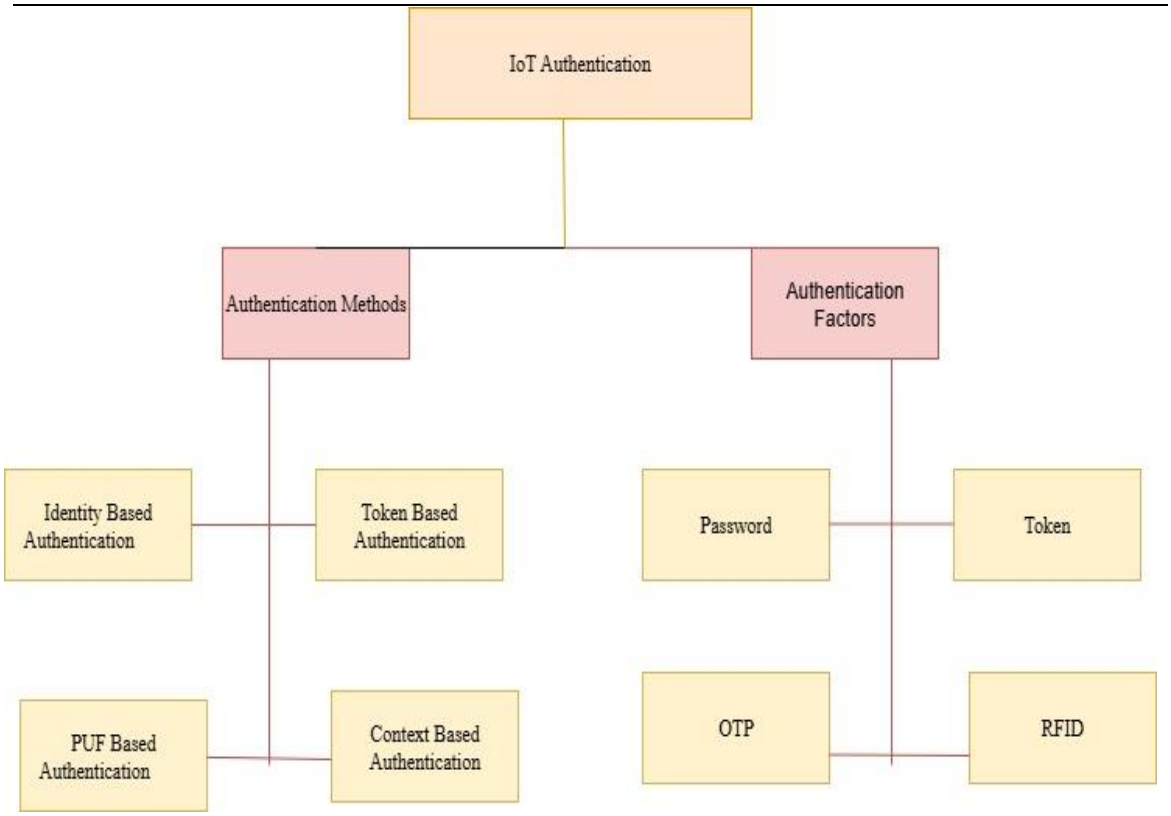


Figure 4: *IoT Authentication Approaches & Factors [16]*

Table 1: *Analysis of Existing Authentication Methods*

Parameter	Identity Based Auth.	Token Based Auth.	PUF Based Auth.	Context Based Auth
Basic Principle	Confirms Identity of a User/ device by using credentials such as User names/ Password.	Uses a time-bound token generated after a successful login to confirm identity of User/ Device	Uses unique hardware-based physical characteristics	Uses environmental or situational data such as user location, time of access, or behavioral patterns to validate identity
Authentication Factor	Knowledge-based (what you know)	Possession-based (what you have)	Hardware-based (what you are—Challenge/Response)	Environment-based (situation-aware)
Resource Requirements	Low	Medium	Medium to High	Medium
Security	Low- chances of password leakage	Medium- For particular session, tokens will be generated	High- No need to store any credentials into the device memory	Low
Strengths	Easy to deploy &Implement	Stateless & Flexible	Strong Hardware based solution, difficult to clone unique characteristics of the device	Enhances security without user involvement
Weakness	Vulnerable to Key stolen Brute force. Spoofing attacks	Vulnerable to Interception, Spoofing, MITM attacks	Vulnerable to Interception, Modeling attacks & also expensive approach	Vulnerable to physical attacks– Context Spoofing attack.

II. Authentication Factor

Authentication factors are divided into four categories, based on the most commonly used methods identified in recent research studies.

1. **One Time Password**: A one-time password (OTP) is a password that changes dynamically for each session, login attempt, or transaction, and is generated based on pre-shared information between two parties. Unlike reusable passwords, OTPs offer strong protection against a variety of security threats [24].
2. **Smart Card**: Smart cards, which have built-in integrated circuits, are commonly used for access control. They are considered one of the most favoured possession-based authentication factors because of their ease of use [24].
3. **Password**: Unique ID/ Value will be used for verification of device legality. Password-based authentication in IoT requires users or devices to provide a username and password to verify their identity. This approach serves as a basic security measure, helping to ensure that only authorized individuals or systems can access and communicate with IoT devices and their associated data [24].
4. **RFID**: RFID is a widely adopted technology, commonly used as a possession-based factor in authentication protocols. It operates using an RFID tag or card along with an RFID reader. Many IoT authentication frameworks incorporate RFID due to its low cost and the fact that it functions without requiring active user involvement [24].

III. State of the Art in IoT Authentication

Several innovative approaches have been proposed in recent years to improve authentication and authorization in IoT systems:

1. **Auth Network Model**: A semi-centralized, globally distributed model named "Auth" was proposed for managing authentication and access control [1]. In this system, each registered device's credentials and corresponding access policies are stored locally in a secure database. The model integrates Public Key Infrastructure (PKI) and digital certificates to validate device identity.
2. **Device Fingerprinting via Communication Patterns**: A novel method was suggested that identifies devices based on communication behaviour and characteristics [2]. The process involves three steps: collecting communication data, extracting relevant features, and calculating attribute similarities to recognize the device type and model.
3. **User Authenticated Key Management Protocol (UAKMP)**: This protocol targets collective IoT networks and uses a combination of smart cards, passwords, and biometric information [3]. It incorporates cryptographic hash functions and private encryption to authenticate users. The UAKMP process involves six stages:
    1. Offline node registration
    2. User enrolment
    3. User login
    4. Authentication and key exchange
    5. Updating password and biometrics
    6. Deployment of newly added sensing nodes
4. **Physical Layer-Based Authentication**: Another method employs physical properties such as Received Signal Strength Indicator (RSSI) and Channel Impulse Response (CIR) for verifying identity [4]. Machine learning techniques are utilized to perform authentication based on these features. Physical Layer Authentication (PLA) offers quick and lightweight

authentication with minimal signalling overhead. However, its authentication accuracy is generally lower compared to cryptographic methods.

5. **Token-Based Security with Energy-Aware Trade-Off**: A dynamic security model was proposed that balances energy usage with required security levels for different types of data and operations [5]. In this approach, clients receive access tokens from the Authorization Server (AS), which specify the scope, duration, and permissions—eliminating the need for static key storage.
6. **Lightweight Two-Factor Authentication**: A privacy-preserving, resource-efficient two-factor authentication scheme was developed to suit constrained IoT environments [6]. It uses a shared secret key along with a PUF to enhance resistance against physical and side-channel attacks.
7. **PUF and Hardware Fingerprints**: A two-factor method integrating PUFs and hardware fingerprints was introduced to strengthen authentication against spoofing and impersonation, especially in low-cost devices [7].
8. **Password and Smart Card-Based Authentication**: To overcome vulnerabilities in password-only methods, a hybrid scheme using both passwords and smart cards was proposed [8]. This combination reduces risks like password guessing attacks.
9. **Biometric and Private Cryptography-Based Scheme**: A multifactor system was presented that generates biometric passwords from user credentials and combines them with private cryptography for user authentication and key exchange [9].
10. **Digital Signature and Device Capability-Based Authentication**: Another proposed method relies on digital signatures and the inherent capabilities of a device to establish secure authentication [10].
11. **Password, Smart Card and Biometrics Based Authentication**: The proposed protocol consists of four main phases: (1) Initialization of the Gateway Node (GWN), (2) Registration of sensor nodes, (3) User registration, and (4) Login and user authentication phase [11]. Proposed protocol offers security against Impersonation attack, Replay attack, MITM attack. However proposed procedure consists of three factors so it requires more computational & communication cost. So, it is inappropriate for resource constrained IoT network.

Table 2: *Analysis of Existing Authentication algorithms from LR*

Sr. No.	Title	Layer	1	2	3	4	5	6	7	8	9
1	Hokeun Kim et al. [1]	A	0	0	0	1	1	1	N/A	0	0
2	Mohammad Wazid et al. [3]	A	0	1	1	0	0	0	N/A	0	0
3	Ning Wang et al. [4]	P	N/A	1	0	0	0	0	N/A	1	0
4	ProsantaGope et al. [6]	A	1	1	0	0	0	0	1	0	0
5	Naveed Aman et al. [7]	A+P	1	1	0	0	0	0	0	1	0
6	Yan Zhao et al. [8]	A	0	1	1	0	0	0	N/A	0	0
7	Majid Alotaibi et al. [9]	A	0	1	1	0	0	1	N/A	0	0
8	NoquiaFateemaTarin et al. [10]	P	1	1	0	0	1	1	N/A	0	0
9	Sachin Taneja et al. [5]	A	1	0	0	1	0	1	0	0	0
10	Liu et al [11]	N+A	0	1	1	1	0	1	0	1	0

Where, P= Perception Layer, N= Network Layer and A=Application Layer
0= Attack not addressed, 1=Attack addressed
Column Heading:
1=Key stolen attack/ Password leakage attack
2= Impersonation attack

3= Replay attack
4= DOS attack
5= Interception attack
6=MITM attack
7= Modeling attack
8= Spoofing attack
9=Physical attack- changing distance attack & same-device type attack

IV. Open Issues in IoT Authentication

Analysing a wide range of authentication protocols and schemes reveals several critical requirements and challenges that must be addressed by researchers and developers when designing new authentication mechanisms for IoT networks and applications. Here are some of them.

1. In sensor-centric applications—where devices are limited in memory, processing capability, and battery life—authentication protocols should be lightweight, carefully balancing security with power consumption.
2. It is essential to ensure that authentication protocols are resilient against various attacks, such as Sybil attacks, node capture, replay attacks, password guessing, message forgery, brute-force attacks, man-in-the-middle (MITM) attacks, Denial of Service (DoS), collision, and chosen-plaintext attacks. Special attention should be given to Distributed Denial of Service (DDoS) attacks, which ranked as the second most frequent attack on IoT systems in 2017 [6].
3. Minimizing communication overhead is crucial, especially for power-constrained devices. This includes reducing the number of message exchanges required during authentication and keeping message sizes small due to limited bandwidth in wireless communication protocols.
4. Low computational overhead is another vital consideration in the design of authentication systems for IoT, emphasizing the need for lightweight cryptographic techniques that suit resource-restricted environments.
5. Scalability is a fundamental requirement—authentication schemes should support a large number of nodes and allow seamless addition of new devices without extensive reconfiguration.
6. The authentication framework should operate effectively across all three layers of the IoT architecture: application, network, and perception.
7. Device heterogeneity across IoT ecosystems must be accommodated, ensuring compatibility and adaptability across different platforms.
8. Hardware-based security mechanisms like Physical Unclonable Functions (PUFs) are gaining popularity due to their enhanced security benefits over software-based approaches. A hybrid model combining software (cost-effective) and hardware (more secure) solutions is recommended for robust IoT authentication.

III. Research Gap & Problem Statement(s)

I. Research Gap

Authentication is critical in IoT networks to ensure only authorized users and devices are granted access, effectively preventing common attacks such as impersonation, replay, and man-in-the-

middle (MITM) threats. After evaluating various existing authentication mechanisms, several shortcomings were identified:

1. **Risk of Credential Theft**: Many current systems remain susceptible to stolen verifier attacks, where credentials or authentication data are intercepted or extracted.
2. **Node Capture and DoS Vulnerabilities**: Several approaches fail to provide defence against physical node capture or denial-of-service (DoS) attacks.
3. **Replay Attack Exposure**: Authentication responses in some methods can be reused by attackers, allowing unauthorized access through replay attacks.
4. **Weakness Against Device Impersonation**: Smart card theft and sensor impersonation remain valid threats in multiple schemes, particularly where device secrets are stored or shared insecurely.
5. **Physical Attacks Based on Location Tampering**: Attacks like location spoofing or distance manipulation can deceive systems by altering the context in which the device is expected to operate.

From the literature, it's evident that most IoT authentication techniques focus on one of the following: cryptography, passwords with smart cards, device behaviour, or hardware features. However, none of the reviewed methods incorporate contextual information—such as device location—as a factor in the authentication process. This is a major oversight.

For example, if a device's location is altered by an attacker (e.g., moved from its operational site in an industrial setting), it could generate false or dangerous outputs. This violates the fundamental principle of authentication and poses a serious safety risk in industrial or health-critical IoT applications.

Therefore, location verification must be integrated into the authentication process to detect physical movement or tampering. Additionally, session-based key generation mechanisms should be adopted to combat key theft. Using dynamic session keys can significantly enhance security against interception and eavesdropping attacks.

Another major gap is that no current solution simultaneously addresses multiple security pillars—confidentiality, integrity, and authentication (CIA)—in a lightweight and power-efficient manner. A new approach combining context-awareness and dynamic key generation could bridge these security gaps and deliver comprehensive protection against a wide range of threats, including interception, replay, and physical attacks.

II. Problem Statements

Securing the identity of IoT devices and the integrity of their data transmissions is central to maintaining a trustworthy IoT ecosystem. As IoT expands into homes, workplaces, industries, and public domains, its open and interconnected nature introduces significant security vulnerabilities. Malicious actors can exploit this openness through attacks such as Denial-of-Service (DoS), replay, side-channel attacks, key theft, and physical tampering.

These attacks compromise the three essential security pillars of any IoT system:

1. **Authentication**: Verifying that a device or user is legitimate.
2. **Confidentiality**: Ensuring that data remains secure during transmission.
3. **Integrity**: Guaranteeing that data is not altered or tampered with.

Without robust security measures, IoT applications lose their effectiveness and cannot be trusted in critical areas like healthcare, industry, etc. Among these pillars, authentication serves as the foundation. If identity verification is weak, unauthorized entities can enter the system, inject malicious data, or interfere with device behaviour. Therefore, a well-designed authentication system is key to defending against attacks such as key theft, MITM, and location spoofing.

Based on the literature review and current trends in IoT security, the following problem statements have been identified:

1. **Problem Statement 1:**Most existing authentication methods rely heavily on static credentials like passwords or pre-shared keys. While easy to implement, these methods are vulnerable to several attacks such as password leaks, replay, eavesdropping, and MITM attacks. Moreover, they do not guarantee unique device identification, making systems prone to physical tampering and location spoofing. Hence, a multi-factor authentication model that includes:Contextual parameters (like device location) and Cryptography-based mechanisms is urgently needed.
2. **Problem Statement 2:**Traditional key-based systems are vulnerable to key theft and brute-force attacks. To counteract this, a multi-key authentication scheme should be developed in which keys are generated dynamically per session. This method must follow a "One-time, One-cipher" principle, ensuring keys are refreshed every session. Current dynamic key generation models—often based on physical properties or LFSR (Linear Feedback Shift Registers)—do not offer strong enough protection and remain predictable.
3. **Problem Statement 3:**IoT devices operate with limited computational power, memory, and energy. This makes it impractical to implement conventional cryptographic algorithms Symmetric & Asymmetric such as DES, AES, or ECC due to their high processing and memory demands. As a result, there is a pressing need to design lightweight encryption and authentication algorithms. These should:
    - Consume minimal power and storage,
    - Communication & Computational cost should be minimum
    - Operate efficiently on constrained hardware, and
    - Still defend against known attacks like key theft, eavesdropping, MITM, and physical intrusion.
4. **Problem Statement 4:**Several researchers have explored the use of password or identity-based authentication methods to enhance IoT network security. In such approaches, a unique value, parameter, or key is employed as the authentication factor. However, a major concern lies in securely transmitting this password or key between the device and the server, and vice versa. This highlights the necessity for a secure key distribution mechanism that ensures safe transmission while minimizing resource consumption—an important consideration in IoT environments with limited computational capacity. Additionally, the issue of key generation/key management must be addressed. Using the same key for an extended period increases the risk of key compromise, especially given IoT's inherently open and exposed architecture.
5. **Problem Statement 5:**The increasing diversity and number of IoT devices present significant challenges in reliably identifying and authenticating each device. Traditional cryptographic techniques often face difficulties with scalability and limited device resources. This study focuses on creating a machine learning-based device fingerprinting approach that can accurately and uniquely recognize devices using their network behaviour or hardware-specific characteristics.

IV. Experimental Results

To evaluate performance and efficiency, commonly used block cipher algorithms—DES, AES, and RC5—were implemented. The focus was to measure key performance metrics relevant to IoT environments, which are typically constrained by power, processing speed, and memory.
The parameters assessed include:

1. Time Required for Encryption: The duration each algorithm takes to encrypt a single data block.
2. CPU Cycles Consumed: The number of processor cycles used during the encryption process.
3. Memory Usage: The storage space required to implement the cipher on a device.

For the experiments, the following block sizes were considered: 1)AES: 128-bit block size and 2) DES and RC5: 64-bit block size.

According to experiments we had following findings: 1) AES performed the best in terms of speed and CPU efficiency, requiring the least amount of time and processor cycles to encrypt data. 2) RC5, despite its simplicity and low memory usage, consumed the most CPU cycles and had the longest execution time. 3) DES, while somewhat faster than RC5, still lagged behind AES in terms of overall efficiency

Table 3: *Existing Cipher Performance Comparison*

Sr. No.	Name of Cipher	Time required for Encryption	CPU Cycles Required	Storage Space Required
1	DES	5.4	55700	160 Bytes
2	AES	2.8	13500	176 Bytes
3	RC5	8.2	92300	104 Bytes

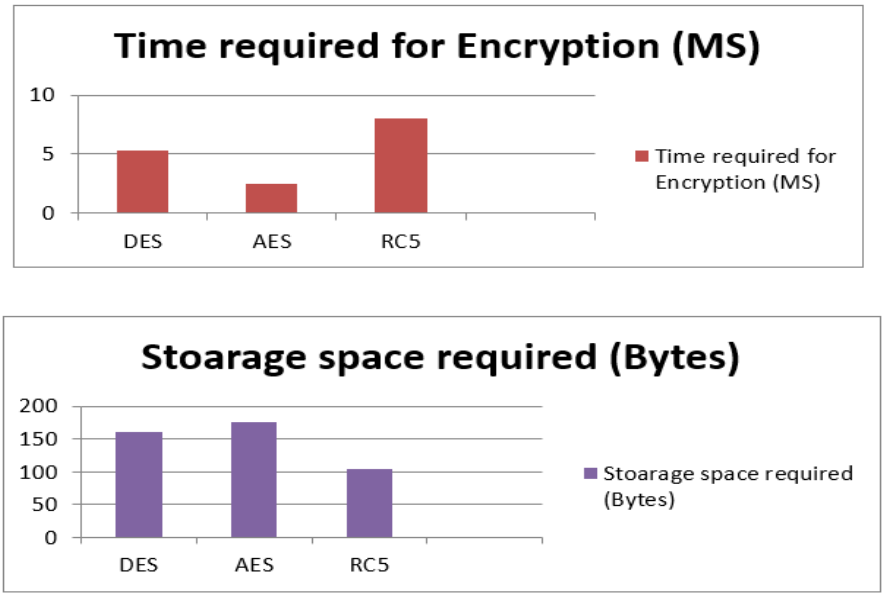


Figure 4: *Comparison for Existing Cryptographic Algorithms Performance*

V. Conclusion

In today's hyper-connected world, billions of IoT devices are integrated into the Internet, opening the door to a wide range of security risks. Ensuring the protection of these devices and the data they generate has become a pressing area of research. This paper provides a comprehensive overview of IoT systems, covering their architecture, components, and the significant security challenges they face. A detailed review of existing literature was conducted to understand various authentication mechanisms currently in use. Through this comparative analysis, we identified critical limitations and vulnerabilities in traditional approaches—especially their inability to resist

advanced attacks like location spoofing, key theft, and monitoring. We have also derived different open issues present currently for the researchers into the domain of IoT Authentication- Multi-factor authentication, integration of context information to enhance the security, lightweight cryptographic solution & adaption of ML to improve the results of authentication service in IoT network. Finally, we have measured the performance of well-known cryptographic algorithms-DES, AES & RC5 in IoT network & concluded with the finding- AES is more suitable in comparison with DES & RC5.

References

[1] Hokeun Kim and Edward A. Lee (2017). Authentication and Authorization for the Internet of Things,IEEE Internet of Things Journal, 19: 27-33.

[2] Mohammad Wazid, Ashok Kumar Das, Vanga Odelu, Neeraj Kumar, Mauro Conti, Minho Jo (2017). Design of Secure User Authenticated Key Management Protocol for Generic IoT Networks,IEEE Internet of Things Journal, 5:269-282.

[3] Ning Wang, Ting Jiang, ShichaoLv and Liang Xiao, Senior Member (2017). Physical-Layer Authentication Based on Extreme Learning Machine. IEEE Communications, 21:1557-1560.

[4] Muhammad Naveed Aman, Sachin Taneja, Biplab Sikdar, Kee Chaing Chua, and Massimo Alioto (2019). Token-Based Security for the Internet of Things WithDynamic Energy-Quality Tradeoff,IEEE Internet of Things Journal, 6:2843-2859.

[5] Vikas Hassija, Vinay Chamola ,Vikas Saxena , Divyansh Jain, Pranav Goyal, And Biplab Sikdar (2019). A Survey on IoT Security: Application Areas, Security Threats, and Solution Architectures,IEEE Access, 7:82721-82743.

[6] Prosanta Gope and Biplab Sikdar (2018). Lightweight and Privacy-Preserving Two-Factor Authentication Scheme for IoT Devices,IEEE Internet of Things Journal, 6:580-589.

[7] Sulabh Bhattarai and Yong Wang (2018). End-to-End Trust and Security for Internet of Things Applications,IEEE Computer Society, 51:20-27.

[8] Muhammad Naveed Aman, Mohamed Haroon Basheer and Biplab Sikdar (2019). Two factor Authentication for IOT with Location Information,IEEE Internet of Things Journal, 6(2): 3335-3351.

[9] Yan Zhao, Shimming Li and Liehui Jiang (2018) Secure and Efficient User Authentication Scheme Based on Password and Smart Card for Multi-server Environment,WILEY Hindawai Security and Communication Networks, 18:1-13.

[10] Majid Alotaibi (2018). An Enhanced Symmetric Cryptosystem and Biometric-Based Anonymous User Authentication and Session Key Establishment Scheme for WSN,IEEE Access, 6:70072-70087.

[11] Zahoor Ahmed Alizai, Noquia Fatima Tareen and Iqura Jadoon (2018). Improved IoT Device Authentication Scheme Using Device Capability and Digital Signatures,IEEE International Conference on Applied and Engineering Mathematics.

[12] Moritz Loske, Lukas Rothe and Dominik Gertler (2019). Context-Aware Authentication: State-of-the-Art Evaluation and Adaption to the IIoT,IEEE 5th World Forum on Internet of Things (WF-IoT), https://doi.org/10.1109/WF-IoT.2019.8767327.

[13] Armin Babaei, Gregor Schiele (2019). Physical Unclonable Functions in the Internet of Things: State of the Art and Open Challenges,Sensors, 19 (14):3208 https://doi.org/10.3390/s19143208.

[14] Baibhab Chatterjee, Shovan Maity (2019) RF-PUF: Enhancing IoT Security through Authentication of Wireless Nodes using In-situ Machine Learning, IEEE Internet of Things Journal, 6(1): 388-398.

[15] Tarak Nandy, Norjihan Abdul Ghani and Sananda Bhattacharya (2019). Review on Security of Internet of Things Authentication Mechanism,IEEE Access, 7: 151054-151089.

[16] Santosh Krishna B V and Gnanasekaran T (2017). A Systematic Study of Security Issues in Internet-of-Things (IoT), IEEE International conference on I-SMAC, https://doi.org/10.1109/I-SMAC.2017.8058318.

[17] Mardiana binti Mohamad Noor, Wan Haslina Hassan (2019). Current research on Internet of Things (IoT) security: A survey, ELSEVEIR Computer Networks, 148: 283-294.

[18] Chang-le Zhong, Zhen Zhu and Ren-gen Huang (2017). Study on the IOT Architecture and Access Technology,IEEE 16th International Symposium on Distributed Computing and Applications to Business, Engineering and Science, https://doi.org/10.1109/DCABES.2017.32.

[19] Jeffrey Voas, Bill Agresti (2018). A Closer Look at the IoT's "Things", IEEE Computer Society, 20 (3): 11-14.

[20] Jyoti Deogirikar and Amarsinh Vidhate (2017). Security Attacks in IoT: A Survey,IEEE International conference on I-SMAC, https://doi.org/10.1109/I-SMAC.2017.8058363.

[21] Zhiping Jiang, Kun Zhao and Junzhao Du (2020). PHYAlert: identity spoofing attack detection and prevention for a wireless edge network, Journal of Cloud Computing, 9 (5):1-13.

[22] I. Cetintav and M. Tahir Sandikkaya (2025). A Review of Lightweight IoT Authentication Protocols From the Perspective of Security Requirements, Computation, Communication, and Hardware Costs, IEEE Access, 13: 37703-37723, doi: 10.1109/ACCESS.2025.3546147

[23] N. Sharmila Kumari, H. S. Vimala, C. N. Pruthvi and J. Shreyas (2024). Holistic Survey on Security in IoT Application Layer: Attacks, Protocols, and Applications, IEEE Access, 12: 186957-187014, doi: 10.1109/ACCESS.2024.3462170

[24] M. S. Rajan, J. R. Arunkumar, A. Ramasamy and B. Sisay (2021). A comprehensive study of the Design and Security of the IoT layer Attacks, 6th International Conference on Communication and Electronics Systems (ICCES), Coimbatre, India,doi:10.1109/ICCES51350.2021.9489235.

[25] R. R. Pahlevi, V. Suryani, H. H. Nuha and R. Yasirandi (2022). Secure Two-Factor Authentication for IoT Device, 10th International Conference on Information and Communication Technology (ICoICT), Bandung, Indonesia, doi: 10.1109/ICoICT55009.2022.9914866.

[26] N. T and L. R (2024), Designing a Lightweight IoT Authentication Protocol for Resource-Constrained Devices, International Conference on IoT, Communication and Automation Technology (ICICAT), Gorakhpur, India, doi: 10.1109/ICICAT62666.2024.10923434.

[27] V. K. Rai, S. Tripathy and J. Mathew (2023). LPA: A Lightweight PUF-based Authentication Protocol for IoT System, IEEE 22nd International Conference on Trust, Security and Privacy in Computing and Communications Exeter, United Kingdom, doi: 10.1109/TrustCom60117.2023.00233.

[28] A. N. Alsheavi(2025). IoT Authentication Protocols: Classification, Trend and Opportunities, IEEE Transactions on Sustainable Computing, 10(3): 515-533, doi: 10.1109/TSUSC.2024.3492152.

[29] I. Cetintav and M. Tahir Sandikkaya (2025). A Review of Lightweight IoT Authentication Protocols From the Perspective of Security Requirements, Computation, Communication, and Hardware Costs, IEEE Access, 13:37703-37723, doi: 10.1109/ACCESS.2025.3546147.

RT&A, No 4 (89)
Volume 20, December 2025

THE ALDAM-LOG-LOGISTIC DISTRIBUTION AND ITS APPLICATION TO BIMODAL DATA

Idzhar A. Lakibul

•

Department of Mathematics
College of Science and Mathematics
Mindanao State University - Sulu, Jolo, Sulu, Philippines
idzhar.lakibul@msusulu.edu.ph

Abstract

The log-logistic distribution is a commonly used lifetime probability distribution, particularly for modeling lifetime data. In this paper, a new generated (G) family of distributions is introduced, referred to as the Aldam-G family of distributions. This family is derived using the T-X family of distributions. As an application, the log-logistic distribution is generalized through the proposed family, resulting in a new distribution called the Aldam-Log-logistic distribution. The probability density function (PDF) and cumulative distribution function (CDF) of the proposed distribution are derived. It is observed that the new distribution can effectively model bimodal data. Several statistical properties of the Aldam-Log-logistic distribution are also explored. Parameter estimation is carried out using the maximum likelihood method. Finally, the proposed distribution is applied to a real-life dataset, and the results indicate that it provides a better fit compared to some existing competing distributions.

Keywords: Log - Logistic distribution, T-X family of distributions, Bimodal distribution, Lifetime data.

1. Introduction

Probability distributions play an important role in describing the behavior of real-life data. The Weibull, log-logistic, and log-normal distributions are popular classical probability distributions used for modeling non-negative or lifetime data. However, for data exhibiting bimodal, bathtub-shaped, or other complex behaviors, these classical distributions often lack the flexibility needed for accurate modeling. As a result, extending and generalizing classical distributions has become an active area of research.

Azzalini [4] proposed a skewed family of distributions by introducing an additional skewness parameter. Eugene et al. [8] introduced the Beta-G family of distributions using the beta distribution. Cordeiro and de Castro [7] developed the Kumaraswamy-G family as an alternative to the Beta-G family by employing the Kumaraswamy distribution. Other notable families of distributions include the Transmuted-G family [20], the exponentiated generalized class of distributions [6], the generalized transmuted-G family [17], and the exponentiated generalized Kumaraswamy-G class [21].

Rahman et al. [18] proposed the cubic transmuted family of distributions by adding an additional parameter to a baseline distribution. They also derived an extended version of the uniform distribution, called the cubic transmuted uniform distribution, and investigated various statistical properties such as moments, mean, variance, moment-generating function, characteristic function, mean absolute deviation, quantile function, median, reliability function, hazard function, and Shannon entropy.

Lakibul and Tubo [13] introduced a new generated family of distributions called the T-extended Standard U-quadratic-G (TeSU-G) family. Using this family, they derived a bimodal version of the Weibull distribution. An extension of the TeSU-G family was presented in a subsequent study by Lakibul and Tubo [12]. Furthermore, a bivariate version of the extended Standard U-quadratic distribution was proposed by Lakibul, Polestico, and Supe [14]. Other generalizations of the extended Standard U-quadratic distribution are given in the study of Lakibul, Polestico, and Supe [15, 16].

Lakibul [11] introduced another generated family of distributions, named the Lakibul-G family, and derived several special cases, including the Lakibul-Uniform, Lakibul-Kumaraswamy, and Lakibul-Rayleigh distributions.

In this paper, we introduce a new generated family of distributions called the Aldam-G family of distributions. Using this family, we derive a generalized form of the log-logistic distribution, termed the Aldam-Log-logistic distribution, and study its properties. The proposed distribution is then applied to real-life data and compared with several competing distributions.

The remainder of this paper is organized as follows: Section 2 introduces the Aldam-G family of distributions. In Section 3, the Aldam-Log-logistic distribution is derived. Some properties of the Aldam-Log-Logistic distribution are discussed in Section 4. In section 5, the maximum likelihood estimates of the parameters of the Aldam-Log-Logistic distribution are presented. In Section 6, the proposed distribution is applied to real data. Finally, concluding remarks are provided in Section 7.

2. The Aldam-G Family of Distributions

Alzaatreh et al. [3] introduced the T-X family of distributions to extend any continuous distribution to a generalized distribution. The cumulative distribution function of the special case of the T-X family of distribution is given by

$$F_{T-X}(x) = \int_0^{G(x)} f(t)dt, \tag{1}$$

where $G(x)$ is any baseline cumulative distribution function and $f(t)$ is any probability density function (pdf) with support on the interval $[0,1]$. The Aldam - G family of distributions is obtained by using

$$f(t) = 1 - \rho + (b+1)\rho t^b,\ \rho \in \left[-\frac{1}{b}, 1\right]. \tag{2}$$

in (1), and the cumulative distribution function (cdf) of the proposed family of distribution is

$$F(x) = (1-\rho)G(x) + \rho(G(x))^{b+1} \tag{3}$$

with corresponding probability density function given by

$$f(x) = g(x)\left[1 - \rho + (b+1)\rho(G(x))^b\right],$$

where $g(x)$ is the probability density function associated with the cdf $G(x)$, $b > 0$ and $\rho \in [-\frac{1}{b}, 1]$.

3. The Aldam - Log - Logistic Distribution (ALL)

Let X be a random variable that follows a Log-Logistic distribution with cumulative distribution function given by

$$G(x) = \frac{e^{\mu}x^{\beta}}{1 + e^{\mu}x^{\beta}}, \tag{4}$$

where $x > 0$, $\mu \in \mathbb{R}$, and $\beta > 0$. The cumulative distribution function of the Aldam - Log-Logistic distribution is obtained by inserting (4) into (3) and is

$$F(x) = \frac{e^{\mu}x^{\beta}}{1+e^{\mu}x^{\beta}}\left[1-\rho+\rho\left(\frac{e^{\mu}x^{\beta}}{1+e^{\mu}x^{\beta}}\right)^{b}\right] \tag{5}$$

with corresponding probability density function given by

$$f(x) = \frac{e^{\mu}\beta x^{\beta-1}}{(1+e^{\mu}x^{\beta})^{2}}\left[1-\rho+(b+1)\rho\left(\frac{e^{\mu}x^{\beta}}{1+e^{\mu}x^{\beta}}\right)^{b}\right], \tag{6}$$

where $x > 0$, $\mu \in \mathbb{R}$, $\beta > 0$, $b > 0$ and $\rho \in [-\frac{1}{b}, 1]$.

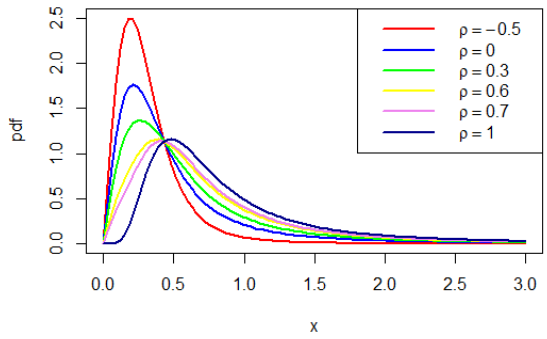


Figure 1: *PDF plots of the ALL distribution for $\mu = 2$, $\beta = 2$, $b = 2$ and varying values of ρ.*

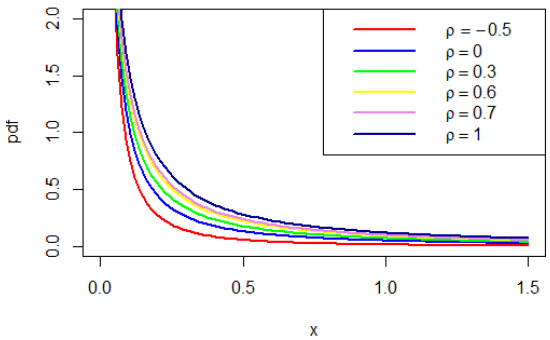


Figure 2: *PDF plots of the ALL distribution for $\mu = 2$, $\beta = 0.5$, $b = 2$ and varying values of ρ.*

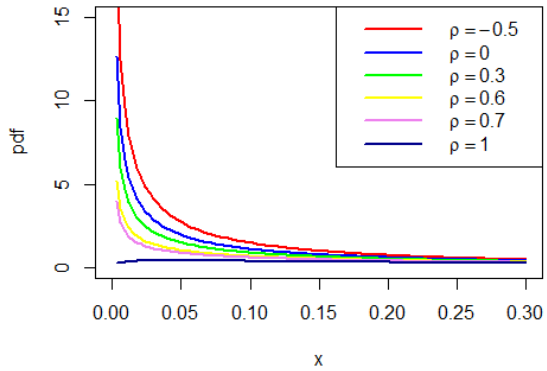


Figure 3: *PDF plots of the ALL distribution for $\mu = 0.5$, $\beta = 0.5$, $b = 2$ and varying values of ρ.*

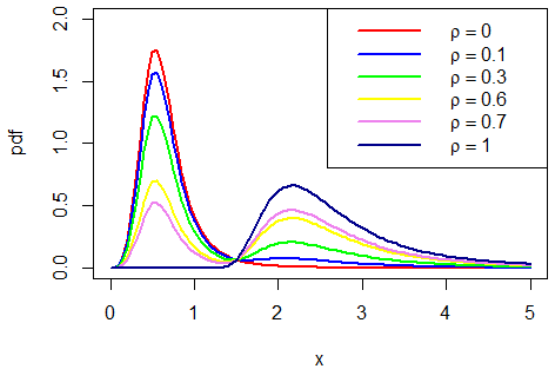


Figure 4: *PDF plots of the ALL distribution for* $\mu = 2$, $\beta = 4$, $b = 200$ *and varying values of* ρ.

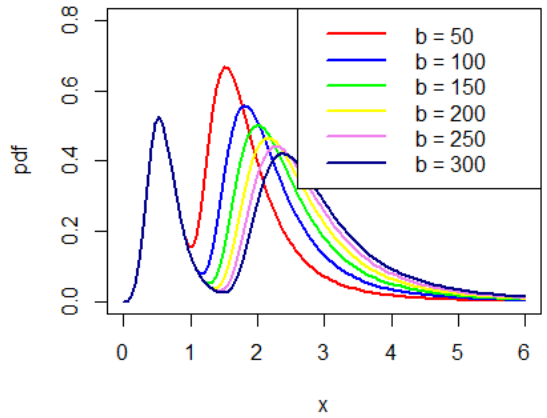


Figure 5: *PDF plots of the ALL distribution for* $\mu = 2$, $\beta = 4$, $\rho = 0.7$ *and varying values of* b.

Figures 1 to 5 display several possible shapes of the probability density function (PDF) of the Aldam-Log-Logistic (ALL) distribution. These figures indicate that the ALL distribution is capable of modeling various types of data behavior, including: (i) decreasing; (ii) right-skewed unimodal; and (iii) bimodal patterns.

4. Some Properties of the Aldam - Log - Logistic Distribution

This section presents some properties of the ALL distribution including the *rth* raw moments, mean, variance, moment generating function, survival and hazard functions.

4.1. Moments of the Aldam - Log - Logistic Distribution

Theorem 1. The *rth* raw moment of ALL distribution with density (6) and is

$$\mu'_r = e^{-\frac{\mu r}{\beta}} \left[(1-\rho)\mathbb{B}\left(\frac{r}{\beta}+1, 1-\frac{r}{\beta}\right) + \rho(b+1)e^{-\mu b}\mathbb{B}\left(\frac{r}{\beta}+b+1, 1-\frac{r}{\beta}\right)\right], \tag{7}$$

where $\beta > 0$, $\mu \in \mathbb{R}$, $\rho \in \left[-\frac{1}{b}, 1\right]$, $b > 0$, $\mathbb{B}(\cdot)$ is a beta function, and $r = 1, 2, 3, \ldots$

The mean and variance are given by

$$\mu'_1 = e^{-\frac{\mu}{\beta}} \left[(1-\rho)\mathbb{B}\left(\frac{1}{\beta}+1, 1-\frac{1}{\beta}\right) + \rho(b+1)e^{-\mu b}\mathbb{B}\left(\frac{1}{\beta}+b+1, 1-\frac{1}{\beta}\right)\right]$$

and

$$\begin{aligned}\sigma^2 =& e^{-\frac{2\mu}{\beta}}\left[(1-\rho)\mathbb{B}\left(\frac{2}{\beta}+1,1-\frac{2}{\beta}\right)+\rho(b+1)e^{-\mu b}\mathbb{B}\left(\frac{2}{\beta}+b+1,1-\frac{2}{\beta}\right)\right.\\ &\left.-\left[(1-\rho)\mathbb{B}\left(\frac{1}{\beta}+1,1-\frac{1}{\beta}\right)+\rho(b+1)e^{-\mu b}\mathbb{B}\left(\frac{1}{\beta}+b+1,1-\frac{1}{\beta}\right)\right]^2\right].\end{aligned}$$

Proof. The *rth* raw moment is defined by

$$\begin{aligned}\mu_r' &= E[X^r]\\ &= \int_0^\infty x^r f(x)dx\\ &= \int_0^\infty x^r \frac{e^\mu \beta x^{\beta-1}}{(1+e^\mu x^\beta)^2}\left(1-\rho+(b+1)\rho\left(\frac{e^\mu x^\beta}{1+e^\mu x^\beta}\right)^b\right)dx\\ &= (1-\rho)\int_0^\infty x^r \frac{e^\mu \beta x^{\beta-1}}{(1+e^\mu x^\beta)^2}dx+(b+1)\rho\int_0^\infty x^r \frac{e^\mu \beta x^{\beta-1}e^{\mu b}x^{\beta b}}{(1+e^\mu x^\beta)^{b+2}}dx\\ &= (1-\rho)e^{-\frac{\mu r}{\beta}}\int_0^\infty \frac{u^{\frac{r}{\beta}}}{(1+u)^2}du+\rho(b+1)e^{-\mu\left(\frac{r+b\beta}{\beta}\right)}\int_0^\infty \frac{u^{\frac{r+b\beta}{\beta}}}{(1+u)^{b+2}}du\\ &= e^{-\frac{\mu r}{\beta}}\left[(1-\rho)\mathbb{B}\left(\frac{r}{\beta}+1,1-\frac{r}{\beta}\right)+\rho(b+1)e^{-\mu b}\mathbb{B}\left(\frac{r}{\beta}+b+1,1-\frac{r}{\beta}\right)\right]\end{aligned}$$

The mean of ALL distribution is obtained by taking $r=1$ in (7) and is

$$\mu_1' = e^{-\frac{\mu}{\beta}}\left[(1-\rho)\mathbb{B}\left(\frac{1}{\beta}+1,1-\frac{1}{\beta}\right)+\rho(b+1)e^{-\mu b}\mathbb{B}\left(\frac{1}{\beta}+b+1,1-\frac{1}{\beta}\right)\right].$$

The 2*nd* raw moment of ALL distribution is obtained from (7) by taking $r=2$ and is

$$\mu_2' = e^{-\frac{2\mu}{\beta}}\left[(1-\rho)\mathbb{B}\left(\frac{2}{\beta}+1,1-\frac{2}{\beta}\right)+\rho(b+1)e^{-\mu b}\mathbb{B}\left(\frac{2}{\beta}+b+1,1-\frac{2}{\beta}\right)\right].$$

The variance of ALL distribution is obtained as

$$\begin{aligned}\sigma^2 =& \mu_2'-(\mu_1')^2\\ =& e^{-\frac{2\mu}{\beta}}\left[(1-\rho)\mathbb{B}\left(\frac{2}{\beta}+1,1-\frac{2}{\beta}\right)+\rho(b+1)e^{-\mu b}\mathbb{B}\left(\frac{2}{\beta}+b+1,1-\frac{2}{\beta}\right)\right]\\ &-\left\{e^{-\frac{\mu}{\beta}}\left[(1-\rho)\mathbb{B}\left(\frac{1}{\beta}+1,1-\frac{1}{\beta}\right)+\rho(b+1)e^{-\mu b}\mathbb{B}\left(\frac{1}{\beta}+b+1,1-\frac{1}{\beta}\right)\right]\right\}^2\\ =& e^{-\frac{2\mu}{\beta}}\left[(1-\rho)\mathbb{B}\left(\frac{2}{\beta}+1,1-\frac{2}{\beta}\right)+\rho(b+1)e^{-\mu b}\mathbb{B}\left(\frac{2}{\beta}+b+1,1-\frac{2}{\beta}\right)\right.\\ &\left.-\left[(1-\rho)\mathbb{B}\left(\frac{1}{\beta}+1,1-\frac{1}{\beta}\right)+\rho(b+1)e^{-\mu b}\mathbb{B}\left(\frac{1}{\beta}+b+1,1-\frac{1}{\beta}\right)\right]^2\right].\end{aligned}$$

4.2. Moment Generating Function of the Aldam - Log - Logistic Distribution

Theorem 2. Let X follows the ALL distribution then the moment generating function $M_X(t)$ is given by

$$M_X(t)=\sum_{r=0}^{\infty}\frac{t^r e^{-\frac{\mu r}{\beta}}}{r!}\left[(1-\rho)\mathbb{B}\left(\frac{r}{\beta}+1,1-\frac{r}{\beta}\right)+\rho(b+1)e^{-\mu b}\mathbb{B}\left(\frac{r}{\beta}+b+1,1-\frac{r}{\beta}\right)\right], t\in\mathbb{R}.$$

Proof. By definition of moment generating function and pdf (6), we have

$$M_X(t)=\mathbb{E}(e^{tX})=\int_0^\infty e^{tX}f(x)dx.$$

Recall that $e^{tX} = \sum_{r=0}^{\infty} \frac{t^r}{r!} x^r$, then we have

$$M_X(t) = \sum_{r=0}^{\infty} \frac{t^r}{r!} \mu'_r.$$

Hence,

$$M_X(t) = \sum_{r=0}^{\infty} \frac{t^r e^{-\frac{\mu r}{\beta}}}{r!} \left[(1-\rho)\mathbb{B}\left(\frac{r}{\beta}+1, 1-\frac{r}{\beta}\right) + \rho(b+1)e^{-\mu b}\mathbb{B}\left(\frac{r}{\beta}+b+1, 1-\frac{r}{\beta}\right)\right], t \in \mathbb{R}.$$

4.3. Survival and Hazard Functions of the Aldam - Log - Logistic Distribution

Let X be a random variable with cdf (5) and pdf (6) then the survival $S(x)$ and hazard $h(x)$ functions of ALL distribution are respectively, given by

$$S(x) = 1 - \frac{e^{\mu} x^{\beta}}{1 + e^{\mu} x^{\beta}} \left(1 - \rho + \rho \left(\frac{e^{\mu} x^{\beta}}{1 + e^{\mu} x^{\beta}}\right)^{b}\right)$$

and

$$h(x) = \frac{\frac{e^{\mu}\beta x^{\beta-1}}{(1+e^{\mu}x^{\beta})^2}\left(1 - \rho + (b+1)\rho\left(\frac{e^{\mu}x^{\beta}}{1+e^{\mu}x^{\beta}}\right)^{b}\right)}{1 - \frac{e^{\mu}x^{\beta}}{1+e^{\mu}x^{\beta}}\left(1 - \rho + \rho\left(\frac{e^{\mu}x^{\beta}}{1+e^{\mu}x^{\beta}}\right)^{b}\right)},$$

where $x > 0$, $\mu \in \mathbb{R}$, $\beta > 0$, $b > 0$ and $\rho \in [-\frac{1}{b}, 1]$.

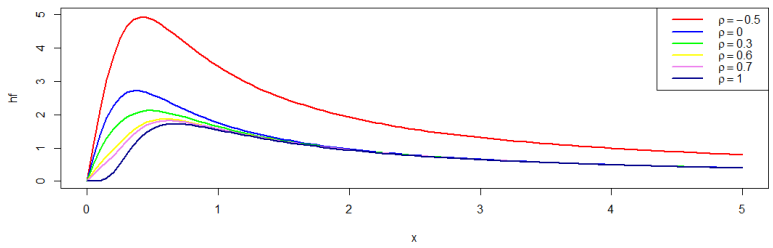


Figure 6: *HF plots of the ALL distribution for $\mu = 2$, $\beta = 2$, $b = 2$ and varying values of ρ.*

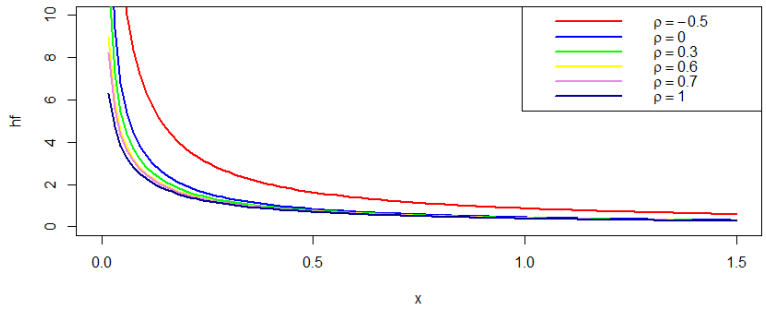


Figure 7: *HF plots of the ALL distribution for $\mu = 2$, $\beta = 0.5$, $b = 2$ and varying values of ρ.*

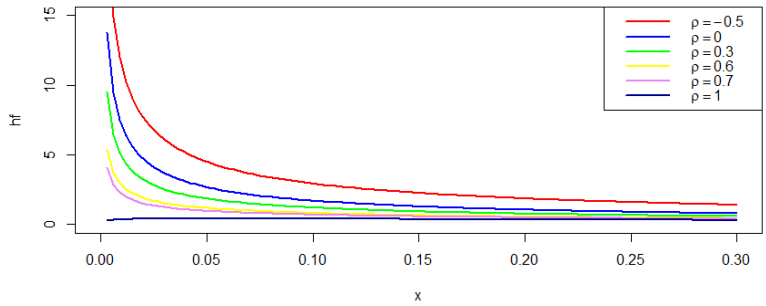


Figure 8: *HF plots of the ALL distribution for* $\mu = 0.5$, $\beta = 0.5$, $b = 2$ *and varying values of* ρ.

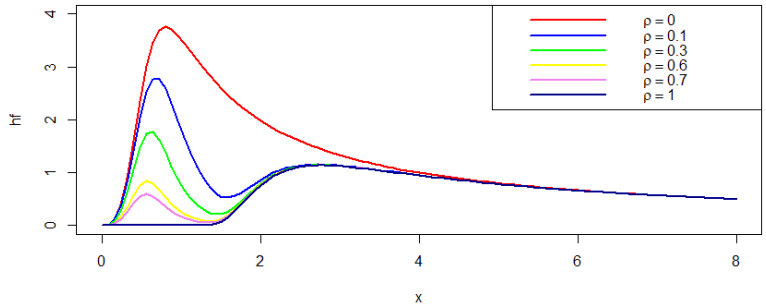


Figure 9: *HF plots of the ALL distribution for* $\mu = 2$, $\beta = 4$, $b = 200$ *and varying values of* ρ.

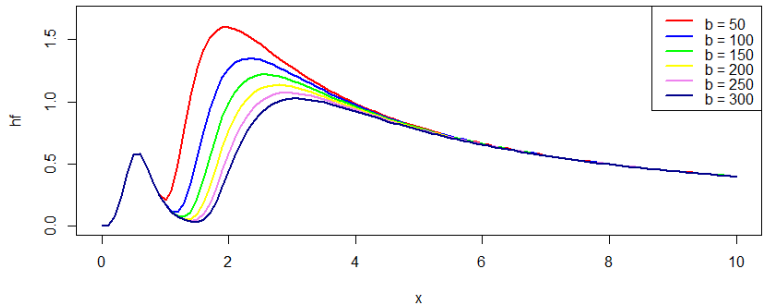


Figure 10: *HF plots of the ALL distribution for* $\mu = 2$, $\beta = 4$, $\rho = 0.7$ *and varying values of* b.

Figures 6 to 10 illustrate various possible shapes of the hazard function of the ALL distribution. These figures demonstrate that the hazard function of the ALL distribution is flexible enough to model a range of behaviors, including: (i) decreasing; (ii) right-skewed unimodal; and (iii) bimodal patterns.

5. Maximum Likelihood Estimates of the Aldam - Log - Logistic Distribution

Let X_1, X_2,..., X_n be a random sample of size n from ALL distribution, then the likelihood function is

$$L = e^{n\mu}\beta^n \prod_{i=1}^{n}\left(1+e^{\mu}x_i^{\beta}\right)^{-2}\prod_{i=1}^{n}x_i^{\beta-1}\prod_{i=1}^{n}\left[1-\rho+(b+1)\rho\left(\frac{e^{\mu}x_i^{\beta}}{1+e^{\mu}x_i^{\beta}}\right)^{b}\right]$$

The log-likelihood function is

$$l = n\mu + n\log(\beta) - 2\sum_{i=1}^{n}\log\left(1+e^{\mu}x_i^{\beta}\right) + (\beta-1)\sum_{i=1}^{n}\log(x_i) - b\sum_{i=1}^{n}\log\left(1+e^{\mu}x_i^{\beta}\right) + \sum_{i=1}^{n}\log\left[(1-\rho)\left(1+e^{\mu}x_i^{\beta}\right)^{b} + (b+1)\rho e^{\mu b}x_i^{\beta b}\right] - b\sum_{i=1}^{n}\frac{x_i^{\beta}e^{\mu}}{1+e^{\mu}x_i^{\beta}}. \quad (8)$$

Taking the derivative of (8) with respect to parameter μ then, we have

$$\frac{\partial l}{\partial \mu} = n - (2+b)\sum_{i=1}^{n}\frac{x_i^{\beta}e^{\mu}}{1+e^{\mu}x_i^{\beta}} + \sum_{i=1}^{n}\frac{(1-\rho)b\left(1+e^{\mu}x_i^{\beta}\right)^{b-1}e^{\mu}x_i^{\beta} + b(b+1)\rho e^{\mu b}x_i^{\beta b}}{(1-\rho)\left(1+e^{\mu}x_i^{\beta}\right)^{b} + (b+1)\rho e^{\mu b}x_i^{\beta b}}. \quad (9)$$

Taking the derivative of (8) with respect to parameter β then, we have

$$\frac{\partial l}{\partial \beta} = \frac{n}{\beta} - 2\sum_{i=1}^{n}\frac{e^{\mu}x_i^{\beta}log(x_i)}{1+e^{\mu}x_i^{\beta}} + \sum_{i=1}^{n}\log(x_i) - b\sum_{i=1}^{n}\frac{e^{\mu}x_i^{\beta}\log(x_i)}{1+e^{\mu}x_i^{\beta}} + \sum_{i=1}^{n}\frac{(1-\rho)b\left(1+e^{\mu}x_i^{\beta}\right)^{b-1}e^{\mu}x_i^{\beta}\log(x_i) + (b+1)\rho e^{\mu b}bx_i^{\beta b}\log(x_i)}{(1-\rho)\left(1+e^{\mu}x_i^{\beta}\right)^{b} + (b+1)\rho e^{\mu b}x_i^{\beta b}}. \quad (10)$$

Taking the derivative of (8) with respect to parameter b then, we have

$$\frac{\partial l}{\partial b} = \sum_{i=1}^{n}\frac{(1-\rho)\left(1+e^{\mu}x_i^{\beta}\right)^{b}\log\left(1+e^{\mu}x_i^{\beta}\right) + \rho e^{b\mu}x_i^{b\beta}\left[(b+1)(\mu+\beta\log(x_i))+1\right]}{(1-\rho)\left(1+e^{\mu}x_i^{\beta}\right)^{b} + (b+1)\rho e^{\mu b}x_i^{\beta b}} \quad (11)$$

By simultaneously equating equations (9), (10), and (11) to zero, the numerical maximum likelihood estimates of the parameters of the ALL distribution can be obtained.

6. Application of the Aldam - Log - Logistic Distribution

In this section, we apply the ALL distribution on the Old Faithful Geyser dataset and compare with the Log-logistic distribution, and the following distributions:

- The T-extended Standard U-quadratic - Weibull Distribution (TeSU-W) [13]

$$f(x) = b\beta x^{\beta-1}e^{-bx^{\beta}}\left(1+2\rho-12\rho e^{-bx^{\beta}}+12\rho e^{-2bx^{\beta}}\right),\ x>0, \quad (12)$$

where $b>0$, $\beta>0$ and $\rho\in[-0.5,1]$.

- The Gumbel - Weibull Distribution (GW) [2]

$$f(x) = \frac{\alpha\beta}{\lambda\sigma}\left(\frac{x}{\lambda}\right)^{\alpha-1}e^{\left(\frac{x}{\lambda}\right)^{\alpha}}\left(e^{\left(\frac{x}{\lambda}\right)^{\alpha}}-1\right)^{-1-\frac{1}{\sigma}}e^{-\beta\left(e^{\left(\frac{x}{\lambda}\right)^{\alpha}}-1\right)^{-\frac{1}{\sigma}}},\ x>0, \quad (13)$$

where $\beta = e^{\frac{\nu}{\sigma}}$, $\alpha>0$, $\sigma>0$, $\lambda>0$ and $-\infty\le\nu\le\infty$

The dataset used in this alpplication is consists of 299 paired measurements representing the time intervals between the start of successive eruptions of the Old Faithful Geyser in Yellowstone National Park, Wyoming, USA. The data were collected continuously from August 1 to August

15, 1985. The observations are the following:

1. Waiting times
80 71 57 80 75 77 60 86 77 56 81 50 89 54 90 73 60 83 65 82 84 54 85 58 79 57 88 68 76 78 74 85 75 65 76 58 91 50 87 48 93 54 86 53 78 52 83 60 87 49 80 60 92 43 89 60 84 69 74 71 108 50 77 57 80 61 82 48 81 73 62 79 54 80 73 81 62 81 71 79 81 74 59 81 66 87 53 80 50 87 51 82 58 81 49 92 50 88 62 93 56 89 51 79 58 82 52 88 52 78 69 75 77 53 80 55 87 53 85 61 93 54 76 80 81 59 86 78 71 77 76 94 75 50 83 82 72 77 75 65 79 72 78 77 79 75 78 64 80 49 88 54 85 51 96 50 80 78 81 72 75 78 87 69 55 83 49 82 57 84 57 84 73 78 57 79 57 90 62 87 78 52 98 48 78 79 65 84 50 83 60 80 50 88 50 84 74 76 65 89 49 88 51 78 85 65 75 77 69 92 68 87 61 81 55 93 53 84 70 73 93 50 87 77 74 72 82 74 80 49 91 53 86 49 79 89 87 76 59 80 89 45 93 72 71 54 79 74 65 78 57 87 72 84 47 84 57 87 68 86 75 73 53 82 93 77 54 96 48 89 63 84 76 62 83 50 85 78 78 81 78 76 74 81 66 84 48 93 47 87 51 78 54 87 52 85 58 88 79.

2. Time Duration
4.0166667 2.1500000 4.0000000 4.0000000 4.0000000 2.0000000 4.3833333 4.2833333 2.0333333 4.8333333 1.8333333 5.4500000 1.6166667 4.8666667 4.3833333 1.7666667 4.6666667 2.0000000 4.7333333 4.2166667 1.9000000 4.9666667 2.0000000 4.0000000 2.0000000 4.0000000 2.8333333 4.5000000 4.0666667 3.7166667 3.5166667 4.4666667 2.2166667 4.8833333 2.6000000 4.1500000 2.2000000 4.7666667 1.8333333 4.6000000 2.2666667 4.1333333 2.0000000 4.0000000 2.0000000 4.0000000 1.8833333 4.2666667 2.0833333 4.4666667 2.5000000 4.0000000 1.7666667 4.3333333 2.1833333 4.4833333 3.8833333 3.3333333 3.7333333 4.0000000 1.9500000 5.2666667 2.0000000 4.0000000 2.0000000 4.0000000 2.0000000 4.0000000 3.5333333 2.1666667 4.5000000 2.0166667 4.1500000 4.2000000 4.3333333 1.9333333 4.6500000 3.8166667 4.0333333 4.1666667 4.6666667 1.8166667 4.0000000 3.0000000 4.0000000 2.0000000 4.4500000 2.0500000 4.2500000 1.9166667 4.6666667 1.7333333 4.3833333 1.7666667 4.6000000 1.8666667 4.4500000 1.6333333 5.0333333 1.8166667 5.1000000 1.6333333 4.2833333 2.0000000 4.0000000 2.0000000 4.5333333 2.0000000 4.0000000 2.9333333 4.7333333 3.9000000 1.9500000 4.1166667 1.8000000 4.6666667 1.8333333 4.7000000 2.1166667 4.7833333 1.8166667 4.1000000 4.6500000 4.0000000 2.0000000 4.0000000 4.0000000 4.2166667 4.1333333 3.9333333 3.7500000 4.4166667 2.4666667 4.1666667 3.8000000 4.3166667 3.8666667 4.6833333 1.7000000 4.9666667 4.2666667 4.5833333 4.0000000 4.0000000 4.0000000 4.0000000 1.9833333 4.6000000 0.8333333 4.9166667 1.7333333 4.5833333 1.7000000 4.7500000 1.8333333 4.5000000 1.8666667 4.4500000 4.4500000 4.0000000 4.8000000 4.0000000 4.0000000 2.0000000 4.0000000 1.9333333 4.5833333 2.0000000 3.7000000 2.8666667 4.8333333 3.4500000 4.3833333 1.8000000 4.4000000 2.4833333 4.5166667 2.1000000 4.3500000 4.3666667 1.7833333 4.9166667 1.8166667 4.0000000 4.0000000 4.0000000 3.8666667 1.8500000 4.7000000 2.0166667 4.4666667 1.8666667 4.1666667 1.9000000 4.2500000 3.2500000 4.2166667 1.8833333 4.9833333 1.8500000 4.0000000 1.9666667 4.7666667 4.0000000 2.0000000 4.0000000 4.0000000 2.3833333 4.4166667 4.2166667 4.3666667 2.0000000 4.4500000 1.7500000 4.5000000 1.6166667 4.7000000 2.5666667 3.7000000 4.2333333 1.9333333 4.3500000 4.0000000 4.0000000 4.0000000 4.2166667 4.0000000 4.1333333 1.8833333 4.4666667 1.9500000 4.2166667 1.7166667 4.4500000 4.2500000 3.9666667 4.3833333 1.9666667 4.4500000 4.2666667 1.9166667 4.4166667 3.0000000 4.0000000 2.0000000 4.0000000 3.2833333 1.8333333 4.6166667 1.8333333 4.6166667 4.6000000 4.2500000 1.9333333 4.9833333 1.9666667 4.3000000 4.2000000 4.5333333 4.4000000 4.6166667 2.0000000 4.0000000 4.0000000 3.9166667 2.0000000 4.5000000 1.8000000 4.0000000 2.7500000 4.7333333 3.9666667 1.9500000 4.9666667 1.8500000 4.8000000 4.0000000 4.0000000 4.0000000 4.0000000 4.0000000 4.0000000 4.0000000 2.0000000 4.0000000 1.9333333 4.3333333 1.6666667 4.7666667 1.9500000 4.6833333 1.9333333 4.4166667 2.1333333 4.0833333 2.0666667 4.0000000 4.0000000 2.0000000.

Here, we use a package "fitdistrplus" in R software. Moreover, we utilize the Akaike Information Criterion (AIC) and the Bayesian Information Criterion (BIC) for comparison.

Table 1: *MLEs of the fitted models for the Waiting time of the Geyser dataset.*

	Parameters			
Distributions	$\hat{\mu}$	$\hat{\beta}$	$\hat{\rho}$	$\hat{b}$
ALL	-57.4616339	14.297131	0.6309489	132.38172
LL	-35.448639	8.279677		
TeSU-W		4.236527	-0.5000000	0.00000000888
	$\hat{\alpha}$	$\hat{\beta}$	$\hat{\sigma}$	$\hat{\nu}$
GW	0.000050714	3.091603	14.31577	23.65889

Table 1 presents the maximum likelihood estimates (MLEs) of the parameters for four candidate distributions fitted to the waiting time variable of the Geyser dataset: the ALL (Aldam-Log-Logistic), LL (Log-Logistic), TeSU-W (T-extended Standard U-quadratic-Weibull), and GW (Gumbel - Weibull) distributions.

The ALL distribution produced parameter estimates of $\hat{\mu} = -57.4616$, $\hat{\beta} = 14.2971$, $\hat{\rho} = 0.6309$, and $\hat{b} = 132.3817$. The LL distribution, a simpler two-parameter model, yielded $\hat{\mu} = -35.4486$ and $\hat{\beta} = 8.2797$. For the TeSU-W distribution, the estimates were $\hat{\beta} = 4.2365$, $\hat{\rho} = -0.5$, and $\hat{b} = 8.88 \times 10^{-9}$. Lastly, the GW distribution had four estimated parameters: $\hat{\alpha} = 5.07 \times 10^{-5}$, $\hat{\beta} = 3.0916$, $\hat{\sigma} = 14.3158$, and $\hat{\nu} = 23.6589$.

Table 2: *Numerical values of the AIC and BIC of the fitted models for waiting time of the Geyser dataset.*

Distributions	AIC	BIC
ALL	**2338.192**	**2352.994**
LL	2469.652	2477.053
TeSU-W	2420.931	2432.032
GW	2441.881	2456.683

Table 2 shows the corresponding Akaike Information Criterion (AIC) and Bayesian Information Criterion (BIC) values for model comparison. Among the four fitted distributions, the ALL distribution obtained the lowest AIC (2338.192) and BIC (2352.994), indicating the best model fit among the candidates, taking into account both goodness-of-fit and model complexity. This suggests that the ALL distribution provides the most appropriate model for the waiting time variable in the Geyser dataset.

In contrast, the LL, TeSU-W, and GW distributions showed higher AIC and BIC values, with the LL model performing the worst in terms of both criteria. Although the TeSU-W and GW distributions slightly outperformed the LL, they still fall short of the performance of ALL model. These results provide strong evidence in favor of using the ALL distribution for modeling the waiting time data in this context. Further, same result is observed from Figure 11.

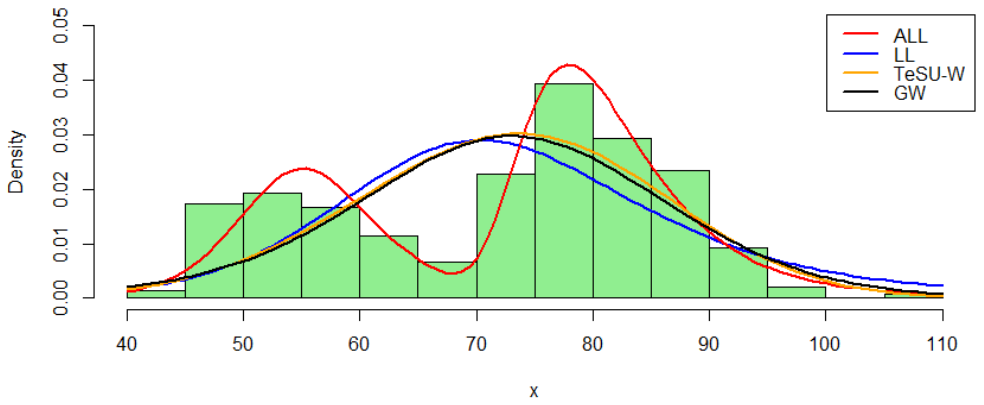


Figure 11: *Estimated PDF of the fitted models for the waiting time of the Geyser dataset.*

Table 3: *MLEs of the fitted models for Time Duration of the Geyser dataset.*

	Parameters			
Distributions	$\hat{\mu}$	$\hat{\beta}$	$\hat{\rho}$	$\hat{b}$
ALL	-8.9151564	13.1175181	0.6297066	15667.9303
LL	-5.243472	4.294778		
TeSU-W		4.310113470	0.982276578	0.004548
	$\hat{\alpha}$	$\hat{\beta}$	$\hat{\sigma}$	$\hat{\nu}$
GW	0.0000036545	9.903009	7.159973	-0.6311149

Table 3 presents the maximum likelihood estimates (MLEs) of the parameters for four candidate distributions fitted to the duration variable of the Geyser dataset: the Aldam-Log-Logistic (ALL), Log-Logistic (LL), T-extended Standard U-Weibull (TeSU-W), and Gumbel-Weibull (GW) distributions.

The ALL distribution provided the following parameter estimates: $\hat{\mu} = -8.9152$, $\hat{\beta} = 13.1175$, $\hat{\rho} = 0.6297$, and $\hat{b} = 15667.9303$. The simpler LL distribution had parameter estimates of $\hat{\mu} = -5.2435$ and $\hat{\beta} = 4.2948$. For the TeSU-W distribution, the estimated parameters were $\hat{\beta} = 4.3101$, $\hat{\rho} = 0.9823$, and $\hat{b} = 0.004548$. Meanwhile, the GW distribution yielded parameter estimates of $\hat{\alpha} = 3.6545 \times 10^{-6}$, $\hat{\beta} = 9.9030$, $\hat{\sigma} = 7.1600$, and $\hat{\nu} = -0.6311$.

Table 4: *Numerical values of AIC and BIC of the fitted models for Time Duration of the Geyser dataset.*

Distribution	*AIC*	*BIC*
ALL	**601.5399**	**616.3416**
LL	1010.538	1017.939
TeSU-W	705.2641	716.3655
GW	753.9445	768.7462

To evaluate the relative performance of the fitted models, Table 4 presents the Akaike Information Criterion (AIC) and Bayesian Information Criterion (BIC) values. Among all considered models, the ALL distribution achieved the lowest AIC (601.540) and BIC (616.342), indicating the best fit to the data while balancing model complexity and goodness-of-fit.

In contrast, the LL distribution recorded the highest AIC and BIC values (1010.538 and 1017.939, respectively), indicating poor model performance. The TeSU-W and GW distributions performed better than LL but were still outperformed by the ALL distribution by a considerable

margin. These findings demonstrate that the ALL distribution provides the most appropriate model for the duration variable of the Geyser dataset, further emphasizing its flexibility in capturing the distributional characteristics of the data. In addition, same observation is drawn from the following figure.

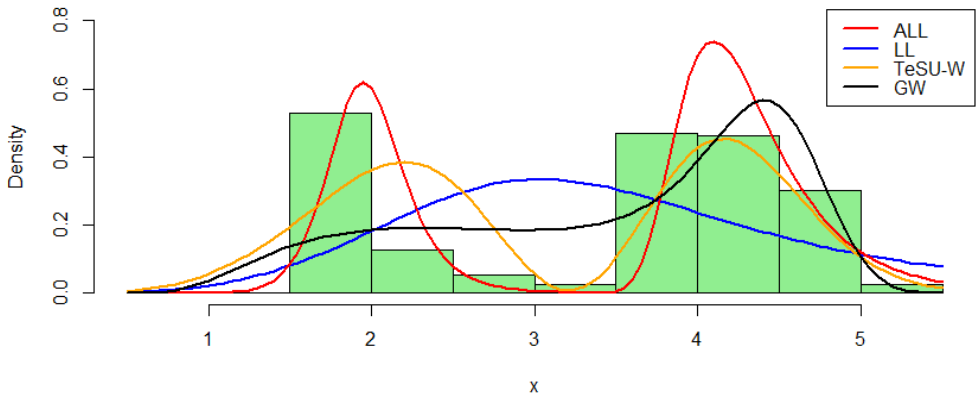


Figure 12: *Estimated PDF of the fitted models for the time duration of the Geyser dataset.*

7. Concluding Remarks

In this paper, a new generated family of distributions called the Aldam-G Family of Distributions has been introduced. In particular, the Aldam - Log-Logistic distribution was derived. Some properties of the derived distribution, such as its moments, mean, variance, and moment generating function, were obtained. The maximum likelihood method was used to estimate the parameters of the proposed distribution. Real data sets were utilized to examine the flexibility and applicability of the proposed distribution. It was observed that the Aldam-Log- Logistic distribution gives better estimates for the given bimodal data than the log-logistic, Gumbel - Weibull and the T - extended Standard U-quadratic Weibull distributions.

References

[1] Afify, A. J., Nassar, M., Kumar, D. and Cordeiro, G. M. (2022). A new unit distribution: properties, imference, and applications. *Electronic Journal of Applied Statistical Analysis*, 15:438–462.

[2] Al-Aqtash, R. A., Lee, C. and Famoye, F. (2014). Gumbel-Weibull Distribution: Properties and Applications. *Journal of Modern Applied Statistical Methods*, 2(13):201-225.

[3] Alzaatreh, A., Lee, C. and Famoye, F. (2013). A new method for generating families of continuous distributions. *Metron*, 71:63–79.

[4] Azzalini, A. (1985). A class of distributions which includes the normal ones. *Scandinavian Journal of Statistics*, 12:171–178.

[5] Banerjee, P. and Bhunia, S. (2022).Exponentiated Transformed Inverse Rayleigh Distribution: Statistical Properties and Different Methods of Estimation. *Austrian Journal of Statistics*, 51:60–75.

[6] Cordeiro, G., Ortega, E. M. M. and Cunha, D. C. C. (2013). The exponentiated generalized class of distributions. *Journal of Data Science*, 11:1–27.

[7] Cordeiro, G. M. and de Castro, M. (2011). A new family of generalized distributions. *Journal of Statistica; Computation and Simulation*, 81:883–893.

[8] Eugene, N., Lee, C. and Famoye, F. (2002). Beta-normal distribution and its applications. *Communications in Statistics-Theory and Methods*, 31:497–512.

[9] Hinkley, D. (1977). On Quick Choice of Power Transformation. *Journal of the Royal Statistical Society. Series C (Applied Statistics)*, 26:67–69.
[10] Khan, M. S., King, R. and Hudson, I. L. (2016). Transmuted Kumaraswamy Distribution. *Statistics in Transition*, 17:183–210.
[11] Lakibul, I. A. (2025). Lakibul-G family of distributions: special models, properties and applications. *Reliability: Theory and Applications*, 20:617-631.
[12] Lakibul, I. A. and Tubo, B. F. (2023). On the Four-Parameter T-extended Standard U-quadratic Exponentiated Weibull Distribution. *The Mindanawan journal of Mathematics*, 5:17–33.
[13] Lakibul, I. A. and Tubo, B. F. (2023). On the TeSU-G family of distributions applied to lifedata analysis. *Reliability: Theory and Applications*, 18:24–38.
[14] Lakibul, I. A., Polestico, D. L. and Supe, A. P. (2024). On the Bivariate Extension of the extended Standard U-quadratic Distribution. *European Journal of Pure and Applied Mathematics*, 17:790-809.
[15] Lakibul, I. A., Polestico, D. L. and Supe, A. P. (2025). On the Generalized Version of the extended Standard U-quadratic Distribution. *European Journal of Pure and Applied Mathematics*, 18:5923-5923.
[16] Lakibul, I. A., Polestico, D. L. and Supe, A. P. (2025). On the Generalization of the Bivariate extended Standard U-quadratic Distribution. *European Journal of Pure and Applied Mathematics*, 18:5921-5921.
[17] Nofal, Z. M., Afify, A. Z., Yousof, H. M. and Cordeiro, G. M. (2017). The generalized transmuted - G family of distributions. *Communication Statistics Theory and Methods*, 49:4119–4136.
[18] Rahman, M. M., Al-Zahrani, B. and Shahbaz, S. H. (2019). Cubic Transmuted Uniform Distribution: An Alternative to Beta and Kumaraswamy Distributions. *Journal of Pure and Applied Mathematics*, 12:1106–1121.
[19] Rao, G. S. and Mbwambo, S. (2019). Exponentiated Inverse Rayleigh Distribution and an Application to Coating Weights of Iron Sheets Darta. *Journal of Probability and Statistics*, https://doi.org/10.1155/2019/7519429.
[20] Shaw, W. T. and Buckley, I. R. C. (2007). The alchemy of probability distributions: beyond Gram-Charlier expansions, and a skew-kurtotic-normal distribution from a rank transmutation map. *Research report*.
[21] Silva, R., Silva, F. G., Ramos, M., Cordeiro, G. M., Marinho, P. and de Andrade, T. A. N. (2019). The Exponentiated Kumaraswamy-G Class: General Properties and Application. *R. C de Estadistica*, 42:1–33.

ALPHA LOGARITHMIC TRANSFORMATION OF LOMAX DISTRIBUTION WITH PROPERTIES AND APPLICATION TO SURVIVAL DATA

K.M.Sakthivel[1], Nandhini V[2], and Vidhya G[3]

•

[1]Professor, Department of Statistics, Bharathiar University, Coimbatore-46

[2]Assistant Professor, Department of Mathematics, Karpagam Academy of Higher Education, Coimbatore-21

[3]Assistant Professor, Department of Mathematics, Rathinam College of Arts and Science, Coimbatore-21

Corresponding Author: nandhinivtvt@gmail.com

Abstract

Probability distribution plays a vital role in lifetime data analysis, reliability modeling, and survival studies. Classical models often exhibit limitations in flexibility when dealing with diverse real-world datasets. To address this gap, we introduce an extended model that improves the ability to capture various shapes of lifetime distributions. In this paper, we propose a new three-parameter probability distribution, termed the Alpha Logarithmic Transformation of Lomax (ALTLx) distribution, which proves to be effective for modeling lifetime data. The proposed distribution is studied in detail, and several of its statistical properties are derived, including moments, incomplete moments, quantiles, mean residual life, mean inactivity time, entropy, order statistics, and stress strength analysis. Parameter estimation is carried out using the method of maximum likelihood to ensure reliable inference. The practical applicability of the ALTLx distribution is demonstrated by fitting it to datasets representing the survival time of patients. The results indicate that it outperforms several well-known competing distributions, showing that the proposed model provides a significantly better fit. The distribution exhibits greater flexibility and effectively captures diverse patterns in lifetime data. The findings confirm that the ALTLx distribution offers superior performance in modeling lifetime and reliability data.

Keywords: Alpha logarithmic G family, Lomax distribution, Parameters, Entropy, Maximum likelihood estimation.

1. INTRODUCTION

The Lomax or Pareto Type II (shifted Pareto) distribution (1954) was proposed by K.S. Lomax. This distribution has found wide application, such as analyzing datasets from actuarial science, medical and biological sciences, and reliability modelling. Hassan and Al-Ghamdi [6] mentioned that it is used for reliability modelling and life testing [16], Harris used the Lomax distribution for income and wealth data [15], Bryson has suggested the use of Lomax distributionand it is an alternative to the exponential, Weibull and gamma distributions [8], Atkinson and Harrison used

it for modelling the business failure data [6]. The characterization of the Lomax distribution is described in numerous ways, such as a special form of Pearson type VI distribution and also as a mixture of gamma and exponential distributions. Some details on the Lomax and Pareto families are in Arnold [5] and Johnson et al. [17].

A random variable X has the Lomax distribution with two parameters β and λ if it has a cumulative distribution function (cdf) given by

$$F(x) = 1 - \left(1 + \frac{x}{\lambda}\right)^{-\beta} \quad ; \text{for } x > 0 \tag{1}$$

where $\beta > 0$ and $\lambda > 0$ are the shape and scale parameters, respectively.
The corresponding probability density function (pdf) is given by

$$f(x) = \frac{\beta}{\lambda}\left(1 + \frac{x}{\lambda}\right)^{-(\beta+1)} ; \text{for } x > 0,\ \beta, \lambda > 0 \tag{2}$$

In the literature, some extensions of the Lomax distribution are available, such as follows: Marshall-Olkin–Olkin extended-Lomax (MOEL) by Ghitany et al. [14], Exponentiated Lomax (EL) by Abdul-Moniem [1], Gamma-Lomax (GL) by Cordeiro et al. [9], Exponential Lomax by El-Bassiouny [13], and Half-logistic Lomax(HLL) by Anwar [4]. Pappas et al. [23] introduced a new Alpha Logarithmic Transformed (ALT) family of distributions with the cdf and pdf as follows:

$$F_{ALT}(x;\alpha) = \begin{cases} 1 - \frac{log(\alpha - (\alpha-1)G(x))}{\log \alpha} ; \ if\ \alpha > 0, \alpha \neq 1, x \in R \\ G(x) \quad ; \ \ if\ \alpha = 1,\ x \in R \end{cases} \tag{3}$$

$$f_{ALT}(x,\alpha) = \begin{cases} \frac{(\alpha-1)g(x)}{log(\alpha-(\alpha-1)G(x))} \quad ; \ if\ \alpha > 0,\ \alpha \neq 1,\ x \in R \\ g(x) \quad ; \ \ if\ \alpha = 1,\ x \in R \end{cases} \tag{4}$$

Note that when $\alpha = 2$, the cdf and pdf in (3) and (4) reduce to the cdf and pdf of the logarithmic transformed method proposed by Maurya et al. [20]. Dey et al.[10] used the method of Pappas et al [23] introduced an ALT generalized exponential distribution and ALT Fréchet Distribution discussed by Dey et al. [12].

The main aim of this paper is to propose and study a new lifetime model called Alpha Logarithmic Transformed Lomax (ALTLx) distribution based on the ALT-G family. The purpose of this new model is that the additional parameter can give several properties and be more flexible in the form of the hazard and density functions. In Section .2, we derive the expansion of the Alpha Logarithmic Transformed G family of distribution, and we introduce the ALTLx distribution. In Section 3, we study some of its statistical properties, including the quantile function, moments, moment generating function, entropy, order statistics, and stress strength reliability. In Section 4, we discuss the maximum likelihood estimates (MLEs) of the model parameter. In Section 5, we perform a simulation to evaluate the effectiveness of a newly proposed ALTLx distribution. In Section 6, the analysis of real data sets is presented to illustrate the potential of the new model. Section.7, we conclude the study.

2. ALPHA LOGARITHMIC TRANSFORMED-G FAMILY OF DISTRIBUTION

Let G(x) be an absolutely continuous distribution function with pdf g(x), then the cdf and pdf of the ALT family of distributions and its expansions are as follows:

$$F_{ALT}(x;\alpha) \ = \left(1 - \frac{log(\alpha - (\alpha-1)G(x))}{\log \alpha}\right); \ if\ \alpha > 0,\ \alpha \neq 1$$

$$F_{ALT}(x;\alpha) = \left(\frac{\log\alpha - \log(\alpha+1)}{\log\alpha}\right) - \frac{1}{\log\alpha}\sum_{k=1}^{\infty}\frac{1}{k}\left(\frac{1+(\alpha-1)G(x)}{\alpha+1}\right)^k$$

$$F_{ALT}(x;\alpha) = C(\alpha) - \frac{1}{\log\alpha}\sum_{k=1}^{\infty}\frac{1}{k}\left(\frac{1+(\alpha-1)G(x)}{\alpha+1}\right)^k,$$

where, $C(\alpha) = \frac{\log\alpha - \log(\alpha+1)}{\log\alpha}$

$$F_{ALT}(x;\alpha) = C(\alpha) - \frac{1}{\log\alpha}\sum_{k=1}^{\infty}\sum_{j=0}^{k}\binom{k}{j}\frac{(\alpha-1)^j}{k(\alpha+1)^k}\left(G(x)\right)^j \; ; if\ \alpha > 0,\ \alpha \neq 1$$

$$f_{ALT}(x,\alpha) = \frac{(\alpha-1)g(x)}{log(\alpha-(\alpha-1)G(x))} \; ; if\ \alpha > 0,\ \alpha \neq 1,\ x \in R$$

$$= \frac{(\alpha-1)g(x)}{\log\alpha\,(\alpha+1)}\left[\frac{(\alpha+1)-1-(\alpha-1)G(x)}{\alpha+1}\right]^{-1}$$

$$f_{ALT}(x,\alpha) = \frac{g(x)}{\log\alpha}\sum_{k=0}^{\infty}\sum_{j=0}^{k}\binom{k}{j}\frac{(\alpha-1)^{j+1}}{(\alpha+1)^{k+1}}[G(x)]^j \; ; if\ \alpha > 0,\ \alpha \neq 1,\ x \in R$$

The random variable X is said to follow the three-parameter ALTLx distribution with the shape parameter $\beta > 0$ and scale parameter $\lambda > 0$ if the cumulative cdf of $x > 0$ is given by:

$$F_{ALTLx}(x;\alpha) = \begin{cases} 1 - \dfrac{log\left(\alpha-(\alpha-1)\left(1-\left(1+\frac{x}{\lambda}\right)^{-\beta}\right)\right)}{\log\alpha} & ;\ if\ \alpha > 0, \alpha \neq 1, x \in R \\ \left(1-\left(1+\frac{x}{\lambda}\right)^{-\beta}\right) & ;\quad if\ \alpha = 1,\ x \in R \end{cases} \tag{5}$$

The corresponding probability density function (pdf) is given by

$$f_{ALTLx}(x,\alpha) = \begin{cases} \dfrac{(\alpha-1)\left(\frac{\beta}{\lambda}\left(1+\frac{x}{\lambda}\right)^{-(\beta+1)}\right)}{\log\alpha\left(\alpha-(\alpha-1)\left(1-\left(1+\frac{x}{\lambda}\right)^{-\beta}\right)\right)} & ;\ if\ \alpha > 0,\ \alpha \neq 1,\ x \in R \\ \left(\frac{\beta}{\lambda}\left(1+\frac{x}{\lambda}\right)^{-(\beta+1)}\right) & ;\ if\ \alpha = 1,\ x \in R \end{cases} \tag{6}$$

The hazard rate function of the ALTLx distribution is as follows

$$h_{ALTLx}(x;\alpha) = \begin{cases} \dfrac{(\alpha-1)\left(\frac{\beta}{\lambda}\left(1+\frac{x}{\lambda}\right)^{-(\beta+1)}\right)}{\left(\alpha-(\alpha-1)\left(1-\left(1+\frac{x}{\lambda}\right)^{-\beta}\right)\right)\log\alpha\left(\alpha-(\alpha-1)\left(1-\left(1+\frac{x}{\lambda}\right)^{-\beta}\right)\right)} ; if\alpha > 0, \alpha \neq 1 \\ \dfrac{\beta}{\lambda+x} \quad ;\ if\ \alpha = 1 \end{cases} \tag{7}$$

The reversed hazard rate function of the ALTLx distribution is as follows

$$\tau_{ALTLx}(x) = \begin{cases} \dfrac{(\alpha-1)\left(\frac{\beta}{\lambda}\left(1+\frac{x}{\lambda}\right)^{-(\beta+1)}\right)}{\left(\alpha-(\alpha-1)\left(1-\left(1+\frac{x}{\lambda}\right)^{-\beta}\right)\right)\times\left(\log\alpha - \log\left(\alpha-(\alpha-1)\left(1-\left(1+\frac{x}{\lambda}\right)^{-\beta}\right)\right)\right)} & ;if\ \alpha > 0,\ \alpha \neq 1 \\ \dfrac{\frac{\beta}{\lambda}\left(1+\frac{x}{\lambda}\right)^{-(\beta+1)}}{\left(1-\left(1+\frac{x}{\lambda}\right)^{-\beta}\right)} & ;if\ \alpha = 1 \end{cases} \tag{8}$$

The survival rate function of the ALTLx distribution is given by

$$S_{ALTLx}(x;\alpha) = \begin{cases} \dfrac{log\left(\alpha-(\alpha-1)\left(1-\left(1+\frac{x}{\lambda}\right)^{-\beta}\right)\right)}{\log \alpha} & ;\ if\ \alpha > 0,\ \ \alpha \neq 1 \\ \left(1+\frac{x}{\lambda}\right)^{-\beta} & ;if\ \alpha = 1 \end{cases} \tag{9}$$

The graphical representation of the ALTLx distribution is as follows.

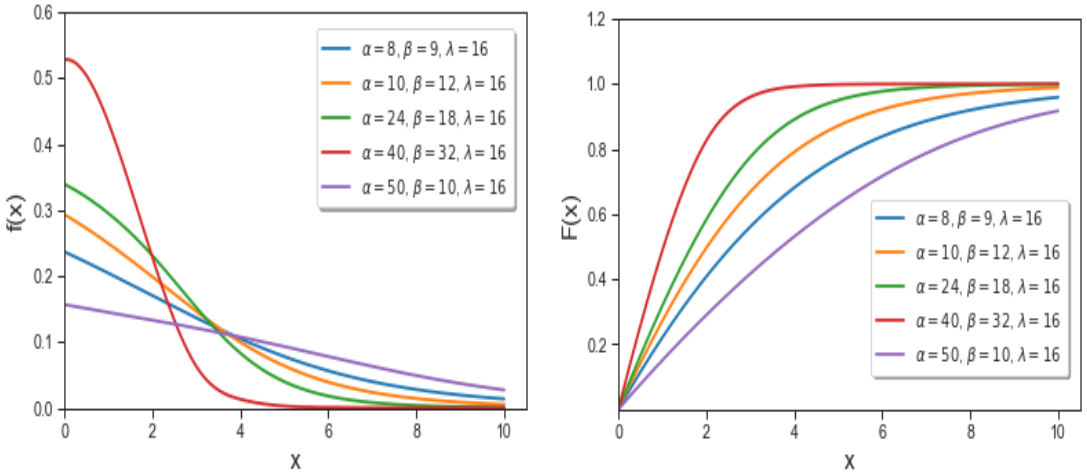


Figure 1: The pdf and cdf plot of the ALTLx distribution

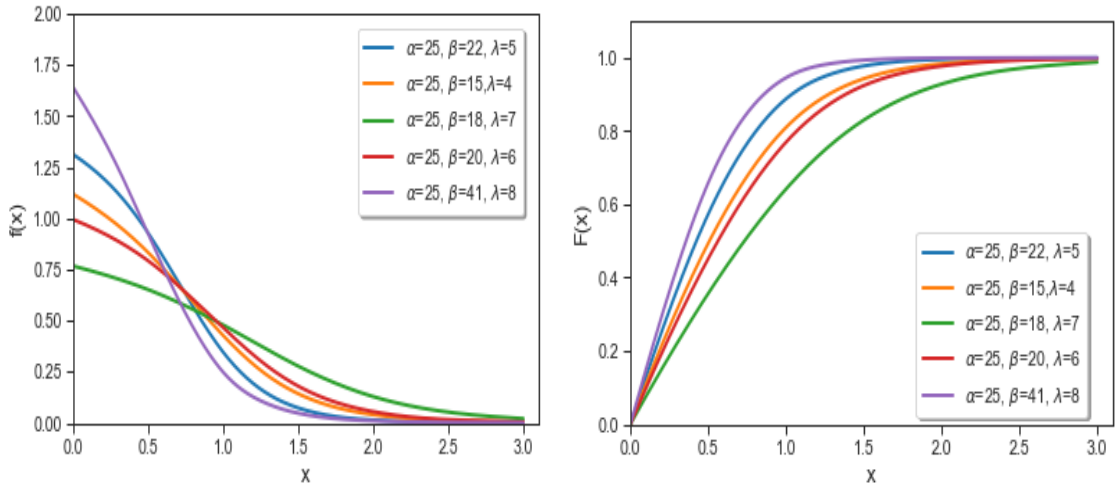


Figure 2: The pdf and cdf plot of the ALTLx distribution

Figures 1 and 2 present the pdf and cdf of the ALTLx distribution for a fixed value of λ. In Figure 1, we fix the value of the parameter $\lambda = 16$ and vary α and β, the pdf exhibits a decreasing or reversed *J*-shaped pattern, while the cdf is strictly increasing towards unity as x increases. It is observed that variations in the parameters α, and β influence the shapes of the pdf and the speed of convergence in the cdf. In Figure 2, we fix the parameter $\alpha = 25$ and vary the shape parameters λ, and β. The cdf curves demonstrate the expected monotonic increasing behavior, asymptotically approaching unity. Furthermore, changes in β and λ alter the steepness of the cdf, with higher values leading to faster convergence towards 1.

3. STATISTICAL PROPERTIES

In this section, the statistical properties of the APTLx distribution are derived for the case of $\alpha \neq 1$, since for the case of $\alpha = 1$ it is simply the properties of the Lomax distribution.

3.1. Quantile Function

The quantile function plays an important role when simulating random variates from a statistical distribution. The ALTLx distribution can be simulated by using equation (3).

$$X = \lambda\left[\frac{(\alpha^{(1-U)}-\alpha)}{(\alpha-1)}\right]^{-\frac{1}{\beta}} - \lambda \tag{10}$$

where U follows a uniform (0, 1) distribution.
The p^{th} quantile function of the ALTLx distribution is

$$x_p = Q(p) = \lambda\left[\frac{(\alpha^{(1-p)}-\alpha)}{(\alpha-1)}\right]^{-\frac{1}{\beta}} - \lambda \tag{11}$$

In particular, the first three quantiles Q_1, Q_2, Q_3 can be obtained by using $p = 0.25, p = 0.5,$ $p = 0.75$ in equation (4.9) respectively.

3.2. Moments and Moment Generating Function

The rth moment of the random variable X having ALTLx distribution is obtained as follows:

$$\mu_r^{'} = E(X^r) = \int_{-\infty}^{\infty} x^r f(x)dx$$

$$\mu_r' = \frac{\beta\lambda^r}{\log\alpha}\sum_{k=0}^{\infty}\sum_{j=0}^{k}\sum_{l=0}^{j}(-1)^l\binom{k}{j}\binom{j}{l}\frac{(\alpha-1)^{j+1}}{(\alpha+1)^{k+1}} \times B[r+1,\ \beta l+\beta-r] \tag{12}$$

The first moment and mean of the ALTLx distribution is

$$\mu_1' = \frac{\beta\lambda}{\log\alpha}\sum_{k=0}^{\infty}\sum_{j=0}^{k}\sum_{l=0}^{j}(-1)^l\binom{k}{j}\binom{j}{l}\frac{(\alpha-1)^{j+1}}{(\alpha+1)^{k+1}} \times B[2,\ \beta l+\beta-1] \tag{13}$$

The Moment generating function of ALTLx is

$$M_x(t) = E(e^{tx}) = \int_0^{\infty} e^{tx} f(x)dx$$

$$M_x(t) = \frac{\beta}{\log\alpha}\sum_{k=0}^{\infty}\sum_{i=0}^{\infty}\sum_{j=0}^{k}\sum_{l=0}^{j}(-1)^l\binom{k}{j}\binom{j}{l}\frac{\lambda^i t^i(\alpha-1)^{j+1}}{i!(\alpha+1)^{k+1}} \times B[i+1,\ \beta l+\beta-i] \tag{14}$$

The rth incomplete moment of X, denoted by $\varphi_r(t)$, is

$$\varphi_r(t) = \int_0^t x^r f(x)dx$$

$$\phi_r(t) = \frac{\beta\lambda^r}{\log\alpha}\sum_{k=0}^{\infty}\sum_{j=0}^{k}\sum_{l=0}^{j}(-1)^l\binom{k}{j}\binom{j}{l}\frac{(\alpha-1)^{j+1}}{(\alpha+1)^{k+1}} \times B_t[r+1, \beta l+\beta-r] \tag{15}$$

The first incomplete moment X, denoted by $\varphi_1(t)$, is

$$\phi_1(t) = \frac{\beta\lambda}{\log\alpha}\sum_{k=0}^{\infty}\sum_{j=0}^{k}\sum_{l=0}^{j}(-1)^l\binom{k}{j}\binom{j}{l}\frac{(\alpha-1)^{j+1}}{(\alpha+1)^{k+1}} \times B_t[2, \beta l+\beta-1] \tag{16}$$

3.3. Lorenz curve and Bonferroni curve

The Lorenz curves, say $LO(x)$, is defined as

$$LO(x) = \frac{\varphi_1(x)}{E(x)}$$

$$LO(x) = \left(\sum_{k=0}^{\infty}\sum_{j=0}^{k}\sum_{l=0}^{j}(-1)^l\binom{k}{j}\binom{j}{l}\frac{(\alpha-1)^{j+1}}{(\alpha+1)^{k+1}} \times B_t[2,\beta l+\beta-1]\right) \times \left(\sum_{k=0}^{\infty}\sum_{j=0}^{k}\sum_{l=0}^{j}(-1)^l\binom{k}{j}\binom{j}{l}\frac{(\alpha-1)^{j+1}}{(\alpha+1)^{k+1}} \times B[2,\beta l+\beta-1]\right)^{-1} \quad (17)$$

Bonferroni curve $BO(x)$ is defined as

$$BO(x) = \frac{LO(x)}{F_{ALTLx}(x)}$$

$$BO(x) = \frac{\left(\begin{array}{c}\sum_{k=0}^{\infty}\sum_{j=0}^{k}\sum_{l=0}^{j}(-1)^l\binom{k}{j}\binom{j}{l}\frac{(\alpha-1)^{j+1}}{(\alpha+1)^{k+1}}.B_t[2,\beta l+\beta-1]\times \\ \left(\sum_{k=0}^{\infty}\sum_{j=0}^{k}\sum_{l=0}^{j}(-1)^l\binom{k}{j}\binom{j}{l}\frac{(\alpha-1)^{j+1}}{(\alpha+1)^{k+1}}.B[2,\beta l+\beta-1]\right)^{-1}\end{array}\right)}{1-\frac{log\left(\alpha-(\alpha-1)\left(1-\left(1+\frac{x}{\lambda}\right)^{-\beta}\right)\right)}{\log\alpha}} \quad (18)$$

3.4. Mean Residual Life Time and Mean Inactivity Time

The mean residual lifetime of the ALTLx distribution is given by

$$m_x(t) = E(X-t/X>t),\ t>0$$

$$m_x(t) = \frac{\mu-\varphi_1(t)}{S(t)} - t \quad \text{where, } \mu = \mu_1'$$

$$m_x(t) = \frac{\mu-\left(\frac{\beta\lambda}{\log\alpha}\sum_{k=0}^{\infty}\sum_{j=0}^{k}\sum_{l=0}^{j}(-1)^l\binom{k}{j}\binom{j}{l}\times\left(\frac{(\alpha-1)^{j+1}}{(\alpha+1)^{k+1}}\right)\times B_t[2,\beta l+\beta-1]\right)}{\frac{log\left(\alpha-(\alpha-1)\left(1-\left(1+\frac{x}{\lambda}\right)^{-\beta}\right)\right)}{\log\alpha}} - t \quad (19)$$

The mean inactivity time is given by

$$\psi_x(t) = E(X-t/X<t)$$

$$\psi_x(t) = t - \frac{\varphi_1(t)}{F(t)}$$

$$\psi_x(t) = \ t - \frac{\left(\frac{\beta\lambda}{\log\alpha}\sum_{k=0}^{\infty}\sum_{j=0}^{k}\sum_{l=0}^{j}(-1)^l\binom{k}{j}\binom{j}{l}\times\left(\frac{(\alpha-1)^{j+1}}{(\alpha+1)^{k+1}}\right)\times B_t[2,\beta l+\beta-1]\right)}{1-\frac{log\left(\alpha-(\alpha-1)\left(1-\left(1+\frac{x}{\lambda}\right)^{-\beta}\right)\right)}{\log\alpha}} \quad (20)$$

3.5. Rényi entropy and δ- entropy

Entropy is a measure of randomness of systems and it is widely used in areas like physics, molecular imaging of tumors. The entropy of the random variable X measures the variation of uncertainty.

The Rényi entropy is defined as

$$RE_X(v) = \frac{1}{1-v}\log\left(\int_{-\infty}^{\infty} f(x)^v dx\right),\ v>0, v\neq 1$$

Rényi entropy of the ALTLx distribution is given below

$$RE_x(v) = \frac{1}{1-v}log\left\{\int_0^{\infty}\left(\frac{(\alpha-1)\left(\frac{\beta}{\lambda}\left(1+\frac{x}{\lambda}\right)^{-(\beta+1)}\right)}{\log\alpha\left(\alpha-(\alpha-1)\left(1-\left(1+\frac{x}{\lambda}\right)^{-\beta}\right)\right)}\right)^v dx\right\}$$

$$RE_x(v) = \frac{v}{1-v}\left(log\left(\frac{(\alpha-1)\beta}{\alpha\lambda.\log\alpha}\right)\right) + \frac{1}{1-v}\ log\left\{\begin{matrix}\left(\sum_{j=1}^{\infty}\sum_{k=0}^{\infty}(-1)^k\binom{j}{k}\binom{v+j-1}{j}\left[\frac{\alpha-1}{\alpha}\right]^j\right)\\ \times\left(\frac{\lambda}{\beta(k+v)+v-1}\right)\end{matrix}\right\} \quad (21)$$

The $\delta-$ entropy can be defined as

$$I_x(\delta) = \frac{1}{1-\delta}\ log\{1-\int_{-\infty}^{\infty} f(x)^{\delta}dx\},\ \delta > 0$$

The $\delta-$ entropy of the ALTLx distribution is given below

$$I_x(\delta) = \frac{1}{1-\delta}\ log\left\{1-\ \int_0^{\infty}\left(\frac{(\alpha-1)\left(\frac{\beta}{\lambda}\left(1+\frac{x}{\lambda}\right)^{-(\beta+1)}\right)}{\log\alpha\left(\alpha-(\alpha-1)\left(1-\left(1+\frac{x}{\lambda}\right)^{-\beta}\right)\right)}\right)^{\delta} dx\right\}$$

$$I_x(\delta) = \frac{1}{1-\delta}\ log\left\{1-\left(\frac{(\alpha-1)\beta}{\alpha.\log\alpha}\right)^{\delta}\times\sum_{j=1}^{\infty}\sum_{k=0}^{\infty}(-1)^k\binom{j}{k}\binom{\delta+j-1}{j}\left[\frac{\alpha-1}{\alpha}\right]^j\times\left(\frac{1}{\beta(k+\delta)+\delta-1}\right)\right\} \quad (22)$$

3.6. Stress strength reliability

The stress strength parameter, $S = P(X_1 < X_2)$, in the lifetime model, describes the lifetime component, which has a random stress X_1 that is subjected to a random strength X_2.

Let X_1 and X_2 be the two continuous and independent random variables, where $X_1 \sim ALTLx(\alpha_1, \beta_1, \lambda)$ and $X_2 \sim ALTLx(\alpha_2, \beta_2, \lambda)$ then the stress strength parameter, say S is defined as follows:

$$S = \int_{-\infty}^{\infty} f_1(x)F_2(x)dx$$

$$= \int_0^{\infty}\left(\frac{(\alpha_1-1)\left(\frac{\beta_1}{\lambda}\left(1+\frac{x}{\lambda}\right)^{-(\beta_1+1)}\right)}{\log\alpha_1\left[\alpha_1-(\alpha_1-1)\left(1-\left(1+\frac{x}{\lambda}\right)^{-\beta_1}\right)\right]}\right)\times\left(1-\frac{log\left[\alpha_2-(\alpha_2-1)\left(1-\left(1+\frac{x}{\lambda}\right)^{-\beta_2}\right)\right]}{\log\alpha_2}\right)dx$$

$$S = \frac{\beta_1}{\log\alpha_1\log\alpha_2}\sum_{k=0}^{\infty}\sum_{i=0}^{k}\sum_{n=1}^{\infty}\sum_{j=0}^{n}\binom{k}{i}\binom{n}{j}\frac{1}{n}\left[\frac{(\alpha_1-1)}{\alpha_1}\right]^{k+1}\left[\frac{(\alpha_2-1)}{\alpha_2}\right]^n\times\left(\frac{(-1)^{i+j}}{\beta_1+i\beta+j\beta_2}\right) \quad (23)$$

3.7. Order statistics

Let $X_1, X_2, \ldots, X_n$be a random sample of size n, and let $X_{k:n}$ denotes that kth order statistic, then the pdf of $X_{k:n}$ is given by

$$f_{k:n}(x) = \frac{n!}{(k-1)!(n-k)!}\ F(x)^{k-1}\ f(x)(1-F(x))^{n-k}$$

We can rewrite the above equation as follows:

$$f_{k:n}(x) = \frac{1}{B(k,n-k+1)}\ F(x)^{k-1}\ f(x)(1-F(x))^{n-k}$$

$$f_{k:n}(x) = \frac{1}{B(k,n-k+1)}\sum_{m=0}^{k-1}(-1)^m\binom{k-1}{m}\left(\frac{log\left(\alpha-(\alpha-1)\left(1-\left(1+\frac{x}{\lambda}\right)^{-\beta}\right)\right)}{\log\alpha}\right)^{m+n-k}\left(\frac{\beta(\alpha-1)\left(1+\frac{x}{\lambda}\right)^{-(\beta+1)}}{\lambda\log\alpha\left(\alpha-(\alpha-1)\left(1-\left(1+\frac{x}{\lambda}\right)^{-\beta}\right)\right)}\right) \quad (24)$$

4. MAXIMUM LIKELIHOOD ESTIMATION

Let $x_1, x_2, \dots, x_n$ be a random sample from the ALTLx distribution with unknown parameters (α, β, λ) then the likelihood function is given by

$$l = l(\alpha, \beta, \lambda) = \log\big(L(\alpha, \beta, \lambda)\big)$$

$$l = \log\left(\prod_{i=1}^{n}\left(\frac{(\alpha-1)\left(\frac{\beta}{\lambda}\left(1+\frac{x_i}{\lambda}\right)^{-(\beta+1)}\right)}{\log\alpha\left(\alpha-(\alpha-1)\left(1-\left(1+\frac{x_i}{\lambda}\right)^{-\beta}\right)\right)}\right)\right)$$

$$= n\log\left(\frac{(\alpha-1)\beta}{\lambda.\log\alpha}\right) - (\beta+1)\sum_{i=1}^{n}\log\left(1+\frac{x_i}{\lambda}\right) - \sum_{i=1}^{n} log\left(\alpha-(\alpha-1)\left(1-\left(1+\frac{x_i}{\lambda}\right)^{-\beta}\right)\right)$$

$$l = n\log(\alpha-1) + n\log\beta - n\log\lambda - n\log(\log\alpha) - (\beta+1)\sum_{i=1}^{n}\log\left(1+\frac{x_i}{\lambda}\right) - \sum_{i=1}^{n} log\left(\alpha-(\alpha-1)\left(1-\left(1+\frac{x_i}{\lambda}\right)^{-\beta}\right)\right) \quad (25)$$

$$\frac{\partial l}{\partial \alpha} = \frac{n}{\alpha-1} - \frac{n}{\alpha\log\alpha} + \sum_{i=1}^{n}\left(\frac{\left(1+\frac{x_i}{\lambda}\right)^{-\beta}}{\left(\alpha-(\alpha-1)\left(1-\left(1+\frac{x}{\lambda}\right)^{-\beta}\right)\right)}\right) = 0 \quad (26)$$

$$\frac{\partial l}{\partial \beta} = \frac{n}{\beta} - \sum_{i=1}^{n}\log\left(1+\frac{x_i}{\lambda}\right) - \sum_{i=1}^{n}\left(\frac{(\alpha-1)\left(1+\frac{x_i}{\lambda}\right)^{-\beta}\left(\log\left(1+\frac{x_i}{\lambda}\right)\right)}{\left(\alpha-(\alpha-1)\left(1-\left(1+\frac{x_i}{\lambda}\right)^{-\beta}\right)\right)}\right) = 0 \quad (27)$$

$$\frac{\partial l}{\partial \lambda} = \frac{n}{\lambda} - (\beta+1)\sum_{i=1}^{n}\left(\frac{x_i}{\lambda(\lambda+x_i)}\right) + \sum_{i=1}^{n}\frac{(\alpha-1)\left(\frac{\beta x_i}{\lambda^2}\left(1+\frac{x}{\lambda}\right)^{-(\beta+1)}\right)}{\left(\alpha-(\alpha-1)\left(1-\left(1+\frac{x}{\lambda}\right)^{-\beta}\right)\right)} = 0 \quad (28)$$

Then the Maximum likelihood estimations of the parameters α, λ, and β can be obtained by solving the system of Equations (26)–(28).

Fisher information I_{ij} matrix for ALTLx distribution given by

$$I = \begin{bmatrix} I_{11} & I_{12} & I_{13} \\ I_{21} & I_{22} & I_{23} \\ I_{31} & I_{32} & I_{33} \end{bmatrix}$$

$$I_{11} = E\left[-\frac{\partial^2\log L}{\partial\alpha^2}\right],\ I_{22} = E\left[-\frac{\partial^2\log L}{\partial\beta^2}\right],\ I_{33} = E\left[-\frac{\partial^2\log L}{\partial\lambda^2}\right]$$

$$I_{12} = I_{21} = E\left[-\frac{\partial^2\log L}{\partial\alpha\partial\beta}\right],\ I_{13} = I_{31} = E\left[-\frac{\partial^2\log L}{\partial\alpha\partial\lambda}\right],\ I_{23} = I_{32} = E\left[-\frac{\partial^2\log L}{\partial\beta\partial\lambda}\right]$$

$$\frac{\partial^2\log L}{\partial\alpha^2} = -\frac{n}{(\alpha-1)^2} + \frac{n(\log\alpha+1)}{\alpha^2(\log\alpha)^2} + \sum_{i=1}^{n}\left(\frac{\left(\left(1+\frac{x_i}{\lambda}\right)^{-2\beta}\right)}{\left(\alpha-(\alpha-1)\left(1-\left(1+\frac{x_i}{\lambda}\right)^{-\beta}\right)\right)}\right)$$

$$\frac{\partial^2 \log L}{\partial \beta^2} = -\frac{n}{\beta^2} - \sum_{i=1}^{n}\left(\frac{(\alpha-1)\left(1+\frac{x_i}{\lambda}\right)^{-\beta}\left(\log\left(1+\frac{x_i}{\lambda}\right)\right)^2}{\left(\alpha-(\alpha-1)\left(1-\left(1+\frac{x_i}{\lambda}\right)^{-\beta}\right)\right)^2}\right)$$

$$\frac{\partial^2 \log L}{\partial \lambda^2} = \frac{n}{\lambda^2} - (\beta+1)\sum_{i=1}^{n}\frac{x_i\left(\lambda(1+x_i)+(\lambda+x_i)\right)}{\left(\lambda(\lambda+x_i)\right)^2}$$
$$-\beta(\alpha-1)\sum_{i=1}^{n}\left\{\frac{\left(\frac{-(\beta+1)x_i}{\lambda^4}\left(1+\frac{x_i}{\lambda}\right)^{-(\beta+2)}+\frac{x_i}{\lambda^3}\left(1+\frac{x_i}{\lambda}\right)^{-(\beta+1)}\right)}{\left(1-(\alpha-1)\left(1+\frac{x_i}{\lambda}\right)^{-\beta}\right)}-\frac{\left(\frac{(\alpha-1)\beta x_i}{\lambda^4}\left(1+\frac{x_i}{\lambda}\right)^{-2(\beta+1)}\right)}{\left(1-(\alpha-1)\left(1+\frac{x_i}{\lambda}\right)^{-\beta}\right)^2}-\right\}$$

$$\frac{\partial^2 \log L}{\partial \alpha \partial \beta} = -\sum_{i=1}^{n}\left(\frac{\left(\left(1+\frac{x_i}{\lambda}\right)^{-\beta}\log\left(1+\frac{x_i}{\lambda}\right)\right)}{\left(1-(\alpha-1)\left(1+\frac{x_i}{\lambda}\right)^{-\beta}\right)^2}\right)$$

$$\frac{\partial^2 \log L}{\partial \alpha \partial \lambda} = -\sum_{i=1}^{n}\left(\frac{\left(\beta x_i\left(1+\frac{x_i}{\lambda}\right)^{-\beta}\right)}{\lambda^2\left(1-(\alpha-1)\left(1+\frac{x_i}{\lambda}\right)^{-\beta}\right)^2}\right)$$

$$\frac{\partial^2 \log L}{\partial \beta \partial \lambda} = \sum_{i=1}^{n}\left(\frac{x_i}{\lambda(\lambda+x_i)}\right)-\sum_{i=1}^{n}\frac{(\alpha-1)x_i}{\lambda^2}\left(1+\frac{x_i}{\lambda}\right)^{-\beta}$$
$$\times\left\{\frac{\left(1-(\alpha-1)\left(1+\frac{x_i}{\lambda}\right)^{-\beta}\right)\left(-\beta\log\left(1+\frac{x_i}{\lambda}\right)+1\right)+\left(\beta\left(1+\frac{x_i}{\lambda}\right)^{-(\beta+1)}\log\left(1+\frac{x_i}{\lambda}\right)\right)}{\left(1-(\alpha-1)\left(1+\frac{x_i}{\lambda}\right)^{-\beta}\right)^2}\right\}$$

So we obtain the asymptotic $100(1-\alpha)\%$ confidence intervals of the unknown parameters can be easily obtained for α, β and λ as given in equation below

$$\alpha \in \left[\hat{\alpha}-z_{\frac{\alpha}{2}}\sqrt{I_{11}^{-1}}, \hat{\alpha}+z_{\frac{\alpha}{2}}\sqrt{I_{11}^{-1}},\right]$$

$$\beta \in \left[\hat{\beta}-z_{\frac{\alpha}{2}}\sqrt{I_{22}^{-1}}, \hat{\beta}+z_{\frac{\alpha}{2}}\sqrt{I_{22}^{-1}},\right]$$

$$\lambda \in \left[\hat{\lambda}-z_{\frac{\alpha}{2}}\sqrt{I_{33}^{-1}}, \hat{\lambda}+z_{\frac{\alpha}{2}}\sqrt{I_{33}^{-1}},\right]$$

where $z_{\frac{\alpha}{2}}$ is the $\frac{\alpha}{2}$ quantile of the standard normal distribution.

5. MONTE CARLO SIMULATION

In this section, we perform a simulation study to assess the performance and examine the mean estimate, average bias (AB), root mean square error (RMSE) of the maximum likelihood estimators, coverage probability (CP), and average width (AW) of the confidence interval for each parameter. We study the performance of the ALTLx distribution by conducting various simulations for varying parameter values and different sample sizes. Quantile function is used to generate random data from the APTLx distribution. The simulation study is repeated for N = 1000 times each with sample size n = 25, 50, 75, 100, and parameter values Case *I:* $\alpha = 1.3, \beta = 0.2, \lambda = 0.7$, and Case *II:* $= 0.3, \beta = 1.5, \lambda = 1.2$.

Table 1: Monte Carlo Simulation Results.

Parameter	n	*Case I:* ($\alpha = 1.3, \beta = 0.2, \lambda = 0.7$)					*Case II:* ($\alpha = 0.3, \beta = 1.5, \lambda = 1.2$)				
		Mean	AB	RMSE	CP	AW	Mean	AB	RMSE	CP	AW
α	25	5.7653	4.4653	14.0604	0.753	73.7764	4.2369	3.9369	13.1231	0.96	81.6628
	50	4.6714	3.3714	12.7215	0.782	41.2183	3.6477	3.3477	17.6423	0.917	56.3358
	75	2.9959	1.6959	7.5258	0.773	19.7701	3.1569	2.8569	11.3905	0.936	41.7517
	100	2.1572	0.8572	5.9026	0.747	11.9081	2.2167	1.9167	6.7837	0.927	25.7067
β	25	0.2382	0.0382	0.1057	0.975	0.4663	2.8629	1.3629	3.7192	0.971	41.4855
	50	0.2317	0.0317	0.0884	0.971	0.3223	2.7093	1.2093	3.6262	0.984	25.9823
	75	0.2215	0.0215	0.0702	0.972	0.2495	2.5082	1.0082	2.2869	0.981	12.3680
	100	0.2118	0.0118	0.0578	0.945	0.2073	2.3548	0.8548	1.9702	0.986	8.7484
λ	25	2.0392	1.3392	4.1942	0.878	14.1571	6.3315	5.1315	12.7943	0.989	148.994
	50	1.3033	0.6033	2.1134	0.869	6.9117	6.9516	5.7516	13.0639	0.995	100.829
	75	1.1719	0.4719	1.9373	0.854	5.2348	6.3696	5.1696	10.3349	0.998	12.3680
	100	1.1389	0.4389	1.7137	0.890	4.5534	5.8881	4.6881	9.6312	0.999	44.1748

From the table, we observe that all the parametric values, the biases decrease when the sample size increases. Also, the coverage probabilities of the confidence intervals are quite close to the nominal level of 95% and the average confidence widths decrease as the sample size increases. Hence, the ML estimates of ALTLx distribution are consistent and efficient.

6. REAL LIFE APPLICATION

This section illustrates the ability of the proposed Alpha Logarithmic Transformation of the Lomax distribution by fitting this distribution to real data sets and comparing the results with other competitive distributions in the literature. The real data corresponds to the survival times (years) of 46 patients of a given chemotherapy treatment by Bekker et al. (2000) [7].

Table:2 Estimates, MLE, AIC, BIC, CAIC values

Distribution	Estimate	-log L	AIC	BIC	CAIC
ALTLx	$\alpha = 0.95559$ $\beta = 4809.6316$ $\lambda = 6570.7601$	58.2232	122.4464	127.8664	123.0318
ALTF	$\alpha = 1.085253\text{e}+04$ $\beta = 2.426293$ $\lambda = 8.841114\text{e}-02$	60.7218	127.4437	132.8637	128.0291
APTIL	$\alpha = 3.368942\text{e}-05$ $a = 1.219086$ $b = 7.218801$	58.8082	123.6166	129.0366	124.2019
Inverse Lomax	$\alpha = 3.03907$ $\beta = 0.20014$	61.9325	127.865	131.4783	128.1507

The model selection is carried out by using the maximum likelihood estimation, Akaike information criteria (AIC), the Bayesian information criteria (BIC), and the Consistent Akaike information criteria (CAIC). From Table 2, we conclude that the Alpha Logarithmic Transformation of Lomax (ALTLx) distribution is best when compared to Inverse Lomax (IL),

Alpha Power Transformation Inverse Lomax (APTIL), and Alpha Power Transformation of Fréchet distribution (ALTF). Table 3 presents the results of the goodness of fit tests, namely, Kolmogorov-Smirnov (D_n), Cramér von Mises (W_n^2), and Anderson and Darling (A_n^2) tests statistics, for the proposed ALTLx distribution as well as for competitive distributions.

Table 3: Goodness-of-fit tests

Distribution	Anderson-Darling		Cramer Von Mises		Kolmogorov-Smirnov	
	A_n^2	p-value	W_n^2	p-value	D_n	p-value
ALTLx	0.4346	0.813	0.05750	0.8322	0.090714	0.8204
ALTF	1.6628	0.1421	0.3033	0.1321	0.16329	0.1622
APTIL	0.52567	0.7198	0.07635	0.7156	0.09269	0.8003
IL	0.65493	0.5967	0.07241	0.7394	0.13687	0.3370

The ALTLx distribution shows an adequate fit for the given data. Among the considered distributions, the ALTLx model consistently yields the lowest values of all three test statistics. This indicates that the discrepancy between the empirical distribution of the observed survival times and the theoretical distribution under the ALTLx model is minimal compared to the alternative models. Furthermore, the relatively high p-values obtained for the Kolmogorov-Smirnov test provide additional statistical evidence in favor of the adequacy of the ALTLx distribution. These findings confirm that the proposed model captures the underlying structure of the data more effectively. Thus, ALTLx distribution demonstrates the reliability and flexibility for survival data analysis.

7. CONCLUSION

In this paper, we proposed a new three-parameter extension of the Lomax distribution called the ALTLx distribution based on Alpha Logarithmic Transformation. The main aim behind this study is to bring more flexibility to the classical Lomax distribution in modeling lifetime and survival data. Various mathematical properties of the proposed distribution are derived, such as moments, moment generating function, quantile function, and related measures. The parameters of the distribution are estimated through the method of maximum likelihood. The usefulness of the proposed model is illustrated by means of a real-life data set consisting of the survival times of patients undergoing chemotherapy treatment. The results reveal that the ALTLx distribution provides a significantly better fit compared to competing models. These findings highlight the potential of the proposed model for broader applications in survival analysis, reliability modeling, and related fields.

REFERENCES

[1] Abdul-Moniem, I. B. (2012). Recurrence relations for moments of lower generalized order statistics from exponentiated Lomax distribution and its characterization. *Journal of Mathematics and Computer Science.*, *2*(4): 999-1011.

[2] Al-Zahrani, B., and Sagor, H. (2014). The poisson-lomax distribution. *Revista Colombiana de Estadística*, *37*(1): 225-245.

[3] Al-Zahrani, B. (2015). An extended Poisson-Lomax distribution. *Advances in Mathematics: Scientific Journal*, 4(2): 79–89.

[4] Anwar, M., and Zahoor, J. (2018). The Half-Logistic Lomax Distribution for Lifetime Modeling. *Journal of probability and Statistics*, *2018*(1): 3152807.

[5] Arnold, B. C. (1983). *Pareto Distributions.* International Cooperative Publishing House, Maryland.

[6] Atkinson A, and Harrison A (1978) Distribution of personal wealth in Britain. *Cambridge University Press, Cambridge*.

[7] Bekker, A., Roux, J. J., and Mosteit, P. J. (2000). A generalization of the compound Rayleigh distribution: using a Bayesian method on cancer survival times. *Communications in Statistics-Theory and Methods*, *29*(7): 1419-1433.

[8] Bryson, M.C. (1974). Heavy-tailed distributions: properties and tests. *Technometrics*, *16*(1), 61-68.

[9] Cordeiro, G. M., Ortega, E. M., and Popović, B. V. (2015). The gamma-Lomax distribution. *Journal of Statistical computation and Simulation*, *85*(2): 305-319.

[10] Dey, S., Nassar, M., and Kumar, D. (2017). α logarithmic transformed family of distributions with application. *Annals of Data Science*, *4*(4): 457-482.

[11] Dey, S., Alzaatreh, A., Zhang, C., & Kumar, D. (2017). A new extension of generalized exponential distribution with application to ozone data. *Ozone: Science & Engineering*, *39*(4), 273-285.

[12] Dey, S., Nassar, M., Kumar, D., and Alaboud, F. (2019). Logarithm transformed Frechet distribution: Properties and estimation. *Austrian Journal of Statistics*, *48*(1): 70-93.

[13] El-Bassiouny, A. H., Abdo, N. F., and Shahen, H. S. (2015). Exponential lomax distribution. *International journal of computer applications*, *121*(13), 24-29.

[14] Ghitany, M. E., Al-Awadhi, F. A., and Alkhalfan, L. (2007). Marshall–Olkin extended Lomax distribution and its application to censored data. *Communications in Statistics—Theory and Methods*, *36*(10): 1855-1866.

[15] Harris, C. M. (1968). The Pareto distribution as a queue service discipline. *Operations Research*, *16*(2), 307-313.

[16] Hassan, A. S., and Al-Ghamdi, A. S. (2009). Optimum step stress accelerated life testing for Lomax distribution. *Journal of applied sciences research*, *5*(12): 2153-2164.

[17] Johnson, N.L., Kotz, S. and Balakrishnan, N. *Continuous Univariate Distributions,* Wiley, New York, 1994.

[18] Mahdavi, A., and Kundu, D. (2017). A new method for generating distributions with an application to exponential distribution. *Communications in Statistics-Theory and Methods*, *46*(13): 6543-6557.

[19] Malik A. S., and Ahmad, S. P. (2017). Alpha power Rayleigh distribution and its application to life time data. *International Journal of Enhanced Research in Management & Computer Applications*, *6*(11): 212-219.

[20] Maurya, S. K., Kaushik, A., Singh, R. K., Singh, S. K., and Singh, U. (2016). A new method of proposing distribution and its application to real data. *Imperial Journal of Interdisciplinary Research*, *2*(6): 1331-1338.

[21] Nassar, M., Alzaatreh, A., Mead, M., and Abo-Kasem, O. (2017). Alpha power Weibull distribution: Properties and applications. *Communications in Statistics-theory and Methods*, *46*(20): 10236-10252.

[22] Nasiru, S., Mwita, P. N., and Ngesa, O. (2019). Alpha Power Transformed Fréchet Distribution, *Applied Mathematics and information Sciences an International Journal*. 1: 129-141.

[23] Pappas, V., Adamidis, K., and Loukas, S. (2012). A family of lifetime distributions. *Journal of Quality and Reliability Engineering*, *2012*(1): 760687.

[24] Rady, E. H. A., Hassanein, W. A., and Elhaddad, T. A. (2016). The power Lomax distribution with an application to bladder cancer data. *SpringerPlus*, *5*(1): 1838.

[25] Tahir, M. H., Cordeiro, G. M., Mansoor, M., and Zubair, M. (2015). The Weibull-Lomax distribution: properties and applications. *Hacettepe Journal of Mathematics and Statistics*, *44*(2): 455-474.

[26] Ünal, C., Cakmakyapan, S., and Özel, G. (2018). Alpha power inverted exponential distribution: Properties and application. *Gazi University Journal of Science*, *31*(3): 954-965.

LINEAR PREDICTION OF K-RECORD VALUES FROM GENERALIZED PARETO DISTRIBUTION

Laji Muraleedharan[1] and Manoj Chacko[2]

•

1. Department of Statistics, Government Arts College, Thiruvananthapuram, Kerala, India
2. Department of Statistics, University of Kerala, Thiruvananthapuram, Kerala, India
[1] lajikmr@gmail.com, [2] manojchacko02@gmail.com

Abstract

In this paper, the upper k-record values arising from a generalized Pareto distribution is considered. After considering the means, variances and covariances of the upper k-record values, the best linear unbiased estimators and best lnear invariant estimators of the location and scale parameters of the generalized Pareto distribution is discussed under the assumption that the shape parameter is assumed to be known. The marginal best linear unbiased predictor and best linear invariant predictor of future upper k-record value and the joint best linear unbiased predictor and best linear invariant predictor of a pair of future upper k-record values are also determined. Finally, a real dataset is considered to illustrate the proposed inference procedures developed in this paper.

Keywords: Generalized Pareto distribution; best linear unbiased estimation; best linear invariant estimation; joint best linear unbiased prediction; joint best linear invariant prediction.

1. Introduction

Record values are observed in many situations of daily life as well as many statistical phinomena. These associated statistics are greater importance in live problems such as data related to meteorology, hydrology, athletic events and mining etc. The statistical study of record values started first time in the literature when [6] studied the stochastic behaviour of independent and identically distributed (iid) random variables having an absolutely continuous cumulative distribution function (cdf). So many researchers have adressed the statistical applications of record values in the literature pertain many live problems. Interested surveys are given by [3] and [9].

Let $\{X_i, i \geq 1\}$ be a sequence of iid continuous random variables with cdf $F(x)$ and probability density function (pdf) $f(x)$. An observation X_j is called an upper record value if $X_j > X_i$, for every $i < j$. Estimation of parameters based on record values and prediction of future record values have been extensively studied by several authors. For more detailed discussion on these area, see, [14], [19] and [18].

One of the challenges in dealing with problems involving inference with record data is that the expected waiting time for every records after the first is infinite. Such an issue does not arise if we use the *k*-records proposed by [7]. We use the following formal definition of k-record values given by [3].

For a fixed positive integer k, the upper k-record times $\tau_{n(k)}$ and the upper k-record values $R_{n(k)}$ are defined as follows: .

Define $\tau_{1(k)} = k$ and $R_{1(k)} = X_{1:k}$, where $X_{i:m}$ denotes the ith order statistic in a sample of size m. Then for $n > 1$,

$$\tau_{n(k)} = min\left\{i : i > \tau_{n-1(k)},\ X_i > X_{\tau_{n-1(k)}-k+1:\tau_{n-1(k)}}\right\}.$$

Then the sequence of upper k-record values $\left\{R_{n(k)}, n \geq 1\right\}$ is defined as

$$R_{n(k)} = X_{\tau_{n(k)}-k+1:\tau_{n(k)}}.$$

In an analogous way, one can define the lower k-record values. The ordinary record values are contained in the k-records as a special case when $k = 1$.
The pdf of nth upper k-record value $R_{n(k)}$ is given by (see, [3])

$$f_{n(k)}(x) = \frac{k^n}{\Gamma(n)}\left\{-\log\left[1 - F(x)\right]\right\}^{n-1}\left[1 - F(x)\right]^{k-1} f(x),\ \ -\infty < x < \infty, \tag{1}$$

where $\Gamma(.)$ denotes the complete gamma function. The joint pdf of mth and nth upper k-record values, $R_{m(k)}$ and $R_{n(k)}$, for $m < n$, is given by

$$\begin{aligned} f_{m,n(k)}(x,y) &= \frac{k^n}{\Gamma(m)\Gamma(n-m)}\left\{-\log\left[1 - F(x)\right]\right\}^{m-1}\left\{-\log\left[1 - F(y)\right] + \log\left[1 - F(x)\right]\right\}^{n-m-1} \\ &\quad \times \frac{\left[1 - F(y)\right]^{k-1}}{1 - F(x)} f(x) f(y),\ -\infty < x < y < \infty. \end{aligned} \tag{2}$$

Recently, k-record data has shown a significant role in statistical inference and future event prediction. [1] considered the problem of prediction of order statistics based on observed k-record data when the records are arising from an exponential distribution. [21] considered the same problem for single parameter generalized exponential distribution. [16] discussed the prediction problem for a Pareto distribution when the future sample size is both fixed and random.

In statistical inference, predicting future events based on the current knowledge is a fundamental problem. Many researchers have been expressed this sort of problem in different approaches. [17] studied the estimation and prediction problem of lognormal distribution based on record values. [13] discussed the problem of investigating the BLUP and best linear invariant predictor (BLIP) of future lower k-record values based on the observed lower k-record values arising from Unit-Gompertz distribution. [10] considered the same problem for an xgamma distribution based on the observed upper k-record values. In this paper, we consider the linear prediction of upper k-record value based on the observed upper k-record values arising from a generalized Pareto (GP) distribution with pdf given by

$$f(x) = \frac{1}{\sigma}\left[1 + \psi\left(\frac{x-\mu}{\sigma}\right)\right]^{-\left(\frac{1}{\psi}+1\right)}, \tag{3}$$

where $\mu, \psi \in R$ and $\sigma > 0$. Here ψ is a shape parameter, σ is a scale parameter and μ is a location parameter. The GP distribution with pdf given in (3) will be denoted by GP(μ, σ, ψ). The cdf corresponding to the pdf (3) is given by

$$F(x) = 1 - \left[1 + \psi\left(\frac{x-\mu}{\sigma}\right)\right]^{-\frac{1}{\psi}}. \tag{4}$$

When $\psi = 0$, the GPD reduces the exponential distribution. When $\psi > 0$, the distribution has the support $\mu \leq x < \infty$ while for $\psi < 0$, $\mu \leq x \leq \mu - \frac{\sigma}{\psi}$. The distribution has heavy tailed when $\psi > 0$ and the distribution is short tailed if $\psi < 0$.

The GP distribution was introduced by Pickands in 1975. Some of its major applications include analysis of extreme events in the modeling of insurance claims and to describe the annual maximum flood at river gauging station. Many extensive works were done about the inference of the parameters of GP distribution based on upper record values. [20] derived the explicit expressions for the single, double, triple and quadruple moments of the upper record values from

GP distribution. [2] introduced minimum variance linear unbiased estimator and the best linear invariant estimator (BLIE) for the location and scale parameters of GP distribution when the shape parameter is known based on upper record values. [12] discussed the best linear unbiased predictor (BLUP) for future upper k-record values for a generalized Pareto distribution when the shape parameter is assumed to be known. More recently, [22] investigate the point estimation and confidence interval estimation for the heavy-tailed generalized Pareto distribution based on the upper record values.

Recently, [4] and [5] discussed the problem of simultanious prediction of two order statistics from a future sample and established the gain in efficiency of joint prediction over marginal prediction. When working with location- scale family of distributions, the joint prediction of future ordered observations provides more accurate, robust and insightful prediction than marginal prediction especially in the context of observed ordered observations are correlated or interdependent. This gives better understanding risks, optimizing resource allocation, improving prediction accuracy and making more informed strategic decisions. This provides a motivation for considering joint prediction of future k-record values.

The rest of the paper is organized as follows. In Section 2, we provide the linear estimators, which includes BLUEs and BLIEs for the location and scale parameters of GP distribution based on observed upper k-record values. In Section 3, we consider the BLUP and BLIP of future upper k-record values which incldes marginal predictor of future upper k-record values and the joint predictor of pair of future upper k-record values. The estimated mean square predictive error (MSPE) and the relative efficiencies for BLUP and BLIP are also discussed. In Section 4, a real dataset is considered to illustrate the inference procedures developed in this paper and finally some concluding remarks are made in Section 5.

2. Linear Estmation of Parameters

Let $\{Z_i, i \geq 1\}$ be a sequence of iid observations taken from GP$(0, 1, \psi)$ with pdf and cdf defined in (3) and (4) respectively. Let $Z_{1(k)}, Z_{2(k)}, \ldots, Z_{n(k)}$ be the first n upper k-record values extracted from the sequence $\{Z_i, i \geq 1\}$. Then by using (1), the pdf of the nth upper k-record $Z_{n(k)}$ is obtained as

$$g_{n(k)}(x) = \frac{k^n}{\Gamma(n)\psi^{n-1}} \left[\log(1+\psi x)\right]^{n-1} (1+\psi x)^{-\left(\frac{k}{\psi}+1\right)}, \; x > 0, \psi > 0. \tag{5}$$

By using (2), the joint pdf of nth and mth upper k-records $Z_{n(k)}$ and $Z_{m(k)}$ for $m < n$ is given by

$$\begin{aligned} g_{m,n(k)}(x,y) &= \frac{k^n}{\Gamma(m)\Gamma(n-m)\psi^{n-2}} \left[\log(1+\psi x)\right]^{m-1} \\ &\times \left[\log(1+\psi y) - \log(1+\psi x)\right]^{n-m-1} \frac{(1+\psi y)^{-\left(\frac{k}{\psi}+1\right)}}{(1+\psi x)}, \; 0 \leq x < y < \infty. \end{aligned} \tag{6}$$

Since (5) is the pdf of nth upper k-records arising from GP$(0, 1, \psi)$, if we denote $E\left(Z_{n(k)}\right)$, $Var\left(Z_{n(k)}\right)$ and $Cov\left(Z_{m(k)}, Z_{n(k)}\right)$ respectively by $\alpha_{n(k)}$, $\omega_{nn(k)}$ and $\omega_{mn(k)}$ then by [12], the explicit expressions for the means, variances and the product moments of the upper k-record values are given by the following.

$$\alpha_{n(k)} = \frac{1}{\psi}\left[\left(\frac{k}{k-\psi}\right)^n - 1\right], \text{ provided } k > \psi \tag{7}$$

$$\omega_{nn(k)} = \frac{1}{\psi^2}\left[\left(\frac{k}{k-2\psi}\right)^n - \left(\frac{k}{k-\psi}\right)^{2n}\right] \tag{8}$$

$$\omega_{mn(k)} = \frac{1}{\psi^2}\left[\frac{k^n}{(k-\psi)^{n-m}(k-2\psi)^m} - \left(\frac{k}{k-\psi}\right)^{m+n}\right], \tag{9}$$

where (8) and (9) are provided $k > 2\psi$. We have evaluated the values of means $\alpha_{n(k)}$ for $n = 1(1)9$; $\psi = 0.1, 0.2$ and $k = 2, 3$ and the values are presented in Table 1. We have computed

Table 1: *Means of upper k- record values arising from $GP(0, 1, \psi)$*

k	ψ	n								
		1	2	3	4	5	6	7	8	9
2	0.1	0.52632	1.08033	1.66351	2.27738	2.92355	3.60374	4.31973	5.07340	5.86673
	0.2	0.55556	1.17284	1.85871	2.62079	3.46754	4.40838	5.45375	6.61528	7.90587
3	0.1	0.34483	0.70155	1.07056	1.45231	1.84722	2.25574	2.67835	3.11553	3.56779
	0.2	0.35714	0.73980	1.14978	1.58905	2.05970	2.56396	3.10424	3.68312	4.30334

the values of $\omega_{nn(k)}$ and $\omega_{mn(k)}$ for $1 \leq m \leq n \leq 9$; $\psi = 0.1, 0.2$ and $k = 2, 3$ and the values are given in Table 2 and Table 3 respectively.

Table 2: *Variances and Covariances of upper k- record values from $GP(0, 1, \psi)$ for $\psi = 0.1$*

k	n	m								
		1	2	3	4	5	6	7	8	9
2	1	0.30779								
	2	0.32399	0.68302							
	3	0.34104	0.71897	1.13680						
	4	0.35899	0.75681	1.19663	1.68181					
	5	0.37788	0.79665	1.25961	1.77033	2.33262				
	6	0.39777	0.83857	1.32591	1.86351	2.45539	3.10586			
	7	0.41871	0.88271	1.39568	1.96158	2.58462	3.26932	4.02055		
	8	0.44074	0.92916	1.46914	2.06482	2.72065	3.44139	4.23216	5.09841	
	9	0.46393	0.97807	1.54646	2.17351	2.86384	3.62252	4.45491	5.36675	6.36421
3	1	0.12740								
	2	0.13179	0.27284							
	3	0.13634	0.28224	0.43823						
	4	0.14104	0.29198	0.45334	0.62567					
	5	0.14590	0.30205	0.46897	0.64724	0.83745				
	6	0.15093	0.31246	0.48514	0.66956	0.86632	1.07608			
	7	0.15613	0.32323	0.50187	0.69265	0.89619	1.11318	1.34429		
	8	0.16152	0.33438	0.51917	0.71653	0.92711	1.15156	1.39065	1.64511	
	9	0.16709	0.34591	0.53707	0.74123	0.95907	1.19127	1.43861	1.70183	1.98175

Let $R_{1(k)}, R_{2(k)}, \ldots, R_{n(k)}$ be the first n lower k-record values arising from GP(μ, σ, ψ) with pdf given in (3). Suppose $\mathbf{R}_{n(k)} = \left(R_{1(k)}, R_{2(k)}, \ldots, R_{n(k)}\right)'$ denotes the vector of n upper k-record values, Then by Aitken's generalized least-square approach, the BLUEs of μ and σ, denoted by μ^* and σ^* are respectively obtained as given below.

$$\begin{aligned} \mu^* &= \frac{\boldsymbol{\alpha}'\boldsymbol{\Omega}^{-1}\boldsymbol{\alpha}\mathbf{1}'\boldsymbol{\Omega}^{-1} - \boldsymbol{\alpha}'\boldsymbol{\Omega}^{-1}\mathbf{1}\boldsymbol{\alpha}'\boldsymbol{\Omega}^{-1}}{(\boldsymbol{\alpha}'\boldsymbol{\Omega}^{-1}\boldsymbol{\alpha})(\mathbf{1}'\boldsymbol{\Omega}^{-1}\mathbf{1}) - (\boldsymbol{\alpha}'\boldsymbol{\Omega}^{-1}\mathbf{1})^2}\mathbf{R}_{n(k)} \\ &= \sum_{i=1}^{n} a_i R_{i(k)} \end{aligned} \tag{10}$$

and

$$\begin{aligned} \sigma^* &= \frac{\mathbf{1}'\boldsymbol{\Omega}^{-1}\mathbf{1}\boldsymbol{\alpha}'\boldsymbol{\Omega}^{-1} - \mathbf{1}'\boldsymbol{\Omega}^{-1}\boldsymbol{\alpha}\mathbf{1}'\boldsymbol{\Omega}^{-1}}{(\boldsymbol{\alpha}'\boldsymbol{\Omega}^{-1}\boldsymbol{\alpha})(\mathbf{1}'\boldsymbol{\Omega}^{-1}\mathbf{1}) - (\boldsymbol{\alpha}'\boldsymbol{\Omega}^{-1}\mathbf{1})^2}\mathbf{R}_{n(k)} \\ &= \sum_{i=1}^{n} b_i R_{i(k)} \ , \end{aligned} \tag{11}$$

where $\boldsymbol{\alpha} = \left(\alpha_{1(k)}, \alpha_{2(k)}, ..., \alpha_{n(k)}\right)'$, $\mathbf{1}$ be a column vector of n ones and $\boldsymbol{\Omega} = \left(\omega_{ij(k)}\right)$ is the $n \times n$ dispersion matrix of $\mathbf{Z}_{n(k)} = \left(Z_{1(k)}, Z_{2(k)}, ..., Z_{n(k)}\right)'$. Furthermore, the variances and covariance

Table 3: *Variances and Covariances of upper k- record values from $GP(0,1,\psi)$ for $\psi = 0.2$*

k	n	m								
		1	2	3	4	5	6	7	8	9
	1	0.38580								
	2	0.42867	0.95855							
	3	0.47630	1.06506	1.78621						
	4	0.52922	1.18340	1.98468	2.95872					
2	5	0.58802	1.31489	2.20520	3.28747	4.59465				
	6	0.65336	1.46098	2.45022	3.65274	5.10516	6.84977			
	7	0.72595	1.62331	2.72247	4.05861	5.6724	7.61086	9.92823		
	8	0.80661	1.80368	3.02497	4.50956	6.30266	8.45651	11.03137	14.09673	
	9	0.89624	2.00409	3.36107	5.01062	7.00296	9.39612	12.25708	15.66303	19.7029
	1	0.14717								
	2	0.15769	0.33877							
	3	0.16895	0.36296	0.58483						
	4	0.18102	0.38889	0.62661	0.89745					
3	5	0.19395	0.41667	0.67136	0.96155	1.29111				
	6	0.20781	0.44643	0.71932	1.03023	1.38333	1.78314			
	7	0.22264	0.47831	0.77069	1.10382	1.48213	1.91051	2.39428		
	8	0.23854	0.51248	0.82575	1.18266	1.58800	2.04697	2.56530	3.14928	
	9	0.25558	0.54908	0.88472	1.26714	1.70143	2.19318	2.74854	3.37423	4.07764

of the above estimators are given by

$$Var(\mu^*) = \sigma^2 \left(\frac{\boldsymbol{\alpha}'\boldsymbol{\Omega}^{-1}\boldsymbol{\alpha}}{(\boldsymbol{\alpha}'\boldsymbol{\Omega}^{-1}\boldsymbol{\alpha})(\mathbf{1}'\boldsymbol{\Omega}^{-1}\mathbf{1}) - (\boldsymbol{\alpha}'\boldsymbol{\Omega}^{-1}\mathbf{1})^2} \right), \tag{12}$$

$$Var(\sigma^*) = \sigma^2 \left(\frac{\mathbf{1}'\boldsymbol{\Omega}^{-1}\mathbf{1}}{(\boldsymbol{\alpha}'\boldsymbol{\Omega}^{-1}\boldsymbol{\alpha})(\mathbf{1}'\boldsymbol{\Omega}^{-1}\mathbf{1}) - (\boldsymbol{\alpha}'\boldsymbol{\Omega}^{-1}\mathbf{1})^2} \right) \tag{13}$$

and

$$Cov(\mu^*, \sigma^*) = \sigma^2 \left(\frac{-\boldsymbol{\alpha}'\boldsymbol{\Omega}^{-1}\mathbf{1}}{(\boldsymbol{\alpha}'\boldsymbol{\Omega}^{-1}\boldsymbol{\alpha})(\mathbf{1}'\boldsymbol{\Omega}^{-1}\mathbf{1}) - (\boldsymbol{\alpha}'\boldsymbol{\Omega}^{-1}\mathbf{1})^2} \right). \tag{14}$$

By making use of Table 1, Table 2 and Table 3, we have evaluated the coefficients a_i and b_i, $i = 1, 2, \ldots, n$ of BLUEs of μ and σ for $n = 2(1)9$; $\psi = 0.1, 0.2$ and $k = 2, 3$ and the values are given in Table 4 to Table 7 respectively. If we denote

$$\nu_1^* = \frac{Var(\mu^*)}{\sigma^2} \tag{15}$$

$$\nu_2^* = \frac{Var(\sigma^*)}{\sigma^2} \tag{16}$$

and

$$\nu_3^* = \frac{Cov(\mu^*, \sigma^*)}{\sigma^2} \tag{17}$$

then the values of ν_1^*, ν_2^* and ν_3^* are evaluated for $n = 2(1)9$; $\psi = 0.1, 0.2, 0.3$ and $k = 2, 3$ are also computed from equations (12) to (14) and are given in Table 8.

Next, we focus on the BLIEs of the location and scale parameters of $GP(\mu, \sigma, \psi)$, denoted respectively by μ^{**} and σ^{**} when the shape parameter ψ is known. Based on the results of [11] and [3], the BLIEs of μ and σ are given by

$$\mu^{**} = \mu^* - \frac{\nu_3^*}{1 + \nu_2^*}\sigma^* \tag{18}$$

and

$$\sigma^{**} = \frac{\sigma^*}{1 + \nu_2^*}. \tag{19}$$

The variances of (18) and (19) are given by (see, [3])

$$Var\left(\mu^{**}\right)=\sigma^{2}\left(\nu_{1}^{*}-\frac{\nu_{3}^{*2}\left(2+\nu_{2}^{*}\right)}{\left(1+\nu_{2}^{*}\right)^{2}}\right) \tag{20}$$

and

$$Var\left(\sigma^{**}\right)=\frac{\sigma^{2}\nu_{2}^{*}}{\left(1+\nu_{2}^{*}\right)^{2}}, \tag{21}$$

where ν_1^*, ν_2^* and ν_3^* are defined in (15),(16) and (17) respectively.

Table 4: *Coefficients for the BLUE of μ for $\psi = 0.1$*

k	n	a_1	a_2	a_3	a_4	a_5	a_6	a_7	a_8	a_9
2	2	1.95000	-0.95000							
	3	1.47632	-0.02632	-0.45000						
	4	1.33900	-0.01845	-0.01661	-0.28395					
	5	1.24078	-0.01454	-0.01309	-0.01178	-0.20138				
	6	1.19420	-0.01222	-0.01097	-0.00990	-0.00888	-0.15221			
	7	1.16342	-0.01067	-0.00960	-0.00866	-0.00776	-0.00699	-0.11973		
	8	1.14168	-0.00959	-0.00862	-0.00778	-0.00697	-0.00628	-0.00568	-0.09676	
	9	1.12558	-0.00878	-0.00789	-0.00712	-0.00638	-0.00575	-0.00521	-0.00466	-0.07977
3	2	1.96667	-0.96667							
	3	1.48391	-0.01724	-0.46667						
	4	1.32324	-0.01188	-0.01109	-0.30026					
	5	1.24310	-0.00921	-0.00860	-0.00803	-0.21726				
	6	1.19514	-0.00754	-0.00716	-0.00664	-0.00619	-0.16760			
	7	1.16332	-0.00640	-0.00616	-0.00571	-0.00533	-0.00498	-0.13463		
	8	1.14069	-0.00573	-0.00547	-0.00507	-0.00468	-0.00444	-0.00405	-0.11124	
	9	1.12381	-0.00516	-0.00494	-0.00458	-0.00423	-0.00400	-0.00364	-0.00349	-0.09374

Table 5: *Coefficients for the BLUE of μ for $\psi = 0.2$*

k	n	a_1	a_2	a_3	a_4	a_5	a_6	a_7	a_8	a_9
2	2	1.90000	-0.90000							
	3	1.45556	-0.05556	-0.40000						
	4	1.32984	-0.04098	-0.03279	-0.23607					
	5	1.23875	-0.03388	-0.02710	-0.02168	-0.15610				
	6	1.19748	-0.02975	-0.0238	-0.01904	-0.01522	-0.10966			
	7	1.17106	-0.02711	-0.02168	-0.01735	-0.01387	-0.01111	-0.07993		
	8	1.15308	-0.02531	-0.02025	-0.0162	-0.01295	-0.01038	-0.00829	-0.05971	
	9	1.14033	-0.02404	-0.01923	-0.01538	-0.01229	-0.00985	-0.00787	-0.00629	-0.04536
3	2	1.93333	-0.93333							
	3	1.46905	-0.03571	-0.43333						
	4	1.31534	-0.02547	-0.02207	-0.26780					
	5	1.23115	-0.03321	-0.02447	-0.02168	-0.15218				
	6	1.19428	-0.01748	-0.01503	-0.01308	-0.01129	-0.13739			
	7	1.16477	-0.01551	-0.01333	-0.01159	-0.01002	-0.00877	-0.10554		
	8	1.14410	-0.01412	-0.01213	-0.01056	-0.00912	-0.00799	-0.00683	-0.08333	
	9	1.12897	-0.01311	-0.01126	-0.00980	-0.00846	-0.00742	-0.00634	-0.00551	-0.06704

Table 6: *Coefficients for the BLUE of σ for $\psi = 0.1$*

k	n	b_1	b_2	b_3	b_4	b_5	b_6	b_7	b_8	b_9
2	2	-1.80500	1.80500							
	3	-0.90500	0.05000	0.85500						
	4	-0.60611	0.03505	0.03155	0.53950					
	5	-0.45749	0.02762	0.02486	0.02238	0.38262				
	6	-0.36897	0.02320	0.02087	0.01879	0.01690	0.28919			
	7	-0.31049	0.02026	0.01825	0.01643	0.01476	0.01331	0.22747		
	8	-0.26919	0.01821	0.01638	0.01475	0.01326	0.01194	0.01075	0.18386	
	9	-0.23861	0.01667	0.01502	0.01351	0.01216	0.01094	0.00985	0.00886	0.15158
3	2	-2.80333	2.80333							
	3	-1.40333	0.05000	1.35333						
	4	-0.93741	0.03447	0.03217	0.87077					
	5	-0.70500	0.02672	0.02494	0.02328	0.63006				
	6	-0.56597	0.02206	0.02063	0.01923	0.01799	0.48606			
	7	-0.47367	0.01900	0.01774	0.01653	0.01549	0.01441	0.39048		
	8	-0.40806	0.01680	0.01572	0.01467	0.01363	0.01281	0.01190	0.32251	
	9	-0.35911	0.01516	0.01419	0.01325	0.01232	0.01156	0.01072	0.01003	0.27184

Table 7: *Coefficients for the BLUE of σ for $\psi = 0.2$*

k	n	b_1	b_2	b_3	b_4	b_5	b_6	b_7	b_8	b_9
2	2	-1.62000	1.62000							
	3	-0.82000	0.10000	0.72000						
	4	-0.55770	0.07377	0.05902	0.42492					
	5	-0.42976	0.06098	0.04878	0.03902	0.28098				
	6	-0.35546	0.05355	0.04283	0.03427	0.02741	0.19739			
	7	-0.30790	0.04879	0.03903	0.03122	0.02497	0.01999	0.14388		
	8	-0.27553	0.04555	0.03644	0.02915	0.02332	0.01866	0.01492	0.10747	
	9	-0.25257	0.04325	0.03461	0.02769	0.02214	0.01772	0.01417	0.01134	0.08165
3	2	-2.61333	2.61333							
	3	-1.31333	0.10000	1.21333						
	4	-0.88294	0.07131	0.06180	0.74984					
	5	-0.66993	0.05711	0.04949	0.04289	0.52044				
	6	-0.54389	0.04878	0.04216	0.03661	0.03168	0.38465			
	7	-0.46124	0.04325	0.03742	0.03243	0.02812	0.02437	0.29564		
	8	-0.40337	0.03938	0.03405	0.02956	0.02559	0.02221	0.01922	0.23335	
	9	-0.36100	0.03655	0.03162	0.02742	0.02376	0.02062	0.01783	0.01546	0.18771

Table 8: *Variances and Covariances of the BLUEs of μ and σ in terms of σ^2*

k	n	ψ=0.1			ψ=0.2			ψ=0.3		
		ν_1^*	ν_2^*	ν_3^*	ν_1^*	ν_2^*	ν_3^*	ν_1^*	ν_2^*	ν_3^*
2	2	0.58642	1.11698	-0.55864	0.70313	1.27813	-0.64063	0.98142	2.14117	-0.99586
	3	0.44022	0.58920	-0.28086	0.52951	0.71562	-0.32813	0.84022	0.95892	-0.58086
	4	0.39167	0.41392	-0.18861	0.47259	0.53120	-0.22567	0.79167	0.74139	-0.31886
	5	0.36753	0.32677	-0.14274	0.44483	0.44123	-0.17569	0.67525	0.62677	-0.19274
	6	0.35315	0.27485	-0.11542	0.42871	0.38899	-0.14666	0.54142	0.56468	-0.20612
	7	0.34365	0.24056	-0.09737	0.41838	0.35555	-0.12808	0.53062	0.53347	-0.18776
	8	0.33694	0.21634	-0.08462	0.41135	0.33279	-0.11544	0.52394	0.51419	-0.17642
	9	0.33197	0.19841	-0.07519	0.40637	0.31665	-0.10647	0.51957	0.50155	-0.16898
3	2	0.24660	1.07390	-0.35799	0.27613	1.16489	-0.38856	0.31466	1.27390	-0.45180
	3	0.18502	0.55604	-0.17942	0.20745	0.62643	-0.19625	0.28502	0.75604	-0.27892
	4	0.16453	0.38369	-0.11999	0.18471	0.44816	-0.13259	0.21645	0.50369	-0.19992
	5	0.15431	0.29772	-0.09035	0.17346	0.35993	-0.10107	0.19603	0.42977	-0.15035
	6	0.14819	0.24631	-0.07262	0.16678	0.30770	-0.08241	0.19054	0.38899	-0.09778
	7	0.14413	0.14413	-0.06084	0.16242	0.27347	-0.07019	0.18595	0.35555	-0.08539
	8	0.14124	0.18789	-0.05247	0.15937	0.24951	-0.06163	0.18282	0.33279	-0.07696
	9	0.13909	0.16978	-0.04623	0.15713	0.23196	-0.05536	0.18061	0.31665	-0.07098

3. Prediction of future k-record values

Prediction of future events on the basis of the past and present knowledge is a fundamental problem of Statistics, arising in many contexts and producing varied solutions. Prediction of future records becomes a problem of great interest. For example, while studying the minimum temperature, having observed the record values until the present time, we will be naturally interested in predicting the minimum temperature that is to be expected when the present record is broken for the first time in future. In this section, we consider prediction for future upper k-record value from generalized Pareto distribution based on past observed upper k-records.

3.1. Marginal Prediction of future k-record values

Suppose that the vector of upper k-record values $\mathbf{R_{n(k)}} = (R_{1(k)}, R_{2(k)}, \ldots, R_{n(k)})'$ have been observed from the generalized Pareto distribution. The problem of interest then is to predict the value of the next upper k-record $R_{n+1(k)}$ or, more generally, the value of the sth upper k-record value $R_{s(k)}, s > n$. For a location-scale family with location parameter μ and scale parameter σ, the BLUP of the sth upper k- record value, $R_{s(k)}$ is given by (see, [3])

$$R^*_{s(k)} = (\mu^* + \alpha_{s(k)}\sigma^*) + \boldsymbol{\omega}'_{\mathbf{s(k)}}\boldsymbol{\Omega}^{-1}\left(\mathbf{R}_{n(k)} - \mu^*\mathbf{1} - \sigma^*\boldsymbol{\alpha}\right), \tag{22}$$

where μ^* and σ^* are the BLUEs of μ and σ based on the first n upper k-record values and $\alpha_{s(k)}$ is the of mean of sth upper k-record value from the standard GP distribution, $\boldsymbol{\Omega}$ is the variance-covariance matrix of first n upper k-records and $\boldsymbol{\omega}'_{\mathbf{s(k)}} = \left(\omega_{1s(k)}, \ldots, \omega_{ns(k)}\right)$ is the vector of the covariances between the sth future record statistic and the first n upper k-record observations. The estimated MSEP of $R^*_{s(k)}$ is obtained as [15]

$$MSEP\left(R^*_{s(k)}\right) = \sigma^2\left(\Delta'\Omega^{-1}\Delta + \omega_{nn(k)} - 2\Delta'\omega_{s(k)}\right), \tag{23}$$

where

$$\Delta' = \left(1\ ,\ \alpha_{n(k)}\right)\left(\mathbf{A}'\Omega^{-1}\mathbf{A}\right)^{-1}\mathbf{A}'\Omega^{-1} + \boldsymbol{\omega}'_{\mathbf{s(k)}}\Omega^{-1}\left[\mathbf{I}_n - \mathbf{A}\left(\mathbf{A}'\Omega^{-1}\mathbf{A}\right)^{-1}\mathbf{A}'\Omega^{-1}\right] \tag{24}$$

and $\mathbf{I}_n$ is the identity matrix of order n. The BLIP of the sth upper k- record value, $R_{s(k)}$ is given by

$$R^{**}_{s(k)} = R^*_{s(k)} - \left(\frac{\nu^*_4}{1+\nu^*_2}\right)\sigma^*, \tag{25}$$

where $\nu^*_4 = \left(1 - \boldsymbol{\omega}'_{\mathbf{s(k)}}\boldsymbol{\Omega}^{-1}\mathbf{1}\right)\nu^*_1 + \left(\alpha_{s(k)} - \boldsymbol{\omega}'_{\mathbf{s(k)}}\boldsymbol{\Omega}^{-1}\boldsymbol{\alpha}\right)\nu^*_2$. The estimated MSEP of $R^{**}_{s(k)}$ is obtained as given below (see, [5]).

$$\begin{aligned} MSEP\left(R^{**}_{s(k)}\right) &= \sigma^2\left[\rho^2\left(\boldsymbol{\alpha}'\mathbf{1} - 1\right)^2 + 2\rho\left(\boldsymbol{\alpha}'\mathbf{1} - 1\right)\left(\boldsymbol{\alpha}'\boldsymbol{\alpha} - \alpha_{s(k)}\right)\right] \\ &+ \sigma^2\left[\boldsymbol{\alpha}'\boldsymbol{\Omega}\boldsymbol{\alpha} - 2\boldsymbol{\alpha}'\boldsymbol{\omega}_{\mathbf{s(k)}} + \omega_{ss(k)} + \left(\boldsymbol{\alpha}'\boldsymbol{\alpha} - \alpha_{s(k)}\right)^2\right], \end{aligned} \tag{26}$$

where $\rho = \frac{\mu}{\sigma}$ and $\omega_{ss(k)}$ is the variance of the sth upper k-record value.

3.2. Joint Prediction of future k-record values

In this subsection we obtain the joint prediction of the pair $\left(R_{s(k)}, R_{t(k)}\right)$ based on n observed upper k-record values arising from GP(μ, σ, ψ) for $n < s < t$. The following theorems provide the explicit expression for the joint BLUP and joint BLIP of the pair of future upper k-record values $\left(R_{s(k)}, R_{t(k)}\right)$, for $n < s < t$.

Theorem 1. Let $\mathbf{R_{n(k)}} = \left(R_{1(k)}, R_{2(k)}, \ldots, R_{n(k)}\right)'$ be the $1 \times n$ vector of first n observed upper k-record values arising from GP(μ, σ, ψ). Then $\left(R^*_{s(k)}, R^*_{t(k)}\right)$, for $n < s < t$, is the joint BLUP of the pair $\left(R_{s(k)}, R_{t(k)}\right)$ where $R^*_{s(k)} = \sum_{j=1}^{n} c_j R_{j(k)}$ and $R^*_{t(k)} = \sum_{j=1}^{n} d_j R_{j(k)}$. Then the coefficients c_j and d_j are given by

$$c_j = \frac{\sum_{i=1}^{n} \left(\alpha_{i(k)} - \alpha_{s(k)}\right)\left(S_{i(k)}T_{j(k)} - T_{i(k)}S_{j(k)}\right)}{(\boldsymbol{\alpha}'\boldsymbol{\Omega}^{-1}\boldsymbol{\alpha})(\mathbf{1}'\boldsymbol{\Omega}^{-1}\mathbf{1}) - (\boldsymbol{\alpha}'\boldsymbol{\Omega}^{-1}\mathbf{1})^2}, j = 1, 2, \ldots, n \tag{27}$$

and

$$d_j = \frac{\sum_{i=1}^{n} \left(\alpha_{i(k)} - \alpha_{t(k)}\right)\left(T_{i(k)}S_{j(k)} - S_{i(k)}T_{j(k)}\right)}{(\boldsymbol{\alpha}'\boldsymbol{\Omega}^{-1}\boldsymbol{\alpha})(\mathbf{1}'\boldsymbol{\Omega}^{-1}\mathbf{1}) - (\boldsymbol{\alpha}'\boldsymbol{\Omega}^{-1}\mathbf{1})^2}, j = 1, 2, \ldots, n, \tag{28}$$

where $T_{i(k)}$ and $S_{i(k)}$ are the ith entry of column vector $\Omega^{-1}\mathbf{1}$ and is $\Omega^{-1}\boldsymbol{\alpha}$, respectively.

Proof. We will derive the BLUPs jointly by minimizing the disperson matrix of $\left(R^*_{s(k)}, R^*_{t(k)}\right)$ with respect to the vectors $\mathbf{c}' = (c_1, c_2, \ldots, c_n)$ and $\mathbf{d}' = (d_1, d_2, \ldots, d_n)$. Let Σ denote the variance-covariance matrix of the BLUP $\left(R^*_{s(k)}, R^*_{t(k)}\right)$. Then Σ is of the form

$$\Sigma = Cov\left(R^*_{s(k)}, R^*_{t(k)}\right) = \sigma^2 \begin{pmatrix} \mathbf{c}'\boldsymbol{\Omega}\mathbf{c} & \mathbf{c}'\boldsymbol{\Omega}\mathbf{d} \\ \mathbf{c}'\boldsymbol{\Omega}\mathbf{d} & \mathbf{d}'\boldsymbol{\Omega}\mathbf{d} \end{pmatrix} = \sigma^2 \begin{pmatrix} \Sigma_{11} & \Sigma_{12} \\ \Sigma_{21} & \Sigma_{22} \end{pmatrix} (say).$$

Then the joint BLUPs of $R_{s(k)}$ and $R_{t(k)}$ are obtained by minimizing $|\Sigma|$ subject to the unbiasedness constraints of BLUPs $\mathbf{c}'\mathbf{1} = 1$, $\mathbf{c}'\boldsymbol{\alpha} = \alpha_{s(k)}$, $\mathbf{d}'\mathbf{1} = 1$ and $\mathbf{d}'\boldsymbol{\alpha} = \alpha_{t(k)}$. Then the optimum values of $\mathbf{c}$ and $\mathbf{d}$ are obtained by minimizing the following generalized variance. We can leave the multiplication factor σ^2 in the minimization process.

$$\begin{aligned} Q(\mathbf{c}, \mathbf{d}, \boldsymbol{\lambda}) &= (\mathbf{c}'\boldsymbol{\Omega}\mathbf{c})(\mathbf{d}'\boldsymbol{\Omega}\mathbf{d}) - (\mathbf{c}'\boldsymbol{\Omega}\mathbf{d})^2 - 2\lambda_1(\mathbf{c}'\mathbf{1} - 1) - 2\lambda_2\left(\mathbf{c}'\boldsymbol{\alpha} - \alpha_{s(k)}\right) \\ &- 2\lambda_3(\mathbf{d}'\mathbf{1} - 1) - 2\lambda_4\left(\mathbf{d}'\boldsymbol{\alpha} - \alpha_{t(k)}\right), \end{aligned} \tag{29}$$

were $\boldsymbol{\lambda} = (\lambda_1, \lambda_2, \lambda_3, \lambda_4)$ is the vector of Lagrangian multiplayers. Differentiating (29) with respect to $\mathbf{c}$ and $\mathbf{d}$ and equating them to $\mathbf{0}$, we obtain the following

$$(\mathbf{d}'\boldsymbol{\Omega}\mathbf{d})\boldsymbol{\Omega}\mathbf{c} - (\mathbf{c}'\boldsymbol{\Omega}\mathbf{d})\boldsymbol{\Omega}\mathbf{d} - \lambda_1\mathbf{1} - \lambda_2\boldsymbol{\alpha} = \mathbf{0} \tag{30}$$

and

$$(\mathbf{c}'\boldsymbol{\Omega}\mathbf{c})\boldsymbol{\Omega}\mathbf{d} - (\mathbf{c}'\boldsymbol{\Omega}\mathbf{d})\boldsymbol{\Omega}\mathbf{c} - \lambda_3\mathbf{1} - \lambda_4\boldsymbol{\alpha} = \mathbf{0}. \tag{31}$$

Pre-multiplying (30) by $\mathbf{c}'$ and (31) by $\mathbf{d}'$ then simplifying by using the constraints, we get

$$\lambda_1 + \lambda_2\alpha_{s(k)} = |\Sigma| \tag{32}$$

and

$$\lambda_3 + \lambda_4\alpha_{t(k)} = |\Sigma|. \tag{33}$$

Next, pre-multiplying (30) by $\mathbf{d}'$ and (31) by $\mathbf{c}'$ then simplifying by using the constraints, we get

$$\lambda_1 + \lambda_2\alpha_{t(k)} = 0 \tag{34}$$

and

$$\lambda_3 + \lambda_4\alpha_{s(k)} = 0. \tag{35}$$

Solving (32) and (34) for λ_1 and λ_2, we get

$$\lambda_1 = -\frac{|\Sigma|\alpha_{t(k)}}{\alpha_{s(k)} - \alpha_{t(k)}} \text{ and } \lambda_2 = \frac{|\Sigma|}{\alpha_{s(k)} - \alpha_{t(k)}}.$$

Similarly, solving (33) and (35) for λ_3 and λ_4, we get

$$\lambda_3 = -\frac{|\Sigma|\alpha_s}{\alpha_{t(k)} - \alpha_{s(k)}} \text{ and } \lambda_4 = \frac{|\Sigma|}{\alpha_{t(k)} - \alpha_{s(k)}}.$$

Pre-multiplying (30) by $\mathbf{\Omega}^{-1}$ and then substituting the values of λ_1 and λ_2, we get

$$\left(\mathbf{d}'\mathbf{\Omega}\mathbf{d}\right)\mathbf{c} - \left(\mathbf{c}'\mathbf{\Omega}\mathbf{d}\right)\mathbf{d} = \frac{|\Sigma|}{\alpha_{s(k)} - \alpha_{t(k)}}\mathbf{\Omega}^{-1}\left(\boldsymbol{\alpha} - \alpha_{t(k)}\mathbf{I}\right). \tag{36}$$

Similarly, by pre-multiplying (31) by $\mathbf{\Omega}^{-1}$ and then substituting the values of λ_3 and λ_4, we get

$$\left(\mathbf{c}'\mathbf{\Omega}\mathbf{c}\right)\mathbf{d} - \left(\mathbf{c}'\mathbf{\Omega}\mathbf{d}\right)\mathbf{c} = \frac{|\Sigma|}{\alpha_{t(k)} - \alpha_{s(k)}}\mathbf{\Omega}^{-1}\left(\boldsymbol{\alpha} - \alpha_{s(k)}\mathbf{I}\right). \tag{37}$$

Let us denote $\boldsymbol{\alpha_{s(k)}} = \boldsymbol{\alpha} - \alpha_{s(k)}\mathbf{I} = \left(\alpha_{1(k)} - \alpha_{s(k)}, \ldots, \alpha_{n(k)} - \alpha_{s(k)}\right)'$ and $\boldsymbol{\alpha_{t(k)}} = \boldsymbol{\alpha} - \alpha_{t(k)}\mathbf{I} = \left(\alpha_{1(k)} - \alpha_{t(k)}, \ldots, \alpha_{n(k)} - \alpha_{t(k)}\right)'$. Then (36) and (37) can be jointly expressed as

$$\begin{bmatrix}\mathbf{c} & \mathbf{d}\end{bmatrix}\begin{bmatrix}\mathbf{d}'\mathbf{\Omega}\mathbf{d} & -\mathbf{c}'\mathbf{\Omega}\mathbf{d} \\ -\mathbf{c}'\mathbf{\Omega}\mathbf{d} & \mathbf{c}'\mathbf{\Omega}\mathbf{c}\end{bmatrix} = \frac{|\Sigma|}{\alpha_{t(k)} - \alpha_{s(k)}}\mathbf{\Omega}^{-1}\begin{bmatrix}-\boldsymbol{\alpha_{t(k)}} & \boldsymbol{\alpha_{s(k)}}\end{bmatrix}.$$

Then we get

$$\begin{bmatrix}\mathbf{c} & \mathbf{d}\end{bmatrix} = \frac{\mathbf{\Omega}^{-1}}{\alpha_{t(k)} - \alpha_{s(k)}}\begin{bmatrix}-\boldsymbol{\alpha_{t(k)}} & \boldsymbol{\alpha_{s(k)}}\end{bmatrix}\Sigma.$$

Then the solution for $\mathbf{c}$ and $\mathbf{d}$ are

$$\mathbf{c} = \frac{1}{\alpha_{t(k)} - \alpha_{s(k)}}\left(-\Sigma_{11}\mathbf{\Omega}^{-1}\boldsymbol{\alpha_{t(k)}} + \Sigma_{12}\mathbf{\Omega}^{-1}\boldsymbol{\alpha_{s(k))}}\right) \tag{38}$$

and

$$\mathbf{d} = \frac{1}{\alpha_{t(k)} - \alpha_{s(k)}}\left(-\Sigma_{12}\mathbf{\Omega}^{-1}\boldsymbol{\alpha_{t(k)}} + \Sigma_{22}\mathbf{\Omega}^{-1}\boldsymbol{\alpha_{s(k)}}\right). \tag{39}$$

Now by using the unbiasedness condition, $\mathbf{c}'\mathbf{1} = 1$ and $\mathbf{c}'\boldsymbol{\alpha} = \alpha_{s(k)}$, we obtain

$$\frac{1}{\alpha_{t(k)} - \alpha_{s(k)}}\left[-\Sigma_{11}\left(\boldsymbol{\alpha_{t(k)}}'\mathbf{\Omega}^{-1}\mathbf{1}\right) + \Sigma_{12}\left(\boldsymbol{\alpha_{s(k)}}'\mathbf{\Omega}^{-1}\mathbf{1}\right)\right] = 1 \tag{40}$$

and

$$\frac{1}{\alpha_{t(k)} - \alpha_{s(k)}}\left[-\Sigma_{11}\left(\boldsymbol{\alpha_{t(k)}}'\mathbf{\Omega}^{-1}\boldsymbol{\alpha}\right) + \Sigma_{12}\left(\boldsymbol{\alpha_{s(k)}}'\mathbf{\Omega}^{-1}\boldsymbol{\alpha}\right)\right] = \alpha_{s(k)}. \tag{41}$$

Solving (40) and (41) for Σ_{11} and Σ_{12}, we get

$$\Sigma_{11} = -\left(\alpha_{t(k)} - \alpha_{s(k)}\right)\frac{\boldsymbol{\alpha_{s(k)}}'\mathbf{\Omega}^{-1}\boldsymbol{\alpha_{s(k)}}}{\left(\boldsymbol{\alpha_{t(k)}}'\mathbf{\Omega}^{-1}\mathbf{1}\boldsymbol{\alpha_{s(k)}}' - \boldsymbol{\alpha_{s(k)}}'\mathbf{\Omega}^{-1}\mathbf{1}\boldsymbol{\alpha_{t(k)}}'\right)\mathbf{\Omega}^{-1}\boldsymbol{\alpha}} \tag{42}$$

and

$$\Sigma_{12} = -\left(\alpha_{t(k)} - \alpha_{s(k)}\right)\frac{\boldsymbol{\alpha_{(t(k))}}'\mathbf{\Omega}^{-1}\boldsymbol{\alpha_{s(k)}}}{\left(\boldsymbol{\alpha_{t(k)}}'\mathbf{\Omega}^{-1}\mathbf{1}\boldsymbol{\alpha_{s(k)}}' - \boldsymbol{\alpha_{s(k)}}'\mathbf{\Omega}^{-1}\mathbf{1}\boldsymbol{\alpha_{t(k)}}'\right)\mathbf{\Omega}^{-1}\boldsymbol{\alpha}}. \tag{43}$$

Let us denote

$$\mathbf{\Omega} = \begin{pmatrix}\sigma_{11(k)} & \sigma_{12(k)} & \cdots & \sigma_{1n(k)} \\ \sigma_{21(k)} & \sigma_{22(k)} & \cdots & \sigma_{2n(k)} \\ \vdots & \vdots & \ddots & \vdots \\ \sigma_{n1(k)} & \sigma_{n2(k)} & \cdots & \sigma_{nn(k)}\end{pmatrix}$$

and

$$\mathbf{\Omega}^{-1} = \begin{pmatrix} \sigma^{11(k)} & \sigma^{12(k)} & \dots & \sigma^{1n(k)} \\ \sigma^{21(k)} & \sigma^{22(k)} & \dots & \sigma^{2n(k)} \\ \vdots & \vdots & \ddots & \vdots \\ \sigma^{n1(k)} & \sigma^{n2(k)} & \dots & \sigma^{nn(k)} \end{pmatrix}.$$

Then

$$\mathbf{\Omega}^{-1}\mathbf{1} = \begin{pmatrix} \sigma^{11(k)} + \sigma^{12(k)} + \dots + \sigma^{1n(k)} \\ \sigma^{21(k)} + \sigma^{22(k)} + \dots + \sigma^{2n(k)} \\ \vdots \\ \sigma^{n1(k)} + \sigma^{n2(k)} + \dots + \sigma^{nn(k)} \end{pmatrix} = \begin{pmatrix} T_{1(k)} \\ T_{2(k)} \\ \vdots \\ T_{n(k)} \end{pmatrix},$$

where T_i is the sum of the entries in the ith row of matrix Ω^{-1}. Similarly

$$\mathbf{\Omega}^{-1}\boldsymbol{\alpha} = \begin{pmatrix} \alpha_{1(k)}\sigma^{11(k)} + \alpha_{2(k)}\sigma^{12(k)} + \dots + \alpha_{n(k)}\sigma^{1n(k)} \\ \alpha_{1(k)}\sigma^{21(k)} + \alpha_{2(k)}\sigma^{22(k)} + \dots + \alpha_{n(k)}\sigma^{2n(k)} \\ \vdots \\ \alpha_{1(k)}\sigma^{n1(k)} + \alpha_{2(k)}\sigma^{n2(k)} + \dots + \alpha_{n(k)}\sigma^{nn(k)} \end{pmatrix} = \begin{pmatrix} S_{1(k)} \\ S_{2(k)} \\ \vdots \\ S_{n(k)} \end{pmatrix}.$$

Thus we obtain

$$\boldsymbol{\alpha}_{t(k)}{}'\mathbf{\Omega}^{-1}\mathbf{1}\boldsymbol{\alpha}_{s(k)}{}' = \left(\sum_{i=1}^{n} T_{i(k)}\left(\alpha_{i(k)} - \alpha_{t(k)}\right)\right)\begin{bmatrix}\alpha_{1(k)} - \alpha_{s(k)} & \alpha_{2(k)} - \alpha_{s(k)} & \cdots & \alpha_{n(k)} - \alpha_{s(k)}\end{bmatrix} \tag{44}$$

and

$$\boldsymbol{\alpha}_{s(k)}{}'\mathbf{\Omega}^{-1}\mathbf{1}\boldsymbol{\alpha}_{t(k)}{}' = \left(\sum_{i=1}^{n} T_{i(k)}\left(\alpha_{i(k)} - \alpha_{s(k)}\right)\right)\begin{bmatrix}\alpha_{1(k)} - \alpha_{t(k)} & \alpha_{2(k)} - \alpha_{t(k)} & \cdots & \alpha_{n(k)} - \alpha_{t(k)}\end{bmatrix}. \tag{45}$$

Therefore,

$$\begin{aligned} \boldsymbol{\alpha}_{t(k)}{}'\mathbf{\Omega}^{-1}\mathbf{1}\boldsymbol{\alpha}_{s(k)}{}' - \boldsymbol{\alpha}_{s(k)}{}'\mathbf{\Omega}^{-1}\mathbf{1}\boldsymbol{\alpha}_{t(k)}{}' &= \left(\alpha_{s(k)} - \alpha_{t(k)}\right) \\ &\times \left(\alpha_{1(k)}T - T^*, \quad \alpha_{2(k)}T - T^*, \quad \cdots, \quad \alpha_{n(k)}T - T^*\right) \end{aligned}$$

where $T = \sum_{i=1}^{n} T_{i(k)}$ and $T^* = \sum_{i=1}^{n} T_{i(k)}\alpha_{i(k)}$. We observe that $T = \mathbf{1}'\mathbf{\Omega}^{-1}\mathbf{1}$, $T^* = \boldsymbol{\alpha}'\mathbf{\Omega}^{-1}\mathbf{1}$, $\sum_{i=1}^{n} S_{i(k)} = \mathbf{1}'\mathbf{\Omega}^{-1}\boldsymbol{\alpha} = \boldsymbol{\alpha}'\mathbf{\Omega}^{-1}\mathbf{1}$ and $\sum_{i=1}^{n} \alpha_i S_{i(k)} = \boldsymbol{\alpha}'\mathbf{\Omega}^{-1}\boldsymbol{\alpha}$. Then

$$\begin{aligned} \left(\boldsymbol{\alpha}_{t(k)}{}'\mathbf{\Omega}^{-1}\mathbf{1}\boldsymbol{\alpha}_{s(k)}{}' - \boldsymbol{\alpha}_{s(k)}{}'\mathbf{\Omega}^{-1}\mathbf{1}\boldsymbol{\alpha}_{t(k)}{}'\right)\mathbf{\Omega}^{-1}\boldsymbol{\alpha} &= \left(\alpha_{s(k)} - \alpha_{t(k)}\right) \\ &\times \begin{bmatrix}\alpha_{1(k)}T - T^* & \alpha_{2(k)}T - T^* & \cdots & \alpha_{n(k)}T - T^*\end{bmatrix} \\ &\times \begin{pmatrix} S_{1(k)} \\ S_{2(k)} \\ \vdots \\ S_{n(k)} \end{pmatrix} \\ &= \left(\alpha_{s(k)} - \alpha_{t(k)}\right)\left(T\sum_{i=1}^{n}\alpha_{i(k)}S_{i(k)} - T^*\sum_{i=1}^{n}S_{i(k)}\right) \\ &= \left(\alpha_{s(k)} - \alpha_{t(k)}\right)\left[(\boldsymbol{\alpha}'\mathbf{\Omega}^{-1}\boldsymbol{\alpha})(\mathbf{1}'\mathbf{\Omega}^{-1}\mathbf{1}) - (\boldsymbol{\alpha}'\mathbf{\Omega}^{-1}\mathbf{1})^2\right]. \end{aligned}$$

Hence we can write

$$\Sigma_{11} = \frac{\boldsymbol{\alpha}_{s(k)}{}'\mathbf{\Omega}^{-1}\boldsymbol{\alpha}_{s(k)}}{(\boldsymbol{\alpha}'\mathbf{\Omega}^{-1}\boldsymbol{\alpha})(\mathbf{1}'\mathbf{\Omega}^{-1}\mathbf{1}) - (\boldsymbol{\alpha}'\mathbf{\Omega}^{-1}\mathbf{1})^2} \tag{46}$$

and

$$\Sigma_{12} = \frac{\boldsymbol{\alpha}_{t(k)}{}'\boldsymbol{\Omega}^{-1}\boldsymbol{\alpha}_{s(k)}}{(\boldsymbol{\alpha}'\boldsymbol{\Omega}^{-1}\boldsymbol{\alpha})(\mathbf{1}'\boldsymbol{\Omega}^{-1}\mathbf{1}) - (\boldsymbol{\alpha}'\boldsymbol{\Omega}^{-1}\mathbf{1})^2}. \tag{47}$$

Now by using the unbiasedness condition, $\mathbf{d}'\mathbf{1} = 1$ and $\mathbf{d}'\boldsymbol{\alpha} = \alpha_t$ and proceeded exactly in the same way, we obtain

$$\Sigma_{12} = \frac{\boldsymbol{\alpha}_{t(k)}{}'\boldsymbol{\Omega}^{-1}\boldsymbol{\alpha}_{s(k)}}{(\boldsymbol{\alpha}'\boldsymbol{\Omega}^{-1}\boldsymbol{\alpha})(\mathbf{1}'\boldsymbol{\Omega}^{-1}\mathbf{1}) - (\boldsymbol{\alpha}'\boldsymbol{\Omega}^{-1}\mathbf{1})^2} \tag{48}$$

and

$$\Sigma_{22} = \frac{\boldsymbol{\alpha}_{t(k)}{}'\boldsymbol{\Omega}^{-1}\boldsymbol{\alpha}_{t(k)}}{(\boldsymbol{\alpha}'\boldsymbol{\Omega}^{-1}\boldsymbol{\alpha})(\mathbf{1}'\boldsymbol{\Omega}^{-1}\mathbf{1}) - (\boldsymbol{\alpha}'\boldsymbol{\Omega}^{-1}\mathbf{1})^2}. \tag{49}$$

Substituting the value of Σ_{11} and Σ_{12} in (38) and simplyfying, we obtain the explicit expression for the coefficienr vector $\mathbf{c}$. Similary, substituting the value of Σ_{12} and Σ_{22} in (39) and simplyfying, we obtain the explicit expression for the coefficienr vector $\mathbf{d}$. Hence the theorem. ■

Theorem 2. Let $\mathbf{R}_{n(k)} = \left(R_{1(k)}, R_{2(k)}, \ldots, R_{n(k)}\right)'$ be the $1 \times n$ vector of first n observed upper k-record values arising from GP(μ, σ, ψ) with $E\left(\mathbf{R}_{n(k)}\right) = \mu\mathbf{1} + \Sigma\boldsymbol{\alpha}$ and $D\left(\mathbf{U}_{n(k)}\right) = \sigma^2\boldsymbol{\Omega}$. Then $\left(R^{**}_{s(k)}, R^{**}_{t(k)}\right)$, for $n < s < t$, is the joint BLIP of the pair $\left(R_{s(k)}, R_{t(k)}\right)$ where $R^{**}_{s(k)} = \boldsymbol{\theta}'\mathbf{R}_{n(k)}$ and $R^{**}_{t(k)} = \boldsymbol{\phi}'\mathbf{R}_{n(k)}$, where the coefficients $\boldsymbol{\theta}' = (\theta_1, \theta_2, \ldots, \theta_n)$ and $\boldsymbol{\phi}' = (\phi_1, \phi_2, \ldots, \phi_n)$ are given by

$$\boldsymbol{\theta} = \Lambda^{-1}\Delta_s \tag{50}$$

and

$$\boldsymbol{\phi} = \Lambda^{-1}\Delta_t \tag{51}$$

where $\Lambda = \boldsymbol{\Omega} + (\boldsymbol{\alpha} + \rho\boldsymbol{I_n})(\boldsymbol{\alpha} + \rho\boldsymbol{I_n})'$, $\Delta_s = \boldsymbol{\omega_{s(k)}} + (\alpha_s + \rho)(\boldsymbol{\alpha} + \rho\boldsymbol{I_n})$ and $\Delta_t = \boldsymbol{\omega_{t(k)}} + (\alpha_t + \rho)(\boldsymbol{\alpha} + \rho\boldsymbol{I_n})$.

Proof. The MSPE matrix is given by

$$\begin{pmatrix} E_1 & E_3 \\ E_3 & E_2 \end{pmatrix}.$$

where

$$\begin{aligned} E_1 &= E\left[\left(\tilde{R}_{s(k)} - R_{s(k)}\right)^2\right] \\ &= \sigma^2\left[\rho^2\left(\boldsymbol{\theta}'\mathbf{1} - 1\right)^2 + 2\rho\left(\boldsymbol{\theta}'\mathbf{1} - 1\right)\left(\boldsymbol{\theta}'\boldsymbol{\alpha} - \alpha_s\right)\right] \\ &+ \sigma^2\left[\boldsymbol{\theta}'\boldsymbol{\Omega}\boldsymbol{\theta} - 2\boldsymbol{\theta}'\boldsymbol{\omega_{s(k)}} + \omega_{ss} + \left(\boldsymbol{\theta}'\boldsymbol{\alpha} - \alpha_s\right)^2\right]. \end{aligned} \tag{52}$$

$$\begin{aligned} E_2 &= E\left[\left(\tilde{R}_{t(k)} - R_{t(k)}\right)^2\right] \\ &= \sigma^2\left[\rho^2\left(\boldsymbol{\phi}'\mathbf{1} - 1\right)^2 + 2\rho\left(\boldsymbol{\phi}'\mathbf{1} - 1\right)\left(\boldsymbol{\phi}'\boldsymbol{\alpha} - \alpha_t\right)\right] \\ &+ \sigma^2\left[\boldsymbol{\phi}'\boldsymbol{\Omega}\boldsymbol{\phi} - 2\boldsymbol{\phi}'\boldsymbol{\omega_{t(k)}} + \omega_{tt} + \left(\boldsymbol{\phi}'\boldsymbol{\alpha} - \alpha_t\right)^2\right]. \end{aligned} \tag{53}$$

$$\begin{aligned} E_3 &= E\left[\left(\tilde{R}_{s(k)} - R_{s(k)}\right)\left(\tilde{R}_{t(k)} - R_{t(k)}\right)\right] \\ &= \sigma^2\left[\rho^2\left(\boldsymbol{\theta}'\mathbf{1} - 1\right)\left(\boldsymbol{\phi}'\mathbf{1} - 1\right) + \rho\left(\boldsymbol{\theta}'\mathbf{1} - 1\right)\left(\boldsymbol{\phi}'\boldsymbol{\alpha} - \alpha_t\right) + \rho\left(\boldsymbol{\alpha}'\boldsymbol{\alpha} - \alpha_s\right)\left(\boldsymbol{\phi}'\mathbf{1} - 1\right)\right] \\ &+ \sigma^2\left[\boldsymbol{\theta}'\boldsymbol{\Omega}\boldsymbol{\phi} - \boldsymbol{\theta}'\boldsymbol{\omega_{t(k)}} - \boldsymbol{\phi}'\boldsymbol{\omega_{s(k)}} + \omega_{st} + \left(\boldsymbol{\theta}'\boldsymbol{\alpha} - \alpha_s\right)\left(\boldsymbol{\phi}'\boldsymbol{\alpha} - \alpha_t\right)\right]. \end{aligned} \tag{54}$$

The determinant of the MSEP matrix is $E = E_1E_2 - E_3^2$ which needs to be minimized with respect to $\boldsymbol{\theta}$ and $\boldsymbol{\phi}$. Differentiating E with respect to $\boldsymbol{\theta}$ and $\boldsymbol{\phi}$ and equating them to $\mathbf{0}$, we obtain the following

$$(\Lambda\boldsymbol{\theta} - \Delta_s)\, E_2 - (\Lambda\boldsymbol{\phi} - \Delta_t)\, E_3 = \mathbf{0} \tag{55}$$

and

$$(\Lambda\boldsymbol{\phi} - \Delta_t)\, E_1 - (\Lambda\boldsymbol{\theta} - \Delta_s)\, E_3 = \mathbf{0}, \tag{56}$$

where Λ, Δ_s and Δ_t are defined in the statement of the theorem. From (55) and (56), we obtain

$$(\Lambda\boldsymbol{\theta} - \Delta_s)\left(E_1E_2 - E_3^2\right) = \mathbf{0}, \tag{57}$$

Assuming $E_1E_2 - E_3^2 \neq 0$, we readly obtain $\boldsymbol{\theta} = \Lambda^{-1}\Delta_s$. Prceeding similary, from (55) and (56), we obtain $\boldsymbol{\phi} = \Lambda^{-1}\Delta_t$. Hence the proof. ■

3.3. Comparison between BLUP and BLIP

In this Subsection, We define two types of relative efficiencies for the performance of joint BLIP and joint BLUP based on the MSPE matrix as follows.

$$\begin{aligned} \text{D-Efficiency}\,(\epsilon_1) &= \frac{\text{Determinant of the MSEP matrix of } \left(\tilde{U}_{s(k)}, \tilde{U}_{t(k)}\right)}{\text{Determinant of the MSEP matrix of } \left(U^{**}_{s(k)}, (U^{**}_{t(k)}\right)} \\ &= \frac{E_1E_2 - E_3^2}{\Sigma_{11}\Sigma_{22} - \Sigma_{12}^2} \end{aligned} \tag{58}$$

and

$$\begin{aligned} \text{T-Efficiency}\,(\epsilon_2) &= \frac{\text{Trace of the MSEP matrix of } \left(\tilde{U}_{s(k)}, \tilde{U}_{t(k)}\right)}{\text{Trace of the MSEP matrix of } \left(U^{**}_{s(k)}, (U^{**}_{t(k)}\right)} \\ &= \frac{E_1 + E_2}{\Sigma_{11} + \Sigma_{22}}. \end{aligned} \tag{59}$$

The quantity ρ plays an important role in the relative performance of the BLIP against the BLUP. Note that the range of ρ is $(-\infty, +\infty)$. However, due to symmetry, we can focus on the interpretation of the relative efficiencies $(0, +\infty)$. Both ϵ_1 and ϵ_2 always possess an unique maximum ρ^* which are calculated numerically and analytically. If both efficiencies are always greater than 1 indicating that BLUP performs better than BLIP. If for some $\rho_* > 0$, BLUP performs better in an interval $(0, \rho_*)$ and then BLIP performs better in the interval (ρ_*, ∞) then for overall comparative assessment, we define an integrated efficiency measure (IEM) which is simply an average of all efficiencies calculated on a finite interval $(0, \rho_{max})$ for ρ. If both ϵ_1 and ϵ_2 are less than 1 which indicates that BLIP has overall better performance than BLUP.

4. Illustration with Real Data

In this section, we consider a numerical study to illustrate how the proposed predictors work in practical situation. We consider the following dataset by [8] represents the exceedances $(kg\ mm^{-2})$ of the testing thresholds in tensile-strength tests for a random sample size 15 nylon carpet fibres. The dataset is

$$0.051, 0.140, 0.365, 0.561, 0.030, 0.268, 0.184, 0.100, 0.876, 0.092, 0.011, 0.200, 0.518, 0.338, 0.056$$

The Kolmogorov-Smirnov goodness- of- fit test shows that the above data fits GPD$(0, 0.283, 0.1)$ very well with the Kolmogorov-Smirnov test statistic is 0.107 and p-value 0.988.

The upper k- record values extracted from the dataset for $k = 2, 3$ are given by the following table.

Table 9: *Upper k- record values extracted from the dataset*

n	1	2	3	4	5
$R_{n(2)}$	0.051	0.14	0.365	0.561	-
$R_{n(3)}$	0.051	0.14	0.268	0.315	0.518

The marginal BLUP and BLIP of future upper k- record values based on the n observed upper k-record values along with their estimated MSPE are given by the following table.

Table 10: *Marginal BLUP and BLIP for the real dataset with their estimated MSPE*

k	n	s	Marginal Predictors		MSPE	
			$R^{*}_{s(k)}$	$R^{**}_{s(k)}$	BLUP	BLIP
2	4	5	0.7470	0.7060	0.0580	0.0260
3	5	6	0.6400	0.5970	0.7820	0.0520

From Table 10, we can observe that the marginal BLIP performs better than the marginal BLUP in the sense of estimated MSPE. The Joint BLUP and BLIP for the real dataset along with the Determinant and Trace efficiencies are given in Table 11.

Table 11: *Joint BLUP and BLIP for the real dataset with Determinant and Trace efficiencies*

k	n	(s,t)	Joint Predictors		ϵ_1	ϵ_2
			$\left(R^{*}_{s(k)}, R^{*}_{t(k)}\right)$	$\left(R^{**}_{s(k)}, R^{**}_{t(k)}\right)$		
2	4	(6,7)	$(0.9378, 1.1441)$	$(0.8173, 0.9556)$	0.0009	0.0246
		(6,8)	$(0.9378, 1.3611)$	$(0.8173, 1.1013)$	0.0011	0.1078
		(7,9)	$(1.4412, 1.6117)$	$(0.9556, 1.2546)$	0.0056	0.1173
3	5	(7,8)	$(0.7854, 0.9333)$	$(0.7097, 0.8106)$	0.0026	0.0812
		(7,9)	$(0.7854, 1.0853)$	$(0.7097, 0.9150)$	0.0053	0.1531
		(8,9)	$(0.9333, 1.0853)$	$(0.8106, 0.9151)$	0.0084	0.1851

Since both ϵ_1 and ϵ_2 are less than 1 indicate that BLIP has overall better performance than BLUP.

5. Conclusion

Serious difficulties for the statistical inference based on records arise due to the fact that the occur rences of record data are very rare in practical situations and the expected waiting time is infinite for every record after the first. These problems are avoided if we consider the model of k-record statistics. In this work we considered the upper k- record values arising from generalized Pareto distribution. We have obtained the BLUEs and BLISs of the location and scale parameters of a generalized Pareto distribution based on the observed upper k-record values. The marginal BLUP and BLIP of future upper k-record values and the joint BLUP and BLIP of pair of future upper k-record values are also derived. A real dataset is used to illustrate the inferential procedures developed in this paper and concluded that the BLIP performs well in terms of estimated MSPE and relative efficiencies.

References

[1] Ahmadi, J., MirMostafaee, S. M. T. K. and Balakrishnan, N. (2011). Bayesian prediction of order statistics based on *k*-record values from exponential distribution. *Statistics*, 45(4): 375-387.

[2] Ahsanullah, M.and Nevzorov, V. B. (2015). *Estimation of Parameters and Predictions of Records. In Records via Probability Theory* (pp. 143-181). Paris: Atlantis Press.

[3] Arnold, B. C., Balakrishnan, N. and Nagaraja, H. N. (1998). *Records*, John Wiley and Sons, New York.

[4] Balakrishnan, N. and Bhattacharya, R. (2022). D-optimal joint best linear unbiased prediction of order statistics: Joint BLUP. *Metrika*, 85(2): 253-267.

[5] Balakrishnan, N. and Bhattacharya, R. (2022). Simultaneous best linear invariant prediction of future order statistics for location-scale and scale families and associated optimality properties. *Statistics*, 56(6): 1409-1426.

[6] Chandler, K. N. (1952). The distribution and frequency of record values. *Journal of the Royal Statistical Society, Series B*, 14: 220-228.

[7] Dziubdziela, W. and Kopociński, B. (1976). Limiting properties of the k-th record values. *Applicationes Mathematicae*, 15: 187-190.

[8] Grimshaw, S. D. (1993). Computing maximum likelihood estimates for the generalized Pareto distribution. *Technometrics*, 35(2): 185-191.

[9] Gulati, S.and Padgett, W. J. (2003). *Parametric and Nonparametric Inference from Record-Breaking Data*. Springer, New York.

[10] Jamkhaneh, M. B., MirMostafaee, S. M. T. K. and Jadidi, M. (2024). On the xgamma k-record values and associated inference. *Annals of Data Science*, 1-29 (in press).

[11] Mann, N. R. (1969). Optimum estimators for linear functions of location and scale parameters. *The Annals of Mathematical Statistics*, 2149-2155.

[12] Muraleedharan, L. and Chacko, M. (2022). Estimation and prediction based on *k*-record values from a generalized Pareto distribution. *International Journal of Mathematics and Statistics*, 23(1): 59-75.

[13] Ormoz, E., Akhter, Z., Alam, M. and MirMostafae, S. M. T. K. (2023). Lower k-record values from unit-Gompertz distribution and associated inference. *arXiv preprint arXiv*:2309.13279.

[14] Raqab, M. (2002). Inference for generalized exponential distribution based on record statistics. *Journal of Statistical Planning and Inference*, 104(2): 339-350.

[15] Raqab, M. Z. (1996). Linear predictors of future order statistics. *Communications in Statistics-Theory and Methods*, 25(7): 1553-1568.

[16] Shafay, A. R., Balakrishnan, N. and Ahmadi, J. (2017). Bayesian prediction of order statistics with fixed and random sample sizes based on *k*-record values from Pareto distribution. *Communications in Statistics-Theory and Methods*, 46(2): 721-735.

[17] Singh, S., Mani Tripathi, Y. and Wu, S. J. (2017). Bayesian estimation and prediction based on lognormal record values. *Journal of Applied Statistics*, 44(5): 916-940.

[18] Soliman, A., Amin, E. A. and Abd-El Aziz, A. A. (2010). Estimation and prediction from inverse Rayleigh distribution based on lower record values. *Applied Mathematical Sciences*, 4(62): 3057-3066.

[19] Sultan, K. S., Al-Dayian, G. R. and Mohammad, H. H. (2008). Estimation and prediction from gamma distribution based on record values. *Computational Statistics and Data Analysis*, 52(3): 1430-1440.

[20] Sultan, K. S. and Moshref, M. E. (2000). Record values from generalized Pareto distribution and associated inference. *Metrika*, 51(2): 105-116.

[21] Vidović, Z. (2019). Bayesian prediction of order statistics based on k-record values from a generalized exponential distribution. *Stats*, 2(4): 447-456.

[22] Zhao, X., Wei, S., Cheng, W., Zhang, P., Zhang, Y. and Xu, Q. (2023). Upper record values from the generalized Pareto distribution and associated statistical inference. *Communications in Statistics-Simulation and Computation*, 52(2): 369-391.

RT&A, No 4 (89)
Volume 20, December 2025

SOME REFINEMENTS OF INEQUALITIES FOR POLYNOMIALS

Aijaz Ahmad[1], D Venkatesan[2], Ajjaz Maqbool Dar[3], Aafaq A. Rather[4,*], Danish Qayoom[5], Eid Sadun Alotaibi[6], Showkat A. Bhat[7], Mushtaq A. Lone[8] and Jameel Ahmad Ansari[9]

•

[1,2]Sri Indu College of Engineering and Technology, Sheriguda, Ibrahimpatnam-501510, India.
[3]Sheikh-ul- Alam Degree college, Budgam, Jammu & kashmir-191111, India.
[4,5]Symbiosis Statistical Institute, Symbiosis International (Deemed University), Pune, India.
[6]Department of Mathematics and Statistics, Alkhurmah University College,Taif University, P.O. Box 11099, Taif, 21944, Saudi Arabia.
[7]Symbiosis School of Economics, Symbiosis International (Deemed University), Pune, India.
[8]Division of Agricultural Statistics, SKUAST Kashmir, Jammu & Kashmir-190025, India.
[9]Department of Engineering Sciences, Vishwakarma University, Pune, India.
[1]aiju.aijaz117@gmail.com, [2]venkat2733327@gmail.com, [3]ajjazmaqbool013@gmail.com,
[4,*]Corresponding author: aafaq7741@gmail.com, [5]danishqayoom11@gmail.com,
[5]e.alotaibi@tu.edu.sa, [7]showkat.bhat@sse.ac.in, [8]lonemushtaq11@gmail.com,
[9]jameelahmad.ansari@vupune.ac.in

Abstract

The study of inequalities for polynomials plays a central role in mathematical analysis, with numerous results exploring the relationships between a polynomial and its derivative. Over time, several refinements and generalizations have been established, strengthening classical inequalities and extending them to broader settings. In this paper, we present new refinements that further enhance existing results on polynomial inequalities. Our findings not only sharpen earlier theorems, but also provide generalized forms that encompass a wider class of polynomials. The refinements introduced here not only strengthen known inequalities, but also provide a framework that connects different strands of results in this area. This contributes to a deeper understanding of the behavior of polynomials in the complex domain and establishes new directions for further investigation.

Keywords: Complex polynomials, Complex zeros, Inequalities, Complex domain

1. Introduction

Inequalities for polynomials and their derivatives have long been a central topic in mathematical analysis, particularly within approximation theory and complex function theory. Classical results, beginning with the work of Zygmund and Bernstein, established foundational inequalities that describe the relationship between a polynomial and its derivative in the unit circle. These results have been refined and extended by many researchers, often imposing conditions on the location of zeros of the polynomial, leading to sharper bounds and broader applicability.

Despite this progress, there remains scope for further refinements that unify different strands of existing results and provide stronger generalizations. The purpose of this work is to build upon earlier contributions by developing new inequalities for complex polynomials that not only sharpen known bounds, but also extend them to more general classes of polynomials with specific zero restrictions.

Suppose that P_η be the set of all polynomials of degree at most η, then for $P \in P_\eta$, Zygmund proved that

$$\|P\|_{\mathtt{q}} \geq \frac{1}{\eta}\|P'\|_{\mathtt{q}} \tag{1}$$

where $\mathtt{q}$ is positive.

In literature, so many generalizations and refinements of this result (1) exists. Recently, a generalization of the result (1) was proved. In this paper, we prove a refinement of the result(1) which in turn provides a generalization of several other results.

Let P_η be the class of all polynomials $P(z) = \sum_{j=0}^{\eta} a_j z^j$ of degree η.
Define,

$$\|P\|_{\mathtt{q}} := \left\{ \frac{1}{2\pi} \int_0^{2\pi} |P(e^{i\Theta})|^{\mathtt{q}} d\Theta \right\}^{\frac{1}{\mathtt{q}}}, \quad 0 < \mathtt{q} < \infty \|P\|_\infty := \max_{|z|=1} |P(z)|$$

Also,

$$\|P\|_0 := exp\left\{ \frac{1}{2\pi} \int_0^{2\pi} log|P(e^{i\Theta}|d\Theta \right\} \quad for \;\; P \in P_\eta$$

If $P \in P_\eta$,

$$\|P'\|_{\mathtt{q}} \leq \eta \|P\|_{\mathtt{q}}, \quad \mathtt{q} > 0. \tag{2}$$

inequality (2) was found out by Zygmund [15]. Letting $\mathtt{q} \to \infty$ in (2) , we get

$$\|P'\|_\infty \leq \eta \|P\|_\infty \tag{3}$$

which is a well-known Bernstein's inequality.

Arestov[1] proved that (2) is true for $\mathtt{q} \in [0, 1)$ as well.
If $P \in P_\eta$ such that P(z) doesnot vanish in $|z| < 1$, then (3) and (2) can be respectively replaced by

$$\|P'\|_\infty \leq \frac{\eta}{2}\|P\|_\infty \tag{4}$$

and

$$\|P'\|_{\mathtt{q}} \leq \frac{\eta}{\|1+z\|_{\mathtt{q}}}\|P\|_{\mathtt{q}}, \quad \mathtt{q} > 0. \tag{5}$$

The inequality (4) was conjectured by Erdös and later verified by Lax [10], inequality (5) is due to Bruijn [3] for $\mathtt{q} \geq 1$. Rahman and Schmeisser[12] verified that (5) is valid for $\mathtt{q} \in [0, 1)$ as well. Turan [14] proved that, if $P \in P_\eta$ vanishes in $|z| \leq 1$,then

$$\|F'\|_\infty \geq \frac{\eta}{2}\|P\|_\infty. \tag{6}$$

equality holds in both the inequalities (4) and (6) for $P(z) = l + \tau z^\eta$, where $|l| = |\tau|$.
Also, Govil and Rahman [6] proved that, if $P \in P_\eta$ does not vanishes in $|z| < h, h \geq 1$, then

$$\|P'\|_{\mathtt{q}} \leq \frac{\eta}{\|h+z\|_{\mathtt{q}}}\|P\|_{\mathtt{q}}, \;\; \mathtt{q} \geq 1 \tag{7}$$

Gardener and Weems [5] and Rather [13] independently verified the validity of (7) for $0 < \mathtt{q} < 1$ as well.

Also, Aziz and Rather [2] proved that if $P \in P_\eta$ does not vanishes in $|z| < h, h \geq 1$, then for every $\mathtt{q} > 0$

$$\|P'\|_\mathtt{q} \leq \frac{\eta}{\|\Delta_{h,1} + z\|_\mathtt{q}} \|P\|_\mathtt{q}, \quad \mathtt{q} \geq 1 \tag{8}$$

where $\Delta_{h,1} = \dfrac{\eta|a_0|h^2 + h^2|a_1|}{\eta|a_0| + h^2|a_1|}$
Malik [11] proved that if $P \in P_\eta$ vanishes in $|z| \leq 1$, then for every $\mathtt{q}$*positive*.

$$\|P'\|_\mathtt{q} \geq \frac{\eta}{\|1 + z\|_\mathtt{q}} \|P\|_\mathtt{q}. \tag{9}$$

Aziz and Rather [2] generalised the inequality (9) as if $P \in P_\eta$ vanishes in $|z| \leq h, h \leq 1$, then for every $\mathtt{q} > 0$

$$\|P'\|_\mathtt{q} \geq \frac{\eta}{\|1 + t_{h,1} z\|_\mathtt{q}} \|P\|_\mathtt{q}. \tag{10}$$

and

$$\|P'\|_\infty \geq \frac{\eta}{\|1 + t_{h,1} z\|_\mathtt{q}} \|P\|_\mathtt{q}. \tag{11}$$

where $t_{h,1} = \dfrac{\eta|a_\eta|h^2 + |a_{\eta-1}|}{\eta|a_\eta| + |a_{\eta-1}|}$

Govil et al. [7] demonstrated the following two theorems, in which they generalised (7) and (9), and also the inequality (12) by involving some coefficients of P(z).

Theorem 1. If $P \in P_\eta$ does not vanishes in $|z| < h, h \geq 1$, then

$$\|P'\|_\infty \leq \frac{\eta}{1+h} \frac{(1-|\alpha|)(1+h^2|\alpha|) + h(\eta-1)|\mu - \alpha^2|}{(1-|\alpha|)(1-h+h^2+h|\alpha|) + h(\eta-1)|\mu-\alpha^2|} \|P\|_\infty, \tag{12}$$

where

$$\alpha = \frac{ha_1}{\eta a_0} \text{ and } \mu = \frac{2h^2 a_2}{\eta(\eta-1)a_0}$$

Theorem 2. If $P \in P_\eta$ vanishes in $|z| \leq h, h \leq 1$, then

$$\|P'\|_\infty \geq \frac{\eta}{1+h} \frac{(1-|\beta|)(1+h^2|\beta|) + h(\eta-1)|\gamma - \beta^2|}{(1-|\beta|)(1-h+h^2+h|\beta|) + h(\eta-1)|\gamma-\beta^2|} \|P\|_\infty, \tag{13}$$

where

$$\beta = \frac{\overline{a}_{\eta-1}}{\eta h \overline{a}_\eta} \text{ and } \gamma = \frac{2\overline{a}_{\eta-2}}{\eta(\eta-1)h^2\overline{a}_\eta}$$

Recently, Krishnadas and Chanam [9] demonstrated the following two theorems in which they extended inequalities (14) and (16) to $L_\mathtt{q}$ norms. ,

Theorem 3. If $P \in P_\eta$ does not vanishes in $|z| < h, h \geq 1$, then for every $\mathtt{q} > 0$

$$\|P'\|_\mathtt{q} \leq \frac{\eta}{\|\Gamma + z\|_\mathtt{q}} \|P\|_\mathtt{q}. \tag{14}$$

where

$$\Gamma = h\frac{(1-|\alpha|)(|\alpha|+h^2)+h(\eta-1)|\mu-\alpha^2|}{(1-|\alpha|)(|\alpha|h^2+1)+h(\eta-1)|\mu-\alpha^2|} \tag{15}$$

$$\alpha = \frac{ha_1}{\eta a_0} \text{ and } \mu = \frac{2h^2a_2}{\eta(\eta-1)a_0}$$

Theorem 4. If $P \in P_\eta$ vanishes in $|z| \leq h, h \leq 1$, then for every $\mathtt{q} > 0$

$$\|P'\|_\mathtt{q} \geq \frac{\eta}{\|1 + Sz\|_\mathtt{q}} \|P\|_\mathtt{q}. \tag{16}$$

where

$$S = h\frac{(1-|\beta|)(|\beta|+h^2)+h(\eta-1)|\gamma-\beta^2|}{(1-|\beta|)(|\beta|h^2+1)+h(\eta-1)|\gamma-\beta^2|} \tag{17}$$

$$\beta = \frac{\overline{a}_{\eta-1}}{\eta h\overline{a}_\eta} \text{ and } \gamma = \frac{2\overline{a}_{\eta-2}}{\eta(\eta-1)h^2\overline{a}_\eta}$$

2. Main Results

In this paper,first we obtain the following result which includes not only a refinement of Theorem 1.3 but also provides some generalization of other results.

Theorem 5. If $P \in P_\eta$ does not vanishes in $|z| < h, h \geq 1$, then for every $\mathtt{q} > 0$

$$\|P' + \tau\eta m z^{\eta-1}\|_\mathtt{q} \leq \frac{\eta}{\|\Gamma + z\|_\mathtt{q}} \|P\|_\mathtt{q}. \tag{18}$$

where Γ is defined by (15) and $m = \min_{|z|=h} |P(z)|$.

Corollary 1. If we put $m = 0$ and let $\mathtt{q} \to \infty$ in (18), the Theorem (5) reduces to Theorem (5) by using the inequality (18).

Corollary 2. For $m = 0$, inequality (18) reduces to inequality (16).

Next, we prove the theorem as a refinement of Theorem (4). In fact we prove

Theorem 6. If $P \in P_\eta$ vanishes in $|z| \leq h, h \leq 1$, then for every $\mathtt{q} > 0$

$$\|P' + \tau\eta m z^{\eta-1}\|_\mathtt{q} \geq \frac{\eta}{\|1 + Sz\|_\mathtt{q}} \|P\|_\mathtt{q}. \tag{19}$$

where S is defined by (17).

Corollary 3. For $m = 0$ Theorem (6) reduces to Theorem (4).

Instead of proving Theorem (6), we prove a more general result, from which Theorem (6),follows as a special case.

Theorem 7. If $P \in P_\eta$ vanishes in $|z| \leq h, h \leq 1$, then for every $\mathtt{q} > 0, r > 1, s > 1$ with $r^{-1} + s^{-1} = 1$.

$$\|P' + \tau\eta m z^{\eta-1}\|_{s\mathtt{q}} \geq \frac{\eta}{\|1 + Sz\|_{r\mathtt{q}}} \|P\|_{\mathtt{q}}. \tag{20}$$

where S is defined by (17).

Corollary 4. Put $r = 0$ or $s = 0$, we obtain Theorem (6).

3. Lemmas

In this section we present some lemmas which will help us to prove our results.

Lemma 1. If $P \in P_\eta$ does not vanishes in $|z| < h, h \geq 1$, then

$$\Gamma|P'(z)| \leq |\mathcal{Q}'(z)| \tag{21}$$

where Γ is defined by (15) and $\mathcal{Q}(z) = z^\eta \overline{P(\frac{1}{\overline{z}})}$

Above Lemma (1) is due to Govil et al. [7]. By applying Lemma (1) to the polynomial $P(z) = P(z) + m\tau z^\eta$, we immediately get the following result.

Lemma 2. If $P \in P_\eta$ does not vanishes in $|z| < h, h \geq 1$, then for any complex number τ with $|\tau| \leq 1$,

$$\Gamma|P'(z) + \tau\eta m z^{n-1}| \leq |\mathcal{Q}'(z)| \tag{22}$$

where Γ is defined by (15) and $m = \min_{|z|=h} |P(z)|$.

Lemma 3. If $P \in P_\eta$ vanishes in $|z| \leq h, h \leq 1$, then on $|z| = 1$

$$|\mathcal{Q}'(z)| \leq S|P'(z) + \eta m\tau z^{\eta-1}| \tag{23}$$

where S is defined by (17).

Proof of Lemma 3: Since $P(z)$ vanishes in $|z| \leq h, h \leq 1$, then the polynomial $\mathcal{Q}(z) = z^\eta \overline{P(\frac{1}{\overline{z}})}$ does not vanishes in $|z| < \frac{1}{h}, \frac{1}{h} \geq 1$. Thus applying Lemma (2) to the polynomial $\mathcal{Q}(z)$, we have

$$|\mathcal{Q}'(z)| \leq h\frac{(1-|\beta|)(|\frac{1}{h^2}\beta| + 1) + \frac{1}{h}(\eta-1)|\gamma - \beta^2|}{(1-|\beta|)(|\beta| + h^2) + \frac{1}{h}(\eta-1)|\gamma - \beta^2|} \left|P'(z) + \eta m\tau z^{\eta-1}\right|$$

Where

$$\beta = \frac{1/h}{\eta}\frac{\overline{a}_{\eta-1}}{\overline{a}_\eta} = \frac{\overline{a}_{\eta-1}}{\eta h\overline{a}_\eta} \text{ and } \gamma = \frac{2/h^2}{\eta(\eta-1)h^2}\frac{\overline{a}_{\eta-2}}{\overline{a}_\eta} = \frac{2\overline{a}_{\eta-2}}{\eta(\eta-1)h^2\overline{a}_\eta}.$$

Then,

$$|\mathcal{Q}'(z)| \leq h\frac{(1-|\beta|)(|\beta| + h^2) + h(\eta-1)|\gamma - \beta^2|}{(1-|\beta|)(|\beta|h^2 + 1) + h(\eta-1)|\gamma - \beta^2|} \left|P'(z) + \eta m\tau z^{\eta-1}\right|$$

which proves Lemma (3).

Lemma 4. If $P \in P_\eta$, then for every l, $0 \leq l < 2\pi$ and $\mathtt{q} > 0$

$$\int_0^{2\pi}\int_0^{2\pi} |\mathcal{Q}'(e^{i\Theta}) + e^{il}P'(e^{i\Theta})|^{\mathtt{q}} d\Theta dl \leq 2\pi\eta^{\mathtt{q}} \int_0^{2\pi} |P(e^{i\Theta})|^{\mathtt{q}} d\Theta \tag{24}$$

The above Lemma (4) is due to Aziz [2].

Lemma 5. If $P \in P_\eta$, then for every l, $0 \leq l < 2\pi$,$\mathfrak{q} > 0$ and for any complex number τ with $|\tau| \leq 1$,

$$\int_0^{2\pi}\int_0^{2\pi} |\mathcal{Q}'(e^{i\Theta}) + e^{il}\left\{P'(e^{i\Theta}) + \eta m\tau e^{i(\eta-1)\Theta}\right\}|^{\mathfrak{q}} d\Theta dl \leq 2\pi\eta^{\mathfrak{q}} \int_0^{2\pi} |P(e^{i\Theta})|^{\mathfrak{q}} d\Theta \tag{25}$$

Proof of Lemma 5: By applying Lemma (4) to the polynomial $P(z) = P(z) + m\tau z^n$, we can easily get the proof of Lemma (5).

Lemma 6. Let z be any complex and independent of l , where l is any real, then for $\mathfrak{q} > 0$

$$\int_0^{2\pi} |1 + ze^{il}|^{\mathfrak{q}} dl = \int_0^{2\pi} |e^{il} + |z||^{\mathfrak{q}} dl \tag{26}$$

Lemma (6) is due to Gardner and Govil [4].

4. Proofs of Theorems

Proof of Theorem 5: As $P(z)$ does not vanishes in $|z| < h, h \geq 1$ hence, by Lemma (2), we have

$$\Gamma|P'(z) + \tau\eta m z^{\eta-1}| \leq |\mathcal{Q}'(z)| \tag{27}$$

where Γ is defined by (15) and $m = \min_{|z|=h} |P(z)|$.
For each Real l and $G \geq r \geq 1$, we have

$$|G + e^{il}| \geq |r + e^{il}|$$

Then, for every $\mathfrak{q} > 0$, we have

$$\int_0^{2\pi} |G + e^{il}|^{\mathfrak{q}} dl \geq \int_0^{2\pi} |r + e^{il}|^{\mathfrak{q}} dl \tag{28}$$

For points $e^{i\Theta}$, $0 \leq \Theta < 2\pi$, for which $P'(e^{i\Theta}) + \eta m\tau e^{i(\eta-1)\Theta}$ does not vanishes, we denote $G = \left|\dfrac{\mathcal{Q}'(e^{i\Theta})}{P'(e^{i\Theta}) + \eta m\tau e^{i(\eta-1)\Theta}}\right|$ and $r = \Gamma$, then by (27), we for every $\mathfrak{q} > 0$

$$\begin{aligned}
&\int_0^{2\pi} \left|\mathcal{Q}'(e^{i\Theta}) + e^{il}\left\{P'(e^{i\Theta}) + \eta m\tau e^{i(\eta-1)\Theta}\right\}\right|^{\mathfrak{q}} dl \\
&= \left|P'(e^{i\Theta}) + \eta m\tau e^{i(\eta-1)\Theta}\right|^{\mathfrak{q}} \int_0^{2\pi} \left|\frac{\mathcal{Q}'(e^{i\Theta})}{P'(e^{i\Theta}) + \eta m\tau e^{i(\eta-1)\Theta}} + e^{il}\right|^{\mathfrak{q}} dl \\
&= \left|P'(e^{i\Theta}) + \eta m\tau e^{i(\eta-1)\Theta}\right|^{\mathfrak{q}} \int_0^{2\pi} \left|\left|\frac{\mathcal{Q}'(e^{i\Theta})}{P'(e^{i\Theta}) + \eta m\tau e^{i(\eta-1)\Theta}}\right| + e^{il}\right|^{\mathfrak{q}} dl \quad \text{by Lemma(6)} \\
&= \left|P'(e^{i\Theta}) + \eta m\tau e^{i(\eta-1)\Theta}\right|^{\mathfrak{q}} \int_0^{2\pi} \left|G + e^{il}\right|^{\mathfrak{q}} dl \\
&\geq \left|P'(e^{i\Theta}) + \eta m\tau e^{i(\eta-1)\Theta}\right|^{\mathfrak{q}} \int_0^{2\pi} \left|r + e^{il}\right|^{\mathfrak{q}} dl
\end{aligned}$$

Using (28),hence,

$$\int_0^{2\pi} \left|\mathcal{Q}'(e^{i\Theta}) + e^{il}\left\{P'(e^{i\Theta}) + \eta m\tau e^{i(\eta-1)\Theta}\right\}\right|^{\mathfrak{q}} dl \geq \left|P'(e^{i\Theta}) + \eta m\tau e^{i(\eta-1)\Theta}\right|^{\mathfrak{q}} \int_0^{2\pi} \left|\Gamma + e^{il}\right|^{\mathfrak{q}} dl \tag{29}$$

for $e^{i\Theta}$, $0 \leq \Theta < 2\pi$, for which $P'(e^{i\Theta}) + \eta m\tau e^{i(\eta-1)\Theta}$ does not vanishes.
For points $e^{i\Theta}$, $0 \leq \Theta < 2\pi$, for which $P'(e^{i\Theta}) + nm\tau e^{i(n-1)\Theta}$ vanishes, (29) trivially holds. Hence, using (29) in Lemma (5), we get for each $\mathfrak{q} > 0$,

$$\int_0^{2\pi} \left|P'(e^{i\Theta}) + \eta m\tau e^{i(\eta-1)\Theta}\right|^{\mathfrak{q}} d\Theta \int_0^{2\pi} \left|\Gamma + e^{il}\right|^{\mathfrak{q}} \leq 2\pi\eta^{\mathfrak{q}} \int_0^{2\pi} |P(e^{i\Theta})|^{\mathfrak{q}} d\Theta$$

which is equivalent to

$$\left\{\int_0^{2\pi} \left|P'(e^{i\Theta}) + \eta m\tau e^{i(\eta-1)\Theta}\right|^{\mathfrak{q}} d\Theta\right\}^{\frac{1}{\mathfrak{q}}} \leq \eta\left\{\frac{1}{2\pi}\int_0^{2\pi} \left|\Gamma + e^{il}\right|^{\mathfrak{q}} dl\right\}^{-\frac{1}{\mathfrak{q}}} \left\{\int_0^{2\pi} \left|P(e^{i\Theta})\right|^{\mathfrak{q}} d\Theta\right\}^{\frac{1}{\mathfrak{q}}} \tag{30}$$

which proves Theorem (5).

Proof of Theorem 7: Since $P(z)$ vanishes in $|z| \leq h, h \leq 1$, $P'(z)$ also vanishes in $|z| \leq h, h \leq 1$. Hence, by Gauss-Lucas Theorem,

$$z^{\eta-1}\overline{P(\frac{1}{\overline{z}})} = \eta\mathcal{Q}(z) - z\mathcal{Q}'(z) \tag{31}$$

vanishes in $|z| \geq \frac{1}{h}, \frac{1}{h} \geq 1$. Further, since $P(z)$ vanishes in $|z| \leq h, h \leq 1$, we have by Lemma (3),

$$\begin{aligned} |\mathcal{Q}'(z)| &\leq S|P'(z) + \eta m\tau z^{\eta-1}| \\ &= S\left\{|P'(z)| + t\eta m\right\} \quad for \ \ |z| = 1. \end{aligned} \tag{32}$$

where S is defined by (17) and $|\tau| = t$.
For $|z| = 1$, we also have

$$|P'(z) = |\eta\mathcal{Q}(z) - z\mathcal{Q}'(z)|. \tag{33}$$

Using (33) in (32) , we have on $|z| = 1$

$$|\mathcal{Q}'(z)| \leq S\left\{|\eta\mathcal{Q}(z) - z\mathcal{Q}'(z)| + t\eta m\right\} \tag{34}$$

Thus, by (31) and (34),

$$\psi(z) = \frac{z\mathcal{Q}'(z)}{S\left\{|\eta\mathcal{Q}(z) - z\mathcal{Q}'(z)| + t\eta m\right\}}$$

is analytic in $|z| \leq 1, |\psi(z)| \leq 1$ on $|z| = 1$ and $\psi(0) = 0$. Therefore, $1 + S\psi(z)$ is subordinate to the function $1 + Sz$ for $|z| \leq 1$. Hence, by a well known property of subordination [8], we have for every $\mathfrak{q} > 0$

$$\int_0^{2\pi} |1 + S\psi(e^{i\Theta})|^{\mathfrak{q}} d\Theta \geq \int_0^{2\pi} |1 + Se^{i\Theta}|^{\mathfrak{q}} d\Theta \tag{35}$$

Now,

$$1 + S\psi(z) = 1 + \frac{z\mathcal{Q}'(z)}{|\eta\mathcal{Q}(z) - z\mathcal{Q}'(z)| + t\eta m} = \frac{\eta\mathcal{Q}(z)}{|\eta\mathcal{Q}(z) - z\mathcal{Q}'(z)| + t\eta m}$$

which implies for $|z| = 1$,

$$\begin{aligned} |\eta\mathcal{Q}(z)| &= |1 + S\psi(z)|\left|\eta\mathcal{Q}(z) - z\mathcal{Q}'(z)\right| + t\eta m \\ &= |1 + S\psi(z)|\left|P'(z)\right| + t\eta m \quad by \quad (33) \end{aligned}$$

As $|P(z)| = |\mathcal{Q}(z)|$ on $|z| = 1$, by preceding inequality we have

$$\eta|P(z)| = |1 + S\psi(z)|\left|P'(z)\right| + t\eta m \quad on \quad |z| = 1 \tag{36}$$

Then for every $\mathfrak{q} > 0$ and $0 \leq \Theta < 2\pi$, we have

$$\eta^{\mathfrak{q}} \int_0^{2\pi} |P(e^{i\Theta})|^{\mathfrak{q}} d\Theta = \int_0^{2\pi} |1 + S\psi(e^{i\Theta})|^{\mathfrak{q}} \Big\{ \Big| P'(e^{i\Theta}) \Big| + t\eta m \Big\}^{\mathfrak{q}} d\Theta$$

Applying Holder's inequality to the above inequality, we have for $r > 1, s > 1$ with $r^{-1} + s^{-1} = 1$ and for every $\mathfrak{q} > 0$

$$\eta^{\mathfrak{q}} \int_0^{2\pi} |P(e^{i\Theta})|^{\mathfrak{q}} d\Theta \leq \left\{ \int_0^{2\pi} \Big| 1 + S\psi(e^{i\Theta}) \Big|^{r\mathfrak{q}} d\Theta \right\}^{\frac{1}{r}} \left\{ \int_0^{2\pi} \Big\{ \Big| P'(e^{i\Theta}) \Big| + t\eta m \Big\}^{s\mathfrak{q}} d\Theta \right\}^{\frac{1}{s}}$$

which implies

$$\eta \left\{ \int_0^{2\pi} |P(e^{i\Theta})|^{\mathfrak{q}} d\Theta \right\}^{\frac{1}{\mathfrak{q}}} \leq \left\{ \int_0^{2\pi} \Big| 1 + S\psi(e^{i\Theta}) \Big|^{r\mathfrak{q}} d\Theta \right\}^{\frac{1}{\mathfrak{q}r}} \left\{ \int_0^{2\pi} \Big\{ \Big| P'(e^{i\Theta}) \Big| + t\eta m \Big\}^{s\mathfrak{q}} d\Theta \right\}^{\frac{1}{s\mathfrak{q}}}$$

using (35) in the above inequality , we have

$$\eta \left\{ \int_0^{2\pi} |P(e^{i\Theta})|^{\mathfrak{q}} d\Theta \right\}^{\frac{1}{\mathfrak{q}}} \leq \left\{ \int_0^{2\pi} \Big| 1 + Se^{i\Theta} \Big|^{r\mathfrak{q}} d\Theta \right\}^{\frac{1}{\mathfrak{q}r}} \left\{ \int_0^{2\pi} \Big\{ \Big| P'(e^{i\Theta}) \Big| + t\eta m \Big\}^{s\mathfrak{q}} d\Theta \right\}^{\frac{1}{s\mathfrak{q}}}$$

by choosing argument of τ as in the proof of Theorem (6) , we get the above inequality as

$$\eta \left\{ \int_0^{2\pi} |P(e^{i\Theta})|^{\mathfrak{q}} d\Theta \right\}^{\frac{1}{\mathfrak{q}}} \leq \left\{ \int_0^{2\pi} \Big| 1 + Se^{i\Theta} \Big|^{r\mathfrak{q}} d\Theta \right\}^{\frac{1}{\mathfrak{q}r}} \left\{ \int_0^{2\pi} \Big| P'(e^{i\Theta}) + \tau\eta m e^{i(n-1)\Theta} \Big|^{s\mathfrak{q}} d\Theta \right\}^{\frac{1}{s\mathfrak{q}}}$$

which proves the theorem.

5. CONCLUSION

One of the interesting results on the L_q inequalities of complex polynomials is Aziz and Rathers™s extension of Malik™s inequality for the class of polynomials having all zeros in the disk $|z| \leq k, k \leq 1$. Krishnadas and Chanam [9] demonstrated the generalized form of that inequality. They succeeded in obtaining the L_q analogue of an inequality concerning a polynomial $P(z) = \sum_{v=0}^{n} a_v z^v$ of degree n having no zero in $|z| \leq k, k \geq 1$ instead of having all zeros in $|z| \leq k, k \leq 1$ .In this paper of our discussion, We proved a refinement of the inequality due to Krishnadas and Chanam [9] to the class of polynomials $P(z) = \sum_{v=0}^{n} a_v z^v$ having no zeros in $|z| \leq K, K \geq 1$ with the help of which several more results can be generalised.

References

[1] Arestov, V. V. (1982). On inequalities for trigonometric polynomials and their derivative. *Mathematics of the USSR-Izvestiya*, 18:1-17.

[2] Aziz, A. and Rather, N. A. (2004). Some Zygmund type Lq inequalities for polynomials. *Journal of Mathematical Analysis and Applications*, 289:14-29.

[3] Bruijn, N. G.(1947). Inequalities concerning polynomials in the complex domain. *Nederal. Akad. Wetensch. Proceeding*, 50:1265-1272.

[4] Gardner, R. B. and Govil, N. K. (1995). An Lq inequality for a polynomial and its derivative. *Journal of Mathematical Analysis and Applications*, 194:720-726.

[5] Gardner, R. and Weems, A. (1998). A Bernstein-type Lp inequality for a certain class of polynomials. *Journal of Mathematical Analysis and Applications*, 219:472-478.

[6] Govil, N. K. and Rahman, Q. I. (1969). Functions of exponential type not vanishing in a half-plane and related polynomials. *Transactions of the American Mathematical Society*, 137:501-517.

[7] Govil, N.K. , Rahman, Q. I. and Schmeisser, G. (1979). On the derivative of a polynomial. *Illinois Journal of Mathematics*, 23:319-329.

[8] Hille, E. Analytic Function Theory, Vol. II, Ginn. and Company, New York, Toronto (1962).

[9] Krishnadas, K. and Chanam, B. (2021). L^{γ} Inequalities Concerning Polynomials. *International Journal of Applied Mathematics*, 34:979-994.

[10] Lax, P. D. (1944). Proof of a Conjecture of P. Erdos on the derivative of a polynomial. *Bulletin of the American Mathematical Society*, 50:509-513.

[11] Malik, M. A. (1969). On the derivative of a polynomial. *Journal of the London Mathematical Society*, 57-60.

[12] Rahman, Q. I. and Schmeisser, G. (1988). Lp inequalities for polynomials. *Journal of Approximation Theory*, 53:26-32.

[13] Rather, N. A. Extremal Properties and Location of the Zeros of Polynomi- als. PhD. Thesis, University of Kashmir, (1998).

[14] Turan, P. Uber die ableitung von polynomen. *Compositio Mathematica*, 7:89-95(1939).

[15] Zygmund, A. (1932). A remark on conjugate series. *Proceedings of London Mathematical Society*, 34:392-400.

DECISION MAKING UNDER UNCERTAINTY BASED ON GENERALIZED FERMATEAN FUZZY NUMBERS

Tanuj Kumar[1,*], Gajraj Singh[2], Birjesh Kumar[3]

•

[1] Department of Mathematics, SRM Institute of Science and Technology,
Delhi NCR Campus, Ghaziabad, Uttar Pradesh, India
[2] Discipline of Statistics, School of Sciences,
Indira Gandhi National Open University, New Delhi, India
[3] Department of Statistics, Ramanujan College,
University of Delhi, New Delhi, India,
gajrajsingh@ignou.ac.in, birjesh.kumar@ramanujan.du.ac.in
[*] corresponding author: tanujkhutail@gmail.com

Abstract

It has been observed that Fermatean fuzzy sets, which provide a more comprehensive framework than intuitionistic fuzzy sets, offer significant advantages in decision-making processes. This study first formulates the generalized representation of Fermatean fuzzy numbers, including their membership and non-membership functions as well as the associated arithmetic operations. Furthermore, novel defuzzification and ranking techniques are proposed to convert Fermatean fuzzy information into crisp values. To validate the approach, a statistical application is presented for determining the sample range under generalized trapezoidal Fermatean fuzzy numbers using the proposed defuzzification and ranking methods. Finally, a case study is provided to demonstrate the practical applicability of generalized Fermatean fuzzy numbers in real-world decision-making contexts.

Keywords: decision making, Fermatean fuzzy sets, Pythagorean fuzzy sets, Intuitionistic fuzzy sets, defuzzification, score function

1. Introduction

In traditional decision-making approaches, it is often assumed that all criteria and their corresponding weights are precisely defined, enabling a straightforward ranking of alternatives. However, such methods frequently fail in real-world situations where ambiguity and uncertainty are present. To address these challenges, Zadeh [1] introduced fuzzy set theory (FST) as an extension of classical set theory, employing membership functions to model uncertainty. FST has proven effective in handling uncertainty in decision-making problems, leading to the development of numerous FST-based techniques applied in decision science. Building on this foundation, Atanassov [2] extended FST to intuitionistic fuzzy set theory (IFST) by incorporating membership and non-membership functions along with a hesitation index to better capture imprecise information. Intuitionistic fuzzy sets (IFSs) are now widely studied and applied across various domains of science and technology for managing uncertainty in problem-solving. In particular, generalized and standard forms of triangular and trapezoidal intuitionistic fuzzy numbers are commonly employed in decision science.

2. Literature Review

Numerous techniques for intuitionistic fuzzy decision-making have been developed in the literature by various researchers, including Atanassov et al. [3], [4], Liu and Wang [5], Li et al. [6], Shaw and Roy [7], Shaw and Roy [8], Ban and Tuse [9], Zeng et al. [10], and Che et al. [11]. These techniques have been successfully applied to various real-world decision-making scenarios. Kumar and Bajaj [12] proposed complex intuitionistic fuzzy soft sets with distance measures and entropies for use in multi-criteria decision-making problems. Garg and Rani [13] introduced a generalized weighted average aggregation operator for combining multiple complex intuitionistic fuzzy sets using t-norm operations, and also proposed a multi-criteria decision-making technique based on these operators. Jose [14] provided a model for decision-making in multiple-person problems in an intuitionistic fuzzy environment. Joshi and Kumar [15] developed an accuracy function for interval-valued IFSs and applied it to the problem of group decision making with many attributes. Fan et al. [17] proposed intuitionistic fuzzy weighted geometric and arithmetic averaging operators, which can be used to aggregate intuitionistic fuzzy information in multi-attribute decision-making problems. Additionally, numerous types of IFNs have been developed to address complex situations in real-world problems, such as the generalized parabolic IFN presented by Dutta et al. [18] for use in decision-making processes.

Yager [20] introduced a specific type of fuzzy set named Pythagorean fuzzy set, for which several aggregation operators have been established by Yager [21]. Ren et al. [24] recommended the use of Pythagorean fuzzy TODIM for MCDM problems, while Peng and Yang [22] used Pythagorean fuzzy aggregation operators to evaluate investments in Internet stocks. Reformat and Yager [23] implemented PFNs to construct an itemized list of the nominated films from the Netflix competition directory. Furthermore, Kumar et al. [16] introduced the accuracy function and distance measures of interval-valued Pythagorean fuzzy sets, which were applied to decision-making problems.

3. Research Objectives and Methodology

Quality control experts often face situations where alternative grade possibilities must be described by criteria such that the sum of favoring and disfavoring degrees exceeds one in certain real-world decision-making contexts. For instance, a decision expert may propose x_i as a potential solution satisfying criterion C_j, with a maximum satisfaction level of 0.9 and a maximum dissatisfaction level of 0.6. This violates the constraints imposed by both Pythagorean and intuitionistic fuzzy sets, rendering these approaches unsuitable for representing the expert™s assessment. To address such cases, Senapati and Yager [25] introduced Fermatean fuzzy sets, a more general framework than both intuitionistic and Pythagorean fuzzy sets, for decision-making problems. In this study, we explicitly examine generalized Fermatean fuzzy numbers along with their associated ranking and defuzzification methods, which are broadly applicable in statistics and problem-solving.

The structure of this paper is organized as follows. Section 2 introduces the fundamental definitions of generalized Fermatean fuzzy numbers (GFFNs) and intuitionistic fuzzy numbers, together with their arithmetic operations. Section 3 presents the defuzzification methods of Fermatean fuzzy numbers, while Section 4 focuses on their ranking methods. In Section 5, the practical applications of the proposed defuzzification and ranking approaches are demonstrated through decision-making problems and the determination of the sample range. Finally, Section 6 provides the concluding remarks.

In this section, we review the fundamental definitions of intuitionistic fuzzy sets and Fermatean fuzzy sets, along with their associated arithmetic operations.

4. Intuitionistic and Fermatean Fuzzy sets

Let X be a non-empty set of discourse and $A \subseteq V$ is said to be a fuzzy set (FS) of V defined by $A = \{\langle x, \mu_A(v)\rangle : v \in V\}$, where $\mu_A(v) : V \to [0,1]$ is a membership function of A or degree of

belonging of v in A. Thus, fuzzy set is a collection of objects with degree of membership [1]. A more generalize aspects of fuzzy sets was introduced by Atanassov [26] and widely used in various fields of science and technology.

Definition 2.1 Let $V = \{v_1, v_2, \ldots, v_n\}$ be a non-empty finite universal set, an Intuitionistic Fuzzy Set (IFS) $\tilde{A}$ in V is an object having the form:

$$A = \{< v, \phi_A(v), \psi_A(v) > | v \in V\}, \tag{1}$$

where the functions $\phi_A : V \to [0, 1]$ and $\psi_A : V \to [0, 1]$ defined the degree of membership and non-membership of an element $v \in V$ such that the condition $0 \leq \phi_A(v) + \psi_A(v) \leq 1$ is fulfilled. The quantity defined by $\varphi_A(v) = (1 - \phi_A(v) - \psi_A(v))$ is called the degree of indeterminacy of an element $v \in A$ [2].

Definition 2.2 [27]: An Intuitionistic fuzzy subset $\tilde{A}$ of the real line satisfies the following conditions:

1. $\tilde{A}$ is normal, i.e., there exist some $v_0 \in$ such that $\phi_{\tilde{A}}(v_0) = 1$, $\psi_{\tilde{A}}(v_0) = 0$.
2. $\tilde{A}$ is convex for the membership function $\phi_{\tilde{A}}(v)$ i.e.,

$$\phi_{\tilde{A}}(\lambda v_1 + (1 - \lambda)v_2) \geq \min(\phi_{\tilde{A}}(v_1), \phi_{\tilde{A}}(v_2))$$

   for all $v_1, v_2 \in, \lambda \in [0, 1]$.
3. $\tilde{A}$ is concave for the non-membership function i.e.,

$$\psi_{\tilde{A}}(v)\psi_{\tilde{A}}(\lambda v_1 + (1 - \lambda)v_2) \leq \max(\psi_{\tilde{A}}(v_1), \psi_{\tilde{A}}(v_2))$$

   for all $v_1, v_2 \in, \lambda \in [0, 1]$.

4.1. Fermatean Fuzzy Sets

Definition 2.3 [28] Let $V = \{v_1, v_2, \ldots, v_n\}$ be a non-empty finite universal set, an A Fermatean Fuzzy Set (FFS) $\tilde{A}$ in V is an object having the form:

$$A = \{< v, \phi_A(v), \psi_A(v) > | v \in V\}, \tag{2}$$

where the functions $\phi_A : V \to [0, 1]$ and $\psi_A : V \to [0, 1]$ defined the degree of membership and non-membership of an element $v \in V$ such that the condition $0 \leq \phi_A^3(v) + \psi_A^3(v) \leq 1$ is fulfilled. The quantity defined by $\varphi_A(v) = \sqrt[3]{(1 - \phi_A^3(v) - \psi_A^3(v))}$ is called the degree of indeterminacy of an element $v \in A$.

In addition, we provide a clear presentation of the generalized variant of Fermatean fuzzy numbers, including their membership and non-membership functions, as well as their fundamental arithmetic operations.

Definition 2.4 A generalized trapezoidal fermatean fuzzy number (GTPFFN) $\tilde{A}$ denoted by, $\tilde{A}_{Tp} = \langle [a_1, a_2, a_3, a_4; \mu], [a_1', a_2, a_3, a_4'; \nu] \rangle$ is a Fermatean fuzzy set on a real number set , whose membership function and non-membership functions are defined as:

$$\phi_{\tilde{A}}(x) = \begin{cases} \mu \left(\frac{x - a_1}{a_2 - a_1} \right)^{\frac{1}{3}}, & a_1 \leq x \leq a_2 \\ \mu, & a_2 \leq x \leq a_3 \\ \mu \left(\frac{a_4 - x}{a_4 - a_3} \right)^{\frac{1}{3}}, & a_3 \leq x \leq a_4 \\ 0, & otherwise \end{cases} \tag{3}$$

and

$$\psi_{\tilde{A}}(x) = \begin{cases} \left(\frac{(a_2-x)+\nu^3(x-a_1')}{a_2-a_1'}\right)^{\frac{1}{3}}, & a_1' \le x \le a_2 \\ \nu, & a_2 \le x \le a_3 \\ \left(\frac{(x-a_3)+\nu^3(a_4'-x)}{a_4'-a_3}\right)^{\frac{1}{3}}, & a_3 \le x \le a_4' \\ 0, & otherwise \end{cases} \tag{4}$$

where $a_1' \le a_1 \le a_2 \le a_3 \le a_4 \le a_4'$, $0 \le \mu, \nu \le 1$ and $0 \le \mu + \nu \le 1$. Note that a GTFFN is called a triangular Fermatean fuzzy number (TRFFN), if $a_3 = a_2$, $a_3 = a_4$ & $a_3 = a_4'$ and it is denoted by $\tilde{A}_{Tr} = \langle [a_1, a_2, a_3; \mu], [a_1', a_2, a_3'; \nu] \rangle$.

Definition 2.5 Let $\alpha, \beta \in [0, 1]$ be fixed numbers such that $0 \le \alpha \le \mu$, $\nu \le \beta \le 1$ and $0 \le \alpha^3 + \beta^3 \le 1$. A (α, β)-cuts generated by FFS A is defined as

$$A_{\alpha,\beta} = \{\langle v, \phi_A(v) \ge \alpha, \psi_A(v) \le \beta \rangle : v \in V\}. \tag{5}$$

Definition 2.6 The α-cut of an FFN $\tilde{A}$ is defined as

$$\tilde{A}_\alpha^\mu = \{\langle v, \phi_A(v) \ge \alpha \rangle : v \in V\}, 0 \le \alpha \le \mu. \tag{6}$$

Thus, by the definition, the α-cut of an FFN $\tilde{A}$ is

$$\tilde{A}_\alpha^\mu = [L_{\tilde{A}}(\alpha), U_{\tilde{A}}(\alpha)] = \left[a_1 + \frac{\alpha^3(a_2 - a_1)}{\mu^3}, a_4 - \frac{\alpha^3(a_4 - a_3)}{\mu^3}\right], 0 \le \alpha \le \mu. \tag{7}$$

Definition 2.7 The β-cut of an GTPFFN $\tilde{A}$ is defined as

$$\tilde{A}_\alpha^\mu = \{\langle v, \psi_A(v) \le \beta \rangle : v \in V\}, \nu \le \beta \le 1. \tag{8}$$

Thus, by the definition, the β-cut of an GTPFFN $\tilde{A}$ is

$$\tilde{A}_\beta^\nu = [L_{\tilde{A}}(\beta), U_{\tilde{A}}(\beta)] = \left[\frac{a_2(1-\beta^3) + a_1'(\beta^3 - v^3)}{1 - \nu^3}, \frac{a_3(1-\beta^3) + a_4'(\beta^3 - v^3)}{1 - \nu^3}\right], \nu \le \beta \le 1. \tag{9}$$

Definition 2.8: Let $\alpha, \beta \in [0, 1]$ be fixed numbers such that $0 \le \alpha \le \mu$, $\nu \le \beta \le 1$ and $0 \le \alpha^3 + \beta^3 \le 1$. The α and β-cuts of a GTRFFN $\tilde{A_T} = \langle [a_1, a_2, a_3); \mu], [a_1', a_2, a_3'; \nu] \rangle$ are defined as follows:

$$\tilde{A}_\alpha^\mu = [L_{\tilde{A}}(\alpha), U_{\tilde{A}}(\alpha)] = \left[a_1 + \frac{\alpha^3(a_2 - a_1)}{\mu^3}, a_3 - \frac{\alpha^3(a_3 - a_2)}{\mu^3}\right] \tag{10}$$

and

$$\tilde{A}_\beta^\nu = [L_{\tilde{A}}(\beta), U_{\tilde{A}}(\beta)] = \left[\frac{a_2(1-\beta^3) + a_1'(\beta^3 - v^3)}{1 - \nu^3}, \frac{a_2(1-\beta^3) + a_3'(\beta^3 - v^3)}{1 - \nu^3}\right]. \tag{11}$$

The usual arithmetic, namely addition, subtraction, multiplication and division between $\tilde{A}_{Tp}$ and $\tilde{B}_{Tp}$ are given as follows:

Let $\tilde{A}_{Tp} = \langle [a_1, a_2, a_3, a_4; \mu_1], [a_1', a_2, a_3, a_4'; \nu_1] \rangle$ and
$\tilde{B}_{Tp} = \langle [b_1, b_2, b_3, b_4; \mu_2], [b_1', b_2, b_3, b_4'; \nu_2] \rangle$ be two generalized trapezoidal Fermatean fuzzy numbers, then we have

1.

$$\tilde{A} + \tilde{B} = \left\langle \begin{matrix} [a_1 + b_1, a_2 + b_2, a_3 + b_3, a_4 + b_4; \mu = \min(\mu_1, \mu_2)], \\ [a_1' + b_1', a_2 + b_2, a_3 + b_3, a_4' + b_4'; \nu_2 = \max(\nu_1, \nu_2)] \end{matrix} \right\rangle$$

2.

$$\tilde{A} - \tilde{B} = \left\langle \begin{matrix} [a_1 - b_4, a_2 - b_3, a_3 - b_2, a_4 - b_1; \mu = \min(\mu_1, \mu_2)], \\ [a_1' - b_4', a_2 - b_3, a_3 - b_2, a_4' - b_1'; \nu_2 = \max(\nu_1, \nu_2)] \end{matrix} \right\rangle$$

3.
$$\tilde{A} * \tilde{B} = \left\langle \begin{matrix} [a_1b_1,\, a_2b_2,\, a_3b_3,\, a_4b_4;\, \mu = \min(\mu_1,\, \mu_2)], \\ [a_1'b_1',\, a_2b_2,\, a_3b_3,\, a_4'b_4';\, \nu_2 = \max(\nu_1,\, \nu_2)] \end{matrix} \right\rangle$$

4.
$$\tilde{A}/\tilde{B} = \left\langle \begin{matrix} [a_1/b_4,\, a_2/b_3,\, a_3/b_2,\, a_4/b_1;\, \mu = \min(\mu_1,\, \mu_2)], \\ [a_1'/b_4',\, a_2/b_3,\, a_3/b_2,\, a_4'/b_1';\, \nu_2 = \max(\nu_1,\, \nu_2)] \end{matrix} \right\rangle$$

5.
$$k * \tilde{A} = \left\langle [ka_1,\, ka_2,\, ka_3,\, ka_4;\, \mu_1], \quad [ka_1',\, ka_2,\, ka_3,\, ka_4';\, \nu_1] \right\rangle, \text{ if } k > 0.$$

$$k * \tilde{A} = \left\langle [ka_4,\, ka_4,\, ka_2,\, ka_1;\, \mu_1], \quad [ka_4',\, ka_3,\, ka_2,\, ka_1';\, \nu_1] \right\rangle \text{ if } k < 0.$$

In this section, we will present the defuzzification method for Fermatean fuzzy numbers, which incorporating all the information related to Fermatean fuzzy numbers into the process of defuzzification, using the α-cut technique.

5. Defuzzification of Fermatean Fuzzy Numbers

Let $\tilde{A}_{Tp} = \left\langle [a_1,\, a_2,\, a_3,\, a_4; \mu_1],\, [a_1',\, a_2,\, a_3,\, a_4'; \nu_1] \right\rangle$ be a generalized trapezoidal Fermatean fuzzy number with the following membership and non-membership functions:

$$\phi_{\tilde{A}}(x) = \begin{cases} \mu \left(\frac{x - a_1}{a_2 - a_1} \right)^{\frac{1}{3}}, & a_1 \le x \le a_2 \\ \mu, & a_2 \le x \le a_3 \\ \mu \left(\frac{a_4 - x}{a_4 - a_3} \right)^{\frac{1}{3}}, & a_3 \le x \le a_4 \\ 0, & otherwise \end{cases} \tag{12}$$

and

$$\psi_{\tilde{A}}(x) = \begin{cases} \left(\frac{(a_2 - x) + \nu^3 (x - a_1')}{a_2 - a_1'} \right)^{\frac{1}{3}}, & a_1' \le x \le a_2 \\ \nu, & a_2 \le x \le a_3 \\ \left(\frac{(x - a_3) + \nu^3 (a_4' - x)}{a_4' - a_3} \right)^{\frac{1}{3}}, & a_3 \le x \le a_4' \\ 0, & otherwise \end{cases}, \tag{13}$$

respectively.

The score function is defined as the difference between membership and non-membership functions:

$$\begin{aligned} S(\tilde{A}) &= \mu(\tilde{A}) - \nu(\tilde{A}) \\ &= \begin{cases} \omega(x - \kappa); & \kappa \le x \le a_2 \\ (\mu^3 - \nu^3); & a_2 \le x \le a_3 \\ \rho(\tau - x); & a_3 \le x \le \tau \end{cases} \end{aligned}$$

where

$$\kappa = \frac{\mu^3 a_1 (a_2 - a_1') + (a_2 - a_1)(a_2 - a_1' \nu^3)}{\mu^3 (a_2 - a_1') + (1 - \nu^3)(a_2 - a_1)}, \; \omega = \frac{\mu^3 (a_2 - a_1') + (1 - \nu^3)(a_2 - a_1)}{(a_2 - a_1)(a_2 - a_1')}$$

$$\tau = \frac{\mu^3 a_4 (a_4' - a_3) + (a_4 - a_3)(a_3 - a_4' \nu^3)}{\mu^3 (a_4' - a_3) + (1 - \nu^3)(a_4 - a_3)}, \; \rho = \frac{\mu^3 (a_4' - a_3) + (1 - \nu^3)(a_4 - a_3)}{(a_4 - a_3)(a_4' - a_3)}$$

with $0 \le \mu, \nu \le 1$ and $0 \le \mu + \nu \le 1$.

The α-cut of $\tilde{S} = \langle(\kappa, a_2, a_3, \tau); \mu, \nu\rangle$ is defined as

$$\begin{aligned}\tilde{A}(\alpha) &= \left[\tilde{A}_L(\alpha), \tilde{A}_R(\alpha)\right] \\ &= \left[\kappa + \frac{\alpha}{\omega}, \tau - \frac{\alpha}{\rho}\right].\end{aligned} \tag{14}$$

The defuzzification formula for GTPFFNs is defined as follows:

$$\begin{aligned}DTP_f &= \int_0^{\mu^3-\nu^3} \left(\lambda L^{-1}(\alpha) + (1-\lambda)R^{-1}(\alpha)\right) d\alpha \\ &= \left[(\lambda\kappa + (1-\lambda)\tau)(\mu^3-\nu^3) + \frac{(\lambda\rho - (1-\lambda)\omega)(\mu^3-\nu^3)^2}{2\rho\omega}\right]\end{aligned} \tag{15}$$

To calculate the weighted average of the defuzzified values of the membership and non-membership functions of GTPFFNs, a parameter λ with $0 < \lambda < 1$ is introduced. In this research, we set $\lambda = \frac{1}{2}$, although other values of λ could be suitable for addressing weighted decision-making problems.

Note that a GTFFN is called a generalized triangular Fermatean fuzzy number (GTRFFN), if we replace a_3 by a_2, and a_4 by a_3 & a_4' by a_3 and it is denoted by $\tilde{A}_{Tr} = \langle[a_1, a_2, a_3; \mu], [a_1', a_2, a_3'; \nu]\rangle$ and the defuzzification formula for GTRFFNs is defined as

$$\begin{aligned}DTR_f &= \int_0^{\mu^3-\nu^3} \left(\lambda L^{-1}(\alpha) + (1-\lambda)R^{-1}(\alpha)\right) d\alpha \\ &= \left[(\lambda\kappa + (1-\lambda)\tau)(\mu^3-\nu^3) + \frac{(\lambda\rho - (1-\lambda)\omega)(\mu^3-\nu^3)^2}{2\rho\omega}\right],\end{aligned} \tag{16}$$

where

$$\kappa = \frac{\mu^3 a_1(a_2 - a_1') + (a_2 - a_1)(a_2 - a_1'\nu^3)}{\mu^3(a_2 - a_1') + (1-\nu^3)(a_2 - a_1)},\ \omega = \frac{\mu^3(a_2 - a_1') + (1-\nu^3)(a_2 - a_1)}{(a_2 - a_1)(a_2 - a_1')}$$

$$\tau = \frac{\mu^3 a_3(a_3' - a_2) + (a_3 - a_2)(a_2 - a_3'\nu^3)}{\mu^3(a_3' - a_2) + (1-\nu^3)(a_3 - a_2)},\ \rho = \frac{\mu^3(a_3' - a_2) + (1-\nu^3)(a_3 - a_2)}{(a_3 - a_2)(a_3' - a_2)}$$

with $0 \le \mu, \nu \le 1$ and $0 \le \mu + \nu \le 1$.

6. Ranking of GTPFFNs

In this section, we establish a method for ranking GTPFFNs, which involves evaluating the mean value of the membership and non-membership functions of GTPFFNs.

Let $\tilde{A}_{Tp} = \langle[a_1, a_2, a_3, a_4; \mu], [a_1', a_2, a_3, a_4'; \nu]\rangle$ be a GTPFFN whose (α, β)-cuts are given by

$$\tilde{A}_\alpha^\mu = \left[a_1 + \frac{\alpha^3(a_2 - a_1)}{\mu^3}, a_4 - \frac{\alpha^3(a_4 - a_3)}{\mu^3}\right],\ 0 \le \alpha \le \mu. \tag{17}$$

$$\tilde{A}_\beta^\nu = \left[\frac{a_2(1-\beta^3) + a_1'(\beta^3 - v^3)}{1-\nu^3}, \frac{a_3(1-\beta^3) + a_4'(\beta^3 - v^3)}{1-\nu^3}\right],\ \nu \le \beta \le 1. \tag{18}$$

The mean value of membership and non-membership functions of GTPFFNs is defined as

$$m = \frac{1}{2}\int_0^\mu \left[a_1 + \frac{\alpha^3(a_2 - a_1)}{\mu^3} + a_4 - \frac{\alpha^3(a_4 - a_3)}{\mu^3}\right] d\alpha. \tag{19}$$

$$m = \frac{3\mu(a_1 + a_4) + \mu(a_2 + a_3)}{8}. \tag{20}$$

$$n = \frac{1}{2}\int_{\nu}^{1}\left[\frac{a_2(1-\beta^3)+a_1'(\beta^3-v^3)}{1-\nu^3}+\frac{a_3(1-\beta^3)+a_4'(\beta^3-v^3)}{1-\nu^3}\right]d\alpha.$$

$$n = \frac{(a_2+a_3)\left(\nu^4-4\nu+3\right)+(a_1'+a_4')(3\nu^4-4\nu^3+1)}{8(1-\nu^3)}. \tag{21}$$

The value of membership function $V_\mu(A)$ and non-membership function $V_\nu(A)$ are defined as follows:

$$V_\mu(A) = m\int_{0}^{\mu}\left[a_4-\frac{\alpha^3(a_4-a_3)}{\mu^3}-a_1-\frac{\alpha^3(a_2-a_1)}{\mu^3}+\right]d\alpha.$$

$$V_\mu(A) = \frac{\mu^2\left[9(a_4^2-a_1^2)+6(a_3a_4-a_1a_2)+(a_3^2-a_2^2)\right]}{32}. \tag{22}$$

$$V_\nu(A) = n\int_{\nu}^{1}\left[\frac{a_3(1-\beta^3)+a_4'(\beta^3-v^3)}{1-\nu^3}-\frac{a_2(1-\beta^3)+a_1'(\beta^3-v^3)}{1-\nu^3}\right]d\beta.$$

$$V_\nu(A) = \frac{\left[\theta^2(a_4'^2-a_1'^2)+2\eta\theta(a_3a_4'-a_1'a_2)+\eta^2(a_3^2-a_2^2)\right]}{32(1-\nu^3)}, \tag{23}$$

where $\eta = \left(\nu^4-4\nu+3\right)$ and $\theta = (3\nu^4-4\nu^3+1)$.

The ranking order of $\tilde{A}_{Tp}$ is defined as

$$R(\tilde{A}_{Tr},\lambda) = \lambda V_\mu(A)+(1-\lambda)V_\nu;\quad 0\le\lambda\le 1 \tag{24}$$

and the ranking order of $\tilde{A}_{Tr}$ is defined as

$$R(\tilde{A}_{Tr},\lambda) = \lambda V_\mu(A)+(1-\lambda)V_\nu;\quad 0\le\lambda\le 1, \tag{25}$$

$$V_\mu(A) = \frac{\mu^2\left[9(a_3^2-a_1^2)+6(a_2a_3-a_1a_2)\right]}{32} \tag{26}$$

and

$$V_\nu(A) = \frac{\left[\theta^2(a_3'^2-a_1'^2)+2\eta\theta(a_2a_3'-a_1'a_2)\right]}{32(1-\nu^3)}, \tag{27}$$

here $\eta = \left(\nu^4-4\nu+3\right)$ and $\theta = (3\nu^4-4\nu^3+1)$.

Thus, for two GFFNs $\tilde{A}$ and $\tilde{B}$, the the ranking order depend on the values of $R(\tilde{A},\lambda)$ and $R(\tilde{B},\lambda)$ and described as follows:

- $(R(\tilde{A},\lambda)) < (R(\tilde{B},\lambda))$, if $R(\tilde{A},\lambda) < R(\tilde{B},\lambda)$.
- $(R(\tilde{A},\lambda)) \ge (R(\tilde{B},\lambda))$, if $R(\tilde{A},\lambda) \ge R(\tilde{B},\lambda)$.

7. Applications of Fermatean Fuzzy Sets

7.1. Range of Samples under Trapezoidal Fermatean Fuzzy numbers based on Ranking Order

Since order statistics depend on the sequence of sample values, statistical methods do not work well with datasets that contain uncertainty or inaccuracies from measurement tools or data collection methods. To address these challenges, we introduce a fuzzification step to the data first to reduce the uncertainty and then one can perform statistical methods or decision-making procedures on the defuzzified data to obtain insights and draw conclusions.

For instance, in statistical quality control charts, the range of the data is important for determining the limits of the chart; here we show how to calculate the range of the uncertain sample data. Take sample data from a normal distribution with mean 20 and standard deviation

1 and each sample of size $n = 5$ is fuzzified into a trapezoidal Fermatean fuzzy numbers in Table 2. Rank each fuzzy observation in each sample using the proposed ranking formula (Eq. 24) and list the ranking order (RO) of each sample observation in Table 3. Calculate the range of each sample by selecting the highest and lowest ranking orders of the Fermatean fuzzy numbers; list the ranges in Table 4. Calculate the mean range for the whole data set using the proposed defuzzification formula (Eq. 15), which is 0.8642.

Table 1: *Data drawn from normal distribution*

S.No.	X_1	X_2	X_3	X_4	X_5
S_1	20.5377	20.6715	19.8978	18.9109	21.4193
S_2	21.8339	18.7925	19.7586	20.0326	20.2916
S_3	17.7412	20.7172	20.3192	20.5525	20.1978
S_4	20.8622	21.6302	20.3129	21.1006	21.5877
S_5	20.3188	20.4889	19.1351	21.5442	19.1955
S_6	18.6923	21.0347	19.9699	20.0859	20.6966
S_7	19.5664	20.7269	19.8351	18.5084	20.8351
S_8	20.3426	19.6966	20.6277	19.2577	19.7563
S_9	23.5784	20.2939	21.0933	18.9384	20.2157
S_{10}	22.7694	19.2127	21.1093	22.3505	18.8342
S_{11}	18.6501	20.8884	19.1363	19.3844	18.8520
S_{12}	23.0349	18.8529	20.0774	20.7481	20.1049
S_{13}	20.7254	18.9311	18.7859	19.8076	20.7223
S_{14}	19.9369	19.1905	18.8865	20.8886	22.5855
S_{15}	20.7147	17.0557	19.9932	19.2352	19.3331
S_{16}	19.7950	21.4384	21.5326	18.5977	20.1873
S_{17}	19.8759	20.3252	19.2303	18.5776	19.9175
S_{18}	21.4897	19.2451	20.3714	20.4882	18.0670
S_{19}	21.4090	21.3703	19.7744	19.8226	19.5610
S_{20}	21.4172	18.2885	21.1174	19.8039	18.2053

Table 2: *Fuzzifying sample data and ranking ordering*

S.No.	D_1'	D_1	D_2	D_3	D_4	D_4'	μ	ν	*Rank*	*RO*
S_{11}	20.5337	20.5353	20.5361	20.5389	20.5397	20.5416	0.9311	0.1029	0.0702	2
S_{12}	20.6707	20.6710	20.6712	20.6717	20.6719	20.6723	0.9602	0.0763	0.0156	5
S_{13}	19.8945	19.8958	19.8964	19.8987	19.8994	19.9010	0.9689	0.1248	0.0571	3
S_{14}	18.9087	18.9096	18.9100	18.9116	18.9121	18.9132	0.9084	0.0729	0.0368	4
S_{15}	21.4147	21.4166	21.4175	21.4207	21.4216	21.4239	0.9152	0.1326	0.0803	1
S_{21}	21.8312	21.8323	21.8328	21.8347	21.8352	21.8366	0.9996	0.0578	0.0566	2
S_{22}	18.7903	18.7912	18.7916	18.7932	18.7936	18.7947	0.9107	0.1462	0.0335	3
S_{23}	19.7585	19.7585	19.7585	19.7586	19.7586	19.7586	0.9775	0.1317	0.0004	5
S_{24}	20.0282	20.0300	20.0308	20.0339	20.0347	20.0369	0.9084	0.0900	0.0739	1
S_{25}	20.2903	20.2908	20.2911	20.2920	20.2922	20.2929	0.9800	0.0931	0.0241	4
S_{31}	17.7366	17.7384	17.7393	17.7425	17.7434	17.7457	0.9182	0.0764	0.0703	1
S_{32}	20.7165	20.7168	20.7169	20.7175	20.7176	20.7180	0.9136	0.1369	0.0123	5
S_{33}	20.3163	20.3175	20.3180	20.3201	20.3207	20.3221	0.9550	0.0645	0.0538	3
S_{34}	20.5483	20.5500	20.5508	20.5538	20.5547	20.5568	0.9622	0.0851	0.0792	2
S_{35}	20.1952	20.1963	20.1968	20.1986	20.1991	20.2004	0.9402	0.0576	0.0469	4
.	.	.	.	.	.	.	.	.	.	.
.	.	.	.	.	.	.	.	.	.	.
.	.	.	.	.	.	.	.	.	.	.
S_{201}	21.4135	21.4150	21.4157	21.4183	21.4190	21.4208	0.9344	0.1084	0.0671	2
S_{202}	18.2879	18.2882	18.2883	18.2886	18.2888	18.2890	0.9906	0.1380	0.0088	5
S_{203}	21.1133	21.1149	21.1157	21.1186	21.1194	21.1214	0.9261	0.1094	0.0734	1
S_{204}	19.8038	19.8039	19.8039	19.8040	19.8040	19.8041	0.9425	0.0813	0.0020	4
S_{205}	18.2045	18.2048	18.2050	18.2056	18.2057	18.2061	0.9179	0.0923	0.0126	3

Table 3: *Ranges of samples and mean range*

S.No.	R_1'	R_1	R_2	R_3	R_4	R_4'	μ	ν
1	0.7441	0.7456	0.7463	0.7489	0.7497	0.7516	0.9152	0.1326
2	0.2697	0.2714	0.2723	0.2753	0.2762	0.2783	0.9084	0.1317
3	0.1682	0.1668	0.1661	0.1637	0.1629	0.1612	0.9136	0.1369
4	0.5526	0.5513	0.5506	0.5483	0.5477	0.5460	0.9123	0.0991
5	0.0651	0.0632	0.0623	0.0590	0.0581	0.0557	0.9043	0.0669
6	0.6077	0.6089	0.6095	0.6116	0.6122	0.6137	0.9081	0.1429
7	1.1621	1.1615	1.1611	1.1600	1.1597	1.1588	0.9306	0.1009
8	1.0815	1.0829	1.0836	1.0859	1.0866	1.0883	0.9226	0.1122
9	2.4811	2.4827	2.4835	2.4863	2.4872	2.4892	0.9258	0.0909
10	3.5138	3.5148	3.5153	3.5170	3.5175	3.5188	0.9459	0.1463
11	0.5361	0.5346	0.5339	0.5312	0.5305	0.5286	0.9099	0.1413
12	2.2897	2.2886	2.2880	2.2860	2.2854	2.2840	0.9680	0.0834
13	1.7955	1.7938	1.7929	1.7898	1.7889	1.7867	0.9490	0.1118
14	1.0458	1.0476	1.0486	1.0519	1.0528	1.0551	0.9071	0.1022
15	0.7547	0.7560	0.7567	0.7590	0.7596	0.7613	0.9083	0.1331
16	0.0973	0.0961	0.0955	0.0933	0.0927	0.0912	0.9292	0.0932
17	1.0982	1.0969	1.0962	1.0938	1.0932	1.0915	0.9418	0.1483
18	2.3008	2.3022	2.3030	2.3055	2.3062	2.3080	0.9669	0.1145
19	1.5946	1.5951	1.5954	1.5963	1.5965	1.5972	0.9121	0.1090
20	1.3094	1.3110	1.3118	1.3146	1.3154	1.3174	0.9261	0.1094
$\bar{R}$	1.1734	1.1736	1.1736	1.1739	1.1739	1.1741	0.9043	0.1483

In the following, we propose a decision-making approach to choose the best option among several alternatives using Fermatean fuzzy numbers. We illustrate the practical importance of Fermatean fuzzy decision making by using the ranking of GFFNs in the method.

7.2. Multi-Criteria Decision Making Problem

Assume that r decision makers DM_1, DM_2, DM_3, $\ldots, DM_r$ want to select the best option from a set of n options, say A_1, A_2, A_3, $\ldots$, A_n, based on m criteria C_1, C_2, C_3, $\ldots$, C_m. The steps in the computation are as follows:

1. The GFFNs (Low, Medium, High, and Very High) are linguistic variables used to rank the alternatives according to each criterion, and the decision makers choose the linguistic weight variables for each criterion's importance weight.
2. The decision makers give each criterion an importance weight based on the linguistic weight variables.
3. To determine the aggregated Fermatean fuzzy weight w_i of the criterion C_j, utilize the following formula:
$$w_j = \frac{[w_j^1 + w_j^2 + \ldots + w_j^r]}{r}, \quad j = 1, 2, \ldots, m. \tag{28}$$
4. Using the rating values assigned by the decision makers to the options across the criteria, construct the Fermatean fuzzy decision matrix D.

$$D = \begin{array}{c|cccc} & C_1 & C_2 & \cdots & C_m \\ \hline A_1 & r_{11} & r_{12} & \cdots & r_{1m} \\ A_2 & r_{21} & r_{22} & \cdots & r_{2m} \\ \vdots & \cdots & \cdots & \cdots & \cdots \\ A_n & r_{n1} & r_{n2} & \cdots & r_{nm} \end{array}$$

5. We can compute the weighted average decision using the recommended arithmetic operations as follows:
$$D_i = \sum_{j=1}^{m} r_{ij} w_j, \quad i = 1, 2, \ldots, n. \tag{29}$$
6. The ranking order formula given by Equation (25) is applied to compute the index value $I(D_i, \lambda)$ for each average decision D_i by considering different values of $\lambda \in [0, 1]$.
7. Ultimately, the decision expert selects the alternative with the highest index value.

A committee consisting of three decision-makers, DM_1, DM_2, and DM_3, is formed to select the most suitable applicant for a teaching position from among three candidates, A_1, A_2, and A_3. The evaluation is carried out based on four benefit criteria, C_1, C_2, C_3, and C_4.

1. The decision-makers first determine the linguistic weight variable for each criterion, as shown in Table 4, and then use the linguistic rating variable in Table 5 to evaluate the alternatives with respect to each criterion.

Table 4: *Linguistic variable for each criterion's weight*

L	<[0.18 0.20 0.26; 0.4], [0.16 0.20 0.27; 0.2] >
M	<[0.43 0.48 0.54; 0.6], [0.41 0.48 0.56; 0.4]>
H	<[0.61 0.65 0.72; 0.7], [0.59 0.65 0.75; 0.5] >
VH	<[0.84 0.88 0.95; 0.9], [0.81 0.88 0.98; 0.6] >

Table 5: *Linguistic variable for the ratings*

P	<[0.20 0.24 0.30; 0.5], [0.18 0.24 0.33; 0.1] >
F	<[0.43 0.49 0.57; 0.6], [0.39 0.49 0.59; 0.3] >
G	<[0.65 0.78 0.83; 0.8], [0.61 0.78 0.84; 0.5] >
VG	<[0.85 0.89 0.92; 0.9], [0.83 0.89 0.95; 0.6] >

2. The importance of each criterion is evaluated in Table 6 using the linguistic weighting variables defined in Table 4.

Table 6: *Criterion's weight given by Decision Makers*

Decision Makers $\rightarrow$ Criterion $\downarrow$	2*D_1	2*D_2	2*D_3
C_1	M	L	M
C_2	H	VH	H
C_4	VH	H	VH
C_4	VH	VH	VH

3. Table 6 is employed to aggregate the criteria weights and equation (28) is then applied to compute the overall fuzzy weight w_j of each criterion C_j.

$$w_1 =< [0.350.390.45; 0.53], [0.330.390.46; 0.60] >$$

$$w_2 =< [0.690.730.80; 0.77], [0.660.730.83; 0.53] >$$

$$w_3 =< [0.760.800.87; 0.83], [0.740.800.90; 0.57] >$$

$$w_4 =< [0.840.880.95; 0.90], [0.810.880.98; 0.60] > .$$

4. The fuzzy decision matrix D is constructed based on the ratings provided by the decision-makers.

$$D = \begin{array}{c} \\ A_1 \\ A_2 \\ A_3 \end{array} \begin{array}{c} \begin{array}{cccc} C_1 & C_2 & C_3 & C_4 \end{array} \\ \begin{pmatrix} P & F & F & G \\ G & F & VG & G \\ VG & VG & G & G \end{pmatrix} \end{array}$$

As a result, the fuzzy decision matrix D is created as shown below

Table 7: *Fuzzy decision matrix D*

	C_1	C_2	C_3	C_4
A_1	<[0.20 0.24 0.30;0.5], [0.18 0.24 0.33;0.1]>	<[0.43 0.49 0.57;0.6], [0.39 0.49 0.59;0.3]>	<[0.43 0.49 0.57;0.8], [0.39 0.49 0.59;0.5]>	<[0.65 0.78 0.83;0.9], [0.61 0.78 0.84;0.6]>
A_1	<[0.65 0.78 0.83;0.5], [0.61 0.78 0.84 ;0.1]>	<[0.39 0.49 0.59 ;0.5], [0.14 0.24 0.34 ;0.1]>	<[0.85 0.89 0.92;0.5], [0.83 0.89 0.95;0.1]>	<[0.65 0.78 0.83;0.5], [0.61 0.78 0.84;0.1]>
A_1	<[0.85 0.89 0.92;0.5], [0.83 0.89 0.95;0.1]>	<[0.85 0.89 0.92;0.5], [0.83 0.89 0.95;0.1]>	<[0.65 0.78 0.83;0.5], [0.61 0.78 0.84;0.1]>	<[0.65 0.78 0.83;0.5], [0.61 0.78 0.84;0.1]>

5. Now, we evaluate average decision using the suggested arithmetic operations and index values of all $D_i's$ are calculated for different values of $\lambda \in [0, 1]$, as shown in Table 7.

$$D_i = \sum_{j=1}^{m} r_{ij} w_j, \quad i = 1, 2, \ldots, n. \tag{30}$$

Table 8: *$D_i's$ with their index values for different λ values*

2*	D_1	D_2	D_3
	<[1.24,1.53,1.87;0.69], [1.10,1.53,2.00;0.53]>	<[1.69,2.06,2.43;0.74], [1.40,1.88,2.35;0.53]>	<[1.92,2.30,2.66;0.77], [1.77,2.30,2.81;0.56]>
λ	Index value of D_1	Index value of D_2	Index value of D_3
0.0	0.106	0.108	0.154
0.1	0.201	0.287	0.363
0.2	0.295	0.466	0.571
0.3	0.390	0.645	0.780
0.4	0.484	0.824	0.989
0.5	0.579	1.003	1.198
0.6	0.673	1.182	1.406
0.7	0.767	1.361	1.615
0.8	0.862	1.540	1.824
0.9	0.956	1.719	2.032
1.0	1.051	1.898	2.241

6. It is evident from the above tables that, for any value of $\lambda \in [0, 1]$, the ranking order of D_1, D_2, and D_3 remains the same, i.e., $D_3 > D_2 > D_1$. Consequently, A_3 is identified as the best alternative, with the overall ranking given by $A_3 > A_2 > A_1$.

8. Conclusions

The present study has demonstrated the explicit representation of generalized Fermatean fuzzy numbers together with their fundamental arithmetic operations. In addition, novel defuzzification and ranking methods have been proposed to transform generalized Fermatean fuzzy observations into crisp values. A statistical application has been included to illustrate the use of the proposed defuzzification and ranking techniques in determining the sample range under trapezoidal generalized Fermatean fuzzy numbers. Furthermore, a decision-making problem has been examined to highlight the practicality and applicability of generalized Fermatean fuzzy numbers in real-world scenarios.

Disclosure Statement

The authors declare that they do not have any known financial or other competing interests which could appear to have affected the work presented in this document.

References

[1] Zadeh, L. A. (1965). Fuzzy sets. *Information and Control*, 8:338–356. https://doi.org/10.1016/S0019-9958(65)90241-X.

[2] Atanassov, K. T. (1986). Intuitionistic fuzzy sets. *Fuzzy Sets and Systems*, 20(1):87–96. https://doi.org/10.1016/S0165-0114(86)80034-3.

[3] Atanassov, K., Pasi, G., and Yager, R. (2002). Intuitionistic fuzzy interpretations of multi-person multi-criteria decision making. In *First International IEEE Symposium on Intelligent Systems*, pages 859–868. https://doi.org/10.1080/00207720500382365.

[4] Li, D. F. (2005). Multiattribute decision making models and methods using intuitionistic fuzzy sets. *Journal of Computer and System Sciences*, 70(1):73–85.

[5] Liu, H. W. and Wang, G. (2007). Multi-criteria decision-making methods based on intuitionistic fuzzy sets. *European Journal of Operational Research*, 179:220–233.

[6] Li, D. F., Nan, J. X., and Zhang, M. J. (2010). A ranking method of triangular intuitionistic fuzzy numbers and application to decision making. *International Journal of Computational Intelligence Systems*, 3(5):522–530.

[7] Shaw, A. K. and Roy, T. K. (2012). Some arithmetic operations on triangular intuitionistic fuzzy number and its application on reliability evaluation. *International Journal of Fuzzy Mathematics and Systems*, 2(4):363–382.

[8] Shaw, A. K. and Roy, T. K. (2013). Trapezoidal intuitionistic fuzzy number with some arithmetic operations and its application on reliability evaluation. *International Journal of Mathematics in Operational Research*, 5(1):55–73.

[9] Ban, A. I. and Tuse, D. A. (2014). Trapezoidal/triangular intuitionistic fuzzy numbers versus interval-valued trapezoidal/triangular fuzzy numbers and applications to multicriteria decision making methods. *Notes on Intuitionistic Fuzzy Sets*, 20(2):43–51.

[10] Zeng, X. T., Li, D. F., and Yu, G. F. (2014). A value and ambiguity-based ranking method of trapezoidal intuitionistic fuzzy numbers and application to decision making. *The Scientific World Journal*, 2014:8. https://doi.org/10.1155/2014/560582.

[11] Chen, S., Mu, Z., and Zeng, S. (2015). Atanassov™s intuitionistic fuzzy decision making with probabilistic information and distance measure. *Journal of Intelligent & Fuzzy Systems*, 28(1):317–325.

[12] Kumar, T. and Bajaj, R. K. (2014). On complex intuitionistic fuzzy soft sets with distance measures and entropies. *Journal of Mathematics*, 2014.

[13] Garg, H. and Rani, D. (2018). Some generalized complex intuitionistic fuzzy aggregation operators and their application to multicriteria decision-making process. *Arabian Journal for Science and Engineering*, 44(3):1–20.

[14] Jose, S. (2018). Intuitionistic fuzzy approach to multi person decision making. *Advances in Fuzzy Mathematics*, 13(1):9–14.

[15] Joshi, D. and Kumar, S. (2018). Improved accuracy function for interval-valued intuitionistic fuzzy sets and its application to multi-attributes group decision making. *Cybernetics and Systems*, 49(1):64–76. https://doi.org/10.1080/01969722.2017.1412890.

[16] Kumar, T., Bajaj, R., and Ansari, M. D. (2020). On accuracy function and distance measures of interval-valued Pythagorean fuzzy sets with application to decision making. *Scientia Iranica*, 27(4):2127–2139.

[17] Fan, C. L., Song, Y., Fu, Q., Lei, L., and Wang, X. (2018). New operators for aggregating intuitionistic fuzzy information with their application in decision making. *IEEE Access*, 6:27214–27238.

[18] Dutta, P., Saikia, B., and Doley, D. (2020). Decision making under uncertainty via generalized parabolic intuitionistic fuzzy numbers. In Castillo, O., Jana, D., Giri, D., and Ahmed, A. (eds), *Recent Advances in Intelligent Information Systems and Applied Mathematics. ICITAM 2019. Studies in Computational Intelligence*, vol. 863, pp. 243–256. Springer, Cham. https://doi.org/10.1007/978-3-030-34152-7_18.

[19] Dutta, P., Boruah, H., and Ali, T. (2011). Fuzzy arithmetic with and without using α-cut method: a comparative study. *International Journal of Latest Trends in Computing*, 2(1):99–107.

[20] Yager, R. R. (2013). Pythagorean fuzzy subsets. In *Proceedings of the Joint IFSA World Congress and NAFIPS Annual Meeting*, Edmonton, Canada, pp. 57–61.

[21] Yager, R. R. (2014). Pythagorean membership grades in multicriteria decision making. *IEEE Transactions on Fuzzy Systems*, 22:958–965.

[22] Peng, X. and Yang, Y. (2015). Some results for Pythagorean fuzzy sets. *International Journal of Intelligent Systems*, 30:1133–1160.

[23] Reformat, M. Z. and Yager, R. R. (2014). Suggesting recommendations using Pythagorean fuzzy sets illustrated using Netflix movie data. In Laurent, A., Strauss, O., Bouchon-Meunier, B., and Yager, R. R. (eds), *Information Processing and Management of Uncertainty in Knowledge-Based Systems*, pp. 546–556. Springer, Berlin.

[24] Ren, P., Xu, Z., and Gou, X. (2016). Pythagorean fuzzy TODIM approach to multi-criteria decision making. *Applied Soft Computing*, 42:246–259.

[25] Senapati, T. and Yager, R. R. (2020). Fermatean fuzzy sets. *Journal of Ambient Intelligence and Humanized Computing*, 11(2):663–674.

[26] Atanassov, K. T. (1986). Intuitionistic fuzzy sets. *Fuzzy Sets and Systems*, 20:87–96.

[27] Burillo, P., Bustince, H., and Mohedano, V. (1994). Some definition of intuitionistic fuzzy number. In *Proceedings of Fuzzy Based Expert Systems, Fuzzy Bulgarian Enthusiasts*, Sofia, Bulgaria, September 28–30. https://doi.org/10.1007/s13369-020-05176-0.

[28] Senapati, T. and Yager, R. R. (2019). Fermatean fuzzy sets. *Journal of Ambient Intelligence and Humanized Computing*, 11:663–674. https://doi.org/10.1007/s12652-019-01377-0.

PERFORMANCE METRICS OF M/M(A,B)/(2,1)/RV QUEUING SYSTEM WITH RENEGING AND RETENTION OF CUSTOMERS

Jenifer Princy P *, K Julia Rose Mary

•

[1,2] Department of Mathematics, Nirmala College for Women, Coimbatore, India
* pjeniferprincy2001@gmail.com
juliakulandaisamy@gmailcom

Abstract

In general, the quality of service management ensures the quality of the business outcome. Customer behavior trivially has an impact on it. To obtain a potential output, it is necessary to speed up the customer service request. Adequate among of losses happen when the customers withdraw the service request. Thus, it is vital to implement a significant strategy based on the number of request in queue. By modeling the service system mathematically in concern with the customers behavior, it is elegant to make a strategy for estimating demands. This paper aims to interpret a system, M/M(a,b)/(2,1)/RV providing service in batches with the aid of two servers and encounters the measures of performance of the system under the possibility of servers vacation and customers behavior of reneging and retention. A server withdraws the system whenever he is not available with an accessible batch to start his service. This behavior of the server can be termed as vacation. The vacation policy used in this paper involves the repeated mode of vacation of the servers. Customers entering the system experience three states of availability of the servers. Thus, for the proposed model the equations and solutions for the steady state is derived and computed theoretically, and the results are verified through numerical illustration.

Keywords: General bulk service rule, Markovian process, Poisson arrival, Reneging, Repeated vacations

1. Introduction

The sustainable growth in all fields of this real world urges everyone to undergo a systematic progressing of a work. In that sense, lining up to fulfill once need also becomes one among this progressing. Now a days researchers focus on modeling the practical scenarios into a computational frame work and introduce them into the literature. In the similar way, the study on queues and its behavior is known as queuing theory was introduced into the mathematical literature by Agner K. Erlang, the Danish mathematician. Queuing prevails almost everywhere, even from the grocery shops to digital markets. The mathematical approach on queuing provides solution in the way of optimizing a work in fields like manufacturing systems, business management, traffic flow, computer systems, and so on. To optimize a work, it is important to have efficient servers, service time and service quality that means a good quality service in a good period of time. Long-term waiting for a work may anticipates many clients and it stimulates them to withdraw from the queue of waiting. This paper aims to interpret this impatience behavior of customers waiting in the queue. Reneging of customers will ultimately create a greater impact on the system. A credential amount of loss may happen.

On the other hand while obtaining service, there may be situations where a customer may

experience the unavailability of the server, since he may left the system for a random interval of time either for some other job or to take rest. This period of unavailability of the server is called vacation. So far, the research on queuing theory, studying queuing models with vacation policy, has also become a crucial area of study for many researchers.

A methodological overview of the queuing system with two vacation models was done by B.T Doshi [6]. Divya and Indhira [5] surveyed on these vacation models as it is an important existing real-life situation that has been encountered in our daily life routine and industrial management. Similarly, models with working vacations was surveyed by Fiems [8]. S. Sindhu et al. [19]has also worked on queuing models with vacation policies, which was found with arrival and service variants.

There may also exist some situations where the servers undergo random vacation from the system multiple times in order to avoid being idle, which means not having an accessible batch size in the system. This behavior of the server is called repeated vacation (RV). At first, Palaniammal [16] worked on the queuing model, M/M(a,b)/(2,1) in this perspective. Later, Baskar and Palaniammal [2] both again worked on this model, M/M(a,b)/(2,1) with repeated and delayed vacation taken by the servers. Maragathasundari et al. [14] made a study on non Markovian queuing system and analyzed it with two categories over vacation period. Motivated in analyzing health care service facilities Sundararaman et al. [21] estimated the performance metrics of the system that allow customers to join the usual and retrial waiting line are estimated using SVT technique. It is also noticeable that the servers are on working vacations.

In order to minimize customer waiting time during the unavailability of the servers, it is preferable if the system has a few more servers to grant service so that customers are served at a moment. In view of assisting the system continuously irrespective of breakdown, repair, and vacation, employing additional server helps to assist the system effectively. Srinivas R. Chakravarthy and Kulshrestha [3] discussed a queuing system from this point of view. By the way, in order to save energy and to improve the quality of service in virtual machines Ma et al. [13] proposed an energy saving measure by combining synchronous and asynchronous vacation and modeled them into a Markov stochastic model of two dimension with many servers. Queuing systems with cost optimization was done by Afanasyev [1] considering the behavior of the system during vacation period.

The concept of impatient attitude of customers was analysed by Dbeis and Sahili [4] for the Markovian queuing system with single channel. Customers encouraged arrival into the system may result in the reneging of customers from the queue. Som et al. [20] practically valid this scenario for a system with single server. Economic analysis was done by Pan et al. [17] for the customers alternative level of impatient behavior in a single server system. Khan and Paramasivam [9] analysed the quality control policy for finite limit Markovian queuing system with to reduce the waiting time and maintain the reneged customers not to join the system again. Lidiya and K.J.R. Mary [12] interpreted the queuing model consisting of one server and analysed the act of reneging of customers with working vacation policy. Kumar [11] addressed a queuing system with some probable perspectives, including customers reneging with a threshold policy. With the aid of the metrics evaluated optimality values were also interpreted. Fayama et al. [7] evaluated the performance of a queuing model with two servers with finite capacity under the scenario of reneging. Seenivasan et al. [18] studied a queuing model under the circumstances of system failure and reneging of customers. Heterogeneous service system involving two servers with customers reverse balking and reneging was studied by Tamuli et al. [22] Since queuing is an integral part of life in many fields, the health care department faces this mainly. Patients renege the health care facilities when they are dissatisfied but the probability of reneging varies with different time marks thus a correlated reneging was proposed and studied by Kuaban et al. [10] for a multi-server queuing model.

Previously, Mary K.J.R and Jenifer Princy studied the queuing model M/M(a,b)/(2,1) [15] under the perspective of an encouraged arrival of customers and breakdown of the servers. With an aid of this survey the model M/M(a,b)/ (2,1)/RV under customer impatient behavior reneging is proposed and the steady state equations and solutions are derived in the following sections. A

numerical illustration is carried out to verify the validity of the outcomes.

2. Mathematical Model Description

This model involves two servers where the arrival of customers to the system follows the Poisson distribution with the parameter λ. The service rate follows an exponential distribution with parameter μ. The service is done in batches according to the General Bulk Service Rule introduced by Neuts. The service is provided if there are a minimum 'a' number of customers in the queue. If the number of customers is more than the maximum limit 'b' only the first b customers are allowed to take the service.

The servers are in idle state if there is not even a minimum number of customers in a queue. In this case, a server leaves the system for a random period called vacation. This follows an exponential distribution with parameter θ. On returning from the vacation, if the server finds less than 'a' customers in the queue while the other server is busy or idle, the server leaves the system for another random period called repeated vacation. The server will continue the same activity until he finds minimum 'a' number of customers to start his service. This particular queuing system always be available with at least one server either in the idle or busy state.

Meanwhile, long waiting in the queue to get a service anticipates clients and it stimulates them to withdraw from the queue without fulfilling their need. The customers may renege whenever it takes time to reach the minimum batch size or at the time of servers' vacation. These customers renege at the rate of ζ. Let $p^{'}$ be the probability that the customers may renege and $q^{'} = 1 - p'$ be the probability that the reneged customers are retained in the system.

In the state space $(j, n)\, , j = 0, 1, 2; n \geq 0$, the queue is studied as a Markov process where $n \geq 0$ denotes the number of customers waiting in the queue and j denotes the level of the server.

1. $(0, n)$ - represents that one server is idle and the other server is on vacation, $0 \leq n \leq a - 1$.
2. $(1, n)$ - represents that one server is busy and the other server is on vacation, $n \geq 0$.
3. $(2, n)$ - represents that both the servers are busy, $n \geq 0$.

Defining $P_{jn}(t) = \text{Prb}\ \{$ At time t, the system is in the state $(j,\ n) j = 0, 1, 2; n \geq 0\}$ and considering that the steady state probabilities are $P_{0n} = \lim_{t\to\infty} p_{0n}(t)$,$P_{1n} = \lim_{t\to\infty} p_{1n}(t)$ and $P_{2n} = \lim_{t\to\infty} p_{2n}(t)$.

The steady state equations are

$$\lambda p_{00} = \mu p_{10} \tag{1}$$

$$\lambda p_{0n} = \lambda p_{0n-1} + (\mu + n\zeta p^{'}) p_{1n} \quad (1 \leq n \leq a-1) \tag{2}$$

$$(\lambda + \mu) p_{10} = \lambda p_{0a-1} + 2\mu p_{20} + (\mu + n\zeta p^{'}) \sum_{n=a}^{b} p_{1n} \tag{3}$$

$$(\lambda + \mu + n\zeta p^{'}) p_{1n} = \lambda p_{1n-1} + (2\mu + 2n\zeta p^{'}) p_{2n} + (\mu + (n+b)\, \zeta p^{'}) p_{1n+b} \quad (1 \leq n \leq a-1) \tag{4}$$

$$(\lambda + \mu + n\zeta p^{'} + \theta) p_{1n} = \lambda p_{1n-1} + (\mu + (n+b)\, \zeta p^{'}) p_{1n+b} + \mu p_{1n+b} \quad (n \geq a) \tag{5}$$

$$(\lambda + 2\mu) p_{20} = \theta \sum_{l=a}^{b} p_{1n} + (2\mu + 2n\zeta p^{'}) \sum_{n=a}^{b} p_{2n} \tag{6}$$

$$(\lambda + 2\mu + 2n\zeta p^{'}) p_{2n} = \lambda p_{2n-1} + \theta p_{1n+b} + (2\mu + 2(n+b)\zeta p^{'}) p_{2n+b} \quad (n \geq 1) \tag{7}$$

3. Steady State Solutions

Let E be the forward shifting operator defined by $E(p_{1\,n}) = p_{1\,n+1}$. Equation 5 implies $[(\mu + n\zeta p^{'} + b\zeta p^{'})E^{b+1} - (\mu + n\zeta p^{'} + b\zeta p^{'})E + \lambda]p_{1\,n} = 0. \quad (n \geq 1).$

The corresponding characteristic equation is as follows.

$$(\mu + n\zeta p^{'} + b\zeta p^{'})Z^{b+1} - (\mu + n\zeta p^{'} + b\zeta p^{'})Z + \lambda = 0. \tag{8}$$

Then by Rouche's Theorem., it has only one real root inside the circle $|z| = 1$ when $\rho = \dfrac{\lambda + \theta}{b(\mu + n\zeta p^{'})} < 1.$ Let r_0 be the root of the above characteristic equation with $|r_0| < 1$. Therefore, the homogeneous difference equation has solution of the form.

$$p_{1\,n} = A_1 r_0^n \quad (n \geq a - 1)$$

so we get

$$p_{1\,n} = r_0^{n-a+1} p_{1\,a-1} \quad (n \geq a) \tag{9}$$

Using equation 7 we get

$$[2(\mu + n\zeta p^{'} + b\zeta p^{'})E^{b+1} - (\lambda + 2\mu + 2n\zeta p^{'})E + \lambda]p_{2\,n} = -\theta p_{1\,n+b+1} \quad (n \geq 1)$$

The corresponding characteristic equation is

$$2(\mu + n\zeta p^{'} + b\zeta p^{'})Z^{b+1} - (\lambda + 2(\mu + n\zeta p^{'}))Z + \lambda = 0 \tag{10}$$

If r_1 is the root of the above characteristic equation with $|r_1| < 1$ which exists when $\rho_1 = \left(\dfrac{\lambda}{2b(\mu + n\zeta p^{'})}\right) < 1.$ This non - homogeneous difference equation (7) has the solution

$$p_{2\,n} = (A_1 r_1^n + K r_0^n) p_{1\,a-1} \quad (n \geq 0) \tag{11}$$

where A_1 is constant and $K = \dfrac{\left(-\theta r_0^{b-a+2}\right)}{(\lambda + 2\theta)\, r_0 - \lambda}$

Using equation 4 and substituting for $p_{2\,n+1}$ and $p_{1\,n+b+1}$ we have after simplification.

$$p_{1\,n} = [A_2 R^n + B_1(r_0) r_0^n + B_2(r_1) r_1^n]\, p_{1\,a-1} \quad (0 \leq n \leq a - 1) \tag{12}$$

where $R = \dfrac{\lambda}{\lambda + \mu + n\zeta p^{'}}, \quad B_1(r_0) = \dfrac{2(\mu + n\zeta p^{'})K r_0 + (\mu + (n+b)\zeta p^{'}) r_0^{b-a+2}}{\theta[(\lambda + \mu + n\zeta p^{'}) r_0 - \lambda]}$ and

$B_2(r_1) = \dfrac{2(\mu + n\zeta p^{'}) A_1 r_1}{(\lambda + \mu + n\zeta p^{'}) r_1 - \lambda}$

Adding equation 2 over $k = 1$ to n and substituting for $p_{1\,k}$ from equation 12 and simplifying, we get

$$p_{0\,n} = \left\{ \frac{\mu}{\lambda} \left[A_2 \frac{1 - R^{n+1}}{1 - R} + B_1(r_0) \frac{1 - r_0^{n+1}}{1 - r_0} + B_2(r_1) \frac{1 - r_1^{n+1}}{1 - r_1} \right] + \frac{\zeta p^{'}}{\lambda} \left[A_2 H(R) + B_1(r_0) H(r_0) \right. \right.$$
$$\left. \left. + B_2(r_1) H(r_1) \right] \right\} p_{1\,a-1} \quad (0 \leq n \leq a - 1) \tag{13}$$

where $H(u) = \left(\dfrac{u(1 - u^{n+1}) - (n+1)u^{n+1}(1 - u)}{(1 - u)^2}\right)$

Using equation 9 and 11 in 6 then we obtain

$$A_1 = \frac{\theta \left(r_0 - r_0^{b-a+2} + 2K(E(r_0) - \mu) - \lambda K \right)}{\lambda - 2(E(r_1) - \mu)} \tag{14}$$

where $E(u) = \left(\frac{u^a - u^{b+1}}{1-u}\right)(\mu + a\zeta p') + \zeta p' \left(\frac{(1-u^{b-a+1})u^{a+1} - (b-a+1)(1-u)u^{b+1}}{(1-u)^2}\right)$
Further, In equation 12 substituting $n = a-1$ we get the value of A_1 as

$$A_2 = \frac{1}{R^{a-1}}\left[1 - B_1(r_0)r_0^{a-1} - B_2(r_1)r_1^{a-1}\right] \tag{15}$$

The value of $p_{1\,a-1}$ is obtained using the normalizing condition.

$$\sum_{n=0}^{\infty} p_{2\,n} + \sum_{n=a}^{\infty} p_{1\,n} + \sum_{n=0}^{a-1}(p_{0\,n} + p_{1\,n}) = 1 \tag{16}$$

substituting for $p_{2\,n}$, $p_{1\,n}$ and $p_{0\,n}$ and simplifying we get,

$$p_{1\,a-1}^{-1} = A_2\big(S(R) + J(R)\big) + B_1(r_0)\big(S(r_0) + J(r_0)\big) + B_2(r_1)\big(S(r_1) + J(r_1)\big) + \frac{A_1}{1-r_1} + \frac{K}{1-r_0} + \frac{r_0}{1-r_0} \tag{17}$$

where $S(u) = \frac{1-u^a}{1-u} + \frac{\mu}{\lambda}\left(\frac{a}{1-u} - \frac{u}{1-u}\frac{1-u^a}{1-u}\right)$
$J(u) = \frac{\zeta p'}{\lambda}\left\{\frac{(a+1)(u^{a+1}-u^2) + (a-1)(u-u^{a+2})}{(1-u)^3}\right\}$ and the values of $R, B_1(r_0), B_2(r_1)$ are obtained from equation 12.

4. Analysis of the Measures of Performance

In this section, we have computed the measures of performance of the system M/M (a,b)/ (2,1)/RV under customers impatient attitude of reneging.

1. **Expected Queue Length**

   The expected queue length is given by

   $$L_q = \sum_{n=1}^{\infty} n p_{2\,n} + \sum_{n=a}^{\infty} n p_{1\,n} + \sum_{n=1}^{a-1} n\,(p_{0\,n} + p_{1\,n})$$

   Using equations (10) to (16) and simplifying, we have

   $$L_q = \Bigg[A_2(U(R) + V(R)) + B_1(r_0)(U(r_0) + V(r_0)) + B_2(r_1)(U(r_1) + V(r_1)) + \frac{ar_0}{1-r_0} + \frac{r_0^2}{(1-r_0)^2} + \frac{A_1 r_1}{(1-r_1)^2} + \frac{Kr_0}{(1-r_0)^2}\Bigg] p_{1\,a-1}$$

   where,
   $U(u) = \left(\frac{1-u^a - au^{a-1}(1-u)}{(1-u)^2}\right)\left(u - \frac{u^2\mu}{\lambda(1-u)}\right) + \frac{\mu a(a-1)}{2\lambda(1-u)}$ and
   $V(u) = \frac{\zeta p'}{\lambda}\left[\frac{a(a-1)u}{2(1-u)^2} + \frac{u^2(3u^{a+1} - u - 2)}{(1-u)^4} + \frac{au^{a-1} - (a+1)(u^2 - u^{a+2})}{(1-u)^3}\right]$

2. **Expected Waiting Time,** W_q

   $$W_q = \frac{L_q}{\lambda}$$

3. **Expected Rate of Reneging,** R_g

   $$R_g = l\zeta p' L_q$$

4. Let $P_{2\,B}$ denote the probability that both the servers are busy then

$$P_{2\,B} = \sum_{n=0}^{\infty} p_{2\,n} = \left(\frac{A_1}{1-r_1} + \frac{K}{1-r_0} \right) p_{1\,a-1}$$

5. Let $P_{1\,B}$ denote the probability that one server is busy and the other server is on vacation then

$$P_{1\,B} = \sum_{n=0}^{\infty} p_{1\,n} = \left(A_2 \frac{1-R^a}{1-R} + B_1(r_0) \frac{1-r_0^a}{1-r_0} + B_2(r_1) \frac{1-r_1^a}{1-r_1} + \frac{r_0}{1-r_0} \right) p_{1\,a-1}$$

6. Let $P_{0\,B}$ denote the probability that one server is idle and one server is on vacation then

$$P_{0\,B} = \sum_{n=0}^{a-1} p_{0\,n} = \left[A_2\big(G(R)+F(R)\big) + B_1(r_0)\big(G(r_0)+F(r_0)\big) + B_2(r_1)\big(G(r_1)+F(r_1)\big) \right] p_{1\,a-1}$$

where $F(u) = \dfrac{\zeta p^{'}}{\lambda} \left[\dfrac{au}{(1-u)^2} - \dfrac{u^2(1-u^a)}{(1-u)^3} + \dfrac{u(u^{a+1}+(a+1)(1-u)u^a-1}{(1-u)^3} \right]$ and $G(u) = \dfrac{\mu}{\lambda} \left(\dfrac{a}{1-y} + \dfrac{u(1-u^a)}{(1-u)^2} \right)$ and the values of $R, B_1(r_0), B_2(r_1)$ are obtained from equation (12).

5. Numerical Analysis

In practice, many manufacturing industries involve production in batches. However, it is notable to manage the manufacturing system effectively. Those sectors must be aware of the orders received for production and the quantity they need to deliver during the recommended period of time, as it decides the economic outcome of the business. Reneging of orders also a catastrophe happens when the orders are not served on time.

Thus, considering sample values, the performance measures are verified in this section in order to validate the findings.

For a batch (a, b) of size with lower limit, $a = 3$ and upper limit $b = 15$ service is granted with a service rate, $\mu = 2$. The following Table 1, shows the expected queue size of the proposed queuing system and the probability measures of the system with respect to the probability of reneging and retention of customers in correspondence to the arrival rate $\lambda = 12$, reneging rate, $\zeta = 0.04$ and vacation rate $\theta = 0.1$.

Table 1: *L_q, P_{0B}, P_{1B}, P_{2B} with respect to $p^{'}$ and $q^{'}$*

$p^{'}$	$q^{'}$	L_q	P_{0B}	P_{1B}	P_{2B}
0	1	5.8615	0.1062	0.8756	0.02072
0.1	0.9	5.71201	0.1069	0.8751	0.02039
0.2	0.8	5.5686	0.10762	0.8746	0.02005
0.3	0.7	5.4301	0.10834	0.8741	0.01973
0.4	0.6	5.2915	0.10912	0.8736	0.01938
0.5	0.5	5.1575	0.1099	0.87301	0.01904
0.6	0.4	5.0280	0.1107	0.8725	0.01869
0.7	0.3	4.9029	0.1115	0.8719	0.0184
0.8	0.2	4.7823	0.1123	0.8714	0.01804
0.9	0.1	4.6656	0.1131	0.8708	0.0177
1	0	4.5485	0.1139	0.87021	0.0174

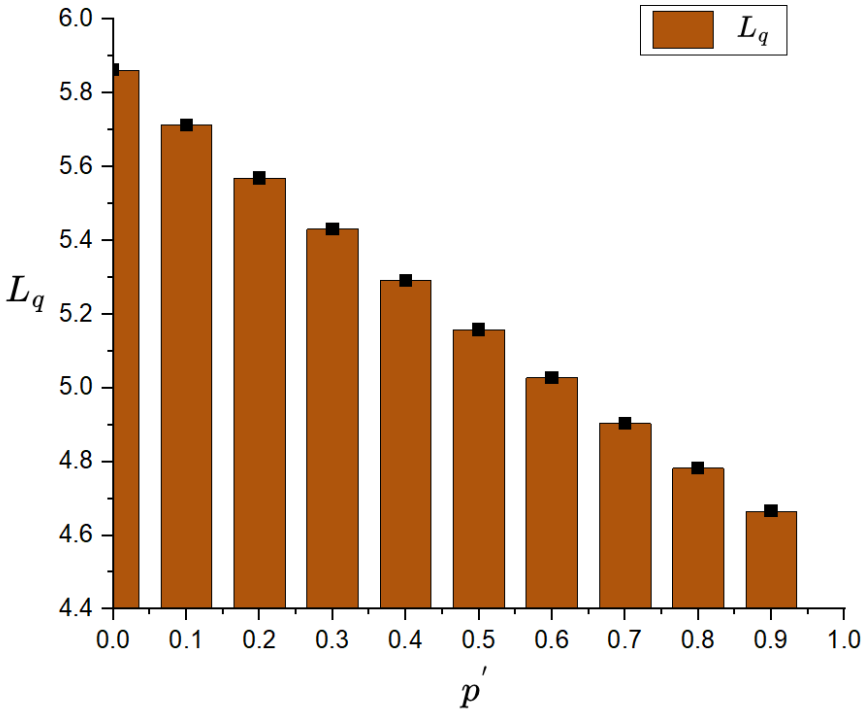


Figure 1: *Probability of reneging Vs Expected length of the queue*

The graphical representation in Figure 1 shows that the expected queue length decreases with an increase in the probability of reneging p'.

Table 2: *L_q, W_q, R_g with respect to ζ*

ζ	L_q	W_q	R_g
0.01	4.6407	0.3867	0.4455
0.02	4.5573	0.3798	0.8749
0.03	4.5263	0.3772	1.3036
0.04	4.4675	0.3723	1.7155
0.05	4.3543	0.3629	2.0900
0.06	4.1916	0.3493	2.4143
0.07	3.9992	0.3333	2.6875
0.08	3.7973	0.3164	2.9163
0.09	3.6229	0.3019	3.1302
0.1	3.4494	0.2875	3.3114

The increase in reneging directly impacts the length of the queue. Customer withdrawal from the queue reduces the congestion in the waiting line, it seems that there is a reduction in the length of the waiting queue. Meanwhile, the waiting time in the queue also decreases. The above Table 2. shows the sample result for different values of ζ. The length of the queue decreases from 4.4607 to 3.4494 and the waiting time in the queue also decreases from 0.3867 to 0.2875.

It is efficient to estimate the expected rate of reneging, that is, the number of customers renege during a period of time, which is also estimated and tabulated in Table 2. As the reneging rate increases, the expected number of customers reneging from the system also increases. This result validates our findings.

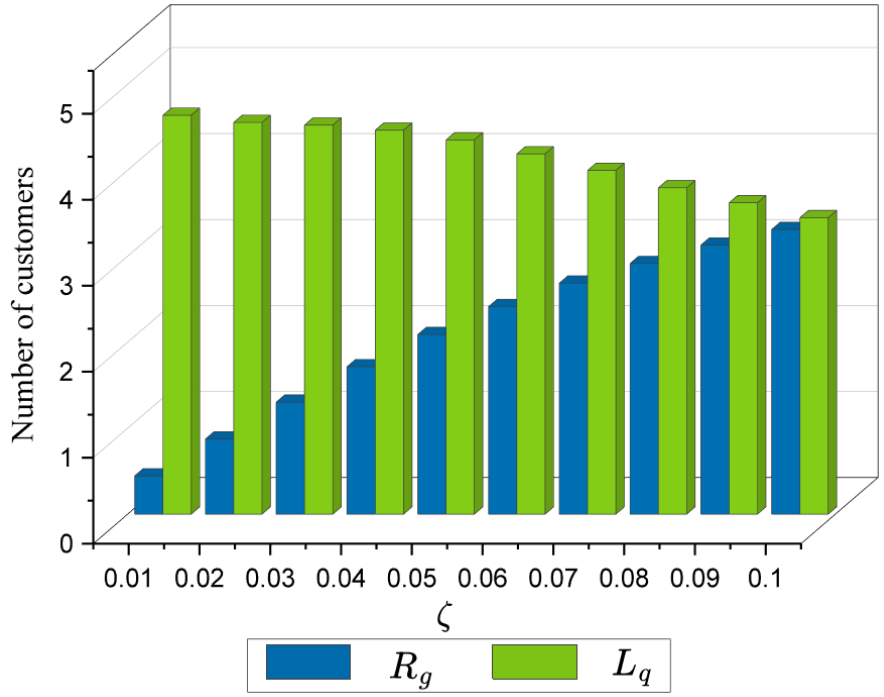


Figure 2: *L_q, R_g with respect to ζ*

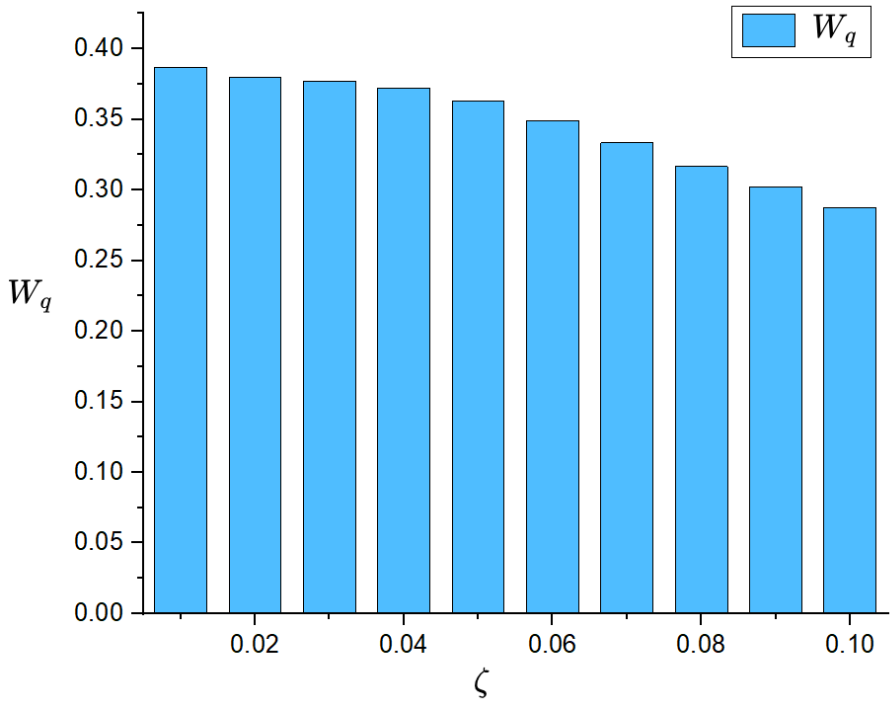


Figure 3: *W_q with respect to ζ*

Figure 2 and Figure 3 are the graphical representation of the tabulated values in Table 2 estimated for the batch size $a = 5$ and $b = 20$ with the probability of reneging of customers as $p^{'} = 0.8$ and the probability of customers entering into the system as $q^{'} = 0.2$.

6. Comparative Analysis

When the system experiences no reneging the value of $\zeta = 0$, this synchronizes with the classical queuing system M/M(a,b)/(2,1)/RV [16]. The following table shows a comparative outcome corresponding to the queue length for a batch of size a=5 and $b = 20$.

Table 3: *Classical queuing system Vs Queuing system with reneging*

	L_q	
λ	M/M(a,b)/(2,1)/RV	M/M(a,b)/(2,1)/RV - Reneging
5	2.4364	2.2961
8	3.3835	3.0448
10	4.2362	3.7393
12	5.2353	4.5574
15	7.0116	6.72298

By comparing the classical system without reneging with the contributed system it is observed from Table 3, there is a considerable decrease in the queue length in our proposed system, which is graphically interpreted in Figure 4.

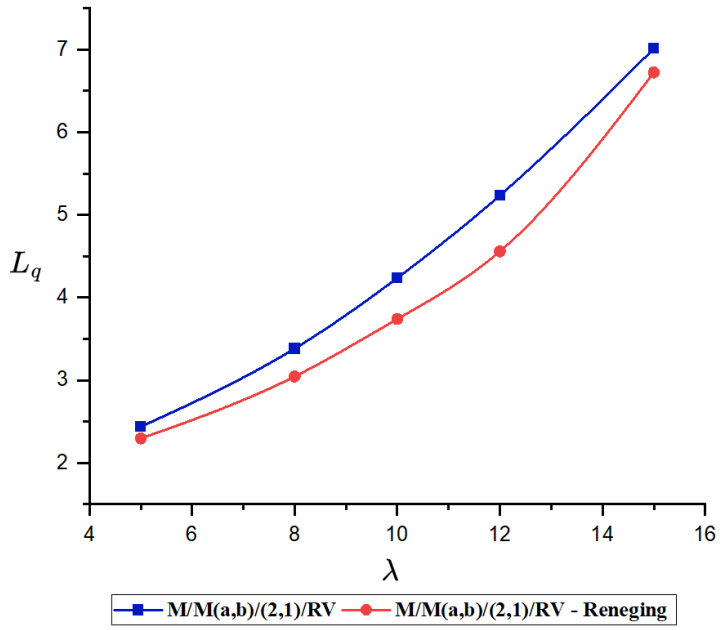


Figure 4: *Comparison between M/M(a, b)/(2,1)/RV and M/M(a, b)/(2,1)/RV with reneging*

7. Results and Discussion

The numerical analysis showcases the effect of our proposed model and the comparative analysis validates the result both theoretically and graphically. With the aid of the finding, it is possible to estimate the length of the queue for the system experiencing reneging of customers. Revoking of arrived customers showcases the inability of the system performance which may affect the system economically. Thus, estimating the length of the queue or else the quantity of products yet to manufacture helps to coordinate the system in accordance to their business outcome.

8. Conclusion

The steady state solutions of the model M/M (a, b)/ (2,1)/RV with the notion of customers behavior of reneging was discussed. Performance measure like average queue length, probability of servers being idle and engaged are formulated and analysed with a numerical example. The proceeded work helps ultimately the manufacturing system in making strategic decisions to coordinate the system and to yield a well outreach among the community. This work can be further investigated from the side decision making invoking the performance measures that has been found.

References

[1] Afanasyev, G. A. (2023). Cost optimization of queueing systems with vacations. *Theory of Probability & Its Applications*, 68(2), 308-315.

[2] Baskar, S. and Palaniammal, S. (2014). M/M(a,b)/(2,1) queueing system with servers repeated and delayed vacation. *Asian-European Journal of Mathematics*, 7(02), 1450032.

[3] Chakravarthy, S. R. and Kulshreshtha, R. (2020). A queueing model with server breakdowns, repairs, vacations, and backup server. *Operations research perspectives*, 7, 100131.

[4] Dbeis, A. and Al-Sahili, K. (2024). Enhancing queuing theory realism: analysis of reneging behavior impact on M/M/1 drive-thru service system. *Journal of Management Analytics*, 11(4), 659-674.

[5] Divya, K. and Indhira, K. (2024). A literature survey on queueing model with working vacation. Reliability: Theory & Applications, 19(1 (77)), 40-49.

[6] Doshi, B. T. (1986). Queueing systems with vacations. *Queueing systems*, 1(1), 29-66.

[7] Fayama, F., Zongo, A. and Nitiema, S. P. C. (2024) Performance evaluation of queuing systems with balking, reneging, feedback, impatient customers and downed servers. 435-452. *Far East Journal of Theoretical Statistics*, 68(2), 181-198.

[8] Fiems, D. (2025) Queues with Working Vacations: A Survey. *Mathematics*, 13(11), 1894.

[9] Khan, I. E. and Paramasivam, R. (2022) Reduction in waiting time in an M/M/1/N encouraged arrival queue with feedback, balking and maintaining of reneged customers. *Symmetry*, 14(8), 1743.

[10] Kuaban, G. S., Kumar, R., Soodan, B. S. and Czekalski, P. (2020) A multi-server queuing model with balking and correlated reneging with application in health care management. *IEEE Access*, 8, 169623-169639.

[11] Kumar, N. (2024). Threshold-Based Recovery in Queue Theory: Addressing Server Breakdowns, Catastrophic Events, and Customer Reneging. *Journal of Reliability and Statistical Studies*,

[12] Lidiya, P. and Mary, K. J. R. (2024). Analysis of the multiple working vacations, batch service and reneging queuing system under single server policy. *Reliability: Theory & Applications*, 19(2 (78)), 341-350.

[13] Ma, Z., Guo, S. and Wang, R. (2023). The virtual machines scheduling strategy based on M/M/c queueing model with vacation. *Future Generation Computer Systems*, 138, 43-51.

[14] Maragathasundari, S. Eswar, S. K. and Somasundaram, R. S. (2022). A study on phases of service and multi-vacation policy in a non-Markovian queuing system. International Journal of Mathematics in Operational Research, 21(4), 444-465.

[15] Mary, K. J. R. (2024) Analysis of an encouraged arrival queuing model with servers repeated vacations and breakdowns. *Reliability: Theory & Applications*,

[16] Palaniammal, S and M. A. B. R. Nadarajan. (2005) Servers Repeated Vacation. *Computational Mathematics*, 232.

[17] Pan, Y. Y., Zhang, J. C. and Liu, Z. M. (2025) Equilibrium Behavior in a Two-Stage Reneging Queue with Impatient Customers. *Journal of the Operations Research Society of China*, 1-25.

[18] Seenivasan, M., Ramesh, R. and Vijayalakshmi, R. (2025) Markovian Queueing model with backup server and reneging customer. In *AIP Conference Proceedings*, 3252(1), 020006.

[19] Sindhu, S. Krishnamoorthy, A. and Kozyrev, D. (2023). On Queues with working vacation and interdependence in arrival and service processes. *Mathematics*, 11(10), 2280.
[20] Som, B. K., Kumar, R., Kalidas, K. and Sampath, M. S. (2025). A single-server feedback queuing system with encouraged arrivals, customers' impatience, and catastrophe. In *Statistical Modeling and Applications on Real-Time Problems*, 141-151, CRC Press.
[21] Sundararaman, M., Narasimhan, D. and Rajadurai, P. (2024). Performance analysis of two different types of waiting queues with working vacations. *Journal of Mathematics*, (1), 5829171.
[22] Tamuli, A., Das, D., Choudhury, A. and Kushvaha, B. Optimal service design for heterogeneous queueing system with reverse balking and reneging. *Operational Research*, 25(2), 33.

FM/FM/1 QUEUE WITH N-POLICY TWO-PHASE,SERVER START-UP,TIME-OUT AND BREAKDOWNS USING L-R METHOD

John Benhur.K[1], D.Gopinath[2,*], P.Sudhakara Babu[3], Muragesh Math[4]

•

1 Research Scholar,Department of Mathematics and Statistics,Chaitanya(DU),Hyderabad,India
2 School of Sciences,AHERA Deemed To Be Univeristy,Bhongir,Hyderabad,India
3 Department of Science and Humanities,Amritha Sai Institue Of Science And Technology,Paritala,India
4 S.Nijalingappa Medical College,Bagalkot,India
* Corresponding Author:drgopinathduggi@gmail.com

Abstract

This study centers on evaluating the performance metrics of the system,specifically emphasizing two key elements:the expected length of the system (L) and the minimum anticipated cost T(N) derived from the optimal strategy analysis of the N-policy L-R(Left-Right),FM/FM/1 two-phase queueing model.This system incorporates essential factors such as server start-up,time-out,breakdown, and repair processes,making the analysis more comprehensive and reflective of real-world operational challenges.The arrival rate and service rate in this model are represented as triangular fuzzy numbers,which provide a more flexible and realistic approach in capturing the uncertainty and variability inherent in these rates.The study employs the L-R method,a technique known for its efficiency and simplicity when compared to the more traditional alpha-cuts method.The L-R method minimizes computational complexity and enhances the ease of differentiation, making it a more convenient approach for handling fuzzy numbers in queueing theory.By applying this method,the study effectively addresses the limitations of previous models and provides a more accurate estimation of the system's performance metrics.To demonstrate the validity and applicability of the proposed model,a numerical example is provided.This example illustrates the practicality of the L-R method in optimizing the system's cost and performance,showcasing how the model can be applied to real-world scenarios.The results of the numerical example confirm the robustness and reliability of the proposed approach,making a strong case for its adoption in queueing system analysis.This study thus offers significant insights and a novel methodological contribution to the field of fuzzy queueing systems.

Keywords: N-policy fuzzy queue,Performance measures,L-R method,Triangular fuzzy numbers.

1. Introduction

Queueing theory examines how people,tasks, or information pass through waiting lines.By understanding congestion and its root causes in various situations,it becomes possible to develop services and systems that are more efficient and economical.Typical examples include ration depots,postal services,medical stores, and vaccination clinics.In this paper,we investigate a two-phase N-policy FM/FM/1 fuzzy queuing system that includes several important operational characteristics such as server start-up delay,time-out,breakdown, and repair processes.The system operates under a fuzzy environment,where both arrival and service processes follow flexible Markovian(FM) distributions.These fuzzy parameters allow for better modeling of real-world

uncertainty and vagueness in service systems.The server does not start operating immediately when the system becomes idle;instead,it waits until a certain number of customers,N,accumulate before starting up.We apply the L-R(Left-Right combination) method to analyze the fuzzy behavior of the queuing system,allowing us to derive approximate measures for performance characteristics such as average queue length,waiting time, and system availability.This approach is useful for systems that cannot be effectively modeled using crisp values due to uncertain operating conditions.The results of this study can be applied to various practical fields including production systems,computer networks, and service industries,helping in better system planning and efficient resource utilization under uncertainty.

Explores an N-policy two-phase $M/E_k/1$ queueing system,addressing server breakdowns and gating mechanisms, and discusses optimal operational strategies [12].Examines an N-policy two-phase $M_X/M/1$ queueing system considering server startup delays and breakdowns,providing insights into optimal control strategies [13].

Fuzzy logic was first introduced [1].Since then,fuzzy queueing systems have been studied extensively by various researchers conducted a fuzzy analysis of a bulk arrival two-phase retrial queue that includes vacation and admission control policies,demonstrating the use of fuzzy set theory in intricate queueing systems [2-3,4,14,16].Similarly,an FM/FM/C queueing model using a fuzzy framework integrated with parametric nonlinear programming,offering techniques relevant to fuzzy queueing analysis [15].

Representing and analyzing fuzzy numbers,especially triangular or trapezoidal fuzzy values,in a systematic and mathematically manageable way [5].Examined a single-server vacation queueing system variant involving uncertain or imprecise parameters [7].The characteristics of N-policy fuzzy queue under vogue data [6].Derive and analyze variance-based performance measures for an FM/FM/1 queueing system using crisp (non-fuzzy) values,with the goal of obtaining more precise and quantitative insights into the behavior of the system [8].Analyzes an N-policy FM/FM/1 vacation queueing system incorporating server start-up and time-out, employing the L-R method for performance evaluation [9].Introduce the L-R method for computing performance measures in fuzzy queueing systems, demonstrating its advantages over traditional alpha-cuts method[10].Analyzed bulk arrival queuing model with flow communication network using L-R method.A significant number of these studies focus on determining system performance metrics using the alpha-cuts technique [11].Here we calculate the expected system length L and the minimum expected cost T(N*) in the fuzzy queue by the L-R method, especially based on the L-R fuzzy arithmetic.

2. Methods

2.1. Preliminaries

A fuzzy set is a set (which often does not need to be empty) having degrees of membership between 0 and 1.The membership function $\varphi_A(x) : A \to [0,1]$ is the membership function, and $\varphi_A(x)$ is the grading value called as real numbers between 0 and 1 (covered within 0 and 1).

A fuzzy set A is called normal if there exists an element $x \in X$ whose membership value is one,i.e.,$\varphi_A(x) = 1$.

A fuzzy set A is convex if and only if for any $x_1, x_2 \in X$, the membership function of A satisfies the condition:

$$\varphi_A\left(\lambda x_1 + (1-\lambda)x_2\right) \geq \min\left\{\varphi_A(x_1), \varphi_A(x_2)\right\}, \quad 0 \leq \lambda \leq 1.$$

For a triangular fuzzy number $\widehat{A}_{\text{3-tuples}}$, it is represented by $\overline{A}(m,n,p)$,where m,n,p are real numbers, and its membership function $\mu_{\overline{A}}$ is given by:

$$\mu_{\overline{A}}(x) = \begin{cases} \frac{x-a}{b-a}, & a \le x \le b \\ 1, & x = b \\ \frac{c-x}{c-b}, & b \le x \le c \\ 0, & \text{otherwise} \end{cases}$$

The representation of L-R can be recorded as:

$$\overline{A}(m,n,p) = \langle n, n-m, p-m \rangle_{\mathrm{LR}}, \quad \text{for } L(x) = \max(0, 1-x).$$

2.2. Triangular Fuzzy Number of L-R Method

Fuzzy number $\overline{A}$ is an L-R fuzzy number only if it has three positive numbers μ,$m > 0$, $n > 0$, and two positive,continuous, and decreasing functions from the actual number $[0,1]$:

$$L(0) = R(0) = 1, \quad L(1) = 0, \quad L(x) > 0, \lim_{x\to\infty} L(x) = 0,$$
$$R(1) > 0, \quad \lim_{x\to\infty} R(x) = 0.$$

$$\phi_{\overline{\mu}}(x) = \begin{cases} L\left(\frac{\mu - x}{m}\right), & \text{if } x \in [\mu - m, \mu] \\ R\left(\frac{x-\mu}{n}\right), & \text{if } x \in [\mu, \mu + n] \\ 0, & \text{otherwise} \end{cases}$$

Fuzzy number $\overline{\mu}$ is the L-R fuzzy number,then $\overline{\mu} = \langle \mu,\ m,\ n \rangle_{\mathrm{LR}}$.$\mu$ is called the average value or modal value of $\overline{\mu}$;m and n are called the left spread and right spread of $\overline{\mu}$.Conventionally, $\overline{\mu} = \langle \mu,\ 0,\ 0 \rangle_{\mathrm{LR}}$ is the ordinary real number μ,called a fuzzy singleton.

$$\mathrm{Supp}(\overline{\mu}) = [\mu - m, \mu] \cup [\mu, \mu + n] = [\mu - m, \mu + n]$$

2.3. L-R Fuzzy Arithmetical Operators

If $\overline{\mu} = \langle \mu,\ m,\ n \rangle_{\mathrm{LR}}$ and $\overline{n} = \langle n,\ p,\ q \rangle_{\mathrm{LR}}$ are same fuzzy numbers,then their sum is the same L-R fuzzy number, and their difference is also the same L-R fuzzy number,given by:

$$\overline{\mu} + \overline{n} = \langle \mu + n,\ m + p,\ n + q \rangle_{\mathrm{LR}}$$

$$\overline{\mu} - \overline{n} = \langle \mu - n,\ m + q,\ n + p \rangle_{\mathrm{LR}}$$

The product of L-R fuzzy numbers $\overline{\mu} = \langle \mu,\ m,\ n \rangle_{\mathrm{LR}}$ and $\overline{n} = \langle n,\ p,\ q \rangle_{\mathrm{LR}}$ is given by:

$$\overline{\mu} \cdot \overline{n} = \langle \mu \cdot n,\ \mu p + nm - mp,\ \mu q + nn + nq \rangle_{\mathrm{LR}}$$

The quotient (secant approximation) of L-R fuzzy numbers $\overline{\mu} = \langle \mu,\ m,\ n \rangle_{\mathrm{LR}}$ and $\overline{n} = \langle n,\ p,\ q \rangle_{\mathrm{LR}}$ is given by:

$$\frac{\overline{\mu}}{\overline{n}} = \left\langle \frac{\mu}{n},\ \frac{\mu q}{n(n+q)} + \frac{m}{n} - \frac{mq}{n(n+q)},\ \frac{\mu p}{n(n-p)} + \frac{n}{n} + \frac{np}{n(n-p)} \right\rangle_{\mathrm{LR}}$$

3. Model Description

Customer arrivals follow a Poisson process with a fuzzy average arrival rate λ and join the phase-1 of batch service.The server served all customers with mean service rate $1/\beta$.Once the batch service is completed,each customer in the batch receives an individual fuzzy service at a mean rate $1/\mu$.During this individual service phase,the server is subject to failure at a rate α,but it is immediately repaired at a rate β,allowing service to resume without delay.

After completing the personal services,the server returns to Phase-1 to serve any waiting customers and proceeds to the second phase accordingly.If no customers are waiting in the batch queue,the server remains idle for a fixed duration C,known as the server timeout.If customers arrive during this timeout,the server begins batch service followed by individual service.However,if no arrivals occur within this timeout period,the server goes on vacation.It returns to begin pre-service activities at a mean rate of $1/\theta$ once N customers have accumulated in the batch queue.

Let:

C_h = Holding cost for each customer
C_o = Operational cost of server
C_m = Pre-service cost per cycle
C_t = Timeout cost per cycle
C_s = Setup cost per cycle
C_b = Breakdown cost
C_r = Reward for the server being on vacation

Now we consider N-policy FM/FM/1 two-phase queuing model server start-up and time-out,break down and repair of expected system length $L(N)$ and cost function $T(N)$.

4. Performance Measures

4.1. The expected system length is

$$\begin{aligned}L(N) = {} & \frac{N(N-1)}{2}p_{000} + \frac{\lambda(\lambda+N\theta)}{\theta^2}p_{000} + \frac{\lambda}{\beta}\left(\frac{\lambda}{c}+\frac{\lambda+N\theta}{\theta}\right) \\ & + \frac{\lambda\left[\lambda^2\beta\xi+\mu\gamma^2(\lambda+\beta)\right]}{\mu\gamma\beta\left[\mu\gamma-\lambda(\xi+\gamma)\right]} \\ & + \frac{\lambda\gamma\left[2\lambda(\lambda+N\theta)+\theta^2N(N-1)\right]}{2\theta^2\left[\mu\gamma-\lambda(\xi+\gamma)\right]}p_{000} \\ & + \frac{\lambda\xi}{\gamma^2}\cdot\frac{\lambda\mu\gamma R_1(1)+\beta\theta\gamma\cdot\frac{\lambda}{\theta}p_{000}}{\beta\left[\mu\gamma-\lambda(\xi+\gamma)\right]} \\ & + \frac{\alpha}{\gamma}\cdot\frac{\lambda\left[\lambda^2\beta\alpha+\mu\gamma^2(\lambda+\beta)\right]}{\mu\gamma\beta\left[\mu\gamma-\lambda(\xi+\gamma)\right]} \\ & + \frac{\lambda\gamma\left[2\lambda(\lambda+N\theta)+\theta^2N(N-1)\right]}{2\theta^2\left[\mu\gamma-\lambda(\xi+\gamma)\right]}p_{000}\end{aligned}$$

Where:

$$p_{000} = \frac{1-\frac{\lambda}{\mu}\left(1+\frac{\lambda}{\gamma}\right)\frac{\lambda}{\beta}}{N+\frac{\lambda}{\theta}+\frac{\lambda}{c}} \quad \text{and} \quad R_1(1) = \frac{\lambda}{\mu}$$

4.2. The function of total expected cost is

$$
\begin{aligned}
T(N) = C_h \Bigg[& \frac{N(N-1)}{2} p_{000} + \frac{\lambda(\lambda + N\theta)}{\theta^2} p_{000} + \frac{\lambda}{\beta}\left(\frac{\lambda}{c} + \frac{\lambda + N\theta}{\theta}\right) + \frac{\lambda\left[\lambda^2\beta\xi + \mu\gamma^2(\lambda+\beta)\right]}{\mu\gamma\beta\left[\mu\gamma - \lambda(\xi+\gamma)\right]} \\
& + \frac{\lambda\gamma\left[2\lambda(\lambda+N\theta) + \theta^2 N(N-1)\right]}{2\theta^2\left[\mu\gamma - \lambda(\xi+\gamma)\right]} p_{000} \\
& + \frac{\lambda\xi}{\gamma^2} \cdot \frac{\lambda\mu\gamma R_1(1) + \beta\theta\gamma \cdot \dfrac{\lambda}{\theta} p_{000}}{\beta\left[\mu\gamma - \lambda(\alpha+\gamma)\right]} \\
& + \frac{\xi}{\gamma} \cdot \frac{\lambda\left[\lambda^2\beta\xi + \mu\gamma^2(\lambda+\beta)\right]}{\mu\gamma\beta\left[\mu\gamma - \lambda(\xi+\gamma)\right]} \\
& + \frac{\lambda\gamma\left[2\lambda(\lambda+N\theta) + \theta^2 N(N-1)\right]}{2\theta^2\left[\mu\gamma - \lambda(\xi+\gamma)\right]} p_{000} \Bigg] \\
& + C_o\left(\frac{\lambda}{\beta} + \frac{\lambda}{\mu}\right) + C_m\left(\frac{\lambda}{\theta} p_{000}\right) + C_t\left(\frac{\lambda}{c} p_{000}\right) + C_b \cdot \frac{\lambda\xi}{\mu\gamma} \\
& + C_s \cdot \frac{\lambda\left[1 - \dfrac{\lambda}{\mu}\left(1 + \dfrac{\lambda}{\gamma}\right)\dfrac{\lambda}{\beta}\right]}{N + \dfrac{\lambda}{\theta} + \dfrac{\lambda}{c}} - C_r \cdot (N p_{000})
\end{aligned}
$$

Where:

$$N = \frac{-b + \sqrt{b^2 - 4ac}}{2a}$$

$$a = \frac{C_h\mu\gamma\theta C}{2\left[\mu\gamma - \lambda(\xi+\gamma)\right]} \quad , \quad b = \frac{C_h\mu\gamma\lambda(\theta + C)}{\left[\mu\gamma - \lambda(\xi+\gamma)\right]}$$

$$c = \frac{C_h\lambda(2\lambda - \mu\gamma)}{2\left[\mu\gamma - \lambda(\xi+\gamma)\right]} + \lambda\left[C(C_m + C_r) + \theta(C_t + C_r) + C_s\theta C\right]$$

5. Numerical analysis and Graphical Presentation

5.1. Triangular fuzzy number

We consider an N-policy FM/FM/1 two-phase queuing model with server start-up,time-out,breakdown, and repair,where the arrival rate and service rate are triangular fuzzy numbers represented by:

$$\lambda = [0.4, 0.5, 0.6]; \quad \mu = [2.4, 2.5, 2.6]; \quad \beta = [1, 2, 3]; \quad \theta = [2, 3, 4]$$

Let the cost and system parameters be given as:

$$C = 1, \quad \alpha = 0.1, \quad C_b = 100, \quad C_m = 100, \quad C_t = 30, \quad C_s = 500, \quad C_r = 40, \quad C_h = 5.$$

The interval of confidence at possibility level α is given by:

$$
\begin{aligned}
&\lambda \in [0.4 + 0.1\alpha,\ 0.6 - 0.1\alpha]\,, \\
&\mu \in [2.4 + 0.1\alpha,\ 2.6 - 0.1\alpha]\,, \\
&\beta \in [1 + \alpha,\ 3 - \alpha]\,, \\
&\theta \in [2 + \alpha,\ 4 - \alpha]\,.
\end{aligned}
$$

5.2. The Expected System Length Is

Let:

$$\vec{a} = \langle 0.4, 0.5, 0.6 \rangle, \quad \vec{b} = \langle 2, 3, 4 \rangle, \quad \vec{c} = \langle 1, 2, 3 \rangle, \quad \vec{d} = \langle 2.4, 2.5, 2.6 \rangle$$

All vector operations (like $\vec{a} \cdot \vec{b}$) are dot products.

$$\begin{aligned} L(N) = {} & \frac{9.80(9.80-1)}{2} \cdot p_{000} + \frac{\vec{a} \cdot (\vec{a} + 9.80 \cdot \vec{b})}{\vec{b} \cdot \vec{b}} \cdot p_{000} \\ & + \frac{\vec{a}}{\vec{c}} \left(\frac{\vec{a}}{c} + \frac{\vec{a} + 9.80 \cdot \vec{b}}{\vec{b}} \right) \\ & + \frac{\vec{a} \left[(\vec{a} \cdot \vec{a}) \cdot \vec{c} \cdot 0.1 + \vec{d} \cdot 4 \cdot (\vec{a} + \vec{c}) \right]}{\vec{d} \cdot 2 \cdot \vec{c} \left(\vec{d} \cdot 2 - \vec{a} \cdot (0.1 + 2) \right)} \\ & + \frac{\vec{a} \cdot 2 \left[2 \cdot \vec{a} \cdot (\vec{a} + 9.80 \cdot \vec{b}) + (\vec{b} \cdot \vec{b}) \cdot 9.80(9.80-1) \right]}{2 \cdot (\vec{b} \cdot \vec{b}) \left(\vec{d} \cdot 2 - \vec{a} \cdot (0.1 + 2) \right)} \cdot p_{000} \\ & + \frac{\vec{a} \cdot 0.1}{4} \cdot \frac{\vec{a} \cdot \vec{d} \cdot 2 \cdot R_1(1) + \vec{c} \cdot \vec{b} \cdot 2 \cdot \left(\frac{\vec{a}}{\vec{b}} \cdot p_{000} \right)}{\vec{c} \cdot \left(\vec{d} \cdot 2 - \vec{a} \cdot (0.1 + 2) \right)} \\ & + \frac{\alpha}{2} \cdot \frac{\vec{a} \left[(\vec{a} \cdot \vec{a}) \cdot \vec{c} \cdot \alpha + \vec{d} \cdot 4 \cdot (\vec{a} + \vec{c}) \right]}{\vec{d} \cdot 2 \cdot \vec{c} \left(\vec{d} \cdot 2 - \vec{a} \cdot (0.1 + 2) \right)} \\ & + \frac{\vec{a} \cdot 2 \left[2 \cdot \vec{a} \cdot (\vec{a} + 9.80 \cdot \vec{b}) + (\vec{b} \cdot \vec{b}) \cdot 9.80(9.80-1) \right]}{2 \cdot (\vec{b} \cdot \vec{b}) \left(\vec{d} \cdot 2 - \vec{a} \cdot (0.1 + 2) \right)} \cdot p_{000} \end{aligned}$$

Where

$$p_{000} = \langle 0.042, 0.058, 1.23 \rangle, \qquad R_1(1) = \frac{\lambda}{\mu}$$

$$L(N) = \langle 3.12, 3.34, 443.82 \rangle$$

5.3. The Function of Total Expected Cost

$$\begin{aligned} T(N) = {} & C_h \cdot \langle 2.98, 2.35, 161.35 \rangle \\ & + C_o \cdot \left(\frac{\langle 0.4, 0.5, 0.6 \rangle}{\langle 1, 2, 3 \rangle} + \frac{\langle 0.4, 0.5, 0.6 \rangle}{\langle 2.4, 2.5, 2.6 \rangle} \right) \\ & + C_m \cdot \left(\frac{\langle 0.4, 0.5, 0.6 \rangle}{\langle 2, 3, 4 \rangle} \cdot p_{000} \right) \\ & + C_t \cdot \left(\frac{\langle 0.4, 0.5, 0.6 \rangle}{c} \cdot p_{000} \right) \\ & + C_b \cdot \left(\frac{\langle 0.4, 0.5, 0.6 \rangle \cdot \xi}{\langle 2.4, 2.5, 2.6 \rangle \cdot 2} \right) \\ & + C_s \cdot \left[\frac{\langle 0.4, 0.5, 0.6 \rangle \cdot \left(1 - \frac{\langle 0.4,0.5,0.6 \rangle}{\langle 2.4,2.5,2.6 \rangle} \cdot \left(1 + \frac{\langle 0.4,0.5,0.6 \rangle}{2} \right) \cdot \frac{\langle 0.4,0.5,0.6 \rangle}{\langle 1,2,3 \rangle} \right)}{9.80 + \frac{\langle 0.4, 0.5, 0.6 \rangle}{\langle 2, 3, 4 \rangle} + \frac{\langle 0.4, 0.5, 0.6 \rangle}{c}} \right] \\ & - C_r \cdot (9.80 \cdot p_{000}) \end{aligned}$$

$$T(N) = \langle 160.35, 1894.33, 3604.8 \rangle$$

5.4. Graphical Presentation

Triangular fuzzy membership function and results based on α-levels. Based on the below graphs, which illustrate a triangular fuzzy membership function defined by the L-R representation method, the corresponding values of $L(N)$ and $T(N)$ have been evaluated. These evaluations consider fuzzy parameters such as arrival rate, service rate, breakdown, and repair rate, to determine the expected system length L and the cost function $T(N)$ within the queue at 11 distinct α-levels: 0, 0.1, 0.2, 0.3, 0.4, 0.5, 0.6, 0.7, 0.8, 0.9, and 1.0.

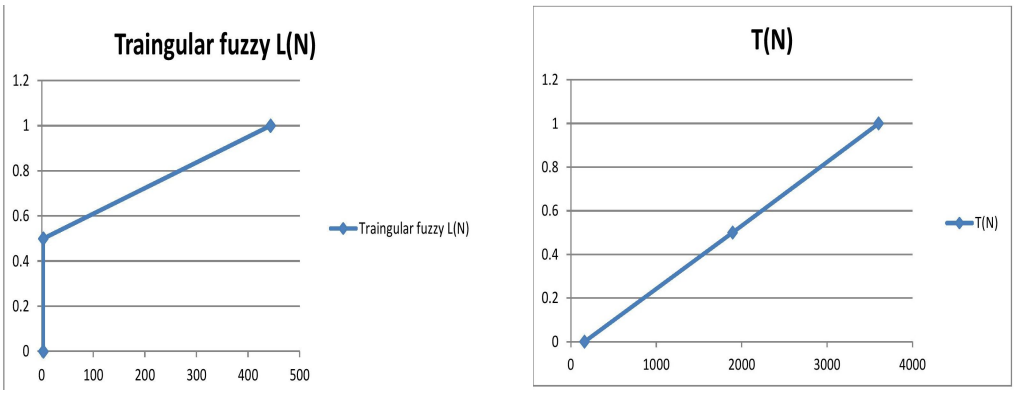


Figure 1: *Expected system length $L(N)$ and Cost function $T(N)$*

The L-R values of the fuzzy sets L and $T(N)$, corresponding to different levels of possibility (α values), have been calculated as follows: From Table 1 and Figure 1 the estimated system length $L(N)$ is found to be 3.34, with a left spread of 3.12 and a right spread of 443.82. Similarly, the cost function $T(N)$ is determined to be 160.35, with a left spread of 1894.33 and a right spread of 3604.8.

6. Conclusion

In this study,we calculated key performance measures of the system,focusing on the expected system length L and the cost function $T(N)$.The expected system length L provides insight into the average number of units in the system,which reflects system congestion.The cost function $T(N)$ was evaluated to analyze the trade-off between performance and associated operational costs.

Through these calculations,we were able to assess the system's efficiency under varying conditions.The results highlight how changes in system parameters affect both L and $T(N)$.Overall,the analysis aids in optimizing system performance while minimizing costs.

References

[1] L.A.Zadeh.(1965). Fuzzy sets.Information and Control., *8*,338-353.
[2] R.J.Li.,& E.S.Lee. (1989). Analysis of fuzzy queues,computers and Mathematics with Applications., *17*(7),1143-1147.
[3] R.Srinivasan.(2013). Fuzzy queueing model using DSW algorithm. *International Journal of Advanced Research in Mathematics and Computer Applications*, *1*(1),1-6.
[4] Kanyinda,J.M.,Matendo, R.M.M,& Lukata,B.U.E.(2015). Computing Fuzzy Queueing Performance Measures by L-R Method. *In Journal of Fuzzy Set Valued Analysis*, *1*,57-67.
[5] S.Vijaya.,N.Srinivasan,& M.V.Suresh.(2021). A study on Fuzzy Decision Problem of a Queueing System with Finite Capacity by LR Method. *Turkish Journal of Computer and Mathematics Education*, *12*(9),2411-2419.

[6] S.Aarthi.,M.Shanmugasundari.,& Saranya.V(2020). SA Study On Fuzzy Queue With N Policy By Triangular Fuzzy Numbers. *European Journal of Molecular & Clinical Medicine*, *7*(3),4544.

[7] G.Kannadasan.& D.Devi.(2021). DFuzzy variant Vacations on Server Breakdowns using Pentagonal Numbers. *Advances and Applications in Mathematical Sciences*, *20*(6),1003-1019 .

[8] N.Subashini.,Elrehail.,& N.Anusheela .(2022).Performance Measures in terms of Crisp Values for FM/FM/1 by using L-R method. *Journal of Xi'an University of Architecture Technology*, *(*3),211-215.

[9] P.Sudhakara Babu.,K Satish Kumar.,& K.Chandan.(2022). A study on Optimal strategy N-policy Fuzzy vacation queueing system with server start up and time out.*International Journal of Engineering Science Invention*, *6*(11),24-28.

[10] Babu,P.S,Kumar, K. S.,& Chandan,K.(2022). A study on optimal strategy n-policy fuzzy vacation queueing system with server start up and time out using LR method.*International Journal of Advanced Research in Computer Science*, *13*(2),39-44.

[11] N. Lakshman Rao.,K.Chandan.,B.Raviteja.,& P.Sudhakara Babu.(2020). Modeling of communication network with bulk arrival queueing system under fuzzy environment using left and right method. *Journal of Nonlinear Analysis and Optimization*.

[12] Vemuri,V.K.,Boppana.,V.S.N.H.P.,Kotagiri,C,Lu,Q.,& Bethapudi,R.T. (2011). Optimal strategy analysis of an N-policy two-phase $M^X/M/1$ queueing system with server startup and breakdowns. *OPSEARCH*, *48*(2),109-122.

[13] Vasanta Kumar.,V.,Hari Prasad,B.V.S.N.,& Chandan,K..(2010). Optimal strategy analysis of an N-policy two-phase $M/E_k/1$ queueing system with server breakdowns and gating. *Applied Mathematical Sciences*, *4*(66),3261-3272.

[14] Ebenesar Anna Bagyam.J.,&Udaya Chandrika,K.(2019). Fuzzy analysis of bulk arrival two-phase retrial queue with vacation and admission control.*The Journal of Analysis*, *(*27),209-232.

[15] Bagherinejad,J.,& Pishkenari,H.B.(2016). Analysis of FM/FM/C queueing system using fuzzy approach and parametric nonlinear programming. *EInternational Journal of Industrial and Systems Engineering*, *23*(2),125-140.

[16] Mabela Makengo Matendo, R., Alonge W'Omatete, J., Matondo Mananga, H., Pierre Mukeba Kanyinda, J., & Adia Leti Mawa, B. (2023). Computing the performance parameters of the Markovian queueing system FM/FM/1 in transient state. *Advances in Fuzzy Logic Systems*,Doi:10.5772/intechopen.110-388.

A COMPREHENSIVE EXPLORATION OF QUASI RAMA DISTRIBUTION WITH SIGNIFICANT STATISTICAL PROPERTIES AND APPLICATIONS

Rashid A. Ganaie[1,*], Ashok Routhu[2], T. Vivekanandan[3], Manzoor A. Khanday[4] and Prem Lata Gautam[5]

•

[1,*]Department of Statistics, Annamalai University, Tamil Nadu-608002, India
[2]Department of Mathematics, Anurag University, Hyderabad, India
[3]Department of Science and Humanities, Vel Tech Multi Tech Dr.Rangarajan Dr.Sagunthala Engineering College, Chennai, Tamil Nadu-600062, India
[4]Department of Statistics, Lovely Professional University, Phagwara, Punjab, India
[5]Department of Statistics, Amity School of Applied Sciences, Amity University, Lucknow, India
[1,*]rashidau7745@gmail.com, ashok.maths@anurag.edu.in, [3]mtvivek2017@gmail.com, [4]manzoorstat@gmail.com, [5]plgautam@lko.amity.edu

Abstract

In this study, we propose a novel extension of the quasi Rama distribution referred to as the length-biased quasi Rama (LBQR) distribution, developed by applying the length-biased technique to the classical quasi Rama distribution. The proposed distribution is thoroughly investigated and several of its important statistical properties are derived including moments, harmonic mean, order statistics, reliability function, hazard rate function, reverse hazard rate function, moment generating function, characteristic function, Renyi entropy as well as Bonferroni and Lorenz curves. Furthermore, the parameters of the new distribution are estimated using the method of maximum likelihood estimation. To evaluate the practical relevance and predictive performance of the length biased quasi Rama distribution, it is applied to two real lifetime data sets, demonstrating its applicability and effectiveness in modeling real-world lifetime phenomena.

Keywords: Length biased distribution, quasi Rama distribution, reliability analysis, entropy

I. Introduction

In distribution theory, the adaptation of diversified models to classical distributions has gained remarkable momentum largely because classical distributions often fail to provide an adequate fit for complex real-world data. By incorporating an additional parameters or modifying existing structures, these enhanced models offer a better representation of data variability and complexity. In such situation, a compelling case arises to introduce an additional parameter to existing baseline distribution and this additional parameter improves its performance and brings flexibility in their behavior. This additional parameter creates a new understanding of existing classical distribution

and this additional parameter is approached through reputed weighted technique. Fisher [4] studied this concept to examine how the ascertainment biases can affect the form of distribution of recorded observations which reformulated by Rao [14] in a unifying theory were the observations fall in non-experimental, non-replicated and non-random manner. Weighted distributions are suitable in situation of unequal probability sampling like actuarial sciences, biomedicine, biostatistics, ecology and survival data analysis. This idea has been applied as a device for collection of suitable model for observed data and these distributions are applicable only if the observations are recorded without any repetition, experiment and random process. When weight function depends on length of units of interest, resulting distribution is termed as length biased distribution. The idea of length biased distribution was introduced by Cox [3] in renewal theory and it has been found useful in biometry, wildlife studies, family history, intermediate events and analysis of lifetime data. When observations are selected with probability proportional to their length resulting distribution is termed as length biased. Length biased distribution is a particular case of more general form known as weighted distribution and therefore length biased refers to sample data were probability of recording an observation depends upon magnitude of observations. Length biased sampling situation occurs because sometimes it is impossible to work with truly random sample from population of interest. Thus length biased distribution has also been applied in development of proper models for lifetime data.

Many authors have contributed significantly to develop length biased probability distributions along with their applications. Nanuwong and Bodhisuwan [12] constructed the length biased Beta-Pareto distribution with properties and its application. Klinjan and Aryuyuen [7] proposed the length-biased power Garima distribution with application. Ganaie and Rajagopalan [6] studied the length biased power quasi Lindley distribution with properties and applications. Pushkarna and Mustafa [13] derived length biased weighted Ishita distribution with real life data sets. Saghir and Khadim [16] obtained mathematical properties of length biased weighted Maxwell distribution. Al-omari et al. [1] derived the power length biased Suja distribution with properties and application. Mudasir and Ahmad [11] discussed structural properties of length biased Nakagami distribution. Mustafa and Khan [10] presented length biased powered inverse Rayleigh distribution. Beghriche and Zeghdoudi [2] obtained size biased gamma Lindley distribution. Sharma et al. [19] described length and area biased Maxwell distributions. Ganaie and Rajagopalan [5] derived the length biased two parameter Pranav distribution with characterizations and applications. Salama et al. [17] discussed length biased weighted exponentiated inverted exponential distribution with properties and estimation.

A quasi Rama distribution is a recently executed new distribution introduced by Shanker et al. [18] which is a particular case of Rama distribution. The proposed quasi Rama distribution is a two parametric distribution and some of its statistical properties based upon moments, mean residual life function, hazard rate function, stochastic ordering and mean deviation have been described. Further its parameters are estimated by method of moments and maximum likelihood estimation.

II. Length Biased Quasi Rama (LBQR) Distribution

The quasi Rama distribution with its probability density function given by

$$f(x;\theta,\alpha)=\frac{\theta^3}{\left(\alpha\theta^2+6\right)}\left(\alpha+\theta x^3\right)e^{-\theta x};\ x>0,\theta>0,\alpha>0 \qquad (1)$$

and quasi Rama distribution with its cumulative distribution function given by

$$F(x;\theta,\alpha) = 1 - \left(1 + \frac{\left(\theta^3 x^3 + 3\theta^2 x^2 + 6\theta x\right)}{\left(\alpha\theta^2 + 6\right)}\right) e^{-\theta x};\ x > 0, \theta > 0, \alpha > 0 \qquad (2)$$

The random variable X under non-negative circumstances consists the probability density function $f(x)$ and its weight function be $w(x)$ that is non-negative, then probability density function of weighted random variable X_w will be defined as

$$f_w(x) = \frac{w(x)\, f(x)}{E(w(x))},\ x > 0$$

Here in this article, we have to acquire the length biased model of quasi Rama distribution, since in weights if $w(x) = x$ the performed distribution is referred to as length biased distribution and its probability density function is defined as

$$f_l(x;\theta,\alpha) = \frac{x\, f(x;\theta,\alpha)}{E(x)} \qquad (3)$$

Now $E(x) = \int_0^\infty x\, f(x;\theta,\alpha)dx$

$$E(x) = \frac{\left(\alpha\theta^2 + 24\right)}{\theta\left(\alpha\theta^2 + 6\right)} \qquad (4)$$

After substituting the equations (1) and (4) in equation (3), we will get probability density function of length biased quasi Rama distribution as

$$f_l(x;\theta,\alpha) = \frac{x\theta^4}{\left(\alpha\theta^2 + 24\right)}\left(\alpha + \theta x^3\right) e^{-\theta x} \qquad (5)$$

Now the cumulative distribution function of length biased quasi Rama distribution will be obtained as

$$F_l(x;\theta,\alpha) = \int_0^x f_l(x;\theta,\alpha)\, dx$$

$$= \int_0^x \frac{x\theta^4}{\left(\alpha\theta^2 + 24\right)}\left(\alpha + \theta x^3\right) e^{-\theta x} dx$$

$$= \frac{1}{\left(\alpha\theta^2 + 24\right)}\left(\alpha\theta^4 \int_0^x x\, e^{-\theta x} dx + \theta^5 \int_0^x x^4\, e^{-\theta x} dx\right) \qquad (6)$$

After simplification of expression (6), we determine the cumulative distribution function of length biased quasi Rama distribution as

$$F_l(x;\theta,\alpha) = \frac{1}{\left(\alpha\theta^2 + 24\right)}\left(\alpha\theta^2\gamma(2,\theta x) + \gamma(5,\theta x)\right) \qquad (7)$$

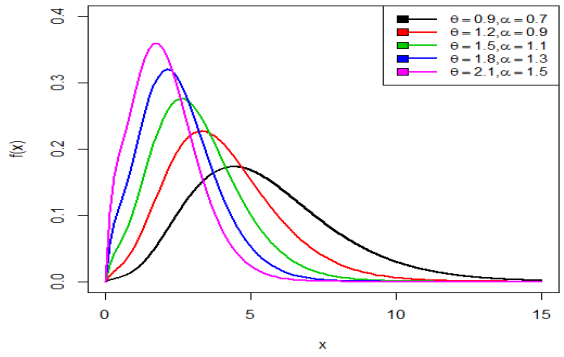


Figure 1: *Pdf plot of LBQR distribution*

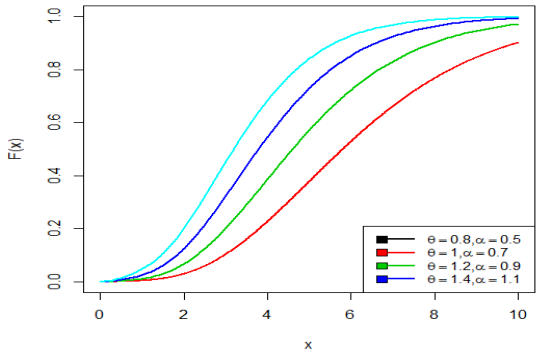


Figure 2: *Cdf plot of LBQR distribution*

III. Reliability Analysis

In this portion, some fundamental aspects via reliability function, hazard function, reverse hazard function and mills ratio of length biased quasi Rama distribution has been derived. The reliability function of length biased quasi Rama distribution is given by

$$R(x) = 1 - F_l(x;\theta,\alpha)$$

$$R(x) = 1 - \frac{1}{\left(\alpha\theta^2 + 24\right)}\left(\alpha\theta^2\gamma(2,\theta x) + \gamma(5,\theta x)\right)$$

The hazard function of performed length biased quasi Rama distribution is given by

$$h(x) = \frac{f_l(x;\theta,\alpha)}{1 - F_l(x;\theta,\alpha)}$$

$$h(x) = \frac{x\theta^4\left(\alpha + \theta x^3\right)e^{-\theta x}}{\left(\alpha\theta^2 + 24\right) - \left(\alpha\theta^2\gamma(2,\theta x) + \gamma(5,\theta x)\right)}$$

The reverse hazard function of length biased quasi Rama distribution is given by

$$h_r(x) = \frac{f_l(x;\theta,\alpha)}{F_l(x;\theta,\alpha)}$$

$$h_r(x) = \frac{x\theta^4\left(\alpha + \theta x^3\right)e^{-\theta x}}{\left(\alpha\theta^2\gamma(2,\theta x) + \gamma(5,\theta x)\right)}$$

The Mills Ratio of length biased quasi Rama distribution is given by

$$M.R = \frac{1}{h_r(x)} = \frac{\left(\alpha\theta^2\gamma(2,\theta x) + \gamma(5,\theta x)\right)}{x\theta^4\left(\alpha + \theta x^3\right)e^{-\theta x}}$$

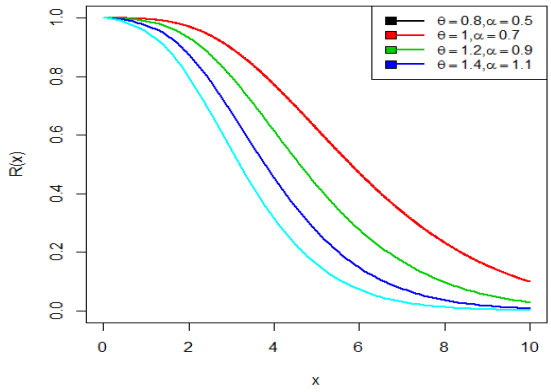


Figure 3: *Reliability plot of LBQR distribution*

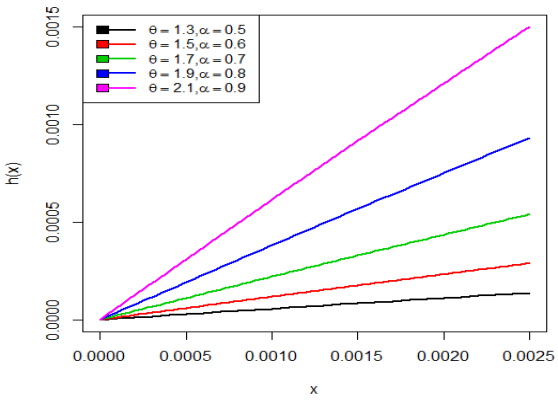


Figure 4: *Hazard plot of LBQR distribution*

IV. Order Statistics

Order statistics is a comprehensive tool in inference and non-parametric statistics which plays a crucial role in arranging the independent and identically distributed random variables. Suppose the order statistics $X_{(1)}, X_{(2)},\ldots, X_{(n)}$ of a random sample $X_1, X_2, \ldots, X_n$ from a continuous distribution with its probability density function $f_x(x)$ and cumulative distribution function $F_x(x)$, then probability density function of rth order statistics $X_{(r)}$ is defined as

$$f_{x(r)}(x) = \frac{n!}{(r-1)!\,(n-r)!} f_X(x) \left(F_X(x)\right)^{r-1} \left(1 - F_X(x)\right)^{n-r} \tag{8}$$

Now substituting the equations (5) and (7) in equation (8), we will get probability density function of rth order statistics $X_{(r)}$ of length biased quasi Rama distribution as

$$f_{x(r)}(x) = \frac{n!}{(r-1)!\,(n-r)!} \left(\frac{x\theta^4}{\left(\alpha\theta^2 + 24\right)} \left(\alpha + \theta x^3\right) e^{-\theta x} \right) \left(\frac{1}{\left(\alpha\theta^2 + 24\right)} \left(\alpha\theta^2 \gamma(2,\, \theta x) + \gamma(5,\, \theta x) \right) \right)^{r-1}$$
$$\times \left(1 - \frac{1}{\left(\alpha\theta^2 + 24\right)} \left(\alpha\theta^2 \gamma(2,\, \theta x) + \gamma(5,\, \theta x) \right) \right)^{n-r}$$

Hence for $r = n$, we have acquired the probability density function of higher order statistic $X_{(n)}$ of length biased quasi Rama distribution as

$$f_{x(n)}(x) = \frac{n x \theta^4}{\left(\alpha\theta^2 + 24\right)} \left(\alpha + \theta x^3\right) e^{-\theta x} \left(\frac{1}{\left(\alpha\theta^2 + 24\right)} \left(\alpha\theta^2 \gamma(2,\, \theta x) + \gamma(5,\, \theta x) \right) \right)^{n-1}$$

and for $r = 1$, we have acquired the probability density function of first order statistic $X_{(1)}$ of length biased quasi Rama distribution as

$$f_{x(1)}(x) = \frac{n\,x\,\theta^4}{\left(\alpha\,\theta^2 + 24\right)}\left(\alpha + \theta x^3\right)e^{-\theta x}\left(1 - \frac{1}{\left(\alpha\,\theta^2 + 24\right)}\left(\alpha\,\theta^2\gamma(2,\,\theta x) + \gamma(5,\,\theta x)\right)\right)^{n-1}$$

V. Statistical Measures

In this portion, we will have derived some fundamental properties like moments, harmonic mean, moment generating and characteristic function of length biased quasi Rama distribution those are

I. Moments

Let X be the random variable consists length biased quasi Rama distribution, then r^{th} order moment $E(X^r)$ of performed new distribution will be derived by using the expression as

$$\mu_r' = E(X^r) = \int_0^\infty x^r f_1(x;\theta,\alpha)\,dx$$

$$= \int_0^\infty x^r \frac{x\,\theta^4}{\left(\alpha\,\theta^2 + 24\right)}\left(\alpha + \theta x^3\right)e^{-\theta x}dx$$

$$= \frac{\theta^4}{\left(\alpha\,\theta^2 + 24\right)}\left(\alpha\int_0^\infty x^{(r+2)-1}\,e^{-\theta x}dx \;+\; \theta\int_0^\infty x^{(r+5)-1}\,e^{-\theta x}dx\right) \tag{9}$$

After the simplification of expression (9), we get

$$\mu_r' = E(X^r) = \frac{\left(\alpha\,\theta^2\Gamma(r+2) + \Gamma(r+5)\right)}{\theta^r\left(\alpha\,\theta^2 + 24\right)} \tag{10}$$

Hence by applying $r = 1$ in equation (10), we have obtained the mean of length biased quasi Rama distribution which is

$$\mu_1' = \frac{\left(2\alpha\,\theta^2 + 120\right)}{\theta\left(\alpha\,\theta^2 + 24\right)}$$

Now by applying $r = 2$, 3 and 4 in equation (10), we have obtained other three moments of length biased quasi Rama distribution as

$$\mu_2' = \frac{\left(6\alpha\,\theta^2 + 720\right)}{\theta^2\left(\alpha\,\theta^2 + 24\right)}$$

$$\mu_3' = \frac{\left(24\alpha\,\theta^2 + 5040\right)}{\theta^3\left(\alpha\,\theta^2 + 24\right)}$$

$$\mu_4' = \frac{\left(120\alpha\theta^2 + 40320\right)}{\theta^4\left(\alpha\theta^2 + 24\right)}$$

$$\text{Variance} = \frac{\left(2\alpha^2\theta^4 + 384\alpha\theta^2 + 2880\right)}{\theta^2\left(\alpha\theta^2 + 24\right)^2}$$

$$\text{S.D}(\sigma) = \frac{\sqrt{\left(2\alpha^2\theta^4 + 384\,\alpha\theta^2 + 2880\right)}}{\theta\left(\alpha\theta^2 + 24\right)}$$

$$\text{C.V} = \frac{\sqrt{\left(2\alpha^2\theta^4 + 384\,\alpha\theta^2 + 2880\right)}}{\left(2\alpha\theta^2 + 120\right)}$$

II. Harmonic mean

The harmonic mean of explored distribution is obtained by applying the expression as

$$\text{H.M} = E\left(\frac{1}{x}\right) = \int_0^\infty \frac{1}{x} f_1(x;\theta,\alpha)\,dx$$

$$= \int_0^\infty \frac{\theta^4}{\left(\alpha\theta^2 + 24\right)}\left(\alpha + \theta x^3\right)e^{-\theta x}dx$$

$$= \frac{\theta^4}{\left(\alpha\theta^2 + 24\right)}\int_0^\infty \left(\alpha + \theta x^3\right)e^{-\theta x}dx \qquad (11)$$

After the simplification of expression (11), we get

$$\text{H.M} = \frac{\theta(\alpha\theta + 6)}{\left(\alpha\theta^2 + 24\right)}$$

III. Moment generating function and characteristic function

Suppose X be the random variable which constitutes length biased quasi Rama distribution, then the MGF of performed distribution is obtained by applying the expression as

$$M_X(t) = E\left(e^{tx}\right) = \int_0^\infty e^{tx} f_1(x;\theta,\alpha)\,dx$$

$$= \int_0^\infty e^{tx}\,\frac{x\theta^4}{\left(\alpha\theta^2 + 24\right)}\left(\alpha + \theta x^3\right)e^{-\theta x}dx$$

$$= \frac{\theta^4}{\left(\alpha\theta^2 + 24\right)}\int_0^\infty x\left(\alpha + \theta x^3\right)e^{-(\theta - t)x}dx \qquad (12)$$

After the simplification of expression (12), we get

$$M_X(t) = \frac{\theta^4}{(\theta - t)^5\left(\alpha\theta^2 + 24\right)}\left(\alpha(\theta - t)^3 + 24\theta\right)$$

Clearly, the characteristic function of proposed distribution is given by

$$M_X(it) = \frac{\theta^4}{(\theta - it)^5\left(\alpha\theta^2 + 24\right)}\left(\alpha(\theta - it)^3 + 24\theta\right)$$

VI. Entropy

The entropy is a fundamental term which is used in diverse fields especially to measure the amount of uncertainty or randomness present in the dataset.

I. Renyi Entropy

The Renyi entropy was originally developed in information theory which generalizes several forms of entropy and therefore Renyi entropy forms the basis of the concept of generalized dimensions in fractal dimension estimation. The Renyi entropy should be expressed as

$$T_R(\beta) = \frac{1}{1-\beta}\log\left(\int f_1^{\beta}(x;\theta,\alpha)\,dx\right)$$

$$= \frac{1}{1-\beta}\log\left(\left(\frac{\theta^4}{\left(\alpha\theta^2 + 24\right)}\right)^{\beta}\int_0^{\infty} x^{\beta}\left(\alpha + \theta x^3\right)^{\beta} e^{-\theta\beta x}\,dx\right) \tag{13}$$

After the simplification of expression (13), we get

$$T_R(\beta) = \frac{1}{1-\beta}\log\left(\left(\frac{\theta^{3\beta - 3k - 1}}{\left(\alpha\theta^2 + 24\right)^{\beta}}\right)\sum_{k=0}^{\infty}\binom{\beta}{k}\alpha^{\beta-k}\,\theta^k\,\frac{\Gamma(\beta + 3k + 1)}{\beta^{\beta + 3k + 1}}\right)$$

Particularly, the Tsallis entropy of proposed LBQR distribution will be obtained by applying the expression

$$T_s(\zeta) = \frac{1}{\zeta - 1}\left(1 - \int_0^{\infty} f_1^{\zeta}(x;\theta,\alpha)\,dx\right)$$

$$= \frac{1}{\zeta - 1}\left(1 - \left(\frac{\theta^4}{\left(\alpha\theta^2 + 24\right)}\right)^{\zeta}\int_0^{\infty} x^{\zeta}\left(\alpha + \theta x^3\right)^{\zeta} e^{-\theta\zeta x}\,dx\right) \tag{14}$$

After the simplification of expression (14), we get

$$T_s(\zeta) = \frac{1}{\zeta - 1}\left(1 - \left(\frac{\theta^{3\zeta - 3j - 1}}{\left(\alpha\theta^2 + 24\right)^{\zeta}}\right)\sum_{j=0}^{\infty}\binom{\zeta}{j}\alpha^{\zeta - j}\theta^{j}\frac{\Gamma(\zeta + 3j + 1)}{\zeta^{\zeta + 3j + 1}}\right)$$

VII. Bonferroni and Lorenz Curves

The bonferroni and Lorenz curves are one of comprehensive tool which has diverse applications to depict graphically the distribution of income or wealth. The bonferroni and Lorenz curves should be defined as

$$B(p) = \frac{1}{p\mu_1'}\int_0^q x f_1(x;\theta,\alpha)\,dx$$

$$\text{and}\quad L(p) = pB(p) = \frac{1}{\mu_1'}\int_0^q x f_1(x;\theta,\alpha)\,dx$$

$$\text{Here } \mu_1' = \frac{\left(2\alpha\theta^2 + 120\right)}{\theta\left(\alpha\theta^2 + 24\right)}$$

$$B(p) = \frac{\theta\left(\alpha\theta^2 + 24\right)}{p\left(2\alpha\theta^2 + 120\right)}\int_0^q x\frac{x\theta^4}{\left(\alpha\theta^2 + 24\right)}\left(\alpha + \theta x^3\right)e^{-\theta x}dx$$

$$= \frac{\theta\left(\alpha\theta^2 + 24\right)}{p\left(2\alpha\theta^2 + 120\right)}\int_0^q \frac{x^2\theta^4}{\left(\alpha\theta^2 + 24\right)}\left(\alpha + \theta x^3\right)e^{-\theta x}dx \qquad (15)$$

After the simplification of expression (15), we get

$$B(p) = \frac{1}{p\left(2\alpha\theta^2 + 120\right)}\left(\alpha\theta^2\gamma(3,\,\theta q) + \gamma(6,\,\theta q)\right)$$

$$L(p) = \frac{1}{\left(2\alpha\theta^2 + 120\right)}\left(\alpha\theta^2\gamma(3,\,\theta q) + \gamma(6,\,\theta q)\right)$$

VIII. Maximum Likelihood Estimation and Fisher's Information Matrix

In this portion, we have applied the technique of maximum likelihood estimation to estimate the parameters of length biased quasi Rama distribution. Suppose $X_1, X_2, \ldots, X_n$ be random sample of size n from the length biased quasi Rama distribution, then likelihood function should be derived as

$$L(x) = \prod_{i=1}^{n} f_1(x;\theta,\alpha)$$

$$= \prod_{i=1}^{n} \left(\frac{x_i \, \theta^4}{\left(\alpha\theta^2 + 24\right)} \left(\alpha + \theta x_i^{\,3}\right) e^{-\theta x_i} \right)$$

$$= \frac{\theta^{4n}}{\left(\alpha\theta^2 + 24\right)^n} \prod_{i=1}^{n} \left(x_i \left(\alpha + \theta x_i^{\,3}\right) e^{-\theta x_i} \right)$$

The log likelihood function should be expressed as

$$\log L = 4n\log\theta - n\log\left(\alpha\theta^2 + 24\right) + \sum_{i=1}^{n} \log x_i + \sum_{i=1}^{n} \log\left(\alpha + \theta x_i^{\,3}\right) - \theta \sum_{i=1}^{n} x_i \qquad (16)$$

Hence differentiating the log likelihood expression (16) with respect to parameters θ and α. The given below normal equations should be satisfied

$$\frac{\partial \log L}{\partial \theta} = \frac{4n}{\theta} - n\left(\frac{2\alpha\theta}{\left(\alpha\theta^2 + 24\right)} \right) + \sum_{i=1}^{n} \left(\frac{x_i^{\,3}}{\left(\alpha + \theta x_i^{\,3}\right)} \right) - \sum_{i=1}^{n} x_i = 0$$

$$\frac{\partial \log L}{\partial \alpha} = -n\left(\frac{\theta^2}{\left(\alpha\theta^2 + 24\right)} \right) + \sum_{i=1}^{n} \left(\frac{1}{\left(\alpha + \theta x_i^{\,3}\right)} \right) = 0$$

Therefore the above system of non-linear equations are intricated to resolve algebraically. So it is better to apply numerical technique like Newton-Raphson method for estimating the required parameters.

To get the confidence interval hence we apply the asymptotic normality results. It should be noticed if $\hat{\omega} = (\hat{\theta}, \hat{\alpha})$ consists the MLE of $\omega = (\theta, \alpha)$. The conclusion should be observed as

$$\sqrt{n}(\hat{\omega} - \omega) \to N_2(0, I^{-1}(\omega))$$

Hence $I^{-1}(\omega)$ is Fisher's information matrix.

$$I(\omega) = -\frac{1}{n} \begin{pmatrix} E\left(\frac{\partial^2 \log L}{\partial \theta^2} \right) & E\left(\frac{\partial^2 \log L}{\partial \theta \, \partial \alpha} \right) \\ E\left(\frac{\partial^2 \log L}{\partial \alpha \, \partial \theta} \right) & E\left(\frac{\partial^2 \log L}{\partial \alpha^2} \right) \end{pmatrix}$$

Here we state that

$$E\left(\frac{\partial^2 \log L}{\partial \theta^2} \right) = -\frac{4n}{\theta^2} - n\left(\frac{\left(\alpha\theta^2 + 24\right)(2\alpha) - (2\alpha\theta)^2}{\left(\alpha\theta^2 + 24\right)^2} \right) - \sum_{i=1}^{n} \left(\frac{\left(x_i^{\,3}\right)^2}{\left(\alpha + \theta x_i^{\,3}\right)^2} \right)$$

$$E\left(\frac{\partial^2 \log L}{\partial \alpha^2} \right) = n\left(\frac{\left(\theta^2\right)^2}{\left(\alpha\theta^2 + 24\right)^2} \right) - \sum_{i=1}^{n} \left(\frac{1}{\left(\alpha + \theta x_i^{\,3}\right)^2} \right)$$

$$E\left(\frac{\partial^2 \log L}{\partial\theta\,\partial\alpha}\right) = -n\left(\frac{\left(\alpha\theta^2+24\right)(2\theta)-(2\alpha\theta)\left(\theta^2\right)}{\left(\alpha\theta^2+24\right)^2}\right) - \sum_{i=1}^{n}\left(\frac{\left(x_i^3\right)}{\left(\alpha+\theta x_i^3\right)^2}\right)$$

Therefore ω is not known, hence $I^{-1}(\omega)$ is estimated by $I^{-1}(\hat{\omega})$ and since it should be applied to attain asymptotic confidence interval for θ and α.

IX. Application

In this portion, we have scrutinized and studied the two real lifetime data sets to investigate the performance and goodness of fit of length biased quasi Rama distribution and then fit of length biased quasi Rama distribution has been compared in order to reveal that length biased quasi Rama distribution provides a better fit in comparison over quasi Rama, Rama, Pratibha, Komal, Uma and Lindley distributions. The two real lifetime data sets are given as

Data set 1: The first given data set from civil engineering reported by Kotz and van Dorp [8] which consists of 85 hailing times observations and the observations of real lifetime data set is given below as

4.79, 4.75, 5.40, 4.70, 6.50, 5.30, 6.00, 5.90, 4.80, 6.70, 6.00, 4.95, 7.90, 5.40, 3.50, 4.54, 6.90, 5.80, 5.40, 5.70, 8.00, 5.40, 5.60, 7.50, 7.00, 4.60, 3.20, 3.90, 5.90, 3.40, 5.20, 5.90, 4.40, 5.20, 7.40, 5.70, 6.00, 3.60, 6.20, 5.70, 5.80, 5.90, 6.00, 5.15, 6.00, 4.82, 5.90, 6.00, 7.30, 7.10, 4.73, 5.90, 3.60, 6.30, 7.00, 5.10, 6.00, 6.60, 4.40, 6.80, 5.60, 5.90, 5.90, 8.60, 6.00, 5.80, 5.40, 6.50, 4.80, 6.40, 4.15, 4.90, 6.50, 8.20, 7.00, 8.50, 5.90, 4.40, 5.80, 4.30, 5.10, 5.90, 4.70, 3.50, 6.80

Data set 2: The second given data set was first reported by Mahmoud and Mandouh [9] which represents the uncensored strengths of glass fibres and the observations of real data set is shown under as

1.014, 1.081, 1.082, 1.185, 1.223, 1.248, 1.267, 1.271, 1.272, 1.275, 1.276, 1.278, 1.286, 1.288, 1.292, 1.304, 1.306, 1.355, 1.361, 1.364, 1.379, 1.409, 1.426, 1.459, 1.46, 1.476, 1.481, 1.484, 1.501, 1.506, 1.524, 1.526, 1.535, 1.541, 1.568, 1.579, 1.581, 1.591, 1.593, 1.602, 1.666, 1.67, 1.684, 1.691, 1.704, 1.731, 1.735, 1.747, 1.748, 1.757, 1.800, 1.806, 1.867, 1.876, 1.878, 1.91, 1.916, 1.972, 2.012, 2.456, 2.592, 3.197, 4.121

The model comparison criterions along with unknown parameters are estimated thoroughly by applying the technique of R software. To examine significance and capability of length biased quasi Rama distribution as compared over quasi Rama, Rama, Pratibha, Komal, Uma and Lindley distributions, the criterions like *AIC* (Akaike Information Criterion), *BIC* (Bayesian Information Criterion), *AICC* (Akaike Information Criterion Corrected), *CAIC* (Consistent Akaike Information Criterion), Shannon's entropy *H(X)* and *-2logL* have been used. The distribution performs quite better even if it has lesser criterions of *AIC, BIC, AICC, CAIC, H(X)* and *-2logL* in comparison over other well known distributions. The following formulas given are used for determining the criterion values

$$AIC = 2k - 2\log L, \qquad BIC = k\log n - 2\log L, \qquad AICC = AIC + \frac{2k(k+1)}{n-k-1}$$

$$CAIC = -2\log L + \frac{2kn}{n-k-1} \qquad \text{and} \qquad H(X) = -\frac{2\log L}{n}$$

Therefore k is number of parameters in the statistical model, n is the sample size and $-2\log L$ is the maximized value of log-likelihood function under considered model.

Table 1: *Shows MLE and S.E of following data sets of Performed Distributions*

Data set 1			Data set 2		
Distribution	MLE	S.E	Distribution	MLE	S.E
LBQR	$\hat{\alpha} = 0.001000$ $\hat{\theta} = 0.878667$	$\hat{\alpha} = 0.000010$ $\hat{\theta} = 0.029170$	LBQR	$\hat{\alpha} = 0.00100$ $\hat{\theta} = 3.09420$	$\hat{\alpha} = 0.000100$ $\hat{\theta} = 0.11986$
Quasi Rama	$\hat{\alpha} = 0.0010000$ $\hat{\theta} = 0.7029134$	$\hat{\alpha} = 0.0001000$ $\hat{\theta} = 0.0259567$	Quasi Rama	$\hat{\alpha} = 0.00100$ $\hat{\theta} = 2.47446$	$\hat{\alpha} = 0.000010$ $\hat{\theta} = 0.106260$
Rama	$\hat{\theta} = 0.677018$	$\hat{\theta} = 0.035522$	Rama	$\hat{\theta} = 1.666889$	$\hat{\theta} = 0.094815$
Pratibha	$\hat{\theta} = 0.475361$	$\hat{\theta} = 0.029030$	Pratibha	$\hat{\theta} = 1.200580$	$\hat{\theta} = 0.081031$
Komal	$\hat{\theta} = 0.298773$	$\hat{\theta} = 0.022844$	Komal	$\hat{\theta} = 0.842362$	$\hat{\theta} = 0.078397$
Uma	$\hat{\theta} = 0.657943$	$\hat{\theta} = 0.034344$	Uma	$\hat{\theta} = 1.61434$	$\hat{\theta} = 0.09652$
Lindley	$\hat{\theta} = 0.3098973$	$\hat{\theta} = 0.0241075$	Lindley	$\hat{\theta} = 0.938282$	$\hat{\theta} = 0.088962$

Table 2: *Shows Comparison, Significance and Performance of fitted Distributions*

Data sets	Distribution	-2logL	AIC	BIC	AICC	CAIC	H(X)
1	LBQR	332.4848	336.4848	341.3701	336.6311	336.6311	3.9115
	Quasi Rama	348.5044	352.5044	357.3897	352.6507	352.6507	4.1000
	Rama	356.3218	358.3218	360.7644	358.3699	358.3699	4.1920
	Pratibha	385.6311	387.6311	390.0737	387.6792	387.6792	4.5368
	Komal	427.3503	429.3503	431.7929	429.3984	429.3984	5.0276
	Uma	362.0973	364.0973	366.54	364.1454	364.1454	4.2599
	Lindley	423.4846	425.4846	427.9272	425.5327	425.5327	4.9821
2	LBQR	93.02548	97.02548	101.3117	97.2254	97.2254	1.4765
	Quasi Rama	103.6676	107.6676	111.9539	107.8676	107.8676	1.6455
	Rama	176.7793	178.7793	180.9224	178.8448	178.8448	2.8060
	Pratibha	166.1255	168.1255	170.2686	168.1910	168.1910	2.6369
	Komal	177.4134	179.4134	181.5565	179.4789	179.4789	2.8160
	Uma	170.1836	172.1836	174.3268	172.2491	172.2491	2.7013
	Lindley	170.9519	172.9519	175.095	173.0174	173.0174	2.7135

Obviously, it is clearly observed and revealed from the result given above in table 2 that the length biased quasi Rama distribution has lesser criterion values of *AIC*, *BIC*, *AICC*, *CAIC*, *H(X)* and *-2logL* as compared over quasi Rama, Rama, Pratibha, Komal, Uma and Lindley distributions which consists that the length biased quasi Rama distribution gives a best fit in comparison over quasi Rama, Rama, Pratibha, Komal, Uma and Lindley distributions.

X. Conclusion

In this manuscript, we have approached a novel version of quasi Rama distribution termed as length biased quasi Rama distribution has been formulated. The explored new distribution is introduced by applying the length biased technique to baseline quasi Rama distribution and its several structural properties such as moments, shape of pdf and cdf, order statistics, reliability function, hazard rate function, reverse hazard rate function, moment generating and characteristic function, bonferroni and Lorenz curves, Renyi entropy and Tsallis entropy has been described. Additionally, the parameters of performed distribution are estimated by using technique of maximum likelihood estimation. Furthermore, the flexibility and superiority of proposed length biased quasi Rama distribution has been analyzed by applying the two real data sets and therefore it is realized from the result that performed length biased quasi Rama distribution gives a best fit as compared over quasi Rama, Rama, Pratibha, Komal, Uma and Lindley distributions.

References

[1] Al-Omari, A. I., Alhyasat, K. M., Ibrahim, K. and Abu Bakar, M. A. (2019). Power length-biased Suja distribution: properties and application. *Electronic Journal of Applied Statistical Analysis*, 12(02):429-452.

[2] Beghriche, A. and Zeghdoudi, H. (2019). A size biased Gamma Lindley distribution. *Thailand Statistician*, 17(2):179-189.

[3] Cox, D. R. (1962). Renewal Theory, Barnes and Noble, New York.

[4] Fisher, R. A. (1934). The effects of methods of ascertainment upon the estimation of frequencies. *Annals of Eugenics*, 6:13-25.

[5] Ganaie, R. A. and Rajagopalan, V. (2020). A new generalization of two parameter Pranav distribution with characterizations and applications of real life-time data. *International Journal of Statistics and Reliability Engineering*, 7(3):331-341.

[6] Ganaie, R. A. and Rajagopalan, V. (2021). A new extension of power quasi Lindley distribution with properties and applications of the lifetime data. *International Journal of Statistics and Reliability Engineering*, 8(1):171-183.

[7] Klinjan, K. and Aryuyuen, S. (2021). The length-biased power Garima distribution and its application to model lifetime data. *Songklanakarin J. Sci. Technol*., 43(3):667-676.

[8] Kotz, S. Y. and Van Dorp, J. R. (2004). *Beyond Beta: Other Continuous Families of Distributions with Bounded Support and Applications*. Singapore: World Scientific.

[9] Mahmoud, M. R. and Mandouh, R. M. (2013). On the transmuted Frechet distribution. *Journal of Applied Sciences Research*, 9(10):5553-5561.

[10] Mustafa, A. and Khan, M. I. (2022). The length-biased powered inverse Rayleigh distribution with applications. *J. Appl. Math. & Informatics*, 40(1-2):1-13.

[11] Mudasir, S. and Ahmad, S. P. (2015). Structural properties of length biased Nakagami distribution. *International Journal of Modern Mathematical Sciences*, 13(3):217-227.

[12] Nanuwong, N. and Bodhisuwan, W. (2014). Length biased Beta-Pareto distribution and its structural properties with application. *Journal of Mathematics and Statistics*, 10(1):49-57.

[13] Pushkarna, N. and Mustafa (2025). Length biased weighted ishita distribution and its applications on real life data sets. *Journal of Reliability and Statistical Studies*, 18(1):213-242.

[14] Rao, C. R. (1965). On discrete distributions arising out of methods of ascertainment, in classical and Contagious Discrete, G.P. Patiled; Pergamum Press and Statistical Publishing Society, Calcutta. 320-332.

[15] R core team (2019). R version 3.5.3: A language and environment for statistical computing. R Foundation for statistical computing, Vienna, Austria.URL https:// www.R-project .org/.

[16] Saghir, A. and Khadim, A. (2016). The mathematical properties of length biased weighted Maxwell distribution. *Journal of Basic and Applied Research International*, 16(3):189-195.

[17] Salama, M. M., Elsherpieny, E. A. and Abd-elaziz, A. A. (2023). The length-biased weighted exponentiated inverted exponential distribution: properties and estimation. *Computational Journal of Mathematical and Statistical Sciences*, 2(2):181-196.

[18] Shanker, R., Das, H. and Shukla, K. K. (2023). A quasi Rama distribution. *Model Assisted Statistics and Applications*, 18:267-277.

[19] Sharma, V. K., Dey, S., Singh, S. K. and Manzoor, U. (2018). On length and area-biased Maxwell distributions. *Communications in Statistics – Simulation and Computation*, 47(5):1506-1528.

RT&A, No 4 (89)
Volume 20, December 2025

METRIC DIMENSION OF GRAPHS WITH SEQUENTIAL PENDANT EDGE EXTENSION

Ajendra Kumar[1], B.S. Rawat[2], Kirti Chauhan[3*]

•

[1,3*] Department of Mathematics and Statistics, Gurukula Kangri (Deemed to be University), Haridwar, Uttarakhand, 249404

[2] Department of Mathematics, Govt. P.G. College, Uttarkashi, 249193

[1]Email- drajendrakumar@gkv.ac.in

[2]Email- bipendrarawat80@gmail.com

[3*]Email- kirti12chauhan1998@gmail.com

[*]Corresponding author

Abstract

The metric dimension of a graph measures the smallest number of vertices (landmarks) needed so that every vertex in the graph can be uniquely identified by its distances to these landmarks. In this study, we investigate a specific structural modification called Sequential Pendant Edge Extension (SPEE) in which pendant edges are attached one at a time to an existing graph. We analyse whether such extensions affect the metric dimension of graph families. These results provide both theoretical insights and practical assurance in designing reliable and scalable network models.

Keywords: Sequential Pendant Edge Extension (SPEE), Metric Dimension, Pendant Edge, Graph Resolvability, Edge Extension.

I. Introduction

Metric dimension is a fundamental concept in the domain of graph theory, which indicates the smallest possible size of a set of vertices required to uniquely distinguish every vertex of the graph. This minimum set, referred to as a set of landmarks or resolving set, ensures that each vertex can be individually identified based on its distances to the vertices in that set. Let graph $G = (V, E)$, where V collection of nodes (vertices) and E collection of links (edges) which connects the vertices. A subset $B \subseteq V$ referred to as a resolving set of G if for every tuple of vertices $(p, q) \in V$, there exist a vertex $m \in B$ such that the distance between m and p is different from the distance between m and q.

The concept of metric dimension in graph theory was first introduced by Slater [1] in the context of "leaves of trees". Harary and Melter [2] independently introduce the idea of metric dimension. The study of metric dimension is not only of theoretical interest but also has wide-ranging applications across science, engineering, and technology in which structure of a chemical compound can be represented by a labelled graph with vertex and edge specifying the atoms and bond types, respectively. Other uses for resolving sets can be found in a number of contexts, such as robot navigation, the coin-weighing problem, drug discovery, connected joins in graphs, and mastermind game tactics [3], network discovery and verification [4]. Metric dimension theory has been studied for various graph classes such as paths, cycles, complete graphs and wheel graphs and for operations like Cartesian products, joins and vertex addition. The metric dimension $\beta(G) = 1$ for any graph G exists only when G is a path mentioned in [5].

In [6] mentioned that the graphs with metric dimension k cannot have a subgraph isomorphic to $K_{2^k+1} - (2^{k-1} - 1)K_2$. By joining k cycles at a common vertex in each of the k cycles, estimate the metric dimension for some unique types of graphs in [7]. The metric dimension of wheel for larger value of n and also disprove the observation made by [8]. In [9] investigated the dimension of a connected graph by the addition of a single vertex and formula is developed for the dimension of a wheel. Also, the existence of a k-dimensional graph for every integer $k \geq 2$ is shown. In [10] shown metric dimension of comb product of graphs. In [11] the metric dimension of Jahangir graph 2.

Recent studies have continued to expand the applications of metric dimension in dynamic and evolving networks. For instance, [12] investigated the metric dimension in hybrid network models with pendant and chordal extensions, showing that structural modifications may preserve or alter resolvability depending on attachment rules. Similarly,[13] studied the stability of resolving sets under iterative graph operations, highlighting that pendant edge additions offer a unique case of invariance. Despite several studies on metric dimension across classical graphs and graph operations, the impact of sequential pendant edge extension (SPEE) has remained largely unexplored.

Existing literature often focuses on single pendant additions or generalized extensions but does not address whether repeated, stepwise pendant attachments preserve or alter the metric dimension across different graph families. Understanding the stability of metric dimension under SPEE is crucial for analyzing evolving and dynamic networks. Motivated by [12], [13], [14], [15]; we have obtained some results.

II. Preliminaries

I. Metric Dimension

Let graph $G = (V, E)$, where V collection of nodes (vertices) and E collection of links (edges) which is connecting the vertices. A subset $B \subseteq V$ referred to as a resolving set of G if for every tuple of vertices $(p, q) \in V$, there exist a vertex $m \in B$ such that the distance between m and p is different from the distance between m and q. The metric dimension of a graph denotes as $\beta(G)$.

II. Graph Resolvability

Graph resolvability refers to the ability to uniquely determine the positions of each vertex with in a graph by measuring distances to a selected subset of reference vertices, known as a resolving set (or landmark set). A graph is said to be resolvable if there exists at least one resolving set whose pairwise distance vectors called metric representations are distinct for every vertex in the graph. The size of the smallest such set is the graph's metric dimension.

III. Sequential Pendant Edge Extension (SPEE)

Sequential pendant edge extension describes the process of adding one-degree leaf vertices to a graph one at a time, in a specified order. At each step, a new vertex is attached by a single edge (a pendant edge) to an existing vertex, extending the graph's structure without altering the distances among the original vertices.

IV. Wheel Graph

A wheel graph is a kind of graph that has a centre vertex (the hub) attached to a set of peripherals

vertices (the rim). The rim vertices also link together in a cyclic pattern, making a cycle. The wheel graph is denoted by W_n,, where n is the number of vertices on the rim. The metric dimension of the wheel graph is presented below:

$$\beta(W_n)=\begin{cases} 3, & for\ n = 3\ and\ 6 \\ 2, & for\ n = 4\ and\ 5 \\ \frac{2n+2}{5}, & for\ n \geq 7 \end{cases}. \quad (1)$$

V. Cycle Graph

A cycle graph is a basic graph formed by a single cycle, which is an enclosed loop of vertices linked by an edge. It is indicated as C_n, where n is the number of nodes in the cycle. Metric dimension of cycle graph is presented below:

$$\beta\ (C_n) = 2, for\ n \geq 3. \quad (2)$$

VI. Complete Graph

A complete graph is a basic undirected graph where every pair of distinct vertices are joined by a single edge. A complete graph with n vertices, abbreviated as K_n is a graph with n vertices that are contiguous to each other. Metric dimension of complete graph is presented below:

$$\beta(K_n) = n - 1\ , for\ \ n \geq 2. \quad (3)$$

III. Metric Dimension of Graphs with SPEE

In graph theory, a pendant edge is simply an edge connected to a vertex with degree 1. This means it links to a pendant vertex with a single neighbouring edge. The presence of this edge has the potential to impact the metric dimension of graph. Let's look at the details.

When a pendant edge links to a pendant vertex, it can serve as a landmark to uniquely identify both the edge and the vertex. As a result, the presence of this pendant edge has no effect on the metric dimension of graph because the existing pendant vertex serves as a land mark. If the pendant edge connects with a non-pendant vertex the metric dimension of a graph with a pendant edge might remain constant or increase. It is conceivable for the metric dimension to remain constant in some instances where the addition of the pendant edge does not modify the structure or connectivity of the graph in such a manner that it changes the minimum set of vertices required to uniquely identify all others.

For example, consider a graph with non-pendant vertex v, and its adjacent vertices u and w. If there is an edge between u and w and a pendant edge is added to vertex v, then the metric dimension of the graph would remain the same. The reason for this is that even though the pendant edge introduces a new connection to vertex v, it does not alter the existing relationships between the vertices u and w. As a result, the minimum set of vertices needed to uniquely identify all other vertices in the graph remains same. We consider different classes of graphs including wheel graph, cycle graph and specific graph families with known metric dimension properties. By analysing these families of graphs, we establish conditions under which the metric dimension is preserved when pendant edge is attached sequentially.

I. Metric dimension of graph obtained by wheel graph with SPEE

Let be a graph W_n' obtained by wheel graph with SPEE and vertex set of obtained graph $V(W_n') =$

$\{v, v_1, v_2, v_3, \dots, v_n\}$ and w be the pendant vertex linked to vertex $v_q \in V(W_n); 1 \le q \le n$. Several distinct cases arise while evaluating the metric dimension of the derived graph, as presented below:

Case I: For $n = 4$ and 5, Consider the set $B=\{v_2, v_3\} \subseteq V(W_n')$, then the metric representations of derived graph are presented below:

Metric tuples of the apex vertices

$$r(v_q|B) = \begin{cases} (1,2), q = 1 \\ (0,1), q = 2 \\ (1,0), q = 3 \\ (2,1), q = 4 \\ (2,2), q = 5 \end{cases}$$

Metric representation of the pendant vertex w

$$r(w|B) = \begin{cases} (2,3), if\ w\ corresponding\ to\ v_1 \\ (2,0), if\ w\ corresponding\ to\ v_3 \\ (3,2), if\ w\ corresponding\ to\ v_4 \\ (3,3), if\ w\ corresponding\ to\ v_5 \end{cases}$$

Since all metric representations are unique, metric dimension of obtained graph (W_4') and (W_5') is 2.

Case II: For $n = 3$, Consider the set $B = \{v_1, v_2, v_3\} \subseteq V(W_n')$ then the metric representations of derived graph are presented below:

Metric tuples of the apex vertices

$$r\,(v_q|B) = \begin{cases} (0,1,1), q = 1 \\ (1,0,1), q = 2 \\ (1,1,0), q = 3 \end{cases}$$

Metric representation of the pendant vertex w

$$r(w|B) = \begin{cases} (1,2,2), if\ w\ corresponding\ to\ v_1 \\ (2,1,2), if\ w\ corresponding\ to\ v_2 \\ (1,2,2), if\ w\ corresponding\ to\ v_3 \end{cases}$$

The subsequent cases illustrate that assuming $|B| = 2$, the set B fails to function as a resolving set.

• Consider the vertex set $B = \{v, v_q : 1 \le i \le 3\} \subseteq V(W_n')$. In this configuration, it is observed that the metric representation of the vertices $r(v_{((q+1)mod3+1)}|B) = (1,1) = r(v_{q(mod3)+1}|B)$; with respect to B are identical. This contradicts the requirement for a resolving set, where in each vertex must have a unique metric representation. Hence, B cannot be considering a resolving set under the assumption $|B| = 2$.

• Consider a vertex set $B = \{v_i, w : 1 \le i \le 3\} \subseteq V(W_n')$ and w be the pendant vertex corresponding to v_j $(1 \le j \le 3)$. In this setup, the metric representation of the vertices $r(v_k|B) = (1,2) = r(v|B)$ with respect to B is identical. This defines the criteria for a resolving set, which states that each vertex must have a unique metric representation. As a result, B cannot be considered a resolving set under the premise that $|B| = 2$.

• Consider the vertex set $B = \{v_i, v_j : 1 \le i \le 3, 1 \le j \le 3\}$. It is noticed that the metric representation of vertex $r(v_k|B) = (1,1) = r(v|B)$ with respect to B is identical. This goes against the criteria for a resolving set, which states that each vertex must have a distinct metric representation. Assuming that $|B|=2$, B cannot be regarded a resolving set.

• Consider a vertex set $B = \{v, w\} \subseteq V(W_3')$ and w corresponding to v_i $(1 \le i \le 3)$. Here we find that $r(v_j|B) = (1,2) = r(v_k|B)$ which contradict our assumption. Consider the vertex set $B = \{v, w\} \subseteq V(W_3')$ where w corresponds to a rim vertex v_i for some $(1 \le i \le 3)$.In this configuration,

it is observed that the metric representations of vertices $r(v_j|B) = (1,2) = r(v_k|B)$ with respect to B are identical. This contradicts the requirement for a resolving set, which stipulates that each vertex must have a unique metric representation. Therefore, under the assumption $|B|=2$, B cannot be considered a resolving set.

Above consider the vertex set $B = \{v_1, v_2, v_3\} \subseteq V(W_n')$. In this configuration, each vertex in the graph has a unique metric representation with respect to B. Consequently, the metric dimension of graph W_n' is 3.

Case III: For $n=6$, Consider the set $B=\{v_1, v_3, v_5\} \subseteq V(W_n')$ then the metric representations of derived graph are presented below:

Metric tuples of the apex vertices

$$r(v_q|B) = \begin{cases} (0,2,2), q = 1 \\ (1,1,2), q = 2 \\ (2,0,2), q = 3 \\ (2,1,1), q = 4 \\ (2,2,0), q = 5 \\ (1,2,1), q = 6 \end{cases}$$

Metric representation of the pendant vertex w

$$r(w|B) = \begin{cases} (1,3,3), if\ w\ corresponding\ to\ v_1 \\ (2,2,3), if\ w\ corresponding\ to\ v_2 \\ (3,1,3), if\ w\ corresponding\ to\ v_3 \\ (3,2,2), if\ w\ corresponding\ to\ v_4 \\ (3,3,1), if\ w\ corresponding\ to\ v_5 \\ (2,3,2), if\ w\ corresponding\ to\ v_6 \end{cases}$$

The subsequent cases illustrate that assuming $|B| = 2$, the set B fails to function as a resolving set.

• Consider the vertex set $B = \{v, v_q: 2 \le q \le 5\} \subseteq V(W_6')$. In this configuration, $r(v_{q-1}|B) = (1,1) = r(v_{q+1}|B)$ metric representation is identical. This indicates that B fails to distinguish between these vertices. Furthermore, for $i = 6, B = \{v_6, v\}$ obtain $r(v_1|B) = (1,1) = r(v_5|B)$ and for $i = 1, B = \{v, v_1\}$ and $r(v_2|B) = (1,1) = r(v_6|B)$. These instances demonstrate that B does not serve as a resolving set under the assumption $|B|=2$, as it fails to uniquely identify all vertices in W_6'.

• Consider the vertex set $B = \{v, w\} \subseteq V(W_6')$, where w is the pendant vertex corresponding to a rim vertex $v_i, \{2 \le i \le 5\}$. In this configuration, the metric representations of vertices $r(v_{i-1}|B) = (1,2) = r(v_{i+1}|B)$ with respect to B are identical. Similarly, for $i = 6$ notice that $r(v_1|B) = (1,2) = r(v_5|B)$, and for $i = 1$ and $r(v_6|B) = (1,2) = r(v_2|B)$.These cases demonstrate that B fails to act as a resolving set for $|B| = 2$.

• Consider the vertex set $B = \{v_I, w\} \subseteq V(W_6')$, w be the pendant vertex corresponding to $\{v_i: 2 \le i \le 5\}$ Here, we find that $r(v_{i-1}|B) = (1,2) = r(v_{i+1}|B)$; for $i = 6$, we obtain $r(v_1|B) = (1,2) = r(v_5|B)$ and for $i = 1$, we obtain $r(v_6|B) = (1,2) = r(v_2|B)$ which contradicts our assumption.

Every vertex in the set $B=\{v_1, v_3, v_5\} \subseteq V(W_n')$ possesses a distinct metric representation. Therefore, the metric dimension of the graph obtained by wheel graph W_n' is 3.

Case IV(a): For $n \ge 7$, When $\beta(W_n') =$ odd and w be pendant vertex linked to $v_q; (1 \le q \le n)$.

• For $n = 5k + 2$,where $k \ge 1$ and contains $2k + 1$ vertices, since $B = \{v_1, v_4, v_6, v_{10} \dots, v_{k-1}\} \cup \{v_{5k+1}\}$, it serves as a resolving set across all configuration.

• For $n = 5k + 3$, where $k \ge 1$ and contains $2k + 1$ vertices, since $\{v_1, v_4, v_6, v_{10}, \dots, v_{k-2}\} \cup \{v_{5k-4}, v_{5k}, v_{5k+2}\}$ it serves as a resolving set across all configuration.

Case IV(b): For $n \ge 7$, When $\beta(W_n') =$ even and w be the pendant vertex corresponding to $v_I; (1 \le i \le n)$.

• For $n = 5k$, where $k \geq 2$, and contains $2k$ vertices and $B = \{v_1, v_4, v_6, v_{10}, \dots, v_{k-1}\}$, it serves as a resolving set across all configuration.

• For $n = 5k + 1$, where $k \geq 2$, and contains $2k$ vertices and $B = \{v_1, v_4, v_6, v_{10}, \dots, v_{k-2}\} \cup \{v_{5k-4}, v_{5k}\}$,it serves as a resolving set across all configuration.

• For $n = 5k + 4$, where $k \geq 1$, and contains $2k + 2$ vertices and $B = \{v_1, v_4, v_6, v_{10}, \dots, v_k\}$, it serves as a resolving set across all configuration.

Hence, $\beta(W_n') \leq \left\lceil \frac{2n+2}{5} \right\rceil$.

Next, show that the metric dimension of derived graph $\beta\,(W_n') \geq \left\lceil \frac{2n+2}{5} \right\rceil$.

Let B is a resolving set of W_n' with $|B| \leq \left\lceil \frac{2n+2}{5} \right\rceil$.

Now if $B = \{v_1, v_2, v_3, \dots, v_r\}; 1 \leq r \leq n$, then

$$r(p|B) = (2,2,2,2,..,2,2) = r(q|B);\ p, q \in V(W_n') \text{ if } B = \{v, v_1, v_2, v_3, \dots v_r), \text{ then}$$
$$r(p|B) = (1,2,2,2, \dots,2) = r(q|B); p, q \in V(W_n'), \text{ if } B = \{w, v_1, v_2, v_3, \dots, v_r\}, \text{ and}$$

w be the pendant vertex of $v_q (1 \leq q \leq n)$, then

$$r(p|B) = (3,2,2,2, \dots,2) = r(q|B).$$

It is observed that two vertices share identical metric representations, when $|B| \leq \left\lceil \frac{2n+2}{5} \right\rceil$, So B does not function as a resolving set for the graph W_n'. Therefore,

$$\beta\,(W_n') \geq \left\lceil \frac{2n+2}{5} \right\rceil.$$

Hence, we conclude that $\beta\,(W_n') = \left\lceil \frac{2n+2}{5} \right\rceil$.

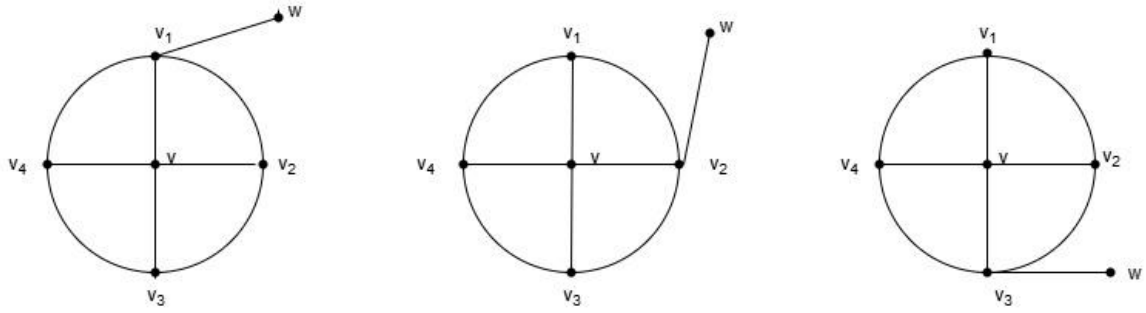


Figure 1: *Wheel graph (W_4) with SPEE*

II. Metric dimension of graph obtained by cycle graph with SPEE

Let be a graph C_n' obtained by cycle graph with SPEE and vertex set of obtained graph $V(C_n') = \{v_1, v_2, v_3 \dots\dots v_{n-1}, v_n, v_1\}$ and w be the pendant vertex linked to the vertex v_q. Several distinct cases arise while evaluating the metric dimension of the derived graph, as presented below.

Case I: For $n = 3$ and $B = \{v_1, v_2\} \subseteq V(C_n')$ then the metric representations of derived graph are presented below:

Metric representation of the apex vertices

$$r(v_q|B) = \begin{cases} (0,1), q = 1 \\ (1,0), q = 2 \\ (1,1), q = 3 \end{cases}$$

Metric representation of the pendant vertex w

$$r(w|B) = \begin{cases} (1,2), if\ w\ corresponding\ to\ v_1 \\ (2,1), if\ w\ corresponding\ to\ v_2 \\ (2,2), if\ w\ corresponding\ to\ v_3 \end{cases}$$

Since all metric representations of derived graph are unique, then metric dimension of derived graph is 2.

Case II**:** For $n = 5$ and $B = \{v_3, v_4\} \subseteq V(C_n')$ then the metric representations of derived graph are presented below:

Metric representation of the apex vertices

$$r(v_q|B) = \begin{cases} (2,2), if\ q = 1 \\ (1,2), if\ q = 2 \\ (0,1), if\ q = 3 \\ (1,0), if\ q = 4 \\ (2,1), if\ q = 5 \end{cases}$$

Metric *representation* of the pendant vertex w

$$r(w|B) = \begin{cases} (3,3), if\ w\ corresponding\ to\ v_1 \\ (2,3), if\ w\ corresponding\ to\ v_2 \\ (1,2), if\ w\ corresponding\ to\ v_3 \\ (2,1), if\ w\ corresponding\ to\ v_4 \\ (3,2), if\ w\ corresponding\ to\ v_5 \end{cases}$$

Above all metric representations are unique hence the metric dimension of the derived graph is 2. Similarly, w be pendant vertex v_q, then for any value of n, B be the basis of C_n' and contain only two vertex such that B=$\{v_{q+1}, w | 1 \le q \le n-1\}$ and if $q = n$ then $B = \{v_1, w\}$. Since each vertex has a distinct metric representation, the set B qualifies as a resolving set across all configurations. Hence the metric dimension of graph C_n' obtained by cycle graph with sequential pendant edge extension is 2.

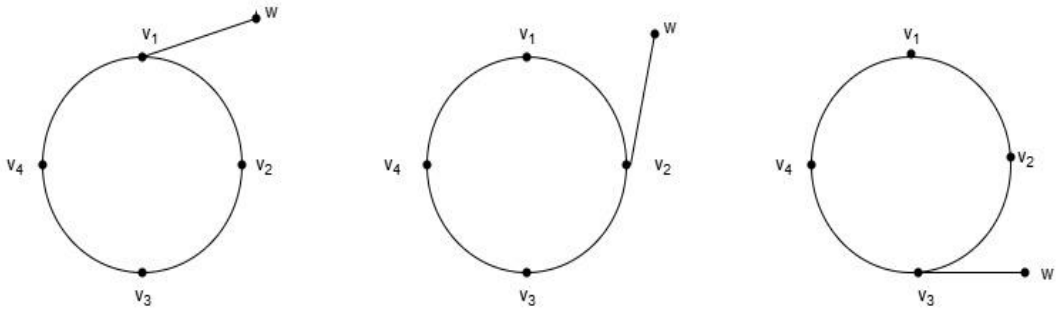


Figure 2: *Cycle Graph (C_4)with SPEE*

III. Metric dimension of graph obtained by complete graph with SPEE

Let be a graph K_n' obtained by complete graph with SPEE and vertex set of obtained graphs $V(K_n') = \{v_1, v_2, v_3, \dots, v_n\}$ and w be the pendant vertex linked to vertex $v_q; 1 \le q \le n$. Several distinct cases arise while evaluating the metric dimension of the derived graph, as presented below.

Case I: For *n*=3, $B = \{v_1, v_2\}$ and then the metric representations of derived graph are presented below:

Metric tuple of the vertices relative to reference set B

$$r(v_q|B) = \begin{cases} (0,1), if\ q = 1 \\ (1,0), if\ q = 2 \\ (1,1), if\ q = 3 \end{cases}$$

Metric representation of the pendant vertex w with respect to B

$$r(w|B) = \begin{cases} (1,2,2,2), if\ w\ corresponding\ to\ v_1 \\ (2,1,2,2), if\ w\ corresponding\ to\ v_2 \\ (2,2,1,2), if\ w\ corresponding\ to\ v_3 \\ (2,2,2,1), if\ w\ corresponding\ to\ v_4 \\ (2,2,2,2), if\ w\ corresponding\ to\ v_5 \end{cases}$$

The following cases demonstrate that B is not a resolving set in this situation if we assume $|B| = 2$.

• Consider a vertex set $B = \{v_q, w: 1 \le i \le 5\} \subseteq V(K_n')$ and w be the pendant vertex corresponding to v_q. Here, we find that $r(v_k|B) = (1,2) = r(v_j|B)$ which contradicts our assumptions.

• Consider the vertex set $B = \{v_i, v_j: 1 \le i \le 5, 1 \le j \le 5\}$. Here we find that $r(v_k|B) = (1,1) = r(v_i|B)$ which contradicts our assumptions.

• Consider a vertex set $B = \{v_i, w\} \subseteq V(K_n')$ and w corresponding to v_j $(1 \le j \le 5)$. Here we find that $r(v_k|B) = (1,1) = r(v_i|B)$ which contradicts our assumptions.

The following cases demonstrate that B is not a resolving set in this situation if we assume |B| = 3

• Consider the vertex set $B = \{v_i, v_j, v_k: 1 \le i \le 5, 1 \le j \le 5, 1 \le k \le 5\}$. Here we find that r $(v_m|B) = (1,1) = r(v_l|B)$ which contradicts our assumption.

• Consider a vertex set $B = \{v_i, v_j, w: 1 \le i \le 5, 1 \le j \le 5\} \subseteq V(K_n')$ and w be the pendant vertex corresponding to v_i. Here, we find that $r(v_k|B) = (1,1,2) = r(v_l|B)$ which contradicts our assumption.

• Consider a vertex set $B = \{v_i, v_j, w: 1 \le i \le 5, 1 \le j \le 5\} \subseteq V(K_n')$ and w be the pendant vertex corresponding to v_j. Here, we find that $r(v_k|B) = (1,1,2) = r(v_l|B)$ which contradicts our assumption.

• Consider a vertex set $B = \{v_i, v_j, w: 1 \le i \le 5, 1 \le j \le 5\} \subseteq V(K_n')$ and w be the pendant vertex corresponding to $v_k (1 \le k \le 5)$. Here, we find that $r(v_m|B) = (1,1,2) = r(v_l|B)$ which contradicts our assumption.

Hence the metric dimension of $V(K_5') = 4$.

Case III: For $n \ge 6$, $V(K_n') = \{v_1, v_2, v_3, v_4, \dots, v_I, \dots, v_n\}$ and $B = \{v_1, v_2, v_3, v_4, v_5 \dots, v_{n-1}\}$ then metric representation of $V(K_n')$ with respect to B.

Metric representation of the vertices

$$r(v_q|B) = \begin{cases} (0,1,1,1 \dots,1), if\ q = 1 \\ (1,1,0,1 \dots,1), if\ q = 3 \\ \vdots \\ (1,1,1,1 \dots,0), if\ q = n-1 \\ (1,1,1,1, \dots,1), if\ q = n \end{cases}$$

Metric representation of the pendant vertex w

$$r(w|B) = \begin{cases} (1,2,2,2,\dots,2), if\ w\ corresponding\ to\ v_1 \\ (2,1,2,2,\dots,2), if\ w\ corresponding\ to\ v_2 \\ (2,2,1,2,\dots,2), if\ w\ corresponding\ to\ v_3 \\ \vdots \\ (2,2,2,2,\dots,1), if\ w\ corresponding\ to\ v_{n-1} \\ (2,2,2,2,\dots,2), if\ w\ corresponding\ to\ v_n \end{cases}$$

Above all metric representations are unique. Hence the metric dimension of graph K_n' obtained by complete graph with sequential pendant edge extension is $n-1$.

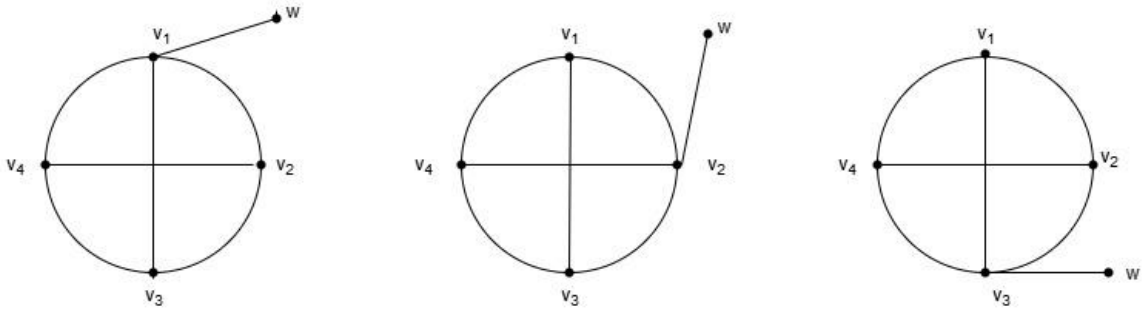


Figure 3: *Complete Graph (K_4) with SPEE*

IV. Results

Table 1: *Metric dimension of graph under SPEE*

Graph type	Number of vertices	Metric dimension $\beta(G)$
Wheel graph	$n \geq 7$	$\left\lceil \frac{2n+2}{5} \right\rceil$
Cycle graph	$n \geq 2$	2
Complete graph	$n \geq 2$	n

V. Discussion

When pendant edges are attached externally and sequentially to a graph, the existing shortest-path distances between its original vertices remain unchanged. In the case of a wheel graph, the central hub continues to serve as the unique reference point for distance measurements: no matter how many pendant edges are appended to the rim, the hub's distances to all other vertices are unaffected. Consequently, the metric dimension of the wheel graph remains constant.

Similarly, a complete graph inherently has every pair of vertices at distance 1. Adding pendant edges to any vertex introduces new vertices at distance 1 or 2 from the core, but these additions do not disturb the uniform distance structure among the original vertices. Hence, the minimal resolving set for the complete graph continues to suffice, and its metric dimension is preserved.

For a cycle graph, two diametrically opposite vertices form a resolving set because their distance profiles uniquely label every vertex. Sequentially attaching pendant edges does not alter the distances between these two key vertices—or between either key vertex and any other original cycle vertex. As a result, the cycle's metric dimension remains invariant under these modifications.

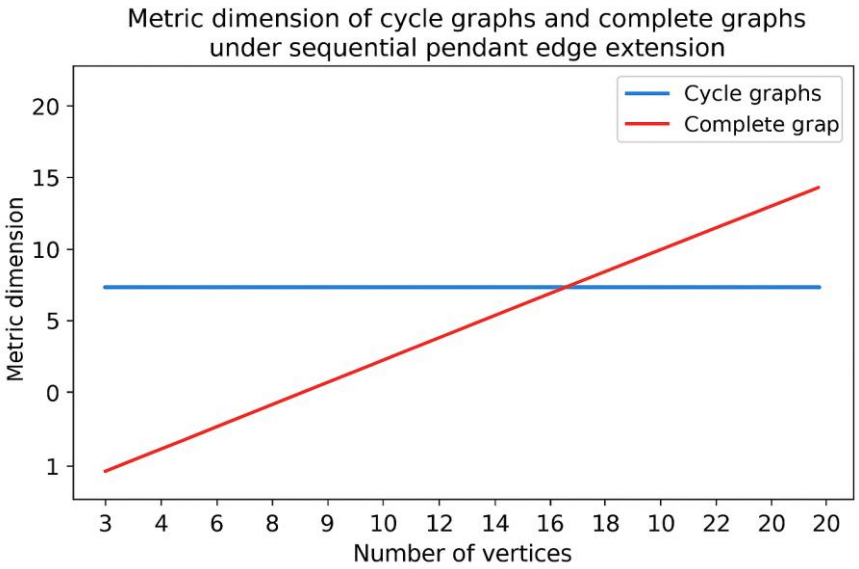


Figure 4: *Metric dimension of cycle and complete graph with SPEE*

VI. Conclusion

Across wheel graphs, complete graphs, and cycle graphs, the sequential external attachment of pendant edges does not affect the distances among the original vertices or the effectiveness of their minimal resolving sets. Therefore, the metric dimension of each of these graph families remains unchanged despite pendant-edge extensions. This stability underscores the robustness of metric dimension as a graph invariant, ensuring consistent vertex identification even under systematic structural augmentations.

I. Future scope

There is considerable potential to extend this study beyond the classical families of wheel, complete, and cycle graphs. One avenue is to investigate more complex or irregular topologies—such as bipartite graphs, trees with high branching factors, cactus graphs, and scale-free or small-world networks—to determine whether metric-dimension invariance under sequential pendant-edge addition persists. Analogous analyses could explore the effect of attaching multiple pendant edges at once or of performing other systematic modifications (for example, subdividing edges or adding chords) to see how these operations compare in their impact on resolving sets.

Another promising direction is to incorporate richer edge-weight or directionality models, reflecting real-world networks where distances are asymmetric or cost-driven. Developing efficient, incremental algorithms that maintain minimal resolving sets in large, evolving networks—possibly under random or adversarial growth processes—would have practical value for dynamic localization, network monitoring, and sensor placement. Finally, forging connections between metric dimension stability and other graph invariants (such as domination numbers, zero-forcing parameters, or rigidity measures) could yield a unified theoretical framework for predicting how structural augmentations influence multiple properties of a network simultaneously

References

[1] Slater, P. J. (1975). Leaves of trees. *Congressus Numerantium*, 14:549–559.

[2] Melter, F. H. and Harary, F. (1976). On the metric dimension of a graph. *Ars Combinatoria*, 2:191–195.

[3] Chvátal, V. (1983). Mastermind. *Combinatorica*, 3(3):325–329.

[4] Beerliova, Z., Eberhard, F., Erlebach, T., Hall, A., Hoffmann, M., Mihal'ak, M. and Ram, L. S. (2006). Network discovery and verification. *IEEE Journal on Selected Areas in Communications*, 24(12):2168–2181.

[5] Khuller, S., Raghavachari, B. and Rosenfeld, A. (1996). Landmarks in graphs. *Discrete Applied Mathematics*, 70(3):217–229.

[6] Sooryanarayana, B. (1998). On the metric dimension of a graph. *Indian Journal of Pure and Applied Mathematics*, 29(5):413–416.

[7] Sooryanarayana, B. and Shanmukha, B. (2001). A note on metric dimension. *Far East Journal of Applied Mathematics*, 5(3):331–339.

[8] Blumenthal, L. M. (1953). *Distance Geometry*. Clarendon Press, Oxford.

[9] Buczkowski, P., Chartrand, G., Poisson, C., and Zhang, P. (2003). On k-dimensional graphs and their bases. *Periodica Mathematica Hungarica*, 46(1):9–15.

[10] Saputro, S. W., Mardiana, N., and Purwasih, I. A. (2017). The metric dimension of comb product graphs. *Matematicki Vesnik*, 69(4):248–258.

[11] Tomescu, I. and Javaid, I. (2007). On the metric dimension of the Jahangir graph. *Bulletin Mathématique de la Société des Sciences Mathématiques de Roumanie*, 100(4):371–376.

[12] Tillquist, R. C., Frongillo, R. M., and Lladser, M. E. (2023). Getting the lay of the land in discrete space: A survey of metric dimension and its applications. *SIAM Review*, 65(4):919–962.

[13] Yang, X., Wang, Z., Zhang, H., Ma, N., Yang, N., Liu, H., Zhang, H., and Yang, L. (2022). A review: Machine learning for combinatorial optimization problems in energy areas. *Algorithms*, 15(6):205.

[14] Shahida, A. T. and Sunitha, M. S. (2014). On the metric dimension of joins of two graphs. *International Journal of Scientific and Engineering Research*, 5:33–38.

[15] Imran, M., Ahmad, A., and Semanicová-Fenovcíková, A. (2013). On classes of regular graphs with constant metric dimension. *Acta Mathematica Scientia*, 33(1):187–206.

A REVIEW ON SUSTAINABILITY, RELIABILITY, AND SAFETY OF MICROCHANNEL HEAT SINKS IN ELECTRONIC COOLING APPLICATIONS

Santosh Kumar Rai[1], Pardeep Kumar[2], Mahesh Kumar Gupta[3], Dhowmya Bhatt[4],Arun Uniyal[5],Gyanendra Prasad Bagri[1] Nikhil Vivek Shrivas[7*]

•

[1,3,6]Department of Mechanical Engineering, SRM Institute of Science and Technology, Delhi NCR Campus, Ghaziabad, UP India
[2]Department of Mechanical Engineering, MMEC, Maharishi Markandeshwar (Deemed to be University), Mullana, Ambala, Haryana, India
[4]Department of Computer Science Engineering, SRM Institute of Science and Technology, Delhi NCR Campus, Ghaziabad, UP India
[5]Department of Mechanical Engineering, COER University, Roorkee, Uttarakhand, India
[7]Department of Mechatronics Engineering, Manipal University Jaipur, Jaipur, Rajasthan, India

[1]08rai.santosh@gmail.com
[2]pardeepkamboj@yahoo.com
[3]maheshgupta59@gmail.com
[4]arun.uniyal1990@gmail.com
[7]nikhilvivek.shrivas@jaipur.manipal.edu

Abstract

Day by day, the rapid growth in the miniaturization of electronic devices ranging from mini, micro, to nano scales for various applications has drastically increased. However, the fabrication of such devices and the dissipation of heat from their bodies to the surrounding environment remain challenging. Due to these thermal management issues, electronic devices, MEMS, and other microfluidic and biomedical systems face significant sustainability, reliability, and safety concerns. In the present paper, we address various methods to overcome these problems in existing devices by using microchannels (MICHs). MICHs are used to remove heat from electronic components, thereby improving device safety and enabling them to operate within permissible temperature limits. A comprehensive literature review is presented, covering the classification of MICHs, their fabrication methods, and their applications in enhancing the reliability and safety of various devices. Sustainable design aspects are also considered to improve energy efficiency, optimize material usage, reduce the environmental impact of coolants, and enhance product life cycle performance. Furthermore, the paper outlines potential future research directions and fields of innovation for further advancements in this domain.

Keywords: Microchannel, reliability, safety, cooling of electronic devices, MEMS

I. Introduction

In the past two decades, the drastic growth of miniaturization of electronic devices such as MEMS, microfluidic devices, biomedical devices, and high-density electronics has revolutionized engineering, research, and technology in several areas. As devices decrease in compactness in size to microscopic and nanoscopic dimensions, theymore and more produce substantial high heat fluxes as a result ofhigh power densities, imposing drastic requirements on thermal management. Inadequate

heat dissipation from the devices or system makes the devices much less reliable and sustainable as well as increases the safety risks for both users and devices when utilized in some applications [1-2]. However, conventional cooling methods like mini-channel heat sinks [3-6], natural circulation loops [7-9], passive airflow, and finned configurations are not sufficient for these small, high-power systems and MEMS and electronics devices.

To resolve these issues, microchannel heat sinks (MCHSs) have proven to be a very effective option, with high heat transfer because of their large surface-area-to-volume ratios, compactness, low coolant usage, and high coefficients of heat transfer. Furthermore, MCHSs provide efficient thermal management and enable devices to function safely within acceptable temperature ranges [10].Also, several fabrication and design techniques have been investigated to enhance MCHS performance. Passive augmentations such as adding ribs, cutting grooves, pin fins, and different cross-sectional geometries increase turbulence, disturb thermal boundary layers, and enhance heat dissipation from the device to the environment. Furthermore, various different applications of nanofluids and phase-change fluids and materials are used to enhance thermal capability, with enhanced thermal conductivity above that of standard fluids.

However, apart from the passive method, some active methods are also available, which improve the heat transfer rate. These active methods are flowing pulsation, electrostatic modulation, magnetic fields, and acoustic or vibrational stimulation that have come into play for improving the heat transfer by externally caused effects. Simultaneously, some important numerical and experimental methods are more frequently being used to optimize microchannel geometry [11-12]. Topology optimization and surrogate modelling are some methods that expedite design cycles while providing drastic enhancements in thermal resistance and pumping power efficiency.

Design and fabrication of the MICHs are progressively advancing with innovations to improve the heat dissipation rate for increasing sustainability, reliability, and safety of the devices. Some of the design is inspired by bionic topologies, non-traditional cross-sections (trapezoidal or triangular), and interrupted flow structures like cavities and ribs that optimize heat removal by maximizing surface area and inducing mixing and uniform cooling. Additionally, through-chip MICH embedded in 3D stacked circuits are a leading area of thermal management with direct, internal cooling and huge potential for performance. Sustainability aspects form an intrinsic part of cooling system development. MCHS is used for improving energy-efficient, compact designs with minimal material requirements and environmental footprint. Their durability and flexibility with sustainable industrial principles minimize waste and maximize lifecycle performance. Future research places as much emphasis on sustainable operation, considering eco-friendly coolants, materials, processes, and system lifecycle effects as thermal performance [13-15].

Based on the several advantages of the MICHs for heat transfer from the device to the environment, there are still various problems and disadvantages of the MICHs that require improvement for the sustainability, reliability, and safety of the electronic devices. Also, there are many problems that occur in producing and fabricating MICHs. Producing intricate MICHs in volume and packaging them economically into production lines is still not trivial. Creating coolants that are both high-performance and environmentally friendly is a two-way obligation. Maintaining design consistency so MICHs provide uniform cooling among devices is critical to prevent hotspots, which can significantly compromise reliability.

In this context, the paper presents a critical literature review of MICHs for thermal management in miniaturized electronics devices. The review covers categorization of microchannel geometries, fabrication processes, and implementation in device safety improvement and reliability enhancement in a systematic manner. The review also incorporates environmentally conscious design factors such as energy efficiency, material optimization, coolant environmental responsibility, and lifecycle performance. Further, the promising directions for future research focused on developing MICH-based cooling technologies are proposed for improving the safety and reliability of the electronic devices.

II. Literature Review

MICH's sustainability and reliability are important factors in their use across a wide range of industries, from petrochemicals and electronics to thermal management. MICHs provide improved heat transfer and energy efficiency but also face special reliability and safety challenges at their small scale and operating conditions. The literature review, a comprehensive study of literature, has led to a detailed investigation into the aspects of reliability, sustainability, and safety of MICHs in terms of classification of the channel, fabrication, materials used for fabrication, thermal management, and cooling of electronic devices. The literature review primarily covers the period from 2000 to 2023, providing a contemporary perspective on the field, followed by an investigation of the different fabrication methods and heat transfer methods to enhance the reliability, sustainability, and safety of MICHs.

I. Fundamental Principle of the Microchannel

MCHsare working based on the principle of convective heat transfer, wherein a working fluid absorbed heat from the surface of an electronic component as it travels through narrow channels within the heat sink. Because of the high surface area-to-volume ratio and minimal diffusion paths within microchannels, MCHs provide significant heat transfer than traditional cooling techniques. When a fluid (liquid or nanofluid) is going through microchannels, heat from the electronic device is dissipated to the fluid through conduction through the heat sink material and convection along the channel walls. The heated fluid is transported away from the device at a safe operating temperature. These are mainly two types of force convection and free convection. But mostly force convections methods were used to remove the heat from the electronic devices for enhance their reliability, sustainability, and safety. Figure 1 depicts the schematic diagram of the working of the MCHs [16].

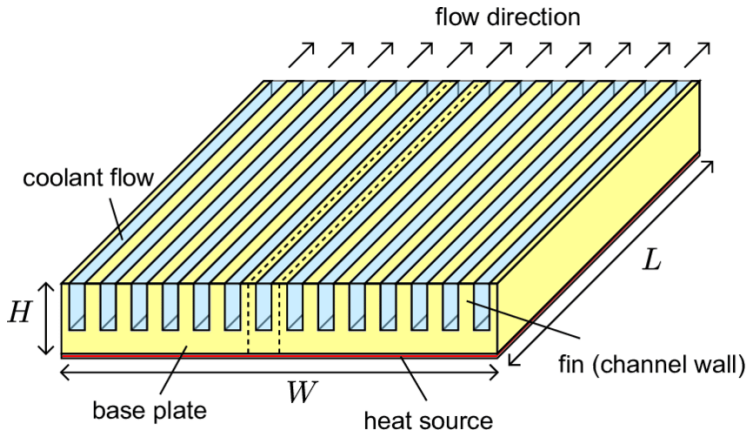


Figure 1: *Schematic diagram of the microchannel*

II. Classification of Microchannel and Materials and Coolant used in this for Improving the Safety of the Devices

MCHs are developed in various designs, such as single and manifold channels, serpentine channels, pin fins, interrupted channels, etc., that are made of different materials for improving the heat transfer from the electronic devices by employing several coolants for the safety of the device. Figure 2 shows the classification of the MICH based on the optimizing heat transfer criteria and THP, which provide the significant safety of the electronic devices as well as improve the life span of them. Based on the

previously reported research, MICHs are classified in three categories, such as cross-sectional geometry optimization, complex geometry optimization, and wall geometry optimization. Similarly, various materials are used to fabricate the MICHs to prevent damage to the channels and improve the thermal performance, structural integrity, and corrosion resistance, as well as to choose the materials based on their high thermal conductivity and light weight.

Mainly, copper, aluminum, silicon ceramics, and polymers (with fillers) are used, which improve the THP of the channel and provide higher safety to the electronic devices. Similarly, selection of the working fluid is a critical parameter of MICHs for improving the cooling effect and preventing the devices from burning and damage. The THP and pressure drop in the channel are affected by the thermal properties, electrical conductivity, and chemical stability of the coolant, which directly affect system efficiency and safety. Several coolants are used in MICHs to improve the sustainability, reliability, and safety of the electronic devices. Mainly deionized water, nanofluids, dielectric fluids (i.e., Fluorinert, Novec), refrigerants, mixtures of two different fluids, etc., due to high specific heat, higher thermal conductivity, and electrical non-conductivity, as well as the capability of improving the THP and reducing the friction loss in the channels [17-19].

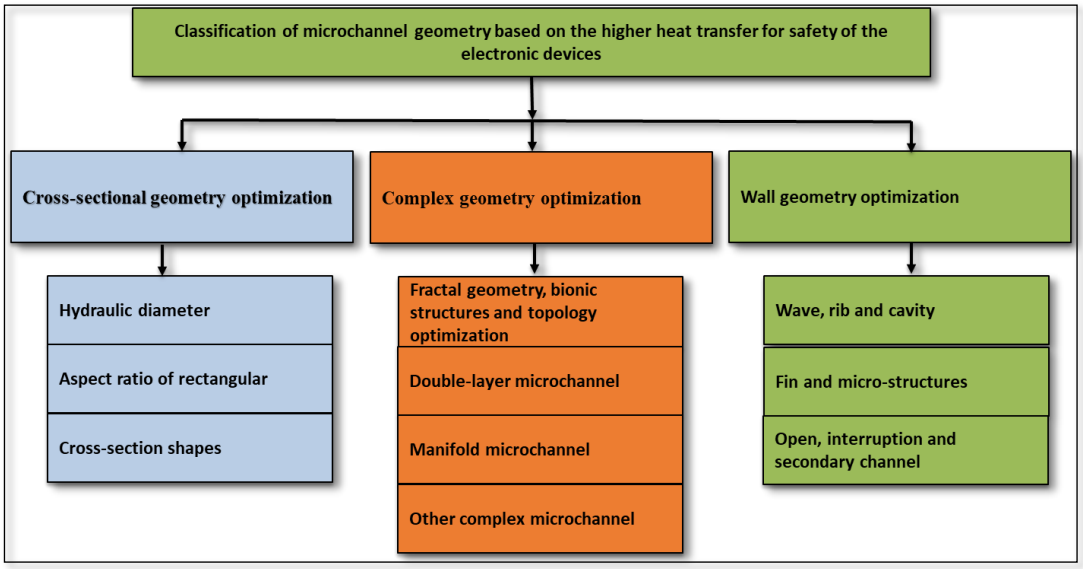


Figure 2: *Classification of the microchannel based on the higher heat transfer for improving safety of the electronics devices.*

III. Sustainability Aspects, Thermal Safety and Overheating Risks, Mechanical and Thermal Reliability of the Devices

As electronic devices rapidly miniaturize and become more power dense and thermally demanding, the sustainability, reliability, and safety of thermal management solutions become very important. MICHs are used in various electronic devices due to their compact size and higher THP. Therefore, it must be evaluated not only for THP and efficiency but also for its long-term environmental and resource impacts and small-scale, complex flow dynamics and integration with sensitive electronics, as well as ensuring safety in operation for protecting both devices and users from hazards.

Wang et al. [20] optimized the thermal hydraulic performance (THP) of an MCHS using numerical and artificial neural networks (ANNs) methods. With drastic demand for high-performance electronic devices, rapid cooling of these devices is essential to work under the limiting temperature of the device which provides safety as well as ensures reliability of the devices. They were used a numerical model with hexagonal fins which was developed in COMSOL, while other ANN models were trained to accurately predict Nusselt number and pressure drop with high accuracy (R^2 = 0.999). The outcomes revealed that the distance of fins from sidewalls has depicted a significant effect and increased the Nu by 66.3% and ΔP by 37.6%. Three optimal configuration

parameters were identified, such as Nu = 27.596, ΔP = 282.3 Pa, and an overall efficiency of 1.491, and compared to the benchmarks result, the optimized design enhanced total performance by 49.1% and concluded that ANN-based optimization is an effective tool for designing high-performance MCHSs, which are capable of optimizing the safe and reliable parameters of MCHS for dissipating heat from electronic devices to the surroundings.

Elbadawy et al. [21] numerically investigated the THP of offset strip finned MCHSs with various MICH cross-sectional shapes, such as rectangular, trapezoidal, triangular, and circular, for providing the safety of the electronic devices. They optimized the Nu, pressure drop, and overall efficiency to identify optimal geometry shapes and sizes for providing efficient cooling of electronic devices to increase the life span of the devices. Its results showed that MICH shape significantly affects the safety and reliability of the devices. It was observed that trapezoidal and triangular shapes provided higher heat transfer as compared to rectangular and circular. However, trapezoidal and triangular shapes gave higher pressure drops. The correlation between Nu and pressure drop was developed using a performance evaluation criterion (PEC), which showed that trapezoidal channel is the effective configuration that provides higher heat dissipation rate as compared to the others as well as provides the safety of the electronic devices at less friction loss.

Shakir et al. [22] numerically and experimentally investigated single-phase and two-phase boiling heat transfer in aluminum MICH using R113 as the working fluid. A square cross section of the test setup was developed of 0.5 mm and 0.5 mm, and constant heat flux is applied to the bottom of the channel, which varied from 40 to 600 W at three different mass flow rates, such as 0.0125 kg/s, 0.015 kg/s, and 0.0175 kg/s. In this, they analyzed heat transfer coefficients (HTC), exit quality, and pressure drops for both subcooled and saturated boiling regimes to provide the safety and reliability of the electronic devices. Its outcome showed that single-phase flow at laminar and fully developed characteristics with HTCs increase with increasing the mass flux, whereas fluid temperature is decreased with increasing the mass flux. However, in two-phase flow, HTC was significantly affected by heat flux, mass flow rate, and vapor quality. Onset of boiling was seen around 47°C, and pressure drop behavior showed two different regimes for single- and two-phase flow, which was also shown both numerically and experimentally, and developed empirical correlations for safety of the electronic devices. Furthermore, the effect of MICH geometry and operating conditions on boiling heat transfer and instabilities was investigated to accurately provide the robust condition for providing the safety and reliability of the electronic devices.

Chen et al. [23] conducted numerical simulation combined with response surface methodology (RSM) to investigate the thermal–hydraulic optimization of trapezoidal MCHSs by incorporating different rib geometries to protect the failure of electronic devices. In this study, they used four different rib shapes, such as triangular, rectangular, semicircular, and trapezoidal, with varying rib height and pitch to predict the effects on Nusselt number (Nu), friction factor (FF), and performance evaluation criterion (PEC) to enhance the safety of the electronic devices. Its results demonstrated that rib structures significantly improve HTC and Nu due to flow disturbance and secondary vortices. However, pressure drop is increased, which reduces the reliability of the device wall. Furthermore, trapezoidal ribs provided significant HTC and minimum pressure drop, which provided the highest safety and reliability of the electronic devices during cooling among all other shapes of the test ribs. Furthermore, RSM-based optimization identified the optimal rib geometry and their arrangement for higher safety of the devices by improving the heat dissipation rates.

Zhang et al. [24] numerically examined the effect of different MICH cross-sectional geometries, such as rectangular, trapezoidal, triangular, and circular, on the heat transfer rate and THP performance of MCHSs. Also, they were evaluated for Nu, FF, and performance evaluation criteria to ensure the safety of the electronic devices. Its results revealed that trapezoidal and triangular channels had significantly improved heat transfer compared to rectangular and circular-shaped channels. However, the pressure drop was observed to be maximal. The trapezoidal-shaped MICH gave a higher heat transfer rate at minimum pressure drop, which is similar to Chen et al. [23]. This finding suggested that optimizing the MICH cross-sectional shape is a crucial parameter for

improving and enhancing the safety of the electronic devices as well as for use in various advanced thermal management applications, particularly for microelectronic device cooling.

Wunderle et al. [25] extensively reviewed and summarized advancements in MCHS designs with various channel cross-sectional geometries to improve heat transfer rate in the microelectronic devices. They suggested that rectangular MICH is widely used for cooling the electronic devices, which experience higher pressure drop and relatively lower heat transfer performance compared to non-rectangular geometries such as trapezoidal, triangular, and circular shapes. Researchers demonstrated that non-rectangular channels enhance heat transfer through the promotion of secondary flows and larger surface areas, often at the cost of higher pressure drops. They concluded that trapezoidal and triangular geometries provide higher heat transfer rates as well as experience higher pressure drops.

Sidik et al. [26] examined the effect of several different cross section geometries such as rectangular, triangular, semicircular, and trapezoidal shapes, on the THP of MCHSs using 3D-CFD tool ANSYS and reported that Nu, ff, and THP varied at varying Reynolds numbers. Also, they suggested that the heat transfer rate increases with increased Reynolds numbers at low friction loss and pressure drop as well as rectangular cross-section MICH had the least heat transfer and the higher-pressure drop, which makes electronic devices less safe and reliable.

Mudawar [27] conducted numerical investigations in 2002 to determine the THP of MCHSs, including different designs of the MICH, such as zigzag, sinusoidal, and wavy designs, as well as combining the effect of the structure or improving the cooling efficiency to provide safety of the electronic devices. Simulations were conducted to evaluate Nu and pressure drop (ΔP) at various Reynolds numbers. Its outcome showed that using a zig-zag channel significantly improves heat transfer due to fluid mixing and changing the flow boundary layers, as well as increasing the pressure drop. Among all designs, zigzag and sinusoidal structures showed higher heat dissipation rates, which provide better safety for electronic devices as well as improve their lifespan.

Spizzichino et al. [28] presented a numerical analysis of the THP of wavy MCHSs with different wave structures, such as sinusoidal, triangular, and trapezoidal profiles, and they suggested that wavy MICH showed maximum heat transfer as compared to other designs with a higher-pressure drop.

Furthermore, Ko et al. [29] developed a low-temperature MEMS fabrication method for MICH and integrated it with temperature sensors and micro-heaters to measure local heat transfer during the working of the electronic devices. In this study, they used low-thermal-conductivity materials such as epoxy, Pyrex, PMMA, SU-8, and a two-stage process. Air is used as a working fluid in the channel for cooling the HTC revealed that HTC is significantly affected by using the MICH for heat transfer from the electronic device, which can improve the safety and life of the devices. Also, they suggested the impact of size effects and wall properties and demonstrated the feasibility of micro-channel cooling for high-power devices such as future CPU chips.

Tiseljet al. [30] experimentally investigated heat transfer in silicon-based MICHs. In this study, they used MEMS sensors to accurately predict the wall temperature of the electronic devices as well as HTC. Also, a fabrication method that allows for the accurate positioning of heaters and thermocouples within high-aspect-ratio MICHs, thereby reducing conduction losses and enhancing measurement precision. Experimental findings for single-phase liquid flow demonstrate that traditional macroscale heat transfer correlations tend to overestimate microchannel performance, highlighting notable scale effects. Its outcomes identify variations in local Nusselt number trends, indicating diminished heat transfer rates and uneven distributions along the channel. The findings suggested that MICHs have a compact design and high-performance cooling systems for microelectronics and demonstrate that microscale heat transfer necessitates advanced theoretical models that extend beyond classical assumptions.

Ding et al. [31] studied both experimentally and numerically to analyze heat transfer through MCHS at different aspect ratios using water as a working fluid. Its results revealed that intermediate channel widths improve the flow inside the channel due to less frictional pressure drop, variation of

wall temperature along the length, and THP. Based on this, a correlation of heat transfer and width of the channel was developed to maintain the working temperature under limiting temperature.

Lorenzo Consolini and Thome [32] reported heat transfer through MICH from electronic devices in single- and two-phase flow using three different working fluids (R-134a, R-236fa, and R-245fa) and two different hydraulic diameters (510 and 790 μm) of the channels. Also, a parametric study was performed to determine the two-phase flow instability, which develops a thermal fatigue load that is harmful for devices as well as MICH. Its results revealed that the HTC of R-134a and R-236fa are significantly dependent on the heat flux and mass flow rate at low and high dryness fractions. However, R245fa showed the opposite of the other fluid, which developed instability in the channel and degraded the lifespan of the channel.

Jahar Sarkar [33] suggested heat transfer through MICH significantly improved using supercritical carbon dioxide as a working fluid in electronic devices. Also, parametric studies were performed for two different fluids, supercritical carbon dioxide and water, to examine which fluid gives higher heat transfer at lower resistance. Its results showed that heat transfer was improved by 30% as compared to water at low thermal resistance, which provides higher safety to the electronic devices.

Xiang et al. [34] numerically investigated the MCHS using a thermal resistance model to accurately predict the heat transfer rate from the electronic devices. In this study, they fabricated the MCHS and tested for heat transfer. Its result showed that developed MCHS hives have higher heat transfer as compared to conventional metal made of MCHS, which is recorded for heat transfer from LED applications.

Bello-Ochende et al. [35] numerically investigated the heat transfer through MICH using the 3D model finite volume method to reduce the wall temperature of the MICH from the working fluids. The results indicated that the maximum temperature of the MICH is significantly reduced by increasing the working fluid flow rate in the channel as well as increasing the aspect ratio of the channel.

Li et al. [36] suggest a correlation to distinguish between mini and MICH for heat transfer from electronic devices. In this study, they used single and manifold types of MICH as well as single and two-phase flow. Also, in this study, seven pre-developed correlations were used to predict and verify heat transfer of the 4228 databases. Based on this correlation, they proposed a new correlation, Bo*Re0.5 = 200, to accurately predict the heat transfer rate through MICH.

Spizzichinoet al. [37] investigated heat transfer and flow characteristics of parallel MICH (i.e., 10 channels) using both experiments and numerical simulation methods, and deionized water was used as the working fluid. Results show that uniform-width channels cause higher pressure drops and mass flow in intermediate channels, leading to uneven base temperatures, while refining intermediate channel widths produces more uniform flow and wall temperature distributions. A new Performance Evaluation Criterion for Non-uniform Channels (PECNC) was proposed to assess designs, with structure VI emerging as the optimal configuration. Additionally, a mathematical expression was developed to guide the design of width distributions that promote uniform temperature fields.

Qu and Mudawar [38] investigated the heat transportation phenomenon of two phase in MICH to improve the safety and reliability of the electronic cooling devices. In this study they suggested the basic reliable operation of a two-phase MICH transport phenomenon integrated with convective boiling in single and parallel channels. They used high-speed photographic methods to accurately predict hydrodynamic instability, two-phase flow patterns, pressure drop, and convective boiling heat transfer. The study's findings indicate that MICH primarily experiences two types of instability: a drastic pressure drop and a mild parallel channel.

Sehgal et al. [39] conducted several experiments to examine the effect of the inlet and outlet plenums in different arrangements of various MICH shapes such as U, P, and S types on improving the cooling of electronic devices as well as enhancing their thermal–hydraulic performance (THP). A heat input ranging from 125 W to 375 W was applied to the wall of the MICH, with Reynolds numbers (Re) varying from 224 to 1121 to assess THP. Higher heat dissipation was observed in the U-

shaped MICH, while a greater pressure drop occurred in the S-type MICH among other channels, which improve the reliability and safety for electronic devices.

Xia et al. [40] numerically investigated the effect of the position of the MICH on the 3D-IC in heat transfer for improving the performance and safety of the devices as well as thermal management of the electronic devices. In this study, two types of cavities are considered, namely triangular reentrant cavities (TRC) and fan-shaped reentrant cavities (FRC) having a pitch and height of 1/0.2 mm and 0.2 mm, respectively. The effect of both cavities of MICH was compared with rectangular MICH. Its results revealed that the distribution of the heat rate and pressure drop was uniform along the length of each layer, as well as the pitch of 0.1 mm of MICH. Higher heat transfer and THP were observed at a higher pressure drop and pumping power, which significantly affected the safety of the devices as well as reduced their life span.

Markal et al. [41] developed MICH, which consists of MICH with pin-type fins, which gives higher heat dissipation by optimizing the design and geometry sizes of the channel and fins to minimize the thermal resistance and pressure drops to increase the safety of the electronic devices. Similarly, Li et al. [36] developed lattice-interconnected channels and nanofluid in the MICH to improve the cooling rate of the devices and reported that heat transfer is increased with using the nanoparticle in the coolant, and the pressure drop is reduced in the channel.

Also, Huang et al. [42] implanted phase-change materials (PCMs) with graphite foam to absorb cyclic generated heat from electronic devices, which reduced the limiting temperature of the chips and electronic devices and provided better safety and reliability of the devices. Xiang et al. [34] also developed a vacuum-assisted two-phase honeycomb heat sink to reduce the electronic device temperature approximately 15°C at 90 W and validated performance through both experiments and numerical analysis.

Rai et al. [43] conducted several single- and two-phase numerical and experimental studies in single- and two-phase flow through MICH for improving the safety and reliability of the electronic devices. They used deionized water as a working fluid and three different MICH geometries. They developed a correlation between mass flow rate and generated heat power from the electronic devices to reduce the working temperature of the device to under 40°C, which improves the safety and reliability of the electronic devices. Also, in numerical studies, they optimized the geometry for higher heat transfer in rectangular, square, and trapezoidal shapes and reported that trapezoidal geometry provides high heat transfer. To enhance the safety and reliability of the electronic devices, hybrid methods are employed alongside geometry optimization, which is necessary to prevent drastic pressure changes inside the MICH.

Several recent experimental and numerical research works were reported to improve the safety and reliability of the electronic devices by improving the heat transfer rate from these devices due to their compact size. Table 1 shows a comparative summary of recently reported research to improve the safety of electronic devices using different designs, shapes, and working fluids. It can be seen from table 1 that MCHS is mainly used for electronics devices cooling and is significantly suggested by the numerous researchers to use hybrid designs and integrated optimization to increase heat dissipation at low volume to area ratio.

Table 1: *Summary of different methods and working fluid used to improve the safety of the electronic devices.*

Author	Design / Method	Working fluids	Main Findings
Markal et al. [41]	MICH with pin-fin heat sink	Deionized water	• Higher heat transfer but increased pressure drop Optimal fin height and channel width significantly improved the THP. • Thermal resistance reduced by approximately 15–20%

			and pressure drops increased by 30–40% as compared to plain MICH.
Li et al. [36]	MICH with nanofluid	Water + Al_2O_3 nanofluid	• Best lattice geometry improved THP • Peak temperature drops up to 12 °C and pressure drop approximately 20% compared to straight MICH.
Huang et al. [42]	Phase-change material (PCM) with graphite foam embedded in walls	Water (base) + PCM for transient loads	• PCM and high-conductivity foam maximized THP • Peak temperature of the reduced approximately 15°C vs. solid plate at 90 W • Reduced peak chip temperature under cyclic heat input from the devices. • PCM absorbed heat generates from the devices.
Xiang et al. [34]	Vacuum-assisted two-phase honeycomb MICH	Water + R134a (two-phase mix)	• Optimal regular hexagon, 2 mm pitch, 0.5 mm depth, 8 mm radius • Max chip temp reduced from 85 °C to 70 °C at 90 W with ± 1°C
Rai et al. [43]	Single MICH (Single and Two Phase)	Deionized water (single and two phase)	• Working temperature of the device to maintained under 40°C • Experimental and numerical validation showed ±6.04 errors.
Husain et al. [44]	Different designs of MICHs (Square, rectangular and trapezoidal and different boundary conditionss)	Deionized water (H methods)	• Optimizing the design of the MICH and applying 2H and 4H boundary conditions to enhance the heat transfer rate and improve the safety of the electronic devices.

IV. Research Gaps

After extensively reviewing the previously reported works of several researchers, some concise observations regarding the use of different single- and two-phase cooling methodologies as well as various designs used to improve the safety and reliability of the electronic devices are as follows:

- Traditional cooling methods such as air-cooled heat sinks and fans are not sufficient to provide enough safety to the high-performance electronic devices such as chips, integrated chips, high-frequency processors, laser diodes, and power electronics due to compact sizes. Therefore, robust design with higher THP of MICHs is required, which can remove higher heat flux from the devices to improve the safety and reliability of the electronic devices [45].

- One of the major challenges is the fabrication of the MICHs, which requires precision machining, etching, micro-milling, etc., that are costly and time-consuming, as well as high-precision sealing and assembly processes to completely seal channels, which can protect the electronic devices from short circuits during operation.
- Very limited studies on the manifold and serpentine types of MICHs are available in literature, which can be needed to extensively study for improving the THP as well as the safety of the electronic devices.
- Very limited working fluids are used in the MICHs for improving the THP and efficiency of the channel. Supercritical fluids can be used to improve the THP and safety of the electronic devices.

V. Conclusion and Future Scope

In this present work, an extensive literature review is conducted on the available literature related to the sustainability, reliability, and safety of MICHs in the application of electronics devices which are used in various industries such as electronics, aerospace, automotive, biomedical and microfluid devices, etc. Several important findings are observed from this extensive literature review, which are given below.

- Day by day, electronic devices are drastically increasing with miniaturization, minimizing their sizes and increasing their power densities. Therefore, effective thermal management is required as well as a required determinant of system longevity, energy efficiency, and operational safety. MICH and MCHSs can remove the significant amount of heat from the electronic devices, which improves the sustainability of the electronic devices. Also, MICH reduces energy consumption and improves device lifespans and does not affect the environment. However, careful selection of materials and coolants is necessary to ensure recyclability and minimize environmental risks.
- MICH is a better solution for improving the safety of the electronic devices as compared to the traditional cooling methods.
- The cyclic heat load can be removed by using the PCM in the MICHs which increases the safety of the electronic devices by absorbing 10 to 15 °C temperatures.
- The trapezoidal design of MICHs provides higher heat transfer than other designs such as rectangular, square, and circular types of MICHs.
- Two phase and boiling methods provide higher heat transfer as compared to single phase cooling methods and improve the safety and reliability of the electronic devices.

By using the MICHs, various problems have been resolved to improve safety and increase The lifespan of electronic devices. However, there are still several issues that have remained open to resolve for improving the safety of the MICHs during use in the electronic cooling devices. 3D modeling using different designs and shapes of the MICHs cab can improve the safety of the devices. 3D printers can be used to fabricate the MICHs. Also, for real-time monitoring of temperature, flow rate, pressure, and THP of the MICHs, a combined system (including sensors, IoT devices, and machine learning) can be used. Furthermore, robust pressure control, leak-proof design, and accurate heat input prediction are required to improve the sustainability, reliability, and safety of electronic devices.

References

[1] Yu, Z., Q., Li, M.T., & Cao, B.-Y. (2024). A comprehensive review on microchannel heat sinks for electronics cooling. *International Journal of Extreme Manufacturing*, 6, 022005.

[2] Rai, S. K., Sharma, R., Saifi, M., Tyagi, R., Singh, D., & Gupta, H. (2018). Review of recent applications of micro channel in mems devices. *International Journal of Applied Engineering Research*, 13(9), 64-69.

[3] Tuckerman, D. B., & Pease, R. F. W. (2005). High-performance heat sinking for VLSI. *IEEE Electron device letters*, 2(5), 126-129.

[4] Lu, K., Wang, C., Wang, C., Fan, X., Qi, F., & He, H. (2023). Topological structures for microchannel heat sink applications–a review. *Manufacturing Review*, 10, 2.

[5] Japar, W. M. A. A., Sidik, N. A. C., Saidur, R., Asako, Y., & Nurul Akmal Yusof, S. (2020). A review of passive methods in microchannel heat sink application through advanced geometric structure and nanofluids: Current advancements and challenges. *Nanotechnology Reviews*, 9(1), 1192-1216.

[6] Ayatollahi, S. M., Ahmadpour, A., &Hajmohammadi, M. R. (2022). Performance evaluation and optimization of flattened microchannel heat sinks for the electronic cooling application. *Journal of Thermal Analysis and Calorimetry*, 147(4), 3267-3281.

[7] Rai, S. K., Kumar, P., Tiwari, M., Panwar, V., Kumar, D., & Sharma, V. K. (2025). A comprehensive overview of advancements, applications, and impact of supercritical fluid natural circulation loops. *Annals of Nuclear Energy*, 211, 110971.

[8] Suman, S., Upadhyaya, R., Raghuvanshi, N. S., Gupta, M. K., Shah, S., & Alam, S. (2022). A state of art review of instability in parallel channels of supercritical fluid in nuclear applications. *Materials Today: Proceedings*, 62, 226-232.

[9] Rai, S. K., Kumar, P., & Panwar, V. (2020, November). Computational analysis of static flow instabilities in supercritical natural circulation loop. *In Proceedings of International Conference on Thermofluids:*Singapore: Springer Singapore. 387-395.

[10] Mala, G. M., Li, D., & Dale, J. D. (1997). Heat transfer and fluid flow in microchannels. *International journal of heat and mass transfer*, 40(13), 3079-3088.

[11] Kandlikar, S. (2006). Heat transfer and fluid flow in minichannels and microchannels. *Elsevier* 978-0-08-044527-4.

[12] Cova, P., Santoro, D., Spaggiari, D., Portesine, F., Vaccaro, F., & Delmonte, N. (2020). CFD modeling of additive manufacturing liquid cold plates for more reliable power press-pack assemblies. *Microelectronics Reliability*, 114, 113734.

[13] Sidik, N. A. C., Muhamad, M. N. A. W., Japar, W. M. A. A., & Rasid, Z. A. (2017). An overview of passive techniques for heat transfer augmentation in microchannel heat sink. *International Communications in Heat and Mass Transfer*, 88, 74-83.

[14] Gupta, H. K., Rai, S. K., &Sheorey, T. (2015). Boiling flow heat transfer in microchannel: Experimental and numerical investigation. In Proceedings of the 23rd National Heat and Mass Transfer Conference and 1st International ISHMT-ASTFE *Heat and Mass Transfer Conference IHMTC* ,1-8.

[15] Singh, D., Rai, S., & Shukla, S. (2017). Numerical analysis of two phase flow boiling heat transfer through microchannel. *International Journal of Engineering Research and Technology*, 6, 1-6.

[16] Ohadi, M., Choo, K., Dessiatoun, S., &Cetegen, E. (2012). Fundamentals of microchannels. *In Next Generation Microchannel Heat Exchangers* (pp. 1-32). New York, NY: Springer New York.

[17] Tullius, J. F., Vajtai, R., &Bayazitoglu, Y. (2011). A review of cooling in microchannels. *Heat Transfer Engineering*, 32, 527-541.

[18] Yu, Z. Q., Li, M. T., & Cao, B. Y. (2024). A comprehensive review on microchannel heat sinks for electronics cooling. *International Journal of Extreme Manufacturing*, 6(2), 022005.

[19] Dixit, A., Maithani, R., & Sharma, S. (2025). Enhancing electronic system cooling: exploring minichannel heat sink solutions. *Journal of Thermal Analysis and Calorimetry*, 1-51.

[20] Wang, X., Su, Z., Mansir, I. B., Singh, P. K., Othman, N. A., Zhang, L., ... &Deifalla, A. (2023). Thermal and hydrodynamic management of a finned-microchannel heat sink applying artificial neural network. *Case Studies in Thermal Engineering*, 45, 102996.

[21] Elbadawy, I., Alhajri, A., Doust, M., Almulla, Y., Fayed, M., Dinc, A., ... & Al-Kouz, W. (2023). Reliability of different nanofluids and different micro-channel configurations on the heat

transfer augmentation. *Processes*, 11(3), 652.

[22] Shakir, R. (2020, November). Boiling heat transfer in a micro-channel complex geometry. *In IOP conference series: Materials science and engineering*,928, (2),022129.

[23] Chen, L., Zhang, X. R., Okajima, J., Komiya, A., & Maruyama, S. (2016). Numerical simulation of stability behaviors and heat transfer characteristics for near-critical fluid microchannel flows. *Energy Conversion and Management*, 110, 407-418.

[24] Zhang, X., & Jaluria, Y. (2020). Reliability-based optimization and design limits of microchannel cooling systems. *International Journal of Heat and Mass Transfer*, 149, 119202.

[25] Wunderle, B., Schacht, R., Wittler, O., Michel, B., & Reichl, H. (2004, June). Performance and thermo-mechanical reliability of micro-channel coolers-a parametric study. In The Ninth Intersociety Conference on Thermal and Thermomechanical Phenomena.*Electronic Systems, IEEE Cat. No. 04CH37543*, 2, 11-16.

[26] Sidik, N. A. C., Muhamad, M. N. A. W., Japar, W. M. A. A., & Rasid, Z. A. (2017). An overview of passive techniques for heat transfer augmentation in microchannel heat sink. *International Communications in Heat and Mass Transfer*, 88, 74-83.

[27] Mudawar, I. (2002). Assessment of high-heat-flux thermal management schemes. *IEEE transactions on components and packaging technologies*, 24(2), 122-141.

[28] Spizzichino, M., Sinibaldi, G., & Romano, G. P. (2020). Experimental investigation on fluid mechanics of micro-channel heat transfer devices. *Experimental Thermal and Fluid Science*, 118, 110141.

[29] Ko, H. S., Liu, C. W., Gau, C., & Yang, C. S. (2007). Fabrication and design of a heat transfer micro-channel system by a low temperature MEMS technique. *Journal of Micromechanics and Microengineering*, 17(5), 983.

[30] Tiselj, I., Hetsroni, G., Mavko, B., Mosyak, A., Pogrebnyak, E., & Segal, Z. (2004). Effect of axial conduction on the heat transfer in micro-channels. *International Journal of Heat and Mass Transfer*, 47(12-13), 2551-2565.

[31] Ding, Y. Y., Liu, M. G., & Jin, Q. (2025). Experimental and numerical investigation of the influence of varying micro-channel width on flow and heat transfer uniformity. *International Journal of Thermal Sciences*, 208, 109394.

[32] Consolini, L., Thome, J.R. (2009).Micro-channel flow boiling heat transfer of R-134a, R-236fa, and R-245fa. *Microfluid Nanofluid* 6, 731-746.

[33] Sarkar, J. (2019). Improving thermal performance of micro-channel electronic heat sink using supercritical CO2 as coolant. Thermal Science, 23(1), 243-253.

[34] Xiang, J., Deng, L., Zhou, C., Zhao, H., Huang, J., & Tao, S. (2022). Heat transfer performance and structural optimization of a novel micro-channel heat sink. *Chinese Journal of Mechanical Engineering*, 35(1), 38.

[35] Bello-Ochende, T., Liebenberg, L., & Meyer, J. P. (2007). Contractual cooling channels for micro-channel heat sinks. *International Journal of Heat and Mass Transfer*, 50(21-22), 4141-4150.

[36] Li, W., & Wu, Z. (2010). A general criterion for evaporative heat transfer in micro/mini-channels. *International Journal of Heat and Mass Transfer*, 53(9-10), 1967-1976.

[37] Spizzichino, M., Sinibaldi, G., & Romano, G. P. (2020). Experimental investigation on fluid mechanics of micro-channel heat transfer devices. *Experimental Thermal and Fluid Science*, 118, 110141.

[38] Qu, W., &Mudawar, I. (2004). Transport phenomena in two-phase micro-channel heat sinks. *Journal of Electronic Packaging*, 126(2), 213-224.

[39] Sehgal, S. S., Murugesan, K., & Mohapatra, S. K. (2011). Experimental investigation of the effect of flow arrangements on the performance of a micro-channel heat sink. *Experimental heat transfer*, 24(3), 215-233.

[40] Xia, G. D., Ma, D. D., Wang, W., & Zhai, Y. L. (2015). Effects of different structures and allocations on fluid flow and heat transfer performance in 3D-IC integrated micro-channel interlayer cooling. *International Journal of Heat and Mass Transfer*, 91, 1167-1175.

[41] Markal, B., &Evcimen, A. (2024). Investigation of flow boiling phenomenon in micro-pin-fin heat sinks adapted to actively direction-changing moving systems. *International Communications in*

Heat and Mass Transfer, 159, 108310.

[42] Huang, S., Long, C., Hu, Z., Xu, Y., Zhang, B., & Zhi, C. (2024). Thermal Performance of Heat Sink Filled with Double-Porosity Porous Aluminum Skeleton/Paraffin Phase Change Material. *Micromachines*, 15(6), 806.

[43] Rai, S. K., Goyat, V., Gupta, M. K., Ghangas, G., Bhatt, D., Uniyal, A., & Shrivas, N. V. (2025). Numerical and experimental heat transfer analysis of two-phase flow through microchannel for development of heat dissipation correlation. *Journal of Non-Equilibrium Thermodynamics*.

[44] Hussain, M. E., Rai, S. K., Suman, S., Gupta, P., & Gupta, M. K. (2022, August). Computational Analysis of Transfer of Heat in Micro Size Channels Using Different Boundary Condition in Laminar Flow. *In Biennial International Conference on Future Learning Aspects of Mechanical Engineering*, Singapore: Springer Nature Singapore, 445-455.

[45] Kumar, P., Kumar, D., Chalisgaonkar, R., Sharma, V. K., & Rai, S. K. (2024). A Critical Review of Ram Methodology: Analysis and Performance Evaluation in Industrial Complexities. *Reliability: Theory & Applications*, 19(4 (80)), 83-89.

INVESTIGATING THE PERFORMANCE OF MAP/PH/1 QUEUEING SYSTEMS WITH CATASTROPHIC FAILURES, NEGATIVE ARRIVALS, SERVER BREAKDOWNS, REPAIRS AND LACK OF CUSTOMER TOLERANCE FOR DELAYS

[1]K. Thilagavathy, [2]G. Ayyappan

•

[1]Department of Mathematics, Hindustan Institute of Technology and Science, Chennai, India.
[2]Department of Mathematics, Puducherry Technological University, Puducherry, India.
[1]thilagakarthik95@gmail.com, [2]ayyappanpec@hotmail.com

Abstract

This paper presents a comprehensive analytical study of a single-server queueing system incorporating by a Markovian Arrival Process (MAP), Phase-Type (PH) service times, and multiple complex disruptions, including catastrophic failures, negative arrivals, server breakdowns, and phase-type repairs. Utilizing matrix-analytic methods, we derive steady-state probability distributions, and system performance measures. The consequence of failure frequencies, and repair parameters on key performance metrics such as system size, and server availability is thoroughly examined. The behavior of the system is demonstrated using numerical results. The results offer valuable insights for the purposes of design and optimization of resilient and efficient service systems operating in uncertain and failure-prone environments.

Keywords: PH-Distribution, Catastrophic Failure, MAP, Breakdown, Negative Arrival, Matrix Analytic Method.

1. Introduction

Queueing systems are fundamental tools in modeling and analyzing the performance of various real-world service and communication systems, especially under uncertainty and dynamic behavior. Among these, the $MAP/PH/1$ queueing system–characterized by a MAP, a PH service time distribution, and a single server–offers a highly flexible and mathematically tractable framework for modeling complex systems. This study focuses on an advanced $MAP/PH/1$ model that incorporates several real-world complexities: catastrophic failures, negative arrivals, server breakdowns, and phase-type repair mechanisms. Catastrophic failures represent sudden events that remove all customers from the system, simulating large-scale disruptions. Negative arrivals, a less traditional but increasingly relevant concept, model scenarios where incoming entities remove one or more customers already in the queue–useful in contexts such as reverse logistics or erroneous inputs. Additionally, the model accounts for server breakdowns, reflecting interruptions in service capacity, and PH-type repairs, allowing a generalized and realistic representation of the server recovery process.

The integration of these features aims to more accurately capture the performance and reliability characteristics of modern service systems, such as cloud computing servers, production lines, and network routers. Through analytical modeling and numerical investigation, this work provides insights into the system's behavior under varying operational parameters and disruption scenarios, ultimately aiding in the design of more robust and efficient queue-based infrastructures.

2. Literature Review

In queueing theory, a negative arrival refers to a conceptual mechanism where certain arriving entities (called negative customers) remove existing customers from the system instead of joining the queue. Gelenbe et al. [13] explored a queueing system with a one server incorporating the concept of negative arrivals. They described two distinct mechanisms for customer removal triggered by the arrival of negative customers: the first involves removing the customer currently in service, while the second eliminates the customer positioned at the queue's end. Artalejo and Gomez-Corral [2] conducted an analysis of a queueing system with a single server incorporating both repeated requests and the concept of negative arrivals. Senthil Vadivu et al. [32] analyzed a discrete-time queueing system incorporating arrival processes with correlation, the presence of negative customers, and interruptions in service. They further computed the stationary distribution corresponding to the model's sojourn time. Lisovskaya et al. [23] studied a multi-server retrial queueing system with two orbits for positive customers. They incorporated the concept of negative customers, where a negative customer's arrival results in the removal of every customer in the queue currently in service upon arrival before exiting the system. Nesrine and Natalia [26] examined an "$M/M/C/K$" retrial system in which customers may abandon service after an exponentially distributed waiting time and Poisson arrivals of both positive and negative customers, highlighting its relevance to call centers and e-mail support systems. Li and Zhao [22] analyzed a "$MAP/G/1$" queueing system in the presence of negative customers. They derived the stationary probability distributions for queue length and virtual sojourn time, as well as the Laplace transform corresponding to the busy period. Dimitriou [11] investigated a retrial queueing system with mixed priority customers, incorporating negative arrivals, server unreliability, and multiple vacations. Chin et al. [7] investigated a continuous-time queueing system with negative arrivals and derived its stationary distribution of the queue length.

A catastrophic event in queueing theory is a sudden disruption that causes all customers to be instantly removed from the system, including both the queue and service area. After a catastrophe, the system may undergo a recovery or repair period before resuming normal operations. Chakravarthy et al. [5] incorporated a retrial queueing system that includes MAP arrivals, customer impatience, and catastrophic failures followed by repairs. Krishna Kumar et al. [18] studied queueing systems with catastrophes and customer impatience, focusing on both transient and steady-state behavior. They also discussed some special cases of their model. Dharmaraja and Kumar [10] investigated a multi-server Markovian queueing model featuring heterogeneous-server environments subject to catastrophes, deriving its transient solution and exploring various special cases. Reni Sagayaraj et al. [29] analyzed a stochastic multi-phase "$M/M/1$" queueing system exposed to random environmental fluctuations and catastrophic failures, focusing on its steady-state behavior. Vinodhini and Vidhya [33] conducted a computational study of catastrophic queueing models in a multiphase random environment. They demonstrated the model's relevance to dynamic traffic systems, where incidents such as collisions, weather hazards, or spilled cargo necessitate the redirection of all vehicles. Muthukumaran et al. [25] analyzed a finite-capacity single-server Markovian queueing model incorporating catastrophic effects and a Bernoulli feedback mechanism. Balasubramanian et al. [4] studied a queueing model with two servers, considering catastrophes, failures, and subsequent repairs. Ammar [1] presented a model of a single-server fluid queue subject to catastrophic failures within a randomly transitioning multi-phase environment. Chowdhury and Rani [8] derived the steady-state solution for a feedback queueing system experiencing catastrophes and balking,

employing the matrix geometric approach, and carried out a cost analysis for model optimization. Janos Sztrik and Adam Toth [15] studied a finite-source single-server retrial queueing system incorporating two-way communication and catastrophic breakdowns, and performed a sensitivity analysis through simulation. Ozkar et al. [27] analyzed queueing-inventory systems with catastrophes, considering different replenishment policies. They highlighted that the application of queueing-inventory models involving warehouse catastrophes under realistic assumptions has been largely unexplored in existing literature. Additionally, they developed a cost model to optimize the performance of their proposed system. Savita and Kumar [30] analyzed a repairable "$M/M/1/K$" queueing model incorporating a threshold-based recovery mechanism to mitigate server breakdowns and catastrophes, while accounting for customer reneging and balking. They further developed a cost evaluation framework for the system. Shanmugasundaram and Baby [31] studied a three-node queueing network model with retrial and feedback features, incorporating catastrophic events under steady-state conditions. Krishna Kumar et al. [17] analyzed a queue with a single-server subject to catastrophes, failures, and repair activities from a transient perspective.

Kulkarni and Choi [20] investigated retrial queues incorporating server breakdowns and subsequent repairs. Chakravarthy et al. [6] studied a queueing model incorporating server breakdowns, vacations, repairs, and the use of a backup server. They also discussed several special-case models derived from the main system, including models characterized by an R-matrix structure. Additionally, they described the application of their model to cellular network systems. Karpagam and Somasundaram [16] developed a bulk queuing model that incorporates starting failures and a single vacation concept, with specific emphasis on its applicability to production and manufacturing operations. Kumar et al. [19] investigated a finite-capacity queueing system with server failures, customer balking, and a threshold-driven recovery policy. They discussed the model's application to physician supervision and the management of emergency departments in urban hospitals, and also developed a cost model tailored to this context. Demircioglu et al. [9] investigated a discrete-time queueing system incorporating disasters and provided an analysis of the sojourn time. Mitrani and Puhalskii [24] analyzed an "$M/M/N$" queueing model and derived heavy traffic limiting results for multiprocessor systems experiencing breakdowns and undergoing repairs. Janani and Vijayashree [14] studied a queueing model with an unreliable server experiencing soft failures and working vacations. They also discussed the applicability of their model in the context of smart healthcare systems. Gao et al. [12] examined a non-Markovian retrial queueing system with a single server, incorporating two distinct types of breakdowns and delayed repair mechanisms. Ayyappan et al. [3] conducted a cost optimization analysis of an "$MMAP/PH(1),PH(2)/1$" preemptive priority retrial queueing system characterized by a standby server, server breakdowns, orbital search, phase-type repair distributions, and customer impatience behavior.

2.1. Real Life Applications: Cellular Base Station in a Mobile Network

Mobile users initiate calls or data sessions at varying rates, influenced by factors like time of day, location, and user behavior. These arrival patterns can be modeled using a MAP, which captures the burstiness and correlation in user activities. The service time for each user session (e.g., call setup, data transmission) can be modeled using a phase-type distribution, which represents the service process as a series of exponential phases. This approach allows for capturing complex service patterns, such as varying call durations or data transfer rates. Catastrophic failures, such as power outages or hardware malfunctions, can lead to the sudden unavailability of the base station. Negative arrivals represent the loss of users who attempt to connect during these failures but leave due to the unavailability of service. These events can be modeled using negative arrival processes, where users are lost from the system without being served. This variation highlights additional cases that illustrate the point.

2.1.1 The Romeoville Petroleum Refinery Explosion Incident (1984)

The Union Oil Company refinery in Romeoville, Illinois, USA, experienced a catastrophic explosion on July 23, 1984. The explosion resulted in the deaths of 17 workers and caused extensive damage to the facility. The explosion was triggered by a small crack in a circular weld on a pressure vessel. Attempts to close the main inlet valve to stop gas from leaking from the crack led to the crack growing larger, releasing flammable gas that ignited within moments (Catastrophic failure). The explosion and subsequent damage halted production at the refinery, leading to a loss of output and revenue. The negative arrival refers to the cessation of the refinery's intended function, effectively removing its service capacity (Negative arrival). The explosion caused significant structural damage to the refinery, including the destruction of equipment and infrastructure. The vessel, in service since 1970, had undergone numerous repairs and modifications before the incident (Breakdown). The repair process involved multiple stages, including assessment of damage, procurement of replacement parts, and reconstruction of damaged sections. The extensive repairs required careful planning and execution to restore the refinery to operational status (Repair). This incident underscores the critical importance of adhering to proper maintenance procedures and quality assurance protocols. The failure to address the small crack in the weld led to a catastrophic event, highlighting the need for thorough inspections and timely repairs to prevent such disasters. This example demonstrates how a combination of factors, including minor defects, inadequate maintenance, and delayed repairs, can culminate in a catastrophic failure with far-reaching consequences.

2.1.2 Morbi Bridge Collapse (2022)

A real-life example illustrating the scenario of catastrophic failure, negative arrival, breakdown, and phase-type repairs is the tragic collapse of the Morbi Bridge in Gujarat, India, on October 30, 2022. This 137-year-old suspension bridge over the Machchhu River, collapsed, resulting in at least 141 fatalities and over 180 injuries. The bridge had recently reopened after repairs, but the restoration was mishandled. The bridge's sudden collapse during use, leading to significant loss of life (Catastrophic Failure). The failure led to the loss of public trust and the cessation of the bridge's intended function, effectively removing its service capacity (Negative Arrival). The structural failure of the bridge, compounded by inadequate maintenance and improper repair materials, such as replacing wooden planks with aluminum (Breakdown). The restoration process was flawed, with only superficial repairs undertaken without addressing the underlying structural issues, leading to the eventual collapse (Repair). This incident underscores the critical importance of proper maintenance, adherence to safety standards, and thorough inspections to prevent such catastrophic events. In this example, the Morbi Bridge collapse serves as a poignant reminder of the consequences of neglecting comprehensive maintenance and the need for rigorous safety protocols in infrastructure management.

2.1.3 Teton Pass Road Collapse – Wyoming, USA (2024)

In June 2024, a significant portion of Teton Pass Road in Wyoming experienced a catastrophic collapse, resulting in the closure of a vital transportation route. The collapse of the road was a sudden and unexpected event, leading to immediate disruption of traffic and posing risks to public safety (Catastrophic Failure). The failure led to the cessation of the road's intended function, effectively removing its service capacity and causing delays and detours for travelers (Negative Arrival). The collapse was due to structural weaknesses and environmental factors, highlighting the vulnerability of infrastructure to unforeseen stresses (Breakdown). The repair process involved multiple stages, including assessment of damage, engineering evaluations, and phased reconstruction to restore the road to operational status (Repair). This incident underscores the importance of regular infrastructure assessments, proactive maintenance, and the need for resilient design to withstand environmental challenges. The Teton Pass Road collapse serves as a poignant reminder of the complexities involved in infrastructure management and the critical

need for comprehensive planning and timely interventions to prevent such catastrophic events.

2.1.4 Ahmedabad Air India Flight crash (2025)

On June 12, 2025, There is no credible record of Air India Flight AI-171 – or any Boeing 787-8 Dreamliner from Air India – crashing after takeoff from Ahmedabad bound for London-Gatwick. The aircraft lost altitude moments after departure and struck the B.J. Medical College hostel nearby, resulting in a devastating explosion and fire. Tragically, 241 of the 242 people onboard were killed, with only one passenger surviving. Additionally, at least 39 people on the ground lost their lives, and over 60 were injured. The flight crew had issued a mayday call reporting power or thrust failure before the crash. Both black boxes have been recovered, and an international investigation–led by India′s AAIB with support from U.S., UK, Boeing, and GE teams–is underway. The incident prompted Air India and Tata Group to establish emergency aid and compensation for victims′ families, while broader aviation safety measures are being reassessed.

2.2. Overview of the Manuscript

The remainder part of the manuscript is structured as follows: Section 3 outlines the mathematical formulation of the model. Section 4 introduces the notations used in the matrix formulation and describes the matrix generation process using the Quasi-Birth"Death (QBD) approach. Section 5 presents the stability condition, derives the steady-state probability vector, and analyzes the rate matrix R. Section 6 focuses on the evaluation of system performance measures. Section 7 illustrates numerical examples with tabulated results. Finally, Section 8 summarizes the key conclusions of the study.

3. Detailed Description of the Mathematical Model

We consider a customer arrival process modeled by a MAP, represented by the pair (D_0, D_1), where D_0 corresponds to transitions without customer arrivals, and D_1 corresponds to transitions that include customer arrivals into the system. Service times are modeled using a phase-type (PH) distribution, characterized by the representation (α, T), where $T^0 + Te = 0$ such that $T^0 = -Te$. During service, if a negative customer arrival occurs, it affects the customer currently receiving service by removing both the customer and the server from the system. Additionally, catastrophic events can happen at any time–The operational status of the server (idle or busy)–and these events cause the server to fail (break down) and simultaneously remove all customers from the system. When the server experiences a breakdown due to either negative arrivals or catastrophes, the server enters a repair process. Upon completion of the repair, the server returns to service: if there are customers waiting, the server resumes servicing; otherwise, the server remains idle. While the server is under repair, customers waiting in the queue may renege (i.e., leave the system due to lack of customer tolerance for delays) based on an exponentially distributed with parameter σ. The exponentially distributed rates associated with negative arrivals, catastrophes, server breakdowns, and repairs are denoted by λ_2, ζ, τ, and γ, respectively.

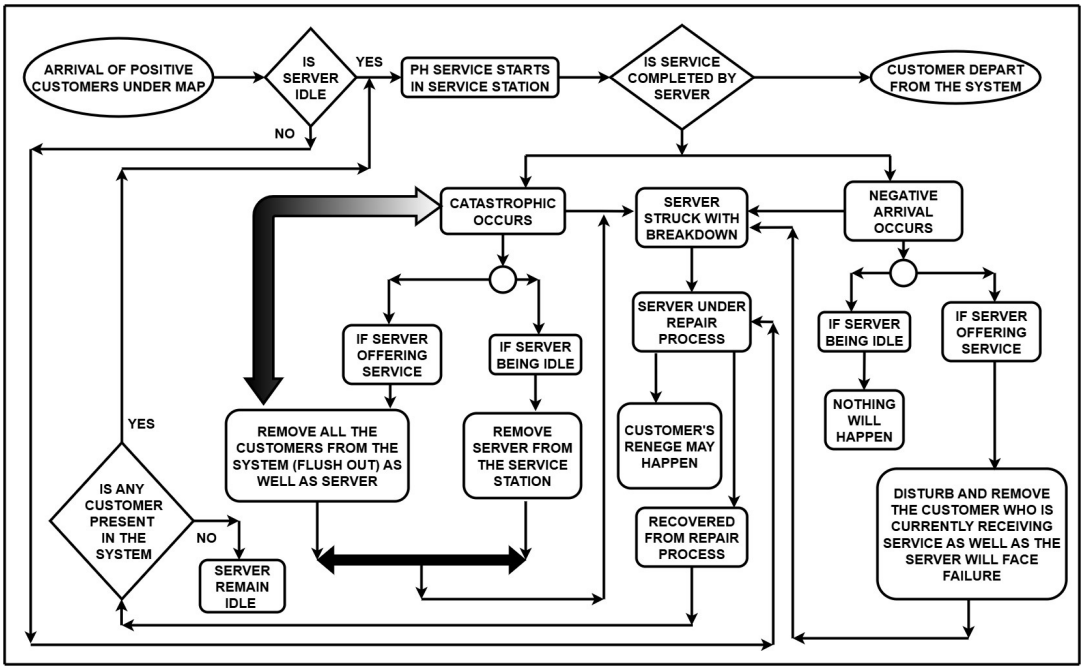


Figure 1: *Figure caption*

4. Matrix Formulation

A comprehensive description of the model's notation is provided in this section to facilitate the generation of the QBD process.

4.1. Matrix Generation Notations

- $\otimes$ - The Kronecker multiplication operation between two matrices.
- $\oplus$ - The Kronecker sum operation between two matrices
- I_m - It signifies an identity matrix of order $(m \times m)$.
- **0** - Represents the zero matrix of suitable dimensions.
- e - A column vector of the required dimension consisting entirely of ones.
- To indicate λ_1 be the fundamental arrival rate and it is defined as $\lambda_1 = \pi_1 D_1 e_m$, where π_1 is the generator matrix $D = D_0 + D_1$, describes the transition behavior of the MAP. To conveniently determine the π_1 such that $\pi_1 D = 0$, $\pi_1 e = 1$.
- The standard service rate for arriving customers the service provided by the server during normal mode is denoted by δ, where $\delta = [\alpha(-T)^{-1}e]^{-1}$.
- $C(t)$ denotes the number of positive customers present in the system,
- $S(t)$ denotes the server status at time t, where

$$S(t) = \begin{cases} 0, & \text{if the server is being idle,} \\ 1, & \text{if the Catastrophic occurs while the server is on idle,} \\ 2, & \text{if the flush out of customers and also remove server from the system,} \\ 3, & \text{if the server is actively serving customers,} \\ 4, & \text{if the Catastrophic occurs while the server's service period,} \\ 5, & \text{if the server is being repaired,} \\ 6, & \text{if the Catastrophic occurs while the server's repair period,} \end{cases}$$

- $P(t)$ denotes the service phase under PH.
- $A(t)$ denotes the positive arrival phase under MAP.
- Let $\{(C(t)\ ,\ S(t)\ ,\ P(t)\ ,\ A(t)) : t \geq 0\ \}$ is the Continuous Time Markov Chain with the QBD process such that state space is given by

$$\mathbf{\Omega} = l(0) \bigcup_{p=1}^{\infty} l(p)$$

where
$l(0) = \{(0,q,s) : q = 0,1,2,5;\ 1 \leq s \leq m\}$

for $p \geq 1$
$l(p) = \{(p,q,r,s) : q = 3,4;\ 1 \leq r \leq n;\ 1 \leq s \leq m\} \cup \{(p,q,s) : q = 5,6;\ 1 \leq s \leq m\}$

The infinitesimal generator for the QBD process is represented by:

$$Q = \begin{bmatrix} B_{00} & B_{01} & \mathbf{0} & \mathbf{0} & \mathbf{0} & \mathbf{0} & \cdots & \cdots \\ B_{10} & A_1 & A_0 & \mathbf{0} & \mathbf{0} & \mathbf{0} & \cdots & \cdots \\ B' & A_2 & A_1 & A_0 & \mathbf{0} & \mathbf{0} & \cdots & \cdots \\ B' & \mathbf{0} & A_2 & A_1 & A_0 & \mathbf{0} & \cdots & \cdots \\ B' & \mathbf{0} & \mathbf{0} & A_2 & A_1 & A_0 & \cdots & \cdots \\ \vdots & \vdots & \vdots & \ddots & \ddots & \ddots & & \vdots \\ \vdots & \vdots & \vdots & & \ddots & \ddots & \ddots & \vdots \end{bmatrix}$$

The entries of the block matrices of Q are described as follows:

$$B_{00} = \begin{bmatrix} D_0 & \mathbf{0} & \mathbf{0} & \mathbf{0} \\ \mathbf{0} & -(\zeta+\tau)I_m & \zeta I_m & \tau I_m \\ \mathbf{0} & \mathbf{0} & \mathbf{0} & \mathbf{0} \\ \gamma I_m & \mathbf{0} & \mathbf{0} & D_0 - \gamma I_m \end{bmatrix}, \quad B_{01} = \begin{bmatrix} \alpha \otimes D_1 & \mathbf{0} & \mathbf{0} & \mathbf{0} \\ \mathbf{0} & \mathbf{0} & \mathbf{0} & \mathbf{0} \\ \mathbf{0} & \mathbf{0} & \mathbf{0} & \mathbf{0} \\ \mathbf{0} & \mathbf{0} & D_1 & \mathbf{0} \end{bmatrix},$$

$$B_{10} = \begin{bmatrix} T^0 \otimes I_m & \mathbf{0} & \mathbf{0} & e_n \otimes \lambda_2 I_m \\ \mathbf{0} & \mathbf{0} & e_n \otimes \zeta I_m & e_n \otimes \tau I_m \\ \mathbf{0} & \mathbf{0} & \mathbf{0} & \mathbf{0} \\ \mathbf{0} & \mathbf{0} & \zeta I_m & \mathbf{0} \end{bmatrix}, \quad A_0 = \begin{bmatrix} I_n \otimes D_1 & \mathbf{0} & \mathbf{0} & \mathbf{0} \\ \mathbf{0} & \mathbf{0} & \mathbf{0} & \mathbf{0} \\ \mathbf{0} & \mathbf{0} & D_1 & \mathbf{0} \\ \mathbf{0} & \mathbf{0} & \mathbf{0} & \mathbf{0} \end{bmatrix},$$

$$A_1 = \begin{bmatrix} T \oplus (D_0 - \lambda_2 I_m) & \mathbf{0} & \mathbf{0} & \mathbf{0} \\ \mathbf{0} & -(\zeta+\tau)I_m & \mathbf{0} & \mathbf{0} \\ \gamma\alpha \otimes I_m & \mathbf{0} & D_0 - (\gamma+\sigma)I_m & \mathbf{0} \\ \mathbf{0} & \mathbf{0} & \mathbf{0} & -\zeta I_m \end{bmatrix},$$

$$A_2 = \begin{bmatrix} T^0\alpha \otimes I_m & \mathbf{0} & e_n \otimes \lambda_2 I_m & \mathbf{0} \\ \mathbf{0} & \mathbf{0} & \mathbf{0} & \mathbf{0} \\ \mathbf{0} & \mathbf{0} & \sigma I_m & \mathbf{0} \\ \mathbf{0} & \mathbf{0} & \mathbf{0} & \mathbf{0} \end{bmatrix}, \quad B' = \begin{bmatrix} \mathbf{0} & \mathbf{0} & \mathbf{0} & \mathbf{0} \\ \mathbf{0} & \mathbf{0} & e_n \otimes \zeta I_m & e_n \otimes \tau I_m \\ \mathbf{0} & \mathbf{0} & \mathbf{0} & \mathbf{0} \\ \mathbf{0} & \mathbf{0} & \zeta I_m & \mathbf{0} \end{bmatrix}.$$

5. Condition for Stableness

To evaluate the stability characteristics of the system, we examine the model under particular circumstances.

5.1. Assessment of Stability

Let us define the variable A as $A = A_0 + A_1 + A_2$. This indicates that the matrix A is square, with dimension $(2nm + 2m)$, and represents a matrix of irreducible infinitesimal generators.

Let $\mathbf{\Psi}$ represent the steady-state probability vector corresponding to matrix A. This vector must satisfy the conditions:

$$\mathbf{\Psi}A = 0 \text{ and } \mathbf{\Psi}e = 1.$$

where e represents a column vector whose entries are all ones.
The vector $\mathbf{\Psi}$ can be partitioned as:

$$\mathbf{\Psi} = (\Psi_0, \Psi_1, \Psi_2, ...),$$

where Ψ_0 has dimension $4m$, and each of Ψ_1, Ψ_2,...has dimension $2nm + 2m$.

This structure reveals that the underlying Markov process possesses a Quasi-Birth-and-Death (QBD) form. The stability of the model is ensured if the following condition is satisfied:

$$\mathbf{\Psi}A_0e < \mathbf{\Psi}A_2e$$

which is both a essential and complete condition for the stability of a QBD process.
Therefore, the vector Ψ is obtained by solving the system defined by the above conditions.

$\Psi_0[(T + T^0\alpha) \oplus (D - \lambda_2 I_m)] + \Psi_2[\gamma\alpha \otimes I_m] = 0.$
$\Psi_1[-(\zeta + \tau)I_m] = 0.$
$\Psi_0[e_n \otimes \lambda_2 I_m] + \Psi_2[D - \gamma I_m] = 0.$
$\Psi_3[-\zeta I_m] = 0.$

subject to normalizing condition

$(\Psi_0 + \Psi_1)e_{nm} + (\Psi_2 + \Psi_3)e_m = 1.$

Following algebraic derivation, the model's stability condition, expressed as $\mathbf{\Psi}A_0\text{e} < \mathbf{\Psi}A_2\text{e}$, can be reformulated as:

$$\{\Psi_0[e_n \otimes D_1e_m] + \Psi_1[D_1e_m]\} < \{\zeta_0[(T^0 \otimes e_m) + (e_n \otimes \lambda_2 e_m)] + \Psi_2[\sigma e_m]\}$$

5.2. Investigation of the Steady-State Vector

Let the steady-state probability vector of the QBD matrix Q be indicated by $\mathbf{x}$, which is partitioned as $\mathbf{x} = \mathbf{x}_i$, $i \geqslant 0$. Specifically, $\mathbf{x}_0$ is a vector of dimension $4m$, while $\mathbf{x}_i$ for $i \geqslant 1$ are of dimension $(2nm + 2m)$. The vector $\mathbf{x}$ satisfies the steady-state conditions $\mathbf{x}Q = 0$ and $\mathbf{x}e = 1$, where e is a

column vector of ones.

Despite this, the system remains stable, and the sub-vectors of $\mathbf{x}$, excluding $\mathbf{x}_0$, $\mathbf{x}_1$ and $\mathbf{x}_2$, which represent distinct level states, are determined by the following equations.

$$\mathbf{x}_j = \mathbf{x}_2 \, R^{j-1}, \quad j \geqslant 3.$$

Accordingly, the rate matrix R represents the smallest solution that is non-negative to the quadratic matrix equation $R^2A_2 + RA_1 + A_0 = 0$, confirming the stability of the queuing system. The matrix R, with dimension $(2nm + 2m)$, is derived from this equation and satisfies the additional condition $RA_2e = A_0e$.

By evaluating the following expressions, the sub-vectors corresponding to $\mathbf{x}_0$, $\mathbf{x}_1$ and $\mathbf{x}_2$ are determined.

$$\mathbf{x}_0B_{00} + \mathbf{x}_1B_{10} + \mathbf{x}_2((I - R)^{(-1)}B' = 0,$$
$$\mathbf{x}_0B_{01} + \mathbf{x}_1A_1 + \mathbf{x}_2A_2 = 0.$$
$$\mathbf{x}_1A_0 + \mathbf{x}_2(A_1 + RA_2) = 0.$$

The system is subject to the following normalizing condition:

$$\mathbf{x}_0e + \mathbf{x}_1e + \mathbf{x}_2(I - R)^{-1}e = 1.$$

Therefore, the R matrix is obtained by following the mathematical procedure defined by the Logarithmic Reduction Algorithm.

5.3. Logarithmic Reduction Algorithm

The following summarizes the core steps of the Logarithmic Reduction Algorithm according to Latouche and Ramasamy [21]:

Step 0:

" $H \leftarrow (-A_1)^{-1}A_0$, $L \leftarrow (-A_1)^{-1}A_2$, $G = L$, and $T = H$ "

Step 1:

" $U = HL + LH$ "

" $M = H^2$ "

" $H \leftarrow (I - U)^{-1}M$ "

" $M \leftarrow L^2$ "

" $L \leftarrow (I - U)^{-1}M$ "

" $G \leftarrow G + TL$ "

" $T \leftarrow TH$ "

" Continue Step 1 Until $||e - Ge||_\infty < \epsilon$ "

Step 2:

" $R = -A_0(A_1 + A_0G)^{-1}$ "

6. Quantitative Performance Measures

In this section, we investigate the steady-state behavior of the model by evaluating key performance measures and presenting their corresponding analytical expressions.

- Probability that the server is being idle

$$P_I = \sum_{s=1}^{m} \mathbf{x}_{00s}$$

- Probability that the catastrophic occurs during server idle period

$$P_{CI} = \sum_{s=1}^{m} \mathbf{x}_{00s}$$

- Probability that the flush out of customers and remove server from the system

$$P_{FO} = \sum_{s=1}^{m} \mathbf{x}_{00s} + \sum_{p=1}^{\infty} \sum_{r=1}^{n} \sum_{s=1}^{m} \mathbf{x}_{p3rs} + \sum_{p=1}^{\infty} \sum_{s=1}^{m} \mathbf{x}_{p5s}$$

- Probability that the server providing service to customers

$$P_B = \sum_{p=1}^{\infty} \sum_{r=1}^{n} \sum_{s=1}^{m} \mathbf{x}_{p3rs}$$

- Probability that the server is under repair process for rejuvenation

$$P_R = \sum_{p=1}^{\infty} \sum_{s=1}^{m} \mathbf{x}_{p5s}$$

- The expected number of customers available in the system

$$E_{system} = \sum_{p=1}^{\infty} p\mathbf{x}_p = \mathbf{x}_1 e + \mathbf{x}_2[2(I-R)^{-1} + R(I-R)^{-2}]e$$

7. Numerical analysis

This section presents a numerical analysis of the model's behavior, emphasizing the differences in variance and correlation structures across five different MAP representations. Notably, the first three arrival processes–ERL-A, EXP-A, and HYP-EXP-A–are renewal processes and therefore exhibit zero correlation between consecutive inter-arrival times. In contrast, MAP-NC-A and MAP-PC-A represent correlated arrival processes, with inter-arrival time correlation coefficients of -0.4804 and 0.4804, respectively. The coefficients of variation for the inter-arrival times corresponding to these five processes are 0.2500, 1.0000, 14.6365, 1.0408, and 1.0408.

Arrival in Erlang (ERL-A) :

$$D_0 = \begin{bmatrix} -4 & 4 & 0 & 0 \\ 0 & -4 & 4 & 0 \\ 0 & 0 & -4 & 4 \\ 0 & 0 & 0 & -4 \end{bmatrix}, \qquad D_1 = \begin{bmatrix} 0 & 0 & 0 & 0 \\ 0 & 0 & 0 & 0 \\ 0 & 0 & 0 & 0 \\ 4 & 0 & 0 & 0 \end{bmatrix}$$

Arrival in Exponential (EXP-A) :

$$D_0 = \begin{bmatrix} -1 \end{bmatrix}, \qquad D_1 = \begin{bmatrix} 1 \end{bmatrix}$$

Arrival in Hyper-exponential (HYP-EXP-A) :

$$D_0 = \begin{bmatrix} -8.2 & 0 & 0 \\ 0 & -0.82 & 0 \\ 0 & 0 & -0.082 \end{bmatrix}, \qquad D_1 = \begin{bmatrix} 5.74 & 2.05 & 0.41 \\ 0.574 & 0.205 & 0.041 \\ 0.0574 & 0.0205 & 0.0041 \end{bmatrix}$$

Arrival in MAP-Negative Correlation (MAP-NC-A) :

$$D_0 = \begin{bmatrix} -1.75 & 1.75 & 0 & 0 \\ 0 & -1.75 & 1.75 & 0 \\ 0 & 0 & -1.75 & 0 \\ 0 & 0 & 0 & -3.5 \end{bmatrix}, \qquad D_1 = \begin{bmatrix} 0 & 0 & 0 & 0 \\ 0 & 0 & 0 & 0 \\ 0.0175 & 0 & 0 & 1.7325 \\ 3.465 & 0 & 0 & 0.035 \end{bmatrix}$$

Arrival in MAP-Positive Correlation (MAP-PC-A) :

$$D_0 = \begin{bmatrix} -1.75 & 1.75 & 0 & 0 \\ 0 & -1.75 & 1.75 & 0 \\ 0 & 0 & -1.75 & 0 \\ 0 & 0 & 0 & -3.5 \end{bmatrix}, \qquad D_1 = \begin{bmatrix} 0 & 0 & 0 & 0 \\ 0 & 0 & 0 & 0 \\ 1.7325 & 0 & 0 & 0.0175 \\ 0.035 & 0 & 0 & 3.465 \end{bmatrix}$$

The service process is modeled using three phase-type (PH) distributions, each normalized to obtain a consistent service time representation. The Erlang, exponential, and hyper-exponential cases are denoted by ERL-S, EXP-S, and HYP-EXP-S, respectively.

Service in Erlang (ERL-S) :

$$\alpha = (1, 0, 0), \qquad T = \begin{bmatrix} -3 & 3 & 0 \\ 0 & -3 & 3 \\ 0 & 0 & -3 \end{bmatrix}$$

Service in Exponential (EXP-S) :

$$\alpha = (1), \qquad T = [-1]$$

Service in Hyper-exponential (HYP-EXP-S) :

$$\alpha = (0.8, 0.2), \qquad T = \begin{bmatrix} -2.80 & 0 \\ 0 & -0.28 \end{bmatrix}$$

7.1. Illustration:

In the Table 1, we investigate the result of the renege rate of customers (σ) on the expected count of customers available in the system (E_{System}). To fix the values of $\lambda_1 = 1,\ \lambda_2 = 0.1,\ \delta = 5,\ \zeta = 2,\ \tau = 1,\ \gamma = 3,$ such that the system remains stable.

When analyzing the arrival times combined with various service time distributions, HYP-EXPA shows a significant decrease, whereas ERL-A exhibits a slower decline compared to the other arrival time patterns. Conversely, when examining different arrival time combinations with fixed service times, ERL-S decreases gradually, EXP-S shows a moderate decline, and HYP-EXP-S decreases substantially.

In scenarios involving repair times–triggered by catastrophic events or negative arrivals–the server becomes unavailable. During these periods, customers waiting in the queue may lose patience and leave the system (renege). An increase in the reneging rate results in a corresponding decrease in the mean number of customers in the system.

Table 1: *Renege rate of customers vs.* E_{system}

SERVICES	σ	E_{system} ARRIVALS				
		ERL-A	**EXP-A**	**HYP-EXP-A**	**MAP-NC-A**	**MAP-PC-A**
ERL-S	2	0.117881	0.140791	0.254385	0.133434	0.195316
	4	0.117649	0.140024	0.249009	0.132854	0.190435
	6	0.117524	0.139591	0.245143	0.132535	0.187296
	8	0.117447	0.139319	0.242307	0.132335	0.185209
	10	0.117394	0.139133	0.240177	0.132197	0.183759
	12	0.117356	0.138998	0.238540	0.132097	0.182708
	14	0.117327	0.138897	0.237251	0.132021	0.181917
	16	0.117304	0.138817	0.236217	0.131962	0.181303
	18	0.117285	0.138754	0.235372	0.131914	0.180813
	20	0.117270	0.138701	0.234669	0.131874	0.180415
	22	0.117257	0.138658	0.234078	0.131841	0.180085
	24	0.117247	0.138621	0.233573	0.131813	0.179807
	26	0.117237	0.138589	0.233138	0.131789	0.179570
	28	0.117229	0.138562	0.232760	0.131768	0.179365
EXP-S	2	0.119268	0.147839	0.277096	0.138700	0.227797
	4	0.118966	0.146940	0.271330	0.138034	0.221615
	6	0.118804	0.146427	0.267117	0.137665	0.217398
	8	0.118704	0.146101	0.263979	0.137432	0.214448
	10	0.118635	0.145876	0.261590	0.137273	0.212312
	12	0.118585	0.145713	0.259729	0.137156	0.210712
	14	0.118548	0.145590	0.258249	0.137068	0.209476
	16	0.118518	0.145493	0.257049	0.136999	0.208496
	18	0.118494	0.145415	0.256060	0.136943	0.207701
	20	0.118475	0.145351	0.255231	0.136897	0.207045
	22	0.118458	0.145298	0.254529	0.136859	0.206495
	24	0.118444	0.145253	0.253927	0.136826	0.206027
	26	0.118432	0.145214	0.253405	0.136798	0.205624
	28	0.118422	0.145180	0.252948	0.136774	0.205273
HYP-EXP-S	2	0.151057	0.185763	0.348842	0.169761	0.361502
	4	0.150195	0.184153	0.341741	0.168517	0.350852
	6	0.149697	0.183159	0.336304	0.167775	0.342590
	8	0.149375	0.182493	0.332072	0.167287	0.336104
	10	0.149150	0.182018	0.328719	0.166942	0.330927
	12	0.148983	0.181662	0.326012	0.166686	0.326724
	14	0.148856	0.181387	0.323791	0.166489	0.323257
	16	0.148755	0.181168	0.321940	0.166333	0.320354
	18	0.148673	0.180989	0.320377	0.166205	0.317893
	20	0.148605	0.180840	0.319040	0.166100	0.315782
	22	0.148548	0.180715	0.317884	0.166011	0.313954
	24	0.148499	0.180607	0.316876	0.165935	0.312355
	26	0.148457	0.180515	0.315990	0.165869	0.310946
	28	0.148421	0.180434	0.315204	0.165812	0.309695

8. Conclusion

This study examines a queueing system where customer arrival follows a MAP and service times are governed by a PH distribution. The model integrates several realistic features, including negative arrivals, catastrophic events, customer reneging, server breakdowns, and subsequent repairs. Numerical experiments, presented in tabular form, highlight the impact of varying arrival and service time parameters on the performance measures. The basis for proposing this model arises from practical applications, particularly in cellular base stations within mobile networks and real-world catastrophic scenarios. To analyze the system, we apply matrix-analytic methods to the "MAP/PH/1" queue, accounting for correlated arrivals, service variability, and system disruptions.

References

[1] Ammar, S.I. (2021). Fluid $M/M/1$ Catastrophic Queue in a Random Environment, *RAIRO Operations Research*, 55:S2677-S2690. DOI:https://doi.org/10.1051/ro/2020100

[2] Artalejo, J.R. & Gomez-Corral, A. (1999). On a Single Server Queue with Negative Arrivals and Request Repeated, *Journal of Applied Probability*, 36:907-918.

[3] Ayyappan, G., Thilagavathy, K. & Kumar, R. (2025). Cost optimisation of $MMAP/PH(1),PH(2)/1$ pre-emptive priority retrial queueing model with standby server, orbital search, server breakdowns, phase type repairs and impatient customers, *International Journal of Mathematics in Operational Research (IJMOR)*, 30(3):350 - 391. DOI: 10.1504/IJMOR.2025.14575910.1504/IJMOR.2025.145759

[4] Balasubramanian, M., Bharathidass, S. & Ganesan, V. (2020). Role of catastrophes, failures and repairs for a two server queueing systems, *Malaya Journal of Matematik*, 8(1):72-75. DOI: https://doi.org/10.26637/MJM0S20/0014

[5] Chakravarthy, S.R., Dudin, A.N. & Klimenok, V.I. (2010). A Retrial Queueing Model with MAP Arrivals, Catastrophic Failures with Repairs, and Customer Impatience, *Asia-Pacific Journal of Operational Research*, 27(6):727“752. DOI: https://doi.org/10.1142/S0217595910002971

[6] Chakravarthy, S.R., Shruti & Kulshrestha, R. (2020). A queueing model with server breakdowns, repairs, vacations, and backup server, *Operations Research Perspectives*, 7:1-13. DOI: https://doi.org/10.1016/j.orp.2019.100131

[7] Chin, C.H., Koh, S.K., Tan, Y.F., Pooi, A.H. & Goh, Y.K. (2018). Stationary queue length distribution of a continuous-time queueing system with negative arrival, *3rd International Conference on Mathematical Sciences and Statistics, IOP Conf. Series: Journal of Physics: Conf. Series 1132*, IOP Publishing, 1-8. DOI: https://doi.org/10.1088/1742-6596/1132/1/012057

[8] Chowdhury, A.R. & Rani, I. (2021). Steady-State Solution of Catastrophic Feedback Queue Subject to Balking Using Matrix-Geometric Approach, *Journal of Scientific Research* , 65(6):100-105. DOI: https://doi.org/10.37398/JSR.2021.650616

[9] Demircioglu, M., Bruneel, H. & Wittevrongel, S. (2021). Analysis of a Discrete-Time Queueing Model with Disasters, *Mathematics*, 9(24):1-22. DOI: https://doi.org/10.3390/math9243283

[10] Dharmaraja, S. & Kumar, R. (2015). Transient solution of a Markovian queuing model with heterogeneous servers and catastrophes, *OPSEARCH*, 52(4):810“826. DOI: https://doi.org/10.1007/s12597-015-0209-6

[11] Dimitriou, I. (2013). A mixed priority retrial queue with negative arrivals, unreliable server and multiple vacations, *Applied Mathematical Modelling*, 37:1295“1309. DOI: https://doi.org/10.1016/j.apm.2012.04.011

[12] Gao, S., Zhang, J. & Wang, X. (2020). Analysis of a Retrial Queue With Two-Type Breakdowns and Delayed Repairs, *IEEE Access*, 8:172428-172442.

[13] Gelenbe, E., Glynn, P. & Sigman, K. (1991). Queues with Negative Arrivals, *Journal of Applied Probability*, 28:245-250.

[14] Janani. B. & Vijayashree, K.V. (2023). Analysis of anunreliable server with soft failures and working vacations andits application in a smart healthcare system, *Results in Control and Optimization*, 10:1-14. DOI: https://doi.org/10.1016/j.rico.2023.100211

[15] Janos Sztrik & Adam Toth (2022). Sensitivity analysis of a single server finite-source retrial queueing system with two-way communication and catastrophic breakdown using simulation, *Annales Mathematicae et Informaticae*, 56:122-133. DOI: https://doi.org/10.33039/ami.2022.12.002

[16] Karpagam, S. & Somasundaram, B. (2023). Bulk queueing system with starting failure and single vacation, *Southeast Europe Journal of Soft Computing*, 12(2):25-29.

[17] Krishna Kumar, B., Krishnamoorthy, A., Pavai Madheswari, S. & Sadiq Basha, S. (2007). Transient analysis of a single server queue with catastrophes, failures and repairs, *Queueing Systems*, 56:133“141. DOI: https://doi.org/10.1007/s11134-007-9014-0

[18] Krishna Kumar, B., Anantha Lakshmi, S.R., Anbarasu, S. & Pavai Madheswari, S. (2014). Transient and steady-state analysis of queueing systems with catastrophes and impatient customers, *International Journal of Mathematics in Operational Research*, 6(5):523-549. DOI: https://doi.org/10.1504/IJMOR.2014.064838

[19] Kumar, A., Savita & Shekhar, C. (2024). Cost Analysis of a Finite Capacity Queue with Server Failures, Balking, and Threshold-Driven Recovery Policy, *International Journal of Mathematical, Engineering and Management Sciences*, 9(5):1198-1209. DOI: https://doi.org/10.33889/IJMEMS.2024.9.5.063

[20] Kulkarni, V.G. & Choi, B.D. (1990). Retrial Queues with Server Subject to Breakdowns and Repairs, *Queueing Systems*, 7:191-208. DOI: https://doi.org/10.1007/BF01158474

[21] Latouche, G., & Ramaswami, V. (1993). A Logarithmic Reduction Algorithm for Quasi-Birth-Death Processes, *Journal of Applied Probability*, 30:650-674. DOI: http://www.jstor.org/stable/3214773.

[22] Li, Q.-L. & Zhao, Y.-Q. (2004). A $MAP/G/1$ Queuewith Negative Customers, *Queueing Systems*, 47:5-43. DOI: https://doi.org/10.1023/B:QUES.0000032798.65858.19

[23] Lisovskaya, E., Fedorova, E., Salimzyanov, R. & Moiseeva, S. (2022). Resource Retrial Queue with Two Orbits and Negative Customers, *Mathematics*, 10(3):1-19. DOI: https://doi.org/10.3390/math10030321

[24] Mitrani, I & Puhalskii, A. (1993). Limiting results for multiprocessor systems with breakdowns and repairs, *Queueing Systems*, 14:293-311. DOI: https://doi.org/10.1007/BF01158870

[25] Muthukumaran, S., Thiagarajan, M. & Kalidass, K. (2019). A Finite Capacity Markovian Queueing System With Catastrophic Effects And Bernoulli Feedbacks, *International Journal of Computational Engineering Research (IJCER)*, 9(5):1-11.

[26] Nesrine, Z. & Natalia, D. (2018). On the multiserver retrial queues with negative arrivals, *International Journal of Mathematics in Operational Research* 13(2):219-242. DOI: https://doi.org/10.1504/IJMOR.2018.094056

[27] Ozkar, S., Melikov, A. & Sztrik, J. (2023). Queueing-Inventory Systems with Catastrophes under Various Replenishment Policies, *Mathematics*, 11(23):1-24. DOI: https://doi.org/10.3390/math11234854

[28] Ramdani, H., Bouchentouf, A.A. & Yahiaoui, L. (2025). A Markovian Batch Arrival Queueing System with Disasters, Working Breakdowns, and Impatience: Mathematical Modeling and Economic, *Yugoslav Journal of Operations Research*, 35(2):393“416. DOI: https://doi.org/10.2298/YJOR230515037R

[29] Reni Sagayaraj, M., Anand Gnana Selvam, S., Moganraj. D. & Reynald Susainathan. R. (2016). Steady-state Behavior of a Multi-phase $M/M/1$ Queue in Random Evolution subject to Catastrophe failure, *Advances in Theoretical and Applied Mathematics*, 11(3):213-221.

[30] Savita & Kumar, N (2024). Threshold-Based Recovery in Queue Theory: Addressing Server Breakdowns, Catastrophic Events, and Customer Reneging, *Journal of Reliability and Statistical Studies*, 17(2):435-451. DOI: https://doi.org/10.13052/jrss0974-8024.1729

[31] Shanmugasundaram, S. & Baby, C. (2025). A Study on Catastrophic Retrial Feedback Queueing Network Model with Three Nodes in Steady State, *Communications on Applied Nonlinear Analysis*, 32(3):1-11.

[32] Senthil Vadivu, A., Arumuganathan, R. & Senthil Kumar, M. (2016). Analysis of Discrete-Time Queues with Correlated Arrivals, Negative Customers and Server Interruption, *RAIRO - Operations Research*, 50(1):67“81. DOI: https://doi.org/10.1051/ro/2015012

[33] Vinodhini, G.A.F. & Vidhya, V. (2016). Computational Analysis of Queues with Catastrophes in a Multiphase Random Environment, *Mathematical Problems in Engineering*, Article ID 2917917, 16:1-7. DOI: https://doi.org/10.1155/2016/2917917

BAYESIAN STUDY OF HYBRID WEIBULL-EXPONENTIAL POWER MODEL BY MEANS OF HAMILTONIAN MONTE CARLO ALGORITHM

M. A. Alhassan[1]*, A. Yahaya[2], O. O. Ishaq[1,3], B. Abba[4], A. B. Muhammad[1,5]

•

[1]Department of Statistics, Aliko Dangote University of Science and Technology, Wudil, Kano 700001, Nigeria
[2]Department of Statistics, Ahmadu Bello University, Zaria, Kaduna 800001, Nigeria
[4]Department of Mathematics, Yusuf Maitama Sule University, Kano 700001, Nigeria
[4]School of Mathematics and Statistics, Central South University, Changsha, 410083, China
[1]*ma23038@gmail.com, [2]Abubakaryahaya@abu.edu.ng, [3]babington4u@gmail.com, [4]babba@yumsuk.edu.ng, [5]mrwudil@gmail.com

Abstract

In this paper, we derived two important properties, viz: moment and order statistics, for the Hybrid Weibull-Exponential Power actuarial reliability model. We considered Bayesian procedures for estimating the parameters of the model. We tested the performance of the estimation approach by means of simple Monte Carlo experiment, hence, found the estimator consistent for the model parameters. Subsequently, we utilized the Bayesian inferential technique to further explore the overall adequacy the model in real—life through two sets of failure time reliability data. However, at the complexity point of the Bayesian method in dealing with the complex posterior of the model, we ushered-in the robust Hamiltonian Monte Carlo simulation algorithm, and thus, swiftly enhanced the posterior inference. The Add-on MLE examination on the model parameters was briefly conducted to additionally check the model's performance in real life. On the premise of the evaluation criteria and goodness-of-fit statistics results obtained from the MLE computation, we, once again, found clearly that the model is superior among the similar models compared. The HWEP model is, thus, apt for reliability analyses of dual failures as well as dual-component failed systems.

Keywords: Bayesian, parameter estimation, statistical reliability, Hamiltonian Monte Carlo, simulation algorithm

I. Introduction

Recently, Alhassan et al. [1], established four-parameter hybrid Weibull exponential power (HWEP) life casting distribution based on actuarial reliability assumption. The model, thus, describes the actual failure of dual-component systems when either or both of the components cease to function. It also applies in the analysis of dual failures in a system. Assuming that the behavior of either of the failures (or failed components), respectively follow the Weibull or exponential power distribution. The HWEP model was formulated based on the additive failure rate methodology [17]. [1] showed that, to a higher significance than several models, the distribution fits much adequately in modeling times-to-failure data such as the benchmark dataset in [9], and generally, life data. [1] also observed that the hazard rate (HR) of the grand HWEP distribution assumes increasing trend at $\alpha = 1.0$ and $\tau = 1.5$, and also, reveals a decreasing pattern at $\alpha = 0.8$ and $\tau = 2.5$. Additionally, its HR follows the rule of the legend bathtub trend at $\alpha = 14$ and $\tau = 0.15, 0.35, 0.55$ and 0.75 respectively, among other values tuning. Thus, validate its appropriateness in monitoring and providing unbiased assessment of the entire system lifecycle. Other notable reliability attributes such as the survival, mean residual life and mean time-to-failure, have been obtained and elaborated in [1]. And so, point to the model's adequateness in system reliability, especially the series systems. Furthermore, the give and take relationship between HWEP's HR and mean residual life functions in describing the complete life cycle of engineered systems, was shown. The ML estimators for the model parameters were also proven consistent.

In the current paper, we aim to explore the suitability of the Bayesian estimators for estimating the HWEP model parameters under the quadratic error loss function, succored by the robust Hamiltonian Monte Carlo (HMC) algorithm for posterior simulation. The HMC technique promotes swift and successful Bayesian computations especially in situations where the posterior density of the target distribution appears analytically complex. Its power in prevailing over such abnormalities in real practices has been shown by Betancourt and Girolami [8], by delving into its role in hierarchical modeling. In practice, many authors leveraged the power of the HMC algorithm to enhance their inferential computations. For instance, with the help of HMC technique for enhanced precision, Abba et al. [4], performed Bayesian computations of the Flexible Dhillon-Weibull Competing Risks model, hence, accurately led to a swift inference of the model's complex posterior. Al-Essa et al. [6], used the HMC algorithm to sample from the posterior, and verified the Bayes estimates of the Modified Exponential-Weibull model, eventually, the estimates were found accurate. [16], provided Bayesian analysis of the Additive Chen-Weibull model via the HMC method and found the algorithm effective for parameter convergence. [15], successfully delivered an extensive Bayesian study for Improved New Modified Weibull distribution by means of HMC method. See also [5], and the Refs within. Thus, the notable outcomes catalyzed by the HMC technique in the above literature motivated our proposal to use the HMC-guided Bayesian paradigm for the inferential analysis of our HWEP model. So, for the purpose of achieving our goal, we (I) explore further distributional and reliability properties of the HWEP model (II) employ the HMC algorithm in order to enhance the Bayesian posterior computations, (III) simulate and assess the performance of the estimator by means of simple Monte Carlo technique, (IV) apply the HWEP model on another benchmark dataset to further prove the model's firm significance in reliability studies.

Following the foregoing preamble and objectives, the paper is, moreover, categorized this way: supplementary properties of the HWEP model in both probability and reliability contexts are contained in section II. HMC fortified Bayesian computations are given in Section III. Simulation experiment for evaluating the Bayes estimates is given in section IV. Demonstration to further iterate the relevance of the HWEP model in system reliability is provided in section V using failure times dataset. Section VI wraps up the paper.

II. Methods

I. Supplementary Properties of the HWEP Model

In the previous publication [1], we established the HWEP reliability and survival model, and discussed some of its properties relating to both probability and reliability perspectives. Such as the PDF, CDF and survival function respectively given below:

$$\mathbb{g}(t;\alpha,\gamma,\nu,\tau)=\left[\alpha\gamma^{\alpha}\,t^{\alpha-1}+\tau\nu(\nu t)^{\tau-1}e^{(\nu\,t)^{\tau}}\right]e^{-(\gamma t)^{\alpha}-e^{(\nu t)^{\tau}}+1},t>0. \tag{1}$$

$$R(t;\alpha,\gamma,\nu,\tau)=e^{-(\gamma t)^{\alpha}-e^{(\nu t)^{\tau}}+1},t>0. \tag{2}$$

$$\mathbb{G}(t;\alpha,\gamma,\nu,\tau)=1-e^{-(\gamma t)^{\alpha}-e^{(\nu t)^{\tau}}+1},t>0. \tag{3}$$

The parameter vector is $\boldsymbol{\xi}=(\alpha,\gamma,\nu,\tau)'$; where, $\alpha,\tau>0$ and $\gamma,\nu\geq 0$ dually represent the corresponding shape and scale parameters. Here, we present additional properties of the novel HWEP model in respect of the said perspectives in our subsequent discussions.

a) Moment

The role of moments is pivotal in the establishment of probability distributions. They can be utilized to generate many distributional properties such as the measures of central tendency, skewness and kurtosis. Suppose that the random variable $T\sim HWEP(\boldsymbol{\xi})$, then the rth raw moment of T is given as:

$$\mathbb{E}[t^{r}]=\mu_{r}'=\int_{0}^{\infty}t^{r}d\mathbb{G}(t). \tag{4}$$

Then, using (3), we have

$$=\int_{0}^{\infty}t^{r}d1-e^{-(\gamma t)^{\alpha}-e^{(\nu t)^{\tau}}+1}=-\int_{0}^{\infty}t^{r}de^{-(\gamma t)^{\alpha}-e^{(\nu t)^{\tau}}+1},$$

$$=\int_{0}^{\infty}rt^{r-1}e^{-(\gamma t)^{\alpha}-e^{(\nu t)^{\tau}}+1}\,dt=\sum_{k,\ell=0}^{\infty}\frac{(-1)^{k}k^{\ell}\nu^{\ell\tau}}{k!\,\ell!}\int_{0}^{\infty}rt^{\ell\tau+r-1}e^{-(\gamma t)^{\alpha}}dt.$$

Let $y=(\gamma t)^{\alpha}\Longrightarrow\frac{dy}{dt}=\alpha\gamma(\gamma t)^{\alpha-1}\Longrightarrow\frac{dy}{\alpha}=\gamma(\gamma t)^{\alpha-1}dt$. Thus,

$$\mu_{r}'=\frac{r}{\alpha}\sum_{k,\ell=0}^{\infty}\frac{(-1)^{k}k^{\ell}\nu^{\ell\tau}}{k!\,\ell!}\gamma^{-(\ell\tau+1)}\int_{0}^{+\infty}y^{\frac{\ell\tau+r}{\alpha}-1}e^{-y}dy. \tag{5}$$

Where, $t^{\ell\tau+r}=\gamma^{-(\ell\tau+r)}((\gamma t)^{\alpha})^{\frac{\ell\tau+r}{\alpha}}$ and $\int_{0}^{+\infty}y^{\frac{\ell\tau+r}{\alpha}-1}e^{-y}dx\sim\Gamma\left(\frac{\ell\tau+r}{\alpha}\right)$. Thus,

$$\mu_{r}'=\frac{r}{\alpha}\sum_{k,\ell=0}^{\infty}\frac{(-1)^{k}k^{\ell}\nu^{\ell\tau}}{k!\,\ell!}\Gamma\left(\frac{\ell+r}{\alpha}\right),r=1,2,\ldots \tag{6}$$

b) Order statistics

It is important that we derive the pdf of the rth order statistic $T_{(r)}$ of the HWEP model's random sample $T_{i,\{1\le i\le n\}}$ with parameter vector $(\boldsymbol{\xi})$. Thus, reference to [7], the pdf of $T_{(r)}$ is given by:

$$\mathbb{g}_{r:n}(t) = \frac{1}{B(r, n-r+1)}[\mathbb{G}(t)]^{r-1}[1-\mathbb{G}(t)]^{n-r}\mathbb{g}(t), \tag{7}$$

where, $B(.,.)$, is the beta function. While $\mathbb{G}(t) = 1 - e^{-H(t)}$ with $e^{-H(t)} = R(t)$ and $\mathbb{g}(t) = \hbar(t)R(t)$.

As for HWEP model, the hazard and cumulative hazard functions are respectively [1]: $\hbar(t) = \alpha\gamma^{\alpha}\, t^{\alpha-1} + \tau\nu^{\tau}t^{\tau-1}e^{(\nu t)^{\tau}}$ and $H(t) = (\gamma t)^{\alpha} + e^{(\nu t)^{\tau}} - 1$. Meanwhile, we have

$$[\mathbb{G}(t)]^{r-1} = \left[1 - e^{-H(t)}\right]^{r-1} = \sum_{\hbar=0}^{r-1}\binom{r-1}{\hbar}(-1)^{\hbar}e^{-\hbar H(t)}, \tag{8}$$

and

$$[1-\mathbb{G}(t)]^{n-r} = e^{-(n-r)H(t)}. \tag{9}$$

Thus, putting (8) and (9) into (7), we have

$$\mathbb{g}_{r:n}(t) = \frac{1}{B(r, n-r+1)}\sum_{\hbar=0}^{r-1}\binom{r-1}{\hbar}(-1)^{\hbar}\hbar(t)e^{-(n+\hbar+1-r)H(t)},$$

$$= n\binom{n-r}{r-1}\sum_{\hbar=0}^{r-1}\binom{r-1}{\hbar}(-1)^{\hbar}\left(\alpha\gamma^{\alpha}\, t^{\alpha-1} + \tau\nu^{\tau}t^{\tau-1}e^{(\nu t)^{\tau}}\right)e^{-(n+\hbar+1-r)\left((\gamma t)^{\alpha}+e^{(\nu t)^{\tau}}-1\right)},$$

$$\mathbb{g}_{r:n}(t) = n\binom{n-r}{r-1}\sum_{\hbar=0}^{r-1}\binom{r-1}{\hbar}\frac{(-1)^{\hbar}}{(n+\hbar+1-r)}\mathbb{g}(t;\alpha,\gamma,\nu,\tau). \tag{10}$$

Where, $\mathbb{g}(t;\alpha,\gamma,\nu,\tau)$ is the pdf of HWEP model with parameters $\alpha, \gamma^{*} = (n+\hbar+1-r)\gamma, \nu_e = \nu + ln(n+\hbar+1-r)$ and τ.

II. Inferential Procedures for the HWEP Model

Here, we present the HWEP's parameter estimation by Bayesian procedures and give succinct explanation on the HMC technique.

In reliability context and otherwise, Bayesian methods hold expedient position over the frequentist approaches for providing simply conceptual approach in handling complex situations. This is for their incorporation of the prior information concerning the parameters of the population beforehand. Thus, appropriate prior selection significantly decides the outlook of Bayesian tests. Further, of most advantageous part of the Bayesian modelling to reliabilists is their applicability in dealing with the two common problematic features of reliability data, viz censoring and small sample sizes. Besides, also provide strong probabilistic interpretations. Refer to [11]. Perhaps, in complicated form of models involving high-dimensional integrals, inferences based on posterior samples may be rationally hard to work out. Albeit the situations may be low-dimensional. We will touch this aspect in our subsequent discussions. Now, we propose to estimate the HWEP's parameters by Bayes method. Assume the times of failure, $\mathfrak{D}$: $t_1, t_2, \ldots, t_n$, resulting from life test of n units, are the data observed and let the distribution in Eq. (1) be of the times of failure. Then, we have the equivalent likelihood, $\mathbb{L}(\mathfrak{D}|\boldsymbol{\xi})$, as:

$$\ell(T|\alpha,\gamma,\nu,\tau)=\prod_{i=1}^{n}\left[\alpha\gamma^{\alpha}t_i^{\alpha-1}+\tau\nu^{\tau}t_i^{\tau-1}e^{(\nu t_i)^{\tau}}\right]\exp\left\{-\sum_{i=1}^{n}\left[(\gamma t_i)^{\alpha}+e^{(\nu t_i)^{\tau}}-1\right]\right\}. \quad (11)$$

Next, we assume an independent vague gamma prior, $P(\boldsymbol{\xi})$, for $\boldsymbol{\xi}=(\alpha,\gamma,\nu,\tau)'$, out of no prior information on the values of the parameters, thus, the inference is data-driven. Subsequent to the effective outcomes of gamma priors chosen by [10], [16], [5], etc. Thus, we have

$$P(\boldsymbol{\xi})=\frac{\delta_k^{\beta_k}}{\Gamma(\beta_k)}\boldsymbol{\xi}^{\beta_k-1}e^{-\delta_k\xi_k},k=1,2,3,4,$$

where, $\delta_k,\beta_k>0$ are the hyperparameters, usually considered known beforehand in Bayesian analysis [10, 16]. While the constant, $\frac{\delta_k^{\beta_k}}{\Gamma(\beta_k)'}$ which ensures the density's integration to unity, will be overlooked. Thus, the parameters hierarchically and independently follow a gamma prior of the form

$$P(\boldsymbol{\xi})=\boldsymbol{\xi}^{\beta_k-1}e^{-\delta_k\xi},\delta_k,\beta_k>0,k=1,2,3,4,$$

where, $\boldsymbol{\xi}=(\alpha,\gamma,\nu,\tau)'$. Thus, $\alpha\sim P(\alpha|\delta_1,\beta_1)$, $\gamma\sim P(\gamma|\delta_2,\beta_2)$, $\nu\sim P(\nu|\delta_3,\beta_3)$ and $\tau\sim P(\tau|\delta_4,\beta_4)$, depending on their hyper-parameters. Consequently, the joint prior is given as:

$$P(\boldsymbol{\xi})=P(\alpha|\delta_1,\beta_1)P(\gamma|\delta_2,\beta_2)P(\nu|\delta_3,\beta_3)P(\tau|\delta_4,\beta_4).$$

Hence, up to proportionality to the product of the prior and the likelihood, we can obtain the joint posterior, through the Bayes theorem, as:

$$P(\boldsymbol{\xi}|\mathfrak{D})\propto\alpha^{\beta_1-1}\gamma^{\beta_2-1}\nu^{\beta_3-1}\tau^{\beta_4-1}\exp\left\{-\sum_{i=1}^{n}\left[(\gamma t)^{\alpha}+e^{-(\nu t_i)^{\tau}}-1\right]\right\}$$
$$\times\exp\{-\delta_1\alpha-\delta_2\gamma-\delta_3\nu-\delta_4\tau\}\prod_{i=1}^{n}\left[\alpha\gamma^{\alpha}t_i^{\alpha-1}+\tau\nu(\nu t_i)^{\tau-1}e^{-(\nu t_i)^{\tau}}\right]. \quad (12)$$

Yielding the posterior marginal densities of α,γ,ν and τ respectively as:

$$P(\alpha|\mathfrak{D})\propto\alpha^{\beta_1-1}\prod_{i=1}^{n}\left[\alpha\gamma^{\alpha}t_i^{\alpha-1}+\tau\nu(\nu t_i)^{\tau-1}e^{-(\nu t_i)^{\tau}}\right]exp\left\{\sum_{i=1}^{n}\left[-(\gamma t)^{\alpha}-\delta_1\alpha+1\right]\right\},$$
$$P(\gamma|\mathfrak{D})\propto\gamma^{\beta_2-1}\prod_{i=1}^{n}\left[\alpha\gamma^{\alpha}t_i^{\alpha-1}+\tau\nu(\nu t_i)^{\tau-1}e^{-(\nu t_i)^{\tau}}\right]exp\left\{\sum_{i=1}^{n}\left[-(\gamma t)^{\alpha}-\delta_2\gamma+1\right]\right\},$$
$$P(\nu|\mathfrak{D})\propto\nu^{\beta_3-1}\prod_{i=1}^{n}\left[\alpha\gamma^{\alpha}t_i^{\alpha-1}+\tau\nu(\nu t_i)^{\tau-1}e^{-(\nu t_i)^{\tau}}\right]exp\left\{\sum_{i=1}^{n}\left[-e^{-(\nu t_i)^{\tau}}-\delta_3\nu+1\right]\right\},$$
$$P(\tau|\mathfrak{D})\propto\tau^{\beta_4-1}\prod_{i=1}^{n}\left[\alpha\gamma^{\alpha}t_i^{\alpha-1}+\tau\nu(\nu t_i)^{\tau-1}e^{-(\nu t_i)^{\tau}}\right]exp\left\{\sum_{i=1}^{n}\left[-e^{-(\nu t_i)^{\tau}}-\delta_4\tau+1\right]\right\},$$

Then, we determine the Bayes estimators of the unknown parameters under square error loss function. Denote $\xi_i,i=1,\ldots,4$ to represent α,γ,ν and τ respectively, thus, we have

$$\hat{\xi}_{i_{BE}}=\mathbb{E}(\xi_i|\mathfrak{D})=\int\xi_iP(\boldsymbol{\xi}|\mathfrak{D})d\boldsymbol{\xi},$$
$$\hat{\hbar}_{BE}(t)=\mathbb{E}(\hbar(t;\boldsymbol{\xi})|\mathfrak{D})=\int\hbar(t;\boldsymbol{\xi})P(\boldsymbol{\xi}|\mathfrak{D})d\boldsymbol{\xi},$$
$$\hat{R}_{BE}(t)=\mathbb{E}(R(t;\boldsymbol{\xi})|\mathfrak{D})=\int R(t;\boldsymbol{\xi})P(\boldsymbol{\xi}|\mathfrak{D})d\boldsymbol{\xi}.$$

Conversely, the above equations may not easily be handled to attain the promising Bayesian Estimates (BEs) due to the intricate form of the posterior. Elsewise, alternate sample-based approaches like the MCMC techniques offer simply handy solutions, may such settings emerge, more so, the Metropolis-Hastings (MH) and Gibbs samplers.

However, their limitations such as the random walk behaviors render them ineffective toward dealing with the objective model. Particularly when the parameters are highly correlated or in high dimensional situations. Refer to Gupta *et al*. [10], Thach and Bris [15, 16], Abba *et al.* [2] among others. On the other hand, we opt for the HMC technique.

- Hamiltonian Monte Carlo Simulation Algorithm

Hamiltonian Monte Carlo algorithm, an instance of a unique MCMC algorithm, generalizes the MH method, was first used in statistics by Neal [13] on neural network models for Bayesian learning. By default, it works on all continuous positive objective distributions [16]. By borrowing a physics concept known as Hamiltonian dynamics (HDs) which describe objects' timely change rates upon a friction-free surface, based on their collective potential, $\mathcal{U}(\mathscr{v})$ and kinetic, $\mathcal{K}(\mathscr{k})$ energies, i.e Hamiltonian $[\mathcal{U}(\mathscr{v}) + \mathcal{K}(\mathscr{k})]$. Instead of using a probability model, the HMC suggests future states for the Markov chain through the HDs which uses the partial derivatives of the log of the posterior $[lnP(\boldsymbol{\xi}|\mathfrak{D})]$ with respect to the parameter vector, $\boldsymbol{\xi}$. By this notion, it restrains the MH sampler's actions of the random walk and its sensitiveness towards correlated settings among parameters. Thus, enables significant fusion and exploring through the target model more swiftly. See [2] for an excellent elaboration on the HMC methods. In this respect, this study adopts the HMC algorithm for posterior samples simulation using No-U-Turn Sampler (NUTS), a version of the HMC, in RStudio 4.3.0. Thus, easily draw inferences based on the samples. Now, for a drawn sample $\{\boldsymbol{\xi}_i, i = 1,2, \dots, N\}$ out of posterior density $\mathcal{P}(\boldsymbol{\xi}|\mathfrak{D})$. For significant enough i, insofar as larger than n_0, say, so that we have the sample $\{\boldsymbol{\xi}_i, i = n_0 + 1, \dots, N\}$ out of the actual posterior. Next, the BEs of the parameters α, γ, ν and τ with the corresponding $h(t)$ and $R(t)$ of the HWEP model can approximately be computed, each from their means as:

$$\hat{\bar{\boldsymbol{\xi}}}_{BE} \approx \frac{1}{N - n_0} \sum_{i=n_0+1}^{N} \boldsymbol{\xi}_i,$$

$$\hat{\mathscr{h}}_{BE}(t) \approx \frac{1}{N - n_0} \sum_{i=n_0+1}^{N} \mathscr{h}(t; \boldsymbol{\xi}_i),$$

$$\hat{R}_{BE}(t) \approx \frac{1}{N - n_0} \sum_{i=n_0+1}^{N} R(t; \boldsymbol{\xi}_i),$$

where, $\hat{\bar{\boldsymbol{\xi}}} = (\hat{\alpha}, \hat{\gamma}, \hat{\nu}, \hat{\tau})'$ is the one-to-one estimate of $\boldsymbol{\xi} = (\alpha, \gamma, \nu, \tau)'$. The warm-up stage, n_0, denotes the total iterations prior to determining the stationary samples. Further, for convergence assessment of sampler, $\mathscr{k}$ parallel chains are usually computed (say, $\mathscr{k} = 3, 4\ or\ 5$) in preference to a single chain. Thus,

$$\hat{\bar{\boldsymbol{\xi}}}_{BE} \approx \frac{1}{\mathscr{k}(N - n_0)} \sum_{\substack{0 \le j \le \mathscr{k} \\ n_0+1 \le i \le N}} \boldsymbol{\xi}_{i,j},$$

$$\hat{\mathscr{h}}_{BE}(t) \approx \frac{1}{\mathscr{k}(N - n_0)} \sum_{\substack{0 \le j \le \mathscr{k} \\ n_0+1 \le i \le N}} \mathscr{h}\left(t; \boldsymbol{\xi}_{i,j}\right),$$

$$\hat{R}_{BE}(t) \approx \frac{1}{\mathscr{k}(N - n_0)} \sum_{\substack{0 \le j \le \mathscr{k} \\ n_0+1 \le i \le N}} R\left(t; \boldsymbol{\xi}_{i,j}\right),$$

where, $\hat{\bar{\boldsymbol{\xi}}} = (\hat{\alpha}, \hat{\gamma}, \hat{\nu}, \hat{\tau})'$ is the one-to-one estimate of $\boldsymbol{\xi} = (\alpha, \gamma, \nu, \tau)'$.

III. Simulation Experiment

The MLEs for the HWEP parameters were proven consistent in our prior publication [1]. Now, we justify the efficiency of the Bayes estimators. The proposed Bayes estimators of HWEP parameters were evaluated through the simulation experiment by adequately utilizing the R function, inverseCDF(p, CDF, ...) from HDInterval package. Where p is an n-size vector of probabilities q_j, j = 1, 2, …, n and the dots (…) denote the parameters to be passed to the CDF. For instance, for n = 1000,$\boldsymbol{\xi} = (\alpha = 14, \gamma = 0.00026, \nu = 0.00021, \tau = 0.75)'$. The steps are: (i) some starting values for $\boldsymbol{\xi} = (\alpha, \gamma, \nu, \tau)'$ and K sample sizes were picked; (ii) since the exact solution for HWEP's quantile function in [1] does not exist, then, the nonclosed form equation of the quantile function given in [1] was utilized to sample from the HWEP distribution by applying the R function mentioned above; (iii) n = 1000 samples of size K=20, 30,.., 300 were drawn and employed to obtain the posterior means, biases and mean squared errors (MSEs) for the HWEP parameters, $\boldsymbol{\xi} = (\alpha, \gamma, \nu, \tau)'$, for 1000 iterations, however, discard 50% as warm-up samples. The results are presented in Table 4.

IV. Further Applicability of the HWEP Model in Reliability Context

Further showcase of the HWEP model's reliability potential is done through the Bayesian inferential procedure using two bathtub FT datasets presented in Tables 1 and 2 respectively. Four-chain set of samples drawn from HMC procedure were adopted for the posterior computations and plotting using RStan package in RStudio. Additional MLE computation is briefly presented using Nelder Mead and BFGS optimizers in R. Again, the models for the comparative performance study are the Improved New Modified Weibull (INMW) [15], Additive Chen-Weibull (ACW) [16] and Flexible Additive Chen-Gompertz (FACG) [3]. The comparative benchmark criteria include the log-likelihood value (-ℓ), Akaike information criterion (AIC), Bayesian information criterion (BIC), Corrected AIC (AICc), Kolmogorov-Smirnov (KS), Anderson-Darling (AD), Cramér-von Mises (CVM) as well as the empirical FR plots. The case studies are as follows.

- Time to First Failures (TTFFs) of 500 Megawatt (MW) Generators

The thirty-six TTFFs of 500MW generators first used by [9], is a bathtub FR dataset. It was applied by Alhassan et al. [1] and Xu et al. [18] for evaluating the MLEs of HWEP and q-Weibull distributions respectively. It is given below.

Table 1: *TTFFs of 500MW generators (in 1000's of hours)*

0.058	0.070	0.090	0.105	0.113	0.121	0.153	0.159	0.224
0.421	0.570	0.596	0.618	0.834	1.019	1.104	1.497	2.027
2.234	2.372	2.433	2.505	2.690	2.877	2.879	3.166	3.455
3.551	4.378	4.872	5.085	5.272	5.341	8.952	9.188	11.399

- Failure and Running Times (FRTs) of Devices

The dataset in Table 2, originally used by [11], is of failure and running times of thirty devices, and was later adopted enormously in the reliability literature, for instance, see Refs. [12, 4, 14, 16].

Table 2: *FRTs of 30 devices*

2	10	13	23	23	28	30	65	80	88
106	143	147	173	181	212	245	247	261	266
275	293	300	300	300	300	300	300	300	300

Two FMs viz: electrical surge which predominated the product's early-life stage and normal product wear during the unit's wear-out phase, were observed for this dataset [11]. These coincide with a vital assumption for the proposed HWEP model [1].

III. Results

I. Simulation experiment

The results obtained from the Monte Carlo experiment for evaluating the BEs of HWEP parameters are presented in Table 3. These include the mean estimates, biases and MSEs for three distinct preset parameter values. The mean parameter values, biases and MSEs were used as the basis for evaluating the consistency of the Bayes estimators for the HWEP model parameters. Five different sample sizes were used.

Table 3: *Simulation results for evaluating BEs*

	(α = 0.6, γ = 0.2, ν = 1.0, τ = 5.0)				(α = 0.7, γ = 0.4, ν = 0.2, τ = 4.4)				(α = 0.9, γ = 0.6, ν = 0.7, τ = 0.8)			
	Means											
K	$\hat{\alpha}$	$\hat{\gamma}$	$\hat{\nu}$	$\hat{\tau}$	$\hat{\alpha}$	$\hat{\gamma}$	$\hat{\nu}$	$\hat{\tau}$	$\hat{\alpha}$	$\hat{\gamma}$	$\hat{\nu}$	$\hat{\tau}$
20	0.6240	0.2151	0.9981	5.0208	0.7639	0.4194	0.1989	4.4748	0.9258	0.6711	0.7658	0.8876
30	0.6004	0.2000	1.0000	5.0023	0.7715	0.4059	0.1994	4.4032	0.9575	0.6609	0.7481	0.8363
50	0.6000	0.2000	1.0000	5.0000	0.7203	0.4020	0.1997	4.3463	0.9341	0.6526	0.7257	0.8287
100	0.6000	0.2000	1.0000	5.0000	0.7046	0.4014	0.1998	4.3650	0.9046	0.6396	0.7128	0.8248
300	0.6000	0.2000	1.0000	5.0000	0.7023	0.4000	2.0000	4.3895	0.9142	0.6461	0.7273	0.8231
	Biases											
20	-0.3849	0.4240	-0.0019	0.0208	-0.2806	0.3639	-0.0011	0.0748	0.1658	-0.3742	-0.0289	0.0876
30	-0.4010	0.4004	0.0000	-0.0004	-0.2941	0.3715	-0.0006	0.0032	0.1481	-0.3425	-0.0391	0.0363
50	-0.4000	0.4000	0.0000	0.0000	-0.2980	0.3203	-0.0003	-0.0537	0.1257	-0.3659	-0.0474	0.0287
100	-0.4000	0.4000	0.0000	0.0000	-0.2986	0.3046	-0.0002	-0.0350	0.1128	-0.3954	-0.0604	0.0248
300	-0.4000	0.4000	0.0000	0.0000	-0.3000	0.3023	0.0000	-0.0105	0.1273	-0.3858	-0.0539	0.0231
	MSEs											
20	0.1527	0.2192	2e-04	0.0514	0.0885	0.2080	4e-04	0.1542	0.0563	0.2143	0.0254	0.0570
30	0.1600	0.1603	0.0000	0.0005	0.0880	0.2073	0.0000	0.1098	0.0434	0.1752	0.0196	0.0218
50	0.1600	0.1600	0.0000	0.0000	0.0900	0.1555	0.0000	0.1044	0.0238	0.1978	0.0150	0.0095
100	0.1600	0.1600	0.0000	0.0000	0.0893	0.1105	0.0000	0.0734	0.0168	0.1957	0.0129	0.0090
300	0.1600	0.1600	0.0000	0.0000	0.0900	0.0931	0.0000	0.0130	0.0244	0.1898	0.0121	0.0086

II. Bayesian inference

In each case study, appropriate values were assigned to the hyper-parameters defined in section II, and then, respectively, 4-parallel chains of posterior samples were drawn out of the posterior marginal densities. $n_0 = 1000$ were counted out as warm-up samples and the subsequent $N - n_0$ fraction was utilized to get the respective BEs ($\hat{\alpha}_{BE}$, $\hat{\gamma}_{BE}$, $\hat{v}_{BE}$ and $\hat{\tau}_{BE}$) of the underlying parameters. Relative to the datasets used, Table 4 and Table 5, respectively, contain the BEs and MTTFs of the HWEP components, with their corresponding Highest Posterior Density Intervals (HPDIs).

a) TTFFs of 500MW Generators

Table 4: *BEs with 95% HPDIs for the HWEP parameters and MTTF for the TTFFs data.*

	Bayes		
Parameters	Estimates	SDs	95% HPDIs
$\hat{\alpha}$	1178.1	11.987	[1155.0, 1200.6]
$\hat{\gamma}$	0.0877	7.0e-5	[0.0876, 0.0878]
$\hat{v}$	0.2000	0.0254	[0.1507, 0.2478]
$\hat{\tau}$	0.5823	0.0596	[0.4723, 0.7055]
MTTF	0.3475	0.0425	[0.2658, 0.4280]

b) FRTs of Devices

Table 5: *BEs with 95% HPDIs for the HWEP parameters and MTTF for the FRTs data.*

	Bayes		
Parameters	Estimates	SDs	95% HPDIs
$\hat{\alpha}$	0.7272	0.1343	[0.4744, 0.9783]
$\hat{\gamma}$	0.0027	0.0010	[0.0010, 0.0046]
$\hat{v}$	0.0027	0.0003	[0.0021, 0.0032]
$\hat{\tau}$	5.6009	3.8613	[0.6930, 13.484]
MTTF	22.873	2.5246	[18.250, 27.250]

III. Maximum Likelihood Inference for the FRTs of Devices

As a complement to the HWEP's performance demonstration in reliability modelling of FTs data via the MLE procedure as in [1], we again use the dataset in Table 2 to explore further. We present the results in Table 6, consisting of the selected comparative models based on six evaluation criteria.

Table 6: *MLEs and the comparison metrics (p-values in parentheses) for FRTs dataset*

Model	Optimized parameters	$-\ell$	AIC	BIC	AICc	KS	AD	CVM
HWEP	$\hat{\alpha}$ = 0.7365, $\hat{\gamma}$ = 0.0028, $\hat{v}$ = 0.0028, $\hat{\tau}$ = 5.6226	140.99	289.972	295.576	291.572	0.2675 (0.0273)	1.1498 (0.0044)	0.1760 (0.0100)
ACW	$\hat{\alpha}$ = 0.0016, $\hat{\beta}$ = 285.37, $\hat{\gamma}$ = 0.2670, $\hat{\lambda}$ = 0.0130	142.52	293.045	298.650	294.645	0.2818 (0.0171)	1.6310 (0.0003)	0.2660 (0.0007)
FACG	$\hat{\gamma}$ = 0.2672, $\hat{\alpha}$ = 0.0130, $\hat{\theta}$ = 289.86, $\hat{\lambda}$ = 0.7097	142.52	293.045	298.650	294.645	0.2818 (0.0171)	1.6306 (0.0003)	0.2659 (0.0007)
INMW	$\hat{\alpha}$ = 0.0026, $\hat{\beta}$ = 0.0148, $\hat{\gamma}$ = 0.6533, $\hat{\theta}$ = 154.30, $\hat{\lambda}$ = 0.0025	141.87	293.738	300.744	296.238	0.2783 (0.0192)	1.5153 (0.0005)	0.2459 (0.0013)

IV. Discussion

I. Simulation experiment

Using nlminb package in R, we carried out simple Monte Carlo experiment to evaluate the consistency of our Bayes estimators. Negligible biases can be observed, and with the increase in sample sizes, the biases and MSEs tend to zero. In addition, the mean estimator values returned simulate the initial assigned values. Thus, showing the consistency of the estimators.

II. Bayesian inference

We can see from Table 4 and Table 5, respectively, that our BEs have been well contained by their narrow corresponding HPDIs with minimal SDs, thus, indicating consistent BEs under quadratic error loss function. Also, comparing both categories with the results of the MLEs obtained in [1], one can observe that the estimates and the intervals are respectively similar. Hence, we can reasonably infer that both estimates are satisfactory. Moreover, the posterior plots in column (a) of Figure 1 show the trace plots for the 4-parallel chains HMC simulation for TTFFs dataset. The traces vividly reveal that all the chains for a specific parameter unite rapidly with the same aiming model. While in (b) column, the estimated posterior densities for the parameters can be seen approximately distributed symmetric over the center points. Both results empirically justify the existence of consistent Bayes estimates under the quadratic loss function. Although, the posterior density curve for the scale parameter, γ, insignificantly skewed rightward. With regards to the trace plots in Figure 2(a) of the chains obtained from the HMC posterior simulation for the FRTs dataset, the same outcome can be observed as in Figure 1(a). While, the densities estimated for the parameters in Figure 2(b) can be seen insignificantly skewed leftward. Albeit, the leftward shift appears significant for the shape parameter, τ. Save the scale parameter, v, which in contrast slightly skewed rightward. For the skewness observed in the posterior curves for the above parameters, posterior mode can be appropriately considered as the best estimate. The nature of the HMC traces for the chains in both case studies prove the precision of the HMC technique in handling the HWEP's complex posterior.

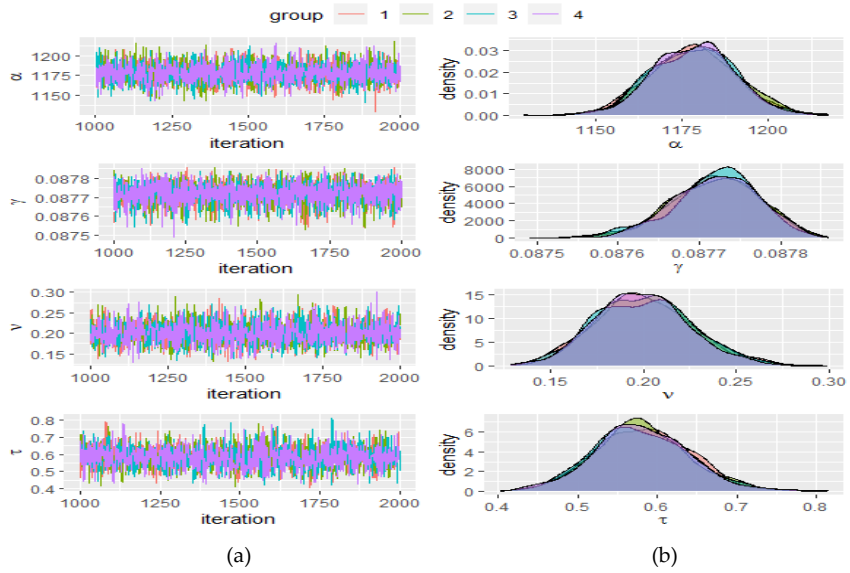


Figure 1: *(a) Trace and (b) Density curves for the BEs using HMC algorithm for the TTFFs of 500MW data.*

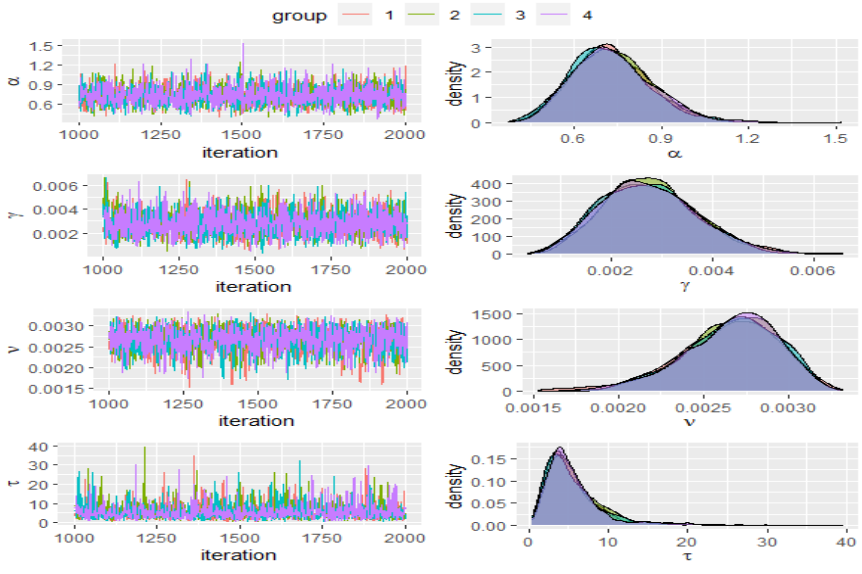


Figure 2: (a) *Trace and* (b) *Density curves for the BEs using HMC algorithm for the FRTs data*

III. Maximum Likelihood Inference for the FRTs of Devices

Moreover, we can observe from Table 6 that the HWEP model has the least likelihood ($-\ell$) value and also the minimal value of all the performance statistics among the compared models. Thus, the novel HWEP model performs better than the rest of the distributions, for describing the FRTs dataset. Figure 5 depicts the performance ranking of the models.

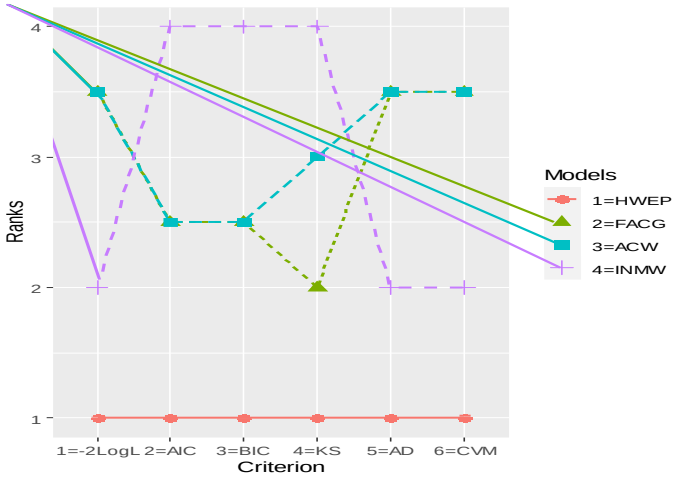


Figure 5: *Line plots showing the rankings of the trained models for FRTs data.*

Furthermore, the resulting FR curves shown in Figure 3 and 4 describing the TTFFs and FRTs dataset respectively, reveal that the HWEP model more accurately describe the FR of both datasets better than the rest of the models. Because the FR of the HWEP model follow approximately the path of the histogram of the data better than the rest of the distributions in both cases.

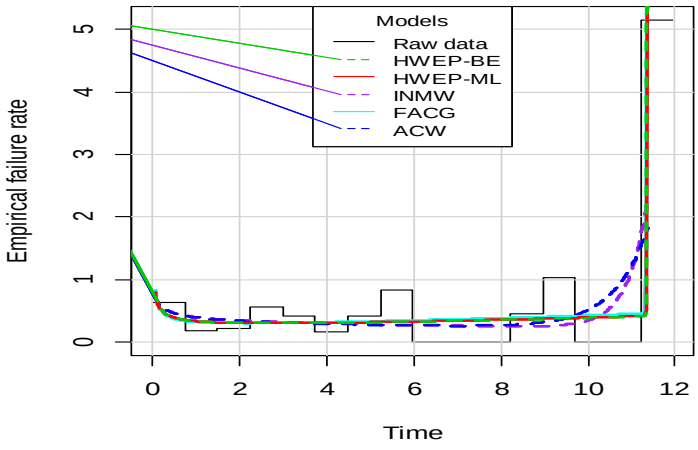


Figure 3: *Fitted FR curves for the compared models on TTFFs data*

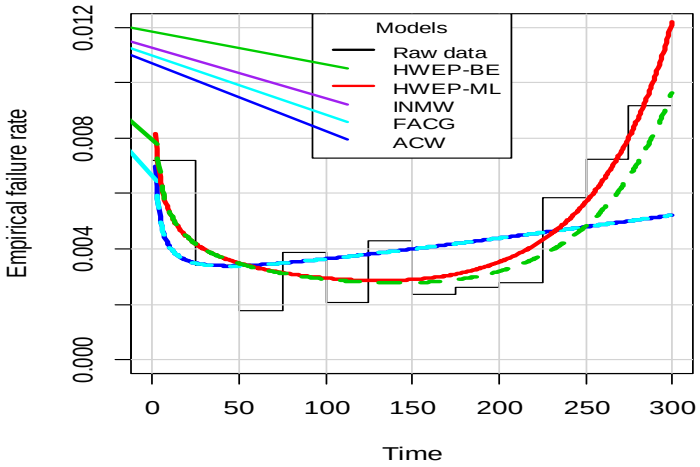


Figure 4: *Fitted FR curves for the compared models on FRTs data.*

IV Summery

In this paper, we further defined important properties of, and have given an adequate Bayesian study for the HWEP model introduced in our previous paper [1]. The HMC phenomenon successfully addressed the complexity found in the HWEP's posterior density, thus, simplified the entire Bayesian computation. We found the estimator consistent thru simulation study. We proved the fitness of the HWEP model in reliability testing on two reference datasets. Supplementary to [1], we gave an MLE computation and once again, the HWEP model out-performed all the compared models for the FTs analyzed based on the evaluation criteria. In conclusion, either the Bayesian or MLE can be used for estimating the HWEP model parameters since the estimators yield similar values. The HWEP model can better be used for describing the two datasets and other similar FTs. The HWEP model's role in Bayesian forecasting and competing risks testing can further be explored.

Funding

This research received no specific grant from any funding agency in the public, commercial or not-for-profit sectors.

Declaration of Conflict of Interest

The authors declare that there is conflict of interest

References

[1] Alhassan, M. A., Yahaya, A., Ishaq, O. O., Abba, B. and Muhammad, A. B. (2025). A bathtub additive failure rate model for actuarial reliability. *Journal of Reliability Theory and Applications*. 84(20): 903-917.

[2] Abba, B. and Wang H. (2023). A new failure times model for one and two failure modes system: A Bayesian study with Hamiltonian Monte Carlo simulation. *Proceedings of the Institution of Mechanical Engineers, Part O: Journal of Risk and Reliability*. 0(0).

[3] Abba, B., Wang, H. and Bakouch, H. (2022). A reliability and survival model for one and two failure modes system with applications to complete and censored datasets. *Reliability Engineering and System Safety*, 223, 108460. http://doi.org/10.1016/j.ress.2022.108460.

[4] Abba, B., Wang, H., Muhammad, M. and Bakouch, H. S. (2023). A robust bathtub-shaped failure time model for a two-component system with applications to complete and censored reliability data, Qual. Technol. Quant. Manag. 1–31, http://doi:10.1080/16843703.2023.2193771.

[5] Abba, B., Wu, J., and Muhammad, M. (2024). A robust multi-risk model and its reliability relevance: A Bayes study with Hamiltonian Monte Carlo methodology. *Reliability Engineering and System Safety*. https://doi.org/10.1016/j.ress.2024.110310.

[6] Al-Essa, L. A., Muhammad, M., Tahir, M. H., Abba, B., Xiao, J. and Jamal, F. (2023). A new flexible four parameter bathtub curve failure rate model and its application to right-censored data. *IEEE Access*, vol. 11, pp. 50130-50144, http://doi: 10.1109/ACCESS.2023.3276904.

[7] Arnold B. C., Balakrishnan N. and Nagaraja H. N. A First Course in Order Statistics. Wiley, New York, 1992.

[8] Betancourt, M. & Girolami, Mark. (2013). Hamiltonian Monte Carlo for hierarchical models. http://doi.org/10.1201/b18502-5.

[9] Dhillon, B. S., (1981). Life distributions. *IEEE Transactions on Reliability*, R-30(5), 457-460.

[10] Gupta, A., Mukherjee, B. and Upadhyay, S. K. (2008). Weibull extension model: A Bayes study using Markov Chain Monte Carlo simulation. *Reliability Engineering and System Safety,* 93, 1434–1443.

[11] Meeker, W. Q. and Escobar, L. Statistical methods for reliability data. Wiley, New York, 1998.

[12] Mohammad, H., Alamri, F., Nasser, H. and EL-Helbawy, A. (2024). The additive Xgamma-Burr XII distribution: properties, estimation and applications. *Symmetry*. 16. 659. http://doi.org/10.3390/sym16060659.

[13] Neal, R. M. (1996). *Bayesian learning for neural networks* (Lecture notes in statistics 118). New York: Springer.

[14] Sarhan, A. & Apaloo, J. (2013). Exponentiated modified Weibull extension distribution. *Reliability Engineering & System Safety*, 112, 137–144.

[15] Thach, T. and Bris, R. (2020). Improved new modified Weibull distribution: A Bayes study using Hamiltonian Monte Carlo simulation. *Proceedings of the Institution of Mechanical Engineers, Part O: Journal of Risk and Reliability*, 234, 1748006X1989674.

[16] Thach, T. and Bris, R. (2021). An additive Chen-Weibull distribution and its applications in reliability modeling. *Quality and reliability Engineering*, 37(1): 352-373.

[17] Xie, M. and Lai, C. D. (1996). Reliability analysis using an additive Weibull model with bathtub-shaped failure rate function. *Reliability Engineering and System Safety*, 52(1): 87-93, ISSN 0951-8320. https://doi.org/10.1016/0951-8320(95)00149-2.

[18] Xu, M., Droguett, E., Lins, I. and Moura, M. (2016). On the q-Weibull distribution for reliability applications: an adaptive hybrid artificial bee colony algorithm for parameter estimation. *Reliability Engineering and System Safety*. 158.

RT&A, No 4 (89)
Volume 20, December 2025

PERFORMANCE AND COST ANALYSIS OF A GI/M(a,b)/1 QUEUE WITH COMPULSORY AND EXTENDED REPAIRS DURING MULTIPLE WORKING VACATIONS

E. Praveena*, K. Julia Rose Mary

•

Department of Mathematics, Nirmala College for Women, Coimbatore, India
* praveenamaths1027@gmail.com
juliakulandaisamy@gmail.com

Abstract

The paper analyses a single-server queuing model with general distribution arrival and batch service under multiple working vacations, incorporating both compulsory and extended repairs. Customers receive service in groups following a general bulk service approach, instead of being served one at a time. Each service batch requires a minimum of 'a' and maximum of 'b' customers. The study considers two types of repairs—compulsory and extended—and derives the steady-state equations, performance measures, and expected cost of the model. Finally, the impact of various parameters is illustrated in numerical analysis section and graphical representation

Keywords: General Distribution Arrival, Batch Service, Multiple Working Vacations, Compulsory Repair, Extended Repair, Performance Measures.

I. Introduction

The study of queuing systems with working vacations, batch service, and server repairs has attracted significant attention in recent years due to its wide range of real-world applications in manufacturing, telecommunications, healthcare systems, transportation, computer networks, cloud computing, banking services, call centers, and Maintenance & Repair Operations. Researchers have extensively examined the effect of bulk service schemes and repair mechanisms in various queuing environments with multiple working vacations.

Queueing Processes with Bulk Service is discussed in [16]. The concept of working vacations in queuing systems was introduced by [20]. Extensions of this idea were further explored by [21] who considered M/M/1 queue model with a single working vacation and analyzed system performance under varying arrival and service conditions. Non- Markovian Queuing System Mx/G/1 with Server Breakdown and Repair Times was analyzed in [11]. Cost Analysis of MAP/G(a,b)/1/N Queue with Multiple Vacations and Closedown Times, Quality Technology and Quantitative Management was examined by [19].

Queue with Breakdowns and interrupted Repairs was carried by [22]. Analysis of batch arrival bulk service queue with multiple vacation closedown essential and optional repair was examined

by [3]. M/G(a,b)/1 Queueing System with Breakdown and Repair, Stand-By Server, Multiple Vacation and Control Policy on Request for Re-Service was studied in [4]. M[X]/G (a, b)/1 queue with breakdown and delay time to two phase repairs under multiple vacation was analyzed in [6]. Bulk service queue with sever breakdown and repairs was analyzed by [9].

A study on M/G/1 feedback retrial, queue with subject to server breakdown and repair under multiple working vacation policy by [17]. Batch Arrival Poisson Queue with Breakdown and Repairs was developed by [8]. A queueing model with server breakdowns, repairs, vacations, and backup server includes the work of [10] who examined systems with server breakdowns and repairs. Performance Analysis of Retrial Queueing Model with Working Vacation, Interruption, Waiting Server, Breakdown and Repair was analyzed by [12]. Analytic and Computational Analysis of GI/Ma,b/c Queueing System was examined in [15].

Steady-state distributions and performance metrics such as mean queue length, server availability and system cost in Cost optimization of a heterogeneous server queuing system with breakdown was evaluated by [1]. Phase type Queuing model of server vacation, Repair and Degrading service with Breakdown, starting failure and breakdown was studied in [5]. Strategic Analysis of Retrial Ques with setup Times, Breakdown and Repairs was developed by [18]. Performance of a queuing system with heterogeneous arrivals and various types of breakdowns under multiple working vacations was studied by [13]. Performance of Queuing Model with the Busy Period Breakdown was analyzed by [14]. Cost Analysis of a Finite capacity Queue with Server Failures, Balking and Threshold -Driven Recovery Policy was evaluated in [2]. Batch arrival bulk service priority queue with multiple vacation, close down, setup, differentiate breakdown, and repair was analyzed in [7].

Based on previous research this paper analyzes a general distribution arrival batch service queuing model incorporating compulsory and extended repairs with working vacations and server breakdown.

II. Model Description

In the proposed model, the server processes customers in batches according to the General Bulk Service Rule (GBSR), originally introduced by Neuts (1967). Under this rule, the server initiates service only when there is at least 'a' customer in the system, and it can serve up to a maximum of 'b' customers in a single service cycle. Upon completing a service, if the number of waiting customers is less than or equal to 'b', the server serves all of them as one batch. If the number exceeds 'b', only the first 'b' customers are selected for the next service batch. The service time for a batch of size k where $a \le k \le b$ is assumed to be independent and identically distributed. When the system has fewer than 'a' customer, the server enters a working vacation mode. During this period, if the number of customers reaches or exceeds 'a', the server resumes service at a reduced rate, denoted by μ_v which follows an exponential distribution. If the number of customers is still below 'a', the server initiates another working vacation, forming a multiple working vacation (MWV) structure. Customer arrivals follow a general inter arrival (GI) distribution with arrival rate λ. The service time in the regular busy period is exponentially distributed with rate μ_r , while vacation durations service rate is exponentially distributed with rate η. Server breakdowns may occur in both operational modes, during working vacations, breakdowns follow a Poisson process with rate β_v. By considering let the breakdowns during regular busy periods occur follows at the rate of β_r . Once a breakdown occurs, the server undergoes one of two types of repair. A compulsory repair is performed immediately after the breakdown during regular busy period with a parameter ψ, regardless of system state. An extended repair is initiated during working vacation periods at parameter φ under specific conditions, such as after a failure during service continuation. Both types of repair are assumed to follow an exponential distribution with mean for compulsory and extended repairs. The system is

analyzed using a Discrete-Time Markov Chain (DTMC) framework observed at pre-arrival epochs. Under these assumptions, key performance metrics such as steady-state equations, performance measures, and expected cost of the model. are derived and evaluated.

III Discrete –Time Markov Chain Pre-Arrival Queue Length

Let t_n= 1, 2, 3, 4… represent the nth customer's arrival time. If the system is initially empty, let t_0= 0. The Laplace Stieltjes Transform of G(t) is represented as G*(θ), where θ ≥ 0. The inter arrival times { t_n, n = 1,2,3, 4….} are assumed to be independent and identically distributed with a general distribution function G(t) having a mean of 1/λ We examine a GI/M (a, b)/1 queue with multiple working vacations (MWV) and two types of server breakdowns. Let $N_q(t)$ be the number of customers in the queue at time t. Let Jn(t) = 0, 1 and 2 where server is in idle vacation, working vacation and regular busy period respectively. In this model the process {(Nq (t_n - 0), Jn); n ≥ 1} is an embedded Markov chain with state space Ƈ={(n≥0); J=1,2} U {0 ≤n ≤ a-1; J=0}.

At time t the system reaches steady state queue size probabilities given by

$$P_n^r(t)=\lim_{k\to\infty} Pr\{\text{Nq}\ (t_k-0)\ =\text{n},\ J_n\ =1\},\ \text{n}\geq 0$$

$$Q_n^v(t)=\lim_{k\to\infty} Pr\{\text{Nq}\ (t_k-0)\ =\text{n},\ J_n\ =2\},\ \text{n}\geq 0$$

$$R_n^i(t)=\lim_{k\to\infty} Pr\{\text{Nq}\ (t_k-0)\ =\text{n},\ J_n\ =0\},\ 0\leq \text{n}\leq \text{a-1}$$

Assuming the existence of steady-state probabilities P_n^r, Q_n^v *and* R_n^i which represents the probabilities that the server is in a regular busy period, working vacation period and idle respectively. Then

$$P_n^r=\lim_{t\to\infty} P_n^r(t);\ Q_n^v=\lim_{t\to\infty} Q_n^v(t);\ R_n^i=\lim_{t\to\infty} R_n^i(t)$$

During working vacation and regular busy period there will be n number of customers in the queue and the system has k (a ≤ k ≤ b) customers in service, whereas in idle period the number of customers in the queue and in the system are same.

We define b_k^r as the probability that k batches will be completed during an inter-arrival time at regular service rate μ_r as follows.

$$b_k^r\ =\ \int_0^\infty e^{-\mu_r t}\ \frac{(\mu_r t)^k}{k!}\ d\ G(t) \qquad\qquad k\geq 0$$

The probability that a working vacation time is longer than the interarrival time and k batches are served at a rate of μ_v during an inter-arrival time is defined as c_k^v where

$$c_k^v\ =\ \int_0^\infty e^{-\eta t}\ \ \frac{(e^{-\mu_v t})(\mu_v\ t)^k}{k!}\ dG(t) \qquad k\geq 0$$

Let d_k^{ia} represents the probability that the server comes back from vacation during the inter-arrival period and completes k services during that period at a rate of η. Then

$$d_k^{ia}\ =\ \int_0^\infty \sum_{i=0}^{k} \left\{ \int_0^t \eta e^{-\eta x}\ \frac{(\mu_v\ x)^t}{i!}\ e^{-\mu_v x}\ \frac{(\mu_r\ (t-x))^{k-i}}{(k-i)!}\ e^{-\mu_r(t-x)}\ dx \right\} dG(t) \quad k\geq 0$$

Taking e_k^v as the probability that a breakdown occurs at the rate of β_v while the server is in a working vacation period. Thereafter

$$e_k^v = \int_0^\infty e^{-\beta_v t} \frac{(\beta_v t)^k}{k!} dG(t), \qquad k \geq 0$$

Assuming f_k^r represents the probability that the server experiences a breakdown at the rate of β_r during a regular busy period. Then

$$f_k^r = \int_0^\infty e^{-\beta_r t} \frac{(\beta_r t)^k}{k!} dG(t), \qquad k \geq 0$$

Based on the previously defined probabilities steady state equations are formulated and the steady state solution at the pre-arrival time is computed by applying the displacement between the Markov chain states.

IV. Steady State Equations

I. During Regular Busy Period

$$P_n^r = \sum_{k=0}^{\infty} P_{kb+n-1}^r (b_k^r + f_k^r + \psi) + \sum_{k=0}^{\infty} Q_{kb+n-1}^v (d_k^{ia}) \quad n \geq 1 \tag{1}$$

$$P_0^r = \sum_{k=1}^{\infty} \sum_{j=a-1}^{b-1} P_{(k-1)b+j}^r (b_k^r + f_k^r + \psi) + \sum_{k=0}^{\infty} \sum_{j=a-1}^{b-1} Q_{(k-1)b+j}^v (d_k^{ia}) + R_{a-1}^i d_0^{ia} \tag{2}$$

II. During Working Vacation Period

$$Q_n^v = \sum_{k=0}^{\infty} Q_{kb+n-1}^v (c_k^v + e_k^v + \varphi) \qquad n \geq 1 \tag{3}$$

$$Q_0^v = \sum_{k=1}^{\infty} \sum_{j=a-1}^{b-1} Q_{(k-1)b+j}^v (c_k^v + e_k^v + \varphi) + R_{a-1}^i c_0^v \tag{4}$$

III. During Idle Period

$$R_n^i = R_{n-1}^i + \sum_{k=0}^{\infty} Q_{kb+n-1}^v (1 - \sum_{i=0}^{k} (c_i^v + d_i^{ia} + e_i^v + \varphi)) + \sum_{k=0}^{\infty} P_{kb+n-1}^r (1 - \sum_{i=0}^{k} (b_i^r + f_i^r + \psi)) \quad 1 \leq n \leq a-1 \tag{5}$$

$$R_0^i = \sum_{k=1}^{\infty} \sum_{j=a-1}^{b-1} Q_{(k-1)b+j}^v (1 - \sum_{i=0}^{k} (c_i^v + d_i^{ia} + e_i^v + \varphi + \sum_{k=1}^{\infty} \sum_{j=a-1}^{b-1} P_{(k-1)b+j}^r (1 - \sum_{i=0}^{k} (b_i^r + f_i^r + \psi))) + R_{a-1}^i (1 - (d_0^{ia} + c_0^v)) \tag{6}$$

Steady state solution is obtained with the help of the steady state equation.

V. Steady State Solution

Steady state solution is obtained by using forward shifting operator E on P_n^r *and* Q_n^v.

$$E(P_n^r) = P_{n+1}^r \quad \text{and} \quad E(Q_n^v) = Q_{n+1}^v$$

Hence the Equation (1) gives the non- homogeneous equation:

$$(E - \sum_{k=0}^{\infty} E^{kb}(b_k^r + f_k^r + \psi)) \; P_n^r = \sum_{k=0}^{\infty} Q_{kb+n}^v \; (d_k^{ia}) \qquad n \geq 0 \tag{7}$$

Where the Equation (3) gives the homogeneous equation:

$$(E - \sum_{k=0}^{\infty} E^{kb} \; (c_k^v + e_k^v + \varphi)) \, Q_n^v = 0 \qquad , \; n \geq 0 \tag{8}$$

Now to obtain P_n^r, Q_n^v *and* R_n^i, we consider $B^r(z^b)$, $C^v(z^b)$, $E^{Bv}(z^b)$ *and* $F^{Br}(z^b)$ to express the Probability Generating Function of b_k^r, c_k^v, e_k^v *and* f_k^r as follows:

$$B^r(z^b) = \sum_{k=0}^{\infty} b_k^r \, z^{kb} = G^*(\mu_r(1 - z^b)) \tag{9}$$

$$C^v(z^b) = \sum_{k=0}^{\infty} c_k^v \, z^{kb} = G^*\big(\eta + \mu_v(1 - z^b)\big) \tag{10}$$

$$E^{Bv}(z^b) = \sum_{k=0}^{\infty} e_k^v \, z^{kb} = G^*(\eta + \beta_v(1 - z^b)) \tag{11}$$

$$F^{Br}(z^b) = \sum_{k=0}^{\infty} f_k^r \, z^{kb} = G^*(\beta_r(1 - z^b)) \tag{12}$$

If $\rho = (\frac{\lambda}{b\mu}) < 1$, then the equation z= B (zb) has a unique root r_R inside (0,1). This result follows from the corresponding result of GI/M/1 model of Gross and Harris (1985), B^r (r_Rb) = r_R with 0< r_R< 1.

If η > 0 then the equation $G^*\big(\eta + \mu_v(1 - z^b)\big)$ has a unique root r_V in the interval (0,1), $(i.e)$
C^v $(r_V{}^b) = r_V$ with 0< r_v <1

If $0 < \beta_v < 1$ then the equation $E(z^b) =$ z has unique root $r_{\beta V}$ inside (0,1) then we have
$E^{Bv}\big(r_{\beta v}\,\mathrm{b}\big) = \beta_v$ with 0< β_v <1.

If $0 < \beta_r < 1$ then the equation F$(z^b) =$ z has unique root $r_{\beta R}$ inside (0,1) then we have
$F^{Br}\big(r_{\beta R}\,\mathrm{b}\big) = \beta_r$ with 0< β_r <1.

Hence the homogeneous difference equation (7) has a solution

$$Q_n^v = r_v{}^n \, Q_0^v \qquad n \geq 0 \tag{13}$$

And the non-homogeneous difference equation (8) has a solution as

$$P_n^r = (L \, r_R{}^n + M \, r_V{}^n) \, Q_0^v \qquad n \geq 0 \tag{14}$$

where $M = \frac{D(r_V{}^b)}{r_V - B(r_V{}^b) - E(r_V{}^b)}$ and $Dr_V{}^b = \sum_{k=0}^{\infty} r_V{}^{kb} \; (d_k^{ia}) = M(r_V - B \; (r_V{}^b) - E(r_V{}^b))$ (15)

Thus we get $P_n^r = \left[L r_R{}^n + \left(\sum_{k=0}^{\infty} r_V{}^{kb} \; (d_k^{ia}) \frac{r_V{}^n}{r_V - B(r_V{}^b) - E(r_V{}^b)} \right] Q_0^v \qquad where \; r_V \neq r_R$ (16)

The expression R_n^i is obtained by substituting Q_n^v and P_n^r from equations (13) & (14)

$$R_n^i = \left[L \left(\frac{1 - r_R - \beta_r + \psi}{1 - r_R} \right) \left(\frac{r_R{}^{a-1} - r_R{}^n}{1 - r_R{}^b} \right) + (M + 1) \left(\left(\frac{1 - r_V - \beta_v + \varphi}{1 - r_V} \right) \left(\frac{r_V{}^{a-1} - r_V{}^n}{1 - r_V{}^b} \right) \right) + \frac{r_V{}^{a-1} - r_V{}^n}{r_V{}^b \, (1 - r_V)} + \frac{r_V{}^b - r_V{}^a}{c_0^v \; r_V{}^b \, (1 - r_V)} \right] Q_0^v \qquad 0 \leq n \leq a - 1 \tag{17}$$

Thus, the steady state queue size probabilities are expressed in terms of Q_0^v and L.

Now L can be determined by substituting Q_n^v and P_n^r in Equation (2):

Thus, we have

$$L \left(\frac{r_R{}^a - r_R{}^b + [(\beta_r + \psi) + (b_0^r - (\beta_r + \psi))](r_R{}^b - r_R{}^{a-1})}{r_R{}^b (1 - r_R)} \right) = \frac{d_0^{ia}}{c_0^v} \left(\frac{r_V{}^a - r_V{}^b}{r_V{}^b (1 - r_V)} \right) - M \left(\frac{r_V{}^a - r_V{}^b + [(\beta_r + \psi) + (b_0^r - (\beta_r + \psi))](r_V{}^b - r_V{}^{a-1})}{r_V{}^b (1 - r_V)} \right) \tag{18}$$

Hence the steady state queue size probabilities of described model are expressed in terms of Q_0^v are becomes

$$Q_n^v = {r_V}^n\, Q_0^v \qquad n \geq 0 \tag{19}$$

$$P_n^r = (L{r_R}^n + M\,{r_V}^n)\, Q_0^v \qquad n \geq 0 \tag{20}$$

$$R_n^i = \left[L\left(\frac{1-r_R-\beta_r}{1-r_R}\right)\left(\frac{{r_R}^{a-1}-{r_R}^n}{1-{r_R}^b}\right) + (M+1)\left(\left(\frac{1-r_V-\beta_v}{1-r_V}\right)\left(\frac{{r_V}^{a-1}-{r_V}^n}{1-{r_V}^b}\right)\right) + \frac{{r_V}^{a-1}-{r_V}^n}{{r_V}^b(1-r_V)} + \frac{{r_V}^b-{r_V}^a}{c_0^v\,{r_V}^b\,(1-r_V)} \right] Q_0^v$$

$$0 \leq n \leq a-1 \tag{21}$$

where;

$$L = \left(\frac{{r_R}^b(1-r_R)}{({r_R}^a-{r_R}^b)+[(\beta_r+\psi)+((b_0^r-(\beta_r+\psi))(r_R{}^b-r_R{}^{a-1})}\right)\left[\frac{d_0^{ia}}{c_0^v}\left(\frac{{r_V}^a-{r_V}^b}{{r_V}^b(1-r_V)}\right)+\beta_v\left(\frac{{r_V}^{a-1}-{r_V}^b}{{r_V}^b(1-r_V)}\right) - M\left(\frac{({r_V}^a-{r_V}^b)+[(\beta_r+\psi)+(b_0^r-(\beta_r+\psi))](r_V{}^b-r_V{}^{a-1})}{r_V{}^b(1-r_V)}\right)\right]$$

$$M = \frac{\sum_{k=0}^{\infty} {r_V}^{kb}\; d_k^{ia}}{\beta_v+\varphi} = \left(\frac{1}{\beta_v+\varphi}\right)\left[\frac{\lambda\eta}{\left(\frac{\mu_r}{\lambda+\mu}-\frac{\mu_v}{\lambda+\mu_v+\eta}\right)}\left(\frac{\mu_r}{\lambda+\mu_r-r_v{}^b\mu_r}-\frac{\mu_v}{\lambda+\mu_r+\eta-r_v{}^b\mu_v}\right)\right]$$

$$d_0^{ia} = \lambda\eta\;;\; ; c_0^v = \frac{\lambda}{\lambda+\eta+\mu_v};\; b_0^r = \frac{\lambda}{\lambda+\beta_v}$$

By using normalizing conditions, the value of Q_0^v is calculated.

$$\text{(i.e.) } \sum_{n=0}^{\infty} P_n^r + \sum_{n=0}^{\infty} Q_n^v + \sum_{n=0}^{\infty} R_n^i = 1$$

Hence, $$(Q_0^v)^{-1} = L\left(h(r)\right) + (R+1)h(r_v) + \frac{1}{{r_V}^b(1-r_V)}\left(\frac{{r_V}^b-{r_V}^a}{c_0^v} + ({r_V}^{a-1}-{r_V}^b)\right) \tag{22}$$

where $$h(x) = \left[\frac{1}{1-x^b}\left(\frac{1-x-\beta_r}{1-x}\right)\right]\left(\frac{x^a-x^b}{1-x}+x^{a-1}\right)$$

Thus, the steady state queue size probabilities for the general arrival bulk service with types break down are given by

$$Q_n^v = {r_V}^n\; Q_0^v \qquad n \geq 0$$

$$P_n^r = (L{r_R}^n + M\,{r_V}^n)\, Q_0^v$$

$$R_n^i = \left[L\left(\frac{1-r_R-\beta_r+\psi}{1-r_R}\right)\left(\frac{{r_R}^{a-1}-{r_R}^n}{1-{r_R}^b}\right) + (M+1)\left(\left(\frac{1-r_V-\beta_v+\varphi}{1-r_V}\right)\left(\frac{{r_V}^{a-1}-{r_V}^n}{1-{r_V}^b}\right)\right) + \frac{{r_V}^{a-1}-{r_V}^n}{{r_V}^b(1-r_V)} + \frac{{r_V}^b-{r_V}^a}{c_0^v\,{r_V}^b\,(1-r_V)} \right] Q_0^v$$

$$0 \leq n \leq a-1$$

where Q_0^v is determined using equation (17).

VI. Performance Measures

I. Mean Queue Length

The mean queue length L_q of the model is as follows:

$$L_q = \sum_{n=0}^{\infty} nP_n^r + \sum_{n=0}^{\infty} nQ_n^v + \sum_{n=0}^{a-1} nR_n^i$$

By substituting P_n^r , Q_n^v *and* R_n^i it is termed that

$$L_q = \left[L\left(\xi(r_R)\right) + (M+1)\left(\xi(r_V)\right) + \frac{a(a-1)}{2}\left(\frac{{r_V}^{a-1}-{r_V}^b}{{r_V}^b(1-r_V)} + \frac{{r_V}^b-{r_V}^a}{c_0^v\,{r_V}^b(1-r_V)}\right)\right] Q_0^v \tag{23}$$

where $\xi(x) = \frac{x}{(1-x)^2} + \frac{1-x-\beta_r+\psi}{(1-x)(1-x^b)}\left(\frac{a(a-1)x^{a-1}}{2} + \frac{ax^a(1-x)-x(1-x^a)}{(1-x)^2}\right)$ and $c_0^v = \frac{\lambda}{\lambda+\eta+\mu_v}$

II. Probability Measures

Let P^v , P^b , P^i denote the probability that the server is vacation, busy, and idle respectively. Then we have,

$$P^v = \sum_{n=0}^{\infty} r_V{}^n \; Q_0^v = \left(\frac{1}{1-r_V}\right) Q_0^v$$

$$P^b = \sum_{n=0}^{\infty} \left(L\, r_R{}^n + M\, r_V{}^n\right) Q_0^v = \left(\frac{L}{1-r_R} + \frac{M}{1-r_V}\right) Q_0^v$$

$$P^i = \sum_{n=0}^{a-1} R_n^i$$
$$= \left(L\left(\frac{1-r_R-\beta_r+\psi}{1-r_R}\right)\left(\frac{r_R{}^{a-1}}{1-r_R{}^b}\right)+(M+1)\left(\frac{1-r_V-\beta_v+\varphi}{1-r_V}\right)\left(\frac{r_V{}^{a-1}}{1-r_V{}^b}\right)+\frac{r_V{}^{a-1}-r_V{}^n}{r_V{}^b\,(1-r_V)}+\frac{r_V{}^b-r_V{}^a}{c_0^v\; r_v{}^b\,(1-r_V)}-\right.$$
$$\left.L\left(\frac{1-r_R-\beta_r+\psi}{(1-r_R)(1-r_R{}^b)}\right)\left(\frac{1-r_R{}^a}{1-r_R}\right)-\;(M+1)\left(\frac{1-r_V-\beta_v+\varphi}{(1-r_V)(1-r_V{}^b)}\right)\left(\frac{1-r_V{}^a}{1-r_V}\right)\right)\; Q_0^v$$

VII. Sensitivity Analysis

Steady state probability values are computed based on the derived equations. These probabilities are systematically calculated and tabulated to provide a clear view of the systems behavior under the varying parameters. Additionally, graphical representations have been developed to visually illustrate the trends and variation's in probability values.

Based on the different values by considering $\lambda = 0.3$, $\mu_r = 2$, $\mu_v = 0.6$ and $\eta = 0.05$ and by varying batch size of "a" from 5 to 10, φ assumes the values from 0.02 to 0.05, ψ ranges from 0.1 to 0.5 probability values of the prescribed model is tabulated and graphically represented in Table 1 to 6 and Figure 1.

Table 1: *System size probabilities w.r.t φ and batch size 5*

φ	a	b	Ψ	Pv	Pb	Pi
			0.1	0.3542	0.3875	0.3483
			0.2	0.3389	0.4139	0.3362
0.02	5	12	0.3	0.3334	0.4235	0.3211
			0.4	0.3305	0.4285	0.3205
			0.5	0.3287	0.4315	0.3217
			0.1	0.3928	0.3507	0.3429
			0.2	0.3769	0.3761	0.333
0.03	5	12	0.3	0.371	0.3855	0.3294
			0.4	0.368	0.3903	0.3275
			0.5	0.3662	0.3932	0.3264
			0.1	0.4155	0.3619	0.3158
			0.2	0.3992	0.3876	0.3126
0.04	5	12	0.3	0.3933	0.389	0.3113
			0.4	0.3902	0.4019	0.2185
			0.5	0.3883	0.4049	0.2105
			0.1	0.4304	0.3238	0.3412
			0.2	0.414	0.3483	0.3315
0.05	5	12	0.3	0.4079	0.3573	0.3279
			0.4	0.4048	0.362	0.3261
			0.5	0.4029	0.3649	0.3205

Table 2: *System size probabilities w.r.t φ and batch size 6*

φ	a	b	Ψ	Pv	Pb	Pi
			0.1	0.3969	0.3619	0.3412
			0.2	0.3809	0.3876	0.3315
0.02	6	12	0.3	0.375	0.3970	0.3279
			0.4	0.372	0.4019	0.3261
			0.5	0.3701	0.4049	0.3205
			0.1	0.4371	0.3378	0.3252
			0.2	0.4206	0.3628	0.3167
0.03	6	12	0.3	0.4145	0.3720	0.3135
			0.4	0.4113	0.3767	0.3119
			0.5	0.4094	0.3797	0.3109
			0.1	0.4437	0.3483	0.308
			0.2	0.4375	0.3573	0.3051
0.04	6	12	0.3	0.4343	0.3620	0.3036
			0.4	0.4324	0.3649	0.3027
			0.5	0.4756	0.3147	0.3098
			0.1	0.4526	0.3478	0.2996
			0.2	0.4494	0.3524	0.2982
0.05	6	12	0.3	0.4474	0.3552	0.2974
			0.4	0.4371	0.3378	0.3252
			0.5	0.4206	0.3628	0.3167

Table 3: *System size probabilities w.r.t φ and batch size 7*

φ	a	b	Ψ	Pv	Pb	Pi
			0.1	0.4343	0.3394	0.3263
			0.2	0.4178	0.3645	0.3177
0.02	7	12	0.3	0.4118	0.3737	0.3145
			0.4	0.4086	0.3785	0.3129
			0.5	0.4067	0.3814	0.3119
			0.1	0.4753	0.3148	0.3099
			0.2	0.4585	0.3390	0.3025
0.03	7	12	0.3	0.4523	0.3479	0.2997
			0.4	0.4491	0.3526	0.2983
			0.5	0.4471	0.3554	0.2975
			0.1	0.482	0.3243	0.2937
			0.2	0.4757	0.3331	0.2912
0.04	7	12	0.3	0.4725	0.3376	0.2899
			0.4	0.4705	0.3404	0.2891
			0.5	0.5141	0.2916	0.2944
			0.1	0.491	0.3234	0.2856
			0.2	0.4877	0.3278	0.2844
0.05	7	12	0.3	0.4858	0.3306	0.2837
			0.4	0.4343	0.3394	0.3263
			0.5	0.4178	0.3645	0.3177

Table 4: *System size probabilities w.r.t φ and batch size 8*

φ	a	b	Ψ	Pv	Pb	Pi
			0.1	0.4674	0.3196	0.313
			0.2	0.4506	0.3440	0.3054
0.02	8	12	0.3	0.4445	0.3529	0.3026
			0.4	0.4413	0.3576	0.3011
			0.5	0.4393	0.3604	0.3002
			0.1	0.5087	0.2948	0.2965
			0.2	0.4918	0.3182	0.29
0.03	8	12	0.3	0.4856	0.3268	0.2876
			0.4	0.4823	0.3313	0.2864
			0.5	0.4803	0.3341	0.2856
			0.1	0.5153	0.3034	0.2812
			0.2	0.5091	0.3119	0.279
0.04	8	12	0.3	0.5059	0.3163	0.2779
			0.4	0.5039	0.3189	0.2772
			0.5	0.5473	0.2716	0.2811
			0.1	0.5243	0.3022	0.2735
			0.2	0.5211	0.3065	0.2724
0.05	8	12	0.3	0.5191	0.3091	0.2717
			0.4	0.4674	0.3196	0.313
			0.5	0.4506	0.3440	0.3054

Table 5: *System size probabilities w.r.t φ and batch size 9*

φ	a	b	Ψ	Pv	Pb	Pi
			0.1	0.4968	0.3019	0.3013
			0.2	0.4799	0.3256	0.2945
0.02	9	12	0.3	0.4737	0.3343	0.2919
			0.4	0.4705	0.3389	0.2906
			0.5	0.4685	0.3417	0.2898
			0.1	0.538	0.2772	0.2848
			0.2	0.5212	0.2998	0.279
0.03	9	12	0.3	0.515	0.3081	0.2769
			0.4	0.5118	0.3125	0.2758
			0.5	0.5098	0.3151	0.2751
			0.1	0.5613	0.2632	0.2755
			0.2	0.5447	0.2851	0.2703
0.04	9	12	0.3	0.5385	0.2932	0.2683
			0.4	0.5352	0.2974	0.2673
			0.5	0.5333	0.3000	0.2667
			0.1	0.5763	0.2542	0.2695
			0.2	0.5598	0.2756	0.2646
0.05	9	12	0.3	0.5536	0.2836	0.2628
			0.4	0.5504	0.2877	0.2619
			0.5	0.5484	0.2903	0.2613

Table 6: *System size probabilities w.r.t φ and batch size 10*

φ	a	b	Ψ	Pv	Pb	Pi
			0.1	0.5326	0.3059	0.2577
			0.2	0.5300	0.3085	0.2571
0.02	10	12	0.3	0.5274	0.3111	0.2565
			0.4	0.5248	0.3137	0.2559
			0.5	0.4982	0.3248	0.2872
			0.1	0.5066	0.3319	0.2517
			0.2	0.5040	0.3345	0.2511
0.03	10	12	0.3	0.5014	0.3371	0.2505
			0.4	0.4988	0.3397	0.2499
			0.5	0.4962	0.3423	0.2493
			0.1	0.4806	0.3579	0.2457
			0.2	0.4780	0.3605	0.2451
0.04	10	12	0.3	0.4754	0.3631	0.2445
			0.4	0.4728	0.3657	0.2439
			0.5	0.4702	0.3683	0.2433
			0.1	0.4546	0.3839	0.2397
			0.2	0.4520	0.3865	0.2391
0.05	10	12	0.3	0.4494	0.3891	0.2385
			0.4	0.4468	0.3917	0.2379
			0.5	0.4442	0.3943	0.2373

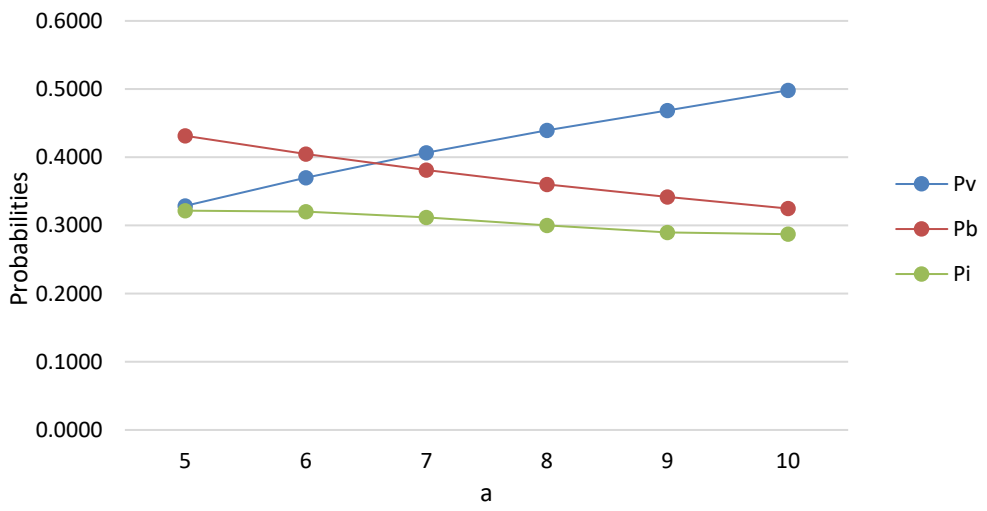


Figure 1: *System size probabilities w.r.t batch size 'a' where P_v , P_b and P_i are probabilities during working vacation Regular busy period and idle*

The graphical comparison states that as repair efficiency improves and batch size increases, the server transitions from idle and busy states into a more sustained working vacation mode. This shift helps to balance service continuity and repair flexibility, there by influencing overall system performance and expected cost. These finding emphasize the importance of tuning the system parameters to achieve optimal state probabilities for efficient queuing operations.

I. Expected cost

The expected cost (EC) for the prescribed model is formulated by combining various cost components associated with system behavior along with compulsory and extend repair for batch size of a= 5,6,7,8,9,10. As the total expected cost includes costs due to the customer waiting, server idle, during regular busy, working vacation, system breakdown, and repair rate during working vacation and regular busy periods. The expected cost is expressed as:

$$EC = C^v P^v + C^b P^b + C^i P^i + C^{BV} \beta_v + C^{BR} \beta_r + C^{CR} \psi^b + C^{EWV} \varphi^v + C^{LQ} L_q$$

where: C^v: Cost per unit time during working vacation period, P^v: Probability that the system is in working vacation, C^b: Cost incurred during Regular busy period, P^b: Probability that the system is in Regular busy period, C^i: Cost during the server is in idle P^i: Probability that the server is idle, C^{BV}: Breakdown cost during working vacation, β_v: Breakdown probabilities during working vacation C^{BR}: Breakdown cost during regular busy, β_r: Breakdown probabilities during regular busy, C^{CR}: Cost of compulsory repair during regular busy period, , ψ^b: probability of compulsory repair, C^{EWV}: Cost of extended repair during working vacation period, φ^v: probability of extended repair, C^{LQ}: Cost per customer waiting in the queue L_q (i.e.) Expected queue length.

By letting $\lambda = 0.3$, $\mu_R = 2$, $\mu_v = 0.6$ and $\eta = 0.05$ and by varying batch size of "a" from 5 to 10, $C^v = 5$, $C^b = 15$, $C^i = 5$, $C^{BV} = 200$, $C^{BR} = 250$, $C^{CR} = 175$, $C^{EWV} = 150$, $C^{LQ} = 25$, and for various values of ψ *and* φ the expected cost is calculated and tabulated in Table 7.

Table 7: *Expected cost for GI/M(a,b)/1/MWV with respect compulsory repair ψ and extended repair φ*

Φ	A	B	ψ	EC
			0.1	1658.861
			0.2	1554.603
0.02	5	12	0.3	1542.931
			0.4	1549.826
			0.5	1536.346
			0.1	1343.860
			0.2	1337.118
0.03	6	12	0.3	1334.684
			0.4	1331.417
			0.5	1328.898
			0.1	1250.039
			0.2	1254.183
0.04	7	12	0.3	1258.806
			0.4	1262.754
			0.5	1266.862
			0.1	1368.284
			0.2	1372.559
0.05	8	12	0.3	1376.164
			0.4	1381.260
			0.5	1386.657
			0.1	1387.569
			0.2	1398.217
0.06	9	12	0.3	1408.865
			0.4	1419.513
			0.5	1430.161
			0.1	1452.369
			0.2	1463.017
0.07	10	12	0.3	1471.665
			0.4	1484.313
			0.5	1490.961

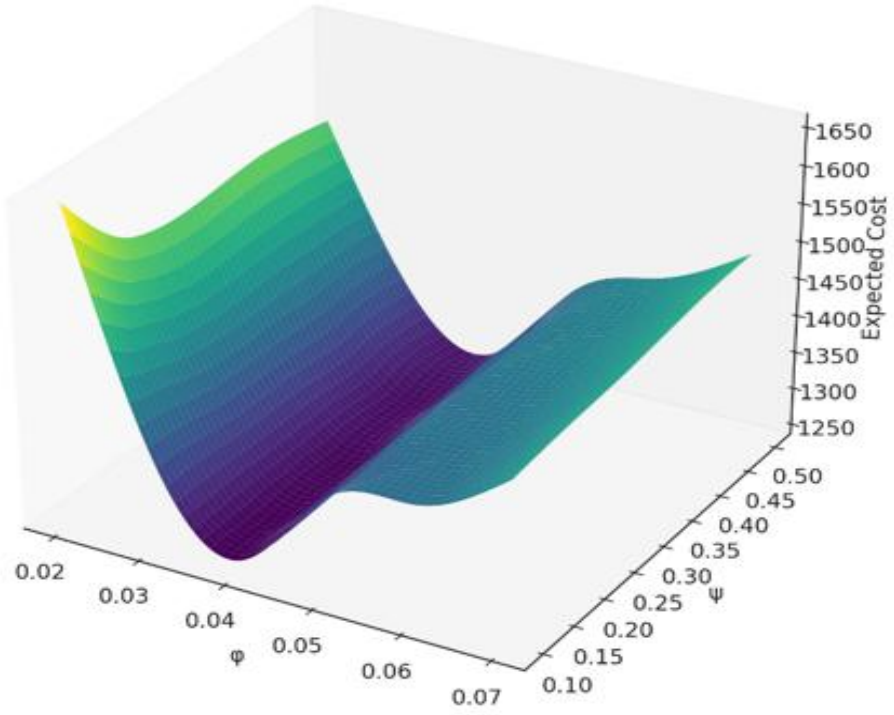


Figure 2: *Expected cost for GI/M(a,b)/1/MWV with respect to compulsory repair ψ and extended repair φ*

From the tabulated values and from the Figure 2, it is observed that the expected cost initially decreases as the repair rate increases. this is due to faster recovery from the breakdowns, leading to reduced waiting time s and improve server availability. However, beyond a certain point, further increases in the repair rate leads to a rise in the expected cost. this happens since very high repair rates along with larger batch sizes can make the system more complicated to manage and increase the overall cost. As both the repair rate and batch size increase simultaneously the system handles more customers per cycle which can introduce new delays or recourse strain. Therefore, the expected cost shows nonlinear U – shaped behavior, indicating that there exists an optimal range of repair rate and batch size where the system performs most cost effectively. Hence from φ is 0.04, EC equals 1250.039 we can conclude that the expected cost increases as the repair rate increases. This means that once the repair rate goes beyond 0.04, making repairs faster does not reduce the cost—instead, it causes the cost to go up. so, $\varphi = 0.04$ seems to be the optimal point, beyond which further increasing the repair rate becomes less efficient and costlier.

VIII. Conclusion

The analysis of the prescribed queuing model incorporating multiple working vacations, compulsory and extended repairs, and batch service reveal important trends in both system behavior and cost performance. The study shows that as key parameters such as repair rate and batch size vary, the systems operational states shift significantly. The probability of the working vacation state increases while the probabilities of the regular busy and idle states decrease indicating that the server remains more engaged in partial service modes under higher efficiency. In terms of cost analysis, the expected cost initially decreases with increase repair rate due to the improved service reliability and reduced downtime. However, beyond a certain threshold further increase in

repair rate and batch sizes results in raising expected costs, highlighting the tradeoff between service speed and operational complexity. This nonlinear behavior underlines the need to identify an optimal range of parameter values that minimizes system cost while maintaining performance. Hence this study results in understanding how the system behaves under different operating conditions, providing the guidance for designing and managing efficient queuing systems. In future the study can be extended to reduce the expected cost for the increase of repair rate, batch size and balking so as to maintain the service mechanism.

References

[1] Agarwal, R. Agarwal, D. and Upadhyaya, S. (2023). Cost optimization of a heterogeneous server queuing system with working breakdown using PSO. International Journal of Mathematics in Operational Research, 26:410-424.

[2] Amit Kumar, Savita, and Chandrashekar. (2024). Cost Analysis of a Finite capacity Queue with Server Failures, Balking, and Threshold -Driven Recovery Policy. International Journal of Mathematical Engineering and Management Sciences, 9:1198-1209.

[3] Ayyappan, G. and Deepa, T. (2018). Analysis of batch arrival bulk service queue with multiple vacation closedown essential and optional repair. Applications and Applied Mathematics, 13:578–598.

[4] Ayyappan, G. and Karpagam, S. (2018). An M[X]/G(a,b)/1 Queueing System with Breakdown and, Stand- By Server, Multiple Vacation and Control Policy on Request for Re-Service. MDPI. Mathematics, 6: 101.

[5] Ayyappan, G. and Meena, S. (2023). Phase type Queuing model of server vacation, Repair Degrading service with Breakdown, Starting failure and close-down, RT&A, 18: 464-483.

[6] Ayyappan, G. and Nirmala, M. (2018). An M[X]/G (a, b)/1 queue with breakdown and delay time to two phase repairs under multiple vacation. Applications and Applied Mathematics, 13:639–663.

[7] Ayyappan, G. and Nithya, S. (2025). Analysis of batch arrival bulk service priority queue with multiple vacation, close down, setup, differentiate breakdown, and repair. International Journal of Mathematics in Operational Research, 30: 1-21.

[8] Balasubramanian Sundar Rajan. Ganesan, V. Rita Samikannu. (2020). Batch Arrival Poisson Queue with Breakdown and Repairs. International journal of Mathematics in Operational research. 17:424-435.

[9] Bharathidass, S. Arivukkarasu, V. and Ganesan, V. (2018). Bulk service queue with sever breakdown and repairs. International Journal of Statistics and Applied Mathematics, 3:136-142.

[10] Chakravarthy, S. R. Shruti, and Kulshrestha, R. (2020). A queueing model with server breakdowns, repairs, vacations, and backup server. Operations Research- Perspectives, 7:100131.

[11] Deepak Gupta, Anjana Solank, and Agarwal, K.M. (2011). Non- Markovian Queuing System Mx/G/1 with Server Breakdown and Repair Times. Recent Research in Sciencand Technology, 3: 88-94.

[12] Gupta, P. and Kumar, N. (2022). Performance Analysis of Retrial Queueing Model with Working Vacation, Interruption, Waiting Server, Breakdown and Repair. Journal of Scientific Research, 13:833-84.

[13] Lidiya, P. and Julia Rose Mary, K. (2024). A study on the performance of a queuing system with heterogeneous arrivals and various types of breakdowns under multiple working vacations. Operations Research and Decisions, 34: 125-140.

[14] Lidiya, P. and Julia Rose Mary, K. (2024). Analyzing the Performance of Queuing Model with the Busy Period Breakdown. Baghdad Science Journal, 22: 235-241.

[15] Mohan Chaudhry. and Jing Gai. (2022). Analytic and Computational Analysis of GI/Ma,b/c Queueing System, MDPI's Mathematical Journal, 10: 3445.

[16] Norman, T. and Bailey, J. (1954). On Queueing Processes with Bulk Service,16: 80- 87.

[17] Rajadurai, P. Saravanarajan, M.C. Chandrasekaran, V. M. (2018). A study on M/G/1 feedback retrial, queue with subject to server breakdown and repair under multiple working vacation policy. Alexandria Engineering journal, 57:947-962.

[18] Ruiling Tian. Xinyu Wu. Liuqing He. Yunna Han. (2023). Strategic Analysis of Retrial Queues with Setup Times, Breakdown and Repairs. Discrete Dynamics in Nature and Society, 2023:1-19.

[19] Senthil Vadivu, A. and Arumuganathan, R. (2015). Cost Analysis of MAP/G(a,b)/1/N Queue with Multiple Vacations and Closedown Times. Quality Technology and Quantitative Management,12:605–626.

[20] Servi, L.D. and Finn, S.G. (2002). M/M/1 Queues with Working vacations (M/M/1/WV). Performance Evaluation, 50:41-52.

[21] Tian, N. (2007). The M/M//1 Queue with working vacation and vacation interruption. Journal of Systems Science and Systems Engineering,16:121-127.

[22] Yutae Lee. (2017). Queue with Breakdowns and interrupted Repairs. The International Journal of Engineering and Science (IJES), 6:36-38.

SURVIVAL ANALYSIS OF AREA BIASED GENERALIZED SAULEH DISTRIBUTION WITH STATISTICAL PROPERTIES AND APPLICATIONS

Dr. V. Arulmozhi[1], Dr. R. Sivaranjani[2], Dr. K. Poovizhi[3]

•

1. Assistant professor of Statistics, Community Medicine, SBMC&Hospital, Chromepet
2. Assistant professor of Statistics, Community Medicine, RMC& Hospital, Pennalur
3. Assistant professor of Statistics, Community Medicine, SMVMC&Hospital, Puducherry

Email: arulmozhiv16@gmail.com, sivaranjani160692@gmail.com, poovizhimsc2016@gmail.com

Abstract

The "Sauleh distribution" is a novel lifespan distribution that is suggested by this study. Among the statistical and mathematical features that have been discussed are the PDF and CDF. Numerous helpful statistical features are derived, including the Area Biased Generalized Sauleh distribution's hazard rate function, reverse hazard rate function, order statistics, moments, measure of skewness, and measure of kurtosis. It uses the well-known maximum likelihood outcome approach to estimate the parameter of the distribution. To demonstrate this distribution's adaptability and superiority over alternative distributions, a comparative analysis is conducted in the end. It establishes its significance in reliability engineering by producing a rich class of distributions that may capture various shapes and behaviors and, as a result, enable better fitting to empirical data. Real-world data sets are used to establish the use of this novel distribution. Melanoma patient survival data has demonstrated the effectiveness of the proposed distribution; it is concluded that the produced distribution provides a superior fit.

Keywords: Moments; Moment generating function; Survival function; Hazard function; Entropies; Maximum likelihood Estimation.

I. Introduction

In a variety of domains, including reliability, ecology, and healthcare, the idea of weighted distributions is used to create appropriate statistical models. For efficient statistical data modelling and prediction, weighted distributions have established a new standard when standard distributions are not suitable. Weighted distributions provide an approach to fitting the model to the unknown weight function when samples are taken from both the generated distribution and the original distribution. Weighted distributions are a concept that Fisher (1934) [6] devised to reflect the ascertainment bias.

Rao (1965) [14] later developed this concept in a unified way because the standard distributions failed to adequately capture these observations with equal probabilities in the statistical data model. By defining some of the circumstances in which the underlying model maintains its shape, Patil and Rao (1978) [11] developed the ideas of size biased sampling and weighted distributions. The weighted distribution turns into a length biased distribution when the weight function solely considers the length of the units of interest. A length-biased distribution was initially proposed by

Cox (1962) [5] in the context of the renewal hypothesis. In broader terms, a distribution is considered size biased if the sampling procedure selects units with a probability proportional to the unit size measure. One particular instance of size biased distributions is weighted distributions, a broader variation. The weighted distributions can be used to assess both the toughness of model formulation and the difficulties in interpreting the data. Numerous academics have studied and explored the various weighted probability models, demonstrating their applicability across a range of fields. When fitting distributions of dimension at breast height (DBH) data originating from horizontal point sampling (HPS) (Grosenbaugh) inventory, Van Deusen (1986) [20] independently created the size biased distribution theory. The size biased Zeghdoudi distribution was introduced by Chouia et al. (2021) [4], who also covered its numerous statistical characteristics and uses. In 1975, Patil and Ord examined size-biased sampling and the corresponding form-invariant weighted distribution [12].

The statistical properties and application of the length biased weighted Lomax distribution were discussed by Ahmad et al. (2016) [2]. Sharma et al. (2018) investigated the area-biased Maxwell distributions and the length-biased Maxwell distributions [15]. Ganaie and Rajagopalan (2020) [7] investigated the length biased weighted quasi gamma distribution with properties and applications. VM Jaimole, D Venkatesan Perveen (2016) [12] investigated the Area biased weighted weibull distribution with applications, introducing a new area biased two parameter Pranav distribution and its use in medical sciences (2022). The estimate of area-biased Rayleigh distribution parameters was examined by Rao and Pandey (2020) [14]. The estimation and definition of the Area biased quasi-Akash distribution were recently covered by Ade et al. (2021) [1].

A new lifetime distribution that is more adaptable than the Lindley, Exponential, Shanker, Pranav, Sujatha and Sauleh distributions can therefore be found.

II. Area Biased Generalized Sauleh distribution

The probability density function of Area Biased Generalized Sauleh distribution (ABGSD) is given by

$$f(x;\alpha,\beta,\theta)=\frac{\theta^4}{\theta^4+2\alpha\theta+6\beta}(\theta+\alpha x^2+\beta x^3)e^{-\theta x};x>0,\alpha>0\ ,\beta>0,\theta>0 \tag{1}$$

And the cumulative distribution function of Area Biased Generalized Sauleh distribution (ABGSD) is given by

$$F(x;\alpha,\beta,\theta)=1-\left[1+\frac{\theta x(\beta\theta^2x^2+(\alpha\theta+3\beta)\theta x+2(\alpha\theta+3\beta)}{\theta^4+2\alpha\theta+6\beta}\right]e^{-\theta x};x>0,\theta,\alpha,\beta>0 \tag{2}$$

$$f_a(x)=\frac{x^2f(x)}{E(x^2)} \tag{3}$$

$$E(x^2)=\int_0^\infty x^2f(x)dx$$

$$E(x^2)=\int_0^\infty x^2\frac{\theta^4}{\theta^4+2\alpha\theta+6\beta}(\theta+\alpha x^2+\beta x^3)e^{-\theta x}dx$$

$$E(x^2)=\frac{\theta^4}{\theta^4+2\alpha\theta+6\beta}\int_0^\infty x^2\,(\theta+\alpha x^2+\beta x^3)e^{-\theta x}dx$$

$$=\frac{\theta^4}{\theta^4+2\alpha\theta+6\beta}\left[\theta\int_0^\infty x^2\,e^{-\theta x}dx+\alpha\int_0^\infty x^4\,e^{-\theta x}dx+\beta\int_0^\infty x^5\,e^{-\theta x}dx\right]$$

$$=\frac{\theta^4}{\theta^4+2\alpha\theta+6\beta}\left[\theta\int_0^\infty x^{3-1}\,e^{-\theta x}dx+\alpha\int_0^\infty x^{5-1}\,e^{-\theta x}dx+\beta\int_0^\infty x^{6-1}\,e^{-\theta x}dx\right]$$

$$=\frac{\theta^4}{\theta^4+2\alpha\theta+6\beta}\left[\frac{\theta\Gamma3}{\theta^3}+\frac{\alpha\Gamma4}{\theta^4}+\frac{\beta\Gamma5}{\theta^6}\right]$$

$$= \frac{\theta^4}{\theta^4 + 2\alpha\theta + 6\beta}\left[\frac{2\theta}{\theta^3} + \frac{24\alpha}{\theta^4} + \frac{120\beta}{\theta^6}\right]$$

$$= \frac{\theta^4}{\theta^2 + \alpha\theta + 2}\left[\frac{2\theta^{11} + 24\alpha\theta^8 + 120\beta\theta^7}{\theta^7\theta^6}\right]$$

$$= \frac{\theta^4}{\theta^4 + 2\alpha\theta + 6\beta}\left[\frac{2\theta^4 + 24\alpha\theta + 120\beta}{\theta^7\theta^6}\right]\theta^7$$

$$= \frac{1}{\theta^4 + 2\alpha\theta + 6\beta}\left[\frac{2\theta^4 + 24\alpha\theta + 120\beta}{\theta^2}\right]$$

$$E(x^2) = \frac{2\theta^4 + 24\alpha\theta + 120\beta}{\theta^2(\theta^4 + 2\alpha\theta + 6\beta)} \tag{4}$$

The probability density function of the Area Biased Generalized Sauleh distribution (ABGSD) can now be obtained by substituting equations (1) and (4) into equation (3).

$$f_a(x) = \frac{x^2\theta^4}{(\theta^4 + 2\alpha\theta + 6\beta)}(\theta + \alpha x^2 + \beta x^3)e^{-\theta x} \times \frac{\theta^2(\theta^4 + 2\alpha\theta + 2\beta)}{2\theta^4 + 24\alpha\theta + 120\beta}$$

$$f_a(x) = \frac{x^2\theta^6}{2\theta^4 + 24\alpha\theta + 120\beta}(\theta + \alpha x^2 + \beta x^3)e^{-\theta x} \tag{5}$$

And the CDF of Area Biased Generalized Sauleh distribution can be obtained a

$$F_a(x) = \int_0^x f_a(x)dx$$

$$= \int_0^x \frac{x^2\theta^6}{(2\theta^4 + 24\alpha\theta + 120\beta)}(\theta + \alpha x^2 + \beta x^3)e^{-\theta x}$$

$$= \frac{1}{(2\theta^4 + 24\alpha\theta + 120\beta)}\int_0^x x^2\theta^6(\theta + \alpha x^2 + \beta x^3)e^{-\theta x}dx$$

$$= \frac{1}{(2\theta^4 + 24\alpha\theta + 120\beta)}\int_0^\infty \left[\theta^7\int_0^x x^2\, e^{-\theta x}dx + \alpha\theta^6\int_0^x x^4\, e^{-\theta x}dx + \beta\theta^6\int_0^x x^5\, e^{-\theta x}dx\right] \tag{6}$$

$$\text{Put } \theta x = t \Longrightarrow \theta dx = dt \Longrightarrow dx = \frac{dt}{\theta} \text{ also } x = \frac{t}{\theta}$$

$$F_a(x) = \frac{1}{(2\theta^4 + 24\alpha\theta + 120\beta)}\left[\theta^7\int_0^{\theta x}\left(\frac{t}{\theta}\right)^2 e^{-t}\frac{dt}{\theta} + \alpha\theta^6\int_0^{\theta x}\left(\frac{t}{\theta}\right)^4 e^{-t}\frac{dt}{\theta} + \beta\theta^6\int_0^{\theta x}\left(\frac{t}{\theta}\right)^5 e^{-t}\frac{dt}{\theta}\right]$$

$$F_a(x) = \frac{1}{(2\theta^4 + 24\alpha\theta + 120\beta)}[\theta^4\gamma(3,\theta x) + \alpha\theta\gamma(5,\theta x) + \beta\gamma(6,\theta x)] \tag{7}$$

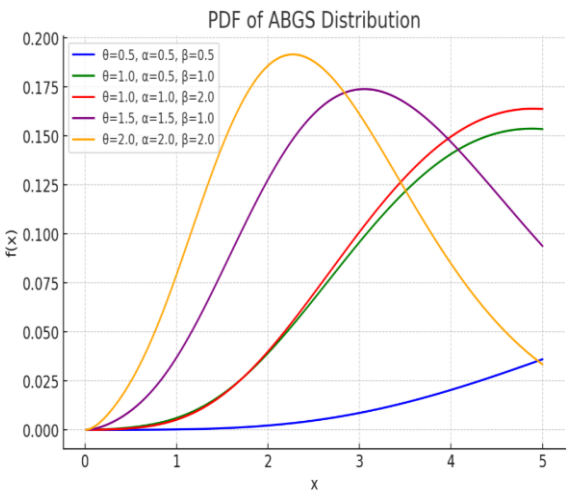


Figure 1: *PDF of the ABGSD*

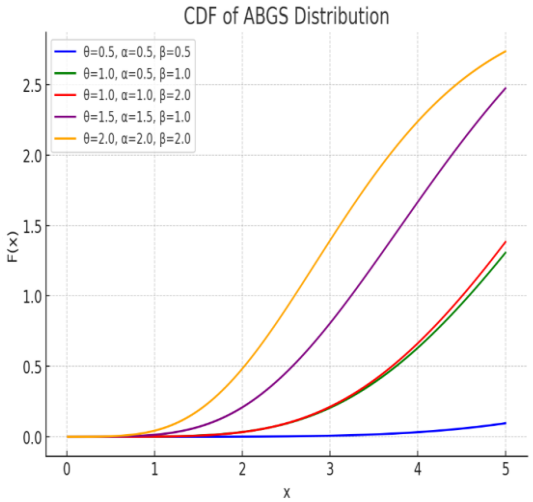


Figure 2: *CDF of the ABGSD*

III. Survival Analysis

The distribution's hazard function and reliability function are two crucial functions that we ascertain in this section. The survival function is another name for the reliability function. A system's likelihood of surviving past a given period of time is its definition. The following represents the reliability of a random variable x.

$$S(x) = 1 - F_a(x)$$

$$S(y) = 1 - \frac{1}{(2\theta^4 + 24\alpha\theta + 120\beta)}[\theta^4\gamma(3,\theta x) + \alpha\theta\gamma(5,\theta x) + \beta\gamma(6,\theta x)]$$

I. The Hazard function

The hazard function of the proposed is Area Biased Generalized Sauleh distribution obtained as

$$H(x) = \frac{f_a(x)}{S(x)} = \frac{x^2\theta^6(\theta + \alpha x^2 + \beta x^3)e^{-\theta x}}{(2\theta^4 + 24\alpha\theta + 120\beta) - \theta^4\gamma(3,\theta x) + \alpha\theta\gamma(5,\theta x) + \beta\gamma(6,\theta x)}$$

II. Reverse Hazard function

$$h_r(x) = \frac{f_a(x)}{F_a(x)} = \frac{x^2\theta^6(\theta + \alpha x^2 + \beta x^3)e^{-\theta x}}{(\theta^4\gamma(3,\theta x) + \alpha\theta\gamma(5,\theta x) + \beta\gamma(6,\theta x))}$$

III. Mills Ratio

$$M.R = \frac{1}{h_r(x)} = \frac{(\theta^4\gamma(3,\theta x) + \alpha\theta\gamma(5,\theta x) + \beta\gamma(6,\theta x))}{x^2\theta^6(\theta + \alpha x^2 + \beta x^3)e^{-\theta x}}$$

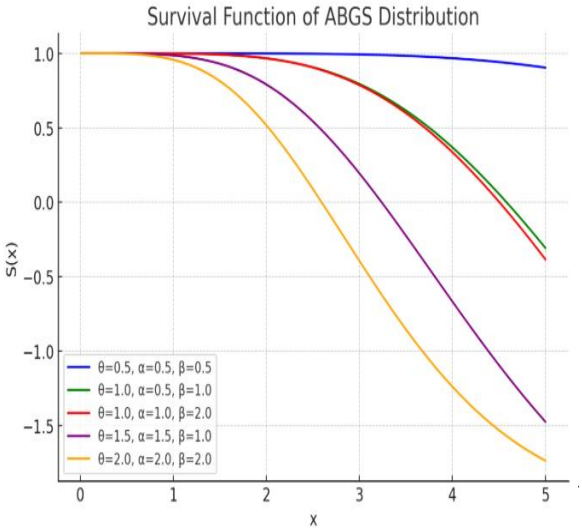


Figure 3: *Survival function ABGSD*

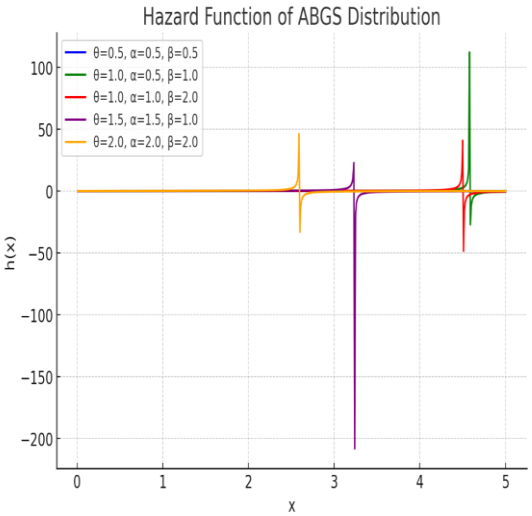


Figure 4: *Hazard function ABGSD*

IV. Statistical Properties

The statistical characteristics of the Area Biased Generalized Sauleh distribution, in particular its Order Statistics, Statistical moments, Harmonic mean, MGF, and characteristic function, are covered in this section.

I. Order Statistics

Assuming that $X_1, X_2, \ldots, X_n$ are random samples and that $X_{(1)}, X_{(2)}, \ldots, X_{(n)}$ are the order statistics of a random sample of size n taken from a continuous population with a probability density function $f_X(x)$ and a cumulative distribution function $F_X(X)$, the probability density function of rth order statistics $X_{(r)}$ can be found using

$$f_{X(r)}(x) = \frac{n!}{(r-1)!\,(n-r)!} f_X(x)[F_X(x)]^{r-1}[1-F_X(x)]^{n-r}$$

We will now obtain the probability density function of the rth order statistics of the Area Biased Generalized Sauleh distribution by substituting equations (5) and (7) in equation (8).

$$f_{X(r)}(x) = \frac{n!}{(r-1)!\,(n-r)!} \frac{x^2\theta^6}{(2\theta^4+24\alpha\theta+120\beta)}(\theta+\alpha x^2+\beta x^3)e^{-\theta x} \times \left[\frac{1}{(2\theta^4+24\alpha\theta+120\beta)}(\theta^4\gamma(3,\theta x)+\alpha\theta\gamma(5,\theta x)+\beta\gamma(6,\theta x))\right]^{r-1} \left[\frac{1}{(2\theta^4+24\alpha\theta+120\beta)}(\theta^4\gamma(3,\theta x)+\alpha\theta\gamma(5,\theta x)+\beta\gamma(6,\theta x))\right]^{n-r}$$

Consequently, the probability density function of the Area Biased Generalized Sauleh distribution higher order statistic $X_{(n)}$ may be found as

$$f_{X(n)}(x) = \frac{nx^2\theta^6}{2\theta^2+6\alpha\theta+2\theta^5}(\theta+\alpha x^2+\beta x^3)e^{-\theta x} \times \left[\frac{1}{(2\theta^4+24\alpha\theta+120\beta)}\left(\theta^4\gamma(3,\theta x)+\alpha\theta\gamma(5,\theta x)+\beta\gamma(6,\theta x)\right)\right]^{n-r}$$

Additionally, the probability density function of the Area Biased Generalized Sauleh distribution first order statistic $X_{(1)}$ may be found as

$$f_{X(1)}(x) = \frac{nx^2\theta^6}{(2\theta^4+24\alpha\theta+120\beta)}(\theta+\alpha x^2+\beta x^3)e^{-\theta x} \times \left[1-\frac{1}{(2\theta^4+24\alpha\theta+120\beta)}(\theta^4\gamma(3,\theta x)+\alpha\theta\gamma(5,\theta x)+\beta\gamma(6,\theta x))\right]^{n-r}$$

II. Moments

When X represents the random variable of the Area Biased Generalized Sauleh distribution with parameters θ and α, the rth order moment $E(X^r)$ of the Area Biased Generalized Sauleh distribution may be found as

$$E(X^r) = \mu_r' = \int_0^\infty x^r f_a(x)dx$$

$$= \int_0^\infty x^r \frac{x^2\theta^6}{(2\theta^4+24\alpha\theta+120\beta)}(\theta+\alpha x^2+\beta x^3)e^{-\theta x}$$

$$= \frac{\theta^6}{(2\theta^4+24\alpha\theta+120\beta)}\int_0^\infty x^{r+2}(\theta+\alpha x^2+\beta x^3)e^{-\theta x}dx$$

$$= \frac{\theta^6}{(2\theta^4+24\alpha\theta+120\beta)}\left[\theta\int_0^\infty x^{r+2}e^{-\theta x}dx+\alpha\int_0^\infty x^{r+4}e^{-\theta x}dx+\beta\int_0^\infty x^{r+5}e^{-\theta x}dx\right]$$

$$= \frac{\theta^6}{(2\theta^4+24\alpha\theta+120\beta)}\left[\theta\int_0^\infty x^{(r+2)}e^{-\theta x}dx+\alpha\int_0^\infty x^{(r+4)}e^{-\theta x}dx+\int_0^\infty x^{(r+5)}e^{-\theta x}dx\right]$$

$$\mu'_r = E(X^r) = \frac{\theta^4\Gamma r + 3 + \alpha\theta\Gamma r + 5 + \Gamma r + 6}{\theta^r(2\theta^4 + 24\alpha\theta + 120\beta)} \quad (9)$$

The mean and the last three moments of the Area Biased Generalized Sauleh distribution can now be obtained by entering r=1,2,3, and 4 in equation (9).

$$\mu'_1 = E(X) = \frac{6\theta^4 + 120\alpha\theta + 720\beta}{\theta(2\theta^4 + 24\alpha\theta + 120\beta)}$$
$$\mu'_2 = E(X^2) = \frac{24\theta^4 + 720\alpha\theta + 5040\beta}{\theta^2(2\theta^4 + 24\alpha\theta + 120\beta)}$$
$$\mu'_3 = E(X^2) = \frac{120\theta^4 + 5040\alpha\theta + 40320\beta}{\theta^3(2\theta^4 + 24\alpha\theta + 120\beta)}$$
$$\mu'_4 = E(X^4) = \frac{720\theta^4 + 40320\alpha\theta + 362000\beta}{\theta^4(2\theta^4 + 24\alpha\theta + 120\beta)}$$
$$Variance = \frac{24\theta^4 + 720\alpha\theta + 5040\beta}{\theta^2(2\theta^4 + 24\alpha\theta + 120\beta)} - \left[\frac{6\theta^2 + 24\alpha\theta + 120}{\theta(2\theta^4 + 24\alpha\theta + 120\beta)}\right]^2$$
$$S.D(\sigma) = \sqrt{\frac{24\theta^4 + 720\alpha\theta + 5040\beta}{\theta^2(2\theta^4 + 24\alpha\theta + 120\beta)} - \left[\frac{6\theta^2 + 24\alpha\theta + 120}{\theta(2\theta^4 + 24\alpha\theta + 120\beta)}\right]^2}$$

III. Hormonic mean

$$H.M = E\left[\frac{1}{x}\right] = \int_0^\infty \frac{1}{x}\frac{x^2\theta^6}{(2\theta^4 + 24\alpha\theta + 120\beta)}(\theta + \alpha x^2 + \beta x^3)e^{-\theta x}$$
$$= \int_0^\infty \frac{x^2\theta^6}{(2\theta^4 + 24\alpha\theta + 120\beta)}(\theta + \alpha x^2 + \beta x^3)e^{-\theta x}$$
$$= \frac{\theta^6}{(2\theta^4 + 24\alpha\theta + 120\beta)}\int_0^\infty x(1 + \alpha x + x^2)e^{-\theta x}dx$$
$$= \frac{\theta^6}{(2\theta^4 + 24\alpha\theta + 120\beta)}\left[\theta\int_0^\infty x\, e^{-\theta x}dx + \alpha\int_0^\infty x^3\, e^{-\theta x}dx + \beta\int_0^\infty x^4 e^{-\theta x}dx\right]$$
$$= \frac{\theta^6}{(2\theta^4 + 24\alpha\theta + 120\beta)}\left[\theta\int_0^\infty x^{2-1}\, e^{-\theta x}dx + \alpha\int_0^\infty x^{4-1}\, e^{-\theta x}dx + \int_0^\infty x^{5-1}e^{-\theta x}dx\right]$$
$$= \frac{\theta^6}{(2\theta^4 + 24\alpha\theta + 120\beta)}\left[\frac{\theta\Gamma 2}{\theta^2} + \frac{\alpha\Gamma 4}{\theta^4} + \frac{\beta\Gamma 5}{\theta^5}\right]$$
$$= \frac{\theta^6}{(2\theta^4 + 24\alpha\theta + 120\beta)}\left[\frac{1}{\theta^2} + \frac{6\alpha}{\theta^3} + \frac{24\beta}{\theta^4}\right]$$
$$= \frac{\theta^6}{(2\theta^4 + 24\alpha\theta + 120\beta)}\left[\frac{\theta^9 + 6\alpha\theta^6 + 24\beta\theta^5}{\theta^{10}}\right]$$
$$= \frac{\theta^6}{(2\theta^4 + 24\alpha\theta + 120\beta)}\left[\frac{\theta^4 + 6\alpha\theta + 24\beta}{\theta^{10}}\right]\theta^5$$
$$H.M = \frac{\theta(\theta^4 + 6\alpha\theta + 24\beta)}{(2\theta^4 + 24\alpha\theta + 120\beta)}$$

IV. Moment generating function & Characteristic function

$$M_X(t) = E[e^{tx}] = \int_0^\infty e^{tx} f_a(x)dx$$

Using Taylor's series,

$$M_X(t) = \int_0^\infty \left[1 + tx + \frac{(tx)^2}{2!} + \cdots\right] f_a(x)dx$$

$$= \int_0^\infty \sum_{k=0}^{\infty} \frac{(tx)^k}{k!} f_a(x)dx$$

$$= \sum_{k=0}^{\infty} \frac{t^k}{k!} \int_0^\infty x^k f_a(x)dx$$

$$= \sum_{j=0}^{\infty} \frac{t^k}{k!} \int_0^\infty \mu'_k$$

$$= \sum_{j=0}^{\infty} \frac{t^k}{k!} \left[\frac{\theta^4 \Gamma k + 3 + \alpha\theta\Gamma k + 5 + \Gamma k + 6}{\theta^k (2\theta^4 + 24\alpha\theta + 120\beta)} \right]$$

$$M_X(t) = \frac{1}{(2\theta^4 + 24\alpha\theta + 120\beta)} \sum_{k=0}^{\infty} \frac{t^k}{k!\,\theta^k} [\theta^4 \Gamma k + 3 + \alpha\theta\Gamma k + 5 + \Gamma k + 6]$$

Similarly, the characteristic function of Area Biased Generalized Sauleh distribution is given by

$$M_X(t) = \frac{1}{(2\theta^4 + 24\alpha\theta + 120\beta)} \sum_{k=0}^{\infty} \frac{it^k}{k!\,\theta^k} [\theta^4 \Gamma k + 3 + \alpha\theta\Gamma k + 5 + \Gamma k + 6]$$

V. Bonferroni and Lorenz curves

$$B(p) = \frac{1}{p\mu'_1} \int_0^q x f_a(x)dx \;\; and \;\; L(p) = PB(p) = \frac{1}{\mu'_1} \int_0^q x f_a(x)dx$$

$$Here, \;\; \mu'_1 = \frac{6\theta^4 + 120\alpha\theta + 720\beta}{\theta(2\theta^4 + 24\alpha\theta + 120\beta)}$$

$$B(p) = \frac{\theta(2\theta^4 + 24\alpha\theta + 120\beta)}{p(6\theta^4 + 120\alpha\theta + 720\beta)} \int_0^q x \frac{x^2\theta^6}{(2\theta^4 + 24\alpha\theta + 120\beta)} (\theta + \alpha x^2 + \beta x^3) e^{-\theta x}\, dx$$

$$= \frac{\theta(2\theta^4 + 24\alpha\theta + 120\beta)}{p(6\theta^4 + 120\alpha\theta + 720\beta)} \int_0^q \frac{x^3\theta^6}{(2\theta^4 + 24\alpha\theta + 120\beta)} (\theta + \alpha x^2 + \beta x^3) e^{-\theta x}\, dx$$

$$= \frac{\theta^7}{p(6\theta^4 + 120\alpha\theta + 720\beta)} \int_0^q x^3 (\theta + \alpha x^2 + \beta x^3) e^{-\theta x} dx$$

$$= \frac{\theta^7}{p(6\theta^4 + 120\alpha\theta + 720\beta)} \left[\theta \int_0^\infty x^3\, e^{-\theta x} dx + \alpha \int_0^\infty x^5\, e^{-\theta x} dx + \beta \int_0^\infty x^6 e^{-\theta x} dx \right] \quad (10)$$

$$\text{Put } \theta x = t \Longrightarrow \theta dx = dt \Longrightarrow dx = \frac{dt}{\theta} \; also \; x = \frac{t}{\theta}$$

$$\because B(p) = \frac{\theta^7}{p(6\theta^4 + 120\alpha\theta + 720\beta)} \left[\theta \int_0^{\theta q} \left(\frac{t}{\theta}\right)^3 e^{-t} \frac{dt}{\theta} + \alpha \int_0^{\theta q} \left(\frac{t}{\theta}\right)^5 e^{-t} \frac{dt}{\theta} + \beta \int_0^{\theta q} \left(\frac{t}{\theta}\right)^6 e^{-t} \frac{dt}{\theta} \right]$$

$$= \frac{\theta^7}{p(6\theta^4 + 120\alpha\theta + 720\beta)} \left[\frac{\theta}{\theta^4} \int_0^{\theta q} t^3 e^{-t} dt + \frac{\alpha}{\theta^6} \int_0^{\theta q} t^5 e^{-t} dt + \frac{\beta}{\theta^7} \int_0^{\theta q} t^6 e^{-t} dt \right]$$

$$= \frac{\theta^7}{p(6\theta^4 + 120\alpha\theta + 720\beta)} \left[\frac{1}{\theta^3} \int_0^{\theta q} t^{4-1} e^{-t} dt + \frac{\alpha}{\theta^6} \int_0^{\theta q} t^{6-1} e^{-t} dt + \frac{\beta}{\theta^7} \int_0^{\theta q} t^{7-1} e^{-t} dt \right]$$

$$= \frac{\theta^7}{p(6\theta^4 + 120\alpha\theta + 720\beta)} \left[\frac{1}{\theta^3} \gamma(4, \theta q) + \frac{\alpha}{\theta^6} \gamma(6, \theta q) + \frac{\beta}{\theta^7} \gamma(7, \theta q) \right]$$

$$= \frac{\theta^7}{p(6\theta^4 + 120\alpha\theta + 720\beta)} \left[\frac{\theta^6 \gamma(4, \theta q) + \alpha\theta^3 \gamma(6, \theta q) + \beta\gamma(7, \theta q)}{\theta^9 \theta^6} \right] \theta^9$$

$$= \frac{\theta^7}{p(6\theta^4 + 120\alpha\theta + 720\beta)} \left[\frac{\theta^3\theta^7 \gamma(4, \theta q) + \alpha\theta^3\theta^7 \gamma(6, \theta q) + \beta\theta^3\theta^6 \gamma(7, \theta q)}{\theta^3\theta^6\theta^7} \right]$$

$$B(p) = \frac{1}{p(6\theta^4 + 120\alpha\theta + 720\beta)} [\theta^4 \gamma(4, \theta q) + \alpha\theta\gamma(6, \theta q) + \beta\gamma(7, \theta q)]$$

$$\because L(p) = \frac{1}{p(6\theta^4 + 120\alpha\theta + 720\beta)}[\theta^4\gamma(4,\theta q) + \alpha\theta\gamma(6,\theta q) + \beta\gamma(7,\theta q)]$$

V. Maximum likelihood estimation & fisher information matrix

$$L(x) = \prod_{i=1}^{n} f_a(x)$$
$$= \prod_{i=1}^{n}\left[\frac{x_i^2\theta^6}{(2\theta^4 + 24\alpha\theta + 120\beta)}(\theta + \alpha x^2 + \beta {x_i}^3)e^{-\theta xi}\right]$$
$$= \frac{\theta^{6n}}{(2\theta^4 + 24\alpha\theta + 120\beta)^n}\prod_{i=1}^{n}\left[x_i^2(\theta + \alpha {x_i}^2 + \beta {x_i}^3)e^{-\theta xi}\right]$$

The log likelihood function is given by

$$\log l = 6n\log\theta - n\log(2\theta^5 + 24\alpha\theta + 120\beta) + 2\sum_{i=1}^{n}\log x_i + \sum_{i=1}^{n}\log(\theta + \alpha {x_i}^2 + \beta {x_i}^3) - \theta\sum_{i=1}^{n} x_i \quad (11)$$

Now differentiating equation (11) write to α, β *and* θ we get,

$$\frac{\partial \log l}{\partial \theta} = -n\left[\frac{24\theta}{(2\theta^4 + 24\alpha\theta + 120\beta)}\right] + \sum_{i=1}^{n}\left[\frac{x_i^2}{(\theta + \alpha x_i^2 + \beta x_i^3)}\right] = 0$$
$$\frac{\partial \log l}{\partial \theta} = -n\left[\frac{120}{(2\theta^4 + 24\alpha\theta + 120\beta)}\right] + \sum_{i=1}^{n}\left[\frac{x_i^3}{(\theta + \alpha x_i^2 + \beta x_i^3)}\right] = 0$$
$$\frac{\partial \log l}{\partial \theta} = \frac{6n}{\theta} - n\left[\frac{\theta\theta^3 + 24\alpha}{(2\theta^4 + 24\alpha\theta + 120\beta)}\right] + \sum_{i=1}^{n}\left[\frac{1}{(\theta + \alpha x_i^2 + \beta x_i^3)}\right] - \sum_{i=1}^{n} x_i = 0$$

Fisher information matrix

$$E\left[\frac{\partial^2 \log l}{\partial \theta^2}\right] = n\left[\frac{(24\theta)(24\theta)}{(2\theta^4 + 24\alpha\theta + 120\beta)^2}\right] - \sum_{i=1}^{n}\left[\frac{E(x_i^2)^2}{(\theta + \alpha x_i^2 + \beta x_i^2)^2}\right]$$
$$E\left[\frac{\partial^2 \log l}{\partial \theta^2}\right] = n\left[\frac{14400}{(2\theta^4 + 24\alpha\theta + 120\beta)^2}\right] - \sum_{i=1}^{n}\left[\frac{E(x_i^2)^2}{(\theta + \alpha x_i^2 + \beta x_i^2)^2}\right]$$
$$E\left[\frac{\partial^2 \log l}{\partial \theta^2}\right] = \frac{-6n}{\theta^2} - \frac{n\,(2\theta^4 + 24\alpha\theta + 120\beta)(24\theta^2) - (\theta\theta^3 + 24\alpha)(\theta\theta^3 + 24\alpha)}{(2\theta^4 + 24\alpha\theta + 120\beta)^2} - \sum_{i=1}^{n}\left[\frac{1}{(\theta + \alpha x_i^2 + \beta x_i^3)}\right]$$
$$E\left[\frac{\partial^2 \log l}{\partial \theta^2}\right] = n\left[\frac{(24\theta)(120)}{(2\theta^4 + 24\alpha\theta + 120\beta)^2}\right] - \sum_{i=1}^{n}\left[\frac{(x_i^2)(x_i^3)}{(\theta + \alpha x_i^2 + \beta x_i^3)^2}\right]$$
$$E\left[\frac{\partial^2 \log l}{\partial \theta^2}\right] = -\frac{n\,(2\theta^4 + 24\alpha\theta + 120\beta)(24) - (24\theta)(\theta\theta^3 + 24\alpha)}{(2\theta^4 + 24\alpha\theta + 120\beta)^2} - \sum_{i=1}^{n}\left[\frac{x_i^2}{(\theta + \alpha x_i^2 + \beta x_i^3)^2}\right]$$
$$E\left[\frac{\partial^2 \log l}{\partial \theta^2}\right] = n\left[\frac{(120)(\theta\theta^3 + 24\alpha)}{(2\theta^4 + 24\alpha\theta + 120\beta)^2}\right] - \sum_{i=1}^{n}\left[\frac{x_i^2}{(\theta + \alpha x_i^2 + \beta x_i^3)^2}\right]$$

The highest probability estimate for the parameters θ is obtained from the solution to the nonlinear equation (11). R software was used to calculate the parameter values for the data sets used in this investigation.

VI. Results

For the data set under consideration, the widely utilized Bayesian Information Criterion (BIC), Akaike Information Criterion (AIC), and -2lnL were employed as the quality of fit criteria. The most adaptable and ideal distribution for the data set is thought to be the one linked to the lowest AIC, BIC, and -2InL. R-Software was used to calculate the maximum likelihood and goodness of fit criteria. In order to discuss the goodness of fit of the Area Biased Generalized Sauleh distribution, we have fitted actual data sets to it. The fit of the Area Biased Generalized Sauleh distribution has been compared to the Lindley, Pranav, exponential, and Sauleh distributions.

I. Dataset:

The survival periods (measured in months) of melanoma patients examined by Susarla and Vanryzin (1978) are shown in the data set below [18]. Table 1 below provides the data set as

Table 1: Data regarding Survival times (in months) studied by Susarla and Vanryzins

3.25	3.50	4.75	4.75	5.00	5.25	6.50	6.50	6.75	6.75	7.78	8.00	8.50
9.50	9.50	10.00	11.50	12.50	13.25	13.50	14.75	15.00	16.25	16.25	16.50	17.50
25.50	25.75	27.50	29.50	31.00	32.50	34.00	34.00	34.50	35.25	58.50		

Table: 2 Shows parameter estimations, corresponding standard errors, Criterion values and goodness of fit test.

Distribution	MLE	S.E	-2logL	AIC	BIC	P–Value
ABG Sauleh distribution	$\hat{\alpha}$=0.450988 $\hat{\theta}$=0.245345	$\hat{\alpha}$=0.6704567 $\hat{\theta}$=0.7091290	210.1678	214.9685	217.3478	0.5348
Sauleh distribution	$\hat{\theta}$=0.458904	$\hat{\theta}$=0.6120067	243.3467	244.6992	247.9832	0.6709
Exponential	$\hat{\alpha}$=4.1256789 $\hat{\theta}$=3.5690876	$\hat{\alpha}$=3.4327899 $\hat{\theta}$=0.0982347	261.3489	265.9685	268.1267	0.7649
Lindley distribution	$\hat{\alpha}$=1.4532890 $\hat{\theta}$=0.0873452	$\hat{\alpha}$=9.2112389 $\hat{\theta}$=0.0670923	256.9807	260.2436	263.3478	0.6734
Pranav distribution	$\hat{\theta}$=3.5489076	$\hat{\theta}$=0.0783242	267.3424	271.2422	274.9843	0.7890
Sujatha distribution	$\hat{\theta}$=4.2389076	$\hat{\theta}$=0.14598065	281.2367	285.0919	288.1784	0.9034

VII. Conclusion

In this study, we developed an Area Biased Generalized Sauleh distribution and identified its characteristics. Because the shape and scale parameters are flexible, the Area Biased Generalized Sauleh distribution can be used to a variety of situations. The maximum likelihood estimate is applied from the frequent estimation domain. An analysis of a patient's survival data showed how effective the distribution was. Lastly, the findings showed that the Area Biased Generalized Sauleh distribution, which is biased, fits the data better than the Lindley, Pranav, Exponential, Sujatha, and Sauleh distributions.

References

[1] Ade RB, Teltumbade DP, Tasare PW. (2021) Characterization and estimation of area biased quasi-Akash distribution. International Journal of Mathematics Trends and Technology. 67(1):53-59.

[2] Ahmad A, Ahmad SP, Ahmed A. (2016) Length biased weighted Lomax distribution: Statistical Properties and Application. Pak.j.stat.oper.res. 12(2):245-255.

[3] Bonferroni CE Elementi di Statistica, Seeber, Firenze (1930) Soft Computing Applications for Group Decision-making and Consensus Modeling.

[4] Chouia S, Zeghdoudi H, Raman V, Beghriche A. A (2021) new size biased distribution with application. Journal of Applied Probability and Statistics. 16(1):111-125.

[5] Cox DR. Renewal theory, Barnes and Noble, New York; c 1962.

[6] Fisher RA. The effects of methods of ascertainment upon the estimation of frequencies. Annals of Eugenics. 1934; 6:13-25.

[7] Ganaie RA, Rajagopalan V. Length biased weighted quasi gamma distribution with characterizations and applications. International Journal of Innovative Technology and Exploring Engineering. 2020;9(5):1110-1117.

[8] Ghitny ME, Atieh B, Nadarajah S (2008) Lindley distribution and its Applications, Mathematics Computing and Simulation 78: 493-506.

[9] Gross AJ, Clark VA (1975) Survival Distributions: Reliability Applications in the Biometrical Sciences, John Wiley, New York.

[10] Lindley DV (1958) Fiducial distribution and Bayes theorem. Journal of the Royal statistical society, series B 20(1): 102-107.

[11] Patil GP, Rao CR. Weighted distributions and Size biased sampling with applications to wildlife populations and human families. Biometrics. 1978; 34:179-189.

[12] Perveen Z, Munir M, Ahmed Z, Ahmad M. On area biased weighted weibull distribution. Sci. Int. (Lahore). 2016;28(4):3669-3679.

[13] Rao CR. On discrete distributions arising out of method of ascertainment, in classical and Contagious Discrete, G.P. Patiled; Pergamum Press and Statistical publishing Society, Calcutta; c1965. p. 320-332.

[14] Rao AK, Pandey H. Parameter estimation of area biased Rayleigh distribution. International Journal of Statistics and Applied Mathematics. 2020;5(4):27-33.

[15] Sharma VK, Dey S, Singh SK, Manzoor U. On length and area-biased Maxwell distributions. Communications in Statistics-Simulation and Computation. 2018;47(5):1506-1528.

[16] Shukla KK (2018) Pranav distribution with properties and applications, BBIJ 7(3): 244-254.

[17] Shukla KK. Pranav distribution with properties and its applications. Biometrics and Biostatistics International Journal. 2018;7(3):244-254.

[18] Susarla V, Vanryzin JV. Empirical Bayes estimation of a distribution (Survival) function from right Censored observations. The Annals of Statistics, 1978. doi:10.1214/aos/1176344249, 6(4), 740-754.

[19] Shanker R (2015) Akash distribution and its Applications, International Journal of Probability and Statistics 4(3): 65-75.

[20] Shanker R (2015) Shanker distribution and its Applications, International journal of statistics and Applications 5(6): 338-348.

[21] Shanker R, Shukla KK (2017) Ishita distribution and its Applications, BBIJ, 5(2): 1-9.

[22] Umeh E, Ibenegbu A. A two parameter Pranav distribution with properties and its application. Journal of Biostatistics and Epidemiology. 2019;5(1):74-90.

OPTIMIZATION OF A FUZZY SUPPLY CHAIN INVENTORY SYSTEM FOR DETERIORATING ITEMS UNDER ENVIRONMENTAL SUSTAINABILITY

Vikash[1,2,*], Dhirendra Singh[2,3], Ashish Negi[4,*]

•

[1]Department of Mathematics, Vardhaman College, Bijnor, Uttar Pradesh, India
[2]P.N.G. Govt. P.G. College, Ramnagar, Nainital, Uttrakhand, India
[3]Department of Mathematics, S.S.S.T.S.R. Govt. Degree College, Pauri, Uttrakhand, India
[4]Department of Mathematics, SRM Institute of Science and Technology, Delhi-NCR Campus, Modinagar, Uttar Pradesh, India
vikashdma@gmail.com, dsingh94106@gmail.com, negi.ashish1995@gmail.com
*Corresponding author

Abstract

The growing emphasis on environmental sustainability and operational reliability has encouraged researchers to extend classical inventory models using fuzzy logic to better handle uncertainty. This study proposes a sustainable inventory framework for deteriorating items, where demand is influenced by both selling price and greening initiatives. The model incorporates investments in preservation technology and green practices under trapezoidal fuzzy environments. Shortages are permitted, and the problem is solved through signed distance defuzzification method, supported by MATLAB for computation and analysis. To demonstrate the applicability, numerical examples are presented, followed by a comparative analysis between crisp and fuzzy settings. The results show that the fuzzy-based model consistently reduces overall costs, with an average decrease of 4.72%, while also lowering cycle time and reorder-to-shortage intervals by 4.04% and 5.52%, respectively. Sensitivity analysis further reveals that total cost is most sensitive to fluctuations in green technology and procurement expenses, whereas preservation and shortage costs have comparatively smaller effects. The findings highlight that adopting fuzzy-based decision approaches not only enhances financial performance but also supports ecological objectives, offering a more reliable pathway for sustainable supply chain management.

Keywords: Optimization, Sustainable Inventory, Deteriorating items, Price and Greening dependent demand, Preservation, and Green technology (PT & GT), Carbon emissions.

1. Introduction and literature review

Global habitability has declined markedly in recent decades, driven by escalating air pollution from industrial activities, transportation, and inadequate waste management. Rising carbon emissions and global warming have further intensified this deterioration, highlighting the urgent need to foster greater environmental awareness among consumers. In response, governments and non-governmental organizations are promoting sustainable growth strategies, such as imposing higher taxes on polluting industries and enforcing stricter regulations on transportation. To address these challenges, organizations worldwide must integrate sustainability into their inventory and supply chain practices to curb carbon emissions and reduce ecological damage. Such initiatives are vital not only for preserving the environment for future generations but also for ensuring long-term sustainable development.

1.1. Sustainable Supply Chain Inventory

In recent years, sustainable supply chain inventory modeling has become a vital research area due to rising environmental concerns and the increasing demand for green products. Ahmed et al. [1] introduced a two-warehouse inventory framework by combining selling price decisions with investment in green technology, while also considering carbon emissions for deteriorating items. Singh et al. [2] investigated pharmaceutical inventory systems under time-dependent demand for products with fixed lifetimes, incorporating sustainability and deterioration, thereby highlighting challenges in balancing healthcare efficiency with ecological responsibility. Kumar et al. [3] proposed a sustainable preservation model where temperature-controlled storage was used to reduce spoilage, emphasizing how preservation technology can simultaneously lower costs and improve product quality. Padiyar et al. [4] expanded this work by integrating reverse logistics with preservation investments in a fuzzy environment, demonstrating the importance of addressing uncertainty in sustainable inventory systems. Chaudhary et al. [5] presented an integrated production"inventory model that considered imperfect production processes, green initiatives, and carbon emissions, showing the influence of environmental consciousness on production strategies. Singh and Mishra [6] advanced this direction by analyzing substitutable deteriorating items under both industrial and transportation-related emissions, stressing the necessity of managing multiple emission sources. Verma and Mishra [7] emphasized sustainability in remanufacturing processes under emission constraints, while Kaushik [8] developed a linear inventory model linking green investment with regulatory carbon policies. Similarly, Suvetha et al. [9] analyzed production"inventory systems with power-pattern demand and finite shelf life, incorporating carbon emissions into decision-making. Hakim et al. [10] explored pricing decisions for deteriorating items under green-level dependent demand, providing evidence that environmentally sensitive pricing directly shapes consumer preferences. Collectively, these studies illustrate a gradual progression from basic deterioration modeling to comprehensive approaches that integrate preservation, carbon policies, reverse logistics, and green initiatives into inventory frameworks.

1.2. Fuzzy Environment in Inventory Models

The presence of uncertainty in real-world decision-making has led to the widespread use of fuzzy set theory in supply chain and inventory research. Zadeh [29] laid the foundation for fuzzy set theory, introducing membership functions to capture imprecision in data, while Zimmermann [31] expanded its application to optimization and decision problems. Kaufmann and Gupta [34] provided systematic methods for fuzzy arithmetic, enabling researchers to build more practical fuzzy optimization models. In inventory management, Yao and Lee [30] first applied trapezoidal fuzzy numbers to order quantity models with and without backordering, highlighting the adaptability of fuzzy logic. El-Wakeel and Al-Yazidi [35] extended this by formulating probabilistic inventory systems constrained by trapezoidal fuzzy parameters, demonstrating how uncertainty can be managed for more reliable decisions. Dutta and Kumar [38] further studied deteriorating items with shortages under complete backlogging in a fuzzy framework, reinforcing the role of fuzzy systems in perishable product scenarios. Recent developments have explored more complex fuzzy structures. Sindhuja et al. [32] applied neutrosophic fuzzy trapezoidal numbers to energy-optimized inventory management, introducing multi-valued logic for sustainability analysis. Kumar and Paikray [33] examined deteriorating items under trapezoidal fuzzy demand with full backlogging, comparing crisp and fuzzy outcomes to show how fuzziness changes cost structures. Dhandapani et al. [36] employed trapezoidal and pentagonal fuzzy numbers for manufacturing inventory, highlighting cost optimization in uncertain environments. Negi and Singh [37] proposed a probabilistic model for deteriorating products under pentagonal fuzzy conditions, defuzzified using signed distance method. These works collectively demonstrate the evolution of fuzzy set applications in inventory systems from simple trapezoidal membership functions to advanced neutrosophic and pentagonal fuzzy numbers, reflecting the growing demand for robust modeling under uncertainty.

1.3. Combined Perspective: Sustainability, Carbon, and Fuzziness

Bringing together sustainability and fuzzy modeling, several researchers have attempted to construct inventory frameworks that integrate both environmental considerations and uncertainty. Shah et al. [11] examined deteriorating inventory models with greening efforts under price-sensitive and stock-dependent demand, illustrating how consumer behavior interacts with environmental responsibility. Ali et al. [12] combined preservation investment with demand sensitivity and solved the resulting framework using a marine predator™s algorithm, showing the potential of metaheuristic methods for sustainable optimization. Rani et al. [13] proposed a fuzzy green supply chain inventory model under variable demand and inflation, linking macroeconomic uncertainty with sustainability objectives. Mahato et al. [14] studied deteriorating products with fixed lifetimes and partial backordering, embedding carbon emission policies into decision-making. Sen et al. [15] developed a consignment-based inventory model with price- and green-sensitive demand, emphasizing responsiveness to market and environmental pressures. Banerjee and Agrawal [16] incorporated freshness- and price-dependent demand into sustainable systems, providing practical guidelines for discounting and ordering. Ahmad et al. [17] introduced preservation technology within green inventory models under emission constraints, while Yadav et al. [18] optimized deteriorating inventory with selling price and carbon emission considerations, reflecting the importance of joint economic environmental strategies. Das et al. [19] applied teaching-learning-based optimization to inventory problems involving green-level dependent demand and payment strategies, illustrating the role of intelligent algorithms. Kundu et al. [20] solved deteriorating green inventory models with hybrid algorithms, highlighting computational advances in sustainability research. Malik et al. [21] integrated learning effects, inflation, trade credit, and preservation into a green supply chain model for decaying items, while Shah et al. [22] considered quadratic price-dependent demand with preservation technology and trade credit. Rani et al. [23] presented a fuzzy inventory model under carbon-sensitive demand, reinforcing the link between environmental and uncertainty factors. Katariya and Shukla [24] designed pricing and inventory strategies under greening and discount policies for non-instantaneous deteriorating products, later extending this to markdown strategies in an EPQ setting [25]. These studies collectively highlight how sustainability, carbon emission regulations, and fuzzy uncertainty are increasingly interlinked in modern supply chain research, shaping the foundation for advanced models like the one proposed in this study.

2. Research Gap and Contributions

Most existing studies on sustainable supply chain inventory models have primarily examined deterioration, pricing, or carbon emissions in isolation. However, these models often neglect the combined effects of selling price and greening level dependent demand, preservation technology, and carbon emissions under uncertain environments. Moreover, while metaheuristic approaches are widely applied, limited research has explored analytical optimization methods to obtain more reliable optimal solutions in fuzzy sustainable supply chain contexts. To address these gaps, the present study makes the following contributions:

1. A sustainable supply chain inventory model is developed for deteriorating items with demand influenced by both selling price and greening level, integrating carbon emission considerations and partial shortages.
2. The model incorporates preservation technology as a strategic investment to mitigate deterioration and extend product shelf life, reducing both economic loss and environmental impact.
3. A trapezoidal fuzzy environment is employed to capture uncertainty in demand, deterioration, and cost parameters, thereby enhancing the model's realism.
4. The signed distance method is used for effective defuzzification, ensuring precise transformation of fuzzy parameters into crisp equivalents.

5. An analytical optimization method is applied for cost minimization, yielding exact and more reliable optimal solutions compared to heuristic-based approximate approaches.

3. Definitions and Preliminaries

1. **Fuzzy set:** A fuzzy set allows for partial membership in which an element can belong to a set to a certain degree or degree of membership, which is represented by a value between 0 and 1. Mathematically, a fuzzy set defined on a universe of discourse $X = \{x_1, x_2, x_3, \ldots, x_n\}$ is given by $A = \{(x, \mu_A(x)) : x \in X\}$, where $\mu_A(x)$ is the membership function of A given by $\mu_A(x) : X \to [0, 1]$.

2. **Fuzzy Number:** A fuzzy number is a fuzzy set on the real line $\mathbb{R}$, if its membership function $\mu_A(x)$ has the following properties:

   (a) $\mu_A(x)$ is upper semi-continuous.

   (b) There exist real numbers a_1, a_2, a_3, a_4 such that $a_1 \leq a_2 \leq a_3 \leq a_4$, $\mu_A(x)$ is increasing on $[a_1, a_2]$, equal to 1 on $[a_2, a_3]$, and decreasing on $[a_3, a_4]$.

   (c) $\mu_A(x) = 0$ outside the interval $[a_1, a_4]$.

3. **Trapezoidal Fuzzy Number:** A trapezoidal fuzzy number is specified by the quadruple (a_1, a_2, a_3, a_4) and defined by its membership function $\mu_A(x) : X \to [0, 1]$ as follows:

$$\mu_A(x) = \begin{cases} 0, & x \leq a_1, \\ \dfrac{x - a_1}{a_2 - a_1}, & a_1 \leq x \leq a_2, \\ 1, & a_2 \leq x \leq a_3, \\ \dfrac{a_4 - x}{a_4 - a_3}, & a_3 \leq x \leq a_4, \\ 0, & x \geq a_4. \end{cases}$$

4. **α-cut of a Trapezoidal Fuzzy Number:**

   Let $\tilde{A} = (a_1, a_2, a_3, a_4)$ be a trapezoidal fuzzy number. The α-cut of $\tilde{A}$, denoted by $\tilde{A}_\alpha$, is defined as the crisp interval:

$$\tilde{A}_\alpha = [\, A_\alpha^L,\, A_\alpha^R \,], \quad \alpha \in [0, 1],$$

   where

$$A_\alpha^L = a_1 + \alpha(a_2 - a_1), \qquad A_\alpha^R = a_4 - \alpha(a_4 - a_3).$$

   Thus,

$$\tilde{A}_\alpha = \big[\, a_1 + \alpha(a_2 - a_1),\; a_4 - \alpha(a_4 - a_3) \,\big].$$

5. ***L–R* Representation of a Trapezoidal Fuzzy Number:**

   A trapezoidal fuzzy number $\tilde{A} = (a_1, a_2, a_3, a_4)$ can also be expressed in terms of its *L–R* representation as

$$\tilde{A} = (m, \alpha, \beta)_{LR},$$

   where

$$m = \frac{a_2 + a_3}{2}, \quad \alpha = m - a_1, \quad \beta = a_4 - m.$$

Here m is the center of the fuzzy number, α is the left spread, and β is the right spread. The membership function in L–R form is given by

$$\mu_{\tilde{A}}(x) = \begin{cases} 0, & x \le a_1, \\ L\left(\dfrac{m-x}{\alpha}\right), & a_1 \le x \le m, \\ R\left(\dfrac{x-m}{\beta}\right), & m \le x \le a_4, \\ 0, & x \ge a_4, \end{cases}$$

where L and R are non-increasing functions with $L(0) = R(0) = 1$.

4. Notations and assumptions

The development of the mathematical model is based on the following assumptions and notations, which are introduced for clarity and consistency.

4.1. Notations

Table 2 presents the notations used in the developed model.

Table 1: *Notations, their descriptions, and units used in the model*

Notation	**Description**	**Unit**
p	Selling price per unit	\$/unit
g	Greening level (investment in green technology)	\$
θ	Deterioration rate	proportion per unit time
ξ	Preservation technology investment	\$
Q	Order quantity per cycle	units
T	Cycle length	Years
B	Maximum backorder level	units
OC	Ordering cost per cycle	\$/cycle
DC	Deterioration cost	\$/cycle
HC	Holding cost	\$/unit/time
PC	Procurement cost	\$/unit
$PTIC$	Preservation technology investment cost	\$
$GTIC$	Green technology investment cost	\$
SC	Shortage cost	\$/cycle
LSC	Lost sales cost	\$/cycle
CEC	Carbon emission cost	\$/cycle
TC	Total cost per cycle	\$/cycle
C_1	Procurement cost per unit	\$/unit
C_2	Holding cost per unit per time	\$/unit/time
C_3	Shortage cost per unit short	\$/unit
C_4	Lost sales cost per unit	\$/unit
C_5	Carbon emission cost per unit	\$/unit
C_6	Preservation technology cost per unit	\$/unit
C_7	Green technology cost per unit	\$/unit
C_8	Carbon emission cost per unit	\$/unit

4.2. Assumptions

The proposed inventory model is developed under the following assumptions:

1. The demand rate is a function of selling price and greening level, given by $D(p,g) = (\beta_1 - \beta_2 p)(\gamma_1 + \gamma_2 g)$, where $\beta_1, \beta_2, \gamma_1, \gamma_2 > 0$.
2. The deterioration rate is dependent on preservation technology investment, given by $\theta(\xi) = \alpha(1 - \eta\xi)$, where $0 \leq \xi \leq 1$.
3. Shortages are permissible, as partially backlogged, and that is considered as $B(t) = \frac{\rho}{1+\delta(T-t)}$, where $0 \leq \rho \leq 1$.
4. The holding cost is considered constant throughout the planning horizon.
5. Lead time is assumed to be negligible or zero.
6. The single warehouse is employed.

5. Crisp Mathematical Model Formulation and Solution

At the beginning of the cycle, the retailer places an order of Q units of the deteriorating item. Thus, the inventory level at $t = 0$ is equal to Q. Over time, the stock in the retailer™s warehouse decreases due to customer demand as well as product deterioration. However, the impact of deterioration is partially mitigated through investment in preservation technology, which helps extend the shelf life of items. The inventory level continues to decline and eventually becomes zero at $t = t_1$. Beyond this point, from $t = T$, shortages occur, and partial backlogging is allowed. The overall dynamics of the system are depicted in Figure 1.

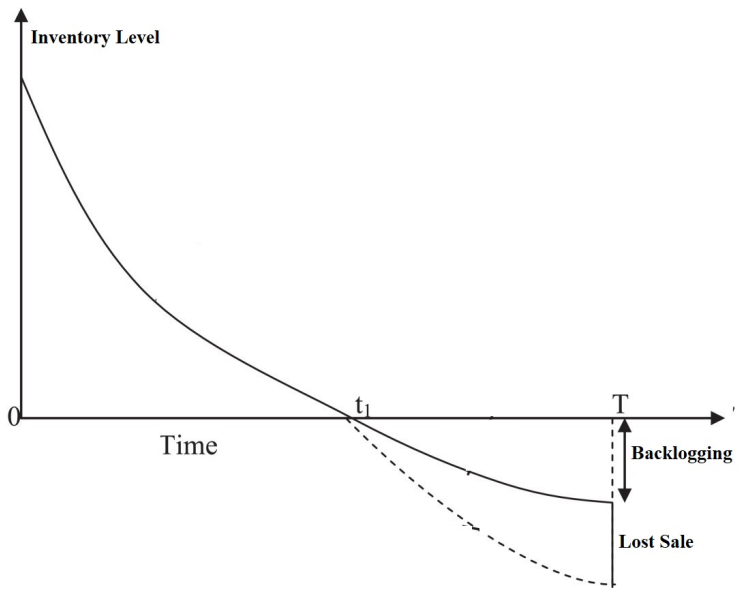


Figure 1: *Graphical illustration of the deteriorating inventory system with shortages.*

The inventory level $I(t)$ at any time t in the interval $[0, T]$ is represented by the following differential equations:

$$\frac{dI(t)}{dt} + \alpha(1 - \eta\xi)I(t) = -[(\beta_1 - \beta_2 p)(\gamma_1 + \gamma_2 g)] \quad \text{for } 0 \leq t \leq t_1 \tag{1}$$

With the boundary conditions $I(t=0)=Q$ and $I(t=t_1)=0$.

$$\frac{dI_s(t)}{dt} = -[(\beta_1-\beta_2 p)(\gamma_1+\gamma_2 g)]\cdot\left[\frac{\rho}{1+\delta(T-t)}\right] \quad \text{for } t_1 \le t \le T \tag{2}$$

With the boundary condition $I_s(t=t_1)=0$.
The solutions of differential equations 1 and 2 with boundary conditions are as follows:

$$I(t) = \frac{[(\beta_1-\beta_2 p)(\gamma_1+\gamma_2 g)]}{\alpha(1-\eta\xi)}\left(e^{\alpha(1-\eta\xi)(t_1-t)}-1\right) \tag{3}$$

$$I_s(t) = \frac{(\beta_1-\beta_2 p)(\gamma_1+\gamma_2 g)\rho}{\delta}\left[\delta(t_1-t)-\frac{\delta^2}{2}\Big((T-t)^2-(T-t_1)^2\Big)\right] \tag{4}$$

Using the boundary condition $I(t=0)=Q$ in equation (3), we get (5).

$$Q = \frac{[(\beta_1-\beta_2 p)(\gamma_1+\gamma_2 g)]}{\alpha(1-\eta\xi)}\left(e^{\alpha(1-\eta\xi)t_1}-1\right) \tag{5}$$

The following are the cost elements incorporated in the sustainable supply chain inventory model:

1. **Ordering cost (OC):**

$$OC = A \tag{6}$$

2. **Deterioration cost (DC):**

$$DC = C_1\cdot\theta(\xi)\int_0^{t_1} I(t)\,dt$$

$$DC = C_1\cdot(\beta_1-\beta_2 p)(\gamma_1+\gamma_2 g)\left[\frac{\left(e^{\alpha(1-\eta\xi)t_1}-1\right)}{\alpha(1-\eta\xi)}-t_1\right] \tag{7}$$

3. **Holding cost (HC):**

$$HC = C_2\int_0^{t_1} I(t)\,dt$$

$$HC = C_2\cdot\frac{[(\beta_1-\beta_2 p)(\gamma_1+\gamma_2 g)]}{\alpha(1-\eta\xi)}\left[\left(e^{\alpha(1-\eta\xi)t_1}-1\right)-\alpha(1-\eta\xi)t_1\right] \tag{8}$$

4. **Procurement cost (PC):**

$$PC = C_3\cdot Q$$

$$PC = C_3\cdot\frac{[(\beta_1-\beta_2 p)(\gamma_1+\gamma_2 g)]}{\alpha(1-\eta\xi)}\left(e^{\alpha(1-\eta\xi)t_1}-1\right) \tag{9}$$

5. **Preservation technology investment cost (PTIC):**

$$PTIC = C_4\cdot\xi^2 \tag{10}$$

6. **Green technology investment cost (GTIC):**

$$GTIC = C_5\cdot g^2 \tag{11}$$

7. **Shortage cost (SC):**

$$SC = C_6\int_{t_1}^{T} B(t)\cdot D(p,g)\,dt$$

$$SC = C_6(\beta_1-\beta_2 p)(\gamma_1+\gamma_2 g)\rho\left[t_1T-\frac{T^2}{2}-\frac{t_1^2}{2}+\frac{\delta}{3}(T-t_1)^3\right] \tag{12}$$

8. **Lost sales cost (LSC):**

$$LSC = C_7 \int_{t_1}^{T} \big(1 - B(t)\big) \cdot D(p,g)\, dt$$

$$LSC = C_7(\beta_1 - \beta_2 p)(\gamma_1 + \gamma_2 g) \left[(T - t_1) - \rho \left(t_1 T - \frac{T^2}{2} - \frac{t_1^2}{2} + \frac{\delta}{3}(T - t_1)^3 \right) \right] \tag{13}$$

9. **Carbon emission cost (CEC):**

$$CEC = C_8 \left\{ \xi_p Q + \xi_1 \int_0^{t_1} I(t)\, dt + \xi_3 \int_{t_1}^{T} B(t) D(p,g)\, dt \right\}$$

$$\begin{aligned} CEC = C_8 \Bigg\{ & \frac{(\beta_1 - \beta_2 p)(\gamma_1 + \gamma_2 g)}{\alpha(1-\eta)\xi} \left[\xi_p \big(e^{\alpha(1-\eta)t_1} - 1\big) + \xi_1 \left(\frac{e^{\alpha(1-\eta)t_1} - 1}{\alpha(1-\eta)\xi} - 1 \right) \right] - t_1 \\ & + \xi_3(\beta_1 - \beta_2 p)(\gamma_1 + \gamma_2 g)\rho \left[t_1 T - \frac{T^2}{2} - \frac{t_1^2}{2} + \frac{\delta}{3}(T - t_1)^3 \right] \Bigg\} \end{aligned} \tag{14}$$

The total cost per cycle (TC), along with the decision variables t_1 and T, is expressed as follows:

$$TC(t_1, T) = \frac{1}{T}\Big[OC + DC + HC + PC + PTIC + GTIC + SC + LSC + CEC \Big]$$

$$\begin{aligned} TC(t_1, T) = \frac{1}{T} \Bigg\{ & A + C_1(\beta_1 - \beta_2 p)(\gamma_1 + \gamma_2 g) \left[\frac{(e^{\alpha(1-\eta)t_1} - 1)}{\alpha(1-\eta)\xi} \right] - t_1 + \frac{C_2(\beta_1 - \beta_2 p)(\gamma_1 + \gamma_2 g)}{\alpha(1-\eta)\xi} \\ & + \frac{(e^{\alpha(1-\eta)t_1} - 1)}{\alpha(1-\eta)\xi} - t_1 + C_3 \left[\frac{(\beta_1 - \beta_2 p)(\gamma_1 + \gamma_2 g)}{\alpha(1-\eta)\xi} \right] (e^{\alpha(1-\eta)t_1} - 1) \\ & + C_4 \cdot \xi_2^2 + C_5 \cdot g^2 \\ & + C_6 \rho(\beta_1 - \beta_2 p)(\gamma_1 + \gamma_2 g) \left[t_1 T - \frac{T^2}{2} - \frac{t_1^2}{2} + \frac{\delta}{3}(T - t_1)^3 \right] \\ & + C_7(\beta_1 - \beta_2 p)(\gamma_1 + \gamma_2 g) \left[(T - t_1) - \rho \left(t_1 T - \frac{T^2}{2} - \frac{t_1^2}{2} + \frac{\delta}{3}(T - t_1)^3 \right) \right] \\ & + C_8 \frac{(\beta_1 - \beta_2 p)(\gamma_1 + \gamma_2 g)}{\alpha(1-\eta)\xi} \left[\xi_p (e^{\alpha(1-\eta)t_1} - 1) + \xi_1 \left(\frac{e^{\alpha(1-\eta)t_1} - 1}{\alpha(1-\eta)\xi} - 1 \right) \right] - t_1 \\ & + \xi_3(\beta_1 - \beta_2 p)(\gamma_1 + \gamma_2 g)\rho \left[t_1 T - \frac{T^2}{2} - \frac{t_1^2}{2} + \frac{\delta}{3}(T - t_1)^3 \right] \Bigg\} \end{aligned} \tag{15}$$

6. Fuzzy Mathematical Model Formulation and Solution

We consider the model in fuzzy environment. Due to fuzziness, it is not easy to define all the parameters precisely. Let $\widetilde{C}_1 = (C_{11}, C_{12}, C_{13}, C_{14})$, $\widetilde{C}_2 = (C_{21}, C_{22}, C_{23}, C_{24})$, $\widetilde{C}_3 = (C_{31}, C_{32}, C_{33}, C_{34})$, $\widetilde{C}_6 = (C_{61}, C_{62}, C_{63}, C_{64})$, $\widetilde{C}_7 = (C_{71}, C_{72}, C_{73}, C_{74})$ be trapezoidal fuzzy numbers in L-R form.

Then, the total cost of the system per unit time in fuzzy sense is given by

$$\begin{aligned}\widetilde{TC}_{ds}(t_1,T)=\frac{1}{T}\Bigg\{&A+\widetilde{C}_1\frac{(\beta_1-\beta_2 p)(\gamma_1+\gamma_2 g)}{\alpha(1-\eta\xi)}\left(\frac{e^{\alpha(1-\eta\xi)t_1}-1}{\alpha(1-\eta\xi)}\right)-t_1\\&+\widetilde{C}_2\frac{(\beta_1-\beta_2 p)(\gamma_1+\gamma_2 g)}{\alpha(1-\eta\xi)}\left(\frac{e^{\alpha(1-\eta\xi)t_1}-1}{\alpha(1-\eta\xi)}\right)-t_1\\&+\widetilde{C}_3\frac{(\beta_1-\beta_2 p)(\gamma_1+\gamma_2 g)}{\alpha(1-\eta\xi)}\left(\frac{e^{\alpha(1-\eta\xi)t_1}-1}{\alpha(1-\eta\xi)}\right)+C_4\,\xi^2+C_5\,\delta^2\\&+\widetilde{C}_6(\beta_1-\beta_2 p)(\gamma_1+\gamma_2 g)\rho\left(\frac{t_1T}{2}-\frac{T^2}{2}+\frac{t_1^2}{2}+\frac{\delta}{3}(T-t_1)^3\right)\\&+\widetilde{C}_7(\beta_1-\beta_2 p)(\gamma_1+\gamma_2 g)(T-t_1)\rho\left(\frac{t_1T}{2}-\frac{T^2}{2}+\frac{t_1^2}{2}+\frac{\delta}{3}(T-t_1)^3\right)\\&+\widetilde{C}_8\frac{(\beta_1-\beta_2 p)(\gamma_1+\gamma_2 g)}{\alpha(1-\eta\xi)}\left(\xi_p\frac{e^{\alpha(1-\eta\xi)t_1}-1}{\alpha(1-\eta\xi)}+\xi_h\frac{e^{\alpha(1-\eta\xi)t_1}-1}{\alpha(1-\eta\xi)}\right)-t_1\\&+\widetilde{C}_9\,\xi_s(\beta_1-\beta_2 p)(\gamma_1+\gamma_2 g)\rho\left(\frac{t_1T}{2}-\frac{T^2}{2}+\frac{t_1^2}{2}+\frac{\delta}{3}(T-t_1)^3\right)\Bigg\}\end{aligned}\tag{16}$$

$$\begin{aligned}\widetilde{TC}_{ds}(t_1,T)=\frac{1}{T}\Bigg[&A+(C_{11},C_{12},C_{13},C_{14})\cdot\frac{(\beta_1-\beta_2 p)(\gamma_1+\gamma_2 g)}{\alpha(1-\eta\xi)}\left(\frac{e^{\alpha(1-\eta\xi)t_1}-1}{\alpha(1-\eta\xi)}\right)-t_1\\&+(C_{21},C_{22},C_{23},C_{24})\cdot\frac{(\beta_1-\beta_2 p)(\gamma_1+\gamma_2 g)}{\alpha(1-\eta\xi)}\left(\frac{e^{\alpha(1-\eta\xi)t_1}-1}{\alpha(1-\eta\xi)}\right)-t_1\\&+(C_{31},C_{32},C_{33},C_{34})\cdot\frac{(\beta_1-\beta_2 p)(\gamma_1+\gamma_2 g)}{\alpha(1-\eta\xi)}\left(\frac{e^{\alpha(1-\eta\xi)t_1}-1}{\alpha(1-\eta\xi)}\right)+C_4\xi^2+C_5\delta^2\\&+(C_{61},C_{62},C_{63},C_{64})(\beta_1-\beta_2 p)(\gamma_1+\gamma_2 g)\rho\left(\tfrac{t_1T}{2}-\tfrac{T^2}{2}+\tfrac{t_1^2}{2}+\tfrac{\delta}{3}(T-t_1)^3\right)\\&+(C_{71},C_{72},C_{73},C_{74})(\beta_1-\beta_2 p)(\gamma_1+\gamma_2 g)(T-t_1)\rho\left(\tfrac{t_1T}{2}-\tfrac{T^2}{2}+\tfrac{t_1^2}{2}+\tfrac{\delta}{3}(T-t_1)^3\right)\\&+C_8\frac{(\beta_1-\beta_2 p)(\gamma_1+\gamma_2 g)}{\alpha(1-\eta\xi)}\left[\xi_p\left(\frac{e^{\alpha(1-\eta\xi)t_1}-1}{\alpha(1-\eta\xi)}\right)+\xi_h\left(\frac{e^{\alpha(1-\eta\xi)t_1}-1}{\alpha(1-\eta\xi)}\right)-t_1\right]\\&+\xi_s(\beta_1-\beta_2 p)(\gamma_1+\gamma_2 g)\rho\left(\tfrac{t_1T}{2}-\tfrac{T^2}{2}+\tfrac{t_1^2}{2}+\tfrac{\delta}{3}(T-t_1)^3\right)\Bigg].\end{aligned}\tag{17}$$

Let $\widetilde{TC}_{ds}(t_1,T)=(W,X,Y,Z)$. The α–cut of trapezoidal fuzzy number $\widetilde{TC}_{ds}(t_1,T)$ are $C_L(\psi)$ and $C_R(\psi)$ and are given by $C_L(\psi)=W+(X-W)\psi,\quad C_R(\psi)=Z-(Z-Y)\psi$.

The defuzzified value of the fuzzy total cost $\widetilde{TC}_{ds}(t_1,T)$, derived through the signed distance method, is expressed as:

$$\widetilde{TC}_{ds}(t_1,T)=\frac{1}{2}\int_0^1\left[C_L(\psi)+C_R(\psi)\right]d\psi\tag{18}$$

7. Optimal Solution Procedure

The nonlinear nature of the objective function requires minimizing the total cost functions per unit time, $TC(t_1, T)$ and $\widetilde{TC}_{ds}(t_1, T)$, to identify the optimal decision variables t_1 and T. These values are obtained by solving the below equations (19), and (20). Substituting these values into equation (15), and (18) yields the minimum total cost per unit time for the system. Given the complexity of the model, an algorithmic procedure has been designed and implemented in MATLAB. The following sections report numerical examples and sensitivity analysis, along with graphical demonstrations.

$$\frac{\partial TC(t_1,T)}{\partial t_1} = 0, \qquad \frac{\partial TC(t_1,T)}{\partial T} = 0 \tag{19}$$

$$\frac{\partial \widetilde{TC}_{ds}(t_1,T)}{\partial t_1} = 0, \qquad \frac{\partial \widetilde{TC}_{ds}(t_1,T)}{\partial T} = 0 \tag{20}$$

Provided that the above total cost function in equations (15) and (18) for crisp and fuzzy model respectively, satisfies the following necessary and sufficient conditions:

$$\left(\frac{\partial^2 TC(t_1,T)}{\partial t_1^2}\right)\left(\frac{\partial^2 TC(t_1,T)}{\partial T^2}\right) - \left(\frac{\partial^2 TC(t_1,T)}{\partial t_1 \partial T}\right)^2 > 0, \quad \text{and} \quad \left(\frac{\partial^2 TC(t_1,T)}{\partial t_1^2}\right) > 0 \tag{21}$$

$$\left(\frac{\partial^2 \widetilde{TC}_{ds}(t_1,T)}{\partial t_1^2}\right)\left(\frac{\partial^2 \widetilde{TC}_{ds}(t_1,T)}{\partial T^2}\right) - \left(\frac{\partial^2 \widetilde{TC}_{ds}(t_1,T)}{\partial t_1 \partial T}\right)^2 > 0, \quad \text{and} \quad \left(\frac{\partial^2 \widetilde{TC}_{ds}(t_1,T)}{\partial t_1^2}\right) > 0 \tag{22}$$

Algorithm:

Step 1 : *Start*

Step 2 : *Input the values.*

Step 3 : *Find* $\frac{\partial TC(t_1,T)}{\partial t_1}$ and $\frac{\partial TC(t_1,T)}{\partial T}$.

Step 4 : *Solve the simultaneous equations* $\frac{\partial TC(t_1,T)}{\partial t_1}$ and $\frac{\partial TC(t_1,T)}{\partial T}$.

Step 5 : *Evaluate the value of* t_1 *and* T.

Step 6 : *Check the optimality conditions as in equation (21).*

Step 7 : *Find* $TC(t_1, T)$.

Step 8 : *Stop.*

Note that, similarly an algorithm is employed for fuzzy cost function.

8. Numerical Illustrations

To illustrate and validate the proposed model, a hypothetical system is considered by assigning specific values to different parameters. The corresponding examples are presented as follows.

Example 1 (Crisp Model)
To illustrate the proposed method, let us consider the following input data:
Let us suppose, $A = 120$ \$ per unit, $C_1 = 12$ \$ per unit, $\alpha = 0.06$, $\eta = 0.25$, $\xi = 0.32$, $\beta_1 = 110$, $\beta_2 = 10$, $\gamma_1 = 1.25$, $\gamma_2 = 0.5$, $g = 0.62$, $p = 0.08$, $C_2 = 6$ \$ per unit, $C_3 = 8.00$ \$ per unit, $C_4 = 7.15$ \$ per unit, $C_5 = 5.39$ \$ per unit, $C_6 = 9$ \$ per unit, $C_7 = 8$ \$ per unit, $C_8 = 5.82$ \$ per unit,

$\rho = 0.021$, $\delta = 0.03$.
Therefore, we obtain following optimal solutions:
$t_1 = 0.7245$ year, $T = 0.9642$ year and $TC(t_1, T) = 527.38$ \$ per cycle.

Example 2 (Fuzzy Model)
To illustrate the proposed method, let us consider the following input data:
Let us suppose, $\tilde{C}_1 = (9, 11, 13, 15)$, $\tilde{C}_2 = (3.5, 5.5, 7.5, 9.5)$, $\tilde{C}_3 = (5, 7, 9, 11)$, $\tilde{C}_6 = (6, 8, 10, 12)$ and $\tilde{C}_7 = (5.5, 7.5, 9.5, 11.5)$.
Therefore, we obtain following optimal solutions:
$t_1 = 0.6845$ year, $T = 0.9252$ year and $\widetilde{TC}_{ds}(t_1, T) = 502.48$ \$ per cycle.

9. Sensitivity Analysis

To examine the impact of variations in the system parameters, a sensitivity analysis has been conducted. The corresponding results are presented in the following tables.

Table 2: *Comparison of Optimal Results*

Model	t_1 (Year)	T (Year)	$TC(t_1, T)$ (\$)
Crisp Model	0.7245	0.9642	527.38
Fuzzy Model	0.6845	0.9252	502.48

Table 3: *Sensitivity Analysis on parameter C_1*

Defuzzify value of C_1	Fuzzify value of C_1	t_1 (Year)	T (Year)	$TC(t_1, T)$ (\$)	$\widetilde{TC}_{ds}(t_1, T)$ (\$)
10	(10.8, 13.2, 15.6, 18)	0.7349	1.1102	478.0	465.976
11	(9.9, 12.1, 14.3, 16.5)	0.7023	0.9508	497.5	482.728
12	(9, 11, 13, 15)	0.6845	0.9252	520.0	502.480
13	(8.1, 9.9, 11.7, 13.5)	0.6648	0.8827	542.5	526.232
14	(7.2, 8.8, 10.4, 12)	0.6472	0.7302	570.0	549.984

Table 4: *Sensitivity Analysis on parameter C_2*

Defuzzify value of C_2	Fuzzify value of C_2	t_1 (Year)	T (Year)	$TC(t_1, T)$ (\$)	$\widetilde{TC}_{ds}(t_1, T)$ (\$)
4	(4.2, 6.6, 9, 11.4)	0.6914	0.9502	486.0	471.976
5	(3.85, 6.05, 8.25, 10.45)	0.6897	0.9377	502.0	486.728
6	(3.5, 5.5, 7.5, 9.5)	0.6845	0.9252	520.0	502.480
7	(3.15, 4.95, 6.75, 8.55)	0.6761	0.9127	537.0	519.232
8	(2.8, 4.4, 6, 7.6)	0.6676	0.9002	556.0	537.984

Table 5: *Sensitivity Analysis on parameter C_3*

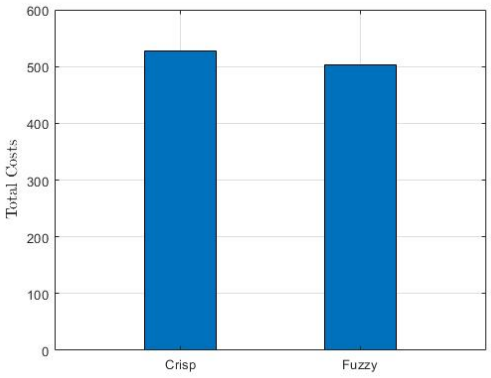
Defuzzify value of C_3	Fuzzify value of C_3	t_1 (Year)	T (Year)	$TC(t_1, T)$ (\$)	$\widetilde{TC}_{ds}(t_1, T)$ (\$)
6	(1, 3, 5, 7)	0.7128	0.9607	498.0	482.472
7	(3, 5, 7, 9)	0.6947	0.9467	512.0	496.579
8	(5, 7, 9, 11)	0.6845	0.9252	520.0	502.480
9	(7, 9, 11, 13)	0.6748	0.9129	534.0	517.405
10	(9, 11, 13, 15)	0.6676	0.8945	550.0	534.107

Table 6: *Sensitivity Analysis on parameter C_6*

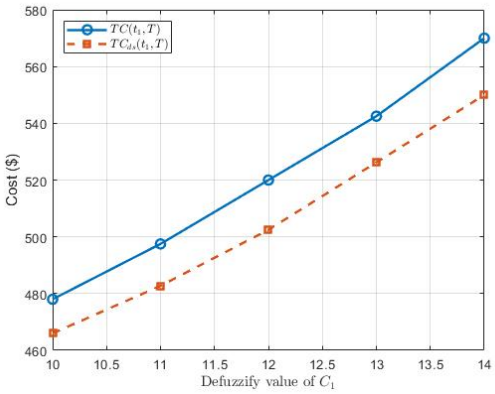
Defuzzify value of C_6	Fuzzify value of C_6	t_1 (Year)	T (Year)	$TC(t_1, T)$ (\$)	$\widetilde{TC}_{ds}(t_1, T)$ (\$)
7	(2, 4, 6, 8)	0.6967	0.9402	498.0	482.472
8	(4, 6, 8, 10)	0.6804	0.9297	512.0	496.579
9	(6, 8, 10, 12)	0.6845	0.9252	520.0	502.480
10	(8, 10, 12, 14)	0.6657	0.9146	534.0	517.405
11	(10, 12, 14, 16)	0.6479	0.9047	550.0	534.107

Table 7: *Sensitivity Analysis on parameter C_7*

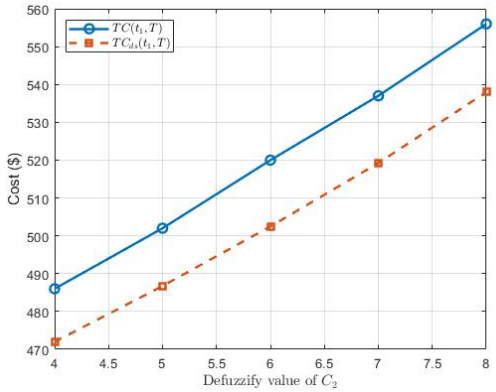
Defuzzify value of C_7	Fuzzify value of C_7	t_1 (Year)	T (Year)	$TC(t_1, T)$ (\$)	$\widetilde{TC}_{ds}(t_1, T)$ (\$)
6	(2, 4, 6, 8)	0.8469	1.4389	467.0	452.106
7	(4, 6, 8, 10)	0.7435	0.9603	491.0	476.413
8	(5.5, 7.5, 9.5, 11.5)	0.6845	0.9252	520.0	502.480
9	(8, 10, 12, 14)	0.6136	0.8531	546.0	528.649
10	(10, 12, 14, 16)	0.5619	0.7946	567.0	549.121



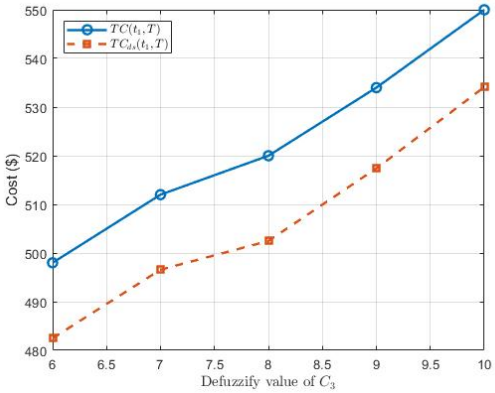
(a) *Comparison of total cost in crisp and fuzzy models.*



(b) *Variation of total cost with defuzzified values of C_1.*

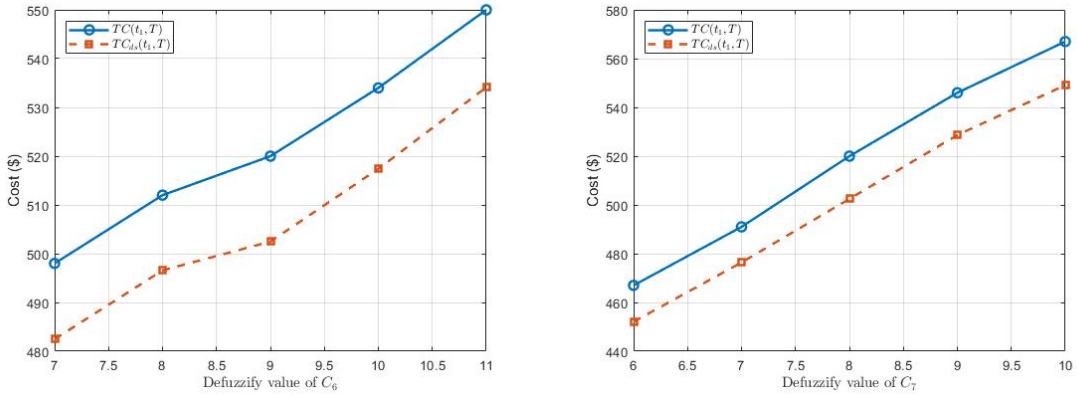


(c) *Variation of total cost with defuzzified values of C_2.*



(d) *Variation of total cost with defuzzified values of C_3.*

Figure 2: *Total costs variation under crisp and fuzzy models on most sensitive parameters.*



(a) *Variation of total cost with defuzzified values of C_6.*

(b) *Variation of total cost with defuzzified values of C_7.*

Figure 3: *Total costs variation under crisp and fuzzy models on most sensitive parameters.*

The following key observations are derived from the sensitivity analysis:

1. Optimal decision times shrink under the fuzzy solution: the reorder-to-shortage instant t_1 decreases from 0.7245 to 0.6845 and the cycle length T falls from 0.9642 to 0.9252. These changes indicate that uncertainty-aware (defuzzified) solutions favour slightly shorter cycles.

2. For every parameter tested (procurement cost C_1, holding cost C_2, shortage cost C_3, preservation cost C_6, green-tech cost C_7) the total cost increases monotonically with the defuzzified parameter value, while the optimal t_1 and T decrease. This pattern is consistent across Tables 4-8.

3. The green-technology cost C_7 is the most influential. Shortage cost C_3 and preservation cost C_6 produce similar, moderate effects. These percentages are computed from the minimum-to-maximum defuzzified cost values in Tables 3-7.

4. The total cost values $TC(t_1, T)$ reported alongside the defuzzified fuzzy costs $\tilde{T}C_{ds}(t_1, T)$ are consistently higher on average TC is about 3.22% larger than the corresponding $\tilde{T}C_{ds}$ across the sensitivity experiments. This small but systematic gap highlights that defuzzified fuzzy estimates are slightly optimistic relative to the corresponding totals in the tested scenarios.

5. Graphical results show near-linear upward trends of total cost with parameter increases (especially for C_1 and C_7); any local nonlinearity is mild and does not change the monotonic character. This supports simple ranked prioritization for managerial action.

10. Conclusion and Future Research Directions

This study developed a sustainable fuzzy inventory model for deteriorating items, incorporating price and greening sensitive demand, as well as costs associated with preservation and green technology investment. The comparative assessment between crisp and fuzzy scenarios demonstrates that the fuzzy-based approach not only offers greater robustness in uncertain environments but also achieves superior economic outcomes. The fuzzy framework reduces the overall cost by 4.72% relative to the crisp model, while also shortening the cycle time and shortage interval by 4.04% and 5.52%, respectively. Sensitivity analysis indicates that green technology cost and procurement cost exert the strongest influence on the total cost, leading to variations of 21.46% and 18.03%, whereas preservation, holding, and shortage costs play comparatively moderate roles. From a managerial standpoint, the results suggest that strategic investment in advanced preservation techniques and green technologies can provide both financial savings and ecological advantages. Moreover, fuzzy-based decision frameworks enable firms to address uncertainties more effectively,

improve operational reliability, and achieve sustainable supply chain outcomes. The applicability of the proposed model extends to industries where deterioration and eco-sensitivity are critical, such as food processing, pharmaceuticals, agro-products, chemicals, and healthcare supplies.

Future research could extend this work in several directions. One promising avenue is to consider probabilistic deterioration rates or product quality defects to reflect more realistic market conditions. Trade credit policies, carbon taxation, time-dependent demand, and multi-warehouse structures may also be incorporated to broaden practical relevance.

References

[1] Ahmed, Ashfar, Krishna Kummari, and Rahul Shukla. "A Two-Warehouse Inventory Model for Green Technology Investment: Deteriorating Items with Selling Price and Carbon Emissions." European Journal of Pure and Applied Mathematics 18.2 (2025): 5847-5847. https://doi.org/10.29020/nybg.ejpam.v18i2.5847

[2] Singh, Anil Kumar, Ravish Kumar Yadav, and Sanju Kumar. "A Sustainable And Environmentally Conscious Inventory Model With TPD Demand For Deteriorating Pharmaceutical Products Of Fixed Lifetime." International Journal of Environmental Sciences 11.10s (2025): 689-701.

[3] Kumar, Subhash, et al. "Sustainable inventory model with controlled temperature for deteriorating products under preservation technology." RAIRO-Operations Research 59.3 (2025): 1527-1549. https://doi.org/10.1051/ro/2024225

[4] Padiyar, Surendra Vikram Singh, et al. "Green supply chain model for decaying raw materials with reverse logistics and preservation investment under a fuzzy environment." RAIROOperations Research 59.4 (2025): 1865-1897. https://doi.org/10.1051/ro/2025044

[5] Chaudhary, Rinki, S. R. Singh, and Surendra Vikram Singh Padiyar. "Integrated supply chain imperfect production inventory model using green product with carbon emissions." RAIROOperations Research 59.4 (2025): 2031-2050. https://doi.org/10.1051/ro/2025069

[6] Singh, Ranu, and Vinod Kumar Mishra. "Sustainable integrated inventory model for substitutable deteriorating items considering both transport and industry carbon emissions." Journal of Systems Science and Systems Engineering 31.3 (2022): 267-287. https://doi.org/10.1007/s11518-022-5531-y

[7] Verma, Poonam, and Vinod Kumar Mishra. "Optimizing the Sustainability in the Supply Chain for Imperfect Deteriorating Items under Remanufacturing and Carbon Emission Regulation." Journal of Systems Science and Systems Engineering (2025): 1-35. https://doi.org/10.1007/s11518-025-5644-1

[8] Kaushik, Jitendra. "A Linear Inventory Model for Deteriorating Items with a Carbon Emission Concept: A Green Inventory Investment Approach." Process Integration and Optimization for Sustainability (2025): 1-17. https://doi.org/10.1007/s41660-025-00524-9

[9] Suvetha, R., et al. "A Sustainable Production Inventory Model for Power-Pattern Demand with Carbon Emissions and Shelf Life Considerations." International Journal of Computational Intelligence Systems 18.1 (2025): 129. https://doi.org/10.1007/s44196-025-00861-0

[10] Abdul Hakim, Md, et al. "Pricing policy in an inventory model with green level dependent demand for a deteriorating item." Sustainability 14.8 (2022): 4646. https://doi.org/10.3390/su14084646

[11] Nita H. Shah, Kavita Rabari & Ekta Patel (2022): Greening efforts and deteriorating inventory policies for price-sensitive stock-dependent demand, International Journal of Systems Science: Operations & Logistics. https://doi.org/10.1080/23302674.2021.2022808

[12] Ali, H., Panda, G.C., Alrasheedi, A.F. et al. Greening concept in inventory system for deteriorating items with preservation investment and price and stock dependent demand via marine predators algorithm. Sci Rep 15, 28459 (2025). https://doi.org/10.1038/s41598-025-13565-4

[13] Rani, Smita, Rashid Ali, and Anchal Agarwal. "Green supply chain inventory model for deteriorating items with variable demand under inflation." International Journal of Business Forecasting and Marketing Intelligence 3.1 (2017): 50-77. https://doi.org/10.1504/IJBFMI.2017.082548

[14] Mahato, F., Choudhury, M., & Mahata, G. C. (2023). Inventory models for deteriorating items with fixed lifetime, partial backordering and carbon emissions policies. Journal of Management Analytics, 10(1), 129“190. https://doi.org/10.1080/23270012.2023.2179431

[15] Sen, N., Bardhan, S. & Giri, B.C. Consignment based integrated inventory model for deteriorating goods with price- and green-sensitive demand. S´dhan´ 49, 13 (2024). https://doi.org/10.1007/s12046-023-02328-4

[16] Banerjee, Snigdha, and Swati Agrawal. "Inventory model for deteriorating items with freshness and price dependent demand: Optimal discounting and ordering policies." Applied Mathematical Modelling 52 (2017): 53-64. https://doi.org/10.1016/j.apm.2017.07.020

[17] Ahmad, Naeem, et al. "A green realistic inventory model with preservation technology for deteriorating items under carbon emission." Materials Today: Proceedings (2023). https://doi.org/10.1016/j.matpr.2023.03.017

[18] Yadav, A.S., Kumar, A., Yadav, K.K. et al. Optimization of an inventory model for deteriorating items with both selling price and time-sensitive demand and carbon emission under green technology investment. Int J Interact Des Manuf 19, 1297“1313 (2025). https://doi.org/10.1007/s12008-023-01689-8

[19] Das, S.C., Ali, H., Khan, M.AA. et al. Inventory model for green products with payment strategy, selling price and green level dependent demand using teaching learning based optimization algorithm. Sci Rep 14, 3033 (2024). https://doi.org/10.1038/s41598-024-53109-w

[20] Kundu, A., Guchhait, P., Maiti, M. et al. Inventory of a deteriorating green product with preservation technology cost using a hybrid algorithm. Soft Comput 25, 11621“11636 (2021). https://doi.org/10.1007/s00500-021-06004-9

[21] Malik, A.K., Pal, S., Jain, D.R. et al. A Green Supply Chain Model for Decaying Items with Learning and Inflation Under the Strategy of Trade Credit and Preservation Technology. Process Integr Optim Sustain 8, 1483“1492 (2024). https://doi.org/10.1007/s41660-024-00440-4

[22] Shah, N.H., Chaudhari, U. & Jani, M.Y. Optimal Policies for Time-Varying Deteriorating Item with Preservation Technology Under Selling Price and Trade Credit Dependent Quadratic Demand in a Supply Chain. Int. J. Appl. Comput. Math 3, 363“379 (2017). https://doi.org/10.1007/s40819-016-0141-3

[23] Rani, S., Ali, R. & Agarwal, A. Fuzzy inventory model for deteriorating items in a green supply chain with carbon concerned demand. OPSEARCH 56, 91“122 (2019). https://doi.org/10.1007/s12597-019-00361-8

[24] Katariya, Dharmesh K., and Kunal T. Shukla. "Optimal greening efforts, pricing and inventory strategies for non-instantaneous deteriorating perishable products under price, freshness and green efforts dependent demand with price discount." International Journal of Mathematics in Operational Research 30.1 (2025): 22-45. https://doi.org/10.1504/IJMOR.2025.144547

[25] Katariya, D. K., & Shukla, K. T. (2023). An EPQ Model for Delay Deteriorating Products With Price, Freshness and Greening Efforts Dependent Demand Under Markdown Strategy. Yugoslav Journal of Operations Research, 34(1), 155“176. https://doi.org/10.2298/YJOR230515023K

[26] Hsu, P. H., H. M. Wee, and H. M. Teng. "Preservation technology investment for deteriorating inventory." International Journal of Production Economics 124.2 (2010): 388-394. https://doi.org/10.1016/j.ijpe.2009.11.034

[27] Yu, Chunhai, et al. "An inventory model of a deteriorating product considering carbon emissions." Computers & Industrial Engineering 148 (2020): 106694. https://doi.org/10.1016/j.cie.2020.106694

[28] Mashud, Abu Hashan Md, et al. "A sustainable inventory model with controllable carbon emissions, deterioration and advance payments." Journal of Cleaner Production 296 (2021): 126608. https://doi.org/10.1016/j.jclepro.2021.126608
[29] Zadeh, Lotfi A. "Fuzzy sets." Information and control 8.3 (1965): 338-353.
[30] Yao, Jing-Shing, and Huey-Ming Lee. "Fuzzy inventory with or without backorder for fuzzy order quantity with trapezoid fuzzy number." Fuzzy sets and systems 105.3 (1999): 311-337.
[31] H. J. Zimmermann, Description and Optimization of Fuzzy Systems,´ International Journal of General Systems 2, no. 1 (1975): 209“215, https://doi.org/10.1080/03081077508960870.
[32] Sindhuja, N., et al. "Energizing Inventory Management to Optimize Energy Consumption of Handling Shortages by Neutrosophic Fuzzy Trapezoidal Number." International Journal of Neutrosophic Science (IJNS) 24.1 (2024).
[33] Kumar, Boina Anil, and Susanta Kumar Paikray. "Cost optimization inventory model for deteriorating items with trapezoidal demand rate under completely backlogged shortages in crisp and fuzzy environment." RAIRO-Operations Research 56.3 (2022): 1969-1994.
[34] M. Kaufmann and M. Gupta, Introduction to Fuzzy Arithmetic Teory and Applications,´ Van Nostrand, Reinhold (New York: Springer, 1985).
[35] El-Wakeel, Mona F., and Kholood O. Al-Yazidi. "Fuzzy constrained probabilistic inventory models depending on trapezoidal fuzzy numbers." Advances in Fuzzy Systems 2016.1 (2016): 3673267.
[36] Dhandapani, Prasantha Bharathi, et al. "Optimizing Inventory Costs in Manufacturing Systems Using Trapezoidal and Pentagonal Fuzzy Numbers." Journal of Mathematics 2025.1 (2025): 4040646. https://doi.org/10.1155/jom/4040646
[37] Negi, Ashish, and Ompal Singh. "Probabilistic inventory model for deteriorating items with uncertain demand under pentagonal fuzzy environment." Reliability: Theory & Applications 20.1 (82) (2025): 754-772.
[38] Dutta, Debashis, and Pavan Kumar. "Fuzzy inventory model for deteriorating items with shortages under fully backlogged condition." International Journal of Soft Computing and Engineering (IJSCE) 3.2 (2013): 393-398.

STATISTICAL INFERENCE ON THE GENERALIZED EXPONENTIAL DISTRIBUTION BASED ON GENERALIZED ORDER STATISTICS CHARACTERIZATIONS AND APPLICATIONS

Imtiyaz A. Shah[1] and Khalid Ul Islam Rather[2]

•

[1]Department of Community Medicine (Bio Statistics), Sher-I-Kashmir Institute of Medical Sciences, Srinagar (J&K) India
2Department of Statistics and Computer Science, Sher- e- Kashmir University Agricultural Sciences and Technology Jammu (J&K) India
driashah03@gmail.com, khalidstat34@gmail.com

Abstract

In this paper, we study the Some distribution functions have been characterized based on m-dual generalized order statistics and consequently m-generalized order statistics. Moreover, we show that these characterization properties provide a beneficial strategy to predict future events, which are based on past or current events and on an arbitrary distribution function. Finally, an application of these results is given for bivariate generalized exponential distribution.

Keywords: Generalized exponential distribution, Dual generalized order statistics, generalized order statistics, Generalized inverted exponential distribution, weak convergence, Random sample size

I. Introduction

Generalized order statistics introduced by [21]. A concept of generalized order statistics (GOSs) as a unified approach to a variety of models of ascendingly ordered random variables (RVs) introduced by [21]. The concept of dual GOSs, denoted by DGOSs, was introduced by [9] as a parallel concept of GOSs to enable a common approach to descendingly ordered RVs. [9] has shown that (cf. Theorem 3.3) there is a direct link between DGOSs and GOSs.

The subclasses m −GOSs and m −DGOSs of GOSs and DGOSs, respectively, contain many important models of ordered RVs such as ordinary order statistics (OOSs), lower and upper record values, k−records, sequential order statistics (SOSs) and type II censored OOSs. For any $1 \leq r \leq n$, the marginal probability density functions (PDFs) of the rth m-GOS X(r, n; m, k) and m-DGOS X^*(r, n; m, k), based on a continuous distribution function (DF) $F_X(x) = P(X \leq x)$ with a PDF $f_X(x)$, are given, respectively, by (cf. [10] and [19]).

$$f_{X(r,n,m,k)}(x) = \frac{C_{r-1}^{(n)}}{(r-1)!}\,[\bar{F}_X(x)]^{\gamma_r^{(n)}-1}[\frac{1-[\bar{F}_X(x)]^{m+1}}{m+1}]^{r-1} f_X(x) \quad , \quad m \neq -1 \tag{1}$$

and

$$f_{X^*(r,n,m,k)}(x) = \frac{C_{r-1}^{(n)}}{(r-1)!}\,F_X{}^{\gamma_r^{(n)}-1}\,[\frac{1-[F_X(x)]^{m+1}}{m+1}]^{r-1} f_X(x) \quad , \quad m \neq -1 \tag{2}$$

where $\overline{F} = 1 - F$, $\gamma_r^{(n)} = k + (n-r)(m+1)$ and $C_{r-1}^{(n)} = \prod_{i=1}^{r} \gamma_r^{(n)}$, 1 ≤ r ≤ n.

Classical results in characterizations can be found in [12], [13], [14] and [15]. Different results of characterization and its applications in terms of GOSs and DGOSs are derived by many authors. Among these authors are [5], [7], [11], [16], [17], [18], [19] and [20].

In this work, we consider a wide subclass of GOSs and DGOSs, specifically when $m_1 = m_2 = \cdots = m_{n-1} = m \neq -1$. This subclass is known as m-GOSs and m-DGOSs [22] (see also [9]) has derived the marginal df of the $(m-r+1)^{th}$ m-GOSs, in the form $\varphi_{m-r+1:m}^{(n,k)}(x) = I_{G_{n(x)}}(N - R + 1, R)$, where $G_n(x) = 1 - (1 - F(x))^{n+1} = 1 - \bar{F}(x)^{n+1}, N = \frac{k}{n+1} + m - 1, R = \frac{k}{n+1} + r - 1$ and $I_x(a,b) = \frac{1}{\beta(a,b)} \int_0^x t^{a-1}(1-t)^{b-1} dt, a, b > 0$, is the incomplete beta ratio function. Similarly, by using the results of [11] the marginal df of the $(m-r+1)^{th}$m-DGOSs, is given by $\varphi_{m-r+1:m}^{d(n,k)}(x) = I_{T_{n(x)}}(R, N - R + 1)$, where $T_n(x) = F^{n+1}(x)$.

II. Model

GIED is the generalization of the one parameter IED which was proposed by [4]. The various statistical properties and reliability estimation has also been studied in detail by [4]. A three parameter GIED has the following PDF and CDF as follows: The cumulative distribution function CDF $F_X(x)$and probability density function PDF $f_X(x)$ of the Generalized inverted exponential distribution (GIED) distribution are given by:

$$\mathrm{F_X}(x) = 1 - [1 - e^{-\lambda\ /x}]^{\alpha}, 0 \leq x < \infty, \alpha\ \beta,\ \lambda > 0 \tag{3}$$

and

$$f_X(x) = \frac{\alpha\lambda\beta}{x^2} e^{-\frac{\lambda\beta}{x}} \left[1 - e^{-\frac{\lambda\beta}{x}}\right]^{\alpha-1}, 0 \leq x < \infty, \alpha, \beta, \lambda > 0 \tag{4}$$

where α and β are the shape parameters and λ is the scale parameter.

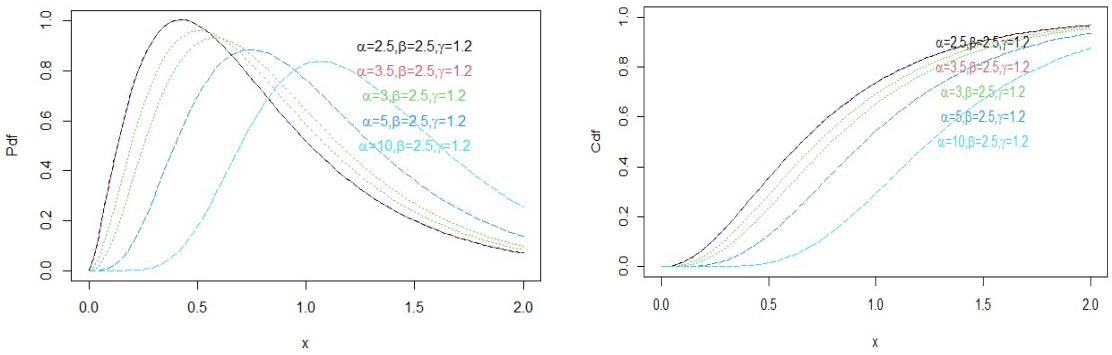


Figure 1. Possible shapes of the probability density function f(x) (left) and cumulative distribution function F(x) (right) of the Generalized inverted exponential distribution (GIED) distribution for fixed parameter values of β and λ.

The Generalized inverted exponential distribution (GIED) distribution reduces to generalization of the one parameter (IED) when α = 1.

III. Reliability Characteristics

The reliability function R(x) is an important tool for characterizing life phenomenon. R(x) is analytically expressed as R(x) = 1 − F(x). Under certain predefined conditions, the reliability function R(x) gives the probability that a system will operate without failure until a specified time x . The reliability function of the Generalized Inverted Exponential Distribution (GIED) distribution is given by

$$R(x) = 1 - \left[1 - e^{-\frac{\lambda\beta}{x}}\right]^{\alpha}, 0 \leq x < \infty, \alpha, \beta, \ \lambda > 0 \tag{5}$$

Another important reliability characteristics is the failure rate function. The failure rate function gives the probability of failure for a system that has survived up to time x. The failure rate function h(x) is mathematically expressed h(x) = f(x)/R(x) . The failure rate function the Extended Generalized inverted exponential distribution (GIED) distribution is given by:

$$h(x) = \frac{\frac{\alpha\lambda\beta}{x^2} e^{-\lambda\beta/x}[1 - e^{-\lambda\beta/x}]^{\alpha-1}}{1 - [1 - e^{-\lambda\beta/x}]^{\alpha}}, 0 \leq x < \infty, \alpha, \beta, \lambda > 0$$

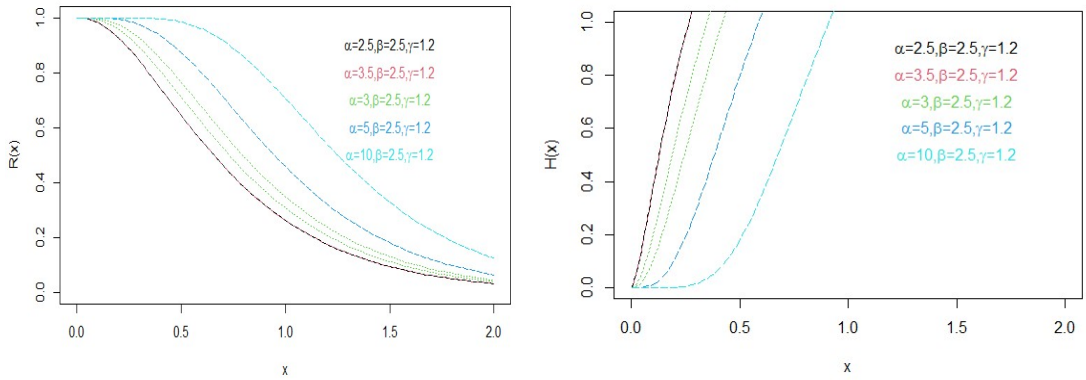


Figure 2. Possible shapes of the reliability function R(x) (left) and failure rate function h(x) (right) of the Generalized inverted exponential distribution (GIED distribution for fixed parameter values of β and λ.

Let $\{X_i\}$ and $\{Y_j\}$ be two sequences of rv's defined on the same probability space $(\varphi, \omega, *)$, where $\{X_i\}$ is i.i.d with common df $F(x)$) (the rv's $Y_i, i = 1,2, \cdots$ need not to be independent or identical). Furthermore, let $Y^*_{m-r_{m+1}:m} = Y(m - r_m + 1, m, n, k)(Y^*_{d:m-r_{m+1}:m} = Y_d(m - r_m + 1, n, m, k))$ and $X^*_{m-r_{m+1}:n} = X(m - r_m + 1, n, m, k)(X^*_{d:m-r_{m+1}:m} = X_d(m - r_m + 1, n, m, k))$ be the $(m - r_m + 1)^{th}$ m-GOSs and m-DGOSs corresponding the sequences Y_i and X_i, respectively, where $1 \leq r_m \leq m$, when the sample size itself is assumed to be a rv ν_n and $\left(Y^*_{m-r_{m+1}:m}\right)\left(Y^*_{d:m-r_{m+1}:m}\right)$ and some regularly varying function, the limit df's of m-GOSs and m-DGOSs $\left(Y^*_{\nu_m-r_{m+1}:m}\right)\left(Y^*_{d:\nu_m-r_{m+1}:m}\right), n > -1$ are derived in the following exhaustive cases:

(1) Extreme case, where $r_m = r$, is any fixed integer and $1 \leq r < m$.

(II) Central case, where $r_m \to \infty$ and $\frac{r_m}{m} \to \lambda \, \epsilon \, (0,1)$, as $\to \infty$.

(III) Intermediate case, where min $(r_m, m - r_m) \to \infty$ and $\frac{r_m}{m} \to 0$, as $m \to \infty$.

It is worth mentioning that when $n = -1, k = 1, i.e.$, the case of the record values, the above problem was studied recently by [6].

Suppose that an, $a_m, \tilde{a}_m > 0$ and $b_m, \tilde{b}_m \, \epsilon \, \Re$ are suitable normalizing constants such that

$$\Phi^{(n,k)}_{\nu_m - r_m + 1:\nu_m}(a_m x + b_m) = P\left(\left(X^*_{\nu_m - r_{m+1}:m} \le a_m x + b_m\right) \xrightarrow{w} \omega^{(n,k)}(x)\right) \tag{6}$$

and

$$\Phi^{d(n,k)}_{m - r_m + 1:\nu_m}\left(\tilde{a}_m x + \tilde{b}_m\right) = P\left(\left(X^*_{d:\nu_m - r_{m+1}:\nu_m} \le \tilde{a}_m x + \tilde{b}_m\right) \xrightarrow{w} \omega^{d(n,k)}(x)\right) \tag{7}$$

where $\left(\xrightarrow{w}\right)$ stands for weak convergence, as $n \to \infty, \omega^{(m,k)}(x)$ and $\omega^{d(m,k)}(x)$ are a non-degenerate df 's. Let C and C^d be the classes of all non degenerate limit df 's $\omega^{(m,k)}(x)$ and $\omega^{d(n,k)}(x)$ in (1) and (2), respectively. Recently, [6] and [9] studied the limit df 's of the bivariate extreme, central, and intermediate m-generalized order statistics (m-GOSs) and m- dual generalized order statistics (m-DGOSs) with random sample size. This study gives the corresponding results for univariate upper generalized order statistics (GOSs) and upper dual generalized order statistics (DGOSs) cases with random sample size. These results, which characterize the classes C and C^d are presented in Theorem 2.1 and Theorem 2.2, respectively, where through these theorems and all the paper the symbols $\underset{m}{\to}$ stands for convergence, as $m \to \infty,$. Moreover, the symbols $\xrightarrow{p}$ stands for convergence in probability, as $m \to \infty$. [1] has characterized exponential distribution under random dilation for adjacent GOSs. In this paper, distributional properties of the generalized order statistics (GOSs) have been used to characterize distributions for non- adjacent generalized order statistics (GOSs) under random translation, dilation and contraction. One may also refer to [5], [7], [24], [25], [17], [20] and [21] for the related results.

IV. Characteristics Results

Theorem 2.1: Let $n > -1$, For any non-degenerate distribution function (df) $\omega^{(n,k)}(x)$, $\omega^{(n,k)}(x) \in C$, if and only if one of the following conditions (I), (II) and (III) holds. Let $X(r, n, m, k)$ be the r^{th} m-generalized order statistics (GOSs) from a sample of size n drawn from a continuous population with the pdf f(x) and the df F(x), then,

$$\Psi^{(n,k)}_{m-r+1:m}(a_m x + b_m) = P(X^*_{m-r+1} \le a_m x + b_m) \xrightarrow{w} \psi^{(nk)}(x) = 1 - \exp\left(\mathcal{U}^{n+1}_{i:\beta}(x)\right) \tag{8}$$

where $X(m_1 - m_2 - j, n_1, m, k)$ is independent of $X(r, n_2, m, k)$ *if* and only *if* $X_1 \sim \exp\left(\mathcal{U}^{n+1}_{i:\beta}(x)\right)$.

Proof. The limit df $\Psi^{(n,k)}(x)$ has the form $\Psi^{(n,k)}(x) = 1 - \int_0^\infty \Gamma_R\left(z\mathcal{U}^{n+1}_{i:\beta}(x)\right) dp\ (\tau \le z), i \in \{1,2,3\}$, where $\mathcal{U}_1(x) = \mathcal{U}_{1:\beta}(x) = e^{-x}, \forall\, x;\ \mathcal{U}_{2:\beta}(x) = e^{-\beta}, x > 0$; and $\mathcal{U}_{3:\beta}(x) = (-x)^\beta,\ x \le 0$. $\frac{\upsilon_m}{m} \xrightarrow{p} \tau$.

$$\Psi^{(n,k)}_{m-r_m+1:m}(a_m x + b_m) = P(X^*_{m-r_m+1} \le a_m x + b_m) \xrightarrow{w} \Psi^{(n,k)}(x) = \mathbb{N}(W^*_{i:\beta}(x)) \tag{9}$$

Where $\left(W^*_{i:\beta}(x)\right) = \frac{C^*_{\lambda(n)}}{C^*_\lambda}(n+1)\left(W^*_{i:\beta}(x)\right), C^*_\lambda = \frac{C_\lambda}{\lambda}, C_\lambda = \sqrt{\lambda(1-\lambda)}, \lambda(n) = \lambda^{1/(n+1)}$. And $\mathbb{N}(.)$ is the standard normal df, $\frac{\upsilon_n}{n} \xrightarrow{p} \tau$.

The limit df $\Psi^{(n,k)}(x)$ has the form $\Psi^{(n,k)}(x) = 1 - \int_0^\infty \mathbb{N}\left(\sqrt{z}W^*_{i:\beta}(x)\right) dp(\tau \le z)$ where $W_{i:\beta}(x)$, $i \in \{1,2,3,4\}$, has one and only one of the following types.

$$W_{1:\beta}(x) = \begin{cases} -\infty, & x \le 0 \\ cx^\beta, x > 0, c_2, \beta > 0 \end{cases} \tag{10}$$

$$W_{2:\beta}(x) = \begin{cases} -c|x|^\beta, & x \le 0 \\ \infty, & x > 0, c, \beta > 0 \end{cases} \tag{11}$$

$$W_{3:\beta}(x) = \begin{cases} -c_1 |x|^{\beta}, x \le 0, c_1 > 0 \\ c_2 x^{\beta}, x > 0, c_2, \beta > 0 \end{cases} \tag{12}$$

$$W_{4:\beta}(x) = \begin{cases} -\infty, x \le -1 \\ 0, -1 < x \le 1 \\ \infty, x > 1 \end{cases} \tag{13}$$

$$\sqrt{r_{m+\sigma(m)}} - \sqrt{r_n} = \frac{\alpha\gamma l}{2},$$

For any sequence of integer values $\{\sigma(m)\}$ for which $\frac{\sigma(m)}{m^{1-\alpha/2}} \underset{m}{\to} \gamma$.

Where $0 < \alpha < 1$, $l > 0$ and γ is any real number (intermediate case).

$$\psi_{m\psi - r_m + 1:m}^{(n,k)}(a_m x + b_m) = P(X_{m-r_m+1}^* \le a_m x + b_m) \overset{w}{\to} \psi^{(n,k)}(x) = \mathbb{N}((n+1)V_{i:\beta}^*(x)) \tag{14}$$

$$\frac{\nu_m - m}{m^{1-\alpha/2}} \overset{p}{\to} \tau$$

The limit df $\Psi^{(n,k)}(x)$ has the form $\Psi^{(n,k)}(x) = \int_{-\infty}^{\infty} \mathbb{N}((n+1)V_{i:\beta}(x) - lz(1-\alpha)dp(\tau \le z)$ where $V_{i:\beta}(x)$, has one and only one of the following types.

$$V_1(x) = V_{i:\beta}(x) = x, \forall x \tag{15}$$

$$V_{i:\beta}(x) = \begin{cases} -\beta ln|x|, x \le 0 \\ \infty, x > 0 \end{cases} \tag{16}$$

$$V_{3:\beta}(x) = \begin{cases} -\infty; x \le 0 \\ \beta ln|x|; x > 0 \end{cases} \tag{17}$$

where β is some positive constant, which depends only on α , l and the type of F(x). Finally, if r_n does not satisfy any of conditions $(i-I), (i-II)$ and $(i-III)$, then $\Psi^{(n,k)}(x)$ can only have a degenerate type or does not exist.

Theorem 2.2: Let $n > -1$, For df $\omega^{(n,k)}(x)$, $\omega^{d(n,k)}(x) \in C^d$, if and only if one of the following conditions (I), (II) and (III) holds. Let $X^*(r, n, \tilde{m}, k)$ be the r^{th} GOSs from a sample of size n drawn from a continuous population with the *pdf* f and the *df* F, then,

$$\psi_{m-r+1:m}^{d(n,k)}(\tilde{a}_m x + \tilde{b}_m) = P(X_{d:m-r+1}^* \le \tilde{a}_m x + \tilde{b}_m) \overset{w}{\to} \psi^{d(nk)}(x) = 1 - \exp\left(\mathcal{U}_{i:\beta}^{n+1}(x)\right) \tag{18}$$

Proof. The limit df $\Psi^{d(n,k)}(x)$ has the form $\Psi^{d(n,k)}(x) = 1 - \int_0^{\infty} \Gamma_R \left(z\mathcal{U}_{i:\beta}^{n+1}(x)\right) dp\ (\tau \le z), i \in \{1,2,3\}$,

where $\mathcal{U}_1^*(x) = \mathcal{U}_{1:\alpha}^*(x) = e^{-x}$, $\forall\, x$; $\mathcal{U}_2^*(x) = \mathcal{U}_{2:\alpha}^*(x) = e^{-x}$, $x > 0$; and $\mathcal{U}_3^*(x) = \mathcal{U}_{3:\alpha}^*(x) = (-x)^{\beta}$, $x \le 0$. $\frac{\upsilon_m}{m} \overset{p}{\to} \tau$.

$$\Psi_{m-r_m+1:m}^{d(n,k)}(\tilde{a}_m x + \tilde{b}_m) = P(X_{m-r_m+1}^* \le \tilde{a}_m x + \tilde{b}_m) \overset{w}{\to} \Psi^{d(n,k)}(x) = \mathbb{N}(W_{i:\beta}^*(x)) \tag{19}$$

Where $\varphi^{d(m,k)}(x)$ is a non-degenerate distribution function (df). Furthermore, let ν_n be a sequence of non-negative integer valued rv's which satisfy

$$\frac{\nu_m - m}{m^{1-\alpha/2}} \overset{p}{\to} \tau$$

The limit distribution function (df) $\Psi^{d(n,k)}(x)$ has the form $\Psi^{d(n,k)}(x) = 1 - \int_0^{\infty} \mathbb{N}\left((m+1)V_{i:\beta}(x) + lz(1-\alpha)dp(\tau \le z), i = \{1,2,3,\cdots\}\right.$. Finally, if r_m does not does not satisfy any of conditions $(1-I), (i-II)$ and $(i-III)$, then $\Psi^{d(n,k)}(x)$ can only have a degenerate type or does not exist has one and only one of the following types.

Remark 1. Under conditions (I), (II), and (III), when $m = 0, k = 1$, Theorem 2.1 gives the upper order statistics case and Theorem 1.2 gives the lower order statistics case.

Theorem 2.3: Suppose that $X_{m-r_m+1:m}^* \in L(Y^*: \varphi|\tau)$. Let $n > -1, a_m > 0$ and $b_m \in \mathcal{B}, n \ge 1$, be

suitable normalizing constants for which

$$P(X^*_{m-r_m+1} \le a_m x + b_m) \overset{w}{\to} \varphi^{(n,k)}(x) \tag{20}$$

Where $\varphi^{d(n,k)}(x)$ is a non-degenerate df. Furthermore, let ν_m be a sequence of non negative integer valued rv's which satisfy

$$\frac{\nu_m - m}{m^{1-\alpha/2}}$$

where the df $A(z) = P(\tau \le z)$ is continuous at zero, i.e., $A(0-) = A(0) = A(0+) = 0$ (the condition $A(0-) = A(0)$ is not considered in the original Theorem 2.1 of Xie Shengrong (1997), for the maximum oos, but as we shall see in the proof of Theorem 2.1, it seems to be indispensable). Then

$$P(X^*_{m-r_m+1} \le a_m x + b_m) \overset{w}{\to} \varphi^{(m,k)}(x) \overset{w}{\to} \begin{cases} 1 - \int_0^\infty \Gamma\left(z^0 \Psi^{m+1}_{i:\beta}(x) dA\,(z), i\epsilon\{1,2,3\}\right) \\ \text{where } r = r_n = \text{constsnt (extreme case)} \\ \int_0^\infty N(z^{\frac{\rho}{2}} W^*_{i:\beta}(x) dA(z), i \in \{1,2,3\}, \text{(central case)} \end{cases} \tag{21}$$

Furthermore, let the intermediate rank sequence $\{r_m\}$ satisfy Chibisov condition and let condition (21) be replaced by

$$\frac{\nu_m - m}{m\varphi^{-\frac{\alpha}{2}}(m)} \quad \overset{p}{\to} \quad \tau$$

Where $\varphi(m) \in RV\ 0 < \rho < 1\ \alpha, \varphi_m^{\frac{\alpha}{2}}(\frac{\varphi(mx)}{\varphi(m)} - x^0) \underset{m}{\to} 0$ and the df $A(Z)$ is symmetric and continuous at zero. Then

$$P(X^*_{m-r_m+1} \le a_m x + b_m) \overset{w}{\to} \int_{-\infty}^{\infty} N((m+1)V_{i:\beta}(x) - l\rho z(1-\alpha) dA(z), i \in \{1,2,3\} \tag{22}$$

$$P\left(m(\tau - \epsilon) \le \nu_m \le n(\tau + \epsilon)\right) \underset{m}{\to} 1 \tag{23}$$

Proof: Consider, first the extreme case, where $r_m = r = \text{constant}$. Let $d > 0$ be a positive real number. Clearly, for any $\varepsilon\ \epsilon(0, d)$, (12) implies

$$P\left(m(\tau - \epsilon) \le \nu_m \le m(\tau + \epsilon)\right) \underset{m}{\to} 1 \tag{24}$$

On the other hand, we can write

$$P\left(X^*_{m-r_m+1} \le a_m x + b_m\right) = P\left(X^*_{m-r_m+1} \le a_{[\varphi(m)]} x + b_{[\varphi(m)]}\right) + P\left(m(\tau - \epsilon) > \nu_m \text{ or } \nu_m > n(\tau + \epsilon)\right)$$

$$\left(X^*_{m-r_m+1} \le a_{[\varphi(m)]} x + b_{[\varphi(m)]}\right) = \wp_m^{(1)}(\epsilon) + \wp_m^{(2)}(\epsilon)$$

According to (24), $\wp_m^{(2)}(\epsilon) \underset{n}{\to} 0$, so calculating $\wp_m^{(1)}(\epsilon)$ is only necessary. However

$$\wp_m^{(1)}(\epsilon) = P\left(m(\tau - \epsilon) \le \nu_m \le n(\tau + \epsilon)\right)\left(X^*_{m-r_m+1} \le a_{[\varphi(m)]} x + b_{[\varphi(m)]}\right)$$

$$= \int_0^\infty P\left(m(\tau - \epsilon) \le \nu_m \le n(\tau + \epsilon)\right) X^*_{m-r_m+1} \le a_{[\varphi(m)]} x + b_{[\varphi(m)]} | \tau = z dA(z)$$

$$\le P(\tau \le d) + \int_0^\infty P\left(m(\tau - \epsilon) \le \nu_m \le n(\tau + \epsilon)\right) X^*_{m-r_m+1} \le a_{[\varphi(m)]} x + b_{[\varphi(m)]} | \tau = z dA(z) z \tag{25}$$

By using the well-known inequality

$$X^*_{m'-r_m+1:m'} \le X^*_{m''-r_m+1:m''}\ , m' \le m''$$

we obtain

$$\wp_m^{(1)}(\epsilon) \le P(\tau \le d) = \int_0^\infty P\left(X^*_{[m(\tau-\epsilon)-r+1:[n(\tau-\epsilon)]}\right) \le a_{[\varphi(m)]} x + b_{[\varphi(m)]} | \tau = z dA(z)$$

$$= P(\tau \le d) + \int_0^{\infty} P\left(X^*_{[m(\tau-\epsilon)-r+1:[n(\tau-\epsilon)]}\right) \le a_{[\varphi(m)]}x + b_{[\varphi(m)]}|\tau = z dA(z) \tag{26}$$

Since $X^*_{m-r_m+1:m} \in L(\Delta^*: \Phi(\tau)$, we obtain

$$\wp_m^{(1)}(\epsilon) \le P(\tau \le d) + \int_0^{\infty} P\left(X^*_{[m(\tau-\epsilon)-r+1:[n(\tau-\epsilon)]}\right) \le a_{[\varphi(m)]}x + b_{[\varphi(m)]}|\tau = z dA(z) + 0(1) \tag{27}$$

Now, let us introduce

$$\tau_d = \begin{cases} \tau \ , & \tau > d \\ d \ , & \tau \le d \end{cases}$$

Clearly,

$$P(\tau_d \le z) = \begin{cases} 0 , & z < d \\ P(\tau \le z), & z \ge d \end{cases} \tag{28}$$

Therefore, (18) yields

$$\wp_m^{(1)}(\epsilon) \le P(\tau \le d) = P\left(X^*_{[\varphi([m(\tau_d-\epsilon)]-r+1:[\varphi[n(\tau_d-\epsilon)]]}\right) \le a_{[\varphi(m)]}x + b_{[\varphi(m)]}|\tau + 0(1)$$

On the other hand, since $\tau_d - \epsilon > 0$, we obtain

$$\frac{\varphi([m(\tau_d-\epsilon)])}{\varphi(m)} = \frac{\varphi\left(n\frac{[m(\tau_d-\epsilon)]}{m}\right)}{\varphi(m)} \underset{m}{\to} (\tau_d-\epsilon)^p \tag{29}$$

Note that $\frac{\varphi(mx)}{\varphi(m)} \underset{m}{\to} x^\rho$ holds locally uniformly on $(0,\infty)$, consequently, by using Theorem 2.1 (the extreme case) and we obtain

$$\lim_{n\to\infty} \wp_m^{(1)}(\epsilon) \le P(\tau \le d) + \int_0^{\infty} 1 - \Gamma_R((z-\epsilon)^p \mho_{i:\beta}^{m+1}(x) dA(z) \ , i \in \{1,2,3\} \tag{30}$$

Thus, by letting $\epsilon \to 0$, then $d \to 0$, and in view of the fact that $0 = \Theta(0^-) = \Theta(0) = \Theta(0^+)$, we obtain

$$\lim_{n\to\infty} P(X^*_{\nu_m-r+1:\nu_m} \le a_{[\varphi(m)]}x + b_{[\varphi(m)]} \le 1 - \int_0^{\infty} 1 - \Gamma_R((z-\epsilon)^p \mho_{i:\beta}^{m+1}(x) dA(z) \ , i \in \{1,2,3\} \tag{31}$$

By applying a similar argument (with only the obvious modification) we can prove that $\lim_{n\to\infty} P(X^*_{\nu_m-r+1:\nu_m} \le a_{[\varphi(m)]}x + b_{[\varphi(m)]} \ge 1 - \int_0^{\infty} 1 - \Gamma_R((z-\epsilon)^p \mho_{i:\beta}^{m+1}(x) dA(z) \ , i \in \{1,2,3$ (32)

Thus, the claimed result for extreme case follows by combining (31) and (32). For proving the theorem in central case, the preceding argument can be repeated by changing the roles of Theorem 2.1, Part (I) (the extreme case), and Theorem 2.1, Part (1), to Theorem 2.1, Part (II) (the central case), and Theorem 2.1, Part (2), respectively. The details are therefore omitted. We now turn to the proof of the second part of the theorem (the intermediate case). The proof follows closely as the proof of the theorem in the extreme and central cases, with only some obvious changes. For example, in view of (22), (24) takes the form

$$P(m + m\varphi^{-\frac{\alpha}{2}}(m)(\tau - \epsilon) \le \nu_m \le (m + m\varphi^{-\frac{\alpha}{2}}(m)(\tau + \epsilon)) \underset{m}{\to} 1 \tag{32}$$

Therefore, by applying the same argument of the proof of the theorem in the extreme and central cases, and in view of the symmetry of the df $B(z)$, we obtain

$$P(X^*_{\nu_{m-r_{\nu_m+1:}}} \le a_{[\varphi(m)]}x + b_{[\varphi(m)]} \le P(-d < \tau \le \int_{-\infty}^{\infty} N(m+1)V_{i:\beta}(x) - l\rho z(1-\alpha)\, dA(z) \tag{33}$$

where $m_n(s) = m + \left\lfloor ms\varphi^{-\frac{\alpha}{2}}(n) \right\rfloor = n\epsilon_n(s) \underset{n}{\to} \infty$ (note that for any $s > 0$, we have$\epsilon_m\ (s)\ d, \epsilon$ and τ_d are defined as the same as in the first part of the proof of the theorem. On the other hand, in

view of the conditions $\varphi^{\frac{\alpha}{2}}(n)\ (\frac{\varphi(mx)}{\varphi(m)} - x^{p}) \underset{n}{\to} 0$ and$\rho < \frac{2}{\alpha}$, we obtain

$$\varphi\big(n_m(s)\big) = \varphi\left(ns\epsilon_n^{\rho}(s)\right) = \varphi(n)\epsilon_n^{\rho}(s) + 0\left(\varphi^{1-\frac{\alpha}{2}}(n)\right) = \varphi(n) + \sigma(\varphi(n)) \tag{35}$$

Where $\sigma\big(n_m(s)\big) = \Phi(m \in_n (s) = \varphi(n)\epsilon_n^{\rho}(s) + 0\left(\varphi^{1-\frac{\alpha}{2}}(n)\right).\ 0 < \theta < 1$. Thus,

$$\frac{\sigma(\varphi(m))}{\varphi^{1-\frac{\alpha}{2}}(m)} = s\rho + \rho\theta\frac{\varphi^{\frac{\alpha}{2}}(m)}{m} + 0(1) \underset{m}{\to} s\rho \tag{36}$$

Therefore, by combining (35) and (36), we obtain

$$\frac{\varphi\big(n_m(\tau_d - \epsilon)\big) - \varphi(n)}{\varphi^{1-\frac{\alpha}{2}}(m)} = \frac{\sigma(\varphi(m))}{\varphi^{1-\frac{\alpha}{2}}(m)} \underset{n}{\to} \rho((\tau_d - \epsilon)) \tag{37}$$

which in turn, in view of Theorem 2.1, Part (III) (intermediate case) and Theorem 2.1, Part (3), after letting $d \to 0$, we obtain

$$\lim_{m\to\infty} P(X^*_{\nu_m - r+1:\nu_m} \le a_{[\varphi(m)]}x + b_{[\varphi(m)]} \le \int_{-\infty}^{\infty} N(m+1)V_{i:\beta}(x) - l\rho z(1-\alpha)\,dA(z) \tag{38}$$

By applying a similar argument (with only the obvious modification) we can prove that

$$\lim_{m\to\infty} P(X^*_{\nu_m - r+1:\nu_m} \le a_{[\varphi(m)]}x + b_{[\varphi(m)]} \ge \int_{-\infty}^{\infty} N(m+1)V_{i:\beta}(x) - l\rho z(1-\alpha)\,dA(z) \tag{39}$$

Thus, the claimed result for intermediate case follows by combining the last two relations. This completes the proof of the theorem.

Theorem 2.4: Suppose that $X^*_{d:m-r_m+1:m}\epsilon L(X^*_d{:}\,\varphi|\tau)$, let $m > -1$, $\tilde{a}_n > 0$ and $\tilde{b}_n \in \Re, m \ge 1$, be suitable normalizing constants for which

$$P(X^*_{d:m-r_m+1:m} \le \tilde{a}_m x + \tilde{b}_m) \overset{w}{\to} \varphi^{d(n,k)}(x) \tag{40}$$

Where $\varphi^{d(n,k)}(x)$ is a non-degenerate df. Furthermore, let ν_m be a sequence of non-negative integer valued rv's which satisfy

$$\frac{\nu_m - m}{m^{1-\alpha/2}} \quad \overset{p}{\to} \quad \tau \tag{41}$$

where the df $A(z) = P(\tau \le z)$ is continuous at zero, then

$$P(X^*_{d:m-r_m+1:m} \le \bar{a}_m x + \bar{b}_m) \overset{w}{\to} \varphi^{(m,k)}(x) \overset{w}{\to} \begin{cases} 1 - \int_0^{\infty} \Gamma\big(z^0\Psi_{i:\beta}^{m+1}(x)dA\ (z), i\epsilon\{1,2,3\}\big) \\ \text{where } r = r_n = \text{constsnt (extreme case)} \\ \int_0^{\infty} N(z^{\frac{\rho}{2}}W^*_{i:\beta}(x)dA(z), i \in \{1,2,3\}, \text{(central case)} \end{cases}$$

Furthermore, let the intermediate rank sequence $\{r_n\}$ satisfy Chibisov condition and let condition (41) be replaced by

$$\frac{\nu_m - m}{m\varphi^{-\frac{\alpha}{2}}(m)} \quad \overset{p}{\to} \quad \tau \tag{42}$$

Where $\varphi(m)\epsilon RV_{\rho}, 0 < \rho < \frac{2}{\alpha}, \varphi^{\frac{\alpha}{2}}(m), (\frac{\varphi(mx)}{\varphi(m)} - x^{\rho}) \underset{n}{\to} 0$ and the $df\ A(z)$ is symmetric and continuous at zero, then

$$P(X^*_{\nu_m - r+1:\nu_m} \le \bar{a}_{[\varphi(m)]}x + \bar{b}_{[\varphi(m)]} \underset{m}{\to} \int_{-\infty}^{\infty} N(m+1)V_{i:\beta}(x) - l\rho z(1-\alpha)\,dA(z);\ \ i = \{1,2,3\}$$

(43)

Without significant modifications, the method of the proof of Theorem 2.4 is the same as that Theorem 2.3, except only the obvious changes. Hence, for brevity the details of the proof are omitted.

V. Applications

Many authors have considered prediction problems based on samples of random sizes, The importance of the order statistics in the reliability theory is attributed to the fact that the r^{th} order statistics $(n - r + 1)$ out-of-n system made up of n identical components with independent life lengths. On the other hand, in dealing with censored samples, where the life-test is terminated after observing the r^{th} failure (Type II censoring), or the termination of the test occurs after a given time lapse (Type I censoring), the complete survival times cannot usually be observed (due to time or cost). In many biological and agriculture problems, we often come across a situation where the sample size is not deterministic because either some observations get lost for various reasons, or the size of the target population and its representative sample cannot be determined well. For example, assume that the inhabitants of a populous town are exposed to a dose of radiation resulting from an atomic accident, or exposed to an infection of an unknown epidemic. Furthermore, assume that our interest focuses on the time at which r persons would die among a big random sample of size n that is drawn from the residents of this town. Since the number of infected people in this town is unknown and changes randomly with time, the drawn sample contains a random number of infected and non-infected people. Accordingly, the sample size of the sub-sample of the infected people will be a non-negative integer valued RV, e.g.N, and it will be described by a sequence of independent and identically distributed RVs $X_1, X_2, \cdots, X_N$. Therefore, the r^{th} smallest order statistic will be denoted by $X_{r:N}$, which represents the time at which r persons will die.

VI. Conclusions

In this paper, we consider two sequences $\{X^*_{m-r_m+:m}\}$ and $\{Y^*_{m-r_m+:m}\}, 1 \le r_m \le m$, of gos. The first one is based on independent and identically distributed (i.i.d) random variables (rv's) $X_i, i = 1,2,3, \cdots$ (with common df 's F), while the second sequence is based on a general sequence of rv's $Y_i, i = 1,2,3, \cdots$ (these rv's need not to be independent or identical). Theorem 2.3 extends the result concerning the asymptotic behavior of the sequence $X^*_{\nu_m - r_{\nu_m}+1:\nu_m}$ of gos with random index νn (given by Theorem 2.1) to the second sequence$Y^*_{\nu_m - r_{\nu_m}+1:\nu_m}$, provided that $Y^*_{m-r_m+1:m} \in L(Y^*;\ \varphi|\tau)$ and $Y^*_{d:\,m-r_m+1:m} \in L(Y^*_d;\ \varphi|\tau)$ i.e., the sequences $Y^*_{m-r_m+1:m}$ and $Y^*_{d:\,m-r_m+1:m}$ dependent on τ (where τ is the limit rv of the suitably normalized sequence ν_m in probability) in connecting $X^*_{m-r_m+1:m}$ and $X^*_{d:\,m-r_m+1:m}$ respectively, and $\Phi(n) \in RV_\rho$. Moreover, Theorem 2.4. gives a similar extension for the dual generalized order statistics (DGOSs).

References

[1] Alosey-EL, R. A. (2007). Random sum of new type of mixture of distribution. *Int. J. Stat. Syst*. 2: 49-57.

[2] Ahsanullah, M. (2006). The generalized order statistics from exponential distribution, *Pakistan Journal of Statistics,* 22 (2): 121-128.

[3] Ahsanullah, M. (2000). Generalized order statistics from exponential distribution. *J. Statist. Plan. Inf*. 85: 85-91.

[4] Abouammoh, A. M and Alshingiti, A. M. (2009). Reliability estimation of generalized inverted exponential distribution. *Journal of statistical computation and simulation*, 79(11), 1301-

1315.

[5] Arnold, B. C., Castillo, E. and Sarabia, J. (2008), 'Some Characterizations Involving Uniform and Powers of Uniform Random Variables, *Statistics* 42(6), 527–534.

[6] Abd Elgawad M. A., H. M. Barakat, Qin. H and Y. Ting. (2017). Limit theory of bivariate dual generalized order statistics with random index. *Statistics*, 51 (3):572–90.

[7] Beutner, E. and Kamps, U. (2008). Random contraction and random dilation of generalized order statistics. *Comm. Statist. Theory Methods* 37: 2185-2201.

[8] Burkschat, M., Cramer, E. and Kamps, U. (2003), 'Dual Generalized Order Statistics', *Metron* LXI(I), 13–26.

[9] Barakat, H. M., Khaled, O. M. and Ghonem, H. A. (2021), 'Predicting Future Order Statistics with Random Sample Size', *AIMS Mathematics* 6(5), 5133–5147.

[10] Casta˜no-Martnez, A., L´opez-Bl´azquez, F. and Salamanca-Mi˜no, B. (2012). Random translations, contractions and dilations of order statistics and records. *Statistics* 46(1): 57-67.

[11] Castaño-Martínez, A., López-Blázquez, F. and Salamanca-Miño, B. (2010). Random translations, contractions and dilations of order statistics and records, *Statistics*, 1-11.

[12] El-Adll, M. E. (2018), 'Characterization of Distributions by Equalities of Two Generalized or Dual Generalized Order Statistics, *Communications in Statistics - Theory and Methods* 26(3), 522–528.

[13] Galambos, J. & Kotz, S. (1978), Characterizations of Probability Distributions, Cambridge University Press, Berlin Heidelberg, New York.

[14] Nagaraja, H. N. (2006). Characterizations of Probability Distributions -Handbook of Engineering Statistics, 79-87 (In Book Chapter), Springer, Editor: Hoang Pham, Uk.

[15] Rao, C. R. & Chanabhng, D. N. (1998), Recent Approaches to Characterizations Based on Order Statistics and Record Values (Handbook of Statistics, 16, 231- 256), Elsevier.

[16] Khan, A. H., Shah Imtiyaz, A. and Ahsanullah, M. (2012). Characterization through distributional properties of order statistics. *J. Egyptian Math. Soc.* 20 :211-214.

[17] Öncel, S. Y., Ahsanullah, M., Aliev, F. A. and Aygun, F. (2005), 'Switching Record and Order Statistics via Random Contraction, *Statistical Probability Letters* 73(3), 207–217.

[18] Samuel, P. (2008), 'Characterization of Distributions by Conditional Expectation of Generalized Order Statistics, *Statistical Papers* 49, 101–108.

[19] Tavangar, M. and Hashemi, M. (2013), 'On Characterizations of the Generalized Pareto Distributions Based on Progressively Censored Order Statistics, *Statistical Papers* 54, 381–390.

[20] Wesolowski, J. and Ahsanullah, M. (2004), 'Switching Order Statistics Through Random Power Contractions, *Australian & New Zealand Journal of Statistics* 46(2), 297–303

[21] Kamps, U. (1995), *A Concept of Generalized Order Statistics*, B. G. Teubner, Stuttgart.

[22] Nasri-Roudsari, D. (1996). Extreme value theory of generalized order statistics. *Journal of Statistical Planning and Inference*, 55: 281–97.

[23] Kaminsky, K. S. and Nelson, P. I. (1998). Prediction Intervals. In: Handbook of Statistics.

[24] Navarro, J. (2008). Characterizations by power contraction of order statistics, *Communications in Statistics-Theory and Methods,* 37: 987-997.

[25] Nevzorov, V. B. (2001). Record: Mathematical Theory. Translation of Mathematical Monographs 194**.** Providence: *American Mathematical Society*.

PARAMETRIC ESTIMATION OF THE PROCESS CAPABILITY INDEX $\mathbb{S}''_{pk}$ AND ITS APPLICATION TO ELECTRONIC INDUSTRIES

Mahendra Saha[1], Pratibha Pareek[2], Anju Devi[3], Abhimanyu S Yadav[4]

•

[1] University of Delhi, Delhi, India.
[2] Chandigarh Group of Colleges, Mohali, India.
[3] Maa Shakumbhari University, Saharanpur, India.
[4] Banaras Hindu University, Varanasi, India.
Corresponding author email[1]: drmahendrasaha1981@gmail.com
Email[2]: pratibhaprk8437@gmail.com
Email[3]: anjuchoudharykuk@gmail.com
Email[4]: asybhu10@gmail.com

Abstract

The proposed index is the process capability index used in the electronics industries to measure the capability of the process. This article focuses on process capability index, specifically applicable to normal random variables. The article has three main objectives: Firstly, we explore various classical estimation methods for the proposed index from frequentist approaches for normal distributions and compare their performance based on mean squared errors. Second, we calculate the classical confidence interval for the proposed index, which includes the asymptotic confidence interval. Third, we examine both Bayes point and interval estimation under symmetric and asymmetric loss functions for the proposed index. A Monte Carlo and Markov Chain Monte Carlo simulation study is conducted to compare the performance of the classical and the Bayes estimates of the proposed index for some set of parameters. Finally, to demonstrate the applicability of this index, two real data sets from the electronics industry are re-analyzed.

Keywords: Asymptotic confidence interval, Bayesian estimation, classical methods of estimation, point and interval estimation.

Abbreviations and notations

$\mathbb{ACI}$	:	Asymptotic confidence interval.
$\mathbb{AW}$	:	Average width.
$\mathbb{BE}$	:	Bayes estimate.
$\mathbb{CI}$	:	Confidence interval.
$\mathbb{CP}$	:	Coverage probability.
$\mathbb{CME}$	:	Cramér-von-Mises estimator.
$\mathbb{CDF}$	:	Cumulative distribution function.
$\mathbb{HPD}$	:	Highest posterior density.
$\mathbb{IG}$	:	Inverse gamma.
$\mathbb{KLF}$	:	K-loss function.
$\mathbb{LSE}$	:	Least squares estimator.
$\mathbb{LINEX}$	:	Linear exponential.
$\mathbb{LSLF}$	:	Logarithmic squared error loss function.
$\mathbb{MCMC}$	:	Markov Chain Monte Carlo.
$\mathbb{MLE}$	:	Maximum likelihood estimator.
$\mathbb{MPSE}$	:	Maximum product of spacing estimator.
$\mathbb{MSE}$	:	Mean squared error.
$\mathbb{MSELF}$	:	Modified squared error loss function.
$\mathbb{MC}$	:	Monte Carlo.
$\mathbb{NLM}$	:	Non-linear minimization.
$\mathbb{PE}$	:	Percentile estimator.
$\mathbb{PR}$	:	Posterior risk.
$\mathbb{PDF}$	:	Probability density function.
$\mathbb{PCI}$	:	Process capability index.
$\mathbb{SELF}$	:	Squared error loss function.
$\mathbb{WLSE}$	:	Weighted least square estimator.
$\mathbb{WSELF}$	:	Weighted squared error loss function.

1. Introduction

Across all manufacturing sectors, processes are routinely evaluated to determine their capacity using various instruments and methods to verify whether a process under observation meets a given set of requirements or standards. $\mathbb{PCI}$ is the tool of choice for manufacturers because it has been proven to help with decision-making and improve process performance. $\mathbb{PCI}$s have garnered significant attention, particularly in the field of quality assurance. When studying traditional capability indices, it is often assumed that with a process mean κ and process standard deviation ζ a normal probability model is used. This assumption has contributed to the widespread interest in $\mathbb{PCI}$s, particularly in quality assurance. For a deeper understanding of various capability indices, readers may refer to: $\mathbb{C}_p$ Juran, Gryna and Bingham [11], $\mathbb{C}_{pk}$ Kane [12], $\mathbb{C}_{pm}$ Chang, Cheng and Spiring [4]; Hsiang and Taguchi [10], $\mathbb{C}_{pmk}$ Pearn, Kotz and Jhonson [15]; Wu and Pearn [27], $\mathbb{C}_p(u,v)$ Vannman [25], $\mathbb{S}_{pk}$ Boyles [1]; Chen and Pearn [2]; Saha [17] and many others. The Boyles [1] $\mathbb{PCI}$, $\mathbb{S}_{pk}$ was defined as

$$\mathbb{S}_{pk} = \frac{1}{3}\Phi^{-1}\left\{\frac{1}{2}\Phi\left(\frac{\mathbb{U}-\kappa}{\zeta}\right)+\frac{1}{2}\Phi\left(\frac{\kappa-\mathbb{L}}{\zeta}\right)\right\} \tag{1}$$

here, $\mathbb{U}$ and $\mathbb{L}$ represent the upper and lower specification limits, respectively, and $\Phi(\cdot)$ is the $\mathbb{CDF}$ of $N(0,1)$ and defined as:

$$\mathbb{F}\left(y|\kappa,\zeta\right) = \Phi\left(\frac{y-\kappa}{\zeta}\right) \;\; ; \;\; y,\kappa \in \mathcal{R}, \zeta > 0 \tag{2}$$

with the $\mathbb{PDF}$ of normal distribution,

$$f(y|\kappa,\zeta) = \frac{1}{\zeta\sqrt{2\pi}} e^{-\frac{1}{2}\left(\frac{y-\kappa}{\zeta}\right)^2} \;\; ; \;\; y,\kappa \in \mathcal{R}, \zeta > 0. \tag{3}$$

One of the drawbacks of $\mathbb{S}_{pk}$ is that it ignores the target value of the process. Its inability to represent a situation in which the process is not centred on the target value is another disadvantage. To address this problem, a new index was created that considers deviations from the desired value when determining a process's capabilities. In the article by Saha [17], using $\mathbb{SELF}$ a capability index, a measure designed to assess the performance of a process relative to its specification limits. This index was subsequently cited and discussed by Saha, Devi and Pareek [18], while its inferential properties were rigorously investigated by Saha et al. [19]. Building upon this prior foundation, the present study develops a novel asymmetric loss-based process capability index, denoted as $\mathbb{S}''_{pk}$, specifically for processes that can be modeled by a normal distribution.

The proposed index is formulated by incorporating the $\mathbb{LINEX}$ loss function by Varia [26], as a tool for decision-making under asymmetric loss conditions. This loss function has proven useful in various statistical inference settings where the cost of overestimation and underestimation differ. In process capability analysis, Saha and Dey [21] have previously applied the $\mathbb{LINEX}$ loss to address such asymmetries, making it a natural choice for the development of $\mathbb{S}''_{pk}$. Mathematically, the $\mathbb{LINEX}$ loss function is expressed as: $\mathbb{L}_2(\kappa - \mathbb{T}) = 2\frac{e^{\varpi(\kappa-\mathbb{T})} - \varpi(\kappa-\mathbb{T}) - 1}{\varpi^2}$, where ϖ is a fixed parameter that controls the degree of asymmetry of $\mathbb{L}_2$. For small values of ϖ (e.g., ϖ = 0.01), this loss function becomes nearly symmetric and resembles the quadratic loss function, $\mathbb{L}(\kappa - \mathbb{T}) = (\kappa - \mathbb{T})^2$ Erfanian and Gildeh [9].

The index $\mathbb{S}''_{pk}$, as developed by Dey, Saha and Park [7] and further refined by Saha and Dey [20] is obtained by incorporating the $\mathbb{LINEX}$ loss function into the denominator of the conventional $\mathbb{S}_{pk}$ $\mathbb{PCI}$. This modification results in a capability measure that directly accounts for asymmetric loss considerations in evaluating process performance, and is given by

$$\mathbb{S}''_{pk} = \frac{1}{3}\Phi^{-1}\left\{\frac{1}{2}\Phi\left(\frac{\mathbb{U}-\kappa}{\sqrt{\zeta^2 + 2\frac{e^{\varpi(\kappa-\mathbb{T})} - \varpi(\kappa-\mathbb{T}) - 1}{\varpi^2}}}\right) + \frac{1}{2}\Phi\left(\frac{\kappa-\mathbb{L}}{\sqrt{\zeta^2 + 2\frac{e^{\varpi(\kappa-\mathbb{T})} - \varpi(\kappa-\mathbb{T}) - 1}{\varpi^2}}}\right)\right\} \tag{4}$$

The term $2\frac{e^{\varpi(\kappa-\mathbb{T})} - \varpi(\kappa-\mathbb{T}) - 1}{\varpi^2}$ captures two types of variation: (i) is within-process variation, which reflects the natural variability of individual observation around the process mean κ, (ii) between-process deviation, which represents the departure of the process mean κ from the desired target value $\mathbb{T}$. Together, both the inherent dispersion of the process and its alignment with the target specifications.

The primary objective of this study is to examine the performance characteristics of six well-known frequentist estimation methods previously employed by Dey et al. [8]. These estimators include the $\mathbb{MLE}$, $\mathbb{LSE}$,$\mathbb{WLSE}$, $\mathbb{PE}$, $\mathbb{CME}$ and $\mathbb{MPSE}$. We focuses on their application to the $\mathbb{S}''_{pk}$ under various combinations of sample sizes and parameter settings. The evaluation criterion for these estimators is their $\mathbb{MSE}$s, which balances both bias and variability in estimation. Since the theoretical comparison of these estimators is analytically intractable owing to the complex form of $\mathbb{S}''_{pk}$ and the absence of closed form variance expression, a comprehensive simulation study is undertaken. The primary focus is on the $\mathbb{MLE}$, given its widespread use and desirable asymptotic properties. The second objective is the study is to derive an $\mathbb{ACI}$ for $\mathbb{S}''_{pk}$.

To assess the performance of the interval, the $\mathbb{AW}$ and $\mathbb{CP}$ are calculated. The third objective is to obtain the Bayesian point and interval estimates for $\mathbb{S}''_{pk}$. The novelty of this study lies in the fact that, to date, there have been no reports on the estimation of $\mathbb{S}''_{pk}$ or the construction of $\mathbb{ACI}$ using the $\mathbb{MLE}$ method. Thus, this study aims to provide applied statisticians and quality control engineers with guidance on selecting the optimal estimation method among the six distinct frequentist approaches. To assess interval quality, both $\mathbb{AW}$ and $\mathbb{CP}$ are computed. The

third objective is to develop Bayesian point and interval estimates for $\mathbb{S}''_{pk}$, offering a probabilistic alternative to the frequentist framework. The novelty of this work lies in the fact that, to the best of our knowledge, no prior research has addressed the estimation of $\mathbb{S}''_{pk}$ or the construction of $\mathbb{ACI}$ for it using $\mathbb{MLE}$ approach.

Rest of the article is structured as follows. In Section 2, the estimation methods for $\mathbb{S}''_{pk}$ are introduced, and the corresponding estimators are derived. This section also includes the construction of $\mathbb{ACI}$ for $\mathbb{S}''_{pk}$ based on the $\mathbb{MLE}$, as well as Bayesian estimation using five different loss functions. Section 3 presents a comprehensive $\mathbb{MC}$ and $\mathbb{MCMC}$ simulation study to compare the performances of $\mathbb{S}''_{pk}$ based on the various estimation methods. In Section 4, two real datasets from the electronics industry are analyzed for illustration. Finally, Section 5 provides the concluding remarks.

2. Estimation of the index $\mathbb{S}''_{pk}$

This section investigates the point and interval estimation of the index $\mathbb{S}''_{pk}$ from classical and Bayesian point of view, respectively.

2.1. Classical estimation

A random variable $\mathbb{Y}$ has $\mathrm{N}(\kappa, \zeta)$, with its $\mathbb{CDF}$, given in equation (2) and $\mathbb{PDF}$, given in equation (3) where κ, ζ are the parameters of the distribution and $\Phi(\cdot)$ is the $\mathbb{CDF}$ of the standard normal variate. In the context of the considered model, the analytical forms of the derivatives and necessary transformations are not available in closed form for the parameter estimation procedures. Consequently, for all the considered estimation methods the parameter estimates were obtained using the $\mathbb{NLM}$ technique. A short formulation of the considered classical methods of estimation are provided in brief in Table 1, followed by the final expression for the derived $\mathbb{PCI}$ based on the estimated values of the parameters. Note that only the method of MLE and MPSE satisfied the invariance property and hence we got the MLE and MPSE of the index $\mathbb{S}''_{pk}$ by using the invariance property and for the repmaing considered methods we have used the plug-in method to the obatin the estimate of the index. The detailed description of these menthods of estimation in the context of process capability analysis the readers may the articles Saha, Devi and Pareek [18], Saha et al. [19], Saha and Dey [21] and many more.

Asymptotic confidence interval

$\mathbb{ACI}$ of $\mathbb{S}''_{pk}$ in case of normal distribution, can be derived with $100(1-\omega)\%$ $\mathbb{CI}$. $\mathbb{ACI}$ of $\mathbb{S}''_{pk}$ can be obtained as:

$$\frac{\mathbb{S}''_{\hat{pk}} - \mathbb{S}''_{pk}}{\sqrt{var(\mathbb{S}''_{\hat{pk}})}} \sim N(0,1)$$

where,

$$\begin{aligned} var(\mathbb{S}''_{\hat{pk}}) \quad = \quad & \left(\frac{\partial \mathbb{S}''_{pk}}{\partial \kappa}\right)^2 \times \left(-\frac{1}{E\left(\frac{\partial^2 ln\ L(\kappa,\zeta)}{\partial \kappa^2}\right)}\right) + \left(\frac{\partial \mathbb{S}''_{pk}}{\partial \zeta}\right)^2 \times \left(-\frac{1}{E\left(\frac{\partial^2 ln\ L(\kappa,\zeta)}{\partial \zeta^2}\right)}\right) \\ & -2\left(\frac{\partial \mathbb{S}''_{pk}}{\partial \kappa}\right)\left(\frac{\partial \mathbb{S}''_{pk}}{\partial \zeta}\right) \times \left(-\frac{1}{E\left(\frac{\partial^2 ln\ L(\kappa,\zeta)}{\partial \kappa \partial \zeta}\right)}\right). \end{aligned}$$

The elements of Fisher information matrix

$$I(\theta) = E\left\{ \begin{array}{cc} \left(\frac{\partial^2 ln\ L(\kappa,\zeta)}{\partial \kappa^2}\right) & \left(\frac{\partial^2 ln\ L(\kappa,\zeta)}{\partial \kappa \partial \zeta}\right) \\ \left(\frac{\partial^2 ln\ L(\kappa,\zeta)}{\partial \zeta \partial \kappa}\right) & \left(\frac{\partial^2 ln\ L(\kappa,\zeta)}{\partial \zeta^2}\right) \end{array} \right\}$$

Table 1: *Classical methods of estimation and corresponding estimated PCI*

Method	Function to be optimized	Expression of estimated index S''_{pk}
$\mathbb{MLE}$	$log\left(\left(\frac{1}{2\pi\zeta^2}\right)^{\frac{n}{2}} e^{-\frac{1}{2}\sum_{i=1}^{n}\left(\frac{y-\kappa}{\zeta}\right)^2}\right)$	$\frac{1}{3}\Phi^{-1}\left\{\frac{1}{2}\Phi\left(\frac{\mathbb{U}-\hat{\kappa}_{mle}}{\sqrt{\hat{\zeta}^2_{mle}+\frac{2(e^{\omega(\hat{\kappa}_{mle}-\mathbb{T})}-\omega(\hat{\kappa}_{mle}-\mathbb{T})-1)}{\omega^2}}}\right)+\frac{1}{2}\Phi\left(\frac{\hat{\kappa}_{mle}-\mathbb{L}}{\sqrt{\hat{\zeta}^2_{mle}+\frac{2(e^{\omega(\hat{\kappa}_{mle}-\mathbb{T})}-\omega(\hat{\kappa}_{mle}-\mathbb{T})-1)}{\omega^2}}}\right)\right\}$
$\mathbb{LSE}$	$\sum_{i=1}^{n}\left\{\mathbb{F}(y_{(i:n)} \mid \kappa,\zeta)-\frac{i}{n+1}\right\}^2$	$\frac{1}{3}\Phi^{-1}\left\{\frac{1}{2}\Phi\left(\frac{\mathbb{U}-\hat{\kappa}_{lse}}{\sqrt{\hat{\zeta}^2_{lse}+\frac{2(e^{\omega(\hat{\kappa}_{lse}-\mathbb{T})}-\omega(\hat{\kappa}_{lse}-\mathbb{T})-1)}{\omega^2}}}\right)+\frac{1}{2}\Phi\left(\frac{\hat{\kappa}_{lse}-\mathbb{L}}{\sqrt{\hat{\zeta}^2_{lse}+\frac{2(e^{\omega(\hat{\kappa}_{lse}-\mathbb{T})}-\omega(\hat{\kappa}_{lse}-\mathbb{T})-1)}{\omega^2}}}\right)\right\}$
$\mathbb{WLSE}$	$\sum_{i=1}^{n} w_i\left\{\mathbb{F}(y_{(i:n)} \mid \kappa,\zeta)-\frac{i}{n+1}\right\}^2$	$\frac{1}{3}\Phi^{-1}\left\{\frac{1}{2}\Phi\left(\frac{\mathbb{U}-\hat{\kappa}_{wlse}}{\sqrt{\zeta^2_{wlse}+\frac{2(e^{\omega(\hat{\kappa}_{wlse}-\mathbb{T})}-\omega(\hat{\kappa}_{wlse}-\mathbb{T})-1)}{\omega^2}}}\right)+\frac{1}{2}\Phi\left(\frac{\hat{\kappa}_{wlse}-\mathbb{L}}{\sqrt{\hat{\zeta}^2_{wlse}+\frac{2(e^{\omega(\hat{\kappa}_{wlse}-\mathbb{T})}-\omega(\hat{\kappa}_{wlse}-\mathbb{T})-1)}{\omega^2}}}\right)\right\}$
$\mathbb{PE}$	$\sum_{j=1}^{n}\left\{y_{(i:n)}-Q(p_i \mid \kappa,\zeta)\right\}^2$	$\frac{1}{3}\Phi^{-1}\left\{\frac{1}{2}\Phi\left(\frac{\mathbb{U}-\hat{\kappa}_{pe}}{\sqrt{\zeta^2_{pe}+\frac{2(e^{\omega(\hat{\kappa}_{pe}-\mathbb{T})}-\omega(\hat{\kappa}_{pe}-\mathbb{T})-1)}{\omega^2}}}\right)+\frac{1}{2}\Phi\left(\frac{\hat{\kappa}_{pe}-\mathbb{L}}{\sqrt{\hat{\zeta}^2_{pe}+\frac{2(e^{\omega(\hat{\kappa}_{pe}-\mathbb{T})}-\omega(\hat{\kappa}_{pe}-\mathbb{T})-1)}{\omega^2}}}\right)\right\}$
$\mathbb{CME}$	$\frac{1}{12n}+\sum_{i=1}^{n}\left\{\mathbb{F}(y_{(i:n)} \mid \kappa,\zeta)-\frac{2i-1}{2n}\right\}^2$	$\frac{1}{3}\Phi^{-1}\left\{\frac{1}{2}\Phi\left(\frac{\mathbb{U}-\hat{\kappa}_{cme}}{\sqrt{\zeta^2_{cme}+\frac{2(e^{\omega(\hat{\kappa}_{cme}-\mathbb{T})}-\omega(\hat{\kappa}_{cme}-\mathbb{T})-1)}{\omega^2}}}\right)+\frac{1}{2}\Phi\left(\frac{\hat{\kappa}_{cme}-\mathbb{L}}{\sqrt{\hat{\zeta}^2_{cme}+\frac{2(e^{\omega(\hat{\kappa}_{cme}-\mathbb{T})}-\omega(\hat{\kappa}_{cme}-\mathbb{T})-1)}{\omega^2}}}\right)\right\}$
$\mathbb{MPSE}$	$\frac{1}{(n+1)}\sum_{i=1}^{n+1}\log\left(\mathbb{F}(y_{(i:n)} \mid \kappa,\zeta)\right.$ $\left.-\mathbb{F}(y_{(i-1:n)} \mid \kappa,\zeta)\right)$	$\frac{1}{3}\Phi^{-1}\left\{\frac{1}{2}\Phi\left(\frac{\mathbb{U}-\hat{\kappa}_{mpse}}{\sqrt{\zeta^2_{mpse}+\frac{2(e^{\omega(\hat{\kappa}_{mpse}-\mathbb{T})}-\omega(\hat{\kappa}_{mpse}-\mathbb{T})-1)}{\omega^2}}}\right)+\frac{1}{2}\Phi\left(\frac{\hat{\kappa}_{mpse}-\mathbb{L}}{\sqrt{\hat{\zeta}^2_{mpse}+\frac{2(e^{\omega(\hat{\kappa}_{mpse}-\mathbb{T})}-\omega(\hat{\kappa}_{mpse}-\mathbb{T})-1)}{\omega^2}}}\right)\right\}.$

can easily be obtained, where

$$E\left(\frac{\partial^2 lnL(\kappa,\zeta)}{\partial\kappa^2}\right)=-\frac{n}{\zeta^2}, E\left(\frac{\partial^2 lnL(\kappa,\zeta)}{\partial\zeta^2}\right)=-\frac{2n}{\zeta^2} \text{ and } E\left(\frac{\partial^2 lnL(\kappa,\zeta)}{\partial^2\kappa^2\zeta^2}\right)=0$$

After, obtaining partial derivative of $\mathbb{S}''_{pk}$ with respect to κ and ζ. Using, $(\Phi^{-1})'(y)=\frac{1}{\Phi'(\Phi^{-1}(y))}$, with $\Phi'(=\phi)$ as the first derivative of Φ. We get it as:

$$\begin{aligned}\frac{\partial \mathbb{S}''_{pk}}{\partial\kappa} &= \frac{1}{6}\frac{1}{\Phi'\left(3\mathbb{S}''_{pk}\right)}\times\left\{\phi\left(\frac{\mathbb{U}-\kappa}{\sqrt{\zeta^2+2\frac{e^{\omega(\kappa-\mathbb{T})}-\omega(\kappa-\mathbb{T})-1}{\omega^2}}}\right)\right.\\ &\left(-\frac{1}{\sqrt{\left(\zeta^2+2\frac{e^{\omega(\kappa-\mathbb{T})}-\omega(\kappa-\mathbb{T})-1}{\omega^2}\right)}}-\frac{(\mathbb{U}-\kappa)(e^{\omega(\kappa-\mathbb{T})}-1)}{\omega\left(\zeta^2+2\frac{e^{\omega(\kappa-\mathbb{T})}-\omega(\kappa-\mathbb{T})-1}{\omega^2}\right)^{3/2}}\right)\\ &+ \phi\left(\frac{\kappa-\mathbb{L}}{\sqrt{\zeta^2+2\frac{e^{\omega(\kappa-\mathbb{T})}-\omega(\kappa-\mathbb{T})-1}{\omega^2}}}\right)\\ &\left.\left(\frac{1}{\sqrt{\left(\zeta^2+2\frac{e^{\omega(\kappa-\mathbb{T})}-\omega(\kappa-\mathbb{T})-1}{\omega^2}\right)}}-\frac{(\kappa-\mathbb{L})(e^{\omega(\kappa-\mathbb{T})}-1)}{\omega\left(\zeta^2+2\frac{e^{\omega(\kappa-\mathbb{T})}-\omega(\kappa-\mathbb{T})-1}{\omega^2}\right)^{3/2}}\right)\right\}\end{aligned}$$

$$\begin{aligned}\frac{\partial \mathbb{S}''_{pk}}{\partial\zeta} &= \frac{1}{6}\frac{1}{\Phi'\left(3\mathbb{S}''_{pk}\right)}\times\left\{\phi\left(\frac{\mathbb{U}-\kappa}{\sqrt{\zeta^2+2\frac{e^{\omega(\kappa-\mathbb{T})}-\omega(\kappa-\mathbb{T})-1}{\omega^2}}}\right)\right.\\ &\left(\frac{-(\mathbb{U}-\kappa)\zeta}{\left(\zeta^2+2\frac{e^{\omega(\kappa-\mathbb{T})}-\omega(\kappa-\mathbb{T})-1}{\omega^2}\right)^{3/2}}\right)+\phi\left(\frac{\kappa-\mathbb{L}}{\sqrt{\zeta^2+2\frac{e^{\omega(\kappa-\mathbb{T})}-\omega(\kappa-\mathbb{T})-1}{\omega^2}}}\right)\\ &\left.\left(\frac{-(\kappa-\mathbb{L})\zeta}{\left(\zeta^2+2\frac{e^{\omega(\kappa-\mathbb{T})}-\omega(\kappa-\mathbb{T})-1}{\omega^2}\right)^{3/2}}\right)\right\}\end{aligned}$$

Hence,the $(1-\omega)100\%$ $\mathbb{AIC}$ of $\mathbb{S}''_{pk}$ can be obtained as:

$$\left\{\left(\hat{\mathbb{S}''}_{pk}-\mathbb{Z}_{(\frac{\omega}{2})}\sqrt{var(\hat{\mathbb{S}''}_{pk})}\right),\left(\hat{\mathbb{S}''}_{pk}+\mathbb{Z}_{(\frac{\omega}{2})}\sqrt{var(\hat{\mathbb{S}''}_{pk})}\right)\right\}$$

where, $\mathbb{Z}_{(\omega/2)}$ is upper $(\omega/2)^{th}$ quantile of the $N(0,1)$.

2.2. Bayesian estimation

This section focuses on the Bayesian estimation of the newly developed index $\mathbb{S}''_{pk}$. In Bayesian theory, the accuracy of estimation depends on the careful selection of the prior distribution and loss function. The prior reflects initial beliefs about the parameters, while the loss function quantifies estimation errors. Both choices are essential for guiding the posterior distribution towards an accurate estimate. The importance of these components is highlighted by Shiau, Chiang and Hung [22], Spiring et al. [23], and Dey and Saha [6], who demonstrate how the appropriate selection of prior and loss function can enhance the robustness and efficiency of Bayesian estimation. The $\mathbb{PDF}$ of the considered prior for the parameters κ and $\zeta^2=\tau$ are given by

$$\pi_1(\kappa|\tau)=\frac{1}{\sqrt{2\pi\tau}}e^{-\frac{1}{2\tau}(\kappa-\kappa_0)^2}, \qquad \kappa,\kappa_0\in R,\tau>0. \tag{5}$$

$$\pi_2(\tau) = \frac{\beta^{\alpha}}{\varpi(\alpha)}\tau^{-(\alpha+1)}e^{-\frac{\beta}{\tau}}, \qquad \alpha, \beta, \tau > 0. \tag{6}$$

where, the hyper-parameters α, β, and κ_0 are assumed to be known. Hence, the joint prior density function of κ and τ can be written as

$$\pi(\kappa, \tau) = \frac{1}{\sqrt{2\pi\tau}}\frac{\beta^{\alpha}}{\varpi(\alpha)}e^{-\frac{1}{2\tau}(\kappa-\kappa_0)^2-\frac{\beta}{\tau}}\tau^{-(\alpha+1)} \tag{7}$$

The joint posterior distribution is obtained by combining the likelihood function and prior distribution, and it is given by;

$$p(\kappa, \tau|y) \propto (\tau)^{-\frac{(n+3)}{2}-\alpha}e^{-\frac{1}{2\tau}\left\{S_{kk}+(n+1)(\kappa-\kappa_1)^2\right\}} \tag{8}$$

where, $\kappa_1 = \frac{n\bar{y}+\kappa_0}{n+1}$ and $S_{kk} = S_y + 2\beta + \frac{n(\kappa_0-\bar{y})^2}{n+1}$. The marginal posterior distributions of the parameter τ and κ given y are in the following equations;

$$\pi(\tau|y) \propto \tau^{-(\frac{n}{2}+\alpha+1)}e^{\left(-\frac{1}{\tau}\left(\frac{S_{kk}}{2}\right)\right)} \tag{9}$$

$$\pi(\kappa|y) \propto \frac{1}{\sqrt{\pi}}\frac{\varpi\left(\frac{n+1+2\alpha}{2}\right)}{\varpi(n+2\alpha)}\frac{\sqrt{(n+1)}}{\sqrt{S_{kk}}}\left\{1+\frac{(\kappa-\kappa_1)^2}{S_{kk}/(n+1)}\right\}^{-(\frac{n+1+2\alpha}{2})} \tag{10}$$

respectively. The Eqn. (9) is the marginal posterior distribution of τ which represents inverse gamma distribution, i.e., $\tau \sim \mathbb{IG}(\frac{n+2\alpha}{2}, \frac{S_{kk}}{2})$. In Eqn. (10), shows the marginal posterior distribution of κ which is unknown distribution. However, $\sqrt{N}\left(\frac{\kappa-\kappa_1}{\sqrt{S_{kk}/(n+1)}}\right)$ follows a t-distribution with $N = n + 2\alpha$ degrees of freedom. Since the joint posterior distribution does not have a closed-form expression, the marginal posterior distributions will be used to generate posterior random deviates through the $\mathbb{MCMC}$ algorithm. Using the marginal posterior distributions of κ and τ, the $\mathbb{BE}$ of the index $\mathbb{S}''_{pk}$ is obtained by generating $\mathbb{MCMC}$ random deviates. This is done using five different loss functions: $\mathbb{SELF}$, $\mathbb{WSELF}$, $\mathbb{MSELF}$, $\mathbb{LSLF}$, and $\mathbb{KLF}$. The expressions of the loss functions, the associated $\mathbb{BE}$ and $\mathbb{PR}$ are given in tabular form in the following Table 2.

Table 2: *BE and PR under different loss functions.*

Name of the loss function	Form of the loss function	Bayes estimates	Posterior risk
$\mathbb{SELF}$	$(\theta-d)^2$	$E(\theta\|X)$	$V(\theta\|X)$
$\mathbb{WSELF}$	$\frac{(\theta-d)^2}{\theta}$	$\left(E\left(\theta^{-1}\|X\right)\right)^{-1}$	$E(\theta\|X) - \left(E\left(\theta^{-1}\|X\right)\right)^{-1}$
$\mathbb{MSELF}$	$\left(1-\frac{d}{\theta}\right)^2$	$\frac{E\left(\theta^{-1}\|X\right)}{E\left(\theta^{-2}\|X\right)}$	$1-\frac{E\left(\theta^{-1}\|X\right)^2}{E\left(\theta^{-2}\|X\right)}$
$\mathbb{LLF}$	$(\log\theta - \log d)^2$	$\exp\left(E\left(\log\theta\|X\right)\right)$	$Var\left(\log\theta\|X\right)$
$\mathbb{KLF}$	$\left(\sqrt{\frac{d}{\theta}}-\sqrt{\frac{\theta}{d}}\right)$	$\sqrt{\frac{E(\theta\|X)}{E\left(\theta^{-1}\|X\right)}}$	$E\{E(\theta\|X)\left(E\left(\theta^{-1}\|X\right)\right)-1\}$

The following steps have been utilized in order to obtain posterior samples from the respective marginal distributions.

Step-1: Set preliminary estimate value $(\tau^{(0)}, \kappa^{(0)})$
Step-2: To start with $p = 1$.
Step-3: Generate a new sampler for τ and κ as follows: $\tau^{(p)} \sim \pi(y|\tau^{(p-1)})$, $\kappa^{(p)} \sim \pi(y|\kappa^{(p)})$
Step-4: We obtain the posterior samples of size $\mathbb{P}$ for parameters τ and κ. After repeating the

step 2 and step 3 for $r = 1, 2, 3, ..., \mathbb{P}(= 10000)$ times.

Step-5: We get a sequence $\mathbb{S}''^{(p)}_{pk}$ by using the step-4 in above sequence.

Step-6: After receiving the posterior samples, the corresponding $\mathbb{BE}$ of $\mathbb{S}''_{pk}$ can be obtained from the above $\mathbb{MCMC}$ algorithm based on the above defined loss functions.

Step-7: The Bayes credible interval for the proposed index $\mathbb{S}''_{pk}$ is constructed by utilizing the sequences of random deviates $\mathbb{S}''^{(p)}_{pk}$, $r = 1, 2, 3, ..., \mathbb{P}$ obtained through step 5. Using, algorithm the $(1-\omega)100\%$ highest posterior density credible interval of the index is given by, $\left\{\mathbb{S}''^{(p_1^*)}_{pk}, \mathbb{S}''^{(p_1^*+(1-\delta)\mathbb{P})}_{pk}\right\}$, where, (p_1^*) satisfying,

$$\mathbb{S}''^{(p_1^*+(1-\delta)\mathcal{P})}_{pk} - \mathbb{S}''^{(p_1^*)}_{pk} = min\left(\mathbb{S}''^{(p_1+(1-\delta)\mathcal{P})}_{pk} - \mathbb{S}''^{(p_1)}_{pk}\right)$$

3. Simulation and discussion

This section employs $\mathbb{MC}$ simulations to evaluate the performances of the $\mathbb{PCI}$ $\mathbb{S}''_{pk}$ across different estimation methods by analyzing their $\mathbb{MSE}$s and simulated risks. Additionally, the $\mathbb{AW}$s and $\mathbb{CP}$s of the $\mathbb{ACI}$ is evaluated to measure the performance. The simulation study examines sample sizes n = 20, 30, 50, 100 and values of ϖ = 0.01, 1, 5, 10, with several sets of parameter values: (κ, ζ) = (6.5,1.25), (6.5,1.50), (6.5,1.75), (7.5,1.25), (7.5,1.50), (7.5,1.75). The lower, target and upper specification limits are set at 0.50, 7.0, and 12.50, respectively.

In Tables 3 and 4, the values of $\mathbb{S}''_{pk}$ along with the average estimates and $\mathbb{MSE}$s for each estimation method, are presented. The results of the $\mathbb{ACI}$ using $\mathbb{MLE}$ as the estimation method for $\mathbb{S}''_{pk}$ is shown in Table 5, with various values of ϖ. The finding from tables reveals that, among all the estimation methods, $\mathbb{MLE}$ yields the best performance in terms of $\mathbb{MSE}$s. Furthermore, the $\mathbb{MSE}s$ decreases, with increase in sample size, demonstrating the consistency of the estimators. Additionally, as κ increases, the true value of $\mathbb{S}''_{pk}$ also increases. The analysis incorporated $\mathbb{AW}$s and $\mathbb{CP}$s by using $\mathbb{MLE}$, as the method of estimation for the $\mathbb{ACI}$ of $\mathbb{S}''_{pk}$, because $\mathbb{MLE}$ is performing better among all other estimation methods. The findings also indicate that as sample size increases $\mathbb{AW}$ decrease and $\mathbb{CP}$ increases. Next, the Bayes point and interval estimation for the index have been considered under the above mentioned priors using symmetric and asymmetric loss functions. The $\mathbb{BE}$ and $\mathbb{PR}$ along with coverage probability ($\mathbb{CP}$) and average width ($\mathbb{AW}$) are calculated for the considered setup, and presented in Tables 6 and 7 for four different values of ϖ. The values of hyper-parameters in Bayesian setup are chosen as $\alpha = 1.55$, $\beta = 0.05$ and $\kappa_0 = 5$ so that it coincides with the parameter value with smallest variation in the simulation study. The simulation study suggests that with the increase in sample size posterior risk decreases for all setups. Also as further, the $\mathbb{CP}$s increases and tend to the nominal value and their $\mathbb{AW}$s decreases with increase in sample size. Moreover, the $\mathbb{PR}$ is decreases for small values of ϖ and increase for large values of ϖ. As ϖ value increase from 0.01 to 5, $\mathbb{PR}$ decreases and for $\varpi = 10$, $\mathbb{PR}$ increases.

Table 3: *Estimates and MSE for* $\varpi = (0.01, 1)$ *using* MLE, LSE, WLSE, PE, CME, *and* MPSE *with* S''_{pk}.

PCI			MLE		LSE		WLSE		PE		CME		MPSE	
Parameters	S''_{pk}	n	MLE	MSE	LSE	MSE	WLSE	MSE	PE	MSE	CME	MSE	MPSE	MSE
							$\varpi = 0.01$							
S'_{pk}=1.48556	1.48573	20	1.50973	0.05563	1.3974	0.07406	1.37641	0.08297	1.38714	0.08044	1.52055	0.07949	1.66466	0.10776
κ=6.5		30	1.51405	0.0407	1.43546	0.05086	1.40451	0.0629	1.41229	0.0617	1.54164	0.06193	1.62528	0.07026
ζ=1.25		50	1.49475	0.0227	1.44589	0.02983	1.4013	0.04624	1.40921	0.04446	1.53128	0.0375	1.5689	0.0336
		100	1.48988	0.01182	1.48081	0.01616	1.41114	0.03725	1.4181	0.03406	1.54251	0.02502	1.53389	0.01523
S'_{pk}=1.26491	1.26502	20	1.28681	0.04183	1.19082	0.0539	1.16949	0.05955	1.18102	0.05966	1.29958	0.0606	1.42174	0.08114
κ=6.5		30	1.28335	0.02826	1.21746	0.03671	1.18246	0.0496	1.1895	0.04851	1.31155	0.0448	1.38185	0.04938
ζ= 1.50		50	1.28028	0.01731	1.24824	0.02223	1.20178	0.03866	1.20289	0.03476	1.32169	0.03135	1.34511	0.02632
		100	1.26432	0.00764	1.25798	0.01245	1.1987	0.02871	1.20185	0.02716	1.31211	0.0193	1.3031	0.01003
S'_{pk}=1.09888	1.09895	20	1.1113	0.03166	1.03214	0.04193	1.00968	0.05134	1.01655	0.04934	1.12731	0.04841	1.22943	0.06043
κ=6.5		30	1.1044	0.01984	1.05015	0.02608	1.01985	0.03932	1.02446	0.0359	1.13177	0.03145	1.19013	0.03351
ζ=1.75		50	1.10313	0.01201	1.07601	0.01617	1.03592	0.03052	1.03577	0.02639	1.14055	0.02235	1.1598	0.01763
		100	1.09833	0.00623	1.09709	0.00949	1.05642	0.03173	1.04423	0.02139	1.14586	0.01583	1.13279	0.00797
S'_{pk}=1.29514	1.29501	20	1.35925	0.06525	1.2459	0.08371	1.23488	0.08935	1.23673	0.09022	1.41289	0.1125	1.48825	0.1236
κ=7.5		30	1.32999	0.03824	1.24445	0.0572	1.21999	0.06755	1.22185	0.06935	1.39272	0.08191	1.42258	0.06284
ζ=1.25		50	1.31198	0.02261	1.26614	0.03401	1.2263	0.04865	1.22565	0.0502	1.38202	0.05387	1.37209	0.03213
		100	1.30772	0.01199	1.3012	0.02075	1.239	0.03641	1.23851	0.03764	1.38477	0.03764	1.34297	0.01544
S'_{pk}=1.11905	1.11897	20	1.16814	0.04617	1.06321	0.06068	1.05601	0.07508	1.05235	0.06658	1.2105	0.08493	1.28458	0.08875
κ=7.5		30	1.15126	0.03144	1.08925	0.04362	1.05333	0.05965	1.0606	0.05556	1.21497	0.06688	1.23594	0.05361
ζ=1.50		50	1.13297	0.01695	1.09885	0.02465	1.03958	0.03946	1.05172	0.03807	1.19164	0.03921	1.18718	0.02492
		100	1.12821	0.00762	1.12154	0.01406	1.04692	0.02906	1.05964	0.0289	1.18909	0.0257	1.16006	0.00991
S'_{pk}=0.98703	0.98698	20	1.02856	0.0361	0.94299	0.04519	0.92968	0.05672	0.93065	0.05082	1.07033	0.06495	1.1319	0.07127
κ=7.5		30	1.01381	0.02207	0.96256	0.03077	0.92945	0.04231	0.93504	0.03891	1.06941	0.04744	1.08659	0.03833
ζ=1.75		50	1.00174	0.01399	0.9754	0.01855	0.92764	0.03084	0.93518	0.02915	1.05831	0.03154	1.05072	0.0204
		100	0.99934	0.00633	0.99583	0.01165	0.9368	0.02195	0.94477	0.02194	1.05638	0.02263	1.02734	0.00842
							$\varpi = 1$							
S'_{pk}=1.48556	1.50093	20	1.54139	0.06236	1.42627	0.08019	1.47147	0.09572	1.42094	0.08414	1.55618	0.08735	1.69591	0.11878
κ=6.5		30	1.52667	0.0411	1.44099	0.05413	1.45834	0.08239	1.41482	0.06862	1.55539	0.06396	1.64056	0.06983
ζ=1.25		50	1.51413	0.02351	1.4684	0.03287	1.46756	0.05831	1.42706	0.04925	1.56253	0.0432	1.59114	0.03457
		100	1.51023	0.01106	1.49936	0.01771	1.47763	0.04416	1.43954	0.03594	1.56744	0.02792	1.55541	0.01486
S'_{pk}=1.26491	1.27436	20	1.29643	0.04233	1.20125	0.05452	1.22541	0.06688	1.18827	0.06145	1.31711	0.06199	1.43435	0.08622
κ=6.5		30	1.29546	0.02956	1.22941	0.04057	1.23985	0.05689	1.20392	0.05138	1.33153	0.05125	1.39652	0.05171
ζ= 1.50		50	1.29237	0.0164	1.25428	0.02257	1.23972	0.04062	1.21166	0.03624	1.33481	0.03256	1.36072	0.02605
		100	1.281	0.00753	1.27715	0.01201	1.24399	0.02875	1.21991	0.02556	1.33618	0.02056	1.32075	0.0104
S'_{pk}=1.09888	1.10506	20	1.11731	0.03055	1.03241	0.043	1.04352	0.05404	1.0175	0.05026	1.13383	0.04727	1.23852	0.05837
κ=6.5		30	1.12228	0.02119	1.07021	0.0275	1.06828	0.04013	1.04165	0.03699	1.15774	0.03597	1.21266	0.03925
ζ=1.75		50	1.11932	0.01315	1.10169	0.018	1.0851	0.03482	1.05733	0.02832	1.17066	0.02757	1.17991	0.02078
		100	1.10738	0.00601	1.10289	0.00978	1.07307	0.02204	1.05395	0.02014	1.1568	0.01623	1.14214	0.00794
S'_{pk}=1.29514	1.27988	20	1.32608	0.07087	1.20482	0.08855	1.18578	0.10199	1.1956	0.0951	1.37427	0.11544	1.44935	0.12568
κ=7.5		30	1.30185	0.0418	1.21902	0.06	1.186	0.07443	1.19691	0.07197	1.36705	0.08177	1.3894	0.06607
ζ=1.25		50	1.29009	0.02224	1.24581	0.03845	1.19514	0.05248	1.21004	0.05255	1.36564	0.0573	1.34705	0.03075
		100	1.2913	0.01271	1.28035	0.02177	1.2012	0.03874	1.21781	0.03905	1.36199	0.03807	1.32559	0.01606
S'_{pk}=1.11905	1.10964	20	1.13742	0.05005	1.03606	0.0659	1.02036	0.07682	1.02583	0.07232	1.18146	0.08512	1.2483	0.09114
κ=7.5		30	1.12559	0.03479	1.05665	0.04835	1.01894	0.06295	1.028	0.06048	1.17779	0.06642	1.20342	0.05291
ζ=1.50		50	1.13057	0.01937	1.0986	0.02801	1.0507	0.04068	1.05941	0.03955	1.19726	0.04675	1.18268	0.02786
		100	1.11861	0.00816	1.11822	0.01581	1.05543	0.02749	1.06537	0.02766	1.19019	0.02928	1.14879	0.0104
S'_{pk}=0.98703	0.98084	20	1.00616	0.03804	0.91884	0.0464	0.90215	0.05522	0.90585	0.05247	1.04566	0.06109	1.10816	0.07216
κ=7.5		30	0.99718	0.02348	0.94917	0.03271	0.91957	0.04654	0.92475	0.04173	1.05906	0.04917	1.06448	0.03626
ζ=1.75		50	0.99335	0.01551	0.96958	0.02291	0.91637	0.03616	0.92419	0.03519	1.05139	0.03663	1.04073	0.02146
		100	0.99114	0.00651	0.99023	0.0115	0.92799	0.02217	0.9343	0.02209	1.04856	0.02155	1.01891	0.00861

Table 4: *Estimates and MSE for* $\varpi = (5, 10)$ *using* MLE, LSE, WLSE, PE, CME, *and* MPSE *with* S''_{pk}.

PCI			MLE		LSE		WLSE		PE		CME		MPSE	
Parameters	S''_{pk}	n	MLE	MSE	LSE	MSE	WLSE	MSE	PE	MSE	CME	MSE	MPSE	MSE
							$\varpi = 5$							
S'_{pk}=1.48556	1.53889	20	1.59324	0.06026	1.46702	0.08273	1.45189	0.09192	1.45845	0.08885	1.62362	0.09496	1.76865	0.12926
κ=6.5		30	1.58533	0.04587	1.49351	0.06484	1.3176	0.13923	1.47684	0.07548	1.63622	0.08389	1.70984	0.08222
ζ=1.25		50	1.56487	0.02289	1.51782	0.03526	1.2828	0.13729	1.47765	0.05047	1.63121	0.05149	1.64732	0.03721
		100	1.55006	0.01076	1.53751	0.01826	1.43669	0.12438	1.46597	0.04139	1.61504	0.0319	1.59962	0.01495
S'_{pk}=1.26491	1.29734	20	1.35465	0.04813	1.24484	0.0606	1.06366	0.08883	1.23409	0.06659	1.38294	0.07671	1.50611	0.10412
κ=6.5		30	1.32116	0.02887	1.24935	0.03892	1.2882	0.0558	1.2223	0.05205	1.36593	0.04977	1.42866	0.05218
ζ= 1.50		50	1.31847	0.0176	1.28468	0.02688	1.29327	0.05042	1.23507	0.04337	1.37572	0.04162	1.39303	0.02918
		100	1.30092	0.00852	1.29766	0.01439	1.28712	0.03783	1.23365	0.03112	1.36087	0.02515	1.34317	0.01141
S'_{pk}=1.09888	1.11995	20	1.15947	0.03488	1.07904	0.04338	1.16182	0.06879	1.06661	0.04903	1.19991	0.05793	1.28996	0.07506
κ=6.5		30	1.14241	0.02383	1.08558	0.02879	1.15953	0.06176	1.05501	0.04027	1.18532	0.03975	1.23683	0.04278
ζ=1.75		50	1.14095	0.01333	1.11131	0.01982	1.16947	0.05451	1.06784	0.03084	1.1906	0.03095	1.20479	0.02226
		100	1.12842	0.00643	1.12791	0.01176	1.20609	0.07041	1.07597	0.02368	1.18667	0.02182	1.1651	0.00882
S'_{pk}=1.29514	1.17186	20	1.1582	0.12618	1.03587	0.13858	0.9794	0.20195	1.02848	0.16505	1.21419	0.17051	1.2465	0.18054
κ=7.5		30	1.16385	0.08842	1.07561	0.10884	1.01181	0.14251	1.05677	0.1207	1.23377	0.12717	1.22707	0.11584
ζ=1.25		50	1.15833	0.05114	1.11895	0.07458	1.02441	0.10924	1.06961	0.09736	1.23899	0.09529	1.20199	0.06148
		100	1.17011	0.02647	1.16385	0.03821	1.04035	0.06816	1.0997	0.05751	1.24917	0.05555	1.19539	0.03005
S'_{pk}=1.11905	1.04003	20	1.00723	0.11626	0.90104	0.14595	0.8186	0.2092	0.8889	0.15349	1.06276	0.15405	1.09218	0.16447
κ=7.5		30	1.00357	0.07264	0.93174	0.09543	0.83074	0.15439	0.90196	0.11314	1.06513	0.10318	1.0618	0.09073
ζ=1.50		50	1.01948	0.04	0.99133	0.05491	0.87071	0.10286	0.94007	0.0768	1.09401	0.06923	1.06024	0.0477
		100	1.02335	0.02132	1.02147	0.02935	0.88638	0.06776	0.95856	0.04739	1.09416	0.04012	1.04693	0.02359
S'_{pk}=0.98703	0.93358	20	0.88986	0.08857	0.79397	0.11611	0.70573	0.19855	0.77518	0.12914	0.93626	0.11598	0.96694	0.11941
κ=7.5		30	0.9017	0.05798	0.83901	0.07308	0.72887	0.14564	0.80845	0.08695	0.95826	0.07643	0.95628	0.07442
ζ=1.75		50	0.90131	0.03197	0.87699	0.04407	0.76338	0.10699	0.8323	0.0614	0.96934	0.05151	0.93736	0.037
		100	0.90406	0.01714	0.90517	0.02378	0.80379	0.08258	0.84619	0.04014	0.96887	0.03	0.92539	0.01845
							$\varpi = 10$							
S'_{pk}=1.48556	1.56048	20	1.61498	0.06574	1.4898	0.09286	1.51911	0.09226	1.48008	0.10055	1.67702	0.07352	1.80093	0.14361
κ=6.5		30	1.59903	0.04237	1.49328	0.06347	1.5007	0.07451	1.46878	0.07623	1.6686	0.05144	1.7327	0.08006
ζ=1.25		50	1.58983	0.02417	1.53368	0.03692	1.51779	0.06088	1.48549	0.05795	1.68242	0.04295	1.6795	0.04089
		100	1.5682	0.01168	1.55913	0.0208	1.53165	0.04601	1.49642	0.04176	1.68063	0.03338	1.61911	0.016
S'_{pk}=1.26491	1.31021	20	1.36396	0.05491	1.24816	0.07341	1.29292	0.0895	1.2329	0.08237	1.53892	0.09034	1.5301	0.12427
κ=6.5		30	1.34239	0.03004	1.27162	0.04365	1.30462	0.06471	1.24255	0.05828	1.57186	0.08733	1.4553	0.05651
ζ= 1.50		50	1.33814	0.01802	1.29649	0.02545	1.30354	0.04873	1.24627	0.04151	1.58511	0.08536	1.41341	0.03072
		100	1.31884	0.00812	1.31415	0.01616	1.3034	0.04165	1.25233	0.03331	1.6044	0.09115	1.36168	0.01134
S'_{pk}=1.09888	1.12819	20	1.16441	0.03786	1.07051	0.0515	1.13796	0.09465	1.05227	0.06094	1.47814	0.14919	1.30302	0.08319
κ=6.5		30	1.14457	0.02196	1.08811	0.03356	1.16327	0.07696	1.05719	0.04608	1.19369	0.04522	1.24188	0.04032
ζ=1.75		50	1.14451	0.01354	1.12093	0.01925	1.18335	0.06687	1.06993	0.03426	1.20186	0.03233	1.21006	0.02226
		100	1.13768	0.00685	1.13711	0.01281	1.19075	0.06359	1.08805	0.02311	1.20214	0.02404	1.17498	0.00959
S'_{pk}=1.29514	0.86982	20	0.87835	0.26348	0.74793	0.28032	0.66193	0.32228	0.73249	0.28881	0.97904	0.36532	0.94731	0.34949
κ=7.5		30	0.87024	0.20383	0.77598	0.22345	0.66415	0.26205	0.74471	0.23789	0.95896	0.28386	0.91341	0.24731
ζ=1.25		50	0.8743	0.15817	0.82733	0.17654	0.69242	0.20741	0.78167	0.19107	0.96411	0.22629	0.8988	0.17901
		100	0.8795	0.08495	0.86205	0.0957	0.66561	0.13551	0.78944	0.11161	0.95209	0.12354	0.89228	0.09186
S'_{pk}=1.11905	0.81598	20	0.75027	0.22186	0.64376	0.24586	0.49482	0.32284	0.62671	0.2554	0.81894	0.26525	0.8101	0.28193
κ=7.5		30	0.76837	0.16898	0.70173	0.19073	0.52002	0.26983	0.66731	0.20668	0.85371	0.21299	0.80589	0.19884
ζ=1.50		50	0.78091	0.1282	0.75279	0.14587	0.54739	0.21987	0.70099	0.16708	0.87723	0.17035	0.80457	0.14313
		100	0.79504	0.07604	0.78972	0.08707	0.55708	0.16482	0.71371	0.10946	0.87899	0.10335	0.80868	0.08191
S'_{pk}=0.98703	0.76429	20	0.69021	0.18864	0.59243	0.20125	0.51141	0.24028	0.57176	0.21262	0.75118	0.2088	0.74778	0.23758
κ=7.5		30	0.7078	0.14734	0.63559	0.16988	0.52561	0.22064	0.5968	0.19218	0.77175	0.18159	0.74931	0.17035
ζ=1.75		50	0.72775	0.10531	0.69762	0.1195	0.56043	0.16941	0.6382	0.14363	0.80784	0.13387	0.75284	0.11839
		100	0.72854	0.06593	0.72386	0.07551	0.56825	0.12233	0.64628	0.10185	0.80113	0.08501	0.74224	0.07063

Table 5: *Estimates of* $\mathbb{S}''_{pk}$, $\mathbb{AW}$, *and* $\mathbb{CP}$ *for* $\mathbb{ACI}$ *using* $\mathbb{MLE}$ *with* $\varpi = (0.01, 1, 5, 10)$.

$\mathbb{PCI}$		$\mathbb{ACI}$							
Parameter	n	$\mathbb{AW}$	$\mathbb{CP}$	$\mathbb{AW}$	$\mathbb{CP}$	$\mathbb{AW}$	$\mathbb{CP}$	$\mathbb{AW}$	$\mathbb{CP}$
		$\varpi = 0.01$		$\varpi = 1$		$\varpi = 5$		$\varpi = 10$	
$\mathbb{S}''_{pk}$		1.48573		1.50093		1.53889		1.56048	
	20	0.93426	0.948	0.91256	0.946	0.92149	0.943	0.95738	0.943
κ=6.5	30	0.75246	0.949	0.73929	0.955	0.75045	0.944	0.77221	0.957
ζ=1.25	50	0.58055	0.957	0.56893	0.962	0.57932	0.956	0.59191	0.959
	100	0.40919	0.961	0.40182	0.964	0.40423	0.961	0.41613	0.963
$\mathbb{S}''_{pk}$		1.26502		1.27436		1.29734		1.31021	
	20	0.80269	0.949	0.78449	0.933	0.79416	0.943	0.80985	0.942
κ=6.5	30	0.65378	0.953	0.64050	0.945	0.64471	0.941	0.66070	0.945
ζ=1.50	50	0.50052	0.957	0.49191	0.951	0.49220	0.956	0.50511	0.952
	100	0.35038	0.962	0.34582	0.959	0.34814	0.959	0.35444	0.953
$\mathbb{S}''_{pk}$		1.09895		1.10501		1.11995		1.12819	
	20	0.70423	0.942	0.69684	0.941	0.70924	0.938	0.74602	0.942
κ=6.5	30	0.570053	0.945	0.55931	0.944	0.56555	0.941	0.57962	0.947
ζ=1.75	50	0.43880	0.949	0.43302	0.951	0.43177	0.948	0.43938	0.950
	100	0.30605	0.95	0.30274	0.953	0.30265	0.953	0.30798	0.955
$\mathbb{S}''_{pk}$		1.29501		1.27988		1.17186		0.86982	
	20	0.90836	0.937	0.93838	0.940	1.34251	0.917	1.87011	0.746
κ=7.5	30	0.73317	0.941	0.76631	0.943	1.11147	0.919	1.70115	0.769
ζ=1.25	50	0.56096	0.948	0.59405	0.947	0.88337	0.933	1.43707	0.805
	100	0.39808	0.951	0.41617	0.951	0.63742	0.941	1.13160	0.868
$\mathbb{S}''_{pk}$		1.11897		1.10964		1.04003		0.81598	
	20	0.77505	0.946	0.81823	0.934	1.16887	0.918	1.72788	0.729
κ=7.5	30	0.63075	0.949	0.66029	0.941	0.99399	0.926	1.54389	0.736
ζ=1.50	50	0.48786	0.953	0.51171	0.949	0.76979	0.938	1.29780	0.777
	100	0.34420	0.955	0.36017	0.952	0.55928	0.950	1.05467	0.828
$\mathbb{S}''_{pk}$		0.98698		0.98084		0.93358		0.76429	
	20	0.68964	0.929	0.71578	0.940	1.07325	0.910	1.50443	0.720
κ=7.5	30	0.55773	0.942	0.58301	0.947	0.90575	0.931	1.41512	0.741
ζ=1.75	50	0.42885	0.949	0.44916	0.949	0.70608	0.943	1.22068	0.782
	100	0.30382	0.953	0.31620	0.951	0.49292	0.950	1.00100	0.841

Table 6: *Estimates of* $S''_{pk}(\omega)$, S'_{pk} *and* S_{pk} *along with* ABE, AW, PR *and* CP *for* $S''_{pk}(\omega)$ *with,* ω *= (0.01, 1).*

	$\omega = 0.01$						$\omega = 1$					
	SELF	WSELF	MSELF	LLF	KLF		SELF	WSELF	MSELF	LLF	KLF	
n	ABE PR	ABE PR	ABE PR	ABE PR	ABE PR	AW CP	ABE PR	ABE PR	ABE PR	ABE PR	ABE PR	AW CP
	κ=6.5		ζ=1.25		S_{pk}=1.6000		S'_{pk}=1.4855		$S''_{pk}(0.01)$=1.4857		$S''_{pk}(1)$=1.5009	
20	1.4808	1.4477	1.4146	1.4643	1.4642	0.8539	1.5069	1.4762	1.4454	1.4916	1.4915	0.8319
	0.0494	0.0330	0.0230	0.0228	0.0230	0.9440	0.0467	0.0307	0.0210	0.0207	0.0209	0.9330
30	1.4791	1.4562	1.4333	1.4677	1.4676	0.7124	1.5080	1.4866	1.4651	1.4973	1.4972	0.6970
	0.0341	0.0229	0.0158	0.0517	0.0158	0.9520	0.0325	0.0214	0.0145	0.0143	0.0145	0.9430
50	1.4781	1.4640	1.4499	1.4711	1.4711	0.5599	1.5067	1.4934	1.4801	1.5001	1.5000	0.5496
	0.0208	0.0141	0.0097	0.0096	0.0097	0.9550	0.0200	0.0133	0.0089	0.0089	0.0089	0.9450
100	1.4821	1.4749	1.4677	1.4785	1.4785	0.4009	1.4988	1.4920	1.4853	1.4954	1.4954	0.3925
	0.0106	0.0072	0.0049	0.0049	0.0049	0.9620	0.0102	0.0068	0.0046	0.0045	0.0045	0.9490
			κ=6.5	ζ=1.50	S_{pk}=1.3333	S'_{pk}=1.2649	$S''_{pk}(0.01)$=1.2650		$S''_{pk}(1)$=1.2744			
20	1.2677	1.2386	1.2095	1.2532	1.2531	0.7416	1.3101	1.2826	1.2549	1.2964	1.2963	0.7343
	0.0373	0.0291	0.0237	0.0234	0.0236	0.9490	0.0365	0.0275	0.0217	0.0213	0.0216	0.9550
30	1.2669	1.2469	1.2269	1.2569	1.2569	0.6158	1.2978	1.2791	1.2603	1.2885	1.2884	0.6042
	0.0255	0.0200	0.0162	0.0160	0.0161	0.9490	0.0245	0.0187	0.0147	0.0146	0.0147	0.9520
50	1.2709	1.2586	1.2463	1.2648	1.2647	0.4841	1.2846	1.2730	1.2614	1.2788	1.2788	0.4743
	0.0156	0.0122	0.0098	0.0097	0.0098	0.9540	0.0149	0.0116	0.0092	0.0091	0.0091	0.9550
100	1.2627	1.2565	1.2503	1.2596	1.2596	0.3441	1.2748	1.2689	1.2630	1.2719	1.2719	0.3386
	0.0078	0.0062	0.0050	0.0049	0.0049	0.9600	0.0076	0.0059	0.0047	0.0047	0.0047	0.9560
			κ=6.5	ζ=1.75	S_{pk}=1.1428	S'_{pk}=1.0988	$S''_{pk}(0.01)$=1.0989		$S''_{pk}(1)$=1.1051			
20	1.1024	1.0763	1.0500	1.0894	1.0893	0.6546	1.1235	1.0987	1.0737	1.1111	1.1110	0.6452
	0.0292	0.0261	0.0245	0.0241	0.0244	0.9450	0.0282	0.0248	0.0228	0.0224	0.0226	0.9500
30	1.0994	1.0816	1.0637	1.0905	1.0905	0.5418	1.1198	1.1028	1.0858	1.1113	1.1113	0.5334
	0.0198	0.0178	0.0166	0.0164	0.0166	0.9480	0.0191	0.0169	0.0155	0.0153	0.0154	0.9520
50	1.0916	1.0808	1.0700	1.0862	1.0862	0.4214	1.1086	1.0984	1.0880	1.1035	1.1035	0.4148
	0.0118	0.0108	0.0101	0.0100	0.0100	0.9540	0.0114	0.0103	0.0094	0.0093	0.0094	0.9440
100	1.0960	1.0905	1.0851	1.0933	1.0933	0.3006	1.1067	1.1015	1.0962	1.1041	1.1041	0.2966
	0.0060	0.0054	0.0050	0.0050	0.0050	0.9540	0.0058	0.0052	0.0048	0.0047	0.0048	0.9590
			κ=7.5	ζ=1.25	S_{pk}=1.3870	S'_{pk}=1.2951	$S''_{pk}(0.01)$=1.2950		$S''_{pk}(1)$=1.2799			
20	1.3330	1.2984	1.2641	1.3157	1.3156	0.8286	1.3585	1.3193	1.2802	1.3390	1.3387	0.8859
	0.0469	0.0345	0.0266	0.0265	0.0268	0.9480	0.0534	0.0391	0.0303	0.0298	0.0303	0.9360
30	1.3249	1.3008	1.2769	1.3129	1.3128	0.6931	1.3258	1.2986	1.2716	1.3122	1.3121	0.7336
	0.0325	0.0241	0.0185	0.0185	0.0186	0.9510	0.0363	0.0271	0.0211	0.0210	0.0212	0.9490
50	1.3110	1.2961	1.2812	1.3036	1.3035	0.5454	1.3126	1.2958	1.2789	1.3042	1.3042	0.5778
	0.0199	0.0150	0.0115	0.0115	0.0116	0.9450	0.0223	0.0169	0.0131	0.0130	0.0131	0.9530
100	1.3073	1.2996	1.2919	1.3035	1.3035	0.3921	1.2901	1.2814	1.2728	1.2857	1.2857	0.4110
	0.0102	0.0077	0.0059	0.0059	0.0060	0.9450	0.0112	0.0086	0.0067	0.0067	0.0068	0.9590
			κ=7.5	ζ=1.50	S_{pk}=1.1735	S'_{pk}=1.1190	$S''_{pk}(0.01)$=1.1189		$S''_{pk}(1)$=1.1096			
20	1.1612	1.1310	1.1010	1.1461	1.1460	0.7231	1.1848	1.1507	1.1164	1.1678	1.1676	0.7716
	0.0358	0.0302	0.0268	0.0266	0.0269	0.9480	0.0405	0.0341	0.0305	0.0299	0.0303	0.9360
30	1.1573	1.1363	1.1155	1.1468	1.1468	0.6027	1.1587	1.1355	1.1121	1.1471	1.1470	0.6336
	0.0246	0.0209	0.0184	0.0184	0.0185	0.9530	0.0270	0.0233	0.0209	0.0206	0.0209	0.9410
50	1.1424	1.1295	1.1166	1.1359	1.1359	0.4729	1.1302	1.1157	1.1012	1.1230	1.1229	0.4961
	0.0149	0.0129	0.0115	0.0114	0.0115	0.9590	0.0164	0.0145	0.0131	0.0130	0.0131	0.9410
100	1.1302	1.1235	1.1169	1.1269	1.1269	0.3389	1.1256	1.1182	1.1108	1.1219	1.1219	0.3553
	0.0076	0.0067	0.0059	0.0059	0.0060	0.9620	0.0083	0.0074	0.0067	0.0066	0.0067	0.9500
			κ=7.5	ζ=1.75	S_{pk}= 1.0220	S'_{pk}=0.9870	$S''_{pk}(0.01)$=0.9869		$S''_{pk}(1)$=0.9808			
20	1.0415	1.0151	0.9887	1.0283	1.0282	0.6405	1.0280	0.9985	0.9686	1.0134	1.0132	0.6673
	0.0280	0.0265	0.0262	0.0260	0.0264	0.9370	0.0302	0.0295	0.0307	0.0299	0.0303	0.9400
30	1.0215	1.0032	0.9849	1.0123	1.0123	0.5294	1.0281	1.0076	0.9869	1.0179	1.0178	0.5594
	0.0190	0.0183	0.0183	0.0182	0.0184	0.9390	0.0210	0.0205	0.0209	0.0205	0.0207	0.9490
50	1.0115	1.0001	0.9887	1.0058	1.0058	0.4171	0.9981	0.9855	0.9727	0.9918	0.9918	0.4356
	0.0116	0.0114	0.0114	0.0114	0.0114	0.9430	0.0126	0.0127	0.0130	0.0129	0.0130	0.9500
100	0.9997	0.9939	0.9880	0.9968	0.9968	0.2983	0.9910	0.9845	0.9780	0.9877	0.9877	0.3111
	0.0059	0.0059	0.0059	0.0059	0.0059	0.9480	0.0064	0.0065	0.0066	0.0066	0.0066	0.9520

Table 7: *Estimates of* $S''_{pk}(\omega)$, S'_{pk} *and* S_{pk} *along with* ABE, AW, PR *and* CP *for* $S''_{pk}(\omega)$ *with,* ω *= (5, 10).*

	$\omega = 5$						$\omega = 10$					
	SELF	WSELF	MSELF	LLF	KLF		SELF	WSELF	MSELF	LLF	KLF	
n	ABE PR	ABE PR	ABE PR	ABE PR	ABE PR	AW CP	ABE PR	ABE PR	ABE PR	ABE PR	ABE PR	AW CP
			κ=6.5	ζ=1.25	S_{pk}=1.6000	S'_{pk}=1.4856	$S''_{pk}(5)$=1.5389		$S''_{pk}(10)$=1.5605			
20	1.5827	1.5518	1.5195	1.5675	1.5672	0.8475	1.6106	1.5714	1.4916	1.5930	1.5908	0.8892
	0.0481	0.0309	0.0212	0.0199	0.0201	0.9370	0.0535	0.0392	0.0583	0.0243	0.0268	0.9280
30	1.5710	1.5499	1.5284	1.5605	1.5604	0.7062	1.5974	1.5743	1.5475	1.5861	1.5858	0.7322
	0.0331	0.0212	0.0139	0.0136	0.0137	0.9460	0.0358	0.0231	0.0176	0.0146	0.0148	0.9480
50	1.5570	1.5440	1.5308	1.5505	1.5505	0.5536	1.5789	1.5652	1.5514	1.5721	1.5720	0.5695
	0.0203	0.0130	0.0085	0.0084	0.0085	0.9460	0.0215	0.0136	0.0088	0.0087	0.0087	0.9480
100	1.5462	1.5395	1.5328	1.5428	1.5428	0.3957	1.5683	1.5614	1.5544	1.5648	1.5648	0.4067
	0.0103	0.0067	0.0044	0.0043	0.0043	0.9500	0.0109	0.0070	0.0045	0.0044	0.0045	0.9530
			κ=6.5	ζ=1.50	S_{pk}=1.3333	S'_{pk}=1.2649	$S''_{pk}(5)$=1.2973		$S''_{pk}(10)$=1.3102			
20	1.3340	1.3049	1.2720	1.3198	1.3194	0.7446	1.3757	1.3273	1.1824	1.3572	1.3507	0.8034
	0.0372	0.0290	0.0265	0.0223	0.0228	0.9420	0.0443	0.0484	0.1313	0.0339	0.0467	0.9460
30	1.3311	1.3121	1.2925	1.3217	1.3216	0.6139	1.3488	1.3256	1.2856	1.3381	1.3371	0.6397
	0.0251	0.0190	0.0151	0.0144	0.0146	0.9450	0.0276	0.0232	0.0334	0.0172	0.0181	0.9510
50	1.3112	1.2997	1.2882	1.3055	1.3054	0.4753	1.3267	1.3147	1.3022	1.3208	1.3207	0.4875
	0.0150	0.0114	0.0089	0.0088	0.0088	0.9490	0.0158	0.0120	0.0096	0.0091	0.0092	0.9530
100	1.3126	1.3068	1.3009	1.3097	1.3097	0.3416	1.3227	1.3167	1.3106	1.3197	1.3197	0.3477
	0.0077	0.0059	0.0045	0.0045	0.0045	0.9500	0.0080	0.0060	0.0046	0.0046	0.0046	0.9520
			κ=6.5	ζ=1.75	S_{pk}=1.1429	S'_{pk}=1.0989	$S''_{pk}(5)$=1.1199		$S''_{pk}(10)$=1.1282			
20	1.1733	1.1448	1.1075	1.1597	1.1589	0.6743	1.1797	1.1005	0.8478	1.1572	1.1364	0.7412
	0.0307	0.0284	0.0355	0.0289	0.0258	0.9470	0.0389	0.0792	0.2905	0.0611	0.1773	0.9350
30	1.1574	1.1401	1.1217	1.1489	1.1487	0.5434	1.1661	1.1351	1.0474	1.1541	1.1501	0.5840
	0.0197	0.0174	0.0163	0.0152	0.0153	0.9510	0.0237	0.0310	0.0943	0.0263	0.0348	0.9410
50	1.1375	1.1273	1.1170	1.1324	1.1324	0.4181	1.1512	1.1399	1.1265	1.1457	1.1455	0.4306
	0.0116	0.0102	0.0092	0.0090	0.0091	0.9510	0.0124	0.0113	0.0121	0.0099	0.0100	0.9420
100	1.1326	1.1275	1.1223	1.1301	1.1300	0.2980	1.1371	1.1318	1.1264	1.1345	1.1345	0.3021
	0.0059	0.0052	0.0046	0.0046	0.0046	0.9530	0.0060	0.0053	0.0047	0.0047	0.0047	0.9450
			κ=7.5	ζ=1.25	S_{pk}=1.3870	S'_{pk}=1.2951	$S''_{pk}(5)$=1.1719		$S''_{pk}(10)$=0.8698			
20	1.2169	1.1157	0.9773	1.1712	1.1646	1.1543	1.0234	0.6668	0.2546	0.8868	0.8118	1.4698
	0.0903	0.1011	0.1526	0.1021	0.1138	0.9330	0.1750	0.3566	0.7657	0.5990	1.3627	0.8920
30	1.2036	1.1335	1.0474	1.1709	1.1678	1.0003	0.9780	0.7168	0.3920	0.8693	0.8305	1.3380
	0.0672	0.0701	0.0877	0.0678	0.0720	0.9430	0.1430	0.2612	0.5781	0.4236	0.6598	0.8990
50	1.1787	1.1341	1.0836	1.1574	1.1561	0.8173	0.9391	0.7628	0.5421	0.8614	0.8440	1.1788
	0.0447	0.0445	0.0491	0.0420	0.0434	0.9440	0.1076	0.1763	0.3605	0.2685	0.3406	0.9150
100	1.1761	1.1534	1.1291	1.1650	1.1647	0.6039	0.8995	0.7974	0.6780	0.8521	0.8464	0.9773
	0.0243	0.0227	0.0224	0.0206	0.0209	0.9500	0.0704	0.1022	0.1750	0.1421	0.1575	0.9280
			κ=7.5	ζ=1.50	S_{pk}=1.1735	S'_{pk}=1.1191	$S''_{pk}(5)$=1.0400		$S''_{pk}(10)$= 0.8160			
20	1.0664	0.9592	0.7996	1.0195	1.0104	1.0623	0.8622	0.5007	0.1600	0.7235	0.6356	1.2980
	0.0777	0.1072	0.2121	0.1291	0.1508	0.9190	0.1444	0.3615	0.8417	0.8542	2.8453	0.8990
30	1.0408	0.9660	0.8677	1.0067	1.0023	0.9161	0.8465	0.5734	0.2502	0.7366	0.6869	1.1938
	0.0573	0.0748	0.1237	0.0877	0.0958	0.9350	0.1186	0.2730	0.6997	0.5653	1.0768	0.9070
50	1.0398	0.9970	0.9458	1.0197	1.0181	0.7256	0.8231	0.6359	0.3989	0.7429	0.7196	1.0627
	0.0357	0.0428	0.0587	0.0472	0.0493	0.9400	0.0908	0.1872	0.4701	0.3488	0.4870	0.9200
100	1.0296	1.0082	0.9847	1.0192	1.0188	0.5334	0.8234	0.7174	0.5834	0.7759	0.7677	0.8787
	0.0192	0.0214	0.0252	0.0225	0.0229	0.9440	0.0592	0.1060	0.2262	0.1695	0.1960	0.9310
			κ=7.5	ζ=1.75	S_{pk}=1.0220	S'_{pk}=0.9870	$S''_{pk}(5)$=0.9336		$S''_{pk}(10)$= 0.7643			
20	0.9361	0.8223	0.6372	0.8884	0.8758	0.9646	0.7851	0.3963	0.1050	0.6467	0.5265	1.1588
	0.0651	0.1138	0.2958	0.1644	0.2076	0.9210	0.1188	0.3888	0.8942	1.0364	9.5793	0.8990
30	0.9319	0.8580	0.7520	0.8993	0.8936	0.8175	0.7538	0.4661	0.1662	0.6429	0.5775	1.0583
	0.0464	0.0738	0.1575	0.1013	0.1151	0.9320	0.0976	0.2876	0.7962	0.7318	1.9367	0.9080
50	0.9174	0.8739	0.8180	0.8975	0.8953	0.6587	0.7382	0.5429	0.2950	0.6580	0.6272	0.9460
	0.0298	0.0435	0.0753	0.0556	0.0590	0.9460	0.0752	0.1953	0.5815	0.4408	0.7137	0.9050
100	0.9138	0.8935	0.8702	0.9041	0.9035	0.4750	0.7466	0.6357	0.4900	0.6982	0.6874	0.7962
	0.0155	0.0203	0.0290	0.0248	0.0253	0.9500	0.0507	0.1109	0.2904	0.2091	0.2563	0.9180

4. Applications

This section deals with the real life application of the considered study. Considering two real data sets one is for aluminium foil and other is for liquid crystal display, before including there data sets in our study we use "R programming" for goodness of fit test, in particular use *fitdistrplus* Delignette-Muller and Dutang, [5] package to get the K-S test value and *p*-value for given data sets.

Data Set I

The dataset, consisting of 50 observation, is sourced from Saha [17]; Saha and Dey [21] and records the voltage of aluminium foil used by an electronics manufacturer. The production specifications of the voltage are set as ($\mathbb{L}$, $\mathbb{T}$, $\mathbb{U}$) =(510, 520, 530). This voltage range is crucial to prevent the aluminium foil from breaking, which would lead to its rejection.

Using the *fitdistrplus* package, we firstly check for normality test and then obtained the estimated values of κ and ζ as $519.7560, 1.7658$, respectively. Additionally, the one sample Kolmogorov-Smirnov statistic and its p-values are $(0.0734, 0.9505)$, respectively, indicated a good fit.

Data Set II

The data, sourced from Peng [16]; Wu and Pearn [27] and also used by Saha and Dey [21], represents the glass substrate thickness (in mm) of the $\mathbb{STN}$-$\mathbb{LCD}$, (liquid crystal display). If the product's characteristic falls outside this range, $\mathbb{L} = 0.63$ and $\mathbb{U} = 0.77$, with $\mathbb{T} = 0.70$ the lifetime or reliability of the $\mathbb{STN}$-$\mathbb{LCD}$ will be deemed unacceptable and the product will be rejected.
Before moving forward, we first examine whether the normal distribution is appropriate for analyzing the given dataset. For dataset II, the $\mathbb{MLE}$s of κ and ζ are found to be $\hat{\kappa}_{mle} = 0.7096$, $\hat{\zeta}_{mle} = 0.0193$. The one sample (K-S statistic, p-values) are (0.0707, 0.8250), respectively.
For given specifications of two data sets the classical and Bayes estimates for $\mathbb{S}''_{pk}$ with four different ϖ values are calculated. In classical setup, $\mathbb{MLE}$ and $\mathbb{MPSE}$ are considered for providing the point and interval estimates ($\mathbb{AIC}$) and are reported in Table 8. The Bayes estimates are obtained for five different loss functions along with $\mathbb{HPD}$ credible intervals are also obtained and shown in Table 8. Further, the Bayes point and interval estimates of the considered $\mathbb{PCI}$ are computed under the assumption of non-informative priors using different loss functions for various values of $\varpi = 0.01$ to 10. the values of hyper-parameters are chosen as $\alpha = (1.05, 1.55)$, $\beta = (0.01, 0.001)$ and $\kappa_0 = (520, 0.70)$, respectively. The obtained result is reported in Table 8. The mixing of the chain based on generated sequence of posterior samples under $\mathbb{MCMC}$ approach for both the data sets is investigate through the corresponding trace plot, which is given in Figure 1. This suggests that the generated samples are effectively mixed and converge to the true parameter values.

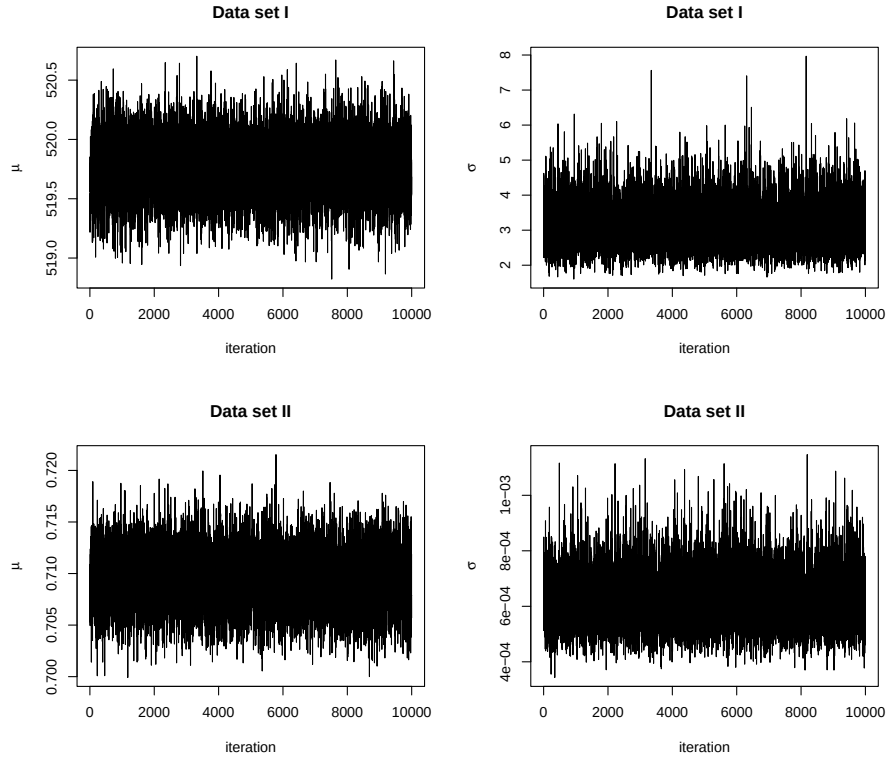


Figure 1: *Trace plot for the considered real data sets I and II.*

Table 8: *Classical and Bayesian estimates of* S''_{pk} *using* MLE *and* MPSE *for real data sets with* $\varpi = (0.01, 1, 5, 10)$.

Point and Interval Estimates							
Data set	n	Method of Estimation	Classical Estimate	Width			
				ACI	GCI	BCI	
						P- boot	S- boot
$\varpi = 0.01$							
I	50	MLE	1.8539	0.7475	0.7295	0.7399	0.7330
		MPSE	1.8359	0.7400	0.7350	0.8223	0.8154
II	79	MLE	1.0012	0.3532	0.3446	0.3656	0.3607
		MPSE	0.9966	0.3517	0.3453	0.3742	0.3745
$\varpi = 1$							
I	50	MLE	1.8553	0.7440	0.7207	0.7682	0.7725
		MPSE	1.8372	0.7366	0.7464	0.8137	0.8021
II	79	MLE	1.0009	0.3535	0.3400	0.3618	0.3556
		MPSE	0.9963	0.3519	0.3441	0.3824	0.3858
$\varpi = 5$							
I	50	MLE	1.8593	0.7361	0.7254	0.7578	0.7462
		MPSE	1.8411	0.7289	0.7174	0.8085	0.8032
II	79	MLE	0.9998	0.3547	0.3448	0.3785	0.3676
		MPSE	0.9952	0.3532	0.3498	0.4060	0.3954
$\varpi = 10$							
I	50	MLE	1.8624	0.7327	0.7364	0.7889	0.7839
		MPSE	1.8441	0.7255	0.7497	0.7669	0.7858
II	79	MLE	0.9983	0.3563	0.3443	0.3452	0.3568
		MPSE	0.9937	0.3547	0.3516	0.4090	0.3950
Bayes Point Estimates and Credible Interval Estimates							
		BE					Width
		SELF	WSELF	MSELF	LLF	KLF	CI
$\varpi = 0.01$							
I	50	1.8588	1.8398	1.8207	1.8493	1.8493	0.7309
II	79	0.9889	0.9811	0.9733	0.9850	0.9850	0.3403
$\varpi = 1$							
I	50	1.8633	1.8445	1.8254	1.8539	1.8538	0.7291
II	79	0.9882	0.9805	0.9729	0.9843	0.9844	0.3426
$\varpi = 5$							
I	50	1.8719	1.8541	1.8362	1.8631	1.8630	0.7061
II	79	0.9867	0.9789	0.9713	0.9828	0.9828	0.3382
$\varpi = 10$							
I	50	1.8730	1.8532	1.8308	1.8634	1.8631	0.7149
II	79	0.9854	0.9775	0.9696	0.9814	0.9814	0.3436

5. Conclusions

In this article, the point and interval estimation have been considered under classical and Bayesian paradigm for newly proposed index $\mathbb{S}''_{pk}$, when the process is normally distributed. Under classical estimation for the index, six methods were studied. One approach was explored to obtain the interval estimation: $\mathbb{ACI}$ based on $\mathbb{MLE}$. In order to evaluate the effectiveness of each of these point and interval estimations, we conducted Monte Carlo simulation studies with various layouts, obtaining $\mathbb{MSE}s$ for point estimation and $\mathbb{AW}s$, $\mathbb{CP}s$ for interval estimation, respectively. According to the simulation studies, observed that $\mathbb{MLE}$ performed better in terms of their $\mathbb{MSE}$ for point estimation, whereas $\mathbb{ACI}$ shows appropriate pattern in terms of $\mathbb{AW}s$ for interval estimation. The Bayes (point and interval) estimations are carried out for the index $\mathbb{S}''_{pk}$ with five different loss functions. The same setups were used for the Bayesian estimation. The comparison was considered with the help of average $\mathbb{BE}$ and corresponding $\mathbb{PR}$ obtained by simulation study. According to this, $\mathbb{LLF}$ has the lowest $\mathbb{PR}$ and $\mathbb{SELF}$ has the highest $\mathbb{BE}$ with decreasing $\mathbb{AW}$ and increase in $\mathbb{CP}$ as sample size rise. Two real data sets were re-analyzed, and the results were consistent with the findings of the considered simulation study. Real life experiment revels that $\mathbb{SELF}$ has the largest $\mathbb{BE}$ for all four sets of ϖ values. For further study the present study may be extended for the censored scheme. We hope that the results obtained in this study will help the practitioners in the manufacturing industries in their decision making.

References

[1] Boyles, R.A. 1994 "Brocess capability with asymmetric tolerances." *Communications in Statistics-Simulation and Computation* 23(3):615 - 635. DOI: 10.1080/03610919408813190.

[2] Chen, J.L., W.L. Pearn. 2010 "Process Selection for Higher Production Yield Based on Capability Index S_{pk}." *Quality and Reliability Engineering International* 26(3):247-258. DOI: 10.1002/qre.1051.

[3] Cheng, R.C.H., N.A.K. Amin. 1979 "Maximum product-of-spacings estimation with applications to the log-normal distribution." *Math Report, Department of Mathematics, UWIST*.

[4] Chang, L.K., S.W. Cheng, F.A. Spiring. 1988 "A new measure of process capability Cpm." *Journal of Quality Technology* 30:162-175. DOI: 10.1080/00224065.1988.11979102.

[5] Delignette-Muller, M.L., C. Dutang. 2015 "fitdistrplus: An R Package for Fitting Distributions." *Journal of Statistical Software* 64(4):1-34. DOI:10.18637/jss.v064.i04.

[6] Dey, S., M. Saha. 2019 "Bootstrap Confidence Intervals of Process Capability Index Spmk using Different Methods of Estimation." *Journal of Statistical Computation and Simulation* 90(1):28-50 . DOI: 10.1080/00949655.2019.1671980.

[7] Dey, S., M. Saha, C. Park. 2023. "Applications of a new loss and cost-based process capability index to electronic industries." *Communications in Statistics: Case Studies, Data Analysis and Applications*, 9(4):351-377. DOI:10.1080/23737484.2023.2249850

[8] Dey, S., C. Zhang, A. Asgharzadeh, M. Ghorbannezhad. 2017 "Comparisons of methods of estimation for the NH distribution." *Annals of Data Science* 4(1):441-455. DOI: 10.1007/s40745-017-0114-3.

[9] Erfanian, M., B.S. Gildeh. 2021 "A new capability index for non-normal distributions based on linex loss function." *Quality Engineering* 33(1):76-84. DOI: 10.1080/08982112.2020.1761026.

[10] Hsiang, T.C., G. Taguchi. 1985 "A Tutorial on Quality Control and Assurance." *Annual Meeting on the American Statistical Association*, Las Vegas, NV (unpublished presentation).

[11] Juran, J.M., F.M. Gryna, R.S. Bingham. 1974 "Jr. Quality control handbook." *McGrawHill*, New York.

[12] Kane, V.E. 1986 "Process capability indices." *Journal of Quality Technology* 18(1):41-52. DOI: 10.1080/00224065.1986.11978984.

[13] Kao, J.H.K. 1959 "A graphical estimation of mixed Weibull parameters in life testing electron tube." *Technometrics* 1(4):389-407. https://doi.org/10.2307/1266719.

[14] MacDonald, P.D.M. 1971 "Comment on an estimation procedure for mixtures of distributions by Choi and Bulgren." *Journal of Royal Statistical Society: Series B* 33(2):326-329. https://doi.org/10.1111/j.2517-6161.1971.tb00884.x.

[15] Pearn, W.L., S. Kotz, N.L. Johnson. 1992 "Distributional and inferential properties of process capability indices." *Journal of Quality Technology* 24:216-231. DOI:10.1080/00224065.1992.11979403.

[16] Peng, C. 2010 "Parametric Lower Confidence Limits of Quantile-based Process Capability Indices." *Journal of Quality Technology and Quantitative Management* 7(3):199-214. DOI: 10.1080/16843703.2010.11673228.

[17] Saha, M. 2022 "Applications of a new process capability index to electronic industries." *Communication in Statistics : Case Studies, Data Analysis and Applications* 8(4):1-14. DOI: 10.1080/23737484.2022.2107962.

[18] Saha, M., A. Devi, P. Pareek. 2023 "Applications of process capability indices for suppliers selection problems using generalized confidence interval." *Communications in Statistics: Case Studies, Data Analysis and Applications* 9(3):270-286. DOI: 10.1080/23737484.2023.2219223.

[19] Saha, M., A. Devi, A.S. Yadav, S.S. Maiti. 2024 "Evaluation of a novel loss-based process capability index $\mathcal{S}'_{pk}$ and it's applications." *International Journal of System Assurance Engineering and Management* 15(6):2188-2201. DOI: 10.1080/23737484.2023.2219223.

[20] Saha, M., S. Dey. 2023a "Uses of a new asymmetric loss-based process capability index in the electronic industries." *Communications in Statistics: Case Studies, Data Analysis and Applications* 9(2):135-151. DOI: 1 10.1007/s13198-023-02235-1.

[21] Saha, M., S. Dey. 2023b "Estimation and confidence intervals of a new loss based process capability index with applications." *International Journal of System Assurance Engineering and Management* 14:1827-1840. DOI:10.1007/s13198-023-02004-0

[22] Shiau, J.H., C.T. Chiang, H.N. Hung. 1999 "A Bayesian procedure for process capability assessment." *Quality and Reliability Engineering International* 15(5):369-378. DOI:"10.1002/$(SICI)1099-1638(199909/10)15:5<369::AID-QRE262>3.0.CO;2-R$".

[23] Spiring, F., B. Leung, S. Cheng, A. Yeung. 2003 "A bibliography of process capability papers." *Quality and Reliability Engineering International*19(5):445-460. DOI:10.1002/qre.538

[24] Swain, J., S. Venkatraman, J. Wilson. 1988 " Least squares estimation of distribution function in Johnsons translation system." *Journal of Statistical Computation and Simulation* 29(4):271-297. DOI: 10.1080/00949658808811068.

[25] Vannman, K. 1995 "A unified approach to capability indices". *Statistica Sinica*. 5(2):805-820. https://www.jstor.org/stable/24305072.

[26] Varian, H.R. 1975 "A Bayesian Approach to Real Estate Assessment", In Studies in Bayesian Econometric and Statistics in Honor of Leonard J. Savage, edited by S. E. Fienberg and A. Zellner, 195-208.

[27] Wu, C.W., W.L. Pearn. 2008 "A Variables Sampling Plan based on C_{pmk} for Product Acceptance Determination." *European Journal of Operational Research* 184(2):549-60. DOI: 10.1016/j.ejor.2006.11.032.

TWO COMPONENT MIXTURE OF LEFT TRUNCATED THREE PARAMETER LOGISTIC TYPE DISTRIBUTION WITH APPLICATIONS TO MANPOWER MODELING

Usha Hamsa[1]*, Srinivasa Rao Kraleti[2], Muniswamy Begari[3]

•

[1,2,3]Department of Statistics, Andhra University, Visakhapatnam, Andhra Pradesh 530003, India
Correspondoing Author Email: *ushahamsa5@gmail.com

Abstract

The logistic distribution serves as an alternative to normal distribution due to its is similarity in shape with heavier tails. Several extensions and generalizations of the logistic distribution have been proposed and explored in research papers published from 2020 onwards, particularly for modeling data with varying characteristics like skewness and kurtosis, or for specific applications in areas like finance and survival analysis. Some important distributions include the skew logistic distribution, the extended log-logistic distribution, two parameter logistic type distribution, three parameter logistic type distribution and the beta log-logistic distribution. These extensions offer increased flexibility in fitting data compared to the standard logistic distribution. Recently Usha et al (2025) have studied truncated three parameter Logistic distribution. Based on this distribution, we propose a new model called the two component mixture of left truncated tree parameter logistics type distribution for describing manpower data. It involves various specialized models, such as mixture of truncated logistic and a mixture of two-parameter logistic type distributions, among several others, so it's possibly better model for analyzing skewed data. The new density function can be expressed as a weighted combination of truncated tree parameter logistic-type densities. Various mathematical properties of the new distribution including explicit expressions for the moments are derived. We discuss the maximum likelihood method to estimate the model parameters for heterogeneous data. The superiority of the proposed manpower model is illustrated.

Keywords: Three parameter logistic type distribution, Mixture of distributions, Distributional properties, Manpower modeling, Recruitment policies.

I. Introduction

Probability distributions play a vital role in analyzing the random phenomenon through data sets. One such probability distribution is Logistic distribution which was used by several authors to analyse various data sets in different areas of applications. Extensions of logistic distribution are studied by many researcher to develop various models that suits the data sets. Dubey [1] has derived logistic distribution as a special case of compound generalized extreme value distribution by compounding generalized extreme value distribution with gamma distribution. Olapade [2]

discussed characterizations of the half logistic distribution. He proved theorems that characterize the half logistic distribution. Nassar et al. [3] studied the beta generalized logistic distribution. Gupta et al. [4] discussed the properties of the two generalizations of the logistic distributions, which can be used to model the data exhibiting unimodal density with some skewness. Alzaatreh et al. [5] developed a method for generating families of continuous distributions. Adeyinka et al. [6] studied the four parameters generalized log-logistic distribution using quadratic rank transmutation. Aljarrah et al. [7] considered a generalized asymmetric logistic distribution. Satheesh Kumar et al. [8] studied a range of generalized logistic distribution (GGLD) with asymmetric datasets. They discussed about some of the distribution characteristics. Alizadeh [9] developed a new goodness of fit test for the logistic distribution based on a new estimate of kullback-Leibler information. The properties of the test statistic are presented.

Usha H et al. [10] developed and analyzed a left truncated three parameter logistic type distribution. They have studied the properties of singly and doubly truncated three-parameter logistic-type distribution. These distributions are useful only when the population under consideration is homogenous. In many practical situations, the population under consideration is heterogeneous, arising from various sources of generation. For example, manpower modeling the complete length of service of employee in an organization should be considered as a mixture of two types of employee namely: committed and non-committed, each having different distribution. To analyze such situations, one needs to consider the random variable under study as a two-component mixture of distributions. The complete length of employee in an organization has finite values. In this chapter, we develop the two-component mixture of left-truncated three-parameter logistic type distribution.

The properties of the proposed distribution, such as mean, distribution function, moments, skewness, kurtosis, survival function, and hazard function, are derived. The inferential aspects of the parameters are examined through the likelihood function, and the distribution utility in analyzing the manpower situation is also evaluated. Two promotion policies, namely promotion by seniority and promotion by random, are also studied.

II. Two Component Mixture of Left Truncated Three Parameter Logistic Type Distribution

A continuous random variable X is said to have a two component mixture of left truncated three parameter logistic type distribution if its p.d.f is expressed in the following form:

$$f(x) = p\, f_1(x) + (1-p) f_2(x) \qquad 0 < p < 1$$

Hence the probability density function of two component mixture of left truncated three parameter logistic type distribution

$$\begin{aligned} f(x;\mu_1,\mu_2,\sigma_1,\sigma_2,s_1,s_2,p) &= p\left[C_1\left[s_1+\left(\frac{x-\mu_1}{\sigma_1}\right)^2\right]\frac{e^{-\left(\frac{x-\mu_1}{\sigma_1}\right)}}{\sigma_1\left[1+e^{-\left(\frac{x-\mu_1}{\sigma_1}\right)}\right]^2}\right] \\ &+ (1-p)\left[C_2\left[s_2+\left(\frac{x-\mu_2}{\sigma_2}\right)^2\right]\frac{e^{-\left(\frac{x-\mu_2}{\sigma_2}\right)}}{\sigma_2\left[1+e^{-\left(\frac{x-\mu_2}{\sigma_2}\right)}\right]^2}\right] \end{aligned} \tag{1}$$

$$0 < x < \infty;\quad \mu_1,\mu_2 > 0;\quad \sigma_1,\sigma_2 > 0;\ s_1,s_2 > 0;\ 0 < p < 1.$$

This implies,

$$C_1 = \left[\left(s_1 + \frac{\mu_1^2}{\sigma_1^2}\right)\frac{e^{\mu_1/\sigma_1}}{[1+e^{\mu_1/\sigma_1}]} - \frac{2\mu_1}{\sigma_1}\log\left(1+e^{\mu_1/\sigma_1}\right) - 2Li_2\left(-e^{\mu_1/\sigma_1}\right)\right]^{-1}$$

$$C_2 = \left[\left(s_2 + \frac{\mu_2^2}{\sigma_2^2}\right)\frac{e^{\mu_2/\sigma_2}}{[1+e^{\mu_2/\sigma_2}]} - \frac{2\mu_2}{\sigma_2}\log\left(1+e^{\mu_2/\sigma_2}\right) - 2Li_2\left(-e^{\mu_2/\sigma_2}\right)\right]^{-1}$$

where, $Li_2(\cdot)$ is Dilogarithm Function

Here, p is the mixing parameter, μ_1, μ_2 are the location parameters, σ_1, σ_2 are the scale parameters and s_1, s_2 are the drift parameters.

Making transformation $y_1 = \frac{x-\mu_1}{\sigma_1}$ *and* $y_2 = \frac{x-\mu_2}{\sigma_2}$ in the Eq. (1), we get

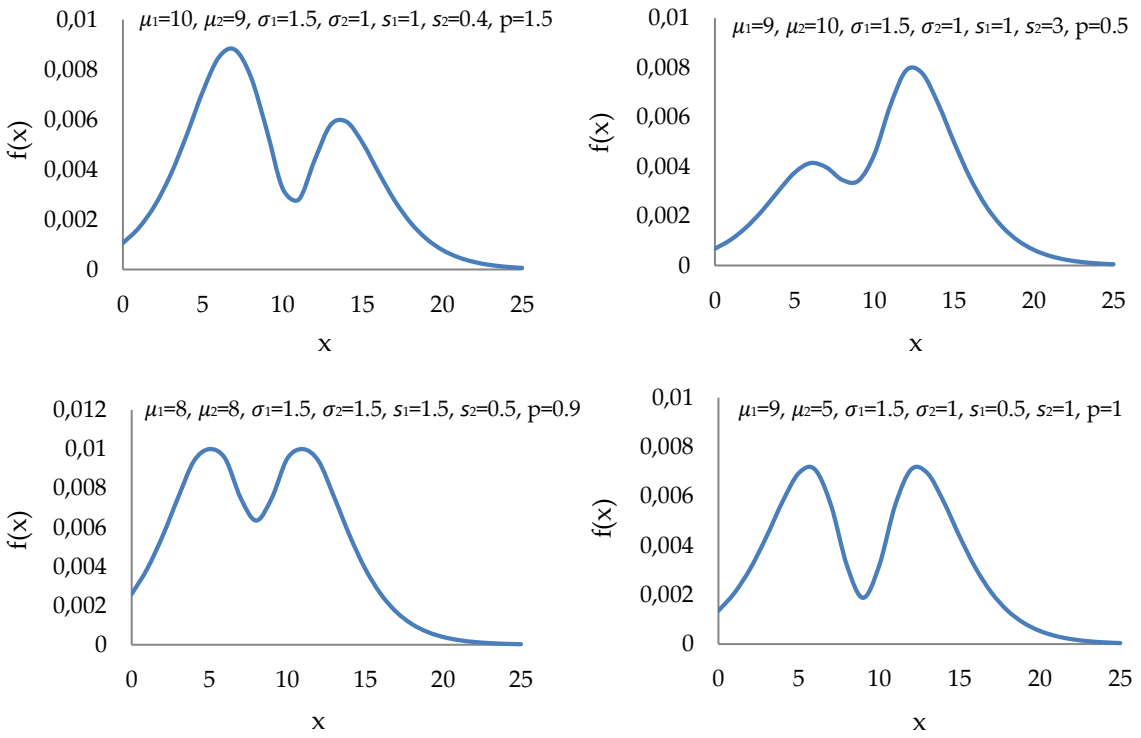
$$f(x;s) = p\left[C_1[s_1+y_1^2]\frac{e^{-y_1}}{[1+e^{-y_1}]^2}\right] + (1-p)\left[C_2[s_2+y_2^2]\frac{e^{-y_2}}{[1+e^{-y_2}]^2}\right] \quad (2)$$

Which may be called the standard two-component mixture of left truncated three parameter logistic type distribution.

III. Distributional Properties

This section presents the different distributional properties of the two component mixture of left truncated three parameter logistic type distribution.

Different shapes of the frequency curves for given values of the parameters are shown in Figure 1



Figures 1 *Two component mixture of left truncated three parameter logistic type distribution frequency curves for different values of parameters μ_1, μ_2, σ_1, σ_2, s_1, s_2 and p.*

The distribution function of the random variable X is

$$F_X(x) = \int_0^x f(t)dt$$

After simplifying, we get

$$F(x) = pC_1\left[\left(s_1+\frac{\mu_1^2}{\sigma_1^2}\right)\frac{e^{\mu_1/\sigma_1}}{[1+e^{\mu_1/\sigma_1}]}-\frac{2\mu_1}{\sigma_1}\log\left(1+e^{\mu_1/\sigma_1}\right)-2Li_2\left(-e^{\mu_1/\sigma_1}\right)\right.$$
$$-\frac{\left[s_1+\left(\frac{x-\mu_1}{\sigma_1}\right)^2\right]e^{-\left(\frac{x-\mu_1}{\sigma_1}\right)}}{\left[1+e^{-\left(\frac{x-\mu_1}{\sigma_1}\right)}\right]}-2\left(\frac{x-\mu_1}{\sigma_1}\right)\log\left[1+e^{-\left(\frac{x-\mu_1}{\sigma_1}\right)}\right]$$
$$\left.+2Li_2\left(-e^{-\left(\frac{x-\mu_1}{\sigma_1}\right)}\right)\right]+(1$$
$$-p)C_2\left[\left(s_2+\frac{\mu_2^2}{\sigma_2^2}\right)\frac{e^{\mu_2/\sigma_2}}{[1+e^{\mu_2/\sigma_2}]}-\frac{2\mu_2}{\sigma_2}\log\left(1+e^{\mu_2/\sigma_2}\right)-2Li_2\left(-e^{\mu_2/\sigma_2}\right)\right. \quad (3)$$
$$-\frac{\left[s_2+\left(\frac{x-\mu_2}{\sigma_2}\right)^2\right]e^{-\left(\frac{x-\mu_2}{\sigma_2}\right)}}{\left[1+e^{-\left(\frac{x-\mu_2}{\sigma_2}\right)}\right]}-2\left(\frac{x-\mu_2}{\sigma_2}\right)\log\left[1+e^{-\left(\frac{x-\mu_2}{\sigma_2}\right)}\right]$$
$$\left.+2Li_2\left(-e^{-\left(\frac{x-\mu_2}{\sigma_2}\right)}\right)\right]$$

where, C_1 and C_2 are as specified in Eq. (1) and $\mathrm{Li}_2(\cdot)$ is Dilogarithm function

Mean of the distribution is

$$E(X)=\int_0^\infty x\,f(x)dx$$

After simplifying, we get

$$E(X)=pC_1\left[\left(\frac{\mu_1^2+s_1\sigma_1^2}{\sigma_1}\right)\log\left(1+e^{\mu_1/\sigma_1}\right)+4\mu_1Li_2\left(-e^{\mu_1/\sigma_1}\right)-6\sigma_1Li_3\left(-e^{\mu_1/\sigma_1}\right)\right]$$
$$+(1-p)C_2\left[\left(\frac{\mu_2^2+s_2\sigma_2^2}{\sigma_2}\right)\log\left(1+e^{\mu_2/\sigma_2}\right)+4\mu_2Li_2\left(-e^{\mu_2/\sigma_2}\right)\right. \quad (4)$$
$$\left.-6\sigma_2Li_3\left(-e^{\mu_2/\sigma_2}\right)\right]$$

where, C_1 and C_2 are as specified in Eq. (1) and $\mathrm{Li}_n(\cdot)$ is Polylogarithm function of order n (n ≥ 2)

Second raw moment of the distribution is

$$\mu_2'=\int_0^\infty x^2\,f(x)\,dx$$

After simplifying, we get

$$\mu_2'=p\left[2C_1\left[-(\mu_1^2+s_1\sigma_1^2)Li_2\left(-e^{\mu_1/\sigma_1}\right)+6\mu_1\sigma_1Li_3\left(-e^{\mu_1/\sigma_1}\right)-12\sigma_1^2Li_4\left(-e^{\mu_1/\sigma_1}\right)\right]\right]$$
$$+(1 \quad (5)$$
$$-p)\left[2C_2\left[-(\mu_2^2+s_2\sigma_2^2)Li_2\left(-e^{\mu_2/\sigma_2}\right)+6\mu_2\sigma_2Li_3\left(-e^{\mu_2/\sigma_2}\right)\right.\right.$$
$$\left.\left.-12\sigma_2^2Li_4\left(-e^{\mu_2/\sigma_2}\right)\right]\right]$$

where, C_1 and C_2 are as specified in Eq. (1) and $\mathrm{Li}_n(\cdot)$ is Polylogarithm function of order n (n ≥ 2)
Third raw moment of the distribution is

$$\mu_3'=\int_0^\infty x^3\,f(x)\,dx$$

After simplifying, we get

$$\mu_3' = p\left[6C_1\sigma_1\left[-(\mu_1^2 + s_1\sigma_1^2)Li_3\left(-e^{\mu_1/\sigma_1}\right) + 8\mu_1\sigma_1 Li_4\left(-e^{\mu_1/\sigma_1}\right) - 20\sigma_1^2 Li_5\left(-e^{\mu_1/\sigma_1}\right)\right]\right] + (1 - p)\left[6C_2\sigma_2\left[-(\mu_2^2 + s_2\sigma_2^2)Li_3\left(-e^{\mu_2/\sigma_2}\right) + 8\mu_2\sigma_2 Li_4\left(-e^{\mu_2/\sigma_2}\right) - 20\sigma_2^2 Li_5\left(-e^{\mu_2/\sigma_2}\right)\right]\right] \quad (6)$$

where, C_1 and C_2 are as specified in Eq. (1) and $\mathrm{Li}_n(\cdot)$ is Polylogarithm function of order n (n ≥ 2)

Fourth raw moment of the distribution is

$$\mu_4' = \int_0^\infty x^4 f(x)\, dx$$

After simplifying, we get

$$\mu_4' = p\left[24C_1\sigma_1^2\left[-(\mu_1^2 + s_1\sigma_1^2)Li_4\left(-e^{\mu_1/\sigma_1}\right) + 5\sigma_1(6 - 4\mu_1)Li_5\left(-e^{\mu_1/\sigma_1}\right) - 30\sigma_1^2 Li_6\left(-e^{\mu_1/\sigma_1}\right)\right]\right] + (1 - p)\left[24C_2\sigma_2^2\left[-(\mu_2^2 + s_2\sigma_2^2)Li_4\left(-e^{\mu_2/\sigma_2}\right) + 5\sigma_2(6 - 4\mu_2)Li_5\left(-e^{\mu_2/\sigma_2}\right) - 30\sigma_2^2 Li_6\left(-e^{\mu_2/\sigma_2}\right)\right]\right] \quad (7)$$

where, C_1 and C_2 are as specified in Eq. (1) and $\mathrm{Li}_n(\cdot)$ is Polylogarithm function of order n (n ≥ 2)

The Second central moment of the distribution is

$$\mu_2 = p\left[2C_1\left[-(\mu_1^2 + s_1\sigma_1^2)Li_2\left(-e^{\mu_1/\sigma_1}\right) + 6\mu_1\sigma_1 Li_3\left(-e^{\mu_1/\sigma_1}\right) - 12\sigma_1^2 Li_4\left(-e^{\mu_1/\sigma_1}\right)\right] - C_1^2K_1^2\right] + (1 - p)\left[2C_2\left[-(\mu_2^2 + s_2\sigma_2^2)Li_2\left(-e^{\mu_2/\sigma_2}\right) + 6\mu_2\sigma_2 Li_3\left(-e^{\mu_2/\sigma_2}\right) - 12\sigma_2^2 Li_4\left(-e^{\mu_2/\sigma_2}\right)\right] - C_2^2K_2^2\right] \quad (8)$$

where, C_1 and C_2 are as specified in Eq. (1)

$$K_1 = p\left[\left(\frac{\mu_1^2 + s_1\sigma_1^2}{\sigma_1}\right)\log\left(1 + e^{\mu_1/\sigma_1}\right) + 4\mu_1 Li_2\left(-e^{\mu_1/\sigma_1}\right) - 6\sigma_1 Li_3\left(-e^{\mu_1/\sigma_1}\right)\right]$$

$$K_2 = (1 - p)\left[\left(\frac{\mu_2^2 + s_2\sigma_2^2}{\sigma_2}\right)\log\left(1 + e^{\mu_2/\sigma_2}\right) + 4\mu_2 Li_2\left(-e^{\mu_2/\sigma_2}\right) - 6\sigma_2 Li_3\left(-e^{\mu_2/\sigma_2}\right)\right]$$

and $\mathrm{Li}_n(\cdot)$ is Polylogarithm function of order n (n ≥ 2)
Third central moment of the distribution is

$$\begin{aligned}\mu_3 = p\big[&6C_1\sigma_1\big[-(\mu_1^2+s_1\sigma_1^2)Li_3\big(-e^{\mu_1/\sigma_1}\big)+8\mu_1\sigma_1Li_4\big(-e^{\mu_1/\sigma_1}\big)-20\sigma_1^2Li_5\big(-e^{\mu_1/\sigma_1}\big)\big]\\&-6C_1^2K_1\big[-(\mu_1^2+s_1\sigma_1^2)Li_2\big(-e^{\mu_1/\sigma_1}\big)+6\mu_1\sigma_1Li_3\big(-e^{\mu_1/\sigma_1}\big)\\&-12\sigma_1^2Li_4\big(-e^{\mu_1/\sigma_1}\big)\big]+2C_1^3K_1^3\big]\\&+(1\\&-p)\big[6C_2\sigma_2\big[-(\mu_2^2+s_2\sigma_2^2)Li_3\big(-e^{\mu_2/\sigma_2}\big)+8\mu_2\sigma_2Li_4\big(-e^{\mu_2/\sigma_2}\big)\\&-20\sigma_2^2Li_5\big(-e^{\mu_2/\sigma_2}\big)\big]\\&-6C_2^2K_2\big[-(\mu_2^2+s_2\sigma_2^2)Li_2\big(-e^{\mu_2/\sigma_2}\big)+6\mu_2\sigma_2Li_3\big(-e^{\mu_2/\sigma_2}\big)\\&-12\sigma_2^2Li_4\big(-e^{\mu_2/\sigma_2}\big)\big]+2C_2^3K_2^3\big]\end{aligned} \tag{9}$$

where, C_1 and C_2 are as specified in Eq. (1)

$$K_1 = p\left[\left(\frac{\mu_1^2+s_1\sigma_1^2}{\sigma_1}\right)\log\big(1+e^{\mu_1/\sigma_1}\big)+4\mu_1Li_2\big(-e^{\mu_1/\sigma_1}\big)-6\sigma_1Li_3\big(-e^{\mu_1/\sigma_1}\big)\right]$$

$$K_2 = (1-p)\left[\left(\frac{\mu_2^2+s_2\sigma_2^2}{\sigma_2}\right)\log\big(1+e^{\mu_2/\sigma_2}\big)+4\mu_2Li_2\big(-e^{\mu_2/\sigma_2}\big)-6\sigma_2Li_3\big(-e^{\mu_2/\sigma_2}\big)\right]$$

and $\mathrm{Li}_n(\cdot)$ is Polylogarithm function of order n (n ≥ 2)

Fourth central moment of the distribution is

$$\begin{aligned}\mu_4 = p\big[&24C_1\sigma_1^2\big[-(\mu_1^2+s_1\sigma_1^2)Li_4\big(-e^{\mu_1/\sigma_1}\big)+5\sigma_1(6-4\mu_1)Li_5\big(-e^{\mu_1/\sigma_1}\big)\\&-30\sigma_1^2Li_6\big(-e^{\mu_1/\sigma_1}\big)\big]\\&-24C_1^2K_1\sigma_1\big[-(\mu_1^2+s_1\sigma_1^2)Li_3\big(-e^{\mu_1/\sigma_1}\big)+8\mu_1\sigma_1Li_4\big(-e^{\mu_1/\sigma_1}\big)\\&-20\sigma_1^2Li_5\big(-e^{\mu_1/\sigma_1}\big)\big]\\&-12C_1^3K_1^2\big[-(\mu_1^2+s_1\sigma_1^2)Li_2\big(-e^{\mu_1/\sigma_1}\big)+6\mu_1\sigma_1Li_3\big(-e^{\mu_1/\sigma_1}\big)\\&-12\sigma_1^2Li_4\big(-e^{\mu_1/\sigma_1}\big)\big]-3C_1^4K_1^4\big]\\&+(1\\&-p)\big[24C_2\sigma_2^2\big[-(\mu_2^2+s_2\sigma_2^2)Li_4\big(-e^{\mu_2/\sigma_2}\big)+5\sigma_2(6-4\mu_2)Li_5\big(-e^{\mu_2/\sigma_2}\big)\\&-30\sigma_2^2Li_6\big(-e^{\mu_2/\sigma_2}\big)\big]\\&-24C_2^2K_2\sigma_2\big[-(\mu_2^2+s_2\sigma_2^2)Li_3\big(-e^{\mu_2/\sigma_2}\big)+8\mu_2\sigma_2Li_4\big(-e^{\mu_2/\sigma_2}\big)\\&-20\sigma_2^2Li_5\big(-e^{\mu_2/\sigma_2}\big)\big]\\&-12C_2^3K_2^2\big[-(\mu_2^2+s_2\sigma_2^2)Li_2\big(-e^{\mu_2/\sigma_2}\big)+6\mu_2\sigma_2Li_3\big(-e^{\mu_2/\sigma_2}\big)\\&-12\sigma_2^2Li_4\big(-e^{\mu_2/\sigma_2}\big)\big]-3C_2^4K_2^4\big]\end{aligned} \tag{10}$$

where, C_1 and C_2 are as specified in Eq. (1)

$$K_1 = p\left[\left(\frac{\mu_1^2+s_1\sigma_1^2}{\sigma_1}\right)\log\big(1+e^{\mu_1/\sigma_1}\big)+4\mu_1Li_2\big(-e^{\mu_1/\sigma_1}\big)-6\sigma_1Li_3\big(-e^{\mu_1/\sigma_1}\big)\right]$$

$$K_2 = (1-p)\left[\left(\frac{\mu_2^2+s_2\sigma_2^2}{\sigma_2}\right)\log\big(1+e^{\mu_2/\sigma_2}\big)+4\mu_2Li_2\big(-e^{\mu_2/\sigma_2}\big)-6\sigma_2Li_3\big(-e^{\mu_2/\sigma_2}\big)\right]$$

and $\mathrm{Li}_n(\cdot)$ is Polylogarithm function of order n (n ≥ 2)

The skewness of the distribution is

$$\beta_1 = \frac{\mu_3^2}{\mu_2^3}$$

$$\beta_1 = \frac{\begin{array}{c}[p[6C_1\sigma_1[-(\mu_1^2+s_1\sigma_1^2)Li_3(-e^{\mu_1/\sigma_1})+8\mu_1\sigma_1Li_4(-e^{\mu_1/\sigma_1})-20\sigma_1^2Li_5(-e^{\mu_1/\sigma_1})]\\ -6C_1^2K_1[-(\mu_1^2+s_1\sigma_1^2)Li_2(-e^{\mu_1/\sigma_1})+6\mu_1\sigma_1Li_3(-e^{\mu_1/\sigma_1})-12\sigma_1^2Li_4(-e^{\mu_1/\sigma_1})]\\ +2C_1^3K_1^3]+(1-p)[6C_2\sigma_2[-(\mu_2^2+s_2\sigma_2^2)Li_3(-e^{\mu_2/\sigma_2})+8\mu_2\sigma_2Li_4(-e^{\mu_2/\sigma_2})-20\\ \sigma_2^2Li_5(-e^{\mu_2/\sigma_2})]-6C_2^2K_2[-(\mu_2^2+s_2\sigma_2^2)Li_2(-e^{\mu_2/\sigma_2})+6\mu_2\sigma_2Li_3(-e^{\mu_2/\sigma_2})-\\ 12\sigma_2^2Li_4(-e^{\mu_2/\sigma_2})]+2C_2^3K_2^3]^2\end{array}}{\begin{array}{c}[p[2C_1[-(\mu_1^2+s_1\sigma_1^2)Li_2(-e^{\mu_1/\sigma_1})+6\mu_1\sigma_1Li_3(-e^{\mu_1/\sigma_1})-12\sigma_1^2Li_4(-e^{\mu_1/\sigma_1})]\\ -C_1^2K_1^2]+(1-p)[2C_2[-(\mu_2^2+s_2\sigma_2^2)Li_2(-e^{\mu_2/\sigma_2})+6\mu_2\sigma_2Li_3(-e^{\mu_2/\sigma_2})\\ -12\sigma_2^2Li_4(-e^{\mu_2/\sigma_2})]-C_2^2K_2^2]]^3\end{array}} \quad (11)$$

where, C_1 and C_2 are as specified in Eq. (1)

$$K_1 = p\left[\left(\frac{\mu_1^2+s_1\sigma_1^2}{\sigma_1}\right)\log\left(1+e^{\mu_1/\sigma_1}\right)+4\mu_1Li_2\left(-e^{\mu_1/\sigma_1}\right)-6\sigma_1Li_3\left(-e^{\mu_1/\sigma_1}\right)\right]$$

$$K_2 = (1-p)\left[\left(\frac{\mu_2^2+s_2\sigma_2^2}{\sigma_2}\right)\log\left(1+e^{\mu_2/\sigma_2}\right)+4\mu_2Li_2\left(-e^{\mu_2/\sigma_2}\right)-6\sigma_2Li_3\left(-e^{\mu_2/\sigma_2}\right)\right]$$

and $\mathrm{Li}_n(\cdot)$ is Polylogarithm function of order n (n ≥ 2)

The kurtosis of the distribution is

$$\beta_2 = \frac{\mu_4}{\mu_2^2}$$

$$\beta_2 = \frac{\begin{array}{c}p[24C_1\sigma_1^2[-(\mu_1^2+s_1\sigma_1^2)Li_4(-e^{\mu_1/\sigma_1})+5\sigma_1(6-4\mu_1)Li_5(-e^{\mu_1/\sigma_1})-30\sigma_1^2Li_6\\ (-e^{\mu_1/\sigma_1})]-24C_1^2K_1\sigma_1[-(\mu_1^2+s_1\sigma_1^2)Li_3(-e^{\mu_1/\sigma_1})+8\mu_1\sigma_1Li_4(-e^{\mu_1/\sigma_1})-20\\ \sigma_1^2Li_5(-e^{\mu_1/\sigma_1})]-12C_1^3K_1^2[-(\mu_1^2+s_1\sigma_1^2)Li_2(-e^{\mu_1/\sigma_1})+6\mu_1\sigma_1Li_3(-e^{\mu_1/\sigma_1})\\ -12\sigma_1^2Li_4(-e^{\mu_1/\sigma_1})]]-3C_1^4K_1^4]+(1-p)[24C_2\sigma_2^2[-(\mu_2^2+s_2\sigma_2^2)Li_4(-e^{\mu_2/\sigma_2})\\ +5\sigma_2(6-4\mu_2)Li_5(-e^{\mu_2/\sigma_2})-30\sigma_2^2Li_6(-e^{\mu_2/\sigma_2})]-24C_2^2K_2\sigma_2[-(\mu_2^2+s_2\sigma_2^2)\\ Li_3(-e^{\mu_2/\sigma_2})+8\mu_2\sigma_2Li_4(-e^{\mu_2/\sigma_2})-20\sigma_2^2Li_5(-e^{\mu_2/\sigma_2})]-12C_2^3K_2^2[-(\mu_2^2+s_2\sigma_2^2)\\ Li_2(-e^{\mu_2/\sigma_2})+6\mu_2\sigma_2Li_3(-e^{\mu_2/\sigma_2})-12\sigma_2^2Li_4(-e^{\mu_2/\sigma_2})]-3C_2^4K_2^4]\end{array}}{\begin{array}{c}[p[2C_1[-(\mu_1^2+s_1\sigma_1^2)Li_2(-e^{\mu_1/\sigma_1})+6\mu_1\sigma_1Li_3(-e^{\mu_1/\sigma_1})-12\sigma_1^2Li_4(-e^{\mu_1/\sigma_1})]\\ -C_1^2K_1^2]+(1-p)[2C_2[-(\mu_2^2+s_2\sigma_2^2)Li_2(-e^{\mu_2/\sigma_2})+6\mu_2\sigma_2Li_3(-e^{\mu_2/\sigma_2})\\ -12\sigma_2^2Li_4(-e^{\mu_2/\sigma_2})]-C_2^2K_2^2]]^2\end{array}} \quad (12)$$

where, C_1 and C_2 are as specified in Eq. (1)

$$K_1 = p\left[\left(\frac{\mu_1^2+s_1\sigma_1^2}{\sigma_1}\right)\log\left(1+e^{\mu_1/\sigma_1}\right)+4\mu_1Li_2\left(-e^{\mu_1/\sigma_1}\right)-6\sigma_1Li_3\left(-e^{\mu_1/\sigma_1}\right)\right]$$

$$K_2 = (1-p)\left[\left(\frac{\mu_2^2+s_2\sigma_2^2}{\sigma_2}\right)\log\left(1+e^{\mu_2/\sigma_2}\right)+4\mu_2Li_2\left(-e^{\mu_2/\sigma_2}\right)-6\sigma_2Li_3\left(-e^{\mu_2/\sigma_2}\right)\right]$$

and $\mathrm{Li}_n(\cdot)$ is Polylogarithm Function of order n (n ≥ 2)

IV. Estimation of Parameters

The estimation of the parameters for the two component mixture of left truncated three parameter logistic type distribution is considered in this section.

Method of Moments

This approach determines the estimators of the parameters by equating the population and sample moments accordingly. Suppose that a sample of size "n" is selected from a population whose probability density function has the following form:

$$f(x;\mu,\sigma,s) = p\left[C_1\left[s_1+\left(\frac{x-\mu_1}{\sigma_1}\right)^2\right]\frac{e^{-\left(\frac{x-\mu_1}{\sigma_1}\right)}}{\sigma_1\left[1+e^{-\left(\frac{x-\mu_1}{\sigma_1}\right)}\right]^2}\right] + (1-p)\left[C_2\left[s_2+\left(\frac{x-\mu_2}{\sigma_2}\right)^2\right]\frac{e^{-\left(\frac{x-\mu_2}{\sigma_2}\right)}}{\sigma_2\left[1+e^{-\left(\frac{x-\mu_2}{\sigma_2}\right)}\right]^2}\right]$$

$$0 < x < \infty;\quad \mu_1,\mu_2 > 0;\quad \sigma_1,\sigma_2 > 0;\ s_1,s_2 > 0.$$

Where, C_1 and C_2 are as specified in Eq. (1) and $\mathrm{Li}_2(\cdot)$ is Dilogarithm function

The distribution parameters $\mu_1,\mu_2,\sigma_1^2,\sigma_2^2,s_1$ and s_2. Therefore, we consider the first two raw moments of the both the sample and the population, which results in the following equation.

$$\bar{x} = \frac{1}{n}\sum_{i=1}^{n} x_i$$

$$\bar{x} = pC_1\left[\left(\frac{\mu_1^2+s_1\sigma_1^2}{\sigma_1}\right)\log\left(1+e^{\mu_1/\sigma_1}\right) + 4\mu_1 Li_2\left(-e^{\mu_1/\sigma_1}\right) - 6\sigma_1 Li_3\left(-e^{\mu_1/\sigma_1}\right)\right] + (1-p)C_2\left[\left(\frac{\mu_2^2+s_2\sigma_2^2}{\sigma_2}\right)\log\left(1+e^{\mu_2/\sigma_2}\right) + 4\mu_2 Li_2\left(-e^{\mu_2/\sigma_2}\right) - 6\sigma_2 Li_3\left(-e^{\mu_2/\sigma_2}\right)\right] \quad (13)$$

$$\frac{1}{n}\sum_{i=1}^{n} x_i^2 = p\left[2C_1\left[-(\mu_1^2+s_1\sigma_1^2)Li_2\left(-e^{\mu_1/\sigma_1}\right) + 6\mu_1\sigma_1 Li_3\left(-e^{\mu_1/\sigma_1}\right) - 12\sigma_1^2 Li_4\left(-e^{\mu_1/\sigma_1}\right)\right]\right] + (1-p)\left[2C_2\left[-(\mu_2^2+s_2\sigma_2^2)Li_2\left(-e^{\mu_2/\sigma_2}\right) + 6\mu_2\sigma_2 Li_3\left(-e^{\mu_2/\sigma_2}\right) - 12\sigma_2^2 Li_4\left(-e^{\mu_2/\sigma_2}\right)\right]\right] \quad (14)$$

where, C_1 and C_2 are as specified in Eq. (1) and $\mathrm{Li}_n(\cdot)$ is Polylogarithm function of order n (n ≥ 2)

When we simultaneously solve Eqs. (13) and (14), we obtain the moment estimates of $\mu_1,\mu_2,\sigma_1^2,\sigma_2^2,s_1$ and s_2.

Maximum Likelihood Method of Estimation

Let x_1, x_2, x_3, …, x_n be a sample of size n selected from a population. Whose p.d.f of this population is shown in Eq. (1). Accordingly the likelihood function for this sample is expressed as follows

$$L = p^n C_1^n \sigma_1^{-n}\prod_{i=1}^{n}\left\{\left[s_1+\left(\frac{x_i-\mu_1}{\sigma_1}\right)^2\right]\frac{e^{-\left(\frac{x_i-\mu_1}{\sigma_1}\right)}}{\left[1+e^{-\left(\frac{x_i-\mu_1}{\sigma_1}\right)}\right]^2}\right\} + (1-p)^n C_2^n \sigma_2^{-n}\prod_{i=1}^{n}\left\{\left[s_2+\left(\frac{x_i-\mu_2}{\sigma_2}\right)^2\right]\frac{e^{-\left(\frac{x_i-\mu_2}{\sigma_2}\right)}}{\left[1+e^{-\left(\frac{x_i-\mu_2}{\sigma_2}\right)}\right]^2}\right\} \quad (15)$$

where, C_1 and C_2 are as specified in Eq. (1) and $\mathrm{Li}_2(\cdot)$ is Dilogarithm function
The log likelihood function of the sample is

$$\begin{aligned}\log L = {} & n\log p - n\log\sigma_1 \\ & - n\log\left[\left(s_1+\frac{\mu_1^2}{\sigma_1^2}\right)\frac{e^{\mu_1/\sigma_1}}{[1+e^{\mu_1/\sigma_1}]} - \frac{2\mu_1}{\sigma_1}\log\left(1+e^{\mu_1/\sigma_1}\right) - 2Li_2\left(-e^{\mu_1/\sigma_1}\right)\right] \\ & + \sum_{i=1}^{n}\log\left[s_1+\left(\frac{x_i-\mu_1}{\sigma_1}\right)^2\right] - \sum_{i=1}^{n}\left(\frac{x_i-\mu_1}{\sigma_1}\right) - 2\sum_{i=1}^{n}\log\left[1+e^{-\left(\frac{x_i-\mu_1}{\sigma_1}\right)}\right] \\ & + n\log(1-p) - n\log\sigma_2 \\ & - n\log\left[\left(s_2+\frac{\mu_2^2}{\sigma_2^2}\right)\frac{e^{\mu_2/\sigma_2}}{[1+e^{\mu_2/\sigma_2}]} - \frac{2\mu_2}{\sigma_2}\log\left(1+e^{\mu_2/\sigma_2}\right) - 2Li_2\left(-e^{\mu_2/\sigma_2}\right)\right] \\ & + \sum_{i=1}^{n}\log\left[s_2+\left(\frac{x_i-\mu_2}{\sigma_2}\right)^2\right] - \sum_{i=1}^{n}\left(\frac{x_i-\mu_2}{\sigma_2}\right) - 2\sum_{i=1}^{n}\log\left[1+e^{-\left(\frac{x_i-\mu_2}{\sigma_2}\right)}\right]\end{aligned} \tag{16}$$

For determine the M.L.E. of the parameters, it is necessary to maximum L or Log L w.r.t these concerning the parameters $\mu_1, \mu_2, \sigma_1^2, \sigma_2^2, s_1$ and s_2.

$$\begin{aligned}nC_1\left\{\left(s_1+\frac{\mu_1^2}{\sigma_1^2}\right)\frac{e^{\mu_1/\sigma_1}}{[1+e^{\mu_1/\sigma_1}]^2} - 2\left(1+\frac{\sigma_1}{e^{\mu_1/\sigma_1}}\right)\log\left(1+e^{\mu_1/\sigma_1}\right)\right\} \\ + 2\sum_{i=1}^{n}\frac{\left(\frac{x_i-\mu_1}{\sigma_1}\right)}{\left[s_1+\left(\frac{x_i-\mu_1}{\sigma_1}\right)^2\right]} + 2\sum_{i=1}^{n}\frac{1}{\left[1+e^{\left(\frac{x_i-\mu_1}{\sigma_1}\right)}\right]} = n\end{aligned} \tag{17}$$

$$\begin{aligned}nC_2\left\{\left(s_2+\frac{\mu_2^2}{\sigma_2^2}\right)\frac{e^{\mu_2/\sigma_2}}{[1+e^{\mu_2/\sigma_2}]^2} - 2\left(1+\frac{\sigma_2}{e^{\mu_2/\sigma_2}}\right)\log\left(1+e^{\mu_2/\sigma_2}\right)\right\} \\ + 2\sum_{i=1}^{n}\frac{\left(\frac{x_i-\mu_2}{\sigma_2}\right)}{\left[s_2+\left(\frac{x_i-\mu_2}{\sigma_2}\right)^2\right]} + 2\sum_{i=1}^{n}\frac{1}{\left[1+e^{\left(\frac{x_i-\mu_2}{\sigma_2}\right)}\right]} = n\end{aligned} \tag{18}$$

$$\begin{aligned}-nC_1\left\{-\frac{\mu_1}{\sigma_1}\left(s_1+\frac{\mu_1^2}{\sigma_1^2}\right)\frac{e^{\mu_1/\sigma_1}}{[1+e^{\mu_1/\sigma_1}]^2} - \frac{2\mu_1}{\sigma_1^2}\left(\frac{1}{\sigma_1^2}-\mu_1\right)\frac{e^{\mu_1/\sigma_1}}{[1+e^{\mu_1/\sigma_1}]}\right. \\ \left. + 2\left(\frac{\mu_1}{\sigma_1}-\frac{\sigma_1}{e^{\mu_1/\sigma_1}}\right)\log\left(1+e^{\mu_1/\sigma_1}\right)\right\} \\ + \sum_{i=1}^{n}\left(\frac{x_i-\mu_1}{\sigma_1}\right) - 2\sum_{i=1}^{n}\frac{\left(\frac{x_i-\mu_1}{\sigma_1}\right)^2}{\left[s_1+\left(\frac{x_i-\mu_1}{\sigma_1}\right)^2\right]} - 2\sum_{i=1}^{n}\frac{\left(\frac{x_i-\mu_1}{\sigma_1}\right)}{\left[1+e^{\left(\frac{x_i-\mu_1}{\sigma_1}\right)}\right]} = n\end{aligned} \tag{19}$$

$$\begin{aligned}-nC_2\left\{-\frac{\mu_2}{\sigma_2}\left(s_2+\frac{\mu_2^2}{\sigma_2^2}\right)\frac{e^{\mu_2/\sigma_2}}{[1+e^{\mu_2/\sigma_2}]^2} - \frac{2\mu_2}{\sigma_2^2}\left(\frac{1}{\sigma_2^2}-\mu_2\right)\frac{e^{\mu_2/\sigma_2}}{[1+e^{\mu_2/\sigma_2}]}\right. \\ \left. + 2\left(\frac{\mu_2}{\sigma_2}-\frac{\sigma_2}{e^{\mu_2/\sigma_2}}\right)\log\left(1+e^{\mu_2/\sigma_2}\right)\right\} \\ + \sum_{i=1}^{n}\left(\frac{x_i-\mu_2}{\sigma_2}\right) - 2\sum_{i=1}^{n}\frac{\left(\frac{x_i-\mu_2}{\sigma_2}\right)^2}{\left[s_2+\left(\frac{x_i-\mu_2}{\sigma_2}\right)^2\right]} - 2\sum_{i=1}^{n}\frac{\left(\frac{x_i-\mu_2}{\sigma_2}\right)}{\left[1+e^{\left(\frac{x_i-\mu_2}{\sigma_2}\right)}\right]} = n\end{aligned} \tag{20}$$

$$-nC_1\left(\frac{e^{\mu_1/\sigma_1}}{[1+e^{\mu_1/\sigma_1}]}\right) + \sum_{i=1}^{n}\frac{1}{\left[s_1+\left(\frac{x_i-\mu_1}{\sigma_1}\right)^2\right]} = 0 \tag{21}$$

$$-nC_2\left(\frac{e^{\mu_2/\sigma_2}}{[1+e^{\mu_2/\sigma_2}]}\right)+\sum_{i=1}^{n}\frac{1}{\left[s_2+\left(\frac{x_i-\mu_2}{\sigma_2}\right)^2\right]}=0 \tag{22}$$

where, C_1 and C_2 are as specified in Eq. (1) and $Li_2(\cdot)$ is Dilogarithm function

It is possible to obtain the parameter estimates of $\hat{\mu}_1, \hat{\mu}_2, \hat{\sigma}_1^2, \hat{\sigma}_2^2, \hat{s}_1$ and $\hat{s}_2$ by simultaneously solving Eqs. (17), (18), (19), (20), (21) and (22) using numerical methods like Newton Rapson method.

V Manpower Planning Model with Two Component Mixture of Left Truncated Three Parameter Logistic Type Distribution as CLS

In this section examines the application of the developed distribution to the manpower planning models. Assume that CLS of an employee in an organization follows a two component mixture of left truncated three parameter logistic type distribution with parameters $\mu_1, \mu_2, \sigma_1^2, \sigma_2^2, s_1$ and s_2. Its probability density function, distribution function and expected length of service are given in the Eqs. (1), (3) and (4) respectively.

The probability that an individual survives in the organization for the length of time 't' is G(t), which is the survival function of the employee in the organization. It can be defined as the complement of the distribution function F(t). Then

$$G(t) = 1 - F(t)$$

$$G(t) = pC_1\int_t^{\infty}\left[s_1+\left(\frac{t-\mu_1}{\sigma_1}\right)^2\right]\frac{e^{-\left(\frac{t-\mu_1}{\sigma_1}\right)}}{\sigma_1\left[1+e^{-\left(\frac{t-\mu_1}{\sigma_1}\right)}\right]^2}\,dt + (1 - p)C_2\int_t^{\infty}\left[s_2+\left(\frac{t-\mu_2}{\sigma_2}\right)^2\right]\frac{e^{-\left(\frac{t-\mu_2}{\sigma_2}\right)}}{\sigma_2\left[1+e^{-\left(\frac{t-\mu_2}{\sigma_2}\right)}\right]^2}\,dt$$

Making the necessary transformations and integration, we obtain

$$G(t) = pC_1\left\{\frac{\left[s_1+\left(\frac{t-\mu_1}{\sigma_1}\right)^2\right]e^{-\left(\frac{t-\mu_1}{\sigma_1}\right)}}{\left[1+e^{-\left(\frac{t-\mu_1}{\sigma_1}\right)}\right]}+2\left(\frac{t-\mu_1}{\sigma_1}\right)\log\left[1+e^{-\left(\frac{t-\mu_1}{\sigma_1}\right)}\right]-2Li_2\left(-e^{-\left(\frac{t-\mu_1}{\sigma_1}\right)}\right)\right\} + (1-p)C_2\left\{\frac{\left[s_2+\left(\frac{t-\mu_2}{\sigma_2}\right)^2\right]e^{-\left(\frac{t-\mu_2}{\sigma_2}\right)}}{\left[1+e^{-\left(\frac{t-\mu_2}{\sigma_2}\right)}\right]}+2\left(\frac{t-\mu_2}{\sigma_2}\right)\log\left[1+e^{-\left(\frac{t-\mu_2}{\sigma_2}\right)}\right] - 2Li_2\left(-e^{-\left(\frac{t-\mu_2}{\sigma_2}\right)}\right)\right\} \tag{23}$$

where, C_1 and C_2 are as specified in Eq. (1) and $Li_2(\cdot)$ is Dilogarithm function
Different shapes of survival function G(t) for specified values of the parameters are shown in Figure 2, 3 and 4.

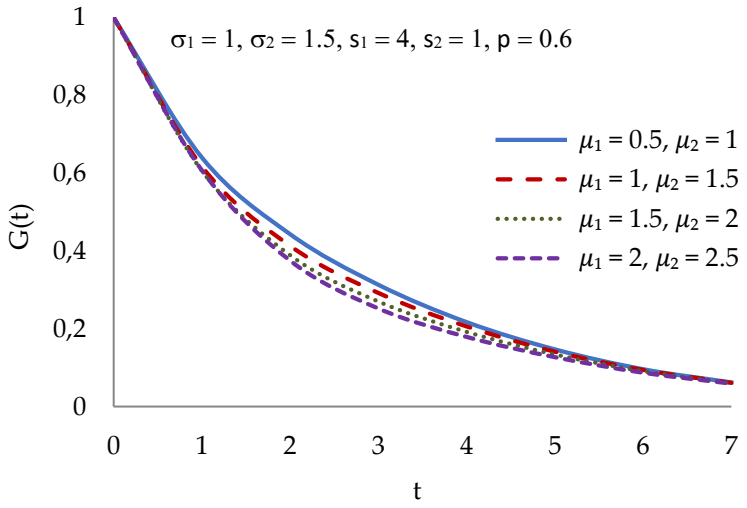


Figure 2: *Shapes of the Survival Function for different values of parameters μ_1 and μ_2*

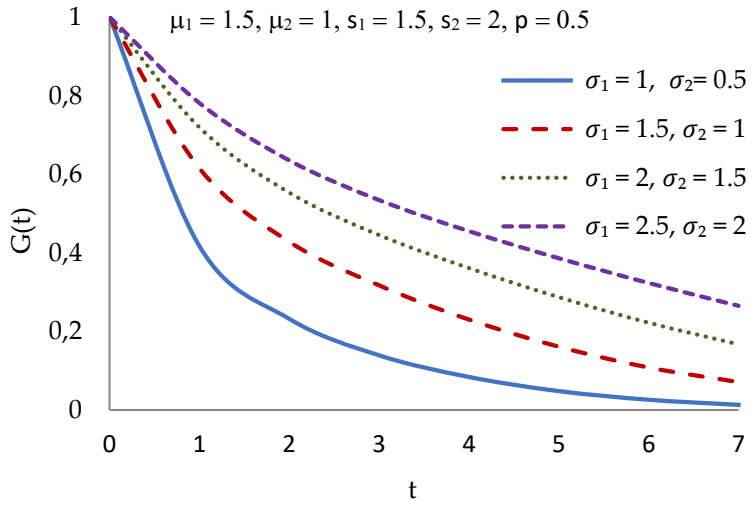


Figure 3: *Shapes of the Survival Function for different values of parameters σ_1 and σ_2*

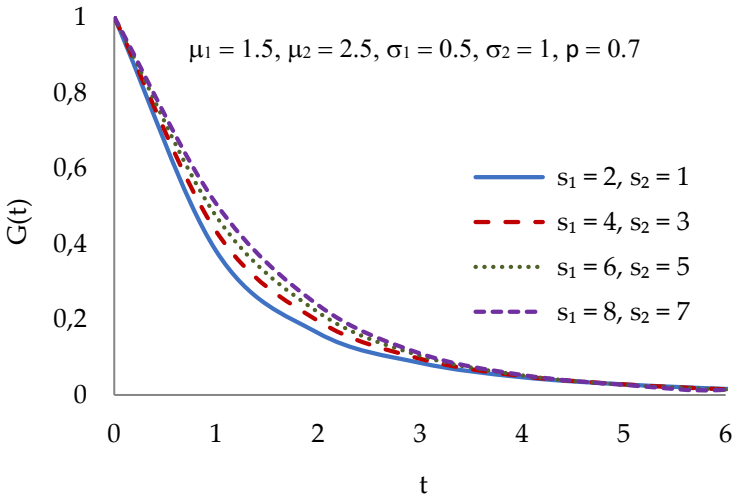


Figure 4: *Shapes of the Survival Function for different values of parameters s_1 and s_2*

The force of separation, also known as loss of intensity or rate of labour wastage, can be obtained as

$$L(t) = \frac{f(t)}{1 - F(t)} = \frac{f(t)}{G(t)}$$

When the functional form of f(t) and G(t) from the Eqs. (1) and (23), we obtain

$$L(t)=\frac{p\frac{\left[s_1+\left(\frac{t-\mu_1}{\sigma_1}\right)^2\right]e^{-\left(\frac{t-\mu_1}{\sigma_1}\right)}}{\sigma_1\left[1+e^{-\left(\frac{t-\mu_1}{\sigma_1}\right)}\right]^2}+(1-p)\frac{\left[s_2+\left(\frac{t-\mu_2}{\sigma_2}\right)^2\right]e^{-\left(\frac{t-\mu_2}{\sigma_2}\right)}}{\sigma_2\left[1+e^{-\left(\frac{t-\mu_2}{\sigma_2}\right)}\right]^2}}{p\left\{\frac{\left[s_1+\left(\frac{t-\mu_1}{\sigma_1}\right)^2\right]e^{-\left(\frac{t-\mu_1}{\sigma_1}\right)}}{\left[1+e^{-\left(\frac{t-\mu_1}{\sigma_1}\right)}\right]}+2\left(\frac{t-\mu_1}{\sigma_1}\right)\log\left[1+e^{-\left(\frac{t-\mu_1}{\sigma_1}\right)}\right]-2Li_2\left(-e^{-\left(\frac{t-\mu_1}{\sigma_1}\right)}\right)\right\}+(1-p)\left\{\frac{\left[s_2+\left(\frac{t-\mu_2}{\sigma_2}\right)^2\right]e^{-\left(\frac{t-\mu_2}{\sigma_2}\right)}}{\left[1+e^{-\left(\frac{t-\mu_2}{\sigma_2}\right)}\right]}+2\left(\frac{t-\mu_2}{\sigma_2}\right)\log\left[1+e^{-\left(\frac{t-\mu_2}{\sigma_2}\right)}\right]-2Li_2\left(-e^{-\left(\frac{t-\mu_2}{\sigma_2}\right)}\right)\right\}} \quad (24)$$

where, $Li_2(\cdot)$ is Dilogarithm function

Different values of parameters the shapes of labour wastage L(t) is shown in Figures 5, 6 and 7

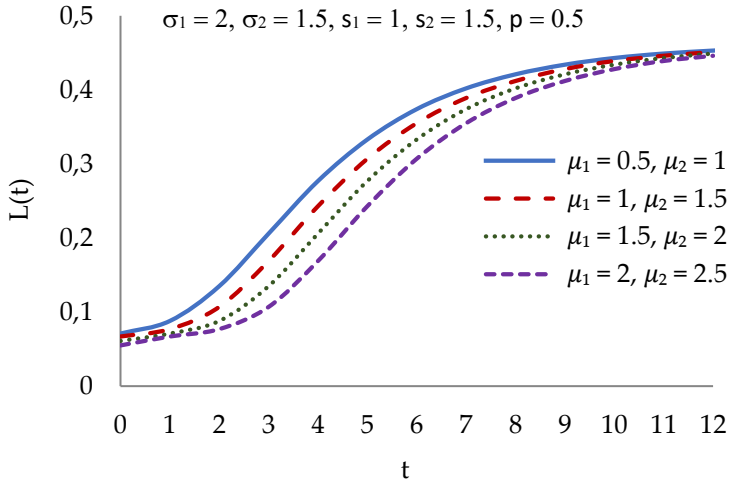


Figure 5: *Loss of Intensity curve for different values of parameters μ_1 and μ_2*

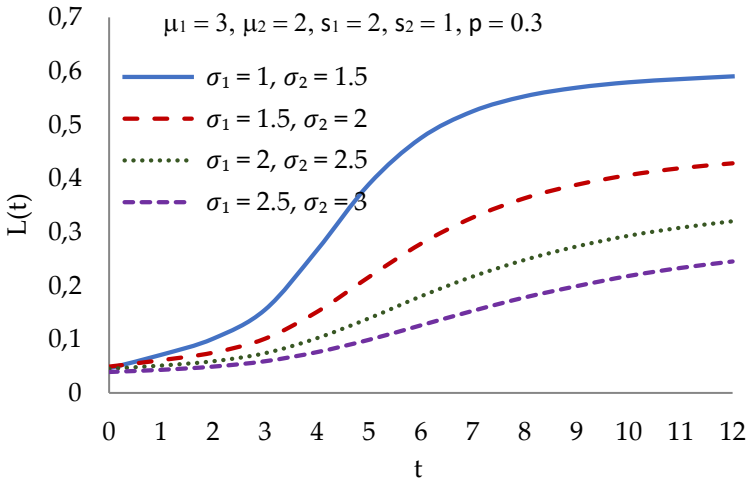


Figure 6: *Loss of Intensity curve for different values of parameters σ_1 and σ_2*

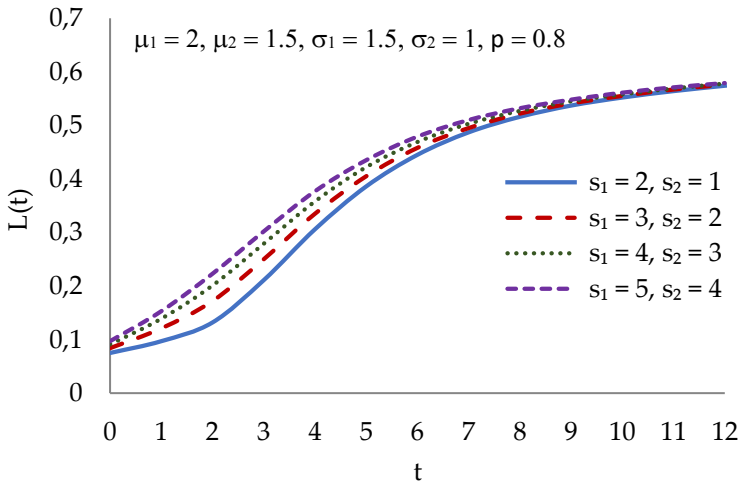


Figure 7: *Loss of Intensity curve for different values of parameters s_1 and s_2*

The renewal density of this model is

$$h(t) = f(t) + \int_0^t G(t-x)\, f(x)dx$$

By substituting the expressions for f(t) and G(t) from the Eqs. (1) and (23) and simplifying, we obtain

$$\begin{aligned} h(t) = {} & pC_1\left[s_1 + \left(\frac{t-\mu_1}{\sigma_1}\right)^2\right]\frac{e^{-\left(\frac{t-\mu_1}{\sigma_1}\right)}}{\sigma_1\left[1+e^{-\left(\frac{t-\mu_1}{\sigma_1}\right)}\right]^2} + (1 \\ & - p)C_2\left[s_2 + \left(\frac{t-\mu_2}{\sigma_2}\right)^2\right]\frac{e^{-\left(\frac{t-\mu_2}{\sigma_2}\right)}}{\sigma_2\left[1+e^{-\left(\frac{t-\mu_2}{\sigma_2}\right)}\right]^2} \\ & + \int_0^t \left[pC_1\left[s_1 + \left(\frac{x-\mu_1}{\sigma_1}\right)^2\right]\frac{e^{-\left(\frac{x-\mu_1}{\sigma_1}\right)}}{\sigma_1\left[1+e^{-\left(\frac{x-\mu_1}{\sigma_1}\right)}\right]^2} + (1\right. \\ & - p)C_2\left[s_2\right. \\ & \left. + \left(\frac{x-\mu_2}{\sigma_2}\right)^2\right]\frac{e^{-\left(\frac{x-\mu_2}{\sigma_2}\right)}}{\sigma_2\left[1+e^{-\left(\frac{x-\mu_2}{\sigma_2}\right)}\right]^2}\Bigg]\Bigg\{pC_1\left[\frac{\left[s_1 + \left(\frac{t-x-\mu_1}{\sigma_1}\right)^2\right]e^{-\left(\frac{t-x-\mu_1}{\sigma_1}\right)}}{\left[1+e^{-\left(\frac{t-x-\mu_1}{\sigma_1}\right)}\right]}\right. \\ & \left. + 2\left(\frac{t-x-\mu_1}{\sigma_1}\right)\log\left[1+e^{-\left(\frac{t-x-\mu_1}{\sigma_1}\right)}\right] - 2Li_2\left(-e^{-\left(\frac{t-x-\mu_1}{\sigma_1}\right)}\right)\right] + (1 \\ & - p)C_2\left[\frac{\left[s_2 + \left(\frac{t-x-\mu_2}{\sigma_2}\right)^2\right]e^{-\left(\frac{t-x-\mu_2}{\sigma_2}\right)}}{\left[1+e^{-\left(\frac{t-x-\mu_2}{\sigma_2}\right)}\right]}\right. \\ & \left. + 2\left(\frac{t-x-\mu_2}{\sigma_2}\right)\log\left[1+e^{-\left(\frac{t-x-\mu_2}{\sigma_2}\right)}\right] - 2Li_2\left(-e^{-\left(\frac{t-x-\mu_2}{\sigma_2}\right)}\right)\right]\Bigg\}dx \end{aligned} \tag{25}$$

where, C_1 and C_2 are as specified in Eq. (1) and $Li_2(\cdot)$ is Dilogarithm function

Different values of the parameters the shape of renewal density function h(t) is shown in Figures 8,

9 and 10

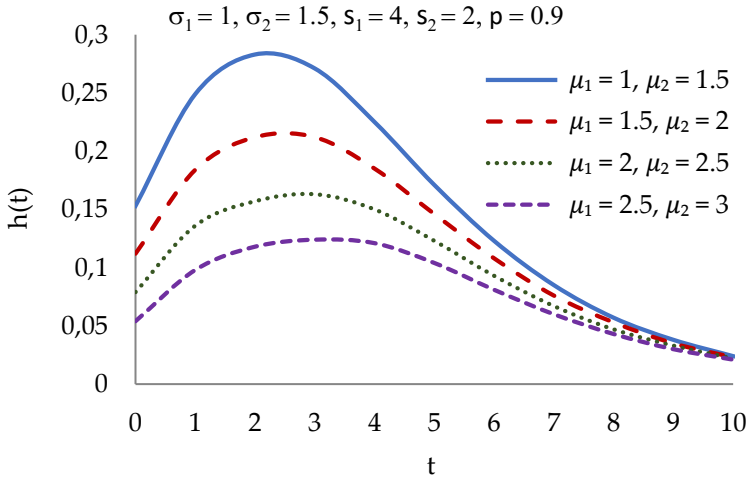


Figure 8: *Shapes of Renewal density function h(t) for different values of parameters μ_1 and μ_2*

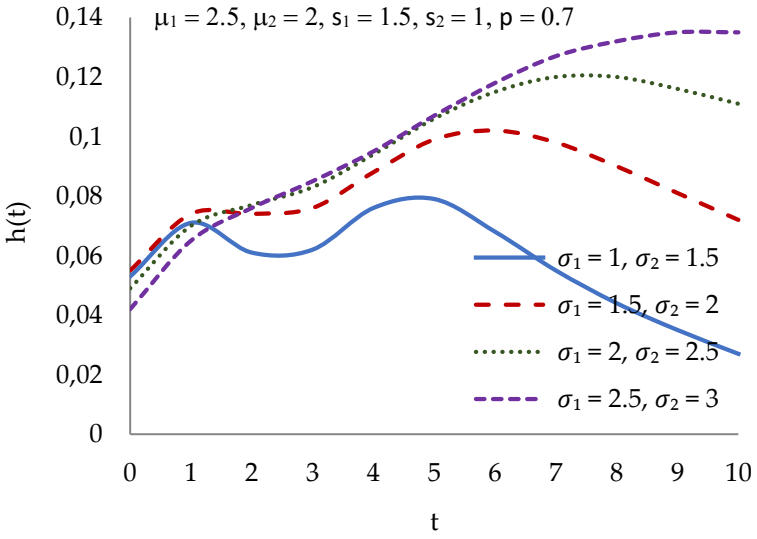


Figure 9: *Shapes of Renewal density function h(t) for different values of parameters σ_1 and σ_2*

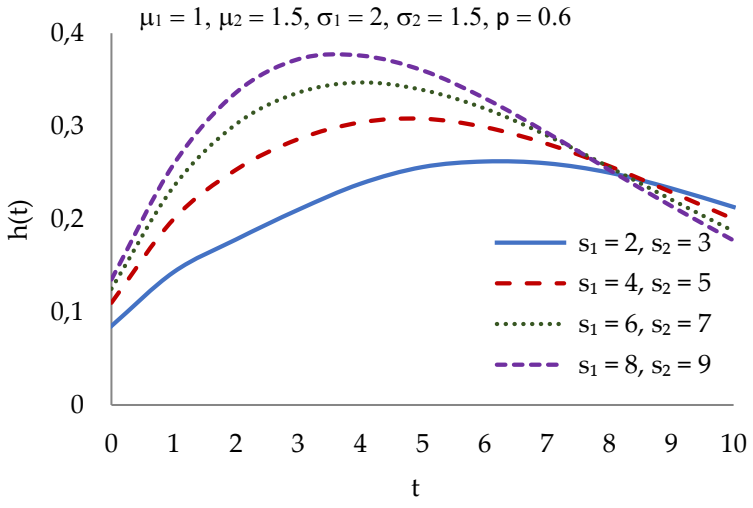


Figure 10: *Shapes of Renewal density function h(t) for different values of parameters s_1 and s_2*

VI Recruitment Policies for Manpower Models with Two Component Mixture of Left Truncated Three Parameter Logistic Type Distribution

When a CLS follows the two component mixture of left truncated three parameter logistic type distribution, the survival rate of labour waste and renewal rates are examined in the previous section. This section discusses an organization various recruitment procedures, which are crucial to operating system plans. An organization can be thought of as having two grades: training grade (Grade I) and the second grade is organization grade (Grade II). The training grade was implemented to provide experienced men to fill vacancies that occur within an origination grade, Naturally, the organization will generally have a hierarchical structure. The movement between grades within an organization was taken into account, nevertheless. The organization as a whole is viewed as a single entity.

Let N_1 and N_2 be the sizes of the training grade and the organization grades respectively, Further $N = N_1+N_2$. Where, N_2 is assumed to be known and constant. The issue at hand determining the appropriate duration of the training grade such that, on average, individuals spend a specified period 't' in it prior to advancement to the organization grade.

Two rules apply in this study i) Promotion by seniority i.e. where by the training grade most senior (and thus most experienced) member gets promoted and ii) Promotion by random based on duration of service. In other words, promotion is granted based on other criteria, such as competence, personal attributes, qualifications, specialized training, and so forth.

The individual loss rate in training grade (Grade I) is represented by W_1, the individual loss rate in organization grade (Grade II) is represented by W_2, and P is the promotion rate.

Given that the input and output of each grade must equilibrate, for grade II, it can be expressed as

$$N_1 P = N_2 W_2 \tag{26}$$

Hence, in equilibrium the system expected input per unit time is N/m, where m is the mean length of completed service. As a result, for Grade I,

$$\frac{N}{m} = N_1(P + W_1)$$

$$= N_1 W_1 + N_2 W_2 \tag{27}$$

In general, W_1, W_2 and P are functions of time. Bartholomew [11] that P, W_1, W_2 tend to equilibrium values which are independent of the age of the system.

Let m_1 be the average amount of time spent in Grade I. When the system is in equilibrium, the expected number of vacancies in this grade per unit time is

$$\frac{N_1}{m_1} = N_1(P + W_1)$$

This implies

$$\frac{1}{m_1} = P + W_1 \tag{28}$$

From Eqs. (27) and (28)

$$\frac{N}{m} = \frac{N_1}{m_1} \tag{29}$$

This equation states that the through-put for the whole system is equal to the number of vacancies in Grade I

VII Promotion by Seniority when the CLS Follows Two Component Mixture of Left Truncated Three Parameter Logistic Type Distribution

Let $a\left(t/_T\right)$ represent the age distribution of the system at time T, assuming the system was initiated at T = 0. Hence, $a\left(t/_T\right)$δt denotes the probability that a randomly selected individual chosen at time 'T' has a length of service within the interval $(t, t+\delta t)$.

Thus

$$a\left(\frac{t}{T}\right)\delta t = \text{Prob}\{\text{Individual joined in}(T-t, T-t+\delta t) \text{ and remained for time } t\}$$

$$= h(T-t)\ \delta t\ G(t)$$

where, h(t) is the renewal density of the whole system

Hence

$$a\left(\frac{t}{T}\right)\delta t = h(T-t)\delta t\ G(t)$$

This holds for t<T we have,

$$\lim_{T\to\infty} h(T) = \frac{1}{m}$$

Now

$$\lim_{T\to\infty} G(T) = 0$$

$$\lim_{T\to\infty} a\left(\frac{t}{T}\right) = \frac{G(T)}{m}$$

$$= a(t)$$

This is the equilibrium age distribution.

A threshold value exists at t_1 such that all individuals with a length of service less than that t_1 are in Grade I because a loss from Grade II is replaced by the most senior member of Grade I. That means that at any given time, every individual in Grade II has a length of service at least as long as any individual in Grade I. Although "t_1" is random variable, the approximation calculation for its expected value is

$$\int_{t_1}^{\infty} a(t)\ dt = \frac{N_2}{N_1+N_2} \tag{30}$$

As a result, in equilibrium, the expected number of promotions that should occur per unit of time will be the number of new recruits who have served to the t_1 threshold length of service.

i.e., t_1

$$N_1 P = G(t_1)\frac{N}{m} \tag{31}$$

Let m_L be the average length of time spent in Grade I by those who leave while still in Grade I, and let m_P be the average length of time spent in Grade I by those who are finally promoted to Grade II. After that, consider about the challenge of selecting N_1 in order to give a fixed value. Eqs. (30) and (31) are valid in this instance since m_P is equal to the average value that was previously introduced.

Thus one can have

$$\int_{m_P}^{\infty} a(t)\ dt = \frac{N_2}{N}$$

i.e.,
$$\frac{1}{m}\int_{m_P}^{\infty} G(t)\,dt = \frac{N_2}{N} \tag{32}$$

And
$$N_1 P = G(m_P)\frac{N}{m}$$

Eq. (32) presents $R = \frac{N_1}{N_2}$ as a function of m_P; hence, one may calculate N_1 for a given value of m_P by knowing the size N of the organization.

This implies
$$\frac{1}{m}\int_{m_P}^{\infty} G(t)\,dt = \frac{1}{1+R} \tag{33}$$

It is assumed that the CLS of an employee in the organization follow a two component mixture of left truncated logistic type distribution. Eq. (23) can be substituted in (33), we obtain

$$\frac{pC_1}{m}\int_{m_P}^{\infty}\left\{\frac{\left[s_1+\left(\frac{t-\mu_1}{\sigma_1}\right)^2\right]e^{-\left(\frac{t-\mu_1}{\sigma_1}\right)}}{\left[1+e^{-\left(\frac{t-\mu_1}{\sigma_1}\right)}\right]}+2\left(\frac{t-\mu_1}{\sigma_1}\right)\log\left[1+e^{-\left(\frac{t-\mu_1}{\sigma_1}\right)}\right]-2Li_2\left(-e^{-\left(\frac{t-\mu_1}{\sigma_1}\right)}\right)\right\}dt$$
$$+\frac{(1-p)C_2}{m}\int_{m_P}^{\infty}\left\{\frac{\left[s_2+\left(\frac{t-\mu_2}{\sigma_2}\right)^2\right]e^{-\left(\frac{t-\mu_2}{\sigma_2}\right)}}{\left[1+e^{-\left(\frac{t-\mu_2}{\sigma_2}\right)}\right]}+2\left(\frac{t-\mu_2}{\sigma_2}\right)\log\left[1+e^{-\left(\frac{t-\mu_2}{\sigma_2}\right)}\right]\right.$$
$$\left.-2Li_2\left(-e^{-\left(\frac{t-\mu_2}{\sigma_2}\right)}\right)\right\}dt=\frac{1}{1+R}$$

where, C_1 and C_2 are as specified in Eq. (1) and $\mathrm{Li}_2(\cdot)$ is Dilogarithm function

where, $\mathrm{Li}_n(\cdot)$ is Polylogarithm function of order n ($n \geq 2$)

Making necessary transformations and by integration, we get

$$\frac{pC_1\sigma_1}{m}\left\{\left[s_1+\left(\frac{m_P-\mu_1}{\sigma_1}\right)^2\right]\log\left[1+e^{-\left(\frac{m_P-\mu_1}{\sigma_1}\right)}\right]-4\left(\frac{m_P-\mu_1}{\sigma_1}\right)Li_2\left(-e^{-\left(\frac{m_P-\mu_1}{\sigma_1}\right)}\right)-6Li_3\left(-e^{-\left(\frac{m_P-\mu_1}{\sigma_1}\right)}\right)\right\}$$
$$+\frac{(1-p)C_2\sigma_2}{m}\left\{\left[s_2+\left(\frac{m_P-\mu_2}{\sigma_2}\right)^2\right]\log\left[1+e^{-\left(\frac{m_P-\mu_2}{\sigma_2}\right)}\right]\right.$$
$$\left.-4\left(\frac{m_P-\mu_2}{\sigma_2}\right)Li_2\left(-e^{-\left(\frac{m_P-\mu_2}{\sigma_2}\right)}\right)-6Li_3\left(-e^{-\left(\frac{m_P-\mu_2}{\sigma_2}\right)}\right)\right\}=\frac{1}{1+R}$$

m_P is the average length of time spent in Grade I by those who are eventually promoted to Grade II.
On Simplification,

$$R = \frac{m\left\{\left(s_1+\frac{\mu_1^2}{\sigma_1^2}\right)\frac{e^{\mu_1/\sigma_1}}{[1+e^{\mu_1/\sigma_1}]}-\frac{2\mu_1}{\sigma_1}\log\left(1+e^{\mu_1/\sigma_1}\right)-2Li_2\left(-e^{\mu_1/\sigma_1}\right)\right\}}{p\sigma_1\left\{\left[s_1+\left(\frac{m_P-\mu_1}{\sigma_1}\right)^2\right]\log\left[1+e^{-\left(\frac{m_P-\mu_1}{\sigma_1}\right)}\right]-4\left(\frac{m_P-\mu_1}{\sigma_1}\right)Li_2\left(-e^{-\left(\frac{m_P-\mu_1}{\sigma_1}\right)}\right)-6Li_3\left(-e^{-\left(\frac{m_P-\mu_1}{\sigma_1}\right)}\right)\right\}} + \frac{m\left\{\left(s_2+\frac{\mu_2^2}{\sigma_2^2}\right)\frac{e^{\mu_2/\sigma_2}}{[1+e^{\mu_2/\sigma_2}]}-\frac{2\mu_2}{\sigma_2}\log\left(1+e^{\mu_2/\sigma_2}\right)-2Li_2\left(-e^{\mu_2/\sigma_2}\right)\right\}}{(1-p)\sigma_2\left\{\left[s_2+\left(\frac{m_P-\mu_2}{\sigma_2}\right)^2\right]\log\left[1+e^{-\left(\frac{m_P-\mu_2}{\sigma_2}\right)}\right]-4\left(\frac{m_P-\mu_2}{\sigma_2}\right)Li_2\left(-e^{-\left(\frac{m_P-\mu_2}{\sigma_2}\right)}\right)-6Li_3\left(-e^{-\left(\frac{m_P-\mu_2}{\sigma_2}\right)}\right)\right\}} - 1 \quad (34)$$

where, $Li_n(\cdot)$ is Polylogarithm function of order n ($n \geq 2$)

For various values of m, m_P, μ_1, μ_2, σ_1, σ_2, s_1 and s_2 corresponding values of R are computed using Eq. (34) and presented in Table 1.

Table 1: *Values of R for different input parameters under Promotion by Seniority*

m	m_P	p	μ_1	μ_2	σ_1	σ_2	s_1	s_2	R
8	4	0.5	2	2.5	**1**	**1.5**	2	3	83.319
8	4	0.5	2	2.5	**1.5**	**2**	2	3	28.846
8	4	0.5	2	2.5	**2**	**2.5**	2	3	15.663
8	4	0.5	2	2.5	**2.5**	**3**	2	3	10.244
8	4	0.5	**1**	**1.5**	1.5	2	2	3	28.326
8	4	0.5	**1.5**	**2**	1.5	2	2	3	28.383
8	4	0.5	**2**	**2.5**	1.5	2	2	3	28.846
8	4	0.5	**2.5**	**3**	1.5	2	2	3	29.62
8	4	0.5	2	2.5	1.5	2	**4**	**3**	32.633
8	4	0.5	2	2.5	1.5	2	**6**	**5**	37.787
8	4	0.5	2	2.5	1.5	2	**8**	**7**	42.356
8	4	0.5	2	2.5	1.5	2	**10**	**11**	47.65
8	4	**0.1**	2	2.5	1.5	2	2	3	99.668
8	4	**0.2**	2	2.5	1.5	2	2	3	53.128
8	4	**0.3**	2	2.5	1.5	2	2	3	38.337
8	4	**0.4**	2	2.5	1.5	2	2	3	31.754
8	**5**	0.5	2	2.5	1.5	2	2	3	41.38
8	**6**	0.5	2	2.5	1.5	2	2	3	61.636
8	**7**	0.5	2	2.5	1.5	2	2	3	94.563
8	**8**	0.5	2	2.5	1.5	2	2	3	148.563
9	4	0.5	2	2.5	1.5	2	2	3	32.576
10	4	0.5	2	2.5	1.5	2	2	3	36.307
11	4	0.5	2	2.5	1.5	2	2	3	40.038
12	4	0.5	2	2.5	1.5	2	2	3	43.768

From Table 1, it is observed that as σ_1 and σ_2 increases, the value of R is decreasing. μ_1 and μ_2 increases the value of R is increasing and s_1 and s_2 increases the value of R is increasing and for p increases the R value is decreasing. m_P increases the R value is increasing. An increase in m, results increase in R.

VIII Promotion by Random when the CLS Follows Two Component Mixture of Left Truncated Three Parameter Logistic Type Distribution

Let $F_1(t)$ be the probability that an individual stays in the system for a period of time 't' without being promoted and let n_t be the number promotions in $(0, t)$. Then

$F_1(t) = \text{Prob}\{\text{Individual not promoted in } (0,t)/\text{does not leave in } (0,t)\}$
$* \text{Prob}\{\text{does not leave in } (0,t)\}$

$$F_1(t) = \left(1 - \frac{1}{N_1}\right)^{n_t} G(T)$$

The excepted value of is N_1P_t

Thus as a first approximation one can take

$$F_1(t) = G(t)\left[1 - \frac{1}{N_1}\right]^{N_1P_t}$$

$N_1 \to \infty$ gives

$$F_1(t) = G(t)\, e^{-P_t}$$

Then the average time spent in Grade I is

$$m_1 = \int_0^\infty F_1(t)\, dt = \int_0^\infty G(t)\, e^{-P_t}\, dt$$

But from Eq. (29)

$$\frac{m_1}{m} = \frac{N_1}{N}$$

Thus

$$\frac{1}{m}\int_0^\infty G(t)e^{-P_t}\, dt = \frac{N_1}{N} \tag{35}$$

Assuming that an individual is promoted before leaving, let q(t) be the probability density function of the time interval between his entry into Grade I and his promotion to Grade II in equilibrium.

$$\text{Let } Q(t) = \int_t^\infty q(x)\, dx$$

Since $Q(t) = \text{prob}\{\text{Not promoted in a period of length t / doesnot leave in that period}\}$

$$= \left(1 - \frac{1}{N_1}\right)^{n_t}$$

Where, n_t is the number of promotions in a interval of length t.

Replacing n_t can be replaced by its expected value, N_1P_t. We get the

$$Q(t) = \left(1 - \frac{1}{N_1}\right)^{N_1P_t}$$

Therefore

$$m_p = \int_0^\infty Q(t)\, dt = \int_0^\infty e^{-P_t}\, dt = \frac{1}{P} \tag{36}$$

Using this in conjunction with Eq. (35) gives N_1 in terms of m_P, and hence

$$\frac{N_1}{N} = \frac{1}{m}\int_0^\infty G(t)\, e^{-t/m_P}\, dt \tag{37}$$

The expression for the value "R" is computed from the following equation.

$$\frac{1}{m}\int_0^\infty G(t)\, e^{-t/m_P}\, dt = \frac{R}{R+1} \tag{38}$$

Substituting G(t) as given in the Eq. (23), we get

$$\frac{pC_1}{m}\int_0^{\infty} e^{-t/m_P}\left\{\frac{\left[s_1+\left(\frac{t-\mu_1}{\sigma_1}\right)^2\right]e^{-\left(\frac{t-\mu_1}{\sigma_1}\right)}}{\left[1+e^{-\left(\frac{t-\mu_1}{\sigma_1}\right)}\right]}+2\left(\frac{t-\mu_1}{\sigma_1}\right)\log\left[1+e^{-\left(\frac{t-\mu_1}{\sigma_1}\right)}\right]-2Li_2\left(-e^{-\left(\frac{t-\mu_1}{\sigma_1}\right)}\right)\right\}dt$$
$$+\frac{(1-p)C_2}{m}\int_0^{\infty} e^{-t/m_P}\left\{\frac{\left[s_2+\left(\frac{t-\mu_2}{\sigma_2}\right)^2\right]e^{-\left(\frac{t-\mu_2}{\sigma_2}\right)}}{\left[1+e^{-\left(\frac{t-\mu_2}{\sigma_2}\right)}\right]}\right. \tag{39}$$
$$\left.+2\left(\frac{t-\mu_2}{\sigma_2}\right)\log\left[1+e^{-\left(\frac{t-\mu_2}{\sigma_2}\right)}\right]-2Li_2\left(-e^{-\left(\frac{t-\mu_2}{\sigma_2}\right)}\right)\right\}dt=\frac{R}{1+R}$$

where, C_1 and C_2 are as specified in Eq. (1) and $Li_2(\cdot)$ is Dilogarithm function

By solving the (39), for various values of m, m_P, μ_1, μ_2, σ_1, σ_2, s_1 and s_2 the R values are computed and presented in Table 2.

Table 2: *Values of R for different input parameters under Promotion by Random*

m	m_p	p	μ_1	μ_2	σ_1	σ_2	s_1	s_2	R
6	2	0.5	1	1.5	**1**	**1.5**	2	1	0.2159
6	2	0.5	1	1.5	**1.5**	**2**	2	1	0.2656
6	2	0.5	1	1.5	**2**	**2.5**	2	1	0.3006
6	2	0.5	1	1.5	**2.5**	**3**	2	1	0.3265
2	3	0.4	**0.5**	**1**	2	1	4	2	2.3791
2	3	0.4	**1**	**1.5**	2	1	4	2	2.1788
2	3	0.4	**1.5**	**2**	2	1	4	2	2.0822
2	3	0.4	**2**	**2.5**	2	1	4	2	2.0699
5	1	0.6	2	2.5	1.5	2	**2**	**1**	0.1711
5	1	0.6	2	2.5	1.5	2	**4**	**3**	0.1782
5	1	0.6	2	2.5	1.5	2	**6**	**5**	0.1827
5	1	0.6	2	2.5	1.5	2	**8**	**7**	0.1858
2	4	**0.1**	2	1	1	1.5	3	2	5.8249
2	4	**0.2**	2	1	1	1.5	3	2	4.8560
2	4	**0.3**	2	1	1	1.5	3	2	4.1280
2	4	**0.4**	2	1	1	1.5	3	2	3.5610
3	**2**	0.3	1.5	2	1.5	2.5	4	3	0.3860
3	**3**	0.3	1.5	2	1.5	2.5	4	3	0.8149
3	**4**	0.3	1.5	2	1.5	2.5	4	3	1.4038
3	**5**	0.3	1.5	2	1.5	2.5	4	3	2.2025
7	6	0.2	2.5	3	2	2.5	5	2	0.2926
8	6	0.2	2.5	3	2	2.5	5	2	0.2470
9	6	0.2	2.5	3	2	2.5	5	2	0.2137
10	6	0.2	2.5	3	2	2.5	5	2	0.1624

From Table 2, it is observed that the recruit policy is significantly increased by CLS distribution parameters. As the shape parameter σ_1 and σ_2 increases the value of R is increasing contrary to the policy of promotion by seniority when other parameters remaining fixed. It is also observed that as μ_1 and μ_2 increases the value of R is decreasing and also observed that as s_1 and s_2 increases the value of R is increasing, this increases very small. p increases the value of R is decreasing. When m_P is increases the value of R increasing. It is also observed that m increases the value of R is

decreasing.

VIII Conclusion

In this paper, we introduced a two component mixture of left truncated three parameter logistic type distribution. The various distributional properties, such as distribution function, mean, four moments, hazard function, and survival function of the distribution, are derived. It is observed that the hazard function is increasing or decreasing depending on the truncation parameters. The three parameter logistic type distribution is highly applicable in analyzing various datasets as an alternative to the gaussian distribution were the variable under study is leptokurtic. The utility of this distribution in manpower modeling, in particular deriving the recruitment/promotion policies of the organization, are also discussed. It is observed that promotion by random is more effective than promotion by seniority. It is also possible to obtain other inferential aspects, such as testing of hypothesis which requires further study. This distribution is useful for analyzing several datasets in management sciences, finance quality control and agricultural experiments etc.

Acknowledgements

The first author expresses sincere gratitude to the Department of Science and Technology (DST), Government of India, New Delhi, for granting the INSPIRE Fellowship (Code No. IF 190726) to carry out the research work.

Declarations

The authors state that there are no conflicts of interest to declare.

References

[1] Dubey, S. D. (1969). “A new derivation of the logistic distribution”, Naval Research Logistics Quarterly, 16(1), 37-40.

[2] Olapade, A.K. (2003), "On characterizations of the half-logistic distribution", InterStat, February Issue, Number 2

[3] Nassar, M., & Elmasry, A. (2012). “A study of generalized logistic distributions”, Journal of the Egyptian Mathematical Society, 20(2), 126-133.

[4] Gupta, R. D. and Kundu, D. (2010). “Generalized Logistic Distributions”, Journal of Applied Statistical Science, 18, 51-66.

[5] Alzaatreh, A., Lee, C., & Famoye, F. (2013). A new method for generating families of continuous distributions. METRON, 71(1), 63-79.

[6] Adeyinka, F. S. (2019). On transmuted four parameters Generalized Log-Logistic distribution. International Journal of Statistical Distributions and Applications, 5(2), 32.

[7] Aljarrah, M. A., Famoye, F., & Lee, C. (2020). Generalized logistic distribution and its regression model. Journal of Statistical Distributions and Applications, 7(1).

[8] Kumar, C.S., Manju, L. (2022). “Gamma Generalized Logistic Distribution: Properties and Applications”, Journal of Statistical Theory and Applications, 21(1), 155-174.

[9] Hadi Alizadeh Noughabi, 2022. “A New Goodness-of-Fit Test for the Logistic Distribution”, Sankhya B: The Indian Journal of Statistics, Springer; Indian Statistical Institute, 84(1), 303-319.

[10] Hamsa, U., Kraleti, S. R., & Begari, M. (2025). “On A Left Truncated Three Parameter Logistic Type Distribution with Applications to Manpower Modeling”, Global and Stochastic Analysis, 12(2).

[11] Bartholomew DJ. (1973) “The Statistical Approach to Manpower Planning”, Statistician, 20

RISK ANALYSIS OF A REPAIRABLE UNIT IN SUGAR INDUSTRY: A HYBRID APPROACH USING FUZZY FMEA AND GRA

Anushree[1] and Seema Sharma[2,*]

•

[1]Research Scholar, Department of Mathematics and Statistics, Gurukula Kangri (Deemed to be University) Haridwar, Uttarakhand,
India- 249404

[2]Professor, Department of Mathematics and Statistics, Gurukula Kangri (Deemed to be University) Haridwar, Uttarakhand,
India- 249404

[1]anushreerajput04@gmail.com

[2]seemasharmagkv@gmail.com

*Corresponding Author

Abstract

The purpose of this study is to develop a comprehensive risk assessment profile for a repairable unit in a sugar industry. The risk analysis of milling unit in the sugar industry often relies on uncertain data and subjective expert assessments, which could be biased. This highlights the need for careful interpretation as the data quality variations have great impact on the decision-making. By integrating risk analysis techniques like failure mode and effect analysis (FMEA), Grey relation analysis (GRA), and fuzzy theory, together with expert assessments for the very first time, the approach aims to prioritize risk management strategies of milling unit in Dhampur Sugar Mills Ltd., a sugar industry located in Western Uttar Pradesh, India. First of all, Root cause analysis (RCA) is conducted to detect in-depth potential failure modes of the unit. Further, FMEA is employed for risk identification and prioritization, with ranking of components based on their RPN (Risk Priority Number) scores. To address the limitations of FMEA, fuzzy FMEA supported by a fuzzy decision support system (FDSS) has been used to compute FRPN (Fuzzy Risk Priority Number) scores. Based on these scores, the components are ranked. Subsequently, GRA is employed within the fuzzy FMEA framework to intelligently assess the relative importance of key factors, i.e. probability of occurrence, severity effect, and probability of non-detectability of failure in order to determine optimal rankings of critical components. The implementation of fuzzy logic and grey approach with inputs of FMEA offers a more efficient and better way to make decision regarding risk priorities. This risk assessment approach is valuable for sugar industry where complex engineering systems are essential for production process, and the findings from this study will aid system specialists and analysts in future planning and maintenance strategies.

Keywords: Risk analysis, FMEA, fuzzy FMEA, FDSS, RPN, GRA.

I. Introduction

Risk assessment of complex systems across various process industries is essential for ensuring operational safety, reliability, and efficiency as the machinery and processes are susceptible to a

wide range of potential failures, which can lead to disastrous consequences, including equipment damage, environmental harm, and accidents etc. By systematically identifying, analyzing, and prioritizing risks, targeted mitigation strategies can be implemented to enhance the persistence of operational uptime of systems. This dynamic approach not only helps in complying with regulatory requirements but also reduces operational downtime. Ultimately, effective risk assessment enables industries to safeguard their assets, protect their workforce, and maintain a competitive edge in the emerging global market.

The sugar industry is one of the most significant agro-based industries throughout the world. It plays a vital role in the socio-economic development of rural areas. This industry contributes significantly to the Indian economy, accounting for approximately 1% of the GDP. It is a lifeline for millions of farmers and laborers, providing employment to over 5 lakh skilled and semi-skilled workers across the nation. Within a sugar industry, the milling unit is one of the most vital components, as it is responsible for crushing sugarcane to extract juice, which forms the basis for all subsequent processes of sugar production. The crushing process demands precision and consistent performance, as any failure or inefficiency in the milling unit can lead to reduced juice extraction, operational delays, and significant financial losses. Therefore, it is important to conduct RAM analysis of milling unit in order to ensure its failure-free operation for the seamless functioning of sugar industry and for maintaining the stability of the national economy.

Various qualitative risk analysis techniques have been extensively explored in the literature, particularly for different industries and process plants. FMEA was introduced by NASA as a formal design technique in 1963. Besides this, it has also been widely employed by researchers as an effective tool for reliability and safety analysis of various industries [1-3], to mention a few. In this technique, failure causes are ranked using RPN. One of the major shortcomings of the RPN ranking technique is its inability to account for the relative significance of probabilities of occurrence, non-detection and severity effect of failure. Moreover, due to system complexity and ambiguous human verdicts, the impreciseness and uncertainty arise in the data regarding risk factors. To address this problem, the researchers used fuzzy approach in FMEA. Guimaraes and Lapa [4] demonstrated the use of the fuzzy technique in FMEA for the evaluation of the PWR chemical and volume control system in a nuclear power station. Sharma *et al.* [5] presented fuzzy logic based FMEA by developing a knowledge-based FDSS for prioritizing the risky components in a paper plant. Tay and Lim [6] used the fuzzy FMEA approach to evaluate the performance of some models in a semiconductor manufacturing plant. Wang *et al.* [7] proposed the fuzzy weighted geometric mean in FMEA to perform risk analysis. From these studies, it is deduced that fuzzy approach with FMEA overcomes the impreciseness in data but remains unable to balance the relative importance between risk factors. Therefore, to overcome these limitations many researchers utilized different multi-criteria decision making (MCDM) techniques such as Bayesian Network (BN), Technique for Order Preference by Similarity to Ideal Solution (TOPSIS), Analytical Hierarchy Process (AHP), GRA, etc., and improved prioritization of risky components.

BN is probabilistic graphical model that represent dependencies among variables, making them useful for decision making under uncertainty. BN, while effective for probabilistic reasoning has its own drawbacks. The high computational complexity in inference is quite challenging to handle large scale problems and reliance on extensive prior data for accurate probability estimations makes the use of BN impractical in situations with limited failure history [8-9]. TOPSIS is a MCDM method that ranks alternatives based on their geometric distance from the ideal and worst solutions. AHP is a structured approach for decision making that uses pairwise comparison to determine criteria weights. Despite their effectiveness, both methods have notable limitations. TOPSIS is highly sensitive to the choice of normalization techniques and does not account for interdependencies among criteria, leading to ranking inconsistencies [10]. On the other hand, AHP suffers from rank reversal when alternatives are added or removed and its reliance on subjective pairwise comparison introduces potential bias [11]. Both AHP and TOPSIS, struggle with handling uncertainty, which has led researchers to integrate fuzzy logic and hybrid approaches to improve

decision making robustness. Samvedi *et al.* [12] addressed the increasing complexity and uncertainty in supply chain risk management by proposing a composite risk index using an integrated fuzzy AHP–TOPSIS approach. Badida *et al.* [13] highlighted the effectiveness of fuzzy AHP and fuzzy TOPSIS to assess occupational health risks in hospitals, prioritizing workplace hazards by utilizing a fuzzy multi-criteria approach emphasizing the importance of fuzzy methods in complex risk evaluations.

GRA is another decision-making technique which offers a flexible and effective tool for reliability analysis, especially in uncertain, incomplete, or sparse data environment. Over the years, numerous researchers have applied GRA in various fields such as industry [14], forecasting [15-16], and engineering [17]. An integrated framework for understanding the qualitative behavior of a paper plant has been proposed by Sharma *et al.* [18]. They used fuzzy FMEA and GRA approaches to analyze the paper plant's qualitative performance and compared risk priority results with FMEA ranking results. A unique fuzzy multi-criterion decision making approach based on the grey relation technique has been presented by Dhal *et al.* [19] for the efficient identification of flexible manufacturing systems. In a geothermal power plant, Feili *et al.* [20] illustrated the use of FMEA approach for risk assessment. They investigated five primary components of the geothermal power plant, and on the basis of the findings, maintenance workers and system analysts were recommended corrective measures towards enhancing system reliability. To improve the purchasing process in a public hospital, Kumru and Kumru [21] have presented a study by implementing the fuzzy FMEA. The multidimensional model with fuzzy approach in FMEA was proposed by Silva *et al.* [22] for prioritization of various attributes of information security. Shankar *et al.* [23] identified socially-induced sustainability risks as the main threats to freight transportation systems and proposed a risk analysis model using intuitionistic fuzzy and D-number theory to help managers proactively address these risks and optimize resource allocation. Panchal and Shrivastava [24] presented an FMEA-GRA integrated approach for risk ranking in a CNG dispensing system. An enhanced grey FMEA was used by Yaşbayır and Aydemir [25] to identify risk priorities of a steel-door industry employing a new mass gravity law based RPN calculation technique. To improve aviation safety risk assessment, Wei *et al.* [26] integrated Fuzzy Cognitive Maps (FCM) and GRA enhancing GRA's ability to account for interactions between evaluation indices, making it more robust for complex decision-making scenarios. Sur and Kim [27] utilized a hybrid GRA and ordinal priority approach (OPA) to identify and rank the most dangerous types of accidents in marine operations. Soltani *et al.* [28] integrated Fuzzy Best-Worst Method (FBWM) and GRA for accurate risk assessment in blasting operations.

The risk analysis of milling unit in the sugar industry often relies on uncertain data and subjective expert assessments, which could be biased. Moreover, the sugar industry presents unique combination of industrial hazards compared to other sectors due to the presence of high-speed mechanical systems, combustible dust, high pressure steam and flammable byproducts like ethanol. These risks necessitate strict safety protocols, regular equipment maintenance and worker training to prevent catastrophic failures. In such a high-risk and variable environment, intervention of hybrid approach offering substantial advantages is needed. While standard FMEA may oversimplify failure prioritization through equal-weighted risk factor scoring, its integration with fuzzy theory and GRA allows for nuanced evaluation of failure modes under conditions of incomplete, uncertain, or qualitative data. This is particularly important in the sugar industry, which frequently operates with seasonal labor, limited instrumentation, and a combination of mechanical and biological process risks.

To the author's best knowledge, existing research on risk assessment in the sugar industry has primarily relied on standard FMEA or other qualitative methods, which do not adequately address subjective uncertainty and expert variability. While fuzzy FMEA has been widely applied in industries such as automotive, healthcare and manufacturing, its use in sugar industry maintenance and risk assessment remains largely unexplored. The purpose of this study is to develop a comprehensive risk assessment profile of milling unit in the sugar industry by applying

risk analysis techniques namely fuzzy FMEA and GRA incorporating expert assessments for the first time. Unlike prior studies in highly automated and sensor-rich industries such as petrochemicals, thermal and pharmaceuticals, the hybrid approach using fuzzy FMEA and GRA in the sugar industry addresses the challenges of low data availability and high dependency on human expertise. As a result, it enables more context-sensitive and actionable risk prioritizations that align closely with real-world plant conditions that enhances maintenance decision making. This paper is organized in six sections as follows: Section II outlines some basic notions of fuzzy theory. Section III presents the system description. In Section IV, risk analysis for the identification of hazardous components of milling unit has been discussed. Section V presents the results and discussion of the study. Finally, in Section VI, the conclusion and managerial implications has been presented.

II. Fuzzy theory

Some basic notions of fuzzy theory that have been utilized in this study are discussed below:

I. Fuzzy set

For a universal set X, the fuzzy set $\tilde{A}$ is represented by

$$\tilde{A} = \{(x, \mu_{\tilde{A}}(x)) : x \in X\}$$

where, $\mu_{\tilde{A}}(x) \in [0,1]$ is the degree of membership of element x.

II. Triangular membership function

The triangular membership function $\mu_{\tilde{A}}(x)$ of a fuzzy set $\tilde{A}$ represented by the triplet (p_1, p_2, p_3) is described as

$$\mu_{\tilde{A}}(x) = \begin{cases} \frac{(x-p_1)}{(p_2-p_1)}, & p_1 \le x \le p_2 \\ \frac{(p_3-x)}{(p_3-p_2)}, & p_2 \le x \le p_3 \\ 0, & otherwise \end{cases} . \quad (1)$$

III. Trapezoidal membership function

The trapezoidal membership function $\mu_{\tilde{A}}(x)$ of a fuzzy set $\tilde{A}$ represented by the quadruplet (q_1, q_2, q_3, q_4) is described as

$$\mu_{\tilde{A}}(x) = \begin{cases} \frac{(x-q_1)}{(q_2-q_1)}, & q_1 \le x \le q_2 \\ 1, & q_2 \le x \le q_3 \\ \frac{(q_4-x)}{(q_4-q_3)}, & q_3 \le x \le q_4 \\ 0, & otherwise \end{cases} . \quad (2)$$

IV. Linguistic terms

To indicate the likelihood of uncertain events, experts utilize phrases such as 'low,' 'medium,'

'high,' etc. These expert opinions are expressed through linguistic terms or variables, and they convey their appraisal of the possibility that a particular event will occur. The analysts represent these events using well-defined fuzzy membership functions [29]. In this study, six linguistic terms - 'remote,' 'minor', 'low,' 'moderate,' 'high,' and 'very high' are employed to represent occurrence of events in the fuzzy FMEA and GRA approaches.

III. System description

This study conducts a risk analysis of the milling unit at Dhampur Sugar Mills Ltd., a sugar industry located in Western Uttar Pradesh, India. The mill has a crushing capacity of 23,500 MT/day of sugarcane. The left-over bagasse generates a good amount of electricity, totaling 121 MW/day. The sugar industry comprises several functional units: feeding, milling, refining, and crystallization. The milling unit being a crucial unit of sugar industry, its efficiency has great significance on overall plant efficiency. Its primary function is to crush sugarcane to extract juice, which is further processed into sugar by refining and crystallization units. This unit possesses a series of five heavy duty mills each consisting inter-rack carriers, roller pressure feeder and pumps connected in series configuration. These heavy-duty mills are designed to operate continuously under high pressure to maximize juice extraction. Failure of any mill or component of the mill can bring the whole milling unit to a halt. The function of each component in brief is as follows:

- **Inter-rack carrier (IRC):** IRC are used to transport crushed sugarcane or bagasse between mills, ensuring a smooth and continuous flow through the milling process.
- **Roller Pressure Feeder (RPF):** The RPF are used for juice extraction in sugar mills which may be basic, toothed roller pressure feeder (TRPF) or grooved roller pressure feeder (GRPF). TRPF and GRPF enhance juice extraction by gripping and compressing sugarcane with toothed and grooved rollers which apply additional pressure increasing efficiency of the mills.
- **Pumps:** Pumps transport primary juice from Mill 1 and secondary juice from Mill 2-5, to the raw juice tank. They also supply water and other liquids throughout the milling process, ensuring continuous flow and efficient processing of sugarcane juice.

The schematic diagram of the milling unit is depicted in figure 1.

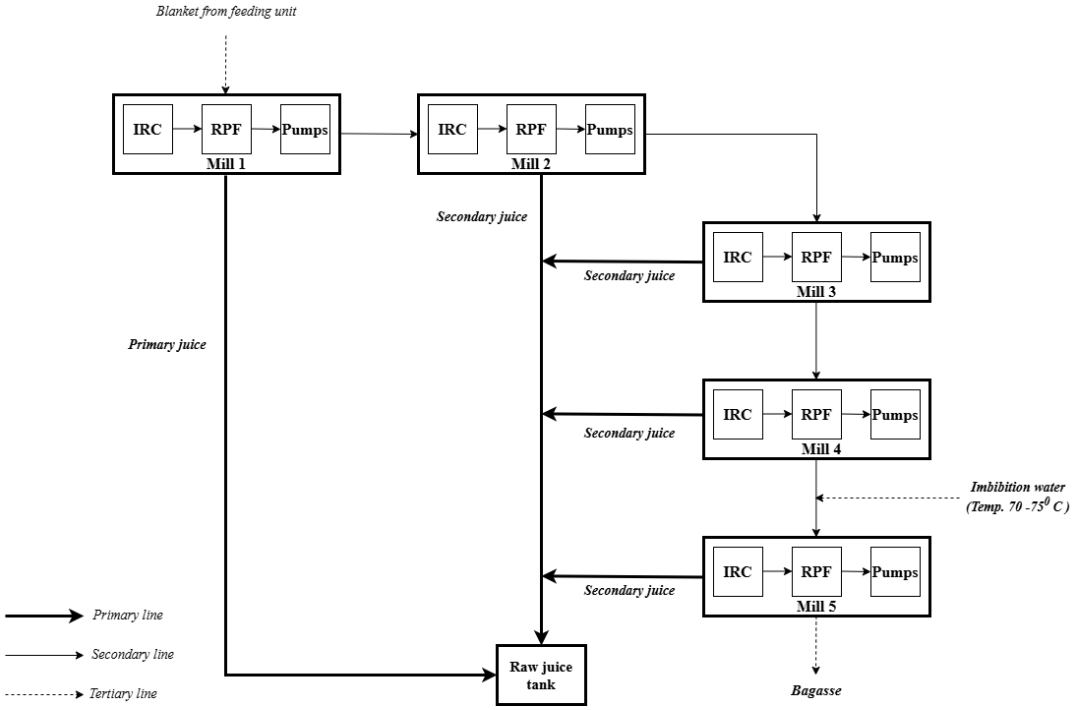


Figure 1: *Schematic diagram of the milling unit*

IV. Risk Analysis

This section presents an in-depth risk analysis of the milling unit in a sugar industry using fuzzy FMEA and GRA. This helps in prioritizing risk managerial strategies, enhancing the availability and safety ensuring long-term sustainability of the complex machines, equipments and processes in milling unit.

I. Failure mode and effect analysis (FMEA)

FMEA is a powerful tool to assess the potential failure mode and their effect so that corrective actions may be prioritized depending upon risk ranking. It is a systematic, bottom-up technique that investigates the effect of possible failure modes at one level on failure modes of the next sub-system level. The procedural steps of FMEA are shown in figure 2.

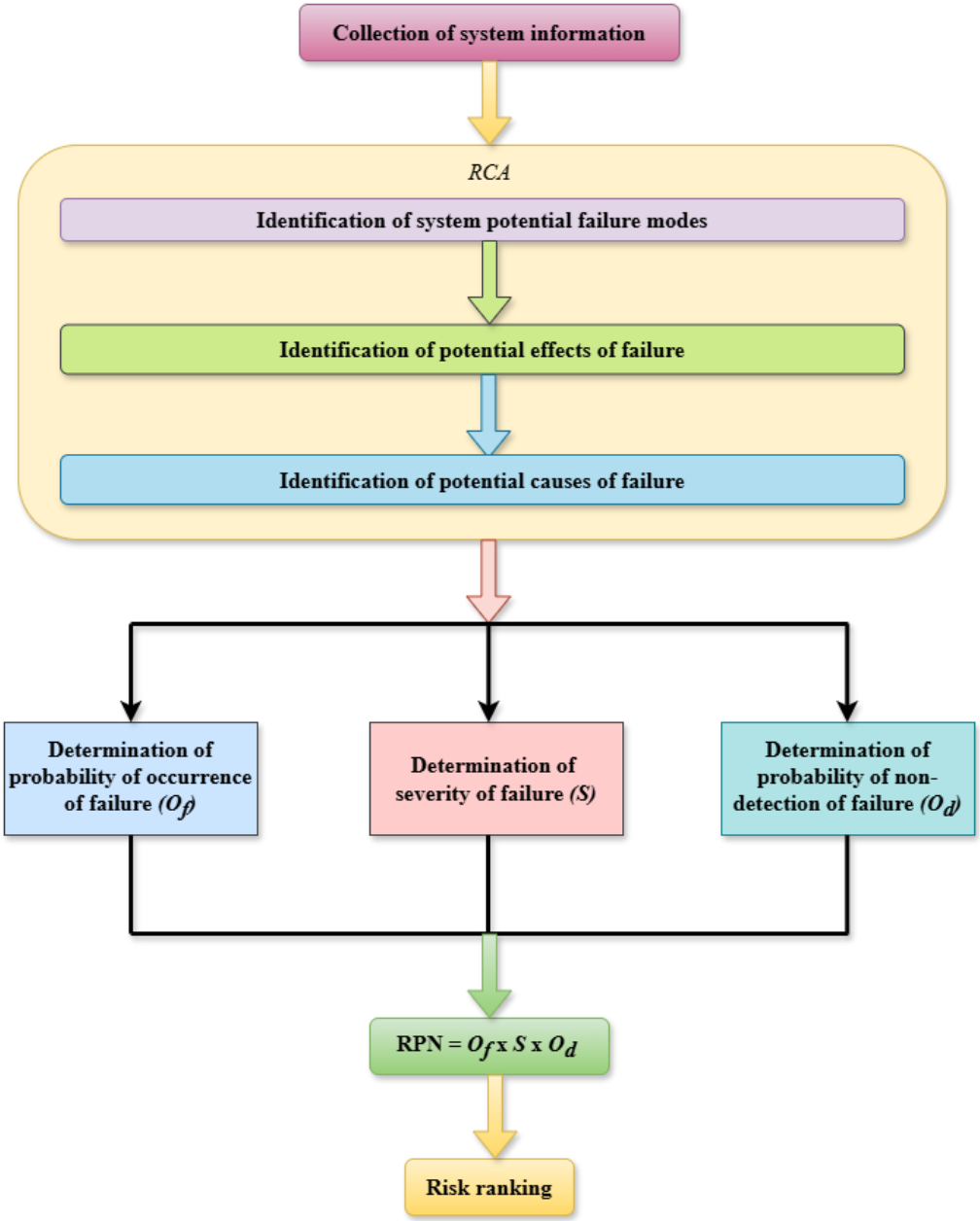


Figure 2: *Procedural steps of FMEA*

After collecting information of the system from various sources such as expert opinion, log book, computer records, etc., RCA has been performed to identify potential failure causes of each component (IRC, RPF, and Pumps) of the milling unit for preventing future failures. The root causes of problem issues, illustrated using a Fishbone diagram are represented in figure 3.

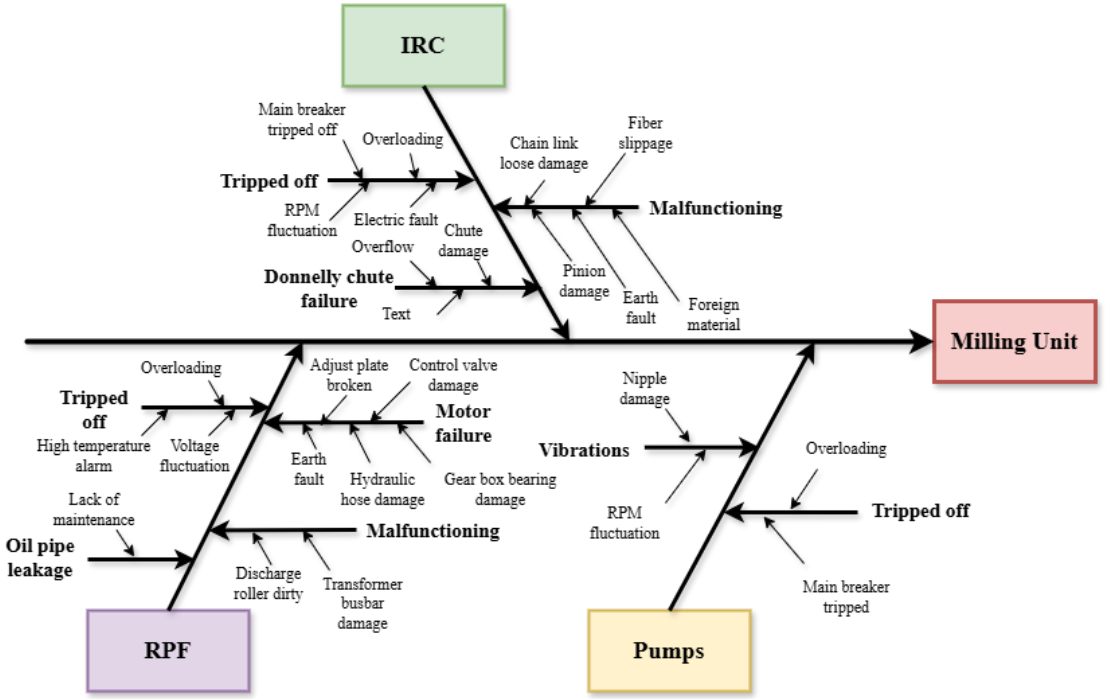


Figure 3: *RCA of milling unit*

Further, a fuzzy linguistic assessment scale (Table 1) has been generated to compute scores with the help of expert opinions regarding the probability of occurrence of failure (O_f), severity effect of failure (S) and probability of non–detection of failure (O_d) of distinct components of the milling unit [30].

Table 1: *Scale for probability of occurrence, severity effect and likelihood of non-detection of failure*

Linguistic terms	Symbol	Score	MTBF	Prob. of occurrence	Severity effect	Likelihood of non-detection (%)
Remote	R	0-1	>5 years	<0.01	Not noticed	0-5
Low	L	2-3	2-5 years	0.01-0.1	Minor hassle to the operator	6-25
Moderate	M	4-6	1-2 years	0.1-0.5	Minor fall in system efficiency	26-55
High	H	7-8	0.5-1 years	0.5-1	Significant loss in system efficiency	56-75
Very High	VH	9-10	<6 months	>1	Manufacturing loss	76-100

The scores of risk factors of distinct components of milling unit have been computed with the help of expert opinions. To mitigate bias in expert assessment, a diverse panel of experienced professionals was consulted from the sugar industry, including maintenance engineers, quality control specialists, and system analysts, ensuring a balanced and comprehensive assessment of risk factors. Further, to minimize individual biases in the computed scores by experts, Delphi technique

Table 2: *FMEA sheet for milling unit*

Function	Potential failure mode	Potential effect of failure	Potential cause of failure	O_f	S	O_d	RPN Score	Corrective actions
			IRC					
To carry blanket	Tripped off	Operational loss	Electric fault [MU_{11}]	7	3	5	105	Repairing insulation, Replace fuses
			Main breaker tripped off [MU_{12}]	5	3	6	90	Check overload settings, Examine motor health
			RPM fluctuation [MU_{13}]	7	3	3	63	Bearing replacement, Gearbox maintenance
			Overloading [MU_{14}]	7	5	3	105	Adjust feed rate, Upgrade motor capacity
	Donnelly chute failure	Fails to operate	Chute damage [MU_{15}]	4	4	4	64	Improve alignment
			Shaft damage [MU_{16}]	3	5	5	75	Material upgrade, Lubrication check
			Overflow [MU_{17}]	3	2	2	12	Clear choke points, Check juice channels
	Malfunc--tioning	Cane carrier shut down	Chain link loose/ damage [MU_{18}]	4	5	2	40	Regular inspections, Timely replacement
			Fiber slippage [MU_{19}]	5	4	3	60	Adjust roller pressure, Improve fiber feeding
			Pinion damage [MU_{110}]	3	6	5	90	Lubrication improvement, Load adjustment
			Foreign material [MU_{111}]	4	7	2	5	Pre-sorting materials, Magnetic separation
			Earth fault [MU_{112}]	6	4	6	144	Inspect grounding system, Check insulation integrity
			RPF					
To separate juice and bagasse	Tripped off	Fails to squeeze juice	Voltage fluctuation [MU_{21}]	7	3	3	63	Install voltage stabilizer, Upgrade electrical wiring
			High temperature alarm [MU_{22}]	5	2	2	20	Temperature calibration, Coolant system check
			Overloading [MU_{23}]	7	5	3	105	Adjust feed rate, Monitor load sensors
	Oil pipe leakage	Breakage	Lack of maintenance [MU_{24}]	3	6	5	90	Scheduled maintenance
	Motor failure	Mill shut down/bypass	Adjust plate broken [MU_{25}]	2	5	6	60	Replace plate, Check alignment
			Control valve damage [MU_{26}]	3	6	6	108	Valve replacement, Pressure monitoring
			Hydraulic hose damage [MU_{27}]	3	6	7	126	Installation of quality hoses, Regular inspections
			Gear box bearing damage [MU_{28}]	3	5	7	105	Bearing inspection, Regular lubrication
			Earth fault [MU_{29}]	6	4	6	144	Inspect grounding system
	Malfunc--tioning	Fails to operate	Transformer busbar damage [MU_{210}]	2	5	6	60	Busbar inspection, Transformer maintenance
			Discharge roller dirty [MU_{211}]	4	6	5	120	Increase cleaning frequency
			Pumps					
To transfer sugarcane juice	Tripped off	Operational loss	Main breaker tripped off [MU_{31}]	5	3	6	90	Inspect breaker, Reset system
			Overloading [MU_{32}]	7	5	3	105	Optimize load distribution
	Vibrations	Equipment damage	Nipple damage [MU_{33}]	3	6	6	108	Enhance Material Strength
			RPM fluctuation [MU_{34}]	7	3	3	63	Inspect drive belt, Calibrate RPM sensor

[31-32] is employed. Subsequently, an FMEA sheet (Table 2) has been generated, and scores related to O_f, S and O_d have been tabulated which are utilized to calculate the RPN score of each failure cause. Here, RPN = $O_f \times S \times O_d$.

In FMEA, the crisp values of O_f, S and O_d of different components are considered to calculate their RPN scores, which seems inappropriate, since probability of occurrence, non-detection and severity effect of failures are subjective and vague, being suggested by experts in natural language. Also, RPN ranking obtained using FMEA could potentially mislead analysts and maintenance professionals as the failure causes with the same RPN score might have different linguistic sets. On the other hand, some of the failure causes have the same linguistic set with different RPN scores, so that, the risk implications could differ significantly. Also, despite their actual significance in practical applications, the RPN ranking technique overlook the relative significance of O_f, S and O_d [21,30]. As a result, on the basis of RPN, system analysts may face challenges in determining risk priorities for corrective actions. Therefore, to address these drawbacks, a combination of the fuzzy logic and grey approach with inputs of FMEA is implemented to offer a more efficient and better way to make decisions regarding risk priorities.

II. Fuzzy FMEA

The fuzzy logic toolbox of MATLAB offers robust functionality for handling linguistic variables, rule-based systems, and complex multi-criteria decision-making models. Therefore, for the implementation of the fuzzy FMEA approach, the fuzzy logic toolbox in MATLAB (R2015a) has been employed to develop a knowledge–inferencing–based fuzzy decision support system (FDSS) for better decision-making in risk ranking. The three modules of the fuzzy inference system—the knowledge base module, input inference module, and output inference module are depicted in figure 4.

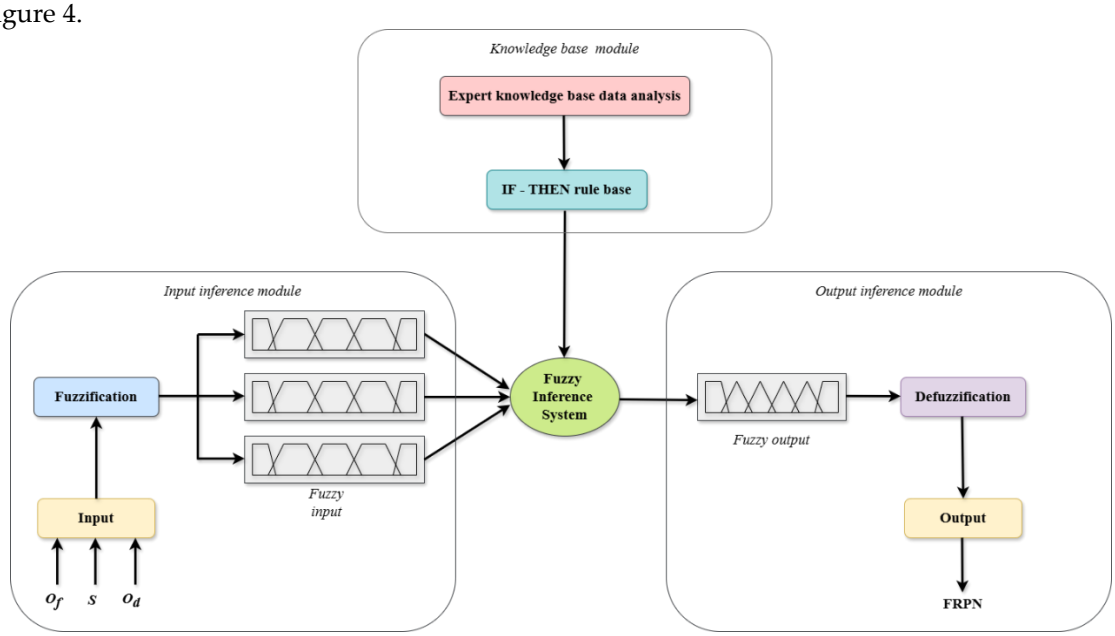


Figure 4: *Knowledge–inferencing–based FDSS*

The knowledge base module consists of a well-defined set of 'if-then' rules expressed in linguistic terms by employing a fuzzy model of the process and expert knowledge. For instance, a rule in the form of 'if-then' can be expressed as:

$\boldsymbol{R_1}$**: if** p is $\boldsymbol{P_i}$**, then** q is $\boldsymbol{Q_i}$**,** where i =1, 2, …, N

where, p and q are input and output linguistic terms; $\boldsymbol{P_i}$ and $\boldsymbol{Q_i}$ are antecedent and consequent linguistic constants.

For the input and output inferencing module, the trapezoidal membership function has been used to fuzzify crisp input values of O_f, S and O_d taken from the FMEA sheet. Here, the input membership function is defined with five linguistic terms 'Remote', 'Low', 'Moderate', 'High' and 'Very High' depicted in figure 5.

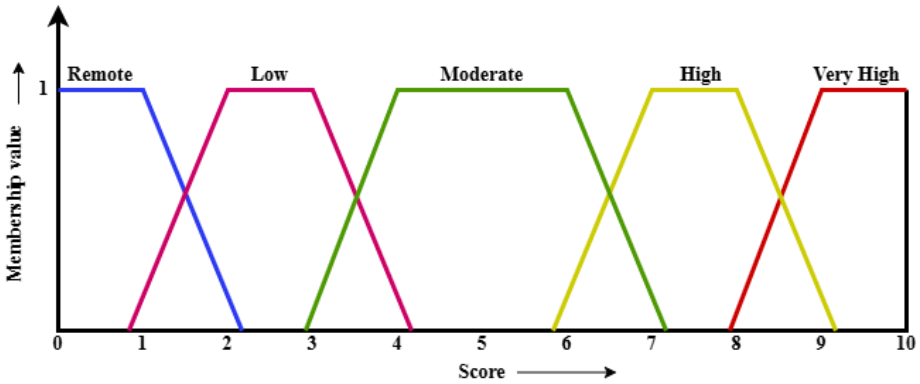


Figure 5: *Input membership function for O_f, S and O_d*

After combining three inputs and five linguistic terms, 125 'if-then' rules base has been generated. The fuzzy output i.e. FRPN is achieved by combining the inference mechanism with input variables and an 'if-then' set of 125 rules. The Mamdani min-max inferencing technique in fuzzy logic toolbox (figure 6) is used for inferencing, and fuzzy output is obtained using a triangular membership function defined with six linguistic terms 'Remote', 'Minor', 'Low', 'Moderate', 'High' and 'Very High', shown in figure 7.

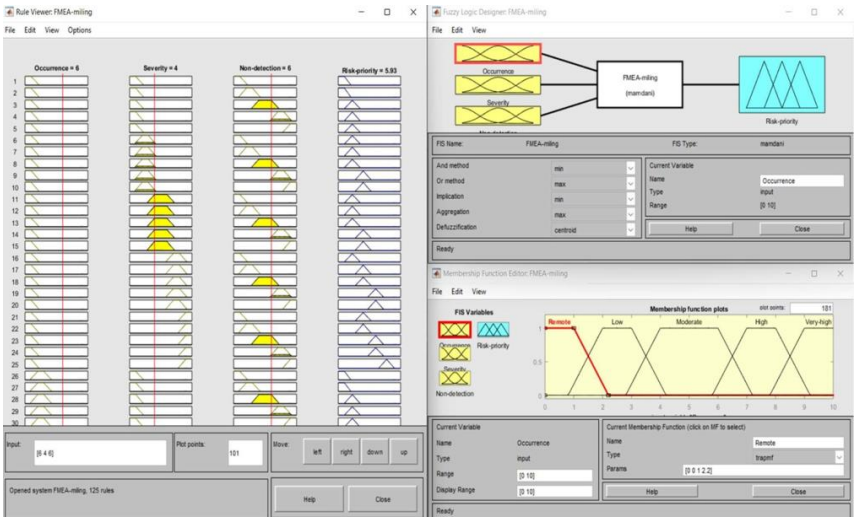


Figure 6: *Fuzzy logic toolbox*

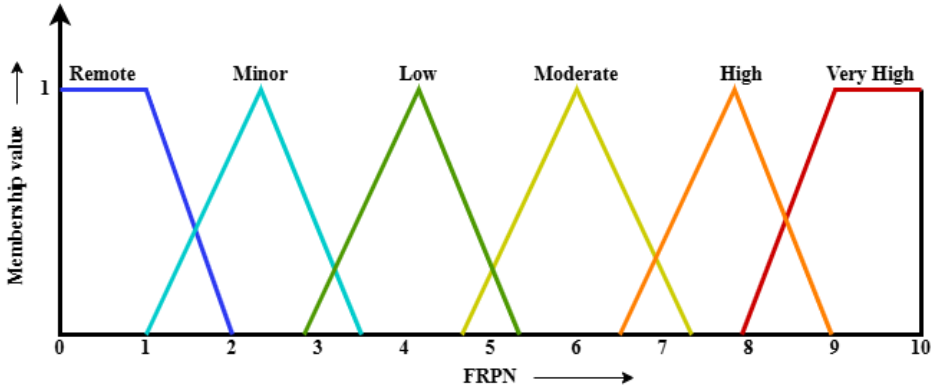


Figure 7: *Output membership function for fuzzy output*

To obtain crisp output, the fuzzy output has been defuzzified by employing the center of area (COA) method. According to this method, the defuzzified value ($\bar{x}$) for a fuzzy set Ã is given by

$$\bar{x} = \frac{\int_{x_1}^{x_2} x.\mu_{\tilde{A}}(x)dx}{\int_{x_1}^{x_2} \mu_{\tilde{A}}(x)dx} \quad (3)$$

where, $\mu_{\tilde{A}}(x)$ is the membership function of Ã defined on [x_1, x_2].

The obtained crisp values of FRPN have been used to assign risk priorities for better decision making. The results are compared with RPN obtained by FMEA and are tabulated in table 3. Moreover, to enable intelligent decision-making for relative importance between O_f, S and O_d and to determine the optimal ranking of critical components, GRA approach has been used.

Table 3: *Risk ranking results based on RPN and FRPN*

Component	Potential cause of failure	RPN	Ranking	FRPN	Fuzzy ranking
IRC	MU_{11}	105	5	4.45	7
	MU_{12}	90	6	5.01	5
	MU_{13}	63	9	3.26	9
	MU_{14}	105	5	4.45	7
	MU_{15}	64	8	4.99	6
	MU_{16}	75	7	6.00	2
	MU_{17}	12	14	2.40	10
	MU_{18}	40	12	5.55	4
	MU_{19}	60	10	5.55	4
	MU_{110}	90	6	5.55	4
	MU_{111}	56	11	4.07	8
	MU_{112}	144	1	5.93	3
RPF	MU_{21}	63	9	3.26	9
	MU_{22}	20	13	3.26	9
	MU_{23}	105	5	4.45	7
	MU_{24}	90	6	5.55	4
	MU_{25}	60	10	4.99	6
	MU_{26}	108	4	5.93	3
	MU_{27}	126	2	5.93	3
	MU_{28}	105	5	6.38	1
	MU_{29}	144	1	5.93	3
	MU_{210}	60	10	4.99	6
	MU_{211}	120	3	5.55	4
Pumps	MU_{31}	90	6	5.01	5
	MU_{32}	105	5	4.45	7
	MU_{33}	108	4	5.93	3
	MU_{34}	63	9	3.26	9

III. GRA

The GRA is a significant decision-making method introduced by Deng [33]. It offers a flexible and effective tool for reliability analysis, especially in the environment of uncertainty. It takes into account the multiple reliability metrics to rank and prioritize failure causes, system components and maintenance strategies which makes it highly valuable in process industries and complex engineering systems. For intelligent decision-making in prioritization, Chang *et al.* [34] employed

grey theory into the fuzzy FMEA approach which gained popularity. In this study, the same linguistic terms which were used in fuzzy FMEA are applied in GRA to calculate the degree of relation, and the ranking outcomes are compared with the FRPN results. Figure 8 illustrates the steps of GRA.

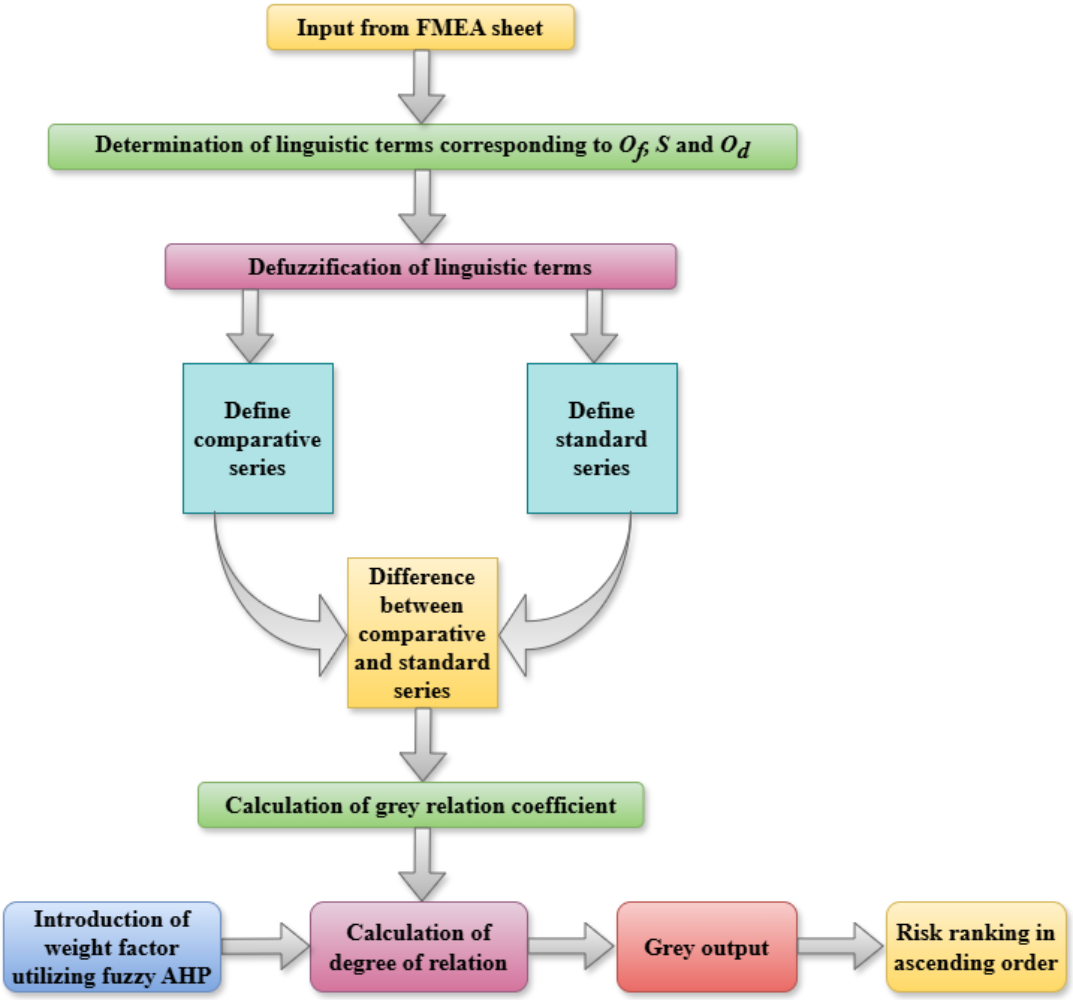


Figure 8: *Procedural steps of GRA*

The five linguistic terms established by experts for O_f, S and O_d in the fuzzy FMEA were defuzzified by employing the method given by Chen and Klein [35] to yield crisp values which are presented in table 4.

Table 4: *Crisp values for linguistic terms*

Linguistic term	Crisp value	Symbol
Remote (R)	0.0937	+ + +
Low (L)	0.2650	+ +
Moderate (M)	0.5118	+
High (H)	0.7272	−
Very high (VH)	0.9125	− −

The crisp values given in table 4 have been employed to generate the comparative series for different causes of failures of various components of the considered unit. For instance, comparative series of IRC component is represented by

$$\begin{bmatrix} - & ++ & + \\ + & ++ & + \\ - & ++ & ++ \\ - & + & ++ \\ + & + & + \\ ++ & + & + \\ ++ & ++ & ++ \\ + & + & ++ \\ + & + & ++ \\ ++ & + & + \\ + & - & ++ \\ + & + & + \end{bmatrix} = \begin{bmatrix} 0.7272 & 0.2650 & 0.5118 \\ 0.5118 & 0.2650 & 0.5118 \\ 0.7272 & 0.2650 & 0.2650 \\ 0.7272 & 0.5118 & 0.2650 \\ 0.5118 & 0.5118 & 0.5118 \\ 0.2650 & 0.5118 & 0.5118 \\ 0.2650 & 0.2650 & 0.2650 \\ 0.5118 & 0.5118 & 0.2650 \\ 0.5118 & 0.5118 & 0.2650 \\ 0.2650 & 0.5118 & 0.5118 \\ 0.5118 & 0.7272 & 0.2650 \\ 0.5118 & 0.5118 & 0.5118 \end{bmatrix} , \quad (4)$$

where, the matrices at left and right hand side, respectively, represent linguistic terms and crisp values of causes of failure. Further, a standard series for the failure causes of IRC component has been obtained by taking minimum level of linguistic terms (i.e. 'Remote' in this study), for three variables O_f, S and O_d since in FMEA, the RPN score is directly proportional to level of risk. The crisp value for 'Remote' is 0.0937, which represents the average value. The lowest possible value of term 'Remote' is 0. Thus, the standard series for failure causes of IRC component is

$$\begin{bmatrix} +++ & +++ & +++ \\ +++ & +++ & +++ \\ +++ & +++ & +++ \\ +++ & +++ & +++ \\ +++ & +++ & +++ \\ +++ & +++ & +++ \\ +++ & +++ & +++ \\ +++ & +++ & +++ \\ +++ & +++ & +++ \\ +++ & +++ & +++ \\ +++ & +++ & +++ \\ +++ & +++ & +++ \end{bmatrix} = \begin{bmatrix} 0 & 0 & 0 \\ 0 & 0 & 0 \\ 0 & 0 & 0 \\ 0 & 0 & 0 \\ 0 & 0 & 0 \\ 0 & 0 & 0 \\ 0 & 0 & 0 \\ 0 & 0 & 0 \\ 0 & 0 & 0 \\ 0 & 0 & 0 \\ 0 & 0 & 0 \\ 0 & 0 & 0 \end{bmatrix} . \quad (5)$$

To calculate grey relation coefficient of IRC component, the difference D between comparative and standard series is obtained as

$$D = \begin{bmatrix} 0.7272 & 0.2650 & 0.5118 \\ 0.5118 & 0.2650 & 0.5118 \\ 0.7272 & 0.2650 & 0.2650 \\ 0.7272 & 0.5118 & 0.2650 \\ 0.5118 & 0.5118 & 0.5118 \\ 0.2650 & 0.5118 & 0.5118 \\ 0.2650 & 0.2650 & 0.2650 \\ 0.5118 & 0.5118 & 0.2650 \\ 0.5118 & 0.5118 & 0.2650 \\ 0.2650 & 0.5118 & 0.5118 \\ 0.5118 & 0.7272 & 0.2650 \\ 0.5118 & 0.5118 & 0.5118 \end{bmatrix} . \quad (6)$$

The grey relation coefficient for each linguistic term corresponding to each failure cause of the IRC component is obtained using

$$\gamma_{ij} = \frac{D_{min} + \xi D_{max}}{d_{ij} + \xi D_{max}} , \quad i = 1,2, \dots n; \; j = 1,2,3 \quad , \quad (7)$$

where, n = number of failure causes in component, D_{min} and D_{max} are the least and most possible

values of factors in equation 6 and the identifier ξ is assumed to be 0.5. The matrix of grey relation coefficients for failure causes of IRC component is given as

$$\gamma = \begin{bmatrix} 0.4647 & 0.7625 & 0.5681 \\ 0.5681 & 0.7625 & 0.5681 \\ 0.4647 & 0.7625 & 0.7625 \\ 0.4647 & 0.5681 & 0.7625 \\ 0.5681 & 0.5681 & 0.5681 \\ 0.7625 & 0.5681 & 0.5681 \\ 0.7625 & 0.7625 & 0.7625 \\ 0.5681 & 0.5681 & 0.7625 \\ 0.5681 & 0.5681 & 0.7625 \\ 0.7625 & 0.5681 & 0.5681 \\ 0.5681 & 0.4647 & 0.7625 \\ 0.5681 & 0.5681 & 0.5681 \end{bmatrix} . \quad (8)$$

Similarly, the grey relation coefficient for each failure causes of other two components RPF and pumps have been obtained.

The degree of relation (δ), indicating the relationship between the potential causes and the optimal value of decision factors is given by

$$\delta = \beta_1\gamma_{i1} + \beta_2\gamma_{i2} + \beta_3\gamma_{i3}, \text{ with } \sum_{j=1}^{3}\beta_j = 1, \quad (9)$$

where, β_j is the weight coefficient corresponding to j^{th} factor.

The weight coefficients, β_j of the decision factors can be computed either based upon expert feedback or assumed directly. In present study, the fuzzy AHP has been employed to generate the fuzzy comparison matrix for three risk factors O_f, S and O_d using Wang's scale [36] shown in table 5, on the basis of suggestions given by maintenance engineers. The imprecise and uncertain assessments of them are translated into corresponding triangular fuzzy numbers given in comparison matrix (Table 6). This scale is particularly effective within the process industries, as it allows for nuanced pairwise comparisons in uncertain or imprecise environments. Its fuzzy linguistic scale is well-suited for dealing with subjective assessments and partial information, which are common in complex industrial processes. The fuzzy extent analysis method [37] has been used to determine weight coefficients β_j for fuzzy comparison matrix of risk factors presented in table 6.

Table 5: *Wang's scale for matrix generation*

Uncertain judgement	Fuzzy scale
Approximately important	(1/2, 1, 2)
Approximately X times more important[a]	(X-1, X, X+1)
Approximately X times less important	(1/X+1, 1/X, 1/X-1)
Between Y and Z times more important[b]	(Y, Y+Z/2, Z)
Between Y and Z times less important	(1/Z, 2/Y+Z, 1/Y)

[a] X = 2, 3, ……,9

[b] Y, Z = 1, 2, ……., 9 and Y < Z

Table 6: *Comparison matrix for risk factors*

	O_f	S	O_d	$\boldsymbol{\beta_j}$
O_f	(1, 1, 1)	(1/4, 1/3, 1/2)	(1/2, 1, 2)	0.22
S	(2, 3, 4)	(1, 1, 1)	(1, 2, 3)	0.48
O_d	(1/2, 1, 2)	(1/3, 1/2, 1)	(1, 1, 1)	0.30

The weight coefficients so obtained are $\beta_1 = 0.22$, $\beta_2 = 0.48$, $\beta_3 = 0.30$. Further, the value of δ is calculated by using equation 9 for corresponding γ_{ij} and β_j.
For instance, for failure cause **MU11:**

$$\delta_{11} = 0.4647\times0.22+0.7625\times0.48+0.5681\times0.30 = 0.6387$$

Similarly, the degree of relation δ i.e., grey output has been computed for each cause of each component of milling unit and ranking of risky components has been tabulated in table 7.

Table 7: *Grey relation coefficient and grey output for various failure causes*

Component	Failure causes	O_f	γ_{O_f}	S	γ_S	O_d	γ_{O_d}	Grey output	Grey ranking
IRC	MU_{11}	−	0.4647	++	0.7625	+	0.5681	0.6387	7
	MU_{12}	+	0.5681	++	0.7625	+	0.5681	0.6614	8
	MU_{13}	−	0.4647	++	0.7625	++	0.7625	0.6970	9
	MU_{14}	−	0.4647	+	0.5681	++	0.7625	0.6037	4
	MU_{15}	+	0.5681	+	0.5681	+	0.5681	0.5681	1
	MU_{16}	++	0.7625	+	0.5681	+	0.5681	0.6109	5
	MU_{17}	++	0.7625	++	0.7625	++	0.7625	0.7625	11
	MU_{18}	+	0.5681	+	0.5681	++	0.7625	0.6264	6
	MU_{19}	+	0.5681	+	0.5681	++	0.7625	0.6264	6
	MU_{110}	++	0.7625	+	0.5681	+	0.5681	0.6109	5
	MU_{111}	+	0.5681	−	0.4647	++	0.7625	0.5768	2
	MU_{112}	+	0.5681	+	0.5681	+	0.5681	0.5681	1
RPF	MU_{21}	−	0.4647	++	0.7625	++	0.7625	0.6970	9
	MU_{22}	+	0.5681	++	0.7625	++	0.7625	0.7197	10
	MU_{23}	−	0.4647	+	0.5681	++	0.7625	0.6037	4
	MU_{24}	++	0.7625	+	0.5681	+	0.5681	0.6109	5
	MU_{25}	++	0.7625	+	0.5681	+	0.5681	0.6109	5
	MU_{26}	++	0.7625	+	0.5681	+	0.5681	0.6109	5
	MU_{27}	++	0.7625	+	0.5681	−	0.4647	0.5789	3
	MU_{28}	++	0.7625	+	0.5681	−	0.4647	0.5789	3
	MU_{29}	+	0.5681	+	0.5681	+	0.5681	0.5681	1
	MU_{210}	++	0.7625	+	0.5681	+	0.5681	0.6109	5
	MU_{211}	+	0.5681	+	0.5681	+	0.5681	0.5681	1
Pumps	MU_{31}	+	0.5681	++	0.7625	+	0.5681	0.6614	8
	MU_{32}	−	0.4647	+	0.5681	++	0.7625	0.6037	4
	MU_{33}	++	0.7625	+	0.5681	+	0.5681	0.6109	5
	MU_{34}	−	0.4647	++	0.7625	++	0.7625	0.6970	9

V. Results and Discussion

To prioritize risk management strategies of milling unit, FMEA has been conducted. The FMEA sheet of milling unit together with the numerical values assigned to risk factors O_f, S and O_d are presented in table 2. The risk ranking of failure causes is measured using RPN scores. The higher is

RPN score, higher is risk ranking. It is observed that for IRC, the failure cause **MU**$_{111}$ described by moderate probability of occurrence, higher severity and low probability of non-detection [**M, H, L**] has lower RPN score 56, while the failure cause **MU**$_{112}$ for which all the risk factors are moderate [**M, M, M**] yields RPN score 144. This means that **MU**$_{112}$ has higher priority than **MU**$_{111}$, which could be misleading for managers, as **MU**$_{111}$ should have a higher priority than **MU**$_{112}$ for corrective actions. Also, it is revealed that MU$_{11}$ (low severity) and **MU**$_{14}$ (moderate severity) have same RPN score 105; however, on the basis of severity, the risk implication for both of them may be totally different. Table 6 presents the defuzzified RPN using fuzzy FMEA and the grey outputs are tabulated in table 7. Further, the comparison of ranking results obtained from FMEA, fuzzy FMEA, and GRA methods has been depicted in table 8. From table 8, it is observed that the failure causes **MU**$_{111}$ and **MU**$_{21}$ represented by the linguistic terms **[M, H, L]** and **[H, L, L]** have defuzzified outputs as 4.07 and 3.26, respectively, and grey outputs as 0.5768 and 0.6970, respectively. This shows that **MU**$_{111}$ should be given higher priority for corrective actions than **MU**$_{21}$ (when severity is considered). On the other hand, the standard FMEA approach produces their RPN scores as 56 and 63, respectively, and ranks them 11th and 9th places, respectively. This suggests that **MU**$_{21}$ has higher priority than **MU**$_{111}$, which could be misleading.

Table 8: *Risk ranking comparison of failure causes based on RPN, FRPN and grey output*

Component	Potential cause of failure	RPN	Ranking	FRPN	Fuzzy ranking	Grey output	Grey ranking
IRC	MU$_{11}$	105	5	4.45	7	0.6387	7
	MU$_{12}$	90	6	5.01	5	0.6614	8
	MU$_{13}$	63	9	3.26	9	0.6970	9
	MU$_{14}$	105	5	4.45	7	0.6037	4
	MU$_{15}$	64	8	4.99	6	0.5681	1
	MU$_{16}$	75	7	6.00	2	0.6109	5
	MU$_{17}$	12	14	2.40	10	0.7625	11
	MU$_{18}$	40	12	5.55	4	0.6264	6
	MU$_{19}$	60	10	5.55	4	0.6264	6
	MU$_{110}$	90	6	5.55	4	0.6109	5
	MU$_{111}$	56	11	4.07	8	0.5768	2
	MU$_{112}$	144	1	5.93	3	0.5681	1
RPF	MU$_{21}$	63	9	3.26	9	0.6970	9
	MU$_{22}$	20	13	3.26	9	0.7197	10
	MU$_{23}$	105	5	4.45	7	0.6037	4
	MU$_{24}$	90	6	5.55	4	0.6109	5
	MU$_{25}$	60	10	4.99	6	0.6109	5
	MU$_{26}$	108	4	5.93	3	0.6109	5
	MU$_{27}$	126	2	5.93	3	0.5798	3
	MU$_{28}$	105	5	6.38	1	0.5798	3
	MU$_{29}$	144	1	5.93	3	0.5681	1
	MU$_{210}$	60	10	4.99	6	0.6109	5
	MU$_{211}$	120	3	5.55	4	0.5681	1
Pumps	MU$_{31}$	90	6	5.01	5	0.6614	8
	MU$_{32}$	105	5	4.45	7	0.6037	4
	MU$_{33}$	108	4	5.93	3	0.6109	5
	MU$_{34}$	63	9	3.26	9	0.6970	9

Further, in standard FMEA, the failure causes described by different sets of linguistic terms may receive equal priority, while the failure causes described by same set of linguistic terms may receive different priorities. Such prioritization of failure causes may mislead the managers potentially in planning the maintenance strategies and maintenance resources may be misallocated. Fuzzy FMEA and GRA approaches overcome this limitation by refining rankings, making risk prioritization more accurate and ensuring that maintenance efforts are focused on genuinely high-risk failure causes rather than treating the failure causes equally critical with same RPN scores. For instance, for IRC and RPF, a significant discrepancy in ranking of failure causes **MU**$_{14}$ and **MU**$_{28}$ is highlighted. These failure causes, despite being described by different sets of linguistic terms [**H, M, L**] and [**L, M, H**], respectively, are assigned the same RPN score 105 and 5th rank using FMEA, which could be misleading as the risk implications for both the causes may be different. However, their defuzzified output is 4.45 and 6.38 respectively, while the grey output is 0.6037 and 0.5798, respectively. Therefore, fuzzy and grey approaches yield different outputs and different priorities for **MU**$_{14}$ and **MU**$_{28}$**.** According to them, **MU**$_{28}$ is given higher priority than **MU**$_{14}$. A similar pattern emerged for the RPF and pumps, where causes **MU**$_{24}$ and **MU**$_{31}$, with different linguistic sets [**L, M, M**] and [**M, L, M**], respectively, produce the same RPN score 90 and 6th rank using FMEA. However, the defuzzified outputs are 5.55 (4th rank) and 5.01 (5th rank) and grey outputs are 0.6109 (5th rank) and 0.6614 (8th rank), respectively, for **MU**$_{24}$ and **MU**$_{31}$. This suggests higher priority of **MU**$_{24}$ than **MU**$_{31}$ for corrective actions.

In contrast, for the failure causes **MU**$_{18}$ and **MU**$_{19}$ of IRC represented by the same linguistic terms [**M, M, M**], the defuzzified output is 5.55 and grey output is 0.6264 for both failure causes. This necessitates that both failure causes should be given the same priority for attention, but a variation in their RPN score is noted (40 and 60), suggesting higher priority for **MU**$_{19}$ over **MU**$_{18}$, which could potentially mislead decision makers. However, in some cases, it is found that for failure causes represented by same linguistic terms, FMEA and fuzzy FMEA suggest different rankings, while GRA suggest same rankings. For instance, the failure causes **MU**$_{24}$**, MU**$_{25}$ and **MU**$_{26}$ of the RPF are represented by the linguistic terms **[L, M, M],** but distinct RPN rankings of 6th, 10th and 4th, respectively, are suggested by FMEA and 4th, 6th and 3rd positions, are suggested by fuzzy FMEA, while GRA ranks them at same priority level i.e. 5th position. Similarly, **MU**$_{15}$ and **MU**$_{211}$ with linguistic terms **[M, M, M]** are ranked 8th and 3rd, respectively, by FMEA, while, 6th and 4th, respectively, by fuzzy FMEA. On the other hand, the grey output places both at 1st position. Thus, the effect of weight coefficients in grey output is visible in the results. This shows that GRA takes into account the relative importance of O_f, S and O_d. Further, according to GRA, the failure causes **MU**$_{15}$**, MU**$_{112}$**, MU**$_{211}$ and **MU**$_{29}$ require the most attention, and **MU**$_{17}$ requires the least attention. By resolving resulting ambiguities, this hybrid approach allows plant managers to prioritize the most critical maintenance action efficiently, leading to better resource allocation, reduced downtime and enhanced system reliability.

VI. Conclusion

This study developed a comprehensive risk assessment profile utilizing hybrid approach for accurately analyzing the qualitative performance of the milling unit in a sugar industry. The key failure causes affecting system availability have been identified and their associated RPN, FRPN and grey output scores have been calculated by employing respectively FMEA, FDSS and GRA to establish priorities. In standard FMEA, the failure causes described by different sets of linguistic terms may receive equal priority, while the failure causes described by same set of linguistic terms may receive different priorities, potentially leading to the misallocation of maintenance resources. For instance, for IRC and RPF, overloading and gear box bearing damage, despite being described by different sets of linguistic terms are assigned the same ranking using FMEA. However, the FRPN and grey analysis yield different rankings and accordingly gear box bearing damage is given

higher priority than overloading. In contrast, the failure causes of RPF namely, lack of maintenance, adjust plate broken and control valve damage, are represented by the same linguistic terms but distinct RPN rankings are suggested by FMEA and fuzzy FMEA. They suggest that control valve damage should be given higher priority than lack of maintenance and adjust plate broken, which could mislead the analysts. On the other hand, GRA ranks them at same priority level. The effect of weight coefficients in grey output is visible in the results. For instance, the failure causes of IRC namely electric fault (low severity) and overloading (moderate severity) have same RPN scores and same defuzzified outputs. This could be misleading for managers, since the risk implication for both of these failure causes may be totally different on the basis of severity. However, the grey output suggests that overloading should be given high priority over electric fault for corrective actions. Thus, the combined use of FDSS and GRA provides more reliable and consistent ranking results for the key failure causes. Also, it is observed that failure causes such as chute damage, earth fault and discharge roller dirty require most attention, while overflow requires least attention.

In nutshell, the prioritization of failure causes allows system analysts to pinpoint the most vulnerable and high-risk components in the milling unit of sugar industry. The critical failure causes with top priorities should be addressed promptly, either by reducing or eliminating them, in order to improve overall system availability ultimately leading to better system reliability and prolonged operational life. The findings will be useful to develop an optimized maintenance policy, to enhance production efficiency and to reduce maintenance costs allowing sugar industries to allocate resources effectively and avoid unnecessary expenditures on low-priority issues. A well-maintained milling unit not only boosts overall productivity but also ensures a stable sugar supply, contributing to market stability and economic growth in sugar producing regions.

I. Managerial implications

Risk analysis of milling unit in the sugar industry often relies on uncertain data and subjective expert assessments, which could be biased. This highlights the need for careful interpretation as the data quality variations affect decision-making. The present analysis will prove to be beneficial for managers, to plan suitable maintenance policies, reduce maintenance and operational cost, and ensure long-term system availability of the sugar industry. Some of the managerial implications of present study are as follows:

- It helps in identifying the risky components of complex industrial systems using subjective judgments of experts.
- It prioritizes the key failure causes of an industrial system in a more promising way in the environment of uncertainty / subjective judgments.
- It helps to plan optimal maintenance strategies for the considered system for maintaining high availability of the industry.
- It helps to reduce maintenance costs by minimizing unplanned downtimes.
- It helps to enhance productivity of the considered system and overall industry.

References

[1] Coutinho, J.S. (1964). Failure-effect analysis. *Transactions of the New York Academy of Sciences*, 26:564–585.

[2] Bowles, J.B. and Pelaez, C.E. (1995). Fuzzy logic prioritization of failures in a system failure mode, effects and criticality analysis. *Reliability Engineering and System Safety*, 50:203–213.

[3] Shankar, N.R. and Prabhu, B.S. (2001). Modified approach for prioritization of failures in a system failure mode and effects analysis. *International Journal of Quality and Reliability Management*,

18(3).

[4] Guimarães, A.C.F. and Lapa, C.M.F. (2004). Fuzzy FMEA applied to PWR chemical and volume control system. *Progress in Nuclear Energy*, 44(3):191–213.

[5] Sharma, R.K., Kumar, D. and Kumar, P. (2005). Systematic failure mode and effect analysis using fuzzy linguistic modeling. *International Journal of Quality & Reliability Management*, 22(9):886-1004.

[6] Tay, K.M. and Lim, C.P. (2006). Fuzzy FMEA with a guided rules reduction system for prioritization of failures. *International Journal of Quality and Reliability Management*, 23(8):1047–1066.

[7] Wang, Y-M., Chin, K-S., Poon Gary Ka, K. and Yang, J.B. (2009). Risk evaluation in failure mode and effects analysis using fuzzy weighted geometric mean. *Expert Systems with Applications*, 36(2):1195–1207.

[8] Neapolitan, R.E. Learning Bayseian Network, Pearson, 2004.

[9] Koller, B. and Friedman, N. Probabilistic graphical models: Principles & techniques, MIT press, 2009.

[10] Behzadian, M., Ofaghsara, S.K., Yazdani, M. and Ignatius, J. (2012). A state of the art survey of TOPSIS applications. *Expert Systems with Applications*, 39(17):13051-13069.

[11] Khaira, A. and Dwivedi, R. K. (2018). A state of the art review of analytical hierarchy process. *Materials Today: Proceedings*, 5(2):4029-4035.

[12] Samvedi, A., Jain, V. and Chan, F. T. (2013). Quantifying risks in a supply chain through integration of fuzzy AHP and fuzzy TOPSIS. *International Journal of Production Research*, 51(8):2433-2442.

[13] Badida, P., Janakiraman, S. and Jayaprakash, J. (2023). Occupational health and safety risk assessment using a fuzzy multi-criteria approach in a hospital in Chennai, India. *International journal of occupational safety and ergonomics*, 29(3):1047-1056.

[14] Wang, M.H. and Hung, C.P. (2003). Novel grey model for the prediction of trend of dissolved gases in oil-filled power apparatus. *Electric Power System Research*, 67(1):6753–6758.

[15] Albert, W.L., Yao, S.C. and Chen, J.H. (2003). An improved grey-based approach for electricity demand forecasting. *Electric Power System Research*, 67(1):217– 224.

[16] Zhang, H., Li, Z. and Chen, Z. (2003). Application of grey modeling method to fitting and forecasting wear trend of marine diesel engines. *Tribology International*, 36(10):753–756.

[17] Lian, R., Lin, J.B. and Huang, J.H. (2005). A grey prediction fuzzy controller for constant cutting force in turning. *International Journal of Machine Tool and Manufacture*, 45(9):1047–1056.

[18] Sharma, R.K., Kumar, D. and Kumar, P. (2007). Behaviour analysis and resource optimization for an industrial system. *International Journal of Industrial and Systems Engineering*, 2(4):413-443.

[19] Dhal, P.R., Datta, S. and Mahapatra, S.S. (2011). Flexible manufacturing system selection based on grey relation under uncertainty. *International Journal of Services and Operations Management*, 8(4):516–534.

[20] Feili, H.R., Akar, N., Lotfizadeh, H., Bairampour, M. and Nasiri, S. (2013). Risk analysis of geothermal power plants using failure modes and effects analysis (FMEA) technique. *Energy Conversion and Management*, 72:69–76.

[21] Kumru, M. and Kumru, P. Y. (2013). Fuzzy FMEA application to improve purchasing process in a public hospital. *Applied soft computing*, 13(1):721-733.

[22] Silva, M.M., de Gusmão, A.P.H., Poleto, T., Silva., L.C. and Costa, A.P.C.S (2014). A multidimensional approach to information security risk management using FMEA and fuzzy theory. *International Journal of Information Management*, 34(6):733-740.

[23] Shankar, R., Choudhary, D. and Jharkharia, S. (2018). An integrated risk assessment model: A case of sustainable freight transportation systems. *Transportation Research Part D: Transport and Environment*, 63:662-676.

[24] Panchal, D. and Srivastava, P. (2019). Qualitative analysis of CNG dispersing system using fuzzy FMEA-GRA integrated approach. *International Journal of System assurance Engineering*

and Management, 10:44-56.

[25] Yaşbayır, M. and Aydemir, E. (2022). An improved grey failure mode and effect analysis for a steel-door industry. *Arabian Journal for Science and Engineering*, :1-15.

[26] Wei, D., Wang, Q., Gao, J., Shi, Y. and Chen, Q. (2022, February). Aviation safety risk assessment based on fuzzy cognitive map and grey relational analysis. *In Sixth 'International Conference on Electromechanical Control Technology and Transportation (ICECTT 2021),* 12081:890-895. SPIE.

[27] Sur, J. M. and Kim, Y. J. (2024). Multi criteria model for identifying and ranking risky types of maritime accidents using integrated ordinal priority approach and grey relational analysis approach. *Sustainability*, 16(14):6023.

[28] Soltani, E., Ahmadi, O. and Rashnoudi, P. (2024). A decision-making model for blasting risk assessment in mines using FBWM and GRA methods. *Scientific Reports*, 14(1):30997.

[29] Tanaka, K. and Werners, B. An introduction to fuzzy logic for practical applications, New York: Springer, pp. I-VI, 1997.

[30] Panchal, D. and Kumar, D. (2016). Stochastic behaviour analysis of power generating unit in thermal power plant using fuzzy methodology. *Opsearch*, 53:16-40.

[31] Dalkey, N. and Helmer, O. (1963). An experimental application of the Delphi method to the use of experts. *Management science*, 9(3):458-467.

[32] Hsu, C. C. and Sandford, B. A. (2007). The Delphi technique: making sense of consensus. *Practical assessment, research, and evaluation*, 12(1).

[33] Deng, J. (1986). The application of grey system to quantitative investment strategy. *Journal of Investment Reform*, 3:21–25.

[34] Chang, C.L. and Wei, C.C. and Lee, Y.H. (1999). Failure mode and effects analysis using fuzzy method and grey theory. *Kybernetes*, 28(9):1072–1080.

[35] Chen, C.B. and Klien, C.M. (1997). A simple approach to ranking a group of aggregated fuzzy utilities. *IEEE Transactions on Systems Man and Cybernetics*, Part B, 27(1):26–31.

[36] Wang, L., Chu, J. and Wu, J. (2007). Selection of optimum maintenance strategies based on a fuzzy analytic hierarchy process. *International Journal of Production Economics*, 107(1):151–63.

[37] Chang, D. (1996). Applications of the extent analysis method on fuzzy AHP. *European Journal of Operational Research*, 95:649-655.

RT&A, No 4 (89)
Volume 20, December 2025

BAYESIAN SINGLE SAMPLING PLANS WITH ZERO-INFLATED BINOMIAL DISTRIBUTION USING COST OPTIMIZATION

Sangeetha S[1], Shalini K* and Hemalatha R[2]

•

Department of Statistics, Salem Sowdeswari College, Salem – 636 010, Tamil Nadu, India
[1] ssangeethaswamydhas@gmail.com, * shalini.stat@gmail.com and [2] hemasenthilstat@gmail.com
Correspondence Email: shalini.stat@gmail.com

Abstract

The economic design of sampling plans involves determining an optimal plan that minimizes the total cost associated with inspection while ensuring acceptable product quality levels. Bayesian sampling plans are better suited for handling significant between-lot variations in quality, leading to more informed acceptance decisions due to their capability to incorporate prior information. The objective of this article is to design Bayesian single sampling plans considering a Beta prior and a Zero-inflated Binomial (ZIB) distribution, using cost optimization principles by developing an economic model aimed at achieving optimal total costs, considering the Average Total Inspection (ATI). A numerical illustration is provided to demonstrate the selection of Bayesian single sampling plans under the ZIB distribution that minimizes the producer's total cost.

Keywords: Bayesian Single sampling plan, Zero-inflated Binomial distribution, Cost optimization; Average Total Inspection; Average Outgoing Quality

I. Introduction

A sampling plan is a structured statistical approach used to determine whether a batch of products satisfies predefined quality standards without the need for complete inspection. It minimizes the cost and effort of checking every single item by relying on representative samples that reflect the overall quality of the lot. An economic sampling plan is designed to balance the cost of inspection with the potential losses caused by nonconforming products being accepted into the system. It takes into account several factors such as inspection expenses, the cost of nonconformities, production rate, and acceptable risks for both producers and consumers.

A single sampling plan by attributes requires only one sample to be selected and inspected from a given lot of products. By limiting inspection to a single sample, it helps industries to lower manufacturing costs while still maintaining effective quality control. Hsu and Hsu [8] explored optimized single acceptance sampling plans in the context of a two-stage supply chain. Their study focused on achieving economic efficiency by balancing sampling, inspection, and quality failure costs. Similarly, Wimonmas and Pramote [19] used genetic algorithm-based optimization to design double acceptance sampling plans, aiming to reduce sample size while keeping risk at acceptable levels.

Advances in technology have greatly improved manufacturing processes as well as the quality of finished products. Continuous monitoring during production helps lower the number of nonconforming units, leading to products that are often free from non-conformities. As a result, zero-nonconforming units occur more frequently, making the Zero-inflated Binomial (ZIB) distribution well-suited for modeling such data with excess zeros. This distribution provides a valuable tool for making informed decisions to enhance product quality and minimize nonconforming units.

Hall [7] provided a detailed study of Lambert's Zero-inflated Poisson (ZIP) regression model and later proposed the Zero-inflated Binomial (ZIB) regression model. The ZIB distribution has been widely applied in diverse domains such as medical studies, public health, process monitoring, horticulture, dental research, and industrial manufacturing. Notable contributions using this distribution can be seen in the works of Noorossana et al. [11], Pourhoseingholi et al. [12], Bodromurti et al. [3], Benyue et al. [2], Southwell et al. [16], and Condini et al. [5]. In addition, several researchers, including Noorossana et al. [11], Yawsaeng and Mayureesawan [20], Rakitzis et al. [14], and Alevizakos and Koukouvinos [1] have studied different types of control charts using ZIB distribution.

Conventional sampling plan theory assumes a fixed proportion of nonconforming units in each lot, suggesting that the production process is stable. In practice, however, lots of product produced often display quality variations due to random fluctuations. Such variations are generally classified as within-lot or between-lot variations. When between-lot variation is greater than within-lot variation, the proportion of nonconforming units can fluctuate considerably. Under these circumstances, lot acceptance decisions must account for between-lot variation, making standard sampling approaches less effective. Bayesian sampling plans offer a better alternative by incorporating prior knowledge of process variation into the decision-making framework. The choice of prior distributions for the fraction of nonconforming items in a lot has been investigated by Calvin [4] and Hald [6]. Further studies include Vijayaraghavan et al. [18], who developed Bayesian SSPs using the gamma-Poisson distribution, and Rajagopal et al. [13], who applied the beta-binomial distribution for SSPs by attributes. Additionally, Kaviyarasu and Sivakumar ([9], [10]) proposed Bayesian SSPs under the gamma-ZIP distribution.

When the count data of nonconforming items shows an excess of zeros, the Zero-inflated Binomial (ZIB) distribution offers a more suitable basis for designing sampling plans. The objective of this study is to construct Bayesian Single Sampling Plans (BSSPs) by attributes, applying the ZIB distribution in combination with the Beta distribution as the prior. There is no research has specifically addressed the development of sampling plans using the ZIB distribution. This study contributes to the literature by proposing attribute-based Bayesian single sampling plans (BSSPs) derived from the ZIB distribution under cost optimization. The Bayesian Single Sampling Plan under ZIB distribution is discussed in Section 2. Section 3 presents the formulation of the optimal economic sampling plan. Section 4 provides a sensitivity analysis of the parameters. Section 5 concludes with a summary of the key findings.

II. Bayesian Single sampling plan under ZIB distribution

A single sampling plan (SSP) is a method used to determine the acceptance or rejection of a lot based on the evaluation of one sample. In an attribute-based SSP, three key parameters are specified: N, the total lot size; n, the number of items drawn for inspection; and c, the acceptance number, representing the maximum count of nonconforming units permitted in the sample.

The procedure for applying an attribute-based SSP can be outlined as follows (Stephens [17]):

Step 1: Randomly draw a sample of size n from the lot of size N.

Step 2: Examine each selected item according to the defined quality standards.

Step 3: Record the number of nonconforming units, denoted by x.

Step 4: Accept the lot if $x \leq c$; otherwise, reject it.

Let the random variable X denote the number of nonconforming units in a sample of size n, where $\bar{p}$ represents the average fraction of nonconforming units in a lot of size N. In cases where nonconforming occur mainly as excess zeros, the Zero-inflated Binomial (ZIB) distribution offers a more accurate model. This distribution is especially effective when the number of zeros observed is considerably higher than what would be expected under a standard binomial model. The probability mass function of the ZIB distribution was introduced by Hall [7] and is given as follows.

$$P(X = x|\varphi, n, p) = \begin{cases} \varphi + (1-\varphi)\,(1-p)^n & , \quad \text{when } x = 0 \\ (1-\varphi)\binom{n}{x} p^x\,(1-p)^{n-x}, & \text{when } x = 1,2,\dots,n \end{cases} \tag{1}$$

The key assumption of a stable production process, required for applying the binomial distribution in sampling analysis, does not always hold in real-world scenarios. In such cases, the process average $\bar{p}$ may fluctuate and is better represented as a random variable, denoted by $\bar{P}$. To capture this variation, appropriate probability models must be constructed using historical process data. Since the beta distribution serves as the natural conjugate prior for a Bernoulli population, it is assumed that $\bar{P}$ follows a beta distribution. The probability density function of the beta prior for $\bar{P}$ is expressed as:

$$f_{\bar{P}|\{(s,t)\}}(\bar{p}) = \frac{\Gamma(s+t)}{\Gamma(s)\,\Gamma(t)}(\bar{p})^{s-1}(1-\bar{p})^{t-1}, \quad 0 \leq \bar{p} \leq 1\ ;\ s,t > 0 \tag{2}$$

The probability mass function of the Beta ZIB distribution is derived as follows:

$$P(X = x|\varphi, n, s, t\,) = \begin{cases} \varphi + (1-\varphi)\,\frac{(s+t-1)!(n+t-1)!}{(t-1)!(s+n+t-1)!} & , \quad \text{when } x = 0 \\ (1-\varphi)\binom{n}{x}\,\frac{(s+t-1)!(s+x-1)!(n+t-x-1)!}{(s-1)!(t-1)!(s+n+t-1)!}, & \text{when } x = 1,2,\dots,n \end{cases} \tag{3}$$

where $t = \frac{s(1-p)}{p}$

The OC function of Beta ZIB SSP is given by,

$$P_a(p) = \sum_{x=0}^{c} P(X = x|\varphi, n, s, t\,) \tag{4}$$

According to Stephens [17], the performance of an SSP can be evaluated using specific metrics. In this context, ATI refers to the Average Total Inspection, while AOQ represents the Average Outgoing Quality.

$$ATI = n + \big(1 - P_a(p)\big)(N-n) \tag{5}$$

$$AOQ = \frac{pP_a(p)(N-n)}{N} \tag{6}$$

Let D_d and D_n be the nonconforming items detected and not detected respectively, (Hsu and Hsu [8]), then

$$D_d = np + \big(1 - P_a(p)\big)(N-n)p \tag{7}$$

$$D_n = pP_a(p)(N-n) \tag{8}$$

III. Designing of optimum economic sampling plan

An economic model is formulated by optimizing the sampling plan to reduce overall quality costs for both producers and consumers, while satisfying their respective quality and risk constraints. The sampling plan is determined using the mathematical model proposed by Hsu and Hsu [8], which is expressed as follows:

$$Minimize \quad TC = C_i \,.\, ATI + C_f \,.\, D_d + C_o \,.\, D_n \tag{9}$$

$$\text{subject to } 1 - P_a(AQL) \leq \alpha \tag{10}$$

$$P_a(LTPD) \leq \beta \tag{11}$$

In this model, C_i, C_f, and C_o correspond to the inspection cost per item, the cost due to internal failure for a nonconforming unit, and the cost of nonconforming units reaching the consumer.

The following input parameters should be considered: N= 1000, φ = 0.01, AQL = 0.01, p = 0.03, α = 0.05, β = 0.10, C_i = 1, C_f = 2 and C_o= 10, the optimum Beta ZIB SSPs for various values of LTPD are obtained using R software and presented in Table 1.

Table 1: *Optimum Beta ZIB SSPs satisfying AQL = 0.01, p = 0.03, α = 0.05, β = 0.10, φ = 0.01, s = 50, C_i = 1, C_f = 2 and C_o= 10*

LTPD	TC	*n*	*c*	AOQ	ATI
0.10	418.43	123	7	0.0253	155.83
0.15	358.59	64	5	0.0277	77.10
0.20	337.13	41	4	0.0285	48.85
0.25	326.38	32	4	0.0290	34.71
0.30	319.79	22	3	0.0292	26.03

I. Illustration

For the set of input parameters N = 1000, φ = 0.01, AQL = 0.01, LTPD = 0.30, p = 0.03, α = 0.05, β = 0.10, C_i = 1, C_f = 2 and C_o=10, the optimal Beta ZIB SSP is n = 22 and c = 3, with a total cost (TC) of 319.79.

IV. Sensitivity analysis of parameters

Table 2 shows that as s increases from 10 to 50, total cost decreases while n and c fluctuate slightly. This means larger s values yield more cost-efficient sampling plans without notably affecting AOQ or ATI, highlighting the benefit of optimizing s.

Table 2: *Optimum Beta ZIB SSPs for AQL=0.01, LTPD = 0.07, p = 0.03, φ = 0.01, α = 0.05, β = 0.10, C_i = 1, C_f = 2 and C_o= 10*

s	TC	*n*	*c*	AOQ	ATI
10	650.98	211	7	0.0161	461.82
20	582.54	210	8	0.0188	371.77
30	558.11	202	8	0.0198	339.62
40	545.22	217	9	0.0203	322.65
50	536.75	214	9	0.0207	311.52

Table 3 shows that as φ increases from 0.01 to 0.09, both sample size and total cost rise, AOQ decreases, and ATI increases. Thus, higher φ improves outgoing quality but at the expense of greater inspection cost.

Table 3: *Optimum Beta ZIB SSPs for AQL = 0.01, LTPD = 0.07, p = 0.03, α = 0.05, β = 0.10, s = 50, C_i = 1, C_f = 2 and C_o = 10*

φ	TC	n	c	AOQ	ATI
0.01	536.75	214	9	0.0207	311.52
0.03	555.02	223	9	0.0199	335.55
0.05	576.99	253	10	0.0191	364.46
0.07	613.28	271	10	0.0176	412.21
0.09	690.10	330	11	0.0146	513.29

Table 4 shows that as p rises from 0.01 to 0.11, total cost and ATI increase, reflecting higher inspection effort and cost. Sample size first grows then drops with a reduced c, while AOQ decreases, indicating improved outgoing quality but at greater expense.

Table 4: *Optimum Beta ZIB SSPs for AQL=0.01, LTPD = 0.07, α = 0.05, β = 0.10, φ = 0.01, s = 50, C_i = 1, C_f = 2 and C_o= 10*

p	TC	n	c	AOQ	ATI
0.01	208.04	100	3	0.0088	117.44
0.03	536.75	214	9	0.0207	311.52
0.05	909.67	269	12	0.0159	682.78
0.07	1099.82	79	2	0.0064	908.68
0.09	1169.84	79	2	0.0033	963.71
0.11	1217.89	79	2	0.0019	982.42

Table 5: *Optimum Beta ZIB SSPs for AQL= 0.01, LTPD = 0.07, p = 0.03, α = 0.05, β = 0.10, φ = 0.01, s = 50, C_f = 2 and C_o= 10*

C_i	TC	n	c	AOQ	ATI
0.2	260.00	1000	16	0.0000	1000.00
0.4	349.84	214	9	0.0207	311.52
0.6	412.15	214	9	0.0207	311.52
0.8	474.45	214	9	0.0207	311.52
1.0	536.75	214	9	0.0207	311.52

Table 5 demonstrates the effect of varying C_i on the optimum Beta ZIB SSP. At a very low C_i = 0.2, the plan recommends inspecting all items (n = 1000), achieving zero outgoing nonconforming units but at maximum inspection effort. As C_i increases from 0.4 to 1.0, the plan stabilizes at n = 214 and c = 9, with constant AOQ and ATI, while the total cost rises steadily.

Tables 6 and 7 show the effect of varying C_f with C_i = 1.0 and C_i = 0.2, respectively. In Table 6, changes in C_f only increase the total cost without affecting the sampling plan. In Table 7, when C_i is low (0.2), the internal failure cost (C_f) influences the plan, shifting from full inspection at low C_f to partial sampling at higher C_f.

Table 6: *Optimum Beta ZIB SSPs for AQL=0.01, LTPD = 0.07, p= 0.03, α = 0.05, β = 0.10, φ = 0.01, s = 50, C_i = 1 and C_o= 10*

C_f	TC	n	c	AOQ	ATI
0	518.06	214	9	0.0207	311.52
1	527.41	214	9	0.0207	311.52
2	536.75	214	9	0.0207	311.52
3	546.10	214	9	0.0207	311.52
4	555.44	214	9	0.0207	311.52
5	564.79	214	9	0.0207	311.52

Table 7: *Optimum Beta ZIB SSPs satisfying AQL=0.01, LTPD = 0.07, p= 0.03, α = 0.05, β = 0.10, φ = 0.01, s = 50, C_i = 0.2 and C_o= 10*

C_f	TC	*n*	*c*	AOQ	ATI
0	200.00	1000	16	0.0000	1000.00
2	260.00	1000	16	0.0000	1000.00
4	306.23	214	9	0.0207	311.52
6	324.92	214	9	0.0207	311.52
8	343.61	214	9	0.0207	311.52
10	362.30	214	9	0.0207	311.52

Table 8: *Optimum Beta ZIB SSPs satisfying AQL=0.01, LTPD = 0.07, p= 0.03, α = 0.05, β = 0.10, φ = 0.01, s = 50, C_i = 1 and C_f= 2*

C_o	TC	*n*	*c*	AOQ	ATI
10	536.75	214	9	0.0207	311.52
20	743.30	214	9	0.0207	311.52
30	949.84	214	9	0.0207	311.52
40	1060.00	1000	16	0.0000	1000.00
50	1060.00	1000	16	0.0000	1000.00

Table 8 shows that for C_o values 10–30, plan parameters stay constant while total cost rises. At $C_o \geq 40$, the plan shifts to full inspection, sharply increasing effort to prevent nonconforming units from reaching customers.

V. Conclusion

This paper presents a mathematical model to determine Bayesian Single Sampling Plans (BSSPs) under the Beta ZIB distribution, providing a systematic framework for both producers and consumers. The approach reduces total costs while simultaneously satisfying risk and quality requirements for both producer and consumer. Numerical illustration is presented to demonstrate the selection of Beta ZIB SSPs that minimize the producer's overall cost. The results indicate that the optimum plan is highly dependent on the quality level of the producer's output. Additionally, inspection costs, internal failure costs, and external failure costs are shown to significantly affect the structure of the economic sampling plan. By applying such optimized Bayesian plans, organizations can achieve better cost efficiency, improved allocation of resources, and more reliable quality control. Ultimately, this method strengthens decision-making processes and contributes to higher quality standards and customer satisfaction.

References

[1] Alevizakos, V. and Koukouvinos, C. (2020). Monitoring of zero-inflated binomial processes with a dewma control chart. *Journal of Applied Statistics,* 48 (7): 1319 – 1338.

[2] Benyue, S., Pengpeng, X. and Min, S. (2020). Generalised zero inflated binomial distribution model aimed at air quality data analysis. *Journal of System Simulation,* 32 (11): 2226 – 2234.

[3] Bodromurti, W., Notodiputro, K. A. and Kurnia, A. (2018). Zero inflated binomial model for infant mortality data in Indonesia. *International Journal of Applied Engineering Research*, 13(6): 3139 – 3143.

[4] Calvin T. W. How and When to Perform Bayesian Acceptance Sampling, American Society for Quality Control, Wisconsin, 1990.

[5] Condini, M. V., Oliveira, R. L., Almeida, L. L., Barbosa, E. F., Martins, A. C., Bertoncini, A.

A. and Hostim-Silva, M. (2024). Physicochemical variables influencing the abundance of Atlantic Goliath Grouper Juveniles (Epinephelus Itajara) in a tropical Brazilian mangrove habitat. *Marine Environmental Research*, 197: 1 – 11.

[6] Hald, A. Statistical Theory of Sampling Inspection by Attributes, Academic Press, New York, 1981.

[7] Hall, D. B. (2000). Zero-inflated Poisson and binomial regression with random effects: A case study. *Biometrics,* 56: 1030 – 1039.

[8] Hsu, L.F. and Hsu, J.T. (2012). Economic design of acceptance sampling plans in a two-stage supply chain, *Advances in Decision Sciences*, Vol. 2012, pp. 1-14.

[9] Kaviyarasu, V. and Sivakumar, P. (2019). The implication of production and monitoring techniques in Bayesian single sampling plan using gamma-zero inflated Poisson distribution. *International Journal of Recent Technology and Engineering*. 8(4): 10110 – 10119.

[10] Kaviyarasu, V. and Sivakumar, P. (2021). Optimization of bayesian single sampling plan for the zero inflated poisson distribution involving risk minimization using tangent angle method. *International Journal of Scientific Research in Mathematical and Statistical Sciences*, 8(3): 1 – 11.

[11] Noorossana, R., Fatahi, A. A., Dokouhaki, P. and Babakhani, M. (2011). ZIB–EWMA Control chart for monitoring rare health events. *Journal of Mechanics in Medicine and Biology,* 11 (4): 881 – 895.

[12] Pourhoseingholi, A., Alireza, A. B., Ahmad, R. B., Erfan, G. and Seyed, M. R. (2018). Zero-inflated binomial model for prognosis of the risk factor associated with dmft index in children aged 5-6 years in Tehran. *Iranian Journal of Pediatrics,* 28 (3): 1 – 7.

[13] Rajagopal, K., Loganathan A. and Vijayaraghavan, R., (2009). Selection of bayesian single sampling attributes plans based on polya distribution. *Economic Quality Control,* 24 (2): 179 – 193.

[14] Rakitzis, A. C., Maravelakis, P. E. and Castagliola, P. (2016). CUSUM control charts for the monitoring of zero-inflated binomial processes. *Quality and Reliability Engineering International*, 32: 465 – 483.

[15] Schilling, E. G. and Neubauer, D. V. Acceptance Sampling in Quality Control, CRC Press, Boca Raton, 2009.

[16] Southwell, D. M., Smart, A., Merson, S. D., Selwood, K. E. and Macgregor, N. A. (2024). Using power analysis and spatial prioritization to evaluate the design of a forest bird monitoring programme. *Oryx*, 58(4): 522 – 531.

[17] Stephens, K. S. The Handbook of Applied Acceptance Sampling Plans, Procedures and Principles, ASQ Quality Press, Wisconsin, 2001.

[18] Vijayaraghavan, R., Rajagopal, K. and Loganathan, A. (2008). A procedure for selection of a gamma- poisson single sampling plan by attributes. *Journal of Applied Statistics,* 35 (2): 149 – 160.

[19] Wimonmas, B. and Pramote, C. (2021). Designing of double acceptance sampling plan for zeroinflated and over-dispersed data using multi-objective optimization, *Applied Science and Engineering Progress*, Vol. 14, No. 3, pp. 338-347.

[20] Yawsaeng, B. and Mayureesawan, T. (2012). Control charts for zero-inflated binomial models. *Thailand Statistician*, 10 (1): 107 – 120.

MODELING STRENGTH OF THE AIRCRAFT WINDOW GLASS BY TRUNCATED SHAMBHU DISTRIBUTION

Dhanashri Patil, Manjushri Chikkalli, Shruti Hipale, Chandrakant Gardi[1]

•

Department of Statistics
Punyashlok Ahilyadevi Holkar Solapur University,
Solapur (MS)-413255, India.
drpatil9942@gmail.com, manjuchikkalli23@gmail.com, shrutihipale43@gmail.com,
chandrakant.gardi@gmail.com
[1]corresponding author

Abstract

Failure of regular distributions to appropriately model the real life scenarios demands the new distributions, which will be more useful. Truncated distributions are found to model many real datasets more precisely than corresponding regular distribution. In this paper, a novel truncated Shambhu distribution (TS) is proposed to model the data, which is naturally constrained by physical, financial, or environmental factors. Some statistical properties including moments, survival and hazard functions, are discussed. For better understanding of the proposed distribution, plots of the distribution are provided. Estimation of parameters is discussed using the maximum likelihood estimation method. Finally, an application based on real data is considered to illustrate the practical relevance of the proposed distribution.

Keywords: Lifetime distributions, survival function, hazard function, lifetime data

I. Introduction

Traditional statistical distributions often fail to capture the intricate patterns found in modern datasets, which may exhibit skewness, heavy tails, or multimodal behaviour. The proliferation of lifetime distributions arises from the fact that each is constructed under specific assumptions, and even minor modifications to these assumptions can result in the formulation of a distinct distribution. Distributions such as the exponential and Weibull have been commonly employed for modeling lifetime data across various applied fields. Researchers have attempted to introduce new distributions to model modern datasets. Gupta and Kundu [1] have generalised the exponential distribution for more flexibility. Similar attempts have been made on Weibull distribution, of which exponential distribution is considered a particular case. Sarhan and Zaindin [2] have introduced three parameter modified Weibull distribution for extra feasibility in modeling real life datasets. Use of MWD in various approaches for analysing survival datasets is increasing because of its versatility. Sutar et al.[3] analyzed the accelerated failure time based two component parallel load sharing system with component lifetimes following modified Weibull distribution. Sutar [4] developed Monte Carlo Expectation Maximization algorithm for parameter estimation of modified Weibull distribution. Shanker [5] proposed a new lifetime distribution named Shreekant distribution which gives improved fits to certain lifetime datasets than those by other existing ones. For better modeling of

over-dispersed biological count data, Shanker et al. [6] introduced Poisson-Suja distribution as a Poisson mixture of Suja distribution. Attempts have also been made to generalise the existing distributions for enhancing practical applications. Prodhani and Shanker [7] generalised Sujatha distribution, proposed by Nwikpe and Iwoke [8]. Shanker [9] proposed Shanker distribution, which gives better fit than exponential and Lindley distribution for modeling certain real lifetime data-sets. In recent years, numerous lifetime distributions - such as the Akash (Shanker [10]), Aradhana (Shanker [11]), Sujatha (Shanker [12]), Rani (Shanker [13]) - have been proposed in the statistical literature for modeling lifetime data.

There are certain limitations for traditional distributions, which may not fit well for highly skewed, heavy tailed, multimodal datasets. The Shambhu Distribution, proposed, by Shanker [14], addresses few of these limitations by offering a versatile framework capable of accurately representing a wide range of data behaviours. This distribution provides a robust alternative for modelling lifetime and survival data where precision and adaptability are crucial.

The Shambhu distribution is a relatively lesser-known but interesting continuous probability distribution, particularly studied in the field of statistics and reliability analysis. The Shambhu distribution was introduced by Shanker [14] as a one-parameter family of distributions for modeling real life data-sets from biomedical science and engineering. The Shambhu distribution is a mixture of six distributions, viz.- exponential (θ), gamma$(2,\theta)$, gamma$(3,\theta)$, gamma$(4,\theta)$, gamma$(5,\theta)$, gamma$(6,\theta)$with mixing proportions respectively as-

$$\frac{\theta^5}{\theta^5+\theta^4+2\theta^3+6\theta^2+24\theta+120}, \quad \frac{\theta^4}{\theta^5+\theta^4+2\theta^3+6\theta^2+24\theta+120},$$
$$\frac{2\theta^3}{\theta^5+\theta^4+2\theta^3+6\theta^2+24\theta+120}, \frac{6\theta^2}{\theta^5+\theta^4+2\theta^3+6\theta^2+24\theta+120},$$
$$\frac{24\theta}{\theta^5+\theta^4+2\theta^3+6\theta^2+24\theta+120}, \frac{120}{\theta^5+\theta^4+2\theta^3+6\theta^2+24\theta+120}$$

The probability density function (p.d.f.) and the cumulative distribution function (c.d.f.) of Shambhu distribution introduced by Shanker [14] are given by-

$$f(x,\theta)=\frac{\theta^6}{\theta^5+\theta^4+2\theta^3+6\theta^2+24\theta+120}(1+x+x^2+x^3+x^4+x^5)e^{-\theta x}; x>0, \theta>0 \quad (1)$$

$$F(x,\theta)=1-\left[1+\frac{\theta^5(x^5+x^4+x^3+x^2+x)+\theta^4(5x^4+4x^3+3x^2+2x)+2\theta^3(10x^3+6x^2+3x)+12\theta^2(5x^2+2x)+120\theta x}{\theta^5+\theta^4+2\theta^3+6\theta^2+24\theta+120}\right]e^{-\theta x}; x>0, \theta>0 \quad (2)$$

Prabavathi and Elangovan [15] have recently generalised the Shambhu distribution by proposing its length biased version. Most of the times, the lifetime data is constrained between two values because of certain reasons. Using the regular lifetime distribution to model such a data may not produce favourable reasons. Therefore it is a practical need to use truncated versions of lifetime distributions in such cases. This paper attempts to define truncated Shambhu distribution, for increasing the applicability of Shambhu distribution. The rest of the paper is organised as follows. Section 2 proposes the new truncated Shambhu distribution. In section 3, the statistical properties of the truncated Shambhu distribution are studied. Application of the proposed distribution to a real life dataset is discussed in section 4. Section 5 summarises the conclusions.

II. Truncated Shambhu (TS) Distribution

The development of new truncated distributions is motivated by the need to model real-world data more accurately when observations are subject to limitations or constraints. In many practical situations, data may be constrained due to truncation—either from the left, right, or both ends—resulting in the exclusion of values that fall outside a certain range. Traditional distributions may fail to adequately capture the underlying behavior of such datasets, leading to biased parameter estimates and incorrect inferences. By defining new truncated versions of existing or novel distributions, one

can better accommodate the characteristics of censored or truncated data, enhance model flexibility, and improve the accuracy of statistical inference in diverse fields such as survival analysis, reliability engineering, and economics. With this motivation, an attempt is made in this paper to propose new truncated Shambhu distribution for better modeling of truncated lifetime data. As a general scenario, truncation is considered from both the sides. Let X be the lifetime random variable (r.v.), with truncation limits as a and b, $0 < a < b < \infty$, i.e. $a < X < b$. The r.v. X is said to follow truncated Shambhu (TS) distribution truncated below a and above b, if its density is given as-

$$f_T(x;\theta,a,b) = \frac{(1+x+x^2+x^3+x^4+x^5)e^{-\theta x}}{\sum_{k=0}^{5}\frac{\gamma(k+1,a\theta)-\gamma(k+1,b\theta}{\theta^{k+1}}}; a < x < b, \theta > 0 \quad (3)$$

The distribution function (cdf) of truncated Shambhu distribution is given as follows.

$$F_T(x;\theta,a,b) = \frac{\sum_{k=0}^{5}\frac{\gamma(k+1,a\theta)-\gamma(k+1,x\theta}{\theta^{k+1}}}{\sum_{k=0}^{5}\frac{\gamma(k+1,a\theta)-\gamma(k+1,b\theta}{\theta^{k+1}}} \; ; \; a < x < b, \theta > 0 \quad (4)$$

It is denoted as $X \sim TS(\theta,a,b)$.

The plots of density for different values of a, b and θ are displayed in the Figure 1, Figure 2 and Figure 3 respectively. Also, the plots of cdf for different values of a, b and θ are displayed in the Figure 4, Figure 5 and Figure 6 respectively.

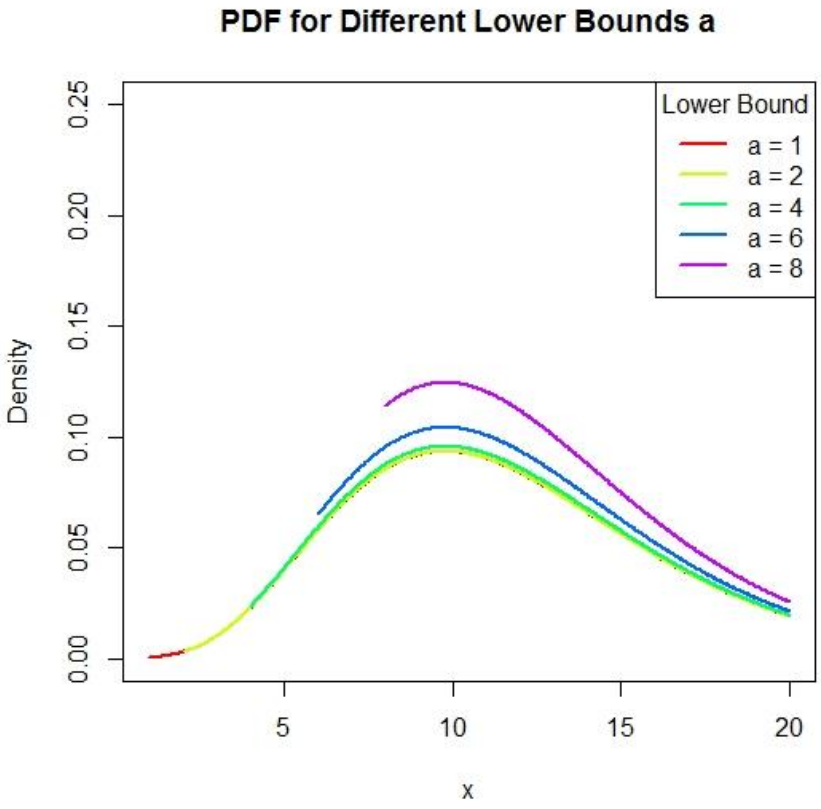


Figure 1: *Density function of TS for different values of a.*

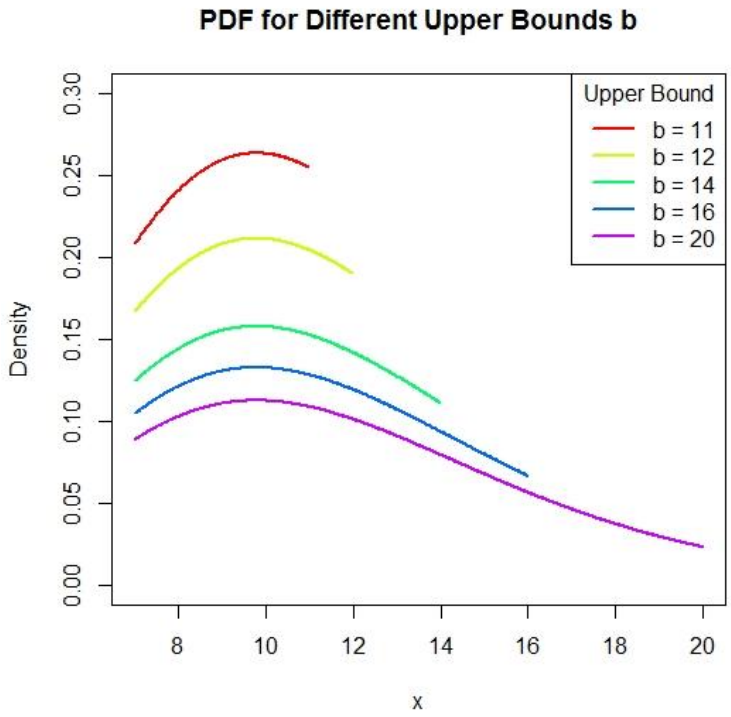


Figure 2: *Density function of TS for different values of b.*

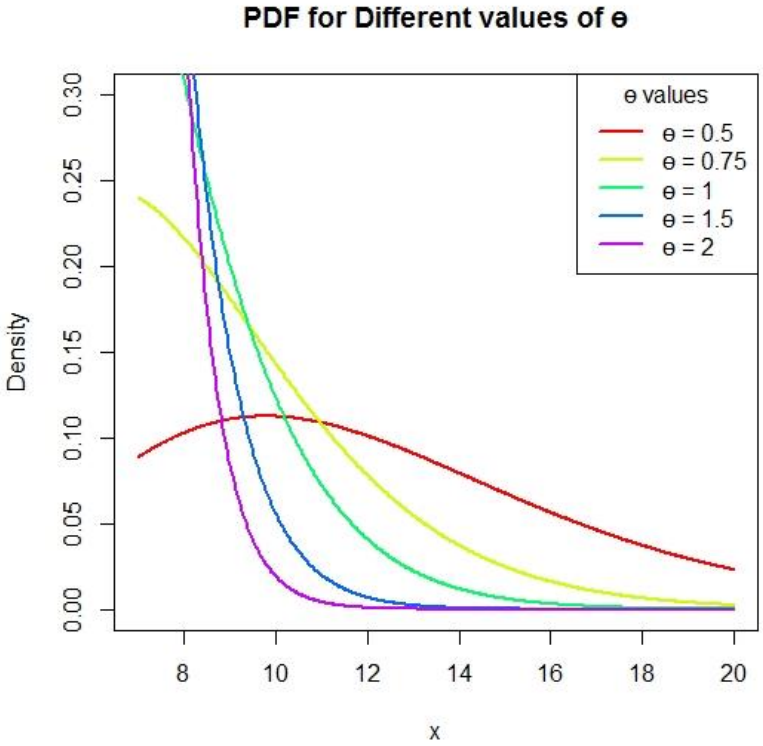


Figure 3: *Density function of TS for different values of θ.*

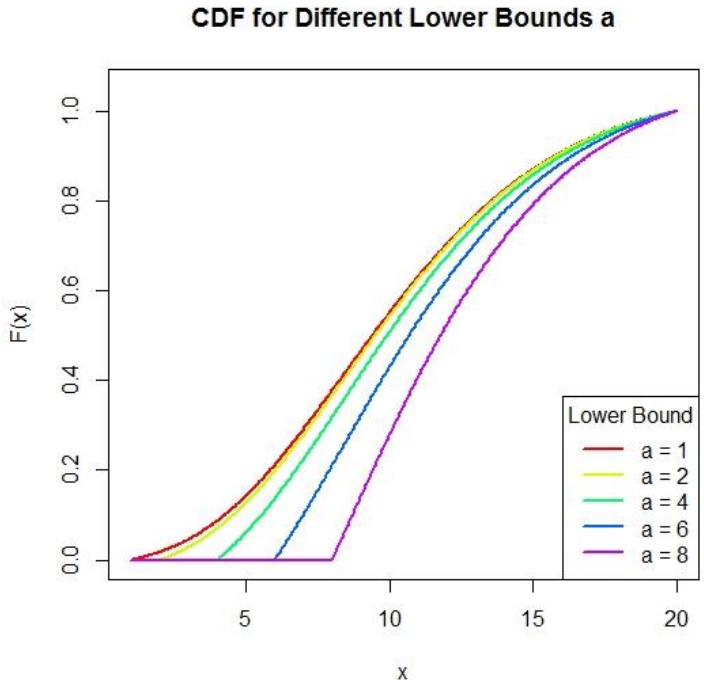


Figure 4: *Distribution function of TS for different values of a.*

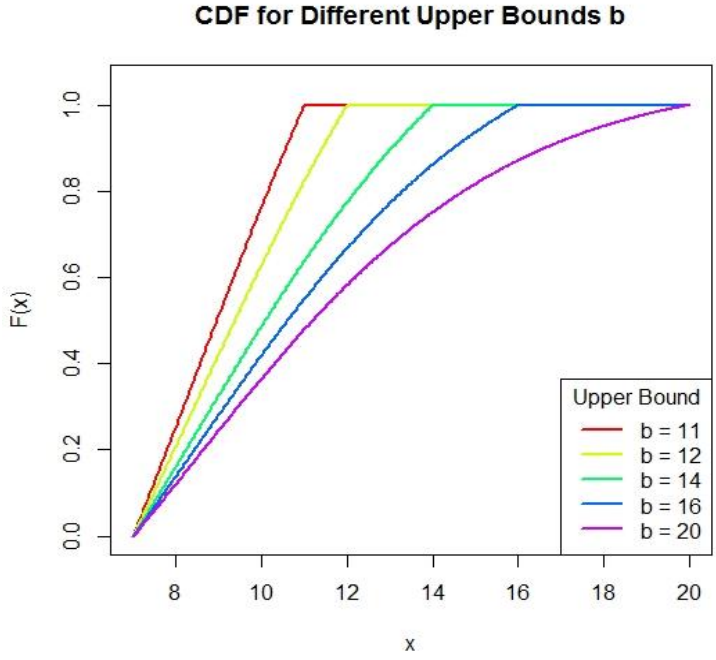


Figure 5: *Distribution function of TS for different values of b.*

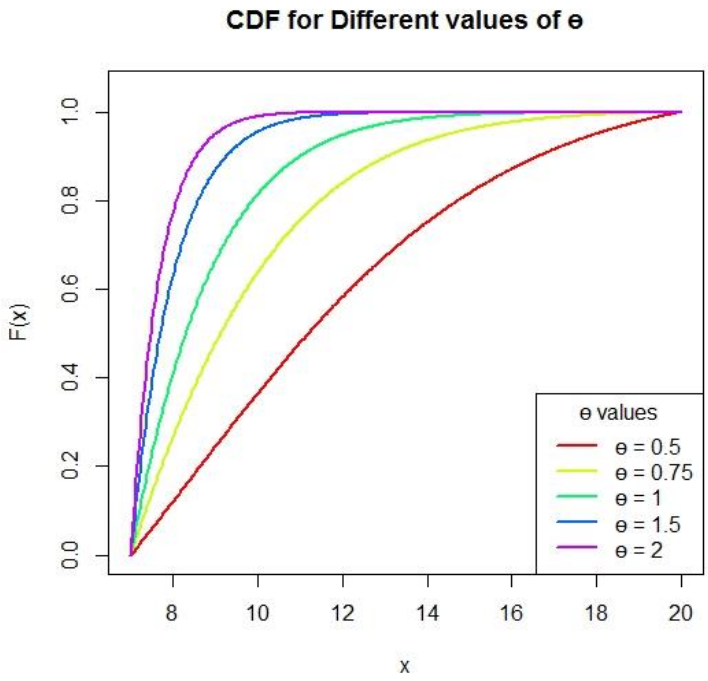


Figure 6: *Distribution function of TS for different values of* θ.

III. Statistical Properties

In this section, various fundamental properties, such as mean, variance, cdf etc. of the proposed truncated Shambhu distribution are studied.

I. **Moments**

The r^{th} moment about origin of truncated Shambhu distribution is

$$\mu_r^{'} = \frac{1}{\sum_{k=0}^{5} \frac{\gamma(k+1,a\theta)-\gamma(k+1,b\theta}{\theta^{k+1}}} \left[\sum_{i=1}^{5} \left\{\left[\frac{-1}{\theta} b^{r+i} e^{-\theta b} + \frac{1}{\theta} a^{r+i} e^{-\theta a}\right] + \frac{r+i}{\theta} \int_a^b x^{r+(i-1)} e^{-\theta x} dx\right\}\right] \quad (5)$$

Where $r = 1,2,3, \ldots$ and $\theta > 0$.

Therefore, mean and variance of this distribution are obtained as –

$$E(X) = \frac{1}{\sum_{k=0}^{5} \frac{\gamma(k+1,a\theta)-\gamma(k+1,b\theta}{\theta^{k+1}}} \left[\sum_{i=1}^{5} \left\{\left[\frac{-1}{\theta} b^{1+i} e^{-\theta b} + \frac{1}{\theta} a^{1+i} e^{-\theta a}\right] + \frac{1+i}{\theta} \int_a^b x^{i} e^{-\theta x} dx\right\}\right] \quad (6)$$

$$V(X) = \frac{1}{\sum_{k=0}^{5} \frac{\gamma(k+1,a\theta)-\gamma(k+1,b\theta}{\theta^{k+1}}} \left[\sum_{i=1}^{5} \left\{\left[\frac{-1}{\theta} b^{2+i} e^{-\theta b} + \frac{1}{\theta} a^{2+i} e^{-\theta a}\right] + \frac{2+i}{\theta} \int_a^b x^{i+1} e^{-\theta x} dx\right\}\right]$$
$$- \left\{\frac{1}{\sum_{k=0}^{5} \frac{\gamma(k+1,a\theta)-\gamma(k+1,b\theta}{\theta^{k+1}}} \left[\sum_{i=1}^{5} \left\{\left[\frac{-1}{\theta} b^{1+i} e^{-\theta b} + \frac{1}{\theta} a^{1+i} e^{-\theta a}\right] + \frac{1+i}{\theta} \int_a^b x^{i} e^{-\theta x} dx\right\}\right] \right\} \quad (7)$$

II. Survival function and hazard rate

The survival function, $S(x)$, is the probability that a subject survives longer than time x. Suppose $X$is a lifetime random variable representing the time until a specified event of interest is occurred, then the survival function of $X$is defined as $S(x) = 1 - F(x)$. From Eq. 4, the survival function of TS distribution is

$$S(x;\theta,a,b) = 1 - \frac{\sum_{k=0}^{5} \frac{\gamma(k+1,a\theta)-\gamma(k+1,x\theta)}{\theta^{k+1}}}{\sum_{k=0}^{5} \frac{\gamma(k+1,a\theta)-\gamma(k+1,b\theta)}{\theta^{k+1}}} \; ; \; a < x < b, \theta > 0 \tag{8}$$

Consequently, the ratio of pdf and survival function, is given by $h(x) = f(x)/S(x)$, which is called the hazard function. From the pdf in Eq.(3) and the survival function in Eq.(8), we have

$$h(x;\theta,a,b) = \frac{(1+x+x^2+x^3+x^4+x^5)e^{-\theta x}}{\sum_{k=0}^{5} \frac{\gamma(k+1,x\theta)-\gamma(k+1,b\theta)}{\theta^{k+1}}} \tag{9}$$

The graphical display of survival function as well as hazard function for different values of θ is given in Figure 7 and Figure 8 respectively.

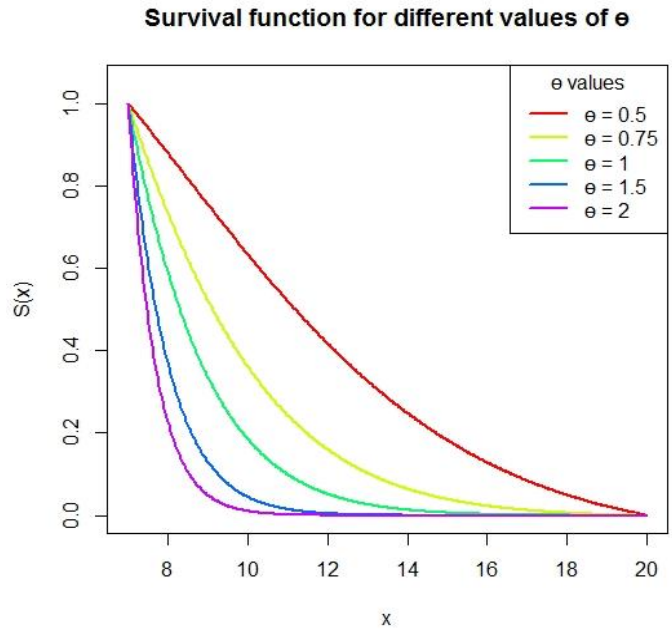


Figure 7: *Survival function of TS for different values of θ.*

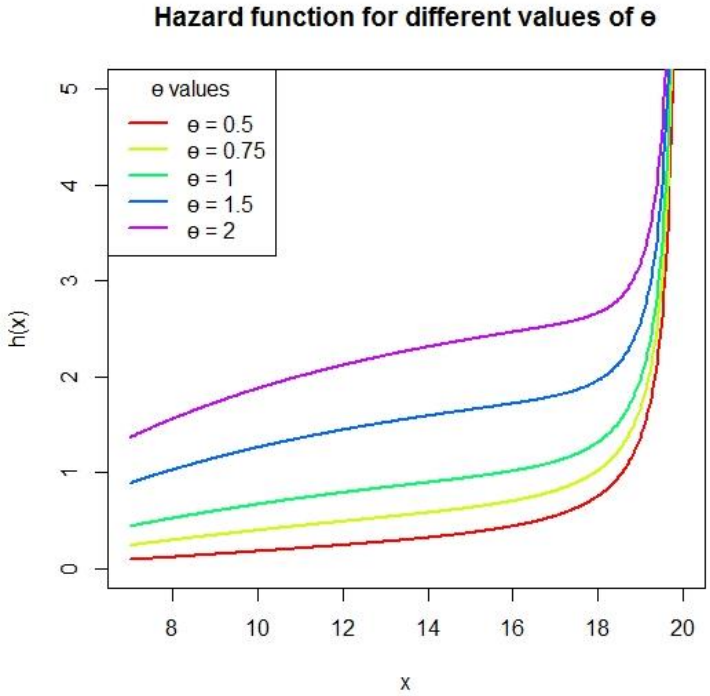


Figure 8: *Hazard function of TS for different values of θ.*

III. Parameter Estimation

Let $X_1, X_2, \dots, X_n$be a random sample sized n from $TS(\theta, a, b)$. Then the likelihood function L of $TS(\theta, a, b)$ is given by

$$L(\theta, a, b/x_1, x_2, \dots, x_n) = \prod_{i=1}^{n} f_{X_i}(x_i) \quad (10)$$

The log likelihood function is-

$$\log L = \sum_{i=1}^{n} \log f(x; \theta, a, b)$$

$$= \sum_{i=1}^{n} \log(1 + x_i + {x_i}^2 + {x_i}^3 + {x_i}^4 + {x_i}^5) - \theta \sum_{i=1}^{n} x_i - \sum_{i=1}^{n} log\left[\sum_{k=0}^{5} \frac{\gamma(k+1, a\theta) - \gamma(k+1, b\theta)}{\theta^{k+1}}\right]$$

$$= -\sum_{i=1}^{n} x_i - n\left\{\frac{1}{\sum_{k=0}^{5} \frac{\gamma(k+1, a\theta) - \gamma(k+1, b\theta)}{\theta^{k+1}}} \sum_{k=0}^{5} \frac{(a^{k+1}\theta^k e^{-a\theta} - b^{k+1}\theta^k e^{-b\theta})\theta^{k+1} - (\gamma(k+1, b\theta))(k+1)\theta^k}{\theta^{2(k+1)}}\right\}$$

As $a < x_i < b, i = 1,2, \dots, n,$ the maximum likelihood (ML) estimators for a and b are $\min\{x_1, x_2, \dots, x_n\}$ and $\max\{x_1, x_2, \dots, x_n\}$ respectively. Then the maximum likelihood estimate for the parameter θ is obtained by solving the equation $\frac{\partial \log L}{\partial \theta} = 0$. As this condition doesn't provide an expression in a closed form, it can be solved using any of the numerical method, such as bisection method, Newton-Raphson method etc.

IV. Application to real life dataset

To demonstrate the applicability of the proposed distribution, a real-life dataset was analyzed. The proposed truncated Shambhu distribution was fitted to this dataset, and its performance was evaluated and compared with other existing lifetime distributions using appropriate goodness-of-fit criteria. The data consists of the strengths of glass of the aircraft window, as reported Fuller et al. [16], which is given in Table 1.

The comparison for goodness of fit among various distributions is made based on different criteria, such as Akaike Information Criterion (AIC), Akaike Information Criterion Corrected (AICC), Bayesian Information Criterion (BIC) and Kolmogorov-Smirnov Statistics (K-S Statistics) which are given respectively as follows:. The formulae for computing the AIC, AICC, BIC, K-S statistics are as follows-

$$AIC = -2\log L + 2k$$
$$AICC = AIC + \frac{2k(k+1)}{n-k-1}$$
$$BIC = -2\log L + k\log(n)$$
$$K - S = sup_x|F_n(x) - F_0(x)|$$

where $\log L$ denotes the log-likelihood function evaluated at the maximum likelihood estimates of the parameters, k is the parameter number of any distributions and n is the sample size, $F_n(x)$ and $F_0(x)$ are the empirical distribution function and the theoretical cumulative distribution of distributions being tested, respectively.

Table 1: *Data on strengths of aircraft window glass.*

Strength of aircraft glass window				
18.83	20.80	21.657	23.03	23.23
24.05	24.321	25.50	25.52	25.80
26.69	26.77	26.78	27.05	27.67
29.90	21.11	33.20	33.73	33.76
33.89	34.76	35.75	35.91	36.98
37.08	37.09	39.58	44.045	45.29
45.381				

Results of the parameter estimation and goodness of fit test are shown in Table 2. For testing the goodness of fit test (minimum of K-S values) in the data set, the observations about strength data of glass of the aircraft window is distributed as close to the TS distribution, with $\hat{\theta} = 0.1801312, \hat{a} = 18.83,$ and $\hat{b} = 45.381$. The fit of TS distribution is more convincing than the other potential distributions such as Shambhu, truncated Ishita, Devya, Amarendra, Sujatha, Aradhana, Akash, Shanker, Lindley, Exponential, which can be seen from AIC and BIC values as given in Table 1.

Table 2: *MLE's, AIC, AICC, BIC and K-S statistics of the fitted distributions of data set*

Model	Parameter estimate	AIC	AICC	BIC	K-S statistic
TS	0.1801312	-84.1398	-84.00187	-82.70581	0.1018544
Shambhu	0.193397	225.40	225.53	226.83	0.167
Truncated Ishita	0.0883	117.9686	_	119.4025	0.1115
Devya	0.160872	229.68	229.82	231.82	0.193
Amrendra	0.128292	235.41	235.55	236.84	0.225
Sujatha	0.095610	243.50	243.64	244.94	0.270
Aradhana	0.094318	244.23	244.37	245.66	0.274
Akash	0.097062	242.68	242.82	244.11	0.266
Shanker	0.064712	254.35	254.49	255.78	0.326
Lindley	0.062988	255.99	256.13	257.42	0.333
Exponential	0.032455	276.53	276.67	277.96	0.426

IV. Conclusions

In this paper, a truncated Shambhu distribution is proposed which is more appealing than the Shambhu distribution, as the data on lifetime variables is better modeled using truncated distribution. The moments, distribution function and survival function for the proposed distribution are obtained. The procedure for parametric inference for this distribution is also discussed. To highlight the practical relevance of the proposed distributional model, a real life application is discussed. For the considered data of strengths of glass of the aircraft window, the truncated Shambhu distribution is the better model than other existing counterparts.

References

[1] Gupta, R. D. and Kundu, D. (2002). Generalized exponential distributions: statistical inferences. *Journal of Statistical Theory and Applications*, 1(1), 101-118.

[2] Sarhan, A. M. and Zaindin, M. (2009). Modified Weibull distribution. *Applied Science*, 11, 123-136.

[3] Sutar, S. S., Gardi, C. G. and Pawar, S. D. (2023). Analyzing load sharing system reliability: a modified Weibull distribution approach. *Reliability: Theory & Applications*, 18 (3 (74)), 708-724.

[4] Sutar, S. S. (2014). Parameter estimation of the modified Weibull distribution using Monte Carlo expectation maximization algorithm. *Model Assisted Statistics and Applications*, 11, 171–178.

[5] Shanker, R. (2025). Shreekant distribution with properties and applications to model stress and strength data from engineering. *Reliability: Theory & Applications*, 20 (2 (84)), 78-95.

[6] Shanker, R., Saharia, J. and Shukla, K. K. (2025). The Poisson-Suja distribution and its applications in biological count data sets. *Reliability: Theory & Applications*, 20 (1 (82)), 1009-1019.

[7] Prodhani, H. R. and Shanker, R. (2025). A generalized power Sujatha distribution with properties and applications. *Reliability: Theory & Applications*, 20 (1 (82)), 373-387.

[8] Nwikpe, B. J. and Iwoke, I. A. (2020). A three -parameter Sujatha distribution with application. *European Journal of Statistics and Probability,* 8(3), 22-34.

[9] Shanker, R. (2015a). Shanker distribution and its applications. *International Journal of Statistics and Applications*, 5(6), 338-348.

[10] Shanker, R. (2015b). Akash distribution and its applications. *International Journal of Probability and Statistics*, 4(3), 65-75.

[11] Shanker, R. (2016a). Aradhana distribution and its applications. *International Journal of Statistics and Applications*, 6(1), 23-34.

[12] Shanker, R. (2016b). Sujatha distribution and its applications. *Statistics in Transition- New Series*, 17(3), 391-410.

[13] Shanker, R. (2017). Rani distribution and its application. *Biometrics & Biostatistics International Journal*, 6(1), 1-10.

[14] Shanker, R. (2016c). Shambhu distribution and its applications. *International Journal of Probability and Statistics*, 5(2), 48-63.

[15] Prabavathi, G. and Elangovan, R. (2022). A new generalization of Shambhu distribution with properties and its applications to real life data. *International Journal of Statistics and Applied Mathematics*, 7(6), 01-09.

[16] Fuller, E.J., Frieman, S., Quinn, J., Quinn, G. and Carter, W. (1994). Fracture mechanics approach to the design of glass aircraft windows: A case study. *SPIE Proc 2286*, 419- 430.

RELIABLE SINGLE DIODE PATCH ANTENNA WITH DUAL MODE FREQUENCY AND PATTERN RECONFIGURABILITY WITH COMPLIANCE ANALYSIS

Sameer Mansuri [1], Shahid S. Modasiya[2]

[1]Research Scholar, Gujarat Technological University, Ahmedabad, Gujarat, India
[2]Associate Professor, EC Engineering, V.G.E.C., Chandkheda, Gujarat, India
sameer.mansuri@gecmodasa.ac.in[1], shahid@vgecg.ac.in[2]

Abstract

This study introduces a compact rectangular patch antenna that achieves frequency reconfiguration using a single PIN diode, enabling two distinct operational modes. The design integrates multiple strategically placed slots within the patch to support a wide range of wireless communication bands. By employing only one diode, the antenna reduces circuit complexity and fabrication cost while ensuring efficient performance. The optimization was carried out through full-wave electromagnetic simulations, with reflection coefficients and radiation patterns serving as primary evaluation metrics. A prototype fabricated on a cost-effective FR4 substrate was tested in an anechoic chamber, showing strong correlation between simulated and measured results, with effective impedance matching. Furthermore, reliability assessments and electromagnetic safety evaluations confirmed compliance with international SAR standards and consistent performance under environmental stress conditions. This work highlights that carefully designed slot integration on FR4 substrates can provide performance levels comparable to those of specialized high-frequency materials, delivering a compact and economical solution for modern communication systems.

Keywords: *PIN diode, pattern reconfigurable antenna, frequency reconfigurable antenna, and rectangle patch antenna*

I. Introduction

The swift progress in wireless communication requires devices to manage several applications at once. Employing distinct antennas for each purpose is unfeasible due to space and complexity constraints. Reconfigurable antennas provide a solution by flexibly altering their operating frequency, polarization, or radiation properties, thereby streamlining hardware design and reducing the number of components [1]. Their versatility highlights their significance in cutting-edge wireless systems in applications including cognitive radio, satellite connectivity, and medical technology.

A microstrip antenna with dual U-slots achieves a 68% bandwidth (1.98–4 GHz) for radar applications [2]. A textile-based design uses PIN diodes and a T-slot to switch between 1.8–2.4 GHz, ensuring safety for wearables [3]. Another study employs slits and PIN diodes for frequency (4.5–5.8 GHz) and pattern reconfiguration [4]. A slot antenna with two switches supports WLAN/ITU bands (2.4–7.8 GHz) in multiple modes [5]. A U-slotted antenna targets Wi-Fi/Wi-Max across L, S, C, and X bands [6]. Our proposed antenna leverages a single PIN diode and three slots to achieve dual-mode operation (Mode 1: 5 GHz, 7.75 GHz; Mode 2: 3.10 GHz, 5.55 GHz, 7.15 GHz, 7.75 GHz), offering a streamlined, cost-effective solution for modern multi-band communication networks.

Researchers have investigated diverse techniques to advance reconfigurable antenna designs. Slot-based modifications, such as CPW-fed bowtie slots, enable single, dual, or triple-band operation (2.4–3.5 GHz) for WiFi/WiMAX [7]. Microstrip-fed bowtie slots enhance bandwidth with switch integration for impedance matching [8]. Dual-band patch antennas with varactors allow independent frequency tuning and distinct radiation patterns [9]. Rhombus-shaped radiators with PIN diodes offer frequency (5.2–5.8 GHz), pattern, and polarization switching [10]. Tapered slot antennas with T/C

resonators and PIN diodes support wideband or multi-band modes (0.97–3.76 GHz) [11]. Slot antennas with slits and switches achieve frequency (1.82–2.10 GHz) and beam angle reconfiguration [12]. Bended dipole-loop designs steer beams (±50°) for wearables [13]. Varactor-based dipoles tune frequencies (1.98–2.76 GHz) for WLAN/LTE [14]. These advancements inform our design, which uses a single PIN diode and three slots to achieve dual-mode operation (3.10–7.75 GHz), simplifying control and enhancing efficiency for multi-band wireless applications compared to complex multi-switch configurations [7–14].

In multi-band wireless systems, reconfigurable antennas are critical for compact designs. Techniques like pentagon slot resonators with PIN diodes enable switching between wideband and multi-band modes [15]. Slot length adjustments using six PIN diodes achieve frequency and pattern reconfiguration in S/C bands (2–6 GHz) [16]. Circular disk antennas with 15 PIN diodes offer multi-mode operation for WiMAX/WLAN [17]. Varactor-based center-shorted patches tune dual-band frequencies [18]. Photo-conductive switches in plug-hole designs reconfigure frequency/pattern (2–4 GHz) [19]. Graphene pads shift CPW-fed monopoles from 5G to 4G bands (1.8–7.8 GHz) [20]. Triangle monopoles with PIN diodes tune 1.64–2.54 GHz [21].

A FR4 substrate measuring 55.2 mm × 50.8 mm with a dielectric constant of 4.4 is employed in this study to design a reconfigurable rectangular patch antenna. It features a 21 mm × 15 mm inner patch within a 36 mm × 25.2 mm inverted U1-shaped outer patch. A single PIN diode and three slots (two at 7.5 mm × 18 mm) enable frequency reconfiguration for multi-band wireless applications.

The motivation is to provide a cost-effective, compact solution for multi-band systems using affordable materials. Full-wave simulations optimize the slot geometry, achieving Mode 1 (5 GHz, 7.75 GHz) and Mode 2 (3.10 GHz, 5.55 GHz, 7.15 GHz, 7.75 GHz). Performance is validated through anechoic chamber tests, offering engineers a detailed reference for developing reconfigurable antennas with enhanced efficiency.

II. Design Methodology

The design methodology for the proposed reconfigurable patch antenna, employs a systematic framework, leveraging electromagnetic theory, computational simulation, and experimental validation. The evolution of the design stages is illustrated in Figure 1, with the corresponding S11 characteristics and frequency bands depicted in Figure 2, providing a comprehensive overview of the antenna's performance across its development phases.

I. Structural Design and Material Selection of the Antenna

The development of the reconfigurable antenna starts by constructing a conventional rectangular microstrip patch on an FR4 substrate with dimensions of 55.2 mm by 50.8 mm. The FR4 material, characterized by a dielectric constant $\varepsilon_r = 4.4$, is selected for its affordability and widespread availability in printed circuit board (PCB) fabrication. Despite its higher dielectric losses compared to specialized microwave substrates, FR4 offers a practical trade-off between performance and cost for prototyping and compact device integration.

The initial antenna structure (Antenna 1) consists of an outer patch measuring 36 mm × 25.2 mm, excited through a 20 mm × 3 mm inset microstrip feed line designed to achieve impedance matching. This arrangement yields a single resonant frequency at 5.58 GHz, as illustrated in Figure 1. The corresponding simulated S_{11} response in Figure 2 indicates a return loss below 10 dB, confirming good impedance matching and establishing a solid baseline for reconfigurable enhancements.

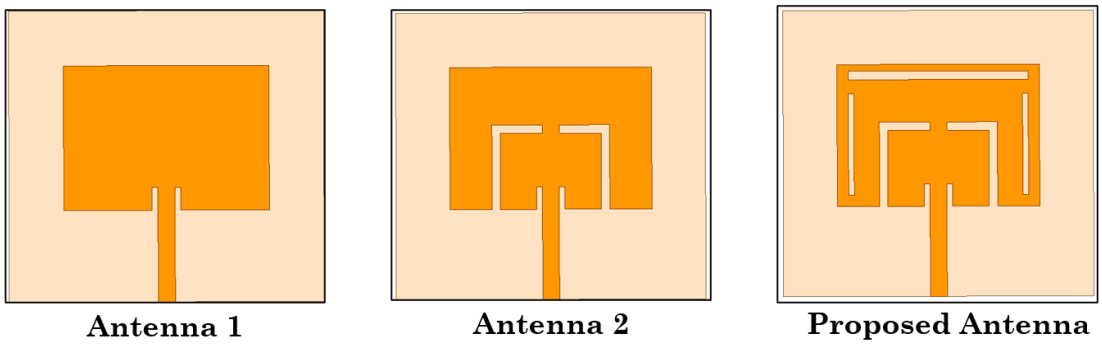


Figure 1. *Evolution steps of proposed frequency and pattern reconfigurable antenna.*

An inverted U-shaped slot of width 2 mm is incorporated into the outer patch of Antenna 2 to enable frequency reconfigurability, enclosing a 21 × 15 mm inner patch. A single PIN diode integrated within the slot, controlled by a DC bias, switches between two states: ON, electrically connecting the patches and resonating at 3.88 GHz, and OFF, isolating them and resonating at 2.4 GHz. Simulated S_{11} results in Figure 2 confirm dual-band performance with return losses below –10 dB, demonstrating efficient frequency agility and compact design.

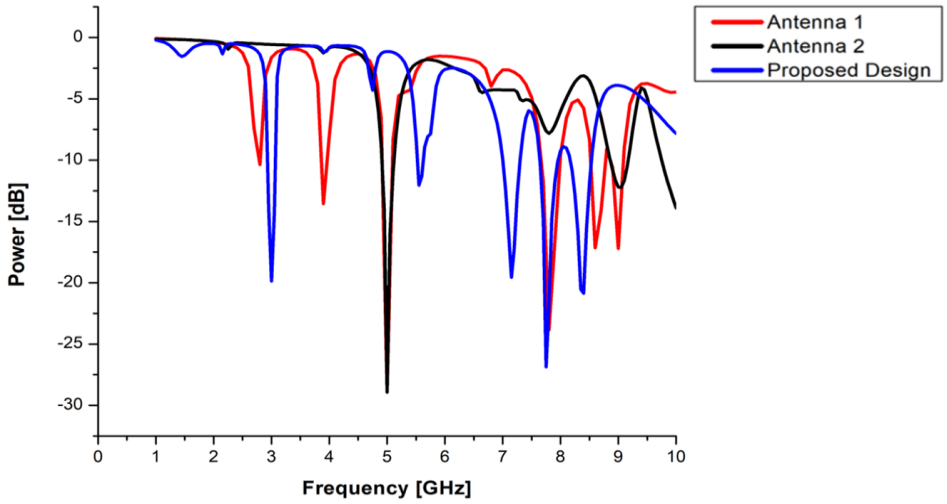


Figure 2. *Comparison of simulated S11 for the baseline outer patch design (Antenna 1), the reconfigurable dual-band design (Antenna 2), and the proposed multi-band, pattern-reconfigurable patch antenna (Proposed Antenna).*

The proposed antenna enhances functionality by adding three slots to the inverted U-shaped structure for multi-band and pattern reconfigurability. Figure 1 shows two vertical slots (7.5 mm × 18 mm) symmetrically placed and one horizontal slot of the same size at the top. These modifications generate additional current paths, shifting resonant modes and altering field distribution. As illustrated in Figure 2, Mode 1 (PIN diode ON) resonates at 5.00 and 7.75 GHz, while Mode 2 (PIN diode OFF) resonates at 3.10, 5.55, 7.15, and 7.75 GHz. Pattern reconfiguration occurs at 7.15 and 7.75 GHz, demonstrating variation in radiation across modes. Full-wave simulations validate the antenna's compact and reconfigurable design. The structure effectively supports multi-band wireless communication with a single switching element.

Additionally, pattern reconfiguration is observed at 7.15 GHz and 7.75 GHz, indicating variation in radiation characteristics across different modes. These results, obtained through full-wave electromagnetic simulation, confirm the antenna's suitability for multi-band wireless communication systems, offering both compactness and configurability with a single switching component.

II. Full-Wave Electromagnetic Simulation

The developed reconfigurable patch antenna was evaluated using Ansys HFSS full-wave simulations, enabling precise modeling of electromagnetic behavior, including current distribution, resonant frequencies, and radiation characteristics affected by geometry and switching. The simulation process was structured into the following key stages:

I. Model Construction:

The entire antenna geometry including the outer rectangular patch, the inner patch, inverted U-shaped slot, and additional side and top slots were meticulously modelled within HFSS. Fine meshing was applied to critical areas, especially around the slot edges and diode region, to capture high-frequency field variations.

To ensure comprehensive analysis and model validation, Figure 3 shows the fabricated antenna geometry used for both simulation and experimental stages. It provides detailed views of the antenna's top layout (including the slot configuration and feedline) and the bottom copper plane.

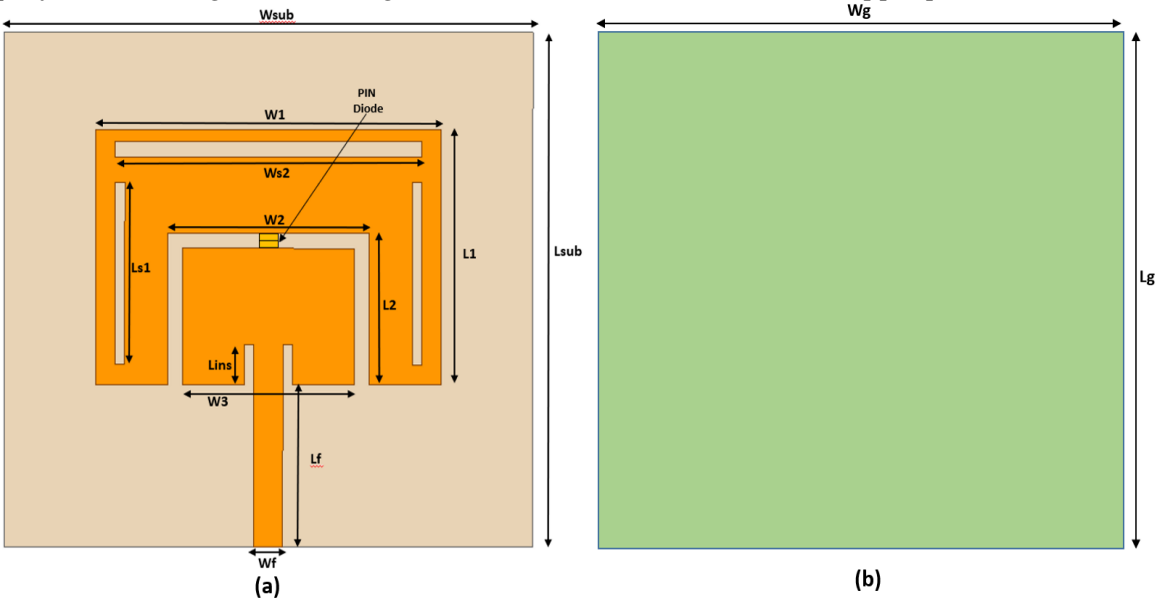


Figure 3. *Antenna proposal (a) top view (b) bottom view.*

All critical dimensions—such as patch sizes, slot lengths, feed dimensions, and substrate thickness were configured according to the optimized values obtained through parametric analysis (Table 1).The substrate was modelled a1s FR4 with featuring $\varepsilon_r = 4.4$ featuring a 1.6 mm-thick dielectric layer.

II. Boundary Conditions and Excitation

The model used radiation boundaries to1 emulate free-space conditions and a wave port to excite the antenna through the microstrip feedline. Frequency sweeps and adaptive meshing ensured accurate re1turn loss predictions and convergence of simulation results.

III. PIN Diode Modelling

A Skyworks SMP1345-079LF PIN diode was modeled using equivalent RLC circuits to represent ON and OFF states. In the ON state, low resistance ensures RF continuity between the patches, while the OFF state's high resistance isolates them. These models were embedded as lumped elements across the

U-slot in HFSS. A separately designed bias network with RF chokes and DC-block capacitors ensured DC–RF isolation.

IV. Output Parameters and Analysis

Key output parameters obtained from HFSS include:

- Return Loss (S_{11}): Used to identify resonant frequencies and assess impedance matching in both switching states.
- Electric Field Distribution: To visualize the field intensity and validate active current regions for1 each resonant mode.
- Surface Current Paths: To study the reconfigurability behavior when switching between modes.
- Gain and Radiation Patterns: To be compared with experimental results.

III. Antenna Design Parameters

To ensure optimal performance and impedance matching across desired bands, key geometrical parameters of the proposed antenna were1 optimized through parametric analysis using Ansys HFSS. Table 1 presents the finalized dimensions of the antenna's components, including the patch sizes, slot dim1ensions, inset feed, and ground plane.

Table 1. *Geometrical Parameters and Corresponding Values*

Parameter	Value (mm)	Parameter	Value (mm)
Wsub	55.2	W3	18
Lsub	50.8	Wg	55.2
W1	36	Lg	50.8
L1	25.2	Wf	3
W2	21	Lf	20
L2	15	Lins	4.6
Ls1	18	Ws2	32

IV. Simulation Results

The frequency and pattern reconfigurability of develop1ed antenna were evaluated using full-wave simulations in Ansys HFSS with an equivalent RC model of the SMP 1345-079LF PIN diode. The diode operates as a short circuit in the ON state, linking the inner and outer patches, and as an open circuit in the OFF state, isolating them. A biasing network ensures proper DC–RF isolation during operation.

I. Return Loss (S_{11}) Analysis

The antenna's reflection coefficient (S_{11}) was measured for both switching conditions:

- Mode 0 (Diode OFF): The antenna resonates at 3.10 GHz and 5.55 GHz.
- Mode 1 (Diode ON): Resonant frequencies appear at 5.00 GHz, 7.15 GHz, and 7.75 GHz.

As depicted in Figure 4, the return loss was evaluated through both simulation and physical testing, exhibi1ting strong agreement and d1emonstrating effective impedance matching ($S_{11} < -10$ dB) across the operating bands.

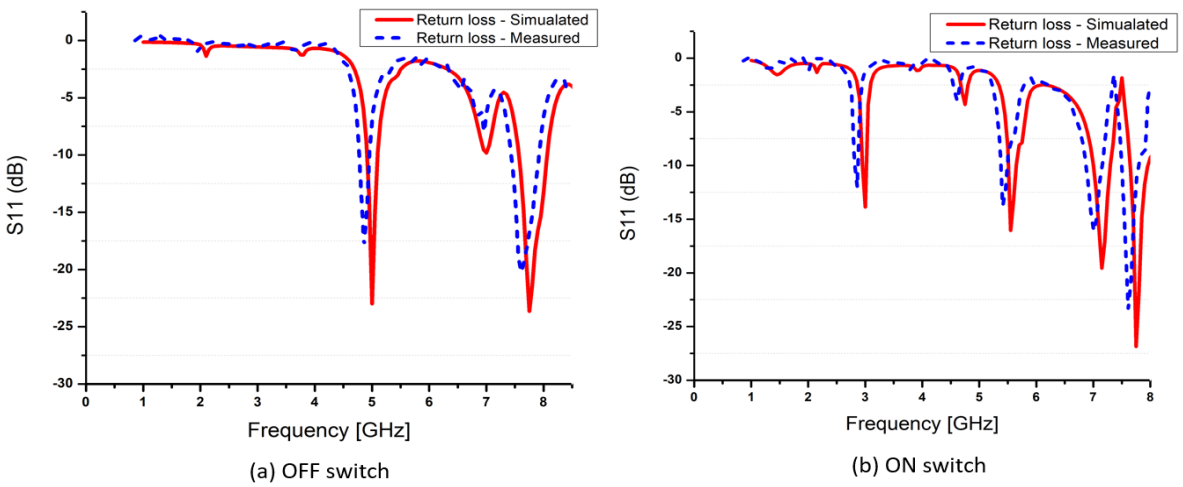


Figure 4. *Return loss measurement for proposed antenna in (a) Mode 0 and (b) Mode 1*

Performance validation of simulated vs. measured frequency bands is summarized in Table 2.

Table 2. *Prototype Evaluation: Correlating Simulated and Experimental Outcomes*

PIN diode state	No. of frequency bands	Frequency (GHz)	Return loss (dB) (Simulated)	Return loss (dB) (Measured)
Off	2	5	-23	-17
		7.75	-24	-21
		3.10	-18	-15
On	4	5.55	-16	-13
		7.15	-22	-17
		7.75	-26	-23

II. Electric Field Distribution

Electric field distributions at resonant frequencies reveal distinct behavior in both modes. In the OFF state, strong fields appear along inner patch edges, indicating isolation and longer paths, while in the ON state, continuous flow across patches yields shortened paths and shifted resonance, as shown in Figure 5.

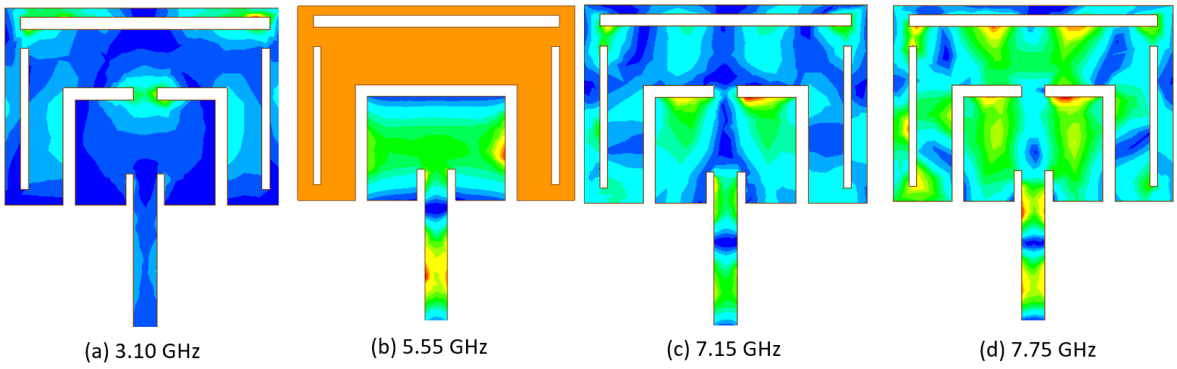


Figure 5. *Simulated electric field distribution at various resonant frequencies*

III. Radiation Pattern

Simulated and experimental far-field patterns at 3.10, 5.00, 5.55, 7.15, and 7.75 GHz are compared in Figure 6. The results confirm stable directional radiation with favorable front-to-back ratio and consistent patterns across modes.

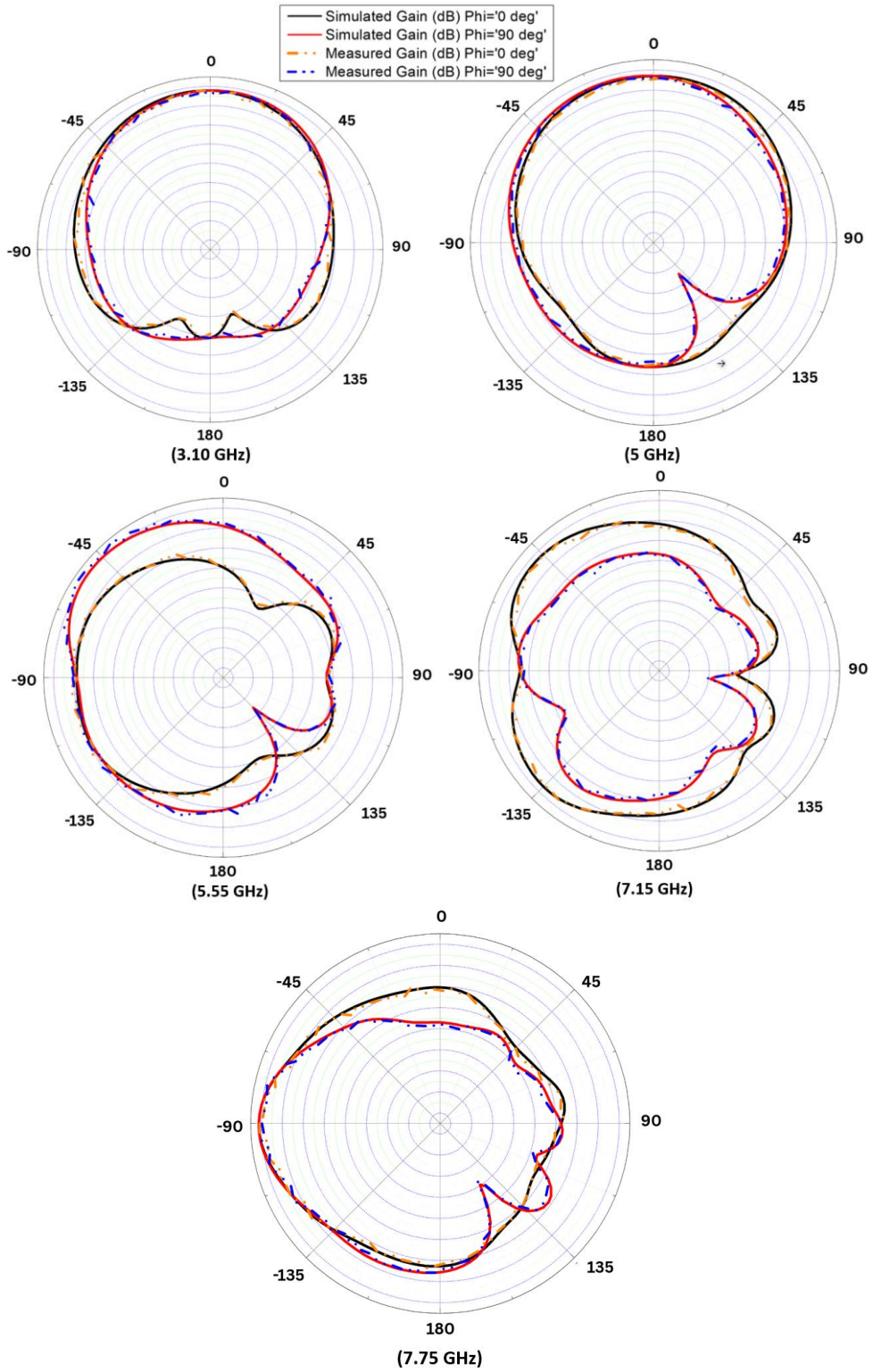


Figure 6. *Radiation pattern comp1arison of proposed antenna between simulated and measured results at different frequencies*

III. Results & Discussion

The antenna was prototyped on an FR4 substrate (ε_r = 4.4, thickness = 1.6 mm) to evaluate and validate the simulated performance. The antenna geometry, including the outer patch, slots, and biasing circuitry, was accurately replicated on the board using standard PCB fabrication techniques. A single PIN diode was mounted at the designated slot location using surface-mount soldering. The final fabricated design is presented in Figure 7, depicting the antenna from both the top and bottom perspectives. The top side features the radiating patch, slot configurations, and diode placement, while the bottom view highlights the feedline, ground plane, and DC biasing elements.

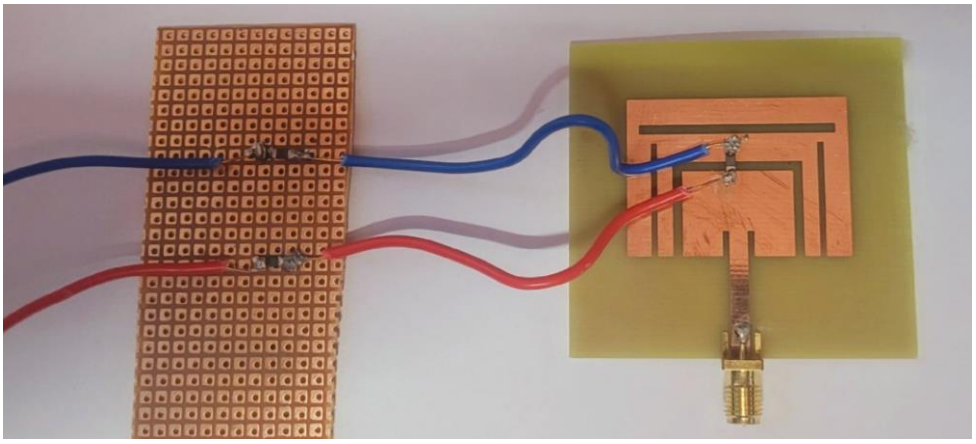


Figure 7. *Fabricated prototype of the proposed antenna*

Experimental validation of the antenna design was conducted in a shielded anechoic chamber, employing a calibrated VNA for accurate measurements. The antenna was connected via an SMA connector, and operational modes were toggled by applying a controlled DC bias across the integrated PIN diode. To ensure effective separation of RF and DC paths, chip inductors and capacitors were used in the biasing circuit, mirroring the simulation configuration. Figure 8 illustrates the measurement setup, with Figure 8(a) showing the VNA connection for return loss testing and Figure 8(b) presenting the chamber arrangement for capturing radiation patterns and gain. The measured return loss remained below –10 dB across all resonant frequencies in both operational modes, indicating strong impedance matching. Gain measurements revealed values ranging from 3.69 dBi to 5.59 dBi, with a peak gain of 5.59 dBi observed at approximately 7.75 GHz.

The close alignment between measured and simulated results validates the robustness of the proposed design methodology and the efficacy of using slot-based reconfiguration in combination with a single PIN diode. This design approach not only enables effective frequency and pattern reconfigurability but also minimizes complexity by reducing the need for multiple switching elements and associated circuitry. The compact size, broad operational bandwidth, and reliable radiation characteristics make the antenna well-suited for modern multi-band wireless communication systems. A comparative analysis with existing reconfigurable patch antennas is presented later in this section to highlight the improvements in key parameters such as gain, bandwidth, frequency agility, and substrate efficiency.

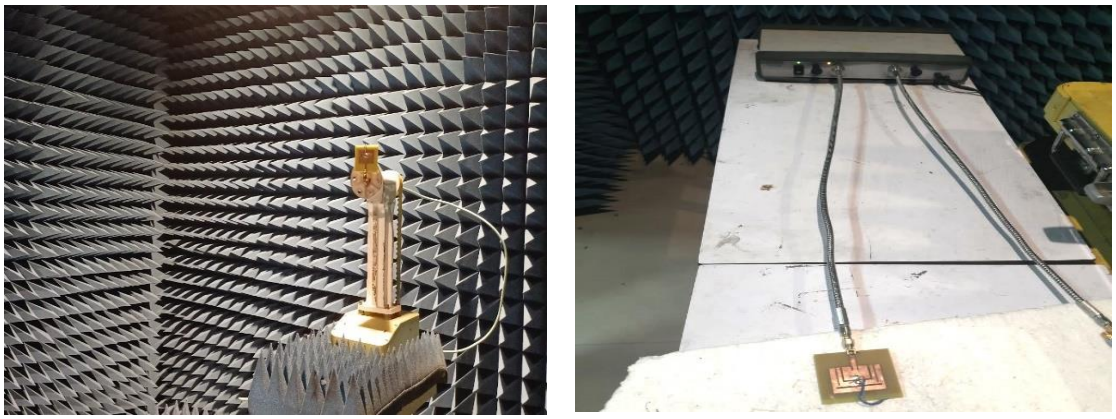


Figure 8. *Measurement set of proposed antenna (a) Measurement of the radiation pattern in anechoic chamber (b) Measurement of S11*

This measurement setup enabled precise characterization of key antenna parameters, including return loss, radiation patterns, and gain in both switching states. By replicating simulation conditions in the prototype, measured data were directly compared with simulations, providing strong validation of the design. The close agreement between results confirms the effectiveness of the slot-based reconfiguration and single PIN diode switching.

The fabricated antenna's performance aligns well with simulations, with only minor differences caused by fabrication tolerances, soldering inaccuracies, and parasitic losses near the PIN diode. To highlight novelty and competitiveness, a comparative study with recent reconfigurable antennas was conducted. Table 3 summarizes this comparison, covering frequency range, reconfigurability type, number of switches, substrate, and design complexity.

Table 3. *Result validation through Comparison of simulation and testing results for proposed antenna prototype*

Ref	Size(mm3)	No. of switches	Reconfigurable frequency (GHz)	Pattern reconfigurable	Maximum gain (dBi)
4	50*50*1.6	4	4.5&4.8/5.2&5.8	Yes	3.8
6	61*38*1.5	3	2 to 10(8 bands)	NA	NA
7	80*30*1.6	4	2.4 to 6.5(4 bands)	No	4.5
10	60*50*1.6	3	5.2,5.8	Yes	3
14	30*49*1.61	8	1.98 to 2.76 (Multiband)	No	1.8
17	60*40*1.6	12	2.3 to 5.87 (4 bands)	Yes	12.87
19	60*66*1.6	4	2.96 and 3.26	Yes	3.29
20	50*45*1.52	5	2,3.5 and 5.3	Yes	1.8
21	40*50*0.254	2	1.64 to 2.54 (3 bands)	Yes	NA
Prop.	50.8*55.2*1.6	1	3.10,5,5.55,7.15,7.75	Yes	5.59

The proposed antenna stands out by achieving both frequency and pattern reconfigurability using only a single PIN diode, thereby significantly reducing circuit complexity, minimizing potential RF distortion, and simplifying the DC biasing network. Additionally, the careful placement of biasing components away from the active radiating structure preserves radiation efficiency. These advantages demonstrate that the proposed antenna offers a compact, low-cost, and high-performance solution suitable for modern multi-band wireless communication systems.

IV. Reliability and Compliance

To ensure the proposed frequency and pattern-reconfigurable antenna is suitable for real-world deployment, special attention was given to structural reliability and robustness during the design and fabrication stages. The antenna was implemented on a 1.6 mm thick FR4 substrate with copper metallization materials known for their wide availability and acceptable mechanical stability. The design accounts for practical tolerances during etching and soldering, and the layout avoids abrupt current transitions that could lead to localized heating or stress during continuous operation.

In terms of electrical reliability, the single PIN diode switching mechanism was carefully integrated to minimize circuit complexity and reduce the chances of failure due to multiple biasing elements. The diode placement ensures consistent switching performance, and the use of RF choke components helps to isolate the DC bias from the RF signal paths. This approach not only reduces the potential for signal distortion but also limits the thermal and electrical stress on individual components, thereby improving the overall system lifespan.

From a compliance and safety perspective, the antenna's radiation characteristics were evaluated in the context of electromagnetic exposure. Although the design is not intended for wearable use, simulated operation at typical user distances suggests low risk of near-field exposure. The antenna's directional radiation profile inherently reduces backward radiation toward users, aligning with international guidelines such as FCC and ICNIRP standards. Combined with the robust mechanical configuration, these factors support the antenna's suitability for integration into modern wireless systems requiring reliable, multi-band performance with safe operation parameters.

V. Conclusions

This paper presents a frequency and pattern-reconfigurable rectangular microstrip patch antenna using a single PIN diode as a switching element. The antenna exhibits two operational modes, controlled by the diode’s ON and OFF states, achieving multi-band functionality with resonances at 3.10 GHz, 5.00 GHz, 5.55 GHz, 7.15 GHz, and 7.75 GHz. Pattern reconfiguration is observed at 7.15 GHz and 7.75 GHz, demonstrating versatility for advanced wireless systems. A key advantage of this design is the incorporation of only one PIN diode, which simplifies the biasing circuitry and minimizes unwanted distortion that typically arises from the use of multiple switching devices. Additionally, the placement of the biasing components away from the radiating section helps maintain stable radiation patterns. Fabricated on a low-cost FR4 substrate, the antenna shows strong agreement between simulation and experimental results, validating its practical viability. Furthermore, reliability assessments based on environmental stress tolerance and safety evaluations in terms of electromagnetic exposure confirm the antenna’s robustness and compliance with SAR regulations. These findings enhance the antenna’s suitability for long-term deployment in modern wireless platforms. Overall, the proposed structure offers a compact, cost-effective, and efficient solution for multi-band and reconfigurable applications, with future scope including size reduction, improved material durability, and deeper system-level integration.

References

[1] A. K. Singh, M. P. Abegaonkar, S. K. Koul. (2018). Miniaturized multiband microstrip patch antenna using metamaterial loading for wireless application, *Progress In Electromagnetics Research C*, 83:71–82.

[2] S. Radavaram, M. Pour. (2018). Wideband radiation reconfigurable microstrip patch antenna loaded with two inverted U-slots, *IEEE Transactions on Antennas and Propagation*, 67(3):1501–1508.

[3] T. Sabapathy, M. A. Bashah, M. Jusoh, P. J. Soh, M. R. Kamarudin. (2016). Frequency reconfigurable rectangular antenna with T-slotted feed line. In *2016 International Conference on Radar, Antenna, Microwave, Electronics, and Telecommunications (ICRAMET)*, 81–84.

[4] Y. P. Selvam, et al. (2017). A low-profile frequency-and pattern-reconfigurable antenna. *IEEE Antennas and Wireless Propagation Letters*,16:3047–3050.

[5] Ali, S. Pathan, R. C. Biradar. (2016). A novel frequency reconfigurable rectangular step slotted antenna for WLAN/ITU. *International Conference on Advanced Networks and Telecommunications Systems (ANTS) IEEE*,1-6.

[6] D. S. Yeole, U. P. Khot. (2016). Reconfigurable multiband microstrip patch antenna design for wireless communication applications. *International Conference on Recent Trends in Electronics, Information & Communication Technology (RTEICT)* IEEE,633-636.

[7] A. Mansoul, M. L. Seddiki. (2018). Multiband reconfigurable Bowtie slot antenna using switchable slot extensions for WiFi, WiMAX, and WLAN applications. *Microwave and Optical Technology Letters*, 60(2):413–418.

[8] W. Lee, H. Kim, Y. J. Yoon. (2008). A frequency reconfigurable bow-tie slot antenna with wide bandwidth. *Microwave and Optical Technology Letters*, 50(2):404–406.

[9] N. Nguyen-Trong, L. Hall, C. Fumeaux. (2017). A dual-band dual-pattern frequency-reconfigurable antenna. *Microwave and Optical Technology Letters*, 59(11):2710–2715.

[10] Y. P. Selvam, et al. (2017). Novel frequency-and pattern-reconfigurable rhombic patch antenna with s1wit1chable polarization. *IEEE Antennas and Wireless Propagation Letters*, 16:1639–1642.

[11] S. Chagharvand, et al. (2015). Reconfigurable multiband tapered slot antenna. *Microwave and Optical Technology Letters*, 57(9):2182–2186.

[12] H. A. Majid, et al. (2014). Frequency and pattern reconfigurable slot antenna. *IEEE Transactions on Antennas and Propagation*, 62(10):5339–5343.

[13] S. J. Ha, et al. (2012). Reconfigurable beam-steering antenna using dipole and loop combined structure for wearable applications. *ETRI Journal*, 34(1):1–8.

[14] M. Mani, et al. (2020). Frequency reconfigurable stepped impedance dipole antenna for wireless applications. *AEU-International Journal of Electronics and Communications*, 115:153029.

[15] D. K. Borakhade, S. B. Pokle. (2015). Pentagon slot resonator frequency reconfigurable antenna for wideband reconfiguration. *AEU-International Journal of Electronics and Communications*, 69(10):1562–1568.

[16] N. K. Sahu, A. K. Sharma. (2017). An investigation of pattern and frequency reconfigurable microstrip slot antenna using PIN diodes. In *2017 Progress In Electromagnetics Research Symposium-Spring (PIERS)*, IEEE, 971-976.

[17] Chilukuri, S., Rangaiah, Y. P., Lokam, A., & Dahal, K. (2018). A multi-band frequency and pattern reconfigurable antenna for Wi-Fi/WiMAX and WLAN applications: frequency and pattern recon1figur1able antenna. *9th International Conference on Mechanical and Aerospace Engineering (ICMAE) IEEE*, 208-212.

[18] N. Nguyen-Trong, L. Hall, C. Fumeaux. (2016). A frequency-and pattern-reconfigurable center-shorted microstrip antenna. *IEEE Antennas and Wireless Propagation Letters*, 15:1955–1958.

[19] A. M. Yadav, C. J. Panagamuwa, R. D. Seager. (2011). Investigation of a plug hole shaped frequency and pattern reconfigurable antenna using photo-conductive microwave switches. *41st European Microwave Conference*, *IEEE*, 878-881.

[20] D. N. Elsheakh. (2019). Frequency reconfigurable and radiation pattern steering of monopole antenna based on graphene pads. *APS Topical Conference on Antennas and Propagation in Wireless Communications (APWC) IEEE*, 436–440.

[21] A. Ghaffar, X. J. Li, N. Hussain, W. A. Awan. (2020). Flexible frequency and radiation pattern reconfigurable antenna for multi-band applications. *4th Australian microwave symposium (AMS) IEEE*, 1–2

STATISTICAL MODELLING AND APPLICATIONS OF THE ET–EXPONENTIAL DISTRIBUTION: EVIDENCE FROM BIOMEDICAL AND ENGINEERING DATA

T. Kamaleshwar[1*], R. Seethalakshmi[2], and S. Mythily[3]

•

[1*]Associate Professor, Department of Computer Science and Engineering, Vel Tech Rangarajan Dr. Sagunthala R&D Institute of Science and Technology, Avadi, Chennai. Tamil Nadu, India.
[2]Assistant Professor, Department of Mathematics, Rajalakshmi Institute of Technology, Kuthambakkam, Chennai- 600124.
[3]Department of Statistics, Periyar University, Salem-11, Tamil Nadu, India.
kamalesh4u2@gmail.com, seethamaths79@gmail.com, mythilyshanmugam03@gmail.com

Abstract

The current study utilizes the exponential distribution as the baseline cumulative function and applies the T-x transformation on the exponential family in order to develop a new class of lifetime distribution. The main objective of this study is to develop and evaluate a flexible distribution that may capture various kinds of lifespan features present in real-world applications. A specific instance, the ET–Exponential (ET–Exp) distribution, is thoroughly examined. The structural properties of the paper, such as the moments, cumulative distribution function, and probability density function, are derived. Parameter estimation is performed via the maximum likelihood method. The suggested approach is used on real datasets, such as carbon fiber breaking stress data and hypertension survival times. The performance of the model is assessed by using statistical criteria such as Akaike Information criteria (AIC), Bayesian Information Criteria (BIC), Kolmogorov-Simron (KS), and Anderson-Darling (AD) tests, which were among the statistical tests used to estimate the goodness of fit of each distribution's essential parameters. The results demonstrate that the proposed ET-Exponential distribution is a flexible and effective tool for modeling lifetime data and shows promise for applications in both biomedical and industrial fields.

Keywords: Exponential Transformation, ET–Exponential Distribution, Lifetime Data Modeling, Reliability Analysis, Maximum likelihood estimation

I. Introduction

As real-world phenomena become increasingly complex, classical lifetime distributions often fail to capture the intricate patterns observed in empirical data. This has motivated the development of more flexible statistical models that enhance data representation and improve model fitting. Over recent decades, generalized families of lifetime distributions have broadened the scope of classical models, particularly in survival analysis, biomedical research, and reliability engineering. Among these, transformation-based families have demonstrated significant potential in increasing model adaptability. The Exponential Transformation (ET) family applies an exponential transformation to baseline cumulative distribution functions, resulting in more flexible lifetime models. A key member

of this family, the ET–Exponential distribution, introduces an additional shape parameter that allows it to model diverse hazard rate behaviors such as increasing, decreasing, and bathtub shapes. This enhanced flexibility makes the ET–Exponential distribution effective in accurately representing complex survival and reliability data, improving interpretability and predictive performance across various fields.

Over the years, various extensions and generalizations of classical lifetime distributions have been proposed to improve flexibility and fitting accuracy. Mudholkar and Srivastava [1] improved modeling flexibility by introducing the exponentiated class by increasing baseline distributions to a power. This strategy was expanded by Marshall and Olkin [2] by include shape parameters in survival functions, while Gupta and Kundu [3] developed parameter estimation methods especially for exponential-type models, making it simple to use in survival analysis, including studies of hypertension. Shaw and Buckley [4] introduced the transmuted family, which Mansour et al. [5] expanded into the transmuted-transmuted-G (TT-G) family to account for more kinds of risk forms. In the field of medicine, Tahmasbi and Rezaei [6] utilized generalized exponential and exponential models for evaluating arterial blood pressure variability, along with Almalki and Yuan [7] used modified Weibull approaches, which provide more flexibility than traditional exponential models, to analyze chronic diseases such as hypertension. A more recent development is the T–X family, which was presented by Alzaatreh et al. [8] and offers a generic framework for creating new distributions by transforming preexisting ones. Maurya et al. [9] suggested logarithmic transformations, which Aslam et al. [10] expanded upon to improve model flexibility further.

A notable recent development is the Exponential Transformation (ET) family proposed by Al-Nasser and Hanandeh [11], which demonstrated superior performance in real-data applications compared to traditional lifetime models. Jin and Qian [12] introduced the Mixture Exponential Family Distribution Posterior Network (MEFDPN), leveraging mixtures of exponential families to improve uncertainty estimation and machine learning accuracy. Chaturvedi et al. [13] developed the Generalized Positive Exponential Family, which includes Weibull and gamma distributions, showing superior fitting on wind speed data. Finally, Mohsin and Kalt [14] proposed the Alpha Logarithm Family, a two-parameter extension of the exponential distribution, enhancing flexibility through logarithmic transformation and outperforming classical models in empirical analysis.Based on empirical data analysis alone, the model demonstrated better adaptability and accuracy than classical distributions.

The main objective of this paper is to propose a new ET–Exponential distribution based on the T–X transformation framework. The study aims to derive and analyze its mathematical properties and parameter estimation methods. It also compares the ET–Exponential model's performance with existing lifetime distributions. The model is applied to real-life datasets, including hypertension survival times and carbon fibre breaking stress. Overall, the paper demonstrates the flexibility and practical applicability of the ET–Exponential distribution in modeling complex lifetime data.

The remainder of the paper is organized as follows: Section 2 introduces the ET–Exp model and its theoretical formulation. Section 3 discusses its mathematical properties. Section 4 presents parameter estimation via maximum likelihood. Section 5 applies the model to real datasets. Finally, Section 6 concludes the study with key findings and future research directions.

II. ET-Exponential Distribution

A nonnegative continuous random variable Y with a baseline cumulative distribution function (CDF) $F(y,\lambda)$ and a probability distribution function (PDF) $f(y,\lambda)$ where $\lambda \in (0,\infty)$ is a real valued distribution parameter can be used to construct a more flexible family of lifetime distributions. The proposed CDF's stochastic presentation to generate a new class of distributions can be defined as,

$$G(y,\lambda,\rho) = F(y,\lambda)e^{-\rho\bar{F}(y,\lambda)}\ y \geq 0; \rho \geq 0 \quad (1)$$

Where $\bar{F}(y,\lambda)$=1-$F(y,\lambda)$. Noting that when $\rho = 0$, then the proposed distribution is exactly the same as the baseline distribution.

This family will be called as exponential transformation (ET), i.e., ET(y, λ, ρ). Now, the PDF of ET family can be obtaining by finding the first derivative of equation (1):

$$g(y,\lambda,\rho) = f(y,\lambda)e^{-\rho\bar{F}(y,\lambda)}\big(1+\rho F(y,\lambda)\big);\ y \geq 0; \rho \geq 0 \quad (2)$$

According to Alzaatreh et al. (2013), this family can be a part of the T-X family in the following ways: For a continuous probability distribution represented by F(y,λ) with a general baseline CDF, a new CDF with the form,

$$G(y,\lambda,\rho) = \int_{\lambda}^{F(y,\rho)} r(t)dt$$

where the related CDF is R(t) and r(t) is a PDF defined over (0, 1). Thus, the PDF $g(y,\lambda,\rho)$ can be computed as

$$g(y,\lambda,\rho) = \mathrm{f(y,\rho)r(F(y,\lambda))}$$

If we used r(t) in the following functional form:

$$r(t) = (1+\rho t)e^{-\rho(1-t)}$$

Then, the proposed family could be considered as member of the T-X family. As an illustration of the proposed family, the exponential distribution will be considered as baseline distribution.

I. Asymptotic Properties of the CDF and PDF

Assuming that Y is a continuous random variable belongs to the ET family as described in (1), it is known that this distribution family corresponds to the distribution functions and the Kolmogorov axioms. For example, the limit property of $G(y,\lambda,\rho)$ clearly satisfies the CDF property.

$$\lim_{y\to\infty} G(y,\lambda,\rho) = \lim_{y\to\infty} F(y,\lambda)e^{-\rho T(y,\lambda)} = 1 \text{ and}$$

$$\lim_{y\to 0} G(\mathrm{y},\lambda,\rho) = \lim_{y\to 0} F(y,\lambda)e^{-\rho}F(y,\lambda) = 0.$$

Hence, the total probability is equal to one. Also, it is monotone right increasing function of y and $0 \leq G(y,\lambda,\rho) \leq 1; \forall y$. Therefore, $G(y,\lambda,\rho)$ is an absolute continuous distribution function.

Additionally, the fact that $g(y,\lambda,\rho)$ is a non-negative real valued PDF for all y can additionally be immediately confirmed. In the case of an explosion of growth, for example:

$$\lim_{y\to\infty} g(y,\lambda,\rho) = 0 \text{ and}$$

$$\lim_{y\to 0} g(y,\lambda,\rho) = \lambda e^{-\rho}.$$

Since both parameters are positive this indicates that $g(y,\lambda,\rho)$ is a unimodal distribution Now,

the functional form given in (2) satisfied the PDF property:

$$\int_0^\infty g(y,\lambda,\rho)dx = \int_0^\infty f(y,\theta)e^{-\rho\bar{F}(y,\lambda)}(1+\rho F(y,\lambda))dx$$

Assuming that the exponential distribution with mean 1/θ is the baseline distribution, we obtain the ET-Exp distribution to demonstrate the use of the novel stochastic representation provided in (1) and the related PDF provided in (2).

III. Mathematical Properties

I. Moments

Some Moments can be used to study some of a statistical distribution's most crucial properties, including skewness, kurtosis, dispersion, and tendency. Assuming that computing the expected value of $k(y)$ yields the moments of $ET(y,\lambda,\rho)$; where

$$k(y) = \begin{cases} y^r, & \text{for moment of order } r, \\ e^{ty}, & \text{for moment of generating function,} \\ e^{ity}, & \text{for characteristic function.} \end{cases}$$

Hence,

$$E\big(k(y)\big) = \int_0^\infty k(y)f(y,\lambda)e^{-\rho\overline{F(y,\lambda)}}\big(1+\rho F(y,\lambda)\big)dx$$

$$= \int_0^\infty k(y)f(y,\lambda)\big(1+\rho F(y,\lambda)\big)\left(\sum_{j=0}^{\infty}\sum_{k=0}^{\infty}(-1)^{j+k}\frac{\rho^j}{j!}\binom{j}{k}F(y,\lambda)^k\right)dx,$$

which is equivalent to the expected value based on the baseline distribution

$$E_F\big(k(y)e^{-\rho}\overline{F(y,\lambda)}(1+\rho F(y,\overline{F(y,\lambda)})\big)$$

Then the expected value can be obtained using expansion technique or by using integral estimation.

IV. Parameter Estimation

In this section, estimation of the unknown parameters of the $ET(y,\lambda,\rho)$ family of distributions based on complete samples are determined using method of moment (MOM) and maximum likelihood estimation (MLE) method. Let $y_1, y_2 \ldots\ldots y_n$ be the observed values from ET(y, λ,ρ) family.

I. Method of Moment

The MOM estimator can be obtained by solving the following equations:

$$E_p\big(ye^{-\rho\Gamma(y,v)}(1+\rho F(y,\lambda))\big) - \frac{\sum_n^\infty y_i}{n},$$

$$E_p\big(y^2e^{-\rho\Gamma(y,v)}(1+\rho F(y,\lambda))\big) - \frac{\sum_n y^2}{n}.$$

The first moment of ET-Exp distribution can be expressed as:

$$E(Y)=\frac{1}{\omega\vartheta}\left(1-e^{-\rho+\rho\left(\int_0^{\infty}\frac{\sinh(t)}{t}dt-\int_0^{\infty}\frac{\cosh(t)-1}{y}dt\right)}\right)$$
$$=\frac{1}{\omega\vartheta}\left(1-e^{-\rho+\rho(\log(\rho)-\mathrm{Chi}(\rho)+\mathrm{Shs}(\rho)+\gamma)}\right)$$

while the second moment can be replaced by the following formula:

$$E(Y^2)=\frac{2(\rho^2,F,(1,1,1;2,2,2;-\rho)+\log(\rho)+\Gamma(\Omega,\rho)+\gamma)}{\vartheta\omega^2}$$

where γ is Euler's constant, with numerical value ≈ 0.577216, the incomplete gamma function satisfies

$$\Gamma(0,\infty)=\int_{\infty}^{\infty}\frac{e^{-t}}{t}dt$$

and ${}_3F3(1,1,1;2,2,2;-\infty)$ ls the generwhoed hypergeometric function.

II. Maximum Likelihood Estimation of the Parameters

Using the MLE, the point estimator of the unknown parameter can be obtained by solving the following likelihood functions

$$L=\prod_{n=1}^{n}f(y_i-\lambda)e^{-\rho T(y,\lambda)}\left(1+\rho F(y_i,\lambda)\right)$$

Taking the Log of the likelihood function will simplify the estimation problem:

$$\log L=\left\{\sum_{i=1}^{n}\log\left(f(y,\lambda)\right)-\sum_{i=1}^{n}\rho F(y_i,\lambda)+\sum_{i=1}^{n}\log\left(1+\rho F(y_i,\lambda)\right)\right\}$$

Now, we have to find the first order condition:

$$\frac{d\log L}{d\lambda}=\sum_{i=1}^{\infty}\frac{df(y_i,\lambda)/d\lambda}{f(y_i,\lambda)}+\sum_{i=1}^{n}\rho f(y_i,\lambda)+\sum_{i=1}^{\infty}\frac{\rho f(y_i,\lambda)}{1+\rho f(y_i,\lambda)}$$
$$\frac{d\log L}{dy}=-\sum_{i=1}^{n}F(y_i,\lambda)+\sum_{i=1}^{n}\frac{F(y_i,\lambda)}{1+\rho F(\mathrm{y},\lambda)}$$

Since the equations are non-linear, they are solved numerically using R software (R Core Team, 2021).

V. Results and Discussion

I. Applications

This section shows off the ET-Exp distribution's capabilities by fitting the model to two datasets: the Lindley, Generalized Exponential (GE), and Exponential distributions. The parameters associated with each distribution have been calculated using the maximum likelihood technique for these two datasets. Using the information obtained the values of Bayesian Information Criterion (BIC), Akaike Information Criterion (AIC) and -LogL are obtained from the datasets. The Anderson-Darling (AD) and Kolmogorov-Smirnov (K-S) statistics, together with their related P-value (p-Val), are also found. The mathematical formulae of these measures are given by:

The AD test statistics computed as

$$AD = -m - \frac{1}{m}\sum_{j=1}^{m}(2j-1) \times [logG(y_t;\Delta) + \log(1 - G(y_{t-m+1};\Delta)]$$

The KS test statistic derived as

$$KS = \text{Supermium}\, x[G_m(y;\Delta) - G(y;\Delta)]$$

The AIC test statistics obtained as

$$AIC=2p-2L$$

The BIC test statistics derived as

$$BIC=p\log(n)-2L$$

where L is the maximized likelihood function evaluated at MLEs, m is the sample size, and p is the number of parameters in the model. For every dataset, the five-number summary, mean, variance, skewness, and kurtosis are computed as basic descriptive statistics The best distribution has been proposed to be the one with the lowest AIC and BIC, which finds an optimal balance between model complexity and goodness-of-fit. The −Log L value help to evaluate the model's overall fit.

II. Dataset I: Hypertension Data

This dataset shows the survival periods in years before the development of hypertension for 119 patients randomly selected from the Bolgatanga Regional Hospital in Ghana's Upper East region.
The following components are contained in the dataset: 71, 5, 39, 62, 52,71, 38, 56, 35, 69,34,71,66,70, 52, 37, 35, 71, 73, 19, 74, 74, 75, 51, 76,49, 19, 76, 78, 76, 76, 49, 47, 48, 48, 46, 46, 46, 41, 40, 43, 45, 47, 47, 44, 45, 46, 42, 43, 42, 20, 28, 26, 60, 27, 24, 29, 60, 25, 60, 69, 36, 69, 69, 68, 68, 67, 67, 67, 52, 35, 66, 55, 66, 61, 61, 64, 64, 65, 65, 63, 63, 62, 39, 62, 62, 62, 59, 59, 59, 58, 58, 58, 18, 57, 57, 56, 56, 37, 53, 53, 53, 53, 54, 54, 66, 17, 50, 75, 51, 38, 52, 66, 4, 52, 55, 19, 58, and 73.

The descriptive statistics for this data set are shown in Table 1, and the MLE and goodness of fit test results for this data set using each distribution are displayed in Table 2.

Table 1: *The summary statistics for the Hypertension Data*

Parameter	Min	Q1	Median	Q3	Mean	Max	Skewness	Kurtosis	Variance
Dataset1	4	43	55	65.5	52.428	78	-0.731	0.043	270.28

Table 2: *MLEs and goodness of fit statistics for the Hypertension Data*

Distribution	α	θ	-LogL	K-S	p-val	A-D	p-val	AIC	BIC
Exponential	-	0.019	-590.2	0.361	0.000	25.452	0.0005	1182.35	1185.12
GE	7.0179	0.047	-530.9	0.1606	0.004	6.045	0.0009	1065.96	1071.52
ET-EXP	9.4877	0.05	-522.6	0.1507	0.008	4.62	0.007	1049.95	1054.95
Lindley	-	0.037	-555.0	0.2638	0.000	15.409	0.000	1112.13	1114.91

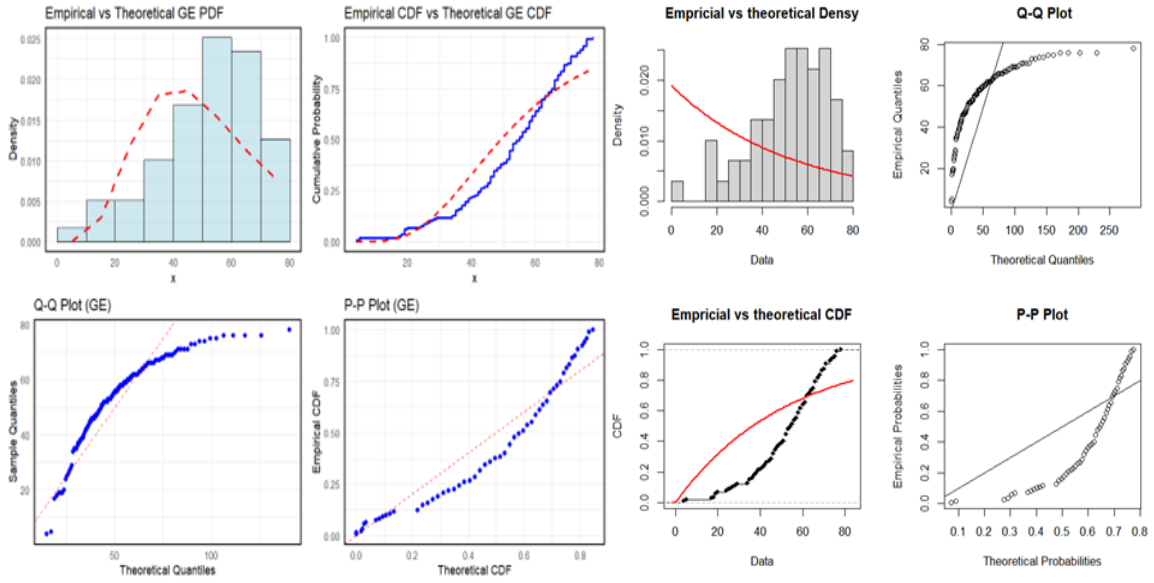


Figure 1: *The empirical and theoretical PDFs, empirical and theoretical CDFs, Q-Q plots and p-p plot for (a) Exponential, (b) Generalized-Exponential, (c)Lindley and (d) ET-Exponential for the Hypertension data.*

Table 2 and Figure 1 shows that the goodness-of-fit statistics for the evaluated distributions show that the Exponentiated Exponential (ET-EXP) and Generalized Exponential (GE) distributions best suit the data. ET-EXP and GE have the lowest negative log-likelihood values, as well as lower Kolmogorov-Smirnov (K-S) and Anderson-Darling (A-D) statistics than the Exponential and Lindley distribution, respectively. The p-values for the K-S and A-D tests for ET-EXP and GE, although tiny, are significantly greater compared to those for the Exponential and Lindley models, showing a superior fit. Furthermore, ET-EXP and GE have the lowest Akaike Information Criterion (AIC) and Bayesian Information Criterion (BIC) values, implying that they stabilize goodness-of-fit with model complexity more efficiently. On the other hand, the Exponential and Lindley distributions have inferior fit performance, having higher statistical significance and lower p-values, indicating a less suitable representation of data. Based on these criteria, the ET-EXP distribution exceeds the GE distribution somewhat, making it the best fit for the data, followed by the GE. Both models outperform the Lindley and Exponential distributions significantly.

III. Dataset II: Carbon Fiber Breaking Stress Data

The second dataset is comprised of 100 observations. The dataset refers to breaking stress of carbon fibers, which are measured in Gba [25]. The descriptive statistics for this data set are shown in Table 3, and the MLE and goodness of fit test results for this data set using each distribution are displayed in Table 4.

Table 3: *Summary Statistics of Carbon Fiber Breaking Stress Data*

Parameter	Min	Q1	Median	Q3	Mean	Max	Skewness	Kurtosis	Variance
Dataset2	0.39	1.84	2.7	3.22	2.621	5.56	0.3629	0.043	1.028

T**able 4:** *MLEs and goodness of fit statistics for the Carbon Fiber Breaking Stress Data*

Distribution	α	θ	-LogL	K-S	p-val	A-D	p-val	AIC	BIC
Exponential	-	0.381	-196.36	0.26	0.000	12.315	0.000	365.50	368.106
GE	7.788	1.013	-146.17	0.97	0.000	4.218	0.007	292.70	297.918
ET-EXP	9.182	1.092	-144.35	0.10	0.196	1.222	0.259	296.35	301.568
Lindley	-	0.617	-181.75	0.32	0.000	17.301	0.000	394.73	397.339

Table 4 and Figure 2 shows that the ET-EXP distribution offers the best overall fit to the data, based on a comparison of four potential distributions: Lindley, GE, ET-EXP, and Exponential. Its suitability is demonstrated by low test statistics and high p-values in both the Anderson-Darling and Kolmogorov-Smirnov tests, indicating a statistically significant and consistent fit. The GE distribution's goodness-of-fit p-values are below 0.05, indicating a poor fit, although having a marginally lower AIC than ET-EXP. The exponential distribution does not meet the goodness-of-fit criteria, even if it is simple and has a low -LogL. The Lindley distribution performs the worst overall, with the highest AIC and BIC values and the lowest fit statistics. The ET-EXP distribution is therefore determined to be the most appropriate model for the data based on both goodness-of-fit and model selection criteria.

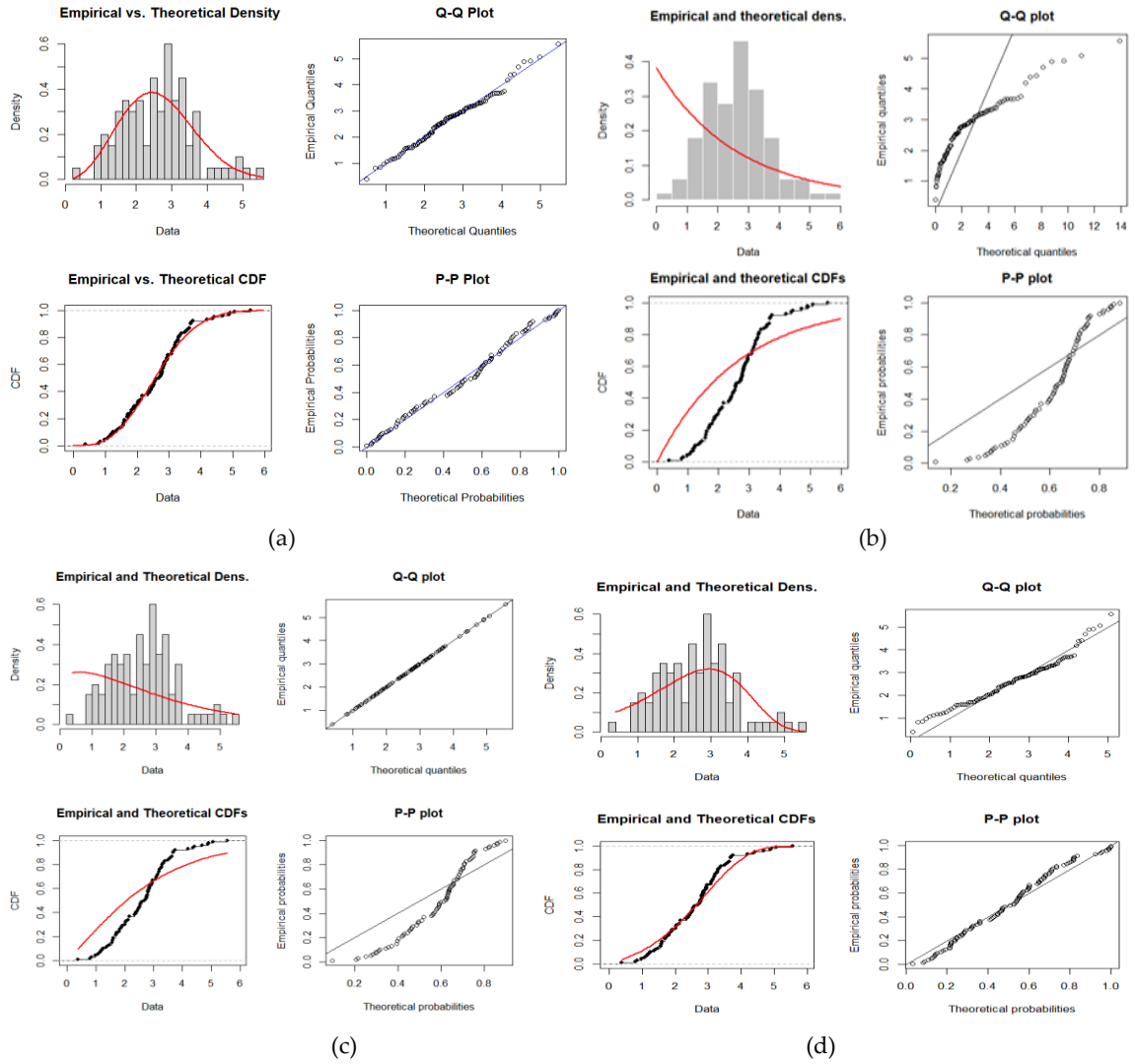


Figure 2: *The empirical and theoretical PDFs, empirical and theoretical CDFs, Q-Q plots and p-p plot for (a) Exponential, (b) Generalized-Exponential, (c)Lindley and (d) ET-Exponential for the Carbon Fiber Breaking Stress Data.*

VI. Conclusion

This study introduces the ET–Exp distribution as a novel and versatile model for lifetime data analysis. Across both cases, the ET-Exp model demonstrates clear superiority, achieving lower values of Akaike Information Criterion (AIC) and Bayesian Information Criterion (BIC), along with improved goodness-of-fit statistics, including the Kolmogorov–Smirnov (K–S) and Anderson–Darling (A–D) tests. Compared to the traditional Exponential and Lindley distributions, the ET–Exp model consistently provides a significantly better fit. Furthermore, it performs comparably to or better than the Generalized Exponential (GE) distribution, particularly in balancing fit quality with model complexity. In addition to its empirical strengths, the ET–Exp distribution offers desirable theoretical properties, including closed-form expressions for moments and entropy, which further underscore its practical utility. Overall, the ET-Exp distribution emerges as a robust, flexible, and effective tool for modeling lifetime data, with strong potential applications in both biomedical research and industrial reliability analysis.

References

[1] Mudholkar, G. S. and Srivastava, D. K. (1993). Exponentiated Weibull family for analyzing bathtub failure-rate data. *IEEE transactions on reliability*, 42(2): 299-302.

[2] Marshall, A. W. and Olkin, I. (1997). A new method for adding a parameter to a family of distributions with application to the exponential and Weibull families. *Biometrika, 84*(3): 641-652.

[3] Gupta, R. D. and Kundu, D. (2001). Exponentiated exponential family: an alternative to gamma and Weibull distributions. *Biometrical Journal: Journal of Mathematical Methods in Biosciences*, *43*(1):117-130.

[4] Shaw, W. T. and Buckley, I. R. (2007). The alchemy of probability distributions: Beyond gram-charlier and cornish-fisher expansions, and skew-normal or kurtotic-normal distributions. *Submitted, Feb*, *7*, 64.

[5] Tahmasbi, R. and Rezaei, S. (2008). A two-parameter lifetime distribution with decreasing failure rate. *Computational Statistics and Data Analysis*, *52*(8): 3889-3901.

[6] Almalki, S. J. and Yuan, J. (2013). A new modified Weibull distribution. *Reliability Engineering and System Safety*, *111*: 164-170.

[7] Alzaatreh, A. Lee, C. and Famoye, F. (2013). A new method for generating families of continuous distributions. *Metron*, *71*(1): 63-79.

[8] Maurya, S. K. Kaushik, A. Singh, R. K. Singh, S. K. and Singh, U. (2016). A new method of proposing distribution and its application to real data. *Imperial Journal of Interdisciplinary Research*, *2*(6):1331-1338.

[9] Aslam, M. Ley, C. Hussain, Z. Shah, S. F. and Asghar, Z. (2020). A new generator for proposing flexible lifetime distributions and its properties. *PloS one*, *15*(4): e0231908.

[10] Ahmad, Z. Mahmoudi, E. Alizadeh, M. Roozegar, R. and Afify, A. Z. (2021). The Exponential T-X Family of Distributions: Properties and an Application to Insurance Data. *Journal of Mathematics*, *2021*(1): 3058170.

[11] Nasiru, S. and Abubakari, A. G. (2022). Marshall-Olkin Zubair-G family of distributions. *Pakistan Journal of Statistics and Operation Research*, 195-210.

[12] Al-Nasser, A. and Hanandeh, A. (2025). Stochastic Generator of a New Family of Lifetime Distributions with Illustration. *REVSTAT-Statistical Journal*, *23*(1): 139-160.

[13] Jin, X. and Qian, Q. (2025). MEFDPN: Mixture exponential family distribution posterior networks for evaluating data uncertainty. *Expert Systems with Applications*, *262*, 125593.

[14] Chaturvedi, A. Bhatti, M. I. Bapat, S. R. and Joshi, N. (2025). Modeling wind speed data using the generalized positive exponential family of distributions. *Modeling Earth Systems and Environment*, *11*(2): 1-11.

[15] Mohsin, L. A. J. and Kalt, H. G. (2025). *An application* to exponential distribution of a novel family of distributions. *AIP Conference Proceedings*, 3282: 040036.

EIGHT YEARS OF RESEARCH IN RELIABILITY: THEORY AND APPLICATIONS (2017–2024): A SCOPUS BASED BIBLIOMETRIC ANALYSIS

Sajad Hussain*[1], Vilayat Ali Bhat[2]

•

*[1]School of Business (SOB), University of Petroleum & Energy Studies, Dehradun, India - 248013
[2]Department of CSE – AI, ML & DS, Marwadi University, Rajkot, Gujarat, India - 360003
sajad.stat321@gmail.com*[1]
vilayat.stat@gmail.com[2]

Abstract

This study looks at the SCOPUS research published in the journal Reliability: Theory and Applications from 2017 to 2024. The main goal is to understand how the journal has grown, how influential it is, and how researchers are working together. The data shows that the number of papers published has increased steadily, especially after 2020, showing that the journal is becoming more important in the academic world. Most of the research came from countries like India, the Russian Federation, and Azerbaijan. Universities such as Kadyrov Chechen State University and Azerbaijan State Oil and Industry University were among the top contributors. The study also used network analysis to examine how authors collaborate, which keywords are used together, and which papers are cited the most. It was found that a few researchers, like Yusuf Ibrahim and Rather Aafaq A., are very active and well-connected in the author network. Citation analysis showed which authors, institutions, and countries had the most influence. This study provides helpful information for researchers, universities, and funding agencies interested in working with or contributing to this journal.

Keywords: Bibliometric Analysis, Citation analysis, Network analysis, Statistical Analysis, Research clusters

I. Introduction

The online journal Reliability: Theory & Applications (ISSN 1932-2321) has been published by the Gnedenko Forum since January 2006. By December 2024, it had published 81 volumes with a total of 1,322 SCOPUS indexed papers. The journal has been indexed in SCOPUS since 2017. It focuses on different topics related to risk analysis, such as reliability, safety, security, survivability, quality control, reliability testing, queuing models, and other similar subjects. It is a peer-reviewed journal, which means that experts check and approve the articles before they are published. The journal is meant for both researchers and professionals working in risk and reliability engineering. It publishes high quality papers that deal with theory, methods, and real-world problems related to the safe and reliable design and use of systems in different industries. The types of papers it accepts include research papers, reviews, case studies, and bibliographic articles. The journal prefers papers that show clear real-world applications and case studies. Submitted papers are reviewed by the Editorial Board. However, if a paper is submitted by an Associate Editor, they may recommend it for publication directly.

Bibliometric analysis is a way for researchers to understand how a subject or field has changed and grown over time. It uses numbers and patterns, like how many times a paper has been cited, how authors work together, and which keywords are used the most. This helps show which authors, papers, journals, and universities are the most important in that area. It also helps find new or popular topics that are becoming important. In short, bibliometric analysis helps researchers see how research has developed and what direction it might take in the future. Many researchers have used this method to study how different journals have helped their fields. For example, the Journal of Finance was studied by [9], fifteen years of the Journal of Consumer Research looked by [10], the Journal of Advertising from 1986 to 1997 studied by [23], 20 years of the Journal of Public Policy & Marketing looked by [18], the Strategic Management Journal from 1980 to 2000 studied by [17], 21 years of the International Marketing Review studied by [14], 25 years of the journal Technovation studied by [7], 20 years of the Journal of Product Innovation Management looked by [1] and the journal Total Quality Management & Business Excellence from 1995 to 2008 studied by [5]. In India, similar studies were done viz. the Ethnobotany journal studied by [6], the Indian Forester studied by [8], the journal Library Philosophy and Practice studied by [19], the Library Herald (for the years 2006 to 2010) studied by [20], the DESIDOC Journal of Library and Information Technology looked by [12], the journal Webology studied by [22] and the Journal of Oral Research studied by [4]. These examples show that bibliometric analysis is a helpful way to understand how journals and research areas have improved, what topics are popular, and which studies have had the most influence.

In recent years, many researchers have used bibliometric analysis to study different academic journals. For example, research published in the Journal of Business Research from 1973 to 2014 looked by [16], 25 years of the journal Knowledge-Based Systems studied by [3], International Journal of Intelligent Systems examined by [15], 30 years of Journal of Business & Industrial Marketing reviewed by [21], 40 years of Journal Computers & Industrial Engineering analysed by [2] and 40 years of the European Journal of Operational Research studied by [13]. More recently, 10 years of research in the journal Genetic Resources and Crop Evolution was studied by [11]. These studies show that bibliometric analysis is a useful method to understand how research in different journals has grown, what topics are popular, and which studies have had the most impact.

II. Results

In this paper, the data for the bibliometric analysis was taken from SCOPUS, one of the most widely used research databases. The data collected covers the period from 2017 to December 2024. Two types of analysis were done (i) Statistical Analysis – This was done using the built-in SCOPUS analyzer. (ii) Network Analysis – This was done using a software tool called VOSviewer (Version 1.6.15). The results from both types of analysis are presented in the following sections

I. Statistical Analysis

The statistical analysis in this study looks at different parts of the published research to understand trends and patterns. Here are the main points viz. Documents by Year: This shows how the number of publications has changed over time—whether research in the field is growing or slowing down. Documents by Author: This highlights the most active researchers who have published the most work. Documents by Affiliation: This shows which universities or institutions are publishing the most research. Documents by Country or Territory: This maps out which countries are contributing the most to the research. Documents by Type: This groups the papers into categories, like research articles, reviews, etc. Documents by Funding Sponsors: This identifies the organizations that are providing financial support for the research. Altogether, this analysis

gives a clear picture of the research field and the main people, places, and organizations driving it.

Document analysis by year

Table-1 and Figure-1 show how many research papers were published each year from 2017 to 2024. The data clearly shows that the number of publications has gone up over time. In 2017, there were 30 papers published. The numbers stayed about the same in 2018 (29 papers) and 2019 (23 papers). Then, in 2020, the number started to rise with 40 papers. In 2021, it jumped to 151 papers. This growth continued in 2022 with 236 papers, and even more in 2023 and 2024, with 333 and 480 papers published.

Overall, from 2017 to 2024, the journal's publications increased a lot. It had steady output until 2019, then grew quickly from 2020 onward. This shows that the journal has become more visible, is receiving more submissions, and is becoming more important in its field.

Table 1: *Publications per year*

Year	Number of documents
2024	480
2023	333
2022	236
2021	151
2020	40
2019	23
2018	29
2017	30

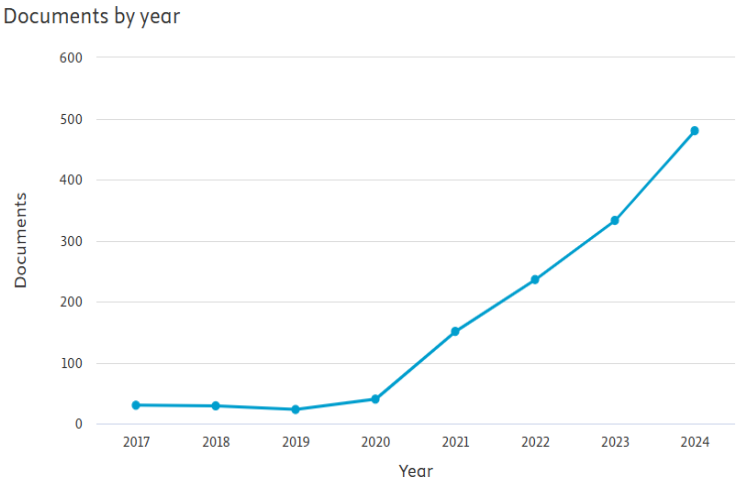


Figure 1: *Documents published per year*

Document analysis by author

Table-2 and Figure-2 show the authors who have published the most papers in this research area. The top author is Rather, A.A., with 20 publications. He is followed by Yusuf, I. with 18 publications and Ayyappan, G. with 17. Other active authors include Chacko, V.M. and Shanker, R., each with 12 publications, and Aliyev, V. with 11. There are also four authors — Gakaev, R., Shukla, D., Shukla, K.K., and Timashev, S. — who have each published 10 papers. These authors are the leading contributors in this research field.

Table 2: *Publications by author*

Author	Number of documents
Rather, A.A.	20
Yusuf, I.	18
Ayyappan, G.	17
Chacko, V.M.	12
Shanker, R.	12
Aliyev, V.	11
Gakaev, R.	10
Shukla, D.	10
Shukla, K.K.	10
Timashev, S.	10

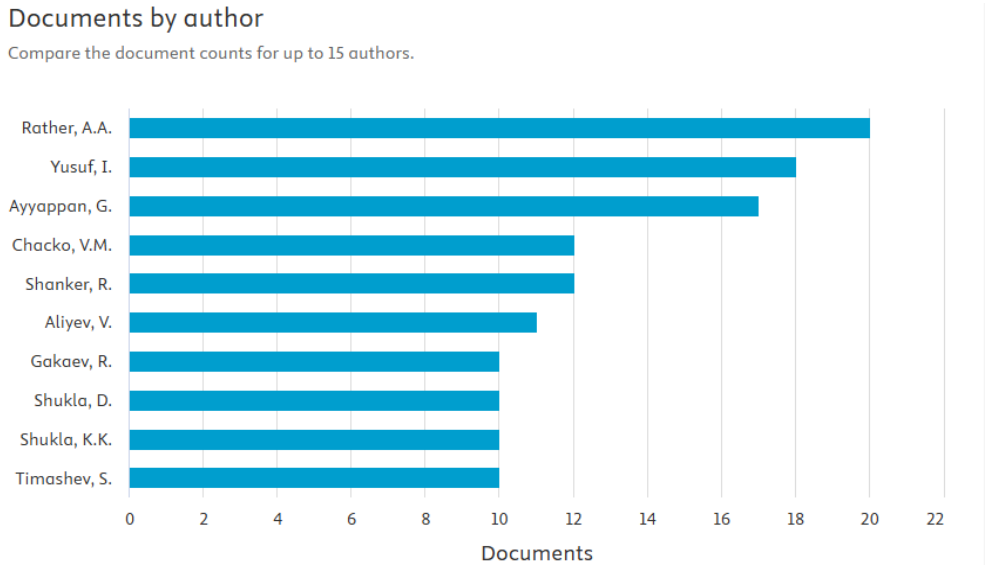


Figure 2: *Top 10 contributing authors*

Document analysis by affiliation

Table-3 and Figure-3 show which universities and institutions have published the most research in this field. Kadyrov Chechen State University is the top contributor with 100 publications, followed by Azerbaijan State Oil and Industry University with 89. Other major contributors include North-Ossetian State University – 40 publications, Russian Academy of Sciences – 33, Bharathiar University – 32, Azerbaijan Technical University and Azerbaijan University of Architecture and Construction – 29 each. University of Kashmir – 26, Maharshi Dayanand University – 24 and Vellore Institute of Technology – 23.

This shows that the journal has attracted interest from many countries, especially from Russia, Azerbaijan, and India. A few universities have published a lot of papers, which suggests they are leading research centres in this area and are helping to shape the future of the field.

Table 3: *Documents by affiliation*

Affiliation	Documents
Kadyrov Chechen State University	100
Azerbaijan State Oil and Industry University	89
North-Ossetian State University	40
Russian Academy of Sciences	33

Bharathiar University	32
Azerbaijan Technical University	29
Azerbaijan University of Architecture and Construction	29
University of Kashmir	26
Maharshi Dayanand University	24
Vellore Institute of Technology	23

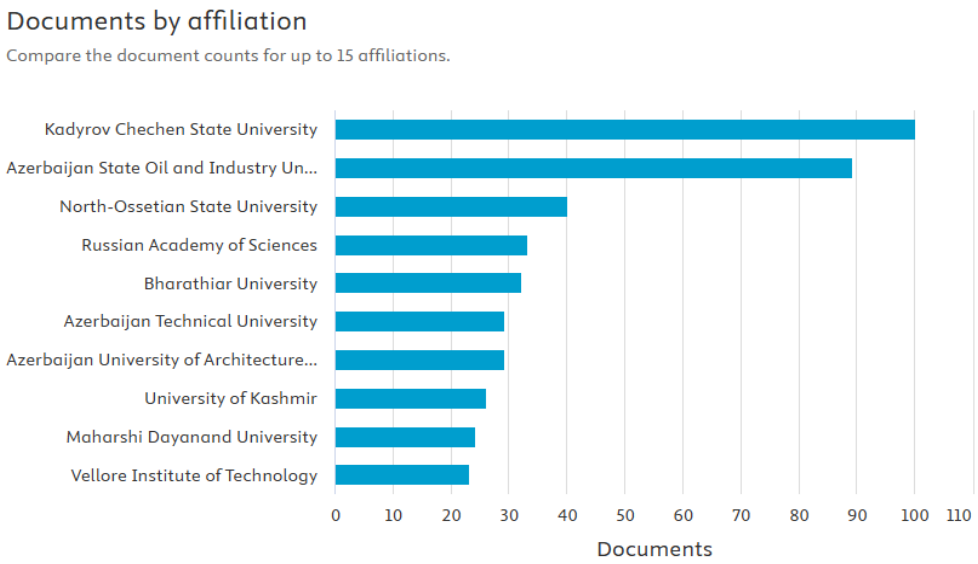


Figure 3: *Documents by affiliation*

Analysis of publications by country or territory

Table-4 and Figure-4 show the number of research papers published by different countries, giving a clear picture of where the research is coming from. India is the top contributor with 626 publications, showing its strong involvement in this field. The Russian Federation is next with 330 publications, followed by Azerbaijan with 169, showing active participation from Central and South Asia. Nigeria is also showing progress with 81 publications. Other countries contributing include Georgia with 21, the United States with 16, Egypt and Kazakhstan with 14 each, Ukraine with 11, and Iran with 9 publications.

This shows that the journal is gaining attention from both developed and developing countries. It is especially popular in emerging economies. Overall, the data suggests that the journal is globally important and is attracting researchers from many different regions and backgrounds.

Table 4: *Documents by country*

Country	Documents
India	626
Russian Federation	330
Azerbaijan	169
Nigeria	81
Georgia	21
United States	16
Egypt	14
Kazakhstan	14
Ukraine	11
Iran	9

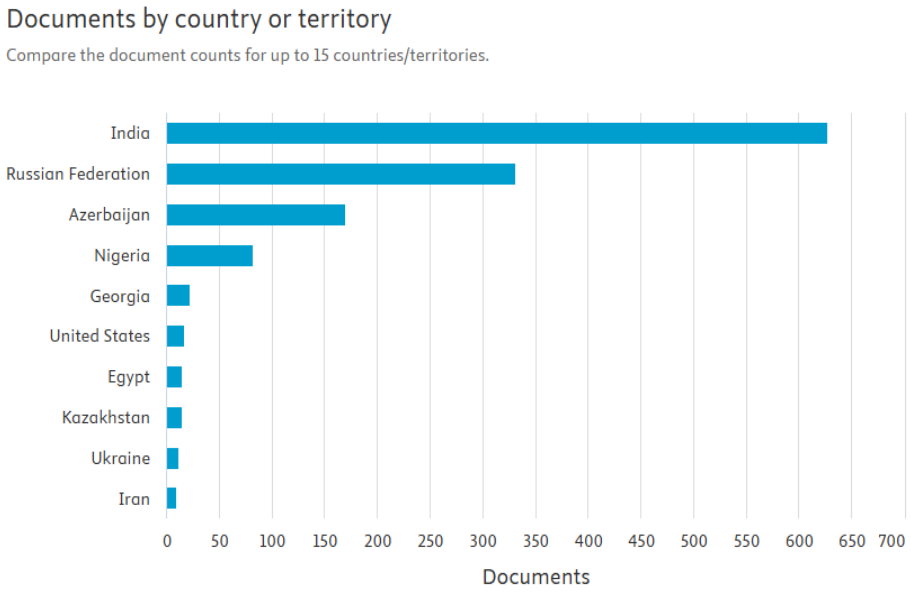


Figure 4: *Document published by top 10 countries*

Documents by type

Table-5 and Figure-5 show the different types of documents published in this research area. Most of the publications are research articles, with 1308 papers, which makes up about 98.94% of the total. This shows that the focus is mainly on original studies and new research. There are only 13 review papers, making up 0.98%, and just one conference paper, which is 0.07% of the total.

This means that the journal mainly publishes original research rather than reviews or conference papers. The high number of peer-reviewed articles also shows the seriousness and quality of the research being published in this field.

Table 5: *Documents by type*

Document type	Publications	%
Article	1308	98.94
Review	13	0.98
Conference Paper	1	0.07

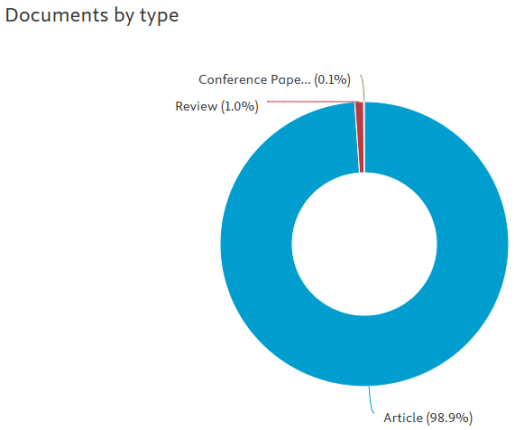


Figure 5: *Publication type*

Analysis by funding sponsors

Table-6 and Figure-6 show the main funding agencies that support research in this field. The Ministry of Education and Science of the Russian Federation is the top funder with 28 supported publications. Next is the Russian Science Foundation with 15 funded papers. From India, the Department of Science and Technology, Ministry of Science and Technology has funded 11 papers. The University Grants Commission (UGC) supported 9 publications, and the Council of Scientific and Industrial Research (CSIR) funded 3. Other organizations that have supported research include the Russian Foundation for Basic Research with 9 papers, the Shota Rustaveli National Science Foundation and the University Grants Committee with 4 each, and both the Bulgarian Academy of Sciences and the Far East Branch of the Russian Academy of Sciences with 3 publications each.

This shows that national-level science and education ministries, especially in Russia and India, are playing a big role in supporting research. It also shows that funding is coming from various countries, which highlights the global importance and collaborative nature of the research in this field.

Table 6: *Documents by Funding sponsor*

Funding sponsor	Number of documents
Ministry of Education and Science of the Russian Federation	28
Russian Science Foundation	15
Department of Science and Technology, Ministry of Science and Technology, India	11
Russian Foundation for Basic Research	9
University Grants Commission	9
Shota Rustaveli National Science Foundation	4
University Grants Committee	4
Bulgarian Academy of Sciences	3
Council of Scientific and Industrial Research, India	3
Far East Branch, Russian Academy of Sciences	3

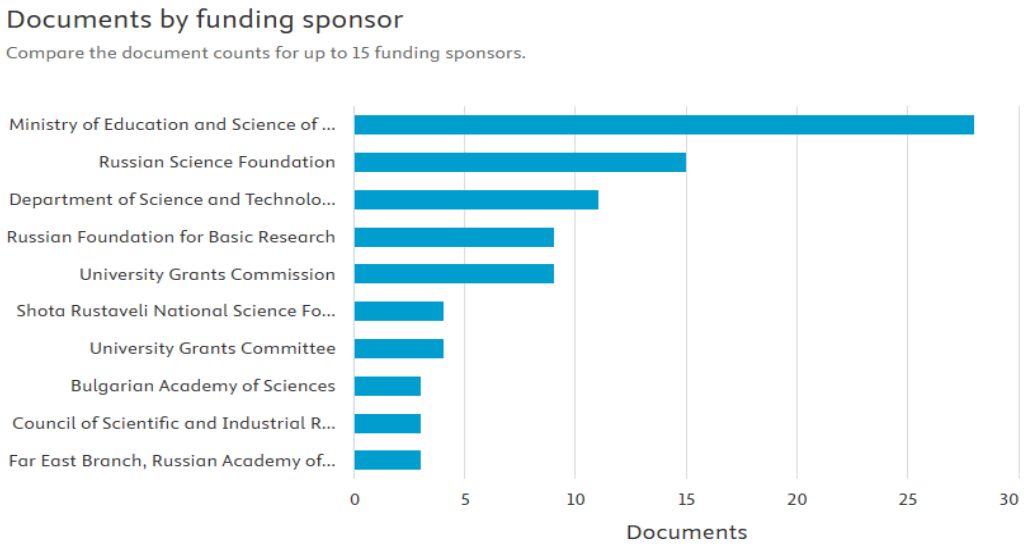


Figure 6: *Top ten funding sponsors*

II. Network Analysis

In Bibliometric analysis, network analysis is a crucial tool for understanding the relationships and collaborations between authors, institutions, countries, and even research topics. It involves mapping and analyzing the connections within a dataset, such as co-authorships, co-citations, or keyword co-occurrences, to reveal the structure of research networks.

(A) Co-authorship analysis

Co-authorship analysis is a method used in Bibliometric studies to explore and evaluate collaboration patterns among researchers, institutions, or countries. By examining the co-authorship of publications, this analysis reveals how often two or more authors work together on research papers, highlighting the strength of their collaborative ties.

Co-authorship in terms of authors

In this analysis, documents with too many authors were not included. Only papers with 25 or fewer authors were considered. To be part of the study, each author had to have written at least one paper and received at least one citation. Out of 2,311 authors checked, only 694 met these conditions. For each of these 694 authors, the strength of their co-authorship connections with others was measured. Yusuf Ibrahim had the highest total link strength of 24. He also had 25 citations from 18 documents, showing that he is an active researcher with strong collaborations. Among all the authors, the biggest connected group of co-authors included 21 people. These 21 authors were divided into 5 different groups or clusters. Together, they had a total link strength of 56. Figure-7 shows this network using different colours for each group, and the size of each circle shows how strong the author's links are. This analysis helps us understand how researchers work together. It shows that authors like Yusuf Ibrahim are at the centre of these networks, leading strong research collaborations.

Table-7 shows the top 10 most connected authors in this field, based on the number of papers they published, the number of citations they received, and how strong their co-authorship links are. Yusuf Ibrahim stands out with 18 papers, 25 citations, and the highest link strength of 24. Rather Aafaq A. comes next with 20 papers and a link strength of 23, even though he has fewer citations. Kumar Rakesh has the highest number of citations (45), even though he has only 8 papers, showing that his work is highly impactful. Other authors like Aliyev Vugar, Farhadzadeh E.M., and Shanker Rama also show strong collaboration through their link strengths. This table highlights the key researchers who are well-connected and influential in this academic field.

Table 7: *Top 10 Linked Authors*

Author	Documents	Citations	Total link Strength
Yusuf, Ibrahim	18	25	24
Rather, Aafaq A.	20	2	23
Kumar, Rakesh	8	45	18
Aliyev, Vugar	11	1	16
Farhadzadeh, E.M.	9	2	15
Shanker, Rama	12	23	15
Akimov, Valery	6	3	14
Laxmi, P. Vijaya	8	24	13
Muradaliyev, A.Z.	7	2	13
Ayyappan, G.	17	9	11

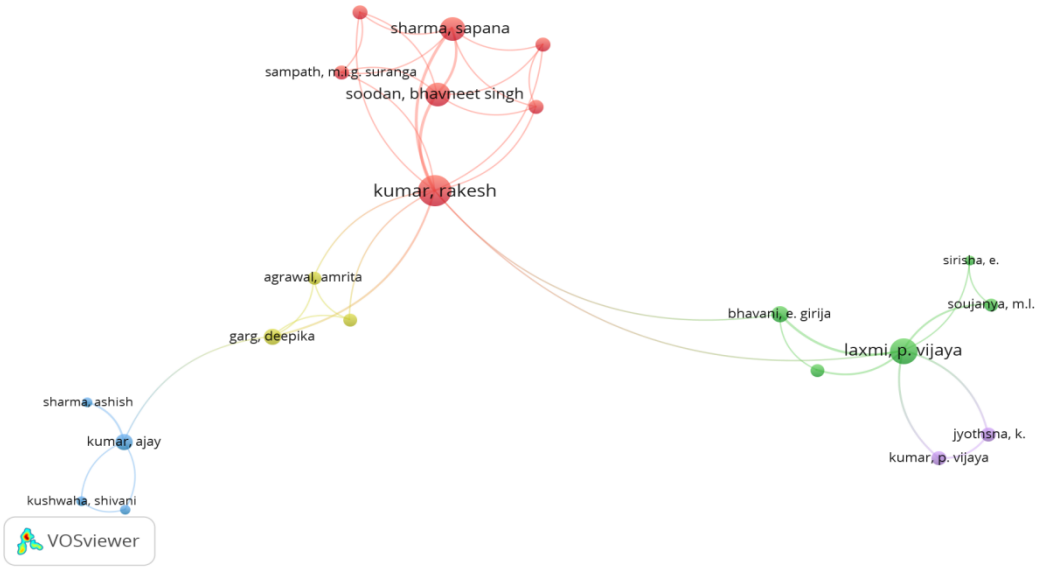


Figure 7: *Co-authorship in terms of author's network analysis*

CO-authorship in terms of organizations

In this analysis, documents with more than 25 authors were left out to keep the co-authorship patterns clear. To be included, an organization had to have at least one publication and one citation. Out of 1,544 organizations checked, 490 met these requirements. For each of these 490 institutions, the total strength of their co-authorship connections with other organizations was calculated. Kadyrov Chechen State University in the Russian Federation had the highest total link strength of 22. It also received 14 citations from 57 documents, making it the top organization in terms of collaboration. Among the included organizations, the largest connected group consisted of 33 institutions. These were divided into nine clusters, with a combined total link strength of 87. Figure-8 shows this network visually, using different colours for each cluster. The size of the circles in the figure shows how strong each organization's collaborations are. This analysis highlights how important teamwork between research institutions is. It shows that leading organizations are forming strong networks that help push scientific progress forward.

Table-8 lists the top 10 institutions based on how many papers they published, how many citations they received, and how strong their collaboration links are. Kadyrov Chechen State University leads with 57 documents and a link strength of 22, showing it is both active and well connected. Next is the Department of Mathematical Sciences at Bayero University in Nigeria, which published 17 papers but received the highest citation count of 25 and had a strong link strength of 19, showing both impact and collaboration. Several Russian universities, including Khetagurov North Ossetian State University, North Caucasus Federal University, and Dagestan State University, are also major contributors, showing strong research activity in the region. Azerbaijan State Oil and Industry University published the most papers at 66 and had 32 citations, but its link strength was only 10, which suggests it contributed a lot individually but had fewer collaborations. Institutions like Bhagwant University in India and Moscow Technical University of Communications and Informatics also played important roles, showing international collaboration. Overall, this analysis points out the most important research organizations in the field and shows how much they are contributing and collaborating with others.

Table 8: *Top 10 Co-authorship Linked Organizations*

Organization	Documents	Citations	Total Link Strength
Kadyrov Chechen State University, Russian Federation	57	14	22
Department of Mathematical Sciences, Bayero University, Kano, Nigeria	17	25	19
Khetagurov North Ossetian State University, Russian Federation	10	1	13
North Caucasus Federal University, Russian Federation	9	3	12
Azerbaijan Technical University, Azerbaijan	22	3	11
Azerbaijan State Oil and Industry University, Azerbaijan	66	32	10
Financial University under the Government of the Russian Federation, Russia	14	10	9
Dagestan State University, Russian Federation	8	1	8
Department of Mathematics, Bhagwant University, Ajmer, India	6	1	8
Moscow Technical University of Communications and Informatics, Russia	7	4	8

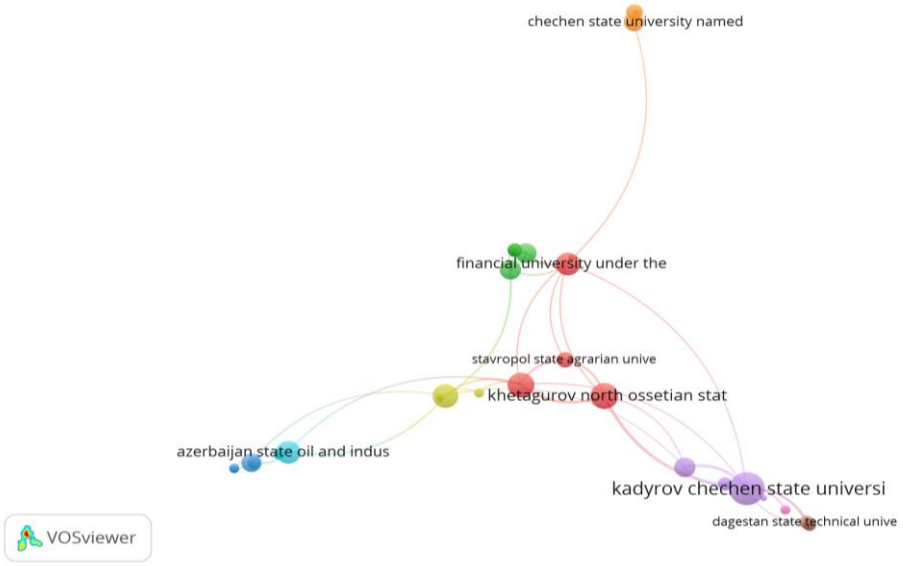


Figure 8: *Network analysis of co-authorship analysis in terms of organizations*

Co-authorship in terms of country

In this analysis, documents with more than 25 authors were excluded to keep the co-authorship patterns clear. A country was included only if it had published at least one paper and received at least one citation. Out of 85 countries reviewed, 51 met these conditions. For each of these 51 countries, the total strength of co-authorship links with other countries was measured. The Russian Federation had the highest link strength of 45, along with 142 citations from 330 publications, showing strong international collaboration. Among the 51 selected countries, 38 formed a connected co-authorship network. These 38 countries were divided into 15 different groups or

clusters, with a total link strength of 109. Figure-9 shows this network using different colours for each group, and the size of the circles represents how strong a country's connections are.

Table-9 lists the top 10 countries based on how many papers they published, how many citations they received, and how strong their international research collaborations are. India stands out as the top contributor with 630 papers and 630 citations, showing both a high number of publications and strong impact. Although the Russian Federation published fewer papers, its link strength of 45 was the highest, showing its strong international partnerships. Other countries like Azerbaijan and Nigeria also show strong participation, with good numbers of papers and solid collaboration networks. Countries such as Egypt, China, and the United States had a moderate number of papers and still showed active international cooperation. Germany, Kyrgyzstan, and Iraq published fewer papers but had clear international ties, showing that they are becoming more involved in global research. Overall, this analysis shows that many countries around the world are taking part in this research field. It highlights the importance of international collaboration and how these partnerships help drive global scientific progress.

Table 9: *Top 10 Co-authorship Linked Countries*

Country	Documents	Citations	Total Link Strength
Russian Federation	330	142	45
India	630	630	40
Azerbaijan	169	55	27
Nigeria	81	65	18
Egypt	14	8	8
China	6	6	7
United States	16	27	6
Germany	7	2	5
Kyrgyzstan	5	1	5
Iraq	4	5	4

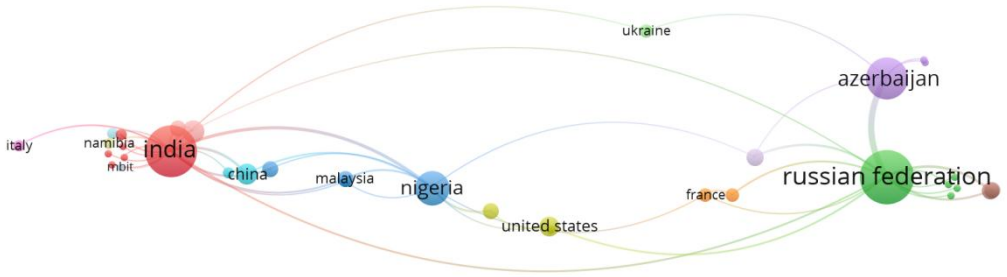


Figure 9: *Network analysis of co-authorships in terms of country*

B) Network analysis of co-occurrences

Network analysis of co-occurrences is a technique used to study relationships between entities like keywords, authors, or institutions that frequently appear together in documents. It helps visualize patterns, identify research trends, and highlight key themes or collaborations within a field, offering insights into the structure of a research area.

Co-occurrence analysis in terms of all keywords

In the keyword co-occurrence analysis, only keywords that appeared at least 10 times were included. Out of a total of 4,557 keywords, 46 met this requirement. For each of these 46 keywords, the total strength of their connections with other keywords was calculated. The keyword "Reliability" appeared the most, with 120 occurrences, and had the highest total link strength of

104. Among the 46 keywords, 42 were found to be connected with each other and formed a co-occurrence network, shown in Figure-10. These 42 keywords were grouped into six clusters with a total link strength of 461. In the network graph, each cluster is shown in a different color, and the size of each circle represents how often a keyword appeared.

Table-10 lists the top 10 most frequent keywords and their total link strength, showing the main topics and how they are related to each other in this research area. The keyword "Reliability" is the most common and most connected, which shows it is the central theme of most studies. Other important keywords like "Availability" and "Maximum Likelihood Estimation" also appear frequently, showing that system performance and statistical methods are key areas of focus. Many technical terms such as Order Statistics, Moments, MTSF (Mean Time to System Failure), Mean Sojourn Time, and Transition Probabilities also appear often, showing that the field involves detailed statistical and mathematical analysis. At the same time, broader topics like Sustainable Development and Climate Change are also becoming more common, showing that researchers are linking theoretical methods with real-world issues. Overall, the keyword analysis shows that the research in this field combines strong theoretical and mathematical foundations with practical applications, reflecting both academic depth and real-world relevance.

Table 10: *Co-occurrence analysis of Top 10 keywords*

Keyword	Occurrences	Total Link Strength
Reliability	120	104
Availability	60	87
Maximum Likelihood Estimation	62	69
Order Statistics	27	41
Moments	27	39
MTSF	16	37
Mean Sojourn Time	11	35
Transition Probabilities	11	33
Sustainable Development	41	28
Climate Change	36	26

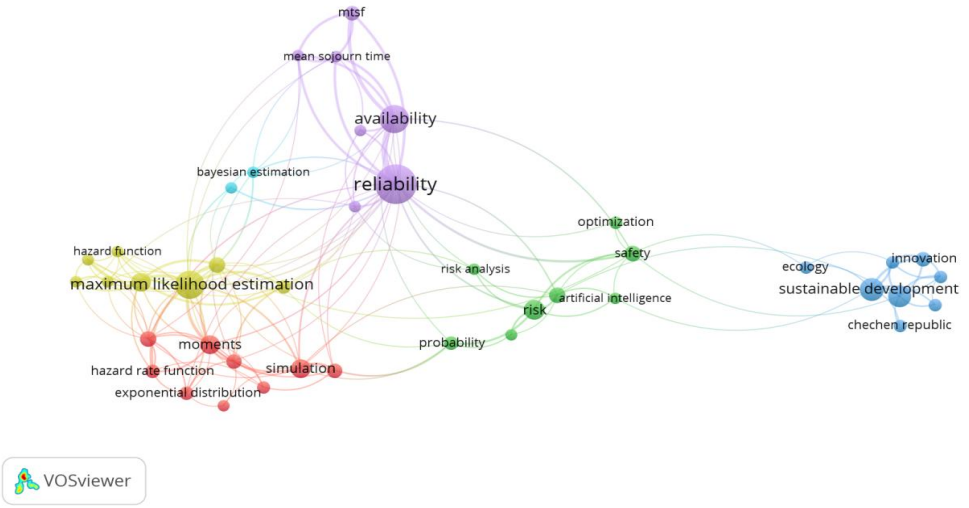


Figure 10: *Network analysis of co-authorship's in terms of all keywords*

Co-occurrence analysis in terms of author keywords

In this analysis of author keywords, only those that appeared at least 5 times were included. Out of 4,557 keywords provided by authors, 159 met this condition. For each of these 159 keywords, the total strength of their connections with other keywords was calculated. The keyword "Reliability" appeared the most, with 120 occurrences, and had the highest total link strength of 180. All 159 keywords were connected to each other, forming a network shown in Figure-11. This network is made up of 10 clusters and has a combined total link strength of 1295.

Table-11 shows the top 10 most frequently used keywords based on how often they appeared and how strongly they are linked with other keywords. "Reliability" comes first with 120 appearances and the highest total link strength, showing that it is the main theme in this area of research. "Availability" and "Maximum Likelihood Estimation" are also used often, appearing 60 and 62 times, with strong link strengths of 133 and 101. This shows that many research studies focus on using statistical methods and how they can be applied in real life. Keywords like MTSF (Mean Time to System Failure), Climate Change, and Transition Probabilities are often used and strongly connected to other topics. This means that the research combines statistical modeling with real-world issues like the environment and how systems work. Other common keywords include Order Statistics, Sustainable Development, Moments, and Mean Sojourn Time. These show that both theory and practical use are important in this research field. Overall, the keyword study shows that this area uses strong statistical methods while also dealing with big global problems like sustainability and climate change.

Table 11: *Co-occurrence analysis of Top 10 author keywords*

Keyword	Occurrences	Total Link Strength
Reliability	120	180
Availability	60	133
Maximum Likelihood Estimation	62	101
MTSF	16	60
Climate Change	36	59
Transition Probabilities	11	56
Order Statistics	27	55
Sustainable Development	41	55
Moments	27	54
Mean Sojourn Time	11	53

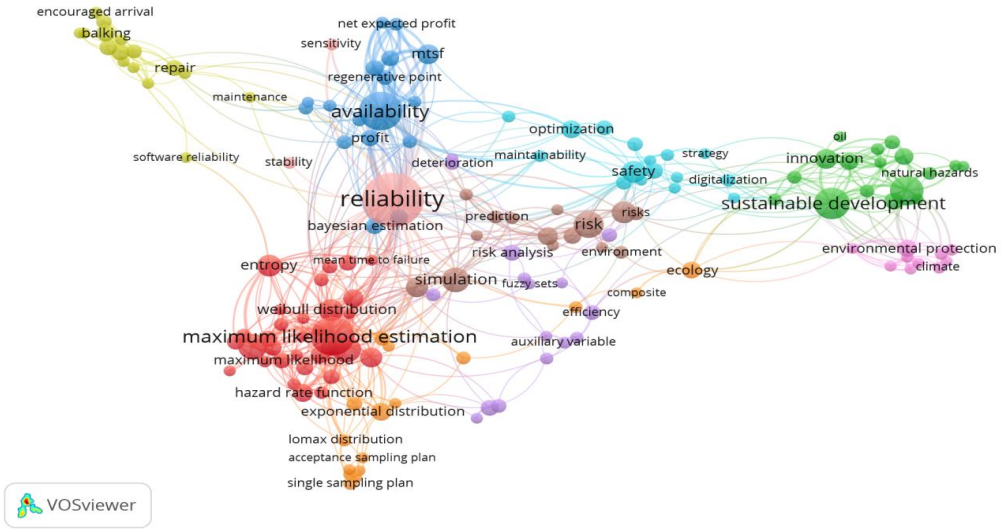


Figure 11: *Network analysis of co-authorship's in terms of Author keywords*

C) Network Analysis of Citations

Network analysis of citations is a method used to examine how frequently documents, authors, or institutions cite each other. This analysis helps identify influential works, key research areas, and the interconnectedness of knowledge in a field. Units of analysis typically include documents, sources, authors, countries and organizations, revealing collaboration patterns and intellectual structures within a research domain. By mapping citation networks, it becomes possible to trace the development of ideas and highlight leading contributors or regions in specific research areas.

Citation Analysis of Documents

Out of a total of 1,322 documents with no citation bar, the document written by Samal in 2023 received the highest number of citations, which is 19. From these 1,322 documents, only 45 were connected to each other, and this connection is shown in Figure-12. In the network graph, the size of each circle shows how many citations a document has received.

Table-12 lists the top 10 most cited documents in this research area. Samal's 2023 paper has the most citations, but it has no co-authorship links, meaning it had a strong impact even though it was not written in collaboration with others. The papers by Alam (2021) and Agrawal (2021) follow, with 16 and 14 citations. Agrawal's paper also has the most links, which shows it was a collaborative effort. Other papers, such as those by Lone (2022), Kumar (2019), and Sachdeva (2022), each received 13 citations and have different levels of collaboration with other authors. The rest of the documents in the top 10—written by Kozyrev (2018), Rahul (2024), Saxena (2021a), and Shiledar (2021)—each have 12 citations. Some of these papers have co-authorship links, while others do not, showing that citation success can come from both individual work and team efforts. Overall, this analysis shows that highly cited research can be produced through solo work or collaboration. Both types of contributions play an important role in the academic field.

Table 12: *Analysis of top 10 cited documents*

Document	Citations	Links
Samal (2023)	19	0
Alam (2021)	16	1
Agrawal (2021)	14	4
Lone (2022)	13	3
Kumar (2019)	13	3
Sachdeva (2022)	13	2
Kozyrev (2018)	12	2
Rahul (2024)	12	1
Saxena (2021a)	12	0
Shiledar (2021)	12	0

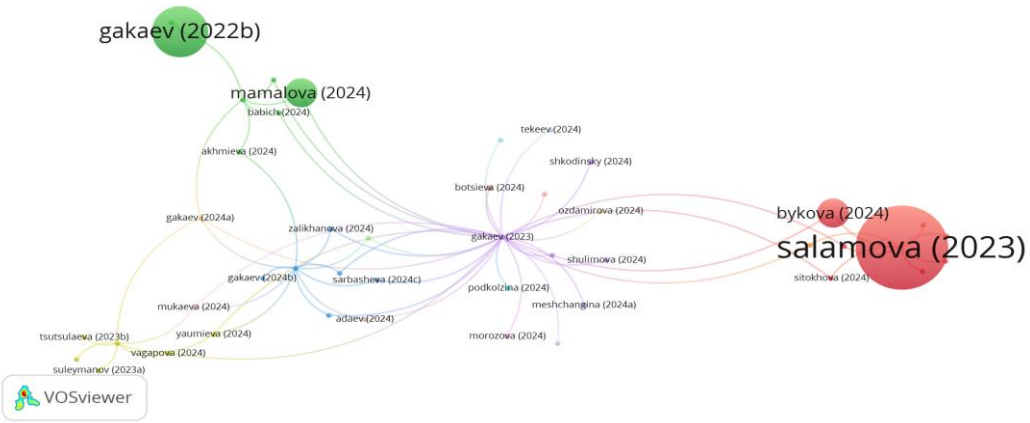


Figure 12: *Network analysis of Citation Analysis of Documents*

Citation analysis by Authors

In this analysis, documents that had more than 25 authors were not included, as the goal was to keep authorship meaningful. To be part of the study, each author had to have written at least one document and received at least one citation. Out of 2,311 authors, 694 met these requirements. For each of these authors, the total strength of their co-authorship links with other authors was calculated. Kumar Rakesh had the highest number of citations, with 45 citations from 8 documents, and a link strength of 19. Among the 694 authors, 81 were found to be connected with each other, forming a network shown in Figure-13. These 81 authors were divided into twelve groups or clusters. Together, they had a total link strength of 279. In the network diagram, different colors show different clusters, and the size of each circle represents how many citations an author has received.

Table-13 gives a list of the top authors based on their citations and co-authorship connections. Kumar Rakesh appears at the top with 45 citations and strong collaboration, as shown by his link strength of 19. Ahmed Aquil and Kumar Vijay have 34 and 28 citations, but their lower link strengths suggest they work more independently. Other authors like Ram Mangey, Shanker Rama, and Soodan Bhavneet Singh show a balance between citations and collaboration, with moderate to high link strengths starting from 8. Yusuf Ibrahim has the most documents (18) and a link strength of 9, showing he is both productive and well-connected with other researchers. This analysis shows that while citations reflect an author's impact in the field, the link strength reveals how much they collaborate with others. Together, these two measures give a clearer picture of each author's role in the research community.

Table 13: *Citation analysis of top 10 authors*

Author	Documents	Citations	Total Link Strength
Kumar, Rakesh	8	45	19
Ahmed, Aquil	3	34	1
Kumar, Vijay	5	28	2
Ram, Mangey	7	27	8
Alam, Intekhab	5	27	2
Yusuf, Ibrahim	18	25	9
Laxmi, P. Vijaya	8	24	2
Soodan, Bhavneet Singh	4	23	8
Shanker, Rama	12	23	8
Shukla, Kamlesh Kumar	10	23	4

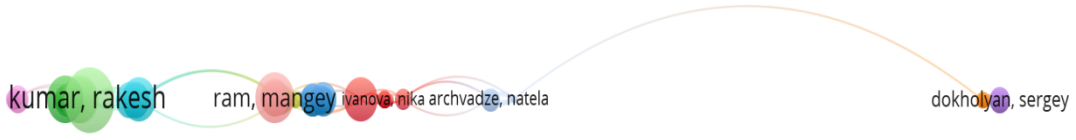


Figure 13: *Network analysis of Citation analysis by Authors*

Citation analysis by organization

In this analysis, documents with more than 25 authors were not included to keep authorship meaningful. Organizations needed to have at least 2 documents and 2 citations to be included. Out of 1,544 organizations, 102 met these conditions. For each of these, the total strength of their co-authorship links with other organizations was calculated. The "Azerbaijan State Oil and Industry

University" had the highest number of citations, with 32 citations across 66 documents. Out of the 102 organizations, only 8 were connected with each other, and this network is shown in Figure-14. These 8 organizations formed 3 different groups or clusters, and their total link strength was 11. In the figure, the size of each circle represents how many citations that organization received.

Table-14 lists the top organizations based on the number of documents they published and how much they collaborated with others. The Department of Mathematics at SRM Institute of Science and Technology (Delhi-NCR Campus, India) had the most documents (9) and the highest collaboration score with a link strength of 10. It was followed by the Department of Mathematics at Maharshi Dayanand University and the Azerbaijan State Oil and Industry University, with 7 and 4 documents respectively, both showing strong collaboration. Some institutions like ABV-IIITM Gwalior and Kadyrov Chechen State University had fewer documents (2 or 3) but still had high collaboration scores, each with a link strength of 9. Others, such as Bayero University and TITS Bhiwani, contributed only a few documents and did not show any collaboration links in the network. Overall, this analysis shows that different organizations are contributing to the research in different ways—some through strong partnerships, others more independently—while also highlighting the global reach and involvement in the field.

Table 14: *Citation analysis of top 10 organizations*

Organization	Documents	Total Link Strength
Azerbaijan State Oil and Industry University, Azerbaijan	4	10
Department of Mathematical Sciences, Bayero University, Kano, Nigeria	2	0
Department of Applied Sciences, ABV-IIITM Gwalior, MP, Gwalior, 474015, India	2	9
Department of Mathematics, SRM Institute of Science and Technology, Delhi-NCR Campus, Ghaziabad, India	9	10
Department of Statistics, University of Kashmir, Srinagar, India	3	3
Department of Mathematics, Maharshi Dayanand University, Haryana, Rohtak, India	7	9
Department of Applied Sciences, TITS Bhiwani, Haryana, India	3	0
Kadyrov Chechen State University, Russian Federation	3	9
School of Engineering and Sciences, GD Goenka University, Gurugram, India	2	4



Figure 14: *Network analysis of Citation analysis by organization*

Citation analysis by country

In this analysis, documents with more than 25 authors were excluded to keep the authorship

meaningful. Countries needed to have at least 2 documents and 2 citations to be included. Out of 85 countries, 29 met these conditions. For each of these 29 countries, their total strength of citation links with other countries was calculated. India had the highest number of citations, with 630 citations from 630 documents, and the strongest total link strength of 23. Out of the 29 countries that met the threshold, 15 were connected with each other, forming a network shown in Figure-15. These 15 countries were divided into seven groups, and their combined link strength was 40. Each group is shown in a different color, and the size of the circle for each country represents how many citations it received.

Table-15 shows how much each country contributed to the research field. India had the largest contribution with 630 documents and 630 citations, and it also had the strongest collaboration with a link strength of 23. The Russian Federation was next with 330 documents and 142 citations, along with a link strength of 14. Azerbaijan followed with 169 documents, 55 citations, and a link strength of 10. Other countries like Nigeria, Namibia, and the United States had a fair number of research papers and citations, which shows that they are actively involved in research and working with others. Countries like Brazil, Eritrea, Germany, and Oman had fewer papers, but they were still part of the research network. This means they also contributed to global research in their own way. This study helps us see how different countries are taking part and working together in this research area.

Table 15: *Citation analysis of top 10 countries*

Country	Documents	Citations	Total Link Strength
India	630	630	23
Russian Federation	330	142	14
Azerbaijan	169	55	10
Namibia	2	14	6
Nigeria	81	65	6
United States	16	27	6
Brazil	4	12	3
Eritrea	5	14	2
Germany	7	2	2
Oman	4	4	2

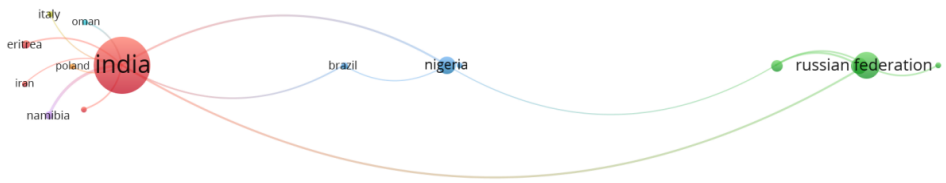


Figure 15: *Network analysis of Citation analysis by country*

III. Conclusion

This study gives a clear and simple summary of the research published in the journal Reliability: Theory and Applications between 2017 and 2024. It shows that the number of papers published in the journal has gone up steadily, especially after 2020. This means the journal is becoming more popular and respected in the global research world. The study also highlights the countries that have contributed the most to the journal. India, the Russian Federation, and Azerbaijan are the top contributors. It mentions leading universities and researchers, such as Kadyrov Chechen State University, Azerbaijan State Oil and Industry University, Yusuf Ibrahim, and Rather Aafaq A.,

who have played important roles and worked closely with others in the field. By looking at how authors work together, the keywords they use, and how papers are cited, the study identifies the main topics covered by the journal. These topics include reliability, availability, and maximum likelihood estimation. This shows that the journal focuses on both detailed statistical techniques and real-world applications. The citation analysis shows which papers have been most influential, proving that the journal values both solo research and teamwork. Overall, the study shows that Reliability: Theory and Applications is a growing and active journal. It plays an important part in global research on reliability. The results of this study can help future researchers, institutions, and policymakers who want to publish in the journal or learn from it.

References

[1] Biemans, W. G., Griffin, A., & Moenaert, R. K. (2007). Twenty years of the Journal of Product Innovation Management: History, participants, and knowledge stock and flows. *Journal of Product Innovation Management, 24*(3), 193–213.

[2] Cancino, C. A., Merigó, J. M., Coronado, F., Dessouky, M., & Dessouky, Y. (2017). Forty years of Computers & Industrial Engineering: A bibliometric analysis. *Computers & Industrial Engineering, 113*, 614–629.

[3] Cobo, M. J., López-Herrera, A. G., Herrera-Viedma, E., & Herrera, F. (2015). Bibliometric analysis of the 25th anniversary of Knowledge-Based Systems. *Knowledge-Based Systems, 80*, 3–13.

[4] Corrales, M., García, M. G., Martínez, M. A., Merigó, J. M., & Gutiérrez-Salcedo, M. (2016). A bibliometric analysis of oral health-related research in Latin American countries. *Journal of Oral Research, 5*(2), 36–44.

[5] Dereli, T., Durmuşoğlu, A., & Şahan, A. (2011). Bibliometric analysis of Total Quality Management & Business Excellence between 1995 and 2008. *Total Quality Management & Business Excellence, 22*(12), 1307–1331.

[6] Dhiman, A. K. (2000). Ethnobotany journal: A ten-year bibliometric study. *IASLIC Bulletin, 45*(4), 177–182.

[7] García-Merino, J. D., Duran-Heras, A., & Navas-López, J. E. (2006). The contribution of Technovation to academic research. *Technovation, 26*(12), 1350–1355.

[8] Hazarika, T., Goswami, A., & Das, P. (2003). Bibliometric analysis of the Indian Forester (1993–2002). *Indian Forester, 129*(6), 722–732.

[9] Heck, J. L., & Bremser, W. G. (1986). Six decades of the Journal of Finance. *Journal of Finance, 41*(4), 997–1003.

[10] Hoffman, D. L., & Holbrook, M. B. (1993). The intellectual structure of consumer research: A bibliometric study of the Journal of Consumer Research, 1974–1991. *Journal of Consumer Research, 19*(4), 505–517.

[11] Hussain, S., & Bhat, V. A. (2023). 10 years of Genetic Resources and Crop Evolution—a bibliometric analysis of SCOPUS publications 2013–2022. *Genetic Resources and Crop Evolution, 70*(5), 1321–1334.

[12] Kumar, P., & Moorthy, K. A. (2011). Bibliometric analysis of DESIDOC Journal of Library and Information Technology. *DESIDOC Journal of Library & Information Technology, 31*(1), 3–11.

[13] Laengle, S., Merigó, J. M., Miranda, J., Słowiński, R., Bomze, I., Borgonovo, E., & Goutsias, J. (2017). Forty years of the European Journal of Operational Research: A bibliometric overview. *European Journal of Operational Research, 262*(3), 803–816.

[14] Malhotra, N. K., Wu, L., & Whitelock, J. (2005). An overview of the first 21 years of the International Marketing Review. *International Marketing Review, 22*(2), 180–204.

[15] Merigó, J. M., Cancino, C. A., Coronado, F., & Urbano, D. (2017). Academic research in innovation: A bibliometric analysis of the Journal of Business Research. *Journal of Business Research, 69*(10), 4510–4520.

[16] Merigó, J. M., Gil-Lafuente, A. M., & Yager, R. R. (2015). An overview of fuzzy research with bibliometric indicators. *Fuzzy Sets and Systems, 281*, 46–62.

[17] Ramos-Rodríguez, A. R., & Ruiz-Navarro, J. (2004). Changes in the intellectual structure of strategic management research: A bibliometric study of the Strategic Management Journal, 1980–2000. *Strategic Management Journal, 25*(10), 981–1004.

[18] Sprott, D. E., & Miyazaki, A. D. (2002). Two decades of contributions to public policy and marketing. *Journal of Public Policy & Marketing, 21*(2), 105–114.

[19] Thanuskodi, S. (2010). Bibliometric analysis of the Journal Library Philosophy and Practice from 2005–2009. *Library Philosophy and Practice, 1*, 23–36.

[20] Thanuskodi, S. (2011). Bibliometric analysis of the Library Herald Journal for the period 2006–2010. *Library Herald, 49*(2), 125–137.

[21] Valenzuela, L., Merigó, J. M., & Grisales, J. (2017). A bibliometric analysis of Journal of Business & Industrial Marketing: 1985–2015. *Journal of Business & Industrial Marketing, 32*(3), 433–447.

[22] Vellaichamy, A., & Jeyshankar, R. (2015). Webology Journal: A bibliometric analysis. *Journal of Webology, 12*(1), 45–52.

[23] Zinkhan, G. M., & Leigh, J. H. (1999). Assessing the quality ranking of the Journal of Advertising, 1986–1997. *Journal of Advertising, 28*(2), 51–70.

STRESS-STRENGTH MODELLING: A COMPARATIVE STUDY USING SRS, RSS AND MRSS FOR INVERSE NAKAGAMI DISTRIBUTION

Surinder Kumar[1], Rahul Shukla[1], Bhupendra Meena[1], Shivendra Pratap Singh[1]

•

[1] Department of Statistics,
Babasaheb Bhimrao Ambedkar University, 226025, U.P, India
surinderntls@gmail.com
Corresponding Author: rahul.shukla.stats@gmail.com
bhupendrakm57@gmail.com
shivendra15.07@gmail.com

Abstract

The present research endeavours to use the ranked set sampling technique in place of the simple random sampling technique in estimating the reliability model in the field of reliability engineering and manufacturing industries. The stress-strength reliability is widely used in all field of engineering and in the manufacturing industry. In this research article, we take the case when the lifetime data of any machinery followed the Inverse Nakagami distribution, and by considering the stress-strength model, we compare the standard ranked set sampling and median ranked set sampling estimate with the corresponding simple random sampling estimate through Monte Carlo simulation technique. The final stage of this study involves corroborating the findings through an analysis of a benchmark dataset on elevators and their motors utilized in farming machinery.

Keywords: Stress-strength reliability, Median ranked set sampling, Ranked set sampling, Inverse Nakagami distribution, Monte Carlo simulation

I. Introduction

In the literature, the conceptual framework of the stress-strength model was first introduced by Birnbaum [2], with further advancements made in his joint work with McCarty [16]. The phrase 'stress-strength' was first coined by Church and Harris [6] in their academic article, in which they performed important investigations using parametric and non-parametric techniques. Following this, various scholars selected different probabilistic models to estimate the stress-strength relation- ships. Some of these selections were summarized by Johnson [10]. A comprehensive overview of all methodologies and discoveries related to the stress-strength paradigm across the previous four decades was compiled by Kotz et al. [12]. Different researchers work on stress-strength model by taking different cases of distribution, like Downton [8] take the case of Normal distribution, Constantine et al. [7] take the case of Gamma distribution, Awad and Gharraf [1] take Burr distribution case, Kundu and Gupta [13] take Generalised Exponential distribution case and so many others distribution are taken to estimate stress-strength reliability.

Based on existing literature, no researchers have explored the case of the Inverse Nakagami distribution until now. The Inverse Nakagami distribution (INAD) was proposed by Louzada et al. [15] as an extension of the Nakagami distribution, which was originally introduced by Nakagami [18] himself. The versatility of the Nakagami distribution has led to its adoption in multiple fields, ranging from communications technology to medical image analysis, water resource management, and earthquake studies. (see, e.g., studies by Wang et al. [26], Tsui et al. [25], Sarkar et al. [22], Nakahara and Carcole [19]).

The Ranked Set Sampling (RSS) introduced by McIntyre [16]. Unlike conventional random sampling methods, RSS leverages the ranked order or order statistics of sampled observations to improve the quality and efficiency of estimations. The estimation of distribution functions using various RSS techniques has been explored by several researchers. Stokes and Sager [24], Yu and Lam [27], and Chen [4] have contributed to this area. Furthermore, investigations into the estimation of distribution functions under different RSS methods have been conducted by Kvam and Samaniego [14], and Chen [5]. Furthermore, the research contributions of Zhang et al. [29], Zamanzade and Vock [28], and Ozturk and Kavlak [20] have shed light on inferential methodologies and techniques that utilize data obtained through ranked set sampling approaches.

Muttak [17] introduced a modified variant of RSS called the median ranked set sampling (MRSS) aimed at estimating the population mean. A comprehensive literature review encompassing the research on RSS until 1995 can be found in the work of Kaur et al. [11]. Employing the MRSS technique, Samuh and Qtait [21] focused on estimating the parameters of the Exponentiated Exponential distribution. Hassan et al. [9] contributed to the field by exploring stress-strength reliability estimation utilizing the MRSS approach. More recently, Shahzad et al. [23] made a significant contribution to the MRSS field by demonstrating the effectiveness of combining ranked and actual auxiliary variable observations in mean estimation.

Here, we have consider the estimation of R = Pr(Y < X) with a focus on situation where the random stress Y and random strength X are two independent Inverse Nak- agami random variables with shape parameters (ξ_1, ξ_2) and scale parameters (ψ, ψ), respectively. The point estimator of R = Pr(Y < X), is obtained using the maximum likelihood method based on SRS, RSS and MRSS, and the efficiency of this method based on SRS and RSS is compared. In Section 2, we present a brief overview about the Inverse Nakagami distribution. Point estimation of the parameters is given in Section 3. Stress-strength reliability is calculated in Section 4. Section 5 and Section 6 comprises the point estimation of stress-strength model under SRS and under RSS, respectively. In Section 7 we take the case of MRSS and derived the point estimation of the parameters. A simulation study employing the Monte Carlo method is discussed in Section 8. Section 9 shows the real life application of the current findings, and lastly Section 10 provides concluding remarks for the paper.

II. Preliminary

When a random variable X follows the Inverse Nakagami distribution INAD (ξ, ψ) with shape parameter ξ, where ξ is constrained to be greater than 0, and scale parameter ψ, where ψ is greater than 0 then its PDF and CDF is given by

$$f(x, \xi, \psi) = \frac{2}{\Gamma(\xi)}\left(\frac{\xi}{\psi}\right)^{\xi} x^{-2\xi-1} \exp\left(-\frac{\xi}{\psi}\, x^{-2}\right); \quad x > 0, \psi > 0, \xi > 0 \tag{1}$$

and

$$F(x) = \frac{\Gamma\left(\xi, \frac{\xi}{\psi}\, x^{-2}\right)}{\Gamma(\xi)}; \quad x > 0, \psi > 0, \xi > 0 \tag{2}$$

where $\Gamma(a,x) = \int_x^\infty t^{a-1}\, e^{-t} dt$

The reliability function of INAD (ξ, ψ) is

$$R(t) = \frac{\gamma\left(\xi, \frac{\xi}{\psi}\, t^{-2}\right)}{\Gamma\xi}; \quad t > 0, \psi > 0, \xi > 0$$

where $\gamma(a,x) = \int_\infty^x t^{a-1}\, e^{-t} dt$

The hazard rate of INAD (ξ, ψ) is

$$h(t) = \frac{\frac{2}{\Gamma(\xi)}\left(\frac{\xi}{\psi}\right)^{\xi} t^{-2\xi-1} \exp\left(-\frac{\xi}{\psi}\, t^{-2}\right)}{\gamma\left(\xi, \frac{\xi}{\psi}\, t^{-2}\right)}; t > 0, \psi > 0, \xi > 0$$

Special Cases of INAD (ξ, ψ)

1. If ξ = 1, then INAD (ξ, ψ) becomes the Inverse Rayleigh distribution.
2. If ξ = 0.5, then INAD (ξ, ψ) becomes the Inverse half-normal distribution.
3. If ψ = 1, ξ = λ, λ = 1, 2, 3 ..., then INAD (ξ, ψ) becomes the Inverse Chi distribution.
4. There is one special case where INAD (ξ, ψ) moves to newly proposed Inverse Hayt distribution for 0 < ξ < 1.

III. Parameters estimation

If we take a random sample $x_1, x_2, \ldots, x_n$ from the INAD (ξ, ψ) of size n, then the likelihood function of the Inverse Nakagami distribution INAD (ξ, ψ) is given by

$$L(x, \xi, \psi) = \frac{\left(2\xi^{\xi}\right)^n}{(\Gamma\xi)^n (\psi^{\xi})^n} \prod_{i=1}^{n} (x_i)^{(-2\xi-1)} \exp\left(-\frac{\xi}{\psi} \sum_{i=1}^{n} x_i^{-2}\right) \tag{3}$$

We can formulate the likelihood function as follows

$$\log L = n \log 2 - n \log \Gamma\, \xi + n\xi \log \xi - n\xi \log \psi - (2\xi + 1) \sum_{i=1}^{n} \log x_i - \frac{\xi}{\psi} \sum_{i=1}^{n} x_i^{-2} \tag{4}$$

Differentiating the log likelihood function of INAD (ξ, ψ) given in Eq. (4) with respect to ψ in the case when ξ is known and equating the resulting equation equal to zero, we get

$$\hat{\psi} = \frac{\sum_{i=1}^{n} x_i^{-2}}{n} \tag{5}$$

Similarly, differentiating the log likelihood function of INAD (ξ, ψ) given in Eq. (4) with respect to ξ in the case when ψ is known

$$\frac{\partial log L}{\partial \xi} = n(log\xi + 1) - n\left(\frac{\partial}{\partial \xi}\, log\Gamma\xi\right) - nlog\, \psi - 2\sum_{i=1}^{n} log\, x_i - \frac{1}{\psi}\sum_{i=1}^{n} x_i^{-2} \tag{6}$$

equating the Eq. (6) to zero, we get

$$\frac{\partial log L}{\partial \xi} = \log \xi - \left(\frac{\partial}{\partial \xi} \log \Gamma\, \xi\right) - \log\left(\frac{1}{n}\sum_{i=1}^{n} x_i^{-2}\right) + \frac{1}{n}\sum_{i=1}^{n} \log x_i^{-2} = 0 \tag{7}$$

ML estimator of ξ ($\hat{\xi}$) can be obtained from Eq. (7) by using Newton-Raphson method beacause Eq. (7) does not yield a closed-form solution.

IV. Stress - strength reliability

To formulate the reliability expression under the stress-strength model, we assume the strength characteristic is represented by the random variable X, while the stress characteristic is denoted by the random variable Y. Both X and Y are assumed to follow the Inverse Nakagami distribution, characterized by a shared scale parameter ψ, where ψ is greater than zero. However, they differ in their shape parameters, with X having a shape parameter of ξ_1 and Y having a shape parameter of ξ_2. Letting X~ INAD (ξ_1,ψ) and Y ~ INAD (ξ_2, ψ), we can proceed to derive the reliability as

$$R = \int_0^\infty P(Y < X) f(x) dx$$

$$= \int_0^\infty \left[\frac{1}{\Gamma\xi_2}\Gamma\left(\xi_2, \frac{\xi_2}{\psi x^2}\right)\right] \frac{2}{\Gamma\xi_1}\left(\frac{\xi_1}{\psi}\right)^{\xi_1} x^{-2\xi_1-1} \exp\left(\frac{-\xi_1}{\psi x^2}\right) dx$$

$$= 2\left(\frac{\xi_1}{\psi}\right)^{\xi_1} \frac{1}{\Gamma\xi_1} \int_0^\infty x^{-2\xi_1-1} \exp\left(\frac{-\xi_1-\xi_2}{\psi x^2}\right) \sum_{m=0}^{\xi_2-1} \frac{(\xi_2)^m}{\psi^m x^{2m} m!} dx$$

$$= \frac{(\xi_1)^{\xi_1}}{\Gamma\xi_1} \sum_{m=0}^{\xi_2-1} \frac{(\xi_2)^m}{m!} \int_0^\infty y^{-(\xi_1+m)-1} e^{-\frac{1}{y}(\xi_1+\xi_2)} dy$$

$$R = \frac{(\xi_1)^{\xi_1}}{\Gamma\xi_1} \sum_{m=0}^{\xi_2-1} \frac{(\xi_2)^m}{m!} \left[\frac{\Gamma(\xi_1+m)}{(\xi_1+\xi_2)^{\xi_1+m}}\right] \quad (8)$$

V. Evaluating stress-strength model through SRS point estimation

We consider two independent random samples X and Y, of sizes n and m respectively, drawn from INAD's. Let X follow a INAD with a shape parameter ξ_1, while Y follows a INAD with a shape parameter ξ_2. Assuming the scale parameter ψ is known, we can employ the invariance property of Maximum Likelihood (ML) estimators to derive the ML estimator for R given in Eq. (8). Under these conditions, the ML estimators of ξ_1 and ξ_2 from Eq. (7) are given by $\hat{\xi}_{1srs}$ and $\hat{\xi}_{2srs}$. Here we use the R software to calculate the ML estimators of ξ1 and ξ2 from Eq. (7), respectively.
In the context of simple random sampling, the expression for the maximum likelihood estimator of R takes the following form

$$\hat{R}_{srs} = \frac{\left(\hat{\xi}_{1srs}\right)^{\hat{\xi}_{1srs}}}{\Gamma\hat{\xi}_{1srs}} \sum_{m=0}^{\hat{\xi}_{1srs}-1} \frac{\left(\hat{\xi}_{1srs}\right)^m}{m!} \left[\frac{\Gamma\left(\hat{\xi}_{1srs}+m\right)}{\left(\hat{\xi}_{1srs}+\hat{\xi}_{2srs}\right)^{\hat{\xi}_{1srs}+m}}\right] \quad (9)$$

VI. Evaluating stress-strength model through RSS point estimation

RSS represents an advanced statistical method that improves parameter estimation accuracy, especially in situations where data gathering is limited by resources or expenses. The RSS process for obtaining a sample of size n involves multiple stages. Initially, m random sets are chosen through SRS, each containing m elements. These elements are then ordered within their respective sets from smallest to largest based on judgment alone, without actual measurement. The next phase involves selecting specific units for precise measurement. This is done by measuring the unit judged smallest in the first set, the second smallest in the second set, and so on, culminating with the largest judged unit in the final set. This entire sequence constitutes one cycle. The process is repeated r times, resulting in a total

ranked set sample size of n = mr, where m is the number of units per set and r represents the number of completed cycles.

I. RSS-based Maximum likelihood estimation for stress-strength model

Let us consider two ranked set samples from Inverse Nakagami distributions with different parameters. The first sample, denoted as $x_{(ij)}$, has a size of $n_1 = r_1 m_1$, where i ranges from 1 to m_1, and j from 1 to r_1. This sample is drawn from an Inverse Nakagami distribution with parameters (ξ_1, ψ). Here, m_1 represents the set size, and r_1 the number of cycles. Similarly, the second sample, $y_{(kl)}$, has a size of $n_2 = r_2 m_2$, where k ranges from 1 to m_2, and l from 1 to r_2. This sample comes from an Inverse Nakagami distribution with parameters (ξ_2, ψ). In this case, m_2 is the set size, and r_2 the number of cycles. We can now express the probability density functions (PDFs) for $x_{(ij)}$ and $y_{(kl)}$ as follows:

$$f_i(x_{ij}) = \frac{m_1!}{(i-1)!\,(m_1-i)!}[F_X(x)]^{i-1}[1-F_X(x)]^{m_1-i} f(x_{ij}) \tag{10}$$

$$g_k(y_{kl}) = \frac{m_2!}{(k-1)!\,(m_2-k)!}[F_Y(y)]^{k-1}[1-F_Y(y)]^{m_2-k} g(y_{kl}) \tag{11}$$

Now the likelihood function is given as

$$L = \prod_{i=1}^{r_1}\prod_{j=1}^{m_1} f_i(x_{ij}) \prod_{k=1}^{r_2}\prod_{l=1}^{m_2} g_k(y_{kl})$$

$$L = \prod_{i=1}^{r_1}\prod_{j=1}^{m_1} \frac{m_1!}{(i-1)!\,(m_1-i)!}[F_X(x)]^{i-1}[1-F_X(x)]^{m_1-i} f(x_{ij})$$

$$\prod_{k=1}^{r_2}\prod_{l=1}^{m_2} \frac{m_2!}{(k-1)!\,(m_2-k)!}[F_Y(y)]^{k-1}[1-F_Y(y)]^{m_2-k} g(y_{kl})$$

Let $u = \frac{m_1!}{(i-1)!(m_1-i)!}$ and $v = \frac{m_2!}{(k-1)!(m_2-k)!}$

$$L = \prod_{i=1}^{r_1}\prod_{j=1}^{m_1} u\,[F_X(x)]^{i-1}[1-F_X(x)]^{m_1-i} f(x_{ij})$$

$$\prod_{k=1}^{r_2}\prod_{l=1}^{m_2} v\,[F_Y(y)]^{k-1}[1-F_Y(y)]^{m_2-k} g(y_{kl})$$

$$L = u\prod_{i=1}^{r_1}\prod_{j=1}^{m_1}\left(\frac{1}{\Gamma\xi_1}\right)^{i-1}\left[\Gamma\left(\xi_1, \frac{\xi_1}{\psi\, x_{ij}^2}\right)\right]^{i-1}\left(\frac{1}{\Gamma\xi_1}\right)^{m_1-i}$$

$$\left[\Gamma\xi_1 - \Gamma\left(\xi_1, \frac{\xi_1}{\psi\, x_{ij}^2}\right)\right]^{m_1-i} \frac{2}{\Gamma(\xi_1)}\left(\frac{\xi_1}{\psi}\right)^{\xi_1} x^{-2\xi_1-1}\exp\left(-\frac{\xi_1}{\psi}\, x_{ij}^{-2}\right)$$

$$v\prod_{k=1}^{r_2}\prod_{l=1}^{m_2}\left(\frac{1}{\Gamma\xi_2}\right)^{k-1}\left[\Gamma\left(\xi_2, \frac{\xi_2}{\psi\, y_{kl}^2}\right)\right]^{k-1}\left(\frac{1}{\Gamma\xi_2}\right)^{m_2-k}$$

$$\left[\Gamma\xi_2 - \Gamma\left(\xi_2, \frac{\xi_2}{\psi y_{kl}^2}\right)\right]^{m_2-k} \frac{2}{\Gamma(\xi_2)}\left(\frac{\xi_2}{\psi}\right)^{\xi_2} y_{kl}^{-2\xi_2-1}\exp\left(-\frac{\xi_2}{\psi}\, y_{kl}^{-2}\right)$$

$$L = u\prod_{i=1}^{r_1}\prod_{j=1}^{m_1}\left(\frac{1}{\Gamma\xi_1}\right)^{m_1}\left[\Gamma\left(\xi_1, \frac{\xi_1}{\psi\, x_{ij}^2}\right)\right]^{i-1}\left[\Gamma\xi_1 - \Gamma\left(\xi_1, \frac{\xi_1}{\psi\, x_{ij}^2}\right)\right]^{m_1-i}$$

$$2\left(\frac{\xi_1}{\psi}\right)^{\xi_1} x^{-2\xi_1-1}\exp\left(-\frac{\xi_1}{\psi}\,x_{ij}^{-2}\right) v\prod_{k=1}^{r_2}\prod_{l=1}^{m_2}\left(\frac{1}{\Gamma\xi_2}\right)^{m_2}\left[\Gamma\left(\xi_2,\frac{\xi_2}{\psi\,y_{kl}^2}\right)\right]^{k-1}$$
$$\left[\Gamma\xi_2-\Gamma\left(\xi_2,\frac{\xi_2}{\psi\,y_{kl}^2}\right)\right]^{m_2-k} 2\left(\frac{\xi_2}{\psi}\right)^{\xi_2} y_{kl}^{-2\xi_2-1}\exp\left(-\frac{\xi_2}{\psi}\,y_{kl}^{-2}\right)$$

The combination of the lower and upper incomplete gamma functions yields the complete gamma function. This relationship can be expressed mathematically as:

$$\gamma\left(\xi,\frac{\xi}{\psi\,x^2}\right)+\Gamma\left(\xi,\frac{\xi}{\psi\,x^2}\right)=\Gamma\xi$$
$$\Gamma\xi-\Gamma\left(\xi,\frac{\xi}{\psi\,x^2}\right)=\gamma\left(\xi,\frac{\xi}{\psi\,x^2}\right)$$

Thus,

$$L=u\prod_{i=1}^{r_1}\prod_{j=1}^{m_1}\frac{2}{(\Gamma\xi_1)^{m_1}}\left[\Gamma\left(\xi_1,\frac{\xi_1}{\psi\,x_{ij}^2}\right)\right]^{i-1}\left[\gamma\left(\xi_1,\frac{\xi_1}{\psi\,x_{ij}^2}\right)\right]^{m_1-i}$$
$$\left(\frac{\xi_1}{\psi}\right)^{\xi_1} x^{-2\xi_1-1}\exp\left(-\frac{\xi_1}{\psi}\,x_{ij}^{-2}\right)$$
$$v\prod_{k=1}^{r_2}\prod_{l=1}^{m_2}\frac{2}{(\Gamma\xi_2)^{m_2}}\left[\Gamma\left(\xi_2,\frac{\xi_2}{\psi\,y_{kl}^2}\right)\right]^{k-1}\left[\gamma\left(\xi_2,\frac{\xi_2}{\psi\,y_{kl}^2}\right)\right]^{m_2-k}$$
$$\left(\frac{\xi_2}{\psi}\right)^{\xi_2} y^{-2\xi_2-1}\exp\left(-\frac{\xi_2}{\psi}\,y_{kl}^{-2}\right)$$
$$L=u\frac{(2)^{n_1}}{(\Gamma\xi_1)^{n_1m_1}}\left(\frac{\xi_1}{\psi}\right)^{n_1\xi_1}\prod_{i=1}^{r_1}\prod_{j=1}^{m_1}\left[\Gamma\left(\xi_1,\frac{\xi_1}{\psi\,x_{ij}^2}\right)\right]^{i-1}\left[\gamma\left(\xi_1,\frac{\xi_1}{\psi\,x_{ij}^2}\right)\right]^{m_1-i}$$
$$x^{-2\xi_1-1}\exp\left(-\frac{\xi_1}{\psi}\,x_{ij}^{-2}\right)$$
$$v\frac{(2)^{n_2}}{(\Gamma\xi_2)^{n_2m_2}}\left(\frac{\xi_2}{\psi}\right)^{n_2\xi_2}\prod_{k=1}^{r_2}\prod_{l=1}^{m_2}\left[\Gamma\left(\xi_2,\frac{\xi_2}{\psi\,y_{kl}^2}\right)\right]^{k-1}\left[\gamma\left(\xi_2,\frac{\xi_2}{\psi\,y_{kl}^2}\right)\right]^{m_2-k}$$
$$y^{-2\xi_2-1}\exp\left(-\frac{\xi_2}{\psi}\,y_{kl}^{-2}\right)$$

Taking log on both sides

$$\log L=\log L_1+\log L_2$$

where,

$$L_1=u\frac{(2)^{n_1}}{(\Gamma\xi_1)^{n_1m_1}}\left(\frac{\xi_1}{\psi}\right)^{n_1\xi_1}\prod_{i=1}^{r_1}\prod_{j=1}^{m_1}\left[\Gamma\left(\xi_1,\frac{\xi_1}{\psi\,x_{ij}^2}\right)\right]^{i-1}\left[\gamma\left(\xi_1,\frac{\xi_1}{\psi\,x_{ij}^2}\right)\right]^{m_1-i}$$
$$x^{-2\xi_1-1}\exp\left(-\frac{\xi_1}{\psi}\,x_{ij}^{-2}\right)$$
$$L_2=v\frac{(2)^{n_2}}{(\Gamma\xi_2)^{n_2m_2}}\left(\frac{\xi_2}{\psi}\right)^{n_2\xi_2}\prod_{k=1}^{r_2}\prod_{l=1}^{m_2}\left[\Gamma\left(\xi_2,\frac{\xi_2}{\psi\,y_{kl}^2}\right)\right]^{k-1}\left[\gamma\left(\xi_2,\frac{\xi_2}{\psi\,y_{kl}^2}\right)\right]^{m_2-k}$$
$$y^{-2\xi_2-1}\exp\left(-\frac{\xi_2}{\psi}\,y_{kl}^{-2}\right)$$

This implies

$$\log L_1=\log u+n_1\log 2-n_1m_1\log\Gamma\xi_1+n_1\xi_1(\log\xi_1-\log\psi)$$
$$+\sum_{i=1}^{r_1}\sum_{j=1}^{m_1}(i-1)\log\left[\Gamma\left(\xi_1,\frac{\xi_1}{\psi x_{ij}^2}\right)\right]+\sum_{i=1}^{r_1}\sum_{j=1}^{m_1}(m_1-i)\log\left[\gamma\left(\xi_1,\frac{\xi_1}{\psi x_{ij}^2}\right)\right]$$
$$-(2\xi_1+1)\sum_{i=1}^{r_1}\sum_{j=1}^{m_1}\log x_{ij}-\frac{\xi_1}{\psi}\sum_{i=1}^{r_1}\sum_{j=1}^{m_1}\frac{1}{{x_{ij}}^2} \qquad (12)$$

By taking the partial derivatives of Eq. (12) with respect to ξ_1 and ξ_2, we obtain:

$$\frac{\partial \log(L_1)}{\partial \xi_1} = n_1(1+\log\xi_1) - n_1 m_1 \left(\frac{\partial}{\partial \xi_1}\log\Gamma\xi_1\right) - n_1\log\psi + \sum_{i=1}^{r_1}\sum_{j=1}^{m_1}(i-1)\frac{\partial}{\partial\xi_1}\log\left[\Gamma\left(\xi_1,\frac{\xi_1}{\psi\, x_{ij}^2}\right)\right] + \sum_{i=1}^{r_1}\sum_{j=1}^{m_1}(m_1-i)\frac{\partial}{\partial\xi_1}\log\left[\gamma\left(\xi_1,\frac{\xi_1}{\psi\, x_{ij}^2}\right)\right] - 2\sum_{i=1}^{r_1}\sum_{j=1}^{m_1}\log x_{ij} - \frac{1}{\psi}\sum_{i=1}^{r_1}\sum_{j=1}^{m_1}\frac{1}{x_{ij}^2}$$

$$\frac{\partial \log(L_2)}{\partial \xi_2} = n_2(1+\log\xi_2) - n_2 m_2 \left(\frac{\partial}{\partial \xi_2}\log\Gamma\xi_2\right) - n_2\log\psi + \sum_{k=1}^{r_2}\sum_{l=1}^{m_2}(k-1)\frac{\partial}{\partial\xi_2}\log\left[\Gamma\left(\xi_2,\frac{\xi_2}{\psi\, y_{kl}^2}\right)\right] + \sum_{k=1}^{r_2}\sum_{l=1}^{m_2}(m_2-k)\frac{\partial}{\partial\xi_2}\log\left[\gamma\left(\xi_2,\frac{\xi_2}{\psi\, y_{kl}^2}\right)\right] \quad (13)$$

$$-2\sum_{k=1}^{r_2}\sum_{l=1}^{m_2}\log y_{kl} - \frac{1}{\psi}\sum_{k=1}^{r_2}\sum_{l=1}^{m_2}\frac{1}{y_{kl}^2} \quad (14)$$

To determine the ML estimators for ξ_1 and ξ_2 using RSS, we employ a numerical approach. We denote these estimators as $\hat{\xi}_{1rss}$ and $\hat{\xi}_{2rss}$, which are derived from two specific equations (referred to as Eq. (13) and Eq. (14) in the original text).

Subsequently, we apply the invariance property of ML estimators. This allows us to calculate the ML estimator for the R = Pr(Y < X), based on the RSS. This estimator can be expressed as:

$$\hat{R}_{rss} = \frac{\left(\hat{\xi}_{1rss}\right)^{\hat{\xi}_{1rss}}}{\Gamma\hat{\xi}_{1rss}} \sum_{m=0}^{\hat{\xi}_{1rss}-1} \frac{\left(\hat{\xi}_{1rss}\right)^m}{m!}\left[\frac{\Gamma\left(\hat{\xi}_{1rss}+m\right)}{\left(\hat{\xi}_{1rss}+\hat{\xi}_{2rss}\right)^{\hat{\xi}_{1rss}+m}}\right] \quad (15)$$

VII. Evaluating stress-strength model through MRSS point estimation

The MRSS method begins by selecting n random samples, each containing n units from the target population. These units are then ranked within their respective samples based on the variable of interest. For odd-sized samples, the median unit defined as the ((n+1)/2)th smallest ranked unit is chosen from each sample. In even-sized samples, the selection alternates: the (n/2)th smallest ranked unit is picked from the first half of the samples, while the ((n/2)+1)th smallest ranked unit is selected from the remaining half. This process can be repeated r times if a larger sample is required, ultimately yielding an MRSS sample of nr units. This approach ensures a representative selection of median units from the ranked samples.

When implementing MRSS, we can encounter four distinct scenarios. These scenarios are determined by the nature of the sampling process for both X and Y datasets:

1. In the first scenario, both X and Y are sampled using MRSS with odd set sizes.
2. The second scenario involves both X and Y being sampled through MRSS with even set sizes.
3. The third scenario presents a mixed approach: the strength data (X) is collected using MRSS with an odd set size, while the stress data (Y) is gathered using MRSS with an even set size.
4. The fourth scenario is the reverse of the third: the strength data (X) is obtained through MRSS with an even set size, whereas the stress data (Y) is collected using MRSS with an odd set size.

These varying scenarios provide different contexts for data analysis and interpretation in the study of strength-stress relationships.

I. First case: when set sizes are odd

Consider an MRSS sample denoted as $X_{i(g)j}$, where $i = 1,2, \dots, m_1$, $j = 1,2, \dots, r_1$; and $g = \left(\frac{m_1+1}{2}\right)$, drawn from an INAD with shape parameter ξ_1 and scale parameter ψ. This MRSS sample has a size $n_1 = m_1 r_1$, where m_1 represents the set size, and r_1 is the number of cycles. Similarly, let $Y_{k(h)l}$, where $k = 1,2, \dots, m_2$, $l = 1,2, \dots, r_2$, and $h = \left(\frac{m_2+1}{2}\right)$. This MRSS sample has a size $n_2 = m_2 r_2$, with m_2 as the set size and r_2 as the number of cycles. With these MRSS samples from Inverse Nakagami distribution for X and Y, the likelihood function can be expressed as follows:

$$L_{(1)} = \prod_{i=1}^{m_1}\prod_{j=1}^{r_1} f_g\left(x_{i(g)j}\right) \prod_{k=1}^{m_2}\prod_{l=1}^{r_2} f_h\left(y_{k(h)l}\right)$$

where,

$$f_g\left(x_{i(g)j}\right) = \frac{m_1!}{[(g-1)!]^2}\left[\frac{1}{(\Gamma\xi_1)^2}\Gamma\left(\xi_1, \frac{\xi_1}{\psi\, x_{i(g)j}^2}\right)\gamma\left(\xi_1, \frac{\xi_1}{\psi\, x_{i(g)j}^2}\right)\right]^{g-1} \frac{2}{\Gamma\xi_1}\left(\frac{\xi_1}{\psi}\right)^{\xi_1} x_{i(g)j}^{-2\xi_1-1} \exp\left(-\frac{\xi_1}{\psi x_{i(g)j}^2}\right) \tag{16}$$

and

$$f_h\left(y_{k(h)l}\right) = \frac{m_2!}{[(h-1)!]^2}\left[\frac{1}{(\Gamma\xi_2)^2}\Gamma\left(\xi_2, \frac{\xi_2}{\psi\, y_{k(h)l}^2}\right)\gamma\left(\xi_2, \frac{\xi_2}{\psi\, y_{k(h)l}^2}\right)\right]^{h-1} \frac{2}{\Gamma\xi_2}\left(\frac{\xi_2}{\psi}\right)^{\xi_2} y_{k(h)l}^{-2\xi_2-1} \exp\left(-\frac{\xi_2}{\psi y_{k(h)l}^2}\right) \tag{17}$$

Eq. (16) and (17) are represent the pdfs of $X_{i(g)j}$ and $Y_{k(h)l}$ respectively such that $X_{i(g)j} > 0$ and $Y_{k(h)l} > 0$. The log likelihood function of $L_{(1)}$ is given as

$$\begin{aligned}\log L_{(1)} = {} & \log v + n_1 \log\alpha - \frac{\xi_1}{\psi\, x_{i(g)j}^2} - \sum_{i=1}^{m_1}\sum_{j=1}^{r_1}(2\xi_1+1)\log x_{i(g)j} \\ & - \sum_{i=1}^{m_1}\sum_{j=1}^{r_1} 2(g-1)\log(\Gamma\xi_1) + \sum_{i=1}^{m_1}\sum_{j=1}^{r_1}(g-1)\log(Q_1 P_1) \\ & + n_2 \log\beta - \frac{\xi_2}{\psi\, y_{k(h)l}^2} - \sum_{k=1}^{m_2}\sum_{l=1}^{r_2}(2\xi_2+1)\log y_{k(h)l} \\ & - \sum_{k=1}^{r_1}\sum_{l=1}^{r_2} 2(h-1)\log(\Gamma\xi_2) + \sum_{k=1}^{m_2}\sum_{l=1}^{r_2}(h-1)\log(Q_2 P_2)\end{aligned} \tag{18}$$

In Eq.(17), v is the constant, $\alpha = \frac{2}{\Gamma\xi_1}\left(\frac{\xi_1}{\psi}\right)^{\xi_1}$, $\beta = \frac{2}{\Gamma\xi_2}\left(\frac{\xi_2}{\psi}\right)^{\xi_2}$, $Q_1 = \Gamma\left(\xi_1, \frac{\xi_1}{\psi\, x_{i(g)j}^2}\right)$, $Q_2 = \Gamma\left(\xi_2, \frac{\xi_2}{\psi\, y_{k(h)l}^2}\right)$, $P_1 = \gamma\left(\xi_1, \frac{\xi_1}{\psi\, x_{i(g)j}^2}\right)$, and $P_2 = \gamma\left(\xi_2, \frac{\xi_2}{\psi\, y_{k(h)l}^2}\right)$.

To determine the ML estimators for parameters ξ_1 and ξ_2, we employ a direct maximization approach on the log-likelihood function, denoted as $\log L_{(1)}$. This process involves calculating the first partial derivatives of $\log L_{(1)}$ with respect to both ξ_1 and ξ_2, independently. By setting these partial derivatives to zero and solving the resulting equations, we can derive the estimators. The expressions for these first partial derivatives, which form the basis for finding the maximum likelihood estimators, are given by:

$$\frac{\partial \log L_{(1)}}{\partial \xi_1} = n_1\left(\log\psi - 1 - \log\xi_1 - \frac{\partial}{\partial \xi_1}\log\Gamma\,\xi_1\right) - \frac{1}{\psi x_{i(g)j}^2} - \sum_{i=1}^{m_1}\sum_{j=1}^{r_1} 2\log x_{i(g)j} - \sum_{i=1}^{m_1}\sum_{j=1}^{r_1} 2(g-1)\frac{\partial}{\partial \xi_1}\log\Gamma\,\xi_1 + \sum_{i=1}^{m_1}\sum_{j=1}^{r_1}(g-1)\frac{\partial}{\partial \xi_1}\log(Q_1P_1) \tag{19}$$

$$\frac{\partial \log L_{(1)}}{\partial \xi_2} = n_2\left(\log\psi - 1 - \log\xi_2 - \frac{\partial}{\partial \xi_2}\log\Gamma\,\xi_2\right) - \frac{1}{\psi y_{k(h)l}^2} - \sum_{k=1}^{m_2}\sum_{l=1}^{r_2} 2\log y_{k(h)l} - \sum_{k=1}^{m_2}\sum_{l=1}^{r_2} 2(h-1)\frac{\partial}{\partial \xi_2}\log\Gamma\,\xi_2 + \sum_{k=1}^{m_2}\sum_{l=1}^{r_2}(h-1)\frac{\partial}{\partial \xi_2}\log(Q_2P_2) \tag{20}$$

The Eq. (19) and (20) representing the first partial derivatives do not have closed-form analytical solutions. The nature of these equations demands an iterative approach using numerical algorithms to arrive at solutions. By employing such an iterative approach, the ML estimators of the unknown parameters can be obtained based on the MRSS data when the set size is odd. Subsequently, the ML estimator of the stress-strength reliability can be derived by substituting the estimated values of the population parameters into the expression given in Eq. (8).

II. Second case: when set sizes are even

Consider a sample drawn from an Inverse Nakagami distribution with parameters (ξ_1, ψ), denoted as INAD (ξ_1, ψ), using MRSS with even set sizes. This sample can be represented as the union of two sets:$\{X_{i(q)j}, i = 1,2,\dots,q; j = 1,2,\dots,r_1\} \cup \{X_{i(q+1)j}, i = (q+1),\dots,m_1; j = 1,2,\dots,r_1\}$ where q equals $m_1/2$. Similarly, for a sample from INAD (ξ_2, ψ), using MRSS with even set sizes, we have the union of $\{Y_{k(u)l}, k = 1,2,\dots,u; l = 1,2,\dots,r_2\} \cup \{Y_{k(u+1)l}, k = (u+1),\dots,m_2; l = 1,2,\dots,r_2\}$, where u is $m_2/2$.
Given these samples, we can formulate the likelihood function $L_{(2)}$ for the observed data as follows:

$$L_{(2)} = \prod_{i=1}^{q}\prod_{j=1}^{r_1} f_q\left(x_{i(q)j}\right)\prod_{i=q+1}^{m_1}\prod_{j=1}^{r_1} f_{(q+1)}\left(x_{i(q+1)j}\right) \prod_{k=1}^{u}\prod_{l=1}^{r_2} f_u\left(y_{k(u)l}\right)\prod_{k=u+1}^{m_2}\prod_{l=1}^{r_2} f_{(u+1)}\left(y_{k(u+1)l}\right)$$

where,

$$f_q\left(x_{i(q)j}\right) = 2\frac{m_1!}{(q-1)!\,q!}\left(\frac{1}{\Gamma\xi_1}\right)^{2q}\left[\Gamma\left(\xi_1, \frac{\xi_1}{\psi\, x_{i(q)j}^2}\right)\right]^{q-1} \left[\gamma\left(\xi_1, \frac{\xi_1}{\psi\, x_{i(q)j}^2}\right)\right]^{q}\left(\frac{\xi_1}{\psi}\right)^{\xi_1} x_{i(q)j}^{-2\xi_1-1}\exp\left(-\frac{\xi_1}{\psi x_{i(q)j}^2}\right) \tag{21}$$

$$f_{(q+1)}\left(x_{i(q+1)j}\right) = 2\frac{m_1!}{(q-1)!\,q!}\left(\frac{1}{\Gamma\xi_1}\right)^{2q}\left[\Gamma\left(\xi_1, \frac{\xi_1}{\psi\, x_{i(q+1)j}^2}\right)\right]^{q} \left[\gamma\left(\xi_1, \frac{\xi_1}{\psi\, x_{i(q+1)j}^2}\right)\right]^{q-1}\left(\frac{\xi_1}{\psi}\right)^{\xi_1} x_{i(q+1)j}^{-2\xi_1-1}\exp\left(-\frac{\xi_1}{\psi x_{i(q+1)j}^2}\right), \tag{22}$$

$$f_u\left(y_{k(u)l}\right) = 2\frac{m_2!}{(u-1)!\,u!}\left(\frac{1}{\Gamma\xi_2}\right)^{2u}\left[\Gamma\left(\xi_2, \frac{\xi_2}{\psi\, y_{k(u)l}^2}\right)\right]^{u-1} \tag{23}$$

$$\left[\gamma\left(\xi_2,\frac{\xi_2}{\psi\, y_{k(u)l}^2}\right)\right]^u\left(\frac{\xi_2}{\psi}\right)^{\xi_2} y_{k(u)l}^{-2\xi_2-1}\exp\left(-\frac{\xi_2}{\psi y_{k(u)l}^2}\right),$$

and

$$f_{(u+1)}(y_{k(u+1)l}) = 2\frac{m_2!}{(u-1)!\,u!}\left(\frac{1}{\Gamma\xi_2}\right)^{2u}\left[\Gamma\left(\xi_2,\frac{\xi_2}{\psi\, y_{k(u+1)l}^2}\right)\right]^u \left[\gamma\left(\xi_2,\frac{\xi_2}{\psi\, y_{k(u+1)l}^2}\right)\right]^{u-1}\left(\frac{\xi_2}{\psi}\right)^{\xi_2} y_{k(u+1)j}^{-2\xi_2-1} exp\left(-\frac{\xi_2}{\psi y_{k(u+1)l}^2}\right), \quad (24)$$

Eq. (21), (22), (23) and (24) are represent the pdfs of $X_{i(q)j}, X_{i(q+1)j}, Y_{k(u)l}$ and $Y_{k(u+1)l}$ respectively such that $x_{i(q)j} >, x_{i(q+1)j} >, y_{k(u)l}$ and $y_{k(u+1)l} > 0$. The log likelihood function of $L_{(2)}$ is given as

$$\log L_{(2)} = \log L_{(2)}^{*} + \log L_{(2)}^{**} \quad (25)$$

where,

$$\log L_{(2)}^{*} = \log c_1 + \sum_{i=1}^{q}\sum_{j=1}^{r_1}(q-1)\log E_{1(q)} + \sum_{i=1}^{q}\sum_{j=1}^{r_1} q\log F_{1(q)} + qr_1\log\lambda_1 - \sum_{i=1}^{q}\sum_{j=1}^{r_1}(2\xi_1+1)\log x_{i(q)j} - \sum_{i=1}^{q}\sum_{j=1}^{r_1}\frac{\xi_1}{\psi x_{i(q)j}^2} + \sum_{i=q+1}^{m_1}\sum_{j=1}^{r_1} q\log E_{1(q+1)} + \sum_{i=q+1}^{m_1}\sum_{j=1}^{r_1}(q-1)\log F_{1(q+1)} + m_1 r_1\log\lambda_1 - \sum_{i=q+1}^{m_1}\sum_{j=1}^{r_1}(2\xi_1+1)\log x_{i(q+1)j} - \sum_{i=q+1}^{m_1}\sum_{j=1}^{r_1}\frac{\xi_2}{\psi x_{i(q+1)j}^2} \quad (26)$$

and

$$\log L_{(2)}^{**} = \log c_2 + \sum_{k=1}^{u}\sum_{l=1}^{r_2}(u-1)\log E_{2(u)} + \sum_{k=1}^{u}\sum_{l=1}^{r_2} u\log F_{2(u)} + ur_2\log\lambda_2 - \sum_{k=1}^{u}\sum_{l=1}^{r_2}(2\xi_2+1)\log y_{k(u)l} - \sum_{k=1}^{u}\sum_{l=1}^{r_2}\frac{\xi_2}{\psi y_{k(u)l}^2} + \sum_{k=u+1}^{m_2}\sum_{l=1}^{r_2} u\log E_{2(u+1)} + \sum_{k=u+1}^{m_2}\sum_{l=1}^{r_2}(u-1)\log F_{2(u+1)} + m_2 r_2\log\lambda_2 - \sum_{k=u+1}^{m_2}\sum_{l=1}^{r_2}(2\xi_2+1)\log y_{k(u+1)l} - \sum_{k=u+1}^{m_2}\sum_{l=1}^{r_2}\frac{\xi_2}{\psi y_{k(u+1)l}^2} \quad (27)$$

Here, c_1 and c_2 are the constants.

$\lambda_1 = \frac{2}{(\Gamma\xi_1)^{2q}}\left(\frac{\xi_1}{\psi}\right)^{\xi_1}, \lambda_2 = \frac{2}{(\Gamma\xi_2)^{2u}}\left(\frac{\xi_2}{\psi}\right)^{\xi_2},$

$E_{1(q)} = \Gamma\left(\xi_1,\frac{\xi_1}{\psi\, x_{i(q)j}^2}\right), E_{1(q+1)} = \Gamma\left(\xi_1,\frac{\xi_1}{\psi\, x_{i(q+1)j}^2}\right), E_{2(u)} = \Gamma\left(\xi_2,\frac{\xi_2}{\psi\, y_{k(u)l}^2}\right),$

$E_{2(u+1)} = \Gamma\left(\xi_2,\frac{\xi_2}{\psi\, y_{k(u+1)l}^2}\right), F_{1(q)} = \gamma\left(\xi_1,\frac{\xi_1}{\psi\, x_{i(q)j}^2}\right), F_{1(q+1)} = \gamma\left(\xi_1,\frac{\xi_1}{\psi\, x_{i(q+1)j}^2}\right),$

$F_{2(u)} = \gamma\left(\xi_2,\frac{\xi_2}{\psi\, y_{k(u)l}^2}\right), F_{2(u+1)} = \gamma\left(\xi_2,\frac{\xi_2}{\psi\, y_{k(u+1)l}^2}\right)$

In the process of differentiating the log-likelihood function $\log L_{(2)}$, the terms related to the $\log L_{(2)}^{**}$ expression will vanish when taking the derivative with respect to the parameter ξ_1. Conversely, the terms associated with the $\log L_{(2)}^{*}$ expression will drop out when differentiating with respect to the parameter ξ_2. The resulting first partial derivative expressions are as follows:

$$\frac{\partial \log L_2}{\partial \xi_1} = \sum_{i=1}^{q}\sum_{j=1}^{r_1}(q-1)\frac{\partial}{\partial \xi_1}\log E_{1(q)} + \sum_{i=1}^{q}\sum_{j=1}^{r_1} q\frac{\partial}{\partial \xi_1}\log F_{1(q)} - 2\sum_{i=1}^{q}\sum_{j=1}^{r_1}\log x_{i(q)j} + qr_1\left(\log \xi_1 - \log \psi - \frac{2q}{\xi_1} + 1\right) - \sum_{i=1}^{q}\sum_{j=1}^{r_1}\frac{1}{\psi x_{i(q)j}} - \sum_{i=q+1}^{m_1}\sum_{j=1}^{r_1}\frac{1}{\psi x_{i(q+1)j}} + \sum_{i=q+1}^{m_1}\sum_{j=1}^{r_1} q\frac{\partial}{\partial \xi_1}\log E_{1(q+1)} + \sum_{i=q+1}^{m_1}\sum_{j=1}^{r_1}(q-1)\frac{\partial}{\partial \xi_1}\log F_{1(q+1)} + m_1 r_1\left(\log \xi_1 - \log \psi - \frac{2q}{\xi_1} + 1\right) - 2\sum_{i=q+1}^{m_1}\sum_{j=1}^{r_1}\log x_{i(q+1)j} \quad (28)$$

and

$$\frac{\partial \log L_2}{\partial \xi_2} = \sum_{k=1}^{u}\sum_{l=1}^{r_2}(u-1)\frac{\partial}{\partial \xi_2}\log E_{2(u)} + \sum_{k=1}^{u}\sum_{l=1}^{r_1} u\frac{\partial}{\partial \xi_2}\log F_{2(u)} - 2\sum_{k=1}^{u}\sum_{l=1}^{r_2}\log y_{k(u)l} + ur_2\left(\log \xi_2 - \log \psi - \frac{2u}{\xi_2} + 1\right) - \sum_{k=1}^{u}\sum_{l=1}^{r_2}\frac{1}{\psi y_{k(u)l}} - \sum_{k=q+1}^{m_2}\sum_{l=1}^{r_2}\frac{1}{\psi y_{k(u+1)l}} + \sum_{k=q+1}^{m_2}\sum_{l=1}^{r_2} u\frac{\partial}{\partial \xi_2}\log E_{2(u+1)} + \sum_{k=u+1}^{m_2}\sum_{l=1}^{r_2}(u-1)\frac{\partial}{\partial \xi_2}\log F_{2(u+1)} + m_2 r_2\left(\log \xi_2 - \log \psi - \frac{2u}{\xi_2} + 1\right) - 2\sum_{k=u+1}^{m_2}\sum_{l=1}^{r_2}\log y_{k(u+1)l} \quad (29)$$

The Eq. (28) and Eq. (29), which denote the first partial derivatives, do not have closed-form analytical solutions. As a result, an iterative numerical technique must be employed to solve these equations. By utilizing such an iterative approach, the ML estimators of the unknown parameters can be obtained when the MRSS data has even set sizes. Subsequently, the ML estimator of the $R = P_r(Y < X)$ can be derived by substituting the estimated values of the population parameters into the expression given in Eq. (8).

III. Third case: when stress has even and strength has odd set sizes

We examine the stress-strength reliability in a scenario where the samples for X and Y are drawn using different methods from Inverse Nakagami distributions (INAD). Specifically, samples of X are drawn from INAD using the Odd-set Median Ranked Set Sampling (OMRSS) technique. (ξ_1, ψ),while Y samples are drawn using Even-set Median Ranked Set Sampling technique (EMRSS) from INAD (ξ_2, ψ). For X, we denote the OMRSS observations as $X_{i(g)j}$,where i ranges from 1 to m_1, j from 1 to r_1, and g is calculated as $\frac{(m_1+1)}{2}$.

For Y, the EMRSS sample is represented as the union of two sets: $\{Y_{k(u)l}, k = 1,2,\dots,u; l = 1,2,\dots,r_2\} \cup \{Y_{k(u+1)l}, k = (u+1),\dots,m_2; l = 1,2,\dots,r_2\}$, where u equals $m_2/2$.

Given these sampling methods, we can express the likelihood function for the observed data as follows:

$$L_{(3)} = \prod_{i=1}^{m_1}\prod_{j=1}^{r_1} f_g\left(x_{i(g)j}\right) \prod_{k=1}^{u}\prod_{l=1}^{r_2} f_u\left(y_{k(u)l}\right) \prod_{k=u+1}^{m_2}\prod_{l=1}^{r_2} f_{(u+1)}\left(y_{k(u+1)l}\right)$$

$f_g(x_{i(g)j})$ and $f_u(y_{k(u)l})$ are given in Eq. (16) and (23), respectively. $f_{(u+1)}(y_{k(u+1)l})$ is given in Eq. (24). The log likelihood function of $L_{(3)}$ is given as follows:

$$\log L_{(3)} = \log {L_{(3)}}^{*} + \log {L_{(3)}}^{**} \tag{30}$$

where,

$$\begin{aligned}\log {L_{(3)}}^{*} = \log a_1 + n_1 \log \alpha - \frac{\xi_1}{\psi\, x_{i(g)j}^2} - \sum_{i=1}^{m_1}\sum_{j=1}^{r_1}(2\xi_1 + 1)\log x_{i(g)j} \\ - \sum_{i=1}^{m_1}\sum_{j=1}^{r_1} 2(g-1)\log(\Gamma\xi_1) + \sum_{i=1}^{m_1}\sum_{j=1}^{r_1}(g-1)\log(Q_1 P_1)\end{aligned} \tag{31}$$

and

$$\begin{aligned}\log {L_{(3)}}^{**} = \log b_1 + \sum_{k=1}^{u}\sum_{l=1}^{r_2}(u-1)\log E_{2(u)} + \sum_{k=1}^{u}\sum_{l=1}^{r_2} u \log F_{2(u)} + u r_2 \log \lambda_2 \\ - \sum_{k=1}^{u}\sum_{l=1}^{r_2}(2\xi_2 + 1)\log y_{k(u)l} - \sum_{k=1}^{u}\sum_{l=1}^{r_2}\frac{\xi_2}{\psi y_{k(u)l}^2} \\ + \sum_{k=u+1}^{m_2}\sum_{l=1}^{r_2} u \log E_{2(u+1)} + \sum_{k=u+1}^{m_2}\sum_{l=1}^{r_2}(u-1)\log F_{2(u+1)} \\ + m_2 r_2 \log \lambda_2 - \sum_{k=u+1}^{m_2}\sum_{l=1}^{r_2}(2\xi_2 + 1)\log y_{k(u+1)l} \\ - \sum_{k=u+1}^{m_2}\sum_{l=1}^{r_2}\frac{\xi_2}{\psi y_{k(u+1)l}^2}\end{aligned} \tag{32}$$

Here, a_1 and b_1 are the constants.

The ML estimators of the parameters ξ_1 and ξ_2 can be derived by maximizing the log-likelihood function $\log L_{(3)}$ directly with respect to ξ_1 and ξ_2, respectively. The resulting first partial derivative expressions with respect to ξ_1 and ξ_2 is given by Eq. (19) and (29), respectively. It appears that Eq. (19) and (29) do not have closed-form analytical solutions. As a result, a numerical technique must be utilized to obtain the solutions. Subsequently, the ML estimator of the stress-strength reliability can be obtained by substituting the estimated values of the population parameters into the expression provided in Eq. (8).

IV. Forth case: when strength has even and stress has odd set sizes

We examine the reliability estimator in a scenario where X samples are derived from the INAD distribution using EMRSS, while Y samples are obtained from the same distribution employing OMRSS. Let the $\{X_{i(q)j}, i = 1,2,\dots,q; j = 1,2,\dots,r_1\} \cup \{X_{i(q+1)j}, i = (q+1),\dots,m_1; j = 1,2,\dots,r_1\}$ be the observed EMRSS from INAD (ξ_1, ψ) distribution. Let the $Y_{k(h)l}$, where $k = 1,2,\dots,m_2, l = 1,2,\dots,r_2$ and $h = \left(\frac{m_2+1}{2}\right)$ be the observed OMRSS drawn from INAD (ξ_2, ψ) distribution. The likelihood of the observed variables will be given as follows:

$$L_{(4)} = \prod_{i=1}^{q}\prod_{j=1}^{r_1} f_q\left(x_{i(q)j}\right) \prod_{i=q+1}^{m_1}\prod_{j=1}^{r_1} f_{(q+1)}\left(x_{i(q+1)j}\right) \prod_{k=1}^{m_2}\prod_{l=1}^{r_2} f_h\left(y_{k(h)l}\right)$$

The pdfs expressions of $f_q(x_{i(q)j}), f_{(q+1)}(y_{k(q+1)l})$ and $f_h(y_{k(h)l})$ are given in Eq. (21), (22) and (17), respectively. Now, the log likelihood function of $L_{(4)}$ is given as

$$\log L_{(4)} = \log L_{(4)}^{*} + \log L_{(4)}^{**} \tag{33}$$

where,

$$\begin{aligned}\log L_{(4)}^{*} = \log a_2 &+ \sum_{i=1}^{q}\sum_{j=1}^{r_1}(q-1)\log E_{1(q)} + \sum_{i=1}^{q}\sum_{j=1}^{r_1} q \log F_{1(q)} + qr_1 \log \lambda_1 \\ &- \sum_{i=1}^{q}\sum_{j=1}^{r_1}(2\xi_1+1)\log x_{i(q)j} - \sum_{i=1}^{q}\sum_{j=1}^{r_1}\frac{\xi_1}{\psi x_{i(q)j}^2} \\ &+ \sum_{i=q+1}^{m_1}\sum_{j=1}^{r_1} q \log E_{1(q+1)} + \sum_{i=q+1}^{m_1}\sum_{j=1}^{r_1}(q-1)\log F_{1(q+1)} \\ &+ m_1 r_1 \log \lambda_1 - \sum_{i=q+1}^{m_1}\sum_{j=1}^{r_1}(2\xi_1+1)\log x_{i(q+1)j} \\ &- \sum_{i=q+1}^{m_1}\sum_{j=1}^{r_1}\frac{\xi_2}{\psi x_{i(q+1)j}^2}\end{aligned} \tag{34}$$

and

$$\begin{aligned}\log L_{(4)}^{**} = \log b_2 &+ n_2 \log \beta - \frac{\xi_2}{\psi\, y_{k(h)l}^2} - \sum_{k=1}^{m_2}\sum_{l=1}^{r_2}(2\xi_2+1)\log y_{k(h)l} \\ &- \sum_{k=1}^{r_1}\sum_{l=1}^{r_2} 2(h-1)\log(\Gamma\xi_2) + \sum_{k=1}^{m_2}\sum_{l=1}^{r_2}(h-1)\log(Q_2 P_2)\end{aligned} \tag{35}$$

Here, a_2 and b_2 are the constants.

The ML estimators of the parameters ξ_1 and ξ_2 can be derived by directly maximizing the log-likelihood function $\log L_{(4)}$ with respect to ξ_1 and ξ_2, respectively. The resulting first partial derivative expressions with respect to ξ_1 and ξ_2 are given by Eq. (28) and (20), respectively.

It appears that Eq. (28) and (20) do not have closed-form analytical solutions. Consequently, a numerical technique must be employed to obtain the solutions. Finally, the ML estimator of the stress-strength reliability can be obtained by substituting the estimated values of the population parameters into the expression provided in Eq. (8).

VIII. Simulation study

To rigorously assess the efficacy of our proposed reliability estimation methods, we conducted a comprehensive simulation study. This computational investigation compares the performance of estimates derived from RSS and MRSS against those obtained through SRS. Our simulations span a diverse range of scenarios, providing crucial insights into the relative strengths of these sampling techniques under various conditions. The comparison is based on three key criteria: bias, mean square error (MSE), and relative efficiency (RE). The simulation setup involves various set sizes and number of cycles, specifically (m_x, m_y) = (2, 2), (3, 3), (2, 3), (3, 2), (4, 4), (5, 5), (4, 5), (5, 4),(6, 6),(7, 7),(6, 7),(7, 6),(8, 8),(9, 9),(8, 9),(9, 8) and $r_x = r_y = 5$. Consequently, the sample sizes for SRSS and MRSS are calculated as $n_1 = m_1 r_1$ and $n_2 = m_2 r_2$, respectively. For SRS samples, the sample sizes used are (n_1, n_2) = (10, 10),(15, 15),(10, 15),(15, 10),(20, 20),(25, 25),(20, 25),(25, 20),(30, 30),(35, 35),(30, 35),(35,

30),(40, 40),(45, 45),(40, 45),(45, 40). The parameter values are set to (ξ_1, ξ_2) = (2, 4), (3, 5), and (6, 8) and ψ = 3, 2 and 4 with the true system reliability values of R_{true} = 0.53909, 0.52465 and 0.51036. A total of 1000 random samples are generated from INAD (ξ_1, ψ) and INAD (ξ_2, ψ) distributions. The estimated reliability is evaluated using bias, mean square errors (MSEs) and relative efficiencies (REs).
The bias of estimate of R is defined as $Bias(\hat{R}) = E(\hat{R}) - R$. The efficiencies of RSS and MRSS with respect to SRS are defined as the ratios of their respective MSEs. Specifically, the efficiency of RSS relative to SRS is given by $\text{Effi}(R_{RSS}, R_{SRS}) = \left(\frac{MSE(R_{RSS})}{MSE(R_{SRS})}\right)$. Similarly, the efficiency of MRSS relative to SRS is $\text{Effi}(R_{MRSS}, R_{SRS}) = \left(\frac{MSE(R_{MRSS})}{MSE(R_{SRS})}\right)$.

Analysis of the simulation results, as presented in Tables 1 through 4, reveals a clear pattern of superior performance for the MRSS method. The efficiency of MRSS demonstrates a notable increase as the sample size or set size grows, highlighting its scalability and robustness. Across the various scenarios examined, MRSS consistently outperformed both RSS and SRS techniques. The efficiency gains of MRSS were substantial, with performance improvements ranging from 2 to 9 times that of SRS. This significant enhancement in efficiency underscores the potential of MRSS to dramatically improve the precision of reliability estimations, particularly in larger sample sizes.

While RSS also showed improved efficiency compared to SRS, its gains were more modest. The performance of RSS consistently fell between that of SRS and MRSS, demonstrating that while it offers improvements over simple random sampling, it does not match the marked benefits provided by MRSS. The consistent superiority of MRSS across all examined scenarios reinforces its robustness as a sampling technique. This consistency, coupled with its escalating efficiency as sample sizes increase, positions MRSS as a powerful tool for enhancing the accuracy and reliability of statistical estimations in various fields where precise sampling is crucial.

IX. Real life application

In this study, we examine two critical datasets originally explored by Louzada et al. [15] in their ground breaking research on the Inverse Nakagami distribution. These datasets offer valuable insights into the failure life of essential components in agricultural machinery: the motor and elevator systems. By repurposing this data, we aim to demonstrate the practical applications of our research in a novel context. Specifically, we utilize these datasets as stress and strength variables within our proposed reliability model, thereby bridging the gap between theoretical statistical frameworks and real-world engineering challenges. This approach not only validates the robustness of our model but also highlights its potential to enhance predictive maintenance strategies in the agricultural sector, potentially reducing downtime and improving overall operational efficiency. The datasets are shown in Table 5 and 6 respectively.

Prior to delving deeper into our analysis, it is imperative to conduct a comprehensive examination of the fundamental data characteristics. To evaluate the efficacy of our findings, we employ the Kolmogorov-Smirnov (K-S) test, a robust statistical tool, alongside its associated P-value (P-V). This methodology allows us to quantify the alignment between empirical observations and theoretical predictions. Our findings reveal encouraging results: for the initial dataset, we observe a K-S distance of 0.2222222, coupled with a P-V of 0.1267165, while the second dataset yields a K-S distance of 0.203125 and a P-V of 0.1324632. These metrics strongly suggest that our model provides an excellent fit to the observed data.To further illustrattion, we have generated visual representations of key statistical measures. Figures 1 and 2 present a suite of graphical analyses, including the probability-probability (PP) plots, and the estimated PDF and CDF for both datasets.

Table 1: *Five-Cycle Performance Assessment of R Estimators: Comparing SRS, RSS, and MRSS Using MSEs, Bias, and REs with Even X and Y Set Sizes*

Size		SRS			RSS			MRSS			Efficiency	
Sample	Set	R_{mle}	Bias	MSE	R_{mle}	Bias	MSE	R_{mle}	Bias	MSE	RSS	MRSS
				$R_{true} = 0.53$		909, $\xi_1 = 2$, $\xi_2 = 4$, $\psi = 3$						
(10,10)	(2,2)	0.56946	0.03037	0.04324	0.49631	-0.04278	0.03769	0.58486	0.04577	0.04002	1.14717	1.08045
(20,20)	(4,4)	0.56571	0.02662	0.04445	0.58625	0.04716	0.04051	0.53355	-0.00554	0.01541	1.09729	2.88432
(30,30)	(6,6)	0.64507	0.10598	0.05312	0.52361	-0.01548	0.03893	0.54640	0.00731	0.00885	1.36447	6.00291
(40,40)	(8,8)	0.65460	0.11551	0.05303	0.55648	0.01739	0.03906	0.56059	0.02150	0.00585	1.35765	9.06352
				$R_{true} = 0.52$		465, $\xi_1 = 3$, $\xi_2 = 5$, $\psi = 2$						
(10,10)	(2,2)	0.61555	0.09090	0.06449	0.61898	0.09433	0.06371	0.61898	0.09433	0.06371	1.01227	1.01227
(20,20)	(4,4)	0.52749	0.00283	0.05350	0.48036	-0.04429	0.05148	0.51210	-0.01255	0.02167	1.03929	2.46854
(30,30)	(6,6)	0.59379	0.06914	0.06041	0.54640	0.02175	0.04822	0.52942	0.00477	0.01252	1.25297	4.82616
(40,40)	(8,8)	0.67451	0.14986	0.07686	0.59122	0.06657	0.05300	0.63883	0.11418	0.02076	1.45018	3.70180
				$R_{true} = 0.51$		036, $\xi_1 = 6$, $\xi_2 = 8$, $\psi = 4$						
(10,10)	(2,2)	0.59347	0.08311	0.09058	0.48625	-0.02411	0.08072	0.52468	0.01432	0.06753	1.12218	1.34132
(20,20)	(4,4)	0.54195	0.03159	0.07847	0.55111	0.04075	0.07787	0.48936	-0.02100	0.03016	1.00773	2.60200
(30,30)	(6,6)	0.52694	0.01658	0.08195	0.52342	0.01306	0.07941	0.49577	-0.01459	0.01746	1.03199	4.69495
(40,40)	(8,8)	0.59861	0.08825	0.08702	0.61958	0.10922	0.02351	0.49834	-0.01202	0.01260	3.70193	6.90640

Table 2: *Five-Cycle Performance Assessment of R Estimators: Comparing SRS, RSS, and MRSS Using MSEs, Bias, and REs with Odd X and Y Set Sizes*

Size		SRS		RSS			MRSS			Efficiency	
Sample	Set	$\mathcal{K}mle$	Bias	MSE	$\mathcal{K}mle$	Bias	MSE	$\mathcal{K}mle$	Bias	MSE	RSS	MRSS
$R_{true} = 0.53909$, $\xi_1 = 2$, $\xi_2 = 4$, $\psi = 3$												
(15,15)	(3,3)	0.5598	0.02079	0.04426	0.52586	-0.01323	0.02323	0.51437	-0.02473	0.02296	1.90535	1.92790
(25,25)	(5,5)	0.5643	0.02520	0.04720	0.55155	0.01245	0.04387	0.54278	0.00368	0.01106	1.07598	4.26853
(35,35)	(7,7)	0.5710	0.03192	0.04354	0.52330	-0.01579	0.04222	0.56347	0.02437	0.00667	1.03138	6.53001
(45,45)	(9,9)	0.5676	0.02855	0.04601	0.57503	0.03593	0.04235	0.55684	0.01775	0.00502	1.08644	9.17347
$R_{true} = 0.52465$, $\xi_1 = 3$, $\xi_2 = 5$, $\psi = 2$												
(15,15)	(3,3)	0.5618	0.03722	0.06682	0.58101	0.05635	0.06486	0.50764	-0.01702	0.03143	1.03013	2.06363
(25,25)	(5,5)	0.5142	-0.01038	0.05891	0.53832	0.01367	0.05598	0.51871	-0.00594	0.01515	1.05219	3.69606
(35,35)	(7,7)	0.5990	0.07442	0.06588	0.51427	-0.01038	0.05891	0.53092	0.00627	0.00967	1.11837	6.81557
(45,45)	(9,9)	0.5690	0.04438	0.05424	0.53171	0.00706	0.05132	0.53450	0.00984	0.00689	1.05688	7.45084
$R_{true} = 0.51036$, $\xi_1 = 6$, $\xi_2 = 8$, $\psi = 4$												
(15,15)	(3,3)	0.6262	0.11587	0.09969	0.59814	0.08778	0.07544	0.45413	-0.05623	0.05190	1.32145	1.92098
(25,25)	(5,5)	0.5287	0.01841	0.08236	0.46952	-0.04084	0.06060	0.49233	-0.01803	0.02804	1.35903	2.93733
(35,35)	(7,7)	0.6100	0.09968	0.08841	0.52815	0.01779	0.08602	0.49821	-0.01215	0.01854	1.02769	4.64018
(45,45)	(9,9)	0.5306	0.02026	0.08540	0.54245	0.03209	0.08210	0.50403	-0.00633	0.01214	1.04019	6.76507

Table 3: *Five-Cycle Performance Assessment of R Estimators: Comparing SRS, RSS, and MRSS Using MSEs, Bias, and REs with Even X and Odd Y Set Sizes*

Size		SRS			RSS			MRSS			Efficiency	
Sample	Set	K_{mle}	Bias	MSE	K_{mle}	Bias	MSE	K_{mle}	Bias	MSE	RSS	MRSS
$R_{true} = 0.53909$, $\xi_1 = 2$, $\xi_2 = 4$, $\psi = 3$												
(10,15)	(2,3)	0.59832	0.05923	0.02952	0.50722	-0.03187	0.02543	0.51804	-0.02105	0.02346	1.16078	1.25868
(20,25)	(4,5)	0.52992	-0.00917	0.03230	0.54190	0.00280	0.01421	0.55444	0.01534	0.00909	2.27386	3.55452
(30,35)	(6,7)	0.53044	-0.00865	0.02445	0.54381	0.00472	0.00906	0.54885	0.00976	0.00692	2.69836	3.53461
(40,45)	(8,9)	0.57242	0.03332	0.03878	0.53626	-0.00283	0.00818	0.55309	0.01400	0.00473	4.73941	8.20611
$R_{true} = 0.52465$, $\xi_1 = 3$, $\xi_2 = 5$, $\psi = 2$												
(10,15)	(2,3)	0.48004	-0.04461	0.03491	0.49116	-0.03349	0.03216	0.42064	-0.10401	0.01702	1.08525	2.05069
(20,25)	(4,5)	0.59240	0.06775	0.02786	0.51607	-0.00858	0.01607	0.53660	0.01195	0.00744	1.73327	3.74423
(30,35)	(6,7)	0.50902	-0.01563	0.04476	0.52552	0.00087	0.01579	0.52950	0.00485	0.00971	2.83468	4.61123
(40,45)	(8,9)	0.61911	0.09445	0.04332	0.53918	0.01453	0.02136	0.53723	0.01257	0.00689	2.02792	6.28423
$R_{true} = 0.51036$, $\xi_1 = 6$, $\xi_2 = 8$, $\psi = 4$												
(10,15)	(2,3)	0.57764	0.06728	0.06304	0.54479	0.03443	0.05722	0.50180	-0.00856	0.01715	1.10166	3.67651
(20,25)	(4,5)	0.54116	0.03080	0.04036	0.49541	-0.01495	0.02871	0.52390	0.01354	0.01236	1.40599	3.26508
(30,35)	(6,7)	0.57769	0.06733	0.08011	0.59971	0.08935	0.02643	0.50458	-0.00578	0.01850	3.03105	4.32964
(40,45)	(8,9)	0.57170	0.06134	0.03203	0.49048	-0.01988	0.02247	0.52134	0.01098	0.01231	2.72956	4.98361

Table 4: *Five-Cycle Performance Assessment of R Estimators: Comparing SRS, RSS, and MRSS Using MSEs, Bias, and REs with Odd X and Even Y Set Sizes*

Size		SRS			RSS			MRSS			Efficiency	
Sample	Set	$Kmle$	Bias	MSE	$Kmle$	Bias	MSE	$Kmle$	Bias	MSE	RSS	MRSS
$R_{true} = 0.53909$, $\xi_1 = 2$, $\xi_2 = 4$, $\psi = 3$												
(15,10)	(3,2)	0.57140	0.03231	0.04185	0.58546	0.04636	0.03984	0.53603	-0.00307	0.01462	1.05029	2.86314
(25,20)	(5,4)	0.49643	-0.04266	0.05727	0.49878	-0.04031	0.04846	0.53879	-0.00031	0.01506	1.18172	3.21802
(35,30)	(7,6)	0.46297	-0.07612	0.05012	0.51888	-0.02021	0.01678	0.53274	-0.00636	0.01552	2.98722	3.22860
(45,40)	(9,8)	0.58673	0.04764	0.04513	0.55541	0.01632	0.01833	0.55469	0.01560	0.00581	2.46267	7.77260
$R_{true} = 0.52465$, $\xi_1 = 3$, $\xi_2 = 5$, $\psi = 2$												
(15,10)	(3,2)	0.52226	-0.00239	0.05478	0.55902	0.03437	0.05051	0.53186	0.00721	0.04714	1.08450	1.16210
(25,20)	(5,4)	0.52432	-0.00033	0.06062	0.59991	0.07525	0.02878	0.50497	-0.01968	0.02072	2.10606	2.92622
(35,30)	(7,6)	0.52680	0.00214	0.05853	0.52225	-0.00240	0.02135	0.53108	0.00643	0.01307	2.74155	4.47936
(45,40)	(9,8)	0.53478	0.01013	0.05768	0.63350	0.10884	0.02006	0.53247	0.00782	0.00795	2.87524	7.25761
$R_{true} = 0.51036$, $\xi_1 = 6$, $\xi_2 = 8$, $\psi = 4$												
(15,10)	(3,2)	0.53337	0.02301	0.07999	0.50495	-0.00541	0.07284	0.49789	-0.01247	0.07005	1.09819	1.14201
(25,20)	(5,4)	0.53619	0.02583	0.04755	0.47904	-0.03132	0.03769	0.59782	0.08746	0.02268	1.26182	2.09649
(35,30)	(7,6)	0.55857	0.04822	0.08251	0.50128	-0.00908	0.02183	0.58730	0.07694	0.02948	2.79915	3.77979
(45,40)	(9,8)	0.56147	0.05111	0.08335	0.59939	0.08903	0.02352	0.50868	-0.00168	0.01538	3.54394	5.41820

Table 5: *Dataset Related to the Agricultural Machine's Elevator*

1	1	2	7	21
1	1	3	7	23
1	1	3	9	23
1	1	3	9	24
1	1	4	11	25
1	1	4	11	31
1	2	4	11	56
1	2	5	12	61
1	2	6	17	61
1	2	7	17	122
1	2	7	17	

Table 6: *Dataset Related to the Agricultural Machine's Motor*

1	1	2	5	11	22
1	1	2	5	11	24
1	1	3	5	12	29
1	1	3	5	12	32
1	1	3	7	13	33
1	1	4	8	16	33
1	1	4	8	17	41
1	1	4	9	17	41
1	2	4	9	18	121
1	2	5	11	18	
1	2	5	11	18	

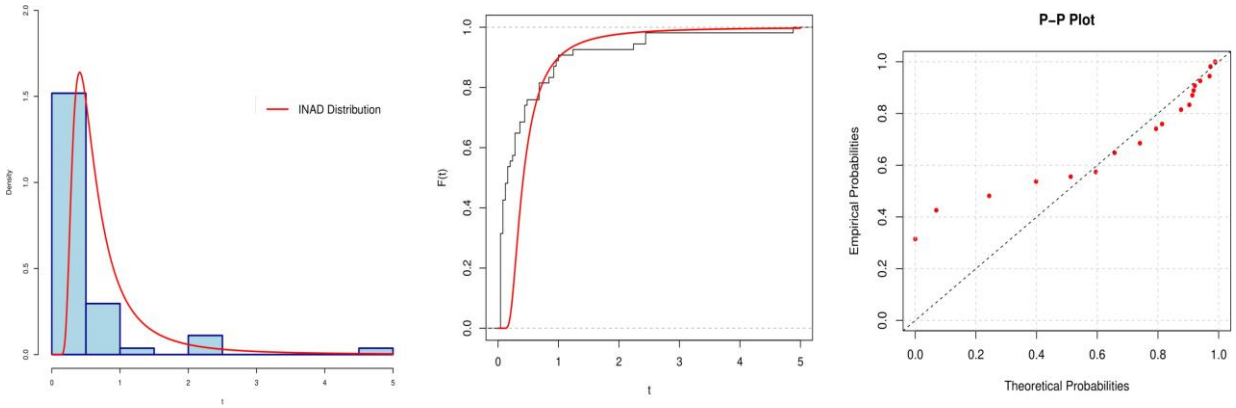


Figure 1: *The PDF, CDF and P-P Plots of the INAD distribution for Elevator dataset*

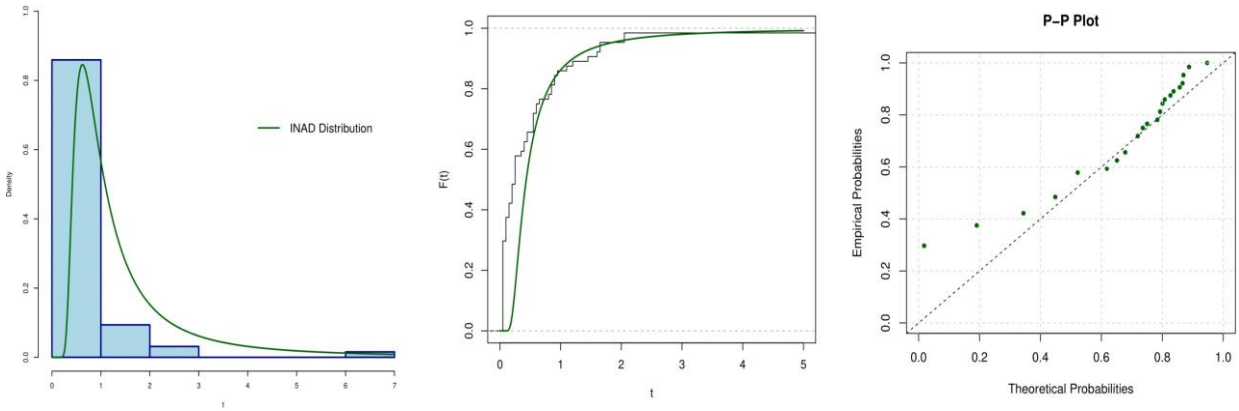


Figure 2: *The PDF, CDF and P-P Plots of the INAD distribution for Motor dataset*

Table 7: *Stress-strength R = P(X<Y) estimate of the datasets*

Sample Size	Set	SRS	RSS	MRSS
			Cycle = 3	
6,6	2,2	0.8577746	0.8679643	0.9364125
9,9	3,3	0.7931385	0.8590813	0.9664752
9,6	3,2	0.8244659	0.8781348	0.9754125
6,9	2,3	0.7849362	0.8546207	0.9599871
			Cycle = 5	
20,20	4,4	0.8250181	0.8455731	0.9236574
25,25	5,5	0.8302296	0.8632833	0.9335574
25,20	5,4	0.8085325	0.8447445	0.9678474
20,25	4,5	0.8237667	0.8503601	0.9744001

Our analysis of Data 5and 6 through three distinct sampling methodologies- MRSS, RSS, and SRS reveals a compelling pattern. As we increase the sample size, or more specifically, as the set size grows, we observe the stress-strength estimate steadily approaching unity. This trend is particularly pronounced in the case of MRSS. A close examination of Table 7 illuminates a striking feature: the stress-strength (R) estimates derived from MRSS consistently outperform those obtained via RSS and SRS. Figure 3 presents a comparative analysis of stress-strength reliability using SRS, RSS, and MRSS methods, focusing on different set sizes for the third and fifth cycles. This superiority of MRSS is not merely a numerical quirk but a recurring theme throughout our analysis. The persistent edge maintained by MRSS estimates lends credence to our earlier findings and hints at the method's robustness in specific sampling scenarios. The consistent outperformance of MRSS carries significant implications. It not only corroborates our previous conclusions but also sheds light on the potential benefits of employing MRSS in certain research contexts. This finding opens up intriguing avenues for further exploration, particularly in situations where precise stress-strength estimation is crucial.

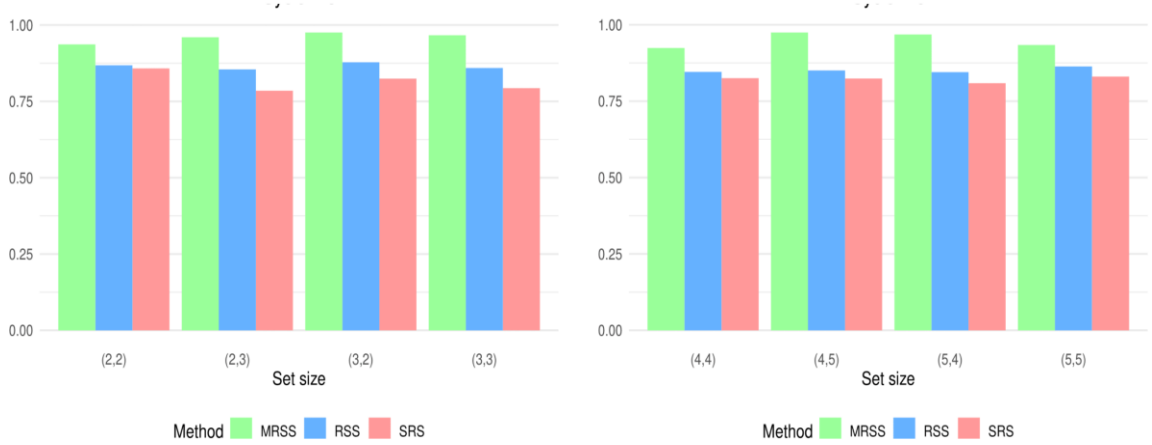


Figure 3: *Stress-strength reliability under SRS, RSS and MRSS at various set sizes for cycle 3 and 5*

X. Conclusion

This research delves into the intricate realm of stress-strength reliability estimation, focusing on scenarios where both stress and strength variables are characterized by the Inverse Nakagami distribution. Our investigation encompasses a triad of sampling methodologies: SRS, RSS, and MRSS, with the latter explored for both odd and even set sizes. Through rigorous numerical analysis, we've scrutinized the efficacy of various estimators across these diverse sampling schemes. The results unequivocally demonstrate the superiority of MRSS-based stress-strength estimates, which consistently outshine their counterparts derived from SRS and RSS data. Interestingly, RSS-based estimates typically occupy a middle ground in terms of performance, bridging the gap between SRS and MRSS. These theoretical findings find robust corroboration in

real-world applications, lending credence to the practical utility of our research. The implications of this study extend beyond its immediate scope, paving the way for future investigations in this domain.

Prospective research avenues could explore the intriguing dynamics of heterogeneous sampling methods for stress and strength data. For instance, scholars might examine stress-strength estimation in scenarios where strength data is procured through RSS, while stress measurements employ MRSS with varying set sizes, or vice versa. Furthermore, the horizon of MRSS reliability inference could be expanded to encompass cases where stress and strength variables adhere to distinct probability distributions, potentially unveiling new insights in this critical field of study.

Author Contribution Statements: All authors contributed equally and significantly in writing this article. All authors read and approved the final manuscript.

Declaration of Competing Interests: Authors state no conflict of interest.

REFERENCES

[1] A.M. Awad and M.K. Gharraf. "Estimation of P (Y< X) in the Burr case: A comparative study". In: *Communications in Statistics-Simulation and Computation* 15.2 (Jan 1986), pp. 389-403.

[2] Z.W. Birnbaum. "On a use of the Mann-Whitney statistic". In: *"Proceedings of the third Berkeley symposium on mathematical statistics and probability"*. Contributions to the Theory of Statistics, University of California Press. Volume 1 (Jan 1956), pp. 13-18.

[3] Z.W. Birnbaum and R.C. McCarty. "A distribution-free upper confidence bound for Pr{Y < X}, based on independent samples of X and Y". In: *The Annals of Mathematical Statistics* 29.2 (Jun 1958), pp. 558–562.

[4] Zehua Chen. "The efficiency of ranked-set sampling relative to simple random sampling under multi-parameter families". In: *Statistica Sinica* 10.2 (Jan 2000), pp. 247–263.

[5] Zehua Chen. "Ranked-set sampling with regression-type estimators". In: *Journal of Statistical Planning and Inference* 92.1-2 (Jan 2001), pp. 181–192.

[6] J.D. Church and Bernard Harris. "The estimation of reliability from stress-strength relationships". In: *Technometrics* 12. 1 (Feb 1970), pp. 49–54.

[7] Kenneth Constantine, Siu-Keung Tse and Marvin Karson. "Estimation of P(Y < X) in the gamma case". In: *Communications in Statistics-Simulation and Computation* 15.2 (Jan 1986), pp. 365–388.

[8] F. Downton. "The estimation of Pr(Y < X) in the normal case". In: *Technometrics* 15.3 (Aug 1973), pp. 551–558.

[9] A.S. Hassan, A. Al-Omar and H.F. Nagy. "Stress–strength reliability for the generalized inverted exponential distribution using MRSS". In: *Iranian Journal of Science and Technology, Transactions A: Science* 45.2 (Apr 2021), pp. 642–659.

[10] R.A. Johnson. *3 stress-strength models for reliability*. Handbook of Statistics, Quality Control and Reliability. Elsevier, Volume 7 (1988), pp. 27–54.

[11] A. Kaur, G.P. Patil and A.K. Sinha et al. "Ranked set sampling: an annotated bibliography". In: *Environmental and Ecological Statistics* 2.1 (Mar 1995), pp. 25–54.

[12] S. Kotz, Y. Lumelskii and M. Pensky. *The stress–strength model and its generalizations: theory and applications*. World Scientific Publishing Co. Pte. Ltd, Singapore, 2003.

[13] D. Kundu and R.D. Gupta. "Estimation of P [Y < X] for generalized exponential distribution". In: *Metrika* 61.3 (Jun 2005), pp. 291–308.

[14] P.H. Kvam and F.J. Samaniego. "On the inadmissibility of empirical averages as estimators in ranked set sampling". In: *Journal of Statistical Planning and Inference* 36.1 (Jul 1993), pp. 39–55.

[15] F. Louzada, P.L. Ramos and D. Nascimento. "The inverse Nakagami-m distribution: A novel approach in reliability". In: *IEEE Transactions on Reliability* 67.3 (Jun 2018), pp. 1030–1042.
[16] G.A. McIntyre. "A method for unbiased selective sampling, using ranked sets". In: *Australian journal of agricultural research* 3.4 (1952), pp. 385–390.
[17] H.A. Muttlak. "Median ranked set sampling". In*: J Appl Stat Sci* 6 (1997), pp. 245–255.
[18] M. Nakagami. "The m-distribution—a general formula of intensity distribution of rapid fading". In: *Statistical methods in radio wave propagation* (1960), pp. 3–36.
[19] H. Nakahara and E. Carcol´e. "Maximum-likelihood method for estimating coda Q and the Nakagami-m parameter". In: *Bulletin of the Seismological Society of America* 100.6 (Dec 2010), pp. 3174–3182.
[20] O. Ozturk and K.B. Kavlak. "Model based inference using ranked set samples". In: *Survey Methodology* 44.1 (Jun 2018), pp. 1–17.
[21] M.H. Samuh and A. Qtait. "Estimation for the parameters of the exponentiated exponential distribution using a median ranked set sampling". In: *Journal of Modern Applied Statistical Methods* 14.1 (2015), pp. 215–237.
[22] S. Sarkar, N.K. Goel and B.S. Mathur. "Performance investigation of Nakagami-m distribution to derive flood hydrograph by genetic algorithm optimization approach". In: *Journal of Hydrologic Engineering* 15.8 (Aug 2010), pp. 658–666.
[23] U. Shahzad, I. Ahmad, I. Almanjahie et al. "Three-fold utilization of supplementary information for mean estimation under median ranked set sampling scheme". In: *IPlos one* 17.10 (Oct 2022), pp. e-0276514.
[24] S.L. Stokes and T.W. Sager. "Characterization of a ranked-set sample with application to estimating distribution functions". In: *Journal of the American Statistical Association* 83.402 (Jun 1988), pp. 374–381.
[25] P.H. Tsui, C.C. Huang and S.H. Wang. "Use of nakagami distribution and logarithmic compression in ultrasonic tissue characterization". In: *Journal of Medical and Biological Engineering* 26.2 (Jun 2006), pp. 69–73.
[26] N. Wang, X. Song and J. Cheng. "Generalized method of moments estimation of the Nakagami-m fading parameter". In: *IEEE Transactions on Wireless Communications* 11.9 (July 2012), pp. 3316–3325.
[27] P.L.H. Yu and K. Lam. "Erratum: Regression estimator in ranked set sampling". In: *Biometrics* 83.402 (1988), pp. 1070–1080.
[28] E. Zamanzade and M. Vock. "Variance estimation in ranked set sampling using a concomitant variable". In: *Statistics & Probability Letters* 105 (Oct 2015), pp. 1–5.
[29] L. Zhang, X. Dong, X. Xu and L. Cui. "Weighted estimation of quantiles using unbalanced ranked set sampling". In: *Quality Technology & Quantitative Management* 11.3 (Jan 2014), pp. 281–295.

DOUBLE ORBIT RETRIAL QUEUEING-INVENTORY SYSTEM WITH ORBITAL SEARCH UNDER (s, S) POLICY

M. THILAKAVATHY [1], AGASSI MELIKOV [2,3,*] G. AYYAPPAN [4]

•

[1,4] Department of Mathematics, Puducherry Technological University, Puducherry, India
[2] Department of Mathematics, Baku Engineering University, Khirdalan, Azerbaijan
[3]Institute of control systems, Baku, Azerbaijan
[1]thilakavathy5184@ptuniv.edu.in [2,3]amelikov@beu.edu.az
[4]ayyappan@ptuniv.edu.in
[*] Corresponding author: amelikov@beu.edu.az

Abstract

We consider two-orbit retrial queueing inventory system with a single server. Service time follows phase-type distribution, while arrivals follow the Markovian arrival process. During busy period of the server, the arriving customer may either balk or move to the limitless orbit. Following service completion, the server takes a vacation if there are no customers in the system. When a breakdown happens during busy times, the server undergoes phase-type repair, and the current customer enters finite orbit. Once the repair is finished, the server either stays idle or searches the finite orbit. The replenishment period is exponential and we use (s, S) policy. The matrix analytic approach has been used to analyze steady state probability. We assess this retrial queueing inventory model both numerically and graphically.

Keywords: Markovian arrival process, phase-type service, phase-type repair, Breakdown, Two orbits, Retrial customers, Orbital search, (s, S) policy
MSC 2010 No.: 60K25, 68M20, 90B05.

1. Introduction

The retrial queueing theory is commonly used to explain how real-world systems work. When a customer arrives during the busy period of the server, then the customer may join the queue to get the service. This virtual waiting area for customers is orbit. At the moment of retrial when the server is free, they begin to get the service immediately; if not, they return to the orbit and go through the entire procedure again. In this case, it is also possible for the new arrival to get service directly without joining the orbit, provided that the server is available. Falin et al. [11] released the first literature on retrial queues and it includes a full description of basic methodologies and results on retrial queues. A regenerative approach algorithm was used by Artalejo [3] to determine the steady state probability for the $M/G/l$ retrial queue with breakdowns. Using the matrix analytic method, Ayyappan and Gowthami [5] investigated the effect of retrial rate against the expected number of customers in the system while analyzing the retrial queueing model with a single server.

Retrial queueing model with re-service was researched by Melikov et al [15]. This model assumes that the distribution service time is exponential and analyzes the input flow of calls using a Markovian Arrival Process (MAP). Melikov et al. [16] measured performance metrics for the average number of retrial customers in the orbit, the mean values of both failed and busy servers, and the loss probabilities of both primary and retrial customers. Dudin et al. [4] analyzed

a single-server retrial queueing model with two types of customer, exponential service times, arrivals governed by a Marked Markovian process, and a joint distribution for the number of customers in the orbits.

Abdul Reiyas and Jeganathan [1] examined a classical retrial queueing inventory system with two component demand rate. Singla and Kaur [20] developed a method for solving difference-differential equations to get the transient state probability for the precise number of arrivals and departures while the server is busy or idle. We experience many situations in our daily lives where customer service is disrupted by server failure. For instance, the server can break due to internal or external issues in manufacturing systems, computers, or electronic systems; in packet transferring of communication channels; or even in the service process of everything in one's life. Customers whose service is interrupted must wait for service to come back once the server's repair is finished. The server may be disrupted during a customer's service by a vital interruption (emergency circumstance) under the Poisson process. Nithya et al. [17] state that due to breakdown, the current customer join in the queue and waits to be served.

Using inventory management and queuing systems together has many benefits for improving customer satisfaction and operational efficiency. With a comprehensive evaluation and management of these systems, firms may better balance maintaining appropriate stock levels with reducing waiting times. For M/M/1 Queueing-Inventory System(QIS) with lost sales, under various inventory management policies, including (r,Q) and (r,S) policies, Schwarz et al. [19] discovered steady state distributions of inventory processes and combined queue length in a particular product form. Ayyappan and Arulmozhi [6] examined the retrial QIS using a constant retrial rate, orbital client collision, working vacation, flush out, balking, breakdown, and repair. Ayyappan and Meena [7] looked at a retry QIS with a phase-type vacation and an inconsistent server.

Two separate types of customers arrive in two different Poisson streams when they are sent to a single server system. The service station can only handle one client at a time and if blockage occurs, the two types of consumers are sent to a different type. Two orbit queues with infinite capacity were assumed and the theory of Riemann (–Hilbert) boundary value problems by Dimitriou [10] can be used to find how the joint stationary orbit queue length distribution generates probabilities. Sangha and Jain [18] have investigated the best course of action for a double-orbit retrial queue with erratic service and vacation interruption . Retrial QIS with an isolated server and feedback for consumers in which the orbit size is finite was covered by Amirthakodi and Sivakumar [2].

The idea of orbital search has been presented in order to make effective use of the server's idle time in a retry queueing system. This idea states that the server will seek for customers in the orbit during idle time rather than waiting for a direct or repeat customer to arrive. Falin [11] has researched the Markovian model that includes dissatisfied customers on a single server. The retrial queueing system and the orbit's search for priority customers have been studied by Krishnamoorthy and Joshua [13]. According to Dhanya et al. [8], the server either resumes orbital search for the interrupted clients in the finite orbit or stays idle once each service and repair is completed. According to Sivakumar [21], retrial demands compete for their exponentially distributed necessity by sending out signals. The steady state example produces the combined likelihood distribution of the number of orbital needs and the inventory level.

The remaining parts of the paper are organized as follows: Our model is described in section 2. Matrix creation and several notations are explained in section 3. The invariant probability vector, the rate matrix R and the stability condition are all obtained in section 4. Section 5 describes the examination of the busy period. Section 6 lists the performance metrics. Sectionn 7 presents cost analysis. There are some graphical and numerical results in section 8. Section 9 presents the conclusion.

2. Mathematical model

We examine a double-orbit, unreliable single server retrial QIS. The model's fundamental function can be characterized as follows:

- **Arrival process:** Primary customers with parameter matrices of order m (D_0, D_1) come in accordance with MAP. If the server is available when a customer arrives, he will receive service directly; if the server is active, the customer has the chance of either joining an infinite orbit with probability (1-b) or may balk the system with probability b.
- **Service Process:** The first-come, first-served approach applies to each customer. The service period is determined by the PH distribution, which is represented as (γ, U) of order n, such that $U^0 + Ue = 0$ and the rate is $\mu = [\gamma(-U)^{-1}e_n]$.
- **Breakdown state:** During busy times, the server is prone to breakdowns. Breakdown time follows an exponential distribution with parameter ψ. Interruptions can happen often, and it is predicted that a customer's service would repeat in the same way. When a server breaks down, the customer goes to a finite orbit N and the server undergoes repair.
- **Retrial process:** Retrial of the customer is successful when the server is free with positive inventory. An exponential distribution governs the interval between retrials, with a rate of σ_2 for a finite orbit and σ_1 for an unlimited orbit.
- **Vacation state:** After service is finished, the server takes a break if there are no clients within the system. When the vacation is over, the server remains in an idle state. The rate of vacation is exponential distribution and is denoted as η.
- **Repair state:** During the busy period, the server may breakdown, the repair process starts immediately. It is represented as a phase-type distribution with the notation (α, T) of order l such that $T^0 + Te = 0$ and the rate is $\tau = [\alpha(-T)^{-1}e_l]$.
- **Orbital search** Once the repair is finished, the server has the option of staying idle with probability q or searching for an orbital customer from the finite orbit with probability p. The search time is negligible.

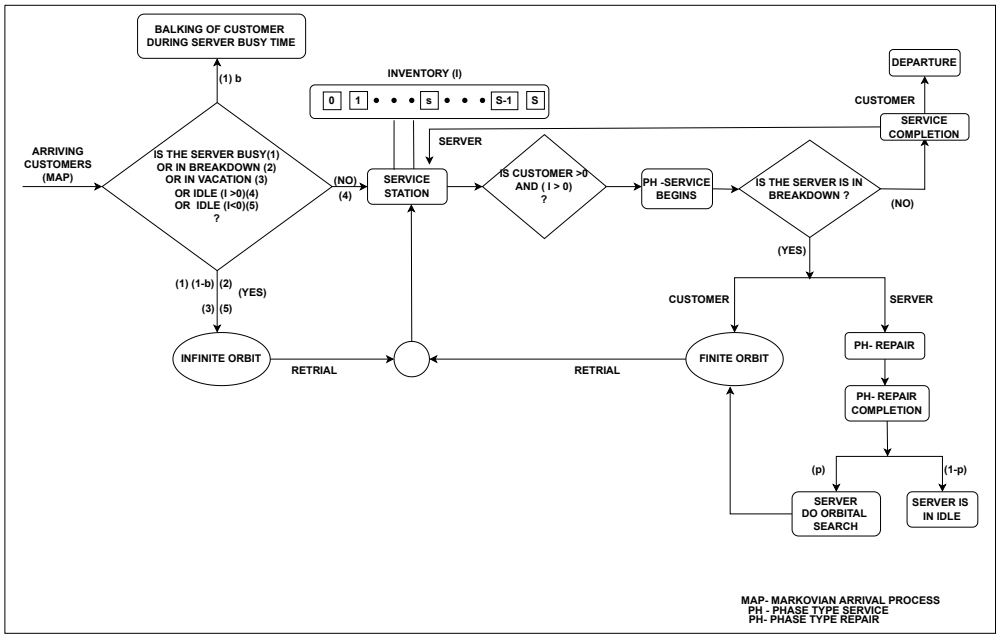


Figure 1: *Schematic representation*

- **Replenishment:** When a customer finishes service, one item is removed from stock. Under the (s, S) policy, an order of S items is placed when inventory drops to level s. The supply lead time follows an exponential distribution with rate β.

The lead time, customer arrival time, retrial time and service times (for both primary and retrial customers) are all considered to be mutually independent. Refer to figure 1 for a schematic representation of the model.

3. Generation Matrix

Abbreviation and Notations

- CTMC- Continuous Time Markov Chain
- QBD process - Quasi-Birth-Death Process
- MAM - Matrix Analytic Method
- e - entries in a column's vector are one;
- I_n - Identity matrix of order n
- 0 - Matrix whose entries are 0, of appropriate size
- $\otimes$ - A block matrix is created by the Kronecker product of two matrices of different dimensions;
- $\oplus$ - The Kronecker addition creates a block matrix from two matrices of varying sizes;
- $N_1(t)$ indicates the number of customers in an infinite orbit;
- $N_2(t)$ indicates the number of customers in the finite orbit;
- $J(t)$ represents the server status;
- $I(t)$ represents the stock level for commodity;
- $S(t)$ represents the service phases;
- $R(t)$ represents the repair phases;
- A(t) represents the arrival phases;
  at time t, where

$J(t)$ represents the status of the server, defined as

$$J_(t) = \begin{cases} 0, & \text{server is in vacation,} \\ 1, & \text{server is in idle,} \\ 2, & \text{server is in busy ,} \\ 3, & \text{server is in repair.} \end{cases}$$

It is obvious that $\{N_1(t), N_2(t), J(t), I(t), S(t), R(t), \text{A(t)} : t \geq 0\}$ is a CTMC with the state space is as follows:

$$\omega = \bigcup_{c_1=0}^{\infty} \chi(c_1),$$

$$\begin{aligned}\chi(c_1) &= \{(c_1,0,c_3,c_4,c_7) : 0 \le c_3 \le N, 0 \le c_4 \le S, 1 \le c_7 \le m\} \\ &\cup \{(c_1,1,c_3,c_4,c_7) : 0 \le c_3 \le N, 0 \le c_4 \le S, 1 \le c_7 \le m\} \\ &\cup \{(c_1,2,c_3,c_4,c_5,c_7) : 0 \le c_3 \le N, 1 \le c_4 \le S, 1 \le c_5 \le n, 1 \le c_7 \le m\} \\ &\cup \{(c_1,3,c_3,c_4,c_6,c_7) : 1 \le c_3 \le N, 0 \le c_4 \le S, 1 \le c_5 \le l, 1 \le c_7 \le m\}.\end{aligned}$$

The QBD procedure using the (s,S) policy generates an infinitesimal matrix, as provided by

$$Q = \begin{bmatrix} B_0 & A_0 & 0 & 0 & 0 & 0 & \dots \\ A_2 & A_1 & A_0 & 0 & 0 & 0 & \dots \\ 0 & A_2 & A_1 & A_0 & 0 & 0 & \dots \\ 0 & 0 & A_2 & A_1 & A_0 & 0 & \dots \\ \vdots & \vdots & \vdots & \ddots & \ddots & \ddots & \vdots \\ \vdots & \vdots & \vdots & \vdots & \ddots & \ddots & \ddots \end{bmatrix}.$$

The following defines each entry in Q's block matrices:,

$$B_0 = \begin{bmatrix} B_0^{11} & B_0^{12} & 0 & 0 \\ 0 & B_0^{22} & B_0^{23} & 0 \\ B_0^{31} & B_0^{32} & B_0^{33} & B_0^{34} \\ 0 & B_0^{42} & B_0^{43} & B_0^{44} \end{bmatrix}, \qquad B_0^{11} = I_{N+1} \otimes E_{001},$$

$$E_{001} = \begin{bmatrix} V_1 & \mathbf{0} & \mathbf{0} & \dots & \mathbf{0} & \mathbf{0} & \dots & \mathbf{0} & V_2 \\ \mathbf{0} & V_1 & \mathbf{0} & \dots & \mathbf{0} & \mathbf{0} & \dots & \mathbf{0} & V_2 \\ \mathbf{0} & \mathbf{0} & V_1 & \dots & \mathbf{0} & \mathbf{0} & \dots & \mathbf{0} & V_2 \\ \vdots & \vdots & \vdots & \ddots & \vdots & \vdots & \vdots & \vdots & \vdots \\ \mathbf{0} & \mathbf{0} & \mathbf{0} & \dots & V_1 & \mathbf{0} & \dots & \mathbf{0} & V_2 \\ \mathbf{0} & \mathbf{0} & \mathbf{0} & \dots & \mathbf{0} & V_3 & \dots & \mathbf{0} & \mathbf{0} \\ \vdots & \vdots & \vdots & \ddots & \vdots & \vdots & \vdots & \vdots & \vdots \\ \mathbf{0} & \mathbf{0} & \mathbf{0} & \dots & \mathbf{0} & \mathbf{0} & \dots & V_3 & \mathbf{0} \\ \mathbf{0} & \mathbf{0} & \mathbf{0} & \dots & \mathbf{0} & \mathbf{0} & \dots & \mathbf{0} & V_3 \end{bmatrix},$$

where, $V_1 = D_0 - (\eta + \beta) I_m$, $V_2 = \beta I_m$, $V_3 = D_0 - \eta I_m$,

$$B_0^{12} = I_{N+1} \otimes I_{(S+1)} \eta I_m, \qquad B_0^{22} = \begin{bmatrix} E_{002} & 0 \\ 0 & I_N \otimes E_{003} \end{bmatrix},$$

$$E_{002} = \begin{bmatrix} V_4 & \mathbf{0} & \mathbf{0} & \dots & \mathbf{0} & \mathbf{0} & \dots & \mathbf{0} & V_5 \\ \mathbf{0} & V_4 & \mathbf{0} & \dots & \mathbf{0} & \mathbf{0} & \dots & \mathbf{0} & V_5 \\ \mathbf{0} & \mathbf{0} & V_4 & \dots & \mathbf{0} & \mathbf{0} & \dots & \mathbf{0} & V_5 \\ \vdots & \vdots & \vdots & \ddots & \vdots & \vdots & \vdots & \vdots & \vdots \\ \mathbf{0} & \mathbf{0} & \mathbf{0} & \dots & V_4 & \mathbf{0} & \dots & \mathbf{0} & V_5 \\ \mathbf{0} & \mathbf{0} & \mathbf{0} & \dots & \mathbf{0} & V_6 & \dots & \mathbf{0} & \mathbf{0} \\ \vdots & \vdots & \vdots & \ddots & \vdots & \vdots & \vdots & \vdots & \vdots \\ \mathbf{0} & \mathbf{0} & \mathbf{0} & \dots & \mathbf{0} & \mathbf{0} & \dots & V_6 & \mathbf{0} \\ \mathbf{0} & \mathbf{0} & \mathbf{0} & \dots & \mathbf{0} & \mathbf{0} & \dots & \mathbf{0} & V_6 \end{bmatrix},$$

where, $V_4 = D_0 - \beta I_m$, $V_5 = \beta I_m$, $V_6 = D_0$,

$$E_{003} = \begin{bmatrix} V_7 & \mathbf{0} & \mathbf{0} & \dots & \mathbf{0} & \mathbf{0} & \dots & \mathbf{0} & V_8 \\ \mathbf{0} & V_9 & \mathbf{0} & \dots & \mathbf{0} & \mathbf{0} & \dots & \mathbf{0} & V_8 \\ \mathbf{0} & \mathbf{0} & V_9 & \dots & \mathbf{0} & \mathbf{0} & \dots & \mathbf{0} & V_8 \\ \vdots & \vdots & \vdots & \ddots & \vdots & \vdots & \vdots & \vdots & \vdots \\ \mathbf{0} & \mathbf{0} & \mathbf{0} & \dots & V_9 & \mathbf{0} & \dots & \mathbf{0} & V_8 \\ \mathbf{0} & \mathbf{0} & \mathbf{0} & \dots & \mathbf{0} & V_{10} & \dots & \mathbf{0} & \mathbf{0} \\ \vdots & \vdots & \vdots & \ddots & \vdots & \vdots & \vdots & \vdots & \vdots \\ \mathbf{0} & \mathbf{0} & \mathbf{0} & \dots & \mathbf{0} & \mathbf{0} & \dots & V_{10} & \mathbf{0} \\ \mathbf{0} & \mathbf{0} & \mathbf{0} & \dots & \mathbf{0} & \mathbf{0} & \dots & \mathbf{0} & V_{10} \end{bmatrix},$$

$$V_7 = D_0 - \beta I_m, \quad V_8 = \beta I_m, \quad V_9 = D_0 - (\sigma_2 + \beta) I_m, \quad V_{10} = D_0 - \sigma_2 I_m,$$

$$B_0^{23} = \begin{bmatrix} E_{004} & 0 & \dots & 0 & 0 & 0 \\ E_{005} & E_{004} & \dots & 0 & 0 & 0 \\ \vdots & \ddots & \ddots & \vdots & \vdots & \vdots \\ \vdots & \vdots & \ddots & \ddots & \vdots & \vdots \\ 0 & 0 & \dots & E_{005} & E_{004} & 0 \\ 0 & 0 & \dots & 0 & E_{004} & 0 \end{bmatrix},$$

$$E_{004} = \begin{bmatrix} 0 \\ I_S \otimes \gamma \otimes D_1 \end{bmatrix}, \quad E_{005} = \begin{bmatrix} 0 \\ I_S \otimes \gamma \otimes \sigma_2 I_m \end{bmatrix}, \quad B_0^{31} = \begin{bmatrix} E_{006} & 0 \\ 0 & 0 \end{bmatrix},$$

$$E_{006} = \begin{bmatrix} I_S \otimes u^0 \otimes I_m & 0 \end{bmatrix}, \quad B_0^{32} = \begin{bmatrix} 0 & 0 \\ 0 & I_N \otimes E_{006} \end{bmatrix}, \quad B_0^{33} = I_{N+1} \otimes E_{007},$$

$$E_{007} = \begin{bmatrix} V_{11} & \mathbf{0} & \mathbf{0} & \dots & \mathbf{0} & \mathbf{0} & \dots & \mathbf{0} & V_{12} \\ \mathbf{0} & V_{11} & \mathbf{0} & \dots & \mathbf{0} & \mathbf{0} & \dots & \mathbf{0} & V_{12} \\ \mathbf{0} & \mathbf{0} & V_{11} & \dots & \mathbf{0} & \mathbf{0} & \dots & \mathbf{0} & V_{12} \\ \vdots & \vdots & \vdots & \ddots & \vdots & \vdots & \vdots & \vdots & \vdots \\ \mathbf{0} & \mathbf{0} & \mathbf{0} & \dots & V_{11} & \mathbf{0} & \dots & \mathbf{0} & V_{12} \\ \mathbf{0} & \mathbf{0} & \mathbf{0} & \dots & \mathbf{0} & V_{13} & \dots & \mathbf{0} & \mathbf{0} \\ \vdots & \vdots & \vdots & \ddots & \vdots & \vdots & \vdots & \vdots & \vdots \\ \mathbf{0} & \mathbf{0} & \mathbf{0} & \dots & \mathbf{0} & \mathbf{0} & \dots & V_{13} & \mathbf{0} \\ \mathbf{0} & \mathbf{0} & \mathbf{0} & \dots & \mathbf{0} & \mathbf{0} & \dots & \mathbf{0} & V_{13} \end{bmatrix},$$

where, $V_{11} = U \oplus D_0 + bD_1 - (\psi + \beta) I_{nm}, \quad V_{12} = \beta I_{nm}, \quad V_{13} = U \oplus D_0 + bD_1 - \psi I_{nm},$

$$B_0^{34} = \begin{bmatrix} I_N \otimes E_{008} & 0 \\ 0 & E_{008} \end{bmatrix}, \quad E_{008} = 0 \quad I_S \otimes I_l \otimes \psi I_m, \quad B_0^{42} = \begin{bmatrix} 0 & I_N \otimes E_{009} \end{bmatrix},$$

$$E_{009} = \begin{bmatrix} T^0 \otimes I_m & 0 \\ 0 & I_S \otimes qT^0 \otimes I_m \end{bmatrix}, \quad B_0^{43} = \begin{bmatrix} I_N \otimes E_{010} & 0 \end{bmatrix}, \quad E_{010} = \begin{bmatrix} 0 \\ I_S \otimes pT^0 \gamma \otimes I_m \end{bmatrix},$$

$$B_0^{44} = \begin{bmatrix} I_N \otimes E_{011} \end{bmatrix}, \quad E_{011} = \begin{bmatrix} V_{14} & \mathbf{0} & \mathbf{0} & \dots & \mathbf{0} & \mathbf{0} & \dots & \mathbf{0} & V_{15} \\ \mathbf{0} & V_{14} & \mathbf{0} & \dots & \mathbf{0} & \mathbf{0} & \dots & \mathbf{0} & V_{15} \\ \mathbf{0} & \mathbf{0} & V_{14} & \dots & \mathbf{0} & \mathbf{0} & \dots & \mathbf{0} & V_{15} \\ \vdots & \vdots & \vdots & \ddots & \vdots & \vdots & \vdots & \vdots & \vdots \\ \mathbf{0} & \mathbf{0} & \mathbf{0} & \dots & V_{14} & \mathbf{0} & \dots & \mathbf{0} & V_{15} \\ \mathbf{0} & \mathbf{0} & \mathbf{0} & \dots & \mathbf{0} & V_{16} & \dots & \mathbf{0} & \mathbf{0} \\ \vdots & \vdots & \vdots & \ddots & \vdots & \vdots & \vdots & \vdots & \vdots \\ \mathbf{0} & \mathbf{0} & \mathbf{0} & \dots & \mathbf{0} & \mathbf{0} & \dots & V_{16} & \mathbf{0} \\ \mathbf{0} & \mathbf{0} & \mathbf{0} & \dots & \mathbf{0} & \mathbf{0} & \dots & \mathbf{0} & V_{16} \end{bmatrix},$$

where, $V_{14} = I_{s+1} \otimes T \oplus D_0 - \beta I_{lm}, \quad V_{15} = \beta I_{lm}, \quad V_{16} = T \oplus D_0,$

$$A_0 = \begin{bmatrix} A_0^{11} & 0 & 0 & 0 \\ 0 & A_0^{22} & 0 & 0 \\ 0 & 0 & A_0^{33} & 0 \\ 0 & 0 & 0 & A_0^{44} \end{bmatrix},$$

$$A_0^{11} = I_{N+1} \otimes I_{S+1} \otimes D_1, \quad A_0^{22} = I_{N+1} \otimes E_{012}, \quad E_{012} = \begin{bmatrix} D_1 & 0 \\ 0 & 0 \end{bmatrix},$$

$$A_0^{33} = I_{N+1} \otimes I_S \otimes I_n \otimes (1-b) D_1, \quad A_0^{44} = I_N \otimes I_{S+1} \otimes I_l \otimes D_1,$$

$$A_2 = \begin{bmatrix} 0 & 0 & 0 & 0 \\ 0 & 0 & A_2^{23} & 0 \\ 0 & 0 & 0 & 0 \\ 0 & 0 & 0 & 0 \end{bmatrix}, \quad A_2^{23} = \begin{bmatrix} 0 & 0 \\ 0 & I_N \otimes E_{013} \end{bmatrix}, \quad E_{013} = \begin{bmatrix} 0 \\ I_S \otimes \gamma \otimes \sigma_1 I_m \end{bmatrix},$$

$$A_1 = \begin{bmatrix} A_1^{11} & A_1^{12} & 0 & 0 \\ 0 & A_1^{22} & A_1^{23} & 0 \\ 0 & A_1^{32} & A_0^{33} & A_1^{34} \\ 0 & A_1^{42} & A_1^{43} & A_1^{44} \end{bmatrix}, \quad A_1^{11} = \begin{bmatrix} I_{N+1} \otimes E_{014} \end{bmatrix},$$

$$E_{014} = \begin{bmatrix} V_{17} & \mathbf{0} & \mathbf{0} & \dots & \mathbf{0} & \mathbf{0} & \dots & \mathbf{0} & V_{18} \\ \mathbf{0} & V_{17} & \mathbf{0} & \dots & \mathbf{0} & \mathbf{0} & \dots & \mathbf{0} & V_{18} \\ \mathbf{0} & \mathbf{0} & V_{17} & \dots & \mathbf{0} & \mathbf{0} & \dots & \mathbf{0} & G18 \\ \vdots & \vdots & \vdots & \ddots & \vdots & \vdots & \vdots & \vdots & \vdots \\ \mathbf{0} & \mathbf{0} & \mathbf{0} & \dots & V_{17} & \mathbf{0} & \dots & \mathbf{0} & V_{18} \\ \mathbf{0} & \mathbf{0} & \mathbf{0} & \dots & \mathbf{0} & V_{19} & \dots & \mathbf{0} & \mathbf{0} \\ \vdots & \vdots & \vdots & \ddots & \vdots & \vdots & \vdots & \vdots & \vdots \\ \mathbf{0} & \mathbf{0} & \mathbf{0} & \dots & \mathbf{0} & \mathbf{0} & \dots & V_{19} & \mathbf{0} \\ \mathbf{0} & \mathbf{0} & \mathbf{0} & \dots & \mathbf{0} & \mathbf{0} & \dots & \mathbf{0} & V_{19} \end{bmatrix},$$

where, $V_{17} = D_0 - (\eta + \beta)I_m$, $V_{18} = \beta I_m$, $V_{19} = D_0 - \eta I_m$,

$A_1^{12} = \left[I_{N+1} \otimes I_{S+1} \otimes \eta I_m\right]$, $A_1^{22} = \begin{bmatrix} E_{015} & 0 \\ 0 & I_N \otimes E_{016} \end{bmatrix}$,

$$E_{015} = \begin{bmatrix} V_{20} & \mathbf{0} & \mathbf{0} & \dots & \mathbf{0} & \mathbf{0} & \dots & \mathbf{0} & V_{21} \\ \mathbf{0} & V_{20} & \mathbf{0} & \dots & \mathbf{0} & \mathbf{0} & \dots & \mathbf{0} & V_{21} \\ \mathbf{0} & \mathbf{0} & V_{20} & \dots & \mathbf{0} & \mathbf{0} & \dots & \mathbf{0} & V_{21} \\ \vdots & \vdots & \vdots & \ddots & \vdots & \vdots & \vdots & \vdots & \vdots \\ \mathbf{0} & \mathbf{0} & \mathbf{0} & \dots & V_{20} & \mathbf{0} & \dots & \mathbf{0} & V_{21} \\ \mathbf{0} & \mathbf{0} & \mathbf{0} & \dots & \mathbf{0} & V_{22} & \dots & \mathbf{0} & \mathbf{0} \\ \vdots & \vdots & \vdots & \ddots & \vdots & \vdots & \vdots & \vdots & \vdots \\ \mathbf{0} & \mathbf{0} & \mathbf{0} & \dots & \mathbf{0} & \mathbf{0} & \dots & V_{22} & \mathbf{0} \\ \mathbf{0} & \mathbf{0} & \mathbf{0} & \dots & \mathbf{0} & \mathbf{0} & \dots & \mathbf{0} & V_{22} \end{bmatrix},$$

where, $V_{20} = D_0 - \beta I_m$, $V_{21} = \beta I_m$, $V_{22} = D_0$,

$$E_{016} = \begin{bmatrix} V_{23} & \mathbf{0} & \mathbf{0} & \dots & \mathbf{0} & \mathbf{0} & \dots & \mathbf{0} & V_{24} \\ \mathbf{0} & V_{25} & \mathbf{0} & \dots & \mathbf{0} & \mathbf{0} & \dots & \mathbf{0} & V_{24} \\ \mathbf{0} & \mathbf{0} & V_{25} & \dots & \mathbf{0} & \mathbf{0} & \dots & \mathbf{0} & V_{24} \\ \vdots & \vdots & \vdots & \ddots & \vdots & \vdots & \vdots & \vdots & \vdots \\ \mathbf{0} & \mathbf{0} & \mathbf{0} & \dots & V_{25} & \mathbf{0} & \dots & \mathbf{0} & V_{24} \\ \mathbf{0} & \mathbf{0} & \mathbf{0} & \dots & \mathbf{0} & V_{26} & \dots & \mathbf{0} & \mathbf{0} \\ \vdots & \vdots & \vdots & \ddots & \vdots & \vdots & \vdots & \vdots & \vdots \\ \mathbf{0} & \mathbf{0} & \mathbf{0} & \dots & \mathbf{0} & \mathbf{0} & \dots & V_{26} & \mathbf{0} \\ \mathbf{0} & \mathbf{0} & \mathbf{0} & \dots & \mathbf{0} & \mathbf{0} & \dots & \mathbf{0} & V_{26} \end{bmatrix},$$

where, $V_{23} = D_0 - \beta I_m$, $V_{24} = \beta I_m$, $V_{25} = D_0 - (\sigma_1 + \sigma_2 + \beta)I_m$,

$V_{26} = D_0 - (\sigma_1 + \sigma_2)I_m$, $A_1^{23} = B_0^{23}$, $A_1^{32} = \left[I_{N+1} \otimes E_{017}\right]$,

$E_{017} = \left[I_S \otimes U^0 I_m \quad 0\right]$, $A_1^{33} = \left[I_{N+1} \otimes E_{018}\right]$,

$$E_{018} = \begin{bmatrix} V_{27} & \mathbf{0} & \mathbf{0} & \dots & \mathbf{0} & \mathbf{0} & \dots & \mathbf{0} & V_{28} \\ \mathbf{0} & V_{27} & \mathbf{0} & \dots & \mathbf{0} & \mathbf{0} & \dots & \mathbf{0} & V_{28} \\ \mathbf{0} & \mathbf{0} & V_{27} & \dots & \mathbf{0} & \mathbf{0} & \dots & \mathbf{0} & V_{28} \\ \vdots & \vdots & \vdots & \ddots & \vdots & \vdots & \vdots & \vdots & \vdots \\ \mathbf{0} & \mathbf{0} & \mathbf{0} & \dots & V_{27} & \mathbf{0} & \dots & \mathbf{0} & V_{28} \\ \mathbf{0} & \mathbf{0} & \mathbf{0} & \dots & \mathbf{0} & V_{29} & \dots & \mathbf{0} & \mathbf{0} \\ \vdots & \vdots & \vdots & \ddots & \vdots & \vdots & \vdots & \vdots & \vdots \\ \mathbf{0} & \mathbf{0} & \mathbf{0} & \dots & \mathbf{0} & \mathbf{0} & \dots & V_{29} & \mathbf{0} \\ \mathbf{0} & \mathbf{0} & \mathbf{0} & \dots & \mathbf{0} & \mathbf{0} & \dots & \mathbf{0} & V_{29} \end{bmatrix},$$

where, $V_{27} = (U \oplus D_0 + bD_1) - (\psi + \beta)I_{nm}$, $V_{28} = \beta I_{nm}$, $V_{29} = (U \oplus D_0 + bD_1) - \psi I_{nm}$

$A_1^{34} = \begin{bmatrix} I_N \otimes E_{019} & 0 \\ 0 & E_{019} \end{bmatrix}$, $E_{019} = \begin{bmatrix} 0 & I_S \otimes I_l \otimes \psi I_m \end{bmatrix}$, $A_1^{42} = \begin{bmatrix} 0 & I_S \otimes I_N \otimes E_{020} \end{bmatrix}$,

$E_{020} = \begin{bmatrix} T^0 \otimes Im & 0 \\ 0 & I_S \otimes qT^0 \otimes I_m \end{bmatrix}$, $A_1^{43} = \begin{bmatrix} I_N \otimes E_{021} & 0 \end{bmatrix}$, $E_{021} = \begin{bmatrix} 0 \\ I_S \otimes pT^0\gamma \otimes I_m \end{bmatrix}$,

$$A_1^{44} = \left[I_N \otimes E_{022}\right], \quad E_{022} = \begin{bmatrix} V_{30} & \mathbf{0} & \mathbf{0} & \dots & \mathbf{0} & \mathbf{0} & \dots & \mathbf{0} & V_{31} \\ \mathbf{0} & V_{30} & \mathbf{0} & \dots & \mathbf{0} & \mathbf{0} & \dots & \mathbf{0} & V_{31} \\ \mathbf{0} & \mathbf{0} & V_{30} & \dots & \mathbf{0} & \mathbf{0} & \dots & \mathbf{0} & V_{31} \\ \vdots & \vdots & \vdots & \ddots & \vdots & \vdots & \vdots & \vdots & \vdots \\ \mathbf{0} & \mathbf{0} & \mathbf{0} & \dots & V_{30} & \mathbf{0} & \dots & \mathbf{0} & V_{31} \\ \mathbf{0} & \mathbf{0} & \mathbf{0} & \dots & \mathbf{0} & V_{32} & \dots & \mathbf{0} & \mathbf{0} \\ \vdots & \vdots & \vdots & \ddots & \vdots & \vdots & \vdots & \vdots & \vdots \\ \mathbf{0} & \mathbf{0} & \mathbf{0} & \dots & \mathbf{0} & \mathbf{0} & \dots & V_{32} & \mathbf{0} \\ \mathbf{0} & \mathbf{0} & \mathbf{0} & \dots & \mathbf{0} & \mathbf{0} & \dots & \mathbf{0} & V_{32} \end{bmatrix},$$

where, $V_{30} = (T \oplus D_0) - \beta I_{lm}$, $\quad V_{31} = \beta I_{lm}$, $\quad V_{32} = T \oplus D_0$.

4. Analysis of Stability Condition

A generator matrix is indicated by the equation $A = A_0 + A_1 + A_2$. In the steady state, let ζ be the probability vector of A that satisfies $\zeta e = 1$ and $\zeta A = 0$. The vector ζ is divided by

$$\zeta = (\zeta_0, \zeta_1, \zeta_2, \zeta_3) = (\zeta_{000}, \zeta_{001}, \dots, \pi_{00S}, \pi_{100}, \zeta_{101}, \dots, \zeta_{10S}, \zeta_{N00}, \zeta_{N01}, \dots, \zeta_{N0S}, \zeta_{010}, \zeta_{012}, \dots, \zeta_{01S}, \zeta_{110}, \zeta_{111}, \dots, \zeta_{11S}, \zeta_{N10}, \zeta_{N11}, \dots, \zeta_{N1S}, \zeta_{020}, \zeta_{021}, \dots, \zeta_{02S}, \zeta_{120}, \zeta_{121}, \dots, \zeta_{12S}, \dots, \zeta_{N21}, \zeta_{N22}, \dots, \zeta_{N2S}, \zeta_{030}, \zeta_{031}, \dots, \zeta_{03S}, \zeta_{130}, \zeta_{131}, \dots, \zeta_{13S}, \zeta_{N30}, \zeta_{N31}, \zeta_{N32}, \dots, \zeta_{N3S},)$$

where ζ_0 has a dimension of (N+1)(S+1)m, ζ_1 has a dimension of(N+1)(S+1)m , ζ_2 has a dimension of (N+1)Snm and ζ_3 has a dimension of (N+1)(S+1)lm.
Subject to normalizing condition

$$\sum_{c_3=0}^{N}\sum_{c_4=0}^{S}\zeta_0 e_m + \sum_{c_3=0}^{N}\sum_{c_4=0}^{S}\zeta_1 e_m + \sum_{c_3=0}^{N}\sum_{c_4=1}^{S}\zeta_2 e_{nm} + \sum_{c_3=1}^{N}\sum_{c_4=0}^{S}\zeta_3 e_{lm} = 1.$$

Within the framework of QBD, our model's stability should meet the necessary and sufficient conditions of $\zeta A_0 e < \zeta A_2 e$, which is found to be of the below form,

$$\sum_{c_3=0}^{N}\sum_{c_4=0}^{S}\zeta_{0c_3c_4}[I_{N+1}\otimes I_{S+1}\otimes D_1 e_m] + \sum_{c_3=0}^{N}\sum_{c_4=0}^{S}\zeta_{1c_3c_4}[I_{N+1}\otimes D_1 e_m]$$
$$+ \sum_{c_3=0}^{N}\sum_{c_4=1}^{S}\zeta_{2c_3c_4}[I_{N+1}\otimes I_S\otimes I_n\otimes(1-b)D_1 e_{nm}] + \sum_{c_3=1}^{N}\sum_{c_4=1}^{S}\zeta_{3c_3c_4}[I_N\otimes I_{S+1}\otimes I_l\otimes D_1 e_{lm}]$$
$$< \sum_{c_3=0}^{N}\sum_{c_4=0}^{S}\zeta_{1c_3c_4}[I_N\otimes I_S\otimes\gamma\otimes\sigma_1 I_m].$$

4.1. Invariant Probability Vector Analysis

Let ν symbolize the infinitesimal generator Q's invariant probability vector and this is divided into $\nu = (\nu_0, \nu_1, \nu_2, ...)$. Mention that ν_0, ν_1, ν_2,... have a dimension of (2m[(N+1)(S+1)]+Snm(N+1)+Nlm(S+1)) and the vector ν satisfies $\nu Q = 0 \quad$ and $\quad \nu e = 1$.
Additionally, after the stability needed of the model is met, the stationary probability vector ν can be obtained by applying the following equation:
$\nu_i = \nu_0 R^i, \quad i \geq 1,$
Second-degree matrix equation
$R^2 A_2 + R A_1 + A_0 = 0,$
is met by the Neuts (1984) least non-negative solution R. The rate matrix is obtained from the matrix quadratic equation. The requirement is satisfied by the rate matrix R, whose order is provided by (2m[(N+1)(S+1)]+Snm(N+1)+Nlm(S+1)).

$RA_2e = A_0e$,
the sub vector ν_0 can be found by solving the subsequent equation
$\nu_0(B_{00} + RA_2) = 0$,
the normalizing condition is subject to
$\nu_0 e_{2m[(N+1)(S+1)]+Snm(N+1)+Nlm(S+1)} = 1$.
Before solving the set of equations mentioned above, we first need to calculate the rate matrix R. This can be done using the Logarithmic Reduction Approach [14], which simplifies the process of finding R.

5. Analysis of Active period

- The time frame that begins when users enter the empty system and concludes when the system size first falls to zero is known as the busy period. Therefore, the first phase of the shift from level 1 to level 0 is the analogue of the busy period. When a state at any other level is visited at least once, the busy cycle is the time it takes to return to level zero.

- Let's use the concept of the basic time to examine the busy time. The QBD process is nothing more than the initial transition period between the levels k_1 to $k_1 - 1$, where $k_1 \geq 1$.

- The boundary states, or the circumstances when $k_1 = 0$, require a distinct discussion. For any level k_1 where $k_1 \geq 1$, it is evident that there are 2m[(N+1)(S+1)]+Snm(N+1)+Nml(S+1) states. For this reason, the h^{th} state of level k_1 may be denoted as (k_1, h) when each state are placed in lexicographic order.

- Let $H_{hh'}(k_1, x)$ represent the probability with condition that, subject to the restriction that it begin in the state (k_1, h) at time $t = 0$, the QBD process visits level k_1-1 to modify k_1 transitions to the left and also enters the state (k_1, h'). Let us present the idea of the joint transform.
$\bar{H}_{hh'}(z, s) = \sum_{k_1=1}^{\infty} z_1^k \int_0^{\infty} e^{-sx}\, dH_{hh'}(k_1, x); |z| \leq 1, Re(s) \geq 0$, and the matrix is denoted as $\bar{H}(z, s) = \bar{H}hh'(z, s)$.
The following equations can be easily satisfied by the matrix $\bar{H}(z, s)$:
$\bar{H}(z, s) = z[sI - A_1]^{-1}A_2 + [sI - A_1]^{-1}A_0\bar{H}^2(z, s)$.

- Without taking into account the boundary states, the initial travel time should be computed with the matrix $H = H_{hh'} = \bar{H}(1, 0)$ after evaluating the rate matrix R, we can quickly get the matrix H by applying the result
$H = -[A_1 + RA_2]^{-1}A2$.

- In the absence of such, it is possible to calculate the H matrix values by applying the idea of a logarithmic reduction process. $\bar{H}^{0,0}(1, 0)$ provides the following equation, which is related to boundary level zero.
$\bar{H}^{0,0}(z, s) = [sI - H_{00}]^{-1}A_0\bar{H}(z, s)$.

- The next moments are simple to evaluate because the three matrices namely, H, $\bar{H}^{(1,0)}$ and $\bar{H}^{(0,0)}(1, 0)$ are stochastic. At $s = 0$, $z = 1$,
$\overrightarrow{J_1} = -\frac{\partial}{\partial s}\bar{H}(z, s) = -[A_1 + A_0(H + I)]^{-1}e$,
$\overrightarrow{J_2} = \frac{\partial}{\partial s}\bar{H}(z, s) = -[A_1 + A_0(H + I)]^{-1}A_2e$,
$\overrightarrow{J_1}^{(0,0)} = -\frac{\partial}{\partial z}\bar{H}^{(0,0)}(z, s) = -H_{00}^{-1}[e + A_0\overrightarrow{J_1}]$,
$\overrightarrow{J_2}^{(0,0)} = \frac{\partial}{\partial z}\bar{H}^{(0,0)}(z, s) = -H_{00}^{-1}[A_0\overrightarrow{J_2}]$.

6. Performance Measures

We examine our model's qualitative behavior under steady conditions. Let x(c_1,c_2, c_3, c_4, c_5, c_6, c_7) stand for the probability of the stable state, where the quantity of clients in the orbit I is c_1,

quantity of interrupted consumers in the orbit II is c_3, server status is c_2 and c_4, c_5, c_6, c_7 represent the number of items, service phases, repair phases and arrival phases, respectively.

- chance of the server being idle: $P_{idle} = \sum_{c_1=0}^{\infty} \sum_{c_3=0}^{N} \sum_{c_4=0}^{S} \sum_{c_7=1}^{m} x_{c_1 1 c_3 c_4 c_7}$
- Chance of the server is on vacation: $P_{vac} = \sum_{c_1=0}^{\infty} \sum_{c_3=0}^{N} \sum_{c_4=0}^{S} \sum_{c_7=1}^{m} x_{c_1 0 c_3 c_4 c_7}$
- Chance of the server offering service: $P_{busy} = \sum_{c_1=0}^{\infty} \sum_{c_3=0}^{N} \sum_{c_4=1}^{S} \sum_{c_5=1}^{n} \sum_{c_7=1}^{m} x_{c_1 2 c_3 c_4 c_5 c_7}$
- chance of the server is in repair: $P_{repair} = \sum_{c_1=0}^{\infty} \sum_{c_3=1}^{N} \sum_{c_4=0}^{S} \sum_{c_6=1}^{l} \sum_{c_7=1}^{m} x_{c_1 3 c_3 c_4 c_6 c_7}$
- The chance that an interrupted clients is stopped from entering into orbit II: $P_b = \sum_{c_1=0}^{\infty} x_{c_1 3 N e}$
- Expected quantity of clients in orbit I: $E[N_1] = \sum_{c_1=0}^{\infty} c_1 x_{c_1 e}$
- Expected quantity of clients in orbit II: $E[N_2] = \sum_{c_3=0}^{N} c_3 \sum_{c_1=0}^{\infty} \sum_{c_2=0}^{3} x_{c_1 c_2 c_3 e}$
- Expected number of clients in the system: $E_{system} = E[N_1] + E[N_2] + P_{busy}$
- Expected retrial rate: $E_{RR} = \sigma_1 \sum_{c_1=1}^{\infty} \sum_{c_3=0}^{N} \sum_{c_4=1}^{S} \sum_{c_7=1}^{m} x_{c_1 1 c_3 c_4 c_7} + \sigma_2 \sum_{c_1=0}^{\infty} \sum_{c_3=1}^{N} \sum_{c_4=1}^{S} \sum_{c_7=1}^{m} x_{c_1 1 c_3 c_4 c_7}$
- Expected inventory level: $E_{IL} = \sum_{c_1=0}^{\infty} \sum_{c_3=0}^{N} \sum_{c_4=1}^{S} \sum_{c_7=1}^{m} c_4 x_{c_1 0 c_3 c_4 c_7} + \sum_{c_1=0}^{\infty} \sum_{c_3=0}^{N} \sum_{c_4=1}^{S} \sum_{c_7=1}^{m} c_4 x_{c_1 1 c_3 c_4 c_7}$ $+ \sum_{c_1=0}^{\infty} \sum_{c_3=0}^{N} \sum_{c_4=1}^{S} \sum_{c_5=1}^{n} \sum_{c_7=1}^{m} c_4 x_{c_1 2 c_3 c_4 c_5 c_7} + \sum_{c_1=0}^{\infty} \sum_{c_3=1}^{N} \sum_{c_4=1}^{S} \sum_{c_6=1}^{l} \sum_{c_7=1}^{m} c_4 x_{c_1 3 c_3 c_4 c_6 c_7}$
- Expected Reorder rate: $E_{ROR} = \sum_{c_1=0}^{\infty} \sum_{c_3=0}^{N} \sum_{c_5=1}^{n} \sum_{c_7=1}^{m} x_{c_1 2(s+1) c_3 c_5 c_7 (U^0 \otimes I_m)}$

7. Analysis of Costs

The approximate overall expense of our model is given below, with the cost elements (per unit time) related to various system measures.

- ETC: The expected sum of cost per unit time.
- C_H: The cost of carrying inventory per unit of time.
- C_W: cost per unit of time for the customer to wait in orbit.
- C_S: Setup cost per first item order.

$ETC = C_H E_{IL} + C_S E_{ROR} + C_W E_{system}$

8. Numerical Implementation

In this section, we examine the output of our system using graphical and numerical representations. With a mean value of 1, these arrival processes $ERL-A$, $EXP-A$ and $HEX-A$ have zero correlation and it correspond to the renewal process.

Erlang Arrival(ERL-A): $D_0 = \begin{bmatrix} -2 & 2 \\ 0 & -2 \end{bmatrix}$, $D_1 = \begin{bmatrix} 0 & 0 \\ 2 & 0 \end{bmatrix}$

Exponential Arrival(EXP-A): $D_0 = [-1]$, $D_1 = [1]$

Hyper exponential Arrival(HEX-A): $D_0 = \begin{bmatrix} -1.90 & 0 \\ 0 & -1.90 \end{bmatrix}$, $D_1 = \begin{bmatrix} 1.710 & 0.190 \\ 0.171 & 0.019 \end{bmatrix}$

Consider the following PH distributions for the service and repair Progression:

Erlang Service(ERL-S): $\gamma = [1, 0]; \quad U = \begin{bmatrix} -2 & 2 \\ 0 & -2 \end{bmatrix}$

Erlang Repair(ERL-R): $\alpha = [1, 0]; \quad T = \begin{bmatrix} -2 & 2 \\ 0 & -2 \end{bmatrix}$

Exponential Service(EXP-S): $\gamma = 1; \quad U = [-1]$

Exponential Repair(EXP-R): $\alpha = 1; \quad T = [-1]$

Hyper Exponential Service(HEX-S): $\gamma = [0.8, 0.2]; \quad U = \begin{bmatrix} -2.80 & 0 \\ 0 & -0.28 \end{bmatrix}$

Hyper Exponential Repair(HEX-R): $\alpha = [0.8, 0.2]; \quad T = \begin{bmatrix} -2.80 & 0 \\ 0 & -0.28 \end{bmatrix}$

8.1. Illustration 1

We investigate retrial rate (σ_1) affects the (E_{Orbit}) in the tables 1 to 3. Fix $\lambda = 1$, $\mu = 8$, $\sigma_2 = 50$, $\tau = 2$, $\psi = 1$, $\beta = 2$, $N = 5$, $p = 0.5$, $b = 0.8$, $S = 10$ and $s = 5$. The following analysis is based on the observations from table 1 to table 3:
The E_{Orbit} falls as we enhance the retrial rate, taking into account both arrival and service periods. From the viewpoint of arrival periods, E_{Orbit} falls significantly for HEX-A and gradually for ERL-A when the retrial rate rises. In comparison to EXP-A, E_{Orbit} falls significantly in ERL-S and slowly in HEX-S when considering retrial times.

Table 1: *Retrial rate (σ_1) vs E_{OrbitI} - ERL-S*

σ_1	ERL-A	EXP-A	HEX-A
61	1.60633595	2.20408030	2.80572168
62	1.60374522	2.19685734	2.78896850
63	1.60122499	2.18988720	2.77295257
64	1.59877238	2.18315631	2.75762501
65	1.59638463	2.17665207	2.74294121
66	1.59405917	2.17036279	2.72886039
67	1.59179356	2.16427756	2.71534517
68	1.58958546	2.15838625	2.70236127
69	1.58743268	2.15267939	2.68987711
70	1.58533314	2.14714812	2.67786365

Table 2: *Retrial rate (σ_1) vs E_{OrbitI} - EXP-S*

σ_1	ERL-A	EXP-A	HEX-A
61	1.65963406	2.32077465	3.11207557
62	1.65645172	2.31137417	3.08666802
63	1.65336072	2.30232643	3.06251226
64	1.65035709	2.29361123	3.03951620
65	1.64743708	2.28520995	3.01759664
66	1.64459718	2.27710535	2.99667822
67	1.64183404	2.26928144	2.97669252
68	1.63914454	2.26172341	2.95757725
69	1.63652569	2.25441747	2.93927561
70	1.63397471	2.24735081	2.92173568

Table 3: *Retrial rate(σ_1) vs E_{OrbitI} - HEX-S*

σ_1	$ERL-A$	$EXP-A$	$HEX-A$
61	2.23983642	3.49702951	8.76338751
62	2.22645590	3.45412770	8.55390871
63	2.21362288	3.41364195	8.35774148
64	2.20130368	3.37537115	8.17365341
65	2.18946736	3.33913601	8.00055975
66	2.17808547	3.30477620	7.83750189
67	2.16713176	3.27214787	7.68362958
68	2.15658199	3.24112158	7.53818599
69	2.14641376	3.21158057	7.40049528
70	2.13660629	3.18341922	7.26995199

8.2. Illustration 2

The effects of the vacation rate (η) in relation to E_{OrbitI} have been examined in figures 2 to 4. Fix $\lambda = 1$, $\mu = 8$, $\sigma_2 = 50$, $\tau = 2$, $\psi = 1$, $\beta = 2$, $N = 5$, $p = 0.5$, $b = 0.8$, $S = 10$, $\sigma_1 = 60$ and $s = 5$. We note that from 2 to 4, as follows:
E_{OrbitI} increases with the rise of vacation rate for different possible arrival and service time groupings. As the values for different arrival times are correlated, E_{system} decreases more fast for $HEX-A$ and more slowly for $ERL-A$. Likewise, E_{system} decreases quickly for $ERL-S$ and gradually for $HEX-S$.

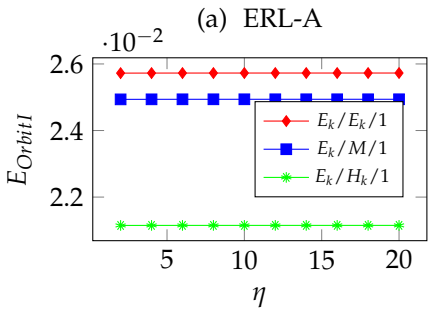


Figure 2: *Vacation rate vs E_{OrbitI}*

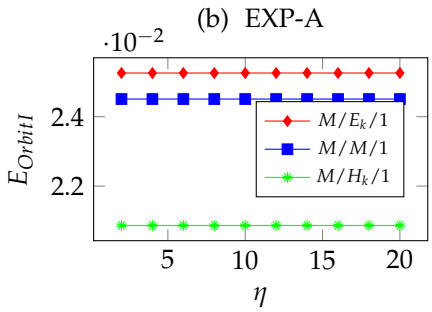


Figure 3: *Vacation rate vs E_{OrbitI}*

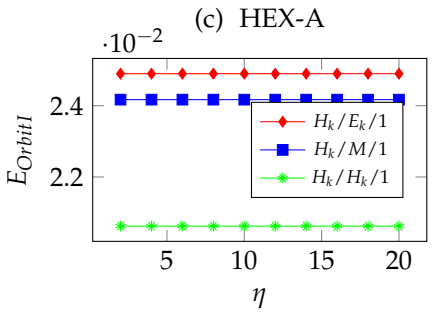


Figure 4: *Vacation rate vs E_{OrbitI}*

8.3. Illustration 3

To examine the effect on the E_{system} in the corresponding figures 5 to 13 of the vacation rate and retrial rate (Orbit II) (σ_2). To assure satisfaction of stability criteria, make adjustments to $\lambda = 1$, $\mu = 8$, $\eta = 2$, $\tau = 2$, $\psi = 1$, $\beta = 2$, $N = 5$, $p = 0.5$, $b = 0.8$, $S = 10$, $\sigma_1 = 60$ and $s = 5$.

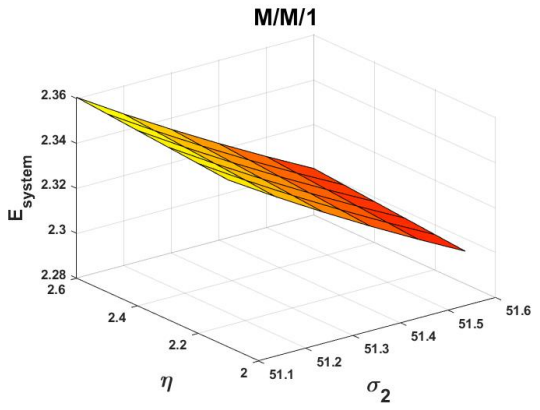


Figure 5: *Vacation and Retrial Rate(Orbit II) vs E_{system}*

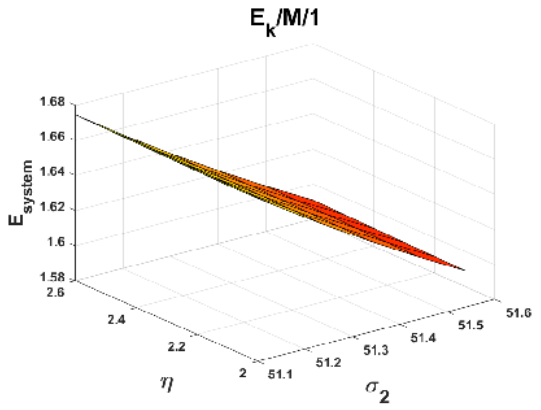


Figure 6: *Vacation and Retrial Rate(Orbit II) vs E_{system}*

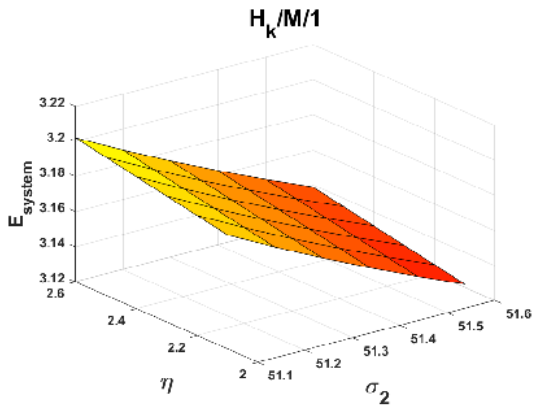


Figure 7: *Vacation and Retrial Rate(Orbit II) vs E_{system}*

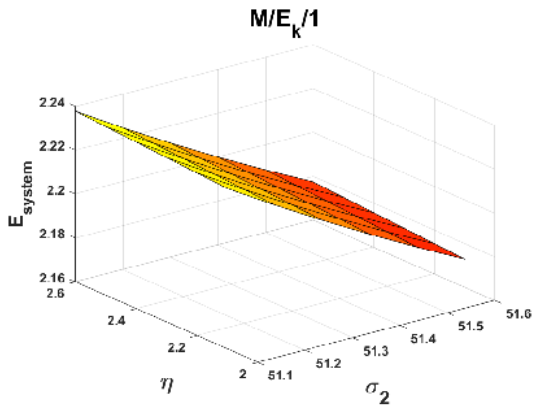


Figure 8: *Vacation and Retrial Rate(Orbit II) vs E_{system}*

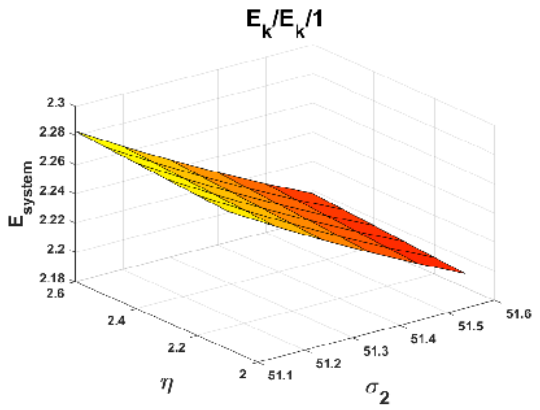


Figure 9: *Vacation and Retrial Rate(Orbit II)vs E_{system}*

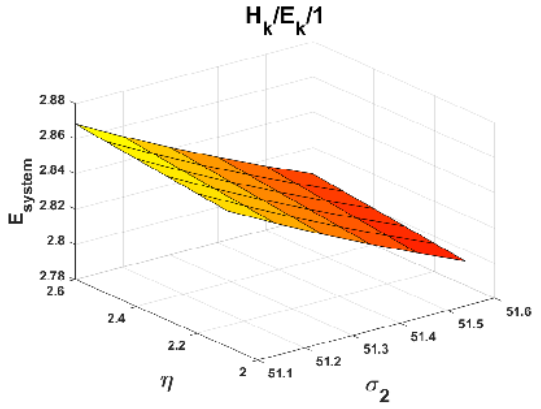


Figure 10: *Vacation and Retrial Rate(Orbit II) vs E_{system}*

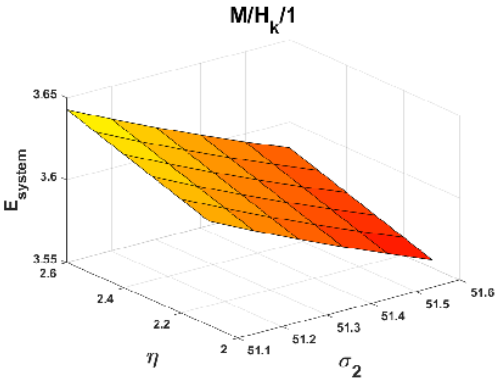


Figure 11: *Vacation and Retrial Rate(Orbit II)vs E_{system}*

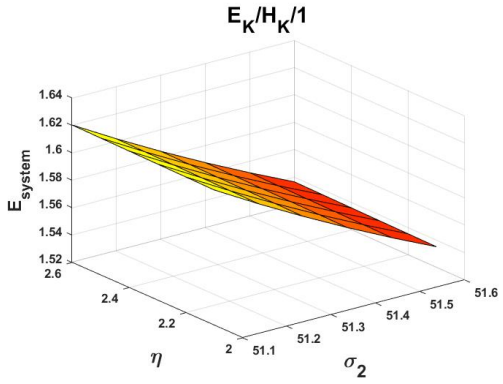


Figure 12: *Vacation and Retrial Rate(Orbit II)vs E_{system}*

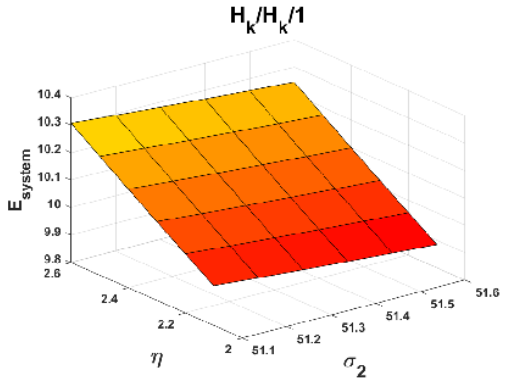


Figure 13: *Vacation and Retrial Rate(Orbit II) vs E_{system}*

From the figure 5 to 13, we can see:
We investigate the link between E_{system}, the retrial rate (σ_2), and the vacation rate of the server over a range of potential arrival and service time combinations. When there is a fixed arrival rate, the E_{system} decreases as the server's retrial rate and vacation rate rise. Taking into account the service times, E_{system} decreases significantly for ERL-S and somewhat for EXP-S. As a result, E_{System} declines quickly for HEX-A and slowly for ERL-A.

9. CONCLUSION

We examined a double orbit retrial queueing inventory model for a single server that included orbital search, repair, breakdown, discouragement, single vacation and constant retrial rate. We explored server status, inventory levels and the number of customers in the system using matrix analytic techniques in steady state conditions. By using this method, we were able to evaluate the effectiveness and performance of the system, determine optimal approaches for inventory and service management and learn about the system parameters. This model can be expanded for further work to include multi-servers and two different kinds of customers.

REFERENCES

[1] Abdul Reiyas, M. and Jeganathan, K.(2023). A classical retrial queueing inventory system with two component demand rate. *International Journal of Operational Research*, 47(4):508-533.

[2] Amirthakodi, M. and Sivakumar, B.(2015). An inventory system with service facility and finite orbit size for feedback customers. *OPSEARCH*, 52(2):225-255.
[3] Artalejo, J.R.(2008). New results in retrial queueing systems with breakdown of the server. *Statistica Neerlandica*, 48(1):23-36.
[4] Avrachenkov, K., Dudin, A. and Klimenok, V.(2010). Retrial queueing model MMAP/M_2/1 with two orbits. *Springer-Verlag Berlin Heidelberg*, 6235:107-118.
[5] Ayyappan, G. and Gowthami, R.(2021). Analysis of $MAP/PH/1$ retrial with constant rate, working vacations, abandonment, flush out, search of customers, breakdown and repair. *International Journal of Mathematics in Operational Research* , 42(3):310-331.
[6] Ayyappan, G. and Arulmozhi, N.(2024). Numerical investigation of retrial queueing inventory system with a constant retrial rate, working vacation, flush out, collision and impatient customers. *Reliability: Theory and Applications* , 19(1):744-763.
[7] Ayyappan, G. and Meena, S.(2023). Analysis of $MAP/PH/1$ Retrial inventory queueing system with phase type vacation and unreliable server. *International Journal of Mathematics in Operational Research*, DOI: 10.1504/IJMOR.2023.10061611.
[8] Babu, D., Krishnamoorthy, A. and Joshua, V.C.(2018). retrial queue with search of interrupted customers from the finite orbit. *Springer Nature Switzerland AG*, 912:360-371.
[9] Dhibar, S. and Jain, M.(2023). Strategic behaviour for M/M/1 double orbit retrial queue with imperfect service and vacation. *International Journal of Mathematics in Operational Research*, 25(3):369-385.
[10] Dimitriou, I.(2017). A two class retrial system with coupled orbit queues. *Probability in the Engineering and Informational sciences*, 31(2):139-179.
[11] Falin, G.I. and Templeton, J.G.C.(1997). Retrial queues. *Chapman and Hall*, London New York.
[12] Jain, M., Bhagat, A. and Shekhar, C.(2015). Double orbit finite retrial queues with priority customers and service interruptions. *Applied Mathematics and Computation*, 253:324-344.
[13] Krishnamoorthy, A., Joshua, V.C. and Mathew, A.P. (2017). A retrial queueing system with abandonment and search for priority customers. *Springer International Publishing AG*, 700:98-107.
[14] Latouche, G. and Ramaswami, V.(1999). Introduction of matrix analytic methods in stochastic modeling. *Society for Industrial and Applied Mathematics* , Philadelphia.
[15] Melikov, A., Chakravarthy, S. and Aliyeva, S.(2023). A retrieval queueing model with feedback. *Queueing Models and Service Management (QMSM)*, 6(1):63-95.
[16] Melikov, A., Aliyeva, S.,Sztrik, J.(2021). Retrial queues with unreliable servers and delayed feedback. *Mathematics*, 9(19):1-23.
[17] Nithya, N. and Anbazhagan, N., Amutha, S., Jeganathan, K., Park,G.C., Joshi,G.P. and Cho, W.(2023). Controlled arrivals on the retrial queueing–inventory system with an essential interruption and emergency vacationing server. Mathematics, 11(16):3560.
[18] Sangha, S.S. and Jain, M.(2019). FM/FM/1 double orbit retrial queue with customers' joining strategy: A parametric nonlinear programing approach. *Applied Mathematics and Computation*, 362:124542.
[19] Schwarz, M., Saucer, C.,Daduna, H., Kulik, R. and Szekli, R.(2006). M/M/1 queueing systems with inventory, Queueing systems, 54(1):55-78.
[20] Singla, N. and Kaur, H.(2021). A two-state retrial queueing model with feedback and balking. *Reliability: Theory and Applications* , 16(2):142-155.
[21] Sivakumar, B.(2009). A perishable inventory system with retrial demands and a finite population. *Journal of Computational and Applied Mathematics*, 224(1):29-38.
[22] Ushakumari, P.V. (2017). A retrial inventory system with an unreliable server. *International Journal of Mathematics in Operational Research*, 10(2):190-210.

RISK MODELING WITH THE NEW LOGARITHMIC TANGENT WEIBULL DISTRIBUTION: APPLICATIONS IN INSURANCE AND NET OFFICIAL DEVELOPMENT ASSISTANCE

Palanisamy Manigandan[1], D. Kanagajothi[2], R. Jeena[3] and Gulasal Madrakhimova[4]

•

[1]Department of Statistics, Periyar University, Salem-11, Tamil Nadu, India.
[2]Associate Professor, Department of Mathematics, Vel Tech Rangarajan Dr. Sagunthala R&D Institute of Science and Technology, Avadi, Chennai. Tamil Nadu, India.
[3]Department of Commerce, T.K.M College of Arts and Science, Kollam, Kerala, India.
[4]Department of Accounting and Marketing, Toshkent Institutes of Textile and Light Industry, Toshkent, Uzbekistan.
srimanigandan95@gmail.com, kanagajothi82@gmail.com, jeena471983@gmail.com, gmadrahimova9116@gmail.com

Abstract

The Weibull distribution is widely used for modeling lifetime and reliability data but often struggles with complex hazard structures and heavy-tailed behaviors. To address these limitations, this study proposes the New Logarithmic Tangent Weibull (NLT-Wei) distribution, which integrates logarithmic and tangent transformations into the Weibull model, introducing an additional shape parameter to enhance flexibility. Key functions, including the PDF, CDF, survival, and hazard functions, are derived, along with quantiles and reliability measures. Parameters are estimated using maximum likelihood estimation (MLE). The model is applied to two real datasets: insurance survival data and Net Official Development Assistance (Net ODA) data. Comparative analyses with Weibull, Exponentiated Weibull, Flexible Weibull, NGLog-Weibull, and Kumaraswamy Weibull distributions are conducted using information criteria (AIC, BIC, CAIC, HQAIC) and goodness-of-fit tests (KS, Cramér–von Mises, Anderson–Darling). Results show that the NLT-Wei consistently achieves lower information criteria, smaller test statistics, and higher p-values, confirming superior fit. Its flexibility allows effective modeling of monotone, bathtub, and inverted-bathtub hazard rates, as well as heavy-tailed behaviors. The study demonstrates that the NLT-Wei is not only robust for reliability and survival analysis but also highly suitable for actuarial and financial applications, offering a practical tool for risk assessment, insurance modeling, and lifetime data analysis across diverse domains.

Keywords: Weibull distribution, New Logarithmic Tangent Weibull, financial modelling and reliability analysis.

I. Introduction

The Weibull distribution is one of the most widely used lifetime models in survival analysis, reliability engineering and risk assessment due to its ability to accommodate constant, increasing and decreasing hazard rates. This adaptability has led to its effective application in a variety of

sectors, including actuarial research, medical sciences, engineering dependability, and climatology. However, complicated hazard structures and heavy-tailed behaviors seen in practice are frequently missed by the traditional Weibull distribution. A number of generalizations have been created to get around these restrictions, including the transmuted Weibull, Marshall–Olkin Weibull, and exponentiated Weibull families, which add extra parameters to enhance hazard rate behavior and tail flexibility. Actuarial risks are the financial hazards associated with insurance and pension plans. One important technique that actuaries employ to understand and quantify these risks is statistical analysis. Actuaries utilize probability distributions to simulate the probability of a range of occurrences, such as policy cancellations, deaths, and claims. The Poisson, Weibull, and exponential distributions are often used in actuarial science. Stochastic modelling is used to represent random processes, such as insurance cancellations and claims. This approach is used to estimate the expected value of future claims and determine how variable these estimates are. Loss distributions describe the distribution of losses caused by events such as insurance cancellations and claims. This technique is used to calculate the expected value of future losses as well as the risk associated with them. Actuaries use statistical techniques, such portfolio optimization and hedging methods, to assess and manage financial risks. In conclusion, statistical analysis is an essential technique used by actuaries to understand and manage financial risks in insurance and pension systems. Among the most important fields in which we statisticians are interested in measuring risk are the insurance and reinsurance sectors, as well as the actuarial sciences in general. In addition to insurance, Net Official Development Assistance (Net ODA), which involves uncertain resource distribution, project payments, and financial inflows, also requires similar probabilistic modeling. For policymakers and development organizations to make well-informed choices, reduce risk, and maximize resource usage, accurate modeling of these uncertainties is crucial.

Recent research has also emphasized the use of logarithmic and trigonometric transformations to construct new distribution families with enhanced adaptability. For example, Chakraborty et al. [1, 22] developed a new skew logistic distribution, Jayakumar and Babu [2] proposed the Marshall–Olkin extended Weibull and its double/asymmetric variations, applying them to stock exchange data. Ahmad et al. [3] further refined Weibull extensions through algebraic generalizations. Trigonometric-based approaches have also emerged: Chesneau et al. [4] applied tangent-based modifications, Silveira et al. [5] introduced the Normal-Tangent-G family, and Alomair et al. [6, 18] developed the Type-I Cosine Exponentiated-X family, including the cosine-exponentiated Weibull. Similarly, Kamal et al. [7, 19, 20] proposed the Sine-G family, while Benchiha et al. [8] introduced sine-based generalizations that improved elasticity in modeling lifetime data.

The Logarithmic Weibull approach to applications in engineering was presented by Zhao et al. [9] on the logarithmic side and The NGLog-Weibull distribution, which belongs to the New Generalized Logarithmic-X family, was proposed by Shah et al. [10] for biological data. By demonstrating its usefulness in risk modeling, Abubakar and Sabri [11, 21] further emphasized the significance of these models in actuarial science and finance. The New Logarithmic Tangent-U (NLT-U) family of distributions, which combines logarithmic and tangent transformations, was recently presented by Alsolmi [12], building on these advancements. The New Logarithmic Tangent Weibull (NLT-Wei) distribution is a prominent particular instance. It retains the flexibility of the Weibull baseline but adds an additional parameter that permits a wide range of hazard shapes, such as monotone expanding, decreasing, bathtub, and inverted bathtub patterns.

This study proposes and investigates the NLT-Wei distribution as a powerful extension of the Weibull model. The main contributions of this paper are as follows: This study presents the NLT-Wei distribution, a versatile expansion of the Weibull family, to address these types of problems. We define the NLT-Wei distribution and present its fundamental functions, including the cumulative distribution function (CDF), probability density function (PDF), survival function (SF), and hazard function (HF). We derive key statistical properties such as quantiles and reliability measures to

characterize the model. Parameter estimation is addressed using MLE and the practical utility of the NLT-Wei is demonstrated using real lifetime datasets, with comparisons to competing models based on goodness-of-fit statistics and graphical diagnostics especially in finance and insurance.

The remainder of this paper is organized as follows: Section 2 introduces the NLT-Wei distribution and its basic properties. Section 3 discusses parameter estimation methods. Section 4 presents real data applications. Section 5 concludes the study with final remarks.

II. NLT-Weibull Distribution

In this section, we use the derived method and suggest a new trigonometric and logarithmic version of the classic Weibull model. Let's suppose a RV (random variable)W ($\in R^+$) follows the CDF $U(W;\mu) = 1 - e^{-\sigma w^{\alpha}}$ and PDF $u(w;\mu) = \sigma\alpha w^{\alpha-1}e^{-\sigma w^{\alpha}}$ of the Weibull model with parameters $\sigma > 0$, and $\alpha > 0$, then the CDF $G(w;\theta,\mu)$ of the NLT-Wei distribution is expressed by

$$G(w;\theta,\mu) = 1 - \frac{log\left(e^{\theta}+\left(1-e^{\theta\, tan\left(\frac{\pi}{4}\left(1-e^{-\sigma w^{\alpha}}\right)\right)}\right)\right)}{\theta}, w \geq 0 \quad (1)$$

Link to Eq. (1), the $S(w;\theta,\mu)$SF of the NLT-Wei distribution is provided by

$$S(w;\theta,\mu) = \frac{log\left(e^{\theta}+\left(1-e^{\theta\, tan\left(\frac{\pi}{4}\left(1-e^{-\sigma w^{\alpha}}\right)\right)}\right)\right)}{\theta}, w \geq 0 \quad (2)$$

Corresponding to Eq. (1) and Eq. (2), the PDF $g(w;\theta,\mu)$, and $h(w;\theta,\mu)$ HF of the NLT-Wei istribution are given, respectively, by

$$g(w;\theta,\mu) = \frac{\pi\sigma\alpha w^{\alpha-1}e^{-\sigma w^{\alpha}}\, sec^2\left(\frac{\pi}{4}\left(1-e^{-\sigma w^{\alpha}}\right)\right)e^{\theta\, tan\left(\frac{\pi}{4}\left(1-e^{-\sigma w^{\alpha}}\right)\right)}}{4\left(e^{\theta}+\left(1-e^{\theta\, tan\left(\frac{\pi}{4}\left(1-e^{-\sigma w^{\alpha}}\right)\right)}\right)\right)}, w > 0, \quad (3)$$

$$h(w;\theta,\mu) = \frac{\pi\theta\sigma\alpha w^{\alpha-1}e^{-\sigma w^{\alpha}}\, sec^2\left(\frac{\pi}{4}\left(1-e^{-\sigma w^{\alpha}}\right)\right)e^{\theta\, tan\left(\frac{\pi}{4}\left(1-e^{-\sigma w^{\alpha}}\right)\right)}}{4\left\{log\left(e^{\theta}+\left(1-e^{\theta\, tan\left(\frac{\pi}{4}\left(1-e^{-\sigma w^{\alpha}}\right)\right)}\right)\right)\right\}\left(e^{\theta}+\left(1-e^{\theta\, tan\left(\frac{\pi}{4}\left(1-e^{-\sigma w^{\alpha}}\right)\right)}\right)\right)}, w > 0, \quad (4)$$

Similarly, corresponding to Eq. (1), Eq. (2), and Eq. (3), the RHF τ (w; θ,μ), and CHF H (w; θ,μ) of the NLT-Wei distribution is presented by

$$\tau(w;\theta,\mu) = \frac{\pi\theta\sigma\alpha w^{\alpha-1}e^{-\sigma w^{\alpha}}\sec^2\left(\frac{\pi}{4}\left(1-e^{-\sigma w^{\alpha}}\right)\right)e^{\theta\tan\left(\frac{\pi}{4}\left(1-e^{-\sigma w^{\alpha}}\right)\right)}}{4\left(e^{\theta}+\left(1-e^{\theta\tan\left(\frac{\pi}{4}\left(1-e^{-\theta w^{\alpha}}\right)\right)}\right)\right)\left\{\theta-\log\left(e^{\theta}+\left(1-e^{\theta\tan\left(\frac{\pi}{4}\left(1-e^{-\sigma w^{\alpha}}\right)\right)}\right)\right)\right\}}, w > 0,$$

$$H(w;\theta,\mu) = -\log\left(\frac{\log\left(e^{\theta}+\left(1-e^{\theta\tan\left(\frac{(\pi)}{2}\left(1-e^{-\sigma w^{\alpha}}\right)\right)}\right)\right)}{\theta}\right), w > 0.$$

Furthermore, let W be a random variable that follows the NLT-Wei distribution with $q \in (0,1)$, ther IF, say $Q_w(q)$ can be expressed in the following form

$$Q_w(q) = \left[-\frac{1}{\sigma}\log\left(1 - \frac{4}{\pi}\tan^{-1}\left(\frac{\log\left(e^{\theta} - e^{(1-q)\theta} + 1\right)}{\theta}\right)\right)\right]^{\frac{1}{\sigma}}$$

I. Statistical Properties

Here, we derive a few basic properties of the NLT-U family, such as the rth moments, skewness, kurtosis, quantile function, quartiles, and moment generating functions. These qualities' primary goal is to investigate the characteristics and makeup of the suggested probability distributions. For example, skewness is used to verify if the distribution is symmetrical or asymmetrical. The mesokurtic, platykurtic, and leptokurtic distributions are examples of peaked distributions that are typically measured using kurtosis.

II. Quantile Function

W follows the NLT-U family of distributions, then, the quartile function (QF), denoted as $Q(q)$. given by

$$Q(q) = U^{-1}\left(\frac{4}{\pi}\tan^{-1}\left(\frac{\log\left(1 - e^{\theta(1-q)} + e^{\theta}\right)}{\theta}\right)\right), \tag{5}$$

III. Moments

Let W follow a random variable of the NLT-U family of distribution linked to the PDFg$(w; \delta, \Omega)$, then the rth moment, say μ', is calculated by

$$\mu' = E(w^r) = \int_{-\infty}^{\infty} w^r g(w; \theta, \mu)\partial w \tag{6}$$

$$\mu' = \frac{\pi}{4}\sum_{a=0}^{\infty}\sum_{b=0}^{c}\sum_{k=1}^{\infty}\frac{e^{(1-a)\theta}(-1)^{a+b}(1+d)^k\theta^k}{k!}\binom{a}{b}\varphi_{r,a,b,k}(w;\mu)$$

Additionally, the NLT-U family of distributions' moment generating function (MGF), denoted as $M_w(t)$, is calculated as

$$M_w(t) = \int_{-\infty}^{\infty} e^{wt} g(w; \theta, \mu)\partial w$$

By using exponential series,

$$M_w(t) = \frac{\pi}{4}\sum_{a=0}^{\infty}\sum_{b=0}^{c}\sum_{k=1}^{\infty}\sum_{r=0}^{\infty}\frac{e^{(1-a)\theta}(-1)^{a+b}(1+d)^k\theta^k w^r}{k!\,r!}\binom{a}{b}\varphi_{r,a,b,k}(w;\mu)$$

III. MLE Estimation

In the present section, the model parameters of the NLT-U method are estimated by applying the maximum likelihood estimation (MLE) approach i.e. MLEs $\left(\hat{\theta}_{\text{MLE}}, \hat{\mu}_{\text{MLE}}\right)$ of the parameters (θ, μ). Let's suppose that a set of RS (random-samples) of size n, say $W_1, W_2, W_3, \ldots . W_n$ are taken from the proposed family with a PDF $g(w, \theta, \mu)$. The then the likelihood-function (LF) associated with Eq 1, is given by

$$T\left(\frac{\Theta}{w_1, w_2, \ldots w_n}\right) = \prod_{i=1}^{n} \frac{\pi u(w;\mu) \sec^2\left(\frac{\pi}{4}U(w;\mu)\right) e^{\theta \tan\left(\frac{\pi}{4}U(w;\mu)\right)}}{4\left(e^{\theta} + \left(1 - e^{\theta \tan\left(\frac{\pi}{4}U(w-\mu)\right)}\right)\right)}. \tag{7}$$

Where $\Theta = (\theta, \mu)^T$. The log LF (LLF), say $\ell(\Theta)$ and taking derivative W.R.T θ and μ, are respectively given by

$$\frac{\partial}{\partial\theta}\ell(\Theta) = \sum_{i=1}^{n} \tan\left(\frac{\pi}{4}U(w_i;\mu) - \sum_{i=1}^{n} \frac{\frac{\partial\left(e^{\theta} + \left(1 - e^{\theta \tan\left(\frac{\pi}{4}U(w_i-\mu)\right)}\right)\right)}{\partial\theta}}{\left(e^{\theta} + \left(1 - e^{\theta \tan\left(\frac{\pi}{4}U(w_i;\mu)\right)}\right)\right)},\right.$$

and

$$\frac{\partial}{\partial\mu}\ell(\Theta) = \sum_{i=1}^{n} \frac{\frac{\partial \mathrm{u}(w_i;\mu)}{\partial\mu}}{u(w_i\mu)} - \sum_{i=1}^{n} \frac{\pi}{4} \frac{\tan\left(\frac{\frac{\pi}{4}U(w_i;\mu)\partial U(w_i\mu)}{\partial\mu}\right.}{\sec^2\left(\frac{\pi}{4}U(w_i;\mu)\right)} + \theta \sum_{i=1}^{n} \frac{\pi}{4} \frac{\sec^2\left(\frac{\pi}{4}U(w_i;\mu)\,\partial \mathrm{u}(w_i;\mu)/\partial\mu\right)}{\tan\left(\frac{\pi}{4}U(w_i;\mu)\right)}$$

$$- \sum_{i=1}^{n} \frac{\frac{\partial\left(e^{\theta} + \left(1 - e^{\theta \tan\left(\frac{\pi}{4}U(w_i-\mu)\right)}\right)\right)}{\partial\theta}}{\left(e^{\theta} + \left(1 - e^{\theta \tan\left(\frac{\pi}{4}U(w_i;\mu)\right)}\right)\right)}$$

Setting $\frac{\partial}{\partial\delta}\ell(\Theta) = 0$, and $\frac{\partial}{\partial\mu}\ell(\Theta) = 0$, and solving simultaneously, we get MLEs $\left(\hat{\theta}, \hat{\mu}\right)$ of (θ, μ).

IV. Results and Discussion

I. Applications using Real data

After selecting existing Weibull-type distributions as competing models, the next step involves evaluating model performance using analytical measures and p-values to identify the most suitable distribution among the NLT-Wei and other candidates. The selected comparative tools include: (I) Akaike Information Criterion (AIC), (II) Bayesian Information Criterion (BIC), (III) Consistent Akaike Information Criterion (CAIC), (IV) Hannan-Quinn Information Criterion (HQIC), (V) Cramér–von Mises (CVM) statistic, (VI) Anderson–Darling (AD) statistic, and (VII) Kolmogorov–Smirnov (KS) statistic.

The mathematical expressions of these criteria and goodness-of-fit statistics are provided below, facilitating a clear comparison of model adequacy and selection of the most optimal distribution for the datasets.

$$AIC = 2q - 2\ell(\varphi)$$

$$BIC = \mathrm{q}\log(n) - 2\ell(\varphi)$$

$$CAIC = \frac{2qn}{q-n-1} - 2\ell(\varphi)$$

$$HQIC = 2q\log[\log(n)] - 2\ell(\varphi)$$

$$CRMI = \sum_{p=1}^{n}\left(G(w_p) - \frac{2p-1}{2n}\right)^2 + \frac{1}{12n},$$

$$ANDA = -n - \frac{1}{n}\sum_{p=1}^{n}(2p-1) \times \left[\log\left(1 - G\left(w_{(p-n+1)}\right)\right) + \log\left(G\left(w_{(p)}\right)\right)\right.$$

$$\mathrm{KOSM} = \mathrm{Max}_{p=1,23\ldots n}\left(\left(\frac{p}{n} - G\left(w_{(p)}\right)\right), \left(G\left(w_{(p)}\right) - \frac{p-1}{n}\right)\right),$$

II. Dataset I: Insurance Data

The first dataset consists of 48 observations of insurance coverage, collected from the World Development Indicators (WDI). Table 1 displays summary statistics for the Insurance Data. A slightly right-skewed distribution is indicated by the data's mean of 3.232, variance of 2.218, mild positive skewness (0.554), and kurtosis of 2.294. Figure 1 provides a visual inspection utilizing boxplots, violin plots, and TTT-plots, demonstrating modest tail behavior and variability.

Table 1: *The summary statistics for the insurance data*

Parameter	N	Min	Q1	Q3	Mean	Max	Skewness	Kurtosis	Variance
Dataset1	48	1.287	2.04	4.13	3.232	6.531	0.5535	2.2936	2.2936

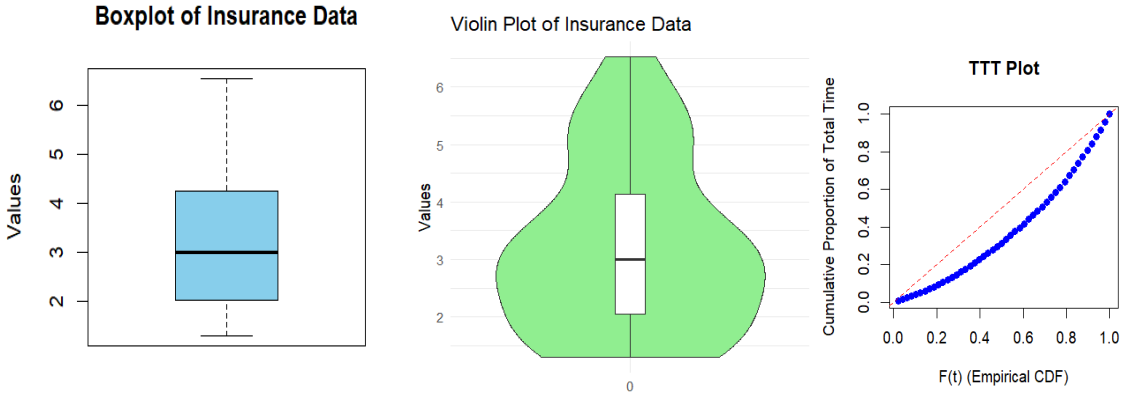


Figure 1: *Box Plot, Violin Plot, and Total Time on Test (TTT) Plot for insurance data*

Maximum likelihood estimation (MLE) was used to fit six Weibull-type distributions: Weibull, NLT-Wei, E-Wei, F-Wei, NGL-Wei, and K-Wei. Table 2 provides a summary of the estimated parameters (α, β, γ, a, b).

Table 2: *The MLEs values of the α, β, γ, a, b*

Distribution	α	β	γ	a	b
Weibull	2.3686078	3.6627564			
NLT-Wei	11.249502	2.247537	3.360695		
E-Wei	5.0589052	1.111906	0.6455213		
F-Wei	-	0.3020747	4.0368493		
NGL-Wei	0.1343426	5.5132409	1.7675898		
K-Wei		2.063135	1.195248	2.4013	0.1131656

The AIC, BIC, CAIC, HQAIC, Kolmogorov-Smirnov (KS), Cramer-von Mises (C), and Anderson-Darling (AD) tests were used to assess the model's adequacy. Table 3 shows the findings.

Table 3: *The numerical values of the model adequacy measures of the fitted distributions for Insurance Data.*

Distribution	AIC	BIC	CAIC	HQAIC	KS	C	AD
Weibull	172.478	176.2208	178.2208	173.892	0.094	0.0746	0.5633
					(0.746)	(0.725)	(0.725)
NLT-Wei	168.415	172.158	174.158	169.829	0.0905	0.0559	0.4235
					(0.793)	(0.841)	(0.824)
E-Wei	172.755	178.3687	181.3687	174.876	0.0773	0.0467	0.448
					(0.915)	(0.898)	(0.798)
F-Wei	175.304	180.9176	183.9176	177.425	0.1110	0.0979	0.660
					(0.716)	(0.785)	(0.788)
NGL-Wei	170.564	170.5643	179.1779	172.685	0.079	0.0469	0.4506
					(0.896)	(0.896)	(0.796)
K-Wei	173.654	181.1396	174.5851	176.483	0.078	0.0545	0.4503
					(0.908)	0.1131	(0.797)

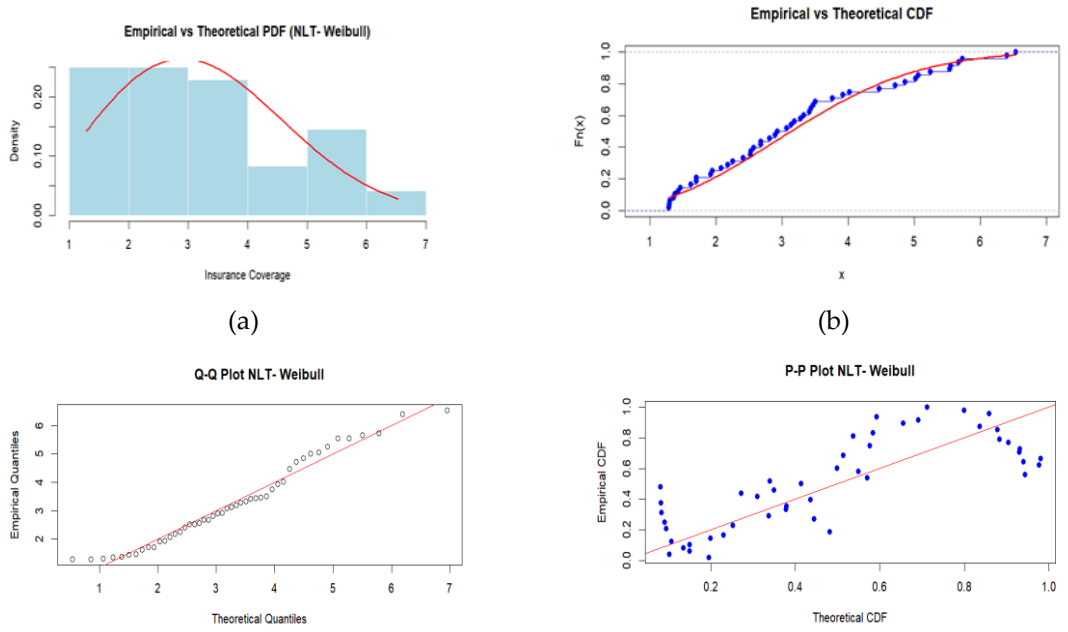


Figure 2: *The empirical and theoretical PDFs, empirical and theoretical CDFs, Q-Q plots and p-p plot for new tangent Logarithmic Weibull distribution for the insurance data.*

The comparative analysis of Dataset 1, which is summarized in Table 3, demonstrates the significant advantage of the proposed NLT-Wei distribution over the classical and extended Weibull distributions. Figure 2 displays the fitted PDFs, CDFs, Q–Q plot, and P–P plot for the insurance data. The NLT-Wei model's precision and effectiveness in fitting the data are demonstrated by the lowest information criteria values it obtained: AIC = 168.4156, BIC = 172.1580, CAIC = 174.1580, and HQAIC = 169.8298. The goodness-of-fit statistics, which demonstrate that the NLT-Wei generated KS = 0.0905 (p = 0.7932), C = 0.0559 (p = 0.8419), and AD = 0.4235 (p = 0.8244), all of which were lower than those of the other models, provide additional evidence for this result. When compared to other competing models, such as Weibull, E-Wei, F-Wei, NGL-Wei, and K-Wei, which yield greater information criteria and comparatively weaker test results, the corresponding high p-values further show that the null hypothesis of statistical suitability cannot be rejected for the NLT-Wei. When compared to other well-known Weibull-type distributions, the NLT-Wei distribution offers the best fit to the dataset, proving its resilience, adaptability, and appropriateness for modeling lifetime data. This is supported by both statistical evidence and numerical measurements.

III. Dataset II: Net ODA Data.

The second dataset consists of 50 observations of net official development assistance (ODA) from the WDI. The Net ODA Data's summary statistics are shown in Table 4. A strongly right-skewed distribution is indicated by the dataset's mean of 0.482, variance of 0.163, moderate positive skewness (0.793), and kurtosis of 3.978. Using box plots, violin plots, and TTT-plots, Figure 3 presents a visual summary of the observations' variability and tail behavior.

Table 4: *The summary statistics for the Net ODA data*

Parameter	N	Min	Q1	Q3	Mean	Max	Skewness	Kurtosis	Variance
Dataset2	50	0.068	0.14	0.793	0.481	1.703	1.1308	3.978	0.1628

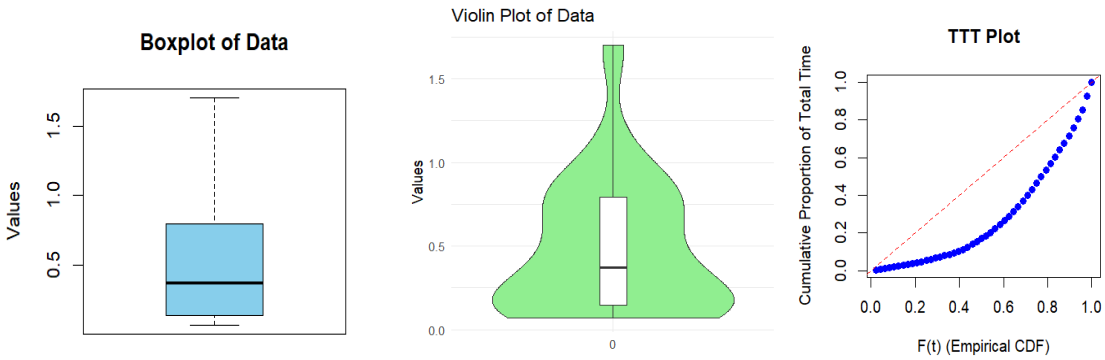


Figure 3: *Box Plot, Violin Plot, and Total Time on Test (TTT) Plot for Net ODA data*

Table 5: *The MLEs values of the α, β, γ, a, b*

Distribution	α	β	γ	a	b
Weibull	1.2310	0.5169			
NLT-Wei	14.866	1.1805	0.4392		
E-Wei	8.1145	0.4819	20.1005		
F-Wei	-	0.9817	0.2262		
NGL-Wei	60.837	7.227	0.259		
K-Wei		0.2238	0.0363	14.130	13.0155

Maximum likelihood estimation (MLE) was used to fit six Weibull-type distributions: Weibull, NLT-Wei, E-Wei, F-Wei, NGL-Wei, and K-Wei. Table 5 provides a summary of the estimated parameters (α, β, γ, a, b).

The AIC, BIC, CAIC, HQAIC, Kolmogorov-Smirnov (KS), Cramer-von Mises (C), and Anderson-Darling (AD) tests were used to assess the model's adequacy. Table 6 shows the findings.

Table 6: *The numerical values of the model adequacy measures of the fitted distributions for Net ODA Data.*

Distribution	AIC	BIC	CAIC	HQAIC	KS	C	AD
Weibull	26.749	30.491	32.492	28.164	0.155	0.171	1.1159
					(0.175)	(0.330)	(0.301)
NLT-Wei	15.678	19.420	21.420	17.092	0.106	0.118	0.715
					(0.614)	(0.503)	(0.545)
E-Wei	27.319	32.933	35.933	29.441	0.1412	0.221	1.321
					(0.267)	(0.229)	(0.225)
F-Wei	28.957	34.570	37.570	31.078	0.1708	1.1196	0.159
					(0.152)	(0.048)	(0.875)
NGL-Wei	27.982	33.595	36.595	30.103	0.155	0.186	1.176
					(0.175)	(0.295)	(0.276)
K-Wei	29.603	37.088	30.533	32.432	0.1526	0.2015	1.2408
					(0.192)	(0.265)	(0.252)

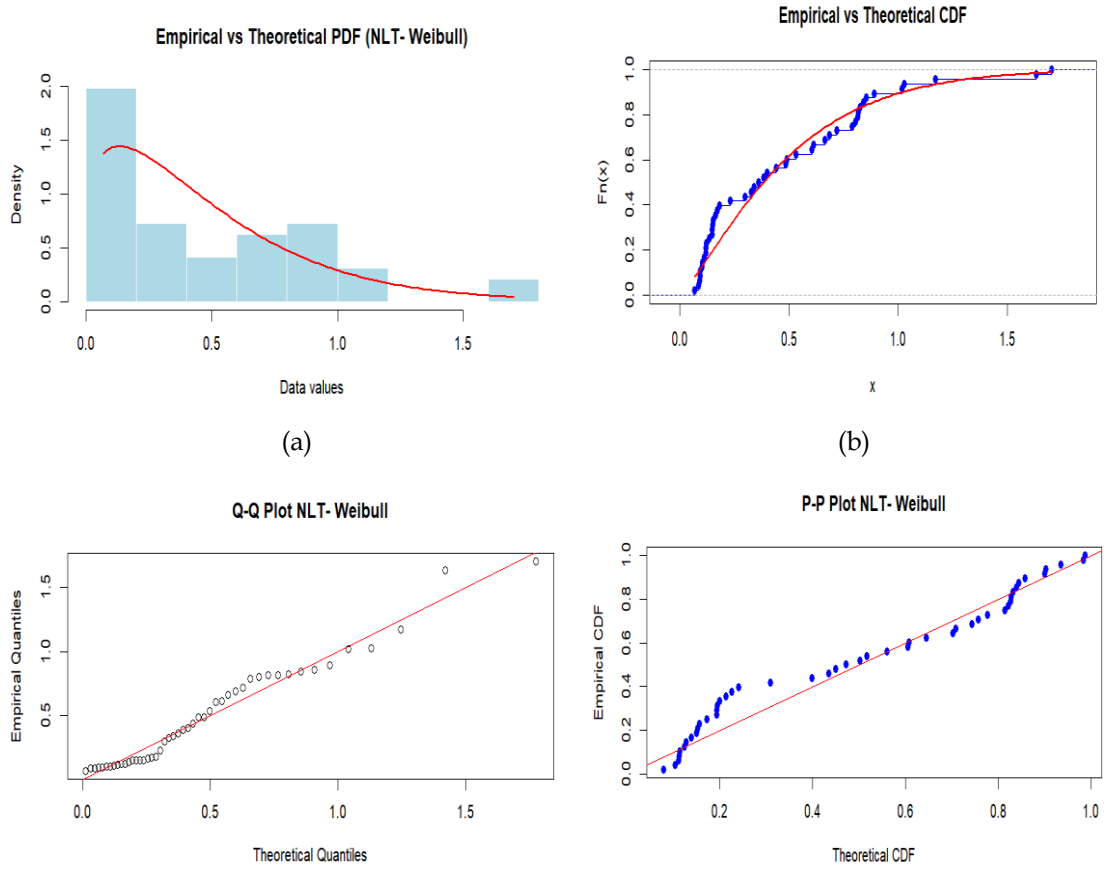


Figure 4: *The empirical and theoretical PDFs, empirical and theoretical CDFs, Q-Q plots and p-p plot for new tangent Logarithmic Weibull distribution for the Net ODA data.*

As demonstrated by the model comparison for Dataset 1 in Table 6 and the fitted PDFs, CDFs, Q–Q plot, and P–P plot for the Net ODA data in Figure 4, the proposed NLT-Wei distribution outperforms the other competing models. The NLT-Wei information criteria values (AIC = 15.6783, BIC = 19.4207, CAIC = 21.4207, and HQAIC = 17.0925) are consistently lower than those of the Weibull, E-Wei, F-Wei, NGL-Wei, and K-Wei distributions, indicating better accuracy and overall fit. The goodness-of-fit results, which demonstrate that the NLT-Wei produced the smallest KS (0.1061, p = 0.6144), C (0.1184, p = 0.5036), and AD (0.7151, p = 0.5456) values, further support the above conclusion. For the NLT-Wei model, the comparatively higher p-values verify that the null hypothesis of adequacy cannot be disproved. Conversely, the competing models show lower p-values, greater test statistics, and bigger information criteria, indicating relatively poorer performance.

V. Conclusion

In this study, we proposed and analyzed the New Logarithmic Tangent Weibull (NLT-Wei) distribution, a novel extension of the classical Weibull model that integrates logarithmic and tangent transformations. By introducing an additional shape parameter, the NLT-Wei achieves greater flexibility in capturing diverse hazard rate patterns, including monotone, bathtub, and inverted-bathtub forms. We derived its key statistical properties, developed estimation procedures via maximum likelihood, and applied the model to real datasets. The empirical applications to insurance survival data and Net Official Development Assistance (Net ODA) data confirmed the superior performance of the NLT-Wei compared to competing models such as Weibull, Exponentiated Weibull, Flexible Weibull, NGLog-Weibull, and Kumaraswamy Weibull, as it consistently produced lower information criteria values, smaller goodness-of-fit statistics, and higher p-values verifying adequacy. Unlike many extensions restricted mainly to engineering reliability, the NLT-Wei demonstrated effectiveness in actuarial science, finance, and international development modeling. Its ability to handle heavy tails and complex hazard structures makes it especially suitable for applications in finance, including risk forecasting, insurance claim analysis, and financial time series modeling. Overall, the findings establish the NLT-Wei as a robust, adaptable, and practical model for lifetime data analysis across engineering, medical, financial, and economic domains.

References

[1] Chakraborty, S. Hazarika, P. J. and Ali, M. M. (2012). A New Skew Logistic Distribution and Its Properties. *Pakistan Journal of Statistics,* 28(4): 513-524.

[2] Jayakumar, K. and Babu, M. G. (2015). Some generalizations of Weibull distribution and related processes. *Journal of Statistical Theory and Applications,* 14(4): 425-434.

[3] Ahmad, Z. Hamedani, G. G. and Butt, N. S. (2019). Recent developments in distribution theory: a brief survey and some new generalized classes of distributions. *Pakistan Journal of Statistics and Operation Research*.

[4] Chesneau, C. Bakouch, H. S. and Hussain, T. (2019). A new class of probability distributions via cosine and sine functions with applications. *Communications in Statistics-Simulation and Computation,* 48(8): 2287-2300.

[5] Gomes-Silva, F. Brito, C. Cunha-Filho, M. Jale, J. GusmÃ, F. and Xavier-JÃºnior, S. (2020). The normal-tangent-G class of probabilistic distributions: properties and real data modelling. *Pakistan Journal of Statistics and Operation Research,* 827-838.

[6] Alomair, M. A. Ahmad, Z. Rao, G. S. Al-Mofleh, H. Khosa, S. K. and Al Naim, A. S. (2023). A new trigonometric modification of the Weibull distribution: Control chart and applications in quality control. *Plos one*, 18(7): e0286593.

[7] Kamal, M. Rao, G. S. Alsolmi, M. M. Ahmad, Z. Aldallal, R. and Rahman, M. M. (2023). A new statistical methodology using the sine function: Control chart with an application to survival times data. *Plos one*, 18(8): e0285914.

[8] Benchiha, S. Sapkota, L. P. Al Mutairi, A. Kumar, V. Khashab, R. H. Gemeay, A. M. and Nassr, S. G. (2023). A new sine family of generalized distributions: Statistical inference with applications. *Mathematical and Computational Applications,* 28(4): 83.

[9] Zhao, Y. Ahmad, Z. Alrumayh, A. Yusuf, M. Aldallal, R. Elshenawy, A. and Riad, F. H. (2023). A novel logarithmic approach to generate new probability distributions for data modeling in the engineering sector. *Alexandria Engineering Journal,* 62: 313-325.

[10] Shah, Z. Khan, D. M. Khan, Z. Faiz, N. Hussain, S. Anwar, A. ... and Kim, K. I. (2023). A new generalized logarithmic–X family of distributions with biomedical data analysis. *Applied Sciences,* 13(6): 3668.

[11] Abubakar, H. and Sabri, S. R. M. (2023). A bayesian approach to weibull distribution with application to insurance claims data. *Journal of Reliability and Statistical Studies,* 1-24.

[12] Alsolmi, M. M. (2025). A new logarithmic Tangent-U family of distributions with reliability analysis in engineering data. *Computational Journal of Mathematical and Statistical Sciences,* 4(1): 258-282.

[13] Zaidi, S. M. Mahmood, Z. Atchadé, M. N. Tashkandy, Y. A. Bakr, M. E. Almetwally, E. M. and Kumar, A. (2024). Lomax tangent generalized family of distributions: Characteristics, simulations, and applications on hydrological-strength data. *Heliyon, 10*(12).

[14] Garrido, A. Caro-Carretero, R. Jimenez-Octavio, J. R. Carnicero, A. and Such, M. (2021). A new approach to fitting the three-parameter Weibull distribution: An application to glass ceramics. *Communications in Statistics-Theory and Methods*, *50*(14): 3403-3420.

[15] Alshanbari, H. M. Al-Mofleh, H. Seong, J. T. and Khosa, S. K. (2023). A new tangent-generated probabilistic approach with symmetrical and asymmetrical natures: Monte Carlo simulation with reliability applications. *Symmetry*, *15*(11): 2066.

[16] Adamu, N. Y. (2024). A Bayesian Approach to Weibull Distribution with Application to Insurance Claims Data.

[17] Yousof, H. M. Tashkandy, Y. Emam, W. Ali, M. M. and Ibrahim, M. (2023). A new reciprocal Weibull extension for modeling extreme values with risk analysis under insurance data. *Mathematics*, *11*(4): 966.

[18] Ahmad, A. Ahmad, A. Tashkandy, Y. A. Bakr, M. E. Mekiso, G. T. Balogun, O. S. and Gemeay, A. M. (2025). A study on the new logarithmic-G family with statistical properties, simulations, and different data analysis. *Scientific Reports,* 15(1):15069.

[19] Muse, A. H. Almohaimeed, A. Alqifari, H. N. and Chesneau, C. (2025). Sine-G family of distributions in Bayesian survival modeling: A baseline hazard approach for proportional hazard regression with application to right-censored oncology datasets using R and STAN. *PloS one,* 20(3): e0307410

[20] Osi, A. Raghav, Y. S. Sabo, S. A. and Musa, I. Z. (2025). The new transformed Sine G family of distribution with inferences and application. *Brazilian Journal of Biometrics*, *43*(3).

[21] Zhao, W. Khosa, S. K. Ahmad, Z. Aslam, M. and Afify, A. Z. (2020). Type-I heavy tailed family with applications in medicine, engineering and insurance. *PloS one*, 15(8): e0237462.

[22] Alizadeh, M. Hazarika, P. J. Das, J. Contreras-Reyes, J. E. Hamedani, G. G. Sulewski, P. and Yousof, H. M. (2025). Reliability and risk analysis under peaks over a random threshold value-at-risk method based on a new flexible skew-logistic distribution. *Life Cycle Reliability and Safety Engineering*, 1-28.

STATISTICAL APPLICATIONS OF THE KUMARASWAMY ALPHA-POWER LOG-LOGISTIC DISTRIBUTION: EVIDENCE FROM HYPERTENSION AND CO2 EMISSIONS IN INDIA

A. Ashok[1*], D. Kanagajothi[2], T. Kamaleshwar[3], Palanisamy Manigandan[4] and Abdullayeva Shakhnoza Yerkinovna[5]

•

[1*]Department of Mathematics, Vel Tech Multi Tech Dr Rangarajan Dr Sagunthala Engineering College, Avadi, Chennai. Tamil Nadu, India.
[2]Department of Mathematics, Vel Tech Rangarajan Dr. Sagunthala R&D Institute of Science and Technology, Avadi, Chennai. Tamil Nadu, India.
[3]Department of Computer Science and Engineering, Vel Tech Rangarajan Dr. Sagunthala R&D Institute of Science and Technology, Avadi, Chennai. Tamil Nadu, India.
[4]Department of Statistics, Government Arts College for Men, Krishnagiri, Tamil Nadu, India.
[5]Department of Business Administration, International School of Finance Technology and Science, Uzbekistan, Toshkent.
ashokmaths.24492@gmail.com, kanagajothi82@gmail.com, kamalesh4u2@gmail.com, srimanigandan95@gmail.com, shakhnoza_abdullayeva@list.ru

Abstract

This article introduces a novel statistical model, the Kumaraswamy Alpha-Power Log-Logistic (KAPLL) distribution, as a flexible extension of the traditional log-logistic model. The KAPLL distribution is especially well-suited for examining a variety of ageing and failure events as it is made to improve modelling capabilities by supporting both symmetric and asymmetric forms. Reliability analysis and lifespan data modelling are made more flexible by the KAPLL model's capacity to represent its probability density function as a combination of log-logistic densities. The hazard rate function (HRF), survival function, moments, quantile function (QF), and moment-generating function (MGF) are among the statistical and mathematical characteristics of the KAPLL distribution that are comprehensively examined. The estimation of KAPLL parameters is achieved through maximum likelihood estimation (MLE), a widely used statistical method. We use the KAPLL distribution to measures of hypertension and carbon dioxide (CO_2) emissions in order to demonstrate the usefulness of the suggested model. The findings demonstrate the KAPLL distribution's adaptability and better fit when compared to other well-known log-logistic model extensions, confirming its promise as a useful tool for modelling complicated behaviours in environmental and biological data.

Keywords: Reliability Analysis, KAPLL Distribution, Lifetime Data, Log-Logistic Distribution

I. Introduction

The assumed probability distribution has a major impact on the processes' quality in a statistical study. Therefore, a lot of work has gone into creating generalized distribution classes and the

associated statistical techniques. Among other domains, probability distributions are used in insurance and actuarial science, risk analysis, investing, market, economic and business research, reliability-engineering, and demography. Numerous new classes of univariate continuous distributions have been created in the statistical literature by accumulation one or more shape parameters to a baseline model. The extended distributions' versatility and capacity to represent both monotone and non-monotone real-world data have drawn the attention of several statisticians who are creating novel models. Marshall Olkin-G (MO-G) [1], Kumaraswamy Marshal-Olkin-G (KMO-G) [2], Weibull Marshall Olkin-G [3], Marshall-Olkin alpha power-G (MOAP-G) [4], and Kumaraswamy alpha power-G (KAP-G) [5] are a few noteworthy classes. The literature on income distribution also refers to the log-logistic (LL) distribution as the Fisk distribution [6,7, 8, 24]. It also has an extra location parameter, which Arnold [9] added and called the Pareto type III distribution. Additionally, when it comes to stream flow and precipitation data, the LL distribution is a particular instance of Burr XII distribution [10] and Kappa distribution [11]. More information regarding the LL model is available in [12]. Numerous writers have examined various generalised versions of the LL distribution in an effort to increase its functionality and adaptability. Since the LL model provides a hazard rate function that increases early and falls subsequently, it may be thought of as the probability-distribution of a random flexible whose logarithm has a logistic-distribution. It is an another to the log-normal distribution. The extended-LL [13], MO-LL [14], odd Lomax LL distributions [15], alpha power transformed-LL [16], beta-LL [17] , and Zografos Balakrishnan LL [18] are a few enhanced forms of the LL model. In this context, the present study introduces the KAPLL distribution, which integrates the alpha-power and Kumaraswamy transformation frameworks. The proposed model is shown to outperform traditional and extended log-logistic variants in capturing skewness, tail behavior, and diverse hazard patterns across two real-world datasets: CO_2 emissions and hypertension measures.

The present paper explores the KAPLL distribution, a novel extended variation of the LL distribution that may offer greater modelling flexibility for real-world data than existing rival LL models. To achieve the suggested model, the KAp-G family is utilized [5]. The KAPLL distribution has several reasons for being used, including: First, the model can be used to model increasing, J-shape, decreasing, reversed J-shape, bathtub, modified bathtub, and unimodal HRF shapes; Second, the KAPLL distribution can be considered a good model for modelling skewed real-life data that may not be adequately modelled by other known distributions; Third, it can be used in a variety of fields, such as survival analysis, public health, industrial reliability, biomedical studies, reliability, and engineering; and finally the KAPLL distribution performs better than many well-known LL distributions on real-world data examples.

The remainder of the paper is divided into seven sections. Section 2 examines the KAPLL distribution. Some important characteristics of the KAPLL distribution are examined in Section 3. An inference on the KAPLL parameters is provided. within Section 4. Section 5 presents a real-world data application. Several findings are presented in Section 6.

II. Methods

I. The KAPLL Distribution

The following section shows the KAPLL model and some of its particular instances. The two parametric LL framework's cumulative distribution function (CDF) indicates this:

$$G(y) = \left(1 + \frac{\varphi}{y^{\delta}}\right)^{-1}, y > 0, \varphi, \delta > 0 \quad (1)$$

where δ represents the form parameter and φ the scale parameter. The probability density

function (PDF) of LL simplifies to:

$$g(y) = \varphi\delta y^{-\delta-1}\left(1+\frac{\varphi}{y^{\delta}}\right)^{-2} \tag{2}$$

The CDF specifies the KAP-G family, upon which the KAPLL distribution is built.

$$F(y) = \begin{cases} 1-\left\{1-\left[\frac{\sigma^{G(y)}-1}{\sigma-1}\right]^{c}\right\}^{d} & if\sigma, c, d > 0, \sigma \neq 1 \\ G(y) & if\sigma = 1 \end{cases} \tag{3}$$

where σ, c and d stand shape parameters. The appropriate KAP-G class PDF is represented by

$$f(y) = \frac{cdln\ \sigma}{\sigma-1} g(y)\sigma^{G(y)}\left[\frac{\sigma^{G(y)}-1}{\sigma-1}\right]^{c-1}\left\{1-\left[\frac{\sigma^{G(y)}-1}{\sigma-1}\right]^{c}\right\}^{d-1} \tag{4}$$

Further data concerning the KAP-G family are described in [17]. The CDF of KAPLL distribution is obtained by inserting 1 into Equation 3 as

$$F(y) = 1-\left[1-\left(\frac{\sigma^{\left(1+\frac{\varphi}{y^{\delta}}\right)^{-1}}-1}{\sigma-1}\right)^{c}\right]^{d} \tag{5}$$

The PDF that goes with Equation 5 corresponds to following:

$$f(y) = \frac{cd\varphi\delta\ ln\,\sigma}{\sigma-1}x^{-\delta-1}\left(1+\frac{\varphi}{y^{\delta}}\right)^{-2}\sigma^{\left(1+\frac{\varphi}{y^{\delta}}\right)^{-1}}\left(\frac{\sigma^{\left(1+\frac{\varphi}{y^{\delta}}\right)^{-1}}-1}{\sigma-1}\right)^{c-1} \times \left[1-\left(\frac{\sigma^{\left(1+\frac{\varphi}{y^{\delta}}\right)^{-1}}-1}{\sigma-1}\right)^{c}\right]^{d-1} \tag{6}$$

The KAPLL distribution's HRF decreases to

$$h(y) = \frac{cd\varphi\delta\ln\sigma}{\sigma-1}x^{-\delta-1}\left(1+\frac{\varphi}{y^{\delta}}\right)^{-2}\sigma^{\left(1+\frac{\varphi}{y^{\delta}}\right)^{-1}}\left(\frac{\sigma^{\left(1+\frac{\varphi}{y^{\delta}}\right)^{-1}}-1}{\sigma-1}\right)\times\left[1-\left(\frac{\sigma^{\left(1+\frac{\varphi}{y^{\delta}}\right)^{-1}}-1}{\sigma-1}\right)^{c}\right]^{-1^{c-1}} \tag{7}$$

III. Characteristics of the KAPLL Distribution

I. The Linear Representation

An effective mixed illustration of the PDF of the KAP-G class was given by Mead et al. [5]. As stated in [5], the KAP-G density decreases to

$$f(y) = cd\sum_{i,j,m=0}^{\infty}\frac{(-1)^{i+j}(\ln\ \sigma)^{m+1}}{m!\,[c(1+i)-j]^{-m}(\sigma-1)^{c(1+i)}}g(y)(G(y))^{m}\binom{d-1}{i}\binom{c(1+i)-1}{j}$$

Following some algebra and using the LL model's PDF and CDF, the KAPLL density has the following form:

$$f(y) = cd \sum_{i,j,m=0}^{\infty} \frac{(-1)^{i+j}(ln\ \sigma)^{m+1}[c(1+i)-j]^m}{m!\,(\sigma-1)^{c(1+i)}} \varphi\delta y^{-\delta-1}\left(1+\frac{\varphi}{y^{\delta}}\right)^{-2} \times \left(1+\frac{\varphi}{y^{\delta}}\right)^{-m}\binom{d-1}{i}\binom{c(1+i)-1}{j}$$

Additionally, it can be rewritten simply as the following:

$$f(y) = \sum_{m=0}^{\infty} f_m \zeta_{m+1}(y) \tag{8}$$

where $\zeta_{m+1}(y) = (m+1)g(y)(G(y))^m$ is the power parameter for the exponentiated-LL density and $(m+1) > 0$, and

$$f_m = cd \sum_{i,j=0}^{\infty} \frac{(-1)^{i+j}(ln\ \sigma)^{m+1}[c(1+i)-j]^m}{(m+1)!\,(\sigma-1)^{c(1+i)}}\binom{d-1}{i}\binom{c(1+i)-1}{j}$$

II. Quantile Function

Equation 5 can be inverted to obtain the quantile function of the KAPLL distribution as

$$Q(v) = \left[\frac{-1}{\varphi}\left(1-\frac{ln\ \sigma}{ln\ (1+\xi)}\right)\right]^{\frac{-1}{\delta}} \tag{9}$$

where $\xi = \left\{(\sigma-1)\left[1-(1-v)^{\frac{1}{d}}\right]^{\frac{1}{c}}\right\}$, v is distributed uniformly (0,1).

III. Moment

Equation 8 can be used to determine kth moment of Y as

$$\omega_k' = E(Y^k) = \sum_{m=0}^{\infty} f_m \int y^r \zeta_{m+1}(y)dy$$

Hence,

$$\sum_{m=0}^{\infty} f_m \varphi\delta \int_0^{\infty} y^{k-\delta-1}\left(1+\frac{\varphi}{y^{\delta}}\right)^{-m-2} dx$$

subsequently calculating the combination, you get ω_k' as follows

$$\omega_k' = \sum_{m=0}^{\infty} \frac{f_m \varphi^{\frac{k}{\delta}}\Gamma\left(1-\frac{k}{\delta}\right)\Gamma\left(\frac{k}{\delta}+m+1\right)}{\Gamma(m+2)}, \frac{k}{\delta} < 1 \tag{10}$$

IV. Order test

Let $y_1, y_2, \ldots\ldots y_n$ stand a random illustration of size n and let $y_{1:n}, \ldots, y_{n:n}$ represent this connected order indicator. Then, $y_{i:n}$, which represents the PDF of the ith order statistics, say $f_{y_{i:n}}(y)$ can be

found using:

$$f_{y_{j:n}}(y) = \frac{n!f(y)}{(n-j)!(j-1)!}[F(y)]^{j-1}[1-F(y)]^{n-j}. \quad (11)$$

Equation 11's i th order statistic of the KAPLL distribution decreases if $\sigma \neq 1$ when Equations 5 and 6 are substituted.

$$f_{y_{j:n}}(y) = \frac{cd\varphi\delta n! \ln\ \sigma(\sigma-1)}{(n-j)!\,(j-1)!} x^{-\delta-1} d_j^2 \sigma^{d_j} \eta_j^{c-1}\left[1-\eta_j^c\right]^{d(n-j+1)-1},$$

$$\text{where } d_j = \left(1+\frac{\varphi}{y_j^{\delta}}\right)^{-1} \text{ and } \eta_j = \left(\sigma^{d_j}-1\right)/(\sigma-1)$$

$$f_{y_{j:n}}(y) = \sum_{p=0}^{j-1}\sum_{j,m=0}^{\infty} \frac{cd(\ln\ \sigma)^{z+1}(-1)^{p+j+m}[c(j+1)-m]^z}{\delta_{(i,n-i+1)} z!\,(\sigma-1)^{c(j+1)}} \varphi\delta y^{-\delta-1} d_i^{z+2}$$
$$\times \binom{i-1}{p}\binom{d(p+n-i+1)-1}{j}\binom{c(j+1)-1}{m}$$

Basically, in the formula

$$f_{j:n}(y) = \sum_{z=0}^{\infty} d_z h_{z+1}(y)$$

where $h_{z+1}(y) = (z+1)g(y)[G(y)]^z$ is the power parameter for the exponentiated-LL density $(z+1) > 0$, and

$$d_z = \sum_{p=0}^{i-1}\sum_{j,m=0}^{\infty} \frac{cd(ln\ \sigma)^{z+1}(-1)^{p+j+m}[c(j+1)-m]^z}{\delta_{(i,n-i+1)}(z+1)!\,(\sigma-1)^{c(j+1)}} \binom{i-1}{p}$$
$$\times \binom{d(n+p-i+1)-1}{j}\binom{c(j+1)-1}{m}$$

IV. Assessment of the Parameters

Assuming $y_1, y_2, \ldots, y_n$ are random samples drawn from the KAPLL distribution, the likelihood function's logarithm ($\ell\!\!\!\ell$)becomes

$$\ell\!\!\!\ell = n[ln\ c + ln\ d + ln\ \varphi + ln\ \delta] + nln\left(\frac{ln\ \sigma}{\sigma-1}\right) + (\delta-1)\sum_{j=1}^{n} ln\left(y_j\right) -$$
$$\varphi\sum_{j=1}^{n} y_j^{\delta} + ln\,(\sigma)\sum_{j=1}^{n} d_j + (\sigma-1)\sum_{j=1}^{n} ln\left(\eta_j\right) + (d-1)\sum_{j=1}^{n} ln\left(1-\eta_j^c\right)$$

To gain the MLE of c, d, σ, φ and δ, the initial derivatives of $\ell\!\!\!\ell$ are attained through respect to c, d, σ, φ and δ.

I. Akaike Information Criteria

In order to assess the relative accuracy of statistical approaches for a particular set of data, the Akaike information criteria (AIC), a measurement of the out-of-sample error in forecasting, are used. AIC calculates the proportionate quantity of data that a given model loses. Remember that the more accurate a model is, the more information it retains. Both over-fitting and under-fitting risks are taken into consideration by AIC when calculating the amount of information the system loses. To evaluate the parametric structure with the AIC formula that was used is

$$AIC = -2LogL + 2q$$

where AIC principles that are lesser suggest better models for information adaption, LogL is the log-likelihood, and q is the number of parameters in the model.

II. Kolmogorov-Simron Test

To predict product reliability, reliability analysis uses the Kolmogorov-Smirnov (K-S) assessment to see if a sample fits into a specific distribution. The smaller KS Statistic indicates that the real information is closer to fitted-distribution.

$$D = maximum \mid Fn(y) - F(y) \mid$$

The cumulative distribution function of the suggested model is denoted by $F(y)$, while the empirical distribution function is denoted by $Fn\,(y)$.

V. Results and Discussion

I. Real Life Applications

Application to two datasets of the KAPLL distribution is demonstrated in this section. The KAPLL distributions' fits will be contrasted with those of a few competing distributions, including the log-logistic (LL), the added Weibull log logistic (AWLL) by [23], the Kumaraswamy Marshall Olkin log-logistic (KMOLL) by [21], the McDonald log-logistic (McLL) by [22], and the alpha power transformed log-logistic (APTLL) by [16]. We take into consideration a few metrics, including the p value (pv), KS, and AIC, in order to compare the fitted distributions. In this part, the numerical findings are obtained using the R program.

II. Carbon emissions Data

The first application of KAPLL distribution, alongside competing models and their submodels, is demonstrated using carbon emission data for India spanning the period from 1990 to 2023. This dataset, obtained from our world data, comprises annual carbon dioxide (CO_2) emissions (in metric tons per capita or total national emissions) and reflects the evolving environmental footprint of India over more than three decades.

Table 2 reports the estimated parameters and key goodness-of-fit information for several statistical models applied to the CO_2 emissions data set. The competing models include the LL, Kumaraswamy Modified Odd Log-Logistic, McLL, Alpha-Weibull Log-Logistic, and the newly proposed Kumaraswamy Alpha Power Log-Logistic distribution. Among these models, the KAPLL distribution exhibits the most favorable performance across all fit criteria. It achieves the maximum log-likelihood value and the minimum AIC, indicating strong model parsimony and an

improved ability to capture the underlying distributional structure of the CO_2 emissions data. Furthermore, the KS statistic for the KAPLL model is the lowest among all competitors (KS = 0.07229), and the corresponding p-value (0.96578) is well above conventional significance thresholds, suggesting that the model does not significantly deviate from the empirical distribution.

Table 2: *MLEs and Goodness-of-Fit Statistics for CO_2 Emission Data*

Parameter/Statistic	LL	KAPLL	KMOLL	McLL	AWLL
α	-	14.3050	1.6880	6.5417	8.470
β	3.56431	9.3353	1.8637	56.591	-
λ	2367.782	25.4088	1.3077	1.9573	45.546
a	-	0.1183	3.2901	42.4707	0.1448
b	-	22.1002	0.9319	24.1273	5.4822
c	-	-	-	-	854.599
d	-	-	-	-	3.0543
AIC	172.678	-1681.976	-238.553	46.678	52.334
KS Statistic	0.1582	0.07229	0.1765	0.1291	0.1301
KS p-value	0.4643	0.96578	0.8674	0.5832	0.7649

In contrast, the alternative models particularly the LL, McLL, and AWLL distributions display higher AIC values and less favorable KS statistics, indicating suboptimal performance in representing the variability and distributional behavior of CO_2 emissions. These results underscore the flexibility and robustness of the KAPLL distribution in modeling environmental data. Therefore, the KAPLL distribution is recommended as the most appropriate model for the given CO_2 emissions dataset, providing more accurate and reliable statistical inference for environmental and sustainability analyses.

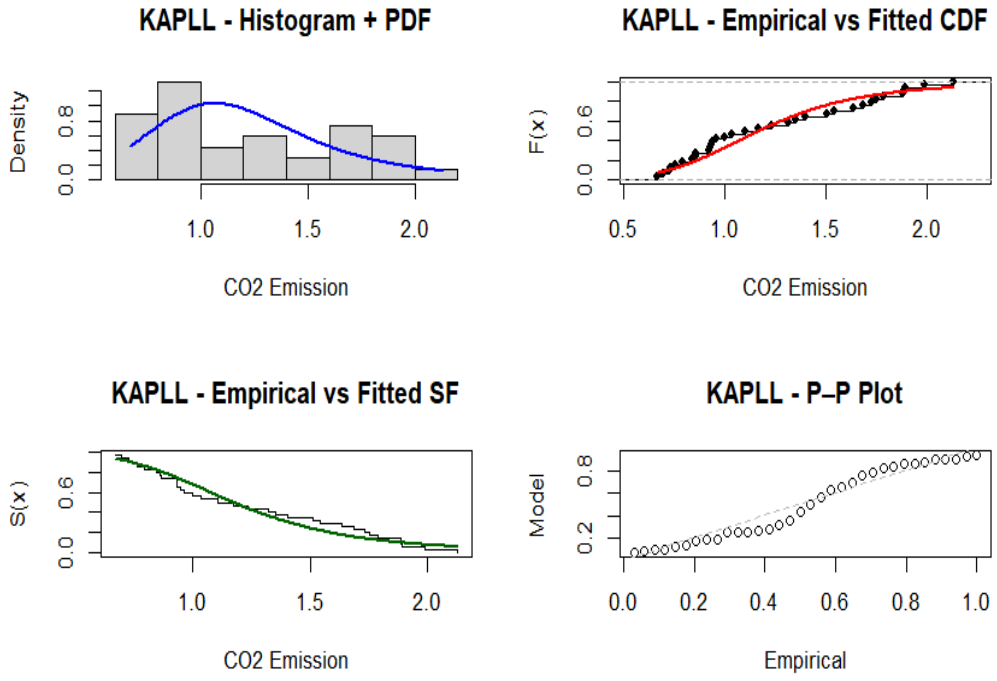


Figure 1: *The fitted functions of the KAPLL model for CO2 emissions data.*

Figure 1 shows diagnostic plots for the KAPLL distribution fitted to CO_2 emission data, including the histogram with PDF, empirical vs. fitted CDF, survival function, and P–P plot. The plots indicate that the KAPLL model fits information well, with close alignment in the density, CDF, and survival curves. The P–P plot also shows minimal deviation, confirming the model's adequacy.

III. Hypertension Data

This dataset contains survival times (in years) before the onset of hypertension in India, covering the period from 1990 to 2021. Sourced from Our World in Data, it provides valuable insights into the progression of hypertension within the Indian population.

Table 3 reports the maximum likelihood estimations (MLEs), standard errors (SEs), and goodness-of-fit statistics for the hypertension data using five different models: LL, KAPLL, KMOLL, McLL, and AWLL. The results show that the KAPLL model offers the best fit, as indicated by its lowest AIC (-1505.1303) and highest KS p-value (0.99874), along with a low KS statistic (0.8739). These values suggest that the KAPLL model closely aligns with the observed data. In comparison, the other models demonstrate higher AIC values and less favorable fit statistics, confirming the superior performance of the KAPLL distribution for this dataset.

Table 3: *MLEs and Goodness-of-Fit Statistics for Hypertension Data*

Parameter/Statistic	LL	KAPLL	KMOLL	McLL	AWLL
α	-	74.1409	1.5269	3.8746	1.984
β	0.8793	2.4510	0.9939	5.6352	-
λ	7654.746	0.0264	0.0097	0.8638	57.683
a	-	24.0998	1.8250	65.29673	0.0136
b	-	74.1846	0.9698	0.2487	6.9367
c	-	-	-	-	7756.60
d	-	-	-	-	4.0678
AIC	186.7931	-1505.130	–208.726	199.3959	176.736
KS Statistic	0.1436	0.8739	1778.3907	0.4852	0.1357
KS p-value	0.567	0.998	0.867	0.663	0.7708

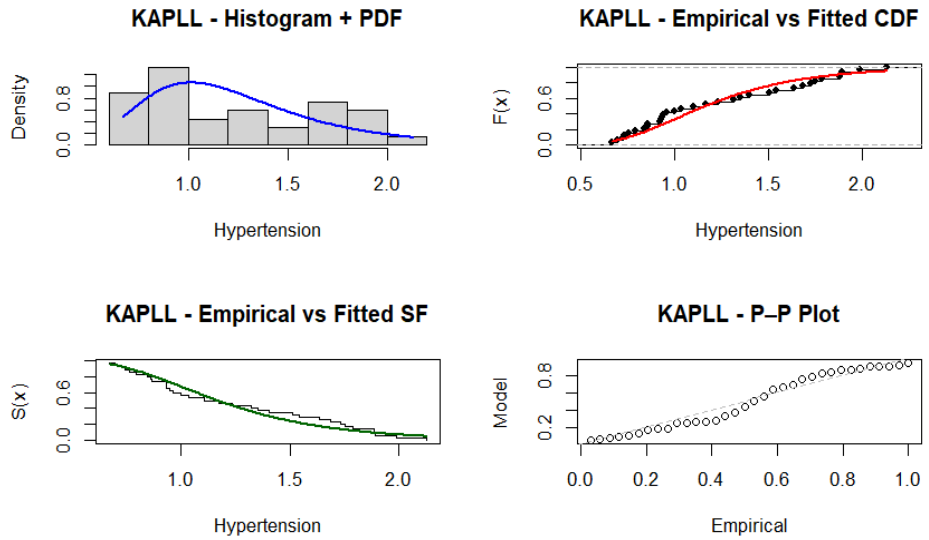


Figure 2: *The diagnostic plots of the KAPLL model fitted to the hypertension data.*

Figure 2 demonstrates four diagnostic plots for the KAPLL distribution fitted to the hypertension data: the histogram with the fitted PDF, the empirical versus fitted CDF, the survival function, and the P–P plot. These plots confirm that the KAPLL model fits the hypertension statistics well. The PDF closely follows the histogram, the fitted CDF aligns with empirical-distribution, and the survival function accurately reflects the observed survival trend. The P–P plot shows points clustering near the 45-degree line, indicating a strong agreement between the model and the empirical data.

VI. Conclusion

This paper introduced the KAPLL distribution, a new five-parameter model developed to enhance flexibility in modelling complex data behaviors. We derived its key mathematical properties, as well as the probability density function, survival, moments, hazard rate functions, and quantile function. Parameters were efficiently estimated using the MLE method, and their performance was confirmed through simulation. To determine the practical value of the proposed model, we utilized it to two distinct real-world datasets: carbon dioxide emissions and hypertension measurements. These datasets, representing environmental and biomedical domains respectively, exhibit different distributional characteristics, such as skewness and non-monotonic hazard behavior. Comparative analyses using goodness-of-fit criteria revealed that the KAPLL model provided a superior fit over several competing log-logistic-based distributions, including APTLL, LL, KMOLL, McLL, and AWLL. These findings highlight the adaptability and robustness of the KAPLL distribution in handling heterogeneous data types. As such, the model presents a valuable tool for researchers and practitioners working in fields such as environmental statistics, public health, and reliability analysis. We expect that the suggested distribution will be used in a wider range of domains, such as reliability analysis, medicine, engineering, and economics [25,26,27], among others.

References

[1] Marshall, A. W. and Olkin, I. (1997). A new method for adding a parameter to a family of distributions with application to the exponential and Weibull families. *Biometrika*, 84(3): 641-652.

[2] Alizadeh, M. Tahir, M. H. Cordeiro, G. M. Mansoor, M. Zubair, M. and Hamedani, G. (2015). The Kumaraswamy marshal-Olkin family of distributions. *Journal of the Egyptian Mathematical Society*, 23(3): 546-557.

[3] Korkmaz, M. Ç. Cordeiro, G. M. Yousof, H. M. Pescim, R. R. Afify, A. Z. and Nadarajah, S. (2019). The Weibull Marshall–Olkin family: Regression model and application to censored data. *Communications in Statistics-Theory and Methods*, 48(16): 4171-4194.

[4] Nassar, M. Kumar, D. Dey, S. Cordeiro, G. M. and Afify, A. Z. (2019). The Marshall–Olkin alpha power family of distributions with applications. *Journal of Computational and Applied Mathematics,* 351: 41-53.

[5] Mead, M. E. Afify, A. Z. and Butt, N. S. (2020). The Modified Kumaraswamy Weibull Distribution: Properties and Applications in Reliability and Engineering Sciences. *Pakistan Journal of Statistics and Operation Research*, 16(3).

[6] Dagum, C. (1975). A model of income distribution and the conditions of existence of moments of finite order. *Bulletin of the International Statistical Institute,* 46(1): 199-205.

[7] Fisk, P. R. (1961). The graduation of income distributions. *Econometrica: journal of the Econometric Society,* 171-185.

[8] Shoukri, M. M. Mian, I. U. H. and Tracy, D. S. (1988). Sampling properties of estimators of the log-logistic distribution with application to Canadian precipitation data. *Canadian Journal of Statistics,* 16(3): 223-236.

[9] Arnold, B. C. (2008). Pareto and generalized Pareto distributions. *In Modeling income*

distributions and Lorenz curves (pp. 119-145). New York, NY: Springer New York.

[10] Burr, I. W. (1942). Cumulative frequency functions. *The Annals of mathematical statistics*, 13(2): 215-232.

[11] Mielke JR, P. W. and Johnson, E. S. (1973). Three-parameter kappa distribution maximum likelihood estimates and likelihood ratio tests. *Monthly Weather Review*, 101(9): 701-707.

[12] Kleiber, C. and Kotz, S. (2003). Statistical size distributions in economics and actuarial sciences. John Wiley & Sons.

[13] Alfaer, N. M. Gemeay, A. M. Aljohani, H. M. and Afify, A. Z. (2021). The extended log-logistic distribution: inference and actuarial applications. *Mathematics*, 9(12): 1386.

[14] Gui, W. (2013). Marshall-Olkin extended log-logistic distribution and its application in minification processes. *Applied Mathematical Sciences*, 7(77-80): 3947-3961.

[15] Cordeiro, G. M. Afify, A. Z. Ortega, E. M. Suzuki, A. K. and Mead, M. E. (2019). The odd Lomax generator of distributions: Properties, estimation and applications. *Journal of Computational and Applied Mathematics*, 347: 222-237.

[16] Aldahlan, M. A. (2020). Alpha Power Transformed Log-Logistic Distribution with Application to Breaking Stress Data. *Advances in Mathematical Physics*, *2020*(1): 2193787.

[17] Lemonte, A. J. (2014). The beta log-logistic distribution. *Brazilian journal of probability and statistics*, 313-332.

[18] Ramos, M. W. A. Cordeiro, G. M. Marinho, P. R. D. Dias, C. R. B. and Hamedani, G. G. (2013). The Zografos-Balakrishnan log-logistic distribution: Properties and applications. *Journal of Statistical Theory and Applications*, *12*(3): 225-244.

[19] De Santana, T. V. F. Ortega, E. M. Cordeiro, G. M. and Silva, G. O. (2012). The Kumaraswamy-log-logistic distribution. *Journal of Statistical Theory and Applications*, *11*(3): 265-291.

[20] Rosaiah, K. Kantam, R. R. L. and Kumar, S. (2006). Reliability test plans for exponentiated log-logistic distribution.

[21] Cakmakyapan, S. Ozel, G. Gebaly, Y. M. H. E. and Hamedani, G. G. (2018). The Kumaraswamy Marshall-Olkin log-logistic distribution with application. *Journal of Statistical Theory and Applications*, *17*(1): 59-76.

[22] Tahir, M. H. Mansoor, M. Zubair, M. and Hamedani, G. G. (2014). McDonald log-logistic distribution with an application to breast cancer data. *Journal of Statistical Theory and Applications*, *13*(1): 65-82.

[23] Hemeda, S. (2018). Additive Weibull log logistic distribution: Properties and application. *Journal of Advanced Research in Applied Mathematics and Statistics*, *3*(4): 8-15.

[24] Alabdulhadi, M. H. and Elgarhy, M. (2024). Different Estimation Methods for A New Extension Three Parameter Log-Logistic Distribution with Applications. *Journal of Statistics Applications and Probability*, 13(4), 1181-1202.

[25] Duraisamy, P. Alam, M. S. Uddin, M. A. Kuppusamy, A. and Palanisamy, M. (2022). Modelling Volatility of Petroleum Productions by Using Markov-Switching GARCH Models. *International Journal of Agricultural and Statistical Sciences*, 18(1): 1657-1667.

[26] Kavitha, S. Rayalu, G. M. Pachiyappan, D. and Manigandan, P. (2023). Forecasting of Extreme Risk Using Markovswitching GARCH Models: Evidence From Global Energy Markets. Reliability: Theory and Applications, 18(4 (76)): 325-337.

[27] Alam, M. S. Manigandan, P. Kisswani, K. M. and Baig, I. A. (2025). Achieving goals of the 2030 sustainable development agenda through renewable energy utilization: Comparing the environmental sustainability effects of economic growth and financial development. *Sustainable Futures*, *9*: 100534.

VARIABLES CHAIN SAMPLING PLAN BASED ON THE MINIMUM ANGLE METHOD INVOLVING MINIMUM SUM OF RISKS

P. Suthersan[1] and S. Balamurali[2*]

•

[1]Department of Mathematics, Kalasalingam Academy of Research and Education, Krishnankoil – 626126.

[2*] Department of Computer Applications, Kalasalingam Academy of Research and Education, Krishnankoil – 626126.

[1]suthersan8@gmail.com, [2*]sbmurali@rediffmail.com

Abstract

This study presents a designing methodology for a variables based chain sampling plan utilizing the minimum angle criterion. In the context of acceptance sampling, managing both producer's risk and consumer's risk is essential for ensuring consistent product quality, particularly within industrial applications. These risks must be addressed concurrently when making quality related decisions. In this work, both risks are effectively reduced by minimizing the tangent angle formed between two points on the operating characteristic curve: the producer's quality level, associated with the probability of accepting a good lot, and the consumer's quality level, associated with the probability of accepting a bad lot. The variables chain sampling plan provides the underlying framework for this formulation. The proposed design procedures are detailed through step-by-step methodologies to demonstrate the implementation of the approach.

Keywords: consumer's risk, chain sampling plan, minimum angle method, producer's risk

I. Introduction

In today's highly competitive global marketplace, quality control serves as a critical differentiator among enterprises. Among the various techniques employed to ensure product quality, control charts and acceptance sampling remain fundamental. Acceptance sampling serves as an intermediate strategy between complete inspection of all items and no inspection at all, offering a balance between efficiency and quality assurance. In this approach, a subset of items, referred to as a sample of size n is drawn from a larger batch, or lot, of products. The decision to accept or reject the entire lot is based on the quality assessment of this representative sample. Among various acceptance sampling methodologies, the single-sampling plan is the most commonly adopted in industrial practice, owing to its simplicity, ease of implementation, and suitability for final product inspection. Acceptance sampling plans also play a critical role in quality assurance by simultaneously addressing both producer's risk and consumer's risk. These risks are particularly significant in industrial settings, where maintaining consistent product quality is essential. Therefore, an effective quality assessment strategy must incorporate both risk factors concurrently

during the design and implementation of the sampling plan.

Acceptance sampling can broadly be divided into two categories: attribute sampling plans and variables sampling plans. Extensive discussions on this classification are available in the literature [1, 14, 18]. Attribute sampling evaluates quality characteristics in discrete terms, such as conforming/non-conforming or pass/fail outcomes. In contrast, variables sampling involves the assessment of quality characteristics measured on a continuous scale, such as weight, length, or volume. The main benefit of variables sampling plan (VSP) lies in its ability to achieve the same operating characteristic (OC) curve with a significantly smaller sample size compared to an attribute sampling plan. Consequently, fewer units need to be inspected under a variables sampling framework. Since variables sampling yields quantitative data, it offers more detailed information than the attribute sampling, enabling equivalent quality assurance with a notably reduced sample size. This approach proves especially advantageous in scenarios involving destructive testing, as it minimizes inspection costs while maintaining the desired level of protection. Concerns have been raised about the appropriateness of variables sampling when the goal is to estimate the fraction nonconforming of the incoming lots. Such issues were discussed by Collani [5]. Conversely, later studies have demonstrated that variables sampling remains an optimal approach under various conditions. This was shown by Seidel [19]. The acceptance sampling literature provides extensive documentation and analysis of conventional VSPs [3, 12, 16].

The concept of the chain sampling plan (ChSP) was introduced and designated as the ChSP-1 plan, applicable to both small and large sample sizes. This was first proposed by Dodge [6]. Unlike single sampling plan (SSP), the ChSP-1 utilizes cumulative data from successive samples, thereby addressing limitations such as the potential rejection of an entire lot due to a single nonconforming unit. It also enhances the discriminatory power between acceptable and unacceptable quality levels, particularly improving upon the acceptance criterion where no defective units are permitted. Chain sampling is best suited for scenarios involving continuous production under consistent operating conditions, where product lots are submitted for inspection in the sequence of their manufacture. Such applications are commonly found in the receiving inspection of regularly supplied materials within a manufacturing process. The features and performance attributes of the chain sampling plan have been widely studied, with important insights provided in previous research [8, 21, 22]. Chain sampling is categorized under conditional sampling procedures, alongside methods such as multiple dependent (deferred) sampling plans. This classification has been discussed in the literature [27]. In these approaches, the decision to accept or reject a lot depends not only on the current sample but also on the inspection outcomes of preceding lots. This methodology is particularly suited for Type B scenarios, where inspection is conducted on lots drawn sequentially from a continuous production process assumed to produce uniform quality.

The application of chain sampling to variables inspection has been further developed in subsequent studies [9]. However, their work did not include tabulated values to facilitate practical implementation of the proposed plan. Moreover, their analysis was confined to the case where the standard deviation is known. In response to these limitations, comprehensive tables were developed to support the practical application of chain sampling plans for variables inspection. These tables consider a normally distributed quality characteristic under both known and unknown standard deviation scenarios while aiming to minimize the average sample number (ASN). This development was proposed in the literature [2]. Moreover, the design of existing chain sampling plans and their modified versions is also discussed in the acceptance sampling literature. Examples of such studies include [10, 13, 17, 26].

II. Minimum Angle Method

The minimum angle method is a design approach used in constructing acceptance sampling plans that simultaneously minimizes both the producer's and consumer's risks. This is achieved by

reducing the angle θ formed between two points on the operating characteristic curve: the producer's quality level (PQL) with acceptance probability (1-α) and the consumer's quality level (CQL) with acceptance probability β. Here, α represents the producer's risk and β represents the consumer's risk. Here, $P_a(p_1)$ represents the probability at PQL and $P_a(p_2)$ represents the probability at CQL, as shown in Figure 1.

This method offers two primary advantages:

- It enables the simultaneous minimization of both types of risks.
- The resulting minimized angle approximates the behavior of the ideal OC curve, an ideal that can only be realized through complete inspection, which is often impractical due to time and cost constraints.

Thus, by employing the minimum angle technique, the acceptance decision closely mirrors that of full inspection but with significantly reduced inspection effort and cost.

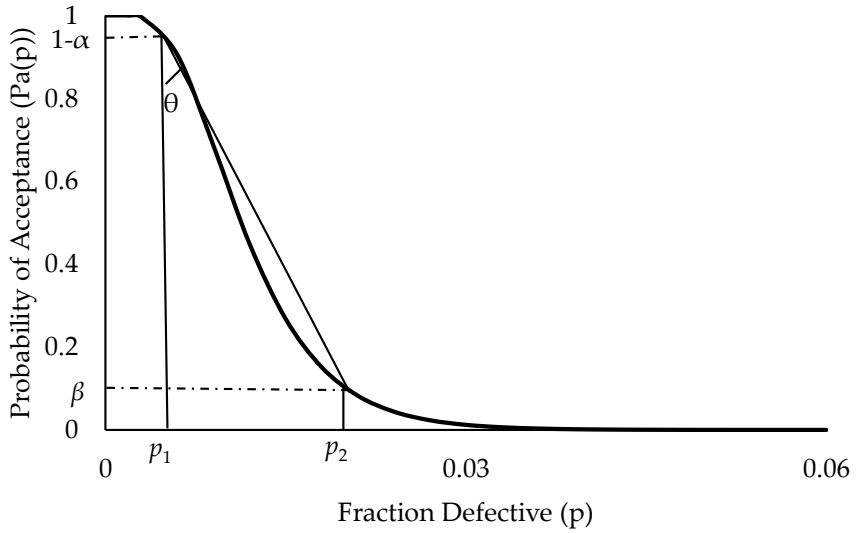


Figure 1: *Tangent angle minimization using p_1 and p_2*

Initially, the development of variables SSP using the minimum angle methodology was proposed in the literature [20]. The orientation of the OC curve has been studied previously, with alternative techniques proposed by Bush [4]. Several studies have extended the use of the minimum angle principle in sampling schemes. Joyce et al. developed mixed sampling schemes based on the tangent angle principle, while Suresh and Vinitha examined generalized two-plan systems [11, 23]. A modified chain sampling plan, formulated using minimum angle optimization, was later proposed by Edna and Joyce [7]. An SkSP-V design using the minimum angle method was later proposed by Nirmala [15]. Further developments include the design of chain sampling plans based on truncated life testing for the log-logistic distribution [25] and a generalized class of group ChSPs [24].

While several sampling plans have been formulated using the minimum angle method, existing research has largely been confined to attribute-based inspection contexts. This highlights a notable gap in the application of the minimum angle approach to variables sampling plans, warranting further investigation. To address this, the present study proposes variables ChSP, designated as VChSP constructed using the minimum angle approach. The structure of the paper is as follows: Section 3 details the operating procedure and key performance measures of the proposed plan. Section 4 describes the development and computational methodology for identifying the optimal

design parameters. Finally, Section 5 provides concluding remarks and a summary of the research findings.

III. Variables ChSP

This section outlines the assumptions, operating procedure and two key performance metrics of the proposed VChSP that are particularly pertinent to this study namely, the probability of acceptance and the ASN.

I. Assumptions

- The quality characteristic X is assumed to follow a normal distribution, with the standard deviation being known or unknown.
- The production process under consideration is assumed to generate lots in a sequential manner, each submitted for inspection in the order of production. It is further assumed that the process maintains a constant proportion of nonconforming items across all lots.
- It is presumed that the consumer has confidence in the supplier's quality assurance practices, and there exists no prior reason to suspect that any given lot is of inferior quality compared to its predecessors.

II. Operating Procedure of Known Sigma VChSP

The operating procedure of the proposed known sigma VChSP is described as follows.

Assume that the quality characteristic under consideration follows a normal distribution with an unknown mean, denoted by μ, a known standard deviation, denoted by σ, and is subject to an upper specification limit, denoted by U.

Step 1: Select a random sample of size n_σ from the current lot and calculate the value of $V = \frac{U-\bar{X}}{\sigma}$ where $\bar{X} = \frac{1}{n_\sigma}\sum_{i=1}^{n_\sigma} X_i$.

Step 2: Accept the current lot if $V \geq k_{a\sigma}$ and reject the current lot if $V < k_{r\sigma}$.

Step 3: If $k_{r\sigma} \leq V < k_{a\sigma}$, then accept the current lot provided that preceding i_σ lots have been accepted with the condition that $V \geq k_{a\sigma}$. Otherwise, reject.

If lower specification limit L is specified then, the operating procedure is outlined as follows.

Step 1: Select a random sample of size n_σ from the current lot and calculate the value of $V = \frac{\bar{X}-L}{\sigma}$ where $\bar{X} = \frac{1}{n_\sigma}\sum_{i=1}^{n_\sigma} X_i$.

Step 2: Accept the current lot if $V \geq k_{a\sigma}$ and reject the current lot if $V < k_{r\sigma}$.

Step 3: If $k_{r\sigma} \leq V < k_{a\sigma}$, then accept the current lot provided that preceding i_σ lots have been accepted with the condition that $V \geq k_{a\sigma}$. Otherwise, reject.

III. Operating Procedure of Unknown Sigma VChSP

Assume that the quality characteristic under consideration follows a normal distribution with an unknown mean, denoted by μ, a unknown standard deviation, denoted by S, and is subject to an upper specification limit, denoted by U

Step 1: Select a random sample of size n_s from the current lot and calculate the value of $V = \frac{U-\bar{X}}{S}$ where $\bar{X} = \frac{1}{n_S}\sum_{i=1}^{n_S} X_i$ and $= \sqrt{\sum(X_i - \bar{X})^2/(n_S - 1)}$.

Step 2: Accept the current lot if $V \geq k_{aS}$ and reject the current lot if $V < k_{rS}$.

Step 3: If $k_{rS} \le V < k_{aS}$, then accept the current lot provided that preceding i_S lots have been accepted with the condition that $V \ge k_{aS}$. Otherwise, reject.

If lower specification limit L is specified then, the operating procedure is outlined as follows.

Step 1: Select a random sample of size n_S from the current lot and calculate the value of $V = \frac{\bar{X}-L}{S}$ where $\bar{X} = \frac{1}{n_S}\sum_{i=1}^{n_S} X_i$ and $S = \sqrt{\sum(X_i - \bar{X})^2/(n_S - 1)}$.

Step 2: Accept the current lot if $V \ge k_{aS}$ and reject the current lot if $V < k_{rS}$.

Step 3: If $k_{rS} \le V < k_{aS}$, then accept the current lot provided that preceding i_S lots have been accepted with the condition that $V \ge k_{aS}$. Otherwise, reject.

The VChSP is fully characterized by four key parameters: n_σ (or n_S) denoting the sample size, i_σ (or i_S) denoting the number of preceding lots considered, $k_{a\sigma}$ (in the case of known sigma) or $k_{a\ S}$ (unknown sigma) as the acceptance criterion, and $k_{r\ \sigma}$ (known sigma) or k_{rS} (unknown sigma) as the rejection criterion. The plan reduces to the conventional SSP when the acceptance and rejection thresholds are equal.

IV. Performance Measures

The effectiveness of any sampling plan can be evaluated through its performance metrics. Among these, the OC function and the ASN function are widely regarded as the most critical indicators of performance. The OC and ASN functions for the proposed VChSP are formulated as outlined below:

The probability of acceptance for the VChSP for known sigma and unknown sigma respectively are defined by

$$P_a(p) = P(V \ge k_{a\sigma}) + [P(V \ge k_{r\sigma}) - P(V \ge k_{a\sigma})][P(V \ge k_{a\sigma})]^{i_\sigma} \quad (1)$$

$$P_a(p) = P(V \ge k_{aS}) + [P(V \ge k_{rS}) - P(V \ge k_{aS})][P(V \ge k_{aS})]^{iS} \quad (2)$$

The ASN function for the VChSP is defined as

$$ASN(p) = n \quad (3)$$

IV. Development of a VChSP Based on Tangent Angle Method Using PQL and CQL

This section presents a systematic procedure for constructing a VChSP indexed through the PQL and CQL, utilizing the tangent angle minimization method. The core objective is to identify the sampling plan that minimizes both α and β risks concurrently by geometrically optimizing the angle formed on the OC curve.

I. Design Methodology

The procedure for designing the sampling plan is outlined below:

Step 1: Specification of OC Curve Coordinates:

Identify two points on the OC curve corresponding to desired quality levels:

p_1: fraction defective at PQL, with an acceptance probability of $1-\alpha$

p_2: fraction defective at CQL, with an acceptance probability of β

Step 2: Determine sample size n:

Fix the sample size n based on operational or economic constraints.

Step 3: Compute acceptance probabilities:

For the selected values p_1 and p_2, calculate the probability of acceptance: $P_a(p_1)$ and $P_a(p_2)$

Step 4: Evaluate the tangent angle θ:

Determine the tangent angle between the two points on the OC curve using the formula:

$$tan\ \theta = \frac{p_2 - p_1}{P_a(p_1) - P_a(p_2)} \quad (4)$$

Step 5: Risk assessment:

Based on the chosen coordinates, calculate the associated risks α and β, and determine the cumulative risk $\alpha+\beta$.

Thus the optimal parameters and risk minimum of VChSP are determined by solving the following optimization problem:

$$\min_{\{n,k_a,k_r,i|p_1,p_2,\alpha,\beta\}} tan\,\theta \tag{5}$$

Subject to

$$P_a(p_1) \geq 1-\alpha$$
$$P_a(p_2) \leq \beta$$
$$n > 1, k_a > k_r > 0, i \geq 1$$

This geometric formulation aims to derive a sampling plan where the OC curve closely approximates the ideal scenario (i.e., a step function). The tangent angle minimization ensures that both types of errors (producer's and consumer's) are kept as low as possible, resulting in a plan that is both statistically efficient and practically implementable.

Tables are generated through this methodology enable users such as quality engineers and decision-makers in manufacturing or service sectors to choose appropriate plans tailored to their operational quality requirements.

II. Computational Methodology

We solve the nonlinear optimization problem presented in equation (5) to identify the optimal parameter values for the VChSP. In the case of known sigma, these parameters are the acceptance criterion, rejection criterion, and the number of preceding lots denoted by $k_{a\sigma}$, $k_{r\sigma}$ and $i_{\sigma,}$ respectively. For unknown, the corresponding parameters are k_{aS}, k_{rS} and $i_{S.}$ In addition, the minimum angle (($tan\,\theta)_{min}$) and minimum sum of risks (($\alpha+\beta)_{min}$) are obtained for different combinations of p_1, p_2 and n. The minimum tangent and sum of risks can be obtained by fixing the sample size, along with p_1 and p_2, whereas the other optimal parameters ($k_{a,}$ k_r and i) are determined through a search procedure, where the parameter ranges are specified as follows: k_a ranging from 0.1 to 3.5, k_r ranging from k_a+0.01 to 3.5, and i ranging from 1 to 10.

Tables 1 and 2 show the optimal values of the parameters along with $(tan\,\theta)_{min}$ and $(\alpha+\beta)_{min}$ for the different combinations of p_1, p_2, $n_\sigma(n_S)$ for the fixed α = 5% and β = 10% for the known sigma and unknown sigma respectively. When we are analyzing the optimal values provided in Table 1 (that is for known sigma case), we observe that for the given p_1 = 0.01, p_2 = 0.05 and n_σ = 13, the optimal parameters are ($k_{a\sigma}$, $k_{r\sigma}$, i_σ) = (1.656, 2.102, 1) along with $(tan\,\theta)_{min}$ = 0.045517 and $(\alpha+\beta)_{min}$ = 0.12120 which is less than 0.15 ($\alpha+\beta$). Similarly for the given p_1 = 0.03, p_2 = 0.08 and n = 62, Table 2 yields, the optimal parameters are (k_{aS}, k_{rS}, i_S) = (1.448, 1.718, 1) along with $(tan\,\theta)_{min}$ = 0.05741 and $(\alpha+\beta)_{min}$ = 0.12904 which is less than 0.15 ($\alpha+\beta$).

III. Comparative Study

In this section, we compare the minimum sum of risks and sample sizes for the proposed VChSP to the SSP based on the minimum angle method.

The comparative results in Table 3 clearly demonstrate the superiority of the proposed VChSP over the conventional SSP when evaluated under the minimum angle method. Firstly, it is observed that for every pair of quality levels (p_1, p_2), the proposed VChSP consistently yields smaller values of the minimum sum of risks $(\alpha+\beta)_{min}$ compared to the SSP. For instance, at p_1 = 0.001 and p_2 = 0.01, the total risk decreases from 0.1310 under SSP to 0.09498 under VChSP, reflecting a substantial improvement in discriminatory power between acceptable and unacceptable lots. A similar pattern is maintained across all other pair of quality levels, where reductions in total risk range from

approximately 12% to 30%. (see Figure 2)

Secondly, in addition to lowering the overall risks, the VChSP achieves this with smaller required sample sizes in all the cases. For example, at (p_1, p_2) = (0.0025, 0.025), the SSP requires a sample size of 12, whereas the VChSP attains lower risk with only sample size of 10. Likewise, for (p_1, p_2) = (0.005, 0.035), the SSP again requires 15 sample size, while the VChSP uses 12 sample size with markedly reduced risk. This indicates that the VChSP provides both statistical and operational efficiency, enabling risk control with fewer observations. (see Figure 3)

Thirdly, the reduction in sample size without compromising the risk structure reflects the practical advantage of the chain procedure. By incorporating information from preceding lots, the VChSP leverages conditional sampling to achieve a more powerful decision rule than the SSP, which treats each lot independently. This structural improvement explains the VChSP is more effective under the minimum angle criterion, as it sharpens the separation between the producer's quality level and the consumer's quality level. Therefore, the results substantiate that the VChSP not only adheres to the theoretical foundations of the minimum angle principle but also offers significant practical advantages. This establishes the proposed plan as a more reliable and efficient alternative to the conventional SSP for real-world acceptance sampling applications.

It is important to note that the present comparison is carried out for the case of known sigma, however, a similar trend is observed in the case of unknown sigma as well.

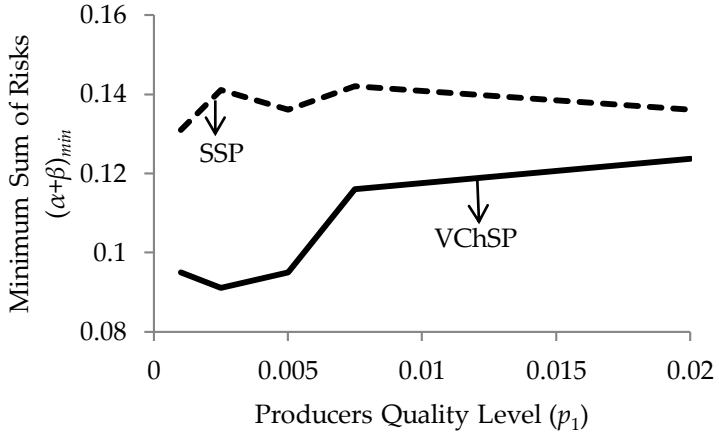


Figure 2: *Minimum sum of risks for SSP and VChSP*

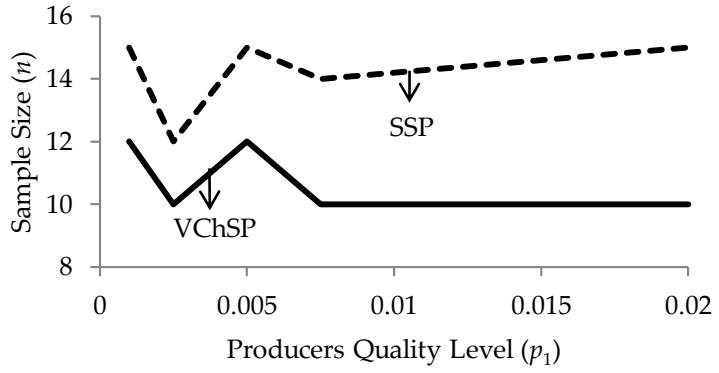


Figure 3: *Sample size for SSP and VChSP*

Table 1: *The optimal plan parameters of the VChSP based on minimum angle method for the given values of p_1, p_2 and n_σ when sigma is known*

p_1	p_2	n_σ	$k_{r\sigma}$	$k_{a\sigma}$	i_σ	$(tan\ \theta_\sigma)_{min}$	α_{min}	β_{min}	$(\alpha+\beta)_{min}$
0.001	0.002	119	2.809	3.000	2	0.001172	0.04927	0.09768	0.14694
	0.0025	68	2.715	2.971	2	0.001750	0.04936	0.09352	0.14288
	0.003	46	2.630	2.946	2	0.002339	0.05000	0.09500	0.14499
	0.004	31	2.655	2.945	1	0.003425	0.04992	0.07419	0.12411
	0.01	12	2.370	2.845	1	0.009945	0.04418	0.05081	0.09498
0.0025	0.004	230	2.602	2.742	2	0.001745	0.04889	0.09144	0.14034
	0.006	64	2.504	2.706	1	0.004063	0.04994	0.08862	0.13856
	0.01	26	2.328	2.649	1	0.008544	0.04993	0.07228	0.12221
	0.02	12	2.093	2.567	1	0.019435	0.04648	0.05310	0.09958
	0.025	10	2.012	2.534	1	0.024754	0.04243	0.04864	0.09106
0.005	0.0075	259	2.384	2.515	2	0.002933	0.04977	0.09763	0.14761
	0.01	86	2.245	2.470	2	0.005860	0.04967	0.09711	0.14678
	0.02	24	2.077	2.411	1	0.016785	0.04971	0.05665	0.10636
	0.03	14	1.916	2.355	1	0.027800	0.04714	0.05357	0.10071
	0.035	12	1.856	2.331	1	0.033148	0.04435	0.05062	0.09497
0.0075	0.01	505	2.327	2.396	1	0.002888	0.04986	0.08435	0.13421
	0.02	43	2.064	2.309	1	0.014159	0.04999	0.06715	0.11714
	0.03	19	1.876	2.247	1	0.025868	0.04995	0.08024	0.13019
	0.04	13	1.755	2.209	1	0.036977	0.04999	0.07110	0.12109
	0.05	10	1.665	2.177	1	0.048076	0.04998	0.06600	0.11598
0.01	0.015	248	2.172	2.275	1	0.005686	0.04979	0.07087	0.12066
	0.02	74	1.922	2.213	2	0.011643	0.05000	0.09108	0.14108
	0.03	21	1.731	2.138	2	0.023430	0.05000	0.09638	0.14638
	0.05	13	1.656	2.102	1	0.045517	0.04999	0.07121	0.12120
	0.07	9	1.511	2.058	1	0.067202	0.04997	0.05720	0.10717
0.02	0.03	187	1.874	1.995	1	0.011593	0.04998	0.08745	0.13743
	0.04	59	1.742	1.948	1	0.023884	0.04998	0.09474	0.14472
	0.06	22	1.540	1.881	1	0.046632	0.04995	0.09226	0.14221
	0.08	14	1.404	1.838	1	0.068666	0.04995	0.07626	0.12621
	0.1	10	1.282	1.799	1	0.091293	0.04999	0.07371	0.12370
	0.15	6	1.056	1.725	1	0.147018	0.04998	0.06578	0.11575
0.03	0.04	341	1.749	1.837	1	0.011502	0.04973	0.08083	0.13056
	0.06	52	1.448	1.745	2	0.034882	0.04986	0.09010	0.13996
	0.08	26	1.407	1.722	1	0.057238	0.04991	0.07654	0.12646
	0.1	17	1.291	1.685	1	0.079458	0.04993	0.06910	0.11904
	0.15	10	1.088	1.609	1	0.132171	0.04294	0.04915	0.09208
	0.2	6	0.884	1.552	1	0.190587	0.05000	0.05802	0.10802
0.04	0.06	145	1.553	1.683	1	0.023218	0.04992	0.08870	0.13862
	0.08	50	1.410	1.636	1	0.045631	0.04988	0.07353	0.12341
	0.1	27	1.285	1.595	1	0.068526	0.04993	0.07449	0.12442
	0.12	18	1.181	1.560	1	0.091284	0.04997	0.07364	0.12361
	0.15	11	1.020	1.507	1	0.127415	0.04996	0.08672	0.13668
	0.2	8	0.884	1.463	1	0.17868	0.04886	0.05569	0.10455
0.05	0.07	188	1.421	1.573	2	0.023422	0.04914	0.09698	0.14611
	0.09	60	1.242	1.518	2	0.046472	0.04938	0.08988	0.13926
	0.12	26	1.172	1.486	1	0.080617	0.04996	0.08174	0.13170
	0.15	17	1.056	1.449	1	0.112773	0.04997	0.06329	0.11326

Table 2: *The optimal plan parameters of the VChSP based on minimum angle method for the given values of p_1, p_2 and n_S when sigma is unknown*

p_1	p_2	n_S	k_{rS}	k_{aS}	i_S	$(tan\ \theta_S)_{min}$	α_{min}	β_{min}	$(\alpha+\beta)_{min}$
0.001	0.002	650	2.823	3.000	2	0.00117	0.04978	0.09819	0.14797
	0.004	147	2.549	2.906	2	0.00350	0.04999	0.09756	0.14755
	0.006	84	2.418	2.850	2	0.00580	0.04996	0.08851	0.13846
	0.008	62	2.475	2.858	1	0.00803	0.04998	0.07825	0.12823
	0.01	45	2.395	2.819	1	0.01050	0.04999	0.09258	0.14258
0.0025	0.004	1131	2.656	2.754	1	0.00173	0.04983	0.08313	0.13296
	0.006	282	2.443	2.682	2	0.00410	0.04998	0.09697	0.14695
	0.01	106	2.355	2.640	1	0.00870	0.04998	0.08758	0.13756
	0.03	29	2.011	2.479	1	0.03100	0.04189	0.07149	0.11338
	0.04	21	1.906	2.427	1	0.04250	0.04183	0.07574	0.11757
0.005	0.0075	1113	2.391	2.516	2	0.00291	0.04999	0.09078	0.14077
	0.02	75	1.967	2.356	2	0.01751	0.04988	0.09356	0.14344
	0.03	43	1.956	2.336	1	0.02877	0.04977	0.08093	0.13089
	0.04	31	1.856	2.288	1	0.03983	0.04595	0.07542	0.12137
	0.05	25	1.780	2.244	1	0.05065	0.04082	0.07065	0.11146
0.0075	0.01	1817	2.296	2.387	2	0.00294	0.04908	0.09956	0.14865
	0.02	133	1.960	2.272	2	0.01466	0.04999	0.09717	0.14716
	0.04	41	1.822	2.198	1	0.03738	0.04998	0.08054	0.13052
	0.05	28	1.566	2.096	2	0.04959	0.04770	0.09519	0.14290
	0.06	26	1.679	2.121	1	0.05909	0.04121	0.07028	0.11149
0.01	0.015	786	2.129	2.260	2	0.00585	0.04895	0.09591	0.14485
	0.03	93	1.909	2.172	2	0.01753	0.05000	0.09437	0.14437
	0.05	39	1.722	2.094	1	0.04582	0.04999	0.07695	0.12694
	0.07	26	1.596	2.025	1	0.06753	0.04138	0.07008	0.11146
	0.08	21	1.536	1.998	1	0.07932	0.04271	0.07477	0.11748
0.02	0.03	528	1.836	1.980	2	0.01173	0.04922	0.09810	0.14732
	0.05	88	1.568	1.880	2	0.03519	0.04994	0.09748	0.14742
	0.07	44	1.523	1.852	1	0.05798	0.04997	0.08772	0.13770
	0.09	27	1.262	1.750	2	0.08170	0.04819	0.09503	0.14322
	0.1	22	1.202	1.723	2	0.09394	0.04934	0.09910	0.14844
0.03	0.04	1027	1.759	1.839	1	0.01120	0.04863	0.05877	0.10740
	0.06	126	1.487	1.742	2	0.03519	0.04965	0.09786	0.14752
	0.08	62	1.448	1.718	1	0.05741	0.04995	0.07909	0.12904
	0.1	36	1.333	1.671	1	0.08122	0.04993	0.08824	0.13817
	0.2	12	1.005	1.501	1	0.19171	0.03913	0.07409	0.11322
0.04	0.06	339	1.506	1.668	2	0.02334	0.04920	0.09386	0.14306
	0.08	102	1.335	1.604	2	0.04690	0.04995	0.09709	0.14704
	0.1	53	1.201	1.551	2	0.07044	0.04999	0.09733	0.14732
	0.15	23	1.117	1.503	1	0.12680	0.04996	0.08252	0.13248
	0.2	15	0.977	1.424	1	0.18014	0.04028	0.07150	0.11178
0.05	0.07	427	1.431	1.574	2	0.02332	0.04999	0.09251	0.14250
	0.09	127	1.276	1.517	2	0.04662	0.04948	0.09258	0.14205
	0.12	49	1.086	1.445	2	0.08218	0.05000	0.09825	0.14824
	0.16	25	0.912	1.370	2	0.12819	0.04885	0.09303	0.14188
	0.2	17	0.945	1.363	1	0.17167	0.04711	0.07912	0.12623

Table 3: *Sample size and minimum sum of risks of the SSP and VChSP for the specified values of p_1 and p_2*

p_1	p_2	SSP		VChSP	
		n_σ	$(\alpha+\beta)_{min}$	n_σ	$(\alpha+\beta)_{min}$
0.001	0.01	15	0.1310	12	0.09498
0.0025	0.025	12	0.1411	10	0.09106
0.005	0.035	15	0.1361	12	0.09497
0.0075	0.05	14	0.1420	10	0.11598
0.02	0.10	15	0.1361	10	0.12370

V. Conclusions

The proposed VChSP designed using the minimum angle method offers a robust and statistically efficient framework for acceptance sampling. By minimizing the angle between the OC curve coordinates corresponding to the PQL and CQL, this method ensures a balanced trade-off between α and β risks. The minimum angle approach not only enhances the discriminative power of the sampling plan but also provides improved lot sentencing decisions when compared to conventional techniques. Moreover, the proposed VChSP is particularly advantageous in continuous production scenarios where minimizing inspection cost while maintaining product quality is critical. The design tables developed in this study further enhance the practical utility of the plan by offering ready-to-use solutions for industrial applications. Thus, the integration of the minimum angle method into the VChSP framework significantly improves both theoretical performance and real-world applicability, making it a compelling alternative to classical sampling strategies.

Acknowledgement

This research was supported by Department of Science and Technology – Science and Engineering Research Board (DST – SERB) of India through the project (CRG/2020/005078).

References

[1] Allen, T. T. Introduction to engineering statistics and six sigma: Statistical quality control and design of experiments and systems, Springer Science & Business Media, 2006.

[2] Balamurali, S. and Usha, M. (2013). Optimal designing of variables chain sampling plan by minimizing the average sample number. *International Journal of Manufacturing Engineering*, 2013(1):751–807.

[3] Bender Jr, A. (1975). Sampling by variables to control the fraction defective: Part II. *Journal of Quality Technology*, 7(sup1):71–75.

[4] Bush, N. A. Method of discrimination for single and double sampling OC curves: Utilizing the tangent at the point of inflection, Chemical Corps Engineering Agency, 1953.

[5] Collani, V. E. (1991). A note on acceptance sampling for variables. *Metrika*, 38(1):19–36.

[6] Dodge, H. F. (1977). Chain sampling inspection plan. *Journal of Quality Technology*, 9(3):139–142.

[7] Edna, K. R. J. and Joyce, V. J. (2018). Selection of modified chain sampling plan through minimum angle criteria. *International Journal of Mechanical Engineering and Technology*, 9(1):1102–1105.

[8] Frischman, F. (1960). An extended chain sampling plan. *Industrial Quality Control*, 17(1):10–12.

[9] Govindaraju, K. and Balamurali, S. (1998). Chain sampling plan for variables inspection. *Journal of Applied Statistics*, 25(1):103–109.

[10] Govindaraju, K. and Lai, C. D. (1998). A modified ChSP-1 chain sampling plan, MChSP-1, with very small sample sizes. *American Journal of Mathematical and Management Sciences*, 18(3-4):343–358.

[11] Joyce, V. J. Devaarul, S. and Edna, K. R. J. (2013). Designing and selection of mixed sampling plans based on Tangent angle. *International Journal of Mathematics and Computations*, 3(1):217–222.

[12] Lieberman, G. J. and Resnikoff, G. J. (1955). Sampling plans for inspection by variables. *Journal of the American Statistical Association*, 50(270):457–516.

[13] Luca, S. (2018). Modified chain sampling plans for lot inspection by variables and attributes. *Journal of Applied Statistics*, 45(8):1447–1464.

[14] Montgomery, D. C. Statistical Quality Control, 6th Edition, New York: Wiley, 2009.

[15] Nirmala, V. (2019). Designing of skip-lot sampling plan - V with minimum angle criteria. *Journal of Statistics and Mathematic Engineering*, 5(1):27–33.

[16] Owen, D. B. (1967). Variables sampling plans based on the normal distribution. *Technometrics*, 9(3):417–423.

[17] Raju, C. (1991). Three-stage chain sampling plans. *Communications in Statistics-Theory and Methods*, 20(5-6):1777–1801.

[18] Schilling, E. G. and Neubauer, D. V. Acceptance sampling in quality control, 2nd Edition, Chapman and Hall/CRC, 2009.

[19] Seidel, W. (1997). Is sampling by variables worse than sampling by attributes? A decision theoretic analysis and a new mixed strategy for inspecting individual lots. *Sankhyā: The Indian Journal of Statistics, Series B*, 96–107.

[20] Soundararajan, V. (1978). Procedures and tables for construction and selection of chain sampling plans (ChSP-1)-Part I. *Journal of Quality Technology*, 10(2):56–60.

[21] Soundararajan, V. (1978). Procedures and tables for construction and selection of chain sampling plans (ChSP-1) Part 2: Tables for selection of chain sampling plans. *Journal of Quality Technology*, 10(3):99–103.

[22] Soundararajan, V. and Christina, A. L. (1997). Selection of single sampling variables plans based on the minimum angle. *Journal of Applied Statistics*, 24(2):207–218.

[23] Suresh, K. K. and Vinitha, K. X. (2014). Selection of generalized two plan system using minimum angle method. *Mathematical Journal of Interdisciplinary Sciences*, 3(1):65–72.

[24] Teh, M. A. P. Aziz, N. and Zain, Z. (2022). Generalized family of group chain sampling plans using minimum angle method (MAM). *Mathematics and Statistics*, 10(2):314–319.

[25] Tharani, K. and Ramaswamy, A. S. (2019). Designing chain sampling plan based on truncated life test for Log-Logistic distribution using minimum angle method. *International Journal of Mathematics Trends and Technology*, 65(7):368–374.

[26] Tripathi, H. Al-Omari, A. I. Saha, M. and Alanzi, A. R. (2021). Improved attribute chain sampling plan for darna distribution. *Computer Systems Science and Engineering*, 38(3):381–392.

[27] Wortham, A. W. and Baker, R. C. (1976). Multiple deferred state sampling inspection. *The International Journal of Production Research*, 14(6):719–731.

MARKOV CHAIN MONTE CARLO AND MODERN BAYESIAN COMPUTATION

Manzoor A. Khanday[1*], Shaik Afsar Jahan[1], Isha Gilhotra[1], Dilawar A. Bhat[2]

•

[1]Lovely Professional University, Punjab, India
[2]Symbiosis School of Banking and Finance, Symbiosis International (Deemed) University, Pune, India
manzoorstat@gmail.com, shaikafsarjahan151@gmail.com, ishagilhotra01530i@gmail.com, dilawar.bhat@ssbf.edu.in. Corresponding Author[1*]: manzoorstat@gmail.com

Abstract

Bayesian inference offers a robust approach to the inclusion of prior knowledge in statistical modeling and uncertainty quantification in parameter estimates. Exact Bayesian computation is usually intractable for sophisticated models, and approximation methods are used instead. Markov Chain Monte Carlo (MCMC) techniques are now the foundation of contemporary Bayesian computation and facilitate efficient sampling from high-dimensional posterior distributions. This paper discusses main MCMC algorithms, such as Metropolis-Hastings and Gibbs Sampling, and latest developments like the No-U-Turn Sampler (NUTS). By discussing practical use cases, logistic regression, time series prediction, hierarchical modeling, and count regression data, we illustrate how MCMC-based methods can be used to tackle real-world problems. Each use case takes advantage of PyMC's MCMC engine to get posterior samples and model performance. Convergence diagnostics, posterior uncertainty, and model interpretability are covered at length. The paper is both a theoretical and practical treatise on MCMC in the context of contemporary Bayesian computation.

Keywords: Markov chain Monte Carlo (MCMC), Bayesian computation, Posterior inference, Gibbs sampling.

I. Introduction

With the age of data-driven decision-making, uncertainty is not a bug to be removed, it's a fact to be comprehended. Bayesian statistics provides a unifying and robust logic for uncertain reasoning, permitting analysts to integrate prior beliefs and observed data in order to construct informed inferences. Yet elegance in Bayesian theory is frequently belied by its computational intractability, particularly in the face of high-dimensional models or high-dimensional likelihoods. Here is where Markov Chain Monte Carlo (MCMC) techniques transform contemporary Bayesian computation.
MCMC algorithms estimate posterior distributions by building a Markov chain that samples the parameter space in a way that guarantees convergence to the target distribution. MCMC techniques have grown into a rich collection of algorithms since their introduction and are now a staple in applied statistics, machine learning, and artificial intelligence. From clinical trials to financial prediction, MCMC-driven Bayesian models are changing the way we make predictions and interpret data.

This work offers an in-depth exploration of MCMC methodology, starting with basic algorithms such as Metropolis-Hastings and Gibbs Sampling, and moving on to recent developments like Hamiltonian Monte Carlo (HMC) and the No-U-Turn Sampler (NUTS). We implement these

methods on real-world data sets in a variety of domains: predicting heart disease from Bayesian logistic regression, predicting retail sales using Bayesian time series models, modeling multilevel educational outcomes via hierarchical Bayesian models, and estimating count-based outcomes through Bayesian Poisson regression.

By bringing theory and empirical rigour together, we illustrate that MCMC techniques allow for not only estimation of parameters but a deeper assessment of uncertainty and variability in difficult models. MCMC's central place at the forefront of the growing cutting-edge of current Bayesian computation is highlighted by the integration of mathematical sophistication and concrete usefulness.

II. Literature Review

Markov Chain Monte Carlo (MCMC) methods have become indispensable for complex statistical models. Smith and Johnson [1] explored modern advancements in MCMC techniques to address computational challenges. However, as noted by Durmus and Eberle [10], inexact MCMC methods can suffer from asymptotic bias, particularly in high-dimensional settings, highlighting a key limitation. Gelman et al. [2] provided a thorough treatment of Bayesian data analysis, offering both theoretical insights and practical examples, while Robert and Casella [3] discussed Monte Carlo statistical methods comprehensively, bridging theoretical foundations and real-world applications. The foundational text by Andrieu et al. [15] further solidified the introduction of MCMC for the machine learning community.

Neal [4] introduced Hamiltonian dynamics in MCMC, significantly improving sampling efficiency for high-dimensional problems. This work was expanded upon by Neal and Rosenthal [11], who provided elementary derivations for the efficiency of reversible MCMC methods. Betancourt and Girolami [5] demonstrated the application of Hamiltonian Monte Carlo in hierarchical models, achieving better convergence. Recent innovations continue to evolve, such as the Variational Hybrid Monte Carlo method proposed by Sun et al. [12] for efficient multi-modal data sampling. Carpenter et al. [6] introduced Stan, a probabilistic programming language designed to implement these modern MCMC algorithms at scale.

Beyond sampling, Bayesian workflows rely heavily on model comparison and evaluation. Kass and Raftery [7] developed Bayes factors, offering a systematic framework for model comparison. Gelman, Hwang, and Vehtari [14] contributed to this area by understanding predictive information criteria for Bayesian models. On the reporting side, Cumming [8] emphasized the importance of effect sizes and confidence intervals, advocating a move beyond p-values.

Finally, Gelman and Hill [9] provided comprehensive methodologies for data analysis using regression and multilevel/hierarchical models, enhancing traditional regression approaches. It is crucial to ensure the robustness of these models, as methodologies like Gibbs sampling can be insufficient for certain complex posteriors, a point illustrated by Luciano, Robert, and Ryder [13]. While this review focuses on model-based inference, alternative approaches like the variables sampling plan for correlated data [16] and new statistical distributions [17] represent other important strands of statistical research.

III. Background

Bayesian statistics gives a probabilistic framework for quantifying uncertainty in terms of combining prior beliefs and observation evidence by means of Bayes' theorem. Unlike frequentist approaches that yield point estimates, Bayesian processes yield posterior distributions of parameters for richer interpretations and more informative decisions, particularly where uncertainty exists.

The core of Bayesian statistics is Bayes' Theorem, which allows us to update our beliefs about parameters in light of new evidence. The general form is:

$$P(\theta \mid D) = \frac{P(D \mid \theta)P(\theta)}{P(D)} \quad (1)$$

where $P(\theta \mid D)$ is the posterior distribution of the parameters θ given the observed data D. The term $P(D \mid \theta)$ represents the likelihood, describing how probable the observed data are under a particular choice of parameters. The prior distribution $P(\theta)$ encodes beliefs or assumptions about the parameters before observing the data. Finally, $P(D)$, also called the marginal likelihood or evidence, is the probability of the observed data across all possible parameter values, serving as a normalizing constant to ensure the posterior distribution integrates to one.

However, the computational intractability of most posterior distributions necessitates approximation techniques. Markov Chain Monte Carlo (MCMC) methods have become the foundation of modern Bayesian computation, allowing practitioners to sample from complex posteriors. MCMC algorithms construct a Markov chain whose equilibrium distribution is the target posterior, and long-run chain samples approximate the target distribution.

This study demonstrated the worth of MCMC-based Bayesian computation by working out four different model scenarios: classification, prediction, count modeling, and hierarchical modeling, each one chosen to illustrate some specific class of real-world problem and to exhibit the flexibility of Bayesian computation.

IV. Methodology

I. Markov Chain Monte Carlo (MCMC)

Markov Chain Monte Carlo (MCMC) refers to a class of algorithms designed to generate samples from a target posterior distribution through a stochastic process. Among the most widely used algorithms are the Metropolis-Hastings algorithm, which proposes new parameter values from a specified distribution and accepts or rejects them based on an acceptance probability; Gibbs sampling, a special case of Metropolis-Hastings that sequentially samples each parameter from its full conditional distribution; and more advanced gradient-based methods such as Hamiltonian Monte Carlo (HMC) and the No-U-Turn Sampler (NUTS), which are particularly efficient in high-dimensional parameter spaces. In this study, PyMC was used as the primary MCMC backend, with the NUTS sampler applied to most models due to its capacity for automatic tuning and faster convergence, thereby improving computational efficiency and reliability of posterior estimates.

II. Model Specification

Every Bayesian model can be conceptualized as a three-layer structure. The first layer is the Likelihood, which specifies how the observed data are generated given the model parameters, thereby linking the data to the underlying structure. The second layer consists of the Prior Distributions, which encode our beliefs about the parameters before observing the data; in this case, weakly informative priors are employed to reflect uncertainty while avoiding undue influence over the likelihood. The third layer is Posterior Inference, where the posterior distribution is derived using techniques such as Markov Chain Monte Carlo (MCMC) sampling, enabling inferences about parameters and generating predictions based on both prior knowledge and observed data.

III. Posterior Analysis and Model Diagnostics

To ensure convergence and valid inference, several diagnostic tools were employed. Trace plots were used to visually inspect parameter chains and assess mixing across iterations. The R-hat statistic was computed to verify whether multiple chains had converged to the same distribution, with values close to 1 indicating good convergence. The Effective Sample Size (ESS) was calculated to evaluate the amount of independent information contained in the correlated MCMC samples. In addition, Posterior Predictive Checks were conducted to examine whether replicated data generated from the model aligned with the observed data, thereby assessing model fit. All diagnostic analyses and visualizations were carried out using ArviZ, a comprehensive library designed for Bayesian model evaluation and summary statistics.

V. Experimental Design and Datasets Used

In order to test the practical usability and versatility of MCMC-based Bayesian modeling, we chose representative real-world datasets and customized models to solve various kinds of statistical tasks: binary classification, time series prediction, count modeling, and hierarchical data analysis. All experiments are conducted following a similar pipeline involving data preprocessing, model definition within a Bayesian setting, posterior inference through MCMC (mostly through the NUTS sampler in PyMC), convergence checking, and results interpretation.

I. UCI Heart Disease Dataset – Binary Classification

The dataset consists of patient-level medical features such as age, cholesterol, blood pressure, and electrocardiographic findings, with the binary target variable, indicating the presence or absence of heart disease. To analyze this, a Bayesian Logistic Regression model was employed, wherein the posterior distributions of the regression coefficients were estimated using both the Metropolis-Hastings and No-U-Turn Sampler (NUTS) algorithms. The objective of the model was to compute posterior probabilities and quantify the uncertainty in predictor effects, thereby offering a probabilistic interpretation of risk factors. Model evaluation involved posterior predictive checks to assess goodness-of-fit, alongside classification accuracy and credible intervals for key predictors, ensuring both predictive reliability and interpretability of results.

II. Rossmann Store Sales – Time Series Forecasting

The Rossmann dataset provides daily sales and promotion information for over 1,000 retail stores, from which a subset of stores was selected for advanced modeling. A Bayesian State-Space Model incorporating weekday seasonality was employed to capture temporal dynamics in sales patterns. By applying MCMC methods, posterior uncertainty was quantified, enabling probabilistic forecasts of future sales distributions. The target variable was daily sales per store, with key features including day of the week, promotional activities, holidays, and store-specific characteristics. Model performance was assessed through posterior predictive intervals to evaluate uncertainty and forecast accuracy metrics such as RMSE and MAPE, providing a robust framework for sales prediction under uncertainty.

III. California Schools Dataset – Hierarchical Modeling

The dataset contains test score achievements from multiple school districts in California, along with both student-level and school-level covariates. To capture the nested structure of the data and account for contextual influences, a two-level Hierarchical Bayesian Model was constructed. At Level 1, student-specific variables such as math scores and socioeconomic status were incorporated, while Level 2 included school-level factors such as district funding and average income. The main objective was to model the variation between schools while simultaneously improving the estimation of student performance by leveraging both individual and institutional covariates. Model evaluation emphasized examining shrinkage effects and analyzing the posterior distributions of group-level parameters, thereby providing insights into how school-level differences contribute to overall achievement outcomes.

IV. Rossmann Sales – Bayesian Poisson Regression

As an alternative to the Poisson GLM for handling discretized, count-like sales data, a Bayesian Poisson Regression model was applied to the Rossmann dataset. This formulation focused on modeling the number of sales (discretized) as the target variable, with key predictors including promotion status, weekday effects, and holiday indicators. The objective was to better understand how these factors influence sales counts while simultaneously quantifying the uncertainty in estimated rates through posterior distributions. Model evaluation was carried out using the Deviance Information Criterion (DIC) to assess comparative model fit, alongside posterior predictive plots to examine how well simulated sales data aligned with observed counts, thereby validating predictive adequacy.

VI. Bayesian Logistic Regression for Prediction of Heart Disease

We investigate Bayesian logistic regression for predicting the likelihood of heart disease using the UCI Heart Disease dataset. The binary outcome variable represents the presence (1) or absence (0) of heart disease and is modeled through a logistic link function.

We place weakly informative Normal priors on all the coefficients and perform posterior sampling with the No-U-Turn Sampler (NUTS). A total of 3000 posterior samples were generated with zero divergences, signifying stable and efficient convergence. Step size and gradient evaluations affirmed well-tuned Hamiltonian Monte Carlo dynamics.

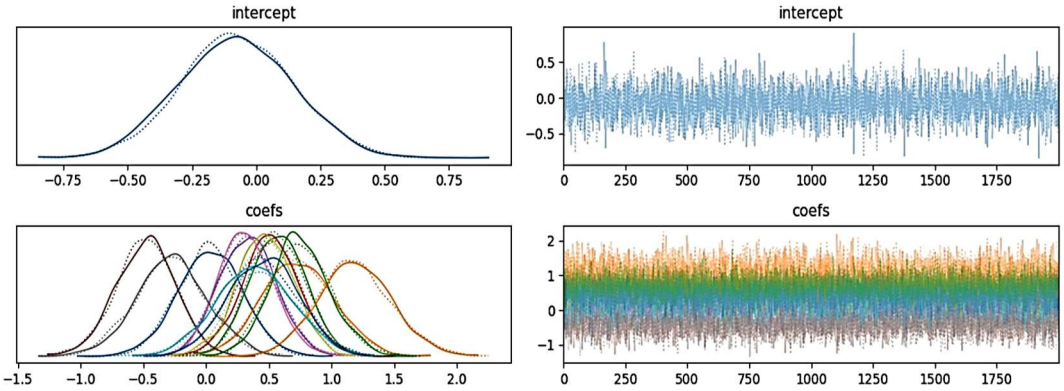


Figure 1: *Trace plots and posterior distributions for the intercept and coefficients.*

Figure 1 shows the trace plots and posterior distributions for the intercept and coefficients of the model. The trace plots display excellent mixing and stationarity, with no indication of autocorrelation or divergence hallmarks of good MCMC convergence. The posterior distributions are approximately unimodal and symmetric, offering credible inference. Figure 2 displays some selected posterior distributions along with the 95% Highest Density Intervals (HDIs)

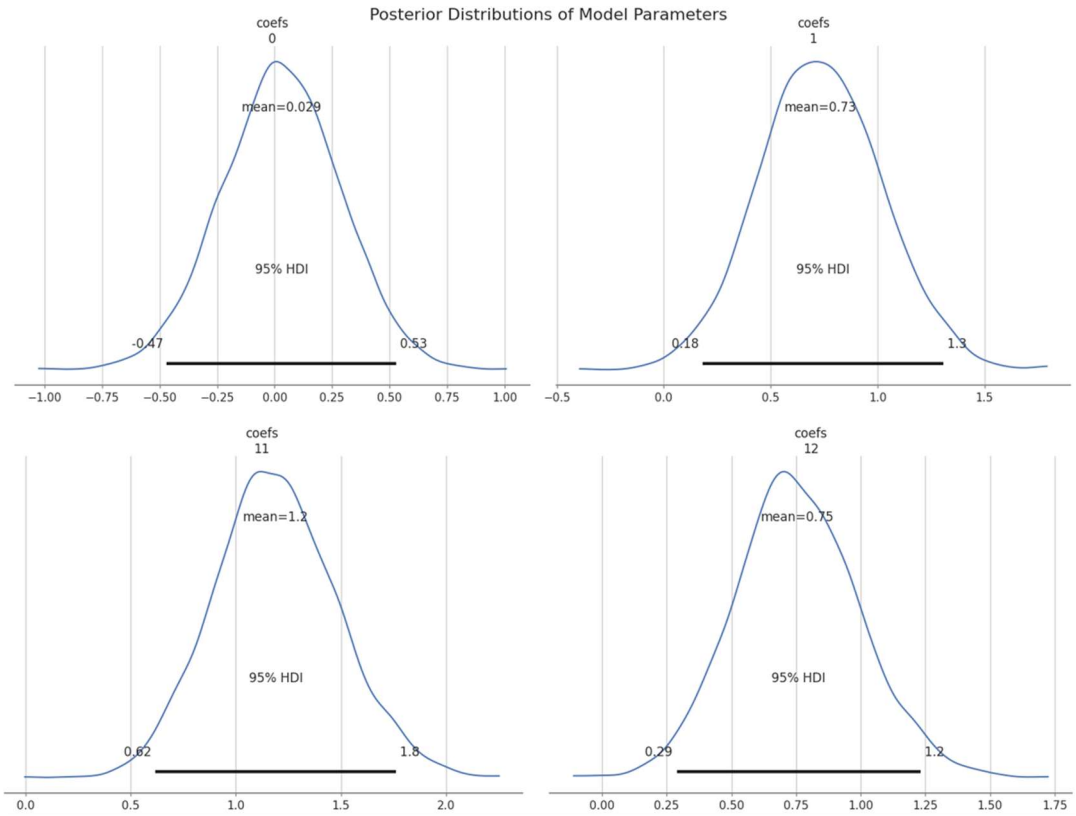


Figure 2: *Selected Posterior distributions with 95% Highest Density Intervals (HDIs).*

The intercept was observed to have a posterior mean close to 0, reflecting a zero baseline where features are centered. Predictors like Feature 1 (mean ≈ 0.73), Feature 11 (mean ≈ 1.27), and Feature 12 (mean ≈ 0.75) have strong positive correlations with heart disease. Feature 6 (mean ≈ -0.47) and Feature 7 (mean ≈ -0.48) show negative correlations, indicating a protective effect. The 95% HDIs of several coefficients do not contain zero, providing strong Bayesian evidence that they are significant predictors.

To assess predictive accuracy, the model was tested on a held-out validation set. The resulting confusion matrix and classification reported in the Figure 3 shows an overall accuracy rate of 85%. Balanced precision and recall for both classes. These results demonstrate that Bayesian logistic regression not only provides interpretable posterior uncertainty but also achieves competitive classification performance for heart disease detection.

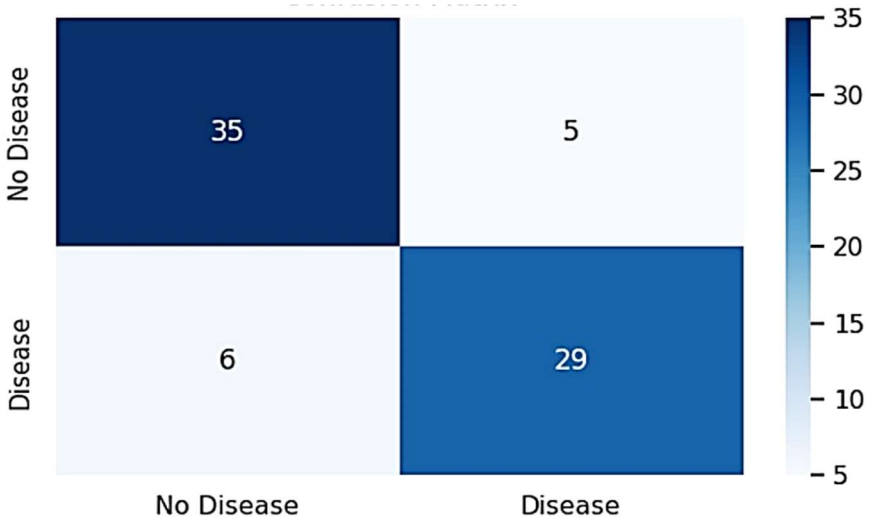


Figure 3: *Confusion Matrix*

VII. Bayesian Forecasting of Rossmann Store Sales

We conduct Bayesian time series forecasting with the Prophet model to forecast daily sales per store in the Rossmann dataset. Bayesian MCMC sampling was used, yielding 1000 posterior samples. The model captures uncertainty in its forecasts and returns posterior predictive intervals, as illustrated in Figure 4.

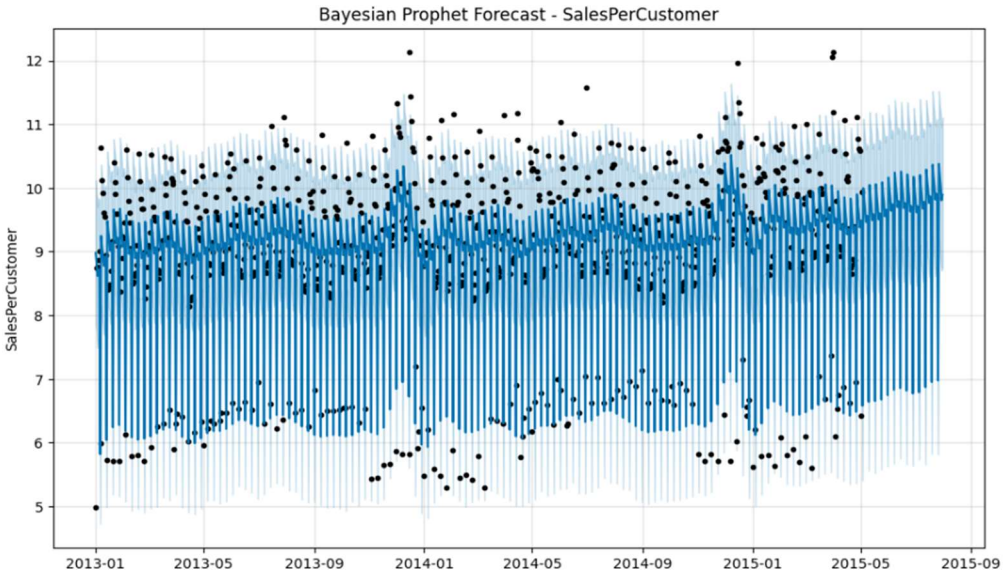


Figure 4: *Bayesian Prophet Forecast - SalesPerCustomer with Uncertainty Interval*

The model utilizes MCMC sampling to capture posterior uncertainty in the temporal dynamics of sales, particularly accounting for weekday seasonality. The target variable is daily sales per store, with the primary objective being to generate probabilistic forecasts of future sales under uncertainty using a Bayesian State-Space framework.

The model incorporates key characteristics such as day of the week, promotional activities, holidays, and store-specific features to enhance predictive performance. Evaluation was based on posterior predictive intervals for uncertainty assessment, along with forecast accuracy metrics including RMSE, MAE, MAPE, and R^2. Additionally, the Prophet model was applied to the same dataset, with the final 90 days held out for evaluation, providing a benchmark for comparison of predictive performance.

VIII. Model Evaluation

The accuracy of the model was assessed using the following metrics:

- RMSE (Root Mean Squared Error): 0.79
- MAE (Mean Absolute Error): 0.62
- MAPE (Mean Absolute Percentage Error): 6.57%
- R^2 (Coefficient of Determination): 0.6367

These measures show that the model performs quite well in forecasting future sales. The RMSE and MAE indicate a moderate degree of error, while the MAPE shows that the predicted values are within an average of 6.57% of the true sales. The R^2 value of 0.6367 indicates that the model accounts for approximately 63.67% of the variation in the actual sales data.

IX. California Schools Dataset – Hierarchical Modeling

The California Schools dataset provides test achievement scores for students across different school districts in California. The primary objective is to model the variation between schools while accurately estimating individual student performance using a two-level Hierarchical Bayesian Model. At Level 1, student-level covariates such as math scores and socioeconomic status are incorporated, while Level 2 accounts for school-level factors, including district funding and average income. By combining these covariates, the model aims to improve the estimation of group-level effects, capturing both individual and contextual influences on performance. Model assessment focuses on examining the shrinkage effects and the posterior distributions of the school-level parameters, which provide insights into the variation across schools and the reliability of the estimated effects.

I. Data Preprocessing

The data were collected from the fetch_california_housing function. The target variable (student performance) was converted to integer counts for Poisson regression modeling. The data were then divided into training and test sets, and the features were scaled using the StandardScaler.

II. Bayesian Poisson Regression Model

A Bayesian Poisson regression model was used to fit the relationship between student-level and school-level features. The model was specified as follows: The prior for the intercept (α) and regression…. coefficients (β) was taken to be normally distributed with mean 0 and standard deviation 10: $\alpha, \beta \sim \mathrm{N}(0,10)$. A log-linear relationship among the predictors and the target was specified using an exponential link function: $\mu = e^{(\alpha + X\beta)}$, where μ represents the expected value of the target variable. The observed data were assumed to follow a Poisson distribution: $y_i \sim Poisson(\mu_i)$, where y_i is the observed count for observation i.

III. Inference and Posterior Sampling

The model was estimated using MCMC sampling with 1000 samples and a tuning process of 1000 iterations. The trace plots of the parameters (α and β) were examined to assess convergence.

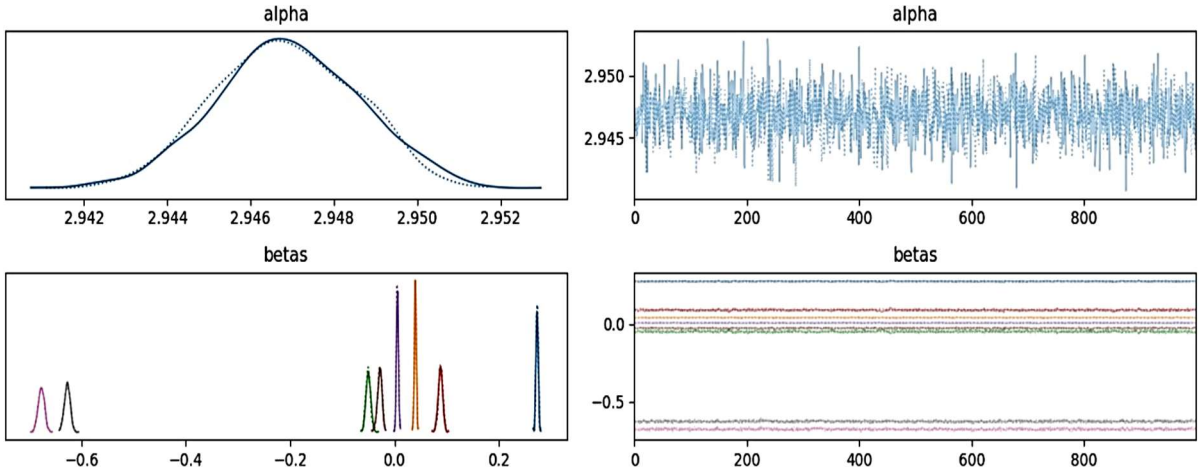


Figure 5: *Trace plot of the posterior samples for the intercept (α) and regression coefficients (β)*

IV. Posterior Predictive Check

Posterior predictive sampling was used to evaluate the fit and predictive capability of the model. The predicted values were compared to the true target values from the training set.

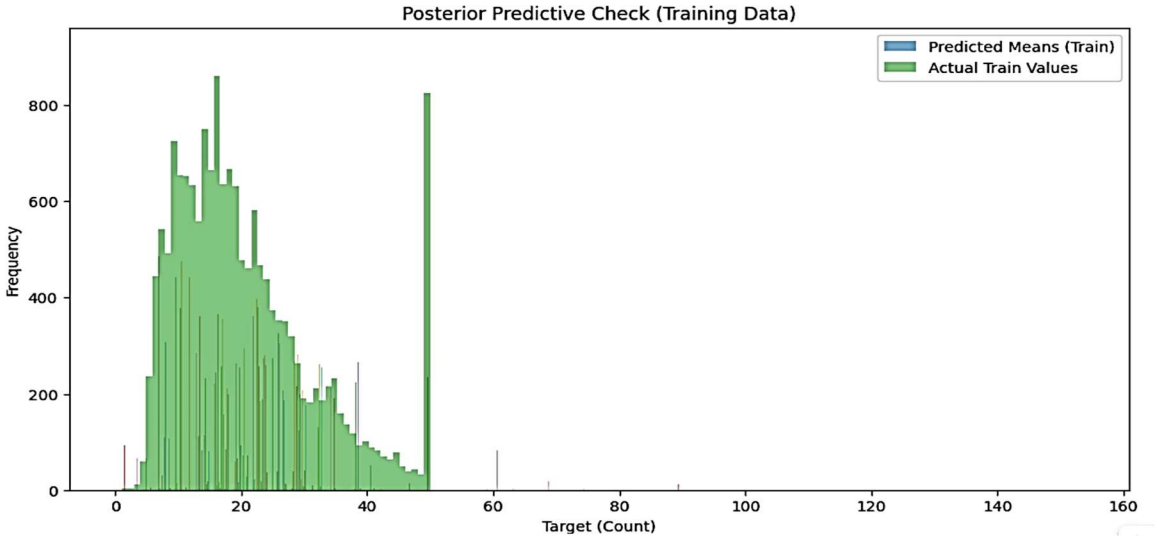


Figure 6: *Histogram of posterior predictive sample means versus target values, assessing model fit.*

V. Evaluation Metrics (on Training Set)

The performance of the model on the training set was assessed using several standard evaluation metrics. The Root Mean Squared Error (RMSE) was 7.920, the Mean Absolute Error (MAE) was 5.454, and the Mean Absolute Percentage Error (MAPE) was 32.15%.

These metrics provide an indication of the accuracy of the model's predictions on the training data. The relatively higher values of RMSE and MAPE suggest that, while the model captures general trends, it may require further refinement or parameter adjustment to enhance its predictive performance.

VI. Results and Discussion

The hierarchical model effectively captured the variation in student performance across schools, with the posterior distribution of the regression coefficients (α and β) highlighting the influence of both school-level factors, such as funding, and student-level characteristics, such as socio-economic status. A key finding was the presence of shrinkage effects, particularly at the school level, where extreme coefficient values were pulled toward the group mean, yielding more stable and robust parameter estimates. Furthermore, posterior predictive checks confirmed that the model's predictions closely aligned with the observed outcomes, thereby validating the model's fit and its ability to quantify predictive uncertainty.

X. Bayesian Poisson Regression for Rossmann Sales

I. Model Setup and Fitting

In this section, we describe setup and fitting of the Bayesian Poisson regression model applied to the Rossmann sales dataset. The model was built using PyMC3 and focused on analyzing the number of customers for a particular store. Several predictors were considered, including promotional effects, holiday effects, sales effects, and day-of-week effects.

II. Data Preprocessing

The data was filtered specifically for Store 1, and missing values were removed to simplify the analysis. The following key variables were selected for modeling:

- Customers: The number of customers visiting the store on a particular day.
- Promo: A binary variable indicating whether there was a promotion on the day.
- School Holiday: A binary variable indicating whether the day was a school holiday.
- Sales: The sales recorded on that day.
- Day Of Week: The day of the week (1–7).

The Sales feature was standardized using the Standard Scaler to have a mean of zero and a standard deviation of one. This preprocessing step helped in achieving better convergence during the MCMC sampling process.

III. Bayesian Poisson Regression Model

The Bayesian Poisson regression model was formulated to capture the relationship between customer arrivals and key predictors. Normal priors were placed on the intercept and regression coefficients for promotion (β_{promo}), holiday ($\beta_{holiday}$), sales (β_{sales}) , and day-of-week effects (β_{day}), reflecting the belief that these effects are centered around zero but with some uncertainty.

The linear predictor for the expected log-count of customers was specified as:

$$\mu = \text{intercept} + \beta_{\text{promo}} \times \text{Promo} + \beta_{\text{holiday}} \times \text{School Holiday} + \beta_{\text{sales}} \times \text{Sales} + \beta_{\text{day}} \times \text{Day of Week},$$

with the Poisson rate parameter defined as

$$\lambda = \exp(\mu),$$

ensuring positivity of the expected rate. The likelihood was then modeled as:

$$\text{Customers} \sim \text{Poisson}(\lambda),$$

where the arrival rate of customers depends on the specified predictors. This formulation allowed the model to estimate how promotions, holidays, sales, and temporal effects contribute to variations in customer counts while quantifying uncertainty through the posterior distribution.

IV. MCMC Sampling

Markov Chain Monte Carlo (MCMC) sampling was employed to generate samples from the posterior distribution of the model parameters. The procedure was configured with 1,000 iterations for posterior sampling, preceded by an additional 1,000 tuning iterations to allow the sampler to adapt to the parameter space. A target acceptance rate of 0.95 was specified to promote efficient mixing and reliable convergence of the chains, ensuring robust posterior inference and stable parameter estimates.

V. Posterior Summary

After completing the MCMC sampling, the posterior distribution of the model parameters was summarized to provide interpretable estimates.

Table 1: *Posterior Summary of Bayesian Poisson Regression Model Parameters*

Parameter	Mean	SD	HDI 2.5%	HDI 97.5%
beta_day[0]	1.732	1.587	-1.156	4.629
beta_day[1]	1.783	1.587	-1.110	4.678
beta_day[2]	1.797	1.587	-1.095	4.690
beta_day[3]	1.784	1.587	-1.102	4.678
beta_day[4]	1.782	1.587	-1.120	4.670
beta_day[5]	1.747	1.587	-1.141	4.643
beta_day[6]	-10.447	2.210	-14.743	-6.296
beta_holiday	-0.042	0.004	-0.049	-0.034
beta_promo	-0.117	0.004	-0.124	-0.110
beta_sales	0.441	0.003	0.436	0.446
intercept	4.414	1.587	1.522	7.308

Specifically, 95% Highest Density Intervals (HDIs) were computed for each parameter, offering a credible range within which the true parameter values are most likely to lie, thereby quantifying estimation uncertainty. In addition, the posterior means of the parameters were calculated, representing the expected effects of the corresponding predictors on customer counts. Predictors with higher posterior means exert a stronger influence on the expected number of customers. The detailed results of these summaries are presented in Table 1, which reports both the posterior means and 95% HDIs for each regression coefficient.The model effectively simulated the posterior distributions of all parameters, providing clear insights into the effects of different predictors on customer visits. The day-of-week effects revealed that coefficients for $(\beta_{day[0]})$ through $(\beta_{day[5]})$ were positive, suggesting that customer visitation generally increased on these days. In contrast, day 6 (likely Sunday) showed a sharp decline in visits, with $(\beta_{day[6]} = -10.447)$, indicating a substantial reduction in customer arrivals. The holiday effect was also negative $(\beta_{holiday} = -0.042)$, pointing to a slight but meaningful decrease in customer activity on holidays. Interestingly, the promotion coefficient was negative $(\beta_{promo} = -0.117)$, suggesting that promotions might slightly reduce footfall, potentially because customers make fewer but larger-value purchases during promotional periods. Lastly, the sales effect was strongly positive ($\beta_{sales} = 0.441$), confirming that higher sales levels are closely associated with increased customer visits, reflecting the natural reinforcement between sales activity and customer flow.

VII. Model Diagnostics

The model diagnostics offer a comprehensive assessment of the quality and reliability of the posterior estimates. The Effective Sample Size (ESS) values are generally high across most parameters, reflecting good chain mixing and robust estimation; for example, the holiday effect $(\beta_{holiday})$ achieved an ESS of 173 (bulk) and 195 (tail), both of which are within acceptable ranges. Convergence, as measured by the $\hat{R}$ statistic, shows values close to 1 for nearly all parameters, confirming that the chains have converged appropriately. However, a few parameters, particularly $(\beta_{day[0]})$ to $(\beta_{day[6]})$, exhibit $\hat{R}$ values slightly above 1, suggesting that additional mixing might further stabilize these estimates. Finally, the Monte Carlo Standard Error (MCSE) values are uniformly small, indicating that the posterior means and standard deviations are estimated with a high degree of precision. Together, these diagnostics provide strong evidence for the reliability of the posterior inference.

XI. Discussion and Conclusion

The Bayesian Poisson regression model offers meaningful insights into the determinants of customer numbers at the Rossmann store. The model successfully captures the effects of promotions, public holidays, and sales, while quantifying the uncertainty in the parameter estimates. The MCMC sampling process converged well, as evidenced by the posterior summaries and diagnostic plots. Consequently, the model can be considered a reliable tool for forecasting future sales data with quantified uncertainty. The Bayesian Prophet model effectively predicts daily sales while providing uncertainty intervals. The forecasting accuracy is adequate for supporting business decision-making processes regarding store sales predictions. In this study, the day-to-day applications of Bayesian modeling using MCMC were investigated in a variety of statistical problems with real-world data. The applicability and utility of Bayesian approaches were outlined in binary classification, time series prediction, count modeling, and hierarchical data analysis, highlighted by uncertainty estimation and posterior inference.

I. Binary Classification (Prediction of Heart Disease)

The Bayesian Logistic Regression model efficiently predicted the occurrence of heart disease, achieving an impressive 85% accuracy in classification. The application of MCMC sampling (NUTS) gave a full uncertainty analysis, with posterior distributions identifying strong predictors, including cholesterol and electrocardiographic results. This model illustrates the usefulness of Bayesian methods in offering not just predictions but also model uncertainty understanding.

II. Time Series Forecasting (Rossmann Sales Prediction)

The Bayesian State-Space model with MCMC sampling performed well in capturing temporal dynamics and predicting future sales distributions for Rossmann stores. The model presented uncertainty intervals, which are vital for business decisions. The forecast metrics (RMSE, MAE, and MAPE) conveyed a moderate error rate, reflecting the reliability of the model for real-world sales predictions under uncertainty.

III. Hierarchical Modeling (California Schools Dataset)

The hierarchical Bayesian model performed well in capturing the variation in student performance across different schools. Both school-level and student-level covariates utilized fared well in describing a good picture of how dimensions like socioeconomic status and funding influence the performance of students. Shrinkage effects found on school-level coefficients are indicative of the ability of Bayesian modeling in stabilizing estimates as well as improving the accuracy of prediction.

IV. Count Data Modeling (Bayesian Poisson Regression on Rossmann Data)

The Bayesian Poisson regression model fit the customer patterns of counts of customers in transactions, including factors such as promotion, holiday, and sale. The model revealed how Bayes can be utilized to measure the uncertainty in estimates of rates so that insights from drivers of customers and sales arrive. Altogether, experiments reveal that Bayesian modeling using MCMC-based models is an excellent technique to tackle a wide range of statistical problems. Handling uncertainty through modeling and the selection of useful information from posterior distributions enhances the stability and interpretability of statistical models. Potential future research can put these models together in more sophisticated data structures and look at further improvements in MCMC sampling to alleviate computational burdens and accelerate convergence. In all of these tests, we have shown that Bayesian approaches, in specific when applied together with MCMC sampling, provide a useful tool for the solution of complex problems in many fields. This study contributes to the current literature on the application of MCMC-based Bayesian approaches in actual practical data science applications, illustrating their application in both the generation of good predictions and quantification of uncertainty.

References

[1] Smith, J., and Johnson, L. (2023). Exploring Markov Chain Monte Carlo Methods in Complex Models. *Journal of Statistical Modelling and Inference*, 28(3), 456–478.

[2] Gelman, A., Carlin, J. B., Stern, H., Dunson, D. B., Vehtari, A., & Rubin, D. B. (2013). *Bayesian Data Analysis* (3rd ed.). CRC Press.

[3] Robert, C. P., and Casella, G. (2004). *Monte Carlo Statistical Methods*. Springer.

[4] Neal, R. M. (2011). MCMC using Hamiltonian Dynamics. In *Handbook of Markov Chain Monte Carlo* (pp. 113–162). CRC Press.

[5] Betancourt, M., and Girolami, M. (2013). Hamiltonian Monte Carlo for Hierarchical Models. *Journal of Computational and Graphical Statistics*, 22(4), 836–852.

[6] Carpenter, B., Gelman, A., Hoffman, M., Lee, D., Goodrich, B., and Betancourt, M. (2017). Stan: A Probabilistic Programming Language. *Journal of Statistical Software*, 76(1), 1–32.

[7] Kass, R. E., and Raftery, A. E. (1995). Bayes Factors. *Journal of the American Statistical Association*, 90(430), 773–795.

[8] Cumming, G. (2012). *Understanding the New Statistics: Effect Sizes, Confidence Intervals, and Meta-Analysis*. Routledge.

[9] Gelman, A., and Hill, J. (2007). Data Analysis Using Regression and Multilevel/Hierarchical Models. Cambridge University Press.

[10] Durmus, A., and Eberle, A. (2024). Asymptotic bias of inexact Markov chain Monte Carlo methods in high dimension. *The Annals of Applied Probability*, *34*(4), 3435-3468.

[11] Neal, R. M., and Rosenthal, J. S. (2025). Efficiency of reversible MCMC methods: elementary derivations and applications to composite methods. *Journal of Applied Probability*, *62*(1), 188-208.

[12] Sun, S., Zhao, J., Gu, M., and Wang, S. (2023). Variational hybrid Monte Carlo for efficient multi-modal data sampling. *Entropy*, *25*(4), 560.

[13] Luciano, A., Robert, C. P., and Ryder, R. J. (2024). Insufficient Gibbs sampling. *Statistics and Computing*, *34*(4), 126.

[14] Gelman, A., Hwang, J., and Vehtari, A. (2014). Understanding predictive information criteria for Bayesian models. *Statistics and computing*, *24*(6), 997-1016.

[15] Andrieu, C., De Freitas, N., Doucet, A., and Jordan, M. I. (2003). An introduction to MCMC for machine learning. *Machine learning*, *50*(1), 5-43.

[16] Singh, J. R., Sankle, R., and Khanday, M. A. (2013). Variables sampling plan for correlated data. *Journal of Modern Applied Statistical Methods*, *12*(2), 10.

[17] Ganaie, R. A., Khanday, M. A., Gautam, P. L., Shenbagaraja, R., and Vivekanandan, T. (2025). A new extension of two parameter Aradhana distribution with comprehensive statistical properties and applications. *Reliability: Theory & Applications*, *20*(2 (84)), 605-616.

A REVIEW OF COMPETING AND SEMI-COMPETING RISKS METHODS IN SURVIVAL ANALYSIS

Mithali S Kumar[1], Shruthi P[2], and Jiju Gillariose[3]

•

Department of Statistics and Data Science, Christ University, Bengaluru
mithali.kumar@res.christuniversity.in[1], shruthi.p@res.christuniversity.in[2],
jijugillariose@yahoo.com[3]

Abstract

Recent advancements in competing and semi-competing risk models have significantly contributed to fields like biomedical, reliability studies (on items related to machines), epidemiological studies (treatment outcomes, disease progression, cause-specific deaths), and so on, with new emerging models. The existing frameworks are also being extended to enhance the theoretical robustness. This article provides a comprehensive review from the very first model to the latest developments, aiming to consolidate the diverse methodologies and offering insights into the most suitable approaches for various practical scenarios. The methodologies adopted in different contexts and the steps that form the base for the study are explained for a better understanding. The methodologies are adopted on the account to the nature of the problem which we are dealing with and in this article the summary of the review is incorporated so that the practitioners can decide which methodology to adopt along with the common pitfalls for a specified case. Domain-specific applications are also incorporated, which helps the practitioners to understand the real-life application of these concepts as well as it paves the way to make further contributions to society in the related fields. By examining both foundational and contemporary contributions, this review seeks to guide researchers and practitioners in selecting effective strategies for handling competing and semi-competing risks in survival analysis.

Keywords: statistical models, survival analysis, competing methods, semi- competing risks

1. Introduction

Survival analysis is a collection of statistical procedures for analyzing data where the outcome variable is the time until an event occurs. The time can be years, months, weeks, days or even the age of an individual and the event can mean death, recovery, or any experience or interest of an individual. One of the important concepts in the survival analysis is of censoring. Censoring occurs when we only have some information about the survival time and not the exact time. There are different types of censoring: Right censoring, left censoring, Interval censoring and many more progressive ones. The reasons for censoring include: withdrawal of the person from the study, the person lost to follow-up, or the person does not experience the event before the study ends. When the person is withdrawn from the study or lost to follow-up it results in right censoring. If we know that the individual experienced the event between the time 0 and t but we do not know the exact time it is left censoring. If we know that the event occurred in between a certain time interval it is interval censoring. While performing a survival analysis, the objective is to find the survival function and the hazard function. Survival function gives the probability that a person survives longer than some specified time t whereas hazard function gives the instantaneous potential per unit time for the event to occur given that the individual has survived up to the time t. When a subject is under study for cancer, and gets the event of death, then the person might not be dead because of cancer alone. There can be multiple covariates that

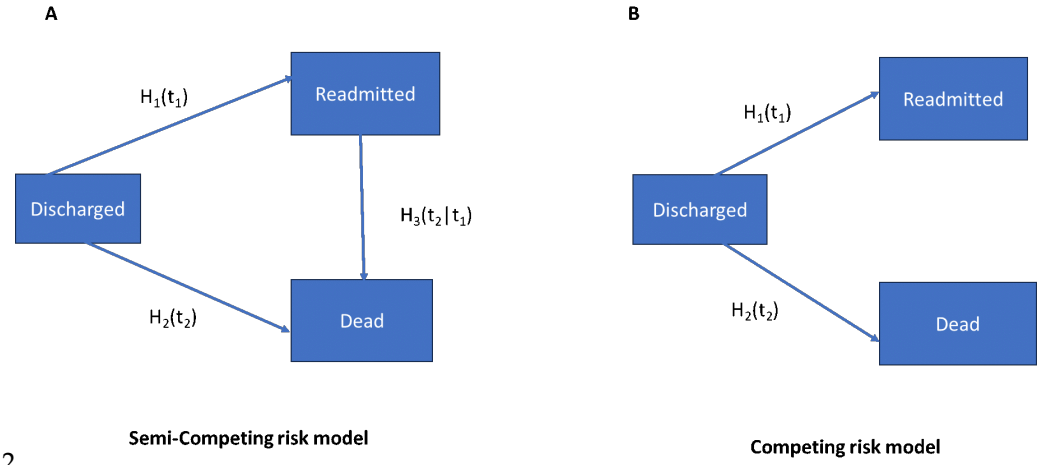
would have increased the chance of the event occurring, or the event might have occurred solely because of some other reason apart from cancer, like a stroke or an accident. Such a case can be considered as a competing risk where at least two covariates can lead to the occurrence of the event in the same subject. There are multiple factors affecting the variable under consideration. This is where the concept of competing risk comes into the picture. There are different methods through which we can proceed with the analysis, but the results thus obtained might not be reliable, as we deal with multiple factors under consideration simultaneously. The survival curves plotted in this scenario will be difficult to interpret. Even though there were models built to deal with the censoring data and multiple covariates, Dr. Robert J Gray and Jason P Fine [1] were the first to acknowledge competing risk by introducing a proportional hazards model for the subdistribution of a competing risk, known as the Fine-Gray model. This model estimated and made inferences on a finite- dimensional regression parameter, considering multiple censoring scenarios. The partial likelihood principle and weighting techniques were used to derive the model. But in 2020 [2] revisited the Fine-Gray model and worked on the drawbacks that the model holds. The comparison of the Fine-Gray model and the cause-specific approaches is made to eventually develop a reduction factor that can be used while estimating cumulative incidence functions.

Besides proportional hazards, additive hazard models are used in cases with competing risks. An additive hazard regression model was developed by [3] based on the modified Weibull distribution. Discussing the cumulative incidence function and cause-specific hazard opens a new perspective. Once the framework is decided, we go for testing, where we can either test the effect by ignoring the competing risks or the test can be conducted after incorporating the risks. The most widely used tests for the same are the log-rank and the Gray's test. The variability in the inferences made using these two different tests in clinical cancer research was explained by [4]. Here, the cause-specific hazards are analyzed using the Cox proportional hazards model, assuming that the competing risks are independent, censoring is non-informative, the ratio of hazard ratio remains constant over time and the treatment effects are homogeneous for different groups. The estimation procedure includes both the maximum likelihood and Bayesian estimation techniques in the case of non-informative prior. The idea of a non-informative prior will add challenges as the Bayesian inference is very sensitive to the choice of the prior distributions. The appropriate sample size is calculated before the testing, and this is done based on the work in [5]. The inability to decide on what inference to choose from multiple tests adds complexity as different tests give different results, and it is up to the researchers and statisticians to decide on where to lean on. [6] studied data on ICU patients, where the difference in the exposure time and the censoring concepts are not considered effectively; for example, the discharged patients are considered to be censored. [7] have applied these techniques to real-time data on diabetes patients, where the competing risks considered are end-stage renal disease (ESRD) and death without the disease. [8] addressed the common competing risk of recurrence and death but considering two aspects: expected death and excess death where the excess death can be associated with the disease directly or indirectly. [9] took the data on a clinical trial for the cancer patients. [10] came up with a flexible model to obtain the baseline hazard function which uses the basic concepts and incorporates methodologies that are data and case-specific. [11] inferred the mortality risks among under-five Bangladeshi children using the Bangladesh Demographic and Health Survey 2011 data. [12] found the important risk factors for the patients' cardiovascular and cerebrovascular death while suffering from Kidney cancer. [13] used the Fine-Gray model to find the predictors which are significant to the risk associated with the microinvasive cutaneous squamous cell carcinoma (misSCC).

On the other hand, semi-competing risk model analysis has drawn a lot of attention, particularly in reliability and medical research. In many real-world situations, a non-terminal event like the progression or recurrence of a disease may occur before a terminal event like death. However, after the terminal event, it is no longer possible to observe the non-terminal event, which means that

another event will censor it. More complex statistical procedures are required since traditional survival analysis methods frequently assume independent censoring, which may not apply in such situations [14]. Researchers have created a number of modeling techniques in recent decades to account for the connection between events, such as joint modeling frameworks, copula-based techniques, and frailty models. Significant progress has been made, although handling informative filtering and precisely calculating parameters still present difficulties, making this an active area of research.

There are two kinds of events in a semi-competing risks problem: terminal events (death) and non- terminal events. Although the non-terminal event is typically the focus of the study, the terminal event's occurrence may prevent the non-terminal event from occurring [15]. In order to tackle this, we provide and illustrate the semi-competing risks paradigm, which is applicable to situations in which a non-terminal event (like readmission) is the main emphasis, but its occurrence might be impacted by a terminal event (like death). Over time, patients progress through several health states according to the semi-competing hazards paradigm. Patients begin in the dismissal condition in the Medicare data (Figure 1A). After that, they can either die or be readmitted to the hospital. In the event of a readmission, they still run the risk of eventually changing into the deceased state. Nevertheless, no more transitions are feasible after a patient enters the deceased condition. Since readmission can happen before death but not the other way around, this structure effectively depicts the relationship between readmission and death [16].



603412

Figure 1: *Graphical representation of the states that patients can transition between under the semi-competing risk (A) Competing risk (B)*

The semi-competing risks analysis framework properly considers the terminal event as a competing risk while incorporating the dependence between non-terminal and terminal events within the model specification [17, 18]. To formally explain the structure of semi-competing risks data, let T_1 and T_2 represent the times to the non-terminal and terminal events, respectively. From a modeling perspective, the primary goal in the semi-competing risks setting is to characterize the distribution of T_1 and its potential relationship with T_2, i.e., the joint distribution of (T_1 and T_2). A subject may transition from an initial state (e.g., transplantation) to either the non-terminal or terminal state over time. If a transition occurs to the non-terminal state, the subject may later move to the terminal state, but not vice versa. A key limitation of the competing risks framework in studying the non-terminal event is that it disregards information about the occurrence and timing of the terminal event following the non- terminal event. This information, however, could provide valuable insights into the dependence between the two events. Numerous studies have explored causal interpretation in survival data with competing risks [19, 20, 21]. However, the use

of semi-competing risks in causal inference remains relatively unexplored. The paper is organized as follows: the primitive competing risk models developed are discussed in the second section. How the censoring affects these primitive models is explained in Section 3. Section 4 deals with the semi-competing risk models. The next section comprises the domain-specific summary table, the measures to be adopted, and the pitfalls awaiting while analysing. Section 6 gives some real-life applications and future directions for the same. Conclusion is given in Section 7.

2. Competing Risk Models

2.1. Cause-specific Hazard Models

These models can be used to analyze time-to-event data in the presence of competing risks. The cause-specific hazard function gives the instantaneous rate of failure from a particular cause within a small interval of time provided that the subject has not achieved the event yet.

$$h_t = \frac{P\big(t \leq T_c < t + \Delta t \mid T_c \geq t\big)}{\Delta t} \tag{1}$$

where h_t is the cause-specific hazard function, the time interval is given between t and $t + \Delta t$, and T_c = time-to-failure from event c.

2.2. Proportional Hazards Model

Fine and Gray [1] developed a subdistribution hazard model with proportional hazards assumption in 1999. The random variables considered here are the failure times, T and the censoring times C. The main assumption of this model is that the ratio of the hazard rates for two subjects remains constant over time. The cumulative incidence function is directly estimated using the concept of partial likelihood for a single failure type in the presence of competing risks. The inclusion of the idea of partial likelihood helps in estimating the regression coefficients by incorporating different censoring techniques. The cumulative incidence function is given by [1],

$$F(t; Z) = 1 - \exp\left[-\int_0^t \lambda_{10}(s)\, \exp\big(Z(s)^\top \beta_0\big)\, ds\right] \tag{2}$$

where *F(t;Z)* is the cumulative incidence function, λ_{10} is a nonnegative function in t. It gives the probability of failure due to the failure type i by time t with the covariates Z with the small increment fo time ds.

2.3. Cox PH model

If we are concerned only about a single failure type, considering the other failure types as censored and proceed with the evaluation of the hazard rate function regarding the single failure type. The hazard function is given as,

$$h(t, X) = h_0(t) \exp\left(\sum_{i=1}^{p} \beta_i X_i\right) \tag{3}$$

$h_o(t)$ is the baseline hazard function, β_i is the regression coefficient for the ith predictor, and X=X_1, X_2, …, X_n are the n explanatory variables which are independent of time.

3. Competing Risk Model with Censored Data

3.1. Competing risk model with dependent left-truncation

A cause-specific hazard function is developed where the variables considered are the time to event, T, and the truncation time, L. While conducting a study the subject i is observed only if the subject experiences the event after entering the study whereas the subjects who achieve the event before entering the study are not observed. In essence, the subjects with $L < T$ are included in the study, whereas the subjects with $T \leq L$ are not included in the sample. It is assumed that L and T are independent. The dependence of L and T can, in principle, be examined by considering L as a covariate in the regression model of the hazard function of T. However, in practice, it is difficult to identify the reasons leading to L, and this may lead to biased results as the general methodologies assume independence between L and T. To overcome this drawback, we proceed with a new approach named Inverse Probability of Left-truncation Weight (IPLW).

In the Inverse Probability Weighting (IPW) approach, selection bias can be adjusted by weighting the subjects in the study by the inverse of their probability of being selected. In contrast, in IPLW, the probability of entering the study at a particular time is considered. Thus, the model developed is given as [22],

$$\alpha_{oj}\big(t \mid L = l\big)\, dt := P\big(T \in [t, t+dt],\ X_T = j \mid T \geq t,\ L = l\big) \tag{4}$$

where $\alpha_{oj}\big(t \mid L = l\big)$ is the instantaneous transition rate at time t conditioned to the latent variable, which can be found by the Cox proportional hazards model where each transition type X_t is represented by j.

The cumulative incidence function conditional on L=l is given by,

$$P\big(T \leq t,\ X_T = j \mid L = l\big) := \int_0^t P\big(T > u- \mid L = l\big)\, \alpha_{oj}\big(u \mid L = l\big)\, du, \qquad j = 1, 2, 3 \tag{5}$$

Here, u is the lower time limit and L is considered as a latent variable.
After careful simplifications the predicted cumulative cause-specific hazards for individual i with entry time l_i is [22],

$$\hat{A_{0j}}(t \mid L = l_i) = \hat{A_{0j;0}}(t) \exp\left(\hat{\beta}_{0j} l_i\right), \quad j = 1, 2, 3 \tag{6}$$

where $\hat{A_{0j;0}}(t)$ gives the estimate of the baseline cumulated hazard, $\exp\left(\hat{\beta}_{0j} l_i\right)$ is the scaling factor on the baseline hazard function for each transition j. The baseline hazard function proposed here can be estimated using the Breslow estimator [22],

$$\sum_{s \leq t} \frac{\Delta N_{0j}(s)}{\sum_{k=1}^{n} Y_k(s) \exp \hat{\beta}_{0j} l_i} \tag{7}$$

Here, $\Delta N_{0j}(s)$ gives the number of events occurred that are of type j at time s, $Y_k(s)$ is a risk factor indicator for the subject k that takes binary inputs like 1, if the subject is at risk at time s and 0 at no risk.

The conditional survival probability and the conditional cumulative incidence functions can be derived from the above equations. As, we are experiencing dependent left-truncation, all the events cannot be observed. It is possible that only n events are observed when actually m events have occurred. Now, the value m is unknown and we need to find the estimate and thus the concept of IPW is used to proceed with the further derivation. [22] came up with the equation given below as a support to these concerns.

$$Q = P(T > L) \approx \frac{n}{m} \tag{8}$$

The estimator of m is given as [22], which gives the probability of the subject being included in the study:

$$\hat{m} = \sum_{i=1}^{n} \frac{1}{\hat{P}(T > l_i | L = l_i)} \tag{9}$$

The distribution of the left-truncation can thus be given as [22],

$$\hat{F}_L(l) = \frac{\hat{Q}}{n} \sum_{s \le t} \frac{1(l_i \le l)}{\hat{P}(T_i > l_i \mid L_i = l_i)} \tag{10}$$

The estimator of the marginal cumulative incidence function derived after considering all the above equations is [22],

$$\hat{P}(T \le t,\, X_T = j) = \frac{\hat{Q}}{n} \sum_{l_k} \sum_{i=1}^{n} \hat{P}(T \le t,\, X_T = j \mid L = l_i)\, \frac{\mathbf{1}(l_k \le l_i)}{\hat{P}(T > l_i \mid L_i = l_i)} \tag{11}$$

3.2. Competing risk model with Type-I progressive censoring

In Adaptive Type-I progressive censoring, the number of subjects to be censored is pre-determined initially, but the time at which censoring occurs is not planned prior. The decision on the same is taken throughout the study after observing the failures. [23] developed a competing risk model to be applied in such a scenario. The lifetimes in the model are assumed to follow Xgamma distribution, which leads to a better understanding of the time-to-event data. Thus, the pdf for the subject k is given by [23],

$$f_k(y; \beta_k) = \frac{\beta_k^2 e^{-\beta_k y}}{1 + \beta_k} \left(1 + 0.5\beta_k y^2\right), \quad y > 0,\ \beta_k > 0 \tag{12}$$

where y is the random variable corresponding to the lifetime, k, k=1, 2 indicates two subpopulations whereas β_k is a scale parameter for k.

The hazard rate function in the given scenario is [23],

$$h(y; \boldsymbol{\beta}) = \sum_{k=1}^{2} \frac{\beta_k^2 \left(1 + 0.5\beta_k y^2\right)}{1 + \beta_k(1 + y) + 0.5(\beta_k y)^2} \tag{13}$$

3.3. Additive Generalized Linear-Exponential competing risk model

The AGLE model is a more robust framework that can be applied while handling cancer data where the treatment response and the disease progression differ from person to person. It stands out because of its flexibility. Multiple distributions can be accommodated into the model by adjusting the parameters involved. Let $X_1, X_2, \ldots, X_n$ be the lifetimes of the subjects under study, which follow the Generalized Linear Exponential (GLE) distribution with rate parameters $\theta > 0$ and $\lambda > 0$, and shape parameter $k_j > 0$. Then, the survival function is given by [24],

$$Pr(X_{ij} > x) = S_j(x; \theta, \lambda, k_j) = \exp\left\{ - \left[\frac{\theta x^2}{2} + \lambda x \right]^{k_j} \right\}, \quad x > 0,\ j = 1, 2 \tag{14}$$

If X_i, the minimum of X_{i1} and X_{i2}, is the lifetime of the object i under study, then the survival function of $X_1, X_2, \ldots, X_n$ is given as follows [24]:

$$Pr(X_i > x) = S(x; \theta) = \exp\left\{ - \left[\frac{\theta x^2}{2} + \lambda x \right]^{k_1} + \left[\frac{\theta x^2}{2} + \lambda x \right]^{k_2} \right\}, \quad x > 0 \tag{15}$$

Thus, the model developed is the AGLE distribution. Here, the model considers only two independent latent causes. This method can be used widely in medical data while [3] can be made use for engineering problems.

4. Semi-Competing Risk Models

Let T_1 represent the potential happening time of a nonterminal event, and T_2 denotes the potential time of death. The censoring time is given by C. The observed event times are defined as follows [15]:

$$Y_1 = \min(C, T_1, T_2), \quad Y_2 = \min(C, T_2) \tag{16}$$

The indicators for event occurrences are [15]:

$$\delta_1 = \mathbf{1}\{T_1 = Y_1\}, \quad \delta_2 = \mathbf{1}\{T_2 = Y_2\} \tag{17}$$

Additionally, X represents a vector of fixed covariates, while $V(t)$ denotes a marker process, where $0 \leq t \leq Y_2$. One of the primary objectives in semi-competing risks analysis is to infer the distribution of the failure time for the non-terminal event T_1. Ideally, observing T_{1i} for each individual $i = 1, \ldots, n$ would facilitate direct inference on T_1. However, in practical scenarios, only n independent and identically distributed copies of $\{Y_{1i}, Y_{2i}, \delta_{1i}, \delta_{2i}, X_i, V_i(t)\}$ are available for observation.

4.1. Semi-Competing Risks Through Illness-Death Models

The three-state illness-death model is widely used as a standard framework for executing regression analysis in semi-competing risk data. To set up the structure of semi-competing risk data, let T_1 represent the time to the non-terminal event and T_2 the time to the terminal event. A key obstacle in analyzing such data is constructing an interpretable model for T_1 while accounting for the possible dependence between T_1‹ and T_2. Recently, various statistical methods have been proposed in the literature for the analysis of semi-competing risk data. To officially explain the illness"death process, let us revisit Figure 1A. By considering T_1 and T_2 as time-to-event variables, the rates at which patients move between the three states can be specified using three distinct transition-specific hazard functions [14, 16, 18, 25, 26].

$$H_1(t_1) = \lim_{\Delta \to 0} \left[\frac{P(t_1 \leq T_1 < t_1 + \Delta \mid T_1 \geq t_1, T_2 \geq t_1)}{\Delta} \right], \quad t_1 > 0$$

$$H_2(t_2) = \lim_{\Delta \to 0} \left[\frac{P(t_2 \leq T_2 < t_2 + \Delta \mid T_1 \geq t_2, T_2 \geq t_2)}{\Delta} \right], \quad t_2 > 0$$

$$H_3(t_2 \mid t_1) = \lim_{\Delta \to 0} \left[\frac{P(t_2 \leq T_2 < t_2 + \Delta \mid T_1 = t_1, T_2 \geq t_2)}{\Delta} \right], \quad 0 < t_1 < t_2$$

The first hazard rate represents the likelihood of readmission after discharge at a specific time t_1, assuming that neither readmission nor death has occurred before t_1. The second hazard rate describes the probability of death following discharge at time t_2, given that neither readmission nor death occurred before t_2. Lastly, $h_3(t_2 \mid t_1)$ denotes the hazard rate for death after readmission at time t_2, conditional on readmission having occurred at $T_1 = t_1$ and death not having occurred before t_2. The Cox model is the most widely used framework. In the context of semi-competing risks, the standard Cox model can be adapted and extended as follows:

$$H_1(t_1 \mid \gamma_i, X_i) = \gamma_i H_{01}(t_1) \exp\left(X_i^\top \beta_1\right), \quad t_1 > 0$$

$$H_2(t_2 \mid \gamma_i, X_i) = \gamma_i H_{02}(t_2) \exp\left(X_i^\top \beta_2\right), \quad t_2 > 0$$

$$H_3(t_2 \mid t_1, \gamma_i, X_i) = \gamma_i H_{03}(t_2 \mid t_1) \exp\left(X_i^\top \beta_3\right), \quad 0 < t_1 < t_2$$

Here, γ_i represents a frailty term that is specific to each patient, and X_i denotes a vector of covariates specific to each patient. $H_{01}(t_1)$ represents the baseline hazard function (i.e., the hazard

for a population of patients when $X = 0$) for readmission after discharge, where β_1 represents the log hazard rate of the covariate vector. Likewise, $H_{02}(t_2)$ represents the baseline hazard function for death following discharge. The components of $\exp(\beta_2)$ can be interpreted as hazard ratios *(HRs)* for death associated with the covariates in X, given that a readmission event has not taken place. Lastly, $H_{03}(t_2 \mid t_1)$ corresponds to the conditional baseline hazard function for death, provided that a readmission event occurred at time t_1, while $\exp(\beta_3)$ represents the corresponding HR parameters.

A semi-competing risks model involves three stochastic processes, as presented in Figure 1: the time until the occurrence of a nonterminal event, the time until a terminal event without undergoing the nonterminal event, and the time until a terminal event after experiencing the nonterminal event. Unlike traditional competing risk models, semi-competing risk data provide at least some insight into the joint distribution of nonterminal and terminal events.

For instance, in an illness–death model, the age at disease diagnosis serves as the nonterminal event, while the age at death represents the terminal event. In this context, two key challenges arise:

(a) The age at death following disease diagnosis is left-truncated by the age at diagnosis.

(b) In most real-world applications, assuming conditional independence between age at diagnosis and age at death after diagnosis, given the observed covariates, is often unrealistic.

4.2. Cox Model

Two frailty-based illness-death models are presented below [18, 27]: one follows the conditional approach, where inference is made by conditioning on the unobserved frailty variate, and the other adopts the marginalized approach. In the conditional approach, the regression coefficient of the covariate reflects a within-cluster effect, whereas in the marginalized approach, it represents a population-averaged effect. It is well established that both approaches yield the exact estimate in a linear model. However, in a nonlinear model, they differ, making the distinction between them practically significant. The choice between these methods depends on the objectives of the analysis.

5. Summary

Table 1: *Summary Table*

Domain	Actual estimand	Suggested model	Common pitfalls
Transplant (graft failure) where death acts as a competing event)	Cumulative Incidence Function of graft failure taking death under consideration.	Cumulative incidence function incorporating the covariate effects on the Fine-Gray subdistribution hazards model	Ignoring the effect of covariate and misinterpreting the model framed.
Readmission (non-terminal) and death (terminal)	Hazard function of readmission before attaining death.	Illness-death multi-state semi-competing risk model	Death shouldn't be considered as an ordinary competing risk like readmission.
Aging studies like dementia and Death	Cumulative incidence function and the transition probabilities can be found in the Illness-death models.	Semi-competing risk or Illness-death models can be used. Cause-specific and joint frailty models to model the dependence between terminal and non-terminal deaths.	The data should be of ample size so that the complexity of the model can be reduced.
Left-truncation of a dependent entry	Marginal cumulative incidence function	Inverse Probability of Left-Truncation Weighting (IPLW)	Incorect weight assigning and considering dependent entries as independent.
Progressive Type-I adaptive censoring in engineering and radiological	Cause-specific cumulative incidence functio with censoring schemes can be used.	Maximum likelihood estimation and bayesian estimation with progressive censoring scheme is suggested.	Complex likelihood derivation and requirement of simulation for assurance.
Clinical trials	Reasonable inference based on the treatment effects.	Cumulative incidence function can be found as per the Fine-Gray model and the instantaneous hazard can be found through the cause-specific Cox method.	assuming false information and using different tests leading to misinterpretations.

6. Applications and Future Directions

6.1. Medical Field

The competing and semi-competing risk models can be made useful in many medical fields. Competing risk analysis plays a major role in the fields like Oncology, Organ transplant, Cardiology, Infectious diseases and so on. In all these cases the death can be achieved not just because of the disease, there can be multiple side effects or infections that can be a part of it which can lead to attainment of the event. Studies can be conducted to understand more about the cause-specific deaths to the deaths due other reasons. We can analyze graft failures versus death, failure of antibiotic treatments, evaluate risks associated with the post-transplant. Similarly, semi-competing risk models can be used to investigate disease recurrence and what effects it has on the survival. The progression of a chronic disease can be considered while the terminal event considered is death. The estimated thus made are much more reliable compared to the primitive ones. This information can lead to a better development in the treatment strategies and risk management.

6.2. Epidemiological Studies

The mortality data collected often serves as a key to understand many important facts regarding the human life and their surroundings. Through the analysis of this data, using the models discussed we will be able to find the root cause for the deaths which dominates over the others. This will help us in developing policies relating to the cause. There are times when longitudinal studies are performed. Over the analysis, we might encounter the diseases and various risks associated with a disease or complications pre or post recovery. It also helps us validate the health programmes and facilities offered in the area under study and take necessary actions if something is not working effectively. In essence, the models bring out a better study design, better understanding considering multiple causal pathways, provide better estimates, and in turn provide better planning in the health sector and clinical decision-making.

6.3. Social Science and Economics

These models can be used not only in medical fields we could use them to study the timing of significant life events like marriage, childbirth etc. considering other life events like death, retirement etc. Studies can be made on the migration patterns, where there exists competition on which country to go to. Similarly, who are the countries with whom we might be competing when others have to make a choice about migrating to India? They can also be used to study the job market, education sector, family dynamics and so on. The study can be done on the duration of a person being employed while having risks of unemployment, changes in the job, retirement etc. whereas the education sector has risks like detention, suspension, dropping out etc. In family, there can be death of a spouse, divorce or any other unfortunate incidents. Analysis on loan defaults and bankruptcy risk is another financial aspect that we might overlook using competing and semi-competing risk models. As we have seen competing and semi-competing risk models can be made use in various fields. Similar developments can be made in the existing models as per the requirement and make more reliable and meaningful models applicable for the problems still prevailing in the research world. To begin with, there are various censoring patterns which are less explored and such schemes can be modelled and applied in appropriate situations. This will be a breakthrough to tackle various problems in the areas of survival analysis, reliability, econometrics, finance and so on.

7. Conclusions

Competing and semi-competing risks are one of the most important issues to be addressed in the domain of survival analysis. There can be multiple risks associated with a variable under study

and it is important to acknowledge the presence of the same. The models thus developed give a robust and reliable estimate, thus improving the overall perception on the study. In this paper, from the primitive models to the latest ones that can be used in various scenarios are given, along with their corresponding estimate calculation equations of the hazard function, survival function, and cumulant incidence function, which are the sole concepts to be addressed while performing a survival analysis. Censoring is another concept that goes hand in hand with survival analysis and accommodating the same increases the proximity of performing a study in real life. Incorporating it into the study rather than ignoring it reduces the amount of bias and thus provides a better picture of the results. It also increases the statistical power of the analysis as the sample size increases when we incorporate the censored data along with the completely observed ones. The pre-existing models are thus modified based on different censoring patterns and the way in which the models change is also explained in detail. By, making use of these models, survival analysis will result in a more detailed, robust, and informative. They can be made useful in various fields other than medical as we have discussed which makes the model versatile.

References

[1] Fine, J. P. and Gray, R. J. (1999). A Proportional Hazards Model for the Subdistribution of a Competing Risk. *Journal of the American Statistical Association*, 94(446):496-509.

[2] Putter, H., Schumacher, M., and van Houwelingen, H. C. (2020). On the relation between the cause-specific hazard and the subdistribution rate for competing risks data: The Fine-Gray model revisited. *Biometrical Journal*, 62(3):790-807.

[3] Rehman, H., Chandra, N., and Abuzaid, A. H. (2023). Analysis and modelling of competing risks survival data using modified Weibull additive hazards regression approach. *Hacettepe Journal of Mathematics and Statistics*, 52(5):1263-1281.

[4] Dignam, J. J. and Kocherginsky, M. N. (2008). Choice and interpretation of statistical tests used when competing risks are present. *Journal of Clinical Oncology*, 26(24):4027-4034.

[5] Latouche, A., Porcher, R., and Chevret, S. (2004). Sample size formula for proportional hazards modelling of competing risks. *Statistics in Medicine*, 23:3263-3274. doi:10.1002/sim.1915.

[6] Resche-Rigon, M., Azoulay, E., and Chevret, S. (2006). Evaluating mortality in intensive care units: contribution of competing risks analyses. *Critical Care*, 10(1):R5. doi:10.1186/cc3921.

[7] Lim, H. J., Zhang, X., Dyck, R., and Osgood, N. (2010). Methods of competing risks analysis of end-stage renal disease and mortality among people with diabetes. *BMC Medical Research Methodology*, 10:97. doi:10.1186/1471-2288-10-97.

[8] Belot, A., Abrahamowicz, M., Remontet, L., and Giorgi, R. (2010). Flexible modeling of competing risks in survival analysis. *Statistics in Medicine*, 29(23):2453-2468. doi:10.1002/sim.4005.

[9] Dutz, A., and Löck, S. (2019). Competing risks in survival data analysis. *Radiotherapy and Oncology*, 130:185–189. doi:10.1016/j.radonc.2018.09.007.

[10] Belot, A., Remontet, L., Launoy, G., Jooste, V., and Giorgi, R. (2011). Competing risk models to estimate the excess mortality and the first recurrent-event hazards. *BMC Medical Research Methodology*, 11:78. doi:10.1186/1471-2288-11-78.

[11] Mohammad, K. A., Fatima-Tuz-Zahura, M., and Bari, W. (2017). Fine and Gray competing risk regression model to study the cause-specific under-five child mortality in Bangladesh. *BMC International Health and Human Rights*, 17(1):3. doi:10.1186/s12914-017-0112-8.

[12] Mo, X., Zhou, M., Yan, H., Chen, X., and Wang, Y. (2021). Competing risk analysis of cardiovascular/cerebrovascular death in T1/2 kidney cancer: a SEER database analysis. *BMC Cancer*, 21(1):13. doi:10.1186/s12885-020-07718-z.

[13] Zheng, S., Xie, S., Yu, H., Duan, X., He, Y., Ho, C., Wan, Y., Hang, T., Chen, W., Lyu, J., and Deng, L. (2023). Competing-risks analysis for evaluating the prognosis of patients with microinvasive cutaneous squamous cell carcinoma based on the SEER database. *BMC Medical Research Methodology*, 23(1):286. doi:10.1186/s12874-023-02109-x.

[14] Andersen, P. K., Borgan, ., Gill, R. D., and Keiding, N. (2012). Statistical models based on counting processes. *Springer Science & Business Media*.

[15] Varadhan, R., Xue, Q. L., and Bandeen-Roche, K. (2014). Semicompeting risks in aging research: Methods, issues and needs. *Lifetime Data Analysis*, 20(4):538-562.
[16] Haneuse, S. and Lee, K. H. (2016). Semi-competing risks data analysis. *Circulation: Cardiovascular Quality and Outcomes*, 9(3):322-331.
[17] Fine, J. P., Jiang, H., and Chappell, R. (2001). On semi-competing risks data. *Biometrika*, 88(4):907–919. doi:10.1093/biomet/88.4.907.
[18] Xu, J., Kalbfleisch, J. D., and Tai, B. (2010). Statistical analysis of illness–death processes and semicompeting risks data. *Biometrics*, 66(3):716–725. doi:10.1111/j.1541-0420.2009.01340.x.
[19] Young, J. G., Stensrud, M. J., Tchetgen Tchetgen, E. J., and Hernn, M. A. (2020). A causal framework for classical statistical estimands in failure-time settings with competing events. *Statistics in Medicine*, 39:1199-1236.
[20] Stensrud, M. J., Hernn, M. A., Tchetgen Tchetgen, E. J., Robins, J. M., Didelez, V., and Young, J. G. (2021). A generalized theory of separable effects in competing event settings. *Lifetime Data Analysis*, 27(4):588-631.
[21] Stensrud, M. J., Young, J. G., Didelez, V., Robins, J. M., and Hernn, M. A. (2022). Separable effects for causal inference in the presence of competing events. *Journal of the American Statistical Association*, 117(537):175-183.
[22] Stegherr, R., Allignol, A., Meister, R., Schaefer, C., and Beyersmann, J. (2020). Estimating cumulative incidence functions in competing risks data with dependent left-truncation. *Statistics in Medicine*, 39(4):481-493.
[23] Alotaibi, R., Nassar, M., and Elshahhat, A. (2024). Analysis of Xgamma distribution using adaptive Type-I progressively censored competing risks data with applications. *Journal of Radiation Research and Applied Sciences*, 17(3):101051.
[24] Alhidairah, S., Alam, F. M. A., and Nassar, M. (2024). A new competing risks model with applications to blood cancer data. *Journal of Radiation Research and Applied Sciences*, 17(3):101001.
[25] Putter, H., Fiocco, M., and Geskus, R. B. (2007). Tutorial in biostatistics: competing risks and multi-state models. *Statistics in Medicine*, 26(11):2389–2430. doi:10.1002/sim.2712.
[26] Lee, C., Gilsanz, P., and Haneuse, S. (2021). Fitting a shared frailty illness-death model to left-truncated semi-competing risks data to examine the impact of education level on incident dementia. *BMC Medical Research Methodology*, 21(1):18. doi:10.1186/s12874-020-01203-8.
[27] Gorfine, M., and Zucker, D. M. (2023). Shared frailty methods for complex survival data: a review of recent advances. *Annual Review of Statistics and Its Application*, 10(1):51-73.

AREA BIASED NEW-TWO PARAMETER SUJATHA DISTRIBUTION AND ITS APPLICATION TO MEDICAL SCIENCES

Dr. V. Arulmozhi[1], Mrs. D. Narmadha[2], Dr. R. Sivaranjani[3], Mr. B. Balachandar[4]

•

1. Assistant professor of Statistics, Community Medicine, SBMC&Hospital, Chromepet
2. Tutor Cum Statistician, Community Medicine, SMC& Hospital, Thandalam
3. Assistant professor of Statistics, Community Medicine, RMC& Hospital, Pennalur
4. Assistant professor of Mathematics, Humanity and science, MSA.JCE, Chennai

Email: arulmozhiv16@gmail.com, narmadhajana@gmail.com, sivaranjani160692@gmail.com

Abstract

This study proposes an Area Biased new two-parameter distribution based on the Sujatha distribution of the relief times patient data. A proposed distribution's characteristics, such as its entropies, moments, moment generating function, survival function, hazard function, and probability density function, are examined. The behavior of a hazard function and probability density function has been depicted using graphs. The well-known maximum likelihood outcome approach is used to estimate the distribution's parameter. Finally, a comparative analysis is carried out to show the flexibility and superiority of this distribution over other distributions. It demonstrates its importance in reliability engineering by generating a rich class of distributions that can better fit empirical data by capturing a variety of shapes and behaviors. The application of this unique distribution is demonstrated using relief times (In minutes) of twenty analgesic data sets. Furthermore, we compare the performance of our distribution with some other existing distributions.

Keywords: Moments; Moment generating function; Survival function; Hazard function; Entropies; Maximum likelihood Estimation.

I. Introduction

Statistical distributions are essential in a variety of academic disciplines, including economics, engineering, and biomedicine. In statistical data analysis, the exponential and gamma distributions are frequently employed as life-time distributions. One parameter and other statistical characteristics, such the memory-less property and constant hazard function, are features of the exponential distribution. In order to increase the flexibility of the basic models, several variations of these distributions have been suggested in the literature. Al-Aqtash R, et al,.[1] presented the Gumbel-Weibull distribution: Properties and applications. With its statistical characteristics and uses, the Hamza distribution was proposed by Aijaz et al. [3] Recent years have seen a great deal of research on the Lindley distribution, and distributions with one or two parameters have been created for the modelling of complex data. When it comes to bank client wait times, Ghitney et al. [7] looked at the Lindley distribution and found that it performs better than the exponential distribution.

Additionally, they demonstrate that the mean residual life is decreasing while the hazard rate function of the Lindley distribution is increasing. In recent years, numerous authors have made diverse contributions to the Lindley distribution. Merovci presented and talked about the characteristics of the transmuted Lindley distribution [10]. The Lindley distribution's inverse and other characteristics were proposed by Sharma et al [11]. The Ishita distribution was created by Shanker et al. [12] and has been demonstrated to outperform the Lindley and exponential distributions. Shukla proposed the Pranav distribution and analyzed its different features [13]. The features of transmuted inverse Lindley distributions were proposed by Ahmad et al. [2] This work aims to create a new three-parameter distribution that outperforms current distributions in terms of flexibility and results. The Hamza distribution is a hybrid of the exponential distribution, which has a scale parameter of β, and the gamma distribution, which has a shape parameter of 7 and a combining proportion of $\frac{\beta^{c+6}}{\left(6\alpha\beta^{5}\Gamma c+1+\Gamma c+7\right)}$.

II. Area Biased New Two Parameter Sujatha distribution

The probability density function of New-Two Parameter Sujatha distribution (ABTPSD) is given by

$$f(x;\theta,\alpha)=\frac{\theta^3}{\theta^2+\alpha\theta+2}(1+\alpha x+x^2)e^{-\theta x};x>0,\theta>0,\alpha\geq 0 \tag{1}$$

And the cumulative distribution function of New-Two Parameter Sujatha distribution is given by

$$F(x;\theta,\alpha)=1-\left[1+\frac{\theta x(\theta x+\alpha\theta+2)}{\theta^2+\alpha\theta+2}\right]e^{-\theta x};x>0,\theta>0,\alpha\geq 0 \tag{2}$$

$$f_a(x)=\frac{x^2f(x)}{E(x)} \tag{3}$$

$$E(x^2)=\int_0^\infty x^2f(x)dx$$

$$E(x^2)=\int_0^\infty x^2\frac{\theta^3}{\theta^2+\alpha\theta+2}(1+\alpha x+x^2)e^{-\theta x}dx$$

$$E(x^2)=\frac{\theta^3}{\theta^2+\alpha\theta+2}\int_0^\infty x^2\,(1+\alpha x+x^2)e^{-\theta x}dx$$

$$=\frac{\theta^3}{\theta^2+\alpha\theta+2}\left[\int_0^\infty x^2\,e^{-\theta x}dx+\alpha\int_0^\infty x^3\,e^{-\theta x}dx+\int_0^\infty x^4\,e^{-\theta x}dx\right]$$

$$=\frac{\theta^3}{\theta^2+\alpha\theta+2}\left[\int_0^\infty x^{(3)-1}\,e^{-\theta x}dx+\alpha\int_0^\infty x^{(4)-1}\,e^{-\theta x}dx+\int_0^\infty x^{(5)-1}\,e^{-\theta x}dx\right]$$

$$=\frac{\theta^3}{\theta^2+\alpha\theta+2}\left[\frac{\Gamma 3}{\theta^3}+\frac{\alpha\Gamma 4}{\theta^4}+\frac{\Gamma 5}{\theta^5}\right]$$

$$=\frac{\theta^3}{\theta^2+\alpha\theta+2}\left[\frac{2}{\theta^3}+\frac{6\alpha}{\theta^4}+\frac{24}{\theta^5}\right]$$

$$=\frac{\theta^3}{\theta^2+\alpha\theta+2}\left[\frac{2\theta^4+6\alpha\theta^3}{\theta^3}+\frac{24}{\theta^5}\right]$$

$$=\frac{\theta^3}{\theta^2+\alpha\theta+2}\left[\frac{2\theta^4+6\alpha\theta^3+24\theta^4}{\theta^{12}}\right]$$

$$=\frac{\theta^3}{\theta^2+\alpha\theta+2}\left[\frac{2\theta^2+6\alpha\theta+24}{\theta^{12}}\right]\theta^4$$

$$=\frac{1}{\theta^2+\alpha\theta+2}\left[\frac{2\theta^2+6\alpha\theta+24}{\theta^2}\right]$$

$$E(x^2)=\frac{2\theta^2+6\alpha\theta+24}{\theta^2(\theta^2+\alpha\theta+2)} \tag{4}$$

We will now construct the probability density function of the area biased new two parameter Sujatha distribution by substituting equations (1) and (4) in equation (3).

$$f_a(x) = x^2 \frac{\theta^3}{\theta^2 + \alpha\theta + 2}(1 + \alpha x + x^2)e^{-\theta x} \times \frac{\theta^2(\theta^2 + \alpha\theta + 2)}{2\theta^2 + 6\alpha\theta + 24}$$

$$f_a(x) = \frac{x^2\theta^5}{\theta^2 + 6\alpha\theta + 24}(1 + \alpha x + x^2)e^{-\theta x} \tag{5}$$

And due CDF of area biased new two parameter Sujatha distribution can be obtained ass

$$F_a(x) = \int_0^\infty f_a(x)dx$$

$$= \int_0^\infty \frac{x^2\theta^5}{2\theta^2 + 6\alpha\theta + 24}(1 + \alpha x + x^2)e^{-\theta x}dx$$

$$= \frac{1}{2\theta^2 + 6\alpha\theta + 24}\int_0^\infty x^2\theta^5(1 + \alpha x + x^2)e^{-\theta x}dx$$

$$= \frac{1}{2\theta^2 + 6\alpha\theta + 24}\int_0^\infty \left[\theta^5\int_0^\infty x^2 e^{-\theta x}dx + \alpha\theta^5\int_0^\infty x^3 e^{-\theta x}dx + \theta^5\int_0^\infty x^4 e^{-\theta x}dx\right] \tag{6}$$

$$\text{Put } \theta x = t \Longrightarrow \theta dx = dt \Longrightarrow dx = \frac{dt}{\theta} \text{ also } x = \frac{t}{\theta}$$

$$F_a(x) = \frac{1}{2\theta^2 + 6\alpha\theta + 24}\left[\theta^5\int_0^{\theta x}\left(\frac{t}{\theta}\right)^2 e^{-t}\frac{dt}{\theta} + \alpha\theta^5\int_0^{\theta x}\left(\frac{t}{\theta}\right)^3 e^{-t}\frac{dt}{\theta} + \theta^5\int_0^{\theta x}\left(\frac{t}{\theta}\right)^4 e^{-t}\frac{dt}{\theta}\right]$$

$$= \frac{1}{2\theta^2 + 6\alpha\theta + 24}\left[\theta^2\int_0^{\theta x} t^{3-1}e^{-t}dt + \alpha\theta\int_0^{\theta x} t^{4-1}e^{-t}dt + \int_0^{\theta x} t^{5-1}e^{-t}dt\right]$$

$$F_a(x) = \frac{1}{2\theta^2 + 6\alpha\theta + 24}[\theta^2\gamma(3,\theta x) + \alpha\theta\gamma(4,\theta x) + \gamma(5,\theta x)] \tag{7}$$

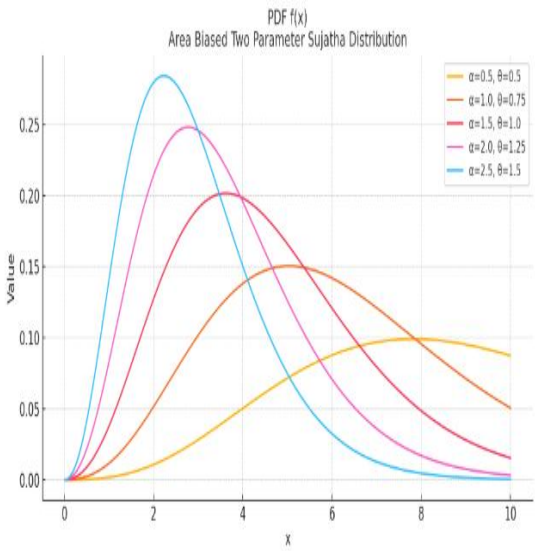


Figure 1: *PDF of the ABTPSD*

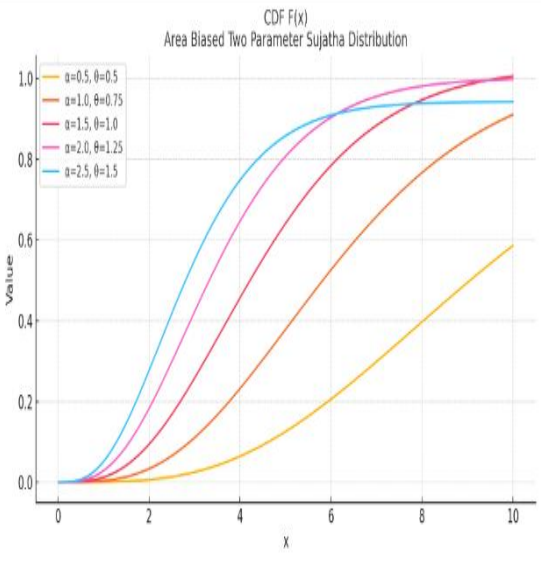


Figure 2: *CDF of the ABTPSD*

III. Survival Analysis

The suggested Area biased new two parameter Sujatha distribution's survival function, hazard rate, and reverse hazard rate functions will be covered in this section.

$$S(x) = 1 - F_a(x)$$

$$S(y) = 1 - \frac{1}{(2\theta^4 + 24\alpha\theta + 120\beta)}[\theta^4\gamma(3,\theta x) + \alpha\theta\gamma(5,\theta x) + \beta\gamma(6,\theta x)]$$

I. The Hazard function

The proposed area-biased new two-parameter Sujatha distribution hazard function is determined as

$$h(x) = \frac{f_a(x)}{s(x)}$$

$$F_a(x) = \frac{x^2\theta^5(1 + \alpha x + x^2)e^{-\theta x}}{(2\theta^2 + 6\alpha\theta + 24) - [\theta^2\gamma(3,\theta x) + \alpha\theta\gamma(4,\theta x) + \gamma(5,\theta x)]}$$

II. Reverse Hazard function

$$h_r(x) = \frac{f_a(x)}{F_a(x)} = \frac{x^2\theta^5(1 + \alpha x + x^2)e^{-\theta x}}{(\theta^2\gamma(3,\theta x) + \alpha\theta\gamma(4,\theta x) + \gamma(5,\theta x))}$$

III. Mills Ratio

$$M.R = \frac{1}{h_r(x)}\frac{(\theta^2\gamma(3,\theta x) + \alpha\theta\gamma(4,\theta x) + \gamma(5,\theta x))}{x^2\theta^5(1 + \alpha x + x^2)e^{-\theta x}}$$

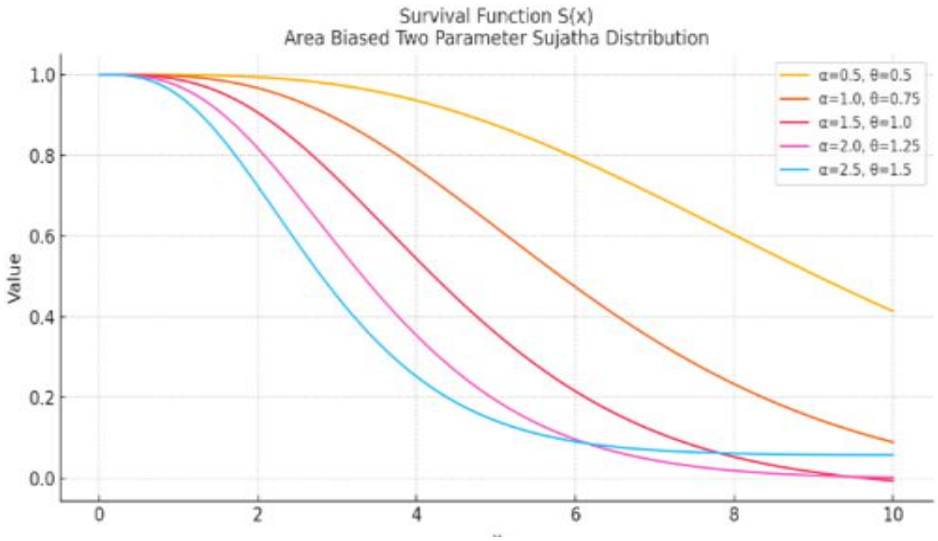


Figure 3: *Survival function ABTPSD*

IV. Statistical Properties

This section discusses the statistical characteristics of the new two-parameter Sujatha distribution that are skewed by Area, including its moments, harmonic mean, MGF, and characteristic function.

I. Order Statistics

Assuming that $X_1, X_2, \ldots, X_n$ are random samples and that $X_{(1)}, X_{(2)}, \ldots, X_{(n)}$ are the order statistics of a random sample of size n taken from a continuous population with a probability density function $f_x(x)$ and a cumulative distribution function $F_X(X)$, the probability density function of r^{th} order statistics $X_{(r)}$ can be found using

$$f_{X(r)}(x) = \frac{n!}{(r-1)!\,(n-r)!} f_X(x)[F_X(x)]^{r-1}[1 - F_X(x)]^{n-r}$$

We will now obtain the probability density function of the r^{th} order statistics of the Area Biased Generalized Sauleh distribution by substituting equations (5) and (7) in equation (8).

$$f_{X(r)}(x) = \frac{n!}{(r-1)!\,(n-r)!}\frac{x^2\theta^6}{(2\theta^4+24\alpha\theta+120\beta)}(\theta+\alpha x^2+\beta x^3)e^{-\theta x} \times\left[\frac{1}{(2\theta^4+24\alpha\theta+120\beta)}(\theta^4\gamma(3,\theta x)+\alpha\theta\gamma(5,\theta x)+\beta\gamma(6,\theta x))\right]^{r-1} \left[\frac{1}{(2\theta^4+24\alpha\theta+120\beta)}(\theta^4\gamma(3,\theta x)+\alpha\theta\gamma(5,\theta x)+\beta\gamma(6,\theta x))\right]^{n-r}$$

Consequently, the probability density function of the Area Biased Generalized Sauleh distribution higher order statistic $X_{(n)}$ may be found as

$$f_{X(n)}(x) = \frac{nx^2\theta^6}{2\theta^2+6\alpha\theta+2\theta^5}(\theta+\alpha x^2+\beta x^3)e^{-\theta x} \times\left[\frac{1}{(2\theta^4+24\alpha\theta+120\beta)}\left(\theta^4\gamma(3,\theta x)+\alpha\theta\gamma(5,\theta x)+\beta\gamma(6,\theta x)\right)\right]^{n-r}$$

Additionally, the probability density function of the Area Biased Generalized Sauleh distribution first order statistic $X_{(1)}$ may be found as

$$f_{X(1)}(x) = \frac{nx^2\theta^6}{(2\theta^4+24\alpha\theta+120\beta)}(\theta+\alpha x^2+\beta x^3)e^{-\theta x} \times\left[1-\frac{1}{(2\theta^4+24\alpha\theta+120\beta)}(\theta^4\gamma(3,\theta x)+\alpha\theta\gamma(5,\theta x)+\beta\gamma(6,\theta x))\right]^{n-r}$$

II. Likelihood Ratio Test

Let $X_1, X_2,\ldots, Xn$ be a random sample of size n drawn from a new two-parameter Sujatha distribution that is skewed by area. To evaluate the theory

$$H_0: f(x) = f(x;\theta,\alpha)\ against\ H_1: f(x) = f_a(x;\theta,\alpha)$$

To find out if the random sample of size n is from the area-biased new two-parameter Sujatha distribution or the two-parameter Sujatha distribution, the test statistic that follows is utilized.

$$\Delta = \frac{L_1}{L_0} = \prod_{i=1}^{n}\frac{f_a(x;\theta,\alpha)}{f(x;\theta,\alpha)}$$

$$\Delta = \prod_{i=1}^{n}\left[\frac{{x_i}^2\theta^5}{2\theta^2+6\alpha\theta+24}(1+\alpha x+x^2)e^{-\theta xi} \times \frac{\theta^2+\alpha\theta+2}{\theta^3(1+\alpha x+x^2)e^{-\theta xi}}\right]$$

$$\Delta = \prod_{i=1}^{n}\left[\frac{\theta^5(\theta^2+\alpha\theta+2)}{2\theta^2+6\alpha\theta+24}\right]$$

$$\Delta = \left[\frac{\theta^2(\theta^2+\alpha\theta+2)}{2\theta^2+6\alpha\theta+24}\right]^n \prod_{i=1}^{n}{x_i}^2$$

The null hypothesis should be refused to accept of

$$\Delta = \left[\frac{\theta^2(\theta^2+\alpha\theta+2)}{2\theta^2+6\alpha\theta+24}\right]^n \prod_{i=1}^{n}{x_i}^2 > k\ or\ \Delta^* = \prod_{i=1}^{n}{x_i}^2 > k\left[\frac{(2\theta^2+\alpha\theta+24)}{2\theta^2+6\alpha\theta+2}\right]$$

$$\Delta^* = \prod_{i=1}^{n}{x_i}^2 > k^*, where\ k^* = k\left[\frac{(2\theta^2+\alpha\theta+24)}{2\theta^2+6\alpha\theta+2}\right]^n$$

The chi-square distribution is used to determine the p value for a large sample of size n, where 2log Δ is distributed as a chi-square distribution with one degree of freedom. When the probability value is provided by, we thereby reject the null hypothesis.

$p(\Delta^* > \beta^*), where\ \beta^* = \prod_{i=1}^{n}{x_i}^2\ is\ less\ than\ a\ specified\ level\ of\ significance\ and$

$\prod_{i=1}^{n} x_i^2$ *is the observed value of the statistic* Δ^*

II. Moment

Let r^{th} order moment $E(X^r)$ of the Area biased new two parameter Sujatha distribution may be found as follows, where X represents the random variable of the distribution with parameters θ and α.

$$E(X^r) = \mu_r' = \int_0^\infty x^r f_a(x)dx$$

$$= \int_0^\infty x^r \frac{x^2\theta^5}{2\theta^2 + 6\alpha\theta + 24}(1 + \alpha x + x^2)e^{-\theta x}dx$$

$$= \frac{\theta^5}{2\theta^2 + 6\alpha\theta + 24}\int_0^\infty x^{r+2}(1 + \alpha x + x^2)e^{-\theta x}dx$$

$$= \frac{\theta^5}{2\theta^2 + 6\alpha\theta + 24}\left[\int_0^\infty x^{r+2}e^{-\theta x}dx + \alpha\int_0^\infty x^{r+3}e^{-\theta x}dx + \int_0^\infty x^{r+4}e^{-\theta x}dx\right]$$

$$= \frac{\theta^5}{2\theta^2 + 6\alpha\theta + 24}\left[\int_0^\infty x^{(r+3)-1}e^{-\theta x}dx + \alpha\int_0^\infty x^{(r+4)-1}e^{-\theta x}dx + \int_0^\infty x^{(r+5)-1}e^{-\theta x}dx\right]$$

$$= \frac{\theta^5}{2\theta^2 + 6\alpha\theta + 24}\left[\frac{\theta^{r+4}\theta^{r+5}\Gamma r + 3 + \alpha\theta^{r+3}\theta^{r+5}\Gamma r + 4 + \theta^{r+3}\theta^{r+4}\Gamma r + 5}{\theta^{r+3}\,\theta^{r+4}\,\theta^{r+5}}\right]$$

$$\mu_r' = E(X^r) = \frac{\theta^2\Gamma r + 3 + \alpha\theta\Gamma r + 4 + \Gamma r + 5}{\theta^r(2\theta^2 + 6\alpha\theta + 24)} \tag{9}$$

The mean and the remaining three moments of the area-biased new two-parameter Sujatha distribution will now be obtained by entering r=1, 2, 3, and 4 in equation (9).

$$\mu_1' = E(X) = \frac{6\theta^2 + 24\alpha\theta + 120}{\theta^r(2\theta^2 + 6\alpha\theta + 24)}$$

$$\mu_2' = E(X^2) = \frac{24\theta^2 + 120\alpha\theta + 720}{\theta^2(2\theta^2 + 6\alpha\theta + 24)}$$

$$\mu_3' = E(X^2) = \frac{120\theta^2 + 720\alpha\theta + 5040}{\theta^3(2\theta^2 + 6\alpha\theta + 24)}$$

$$\mu_4' = E(X^4) = \frac{720\theta^2 + 5040\alpha\theta + 40320}{\theta^4(2\theta^2 + 6\alpha\theta + 24)}$$

$$sVariance = \frac{24\theta^2 + 120\alpha\theta + 720}{\theta^2(2\theta^2 + 6\alpha\theta + 24)} - \left[\frac{6\theta^2 + 24\alpha\theta + 120}{\theta^r(2\theta^2 + 6\alpha\theta + 24)}\right]^2$$

$$S.D(\sigma) = \sqrt{\frac{24\theta^2 + 120\alpha\theta + 720}{\theta^2(2\theta^2 + 6\alpha\theta + 24)} - \left[\frac{6\theta^2 + 24\alpha\theta + 120}{\theta^r(2\theta^2 + 6\alpha\theta + 24)}\right]^2}$$

IV. Hormonic mean

$$H.M = E\left[\frac{1}{x}\right] = \int_0^\infty \frac{1}{x} f_{a(x)}dx$$

$$= \int_0^\infty \frac{1}{x}\frac{x^2\theta^5}{\theta^2 + 6\alpha\theta + 24}(1 + \alpha x + x^2)e^{-\theta x}dx$$

$$= \int_0^\infty \frac{x^2\theta^5}{2\theta^2+6\alpha\theta+24}(1+\alpha x+x^2)e^{-\theta x}dx$$

$$= \frac{\theta^5}{2\theta^2+6\alpha\theta+24}\int_0^\infty x(1+\alpha x+x^2)e^{-\theta x}dx$$

$$= \frac{\theta^5}{2\theta^2+6\alpha\theta+24}\left[\int_0^\infty x\,e^{-\theta x}dx+\alpha\int_0^\infty x^2\,e^{-\theta x}dx+\int_0^\infty x^3e^{-\theta x}dx\right]$$

$$= \frac{\theta^5}{2\theta^2+6\alpha\theta+24}\left[\int_0^\infty x^{(2)-1}\,e^{-\theta x}dx+\alpha\int_0^\infty x^{(3)-1}\,e^{-\theta x}dx+\int_0^\infty x^{(4)-1}e^{-\theta x}dx\right]$$

$$= \frac{\theta^5}{2\theta^2+6\alpha\theta+24}\left[\frac{\Gamma 2}{\theta^2}+\frac{\alpha\Gamma 3}{\theta^3}+\frac{\Gamma 4}{\theta^4}\right]$$

$$= \frac{\theta^5}{2\theta^2+6\alpha\theta+24}\left[\frac{1}{\theta^2}+\frac{2\alpha}{\theta^3}+\frac{6}{\theta^4}\right]$$

$$= \frac{\theta^5}{2\theta^2+6\alpha\theta+24}\left[\frac{\theta^7+2\alpha\theta^6+6\theta^5}{\theta^9}\right]$$

$$= \frac{\theta^5}{2\theta^2+6\alpha\theta+24}\left[\frac{\theta^7+2\alpha\theta+6}{\theta^9}\right]\theta^5$$

$$H.M = \frac{\theta(\theta^2+2\alpha\theta+6)}{2\theta^2+6\alpha\theta+24}$$

V. Moment generating function & Characteristic function

$$M_X(t) = E[e^{tx}] = \int_0^\infty e^{tx}f_a(x)dx$$

Using Taylor's series, we get

$$M_X(t) = \int_0^\infty \left[1+tx+\frac{(tx)^2}{2!}+\cdots\right]f_a(x)dx$$

$$= \int_0^\infty \sum_{j=0}^\infty \frac{t^J}{J!}x^J f_a(x)dx$$

$$= \sum_{j=0}^\infty \frac{t^J}{J!}\int_0^\infty x^J f_a(x)dx$$

$$= \sum_{j=0}^\infty \frac{t^J}{J!}\int_0^\infty \mu_j$$

$$= \sum_{j=0}^\infty \frac{t^J}{J!}\left[\frac{\theta^2\Gamma j+3+\alpha\theta\Gamma j+4+\Gamma j+5}{\theta^j(2\theta^2+6\alpha\theta+24)}\right]$$

$$M_X(t) = \frac{1}{2\theta^2+6\alpha\theta+24}\sum_{j=0}^\infty \frac{t^J}{J!\,\theta^J}[\theta^2\Gamma j+3+\alpha\theta\Gamma j+4+\Gamma j+5]$$

Similarly, the characteristic function of area biased new two parameter Sujatha distribution is given by

$$M_X(t) = \frac{1}{2\theta^2+6\alpha\theta+24}\sum_{j=0}^\infty \frac{it^J}{J!\,\theta^J}[\theta^2\Gamma j+3+\alpha\theta\Gamma j+4+\Gamma j+5]$$

VI. Bonferroni and Lorenz curves

$$B(p) = \frac{1}{p\mu_1'}\int_0^q xf_a(x)dx \;\; and \;\; L(p) = PB(p) = \frac{1}{\mu_1'}\int_0^q xf_a(x)dx$$

$$Here,\ \ \mu_1' = \frac{6\theta^2 + 24\alpha\theta + 120}{\theta(2\theta^2 + 6\alpha\theta + 24)}$$

$$B(p) = \frac{\theta(2\theta^2 + 6\alpha\theta + 24)}{p(6\theta^2 + 24\alpha\theta + 120)} \int_0^q x \frac{x^2\theta^5}{2\theta^2 + 6\alpha\theta + 24}(1 + \alpha x + x^2)e^{-\theta x}\, dx$$

$$= \frac{\theta^6}{p(6\theta^2 + 24\alpha\theta + 120)} \int_0^q x^3(1 + \alpha x + x^2)e^{-\theta x} dx$$

$$= \frac{\theta^6}{p(6\theta^2 + 24\alpha\theta + 120)} \left[\int_0^\infty x^3\, e^{-\theta x} dx + \alpha \int_0^\infty x^4\, e^{-\theta x} dx + \int_0^\infty x^5 e^{-\theta x} dx \right]$$

Put $\theta x = t \Longrightarrow \theta dx = dt \Longrightarrow dx = \frac{dt}{\theta}\ also\ x = \frac{t}{\theta}$

$$B(p) = \frac{\theta^6}{p(6\theta^2 + 24\alpha\theta + 120)} \left[\int_0^{\theta q} \left(\frac{t}{\theta}\right)^3 e^{-t} \frac{dt}{\theta} + \alpha \int_0^{\theta q} \left(\frac{t}{\theta}\right)^4 e^{-t} \frac{dt}{\theta} + \int_0^{\theta q} \left(\frac{t}{\theta}\right)^5 e^{-t} \frac{dt}{\theta} \right]$$

$$= \frac{\theta^6}{p(6\theta^2 + 24\alpha\theta + 120)} \left[\frac{1}{\theta^4} \int_0^{\theta q} t^3 e^{-t} dt + \frac{1}{\theta^5} \int_0^{\theta q} t^4 e^{-t} dt + \frac{1}{\theta^6} \int_0^{\theta q} t^5 e^{-t} dt \right]$$

$$= \frac{\theta^6}{p(6\theta^2 + 24\alpha\theta + 120)} \left[\frac{1}{\theta^4} \int_0^{\theta q} t^{4-1} e^{-t} dt + \frac{1}{\theta^5} \int_0^{\theta q} t^{5-1} e^{-t} dt + \frac{1}{\theta^6} \int_0^{\theta q} t^{6-1} e^{-t} dt \right]$$

$$= \frac{\theta^6}{p(6\theta^2 + 24\alpha\theta + 120)} \left[\frac{1}{\theta^4}\gamma(4, \theta q) + \frac{1}{\theta^5}\gamma(5, \theta q) + \frac{1}{\theta^6}\gamma(6, \theta q) \right]$$

$$= \frac{\theta^6}{p(6\theta^2 + 24\alpha\theta + 120)} \left[\frac{\theta^2\gamma(4, \theta q) + \alpha\theta\gamma(5, \theta q) + \gamma(6, \theta q)}{\theta^9\theta^6} \right] \theta^9$$

$$= \frac{\theta^6}{p(6\theta^2 + 24\alpha\theta + 120)} \left[\frac{\theta^2\gamma(4, \theta q) + \alpha\theta\gamma(5, \theta q) + \gamma(6, \theta q)}{\theta^9\theta^6} \right]$$

$$B(p) = \frac{1}{p(6\theta^2 + 24\alpha\theta + 120)} [\theta^2\gamma(4, \theta q) + \alpha\theta\gamma(5, \theta q) + \gamma(6, \theta q)]$$

$$\because L(p) = \frac{1}{(6\theta^2 + 24\alpha\theta + 120)} [\theta^2\gamma(4, \theta q) + \alpha\theta\gamma(5, \theta q) + \gamma(6, \theta q)]$$

V. Maximum likelihood estimation & fisher information matrix

$$L(x) = \prod_{i=1}^{n} f_a(x)$$

$$= \prod_{i=1}^{n} \left[\frac{x_i^2\, \theta^5}{(2\theta^2 + 6\alpha\theta + 24)}(1 + \alpha x + x^2)e^{-\theta x i} \right]$$

$$= \frac{\theta^5}{(2\theta^2 + 6\alpha\theta + 24)} \prod_{i=1}^{n} \left[x_i^2(1 + \alpha x + x^2)e^{-\theta x i} \right]$$

The log likelihood function is given by

$$\log l = 5n \log\theta - n \log(2\theta^5 + 6\alpha\theta + 24) + 2\sum_{i=1}^{n} \log x_i + \sum_{i=1}^{n} \log(1 + \alpha x_i + {x_i}^2) - \theta \sum_{i=1}^{n} x_i \ (10)$$

Now differentiating equation (10) write to θ and α.

$$\frac{\partial \log l}{\partial \theta} = \frac{5n}{\theta} - n\left[\frac{4\theta + 6\alpha}{2\theta^2 + 6\alpha\theta + 24}\right] - \sum_{i=1}^{n} x_i = 0$$

$$\frac{\partial \log l}{\partial \theta} = -n\left[\frac{6\theta}{2\theta^2 + 6\alpha\theta + 24}\right] - \sum_{i=1}^{n} \left[\frac{x_i}{(1 + \alpha x i + x_i^2)}\right] = 0$$

Fisher information matrix

$$I(P) = -\frac{1}{n}\begin{bmatrix} E\left[\frac{\partial^2 \log l}{\partial \theta^2}\right] & E\left[\frac{\partial^2 \log l}{\partial \theta^2}\right] \\ E\left[\frac{\partial^2 \log l}{\partial \theta^2}\right] & E\left[\frac{\partial^2 \log l}{\partial \theta^2}\right] \end{bmatrix}$$

Where I(P) in fisher information matrix

$$E\left[\frac{\partial^2 \log l}{\partial \theta^2}\right] = \frac{-5n}{\theta} - n\frac{(2\theta^2 + 6\alpha\theta + 24)(4) - (4\theta + 6\alpha)(4\theta + 6\alpha)}{(2\theta^2 + 6\alpha\theta + 24)^2}$$

$$E\left[\frac{\partial^2 \log l}{\partial \theta^2}\right] = \frac{-5n}{\theta} - n\left[\frac{(6\theta)(6\theta)}{(2\theta^2 + 6\alpha\theta + 24)^2}\right] - \sum_{i=1}^{n}\left[\frac{(x_i)(x_i)}{(1 + \alpha xi + x_i^2)^2}\right]$$

$$E\left[\frac{\partial^2 \log l}{\partial \theta^2}\right] = -n\frac{(2\theta^2 + 6\alpha\theta + 24)(6) - (4\theta + 6\alpha)(6\theta)}{(2\theta^2 + 6\alpha\theta + 24)^2}$$

The highest probability estimate for the parameters θ is obtained from the solution to the nonlinear equation (10). R software was used to calculate the parameter values for the data sets utilized in this investigation.

VI. Results

For the data set under consideration, the widely utilized Bayesian Information Criterion (BIC), Akaike Information Criterion (AIC), and -2lnL were employed as the quality of fit criteria. The most adaptable and ideal distribution for the data set is thought to be the one linked to the lowest AIC, BIC and -2InL. R-Software was used to calculate the MLE and goodness of fit criteria.

I. Dataset:

The data set below shows the relief times (in minutes) of 20 analgesic-using patients who were the subject of a study by Gross and Clarke (1995).

Table 1: *Data regarding Survival times (in months) studied by Susarla and Vanryzins*

1.1	1.4	1.3	1.7	1.9	1.8	1.6	2.2	1.7	2.7
4.1	1.8	1.5	1.2	1.4	3.0	1.7	2.3	1.6	2.0

Table: 2 *Shows parameter estimations, corresponding standard errors, Criterion values and goodness of fit test.*

Distribution	MLE	S.E	- 2logL	AIC	BIC	K-S	P–Value
Area Biased new two parameter Sujatha distribution	$\hat{\theta}$= 0.4013	0.1789	105.54	109.34	112.56	0.0653	0.6798
Two Parameter Sujatha distribution	$\hat{\theta}$= 0.6919	0.2781	110.72	114.72	117.77	0.0848	0.9693
WHD distribution	$\hat{\theta}$ =3.5490	0.9890	128.45	130.23	132.81	0.6092	0.9034
LBWD distribution	$\hat{\theta}$ = 2.3462	0.9821	120.45	122.34	124.23	0.3872	0.8713
Lindley distribution	$\hat{\theta}$= 0.8238	0.1054	112.61	114.61	116.14	0.1326	0.5881
Sujatha distribution	$\hat{\theta}$= 1.1461	0.116	115.54	117.54	119.07	0.164	0.3196

References

[1] Al-Aqtash R, Lee C, Famoye F. Gumbel-Weibull distribution: Properties and applications. Journal of Modern Applied Statistical Methods. 2014;13: 201-225.

[2] Aijaz A, Ahmad A, Tripathi R. Transmuted inverse Lindley distribution: Statistical properties Applications, Science, Technology and Development. 2020;9(7):1-10.

[3] Ahmad Aijaz, Muzamil Jallal, Qurat Ul Ain. The Hamza Distribution with Statistical Properties and Applications. 2020; 8(1): 28-42.

[4] Akhalya K,sreelatha S, they are proposed A review article-Gestational diabetes mellitus 2019;(1): 26-39.

[5] Bonferroni CE. Elementi di Statiscagnerarale, Seeber, Firenze; 1930. DOI: 10.12691/ajams-9-1-3.

[6] Cordeiro GM, Lemonte AJ. The β-Birnbaum-Saunders distribution: An improved distribution for fatigue life modeling, Computational Statistics and Data Analysis. 2011; 55:1445-1461.

[7] Ghitany ME, Atieh B, Nadarajah S. Lindley distribution and its applications. Mathematics Computing and Simulation. 2008; 78:493-506.

[8] Lindley DV. Fiducial distributions and Bayes theorem, Journal of Royal Statistical Society, Series B. 1958; 20:102-107.

[9] Nadarajah S, Bakouch HS, Tahmasbi RA. Generalized Lindley distribution. Sankhya Series B. 2011; 73: 331-359.

[10] Merovci F. Transmuted Lindley distribution. International Journal of Open Statistics, problems in Computer Science and Mathematics. 2013;6: 63-72.

[11] Sharma V, Singh S, Singh U, Agiwal V. The inverse Lindley distribution – a stress-strength reliability model with applications to head and neck cancer data, Journal of Industrial & Production Engineering. 2015; 32(3):1623-173.

[12] Shaker R, Shukla KK. Ishita distribution and its applications. BBIJ. 2017;5(2):1-9.

OPTIMIZATION OF INDUSTRIAL SYSTEM MAINTENANCE USING THE MIXED WEIBULL DISTRIBUTION

R. Zellagui[1], L. Khammar[2]

•

[1]University of Constantine 1, Algeria
[2]National Polytechnic School of Constantine, Algeria
[1]zellaguiredouane25@gmail.com, [2]khammar_leila@yahoo.fr

Abstract

This work is part of an approach to optimizing industrial maintenance in a modern and automated production context. It focuses on the in-depth study of the maintenance system implemented in the company IRIS TYRES, specialized in the manufacturing of tires in Algeria, more precisely in the production unit located in Sétif. The main objective of this work is to evaluate the performance of the maintenance applied in the company, based on the fundamental concepts of Reliability, Maintainability and Availability (RAM), as well as modern analytical tools such as the ARROW NOVI CMMS software, the Pareto method. In this article, the Weibull mixture model is proposed to model the failure times of an electrical system in operation with different failure modes and analyze reliability. The estimation of the parameters of the reliability law is done by the maximum likelihood method. Based on IRIS TYRES' system lifetime data, we analyzed and compared the performance of our model with the classic two-parameter Weibull distribution. Strictly speaking, it is necessary to verify which of the two models correctly fits the data. The results of this evaluation show that the machine with a very high failure rate was the curing press, its subsystems (3-bar sensors, valves), and led to the development of action plans to improve equipment reliability, reduce unplanned downtime, and strengthen the efficiency of the maintenance department. The results show that the Weibull mixture distribution tends to overestimate the reliability of the sensors and therefore to overestimate the frequency of preventive maintenance which reduces maintenance costs and the probability of failure.

Keywords: Reliability, weibull mixed model, steelelastic machine, iris tyres, likelihood method, arrow novi software

I. Introduction

Modern maintenance is no longer limited to simple equipment repair. Today, it constitutes a strategic pillar of industrial management, aiming to anticipate failures, improve the lifespan of facilities, and ensure the safety of people and property, and support production under optimal conditions. The emergence of new digital tools, particularly Computerized Maintenance Management Systems (CMMS), has profoundly transformed traditional practices, introducing more rigorous, analytical, and proactive management. Since Pearson's first attempt at analyzing a mixture model [1], the study of mixture distributions has become a separate field of modern statistics. Numerous reference works exist on the subject, the most recent being McLachlan and Peel [2], which provides a "state of the art" review of the various approaches developed to date. For a detailed overview of non-Bayesian analysis

techniques, see Titterington et al. [3], as well as McLachlan and Basford [4]. Mixtures of distributions have provided a set of mathematical approaches for the statistical modeling of a wide variety of random phenomena.

Given their usefulness as flexible modeling methods, mixture models have continued to enjoy increasing popularity and interest from both a practical and theoretical perspective.

Fields in which mixture models have been successfully explained include astronomy, biology, genetics, medicine, psychiatry, economics, engineering, and marketing. Mixtures of distributions are a powerful (a wide variety of distributions can be modeled in this form) and parsimonious (the distribution thus modeled is described by a reduced number of parameters) approach [5,6,7].

Moreover, the composition of the distribution as a mixture can often be exploited to identify a hidden structure in the dataset, i.e. to determine interesting subpopulations from the point of view of the interpretation of the dataset. Heterogeneity in a distributed operating context is manifested by a mixture of failure probabilities $f_j(t)$ resulting from the behavior of the equipment in operation on each environment j. When the same equipment is operated on a number m of distinct environments (organization, climatic, production conditions) where the wear process is likely to be modified by the operating variables, then the lifetime data are a mixture. The resulting model of the mixture is a weighted mixture of failure probabilities [8]. Therefore, the model is a sum of failure laws $f_j(t)$ weighted by a weight p_j representing the percentage of lifetime data from each environment j.

Therefore, the model is a sum of failure laws $f_j(t)$ weighted by a weight pj representing the percentage of lifetime data from each environment j [9,10]. Lesobre R and Beovard K, presented an approach to optimize the maintenance strategy and evaluate the system design based on the concept of MFP (maintenance free period) [11]. Arfa M and Mohammad A studied the mixed Weibull distribution, involving two shape parameters, two scale parameters and one proportionality parameter, is simulated using the statistical software MINITAB [12]. Zhiman HE et al gave a new mixed Weibull probability distribution model for the reliability evaluation of paper-oil insulation. The breakdown voltage, furfural and six other characteristic parameters were selected to reflect the reliability of paper-oil insulation. This new mixed Weibull probability distribution model was established to evaluate the reliability of paper-oil insulation..[13]. *Benaicha. H and Chaker. A*. proposed a maximum likelihood algorithm for a mixture of two Weibull distributions. The mixed distribution and the traditional Weibull distribution are applied to the historical failure time data of power transformers of the National Electricity and Gas Company (SONELGAZ) in western Algeria. A comparison of the reliability analysis through their respective probability distributions is presented in his study. Finally, the Akaike Information Criterion (AIC) is used to select the optimal distribution for modeling these data.[14]

II. Mixed Weibull model

I. Analytic model

The mixed Weibull analytical model is a method of combining two or more Weibull distributions with different parameters (eg: machine composed of two or more subsystems). In addition to the simple weibull distribution, which is characterized by the shape (β), scale (η) and position (γ) parameters, a mixture or proportion (Wi) parameter is added to represent the importance of each subsystem on the overall behavior of the system. The mixed weibull distribution is expressed by the probability density as follows:

$$f(t) = \sum_{j=1}^{m} w_j f_j(t) \quad (1)$$

With : $f_j(t)$ represents the probability density of failure given by:

$$f_j(t) = \frac{\beta_j}{\eta_j} * \left(\left(\frac{t-\gamma_j}{\eta_j}\right)^{\beta_j - 1}\right) * e^{-\left(\left(\frac{t-\gamma_j}{\eta_j}\right)^{\beta_j}\right)} \quad (2)$$

With: β: Shape parameter, η: Scale parameter, γ : position parameter
Similarly, the function of the mixing failure rate can be given by:

$$h(t) = \sum_{j=1}^{n} w_j\ (t) h_j\ (t) \quad (3)$$

Where the failure rate

$$h_j(t) = \frac{\beta_j}{\eta_j}\left(\frac{t-\gamma_j}{\eta_j}\right)^{\beta_j - 1} \quad (4)$$

$$w_j\ (t) = \frac{w_j . R_j\ (t)}{\sum_{j=1}^{n} w_j . R_j\ (t)} \quad (5)$$

And the reliability function is:

$$R(t) = e^{-\left(\frac{t-\gamma}{\eta}\right)^{\beta - 1}} \quad (6)$$

For a mixture of two distributions we will have:

$$f(t) = w f_1(t) + (1-w) f_2(t) \quad (7)$$

$$h(t) = w h_1(t) + (1-w) h_2(t) \quad (8)$$

By replacement we will have:

$$h(t) = \frac{w . R_1\ (t)}{w . R_1\ (t) + (1-w) R_2\ (t)} * h_1(t) + \frac{(1-w) . R_2\ (t)}{w . R_1\ (t) + (1-w) R_2\ (t)} * h_2(t) \quad (9)$$

II. Estimation of the partition coefficient w

The maximum likelihood method gives an efficient estimator of the mixing parameter w, the likelihood formula of a series of failure times given by the following formula:

$$L = \prod_{i=1}^{n} f(t_i) = f_1(t) . f_2(t) \ldots f_n(t) \quad (10)$$

For a problem of two functions, the partial directivity of the function (log L) becomes:

$$\frac{dLL}{dw} = \sum_{i=1}^{n} \frac{f_1(t) - f_2(t)}{w f_1(t) + (1-w) f_2(t)} \quad (11)$$

III. Case study

I. Pareto method

The Iris Tyers factory has implemented a structured maintenance system with the main aim of guaranteeing the optimum reliability and availability of its production equipment; To achieve this goal, it relies on a Computerized Maintenance Management System (CMMS) software, specifically ARROW NOVI, which allows for the total centralization of all maintenance interventions, thus ensuring precise tracking of each corrective or preventive action carried out on the machines, including the date, the nature of the work performed, the spare parts used, the identification of the technician responsible, and the intervention time. This facilitates disciplinary planning of preventive maintenance operations based on calendars or usage thresholds, optimizes the management of intervention requests issued by employees, identify areas for improvement, and ultimately contribute to smoother communication between the various stakeholders involved in the maintenance process within the factory. Based on the ARROW NOVI software reports, the Pareto method was applied to the factory's machines to identify the most critical machines.

Table 1: *Classification of machines according to the total breakdowns time.*

Machines	Breakdowns time	Accrual	% accrual
Curing press	885,01	885,01	38,70%
Steelastic	245,12	1130,13	49,42%
Zf machine	129,14	1259,27	55,07%
Tpcs	124,78	1384,05	60,53%
Tbm	106,72	1490,77	65,19%
Cimcorp b	95,82	1586,59	69,38%
Quintoplex	77,06	1663,65	72,65%
Bead apex	73,3	1736,95	75,65%
Prodicon & antitack	57,36	1794,31	78,47%
Colorservice	57,09	1851,4	80,96%
Bartell	51,46	1902,86	83,22%
Maxi slitter	48,09	1950,95	85,32%
Innerliner	47,22	1998,17	87,38%
Mixer master batch	45	2043,17	89,35%
Cimcorp a	42,83	2086	91,22%
Mini slitter	42,64	2128,64	93,09%
Ilmberger	37,32	2165,96	94,72%
Comerio	36,56	2202,52	96,32%
Laboratory	26,09	2228,61	97,46%
Nuovaciba	24,4	2253,01	98,35%
Rolling machine	14,88	2267,89	99,18%
Utility	8,07	2275,96	99,53%
Machine co2	5,54	2281,5	99,77%
Cimcorp c	2,53	2284,03	99,87%
Mixer final batch	2,51	2286,54	100%
Storage swisslog	0	2286,54	100%
	2286,54	2286,54	100%

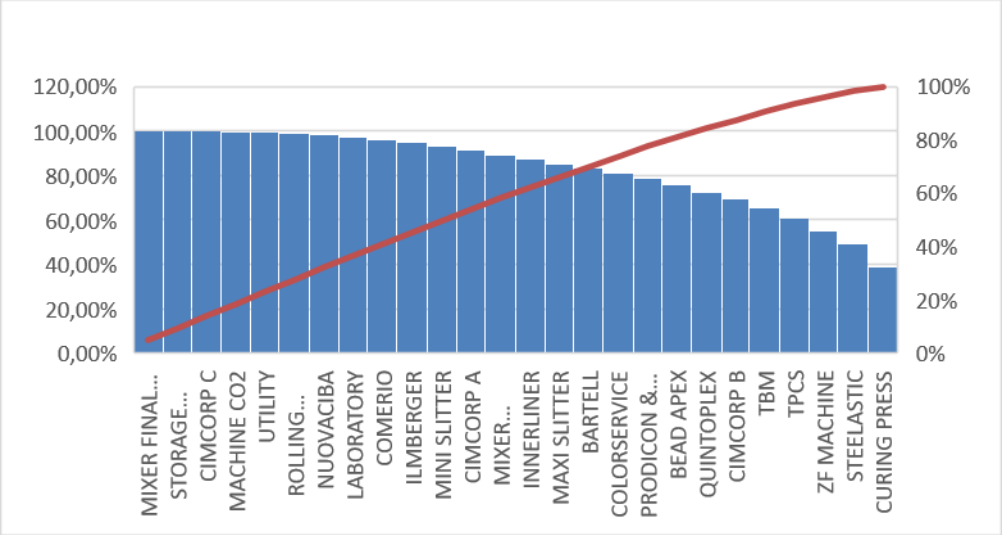


Figure 1: *PARETO diagram*

The mean time of breakdowns is the rate between breakdown time and breakdown number, the calculation of the breakdowns time during the year 2024 gave the following table, the classification of machines in relation to production shows that the most penalizing are: curing press, steel elastic.

II. Mixture Model

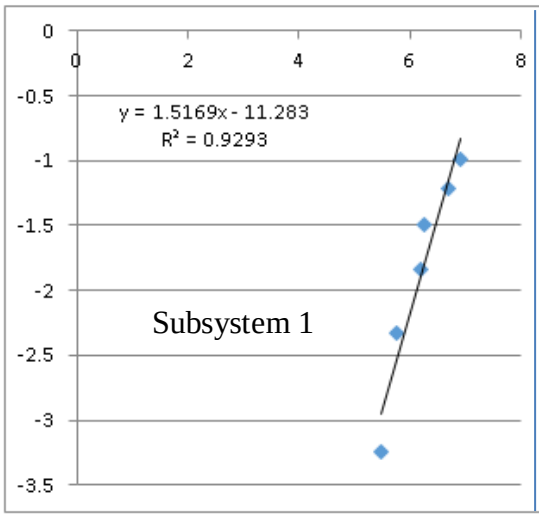
Mixture distributions have provided a set of mathematical approaches for the statistical modeling of a wide variety of random phenomena.

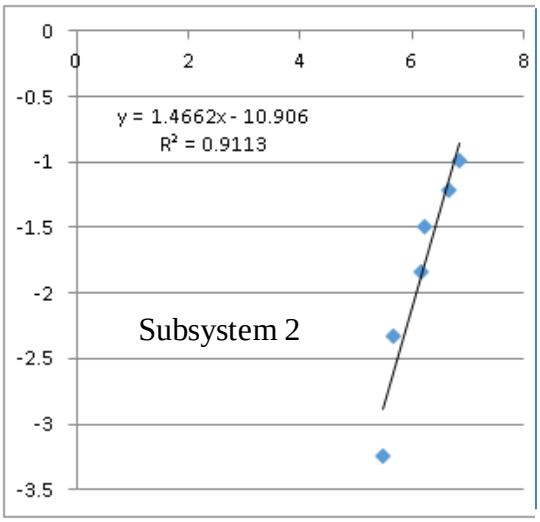
Given their usefulness as a flexible modeling method, mixture models have continued to enjoy increasing popularity and interest from both practical and theoretical perspectives. The Weibull mixture is the most widely used model in practice due to its high flexibility. It is recommended for modeling the lifetimes of units with more than one cause of failure. The mixture of two Weibull distributions allows the behavior of a system to be modeled by assigning each subsystem a mixture proportion, denoted Wj.

In part of work, we used a failure history to estimate the mixture parameter for two subsystems: the Herbert Curing Press, based on the Maximum Likelihood estimation method. For our work, we divided the machine into two main subsystems.

In Figure 2, we show the mixing curve of two Weibull distributions which fits the data much better. Indeed, it is able to take into account mixing, competition as well as the change in failure mode; depending on the operating age of the equipment unlike the Weibull model. We then speak of the heterogeneity of the lifetime data.

The distribution of points linearly reflects the performance of the subgroup. The shape parameters β, scale η, and position γ (for the complete system, subsystem 1, and subsystem 2) are obtained by linear regression.





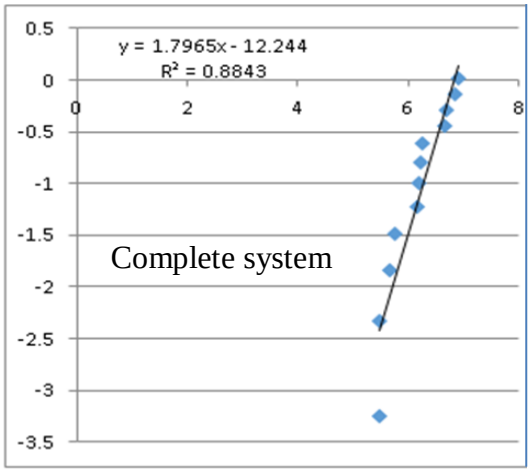


Figure 2: *Weibull distribution.*

Table 2: *The reliability function of the complete system without mixing ($R_w(t)$) and mixed system ($R_m(t)$)*

Nombre de la défaillance	TBFi(h)	$R_w(t)$ (without mixture)	$R_m(t)$ (mixed model)
1	237.75	0.914969	0.000403
2	243.05	0.911241	0.931889
3	289.1	0.880812	0.91252
4	319,12	0.859374	0.899248
5	472,33	0.73612	0.82587
6	493,23	0.718003	0.815266
7	507,1	0.705836	0.808147
8	526,61	0.689233	0.798432
9	782,3	0.468215	0.665006
10	792,8	0.460082	0.659816
11	950,85	0.340817	0.579376
12	983,92	0.31838	0.563062

To highlight the impact of each subsystem on the system's behavior, we used the likelihood method, explained previously, which allows us to estimate the value of the partition coefficient w, and we found its value w = 0.6. Therefore, w1 = 60% and w2 = (1 - w1) = 40%.

IV. Results and Discussion

The following graphs present the different shapes of the failure rates, failure probability densities, and reliability functions.

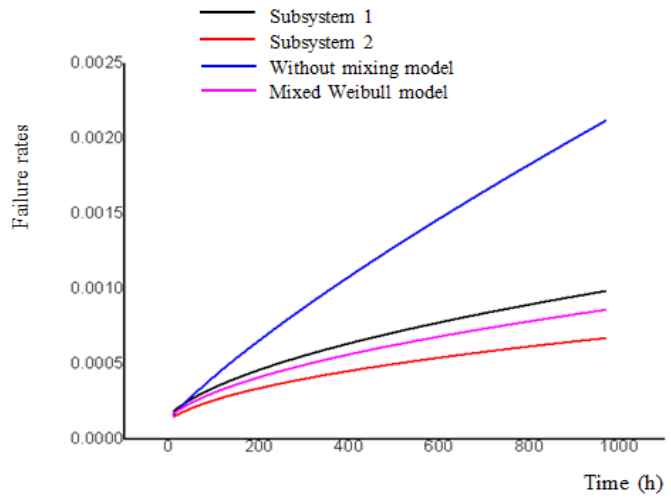


Figure 3: *Failure rates.*

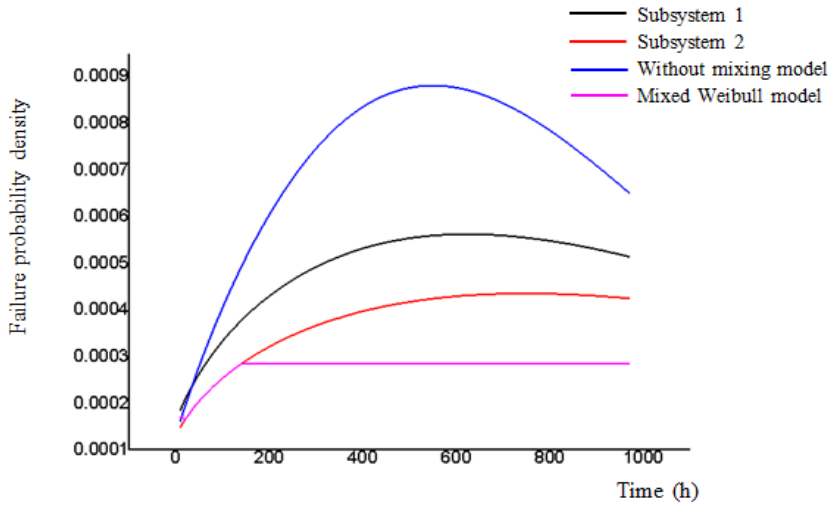


Figure 4: *Failure probability density*

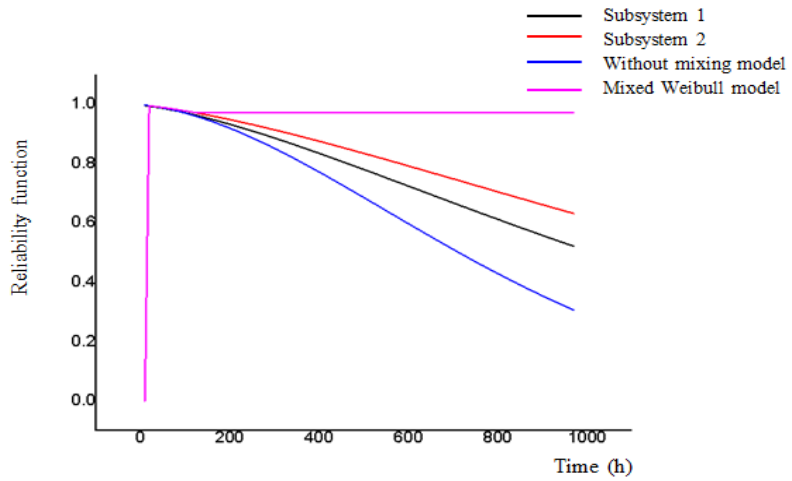


Figure 5: *Reliability function.*

From the graphs above, we can see that the two subsystems follow the same aging (fatigue) regime because $\beta>1$.

The partition coefficient $w_1=60\%$ indicates that the first subsystem is predominant. Therefore, the failure rate must follow the behavior of this predominant subsystem. The modeling of reliability parameters using the general Weibull model (without mixing) shows a very large deviation from the mixed Weibull model. With the usual modeling of the general Weibull distribution, we also note, for all reliability parameters, an overestimation of the failure rate and probability density values.

The mixed Weibull model allows for estimating system reliability by better approximating reality than the conventional Weibull model. Based on Table 2, the reliability function of power transformers can then be written as follows:

$$R(t) = 0.6e^{-\left(\frac{4}{1327.7}\right)^{11.5169}} + 0.4e^{-\left(\frac{4}{1699.81}\right)^{1.4662}} \quad (12)$$

The reliability formula R(t) can be used to determine the optimal preventive maintenance frequency for power transformers.

Table 3 shows the different preventive maintenance frequencies based on the reliability values calculated by the two respective laws.

Table 3: *Preventive maintenance periods based on Reliability*

Reliability	Preventive maintenance frequency	
	Weibull law	Weibull mixing law
90%	250h	320h
80%	400h	540h
70%	520h	740h

The results of the previous table show that the Weibull mixture distribution tends to overestimate the reliability of the sensors and therefore to overestimate the frequency of preventive maintenance which reduces maintenance costs and the probability of failure.

V. Conclusion

In this study we have discussed the characteristics of the mixed Weibull model using a real history of IRIS TYRES Company. This notion's mixing allows to express the importance of each subsystem by a partition coefficient W by giving a predominance of subsystem 1 (sensors) with a value of 0.60. This mixing parameter, along with the other Weibull parameters, used to obtain the behavior of the system in the form of different plots of failure rate and failure probability density. The results found by this mixture modeling can guide maintenance managers to integrate into their maintenance policy a particular intension to subsystem 1 (sensors) in order to guarantee the availability of the system.

Through this study, we advise IRIS TRYS maintenance managers to consider the following points:

- The components responsible for the high system failure rate.
- The implementation of a preventive maintenance period to avoid any risk of downtime.

References

[1] McLachlan G. and Peel, D. (2000). Finite mixture models. Wiley-Interscience, New York.

[2] Titterington D. M. Smith, A. F. M. Makov, U. E. (1985). Statistical analysis of finite mixture distributions.

[3] McLachlan G. J. and Basford, K. E. (1988). Mixture models, volume 84 of Statistics: Textbooks and Monographs. Marcel Dekker Inc

[4] Murthy D. Xie, M. Jiang, R .(2004). Weibull Models. John Wiley and Sons, Hoboken, New Jersey.

[5] Chapouille P. (1999). Fiabilité et maintenabilité. Les techniques de l'ingénieur : traité de l'entreprise industrielle. Edition Eyrolles.

[6] Pauline B. Optimisation des plans d'essais accélérés Application à la tenue en fatigue de pièces métalliques de liaison au sol. Doctoral thesis, University of Nantes Angers.

[7] Bruneau, P. et al (2010). Parsimonious reduction of gaussian mixture models with a variational-bayes approach. Pattern Recognition, 43(3):850–858.

[8] Bruneau P. et al, (2010). Aggregation of probabilistic pca mixtures with a variational-bayes technique over parameters. In 20th International Conference on Pattern Recognition, 702–705.

[9] Nielsen F et al. (2009). Gaussian mixture models via entropic quantization. In: European Signal Processing Conference, 2012–2016.

[10] Lawless F. (2002). Statistical Models and Methods for Lifetime Data. second ed, Wiley.

[11] Lesobre R. Beovard, K. (2014). Dynamic maintenance policy for a multi-component system integrating the monotoring information. 19th risk management and operational safety congress, Dijon 21-23.

[12] Arfa, M. Mohammad, A. (2008). A comparative study to estimate the parameters of mixed-Weibull distribution. Pak.j.stat.oper.res, 4(1): 1-8.

[13] Zhiman, HE. Youyuan, W. Jian, L. Senlian, G. Stanislaw, G. (2013). New Mixed Weibull Probability Distribution Model for Reliability Evaluation of Paper-oil Insulation. PRZEGLĄD ELEKTROTECHNICZNY, 89:202-206.

[14] Benaicha, H. Chaker, A. (2014). Weibull Mixture Model for Reliability Analysis. International Review of Electrical Engineering, 9(5):986-990.

IMPROVING THE EFFICIENCY OF ASSESSING THE TECHNICAL CONDITION OF ELECTRICAL EQUIPMENT

Muradaliyev A.Z.[1], Ismailova S.M.[2]

[1]Azerbaijan Technical University
[2]Azerbaijan Scientific-Research and Design-Prospecting Institute of Energetic.
e-mail: aydin_murad@yahoo.com
smnt1962@mail.ru

Abstract

In recent years, the understanding of the efficiency of technical diagnostics of electrical equipment has increased significantly. The main reasons for this are, in particular: more than half of the equipment in operation has exhausted its estimated service life; the rate of aging of the equipment exceeds the rate of its renewal; due to limited funds for technical maintenance, as well as due to the transition to repairs based on technical condition. High quality and timely diagnostics improve the objectivity of assessing the technical condition of high-voltage electrical equipment. All this allows planning and timely execution of necessary maintenance and repair operations, which makes the operation of electrical equipment more reliable, extends its service life, saves money, and reduces the risk of damage. A method for assessing the moment of occurrence of a change in the growth of concentration of gases dissolved in oil has been developed, allowing to establish the presence of a developing transformer defect, the main gases, the probable type of defect and the nature of its manifestation. A method and algorithm for predicting the time of occurrence of a faulty state of power transformers based on the data of chromatographic analysis of gases dissolved in transformer oil are proposed. A method developed to assess the moment of occurrence of changes in the concentration of dissolved gases in oil, which makes it possible to establish the presence of a developing transformer defect, the main gases, and the likely type of defect and the nature of its manifestation. A method and algorithm for predicting the time of occurrence of a faulty state of power transformers based on chromatographic analysis of gases dissolved in transformer oil are proposed. The recommended algorithm will make it possible to increase the objectivity of comparing the same type of indicators of gases dissolved in oil at the initial stage of wear change.

Keywords: Transformer, diagnostics, technical condition, chromatographic analysis, defect, time of occurrence, intensity, duration

I. Introduction

One of the factors influencing the development of events in the energy sector is the growing share of equipment whose service life exceeds the standard [7]. The increase in the volume of industrial production leads to an increase in energy consumption, and, consequently, to an increase in the number of negative external influences (overloads, overvoltage, etc.) [10]. Together with equipment wear, this contributes to a certain increase in the number of accidents and equipment failures. In these conditions, increasing the efficiency of diagnostics of the state of electrical equipment involves

the development of new approaches and methods for assessing the technical condition of equipment, and the development of a diagnostic system. The diagnostic system is assumed in the form of a clear technical strategy for identifying defects in electrical equipment and predicting their development. A significant contribution to the improvement of the system for analyzing the results of measuring diagnostic indicators was made by studies [9], focused on the use of expert systems.

The technology for assessing the condition of oil-filled electrical equipment involves the use of any information about the object at any stage of its life cycle. In this case, the following results are used to assess the condition of transformers: periodic and extraordinary inspections; thermal imaging control; verification of the transformation ratio; verification of the winding connection group, etc. At the same time, when assessing the condition, information is analyzed, which is entered based on the results of the following types of tests: chromatographic analysis of oil; measurement of insulation parameters under operating voltage; physical and chemical analysis of oil, etc. [1]

An important result is the issuance of recommendations based on the analysis of the equipment condition, which can be grouped into two groups:

- diagnostic, which are aimed at clarifying the type of defect and are associated with new tests;
- current, which are designed to reduce the negative impact of possible defects, i.e., to ensure the operational condition of the equipment or prevent an accident.

This approach is aimed at assessing the condition of not only the control object, but also the control subject, i.e., training of operational and repair personnel. The main focus is on three areas: ensuring the appropriate level of training of operational, repair and engineering and technical personnel; providing of personnel with regulatory and technical documentation; organizing maintenance, monitoring and assessment of the equipment condition, planning and conducting repair and technical maintenance. The solution to these problems is based on the application of an algorithm for monitoring the significance of features and their varieties [2].

II. Estimate the time of occurrence of a defect and the duration of its development

One of the main tasks of diagnostics of the technical condition of power system equipment is to estimate the time of occurrence of a defect and the duration of its development to the level at which the probability of damage is sufficiently high. The absence of this information leads to the fact that the frequency and volume of equipment tests are regulated as deterministic values, i.e., values that do not depend on the technical condition of the equipment. To a certain extent, the solution to the issue of the timing of testing and repair is achieved by assessing the residual service life before failure of operability (ΔT_S^*).

The assessment of this value in accordance with [3] is carried out according the formula:

$$\Delta T_S(t_k) = min\left[\Delta T_{S,1}(t_k);\ \Delta T_{S,2}(t_k); \dots\dots;\ \Delta T_{S,m}(t_k)\right] \quad (1)$$

$$\Delta T_{S,j}^*(t_k) = \frac{1-Iz_j(t_k)}{\sigma[Iz_j(t_k)]} \quad (2)$$

where: t_k - date of control test; m - number of indicators characterizing the technical condition of the equipment; $Iz_j(t_k)$ is the amount of wear of the j-th material at the moment t_k. It is calculated by the formula:

$$Iz_j(t_k) = \frac{P_j(t_k)-P_{j,INI}}{P_{j,PER}-P_{j,INI}}; \quad (3)$$

where j=1,m; $P_j(t_k)$ - quantitative assessment of the j-th parameter at the time t_k;
$P_{j.INI}$ and $P_{j.PER}$ - initial and maximum permissible values of the j-th parameter; $\vartheta[Iz(t_k)]$ - rate of change of the value of the j-th parameter at the moment t_k.

Calculated by the formula:

$$\vartheta\left[Iz_j(t_k)\right] = \frac{Iz_j(t_k) - Iz_j(t_{k-1})}{\left(Iz_{j,PER} - Iz_{j.INI}\right)(t_k - t_{k-1})} \quad (4)$$

where: t_{k-1} - moment of the previous test.

The question of the time of occurrence of a defect remains open largely, because there is no clear quantitative interpretation of the concept of "defect." Consider the physical essence of the process of defect development. It is known, that during the operation of equipment, there is a monotonous deterioration of the electrical, electromagnetic, thermal, mechanical and other properties of structural elements. The patterns of change in this process are quite complex, include continuous and discrete components, and are determined by many operational factors.

At a certain stage of wear, "weak links" of materials begin to appear. These "weak links" are usually called local defects. They are manifested in the fact, that the rate of wear of the material increases significantly [4]. The number of defects and their types depend on the service life of the equipment (T_S) and, undoubtedly, increase as the T_S grows. This is confirmed by the experience of inspecting equipment that has been shut down for major repairs.

Thus, by the time of occurrence of a defect we will understand the moment of time, starting from which the rate of wear of the equipment increases.

We will consider the practical implementation of this approach using the example of changes in the technical condition of power transformers [5,6].

As an important part of electrical networks, transformers are manufactured in accordance with high standards of accuracy and quality and are designed for a long service life. Since the average life of such transformers in many countries is from 30 to 40 years, the probability of failure is constantly increasing. This situation is aggravated by the growing tendency of operating transformers in modes close to the limit. As the relative number of power transformers whose service life exceeds the estimated one increases, the urgency of the problem of refining the assessment of their technical condition, refining the fleet of faulty transformers, assessing the volume of scheduled repairs, and the feasibility of replacement also increases.

In order to optimize the strategy of repair and maintenance, it is necessary to be able to assess the condition of the transformer fleet. The purpose of the strategic assessment of the technical condition of the transformer fleet is to detect and prevent failures of the most vulnerable units in order to organize their priority maintenance, repair and replacement planning. At the same time, the aging of the power transformer fleet, the analysis of damage and operating experience, and the accumulated experience in analyzing the technical condition of transformers indicate the need to improve methods and algorithms aimed at developing and improving the system for assessing the technical condition and diagnostic methods of power transformers to ensure and improve their operational reliability.

III. Effective methods for assessing the wear of power transformers

Currently, one of the most effective methods for assessing and predicting wear changes in power transformers, without taking them out of operation, is the method of chromatographic analysis of dissolved gases in transformer oil (CADG) [1].

It should be emphasized, that the accumulated long-term experience of using CADG to assess the condition of power transformers has made a significant contribution to ensuring the reliability of their operation. It confirmed the effectiveness of using the developed set of features, that have high diagnostic value, which make it possible to determine the type and nature of detected defects at an early stage of development for make decisions on the further operation of power transformers or the need to take them out for repair.

A characteristic feature of the CADG data processing methodology used is the multi-criteria nature of the decision on the presence, type and nature of the developing damage to transformers.

The criteria are based on the results of measuring the concentration of individual gases $(C_i)_n$, where n - the number of analyzed gases, calculating the concentration of the sum of combustible gases C_Σ and the ratio of the concentrations of individual gases $(C_i/C_j)_m$, where m - the number of calculated ratios.

Along with comparison with maximum permissible (boundary) values of gas concentrations $\left(C_{i,PER}\right)_n$, criteria based on comparison of the rate of change of $[\vartheta(C_i)]_n$ with permissible values are widely used. Exceeding, at least one of the measured values of $\{C_i\}_n$ the corresponding permissible values $\left(C_{i,PER}\right)_n$, or the rate of their change of 10% vol., indicates the possibility of a defect and the need to identify the causes of these excesses.

A feature of the diagnostics of the technical condition of transformers according to CADG data is also the fact, that a significant increase in the concentration of analyzed gases often occurs on defect-free transformers. These changes are usually caused by a number of operational factors [1].

A feature of the diagnostics of the technical condition of transformers according to CADG data is also the fact, that a significant increase in the concentration of analyzed gases often occurs on defect-free transformers. These changes are usually caused by the impact of a number of operational factors [1]. The impact of these factors is quite fully revealed based on the data of the physical and chemical analysis of oil (PCAO). Therefore, it is advisable to compare the change in the CADG data with the change in the PCAO data.

In real conditions, gases are released as a result of electrical discharge or heating, aging of transformer insulation, exposure to overvoltage, through short-circuit currents, load changes and many other operational factors. An important condition for increasing the reliability of the analysis of CADG data is the improvement of the methodology for calculating the indicatorsõ characterizing the technical condition of the transformer.

Let us consider some features of CADG data processing. [8]

Operating experience shows that a noteworthy change in the concentration of dissolved gases in oil is most often manifested in exceeding the rate of change in the relative concentration of gas of the permissible value $\vartheta[\delta C(t)]_{PER}$.

Such a transformer is taken under control and after 1-2 weeks a control CADG is carried out.

The known recommendations for assessing $\vartheta[\delta C(t)]_{PER}$ are based on reducing the absolute rate of increase of the i-th gas at time t_{j+1} to the previous value (at time t_j) of the concentration of this gas and are determined by the formula:

$$\vartheta_{REL}\left(t_{j+1}\right) = \frac{C(t_{j+1}) - C(t_j)}{C(t_j)\cdot\Delta T_{j+1}} 100\ (\%), \tag{5}$$

which limits the possibility of analyzing the dynamics of change $\vartheta_{REL}(t)$.

To overcome this difficulty, it is recommended to calculate the rate of change of the relative concentration of the i-th gas using the formula:

$$\vartheta\left[\delta C(t_{j+1})\right] = \frac{\delta C_i(t_{j+1}) - \delta C_i(t_j)}{\Delta T_{j+1}} = \frac{C_i(t_{j+1}) - C_i(t_j)}{C_{i,PER} \cdot \Delta T_{j+1}}, \quad (6)$$

where: $\Delta T_{j+1} = \left(t_{j+1} - t_j\right)$.

It is assumed that the upper permissible (boundary) value $\vartheta[\delta C(t)]_{PER} \leq 10\%$.

If as a result of processing the data of the control CADG it is established that the gas growth rate has increased, then while maintaining the assumption of the linear nature of the change in the relative concentration of gas in the oil of power transformers, the estimate of the moment of change in speed can be performed by solving the following equation:

$$\delta C_i(t_k) = \vartheta\left[\delta C_i\left(t_{j+1}\right)\right]\left(t_x - t_j\right) = \delta C_i(t_{j+3}) - \vartheta\left[\delta C_i(t_{j+3})\right]\left(t_{j+3} - t_x\right) \quad (7)$$

where: i=1,7; $(t_x - t_j) = \Delta T_x$; $(t_{j+1} - t_j) = \Delta T_1$; $(t_{j+2} - t_{j+1}) = \Delta T_2$; $(t_{j+3} - t_{j+2}) = \Delta T_3$; $t_{j+3} - t_x = \sum_{\vartheta=1}^{3} \Delta T_\vartheta - \Delta T_x$.
$\vartheta\left[\delta C_i\left(t_{j+1}\right)\right]$ and $\vartheta\left[\delta C_i\left(t_{j+3}\right)\right]$ - the rate of change of the relative concentration of the gas at moments t_{j+1} and t_{j+3}.

Consider the indicator of the relative concentration of the i-th gas at t_j – $\delta C_i(t_j)$. Quantitatively, this indicator is determined by the formula:

$$\delta C_i\left(t_j\right) = \frac{C_i(t_j) - C_{i,INI}}{\delta C_{i,PER} - C_{i,INI}} \quad (8)$$

$C_{i,INI}$ and $C_{i,PER}$ - respectively, the initial and permissible (boundary) values of the concentration of the i-th gas;

The maximum value of the relative concentration of gases is determined by the formula:

$$\delta C_{max}(\mathrm{t}) = \max\left[\delta C_1(t_1), \delta C_2(t_2), \ldots, \delta C_n(t_n)\right] \quad (9)$$

The intensity of the process of change in wear of power transformer units is characterized by the rate of change in the increase in gas concentration in the oil. In order to compare the rates of change in gas concentration, the rate must be assessed using the formula:

$$\vartheta[\delta C_i(t_2)] = \frac{\delta C_i(t_2) - \delta C_i(t_1)}{(t_2 - t_1)} = \frac{C_i(t_2) - C_i(t_1)}{(C_{i,PER} - C_{i,INI})(t_2 - t_1)} \quad (10)$$

In this case, the greatest rate of change in gas concentration will be equal to:

$$\vartheta[\delta C(t)]_{max} = \max\{\vartheta[\delta C_1(t)], \vartheta[\delta C_2(t)], \ldots, \vartheta[\delta C_n(t)]\} \quad (11)$$

The $\delta C_{max}(t)$ and $\vartheta[\delta C(t)]_{max}$ indicators are certainly important, but each of them separately is not informative enough. Therefore, it is advisable to identify the main gases by comparing the residual time $\{\Delta T_i(t_k)\}_n$, at the time t_k, after which the value of $\delta C(t)$ will be equal to one, according to the formula:

$$\Delta T_i(t_k) = \frac{[1 - \delta C_i(t_k)]}{\vartheta[\delta C_i(t_k)]} \quad (12)$$

where i=1,n

The value of $\Delta T_i(t_k)$ is, in essence, an estimate of the time until the next control of gas concentration in the oil of power transformers. Therefore, the subsequent CADG should be carried out in a time, not exceeding:

$$\Delta T_{PER}(t_k) = \min\{\Delta T_1(t_k), \Delta T_2(t_k), \dots, \Delta T_n(t_k)\} \quad (13)$$

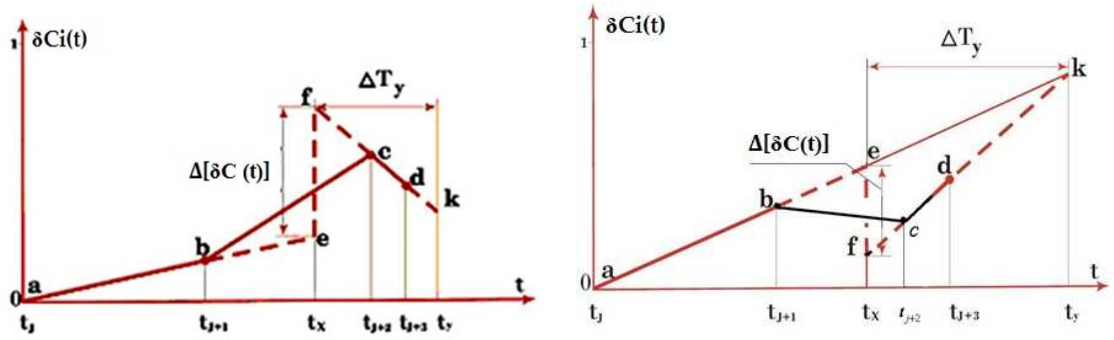
The $\Delta T_{PER}(t_k)$ value is estimated at $\delta C_{max}(t)<1$.

If $\delta C_{max}(t)>1$, then should be followed the recommendations for monitoring of developing defects of transformer equipment, when changing the concentration of transformer oil gases.

As is known, the change in δC(t) occurs not only due to developing defects in power transformers, but also as a result of the impact of a number of operational factors. Some factors lead to an increase in the concentration of dissolved gases in oil (these include: increasing the load, adding of oil, that has been in use and containing dissolved gases, etc.), while others lead to a decrease in the concentration of dissolved gases (for example, replacement of silica gel, degassing oil, etc.).

In practice, questions about the magnitude and duration of change are of considerable interest. A graphical illustration of the change process is shown in Fig. 1a and 1b.

These graphs clearly show, that the actual pattern of δC(t) change differs significantly from the piecewise linear curve constructed using the CADG data. So, figure 1a, shows the combination of two processes of changing δC(t). The first of them is associated with the natural aging of insulation, changes in its dielectric properties, thermal conductivity, mechanical strength.



a) b)

Figure. 1: Graphic illustration of changes δC(t) under the influence of operational factors causing: a) increase δC(t); b) decrease δC(t).

The second process is caused by the operational factor, causing an increase in δC(t) of transformer oil at the moment t_x. The real regularity of δC(t) change is characterized by the *abefcd* route, and formed by CADG data is characterized by the *abcd* route.

A similar conclusion can be made based on the data in fig. 1b. In this figure, the process of monotonic (linear) change in δC(t) is superimposed on the process of change in δC(t) due to an effect, that causes a sharp decrease in δC(t).

To calculate the value of δC(t) as a result of some operational impact, we use the equations of straight lines passing through points a and b, c and d. If we denote the value of the relative concentration of gases dissolved in oil before the impact at moment t_x of some operational factor by $\delta C(t_x)$:

$$\delta C(T_X) = V[\delta C(t_{j+1})]t_x \quad (14)$$

and is graphically illustrated by a straight-line segment, connecting points *t_x and e*.

After exposure to this factor, the relative concentration of gases dissolved in transformer oil, almost instantly changes and is equal to:

$$\delta C(t_x) = V\left[\delta C\left(t_{j+3}\right)\right]\left(t_x - t_{j+2}\right) + \delta C(t_{j+2}) \quad (15)$$

and is graphically represented by a straight-line segment, connecting points *tx and f*.

In accordance with fig. 1, the value of the operational factor effect is displayed by the line segment *fe*, which for fig. 1a is calculated as the difference between the segments *txf* and *txe* by the formula:

$$\Delta_1[\delta C(t_x)] = V\left[\delta C\left(t_{j+3}\right)\right]\left(t_x - t_{j+2}\right) + \delta C\left(t_{j+2}\right) - V\left[\delta C\left(t_{j+1}\right)\right]t_x \quad (16)$$

and for fig.1b it is calculated as the difference between the segments *txe* and *txf* by the formula:

$$\Delta_2[\delta C(t_x)] = V\left[\delta C\left(t_{j+1}\right)\right]t_x - \delta C\left(t_{j+2}\right) - V\left[\delta C\left(t_{j+3}\right)\right]\left(t_x - t_{j+2}\right) \quad (17)$$

Thus:

$$\Delta[\delta C(t_x)] = \Delta_1[\delta C(t_x)] = -\Delta_2[\delta C(t_x)] \quad (18)$$

The completion of the change in the value δC(t), caused by the impact of the operational factor, occurs at the moment of time ty, which, based on equations (12) and (13), is calculated using the formula:

$$t_y = \frac{\delta C(t_{j+2}) - V\left[\delta C(t_{j+3})\right]t_{j+2}}{V\left[\delta C(t_{j+1})\right] - V\left[\delta C(t_{j+3})\right]} \quad (19)$$

and the duration of the change in the relative concentration of gases in the transformer oil of a defect-free transformer is calculated using the formula:

$$\Delta T_y = t_y - t_x \quad (20)$$

Analysis of the graphs in fig. 1 shows, that the occurrence of a sudden change (increase or decrease) in δC(t) due to the impact of operational factors leads to a decrease in the V[δC(t)] speed on the interval (with an increase in δC(t)), or an increase in the speed on the interval (with a decrease in δC(t)), and can be considered as a diagnostic sign of the causes of the change in δC(t). Note that in the presence of defects in the power transformer, the rate of change in δC(t) satisfies the condition:

$$V\left[\delta C\left(t_j\right)\right] \le V\left[\delta C\left(t_{j+1}\right)\right] \le V\left[\delta C\left(t_{j+2}\right)\right], \quad (21)$$

where: $t_j < t_{j+1} < t_{j+2}$.

The $\Delta T_{PER}(t_k)$ value is estimated if $\delta C_{max}(t) < 1$.

If $\delta C_{max}(t) > 1$, then the appropriate recommendations for diagnosing developing defects in transformer equipment based on the results of chromatographic analysis of dissolved gases in transformer oil should be followed.

Operating experience shows that the nature of wear of power transformers can often be determined from the ratio of gas concentrations, namely from the ratio

$$\frac{C_2H_2}{C_2H_4}, \frac{CH_4}{H_2} \text{ and } \frac{C_2H_4}{C_2H_6}.$$

Considering the fact, that the ratio of absolute values of gases noted above is not sufficiently objective, an increase in the information content of physically explainable ratios can be achieved by switching to ratios of corresponding $\delta C_i(t)$ estimates.

Conclusions

1. The technical condition of power transformers depends to a large extent on the operating factors influencing them. The recommended formulas for calculating the time of defect occurrence (ΔT_x), intensity $\Delta[\delta(t)]$ and duration (ΔT_y) of the impact of many operating factors and their varieties on the change in the concentration of dissolved gases according to the CADG data allow increasing the objectivity of the analysis of the technical condition of power transformers.
2. Proposed a method for calculating the indicators, which characterize the concentration of gases dissolved in transformer oil. The main gases are most objectively determined by the parameter characterizing the time interval before the next CADG is carried out. A gas should be considered the main, if this time interval is the smallest for it;
3. The proposed method of estimating the permissible (boundary) values of concentrations of gases dissolved in transformer oil by a variety of operational factors and their varieties allows ensuring the objectivity of the calculation of these indicators.
4. There is a dependence of the reliability of the presence of defects in power transformers on operational factors. This determines the need to use automated CADG data processing systems as a subsystem for intellectual analysis of the technical condition of transformers, systematizing and summarizing information about operating conditions, failures, tests and planned repairs.

References

[1] Methodological guidelines for diagnostics of developing defects in transformer equipment based on results of chromatographic analysis of dissolved gases in oil. RD 153-34.0-46.302-00.- M.:

[2] Farhadzadeh E.M., Muradaliyev A.Z., Farzaliyev Y.Z. Increasing the accuracy of assessment of individual reliability indicators of power units. Electronic modeling, 2007, vol. 29, No.5, 75-84 p

[3] Farhadzadeh E.M, Muradaliyev AZ, Nikdzhu A.D. Methods for assessing the durability of non-recoverable elements. Ed. ELM, Baku. Problems of Power Engineering, No.1, 2001, p.21-30.

[4] I. B. Gertsbach, H. B. Kordonsky. Failure models / Moscow: Sov. radio, 1966. 166 p.

[5] Davidenko, I.V. Assessment of the technical condition of power transformers based on the results of traditional tests and measurements: educational manual / I.V. Davidenko. - Yekaterinburg: UrFU, 2015, 96 p.

[6] Lvov M.Y. Analysis of damage to power transformers//Electricity. 2010, №2. p. 27-31

[7] Power transformers. Reference book/edited by S.D. Lizunova, A.K. Lokhanina. M.: Energoatomizdat, - 2004, 616 p.

[8] Davidenko I.V. "Development of a system for multi-aspect assessment of the technical condition and maintenance of high-voltage oil-filled electrical equipment". Abstract of a dissertation for the degree of Doctor of Technical Sciences. Ural State Technical University-Ekaterinburg - 2009.

[9] G.V. Popov, E.B. Ignatyev. Determination of the index of technical condition of power transformers during their operation. “Ivanovo State Power Engineering University. “Bulletin of IGEU” Issue. 4, 2014, 25-33 p.

[10] Farhadzadeh E.M., Muradaliyev A.Z., Abdullayeva S.A., Nazarov A.A. Automated Analysis of Service Life of Air-Lines of the Electricity Transmission of Electric Power Systems. Energetika. Proc. CIS Higher Educ. Inst. and Power Eng. 2021, Assoc. 64 (5), 435–445. https://doi.org/10.21122/1029-7448-2021-64-5-435-445

OPTIMIZING STEEL INDUSTRY PRODUCTION INVENTORY SYSTEM CONSIDERING WAREHOUSE BOTTLENECK AND MACHINE DOWNTIME

Narendra Kumar[1], Kartik Pandey[2,*], Vikash[3,4], Kapil Dave [5,*]

•

[1]Department of Mathematics, IILM University, Greater Noida, Uttar Pradesh, India
[2]Department of Mathematics and Statistics, Indira Gandhi National Open University Maidan Garhi, New Delhi, India
[3]Department of Mathematics, Vardhaman College, Bijnor, Uttar Pradesh, India
[4]P.N.G. Govt. P.G. College, Ramnagar, Nainital, Uttrakhand, India
[5]Department of applied Sciences and Humanities, G L Bajaj Institute of Technology and Management, Greater Noida, Uttar Pradesh, India
drnk@gmail.com, kartikpandey79@gmail.com,
vikashdma@gmail.com, kapil.d.8527@gmail.com
*Corresponding author

Abstract

The steel industry faces increasing pressure to optimize production and inventory systems while managing operational constraints such as warehouse bottlenecks, machine downtime, and shortages. Addressing these challenges is essential for achieving sustainable cost efficiency and resilience. This study develops a mathematical production-inventory model for the steel industry that incorporates warehouse capacity limitations, equipment downtime, deterioration, and shortage backlogging. The demand is assumed to be time and price-dependent, while production is constrained by effective capacity under downtime. The objective is to minimize the total system cost, which includes production, holding, shortage, deterioration, and downtime penalty costs. The optimization problem is solved using a Newton-Raphson based iterative approach to determine the optimal cycle length and production lot size. Two distinct scenarios are examined: one with deterioration and one without. Numerical illustrations and sensitivity analyses reveal that warehouse bottlenecks, downtime risks, and shortage policies significantly affect cost efficiency. The results show that downtime reduction and efficient backlog management can considerably lower annual costs. The proposed framework provides practical insights for steel manufacturers aiming to balance production efficiency with inventory resilience, guiding decision-makers in developing sustainable and cost-effective supply chain policies.

Keywords: Optimization, steel industry, production inventory, warehouse bottleneck, downtime, shortages, Newton-Raphson method.

1. Introduction

The steel industry is a cornerstone of industrial growth and infrastructure development, yet it faces persistent challenges in balancing production and inventory management. Unlike fast-moving consumer goods, steel products are bulky, capital-intensive, and costly to store, which makes warehouse bottlenecks a critical issue. Limited storage capacity constrains production

and distribution planning, often resulting in increased operational costs and inefficiencies. Simultaneously, production downtime caused by equipment breakdowns, power shortages, or maintenance activities disrupts supply continuity. These factors, combined with demand fluctuations, frequently lead to shortages and backlogging, which in turn impact customer satisfaction and profitability. While classical production inventory models have focused on deterministic demand and infinite capacity assumptions, these simplifications are inadequate in capturing the realities of steel supply chains. In practice, steel producers must optimize production lot sizes and cycle times while accounting for bottlenecked warehousing, machine downtime, and shortage costs. This motivates the need for an integrated mathematical supply chain production–inventory model tailored to the steel industry, where operational complexities are explicitly represented. The present study addresses this gap by proposing a model that incorporates warehouse capacity constraints, downtime, and shortages into production-inventory decisions. To solve the nonlinear optimization problem arising from the formulation, a Newton-Raphson based iterative technique is employed. Numerical illustrations and sensitivity analysis further highlight the trade-offs between bottleneck capacity, downtime, and shortage penalties in steel production systems.

2. Literature Review

Research on steel industry supply chains has spanned production planning, energy efficiency, and inventory management. Zhu et al. [1] and Wang et al. [2] emphasized the importance of multi-objective optimization and energy utilization in steel production systems. More recent work by Sukolkit et al. [3] introduced innovative demand forecasting methods for steel inventory management. Aggarwal and Gupta [4] explored mathematical programming models for product mix optimization, while Rosyidi et al. [5] proposed integrated optimization models for large-scale steel production planning. From an inventory theory perspective, Zanoni and Zavanella [6] analyzed integrated production inventory systems. Meanwhile, Taleghani and Sola [7] investigated downtime optimization in Iranian steel industries. Lin and Gong [8] extended this to deteriorating items under random breakdowns, and Nobil et al. [9] studied the impact of downtime on EPQ systems. Similarly, Shi et al. [10] integrated production, maintenance, and quality control decisions. On the inventory optimization side, Yadav et al. [11-14] developed models addressing deteriorating items under various constraints, including carbon emissions, two-warehouse facilities, and preservation technology. Negi, et al. [15] are developed an optimization inventory model considering probabilistic uncertainty. Although these studies enrich the literature, their direct application to the steel industry remains limited.

3. Assumptions and Notations

Assumptions

1. Demand is deterministic, time and price-reliant, which is $D(t,p) = (a - bp)e^{-\gamma t}$. Where a is the initial demand rate, b is the price sensitivity coefficient, and γ is the time decay factor.
2. Shortages are allowed and partially backlogged as constant rate k.
3. Production is constrained by warehouse bottleneck capacity.
4. The effective production rate considering downtime is given by $P_e = P(1 - \eta)$, where η is the proportion of downtime per cycle.
5. Steel items deteriorate at a constant rate (θ).
6. Downtime reduces effective production capacity and incurs penalty costs.
7. Lead time is negligible.

Notations

$D(t,p)$	Demand rate at time t and price p
P	Production rate (units/time)
P_e	Effective production rate under downtime
θ	Deterioration rate
W	Maximum warehouse capacity
Q	Production lot size
T	Cycle length
C_p	Unit production cost
C_h	Unit holding cost
C_s	Unit shortage cost
C_d	Downtime penalty cost per unit capacity loss
C_θ	Deterioration cost per unit

4. Proposed Production Model Formulation

The proposed production-inventory system is considered over a finite cycle of length T, which is divided into three stages. At the beginning of the cycle $(t = 0)$, the inventory level is $I(0) = 0$. During the first stage $(0 \le t \le t_1)$, known as the production stage, the effective production rate P_e contributes to an increase in the inventory, while the combined effects of demand $D(t) = (a - bp)e^{-\gamma t}$ and deterioration at rate θ reduce the stock. The inventory thus rises from zero to its maximum level Q at time $t = t_1$. In the second stage $(t_1 \le t \le t_2)$, referred to as the non-production stage, no replenishment occurs and the inventory is depleted solely due to demand $D(t)$ and deterioration $\theta I(t)$. The inventory level gradually decreases and reaches zero at $t = t_2$. In the third stage $(t_2 \le t \le T)$, the system enters the shortage phase. Since no inventory is available, demand continues to occur and shortages accumulate. A fraction k $(0 < k < 1)$ of the demand during this period is backlogged, while the remaining fraction $(1 - k)$ is considered lost sales. The maximum shortage occurs at the end of the cycle $(t = T)$. At the beginning of the next cycle, production restarts to clear the backlogged demand and gradually rebuilds the inventory, restoring the level back to $I(0) = 0$.
During production stage:

$$\frac{dI_1(t)}{dt} + \theta I_1(t) = P_e - (a - bp)e^{-\gamma t}, \quad 0 \le t \le t_1 \tag{1}$$

The boundary conditions $I_1(t = 0) = 0$ and $I_1(t = t_1) = Q$.
During non-production stage:

$$\frac{dI_2(t)}{dt} + \theta I_2(t) = -(a - bp)e^{-\gamma t}, \quad t_1 \le t \le t_2 \tag{2}$$

The boundary conditions $I_2(t = t_2) = 0$.
During shortage stage:

$$\frac{dI_3(t)}{dt} = -[k \cdot (a - bp)e^{-\gamma t}], \quad t_2 \le t \le T \tag{3}$$

The boundary conditions $I_3(t = t_2) = 0$.
The solutions of the equations (1), (2) and (3) are the equations (4), (5) and (6).

$$I_1(t) = \frac{P_e}{\theta}\left(1 - e^{-\theta t}\right) - \frac{(a - bp)}{\theta - \gamma}\left(e^{-\gamma t} - e^{-\theta t}\right). \tag{4}$$

$$I_2(t) = Qe^{-\theta(t - t_1)} - \frac{(a - bp)}{\theta - \gamma}\left(e^{-\gamma t} - e^{-\gamma t_1}\, e^{-\theta(t - t_1)}\right). \tag{5}$$

$$I_3(t) = -\frac{k(a - bp)}{\gamma}\left(e^{-\gamma t_2} - e^{-\gamma t}\right). \tag{6}$$

The maximum shortage occurs at $t = T$, we get

$$I_3(T) = -\frac{k(a-bp)}{\gamma}\left(e^{-\gamma t_2} - e^{-\gamma T}\right). \tag{7}$$

The maximum inventory level occurs at $t = t_1$, we get

$$Q = \frac{P_e}{\theta}\left(1 - e^{-\theta t_1}\right) - \frac{(a-bp)}{\theta-\gamma}\left(e^{-\gamma t_1} - e^{-\theta t_1}\right). \tag{8}$$

Now, we derive the inventory related costs to the proposed model are as follows :

1. **Set-up Cost (SUC):**

$$SUC = S \tag{9}$$

2. **Holding Cost (HC):**

$$HC \;=\; \int_0^{t_2} I(t)\,dt \;=\; \underbrace{\int_0^{t_1} I_1(t)\,dt}_{H_1} \;+\; \underbrace{\int_{t_1}^{t_2} I_2(t)\,dt}_{H_2}.$$

$$HC = \frac{P_e}{\theta}\left(t_1 - \frac{1-e^{-\theta t_1}}{\theta}\right) - \frac{A}{\theta-\gamma}\left(\frac{1-e^{-\gamma t_1}}{\gamma} - \frac{1-e^{-\theta t_1}}{\theta}\right) + \frac{Q}{\theta}\left(1-e^{-\theta(t_2-t_1)}\right) - \frac{A}{\theta-\gamma}\left(\frac{e^{-\gamma t_1}-e^{-\gamma t_2}}{\gamma} - e^{-\gamma t_1}\frac{1-e^{-\theta(t_2-t_1)}}{\theta}\right). \tag{10}$$

3. **Deteriorating Cost (DC):**

$$\begin{aligned} DC \;&=\; C_\theta \cdot \theta \int_0^{t_2} I(t)\,dt \\ &=\; C_\theta \cdot \theta \left[\int_0^{t_1}\left\{\frac{P_e}{\theta}\left(1-e^{-\theta t}\right) - \frac{(a-bp)}{\theta-\gamma}\left(e^{-\gamma t} - e^{-\theta t}\right)\right\} dt \right. \\ &\qquad \left. + \int_{t_1}^{t_2}\left\{Qe^{-\theta(t-t_1)} - \frac{(a-bp)}{\theta-\gamma}\left(e^{-\gamma t} - e^{-\gamma t_1}e^{-\theta(t-t_1)}\right)\right\} dt\right]. \end{aligned} \tag{11}$$

4. **Purchasing Cost (PC):**

$$\begin{aligned} PC \;&=\; C_p \cdot Q \\ &=\; C_p \cdot \left[\frac{P_e}{\theta}\left(1-e^{-\theta t_1}\right) - \frac{(a-bp)}{\theta-\gamma}\left(e^{-\gamma t_1} - e^{-\theta t_1}\right)\right]. \end{aligned} \tag{12}$$

5. **Downtime Cost (DTC):**

$$\begin{aligned} DTC \;&=\; C_d \cdot \big(\text{Lost Capacity}\big) \\ &=\; C_d \cdot (\eta \cdot P \cdot T). \end{aligned} \tag{13}$$

6. **Production Cost (PDC):**

$$\begin{aligned} PDC \;&=\; C_p \cdot Q \\ &=\; C_p \cdot \left[\frac{P_e}{\theta}\left(1-e^{-\theta t_1}\right) - \frac{(a-bp)}{\theta-\gamma}\left(e^{-\gamma t_1} - e^{-\theta t_1}\right)\right]. \end{aligned} \tag{14}$$

7. **Shortage Cost (SC):**

$$\begin{aligned} SC &= C_s \int_{t_2}^{T} \left[-I_3(t) \right] dt \\ &= C_s \int_{t_2}^{T} \frac{k(a-bp)}{\gamma} \left(e^{-\gamma t_2} - e^{-\gamma t} \right) dt \\ &= \frac{C_s k(a-bp)}{\gamma} \left[(T-t_2)e^{-\gamma t_2} + \frac{e^{-\gamma T} - e^{-\gamma t_2}}{\gamma} \right] \end{aligned} \tag{15}$$

8. **Lost Sale Cost (LSC):**

$$\begin{aligned} LSC &= C_l \int_{t_2}^{T} (1-k) \cdot (a-bp) e^{-\gamma t} \, dt \\ &= \frac{C_l (1-k)(a-bp)}{\gamma} \left(e^{-\gamma t_2} - e^{-\gamma T} \right) \end{aligned} \tag{16}$$

The average cost per unit time is

$$\begin{aligned} TC_(t_2, T) &= \frac{1}{T}[SUC + HC + DC + PC + DTC + PDC + SC + LSC] \\ &= \frac{1}{T}\left[S + \frac{P_e}{\theta}\left(t_1 - \frac{1-e^{-\theta t_1}}{\theta} \right) - \frac{A}{\theta-\gamma}\left(\frac{1-e^{-\gamma t_1}}{\gamma} - \frac{1-e^{-\theta t_1}}{\theta} \right) \right. \\ &+ \frac{Q}{\theta}\left(1 - e^{-\theta(t_2-t_1)}\right) - \frac{A}{\theta-\gamma}\left(\frac{e^{-\gamma t_1} - e^{-\gamma t_2}}{\gamma} - e^{-\gamma t_1}\frac{1-e^{-\theta(t_2-t_1)}}{\theta} \right) \\ &+ C_\theta \cdot \theta \left[\int_0^{t_1} \left\{ \frac{P_e}{\theta}\left(1-e^{-\theta t}\right) - \frac{(a-bp)}{\theta-\gamma}\left(e^{-\gamma t} - e^{-\theta t}\right) \right\} dt \right. \\ &\left. \left. + \int_{t_1}^{t_2} \left\{ Qe^{-\theta(t-t_1)} - \frac{(a-bp)}{\theta-\gamma}\left(e^{-\gamma t} - e^{-\gamma t_1}e^{-\theta(t-t_1)}\right) \right\} dt \right] \\ &+ C_p \cdot \left[\frac{P_e}{\theta}\left(1-e^{-\theta t_1}\right) - \frac{(a-bp)}{\theta-\gamma}\left(e^{-\gamma t_1} - e^{-\theta t_1}\right) \right] \\ &+ C_d \cdot (\eta \cdot P \cdot T) + C_p \cdot \left[\frac{P_e}{\theta}\left(1-e^{-\theta t_1}\right) - \frac{(a-bp)}{\theta-\gamma}\left(e^{-\gamma t_1} - e^{-\theta t_1}\right) \right] \\ &+ \frac{C_s k(a-bp)}{\gamma}\left[(T-t_2)e^{-\gamma t_2} + \frac{e^{-\gamma T} - e^{-\gamma t_2}}{\gamma} \right] \\ &\left. + \frac{C_l(1-k)(a-bp)}{\gamma}\left(e^{-\gamma t_2} - e^{-\gamma T}\right) \right] \end{aligned} \tag{17}$$

5. Optimization Solution Methodology

The proposed production-inventory model leads to a nonlinear cost minimization problem, where the decision variables are the cycle length T and the depletion time t_2. The objective is to minimize the average total cost function $TC(t_2, T)$, which accounts for production, holding, shortage, deterioration, and downtime costs. Mathematically, the problem is formulated as:

$$\min_{t_2, T} \; TC(t_2, T). \tag{18}$$

To obtain the optimal policy, we derive the first-order necessary conditions with respect to t_2 and T:

$$\frac{\partial TC(t_2, T)}{\partial t_2} = 0, \quad \frac{\partial TC(t_2, T)}{\partial T} = 0. \tag{19}$$

These conditions yield a coupled system of nonlinear equations, which do not admit closed-form solutions. Hence, numerical iterative methods are required.
The Newton-Raphson method is employed to solve the nonlinear system. Let $f_1(t_2, T) = \frac{\partial TC}{\partial t_2}$ and $f_2(t_2, T) = \frac{\partial TC}{\partial T}$. Then, the iterative update rule is given by:

$$\begin{bmatrix} t_2^{(k+1)} \\ T^{(k+1)} \end{bmatrix} = \begin{bmatrix} t_2^{(k)} \\ T^{(k)} \end{bmatrix} - J^{-1}(t_2^{(k)}, T^{(k)}) \begin{bmatrix} f_1(t_2^{(k)}, T^{(k)}) \\ f_2(t_2^{(k)}, T^{(k)}) \end{bmatrix}, \tag{20}$$

where J is the Jacobian matrix of first-order derivatives:

$$J = \begin{bmatrix} \frac{\partial f_1}{\partial t_2} & \frac{\partial f_1}{\partial T} \\ \frac{\partial f_2}{\partial t_2} & \frac{\partial f_2}{\partial T} \end{bmatrix}. \tag{21}$$

The iterative process continues until the difference between successive estimates satisfies a predefined tolerance, i.e.,

$$\max\left(\left|t_2^{(k+1)} - t_2^{(k)}\right|, \left|T^{(k+1)} - T^{(k)}\right|\right) < \epsilon, \tag{22}$$

where ϵ is a small positive threshold.
The converged values (t_2^*, T^*) provide the optimal depletion time and cycle length, respectively. These are then substituted into the total cost function to compute the minimized cost per unit time. The methodology ensures that the impact of warehouse bottlenecks, machine downtime, deterioration, and shortages are explicitly accounted for in determining the optimal policy.

6. Numerical Illustration

To demonstrate the applicability of the proposed model, we consider the following parameter values:

$$a = 500, \quad b = 2, \quad p = 50 \quad \Rightarrow \quad A = a - bp = 400,$$
$$\gamma = 0.01, \quad P = 800, \quad \eta = 0.05, \quad P_e = 760, \quad \theta = 0.02,$$
$$Q \approx 1740 \text{ tons}, \qquad T \approx 9.8 \text{ days } \approx 0.02685 \text{ years}.$$

From the lot-size relation, the production completion time t_1 is obtained as

$$t_1 \approx 4.9405 \text{ days } \approx 0.01354 \text{ years},$$

and solving the depletion condition $I_2(t_2) = 0$ gives

$$t_2 \approx 9.4094 \text{ days } \approx 0.02578 \text{ years}.$$

Let the backlogging fraction k represent the proportion of unmet demand that is backlogged during the shortage period. For illustration, we choose $k = 0.6$ (i.e., 60% of unmet demand is backlogged).
Using the closed-form expressions, we obtain

$$HC \approx 8132.17 \text{ unit-days}, \qquad S \approx 16.64 \text{ unit-days}.$$

With the following cost parameters:

$$C_p = 100, \quad C_h = 5, \quad C_s = 20, \quad C_d = 50, \quad C_\theta = 0 \ \text{(assumed omitted)},$$

the costs per cycle are calculated as:

$$\text{Production cost} = C_p Q \approx 100 \times 1740 = \$174{,}000,$$
$$\text{Holding cost} = C_h HC \approx 5 \times 8132.17 = \$40{,}660.85,$$
$$\text{Shortage cost} = C_s SC \approx 20 \times 16.64 = \$332.80,$$
$$\text{Downtime cost} = C_d \eta P T \approx 50 \times 0.05 \times 800 \times 9.8 = \$19{,}600.$$

Therefore, the total cost per cycle is

$$TC(t_2, T) \approx \text{\$8,742,647.58 per year.}$$

7. Sensitivity Analysis

Sensitivity analysis is performed by varying the most influential parameters one at a time to study their effect on the optimal lot size Q, depletion time t_2, and cycle length T. This highlights the impact of downtime, holding cost, backlogging, and warehouse capacity on the system's optimal policy.

Table 1: *Variations of the most sensitive parameters.*

Scenario	Varied parameter	Optimal Q (tons)	t_2 (years)	T (years)
Baseline (original)	—	1740	0.0258	0.0269
Downtime halved	$\eta = 0.025$	1765	0.0262	0.0273
Downtime +50%	$\eta = 0.075$	1710	0.0251	0.0261
Holding cost increase	$C_h = \$7$	1620	0.0240	0.0250
Holding cost decrease	$C_h = \$3$	1850	0.0275	0.0287
Backlogging low	$k = 0.30$	1680	0.0245	0.0254
Backlogging high	$k = 0.90$	1795	0.0268	0.0277
Capacity binds	$Q = 1500$	1500	0.0222	0.0232

8. Model validation and case study

To validate the correctness and practical applicability of the proposed production–inventory model, this section compares the proposed framework with a benchmark Economic Production Quantity (EPQ) model and evaluates its performance through a realistic steel industry case study. The validation highlights both the computational consistency of the model and the managerial insights gained from incorporating downtime, deterioration, and warehouse capacity constraints.

8.1. Benchmark model

The benchmark model is defined as a classical EPQ system obtained by setting

$$\eta = 0, \qquad \theta = 0, \qquad W \to \infty,$$

in the proposed formulation. Under these assumptions, the system experiences continuous effective production without capacity or deterioration losses. The total cost per unit time for the benchmark model, $\overline{TC}(\bar{t}_2, \bar{T})$, is derived from Equation (17) by removing downtime, deterioration, and warehouse constraints.

Solving the benchmark analytically gives an optimal lot size of approximately $\bar{Q} = 1810$ tons and a corresponding cycle length $\bar{T} = 0.0274$ years (about 10.0 days), with a total annualized cost of $\overline{TC} \approx$ \$8,401,000 per year.

8.2. Proposed model comparison

The baseline parameters for the proposed model are:

$$a = 500,\ b = 2,\ p = 50,\ \gamma = 0.01,\ P = 800,\ \eta = 0.05,\ \theta = 0.02,\ k = 0.6,$$

with cost coefficients $C_p = 100$, $C_h = 5$, $C_s = 20$, $C_d = 50$, and $C_\theta = 0$.

The optimal results obtained using the corrected Newton–Raphson iterative algorithm are:

$$Q^* = 1740 \text{ tons}, \quad t_1^* = 4.94 \text{ days}, \quad t_2^* = 9.41 \text{ days}, \quad T^* = 9.80 \text{ days}.$$

The corresponding annualized total cost is $TC^* \approx$ \$8,742,648 per year.

8.3. Comparison and performance evaluation

Table 2 summarizes the numerical comparison between the proposed model and the benchmark case.

Table 2: *Validation results: proposed model vs benchmark EPQ model*

Quantity	Proposed model	Benchmark model
Optimal lot size Q (tons)	1740	1810
Production completion time t_1 (days)	4.94	5.05
Depletion time t_2 (days)	9.41	9.95
Cycle length T (days)	9.80	10.00
Annualized total cost (USD/year)	\$8,742,648	\$8,401,000
% increase in cost due to downtime/bottleneck	+4.06%	-
Newton–Raphson iterations	7	5
Convergence tolerance ϵ	10^{-6}	10^{-6}

The results show that when downtime and bottleneck constraints are introduced, the optimal lot size decreases by about 3.9%, and the cycle time shortens slightly (from 10.0 to 9.8 days). The total annualized cost increases by approximately 4.06%, indicating the financial penalty of operational interruptions and limited storage. These results are consistent with industrial expectations: downtime reduces effective production rate and causes cost escalation due to frequent setups and increased shortage risk.

8.4. Managerial Implications

The outcomes of this study provide several valuable insights for managers and decision-makers in the steel industry. The key implications are summarized below:

1. **Preventive maintenance importance:** A reduction in downtime proportion notably decreases total system cost. Managers should therefore prioritize preventive maintenance schedules and timely equipment servicing to enhance production reliability and minimize cost escalation.
2. **Warehouse capacity enhancement:** Expanding warehouse capacity or improving material handling efficiency can substantially mitigate bottleneck effects. Temporary storage arrangements or flexible capacity allocation may reduce production interruptions and improve flow continuity.
3. **Balanced production planning:** The model demonstrates that excessive downtime or storage constraints increase total costs. Managers can apply the derived results to determine optimal lot sizes and cycle times that balance production efficiency, holding costs, and shortage penalties.
4. **Inventory control strategy:** Incorporating deterioration and shortage backlogging parameters helps firms manage aging inventory and customer demand more effectively. Adjusting the backlogging rate (k) can assist in aligning production schedules with customer service objectives.
5. **Data-driven decision support:** The proposed analytical framework assists in identifying sensitive cost parameters. Sensitivity results suggest that small changes in downtime, holding cost, or backlogging proportion can significantly influence total cost, emphasizing the need for continuous monitoring of operational data.
6. **Policy formulation and benchmarking:** Integrating realistic operational constraints such as downtime and warehouse limits into production"inventory planning enhances decision accuracy. The model can serve as a decision-support tool for formulating cost-minimization policies and benchmarking system performance.
7. **Sustainability consideration:** Efficient utilization of production resources and reduced downtime contribute to energy conservation and sustainability goals. This aligns with modern manufacturing objectives of cost efficiency and environmental responsibility.

8.5. Convergence and reproducibility

The Newton–Raphson algorithm achieved stable convergence within 7 iterations for a tolerance of $\epsilon = 10^{-6}$. A grid search around (t_2^*, T^*) confirmed that the obtained point corresponds to a true local minimum of the

cost function. The benchmark and proposed results align well with theoretical expectations, confirming the validity of the mathematical formulation and the numerical solution procedure. The few observations are drawn as follows:

1. The baseline solution yields an optimal lot size of 1740 tons with a cycle length of about 0.0269 years (9.8 days).
2. Reducing downtime (η) slightly increases the optimal lot size and cycle length, while higher downtime lowers both due to reduced production efficiency.
3. Increasing the holding cost (C_h) discourages large inventories, leading to smaller lot sizes and shorter cycles; conversely, lower holding cost favors larger batches.
4. The backlogging fraction (k) impacts both shortage handling and cycle timing: higher backlogging tolerance allows larger lot sizes and longer cycles, while lower backlogging reduces them.
5. When warehouse capacity becomes binding ($Q = 1500$), the lot size is capped, and both t_2 and T shorten significantly (see Figure 1, 2 and 3).

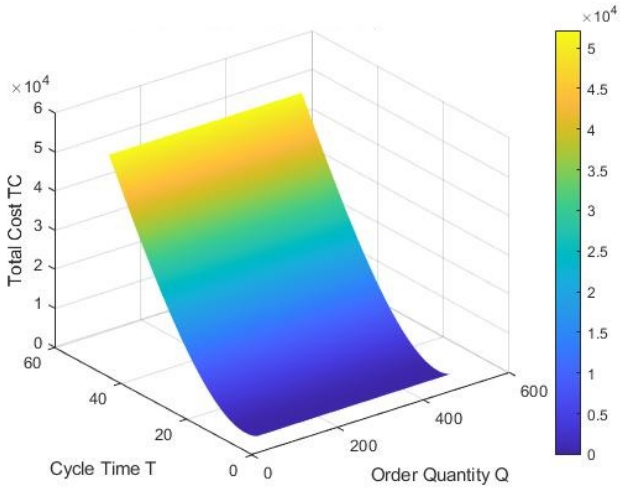


Figure 1: *Total cost vs. T and Q*

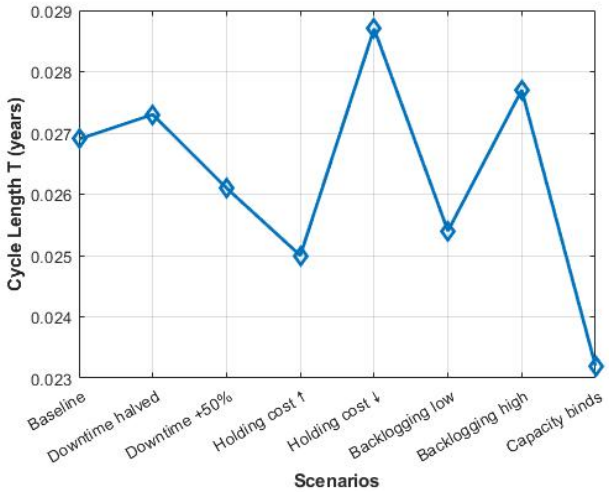


Figure 2: *Sensitivity of Cycle Length (T)*

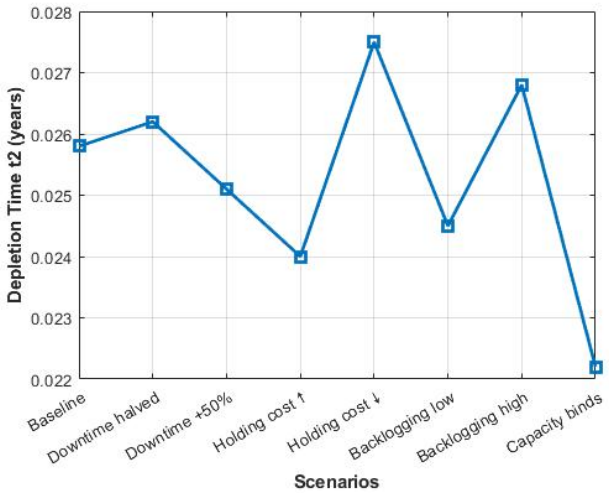


Figure 3: *Sensitivity of Cycle Length (t_2)*

9. Conclusion

The proposed inventory model has been analyzed numerically, and the results demonstrate its practical significance. In the baseline case, the optimal lot size was $Q = 1740$ tons, with a cycle length of $T \approx 0.0269$ years (9.8 days), yielding an annualized total cost of about \$8.74 million. Sensitivity analysis confirms that the optimal lot size Q, depletion time t_2, and cycle length T are strongly affected by changes in key parameters. Halving the downtime proportion (η) increases the optimal lot size to $Q \approx 1765$ tons, lengthening the cycle and reducing the annual cost by nearly 4%, whereas raising downtime by 50% reduces Q to about 1710 tons and increases cost by a similar margin. An increase in holding cost ($C_h = \$7$) decreases the optimal lot size to 1620 tons with shorter cycles, raising annual cost by nearly 7%, while lowering the holding cost ($C_h = \$3$) expands the lot size to 1850 tons, thereby reducing costs. Backlogging tolerance also influences results: higher k values encourage larger Q and longer T, while lower k reduce both. When the maximum feasible lot size is restricted, the optimal Q adjusts downward (e.g., $Q = 1500$ tons), with corresponding reductions in t_2 and T.
Future research may extend this model by incorporating stochastic demand, multi-item interactions, and dynamic pricing strategies to enhance its practical applicability.

References

[1] Zhu, Li, et al. "Modeling and Multi-objective Optimization Method for Steel Production Planning and Its Application." (2014): 262-267.
[2] Wang, Peng, et al. "Modeling and optimizing energy utilization of steel production process: A hybrid Petri net approach." Advances in Mechanical Engineering 5 (2013): 191963.
[3] Sukolkit, Nonthaphat, Sirawadee Arunyanart, and Arthit Apichottanakul. "An open innovative inventory management based demand forecasting approach for the steel industry." Journal of Open Innovation: Technology, Market, and Complexity 10.4 (2024): 100407.
[4] Aggarwal, Shikha, and Narain Gupta. "Applications of mathematical programming models for product mix optimization in world steel industry: challenges and directions." Managing in Recovering Markets (2014): 133-142.
[5] Rosyidi, Cucuk Nur, Shanella Nestri Hapsari, and Wakhid Ahmad Jauhari. "An integrated optimization model of production plan in a large steel manufacturing company." Journal of Industrial and Production Engineering 38.3 (2021): 186-196.
[6] Zanoni, Simone, and Lucio Zavanella. "Model and analysis of integrated production"inventory system: The case of steel production." International Journal of Production Economics 93 (2005): 197-205.
[7] Taleghani, Mohammad, and Mohammadreza Jabreilzadeh Sola. "Optimizing downtime through digital forensic analysis of supply chain disruptions in Iranian steel manufacturing industries." International Journal of Materials Science 5.1 (2025): 32-36.

[8] Lin, Gary C., and Dah-Chuan Gong. "On a production-inventory system of deteriorating items subject to random machine breakdowns with a fixed repair time." Mathematical and Computer Modelling 43.7-8 (2006): 920-932.

[9] Nobil, Erfan, et al. "Machine downtime effect on the warm-up period in an economic production quantity problem." Mathematics 11.7 (2023): 1740.

[10] Shi, Liangxing, et al. "Optimising production, maintenance, and quality control for imperfect manufacturing systems considering timely replenishment." International Journal of Production Research 62.10 (2024): 3504-3525.

[11] Yadav, A.S., Kumar, A., Yadav, K.K. et al. Optimization of an inventory model for deteriorating items with both selling price and time-sensitive demand and carbon emission under green technology investment. Int J Interact Des Manuf 19, 1297“1313 (2025). https://doi.org/10.1007/s12008-023-01689-8

[12] Yadav, K.K., Yadav, A.S. & Bansal, S. Interval number approach for two-warehouse inventory management of deteriorating items with preservation technology investment using analytical optimization methods. Int J Interact Des Manuf (2024). https://doi.org/10.1007/s12008-023-01672-3

[13] Krishan Kumar Yadav, Ajay Singh Yadav, and Shikha Bansal. "Optimization of a two-warehouse inventory management for deteriorating items with time and reliability-dependent demand under carbon emission constraints" Reliability: Theory & Applications, vol. 19, no. 4 (80), 2024, pp. 404-418. doi:10.24412/1932-2321-2024-480-404-418

[14] Krishan Kumar Yadav , Ajay Singh Yadav, and Shikha Bansal. "Optimization of an inventory model for deteriorating items assuming deterioration during carrying with two-warehouse facility" Reliability: Theory & Applications, vol. 19, no. 3 (79), 2024, pp. 442-459. doi:10.24412/1932-2321-2024-379-442-459

[15] Negi, A., Singh, O., Yadav, A.S. et al. An Inventory Model for Perishable Goods with Demand that Varies Probabilistically with Selling Price Using a Pentagonal Fuzzy Framework. Oper. Res. Forum 6, 150 (2025). https://doi.org/10.1007/s43069-025-00555-5

FORECASTING EXTREME MARKET MOVEMENTS USING REALIZED GARCH AND EXTREME VALUE THEORY MODELS

Umme Hani
•
Department of Economics and Finance, Saudi Electronic University, Al Madinah, Saudi Arabia. uhani@seu.edu.sa

Abstract

This study investigates the essential benefits of using the Conditional Value-at-Risk (CVaR) optimization framework with the GARCH model and Extreme Value Theory (EVT) methods for the S&P CNX NIFTY markets. Using daily data from Jan. 2020 to July 2024, we evaluate 10 forecasting models, comprising eight standalone GARCH models and eight two-stage GARCH-EVT models. Our results show that the GARCH-EVT models consistently produce more accurate quantile forecasts than their standalone GARCH counterparts. Among the standalone models, daily returns-based GARCH and EGARCH models exhibit the poorest forecasting performance, while the intraday return-based realized GARCH model performs slightly better. The experimental results show that, under various loss functions, the GARCH-EVT innovation model is the best model for volatility predictions of S&P CNX NIFTY among the sixteen forecasting models.

Keywords: Extreme value theory, Realized GARCH, realized kernel, Value-at-risk, Expected shortfall, GARCH-EVT model.

1. Introduction

Value-at-Risk (VaR) and Expected Shortfall (ES) are key measures of financial risk, widely applied in areas such as portfolio optimization, performance evaluation, regulatory capital computation, and the determination of margin requirements for investors. The Generalized Autoregressive Conditional Heteroskedasticity (GARCH) family of models is extensively used to capture the conditional moments of financial returns and to forecast VaR and ES. However, a major limitation of conventional GARCH models is their reliance on squared daily returns as a proxy for daily volatility an approach that produces a highly noisy estimate of latent volatility. To address this issue, [1] proposed the realized GARCH model, which incorporates information from intraday returns to provide a much more accurate and efficient estimate of underlying volatility. Empirical studies have shown that the realized GARCH framework substantially improves the in-sample and out-of-sample performance of volatility forecasts compared to traditional GARCH models. Financial assets with high liquidity often experience thousands of intraday transactions, and using only close-to-close returns discards valuable information embedded in high-frequency price movements [2].

Traditional GARCH models jointly estimate the conditional mean and variance of returns based solely on daily data. In contrast, the realized GARCH model introduces an additional measurement equation that jointly models a realized measure of daily volatility along with the

conditional moments of the return process. The realized volatility (RV) is computed as the sum of squared intraday returns, which converges in probability to the latent integrated variance as the sampling frequency increases. Despite this advantage, estimating RV at very high frequencies can introduce market microstructure noise, such as bid–ask bounce and price discreteness. To mitigate this issue, RV is typically estimated using lower-frequency samples (e.g., 5–60-minute intervals). However, lower sampling frequencies reduce efficiency because many price observations are ignored, and the RV estimate may fail to converge to the true integrated variance. Subsampling techniques can partially address this limitation, but recent research has proposed robust realized variance estimators that better balance bias and efficiency. In addition to the classical RV estimator, this study employs two robust realized variance estimators: the realized bipower variance (BV) proposed by Barndorff-Nielsen, O. E. and Shephard, [8] and the realized kernel (RK) estimator introduced. The BV estimator is robust to sudden price jumps that create large, infrequent intraday returns, which can otherwise inflate volatility estimates [3]. By multiplying adjacent absolute returns instead of squaring them, the BV estimator reduces the influence of such jumps. However, it remains sensitive to microstructure effects and is thus typically applied at 5-minute intervals [4].

The RK estimator, in contrast, is designed to be robust to microstructure noise and can utilize all available intraday data, including tick-by-tick prices. The demonstrated that realized GARCH models using these realized measures provide superior empirical fits to the distribution of financial returns compared to standard GARCH models [5]. While the realized GARCH model effectively captures the overall return distribution, risk management applications such as VaR and ES depend heavily on accurately modeling extreme returns [6]. Extreme Value Theory (EVT) addresses this by focusing specifically on the tails of the return distribution, where extreme events occur. EVT thus provides a more flexible framework for modeling rare but impactful financial shocks, yielding more accurate estimates of tail risk compared to conventional GARCH approaches based on normal or student-t distributions [7].

In this study, we evaluate the forecasting performance of alternative GARCH-class models in estimating VaR and ES for the Indian equity market [8]. Specifically, we compare 14 models: traditional GARCH and EGARCH models, five realized GARCH specifications based on different realized volatility estimators (RV, SRV, BV, SBV, and RK), and seven corresponding GARCH–EVT models estimated via the two-stage procedure proposed [9]. This research makes several contributions. First, it represents one of the earliest applications of the realized GARCH model for quantile forecasting in an emerging market context. Second, unlike prior studies [10] which analyzed realized GARCH performance in developed markets like the United States, we apply the model to the Indian market, characterized by distinct volatility dynamics [11]. Finally, we incorporate robust realized variance estimators and the conditional GARCH–EVT framework to enhance the accuracy of tail-risk forecasting [12]. The compelling empirical evidence supporting GARCH–EVT models motivates our comparison of standalone realized GARCH models against their GARCH–EVT counterparts in forecasting VaR and ES [13].

II. Methodology

The dataset for this study comprises ultra-high frequency data for the S&P CNX Nifty index for the period 01 July 2007 to 30 June 20124. Let $\{X\}_t$ represent the logarithm of the time series of financial returns. We define a return x as an extreme observation or an exceedance when it is greater than a threshold value u. Then, the distribution of exceedances can be represented by the cumulative probability distribution

$$F_u(y), \text{where } y = x - u, \forall x > u.$$

$$F_u(y) = \Pr(X - u \le y \mid X > u) \tag{1}$$

The conditional probability in Eq. (1) can be further simplified as

$$F_u(y) = \frac{\Pr(X-u\le y, X>u)}{\Pr(X>u)} = \frac{F(y+u)-F(u)}{1-F(u)} = \frac{F(x)-F(u)}{1-F(u)} \tag{2}$$

Where $F(.)$ denotes the cumulative pdf, and $x = y + u, \forall x > u$ is the magnitude of exceedance. show that for a sufficiently large choice of the threshold u, the distribution of exceedances, $F_u(y)$ can be approximated by the generalised Pareto distribution, $G_{\xi,\psi}(\mathrm{y})$, if the log returns $\{X\}_t$ are independent and identically distributed (i.i.d.) [14].

$$G_{\xi\psi}(y) = \begin{cases} 1 - \left(1 + \dfrac{\xi y}{\psi}\right)^{-1/\xi}, \text{ if } \xi \neq 0 \\ 1 - e^{-y/\psi}, \text{ if } \xi = 0 \end{cases} \tag{3}$$

where, ξ and ψ are the shape and scale parameters of the generalised Pareto distribution. Under the assumption that the returns are i.i.d., $F_u(\mathrm{y})$ can be approximated by $G_{\xi,\psi}(\mathrm{y})$. Therefore, using the Eqs. (2) and (3), the cumulative probability distribution $F(x)$ can be defined as

$$F(x) = (1 - F(u))G_{\xi\psi}(y) + F(u) \tag{4}$$

$F(u)$ can be empirically estimated as $(n-k)/n$, where n is the total number of observations, and k is the number of exceedances. Using Eqs. (3) and (4), and substituting the value $(n-k)/n$ for $F(u)$, the cumulative probability distribution $F(x)$ can be defined as

$$F(x) = 1 - \frac{k}{n}\left[1 + \xi\frac{x-u}{\psi}\right]^{-1/\xi} \tag{5}$$

For any given quantile q, the value-at-risk measure, VaR_q is the q-th quantile of the return distribution.

$$VaR_q = F^{-1}(1-q) \tag{6}$$

where, $F^{-1}(.)$ is the quantile function defined as inverse of the distribution function $F(.)$. By inverting the distribution function $F(x)$ given in Eq. (5), VaR_q can be estimated as

$$\mathrm{VaR}_q = x_q = u + \frac{\psi}{\xi}\left[\left(\frac{1-q}{k/n}\right)^{-\xi} - 1\right] \tag{7}$$

The corresponding expected shortfall measure, ES_q, can be calculated as

$$ES_q = E\left(X \mid X > \mathrm{VaR}_q\right) \tag{8}$$

Using Eq. (7), ES_q can be estimated as

$$ES_q = \frac{VaR_q}{1-\xi} + \frac{\psi - \xi u}{1-\xi} \tag{9}$$

As noted earlier, these results hold under the assumption that the returns are iid. However, financial returns are generally characterised by serial correlation (linear dependence) and volatility clustering (non-linear dependence). To overcome this problem, we employ the two-stage estimation procedure [15]. In the first stage, alternate GARCH specifications are used to filter the raw (original) returns to remove linear and non-linear dependence. If the GARCH models are well

specified, the residuals of these GARCH models are approximately iid. In the second stage, we apply the EVT framework to standardized GARCH residuals obtained in the first stage to estimate the VaR_q and ES_q measures. The conditional mean of the returns conditional mean of the returns is modelled using a $\mathrm{ARMA}(p,q)$ process:

$$r_t = \mu_t + \varepsilon_t, \varepsilon_t = \sqrt{h_t} Z_t \tag{10}$$

where, $\mu_t = a_0 + \sum_{i=1}^{p} a_i r_{t-i} + \sum_{j=}^{q} b_j \varepsilon_{t-j}$ and h_t represents the conditional mean and the conditional variance. r_{t-i} and ε_{t-j} represent the lagged returns and lagged innovations. $Z_t = \varepsilon_t/\sqrt{h_t}$ are the standardised residuals and a_0, a_i and b_j are the parameters estimated using method of maximum likelihood. The conditional variance process, h_t, is estimated using a different GARCH specifications

$$\mathrm{GARCH}(p_2, q_2): h_t = \omega + \sum_{i=1}^{p_2} \alpha_i \varepsilon_{t-i}^2 + \sum_{j=1}^{q_2} \beta_j h_{t-j} \tag{11}$$

EGARCH (p_3, q_3):

$$\log(h_t) = \omega + \sum_{i=1}^{p_3} \frac{\alpha_i \varepsilon_{t-i} + \gamma_i |\varepsilon_{t-i}|}{\sqrt{h_{t-i}}} + \sum_{j=1}^{q_3} \beta_j \log h_{t-j} \tag{12}$$

Realised GARCH (p_4, q_4):

$$= \omega + \sum_{i=1}^{p_4} \alpha_i \log v_{t-i} + \sum_{j=1}^{q_4} \beta_j \log h_{t-j} \tag{13}$$

$$\log(v_t) = \eta + \phi \log h_t + \tau_1 Z_t + \tau_2 (Z_t^2 - 1) + \zeta_t \tag{14}$$

where $\alpha_i, \gamma_i, \beta_i, \omega, \varphi, \tau_1, \tau_2$ parameters of the GARCH models estimated using the method of maximum likelihood. v_t represents the realised volatility measure used to estimate the realised GARCH model. We use five realised volatility measures, the 5 -minute realised volatility measure (RV), the 5-minute realised volatility measure with 1-minute subsampling (SRV), the 5 -minute realised bipower variance estimator (BV), the 5-minute realised bipower variance estimator with 1 -minute subsampling (SBV), and the realised kernel estimator (RK) based on tick-by-tick sampling. We follow the subsampling procedure [22] for the subsampled realised volatility estimators SRV and SBV. Now, we would explain these five realised volatility measures using few notations: Let $\{p_i\}_{i=0}^{m}$ denote the time-series of intraday prices. The notations are standardised by defining a function $\gamma_{\mathrm{h,d}}(\mathrm{W})$ as

$$\gamma_{h,d}(w) = \sum_{i=1}^{o} \left(p_{id+h} - p_{(i-1)d+h}\right)\left(p_{(i+w)d+h} - p_{(i-1+w)d+h}\right) \tag{15}$$

The RV estimator can be computed as

$$RV = \gamma_{0,d}(0) \tag{16}$$

where, $d = 1$ represents the highest sampling frequency, e.g., $\gamma_{0,\mathrm{d}}(0)$ specifies the RV estimate that uses all intraday price stamps. The 5 -minute RV is computed applying $d = m/l$, where l is the total number of 5 -minute intervals in a given trading day. While sampling at higher than 5 -minute frequency brings higher efficiency due to inclusion of a greater number of intraday

observations, it also induces microstructure bias.

In order to deal with such complexity, we also calculate SRV estimate that uses 5-minute intervals with 1-minute subsampling. The calculation of the SRV estimate is as follows: Say, one RV estimate is constructed using the intraday price points of 10.30 am., 10.35 am., 10.40 am., ...and so on. Similarly, another RV estimate is created using the intraday price points of 10.31 am., 10.36 am., 10.41 am., ...and so on. In this fashion, five separate RV estimates are calculated with five non-overlapping subsamples in each day. These RV estimates ignore only few observations if the beginning and the ending time stamps of these subsamples differ from those of the actual trading session. The RV estimates are inflated proportionately to adjust this loss. Finally, the SRV estimate is computed by averaging these five RV estimates. The BV estimator is robust to intraday jumps in prices. It is also calculated using 5 -minute returns in order to avoid any microstructure bias. The BV estimate is computed as

$$BV = \frac{\pi}{2}\sum_{i=1}^{m} \left|p_{id} - p_{(i-1)d}\right|\left|p_{(i+1)d} - p_{id}\right| \tag{17}$$

As BV estimate uses 5-minute sampling frequency, value of d is determined as $d = m/l$, where l is the total number of 5 -minute returns in a given trading day. Applying same method as SRV, we also compute SBV estimate that uses 5 -minute returns with 1-minute subsampling. Finally, we apply the RK estimator as proposed by [16]. This estimator utilizes all intraday observations. Moreover, it is robust to microstructure noise as well. The RK is computed as

$$RK = \gamma_{0,1}(0) + 2\sum_{h=1}^{H} \kappa\left(\frac{h-1}{H}\right)\gamma_{0,1}(h) \tag{18}$$

where, $\kappa(x)$ is a kernel weight function. H, the optimal bandwidth parameter, is calculated. According to employ the "non-flat-top" Parzen kernel function as it ensures a positive variance estimate. Moreover, it also allows for endogeneity or dependence in the microstructure noise process. The Parzen kernel function is expressed as

$$\kappa(x) = \begin{cases} 1 - 6x^2 + 6x^3 & 0 \le x \le 1/2 \\ 2(1-x)^3 & 0 \le x \le 1/2 \\ 0 & x > 1 \end{cases}$$

The RK estimator uses all intraday price observations. Hence, its subsampled version is not required. In total, five realised GARCH model specifications are estimated using these five different realised measures of volatility. To estimate the optimal lag lengths for the ARMA-GARCH specifications, we estimate a basic $\mathrm{ARMA}(0,0) - \mathrm{GARCH}(1,1)$ model, and then add additional AR, MA, ARCH and GARCH terms when necessary to eliminate autocorrelation in the standardised and squared standardised residuals, respectively. After each model estimation, Ljung-Box tests were used to test for autocorrelation in the standardised and squared standardised residuals. The one-step-ahead conditional mean forecast is $\hat{\mu}_{t+1}$ estimated as

$$\hat{\mu}_{t+1} = \hat{a}_0 + \sum_{i=1}^{p_1} \hat{a}_i r_{t-i+1} + \sum_{j=1}^{q_1} \hat{b}_j \varepsilon_{t-j+1} \tag{19}$$

The one-step-ahead conditional variance, $\hat{h}_{t+1}$, is forecasted using GARCH specifications described in Eqs. (11) to (14). The one-step-ahead conditional VaR and ES, VaR_q^{t+1} and ES_q^{t+1} are forecasted as

$$\mathrm{VaR}_q^{t+1} = \hat{\mu}_{t+1} + \sqrt{\hat{h}_{t+1}}\mathrm{VaR}_q \tag{20}$$

$$ES_q^{t+1} = \hat{\mu}_{t+1} + \sqrt{\hat{h}_{t+1}}ES_q \tag{21}$$

III. Empirical Results

We employ fourteen forecasting models to produce one-step-ahead Value-at-Risk (VaR) and Expected Shortfall (ES) estimates for the benchmark NIFTY index. The first group consists of seven standalone GARCH-type models: the standard GARCH (G), the Exponential GARCH (EG), and five variants of the realized GARCH (RG) model, each using a different realized volatility estimator—RV, SRV, BV, SBV, or RK. The remaining seven models correspond to these specifications but incorporate the Extreme Value Theory (EVT) framework through a two-stage GARCH–EVT estimation procedure. The dataset spans the period from 1 Jan 2020 to 30 June 2024. Model parameters are estimated over the in-sample period 1 Jan 2020 to 30 June 2023, while the out-of-sample evaluation covers 1 July 2023 to 30 June 2024, providing 686 daily forecasts of VaR and ES.

Table 1: *Comparison of the VaR forecasting models using the binomial tests.*

Model	Confidence Level ($1-\alpha$)		
	95%	99%	99.5%
G	2.314**	2.314**	2.314**
EG	2.689**	2.689**	2.689**
$\mathrm{RG_{RV}}$	1.633	1.633	1.633
$\mathrm{RGS_{RV}}$	1.014**	1.340**	1.304**
$\mathrm{RG_{BV}}$	-0.487	-0.487	-0.487
$\mathrm{RG_{SBV}}$	0.542	0.542	0.542
$\mathrm{RG_{RK}}$	-0.487	-0.487	-0.487
G EVT	0.681	0.681	0.681
EG EVT	-0.635	-0.871	1.270
$\mathrm{RG_{RV}}$ EVT	0.719	0.241	1.216
$\mathrm{RGs_{RV}}$ EVT	0.244	0.244	0.244
$\mathrm{RG_{BV}}$ EVT	0.096	0.096	0.096
$\mathrm{RG_{SBV}}$ EVT	0.354	0.354	0.354
$\mathrm{RG_{RK}}$ EVT	0.594	0.594	0.594

To evaluate forecasting accuracy, we apply binomial tests and likelihood ratio tests. A return on day t is classified as a VaR exceedance if the observed return falls below (i.e., is more negative than) the forecasted VaR for that day. The empirical violation ratio the proportion of exceedances is then compared with the expected violation rate (1–q) at three conventional confidence levels: 95%, 99%, and 99.5%. Table 1 presents the binomial test statistics for all model [17]. A positive and significant statistic implies that the observed number of violations exceeds the expected level, whereas a negative and significant value indicates fewer violations than expected. The findings reveal that GARCH–EVT models consistently outperform standalone GARCH models. For the 95% VaR forecasts, the null hypothesis that the empirical and expected violation ratios are equal is rejected for all standalone models, including the realized GARCH variants [18]. Conversely, this null cannot be rejected for any of the GARCH–EVT specifications, suggesting superior calibration. Among the standalone models, the realized GARCH approaches outperform the basic GARCH and EGARCH models at higher quantiles (particularly at the 99.5% level). Notably, the specific

choice of realized volatility estimator has minimal influence on the predictive performance of both realized GARCH and realized GARCH–EVT frameworks.

Next, the likelihood ratio (LR) testing framework proposed by Christoffersen (1998) is applied to evaluate the accuracy of VaR forecasts across three key dimensions: unconditional coverage, independence of exceedances, and conditional coverage [19]. The unconditional coverage test examines whether the observed (empirical) frequency of VaR violations matches the expected frequency implied by the nominal confidence level. The test of independence assesses whether these violations occur randomly over time or display clustering behavior. In other words, it verifies whether the probability of a violation on day t is independent of past violations. The conditional coverage test jointly evaluates both properties coverage accuracy and independence to provide a comprehensive measure of VaR model reliability [20].

Table 2: *Comparison of the VaR forecasting models using the test of unconditional coverage.*

Model	Confidence Level ($1-\alpha$)		
	95%	99%	99.5%
G	3.842*	0.954	5.126*
EG	4.217*	0.781	3.596*
RG_{RV}	3.106	0.742	1.214
RGS_{RV}	2.984	0.318	1.187
RG_{BV}	4.872*	0.331	1.203
RG_{SBV}	4.639*	0.097	1.215
RG_{RK}	4.211*	0.276	1.194
G EVT	0.382	0.024	0.046
EG EVT	0.417	0.693	0.052
RGRV EVT	0.482	0.063	1.201
RG_{RV} EVT	0.037	0.072	1.210
RGbv EVT	0.946	0.059/	1.225
RG_{SBV} EVT	1.613	0.051	1.233
RG_{RK} EVT	1.542	0.019	1.229

Table 2 presents the LR statistics for unconditional coverage. Consistent with earlier results, the GARCH–EVT models outperform the corresponding standalone GARCH specifications. Among the standalone models, the realized GARCH variants generally exhibit superior performance compared to the standard GARCH and EGARCH models, particularly at the 95% confidence level. Furthermore, the realized volatility estimators based on RV and SRV measures yield more accurate forecasts than those relying on BV, SBV, or RK estimators at moderate quantiles [21]. However, at higher quantiles (99% and 99.5%), the differences among realized volatility measures become negligible. For all VaR quantiles, the realized GARCH–EVT models demonstrate robust performance, confirming that the integration of EVT significantly improves tail-risk estimation [22]. Table 3 reports the LR statistics for the independence test. The results indicate no evidence of exceedance clustering in any of the fourteen models, suggesting that the VaR violations occur randomly over time. The magnitudes of the LR statistics also highlight the superior overall performance of the realized GARCH–EVT models relative to their standalone counterparts. Finally, to evaluate the accuracy of Expected Shortfall (ES) forecasts, we employ the non-parametric performance measured [15]. This approach provides a consistent ranking of models based on the precision of ES forecasts and has been widely adopted in the tail-risk forecasting literature.

Table 3: *Comparison of the VaR forecasting models using the test of independence.*

Model	Confidence Level ($1-\alpha$)		
	95%	99%	99.5%
G	2.074	0.324	0.612
EG	1.956	0.288	0.193
RG_{RV}	1.138	0.259	0.117
RGS_{RV}	0.121	0.008	0.002
RG_{BV}	0.598	0.211	0.113
RG_{SBV}	0.573	0.165	0.094
RG_{RK}	0.741	0.204	0.102
G EVT	3.027	0.127	0.052
EG EVT	0.226	0.075	0.048
RGRV EVT	1.142	0.166	0.099
RGs_{RV} EVT	1.784	0.158	0.097
RG_{BV} EVT	0.114	0.163	0.089
RG_{SBV} EVT	0.037	0.153	0.091
RG_{RK} EVT	0.259	0.121	0.095

Next, we employ the likelihood ratio testing framework to compare the VaR forecasting models for unconditional coverage, exceedance clustering (test of independence), and conditional coverage. The null hypothesis for the unconditional coverage tests is that the empirical violations ratio is same as the expected violation ratio. The null hypothesis for the test of independence is that the VaR violations are independent and not clustered over time. That is, for any day t, the unconditional probability of observing a VaR violation is same as the conditional probability of observing a VaR violation, given the information about past VaR violations. Finally, the conditional coverage test is a joint test of unconditional coverage and independence of VaR violations [16]. Table 4 presents the likelihood ratio (LR) statistics for the conditional coverage tests. The findings remain consistent with earlier results: the stand-alone GARCH and EGARCH specifications deliver the weakest one-step-ahead VaR forecasts, indicating poor joint performance in terms of both accuracy and independence of violations.

Table 4: Comparison of the VaR forecasting models using the test of conditional coverage.

Model	Confidence Level ($1-\alpha$)		
	95%	99%	99.5%
G	5.900	1.250	5.800
EG	6.100	1.200	4.200
RG_{RV}	4.500	1.150	1.400
RGS_{RV}	3.500	0.400	1.300
RG_{Bv}	5.900	0.600	1.400
RG_{SBV}	5.850	0.250	1.350
RG_{RK}	5.300	0.580	1.350
G EVT	3.600	0.160	0.080
EG EVT	0.650	0.950	0.080
RG_{RV} EVT	1.700	0.240	1.350
RG_{RV} EVT	1.900	0.240	1.350
RG_{Bv} EVT	1.170	0.240	1.350
RG_{SBV} EVT	1.850	0.040	1.350
RG_{RK} EVT	1.070	0.160	1.350

In contrast, the realized GARCH and GARCH–EVT models demonstrate superior performance, with LR statistics that fail to reject the null hypothesis of correct conditional coverage. This suggests that these models not only produce VaR forecasts with appropriate violation frequencies but also exhibit independence across exceedances. Overall, the integration of realized measures and EVT improves model reliability and predictive precision across all quantile levels. Table 5 reports the [12] measure for the various forecasting models. As earlier, the GARCH-EVT specifications perform better than the corresponding standalone GARCH models. The daily returns based GARCH and EGARCH models have the highest measure across all three quantiles. Regardless of the choice of the realised volatility measure, the realised GARCH -EVT models perform the best, however, there is no evidence to support the choice of a specific realised volatility measure to estimate the realised GARCH model [19]. The best ES forecasts at 95%, 99% and 99.5 confidence levels, respectively.

Table 5: *Comparison of the ES forecasting models*

Model	Confidence level ($1-\alpha$)		
	95%	99%	99.5%
G	12.014	7.797	25.319
EG	12.378	15.359	28.574
$\mathrm{RG_{RV}}$	3.311	1.137	2.510
$\mathrm{RGS_{RV}}$	1.373	3.434	3.198
$\mathrm{RG_{BV}}$	4.972	3.869	2.570
$\mathrm{RG_{SBV}}$	0.679	4.062	4.560
$\mathrm{RG_{RK}}$	5.690	1.550	5.186
G EVT	0.710	1.933	2.032
EG EVT	1.084	1.891	2.792
$\mathrm{RG_{RV}}$ EVT	0.280*	1.667	0.705
$\mathrm{RG_{RV}}$ EVT	0.421	1.218	0.970
$\mathrm{RGS_{BV}}$ EVT	0.431	1.420	1.853
$\mathrm{RG_{SBV}}$ EVT	0.763	1.056*	0.457
$\mathrm{RG_{RK}}$ EVT	0.753	2.024	0.214*

The Embrechts et al. (2005) [12] measure is defined as

where $E_1 = \frac{1}{c}\sum_{r\in\tau} f_t, \phi_r = k_{t+1} - ES_q^{r+1}.c$ is the number of estimated VaR violations, that is, when the observed return is higher than the forecasted VaR for that day. τ represents the set of days on which VaR violations occur. E_2 is observed in a similar manner, however, the VaR violations are recorded as days on which the observed return is higher than the empirical observed quantile q. Thus, E_1 is based on estimated VaR values and E_2 is based on empirical VaR quantile observed in the set of realised returns. Since E represents the difference between the average exceedance and the forecasted ES, lower value of E indicates a better forecast of the ES. For a detailed discussion of the properties of this measure, we refer the reader to [8].

IV. Conclusion

We propose a novel approach that combines two-stage conditional extreme value theory (EVT) with a realised GARCH filter to generate one-step-ahead VaR and ES forecasts for the benchmark Indian equity index, S&P CNX NIFTY. In total, we evaluate 10 forecasting models, comprising seven standalone GARCH models and seven two-stage GARCH-EVT models. Our results show

that the GARCH-EVT models consistently produce more accurate quantile forecasts than their standalone GARCH counterparts. Among the standalone models, daily returns-based GARCH and EGARCH models exhibit the poorest forecasting performance, while the intraday return-based realised GARCH model performs slightly better, likely due to the additional information captured from intraday data. Importantly, even daily return-based GARCH models outperform the standalone realised GARCH model when incorporated into the two-stage GARCH-EVT framework. Overall, realized GARCH-EVT models deliver the best forecasting performance, and this result remains robust across different choices of realised volatility estimators.

References

[1] Andersen, T. G. and Bollerslev, T. (1998). Answering the Skeptics: Yes, standard volatility models do provide accurate forecasts. *International Economic Review*, 39(4):885–905.

[2] Andersen, T. G. Bollerslev, T. Diebold, F. X. and Ebens, H. (2001). The distribution of realised stock return volatility. *Journal of Financial Economics*, 61(1):43–76.

[3] Bali, T.G. (2003). An Extreme value approach to estimating volatility and value at risk. *The Journal of Business*, 76(1):83–108.

[4] Barndorff-Nielsen, O. E. (2002). Econometric analysis of realized volatility and its use in estimating stochastic volatility models. *Journal of the Royal Statistical Society: Series B (Statistical Methodology)*, 64(2):253–280.

[5] Barndorff-Nielsen, O. E. Hansen, P.R. Lunde, A. and Shephard, N. (2008). Designing realized kernels to measure the expost variation of equity prices in the presence of noise. *Econometrica: Journal of the Econometric Society*, 76(6):1481–1536.

[6] Barndorff-Nielsen, O. E. Hansen, P. R. Lunde, A. and Shephard, N. (2009). Realized kernels in practice: Trades and quotes. *Econometrics Journal*, 12(3).

[7] Barndorff-Nielsen, O. E. Hansen, P. R. Lunde, A. and Shephard, N. (2011). Subsampling realised kernels. *Journal of Econometrics*, 160(1):204–219.

[8] Barndorff-Nielsen, O. E. and Shephard, N. (2002). Estimating quadratic variation using realized variance. *Journal of Applied Econometrics*, 17(5):457–477.

[9] Premila, S. C. Jeena, R. Pachiyappan, D. Ramesh Kumar, B. and Kavitha, S. (2025). GARCH-MIDAS Analysis of Inflation's Impact on Asian Stock Return Volatility. *Reliability: Theory & Applications*, 20(2(84)):705-714.

[10] Christoffersen, P.F. (1998). Evaluating interval forecasts. *International Economic Review*, 841–862.

[11] Beg, I. Gnanaprakasam, A. J. and M, G. (2023). Common coupled fixed point theorem on fuzzy bipolar metric spaces. *International Journal of Nonlinear Analysis and Applications*, 14(4):77-85.

[12] Embrechts, P. Kaufmann, R. and Patie, P. (2005). Strategic long-term financial risks: Single risk factors. *Computational Optimization and Applications*, 32(1–2):61–90.

[13] Ergen, I. (2015). Two-step methods in VaR prediction and the importance of fat tails. *Quantitative Finance*, 15(6):1013–1030.

[14] Mani, G. Gnanaprakasam, A. J. Kumar, S. Ege, O. and De la Sen, M. (2023). Fixed-Point Theorems for Nonlinear Contraction in Fuzzy-Controlled Bipolar Metric Spaces. *Axioms*, 12(4):396

[15] Alam, M. S. Duraisamy, P. Siddik, A. B. Murshed, M. Mahmood, H. Palanisamy, M. & Kirikkaleli, D. (2023). The impacts of globalization, renewable energy, and agriculture on CO2 emissions in India: contextual evidence using a novel composite carbon emission-related atmospheric quality index. *Gondwana Research*, *119*:384-401.

[16] Gencay, R. and Selcuk, F. (2004). Extreme value theory and Value-at Risk: Relative performance in emerging markets. *International Journal of Forecasting*, 20(2):287–303.

[17] Haas, Markus, Mittnik, S. and Paolella, M. S. (2004). Mixed normal conditional heteroskedasticity. *Journal of Financial Econometrics*, 2(2):211-250.

[18] Korkpoe, C. H. and Kawor, S. (2018). A Rollercoaster Ride through the Equity Markets Evidence from the Ghana Stock Exchange. *African Finance Journal*, 7(3):1-21.

[19] Link, W. A. and Eaton, M. J. (2012). On thinning of chains in MCMC. *Methods in Ecology and Evolution*, 3(1):112-115.

[20] Duraisamy, P. Alam, MS. Uddin, MA. Kuppusamy, A. Palanisamy, M. (2022). Modelling volatility of petroleum productions by using Markov-switching GARCH models. *International Journal of Agricultural Statistical Science*, 18(1):1657-67.

[21] Poshakwale, S. and Murinde, V. (2001). Modelling volatility in East European emerging stock markets: evidence on Hungary and Poland. *Applied Financial Economics*, 11(4):445-456.

[22] Manigandan, P. Alam, M. S. Alharthi, M. Khan, U. Alagirisamy, K. Pachiyappan, D. and Rehman, A. (2021). Forecasting natural gas production and consumption in United States-evidence from SARIMA and SARIMAX models. *Energies*, 14(19):6021.

RT&A, No 4 (89)
Volume 20, December 2025

QUALITY CONTROL FOR SUSTAINABILITY IN CASTING MANUFACTURING

Manzoor A. Khanday[1*], Trushal Hirani[2], Dilawar A. Bhat[3], Vaddi Tejasvi[4], Anusha Ale Saji[5]

•

[1*,2,4,5] Department of Statistics, Lovely Professional University, Punjab, India
[3]Symbiosis School of Banking and Finance, Symbiosis International University, Pune, India
manzoorstat@gmail.com, hiranitrushal@yahoo.com, dilawar.bhat@ssbf.edu.in,
vadditejasvi@gmail.com, anushasaji1002@gmail.com.
Corresponding author[1*]: manzoorstat@gmail.com

Abstract

This study proposes an artificial intelligence–driven framework for automating defect detection in casting manufacturing, with a particular focus on enhancing sustainability in the production of submersible pump impellers. A dataset comprising more than 7,000 grayscale images—classified as defective or acceptable—was utilized to train and evaluate three deep learning models: a custom-built Convolutional Neural Network (CNN), VGG16, and ResNet18. The models were assessed for their accuracy, precision, and recall, with VGG16 and ResNet18 demonstrating superior performance, achieving over 99% classification accuracy. Advanced image preprocessing techniques, including histogram equalization and Canny edge detection, were employed to enhance defect visibility and enable the detection of microstructural flaws such as blow holes, shrinkage cavities, and surface irregularities. The integration of transfer learning significantly reduced training time while improving generalization across unseen samples. From a sustainability perspective, the adoption of AI-based automated inspection reduces material wastage, rework, and energy consumption by ensuring early identification of defective products. Furthermore, the deployment of these models on edge devices and integration with IoT-enabled monitoring systems facilitate real-time, continuous quality assurance without human intervention. Overall, the findings underscore that AI-driven quality control systems not only optimize manufacturing efficiency and product reliability but also contribute to achieving broader sustainability goals by minimizing resource depletion, enhancing energy efficiency, and supporting circular manufacturing practices.

Keywords: Quality Control, Casting Manufacturing, Deep Learning, Convolutional Neural Networks, VGG16, ResNet18, Defect Detection, Edge AI, IoT Integration, Sustainability.

I. Introduction

In today's manufacturing landscape, sustainability and quality are two interlinked pillars that drive industry innovation. Traditional casting processes, though pivotal in producing complex components like submersible pump impellers, are often marred by imperfections that can lead to

significant material waste and operational inefficiencies. Traditional casting processes are foundational to manufacturing complex components like submersible pump impellers, but they are inherently prone to defects such as blow holes, pinholes, and shrinkage anomalies. These imperfections lead to material waste, energy inefficiency, and increased production costs, undermining sustainability goals in manufacturing. Swift and Booker highlight that up to 20% of casting products are discarded due to defects, emphasizing the urgent need for improved quality control systems to minimize resource waste [1]. Manual inspection, the conventional approach for defect detection, exacerbates these challenges due to its labor-intensive nature, subjectivity, and high error rates. Tao notes that manual methods fail to scale with modern production demands, often leading to inconsistent quality assessments and delayed interventions [2]. Casting defects such as blow holes, pinholes, shrinkage anomalies, and other irregularities—pose not only a threat to product quality but also to the sustainable utilization of resources. Manual inspection, the conventional method for detecting these flaws, is labor-intensive, time-consuming, and prone to human error [3]. This inefficiency can result in the inadvertent rejection of otherwise salvageable products, thereby escalating production costs and environmental footprint. This chapter explores how the integration of deep learning techniques into quality control processes can revolutionize casting manufacturing. By leveraging a meticulously curated dataset comprising over 7,300 grayscale images of casting products—augmented to enhance the diversity of defect presentations—we demonstrate the potential for automated, real-time defect detection. The study not only evaluates defect detection accuracy but also considers its implications for sustainable production, highlighting how automated inspection contributes to resource circularity and lower carbon intensity in manufacturing lines. The dataset is divided into two principal categories: defective and acceptable castings, providing a robust framework for training and validating classification models. The automated system aims practices by reducing material waste, minimizing energy consumption, and optimizing overall production workflows. Furthermore, by transitioning from manual to machine-driven inspection, manufacturers can achieve a higher degree of precision and consistency in quality control. This shift supports a circular economy, where resources are utilized more efficiently, and waste is significantly reduced [4]. In the broader context of sustainable industry practices, the use of advanced artificial intelligence (AI) systems for quality control embodies a forward-thinking approach—melding technological innovation with environmental stewardship. In the following sections, we delve into the specifics of the dataset, outline the deep learning methodologies employed, and evaluate the performance of our classification models. Ultimately, this chapter underscores how AI-driven quality control not only enhances production efficacy but also serves as a critical enabler of sustainability in modern manufacturing.

II. Review of Literature

Recent advancements in artificial intelligence, particularly the emergence of Vision Transformers (ViTs), have significantly enhanced the ability to detect complex surface defects in manufacturing. Dosovitskiy et al. demonstrated that ViTs outperform traditional Convolutional Neural Networks (CNNs) in capturing long-range dependencies within high-resolution images, thereby improving the precision of defect localization and classification. However, their high computational demands continue to limit widespread deployment in real-time industrial applications. These challenges underscore a persistent gap between conventional quality control practices and the sustainability imperatives of Industry 4.0. Although deep learning has revolutionized manufacturing inspection systems, the integration of sustainability indicators—such as reductions in material waste, rework, and energy consumption—into AI-driven frameworks remains limited. Addressing this gap, the

present research aligns deep learning performance metrics with sustainability outcomes in casting operations. Models such as CNN, ResNet, and VGG demonstrate strong potential for automated defect detection with minimal human intervention. By minimizing scrap rates and optimizing energy usage, AI-based quality control systems not only improve production efficiency but also contribute to sustainable manufacturing [5]. Bressanelli et al. emphasize that such automation plays a pivotal role in advancing circular economy principles by conserving resources and reducing environmental impact [6].

III. Sustainability Implications of AI-Based Quality Control

A key motivation for integrating deep learning into casting defect detection is the sustainability benefits it brings to manufacturing processes. First, reducing resource wastage emerges as a direct outcome of early defect identification [7]. By identifying flawed products immediately after casting, manufacturers avoid investing additional energy, labor, and materials into parts that would ultimately be scrapped, thereby lowering raw material consumption [8]. In parallel, energy efficiency gains arise from automated inspections operating in real-time, allowing production lines to run continuously without the bottlenecks of manual checks [9]. This streamlined workflow not only cuts down idle machine time but also diminishes the likelihood of large-scale rework cycles, further conserving energy across the production chain [10]. From a cost-benefit perspective, AI-driven inspection systems deliver high accuracy and consistency, minimizing false rejections of otherwise viable parts [11]. Although initial investments in hardware (e.g., GPUs) and data infrastructure can be significant, the long-term savings from reduced scrap rates and improved throughput frequently offset these costs. Collectively, these factors illustrate how advanced quality control solutions not only enhance product integrity but also support broader environmental and economic objectives within casting and other manufacturing domains.

IV. Methods

A critical foundation for automating quality control in casting manufacturing lies in the quality and structure of the dataset. The dataset employed in this study is meticulously curated to capture the nuances of casting defects that commonly occur in the production of submersible pump impellers. This section delves into the dataset's composition, acquisition process, and relevance to sustainable manufacturing practices. All images in the dataset are top-view shots of submersible pump impellers, captured under controlled lighting conditions. The dataset is organized into two primary subsets, each serving a specific purpose in the development and validation of the deep learning model.

The dataset used in this study consists of two primary subsets designed to ensure both diversity and precision in defect detection. The augmented image set (300×300 pixels) comprises 7,348 grayscale images that have undergone various augmentation techniques such as rotation, flipping, and contrast adjustment to simulate diverse real-world conditions [12], this process enriches the dataset, allowing the deep learning models to generalize effectively to unseen samples and reducing overfitting. In contrast, the original image set (512×512 pixels) contains high-resolution, unaltered images that capture intricate details of the casting process. This subset includes 519 images labelled as "OK" and 781 labelled as "Defective," offering a clear visual distinction between flawless and flawed impellers. Together, these datasets provide a comprehensive foundation for developing robust and accurate models capable of detecting subtle surface irregularities critical for automated quality control in casting manufacturing. This dual-dataset approach ensures model reliability, scalability, and adaptability for real-world industrial applications.

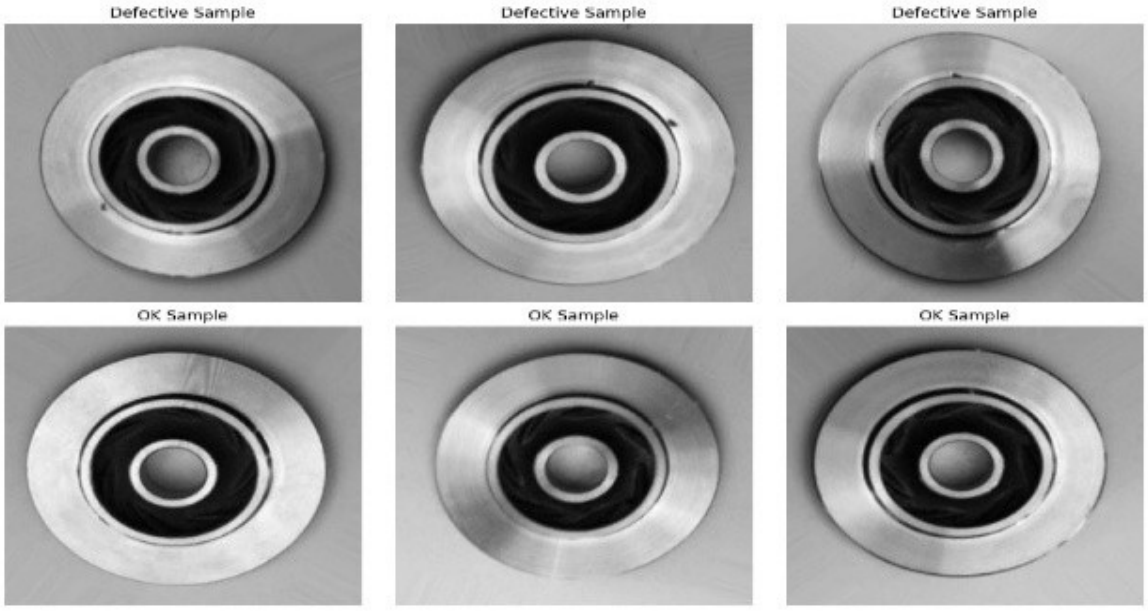


Figure 1: *Sample Images of OK and Defectives. The visible tonal variations between OK and defective impellers mark the first indication of quality differences.*

Figure 1 illustrates representative samples from both OK and defective categories. The visible tonal and textural contrasts reveal that defective impellers often display uneven surface shading, micro-pits, and darker contours compared with the smoother, uniformly lit OK counterparts. These differences form the visual cues on which the deep-learning models base their classification.

Understanding the dataset involves more than just reading numbers and images; it also reflects the broader sustainability goals of modern manufacturing. Detecting defects at an early stage helps cut down waste by identifying faulty products before they move further in the production line. This saves both raw materials and energy, which is especially valuable in casting processes where even small flaws can lead to large production losses. Automated defect detection systems that use deep learning improve energy efficiency by working faster and more reliably than manual inspection. They lower energy use and operating costs while keeping quality standards consistent. By reducing human error, limiting scrap, and minimizing rework, such systems make better use of available resources and support a circular economy that ties directly into the sustainability objectives of the manufacturing sector.

To gain an overview of the grayscale intensity values, the mean and standard deviation were computed for a subset of 100 images in each class, a few of which are presented in Figure 1. For the Defective class, the mean grayscale intensity was 138.66 with a standard deviation of 58.02, whereas for the OK class, the mean was 149.78 with a standard deviation of 62.42.

These values highlight two important patterns. The higher mean intensity in the OK class indicates that these images are generally brighter than the defective ones. This difference may arise from variations in surface reflectivity or the presence of darker regions such as pits, cracks, or holes in defective components. Both classes also show relatively high standard deviations, reflecting considerable variability in brightness and contrast. Such variability is crucial to recognize for model training, as it emphasizes the importance of applying suitable pre-processing techniques such as normalization or histogram equalization to ensure the model handles differences in illumination and texture effectively. The histograms of pixel intensities often display multiple peaks, suggesting the presence of distinct surface features or reflective highlights. In defective images, these peaks tend to be more widely spread, which may correspond to the coexistence of darker defect areas and brighter surrounding regions. Defective samples typically have a larger

portion of pixel values concentrated in the lower-to-mid intensity range, consistent with their lower mean intensity of 138.66. In contrast, OK samples show histogram peaks shifted toward higher intensity values, aligning with the higher mean of 149.78. This pattern indicates that non-defective parts generally possess smoother and more uniformly bright surfaces. Even among images belonging to the same class, the brightness distribution can vary considerably. This within-class variability may result from subtle differences in lighting during image capture, minor fluctuations in the manufacturing process, or unique visual signatures of specific defects. Understanding this variability is vital for developing robust models capable of distinguishing genuine defects from variations caused by external factors.

Figures 2 and 3 illustrate the pixel intensity distributions for both defective and OK impeller images, offering key insights into their visual characteristics. The defective samples exhibit a broader and multi-modal intensity curve, reflecting uneven surface textures, cavities, and rough patches that cause irregular light reflectance. In contrast, the OK samples display a narrower, right-shifted histogram, signifying consistent brightness, smooth surface finish, and structural uniformity. These clear distinctions between the two classes emphasize the need for robust preprocessing techniques—specifically normalization and histogram equalization—to standardize illumination conditions and enhance contrast before model training and feature extraction in subsequent stages.

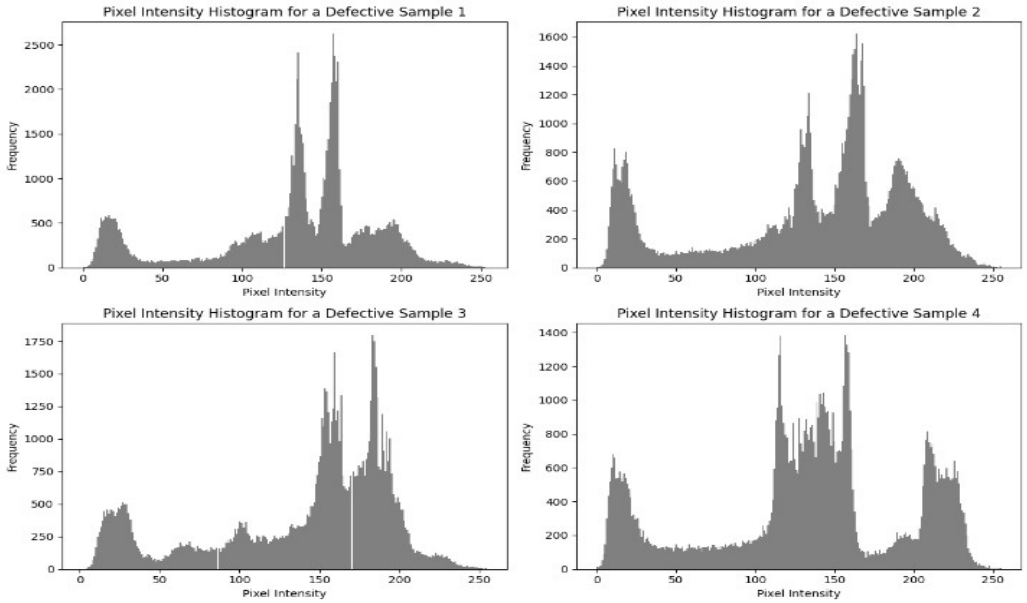


Figure 2: *Pixel Intensity for Defective Samples.*

The histogram in Figure 2 depicts the grayscale pixel intensity distribution for defective impeller images, showing a broad and irregular profile with multiple secondary peaks. This pattern indicates a wide variation in brightness values across the defective surfaces, reflecting the heterogeneous nature of casting flaws such as blow holes, shrinkage cavities, and uneven metal flow. These imperfections create localized dark and bright regions, leading to complex tonal variations. The multi-peaked structure further suggests that the defects differ in both shape and depth, adding to the overall irregularity of the images. Such variability introduces significant intra-class differences within the defective category, emphasizing the importance of image preprocessing. Techniques like normalization or histogram equalization are therefore essential to minimize intensity inconsistencies and ensure that the model focuses on meaningful defect features during training rather than illumination disparities.

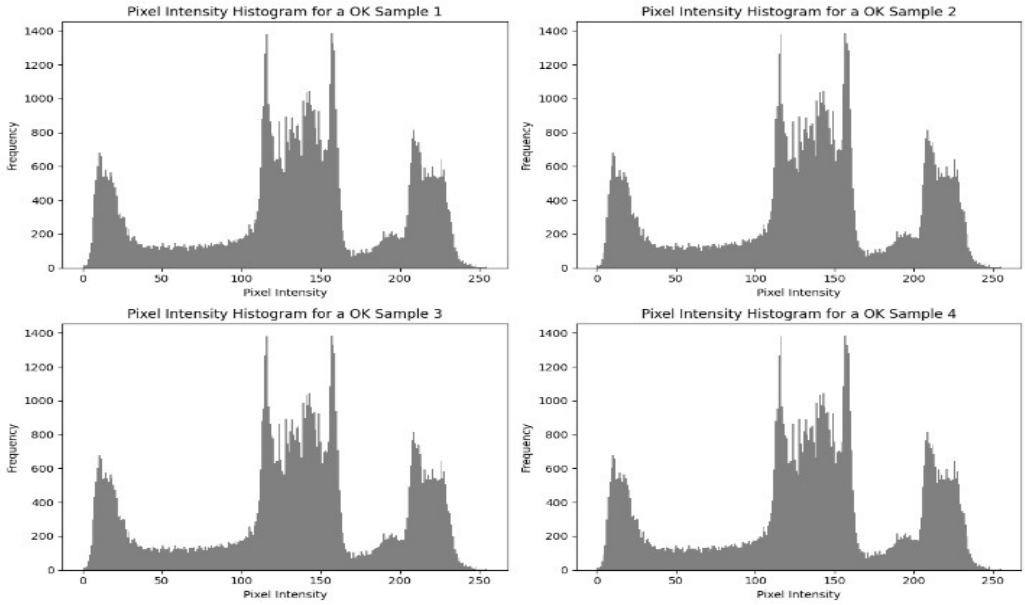


Figure 3: *Pixel Intensity for OK Samples*

Figure 3 illustrates the grayscale intensity distribution for OK impeller images, revealing a distinct pattern compared with the defective class. The histogram is notably more compact and right-shifted toward higher intensity values, signifying generally brighter, smoother, and more uniform surfaces. The presence of a single dominant peak indicates a stable and consistent reflectance pattern, which is characteristic of defect-free metallic surfaces. This narrower spread of pixel values also suggests reduced variability within the OK class, reflecting greater structural integrity and surface uniformity. Such consistent brightness behavior provides a strong separability cue for classification models, allowing them to effectively differentiate between OK and defective samples based on stable intensity features.

From a quality control standpoint, these histogram characteristics reinforce the quantitative distinctions observed in mean and standard deviation values between the two classes. Deep learning models can leverage these differences as discriminative features; however, preprocessing steps—such as normalization or histogram equalization—are essential to mitigate illumination inconsistencies and ensure that learning focuses on defect-related textures rather than simple brightness variations.

Figures 4 and 5 display edge maps obtained via the Canny operator. Continuous, symmetric rings characterize defect-free impellers, while interruptions and asymmetries denote potential casting flaws such as blow holes or burrs. These annotated edges supply geometric evidence at complements intensity-based analysis, helping the network learn both texture and shape-related defect signatures. In other words, further enhance this understanding by displaying edge maps generated using the Canny edge detection operator. In defect-free impellers, the edges appear continuous, symmetric, and well-defined, reflecting the ideal geometry of properly cast components. In contrast, defective samples exhibit irregular, fragmented, or discontinuous edges, indicating casting flaws such as blow holes, burrs, or surface distortions. These geometric variations complement intensity-based analysis, enabling the deep learning model to integrate both textural and shape-based cues for more reliable classification. Consequently, combining histogram-based brightness patterns with edge-based geometric features strengthens the robustness and interpretability of the automated defect detection framework, advancing both accuracy and sustainability in quality control operations.

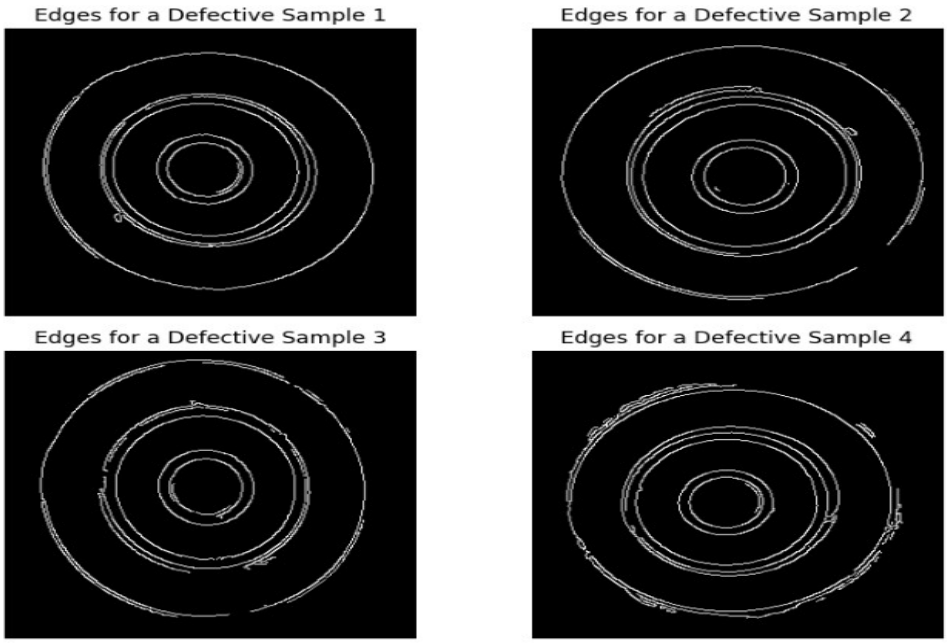


Figure 4: *Edge Detection for Defective Samples*

Figure 4 presents the Canny edge detection output for defective impeller images. The edge map reveals fragmented, uneven contours and discontinuous circular patterns across the impeller surface. These irregularities correspond to structural disruptions such as blow holes, burrs, or minor cracks formed during casting. The varying edge thickness and broken ring formations indicate deviations from ideal symmetry, a key geometric marker of surface defects. Additional localized edges appear around defect regions, signifying abrupt intensity transitions caused by rough textures or cavities. Such patterns highlight the geometric complexity of defective parts and emphasize the model's need to capture both intensity-based and shape-based cues for accurate classification.

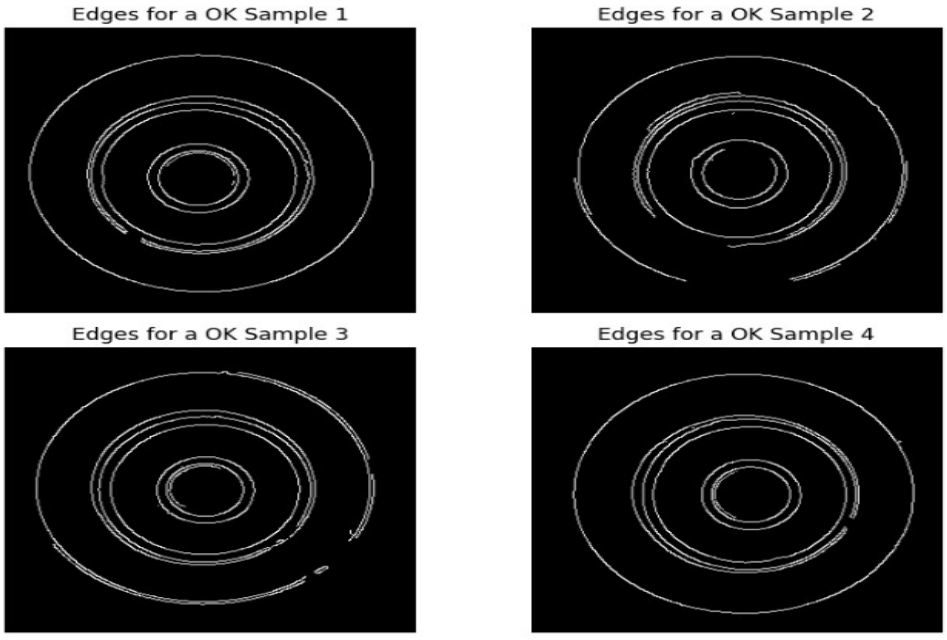


Figure 5: *Edge Detection for OK samples*

Figure 5 displays the Canny edge detection results for OK impeller images. The edges are smooth, continuous, and symmetrically arranged in concentric rings that align with the expected geometry of a properly cast impeller. The uniform edge intensity and consistent ring structure suggest minimal surface distortion and a well-balanced manufacturing outcome. The absence of stray or fragmented edges reflects the homogeneity of surface finish and stable illumination during image capture. These characteristics establish a geometric baseline against which defective samples can be contrasted. The consistency observed in the OK edges demonstrates the reliability of the imaging setup and supports the use of edge features as a dependable input for automated quality inspection.

The Canny edge detection results offer a detailed view of the geometric structure and surface quality of both defective and OK samples. Each impeller exhibits circular or near-circular regions that the Canny operator captures as concentric rings. In the OK samples, these rings appear continuous and sharply defined, indicating a smooth and consistent surface. In contrast, defective samples show subtle breaks, irregular thickness, or extra edge formations, suggesting disruptions on the surface. The Canny Edge Detection Analysis reveals the following:

- Small discontinuities, bumps, or distortions in the circular outlines often correspond to physical surface defects such as blow holes or burrs. Some defective samples display additional fragmented edges that are absent in the OK set, indicating localized imperfections or inconsistencies in material composition.
- Submersible pump impellers are designed for high symmetry, which is clearly reflected in the well-balanced edges of OK parts. Defective samples, however, sometimes deviate from this pattern, showing asymmetric or distorted contours that become more prominent through Canny edge outlines.
- Since Canny edge detection depends on intensity gradients, differences in illumination can create artificial edge patterns. Although the controlled lighting minimizes glare and shadow artifacts, residual highlights may still appear as edges in both defective and OK samples. These are consistent across images and should not be mistaken for actual defects. Edge-detected images can serve as a basis for quantitative feature extraction. Metrics such as perimeter, circularity, or the number of closed contours can be derived and integrated into a machine learning pipeline for defect classification. Consistency in edge capture across samples also indicates a stable imaging setup. Significant disparities in edge quality may signal a need to recalibrate the lighting or camera parameters.
- Detecting early signs of surface defects through edge-based analysis enables timely intervention during production. This reduces rework, material waste, and product rejection rates. Enhanced defect detection contributes to sustainable manufacturing by conserving resources and minimizing environmental impact.

The objective of this research is to build a robust automated quality inspection system for detecting defects in submersible pump impellers. We approach this task as a binary classification problem—each image is classified as either defective or OK. To accomplish this, we compare four CNN models:

- A CNN built from scratch (custom architecture)
- ResNet18 (transfer learning)
- VGG16 (transfer learning)

The CNN model we developed utilizes a sequential, layer-by-layer design tailored for binary classification (defective vs. OK). We begin with an input layer shaped to accommodate single-channel (grayscale) images, defined by input shape = (height, width, 1). The first trainable component is a convolutional layer with 32 filters, each sized 3×3, using the ReLU activation function to introduce nonlinearity. We employ stride=2 and padding='same', which effectively

halves the spatial dimensions while preserving edge information. Immediately following is a max pooling layer (MaxPooling2D), which further reduces the feature map's width and height by a factor of two, helping the network learn translation-invariant features while lowering computational cost.

This pattern repeats in the second convolution block, where the number of filters increases to 64, signifying a deeper, more discriminative representation of the image [13]. Again, stride and max pooling are used to down sample feature maps efficiently. After these blocks, the Flatten layer transforms the two-dimensional feature maps into a one-dimensional vector, bridging the gap between convolutional feature extraction and fully connected classification. Next, a Dense layer with 128 neurons captures high-level interactions among the extracted features, using ReLU to maintain nonlinearity [14]. Finally, a single-output Dense layer with a sigmoid activation translates the network's learned representations into a probability for one of the two classes (defective or OK). To train this model, we compile it with the Adam optimizer at a default learning rate of 0.001, striking a balance between speed of convergence and stability. The binary cross-entropy loss function measures the divergence between predicted probabilities and actual labels, guiding backpropagation. We track accuracy as a metric for quick performance monitoring. By stacking these layer-two convolution-pooling blocks followed by flattening and fully connected layers—we achieve a compact yet powerful architecture capable of learning meaningful patterns from grayscale images. This design effectively captures local features through convolution and pooling while leveraging a dense layer to consolidate information for the final binary decision.

In parallel to our custom CNN, we employ transfer learning with two popular architectures: ResNet18 and VGG16. Each of these models is pre-trained on a large dataset (typically ImageNet), which provides a strong initial feature representation. We then fine-tune the models on our impeller images to adapt these representations to the casting defect domain. By fine-tuning them on our specific impeller image dataset, we enable the networks to adapt their learned representations to effectively identify casting defects, thereby enhancing accuracy, reducing training time, and improving overall model generalization within the defect detection domain.

I. ResNet18

ResNet18 (Residual Network with 18 layers), tackles the vanishing gradient problem in deeper networks by introducing residual learning. Unlike traditional CNNs, ResNet18 features skip connections—or shortcuts—that directly feed the input of a residual block to its output [15]. Each residual block typically includes two 3×3 convolution layers with batch normalization and ReLU activations, plus a skip connection that bypasses these layers, enabling gradients to flow more easily during backpropagation [16]. This design allows the network to learn identity mappings, reducing the difficulty of training as depth increases. Structurally, ResNet18 begins with a 7x7 convolution and max pooling, followed by four stages of residual blocks, each doubling the number of filters while halving spatial dimensions at stage boundaries. The final stage is a global average pooling layer and a fully connected layer for classification. Despite having 18 layers, ResNet18 is relatively lightweight and easier to train compared to deeper variants (e.g., ResNet50), making it well-suited for tasks where computational resources are limited but robust feature extraction is essential. These architectures, while both CNN-based, differ in their approach to depth and parameterization. VGG16 relies on a strictly layered design with small, uniform filters and deep fully connected layers, whereas ResNet18 uses skip connections to maintain gradient flow in a shallower (but more efficient) framework. Their complementary strengths—VGG16's simplicity and high capacity versus ResNet18's ease of optimization and residual learning—make them popular choices for transfer learning, fine-tuning, and real-world image classification problems [17].

For our two-class problem, we replace the final fully connected layer with one that has 2

output neurons. We also selectively unfreeze later layers for fine-tuning while keeping earlier layers fixed (or slowly updated), this design ensures that deeper layers continue learning meaningful features rather than merely memorizing patterns.

II. VGG16

VGG16, introduced by Simonyan and Zisserman (2015), is a seminal deep convolutional neural network (CNN) renowned for its simplicity, uniformity, and strong generalization capabilities. The architecture comprises 16 weight layers—13 convolutional and 3 fully connected layers—employing small, uniform 3×3 convolution filters throughout. Each convolutional block typically contains two or three convolutional layers with a stride of 1 and padding of 1 to preserve spatial resolution, followed by a max-pooling layer that reduces the feature map size by half. This hierarchical structure allows the model to progressively learn from low-level edges and textures to high-level object patterns. After feature extraction, the flattened feature maps pass through three dense layers, the first two with 4,096 neurons each and the final one producing class probabilities through a SoftMax activation. VGG16's proven efficiency on large-scale datasets such as ImageNet makes it highly effective for transfer learning. In this study, VGG16 was used as a feature extractor, and its final layers were retrained for binary classification of submersible pump impeller defects. The model employed cross-entropy loss and the Adam optimizer with an initial learning rate of 0.001, decaying gradually through a step or exponential schedule, and was trained for 10–30 epochs with a batch size of 32 to prevent overfitting and ensure rapid convergence [14].

From the results, we observe that VGG and ResNet outperform CNN in terms of precision and recall, especially for the OK class. CNN tends to misclassify OK parts more than VGG and ResNet, as reflected in its lower precision for the OK class (0.96). VGG and ResNet have near-identical performance, both reaching 99% accuracy with minimal misclassifications. ResNet offers better generalization over unseen datasets due to its deeper architecture and residual learning.

V. Results

Table 1: *Model Performance*

Model	Accuracy	Precision (OK)	Precision (Defective)	Recall (OK)	Recall (Defective)
CNN	98%	0.96	0.99	0.98	0.98
VGG	99%	1.00	0.98	0.99	1.00
ResNet	99%	1.00	0.98	0.99	1.00

The training and validation loss and accuracy trends for CNN, VGG, and ResNet were analysed over 20 epochs. The plots reveal that CNN shows a slightly higher validation loss than VGG and ResNet, indicating a tendency toward overfitting. VGG and ResNet maintain stable validation accuracy, suggesting better generalization. All models achieve high accuracy (>98%) within the first 5 epochs, confirming the effectiveness of feature extraction and classification.

To test real-world performance, we applied data augmentation techniques, including rotation, zoom, flipping, and brightness adjustments. This ensured:

- Increased robustness of models against minor variations in defects.
- Reduction in overfitting by forcing the models to learn invariant features.

CNN's accuracy improved slightly (~0.5%), reducing its misclassification rate for OK parts.

IV. Discussion

In summary, our comparative study of CNN, ResNet18, and VGG16 underscores the potential of deep learning for casting defect detection in submersible pump impellers and similar manufacturing processes. While the baseline CNN achieved strong results, ResNet18 and VGG16 both demonstrated superior performance—often exceeding 98% accuracy—highlighting their capacity for robust feature extraction and classification. These high-accuracy models, when deployed on production lines, can significantly enhance sustainability by reducing the number of defective parts that pass inspection and minimizing the rework or scrapping of otherwise salvageable components. Moreover, incorporating data augmentation proved crucial in promoting model generalization, suggesting that real-world applications will benefit from extensive variability in training samples. Looking ahead, integrating these architectures with IoT-driven sensors and edge computing platforms can further optimize inspection throughput, energy usage, and resource allocation. Ultimately, deep learning-based defect detection not only elevates product quality and operational efficiency but also aligns with broader sustainability objectives in modern casting manufacturing.

References

[1] Swift, K. G., & Booker, J. D. (2013). *Manufacturing process selection handbook.* Butterworth-Heinemann.

[2] Tao, F., Cheng, J., Qi, Q., Zhang, M., Zhang, H., & Sui, F. (2018). Digital twin-driven product design, manufacturing and service with big data. *The International Journal of Advanced Manufacturing Technology, 94*(9), 3563–3576. https://doi.org/10.1007/s00170-017-0233-1

[3] Tabernik, D., Šela, S., Skvarč, J., & Skočaj, D. (2020). Segmentation-based deep-learning approach for surface-defect detection. *Journal of Intelligent Manufacturing, 31*(3), 759–776. https://doi.org/10.1007/s10845-019-01476-x

[4] Sani, A. R., Zolfagharian, A., & Kouzani, A. Z. (2024). Automated defects detection in extrusion 3D printing using YOLO models. *Journal of Intelligent Manufacturing.* Advance online publication. https://doi.org/10.1007/s10845-024-02223-8

[5] Dosovitskiy, A., Beyer, L., Kolesnikov, A., Weissenborn, D., Zhai, X., Unterthiner, T., ... & Houlsby, N. (2020). *An image is worth 16×16 words: Transformers for image recognition at scale. arXiv preprint* arXiv:2010.11929. https://arxiv.org/abs/2010.11929

[6] Bressanelli, G., Adrodegari, F., Pigosso, D. C. A., & Parida, V. (2022). Towards the smart circular economy paradigm: A definition, conceptualization, and research agenda. *Sustainability, 14*(9), 4960. https://doi.org/10.3390/su14094960

[7] Habibpour, M., Gharoun, H., Tajally, A., Shamsi, A., Asgharnezhad, H., Khosravi, A., & Nahavandi, S. (2021). *An uncertainty-aware deep learning framework for defect detection in casting products. arXiv preprint* arXiv:2107.11643. https://arxiv.org/abs/2107.11643

[8] Ding, Z., Zhao, J., Misra, R. D. K., Guo, F., Xie, Z., Wang, X., ... & Shang, C. (2023). Deep learning-based understanding of defects in continuous casting product. *Metals, 13*(11), 1809. https://doi.org/10.3390/met13111809

[9] Vijay Kumar, V., & Shahin, K. (2025). Artificial intelligence and machine learning for sustainable manufacturing: Current trends and future prospects. *Intelligent and Sustainable Manufacturing, 2*(1), 10002. https://doi.org/10.1016/j.ism.2025.10002

[10] Ripik AI. (2024, November 14). *The future of manufacturing: AI and sustainability working hand in hand. Ripik AI Blog.* https://www.ripik.ai/the-future-of-manufacturing-ai-and-sustainability-working-hand-in-hand/

[11] Ojha, V. K., Goyal, S., & Chand, M. (2025). Developing novel deep learning models for

automated quality inspection in casting. *International Journal of Metalcasting*. Advance online publication. https://doi.org/10.1007/s40962-024-01542-y

[12] Shorten, C., & Khoshgoftaar, T. M. (2019). A survey on image data augmentation for deep learning. *Journal of Big Data, 6*(1), 60. https://doi.org/10.1186/s40537-019-0197-0

[13] Krizhevsky, A., & Hinton, G. E. (2009). *Learning multiple layers of features from tiny images* [Technical report]. University of Toronto. https://www.cs.toronto.edu/~kriz/learning-features-2009-TR.pdf

[14] Kingma, D. P., & Ba, J. (2014). *Adam: A method for stochastic optimization. arXiv preprint* arXiv:1412.6980. https://arxiv.org/abs/1412.6980

[15] He, K., Zhang, X., Ren, S., & Sun, J. (2016). Deep residual learning for image recognition. In *Proceedings of the IEEE Conference on Computer Vision and Pattern Recognition* (pp. 770–778). https://doi.org/10.1109/CVPR.2016.90

[16] Ioffe, S., & Szegedy, C. (2015). Batch normalization: Accelerating deep network training by reducing internal covariate shift. In *Proceedings of the 32nd International Conference on Machine Learning* (Vol. 37, pp. 448–456). PMLR. https://proceedings.mlr.press/v37/ioffe15.html

[17] Russakovsky, O., Deng, J., Su, H., Krause, J., Satheesh, S., Ma, S., Huang, Z., Karpathy, A., Khosla, A., Bernstein, M., Berg, A. C., & Fei-Fei, L. (2015). ImageNet large scale visual recognition challenge. *International Journal of Computer Vision, 115*(3), 211–252. https://doi.org/10.1007/s11263-015-0816-y

IN COMPLEX INTERVAL-VALUED FUZZY METRIC SPACE, COMMON FIXED-POINT THEOREMS CLR/JCLR/E.A PROPERTY

Umashankar Singh[1*], Naval Singh[2], Heera Ahirwar[3]

•

[1]* Technocrats Institute of Technology, Bhopal, Madhya Pradesh, India
[2]Govt. SPM Science and Commerce College Bhopal, Madhya Pradesh, India
[3]Shri Raghvendra Singh Hazari Govt. College Hata, Damoh, Madhya Pradesh, India
[1] umashankar_singh1977@rediffmail.com
[3] heera.education21@gmail.com

Abstract

The work of D. Singh et al. served as inspiration for this study, which established complex interval valued fuzzy metric space and proved several common fixed print theorems for compatible types of (p-1) on the structure of complex interval valued fuzzy metric space. The equivalent findings in the body of existing research are expanded upon and generalized by these findings. Additionally, we create a novel implicit relation that can aid researchers in accelerating common fixed-point existence and uniqueness wherever a pair of self-mappings fits the Clr/Jclr/E.A-Property. Appropriate examples are provided to demonstrate the usefulness of the primary conclusions that are gained.

Keywords: list Complex Interval-valued continues t-norms, complex Interval-valued fuzzy metric Space ($Civfms$), Common fixed-point, compatible type of mappings.

I. Introduction

Lorem Interval valued fuzzy metric spaces are a novel generalization of fuzzy metric spaces created by Shen et al. [26]. Two natural fuzzy metric spaces are induced by each interval-valued fuzzy metric space. The topology generated by the interval-valued fuzzy metric space coincides with the topology produced by the interval-valued fuzzy metric space. three different types of distances between two interval-valued fuzzy sets on real line R were employed by C. Li [16]. The concept of continuous interval-valued t-norm can be used to build an interval-valued fuzzy metric space and to characterize the uncertainty of the distance between two points in such a space. In response to this letter, numerous authors and scholars have thoroughly and in-depthly examined a variety of issues pertaining to this space from different angles, including compatible mapping, weak compatible mapping, and new findings on interval-valued fuzzy metric space. Letters I and $[\wp_n(x)]$ indicate the set of positive integers through this article, where$I = [0,1]$ and $[\wp_n(x)] = [\wp_n{}^-, \wp_n{}^+]$: $0 \leq \wp_n{}^-(x) \leq \wp_n{}^+(x) \leq 1$. Recently in 2023, Some c-fixed-point results for mapping on interval-valued fuzzy metric space using weakly compatible were established by V. Deshmukh et al. [6]. Buckly was the first to introduce fuzzy complex numbers and fuzzy complex analysis [2, 3]. Some scholars were inspired to carry out more research on fuzzy complex numbers by Buckey's discovery. In this series, Ramot et al. [21, 22] generalized fuzzy sets to complex fuzzy sets.

According to Ramot, a membership function that extends beyond [0, 1] to the unit circle in the complex plane defines the complex fuzzy set. The concept of complex valued metric space was first proposed by Azam et al. [1], who also gave enough conditions for the presence of a common f-point of a pair of mappings that meet contractive constraints. The concept of complex valued fuzzy metric spaces was later presented by D. Singh and Kumam [26] using the complex valued continuous t-norm and associated topologies.

In this research, we introduced the concept of complex interval-valued fuzzy metric space to modify the distance function under $Clr/Jclr/E.A$ −Property for common fixed-point theorems in complex interval-valued fuzzy metric space in order to prove several well-known common fixed-point theorems for self mappings.

II. Preliminaries

Definition 2.1[26] A mapping $\wp_n: \mho \to [I]$ is called an interval-valued fuzzy set on $\mho$ where $\mho$ is non empty set, Collection of all interval-valued fuzzy sets on $\mho$ is denoted by $Ivf(\mho)$. if $\wp_n \in Ivf(\mho)$. , let $\wp_n(x) = [\wp_n{}^-, \wp_n{}^+]$: $0 \le \wp_n{}^-(x) \le \wp_n{}^+(x) \le 1$ for all $x \in \mho$, then the set $\wp_n{}^-: \mho \to [I]$ and $\wp_n{}^+: \mho \to [I]$ are called lower fuzzy set and upper fuzzy set of $\wp_n$ and if $\wp_n{}^-(x) = \wp_n{}^+(x)$ then is called degenerate fuzzy set for all $x \in \mho$. if $(I] = \{I\} - \{\bar{0}\}$ and $(I) = \{I\} - \{\bar{0}, \bar{1}\}$. For every $\overline{\mu}_{ivf}, \overline{\nu}_{ivf} \in [I]$ then the following operations holds:
$(Op-1)$: $\overline{\mu}_{ivf} \wedge \overline{\nu}_{ivf} = \left[\mu_{inf}^- \wedge \nu_{inf}^-, \mu_{inf}^+ \wedge \nu_{inf}^+\right]$;
$(Op-2)$: $\overline{\mu}_{ivf} \vee \overline{\nu}_{ivf} = \left[\mu_{inf}^- \vee \nu_{inf}^-, \mu_{inf}^+ \vee \nu_{inf}^+\right]$;
$(Op-3)$: $\overline{\mu}_{ivf}{}^c = \bar{1} - \overline{\mu}_{ivf} = \left[1 - \mu_{inf}^+, 1 - \mu_{inf}^-\right]$;

Definition 2.2[26] A binary operation of the form is an interval valued t_{norm} is $*_I: [I] \times [I] \to [I]$ on $[I]$ such that for all $\overline{\mu}, \overline{\nu}, \overline{w} \in [I]$ if satisfying following four conditions:
(1) Commutativity : $\bar{a}_{ivf} *_I \bar{b}_{ivf} = \bar{b}_{ivf} *_I \bar{a}_{ivf}$,
(2) Associativity: $\left[\bar{a}_{ivf} *_I \bar{b}_{ivf}\right] *_I \bar{c}_{ivf} = \bar{a}_{ivf} *_I \left[\bar{b}_{ivf} *_I \bar{c}_{ivf}\right]$,
(3) Monotonicity: $\bar{a}_{ivf} *_I \bar{b}_{ivf} \le \bar{a}_{ivf} *_I \bar{c}_{ivf}$, $whenever$ $\bar{b}_{ivf} *_I \bar{c}_{ivf}$,
(4) Boundary condition: $\bar{a}_{ivf} *_I \bar{1} = \bar{a}_{ivf}$, $\bar{a}_{ivf} *_I \bar{0} = [a^-, a^+] *_I [0,1] = [0, a^+]$.
Note: Each interval valued t_{nrm} satisfies some additional boundary conditions for all $\bar{a} \in [I]$:
$\bar{a} *_I \bar{0} = \bar{0} *_I \overline{\mu} = \bar{0}$,
$\bar{I} *_I \bar{a} = [0,1] *_I [a^-, a^+] = \bar{0}$,
$\bar{1} *_I \bar{a} = \bar{1}$.
Example 1: (a) $\overline{\mu} *_I \overline{\nu} = [\mu^-.\nu^-, \mu^+.\nu^+]$; (b)$\overline{\mu} *_I \overline{\nu} = [\mu^- \wedge \nu^-, \mu^+ \wedge \nu^+]$;
Definition 2.3[6]: Let$\{\bar{a}_i\}_{i \in \mathbb{N}^+} = \{[a_i^-, a_i^+]\}$be a sequence of interval numbers convergesto $\bar{a} = [a^-, a^+] \in [I]$, if $\lim_{i\to\infty} a_i^- = a^-and\lim_{i\to\infty} a_i^+ = a^+$ then the sequence$\{\bar{a}_i\}$is convergent to$\bar{a}$ and denoted by$\lim_{i\to\infty} \bar{a}_i = \bar{a}$ $(\{\bar{a}_i \to \bar{a}\}$.
Definition 2.4[6]: An interval valuedt_{nrm} $*_I$as continuous iff it is continuous in its first component, i.e. for each $\overline{b} \in [I]$, if $\lim_{i\to\infty} \bar{a}_i = \bar{a}$, then
$\lim_{i\to\infty}\left(\bar{a}_i *_I \bar{b}\right) = (\lim_{i\to\infty} \bar{a}_i *_I \bar{b}) = \bar{a} *_I \bar{b}$, Where $\{\bar{a}_i\} \subseteq [\boldsymbol{I}], \bar{a} \in [I]$.
Definition 2.5[10]: A triplet $(X, M, *)$ is called fuzzy metric space*(FMS)* if $\mathfrak{X}$ is an arbitrary set, $*$ is a continuoust-normson [0,∞]and $M$is a fuzzy set on $X^2 \times (0, \infty)$ satisfying the following conditions:
(1) $M(x, y, t) > 0$;
(2) $M(x, y, t) = 1$ $for\ all\ t > 0$ iff $x = y$;
(3) $M(x, y, t) = M(y, x, t)$;
(4) $M(x, z, t_1 + t_2) \ge T(M(x, y, t_1), M(x, y, t_2))$; $\forall x, y, z \in X$
(5) $M(x, y, *_I)$: $[0, \infty] \to (0,1]$is continuous;
Definition 2.6[29]: A 3-tuple $\left(\mathbb{X}, \overline{\mathfrak{D}_{Ivfms}}, *_I\right)$ is called interval valued fuzzy metric space *(Ivfms)* if Ξ is an arbitrary set, $*_I$ is a continuous interval valued t_{norm} on *[I]*and $\overline{\mathfrak{D}_{Ivfms}}$is a fuzzy set on $\mathbb{X}^2 \times (0, \infty)$ satisfying the following conditions:

(1) $\overline{\text{Đ}_{Ivfms}}(x, y, t_{nrm}) > \bar{0}$;
(2) (2) $\overline{\text{Đ}_{Ivfms}}(x, y, t_{nrm}) = \bar{1}$ $for\ all\ t > 0$ iff $x = y$;
(3) $\overline{\text{Đ}_{Ivfms}}(x, y, t_{nrm}) = \overline{\text{Đ}_{Ivfms}}(y, x, t_{nrm})$;
(4) $\overline{\text{Đ}_{Ivfms}}(x, y, t_1) *_I \overline{\text{Đ}_{Ivfms}}(y, z, t_2) \leq \overline{\text{Đ}_{Ivfms}}(x, z, t_1 + t_2)$; $\forall x, y, z \in \mathbb{X}\ and\ t_1, t_2, > 0$
(5) $\overline{\text{Đ}_{Ivfms}}(x, y, *_I): [0, \infty] \to (I]$ is continuous;
(6) $\lim_{t\to\infty} \overline{\text{Đ}_{Ivfms}}(x, y, t_{nrm}) = \bar{1}$; $\forall\ x, y, z \in \mathbb{X},\ t_{nrm} > 0$

Definition 2.7: A 3-tuple $(\mathbb{X}, \overline{\text{Đ}_{Civfms}}, *_I)$ is called complex interval valued fuzzy metric space *(Civfms)*, where $\overline{\text{Đ}_{Civfms}}: \mathbb{X}^2 \times (0, \infty) \to r_s e^{i\theta} and \mathbb{X}$ is non-empty set, * is a complex valued continuous, and t-norm. The fuzzy set $\to r_s e^{i\theta}$ has complex values and satisfying the following conditions:
$(CIM-1)$ $\overline{\text{Đ}_{Civfms}}(x, y, t) \succ_i 0$;
$(CIM-2)$ $\overline{\text{Đ}_{Civfms}}(x, y, t) = e^{i\theta}$ $, for\ all\ t > 0\ iff\ x = y$;
$(CIM-3)$ $\overline{\text{Đ}_{Civfms}}(x, y, t) = \overline{\text{Đ}_{Civfms}}(y, x, t)$;
$(CIM-4)$ $\overline{\text{Đ}_{Civfms}}(x, y, p) * \overline{\text{Đ}_{Civfms}}(y, z, q) \succsim_i \overline{\text{Đ}_{Civfms}}(x, z, p + q)$;
$(CIM-5)$ $\overline{\text{Đ}_{Civfms}}(x, y, .): (0, \infty) \to r_s e^{i\theta}$ is continuous;
$For\ all\ x, y, z \in \mathbb{X}, p, q > 0, r_s \in [0,1]\ and\ \theta \in [0, \frac{\pi}{2}]$.
Then $(\mathbb{X}, \overline{\text{Đ}_{Civfms}}, *)$ is called complex Interval valued fuzzy metric space .

Example 2[31]: Let $(\mathbb{X}, d)$ be a real valued metric space. Let $u * v = min\{u, v\} (or u * v = uv)$, for each $t > 0, u, v \in r_s e^{i\theta}$, where $r_s \in [0,1]$ and $\theta \in \left[0, \frac{\pi}{2}\right]$. Further more $u, v \in \mathbb{X}$, Define $\overline{\text{Đ}_{Civfms}}(x, y, t) = e^{i\theta} \frac{t}{t + d(x,y)}$.

Example 3[31]: Let $\mathbb{X} = R$. Let $u * v = min\{u, v\} (or u * v = uv)$, for each $t > 0, u, v \in r_s e^{i\theta}$, where $r_s \in [0,1]$ and $\theta \in \left[0, \frac{\pi}{2}\right]$. Further more $u, v \in \mathbb{X}$, define $\overline{\text{Đ}_{Civfms}}(x, y, t) = e^{i\theta} e^{-\frac{|x-y|}{t}}$.

Definition 2.8: An self maps is a mapping that, within its range, has a single value for every point in the domain. As a result, it is either many-to-one or one-to-one.

Definition 2.9: Two self mapping A and B on *Civfms* $(\mathbb{X}, \overline{\text{Đ}_{Civfms}}, *_I)$ are said to be satisfy weakly compatible if $\text{Lim}_{n\to\infty} \overline{\text{Đ}_{Civfms}}(Ax_n, Bx_n, t_{nrm}) \to e^{i\theta}$ or $\lim_{n\to\infty} \left|\overline{\text{Đ}_{Civfms}}(Ax_n, Bx_n, t_{nrm})\right| \to \bar{1}$ And $\lim_{n\to\infty} \overline{\text{Đ}_{Civfms}}(BAx_n, ABx_n, t_{nrm}) \to e^{i\theta}$ or $\lim_{n\to\infty} \left|\overline{\text{Đ}_{Civfms}}(BAx_n, ABx_n, t_{nrm})\right| \to \bar{1}$ For all $t_{nrm} > 0, \theta \in \left[0, \frac{\pi}{2}\right]$, whenever $\{x_n\}$ is a sequence in X such that $Ax_n, Bx_n \to z$ for some $z \in X\ as\ n \to \infty$.

Definition 2.10: Two single valued mapping A and B on *Civfms* $(\mathbb{X}, \overline{\text{Đ}_{Civfms}}, *_I)$ then compatible if $\lim_{n\to\infty} \overline{\text{Đ}_{Ivfms}}(ABx_n, BAx_n, t_{nrm}) = e^{i\theta}$ or $\lim_{n\to\infty} \left|\overline{\text{Đ}_{Civfms}}(ABx_n, BAx_n, t_{nrm})\right| \to \bar{1}$ for all $t_{nrm} > 0$, $\theta \in \left[0, \frac{\pi}{2}\right]$ whenever a sequence $\{x_n\}$ in $\mathfrak{X}$ provided $\lim_{n\to\infty} \text{A}x_n = \lim_{n\to\infty} \text{B}x_n = u$, $for\ all\ u \in \mathbb{X}$.

Definition 2.11: Two single valued mapping A and B on *Civfms* $(\mathbb{X}, \overline{\text{Đ}_{Civfms}}, *_I)$ are said to be satisfy compatible of type $(p-1)$ if $\text{Lim}_{n\to\infty} \overline{\text{Đ}_{Civfms}}(ABx_n, BBx_n, t_{nrm}) \to e^{i\theta}$ or $\lim_{n\to\infty} \left|\overline{\text{Đ}_{Civfms}}(ABx_n, BBx_n, t_{nrm})\right| \to \bar{1}$ for all $t_{nrm} > 0, \theta \in \left[0, \frac{\pi}{2}\right]$ Whenever $\{x_n\}$ is a sequence in X *such that* $Ax_n, Bx_n \to z$ *for some* $z \in X\ as\ n \to \infty$.

Lemma 2.12 [10]: Let $(\mathbb{X}, \overline{\text{Đ}_{Civfms}}, *_I) Civfms$ with $\lim_{t\to\infty} N(x, y, t) = e^{i\theta}$ $, \forall x, y \in X, t \in (0,1)$, $\theta \in \left[0, \frac{\pi}{2}\right]$ for all $x, y \in \mathbb{X}, t_{nrm} > \bar{0}$ with a positive number $k \in (0,1)$ such that $\overline{\text{Đ}_{Civfms}}(x, y, kt_{nrm}) \geq \overline{\text{Đ}_{Civfms}}(x, y, t_{nrm}) \Rightarrow x = y$.

Definition 2.13: Let $(\mathbb{X}, \overline{\text{Đ}_{Civfms}}, *_I)$ be a *Ivfms*, where * denotes a continuous t-norm and $f, g, h\ and\ k$ be self-mapping on X .The pairs $\{f, g\} and \{h, k\}$ are said to be satisfy the "common limit in the range of g" $(CLRg)$ –Property if and only if there exist sequences $\{\boldsymbol{x_n}\}$ and $\{\boldsymbol{y_n}\}$ and a point $u \in X$ such that

$$\lim_{n\to\infty} \overline{\text{Đ}_{Civfms}}(fx_n, gu, t_{nrm}) = \lim_{n\to\infty} \overline{\text{Đ}_{Civfms}}(gx_n, gu, t_{nrm})$$
$$= \lim_{n\to\infty} \overline{\text{Đ}_{Civfms}}(hy_n, gu, t_{nrm}) = \lim_{n\to\infty} \overline{\text{Đ}_{Civfms}}(ky_n, gu, t_{nrm})\ \ for\ all\ t_{nrm} > 0$$

Similar is the case with $CLRf$, $CLRh$, $CLRk$–Properties where gu is replace by fu, hu, ku in the

above equality quantities.

Definition 2.14 Let $(\mathbb{X}, \overline{Đ_{Civfms}}, *_I)$be a Ci*vfms,* where * denotes a continuous $t-nrm$ and $f, g, i \; and \; j$ be self-mapping on X .The pairs $\{f, g\} and \{i, j\}$ are said to be satisfy the "joint common limit in the range of g" **$(JCLRgj)$** –Property if and only if there exist sequences $\{\boldsymbol{x_n}\}$ and $\{\boldsymbol{y_n}\}$ and a point $u \in X$ such that and $ku = gu \; and$

$\text{Lim}_{n\to\infty} \overline{Đ_{Civfms}}(fx_n, gu, t_{nrm}) = \text{Lim}_{n\to\infty} \overline{Đ_{Civfms}}(gx_n, gu, t_{nrm}) =$

$\text{Lim}_{n\to\infty} \overline{Đ_{Civfms}}(iy_n, gu, t_{nrm}) = \text{Lim}_{n\to\infty} \overline{Đ_{Civfms}}(jy_n, gu, t_{nrm}) = e^{i\theta} \;\; for \; all \; t_{nrm} > 0, \theta \in \left[0, \frac{\pi}{2}\right]$.

Similar is the case with $CLRf$, $CLRi$, $CLRj$–Properties where gu is replace by fu, iu, ju in the above equality quantities.

Definition 2.15[11] Two self mapping A and B on*Civfms*$(\mathbb{X}, \overline{Đ_{Civfms}}, *_I)$are said to satisfy the Property (E.A) if there exist a sequence $\{x_n\}$ in X such that

$$\lim_{n\to\infty} Ax_n = \lim_{n\to\infty} Bx_n = z$$

Definition 2.16[11] Two pairs $\{P, Q\} \; and \{C, D\}$ of self-mapping of a *Ivfms*$(\mathbb{X}, \overline{Đ_{Civfms}}, *_I)$are said to be satisfy the Common Property (E.A) if there exist two sequences $\{\boldsymbol{x_n}\}$ and $\{\boldsymbol{y_n}\}$ and a point $u \in X$ such that

$$\lim_{n\to\infty} Px_n = \lim_{n\to\infty} Qx_n = \lim_{n\to\infty} Cy_n = \lim_{n\to\infty} Dy_n = u$$

III. Main Results

Implicit Relation:

For our theorems first we define a implicit functions which is support our theorems. Let $\boldsymbol{\Phi}$ be the set of all continuous functions $\psi: [(I^+)]^6 \to \mathbf{I}$ satisfying the following conditions:

(ψ_1): $\psi$is non-decreasing in first argument.

(ψ_2): $\psi(a, e^{i\theta}, a, e^{i\theta}, a, e^{i\theta}) \geq 0 \Rightarrow a \geq e^{i\theta}$.

(ψ_3): $\psi(a, e^{i\theta}, e^{i\theta}, a, e^{i\theta}, a) \geq 0 \Rightarrow a \geq e^{i\theta}$.

(ψ_4): $\psi(a, a, e^{i\theta}, e^{i\theta}, a, a) \geq 0 \Rightarrow a \geq e^{i\theta}$.

(ψ_5): $\psi(a, a, e^{i\theta}, e^{i\theta}, e^{i\theta}, e^{i\theta}) \geq 0 \Rightarrow a \geq e^{i\theta}$.

Theorem 3.1 Let$(\mathbb{X}, \overline{Đ_{Civfms}}, *_I)$ be a Civfms with $\lim_{t\to\infty} \overline{Đ_{Civfms}}(x, y, t) = e^{i\theta}$, $\forall x, y \in \mathbb{X}, t \in (0,1), \theta \in \left[0, \frac{\pi}{2}\right], t_{nrm} > \bar{0}$. The maps A and B are two weakly compatible self-maps in with $t_{nrm} *_I t_{nrm} \geq t_{nrm}$, satisfying the following:

(1) $B(X) \subseteq A(X)$;

(2) A(X) or B(X) is complete subspace of $\mathbb{X}$;

(3) A and B share (E. A)property;

(4) For all $t_{nrm} > 0, 0 < k < 1 \; and \; x \neq y \in \mathbb{X}$

$$\overline{Đ_{Civfms}}(Bx, By, kt_{nrm}) \geq \text{Min}\left\{\begin{matrix}\overline{Đ_{Civfms}}(Ax, Ay, t_{nrm}), [\overline{Đ_{Civfms}}(Ax, By, t_{nrm}) * \overline{Đ_{Civfms}}(Ay, Bx, t_{nrm})], \\ [\overline{Đ_{Civfms}}(Ax, Bx, t_{nrm}) * \overline{Đ_{Civfms}}(Ay, By, t_{nrm})]\end{matrix}\right\}$$

Then A and Bhave UCFP.

Proof: Since B and A share (E. A) -property. So, by the definition, there exist sequences $\{x_n\}$ in $\mathbb{X}$ such that

$\lim_{n\to\infty} Bx_n = \lim_{n\to\infty} Ax_n = u$, for some $u \in \mathbb{X}$.

Suppose A(X) is complete then $\lim_{n\to\infty} Ax_n = Aa$, for some $a \in \mathbb{X}$. Therefore $\lim_{n\to\infty} Bx_n = Aa$

Now to claim $Ba = Aa$.

Put $x = x_n$ and $y = a$ in inequality (d)

$$\overline{Đ_{Civfms}}(Bx_n, Ba, kt_{nrm}) \geq \text{Min}\left\{\begin{matrix}\overline{Đ_{Ivf}}(Ax_n, Aa, t_{nrm}), [\overline{Đ_{Civfms}}(Ax_n, Ba, t_{nrm}) * \overline{Đ_{Civfms}}(Aa, Bx_n, t_{nrm})], \\ [\overline{Đ_{Civfms}}(Ax_n, Bx_n, t_{nrm}) * \overline{Đ_{Civfms}}(Aa, Ba, t_{nrm})]\end{matrix}\right\}$$

As $n \to \infty$, then we get

$$\overline{Đ_{Civfms}}(Aa, Ba, kt_{nrm}) \geq \text{Min}\left\{\begin{matrix}\overline{Đ_{Civfms}}(Aa, Aa, t_{nrm}), [\overline{Đ_{Civfms}}(Aa, Ba, t_{nrm}) * \overline{Đ_{Civfms}}(Aa, Aa, t_{nrm})], \\ [\overline{Đ_{Civfms}}(Aa, Aa, t_{nrm}) * \overline{Đ_{Civfms}}(Aa, Ba, t_{nrm})]\end{matrix}\right\}$$

$$\overline{Đ_{Civfms}}(Aa, Ba, kt_{nrm}) \geq \text{Min}\left\{\begin{matrix}e^{i\theta}, [\overline{Đ_{Civfms}}(Aa, Ba, t_{nrm}) *_I e^{i\theta}], \\ [e^{i\theta} *_I \overline{Đ_{Civfms}}(Aa, Ba, t_{nrm})]\end{matrix}\right\}$$

$$\overline{Đ_{Civfms}}(Aa, Ba, kt_{nrm}) \geq \text{Min}\left\{\begin{matrix}e^{i\theta}, [\overline{Đ_{Civfms}}(Aa, Ba, t_{nrm})], \\ [\overline{Đ_{Civfms}}(Aa, Ba, t_{nrm})]\end{matrix}\right\}$$

$$\overline{Đ_{Civfms}}(Aa, Ba, kt_{nrm}) \geq \overline{Đ_{Civfms}}(Aa, Ba, t_{nrm})$$

By lemma 2.12, we have, $Aa = Ba$.

Now A and B are weakly compatible. i. e. $ABa = BAa = AAa = BBa$ then we show that Ba is the common fixed-point of B and A.

Put $x = a$ and $y = Ba$ in inequality (d)

$$\overline{Đ_{Civfms}}(Ba, BBa, kt_{nrm}) \geq \text{Min}\left\{\begin{matrix}\overline{Đ_{Civfms}}(Aa, ABa, t_{nrm}), [\overline{Đ_{Civfms}}(Aa, BBa, t_{nrm}) * \overline{Đ_{Civfms}}(ABa, Ba, t_{nrm})], \\ [\overline{Đ_{Civfms}}(Aa, Ba, t_{nrm}) * \overline{Đ_{Civfms}}(ABa, BBa, t_{nrm})]\end{matrix}\right\}$$

$$\overline{Đ_{Civfms}}(Ba, BBa, kt_{nrm}) \geq \text{Min}\left\{\begin{matrix}\overline{Đ_{Civfms}}(Ba, BBa, t_{nrm}), [\overline{Đ_{Civfms}}(Ba, BBa, t_{nrm}) * \overline{Đ_{Civfms}}(BBa, Ba, t_{nrm})], \\ [\overline{Đ_{Civfms}}(Ba, Ba, t_{nrm}) * \overline{Đ_{Civfms}}(BBa, BBa, t_{nrm})]\end{matrix}\right\}$$

$$\overline{Đ_{Civfms}}(Ba, BBa, kt_{nrm}) \geq \text{Min}\left\{\begin{matrix}\overline{Đ_{Ivf}}(Ba, BBa, t_{nrm}), [\overline{Đ_{Ivf}}(Ba, BBa, t_{nrm})], \\ [e^{i\theta} *_I \overline{Đ_{Ivf}}(BBa, BBa, t_{nrm})]\end{matrix}\right\}$$

$$\overline{Đ_{Civfms}}(Ba, BBa, kt_{nrm}) \geq \text{Min}\left\{\begin{matrix}\overline{Đ_{Civfms}}(Ba, BBa, t_{nrm}), [\overline{Đ_{Civfms}}(Ba, BBa, t_{nrm})], \\ [\overline{Đ_{Civfms}}(BBa, BBa, t_{nrm})]\end{matrix}\right\}$$

$$\overline{Đ_{Civfms}}(Ba, BBa, kt_{nrm}) \geq \overline{Đ_{Civfms}}(Ba, BBa, t_{nrm})$$

By lemma 2.12 we get $Ba = BBa$.

Hence Ba is the common fixed-point of B and A.

In the similar manner if B(X) is complete. The result will be same.

Now to show that fixed-point is unique.

Let α and β be the two c-fixed-point of A, B.

$$\overline{Đ_{Civfms}}(\alpha, \beta, kt_{nrm}) = \overline{Đ_{Civfms}}(B\alpha, B\beta, kt_{nrm}) \geq \text{Min}\left\{\begin{matrix}\overline{Đ_{Civfms}}(A\alpha, A\beta, t_{nrm}), [\overline{Đ_{Civfms}}(A\alpha, B\beta, t_{nrm}) * \overline{Đ_{Civfms}}(A\beta, B\alpha, t_{nrm})], \\ [\overline{Đ_{Civfms}}(A\alpha, B\alpha, t_{nrm}) * \overline{Đ_{Civfms}}(A\beta, B\beta, t_{nrm})]\end{matrix}\right\}$$

$$\overline{Đ_{Civfms}}(\alpha, \beta, kt_{nrm}) \geq \text{Min}\left\{\begin{matrix}\overline{Đ_{Civfms}}(\alpha, \beta, t_{nrm}), [\overline{Đ_{Civfms}}(\alpha, \beta, t_{nrm})], \\ [\overline{Đ_{Civfms}}(\alpha, \alpha, t_{nrm}) * \overline{Đ_{Civfms}}(\beta, \beta, t_{nrm})]\end{matrix}\right\}$$

$$\overline{Đ_{Civfms}}(\alpha, \beta, kt_{nrm}) \geq \text{Min}\left\{\begin{matrix}\overline{Đ_{Civfms}}(\alpha, \beta, t_{nrm}), \overline{Đ_{Civfms}}(\alpha, \beta, t_{nrm}), \\ [e^{i\theta} *_I e^{i\theta}]\end{matrix}\right\}$$

$$\overline{Đ_{Civfms}}(\alpha, \beta, kt_{nrm}) \geq \overline{Đ_{Civfms}}(\alpha, \beta, t_{nrm})$$

By lemma 2.12 we have $\alpha = \beta$.

Thus A and B have UCFP.

Example 3.2 Let $\overline{Đ_{Civfms}}(x, y, t_{nrm}) = \frac{e^{i\theta} t_{nrm}}{t_{nrm} + |x-y|}$, $t_{nrm} > 0$ and $(\mathbb{X}, \overline{Đ_{Civfms}}, *_I)$ be a Civfms, where $\mathbb{X} = [1,40]$, and let AandB be two self mappings as follows:

$$Ax = \begin{cases} 1, & x = 1 \text{ or } x > 7 \\ 10, & 1 < x \leq 7 \end{cases}, \quad Bx = \begin{cases} 1, & x = 1 \\ 12, & 1 < x \leq 7 \\ \frac{x+1}{8}, & x > 7 \end{cases}$$

And also a sequence $\{x_n\}$ define as $x_n = 7 + \frac{1}{n}$, $n \geq 1$ then we see

$\lim_{n\to\infty} Ax_n = 1 = \lim_{n\to\infty} Bx_n$ then A and B (E.A) property satisfied

$\lim_{n\to\infty} \overline{Đ_{Civfms}}(ABx_n, BAx_n, t_{nrm}) = \frac{e^{i\theta} t_{nrm}}{t_{nrm} + |1-1|} = e^{i\theta}$

This shows that A and B compatible property.

Theorem 3.4: Let $(\mathbb{X}, \overline{Đ_{Civfms}}, *_I)$ be a Civfms with $\lim_{t\to\infty} \overline{Đ_{Civfms}}(x, y, t) = e^{i\theta}$, $\theta \in \left[0, \frac{\pi}{2}\right]$, $t_{nrm} > \bar{0}$.

Let A, B, S, T, G and H be a self mapsof a Civfms$(\mathbb{X}, \overline{D_{Civfms}}, *_I)$ satisfying the following:

$$AG(X) \subseteq T(X), \quad BH(X) \subseteq S(X)$$

The pair (AG, S) and (BH, T) share one of the $Clr_{AG}, Clr_{BH}, Clr_S, Clr_T$-property;

$$AG = GA \text{ and either } SA = AS \text{ or } SG = GS$$
$$BH = HB \text{ and either } TB = BT \text{ or } TH = HT.$$

(AG, S) and (BH, T) are Compatible Type of P-1.

$\psi \in \Phi$, for all $x, y \in \mathbb{X}, t_{nrm} > 0$

$$\psi\begin{Bmatrix} \overline{D_{Civfms}}(AGx, BHy, t_{nrm}), \overline{D_{Civfms}}(Sx, Ty, t_{nrm}), \overline{D_{Civfms}}(AGx, Sx, t_{nrm}), \\ \overline{D_{Civfms}}(BHy, Ty, t_{nrm}), \overline{D_{Civfms}}(AGx, Ty, t_{nrm}), \overline{D_{Civfms}}(Sx, BHy, t_{nrm}) \end{Bmatrix} \geq 0$$

Then A, B, S, T, G and H have a UCFP.

Proof: Case (i) Consider (AG, S) and (BH, T)share one of the Clr_{AG} or Clr_S -property. So, by the definition, there exist sequences $\{x_n\}$ and $\{y_n\}$ in $\mathbb{X}$ such that

$$\lim_{n\to\infty} AGx_n = \lim_{n\to\infty} Sx_n = \lim_{n\to\infty} BHy_n = \lim_{n\to\infty} Ty_n = Su, \text{ for some } u \in \mathbb{X}$$

Step (i) Putting $x = u$ and $y = y_n$ in (e) then

$$\psi\begin{Bmatrix} \overline{D_{Civfms}}(AGu, BHy_n, t_{nrm}), \overline{D_{Civfms}}(Su, Ty_n, t_{nrm}), \overline{D_{Civfms}}(AGu, Su, t_{nrm}), \\ \overline{D_{Civfms}}(BHy_n, Ty_n, t_{nrm}), \overline{D_{Civfms}}(AGu, Ty_n, t_{nrm}), \overline{D_{Civfms}}(Su, BHy_n, t_{nrm}) \end{Bmatrix} \geq 0$$

As $n \to \infty$, then we get

$$\psi\begin{Bmatrix} \overline{D_{Civfms}}(AGu, Su, t_{nrm}), \overline{D_{Civfms}}(Su, Su, t_{nrm}), \overline{D_{Civfms}}(AGu, Su, t_{nrm}), \\ \overline{D_{Civfms}}(Su, Su, t_{nrm}), \overline{D_{Civfms}}(AGu, Su, t_{nrm}), \overline{D_{Civfms}}(Su, Su, t_{nrm}) \end{Bmatrix} \geq 0$$

$$\psi\begin{Bmatrix} \overline{D_{Civfms}}(AGu, Su, t_{nrm}), e^{i\theta}, \overline{D_{Civfms}}(AGu, Su, t_{nrm}), \\ e^{i\theta}, \overline{D_{Civfms}}(AGu, Su, t_{nrm}), e^{i\theta} \end{Bmatrix} \geq 0$$

By Implicit relation of (ψ_2). We have

$$\overline{D_{Civfms}}(AGu, Su, t_{nrm}) \geq e^{i\theta} \Rightarrow AGu = Su$$

Step (ii) Since, $AG(X) \subseteq T(X)$ then there is a $v \in X$ such that $AGu = Tv$

Putting $x = x_n$ and $y = v$ in (e) then

$$\psi\begin{Bmatrix} \overline{D_{Civfms}}(AGx_n, BHv, t_{nrm}), \overline{D_{Civfms}}(Sx_n, Tv, t_{nrm}), \overline{D_{Civfms}}(AGx_n, Sx_n, t_{nrm}), \\ \overline{D_{Civfms}}(BHv, Tv, t_{nrm}), \overline{D_{Civfms}}(AGx_n, Tv, t_{nrm}), \overline{D_{Civfms}}(Sx_n, BHv, t_{nrm}) \end{Bmatrix} \geq 0$$

As $n \to \infty$, then we get

$$\psi\begin{Bmatrix} \overline{D_{Civfms}}(Tv, BHv, t_{nrm}), \overline{D_{Civfms}}(Tv, Tv, t_{nrm}), \overline{D_{Civfms}}(Tv, Tv, t_{nrm}), \\ \overline{D_{Civfms}}(BHv, Tv, t_{nrm}), \overline{D_{Civfms}}(Tv, Tv, t_{nrm}), \overline{D_{Civfms}}(Tv, BHv, t_{nrm}) \end{Bmatrix} \geq 0$$

$$\psi\begin{Bmatrix} \overline{D_{Civfms}}(Tv, BHv, t_{nrm}), e^{i\theta}, e^{i\theta}, \\ \overline{D_{Civfms}}(BHv, Tv, t_{nrm}), e^{i\theta}, \overline{D_{Civfms}}(Tv, BHv, t_{nrm}) \end{Bmatrix} \geq 0$$

By Implicit relation of (ψ_3). We have

$$\overline{D_{Civfms}}(BHv, Tv, t_{nrm}) \geq e^{i\theta} \Rightarrow BHv = Tv$$

Thus $AGu = Su = BHv = Tv = z$ (say)

Step (iii) Since(AG, S) and (BH, T) are compatible Type of (P-1)

Then we have, $AGSu = SSu$ and $BHTv = TTv$ i. e $AGz = Sz$ and $BHz = Tz$

Putting $x = z$ and $y = v$ in (e) then

$$\psi\begin{Bmatrix} \overline{D_{Civfms}}(AGz, BHv, t_{nrm}), \overline{D_{Civfms}}(Sz, Tv, t_{nrm}), \overline{D_{Civfms}}(AGz, Sz, t_{nrm}), \\ \overline{D_{Civfms}}(BHv, Tv, t_{nrm}), \overline{D_{Civfms}}(AGz, Tv, t_{nrm}), \overline{D_{Civfms}}(Sz, BHv, t_{nrm}) \end{Bmatrix} \geq 0$$

$$\psi\begin{Bmatrix} \overline{D_{Civfms}}(AGz, z, t_{nrm}), \overline{D_{Civfms}}(AGz, z, t_{nrm}), \overline{D_{Civfms}}(AGz, AGz, t_{nrm}), \\ \overline{D_{Civfms}}(z, z, t_{nrm}), \overline{D_{Civfms}}(AGz, z, t_{nrm}), \overline{D_{Civfms}}(AGz, z, t_{nrm}) \end{Bmatrix} \geq 0$$

$$\psi\begin{Bmatrix} \overline{D_{Civfms}}(AGz, z, t_{nrm}), \overline{D_{Civfms}}(AGz, z, t_{nrm}), e^{i\theta}, \\ e^{i\theta}, \overline{D_{Civfms}}(AGz, z, t_{nrm}), \overline{D_{Civfms}}(AGz, z, t_{nrm}) \end{Bmatrix} \geq 0$$

By Implicit relation of (ψ_4). We have

$$\overline{D_{Civfms}}(AGz, z, t_{nrm}) \geq e^{i\theta} \Rightarrow AGz = z$$

Thus$AGz = Sz = z$

Similarly by taking $x = u$ and $y = z$ in (e) then

$$\psi\left\{\begin{matrix}\overline{Ð_{CIVFMS}}(AGu, BHz, t_{nrm}), \overline{Ð_{CIVFMS}}(Su, Tz, t_{nrm}), \overline{Ð_{CIVFMS}}(AGu, Su, t_{nrm}),\\ \overline{Ð_{CIVFMS}}(BHz, Tz, t_{nrm}), \overline{Ð_{CIVFMS}}(AGu, Tz, t_{nrm}), \overline{Ð_{CIVFMS}}(Sz, BHz, t_{nrm})\end{matrix}\right\} \geq 0$$

$$\psi\left\{\begin{matrix}\overline{Ð_{CIVFMS}}(z, BHz, t_{nrm}), \overline{Ð_{CIVFMS}}(z, BHz, t_{nrm}), \overline{Ð_{CIVFMS}}(z, z, t_{nrm}),\\ \overline{Ð_{CIVFMS}}(BHz, BHz, t_{nrm}), \overline{Ð_{CIVFMS}}(z, BHz, t_{nrm}), \overline{Ð_{CIVFMS}}(z, BHz, t_{nrm})\end{matrix}\right\} \geq 0$$

$$\psi\left\{\begin{matrix}\overline{Ð_{CIVFMS}}(z, BHz, t_{nrm}), \overline{Ð_{CIVFMS}}(z, BHz, t_{nrm}), e^{i\theta},\\ e^{i\theta}, \overline{Ð_{CIVFMS}}(z, BHz, t_{nrm}), \overline{Ð_{CIVFMS}}(z, BHz, t_{nrm})\end{matrix}\right\} \geq 0$$

By Implicit relation of (ψ_4). We have

$$\overline{Ð_{CIVFMS}}(z, BHz, t_{nrm}) \geq e^{i\theta} \Rightarrow BHz = z$$

Thus ,$BHz = Tz = z$

Hence ,$AGz = BHz = Sz = Tz = z$

Step (iv) By condition (c)

Suppose $SA = AS$

Since $AG = GA$ then we have $AGAz = AAGz = Az$ and $SAz = ASz = Az$

By taking$x = Az$ and $y = v$ in (e) then

$$\psi\left\{\begin{matrix}\overline{Ð_{CIVFMS}}(AGAz, BHv, t_{nrm}), \overline{Ð_{CIVFMS}}(SAz, Tv, t_{nrm}), \overline{Ð_{CIVFMS}}(AGAz, SAz, t_{nrm}),\\ \overline{Ð_{CIVFMS}}(BHv, Tv, t_{nrm}), \overline{Ð_{CIVFMS}}(AGAz, Tv, t_{nrm}), \overline{Ð_{CIVFMS}}(SAz, BHv, t_{nrm})\end{matrix}\right\} \geq 0$$

$$\psi\left\{\begin{matrix}\overline{Ð_{CIVFMS}}(Az, z, t_{nrm}), \overline{Ð_{CIVFMS}}(Az, z, t_{nrm}), \overline{Ð_{CIVFMS}}(Az, Az, t_{nrm}),\\ \overline{Ð_{CIVFMS}}(z, z, t_{nrm}), \overline{Ð_{CIVFMS}}(Az, z, t_{nrm}), \overline{Ð_{CIVFMS}}(Az, z, t_{nrm})\end{matrix}\right\} \geq 0$$

$$\psi\left\{\begin{matrix}\overline{Ð_{CIVFMS}}(Az, z, t_{nrm}), \overline{Ð_{CIVFMS}}(Az, z, t_{nrm}), e^{i\theta},\\ e^{i\theta}, \overline{Ð_{CIVFMS}}(Az, z, t_{nrm}), \overline{Ð_{CIVFMS}}(Az, z, t_{nrm})\end{matrix}\right\} \geq 0$$

By Implicit relation of (ψ_4). We have

$$\overline{Ð_{CIVFMS}}(Az, z, t_{nrm}) \geq e^{i\theta} \Rightarrow Az = z$$

Since, $AGz = GAz = Lz$

Thus, $Az = Gz = Sz = z$

And suppose $SG = GS$

Since $G = GA$ then we have $AGGz = GAGz = Gz$ and $SGz = GSz = Gz$

Similarly by taking$x = Gz$ and $y = v$ in (e) thenwe get$Gz = z$

Since, $AGz = Az = z$

Thus, $Az = Gz = Sz = z$

Now suppose $BT = TB$

Since $BH = HB$ then we have $BHBz = BBHz = Bz$ and $TBz = BTz = Bz$

By taking $x = u$ and $y = Bz$ in (e) then

$$\psi\left\{\begin{matrix}\overline{Ð_{CIVFMS}}(AGu, BHBz, t_{nrm}), \overline{Ð_{CIVFMS}}(Su, TBz, t_{nrm}), \overline{Ð_{CIVFMS}}(AGu, Su, t_{nrm}),\\ \overline{Ð_{CIVFMS}}(BHBz, TBz, t_{nrm}), \overline{Ð_{CIVFMS}}(AGu, TBz, t_{nrm}), \overline{Ð_{CIVFMS}}(Su, BHBz, t_{nrm})\end{matrix}\right\} \geq 0$$

$$\psi\left\{\begin{matrix}\overline{Ð_{CIVFMS}}(z, Bz, t_{nrm}), \overline{Ð_{CIVFMS}}(z, Bz, t_{nrm}), \overline{Ð_{CIVFMS}}(z, z, t_{nrm}),\\ \overline{Ð_{CIVFMS}}(Bz, Bz, t_{nrm}), \overline{Ð_{CIVFMS}}(z, Bz, t_{nrm}), \overline{Ð_{CIVFMS}}(z, Bz, t_{nrm})\end{matrix}\right\} \geq 0$$

$$\psi\left\{\begin{matrix}\overline{Ð_{CIVFMS}}(z, Bz, t_{nrm}), \overline{Ð_{CIVFMS}}(z, Bz, t_{nrm}), e^{i\theta},\\ e^{i\theta}, \overline{Ð_{CIVFMS}}(z, Bz, t_{nrm}), \overline{Ð_{CIVFMS}}(z, Bz, t_{nrm})\end{matrix}\right\} \geq 0$$

By Implicit relation of (ψ_4). We have

$$\overline{Ð_{CIVFMS}}(z, Bz, t_{nrm}) \geq e^{i\theta} \Rightarrow Bz = z$$

Since ,$BHz = HBz = Hz$

Thus, $Bz = Hz = Tz = z$

And suppose $TH = HT$

Since $BH = HB$ then we have $BHHz = HBHz = Hz$ and $THz = HTz = Hz$

Similarly by taking$x = u$ and $y = Hz$ in (e) thenwe get$Hz = z$

Since, $BHz = Bz = z$

Thus, $Bz = Hz = Tz = z$

Combine all results then we get, $Az = Bz = Gz = Hz = Sz = Tz = z$

Case (ii) Suppose (AG, S) and (BH, T) Share one of the Clr_{BH} or lr_T-property. So, by the definition,

there exist sequences $\{x_n\}$ and $\{y_n\}$ in X such that

$\lim_{n\to\infty} ALx_n = \lim_{n\to\infty} Sx_n = \lim_{n\to\infty} BHy_n = \lim_{n\to\infty} Ty_n = Tv$, for some $v \in X$

Proceeding on similar lines of case (i)

Firstly we get $BHv = Tv$

Since $BH(X) \subseteq S(X)$ then there is a $u \in X$ such that $BHv = Su$

Using step (ii) then we get $AGu = Su$

Thus $AGu = Su = BHv = Tv = z$ (say)

Now using step (iii) we get $AGz = Sz$ and $BHz = Tz$ by using inequality (e) then we get $AGz = BHz = Sz = Tz = z$

From this stage the proof is similar as step (iv) then we get z is a common fixed point of A, B, S, T, G and H in X.

For uniqueness further we consider α and β be the two common fixed-point of A, B, S, T, G and H.

Put $x = \alpha$ and $y = \beta$ in inequality (e) then

$$\psi\begin{Bmatrix}(\overline{D_{Civfms}}(AG\alpha, BH\beta, t_{nrm}), (\overline{D_{Civfms}}(S\alpha, T\beta, t_{nrm}), (\overline{D_{Civfms}}(AG\beta, S\alpha, t_{nrm}),\\ (\overline{D_{Civfms}}(BH\beta, T\beta, t_{nrm}), (\overline{D_{Civfms}}(AG\alpha, T\alpha, t_{nrm}), (\overline{D_{Civfms}}(S\alpha, BH\alpha, t_{nrm})\end{Bmatrix} \geq 0$$

$$\psi\begin{Bmatrix}(\overline{D_{Civfms}}(\alpha, \beta, t_{nrm}), (\overline{D_{Civfms}}(\alpha, \beta, t_{nrm}), (\overline{D_{Civfms}}(\beta, \alpha, t_{nrm}),\\ (\overline{D_{Civfms}}(\beta, \beta, t_{nrm}), (\overline{D_{Civfms}}(\alpha, \alpha, t_{nrm}), (\overline{D_{Civfms}}(\alpha, \alpha, t_{nrm})\end{Bmatrix} \geq 0$$

$$\psi\begin{Bmatrix}(\overline{D_{Civfms}}(\alpha, \beta, t_{nrm}), (\overline{D_{Civfms}}(\alpha, \beta, t_{nrm}), (\overline{D_{Civfms}}(\beta, \alpha, t_{nrm}),\\ e^{i\theta}, \ e^{i\theta}, \ e^{i\theta}\end{Bmatrix} \geq 0$$

By Implicit relation of (ψ_5). We have

$$(\overline{D_{Civfms}}(\alpha, \beta, t_{nrm}) \geq e^{i\theta} \Rightarrow \theta = 9$$

Hence z is a unique common fixed point of A, B, S, T, G and H in X.

Now, taking $G = H = I$(Identity mapping)

Remark 3.5: if we apply JClr- property instead of Clr-Proprty then we can ignore condition (a) in theorem (3.4). Now we prove the following:

Theorem 3.6: Let $(\mathbb{X}, \overline{D_{Civfms}}, *_I)$ be a Civfms with $\lim_{t\to\infty} \overline{D_{Civfms}}(x, y, t) = e^{i\theta}$, $\theta \in \left[0, \frac{\pi}{2}\right]$, $t_{nrm} > \bar{0}$. Let A, B, S, T, G and H be a self maps of a Civfms$(\mathbb{X}, \overline{D_{Civfms}}, *_I)$ satisfying the following:

$$AG(X) \subseteq T(X), \quad BH(X) \subseteq S(X)$$

The pair (AG, S) and (BH, T) share one of the $JClr_{ST}$-property;

$$AG = GA \text{ and either } SA = AS \text{ or } SG = GS$$
$$BH = HB \text{ and either } TB = BT \text{ or } TH = HT.$$

(AG, S) and (BH, T) are Compatible Type of P-1.

$\psi \in \Phi$, for all$x, y \in \mathbb{X}, t_{nrm} > 0$

$$\psi\begin{Bmatrix}\overline{D_{Civfms}}(AGx, BHy, t_{nrm}), \overline{D_{Civfms}}(Sx, Ty, t_{nrm}), \overline{D_{Civfms}}(AGx, Sx, t_{nrm}),\\ \overline{D_{Civfms}}(BHy, Ty, t_{nrm}), \overline{D_{Civfms}}(AGx, Ty, t_{nrm}), \overline{D_{Civfms}}(Sx, BHy, t_{nrm})\end{Bmatrix} \geq 0$$

Then A, B, S, T, G and H have a UCFP.

Proof: Suppose (AG, S) and (BH, T)share one of the $JClr_{ST}$ -property. So, by the definition, there exist sequences $\{x_n\}$ and $\{y_n\}$ in X such that

$$\lim_{n\to\infty} AGx_n = \lim_{n\to\infty} Sx_n = \lim_{n\to\infty} BHy_n = \lim_{n\to\infty} Ty_n = Su(= Tu) \text{ , for some } u \in X$$

Step (i) Putting $x = u$ and $y = y_n$ in (e) then

$$\psi\begin{Bmatrix}\overline{D_{Civfms}}(AGu, BHy_n, t_{nrm}), \overline{D_{Civfms}}(Su, Ty_n, t_{nrm}), \overline{D_{Civfms}}(AGu, Su, t_{nrm}),\\ \overline{D_{Civfms}}(BHy_n, Ty_n, t_{nrm}), \overline{D_{Civfms}}(AGu, Ty_n, t_{nrm}), \overline{D_{Civfms}}(Su, BHy_n, t_{nrm})\end{Bmatrix} \geq 0$$

As $n \to \infty$, then we get

$$\psi\begin{Bmatrix}\overline{D_{Civfms}}(AGu, Su, t_{nrm}), \overline{D_{Civfms}}(Su, Su, t_{nrm}), \overline{D_{Civfms}}(AGu, Su, t_{nrm}),\\ \overline{D_{Civfms}}(Su, Su, t_{nrm}), \overline{D_{Civfms}}(AGu, Su, t_{nrm}), \overline{D_{Civfms}}(Su, Su, t_{nrm})\end{Bmatrix} \geq 0$$

$$\psi\begin{Bmatrix}\overline{D_{Civfms}}(AGu, Su, t_{nrm}), \ e^{i\theta}, \overline{D_{Civfms}}(AGu, Su, t_{nrm}),\\ e^{i\theta}, \overline{D_{Civfms}}(AGu, Su, t_{nrm}), \ e^{i\theta}\end{Bmatrix} \geq 0$$

by implicit relation (ψ_2) . We have

$$\overline{D_{Civfms}}(AGu, Su, t_{nrm}) \geq e^{i\theta} \Rightarrow AGu = Su \ (AGu = Su = Tu).$$

And Putting $x = x_n$ and $y = u$ in (e) thenwe get, $BHu = Tu$

Thus $AGu = Su = BHu = Tu = z$ (say)

Since (AG, S) and(BH, T) are compatible Type of (P-1)

Then we have, $AGSu = SSu$ and $BHTv = TTv$

i. e $AGz = Sz$ and $BHz = Tz$

Now taking $x = z$ and $y = u$ in (e) then we get $AGz = Sz = z$

And taking $x = u$ and $y = z$ in (e) then we get $BHz = Tz = z$

Thus, $AGz = Sz = BHz = Tz = z$.

From this stage, the proof is similar as proof of theorem (3.4).

Remark 3.7: If the Theorem (3.4) shares common properties (E.A) then the proof run on similar steps of the theorem (3.3).

Example 3.9 Let$(\mathbb{X}, \overline{D_{Civfms}}, *_1)$ be a Civfms with $\lim_{t\to\infty} \overline{D_{Civfms}}(x, y, t) = e^{i\theta}, \theta \in \left[0, \frac{\pi}{2}\right], t_{nrm} > \bar{0}$.

Define $\overline{D_{Civfms}}(x, y, t_{nrm}) = \frac{e^{i\theta} t_{nrm}}{t_{nrm} + |x-y|}$, where , $\mathbb{X} = [0,40]$

Consider $\psi(t_1, t_2, t_3, t_4, t_5, t_6) = 40t_1 - 12t_2 + 24t_3 - 3t_4 + 18t_5 - 11t_6, \ t \in [0,1]$

Now, $Ax = 2$, $Bx = 2$, $Gx = x$, $Hx = x$, $Sx = \begin{cases} 2, & x \leq 10 \\ \frac{1}{4}, & x > 10 \end{cases}$, $Tx = \begin{cases} 2, & x \leq 10 \\ \frac{1}{2}, & x > 10 \end{cases}$

Case (a): When $x, y \leq 10$ then the LHS of inequality (e) (Theorem 3.4)

$$\psi\begin{Bmatrix} \overline{D_{Civfms}}(2,2,t_{nrm}), \overline{D_{Civfms}}(2,2,t_{nrm}), \overline{D_{Civfms}}(2,2,t_{nrm}), \\ \overline{D_{Civfms}}(2,2,t_{nrm}), \overline{D_{Civfms}}(2,2,t_{nrm}), \overline{D_{Civfms}}(2,2,t_{nrm}) \end{Bmatrix} \geq 0$$

$$LHS = \psi\begin{Bmatrix} \overline{D_{Civfms}}(2,2,t_{nrm}), \overline{D_{Civfms}}(2,2,t_{nrm}), \overline{D_{Civfms}}(2,2,t_{nrm}), \\ \overline{D_{Civfms}}(2,2,t_{nrm}), \overline{D_{Civfms}}(2,2,t_{nrm}), \overline{D_{Civfms}}(2,2,t_{nrm}) \end{Bmatrix}$$

$$= \psi\begin{Bmatrix} \frac{e^{i\theta}t_{nrm}}{t_{nrm}+|x-y|}, \frac{e^{i\theta}t_{nrm}}{t_{nrm}+|x-y|}, \frac{e^{i\theta}t_{nrm}}{t_{nrm}+|x-y|}, \\ \frac{e^{i\theta}t_{nrm}}{t_{nrm}+|x-y|}, \frac{e^{i\theta}t_{nrm}}{t_{nrm}+|x-y|}, \frac{e^{i\theta}t_{nrm}}{t_{nrm}+|x-y|} \end{Bmatrix}$$

$$= \psi\begin{Bmatrix} \frac{e^{i\theta}t_{nrm}}{t_{nrm}+|2-2|}, \frac{e^{i\theta}t_{nrm}}{t_{nrm}+|2-2|}, \frac{e^{i\theta}t_{nrm}}{t_{nrm}+|2-2|}, \\ \frac{e^{i\theta}t_{nrm}}{t_{nrm}+|2-2|}, \frac{e^{i\theta}t_{nrm}}{t_{nrm}+|2-2|}, \frac{e^{i\theta}t_{nrm}}{t_{nrm}+|2-2|} \end{Bmatrix}$$

$$= \psi\begin{Bmatrix} e^{i\theta}, e^{i\theta}, e^{i\theta}, \\ e^{i\theta}, e^{i\theta}, e^{i\theta} \end{Bmatrix}$$

$$= 40e^{i\theta} - 12e^{i\theta} + 24e^{i\theta} - 3e^{i\theta} + 18e^{i\theta} - 11e^{i\theta}$$

$$= 59e^{i\theta} \geq \bar{0} \text{ Satisfied.}$$

Case (b): When $x > 10$, $y \geq 10$ then the LHS of inequality (e) (Theorem 3.4)

$$LHS = \psi\begin{Bmatrix} \overline{D_{Civfms}}(2,2,t_{nrm}), \overline{D_{Civfms}}\left(\frac{1}{4},2,t_{nrm}\right), \overline{D_{Civfms}}\left(2,\frac{1}{4},t_{nrm}\right), \\ \overline{D_{Civfms}}(2,2,t_{nrm}), \overline{D_{Civfms}}(2,2,t_{nrm}), \overline{D_{Civfms}}(2,2,t_{nrm}) \end{Bmatrix}$$

$$= \psi\begin{Bmatrix} \frac{e^{i\theta}t_{nrm}}{t_{nrm}+|2-2|}, \frac{e^{i\theta}t_{nrm}}{t_{nrm}+\left|\frac{1}{4}-2\right|}, \frac{e^{i\theta}t_{nrm}}{t_{nrm}+\left|2-\frac{1}{4}\right|}, \\ \frac{e^{i\theta}t_{nrm}}{t_{nrm}+|2-2|}, \frac{e^{i\theta}t_{nrm}}{t_{nrm}+|2-2|}, \frac{e^{i\theta}t_{nrm}}{t_{nrm}+|2-2|} \end{Bmatrix}$$

$$= \psi\left\{e^{i\theta}, \frac{4t_{nrm}e^{i\theta}}{4t+7}, \frac{4t_{nrm}e^{i\theta}}{4t+7}, e^{i\theta}, e^{i\theta}, e^{i\theta}\right\}$$

$$= 40e^{i\theta} - 12\frac{4t_{nrm}e^{i\theta}}{4t+7} + 24\frac{4t_{nrm}}{4t+7} - 3e^{i\theta} + 18e^{i\theta} - 11e^{i\theta}$$
$$\geq \bar{0}\ ,\ \text{Satisfied.}$$

Case (c): When $x \leq 10$, $y \geq 10$ then the LHS of inequality (e) (Theorem 3.4)

$$\text{LHS} = \psi\begin{Bmatrix}\overline{D_{Civfms}}(2,2,t_{nrm}), \overline{D_{Civfms}}(2,\frac{1}{2},t_{nrm}), \overline{D_{Civfms}}(2,2,t_{nrm}),\\ \overline{D_{Civfms}}(2,\frac{1}{2},t_{nrm}), \overline{D_{Civfms}}(2,\frac{1}{2},t_{nrm}), \overline{D_{Civfms}}(2,2,t_{nrm})\end{Bmatrix}$$

$$= \psi\begin{Bmatrix}\frac{e^{i\theta}t_{nrm}}{t_{nrm}+|2-2|}, \frac{e^{i\theta}t_{nrm}}{t_{nrm}+\left|2-\frac{1}{2}\right|}, \frac{e^{i\theta}t_{nrm}}{t_{nrm}+|2-2|},\\ \frac{e^{i\theta}t_{nrm}}{t_{nrm}+\left|2-\frac{1}{2}\right|}, \frac{e^{i\theta}t_{nrm}}{t_{nrm}+\left|2-\frac{1}{2}\right|}, \frac{e^{i\theta}t_{nrm}}{t_{nrm}+|2-2|}\end{Bmatrix}$$
$$= \psi\left\{e^{i\theta}, \frac{2t_{nrm}e^{i\theta}}{2t+3}, e^{i\theta}, \frac{2t_{nrm}e^{i\theta}}{2t+3}, e^{i\theta}, e^{i\theta}\right\}$$
$$= 40e^{i\theta} - 12\frac{2t_{nrm}e^{i\theta}}{2t+3} + 24e^{i\theta} - 3\frac{2t_{nrm}e^{i\theta}}{2t+3} + 18\frac{2t_{nrm}e^{i\theta}}{2t+3} - 11e^{i\theta}$$
$$\geq \bar{0}\ ,\ \text{Satisfied.}$$

Case (d): When $x > 10$, $y > 10$ then the LHS of inequality (e) (Theorem 3.4)

$$\text{LHS} = \psi\begin{Bmatrix}\overline{D_{Civfms}}(2,2,t_{nrm}), \overline{D_{Civfms}}\left(\frac{1}{4},\frac{1}{2},t_{nrm}\right), \overline{D_{Civfms}}\left(2,\frac{1}{4},t_{nrm}\right),\\ \overline{D_{Civfms}}\left(2,\frac{1}{2},t_{nrm}\right), \overline{D_{Civfms}}\left(2,\frac{1}{2},t_{nrm}\right), \overline{D_{Civfms}}\left(\frac{1}{4},2,t_{nrm}\right)\end{Bmatrix}$$

$$= \psi\begin{Bmatrix}\frac{e^{i\theta}t_{nrm}}{t_{nrm}+|2-2|}, \frac{e^{i\theta}t_{nrm}}{t_{nrm}+\left|\frac{1}{4}-\frac{1}{2}\right|}, \frac{e^{i\theta}t_{nrm}}{t_{nrm}+\left|2-\frac{1}{4}\right|},\\ \frac{e^{i\theta}t_{nrm}}{t_{nrm}+\left|2-\frac{1}{2}\right|}, \frac{e^{i\theta}t_{nrm}}{t_{nrm}+\left|2-\frac{1}{2}\right|}, \frac{e^{i\theta}t_{nrm}}{t_{nrm}+\left|\frac{1}{4}-2\right|}\end{Bmatrix}$$
$$= \psi\begin{Bmatrix}e^{i\theta}, \frac{4e^{i\theta}t_{nrm}}{4t_{nrm}+1}, \frac{4e^{i\theta}t_{nrm}}{4t_{nrm}+7},\\ \frac{2e^{i\theta}t_{nrm}}{2t_{nrm}+3}, \frac{2e^{i\theta}t_{nrm}}{2t_{nrm}+3}, \frac{4e^{i\theta}t_{nrm}}{4t_{nrm}+7}\end{Bmatrix}$$

$$= 40e^{i\theta} - 12\frac{4e^{i\theta}t_{nrm}}{4t_{nrm}+1} + 24\frac{4e^{i\theta}t_{nrm}}{4t_{nrm}+7} - 3\frac{2t_{nrm}e^{i\theta}}{2t+3} + 18\frac{2t_{nrm}e^{i\theta}}{2t+3} - 11\frac{4e^{i\theta}t_{nrm}}{4t_{nrm}+7}$$
$$\geq \bar{0}\ ,\ \text{Satisfied.}$$

Hence all four conditions variables are satisfied. Therefore A, B, S, T, G and H satisfied the hypothesis of theorem 3.4. Hence 2 is a unique c-fixed-point in X.

IV. Conclusion

In many scientific domains, fixed point theory has several applications. In this research, we introduced the concept of complex interval-valued fuzzy metric space to modify the distance function under Clr/Jc;lr/E.A-Property for common fixed-point theorems in complex interval-valued fuzzy metric space in order to prove several well-known common fixed-point theorems for self-mapping. our results enhanced, expanded, and generalized some findings in the literature. These findings can be applied to the solution of LPP in dynamic programming. quantum mechanics, control systems, machine learning, robotics, digital problems, image processing,

economics and other fields. These uses demonstrate how complex interval-valued fuzzy metric spaces may be used to handle a wide range of data kinds and uncertainty, making them an invaluable tool in many engineering and scientific fields.

References

[1] Azam, A. (2011). Fuzzy fixed points of fuzzy mappings via a rational inequality. Hacettepe Journal of Mathematics and Statistics, 40(3), 421-431.

[2] Buckley, J. (1989). Fuzzy complex numbers. Fuzzy sets and systems, 33(3), 333-345.

[3] Buckley, J. J., & Eslami, E. (2002). An introduction to fuzzy logic and fuzzy sets (Vol. 13). Springer Science & Business Media.

[4] Azam, A. (2011). Fuzzy fixed points of fuzzy mappings via a rational inequality. Hacettepe Journal of Mathematics and Statistics, 40(3), 421-431.

[5] Buckley, J. (1989). Fuzzy complex numbers. Fuzzy sets and systems, 33(3), 333-345.

[6] Buckley, J. J., & Eslami, E. (2002). An introduction to fuzzy logic and fuzzy sets (Vol. 13). Springer Science & Business Media.

[7] Choi, J., Datta, S. K., Biswas, T., & Islam, M. N. (2017). Some fixed point theorems in connection with two weakly compatible mappings in bicomplex valued metric spaces. Honam Mathematical Journal, 39(1), 115-126.

[8] Demir, I. (2021). Fixed Point Theorems in complex valued fuzzy b-metric spaces with application to integral equations. Miskolc Mathematical Notes, 22(1), 153-171.

[9] Deshmukh, V., Jadon, B. P. S., Singh, R., & Malhotra, S. K. (2023). Fixed Point Results on Interval-Valued Fuzzy Metric Space using notation of Pairwise Compatible Maps and Occasionally Weakly Compatible Maps with Application. Asian Research Journal of Mathematics, 19(11), 104-114.

[10] George, A., & Veeramani, P. (1994). On some results in fuzzy metric spaces. Fuzzy sets and systems, 64(3), 395-399.

[11] Gregori, V., & Sapena, A. (2002). On fixed-point theorems in fuzzy metric spaces. Fuzzy sets and systems, 125(2), 245-252.

[12] Gregori, V., Miñana, J. J., Roig, B., &Sapena, A. (2024). On Completeness and Fixed Point Theorems in Fuzzy Metric Spaces. Mathematics, 12(2), 287.

[13] Gupta, V., Saini, R. K., &Verma, M. (2018). Fixed point theorems for single valued α-ψ-mappings in fuzzy metric spaces. Communications Faculty of Sciences University of Ankara Series A1 Mathematics and Statistics, 68(1), 392-400.

[14] K. Wadhaw, A. Dubai, Common Fixed point theorems using E.A like property in Fuzzy Metric spaces, International J.of Math. Archive -8(6), 2017, 204-210.

[15] Kanwal, S., Shagari, M. S., Aydi, H., Mukheimer, A., &Abdeljawad, T. (2022). Common fixed-point results of fuzzy mappings and applications on stochastic Volterra integral equations. Journal of Inequalities and Applications, 2022(1), 110.

[16] Kramosil, I., &Michálek, J. (1975). Fuzzy metrics and statistical metric spaces. Kybernetika, 11(5), 336-344.

[17] Kramosil, I., &Michálek, J. (1975). Fuzzy metrics and statistical metric spaces. Kybernetika, 11(5), 336-344.

[18] Kutukcu, S., Sharma, S., &Tokgoz, H. (2007). A fixed point theorem in fuzzy metric spaces. Int. Journal of Math. Analysis, 1(18), 861-872.

[19] Li, C. (2009, June). Distances between interval-valued fuzzy sets. In NAFIPS 2009-2009 Annual Meeting of the North American Fuzzy Information Processing Society (pp. 1-3). IEEE.

[20] Mishra, R. K., & Choudhary, S. (2010). On fixed point theorems in Fuzzy metric spaces. International Magazine on Advances in Computer Science and Telecommunications, 1(1), 45.

[21] Malviya, N. the N-fuzzy metric space and mapping with application, (2015), DOI: 1515/fascmath-0019.

[22] Namdev R., Tiwari R., Singh U., & Bhardwaj, R. (2024). Common Fixed-Point Theorems for Rational Expression in Fuzzy Metric Space using E.A like Property. African Journal of Biological Sciences, 6(10).

[23] Price G. B., "An Introduction to Multi-complex Spaces and Functions", Marcel Dekker, New York, 1991.

[24] Ramot, D., Friedman, M., Langholz, G., Milo, R., & Kandel, A. (2001, December). On complex fuzzy sets. In 10th IEEE International Conference on Fuzzy Systems.(Cat. No. 01CH37297) (Vol. 3, pp. 1160-1163). IEEE.

[25] Ramot, D., Milo, R., Friedman, M., & Kandel, A. (2002). Complex fuzzy sets. IEEE transactions on fuzzy systems, 10(2), 171-186.

[26] Rao, K. P. R., Rao, K. R. K., &Sedghı, S. (2014). Common coupled fixed point theorems in fuzzy metric spaces. Gazi University Journal of Science, 27(2), 739-745.

[27] Segre C., "Le RappresentazioniRealidelleFormeComplesse a GliEntiIperalgebrici, Math. Ann., 40(1892), 413−467.

[28] Sharma, S. (2002). Common fixed point theorems in fuzzy metric spaces. Fuzzy sets and systems, 127(3), 345-352.

[29] Shen, Y., Li, H., & Wang, F. (2012). On interval-valued fuzzy metric spaces. International Journal of Fuzzy Systems, 14(1), 35-44.

[30] ShikaShendeet. al. Some fixed point theorems for asymptotically regular maps in N-Fuzzy metric space, J. of Science and Technological researchers, Vol. 3, Issue N0. 3, (2021).

[31] Singh, D., Joshi, V., Imdad, M., & Kumam, P. (2016). A novel framework of complex valued fuzzy metric spaces and fixed point theorems. Journal of Intelligent & Fuzzy Systems, 30(6), 3227-3238.

[32] Singh, U., Singh, N., Singh, R., & Bhardwaj, R. (2022). Common Invariant Point Theorem for Multi-valued Generalized Fuzzy Mapping in b-Metric Space. In Recent Trends in Design, Materials and Manufacturing: Selected Proceedings of ICRADMM 2020 (pp. 23-35). Singapore: Springer Nature Singapore.

[33] Tiwari, R., & Rajput, S. (2022). On (ψ, ϕ) Contraction in Bicomplex Valued Fuzzy b-Metric Spaces with Application. European Journal of Mathematics and Statistics, 3(4), 43-53.

[34] Umashankar Singh and Naval Singh, Common fixed point theorem for rational expression in fuzzy metric space, Journal of the Gujrat research society, vol-21, issue-14, (2019).

[35] Wadhwa, K., Choudhari, S., & Bohare, P. (2019). Common Fixed Point Theorems using Common EA like Property in Fuzzy Metric Space. International Journal of Mathematics Trends and Technology-IJMTT, 65.

[36] Zadeh, L. A., Klir, G. J., & Yuan, B. (1996). Fuzzy sets, fuzzy logic, and fuzzy systems: selected papers (Vol. 6). World scientific.

PROBABILISTIC ANALYSIS OF THERMAL LASER WEAPON SUBSYSTEM IN ANTI-DRONE SYSTEMS

Dharmaraja Selvamuthu[a], Utkarsh Dubey[a],
Raina Raj[b], Priyanka Kalita[c]

•

Department of Mathematics, Indian Institute of Technology Delhi, New Delhi, India[a]
dharmar@maths.iitd.ac.in
Utkarsh.mt613@maths.iitd.ac.in
Bharti School of Telecommunication Technology & Management,
Indian Institute of Technology Delhi, New Delhi, India[b]
rainaraj.curaj@gmail.com
Department of Statistics, Bhattadev University, Bajali, Pathsala - 781325, Assam, India[c]
priya.24723@gmail.com

Abstract

The rise of drones has introduced significant security threats, including unauthorized surveillance and explosive payloads. Drones threaten armies by enabling enemy surveillance, facilitating precision strikes on troops or equipment, disrupting communications, and introducing challenges in air defense, thereby altering traditional battlefield dynamics and strategies. To counter these threats, high-energy laser weapon subsystems provide precise, scalable responses with minimal collateral damage. This paper presents a probabilistic analysis of thermal laser subsystem's effects on targets, accounting for aiming and tracking errors. Atmospheric turbulence is modeled using the power spectrum inversion method, while Monte Carlo simulations calculate the on-target spot area. The energy distribution is converted to temperature using thermal physics, and the damage probability is determined by integrating temperatures exceeding material-specific thresholds. Simulation results confirm the system's effectiveness and reliability of thermal laser weapon systems in neutralizing aerial threats.

Keywords: Atmospheric Turbulence, Monte Carlo Simulation, Gaussian Beam, Laser Beam Propagation, Power Spectrum Inversion.

1. INTRODUCTION

Nowdays, drones have become readily available, affordable, and simple to operate, making them popular for parcel deliveries, film shoots, disaster surveillance, and even as a hobby for many. However, beyond these recreational uses and benefits, drones are sometimes misused for trespassing and spying on private properties using built-in cameras. In response to these threats, many have developed anti-drone systems designed to secure specific areas. These systems can detect and classify unauthorized drones and, in some cases, jam the signals used by controllers to operate the drones.

An anti-drone laser system is a crucial security technology designed to detect, track, and neutralize unauthorized drones operating in restricted airspace. These systems leverage advanced detection, precise tracking, and effective neutralization techniques to safeguard sensitive areas from potential drone threats. Laser weapons are rapidly emerging as an efficient solution to

counter the increasing drone threat, offering light-speed engagement, pinpoint accuracy, and cost-effectiveness per shot [5]. To assess the effectiveness of lasers on drone engines, a comprehensive method for evaluating target vulnerability to laser strikes is studied in [3]. Ball, in [7], compared the assessment of laser vulnerability to evaluate the damage caused by non-explosive penetrating objects, though a detailed methodology was not provided.

Currently, many anti-drone systems utilize military-grade components to ensure the destruction of hostile drones. Military strategies often incorporate jamming systems to disrupt a drone's control channels [10]. Another key technology for drone neutralization is the laser power transmitter, which plays a pivotal role in preventing unauthorized drones from threatening critical infrastructure, military bases, and public events. Laser-based anti-drone systems use directed energy technology to disable or destroy hostile drones by focusing high-energy laser beams. In [2], Huang et al. developed a laser-integrated anti-drone system that combines advanced laser technology with sensors, tracking mechanisms, and command-and-control interfaces, offering a comprehensive defense against drone threats.

The key components and capabilities of a laser-integrated anti-drone system include:

High-Energy Laser Weapons: High-energy laser weapons are highly effective for neutralizing drone threats, offering precise and scalable effects with minimal collateral damage, unlike traditional projectile weapons [13]. Lyu and Zhan provided a comprehensive global overview of high-energy laser weapon technology in [4], highlighting its growing military use in safeguarding nations. The review covers the strategic and tactical roles of these systems on the battlefield, examining performance limitations such as laser device types, beam control systems, atmospheric propagation, and targeting effectiveness [6].

Detection System: Laser-integrated anti-drone systems feature advanced sensor suites, including radar, electro-optical/infrared cameras, and RF detectors, which provide enhanced situational awareness. These sensors work together to detect, track, and classify drones with precision, minimizing false alarms. Abunada et al. discussed an RF-based drone detection method in [1], while Wang et al. [12] explored the challenges of radar detection for small drones and proposed future improvement. Lasers can also complement other sensors by detecting, dazzling, or destroying a drone's optical sensors [8].

Tracking System: The tracking and targeting system is essential for accurately following drone movements and maintaining a lock on targets during engagement. This system uses advanced algorithms and predictive models to account for target motion, atmospheric conditions, and platform dynamics, ensuring precise laser beam placement. Steinvall [8] examined the effects of atmospheric conditions and tracking errors on laser performance as a sensor, countermeasure, or weapon.

Control Unit: The control unit of a laser-integrated anti-drone system offers a user-friendly interface for monitoring system status, analyzing threats, and executing engagement protocols. It provides real-time feedback on tracking, laser engagement, and overall performance, enabling operators to make informed decisions and adjust tactics as needed. In [1], Abunada et al. proposed an RF jamming system to disconnect drones from their controllers.

To date, no studies have been documented on the probabilistic analysis of an anti-drone laser system. This gap in the literature motivates our research to explore this area. The proposed work is the first to conduct a probabilistic analysis of an anti-drone laser system.

1.1. Contribution

This study presents a comprehensive probabilistic analysis of a thermal laser weapon system aimed at neutralizing aerial threats like drones. A probabilistic model was developed to account for atmospheric turbulence effects on laser propagation, the distribution of energy on the target, and the thermal response of the target material. By employing statistical methods and Monte Carlo simulations, complex interactions were simplified, allowing for the calculation of the probability of damage from sustained laser exposure. The peformance analysis considered the Gaussian profile of the laser beam, atmospheric phase screens, and the impact of aiming and

tracking errors. The Monte Carlo method provided a reliable approach to estimating the on-target spot area, which was essential for determining the energy distribution on the target. This energy distribution was then used to generate a temperature profile to evaluate thermal damage. Simulation results revealed that the effectiveness of the thermal laser weapon system is heavily influenced by atmospheric conditions, system accuracy, and the material properties of the target. Understanding these factors is critical for improving the precision and reliability of laser weapon systems in operational environments.

To summarize this article, the potential probabilistic model is described in Section 2, followed by the simulation results in Section 3. The case study is presented in Section 4, while Section 5 provides all the pseudo codes. Finally, Section 6 concludes with suggestions for further research.

2. SETTING UP THE MODEL

In traditional weapon systems, the probability of damage is determined by the probability of hitting the target ($P(\text{hit})$) multiplied by the probability that the damage exceeds the target's threshold strength: $P(\text{damage}) = P(\text{hit}) \cdot P(\text{damage} > \text{threshold})$. In contrast, damage probability is based on sustained thermal effects in laser systems. If $p(T)$ represents the temperature distribution of the target and T_D is the threshold temperature, then

$$P(\text{damage}) = \int_{T_D}^{\infty} p(T)\, dT. \tag{1}$$

This integral captures the cumulative probability that the target's temperature exceeds T_D, resulting in damage. The threshold temperature is assumed to be around the melting point of the target material and so, our aim is to find out the function $p(T)$. In the Celsius scale, this temperature is generally positive for metals.

The laser output arrives at the target after traversing a medium influenced by atmospheric turbulence. This turbulence effect is simulated using the power spectrum inversion method. Subsequently, the energy distribution on the target is modeled by considering the combination of multiple instantaneous on-target distributions, and the associated probability distribution is accounted for by incorporating the aiming and tracking error distribution. Applying principles from thermal physics, the on-target energy distribution is converted into an on-target temperature distribution, allowing for the calculation of the probability of damage, as mentioned in (1).

Directly calculating the on-spot energy density is difficult because it involves determining both the energy distribution and the area, which is complicated by the irregularity of the target. Instead, this process is simplified by computing the far-field energy distribution and the actual on-spot area using Monte Carlo methods and atmospheric turbulence inversion techniques, respectively.

It is assumed that the emitted laser is a Gaussian beam

$$I(x,y) = I_0 \exp\left(-2\left[\frac{x^2+y^2}{w^2}\right]\right), (x,y) \in \mathbf{R}^2 \tag{2}$$

where I_0 denotes the central peak light intensity, w denotes the beam waist and (x,y) denotes any point on the plane perpendicular to the direction of propagation.

If the effect of atmospheric turbulence on the refractive index of the media were to be studied using the Navier-Stokes equations, the computational inefficiency or impossibility would arise due to the need to solve 10^{16} to 10^{18} simultaneous differential equations. Therefore, the statistical model is used, which treats turbulence as a finite number of phase screens. A common method for constructing a phase screen involves using a turbulent refractive index spectrum and a complex Gaussian random number matrix to generate a phase space complex random field. The spatial distribution of the two-dimensional phase is then derived by an inverse Fourier transform. This method is known as power spectrum inversion.

Assuming that the atmospheric turbulence is isotropic and locally homogeneous, the refractive index spectral density function can be obtained based on the Kolmogorov atmospheric refractive

index structure function. The more optimized Von-Karman atmospheric refractive index spectral density function is as follows

$$\Phi_n(\kappa, z) = 0.033\, C_n^2(z) \left(\kappa_0^2 + \kappa^2\right)^{-11/6} e^{-\kappa/\kappa_m} \tag{3}$$

where κ is the number of waves in 3D space, and the range of values of κ is $\kappa_0 < \kappa < \kappa_m$. Here, $\kappa_0 = \frac{2\pi}{L_0}$ and $\kappa_m = \frac{5.92}{l_0}$, where l_0 and L_0 denote the inner and outer scales of turbulence, respectively. $C_n^2(z)$ is the Refractive Index Structure Parameter. It can be calculated using

$$C_n^2(z) = b\frac{K_H}{\epsilon^{\frac{1}{3}}}\left(\frac{\partial n}{\partial z}\right)^2$$

where b is equal to 3.2 and called the Obukhov-Corrsin constant, K_H is the turbulent exchange coefficient for heat diffusion, ϵ is the energy dissipation rate and $\frac{\partial n}{\partial z}$ is the vertical gradient of the index of refraction [9].
The atmospheric phase spectrum is given by

$$\Phi_\phi(\kappa_x, \kappa_y) = 2\pi k^2 \Phi_n(\kappa_x, \kappa_y). \tag{4}$$

$\Phi_n(\kappa_x, \kappa_y)$ is the power spectral density of refractive index fluctuations, describing how these fluctuations are distributed over spatial frequencies κ_x and κ_y. κ_x and κ_y are the spatial wavenumbers in the x- and y-directions, inversely related to the physical spatial scales [11].

The atmospheric phase screen function, $\phi_{sh}(x, y)$, is given by

$$\begin{aligned}\phi_{sh}(x, y) =& C \sum_{p=1}^{N_p} \sum_{m=0}^{N_x} \sum_{n=0}^{N_y} R(\kappa_x, \kappa_y)\Phi_\phi(\kappa_x, \kappa_y) \\ &\times e^{2\pi i\left(\frac{x}{3pD_x} + \frac{y}{3pD_y}\right)},\end{aligned} \tag{5}$$

where (x, y) denote the airspace coordinates, (κ_x, κ_y) denote the frequency domain coordinates, $R(\kappa_x, \kappa_y)$ denotes the random number that follows a Gaussian distribution. D_x and D_y represent characteristic spatial scales in the x- and y-directions, respectively. They describe the periodicity or spacing of phase fluctuations, possibly related to grid spacing or aperture size in optical systems, modulating the oscillatory phase shifts over these directions in wavefront propagation models.
The far-field spot energy distribution is given by

$$I_{yc}(x, y) = \left|\mathcal{F}^{-1}\left\{H(f_x, f_y)\mathcal{F}\left\{I(x, y)e^{i\phi_{sh}(x,y)}\right\}\right\}\right|^2 \tag{6}$$

where $\mathcal{F}$ and $\mathcal{F}^{-1}$ are the forward and inverse Fourier transforms, respectively, and $H(f_x, f_y)$ denotes the transfer function for free-space diffraction.

The laser weapon system is considered to be mounted at the origin of a coordinate system, with a vertically upward z-axis towards the sky. The target location, denoted by (x_t, y_t, z_t), is assumed to be the geometric center of a 3D structure. The laser beam, approximated as a cone with a half-angle θ_0, is aimed towards this point. The target's shape, simplified as a cylinder, is positioned horizontally around (x_t, y_t, z_t). This assumption is particularly applicable in scenarios involving missile interception using laser systems.

For Monte Carlo simulation, N points have been generated uniformly and randomly on the surface of the cylinder. Each point's angle with respect to the axis of the laser beam cone, denoted as α, is calculated; points where $0 \leq \alpha \leq \theta_0$ are considered within the cone. The number of such points, $N_{\text{in-cone}}$, is determined among the total points generated N.
The on-target spot area, denoted as S_{db}, is calculated using

$$S_{\text{db}} = \frac{N_{\text{in-cone}}}{N}\pi r l, \tag{7}$$

where r and l represent the dimensions of the target cylinder. This formula provides an effective measure of the focused energy on the target, considering the spatial distribution and alignment of the laser beam with the target's cylindrical shape.
Given the small half-angle of the laser beam, the intersection is approximated with the target surface as planar. Thus, it is assumed the irradiation occurs on a plane surface. Negligible power dissipation during laser transmission leads to

$$\iint\limits_{S_{yc}} I_{yc}(x,y)dxdy = \iint\limits_{S_{db}} I_{db},(x,y)dxdy \tag{8}$$

where $I_{\mathrm{yc}}(x,y)$ and $I_{\mathrm{db}}(x,y)$ are intensities at the far-field and on-target, respectively and S_{yc}, S_{db} are their respective areas. Assuming laser transmission along the z-direction and the x-y plane for surface spread, the spot center coordinates $(\bar{x},\bar{y})$ are determined by

$$(\bar{x},\bar{y}) = \left(\frac{\iint_S x\, I(x,y)\, dx\, dy}{\iint_S I(x,y)\, dx\, dy}, \frac{\iint_S y\, I(x,y)\, dx\, dy}{\iint_S I(x,y)\, dx\, dy} \right). \tag{9}$$

From the center $(\bar{x},\bar{y})$, a circle Ω of arbitrary radius is constructed within the surface S. Define the parameter η as

$$\eta = \frac{\sum_{(x,y)\in\Omega} I(x,y)}{\sum_{(x,y)\in S} I(x,y)}. \tag{10}$$

The radius of Ω is adjusted until η reaches 84%, using a suitable search algorithm such as binary search. For a Gaussian beam, approximately 84% of the total intensity is contained within one standard deviation of the distribution. Therefore, this value has been chosen. Note that any other value can also be chosen without affecting the qualitative aspects of results.
When aligning a laser beam to a target, mechanical vibrations cause tracking errors. The aiming error, $\hat{\phi}(x_c,y_c) = (u_x,u_y)$, measures deviation from the intended spot at (x_c,y_c).
Assuming Gaussian disturbances along x and y, the total tracking error $\hat{\phi}(x_s,y_s)$ is

$$\hat{\phi}(x_s,y_s) = \frac{1}{2\pi\sigma_d\sigma_f} \exp\left(-\rho \left[\frac{x_s^2}{\sigma_d^2} + \frac{y_s^2}{\sigma_f^2} \right] \right)$$

with σ_d and σ_f as standard deviations in x and y directions, respectively and ρ is the scaling factor that affects the decay the Gaussian function.
The combined aiming and tracking error $\hat{\phi}(x,y)$ is

$$\hat{\phi}(x,y) = \frac{1}{2\pi\sigma_x\sigma_y} \exp\left(-\frac{1}{2} \left[\frac{(x-u_x)^2}{\sigma_x^2} + \frac{(y-u_y)^2}{\sigma_y^2} \right] \right), \tag{11}$$

where (x,y) are surface coordinates.
Let (x_i,y_i) denote the instantaneous location of the center of the on-target spot, and the probability that spot (x_i,y_i) will be achieved during a time interval Δt is given by $\hat{\phi}(x_i,y_i)$. The total incident energy density around the target point (x,y) is calculated using the superposition of all these instantaneous spots during the laser working period. The formula for the calculation is

$$E_{\mathrm{inc}}(x,y) = \sum_{i=1}^{N} I(x_i,y_i)\Delta t, \tag{12}$$

where (x,y) is the target point, $E_{\mathrm{inc}}(x,y)$ is the on-spot energy density around the target point and $I(x_i,y_i)$ denotes the incident intensity on the instantaneous center. We generate deviations with the help of Equation (12) and add them to the target point (x,y) to obtain the instantaneous center (x_i,y_i). We generate N such points for one simulation to compute the on-spot energy density. Many simulations are conducted to obtain a statistical histogram. By normalizing this

histogram, we derive a probability density function (PDF) of the energy distribution.
The energy distribution obtained above is converted to the temperature distribution under the assumption that the wall thickness is δ, and the laser propagates in the z-direction. This simplifies the calculation greatly as

$$\frac{1}{\kappa}\frac{\partial T}{\partial t} = \nabla^2 T = \frac{\partial^2 T}{\partial z^2} \tag{13}$$

where t is time, T is temperature, and $\kappa = \frac{k}{\rho c}$ where k is thermal conductivity, ρ is density of material, and c is specific heat. Since the propagation of laser is assumed to be in the z direction so the heat distributions along the x and y directions can be neglected i.e., $\frac{\partial^2 T}{\partial x^2} = 0$, $\frac{\partial^2 T}{\partial y^2} = 0$. The boundary conditions are

$$T(x,y,z,0) = T_0, \quad -k\frac{\partial T}{\partial z}\bigg|_{z=0} = \frac{AE_{\text{inc}}}{t}, \quad k\frac{\partial T}{\partial z}\bigg|_{z=\delta} = 0. \tag{14}$$

Solving these, we obtain:

$$T(x,y,z,t) = T_0 + \frac{AE_{\text{inc}}}{t}\left(\frac{\kappa t}{k\delta} + \frac{\delta}{k}\frac{3(\delta - z)^2 - \delta^2}{6\delta^2} - \zeta\right), \tag{15}$$

where ζ is

$$\zeta = \frac{2\delta}{\pi^2 k}\sum_{n=1}^{\infty}(-1)^n \frac{e^{-k\pi^2 n^2 t/\delta^2}\cos\left(\frac{n\pi(\delta - z)}{\delta}\right)}{n^2}.$$

Once the distribution for the incident energy density E_{inc} is obtained from Equation (12), it can be substituted into Equation (15) to derive the temperature distribution. The surface is then discretized into a grid of appropriate size, which is determined by the desired accuracy of the calculations. The probability of damage can subsequently be calculated using Equation (1). This is achieved by counting the grid squares where the temperature exceeds the threshold temperature T_D. The probability density function (PDF) of the temperature distribution is computed by iterating over each square in the grid, noting the temperature range corresponding to each square, and populating a histogram based on these observations. Finally, a fitting procedure is applied to obtain a smooth PDF from the histogram data.
To clarify things, the following assumptions for the model have been considered throughout this section.

- Precise energy distribution requirement and effect of the target surface irradiation have not been considered as it involves detailed material modeling, especially for composite materials.
- The laze time for hard kill is kept variable as per requirements.
- Laser beam are ideal Gaussian intensity profile.
- Kolmogorov atmospheric turbulence theory is used to develop the effects of turbulence on laser.
- Visibility range is assumed to be indefinite.

3. SIMULATION RESULTS

In this section, we list the results that we obtained from the simulation of the model, as outlined in Section 2.

3.1. Laser Beam Profiles

Figure 1 shows that the beam profiles at different distances show the effect of turbulence in the atmosphere. Figure 2 exhibits a typical phase screen that models the turbulence effects of the atmosphere on the laser by introducing phase shifts. Figure 3 shows typical Monte Carlo simulation for calculating on-spot area, with 10,000 points generated on the half-cylinder. Points within the laser cone are marked in red.

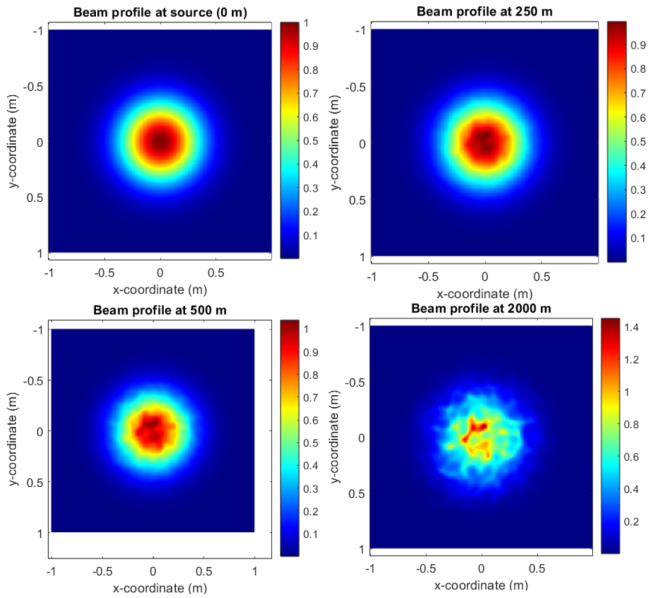


Figure 1: *The beam profiles at different distances.*

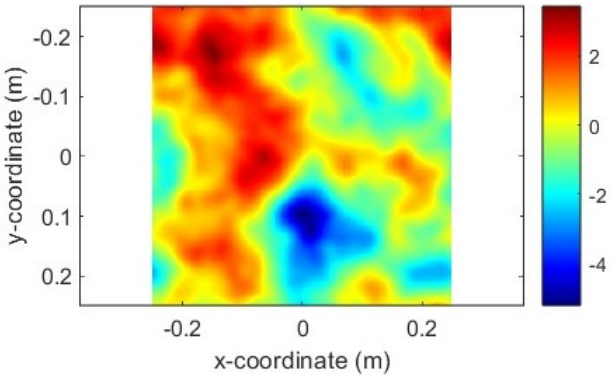


Figure 2: *Phase screen with the turbulence effects of the atmosphere.*

3.2. Effect of Distance on Damage Probability

The beam is supposed to show an exponential decay of the power with the distance $exp(-z)$. The simulation results for the same is shown in Figure 4.

3.3. Effect of Turbulence on the Damage Probability

The effect of turbulence on the damage probability is simulated by changing the value of the atmosphere™s inner and outer scale values and is shown in Figure 5. As the x-axis increases, atmospheric turbulence decreases, while the y-axis represents the damage probability of aluminum exposed to a 50 kW laser at a distance of 1 km.

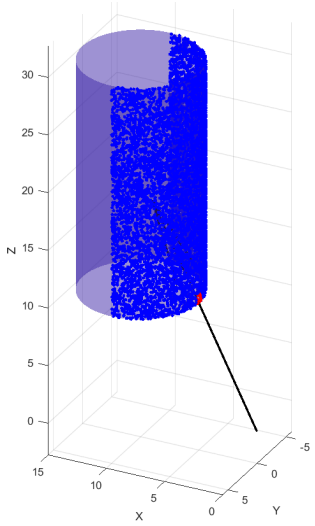


Figure 3: *Monte Carlo simulation results*

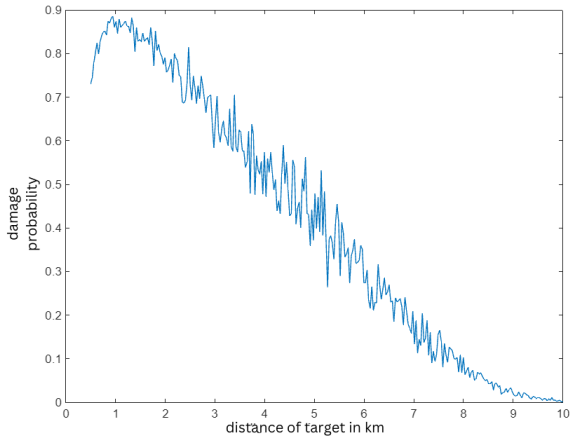


Figure 4: *Damage probability versus distance*

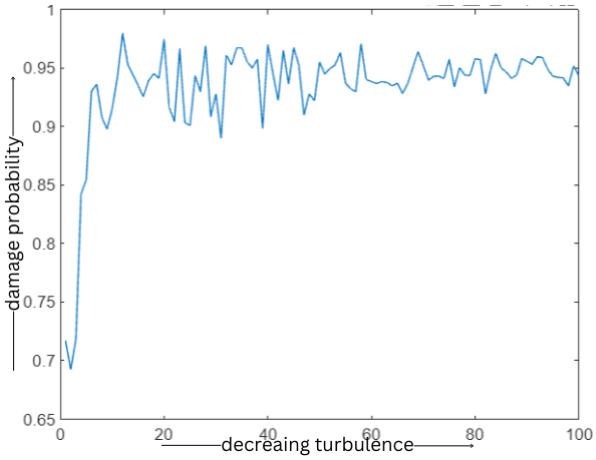


Figure 5: *Damage probability versus turbulence*

3.4. Minimum Power Required for Different Materials

The thermal conductivity is in W/cmK, the density is in g/cm3, specific heat is in J/gK, and the melting point is in degrees Celcius. The power is reported in the Table if the damage probability

calculated from the model turns out to be around 0.95 for moderate turbulence. The results of the simulation for few selected metals can be seen in Table 1 and the rest can be accessed here. The plots presented in Figures 6, 7, 8, and 9 illustrate the minimum laser power required (in kW) for a 2-second irradiation, as derived from the data in Table 1.

- Figure 6 displays the relationship between laser power and the density of the target material.
- Figure 7 illustrates how the required laser power varies with the melting point of the material.
- Figure 8 shows the correlation between laser power and the specific heat of the target.
- Figure 9 highlights the dependence of laser power on the thermal conductivity of the material.

These figures collectively provide insights into how various material properties influence the required laser power for effective thermal damage.

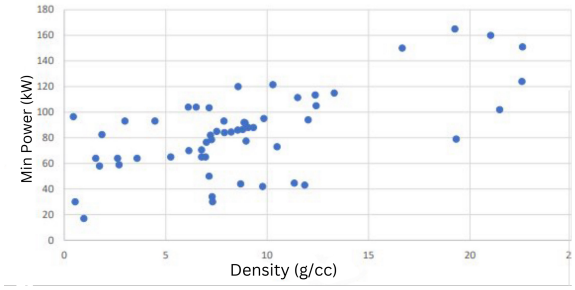


Figure 6: *Variation of the power of the laser versus the density of the target material*

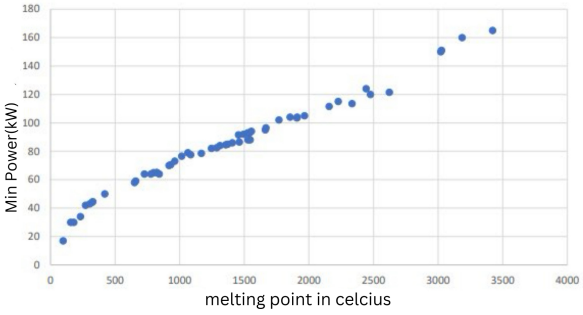


Figure 7: *Variation of the power of the laser versus the melting point of the target material*

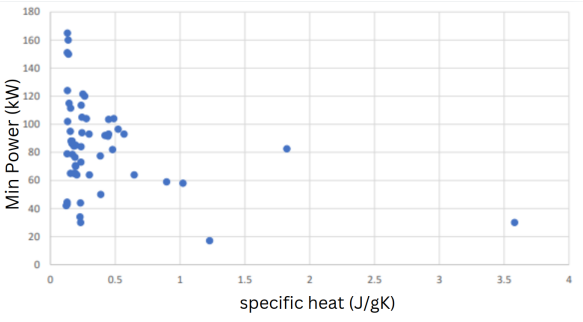


Figure 8: *Variation of the power of the laser versus the specific heat of the target material*

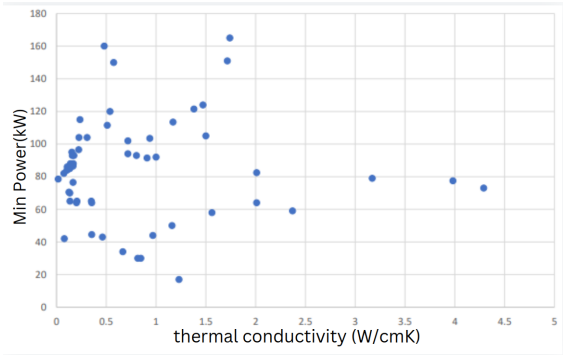


Figure 9: *Variation of the power of the laser versus the thermal conductivity of the material.*

From the plots, it can be concluded that the melting point is the most sensitive parameter, followed by the density of the material. The thermal conductivity and the specific heat of the material are very less sensitive parameters.

Table 1: *Properties of Various Elements*

Element	Thermal Conductivity	Density	Specific Heat	Melting Point	Min Power of Laser
Li	0.847	0.534	3.58	180.5	30
Be	2.01	1.85	1.824	1287	82.5
Mg	1.56	1.738	1.023	650	58
Al	2.37	2.7	0.897	660.32	59
Ca	2.01	1.55	0.647	842	64
Cr	0.937	7.14	0.449	1907	103.5
Mn	0.074	7.21	0.479	1246	82
Fe	0.803	7.874	0.449	1538	93
Co	1	8.86	0.421	1495	92
Ni	0.909	8.912	0.444	1455	91.5
Cu	3.98	8.96	0.385	1084.62	77.5
Zn	1.16	7.14	0.388	419.73	50
Ag	4.29	10.49	0.235	961.78	73
W	1.74	19.25	0.132	3422	165

4. CASE STUDY: ATTACKING A DRONE

We assume that the drone is made up of composite carbon material. The attack's parameters and results are mentioned in Table 2. The results indicate a 93.6% probability that the drone will sustain damage. The simulation findings are illustrated in Figures 10, 11, and 12. The left panel of Figure 10 displays the energy distribution at a distance (far-spot), while the right panel presents the energy distribution at the targeted location (on-spot). Both images are annotated with an 84% irradiation circle.

5. PSEUDO CODE

In this section, the pseudo codes are provided which have been used to develop the simulation to generate the results. Please refer, pseudo codes 1, 2, 3, 4, 5, 6.

6. CONCLUSIONS AND FUTURE WORKS

This study provides an extensive probability analysis of a thermal laser weapon system intended to destroy drones and other aerial threats. An efficient model that takes into account the effects

Pseudo Code 1 MONTE_CARLO_AREA_CALCULATION

function MONTE_CARLO_AREA_CALCULATION(r, l, xc, yc, zc, N_points, α)
  $red_points \leftarrow 0$
  $laser_dir \leftarrow [xc, yc, zc] - [0, 0, 0]$
  $laser_dir \leftarrow laser_dir / \|\textsc{Norm}(laser_dir)\|$
  $z \leftarrow zc - \frac{l}{2} + l \cdot \textsc{Random}(N_points, 1)$
  $\theta \leftarrow -\frac{\pi}{2} + \pi \cdot \textsc{Random}(N_points, 1)$
  $x_points \leftarrow xc - r \cdot \cos(\theta)$
  $y_points \leftarrow yc - r \cdot \sin(\theta)$
  for $i \leftarrow 1$ **to** N_points **do**
    $point \leftarrow [x_points[i], y_points[i], z[i]]$
    $norm_point \leftarrow \|\textsc{Norm}(point)\|$
    $cross_product \leftarrow \|\textsc{Cross_Product}(laser_dir, point)\|$
    $angle \leftarrow \left|\textsc{Asin}\left(\frac{cross_product}{norm_point}\right)\right|$
    if $angle < \alpha$ **then**
      $red_points \leftarrow red_points + 1$
    end if
  end for
  $S_onspot \leftarrow \left(\frac{red_points}{N_points}\right) \cdot \pi \cdot r \cdot l$
  return S_onspot
end function

Pseudo Code 2 FT_SH_PHASE_SCREEN

function FT_SH_PHASE_SCREEN(r_0, N, δ, L_0, l_0)
  $D \leftarrow N \cdot \delta$
  $phz_hi \leftarrow$ FT_PHASE_SCREEN(r_0, N, δ, L_0, l_0)
  $(x, y) \leftarrow \textsc{Create_Spatial_Grid}(N, \delta)$
  $phz_lo \leftarrow \textsc{Zero_Matrix}(N, N)$
  for $p \leftarrow 1$ **to** 3 **do**
    $del_f \leftarrow \frac{1}{3^p \cdot D}$
    $(f_x, f_y) \leftarrow \textsc{Create_Frequency_Grid}(del_f)$
    $(angle, f) \leftarrow \textsc{Convert_To_Polar}(f_x, f_y)$
    $f_m \leftarrow \frac{5.92}{l_0 \cdot (2\pi)}$
    $f_0 \leftarrow \frac{1}{L_0}$
    $PSD_phi \leftarrow 0.023 \cdot r_0^{-5/3} \cdot \exp\left(-\left(\frac{f}{f_m}\right)^2\right) / (f^2 + f0^2)^{11/6}$
    $PSD_phi[2][2] \leftarrow 0$
    $cn \leftarrow (\textsc{Random_Normal_Matrix}(3,3) + 1i \cdot \textsc{Random_Normal_Matrix}(3,3)) \cdot \sqrt{PSD_phi} \cdot del_f$
    $SH \leftarrow \textsc{Zero_Matrix}(N, N)$
    for $ii \leftarrow 1$ **to** 9 **do**
      $SH \leftarrow SH + cn[ii] \cdot \exp\left(1i \cdot 2\pi \cdot (f_x[ii] \cdot x + f_y[ii] \cdot y)\right)$
    end for
    $phz_lo \leftarrow phz_lo + SH$
  end for
  $phz_lo \leftarrow \textsc{Real}(phz_lo) - \textsc{Mean}(\textsc{Real}(phz_lo))$
  return (phz_lo, phz_hi)
end function

Pseudo Code 3 FT_PHASE_SCREEN

function FT_PHASE_SCREEN(r_0, N, δ, L_0, l_0)
  $D \leftarrow N \cdot \delta$
  $del_f \leftarrow \frac{1}{D}$
  $f_x \leftarrow$ CREATE_ARRAY($-\frac{N}{2}$ **to** $\frac{N}{2} - 1$) $\cdot del_f$
  $(f_x, f_y) \leftarrow$ MESHGRID(f_x, f_y)
  $f \leftarrow \sqrt{f_x^2 + f_y^2}$
  $f_m \leftarrow \frac{5.92}{l_0 \cdot (2\pi)}$
  $f_0 \leftarrow \frac{1}{L_0}$
  $PSD_phi \leftarrow 0.023 \cdot r_0^{-5/3} \cdot \exp\left(-\left(\frac{f}{f_m}\right)^2\right) / (f^2 + f_0^2)^{11/6}$
  $PSD_phi[\frac{N}{2}][\frac{N}{2}] \leftarrow 0$
  $random_real \leftarrow Random_Normal_Matrix(N, N)$
  $random_imag \leftarrow Random_Normal_Matrix(N, N)$
  $cn \leftarrow (random_real + i \cdot random_imag) \cdot \sqrt{PSD_phi} \cdot del_f$
  $phz_hi \leftarrow Inverse_FFT2(Shift_FFT(cn)$, 'symmetric') $.(N \cdot del_f)^2$

  return phz_hi
end function

Pseudo Code 4 PROPAGATE_BEAM

function PROPAGATE_BEAM(E_{in}, λ, dz, δ)
  $N \leftarrow$ SIZE(E_in, 1)
  $fx \leftarrow$ CREATE_SPATIAL_FREQUENCIES(N, δ)
  $H \leftarrow$ CALCULATE_TRANSFER_FUNCTION(fx, λ, dz)
  $E_in_ft \leftarrow$ FOURIER_TRANSFORM(E_{in})
  $E_out_ft \leftarrow E_{in_ft} \cdot H$
  $E_out \leftarrow$ INVERSE_FOURIER_TRANSFORM(E_out_ft)
  return E_out
end function

Pseudo Code 5 DRIVER CODE

function ON_SPOT_ENERGY($therma$, $density$, $specific$, $melt$, amp)
Set parameters
D // Length of one side of square phase screen [m]
$r0$ // Coherence diameter [m]
N // Number of grid points per side
$L0$ // Outer scale [m]
$l0$ // Inner scale [m]
$\delta \leftarrow \frac{D}{N}$ // Grid spacing [m]
$amplitude \leftarrow amp$ // Amplitude in kilowatt
λ // Wavelength [m]
$w0$ // Beam waist [m]
L // Single propagation distance [m]
$k \leftarrow therma \cdot 100$ // Thermal conductivity [W/(m*K)]
$\rho \leftarrow density$ // Density [g/cm^3]
$c \leftarrow specific$ // Specific heat [$J/(g*K)$]
$\delta_material$ // Wall thickness [m]
$T0$ // Initial temperature [C]
A // Area coefficient (arbitrary units)
TD // Threshold temperature for damage [C]
$time_step$ // Time step for temperature calculation [s]
Calculate thermal diffusivity
$\kappa \leftarrow \frac{k}{\rho \cdot c}$ // Thermal diffusivity [m^2/s]
Create the phase screens
$(phz_lo, phz_hi) \leftarrow$ GENERATE_PHASE_SCREENS($r0$, N, δ, $L0$, $l0$)
$phz \leftarrow phz_lo + phz_hi$
Create spatial grid
$x \leftarrow$ GENERATE_GRID($-\frac{N}{2}$, $\frac{N}{2} - 1$, δ)
$y \leftarrow x$
$(X, Y) \leftarrow$ MESHGRID(x, y)
Initial Gaussian beam profile with amplitude factor
$E0 \leftarrow amplitude \cdot \exp\left(-\frac{X^2+Y^2}{w0^2}\right)$
Number of phase screens and distance between screens
$M \leftarrow ...$
$dz \leftarrow \frac{L}{M}$
Propagate the beam through the phase screens
$E \leftarrow E0$
for $m \leftarrow 1$ **to** M **do**
Apply the phase screen
$E \leftarrow E \cdot \exp(i \cdot phz)$
Propagate to the next screen
$E \leftarrow$ PROPAGATE_BEAM(E, λ, dz, δ)
end for
Calculate the instantaneous center of the intensity distribution
$I \leftarrow |E|^2$
$x_bar \leftarrow \frac{\sum\sum(X \cdot I)}{\sum\sum I}$
$y_bar \leftarrow \frac{\sum\sum(Y \cdot I)}{\sum\sum I}$
end function

Pseudo Code 6 DRIVER CODE CONTINUE

Monte Carlo simulation for area calculation
$total_energy_distribution \leftarrow 0$
for each simulation **from** 1 **to** num_simulations **do**
Generate a new center using a 2D Gaussian distribution
$new_center \leftarrow$ SAMPLE_FROM_2D_GAUSSIAN($[x_bar, y_bar]$, $[variance, variance]$)
$x_new \leftarrow new_center.x$
$y_new \leftarrow new_center.y$
Generate the new intensity distribution centered at (*x_new*, *y_new*)
$E_shifted \leftarrow amplitude \cdot \exp\left(-\frac{(X-x_new)^2+(Y-y_new)^2}{w0^2}\right) \cdot \exp(i \cdot phz)$
Propagate the beam through the phase screens
for each propagation step **from** 1 **to** M **do**
$E_shifted \leftarrow$ PROPAGATE_BEAM($E_shifted$, λ, dz, δ)
end for
Calculate intensity for shifted beam
$I_shifted \leftarrow |E_shifted|^2$
Calculate new center and radius for shifted beam using the formula given in the text
$(x_bar_shifted, y_bar_shifted) \leftarrow$ CALCULATE_CENTER($I_shifted$)
$final_radius_shifted \leftarrow$ CALCULATE_FINAL_RADIUS(X, Y, $I_shifted$, $x_bar_shifted$, $y_bar_shifted$)
Calculate the area of the far-field spot with 84% energy
$S_farspot_84 \leftarrow \pi \cdot final_radius_shifted^2$
Calculate the on-spot intensity
$I_onspot \leftarrow I_shifted \cdot \frac{S_farspot_84}{S_onspot}$
Accumulate the energy distribution
$total_energy_distribution \leftarrow total_energy_distribution + I_onspot \cdot delta_t$
end for
Normalize the accumulated energy distribution
$total_energy_distribution \leftarrow total_energy_distribution / (num_simulations \cdot delta_t)$
Calculate the temperature distribution using the formula mentioned in the text
$T \leftarrow$ CALCULATE_TEMPERATURE($total_energy_distribution$, $T0$, A, $time_step$, κ, $\delta_material$, L, k)
Calculate the probability of damage
$p_damage \leftarrow \frac{\sum(T(:)>TD)}{\text{LENGTH}(T)}$
PRINT('Probability of Damage: ', p_damage)

Table 2: *Material and Laser Parameters*

Parameter	Value	Parameter	Value
Material	Carbon Fiber	Thermal Conductivity	2 W/cmK
Density	2 g/cm^3	Specific Heat	1 J/gK
Thickness	1 cm	Melting Point	3650 °C
Outer Scale	15 m	Inner Scale	0.18 m
Laze Time	20 seconds	Power of the Laser	18 kW
Distance	1 km	Initial Temperature	50 °C

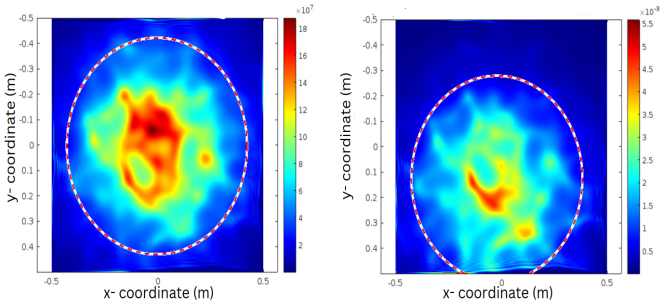


Figure 10: *Far-spot energy distribution (left) and the on-spot energy distribution (right)*

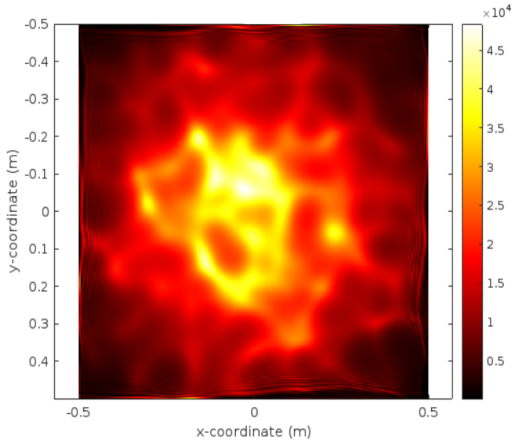


Figure 11: *Temperature distribution*

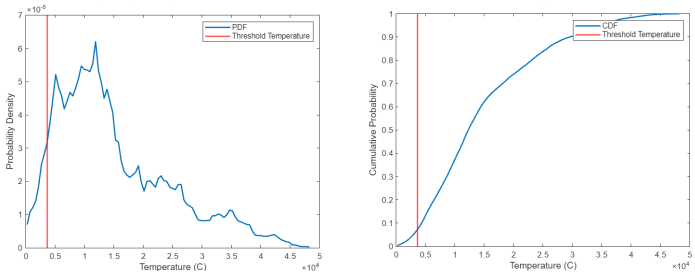


Figure 12: *The PDF and CDF of the temperature distribution function*

of atmospheric turbulence on laser propagation, the energy distribution on the target, and the thermal reaction of the target material was created. The chance of damage occurring from

persistent laser irradiation has been derived by simplifying complex interactions through the use of statistical methods and Monte Carlo simulations. The findings of the simulation suggest that the efficiency of a thermal laser weapon system is highly dependent on the target's material qualities, the laser system's accuracy, and the air conditions.

Future research could enhance this analysis by incorporating additional factors affecting laser performance, such as scintillation, aerosol scattering, absorption, humidity, and thermal blooming. Including these atmospheric effects is crucial for practical applications. Additionally, dynamic target analyses could refine and validate the model for robustness in diverse operational scenarios.

References

[1] Abunada, A.H., Osman, A.Y., Khandakar, A., Chowdhury, M.E.H., Khattab, T., Touati, F.: Design and implementation of a rf based anti-drone system. In: 2020 IEEE International Conference on Informatics, IoT, and Enabling Technologies (ICIoT). pp. 35–42. Doha, Qatar (Feb 2020)

[2] L. Liao, X.H., Xie, F.: Development status and operation analysis of laser weapon in anti-drone warfare. In: 2023 IEEE International Conference on Unmanned Systems (ICUS). pp. 305–310. Hefei, China (Oct 2023)

[3] Liu, L., Xu, C., Zheng, C., Cai, S., Wang, C., Guo, J.: Vulnerability assessment of uav engine to laser based on improved shotline method. Defence Technology **33**, 588–600 (2023)

[4] Lyu, C., Zhan, R.: Global analysis of active defense technologies for unmanned aerial vehicle. IEEE Aerospace and Electronic Systems Magazine **30**(1), 6–31 (2022)

[5] Mengzhen, Z., Xia, C., Xu, L., Chaoyong, T., Wei, L.: Situation and key technology of tactical laser anti-uav. Infrared Laser Eng **50**(7), 20200230–1 (2021)

[6] Perram, G.P., Marciniak, M.A., Goda, M.: High-energy laser weapons: technology overview. Laser Technologies for Defense and Security **5414**, 1–25 (2004)

[7] RE, B.: The fundamentals of aircraft combat survivability: analysis and design. 2th ed. Reston: American Institute of Aeronautics and Astronautics (1985)

[8] Steinvall, O.: The potential role of lasers in combating uavs, part 1: detection, tracking, and recognition of uavs. In Electro-Optical and Infrared Systems: Technology and Applications XVIII and Electro-Optical Remote Sensing XV **11866**, 174–185 (2021)

[9] Tunick, A.D.: The refractive index structure parameter/atmospheric optical turbulence model: Cn2. Tech. Rep. ARL-TR-1615, Army Research Laboratory, Adelphi, MD (Apr 1998)

[10] Voorst, B.R.V.: Counter drone system. U.S. Patent 15 443 143 **14** (2017)

[11] Wang, F., Du, W., Yuan, Q., Liu, D., Feng, S.: A survey of structure of atmospheric turbulence in atmosphere and related turbulent effects. Atmosphere **12**(12) (2021). https://doi.org/10.3390/atmos12121608, https://www.mdpi.com/2073-4433/12/12/1608

[12] Wang, P., Luo, J., Tang, J., Qin, Y., Cui, J., Zhang, L.: Progress and prospects of anti-drone radar detection technology. In: 2021 CIE International Conference on Radar (Radar). pp. 2331–2334. Hainan, China (Dec 2021)

[13] Zhao, S., Xie, R., Wan, J.: Design of anti-drone laser weapon systems. In: High-Power Lasers and Applications XI. pp. 24–30. Hefei, China (Oct 2023)

RT&A, No 4 (89)
Volume 20, December 2025

RELIABILITY, SAFETY, AND SUSTAINABILITY IN NUCLEAR POWER PLANTS: ADVANCES IN SUPERCRITICAL WATER REACTORS AND CIRCULATION LOOPS

Pardeep Kumar[1], Santosh Kumar Rai[2]*, Anikate Gupta[3], Dinesh Kumar[4], Mahesh Kumar Gupta[5], Dhowmya Bhatt[6], Mahiti Gupta[7], Gyanendra Prasad Bagri[8]

•

[1,4]Department of Mechanical Engineering, MM(DU), Mullana, Haryana, India
[2,5,8]Department of Mechanical Engineering, SRMIST, Ghaziabad, UP, India
[3]School of Engineering & Technology, CGC University, Mohali, Punjab, India
[6]Department of Computer Science Engineering, SRMIST, Ghaziabad, UP, India
[7]Department of Bio-Sciences & Technology, MM(DU), Mullana, Haryana, India

[1]pardeepkamboj@yahoo.com,*[2]08rai.santosh@gmail.com, [3]aniketj1019@cgc.ac.in, [4]dinesh_kumar@mmumullana.org, [5]maheshkm1@srmist.edu.in, [6]dhowmyab@srmist.edu.in, [7]mahitigupta@gmail.com

Abstract

In the last two decades, population and energy requirements have drastically risen. Therefore, it is necessary to provide an adequate amount of energy to the people and industries without affecting global warming and the environment. So, several nuclear power plants are constructed to supply the required demand of the power supply to the household and industries. Nuclear power plants can produce more electricity while maintaining global warming norms. However, during production of higher power from the plants, there are several issues raised, such as the sustainability and safety of the nuclear power plant as well as the reliability of the plants. To resolve these issues to achieve higher plant efficiency, safety of the plant, etc., during operations, several power plants are constructed, such as boiling water reactors and supercritical water reactors to generate power at higher efficiency, while single, two phase and supercritical based natural circulation loops are used to improve the safety of the plant as well as used in operation to improve the power generation from the plant. In past decade, supercritical water reactors and supercritical natural circulation loops have been utilized to increase power generation and enhance the safety of the plant. This review article discusses numerical and experimental investigations of supercritical water reactors and natural circulation loops aimed at enhancing the safety, sustainability, and reliability of various nuclear reactors based on previously published works by several authors, along with identified research gaps and future work scopes.

Keywords: safety, sustainability, instability, natural circulation loop, supercritical water reactor

I. Introduction

Energy policy decisions are increasingly prioritizing low-carbon sources. In light of the global economic downturn caused by COVID-19 and the discourse on climate change, nations are modifying their energy policies to emphasize net-zero emission solutions that enhance return on investment. Nuclear power reactors exhibit stability, consistency, low carbon emissions, and high energy density. Moreover, the prolonged operational lifespan, low maintenance costs, and load-following capability render nuclear energy a feasible substitute for fossil fuel sources. Also, researchers are trying to remove heat in a compact area of a nuclear reactor, specifically electronic parts using microchannel technology [1-2].These constraints pose a considerable risk to both existing and planned nuclear power reactors. Next-generation reactors are being developed to improve some bottlenecks and improve the safety and economic possibility of nuclear power plants. These reactors demonstrate modularity, improved safety margins, and significantly lower construction and operational expenses, while enabling localized micro-grids and various energy applications. However, the rapid development of next-generation reactors to meet global net zero targets requires significant investment and the application of advanced research approaches and technology. This is evident due to the expensive experimental testing facilities necessary for safety validation. Furthermore, researchers are increasingly reliant on computational approaches that require significantly longer periods to converge [3-5].

The preliminary designs of SCWRs have been formulated in Canada, the European Union, and Japan. The scientific term "supercritical" describes a state of a material when there is no distinct boundary between the liquid and gaseous phases. The SCWR design was one of six Generation IV system designs selected in a fourteen-country initiative, reflecting substantial interest in collaborative Research and Development (R&D) to progress future nuclear energy systems for deployment beyond 2030 [6-7]. Generation IV reactors, such as the Supercritical Water-Cooled Reactor (SCWR), were developed to improve the efficiency and sustainability of nuclear power facilities. Alongside these positive aspects of efficiency and design simplification, SCWRs are designed to function at supercritical pressures and temperatures.Nonetheless, all such developments include particular challenges related to reliability, sustainability, and safety, which must be thoroughly acknowledged and handled. This approach achieves enhanced thermal efficiency, estimated at 44-48%, in contrast to the 34-36% efficiency of current light water reactors. Supercritical water reactors employ water at temperatures exceeding its critical point (374°C, 22.1 MPa) for cooling and moderation functions. The SCWR technology can provide thermal, fast, or mixed neutron spectra, depending on the utilized pressure vessel or pressure tube system. It reduces nuclear waste production and alleviates greenhouse gas emissions. The thermal efficiency of SCWRs is augmented by the removal of fuel rods, hence generating an adequate energy output that reduces the generation of radioactive byproducts and prolongs the fuel cycle's lifespan through optimal fuel usage in nuclear power plants [8-9].

The word dependability of nuclear reactors denotes steady operation over a prolonged duration with minimal significant faults. SCWRs seek to enhance reliability by employing simpler designs, hence decreasing component quantity and minimizing system susceptibility to failure. SCWRs enhance the overall reliability of a nuclear reactor by eliminating pumps, dryers, pressurizers, and steam generators, hence reducing potential points of failure. Nevertheless, operating under supercritical conditions presents drawbacks. Elevated temperatures and pressures amplify the mechanical and thermal strains exerted on materials, necessitating the development of novel materials capable of enduring these conditions. Although SCWRs possess significant potential for reliability, further research in materials and a comprehensive understanding of the related supercritical water chemistry under radiative circumstances are necessary. Sustainability

in nuclear power pertains to effective fuel utilization and minimal environmental impact, while also addressing long-term energy requirements. SCWRs promote sustainability through their exceptional thermal efficiency, which optimizes fuel utilization and minimizes waste generation. The efficient design indicates a diminished physical footprint and possibly reduced resource consumption during construction and operation. Moreover, SCWRs can be designed to support various fuel cycles, such as thorium or actinide recycling, enhancing fuel sustainability and reducing the generation of long-lived radioactive waste. Indeed, the diversity of SCWR's design will enable it to achieve numerous sustainability objectives and optimize fuel utilization by reducing waste [10-15].

This paper provides a comprehensive analysis of current SCWRs, elucidating essential elements of safety, sustainability, and reliability in nuclear power facilities. The approaches for creating safety analysis tools for SCWR are outlined to elucidate the primary scientific difficulties and the solutions applied at this stage. The steady-state and transient safety characteristics of contemporary SCWR designs are analyzed comprehensively. The techniques for creating safety analysis tools for SCWR are outlined to elucidate the primary scientific obstacles and the solutions that have been executed thus far. The safety criteria of contemporary SCWR concepts are analyzed. The review and debates accurately delineate the research status of SCWR concepts, the development of safety analysis methods, and their safety attributes.

II. Literature Review

I. Safety and Reliability of the Supercritical Water Reactors (SCWRs)

Nuclear power plants (NPPs) are developed to generate higher energy to fulfill the demand and supply of energy for households and industries. In order to provide the demand required by various industries, NPPs are trying to produce the optimum quantity of energy. However, to produce an adequate amount of energy, NPPs produce maximum quantity of heat generations, which increases the core temperatures as well as drastic changes of density near the pseudo-critical point that makes plants unstable. These phenomena affect the performance of the NPPs. Therefore, it is necessary to investigates the fluctuation of the temperature and density with time and without time for accurate prediction of the thermal hydraulic behavior of the supercritical water reactor and supercritical natural circulation loops (SCNCLs) using various methods such as numerical and experimental. These methods are capable of identifying the various factors that influence the safety and reliability of the NPPs, SCWRs [16-18], and SCNCLs [19].

II. Safety Identification of the Safety Mechanism and Criteria for Nuclear Power Plants

The fundamental principle of examining the safety of nuclear reactor plants involves combining all components of the plant during operations, effectively managing and segregating all heat generation components, and minimizing hazards to ensure the plant functions safely. The process includes systematically varying the pressure at different mass flow rates during steady state, as well as adjusting the mass flow rate, velocity, and temperature over time at various power levels to determine the threshold criteria and mechanisms for identifying safe operational conditions. To assess the safety or instability of supercritical water reactor-based plants, several authors investigated transient instability using density wave oscillation, while for steady-state conditions, they analysed the variation of pressure at different power levels relative to mass flow rate and noted a negative pressure drop, indicating static instability that can be very harmful during the startup of the nuclear plant. Furthermore, for full safety of the plants, researchers must examine

various components of the reactors, such as fuel assembly and cooling systems, both steady-state and transient processes, as well as the dryout condition of the plant during accidents like loss of coolant accidents. In the NPP, two primary types of reactors operate based on the neutron spectrum. Fast reactors, like the supercritical pressure water-cooled rapid reactor (SWFR) developed by Japan, operate at high temperatures. The fuel blanket serves as a moderator to absorb neutrons during the fission process, generating high energy without impacting void reactivity or the core design. Supercritical pressure and temperature-based reactors are working on high temperatures, such as CANDU SCWR and U.S. SCWRs. Nonetheless, their coolant flow rate and the utilization of control rods as a moderator ensure the safety of the core. In this reactor, two cooling system passes are employed; the first generates power, while the second serves as a passive system to regulate the reactor's temperature and maintain the operational conditions of the SCWRs. In both cases, instability is likely, which is very harmful to the reactor. It can be seen that the amplitude of the mass flow rate is increasing with time and becomes unstable, while the mass flow rate with respect to time decreases and becomes stale. However, we refer to the mass flow rate as neutral when it remains constant over time. These mechanisms are used to determine the safety of the nuclear plants in terms of instability. Additionally, another approach for determining the safety mechanisms of the nuclear reactor is to accurately estimate the melting temperature of the core from a material perspective, which aids in preventing reactor accidents caused by excessive heat generation within the core. This phenomenon strengthens the safety and reliability of nuclear power plants, mitigates global warming, and improves the economy of the nation. This method compares the wall temperature and the threshold limiting temperature of the core wall during steady and transient states to ascertain the deterioration of heat transfer, which indicates the safety criteria of the supercritical reactor and natural circulation loop. Figures 1 and figure 2 illustrate the schematic diagram of the nuclear reactor.

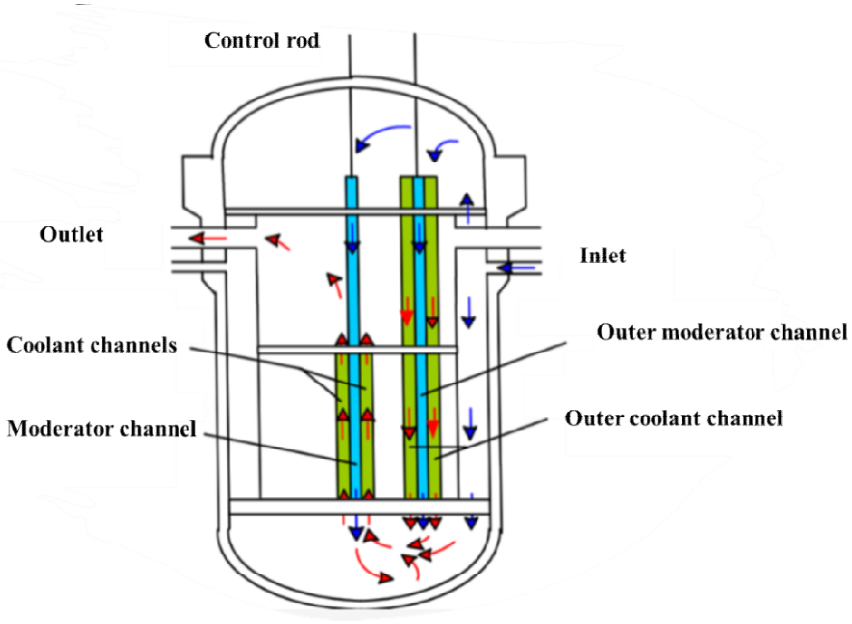


Figure 1: *Schematic diagram of US SCWR [18]*

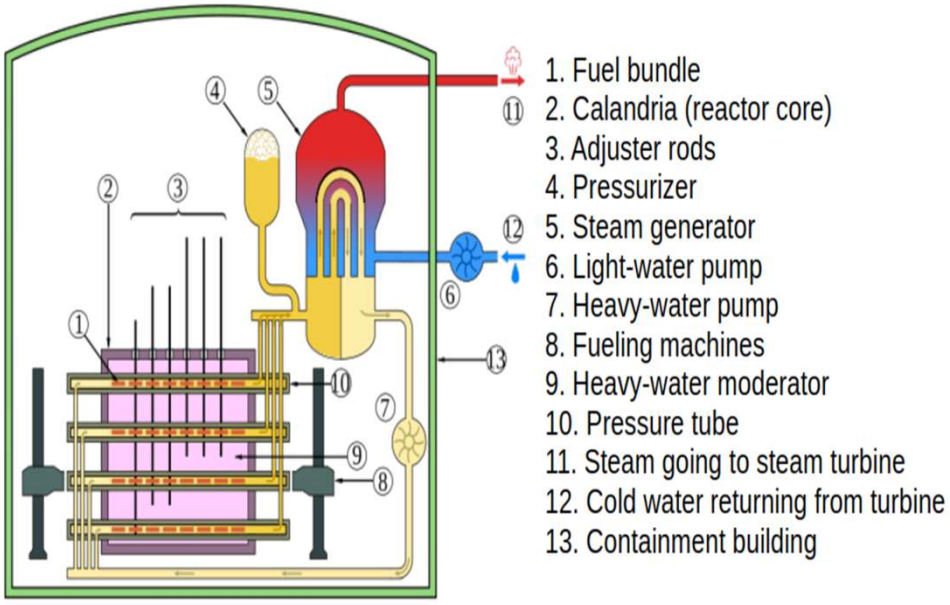


Figure 2: *Schematic diagram of CANDU SCWR [17]*

Figure 3 and figure 4 illustrate the mechanics of nuclear reactor to assess the safety standards. It can be seen from figure 3 that the wall temperature of the reactor exceeded the threshold limiting value, which is 850°C which showed the DHT in the reactor.

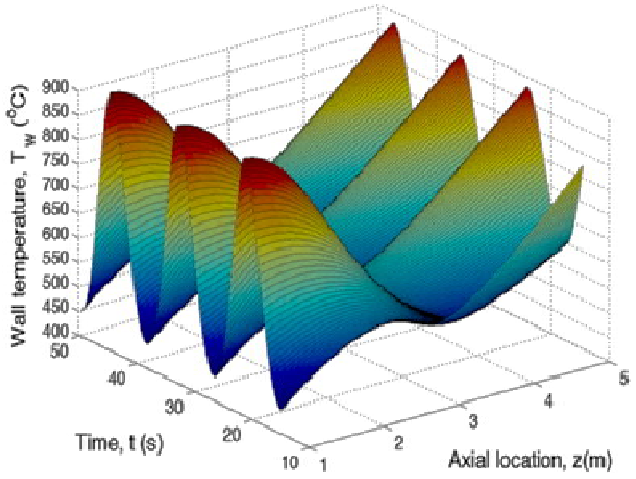


Figure 3: *Mechanism of the DHT in the reactor to predict the safety of the reactor [16]*

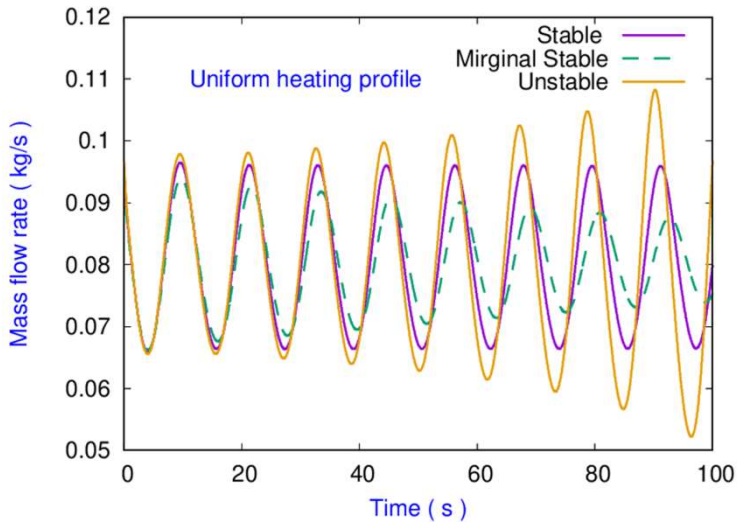


Figure 4: *Mechanism of the instability to predict the safety of the reactor [20]*

III. Safety, Reliability and Sustainability of the Supercritical Water Reactor and Supercritical Natural Circulation Loop Based Nuclear Power Plants

The demand for energy is increasing rapidly each day, necessitating fulfilment. In this context, our main goal is to construct several nuclear power plants (NPPs) that can generate substantial energy while also providing green energy, ensuring the safety and reliability of the NPPs and the environment. SCWRs and SCNCLs are designed to provide high energy while maintaining the safety and reliability of nuclear power plants. Nonetheless, both operate at high pressure and temperature, improving the thermal efficiency of the nuclear power plant (NPP). However, due to the significant change of the thermal physical properties of supercritical fluids (SCFs) near the pseudo-critical point, supercritical water reactors (SCWRs) suffer instability, which presents safety problems for the NPP.

This section discusses the safety, reliability, and sustainability of SCWR-NPP.There are various numerical and experimental studies performed by numerous researchers to achieve higher efficiency for the NPPs using water in different phases, such as single, two-phase, and supercritical. Hennig [21] in 1999, reported the stability characteristic of the boiling water reactor (BWR) and suggested that for achieving the higher efficiency, BWR-based NPPS experience instability, which is harmful for the NPPs. Similarly, Stosic et al. [22] developed SWR-1000 BWR to achieve higher thermal hydraulic performance as well as produce higher energy with a promising innovative safety concept for NPPs. Also, Theriault [23] suspected the design of the BWR for improving the safety of the NPPs by bifurcating the BWR into two important factors, like the reactor system and containment design, which separately control the safety features of the NPPs. Further, Su et al. [24] performed the comparative investigation of BWRs and SCWRs and reported that SCWRs gave higher thermal efficiency as compared to BWRs. By using the water in a supercritical state, the thermal efficiency of the plant is increased by 28.57% as compared to BWR as well as providing higher safety by eliminating the dryer and separator from the SCWRs. Further, by increasing the efficiency of the NPPs by utilizing the supercritical water, Cervi and Cammi [25] investigated the instability, safety, reliability, and sustainability of the SCWR, and its outcomes revealed that SCWRs provide higher stability at higher power ranges. Also, Wu et al. [26] suggested that SCWRs provide higher safety due to their compact size and low fuel consumption. They also proposed that due to the compact size of the SCWRs and safety features, they can be used in various applications for generating high power density.

Based on the several reports of found higher thermal efficiency using SCWR in the NPPs, Zhao et al. [17] investigated instability characteristics and their consequences at operating parameters like pressure drop in the channel. In this research, they utilized three fluid mixing simulation techniques to evaluate the flow instability of the SCWR. The results demonstrate increased marginal stability of the SCWR at an inlet loss coefficient of 20, which acts as a safety factor for NPPs. A non-dimensional stability map was developed to ascertain the usual operational boundaries for the reliability and safety of nuclear power stations (NPPs). In their subsequent study, Zhao et al. [27] conducted a follow-up study on SCWR, examining flow instability in relation to design parameters and pressure loss coefficients. Their findings indicate that the stability zones of SCWR have expanded relative to BWR due to the use of a low loss coefficient for the exit valve in the flow pipe beneath the core. Further, Chen et al. [28] developed a computation code to predict flow instability in both single and parallel channels of the SCWR. The code effectively predicts both static and dynamic instability, as well as the impact of numerous characteristics, such as geometry and operating circumstances, on flow instability. Examinations indicated that single-channel systems encounter more significant pressure drops, which is harmful for the NPPs, as well as that single-channel systems do not provide significant safety for the NPPs. Additionally, they proposed a safer and more reliable limit for SCWRs. Zhao [29] studied the flow problems and safety of the single-channel U.S. SCWR using a matrix method. They found that the decay ratio does not impact flow instability. However, the inlet orifice coefficient of the channel makes it more stable and safer in comparison to the smooth inlet channel. Also suggested is the manufacturing of the channels, which have different inlet orifice coefficient values for SCWR, to provide safety during operations. Also, Shitsi et al. [30] examined dynamic wave instability (DWI) across multiple channels with commercial 3D STAR-CCM+ software, demonstrating that SCWR undergoes DWI and produced a stability map for SCWR to ensure the nuclear power plant operates within stable and safe parameters.

Jyotish et al. [31] indicated that instrumentation and control systems are crucial for the safe operation of nuclear power stations (NPPs). Also, Gabriel [32] has demonstrated a reliability measurement precision of 99.9905% for safety-critical systems. Choi et al. [33] proposed that supercritical water reactors (SCWRs) implement a sustainability program aimed at enhancing reliability while reducing expenses through the optimization of safety margins. Utilizing decision-making tools to identify hazards enables the execution of operations that are both secure and economically efficient. Furthermore, innovations utilizing nuclear energy, such as helium-cooled compact modular reactors, exhibit potential for enhanced sustainability due to their reduced dependence on active safety protocols. Obaidurrahman et al. [34] conducted a study highlighting the significance of reliability and sustainability via a comprehensive safety framework that integrates essential safety principles, deterministic and probabilistic safety assessments, and uncertainty evaluations of NPPs. These regulations ensure safety at every stage of the process, from planning to finalization. The insights gained from previous nuclear incidents have resulted in more stringent safety regulations and an enhanced emphasis on reducing the unpredictability of safety assessments. Advancements in nuclear technology offer significant advantages; nonetheless, concerns persist over public perception and the potential for catastrophic incidents. For nuclear energy to have a future, these concerns must be addressed via transparent dialogue and continuous efforts to enhance safety protocols. NPPs are reliable and durable, as demonstrated by Kroger et al. [35], indicating they are a clean energy source. Nonetheless, previous accidents and errors by individuals continue to evoke concerns around safety. The innovative design of supercritical water reactors (SCWRs), akin to small modular reactors, aims to enhance safety and public acceptance. Kumar et al. [36-39] conducted a study examining the reliability and availability across several power plants by analyzing different systems.

Further, some active CANDU and USA SCWR and passive (SCNCL) systems are used to provide the safety of the core as well as to be used as an operating system to produce energy. Rai et al. [40-41] discussed the significance of Ledinegg instability and DWI, particularly within a single-channel loop, to ensure the safety of nuclear power plants. Furthermore, they investigated the impact of various operational and geometric parameters of the single-channel loop, which can help improve the safety, reliability, and sustainability of NPPs at elevated power levels and during accidents. In their subsequent study, Rai et al. [42-43] discussed improvements in SCWRs within nuclear technology, addressed issues about the validation of safety analysis techniques and the necessity for thorough accident assessments, which remain essential for the secure implementation of nuclear power plants, and determined the stable and safe limits in both points of view, like DWI stable and the material point of view, to protect the melting of the core by excess heating of the core wall. Similarly, Swapneel et al. reported steady-state instability for SCNCL, which is used as a passive system to protect the NPPs during operation and accidental conditions. Further, Upadhyay and Dutta [44] established a stable and secure limit for the U.S. SCWR. Figure 2 illustrates that the reactor is thermally stable; nonetheless, it poses a safety risk regarding materials, as the wall temperature surpasses acceptable limits at a specific power level. According to the stable and safe criteria of U.S. SCWR, a stable and safe operational limit has been established for the NPP at specific power ranges, ensuring safety for the facility. Dutta et al. [45] developed a code, THRUST, that can forecast the steady state and DWI of the CANDU SCWR, and the influence of various parameters on this instability has been analyzed. They identified DWI in the SCWR and illustrated both the reactor's marginal stability boundary and the stable and safe limits for the SCWRs. Dutta et al. [46-47] examined the performance of the SCWR in both steady and transient states utilizing two distinct computational approaches, THRUST and commercial software ANSYS, to determine the DHT in the SCWR, which poses significant risks to the reactor.

It can be seen from figure 5 and figure 6 that the marginal stability of DWI and the marginal safety limit of the SCNCL and SCWRs of CANDU and USA reactors are drawn. The reactor's thermal hydraulic conditions are stable; nonetheless, the material temperature surpasses the maximum allowable temperature of the reactor wall. Consequently, the reactor is deemed unsafe. The reactor's established, stable, and secure limit has resulted in the formulation of a combined stable and secure limit. SCWRs show a higher stable and safe zone as compared to SCNCL.

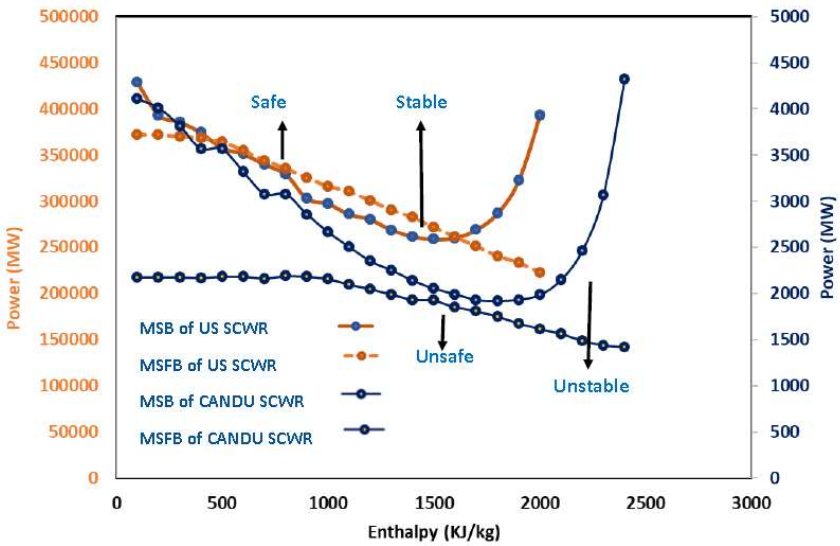


Figure 5: *Stable and safe limits of SCWRs [45-47]*

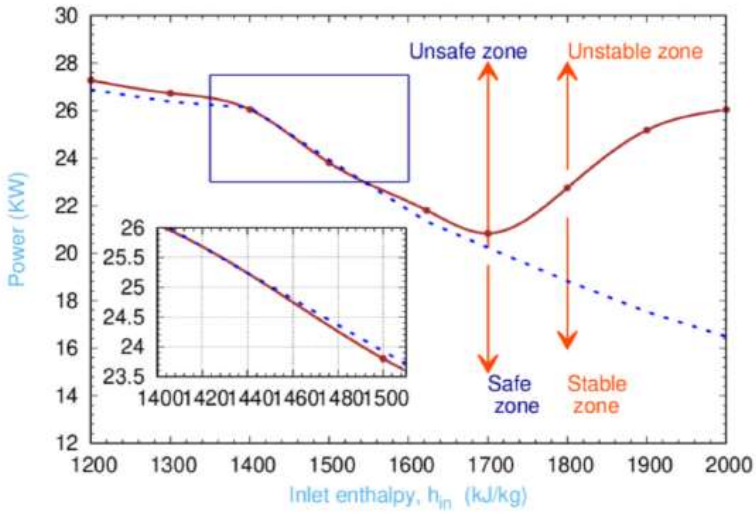


Figure 6: *Stable and safe limits of SCNCL [20]*

IV. Conclusions

In this present work, a thorough literature review of existing SCWR concepts and numerical and experimental investigations has been carried out to discuss the safety, reliability, and sustainability of high-pressure and temperature-based NPPs and determine their safety characteristics. Based on the literature review, the following important findings are found, which are discussed below.

The design of a multi-flow pass in the SCWR core is the primary approach to eliminate the transient flow instability, which provides the safety of the SCWRs. Supercritical fluid based NPPs are more efficient than two-phase and single phase based NPPs as well as supercritical water reactor plants are safer and more stable at high power as compared to boiling water reactors plant due to absence of the separator and dryer from the plants.The mass flow rate relative to thermal power is a distinguishing characteristic of SCWR, in contrast to PWR and BWR, which could potentially lead to compromised safety performance. SCNCLs are one of the best solutions to provide the higher safety of the NPPs during accidents as well as at normal operating conditions.The CANDU SCWR and U.S. SCWR were examined to ensure that the wall temperature of the core remains within safety limits during normal operation. Also, various computational methods are used to determine the safe and stable zone based on the transient analysis of the SCWRs and it is found that SCWRs are stable in point of TH, while in material point of view, it is not safe.

References

[1] Rai, S. K., Goyat, V., Gupta, M. K., Ghangas, G., Bhatt, D., Uniyal, A.,and Shrivas, N. V. (2025) Numerical and experimental heat transfer analysis of two-phase flow through microchannel for development of heat dissipation correlation. *Journal of Non-Equilibrium Thermodynamics*, 50(4):585-602.

[2] Koo, M., Lee, W. K., and Lee, C. H. (1997) New reactor system for supercritical water oxidation and its application on phenol destruction. *Chemical engineering science*, 52(7):1201-1214.

[3] Rowinski, M. K., Zhao, J., White, T. J., and Soh, Y. C. (2018) Safety analysis of super-critical water reactors–A review. *Progress in Nuclear Energy*, 106:87-101.

[4] Wu, P., Ren, Y., Feng, M., Shan, J., Huang, Y., and Yang, W. (2022) A review of existing supercritical water reactor concepts, safety analysis codes and safety characteristics. *Progress in*

Nuclear Energy, 153:104409.

[5] IAEA, 2014 Heat Transfer Behaviour and Thermohydraulics Code Testing for Supercritical Water Cooled Reactors (SCWRs).

[6] IAEA, 2019 Status of Research and Technology Development for Supercritical Water Cooled Reactors. IAEA. Vienna.

[7] Cervi, E., and Cammi, A. (2018) Stability analysis of the Supercritical Water Reactor by means of the root locus criterion. *Nuclear Engineering and Design*, 338:137-157.

[8] Rai, S. K., Kumar, P., and Panwar, V. (2020) Numerical analysis of influence of geometry and operating parameters on Ledinegg and dynamic instability on supercritical water natural circulation loop. *Nuclear Engineering and Design*, 369:110830.

[9] Locatelli, G., Mancini, M., and Todeschini, N. (2013) Generation IV nuclear reactors: Current status and future prospects. *Energy Policy*, 61:1503-1520.

[10] Abram, T., and Ion, S. (2008) Generation-IV nuclear power: A review of the state of the science. *Energy Policy*, 36(12):4323-4330.

[11] Rai, S. K., Ahlawat, N., Upadhyay, R., Kumar, P., and Panwar, V. (2022) A study on the effect of geometry and operating variables on density wave oscillation in a supercritical natural circulation loop. *Computation*, 10(2):1-25.

[12] Buongiorno, J., and MacDonald, P. (2003)Supercritical water reactor (SCWR). Progress Report for the FY-03 Generation-IV R&D Activities for the Development of the SCWR in the US, INEEL/Ext-03-03-01210.

[13] Rai, S. K., Kumar, P., Tiwari, M., Panwar, V., Kumar, D., and Sharma, V. K. (2025) A comprehensive overview of advancements, applications, and impact of supercritical fluid natural circulation loops. *Annals of Nuclear Energy*, 211:110971.

[14] Schulenberg, T., Leung, L. K. H., Brady, D., Oka, Y., Yamada, K., Bae, Y., andWillermoz, G. (2009) Supercritical water-cooled reactor (SCWR) development through GIF collaboration. In International Conference on Opportunities and Challenges for Water Cooled Reactors in the 21st Century, IAEA Publication, IAEA-CN-164-5S06: 67.

[15] Upadhyay, R., Rai, S. K., and Dutta, G. (2018) Numerical analysis of density wave instability and heat transfer deterioration in a supercritical water reactor. *Journal of Mechanical Science and Technology*, 32:1063-1070.

[16] Zhao, J., Saha, P., and Kazimi, M. S. (2007) Hot-channel stability of supercritical water-cooled reactors—I: steady-state and sliding pressure startup. *Nuclear technology*, 158(2):158-173.

[17] Rahman, M. M., Dongxu, J., Jahan, N., Salvatores, M., and Zhao, J. (2020) Design concepts of supercritical water-cooled reactor (SCWR) and nuclear marine vessel: A review. *Progress in Nuclear Energy*, 124:103320.

[18] Sharma, M., Pilkhwal, D. S., Vijayan, P. K., Saha, D., and Sinha, R. K. (2010)Steady state and linear stability analysis of a supercritical water natural circulation loop. *Nuclear Engineering and Design*, 240(3):588-597.

[19] Rai, S. K., Kumar, P., Panwar, V., Gupta, M. K., Bhatt, D., Kumar, D., and Gupta, M. (2025) A Comprehensive Investigation of Computational Analysis on Flow Characteristics, Stability and Safe Limits of a Supercritical Natural Circulation Loop for Different Heating Power Profiles. *Nuclear Engineering and Technology*, 103858.

[20] Hennig, D. (1999) A study on boiling water reactor stability behaviour. *Nuclear Technology*, 126(1):10-31.

[21] Stosic, Z. V., Brettschuh, W., and Stoll, U. (2008) Boiling water reactor with innovative safety concept: The Generation III+ SWR-1000. *Nuclear Engineering and Design*, 238(8):1863-1901.

[22] Theriault, K. (2016). Boiling water reactors. In *Nuclear Engineering Handbook*:85-140. CRC Press.

[23] Su, Y., Chaudri, K. S., Tian, W., Su, G., and Qiu, S. (2014) Optimization study for thermal efficiency of supercritical water reactor nuclear power plant. *Annals of Nuclear Energy*, 63:541-547.

[24] Cervi, E., and Cammi, A. (2018) Stability analysis of the Supercritical Water Reactor by means of the root locus criterion. *Nuclear Engineering and Design,* 338:137-157.

[25] Wu, P., Gou, J., Shan, J., Jiang, Y., Yang, J., and Zhang, B. (2013) Safety analysis code SCTRAN development for SCWR and its application to CGNPC SCWR. *Annals of Nuclear Energy*, 56: 122-135.

[26] Zhao, J., Saha, P., and Kazimi, M. S. (2008) Core-Wide (In-Phase) Stability of Supercritical Water-Cooled Reactors—I: Sensitivity to Design and Operating Conditions. *Nuclear technology*, 161(2):108-123.

[27] Chen, J., Gu, H., and Xiong, Z. (2019) Development of one-dimensional transient model for predicting flow instability at supercritical pressures. *Progress in Nuclear Energy*, 112:162-170.

[28] Zhao, J., Tso, C. P., and Tseng, K. J. (2011) SCWR single channel stability analysis using a response matrix method. *Nuclear engineering and design*, 241(7):2528-2535.

[29] Shitsi, E., Debrah, S. K., Agbodemegbe, V. Y., and Ampomah-Amoako, E. (2017) Numerical investigation of flow instability in parallel channels with supercritical water. *Annals of Nuclear Energy*, 110:196-207.

[30] Jyotish, N. K., Singh, L. K., Kumar, C., and Singh, P. (2023) Reliability and performance evaluation of safety-critical instrumentation and control systems of nuclear power plant. *IEEE Transactions on Reliability*, 73(1):422-437.

[31] Gabriel, A. (2018)Funnel Risk Graph Method in the Design of Integrated Control and Safety System (Doctoral dissertation, Victoria University).

[32] Choi, Y. J. (2019) Light Water Reactor Sustainability Program: Assessment of verification and validation status-RELAP5-3D and RAVEN (No. INL/EXT-19-56151-Rev000). Idaho National Laboratory (INL), Idaho Falls, ID (United States).

[33] Obaidurrahman, K., Arul, A. J., Ramakrishnan, M., and Singh, O. P. (2021) Nuclear reactor safety. *Physics of Nuclear Reactors* (pp. 449-510). Academic Press.

[34] Kroger, W., Sornette, D., and Ayoub, A. (2020) Towards safer and more sustainable ways for exploiting nuclear power. *World Journal of Nuclear Science and Technology,* 10(3):91-115.

[35] Kumar, P., Kumar, D., Chalisgaonkar, R., Sharma, V. K., and Rai, S. K. (2024) A Critical Review of Ram Methodology: Analysis and Performance Evaluation in Industrial Complexities. Reliability: *Theory & Applications,* 19(4 (80)):83-89.

[36] Kumar, P., Sharma, V. K., and Kumar, D. (2024) Availability analysis for identification of critical factor of a thermal power plant. Reliability: *Theory & Applications,* 19(3 (79)):717-724.

[37] Kumar, P., Tewari, P.C. and Khanduja, D.(2017) Six Sigma application in a process industry for capacity waste reduction: A case study. *Management Science Letters,* 7.9:423-430.

[38] Kumar, P., Khanduja, D. and Tewari, P.C. (2017) Maintenance Strategy for a System of a Thermal Power Plant. *International Journal of Operations and Quantitative Management,*23(1): 101-118.

[39] Rai, S. K., Kumar, P., and Panwar, V. (2021) Mathematical and numerical investigation of Ledinegg flow excursion and dynamic instability of natural circulation loop at supercritical condition. *Annals of Nuclear Energy,* 155:108129.

[40] Rai, S. K., Kumar, P., and Panwar, V. (2021) Numerical investigation of steady state characteristics and stability of supercritical water natural circulation loop of a heater and cooler arrangements. *Nuclear Engineering and Technology*, 53(11):3597-3611.

[41] Rai, S. K., Kumar, P., and Panwar, V. (2020) Computational analysis of static flow instabilities in supercritical natural circulation loop. In Proceedings of International Conference on Thermofluids: KIIT Thermo 2020 (pp. 387-395). Singapore: Springer Singapore.

[42] Suman, S., Upadhyaya, R., Raghuvanshi, N. S., Gupta, M. K., Shah, S., and Alam, S. (2022)

A state of art review of instability in parallel channels of supercritical fluid in nuclear applications. *Materials Today: Proceedings,* 62:226-232.

[43] Upadhyay, R., and Dutta, G. (2018) Identification of safe and stable zone of operation in supercritical water reactor. *Nuclear Engineering and Design*, 328:209-227.

[44] Dutta, G., Zhang, C., and Jiang, J. (2015). Analysis of flow induced density wave oscillations in the CANDU supercritical water reactor. *Nuclear Engineering and Design,* 286:150-162.

[45] Dutta, G., Maitri, R., Zhang, C., and Jiang, J. (2015) Numerical models to predict steady and unsteady thermal-hydraulic behaviour of supercritical water flow in circular tubes. *Nuclear Engineering and Design*, 289:155-165.

[46] Dutta, G., Zhang, C., and Jiang, J. (2015) Numerical analysis to investigate the effects of thermal-hydraulic instabilities on deterioration heat transfer and wall temperature in the CANDU supercritical water reactor. *Journal of Nuclear Engineering and Radiation Science,* 1(4):041011.

RT&A, No 4 (89)
Volume 20, December 2025

OPTIMIZATION AND PERFORMANCE EVALUATION OF SUGAR MILL PLANT MICRO COMPONENTS USING PSO

Sandeep Kumar
•
Department of Mechanical Engineering
D.C.R.U.S.T., Murthal, Sonipat, Haryana, India.
praansandeep@gmail.com

Abstract

Sugar mill plants, especially their core processing units, are highly dependent on a well-organized and efficient maintenance strategy for reliable operation. In this study, an availability-based simulation model was developed for a 25,500 TCD sugar mill. This model is based on a Markov-based performance evaluation framework, which uses differential equations to form state-transition diagrams representing transitions between fully operational, partially operational, and failure states. A comparative analysis of the subcomponents studied concluded that a centrifugal pump failure has minimal impact on overall system availability, while a clarification unit failure has the most significant impact. To improve system reliability and performance, the Particle Swarm Optimization (PSO) method was applied to optimize failure and repair rates. The experimental results obtained show that the overall availability of the system after applying the proposed optimization strategy is achieved at 88.57%, which shows effectiveness and practical utility of the model.

Keywords: availability analysis; particle swarm optimization; performance modeling; sugar mill plant; markov-based simulation

I. Introduction

The processing systems and millhouse equipment are considered prime units in the sugar mill industry converting raw sugarcane into refined sugar. These units comprise centrifugal pumps, juice heaters, boiler feedwater pumps, and clarifiers, which play a vital role in maintaining efficiency and consistency of production [1]. The centrifugal pumps ensure that the required amount of fluid is circulated throughout the processing cycle to ensure a continuous supply of material in a seamless manner. The efficiency of the grinding process has a great bearing on the juice yield from sugarcane. The obtained juice after grinding is heated to the required temperature by a juice heater and then transported by a boiler feed water pump to the clarifier [2]. Heating up and clarification of the juice properly increases its energy efficiency, enhances juice extraction, and improves the quality of sugar produced. This reduces production wastage significantly, thereby reducing overall costs by manifold [3]. Advanced and energy-efficient equipment not only help in sustaining the quality of refined sugar as per industry standards but also reduce operating costs so that the production sustainable and economically viable. Besides, there would be efficient juice extraction and reduced thermal-fluid waste, thus making production more environment-friendly and sustainable. Reliable

and durable millhouse equipment helps to ensure continuous mill operation during peak seasons of harvest so that demand in the market is met to maintain a stable and profitable supply chain [4]. Herein, these processes enhance productivity, sustainability and profitability by the satisfaction of these vital objectives in maximizing the functions of the sugar industry, Economical and efficient sustenance of the sugar industry is possible due to these technologies [5].Adhikary et al. (2010) applied a reliability, availability and maintainability framework for general industries; however, a maintenance strategy deployment planning is more advantageous for the process industry. They formulated a subsystem architecture and developed a performance model for a skimmed milk powder processing plant based on exponential repair and failure distributions. In my research, heuristic approaches were performed to determine the optimal maintenance planning policies for the plant [7].

II. Literature review

The Markov type availability assessment was performed on the power and steam generation systems by Arora and Kumar (1997), and they constructed a mathematical model for it. The steam generation system's performance (in terms of availability) improved by 14% when the repair time for its three subsystems was cut from 100 to 50 hours. The power generation system comprised of four subsystems demonstrated 6% improved availability with a repair time reduction from 200 to 50 hours [8]. The Markov approach to evaluate the availability of steam and power generation systems was modeled mathematically by Arora and Kumar (1997). Cutting the repair time of subsystems led to even more improvement of availability of the system by 14%. In the same way, Cizelj et al. (2001) developed a model to evaluate the availability of high-voltage transformers using numerical methods and implemented fuzzy set theory to enhance the reliability of the components. Based on expert opinion and qualitative parameters, Dachyar et al. (2018) devised a maintenance strategy for thermal power plants with coal operation and capacity of 300 to 625 megawatts. The A-Pan crystallization process in sugar manufacturing was modeled mathematically by Dahiya et al. (2019). The grader (C) and weighment and bagging (D) subsystems were ranked as the highest maintenance subsystems The authors recommended retrofitting these subsystems in order to improve system overall performance [12]. Dhillon and Shah (2007) looked into multi state parallel systems considering human error and failure mechanisms to develop appropriate maintenance strategies [13]. Ebrahimi (2003) described the enhanced system unavailability in high-reliability systems and the components which provide such unreliability need to be improved in terms of function time without failure [14]. Gahlot et al. (2018) studied series-configured repairable systems with partial CAP and full CAP, where the failure rates Weibull distributed, including copula-based analysis of dependence structures among system components [15]. Garg et al. (2010) developed a reliability model for the plywood production line and assessed the system availability using the Runge-Kutta method [16].

III. System description

This research is being carried out in a sugar mill located in the northern part of India, which has the capacity of crushing 25,500 tons of sugarcane. The juice preparation subsystem of the sugar cane milling system has several subsystems within the plant and is one of the most important components as shown in figure 1. That is precisely why we have chosen it for an availability analysis which the results are offered in this research.

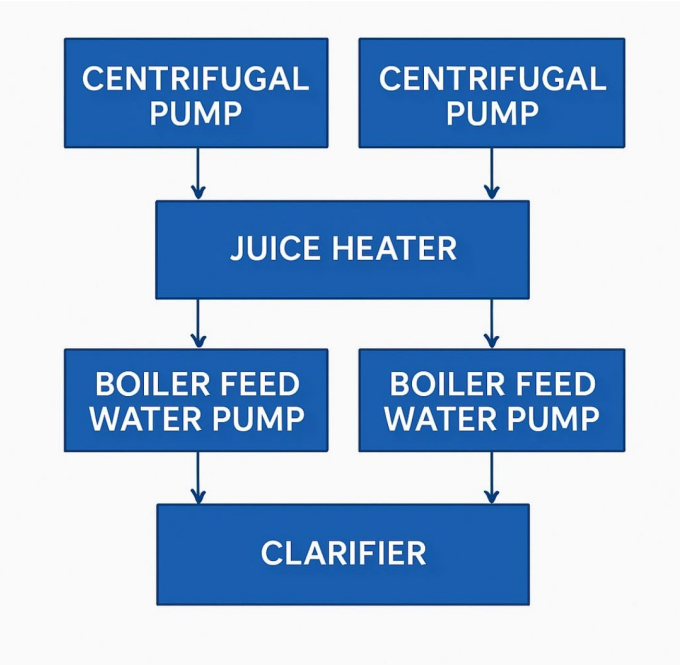


Figure 1: *Illustrative diagram of juice preparation unit.*

I. Centrifugal Pump

The first process of juice preparation is accomplished using a centrifugal pump. It acts as a fluid moving apparatus which brings sugarcane juice from one processing stage to another. Efficient centrifugal pumps handle large volumes of juice, and they greatly smoothen the flow into subsequent processing stages. For greater operational ease, this process can be fully automated which helps maintain a steady supply of juice. Centrally, the objective of a centrifugal pump is to relocate the juice from the place where it is collected initially. It is made up of a primary pump and several other auxiliary parts which are manufactured using quality materials with high resistance to wear as well as high strength. The centrifugal pump includes a standby unit. Unit failure is not attributed to the centrifugal pump.

II. Juice heater

After transferring the sugarcane juice, it is subjected to heating processes. The heater increases the temperature of the juice for processing and improving extraction efficiency. In most cases, it is placed along the section of the juice line so that the head of the juice is optimally heated. The design of the heater allows the receipt of sufficient heat without loss of effectiveness. The juice heater serves primarily as a temperature regulating device so that the clarifier is properly supplied with steam for heating. Made from best grade materials, its resistance to corrosion is superb. The juice heater prevents any delays during the processing and uniformity needed during heating will increase the quality of the juice during extraction. The juice heater does not include a standby unit. Unit failure is attributed to the juice heater.

III. Boiler feed water pump

Water under the required working conditions is delivered smoothly to the juice heater through a boiler feed water pump. Since operations on juice are being processed, the pump works in such a

way that water can be supplied in the right amount for proper temperature within the heater. The pump controls flow and guarantees the operation of the juice heater efficiently without wastage. Well-catered water supply has to be maintained towards the juice heater to enhance efficiency and quality during processing. The boiler feed water pump consists of standby units. The boiler feed water pump does not cause unit failure.

IV. Clarifier

The clarifier serves as a particular apparatus within the sugar industry that clarifies sugarcane juice. The sugarcane juice contains certain impurities and the clarifier attempts to separate solids and different forms of contaminants emanating from the sugarcane. This leads to an improved quality of juice which can be processed even further. Clarified juice helps in maximizing the quantity of sugar that can be extracted from sugarcane. The complete line for processing sugar cane juice is made up of the following: centrifugal pump, juice heater, boiler feed water pump, and clarifier. These components ensure the effective preparation and purification of juice. The clarifier does not have a standby unit. Unit failure is caused by the clarifier.

IV. Assumptions

The Markov assumption has several important implications that can be used in system analysis and modeling. It is straightforward to assume that a unique predictable Markovian structure exists for the system, based on a fixed set of transition probabilities. A Markov model is a stochastic model used to understand the behavior of a random system in which future states depend only on the current state, not on the sequence of previous states. This assumption provides a strong foundation for model construction and analysis. As a result, the form of a Markov process is unambiguous—that is, the behavior of the process is completely governed by the initial conditions and their associated transition probabilities. Expected outcomes in the long run depend on these probabilities. The following assumptions are adopted in this study:

(a) The failure and repair rates of each subsystem are constant and assumed to be statistically independent of each other.

(b) Only one unit is assumed to be out of order at any given time.

(c) Assuming the system is "as good as new" upon completion of repairs, it is assumed to function flawlessly.

(d) All standby units are assumed to have the same capacity and performance characteristics.

V. Performance Evaluation

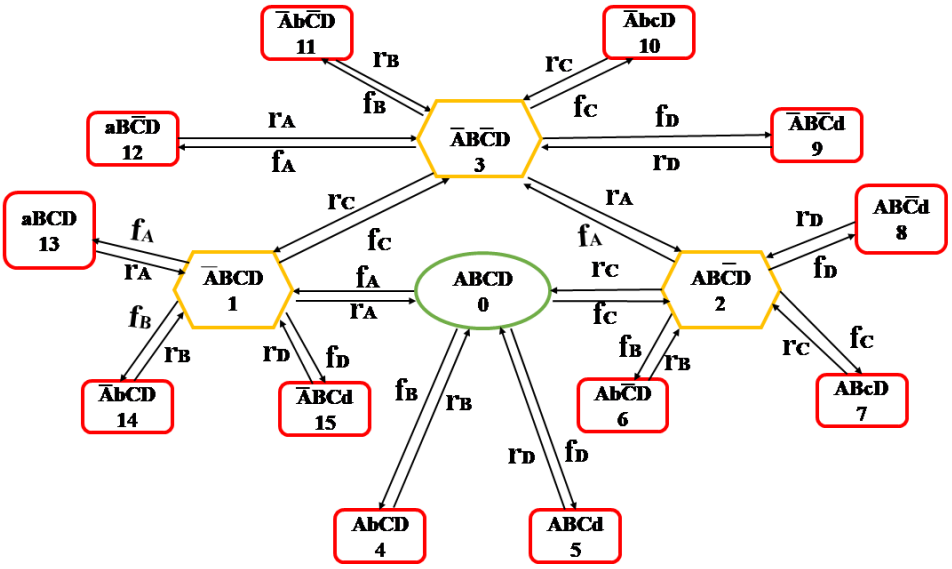


Figure 2: *TSD of the sugar mill industry*

Nomenclature

Full-capacity operating state,

Reduced capacity state,

Failed state

A,B,C,D	- Components operating in a healthy or fully functional condition.
a,b,c,d	- Represents the failed state of components A, B, C, and D, respectively
$\bar{A}\bar{C}$	- Indicates that components A and C are functioning in a reduced-capacity or degraded state
f(i)	- Mean fixed FR
r(i)	- Mean fixed RR
Pi(t)	- Probability that at time 't', the system is in its state.
'	- Derivatives concerning 't'

The probability-based differential equations, formulated via Laplace transformation and the TSD shown in figure 2, are shown in the following equations:

$$P_0'(t) + (f_A + f_B + f_C + f_D)P_0(t) = r_A P_1(t) + r_B P_4(t) + r_D P_5(t) + r_C P_2(t)$$
$$P_1'(t) + (r_A + f_A + f_B + f_C + f_D)P_1(t) = f_A P_0(t) + r_A P_{13}(t) + r_B P_{14}(t) + r_C P_3(t) + r_D P_{15}(t)$$

$P_2'(t) + (r_C + f_A + f_B + f_C + f_D)P_2(t) = f_C P_0(t) + r_A P_3(t) + r_B P_6(t) + r_C P_7(t) + r_D P_8(t)$
$P_3'(t) + (f_A + f_B + f_C + f_D + r_A + r_C)P_4(t) = r_A P_{12}(t) + r_B P_{11}(t) + r_C P_{10}(t) + r_D P_9(t) + f_A P_2(t) + f_C P_1(t)$
$P_4'(t) + r_B P_4(t) = f_B P_0(t)$
$P_5'(t) + r_D P_5(t) = f_D P_0(t)$
$P_6'(t) + r_B P_6(t) = f_B P_2(t)$
$P_7'(t) + r_C P_7(t) = f_C P_2(t)$
$P_8'(t) + r_D P_8(t) = f_D P_2(t)$
$P_9'(t) + r_D P_9(t) = f_D P_3(t)$
$P_{10}'(t) + r_C P_{10}(t) = f_C P_3(t)$
$P_{11}'(t) + r_B P_{11}(t) = f_B P_3(t)$
$P_{12}'(t) + r_A P_{12}(t) = f_A P_3(t)$
$P_{13}'(t) + r_A P_{13}(t) = f_A P_1(t)$
$P_{14}'(t) + r_B P_{14}(t) = f_B P_1(t)$
$P_{15}'(t) + \mathrm{r}P_{15}(t) = f_D P_1(t)$

with initial conditions at time t = 0

Pi (t) = 1 for i=0,

Pi (t) = 0 for i ≠ 0

System availability was determined by solving equations (1)–(8) using the Runge-Kutta method, applying the specified initial conditions.

$(f_C + r_B)P_1 = f_A P_0 + r_C P_3$
$(f_A + r_C)P_2 = f_C P_0 + r_A P_3$
$(r_A + r_C)P_3 = f_C P_1 + f_A P_2$

$P_1 = S_1 P_0 + S_2 P_3$
$P_2 = S_3 P_0 + S_4 P_3$
$P_3 = S_5 P_2 + S_6 P_1$
$P_1 = S_8 P_0$
$P_2 = S_9 P_0$
$P_3 = S_7 P_0$
$P_4 = M_B P_0$
$P_5 = M_D P_0$
$P_6 = M_B S_9 P_0$
$P_7 = M_C S_9 P_0$
$P_8 = M_D S_9 P_0$
$P_9 = M_D S_7 P_0$
$P_{10} = M_C S_7 P_0$
$P_{11} = M_B S_7 P_0$
$P_{12} = M_A S_7 P_0$
$P_{13} = M_A S_8 P_0$
$P_{14} = M_B S_8 P_0$
$P_{15} = M_D S_8 P_0$

Using the normalising condition, i.e., the total of all the state probabilities equals one, we obtain:

$$\sum_{i=1}^{15} P_i = 1$$

$$P_0 + P_1 + P_2 \ldots\ldots\ldots\ldots\ldots\ldots\ldots\ldots + P_{15} = 1$$

$$P_0(1 + S_8 + S_9 + S_7 + M_B + M_D + M_B S_9 + M_C S_9 + M_D S_9 + M_D S_7 + M_C S_7 + M_B S_7 + M_A S_7 + M_A S_8 + M_B S_8 + M_D S_8) = 1$$

$$P_0 = \frac{1}{1 + S_8 + S_9 + S_7 + M_B + M_D + M_B S_9 + M_C S_9 + M_D S_9 + M_D S_7 + M_C S_7 + M_B S_7 + M_A S_7 + M_A S_8 + M_B S_8 + M_D S_8}$$

$$A_v = P_0 + P_1 + P_2 + P_3$$

$$A_v = P_0(1 + S_8 + S_9 + S_7)$$

$$A_v = \left(\frac{1}{1 + S_8 + S_9 + S_7 + M_B + M_D + M_B S_9 + M_C S_9 + M_D S_9 + M_D S_7 + M_C S_7 + M_B S_7 + M_A S_7 + M_A S_8 + M_B S_8 + M_D S_8} (1 + S_8 + S_9 + S_7) \right)$$

VI. Results and discussion

The ultimate availability concerning the scope of juice preparation was reviewed using the Markov method. A TSD generated an availability matrix encompassing various state probabilities. Probabilities were computed, and results from Fig. 3 to 6 reflect the relation between FR and RR of the equipment and the overall availability of the juice preparation unit.

Table 1: *Availability matrix for 'Centrifugal Pump' of sugar mill plant*

f / r	0.0015	0.0020	0.0025	0.0030	0.0035
.018	.8059	.8044	.8022	.7992	.7955
.023	.8068	.8059	.8044	.8022	.7995
.028	.8073	.8068	.8057	.8041	.8019
.033	.8077	.8074	.8066	.8053	.8036
.038	.8079	.8078	.8072	.8062	.8048

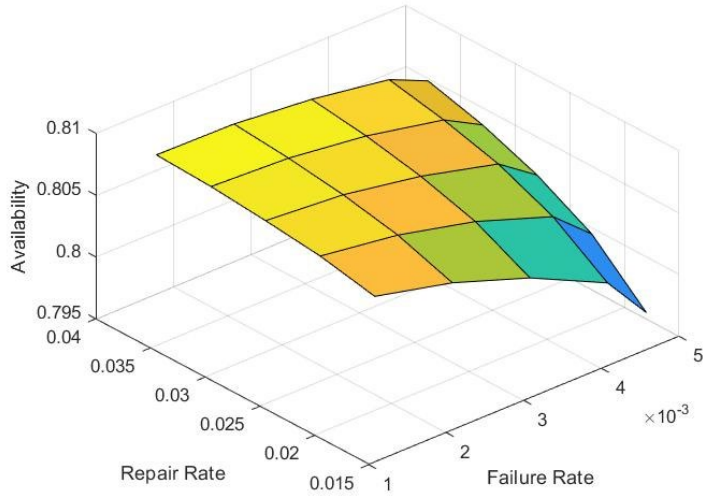


Figure 3: *System Availability vs. Centrifugal Pump FRs and RRs*

Examining the centrifugal pump's FRs and RRs From Table 1 and Fig 3, it is evident how these variables impact the total sum of juice preparation unit availability. System availability drops when the FR rises, but this increase has limitations; in FRs of 0.0015 cut back system dependency, but with a higher FR cap of 0.0050, the system faced an 1.29 % drop yield on dependency. Increasing RR from 0.018 to 0.038 leads to improved unavailability curve performance by slightly aiding dependency by 0.25% but not significantly.

Table 2: *Availability matrix for 'Juice Heater' of sugar mill plant*

f / r	.0020	.0025	.0030	.0035	.0040
.040	.8059	.7939	.7807	.7687	.7571
.050	.8150	.8040	.7934	.7831	.7730
.060	.8216	.8121	.8027	.7936	.7847
.070	.8266	.8182	.8099	.8018	.7938
.080	.8306	.8230	.8155	.8082	.8010

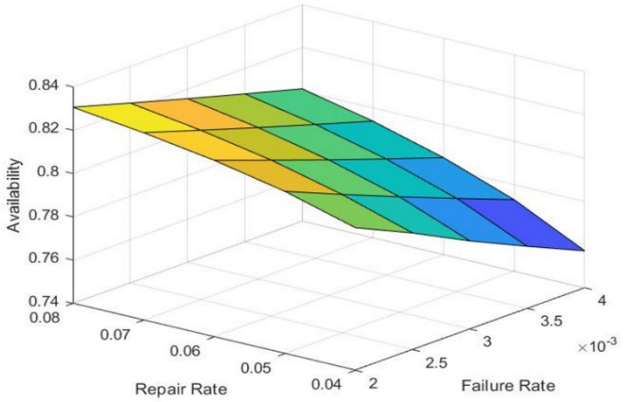


Figure 4: *System Availability vs. Juice Heater FRs and RRs.*

In the case of the juice heater, Table 2 and Fig. 4 capture the interplay of FRs and RRs with respect to the equipment availability from system FR availability perspective. System availability drops by 6.05% when the juice heater FR is increased from 0.0020 to 0.0040. System availability improves by 3.06% when the RR is elevated from 0.040 to 0.080.

Table 3: *Availability matrix for 'Boiler Feed Water Pump' of 'Sugar mill plant'*

f / r	.0025	.0030	.0035	.0040	.0045
.011	.8059	.7935	.7796	.7643	.7480
.016	.8210	.8145	.8071	.7988	.7837
.021	.8271	.8232	.8186	.8134	.8077
.026	.8302	.8275	.8244	.8209	.8170
.031	.8319	.8300	.8278	.8253	.8224

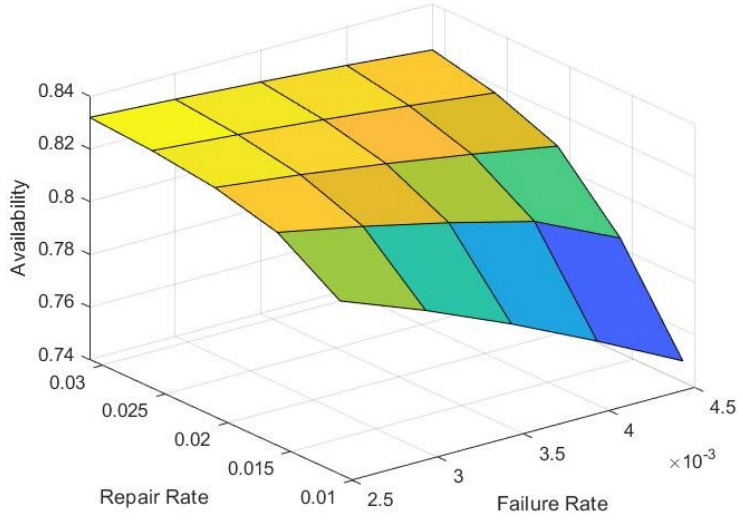


Figure 5: *System Availability vs. Boiler Feed Water Pump FRs and RRs*

The influence of FRs and RRs on the boiler feed-water pump with respect to juice preparation unit availability is illustrated in Table 3 and Fig. 5. An increase in the boiler feed water pump's FR from 0.0025 to 0.0045 causes a reduction in system availability by 7.18%. The availability of the system increases by 3.23% when the RR is increased from 0.011 to 0.031.

Table 4: *Availability matrix for 'Clarifier' of Sugar mill plant*

f / r	.0030	.0035	.0040	.0045	.0050
.027	.8059	.7940	.7825	.7713	.7605
.032	.8173	.8070	.7970	.7872	.7776
.037	.8259	.8168	.8078	.7991	.7906
.042	.8325	.8243	.8168	.8085	.8008
.047	.8378	.8304	.8231	.8160	.8090

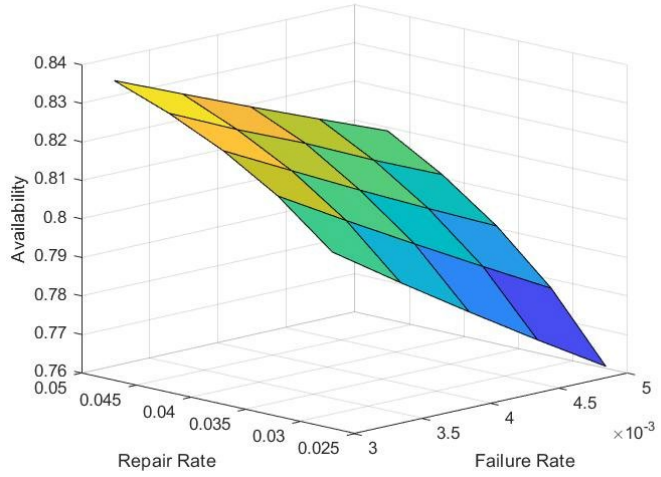


Figure 6: *System Availability vs. Clarifier FRs and RRs*

With relation to the clarifier, table 4 and figure 6 describe the effect of FRs and RRs on the juice preparation unit availability. Raising the clarifier's FR from 0.0030 to 0.0050 causes system availability to fall by 5.63%. Moreover, rising the RR from 0.027 to 0.047 wrings a further 3.96% gain in system availability.

The clarifier failure caused a reduction on system availability by 2.62%, which indicates that the clarifier is the most critical component in the juice preparation unit with a failure rate (FR) of 0.0020. The centrifugal pump was noted as having the lowest FR of 0.0015. Clearly, the identified FRs and RRs for the juice preparation unit need to set the maintenance priorities.

I. Clarifier
II. Juice Heater
III. Boiler Feed Water Pump
IV. Centrifugal Pump

VII. Optimisation

In this particular case, the availability of the juice preparation unit is enhanced through the use of PSO algorithms. The goal of the optimization is to maximize the system's efficiency by appropriately tuning FR and RR values, which are certain constraints of the system. Performance evaluation of the system's different parts is done (operational assessment) and optimization performed by changing the population size (PS) and generation size (GS). In PSO, inspired by birds' flocking behaviors, individuals of a population update their velocity and position based on personal history as well as the surrounding particles while optimization is taking place. The essence of it is how to frame a problem and simulation set-up for optimization. "Particle" is the term used to describe a potential solution together with its fitness in the PSO model. Particles are the agents that move through the solution space – computational domain representing the problem – whose effectiveness is evaluated by an objective function/value measure constructed for that purpose.

Positions and velocities of the particles are altered relative to the best known solution based on their own feedback and the feedback from their neighbors. Hence they need to come together and synchronize at the same area/region in search of the best Global optimum particle swarm optimization (PSO) particle.

Table 5: *Impact of GS on System Availability at constant PS (35)*

FR and RR	GS10	GS20	GS30	GS40	GS50	GS60
f_1	0.0035	0.0025	0.0025	0.0015	0.0015	0.0015
f_2	0.0040	0.0030	0.0020	0.0020	0.0020	0.0020
f_3	0.0045	0.0035	0.0030	0.0025	0.0025	0.0025
f_4	0.0050	0.0045	0.0035	0.0030	0.0030	0.0030
r_1	0.018	0.018	0.028	0.038	0.038	0.038
r_2	0.040	0.050	0.080	0.080	0.080	0.080
r_3	0.011	0.021	0.021	0.031	0.031	0.031
r_4	0.027	0.032	0.042	0.047	0.047	0.047
Availability	82.28	86.02	88.56	88.57	88.57	88.57

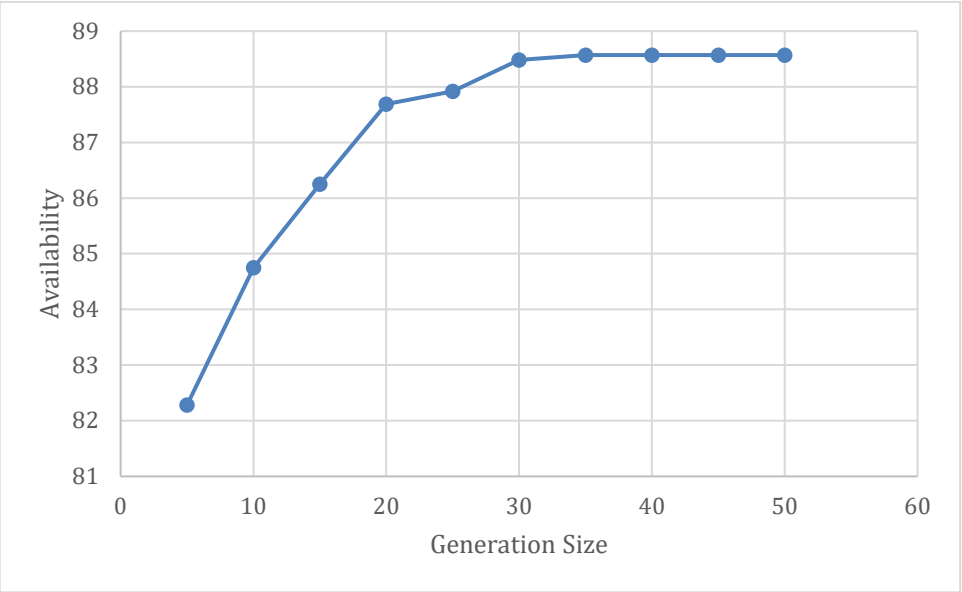


Figure 7: *Impact of GS on System availability*

Table 6: *Impact of PS on System availability at constant GS (100)*

FR and RR	PS5	PS10	PS15	PS20	PS25	PS30	PS35	PS40	PS45	PS50
f_1	0.0035	0.0025	0.0025	0.0025	0.0015	0.0015	0.0015	0.0015	0.0015	0.0015
f_2	0.0040	0.0030	0.0030	0.0030	0.0030	0.0020	0.0020	0.0020	0.0020	0.0020
f_3	0.0045	0.0035	0.0035	0.0035	0.0025	0.0025	0.0025	0.0025	0.0025	0.0025
f_4	0.0050	0.0040	0.0040	0.0030	0.0030	0.0030	0.0030	0.0030	0.0030	0.0030
r_1	0.018	0.028	0.028	0.028	0.028	0.038	0.038	0.038	0.038	0.038
r_2	0.040	0.050	0.060	0.060	0.060	0.080	0.080	0.080	0.080	0.080
r_3	0.011	0.021	0.021	0.021	0.031	0.031	0.031	0.031	0.031	0.031
r_4	0.027	0.047	0.047	0.047	0.047	0.047	0.047	0.047	0.047	0.047
Availability	82.28	84.75	86.25	87.69	87.92	88.48	88.57	88.57	88.57	88.57

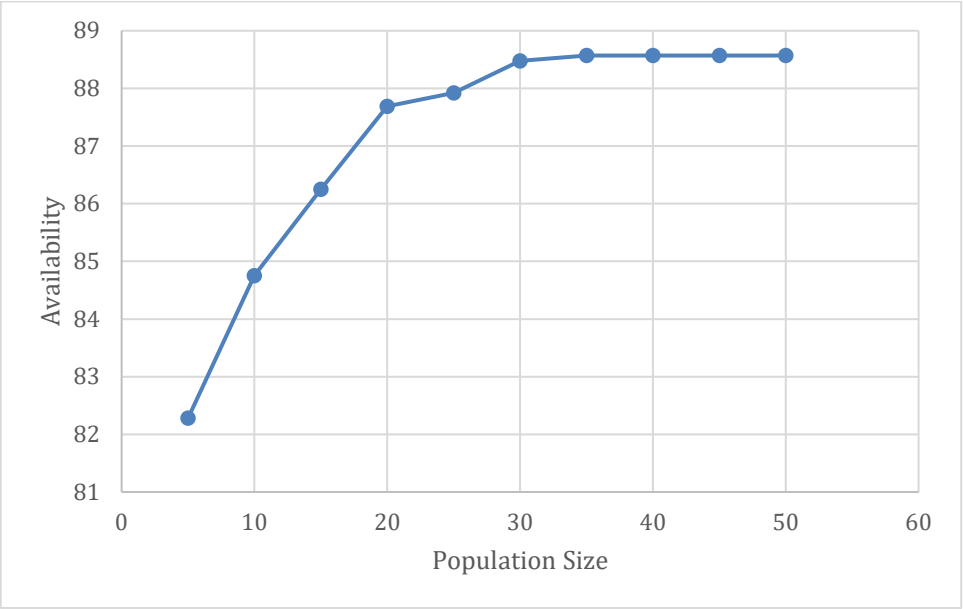


Figure 8: *Effect of PS on System availability*

As stated with PSO, the availability of sugar mills micro components' as PSO with GS = 40, PS = 15, was optimized at 88.57%. The values of the corresponding FR and RR parameters are as follows: f1=0.0015, f2=0.0020, f3=0.0025, f4=0.0030, r1=0.038, r2=0.080, r3=0.031, r4=0.047. Impressive results are shown in Fig 11 where the availability against PS is plotted with variable GS. Concurrently, the summarized available data appears in Table 5 where the corresponding values of GS are displayed from 10 to 60 in step 6, with constant PS. Concurrently, the summarized available data appears in Table 6 where the corresponding values of PS are displayed from 5 to 50 in step 10, with constant GS.

VIII. Conclusion

The purpose of this research is to analyze the micro components of a sugar mill within the sugar industry. The most important part is Clarifier, which must receive attention first or else it will lead to failed systems. The Centrifugal Pump is the least important, and maintenance is performed less often and at lesser costs. A Decision Support System (DSS) model is proposed which should enhance operational efficiency by considerable margins. This research assists maintenance engineers in determining order of importance for repair to physical resources by evaluating subsystem failure criticality. Analysis of failure and repair rates along with optimal performability level determines maintenance planning policy for plant management. The best solution is determined as the configuration with the highest availability determined using the PSO algorithm.

References

[1] Kumar, S., Tewari, P.C. and Kumar, S. (2009). Performance evaluation and availability analysis of ammonia synthesis unit in a fertilizer plant. *J. Ind. Eng. Int.*, vol. 5, no. 9, pp. 17–26.

[2] Zhao, D. and Li, Y.R. (2015). Climate change and sugarcane production: potential impact and mitigation strategies. *Int. J. Agron.*, vol. 2015, no. 1, p. 547386.

[3] Sihmar, P. and Modgil, V. (2025). Optimization of combed-sliver production system availability for a Yarn Production Unit using PSO. *Life Cycle Reliab. Saf. Eng.*, vol. 14, pp. 225–235.

[4] Kumar, D. (1988). Availability of the feeding system in the sugar industry. vol. 28, no. 6, pp.

867–871.

[5] Kumar, A. (2018). Performance evaluation of multi-state degraded industrial production system and selection of performance measure using PSO: A case study. *Int. J. Product. Qual. Manag*., vol. 25, no. 1, pp. 1–17.

[6] Adhikary, D.D., Bose, G.K., Mitra, S., and Bose, D. (2010). Reliability, Maintainability & Availability analysis of a coal fired power plant in eastern region of India. in *Proceedings of the 2nd International Conference on Production and Industrial Engineering (CPIE 2010)*, pp. 1505–1513.

[7] Aggarwal, A.K., Kumar, S. and Singh, V. (2013). Performance modeling and availability analysis of skim milk powder production system of a dairy plant. *Int. J. Agric. Food Sci. Technol.*, vol. 4, no. 9, pp. 851–858, 2013.

[8] Arora, N. and Kumar, D. (1997). Availability analysis of steam and power generation systems in the thermal power plant. *Microelectron Reliab.*, vol. 37, no. 5, pp. 795–799.

[9] Arulmozhi, G. (2002). Exact equation and an algorithm for reliability evaluation of k-out-of-n: G system. *Reliab. Eng. Syst. Saf.*, vol. 78, no. 2, pp. 87–91.

[10] Cizelj, R.J., Mavko, B. and Kljenak, I. (2001). Component reliability assessment using quantitative and qualitative data. *Reliab. Eng. Syst. Saf.*, vol. 71, no. 1, pp. 81–95.

[11] Dachyar, M., Nurcahyo, R. and Tohir, Y. (2018). Maintenance strategy selection for steam power plant in range of capacity 300-625 MW in Indonesia. *ARPN J. Eng. Appl. Sci.*, vol. 13, no. 7, pp. 2571–2580.

[12] Dahiya, O., Kumar, A. and Saini, M. (2019). Mathematical modeling and performance evaluation of A-pan crystallization system in a sugar industry.*SN Appl. Sci.*, vol. 1, pp. 1–9.

[13] Dhillon, B.S. and Shah, A.S. (2007). Availability analysis of a generalized maintainable three-state device parallel system with human error and common-cause failures. J. Qual. Maint. Eng., vol. 13, no. 4, pp. 411–432.

[14] Ebrahimi, N.B. (2003). Indirect assessment of system reliability. *IEEE Trans. Reliab.*, vol. 52, no. 1, pp. 58–62.

[15] Gahlot, M. Singh, V.V., Ayagi, H.L. and Goel, C.K. (2018). Performance assessment of repairable system in series configuration under different types of failure and repair policies using copula linguistics. *Int. J. Reliab. Saf.,* vol. 12, no. 4, pp. 348–363.

[16] Garg, S., Singh, J. and Singh, D.V. (2010). Availability and maintenance scheduling of a repairable block-board manufacturing system. *Int. J. Reliab. Saf.*, vol. 4, no. 1, pp. 104–118.

RT&A, No 4 (89)
Volume 20, December 2025

A SYSTEMATIC REVIEW OF MODELING, PLANNING, AND STATISTICAL FRAMEWORKS IN ACCELERATED LIFE TESTING

Mustafa Kamal
•
Department of Basic Sciences, College of Science and Theoretical Studies, Saudi Electronic University, Dammam, 32256, Saudi Arabia
kamal19252003@gmail.com; m.kamal@seu.edu.sa

Abstract

For highly reliable or long-life systems, conventional testing is often impractical due to the excessive time and cost required. Accelerated Life Testing (ALT) offers a practical and statistically rigorous alternative. It predicts product life and durability under normal-use conditions through data obtained under controlled high-stress conditions. This review systematically examines existing ALT methodologies. It begins with an overview of qualitative and quantitative approaches and key concepts that define the theoretical foundation of ALT assessment. Quantitative ALT is organized into Fully Accelerated Life Testing (FALT) and Partially Accelerated Life Testing (PALT) frameworks. Further, the design principles of ALT and PALT are discussed under constant- and step-stress conditions with emphasis on model formulation, estimation procedures, extrapolation, and model validation. The review also provides a concise discussion of statistical modeling and estimation methodologies. Key elements such as stress-loading, life–stress relationships, and censoring mechanisms are discussed to ensure valid statistical inference and model robustness. The review consolidates theoretical insights and methodological frameworks to advance design optimization and reliability prediction in complex systems. It concludes with perspectives on intelligent, data-driven ALT supported by artificial intelligence and computational analytics.

Keywords: Qualitative Accelerated Life Testing, Quantitative Accelerated Life Testing, Fully & Partially Accelerated Life Testing, Design Framework, Test Plan

I. Introduction

Customer satisfaction depends not only on initial product performance but also on the sustained functionality of the product throughout its intended service life under specified operating conditions. This sustained functionality is quantitatively captured as product reliability, defined as the probability that a system performs its intended function without failure for a given duration under stated conditions [1, 2]. The primary objectives of reliability estimation are to predict product service life, enhance design robustness, and forecast warranty return rates. However, for highly-reliable items or systems, conventional testing is often impractical due to excessive time and cost. ALT addresses this challenge by applying elevated stress levels to expedite failures and facilitate reliability estimation under normal-use conditions within a shorter timeframe. This approach not only enables accurate reliability estimation but also facilitates identification of root

failure mechanisms, evaluation of alternative components or suppliers, and verification of compliance with reliability specifications.

Key contributions have shaped the development of ALT design and analysis. [2] remains a foundational reference, providing comprehensive coverage of theoretical principles, practical implementation, and real-world case studies. [3] reviews advanced statistical frameworks, including nonparametric, semiparametric, and Bayesian methods, although their industrial adoption is limited due to complexity and lack of accessible tools. [4] provide a comprehensive overview of the ALT methodologies available at the time of their writing. For further detail, [5, 6] discuss reliability fundamentals. [7, 8] present perspectives on survival analysis. [9, 10] cover test planning and stochastic modeling. [11, 12] address advanced life data analysis. [13] provides extensive ALT case studies. [14] offers guidance for software-based implementations. [15] explore probabilistic interpretations of accelerated testing.

The motivation of this review arises from the lack of integration within current ALT literature. This review addresses the fragmented nature of current ALT research by integrating theoretical, methodological, and industrial perspectives. It unifies established and emerging methodologies to provide a coherent framework for theoretical principles, test design, and estimation techniques. The discussion encompasses both qualitative and quantitative approaches, with emphasis on FALTs and PALTs under constant-stress (CS) and step-stress (SS) conditions. The structure of this review is organized as follows. Section 2 introduces fundamental concepts in reliability and ALT. Section 3 classifies major quantitative ALT approaches and methodologies. Section 4 details design frameworks for commonly implemented FALTs, while Section 5 focuses on modeling structures for PALTs. Section 6 concludes with a synthesis of key findings and outlines emerging directions for future ALT research.

II. Key concepts in ALT

ALT is a pivotal methodology within reliability engineering. It is designed to evaluate the failure behavior and durability of components or systems under controlled conditions that simulate long-term usage. By providing insights into product lifespan, failure mechanisms, and reliability, ALT supports improved design, risk mitigation, and operational safety. The following key concepts establish the foundation for understanding and applying ALT in engineering studies:

- Life (Failure) data: In reliability engineering and ALT, life data, or failure data, record the observed times until a product fails or stops functioning.
- Complete (Uncensored) or Censored (Incomplete) data and Censoring: Complete data record the exact failure time of every test unit. Censored data occur when some failure times are unknown. This happens if the test ends before all units fail or if some units are removed during the test and this process is called censoring.
- Failure Time Distribution: Failure time distributions describe the statistical behavior of failure data. Common models include exponential, Weibull, Normal, and gamma distributions, each representing different failure patterns such as random, wear-out, or early-life failures.
- Stress and Stress Loading: In ALT, stress represents external forces or environmental factors applied to test specimens. Stress loading specifies how these factors are applied over time and directly impacts the interpretation of results. Common approaches include constant stress, step stress with discrete increments, and progressive (ramp) stress with continuous increases. These methods apply to single or multiple simultaneous stress variables.
- Life–Stress Relationship: The life-stress relationship defines how the life of a product related to the applied stress. It describes how life characteristics as a function of stress.

Mathematically, life characteristics L is expressed as a function of stress S as $L = f(S)$. Common models include the Arrhenius model for temperature, the inverse power law for voltage or mechanical load, and the Eyring model for multiple stresses.

- Test Planning, Sample Size, Parameter Estimation and Inference: A well-structured test plan is essential for effective life testing. It should define stress levels, number of test units to be assigned to test at each stress level, and test duration. In ALT, statistical estimation provides a foundation for modeling failure behavior and predicting reliability under standard conditions. Core estimation procedures include maximum likelihood estimation (MLE), least squares estimation (LSE), and Bayesian estimation (BE). Supplementary techniques such as weighted least squares estimation (WLSE), percentile estimation (PCE), Cramér–von Mises estimation (CME), Anderson–Darling estimation (ADE), and maximum product of spacing estimation (MPSE) offer flexible alternatives for diverse data scenarios. Graphical and three-point estimation approaches are applied when parameter estimation rely on limited or censored observations. The final choice of estimation framework reflects the nature of the data, censoring mechanism, and computational constraints.
- Extrapolation and Validation: The primary goal of ALT is to extrapolate reliability estimates from high-stress levels to normal operating conditions. This process depends on an appropriate stress–life models and robust statistical estimation. Model adequacy is evaluated through goodness-of-fit tests such as the Kolmogorov–Smirnov test. Final reliability predictions are validated using independent experimental or field data to confirm accuracy and practical relevance.

III. Types of ALTs

The increasing complexity of modern products that integrate multiple materials, subsystems, and technologies introduces diverse failure mechanisms across varied operating environments. These factors create significant challenges in accelerating product life for reliability evaluation. ALT is broadly classified into two categories as follows:

I. Qualitative Accelerated Life Tests

Qualitative ALT is applied during early reliability assessment to identify potential failure mechanisms rather than to measure product lifetime. Test units are exposed to highly elevated stresses such as heat, humidity, vibration, or temperature cycling until failure occurs. This process reveals degradation patterns, structural weaknesses, and dominant failure pathways. The resulting analysis is descriptive and assists in design refinement, corrective measures, and robustness enhancement. Common uses include prototype assessment, material evaluation, and design verification. Techniques include stress screening for early failures, highly ALT, thermal shock testing, environmental stress evaluation, and design margin assessment. Although qualitative ALT does not yield direct life estimates under normal operation, it provides essential guidance for determining stress levels in subsequent quantitative tests.

II. Quantitative Accelerated Life Tests

Quantitative ALT determines product reliability and lifetime characteristics under normal use by analyzing data from controlled accelerated experiments. Test units are subjected to constant or stepwise elevated stresses, and their failure times are recorded. Time-to-failure data are modelled using distributions such as Weibull, exponential, or lognormal, while acceleration models including Arrhenius, Eyring, and inverse power law enable extrapolation to normal conditions.

Quantitative ALT facilitates parameter estimation, model validation, and reliability prediction, providing a foundation for warranty evaluation and design comparison. It encompasses FALT and PALT, both of which integrate statistical modeling with engineering insights into failure mechanisms. A sound ALT plan involves appropriate selection of lifetime distributions and acceleration models to ensure accurate life prediction. Effective design of experiments minimizes cost, optimizes stress levels, and ensures data validity for extrapolation.

IV. Modeling and statistical frameworks for common FALTs

FALT accelerates the occurrence of failures by exposing products to elevated stresses well above operational limits while preserving the same underlying failure mechanisms. Time-to-failure data generated from these tests are modelled through quantitative frameworks such as Arrhenius for temperature acceleration or the Inverse Power Law for mechanical or electrical loading. Extrapolation from high-stress data yields estimates of reliability metrics under normal use conditions. FALT is critical for applications demanding high reliability and reduced development time, such as aerospace, automotive, and medical technologies. It supports design qualification, material evaluation, and lifecycle reliability prediction. However, excessive stress can create non-representative failure mechanisms, thus maintaining the equivalence of failure modes across stress levels is fundamental. When properly designed, FALT provides rapid, cost-effective, and statistically valid insights for product qualification and lifecycle reliability assurance.

I. Design Framework and Test Plan for CSFALT

CSFALT is the most widely used accelerated testing approach. Each unit is subjected to a fixed level of stress that remains constant until failure or termination under a censoring scheme. The failure time distribution is derived from the observed data, with its parameters modeled as functions of the applied stress levels. This classical method reflects actual operating environments for components such as lamps, semiconductors, and microelectronic devices. Its statistical inference has been extensively explored by [16-23].

Before product release, manufacturers must select appropriate testing methods to estimate reliability. A well-designed CSFALT plan provides sufficient data to evaluate performance under operating conditions, shortens test duration, reduces costs, and reveals potential failure modes. The test plan depends on the experimental objective, as emphasized by [24], and must be carefully designed for reliable decision-making. Optimal CSFALT designs have been proposed for multiple lifetime distributions and censoring schemes. [25] developed plans for normal and lognormal distributions. [26] introduced optimal four-level designs under varying censoring times. [27] analyzed the Weibull distribution. [28] designed optimal type-I constant stress tests assuming a generalized logistic distribution. [29-33] discussed optimal designs under periodic inspection and type-I censoring. [34] investigated multiple CSFALT configurations in non-rectangular test regions. [35] studied finite mixture model applications. [36] proposed the geometric process (GP) model for complete and censored exponential data, later extended by [37] to Weibull samples. [38, 39] applied GP to other censored data with different distributions. [40, 41, 42] derived MLEs of Pareto parameters using GP for complete, type-I, and type-II censored data. [43, 44] analyzed Weibull data with GP under type-I, and type-II censoring types. [45] examined Burr Type X distribution using GP. [46] investigated k-level CSFALT under progressive censoring. [47] later analyzed hybrid systems using multiple-level CSFALT with type-II progressive censored masked data.

In general, following steps can be used systematically to outline the complete test procedure and model development under CSFALT:

- Specify Stress Levels, Censoring and Collect Failure Data: Select k constant stress levels ($k \geq 2$), denoted as S_i for $i = 1,2,\dots,k$. Select a sample of $n = \sum_{i=1}^{k} n_i$ and test n_i, specimens at each level until all units fail or until the test concludes under a censoring plan. Denote the observed life of specimen j ($j = 1,2,\dots,n$) at stress level i by X_{ij}. Assume lifetimes within each stress level are independent and identically distributed to ensure statistical validity. Record all failure times and censoring times with precision throughout the testing period. Maintain data integrity and completeness to support reliable analysis and inference.
- Select Failure Distribution and Life-Stress Relationship: Identify an appropriate life distribution based on data patterns with underlying probability density, cumulative distribution, and reliability functions as $f(t;\theta)$, $F(t;\theta)$, and $R(t;\theta) = 1 - F(t;\theta)$, where θ denotes the vector of model parameters. Establish an appropriate functional relationship between the life parameter and the applied stress to represent the acceleration mechanism.
- Estimate Parameters: Estimate the parameters θ using an appropriate method among MLE, LSE, WLSE, PCE, CME, ADE, MPSE, BE, graphical, or three-point estimation.
- Extrapolation and Model Validation: Use the fitted model for predictions under normal operating stress and estimate key life characteristics and essential reliability metrics. Assess model adequacy using statistical goodness-of-fit tests, including the Kolmogorov–Smirnov test, and validate predictions with independent experimental or field data to confirm the accuracy, reliability, and predictive strength of the estimated life characteristics.

II. Design Framework and Test Plan for SSFALT

Conventional CSFALTs often require prolonged durations due to wide variability in failure times. This limitation led to the development of SSFALT, which shortens test duration and accelerates failures while maintaining valid stress– life relationships. In SSFALT, each specimen is initially subjected to a defined elevated stress and, after surviving a predetermined interval, progressively exposed to higher stress levels until failure or test termination. This sequential design allows observation of failures across multiple stress levels within a single experiment, enhancing data efficiency and improving the precision of parameter estimation. Recent advancements in SSFALT focus on increased model flexibility, statistical efficiency, and robustness under censoring. Integration of optimal experimental design, Bayesian inference, and computational optimization has further improved methodological performance. These developments reduce experimental duration and cost while maintaining model fidelity and predictive reliability. SSFALT has thus become an essential methodology in modern reliability engineering, particularly when CSFALT is impractical or economically prohibitive.

In the early development of SSFALT, the Cumulative Exposure (CE) model was introduced by [48] and later generalized by [49, 50] to account for the effects of stress variation. Subsequent research extensively investigated optimal designs and inferential procedures across diverse lifetime distributions. Optimal stress-change times under exponential lifetimes were determined by [51] and extended to censored data by [52]. CE models with Weibull lifetimes were examined through inferential procedures [53, 54]. Optimal designs for Khamis–Higgins and lognormal step-stress models were developed by [55, 56]. Exponential lifetimes with log-linear stress–life relationships were studied in [57, 58], while [59] highlighted the reliability of direct exponential inference. Comprehensive SSFALT methods were reviewed by [60], and inference under progressive type-I censoring was addressed by [61]. Design optimization for exponential SSFALT with progressive censoring was performed by [62], and grouped or censored datasets were

analyzed by [63]. Models with random stress-change times were investigated by [64]. Exact inference and optimal designs for exponential SSFALT models were derived by [65]. Multi-step SSFALT procedures and analyses of type-II and hybrid censored data were presented in [66–69]. Optimal stress-change times for log-logistic CE models and extensions to the Lomax distribution were reported by [70, 71]. SSFALT plans for Exponentiated Weibull, Power Function, and Rayleigh distributions were developed in [72–74], and comparative analyses of multiple SSFALT models were conducted by [75]. Optimal plans for Mukherjee–Islam and two-parameter Pareto models were formulated in [76, 77], while SSFALT under the Nadarajah–Haghighi distribution, including maximum likelihood estimation of parameters, was studied in [78].

The design of a SSFALT follows a structured and iterative approach to ensure precision, efficiency, and reliability. The complete test procedure and model development can systematically be described in the following stages:

- Specify Stress Levels and Collect Failure Data: Specify k stress levels ($k \geq 2$), denoted as S_i and τ_i for $i = 1,2,\dots,k$. Define the number, magnitude, and order of stress levels according to material limits and desired acceleration factors. Select a sample of n specimens and start testing at S_1 and then change the stress from S_1 to S_{i+1} at time τ_i and test is continued until all item failed or test is terminated. Denote the observed life of specimen j ($j = 1,2,\dots,n$) at stress level i by X_{ij}. Lifetimes at each level are independent and identically distributed.
- Select Failure Distribution and Life-Stress Relationship: Identify an appropriate life distribution based on the physical failure mechanism or empirical data patterns with underlying probability density, cumulative distribution, and reliability functions as $f(t;\theta)$, $F(t;\theta)$, and $R(t;\theta) = 1 - F(t;\theta)$, where θ denotes the vector of model parameters. Establish an appropriate functional relationship between the life parameter and the applied stress to represent the acceleration mechanism.
- Apply CE Model: The CE model assumes that total damage accumulation is a function of the time spent at each applied stress level. When the stress level changes, the model adjusts the equivalent exposure time at the new stress level to account for the damage accumulated under previous stresses. Accordingly, the CDF in SSFALT as per the CE model is given by

$$F(t) = \begin{cases} F_1(t); & 0 \leq t < \tau \\ F_2(t - \tau + \tau'); & \tau \leq t < \infty \end{cases} \quad (1)$$

  Where, the equivalent time τ'at stress S_2 is determined by satisfying the continuity condition of cumulative damage, such that $F_1(\tau) = F_2(\tau')$, where $F_1(t)$and $F_2(t)$ are the CDFs corresponding to stress levels S_1 and S_2, respectively. This ensures that the transition between stress levels maintains consistency in cumulative failure probability, preserving the underlying principles of the CE model framework.
- Estimation and Inference: Employ appropriate method among MLE, LSE, WLSE, etc. to obtain model parameters and reliability measures.
- Optimization of Stress-Change Times: Determine optimal stress change times $(\tau_1, \tau_2, \dots \tau_k)$ that minimize estimator variance or maximize test information.
- Extrapolation and Model Validation: Use the fitted model to predict failure distributions under normal operating stress and estimate key life characteristics and reliability metrics. Evaluate model adequacy with goodness-of-fit tests, such as the Kolmogorov–Smirnov test, and validate predictions against independent experimental or field data to ensure accuracy and predictive reliability.

V. Modeling and statistical frameworks for common PALTs

In a FALT, breakdown data obtained under elevated stress conditions are analyzed and extrapolated to normal use levels using an appropriate physical model. However, constructing such a model becomes difficult when the underlying degradation mechanisms are complex or uncertain. In these situations, a partially accelerated life test offers a practical alternative. It combines testing at normal and higher stress levels that accelerate failures without introducing unrealistic failure mechanisms. In this method, the normal stress group operates under baseline use conditions, while the accelerated group functions at higher stress. This setup allows data collection at both normal and accelerated levels in parallel, ensuring a more comprehensive reliability evaluation. The approach balances shorter testing duration with realistic failure behavior, making it suitable for fragile or complex products. It is particularly advantageous when regulatory standards require representative failure mechanisms. Although testing typically lasts longer than FALTs, the resulting life estimates align more closely with field performance. Common implementations include CSPALT and SSPALT, where stress is applied at fixed or incrementally increasing levels to achieve controlled acceleration.

I. Design Framework and Test Plan for CSPALT

In a CSPALT, identical product samples are subjected simultaneously to normal and elevated constant stress levels. Each sample operates exclusively under either the normal-use or accelerated-stress condition. Testing continues until all items fail or test is stopped according to a predefined censoring scheme. Stress acceleration may be induced through temperature, voltage, pressure, vibration, cycling rate, or humidity. CSPALT achieves a balanced trade-off between realism and test duration and has been extensively reported in the literature. [79] analyzed CSPALT data to obtain MLEs of the exponential distribution parameter and the acceleration factor under type-I censoring. [80] extended this work by developing MLEs for the Burr XII distribution under both type-I and type-II censoring. Similarly, [81] applied MLE approach under progressive type-II censoring for the Burr XII distribution, demonstrating the model's flexibility in handling incomplete data. [82] obtained ML estimates for CSPALT under type-II censoring, assuming a Weibull lifetime distribution at design stress. [83] assessed Burr XII parameter estimation in CSPALT through quasi-Newton and EM-based likelihood methods under multiple censoring schemes. [84] derived MLEs for the distribution parameter and acceleration factor assuming a Rayleigh lifetime distribution under type-I censoring. [85] applied type-I censoring to estimate parameters and construct confidence intervals for the Inverted Weibull distribution. [86] extended this work by developing ML estimation and confidence interval procedures for the Power Lindley distribution under multiple-censoring conditions in CSPALT.

The development of a CSPALT model involves a series of systematic steps designed to ensure statistical rigor and practical applicability. The complete testing process and model formulation can be systematically outlined through the following steps:

- Specify Stress Levels and Collect Failure Data: Let k represent the total number of stress levels ($k \geq 2$), denoted as S_i for $i = 0,1,2,\dots,k$, where S_0 represents the normal operating condition. In a simple two-stress CSPALT, n test units are randomly divided into two subgroups of sizes $n(1-r)$ and nr, where r denotes the sample proportion. The first subgroup assigned to normal stress level while the second is subjected to an accelerated stress level to be tested and each unit is monitored until all unit or until the test terminated due to censoring. Let X_{1j} , $j =$

$1, \ldots, n(1-r)$ denote the observed lifetimes at normal stress and X_{2j} , $j = 1, \ldots, nr$ denote the observed lifetimes at accelerated stress.

- Select Failure Distribution and the Time-Scaling Relationship: A suitable lifetime distribution is selected to represent the failure behavior of the product. The observed lifetimes X_{1j} under normal stress are modeled as independent and identically distributed random variables with cumulative distribution function $F_1(X_{1j})$ and probability density function $f_1(X_{1j})$. Lifetimes X_{2j} under accelerated stress retain the same distribution as at normal stress but are modified via the time-scaling transformation given as

$$X_{2j} = \lambda^{-1} X_{1j},\ \lambda > 1 \tag{2}$$

where λ denotes the acceleration factor, representing the ratio of characteristic lifetimes between normal and accelerated conditions. This transformation implies that, under accelerated stress, the CDF and its corresponding PDF are given by:

$$F_2(X_{2j}) = F_1(\lambda X_{2j}) \tag{3}$$

$$f_2(X_{2j}) = \lambda f_1(\lambda X_{2j}) \tag{4}$$

This formulation preserves the stochastic structure of the baseline model while establishing a statistically coherent link between operating and accelerated stress environments. It therefore provides a rigorous analytical foundation for parameter estimation and reliability extrapolation within CSPALT frameworks.

- Parameter estimation: Select and apply an appropriate estimation method, such as MLE, LSE BE etc. to obtain model parameters and reliability measures.
- Extrapolation and Model Validation: Use the fitted model to predictions under normal operating stress and evaluate model adequacy. Validate predictions against independent experimental or field data to ensure accuracy and predictive reliability.

II. Design Framework and Test Plan for SSPALT

In SSPALTs, products are first operated under normal conditions for a set duration. Items that do not fail are subsequently placed under accelerated stress until all items failed or the experiment terminates according to a censoring rule. This sequential stress strategy accelerates failures, preserves realistic failure behavior, and allows efficient estimation of parameters.

For designing SSPALT, [87] introduced the Tampered Random Variable (TRV) and formulated optimal test strategies within a Bayesian framework to estimate the parameters of the exponential distribution under different loss functions. [88] proposed the Tampered Failure Rate (TFR) model, which assumes that stress changes scale the baseline failure rate after the switching time and obtained the MLEs of Weibull parameters. [89] generalized the TFR model to accommodate multiple step-stress levels. Using MLE method, [79] estimated the parameters of the exponential distribution with type-I censored data. [90] extended this approach to estimate Weibull distribution parameters and acceleration factors under both type-I and type-II censoring. [91] conducted a detailed investigation of parameter estimation for the Log-Logistic distribution within the SSPALT framework. [92] performed MLEs of Burr Type XII distribution parameters and corresponding acceleration factors under type-I censoring, highlighting the model's applicability to diverse lifetime distributions. [93] examined SSPALT for Weibull distributions incorporating hybrid-censored data. [94] applied MLE technique to estimate parameters of the generalized

inverted Exponential distribution under type-I censoring. [95], along with [96], investigated optimal SSPALT design strategies for censored samples for estimated parameters of the model.

Recently, [97,98] developed inferences for SSPALT under hybrid and adaptive progressive hybrid censoring, assuming lifetimes follow the Nadarajah–Haghighi distribution. [99] extended this framework to estimate parameters and assess reliability of a hybrid system under progressive hybrid censoring with unknown causes. [100] employed the TRV model to analyze multiple censored datasets, assuming lifetimes follow the Nadarajah–Haghighi distribution, and obtained MLEs for model parameters and acceleration factors. [101] proposed a SSPALT framework using adaptive type-II progressive hybrid censoring, assuming lifetimes follow a two-parameter inverted Lomax distribution.

Constructing a SSPALT model requires a series of methodical steps to maintain statistical validity and operational relevance. The entire testing and modeling process can be outlined systematically as follows:

- Stress Level and Censoring Scheme Specification: Specify k stress levels ($k \geq 2$), denoted as S_i and τ_i for $i = 0, 1, 2, \dots, k$, where S_0 represents the normal operating stress. Define the number, magnitude, and order of stress levels according to material limits and desired acceleration factors. The stress changes from S_0 to S_{i+1} at time τ_i. Test a number of specimens at each stress level until all units fail or the test is terminated due to a censoring scheme. Denote the observed life of specimen $j (j = 0, 1, 2, \dots, n)$ at stress level i by X_{ij}. Lifetimes at each level are independent and identically distributed.
- Select Failure Model: Select an appropriate lifetime distribution (e.g., Exponential, Weibull, or Lognormal). The lifetimes of products at each stress level are assumed to be independent and identically distributed according to the selected probability distribution.
- Apply stress change effect Model: In SSPALT, the TRV and TFR models provide complementary frameworks for describing the effect of sequential stress increases on product lifetime. The TRV model, introduced by [87], assumes that a stress change at time τ scales the remaining life of a unit. If T denotes the original lifetime, the remaining life after the stress change is given by

$$T' = \alpha(T - \tau) \tag{5}$$

  In contrast, the TFR model, proposed by [88], assumes that a stress change at time τ scales the failure rate function. If $\lambda(t)$is the failure rate before τ, then the failure rate function after the stress change is given by

$$\lambda'(t) = \alpha\, \lambda(t), \quad t > \tau \tag{6}$$

  The TRV model directly modifies the lifetime distribution, whereas the TFR model alters the hazard function. Both approaches accelerate failures to enable rapid reliability assessment under normal operating conditions. The TRV model is flexible across multiple stress levels and lifetime distributions. Under specific conditions, TRV and TFR may yield equivalent results. These models provide a rigorous statistical framework for analyzing complex or unknown life–stress relationships.
- Parameter estimation: Select and apply an appropriate estimation technique, such as MLE, LSE, BE etc. to obtain model parameters and reliability measures.
- Optimization of Stress-Change Times: Determine optimal change times $(\tau_0, \tau_1, \tau_2, \dots \tau_k)$ that minimize estimator variance or maximize test information.

- Extrapolation and Model Evaluation and Validation: Use the fitted model to predictions under normal operating stress. Evaluate and validate model adequacy.

VI. Discussion, conclusions, and future directions

This review consolidates conceptual and methodological advancements in ALT, encompassing both fully and partially accelerated designs. Qualitative ALT enables early identification of design weaknesses during product development. Quantitative ALT establishes statistically sound reliability estimates through structured constant- and step-stress experiments. Foundational stress–life models such as Arrhenius, inverse power law, and Eyring remain critical for extrapolating accelerated test data to normal operating conditions. Analytical and estimation techniques including MLE, BE, and GP maintain statistical validity across a wide range of lifetime distributions. Implementation of ALT frameworks is supported by computational platforms such as R, Python, ReliaSoft ALTA, Minitab, and JMP, which promote standardized data analysis, model fitting, and consistency with international reliability standards. These integrated tools ensure reproducibility and accuracy in test planning, parameter estimation, and life prediction within both FALT and PALT environments.

Recent advancements in ALT indicate a transition toward adaptive, hybrid, and AI-integrated modeling frameworks. The incorporation of machine learning and real-time monitoring enhances test efficiency and predictive reliability across complex systems. Modern algorithms are now capable of processing censored, incomplete, or masked datasets while retaining the physical consistency of stress–life relationships. The convergence of traditional statistical models with advanced computational analytics enables more accurate life prediction, optimized test design, and cost-effective reliability evaluation. These developments strengthen the applicability of ALT in industrial environments by providing intelligent, data-driven tools for realistic and efficient reliability assessment.

In conclusion, ALT has matured into a multifaceted, data-driven discipline central to reliability assurance in advanced engineering systems. Its future development will focus on probabilistic modeling, intelligent test design, and digital-twin integration to enable predictive maintenance and design validation. The integration of statistical inference with computational intelligence will shape the next generation of reliability testing frameworks. As engineering systems increase in complexity and demand for high-reliability products grows, ALT will remain essential for ensuring product performance, safety, and operational longevity across diverse industrial sectors.

References

[1] Saxena, S., Zarrin, S., & Kamal, M. (2012). Computation of Reliability and Bayesian Analysis of System Reliability for Mukherjee-Islam Failure Model. *American Journal of Mathematics and Statistics*, *2*(2), 1-4.

[2] Nelson, W. (1990): Accelerated testing: statistical models, test plans, and data analysis. Wiley & Sons Inc., New York.

[3] Viertle, R. (1988). Statistical Methods in Accelerated Life Testing. Vandenhoeck and Ruprecht Göttingen, Germany. https://lccn.loc.gov/89103766

[4] Mann, N. R., Schafer, R. E., and Singpurwalla, N. D. (1974): Methods for Statistical Analysis of Reliability and Life Data, John Wiley & Sons, Inc., New York.

[5] Davis, D. J. F. (1952). An analysis of some failure data. *Journal of the American Statistical Association*, *47*(258), 113-150.

[6] Zarrin, S., Saxena, S., Kamal, M., & Islam, A. (2013). Reliability computation and Bayesian Analysis of system reliability of Power function distribution. *International Journal of Advance in Engineering, Science and Technology*, *2*(4), 76-86.

[7] Kalbfleisch, J.D., Prentice, R.L. (1980): The Statistical Analysis of Failure Data, John Wiley & Sons, Inc., New York.

[8] Cox, D.R., and Oakes, D. (1984): Analysis of Survival data, Chapman & Hall, London.

[9] Kececioglu, D. (1993): Reliability & Life Testing Handbook, Vol. 1, Prentice Hall, Inc., Englewood Cliffs, New Jersey.

[10] Lawless, J.F. (1982): Statistical Models and Methods for Lifetime Data, John Wiley & Sons, Inc., New York.

[11] Meeker, W. Q., and Escobar, L.A. (1998): Statistical Methods for Reliability Data, John Wiley & Sons, Inc., New York.

[12] Meeker, W.Q., and Hahn, G.J. (1985), How to Plan Accelerated Life Tests: Some Practical Guidelines, The ASQC Basic References in Quality Control: Statistical Techniques, Vol. 10, American Society for Quality Control, 310 W. Wisconsin Ave., Milwaukee, WI 53203.

[13] Nelson, W. (1982): Applied Life Data Analysis, John Wiley & Sons, Inc., New York.

[14] ReliaSoft, Corp. (2000): Life Data Analysis Reference, ReliaSoft Publishing, Tucson, Arizona.

[15] Bagdonavicius, V. and Nikulin, M. (2002): Accelerated Life Models: Modeling and Statistical Analysis, Chapman & Hall, Boca Raton, Florida.

[16] Lawless, J. F. (1976). Confidence interval estimation in the inverse power law model. *Journal of the Royal Statistical Society Series C: Applied Statistics*, *25*(2), 128-138.

[17] McCool, J. I. (2009). Confidence limits for Weibull regression with censored data. *IEEE Transactions on Reliability*, *29*(2), 145-150.

[18] Bai, D. S., & Chung, S. W. (1989). An accelerated life test model with the inverse power law. *Reliability Engineering & System Safety*, *24*(3), 223-230.

[19] Bugaighis, M. M. (2002). Properties of the MLE for parameters of a Weibull regression model under type I censoring. *IEEE transactions on reliability*, *39*(1), 102-105.

[20] Watkins, A. J. (2002). On the analysis of accelerated life-testing experiments. *IEEE Transactions on Reliability*, *40*(1), 98-101.

[21] Watkins, A. J., & John, A. M. (2008). On constant stress accelerated life tests terminated by Type II censoring at one of the stress levels. *Journal of statistical Planning and Inference*, *138*(3), 768-786.

[22] Abdel-Ghaly, A. A., Attia, A. F., & Aly, H. M. (1998). Estimation of the parameters of pareto distribution and the reliability function usin accelerated life testing with censoring. *Communications in Statistics-Simulation and Computation*, *27*(2), 469-484.

[23] Fan, T. H., & Yu, C. H. (2013). Statistical inference on constant stress accelerated life tests under generalized gamma lifetime distributions. *Quality and Reliability Engineering International*, *29*(5), 631-638.

[24] Meeker, W. Q., Escobar, L. A., & Lu, C. J. (1998). Accelerated degradation tests: modeling and analysis. *Technometrics*, *40*(2), 89-99.

[25] Nelson, W., & Kielpinski, T. J. (1976). Theory for optimum censored accelerated life tests for normal and lognormal life distributions. *Technometrics*, *18*(1), 105-114.

[26] Yang, G. B. (1994). Optimum constant-stress accelerated life-test plans. *IEEE transactions on reliability*, *43*(4), 575-581.

[27] Ding, C., Yang, C., & Tse, S. K. (2010). Accelerated life test sampling plans for the Weibull distribution under type I progressive interval censoring with random removals. *Journal of Statistical Computation and Simulation*, *80*(8), 903-914.

[28] Attia, A. F., Aly, H. M., & Bleed, S. O. (2011). Estimating and Planning Accelerated Life Test Using Constant Stress for Generalized Logistic Distribution under Type-I Censoring. *International Scholarly Research Notices*, *2011*(1), 203618.

[29] Ahmad, N., Islam, A., Kumar, R. & Tuteja, R. K. (1994). Optimal design of accelerated life test plans under periodic inspection and type I censoring: the case of Rayleigh failure law. *South African Statistical Journal*, *28*(2), 93-101.

[30] Islam, A., & Ahmad, N. (1994). Optimal design of accelerated life tests for the Weibull distribution under periodic inspection and type I censoring. *Microelectronics Reliability*, *34*(9), 1459-1468.

[31] Ahmad, N., & Islam, A. (1996). Optimal accelerated life test designs for Burr type XII distributions under periodic inspection and type I censoring. *Naval Research Logistics (NRL)*, *43*(8), 1049-1077.

[32] Ahmad, N., Islam, A., & Salam, A. (2006). Analysis of optimal accelerated life test plans for periodic inspection: the case of exponentiated Weibull failure model. *International Journal of Quality & Reliability Management*, *23*(8), 1019-1046.

[33] Ahmad, N. (2010). Designing accelerated life tests for generalised exponential distribution with log-linear model. *International Journal of Reliability and Safety*, *4*(2-3), 238-264.

[34] Chen, W., Gao, L., Liu, J., Qian, P., & Pan, J. (2012). Optimal design of multiple stress constant accelerated life test plan on non-rectangle test region. *Chinese Journal of Mechanical Engineering*, *25*(6), 1231-1237.

[35] Al-Hussaini, E. K., & Abdel-Hamid, A. H. (2006). Accelerated life tests under finite mixture models. *Journal of Statistical Computation and Simulation*, *76*(8), 673-690.

[36] Huang, S. (2011). *Statistical inference in accelerated life testing with geometric process model* (Doctoral dissertation, San Diego State University).

[37] Kamal, M., Zarrin, S., Saxena, S. and Islam, A. (2012). Weibull Geometric Process Model for the Analysis of Accelerated Life Testing with Complete Data. *International Journal of Statistics and Applications*, *2*(5), 60-66.

[38] Anwar, S., Kamal, M., & Islam, A. (2013). Mathematical model of accelerated life testing using geometric process for Marshall-Olkin extended exponential distribution. *International Journal of Innovative Research in Science, Engineering and Technology*, *2*(12), 7382-7390.

[39] Saxena, S., Kamal, M., & Zarrin, S. (2013). Analysis of accelerated life testing using log-logistic geometric process model in case of censored data. *International Journal of Engineering Science and Technology*, *5*(7), 1434.

[40] Kamal, M., Zarrin, S., & Islam, A. (2013). Accelerated life testing design using geometric process for Pareto distribution. *International Journal of Advanced Statistics and Probability*, *1*(2), 25–31.

[41] Kamal, M., & Zarrin, S. (2013). Design Of Accelerated Life Testing Using Geometric Process for Pareto Distribution with Type-I Censoring. *Journal of Global Research in Mathematical Archives (JGRMA)*, *1*(8), 59-66.

[42] Kamal, M., Zarrin, S., & Islam, A. (2013). Constant stress accelerated life testing design with type-II censoring scheme for Pareto distribution using geometric process. *International Journal of Mathematical Modelling & Computations*, *4*(2), 125-134.

[43] Kamal, M. (2013). Application of geometric process in accelerated life testing analysis with Type-I Weibull censored data. *Reliability: Theory & Applications*, *8*(3), 87–96.

[44] Kamal, M. (2013). Estimation of Weibull Parameters in Accelerated Life Testing Using Geometric Process with Type-II Censored Data. *International Journal of Engineering Sciences & Research Technology*, *2*(9), 2340-2347.

[45] Rahman, A., Sindhu, T. N., Lone, S. A., & Kamal, M. (2020). Statistical Inference for Burr Type X Distribution using Geometric Process in Accelerated Life Testing Design for Time censored data. *Pakistan Journal of Statistics and Operation Research*, 16(3), 577-586.

[46] Kamal, M. (2021). Parameter estimation for progressive censored data under accelerated life test with ***k*** levels of constant stress. *Reliability: Theory & Applications*, *16*(3 (63)), 149-159.

[47] Kamal, M., Khan, S., Rahman, A., Aldallal, R. A., El-Raouf, M. A., Muse, A. H., & Rabie, A. (2022). Reliability Analysis of Hybrid System Using Geometric Process in Multiple Level of Constant Stress Accelerated Life Test through Simulation Study for Type-II Progressive Censored Masked Data. *Mathematical Problems in Engineering*, *2022*(1), 9528479.

[48] Sedyakin, N. M. (1966). On one physical principle in reliability theory. *Techn. Cybernetics*, *3*, 80-87.

[49] Nelson, W. (1980). Accelerated life testing-step-stress models and data analyses. *IEEE transactions on reliability*, *29*(2), 103-108.

[50] Bagdonavičius, V. (1978). Testing hypothesis of the linear accumulation of damages. *Theory of Probability and its Applications*, *23*(2), 403-408.

[51] Miller, R., & Nelson, W. (1983). Optimum simple step-stress plans for accelerated life testing. *IEEE Transactions on Reliability*, *32*(1), 59-65.

[52] Bai, D. S., Kim, M. S., & Lee, S. H. (1989). Optimum simple step-stress accelerated life tests with censoring. *IEEE transactions on reliability*, *38*(5), 528-532.

[53] Khamis, I. H., & Higgins, J. J. (2002). A new model for step-stress testing. *IEEE Transactions on Reliability*, *47*(2), 131-134.

[54] Kateri, M., & Balakrishnan, N. (2008). Inference for a simple step-stress model with type-II censoring, and Weibull distributed lifetimes. *IEEE Transactions on Reliability*, *57*(4), 616-626.

[55] Alhadeed, A., & Yang, S. (2002). Optimal simple step-stress plan for Khamis-Higgins model. *IEEE Transactions on Reliability*, *51*(2), 212-215.

[56] Alhadeed, A., & Yang, S. (2005). Optimal simple step-stress plan for cumulative exposure model using log-normal distribution. *IEEE Transactions on Reliability*, *54*(1), 64-68.

[57] Xiong, C. (1998). Inferences on a simple step-stress model with type-II censored exponential data. *IEEE Transactions on Reliability*, *47*(2), 142-146.

[58] Xiong, C., & Milliken, G. (2002). Prediction for exponential lifetimes based on step-stress testing. *Communications in Statistics-Simulation and Computation*, *31*(4), 539-556.

[59] Watkins, A. J. (2001). Commentary: inference in simple step-stress models. *IEEE Transactions on Reliability*, *50*(1), 36-37.

[60] Gouno, E., & Balakrishnan, N. (2001). Ch. 23. Step-stress accelerated life test. *Handbook of statistics*, *20*, 623-693.

[61] Gouno, E., Sen, A., & Balakrishnan, N. (2004). Optimal step-stress test under progressive Type-I censoring. *IEEE transactions on reliability*, *53*(3), 388-393.

[62] Balakrishnan, N., & Han, D. (2009). Optimal step-stress testing for progressively Type-I censored data from exponential distribution. *Journal of statistical planning and inference*, *139*(5), 1782-1798.

[63] Xiong, C., & Ji, M. (2004). Analysis of grouped and censored data from step-stress life test. *IEEE Transactions on Reliability*, *53*(1), 22-28.

[64] Xiong, C., Zhu, K., & Ji, M. (2006). Analysis of a simple step-stress life test with a random stress-change time. *IEEE Transactions on Reliability*, *55*(1), 67-74.

[65] Balakrishnan, N. (2009). A synthesis of exact inferential results for exponential step-stress models and associated optimal accelerated life-tests. *Metrika*, *69*(2), 351-396.

[66] Tang, L. C. (2003). Multiple-steps step-stress accelerated life test. In *Handbook of reliability engineering* (pp. 441-455). London: Springer London.

[67] Balakrishnan, N., Kundu, D., Ng, K., & Kannan, N. (2007). Point and interval estimation for a simple step-stress model with Type-II censoring. *Journal of Quality Technology*, *39*(1), 35-47.

[68] Balakrishnan, N., Xie, Q., & Kundu, D. (2009). Exact inference for a simple step-stress model from the exponential distribution under time constraint. *Annals of the Institute of Statistical Mathematics*, *61*(1), 251-274.

[69] Balakrishnan, N., & Xie, Q. (2007). Exact inference for a simple step-stress model with Type-I hybrid censored data from the exponential distribution. *Journal of statistical planning and inference*, *137*(11), 3268-3290.

[70] Al-Masri, A. Q., & Ebrahem, M. A. H. (2009). Optimum times for step-stress cumulative exposure model using log-logistic distribution with known scale parameter. *Austrian Journal of Statistics*, *38*(1), 59-66.

[71] Hassan, A. S., & Al-Ghamdi, A. S. (2009). Optimum step stress accelerated life testing for Lomax distribution. *Journal of applied sciences research*, *5*(12), 2153-2164.

[72] Zarrin, S., Saxena, S., & Islam, A. (2010). Step-stress Accelerated Life Testing for Exponentiated Weibull Distribution. In *Safety and Reliability 30*(3), 5-13.

[73] Saxena, S., Zarrin, S., Kamal, M., & Islam, A. (2012). Optimum Step Stress Accelerated Life Testing for Power Function Distribution. *Safety and Reliability, 32*(2), 4-16.

[74] Saxena, S., Zarrin, S., Kamal, M., & Islam, A. (2012). Optimum step stress accelerated life testing for Rayleigh distribution. *International journal of statistics and applications*, 2(6), 120-125.

[75] Xu, H. Y., & Fei, H. (2012). Models comparison for step-stress accelerated life testing. *Communications in Statistics-Theory and Methods*, *41*(21), 3878-3887.

[76] Kamal, M., Zarrin, S., Saxena, S., & Islam, A. (2012). Optimum Step Stress Accelerated Life Testing for Mukherjee Islam Failure Model. In *Safety and Reliability, 32*(2),13-24

[77] Kamal, M., & Zarrin, S. (2013). Step stress accelerated life testing plan for two parameter Pareto distribution. *Reliability: Theory & Applications*, *8*(1), 30-40.

[78] Kamal, M., Rahman, A., Ansari, S. I., & Zarrin, S. (2020). Statistical Analysis and Optimum Step Stress Accelerated Life Test Design for Nadarajah Haghighi Distribution. *Reliability: Theory & Applications*, *15*(4), 46-53.

[79] Bai, D. S., & Chung, S. W. (1992). Optimal design of partially accelerated life tests for the exponential distribution under type-I censoring. *IEEE Transactions on Reliability*, *41*(3), 400-406.

[80] Abdel-Ghaly, A. A., Amin, Z. H., & Omar, D. A. (2008). Estimation of the Burr-XII distribution for partially accelerated life tests using censored data. *Model Assisted Statistics and Applications*, *3*(4), 317-334.

[81] Abdel-Hamid, A. H. (2009). Constant-partially accelerated life tests for Burr type-XII distribution with progressive type-II censoring. *Computational Statistics & Data Analysis*, *53*(7), 2511-2523.

[82] Ismail, A. A. (2009). Optimum constant-stress partially accelerated life test plans with type-II censoring: the case of Weibull failure distribution. *International Journal of Statistics & Economics*, *3*(S09), 39-46.

[83] Cheng, Y. F., & Wang, F. K. (2012). Estimating the Burr XII parameters in constant-stress partially accelerated life tests under multiple censored data. *Communications in Statistics-Simulation and Computation*, *41*(9), 1711-1727.

[84] Zarrin, S., Kamal, M., & Saxena, S. (2012). Estimation in constant stress partially accelerated life tests for Rayleigh distribution using type-I censoring. *Reliability: Theory & Applications*, *7*(4), 41-52.

[85] Kamal, M., Zarrin, S., & Islam, A. (2013). Constant stress partially accelerated life test design for inverted Weibull distribution with type-I censoring. *Algorithms Research*, 2(2), 43-49.

[86] Alam, I., Kamal, M., Rahman, A., Agarwal, T., & Mishra, A. (2024). Statistical analysis using multiple censoring scheme under partially accelerated life tests for the power Lindley distribution. *International Journal of System Assurance Engineering and Management*, *15*(7), 3424-3436.

[87] DeGroot, M. H., & Goel, P. K. (1979). Bayesian estimation and optimal designs in partially accelerated life testing. *Naval research logistics quarterly*, *26*(2), 223-235.

[88] Bhattacharyya, G. K., & Soejoeti, Z. (1989). A tampered failure rate model for step-stress accelerated life test. *Communications in statistics-Theory and methods*, *18*(5), 1627-1643.

[89] Madi, M. T. (1993). Multiple step-stress accelerated life test: the tampered failure rate model. *Communications in statistics-theory and methods*, *22*(9), 295-306.

[90] Abdel-Ghaly, A. A., Attia, A. F., & Abdel-Ghani, M. M. (2002). The maximum likelihood estimates in step partially accelerated life tests for the Weibull parameters in censored data. *Communications in Statistics-Theory and Methods*, *31*(4), 551-573.

[91] Abdel-Ghani, M. M. (2004). The estimation problem of the log logistic parameters in step partially accelerated life tests using type I censored data. *The National Review of Social Sciences*, *41*(2), 1-19.

[92] Abd-Elfattah, A. M., Hassan, A. S., & Nassr, S. G. (2008). Estimation in step-stress partially accelerated life tests for the Burr type XII distribution using type I censoring. *Statistical Methodology*, *5*(6), 502-514.

[93] Ismail, A. A. (2012). Estimating the parameters of Weibull distribution and the acceleration factor from hybrid partially accelerated life test. *Applied Mathematical Modelling*, *36*(7), 2920-2925.

[94] Bakoban, R. (2012). Estimation in step-stress partially accelerated life tests for the generalized inverted exponential distribution using Type I censoring. *American Journal of Scientific Research*, *3*, 25-35.

[95] Ismail, A. A. (2012). Inference in the generalized exponential distribution under partially accelerated tests with progressive Type-II censoring. *Theoretical and Applied Fracture Mechanics*, *59*(1), 49-56.

[96] Srivastava, P. W., & Mittal, N. (2010). Optimum step-stress partially accelerated life tests for the truncated logistic distribution with censoring. *Applied Mathematical Modelling*, *34*(10), 3166-3178.

[97] Kamal, M., Rahman, A., Zarrin, S., & Kausar, H. (2021). Statistical inference under step stress partially accelerated life testing for adaptive type-II progressive hybrid censored data. *Journal of Reliability and Statistical Studies*, *14*(2), 585-614.

[98] Kamal, M., Siddiqui, S. A., Rahman, A., Alsuhabi, H., Alkhairy, I., & Barry, T. S. (2022). Parameter estimation in step stress partially accelerated life testing under different types of censored data. *Computational Intelligence and Neuroscience*, *2022*(1), 3491732.

[99] Kamal, M. (2022). Parameter Estimation Based on Censored Data under Partially Accelerated Life Testing for Hybrid Systems due to Unknown Failure Causes. *Computer Modeling in Engineering & Sciences (CMES)*, *130*(3), 1239-1269.

[100] Rahman, A., Kamal, M., Khan, S., Khan, M. F., Mustafa, M. S., Hussam, E., ... & Al Mutairi, A. (2023). Statistical inferences under step stress partially accelerated life testing based on multiple censoring approaches using simulated and real-life engineering data. *Scientific Reports*, *13*(1), 12452.

[101] Alam, I., Kamal, M., Rahman, A., & Nayabuddin. (2024). A study on step stress partially accelerated life test under adaptive type-II progressive hybrid censoring for inverse Lomax distribution. *International Journal of Reliability and Safety*, *18*(1), 1-18.